Vol. 72, No. 1 / 2024

e: ISSN 2068 – 2239
p: ISSN 2068 – 4215

INMATEH – AGRICULTURAL ENGINEERING

JANUARY - APRIL

Managing Editorial Board - INMA Bucharest

INMATEH - Agricultural Engineering **journal is indexed in the next international databases:**
ELSEVIER /SciVerse SCOPUS, CLARIVATE - WEB of SCIENCE- Emerging Sources Citation Index (ESCI), ULRICHS Web: Global Serials Directory, CABI, SCIPIO, Index COPERNICUS International, EBSCO Publishing, Elektronische Zeitschriftenbibliothek

INMATEH - Agricultural Engineering
vol. 72, no.1 / 2024
e-ISSN: 2068 – 2239; p: ISSN: 2068 – 4215

https://inmateh.eu/ *E-mail: inmatehjournal@gmail.com*

Edited by: INMA Bucharest

National Institute for Research-Development of Machines and Installations
Designed for Agriculture and Food Industry - INMA Bucharest
6, Ion Ionescu de la Brad Bvd., sector 1, Bucharest, ROMANIA

CONTENT

		Page(s)
1.	**ESTABLISHMENT AND APPLICATION OF SOIL FERTILIZATION PRESCRIPTION CHART / *土壤施肥处方图的建立和应用*** **Haozheng SUN*[1)], Fanxia KONG*[1)], Jiankun LI[*3)], Lili YI*[1)], Yubin LAN*[1,2)], Xin HAN*[1)], Duanyang GENG*[1)], Qiang GAO[*3)]** [1)]School of Agricultural Engineering and Food Science, Shandong University of Technology, Zibo / China [2)]Shandong Provincial Engineering Technology Research Centre for Agricultural Aviation Intelligent Equipment, Zibo / China [3)] Weichai Lovol Intelligent Agricultural Technology Co. Ltd, Weifang/ China	11
2.	**SIMULATION ANALYSIS AND OPTIMIZATION OF SOIL CUTTING OF ROTARY BLADE BY ANSYS/LS-DYNA / *基于 ANSYS/LS-Dyna 旋耕刀切土仿真分析及优化*** **Wusong XIAO [1)], Po NIU [*1)], Pan WANG [*2)], Yingjie XIE [3)], Fei XIA [4)]** [1)]College of Mechanical Engineering, Chongqing Three Gorges University, Chongqing/China; [2)]Sichuan Academy of Agricultural Machinery Science, Sichuan/China; [3)]Chongqing Agricultural Mechanization Technology Extension Station, Chongqing/China; [4)]Chongqing Kaizhou District Agriculture Service Center, Chongqing/China	22
3.	**DEVELOPMENT AND EVALUATION OF A CONTINUOUS FLOW BIOCHAR UNIT USING RICE HUSK BIOMASS / *تطوير وتقييم وحدة الفحم الحيوي ذات التدفق المستمر للكتلة الحيوية لقشور الأرز*** **Hesham A. FARAG, Mohamed M. EL-KHOLY, Mahmoud OKASHA[*], Ahmed E. AZAB, Ahmed E. KHATER, Reham M. KAMEL** Agricultural Engineering Research Institute (AEnRI), Agricultural Research Center (ARC), Giza 12611 / Egypt	33
4.	**DESIGN AND EXPERIMENT OF AN AUTOMATIC GIRDLING DEVICE FOR ECONOMIC TREE TRUNK INSPIRED BY CAM MECHANISM / *凸轮原理启发的经济林树干自动环剥装置的设计与实验研究*** **Zhenkun ZHI, Haifeng LUO[*)]** School of Engineering, Beijing Forestry University, Beijing/ China	45
5.	**DESIGN AND EVALUATION OF A LOCALLY- DESIGNED PEANUT DIGGER** **Rosalinda L. ABAD*; Frank Michael L. JACLA; Hipolito C. BUCCAT; Paul James C. GAÑOLA; Alliver P. SAPITULA** Don Mariano Marcos Memorial State University [DMMMSU], La Union, Philippines	57
6.	**SUNFLOWER PLANTING MACHINERY ELECTRIFICATION TRANSFORMATION AND CONTROL SYSTEM DESIGN / *葵花种植机械电动化改造及控制系统设计*** **Guoxing CAI[1)], Haijun LI*[1)], Dabo LU[2)], Renjie WANG[1)], Kaiyuan WANG[1)], Subo QIN[1)], Zhiqiang WU[1)]** [1)] College of Electrical and Mechanical Engineering, Inner Mongolia Agricultural University, Hohhot / China; [2)] Inner Mongolia Dabo Jintian Machinery Company Limited, Bayannur / China	67
7.	**PARAMETERS CALIBRATION FOR DISCRETE ELEMENT MODEL SIMULATION OF WHITE KIDNEY BEAN SEEDS / *白芸豆种子离散元模型仿真参数标定*** **Huhu YANG[1,2)]，Junlin HE *[1)]，Jiaxuan LU[1)]，Tao WANG[1)]，Yuehua WANG[1)]，Yanxi GUO[1)]** [1)]College of Agricultural Engineering, Shanxi Agricultural University, Taigu, China; [2)]Dryland Farm Machinery Key Technology and Equipment Key Laboratory of Shanxi province, Taigu, China	77
8.	**RESEARCH ON THE ANTI-CRUSHING MECHANISM OF CORN GRAIN PNEUMATIC CONVEYING PROCESS UNDER THE INFLUENCE OF MULTI-PARAMETER COUPLING / *多参数耦合影响的玉米颗粒气力输送过程抗破碎机理探究*** **Mingxu WANG[1,2)], Jiangfeng OUYANG[1)], Ziiyan ZHAO[1)], Runze WU[3)]** [1)]School of Mechanical & Electrical Engineering, Henan University of Technology, Zhengzhou, China [2)]Henan Key Laboratory of Grain and Oil Storage Facility & Safety, Henan University of Technology, China [3)]Dalian University of Technology Panjin Campus, Panjin, China	87
9.	**REAL-TIME GRAPE DISEASE DETECTION MODEL BASED ON IMPROVED YOLOv8s / *基于改进 YOLOv8s 的实时葡萄病害检测模型*** **Jinglong REN, Huili ZHANG*), Guangyuan WANG, Chenlong DAI, Fei TENG, Moxian LI** College of Mechanical and Electrical Engineering, Qingdao Agricultural University / China	96
10.	**DESIGN AND EXPERIMENTATION OF A POTATO PLANTER MISSED AND REPEATED PLANTING DETECTION SYSTEM BASED ON YOLOv7-TINY MODEL / *基于 YOLOv7-tiny 模型的马铃薯播种机漏重播检测系统的设计与试验*** **Shengchun QI[1)], Zhiguo PAN[1)], Ranbing YANG[1, 2)], Huan ZHANG*[1)], Xinyu GUO[1)], Weijing WANG[1)], Sha LIU[1)], Zhen LIU[1)], Jie MU[1)], Binxuan GENG[)]** [1)] College of Mechanical and Electrical Engineering, Qingdao Agricultural University, Qingdao, China [2)] College of Mechanical and Electrical Engineering, Hainan University, Haikou, China	106
11.	**DESIGN AND EXPERIMENTAL STUDY OF PEANUT PLANTER WITH HIGH-SPEED OPERATION AND CONTROLLABLE SOWING DEPTH / *高速作业种肥播深可控的花生播种机的设计与试验研究*** **Moxian LI[1)], Xueliang CHANG[1)], Xiaoning HE[1)], Ning ZHANG[1)], Wei LIU[2)], Zhixin LIU[1)], Tongtong DONG[1)] Shuqi SHANG*[1)], Dongwei WANG[1)], Maomao ZOU[1)], Yunkang LI[1)], Zhenjia MA[1)]** [1)]Qingdao Agricultural University, College of Mechanical and Electrical Engineering /China; [2)] Shandong Yuanquan Mechanical Co/China	117
12.	**CROP TYPE MAPPING USING MACHINE LEARNING-BASED APPROACH AND SENTINEL-2: STUDY IN LUMAJANG, EAST JAVA, INDONESIA / *PEMETAAN JENIS TANAMAN MENGGUNAKAN PENDEKATAN MACHINE LEARNING DAN SENTINEL-2: STUDI DI LUMAJANG, JAWA TIMUR, INDONESIA*** **Irsyam MAHRUS [1)], Indarto INDARTO *[1)], Khristianto WHENY [1)], Kurnianto FAHMI [1)]** [1)] Research Group of Agroindustrial and Food Safety (Keris Dimas KPPI), Research Centre (LP2M), University of Jember / Indonesia	129

		Page(s)
13.	**OPTIMISATION BY COUPLED RECURDYN-EDEM SIMULATION: OPTIMISATION TESTS OF A THREE-STAGE LOW-LOSS SEPARATION DEVICE FOR POTATO SOIL / *RecurDyn-EDEM 耦合仿真优化：三段式薯土低损分离装置优化试验*** **Zhixin LIU, Shuqi SHANG*), Shikuan MA, Yaxiu HOU, Tongtong DONG, Xiaoning HE** College of Electrical and Mechanical Engineering, Qingdao Agricultural University, Qingdao/ China	138
14.	**SIMULATION AND EXPERIMENT OF MONORAIL ANTI-FROST MACHINE IN HILLY ORCHARD / *丘陵山地果园单轨式防霜机的仿真与试验*** **Qingfu GONG [1)], Yuepeng SONG[1,2)], Wei MA[3)], Hongmei ZHANG [1)], Xiang HAN[1)], Ang GAO [1)], Longlong REN [1,2*)]** [1)] Shandong Agricultural University, College of Mechanical and Electrical Engineering / China; [2)] Shandong Provincial Engineering Laboratory of Agricultural Equipment Intelligence / China; [3)] Institute of Urban Agriculture, Chinese Academy of Agricultural Sciences / China	148
15.	**DESIGN AND EXPERIMENT OF PRECISION SEED METERING PLATE FOR EDIBLE SUNFLOOWER BY ADDING SEED GUIDE BAR / *增加导种条式食葵精量排种盘设计及试验*** **Fengli LI[1)], Jianghui CHEN[1)], Keyi LIU[1)], Jia ZHANG[1)], Yaou ZHANG[1)], Junchi YIN[1)], Fei LIU[2)], Manquan ZHAO [*2)]** [1)]College of Mechanical and Electrical Engineering, Xinjiang Institute of Engineering, Urumqi, China; [2)]College of Mechanical and Electrical Engineering, Inner Mongolia Agricultural University, Hohhot, China	162
16.	**INTENSIFICATION OF APPLE DRYING USING CONVECTIVE AND COMBINED METHODS OF DEHYDRATION / *ІНТЕНСИФІКАЦІЯ СУШІННЯ ЯБЛУК ПРИ КОНВЕКТИВНОМУ ТА КОМБІНОВАНОМУ СПОСОБАХ ЗНЕВОДНЕННЯ*** **Vadim PAZIUK[1)], Olena HUSAROVA[2)], Valentyna BANDURA[3)]; Larysa FIALKOVSKA [4)]** [1)] Institute of Engineering Thermophysics of the National Academy of Sciences of Ukraine; [2)] National Technical University of Ukraine “Igor Sikorsky Kyiv Polytechnic Institute”, Institute of Engineering Thermophysics of the National Academy of Sciences of Ukraine; [3)] National University of Life and Environmental Sciences of Ukraine, Ukraine; [4)] Vinnytsia Trade and Economics Institute, State Trade and Economics University, Ukraine	173
17.	**APPLE DETECTION METHOD IN THE NATURAL ENVIRONMENT BASED ON IMPROVED YOLOv5 / *基于改进 YOLOv5 的自然环境下苹果检测方法*** **Yongpeng CHEN, Yi NIU, Weidong CHENG*), Laining ZHENG, Dongchao SUN** School of Agricultural Engineering and Food Science, Shandong University of Technology, Zibo, China	183
18.	**DESIGN AND EXPERIMENT OF NO-TILLAGE PRECISION PLANTERS WITH STAGGERED SEEDLING BELTS FOR SOYBEAN / *交错苗带式大豆精量免耕播种机设计与试验*** **Chuang MA, Weipeng CHEN, Shandong YANG*, Peisong DIAO, Yinping ZHANG, Zengjia LUO, Zhanyang WANG** Shandong University of Technology, Collage of Agricultural Engineering and Food Science, ZiBo, China	193
19.	**STUDY ON HIGH-TEMPERATURE AEROBIC FERMENTATION TECHNOLOGY OF KITCHEN WASTE / *餐厨垃圾高温好氧发酵工艺的研究*** **Yupeng JIANG; Aiping SHI*); Feng LIANG; Jun YANG** College of Agricultural Engineering, Jiangsu University, Zhenjiang, China	203
20.	**EFFECT OF NOZZLE ANGLE OF PLANT PROTECTION UNMANNED AERIAL VEHICLE ON DROPLET DEPOSITION DISTRIBUTION / *植保无人机喷头角度对雾滴沉积分布的影响*** **Zhihao BIAN[1,3)], Yubin LAN*[1,2,3)], Meng WANG[1,3)], Changfeng SHAN [1,3)], Haozheng GU [1,3)], Jingang HAN [1,3)]** [1)] School of Agricultural Engineering and Food Science, Shandong University of Technology, Zibo / China; [2)] College of Electronic Engineering, College of Artificial Intelligence, South China Agricultural University, Guangzhou / China; [3)] National Key Laboratory of Green Pesticide, Guangzhou / China	214
21.	**3D MULTI-OBJECTIVE FLIGHT PATH OPTIMIZATION OF AGRICULTURAL PLANT PROTECTION UAVS BASED ON EMSDBO ALGORITHM / *基于 EMSDBO 算法农业植保无人机三维航迹多目标优化研究*** **Hexia Chu*[1)], Hongxing Liu[2)]** [1)] Department of Mathematics Education, Zhumadian Preschool Education College, Zhumadian, Henan, China [2)] School of Mathematics and Statistics, Henan University, Kaifeng, Henan, China	224
22.	**KINEMATIC SIMULATION AND EXPERIMENTAL ANALYSIS OF A ROLLER BRANCH PICKING MECHANISM / *辊式枝条捡拾机构运动学仿真与试验分析*** **Aiqian YANG[1)], Hui LI[1*)], Junfang ZHANG[1)], Xin YANG[2)]** [1)] Hengshui University, Hengshui, China; [2)] College of Mechanical and Electrical Engineering, Hebei Agricultural University, Baoding, China	235
23.	**DESIGNING AND CALIBRATION OF A LOW-COST MULTI-POINT SOIL MOISTURE MONITORING SYSTEM FOR PRECISION AGRICULTURE / *REALIZAREA ȘI CALIBRAREA UNUI SISTEM, CU COSTURI REDUSE, DE MONITORIZAREA UMIDITĂȚII SOLULUI IN MAI MULTE PUNCTE PENTRU AGRICULTURĂ DE PRECIZIE*** **Ioan Aurel CHERECHES [1)]; Ferenc GASPAR *[1)]; Ioan Alin DANCI [2)]** [1)] Department of Automotive Engineering and Transports, Faculty of Automotive, Mechatronics and Mechanical Engineering, Technical University of Cluj-Napoca / Romania, [2)] Department of Engineering Design and Robotics, Technical University of Cluj-Napoca / Romania	245
24.	**DESIGN AND PERFORMANCE TEST OF REMOTE DRIVING CONTROL SYSTEM OF SMALL AGRICULTURAL HYDRAULIC CHASSIS / *小型农用液压底盘远程驾驶控制系统的设计与试验*** **Xiaorong LÜ[#1)], Yuan FU[#1)], Xinping CHENG[2)], Fugui ZHANG[1)], Yuancai LEN[1)], Dandan HAN[1*)]** [1)] College of Machinery & Electronics, Sichuan Agricultural University, Yaan, Sichuan, China [2)]Chengdu Wenjiang Science and Technology Industrial Development Park, Chengdu, Sichuan, China	255

		Page(s)
25.	**ANALYSIS AND MANAGEMENT OF ORGANIC AGRICULTURE DEVELOPMENT IN EASTERN EUROPEAN COUNTRIES / *ANALIZA I ZARZĄDZANIE ROZWOJEM ORGANICZNEGO ROLNICTWA W KRAJACH EUROPY WSCHODNIEJ*** **Nadiia SHMYGOL[1)], Władysława ŁUCZKA[2)], Nataliia GAVKALOVA[3)], Zhanna HARBAR [4)], Viktor KOVAL [5)] and Lucian-Ionel CIOCA[6,7,*)]** [1)]Warsaw University of Technology, Warsaw; [2)]University of Life Sciences in Poznań; [3)]Warsaw University of Technology, Warsaw; [4)]Vinnytsia National Agrarian University, Vinnytsia, Ukraine; [5)]Izmail State University of Humanities, Izmail, Ukraine; [6)]Lucian Blaga University of Sibiu, Sibiu, Romania; [7)]Academy of Romanian Scientists, 3 Ilfov, Bucharest, Romania	265
26.	**DETECTION OF APPLE LEAF DISEASES TARGET BASED ON IMPROVED YOLOv7 / *基于改进 YOLOv7 的苹果叶病害目标检测*** **Lingqing FENG, Yujing LIU*), Hua YANG, Zongwei JIA, Jiaxiong GUAN, Huiru Zhu, Yiming HOU** College of Information Science and Engineering, Shanxi Agricultural University, Taigu/China	280
27.	**ONLINE DETECTION OF SOLUBLE SOLID CONTENT IN FRESH JUJUBE BASED ON VISIBLE / NEAR-INFRARED SPECTROSCOPY / *基于可见/近红外光谱的鲜枣可溶性固形物在线检测*** **Bin WANG [1)], Lili LI [*1)]** [1)] College of Information Science and Engineering, Shanxi Agricultural University, Taigu / China	291
28.	**OPTIMIZATION DESIGN ANALYSIS OF MOVABLE ROTATING PLATE TYPE GRADING DEVICE FOR POTATO / *活动转板式马铃薯分级装置优化设计分析*** **Haohao ZHAO, Weigang DENG*, Zhiqi REN, Chenglong LIU, Dong YAN, Yansong CAI, Zexin ZHAO** College of Mechanical and Electrical Engineering, Inner Mongolia Agricultural University, Hohhot, China	299
29.	**SIMULATION AND TEST OF FILLING PERFORMANCE OF PNEUMATIC PRECISION SEED METERING DEVICE BASED ON EDEM SOFTWARE / *基于 EDEM 软件的气压式精量排种器充种性能模拟与试验*** **Wenqi GUO, Wenyi ZHANG, Yunxia WANG, Youqiang DING, Bin QI*[1]** Nanjing Institute of Agricultural Mechanization, Ministry of Agriculture and Rural Affairs, Nanjing / China	313
30.	**EXPERIMENTAL STUDY ON THE SEEDING PERFORMANCE OF THE SPOON-WHEEL MAIZE SEED-METERING DEVICE UNDER VIBRATION CONDITIONS / *勺轮式排种器在振动条件下的排种性能试验研究*** **Qing WANG, Dandan HAN*, You XU, Yuxia HUANG, Chao TANG, Wei LI** College of Mechanical and Electrical Engineering, Sichuan Agricultural University, Ya'an, China	324
31.	**PARAMETER CALIBRATION FOR DISCRETE ELEMENT SIMULATION OF CUTTING DECK CLEANING IN SMALL PLOT WHEAT COMBINE HARVESTER / *小区小麦联合收获机割台清理离散元仿真参数标定*** **Yong DING[1)], Jian ZHANG[2)], Zhiguo PAN*[1)], Weijing WANG[1)], Qi LIU[1)], Shuai WANG[1)], Zhenjia MA[1)], Xiaokang WANG[1)]** [1)] College of Mechanical and Electrical Engineering, Qingdao Agricultural University, Qingdao, China [2)] College of Mechanical and Electrical Engineering, Hainan University, Haikou, China	339
32.	**INVESTIGATION OF THE MICROSCOPIC DAMAGE MECHANISM OF BAIJIU YEAST SPRAY DRYING / *白酒酵母喷雾干燥微观损伤机制探究*** **Feng-Kui XIONG[1, 2)], Jing-Yu LI[1)], Yue-Jin YUAN[2*)], Ying-Ying XU[2)], Guang-Zhong HU[1)]** [1)]College of Mechanical Engineering, Sichuan University of Science & Engineering, Yibin, Sichuan / China; [2)]College of Mechanical & Electrical Engineering, Shaanxi University of Science & Technology, Shaanxi / China	352
33.	**PARAMETER CALIBRATION AND DISCRETE ELEMENT MODEL OF HIGHLAND BARLEY STEM BASED ON EDEM / *基于 EDEM 的青稞茎秆离散元参数标定*** **Fan JIN[1)], Dejiang LIU*[1)] , Chengyi ZHONG[1*)], Keheng YAO[1)] , Jian TONG[2)] , Zhibing JIANG[2)]** [1)] Nanjing Institute of Agriculture Mechanization, Ministry of Agriculture and Rural Affairs, Nanjing, China [2)] Tibet Academy of Agricultural and Animal Husbandry Sciences, Lhasa, China	363
34.	**PARTICLE MOTION OF COATED CORN SEED ACCUMULATION PROCESS BASED ON DISCRETE ELEMENT METHOD / *基于离散元法的包衣玉米种子堆积过程颗粒运动研究*** **Shihao WANG [1)], Shouhao XIA [1)], Yongxin CHEN [1)], Chao LOU [1)], Dinglin REN [1)], Zhaodong LI*[1, 2)]** [1)] College of Engineering, Anhui Agricultural University, Hefei, Anhui, China [2)] Engineering Laboratory of Intelligent Agricultural Machinery Equipment, Anhui, Hefei, China	375
35.	**RESEARCH ON THE CONSTRUCTION METHOD OF HIGH PRECISION 3D POINT CLOUD MAP FOR AGRICULTURAL ENVIRONMENTS / *农业环境高精度三维点云地图构建方法研究*** **Bo ZHAO[1)], Suchun LIU[1)], Xiufeng Zhao[2)], Licheng ZHU[1*)], Tianfu ZHANG[1)], Zhenhao HAN[1)], Weipeng ZHANG[1)]** [1)] National Key Laboratory of Agricultural Equipment Technology, China Academy of Agricultural Mechanization Science Group Co., Ltd, Beijing, China; [2)] Nong'an County Agricultural Mechanization Technology Promotion Station, Changchun, Jili, China	391
36.	**ACCURATE NON-DESTRUCTIVE TESTING METHOD FOR POTATO SPROUTS FOCUSING ON DEFORMABLE ATTENTION / *聚焦可变形注意力的马铃薯芽苗精确无损检测方法*** **Binxuan GENG[1)], Guowei DAI[2)], Huan ZHANG[1,*)], Shengchun QI[1)], Christine DEWI[3)]** [1)] Faculty of Mechanical and Electrical Engineering, Qingdao Agricultural University, Qingdao / China; [2)] Agricultural Information Institute of CAAS, Beijing / China; [3)] Faculty of Information Technology, Satya Wacana Christian University Salatiga / Indonesia	402
37.	**DESIGN AND TEST OF DOUBLE-SHAFT TYPE SWEET POTATO HAULM CUTTING RETURN MACHINE / *双轴式甘薯打秧还田机设计与试验*** **Kuan QIN*), Yun ZHAO, Rui YANG** College of Engineering, Anhui Agricultural University, Anhui, Hefei / China	414

		Page(s)
38.	**DESIGN OF ENERGY MANAGEMENT STRATEGY FOR DUAL-MOTOR-DRIVEN ELECTRIC TRACTORS / *双电机驱动电动拖拉机能量管理策略的研究*** **Jun YANG[1)], Aiping SHI[*1)], Yupeng JIANG[1)], Bochuan DING[1)]** College of Agricultural Engineering, Jiangsu University, Zhenjiang, China	429
39.	**MEASUREMENT OF THE PHYSICAL PARAMETERS OF PEANUT SEEDS AND CALIBRATION OF THE DISCRETE ELEMENT PARAMETERS / *花生籽粒物理参数测定与离散元参数标定*** **Hongwei Diao[1)], Wenlong Ye[2)], Zhicheng Zhang[1)], Xin Liu[1)], Fandi Zeng[*1)], Xuying Li[*2)], Ji Cui[2)], Zhihuan Zhao[1)]** [1)] Shandong Agriculture and Engineering University, College of Mechanical and Electronic Engineering, Jinan, China; [2)] Inner Mongolia Agricultural University, College of Mechanical and Electrical Engineering, Hohhot, China.	444
40.	**FORCE ANALYSIS OF A ROTARY TILLER WITH A VERTICAL ROTATION AXIS / *ՈՒՂՂԱՁԻԳ ՊՏՏՄԱՆ ԱՌԱՆՑՔՈՎ ՀՈՂԱՄՇԱԿ ՃՐԵՋԻ ՈՒԺԱՅԻՆ ՎԵՐԼՈՒԾՈՒԹՅՈՒՆ*** **Arshaluys TARVERDYAN, Artur ALTUNYAN [*)], Albert GRIGORYAN** Scientific Research Institute for Agricultural Mechanization and Automation, Armenian National Agrarian University, Yerevan, Armenia	454
41.	**JOINT OPTIMIZATION OF COLD-CHAIN PICK-UP VEHICLE ROUTING AND CARGO ALLOCATION FOR FRESH AGRICULTURAL PRODUCTS / *生鲜农产品冷链集货车辆路径与货物配载联合优化研究*** **Jingqiong WU[*1,2)]; Xuke WU[1)]; Jiabo HUANG[1)]** [1)]School of Traffic Engineering, Kunming University of Science and Technology, Kunming, Yunnan, China; [2)]Yunnan Engineering Research Center of Modern Logistics, Kunming Yunnan, China	466
42.	**FIELD TRAVERSAL PATH PLANNING FOR AGRICULTURAL ROBOTS IN HILLY AREAS BASED ON DISCRETE ARTIFICIAL BEE COLONY ALGORITHM / *基于离散人工蜂群算法的农业机器人丘陵地区农田遍历路径规划*** **Xiaodong LOU [1)], Zheng LI [*2)]** [1)] College of Digital Commerce, Zhejiang Business Technology Institute, Ningbo, Zhejiang/ China [2)] School of Teacher Education, Shaoxing University, Shaoxing, Zhejiang/ China	480
43.	**STUDY ON THE DETERMINATION OF PHYSICAL AND MECHANICAL PROPERTIES OF LAVENDER / *薰衣草物理力学特性的测定研究*** **Yang LI [1)], Yanmin TAO [2)], Yulong CHEN [3)], Yiteng LEI [*1)]** [1)] School of Electronic and Engineering, Yili Normal University, Yining, Yili, China; [2)] Shandong Kexiang Intelligent Technology Co., Ltd., Jinan, China; [3)]College of Agricultural Engineering and Food Science, Shandong University of Technology, Zibo, China	492
44.	**REVIEW ON THE DEVELOPMENT OF LAVENDER HARVESTING TECHNIQUES / *薰衣草收获技术发展综述*** **Yang LI [1)], Yanmin TAO [2)], Yulong CHEN [3)], Yiteng LEI [*1)]** [1)] School of Electronic and Engineering, Yili Normal University, Yining, Yili, China; [2)] Shandong Kexiang Intelligent Technology Co., Ltd., Jinan, China; [3)] College of Agricultural Engineering and Food Science, Shandong University of Technology, Zibo, China	501
45.	**TRAJECTORY PLANNING FOR COLLABORATIVE OPERATION OF MULTIPLE AGRICULTURAL HANDLING ROBOTS BASED ON IMPROVED WHALE OPTIMIZATION ALGORITHM / *基于改进鲸鱼优化算法的多农业搬运机器人协同作业轨迹规划研究*** **Jiahao LAN, Yunjie MA [*)]** School of Economics and Management, Ningbo University of Technology, Ningbo, Ningbo/China	514
46.	**EXPERIMENTAL RESEARCH ON THE STABILITY OF A SPRAY BOOM WITH AN ACTIVE AND PASSIVE PENDULUM SUSPENSION / *摆式主被动悬架喷雾机喷杆稳定性试验研究*** **Fang LI[1)], Xiaohu BAI[*2)]** [1)] School of Information and Control Engineering, Liaoning Petrochemical University, Fushun/China; [2)] College of Engineering, Shenyang Agricultural University, Shenyang/China	525
47.	**DESIGN AND EXPERIMENTAL STUDY OF HORIZONTAL-SHAFT ROLLER-TYPE COTTON STALK PULLER BASED ON RESPONSE SURFACE METHOD / *基于响应曲面法的横轴对辊式棉花拔秆机的设计与试验研究*** **Dangqin Xue[1)*], Zhouming Gao[2)], Jiaxi Zhang[2)]** [1)] Nanyang Institute of Technology, Nanyang, Henan, China; [2)] Xinjiang Agricultural University, Urumqi, Xinjiang, China	535
48.	**PRELIMINARY RESEARCHES ON SOME TECHNICAL-FUNCTIONAL PARAMETERS OF AN EXPERIMENTAL MODEL OF CONVECTIVE DRYER WITH TOTAL ENERGY INDEPENDENCE/ *CERCETĂRI PRELIMINARE ASUPRA UNOR PARAMETRI TEHNICO-FUNCȚIONALI AI UNUI MODEL EXPERIMENTAL DE USCĂTOR CONVECTIV CU INDEPENDENȚĂ ENERGETICĂ TOTALĂ*** **Cristian SORICĂ[1*)], Andrei PĂTRUȚ[2)], Gheorghe ȘOVĂIALĂ[3)], Elena SORICĂ[1)], Laurențiu VLĂDUȚOIU[1)], Mario CRISTEA[1)], Gabriela MATACHE[3)] , Ioan PAVEL[3)]** [1)]INMA Bucharest, No. 6 Ion Ionescu de la Brad Blvd., Bucharest, Romania [2)]CALORIS GROUP S.R.L., No. 8A Berceni Road, Bucharest, Romania [3)]INOE 2000-IHP, No.14 Cuțitul de Argint Street, Bucharest, Romania	547
49.	**OPTIMIZATION AND EXPERIMENT ON MECHANICAL VIBRATION HARVESTING PROCESS PARAMETERS OF MULBERRY / *桑葚机械振动收获参数优化与试验研究*** **Junming Hou, Yachen Yu, Ziyuan Tang, Liang Zhang, Jiuyu Jin, Wei Wang** Shenyang Agricultural University, College of Engineering / China	557
50.	**DESIGN AND EXPERIMENT OF SWING TYPE SYNCHRONOUS MULCHING FOR RICE DIRECT SEEDER / *悬摆式同步覆土水稻直播机的设计与试验*** **Jiajia YU[1,2)], Zhongyan TAO[1,2)], Liping XIAO[1,2)], Jun'an LIU[1,2)], Xiongfei CHEN[1,2*)], Muhua LIU[1,2)], Nan HUANG[1,2)], Wei DONG[1,2)]** [1)] College of Engineering, Jiangxi Agricultural University, Nanchan, China [2)] Key Laboratory of Modern Agricultural Equipment library, Nanchang, China	569

		Page(s)
51.	**STUDY OF FIBER DEFORMATION OF ELASTIC BRUSH-LIKE SCREWS DURING GRAIN MATERIAL TRANSPORTATION / *ДОСЛІДЖЕННЯ ДЕФОРМАЦІЇ ВОЛОКОН ЕЛАСТИЧНИХ ЩІТКОПОДІБНИХ ШНЕКІВ ПРИ ТРАНСПОРТУВАННІ ЗЕРНОВОГО МАТЕРІАЛУ*** **Andrii DIACHUN, Ivan GEVKO, Oleg LYASHUK, Andrii STANKO, Andrii PIK, Yuri OMELYANSKYI** Ternopil Ivan Puluj National Technical University, Ukraine	579
52.	**DESIGN AND EXPERIMENT ON CUTTING AND CRUSHING DEVICE OF SIDE-SWEEPING STRAW RETURNING MACHINE / *侧扫式秸秆还田机切割粉碎装置设计与试验*** **Ruili WANG[1)], Deshuai LI[1)], Shuai LI[1)], Tong REN[1)], Hongbo BAI[2)], Yashuang JIN[2)], Wei WANG[1,*)], Satyanarayan R.S. DEV[3)]** [1)] College of Engineering, Shenyang Agricultural University, Shenyang 100866, China [2)] Yushu City Enyu Township Comprehensive Service Center, Changchun 130408, China [3)] College of Agriculture and Food Sciences, Florida A&M University, Tallahassee, FL 32307, USA	589
53.	**REAL-TIME WHEAT DETECTION BASED ON LIGHTWEIGHT DEEP LEARNING NETWORK REPYOLO MODEL / *基于轻量级深度学习网络 RepYOLO 模型的麦穗实时检测*** **Zhifang BI[1)], Yanwen LI[2)], Jiaxiong GUAN[2)], Xiaoying ZHANG[*3)]** [1)] Department of Basic Courses, Shanxi Agricultural University, Shanxi / China [2)] College of Information Science and Engineering, Shanxi Agricultural University, Shanxi / China [3)] School of Software, Shanxi Agricultural University, Shanxi / China	601
54.	**NUMERICAL AND EXPERIMENTAL ANALYSIS OF THE ABRASIVE WEAR OF TWO STEELS USED IN TILLAGE TOOLS / *ANÁLISIS NUMÉRICO Y EXPERIMENTAL DEL DESGASTE ABRASIVO DE DOS ACEROS UTILIZADOS EN APEROS DE LABRANZA*** **Ángel, SÁNCHEZ-IZNAGA[1)]; Carlos, MONTES-RODRÍGUEZ[2*)]; Roberto, TORRES-RODRÍGUEZ[3)]; Nadia GONZÁLEZ-LÓPEZ[2)]; Julio PÉREZ-GUERRERO[3)]; Carlos RECAREY-MORFA[4)]; Miguel HERRERA-SUÁREZ[3)].** [1)]University of Cienfuegos. Collaboration between the University of Cienfuegos and the Metropolitan University of Ecuador; [2)]Technical University of Manabi, Faculty of Basic Sciences. Department of Physics / Ecuador; [3)]Technical University of Manabi, Faculty of Engineering and Applied Sciences, Department of Mechanics / Ecuador; [4)]Central University of Las Villas, International Centre for Numerical Methods in Engineering / Cuba	611
55.	**THE INFLUENCE OF WORKING SPEED ON THE QUALITY PARAMETERS FOR SPRAYING IN VINEYARDS / *INFLUENȚA VITEZEI DE LUCRU ASUPRA PARAMETRILOR CALITATIVI LA EFECTUAREA LUCRĂRILOR DE STROPIT ÎN VII*** **Tibor RITTNER, Alexandru Bogdan GHEȚE*, Ovidiu MARIAN, Ovidiu RANTA, Valentin CRIȘAN, Cătălin BOGDAN, Molnar ADRIAN** University of Agricultural Sciences and Veterinary Medicine Cluj-Napoca, Romania	621
56.	**USING SOLAR ENERGY AS NON-CONVENTIONAL ALTERNATIVE ENERGY IN SMALL AND MEDIUM-SIZED FARMS / *UTILIZAREA ENERGIEI SOLARE CA SURSĂ ALATERNATIVĂ NECONVENȚIONALĂ DE ENERGIE ÎN FERMELE DE DIMENSIUNI MICI ŞI MEDII*** **Mario CRISTEA[1)], Nicolae-Valentin VLĂDUȚ[1*)], Nicoleta UNGUREANU[2*)]** [1)]INMA Bucharest / Romania; [2)]POLITEHNICA Bucharest / Romania	631
57.	**ASPECTS REGARDING THE USE OF SOLAR ENERGY IN SMALL AND MEDIUM FARMS / *ASPECTE PRIVIND UTILIZAREA ENERGIEI SOLARE ÎN FERMELE MICI ŞI MEDII*** **Mario CRISTEA[1)], Nicolae-Valentin VLĂDUȚ[1*)], Georgiana MOICEANU[2*)]** [1)]INMA Bucharest / Romania; [2)]POLITEHNICA Bucharest / Romania	644
58.	**DESIGN AND MECHANISM STUDY OF SEED FILLING ROOM WITH STAGGERED ORIENTED PLATES AND VIBRATION / *交叉导流式振动种箱设计与机理研究*** **Zhiye MO, Fangyuan LU*), Mengqi ZHANG, Chong TAO, Bolong WANG, Guohai ZHANG** School of Agricultural Engineering and Food Science, Shandong University of Technology, Zibo/ China	653
59.	**TECHNICAL SOLUTIONS FOR BIOMASS ESTIMATION ACCORDING TO THE CONCEPT OF AQUACULTURE 4.0 / *SOLUȚII TEHNICE PENTRU ESTIMAREA BIOMASEI CONFORM CONCEPTULUI DE ACVACULTURĂ 4.0*** **Dan CUJBESCU[1)], Dragoș DUMITRU*[1)], Iulian VOICEA*[1)], Cătălin PERSU[1)], Iuliana GĂGEANU[1)], Alexandru IONESCU[1)], Ana Maria TĂBĂRAȘU[1)], Dragoș ANGHELACHE[1)]** National Institute of Research – Development for Machines and Installations Designed to Agriculture and Food Industry, Romania	663
60.	**STUDY ON SINGLE-BRANCH COMBING OF *Cerasus humilis* / *钙果单枝梳脱试验研究*** **Shilei KANG[1,2)], Junlin HE*[1,2)], Tao WANG[1)]** [1)]College of Agricultural Engineering, Shanxi Agricultural University, Taigu, China; [2)]Dryland Farm Machinery Key Technology and Equipment Key Laboratory of Shanxi Province, Taigu, China	679
61.	**CHERRY SEGMENTATION AND IDENTIFICATION BASED ON DEEPLABV3 IN COMPLEX ORCHARD ENVIRONMENT / *基于 DeepLabV3 的复杂果园环境下樱桃分割与识别*** **Jinlong WU*[,1,2)], Ronghui MIAO[1,2)]** [1)] College of information science and engineering, Shanxi agricultural university, Taigu / China; [2)] College of agricultural engineering, Shanxi agricultural university, Taigu / China	689
62.	**DESIGN AND TESTING OF A COTTON STALK CLAMP-PULLING TEST BENCH / *棉秆对夹拉拔试验台设计与试验*** **Jiaxi ZHANG*[1,2)], Zhenkun LI[1)], Gang GUO [1)], Yasenjiang BAIKELI[1)], Yichao WANG[1)], Jialin CAI[1)], Zhenwei WANG[1,3)]** [1)]Xinjiang Agricultural University, School of Mechanical and Electrical Engineering, Urumqi / China; [2)]Xinjiang Key Laboratory of Intelligent Agricultural Equipment, Urumqi / China [3)] Nanjing Institute of Agricultural Mechanization, Ministry of Agriculture and Rural Affairs / China	699
63.	**DESIGN AND EXPERIMENT OF MULTI-FRUIT GRIPPING AND CUTTING LINKAGE KIWIFRUIT PICKING END-EFFECTOR / *多果夹持切割联动式猕猴桃采摘末端执行器设计与试验*** **Min FU*, Jianan CAI, Shike GUO, Lei CHEN, Chengmeng WANG, Gangqiang YANG, Xiaoman CUI** Northeast Forestry University, College of Mechanical and Electrical Engineering, Harbin / China	710

		Page(s)
64.	**RESEARCH ON THE RESPONSE MECHANISM OF CLAMPING POINT POSITION TO THE VIBRATION PROPAGATION CHARACTERISTICS OF WOODEN MATERIALS /** ***夹持点位置对木质材料振动传播特性的响应机理研究*** **Xingdong SUN*[1)], Yukai ZHENG[1)], Yuhang SUI[1)], Delin WU[1)], Rongyan WANG[1)], Yangyang LIU[1)], Jianfei ZHOU[1)]** [1)]School of Engineering, Anhui Agricultural University, Hefei, China	720
65.	**DESIGN AND TESTING OF SEED PUSH WHEEL FOR HIGH-SPEED PRECISION SEED METERING DEVICE FOR CORN WITH INTERNAL SEED FILLING AND POSITIVE PRESSURE AIRFLOW /** ***玉米内充气压式高速精量排种器推种轮设计与试验*** **Xin DU, Qianhao YU, Shufa CHEN, Qixin SUN, Han ZHANG, Changqing LIU*** School of Mechanical Engineering, Jiangsu Ocean University, Lianyungang / China	731
66.	**SIMULATION ANALYSIS AND TEST OF EDEM-BASED TWIN SPIRAL PROPELLER FOR MUDFLAT AQUACULTURE /** ***基于 EDEM 的滩涂养殖双螺旋推进器仿真分析与试验*** **Maomao ZOU[1)], Rui ZHANG*[1)], Xiwen ZHANG[1)], Xiaoning HE[1)], Shuqi SHANG[13)], Xuegeng CHEN[12)], Zhenjia MA[1)], Moxian LI[1)], Yunkang LI[1)], Wenjie LI[1)], Haozhe WEI[1)], Yutao LI[1)]** [1)] College of Mechanical and Electrical Engineering, Qingdao Agricultural University, Qingdao, China; [2)] Shihezi University, Shihezi, China; [3)] Key Laboratory of Intelligent Agricultural Machinery and Equipment for Saline and Alkaline Land, Ministry	741
67.	**DETERMINANTS OF AI-BASED APPLICATIONS ADOPTION IN THE AGRICULTURAL SECTOR – MULTI-GROUP ANALYSIS /** **ปัจจัยกำหนดการนำแอปพลิเคชันที่ใช้ AI มาใช้ในภาคเกษตรกรรม – การวิเคราะห์แบบหลายกลุ่ม** **Vasu KEERATIVUTISEST [1)], Wornchanok CHAIYASOONTHORN[1)], Bilal KHALID[1)], Beata ŚLUSARCZYK[1,3)], Singha CHAVEESUK*[1)]** [1)] KMITL Business School, King Mongkut's Institute of Technology Ladkrabang, Thailand [2)] North-West University, Trade and Development, Private Bag X1290, 2520 Potchefstroom, South Africa [3)] Faculty of Management, Czestochowa University of Technology, Poland	750
68.	**SATELLITE IMAGERY USAGE IN AGRICULTURE. CASE STUDY /** ***UTILIZAREA IMAGINILOR SATELITARE ÎN AGRICULTURĂ. STUDIU DE CAZ*** **Anca Daniela MOICEANU[1)], Georgiana MOICEANU[2)], Gigel PARASCHIV*[2)], Mario CRISTEA*[3)]** [1)] Aider Association / Romania; [2)] National University of Science and Technology "POLITEHNICA" Bucharest / Romania; [3)] National Institute for Research-Development of Machines and Installations Designed for Agriculture and Food Industry - INMA Bucharest/ Romania	765
69.	**DESIGN AND EXPERIMENT OF SEED-FILLING COMPONENT FOR RICE HOLE SEEDER /** ***水稻穴播器取种装置设计与试验*** **Huyang TANG[1)], Gang WANG[1)], Bo ZHOU[1)], Yu WAN[1)], Fuming KUANG[1)], Wei XIONG[1)], Dequan ZHU[1)], Shun ZHANG*[1, 2)]** [1)] College of Engineering, Anhui Agricultural University, Hefei, Anhui, 230036, China [2)] Engineering Laboratory of Intelligent Agricultural Machinery Equipment, Anhui, Hefei, China	775
70.	**NUMERICAL SIMULATION OF THE INFLUENCE OF SOME GEOMETRIC PARAMETERS ON THE DECONTAMINATION QUALITY OF A NON-LAMBERTIAN TYPE DETECTOR, USING A UV-C LEDs MATRIX /** ***SIMULARE NUMERICĂ A INFLUENȚEI UNOR PARAMETRI GEOMETRICI ASUPRA CALITATII DECONTAMINARII UNUI RECEPTOR DE TIP NON-LAMBERTIAN, UTILIZAND O MATRICE DE LED-uri UV-C*** **Cristian SORICĂ[1)], Mario CRISTEA[1*)], Valentin VLĂDUȚ[1)]** [1)]INMA Bucharest, No. 6 Ion Ionescu de la Brad Blvd., Bucharest, Romania	788
71.	**DESIGN AND TEST OF THRESHING AND CLEANING DEVICE FOR *CYPERUS ESCULENTUS L.* COMBINE HARVESTER /** ***油莎豆联合收获机用脱粒清选装置设计与试验*** **Zixuan ZHANG[1)], Honglei JIANG[1)], Xiaoning HE*[1)], Fangyan ZHANG[1)], Jiasheng WANG[1)], Dongwei WANG[1)]** [1)]College of Electromechanical Engineering, Qingdao Agricultural University, Qingdao 266109, China	798
72.	**DESIGN AND EXPERIMENT OF SPRAY BOOM INCLINATION CONTROL SYSTEM /** ***喷杆倾角控制系统的设计与实验*** **Fang LI[1)], Xiaohu BAI*[2)]** [1)] School of Information and Control Engineering, Liaoning Petrochemical University, Fushun/China; [2)] College of Engineering, Shenyang Agricultural University, Shenyang/China	809
73.	**DESIGN AND TESTING OF 4YZ-6 FRESH CORN HARVESTER GRAIN SPLITTING FRONT END COMPONENT /** ***鲜食玉米联合收获机分禾前端研究与试验*** **Zhibo LI, Tong YE, Meiling NIE, Haitao LAN, Xin ZHANG, Wei ZHAO** Heilongjiang Academy of Agricultural Machinery Engineering, Harbin, China	820
74.	**EVOLUTION AND TECHNOLOGICAL DEVELOPMENT OF AUTOMATIC TRANSPLANTERS FOR VEGETABLES: A REVIEW /** ***EVOLUCIÓN Y DESARROLLO TECNOLÓGICO DE LAS TRASPLANTADORAS AUTOMÁTICAS PARA HORTALIZAS: UNA REVISIÓN*** **Gaudencio GRANDE[1]; Martín HIDALGO-REYES*[2)]; Pedro CRUZ[2)]; Noe VELÁZQUEZ[3)]** [1)]Graduate Program of Agricultural Engineering and Integral Use of Water, Universidad Autonoma Chapingo / Mexico; [*2)] Agricultural Mechanical Engineering Department, Universidad Autonoma Chapingo / Mexico; [3)] Irrigation Department, Universidad Autonoma Chapingo / Mexico	830
75.	**TECHNOLOGIES AND CONSTRUCTIVE SOLUTIONS REGARDING THE INTER-ROW MANAGEMENT OF VINEYARD AND FRUIT TREES /** ***TEHNOLOGII ȘI SOLUȚII CONSTRUCTIVE PRIVIND MANAGEMENTUL INTERVALULUI DINTRE RÂNDURILE DE VIȚĂ DE VIE ȘI POMI FRUCTIFERI*** **Dragoș DUMITRU[1)], Carmen BĂLȚATU*[1)], Eugen MARIN[1)], Gabriel-Valentin GHEORGHE[1)], MANEA Dragoș[1)], Marinela MATEESCU[1)], Melania-Elena CISMARU[1)]** [1)] INMA Bucharest/ Romania	848

ESTABLISHMENT AND APPLICATION OF SOIL FERTILIZATION PRESCRIPTION CHART
/
土壤施肥处方图的建立和应用

Fanxia KONG*[1)], Haozheng SUN[1)], Jiankun LI[3)], Baixu LIU[1)], Lili YI[1)], Yubin LAN[1,2)], Xin HAN[1)], Duanyang GENG[1)], Qiang GAO[3)]

[1)]School of Agricultural Engineering and Food Science, Shandong University of Technology, Zibo/ China
[2)]Shandong Provincial Engineering Technology Research Centre for Agricultural Aviation Intelligent Equipment, Zibo/ China
[3)] Weichai Lovol Intelligent Agricultural Technology Co. Ltd, Weifang/ China
Tel:+8618653372858;E-mail: kfx0309@163.com
Corresponding author: Fanxia Kong
DOI: https://doi.org/10.35633/inmateh-72-01

***Keywords**: soil characteristics; soil fertilization prescription chart; spatial interpolation; variable rate fertilization*

ABSTRACT
Precision soil fertilization is an important aspect of smart precision agriculture development, and the fertilization prescription map is a prerequisite for precision fertilization. Taking grapevine soil information as an example, this study explores the impact of different sampling densities on the accuracy of soil nutrient distribution. Experimental trials were conducted using sampling densities of 1m x 1m, 3m x 3m, 6m x 6m, 9m x 9m, and 12m x 12m, with the optimal sampling density determined to be 6m x 6m. Nutrient distribution maps were created using Bigemap and ArcGIS software, and based on nutrient balance calculations using ArcGIS software, fertilization prescription maps were developed. Furthermore, precise fertilization schemes for nitrogen, phosphorus, and potassium fertilizers were formulated based on the prescription maps. This study provides methodological and data support for research on precision soil fertilization.

摘要
土壤精准施肥是智慧精准农业发展的重要方面，施肥处方图是精准施肥的前提。本文以葡萄园土壤信息为例，探索了不同采样密度对土壤养分分布准确度的影响，以 1m x 1m, 3m x 3m, 6m x 6m, 9m x 9m, and 12m x 12m, 为例进行了试验，确定了最佳采样密度为 6m x 6m，使用 Bigemap 和 ArcGIS 软件绘制了养分分布图，根据养分平衡法运用 ArcGIS 软件得出相应的施肥处方图，并基于处方图给出了氮、磷、钾三种肥料的精准施肥方案，为土壤精准施肥研究提供了方法支持和数据支持。

INTRODUCTION
Precision agriculture represents the future trend in agricultural production, with precise soil fertilization being a crucial component of smart farming. China has made significant strides in the development of precise fertilization prescription charts *(An et al., 2017)*, fertilization control algorithms *(Liu et al., 2021; Zhang et al., 2021)*, as well as fertilization systems and mechanisms *(Bai et al., 2021; Jin et al., 2018; Li et al., 2016; Shi et al., 2017; Yuan et al., 2014)*. Moreover, international research efforts have also contributed to advancements in precise fertilization *(Chung et al., 2018; Kabir et al., 2018; Marius et al., 2021; Saleem et al., 2013; Reyes et al., 2015; Yang., 2001)*. The acquisition of fertilization prescription charts is fundamental to precision fertilization.

Currently, research in various aspects of precision fertilization, including the accuracy of prescription charts, efficiency of acquisition, acquisition costs, and the reliability of precision fertilization plans, falls short of meeting the demands of smart precision agriculture development. *Xu et al., (2011),* used Web Services, metadata, spatial interpolation and AJAX technologies, combined with VS2005, ArcGIS 9.3 and SQL Server 2005 and other software, in their paper. NET platform built "WebGIS based wheat precision fertilization decision system", realized the production of wheat prescription map. *Yuan et al., (2013),* studied the soil sampling strategy and the generation method of nutrient distribution map. One soil sample was selected every 10 ridges, and one soil sample was taken from each ridge at an interval of 10 m. The national standard method and rapid measurement method were used to detect the nutrient content. However, the traditional methods of soil sample collection and laboratory testing are not only time-consuming and laborious, but also costly. This can be difficult to achieve for large areas of farmland, limiting the popularity of precision fertilization techniques.

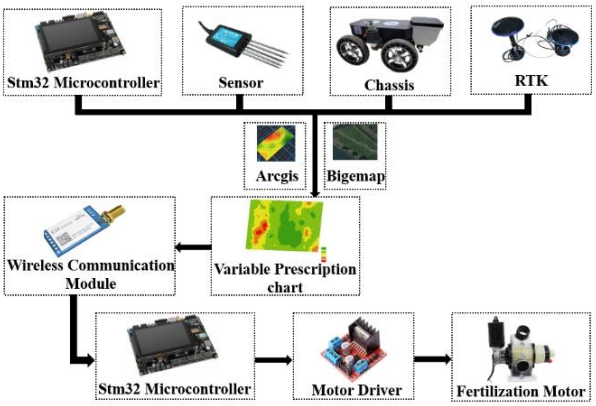

Fig. 1 – System frame diagram

The system frame diagram of this paper is shown in the Fig 1. To address the issue of low efficiency in soil information collection for precision fertilization prescription maps, this study employs an STM32 microcontroller, soil sensors, and Real-Time Kinematic (RTK) technology mounted on a chassis to collect soil information and create fertilization prescription maps. The study investigates the impact of different sampling densities on the accuracy of soil nutrient distribution and determines the optimal sampling density. The prescription map files are transmitted wirelessly to the fertilizer motor control system to achieve variable rate fertilization by controlling the motor speed. This research provides a cost-effective data acquisition method and a more accurate precision fertilization scheme for soil precision fertilization, thereby advancing the development of precision agriculture.

MATERIALS AND METHODS

Soil information collection system

There are various methods for detecting soil information *(Yang et al., 2010; Zhai et al., 2022)*, and in this study, an indirect measurement approach based on soil electrical conductivity was chosen due to its rapid response, cost-effectiveness, and durability. It has been selected a sensor that measures soil nutrient values through electrical conductivity to establish a soil information collection system.

It was opted for the high-precision, rapidly responsive JXBS-3001-TR soil comprehensive sensor in our soil information collection system. This sensor exhibits high accuracy, fast response times, stable output, and is minimally influenced by soil salinity, making it suitable for various soil types. The sensor operates within a voltage range of 12-24V and can withstand temperatures from -40°C to 80°C, thereby complying with our experimental environmental requirements.

The soil information collection system comprises an STM32f429IGT6 development board and the soil comprehensive sensor. It incorporates the SP3485 level-shifting chip and a power module, with sensor readings displayed via a 4.3-inch RGB LCD touch screen module. The hardware configuration features a 485 bus interface, with the sensor functioning as a slave device and its device address set to 0x01. The hardware connection of the system is illustrated in Fig 2.

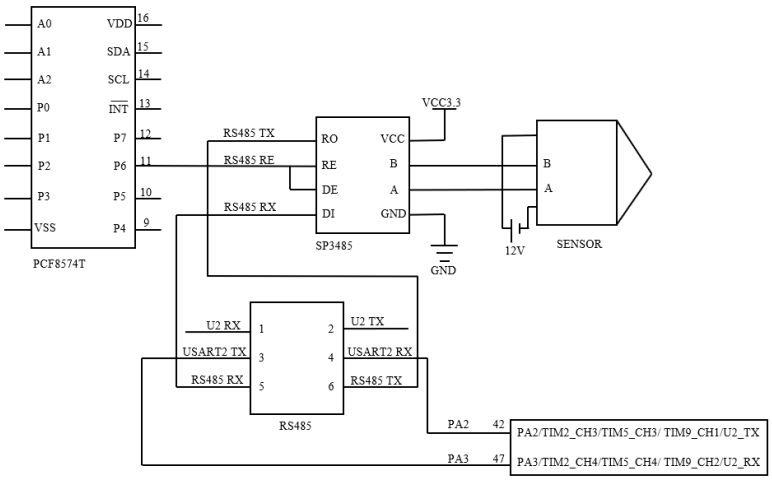

Fig. 2 – Hardware connection chart

In the process of communication between the sensor and the development board, it is essential to predefine various parameters of the communication protocol, such as the baud rate, data bits, parity bits, and stop bits. To ensure the reliability and security of communication, error detection and validation measures, such as parity checks and CRC checks, need to be implemented. These measures effectively mitigate the occurrence of errors and data inaccuracies that may arise during communication. The soil sensor and STM32 development board employ the Modbus RTU communication protocol. The communication data frame formats are outlined in Tables 1 and 2.

Table 1

Query frame

Address code	Function code	Start Address	Data Length	Check bit low	Check bit high
1byte	1byte	2byte	2byte	1byte	1byte

Table 2

Response frame

Address code	Function code	Valid byte	Data area 1	Data area 2	Data area N	Check code
1byte	1byte	1byte	2byte	2byte	2byte	2byte

When utilizing this protocol for data transmission, it is imperative to initialize the system and configure the 485 interfaces for transmission mode. Subsequently, the host sends a query frame to the slave sensor. Upon receiving the query frame, the slave responds with an acknowledgment frame. At this point, the host's receive buffer is cleared, and it switches to receive mode to receive data from the slave.

During the data reception process, the system undergoes a series of checks. Initially, it verifies whether it has received a response from the slave. If a response is received, the system proceeds to confirm whether the received slave address matches 0x01. If the slave address is correct, the system calculates the CRC checksum and compares it with the checksum in the acknowledgment frame. If they match, the system converts the hexadecimal data to decimal and outputs it. In case of a mismatch, the system returns to the initialization phase to resend the query frame.

In this study, programming was performed using the Keil uVision5 software platform, and the entire program flow is depicted in Fig. 3.

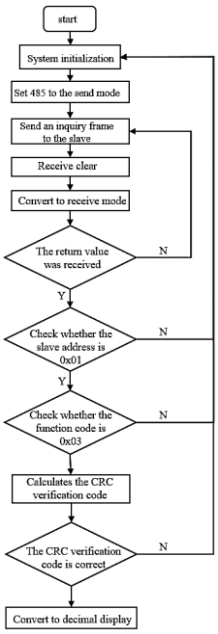

Fig. 3 – Program flow chart

Soil information collection test

To investigate the uniformity of soil nutrient distribution and the impact of sampling density on prescription charts, a rectangular plot measuring 132 meters by 144 meters was selected within the Qianmuyuan Garden Grape Base, located in Huantai County, Zibo City, Shandong Province, China (N37.07420°, E117.91777°).

This site is situated in a temperate monsoon climate region, characterized by yellow-brown soil. The experimental site within the Qianmuyuan Grape Base is of substantial scale and representational significance.

The cultivation pattern in the Qianmuyuan Garden Grape Base follows a ridge-planting approach, where grapevines are planted in a single row on each ridge, with row spacing set at 3 meters.

Bigemap GIS Office software was used to locate the test site through the map query function, as shown in Fig. 4.

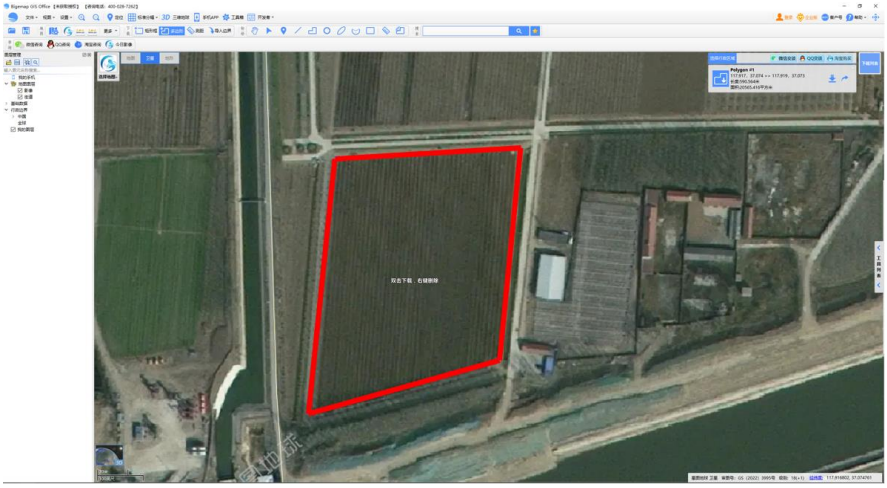

Fig. 4 – The test site

To examine the uniformity of soil nutrient distribution and assess the influence of sampling density on prescription charts, sampling points were selected at various intervals, specifically 1 meter, 3 meters, 6 meters, 9 meters, and 12 meters apart. This equates to a grid pattern of 1m x 1m, 3m x 3m, 6m x 6m, 9m x 9m, and 12m x 12m, respectively, with samples collected at the geometric center of each grid. Each sampling method consisted of 100 samples, resulting in a total of 500 sampling points.

The soil information collection method employed in this study involves selecting sampling points at positions approximately 0.6m away from the grapevine roots, at a depth of 0.2m. Location information is obtained through GNSS-RTK real-time positioning, which offers centimeter-level accuracy. To simultaneously capture both the position information and nutrient content at the sampling points, a sensor is installed on the chassis of a remote-controlled vehicle.

At the front of the vehicle, a drilling device is mounted, affixed to a rod using 3D-printed fixtures. The up-and-down motion of the electric actuator, controlling the drilling operation, is managed by manipulating the high and low levels of an STM32 microcontroller. The steel needle of the sensor measures 0.07m in length, allowing for the collection of soil information at a depth of 0.2m. By controlling the electric actuator, the drilling device creates a hole with a depth of 0.13 meters to reach the required depth. Additionally, GNSS-RTK is used to connect the computer and serial port assistant software, enabling real-time acquisition of the sampling point's location information.

Fig. 5 – Soil collection test

The Christiansen uniformity coefficient is an indicator used to measure the uniformity of nutrient distribution in soil. It effectively reflects the deviation of nutrient distribution across the field from the mean value. This coefficient is calculated by assessing the differences between nutrient content at each sampling point and the mean value, followed by a standardization process. A higher numerical value indicates a more uniform distribution of soil nutrients, whereas a lower value suggests non-uniformity. The formula for calculating the Christiansen uniformity coefficient is as follows:

$$C_{uc} = 100 * \left(1 - \frac{\sum_{i=1}^{n} \left| w_i - \overline{w} \right|}{\sum_{i=1}^{n} w_i} \right) \quad (1)$$

where:

C_{uc} is Christiansen uniformity coefficient; n is the number of soil sampling sites; w_i is nutrient content at the i soil sampling site; $\overline{w}$ is the average nutrient content of the soil sampling site.

The soil nutrient data at various sampling densities were extracted, and the Christiansen Uniformity Coefficient for different sampling densities was computed using Equation (4), yielding the results as presented in Table 4.

Table 4

Christiansen uniformity coefficient at different sampling densities

Sampling density	Christiansen uniformity coefficient		
(m×m)	Rapidly available nitrogen	Rapidly available phosphorus	Rapidly available potassium
12×12	76.11%	77.58%	78.07%
9×9	82.89%	81.71%	83.18%
6×6	86.80%	85.96%	87.77%
3×3	88.32%	87.13%	88.59%
1×1	90.03%	89.03%	90.38%

From the data presented in Table 4, it is evident that, as the sampling density decreases below 6m x 6m, the soil's readily available nitrogen content remains stable within the range of 85% to 91% when compared to denser sampling densities. Similarly, the readily available phosphorus content stabilizes within the range of 85% to 90%, while the readily available potassium content stabilizes within the range of 87% to 92%. These findings indicate a relatively close uniformity in nutrient distribution among different sampling densities.

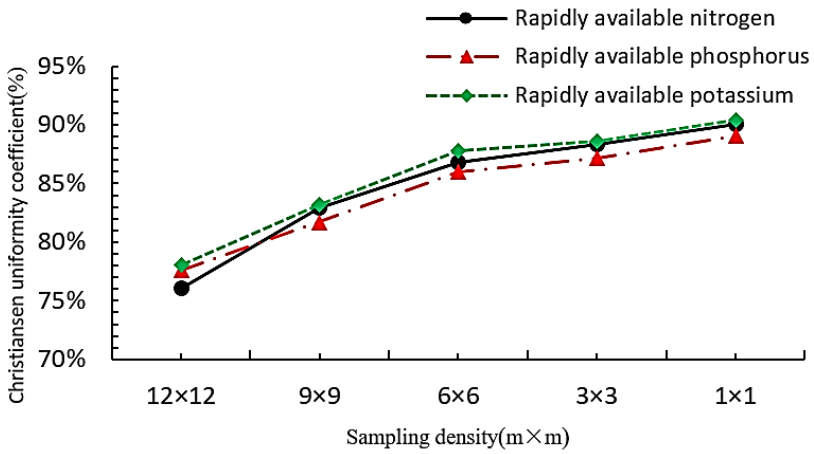

Fig. 6 – Variation map of nutrient distribution uniformity

Moreover, as illustrated in Fig 6, it can be observed that starting from the 12m x 12m sampling density, with an increase in sampling density, the uniformity of nutrient distribution gradually improves. At a sampling density of 6m x 6m, all three nutrient profiles exhibit a turning point, beyond which the slope of the curves noticeably decreases, indicating a reduction in the rate of uniformity change. Therefore, a sampling density of 6m x 6m can be employed for experimentation.

Subsequently, with a sampling density of 6m x 6m, a total of 378 sampling points were re-sampled, and the distribution of these sampling points is depicted in the following Fig. 7.

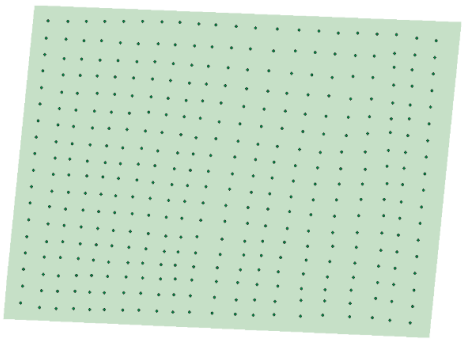

Fig. 7 – Distribution of sampling points

The experimental data obtained with a grid sampling density of 6m x 6m are presented in Table 5. From the data in Table 5, it can be observed that the coefficient of variation for readily available nitrogen, phosphorus, and potassium distribution in the experimental area is approximately 20%, indicating a relatively low level of variation and relatively uniform distribution. The kurtosis values are 5.4425, 5.4027, and 5.1216, all of which exceed the kurtosis of 3 for a normal distribution. This suggests that, compared to a normal distribution, the probability density distribution curves for these three elements have sharper peaks and are steeper. The skewness for all three elements is greater than zero, indicating a leftward skewness in data distribution compared to a normal distribution. This implies the presence of significant outliers, with a long tail trailing on the right side in the histogram, which corresponds to areas in the experimental field with higher levels of readily available nitrogen, phosphorus, and potassium content.

Table 5

Christiansen uniformity coefficient at sampling density 6m × 6m

Item	Minimum value [mg/kg]	Maximum value [mg/kg]	Md-value [mg/kg]	Mean value [mg/kg]	Standard deviation [mg/kg]	Coefficient of variation [%]	Kurtosis	Skewness
N	6	31	17	16.643	3.4782	20.8989	5.4425	0.73429
P	13	41	23	23.751	5.4953	23.1371	5.4027	1.2861
K	29	101	54.5	56.841	13.883	24.4243	5.1216	1.2943

A grid sampling density of 6m x 6m strikes a favorable balance between data precision and the labor costs associated with sampling. In comparison to higher-density sampling, it reduces the workload involved in data collection and processing, while simultaneously offering improved data precision relative to lower-density sampling.

Establishment of soil nutrient distribution map

Since the collected soil nutrient data and coordinate points are discrete, obtaining continuous demand values for readily available nitrogen, phosphorus, and potassium within the field requires the conversion of point data into spatial data through interpolation methods.

The Ordinary Kriging method, suitable for flatland areas, is employed to transform the discrete point-based data into spatial data *(Li et al., 2012)*. The calculation formula for this method is as follows:

$$\hat{Z}(S_0) = \sum_{i=1}^{N} \lambda_i Z(S_i) \quad (2)$$

where:

$\hat{Z}(S_0)$ is estimated value of point(x_0,y_0); λ_i is the unknown weight of the measured value at position i; S_0 is predicted position; N is number of measured values.

The fundamental concept underlying this approach involves treating the neighboring known points of the points to be interpolated as a random field. By seeking the optimal spatial autocorrelation function model to depict the spatial variability of this random field, the model is then used for interpolation at the unknown points.

Based on the soil nutrient content data collected at a sampling density of 6m x 6m and utilizing the Ordinary Kriging interpolation method, the resulting soil nutrient distribution map is presented below, showcasing a gradual increase in nutrient content from 1 to 10.

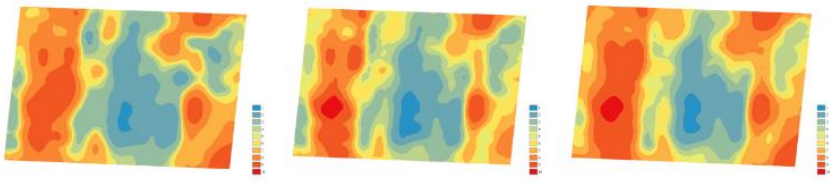

a). Nitrogen *b). Phosphorus* *c). Potassium*

Fig. 8 – The nutrient distribution map

The construction and experimental methods of the fertilization system

In order to test whether the adjustable fertilizer application range of the device and the control system can meet the requirements of fertilizer application, and to verify the accuracy and stability of variable fertilization, laboratory experiments were carried out.

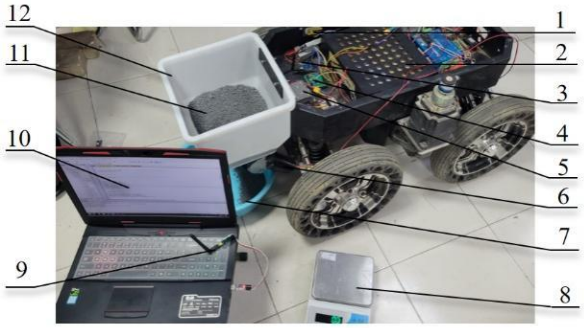

Fig. 9 – Variable fertilization laboratory test

1. Stm32 development board; 2. 48V vehicle power supply; 3. Wireless transmission module; 4.stm32 development board; 5. 48V to 12V step-down module; 6. Fertilizer motor; 7. Plastic basin; 8. Electronic scale; 9. Wireless transmission module; 10. Computer; 11. Fertilizer; 12. Fertilizer box

The indoor simulated variable fertilization experiment is shown in Fig 9. The discharge amounts of urea, superphosphate and potassium nitrate were calibrated at 8, 16, 24, 32, 40, 48, 56, 64 and 72 r/min with the fertilizer dispenser. The relationship between fertilizer discharge and rotational speed of three kinds of fertilizers was studied.

RESULTS

Application of soil fertilization prescription map in variable fertilization

The primary methods for determining fertilization quantities include the Nutrient Balance Method, the Nutrient Surplus/Deficiency Index Method, and the Fertilizer Response Function Method, each of which has its own advantages and disadvantages. The Nutrient Balance Method estimates soil fertilizer supply by measuring soil nutrient content and basic yield. Among these three methods, this approach is better suited for this experiment, where fertilizer quantities are determined through soil nutrient testing. The formula for calculation is as follows:

$$U_N = \frac{V_N S - 0.16\omega_s \mu_N}{\omega_f \eta_{Nf}} \quad (3)$$

where: U_N is rate of fertilizer application; V_N is nutrient uptake per unit yield of crop; S is target yield. (The 3-year average yield of local crops is increased by 10% to 15%); 0.16 is the conversion coefficient represents the nutrient coefficient that the soil available nutrients can be converted into the arable layer of each mu of land; ω_S is soil available nutrient test value; μ_N is correction coefficient of available nutrient; ω_f is nutrient content in fertilizer; η_M is fertilizer utilization rate.

Through consultation with local experts in grape cultivation, it has been determined that for every 100kg of grape fruit production, the absorption of pure nutrients is as follows: 0.6 kg of nitrogen (N), 0.3 kg of phosphorus (P_2O_5), and 0.72 kg of potassium (K_2O). Urea contains 46% nitrogen (N), calcium superphosphate contains 16% phosphorus (P_2O_5), and potassium chloride contains 60% potassium (K_2O).

The soil available nutrient correction factors are set as follows: in the unfertilized area, the nutrient quantity absorbed by crops per hectare is multiplied by 100%.

Generally, the soil available nutrient correction factors fall within the range of 0.3 to 0.7 for available nitrogen, 0.4 to 0.5 for available phosphorus, and 0.5 to 0.85 for available potassium. The arithmetic mean between the maximum and minimum values is taken. Nutrient utilization efficiency is typically in the range of 20% to 40% for nitrogen, 15% to 25% for phosphorus, and 40% to 60% for potassium. Again, the arithmetic mean between the maximum and minimum values is used, resulting in nitrogen fertilizer utilization of 30%, phosphorus fertilizer utilization of 20%, and potassium fertilizer utilization of 50%.

The calculated fertilizer quantities are divided into five equal levels, corresponding to five different application rates. Three types of fertilizers (urea, calcium superphosphate, and potassium chloride) are applied using a fertilizer distributor at different rotational speeds to calibrate the application rates.

The spacing between ridges in the experimental area is approximately 3 meters, and the distance between grape trees is approximately 1.5 meters. Consequently, a grid of 1.5m x 3m is superimposed on the nutrient distribution map, where each grid represents a fertilization unit. Using the lower-left corner of the study area as the origin, a Y-axis is drawn to the upper-left corner to determine the grid's row width and row height, thereby creating the grid. Subsequently, the obtained grid and the points within each grid are clipped to fit within the study area, as depicted in Fig 10.

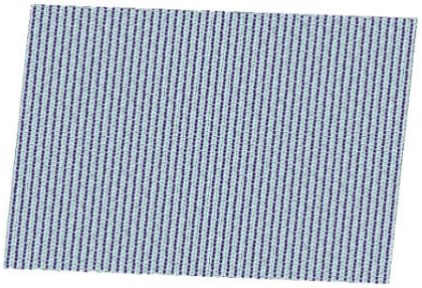

Fig. 10 – Clipped grid

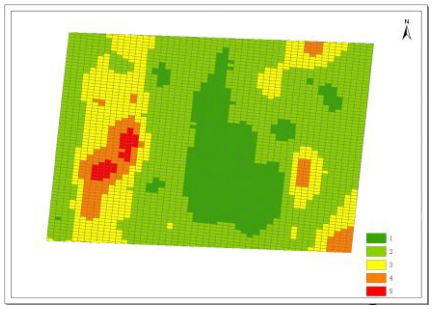

Fig. 11 – Fertilization prescription chart of nitrogen

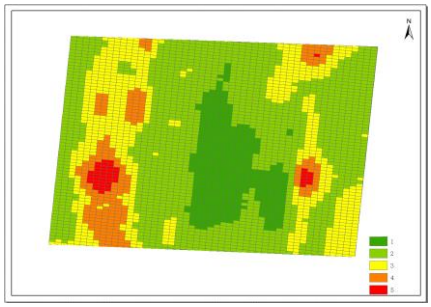

Fig. 12 – Fertilization prescription chart of phosphate

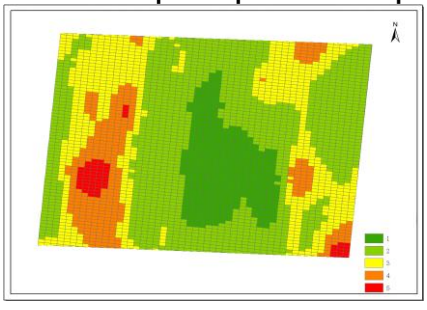

Fig. 13 – Fertilization prescription chart of potassium

As shown in Fig. 11 to Fig. 13, fertilization level 1 corresponds to the regions within the nutrient distribution map with lower nutrient content, resulting in the maximum required fertilizer application, and so forth, with fertilization level 5 requiring the least amount of fertilizer.

Soil nutrient levels directly affect crop yield *(Li et al., 2022)*, so the variation of nutrients in different regions is the starting point and basis for variable fertilization. The exported prescription chart in CSV format is wirelessly transmitted from the computer to the onboard microcontroller via a wireless communication module. Upon receiving the prescription chart information, the microcontroller calculates the desired fertilizer quantities for urea, calcium superphosphate, and potassium chloride at its current location. Subsequently, this information is transmitted to the fertilizer distribution shaft control motor, allowing for the adjustment of the distribution shaft's rotational speed. This process enables variable-rate fertilization operations, as illustrated in Fig. 14.

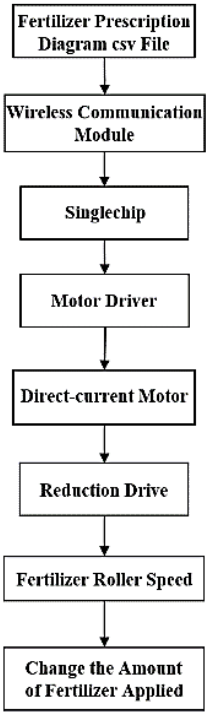

Fig. 14 – Flow chart of variable fertilizer control system

Laboratory test of fertilization system

During calibration, a plastic basin is placed under the fertilizer box, and the fertilizer is weighed by an electronic scale. Each fertilizer was tested for 10 times at each speed. The unitary linear regression analysis was carried out on fertilizer discharge and rotational speed, and the unitary linear regression model between fertilizer discharge and rotational speed was obtained:

$$M_f = an + b \tag{4}$$

where: M is the fertilizer discharge per minute of the fertilizer dispenser, n is the rotation speed of the fertilizer wheel, and a,b is the coefficient and constant of the unitary linear regression model. The a,b values corresponding to the three fertilizers are different.

Table 6

Regression results and significance test

	a	b	R^2	P-value
urea	29.644	357.95	0.9827	2.84×10-6
superphosphate	65.328	382.65	0.9915	6.71×10-7
potassium	34.004	-26.375	0.9893	1.04×10-6

As can be seen from Table 6, the determination coefficient R^2 of the linear regression model established by the fertilizer discharge amount of three fertilizers and the rotation speed of the fertilizer discharge wheel is no less than 0.98, and the P value is less than 0.0001. Therefore, the linear regression equations established between the fertilizer discharge amount of three fertilizers and the rotation speed of the fertilizer discharge wheel are particularly significant and have a high degree of fit, showing a linear relationship with a confidence of 99.99%.

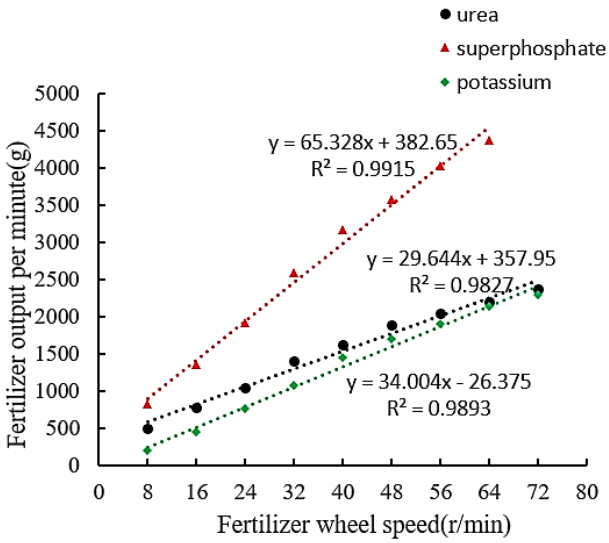

Fig. 15 – Relationship between fertilizer discharge and speed change

The amount of fertilizer applied by each fertilizer is calculated through the prescription diagram, and the corresponding rotation speed of the fertilizer wheel can be obtained by bringing it into the regression equation. Then variable fertilization can be carried out by adjusting the PWM duty ratio to reach the required rotation speed.

In summary, the use of prescription diagrams to calculate fertilizer application rates, coupled with adjusting the rotation speed of the fertilizer wheel through regression equations, has enabled variable-rate fertilization. This method, achieved through PWM duty ratio adjustments, provides a precise means of achieving the required rotation speeds. These findings are crucial for advancing precision agriculture practices. However, further research is needed to compare these results with those from other countries or regions to gain a comprehensive understanding of variable-rate fertilization systems worldwide.

CONCLUSIONS

This study proposed an effective variable fertilization method by integrating soil sensor technology and geographic information systems, providing technical support and theoretical guidance for agricultural production.

An indoor fertilization experiment was conducted, and a linear regression equation was established between the discharge of three types of fertilizers and the rotation speed of the fertilizer wheel to further guide variable fertilization. The results of this study are of great significance for improving the efficiency of fertilization in vineyards, reducing fertilization costs, and promoting the development of precision agriculture.

ACKNOWLEDGMENT

This work was supported by the Natural Science Foundation of Shandong Province, No. ZR202111290044 and Shandong Province Modern Agricultural Industrial Technology System Innovation Team Project (SDAIT-02-02).

REFERENCES

[1] An X., Fu W., Wei X., et al. (2017). Evaluation of Four-element Variable Rate Application of Fertilization Based on Maps (基于处方图的垄作玉米四要素变量施肥机作业效果评价). *Transactions of the Chinese Society for Agricultural Machinery*, Vol. 48, Issue S1: 66-70.

[2] Bai Q., Zhang X, Luo H., et al. (2021). Control system for auto-targeting precision variable-rate fertilization of fruit trees in a greenhouse orchard (设施果园自动对靶精准变量施肥控制系统). *Transactions of CSAE*, Vol. 37, Issue 12: 28-35.

[3] Chung S.O., Kabir M.S.N, Kim Y.J. (2018). Variable Fertilizer Recommendation by Image-based Grass Growth Status. *IFAC-PapersOnLine,* Vol. 51, Issue 17: 10-13.

[4] Jin X., Li Q., Yuan Y., et al. (2018). Design and Test of 2BFJ-24 Type Variable Fertilizer and Wheat Precision Seed Sowing Machine (2BFJ-24 型小麦精量播种变量施肥机设计与试验). *Transactions of the Chinese Society for Agricultural Machinery*, Vol. 49, Issue 05: 84-92.

[5] Kabir M., Chung S., Jang B., et al. (2018). Variable Fertilizer Recommendation by Image-based Grass Growth Status. *IFAC-PapersOnLine*, Vol. 51, Issue 17: 10-13.

[6] Li M., Wen X., Zhou F. (2016). Working Parameters Optimization and Experiment of Precision Hole Fertilization Control Mechanism for Intertilled Crop (中耕作物精准穴施肥控制机构工作参数优化与试验). *Transactions of the Chinese Society for Agricultural Machinery*, Vol. 47, Issue 09: 37-43.

[7] Li X., Liu D., Wang X., et al. (2022). Screening and monitoring of soil fertility stress using ensemble empirical mode decomposition (基于集合经验模态分解算法的土壤肥力胁迫甄别与监测). *Transactions of CSAE*, Vol. 38, Issue 21: 137-146.

[8] Li Z., Zhao G., Zhao Q., et al. (2012). Comparison of Spatial Interpolation Methods for Soil Nutrients in Cultivated Land Fertility Evaluation (县域耕地地力评价中土壤养分空间插值方法的比较研究).*Chinese Agricultural Science Bulletin*, Vol. 28, Issue 20: 230-236.

[9] Liu G., Hu H., Huang J., et al. (2021). Lag Time Detection and Position Correction Method of Variable Rate Fertilization (变量施肥滞后时间检测与位置修正方法研究). *Transactions of the Chinese Society for Agricultural Machinery*, Vol. 52, Issue S1: 74-80.

[10] Marius K., Bručienė I., Jasinskas A., et al. (2021). Comparative analysis of energy and GHG emissions using fixed and variable fertilization rates. *Agronomy*, Vol. 11, Issue 01: 138.

[11] Reyes J. F., Esquivel W., Cifuentes D., et al. (2015). Field testing of an automatic control system for variable rate fertilizer application. *Comput. Electron. Agric.,* Vol. 113, 260-265.

[12] Saleem S., Zaman Q., Schumann A., et al. (2013). Impact of variable rate fertilization on subsurface water contamination in wild blueberry cropping system. *Applied engineering in agriculture*, Vol. 29, Issue 2: 225-232, United States.

[13] Shi Y., Chen M., Wan X., et al. (2017). Analysis and Experiment of Fertilizing Performance for Precision Fertilizer Applicator in Rice and Wheat Fields (稻麦精准变量施肥机排肥性能分析与试验). *Transactions of the Chinese Society for Agricultural Machinery*, Vol. 48, Issue 07: 97-103.

[14] Xu X., Zhang H., Xi L., et al. (2011). Decision-making System for Wheat Precision Fertilization Based on WebGIS (基于 WebGIS 的小麦精准施肥决策系统) *Transactions of CSAE*, Vol. 27, Issue S2: 94-98.

[15] Yang S., Yang W., Wang Y. (2010). Remote Collecting and Monitoring System of Soil Moisture Content Information. *Transactions of the Chinese Society for Agricultural Machinery*, Vol. 41, Issue 9: 173-177.

[16] Yang C. (2001). A variable rate applicator for controlling rates of two liquid fertilizers *Applied engineering in agriculture*, Vol. 17, Issue 3: 409.

[17] Yuan J., Liu Q., Liu X., et al. (2014). Granular Multi-flows Fertilization Process Simulation and Tube Structure Optimization in Nutrient Proportion of Variable Rate Fertilization (多肥料变比变量施肥过程模拟与排落肥结构优化). *Transactions of the Chinese Society for Agricultural Machinery*, Vol. 45, Issue 11: 81-87.

[18] Yuan Y., LI S., Fang X., et al. (2013). Decision Support System of N, P and K Ratio Fertilization (氮磷钾配比施肥决策支持系统) *Transactions of the Chinese Society for Agricultural Machinery*, Vol. 44, Issue 08: 240-244+223.

[19] Zhai C., Yang S., Wang X., et al. (2022). Status and Prospect of Intelligent Measurement and Control Technology for Agricultural Equipment (农机装备智能测控技术研究现状与展望). *Transactions of the Chinese Society for Agricultural Machinery*, Vol. 53, Issue 04: 1-20.

[20] Zhang J., Yan S., Ji W., et al. (2021). Precision Fertilization Control System Research for Solid Fertilizers Based on Incremental PID Control Algorithm (基于增量式 PID 算法的多种固体肥精确施控系统研究). *Transactions of the Chinese Society for Agricultural Machinery*, Vol. 52, Issue 03: 99-106.

SIMULATION ANALYSIS AND OPTIMIZATION OF SOIL CUTTING OF ROTARY BLADE BY ANSYS/LS-DYNA
/
基于 ANSYS/LS-Dyna 旋耕刀切土仿真分析及优化

Wusong XIAO [1], Po NIU [*1], Pan WANG [*2], Yingjie XIE [3], Fei XIA [4]
[1]College of Mechanical Engineering, Chongqing Three Gorges University, Chongqing/China;
[2]Sichuan Academy of Agricultural Machinery Science, Sichuan/China;
[3]Chongqing Agricultural Mechanization Technology Extension Station, Chongqing/China;
[4]Chongqing Kaizhou District Agriculture Service Center, Chongqing/China
Tel: +86 18883367182; E-mail: niupo205@163.com
Corresponding author: Po Niu, Pan Wang
DOI: https://doi.org/10.35633/inmateh-72-02

Keywords: *rotary blade, numerical simulation, SPH, optimization*

ABSTRACT
Mini-tiller is an indispensable agricultural machinery in hilly and mountainous areas of China. Rotary blade is an important working part of mini-tiller, which directly affects the operation quality and power consumption of mini-tiller. In order to reduce the cutting resistance and power consumption of the rotary blade of mini-tiller, the cutting process of the rotary blade was analyzed by numerical simulation, and the tangential bending radius (R), bending angle (β) and edge thickness (c) of the rotary blade were selected as factors to optimize it. After comparing the cutting resistance and cutting power consumption of the rotary blade before and after optimization, the results show that the cutting force of the optimized rotary blade is smaller than that of the rotary blade before optimization. The cutting power consumption of the optimized rotary blade is 2.4% lower than that of the unoptimized rotary blade, which achieves the purpose of drag reduction and consumption reduction.

摘要
微耕机是我国丘陵山区不可或缺的农业机械，旋耕弯刀是其重要的工作部件，直接影响其作业质量与功耗。为降低微耕机旋耕弯刀的切削阻力和功耗，本文通过数值模拟的方法对旋耕弯刀切土过程进行了分析，并选取旋耕弯刀的正切部弯折半径（R），弯折角（β），刃口厚度（c）作为因子对其进行了优化，优化前后旋耕弯刀的切削阻力和切土功耗的对比结果表明优化后的旋耕弯刀切削力小于优化前旋耕弯刀的切削力，旋耕弯刀切土功耗较优化前的旋耕弯刀切土功耗降低了2.4%，达到了减阻降耗的目的。

INTRODUCTION

Mini-tiller is an indispensable agricultural machinery in hilly and mountainous areas of China, which is mainly used for tillage and soil preparation in paddy fields and dry fields *(Niu et al.,2017)*. During the operation of the mini-tiller, the power is transmitted to the rotary blade through the conveying device. The rotary blade cuts the soil and completes the operations of cutting soil, crushing soil, and throwing soil (*Sun et al., 2022*). At the same time, the rotary blade is subjected to the reaction force of the soil and pushes the mini-tiller forward *(Li et al., 2016)*. Therefore, the cutting resistance of rotary tiller bend is not only related to the working quality of mini-tiller, but also the main influencing factor of mini-tiller power consumption. How to reduce the cutting resistance of rotary blade in the operation process of mini-tiller is the key link to improve the operation performance of mini-tiller and reduce the power consumption of mini-tiller.

At present, the research on rotary blade mainly focuses on the soil cutting process of rotary blade. Mootaz Abo-Elnor et al. simulated the interaction between rotary blades and soil using numerical simulation *(Mootaz et al., 2004)*. Jafar Habibi Asl selected three types of rotary blades, C-shaped, L-shaped and RC-shaped, for a comparative experiment on cutting power consumption by establishing a mathematical model of power consumption, revealing that the cutting power consumption of RC-type rotary blade was lower than that of the other two types *(Jafar., 2009)*.

Wusong Xiao, M.S. Stud. Eng.; Po Niu, Assoc. Prof. Ph.D. Eng.; Pan Wang, Senior engineer. M.S. Eng.; Yingjie Xie, Senior engineer. M.S. Eng.; Fei Xia, Senior engineer. M.S. Eng.

Alavi and Hojati numerically simulated the process of rotary blades cutting soil using the finite element method, and the results showed that increasing the forward speed of the machinery would reduce soil stress, while increasing the rotary speed of rotary blades and soil moisture content would increase soil stress *(Alavi et al., 2012).* To optimize the geometry of rotary blades, Matin M.A. et al. studied the torque, power consumption, and energy characteristics of three types of blades (conventional, half-width and straight) at four rotary speeds (125, 250, 375 and 500 rpm). Through testing, the average and maximum power of all blades increased with the increase in rotary speed. At a rotary speed of 500 r/min, the power consumption of straight blade was 25% lower than that of conventional blade *(Matin M.A., 2015)*; Subrata Kumar Mandal et al. optimized the energy consumption of L-shaped rotary blade by establishing a mathematical model *(Subrata et al., 2016)*. Li Shoutai and Li Yunwu used SPH method to simulate the soil cutting process of rotary blade *(Li et al.,2018; Li et al., 2019)*; Zhu Liuxian and Sun Yong et al. used the finite element method to analyze the soil cutting process of rotary blade roller *(Zhu., 2020)*; Nelson Richard Makange et al. studied the mechanical properties between rotary blades and soil at different rotary speeds and tillage depths using the discrete element method (DEM) *(Nelson et al., 2020)*. Yeon-Soo Kim et al. predicted and analyzed the cutting force of rotary blades with tillage depth as a function, and analyzed the impact of different tillage depths on soil properties based on DEM, providing a theoretical basis for the design of agricultural machinery *(Yeon-Soo et al., 2021)*. Zhu et al. conducted an optimization analysis using DEM on the performance of rotary blades for cutting soil and crushing stubble *(Zhu et al., 2022)*. However, most studies have focused on the interaction between the soil and the rotary blade, while there has been relatively little research on the optimization of the structure and cutting power consumption of the rotary blade. The structure and geometric parameters of rotary blade directly affect the power consumption of soil cutting. A reasonable structure of rotary blade can reduce the cutting resistance and reduce the cutting power consumption *(Du et al., 2020)*. Therefore, this paper selects the rotary blade of the mini-tiller as the research object, and analyzes the soil cutting process of the rotary blade by numerical simulation. The tangent bending radius (R), bending angle (β) and blade thickness (c) of the rotary blade are selected as the test factors to optimize the rotary blade. Through the analysis of the numerical simulation results before and after, the optimal combination of the lowest power consumption of the rotary blade in the soil cutting process is obtained. This provides a theoretical basis and reference for the optimization of rotary blade and the performance improvement of mini-tiller.

MATERIALS AND METHODS

The main structure and parameter name of rotary blade

The structure of rotary blade is mainly composed of side cutting edge, positive cutting edge, handle and installation hole. The structure is shown in Fig.1. *(Md.A.Matin et al., 2021)*.

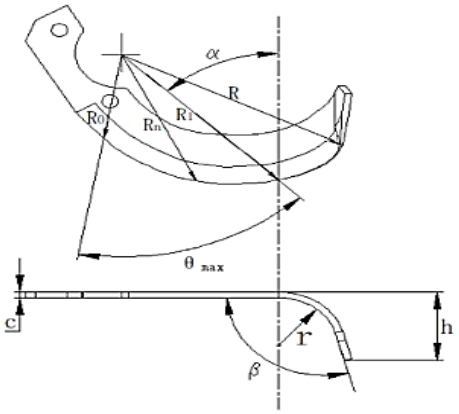

Fig. 1 – Rotary blade construction

R-rotation radius, R_0-initial radius of side-cutting edge, R_1-terminal radius of side-cutting edge, R_n-radius of any point of side-cutting edge, α - angle between end radius of side-cutting edge and bending line, θ_{max}-wrap angle of side-cutting edge, β-bending angle, r - bending radius, h-working width

Motion analysis of rotary blade

In the operation process of the mini-tiller, on the one hand, the rotary blade rotates around the cutter shaft, and on the other hand, it moves forward with the machine. Therefore, the absolute motion of the rotary blade is the vector sum of its rotary motion and forward motion, and the motion trajectory is a trochoid *(Fang et al., 2020)*.

Taking the knife roller rotation center as the coordinate origin, the forward direction of the rotary tiller is the positive direction of the x-axis, and the y-axis is positive downward. The coordinate system shown in Fig. 2 is established *(Zhang et al., 2022)*.

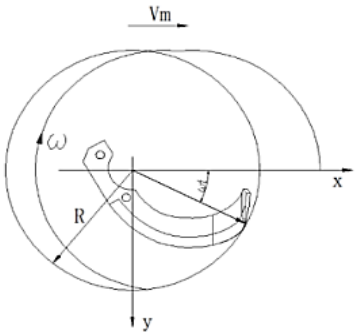

Fig. 2 – Trajectory diagram of rotary blade

If the forward speed of the micro tillage machine is v_m, the angular velocity of the rotary blade is ω. The motion equation is as follow *(Abdullah Al Musabbir et al., 2022):*

$$x = R\cos\omega t + v_m t \tag{1}$$

$$y = R\sin\omega t \tag{2}$$

R - rotary radius of blade roller [mm];
ω - rotational angular velocity of rotary blade [rad/s];
v_m - forward speed of Mini-tiller [m/s];
t - time [s].

From the formulas (1) and (2), it can be seen that the x coordinate and y coordinate corresponding to the end point of the rotary tiller bender in the rectangular coordinate system change with time, and the time there is the independent variable *(Matin MA et al., 2014)*. Therefore, the speed of the tool on the x axis and the speed on the y axis can be obtained only by deriving the formulas (1) and (2) respectively:

$$v_x = \frac{dx}{dt} = v_m - R\omega\sin\omega t \tag{3}$$

$$v_y = \frac{dy}{dt} = R\omega\cos\omega t \tag{4}$$

v_x-velocity component in x-axis direction
v_y-velocity component in y-axis direction

According to the formula (3) and formula (4), the absolute speed of the rotary blade at work can be obtained:

$$v = \sqrt{v_x^2 + v_y^2} = \sqrt{v_m^2 + R^2\omega - 2v_m\omega\sin\omega t} \tag{5}$$

v - absolute speed of rotary blade in the working process [m/s]

Linear velocity formula of the end point of the rotary blade is:

$$v_p = R\omega \tag{6}$$

v_p - linear velocity of the end point of the rotary blade

Rotary tillage speed ratio λ is

$$\lambda = \frac{v_p}{v_m} = \frac{R\omega}{v_m} \tag{7}$$

$$v_x = v_m - R\omega\sin\omega t = v_m(1 - \lambda\sin\omega t) \tag{8}$$

When the rotary blade cuts the soil backwards, it is necessary to make $v_x < 0$. From the formulas (7) and (8), it can be seen that $\lambda > 1$. Therefore, the circular line speed of the end point of the rotary blade is greater than the forward speed of the rotary tiller. The cutting trajectory of the rotary blade is shown in Fig. 2.

Finite element model of rotary blade

The rotary blade model established in UG 10.0 is saved in *CATPart or *IGES format and imported into ANSYS/Ls-dyna. The unit type of rotary blade is set to “Thin shell 163”, and the unit is defined as a constant *(Tagar et al., 2015)*. The material of the tool is set to be a rigid body type material, the density is defined as 7800 kg/m^3, the Young's modulus is defined as 207 GPa, and the Poisson's ratio is defined as 0.35 *(Ma et al., 2022)*. The unit size of the grid is set to 1 mm, and the free grid is divided and checked and optimized. The number of units is 25274, and the number of unit nodes is 25254. The finite element model of the rotary blade is shown in Fig. 3 *(Li et al., 2019)*. The finite element model of the rotary blade is saved in the form of *k* files.

Fig. 3 – Finite element model of rotary blade

Establishment of finite element model of soil

By consulting the literature, the common cultivated soil in hilly and mountainous areas was selected as the basis for soil parameter setting, as shown in table 1 *(Manuwa, 2009; A.A. Tagar et al., 2014)*. The finite element model of the rotary blade is imported into Ls-Prepost, and the SPH soil model is established according to the global coordinate system of the rotary blade *(Zeng et al., 2021; Lu et al., 2014)*. The soil material is MAT147 material model *(Bahrami et al., 2020)*, the length of the soil is 400 mm, the width is 300 mm, and the height is 200 mm. The soil model is shown in Fig. 4 *(Zhang et al., 2019)*.

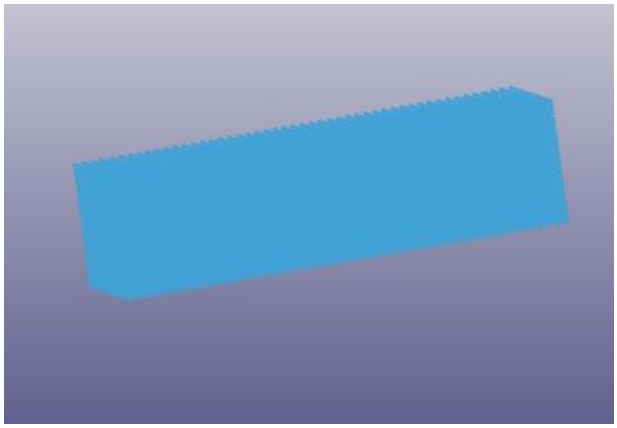

Fig. 4 – SPH Model of Soil

Table 1

Soil parameters

Parameter name	Soil density [kg/m^3]	Bulk modulus [Pa]	Specific gravity of soil particle	Water content [%]	Shear modulus [Pa]	Internal friction angle [radian]
Value selection	2350	3.5e+7	2.68	21	2.0e+7	0.436

Setting of boundary conditions

According to the actual situation of soil cutting by rotary blade, the degree of freedom of movement of the bottom and both sides of the soil model in the x, y and z directions is constrained. The rotary blade rotates around the cutter shaft and moves forward with the unit.

Therefore, the degree of freedom of rotation and movement of the rotary blade in the y-axis direction, the degree of freedom of rotation in the x-axis direction and the degree of freedom of movement in the z-axis direction are constrained. AUTOMATIC_NODES_TO_SUFACE is used to set the contact between the rotary blade and the soil to ensure that the surface unit of the soil can be automatically defined by the program even in the case of cutting failure *(Li et al., 2018)*.

The forward speed of the rotary blade is set to 0.25 m/s, the rotation angular velocity is set to 0.022 rad/s, the calculation time step is set to 0.1 ms, and the forced termination time is set to 300 ms *(Viktor et al., 2018)*.

Parameter optimization of rotary blade

Through the numerical simulation analysis process analysis and related data, the tangent bending radius (R), bending angle (β), and edge thickness (C) were selected as the test factors for optimizing the rotary blade.

Quadratic regression orthogonal design

(1) Determine the number of tests

Number of combined design trials

$$N = m_c + 2p + m_0 \tag{9}$$

In the formula, m_c is the number of comprehensive test points with two levels of each factor; p is the number of test factors; m_0 is the number of repeated tests with zero level for each factor.

Three factors were selected in this experiment, that is, $p = 3$, $m_c = 8$, and three groups were arranged at the zero level, that is, $m_0 = 3$, so the total number of tests can be obtained as $N = 17$. According to the r^2 value table, $r^2 = 1.831$, that is, the asterisk arm $r = 1.353$.

(2) Coding of factor level

The range of bending radius (R) is 30 mm -50 mm and the range of bending angle (β) is $90\text{-}120^{o}$. The value range of edge thickness (C) is 0.5 mm-1.5 mm.

The coding formula of horizontal factor is:

$$\begin{cases} z_{0j} = \dfrac{z_{1j} + z_{2j}}{2} \\ \Delta j = \dfrac{z_{2j} - z_{0j}}{r} = \dfrac{z_{2j} - z_{1j}}{2r} \\ x_j = \dfrac{z_j - z_{0j}}{\Delta j} \end{cases} \tag{10}$$

In the formula, z_{2j} and z_{1j} are the upper and lower limits of factor z_j respectively, and Δj is the change interval of factor z_j. According to formula (10), the three factors are coded, and the coding of the factor levels is shown in Table 2.

Table 2

Coding table of factor levels

x_j	z_j	R [mm]	β [º]	C [mm]
r	z_{2j}	50	120	1.5
1	$z_{0j} + \Delta j$	47.39	116.09	1.37
0	z_{0j}	40	105	1
-1	$z_{0j} - \Delta j$	32.61	93.91	0.63
-r	z_{1j}	30	90	0.5
Δj	$z_{2j} - z_{0j}/r$	7.39	11.09	0.37
Coding formula	$z_j - z_{0j}/\Delta j$	$x_1 = R - 40/7.39$	$x_2 = \beta - 105/11.09$	$x_2 = C - 1/0.37$

(3) Preparation of test plan

The quadratic orthogonal combination test plan and the corresponding rotary blade cutting simulation power are shown in Table 3.

Table 3

Analysis table of test plan

Test number	x_0	x_1	x_2	x_3	p [kW]
1	1	1	1	1	0.4980
2	1	1	1	-1	0.6053
3	1	1	-1	1	0.6112
4	1	1	-1	-1	0.6367
5	1	-1	1	1	0.4986
6	1	-1	1	-1	0.5642
7	1	-1	-1	1	0.5150
8	1	-1	-1	-1	0.5213
9	1	1.353	0	0	0.5782
10	1	-1.353	0	0	0.5712
11	1	0	1.353	0	0.5412
12	1	0	-1.353	0	0.6435
13	1	0	0	1.353	0.5086
14	1	0	0	-1.353	0.5420
15	1	0	0	0	0.5980
16	1	0	0	0	0.6160
17	1	0	0	0	0.6200

(4) The test scheme analysis table is imported into excel, and the interaction terms and centralization of factors x_1, x_2 and x_3 are compiled. The coefficients, variances and analysis results of the regression equation are calculated as shown in Table 4.

Table 4

Analysis results

Variation source	B_j	a_j	b_j	SS_j	F_j	α_j
x_0	9.687	17	0.567			
x_1	0.263	11.661	0.0225	5.912e-3	9.271	0.01 ~ 0.05
x_2	-0.270	11.661	-0.0231	6.266e-3	9.826	0.01 ~ 0.05
x_3	-0.263	11.661	-0.0226	5.963e-3	9.351	0.01 ~ 0.05
x_1x_2	-0.170	8	-0.0212	3.617e-3	5.672	0.01 ~ 0.05
x_1x_3	-0.060	8	-0.0075	4.490e-4	0.704	>0.25
x_2x_3	-0.155	8	-0.0193	2.999e-3	4.703	0.25
x_1'	-0.071	6.703	-0.0106	7.540e-4	1.182	>0.25
x_2'	-0.006	6.703	-0.0009	6.260e-6	9.82e-3	>0.25
x_3'	-0.251	6.703	-0.0375	9.471e-3	14.852	0.01

It can be seen from Table 5 that the values of α_{13}, α_1' and α_2' are greater than 0.25, indicating that the significance level of regression coefficients of x_1x_3, x_1' and x_2' are not significant, and should be removed from the regression equation.

The values of α_1,α_2,α_3 and α_{12} are all between 0.01 and 0.05, the value of α_{23} is less than 0.25, and the value of α_3' is less than 0.01, indicating that the significance level of regression coefficients of x_1, x_2, x_3, x_1x_2, x_2x_3, x_3' is significant, and the significance level of regression coefficients of x_3' is very significant, which should be retained in the regression equation.

Therefore, the regression equation is:

$$P = 0.5927 + 0.0225x_1 - 0.0231x_2 - 0.0226x_3 - 0.0212x_1x_2 - 0.0193x_2x_3 - 0.0375x_3^2 \quad (11)$$

(5) Calculation of sum of squares and F test

The total deviation sum of squares and the degree of freedom are:

$$ss_{total} = \sum_{i=1}^{N} p_i^2 - \frac{1}{N}\left(\sum_{i=1}^{N} P_i\right)^2 = \sum_{i=1}^{17} p_i^2 - \frac{1}{17}\left(\sum_{i=1}^{17} p_i\right)^2 = 0.0399 \quad (12)$$

$$df_{total} = N - 1 = 16 \quad (13)$$

The regression equation consists of six variables. Regression sum of square and regression degree of freedom are:

$$ss_{regression} = \sum_{i=1}^{6} ss_j = 0.034228 \quad (14)$$

$$df_{regression} = 6 \quad (15)$$

The sum of error squares and the degree of freedom of error are:

$$ss_e = \sum_{i=1}^{3} (p_{0i} - 0.6058) = 1.7E-4 \quad (16)$$

$$df_e = m - 1 = 2 \quad (17)$$

Residual sum of square and degree of freedom are:

$$ss_{residual} = ss_{total} - ss_{regression} = 5.673E-3 \quad (18)$$

$$df_{residual} = df_{total} - df_{regression} = 10 \quad (19)$$

Lack of fit sum of squares and degrees of freedom are

$$ss_{Lf} = ss_{residual} - ss_e = 5.503E-3 \quad (20)$$

$$df_{Lf} = df_{residual} - df_e = 8 \quad (21)$$

Regression equation test:

$$F_{regression} = \frac{ss_{regression}/df_{regression}}{ss_{residual}/df_{residual}} = 10.056 > F_{0.01}(6,10) = 5.385 \quad (22)$$

Lack of fit test:

$$F_{Lf} = \frac{ss_{Lf}/df_{Lf}}{ss_e/df_e} = 8.0926 < F_{0.1}(8,2) = 9.3667 \quad (23)$$

After regression equation test and lack of fit test, the significance level of regression equation (11) is $\alpha = 0.01$, that is, the regression of regression equation is particularly significant.

Parameter optimization of rotary blade

The objective function (11) is established with the goal of minimizing the power consumption of rotary blade. The constraint condition is:

$$\begin{cases} x_1 \in [-1.353, 1.353] \\ x_2 \in [-1.353, 1.353] \\ x_3 \in [-1.353, 1.353] \end{cases} \quad (24)$$

According to the optimized objective function and constraint conditions, the optimal solution of the minimum value of the objective function is x_1=0.96, $x_2 = -0.48$, $x_3 = 0.0468$, that is, R=47.09 mm, $\beta = 99.8^\circ$, $c = 1.017\text{mm}$. The theoretical power consumption of soil cutting is 0.4921 kW. According to the optimized parameters of the rotary blade, the rotary blade model is optimized, and the soil cutting dynamics simulation of the optimized rotary blade is carried out.

RESULTS

In the process of cutting soil, the side cutting edge of the rotary blade which is close to the soil first cuts the soil along the longitudinal direction to realize the function of cutting soil. Under the extrusion of the rotary blade, the soil begins to undergo plastic deformation. As the rotary blade rotates around the cutter shaft, the tillage depth of the rotary blade gradually deepens, and the tangent edge and the tangent part begin to contact the soil. The rotary blade cuts the soil horizontally. The contact area between the rotary blade and the soil continues to increase, and the shear and extrusion of the soil continue to increase. The soil unit is invalidated and deleted and broken along the blade surface. Under the combined action of the side cutting edge, the side cutting edge, the side cutting part, the tangent part and the back of the rotary blade, the soil is squeezed and deformed and finally broken and flipped, so as to achieve the effect of breaking soil, breaking soil, throwing soil and weeding by the rotary blade. The simulation results of the rotary blade cutting soil at a certain time are shown in Fig.5.

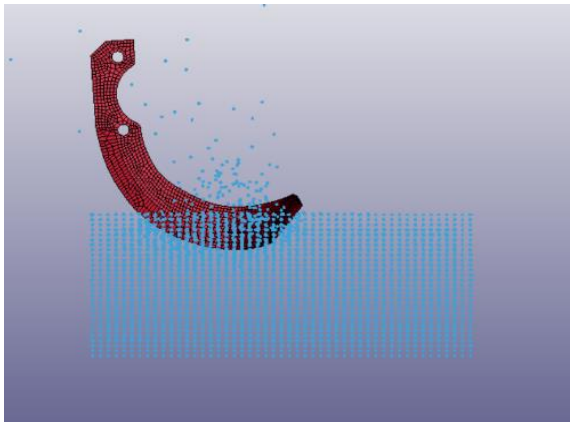

Fig. 5 – Simulation results of rotary blade cutting soil at a certain moment

The time history curve of the cutting force of the rotary blade before and after optimization is shown in Figs. 6(a) and 6(b). According to the time history curve of the cutting force, in a rotation cycle, the rotary blade begins to cut the soil, and the soil is squeezed by the rotary blade. The elastic deformation occurs, and the cutting force increases with the increase of the tillage depth of the rotary blade. When the tillage depth of the rotary blade is the largest, the cutting resistance reaches the maximum value of 1.04 kN. The rotary blade continues to do rotary motion, and the cutting force decreases with the decrease of tillage depth. When the soil is cut, the cutting force becomes 0 kN when the rotary blade leaves the soil, which is consistent with the force of the rotary blade in the actual operation. By comparing the time history curves of the cutting force of the rotary blade before and after optimization, it can be seen that the cutting force of the optimized rotary blade is smaller than that of the rotary blade before optimization, indicating that the optimization of the rotary blade has played a role in reducing the cutting force of the rotary blade.

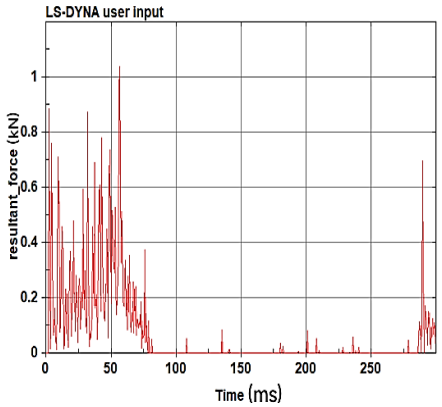

Fig.6(a) – Time history curve of cutting force before optimization

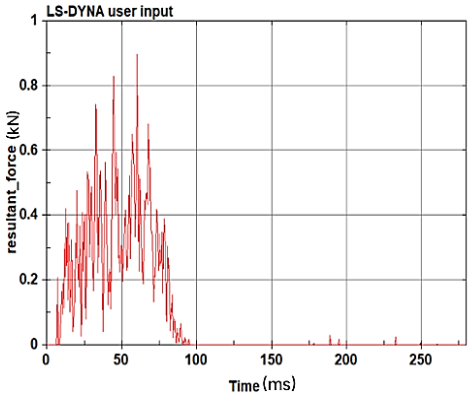

Fig. 6(b) – Time history curve of cutting force after optimization

In the LS-PrePost (post-processing software), the time-history curves of the total energy of the rotary blade before and after optimization are shown in figs. 7(a) and 7(b). It can be seen that when the rotary blade starts to cut the soil, the cutting energy increases. With the rotation of the rotary blade, the tillage depth continues to deepen, the area of contact between the rotary blade and the soil continues to increase, and the energy consumed by the soil is also increasing.

The total energy reaches the maximum value of 295J after the rotary blade completed one cutting of the soil, and tends to be stable, which is consistent with the actual working conditions. The soil cutting energy data of the rotary blade before and after optimization are imported into Excel respectively. The soil cutting power consumption of the rotary blade before optimization is 0.507 kW, and the soil cutting power consumption of the optimized rotary blade is 0.495 kW. Through comparative calculation, the soil cutting power consumption of the optimized rotary blade is 2.4% lower than that before optimization, which achieves the purpose of optimization.

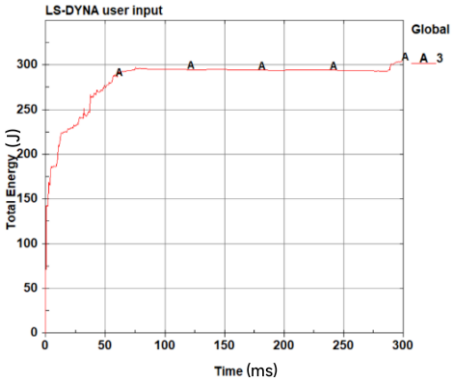

Fig. 7(a) – Energy time history diagram before optimization

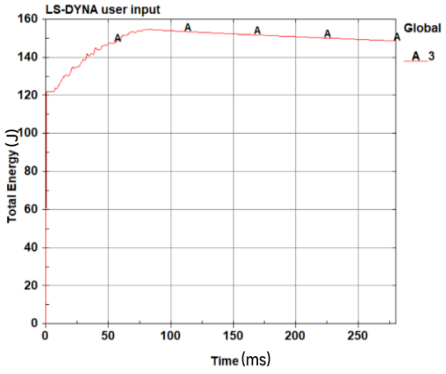

Fig. 7(b) – Energy time history diagram after optimization

CONCLUSIONS

(1) From the cutting force curve of the rotary blade before optimization, it can be seen that the cutting force increases with the increase of the tillage depth of the rotary blade. When the tillage depth of the rotary blade is the largest, the cutting resistance reaches the maximum value of 1.04 kN. The rotary blade continues to do rotary motion, and the cutting force decreases with the decrease of tillage depth. When the soil cutting is completed, the rotary blade leaves the soil and the cutting force becomes 0 kN, which is consistent with the force of the rotary blade in the actual operation.

(2) From the cutting power consumption curve of the rotary blade before optimization, it can be seen that the cutting power consumption of the rotary blade increases with the increase of the tillage depth of the rotary blade. When the cutting is completed, the rotary blade leaves the soil, and the cutting power consumption reaches the maximum value of 295 J and tends to be stable, which is consistent with the actual working conditions.

(3) Through the orthogonal test, the geometric parameters of the rotary blade were optimized. The cutting force rate of the optimized rotary blade was lower than that of the rotary blade before optimization, and the energy consumption of cutting soil was reduced by 2.4% compared with that before optimization. This provides a theoretical basis and reference for the improvement of the comprehensive performance of the micro-tiller and the optimization of the rotary tiller.

ACKNOWLEDGEMENT

The work was supported by the Chongqing Municipal Education Commission (KJQN202101207),and the Chongqing Wanzhou District Science and Technology Bureau (202206051958331768), and the Start-up fee for scientific research of high-level talents in Chongqing Three Gorges University (2014/0903341).

REFERENCES

[1] Abdullah Al Musabbir., Md Abedur Rahman., et al. (2022) Performance Evaluation of New Rotary Blades and Roller Cutter of Versatile Multi-Crop Planter on Residue Management, *Sarhad Journal of Agriculture*, 38(05):211-221. https://doi.org/10.17582/journal.sja/2022/38.5.211.221

[2] Alavi N. and Hojati R. (2012) Modeling the soil cutting process in rotary tillers using finite element method. Journal of Agricultural Technology 8(1): 27-37. https://doi.org/10.1016/j.jclepro.2011.05.006

[3] Chengcheng Ma., Shujuan Yi.,et al. (2022) A rotary blade design for paddy fields with long rice straw based on EDEM, *Engenharia Agrícola*, 43(03):62-72, https://doi.org/10.1590/1809-4430

[4] Du F., Liu J. (2020). Optimal combination and soil cutting analysis of rotary tillage knife in micro tiller based on orthogonal optimization (基于正交优化的微耕机旋耕刀优化组合及切土分析). *Ningxia Engineering Technology*, 19(04): 302-307+313. https://doi.org/10.3969/j.issn.1671-7244.2020.04.004

[5] Gongshuo Zhang, Zhiqing Zhang, et al. (2019) Soil-cutting simulation and parameter optimization of rotary blade's three-axis resistances by response surface method, *Computers and Electronics in Agriculture*, 164:104902. https://doi.org/10.1016/j.compag.2019.104902

[6] Hao Zhu.,Xiaoning He., et al. (2022) Evaluation of Soil-Cutting and Plant-Crushing Performance of Rotary Blades with Double-Eccentric Circular-Edge Curve for Harvesting Cyperus esculentus, *Advances in Agricultural Engineering Technologies and Application*, 12(06):862. https://doi.org/10.3390/agriculture12060862

[7] Huimin Fang.,Qingyi Zhang., Farman Ali Chandio.,et al. (2016) Effect of straw length and rotavator kinematic parameter on soil and straw movement by a rotary blade. *Engineering in Agriculture, Environment and Food*, 09(03):235-241, https://doi.org/10.1016/j.eaef.2016.01.001

[8] Jafar Habibi Asl., Surendra Singh. (2009). Optimization and evaluation of rotary tiller blades: Computer solution of mathematical relations. *Soil & Tillage Research*, 106(1):1-7. https://doi.org/10.1016/j.still.2009.09.011

[9] Jiang T., Zhang X., et al. (2009). 3D Numerical Simulation and Optimization of Soil Cutting Tools Based on SPH Method (基于 SPH 法的土壤切削刀具三维数值模拟及优化). *Electromechanical Engineering*, 26(6): 44-46. https://doi.org/10.3969/j.issn.1001-4551.2009.06.013

[10] Li S., Chen X., Chen W., et al. (2018). Soil-cutting simulation and parameter optimization of handheld tiller's rotary blade by Smoothed Particle Hydrodynamics modelling and Taguchi method. *Journal of cleaner production*, 179:55-62. https://doi.org/10.1016/j.jclepro.2017.12.228

[11] Li Y., Zhang G., et al. (2019). Development of sectional spiral rotary tillage cutter for low-power small vertical shaft deep plow (低功耗小型立轴式深耕机分段螺旋旋耕刀具的研制). *Journal of Agricultural Engineering*, 35(4):80-88. https://doi.org/10.11975/j.issn.1002-6819.2019.04.009

[12] Lu C., He J., et al. (2014). Simulation of soil cutting process of plane cutter based on SPH algorithm (基于 SPH 算法的平面刀土壤切削过程模拟). *Journal of Agricultural Machinery*, (8):134-139. https://doi.org/10.6041/j.issn.1000-1298.2014.08.022

[13] Manuwa S.I. (2009). Performance evaluation of tillage tines operation under different depths in a sandy clay loam soil. *Soil & Tillage Research*, 103(2): 399-402. https://doi.org/10.1016/j.still.2008.12.004

[14] Matin M.A., Fielke J.M., Desbiolles J.M.A. (2015). Torque and energy characteristics for strip-tillage cultivation when cutting furrows using three designs of rotary blade. *Biosystems Engineering*, 129(1): 329–340. https://doi.org/10.1016/j.biosystemseng.2014.11.008

[15] Matin M.A., Fielke J.M., Desbiolles J. (2014) Furrow parameters in rotary strip-tillage: effect of blade geometry and rotary speed. *Biosystems Engineering*, 118: 7-15. https://doi.org/10.1016/j.biosystemseng.2013.10.015

[16] Md. A. Matin., Md. I. Hossain., et al. (2021) Optimal design and setting of rotary strip-tiller blades to intensify dry season cropping in Asian wet clay soil conditions, *Soil and Tillage Research*, 02(07):235-245. https://doi.org/10.1016/j.still.2020.104854

[17] Milkevych Viktor, Munkholm J. Lars, et al. (2018) Modelling approach for soil displacement in tillage using discrete element method, *Soil & Tillage Research*, 183:60-71. https://doi.org/10.1016/j.still.2018.05.017

[18] Mootaz Abo-Elnor., R Hamilton., et al. (2004). Simulation of soil–blade interaction for sandy soil using advanced 3D finite element analysis. *Soil & Tillage Research*, 75(1): 61–73. https://doi.org/10.1016/s0167-1987(03)00156-9

[19] Mostafa Bahrami, Mojtaba Naderi-Boldaji, et al. (2020) Simulation of plate sinkage in soil using discrete element modelling: Calibration of model parameters and experimental validation, *Soil & Tillage Research*, 203:104700. https://doi.org/10.1016/j.still.2020.104700

[20] Nelson Richard Makange, Changying Ji, et al. (2020) Prediction of cutting forces and soil behavior with discrete element simulation, *Computers and Electronics in Agriculture*, 179,5848. https://doi.org/10.1016/j.compag.2020.105848

[21] Niu P., Yang M.J., Chen J., et al. Structural optimization of handrail of a handheld tiller by vibration modal analysis, *INMATEH-Agricultural Engineering*, 2017, 52(2): 91-98.

[22] Li S.T., Yang L., Niu P., et al. Design and study on the edge curve of blade of a handheld tiller's rotary blade, *INMATEH-Agricultural Engineering*, 2016, 51(3): 5-12.

[23] Shoutai Li, Xiaobing Chen, et al. (2018) Soil-cutting simulation and parameter optimization of handheld tiller's rotary blade by Smoothed Particle Hydrodynamics modelling and Taguchi method, *Journal of*

Cleaner Production, 179:55-62. https://doi.org/10.1016/j.jclepro.2017.12.228

[24] Subrata Kumar Mandalt., Basudeb Bhattacharyya‡., et al. (2016). Design Optimization of Rotary Tiller Blade using Specific Energy Requirement. *International Journal of Current Engineering and Technology*, 6(04),1257-1263. https://doi.org/10.14741/Ijcet/22774106/6.4.2015.31

[25] Sun Y., Zhu L., et al. (2022). Design and Simulation Analysis of the Mini-Tiller Rotary Blade Roller (微耕机旋耕刀辊的设计与仿真分析). *Mechanical Research & Application*, 35(03):34-36+42. https://doi.org/10.16576/j.ISSN.1007-4414.2022.03.010

[26] Tagar A.A., Changying Ji et al. (2014) Soil failure patterns and draft as influenced by consistency limits: An evaluation of the remolded soil cutting test, *Soil & Tillage Research*, 137:58-66. https://doi.org/10.1016/j.still.2013.12.001

[27] Tagar A A, Ji C Y, Jan A, Julien M, Chen S Q, Ding Q S, et al. (2015) Finite element simulation of soil failure patterns under soil bin and field testing conditions. *Soil & Tillage Research*, 145: 157–170. https://doi.org/10.1016/j.still.2014.09.006

[28] Xiao M., Buttons, et al. (2022). Design and analysis of torsion reduction and consumption reduction performance of self-excited vibration rotary tillage knife (自激振动旋耕刀设计与减扭降耗性能分析). *Transactions of the Chinese Society for Agricultural Machinery*, 53(11):52-63. https://doi.org/10.6041/j.issn.1000-1298.2022.11.006

[29] Xiongye Zhang, Lixin Zhang, Xue Hu, et al. (2022) Simulation of Soil Cutting and Power Consumption Optimization of a Typical Rotary Tillage Soil Blade. *Applications of Computer Science in Agricultural Engineering*. 12(16):8177, https://doi.org/10.3390/app12168177

[30] Yanshan Yang, John Fielke, et al. (2018) Field experimental study on optimal design of the rotary strip-till tools applied in rice-wheat rotation cropping system, *International Journal of Agricultural and Biological Engineering*, 11(02):88-94. https://doi.org/10.25165/j.ijabe.20181102.3347

[31] Yeon-Soo Kim, Md. Abu Ayub Siddique, et al. (2021) DEM simulation for draft force prediction of moldboard plow according to the tillage depth in cohesive soil, *Computers and Electronics in Agriculture*, 189, 10638. https://doi.org/10.1016/j.compag.2021.106368

[32] Zeng Z., Ma X., et al. (2021). Application status and prospect of discrete element method in agricultural engineering research (离散元法在农业工程研究中的应用现状和展望). *Transactions of the Chinese Society for Agricultural Machinery,* 52(04):1-20. https://doi.org/10.6041/j.issn.1000-1298.2021.04.001

[33] Zhu L., Sun Y., et al. (2020). Simulation of Cutting Soil of the Mini-tiller Rotary Blade Roller Based on Finite Element Method (基于有限元法的微耕机旋耕刀辊切削土壤仿真). *Journal of Agricultural Mechanization Research*, 42(09), 8177. https://doi.org/10.13427/j.cnki.njyi.2020.09.007

DEVELOPMENT AND EVALUATION OF A CONTINUOUS FLOW BIOCHAR UNIT USING RICE HUSK BIOMASS

/

تطوير وتقييم وحدة الفحم الحيوي ذات التدفق المستمر للكتلة الحيوية لقشور الأرز

Hesham A. FARAG, Mohamed M. EL-KHOLY, Mahmoud OKASHA*, Ahmed E. AZAB, Ahmed E. KHATER, Reham M. KAMEL

Agricultural Engineering Research Institute (AEnRI), Agricultural Research Center (ARC), Giza 12611/ Egypt

Tel: +20-1003133841; E-mail: mahmoudokasha1988@yahoo.com

Corresponding author: Mahmoud Okasha

DOI: https://doi.org/10.35633/inmateh-72-03

Keywords: *Rice husk; Biochar; Pyrolysis; Continuous flow*

ABSTRACT

This study aims to develop and evaluate a locally manufactured carbonization unit with a screw conveyor. Various carbonization temperatures (350, 400, and 450°C) and feeding rates (50, 75, and 100 kg/h) were examined to determine optimal conditions for producing biochar from rice husk (RH). The results revealed that increasing the pyrolysis temperature from 350 to 450°C decreased RH biochar yield, while increasing the feeding rate from 50 to 100 kg/h increased it. Ash content was 22.4% at 350°C for 100 kg/h, and the maximum value was 31.4% at 450°C and 50 kg/h. The BET surface area of the biochar increased from 105.71 to 312.32 m^2/g at 450°C, with slight non-significant changes at a 100 kg/h feed rate. RH biochar showed decreasing H and O values with higher temperatures and lower feed rates. RH biochar at 450°C and 50 kg/h showed increased macro porosity and surface area, rendering it suitable for agricultural application as a soil amendment.

الملخص

تهدف هذه الدراسة إلى تطوير وتقييم وحدة انحلال حراري مستمر من النوع اللولبي محلي الصنع. تم تقييم الوحدة عند درجات تحلل حراري مختلفة (350، 400 و450 درجة مئوية) ومعدلات تغذية (50، 75 و100 كجم/ساعة) لتحديد الظروف المثالية لإنتاج الفحم الحيوي من قشر الأرز. وأظهرت النتائج أن بزيادة درجة التحلل الحراري من 350 إلى 450 درجة مئوية أدت الى انخفاض إنتاجية الفحم الحيوي الناتج من قشر الأرز، بينما بزيادة معدل التغذية من 50 إلى 100 كجم/ساعة أدت الى زيادة إنتاجية الفحم الحيوي. بلغ محتوى الرماد 22.4٪ عند درجة تحلل حراري 350 درجة مئوية ومعدل تغذية 100 كجم/ساعة، وكانت القيمة القصوى 31.4٪ عند 450 درجة مئوية و50 كجم/ساعة. زادت قيمة مساحة سطح *BET* للفحم الحيوي الناتج من 105.71 إلى 312.32 م^2/جم عند 450 درجة مئوية، مع تغييرات طفيفة وغير معنوية عند معدل تغذية 100 كجم/ساعة. أظهر الفحم الحيوي الناتج من قشر الأرز انخفاضًا في قيم الهيدروجين والاكسجين مع درجات الحرارة المرتفعة ومعدلات التغذية المنخفضة. أظهر الفحم الحيوي الناتج من قشر الأرز عند درجة تحلل حراري 450 درجة مئوية ومعدل تغذية 50 كجم/ساعة زيادة في المسامية الكلية ومساحة السطح، مما يجعله مناسبًا للتطبيق الزراعي كمحسن للتربة.

INTRODUCTION

Annually, large amounts of biomass by-products are produced as a result of human activities. Agriculture ranks as one of the most common human activities that produce large amounts of biomass, and the incorrect treatments for these by-products make it harmful to the environment and help to increase the destructive impacts of climate change. The climate change phenomenon is undeniably one of the utmost pressing concerns globally. Global warming is a consequence of the mounting levels of carbon dioxide and different greenhouse gases in the atmosphere. The climate crisis likely will require a large quantity of CO2 to be removed from the atmosphere. Biochar production for agricultural use has a good potential for solving the global warming problem. Its storage in soils has been suggested to decrease climate change by sequestering carbon inside the soil. It has a long period of stability, lasting hundreds to thousands of years (*Sun et al., 2020; Ren et al., 2022*).

Biochar is a carbon-rich black solid, mainly generated from biomass through pyrolysis processes; pyrolysis allows producing biochar by heating in the lack of oxygen. Besides the biochar, the pyrolysis processes also give other products like bio-oils and synthesis gas or syngas that could be further used as renewable fuels (*Sun et al., 2020*). Moreover, biochar has attained extensive interest globally owing to its verified capacity to enhance soil health (*Ren et al., 2023*), soil fertility (*Ding et al., 2016*), and increased water-holding capacity as an inexpensive sorbent (*Qu et al., 2021*). Due to these reasons, developing pyrolysis technologies for biochar production continues to be an urgent task on a global scale. The word pyrolysis has two Ancient Greek Words; the first is Pyro, which means fire, and the second is Lysis, which means separating (*Ibrahim, 2020*). Pyrolysis is the thermal degradation of biomass that occurs due to a lack of oxygen at

temperatures varying from 300 to 800°C. In a three-stage reaction, pyrolysis necessitates using kilns and furnaces to heat the biomass. At the first manufacturing stage, the biomass loses water and other wastes. The residue is then pyrolyzed again, and biochar is formed. Ultimately, the biochar decomposes to generate the carbon-rich charcoal employed in applications (*Demirbas, 2004*). The pyrolysis process can be categorized as slow, quick, rapid, and flush. Although there are no significant differences between these alternatives and their derivatives, slow pyrolysis is the proper method for producing the target biochar (*Demirbas et al., 2006*).

Rice husk (RH) is one of the most used raw materials in producing biochar. Moreover, RH is a plentiful by-product in rice-producing countries. Around 822 million tons of rice husks are produced globally; however, they are underutilized because of the limited recycling options (*Dunnigan et al., 2018*). Rice plays a pivotal role in agricultural sector of Egypt. In 2019, over 503,000 hectares of rice were planted. This area produced about 0.9 million tons of rice husk. This important rice by-product should be considered a sustainable national source instead of being left or burned, causing terrible environmental and health hazards. Conversion of RH to biochar has good potential and benefits for sustainable waste recycling, energy production, carbon sequestration, soil quality enhancement, and improved plant growth (*Abrishamkesh et al., 2015*).

Biochar can be used as a soil conditioner, improving plant growth by providing and keeping nutrients and offering further services, including enhancing biological and physical properties of the soil (*Lehmann and Rondon, 2006*). Biochar has a higher porosity and surface area than other soil organic matter (SOM) types. It can enhance soil structure and water retention by improving soil aggregation and texture (*McElligott et al., 2011*). Biochar also affects the soil bulk density, which might decrease by adding biochar, particularly at high application rates, because of its relatively lower bulk density than mineral particles (*Lehmann and Joseph, 2015*). The organic carbon of the biochar improves soil aggregation and aggregate stability. Furthermore, changes in soil structure enhance soil water retention and infiltration, resulting in less runoff and erosion (*Gwenzi et al., 2015*). Some soil characteristics, on the other hand, may improve over time rather than immediately after treatment (*Mukherjee and Lal, 2014*).

Biochar-producing systems are categorized as gasifiers or pyrolizers and, depending on the technology utilized, create three distinct products: biochar, syngas, and bio-oil (*Scholz et al., 2014*). Currently, waste and biomass management by the thermo-pyrolysis process to produce high-value products requires the improvement of more selective, controlled, multi-product, and integrated pyrolysis units. Pyrolysis furnaces should be designed and manufactured with a perfect model in mind; Even if a usual formula has produced relevant results in other contexts, it should be applied carefully. *El-Sheikha and Hegazy* (*2020*) designed and assessed a biochar pyrolysis kiln to produce biochar from two agricultural residues (i.e., rice straw and date palm fronds). Their results revealed the possibility of utilizing agricultural residues to produce biochar. In the same trend, a double-chamber down draft (DcDD) pyrolizer was constructed and tested using rice husk to produce biochar. Its results indicated that the DcDD reactor is an appropriate choice for turning waste biomass into biochar that improves the soil characteristics in agricultural settings (*Alahakoon et al., 2022*).

Therefore, this study aims to use rice husk as a biomass feedstock to produce superior-quality biochar using a continuous screw-type pyrolysis furnace that features easy operation and maintenance.

MATERIALS AND METHODS

Description of biochar-producing system

The biochar-producing system consists of the following main units (i.e., feeding unit, carbonization unit with horizontal screw conveyor, biochar outlet unit, filtration and condensing units, and the control unit), as shown in Fig.1.

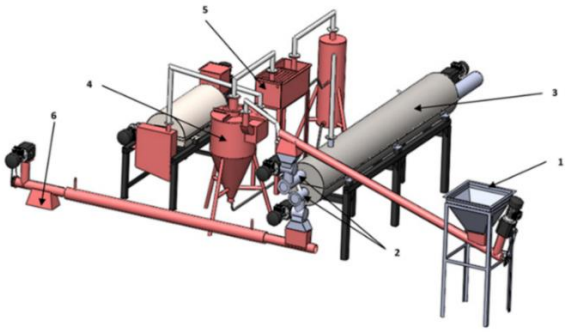

Fig. 1 – 3D view of the continuous screw model of the biochar system

1 – Feeding unit; 2 – Horizontal screw conveyor; 3 – Carbonization unit chassis; 4 – Cyclone; 5 – Condenser unit; 6 – Biochar outlet unit

The feeding unit

The feeding unit comprises a raw material feeding hopper and an inclined raw feeding screw. A square-shaped raw material hopper made of an iron sheet with a thickness of 3 mm, dimensions of 80 × 80 × 65 cm, and a slope angle of 60° on all sides was used to feed the system with rice husk. The feeding hopper is fixed within four supporting legs with a length of 173 cm. The inclined feeding screw has a 12.5° inclination angle, a 450 cm length, a 15.2 cm diameter, and a 10.1 cm screw pitch, enclosed in a tubular housing with a 16.0 cm diameter. A 1.5 kW three-phase electric motor powered the inclined feeding screw with a reduction gearbox to elevate the RH from the feeding hopper to the screw conveyor in the carbonization unit. A 0.55 kW three-phase motor feeds RH to the carbonization unit.

Horizontal screw conveyor and carbonization unit

The horizontal screw conveyor conveys the rice husk (raw material) into the carbonization unit. A horizontal screw with a two-ways carbonization cylinder was chosen to reduce the total length of the carbonization unit. The horizontal screw with a two-way (forward and backward) carbonization cylinder has the same diameter and pitch of 15.2 cm. The length of the forward screw is 520 cm, whereas the backward screw measures 475 cm in length, and each screw is powered by a three-phase electric motor with a power of 2.2 kW. The two-way screws are placed in a tubular housing with a diameter of 16 cm. The carbonization unit consists of a heating stove and carbonization cylinders. The heating stove is the outer body of the carbonization chamber and consists of a double-layer cylinder. A thermal insulator was placed between the double cylinder for energy-saving purposes. The carbonization chamber is the essential part of the carbonization unit, where the thermo-pyrolysis process occurs, and the other parts are linked to this part. The inner cylinder (pyrolysis chamber) is made of steel with a thickness of 10 mm and an internal diameter of 15.24 cm. It is also airtight to withstand temperatures above 800°C and achieve low oxygen levels during pyrolysis. The carbonization tank length is 535 cm, and the diameter is 75 cm. Two K-type thermocouples were located along the horizontal axis of the outer cylinder. The thermocouples with an accuracy of ±2.5°C and a temperature range of 0–1600°C with a probe diameter of 13 mm and length of 35 cm were used to measure the internal chamber temperature. The carbonization unit was heated through a flame hole placed at the beginning of the unit with an internal diameter of 15 cm. During operation, the exhaust gases exit through a smokestack on the top of the carbonization tank.

Carbonization unit chassis

The carbonization unit chassis is made of square hollow steel sections shaped (10 × 10 cm) with a thickness of 3 mm and overall dimensions of 400 × 97.5 × 135 cm (L × W × H), respectively. It was used to carry the carbonization unit and the screw conveyor. In addition, the chassis has six subsidizing legs in a square hollow section (10 × 10 cm) with a thickness of 3 mm to attain the required operating height.

The filtration and condensing units

Developed biochar system generated steam, fumes, and dust. It has a cyclone, condenser, dry scrubber, and steel connecting tubes. The ignition sources in this system are feedstock or syngas. The fume treatment unit processes the smoke, where it is separated into distinct elements; coal tar is discharged from the cyclone, while bio-oil emerges from the dry scrubber. A condensing unit comprises a condenser (heat exchanger) and a suction fan. The condenser, which had a water cooler, was used to cool the gas and generate liquid distillate compounds (bio-oil) through condensation. A 13.2 V DC motor-driven suction fan was employed to draw the generated syngas and additional vapors from the syngas tank, pushing them through the firing system to decrease fuel consumption. The condenser of the filtration unit concentrates the vapor to produce the bio-oil, and the other gas mix is directed to the filter groups to produce syngas, which is stored in the syngas tank and used in the firing system to reduce fuel consumption. For the last stage, a dry scrubber comprises a cylinder of 50 cm in diameter and 1.5 m in height. It was used to separate the steam from the condenser to produce syngas to reuse for ignition, provide the energy needed to heat the reactor and obtain bio-oil.

The biochar outlet unit

This unit comprises a horizontal screw with a length of 450 cm; it has the same diameter and pitch of 15.2 cm and is operated by a three-phase motor with a power of 1.1 kW. The horizontal screw of biochar is placed in a tubular housing with a diameter of 16.0 cm, and at the end of this screw, a biochar outlet is assembled.

The control unit

The control unit has switches to turn on and off the motors, an inverter (model: ATV71HU22N4Z Schneider Electric, Taiwan) to control and change the speeds of the feeding motors, an indicator linked to the temperature sensors to display the temperature inside the reactor, and a voltmeter indicator to display the voltage and amperage while the motors are running.

Raw materials

Rice husk was utilized as a raw material to yield biochar using the developed screw continues model reactor. The rice husk was obtained from local medium-scale mills in Kafr El-Sheikh, Egypt. Before being used in the trials, the obtained rice husks were air-dried and stored. The proximate and elemental RH analyses were determined using the Perkin Elmer Thermo gravimetric analyzer and EA 1112 elemental analyzer, and the results are recorded in Table 1.

Table 1

Elemental and proximate analysis of rice husk (raw material)

Elemental analysis	**Value**
Carbon (wt%)	40.89 ± 4.25
Hydrogen (wt%)	3.56 ± 0.48
Nitrogen (wt%)	4.73 ± 0.26
Oxygen (wt%)	53.72 ± 6.30
Proximate analysis	**Value**
Bulk density (kg/cm^3)	120 ± 11.65
Moisture (%)	11.9 ± 0.38
Ash (dry) (%)	8.67 ± 1.25
Fixed carbon (%)	15.68 ± 1.06
Volatile compounds (%)	74.52 ± 5.94

* The data was expressed using the mean ± standard deviation (SD).

Experimental site

The biochar system was constructed and evaluated by the Agricultural Engineering Research Institute in cooperation with the Academy of Scientific Research and Technology. The Experimental investigations were executed in Egypt at the Rice Mechanization Center, Kafr El-Sheikh Governorate, at coordinates 31°06′58.67″ N latitude and 30°51′17.53″ E longitude.

Methods

First, the ignition of the carbonization unit was achieved by utilizing a Liquefied Petroleum Gas (LPG) cylinder. (43.1 MJ/kg calorific value) for 100% energy supply; when the unit reached 250-450°C, syngas shared about 50% of the energy needed for the carbonization process, saving about 50% of energy cost. According to the previous references, biochar is produced at temperatures between 250-450°C, depending on the source of residues and the quality needed. Rice husk residual (Sakha 101 cv., *Oryza sativa* L.) was carbonized under different degrees of carbonization temperature (350, 400, and 450°C) plus feeding rates of 50, 75, and 100 kg/h to optimize the production of biochar from RH. Each temperature or residence time has been controlled using the electrical control panel. Before feeding the RH (raw material) to start the pyrolysis process, the reactor should be at the desired temperature for executing the trials. The energy supply from the heat source should be greater during startup than at a steady state. Thus, the system takes approximately 2 hours at the beginning of the process to reach the pyrolysis temperature, relying on radial temperature gradient of the pyrolysis chamber. The indirect heating system of this study dilutes syngas less than direct heating. Consequently, concentrated syngas could produce biochar for combustion zone energy (*Joardder et al., 2017*).

Scanning electron microscopy (SEM) and Fourier transform infrared spectroscopy (FTIR) analysis

Scanning electron microscopy (SEM, Hitachi, S-570) was used according to *Liu et al.* (*2015*) to evaluate the biochar samples' morphological alterations with a high vacuum at a 20 kV accelerating voltage and a 6000x magnification magnitude. Fourier transform infrared spectroscopy (FTIR) was also assigned between 600 and 4000 cm^{-1} utilizing the method of attenuated total reflectance (ATR). Moreover, 0.5 mg of each sample was put into the Ge window of Nicolet FTIR instrument, equipped with an ATR attachment, after being ground to a 0.1 mm particle size. A KBr beam sampler was used to analyze the samples' spectra, conducting over 256 scans. The FTIR data was acquired with 4 cm^{-1} resolution and 32 scans using a diamond ATR attachment.

Biochar yield and physical properties

The determination of biochar yield was performed following the procedure described by *Lynch and Joseph* (*2010*), as shown in Eq. 1:

$$Biochar\ yield\ (\%) = \frac{M_1}{M_2} \times 100 \quad (1)$$

where: M_1 stands for the mass of the biochar [g], and M_2 stands for the mass of air-dried raw materials [g].

The ash content was calculated using the dry combustion technique. Briefly, 5.0 g of biochar was heated to 500°C for 8 h. Once the crucible had reached the ambient temperature, it underwent re-weighing (*Song and Guo, 2012*). Finally, the ash percentage was determined using Eq. 2:

$$Ash\ content\ (\%) = \frac{M_{Ash}}{M_1} \times 100 \quad (2)$$

where M_{Ash} is the ash mass [g].

The specific surface area and total pore volume of the biochar can be determined using the Brunauer-Emmett-Teller method and an Autosorb-1 surface area analyzer (Quantochrome Instruments, USA).

Elemental analysis

The carbon (C), oxygen (O), hydrogen (H), and nitrogen (N) content of the biochar was calculated utilizing an X-ray fluorescence spectrometer (XRF) manufactured by Malvern Panalytical Almelo in the Netherlands (CNHOS). The Bray II technique determined the amount of (P) *(Bray and Kurtz, 1945*). The approach outlined by *Samsuri et al.* (*2014*) was employed to analyze the tradable elements, such as magnesium (Mg), potassium (K), silicon (Si), and aluminum (Al).

PH, electric conductivity (EC), and cation exchange capacity (CEC)

The method developed by *Savova et al.* (*2001*) was utilized to determine the pH of biochar. In a 100mL conical flask, 4.0 g of biochar was dissolved in water. The flask was prepared by filling it with boiling water, which was subsequently covered with a watch glass and allowed to cool. The supernatant was then drained. The supernatant was allowed to cool to ambient temperature before pH was measured by a Metrohm 827 pH Lab (USA). The EC of the biochar was measured utilizing the CON 700 EC meter (Eutech Instruments, USA) after wetting it with deionized water at a solid-to-water ratio of 1:5 and agitating the mixture for 24 h.

Song and Guo (*2012*) method was used to measure the cation exchange capacity (CEC). In a 50-mL Falcon tube, about 0.50 g of biochar was mixed with 40 mL of 1 M ammonium acetate. Then, the mixture was carefully stirred for a complete 24-hour timeframe. A vacuum pump was used to filter the mixture, and after that, 40 mL of ammonium acetate was added. Then, 30 mL of isopropanol was decanted into the vacuum pump in three equal portions. 50-mL dosages of 1 M KCl were used to leach the remaining biochar, and the leachate was collected. An auto-analyzer (QuikChem 8000 Series FIA+ System; Lachat Instruments, USA) was utilized to quantify the extracted NH4+ content, while atomic absorption spectrometry (AAnalyst 400; PerkinElmer, USA) was employed to assess exchangeable cations of the biochar.

Statistical analysis

An SPSS 26.0 program (IBM Corporation, USA) was used to analyze the data. For multiple comparisons, two-way analysis of variance (ANOVA) and post hoc (Tukey test) were employed. Differences were considered statistically significant at a level of 0.05.

RESULTS AND DISCUSSION

SEM and FTIR analysis

Figure 2 illustrates the cellular microstructure of the biochar (shown by SEM microscopy), which consists of numerous hollow channels of varying diameters formed from tracheid cells. The SEM micrographs displayed the porous structures of the resultant biochar, revealing different sizes and shapes of the micropores, and mesopores. The biochar produced at a temperature of 350°C retained unaltered tissue, leading to incomplete pore formation. Nevertheless, when exposed to a temperature of 450°C, the morphology of the biochar underwent a transformation resembling a honeycomb structure, wherein larger holes interconnected cylindrical holes. Biochar featuring well-structured pore arrangements shows a considerable BET surface area and adsorptive capacity, as indicated by *Guo and Lua* (*1998*). Once the biochar was heated at 450°C, noticeable surface cracks and shrinkage became apparent across different feeding rates. Excessively porous, hollow, spherical particles and well-structured pyrolyzed biochar at 450°C are seen in Fig. 2 [c, f, and i]. The thin walls of the buildings gave them a fragile appearance. The structure of biochar displayed increased organization with an elevation in pyrolysis temperature and with a decrease in the number of micropores and a higher number of large pores. This result is similar to *Claoston et al.* (*2014*).

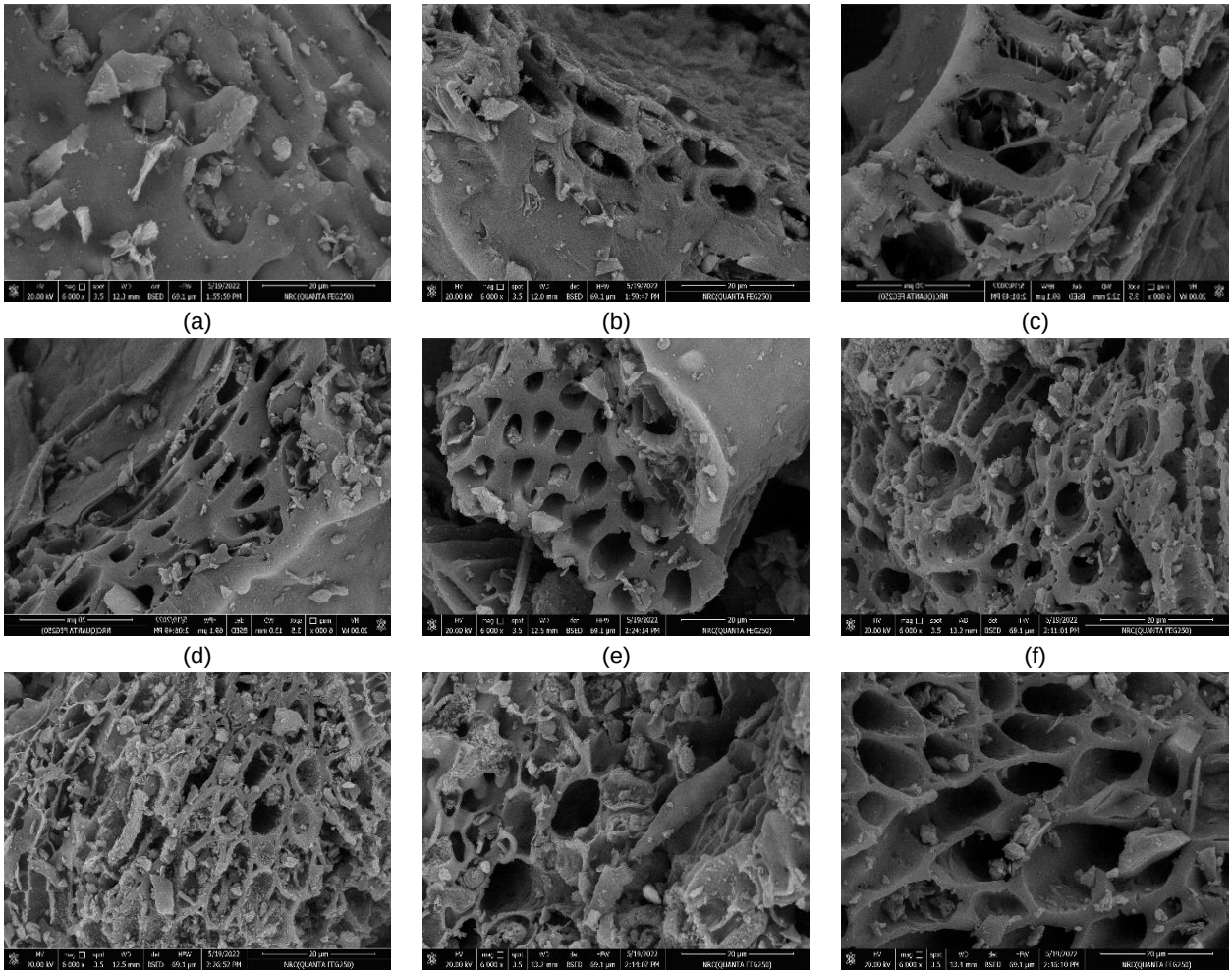

Fig. 2 – SEM images as a function of the pyrolysis temperatures of 350°C (a, b, and c), 400°C (d, e, and f), and 450°C (g, h, and i) for feeding rates of 50, 75, and 100 kg/h from left to right for every row, respectively

Fourier transforms infrared (FTIR) spectra of biochar prepared from RH as a function of wavenumber at different pyrolysis temperatures are presented in Fig. 3. Table 2 shows the specific chemical bonding and transmittance observed by FTIR. The change in biochar surface functional groups as a heating function was studied with (FTIR) spectroscopy. The chemical response of the surface also controls adsorption behavior, specifically chemically adsorbed oxygen in different forms of functional groups, in addition to porosity. FTIR was effectively used to investigate the impact of temperature on biochar, but due to the absence of discernible variation in intensity under varied feeding rates, the results from this experiment were omitted.

Table 2 details chemical bonding, peak position, and transmittance. Most FTIR provides characteristics from organic functional groups for analyzing the organic components of the biochar. The peak detected at 3505.35 cm^{-1} is presumably a result of the stretching of organic O-H bonds, potentially arising from water within the sample or minerals possessing hydroxyl groups. An increase in temperature from 350°C to 450°C reduces the intensity of the hydroxyl peak, indicating the degradation of hydroxyl groups and the subsequent release of hydrogen and oxygen atoms. C=C asymmetric stretching occurs at 1579.43 cm^{-1}, indicated as a G band in (*Keiluweit et al., 2010*), due to the sp2-hybridization bonding of carbon atoms in the aromatic group of lignin. With the increase in temperature from 350°C to 450°C, the intensity of C-H bending dropped, leading to the gaseous product CH4 in the same trend (*Armynah et al., 2018*). Because of the sp3-hybridization bonding of carbon atoms, the transmittance at 1087 cm^{-1} occurred (*Keiluweit et al., 2010; Armynah et al., 2018*), but the range of 1060.71–1079.99 cm^{-1} was achieved as symmetric C-O stretching for lignin, cellulose, and hemicellulose. The presence of aromatic with C-C stretching is suggested by the transmission peak of 1451.92 cm^{-1} (ester and phenol) (*Claoston et al., 2014*). Nonetheless, a C-H bending peak was detected at 792 cm^{-1}, indicating the existence of alkynes. Gases CO2 and CH4 are created when the husk is heated, and the FTIR confirms that these gases correspond to the peaks attributed to the cellulose, hemicellulose, and lignin content of the biomass (*Ma et al., 2015*).

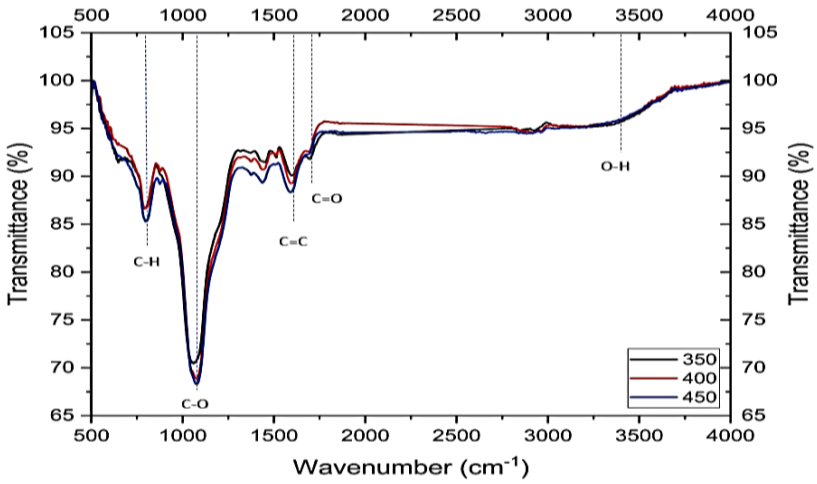

Fig. 3 – FTIR spectra of rice husk biochar as a function of wavenumber at different pyrolysis temperatures

Table 2

Peak position and intensity of chemical bonds of RH as a function of pyrolysis temperature utilizing Fourier transform infrared (FTIR)

Chemical bond	Peak position and intensity		
	350°C	**400°C**	**450°C**
O-H stretching (Lignin, Hemicellulose, Cellulose)	3509.93 cm^{-1}	3506.54 cm^{-1}	3505.35 cm^{-1}
	96.82	96.57	96.93
C=O Stretching (Lignin)	Peak no observed	Peak no observed	Peak no observed
	-	-	-
C=C Asymmetric Stretching (Lignin)	1579.43 cm^{-1}	1592.09 cm^{-1}	1590.73 cm^{-1}
	90.71	89.26	88.43
C-O Stretching (Hemicellulose)	Peak no observed	Peak no observed	Peak no observed
	-	-	-
C-C Stretching (Hemicellulose)	1451.92 cm^{-1}	1441.31 cm^{-1}	1436.64 cm^{-1}
	88.34	90.71	97.47
C-O Stretching C-OH Bending (Hemicellulose, Cellulose)	1074.21 cm^{-1}	1060.71 cm^{-1}	1079.99 cm^{-1}
	68.32	68.86	70.46
C-H Bending (Lignin)	791.09 cm^{-1}	799.68 cm^{-1}	797.11 cm^{-1}
	80.33	79.74	78.50

Elemental analysis

Table 3 shows the elemental composition of RH biochar. At feeding rates of 50 and 100 kg/h, the carbon content (C) exhibited a range of 63.34% to 79.14% and 693.4% to 77.33%, respectively. The maximum value of 79.14% was achieved at a 50 kg/h feeding rate and a pyrolysis temperature of 450°C. The high carbon content of biochar with higher pyrolysis temperatures suggests that higher pyrolysis temperatures promote carbonation (*Chen et al., 2012; Nan et al., 2021*). This reduction was caused by the high level of polymerization of the biochar, which resulted in a more condensed carbon structure (*Tomczyk et al., 2020*). The increase in carbon may also be a reason for losing oxygen and hydrogen from the biochar as the pyrolysis temperature rises (*Antal and Grønli, 2003*). In opposition, H and O dropped with increasing carbonization temperature, as *Keiluweit et al.* (*2010*) and *Southavong et al.* (*2018*) also demonstrated.

At both the minimum and maximum feeding rates, the total nitrogen content decreased from 1.74 to 1.36% and 1.54 to 1.45%, respectively, as the corresponding pyrolysis temperature increased (Table 3). The reason is that when the plant biomass is pyrolyzed, its nitrogen-containing structures, including amino acids, amino sugars, and amines, are converted into heterocyclic N aromatic structures (*Cao and Harris, 2010*). This means that the nitrogen will be available and will not decompose immediately but will be released with increasing duration of carbonation.

As shown in Table 3, the element components also display P, K, Mg, Al, and Si for the generated biochar from RH. According to X-ray fluorescence spectroscopy (XRF) results, the considerable ash elements in RH biomass are P, K, and Si. At 450°C pyrolysis temperature and 50 kg/h feeding rate, their respective values are 0.54, 1.64, and 42.14 g/kg.

Table 3

Elemental analysis of rice husk biochar for each specific treatment

Biochar characteristics	Pyrolysis temperature, °C	350°C			400°C			450°C		
	Feeding rate, kg/h	50	75	100	50	75	100	50	75	100
Elemental analysis	Carbon (%)	63.34 ± 4.05 c	62.92 ± 2.99 c	61.3 ± 3.85 c	73.73 ± 6.62 b	73.68 ± 5.36 b	72.18 ± 6.78 b	79.14 ± 4.26 a	78.68 ± 5.01 a	77.38 ± 2.87 ab
	Hydrogen (%)	4.80 ± 0.21 a	4.10 ± 0.12 b	3.81 ± 0.41 c	1.04 ± 0.35 f	2.07 ± 0.25 de	2.25 ± 0.27 d	1.08 ± 0.13 f	1.90 ± 0.00 e	1.00 ± 0.00 f
	Oxygen (%)	20.01 ± 2.36 d	22.74 ± 4.05 bc	22.01 ± 3.84 c	27.58 ± 2.89 ab	24.03 ± 4.66 b	24.23 ± 1.56 b	28.02 ± 2.01 a	28.70 ± 0.99 a	21.99 ± 3.68 c
	N (%)	1.74 ± 0.02 a	1.63 ± 0.04 bc	1.54 ± 0.03 c	1.60 ± 0.02 bc	1.57 ± 0.05 c	1.66 ± 0.09 b	1.36 ± 0.10 e	1.40 ± 0.06 de	1.45 ± 0.01 d
	P, g/kg	0.38 ± 0.08 c	0.36 ± 0.02 c	0.35 ± 0.00 c	0.45 ± 0.00 b	0.41 ± 0.02 bc	0.42 ± 0.01 bc	0.54 ± 0.02 a	0.52 ± 0.03 ab	0.51 ± 0.00 ab
	K, g/kg	0.13 ± 0.01 g	0.05 ± 0.00 h	0.31 ± 0.01 f	0.53 ± 0.05 d	0.41 ± 0.01 e	0.30 ± 0.02 f	1.64 ± 0.07 a	0.62 ± 0.01 c	0.77 ± 0.03 b
	Mg, g/kg	0.04 ± 0.00 d	0.05 ± 0.00 d	0.05 ± 0.00 d	0.14 ± 0.01 b	0.10 ± 0.00 c	0.07 ± 0.00 cd	0.23 ± 0.02 a	0.15 ± 0.00 b	0.12 ± 0.00 bc
	Al, g/kg	0.41 ± 0.02 e	2.00 ± 0.03 b	0.39 ± 0.04 e	0.25 ± 0.04 f	0.96 ± 0.00 c	0.17 ± 0.02 g	0.47 ± 0.01d	0.87 ± 0.06 cd	5.66 ± 0.07 a
	Si, g/kg	35.7 ± 2.86 b	36.85 ±4.36 b	37.33 ± 5.34 b	43.3 ± 4.56 a	38.55 ± 1.09 ab	39.61 ± 2.85 ab	42.14 ± 1.25 a	42.84 ± 5.27 a	32.24 ± 4.00 c

Physical properties of the produced biochar

Table 4 displays the physical properties of the biochar derived from RH. The ash content within the resulting biochar experienced a 33% increase when the temperature was raised from 350°C to 400°C, after which it remained constant at higher temperatures. The ash content increases and stabilizes at 19% for grass charcoal, as stated by *Li et al.* (*2013*).

Biochar yield decreased from 45.8% to 39.1% when the pyrolysis temperature was raised from 350°C to 400°C at the feeding rate of 100 kg/h. Furthermore, elevating the pyrolysis temperature from 400°C to 450°C at a 100 kg/h feeding rate decreased biochar yield from 39.1% to 34.2%. Meanwhile, the biochar production rate decreased from 43.6% to 33.9% and from 37.2% to 30.0% as the temperature increased from 350°C to 450°C, at 75 and 50 kg/h feeding rates, in order, as illustrated in Table 4.

The BET surface areas of the generated biochar increased as the pyrolysis temperature within the examined range of 350–450°C rose, as indicated in Table 4. At a feeding rate of 50 kg/h, the BET surface areas for pyrolysis temperatures of 350, 400, and 450°C were 125.71 m^2/g, 210.75 m^2/g, and 312.32 m^2/g, in order. Similarly, at a 100 kg/h feeding rate, the counterparts' BET surface areas were 105.71 m^2/g, 187.91 m^2/g, and 283.64 m^2/g, in order. The values in question were higher when the pyrolysis temperature reached 450°C, likely due to the intense reactions at this temperature, leading to biochar characterized by mesoporous pores. At high pyrolysis temperatures, a rise in surface area is generally caused by removing volatile material, which increases micropore volume (*Ahmad et al., 2012; Tomczyk et al., 2020*).

Table 4

Physical properties of rice husk biochar yielded at various pyrolysis temperatures and feeding rates

Pyrolysis temperature, °C	Feeding rate, kg/h	Physical properties		
		Biochar yield (%)	Ash content (%)	BET surface area (m^2/g)
350	50	37.2 ± 0.39 bc	23.2 ± 4.76 d	125.71 ± 3.52 d
	75	43.6 ± 2.65 ab	23.2 ± 1.85 d	118.63 ± 0.95 de
	100	45.8 ± 1.23 a	22.4 ± 2.96 d	105.71 ± 1.26 e
400	50	33.1 ± 0.58 c	31.0 ± 2.06 a	210.75 ± 0.98 b
	75	36.8 ± 0.36 bc	30.1 ± 1.07 ab	193.28 ± 2.05 bc
	100	39.1 ± 0.43 b	28.3 ± 0.95 b	187.91 ± 1.98 c
450	50	30.0 ± 3.95 d	31.4 ± 5.05 a	312.32 ± 3.75 a
	75	33.9 ± 2.36 c	28.6 ± 0.58 b	300.39 ± 4.95 a
	100	34.2 ± 1.25 cd	27.2 ± 0.93 c	283.64 ± 2.87 ab

**The data were presented using the mean ± standard deviation (SD), and significant differences (P<0.05) at a 5% significance level were denoted by distinct lowercase letters next to the means.*

PH, electric conductivity (EC), and cation exchange capacity (CEC)

The pH values of biochar ranged from 7.55 to 8.40, and there was a non-significant increase (p>0) in pH with the increase in pyrolysis temperature and down feeding rate, as shown in Fig.4[A]. *Wu et al.* (*2012*) reported a similar finding. PH values of biochar produced from bamboo were around 8.2, according to *Abrishamkesh et al*. (*2015*), which is comparable to the biochar generated from rice husk. After pyrolysis, pH values change to a more alkaline value and may be applied to acidic soils for agricultural purposes like paddy cultivation (*Shen et al., 2014*). The results of this investigation show that the pyrolysis temperature greatly impacts the pH of rice husk biochar more than the feeding rate. *Wu et al.* (*2012*) and *Southavong et al.* (*2018*) also reached an identical conclusion. Nevertheless, studies of bamboo and rice husk biochar production showed that feeding rate had impacts on the physiochemistry, morphology, and spectroscopy of the biochar comparable to those of temperature (*Peng et al., 2011; Cantrell et al., 2012*).

EC increased with the biochar pyrolysis temperature. The EC was 0.206, 0.304, and 0.402 ds/m for 350, 400, and 450°C at 100 kg/h and increased to 0.253, 0.338, and 0.457 at 50 kg/h, respectively (Fig. 4[B]). When the temperature rose and the feed rate decreased, the ash content also increased, matching the rising trend in EC. Components previously dispersed throughout the ash content became concentrated there due to the loss of volatiles (*Cantrell et al., 2012*). This is because the K+ ion is more mobile in biochar, with a higher percentage of mineral ash probably having a greater electrical conductivity (*Joseph et al., 2007*).

Variance analysis also indicated no significant changes (p > 0.05) between the feeding rate of RH. In addition, the results illustrated in Fig. 4[C] present the CEC of biochar significantly reduced as the pyrolysis temperature increased (p < 0.05). CEC was 31.47, 26.70, and 22.71 cmol/kg for 350, 400, and 450°C at 50 kg/h and 32.45, 28.16, and 24.50 cmol/kg at 100 kg/h, respectively, which is consistent with *Graber et al.* (*2017*), *Huff et al.* (*2018*), and *Domingues et al.* (*2020*). When the temperature of the pyrolysis process rises, the aromatic carbon oxidation and the production of carboxyl groups in biochar contribute to a drop in the CEC (*Graber et al., 2017*). The prevalent phenolic, quinone, hydroxyl, and carbonyl groups also affect the CEC of biochar. The FTIR spectra (Fig. 3) reveal that free –OH bonds declined with increasing pyrolysis temperatures. *McBeath and Smernik* (*2009*) stated that the aromatization of carbon might have lowered the CEC in the ash of biochar created at high temperatures of 450°C.

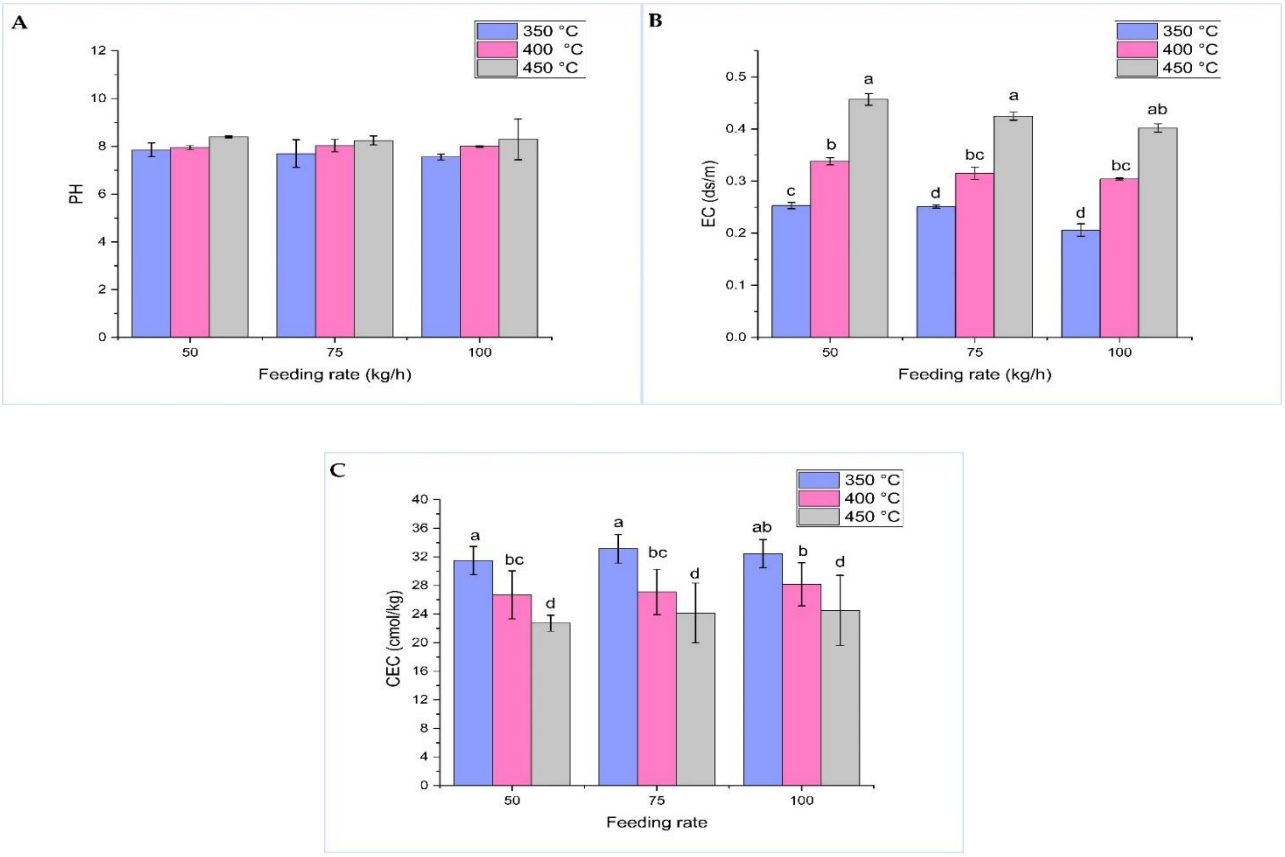

Fig. 4 – Influence of the pyrolysis temperatures (350, 400, and 450°C) and feeding rate (50, 75, and 100 kg/h) on pH [A], EC [B], and CEC [C]

CONCLUSIONS

The biochar yield from rice husk biomass decreased as pyrolysis temperature increased but slightly increased as the feed rate increased. The maximum value of biochar ash content was obtained at a pyrolysis temperature of 450°C and a feeding rate of 50 kg/h. The BET surface area of the produced biochar mainly increased with increasing pyrolysis temperature, while the feeding rate was slightly affected. Both H and O values of the produced biochar increased with pyrolysis temperature and decreased with increased feeding rate. In contrast, an inverse pattern was observed for C and N values. The EC increased with the increase in pyrolysis temperature and decreased with the increase in feeding rate, while the CEC values showed an opposite trend. In general, biochar produced from rice husk (RH) at a pyrolysis temperature of 450°C and a feeding rate of 50 kg/h exhibited favorable chemical and physical features appropriate for enhancing soil quality.

ACKNOWLEDGEMENT

The authors are most grateful to the Academy of Scientific Research and Technology (ASRT), Egypt, for funding the "Recycling of Agricultural Waste for Various Economic Products" project with ID No: 4539. The authors express their gratitude to the staff of the Agricultural Engineering Research Institute (AEnRI), Agricultural Research Center (ARC), Giza, Egypt, for their assistance with technical matters.

REFERENCES

[1] Abrishamkesh, S., Gorji, M., Asadi, H., Bagheri-Marandi, G.H., & Pourbabaee, A.A. (2015). Effects of rice husk biochar application on the properties of alkaline soil and lentil growth. *Plant Soil Environ. 61*(11), 475–482. http://dx.doi.org/10.17221/117/2015-PSE

[2] Ahmad, M., Lee, S.S., Dou, X., Mohan, D., Sung, J-K., Yang, J.E., & Ok, Y.S. (2012). Effects of pyrolysis temperature on soybean stover-and peanut shell-derived biochar properties and TCE adsorption in water. *Bioresour. Technol*. *118*, 536–544. https://doi.org/10.1016/j.biortech.2012.05.042

[3] Alahakoon, A., Karunarathna, A.K., Dharmakeerthi, R.S., & Silva, F. (2022). Design and Development of a Double-chamber Down Draft (DcDD) Pyrolyzer for Biochar Production from Rice Husk. *J. Biosyst. Eng. 47*, 458–467. http://dx.doi.org/10.1007/s42853-022-00159-5

[4] Antal, M.J., & Grønli, M. (2003). The art, science, and technology of charcoal production. *Ind. Eng. Chem. Res. 42*(8), 1619–1640. http://dx.doi.org/10.1021/ie0207919

[5] Armynah, B., Djafar, Z., Piarah, W.H., & Tahir, D. (2018). Analysis of chemical and physical properties of biochar from rice husk biomass. *J. Phys. Conf. Ser. 979*, 12038. http://dx.doi.org/10.1088/1742-6596/979/1/012038

[6] Bray, R.H., & Kurtz, L.T. (1945). Determination of total, organic, and available forms of phosphorus in soils. *Soil Sci. 59*(1), 39–45. http://dx.doi.org/10.1097/00010694-194501000-00006

[7] Cantrell, K.B., Hunt, P.G., Uchimiya, M., Novak, J.M., Ro, & K.S. (2012). Impact of pyrolysis temperature and manure source on physicochemical characteristics of biochar. *Bioresour. Technol. 107*, 419–428. http://dx.doi.org/10.1016/j.biortech.2011.11.084

[8] Cao, X., & Harris, W. (2010). Properties of dairy-manure-derived biochar pertinent to its potential use in remediation. *Bioresour. Technol. 101*(14), 5222–5228. https://doi.org/10.1016/j.biortech.2010.02.052

[9] Chen, Y., Yang, H., Wang, X., Zhang, S., & Chen, H. (2012). Biomass-based pyrolytic polygeneration system on cotton stalk pyrolysis: influence of temperature. *Bioresour. Technol. 107*, 411–418. https://doi.org/10.1016/j.biortech.2011.10.074

[10] Claoston, N., Samsuri, A.W., Ahmad Husni, M.H., & Mohd Amran, M.S. (2014). Effects of pyrolysis temperature on the physicochemical properties of empty fruit bunch and rice husk biochars. *Waste Manag. Res. 32*(4), 331–339. https://doi.org/10.1177/0734242x14525822

[11] Demirbas, A. (2004). Effects of temperature and particle size on bio-char yield from pyrolysis of agricultural residues. *J. Anal. Appl. Pyrolysis 72*(2), 243–248. http://dx.doi.org/10.1016/j.jaap.2004.07.003

[12] Demirbas, A., Pehlivan, E., & Altun, T. (2006). Potential evolution of Turkish agricultural residues as bio-gas, bio-char and bio-oil sources. *Int. J. Hydrogen Energy 31*(5), 613–620. http://dx.doi.org/10.1016/j.ijhydene.2005.06.003

[13] Ding, Y., Liu, Y., Liu, S., Li, Z., Tan, X., Huang, X., Zeng, G., Zhou, L., & Zheng, B. (2016). Biochar to improve soil fertility. A review. *Agron. Sustain. Dev. 36*, 1–18. http://dx.doi.org/10.1007/s13593-016-0372-z

[14] Domingues, R.R., Sánchez-Monedero, M.A., Spokas, K.A., Melo, L.C.A., Trugilho, P.F., Valenciano, M.N., & Silva, C.A. (2020). Enhancing cation exchange capacity of weathered soils using biochar: Feedstock, pyrolysis conditions and addition rate. *Agronomy 10*(6), 824. https://doi.org/10.3390/agronomy10060824

[15] Dunnigan, L., Ashman, P.J., Zhang, X., & Kwong, C.W. (2018). Production of biochar from rice husk: Particulate emissions from the combustion of raw pyrolysis volatiles. *J. Clean Prod. 172*, 1639–1645. http://dx.doi.org/10.1016/j.jclepro.2016.11.107

[16] El-Sheikha, A.M., & Hegazy, R.A. (2020). Designing and Evaluating Biochar Pyrolysis Kiln. *J. Soil Sci. Agric. Eng. 11*(12), 701–707. https://dx.doi.org/10.21608/jssae.2020.159761

[17] Graber, E.R., Singh, B., Hanley, K., & Lehmann, J. (2017). Determination of cation exchange capacity in biochar. Biochar A Guid to Anal methods. Australia CSIRO. 74–84.

[18] Guo, J., & Lua, A.C. (1998). Characterization of chars pyrolyzed from oil palm stones for the preparation of activated carbons. *J. Anal. Appl. Pyrolysis 46*(2), 113–125.

[19] Gwenzi, W., Chaukura, N., Mukome, F.N.D., Machado, S., & Nyamasoka, B. (2015). Biochar production and applications in sub-Saharan Africa: Opportunities, constraints, risks and uncertainties. *J. Environ. Manage. 150*, 250–261. https://doi.org/10.1016/j.jenvman.2014.11.027

[20] Huff, M.D., Marshall, S., Saeed, H.A., Lee, & J.W. (2018). Surface oxygenation of biochar through ozonization for dramatically enhancing cation exchange capacity. *Bioresour. Bioprocess. 5*, 1–9. http://dx.doi.org/10.1186/s40643-018-0205-9

[21] Ibrahim, H.A-H. (2020). Introductory chapter: pyrolysis. Recent Adv Pyrolysis. London, United Kingdom: IntechOpen. http://dx.doi.org/10.5772/intechopen.90366

[22] Joardder, M.U.H., Halder, P.K., Rahim, M.A., & Masud, M.H. (2017). Solar pyrolysis: converting waste into asset using solar energy. *Clean Energy Sustain. Dev.* 213–235. https://doi.org/10.1016/B978-0-12-805423-9.00008-9

[23] Joseph, S.D., Downie, A., Munroe, P., Crosky, A., & Lehmann, J. (2007). Biochar for carbon sequestration, reduction of greenhouse gas emissions and enhancement of soil fertility; a review of the materials science. *Proc. Aust. Combust. Symp.* 130–133.

[24] Keiluweit, M., Nico, P.S., Johnson, M.G., & Kleber, M. (2010). Dynamic molecular structure of plant biomass-derived black carbon (biochar). *Environ. Sci. Technol. 44*(4), 1247–1253. https://doi.org/10.1021/es9031419

[25] Lehmann, J., & Joseph, S. (2015). Biochar for environmental management: an introduction. *Biochar Environ. Manag. Routledge*, 1–13.

[26] Lehmann, J., & Rondon, M. (2006). Bio-char soil management on highly weathered soils in the humid tropics, Biol approaches to Sustain soil Syst. CRC Press Boca Raton, FL;113, e530. http://dx.doi.org/10.1201/9781420017113.ch36

[27] Li, F., Cao, X., Zhao, L., Yang, F., Wang, J., & Wang, S. (2013). Short-term effects of raw rice straw and its derived biochar on greenhouse gas emission in five typical soils in China. *Soil Sci. Plant Nutr. 59*(5), 800–811. http://dx.doi.org/10.1080/00380768.2013.821391

[28] Liu, W-J., Jiang, H., & Yu, H-Q. (2015). Development of biochar-based functional materials: toward a sustainable platform carbon material. *Chem. Rev. 115*(22), 12251–12285. https://doi.org/10.1021/acs.chemrev.5b00195

[29] Lone, A.H., Najar, G.R., Ganie, M.A., Sofi, J.A., & Ali, T. (2015). Biochar for Sustainable Soil Health: A Review of Prospects and Concerns. *Pedosphere 25*(5), 639–653. http://dx.doi.org/10.1016/S1002-0160(15)30045-X

[30] Lynch, J., & Joseph, S. (2010). Guidelines for the development and testing of pyrolysis plants to produce biochar. Int. Biochar Initiat London, UK.

[31] Ma, Z., Chen, D., Gu, J., Bao, B., & Zhang, Q. (2015). Determination of pyrolysis characteristics and kinetics of palm kernel shell using TGA–FTIR and model-free integral methods. *Energy Convers. Manag. 89*, 251–259. http://dx.doi.org/10.1016/j.enconman.2014.09.074

[32] McBeath, A.V., & Smernik, R.J. (2009). Variation in the degree of aromatic condensation of chars. *Org. Geochem. 40*(12), 1161–1168. https://doi.org/10.1016/j.orggeochem.2009.09.006

[33] McElligott, K.M., Page-Dumroese, D.S., Coleman, M., & McElligott, K. (2011). Bioenergy production systems and biochar application in forests: Potential for renewable energy, soil enhancement, and carbon sequestration, US Department of Agriculture, Forest Service, Rocky Mountain Research. https://doi.org/10.2737/RMRS-RN-46

[34] Mukherjee, A., & Lal, R. (2014). The biochar dilemma. *Soil Res. 52*(3), 217–230. http://dx.doi.org/10.1071/SR13359

[35] Nan, H., Yin, J., Yang, F., Luo, Y., Zhao, L., & Cao, X. (2021). Pyrolysis temperature-dependent carbon retention and stability of biochar with participation of calcium: Implications to carbon sequestration. *Environ. Pollut. 287*, 117566. https://doi.org/10.1016/j.envpol.2021.117566

[36] Peng, X., Ye, L.L., Wang, C.H., Zhou, H., & Sun, B. (2011). Temperature-and duration-dependent rice straw-derived biochar: Characteristics and its effects on soil properties of an Ultisol in southern China. *Soil Tillage Res. 112*(2), 159–166. http://dx.doi.org/10.1016/j.still.2011.01.002

[37] Qu, J., Wang, Y., Tian, X., Jiang, Z., Deng, F., Tao, Y., Jiang, Q., Wang, L., & Zhang, Y. (2021). KOH-activated porous biochar with high specific surface area for adsorptive removal of chromium (VI) and naphthalene from water: Affecting factors, mechanisms and reusability exploration. *J. Hazard Mater. 401*, 123292. https://doi.org/10.1016/j.jhazmat.2020.123292

[38] Ren, D., Zhang, L., Huang, W., Cheng, H., He, T., & Meng, J. (2022). Design and test of key components of biochar return machine based on rocky. *INMATEH - Agricultural Engineering, 68*(3), 607–616. https://doi.org/10.35633/inmateh-68-60

[39] Ren, H., Guo, H., Shafiqul Islam, M., Zaki, H.E.M., Wang, Z., Wang, H., Qi, X., Guo, J., Sun, L., Wang, Q., Li, B., Li, G., & Radwan, K. (2023). Improvement effect of biochar on soil microbial community structure and metabolites of decline disease bayberry. *Front. Microbiol. 14*, 1154886. https://doi.org/10.3389/fmicb.2023.1154886

[40] Samsuri, A.W., Sadegh-Zadeh, F., & Seh-Bardan, B.J. (2014). Characterization of biochars produced from oil palm and rice husks and their adsorption capacities for heavy metals. *Int. J. Environ. Sci. Technol. 11*, 967–976. http://dx.doi.org/10.1007/s13762-013-0291-3

[41] Savova, D., Apak, E., Ekinci, E., Yardim, F., Petrov, N., Budinova, T., Razvigorova, M., & Minkova, V. (2001). Biomass conversion to carbon adsorbents and gas. *Biomass and Bioenergy 21*(2), 133–142. https://doi.org/10.1016/S0961-9534(01)00027-7

[42] Scholz, S.B., Sembres, T., Roberts, K., Whitman, T., Wilson, K., & Lehmann, J. (2014). Biochar systems for smallholders in developing countries: leveraging current knowledge and exploring future potential for climate-smart agriculture, World Bank Publications. http://hdl.handle.net/10986/18781

[43] Shen, J., Tang, H., Liu, J., Wang, C., Li, Y., Ge, T., Jones, D.L., & Wu, J. (2014). Contrasting effects of straw and straw-derived biochar amendments on greenhouse gas emissions within double rice cropping systems. *Agric. Ecosyst. Environ. 188*, 264–274. http://dx.doi.org/10.1016/j.agee.2014.03.002

[44] Song, W., & Guo, M. (2012). Quality variations of poultry litter biochar generated at different pyrolysis temperatures. *J. Anal. Appl. Pyrolysis 94*, 138–145. http://dx.doi.org/10.1016/j.jaap.2011.11.018

[45] Southavong, S., Ismail, M.R., Preston, T.R., Saud, H.M., & Ismail, R. (2018). Effects of pyrolysis temperature and residence time on rice straw-derived biochar for soil application. *Int. J. Plant Soil Sci. 23*(3), 1–11. http://dx.doi.org/10.9734/IJPSS/2018/42197

[46] Sun, X., Atiyeh, H.K., Li, M., & Chen, Y. (2020). Biochar facilitated bioprocessing and biorefinery for productions of biofuel and chemicals: A review. *Bioresour. Technol. 295*, 122252. https://doi.org/10.1016/j.biortech.2019.122252

[47] Tomczyk, A., Sokołowska, Z., & Boguta, P. (2020). Biochar physicochemical properties: pyrolysis temperature and feedstock kind effects. *Rev. Environ. Sci. BioTechnol. 19*, 191–215. https://link.springer.com/article/10.1007/s11157-020-09523-3

[48] Wu, W., Yang, M., Feng, Q., McGrouther, K., Wang, H., Lu, H., & Chen, Y. (2012). Chemical characterization of rice straw-derived biochar for soil amendment. *Biomass and Bioenergy 47*, 268–276. http://dx.doi.org/10.1016/j.biombioe.2012.09.034

DESIGN AND EXPERIMENT OF AN AUTOMATIC GIRDLING DEVICE FOR ECONOMIC TREE TRUNK INSPIRED BY CAM MECHANISM
/
凸轮原理启发的经济林树干自动环剥装置的设计与实验研究

Zhenkun ZHI[1)], Haifeng LUO[*)]
[1)]School of Engineering, Beijing Forestry University, Beijing/ China;
Tel: 8601062338144; E-mail: luohaifeng@bjfu.edu.cn
DOI: https://doi.org/10.35633/inmateh-72-04

Keywords: *cam mechanism, half-ring, tree trunk profile scanning, trajectory calculating, chainsaws*

ABSTRACT
In order to solve the problem of complicated processes, low efficiency and high cost of economic tree trunks girdling, inspired by cam mechanism this study developed a new type of automatic half-ring girdling device, which can automatically complete a series of operations, including the tree trunk profile scanning, girdling trajectory calculating and automatic bark cutting. A pair of laser rangefinders and guide screws were symmetrically arranged on a half-ring rotating rail, which could rotate around the tree trunk, and two chainsaws assembled above the guide screws were controlled to move radially. The laptop was used as upper computer, and a 4-axis motion control card was used as the lower computer, which constituted the control system of precise movement. The programs of the tree trunk profile scanning, the xylem profile curve fitting and the chainsaw centre trajectory calculation were designed in LabVIEW. The scanning tests and girdling experiments were carried out on the different sections of the tree trunks in the laboratory. The feasibility of the automatic girdling device for economic tree trunks was verified with one complete and automatic girdling operation finished by this device, which took 150 seconds, and the error range of automatic girdling was within ±2mm. This device improves the automation degree of girdling operation and provides a support for the development of economic forestry.

摘要
为解决经济林树木开甲存在流程复杂，效率低，成本高的问题，受凸轮原理启发，本文设计一种新型自动化半环开甲装置，自动完成树干轮廓扫描，环剥轨迹计算，自动切割树皮等操作。该装置在半环转动支架上对称安装了一对称双激光测距仪、丝杠，半环支架可环绕树干旋转运动。丝杠上面安装的手持电锯能够实现径向运动。以 LabVIEW 为上位机，以 4 轴运动控制卡作为下位机，构成精确运动的控制系统。在 LabVIEW 中完成了树干轮廓扫描、木质部轮廓曲线拟合、电锯中心轨迹计算等程序设计。在实验室中对树干不同的截面进行了测量实验和环剥实验。完整自动的开甲操作证实了该经济林开甲装置的可行性，该装置单次自动环剥时间为 150 秒，开甲精度为±2mm。该装置提高了开甲操作的自动化程度，为经济林产业提供了支撑。

INTRODUCTION

Girdling is defined as the removal of a ring of bark or phloem, mainly around the trunk or branch, which has the immediate effect of blocking the phloem transport pathway, thereby eliciting the accumulation of carbohydrates above the girdle *(Goren et al., 2004; Oberhunber et al., 2017)*. In 1686, Marcello Malpighi carried out the classical experiment of organic solute migration with removal of the bark around the trunk of a tree in a circular pattern. Since Kobel studied the physiological mechanism of flower promotion by ring cutting from the perspective of C/N ratio in 1931, many scholars had carried out in-depth studies from different perspectives such as nutrition, hormone and nucleic acid. Particularly, girdling often promotes flower-bud initiation, fruit set and growth, and increases yield, but reduces vegetative growth. Thus, girdling is widely applied for hundreds of years in trees horticultural practice because of these benefits *(Wilkie et al., 2008; De Schepper and Steppe, 2011)*. The jujube tree is an important economic crop native to China, which accounts for more than 98% of the total cultivated area in the world. Girdling jujube trees at the right stage of growth can effectively increase the fruit set rate of jujube trees, improve fruit quality, and increase production at the same time (*Ye et al., 2019*). Therefore, girdling is often used to regulate the growth of fruit trees and promote fruit development.

Girdling improves the fruit-set rate of citrus *(Yang et al., 2013)*, persimmon *(Juan et al., 2009)*, grape *(Zhu et al., 2022)*, tomato *(Chai et al., 2021)*, and finally increases the fruit yield. Therefore, girdling technology is widely used in economic forestry.

The using of different tools directly affects the girdling efficiency of fruit trees, ultimately the yield of economic trees. Traditionally, girdling is accomplished by workers using simple hand-held knives to remove the tree bark. The typical girdling tools are "Z" type girdling knife, triangular double-edged ring cutter knife, curved bar double-edged ring cutter, L-shaped ring stripper, pulley girdling knife, double curved blade ring stripping shears, three-blade ring stripper *(Duan, 2007)*. The structures of these girdling tools are simple and the effects of girdling depend largely on the experience of workers. Girdling work is labour-intensive and time-consuming, and this problem becomes serious when huge amount of fruit trees needs to be girdled within a short period, especially with the yearly reduction of the workforce. In response to the problems of low quality and efficiency of general artificial girdling tools, an electric type jujube girdling device was designed *(Xie, et al., 2018)*. This type of girdling device solved the problem of maintaining relative fixation with the trunk during girdling, but it led to another problem of uncontrollable girdling breakage rate by fixing the tool to perform girdling at the same depth. *Li, et al., (2019)*, designed a handheld small girdling device, which improved the efficiency of cutting bark, but the accuracy of girdling was also dependent on workers' experience. Although the electric girdling tools increased the speed of working, accuracy and efficiency of traditional girdling still varied from person to person.

In this paper, a new automatic girdling device is designed to improve girdling accuracy on the basis of ensuring efficiency of girdling. A half-ring symmetrical mechanical structure is adopted on the device, and actuators and scanning sensors are selected based on the requirements of economic trees girdling. The control flow is completed according to the structure of the girdling device and the girdling process, and girdling programs are designed in LabVIEW. Three levels of error analysis are carried out by scanning tests and girdling experiments in laboratory.

MATERIALS AND METHODS

The economic trees that need to increase production, should be girdled when they are older than 7 years or the trunk diameters are greater than 10 cm. Nearly half of the time of flowering is the best time to be girdled. One of the manual girdling methods is shown in Fig. 1. The operators select a position 30 cm above the ground, and the old bark is removed from the tree trunk by a sickle. The width of the excised skin should be widened to 2 cm, and the inner phloem exposes a circle with a width of 1 cm. The upper part of the phloem needs to be cut by tools after peeling horizontally to the xylem of the tree, and it is cross cut obliquely at the lower part of the phloem to the xylem. The final incision width should be controlled at about 0.5 cm. Due to the different sizes of tree trunks and the experience of workers, the time for manual girdling usually varies from minutes to half an hour. In some regions of China, experienced workers girdle about 200 trees for 400-500 yuan (RMB) a day.

Fig. 1 – Manual girdling

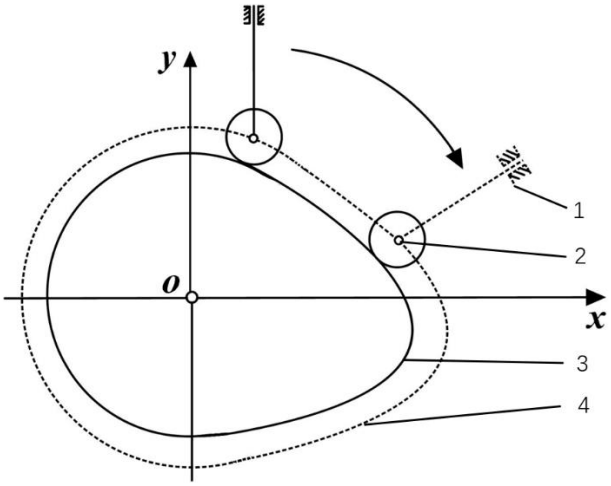

Fig. 2 – The inversion of cam
1–Guide; 2–Roller; 3–Cam; 4–The trajectory of roller centre;

Core mechanisms

As shown in Fig. 2, an irregularly shaped cam (3) is fixed at point O. The roller (2) can be rotated relative to the cam together with the guide, and also be moved radially inside the guide (1). The trajectory (4) of the roller can be formed by synthetic motion of radial slide and rotation. In this paper, the xylem of the tree trunk is taken as the cam, and the chainsaw for girdling is considered as the roller. Based on the principle of inversion of cam mechanism shown in Fig. 2, the trajectory (4) of the chainsaw's centre can be obtained for the automatic girdling method.

The core working principle of the device is shown in Fig. 3. A pair of chainsaws (3), guide screws (2) and laser rangefinders (1) are mounted symmetrically at the end of the half-ring rail (6). As shown in Fig. 3a, the profile of the tree trunk is scanned by the device. The scanning starts at the horizontal initial position (7). The half-ring rail rotates counter clockwise around the tree trunk, and at the same time the laser rangefinders start measuring along the red dashed circle. The distance between the laser rangefinders and the tree trunk is measured by the laser rangefinders at a certain frequency in the process of rotational movement. The half-ring rail reaches the opposite horizontal position (8) after the scanning of the tree trunk profile. The external profile of the tree trunk (5) is obtained, and the xylem profile curve (4) is acquired by algorithms. The girdling process of the device is shown in Fig. 3b. The half-ring rail rotates clockwise, and the chainsaws are driven to girdle based on trajectory mentioned in Fig. 2. The device completes girdling when the half-ring rail rotates to the initial position (7) in Fig. 3a.

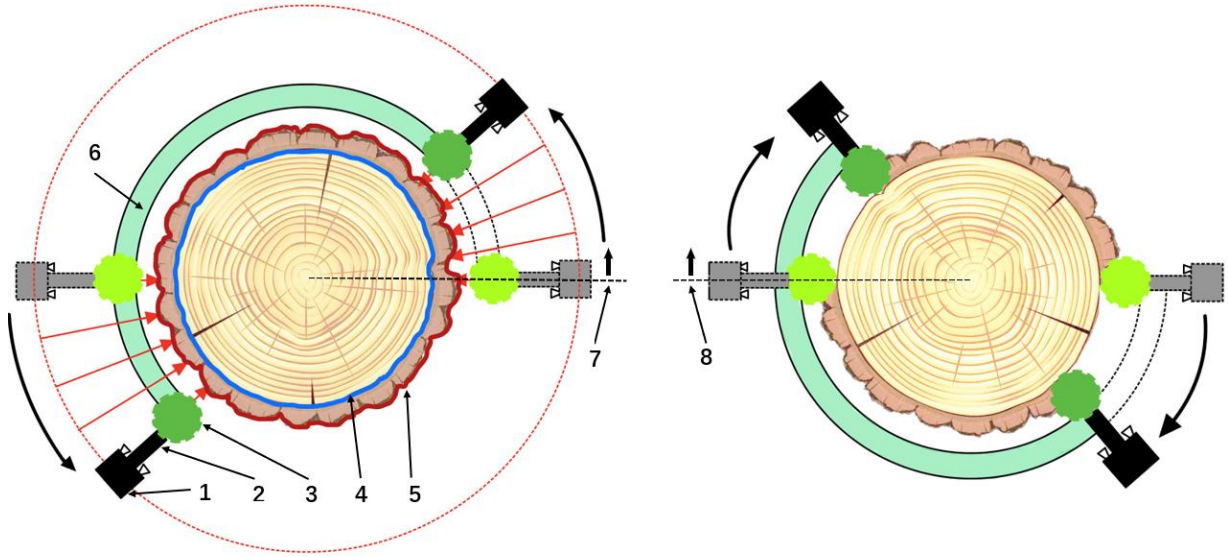

Fig. 3 – The girdling device mechanism

a) The scanning process; b) The girdling process

1-Laser rangefinders; 2-Guide screws; 3-Chainsaws; 4-Xylem profile curve; 5-Tree trunk profile curve; 6-Half-ring rail; 7-Initial position of scanning; 8-Initial position of girdling

As shown in Fig. 4, the motion centre O of the half-ring rail is taken as the origin of the cartesian coordinate system, and curve C is the trajectory of the half-ring rail. The xylem profile curve s is obtained by calculating based on the tree trunk profile, and its polar coordinate equation is $s=s(\varphi)$. The instantaneous girdling state of the chainsaw with B as the centre at the cutting point A is shown in Fig. 4. The polar coordinate of point A is $(\varphi, s(\varphi))$. The tangent line of A point on the curve s is l'. The common normal line through A point is l, and the angle between l and the positive direction of x axis is β, then the cartesian coordinate of A point is:

$$\begin{aligned} x &= s\cos\varphi \\ y &= s\sin\varphi \end{aligned} \tag{1}$$

Line l and l' are perpendicular to each other, the trigonometric function of the angle β is:

$$\tan\beta = -\frac{dx}{dy} \tag{2}$$

$$\sin\beta = \frac{dx/d\varphi}{\sqrt{(dx/d\varphi)^2 + (dy/d\varphi)^2}} \tag{3}$$

$$\cos\beta = \frac{-dy/d\varphi}{\sqrt{(dx/d\varphi)^2 + (dy/d\varphi)^2}} \tag{4}$$

The radius of the chainsaw is R, and the coordinate of $B(X,Y)$ on the central trajectory of the chainsaw is obtained as follows :

$$\begin{aligned} X &= x + R\cos\beta \\ Y &= y + R\sin\beta \end{aligned} \tag{5}$$

In order to be used directly in control program, the cartesian coordinate on trajectory B is transformed into a polar coordinate relative to point O as follows.

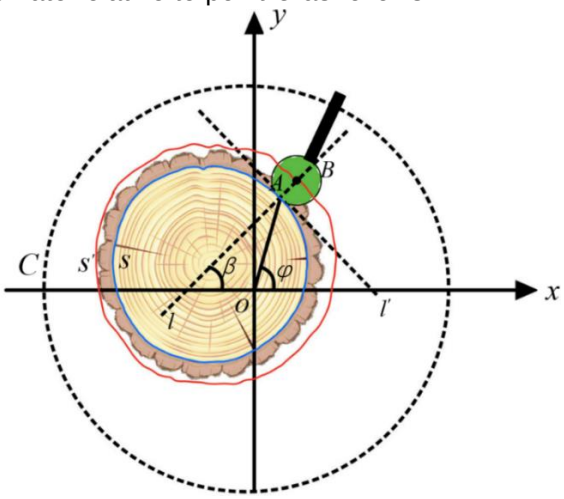

Fig. 4 – The principle of the trajectory of the chainsaw's centre

Overall structure

The mechanical structure of the device is shown in Fig. 5. The half-ring rail (5) is driven by stepper motor (1) to rotate around the tree trunk (6) though gearing. Two laser rangefinders (2) are symmetrically installed at both ends of the half-ring rail, which realizes the scanning of the tree trunk in rotational movement. The guide screws and chainsaws are mounted at the end of the half-ring rail by the way the same to laser rangefinders. The guide screws are driven by motors to realize the radial movement. Girdling can be completed by the chainsaws with synthetic movement of radial movement and rotational movement.

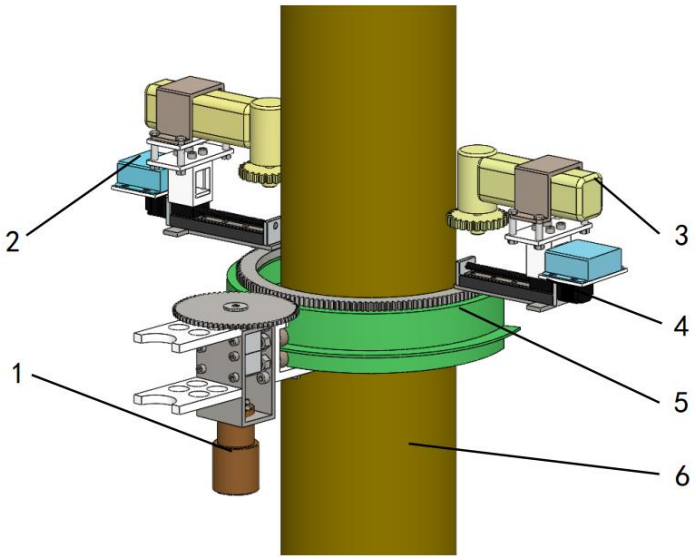

Fig. 5 – The girdling device

1-Stepper motor; 2-Laser rangefinders; 3-Chainsaws; 4-Guide screw motors; 5-Half-ring rail; 6-Tree trunk

Control system

The overall hardware system of the girdling device is shown in Fig. 6. The laptop based on x64 Intel (R) i7 processor is selected as the upper computer of the device control system. *Art* 1020 motion control card is selected as the lower computer. *Art* 1020 is a four-axis servo/stepper motor motion control card with the USB bus, which can complete various complex control requirements of servo / stepper motor. The motors in this girdling device are controlled by *Art* 1020 precisely. Guide screw motors and stepper motor are used as the drive system, and the laser rangefinders are the sensors of the scanning system. The transmission of scanning signals and control signals between laptop and laser rangefinders is realized through USB bus. The hardware parameters are shown in Table 1.

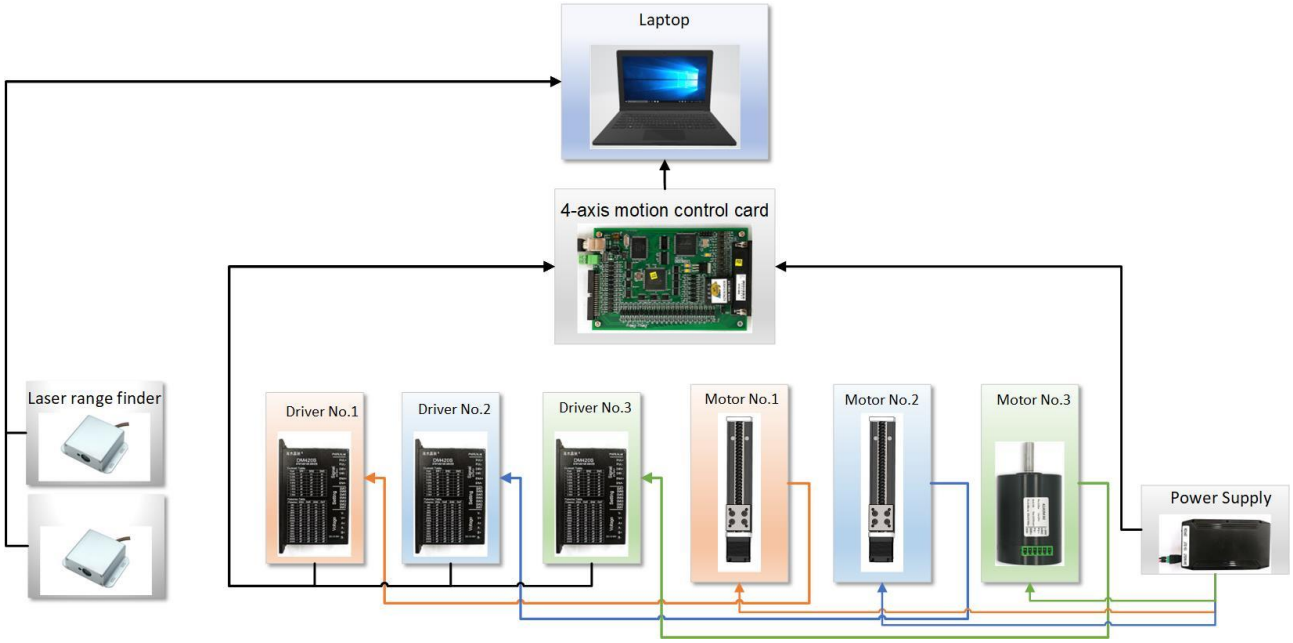

Fig. 6 – Hardware system of girdling device

Table 1

Main technical parameters

Parameter	Value	Units
Scanning Frequency	1~20	Hz
Stepper motor torque	20	N·m
Stepper motor power	50	W
Accuracy of guide screw	0.125	mm
Motor response frequency	≤80k	Hz
Laser rangefinder measurement accuracy	±0.05	mm

The block diagram of the control system program is shown in Fig. 7. In order to ensure the accuracy of the movement, the initialization of the girdling device control system is first carried out. The parameters including the emission frequency of laser rangefinders, scanning time and cutting time are set after initialization. Then the half-ring rail is driven by the stepper motor to rotate around the tree trunk. simultaneously, the laser rangefinders are started to scan the tree trunk. The half-ring rail rotates to the position (8) as mentioned in Fig. 3b after finishing scanning. The polar coordinate points of the tree trunk external profile are saved in a txt file. The data processing includes two algorithms. Since an explicit function between the bark profile and its xylem profile has not been defined in the papers, this paper proposes the interval minimum algorithm. Analysis of the bark and xylem structure through the trunk cross-section shows that the change in curvature of the xylem profile surface is much smaller than that of the bark profile surface. The measured polar coordinate points saved in the txt file are grouped into equal intervals according to the scanning direction. The first smallest value in the interval is selected as the representative point close to the xylem. The interval minimum curve is obtained by linear fitting of these selected points. Then the xylem profile curve, which is also the curve s mentioned in Fig. 4, is obtained according to the thickness value of the tree bark. The trajectory of the chainsaw centre is obtained by the cam inversion algorithm based on the equation (5). The cutting operation starts at the position (8) in Fig. 3b.

The laptop converts the polar coordinate points of chainsaw centre trajectory into pulse signals to 4-aix motion control card. The stepper motor and the guide screw motors are controlled according to the pulse signals, and the girdling is carried out with the half-ring rail moving clockwise. The girdling operation of the tree trunk is completed by chainsaws with radial and rotational synthetic movement.

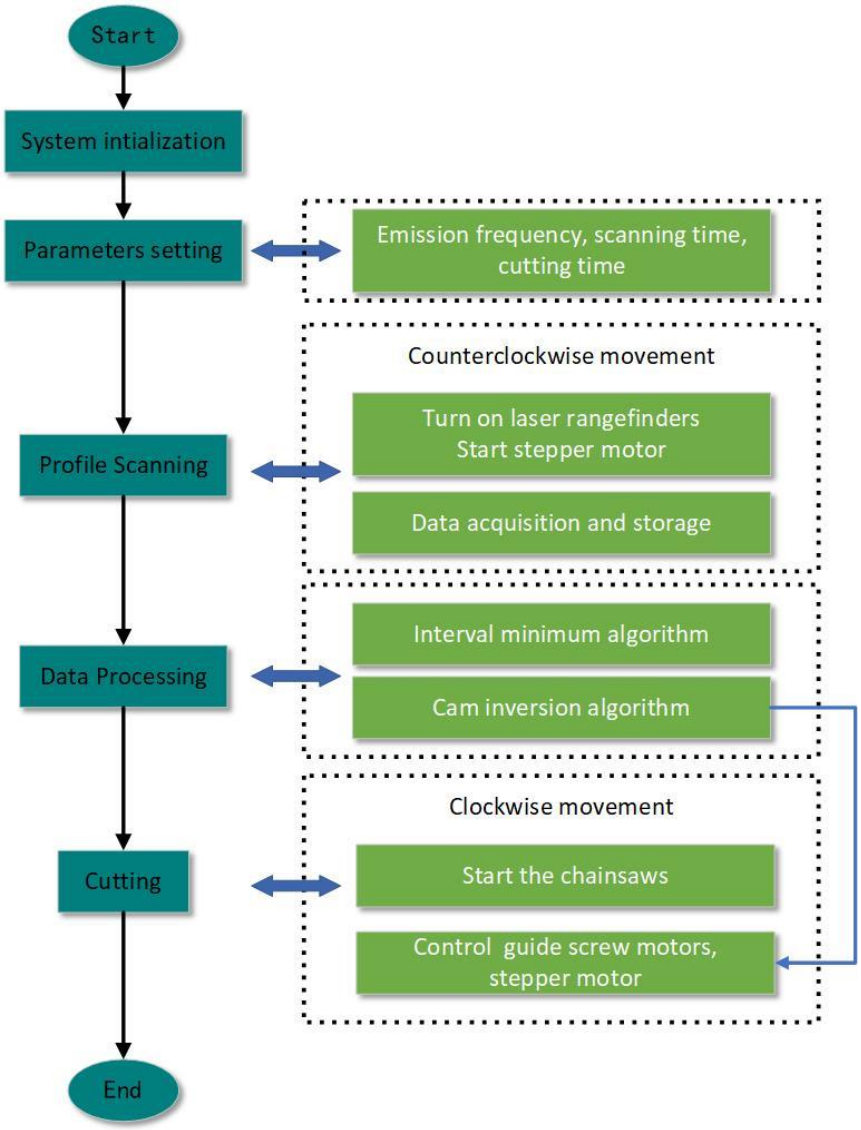

Fig. 7 – Control system program block diagram

As shown in Fig.8, the operation panel of the girdling device control system is designed in LabVIEW. The operation panel includes the parameters setting, the status prompt of the completed process, the real-time display of scanning state and cutting state, and the schematic display of current girdling state. The scanning time, scanning frequency and cutting time can be set on the panel based on different girdling requirements of economic tree trunks. The process of girdling can be divided into four parts according to control system program block diagram, and every part can be controlled individually by the button in the panel. Every finished part can be prompted by the indicator light behind the corresponding button. In the part of real-time scanning, the scanning and cutting process of the tree trunk profile can be shown in the polar coordinate system in real time.

As shown in the polar coordinate system, the red curve is the profile of the tree trunk, and the brown curve is the profile of the xylem calculated by algorithm. The corresponding state in the part of real-time scanning is shown in form of pictures in the part of process. According to the real-time feedback in the panel, the operator can control the operation condition of the girdling device.

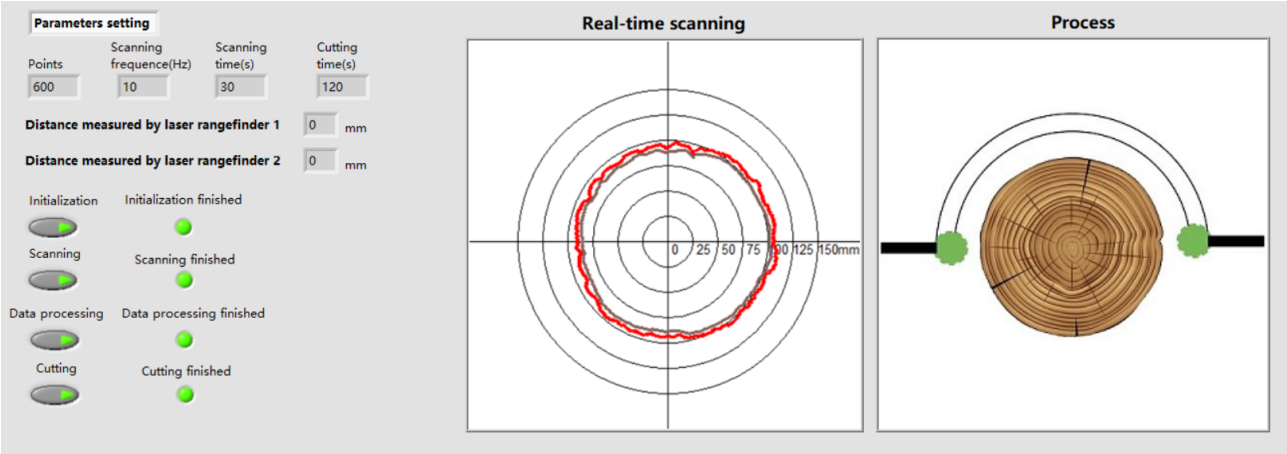

Fig. 8 – The operation panel of the control system

RESULTS AND DISCUSSION

Scanning system error

In the whole process of girdling, the scanning of the external profile of the tree trunk was completed first, and the scanning result was directly related to the accuracy of the centre point trajectory of the chainsaws obtained from the cam inversion algorithm. Therefore, the error analysis of the scanning system of the girdling device is carried out first. RA7525SE-1005 is a six-axis absolute arm, which can realize high-precision contact measurement. The measurement radius range of RA7525SE-1005 is 1.2 meters, and the measurement point repeatability accuracy is 0.050 mm. It can accurately measure the 3D coordinates of spatial points in its radius range. The cross sections of the same tree trunk were measured by the device and the RA7525SE-1005 respectively. In this experiment, a wooden pile only with its xylem was selected to be scanned. The profile scanning with the girdling device was shown in Fig.9, and the profile measurement with RA7525SE-1005 was shown in Fig.10.

Fig. 9 – Profile scanning with the girdling device
1-Girdling mechanical structure; 2-Control box; 3-Power; 4-Laptop;

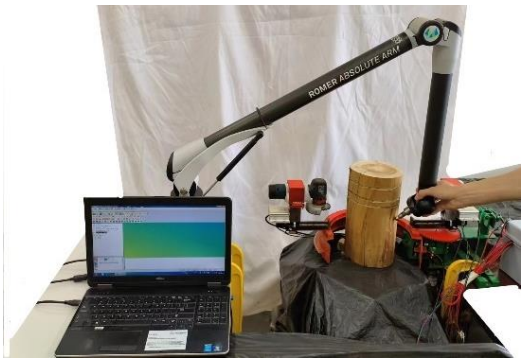

Fig. 10 – Profile measurement with RA7525SE-1005

The same positions of the wooden pile were measured by RA7525SE-1005 and the girdling device. In the ten groups of scanning experiments, the scanning frequency of the laser rangefinders was 10 Hz, and the scanning time was from 7.5 s to 30 s.

The number of scanning points by the girdling device was from 150 to 600, and number of points measured by RA7525SE-1005 was 50. In order to better calculate the result error between the result measured by RA7525SE-1005 and the result scanned by girdling device, the measurement result of RA7525SE-1005 was fitted by first order. The measurement results were shown in Fig. 11.

Data 1 is the measurement result of RA7525SE-1005, and data 2 to data 11 were scanning results by the girdling device. Due to the high measurement precision of RA7525SE-1005, data 1 mentioned in Fig. 11 was taken as the standard value. In the polar coordinate system, the difference between points (data 2 to data 11) scanned by the girdling device and the fitted curve (data 1) at the corresponding angle was used as the error of the measurement system.

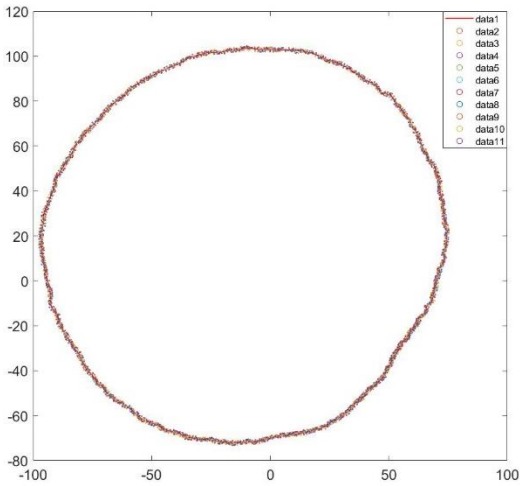

Fig. 11 – The measurement results

The error calculation results were shown in Table 2, including the measurement error maximum, measurement error minimum, measurement error average and root mean square error of measurement system. It can be concluded that the tree trunk profile scanning average error of the device was within 1 mm. With the increase of the number of measurement points, the error decreased in all four aspects. When the number of points measured reached 600, the average error stabilized within 0.5 mm and the root mean square error remained at a low level.

Table 2

Error of scanning system

Number of scanning points by girdling device	Number of measurement points by RA7525SE-1005	Maximum error (mm)	Minimum error(mm)	Average error(mm)	Root mean square error
150	50	1.994	-2.030	0.783	1.0293
200	50	1.984	-1.999	0.690	0.9909
250	50	1.979	-1.999	0.681	0.9350
300	50	1.977	-1.998	0.572	0.8133
350	50	1.953	-1.998	0.536	0.7872
400	50	1.918	-1.997	0.521	0.7805
450	50	1.853	-1.997	0.501	0.7486
500	50	1.758	-1.982	0.443	0.6610
550	50	1.740	-1.458	0.408	0.6316
600	50	1.668	-1.329	0.408	0.2828

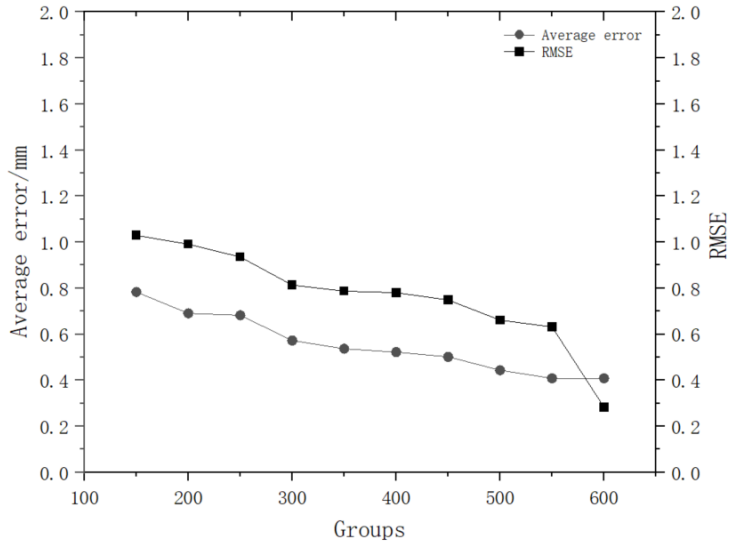

Fig. 12 – Error of scanning system

Control system and algorithm error

In this experiment, a wooden pile only with its xylem was selected to be cut. In the process of cutting, the error includes the scanning error, the motion control error and the calculation error of the cam inversion algorithm mentioned in Fig. 7. In order to reduce the impact of scanning error, 600 points were selected in the process of profile scanning. In this experiment, the wooden file was scanned in 30 seconds, and the chainsaw centre trajectory calculated by the cam inversion algorithm was performed in 120 seconds.

The process of scanning and cutting were shown in Fig. 13 and Fig. 14. In Fig. 15, the red curve was the profile of the wooden pile, and it was used as the curve s in Fig. 4, and the brown curve was the cutting profile. In this experiment, the cutting depth was 5 mm. The cutting depth errors were measured by 50 index vernier scale. There were ten groups of girdling experiments were carried out, and the number of error measurement points was 100 in each group.

Fig. 13 – Scanning

Fig. 14 – Cutting

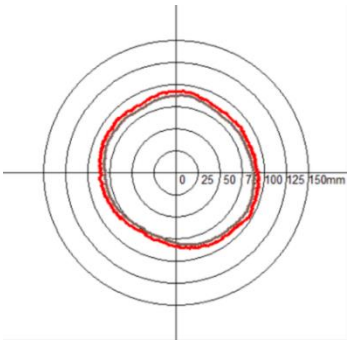

Fig. 15 – Scanning profile and cutting profile

Table 3

Error of control system and algorithm

Experimental group	Number of measurement points	Maximum error (mm)	Minimum error (mm)	Average error (mm)	Root mean square error
1	100	1.68	-1.56	0.74	0.8704
2	100	1.84	-1.48	0.68	0.8304
3	100	1.88	-1.78	0.64	0.7631
4	100	1.68	-1.78	0.74	0.9013
5	100	1.56	-1.86	0.58	0.7055
6	100	1.54	-1.84	0.76	0.9231
7	100	1.20	-1.78	0.70	0.8166
8	100	1.86	-1.84	0.78	0.9222
9	100	1.54	-1.86	0.74	0.8787
10	100	1.82	-1.82	0.68	0.8353

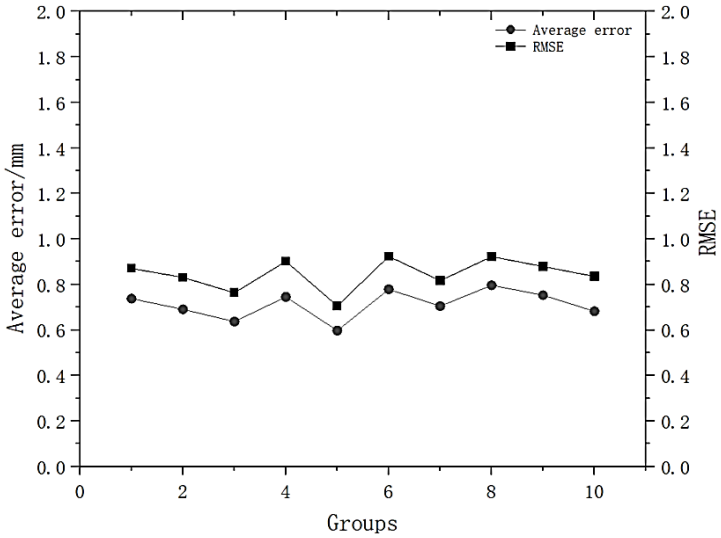

Fig. 16 – Error of control system and algorithm

The maximum measurement error, the minimum measurement error, the average measurement error and root mean square error were shown in Table 3, and the error generated by the control system and the cam inversion algorithm was generally larger than the error in the last experiment.

From the trend of the curves in Fig. 16, the average errors were relatively stable in the range of 0.6-0.8 mm. Under the same experimental conditions, the root mean square errors of the ten groups were maintained at a low level, and the accuracy of motion control and calculation in the cam inversion algorithm was stable.

Girdling operation error

In this experiment, a wooden pile with its complete bark structure was selected to be girdled. In order to ensure the accuracy of the scanning profile, the number of measurement points was 600 in the process of scanning. In this experiment, the device took 30 seconds to scan the wooden pile, and it took 120 seconds for the chainsaws to perform girdling. The difference between the surface after girdling and the xylem of the wooden pile was defined as the girdling overall error, and the errors were measured by 50 index vernier scale. The processes of scanning and girdling were shown in Fig.17 and Fig.18. In Fig.19, the red curve was the scanning profile of the wooden pile, and the brown curve was the girdling profile at the corresponding cross-section of the wooden pile. The xylem profile was obtained by the interval minimum algorithm mentioned in Fig. 7.

Fig. 17 – Scanning

Fig. 18 – Girdling

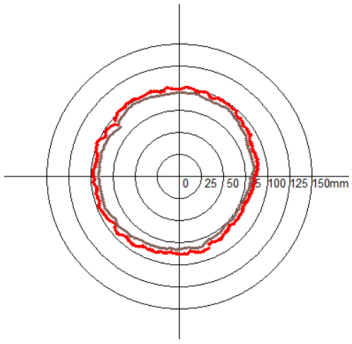

Fig. 19 – Scanning profile and xylem profile

Table 4

Error of the girdling device

Experimental group	Number of measurement points	Maximum error (mm)	Minimum error(mm)	Average error(mm)	Root mean square error
1	100	1.98	-1.98	1.04	1.1882
2	100	1.94	-1.92	0.96	1.1145
3	100	1.96	-1.92	1.12	1.1742
4	100	1.98	-1.95	0.84	1.0198
5	100	1.96	-1.98	0.99	1.1649
6	100	1.96	-1.96	0.96	1.1344
7	100	1.96	-1.94	0.98	1.1401
8	100	1.96	-1.92	0.94	1.1246
9	100	1.98	-1.96	1.06	1.2205
10	100	1.94	-1.94	1.02	1.1578

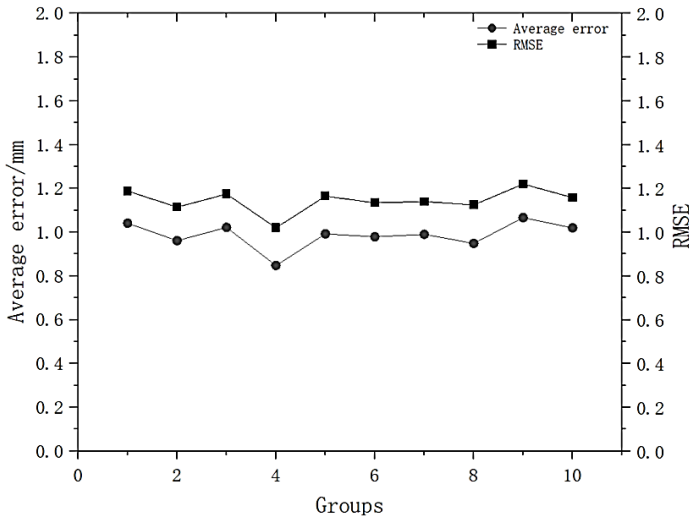

Fig. 20 –Error of the girdling device

The error generated by girdling was accumulated by the profile scanning error, motion control error and calculation error from algorithm. The new error in this experiment was from the calculation error in interval minimum algorithm. Because only one point was selected from the interval, there were differences between the calculated xylem profile by the interval minimum algorithm and the real xylem profile. The error was accumulated, and it effected the calculation in the cam inversion algorithm. The maximum error, minimum error, average error and root mean square error were shown in Table 4. The trends of average error and root mean square error were shown in Fig. 20. The comprehensive error of girdling was within ±2 mm, and the average error was within 1.1 mm, and the girdling error of this device was relatively stable.

CONCLUSIONS

(1) The mechanical structure for the automatic girdling device was verified. In the rotation process of the half-ring rail, the scanning of the tree trunk profile was realized by two symmetrical laser rangefinders at the end of the half-ring rail. In the combined motion of the half-ring rail rotational motion and the guide screws radial motion, the girdling of the tree trunk was realized by two chainsaws above the guide screws.

(2) The control program for the girdling operation was implemented in LabVIEW, and the feasibility of the control program was proved within the girdling experiments. The minimum interval algorithm was presented to acquire the xylem profile according to tree trunk profile. The cam inversion algorithm was proposed to obtain the chainsaw centre trajectory according to the xylem profile.

(3) The error analysis experiments of the device were divided into three steps. The error analysis of the device scanning system was carried out by comparing with the measurement result from the RA7525SE-1005. The motion control error and algorithm calculation error were obtained by cutting the wooden pile only with the xylem. The girdling operation error was tested by girdling the complete trunk. The girdling error is within ±2 mm and the overall time of girdling is within 150 seconds, and the accuracy and efficiency for economic tree trunk girdling can be improved with this device.

ACKNOWLEDGEMENT

This work is supported by the Fundamental Research Funds for the Central Universities (2017ZY46) and 2023HXKFGXY002.

REFERENCES

[1] Chai, L., Li, Q., Wang, H., Wang, C., Xu, H., Jiang, W., (2021). Girdling alters carbohydrate allocation to increase fruit size and advance harvest in tomato production, *Scientia Horticulturae*, Vol.276, Amsterdam/ Netherlands.

[2] De Schepper, V., Steppe, K., (2011). Tree girdling responses simulated by a water and carbon transport model. *Annals of Botany*, Vol.108, Issue 6, pp.1147–1154, Oxford/England.

[3] Duan, L., (2007). Review of girdling knife development and innovative tool outlook (环剥刀研制的回顾与创新刀具展望), *Shanxi Fruits*, Vol.1, pp.37–38, 39, Shanxi/China.

[4] Goren, R., Huberman, M., Goldschmidt, E.E., 2004. Girdling: physiological and horticultural aspects. *Hortic. Rev*. 30, 1–36. https://doi.org/10.1002/9780470650837.ch1.

[5] Gülden G., Atalba M.C., Guler H., (2020), Chaotic Systems Based Real-Time Implementation of Visual Cryptography Using LabVIEW. *Traitement du Signal*, Vol 37, Issue 4, pp. 639 -645, Turkey;

[6] Juan, M., Mesejo, C., Martínez-Fuentes, A., Reig, et al., (2009), Branch scoring encourages fruit development and climacteric in persimmon. *Scientia Horticulturae*, Vol.122, Issue 3, pp.497–500, Amsterdam / Netherlands.

[7] Li, H., Xie, J., (2019). Research Status and Countermeasures of Jujube Girdling Technology (枣树环剥技术研究现状与对策), *Journal of Tarim University*, Vol.31, Issue 1, pp.89–93, Xinjiang/China.

[8] Michailidis M., Karagiannis E., Tanou G., et al., (2020). Proteomic and metabolic analysis reveals novel sweet cherry fruit development regulatory points influenced by girdling. *Plant Physiol Biochem*, Vol.149, pp.233–244. Issy-les-Moulineaux / France.

[9] Oberhunber, W., Gruber, A., Lethaus, G., Winkler, A., Wieser, G. (2017). Stem girdling indicates prioritized carbon allocation to the root system at the expense of radial stem growth in Norway spruce under drought conditions, *Environmental and Experimental Botany*, Vol.138, pp.109–118, Austria.

[10] Olofsson, K., Holmgren, J., (2016). Single Tree Stem Profile Detection Using Terrestrial Laser Scanner Data, Flatness Saliency Features and Curvature Properties, *Forests*, Vol.7, Issue.9, pp.1-23, Basel / Switzerland.

[11] Wilkie, J.D., Sedgley, M., Olesen, T., (2008), Regulation of floral initiation in horticultural trees. *Journal of Experimental Botany*, Vol. 59, Issue 12, pp. 3215–3228, NSW / Australia. https://doi.org/10.1093/jxb/ern188.

[12] Xie, J., Li, H., Jiang, X., et al., (2018). Research and Design of Electric Type Jujube Tree Ring Cutting Machine (电动式枣树环剥机的设计研究), *Science & Technology Vision*. pp.64–65, Xinjiang/China.

[13] Yang, X., Wang, F., Jaime, A.T.D.S., Zhong, J., et al., (2013), Branch girdling at fruit green mature stage affects fruit ascorbic acid contents and expression of genes involved in l-galactose pathway in citrus. New Zealand Journal of Crop and Horticultural Science, Vol.41, Issue 1, pp.23–31, Beijing / China.

[14] Ye, B., Xie, S., Zhang, J., et al., (2019). Effect of Ring Peeling on Jujube Growth and Fruit Quality (枣树环剥对枣树生长及果实品质的影响), *Agricultural technology and equipment*, pp.30–32, Gansu/China.

[15] Zhang X., Hou Z., Dai N., (2021), Design and experiment of a new rotary coating machine based on LabVIEW. *INMATEH Agricultural Engineering*, Vol 65, Issue 3, pp. 91-100, China. https://doi.org/10.35633/inmateh-65-10

[16] Zhu, M., Yu, J., Xu, Yang, G., (2022). Effect of Girdling on Anthocyanin Content and Quality of Spine Grape Berries. *Journal of Plant Growth Regulation*, Vol.41, Issue 1, pp.65–73, New York/American.

DESIGN AND EVALUATION OF A LOCALLY- DESIGNED PEANUT DIGGER

Rosalinda L. ABAD*; Frank Michael L. JACLA; Hipolito C. BUCCAT; Paul James C. GAÑOLA; Alliver P. SAPITULA

Don Mariano Marcos Memorial State University [DMMMSU], La Union, Philippines;
Tel: 09695875675; E-mail: rabad@dmmmsu.edu.ph/rlabad@up.edu.ph
DOI: https://doi.org/10.35633/inmateh-72-05

Keywords: *agricultural machinery, hand tractor, peanut digger, Philippines-designed*

ABSTRACT

Manual peanut digging in the Philippines is still a practice due to the unavailability of low-cost mechanical diggers adaptable to local field conditions. Hence, the peanut digger design and evaluation were developed. The design involves benchmarking local field practices, ANSYS analysis of the digger blade, and CAD drawing. It is designed to dig, lift, convey, and drop the peanut stalk in a windrow. Its main parts are the main frame, digger blade, belt stalk conveyor, power transmission system, and hitching system. The pulling force and power requirement for the peanut digger is 1,387.48 N and 2.0 hp, respectively. The performance measures are the belt stalk conveyor speed levels at 205 rpm, 410 rpm, and 615 rpm, replicated three (3) times with three (3) plots per replication. They revealed an actual field capacity, digging efficiency, and mechanical physical damage of 0.025 ha/h, 95.31%, and 0.56%, respectively. Investing in the machine is economically viable with a benefit-cost ratio (BCR) of 2.09, a break-even point (BEP) of 5.33 ha/yr, and a payback period of 1.60 years. This implies that digging operations wider than 5.33 ha/yr start profit generation for farmers.

INTRODUCTION

Globally, the peanut is the 13th most important food crop, 50% of the total production is used as raw material for the manufacture of peanut oil, 37% for confectionery, and 12% for seed purposes *(Food and Agriculture Organization of the United Nations [FAO], 2002)*. It is the Philippines' second most important food legume, with slightly increasing production from 29,194.81 MT to 29,300.78 MT from 2015 to 2019, planted in 27,500 to 28,102 ha. This production came from the highest-producing provinces of Pangasinan (20.6%) equivalent to 6.03 thousand MT, La Union (9.3%) of 2.72 thousand MT, Lanao del Norte (6.4%) of 1.87 thousand MT, Cagayan (5.8%) of 1.70 thousand MT, Ilocos Sur (5.5%) of 1.60 thousand MT, and 15.37 thousand MT (52.3%) in the rest of the provinces *(Department of Agriculture [DA], 2021)*.

Peanuts can be grown in all climatic conditions in the country. In Ilocos Region, it is grown throughout the year. During the dry season, it is planted from October to January, and March to June for the wet season. Planting is done manually using conventional tools for drilling seed at 10 to 15 cm planting depth. Harvesting is done by either manual uprooting or a carabao-drawn plow at 15 cm to 20 cm depth. Without a carabao, digging requires up to 25 man-days/ha and another 10 man-days/ha for manual stripping of pods *(Department of Agriculture-Bureau of Plant Industry [DA-BPI], n.d.)*. A total of 35 man-days/ha with a cost of Philippine Pesos PHP13,020.00, considering the upgraded wage rate of PhP372.00/day *(Department of Labor and Employment [DOLE], 2022)*.

Manual harvesting is laborious and costly and could incur a total loss of as high as 20.23% or 621.06 kg/ha of the total production *(Mishamandani et al., 2014)*. This loss results from manual digging, which dislodges pods from the root system and over-maturity during the digging operation *(Warner et al. 2015)*. To reduce losses and costs, advanced countries use self-propelled peanut diggers and harvesters or four-wheel tractor-pulled diggers and harvesters *(Yang et al., 2022).* Through inclusive research and development, China developed a peanut picking-up harvester driven by a four-wheel tractor with a chain nylon elastic tooth pick-up device, transmission device, take-off equipment, cleaning equipment, and elevator set fruit device parts with a high capacity of 886 kg/hr *(Wang et al., 2013).* 90% of peanut farmers in India use four-wheel tractor peanut harvesters with strippers. Other advanced countries such as South Africa, Israel, France, and the United States have established peanut harvester manufacturing factories meeting the widespread need for mechanization *(Negrete, 2019).*

[1] *Rosalinda Abad, M.S. Agri. Eng.; Frank Michael L. Jacla M.A. Tech. Edu.; Hipolito C. Buccat, B. S Agri. Eng.; Paul James C. Gañola, M.S. Agri. Eng; and Alliver P. Sapitula, M. Eng. in E.E*

Westler et al. (2017), Camara (2016), and Zerbato (2013), as cited by *Negrete (2019)* claimed that mechanizing peanut production from planting to harvesting is important for increased production and profitability. In the Philippines, where the mechanization level is low at 1.23 hp/ha, only rice and corn are intermediate to highly mechanized at 2.31 hp/ha *(Philippine Center for Postharvest Development and Mechanization [PhilMech], 2018).* Only the land preparation is mechanized for other crops, such as peanuts. *Briones (2021)* cited that the weak growth in the agriculture sector in the Philippines is due to slow growth in factors of production and productivity. Labor is declining, and arable lands are converted to industrial infrastructures with an average farm size of 1.29 ha. Considering small parcels of land and other constraints impeding agriculture growth, developing small machines suitable to the field conditions is timely and necessary. Adopting imported machines could be one intervention. However, it is expensive and impractical. The working size and capacity, the complexity of the design, and the availability of spare parts during repair and maintenance are some of the important considerations.

With all these undeniable status quo of peanut production, it is an avenue to contribute to addressing the specific need of reducing labor and cost of manual operation for digging. Thus, the design and performance evaluation of a locally designed peanut digger was conceptualized. Specifically, design the peanut digger adaptable to hand tractors and local farming conditions; fabricate the machine made of locally standard available materials; evaluate the performance in terms of Actual Field Capacity (AFC), digging efficiency, Mechanical Physical Damage (MPD); and calculate economics returns using the machine. According to *(Philippine Center for Postharvest Development and Mechanization [PhilMech], 2018),* 53% of farmers owned hand tractors and 90% used mechanical power for land preparation. Developing a peanut digger could maximize the availability of hand tractors; to be used not just for land preparation and transportation but for other field operations. Using a hand tractor as a prime mover could boost sustainable utilization, marketability, and adoption of locally developed machinery.

MATERIALS AND METHODS

Design of machine components

The machine for digging peanuts is driven by a hand tractor of 7 HP (Fig. 1). As the hand tractor moves forward, the digger blade is pulled through the soil underneath one (1) row of peanut, uprooting the root system while being transported into the belt stalk conveyor. The belt stalk conveyor is a locking mechanism of uprooted peanut stalk while conveying it to one side of the plot.

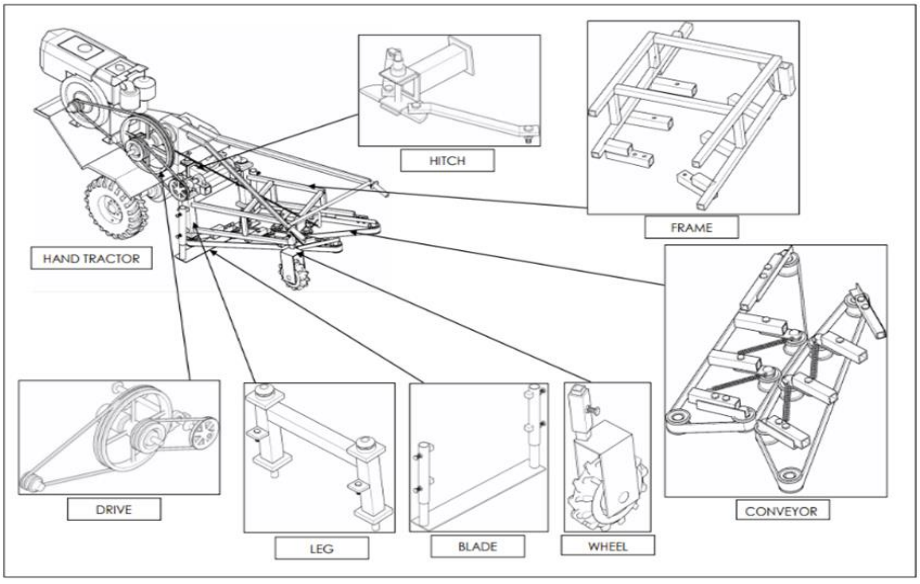

Fig. 1 – Major parts of the peanut digger

The mainframe is the foundation of peanut digger stability during operation. It is the mounting structure supporting the digger blade, belt stalk conveyor, and power transmission system. The digger blade is the penetrating medium uprooting the root system of peanuts from the field plots. It was designed with a working width of 377 mm to uproot one (1) row of peanuts and inclined at 12 º to the horizontal. The calculation of traction resistance with a free-body diagram (FBD) (Fig. 2) is based on the method used by *Liu et al. (2014).* Equation (1) was used in calculating digging blade traction resistance.

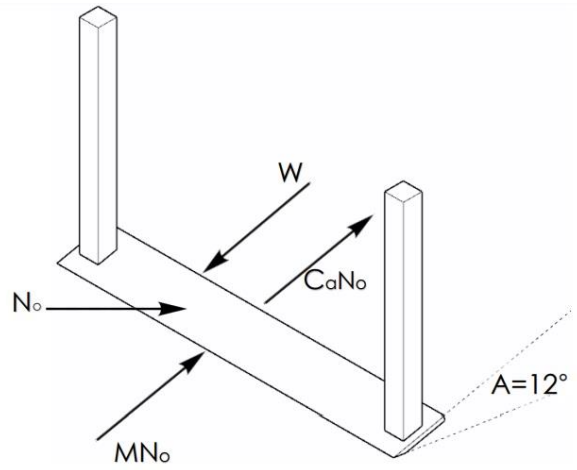

Fig. 2 – FBD of digging blade considering soil mechanics

The digger blade is the most forced member of the peanut digger during operation. It uses static structural analysis in ANSYS to obtain the required thickness of the digger blade. This is also to solve the total deformation, equivalent stress, and the equivalent elastic strain of the digger blade.

The belt-stalk conveyor is the holding mechanism of the uprooted peanut stalk from the digger blade, then it discharges the stalk to one side of the plot. It is composed of roller mechanisms meshing together to hold the peanut stalk simultaneously during the digging operation. The rotating speed of 410 rpm is synchronized to the forward speed of the hand tractor, ensuring stalk holding capacity, and avoiding the piling up of stalk in the digger blade.

The power transmission system provides a controlled application of power into the peanut digger. From the engine power, it uses a gearbox composed of sets of gears providing speed and torque conversions and rotating for the belt stalk conveyor assembly. The diameter of pulleys, length of belts, and number of teeth of spur gears were calculated and adapted to *PNS/PAES301:2000* and *PNS/PAES303:2000.*

Draft force is the energy used to overcome soil resistance and cut and invert the soil during tillage operation *(Almaliki, 2018).* The impact of draft force on the peanut digger depends on the type of soil, working width, harvesting depth, and running speed. The calculation of draft requirements of the peanut digger is assumed to be like the moldboard plow. Equations (1) and (2) adopted from the *American Society of Agricultural Engineers [ASAE] Standards (2000) and Coates (2002)* were used. The power requirement is the total power needed for the hand tractor and the peanut digger. This was calculated considering the power requirement for the digging blade and the belt stalk conveyor. Equations (3) to (5) were used to compute the total power requirement of the machine adopted from *Alhaseen et al. (2015).*

$$W = [N_o \times sin(\alpha)] + [\mu\, N_o \times cos(\alpha)] + [C_a\, N_o \times cos(\alpha)] \quad \text{[N]} \tag{1}$$

$$D = Fi \times [A + B(S) + C(S^2)] \times Wm \quad \text{[kN]} \tag{2}$$

$$HP_{draft} = \frac{D_a \times S}{C} \text{ [hp]} \tag{3}$$

$$P_{TDB} = \frac{D \times S}{C} \text{ [hp]} \tag{4}$$

$$T_{HP} = P_{DB} + P_{STD} \text{ [hp]} \tag{5}$$

where:

W - digging blade traction resistance, [N], A - digging blade tilt angle [°], μ - soil to metal friction factor [0.675], C_a - soil adhesion coefficient [30 $\mathrm{kN/cm^2}$], N_o - blade surface area [$\mathrm{cm^2}$], i - a dimensionless soil texture adjustment parameter, A,B & C - machine-specific parameters, S - forward speed of the hand tractor [$\mathrm{km/h}$], Wm - machine working width [m], D_a - adjusted draft value [kg], HP_{draft} - horsepower due to adjusted draft caused by speed [hp], S - forward speed of hand tractor [$\mathrm{km/h}$], C - conversion factor for hp, P_{TDB} - total drawbar power [hp], D– Total draft [kN], T_{HP} - total power requirement of the peanut digger [hp], P_{DB} - power requirement of digger blade [hp], P_{STD} - power requirement of belt stalk conveyor [hp]

Description of fabricated peanut digger

The prototype peanut digger was fabricated involving cutting, welding, boring, bending, and machining. The fabrication commenced with the main frame. It is made with 50 and 25-mm steel square tubes welded together. It is equipped with a wheel for easy mobility during operation and transport.

Said mainframe is the mounting structure of the digger blade, belt stalk conveyor, and power transmission system. It also has (2) two-depth adjustments to address the unevenness of field plots from 15 to 30 cm digging depth.

The power transmission consists of belts, pulleys, spur gears, and power shafts for transferring power from the engine to the moving assemblies of the peanut digger. The pulley combinations of 3, 16, 6, and 4 inches maintain the rotation of the belt stalk conveyor at 410 rpm. Said power shafts are attached to the mainframe using pillow blocks and flange bearings. The digger blade of 38 cm working width is made of an 8 mm leaf spring steel plate. It is bolted to the front portion of the main frame with adjustments from 10 to 20 cm digging depth. The land preparation is manually done. Thus, the digger blade is adjustable to address the unevenness of fields. The belt stalk conveyor comprises a series of rollers, springs, and two (2) endless belts. Said rollers have meshing mechanisms to hold the peanut stalks, convey, and drop them to one side of the plot. Said belt stalk conveyor is made with a rubberized timing belt for tight gripping during the operation. The hitch assembly was assembled based on the standard one-hole hitch specified in *PNS/PAES107:2000*; where the pin sleeve and hitch frame were adaptable to the hand tractor. Said hitch system support is made with a 6 mm thick plate to counteract draft or pull force during the digging operation. It is also full-weld and equipped with bolts and nuts to ensure tightening of support and stability eliminating the swiveling in the hitch system.

Research design

The peanut digger belt stalk conveyor speed levels were used as the performance measure. These are 205 rpm, 410 rpm, and 615 rpm. It was replicated three (3) times with three (3) plots per replication (0.3 x 10 m/plot), having a total experimental area of 81 m^2 excluding headlands. The evaluative parameters are the Actual Field Capacity (AFC), digging efficiency, and mechanical physical damage. Since it has only one (1) performance measure, one (1) operator, and the forward speed and engine speed (with load) are the same throughout the performance evaluation, the single factor- One-way ANOVA in Completely Randomized Design (CRD) was used. The data were analyzed using the Statistical Tool for Agricultural Research (STAR) (Version 2.0.1) developed by the International Rice Research Institute (IRRI).

The Actual Field Capacity (AFC) is the actual area of operation unit operation time. The total area covered was measured per plot before the start of the test. The turning time was measured from the plot's end to the next plot's start. The total operation time includes the unproductive time (i.e., adjustment and turning time) and the productive time (time during simultaneous operation without failure). The AFC was computed using equation (6) adopted from *PNS/PAES160:2011*.

The digging efficiency (DE) is the mass ratio of the lifted pods over the plot's unlifted/still buried pods and the mechanical physical damage. After digging using the machine in each plot, unlifted pods were manually dug, collected, and weighed. Also, the lifted pods were manually inspected for damage detection. The digging efficiency was determined using equation (7), adopted from *Ibrahim et al. (2008).*

The mechanical physical damage (MPD) is the total weight of cracked and broken pods collected after the digging operation per replication. Manual inspection of damages was implemented after the manual separation of peanut pods from the stalk and collection of exposed pods in the plots. The MPD was determined using equation (8) adopted from *Mishamandani et al. (2014).*

$$AFC = A/(Tp + Tn) \text{ [ha/h]} \quad (6)$$

$$DE = [Rt - (D+MPD)]/Rt \text{ [\%]} \quad (7)$$

$$MPD = C/Tp \text{ [\%]} \quad (8)$$

where:

AFC - actual field capacity [ha/h], A - area operated [ha], T_{p}- productive time [h], T_{n}- non-productive time [h], DE - digging efficiency [%], Rt - total weight of lifted peanut pods [kg], D - unlifted peanut pods [kg], MPD - mechanical physical damage of the machine [kg], C - weight of damaged pods collected from the sampling area [kg], T_P - total weight of peanut pods collected from the sampling area [kg]

Investment viability of peanut digger farmers' level

The three (3) parameters adopted in calculating the investment viability of the machine farmers' level are the break-even point, payback period, and benefit/cost ratio. The tractor cost or the cost of operation was calculated and included in the variable cost (VC).

Two (2) farmers implemented the manual digging of peanuts. This is to eliminate bias in data collection for manual digging capacity and machine operation.

The data for manual digging capacity in ha/h used in the calculation is the work actual duration of the two (2) farmers. The peanuts are not in plots and are manually planted. Thus, removing 1 hill side by side was implemented to give way for the wheels of the hand tractor.

The average time for manual digging was converted to PhP46.50/h, the allowable wage for agricultural works (plantation) *(Department of Labor and Employment [DOLE], 2022).* The fuel consumption of the machine is calculated using the current price of PhP71.80/li *(Department of Energy [DOE], 2022).*

The BEP analysis shows the point where there is enough revenue to pay all associated costs. It is the intersection point of total gross revenue and total cost. The BEP is a point where neither profit nor loss is made and known. Equations (9) to (17) were used to calculate BEP.

The PP points out the duration it will recover the investment or the duration in years where cash outflows and inflows are equal. It is also known as the simple payout method that concerns the recovery of investments rather than profitability. Equation (18) was used to calculate the payback period.

The BCR is the ratio of discounted benefits versus all associated costs. Project proponents use this standard procedure to make smart decisions on project investing. If the BCR > 1.0, the project is feasible. Therefore, investment is viable. However, if BCR < 1.0, the project is not feasible, the investment is not viable or recommendable.

Equations (19) to (21) were used to calculate BCR.

$$IC = COM + L \quad \text{[PhP]} \tag{9}$$

$$SV = 10\%\ IC \quad \text{[PhP]} \tag{10}$$

$$D = (IC - SV) / n \quad \text{[PhP/yr]} \tag{11}$$

$$FC = D + I + TIS \quad \text{[PhP/yr]} \tag{12}$$

$$VC = Cp + Cl + RM + Clu + Ct \quad \text{[PhP/yr]} \tag{13}$$

$$THC = FC + VC \quad \text{[PhP/ha]} \tag{14}$$

$$HC = (VC / C) * T \quad \text{[PhP/ha]} \tag{15}$$

$$BEP = (FC / Cr) - Bc \quad \text{[ha]} \tag{16}$$

$$ANI = C * T * (Cr - Tc) \quad \text{[PhP/yr]} \tag{17}$$

$$PP = IC / ANI \quad \text{[yr]} \tag{18}$$

$$PWB = AGI\ (P/A, I\%, N) \quad \text{[PhP]} \tag{19}$$

$$PWC = ATC\ (P/A, I\%, N) - SV\ (P/F, I\%, N) \quad \text{[PhP]} \tag{20}$$

$$BCR = PWB / (PWC + IC) \tag{21}$$

where:

IC- investment cost of the machine, [PhP]; COM- total cost of the materials, [PhP]; L-cost of labor of fabrication, [PhP]; SV- salvage value of investment cost, [PhP]; D- depreciation cost, [PhP/yr]; n -life span [yr]; FC- annual fixed cost [PhP/yr]; VC- variable cost [PhP/yr]; TIS – taxes, insurance, and shelter [PhP/yr]; I- interest on investment [PhP/yr]; C_p- cost of fuel [PhP/yr]; CI - cost of labor [PhP/yr]; Clu- cost of lubrication [PhP/yr]; Ct - cost of using the hand tractor [PhP/yr]; RM - repair and maintenance cost [PhP/yr]; THC - total peanut digging cost [PhP/ha]; C - digging capacity of the machine [ha/h]; HC-peanut digging cost [PhP/ha]; T annual operating time [ha/yr]; Cr - custom rate [PhP/ha]; BEP - total number of hectares the peanut digger will work to recover the IC [ha]; ANI - annual net income [PhP/yr]; TC- annual cost [PhP/yr]; PWB - present worth benefits [PhP]; AGI - annual gross income [PhP/yr]; I% - interest rate in investment cost [12%/yr]; PWC - present worth costs [PhP]; ATC- annual total costs [PhP]

RESULTS

Design ANSYS analysis on the digger blade

The depth, width, dip angle, and soil volume affect the digging soil resistance on the digger blade. The depth and width of the digger blade have a considerable effect because it defines the area of soil resistance. The maximum stress (Fig. 3a) of 17.4 MPa is much smaller than the allowable stress of mild steel of 155 to 165 MPa.

The maximum deformation (Fig. 3b) is 0.53644 mm. The red indicates that maximum deformation occurs at the middle part of the blade. Conversely, the maximum strain (Fig. 3c) was 9.36 e-5. It conveys that the deformation ratio to the blade's original dimension is 0.0000936, which is within the limit of proportionality.

It means no permanent deformation will occur, and the digger blade will return to its original shape after the operation. Thus, the 8 mm leaf spring hard steel can withstand the 77.44 N working traction resistance without breaking.

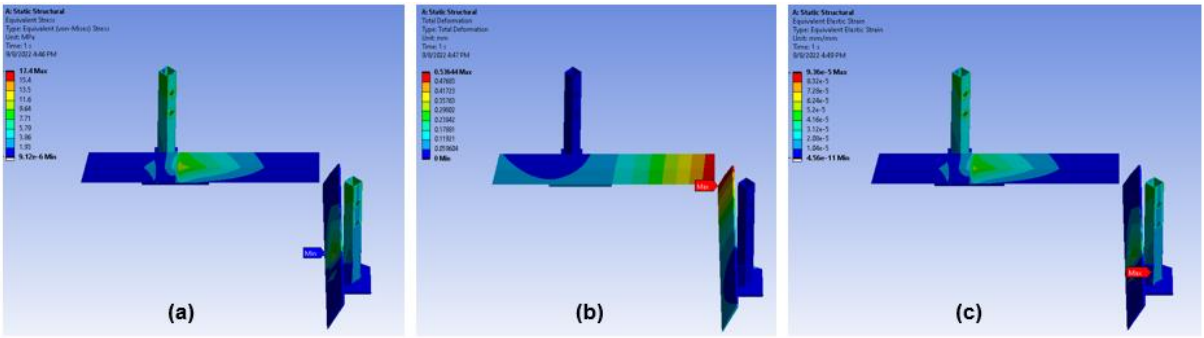

Fig. 3 – Digger Blade ANSYS

(a) stress map of the digger blade, (d) deformation map of the digger blade, and (c) strain map of the digger blade

Fabricated peanut digger prototype

The peanut digger (Fig. 4) is developed for digging, lifting, conveying, and dropping peanut stalks to one side of the plot simultaneously in one operation. It is an implement adaptable to a Philippine-designed hand tractor or "kuliglig" that lifts a 30 cm wide plot planted with 1 to 2 hills of peanut. It weighs 55 kg for ease of transportation, hitching, and operation. It has an overall dimension of 1,070 x 620 x 550 mm (l x w x h), giving ample space for the operator's movement at the back of the hand tractor. The peanut digger is mounted at the rear portion of the hand tractor through a single-point hitch. The lever operation of the peanut digger is synchronous to the forward speed of the hand tractor. As the hand tractor moves forward, it engages the operation of the peanut digger. It is equipped with a single wheel to maintain the digger blade depth and support the weight for mobility and ease of operation. The pulling force or draft for the hand tractor to propel the peanut digger is 1,625.85 N at a forward speed of 1.93 km/h. The power requirement is 2.0 HP, which is lower than the available power of the hand tractor engine of 7 HP.

Fig. 4 – The locally-designed peanut digger hitched to the hand tractor or "kuliglig"

Actual field capacity (AFC)

The Analysis of Variance (ANOVA) at a 5% significance level, revealed a significant difference among the three (3) speed levels. It indicates that the speed of the belt stalk conveyor affects the AFC shown in Table 1. It is known that the Philippine hand tractor has only one forward speed and no reverse (PNS/PAES 111:2000). Said forward speed is designed for the pacing of the human as its machine operator. The digging depth is set at one (1) depth adjustment. Thus, the digging blade load bearing during operation is the same. However, increasing the belt stalk conveyor speed increases the AFC. Studies revealed that the belt stalk conveyor speed should be slightly faster than the forward speed of the hand tractor to avoid piling up of vines ahead of picking up *(Bader 2012, cited by Kirk et al., 2017*). The conveyor speed should also be synchronized with the forward speed to avoid dragging and snatching peanut stalks *(Roberson, 2016, cited by Kirk et al., 2017).*

The results revealed that when the belt stalk conveyor rotates too slowly at 205 rpm, it causes the stalk to pile up at the bottom of the conveyor, causing excessive agitation of the stalk, thereby stopping the rotation of the conveyor. As it stops, it increases the operation time, reducing the AFC. As it needs manual removal of piled stalks before continuing the digging operation. During the field test, from the length of the 10 m field plot, it stopped 4 to 5 times as the peanut stalk piled up at the bottom of the conveyor, prolonging the operation time when manually removed. Comparing it to higher rotation speeds at 410 and 615 rpm, the AFC is higher as the speed of the conveyor is synchronized to the forward speed of the hand tractor at 1.93 km/h. The AFC at 0.025 ha/h is five times higher than that of manual digging at 0.0049 ha/h, gathered during the field test. This agrees with the *Department of Agriculture-Bureau of Plant Industry [DA-BPI], (n.d.)* that manual digging requires 20 to 25 man-days/ ha. Converting said the manual capacity of 0.0049 ha/h is almost 26 man-days/ha.

Table 1

ANOVA of actual field capacity [AFC], digging efficiency [DE], and mechanical physical damage [MPD]

Performance Measure	AFC	DE	MPD
[rpm]	[ha/h]	[%]	[%]
205	0.008[b]	83.07[b]	1.06
410	0.025[a]	95.31[a]	0.56
615	0.023[a]	94.52[a]	0.24

**Means with same letter superscript is significant at a 5% level of significance*

Digging efficiency

The DE of the peanut digger shown in Table 1 revealed a significant difference at a 5% significance level. The lower the speed of the belt stalk conveyor at 205 rpm, the lower the digging efficiency. During operation, at 205 rpm, peanut stalks piled up into the bottom of the conveyor, dragging and causing the stripping of pods into the ground. Stripped/dislodged pods are dropped into the ground, thus, increasing the pod losses. According to *Warner et al. (2015),* losses came from dislodged pods due to manual uprooting and over-maturity of peanuts. The variety planted as a test crop is UPL Pn-10, and the maturity is 98 to 100 days upon planting. During the field test, the maturity exceeds 114 days. Thus, it is noticed that some pod losses manually picked in the ground, dislodged from the root system during the operation are easily cracked, and pegs are decayed.

Mechanical physical damage

The MPD of the peanut digger shown in Table 1 revealed no significant difference at a 5% significance level. It means that during operation, different speed levels could be used. However, considering the higher AFC of 410 rpm at 0.025 ha/h and the Mechanical physical damage is 0.56 %, it is favorable to use this speed level. These MPDs incurred are caused by the cutting in the digger blade or the dragging and agitation into the belt stalk conveyor. The piling up of stalk in the belt stalk conveyor caused pods to crack, especially those pods near the stalk. This MPD is lower than manual digging at 20.23% *(Mishamandani, et al., 2014).*

Investment viability of the peanut digger (farmer's level)

The investment analysis determines whether the machine is viable for digging peanuts. The assumptions used (Table 2) consider the investment cost of the machine of PhP47,866.00, covering the total cost of materials and fabrication labor. The Annual Fixed Cost (AFC) was PhP13,334.10/yr. It is the incurred cost due to depreciation of the machine with a 5-year lifespan, interest on investment of 12%, housing, taxes, and insurance. The Variable Cost (VC) was PhP118.49/hr. It is the total incurred cost for fuel at PhP71.80/li; lubricant cost, repair, and maintenance; labor cost at PhP46.50/h; and tractor cost. The tractor cost of PhP43.20/h was included as a variable cost since the hand tractor propelled the peanut digger. The calculation yielded Fig. 5 and Table 2. Figure 5 illustrates the BEP curve (ha/yr); Table 3 shows the summarized investment parameters of the peanut digger.

Table 2

Assumptions in the investment cost analysis of peanut digger

Particulars	Hand tractor	Peanut Digger
Purchase Price [PhP]	60,000.00	47,866.00
Salvage value [%]	10.00	10.00
Years [n]	10.00	7.00

Particulars	Hand tractor	Peanut Digger
Fuel consumption [l/h]		0.78
Fuel price per liter, PhP/l		71.80
Repair and maintenance [% PhP/100 h]	1.20	1.00
Rate of interest [%]	20.00	20.00
TIS [%]	4.00	4.00
Labor cost [PhP/day]		372.00
Annual hours [h/yr]	400.00	
Capacity [ha/h]		0.025
A. Fixed Cost Items		
Depreciation	5,400.00	6,154.20
Interest on investment	6,600.00	5,265.26
TIS	2,400.00	1,914.64
Total Annual FC [PhP/yr]	14,400.00	13,334.10
B. Variable Costs		
Fuel cost		56.00
Lubricant cost		11.20
Repair and maintenance	7.20	4.79
Labor		46.50
Tractor cost	43.20	
Total VC [PhP/h]	118.49	

Table 3

Summary of investment viability (farmer's level) of the peanut digger

Particulars	Value
Total annual fixed cost [PhP/yr]	13,334.10
Total variable cost [PhP/yr]	118.49
Digging cost [PhP/ha]	5,010.28
Net income generated [PhP/yr]	29,741.24
Break-even point [ha/yr]	5.33
Payback period [yr]	1.6
BCR	2.04

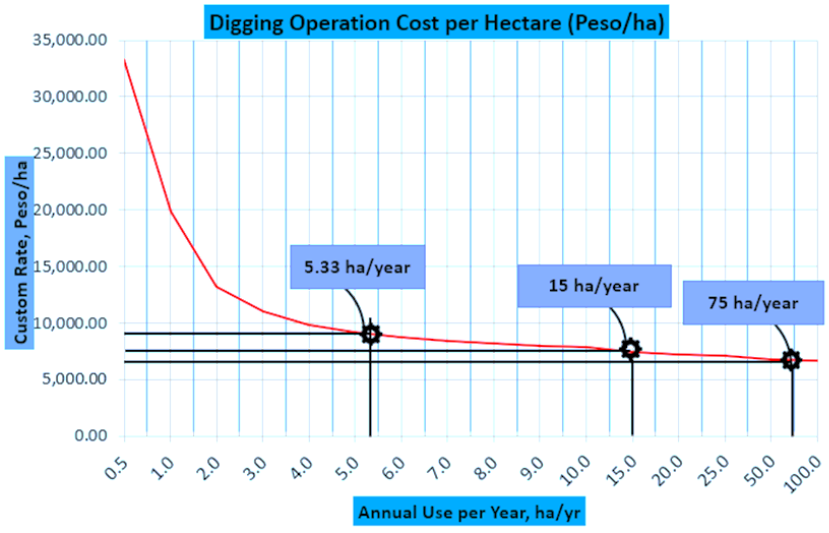

Fig. 5 – BEP point curve (ha/yr) of utilization

The cultivation of peanuts is twice a year. With this, the peanut digger was assumed to be operating at 25 days per cropping season or 400 hours/yr. Calculating using the digging capacity of 0.025ha/hr, the computed annual capacity is 10 ha/yr.

The rent of the machine or custom rate is assumed to be equal to the manual digging cost of PhP9,047.19/ha. This was calculated from the manual digging capacity of 0.0049 ha/h (gathered data during the field test).

The BEP yielded at 5. 33 ha/yr. This signifies that the peanut digger needs to finish or operate at the required BEP to recover the gross revenue. As the peanut digger increases its working capacity beyond the BEP, it will generate profit. The BEP is low and favorable as the harvesting season is one (1) month or more, thus, the 5.33 ha/yr could be finished in 15 to 20 days for continuous operation. From Fig. 5, the peanut digger increases its working capacity from BEP of 5. 33ha/yr to 15 ha/yr or higher at 75 ha/yr, the custom rate of the machine gets lower. The rent of PhP9,047.19/ha could be reduced, or as the machine is maximized, it adds profit to farmers by reducing the renting cost or custom rate. Investing in the machine is viable with a BCR of 2.09. However, if the farmer does not own the required BEP, it is best to rent the peanut digger. But, if land consolidation or grouping of fields is practiced to meet the BEP, investing is viable and recommendable.

Cost comparison of manual and mechanical digging of peanut

Due to the increasing cost of manual labor of PhP9,047.19/ha and 26 man-days/ha, utilizing the peanut digger reduces the associated cost and duration of the operation. From the results, the cost of the machine is PhP5,010.28 and requires a labor of 13 man-days/ha. The cost reduction of PhP4,036.91 implies a significant increase in farmers' profit. The reduction of 13 man-days/ha implies less labor requirement that could answer the labor shortage in the coming years. During the peak season of peanut harvesting, when labor is scarce, the adoption of the machine is timely and effective.

CONCLUSIONS

This research achieved its objectives. The peanut digger adapted to a hand tractor is effective in the digging of peanuts. It is suitable for local field conditions, light in weight, and easy to operate. It is simple in design that a local manufacturer could fabricate using standard available materials. Its main parts are bolted for easy assembly and disassembly during repair and maintenance. Using the machine decreases the manual labor requirement by 50% and the digging cost by 55.40%. Realizing this significant outcome of developing the machine, adopting the peanut digger could increase the production and profitability of peanut farmers in the country. Further, based on the results, it needs further research to increase machine performance, perform standard tests, and farmers' acceptability as the entry for technology commercialization.

ACKNOWLEDGEMENT

The researchers acknowledge the Department of Science and Technology - Metals Industry Research and Development Center (DOST-MIRDC), the funding agency, for giving importance to the advancement of peanut field operations through mechanization in the country; to Don Mariano Marcos Memorial State University, the implementing agency, for supporting all project activities; and the peanut farmers of Birunget Peanut Farmers' Cooperative for their admirable cooperation, especially to Mr. Donato F. Fuselero, the cooperative president, for committing his field as a research area for the actual field test of the peanut digger.

REFERENCES

[1] Alhaseen, I. A., Sharif, A.S., Ali, Z.A. and Alamein, A.A., (2015). *Design of a one-row potato digger harvester*. http://api.uofk.edu:8080/api/core/bitstreams/6d366667-c68d-4ed89cec6dc28234ce33/ content

[2] Almaliki, S., (2018). Simulation of draft force for three types of plows using response surface method under various field conditions. *The Iraqi Journal of Agricultural Sciences,* 49(6):1123-1124.

[3] American Society of Agricultural Engineers (2000). *Agricultural machinery management*. ASAE EP496.2 DEC99:

[4] Briones, R., (2021). Philippine agriculture: Current state, challenges, and ways forward. https://pidswebs.pids.gov.ph/CDN/PUBLICATIONS/pidspn2112.pdf?fbclid=IwAR3RvKz1Ya2J13utihtCI2SqYcj46HrKQbtt2sx1Tyb7IG65elnjz2Gd2ks

[5] Coates, W., (2002). Agricultural Machinery Management. The University of Arizona Cooperative Extension. https://cals.arizona.edu/crop/equipment/agmachinerymgt. html

[6] Department of Agriculture-Bureau of Plant Industry [DA-BPI]., (n.d). Organic peanut seed production. https://library.buplant.da.gov.ph/images/1640937055Organic%20Peanut%20Seed%20Production.pdf
[7] Department of Agriculture [DA]. (2021). Investment guide for peanut. https://www.da.gov.ph/wp-content/uploads/2021/04/Investment-Guide-for-Peanut.pdf
[8] Department of Energy [DOE]., (2022). Prevailing Retail Prices of Liquid Petroleum Products (LPP) in the Key Cities/Municipalities in Northern Luzon as per Price Movement on January 21, 2022. https://www.doe.gov.ph/sites/default/files/pdf/price_watch/petro_nluz_2022-jan-21.pdf
[9] Department of Labor and Employment [DOLE]., (2022). Current Daily Minimum Wage Rates Region I (Ilocos). https://nwpc.dole.gov.ph/regionandwages/region-i-ilocos/
[10] Food and Agriculture Organization of the United Nations [FAO-UN]., (2002). Groundnut post-harvest operations. https://www.fao.org/fileadmin/user_upload/inpho/docs/Post_Harvest_Compendium_-Groundnut.pdf
[11] Ibrahim, M.M., Amin, E. and Farag, A., (2008). Developing a multi-purpose digger for harvesting root crops. *Misr Journal of Agricultural Engineering.,* 25(4):1225-1239.
[12] Kirk, K., Warner, A., Thomas, J., Fogle, B., Anco, D., and Massey, H., (2017). Impact of Ground Speed and Conveyor Speed on Peanut Digging. https://doi.org/10.13031/aim.201701600
[13] Liu, S., Weng, S., Liao, Y., and Zhu, D., (2014). Structural bionic design for digging shovel of cassava harvester considering soil mechanics. *Applied Bionics and Biomechanics.* Vol. 11. pp1-11.
[14] Mishamandani, A., Abdollahpoor, A., Moghaddam, M., and Navid, H., (2014). Comparing of Peanut Harvesting Loss in Mechanical and Manual Methods. *International Journal of Advanced Biological and Biomedical Research*, 2(5):1475-1483
[15] Negrete, J., (2019). The Role of Agricultural Mechanization in Food Security. Journal of Agricultural Research Advances. https ://www.researchgate.net./publication/33647191
[16] Philippine National Standards/Philippine Agricultural Engineering Standard (2000). *Engineering Materials - V-belts and Pulleys for Agricultural Machines- Specifications and Applications* (PNS/PAES 301:2000)
[17] Philippine National Standards/Philippine Agricultural Engineering Standard (2000). *Engineering Materials –Roller Chains and Sprockets for Agricultural Machines- Specifications and Applications* (PNS/PAES 303:2000)
[18] Philippine National Standards/Philippine Agricultural Engineering Standard (2000). *Agricultural Machinery – Hitch for Walking-type Agricultural Tractor – Specifications* (PNS/PAES 107: 2000)
[19] Philippine National Standards/Philippine Agricultural Engineering Standard (2011). *Agricultural Machinery – Sugarcane Planter – Methods of Test* (PNS/PAES 160:2011)
[20] Philippine Center for Postharvest Development and Mechanization (PHilMech)., (2018). On-Farm Mechanization Of Paddy in The Philippines. *Asian Journal of Postharvest and Mechanization* Vol. 1, No. 1.
[21] Warner, A., Kirk, K., Thomas, J., White, W., Peele, J., Massey, H., and Fogle, B., (2015). *Peanut Digging Losses Across Soil Moisture Contents*. https://www.clemson.edu/cafls/research/edisto/faculty/kirk/PapersAndPresentations/PeanutDigger/ASABE%20152190009.pdf
[22] Wang, D., Shugi, S., and Kun, H., (2013). Design and test of 4HJL-2 harvester for peanut picking-up and fruit-picking. *Transactions of the Chinese Society of Agricultural Engineering, Vol. 29, Number 11* pp. 27-36(10).
[23] Yang, H., Cao, M., Wang, B., Hu, Z., Xu, H., Wang, S., and Yu, Z., (2022). Design and Test of a Tangential-Axial Flow Picking Device for Peanut Combine Harvesting. *Agriculture*, Vol 12(2) pp.179.

SUNFLOWER PLANTING MACHINERY ELECTRIFICATION TRANSFORMATION AND CONTROL SYSTEM DESIGN

/

葵花种植机械电动化改造及控制系统设计

Guoxing CAI[1)], Haijun LI[*1)], Dabo LU[2)], Renjie WANG[1)], Kaiyuan WANG[1)], Subo QIN[1)], Zhiqiang WU[1)]

[1)] College of Electrical and Mechanical Engineering, Inner Mongolia Agricultural University, Hohhot / China;

[2)] Inner Mongolia Dabo Jintian Machinery Company Limited, Bayannur / China

Tel: +86 13848129323; E-mail: lhj70927@sina.com

Corresponding author: Haijun Li

DOI: https://doi.org/10.35633/inmateh-72-06

Keywords: *sunflower mulching planter, kinematic modeling, control system, Linux system*

ABSTRACT

This research aimed to address the issue of physical damage caused by long-term work in high-saline fields by electrifying sunflower growing machinery and designing control systems. Firstly, the method of establishing the equation of motion is used to obtain the parameters to carry out motorization modification, and then the control system is built using STM32 as the main controller, which has the functions of control, data acquisition, and alarm. The feasibility and stability of the study are verified by using a model vehicle to conduct tests of straight-line driving and steering in a simulated high-saline field.

摘要

本研究的重点是通过对葵花种植机械进行电气化改造和设计控制系统解决工作人员长时间在高盐碱地工作对身体有损伤的问题。首先采用建立运动方程的方法获取参数从而进行电动化改造，然后使用 STM32 作为主控制器搭建控制系统，该系统具有控制、数据采集和报警的功能。使用模型车在模拟的高盐碱地进行直线行驶和转向的试验验证该研究的可行性和稳定性。

INTRODUCTION

Seeders are widely used in agriculture, especially in harsh environments to reduce the labor intensity of manual seeding to a large extent. With the development of the agricultural economy, automatic control technology, and intelligent technology in agricultural production in a wide range of applications, the economy and precision of the seeding machine have reached a higher level *(Yang et al., 2022; Bi Yajuan, 2021; Liang et al., 2024; Chen et al., 2024)*. Sunflowers can grow in slightly acidic and alkaline environments with a pH of 6.0 to 7.5, making them well-suited to growing in saline soils. However, they still need to be watered heavily in the spring before planting to reduce salinity *(Fatima et al., 2021)*. There are many problems such as traveling difficulty, insufficient steering ability, poor steering accuracy, serious skidding, and so on, which cause a high degree of dependence on manual labor when the planter works in the saline land after the watering to reduce the salinity.

In agricultural machinery, Internal Combustion Engine (ICE) is usually fueled with diesel, although some bio-fuel blends have been proposed in the literature to reduce emissions *(Lovarelli et al., 2019)*. Some scholars proposed that the electric drive intelligent high-speed precision sowing machine still needs a tractor for traction *(Liang et al., 2023)*. Some scholars have investigated fully electric small-family agricultural tractors using a single permanent magnet motor and lead-acid batteries, which can permit changes in track width and ground clearance *(Das et al., 2019; Gurusamy et al., 2015; Brenna et al., 2018)*. This paper takes the 2BQKS-2 diesel self-propelled air-absorbing sunflower mulching seeder produced by Inner Mongolia Dabo Jintian Machinery Co. Ltd. as a prototype for electrification transformation, and the transformed seeder is easier to realize the control of speed and direction. Moreover, the motorized transformation of the seeder lays the foundation for the subsequent intelligent transformation, and the remote control of the seeder by the staff can avoid skin irritation, and respiratory and neurological injuries caused by working on the saline soil for a long time.

Guoxing Cai, M.S. Stud. Eng.; Haijun Li, Prof, M.S. ENG.; Renjie Wang, M.S. Stud. Eng; Kaiyuan Wang, M.S. Stud. Eng; Subo Qin, M.S. Stud. Eng; Zhiqiang Wu, MS. Stud. Eng.; Dabo Lu, P&D*

The control system uses the Proportion-Integration-Differentiation (PID) algorithm, but the steering controller under the PID method has problems of large overshoot and low accuracy *(Xiong et al., 2020; Li et al., 2019; Shen et al., 2019)*. Therefore, the kinematic analysis of slip steering under the world coordinate system is carried out first, and the control parameters of the PID algorithm are optimized according to the equations of motion, to solve the two problems mentioned above, and also to better solve the problems of misalignment of crop rows and inconsistency of row spacing, which facilitates the subsequent mechanization of fertilizer application, drug spreading, harvesting and other mechanized operations.

MATERIALS AND METHODS

Slip steering kinematic analysis

The steering mode of the seeder studied in this paper is selected to increase the steering mode, that is, the speed of the outer wheels is accelerated, and this steering mode can keep the speed of the geometric center of the vehicle unchanged, to be closer to the true steering motion of the vehicle *(Ding Dong, 2021)*. The 2BQKS-2 self-propelled air-absorbent sunflower mulching planter is center-symmetric, as shown in Fig. 1. The body size of the seeder is 2.6X1.3 m, wheelbase is 1.1 m, axle distance is 2 m, the weight of the whole machine is about 460 kg, and the speed is 4-7 km/h. The analysis after that does not take into account the effect of different terrain on the friction of the wheels and the steering radius, and the friction coefficient of the tires and the ground is stable and unchanged, the rotation speeds of the wheels at the same side are the same and the center of gravity of the vehicle does not change with the steering. The traveling path of the planter is shown in Fig. 2.

Fig. 1 - 2BQK-2 type sunflower seeder

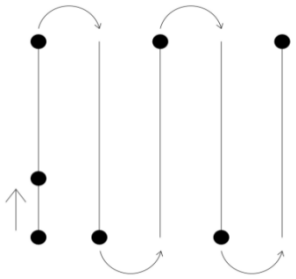

Fig. 2 - Traveling path of the planter

Straight-line travel is achieved when the speed and direction of the vehicle's inner and outer tires are aligned. The speed of the collection center when the vehicle travels in a straight line is also equal to the linear speed of the wheels, and the equation of linear motion is shown in Equation (1):

$$\begin{bmatrix} V_1 \\ V_2 \\ V_3 \\ V_4 \end{bmatrix} = \begin{bmatrix} R_1 \\ R_2 \\ R_3 \\ R_4 \end{bmatrix} \quad (1)$$

where: V_i is the linear velocity of the wheel, [m/s]; R_i is the corresponding angular velocity of the wheel, [rad/s]; 1 is the left front wheel; 2 is the right front wheel; 3 is the left rear wheel; 4 is the right rear wheel.

The slip steering process of a four-wheeled vehicle can be viewed as a combination of lateral and vertical motions, as shown in Fig. 3.

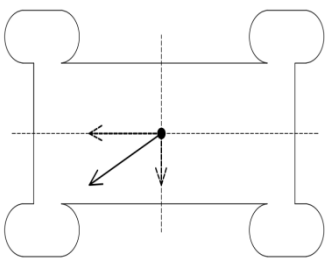

Fig. 3 - Slip steering synthesis

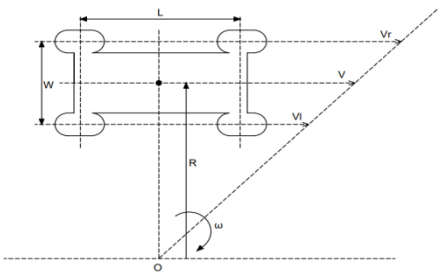

Fig. 4 - Schematic of steering with a large radius

Take left steering as an example, when the inner and outer wheels of the planter rotate at different speeds in the same direction when the movement relationship is shown in Fig. 4.

Taking clockwise steering as the positive direction and O as the center of rotation, then theoretically the speed of the geometric center of the planter, the angular speed of rotation, and the radius of steering are calculated as follows:

$$V = \frac{V_r + V_l}{2} \tag{2}$$

$$\omega = \frac{V}{R} = \frac{V_l}{R - \frac{\omega}{2}} = \frac{V_r}{R + \frac{\omega}{2}} \tag{3}$$

$$R = \frac{W}{2} \cdot \frac{V_r + V_l}{V_r - V_l} > \frac{W}{2} \tag{4}$$

where:

V is the speed of the geometric center, [m/s]; ω is rotational angular velocity, [rad/s]; R is turning radius, [m]; W is the wheelbase, [m]; L is the axle distance, [m]; V_l is the speed of the left wheel, [m/s]; V_r is the speed of the right wheel, [m/s].

When the inner and outer wheels of the planter rotate at different speeds in different directions and also in different simultaneous motion relationships as shown in Figure 5, the theoretical speed of the geometric center of the vehicle and the angular velocity of rotation are shown in Equations 2 and 3 with the direction of the right-hand wheel as the positive direction. The theoretical steering radius of the whole vehicle is:

$$R = \frac{W}{2} \bullet \frac{V_r + V_l}{V_r - V_l} < \frac{W}{2} \tag{5}$$

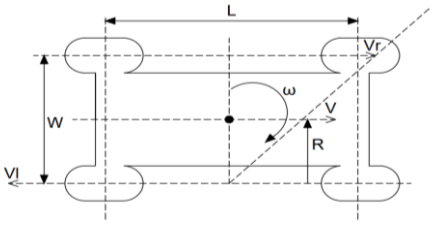

Fig. 5 - Schematic of steering with a small radius

When the inner and outer wheels of the planter rotate at the same speed in different directions, the body speed V=0 from Equation 2, that is, in-situ steering, in the ideal case the steering radius R=0, and the formula for angular velocity is as follows:

$$\omega = \frac{V_r}{\frac{W}{2}} = -\frac{V_l}{\frac{W}{2}} \tag{6}$$

Slip Steering Dynamics Analysis

The actual working environment is more complex, and the analysis of the drive of the planter in different situations allows for better motorization and is also the basis of the control system. The following analysis is carried out under ideal conditions.

When the vehicle is traveling in a straight line, it must be ensured that the total driving force of the driving wheels is greater than the friction force between the wheels and the ground. From the perspective of dynamics analysis, when steering the two sides of the wheels will produce a driving force difference, the formation of steering driving moment, the direction of the moment points to the inside of the wheel. At the same time, a steering resistance moment is generated between the tire and the ground, whose direction is opposite to the driving moment. To realize steering, the driving moment must be greater than the resistance moment.

The rolling resistance coefficient is assumed to be constant when steering, the same as when traveling in a straight line. Rolling resistance is always opposite to the direction of wheel rotation, and the kinematic characteristics of the vehicle are different depending on the steering radius. When steering, the moment generated by rolling resistance may be the driving moment or resistance moment. When steering with a large radius, the direction of rotation of the tires on both sides and the direction of the moment generated by rolling resistance are the same; while when steering with a small radius, the direction of rotation of the tires on both sides is different and the direction of the moment generated by rolling resistance is opposite.

When a planter is steered, the tires create a sliding motion in the soil and therefore are also affected by sliding resistance. So, the seeder is affected by rolling resistance and sliding resistance when steering in a large radius, and the total drive force of the vehicle has to overcome the effects of all the resistance, and also the effects of gravity when the vehicle is traveling on a ramp. Assuming that the total driving force is equally distributed among the four tires, the required driving force for each tire is calculated as follows:

$$F > \frac{G \cdot f \cdot cos\alpha + G \cdot \mu \cdot cos\alpha + G \cdot sin\alpha}{4} \tag{7}$$

where:

F is the required driving force per tire, [N]; G is the weight of the whole vehicle, [mg]; f is the rolling resistance coefficient, which generally takes a value between 0.1 and 0.25; μ is the longitudinal maximum attachment coefficient for complete slip; α is the inclination angle of the ramp, [°].

Electrification conversion

Currently, the mainstream motor directions are permanent magnet synchronous motor and AC asynchronous motor. The seeder often repeatedly starts and stops, frequently accelerates and decelerates and the maximum running speed is small, so the permanent magnet synchronous motor is selected. The drive mode of the motor is shown in Fig. 6.

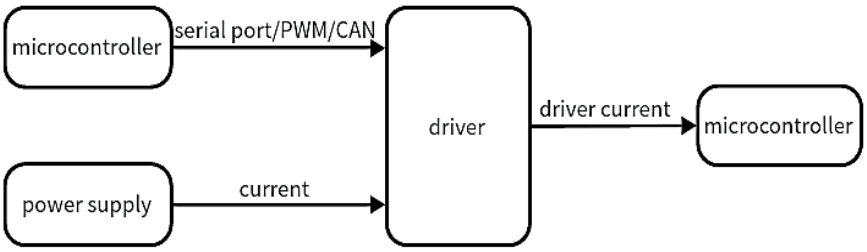

Fig. 6 - Motor drive type

Assuming that the traveling motor has no reducer, the rated speed of the drive motor is calculated as shown in Equation 8. The power required by the seeder when climbing a slope is greater than the power required for traveling in a straight line on level ground, so the rated power of the motor is based on the power required for climbing a slope as a reference, and the rated power is calculated based on Equation 7, as shown in Equation 9.

$$n = \frac{V_{max}}{2\pi r \times 0.8} \tag{8}$$

$$P = \frac{1}{0.96n}\left(\frac{f \cdot mg \cdot cos\,\alpha}{3600}V_{max} + \frac{mg \cdot sin\,\alpha}{3600}V_{max}\right) \tag{9}$$

where:

n is the number of motors; V_{max} is the maximum travel speed, [m/s]; r is the tire radius in Equation 8; P is the rated power of the motor, [W].

The minimum torque requirement for planter operation in a full-service environment is 80% of the rated torque requirement, and the minimum torque requirement necessary for operation on a ramp is the maximum, with the rated torque (T) calculated as follows:

$$T = mgr(f\cos\alpha + \sin\alpha)/(0.8n\eta) \quad (10)$$

The battery energy source of the planter is based on the original fuel tank capacity to select the ternary lithium battery with a weight of 160 kg and an energy density of about 200 Wh/kg, and the calculation of the battery's operating hours (H) under full charge is as follows:

$$H = 160 \times 200/(4P) \quad (11)$$

Overall design

The control system of the seeder is mainly designed, and the control system is divided into two parts: the motion control system and the main control system.

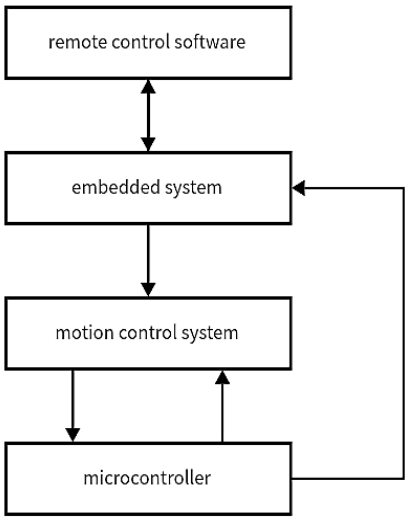

Fig. 7 - Structural sketch of the control system of the planter

Motion Control System

The motion control system is the core of the whole system, with a microcontroller as the main controller, choose the STM32F103 chip. The block diagram of the control system is shown in Figure 8. The microcontroller controls the motor rotation through the motor driver, and the communication method with the motor driver is selected as Pulse-width-modulation (PWM) control, and the PWM control method can reduce the system cost and power consumption *(Guo Yanhong, 2010)*. The resolution of the PWM control method is adjusted to 10 KHz in the simulation software. Speed monitoring of the actual speed of the motor is carried out through the Hall encoder, which uses a quadruple-frequency measurement method, which is not only highly resistant to interference but also capable of realizing accurate position control. The conversion relationship between the encoder value and the speed of the planter is calculated using the following method:

$$V = CONT \cdot \frac{1}{f} \cdot S \cdot \delta \quad (12)$$

where:

$CONT$ denotes the encoder count, f is the sampling rate, S is the tire circumference, and δ is the encoder accuracy.

From Equation 2 and Equation 3, it can be seen that the speed of the motor can be expressed by the linear speed and steering target angular speed. Therefore, the linear velocity and the steering target angular velocity are used as the control signals of the master control system and finally converted to the target signal of the motor. To compensate for the discontinuity of the sensor in time series data acquisition, the STM32 microcontroller discretizes the data by using the first order difference and iterative integral at the time of the timer interrupt, and the frequency at which the timer interrupt occurs in this study is set to 200 Hz. According to the discretized data, PID control can achieve the control of the motor. The motion control flowchart is shown in Figure 9.

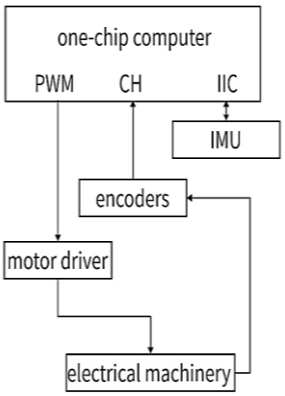

Fig. 8 - Motion control system diagram

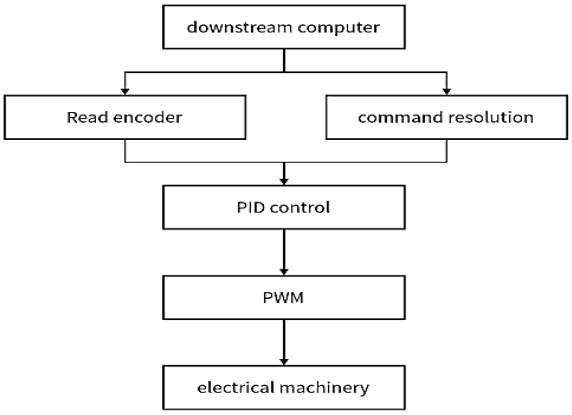

Fig. 9 - Motion control flowchart

The actual working conditions when the seeder is working are complex, to get the real condition of the vehicle, it is also necessary to use the MPU6050 module in the Inertial Measurement Module (IMU), which realizes the function of communicating with the microcontroller and connecting to other sensors through two IIC interfaces.

Master Control System

The main control system is developed using a high-performance embedded processor and an open-source operating system. The embedded system consists of a hardware layer, a driver layer, and a software layer. The hardware layer includes various hardware devices such as serial port, processor, camera, WIFI, etc.; the driver layer is responsible for providing the driver of the corresponding device in the hardware layer so that the upper layer of user software can call the hardware functions; the top layer is the user software layer, which is the place to realize the user's logical functions. In this layer, users can write code to realize various functions and logical operations.

The microcontroller communicates with the main control system through the serial port, mainly realizing the reception of control commands sent by the main control system and the sending of information collected by the sensors. This research considers the richness of the system ecology and the convenience of system editing and uses an embedded Linux system to complete the platform construction. Users can get the Linux source code for free, and then complete the transformation according to their own needs *(Lin Jimin, 2010)*. The WIFI driver is not included in the Linux source code and needs to be transplanted. The HI3881 WIFI chip is selected for WIFI, which has a standard broadband of 20 MHz and a maximum physical layer rate of 72.2 Mbit/s. The camera is equipped with the UVC protocol. The camera is equipped with UVC protocol devices, only in the source code for USB configuration and open the kernel module code. MJPG technology is selected for video monitoring, which is characterized by low performance requirements for the system and high clarity, and can simultaneously capture images and data output, which is suitable for field environments with complex working conditions.

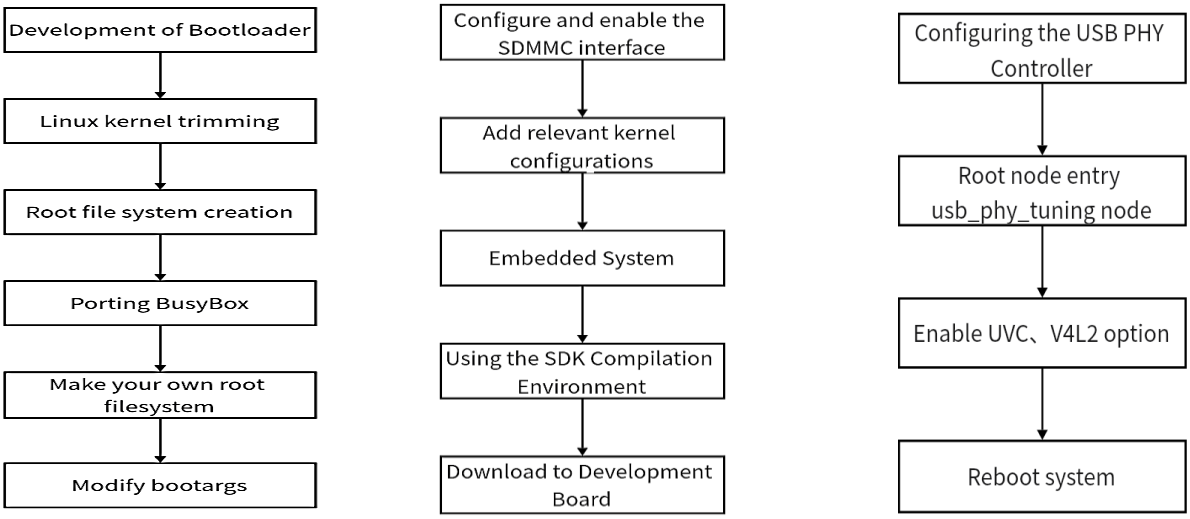

Fig. 10 - Embedded system, WIFI, and Camera operation steps

RESULTS

Control system stability test

This test selected the model vehicle for technical verification, the microcontroller as the core of the motion control system installed in the middle of the chassis mezzanine, and the main control system is installed in the ground above the front end of the vehicle placed in the camera used to monitor the road conditions. Based on the soil water content and soil density after irrigation and alkali reduction in Bayannur City provided by Inner Mongolia Dabo Jintian Machinery Co., Ltd, the test field was manually watered, and the test was conducted when the data from the soil temperature and humidity sensors were the same as the basic data.

Fig. 11 - Plow land

Fig. 12 - Flatten out the land

Fig. 13 - Comparison of land

Fig. 14 - Test model vehicles

Linear Offset Error Test

Straight-line offset error tests were conducted in a 40-meter-long test field, with 10 meters as a group for three sets of comparative tests. The starting point of the vehicle in each set of tests was 50 cm away from the edge of the test field, the edge of the test field was a straight line, and the attitude of the vehicle at the starting point was positioned parallel to the edge of the test field. In each group of experiments, a measurement point was set at every one-meter interval, and at each measurement point, the offset of the vehicle's straight driving was obtained by measuring the distance between the vehicle and the edge of the test field. The results of the experiments are shown in Fig. 15, which can be seen from the experimental results:

(1) With the increase of driving distance, the soil adhered to the tires of the model vehicle increases, resulting in a gradual increase in the amount of straight line offset, but due to the algorithm of bias correction, the offset error is within the design allowable error range of 10 cm.

(2) The vehicle is generally in a pothole each time the offset is large, and the increase in torque causes the vehicle to leave the pothole with a larger offset.

Table 1

Distance of rutting from the edge of the test field

Measuring point	The first time [cm]	The second time [cm]	The third time [cm]
0	50	50	50
1	50.4	50.8	50.5
2	49.9	51.5	50.3
3	49.6	51.2	50.0
4	49.8	50.7	50.4
5	49.4	51.1	50.5
6	49.0	51.4	49.9
7	48.6	50.9	49.0
8	48.9	49.3	49.4
9	48.2	49.7	49.9
10	48.7	49.3	49.3

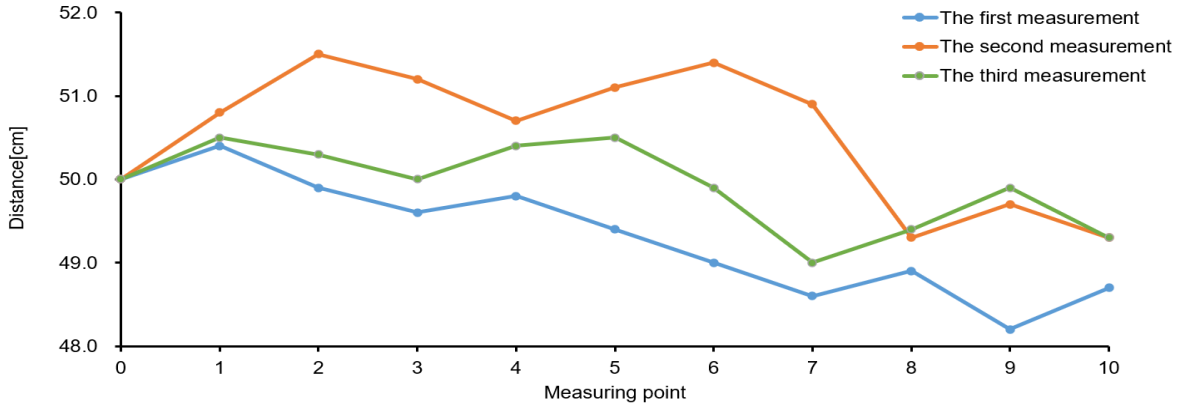

Fig. 15 - Plot of linear offsets for model vehicles

Fig. 16 - Trace diagrams for traveling in a straight line

Steering experiments on model vehicles

Tests were conducted on the model vehicle to evaluate its steering capabilities across different steering radii, including both large and small radii. The results suggest that the control system proposed in this study effectively facilitates the execution of steering maneuvers by the model vehicle, meeting diverse operational requirements with precision.

Fig. 17 - Trace diagrams for large-radius steering

Fig. 18 - Trace diagrams for small-radius steering

CONCLUSIONS

Aiming at the current problem of high dependence on manpower for seeders, the original diesel seeder was motorized from a practical point of view after dynamics and kinematics analysis. The control system of the planter was developed in two layers in the form of layered development. The control system is divided into the motion control system and the main control system, and the logic between the two systems is close and the division of labor is clear. The motion control system is based on the STM32 platform, which realizes the monitoring of the speed and motion attitude of the planter by cooperating with the encoder and IMU module; the master control system takes Linux as the platform, which realizes the communication with the motion control system and the monitoring of the working condition of the planter. The remote-control software realizes the function of human-machine interaction, which lays the foundation for the realization of unmanned driving. The stability test of the control system was carried out by using a model vehicle, and the test showed that the control system designed in this paper is stable and reliable, and meets the needs in actual production. Through the electrification of sunflower growing machinery and the design of the control system, the seeding machine can reduce the pollution of the environment and human injury.

ACKNOWLEDGEMENT

The authors were funded for this project by the Natural Science Foundation of Inner Mongolia Autonomous Region (No.2019MS03069).

REFERENCES

[1] Bi Yajuan, (2021). Comparison of advantages and disadvantages of rice machine direct seeding and machine transplanting and application considerations (水稻机直播与机插秧优缺点对比与应用注意事项). *Agricultural Machinery Use and Maintenance*, Vol. 11, pp. 155-156, China.

[2] Brenna M., Foiadelli F., Leone C., Longo M., and Zaninelli D., (2018). Feasibility proposal for heavy duty farm tractor. *2018 International Conference of Electrical and Electronic Technologies for Automotive*, pp. 1-6, Italy.

[3] Chen Huaxin, LI Shuai, (2024). Optimization of tractor hydraulic motor gears based on parametric design (基于参数化设计的拖拉机液压马达齿轮优化). *Agricultural Mechanization Research*, Vol. 46, pp. 233-237, China.

[4] Das A., Jain Y., Agrewale M.R.B., Bhateshvar Y.K., (2019). Design of a concept electric mini tractor. *2019 IEEE Transportation Electrification Conference*, pp. 1-7, India.

[5] Ding Dong, (2021). Research on slip steering control of small four-wheel independent drive vehicles (小型四轮独立驱动车辆滑移转向控制研究). *Xiamen Institute of Technology*. China.

[6] Guo Yanhong, (2010). Application of wireless sensor networks in building temperature monitoring system (无线传感器网络在楼宇温度监控系统中的应用研究). *Taiyuan University of Technology*, China.

[7] Gurusamy S.K. and Devaradjane G., (2015). Electrical tractive equipment design for small & marginal farm mechanization. *2015 IEEE International Transportation Electrification Conference (ITEC)*, pp. 1-6, India.

[8] Li Jun, Tang Shuang, Zhou Wei, (2019). A model predictive path tracking method considering vehicle stability (考虑车辆稳定性的模型预测路径跟踪方法). *Journal of Huaqiao University (Natural Science)*, Vol. 40, pp. 574-579, China.

[9] Liang Chao, Wang Hongzhen, Bao Xiaozhim, Zhang Qi. (2024). Research on a path tracking method for an autonomous seeder in paddy field (一种稻田自主播种机的路径跟踪方法的研究). *Agricultural Mechanization Research*, Vol. 46(03) pp. 52-56, China.

[10] Liang Lijun, et al. (2023). Development of 2BQD series of electrically-driven intelligent high-speed precision sowing machine (2BQD 系列电驱智能高速精播机的研制). *Agricultural Machinery Use and Maintenance*, Vol. 07, pp. 06-10, China.

[11] Lin Jimin, Wu Yi, Lin Xiao, (2010). Construction and application of Linux-based embedded system development platform (基于 Linux 嵌入式系统开发平台的构建及应用). *Modern Electronic Technology*, Vol.18, pp. 30-34, China.

[12] Lovarelli D. and Bacenetti J., (2019). Exhaust gases emissions from agricultural tractors: State of the art and future perspectives for machinery operators. *Biosystems Engineering*, Vol.186, pp. 204-213, Italy.

[13] Shen Peng, Cao Kai, Liu Bingzheng, et al, (2019). An unmanned path tracking method combined with a planning layer (一种结合规划层的无人驾驶路径跟踪方法). *Journal of Shandong University of Technology (Natural Science Edition)*, Vol. 33(06), pp. 50-55, China.

[14] Tahmish Fatima, Naveen Kumar Arora. (2021). Pseudomonas entomophila PE3 and its exopolys-accharides as biostimulants for enhancing growth, yield and tolerance responses of sunflower u-nder saline conditions. *Microbiological research*, Vol. 244, India.

[15] Xiong Yong, Zhang Jia, Huang Kaisheng, et al (2020). Optimal control-based path tracking method for dual-jet-propelled unmanned craft (基于最优控制的双喷推无人艇路径跟踪方法). *Ship Engineering*, Vol.42(02), pp. 20-27, China.

[16] Yang Yun, Liu Tingting (2022). Calculation of slip and path planning for agricultural robots based on machine learning (基于机器学习的农业机器人滑移量计算及路径规划). *Agricultural Mechanization Research*, Vol. 44(09), pp. 264-268, China.

PARAMETERS CALIBRATION FOR DISCRETE ELEMENT MODEL SIMULATION OF WHITE KIDNEY BEAN SEEDS
/
白芸豆种子离散元模型仿真参数标定

Huhu YANG[1,2)], Junlin HE *[1)], Jiaxuan LU[1)], Tao WANG[1)], Yuehua WANG[1)], Yanxi GUO[1)]

[1)]College of Agricultural Engineering, Shanxi Agricultural University, Taigu 030801, China;
[2)]Dryland Farm Machinery Key Technology and Equipment Key Laboratory of Shanxi province, Taigu 030801, China;
Tel: +86-0354-6288400; E-mail: hejunlin26@126.com
DOI: https://doi.org/10.35633/inmateh-72-07

Keywords: *White kidney bean; discrete element model; parameter calibration; the steepest climbing test*

ABSTRACT

This paper addresses the problem of the lack of intrinsic and contact parameters when applying the discrete element method to simulate and analyze the key aspects of white kidney bean seed sowing, harvesting and clearing. The experiment took white kidney bean seeds as the research object, measured the intrinsic parameters of white kidney bean seeds by using the universal testing machine, and measured the collision recovery coefficient of 0.445, static friction coefficient of 0.452 and rolling friction coefficient of 0.091 between white kidney bean seeds and Q235 steel plate by physical test and EDEM discrete element simulation parameter calibration. The stacking experiment was carried out by the cylinder lifting method, numerical processing was performed with MATLAB, and the actual stacking angle of white kidney bean seeds was 31.28°. The steepest climbing test was designed with the interspecific contact parameters as factors and the relative error between the actual and simulated stacking angles as indicators. The optimal combination of the interspecific contact parameters of white kidney bean was determined by response surface optimization analysis, and the interspecific collision recovery coefficient of white kidney bean was obtained as 0.39, static friction coefficient was 0.53, rolling friction coefficient was 0.092. Using the optimal parameters for the simulation test, the relative error between the actual stacking angle of white kidney bean seeds and the simulated stacking angle was 1.63%, indicating that the calibrated simulated contact parameters were reliable and could provide reference for the discrete element simulation of white kidney bean seeds.

摘要

针对应用离散元法对白芸豆播种、收获和清选等关键环节进行仿真分析时，缺乏本征参数和接触参数的问题。该实验以白芸豆种子为研究对象，使用万能试验机测得白芸豆种子本征参数，通过物理试验和EDEM离散元仿真参数标定，测定白芸豆种子与Q235钢板之间的碰撞恢复系数为0.445、静摩擦系数为0.452、滚动摩擦系数为0.091。采用圆筒提升法进行堆积试验，用MATLAB对堆积图像进行数值处理，得到白芸豆种子实际堆积角为31.28°。以种间接触参数为因素，以实际堆积角和仿真堆积角的相对误差为标准，进行最陡爬坡试验，通过响应面优化分析确定白芸豆种间接触参数最优组合，确定白芸豆种间碰撞恢复系数为0.39，[1]静摩擦系数为0.53，滚动摩擦系数为0.092。利用最优参数进行仿真验证，结果显示白芸豆种子实际堆积角与仿真堆积角相对误差为1.63%，表明所标定的接触参数具有可靠性，可为白芸豆种子离散元仿真提供参考。

INTRODUCTION

White kidney beans are biologically known as Phaseolus vulgaris, also known as string beans and white beans (*Phaseolus., 2021*), and are native to Mexico, Argentina and other parts of the Americas. China began to introduce cultivation at the end of the 16th century. White kidney beans are one of the most important edible bean crops in China. At present, it is widely planted in various provinces and cities in China, among which Yunnan, Guizhou, Sichuan, Gansu, Inner Mongolia and other provinces have the widest planting area. China is the world's major producer and exporter of kidney beans, and its output ranks third in the world, after India and Brazil. Moreover, white kidney beans are a kind of medicinal and food plant with high nutritional and medicinal value, and have great development potential and economic prospects (*Niu et al., 2020; Zheng et al., 2022; Zi et al., 2015*).

[1] *Huhu Yang, As.M.S.Stud.; Junlin He, Prof.Ph.D.Eng.; Jiaxuan LU, As.M.S.Stud.; Tao Wang, As.M.S.Stud.; Yuehua Wang, As.M.S.Stud.;Yanxi Guo, As.M.S.Stud.*

With the development of discrete element theory and simulation technology, the application of discrete element methods in the field of agricultural engineering is becoming more and more widespread. By applying the discrete element method to simulate the seed sowing and clearing process, it can be visually analyzed the movement of seeds in a complex environment, and then the structural design of seeders can be optimized. (*Dun et al., 2020; Han et al., 2017*). In the simulation using the EDEM-FLUENT gas-solid coupling method, the intrinsic parameters (density, Poisson's ratio and shear modulus) of the discrete element model need to be input to define the contact parameters between the crop and the equipment material and between the crops. The intrinsic parameters can be obtained by physical test measurements, but the interspecies contact parameters are not easy to obtain accurate values by test measurements, so the parameters need to be calibrated to obtain accurate values (*Zhang et al., 2022*).

Domestic and foreign scholars have calibrated the discrete element simulation parameters of Agropyron, Mung-been, Fresh lotus seed, Peanut, Soybean, Panax notoginseng, and broad bean seeds (*Hou et al., 2020; Zhang et al., 2017; Zhang et al., 2023; Wu et al., 2020; Yu et al., 2020; Wang et al., 2023*), and the results showed that the contact parameters varied among different crops, but little has been reported about the parameter calibration of white kidney bean seeds. The experiment takes white kidney bean seeds as the research object and establishes the discrete element model of white kidney bean seeds based on their three-dimensional size with the basic unit ball combination method in EDEM, and conducts simulation tests to calibrate the contact parameters between white kidney bean seeds and Q235 steel plates, and determines the optimal combination of contact parameters between white kidney bean seeds through stacking tests, steepest climbing tests, quadratic orthogonal rotation combination tests and response surface optimization analysis, in order to provide reference for the structural optimization of white kidney bean seed dischargers and the simulation design of clearing devices.

MATERIALS AND METHODS

Determination of intrinsic parameters and discrete element model of white kidney beans

Three-dimensional size

To accurately establish the three-dimensional model and discrete element model of white kidney bean seeds, 300 white kidney bean seeds without damage and mildew were randomly selected, and the three-dimensional size (length L, width W, thickness T) of white kidney bean seeds were measured by electronic vernier caliper (accuracy 0.01 mm). The average length L of white kidney bean seeds was 9.76 mm, the average width W was 6.07 mm, and the average thickness T was 5.39 mm. The length, width, thickness and equivalent diameter of white kidney bean seeds are approximately subject to normal distribution (Fig. 1). The length range is 7.5 ~ 13.0 mm, the width range is 5.0 ~ 7.2 mm, and the thickness range is 4.0 ~ 6.6 mm. According to the formula (1,2), the equivalent diameter (D_p) is 6.83 mm and the sphericity (φ) is 70.19%.

$$D_p = \sqrt[3]{L \cdot W \cdot T} \tag{1}$$

$$\varphi = \frac{\sqrt[3]{L \cdot W \cdot T}}{L} \tag{2}$$

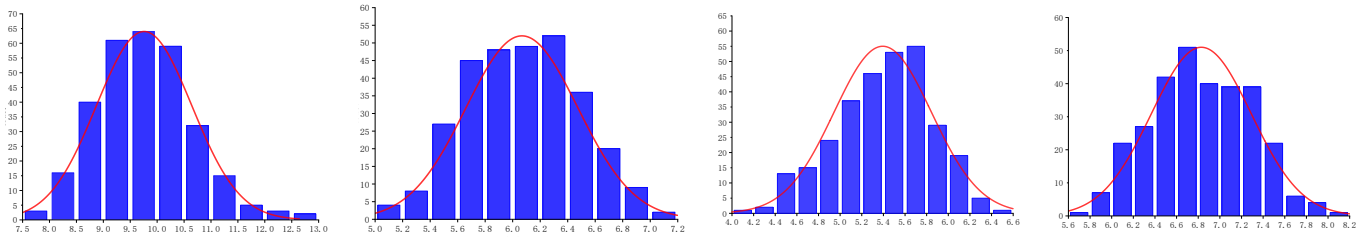

(a) length (b) width (c) thickness (d) equivalent diameter

Fig. 1 - Probability density distribution of triaxial dimensions

Thousand seed weight, density and moisture content

Randomly select 1000 white kidney bean seeds, using an electronic balance (accuracy 0.01g) to measure their weight m_1; in order to measure the results accurately, measure five times to obtain the average value, measured the amount of white kidney bean seeds thousand seed weight is 249.20g.

Using the drainage method to measure the density of white kidney bean seeds, weigh 30 g of white kidney bean seeds with an electronic balance, put the white kidney bean seeds into a measuring cylinder with a certain volume of water, record the volume V_1 before putting in the seeds and the volume V_2 after putting in the seeds, make multiple measurements, and measure the density as being 1363.60 kg/m3.

The water content of white kidney bean seeds was measured with a constant temperature drying oven, weighing the mass of m_1 seed samples, placing the seed samples into the drying oven, setting the temperature at 105°C, weighing every 2h until the sample mass no longer changes, and recording the mass of the sample at this time, m_2, then the water content of the white kidney bean seeds is $(m_1-m_2)/m_1\times100\%$.

Poisson ratio

Poisson ratio of white kidney bean seeds was measured by compression test using the universal material testing machine. 10 white kidney bean seeds were randomly selected, the length (axial) and width (transverse) of the original size were recorded. A universal testing machine was used at a speed of 5 mm/min on the white kidney bean seeds for compression, and the measurement of compression after the axial and transverse deformation of the white kidney bean seeds was performed. Poisson's ratio was calculated from formula (3) and the results were averaged.

$$\mu = \frac{w/W}{l/L} = \frac{(H_1 - H_2)/W}{(A_1 - A_2)/L} \tag{3}$$

where:

μ is Poisson ratio; w is transverse deformation, mm; l is axial deformation, mm; W is the width of white kidney bean seeds, mm; L is the length of white kidney bean seeds, mm; H_1 is the width of white kidney bean seeds after rupture, mm; H_2 is the original width of white kidney bean seeds, mm; A_1 is the original length of white kidney bean seeds, mm; A_2 is the length of white kidney bean seeds after rupture, mm.

Elastic modulus and shear modulus

The elastic modulus is a scale used to measure the resistance of the material to elastic deformation. 10 white kidney bean seeds were randomly selected and placed on the circular platform of the universal testing machine, and the load was applied to the white kidney bean seeds using a circular indenter with a loading speed of 5 mm/min, and the load F and deformation (ΔL) were recorded. 10 white kidney bean seeds were repeated in turn, and the above test was calculated from equation (4,5,6). The average value of elastic modulus E was 128.30 MPa and the average value of shear modulus G was 343.84 MPa.

$$E = \left(\frac{F}{A}\right)\Big/\varepsilon \tag{4}$$

$$\varepsilon = \frac{\lim}{L_1 \to 0}\left(\frac{\Delta L}{L_1}\right) \tag{5}$$

$$G = \frac{E}{2(1+\mu)} \tag{6}$$

where: E is the elastic modulus, MPa; F is the axial load on the white kidney bean seeds, N; A is the contact area, mm^2; ε is the strain; ΔL is the deformation of white kidney bean seeds after compression, mm; G is the shear modulus, MPa; μ is the Poisson ratio of white kidney bean seeds.

Discrete element model of white kidney bean seed

According to the three-dimensional size and shape of white kidney bean seeds, the three-dimensional model of white kidney bean seeds was established in SOLIDWORKS, the built three-dimensional model was imported into EDEM software, and the basic spherical unit combination method was used to establish the discrete element simulation model of white kidney bean seeds, using 12 different radii of spherical particles filled until close to the real thing, white kidney bean seed particles and discrete element model (Fig. 2).

In physical experiments, the surface of white kidney bean seeds and steel plates are smooth and almost free of adhesion, so the Hertz-Mindlin no-slip contact model is selected in EDEM simulation. The intrinsic parameters of white kidney bean seeds and Q235 steel in EDEM simulation tests are obtained through experiments and literature review, as shown in Table 1.



(a) White kidney bean seed (b) Three-dimensional model (c) Discrete element model

Fig. 2 - White kidney bean seed particle and discrete element model

Table 1

White kidney bean seed, Q235 steel intrinsic parameters

Materials	Poisson ratio (μ)	Shear modulus (G / MPa)	Elastic modulus (E / MPa)	Density ($\rho/kg.m^3$)
White kidney bean seed	0.34	128.30	343.84	1363.60
Q235 steel	0.30	700.00	1820.00	7800.00

Calibration of contact parameters between white kidney bean seeds and Q235 steel plates

Collision recovery factor

The experiment used the free fall method to measure the collision recovery coefficient from white kidney bean seeds to Q235 steel, the experiment used Q235 steel plate as the bottom plate of the test bench, the white kidney bean seeds were free falling from the height H_1 (360 mm) to Q235 steel plate. The process was recorded using a video camera, and the video was processed to mark the maximum height H_2 that the white kidney bean seeds popped up after falling after the test. The test was repeated 10 times, its average value was calculated, white kidney bean seeds and Q235 collision was measured after popping up the maximum height of the average H_2=71mm. It was calculated by the formula (7) to get white kidney bean seeds collision recovery coefficient e which is 0.429.

$$x_1 = \frac{v_2}{v_1} = \frac{\sqrt{2gH_2}}{\sqrt{2gH_1}} \tag{7}$$

The static and rolling friction coefficients between white kidney bean seeds and Q235 steel plates and the contact parameters between white kidney bean seeds have no effect on the height of pop-up after collision of white kidney bean seeds. In the EDEM simulation test, set the parameters other than the collision recovery coefficient between white kidney bean seeds and Q235 steel to 0. After the pre-simulation test, set the range of collision recovery coefficient between white kidney bean seeds and Q235 steel plate to 0.3~0.6, design 7 groups of simulation tests, repeat each group of tests 10 times, and take the average value of simulation results. The curve fitting of the experimental results is shown in Fig. 5.

The fitted equation is shown in equation (8).

$$h = 332.952x_1^2 + 14.9x_1 - 1.827 \quad (R^2 = 0.9986) \tag{8}$$

The physical test white kidney bean seeds and Q235 steel plate maximum pop-up height average value of 71 mm was substituted into the formula (8), to obtain x_1 = 0.445. The simulation was verified in EDEM software, and the average value was calculated by repeating 10 tests. The relative error between the maximum height of pop-up after the simulation test and the maximum height of pop-up in the actual test was 3.5%, indicating that the difference between the simulation test and the actual test result was not significant, so the collision recovery coefficient between white kidney bean seeds and Q235 steel plate x_1=0.445 was determined in the EDEM simulation test.

Static friction coefficient

The size of the coefficient of friction is generally affected by the roughness of the object's surface, material, temperature, load, etc. The coefficient of static friction is the ratio of the maximum static friction force on the object in the friction pair to the normal pressure on it. In this test, the static friction coefficient between white kidney bean seeds and Q235 steel is measured by the slanting method (Fig.3).The white kidney bean seed adhesion plate is placed on the surface of the Q235 steel measuring plate, the other end of the measuring plate is slowly pulled up by an asynchronous motor, the measuring plate is tilted from the horizontal state and the state of white kidney beans on the measuring plate is carefully observed. When the white kidney bean

adhesion plate is found to start sliding downward, the stop button is immediately pressed, the angle α is recorded, and the test results are repeated 10 times to take the average value. The static friction coefficient between the white kidney bean seeds and the Q235 steel plate was calculated from f=tanα as 0.58.

(a) Physical test (b) Simulation experiment

Fig. 3 - Static friction coefficient calibration

The rolling friction coefficient between the white kidney bean seeds and the Q235 steel plate, as well as the static friction coefficient, rolling friction coefficient and collision recovery coefficient between the white kidney bean seeds had no effect on the tilt angle of the Q235 steel measuring plate. The collision recovery coefficient between white kidney bean seeds and Q235 steel plate was set to the already calibrated parameter 0.445 during the EDEM simulation test. After a large number of pre-simulation tests, the static friction coefficient between white kidney bean seeds and Q235 steel plate was determined to be 0.30~0.60. 7 groups of simulation tests were designed, and each group of tests was conducted ten times, and the results were taken as the average value. The curve fitting of the experimental results is shown in Fig.5.

The fitted equation is shown in equation (9).

$$y = 4.2381x_2^2 + 44.5643x_2 - 21.0174 \quad \left(R^2 = 0.9988\right) \tag{9}$$

Substituting the inclination angle of 24.15° of the bench test, the coefficient of static friction x_2=0.452 was obtained. Simulation tests were carried out in EDEM, and the average value was repeated 10 times, and the simulated inclination angle was measured as 25.31°, and the relative error with the actual inclination angle obtained from the bench test was 4.8%, and the results were basically the same so that it can be determined that the coefficient of static friction between the seeds of the white kidney bean and the Q235 steel plate is x_2=0.452.

Rolling friction coefficient

The rolling friction coefficient between white kidney bean seeds and Q235 steel plate was measured using the slant method, as shown in Fig.4. The white kidney bean seeds were placed on a steel plate with an inclination angle of β. After several preliminary experiments, the inclination angle β = 30° was initially determined. Release the white kidney bean seeds from S=50 mm with an initial velocity of 0, and record the rolling distance in the horizontal plane when the seeds completely stop rolling L. Assuming that the seeds are only affected by rolling friction in the rolling process, the rolling friction coefficient is calculated by the formula (10). The test was repeated 10 times, and the average value of rolling distance of white kidney bean seeds in the horizontal plane was measured to be 251.7 mm, and the rolling friction coefficient was 0.09.

$$mg\,S \cdot \sin\beta = mg\left(S \cdot \cos\beta + L\right)X \tag{10}$$

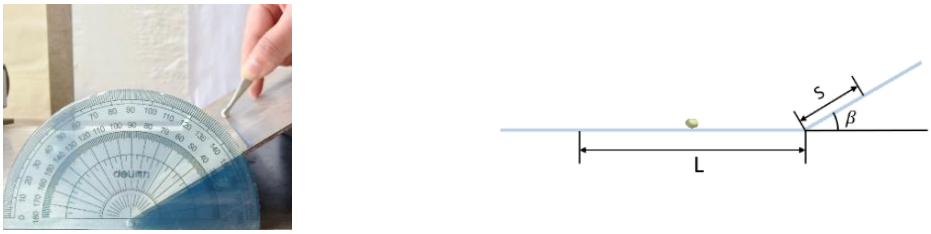

(a) Physical test (b) Simulation experiment

Fig. 4- Static friction coefficient calibration

In the simulation test, the parameters that have been calibrated are used to set the collision recovery coefficient x_1=0.445 and the static friction coefficient x_2=0.452 between the white kidney bean seeds and the Q235 steel plate. Other parameters have no effect on the horizontal rolling distance, and they are all set to 0 to avoid interference. After the previous pre-simulation work, the range of the rolling friction coefficient x_3

between the white kidney bean seeds and the Q235 steel plate is taken as 0.06~0.12. Seven groups of tests are designed, each group of tests is carried out 10 times, and the results are averaged. The curve fitting of the experimental results is shown in Fig.5. The fitted equation is shown in equation (11).

$$L = 28350x_3^2 - 8441.86x_3 + 770.72 \quad \left(R^2 = 0.9976\right) \tag{11}$$

The horizontal rolling distance L=237.2 mm of the white kidney bean seed of the bench test is substituted into equation (11) to obtain x_3=0.091. Simulation is carried out to verify that the horizontal rolling distance of the simulation test is 226.28 mm, and the relative error with the actual measured distance is 4.6%, which indicates that the simulation result after calibration is basically the same as that of the bench test. Therefore, the rolling friction coefficient between the white kidney bean seeds and the Q235 steel plate was determined as x_3=0.091.

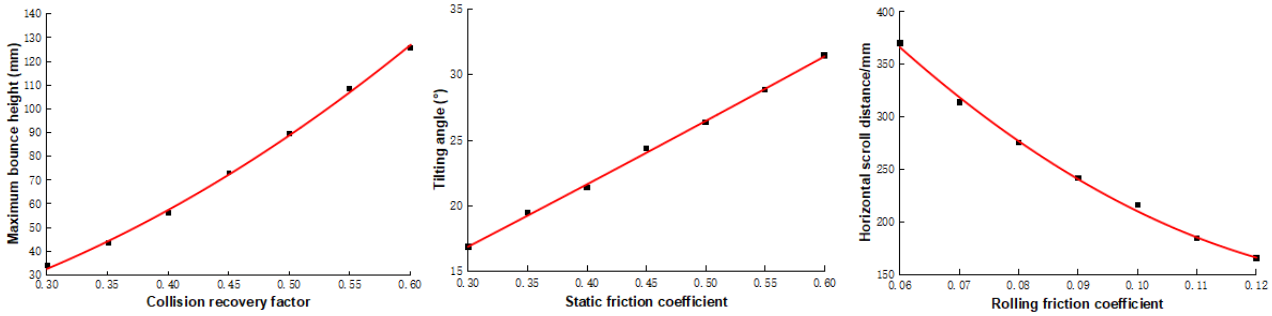

Fig. 5 - Calibration of contact parameters of white kidney bean seeds with Q235 steel plates

RESULTS

Calibration of interspecific contact parameters for white kidney bean

Stacking test

The collision recovery coefficient, static friction coefficient and rolling friction coefficient between seeds have an effect on the stacking angle of white kidney bean seeds during the stacking and molding process. In this test, the bottomless cylinder lifting method was used to measure the actual stacking angle of white kidney bean seeds. During the test, a Q235 steel cylinder (inner diameter of 36 mm, height of 350 mm) was placed vertically on the horizontal steel surface of the test bench, 1,000 white kidney bean seeds were put into the cylinder, and the operating speed of the stepping motor was set so that the cylinder was lifted at a uniform speed of 20 mm/s, and the stacking slope and horizontal angle formed by natural stacking under gravity were the angle of stacking between white kidney bean seeds and the horizontal clamping angle. The natural accumulation of white kidney bean seeds in the cylinder under the action of gravity formed by the accumulation of the slope and the horizontal angle is the accumulation angle of white kidney bean seeds.

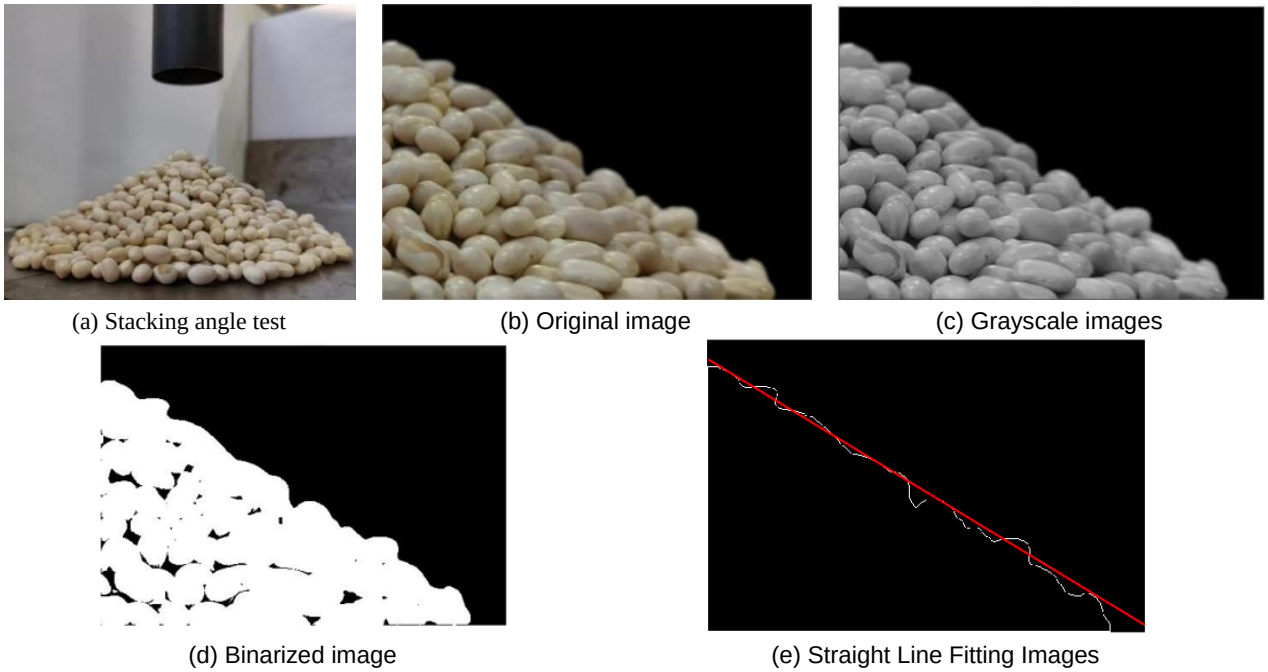

(a) Stacking angle test (b) Original image (c) Grayscale images

(d) Binarized image (e) Straight Line Fitting Images

Fig. 6 - Stacking angle image processing

A high-definition camera was used to capture the image of white kidney bean seed stacking, and MATLAB was used to process the stacking image in grayscale, binarization, hole filling, and extraction of contour curves (Fig.6), and finally, a straight line was fitted to the extracted contour curves using the least-squares method, and the mean value of the stacking angle of the white kidney bean seed θ = 31.28° was obtained from the slope of the fitted straight line.

Steepest Climb Test

In order to determine the values of the interspecies collision recovery coefficient, static friction coefficient and rolling friction coefficient of white kidney bean, the steepest climb experiment was designed by taking the actual stacking angle measured by bench test as the control, the interspecies collision recovery coefficient, static friction coefficient and rolling friction coefficient of white kidney bean as the test factors, and the relative error δ between the actual stacking angle and the simulated stacking angle as the criterion. The steepest climb design scheme and results are shown in Table 2.

The relative error δ between the simulated stacking angle and the actual stacking angle is calculated as (12).

$$\delta = \left| \frac{\theta' - \theta}{\theta} \right| \times 100\% \quad (12)$$

Table 2

Steepest climb test program and results

Test number	Test factors			Test results	
	Collision recovery coefficient X_1	Static friction coefficient X_2	Rolling friction coefficient X_3	Simulation stacking angle	Relative error δ /%
1	0.34	0.30	0.065	27.22	12.97
2	0.37	0.35	0.075	28.93	7.51
3	0.40	0.40	0.085	29.54	5.56
4	0.43	0.45	0.095	30.83	1.44
5	0.46	0.50	0.105	33.54	7.23
6	0.49	0.55	0.115	34.23	9.43
7	0.52	0.60	0.125	35.63	13.91

As can be seen from Table 2, the stacking angles obtained from the simulation of different parameter combinations are different, and the relative errors show a tendency of decreasing and then increasing, and the relative error between the simulated stacking angle and the actual stacking angle of the 4th group is the smallest. Therefore, the 4th group of test factors is selected as the 0-level test factors of the quadratic orthogonal rotational combination design test, and the 3rd and 5th groups are selected as the -1 and 1-level test factors, respectively.

Quadratic orthogonal rotating combination test

In order to determine the optimal combination of white kidney bean interspecific contact parameters (collision recovery coefficient x_1, static friction coefficient x_2, and rolling friction coefficient x_3) in the EDEM simulation test, a three-factor, five-level quadratic orthogonal rotational combination test was conducted, and the factor codes for the simulation test are shown in Table 3, and the experimental scheme and results are shown in Table 4, with the test factor codes A, B, and C representing the collision recovery coefficient x_1, the static friction coefficient x_2, and the rolling friction coefficient x_3 of the white kidney bean interspecific contact, respectively.

Table 3

Simulation test factor codes

Code	Test factors		
	Collision recovery coefficient X_1	Static friction coefficient X_2	Rolling friction coefficient X_3
-1.682	0.37	0.35	0.075
-1	0.40	0.40	0.085
0	0.43	0.45	0.095
1	0.46	0.50	0.105
1.682	0.49	0.55	0.115

Multiple regression was fitted to the test data (Table 4) using Design-Expert 8.0.6, and the fitted equation for the relative error in stacking angle was obtained as equation (13).

$$\delta = 897.17 - 2211.69A - 1064.91B - 3974.84C + 1600.14AB + 2459.99AC + 459.99BC + 1484.22A^2 + 372.32B^2 + 14902.63C^2 \quad (13)$$

The ANOVA results of the regression equation are shown in Table 5, with a quadratic regression model (P<0.0001), a loss of fit term (P=0.8557>0.05), and a coefficient of determination R^2=0.9887, which indicates that the regression model is well fitted and no loss of fit occurs, suggesting that the model is significant, accurate, and predictive. A, C, AB, AC, A^2, B^2, and C^2 have highly significant effects on the relative error δ, and B and BC have non-significant effects on δ, indicating that the effects of the relevant test factors on the response values are not simple linear relationships, and there is a quadratic relationship.

Table 4

Experiment scheme and results

Number	Test factors			δ/%	Number	Test factors			δ/%
	A	B	C			A	B	C	
1	0.40	0.40	0.085	8.76	**13**	0.43	0.45	0.075	6.88
2	0.46	0.40	0.085	3.40	**14**	0.43	0.45	0.115	11.68
3	0.40	0.50	0.085	3.51	**15**	0.43	0.45	0.095	3.58
4	0.46	0.50	0.075	10.03	**16**	0.43	0.45	0.095	2.86
5	0.40	0.40	0.105	9.27	**17**	0.43	0.45	0.095	3.05
6	0.46	0.40	0.105	6.75	**18**	0.43	0.45	0.095	2.66
7	0.40	0.50	0.105	4.82	**29**	0.43	0.45	0.095	2.49
8	0.46	0.50	0.105	11.93	**20**	0.43	0.45	0.095	3.67
9	0.37	0.45	0.095	7.24	**21**	0.43	0.45	0.095	3.45
10	0.49	0.45	0.095	9.96	**22**	0.43	0.45	0.095	3.71
11	0.43	0.35	0.095	6.62	**23**	0.43	0.45	0.095	3.74
12	0.43	0.55	0.095	7.34					

Table 5

Variance analysis of regression equation

Source of variation	Sum of Squares	Degree of Freedom	Mean Square	F Value	P Value
Model	204.90	9	22.77	126.86	<0.0001**
A	4.84	1	4.84	26.96	0.0002**
B	0.095	1	0.095	0.53	0.4808
C	24.74	1	24.74	137.84	<0.0001**
AB	44.39	1	44.39	247.37	<0.0001**
AC	5.11	1	5.11	28.50	0.0001**
BC	0.49	1	0.49	2.72	0.1230
A^2	50.44	1	50.44	281.09	<0.0001**
B^2	24.49	1	24.49	136.48	<0.0001**
C^2	70.15	1	70.15	390.92	<0.0001**
Residual	2.33	13	0.18		
Lack of fit	0.44	5	0.088	0.37	0.8557
Pure error	1.89	8	0.24		
Sum	207.23	22			

Note: P<0.05(significant,); P<0.01(highly significant,**)*

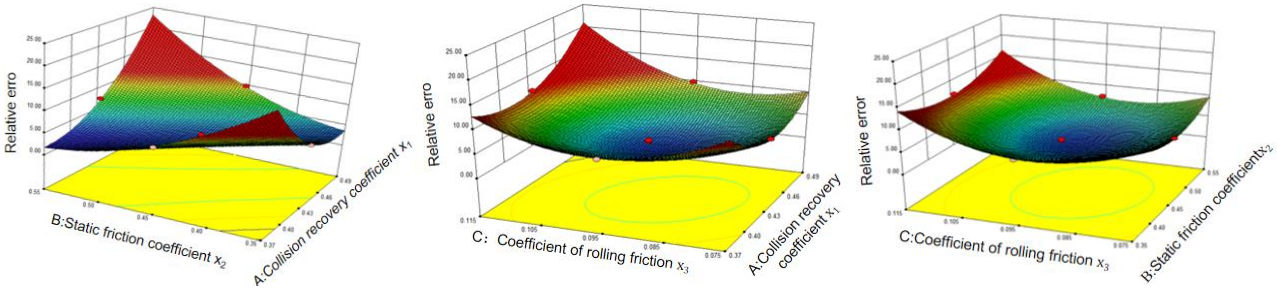

Fig. 7- Response surface of relative error and test factor

Response surface analysis using Design-Expert 8.0.6 software can visually analyze the effects of interactions among factors on the test indexes, and the effects of interactions among factors on the relative error δ of the stacking angle of white kidney beans are shown in Figure 7. With the increase of A (collision recovery coefficient x_1), B (static friction coefficient x_2) and C (rolling friction coefficient x_3), the relative error δ of the stacking angle of white kidney beans all decreased firstly and then increased.

Optimal parameter combination determination and validation

Through Design-Expert 8.0.6, with the objective of minimizing the relative error between the simulated stacking angle and the actual stacking angle, the regression equations are optimally solved, the response surface is analyzed, and the optimal solution is sought for the model. The system of objective and constraint equations is shown in equation (14)

$$\begin{cases} \min Y(X_1, X_2, X_3) \\ s.t \begin{cases} 0.37 \leqslant X_1 \leqslant 0.49 \\ 0.35 \leqslant X_2 \leqslant 0.55 \\ 0.075 \leqslant X_3 \leqslant 0.115 \end{cases} \end{cases} \quad (14)$$

The finalized coefficient of recovery of white kidney bean interspecific collision x_1 was 0.39, static friction coefficient x_2 was 0.53 and rolling friction coefficient x_3 was 0.092. The white kidney bean seed stacking angle test was carried out with optimal parameter combinations and replications were performed 10 times. The simulation test stacking angle is shown in Fig. 8. The stacking angle obtained from the simulation test is 31.79°, and the actual measured stacking angle of the bench test is 31.28°. The relative error between the actual measured stacking angle and the simulation stacking angle is 1.63%, which indicates that the contact parameters calibrated by this discrete element model are accurate and reliable, and can be used in the subsequent EDEM simulation test.

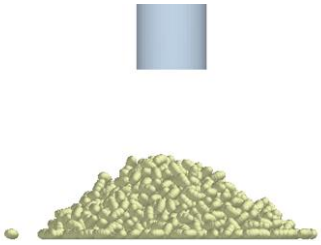

Fig. 8 - Simulation of accumulation angle experiment of white kidney bean

CONCLUSIONS

In this paper, white kidney bean seeds were used as the research object to measure the physical characteristics of white kidney bean seeds. The mean values of the triaxial dimensions of white kidney bean seeds were 9.76 mm, 6.07 mm and 5.39 mm for length, width and thickness respectively, and the triaxial dimensions conformed to normal distribution. Through experimental measurements, the Poisson's ratio of white kidney bean seeds is 0.34, the elastic modulus is 128.30 MPa, and the shear modulus is 348.34 MPa. In EDEM, the Hertz-Mindlin contact model was selected to build a discrete elemental model of the white kidney bean seeds, and the contact parameters of the white kidney bean seeds and Q235 steel were calibrated. The collision recovery coefficient between the white kidney bean seeds and Q235 steel was measured to be 0.429, the static friction coefficient was 0.452, and the rolling friction coefficient was 0.091.

The white kidney bean seed stacking angle test was carried out, and MATLAB was used to process the stacking angle pictures, extract the boundary contours, and perform curve fitting to obtain the actual stacking angle of 31.28°. With the objective of minimizing the relative error δ between the actual stacking angle and the simulated stacking angle, the steepest-climbing test and the quadratic orthogonal rotational combination test were designed for optimization solving, and the optimal combination of the contact parameters between the white kidney bean species was determined: the coefficient of recovery of the collision between the species of the white kidney bean was 0.39, the coefficient of static friction was 0.53, and the coefficient of rolling friction was 0.092, respectively. The simulated stacking angle test is carried out with the optimal parameter combination, and the simulated stacking angle is measured to be 31.79°, and the relative error with the actual stacking angle is 1.63%, which indicates that the discrete element model and the calibrated contact parameters are accurate and reliable.

ACKNOWLEDGEMENT

This research was supported by the science and technology Innovation Fund project of Shanxi Agricultural University (Zdpy201802 and Zdpy201906).

REFERENCES

[1] Dun G.Q., Fan X.R., Yang Y.Z., Li H.S., Wang C.F., Chen H.T., Du J.X, (2020), Improved design and experiment of a plug-in soybean seed metering device based on discrete element (基于离散元的插装式大豆排种器改进设计及试验), *Journal of Huazhong Agricultural University*, Wuhan/China, vol.39, issue 3, pp.135-144;

[2] Han D.D., Zhang D.X., Yang L., Cui T., Ding Y.Q., Bian X.H., (2017), Optimization and experiment of inside-filling air-blowing seed metering device based on EDEM-CFD (基于 EDEM-CFD 耦合的内充气吹式排种器优化与试验), *Transactions of the Chinese Society for Agricultural Machinery*, Beijing/China, vol.48, issue 11, pp.43-51;

[3] Hou Z.F., Dai N.Z., Chen Z., Qiu Y., Zhang W.X., (2020), Measurement and calibration of physical property parameters for Agropyron seeds in a discrete element simulation (冰草种子物性参数测定与离散元仿真参数标定), *Transactions of the Chinese Society of Agricultural Engineering*, Beijing/China, vol.36, issue 24, pp.46-54;

[4] Niu Y Z., Mao X., Yi S.J., Tao G.X. (2020), Compression characteristics test of mature white kidney bean (成熟期白芸豆压缩特性试验), *Journal of Agricultural Mechanization Research*, Harbin /China, vol.42, issue 4, pp.125-131;

[5] Phaseolus vulgaris L. (2021). *Molecular Plant Breeding*, Haikou/China, vol19, issue 5, pp1746;

[6] Wu M C., Cong J L., Yan Q., Zhu T., Peng X Y., Wang Y S, (2020), Calibration and experiments for discrete element simulation parameters of peanut seed particles (花生种子颗粒离散元仿真参数标定与试验), *Transactions of the Chinese Society of Agricultural Engineering*, Beijing/China, vol.36, issue 23, pp.30-38;

[7] Wang Y H., He J L., Yang H H., Guo Y X., Lu J X, (2023), Simulation parameter calibration of broad bean seed discrete element model (蚕豆种子离散元模型仿真参数标定), *Agricultural Engineering*, Beijing/China, vol.13, issue 1, pp.79-84;

[8] Yu Q.X., Liu Y., Chen X.B., Sun K., Lai Q.H., (2020), Calibration and experiment of simulation parameters for panax notoginseng seeds based on DEM (基于离散元的三七种子仿真参数标定与试验), *Transactions of the Chinese Society of Agricultural Engineering*, Beijing/China, vol.51, issue 2, pp.123-132;

[9] Zheng H.J., Zhu X.C., Li Y.J., Zhou X.Y., Liu J.Y., Tang Y., Wang Y.L., Yang X.Q., Zhang H.J., Shen Y.B., Li M.M., (2022), A review of functional components, bioactivities and product development of white kidney bean (白芸豆功能成分、生物活性及其产品开发研究进展), *Journal of the Chinese Cereals and Oils Association*, Beijing/China, vol.37, issue 12, pp.277-285;

[10] Zi Y., Wang C.Q., Chen X.M., Chen T., Li X.F., Hao Z.P., Yu W.J., (2015), Preparation and thermal stability of white kidney bean inhibitory activity (具有 α-淀粉酶抑制活性的白芸豆多肽的制备及其热稳定性研究), *Food Science*, Beijing/China, vol.36, issue 13, pp.190-195;

[11] Zhang S.W., Zhang R.Y., Chen T.Y., Fu J., Yuan H.F., (2022), Calibration of simulation parameters of Mung-been seeds using discrete element method and verification of seed-metering test (绿豆种子离散元仿真参数标定与排种试验), *Transactions of the Chinese Society for Agricultural Machinery*, Beijing/China, vol.53, issue 3, pp.71-79;

[12] Zhang T., Liu F., Zhao M Q., Liu Y Q., Li F L., Ma Q., Zhang Y., Zhou P, (2017), Measurement of physical parameters of contact between soybean seed and seed metering device and discrete element simulation calibration (大豆种子与排种器接触物理参数的测定与离散元仿真标定), *Journal of China Agricultural university*, Beijing/China, vol.22, issue 9, pp.86-92;

[13] Zhang G.Z., Zhang Q.H., Jiao J., Chen Y.X., Liang S., Liu H.P., (2023), Parameters calibration of discrete element simulation for fresh lotus seeds (鲜莲籽离散元仿真参数标定), *Journal of South China Agricultural University*, Guangzhou/China, vol.44, issue 1, pp.170-178;

RESEARCH ON THE ANTI-CRUSHING MECHANISM OF CORN GRAIN PNEUMATIC CONVEYING PROCESS UNDER THE INFLUENCE OF MULTI-PARAMETER COUPLING

/

多参数耦合影响的玉米颗粒气力输送过程抗破碎机理探究

Mingxu WANG[1,2], Jiangfeng OUYANG[1], Ziiyan ZHAO[1], Runze WU[3]
[1]School of Mechanical & Electrical Engineering, Henan University of Technology, Zhengzhou 450001, China
[2]Henan Key Laboratory of Grain and Oil Storage Facility & Safety, Henan University of Technology, Zhengzhou 450001, China
[3]Dalian University of Technology Panjin Campus, Panjin 124000, China
Tel: 18623717728.; E-mail: wmx20032002@163.com
DOI: https://doi.org/10.35633/inmateh-72-08

Keywords：*pneumatic conveying; corn crushing; response surface experiments; multi parameter coupling; shatterproof; mechanistic investigation*

ABSTRACT

In order to reduce the crushing rate and energy consumption of corn kernels in the pneumatic conveying process, this paper firstly used the conveying wind speed, material-air ratio and corn kernel moisture content as the influencing factors in the conveying process to conduct single-factor simulation experiments. Then, a test platform was created for the pneumatic conveying of grain particles and an orthogonal test was conducted using the crushing rate and pipeline pressure drop as conveying performance indices. A regression equation model was then created that connected each test index to each factor in turn. Lastly, it was used the response surface method for multi-objective optimization to determine the ideal parameter combinations for the conveying wind speed, which was 25.42 m/s, the material to gas ratio, which was 10, and the moisture content, which was 13.912%. At this time, the corresponding pneumatic conveying indexes are 1.112% crushing rate, 8.725 kPa pressure drop, and 0.328 kg/s conveying capacity, which provide theoretical and experimental bases for the prevention of crushing and the reduction of energy consumption during the pneumatic conveying of grain particles.

摘要

为降低玉米籽粒在气力输送过程中的破碎率、减小能耗，本文将输送过程中输送风速、料气比和玉米籽粒含水率作为影响因素分别进行单因素仿真实验，然后，设计并搭建粮食颗粒气力输送试验平台，以破碎率和管道压降为输送性能指标进行正交试验，分别建立起各试验指标与各因素之间的回归方程模型，最后，利用响应面法进行多目标优化，得到最优参数组合为输送风速为25.42m/s，料气比为10，含水率为13.912%。此时对应的气力输送指标分别为破碎率为1.112%，压降为8.725kPa，此时的输送能力为0.328kg/s。为粮食颗粒气力输送过程防破碎和降低能耗提供理论和试验依据。

INTRODUCTION

Pneumatic conveying is a high-efficiency, flexible process arrangement, airtight environmental protection, safe, and reliable conveying method that is widely used in the storage of grain particles in logistics as well as in various aspects of the production and processing of food, feed, and industrial raw materials. Agricultural materials are widely used in the production and processing of food, feed, and industrial raw materials. Particle crushing is a necessary component of pneumatic conveying technology because of the inevitable collision behavior of particles and pipe walls. Therefore, the study of the interaction behavior between the particle motion distribution and the flow field in the gas-solid two-phase interaction process is a must to reveal the mechanism of corn grain crushing and reduce energy consumption.

The crushing properties of grain particles are influenced by a variety of variables. It is challenging to learn about the microscopic dynamics of a pneumatic conveying system by experimentation alone. For analyzing gas-solid two-phase flow, computational fluid dynamics with discrete element coupling is the best method. Hall studied the impact test that was carried out under the same conditions, the degree of damage depended on the type of grain, which was tested for wheat, rice, soybeans and corn, and corn was the most prone to breakage, followed by soybeans (*Hall et al,1974*). Kendall found that large grains are more likely to be damaged than small grains (*Kendall K.,1978*).

The reason is that when the particles are small, the stress required for crack propagation increases. At the same time, larger grains have larger mass, so they are subjected to greater impact force during the impact process. Chen conducted compression, friction and repeated impact tests on corn grains and wheat respectively, and the results showed that corn grains and wheat were sensitive to compression and impact loads, and friction brought little damage to these two grains, and both of them had good anti-wear ability (*Chen et al, 2021*). Shamba studied wheat and rye seeds and found that when the water content is below a certain limit, the damage sensitivity decreases with the increase of grain water content (*Shahbaz et al, 2012*). Grains with low water content are more likely to be broken, because they are more brittle, less elastic and have lower fracture energy than grains with high water content. Su measured the physical mechanics of different types of corn grains and studied the damage resistance and compression characteristics of bulk corn through compression experiments on bulk corn (*Su et al, 2019*). It was found that when the water content increased from 12% to 31%, the crushing rate, maximum shape variable and deformation energy of corn grains all increased, while the hardness decreased with the increase of water content. Salman used a continuous airflow gun to take fertilizer particles as the experimental material, and experimentally studied the effects of impact angle, impact velocity and impact frequency on the breakage rate of single particles (*Salman et al, 2002*). It was found that when the impact angle is larger, a smaller impact velocity leads to a higher crushing rate, and when the impact angle is smaller, increasing the number of impacts does not lead to a higher crushing rate, and it was also found that an increase in particle size leads to a sharp increase in particle crushing rate. A small impact velocity will lead to a higher crushing rate. The study found that when the impact angle is small, increasing the crushing frequency will not lead to an increase in the crushing rate. At the same time, it was found that increasing the particle size will lead to a sharp increase in the crushing rate.

However, all of these efforts have looked at one factor at a time. The combined effect of multiple factors is ignored. Peng conducted an experimental study on the collision process between the larvae of the black water fly and the wall, and analyzed factors such as collision material, falling height, material thickness, collision angle, falling direction, and water content, and concluded the relationship between the larvae of the black water fly and the above factors (*Peng et al, 2021*). Liu used high-speed photography technology combined with three-dimensional dynamic coordinates to analyze the collision process of oil sunflower seeds, and established regression equations of falling height, material thickness, collision angle, water content and recovery coefficient (*Liu et al, 2020*). The conventional orthogonal design technique is a mathematically based design approach that may determine the optimal arrangement of various component levels. But because orthogonal design can only be used to evaluate discrete data, it has limited precision and unpredictable results. The response surface approach may create a high-precision regression equation using a nonlinear model, make accurate predictions, and identify the ideal process conditions. As a result, employing the response surface approach to examine the variables impacting corn crushing rate is more trustworthy.

In summary, the single factor analysis of the three factors which affect the crushing rate of maize was carried out. Secondly, a multi-bend pneumatic conveying platform for grain particles was built. Finally, by synthesizing the influence of different factors on particle breakage and pipeline pressure drop, the influence of different factors on the crushing rate and pipeline pressure drop is obtained, and the influence law and principle are analyzed. The response surface method is adopted to comprehensively analyze the influence of each factor, and the optimal parameter ratio is obtained. The reliability of the multi-objective optimization model is verified, which provides theoretical and experimental basis for preventing crushing and reducing energy consumption during the pneumatic conveying of grain particles.

MATERIALS AND METHODS

System architecture

Based on the findings of the investigation into the relationship between corn kernels and the flow field in the pipeline, an experimental platform for pneumatically conveying grain particles in conjunction with curved pipe was constructed in order to examine the influence law of various factors on the effect of pneumatic conveying of corn kernels. As shown in Fig.1, the experimental platform for positive pressure pneumatic conveying of grain particles is mainly composed of Roots blower, vortex flowmeter, rotary unloader, hopper, frequency converter, cyclone separator, glass sight glass, pressure transducer, signal acquisition system, high-speed camera and PLC control cabinet. The Jinkong JGR-80H Roots blower supplies the air for the experimental platform. It has a rated flow rate of 3.07 m3/min, a rated power of 7.5 kw, and a pressure range of 0–63.7 KPa. The conveying wind speed can be controlled and measured by measuring the air flow with a vortex flowmeter.

Vortex flowmeter being connected to the air inlet of the rotary unloader, corn kernels and other food particles can be fed through the hopper on the rotary unloader, through the rotating unloader uniformly into the gas-solid injector, the material in the gas-solid injector and the airflow is fully mixed, with the conveying airflow into the initial section of the straight tube for acceleration. In order to avoid the effect of different wall materials at bend on the test results, it was chosen to connect a better wear-resistant glass pipe sight glass before and after the 180° bend, and measure the particle velocity with a high-speed camera to record the particle movement before and after the bend. In order to study the flow characteristics more comprehensively, the test platform is designed with multiple 180° bends to realize long-distance conveying tests in the laboratory space. Corn kernel is transported in the pipe under the action of conveying airflow, and then finally the cyclone separator is used to separate the gas and solid and collect the materials.

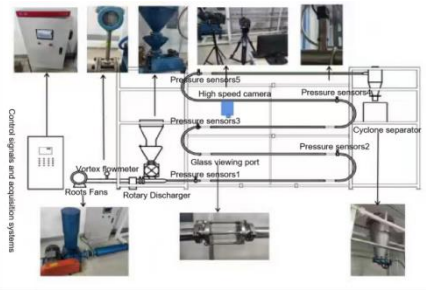

Fig. 1 - Multi-bend Pneumatic Conveying Test Platform for Grain Pellets

Control and signal acquisition system test equipment

The control and signal acquisition system of this test platform is mainly composed of pressure sensor, vortex flow meter, frequency converter, PLC control cabinet and dynamic signal measurement and control system. The model of the pressure sensor is Lester LST-131 diaphragm sheet pressure sensor made of diffusion silicon, powered by 24V DC power supply, and the range of the pressure sensor is 0-100kPa. With the change of the airflow pressure in the pipeline, the pressure sensor outputs a 4-20 mA current signal corresponding to the pressure of the airflow, and the pressure sensors 1 to 5 are distributed in different positions of the pipeline, as shown in Fig. 1. The output signals of the experimental process are transmitted to the self-developed dynamic signal measurement and control system through the signal acquisition instrument, and the main interface of the system is shown in Fig. 2. The vortex flowmeter is PFT-LUGB-2305-N vortex flowmeter, with a nominal diameter of DN50, nominal pressure of 1.6 MPa, accuracy of 1.5 grade, and a measurable flow range of 30-300 m^3/h.

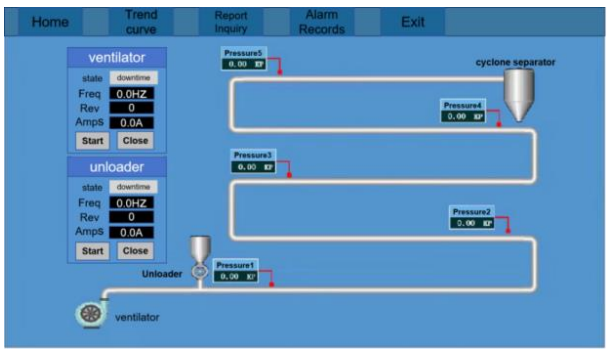

Fig. 2 - Dynamic signal measurement and control systems

Experimental program

First, fix the bend pipe on the test stand, make good connections and check the sealing ring status, then, open the dynamic signal measurement and control software, adjust the frequency converter connected to the Roots fan and the frequency converter connected to the unloader to the required experimental settings; when the Roots fan enters into a stable conveying state, the vortex meter shows that the flow rate is the same as the expected conveying wind speed, add prepared corn kernels to the hopper; use the high-speed camera to record the movement status and position distribution in the pipe before and after entering the bend pipe; finally, re-sieve the broken kernels after conveying and save the pressure signal data. Use high-speed camera to record the movement of corn kernels before and after entering the pipe and the position distribution in the pipe; finally, the pressure signal data was saved and the conveyed corn grains were re-screened to screen out the broken corn grains and weighed. The morphology of the broken corn grains is shown in Fig. 3.

Fig. 3 - Example of corn kernel breakage

RESULTS

Particle motion analysis

A high-speed video camera was used to film the movement of corn kernels in the pipe and to analyze the average particle velocity before and after the bend. Measure the position of a particular corn kernel at time $t(x_t,y_t)$, as shown in Fig. 4(a), the position of the grain (x_{t+5},y_{t+5}) at the moment $(t+5)$ after 5 frames is measured, as shown in Fig. 4(b), and the distance between these two positions divided by the time of 5 frames is obtained as the moving speed of this corn kernel. In the conveying process every 1000 frames randomly selected 5 corn kernels to record the particle moving speed, a total of 5 groups of average speeds were recorded and the experimental data are shown in Table 1.

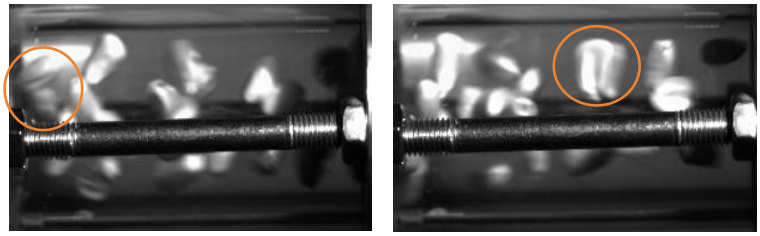

a) moment t **b) moment t+5**

Fig. 4 - Corn kernel grain movement

Analysis of pressure drop test results

The static pressure signals of the four pressure sensors in the flow field of the conveyor pipe, corresponding to the pressure signals of the four pressure sensors are shown in Fig.5. When the material enters the conveying pipeline, the pressure inside the pipeline will rise significantly as the material passes through, the values of the pressure sensors are recorded, and the pressure drop between different points can be calculated by calculating the difference between them. The variation of conveyed energy consumption under different test conditions can be obtained by recording the pressure drop between pressure sensors 1 and 4.

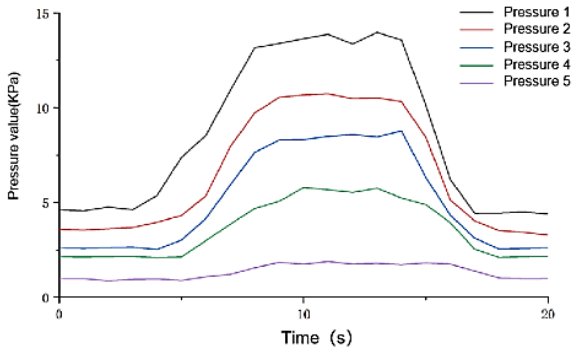

Fig. 5 - Pressure signal diagrams for different measurement points

Response surface method test results and analysis

The conveying air speeds of the corn kernels were selected as 25 m/s, 29 m/s and 33 m/s, the material-air ratios were controlled by the frequency conversion of the unloader, and the selected material-air ratios were 6, 8 and 10. The moisture contents of the corn kernels were 10%, 12% and 14%. The specific test coefficients and levels are shown in Table 1.

Table 1

Combined elbow pneumatic conveying test factors and levels

Level	Factor		
	Conveying wind speed (m/s)	Material-to-gas ratio	Moisture content (%)
-1	25	6	10.0
0	29	8	12.0
1	33	10	14.0

Desing-Expert software was utilized to create orthogonal tests in accordance with the Box-Behnken model, taking into account the orthogonal design elements indicated in Table1. Approximate experiments on the conveying process were conducted using the pneumatic conveying platform for grain particles, and the crushing rate and pipeline pressure drop under various parameter combinations were computed. The outcomes were displayed in Table 2. Each index findings in the table were calculated by averaging the outcomes of three separate, repeated experiments.

Table 2

Design of the orthogonal tests

Serial Number	Factor			Crushing rate Y_1	Pipe pressure drop Y_2
	Conveying wind speed X_1	Material-to-gas ratio X_2	Moisture content X_3		
1	-1	-1	0	1.495	6.62
2	1	1	0	4.705	15.31
3	0	0	0	2.885	9.64
4	1	0	1	4.596	13.97
5	0	0	0	2.831	9.78
6	-1	0	1	1.112	7.6
7	1	0	-1	5.437	13.53
8	-1	1	0	1.243	8.41
9	0	1	1	2.383	11.26
10	-1	0	-1	1.561	7.61
11	1	-1	0	5.143	11.95
12	0	-1	1	2.752	7.91
13	0	0	0	2.794	9.86
14	0	1	-1	3.285	10.37
15	0	-1	-1	3.328	7.52

Regression Equation for Crushing Rate

Table 3 shows that X_1, X_2, X_3, X_1X_3, and X_{12} are extremely significant at the α = 0.05 level. The regression equation between crushing rate Y_1 and the factors was obtained as shown in equation (3):

$$Y_1 = 2.84 + 1.81X_1 - 0.138X_2 - 0.346X_3 - 0.098X_1X_3 - 0.082X_2X_3 + 0.274X_1^2 \quad (3)$$

Table3

Variance analysis of crushing rate regression equation

Source	Mean Square	df	Sum of Squares	F Valve	p Valve
Model	27.64	9	3.07	588.84	< 0.0001**
X_1	26.17	1	26.17	5017.83	< 0.0001**
X_2	0.1518	1	0.1518	29.10	0.003**
X_3	0.9577	1	0.9577	183.62	< 0.0001**
X_1X_2	0.0086	1	0.0086	1.66	0.2542
X_1X_3	0.0384	1	0.0384	7.37	0.0421*
X_2X_3	0.0266	1	0.0266	5.09	0.0705
X_1^2	0.2786	1	0.2786	53.4	0.008**

Source	Mean Square	df	Sum of Squares	F Valve	p Valve
X_2^2	0.0046	1	0.0046	0.875	0.3924
X_3^2	0.0157	1	0.0157	3.01	0.1435
Residual	0.0261	5	0.0052		
Lack of Fit	0.0219	3	0.0073	3.48	0.231
Pure Error	0.0042	2	0.0021		
Cor Total	27.67	14			

Pipe pressure drop regression equation

The R^2=0.997>0.8 of the pipeline pressure drop regression model derived from this multifactor calculation indicates that the regression equation can better reflect the actual situation and the degree of fit is excellent. Adjustment $Radj^2$=0.993 and prediction $Rpre^2$=0.962 are basically consistent with each other, the difference between the two is within 0.2, indicating that the regression model is more accurate.

In Table 4, and it can be seen that X_1, X_2, X_3, X_1X_2, X_{12} are extremely significant at the level of α = 0.05. The P value greater than 0.1 indicates that the item of the model is not significant, the reduction of these items in the degree of influence and trend analysis will help to improve the model. After removing the insignificant terms with P-value greater than 0.1, the regression equation between the pipe pressure drop Y_2 and the factors was obtained as shown in equation (4):

$$Y_2 = 9.76 + 3.06X_1 + 1.42X_2 + 0.214X_3 + 0.393X_1X_3 + 1.11X_1^2 - 0.3X_3^2 \quad (4)$$

Table 4

Variance analysis of pipe pressure drop regression equation

Source	Mean Square	df	Sum of Squares	F Valve	p Valve
Model	97.71	9	10.86	214.25	< 0.0001**
X_1	75.15	1	75.15	1483.05	< 0.0001**
X_2	16.10	1	16.10	317.77	< 0.0001**
X_3	0.3655	1	0.3655	7.21	0.0435*
X_1X_2	0.6162	1	0.6162	12.16	0.0175*
X_1X_3	0.0506	1	0.0506	0.9990	0.3634
X_2X_3	0.0625	1	0.0625	1.23	0.3173
X_1^2	4.57	1	4.57	90.18	0.0002**
X_2^2	0.3323	1	0.3323	6.56	0.0506
X_3^2	0.1404	1	0.1404	2.77	0.1569
Residual	0.2534	5	0.0507		
Lack of Fit	0.2286	3	0.0762	6.14	0.1432
Pure Error	0.0248	2	0.0124		
Cor Total	97.97	14			

The contribution of each factor to the indicator is shown in Table 5.

Table 5

Degree of influence of factors on indicators

Norm	Impact factor contribution rate								
	X_1	X_2	X_3	$X1X_2$	X_1X_3	X_2X_3	X_{12}	X_{22}	X_{32}
Y_1	1.809	-0.138	-0.346	—	-0.098	-0.082	0.275	—	—
Y_2	3.065	1.419	0.214	0.393	—	—	1.113	-0.3	—
arrange in order $\frac{Y_1}{Y_2}$	X1>X3>X12>X2>X1X3>X2X3								
	X1>X2>X12>X1X2>X22>X3								

Analysis of the influence law of each factor on the crushing rate

The one-way relationship between the crushing rate and each factor is negatively correlated with the water content and the material-gas ratio, except for the positive correlation with the wind speed. From the ANOVA results in Table 3, it can be seen that the p-value of conveying wind speed-water content (X_1-X_3) and material-gas ratio-water content (X_2-X_3) is <0.1, which is more significant to the crushing rate, in the above case, the Design-Expert software was used to draw the three-dimensional response surface analysis graphs of conveying wind speed-water content (X_1-X_3) and material-gas ratio-water content (X_2-X_3) on crushing rate. From Fig. 6(a), it can be seen that the crushing rate generated by the conveying wind speed is much greater than that by the moisture content; if the moisture content is small, the crushing rate with the wind speed changes faster, so in the design of grain particle pneumatic conveying system attention should be paid to conveying the lower moisture content of the particles to reduce the wind speed; from Fig. 4(b), it can be seen that the crushing rate is affected by the material-gas ratio and the water content, the material-gas ratio and water content (X_2 - X_3) on the three-dimensional response surface analysis. It can be seen from Fig. 6(b) that the crushing rate is affected by the ratio of material and gas and water content in a similar way, and the crushing rate is the smallest when the ratio of material and gas and water content are the largest.

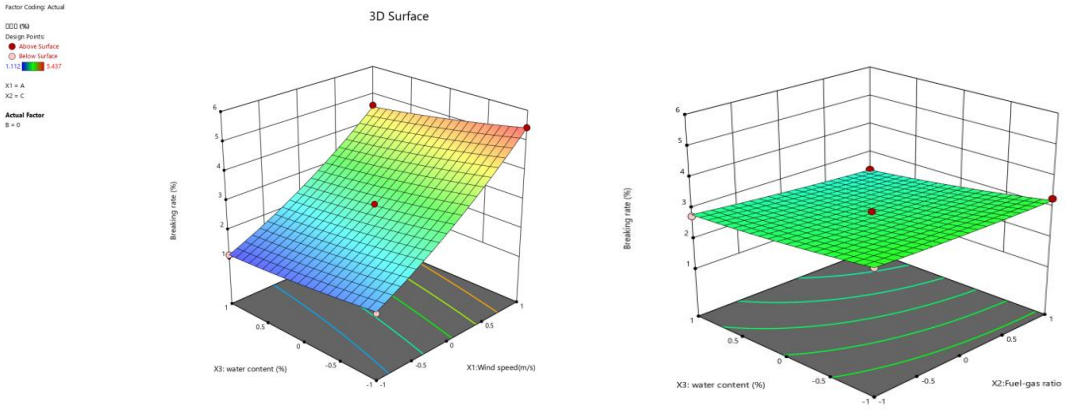

(a) (b)

Fig. 6 - Crushing rate response surface analysis

Analysis of the influence pattern of each factor on pipeline pressure drop

From the ANOVA results in Table 5, it can be seen that the p-value of conveying wind speed - material-gas ratio (X_1-X_2) is <0.1, which has a more significant effect on the pressure drop of the pipeline. In the above case, the three-dimensional response surface analysis of conveying wind speed - material-gas ratio (X_1-X_2) on the pressure drop of the pipeline is plotted using Design-Expert software. From Fig. 5, it can be seen that the pipeline pressure drop by conveying wind speed is greater than by the influence of the material gas ratio, when the material-to-gas ratio is larger, the duct pressure drop varies more rapidly with the wind speed, that is, when the material gas is relatively large, the low air velocity will make the pipeline pressure drop up to too large, resulting in waste of energy consumption.

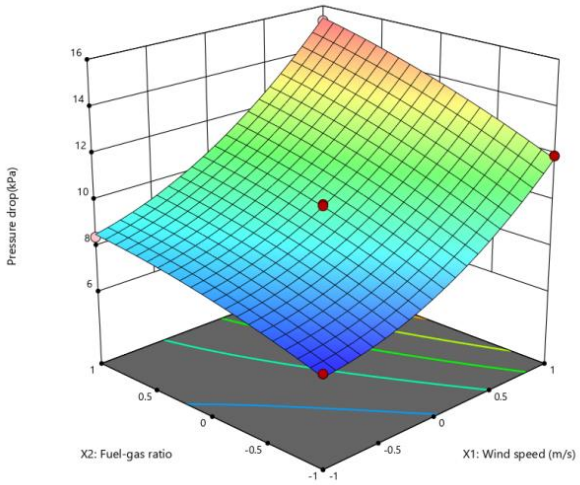

Fig. 5 - Pipeline pressure drop response surface analysis

CONCLUSIONS

In this paper, taking the minimum crushing rate, minimum pipeline pressure drop and maximum conveying capacity as the target, the three regression equation models established are used to do multi-objective optimization and solving, and the optimal parameter combinations are conveying wind speed of 25.42 m/s, material/gas ratio of 10, moisture content of 13.912%, and the corresponding pneumatic conveying indexes are 1.112% crushing rate, 8.725 kPa pressure drop, and 0.328 kg conveying capacity. The conveying capacity is 0.328 kg/s. The multi-objective optimization results were verified experimentally, and the indicators obtained from the verification were 1.143% crushing rate and 8.408 kPa pipeline pressure drop, and the relative error between the experimental value and the theoretical optimization value was within 8%, which verified the reliability of this multi-objective optimization model. In the process of corn grain conveying, controlling the conveying wind speed and material-air ratio can reduce the crushing rate of corn grains, reduce the energy consumption in the process of pneumatic conveying, so as to achieve the purpose of energy saving.

ACKNOWLEDGEMENT

This research was supported by Training plan of young backbone teachers in colleges and universities in Henan Province (2020GGJS088), Opening subject of Henan key laboratory of grain and oil storage construction and safety (2021KF-B02) and Science and Technology Research Project of Henan (No. 232103810084).

REFERENCES

[1] Chen Z.P.，Wassgren C., Ambrose R.P.K. (2021) Measured damage resistance of corn and wheat kernels to compression, friction, and repeated impacts [J]. *Powder Technology*, 380: 638-648.

[2] Du Jun, Hu Guoming, Fang Ziqiang, et al. (2014) Numerical simulation of bent tube dilute phase pneumatic conveying by CFD-DEM method (弯管稀相气力输送 CFD-DEM 法数值模拟) *Journal of National University of Defense Technology*, 36(04):134-139.

[3] Feng-Yao Zhang. (2019) Research on physical and mechanical properties and fine-scale mechanism of soybean particles based on discrete element method. *Henan University of Technology,* 2019.

[4] Gao Tianbao, Li Yong. (2006) Grain particle crushing in pneumatic conveying process (气力输送过程中的粮食颗粒破碎问题) *Grain and Feed Industry*, (12):13-15.

[5] Hall G.E. (1974) Damage during handling of shelled corn and soybeans [J]. *Trans. ASAE*, 17(2):335-338.

[6] Ji Y., Liu S., Li J. (2018) Experimental and numerical studies on dense-phase pneumatic conveying of spraying material in venturi [J]. *Powder Technology,* 339:419-433.

[7] Kendall K. (1978) The impossibility of comminuting small particles by compression. *Nature*, 272(5655): 710-711.

[8] Li Hongcheng, Zeng Rong, Yang Tianyuan, et al. (2022) Experimental study on impact crushing characteristics of corn kernels (玉米籽粒冲击破碎特性试验研究) *Journal of Agricultural Engineering,* 38(07):29-37.

[9] Liang Tao, Li Ping, et al. (2021) Research on basic physical properties and mechanical damage law of corn seeds (玉米种子基本物性及机械损伤规律研究) *Seed*, 40(11):46-53.

[10] Liu Yang, Zong Wangyuan, Ma Lina, et al. (2020) Determination of three-dimensional collision recovery coefficient of oil sunflower seeds using high-speed photography (采用高速摄影技术测定油葵籽粒三维碰撞恢复系数). *Journal of Agricultural Engineering*, 36(04):44-53.

[11] Li Xinping, Gao Lianxing, Ma Fuli. (2007) Finite element analysis of mechanical properties of corn seeds (玉米种子力学特性的有限元分析). *Journal of Agricultural Machinery* (10): 64-67+72.

[12] Lu Zhou, Liu Xuedong, Pan Bing. (2011) Numerical simulation of columnar particle transportation process in a curved pipe based on CFD-DEM method (基于 CFD-DEM 方法的柱状颗粒在弯管中输送过程的数值模拟). China Powder Technology, 17(05):65-69.

[13] Peng Caiwang, Zhou Ting, Song Shisheng et al. (2021) Determination of collision recovery coefficient of black gadfly larvae based on Hertz contact theory (基于 Hertz 接触理论的黑水虻幼虫碰撞恢复系数测定). *Journal of Agricultural Machinery*, 52(11):125-134.

[14] Salman A.D.，Hounslow M.J., Verba A. (2002) Particle fragmentation in dilute phase pneumatic conveying [J]. *Powder Technology*, 126(2002):109-115.

[15] Shahbazi F., Dowlatshah A., Valizadeh S. (2012) Breakage Susceptibility of Wheat and Triticale Seeds Related to Moisture Content and Impact Energy [J]. *Cercetari agronomice in Moldova*, 45(3).

[16] Su Y., Cui T., Zhang D.X. et al. (2019) Damage resistance and compressive properties of bulk maize kernels at varying pressing factors: Experiments and modeling [J]. *Journal of Food Process Engineering*, 42(7).

[17] Wang Bo, Wang Jun, Du Dongdong. (2018) Finite element analysis of the dynamic process of corn kernel collision damage based on HyperMesh and LS-DYNA (基于 HyperMesh 和 LS-DYNA 的玉米籽粒碰撞损伤动态过程的有限元分析). *Journal of Zhejiang University (Agricultural and Life Sciences Edition)*, 44(04): 465-475.

[18] Ye Fangping, Li Yu, Hu Jiquan, et al. (2017) Research on pneumatic conveying characteristics based on particle dynamics theory (基于颗粒动力学理论的气力输送特性研究) *Journal of Wuhan University of Technology,* (5):47-52.

[19] Zhang Chunyan, Ma Chao, Yan Fei. (2018) Gas-solid two-phase flow characteristics in bends with different bend-to-diameter ratios based on CFD-DEM method (基于 CFD-DEM 方法的不同弯径比弯管中气固两相流动特性) *Journal of Jiangsu University of Science and Technology (Natural Science Edition),* 32(06):803-808.

[20] Zhao Zhan, Li Yaoming, Chen Yi, et al. (2013) Research on mechanical characteristics of rice seed collision (水稻籽粒碰撞力学特性研究). *Journal of Agricultural Machinery*, 44(06): 88-92.

REAL-TIME GRAPE DISEASE DETECTION MODEL BASED ON IMPROVED YOLOv8s
/
基于改进 YOLOv8s 的实时葡萄病害检测模型

Jinglong REN[1)], Huili ZHANG*[1)], Guangyuan WANG[1)], Chenlong DAI[1)], Fei TENG[1)], Moxian LI[1)]

[1)]College of Mechanical and Electrical Engineering, Qingdao Agricultural University / China

Tel: +86-13605424499.; E-mail: zhhuili73@163.com

DOI: https://doi.org/10.35633/inmateh-72-09

Keywords: *MobileNetV3, YOLOv8s, Grape Leaves, Disease, Image Recognition*

ABSTRACT

This research is dedicated to enhancing the accuracy and processing speed of grape disease recognition. As a result, a real-time grape disease detection model named MSCI-YOLOv8s, based on an improved YOLOv8s framework is proposed. The primary innovation of this model lies in replacing the backbone network of the original YOLOv8s with the more efficient MobileNetV3. This alteration not only strengthens the ability of the model to capture features of various disease manifestations in grape leaf images but also improves its generalization capabilities and stability. Additionally, the model incorporates the SPPFCSPC pyramid pooling structure, which maintains the stability of the receptive field while significantly enhancing processing speed. The integration of the CBAM attention mechanism further accentuates the ability of the model to identify key features, substantially increasing the accuracy of disease detection. Moreover, the model employs Inner-SIoU as the loss function, optimizing the precision of bounding box regression and accelerating model convergence, thereby further enhancing detection efficiency. Rigorous testing has shown that the MSCI-YOLOv8s model achieves an impressive average precision (mAP) of 97.7%, with an inference time of just 37.2 milliseconds and a memory footprint of 39.3 MB. These advancements render the MSCI-YOLOv8s not only highly efficient but also extremely practical for real-time grape disease detection, meeting the actual demands of grape orchard disease identification and demonstrating significant potential for application.

摘要

本研究致力于提升葡萄病害识别的准确性与处理速度，因此提出了一款基于改进的 YOLOv8s 模型的实时葡萄病害检测模型，命名为 MSCI-YOLOv8s。该模型的核心创新在于将原 YOLOv8s 的主干网络替换为更高效的 MobileNetV3，此举不仅增强了模型捕捉葡萄叶片图像中不同尺度病害特征的能力，同时也提高了其泛化性与稳定性。此外，模型整合了 SPPFCSPC 金字塔池化结构，不仅保持了感受野的稳定性，还实现了处理速度的显著提升。引入的CBAM 注意力机制进一步加强了模型对关键特征的识别，显著提高了病害检测的准确度。模型还采用了 Inner-SIoU 作为损失函数，以优化边界框回归的精度并加快模型收敛，从而进一步提升了检测效率。经过严格测试，MSCI-YOLOv8s 模型实现了 97.7%的平均精度（mAP），推理时间仅需 37.2 毫秒，内存占用为39.3MB，表现卓越。这些改进使得 MSCI-YOLOv8s 在实时葡萄病害检测方面不仅效率高，且具备强大的实用性，完全符合葡萄果园病害识别的实际需求，展现了巨大的应用前景。

INTRODUCTION

Crop health monitoring plays a crucial role in ensuring the yield and quality of agricultural products and is an indispensable part of the development of precision agriculture (*Sishodia et al., 2020; Sharma et al., 2020; Farooq et al., 2019*). Grapes, in particular, as a widely cultivated economic crop globally, are not only nutritionally rich but also have significant medicinal value (*Georgiev et al., 2014; Ananga et al., 2013; Perestrelo et al.,2014*). However, crops like grapes face attacks from various diseases every year, leading to severe yield losses and posing a significant threat to global food security (*Nicholas et al., 2012*). Therefore, developing a method for timely and accurate identification of crop diseases is particularly important. This not only reduces the yield loss caused by diseases but also helps to improve the efficiency of pesticide use, making it a key component of crop disease management.

[1] *Jinglong REN, Ph.D.Stud.Eng; Huili ZHANG,Prof.Ph.D.Eng; Guangyuan WANG, Ph.D.Stud.Eng; Chenlong DAI, Ph.D.Stud.Eng; Fei TENG, Ph.D.Stud.Eng; Moxian LI, Ph.D.Stud.Eng*

Although traditional methods of crop disease identification rely on manual observation and laboratory analysis, these methods are inefficient, complex, and fail to meet the practical needs of modern agricultural production. With the rapid development of artificial intelligence technology, machine vision and image processing techniques have been widely applied in the field of crop disease identification (*Singh et al., 2024*). While traditional machine vision methods classify diseases by analysing features like colour, shape, and texture, these methods are inefficient and struggle to adapt to the rapidly changing needs of agriculture (*Thakur et al., 2023; Ibrahimi et al., 2023; Salman et al., 2023*). This study effectively tackles the rapid detection and identification of diseases in natural environments by integrating a multi-target detection model with manual labelling, data augmentation, and parameter optimization techniques. By integrating multi-target detection models, manual labelling, data augmentation, and parameter optimization techniques, and incorporating a coordinate attention mechanism into the backbone network, the accuracy and speed of detection have been effectively improved. (*Jing HAO et al., 2022; Ye XIA et al., 2023*). Through self-supervised learning, deep learning methods can automatically learn and extract features, effectively overcoming the limitations of traditional machine learning methods and showing great potential in disease identification.

In the realm of grape leaf disease identification and management, there is an urgent need for a method capable of rapid and precise execution. In response to the limitations of existing approaches, this study has developed an innovative real-time detection model named MSCI-YOLOv8s stability (*Yang et al., 2023; Jia et al., 2023*). This model combines an improved YOLOv8s framework with the efficient MobileNetV3 backbone network, showcasing superior performance in extracting multi-scale disease features from grape leaf images and enhanced generalization and stability (*Wang et al., 2023; Niu et al., 2023*). To further increase processing speed, the SPPFCSPC pyramid pooling structure have been employed, optimizing the spatial reception capacity of the model (*Zhang et al., 2023*). Moreover, the integrated CBAM attention mechanism has improved the precision in identifying key features, significantly boosting the accuracy of disease detection. The utilization of the Inner-SIoU loss function has refined the accuracy of bounding box regression and expedited model convergence. Experimental results prove that the MSCI-YOLOv8s model, with its swift and accurate detection capabilities, meets the practical demands of orchard disease identification and lays a foundation for technological advancements in precision agriculture.

MATERIALS AND METHODS

Dataset

In this study, the focus was on several common diseases in grape leaves, including Black Rot, Leaf Blight, Downy Mildew, Anthracnose, Rust, and Black Measles. Specifically, four primary conditions for in-depth investigation were selected: Black Spot, Leaf Blight, Black Measles, and Healthy leaves. These specific diseases and the healthy state constituted the focal point of our research, aiming to enhance the accuracy and efficiency of our model in detecting grape leaf diseases through comprehensive analysis and recognition of these conditions.

To construct the dataset, a Sony Alpha 6400 camera was utilized to capture images of grape leaves affected by the aforementioned diseases and healthy leaves under various time and weather conditions, and from multiple angles. In total, 3,970 images were collected. To further enrich the dataset and increase the number of images, 500 grape leaf disease images were also incorporated from three public datasets: Plant Village, Plant Pathology, and Ai Studio, bringing the total number of images to 4,470 (*Goncharov et al., 2019; Agrios G.N. et al., 1978*). These carefully selected and diverse images provided a comprehensive and rich perspective for this research, aiding in enhancing the generalization ability and recognition efficiency of our model. Example images from the dataset are displayed in Figure 1, reflecting the diversity of grape leaves with different disease types.

In this study, the collected raw images of grape leaves were subjected to a series of data augmentation processes to enhance the diversity of the dataset and the generalization ability of the model. These augmentation techniques included image flipping, mirroring, translation, noise addition, and brightness adjustment. These manipulations not only increased the adaptability and robustness of the samples but also helped to improve the ability of the model to recognize grape leaf diseases in natural environments and strengthen the retention of label information.

After the aforementioned data augmentation methods, a total of 17,880 images of grape leaves were obtained. Subsequently, these augmented images were manually annotated using the LabelImg tool, and labels were created for the grape leaf disease dataset in the YOLO format. These labels included Black Rot, Leaf Blight, Black Measles, and Healthy.

To ensure the scientific validity and effectiveness of the training, the dataset of 17,880 images was randomly and evenly distributed into training, validation, and testing sets in an 8:1:1 ratio. The specific number of images for each category is summarized in Table 1. Through this approach, a grape leaf disease recognition dataset was successfully constructed for the experiments in this study.

Table 1

Disease Dataset

Labels	Training Dataset	Validation Dataset	Test Dataset	Total Number of Images
Block_Rot	3776	472	472	4720
Leaf_Blight	3400	425	425	4250
Black_Measles	3800	475	475	4750
Healthy	3328	416	416	4160
Totals	14304	1788	1788	17880

Yolov8 Model

YOLOv8 represents the latest advancement in the YOLO (You Only Look Once) series of models, demonstrating exceptional performance in tasks such as object detection, image classification, and instance segmentation. Developed by Ultralytics, the company that previously released the highly influential YOLOv5 model, YOLOv8 incorporates numerous improvements and updates in its architectural design and development experience compared to YOLOv5. These modifications draw from the optimization strategies of many outstanding YOLO algorithms, propelling YOLOv8 to a new state-of-the-art (SOTA) level and achieving significant enhancements in object recognition performance.

Despite the commendable achievements in detection accuracy, YOLOv8 still has room for improvement in practical production environments. Currently, the model faces challenges in handling the impact of changes in the shape and size of targets on detection accuracy, reducing confusion due to similar features, and enhancing the speed of model recognition. To better adapt to the demands of real-world applications, YOLOv8 requires further optimization and refinement, strengthening its performance and practicality in various complex scenarios.

Improving the YoloV8s Model

To address the existing issues with YOLOv8 and further improve its accuracy and speed to better meet the needs of practical production, this study has made the following improvements:

1) By replacing the backbone feature extraction network of the original YOLOv8 model with MobileNetV3, a lightweight deep learning model optimized for mobile and embedded devices has been effectively integrated. MobileNetV3 significantly reduces model parameters and computational demands, greatly enhancing operational efficiency on devices with limited computing resources. This optimization makes the model more suitable for deployment on edge devices, such as smartphones or other portable devices, which is crucial for real-time disease detection applications.

2) In optimizing the original YOLOv8 model, its standard SPPF (Spatial Pyramid Pooling in Fast R-CNN) pyramid pooling was replaced with an innovative SPPFCSPC pyramid pooling. This improvement achieves a speed increase while maintaining the receptive field. This strategic modification not only optimizes the efficiency of the model, but also preserves its ability to effectively process spatial information, a key factor in achieving accurate detection.

3) Incorporating the new RFA (Receptive Field Attention) mechanism into the model reduces information loss and enhances feature information, facilitating feature extraction and accelerating recognition speed. This improvement further enhances the recognition performance of the model, making it more efficient and accurate in processing key features, which is vital for tasks requiring high precision and efficiency.

4) After replacing the original CIoU (Complete Intersection over Union) loss function of YOLOv8 with the Inner-SIoU loss function, the improved loss function aids the model in focusing on high-quality bounding boxes. This change not only improves the detection accuracy of the model but also accelerates the convergence process, thereby enhancing target recognition speed. This modification is a strategic improvement that significantly enhances the overall performance of the model, especially in tasks that require precise localization and rapid processing.

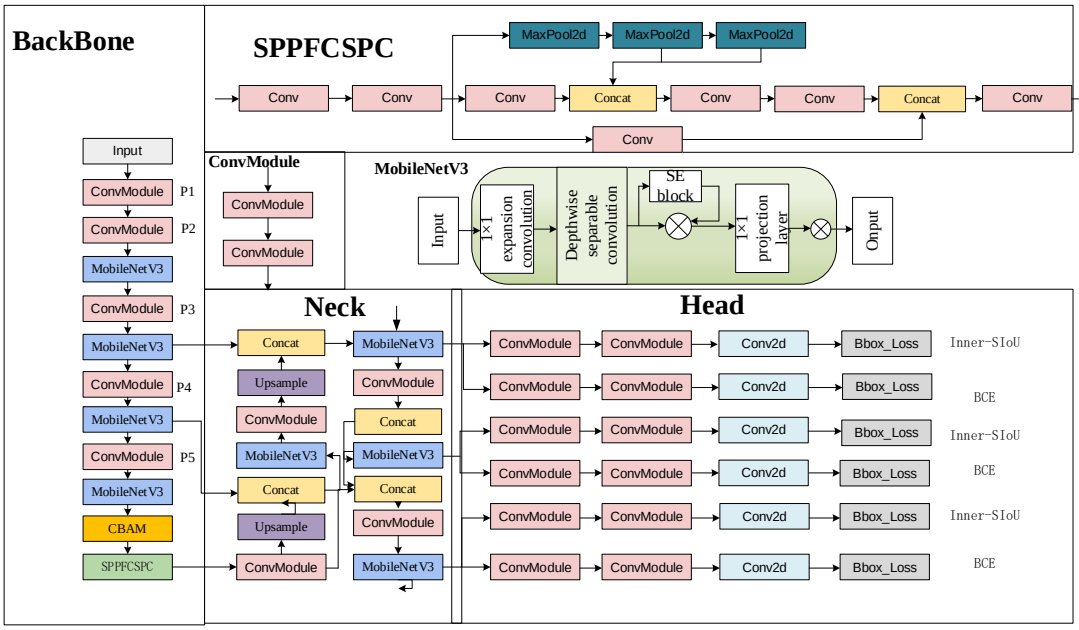

Fig. 1 - MSCI-YOLOv8s Network Structure

MobileNetV3 Feature Extraction Network

To enhance the accuracy and speed of grape leaf disease recognition based on the YOLOv8 model, this study has employed various modules for improvement, aiming to achieve superior recognition performance. MobileNetV3 was chosen as the backbone feature extraction network. MobileNetV3 is a lightweight deep learning model optimized for mobile and embedded devices, renowned for its efficient depthwise separable convolutions and other techniques. It significantly reduces the parameter count and computational needs of the model while achieving a good balance between accuracy and speed, making it highly suitable for real-time disease recognition applications.

MobileNetV3 is an efficient, lightweight deep learning model particularly apt for disease recognition on mobile and embedded devices. It drastically cuts down on the number of parameters and computational demands of the model through depthwise separable convolutions, allowing for rapid operation on resource-constrained devices. The network architecture, automatically designed using Network Architecture Search (NAS) technology, along with the incorporation of the H-swish activation function and Squeeze-and-Excitation (SE) module, ensures that MobileNetV3 remains lightweight while optimizing its feature extraction and representation capabilities. The specific structure employed in this paper is MobileNetV3-Small, as illustrated in Figure 2. This makes MobileNetV3 highly suitable for disease recognition applications, such as real-time monitoring of crop diseases and automated analysis of plant health conditions. Its efficient performance and accurate feature recognition capabilities make it an ideal choice for implementing disease recognition in mobile devices and embedded systems.

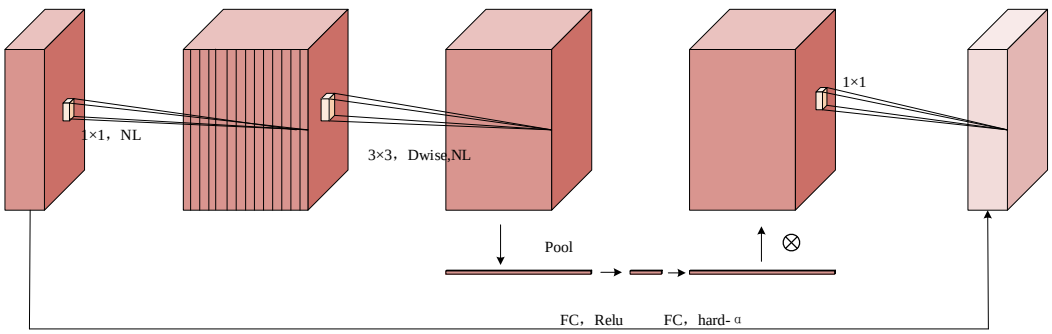

Fig. 2 - MobileNetV3-Small Architecture Diagram

SPPFCSPC Pyramid Pooling

After successfully replacing the backbone feature extraction network of the YOLOv8 model with MobileNetV3, the model achieved significant performance improvements.

To further enhance this effect, this study introduced three additional improvement modules, particularly the SPPFCSPC novel pyramid pooling, which effectively accelerated the processing speed for grape leaf disease recognition. The lightweight nature of MobileNetV3, combined with these innovative improvements, significantly increased processing efficiency while maintaining high-precision recognition.

The Spatial Pyramid Pooling (SPP) module aims to address two key issues: firstly, preventing image distortion caused by cropping and scaling of image regions, and secondly, reducing redundancy in feature extraction by convolutional neural networks. The SPP module accelerates the generation of candidate boxes and saves computational resources through these improvements. With continuous technological evolution, various efficient pyramid pooling structures have emerged. Different versions of the YOLO series exhibit diverse applications of this technology. For example, YOLOv5 and YOLOv8 have adopted the SPPF pyramid pooling structure in their source code, while YOLOv7 has utilized the SPPCSPC pyramid pooling. Each structure has its unique advantages and limitations, reflecting the specific needs and optimization directions of different YOLO model versions in processing images. The application of these pyramid pooling structures has significantly enhanced the adaptability and efficiency of models in various complex environments, achieving more precise and faster performance in object detection.

Specifically, the depthwise separable convolutions and efficient network structure design of MobileNetV3 ensure accurate feature extraction while reducing computational load. Combined with the SPPFCSPC pyramid pooling, it further optimizes the ability of the model to capture features at different scales, enhancing the sensitivity of disease recognition. These improvements work together to significantly enhance the practicality of the model in grape disease recognition, making it more suitable for rapidly and accurately handling complex agricultural disease recognition tasks. In summary, these integrated improvements showcase higher efficiency and precision in the application of grape disease recognition.

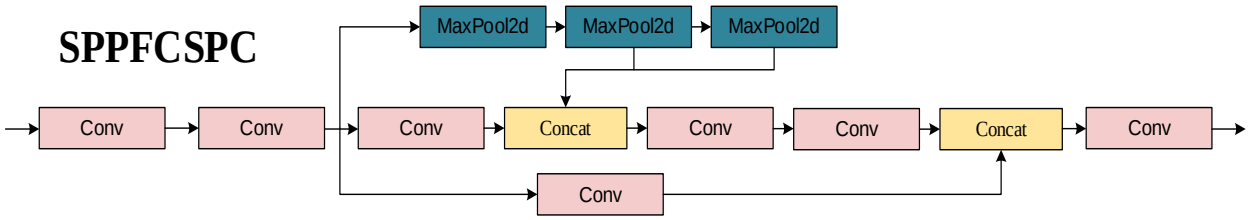

Fig. 3 - SPPFCSPC Structure Diagram

CBAM Attention

This article introduces an attention mechanism known as CBAM (Convolutional Block Attention Module), which plays a pivotal role in various image processing tasks, particularly in the recognition of grape leaf diseases. The main feature of the CBAM attention mechanism is its ability to effectively focus on key parts of an image, especially when dealing with diseased spots on grape leaves. By efficiently selecting features and concentrating on critical areas, it enhances the accuracy of recognition.

The structural design of CBAM is both ingenious and efficient, combining sequential channel and spatial attention methods to fully harness the advantages of both types of attention mechanisms. This design allows CBAM to be flexibly embedded into various convolutional neural network architectures, enhancing the performance of both shallow and deep models in a stable manner. CBAM demonstrates good adaptability to data and robustness, particularly suitable for recognizing grape leaf diseases in variable and complex scenarios.

Overall, the introduction of the CBAM attention mechanism offers an efficient and precise solution in the field of image processing, especially in the domain of grape leaf disease recognition. It enables models to focus more on the key features of images while maintaining outstanding performance. This innovation plays a significant role in enhancing accuracy and practicality in real-world applications.

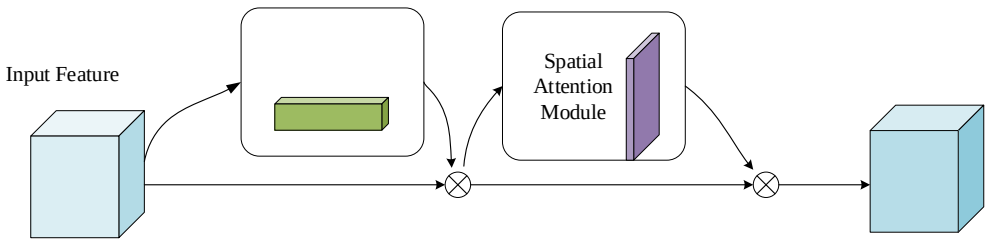

Fig. 4 - CBAM Attention Mechanism Principle Diagram

Inner-SIoU Loss Function

In the original YOLOv8 model, the CIoU (Complete Intersection over Union) loss function was used, which, although accounting for key geometric factors such as overlap area, centre point distance, and aspect ratio, has shortcomings in ensuring precise alignment of bounding boxes (BBoxes), a critical factor affecting the recognition accuracy of the model.

To address this, the Inner-SIoU loss function was adopted in place of the original CIoU loss function in this study. The Inner-SIoU loss function focuses on optimizing the alignment accuracy between predicted and actual bounding boxes, which is crucial for enhancing the accuracy of grape leaf disease recognition. It minimizes the discrepancy in the internal regions of the predicted and actual bounding boxes, rather than just their outer contours, thereby capturing the exact location and shape of disease spots more accurately. Additionally, the Inner-SIoU loss function features rapid convergence and excellent localization effects. By precisely calculating the overlap area, it effectively handles complex cases with less overlap, particularly excelling in images of grape leaves with complex backgrounds or smaller disease spots. The specific formula is as follows:

$$L_{Inner-SIoU} = L_{SIoU} + IoU - \frac{(min(b_r^{gt}, b_r) - max(b_l^{gt}, b_l)) * (min(b_b^{gt}, b_b) - max(b_t^{gt}, b_t))}{(w^{gt} * h^{gt}) * (ratio)^2 + (w * h) * (ratio)^2 - inter} \quad (1)$$

In this formula, w^{gt} and h^{gt} denote the width and height of the target box, while w and h represent the width and height of the predicted box. The term inter refers to the intersection of the predicted and target boxes. The ratio is a scaling factor that controls the size of the auxiliary bounding boxes used in the calculation.

Overall, the application of the Inner-SIoU loss function has significantly enhanced both the accuracy and speed of the grape disease recognition model developed in this study, better fulfilling the practical requirements for efficient and accurate disease detection. This improvement has substantially increased the practicality and efficacy of the model, marking a significant advancement in the field of disease recognition.

Experimental Environment Configuration and Training Parameter Settings

The experiments for this study were conducted under uniform conditions on a single server. The server specifications included a 15-core Intel(R) Xeon(R) Platinum 8358P CPU @ 2.60GHz, an NVIDIA GeForce RTX 3090 GPU with 24GB of memory, 80GB of RAM, a 1TB solid-state drive, and the Linux Ubuntu 20.04 operating system. The software environment comprised PyTorch 2.0.0, Cuda 11.8, Cudnn 8.6.0, and Python 3.8.

In these experiments, training parameters were meticulously calibrated to ensure optimal learning performance of the model. The image input size was set to 640×640 pixels, standardizing all input data to this resolution. Regarding batch size, a Batch=100 setting was opted for, meaning that each batch processed 100 images. To thoroughly train the model, the number of iterations (Epochs) was set to 500, ensuring that the model had ample time to learn and adjust its weights. The initial learning rate was set at Lr0=0.01, providing a balanced starting point that was neither too fast to miss critical learning opportunities nor too slow to impede training efficiency. To monitor and save training progress timely, weight parameters were saved after every 50 iterations.

Evaluation Metrics

In this study, Precision (P), Recall (R), and mean Average Precision (mAP) were meticulously selected as the core metrics for evaluating the accuracy of the model. Precision P primarily measures the similarity between the predicted target area and the actual target area, while Recall R is used to assess the ability of the model to correctly identify target categories, that is, the proportion of accurately identified targets to the total number of targets required to be recognized.

To comprehensively evaluate the performance of the model, inference time and network parameter count were also incorporated into our assessment system to reflect the real-time performance of the model and computational resource efficiency. These metrics were calculated based on the number of true positive samples (TP), false positive samples (FP), and the total number of samples (N). For each grape leaf disease category, its Average Precision (APi) was calculated separately, derived from a specific formula designed to accurately reflect the recognition precision of each category. These comprehensive evaluation metrics allow us to thoroughly and accurately assess performance of the model in grape leaf disease recognition, ensuring its effectiveness and reliability in practical applications. The number of true positive samples (TP), false positive samples (FP), and the total number of samples (N) are used to calculate the metrics, with the Average Precision (AP) for each grape disease category derived from a specific formula. The formula is as follows:

$$AP_i = \frac{\frac{TP}{TP+FP}}{N} \quad (2)$$

$$mAP = \frac{\sum_{i=1}^{Q} AP_i}{Q} \times 100\% \quad (3)$$

$$P = \frac{TP}{TP+Fp} \quad (4)$$

$$R = \frac{TP}{P} \quad (5)$$

RESULTS AND ANALYSIS

Grape Leaf Disease Recognition

Upon the successful completion of the training phase of the MSCI model, the optimally performing weight file, best.pt, was acquired. Subsequently, using images from the test set, an exhaustive evaluation of the MSCI model specific performance in grape leaf disease recognition was conducted. To visually demonstrate the results of the disease recognition experiment, the outcomes are presented in the form of a confusion matrix, as shown in Figure 5.

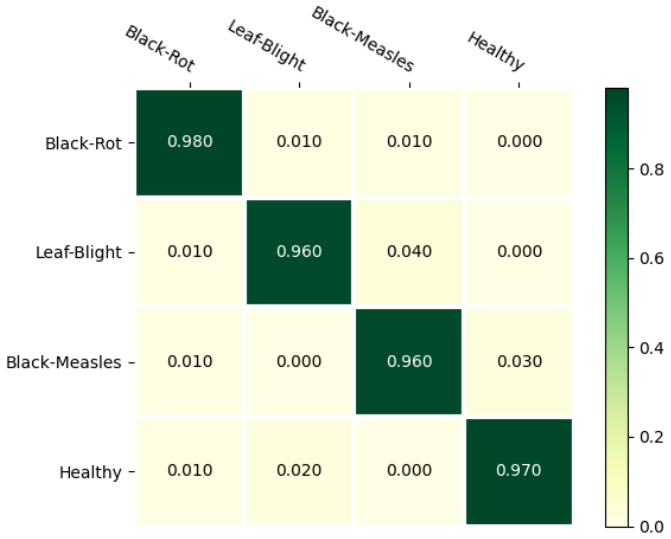

Fig. 5 - Predicted Label

Ablation Experiment

To assess the contribution of the MobileNetV3 backbone feature extraction network and the improvements made by the other three modules to the grape leaf disease recognition model, this study designed a series of ablation experiments. These experiments included evaluations of the original YOLOv8 model and the modified YOLOv8 model with MobileNetV3 as the backbone network. Through such comparisons, the significant impact of integrating MobileNetV3 as the backbone feature extraction network on model performance could be more intuitively understood.

Furthermore, in this study, Grad-CAM (Gradient-weighted Class Activation Mapping) technology for visual analysis of both the pre-improved YOLOv8 model and the post-improved MSRI model was also employed (*Selvaraju et al., 2016*). This method allowed to visually assess the MSRI model, particularly in analysing how the model focuses on key parts of grape leaves. This visualization technique enabled to intuitively understand and compare the level of attention and precision the model, pre- and post-improvement, gave to leaf disease features.

In the visualization results, as shown in the figure 6, the ability of the model before and after improvement to focus on key parts of the leaf was displayed. This not only revealed the mechanism of the model in disease recognition but also showcased the superiority of the MSRI model in capturing key features. These visual analyses provide a clearer understanding of how model improvements impact the precision of disease detection, offering valuable perspectives and foundations for future research.

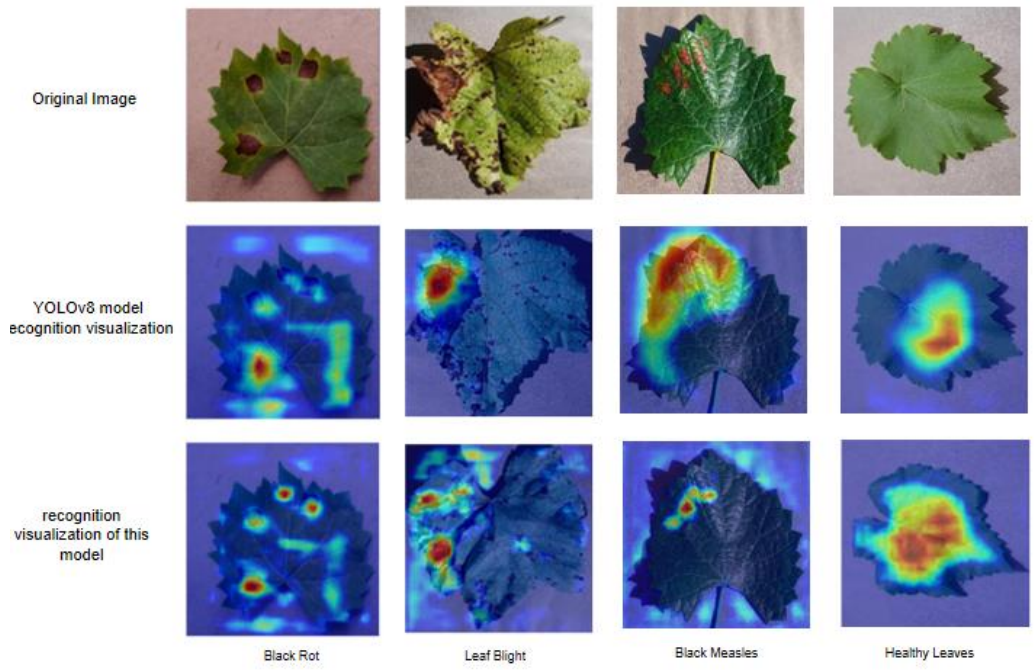

Fig. 6 - Visualization of the Model Focus on Key Leaf Positions Before and After Improvement

As indicated by the data in Table 2 and Figure 7, without any module improvements to the YOLOv8 model, it managed to achieve a grape disease recognition accuracy of 89.6%. While this result is somewhat acceptable, there is a considerable scope for optimization, particularly for real-world application scenarios. To enhance the recognition accuracy, the model was augmented with three modules: SPPFCSPC, CBAM, and Inner-SIoU. Although these improvements resulted in a slight increase in accuracy, the gains were limited, and they also led to higher memory usage and a slight reduction in inference speed. However, when these three modules were integrated into the model simultaneously, the accuracy significantly increased to 97.7%. This marked improvement demonstrates that these three enhancement modules have a distinctly positive impact on bolstering the performance of the grape disease recognition model.

Table 2

Ablation Experiment

Experiment Number	Backbone Network	Pyramid Pooling	Attention Mechanism	Loss Function	mAP / %	Memory Usage / MB	IT / ms
1	Yolov8s	-	-	CIoU	89.6	23.4	58.1
2	MobileNetV3	-	-	CIoU	92.4	27.6	50.2
3	MobileNetV3	SPPFCSPC	-	CIoU	93.1	29.7	47.2
4	MobileNetV3	SPPFCSPC	CBAM	CIoU	94.6	34.7	38.5
5	MobileNetV3	SPPFCSPC	CBAM	Inner-SIoU	97.7	39.3	37.2

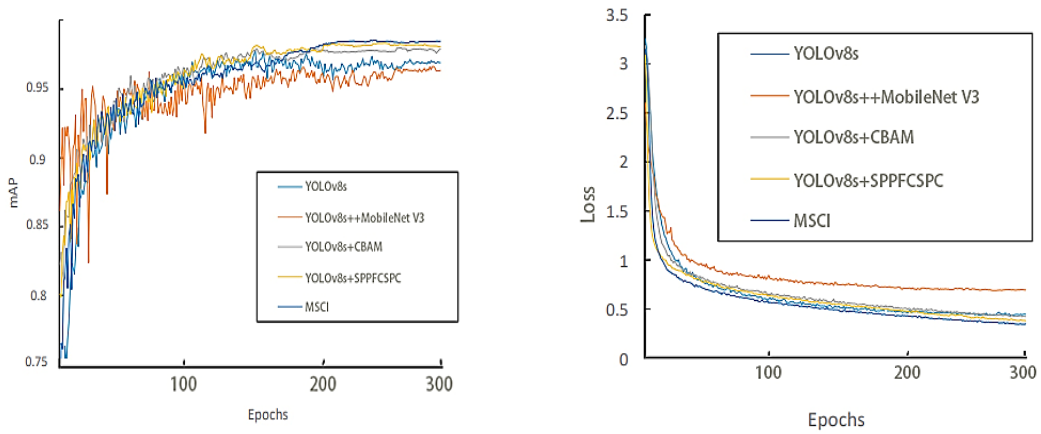

Fig. 7 - mAP Curve and Loss Curve

Comparison of Detection Performance of Different Models

To evaluate the efficiency of the improved algorithm proposed in this article, comparative experiments were conducted with Faster R-CNN, SSD, YOLOv4, YOLOv5, and YOLOv7, as shown in Tabel 9. The experimental results demonstrate that the algorithm in this study excels in accuracy, recall rate, mAP, frame rate, and model size. In particular, it achieved a mAP of 97.7% and a detection speed of 119.81 FPS, meeting the requirements for real-time detection. The model size is 19.40 MB, comparable to YOLOv8 but with superior performance. The algorithm has achieved excellent results in terms of real-time performance, detection accuracy, and efficiency.

Table 3

Comparison results of the models

Network	P(%)	R(%)	mAP(%)	FPS	Model Size(M)	Network	P(%)
Faster-R-CNN	82.36	88.56	80.78	9	523	Faster-R-CNN	82.36
SSD	78.23	73.89	76.68	18	92	SSD	78.23
YOLOv4	89.63	85.23	88.38	52	22.3	YOLOv4	89.63
YOLOv5	91.35	89.20	91.23	90	15	YOLOv5	91.35
YOLOv7	92.56	90.19	91.96	101	12	YOLOv7	92.56
YOLOv8	92.63	91.20	92.00	151	23	YOLOv8	92.63
MSCI	97.70	93.00	94.03	119.81	19.40	MSCI	97.70

RESULTS

This study successfully developed an efficient and real-time grape disease detection model based on an improved YOLOv8s, named MSCI-YOLOv8s, aimed at significantly enhancing the accuracy and speed of grape disease detection. By replacing the backbone network of the YOLOv8s model with MobileNetV3 and embedding an SPPFCSPC pyramid pooling structure, the ability of the model to capture various scale disease features in grape leaf images was enhanced. This not only improved the generalization ability and stability of the model, but also, by introducing the CBAM attention mechanism, further enhanced the focus on key features, thereby increasing the accuracy of disease detection. Moreover, using Inner-SIoU as the loss function, the precision of the model in bounding box regression was enhanced and the convergence of the model was accelerated, thus improving detection efficiency. With these improvements, the MSCI-YOLOv8 model demonstrates outstanding performance in real-time grape disease detection, showing high application value and practical operational potential. The results of this study not only provide strong technical support for the accurate identification and timely treatment of grape diseases but also offer an effective reference model for similar agricultural image recognition tasks. With further optimization and customization, this model is expected to play a broader role in precision agriculture and intelligent monitoring.

ACKNOWLEDGEMENT

This research received support from the Shandong Key Research and Development Programme in the Public Welfare Field (Project No: 2018GGX104012), titled "Key Technology Research and Industrialization of High-Frequency Isolation Power Battery Detection System."

REFERENCES

[1] Ananga A, Georgiev V, Ochieng J,. (2013). Production of anthocyanins in grape cell cultures: a potential source of raw material for pharmaceutical, food, and cosmetic industries. *The Mediterranean genetic code-grapevine and olive*, 1(0): 247-287, Croatia.

[2] Agrios G N. (2005). Plant pathology[M]. *Elsevier*, United States.

[3] Farooq M S, Riaz S, Abid A, (2019). A Survey on the Role of IoT in Agriculture for the Implementation of Smart Farming. *Ieee Access*, 7: 156237-156271, Pakistan.

[4] Georgiev V, Ananga A, Tsolova V., (2014). Recent advances and uses of grape flavonoids as nutraceuticals. *Nutrients*, 6(1): 391-415, United States.

[5] Goncharov P, Ososkov G, Nechaevskiy A, (2019). Disease detection on the plant leaves by deep, *Remote Sensing*, 15(17): 4356, China.

[6] Ibrahimi A E, Akchioui N E., (2023). A review on plant diseases detection using artificial intelligence techniques[C]//AIP Conference Proceedings. *AIP Publishing*, 2814(1), Morocco.
[7] learning[C]//Advances in Neural Computation, Machine Learning, and Cognitive Research II: Selected Papers from the XX International Conference on Neuroinformatics, October 8-12, 2018, Moscow, *Russia. Springer International Publishing*, 151-159, Belarus.
[8] Jia L, Wang T, Chen Y, (2023). MobileNet-CA-YOLO: An Improved YOLOv7 Based on the MobileNetV3 and Attention Mechanism for Rice Pests and Diseases Detection[J]. *Agriculture*, 13(7): 1285, China.
[9] Niu K, Wang C, Xu J, (2023). An Improved YOLOv5s-Seg Detection and Segmentation Model for the Accurate Identification of Forest Fires Based on UAV Infrared Image. *Remote Sensing*, 15(19): 4694 China.
[10] Nicholas K A, Durham W H., (2012). Farm-scale adaptation and vulnerability to environmental stresses: Insights from winegrowing in Northern California. *Global Environmental Change*, 22(2): 483-494, United States.
[11] Salman Z, Muhammad A, Piran M J, (2023). Crop-saving with AI: latest trends in deep learning techniques for plant pathology. *Frontiers in Plant Science*,14, Korea.
[12] Selvaraju R R, Das A, Vedantam R, (2016). Grad-CAM: Why did you say that [J]. *arXiv preprint arXiv:1611.07450*, United States.
[13] Sharma A, Jain A, Gupta P, (2020). Machine learning applications for precision agriculture: A comprehensive review. *IEEE Access*, 9: 4843-4873, India.
[14] Singh B K, Delgado-Baquerizo M, Egidi E, (2023). Climate change impacts on plant pathogens, food security and paths forward. *Nature Reviews Microbiology*, 1-17, Morocco.
[15] Sishodia R.P., Ray R. L., Singh S. K., (2020). Applications of remote sensing in precision agriculture: A review. *Remote Sensing*, 12(19): 3136, United States.
[16] Thakur A, Venu S, Gurusamy M., (2023). An extensive review on agricultural robots with a focus on their perception systems. *Computers and Electronics in Agriculture*, 212: 108146, India.
[17] Wang Z, Ye R, Xu Y, (2023). Research on Meteorological Equipment Identification and Monitoring Algorithm Based on Yolov8. *Available at SSRN 4665653*, China.
[18] Yang Y, Han J., (2023). Real-Time object detector based MobileNetV3 for UAV applications[J]. *Multimedia Tools and Applications*, 82(12): 18709-18725, China.
[19] Ye XIA, Xiaohui LEI, Andreas HERBST., (2023). Research on Pear Inflorescence Recognition Based on Fusion Attention Mechanism with YOLOv5. *INMATEH - Agricultural Engineering,* 69(01), China.
[20] Zongwei JIA, Jing HAO, Yiming HOU., (2022). Study on Rapid Detection and Identification of Multi category Apple Leaf Disease. *INMATEH - Agricultural Engineering,* 67(06), China.
[21] Zhang H, Xu C, Zhang S., (2023). Inner-IoU: More Effective Intersection over Union Loss with Auxiliary Bounding Box[J]. *arXiv preprint arXiv:2311.02877*, China.
[22] Zhang Y, Wang H, Liu J, (2023). A lightweight winter wheat planting area extraction model based on improved DeepLabv3+ and CBAM. *Remote Sensing*, 15(17): 4156, China.

DESIGN AND EXPERIMENTATION OF A POTATO PLANTER MISSED AND REPEATED PLANTING DETECTION SYSTEM BASED ON YOLOv7-TINY MODEL

/

基于 YOLOv7-tiny 模型的马铃薯播种机漏重播检测系统的设计与试验

Huan ZHANG[1)], Shengchun QI[1)], Ranbing YANG[1, 2)], Zhiguo PAN*[1)], Xinyu GUO[1)], Weijing WANG[1)], Sha LIU[1)], Zhen LIU[1)], Jie MU[1)], Binxuan GENG[1)]

[1)] College of Mechanical and Electrical Engineering, Qingdao Agricultural University, Qingdao 266109, China

[2)] College of Mechanical and Electrical Engineering, Hainan University, Haikou 570228, China

Tel: 15318715305; E-mail: peter_panzg@163.com

DOI: https://doi.org/10.35633/inmateh-72-10

Keywords: *object detection, real-time monitoring, positioning acquisition, agriculture technology*

ABSTRACT

In response to the issues of missed and repeated planting during the operation of the chain-spoon type potato planter in China, as well as the low recognition rate for missed planting and the difficulty in identifying repeated planting using existing detection methods, an innovative Potato Planter Missed and Repeated Planting Detection System has been designed. This system is built with a PLC as the lower-level controller and an industrial computer as the core, incorporating the YOLO object detection algorithm for detecting missed and repeated plantings during the operation of the potato planter. Using the YOLOv7-tiny object detection network model as the core, and combining model training with hardware integration, the system performs real-time detection of the potato seed situation within the seed spoon during the operation of the potato planter. It can quickly distinguish between normal planting, missed planting, and repeated planting scenarios. By incorporating the working principles of the planter, the system designs a positioning logic to identify the actual coordinates of missed and repeated planting locations when a lack or excess of planting is detected. This is achieved through the positioning module, enhancing the system's capability to accurately obtain coordinate information for actual missed and repeated planting positions. The system was deployed and tested on a 2CM-2C potato planter. The results indicate that the detection accuracy for missed and repeated plantings reached 96.07% and 93.98%, respectively. Compared to traditional sensor detection methods, the system improved the accuracy of missed planting detection by 5.29%. Additionally, it successfully implemented the functionality of detecting repeated plantings, achieving accurate monitoring of quality-related information during the operation of the potato planter.

摘要

针对我国链勺式马铃薯播种机作业过程中存在漏播、重播以及现有的检测方法对漏播的识别率较低且难以识别重播的问题，创新设计了一种以 PLC 为下位机，以工控机为核心搭载 YOLO 目标检测算法的马铃薯播种机漏重播检测系统。以 YOLOv7-tiny 目标检测网络模型为主体，经过模型训练与硬件相结合，在马铃薯播种机工作过程中对种勺内种薯情况进行实时检测，能够快速区分正常种、缺种及重种等情况。结合播种机的工作原理设计定位逻辑，实现在检测到缺种、重种情况时通过定位模块完成对实际漏播、重播位置坐标信息的获取。将该系统部署在 2CM-2C 马铃薯播种机上进行相关试验测试，结果表明：该系统对于漏播、重播的检测准确度分别达到 96.07%与 93.98%，与传统传感器检测方法相比，漏播检测精度提高 5.29%，并且实现了重播检测的功能，实现对马铃薯播种机作业质量相关信息的准确检测。

INTRODUCTION

The potato is a root food crop second only to maize, wheat and rice. China is the largest potato-growing country *(Li et al., 2020)*. The potato planter is a crucial implement for the development of the potato industry, and its operational quality directly affects the growth and development of potatoes, thus indirectly impacting potato yields *(Li et al., 2024)*. In recent years, the mechanization level of potato planting in China has continuously improved, but the level of intelligence remains relatively low *(Ma et al., 2023)*. In the process of potato planting, it is essential to accurately control various key indicators. The phenomena of missed and repeated plantings caused by changes in the quantity of seed potatoes in the seed spoon significantly affect the quality of planting *(Li et al., 2023)*.

In response to the issue of missed planting, domestic experts and scholars have gradually delved into research. Zhang Xiaodong and others designed an automatic compensation system for a potato planter using

infrared photoelectric sensors, a microcontroller, and a stepper motor *(Zhang et al., 2013)*. Liu Quanwei and others designed a missed planting compensation system for a potato planter based on the ATmega16 microcontroller, and wrote the monitoring and compensation system program in the C language *(Liu et al., 2013)*. Wang Guanping proposed a new compensation solution for missed planting detection using the PIC16F877 microcontroller, which consists of a circuit for generating signals from missed planting detection, an infrared missed planting detection circuit, and a nest-eye wheel-type planting system *(Wang et al., 2016)*. Currently, the mainstream method for detecting missed planting in potatoes mostly involves sensors to detect whether there are seed potatoes in the seed spoon. However, this method is prone to interference from external factors, resulting in detection errors and difficulty in identifying whether there is a phenomenon of repeated planting during the planting process.

With the development of computer vision technology, deep learning methods utilizing deep neural networks can autonomously learn various features in images and perform feature fusion, achieving intelligent detection of targets. These methods are gradually being widely applied in various recognitions within agricultural environments *(Li et al., 2023)*. Given the current issues in potato planter planting quality detection, this paper proposes an image processing-based missed and repeated planting detection technology. This technology can not only detect replanting but also further improve the accuracy of missed planting detection. Combined with a positioning module, it obtains information on the locations of missed and repeated plantings, thereby providing a statistical analysis of the planting quality in the target field.

MATERIALS AND METHODS

Overall design of the system

The Potato Planter Missed and Repeated Planting Detection System is based on the 2CM-2C potato planter as its working platform. It consists of a DF30 industrial camera, an industrial control computer, SIEMENS S7-200SMART PLC, and a positioning module, all integrated with a display screen. The primary working principle involves the industrial control computer carrying a pre-trained target detection neural network model. The industrial camera captures real-time images of each seed bucket during the potato planting process. This facilitates real-time detection and differentiation of the potato seed situation within each spoon. Upon detecting instances of missed or repeated planting, signals are sent to the PLC. The PLC, in turn, sends commands to the positioning module to acquire corresponding coordinates of the planting positions. This process enables accurate monitoring of missed and repeated planting information during the planting operation in the target field.

Detection scheme design

In the mechanized planting process of potatoes, the quantity of potato pieces taken from the seed box by the seed spoon, driven by the planting chain, is a crucial factor influencing planting quality *(Lei et al., 2022)*. Therefore, considering the potato pieces within the seed spoon as the detection target, the detection method involves assessing the quantity of potatoes in each seed spoon to determine whether there is a phenomenon of missed or repeated planting at the corresponding planting point. To ensure the integrity of the target image and the accuracy of the detection results, the imaging device is installed directly above the ascending end of the planting chain, focusing on the topmost seed spoon as it enters the planting tube. As the planting chain rotates, the top seed spoon moves into the planting tube, and the seed spoons below sequentially reach the detection position for assessment, repeating this process to complete the detection of each seed spoon. The schematic diagram of the missed and repeated planting detection is illustrated in Figure 1.

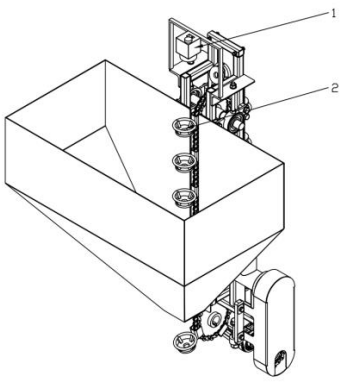

Fig. 1 - The schematic diagram for missed and repeated planting detection
1. The Camera Installation Position; 2. The Detection Target

Situation analysis of detection targets

Based on the image capture position, the condition of potato pieces within the seed spoon can be primarily classified into the following four scenarios: when there is only one potato piece inside the seed spoon, it is considered a normal situation, as shown in Figure 2a; if there are no potato pieces inside the seed spoon, it indicates a situation of missing planting, as illustrated in Figure 2b, which can lead to the phenomenon of missed planting during seeding; if there are two or more potato pieces inside the seed spoon, it indicates a situation of repeated planting, as depicted in Figure 2c, which can lead to the phenomenon of repeated planting during seeding; when the planting chain is in motion, there may be partial overlap in the images during the alternating process of the target seed spoon, making it challenging for the image capture device to collect complete seed spoon information. To prevent erroneous judgments in such cases, this condition is defined as incomplete recognition, as shown in Figure 2d.

a b c d

Fig. 2 - Situation analysis of detection targets

a. Normal situation; b. Situation of missing planting; c. Situation of repeated planting; d. Incomplete recognition.

Image acquisition

The image capture location is in Jiaozhou City, Shandong Province, China. The potato variety used in this study is Dutch 15. Potato seed pieces were cut, with each piece's weight controlled between 45-50g, ensuring 1-2 sprouts per piece. Using the 2CM-2C potato planter from Qingdao Hongzhu Agricultural Machinery Co., Ltd. as the platform, industrial cameras were employed for image acquisition. The cut potato pieces were placed in the target seed spoon to simulate normal planting, missed planting, and repeated planting scenarios. Static shots were taken of the target, capturing 300 images. To ensure the continuity and authenticity of the detection, potato pieces were poured into the seed box, and the movement of the seed spoon was recorded in videos during the planter's operation. From the video, 900 images were extracted. All images had a resolution of 640×640 pixels and were uniformly saved in .JPG format. Part of the image data from static shots and video extraction is shown in Figure 3.

Fig. 3 - Partial image data

Dataset construction

After filtering the collected images, the annotation process was performed using the visual image annotation tool Labelimg to label the potato pieces within each seed spoon. The annotated labels are utilized for classification and object detection tasks. In alignment with the previously discussed detection target scenarios, four labels were set: 'Normal,' 'Repeat,' 'Missing,' and 'Incomplete.' These labels correspond to the normal planting, repeated planting, missed planting, and incomplete recognition scenarios during the detection process.

Due to the complex and dynamic field operating environment of the potato planter, to ensure accurate model training and enhance the model's ability to recognize potato pieces in different scenarios and environments, data augmentation techniques were applied to the collected image data. Operations such as adding noise, adjusting brightness, cropping, panning, rotation and cut-out were performed for data augmentation (*Su et al., 2023; Nithya R et al., 2022*). The enhancement effect is illustrated in Figure 4, and the total number of augmented images reached 5400. The dataset was then divided into training, testing, and validation sets with a ratio of 7:1:2, comprising 3780 images for training, 540 for testing, and 1080 for validation.

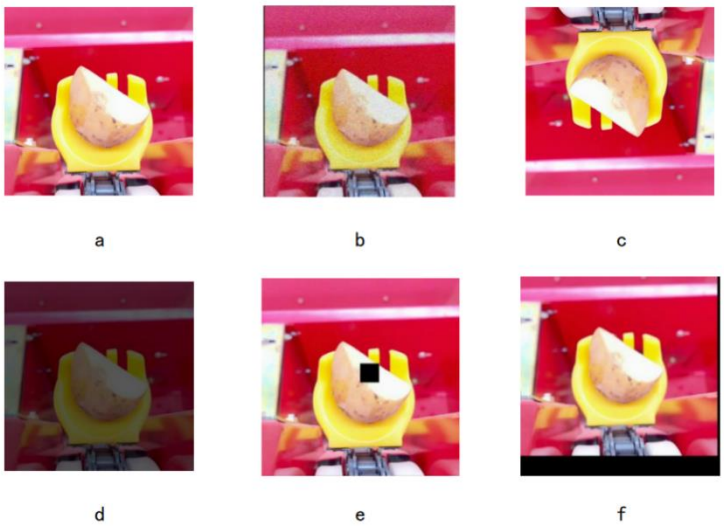

Fig. 4 - Example of data augmentation
a. Original figure; b. Adding noise; c. Rotation; d. Adjusting brightness; e. Cut-out; f. Panning.

Model training

The model selected is YOLOv7-tiny, a streamlined version based on YOLOv7. It is more lightweight and adopts a cascaded model scaling strategy. While ensuring detection accuracy, it achieves fewer parameters and faster detection speed *(Wang et al., 2023)*. This model is suitable for real-time detection requirements in the context of missed and repeated planting during the potato planting process.

The hardware used for training the model is a laptop running Windows 11 (64-bit), equipped with an AMD Ryzen 7 5800H processor, NVIDIA GeForce RTX 3050 Ti GPU. The training environment is set up with Python 3.9.17, PyTorch 1.12.1, and CUDA and cuDNN versions 11.6 and 8.4, respectively.

The training utilized the weight file YOLOv7-tiny.pt. The dataset was iterated for 300 epochs during training, with a batch size of 16 samples per iteration and one weight update performed afterward. To enhance speed while maintaining recognition accuracy, the input image size was set to 480×480. The entire training process took 7 hours and 36 minutes.

Analysis of training results

In order to better evaluate the detection performance of the model in recognizing missed and repeated planting in potatoes, this study employs metrics such as Precision (P), Recall (R), F1 Score, Average Precision (AP), and Mean Average Precision (mAP) as evaluation indicators *(Zhang et al., 2023; Yi et al., 2020; Tian et al., 2023)*. Precision is the proportion of correctly predicted positive samples among the total positive samples in the model's predictions. Recall reflects the model's ability to find positive samples. F1 Score, Mean Average Precision, and Average Precision are all related to Precision and Recall *(Li et al., 2023; Chang et al., 2023)*. The calculations for these evaluation metrics are as follows:

$$P = \frac{TP}{TP + FP} \tag{1}$$

$$R = \frac{FP}{FP + TN} \tag{2}$$

$$F1 = 2 \cdot \frac{P \cdot R}{P + R} \tag{3}$$

$$AP = \int_0^1 P \cdot (R) dR \tag{4}$$

$$\mathrm{m}AP = \frac{1}{N} \sum_{i=1}^{N} AP_i \tag{5}$$

TP (True Positives): the number of samples correctly classified as positive. FP (False Positives): the number of samples incorrectly classified as positive.TN (True Negatives): the number of samples correctly classified as negative. FN (False Negatives): the number of samples incorrectly classified as negative.

The accuracy curve (P_curve) and recall curve (R_curve) obtained during training are shown in Figures 5(a) and 5(b), respectively. The F1 Score is the harmonic mean of precision and recall *(Zheng et al., 2023)*, and the F1 curve is depicted in Figure 5(c). By calculating the precision and recall, the precision-recall curve (PR curve) can be plotted. This curve has recall as the horizontal axis and precision as the vertical axis *(Wu et al., 2023)*. The area under the PR curve is the Average Precision (AP), and the average of AP for all classes is the Mean Average Precision (mAP). The mAP value reflects the overall recognition and classification accuracy performance of the network for object detection *(Zheng et al., 2023).* The accuracy-recall curve obtained during training is shown in Figure 5(d), where the average precision (AP) for each label exceeds 99%, and the mean average precision (mAP) reaches 99.6%. The loss function results and confusion matrix for the trained model are illustrated in Figures 5(e) and 5(f), respectively.

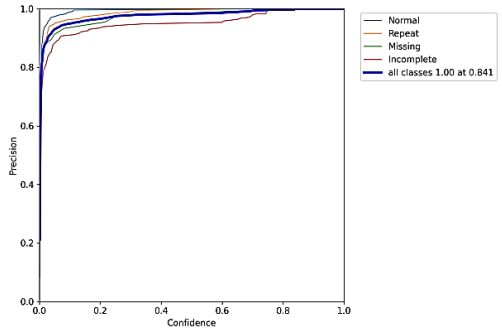

a)

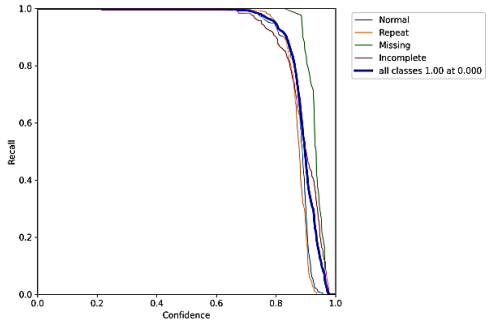

b)

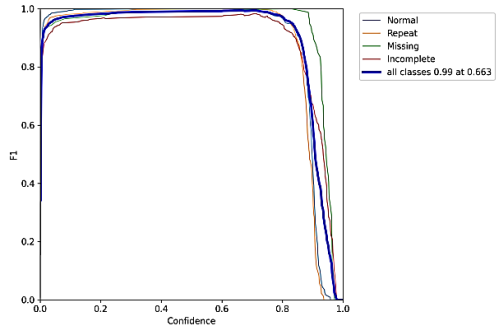

c)

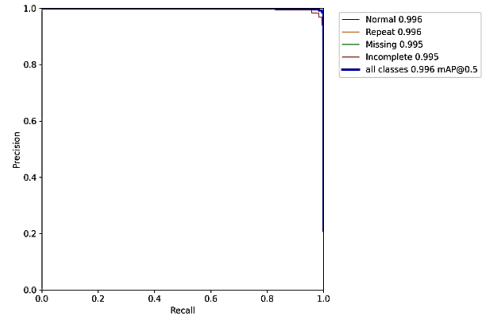

d)

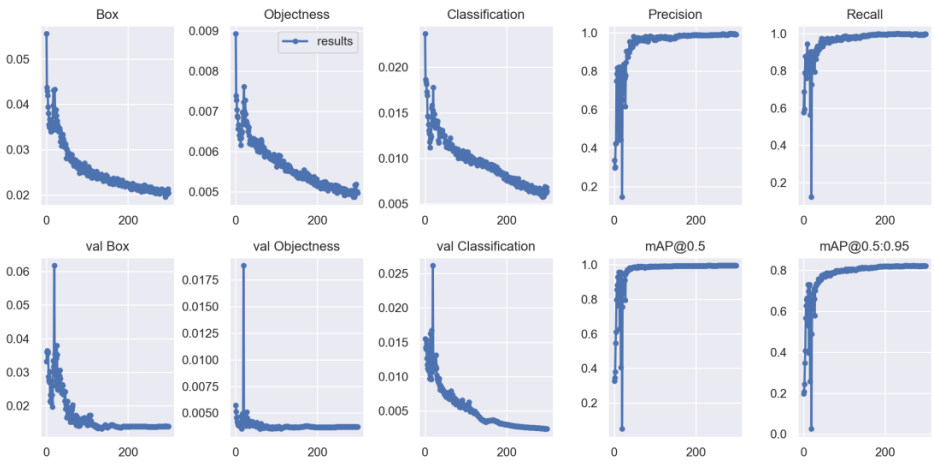

e)

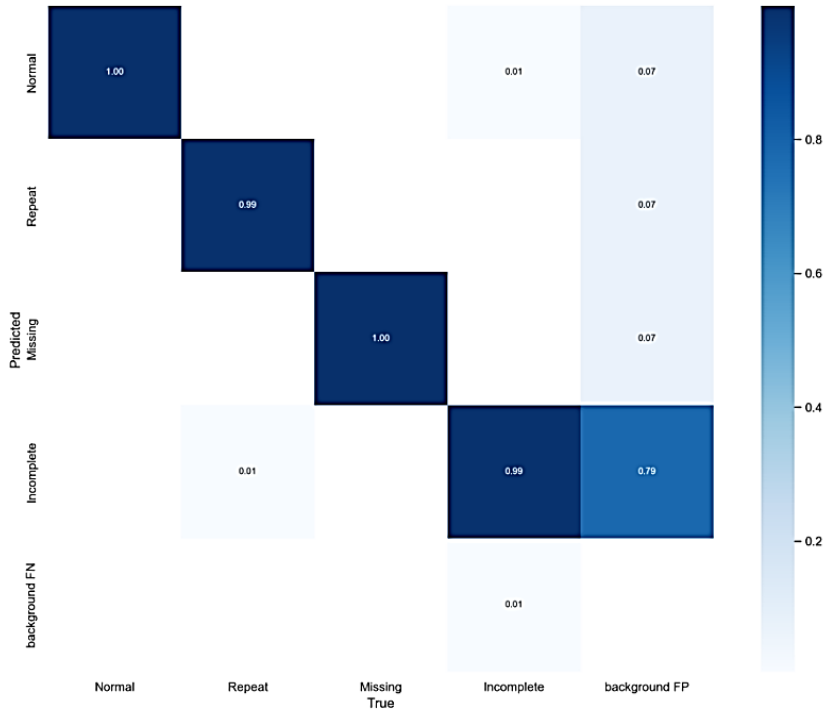

f)

Fig. 5 - Model training results

a. P_curve; b. R_curve; c. F1_curve; d. PR_curve; e. Results; f. Confusion_matrix.

Since the batch size is set to 16, 16 images are read at a time. The actual labels and accuracy of the first round of the validation set are shown in Figure 6(a). In addition, the model was validated using video images with a resolution of 480P/30fps and a duration of 30 seconds, containing 29 seed spoons, including 15 normal plantings, 6 missed plantings, and 8 repeated plantings. During the validation process, 927 frames were extracted for detection, taking 19.927 seconds, and achieving a detection accuracy of 100%. Some screenshots of the video detection results are shown in Figures 6(b) and 6(c).

a b c

Fig. 6 - The results of the validation set and video detection

a. The first round of the validation; b. Screenshot1; c. Screenshot

Transfer model

To ensure compatibility with the hardware of the system and the planter, and to better achieve real-time detection, the trained model was transferred to the industrial control computer. The industrial control computer has a relatively small size, is easy to install, and runs on the Windows 10 operating system. In terms of environment configuration, Python version 3.9.17 and PyTorch version 1.12.1 were used, with the model running on the CPU.

The design of the positioning scheme

Since the detection device is located above the planting chain, and the detection target is the upper end of the planting chain as it ascends, the actual planting coordinates of the potato should be the position coordinates after the potato falls into the soil during the planting process. Therefore, the movement of the

potato from detection to soil entry needs to be analysed, and the time duration *t* for this movement is calculated. After the image recognition module identifies a missed or repeated planting, it sends a signal to the PLC. The PLC, after a time interval *t*, sends a command to the positioning module for reading and parsing the positioning data. This process allows obtaining relatively accurate coordinates for the missed and repeated plantings.

Analysis of potato movement

The movement of the potato inside the seed spoon, from detection to entering the soil, can be roughly divided into three parts. The first part is when the potato reaches position 1, it rotates 180° with the seed spoon, enters the planting tube, and reaches position 2. The second part is when the potato moves with the planting chain in the planting tube from position 2 to position 3. The third part is when the potato leaves the planting tube (position 3) and falls to the soil (position 4). The motion diagram is shown in Figure 7.

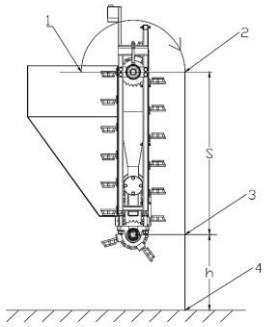

Fig. 7 - Schematic diagram of seed potato movement
1. Position 1; 2. Position 2; 3. Position 3; 4. Position 4.

Calculation of seed potato campaign time

Based on the previous analysis of the movement of the seed potato from detection to entering the soil, the calculation for the movement time *t* is as follows:

The forward speed of the planter is v_0, and the radius of the ground wheel is *r*. Therefore, the rotational speed of the ground wheel is given by:

$$n_1 = \frac{v_0}{2\pi r} \tag{6}$$

The planting chain is driven by the ground wheel, and the tooth number of the ground wheel sprocket is z_1, while the tooth number of the planting chain sprocket is z_2. Therefore, the transmission ratio between the ground wheel and the planting device is given by i:

$$i = \frac{n_1}{n_2} = \frac{z_2}{z_1} \tag{7}$$

Based on the transmission ratio i, the rotational speed of the planting chain sprocket, n_2, can be obtained as:

$$n_2 = \frac{n_1 z_1}{z_2} \tag{8}$$

The tooth spacing of the seed discharge chain is *p*. The linear velocity v_1 of the seed discharge chain can be calculated as:

$$v_1 = \frac{n_2 z_2 p}{60 \times 1000} = \frac{n_1 z_1 p}{60 \times 1000}. \tag{9}$$

In this case, for the convenience of calculation, the first part of the motion is considered as uniform circular motion. The trajectory of the first part of the motion is a concentric circle with the sprocket of the planting chain. The radius of the planting chain sprocket is r_1, and the angular velocity is equal as well as the movement time.

Therefore, the first part of the movement time t_1 is calculated as:

$$t_1 = \frac{\pi r_1}{v_1} = \frac{60 \times 1000 \cdot \pi r_1}{n_1 z_1 p} \tag{10}$$

The distance from the end of the first part of the motion to the position where the seed leaves the planting tube is denoted as s. In the second part, the seed follows the spoon for uniform motion. Therefore, the second part of the motion time t_2 is calculated as:

$$t_2 = \frac{s}{v_1} = \frac{60 \times 1000 s}{n_1 z_1 p} \tag{11}$$

In the third part of the motion, the vertical direction is free fall motion and the horizontal direction is uniform motion (the forward speed of the planter). Given that this segment of motion time is only related to the height, let h be the height from the position where the seed leaves the planting tube to the ground. Therefore, the third part of the motion time t_3 is the free fall time of the seed:

$$h = \frac{1}{2} g t_3^{\,2} \tag{12}$$

$$t_3 = \sqrt{\frac{2h}{g}} \tag{13}$$

The total time of motion is the sum of the three parts of motion time. Combining the above formulas, the total time required for the entire motion process is denoted as t:

$$t = t_1 + t_2 + t_3 = \frac{120000(\pi r_1 + s)\pi r}{v_0 z_1 p} + \sqrt{\frac{2h}{g}} \tag{14}$$

RESULTS

Experimental preparation

To ensure that the developed image recognition-based potato planter skip-seeding detection system meets the practical requirements of agricultural production, experiments were conducted on the relevant functions of the system in the potato test fields in Jiaozhou. The potato variety used for the experiment is Dutch 15, and diced seed potatoes were employed, with each piece controlled to a mass of 45-50 g and a diameter of 30-50 mm, as illustrated in Figure 8. The experimental equipment used was the 2CM-2C one-ridge, two-row potato planter. The potato planter skip-seeding detection system was assembled and fixed according to the design scheme, integrating it with the structure of the planter. Basic functionality of each component was checked to ensure its proper operation. The assembly of the system is shown in Figure 9.

Fig. 8 - Seed potato cubes

Fig. 9 - System assembly

Comparison experiment on missed and repeated planting detection accuracy

In this study, field experiments were conducted to compare the proposed target detection scheme based on the YOLO model with the traditional optoelectronic sensor-based detection scheme. Both detection schemes were simultaneously applied using the same planter to assess missed and repeated planting situations, as well as the detection performance of the two schemes. The field experiment is illustrated in Fig.10.

Fig. 10 - Field experiment

2CM-2C planter with a single row of 19 seed spoons was tested for missed and repeated seeding under the same chain speed (0.35 m/s). The rotating cycles were set at 10, 15, 20, 25, and 30, respectively. The number of detected and actual instances of missed and repeated seeding were recorded during the planting process, aiming to calculate the detection accuracy. The comparative experimental results of missed and repeated planting detection are shown in Tables 1 and 2.

Table 1

The comparative experimental results of missed planting detection

Test	Number of rotating cycles	Seeding number	Scheme	Number of missed plantings detected	Actual number of missed plantings	Accuracy	Missed planting rate
1	10	190	1	16	17	94.12%	8.94%
			2	16		94.12%	
2	15	285	1	21	23	91.30%	8.07%
			2	22		95.65%	
3	20	380	1	30	34	88.23%	8.95%
			2	33		97.05%	
4	25	475	1	38	42	90.48%	8.84%
			2	41		97.62%	
5	30	570	1	44	49	89.79%	8.59%
			2	47		95.92%	

Table 1 presents the experimental data for missed planting detection, while Table 2 provides the experimental data for repeated planting detection. Where Scheme 1 is based on the photodetector detection system, and Scheme 2 is based on the YOLOv7-tiny model detection system.

Table 2

The comparative experimental results of repeated planting detection

Test	Number of rotating cycles	Seeding number	Scheme	Number of repeated plantings detected	Actual number of repeated plantings	Accuracy	Repeated planting rate
1	10	190	1	-	18	-	9.47%
			2	17		94.44%	
2	15	285	1	-	28	-	9.82%
			2	26		92.86%	
3	20	380	1	-	37	-	9.73%
			2	35		94.59%	
4	25	475	1	-	46	-	9.68%
			2	43		93.47%	
5	30	570	1	-	55	-	9.65%
			2	52		94.54%	

Based on the above results, it can be seen that during the experiment, the average missed planting rate of the planter was 8.68%, and the average repeated planting rate was 9.67%. Scheme 1 achieved an average accuracy of 90.78% in missed planting detection, with no repeated planting identification function. Compared to Scheme 1, Scheme 2 achieved an average accuracy of 96.07% in missed planting detection, an improvement of 5.29%. It also implemented replanting detection with an accuracy of 93.98%.

Missed and repeated planting positioning information acquisition

In the above experiments, the positioning module obtained the coordinate information of the actual seeding positions for missed and repeated instances based on the detection results. Partial coordinates information for missed and repeated seeding positions is provided in Table 3.

Partial coordinates information for missed and repeated seeding positions **Table 3**

Location point	Longitude coordinates	Latitude coordinates
Row 1, North to South repeated planting 4	120°03′12.00784″E	36°27′29.67500″N
Row 3, North to South missed planting 1	120°03′12.03886″E	36°27′30.11943″N
Row 5, North to South missed planting 6	120°03′12.28203″E	36°27′28.92467″N
Row 6, North to South repeated planting 11	120°03′12.60862″E	36°27′27.18578″N
Row 8, North to South repeated planting 9	120°03′12.35399″E	36°27′29.09525″N
Row 9, North to South repeated planting 4	120°03′12.31591″E	36°27′29.88054″N
Row 10, North to South missed planting 7	120°03′12.86716″E	36°27′26.58084″N

CONCLUSIONS

This paper addresses the issues of low accuracy in detecting missed seeding and the difficulty in detecting repeated seeding during the potato planting process using existing detection methods. It proposes a missed and repeated seeding detection method based on the YOLOv7-tiny model and combines it with hardware to form a comprehensive detection system. Experimental tests conducted at a seeding chain line speed of 0.35 m/s show that the detection accuracy for missed seeding can reach 96.07%. Compared to traditional methods using photoelectric sensors, the accuracy for missed seeding detection has improved by 5.29%. The system also successfully detects repeated seeding with an accuracy of 93.98%. Furthermore, it acquires the coordinates of the missed and repeated seeding positions during detection in real-time.

The design and functionality implementation of this system address the deficiencies of traditional detection methods, enhancing the detection capability for missed and repeated plantings. It achieves precise monitoring of the operational quality of potato planters and the planting conditions in specific areas, thereby advancing the information level of mechanized potato planting.

ACKNOWLEDGEMENT

This research, titled " Design and Experimentation of a Potato Planter Missed and Repeated Planting Detection System based on YOLOv7-tiny Model ", was funded by the Ministry of Finance and the Ministry of Agriculture and Rural Development under the Special Project for the Construction of National Modern Agricultural Industrial Technology System (CARS-10-P32), the National Key Research and Development Program (2023YFD2000902), and the Research Fund Project for Senior Talents of Qingdao Agricultural University (1116002).

REFERENCES

[1] Chang, R., et al. (2023) Research on Insulator Defect Detection Based on Improved YOLOv7 and Multi-UAV Cooperative System [J]. *Coatings,*13(5):

[2] Lei, X.L., et al. (2022) Design and test of leakage detection and replanting system for potato planter [J]. *Journal of China Agricultural University*, 27(12):234-244.

[3] Li, J.H., et al. (2023) Real-time pineapple detection for agricultural robot via lightweight YOLOv7-tiny model. *Procedia Computer Science* 226:92-98.

[4] Li, P., et al. (2023) Research on the design of leakage monitoring and replanting system of potato planter [J]. *Agricultural Mechanization Research*, 45(12):81-88.

[5] Li, P.W., et al. (2024) Current status and outlook of the development of potato precision seeding technology [J]. *Agricultural Equipment and Vehicle Engineering*, 62(01):29-33.

[6] Liu, Q.W., et al. (2013) Design and research on the compensation system of leakage sowing for 2CM-2 potato planter[J]. *Arid Region Agricultural Research*, 31(03):260-266.

[7] Li, Y., et al. (2020) Analysis of production characteristics, limiting factors and countermeasures in China's main potato producing areas [J]. *China Potato*, 34(06):374-382.

[8] Li, Z.W., et al. (2023) An Enhanced Deep Learning Model for Obstacle and Traffic Light Detection Based on YOLOv5 [J]. *Electronics*, 12(10):

[9] Ma, T., et al. (2023) Development status and analysis of potato mechanization in China [J]. *Hebei Agricultural Machinery*, (15):7-9.

[10] Nithya R., et al. (2022) A Smart Parking System: An IoT Based Computer Vision Approach for Free Parking Spot Detection Using Faster R-CNN with YOLOv3 Method. *Wireless Personal Communications* 125(4):3205-3225.

[11] Su, P.Y., et al. (2023) Improvement of the YOLOv5 Model in the Optimization of the Brown Spot Disease Recognition Algorithm of Kidney Bean [J]. *Plants*, 12(21):

[12] Tian, Y.X., et al. (2023) A New Lunar Dome Detection Method Based on Improved YOLOv7 [J]. *Sensors*, 23(19):

[13] Wang, G.P., et al. (2016) Development of a potato leakage detection and compensation device [J]. *Agricultural Modernization Research*, 37(05):1008-1014.

[14] Wang, W.J., et al. (2023) Improved YOLOv7-Based Algorithm for Detecting Foreign Objects on the Roof of a Subway Vehicle [J]. *Sensors*, 23(23):

[15] Wu, W., et al. (2023) Ship Detection and Recognition Based on Improved YOLOv7 [J]. *Computers, Materials Continua*, 76(1):489-498.

[16] Yi, S., et al. (2020) Pheasant identification method based on enhanced Tiny-YOLOV3 model [J]. *Journal of Agricultural Engineering,* 36(13):141-147.
[17] Zhang, L.H., et al. (2023) Improved Object Detection Method Utilizing YOLOv7-Tiny for Unmanned Aerial Vehicle Photographic Imagery [J]. *Algorithms*, 16(11):
[18] Zhang, X.D., et al. (2013) Design of automatic compensation system for potato planter [J]. *Journal of Gansu Agricultural University*, 48(01):145-149+155.
[19] Zheng, L.S., et al. (2023) Tank vehicle detection method based on improved YOLOv7-tiny [J]. *Journal of Weapons and Equipment Engineering*, 44(12):285-292.
[20] Zheng, Z.H., et al. (2023) EW-YOLOv7: A Lightweight and Effective Detection Model for Small Defects in Electrowetting Display [J]. *Processes*, 11(7):

DESIGN AND EXPERIMENTAL STUDY OF PEANUT PLANTER WITH HIGH-SPEED OPERATION AND CONTROLLABLE SOWING DEPTH

/

高速作业种肥播深可控的花生播种机的设计与试验研究

Moxian LI[1)], Xueliang CHANG[1)], Xiaoning HE[1)], Ning ZHANG[1)], Wei LIU[2)], Zhixin LIU[1)], Tongtong DONG[1)]
Shuqi SHANG*[1)], Dongwei WANG[1)], Maomao ZOU[1)], Yunkang LI[1)], Zhenjia MA[1)]
[1)]Qingdao Agricultural University, College of Mechanical and Electrical Engineering /China;
[2)] Shandong Yuanquan Mechanical Co /China
Tel:+86-13884956252; E-mail: sqshang@qau.edu.cn
DOI: https://doi.org/10.35633/inmateh-72-11

Keywords: *Peanut planter，Seed fertilizer consistency, Improved PID algorithm, Sowing depth*

ABSTRACT

Aiming at the traditional peanut planter seed and fertilizer sowing depth inconsistency caused by seed burning and injury, fertilizer waste and low seed emergence rate, the design of a peanut planter with high-speed operation and controllable seed and fertilizer sowing depth was performed. The laser sensor is added to detect the height of the ridge and the furrow opener position feedback, and the speed sensor detects the operating speed of the peanut planter. The mechanical analysis of the four-link rod clarifies the control principle, improves the PID algorithm of the integral term, designs the control strategy based on the operating speed of the planter, controls the electro-hydraulic system, and realizes the sowing and fertilizing depth adjustment of the furrow opener. Through the design of three-factor three-level orthogonal simulation test, it is concluded that the vehicle speed and height deviation value are significant factors affecting the sowing and application depth, and under the verification of the field test, it is obtained that when the sowing depth is 50 mm under the speed of 3 km/h, the dynamic sowing depth qualification rate is 96.26%, and the maximum coefficient of variation of the sowing depth is 2.58%, which improves the effect of the existing control of the sowing depth of the peanut by 6.05%, and reduces the variation of the sowing depth by 2.85%. The research has demonstrated superior performance compared to traditional mechanical adjustment in regulating the planting depth of peanuts, thereby achieving the intended design objective.

摘要

针对传统花生播种机种肥的播施深度不一致造成烧种伤种、肥力浪费以及种子出苗率低的问题，设计一款具备高速作业种肥一致可控的花生播种机。增添激光传感器对垄面高度检测以及开沟器位置反馈、速度传感器检测花生播种机的作业速度。对四连杆进行力学分析明确控制原理，改进积分项的 PID 算法，设计基于播种机作业速度的控制策略，控制电液系统，实现开沟器的播施深度调节。通过设计三因素三水平正交仿真试验，得出车速和高度偏差值是对播施深度影响的显著因素，在田间试验验证下，得到在 3km/h 的速度下播深为 50mm 时，动态播深合格率为 96.26%，最大播深变异系数为 2.58%，比现有的花生播种深度控制效果提升 6.05%，播深变异降低 2.85%。在调节花生播深方面，与传统的机械调节相比，该方法有更优越的性能，实现了预期的设计目标。

INTRODUCTION

Peanut is one of the top ten oilseed crops in China, and it is of great significance to improve peanut production in China *(Zhang et al., 2005)*. The depth of peanut seed fertilizer application will affect the seedling emergence and growth condition, the depth of fertilizer application is too deep and far away from the peanut seeds, resulting in less nutrient absorption by peanuts, which not only wastes the fertilizer, but also affects the seedling growth of peanuts, thus affecting the yield of peanuts; the depth of fertilizer application is too shallow, and is closer to the peanut seeds, which results in seed burning and seed injury, and also affects the yield of peanuts. Similarly for peanut seeds from the ridge surface, too deep or too shallow will also affect the seedling emergence rate, so the development of more precise sowing machinery is the key to improve the yield *(Wan et al., 2020; Wu et al., 2015).*

[1]*Moxian LI, Ph.D.Stud.Eng; Xueliang CHANG, Ph.D.Stud.Eng; Xiaoning HE, Prof.Ph.D.Eng; Ning ZHANG,. Ph.D.Eng; Wei LIU, Ph.D.Eng; Zhixin LIU, Ph.D.Stud.Eng; Tongtong Dong, Ph.D.Stud.Eng; Shuqi SHANG*, Prof.Ph.D.Eng; Dongwei WANG, Prof.Ph.D.Eng; Maomao ZOU, Ph.D.Stud.Eng; Yunkang LI, Ph.D.Stud.Eng; Zhenjia MA, Ph.D. Ph.D.Stud.Eng*

At present, there are many types of peanut seeding machines developed both domestically and abroad, and their functions are different, but they all have a commonality in terms of the problem, i.e., there is a low pass rate of peanut seed and fertilizer sowing depth *(Wang et al., 2021; Lü et al., 2012; Lü et al., 2015).* Therefore, in order to enhance the precision of peanut sowing depth, scholars at home and abroad have conducted research in the field of sowing depth control. Sowing depth adjustment is mainly divided into two ways, one is active imitation adjustment, the other is passive imitation adjustment, most of the seeder companies in the market use mechanical passive imitation such as depth limiting wheels, which is a little bit insufficient in terms of the precision of the sowing depth compared to the active imitation *(Yang et al., 2016).* In the late 20th century, foreign agricultural machinery enterprises have begun to conduct research in the field of deep control, and carry out active copying of agricultural machinery with the help of electronic equipment and intelligence. For example, MOLATUDI in the United States and other research in the field of corn sowing depth, to explore the seedling emergence rate and seedling growth *(Molatudi R.L, et al., 2009; Mock J.J., et al., 1977)*. The German company Amazone has carried out research in the field of furrowing depth, where the control of sowing depth is achieved by using an ultrasonic sensor as a detection device and a hydraulic system as a control device *(Zhao et al., 1989)*. At the same time, in 2015, foreign researchers also carried out in-depth research on the field of sowing depth, such as that of furrowing depth based on the ISO communication protocol using angle sensors and ultrasonic range sensors, controlling the hydraulic system pressure to achieve the adjustment of sowing depth *(Pasi S. et al., 2015)*.

In 2012, Kiani S designed a non-contact control device in the field of furrow depth, which used ultrasonic sensors to measure the distance between the soil surface and the furrow, and adjusted the sowing depth by adjusting the hydraulic system. *(Kiani S. et al., 2012)*. With the intelligent development of agricultural machinery, domestic researchers have strengthened the research on active mimicry in the field of sowing depth. In 2009, Li achieved the adjustment of sowing depth in the field of furrowing depth by developing an automatic control system and a furrowing depth adjustment device *(Li et al., 2009; Li et al., 2010)*. In 2012, Hu Jun designed a ground profiling sensing device in the field of furrowing depth to control the furrow opener to achieve the adjustment of furrowing depth *(Hu et al., 2012)*.

In 2016, Li Yuhuan designed a device to adjust the sowing depth using a PLC-controlled electric actuator *(Li et al., 2016).* In 2020, Bai Huijuan designed a sowing device, which realizes the adjustment of sowing depth through control of pressure parameters by PLC *(Bai et al., 2020)*. In 2022, Liu designed an adaptive profiling cutter in the field of cutter height control, which uses profiling ground wheels and inclination sensors, and through a fuzzy Proportional-Integral-Derivative (PID) control system, it accomplished a rapid and accurate positioning in the height of the cutter *(Liu et al., 2022)*. In 2022, Ding explored the relationship between monomers and soil mechanics in the field of rice and wheat sowing depth, designed sowing monomers and developed an intelligent soil mechanics on-line testing system to complete the adjustment of rice and wheat sowing depth *(Ding et al., 2022).* In 2023, in the field of wheat sowing depth control, Xue designed a sowing depth control device for suppressor roller position by using a rope displacement sensor and a biaxial inclination sensor, and proposed a fuzzy PID control method based on sowing depth feedback to complete the adjustment of sowing depth *(Xue et al., 2023)*. Although currently there is quite a lot of research in the field of sowing depth control, the application of sowing depth control technology in peanut is still less, and the actual farmland surface morphology is complex and irregular, while peanut is not the same as other crops.

In view of this, the paper researches the seed and fertilizer sowing depth and sowing depth of peanut under high-speed operation, and designs a peanut sowing machine with the ability to control the sowing depth of peanut and the seed and fertilizer consistency, to provide a new type of idea for the in-depth research on the sowing depth control technology of peanut.

MATERIALS AND METHODS

Structural design of a peanut planter with controllable seed and fertilizer sowing depth for high-speed operation

The structure of a peanut planter with high-speed operation and controllable seed and fertilizer sowing depth is shown in Figure 1. It mainly consists of a fertilizer application device, a seed discharge device, a collection and control device, etc.; where in the fertilizer application device includes a fertilizer box and a fertilizer opener; the seed discharge device includes a seed box and a disc opener, and the collection and control device includes a laser sensor, a speed sensor, a hydraulic system, a parallel four-link rod, a control box, and a ground wheel.

Structural design of a peanut planter with controllable seed and fertilizer sowing depth for high-speed operation

Peanut planter collection control device in the collection unit includes laser sensors, speed sensors, used for peanut ridge height and planter operating speed for real-time collection; data collection success through the transmission and processing module will be sent to the central processing unit PLC data, PLC data computing control hydraulic system adjusts the parallel four linkage to achieve the disc opener and fertilizer opener position adjustment. The laser sensor on the connecting rod of the disc opener collects and feeds back the data of the height to the ground to the central processing unit Programmable Logic Controller (PLC), and completes the feedback to the opener. The PLC will record real-time data and display it on the terminal display. The working principle of the high-speed operation of seed and fertilizer sowing depth control is shown in Figure 2.

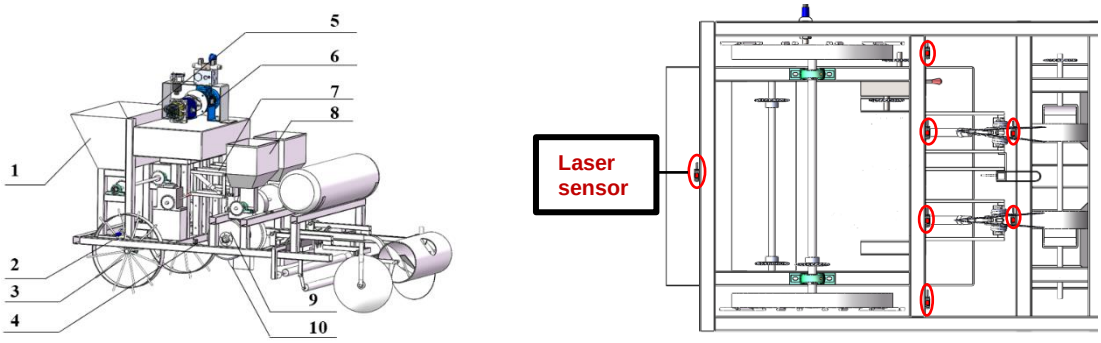

Fig. 1 - Structural design of a peanut planter with controllable seed and fertilizer sowing depth for high-speed operation

1. Fertilizer box; 2. Speed sensor; 3. Ground wheel; 4. Laser sensor; 5. Control box; 6. Hydraulic system; 7. Parallel four-link; 8. Seed box; 9. Disc opener; 10. Fertilizer opener

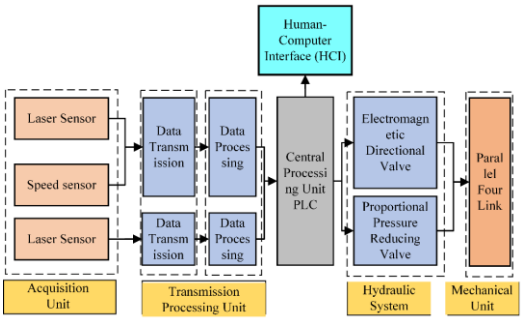

Fig. 2 - Working principle diagram of controllable seed and fertilizer sowing depth for high-speed operation

Theoretical calculation of the operating principle

- Theoretical Calculation of Ranging Principle

This study adopts the direct measurement method of multi-laser sensors to measure the attitude offset of the planter using laser sensors *1, 2, 3*. Each of the three laser sensors transmits the measured distances to the PLC. If the three distances are equal, the planter is not tilted. If the three distances are not equal, it is necessary to calculate the differences between the data measured by laser sensors 4 and 5 from and the data measured by laser sensors 6 and 7. The result will be used next time.
Laser sensor ranging principle is shown in Figure 3.

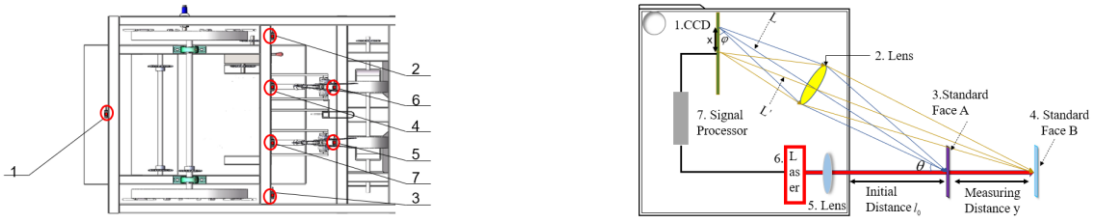

Fig. 3 - Ranging principle diagram of laser triangular reflective displacement sensor

Assuming that the distance moved by the image point on the Charge-Coupled Device (CCD) is x and the distance moved by the surface of the object to be measured is y, Equation (1) is obtained from the similarity triangle:

$$\frac{L'}{x} = \frac{L + y\cos\theta}{y\sin\theta} \quad (1)$$

Equation (1) is collapsed to obtain equation (2):

$$y = \frac{xL}{L'\sin\theta - x\cos\theta} \quad (2)$$

where:

L is the distance from the intersection point of the optical axis of the laser beam to the front principal surface of the receiving lens, (mm);

L' is the distance from the rear principal surface of the receiving lens to the center point of the imaging surface, (mm);

θ is the angle between the optical axis of the laser beam and the optical axis of the receiving lens, (°).

- Control principle calculation

The hydraulic cylinder is mounted on the parallel four-link, when the hydraulic system receives the control command from the central processing unit PLC will complete the expansion and contraction according to the command that is, the parallel four-link will appear in the position of the following Fig. 4, the state I and the state Ⅱ corresponds to the limit state of the upper and lower four-link.

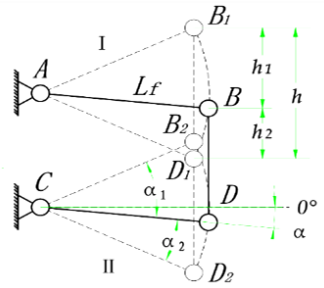

Fig. 4 - Schematic diagram of parallel four-link up and down control volume

Points A and C of the four-link mechanism are fixed with the crossbeam, and points B and D are hinged with the furrow opener connecting rods. AB and CD connecting rods are the upper and lower rods of the profiling mechanism respectively. The BD rod floats up and down along the ground undulation to complete the control when working, and the formula for its control volume is:

$$h = L_f(\sin(\alpha + \alpha_1) + \sin(\alpha_2 - \alpha)) \quad (3)$$

$$h = h_1 + h_2 \quad (4)$$

where:

h is the total control amount, (mm);

h_1 - the upper control amount, (mm);

h_2 - the lower control amount, (mm);

L_f - the length of the connecting rod of the four-bar mechanism, (mm);

α_1 - the upper control angle, (°);

α_2 - the lower control angle, (°);

α - the traction angle, (°).

From equation (3) and equation (4), it can be seen that when the upper and lower control amounts of the four-link are the same, the longer the length of the linkage, the smaller the range of variation of the imitation angle. The change of traction angle depends on the direction of the tractor traction planter frame; in order to ensure that the sowing operation process of the furrow opener works stably, the value of the traction angle should be as small as possible. According to the requirements of peanut agronomic planting, the total control is 50 mm in general.

Selection of detection devices in the seeding depth control system of a peanut planter running at high speeds

The contact detection method has a certain hysteresis and is not applicable to the high-speed working conditions of this study. Therefore, the non-contact method is selected for this study. The BL-400NZ laser sensor selected for this study meets the requirements in terms of sensitivity, accuracy and resolution. The maximum distance of this sensor is 250 mm and the specific parameters are shown in Table 1.

Table 1

Main technical parameters of laser sensors

Technical specifications	Parameters	Technical specifications	Parameters
Model	BL-400NZ	Voltage	24 V
Measuring range	200-600 mm	Signal Output	digital quantity
Accuracy	0.8 mm	Serial Port Type	RS485
Switching frequency	160 hz	Operating Temperature	-20-40℃
Response time	6.25 ms	Protection Class	IP67

The LJA30M-40N1 inductive proximity switch operates at 24 volts and is a reliable sensor with a fast frequency response and adjustable detection distance. It is mounted close to the ground wheel and is used to detect the number of times the axle of the ground wheel passes during operation. Based on the number of contacts in a specified time, the forward speed of the peanut planter can be obtained by calculation. Its specific working parameters are shown in Table 2.

Table 2

Main technical parameters of laser sensors

Technical specifications	Parameters	Technical specifications	Parameters
Model	LJA30M-40N1	Detection distance	0-40 mm adjustable
Working Voltage	DC6~36V	Object detection	Metal
Output form	PNP normally open	Sensing method	Inductive
Output current	300mA	Response time	1 ms

High-speed operation seed fertilizer sowing depth controllable peanut planter software design

This study uses Portal v16 software to compile the control program. After the sowing depth control system is activated, it is necessary to input the set parameters in the terminal display. The PLC saves the set parameters and receives the data transmitted by the sensors in real time. At the same time, the PLC calculates according to the compiled algorithm and outputs PWM signals to the hydraulic system, realizing the adjustment of the sowing depth of peanuts. Laser sensors 6 and 7 transmit the detected data from the fertilizer opener and disc furrow to the PLC in real time, forming a closed-loop control system. The control program flow chart is shown in Figure 5.

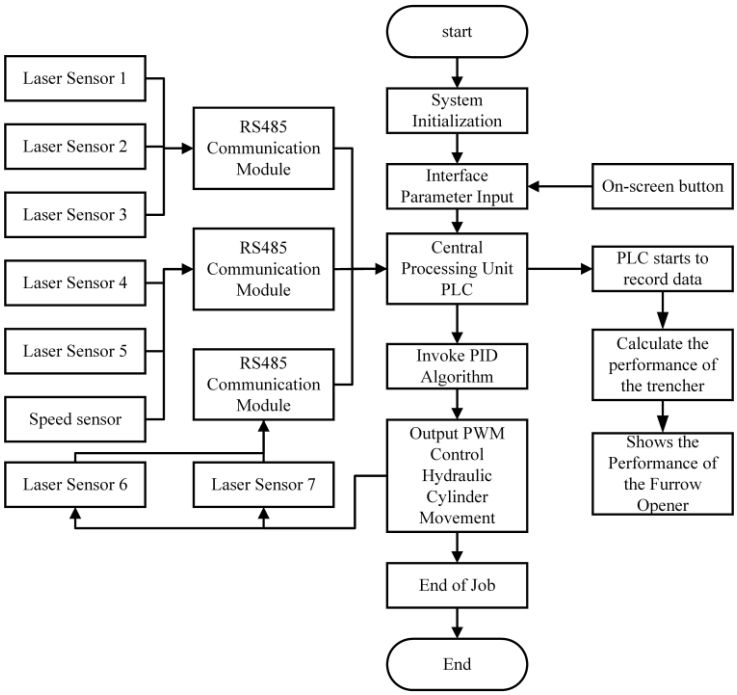

Fig. 5 - High-speed operation seed fertilizer sowing depth controllable peanut planter control program flow chart

Control strategy of peanut planter with controllable seed and fertilizer sowing depth for high-speed operation

- Improved PID control algorithm

For the current most commonly used automatic control feedback technology using PID algorithm to reduce the uncertainty of the system, the control law is shown in equation (5), because the data collected is discrete. Therefore, the PID algorithm is designed discretely in this study and the sampling time is set.

$$e(t) = K_P\left(e(t) + \frac{1}{T_I}\int e(t)dt + T_D\frac{de(t)}{dt}\right) + M \quad (5)$$

From Eq. (5), can be obtained the discretization Eq. (6) and Eq. (7):

$$u(n) = k_p\left\{e(n) + \frac{T}{T_I}\sum_{j=0}^{n} e(j) + \frac{T_D}{T}[e(n) - e(n-1)]\right\} \quad (6)$$

$$u(n) = k_p e(t) + k_i\sum_{j=0}^{n} e(j)T + k_d\frac{[e(n)-e(n-1)]}{T} \quad (7)$$

where: $k_i=k_p/T_I$, $k_d=k_p*T_D$; T is the sampling period;

n is the number of samples, $n=1, 2.....$, $e(n-1)$ and $e(n)$ are at $(n-1)$ and n times.

When the seeding depth is adjusted, the control system is required to adjust the PWM signal. In this process, the PID algorithm will have the phenomenon of error accumulation, leading to the oversaturation of the integral. To avoid the above situation, the idea of this study is to weaken the influence of the integral term when the system difference is too large; when the difference of the system is small, the integral term should be strengthened, and the cumulative speed of the integral term should be adjusted, so as to synchronize with the difference of the change. Therefore, a coefficient $\int(e(n))$ is added, which is a function of $e(n)$. When the absolute value of $e(n)$ increases, its integral decreases; when the absolute value of $e(n)$ decreases, its integral increases. The expression formula is shown in (8):

$$u_i(n) = n_I\{\sum_{i=0}^{n-1} e(i) + \int(e(n))e(n)\}T \quad (8)$$

The functional relationship between $\int(e(n))$ and $|e(n)|$ is equation (9):

$$\int(e(n)) = \begin{cases} 1, (|e(n)| \le B) \\ \frac{A-|e(n)|+B}{A}, (B < |e(n)| \le A+B) \\ 0, (|e(n)| > A+B) \end{cases} \quad (9)$$

So that $\int(e(n))$ function value change interval is [0,1], when $|e(n)|$ is greater than the set $A+B$, its function value is 0; when $|e(n)|$ is less than or equal to B, its function value is 1; if it is in the middle of the two, its function value will be accumulated. Therefore, the formula of the letter PID algorithm with improved integral term is:

$$u(n) = k_p e(n) + k_I\{\sum_{i=0}^{n-1} e(i) + \int(e(n))e(n)\}T + k_D[e(n) - e(n-1)] \quad (10)$$

In figure 6, the unit step response between the improved PID and the traditional PID can be seen. When the deviation between the target value and the actual value is the largest, the integral coefficient of the improved PID is 0, and the integral coefficient changes with $e(n)$, while the integral coefficient of the traditional PID does not change.

- Based on speed detection

In the operation of peanut planter, in order to improve the operation efficiency and improve the operation speed on the basis of ensuring the qualified rate of sowing depth, different sowing speed has different requirements for the response time of this study. Therefore, in order to improve the driving speed in different operations, the high, medium and low speed regions are divided, and different proportion, integral and differential parameters are set for each region. The PID algorithm flow chart of the control strategy based on speed detection is shown in Figure 7.

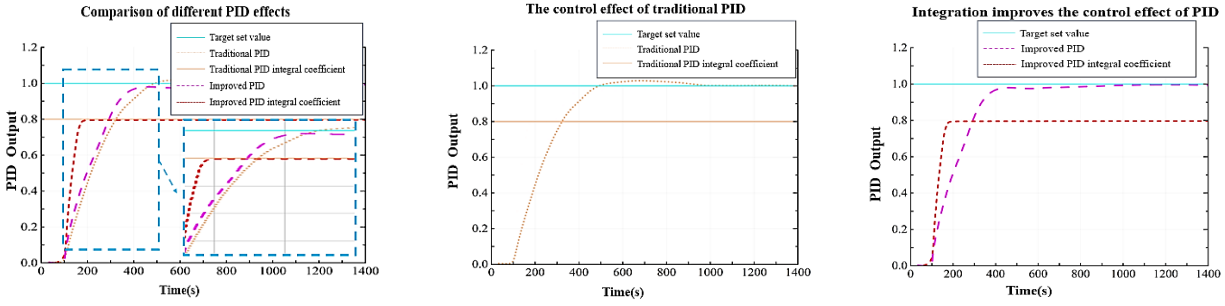

Fig. 6 - Comparison of integral improved PID and traditional PID

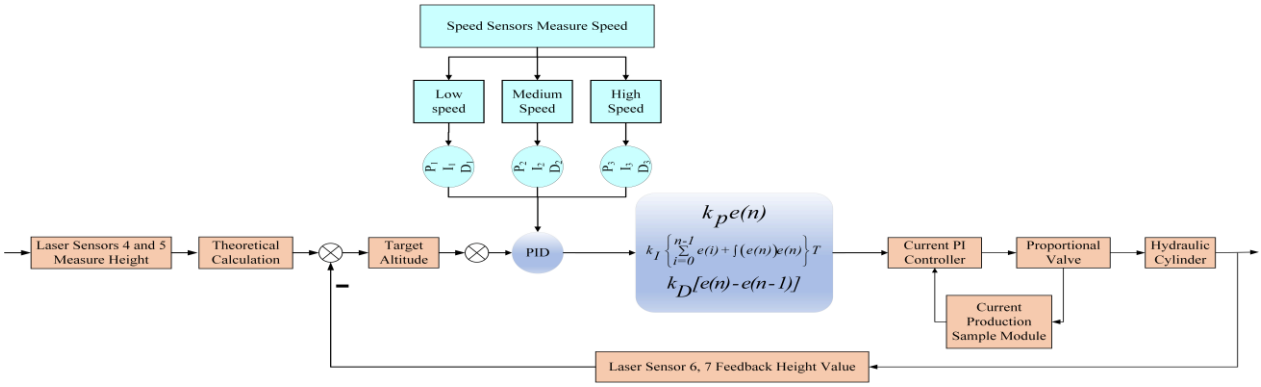

Fig. 7 - Flow chart of control strategy PID algorithm based on speed detection

Orthogonal test of qualified rate of sowing depth

In order to verify that the sowing depth effect of peanut planter is affected by factors such as vehicle speed and height deviation value (height deviation value between the two points in front of the ridge is referred to as height deviation value), the influencing factors of sowing depth effect driven by hydraulic cylinder are further explored, and a three-factor and three-level simulation test is carried out. Taking the sowing depth of peanut seeder as the research object, ignoring the influence of external working conditions, the speed, height deviation value and sowing depth were selected as the test factors, and the qualified rate of sowing depth was taken as the test index, which were expressed by A, B and C respectively. The planter can achieve a working speed of 3 to 7 km/h and a sowing depth of 40 to 60 millimeters. Orthogonal test was used to study the influence of factors on the qualified rate of sowing depth. The factors and level design are shown in Table 3.

Table 3

Sowing depth qualification rate test factor level coding table

Coding	Factor		
	A: Speed v / km·h^{-1}	B: Height deviation h/mm	C: Sowing depth setting h/mm
-1	3.0	0	40
0	5.0	25	50
1	7.0	50	60

In the EDEM simulation test, the response surface model of the qualified rate of sowing depth was constructed with three factors as independent variables and the qualified rate of sowing depth as the evaluation index. The test results are shown in table 4.

Table 4

Sowing depth qualification rate test program and results

Test number	Experimental factors			Response value
	A: Speed km·h^{-1}	B: Height deviation h/mm	C: Sowing depth setting h/mm	P: Qualified rate of sowing depth %
1	3	50	50	93.35
2	3	25	40	95.45
3	3	0	50	98
4	3	25	60	94.06
5	5	25	50	88.25
6	5	50	60	87.95
7	5	25	50	88.3
8	5	0	60	91.35
9	5	50	40	88.2
10	5	25	50	90
11	5	25	50	88.65
12	5	25	50	88.75

Test number	Experimental factors			Response value
	A: Speed km·h^{-1}	B: Height deviation h/mm	C: Sowing depth setting h/mm	P: Qualified rate of sowing depth %
13	5	0	40	92.45
14	7	25	40	86.8
15	7	0	50	87.15
16	7	25	60	86.55
17	7	50	50	85.92

Table 5

Analysis of variance of sowing depth qualification rate model

Source	Sum of squares	Degrees of freedom	Mean square	F-value	P-value
Model	189.86	9	21.10	49.54	< 0.0001**
A	148.26	1	148.26	348.16	< 0.0001**
B	22.88	1	22.88	53.73	0.0002**
C	1.12	1	1.12	2.62	0.1493
AB	2.92	1	2.92	6.87	0.0344
AC	0.3249	1	0.3249	0.7630	0.4114
BC	0.1806	1	0.1806	0.4242	0.5357
A^2	9.74	1	9.74	22.88	0.0020**
B^2	2.65	1	2.65	6.23	0.0412
C^2	0.6864	1	0.6864	1.61	0.2448
Residual	2.98	7	0.4258		
Loss of fit Term	0.9639	3	0.3213	0.6372	0.6295
Pure error	2.02	4	0.5043		
Total error	192.84	16			

*Note:**denotes the difference is very significant (P ≤ 0.01).*

The data in the table were fitted by quadratic multiple regression, and the results of variance analysis on the qualified rate of sowing depth were obtained by Design-Expert software, as shown in Table 5.

According to the data samples of the table, the quadratic polynomial regression model of the qualified rate of sowing depth is obtained, that is:

$$P = 88.79 - 4.31A - 1.69B - 0.374C + 0.855AB + 0.285AB + 0.213BC + 1.52A^2 + 0.794B^2 + 0.404C^2 \quad (11)$$

where:

P is the qualified rate of sowing depth;

A is the speed;

B is the height deviation value;

C is the sowing depth.

According to the variance analysis results of the regression model, the P value of the regression model is less than 0.01, indicating that the regression model is extremely significant. The P value of the model's mismatch term is 0.6295, indicating that the regression model has a high degree of fitting. Through the P value of vehicle speed, height deviation value and sowing depth, it can be judged that the influence of three test factors on the qualified rate of sowing depth from large to small is vehicle speed, height deviation value and sowing depth. The adjusted coefficient of determination of the regression model is 0.9647, indicating that the model can explain 96.47 % of the corresponding changes, and only 3.53 % of the data cannot be explained by the model. The determination coefficient of the model is R^2 = 0.9845, close to 1, and the coefficient of variation and precision are 0.9037 and 23.9612, respectively, indicating that the test data and the net rate fitting regression model have high reliability.

The response surface method was used to study the influencing factors of the qualified rate of sowing depth. As shown in Fig. 8, the Model Graphs module in Design Expert 13 was used to obtain the corresponding surface of each test factor on the qualified rate of sowing depth.

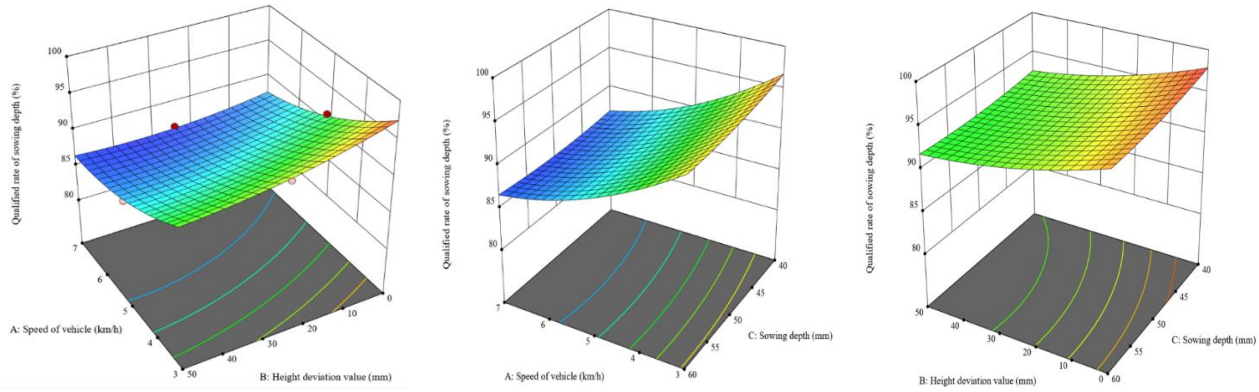

Fig. 8 - The corresponding surface of each test factor on the qualified rate of sowing depth

It can be seen that the qualified rate of sowing depth decreases with the increase of vehicle speed and decreases with the increase of height difference, while the qualified rate of sowing depth is not significantly affected by the setting of sowing depth.

Field experiment

In order to verify the rationality of peanut seeder and control strategy with seed and fertilizer sowing depth control and sowing control, a comparative test was carried out in a real and complex field environment. On October 15, 2023, it was carried out in the test base of Xizhujia Village, Yishui County, Linyi City, Shandong Province. The test machine was a 2MB-1 / 2 peanut planter manufactured by Shandong Yuanyuan Machinery Co., Ltd., and the peanut seed model was Luhua peanut.

- Test method

The traditional 2MB-1/2 peanut planter with one ridge and two rows produced by Shandong Yuanyuan Machinery Co. Ltd. was used for comparative test. The test personnel were the employees of the company, and the depth of seed and fertilizer application was positioned at different operating speeds. The test parameters refer to the agronomic standards of peanuts in Shandong Province formulated by Shandong Agricultural and Rural Bureau. The sowing depth of peanuts was set to 40 mm, 50 mm and 60 mm. The fertilization depth was 70 mm below the peanut seeds. The operating speed was set to 3 km/h, 5 km/h and 7 km/h, and the seed spacing of peanuts is set to 25 cm. In order to eliminate the instability of the operation speed of the peanut planter when it started or stopped, a plot with a length of 100 meters and a width of 40 meters was selected, and the middle area of 15 meters from both ends of the ground was selected for random measurement. The field experiment is shown in Fig. 9.

Fig. 9 - Field experiment diagram

During the measurement, the ridge surface height was first flatly marked, and then the soil above the fertilizer and seed was scraped clean. The height between the leaked fertilizer and seed, the seed and the ridge surface soil layer were measured, and 10 sets of measurements were performed. Each group selected 50 seeds, and some of the data are shown in Figure 10.

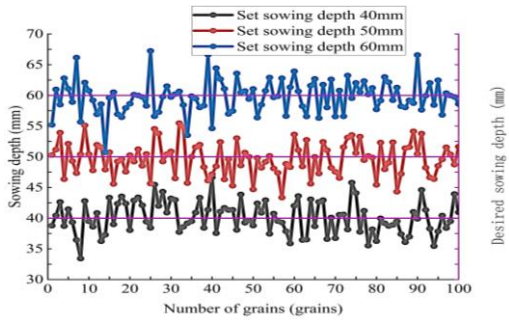

a) When the speed is 3 km/h, the field data of active adjustment methods with different sowing depths are set

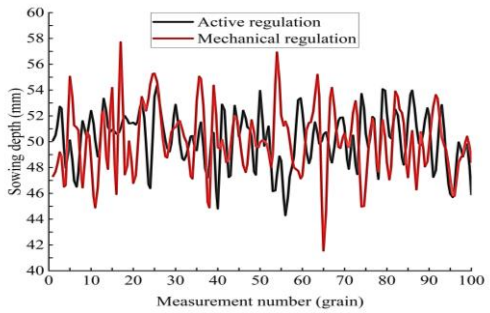

b) The field data of two adjustment methods when the sowing depth is set to 50 mm at the speed of 3 km/h

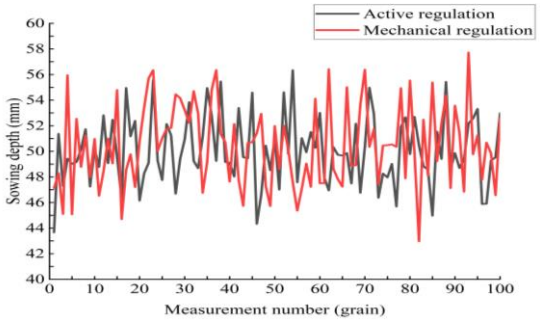

c) The field data of two adjustment methods when the sowing depth is set to 50 mm at the speed of 5 km/h

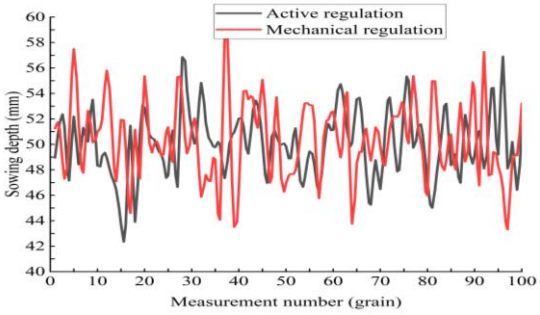

d) The field data of two adjustment methods when the sowing depth is set to 50 mm at the speed of 7 km/h

Fig. 10 - Part of the field test data

- Test result analysis

According to the calculation formula of each calculation parameter, the experimental data of two different methods are analyzed. The results are shown in Table 6.

$$\bar{h} = \frac{\sum h_i}{N} \quad (12)$$

$$\eta = \frac{n}{N} \times 100\% \quad (13)$$

$$s_h = \sqrt{\frac{\sum (h_i - h)^2}{N}} \quad (14)$$

$$V_h = \frac{S_h}{\bar{h}} \times 100\% \quad (15)$$

where:

H is the qualified rate of sowing depth, %;
n - the qualified number of sowing depth, grain;
n - the total number of measuring points of sowing depth, grain;
h_i - the measured value of sowing depth, mm;
S_h - the standard deviation of sowing depth, mm;
V_h - the coefficient of variation of sowing depth, %.
$\bar{h}$ - the average sowing depth, mm.

Table 6

Comparison of results of each test data

Measuring parameters							Adjustment mode
Peanut planter operating speed / km/h	3	5	7	3	3	3	
Peanut seed depth after sowing / mm	50	50	50	40	50	60	
Mean value of peanut seed depth after sowing / mm	50.8	47.54	45.04	41.2	48.68	44.36	Dynamic
	46.12	53.83	40.56	45.62	53.26	44.27	Mechanical

Measuring parameters							Adjustment mode
Pass rate of peanut seed depth after sowing / %	94.26	90.57	85.69	94.03	94.26	92.68	Dynamic
	90.21	83.46	75.25	90.67	90.21	88.52	Mechanical
Standard deviation of peanut seed depth after sowing / mm	2.58	3.34	5.19	2.32	2.02	4.89	Dynamic
	4.03	5.17	6.95	4.95	4.56	5.51	Mechanical
Coefficient of variation of peanut seed depth after sowing / %	4.09	5.26	6.14	5.29	3.95	5.54	Dynamic
	7.24	10.75	13.98	6.96	6.63	12.49	Mechanical

It is known from the test results that the average sowing depth caused by the active adjustment method has little change compared with the traditional mechanical adjustment under different speeds of the seeder, and the maximum error occurs at the speed of 7 km/h, which is 4.96 mm. It is 4.48 mm higher than that of traditional mechanical adjustment. From the qualified rate of sowing depth, it can be seen that the qualified rate is high and the change range is relatively small. The qualified rate of sowing in high-speed operation is not less than 85%, which meets the agronomic requirements of peanut sowing. In terms of the standard deviation of sowing depth and the coefficient of variation of sowing depth, the active adjustment method is also more advantageous than the passive mechanical adjustment. In the low speed 3 km/h operation, the active adjustment method is not much different from the set sowing depth value, and the performance of the sowing depth consistency adjustment is better, and the purpose of the system design is realized.

CONCLUSIONS

(1) A peanut planter is designed, which can control the depth of peanut sowing and keep a constant distance between seed and fertilizer. The laser sensor and speed sensor measuring device were used to detect the working speed of the planter and the position of the fertilizer opener and the disc opener in real time, and the real-time control was completed by the hydraulic system.

(2) According to the actual operation of the peanut planter, the integral coefficient of the traditional PID algorithm is improved and applied to the control strategy of the peanut planter to achieve faster response speed and accuracy.

(3) Under different operating speeds and different sowing depth measurements, the developed peanut planter with controlled peanut sowing depth and with a constant distance kept between seed and fertilizer has more obvious advantages in the average sowing depth, the qualified rate of sowing depth, the standard deviation of sowing depth and the coefficient of variation of sowing depth than the traditional mechanical passive peanut planter in the adjustment of sowing depth consistency.

ACKNOWLEDGEMENT

The authors were funded for this project by the Key R & D Program of Shandong Province (2021CXGC010813) and national Key R & D Program (2022YFD2300100) and national Modern Agricultural Industry Technology System (CARS-13).

REFERENCES

[1] Bai H., Fang Z., Wang D., et al., (2019). Design and experiment of Integrated Control System for sowing depth and compaction degree of Maize sower (玉米播种机播深和压实度综合控制系统设计与试验). *Journal of Agricultural Machinery,* Vol. 51, pp.61-72, Beijing/China.

[2] Ding Q., et al., (2022). Field bench test of seeding monomer based on precise sowing depth control objective (基于精确播深控制目标的播种单体田间台架试验). *Journal of Agricultural Machinery,* Vol. 53, pp.100-108, Beijing/China.

[3] Hu J., et al., (2012). *Theory and experimental research of sowing depth control for precision seeder (精密播种单体播深控制的理论与试验研究).* Doctoral dissertation, Jilin University, Jinlin/China.

[4] Kiani S. (2012). Automatic on-line depth control for seeding units using a non-contacting ultrasonic sensor. *International Journal of Natural & Engineering Science*, Vol. 6, pp.39-42, USA

[5] Li H., et al., (2009). *Automatic adjustment device for ditching depth of no-sowing machine*, Patent, CN201623979U, China.
[6] Liu W., et al., (2022). Performance test and analysis of adaptive copying cutting table for regenerated rice based on fuzzy PID control (基于模糊 PID 控制的再生稻自适应仿形割台性能试验与分析). *Transactions of the Chinese Society of Agricultural Engineering,* vol. 38, no.10, pp.1-9, Beijing/China
[7] Li Y., Meng P., Geng D., et al., Intelligent system for adjusting and controlling corn seeding depth (玉米播种深度智能调控系统研究), *Transactions of the Chinese Society for Agricultural Machinery*，vol. 47, pp. 62-68, Beijing/China
[8] Li H., (2010), *An adjustment device applied to deep sowing automatic control system*, Patent, CN101785386A, China.
[9] Lü X., Liu M., Wang H., et al., (2012). Progress in peanut film seeding technology and equipment research and development (花生膜上播种技术及其设备研究进展), *Chinese Journal of Agricultural Mechanization*, vol.01, pp. 88-92, Jiangsu/China.
[10] Lü X., Hu Z., Liu M., et al., (2015). Design and Experiment of BQHM-2 Peanut Cover Hole Planter (2-BQHM 型花生覆膜穴播机的设计与试验), *Journal of South China Agricultural University,* vol.01, pp. 96-100, Guangdong/China.
[11] Molatudi R. L, Mariga I. K., et al., (2009) The effect of maize seed size and depth of planting on seedling emergence and seedling vigour. *Journal of Applied Sciences Research*，vol.05, pp. 2234-2237. USA
[12] Mock J.J, Erbach D.C., et al., (1977) Influence of conservation tillage environments on growth and productivity of corn. *Agronomy Journal*, vol.69, pp. 337－340．USA
[13] Pasi S., Timo O., et al., (2015). Automatic working depth control for seed drill using ISO 11783 remote control messages. *Computers & Electronics in Agriculture*, vol.116, pp. 30—35. England.
[14] Wan S., Zhang J., et al., (2020) Significant Changes in Peanut Planting Technology - Single Seed Precision Sowing. (花生种植技术的重大变革-单粒精播), *China Oil Crop Journal*, vol.42, pp. 927-933. Hubei/China
[15] Wu D., Zheng Y., et al., (2015) The effect of clearing under different sowing depths on the growth, development, and yield of peanuts (不同播深下清棵对花生生长发育及产量的影响)， *Anhui Agricultural Science*, vol.10, pp. 40-43. Anhui/China.
[16] Wang Q., Xu Q., Lu C., et al., (2021). Research Status and Development of Key Technologies for Intelligent Notill Sowing (免耕播种智能化关键技术研究现状与发展), *Journal of South China Agricultural University*, Vol. 42, pp. 27-35. Guangdong/China.
[17] Xue B., et al., (2023) Research on wheat sowing depth control system based on adaptive fuzzy PID (基于自适应模糊 PID 的小麦播深控制系统研究) *Journal of Agricultural Machinery,* Vol. 54, pp.93-102. Beijing/China.
[18] Yang L., Yan B., Zhang D., et al., (2016) Research progress on precision corn sowing technology(玉米精密播种技术研究进展). *Journal of Agricultural Machinery*, Vol. 47, pp. 38-48. Beijing/China.
[19] Zhang Z, Hu W, et al. (2005) The advantage analysis and development of the peanut production of China (中国花生生产的发展与优势分析), *Journal of Peanut Science*, Vol.34, pp.6-10. Shandong/China.
[20] Zhao H., et al., (1989) Ultrasonic detector mounted on a furrow opener. (装在开沟器上的超声波探测器), *Grain and Oil Processing and Food Machinery,* Vol.1, pp.45. Beijing/China.

CROP TYPE MAPPING USING MACHINE LEARNING-BASED APPROACH AND SENTINEL-2: STUDY IN LUMAJANG, EAST JAVA, INDONESIA
/
PEMETAAN JENIS TANAMAN MENGGUNAKAN PENDEKATAN MACHINE LEARNING DAN SENTINEL-2: STUDI DI LUMAJANG, JAWA TIMUR, INDONESIA

Irsyam MAHRUS [1)], Indarto INDARTO *[1)], Khristianto WHENY [1)], Kurnianto FAHMI [1)]
[1)] Research Group of Agroindustrial and Food Safety (Keris Dimas KPPI), Research Centre (LP2M), University of Jember / Indonesia;
Tel: +62 813-4444-5615; E-mail: indarto.ftp@unej.ac.id
DOI: https://doi.org/10.35633/inmateh-72-12

Keywords: *Crop-type mapping, Sentinel-2, Random Forest, Lumajang*

ABSTRACT
In general, sentinel-2 imagery can be used for crop mapping. Crop types mapping aims to develop future strategies for sustainable agricultural systems. This study used Sentinel-2 from June 25 to July 6, 2023, with 10% cloud cover. The research was conducted in Pasrujambe and Candipuro sub-districts (± 242.23 km^2). The image is processed using a random forest on the GEE platform. Accuracy was generated using a confusion matrix with an overall accuracy of 85.82% and a kappa of 71.19%. Five main types of land use/cover were produced, namely: paddy (17.31%), sugarcane (0.93%), vegetation (69.74%), sand (7.4%) and built-up land (4.59%).

ABSTRAK
Secara umum, citra sentinel-2 dapat digunakan untuk pemetaan tanaman. Pemetaan jenis tanaman bertujuan untuk mengembangkan strategi masa depan untuk sistem pertanian berkelanjutan. Penelitian ini menggunakan Sentinel-2 pada tanggal 25 Juni hingga 6 Juli 2023 dengan tutupan awan 10%. Penelitian dilakukan di Kecamatan Pasrujambe dan Candipuro (± 242,23 km2). Gambar diproses menggunakan random forest pada platform GEE. Akurasi dihasilkan menggunakan matriks konfusi dengan akurasi keseluruhan sebesar 85,82% dan kappa sebesar 71,19%. Lima jenis penggunaan/tutupan lahan utama yang dihasilkan, yaitu: padi (17,31%), tebu (0,93%), vegetasi (69,74%), pasir (7,4%) dan lahan terbangun (4,59%).

INTRODUCTION

Crop Type Mapping indicates the intensity of land use in an area to develop sustainable future policy strategies in agriculture, plantations, and the like, both economically and ecologically *(Blickensdörfer et al., 2022).* In the agricultural sector, up-to-date information can be obtained by mapping crop types for planning and recognizing food security threats and their sustainability *(Hegarty-Craver et al., 2020).* Crop identification concerning the field of plant phenology, including the growth stage, has been carried out using remote sensing data *(Erdanaev et al., 2022a).* Remote sensing is a technique that has been proven effective in producing specific information on land cover and plant species *(Sun et al., 2020)*, both for its application in narrow *(Salas et al., 2020)* and large areas *(Griffiths et al., 2019).*

The Sentinel 2 platform is a remote sensing data widely used to map crop types in an area because of its multispectral sensor capabilities with 10 m, 20 m, and 60 m resolution and has an ideal wavelength *(Prins & Van Niekerk, 2021).* Several studies related to the mapping of crop types have been carried out, such as using sentinel 2 for crop type identification in small-plot agriculture land, which has a high accuracy value *(Gumma et al., 2022).* Xie and Niculescu 2022 *(Xie & Niculescu, 2022)* evaluated the Sentinel 2 image to map winter crops in the growing season. Furthermore, depending on the high precipitation frequency in their study location, they use Sentinel-1 C-band SAR data to monitor crop phenology. Sentinel-2 time series data for land cover mapping can reduce misclassification in its application to precision farming activities. It can also identify land cover features with small coverage, such as small fields, roads, and rivers *(Liu et al., 2020; Tran et al., 2022).* Different classification approaches and methods followed by pixel-based and object-based classifications were performed and evaluated using the Google Earth Engine (GEE) platform. No research can be found on mapping crop types using sentinel 2 in the Pasrujambe and Candipuro District of Lumajang.

Crop-type maps can be generated using a machine-learning approach applied to satellite images. Many studies on crop-type mapping used various machine-learning algorithms and Sentinel-2 data *(Alami Machichi et al., 2023; Luo et al., 2023).*

Machine Learning (ML) is a machine developed based on artificial intelligence (AI) to collect data independently using designed algorithms to imitate how humans learn (source). Machine learning has more features, such as simple operation, swiftness of operations, and the ability to process different data types (source). The use of machine learning for remote sensing, including Random Forests (RF), Neural Networks (NN), Support Vector Machines (SVM), and other processing methods, have proliferated with a high degree of accuracy *(Feng et al., 2019).* In several studies of various algorithms of machine learning for crop type identification, the random forest was recognized as one of the most efficient and accurate algorithms *(Akbari et al., 2020; Kpienbaareh et al., 2021; Wei et al., 2023).*

The objectives of this study are (1) to generate crop-type maps using 10 m Sentinel 2 of Pasrujambe and Candipuro District, Lumajang, and (2) to evaluate the random forest algorithm used to generate crop-type maps in the study area. The accuracy of the classification result is assessed using a confusion matrix derived from field data collection. Crop types have been widely mapped in large areas, and plant varieties have been uniform. This research was conducted in a limited area with various field sizes and plant varieties.

MATERIALS AND METHODS

Study Area

Two study areas were selected for crop type mapping, including Candipuro and Pasrujambe District, located in Lumajang Regency (Figure 1) and covering an area of 242.23 km2. Pasrujambe district, specifically, is located approximately 23 km south of the center of Lumajang city, with an average altitude of 75-2500 meters above sea level, and has an average rainfall of 952 mm with rainy days for 220 days within a year. Most of the Pasrujambe area is the mountainous area of Mount Semeru, and nearly 50% of its land cover is dense vegetation. Meanwhile, Candipuro District is 322 meters above sea level with a 2018 mm/year of rainfall.

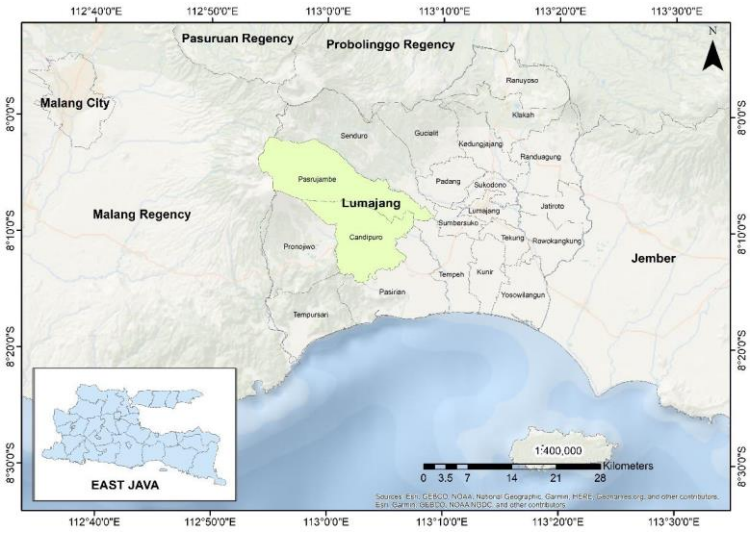

Fig. 1 - Study area in Candipuro and Pasrujambe District, Lumajang Regency

Input Data

Satellite Data

Spectral information from sentinel-2 imagery recorded in 2023 was used in this study. Sentinel-2 is a multispectral imaging mission based on a constellation of two high-resolution satellites launched in the sun-synchronous orbit *(Agency, 2015).* This study used time series data of Sentinel-2 from June 25 to July 6, 2023, with a minimum cloud cover of 10%. Due to the topography and climate conditions in the study area, the recorded images have a heavy cloud cover, and it is not easy to obtain satellite imagery with clear cloud cover.

Field Data Collection and Sampling

Field data on crop types were identified and collected from June to July 2023. The coordinates were recorded on each field using a GPS device at the center of the field boundaries. Crop types in each field were collected using a photo camera. One hundred sixty (160) ground truth samples from different crop types were collected, including paddy, built-up area, river, sugarcane, and dense vegetation (forest area, pine, teak plantations, and sengon trees). Field data collection is adjusted to the actual condition of vegetation cover in the field.

Fig. 2 - Example of field data in the study area captured using a digital camera and drone

Field data is used as a reference for making training areas. To improve the creation of training samples, Google Earth imagery was used to identify other types of land cover that are difficult to reach in the field data collection process. The training sample was divided into 70% training data and 30% validation data, as described by *(Adam et al., 2014)*. 70% of training data (31896 pixels) is used as input for classification, and 30% (13726 pixels) is used to validate the algorithm and assess the accuracy *(Shaharum et al., 2020).* The training data was used for training of the random forest classifier, while the validation data was used for accuracy assessment *(Adam et al., 2014)*. Optimization of the random forest parameters was done by repeated k-fold cross-validation using only the training sample *(Duro et al., 2012).*

Five (5) classes were identified and created using GEE, including built-up areas, sand, vegetation, paddy, and sugarcane. Samples were created using a polygon format. Table 1 illustrates the classes and number of each sample.

Table 1

Summary of the number of samples and the classes

Class	Number of samples (pixel)	Percentage (%)
Built-up Area	1229	3.27
Sand	11109	29.53
Vegetation	23062	61.31
Paddy	1184	3.15
Sugarcane	1032	2.74

Image Processing

The image processing was performed using the Google Earth Engine (GEE) platform. GEE provides a set of pixel-based classifiers to map crop types *(Shelestov et al., 2017).* GEE is used to collect a set of Sentinel-2 time series data, vegetation index transformation, and create a crop classification raster by performing a random forest classifier. A random forest classifier was used to produce crop-type maps and combine multiple vegetation indices to improve accuracy. The proposed workflow of the methodology of this study is shown in Figure 3.

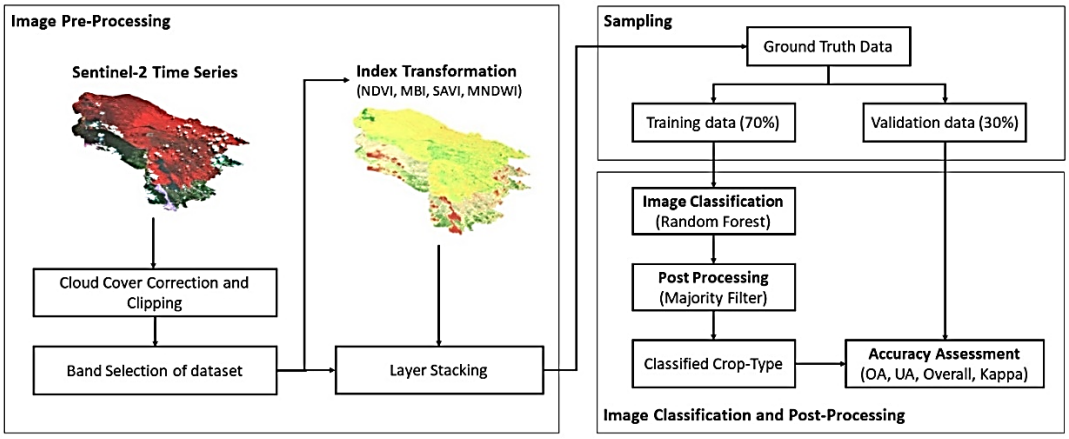

Fig. 3 - The workflow of this study was conducted in GEE to produce a crop-type map

a. Vegetation indices

Multiple vegetation indices were calculated as classification input data, including the Normalised Difference Vegetation Index (NDVI), Modified Bare Soil Index (MBI), Soil Adjusted Vegetation Index (SAVI), and Modified Normalised Difference Water Index (MNDWI). Each vegetation indices equation is shown in Table 2.

Table 2

Vegetation indices and the equation used in this study

Index	Formula	References
NDVI	(NIR – Red) / (NIR + Red)	*(Nouri et al., 2017)*
MBI	((SWIR1 – SWIR2 – NIR) / (SWIR1 + SWIR2 + NIR) + f))	*(Nguyen et al., 2021)*
SAVI	((NIR – Red) / (NIR + Red + L)(1 + L))	*(Huete et al., 1992)*
MNDWI	(Green – SWIR) / (Green + SWIR)	*(Xu, 2006)*

NDVI is an index widely used to produce crop-type classification maps *(Erdanaev et al., 2022b; HAO et al., 2020; Tariq et al., 2022)* by comparing the differences in the reflectance values of the red band (Red) and the near-infrared (NIR) band. NDVI values ranged from -1 to 1 *(Nouri et al., 2017)* and were calculated using the equation in Table 3.

MBI is used to distinguish between agricultural and non-agricultural fields. Specifically, it can identify bare soil and fallow land *(Nguyen et al., 2021).* The MBI value ranges from -0.5 to +1.5, where a higher MBI value indicates vacant land while a lower value indicates a body of water or vegetation. In MBI, an additional factor f is used with a value of 0.5 and is calculated using the equation in Table 3.

SAVI is a vegetation index aimed at minimizing the influence of soil on the calculation of vegetation values by using the L value as a soil adjustment factor. It has a value ranging from -1 to 1. The L value differs for each vegetation cover type, specifically 0 or 0.25 for dense vegetation, 1 for sparse vegetation, and 0.5 for moderate vegetation cover.

MNDWI is a modified form of NDWI *(McFeeters, 1996),* which computes using the SWIR band. This index is needed to delineate water bodies against other land covers.

b. Random Forest

Random Forest (RF) is a non-parametric supervised machine learning classification method. RF is a collection of decision trees combined to reduce variance and make data predictions more accurate. It can be used for classification and regression analysis *(Shaharum et al., 2020).* The random forest was selected because it is widely used and performs well for crop-type mapping.

RESULTS

Accuracy Assessment

The accuracy assessment was performed using the AcATaMa plugin provided by QGIS software. For sampling, response planning, and estimating in a framework for design-based inference, the AcATaMa plugin is a feature that offers thorough support *(Llano, 2019).* The crop type classification thematic map was evaluated using a confusion matrix (Table 3).

Table 3

Accuracy assessment of crop-type map

Class	Built-Up Area	Sand	Vegetation	Paddy	Sugarcane	Total	User Accuracy
Built-Up Area	36	3	0	6	1	46	78.26
Sand	1	48	9	18	1	77	62
Vegetation	3	3	665	60	8	739	89.99
Paddy	11	5	10	144	5	175	82.29
Sugarcane	0	0	1	3	3	7	43
Total	51	59	685	231	18	1044	
Producer Accuracy	70.59	81	97.08	62.34	17		
Overall Accuracy = 85.82%, Kappa Accuracy = 71.19%							

Table 4 - shows the accuracy of thematic maps, including PA, UA, OA, and Kappa. In general, crop type classification with NDVI, MBI, SAVI, and MNDWI index combination using RF classifier produced the accuracy derived from the confusion matrix shows good value where the Kappa of 71.19% and OA of 85.82%. In this study, paddy and sugarcane are the crop types that can be recognized. However, UA and PA of the sugarcane class showed the smallest value. The sugarcane class has a UA of 43% and a PA of 17%.

Identifying the crop type in Candipuro and Pasrujambe, Lumajang Regency is challenging due to the climatological and geographical conditions. The study area is a hillside area of Mount Semeru with relatively high rainfall, causing the image used as input for classification not to be free from cloud cover. On the other hand, the agricultural conditions in the study area are heterogeneous, and many farmers plant crops using an intercropping system. Due to the condition, the classification result is ambiguous.

This research uses limited sentinel-2 images and training samples illustrated in Table 2, recorded from June 25 to July 6, 2023. The classification accuracy can be improved using crop type label data in several years as training and test data. The experiment by Zhi et al. *(Zhi et al., 2022)* shows that classification accuracy will be low if only using data on plant species in one year. However, the accuracy can be increased when the coupling crop label from several years is used to classify crops, especially paddy and maize.

Thematic Maps of Crop Type Classification

This study used sentinel-2 level 2-A time series data computed by the GEE platform. The images were processed using an RF Classifier provided by GEE. The crop-type classification map identified using Sentinel-2 imagery obtained five (5) classes consisting of (1) built-up area, (2) sand, (3) vegetation, (4) paddy, and (5) sugarcane presented in Figure 3. The types of plant cover are identified using field data collection.

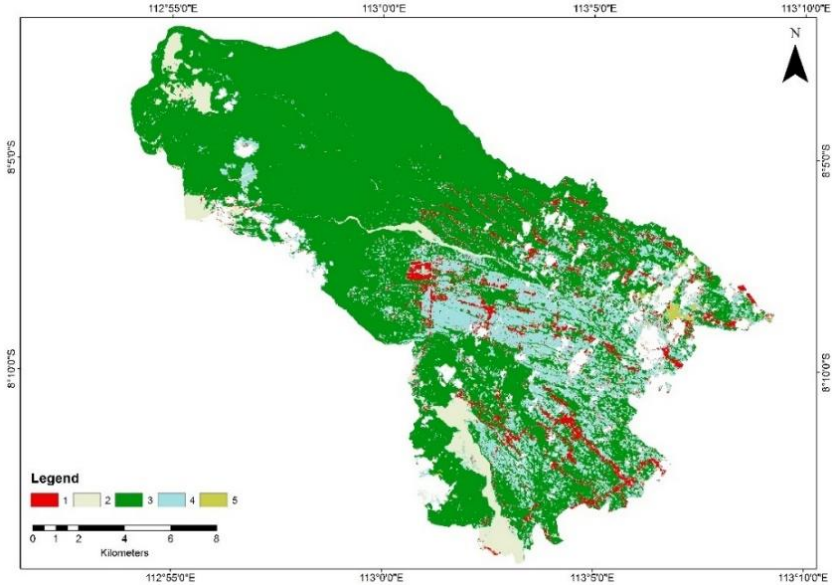

Fig. 3 - Thematic map of crop type classification of Candipuro and Pasrujambe, Lumajang Regency

Table 5- shows the area of each class, where two dominant food crops identified in the study area are paddy and sugarcane. In the study area, primary forests, pines, teak plantations, and sengon trees comprise most vegetation cover. Respectively, the classification results show that the paddy area is 46.22 ha (17.31%) and sugarcane is 2.49% (0.93%). In our study area, vegetation accounted for 69.74% of the total estimated area, so its effect on overall accuracy was relatively significant. Furthermore, the Built-Up Area shows an estimated area of 12.25 ha or approximately 4.59%, and sand of 19.87 ha or 7.44% of the study area.

Table 4

Summary of per-class estimated area

Class	Area (ha)	Percentage (%)
Built-Up Area	12.25	4.59
Sand	19.87	7.44
Vegetation	186.26	69.74
Paddy	46.22	17.31
Sugarcane	2.49	0.93
Total	267.09	100

DISCUSSION

Crop-type mapping is essential for various applications, especially in agriculture. However, mapping crop types in Candipuro and Pasrujambe Districts is challenging because this region is a heterogeneous environment with climatological and geographical conditions and temporal and spatial resolution of images. After all, the region has a tropical climate. Another challenge faced was the availability of cloud-free and shadow-free data, making it difficult to find optimal solutions for cloud-free temporal and composite resolution, leading to a lot of data loss. The solution offered for further studies is using Sentinel-1 images and a fusion of Sentinel-1 and Sentinel-2 images. Sentinel-1 uses a microwave sensor and operates day and night without any weather barriers, thus offering cloud-free data. The experiments conducted by Guo et al. and Kpeinbaareh et al. *(Guo et al., 2018; Kpienbaareh et al., 2021)* showed that fusing Sentinel-1 and Sentinel-2 data could improve the classification results of plant species in Northern Germany and Northern Malawi. In this research, the focus was on the uses of Sentinel-2 images combined with several vegetation indices (i.e., NDVI, MBI, SAVI, MNDWI) processed on the GEE cloud platform using an RF classifier to produce a thematic crop type map in Candipuro and Pasrujambe District, Lumajang Regency.

Random forest is an algorithm widely used in various studies and proved more accurate *(Dakir et al., 2023; Hudait & Patel, 2022).* Our result showed that the RF classifier can distinguish crop types in this study area in terms of overall accuracy (Table 4-). The overall accuracy obtained was 85.82%, and the kappa value of 71.19%. The causal factor that affects the accuracy is the occurrence of misclassification. For example, in this study, misclassification occurred due to similarities in pixel value between paddy (Band 02 = 0.1288, Band 03 = 0.1479, and Band 04 = 0.126) and vegetation (Band 02 =0.1238, Band 03 = 0.1385, Band 04 = 0.1206). Figure 4a shows how the paddy is classified as vegetation. A comparison of similarities between rice and vegetation in Sentinel-2 imagery is shown in Figure 4.

(a) (b) (c)

Fig. 4 - Comparison of the classified map, Sentinel-2 dataset, and Google image

This study uses the GEE cloud computing as a data processing platform. GEE is a geospatial analysis platform that provides multiple processing algorithms, an extensive database, and computing power and facilitates large amounts of high-resolution imagery to map crop types *(Liu et al., 2020).* Data processing by conventional methods (without cloud computing) will take quite a long time. With GEE, processing can be completed in just a few seconds, allowing for fast decision-making *(Shelestov et al., 2017).*

CONCLUSIONS

Crop-type maps in Candipuro and Pasrujambe Districts are generated using a machine learning approach provided by the Google Earth Engine (GEE) cloud computing platform. This study used Sentinel-2 time series data provided in large and free by GEE. The image was processed using a random forest classifier and showed an overall accuracy of about 85.82% and a kappa value of 71.19%. However, because of the climatological and geographical characteristics, identifying the crop type in the research area is difficult. The research region is a hillside area of Mount Semeru with relatively high rainfall, resulting in cloud cover in the photograph utilized as input for classification. On the other hand, the agricultural conditions in the research area are varied, and many farmers produce crops using an intercropping technique.

ACKNOWLEDGEMENT

The authors thank Hibah Internal Universitas Jember Skim Penelitian Produktivitas Guru Besar (PRGB) Tahun 2023 SK. Rektor Universitas Jember Nomor: 7575/UN25/KP/2023, all field personnel, and all parties involved in the research.

REFERENCES

[1] Adam, E., Mutanga, O., Odindi, J., & Abdel-Rahman, E. M. (2014). Land-use/cover classification in a heterogeneous coastal landscape using RapidEye imagery: evaluating the performance of random forest and support vector machines classifiers. *International Journal of Remote Sensing*, *35*(10), 3440–3458. https://doi.org/10.1080/01431161.2014.903435

[2] Agency, E. S. (2015). *SENTINEL-2 User Handbook Sentinel-2 User Handbook SENTINEL-2 User Handbook*. *1*, 1–64.

[3] Akbari, E., Boloorani, A. D., Samany, N. N., Hamzeh, S., Soufizadeh, S., & Pignatti, S. (2020). Crop Mapping Using Random and Particle Swarm Optimization based on Multi-Temporal Sentinel-2. *Remote Sensing*, *12*(9), 1–21. https://doi.org/10.3390/rs12091449

[4] Alami Machichi, M., mansouri, loubna El, imani, yasmina, Bourja, O., Lahlou, O., Zennayi, Y., Bourzeix, F., Hanadé Houmma, I., & Hadria, R. (2023). Crop mapping using supervised machine learning and deep learning: a systematic literature review. *International Journal of Remote Sensing*, *44*(8), 2717–2753. https://doi.org/10.1080/01431161.2023.2205984

[5] Blickensdörfer, L., Schwieder, M., Pflugmacher, D., Nendel, C., Erasmi, S., & Hostert, P. (2022). Mapping of crop types and crop sequences with combined time series of Sentinel-1, Sentinel-2 and Landsat 8 data for Germany. *Remote Sensing of Environment*, *269*(January), 112831. https://doi.org/10.1016/j.rse.2021.112831

[6] Dakir, A., Barramou, F., & Alami, O. B. (2023). Towards a Machine Learning-based Model for Automated Crop Type Mapping. *International Journal of Advanced Computer Science and Applications*. https://doi.org/10.14569/IJACSA.2023.0140185

[7] Duro, D. C., Franklin, S. E., & Dubé, M. G. (2012). A comparison of pixel-based and object-based image analysis with selected machine learning algorithms for the classification of agricultural landscapes using SPOT-5 HRG imagery. *Remote Sensing of Environment*, *118*, 259–272. https://doi.org/10.1016/j.rse.2011.11.020

[8] Erdanaev, E., Kappas, M., & Wyss, D. (2022a). Irrigated Crop Types Mapping in Tashkent Province of Uzbekistan with Remote Sensing-Based Classification Methods. *Sensors*. https://doi.org/10.3390/s22155683

[9] Erdanaev, E., Kappas, M., & Wyss, D. (2022b). The Identification of Irrigated Crop Types Using Support Vector Machine, Random Forest and Maximum Likelihood Classification Methods with Sentinel-2 Data in 2018: Tashkent Province, Uzbekistan. *International Journal of Geoinformatics*. https://doi.org/10.52939/ijg.v18i2.2151

[10] Feng, S., Zhao, J., Liu, T., Zhang, H., Zhang, Z., & Guo, X. (2019). Crop Type Identification and Mapping Using Machine Learning Algorithms and Sentinel-2 Time Series Data. *IEEE Journal of Selected Topics in Applied Earth Observations and Remote Sensing*, *12*(9), 3295–3306. https://doi.org/10.1109/JSTARS.2019.2922469

[11] Griffiths, P., Nendel, C., & Hostert, P. (2019). Intra-annual reflectance composites from Sentinel-2 and Landsat for national-scale crop and land cover mapping. *Remote Sensing of Environment*. https://doi.org/10.1016/j.rse.2018.10.031

[12] Gumma, M. K., Tummala, K., Dixit, S., Collivignarelli, F., Holecz, F., Kolli, R. N., & Whitbread, A. M. (2022). Crop type identification and spatial mapping using Sentinel-2 satellite data with focus on field-level information. *Geocarto International*. https://doi.org/10.1080/10106049.2020.1805029

[13] Guo, J., Wei, P.-L., Liu, J., Jin, B., Su, B.-F., & Zhou, Z.-S. (2018). Crop Classification Based on Differential Characteristics of H/α Scattering Parameters for Multitemporal Quad- and Dual-Polarization SAR Images. *IEEE Transactions on Geoscience and Remote Sensing*. https://doi.org/10.1109/tgrs.2018.2832054

[14] HAO, P. yu, TANG, H. jun, CHEN, Z. xin, MENG, Q. yan, & KANG, Y. peng. (2020). Early-season crop type mapping using 30-m reference time series. *Journal of Integrative Agriculture*. https://doi.org/10.1016/S2095-3119(19)62812-1

[15] Hegarty-Craver, M., Polly, J., O'Neil, M., Ujeneza, N., Rineer, J., Beach, R. H., Lapidus, D., & Temple, D. S. (2020). Remote crop mapping at scale: Using satellite imagery and UAV-acquired data as ground truth. *Remote Sensing*. https://doi.org/10.3390/rs12121984

[16] Hudait, M., & Patel, P. P. (2022). Crop-type mapping and acreage estimation in smallholding plots using Sentinel-2 images and machine learning algorithms: Some comparisons. *Egyptian Journal of Remote Sensing and Space Science*. https://doi.org/10.1016/j.ejrs.2022.01.004

[17] Huete, A. R., Hua, G., Qi, J., Chehbouni, A., & van Leeuwen, W. J. D. (1992). Normalization of multidirectional red and NIR reflectances with the SAVI. *Remote Sensing of Environment*. https://doi.org/10.1016/0034-4257(92)90074-T

[18] Kpienbaareh, D., Sun, X., Wang, J., Luginaah, I., Bezner Kerr, R., Lupafya, E., & Dakishoni, L. (2021). Crop Type and Land Cover Mapping in Northern Malawi Using the Integration of Sentinel-1, Sentinel-2, and PlanetScope Satellite Data. *Remote Sensing*, *13*(4), 700. https://doi.org/10.3390/rs13040700

[19] Liu, L., Xiao, X., Qin, Y., Wang, J., Xu, X., Hu, Y., & Qiao, Z. (2020). Mapping cropping intensity in China using time series Landsat and Sentinel-2 images and Google Earth Engine. *Remote Sensing of Environment*, *239*, 111624. https://doi.org/10.1016/j.rse.2019.111624

[20] Llano, X. C. (2019). *AcATaMa - QGIS plugin for Accuracy Assessment of Thematic Maps*. https://plugins.qgis.org/plugins/AcATaMa/

[21] Luo, K., Lu, L., Xie, Y., Chen, F., Yin, F., & Li, Q. (2023). Crop type mapping in the central part of the North China Plain using Sentinel-2 time series and machine learning. *Computers and Electronics in Agriculture*, *205*, 107577. https://doi.org/10.1016/j.compag.2022.107577

[22] McFeeters, S. K. (1996). The use of the Normalized Difference Water Index (NDWI) in the delineation of open water features. *International Journal of Remote Sensing*. https://doi.org/10.1080/01431169608948714

[23] Nguyen, C. T., Chidthaisong, A., Kieu Diem, P., & Huo, L.-Z. (2021). A Modified Bare Soil Index to Identify Bare Land Features during Agricultural Fallow-Period in Southeast Asia Using Landsat 8. *Land*, *10*(3), 231. https://doi.org/10.3390/land10030231

[24] Nouri, H., Anderson, S., Sutton, P., Beecham, S., Nagler, P., Jarchow, C. J., & Roberts, D. A. (2017). NDVI, scale invariance and the modifiable areal unit problem: An assessment of vegetation in the Adelaide Parklands. *Science of The Total Environment*, *584–585*, 11–18. https://doi.org/https://doi.org/10.1016/j.scitotenv.2017.01.130

[25] Prins, A. J., & Van Niekerk, A. (2021). Crop type mapping using LiDAR, Sentinel-2 and aerial imagery with machine learning algorithms. *Geo-Spatial Information Science*, *24*(2), 215–227. https://doi.org/10.1080/10095020.2020.1782776

[26] Salas, E. A. L., Subburayalu, S. K., Slater, B., Zhao, K., Bhattacharya, B., Tripathy, R., Das, A., Nigam, R., Dave, R., & Parekh, P. (2020). Mapping crop types in fragmented arable landscapes using AVIRIS-NG imagery and limited field data. *International Journal of Image and Data Fusion*. https://doi.org/10.1080/19479832.2019.1706646

[27] Shaharum, N. S. N., Shafri, H. Z. M., Ghani, W. A. W. A. K., Samsatli, S., Al-Habshi, M. M. A., & Yusuf, B. (2020). Oil palm mapping over Peninsular Malaysia using Google Earth Engine and machine learning algorithms. *Remote Sensing Applications: Society and Environment*. https://doi.org/10.1016/j.rsase.2020.100287

[28] Shelestov, A., Lavreniuk, M., Kussul, N., Novikov, A., & Skakun, S. (2017). Exploring Google Earth Engine Platform for Big Data Processing: Classification of Multi-Temporal Satellite Imagery for Crop Mapping. *Frontiers in Earth Science*, *5*. https://doi.org/10.3389/feart.2017.00017

[29] Sun, L., Chen, J., Guo, S., Deng, X., & Han, Y. (2020). Integration of time series sentinel-1 and sentinel-2 imagery for crop type mapping over oasis agricultural areas. *Remote Sensing*. https://doi.org/10.3390/RS12010158

[30] Tariq, A., Yan, J., Gagnon, A. S., Riaz Khan, M., & Mumtaz, F. (2022). Mapping of cropland, cropping patterns and crop types by combining optical remote sensing images with decision tree classifier and random forest. *Geo-Spatial Information Science*. https://doi.org/10.1080/10095020.2022.2100287

[31] Tran, K. H., Zhang, H. K., McMaine, J. T., Zhang, X., & Luo, D. (2022). 10 m crop type mapping using Sentinel-2 reflectance and 30 m cropland data layer product. *International Journal of Applied Earth Observation and Geoinformation*, *107*, 102692. https://doi.org/10.1016/j.jag.2022.102692

[32] Wei, P., Ye, H., Qiao, S., Liu, R., Nie, C., Zhang, B., Song, L., & Huang, S. (2023). Early Crop Mapping Based on Sentinel-2 Time-Series Data and the Random Forest Algorithm. *Remote Sensing*, *15*(13), 3212. https://doi.org/10.3390/rs15133212

[33] Xie, G., & Niculescu, S. (2022). Mapping Crop Types Using Sentinel-2 Data Machine Learning and Monitoring Crop Phenology with Sentinel-1 Backscatter Time Series in Pays de Brest, Brittany, France. *Remote Sensing*, *14*(18), 4437. https://doi.org/10.3390/rs14184437

[34] Xu, H. (2006). Modification of normalised difference water index (NDWI) to enhance open water features in remotely sensed imagery. *International Journal of Remote Sensing*. https://doi.org/10.1080/01431160600589179

[35] Zhi, F., Dong, Z., Guga, S., Bao, Y., Han, A., Zhang, J., & Bao, Y. (2022). Rapid and Automated Mapping of Crop Type in Jilin Province Using Historical Crop Labels and the Google Earth Engine. *Remote Sensing*. https://doi.org/10.3390/rs14164028

OPTIMISATION BY COUPLED RECURDYN-EDEM SIMULATION: OPTIMISATION TESTS OF A THREE-STAGE LOW-LOSS SEPARATION DEVICE FOR POTATO SOIL
/
RecurDyn-EDEM 耦合仿真优化：三段式薯土低损分离装置优化试验

Zhixin LIU, Shuqi SHANG*), Shikuan MA, Yaxiu HOU, Tongtong DONG, Xiaoning HE
College of Electrical and Mechanical Engineering, Qingdao Agricultural University, Qingdao/ China
Corresponding author: Shuqi SHANG
Tel: +8613884956252; E-mail: sqshang@qau.edu.cn
DOI: https://doi.org/10.35633/inmateh-72-13

Keywords: *Potato soil separation device, RecurDyn, EDEM, Co-simulation*

ABSTRACT

Aiming at the potato soil separation device of potato harvester, which generally has the problem of potato high damage in potato-soil separation, a three-stage potato soil low-loss separation device was developed, and orthogonal experiments were designed with the help of RecurDyn-EDEM coupled simulation method. A field bench was built for verification tests. The test proved that: when the lift transport chain speed was 1.40 m/s, travel speed was 0.60 m/s, amplitude was 32.0 mm, the impurity rate was 1.49% and the average force on potato was 1.801 N. The potato damage rate was 2.7%, indicating that the design of the three-stage potato soil low-loss separator device worked well.

摘要

针对马铃薯收获机薯土分离装置普遍存在的薯土分离损伤高等问题，研制出一种三段式薯土低损分离装置，借助 RecurDyn-EDEM 耦合仿真方法设计正交实验。并搭建田间台架进行验证试验，试验证明：当升运链速度为 1.40m/s、行进速度为 0.60m/s、振幅 32.0mm 时，含杂率 1.49%，马铃薯平均受力为 1.801N，伤薯率 2.7%，表明设计的三段式薯土低损分离装置工作性能良好。

INTRODUCTION

Native to South America and introduced to China in the 17th century, the potato, as the world's fourth-largest food, has played an important role in reducing poverty and achieving sustainable development of human society (*Ren et al., 2022*). As a key link in the mechanization of potatoes, potato harvester is of great significance in improving labour efficiency and increasing production and income in the potato industry. The structure of similar foreign machinery and equipment is complicated, which affects the effect of potato soil separation and potato harvesting damage and is not adapted to China's potato planting mode (*Li et al., 2020; Baritelle et al. 2000; Du et al., 2019*).

Given the problems of potato mechanised harvesting, experts and scholars mainly analyse the range of length of the lifting chain of potato harvester potato soil separation device, the structural parameters of the Jitter and the working condition of the agricultural equipment, and optimise them in combination with the field trials (*Hu, 2018; Zhou et al., 2019*). Roger C. Brook used the MSU-USDA Instrumentation Sphere (IS) to analyse the structure of seven different structures of potato harvesters with a total of 28 different potato harvesting machines, to optimise their performance, to measure the effects of chain speed, equipment travel speed, chain type and drop height on harvesting results for each harvester, providing a range of data for harvester testing and development (*Roger C.B., 2008*). In addition, Alexey Dorokhov et al research has shown that damage due to the operation of potato-soil separating devices during mechanized harvesting of potato tubers accounts for 95% of mechanized damage to potatoes (*Dorokhov et al., 2022*). In another paper, the researcher pointed out that vibratory soil breaking is more efficient due to the fact that the effect of the external force is constant in a specific (limited) area of the soil mass (*Dorokhov et al., 2022*). Yakov Lobachevsky et al. used Raman LIDAR to analyse the cut surface of impacted potato tubers in a study of potato damage to assess potato tuber damage (*Lobachevsky et al., 2022*). Matmurodov et al. proposed a potato harvester solution that can separate impurities from potato tuber components multiple times, and the transmission mechanism of a newly developed crochet potato harvester was a mathematical simulation (*Matmurodov et al., 2020*).

Zhixin LIU, M.S. Stud. Eng; Shuqi SHANG, Prof. Ph.D. Eng; Shikuan MA, M.S. Stud. Eng; Yaxiu HOU, M.S. Stud. Eng; Tongtong DONG, M.S. Stud. Eng; Xiaoning HE, Prof. Ph.D. Eng.

Murodov et al. proposed a scheme of potato harvester with screw lift separator and verified the main parameters of centrifugal separation screw lift separator *(Murodov et al., 2022)*. Wei Zhongcai et al. designed a potato harvester based on the vibration separation section and wave separation section and analysed the separation sieve and potato movement characteristics of the equipment, and it was difficult to reflect the real chain movement state because the simulation model did not see the coupled simulation (*Wei et al., 2018*). In addition, the team designed a crawler self-propelled sorting potato harvester for the hilly mountainous operating environment, which has a large adhesion force, high-frequency and low-amplitude vibration soil crushing, it has technical advantages such as high adhesion force, high-frequency and low-amplitude vibration soil crushing, automatic row-to-row digging, manually-assisted sorting and hydraulic drive mode (*Wei et al., 2023*). Zhao Xiang et al. used the gliding motion vibration equation to model the mechanics of the oscillating separating screen of the potato digger and carried out the theoretical analysis of the motion, but there was no analysis of the lifting chain and jitter wheel of the transport sub-mechanism (*Zhao et al., 2021*). Li Yanbin et al. designed a potato harvester multi-stage conveying and separating device, analysed the multi-stage conveying and separating device and the motion characteristics of the potato-soil mixture and verified that the conveying and separating sieve produces a "high-frequency and low-amplitude" cyclic motion, but did not analyse the shaking wheel and chain (*Li et al., 2021)*. Zhang Zhaoguo et al. designed a multistage separation buffer potato harvester for potato mechanisation in Yunnan mountainous clay conditions, analysed the collision characteristics of the soil in the conveying and separation process, and determined the factors affecting the effect of separation and crushing, but did not analyse the vibration of the lifting chain (*Zhang et al., 2021*). Wang Xingdong et al. simulated the collision effect between potato and lifting chain based on the results of ADAMS dynamics rigid-flexible collision calculations, and proposed a method to assess the impact of collision on tubers to predict the effect of tuber desliming and damage rate, but did not study the interaction between the soil and potato of the lifting chain in-depth *(Wang et al., 2018)*. Currently, EDEM software is increasingly being used in the agricultural field. Jun-Hee Byum et al. designed and fabricated an experimental setup to simulate the analytical factorization of a chili pepper harvester and conducted analytical factorization experiments to determine the card-cleaner type of the chili pepper harvester that can be mounted in the chili pepper harvester with the help of EDEM software (*Jun-Hee, 2018*). *Je Lim et al. (2016)* used EDEM software to simulate the conveyance performance of the separating system of a peanut harvester.

In summary, there are more studies on potato soil separation devices in China, but the depth of the analysis of the role of potato soil separation structure on the material is not deep enough, and there is no vibration analysis of the lifting chain as well as coupling simulation analysis.

To solve the above problems, this paper designs a three-stage potato soil separation device based on kinetic analysis and sieving principle analysis, and with the help of the method of response surface experimental design and RecurDyn-EDEM coupled simulation as a means of structural optimization and parameter design, finally builds a field bench test to verify the working effect of the three-stage potato soil separation device.

MATERIALS AND METHODS

System architecture

The three-stage low-loss potato soil separation device designed in this paper has main parts including guide wheel, Jitter wheel, positioning wheels, side plate, lifting chain with bar, driving wheel and so on. As the main core component of the potato harvester, the three-stage low-loss potato soil separation device can vibrate, crush, sieve and transport the potato soil mixture on the lifting chain, and its structure and motion parameters are directly related to the effect of potato soil separation and operation quality. The working width of the three-section potato soil low-loss separation device is 900 mm, the structure is shown in Figure 1,2, divided into three working sections: material feeding section, vibration crushing section and screening section, the material feeding section is 400 mm long, the vibration crushing section is 500 mm long, and the screening section is 300 mm long, to satisfy the requirements of material transport, the inclination angle of the lifting chain should be less than the friction angle of the material, and the design manual of agricultural machinery has shown that the potato soil separation effect and operation quality are directly related to its structure and motion parameters. According to the design manual of agricultural machinery, the rolling friction angle of potato on 65Mn is 9 º ~ 37 º, the rolling friction angle of sand and sandy loam (cohesion) on 65Mn is 26 º 30 ´ ~ 35 º, the rolling friction angle of sand and sandy loam (loose) on 65Mn is 14 º ~ 26 º 30 ´. Therefore, it can be concluded that the inclination angle of the three working section of the lifting chain $\alpha_1 \leq 26$ º, $\alpha_2 \leq 14$ º, $\alpha_3 \leq 9$ º, to facilitate the processing and installation of parts, take $\alpha_1 = 22$ º, $\alpha_2 = 12$ º, $\alpha_3 = 8$ º.

The three working sections of the three-stage potato soil low-loss separation device: material feeding section, vibration crushing section and screening section. In the work, the potato mixture first arrives at the material feeding section, at the same time the portion of the potato mixture with dimensions smaller than the spacing of the conveyor bars falls through the gap in the conveyor bars of the lifting chain, most of the remaining material continues to be transported along the lifting chain; in the vibration of the broken soil section, the Jitter wheel rotationally impacts conveyor bars, while driving the potato mixture to do a certain frequency and amplitude of reciprocating vibration, crushing the larger pieces of soil, so that the soil attached to the potato off. The soil falls to the ground along the gap between the bars, and the remaining material is transported to the screening and de-soiling section for further screening, which ultimately achieves the functions of material transport, vibration soil crushing and material screening.

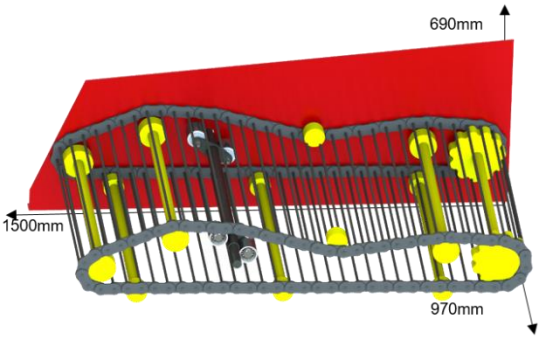

Fig. 1 - Side sectional view of the three-stage potato soil separation device

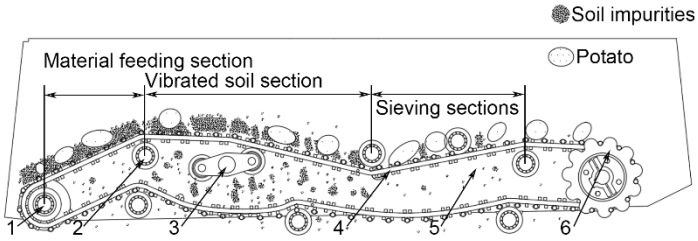

Fig. 2 - Working principle of three-stage potato soil separator

1 Guide wheel; 2 Positioning wheels; 3 Jitter wheel; 4 Lifting chain with bar; 5 Side plate; 6 Drive wheel

Orthogonal test of coupled simulation of potato soil separation device

To explore the optimal operating parameters, as well as the relationship with the potato force and potato soil separation ability, it is necessary to carry out the response surface test on the lifting chain with the help of a simulation test. Through the parameter design and analysis of the device, the lifting chain linear speed, the harvester travel speed (hereinafter referred to as travel speed) and the Jitter wheel from the lifting chain straight line distance (hereinafter referred to as the Jitter wheel distance) range were initially determined. The RecurDyn-EDEM coupled simulation model of the potato harvester soil separation device is established and then the simulation test of potato soil separation is carried out to deeply analyse the influence of the above three parameters on the effect of potato soil separation and tuber damage, in order to come up with the optimal parameter combination.

The discrete element model calibration object used in the experiment was taken from the experimental field of Qingdao Hongzhu Agricultural Machinery Co., Ltd. in Qingdao City, Shandong Province (120.06811°N, 36.43653°E), and the soil in the planting area was yellow loam, with loose surface soil and small lumps, and the subsoil had a certain degree of adhesion, and there were large lumps after excavation. To simulate the soil during the potato harvesting period, two kinds of particles, surface (loose) - and subsoil (cemented), were established to construct the potato harvesting granular bed. As shown in Figure 3.

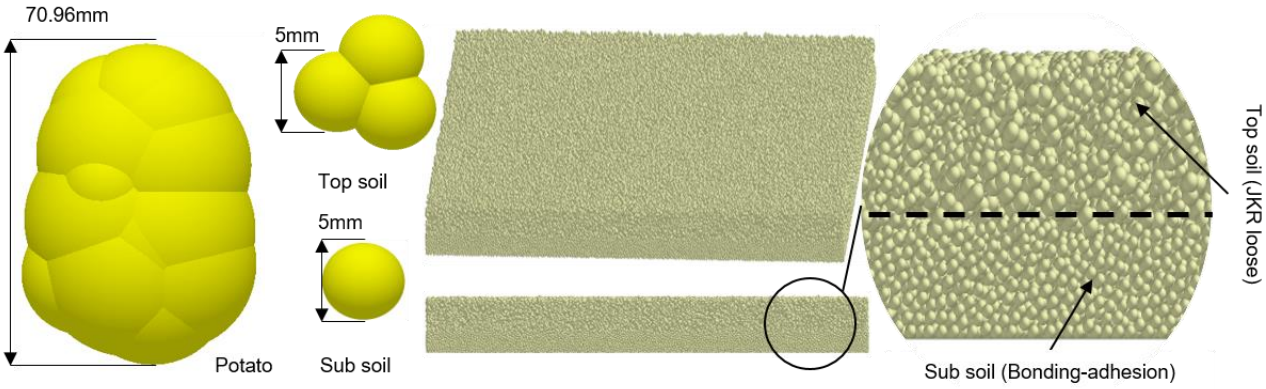

Fig. 3 - Discrete element simulation particle modelling

The surface particles were tri-spherical, bonded by the Hertz Mindlin with the JKR model, with diameters ranging from 2.5-5.0 mm. The bottom particles were based on the Hertz Mindlin with bonding model, using

single-spherical particles with a diameter of 2.5 mm, and were bonded by the Hertz Mindlin with JKR model between the two types of soil particles, and between the soil particles and the potato, with JKR parameters set at 12 J/m3 between the soil and 7.5 J/m^3 between the soil and the potato. According to the JKR model, the JKR parameter was set at 12 J/m^3 between the soils and 7.5 J/m^3 between the soils and the potatoes.
The overall size of the particle bed was 1000mm*200mm*900mm, the bottom particles were generated by static particle factory in EDEM with a thickness of 100 mm, and the surface particles were generated dynamically with a thickness of about 65 mm, and the intrinsic parameters and contact parameters of each discrete elemental cell are shown in Tables 1 to 3.

Table 1

Particle intrinsic parameters

Material	Densities/kg·m^{-3}	Poisson's ratio	Shear modulus/Pa
Sub-soil	2400	0.25	1e+07
Top-soil	2400	0.25	1e+07
Potato	1058	0.48	1.58e+08
Steel	7800	0.3	7.984e+10

Table 2

Bonding parameters of particles

Parametric	Sub-soil-sub-soil
Unit normal stiffness / N·m^{-3}	1.8e+06
Unit tangential stiffness / N·m^{-3}	1.4e+06
Normal strength / Pa	189000
Shear strength / Pa	106000
Bonding radius / mm	3

Table 3

Discrete element material contact parameters

Parametric	Crash recovery factor	Static friction factor	Kinetic friction factor
Sub-soil-sub-soil	0.15	0.8	0.05
Sub-soil-top-soil	0.61	0.5	0.2
Sub-soil-potato	0.25	0.21	0.013
Sub-soil-steel	0.7	0.6	0.015
Top-soil-top-soil	0.6	0.5	0.4
Top-soil-potato	0.206	0.2	0.13
Top-soil-steel	0.6	0.5	0.05
Potato-potato	0.313	0.36	0.1
Potato-steel	0.36	0.41	0.06

Simulation model construction based on RecurDyn-EDEM

Constructing the three-dimensional model of the key components of the potato soil separation device of the potato harvester is an important part of the simulation, the design and modelling of the lifting chain rod of the potato soil separation device is carried out in SolidWorks, and imported into RecurDyn in STEP format to add the moving and fixed vice and the contact between the parts. The External SPI is further exported to the EDEM through the RecurDyn software coupling interface, and the modeling rendering diagrams are shown in Figures 4 and 5.

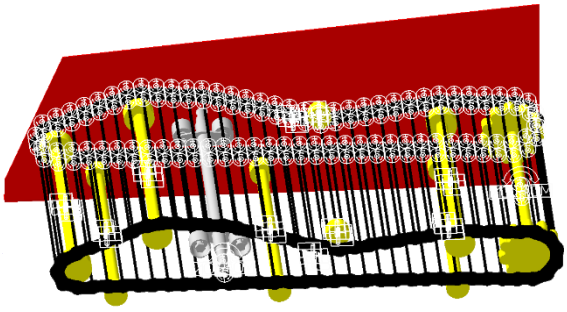

Fig. 4 - Multibody dynamics model motion pair added

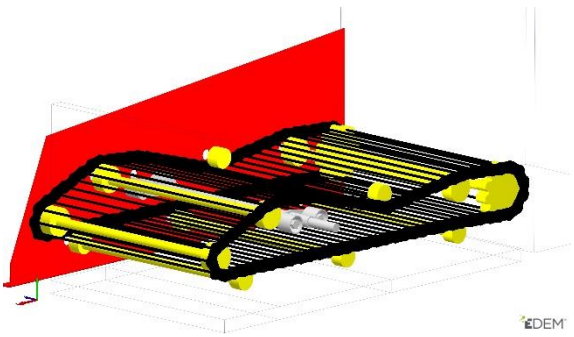

Fig. 5 - EDEM model

Considering the large particle velocity, to guarantee the reliability of the results, 1% of Rayleigh time is used as the minimum simulation step. A single simulation requires 746,250 soil particles, including 59 potatoes, and the simulation time is 5-7 s. It is estimated that the simulation takes 136-172 hours.

SIMULATION OF ORTHOGONAL TESTS

Design of test programme

The test program is shown in Table 4, taking the lifting chain linear speed, travel speed and jitter wheel position as the test factors, and the impurity content rate and average potato force as the evaluation indexes. According to "NY/T648-2015 Technical specification for quality evaluation of potato harvester", the impurity rate Y_1 is calculated as follows:

$$Y_1 = \frac{Q_2}{Q_2 + Q_1} \times 100\% \quad (1)$$

where Q_2 is the mass of impurities (soil in this paper), Q_1 is the mass of harvested potatoes, the experimental test factors coded as shown in Table 5. The test programme and results are shown in Table 5.

Table 4

Test factor coding

Encodings	Experimental factors		
	A: Lifting chain linear speed / m·s^{-1}	B: travel speed / m·s^{-1}	C: Jitter wheel position / mm
-1	0.8	0.6	30
0	1.1	0.9	65
1	1.4	1.2	100

Table 5

Test scheme and results

Serial number	Experimental factors			Y_1 / %	Y_2 / N
	A	B	C		
1	0	0	0	1.30	2.15
2	1	0	-1	1.10	2.59
3	0	1	-1	1.50	2.59
4	0	0	0	1.20	2.17
5	0	0	0	1.30	2.31
6	0	0	0	1.20	2.41
7	-1	0	1	0.96	2.93
8	1	0	1	1.60	0.90
9	0	-1	1	1.59	1.72
10	0	0	0	1.30	2.18
11	1	1	0	1.73	1.26
12	1	1	0	1.12	2.13
13	-1	1	0	0.85	3.34
14	0	1	1	1.51	1.23
15	-1	1	0	0.96	2.99
16	-1	0	1	0.79	3.68
17	0	-1	1	0.91	3.19

The simulation test procedure is shown in Figure 6.

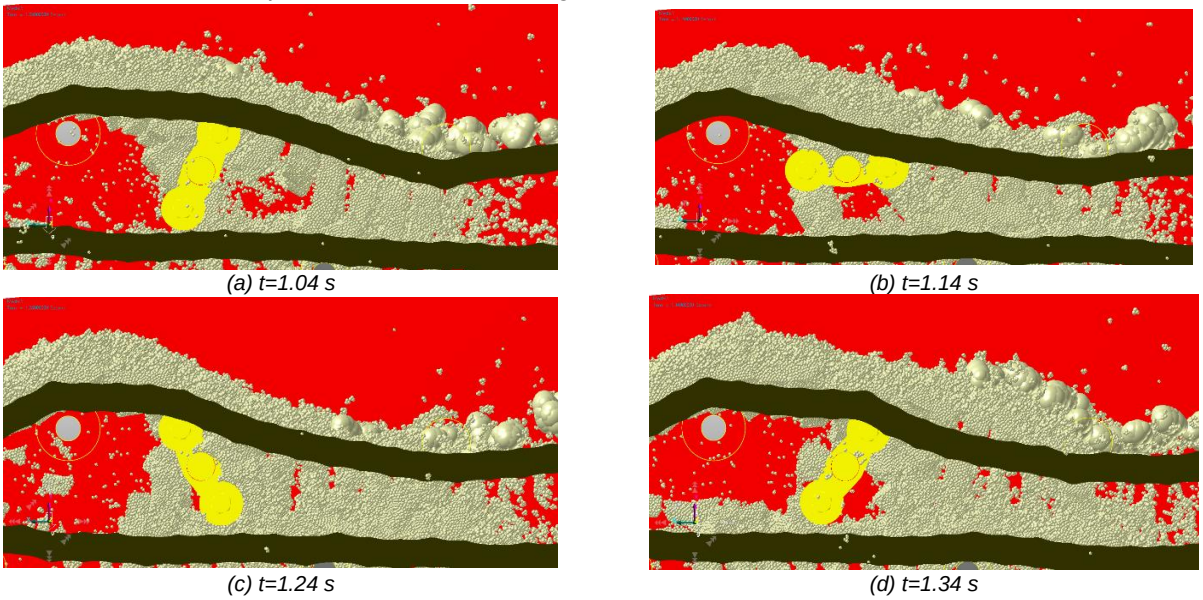

(a) t=1.04 s *(b) t=1.14 s*

(c) t=1.24 s *(d) t=1.34 s*

Fig. 6 - Coupled simulation process

RESULTS

Analysis of test results

Using Design-Expert software to analyse the test results, to get the regression equations of the impurity rate and average force, the results of ANOVA are shown in Table 6. For the regression model of impurity rate A, B, C, AB and A^2 for the impact of impurity rate is extremely significant (P<0.01), and the effects of AC and BC on this index were significant (P<0.05). The order of influence of the main terms of impurity rate is A, B, C. For the regression model of the average force on potatoes, A, B, C, AC and A^2 for the impact of impurity rate is extremely significant (P<0.01), AC and BC for this indicator is significant (P<0.05). The order of influence of the main terms of the average force on potatoes is A, C and B. The regression model was fitted using the software.

Using the software to carry out multiple regression fitting analysis, excluding the insignificant items, to establish the regression equation between the impurity rate, the average force and the significant factors:

$$Y_1 = 2.54914A - 1.31972B + 0.003827C + 1.38889AB + 0.007934AC - 0.008938BC - 1.58583A^2 - 0.534829 \quad (2)$$

$$Y_2 = -6.22968A + 2.02115B + 0.001663C - 1.44444AB - 0.002619AC + 2.93611A^2 + 7.14033 \quad (3)$$

The regression equations for impurity rate and average force are highly reliable, and the optimal parameter combinations for each factor can be solved based on the above two regression models.

Table 6

Impurities and Average Force Variance Analysis

Variance (statistics)	Impurity rate / %		Average force / N	
Source	F	P	F	P
models	36.84	< 0.0001	96.17	< 0.0001
A	142.90	< 0.0001	425.63	< 0.0001
B	84.08	< 0.0001	61.85	< 0.0001
C	40.75	0.0004	321.89	< 0.0001
AB	18.18	0.0037	6.27	0.0408
AC	8.07	0.0250	20.48	0.0027
BC	10.25	0.0150	0.2805	0.6128
A²	24.95	0.0016	27.26	0.0012
B²	3.10	0.1216	2.39	0.1660
C²	0.0579	0.8168	0.1095	0.7504
lost proposal	1.34	0.3795	0.6671	0.6149

Analysis of the effect of interaction on the test indexes

Through the software, as shown in Figures 7 and 8, the response surface of the interaction of the three factors on the influence of impurity rate Y_1 and average force Y_2 were obtained.

(1) Analysis of the effect of interaction on impurity rate

As can be seen from Fig. 7, there is a positive correlation between the impurity rate Y_1 and the lifting chain linear speed A, travelling speed B, and Jitter wheel position C. The interaction of the three factors on the impurity rate Y_1 is shown in Fig. 7. For the interaction of AB factors, when the travelling speed B is at a low level, the change of the impurity rate Y_1 with the lifting chain linear speed A is slower, mainly because when the travelling speed is slower, the feeding amount is lower, and the lifting chain can deal with the current soil, and vice versa, the impurity rate Y_1 will be increased accordingly; for the interaction of AC factors, when the jittering wheel position C is at a high level, the effect of the lifting chain linear speed A on the impurity rate Y_1 is more significant than that at the low level, and this is because the simulation shows a positive correlation between the speed of the lifting chain line and the impurity rate Y_1. This is because the soil particles of the simulation have a large degree of adhesion, and the amplitude of the shaking wheel of the lifting chain is related to the crushing of the soil, which helps the lifting chain to sieve the soil. The impurity rate is minimized when the shaking wheel is positioned and moves at a low level.

(2) Analysis of the effect of interaction on the average force on potato

The potato average force response surface is shown in Figure 8, and the lifting chain linear speed A, travelling speed B and Jitter wheel position C are negatively correlated with the average force Y_2. For the AB interaction, travelling speed at a high level of the lifting chain linear speed changes on the average force effect

is smaller, due to the faster travelling speed, so that the feeding volume is larger, while the lifting chain linear speed is faster, the potato in the lifting chain residence time is less, the number of collisions is less, and the soil protection effect is better, the Jitter effect makes the potato force be reduced, so the two factors are at a high level, the average force is the lowest. AC interaction effect is more significant than that of AB, but the lowest average force is still at a high level. This is due to the fact that the shaking wheel is farther away from the position of the lifting chain, the amplitude of the forced vibration of the lifting chain is smaller, so that the force is smaller, and at the same time the linear speed increases, the potato stay in the lifting chain time decreases, further reducing the number of collisions, the two together reducing the average force on the potatoes.

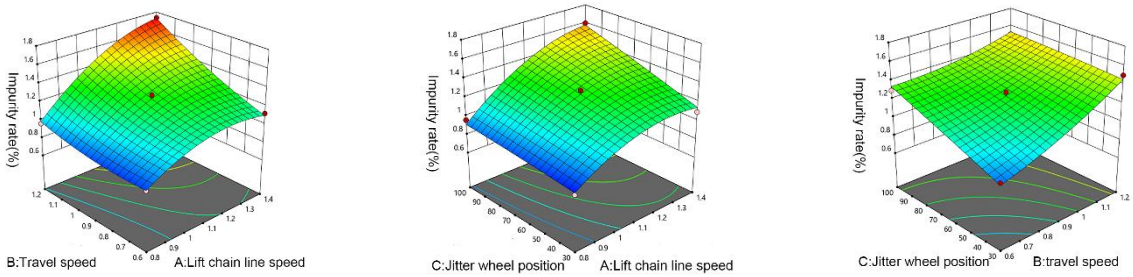

Fig. 7 - Response surface of factor interactions on impurity rate

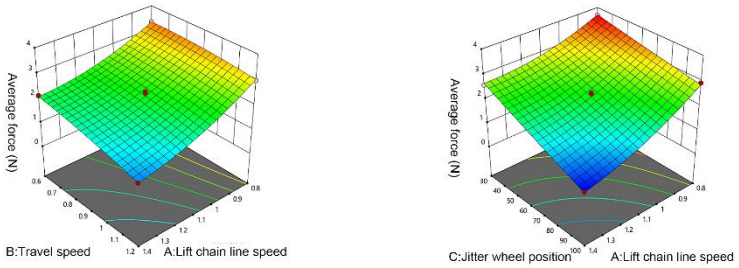

Fig. 8 - Response surface of factor interactions to the average force applied

Combination solution of the optimal value of experimental factors

According to the above test results and regression equation, the minimum impurity rate and average force are taken as the optimization objectives, and the linear speed, travel speed and jitter wheel position of the lifting chain are taken as the optimization objects, the regression model is optimized, and its objective function and constraint conditions are:

$$\begin{cases} \min Y_1(A,B,C) \\ \min Y_2(A,B,C) \\ X_1, X_2, X_3 \subseteq (-1,1) \end{cases} \quad (4)$$

Finally, when the lifting chain linear speed is 1.40 m/s, the travel speed is 0.60 m/s, when the jitter wheel position is 70.701 mm (the theoretical amplitude is 32.299 mm), the impurity content is 1.151 %, and the average force is 1.942 N.

Bench validation experiments

Testing material

According to the design parameters of the device and the factors optimized by the simulation test, a three-stage potato-soil separation performance test bench was built. The test equipment was modified and processed by Qingdao Hongzhu Agricultural Machinery Co., Ltd. according to the test requirements. The test equipment is shown in Figures 9, 10, 11. The test equipment includes an electronic potato, frequency converter, horizontal conveyor belt, potato test bench and tachometer.

Bench test

The test site was the test field of Qingdao Hongzhu Agricultural Machinery Co., Ltd, Qingdao City, Shandong Province (120.06811°N, 36.43653°E), and the test bench was modified by an amplitude of 32 mm, with working parameters following a travelling speed of 0.6 m/s, and lifting chain linear speed of 1.4 m/s for the test. The acceleration sensor of the electronic potato was used to record the acceleration of the electronic potato when the equipment was working, and the force was calculated by multiplying the mass of the electronic potato. As the test results show in Table 7, after five repetitions, the average force of electronic potato is 1.801 N, impurity rate is 1.49%. The impurities rate in the test was higher than in the simulation tests due to the

presence of weeds and other impurities such as rhizome stones. However, the protective effect of the soil resulted in less damage to the potato block in the test compared to the simulation. The results are consistent with the optimisation and prediction of the simulated response surface test. For the index of potato damage rate, the result of this test is 2.7%, which is better than the results of other studies *(Lv et al., 2020)*.

Fig. 9 - Electronic potato

Fig. 10 - Rotating speed meter

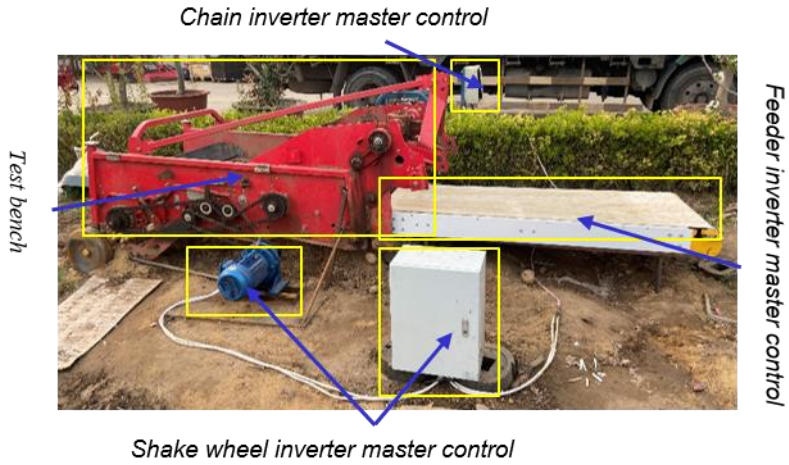

Fig. 11 - Three-stage potato soil separation performance test bench

Table 7

Bench test results

Num	1	2	3	4	5	Average
Average Force(N)	1.790	1.770	1.793	1.840	1.812	1.801

CONCLUSIONS

(1) In this paper, a three-stage potato-soil separation device is designed by analysing the working principle of the device and the forced vibration analysis of the lifting chain. The device is divided into three working sections: material feeding section, vibrating soil crushing section and screening soil removal section, and the mechanism of each working section is analysed.

(2) The multi-body dynamics model of potato-soil mixed granular bed and potato-soil separation device was established. The response surface simulation test of a three-stage potato-soil separation device based on RecurDyn-EDEM coupling simulation was designed with impurity rate and average force as evaluation indexes, and the linear speed of the lifting chain, travel speed and position of shaking wheel as factors. The results were optimized by regression. The results showed that when the speed of the lifting chain was 1.40 m/s, the travel speed was 0.60 m/s, and the distance between the shaking wheel and lifting chain was 70.70 mm (theoretical amplitude was 32.30 mm), the impurity rate was 1.151 %. The average force was 1.942 N.

(3) In this paper, the three-stage potato-soil separation device is designed and optimized, and a three-stage potato-soil separation performance test bench is built to verify the simulation results. Five repetitions are made and the average force of electronic potato is 1.801 N, impurity rate of 1.49%, the potato damage rate is 2.7%. The test results are similar to the simulation test results, which verifies the reliability of the simulation test.

ACKNOWLEDGEMENT

The authors were funded for this project by the Taishan Industry Leading Talents Project (No. LJNY202104) and the science and technology project of Xinjiang Production and Construction Corps (No. QNYCX22092).

REFERENCES

[1] Baritelle A., Hyde G., Thornton R., Bajema R. (2000). A classification system for impact-related defects in potato tubers. *American Journal of Potato Research*, Vol. 77, pp. 143-148, USA.

[2] Dorokhov A., Didmanidze O., Aksenov A. (2022). The Results of Studies on the Assessment of the Destruction of Soil Clods during Combine Harvesting of Potatoes. *Agriculture*, Vol. 12, pp. 2024, Russia.

[3] Dorokhov A., Ponomarev A., Zernov V. (2022). The Results of Laboratory Studies of the Device for Evaluation of Suitability of Potato Tubers for Mechanized Harvesting. *Applied Sciences*, Vol. 12, pp.2171, Russia.

[4] Du M., Wang J., Wang W., Yu W., Yang H. (2019). Development status and trend of potato combine harvester (马铃薯联合收获机现状及发展趋势). *Agricultural Machinery Using & Maintenance*, Vol. 08, pp. 15-17, China.

[5] Hu B. (2018). Study on potato dropping damage mechanism and damage-proof device. Chengdu (马铃薯跌落损伤机理与防损伤装置研究): *Xihua University*. China.

[6] Je Lim, Myoung–Ho Kim, Seong–Min Kim. (2016). Transport Performance Simulation of Separating System for Self–propelled Peanut Harvester using EDEM Software. *Journal of the Faculty of Agriculture*, Vol. 61, pp. 361-365, Japan.

[7] Jun Hee B., Ju Seok N., Jung Seob C. (2018). Analysis of the Separating Performance of a Card Cleaner for Pepper Harvester using EDEM Software. *Journal of the Faculty of Agriculture*, Vol. 63, pp. 347-354, Japan.

[8] Li Y., Zhang Z., Wang Y., Wang H. Pang Y., Zhang Z. (2021). Design and Experiment of Multistage Conveying and Separating Device for Potato Harvester (马铃薯收获机多级输送分离装置设计与试验). *Journal of Shenyang Agricultural University*, Vol. 52, pp. 758-768, China.

[9] Li Z., Chang Q., Liu J., Dong X. (2020). Development Status and Trend of Domestic and Overseas Potato Harvesters (国内外马铃薯收获机械发展现状及趋势). *Modern manufacturing technology and equipment*, Vol. 56, pp. 207-208, China.

[10] Lobachevsky Y., Dorokhov A., Aksenov A. (2022). RAMAN and Fluorimetric Scattering Lidar Facilitated to Detect Damaged Potatoes by Determination of Spectra. *Applied Sciences*, Vol. 12, pp. 5391, Russia.

[11] Lv J., Yang X., Lv Y., Li Z., Li J., Du C. (2020). Analysis and Experiment of Potato Damage in Process of Lifting and Separating Potato Excavator (马铃薯挖掘机升运分离过程块茎损伤机理分析与试验). *Journal of Agricultural Machinery*, Vol. 51, pp. 103-113, China.

[12] Matmurodov F., Dustkulov A., Abdiyev N. (2020) Mathematical simulation of transfer mechanisms of crocheting potato harvesting machine. *IOP Conference Series: Materials Science and Engineering*, Vol. 883, pp. 012176, Uzbekistan.

[13] Murodov R. K., Nishonov K. K., Bayboboev N. G. (2022). Influence of elevator parameters with centrifugal separation on soil separation from potato tubers. *IOP Conference Series: Earth and Environmental Science (1)*. Vol. 1112, pp. 012072, Uzbekistan.

[14] Ren S., Sun B., Meng Y., Zheng Y. (2022). The Present Situation and Development Tendency of Potato Harvester and Its Key Components (马铃薯收获机及其关键部件的现状和发展趋势). *Forestry machinery and woodworking equipment*, Vol. 50, pp. 45-49, China.

[15] Roger C.B. (2008). Impact testing of potato harvesting equipment. *American Potato Journal*, Vol. 70, pp.243-256, USA.

[16] Wang X, Wen H, Zeng Y, Xie S. (2018). Analysis of Movement and Impact of Tubers on Elevator Belt of Potato Harvest (马铃薯收获机升运带块茎运动碰撞分析). *Journal of Agricultural Mechanization Research*, Vol. 40, pp. 29-33+39, China.

[17] Wei Z, Li H, Sun C, Li X, Liu W, Su G, Wang F. (2018). Improvement of potato harvester with two segment of vibration and wave separation (振动与波浪二级分离马铃薯收获机改进). *Journal of Agricultural Engineering*, Vol. 34, pp. 42-52, China.

[18] Wei Z, Wang X, Li X, Wang F, Li Z, Jin C. (2023). Design and Experiment of Crawler Self-propelled Sorting Type Potato Harvester (履带自走式分拣型马铃薯收获机设计与试验). *Journal of Agricultural Machinery*, Vol. 54, pp. 95-106, China.

[19] Zhang Z, Wang H, Li Y, Yang X, IBRAHIM I, Zhang Z. (2021). Design and Experiment of Multi- stage Separation Buffer Potato Harvester (多级分离缓冲马铃薯收获机设计与试验). *Journal of Agricultural Machinery*, Vol. 52, pp. 96-109, China.

[20] Zhao X. (2021). Dynamic Analysis and Experimental Research on the Swing Separation Screen of Potato Excavator (马铃薯挖掘机摆动分离筛动力学分析与试验研究). *Baotou: Inner Mongolia University of Science and Technology*, China.

[21] Zhou W, Chen W, Guo B. (2019). Damage Factors and Experimental Study on Mechanized Potato Harvesting Process (马铃薯机械化收获过程的损伤因素及试验研究). *Agriculture and Technology*, Vol. 39, pp. 50-51, China.

SIMULATION AND EXPERIMENT OF MONORAIL ANTI-FROST MACHINE IN HILLY ORCHARD
/
丘陵山地果园单轨式防霜机的仿真与试验

Qingfu GONG [1], Yuepeng SONG[1,2], Wei MA[3], Hongmei ZHANG [1], Xiang HAN[1], Ang GAO [1], Longlong REN [1,2*]
[1] Shandong Agricultural University, College of Mechanical and Electrical Engineering/ China;
[2] Shandong Provincial Engineering Laboratory of Agricultural Equipment Intelligence/ China;
[3] Institute of Urban Agriculture, Chinese Academy of Agricultural Sciences/ China
E-mail: renlonglong@sdau.edu.cn
DOI: https://doi.org/10.35633/inmateh-72-14

Keywords: *Frost; Frost protection wind machine; Hilly Orchard; Fluent; Simulation; Diffusion*

ABSTRACT
In order to solve the problems of artificial operation, high labor intensity and low efficiency of frost prevention in hilly orchards, this study focused on hilly orchards and designed a smoke frost prevention machine based on the agronomic requirements for frost prevention in hilly orchards. Utilizing Fluent software, a simulation analysis was conducted on the spatiotemporal distribution characteristics of smoke mass concentration and temperature during the smoke diffusion process based on the discrete phase model. The results indicated continuous emission of smoke at a velocity of 6 m/s, with smoke plume volume gradually increasing and reaching a stable diffusion state after 9 seconds. Based on the established smoke diffusion simulation model, an orthogonal experimental analysis of the working parameters at the smoke outlet of the frost prevention machine was conducted using the warming amplitude near the canopy as an index. The optimal combination of working parameters at the smoke outlet was determined to be a smoke outlet velocity of 6 m/s, a smoke outlet angle of 60°, and a smoke outlet diameter of 140 mm. The field experiments demonstrated that the frost prevention machine operating at a speed of 0.6 m/s continuously for 0.5 hours could increase the temperature within the range of 1.5 m to 4 m above ground level by approximately 1.7°C. This research is of great significance to reduce the frost disaster loss of hilly orchards and improve the economic benefits of hilly orchards.

摘要
为了解决丘陵果园防霜以人工作业为主、劳动强度大、作业效率低的问题，本文以丘陵果园为研究对象，基于丘陵果园防霜冻的农艺要求，设计了一种基于丘陵果园输运轨道的烟雾防霜机。借助 Fluent 软件，基于离散相模型对烟雾扩散过程中烟雾质量浓度和温度的时空分布特性进行仿真分析，结果表明烟雾以 6 m/s 的速度持续喷发，烟羽体积逐渐增大，9s 后，烟雾达到稳定扩散状态；基于建立的烟雾扩散仿真模型，以果树冠层附近的增温幅度为指标，对防霜机烟雾出口处的工作参数进行正交试验分析，结果表明防霜机烟雾出口处的工作参数最佳组合为烟雾出口速度为 6m/s，烟雾出口角度为 60°，烟雾出口直径为 140 mm。田间试验结果表明，防霜机以 0.6 m/s 的运行速度连续作业 0.5 h，可将工作区域 1.5 m 至 4 m 高度范围内的温度升高约 1.7° C。该研究对降低丘陵果园霜冻灾害损失，提升丘陵果园经济效益具有重要意义。

INTRODUCTION
In recent years, extreme weather such as frost caused by spring low temperatures has occurred frequently *(Ferrez et al., 2011)*. Affected by the geographical environment, frost damage caused by low temperatures has become one of the main natural disasters. Frost damage caused by low temperatures often occurs during the flowering period of fruit trees. If there are no effective protective measures, it is easy to cause a large-scale production reduction or even extinction, which brings serious economic losses to fruit farmers *(Li et al., 2018; Zhang et al., 2019)*.

Frost prevention in the orchard is not only a crucial method for addressing frost disasters but also a key aspect in managing the flowering period of fruit tree *(Ran et al., 2020)*. Research on anti-frost technology of orchards is relatively early and mature. Mechanized frost prevention has become an important technical means to prevent frost *(Beyá-Marshall et al., 2019)*. At present, the domestic frost protection measures in orchards are mainly based on traditional frost prevention methods such as artificial flooding, chemical whitening of the tree trunks, smoke and tree canopy covering. The problems of consuming a significant amount of time and energy and wasting resources have seriously affected the sustainable and healthy development

of the fruit industry *(Dai et al., 2009)*. Therefore, mechanized frost prevention operations will play a crucial role in protecting orchards from frost. At present, foreign research on anti-frost machines is relatively early. There are many types of anti-frost machines in foreign countries and the degree of mechanization is relatively high *(Augspurger, 2013)*. According to the principle of anti-frost, anti-frost machines mainly include air-assisted anti-frost machines, suction-exhaust anti-frost machines, anti-frost helicopters, and warm-wind anti-frost machines *(Reese et al., 1969; Mikio et al., 2007; Vincent et al., 2020; Yazdanpanah et al., 2011; Battany, 2012; Poling, 2008; Hu et al., 2015)*.

The existing anti-frost machines are dedicated to special machines and have a single function, which results in a low utilization rate and a high idle rate. The low utilization rate of agricultural machines is one of the important reasons for the increase in the cost of agricultural machines and the difficulty in the promotion and application of agricultural machines *(Zhang et al., 2016)*. Therefore, in order to reduce the idle power equipment of agricultural machinery, the design of the anti-frost machine in hilly orchards should adopt the method of combining agricultural machines and power equipment in the hilly orchard to realize the anti-frost working. According to the developing status of domestic hilly orchard power machinery, it can be known that the hilly orchard transportation track tractor which has strong transportation capacity, small and exquisite structure design *(Liu., 2018; Yan et al., 2023; Song et al., 2017)*, and the ability to overcome terrain obstacles is the best choice for the power equipment of anti-frost machine in the hilly orchard.

According to the agronomic requirements for frost protection in hilly orchards, a smoke anti-frost machine based on the monorail transport track of hilly orchards, which reduces the frost disasters and the economic losses of orchards, was developed. The smoke anti-frost machine developed in combination with the existing power equipment of the hilly orchard realizes the mechanized anti-frost working. At the same time, it is of great significance to reduce the cost of frost prevention in orchards and increase the income of fruit growers.

MATERIALS AND METHODS

Whole structure and working principle

Whole structure

Combined with the above analysis, a smoke anti-frost machine based on the transportation track of hilly orchard was designed, as shown in Figure 1.

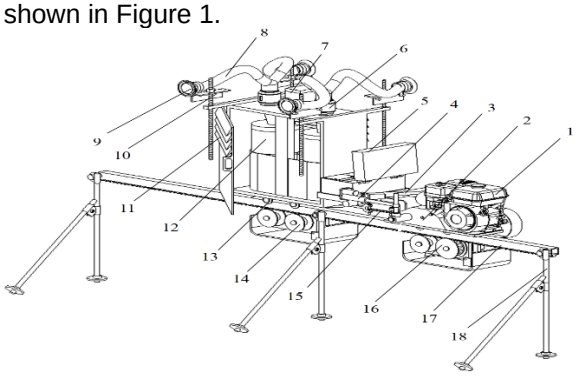

Fig. 1 - Structure diagram of frost protection smoke machine based on transportation track of hilly orchard

1. Gasoline engine; 2. Clutch device; 3.Electric push rod device 1; 4.Electric push rod device 2; 5.Control cabinet; 6.fan; 7.DC power supply box; 8.Hose for transporting smoke; 9.Smoke outlet; 10.Adjusting device for smoke outlet; 11.Vent; 12.Smoke generating agent placement box; 13.Bearing wheel; 14.Guide wheel; 15.Junction device; 16.Drive pin wheel; 17.Track; 18.Support frame

Working principle

The whole structure is mainly composed of the transportation track tractor, the smoke generation and transportation components, and the control cabinet. Smoke generation and transportation components are connected to the transportation track tractor by the junction device. The tractor drives the movement of the smoke transportation components to realize the mobile anti-frost operation in hilly orchards. During the anti-frost operation, the operation of the anti-frost machine is mainly controlled by the electric push rod device.

The smoke generation and transportation components of the anti-frost machine are mainly composed of smoke-generator, fan, and system control components. The control system of smoke generation and transportation components is mainly based on the programmable controller, which completes the generation and output of smoke by controlling the ignition of the smoke-generating agent and the opening and closing of the fan. The smoke-generating agent burns with oxygen to generate highly dispersed oxide particles, which quickly diffuse under the action of the fan and form a large amount of smoke.

Smoke floats in the air at a certain height for a long time, forming a smoke screen. The smoke screen can effectively reduce the heat radiation loss of the soil and fruit trees. At the same time, the large amount of smoke generated dissolves the damp and cold air in the frost orchard into water and releases a certain amount of latent heat, which can effectively increase the temperature of the surrounding environment and achieve the purpose of frost prevention in the orchard.

Main technical parameters

According to the topographical distribution characteristics of hilly orchards in northern China and the design requirements of the planting characteristics of fruit trees on the frost-proof machine, the overall design parameters of the smoke anti-frost machine in hilly orchards were preliminarily determined, as shown in Table 1.

Table 1

Table of main technical parameters

Item	Design parameters of the prototype
Auxiliary Power of tractor	Gasoline engine
Size of the whole machine (length ×width ×height/cm)	160×40×160
Operating speed（m/s）	0.5~1
Remote control distance（m）	≥100
Amplitude of warming when the anti-frost machine works for 0.5 h（℃）	≥1.5

CFD numerical simulation analysis of smoke diffusion based on Fluent

Based on the discrete-phase multi-phase flow model, Fluent software was used to simulate the diffusion process of smoke. The law of smoke diffusion was obtained by analyzing the mass concentration of smoke particles and temporal and spatial distribution characteristics of temperature. At the same time, to explore the influence law of the working parameters of the smoke outlet on the warming magnitude of the orchard environment and provide a theoretical basis for the optimization design of the anti-frost machine, three factors and three levels orthogonal experiment was carried out by selecting the speed of the smoke outlet, the angle of the smoke outlet and the diameter of the smoke outlet as the inspection factors, taking environmental warming amplitude as evaluation index and using discrete phase smoke diffusion model and method of orthogonal experiment.

CFD simulation and numerical model of smoke diffusion

The smoke diffusion process is a typical discrete-phase diffusion model. In view of the fact that airflow and the diffusion movement of smoke particles should be fully considered when establishing the simulation model, the method of combining Euler-Lagrange with coordinates was used to simulate. In the calculation process of the two-phase flow numerical model of the Euler-Lagrange method, the air-fluid was considered as a continuous phase and its flow characteristics under Euler coordinates were studied. In addition, smoke particles were considered as discrete phases and the movement of particles in the flow field over time under Lagrange coordinates was tracked *(Song et al., 2017)*.

(1) Numerical model of air flow

In this paper, the governing equations of turbulent kinetic energy k, turbulent dissipation rate ε, turbulent viscosity μ_t and turbulent time-averaged parameters were established by using Realizable $k-\varepsilon$ turbulence model.

The calculation control equations of k and ε are as follows:

$$\frac{\partial(\rho k)}{\partial t}+\frac{\partial(\rho k\mu_i)}{\partial x_i}=\frac{\partial}{\partial x_j}\left[\left(\mu+\frac{\mu_t}{\sigma_k}\right)\frac{\partial k}{\partial j_k}\right]+G_k-\rho\varepsilon \quad (1)$$

$$\frac{\partial(\rho\varepsilon)}{\partial t}+\frac{\partial(\rho\varepsilon u_i)}{\partial x_i}=\frac{\partial}{\partial x_j}\left[\left(\mu+\frac{\mu_t}{\sigma_\varepsilon}\right)\frac{\partial\varepsilon}{\partial x_j}\right]+C_1\varepsilon\frac{G_k}{k}-C_2\rho\frac{\varepsilon^2}{k} \quad (2)$$

In the above formula, k is the Turbulent kinetic energy; ε is the Turbulent dissipation rate; σ_k is the Turbulent Prandtl number corresponding to turbulent kinetic energy k; σ_ε is the Turbulent Prandtl number corresponding to Turbulent dissipation rate ε; C_1 and C_2 are the Empirical constant; G_k is the Turbulent kinetic energy derived from average velocity gradient.

(2) Numerical model of smoke particles

In the process of solving the two-phase flow discrete phase numerical model based on the Euler-Lagrange coordinate method, the fluid was taken as the continuous phase and the force balance differential equation and trajectory differential equation of the particle were integrated. Finally, the velocity and trajectory of each position of the particle were obtained *(Jian et al., 2020)*. The particle x-axis force balance equation and trajectory equation expression are, respectively:

$$\frac{du_p}{dt} = F_D(v_t - v_p) + (\rho_p - \rho)\frac{g_x}{\rho_p} + F_x \quad (3)$$

$$\frac{dx}{dt} = v_p \quad (4)$$

In the above formula, v_t is the fluid phase velocity in the x-axis direction; v_p is the particle velocity in the x-axis direction; ρ_p is the packing density of particle; F_x is the other forces per unit mass; $F_D(v_t - v_p)$ is the drag function per unit mass of particles.

The fuming agent material selected by the anti-frost machine in the orchard is mainly composed of manganese dioxide, iron trioxide, barium nitrate, and potassium permanganate. The smoke-generating agent will generate tiny solid particles after burning. The particle size of the smoke particles generated by the combustion of smoke-generating agent obeys the Rosin-Rammler distribution *(González-Tello et al., 2008)*. The expression of Rosin-Rammler distribution function is *(Delagarmmatikas et al., 2010)*:

$$F(d) = 1 - \exp[1 - \beta d^n] \quad (5)$$

In the above formula, β is the characteristic parameter; d is the particle size; n is the distribution index; $F(d)$ is the cumulative percentage of particle size less than d.

Establishment of smoke diffusion simulation model

In the simulation analysis of CFD fluid, it is crucial to determine a reasonable calculation domain. The smoke anti-frost machine designed in this paper can perform dynamic cycle operation along the transportation track of hilly orchard. Therefore, the size of the computational domain and the structure of the anti-frost machine should be simplified under the premise of ensuring the reliability of the simulation results when exploring the law of smoke diffusion. The simplified simulation model is: under the condition of airflow velocity of 1 m/s, smoke particles with a certain temperature and velocity are ejected from the smoke outlet and diffuse in the environment; assuming that the vertical height of the smoke outlet from the ground is 1000 mm, the angle of the smoke outlet is 60°, the diameter of the smoke outlet is 100 mm, and the computational domain of the model is a cube of 1000 mm×1000 mm × 1000 mm. At the same time, in order to facilitate the study of the temporal and spatial characteristics of smoke in the flow field, a typical plane of z = 0 was established, as shown in Figure 2 (a).

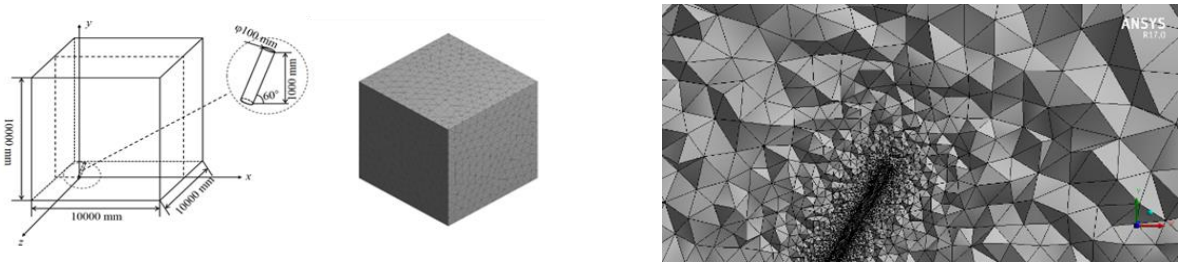

a) Physical model size of computational domain b) Unstructured grid division

Fig. 2 - Computational domain size and unstructured grids generation

RESULTS

Analysis of the smoke diffusion process

Figure 3 (a) ~ (h) are the cloud diagrams of the smoke mass concentration distribution at the typical time within 1 ~ 15 s on the z=0 section. According to Figure 3, it can be seen that as smoke continues to erupt at 6 m/s, smoke diffuses horizontally along the x-axis due to the influence of airflow. The volume of plume (Smoke flow's shape at punctiform emission sources) gradually increased within 1 s - 7 s. The plume had an inverted V shape; with the increase of the eruption time of smoke, the smoke diffusion reached a steady state after 9 s.

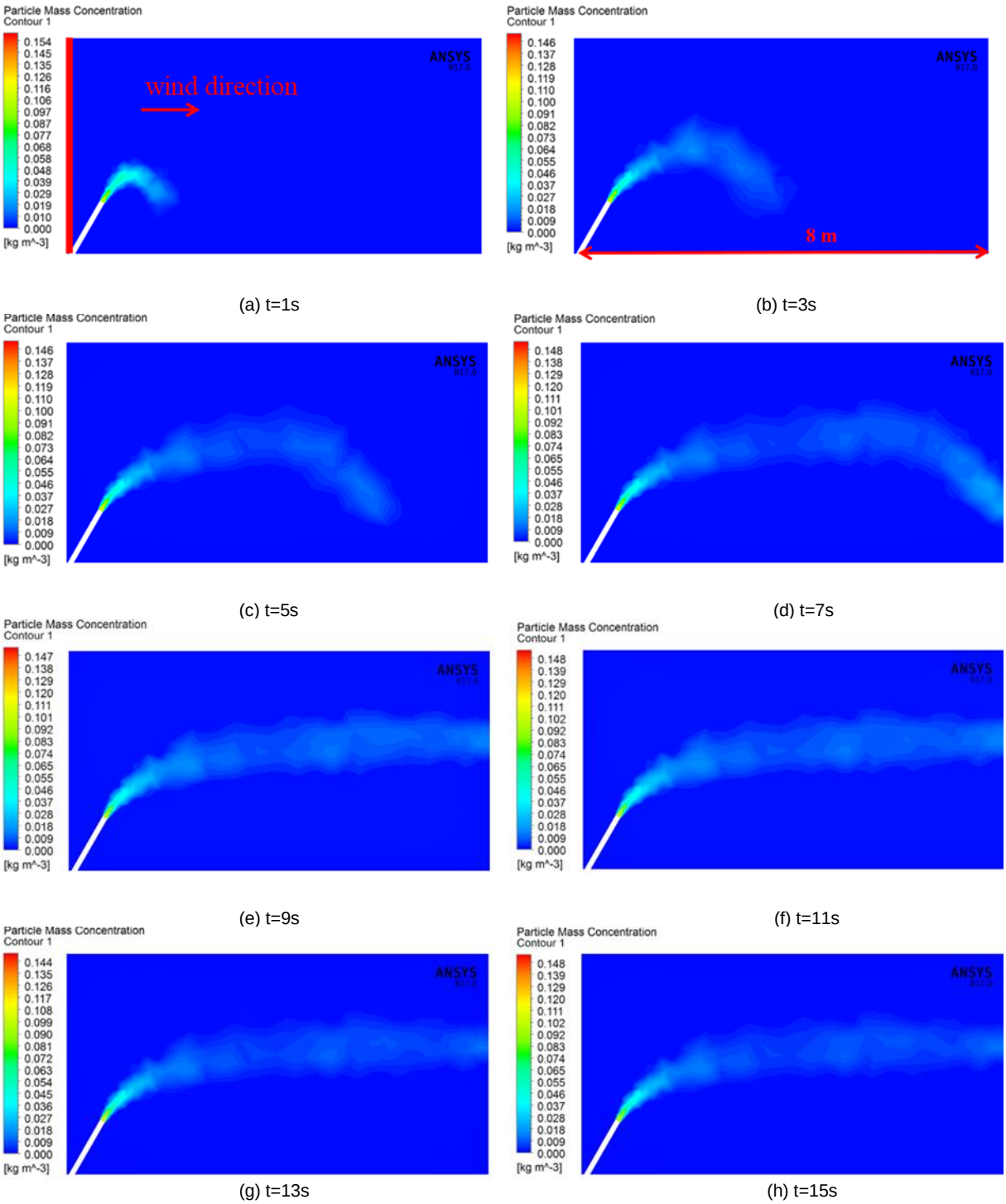

Fig. 3 - Distributions of smoke mass concentration at different times

In order to further study the variation law of smoke mass concentration in the diffusion process of smoke along the x-axis, the center of the bottom of the smoke outlet was taken as the origin of the coordinates, the horizontal distance as the x-axis and the smoke mass concentration at a height of 2 m on the z=0 section as y-axis. Figure 4 shows the variation curve of smoke particle mass concentration. It can be seen from Figure 4 that when x=0, the mass concentration of smoke is 0. As the distance increases, the mass concentration of smoke first increased and then decreased. In the BC section of the curve, the main reason for the increase in smoke mass concentration is that the smoke outlet is 60° to the x-axis. Affected by the direction of wind flow, the diffusion tilt amplitude of the plume gradually decreased, and finally is parallel to the x-axis. In the CD section of the curve, the main reason for the fluctuation of the smoke mass concentration is that the shape of the plume formed during the horizontal diffusion of the smoke is relatively irregular.

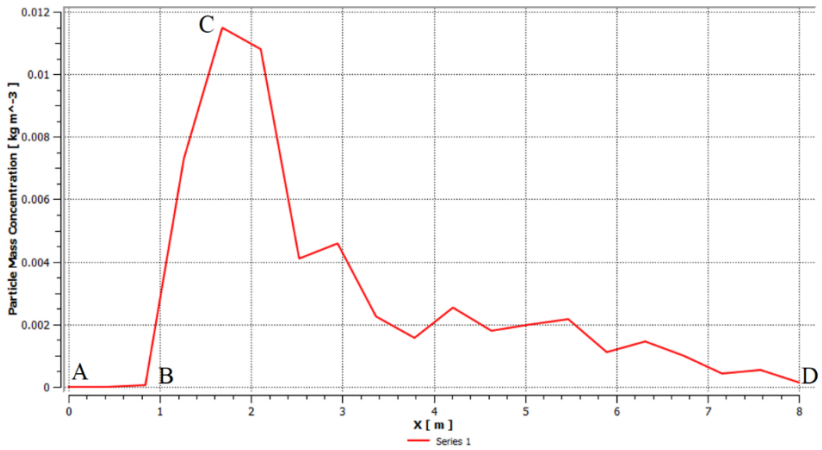

Fig. 4 -The relationship between smoke mass concentration and horizontal distance

Analysis of smoke diffusion temperature field

In order to obtain the space-time variation law of the temperature field in the process of smoke diffusion, the smoke diffusion temperature field at typical moments on the z=0 plane was analyzed. The cloud chart of the smoke diffusion temperature on the z=0 plane is shown in Figure 5(a)~(h). It can be seen from Figure 5 that in a low-temperature environment of 271.15 k (-2 ℃), the high-temperature smoke sprayed from the smoke outlet continuously exchanged heat with the cold air and the temperature of the smoke gradually decreased; High-temperature smoke was mainly concentrated in the center of the plume. As the volume of the plume increased, the temperature at the edge of the plume gradually decreased.

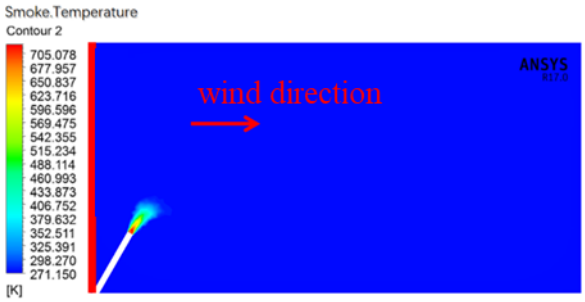

(a) t=1s

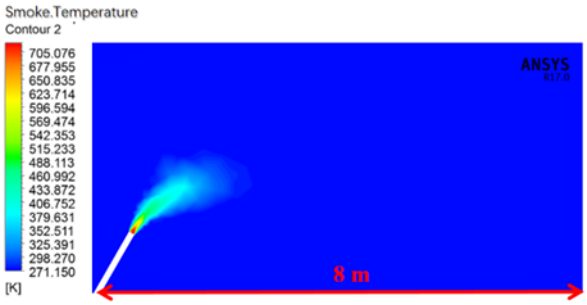

(b) t=3s

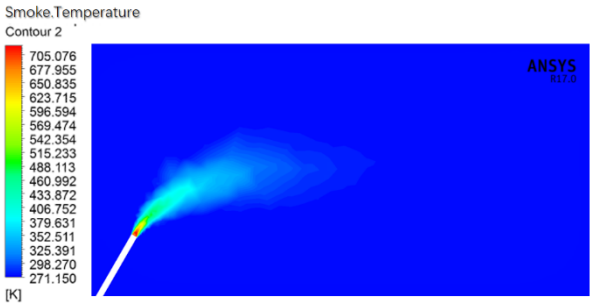

(c) t=5s

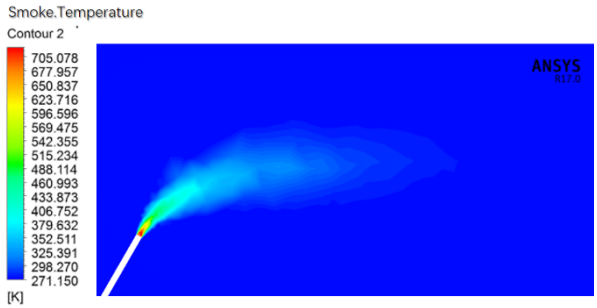

(d) t=7s

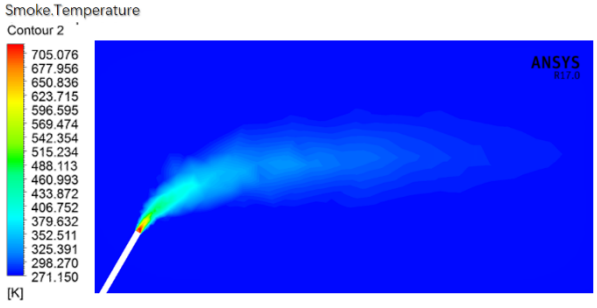

(e) t=9s

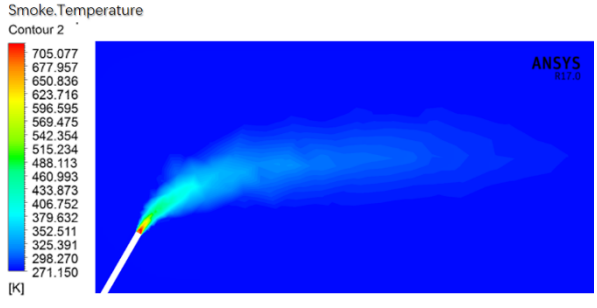

(f) t=11s

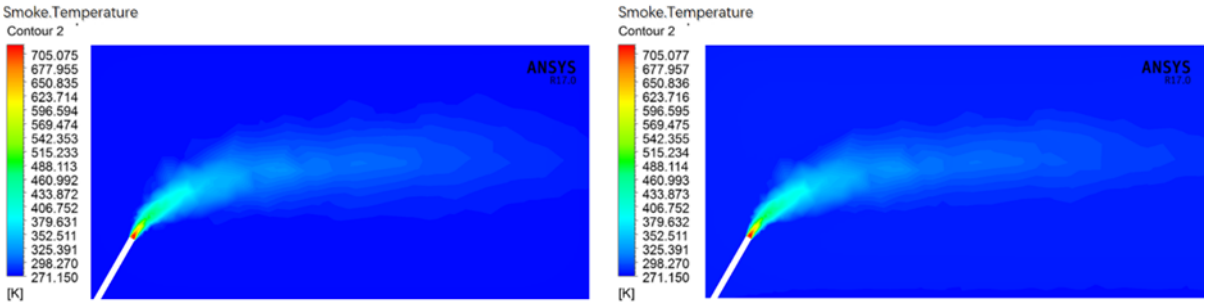

(g) t=13s (h) t=15s

Fig. 5 - Spatial temperature field distribution at different times

By observing the cloud chart of smoke diffusion in Figure 3 and Figure 5, it was found that during the smoke diffusion process, the spatial and temporal distribution characteristics of smoke mass concentration and temperature are basically consistent. In order to further study the spatial and temporal distribution characteristics of the smoke diffusion temperature, the same method as above was used to establish the variation curves of smoke particle temperature with x-axis and y-axis directions, as shown in Fig. 6 and Fig. 7, respectively.

From the variation curve of smoke temperature with x-axis in Fig. 6, it can be seen that during the process of smoke diffusion, the smoke temperature along the x-axis direction showed a sharp increase first and then slowly decreased. The reason for the sharp increase of smoke temperature in BC section is the same as the change of smoke mass con-centration curve. From the variation curve of smoke temperature with the y-axis direction in Fig. 7, it is known that when x=4 m, with the increase of y, the temperature of smoke particles first increased and then decreased, and finally the same as the changing trend of the ambient temperature. It can be seen that the temperature of the smoke particles at the center of the plume is the highest and the temperature gradually decreased as the plume spread from the center to the surroundings, which is consistent with the analysis conclusion in Figure 4. At the same time, it can be seen from the FH section of the curve in Fig. 7 that under certain simulation conditions, the diffusion height of smoke along the y-axis direction is about 2.05 m.

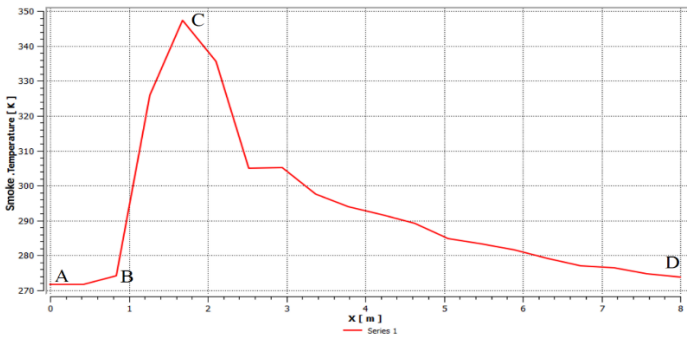

Fig.6 -The relationship between smoke temperature and horizontal distance

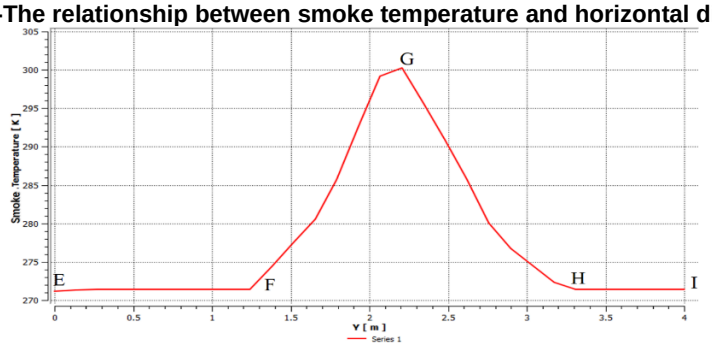

Fig. 7 - The relationship between smoke temperature and vertical distance

Design of orthogonal test

The rapid spread of smoke in a certain area of the orchard is an important measure to improve the anti-frost effect of the orchard. Combined with the structural design of the smoke anti-frost machine in this article, it can be seen that the diffusion effect of the smoke is mainly related to the parameters of the smoke outlet. To study the influence of smoke outlet on the distribution of smoke under different working parameters, the

orthogonal test method was adopted and the velocity of smoke outlet (A), the angle of smoke outlet (B), and the diameter of smoke outlet (C) were taken as the test factors. The level of each factor is three. Taking the warming amplitude near fruit tree canopy (z=0 section, 1.5 m≤y≤3.5 m, 0 m≤x≤8 m) as the index, three factors and three levels of virtual orthogonal experiments were established and the influence of smoke outlet on smoke diffusion under different working parameters was explored.

It can be seen from the overall structure design of the anti-frost machine in hilly orchard that the fan is a key component of the anti-frost machine and the airflow velocity of the smoke outlet has an important influence on the diffusion state of smoke. Low transport efficiency, high transport height, and excessively high or low smoke outlet speed are not conducive to the spread of smoke near the fruit tree canopy. Combined with the actual situation of the northern hilly orchard, it is known that: the velocity of smoke outlet (A) should be 6 m/s~10 m/s, the angle of smoke outlet (B) should be 0 ° ~ 60 ° and the diameter of the smoke outlet (C) should be 60 mm ~ 140 mm. The test Factor Level is shown in Table 2.

Table 2

Test Factor Level of Virtual experiment

Level	Factor		
	(A) The velocity of the smoke outlet（m/s）	(B) The angle of the smoke outlet（°）	(C) The diameter of the smoke outlet（mm）
1	6	0	60
2	8	30	100
3	10	60	140

According to the test factor level in Table 2, orthogonal table L9 (34) was chosen for orthogonal test design. The test scheme is shown in Table 3 and the fourth column in the table is blank.

According to the test data in Table 3, based on the smoke diffusion simulation model, the parameters of simulation model and related boundary conditions were modified and the calculations were finally performed. After the simulation calculation, by collecting and analyzing the data in the CFD-Post post-processing simulation module and filling the obtained data in Table 3 for analysis and calculation, the optimal combination of the primary and secondary order of the factors that affect the warming magnitude and the working parameters was obtained. The orthogonal test design and results are shown in Table 3.

Table 3

Test plan and results

Serial number	Factor				Result Warming magnitude (℃)
	A The velocity of smoke exit (m/s)	B The angle of smoke outlet (°)	C The diameter of smoke outlet (mm)	D (null)	
1	1（6）	1（0）	1（60）	1	0.148
2	1	2（30）	2（100）	2	0.796
3	1	3（60）	3（140）	3	2.043
4	2（8）	1	2	3	0.482
5	2	2	3	1	1.263
6	2	3	1	2	1.329
7	3（10）	1	3	2	0.563
8	3	2	1	3	0.669
9	3	3	2	1	1.989
K_{1j}	2.987	1.193	2.146	3.400	The primary and secondary order of the factors is: BCA The better plan is: $B_3C_3A_1$
K_{2j}	3.074	2.728	3.267	2.688	
K_{3j}	3.221	5.361	3.869	3.194	
k_{1j}	0.996	0.398	0.715	1.133	
K_{2j}	1.025	0.909	1.089	0.896	
K_{3j}	1.074	1.787	1.290	1.065	
R_j	0.078	1.389	0.575	0.237	

Note: K_{1j}, K_{2j}, K_{3j} - the sum of data for each factor column corresponding to level (1,2,3); k_{1j}, k_{2j}, k_{3j} - the comprehensive average of the level data of each factor column; R_j - extreme difference

Analysis of Orthogonal Test Results

It can be seen from the data analysis in Table 3 that the minimum value of warming magnitude near the fruit tree canopy is 0.148 °C and the maximum value is 2.043 °C. At the same time, the greater the warming amplitude, the better the diffusion effect of smoke in the canopy of fruit trees. When the warming magnitude is used as the evaluation index, it was found that the primary and secondary order of the three factors affecting the smoke diffusion effect of the fruit tree canopy was (B) the angle of smoke outlet >(C) the diameter of smoke outlet >(A) the velocity of smoke outlet.

In order to obtain the variation trend of warming magnitude near fruit tree canopy with three factors and three levels, the horizontal values of the factors in Table 3 were used as the abscissas and the values of k_{1j}, k_{2j}, and k_{3j} as the ordinates to draw the effect curve between the influencing factors and the warming magnitude near the fruit tree canopy, as shown in Figure 8. Through the variation trend of the curve in Figure 8, it can be intuitively obtained that the optimal level of the working parameters at the smoke outlet of the anti-frost machine is $B_3C_3A_1$ when the warming magnitude is the largest near the fruit tree canopy. That is, when the velocity of smoke outlet is 6 m /s, the angle of smoke outlet is 60° and the diameter of smoke outlet is 140 mm, the warming magnitude is the largest.

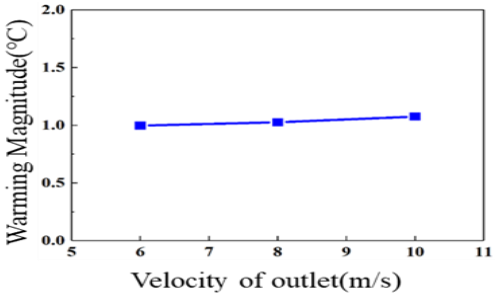

a) Effect curve of the velocity of smoke outlet and warming magnitude

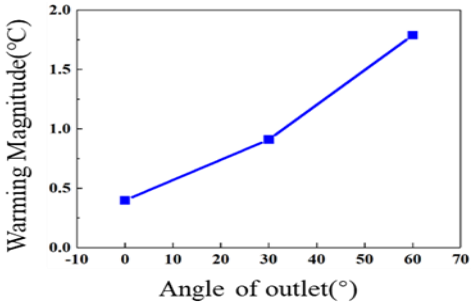

(b) Effect curve of the angle of smoke outlet and warming magnitude

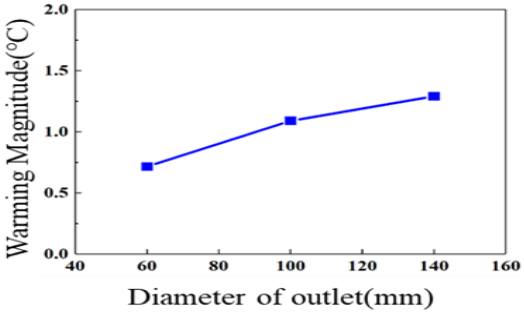

c) Effect curve of the diameter of smoke outlet and warming magnitude

Fig. 8 - Effect curve of influence factors and warming magnitude

It can be seen from the effect curves of Figure 8 (a) ~ (c) that the warming magnitude near the fruit tree canopy is positively correlated with the velocity of smoke outlet, the angle of smoke outlet, and the diameter of smoke outlet. In the process of the velocity of smoke outlet from 6 m/s to 10 m/s, the warming magnitude showed a steady upward trend with the increase of the velocity of smoke outlet. The reason may be that with the gradual increase of the velocity of smoke outlet, the efficiency of smoke delivery increased, but the upward trend was slow. It can be seen that the velocity of smoke outlet had little effect on the warming magnitude near the fruit tree canopy. In the process of the angle of smoke outlet from 0° to 60°, the warming magnitude showed a significant upward trend with the increase of the angle of smoke outlet. The larger the angle of smoke outlet, the greater the temperature increase. The main reason is that with the increase of angle of smoke outlet, the vertical diffusion height of smoke increased, the mass concentration of smoke near the canopy of fruit trees increased and the warming amplitude increased. It can be seen that the angle of smoke outlet had a significant effect on the height of smoke diffusion. In the process of diameter of smoke outlet from 60 mm to 140 mm, the warming magnitude increased with the increase of the diameter of smoke outlet. The main reason is that as the diameter of smoke outlet increased, the efficiency of smoke delivery increased and the velocity of smoke diffusion increased. However, the upward trend of warming magnitude slowed down with the diameter of smoke outlet further increased.

Through the above analysis, the primary and secondary order of the test factors, the optimal combination of working parameters, and the variation trend of the warming magnitude near the fruit tree canopy with the three-factor parameters were obtained. It is impossible to accurately explain the importance of each factor on the test results by range analysis and effect curve analysis. Therefore, in order to further clarify the significance of the influence of each factor level on the warming amplitude, variances were analyzed based on the orthogonal test data in Table 3 by using statistical software SPSS Statistics 23. The results of variance analysis are shown in Table 4.

Table 4

Analysis of variance

Index	Origin	Degree of freedom df	Quadratic	Mean square	F	Significance
Warming amplitude	Modified model	6	3.481	0.580	12.968	0.073
	Intercept	1	9.573	9.573	213.940	0.005
	A	2	0.009	0.005	0.104	0.906
	B	2	2.962	1.481	33.102	0.029
	C	2	0.510	0.255	5.696	0.149
	Error	2	0.089	0.045		
	Total	9	13.144			
	Total after correction	8	3.571			

Note: 1 - The square of R = 0.975 (the square of adjusted R = 0.900); 2- When P <0.01, the degree of influence is extremely significant, when 0.01 <P <0.05, the degree of influence is significant, and when P >0.05, the degree of influence is insignificant

It can be seen from the results of the variance analysis in Table 4 that the angle of smoke outlet has a significant impact on the warming magnitude near the fruit tree canopy and the velocity of smoke outlet has no significant effect on the warming magnitude. It can be seen from the significant results of the variance analysis that the order of the influence of each factor on the warming magnitude near the fruit tree canopy is (B) the angle of smoke outlet > (C) the diameter of smoke outlet > (A) the velocity of smoke outlet. The results of variance analysis are consistent with those of range analysis.

Therefore, an adjusting device for angle at the smoke outlet should be designed. Properly increasing the angle of smoke outlet can increase the height of smoke diffusion and improve the efficiency of smoke diffusion near the fruit tree canopy. In view of the fact that the diameter of smoke outlet and the wind velocity have little influence on the smoke diffusion height, the delivery efficiency of smoke can be increased by appropriately increasing the wind velocity and diameter of the fan.

Field experiment

After the prototype is completed, it can effectively be tested whether the smoke anti-frost machine can meet the requirements of frost protection and intelligent control in orchard field. At the same time, the structure of the smoke anti-frost machine in hilly orchards should be further optimized based on the results of field test.

Based on the agronomic requirements of frost prevention in hilly orchards, the optimal design of working parameters at the smoke outlet of the anti-frost machine showed that the angle of smoke outlet had a significant effect on the diffusion height of smoke. Therefore, in order to improve the diffusion effect of smoke, it is necessary to increase the angle of smoke outlet and install a height adjustment device at the smoke outlet during the processing of the smoke anti-frost machine. The prototype of smoke anti-frost machine based on hilly orchard transport track is shown in Figure 9.

The test site is the horticulture experimental station of the south campus of Shandong Agricultural University, and the test time is January 18, 2022. The height of fruit trees in the orchard is relatively high, the height of the fruit tree canopy is generally concentrated in 3~4 m, the spacing of fruit trees is 1~1.5 m and the row spacing of fruit trees is 3~4 m.

The supporting power of the prototype adopts a remote-controlled hilly orchard track tractor. The smoke-generating and conveying parts are hauled and operated by the tractor. The transportation track is a key component for the mobile operation of the prototype. During the installation process, it is necessary to determine the appropriate track position by observing the topographic features of the orchard.

When installing the track, it is necessary to ensure that the track plane is parallel to the ground, which is conducive to the stable operation of the prototype. After the track installation is completed, the track tractor and smoke-generating and conveying parts of hilly orchard were imported into the track and the prototype was debugged. The situation of orchard and the prototype of smoke anti-frost machine are shown in Figure 9.

Fig. 9 - Hilly orchard frost protection smoke machine

Analysis of test content and result

The frost protection principle of the smoke anti-frost machine showed that the smoke generated by the anti-frost machine can float for a long time to form a smoke layer in the air at a certain height, which effectively reduced the heat radiation loss of soil and fruit trees. At the same time, a large amount of smoke generated by the smoke generation agent dissolved the wet and cold air in the frost orchard into water and released certain latent heat, which effectively improved the temperature of the surrounding environment and achieved the purpose of orchard frost prevention. In order to explore the anti-frost effect of the smoke anti-frost machine, a comparative experiment was carried out on frost prevention effect by taking the warming magnitude of the orchard as the evaluation index after the anti-frost machine worked for 0.5 hours, the frost machine operating orchard as the work area and the non-operating orchard as the contrast area. The working area and the comparison area of the orchard are both 667 m^2.

Before the start of the experiment, 24 temperature monitoring points were set up in the contrast area and the work area respectively, and a temperature recorder was placed at a height of 1.5 ~ 4 m from the ground. The installation position of some RC-4 temperature recorders is shown in Figure 10.

Fig. 10 - Installation of RC-4 temperature recorder

As shown in Figure 11 (a), the orchard smoke anti-frost machine and control button was started to control the prototype to run continuously along the orchard track by using remote controller. As shown in Figure 11(b), all temperature recorders in the work area and the contrast area were started and the temperature changes in the orchard were recorded when the smoke in the work area of the orchard was sufficiently diffused.

(a) Start anti-frost machine (b) Anti-frost machine operation in the orchard

Fig. 11- Hilly orchard frost protection smoke machine operation

After the test, all the data monitored by the temperature recorder were exported and sorted out. The comparison result of the temperature space-time distribution of the comparison area and the work area was obtained by using the grid data interpolation function method, as shown in Figure 12. It can be seen from Figure 12 (a) that before the start of the experiment, the temperature of the orchard in the contrast area was -1.6℃. As time went by, the temperature of the orchard in the contrast area began to gradually decrease. After 0.5 h, the temperature of the orchard in the contrast area dropped to -2.2℃ and the temperature in the contrast area dropped by 0.6℃ within 0.5 h. It can be seen from Figure 12 (b) that the initial temperature is -1.5℃ when the smoke fully diffused in the work area and the temperature in the work area did not change significantly when the anti-frost machine worked for 0.3 hours. With the further increase of the working time of the anti-frost machine, the temperature of the orchard began to show an obvious upward trend. After the anti-frost machine worked for 0.5 hours, the temperature in the work area increased by 1.7℃. The heating effect was relatively significant.

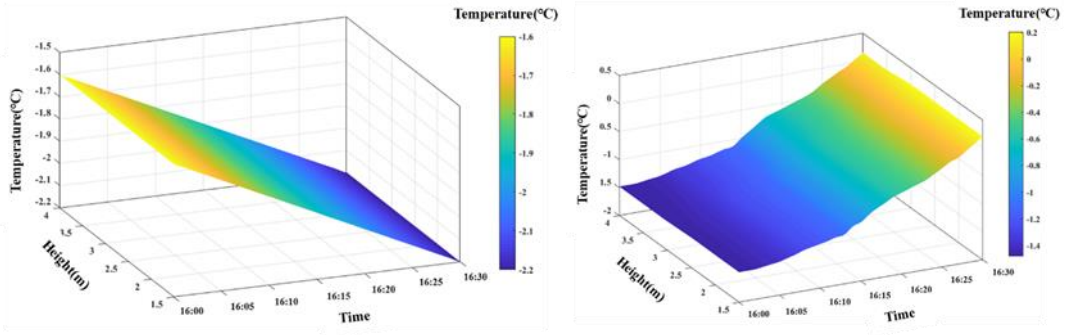

(a) Orchard test comparison area (b) Orchard test working area

Fig. 12 - Temporal and spatial distribution of temperature at different heights in the contrast area and the work area

It can be seen from the result analysis of the above comparative test that the prototype can effectively improve the temperature within the height range of 1.5 m ~ 4 m in the work area. After continuous operation for 0.5 h, the prototype can increase the temperature of the work area by 1.7 °C, which can provide effective protection against orchard frost. However, since the temperature rise in the orchard is relatively slow during the smoke anti-frost operation, when carrying out frost prevention operations in orchards, the smoke anti-frost machine should be opened in advance before the orchard temperature drops to the critical value of frost temperature to improve the anti-frost effect of orchards.

After the operation of the anti-frost machine, the orchard smoke gradually spread, and a thicker smoke screen can be formed at the height of 1.5 to 3 m in the orchard, as shown in Figure 13. The production of the smoke layer can effectively slow down the descending speed of cold air and reduce the heat radiation loss of soil and plants. The smoke layer has the effect of heat preservation, which can provide effective protection for orchard frost. At the same time, according to the actual requirements, the operation time of the smoke anti-frost machine can be adjusted to effectively reduce the cost.

Fig. 13 - Orchard smoke layer effect

CONCLUSIONS

In order to improve the mechanized anti-frost operation of hilly orchards, a smoke anti-frost machine was designed based on the transportation track of hilly orchard by using computer numerical simulation and electronic control technology. The main work and conclusions of this paper are as follows:

(1) The fluid dynamics simulation was established by Fluent, and the diffusion process of smoke was simulated and analyzed based on the discrete phase model. The simulation results showed that smoke erupted continuously at a speed of 6 m/s from the exit and gradually spread horizontally due to the influence of the wind direction. Within 1 ~ 7 s, the volume of the plume increased gradually and the plume had an inverted V-shaped. After 9 s, the smoke reached a stable diffusion state. During the diffusion process, high-temperature smoke was mainly concentrated in the center of the plume. As the volume of the plume increased, the smoke continuously exchanged heat with the cold air and the temperature of the smoke gradually decreased to the ambient temperature.

(2) Using the orthogonal test method, the virtual orthogonal test of three factors and three levels was carried out on the working parameters of the smoke outlet of the anti-frosting machine, which affected the smoke diffusion. The primary and secondary order of the three factors affecting the canopy temperature increase of fruit trees was obtained: the angle of smoke outlet > the diameter of smoke outlet > the velocity of smoke outlet. When the warming magnitude near the fruit tree canopy is the largest, the best combination of working parameters at the smoke outlet is that the velocity of smoke is 6 m/s, the angle of smoke outlet is 60° and the diameter of smoke outlet is 140 mm. At the same time, the influence of working parameters at smoke outlets on smoke diffusion should be further explored and theoretical support for the structural design of smoke outlets should be provided.

(3) Field experiments showed that the prototype was running stably. When the prototype worked continuously at a speed of 0.6 m / s for 0.5 h, the temperature within the height range of 1.5 to 4 m in the work area could be increased by about 1.7°C. The anti-frost machine can form a thick smoke layer at the height of 1.5~3 m in the orchard, which can provide better frost protection and improve the economic benefits of orchards.

ACKNOWLEDGEMENT

This work was sponsored by National key research and development "13th Five Year Plan" project (2016YFD0701701); Shandong modern agricultural industrial technology system - special fund for fruit innovation team (SDAIT-06-12) - special fund for fruit facilities, machinery and equipment post.

REFERENCES

[1] Augspurger, C.K., (2013). Reconstructing patterns of temperature, phenology, and frost damage over 124 years: Spring damage risk is increasing. *Ecology*, Vol. 94, pp.41-50.

[2] Battany, M.C., (2012). Vineyard frost protection with upward-blowing wind machines. *Agricultural and Forest Meteorology*, Vol.157, pp.39-48.

[3] Beyá-Marshall, V., Herrera, J., Santibáñez, F., et al., (2019). Microclimate modification under the effect of stationary and portable wind machines. *Agricultural and Forest Meteorology*, Vol.269-270, pp.351-363.

[4] Dai, Q.I., Zhang, S.B., Li, P.P., Hu, Y.G., (2009). Frost Protection Effects and Control of Wind Machine for Tea Garden under Temperature Inversion during Early Spring (茶园高架风扇防霜效果试验与控制系统设计). *Agricultural technology and equipment*, pp.34-37.

[5] Delagarmmatikas, G., Tsimas, S., (2010). Grinding process simulation based on Rosin-Rammler equation. *Chemical Engineering Communications*, Vol.191, pp.1362-1378.

[6] Ferrez, J., Davison, A.C., Rebetez, M., (2011). Extreme temperature analysis under forest cover compared to an open field. *Agricultural and Forest Meteorology*, Vol.151, pp.992-1001.

[7] González-Tello, P., Camacho, F., Vicaria, J. M., González, P. A, (2008). A modified Nukiyama–Tanasawa distribution function and a Rosin–Rammler model for the particle-size-distribution analysis. *Powder Technology*, Vol.186, pp.278-281.

[8] Hu, Y.G., Liu, S.Z., Wu, W.Y., Wang, J.Z., Shen, J.W., (2015). Optimal flight parameters of unmanned helicopter for tea plantation frost protection. *International Journal Agricultural and Biological Engineering*, Vol.8, pp.50-57.

[9] Jian, L.A., Ji, A., Zw, A., et al, (2020). Practical tracking control with prescribed transient performance for Euler-Lagrange equation – Science Direct. *Journal of the Franklin Institute*, Vol.357, pp.5809-5830

[10] Li, C.F., Dong, Z., Qin, S.J., Zhao J.X., (2018). Occurrence and prevention of orchard frost (果园霜冻的发生与预防). *Anhui Agricultural Science Bulletin*, Vol.24, pp.47-48+90.

[11] Liu, H., (2018). Research on rack tooth forms of self-propelled monorail mountain orchard transporter (自走式单轨道山地果园运输机轨道齿条齿形研究). *Huazhong Agricultural University*.

[12] Mikio, F., Shinsuki, A., (2007). Frost prevention fan apparatus having automatic folding type neck mechanism: JP, JP2007000096.

[13] Poling, E.B., (2008). Spring cold injury to winegrapes and protection strategies and methods. *HortScience A Publication of the American Society for Horticultural Science*, 2008, Vol.43, pp.1652-166.

[14] Ran, K., Wang, H.W., Wei, S.W., et al., (2020). Investigation Report on Freezing Injury of Pear in Midwestern Shandong Province (山东中西部梨产区幼果期冻害调研报告). *Fruit Growers' Friend*, Vol.216(05), pp.12-14+50.

[15] Reese, R.L., Gerber, J.F., (1969). Empirical description of cold protection provided by a wind machine. *J Amer Soc Hort Sci*.

[16] Song, J.F., Hu, X.F., (2017). A mathematical model to calculate the separation efficiency of streamlined plate gas-liquid separator. *Separation and Purification Technology*, Vol.178.

[17] Song, Y.P., Zhang H.M., Gao D.S., Ren L.L., Zhang Z.H, Geng X.Y., (2019). Development status and trend of domestic orchard transportation machinery in hilly and mountainous areas (国内丘陵山地果园运输机械发展现状与趋势). *Journal of Chinese Agricultural Mechanization*, Vol.40, pp.50-55+67.

[18] Vincent W.J. Heusinkveld, J. Antoon van Hooft, Bart Schilperoort, Peter Baas, Marie-Claire ten Veldhuis, Bas J.H. van de Wiel, (2020). Towards a physics-based understanding of fruit frost protection using wind machines. *Agricultural and Forest Meteorology*, Vol. 282–283.

[19] Yan, J.M., G, R., Z, W., et al, (2023). Development and application of hilly and mountainous bamboo monorail transporter (丘陵山地竹林单轨运输机研发与应用). *World Bamboo and Rattan Newsletter*, Vol. 21(01), pp.112-115.

[20] Yazdanpanah, H., Stigter, C.J., (2011). Selective inverted sink efficiency for spring frost protection in almond orchards northwest of Isfahan. *Theoretical and Applied Climatology*, Vol.105, pp.27-35.

[21] Zhang, J.D., Liu, Q.M., Chen, X.H., Bi, C.H., Wang, Y.S., (2019). Technical Measures for Preventing Frost in Spring of Orchard in Yimeng Mountain Area (沂蒙山区果园春季防霜冻技术措施). *Bulletin of Agricultural Science and Technology*, pp.338-339+350.

[22] Zhang, Q., Wang, W., Liao J.A., (2016). Study the status of fertilizing and ditching machines in orchards at home and abroad (国内外果园施肥开沟机的研究现状). *Journal of Agricultural Mechanization Research*, Vol.38, pp. 264-268.

DESIGN AND EXPERIMENT OF PRECISION SEED METERING PLATE FOR EDIBLE SUNFLOOWER BY ADDING SEED GUIDE BAR

/

增加导种条式食葵精量排种盘设计及试验

Fengli LI[1)], Jianghui CHEN[1)], Keyi LIU[1)], Jia ZHANG[1)], Yaou ZHANG[1)], Junchi YIN[1)], Fei LIU[2)], Manquan ZHAO [*2)]

[1)]College of Mechanical and Electrical Engineering, Xinjiang Institute of Engineering, Urumqi 830023, China;

[2)]College of Mechanical and Electrical Engineering, Inner Mongolia Agricultural University, Hohhot 010018, China;

Tel: +86 13139630536; E-mail: lifid@126.com

DOI: https://doi.org/10.35633/inmateh-72-15

Keywords: *air suction metering device, edible sunflower, adsorption stance, high-speed camera technology, seeding performance*

ABSTRACT

In order to solve the problems of easy seed shedding and poor seed population mobility during sowing, a precision seed metering tray for edible sunflowers with seed guide strips was designed in this paper. This article aims to adjust the adsorption posture of sunflower seeds by designing three types of structures: triangular seed guide strip, rectangular seed guide strip, and diamond seed guide strip. Seed population motion simulation and seeding performance experiments were conducted on the seeder. The experimental results show that adding a triangular seed guide strip to the seeding tray has the best disturbance effect on the seed population, with the highest proportion of seeds in the first adsorption stance seed (the seed centroid was adsorbed) and the highest qualification index. The working parameters for the best seed metering performance were obtained: the rotating speed of the seed metering disc was 8.41 r/min, and the vacuum degree was 3.5 kPa.

摘要

为提高气吸式食葵排种器的排种性能，解决播种过程中种子易脱落、种群流动性差等问题，本文以调整食葵种子的吸附姿态为切入点，对气吸式排种器排种盘进行了设计改进，设计了三角形导种条、矩形导种条、菱形导种条 3 种结构，并对排种器进行了种群运动仿真和排种性能试验。试验结果表明，增加三角形导种条的排种盘，对种群扰动效果最好，姿态一（种子质心被吸附）种子比例最高，合格指数最高。得到三角形导种条排种盘排种性能最佳时的工作参数：排种盘转速 8.41 r/min，真空度 3.5 kPa。

INTRODUCTION

As an important cash crop in China, edible sunflower cultivation is an important link in its production process. The air-suction seed metering device has low requirements for seed shape, strong adaptability, and good versatility, especially for seeds with irregular shapes. However, for seeds with large sizes and irregular shapes, it needs to have good mobility in the seed chamber.

Some studies have improved the seeding performance of seeds by improving the structure of the seeding tray (*Sun et al., 2020; Ye et al., 2021; Zhang et al., 2021; Dylan et al., 2013; Yazgi et al., 2014; Neto et al., 2012; Khobragade et al., 2012; Karael, 2009*). Electronically controlled seed singulation devices was being studied (*Cristian et al., 2015*). Onal et al used CFD software to simulate the seeding process of the metering device and analyzed the velocity and pressure fields of the rice bud seeds during the filling process (*Onal et al., 2012*).

Some studies used EDEM software to simulate seed population motion (*Tijskens et al., 2003*) and analyze the impact of working parameters on seed population motion (*Zhu et al., 2023; Wang et al., 2023; Dong et al., 2022*). Because increasing seed population mobility in the seed filling area can help improve seed filling performance, some scholars have designed and improved the seeding tray to increase population mobility in the seed filling area. It was verified the conclusion that improving the seeding tray can improve seed population mobility by using EDEM software to simulate population movement (*Wang et al., 2021; Boac et al., 2010; Zhang et al., 2021; Min et al., 2017*). Some scholars also used EDEM software to simulate and analyze the filling performance of seeds (*John et al., 2018; Lysych et al., 2023*).

Recently, some domestic and foreign scholars have used the coupling method of Discrete Element Method (DEM) and Computational Fluid Dynamics (CFD) to simulate the working process of an air suction seeder and analyze relevant parameters, such as the seed motion in the airflow field (*Han et al., 2018*).

In summary, the scholars mentioned above have conducted in-depth research on the flow of seeds in the seed chamber during the air suction seed metering process and achieved good results. However, there are few reports on edible sunflowers' fluidity and adsorption stance in the air suction seeder chamber. According to previous research (*Li et al., 2018*), there are three main adsorption stances when suction holes adsorb edible sunflower seeds. The first adsorption stance is that the seed centroid is adsorbed; The second adsorption stance is that one end of the seed is adsorbed; The third adsorption stance is that the tip of the seed is sucked into the suction hole. And the first adsorption stance is relatively stable. As well as the higher the proportion, the better the seeding performance. This article took the 2BM-5 air suction seeder as the research object to study the adsorption stability of seeds with different adsorption stances. The ultimate goal is to improve the seeding performance of the air suction seeder by improving the structure of the seeding tray, discrete element simulation, and indoor experiments.

MATERIALS AND METHODS

COMPOSITION AND WORKING PRINCIPLE OF THE AIR-SUCTION PRECISION METERING DEVICE

The air-suction precision metering device is shown in Fig.1. The working principle of the air-suction precision metering device is as follows: the seed metering disc separates the vacuum chamber from the seed chamber. Moreover, the vacuum chamber is connected to the fan through a hose. When the fan is working, the vacuum chamber generates negative pressure. Then, the suction force is formed at the suction hole of the seed tray, which adsorbs the seeds in the seed chamber. The seeds rotate along with the seeding tray to the seeding area. Because the pressure in the vacuum chamber disappears, all seeds are seeded under the action of gravity.

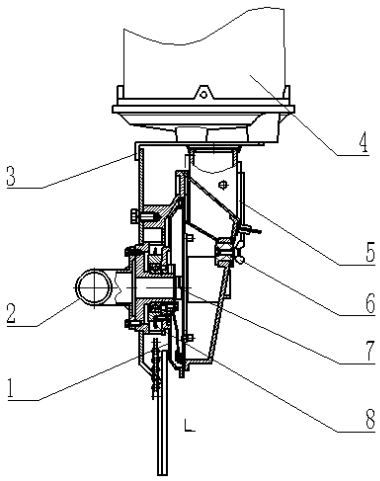

Fig. 1 - Structure of the air suction seed metering device

1- Vacuum chamber; 2- Inlet pipe; 3- Seed metering housing; 4- Seedbox; 5- Seed storage device; 6- Limit plate; 7- Seed metering disc; 8- Seed metering sprocket

DESIGN AND ANALYSIS OF PLANTER PLATE STRUCTURE

Seed sizes of edible sunflower and parameters of planter plate

Randomly selected 100 confectionery edible sunflower seeds and measured their length (L), width (W), and thickness (H) using a vernier caliper with an accuracy of 0.02 mm (Fig. 2). The average of the experimental results shows that the length, width, and thickness of confectionery edible sunflower seeds are 16.11, 7.6, and 4.29 mm, respectively.

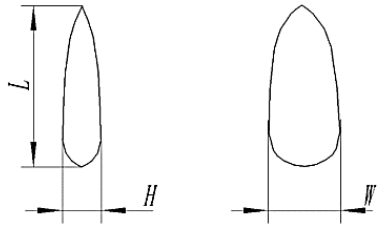

Fig. 2 - Diagram of the triaxial size of edible sunflower seed

The basic parameters of the planter plate are as follows: diameter is 200 mm, thickness is 2 mm, rotation radius of the suction hole center is 82.5 mm, and suction hole diameter is 5 mm (Fig. 3).

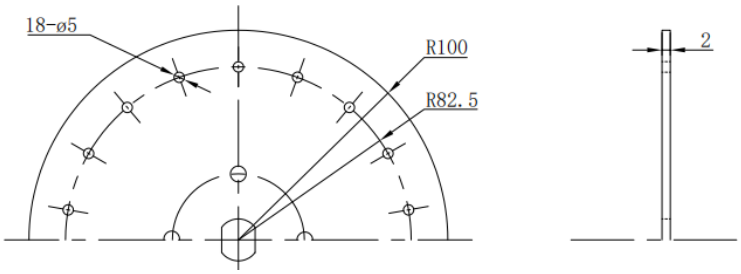

Fig. 3 - Schematic diagram of the planter plate structure

The structure design of the planter plate

As shown in Fig. 4, the seed guide strip is evenly arranged along the circumference of the outer tangent circle of the suction hole. Its one side is perpendicular to the connector of the center of the seeding disc and the center of the suction hole. At the same time, it is tangent to the suction hole, with the tangent point being the midpoint of this edge. An isosceles triangle is selected as the shape of the seed guide strip, with a bottom edge of 8 mm. The longer the seed guide strip length, the more obvious the stirring effect on the seeds. Therefore, the length of L_s of the seed guide strip should be greater than the average length of the seeds.

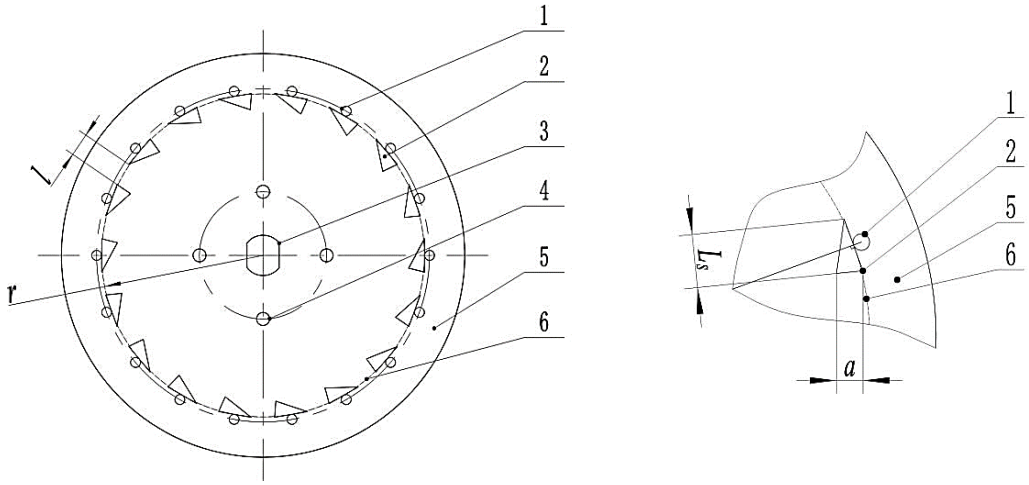

Fig. 4 - Arrangement position of triangle guide strip

1- Suction hole; 2- Triangle seed guide; 3- Power transmission hole; 4- Installation hole; 5- Seed tray; 6- The circle on the inner side of the suction hole edge line

However, the size of the seed chamber must be considered, as well as the distance l between the two seed guide strips. If l is too small, it is easy to grip the seeds. Hence, l should be greater than or equal to $\frac{L}{2}$. The length of the seed guide strip is as follows:

$$L \leq L_S \leq \frac{1}{9}\pi r - \frac{L}{2} \quad (1)$$

In Eq.(1), L_S is the height of the triangular seed guide strip, mm; r is the radius of the circle tangent to the suction hole, mm. To prevent excess seeds from being adsorbed by suction holes and difficult to fall off, as well as to carry excess seeds to the seed feeding area during the rotation of the seeding disc, its thickness is as follows:

$$H_S \leq H \quad (2)$$

In Eq.(2), H_S is the thickness of the triangular seed guide strip, mm. The final length and thickness of the seed guide strip were determined to be 18 mm and 2 mm.

As shown in Fig. 5, the center line of the length direction of the seed guide strip coincides with the line connecting the center of the suction hole and the center of the seeding disc, and the short side of the rectangle is tangent to the suction hole. Considering the size of the seed mixing wheel and seed chamber, the length L_j of the rectangular seed guide strip is 12 mm. The width W_j of the seed guide strip is designed based on the seed width, which is 6 mm.

To prevent the seed guide strip from carrying the seeds to the seeding area when the seeding disc rotates, the thickness of the guide strip is 2 mm. The seed guide strip was chamfered to enhance the fluidity of the seeds at the suction hole.

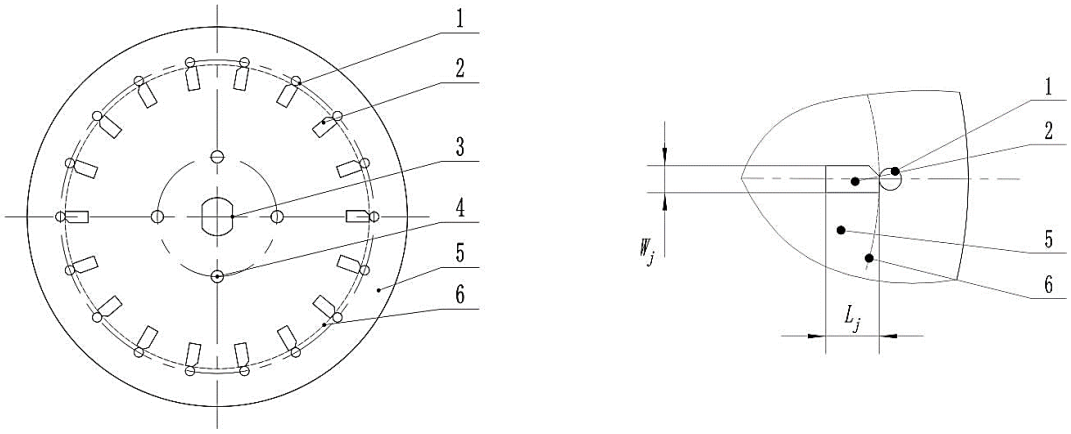

Fig. 5 - Arrangement position of the rectangle guide strip

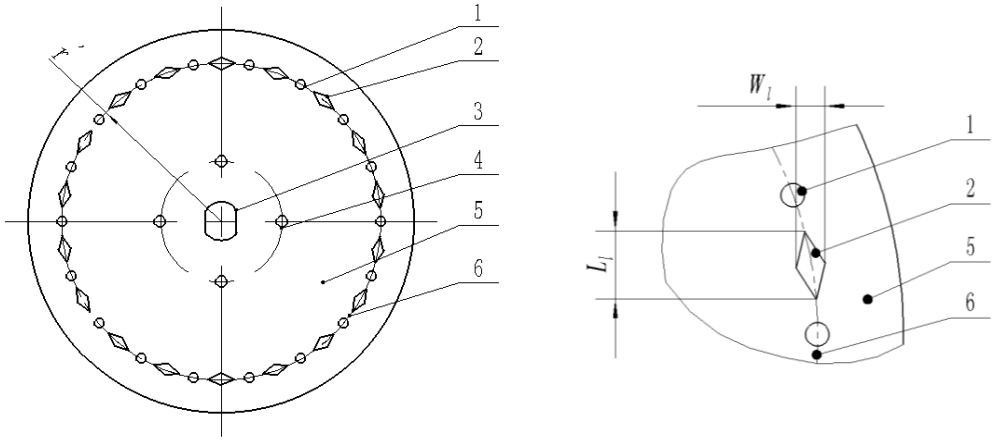

Fig. 6 - Arrangement position of the rhombus guide strip

The length direction of the diamond-shaped seed guide strip is evenly arranged along the circle where the center of the suction hole is located. Also, the seed guide strip is located in the middle of the two suction holes. The arrangement diagram is shown in Fig.6. W_l is similar to the seed width, which is 6 mm. Then, the thickness is 2 mm. The length of the seed guide strip is as follows:

$$L_l \leq \frac{1}{9}\pi r' - L \tag{3}$$

In Eq.(3), r' is the radius of the circle where the center of the suction hole is located, mm; L_l is the length of the diamond shaped seed guide strip, mm. L_l is determined as 14 mm. The dimensions of three kinds guide bars are shown in Fig. 7.

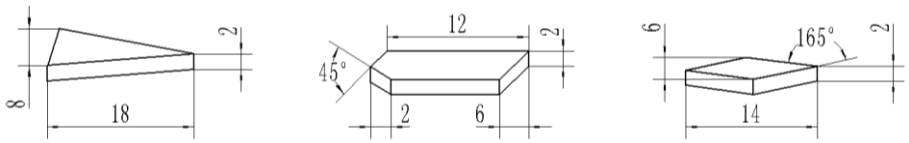

Fig. 7 - The sizes for seed guide strips

Force analysis of the seed on the seed guide strip

Due to the same force situation on the triangular and rectangular seed guide strips during the seed carrying process, the seed on the triangular seed guide strips was analyzed as the object (Fig.8). It is assumed that all external forces act on the centroid of the seed, with the seed centroid as the origin o. The rotation direction of the seeding disk was the oi direction. The Oj direction was the direction from the center of mass points to the center of the seeding disc. Moreover, the direction perpendicular to the plane of the seeding disk was the ok direction. Finally, a natural coordinate system was established. If the seed did not roll, there must be:

$$(F_S' - N_k)\frac{d}{2} = Q_1\frac{H}{2} \tag{4}$$

In Eq.(4), Q_1 is the combined force of G, F_e, N_3, F_3, F_{2j} and F_{2i}, N; F_S' is the suction force on the seed on the seed guide strip, N; N_3 is the binding force of the seed guide strip on the seed, N; F_3 is the frictional force between the seed and the seed guide strip, $F_3 = f_3 N_3$; f_3 is the friction coefficient between the seed guide and the seed; F_{2i} is the component of the frictional force between the seed and the seeding disc in the oi direction, N; F_{2j} is the component of the frictional force between the seed and the seeding disc in the oj direction, N; G is the gravity of the seed, N; F_e is the inertial force involved, N; N_k is the binding force of the suction hole on the seed, N, d is the diameter of the suction hole, mm.

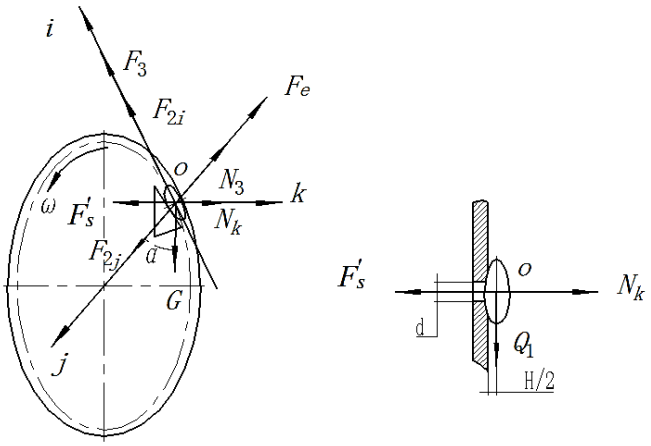

Fig. 8 - Stress analysis of the critical state of seed adsorption

When $N_k = 0$, it is the critical state for seed adsorption, where:

$$F_S' \frac{d}{2} = Q_1 \frac{H}{2} \tag{5}$$

In Eq. (5), $F_S' = P_1' \frac{\pi d^2}{4}$,$Q_1 = \sqrt{(F_3 - G\sin\alpha)^2 + (G\cos\alpha - F_e - N_3)^2}$, $P_1'$is the critical adsorption vacuum of the suction chamber when the seed on the seed guide strip does not roll, kPa.

Each force is introduced into Eq.(5), then it can be obtained:

$$P_1' = \frac{4H}{\pi d^3}\sqrt{(F_3 - G\sin\alpha)^2 + (G\cos\alpha - F_e - N_3)^2} \tag{6}$$

According to previous research (*Li et al., 2018*), the non-rolling critical vacuum degree of the adsorbed seed for the first adsorption stance during the seed-carrying process without a guide strip is:

$$P_1'' = \frac{4H}{\pi d^3}\sqrt{G^2\sin^2\alpha + (G\cos\alpha - F_e)^2} \tag{7}$$

Due to $F_3 < N_e$, the comparison between equations (6) and (7), it can be seen that $P_1' < P_1''$. Therefore, adding triangular and rectangular seed guide strips on the seeding tray can reduce the vacuum degree of seed carrying. Under the same vacuum degree, adding triangular and rectangular seed guide strips will result in a more stable seed state adsorbed.

SEED MOTION SIMULATION

This paper analyzes the seed motion simulation through discrete element software. The purpose is to explore the disturbance effect of different structure seed guides on the seeds.

Set global variable parameters

The surface of sunflower seeds is smooth without adhesion, and Hertz Mindlin (no slip) is selected as the simulation contact model. The other parameters are shown in Tab. 1.

Table 1

Global variable parameter setting

Item	Property	Value
Edible sunflower	Poisson's ratio	0.35
	Shear modulus/MPa	26.73
	Density/kg·m^{-3}	476.92

Item	Property	Value
Seed plate	Poisson's ratio	0.3
	Shear modulus/MPa	70000
	Density/kg·m^{-3}	7800
Seed chamber	Poisson's ratio	0.5
	Shear modulus/MPa	35
	Density/kg·m^{-3}	1180
Seed stirring device	Poisson's ratio	0.39
	Shear modulus/MPa	71.94
	Density/kg·m^{-3}	1050
Edible sunflower-edible sunflower	Static friction coefficient	0.34
	Dynamic friction coefficient	0.12
	Impact recovery factor	0.42
Edible sunflower-seed plate	Static friction coefficient	0.43
	Dynamic friction coefficient	0.1
	Impact recovery factor	0.51
Edible sunflower-seed chamber	Static friction coefficient	0.45
	Dynamic friction coefficient	0.19
	Impact recovery factor	0.49
Edible sunflower-seed stirring device	Static friction coefficient	0.43
	Dynamic friction coefficient	0.14
	Impact recovery factor	0.48

Establishment of the model for edible sunflower

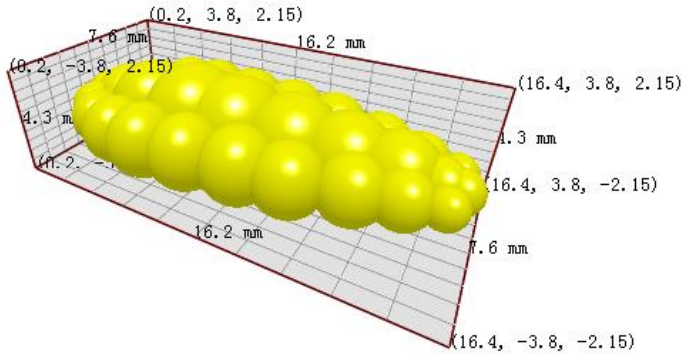

Fig. 9 - The seed model of edible sunflower

When establishing the edible sunflower seed model, adjust the length, width, and thickness of the seed model to 16.2 mm, 7.6 mm, and 4.3mm, respectively. The seed model is composed of 30 balls, as shown in Fig.9.

Establishment of the seeder model

The simplified air suction precision seeder consisted of three parts: seed chamber, seed tray, and seed stirring device (including seed stirring wheel and guide strips). The variable parameters of these three parts were set according to Table 1. The particle factory was built on the upper part of the seed chamber of the seeder, and the total number of particles was 2000. The simulation time step was 2.6×10^{-6} seconds. The total simulation time was 8 seconds, and the output time step was 0.05 seconds. The working conditions of the seeder during simulation were set as follows: the amplitude in the y-direction was 3 mm, and the vibration frequency was 5 Hz; The rotation speed of the seeding disc and the stirring wheel was 8.41 r/min. The starting time for vibration and rotation was 1.2 seconds. The seeder began to operate when all seeds were generated by the particle factory and the population motion state was stable.

RESULTS

SEED MOTION SIMULATION EXPERIMENT AND RESULT ANALYSIS

Test design

The impact of seed guide strips on seed disturbance was studied. Then, non-seed guide strips (disc A), triangular seed guide strips (disc B), rectangular seed guide strips (disc C), and diamond seed guide strips (disc D) were selected as experimental factors. These seeds in the suction area next to the seeding tray were chosen as the research object (Fig.10). The disturbance effect of different seed guides on seeds was evaluated with the average velocity and displacement in the y direction of the seeds. Using the post-processing function of EDEM software, the y-direction average velocity and average displacement of the seed population within the simulation time of 1.2-8 seconds were output.

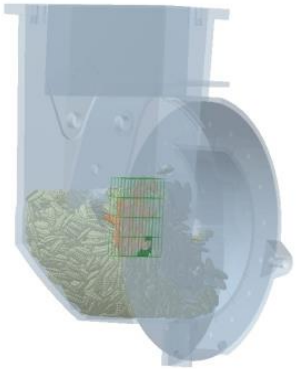

Fig. 10 - Seed absorption area position

Test results and analysis

Test results are shown in Table 2. The average velocity and displacement in the y-direction of disc B, C and D are improved. Therefore, with the addition of seed guide strips, the disturbance effect of the seed population in the suction hole area is strengthened. Among them, disk B has the best disturbance effect.

Table 2

Average velocity and displacement in the y-direction of the seed population

Seed plate	Average velocity in y direction/(m/s)	Average displacement in y direction/mm
Disc A	0.008	1.51
Disc B	0.017	3.16
Disc C	0.015	3.01
Disc D	0.009	2.17

SEED METERING PERFORMANCE TEST AND RESULT ANALYSIS

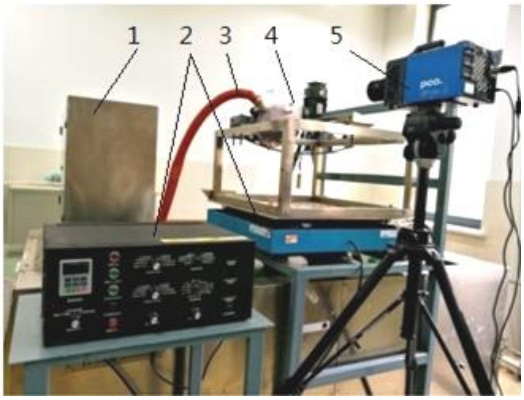

Fig. 11 - Arrangement position of triangle guide strip

1- JPS-12 type seed metering performance test-bed; 2- Suction electromagnetic vibration table; 3- Pneumatic system; 4- Suction seed metering device; 5- High speed camera

As shown in Fig. 11, the seeding performance test was conducted on the JPS-12 seeding performance detection test bench, and the high-speed camera is placed in front of the seeding device to capture and record the seeding process.

Single factor seeding performance test and result analysis

Test design

As shown in Fig.12, the structural parameters of the seed guide strip were selected as experimental factors, and the seeding performance and the seed adsorption stance were evaluated as evaluation indicators for single factor seeding performance test. The working parameters during the experiment were as follows: The speed of the seeding disc was 8.41 r/min. The vacuum degree was 3.5 kPa. The amplitude of the seeding device was 3 mm. The height of the seeding layer was 60 mm. Each group of experiments was repeated three times, and 250 particle pitches were taken for each experiment when the test bench was running smoothly and the corresponding seed adsorption stances were recorded.

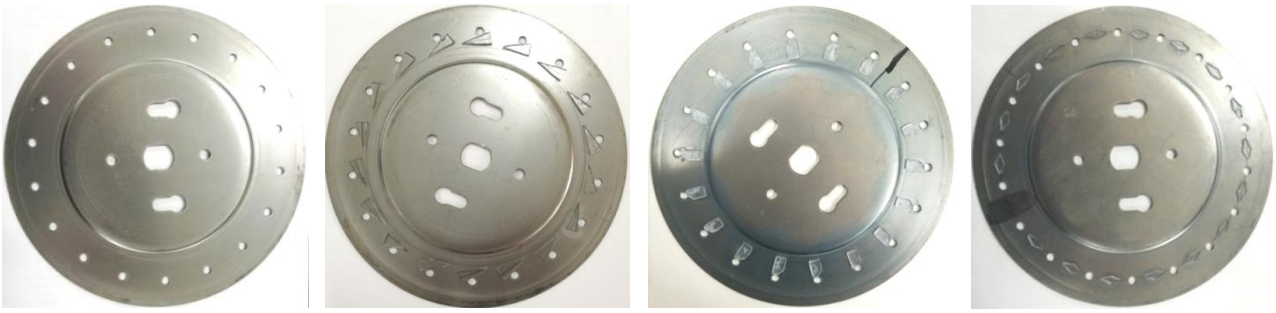

a. Disc A *b. Disc B* *c. Disc C* *d. Disc D*

Fig. 12 - Four different types of planter plates of edible sunflower

Test results and analysis

As shown in Table 3, the proportion of the first adsorption stance is increased for disk B, C and D, while the proportion of the second adsorption stance and the third adsorption stance are decreased. The seed adsorption stance of disc B is the best.

Table 3

Effect of each planter plate on the adsorption stance of edible sunflower seeds

Type of seed metering tray	The first adsorption stance/%	The second adsorption stance/%	The third adsorption stance/%	No stance/%
Disc A	71.36	12.39	10.24	6.01
Disc B	87.74	1.11	8.04	3.11
Disc C	76.7	8.16	9.01	6.13
Disc D	74.6	10.16	9.73	5.51

As shown in Table 4, the qualified index of disc B, C and D is increased, while the repeat index sowing and leak index are decreased. Among them, the qualified index is highest for disc B, while the repeat sowing index and leak index are the lowest.

Table 4

Seeding performance of each planter plate in edible sunflower

Type of seed metering tray	Qualified index (%)	Repeat sowing index (%)	Leak index (%)
Disc A	79.21	14.78	6.01
Disc B	91.57	5.32	3.11
Disc C	84.03	10.68	5.29
Disc D	80.78	13.71	5.51

Dual factor seeding performance test and result analysis

Test design

Through single-factor experiments, it was determined that disc B was more suitable for sowing edible sunflowers, so disc B was selected as the experimental object. A dual-factor seeding performance test was conducted. The rotation speed of the seeding disc and vacuum degree were used as experimental factors. Then, the seeding performance and the seed adsorption stance were recorded. The level of experimental factors is shown in Table 5. Each group of experiments was repeated three times, and 250 particle pitches were taken for each experiment when the test bench ran smoothly. The corresponding seed adsorption stances were taken notes.

Table 5

Test factor level of edible sunflower

Factor	Level				
	1	2	3	4	5
The planter plate speed / (r/min)	6.29	7.35	8.41	9.47	10.53
Vacuum degree / kPa	2.3	2.9	3.5	4.1	4.7

Test results and analysis

The average value of three repeated experiments was taken as the experimental result. The surface graph is shown in Fig. 13. As the rotational speed increases, the qualified index shows an up-down trend, it is the highest with a vacuum degree of 3.5 kPa and a rotation speed of 8.41 r/min. Except for the vacuum degree of 4.7 kPa, the repeat sowing index under all other vacuum degrees showed a downward trend, it is the lowest with a vacuum degree of 2.3 kPa and a rotation speed of 10.53 r/min. The leak index shows an upward trend, it is the lowest with a vacuum degree of 4.7 kPa and a rotation speed of 6.29 r/min. The proportion of the first adsorption stance shows an up-down trend, it is the highest with a vacuum degree of 3.5 kPa and a rotation speed of 8.41 r/min. The change trend of the proportion of the second adsorption stance is not apparent, it is the lowest with a vacuum degree of 3.5 kPa and a rotation speed of 8.41 r/min. When the vacuum degree is 2.3 kPa and 4.7 kPa, the proportion of the third adsorption stance shows a downward trend, while under other vacuum degrees, it shows a down-up trend. It is the lowest with a vacuum degree of 2.3 kPa and a rotation speed of 10.53 r/min. The optimal working parameters for planting edible sunflowers reasonably and densely are a vacuum degree of 3.5 kPa and a rotation speed of the seeding disc of 8.41 r/min.

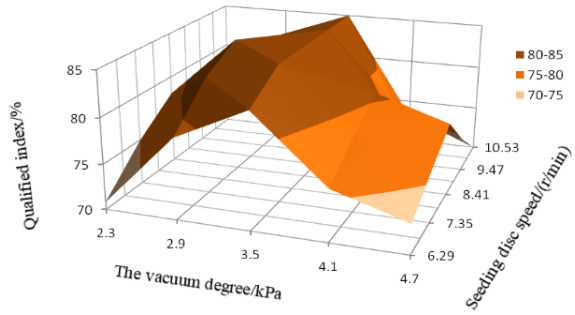

a. Qualified index

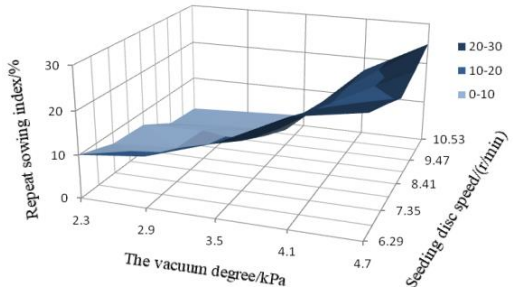

b. Repeat sowing index

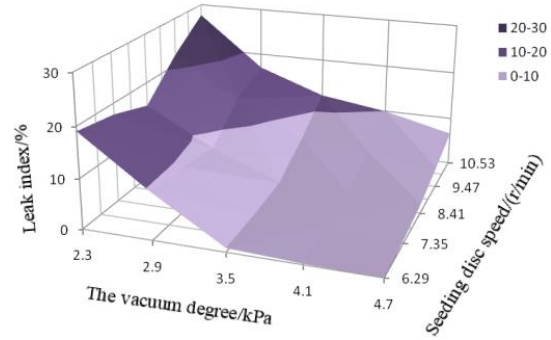

c. Leak index

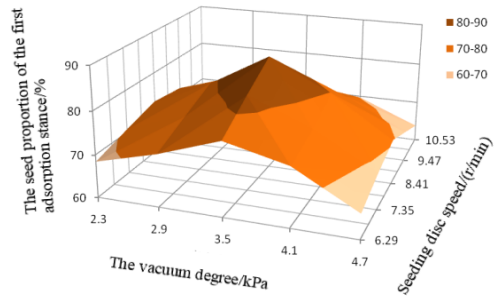

d. The seed proportion of the first adsorption stance

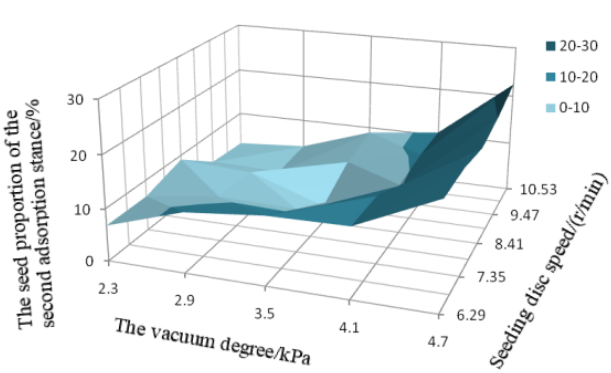

e. The seed proportion of the second adsorption stance

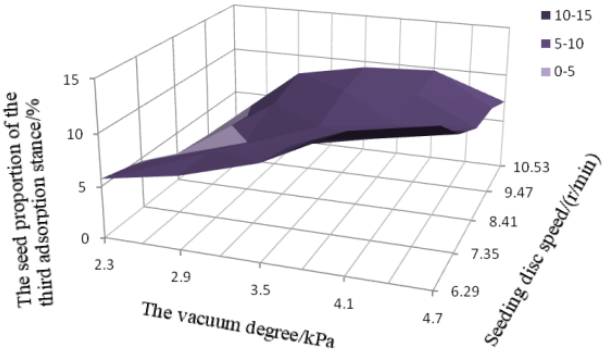

f. The seed proportion of the third adsorption stance

Fig. 13 - The influence surface graph of the seeding performance and adsorption stance

CONCLUSIONS

In this paper, three types of seed guide strip structures were designed. By analyzing the force on the seeds on the guide strip, adding triangular and rectangular guide strips can reduce the vacuum degree of seed carrying. By simulating and analyzing the seed population movement, it can be seen that the average velocity and displacement in the y-direction of disc B, C and D have increased. Therefore, the disturbance effect on the seed population in the suction hole area was enhanced by adding guide strips. A single-factor seeding performance test was conducted. It can be obtained that the seed adsorption stances were adjusted for disc B, C and D. In these three types of seeding trays, the proportion of the first adsorption stance for seeds was increased. Disc B has the highest proportion of the first adsorption stance for seeds and the best seeding performance. The dual factor seeding performance test was carried out, and the best working parameters were obtained. The effect of the improved seeding tray on the seeding performance of Mengjichang 3638C sunflower seeds was studied in this paper. However, there is a wide variety of edible sunflower seeds, and the shape and position of the seed guide need to be optimized and improved.

ACKNOWLEDGEMENT

The supports of the Natural Science Foundation of Xinjiang Uygur Autonomous Region (2022D01B19) and Doctoral Research Initiation Fund Project of Xinjiang Institute of Engineering (2020xgy042302) for this research are greatly appreciated.

REFERENCES

[1] Boac, J.M., Casada, M.E., Maghiang R.G., et al, (2010). Material and interaction properties of selected grains and oilseeds for modeling discrete particles, *Transactions of the ASABE*: 53(4):1201-1216.

[2] Cristian I., Octavian P. (2015). A New Concept for Seed Precision Planting. *Agriculture and Agricultural Science Procedia*, 6:38-43.

[3] Dong X.Q., Zheng H.N., Jia X., et al, (2022), Calibration and experiments of the discrete element simulation parameters for rice bud damage. *INMATEH-Agricultural Engineering*, 68(3):659-668.

[4] Dylan S., J., Dianne C.H., Andrew L.G., (2013), Precision metering of Santalum spicatum (Australian Sandalwood) seeds, *Biosystems Engineering*,115(2):171-183.

[5] Han D.D., Zhang D.X., Jing H.R. et al, (2018), DEM-CFD coupling simulation and optimization of an inside-filling air-blowing maize precision seed-metering device. *Computers and Electronics in Agriculture*, 150: 426-438.

[6] John M.T., Wang D.C., Ma W.P. et al, (2018), Design and optimization of the vertical plate metering device for alfalfa seeds precision based on engineering discrete element method (EDEM). *Innovative Systems Design and Engineering*, 9(6): 16-22.

[7] Karael D. (2009), Performance of a modified precision vacuum seeder for no-till sowing of maize and soybean． *Soil and Tillage Research*, 104(1) :121-125．

[8] Khobragade H.M., Kamble A.K., Dave A.K. (2012), Performance evaluation of pneumatic seed metering device for paddy in puddle. *International Journal of Agricultural Engineering*，5(1) : 98-102．

[9] Li F.L., Chen J.H., Liu F. et al, (2018), Influence of seed adsorption stance on seeding performance based on high speed camera technology (*基于高速摄像技术种子吸附姿态对排种性能的影响*) *Journal of China Agricultural University*, 23(4): 128-136.

[10] Lysych M.N., Chernyshev V.V., Nagaytsev V.M., (2021), Design and simulation of seed metering device for aero sowing of forest pelleted seeds. *International Conference on IT in Business and Industry*, 2032: 1-7.

[11] Min S.W., Dooyum D.U., Sang M.S., et al, (2017), Development of seeder for mixed planting of corn and soybeans, *International Journal of Agricultural and Biological Engineering*,10(3):95-101.

[12] Neto W.H.P., Justino A., Namur T.R., et al, (2012), Comparison of metering mechanisms of corn seed (Comparação entre mecanismos dosadores de sementes demilho), *Engenharia Agrícola*, 32(5):981-988.

[13] Onal I., Degirjviencioglu A., Yazgi A., (2012), An evaluation of seed spacing accuracy of a vacuum type precision metering unit based on theoretical considerations and experiments, *Turkish Journal of Agriculture Forestry*, 36(2):133-144.

[14] Sun D., Cui Q.L., Zhang Y.Q., et al, (2020), Performance test of the 2BDE-2 type millet fine and small-amount electric seeder. *INMATEH-Agricultural Engineering*, 60(1):129-136.

[15] Tijskens E, Ramon H, Baerdemaeker J D. (2003). Discrete element modelling for process simulation in agriculture. *Journal of Sound and Vibration*, 266:493-514.
[16] Wang Y.B., Li H.W., Wang Q.J., et al, (2021), Experiment and parameters optimization of seed distributor of mechanical wheat shooting seed-metering device. *INMATEH-Agricultural Engineering*, 63(1):29-40.
[17] Wang Y.C., Kang X.Q., Wang G.Q., et al, (2023), Numerical analysis of friction-filling performance of friction-type vertical disc precision seed-metering device based on EDEM. *Agriculture*,13(12):2183
[18] Yazgi A., Degirmencioglu A., (2014), Measurement of seed spacing uniformity performance of a precision metering unit as function of the number of holes on vacuum plate, *Measurement*, 56:128-135.
[19] Ye S.B., Zheng D.C., Li W., et al, (2021), Design and test of negative pressure chamber rotary buckwheat seed metering device. *INMATEH-Agricultural Engineering*, 64(2):185-194.
[20] Zhu H.B., Wu X., Bai L.Z., et al, (2023), Design and experiment of a soybean shaftless spiral seed discharge and seed delivery device. *Scientific Reports*, 13(1):20751-20751.
[21] Zhang K.X., Zhang L., Ding Y. et al, (2021), Design and test of air-suction pepper seed metering device based on air supply and quantitative seed supply, *INMATEH-Agricultural Engineering*, 64(2):345-354.
[22] Zhang X.S., Zhu D.Q., Xue K., et al, (2021), Parameter optimization and experiment of slider-hole-wheel seed-metering device based on discrete element method, *INMATEH-Agricultural Engineering*, 65(3):410-420.

INTENSIFICATION OF APPLE DRYING USING CONVECTIVE AND COMBINED METHODS OF DEHYDRATION
/
ІНТЕНСИФІКАЦІЯ СУШІННЯ ЯБЛУК ПРИ КОНВЕКТИВНОМУ ТА КОМБІНОВАНОМУ СПОСОБАХ ЗНЕВОДНЕННЯ

Vadim PAZIUK[1)], Olena HUSAROVA[2)], Valentyna BANDURA [*3)]; Larysa FIALKOVSKA [4)]
[1)] Institute of Engineering Thermophysics of the National Academy of Sciences of Ukraine;
[2)] National Technical University of Ukraine "Igor Sikorsky Kyiv Polytechnic Institute", Institute of Engineering Thermophysics of the National Academy of Sciences of Ukraine;
[3)] National University of Life and Environmental Sciences of Ukraine, Ukraine;
[4)] Vinnytsia Trade and Economics Institute, State Trade and Economics University, Ukraine
DOI: https://doi.org/10.35633/inmateh-72-16

***Keywords**: convective, combined drying, apples, energy efficiency, duration of drying, rebinder number, recoverability.*

ABSTRACT

The paper examines the intensification of drying apple slices to low residual moisture content. It is proposed to use an energy-efficient multi-stage mode of convective drying at 80/60 °C and a combined multi-stage mode with IR radiation and IR convective heating (100 W) + 60°C / 60°C. The paper presents the temperature and kinetic curves and changes in drying speed for the studied dehydration regimes. A formula was obtained for determining the total duration of the process of drying apple slices using a combined method, and a dependence of the Rebinder number for the studied dehydration modes was constructed. Based on the experimental data analysis and generalization of research results, a method of determining the drying intensity based on the average moisture exchange and the average temperature of material heating per minute, at the first stage of drying and during the entire drying time, was proposed for the first time. The efficacy of the proposed modes is confirmed by a reduction in drying duration 1.9 times compared to the stationary mode at a coolant temperature of 60 °C. The obtained dried product is characterized by high recoverability (78–80%) and appropriate organoleptic properties.

АНОТАЦІЯ

У статті розглянуто інтенсифікацію процесу сушіння яблучних пластинок до низької залишкової вологості. Запропоновано використовувати енергоефективний ступеневий режим конвективного сушіння 80/60 °С та ступеневий комбінований режим з поєднанням ІЧ-випромінювання та конвективного нагріву ІЧ (100 Вт)+60 °С / 60 °С. У статті представлено температурні та кінетичні криві та зміну швидкості сушіння для досліджуваних режимів зневоднення. Одержано формулу для визначення загальної тривалості процесу сушіння яблучних пластинок комбінованим способом, побудовано залежність числа Ребіндера для досліджуваних режимів зневоднення. На підставі аналізу експериментальних даних та узагальненні результатів досліджень вперше запропоновано спосіб визначення інтенсивності сушіння по середній вологовіддачі та середній температурі прогрівання матеріалу за хвилину, на першому етапі сушіння та за весь час сушіння. Ефективність запропонованих режимів підтверджується скороченням тривалості процесу сушіння у 1,9 рази порівняно з стаціонарним режимом при температурі теплоносія 60°С. Отриманий сушений продукт характеризується високою відновлюваністю (78–80%) та належними органолептичними властивостями.

INTRODUCTION

Drying is a well-known procedure for removing and retaining free moisture, increasing shelf life, and reducing transport weight (*Hany et al., 2022; Bulgakov et al., 2018)*. Apples are the most common type of fruit that is available in the diet throughout the year. They contain a large amount of vitamins such as C, B_1, B_2, P, and E, as well as manganese, potassium, and easily digestible iron. Apples are hypoallergenic and almost everyone can consume them *(Campeanu et al., 2009).*

[1] *Vadim Paziuk, Doctor of Technical Sciences; Olena Husarova, Candidate of Technical Sciences; Valentyna Bandura, Doctor of Technical Sciences; Larysa Fialkovska, Candidate of Technical Sciences*

Medium-ripe apples with a large amount of aromatic and flavoring substances are suitable for drying. For convenient and quick drying of apples and the possibility of giving them a necessary shape, they are pre-cut into circles, plates, slices, or cubes. As previously shown *(Bessarab and Shutyuk, 2002),* it is advisable to use apples with a diameter of more than 50 mm for drying. Small apples can be used to make more crushed material, but the processing of fruits with a diameter of less than 30...35 mm is impractical due to the increase in waste.

Analysis of recent research and publications

A convective drying method is used at low temperatures of the coolant to dehydrate apples, which is an energy-consuming and long-term process. Therefore, other methods are used for drying, including infrared radiation, high-frequency currents, ultrasound, etc.

One of the effective drying methods for improving the quality of food products and reducing the duration of the drying process is the introduction of heat through infrared radiation. As previously shown *(El-Mesery et al., 2023),* infrared-dried apple slice quality was evaluated experimentally and statistically in terms of the drying period, rehydration ratio, color, and shrinkage as a function of infrared intensity levels, slice thicknesses, and air velocity. Apple slices were dried at infrared intensities of 0.130, 0.225, and 0.341 W/cm2, air velocities of 1.0, 0.5, and 1.5 m/s, and slice thicknesses of 6, 4, and 2 mm. Throughout the procedure, the dried slices were reduced from an initial moisture content of 87.5 %–11 % (w.b.). According to the findings, the drying time needed to decrease the moisture level of sliced apples to roughly 0.12 g water/g dry matter ranged from 200 to 280 min, 170–240 min, and 130–190 min at infrared radiation intensities of 0.130, 0.225, and 0.341 W/cm^2, respectively. Water activity values for dried apple slices ranged from 0.371 to 0.450. The rehydration ratio increased with increasing air velocity and reduced with increased infrared radiation intensity. In contrast, the shrinkage ratio increased with increased infrared radiation intensity and decreased with increased air velocity. Slices of fresh and dry apples had a more significant overall color difference as radiation intensity and air velocity increased.

A study of innovative equipment for drying fruit and vegetable slices under IR radiation conditions was conducted *(Burdo et al., 2018).* An experimental stand and research methodology were developed. The structure of the equation for calculating the mass transfer coefficient was proposed. The base of experimental data was summarized in the equation in similarity numbers. The equation makes it possible to calculate the mass transfer coefficient with an error within +- 15%. The influence of the power of IR radiation on the kinetics of the drying process of fruit and vegetable slices was determined. A comparison of experimental data on the drying of slices under the conditions of microwave and infrared radiation was carried out.

The effect of infrared radiation is quite significant when drying other raw materials as well. Based on experimental studies of grain material dehydration, Bandura, V. et al. (2018) found that under the increase in the power of the IR source from 400 to 500 W, the drying time from the initial moisture content of the material of 11% to 8.75% decreases from 9 to 7 minutes. It was determined that the Rebinder criterion characterizing the moisture-thermal characteristics of the material decreases when reducing its moisture content from 0.04 at 11% to 0.01 at 9%. Microwave energy also has a significant effect on the drying process (Bandura V. et al. (2023)).

There is a known method of drying, according to which apples are dehydrated by a combination of pre-IR treatment and convective drying. Short-term treatment with IR radiation at E = 20 kW/m^2 was carried out for 90 and 120 s. When the process lasts for 90 s, the internal layers of raw materials are heated to the temperature of 70 °C, and when it lasts for 120 s to 82 °C. IR pre-treatment removes up to 15% of moisture within 90 s, and the drying time is reduced by 23%, but when the drying time is 120 s, up to 25% of the moisture is removed with a 62% reduction in the duration of the process compared to only the convective drying method at a coolant temperature of 60 °C. Pre-IR treatment reduces the content of vitamin C in apples to 95%, but due to the reduction of the duration of drying, the content of vitamin C is 65-70%, which exceeds the content of vitamin C when using convective drying by 15-20% *(Snezhkin et al., 2001).*

The use of this drying method is not advisable, since the maximum allowable temperature of the material is exceeded, which is a determining parameter when drying plant heat-labile raw materials.

The purpose of this research is to intensify the process of drying apple slices to low residual moisture content without losing biologically active substances of fresh raw materials.

To achieve the goal, it is necessary to solve the following tasks:

- to establish kinetic regularities of the process of drying apple slices by convective and combined methods;
- to develop dehydration modes using a combined drying method;
- to investigate the intensity of the developed drying methods;
- to calculate the total duration of the drying process of apple slices using a combined method of dehydration;
- to determine the criterion for optimizing the drying process;
- to evaluate the recoverability and organoleptic indicators of the obtained dried product.

MATERIALS AND METHODS

The investigation of the process of dehydration of apples aimed at studying the main patterns of heat and mass transfer was carried out on the experimental drying stand, the schematic diagram of which is shown in Fig. 1 *(Paziuk et al., 2018).*

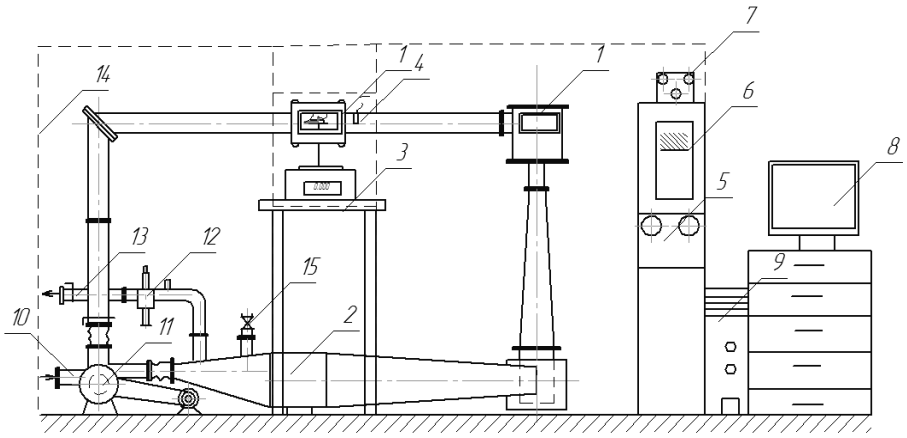

Fig. 1 - Scheme of an experimental drying stand for the study of heat and mass exchange processes during dehydration of apples

1 – drying chambers; 2 – air heating section; 3 – scales with a stand; 4 – resistance thermometer; 5 – control panel; 6 – potentiometer; 7 – air temperature regulator; 8 – monitor; 9 – workstation system unit; 10 – nozzle for mixing the coolant with ambient air; 11 – fan; 12 – psychrometer; 13 – air discharge nozzle for subsequent mixing; 14 – thermal insulation frame; 15 – a steam supply nozzle with a needle valve

The experimental stand consists of a system of insulated air ducts with devices for heating and circulation of the coolant, drying chambers, a system for controlling the temperature of the coolant, automatic collection and processing of information about the course of the material dehydration process.

The air heating section (2) is made in the form of a rectangular box, in which a three-section electric heater with a capacity of 10 kW is placed. To ensure accurate maintenance of the set temperature, the heater is connected to an automatic regulation system and TSM-50 resistance thermometers (4). It enables to maintain the temperature of the coolant in automatic mode with an accuracy of ±0.1°C.

The movement of the coolant occurs with the help of a centrifugal fan (11) of medium pressure. Changing the speed of the coolant is achieved by adjusting the frequency of rotation of the fan (11) on the control panel (5). The ratio between exhaust and fresh air can be adjusted with the help of dampers on the nozzles (10) and (13). The air velocity in the drying chambers was measured using an anemometer MS-13.

The stand is equipped with an automated system for information collection and processing, which includes a computer, AD-500 digital scales, a specially developed automated program, a temperature measurement channel consisting of an analog-digital converter, and an interface. Analog signals from thermoelectric sensors were converted into digital form by an ADC (i-7018) and transmitted to a computer using an interface (i-7520).

Experimental studies of drying apples were carried out in the following sequence:

1. Choosing a variety of apples. The selected variety of Jonagold apples has a red color and a balanced sweet taste (yield of 2023, harvested in Vinnytsia region, Ukraine).

2. Preparation of apples for drying. Apples were washed under running water and cut into slices 4...5 mm thick, 8...10 mm wide, and 60...65 mm long, with seeds removed.

3. Drying apple slices to a low residual moisture content of 5%.

4. Based on the experimental data, there were constructed drying kinetics curves $W = f(\tau)$, drying speed curves $dW/d\tau = f(W)$, obtained by numerical differentiation of drying curves, as well as material heating temperature curves $\theta = f(\tau)$.

5. To determine the quality of the obtained product and check the correctness of the developed dehydration regimes, a study was conducted to determine the coefficient of swelling and recoverability according to the methodology given in the publications *(Husarova, 2020).*

Since long-term thermal action negatively affects the quality of dried apple products, the main emphasis should be made on using the maximum allowable temperatures of the material and reducing the duration of the process when developing dehydration regimes.

The maximum permissible temperature for heating apples, as a rule, does not exceed 60 °C and is determined *(Husarova, 2020)* by the following items:

1) thermosensitivity of the protein complex;

2) thermal decomposition of sugars, which is accompanied by the formation of dark-colored substances;

3) reactions of non-enzymatic darkening during the interaction of sugars with amino acids.

Dehydration of apple slices was carried out by two methods of drying:

- convective – using stationary (60, 80 °C) and multi-stage (80/60 °C) modes;
- combined multi-stage infrared-convective mode – IR (100 W) + 60 °C / 60 °C.

Multi-stage convective drying was carried out as follows: at the beginning of the process, the temperature of the coolant was 80 °C, as the material warmed up to 55 °C, the temperature of the coolant was lowered to 60 °C, and it maintained at this level until the end of the process.

Combined multi-stage infrared-convective drying consists of two stages: the first one is a combined drying at IR (100 W) + 60 °C, and the second one is a convective drying at 60 °C. In the first stage, drying takes place with a combination of two methods of drying, in particular, IR and convective drying, and when the material reaches a temperature of 59 °C, IR radiation is turned off, and then only convective dehydration takes place at the temperature of 60 °C.

RESULTS

Intensification of the process of drying apple slices due to multi-stage convective dehydration

Determination of the duration of drying apple slices was carried out at coolant temperatures of 60, 80, 80/60 °C (Fig. 2).

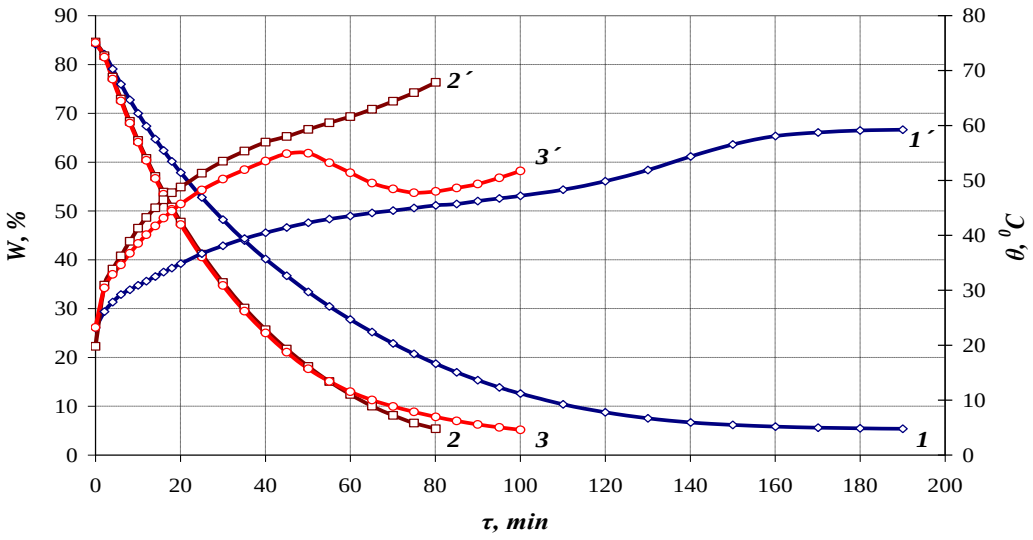

Fig. 2 - Influence of a coolant temperature on the kinetics of the process of drying apple slices with dimensions of 5×10×65 mm, *V*= 1.5 m/s, *d* = 10 g/kg of dry air: *1, 1´ – 60 °C; 2, 2´ – 80 °C; 3, 3´ – 80/60 °C*

An increase in the temperature of the coolant from 60 to 80°C (curves 1, 2) reduces the drying time by 2.38 times. Drying was carried out from the initial relative moisture content of 84% to the final moisture content of 5%.

According to curve 2´, under a coolant temperature of 80°C, the final temperature of heating the material reached 68.2°C, which was higher than the permissible level of 60°C, so the coolant temperature must be reduced.

Using a multi-stage drying mode of 80/60°C is suggested. In the first stage, which lasts for 50 minutes, this mode intensifies the process due to the use of a drying temperature of 80°C, which ensures intensive removal of most moisture from the material (curves 3, 3´). Then, when the material reached a current moisture content of 18% and was heated to 55°C, the temperature of the coolant was lowered to 60 °C and maintained at this level throughout the second stage of drying until the end of the process.

In this case, the drying time increases to 100 min compared to the 80°C drying mode (curves 2, 3), but the final heating temperature in the middle of the material does not exceed 51.7°C, which is 16.5°C less (curve 2´, 3´) and guarantees compliance with the maximum temperature of raw material.

Compared to the stationary mode of dehydration at 60°C (curve 1), the duration of the process is reduced by 90 minutes.

The use of a multi-stage mode of 80/60 °C preserves biologically active substances in dried apple slices and intensifies the drying process.

To characterize the drying process, curves of the drying speed of apple slices were constructed (Fig.3). The drying process takes place in the period of falling drying speed.

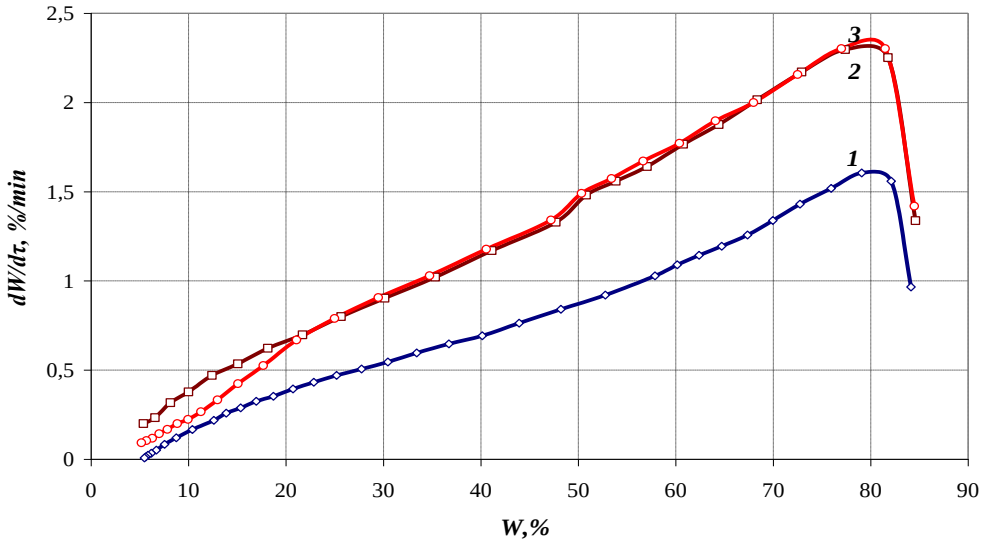

Fig. 3 - Influence of the coolant temperature on the speed of drying apple slices with dimensions of 5×10×65 mm, *V*= 1.5 m/s, *d* = 10 g/kg of dry air
1 – 60°C; 2 – 80°C; 3 – 80/60°C

According to Fig. 3, in the 80 and 80/60 °C drying modes (curves 2, 3), the maximum speed values are 2.3%/min, which is 1.43 times higher than in 60°C drying mode (curve 1). The decrease in the intensity of drying at the end of the process in the multi-step mode of 80/60°C is associated with a decrease in the temperature of the coolant to the level of the maximum permissible temperature for heating the raw material.

Intensification of the process of drying apple slices by a multi-stage combined infrared-convective method (IR radiation E= 3.8 kW/m^2)

According to Fig. 4, the use of a multi-step combined drying mode IR (100 W) + 60°C / 60°C compared to the stationary mode of 60°C (curves 1, 3) allows to reduce the duration of the process by 90 min or 1.9 times. A comparison of two-step, convective, and combined modes (curves 2, 3) indicates that the duration of drying is the same and lasts 100 minutes. These curves have different nature, and to analyze the intensity of drying apple slices, an additional analysis is required, which is given below and shown in Fig. 5-7.

Temperature curves 1´– 3´ describe the nature of the process of drying apple slices (Fig. 4). At a coolant temperature of 60 °C (curve 1´) the drying process proceeds slowly, with a gradual increase in the temperature of the material to 59.2 °C and long-term uniform removal of moisture from the material.

The difference between the multi-step combined drying mode IR (100 W) + 60°C / 60°C and the 80/60°C multi-stage convective drying mode is that heating occurs faster, already at the 35th minute, until the material reaches the temperature of 59°C (curve 3´, point C). The final temperature of heating the material in the combined mode is higher than that one in the convective mode and reaches 56°C.

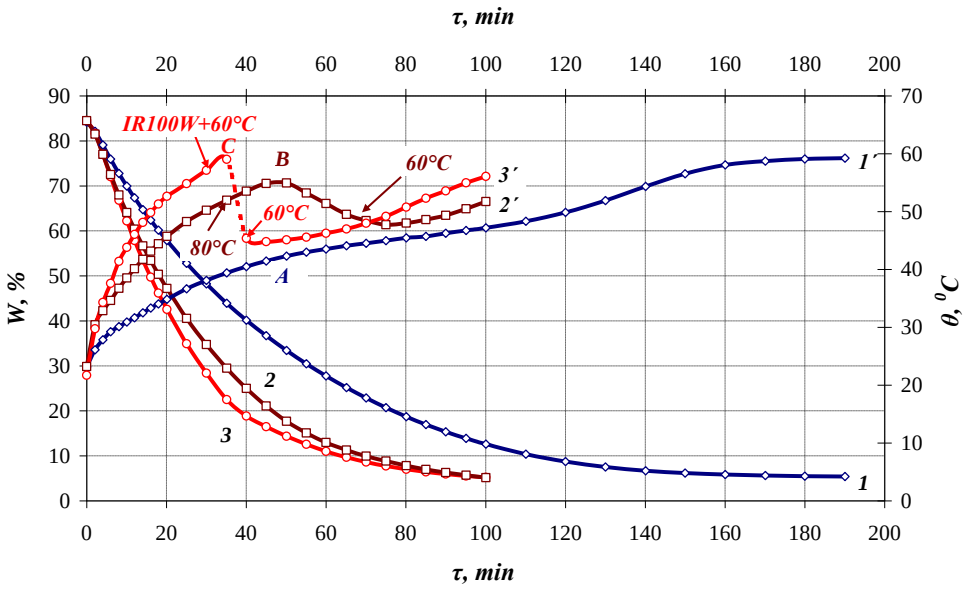

Fig. 4 - Influence of the drying modes on the kinetics of the process of dehydrating apple slices with dimensions of 5×10×65 mm, *V*= 1.5 m/s, *d* = 10 g/kg of dry air

1, 1´ – 60 °C; 2, 2´ – 80/60 °C; 3, 3´ – IR (100 W)+ 60 °C / 60 °C. A, B, C are points of comparison and changes in drying modes

The intensity of the process of drying apple slices shown in Fig. 5 is estimated by the values of the maximum drying speed.

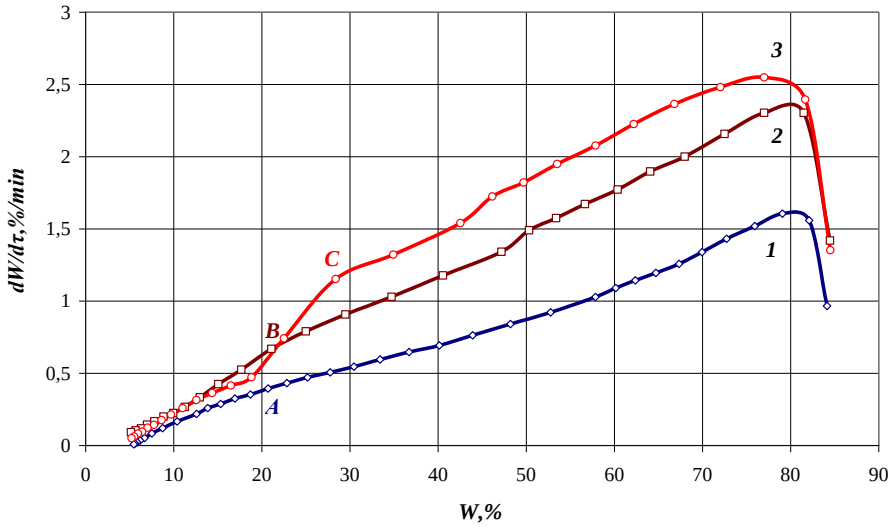

Fig. 5 - Influence of drying modes on the speed of dehydrating apple slices with dimensions of 5×10×65 mm, *V*= 1.5 m/s, *d* = 10 g/kg of dry air

1 – 60 °C; 2 – 80/60 °C; 3 – IR (100 W) + 60 °C / 60 °C. A, B, C are points of comparison and changes in drying modes

Thus, the combined IR drying mode (100 W) + 60 °C / 60 °C (curve 3) is the most intense. It enables to increase a maximum speed compared to the drying mode of 60 °C by 1.58 times, and the multi-stage mode of 80/60 °C by 1.1 times.

When applying a multi-stage combined infrared-convective mode (curve 3, Fig. 5), a decrease in the drying speed is observed when the material reaches a moisture content of 23% (point C), which is associated with turning off the IR radiation and a sharp drop in the temperature of the material. Due to this, both multi-step modes have the same drying time.

Study of the kinetics of the process of dehydrating apple slices, determination of the drying process duration

To study the kinetics of drying apples by the combined infrared-convective method, the drying kinetics curve in semi-logarithmic coordinates lgW – *(N·τ)* will be presented in Fig. 6 *(Paziuk et al., 2021)*.

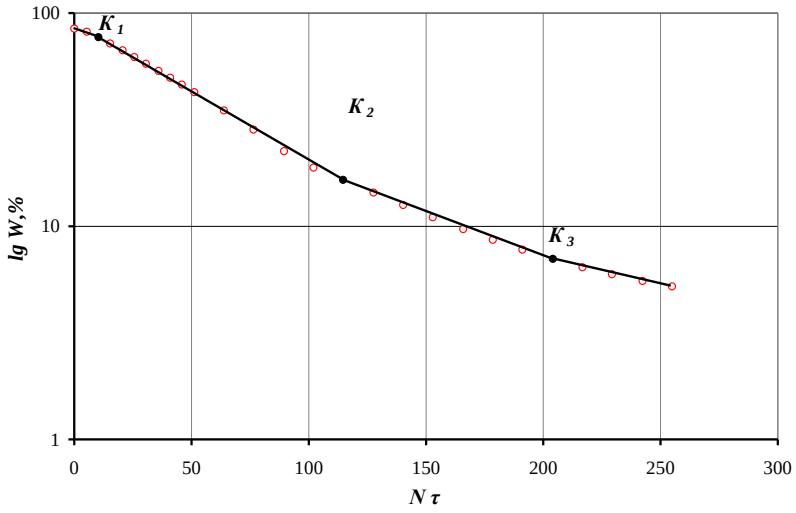

Fig. 6 - The curve of kinetics of drying apple slices with dimensions 5×10×65 mm, V= 1.5 m/s, d = 10 g/kg of dry air in coordinates lg*W* – (*N·τ*)

In the mathematical description of the kinetics of moisture exchange during drying in the second period, it is necessary to consider empirical coefficients (K_i), which are substantiated by the properties of this material. These coefficients are determined directly according to the experiment on drying.

The relative drying coefficient χ_i is determined only by the form of moisture connection with the material, its structure, density and does not depend on the processing mode.

The values of the relative drying coefficients of apple slices in the second period are determined according to the formulas (1 - 3):

$$\chi_1 = \frac{\lg W_{K_1} - \lg W_{K_2}}{N\tau_1} = \frac{\lg 77 - \lg 16.49}{104.3} \approx 0.0064 \quad (1)$$

$$\chi_2 = \frac{\lg W_{K_2} - \lg W_{K_3}}{N\tau_2} = \frac{\lg 16.49 - \lg 7}{89} \approx 0.0042 \quad (2)$$

$$\chi_3 = \frac{\lg W_{K_3} - \lg W_{K}}{N\tau_2} = \frac{\lg 7 - \lg 5.22}{50.8} \approx 0.0024 \quad (3)$$

The drying coefficients in the second drying period are determined by the dependences (4 -5):

$$K_1 = \chi_1 \cdot N = 0.0064 \cdot 2.54 \approx 0.0163 XB^{-1} \quad (4)$$

$$K_2 = \chi_2 \cdot N = 0.0042 \cdot 2.54 \approx 0.0107 XB^{-1}. \quad (5)$$

$$K_3 = \chi_3 \cdot N = 0.0024 \cdot 2.54 \approx 0.0061 XB^{-1} \quad (6)$$

The total duration of the process is determined by the dependence (7):

$$\tau_T = \frac{1}{N}\left(\frac{1}{\chi_1}\lg\frac{W_{K_1}}{W_{K_2}} + \frac{1}{\chi_2}\lg\frac{W_{K_2}}{W_{K_3}} + \frac{1}{\chi_3}\lg\frac{W_{K_3}}{W_{K}}\right) \quad (7)$$

Having substituted the values of relative drying coefficients χ_i and critical moisture content W_{K_i}, the total duration of the drying process is obtained:

$$\tau_T = \frac{1}{2.54}\left(\frac{1}{0.0064}\lg\frac{77}{16.49} + \frac{1}{0.0042}\lg\frac{16.49}{7} + \frac{1}{0.0024}\lg\frac{7}{5.22}\right) \approx 97\,\text{min}$$

According to experimental data, drying lasts100 minutes under the combined mode, i.e. the deviation of the experimental value from the theoretical one is 3%.

The study of the process of heat and mass transfer when drying apple slices

To describe the process of heat and mass transfer when drying apple slices, the Rebinder number will be used. The Rebinder number is equal to the ratio of the amount of heat required to heat the material to the amount of heat required to evaporate moisture from it during an infinitesimally small time period. It is also called a criterion for optimizing the drying process.

$$Rb = b\frac{c}{r} \tag{8}$$

where:

b – temperature coefficient of drying; c – specific heat capacity of the material, kJ/kg K;

r – specific heat of moisture evaporation, kJ/kg.

The temperature coefficient of drying b is the derivative of the average temperature of the material θ from the moisture content of the material W:

$$b = \frac{d\bar{\theta}}{d\overline{W}} \tag{9}$$

Analysis of the Rebinder number during drying of apple slices, under the studied dehydration modes, shows that the process of heat and mass transfer is initially inefficient, most of the energy is spent on heating the material, and not on evaporating moisture from it (Fig. 7).

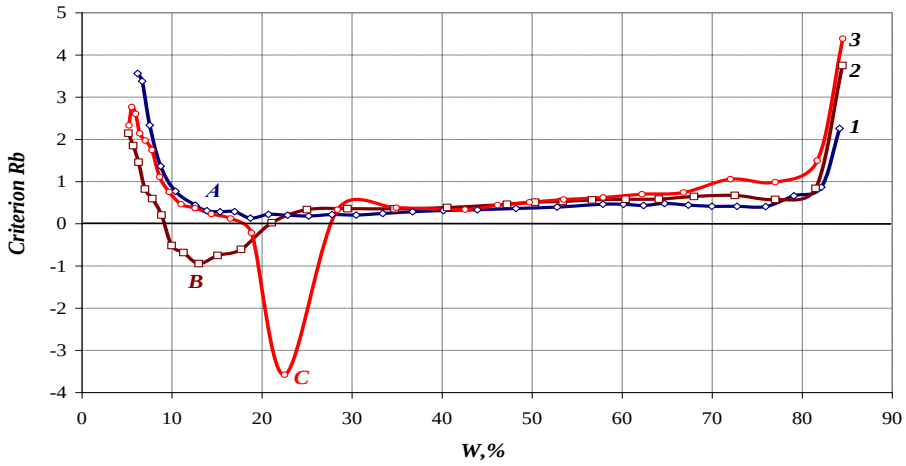

Fig. 7 - Influence of the drying mode on the change in the Rebinder number when drying apple slices with dimensions of 5×10×65 mm, *V*= 1.5 m/s, *d* = 10 g/kg of dry air

1 – 60 °C; 2 – 80/60 °C; 3 – IR (100 W) + 60 °C / 60 °C

A, B, C – points of comparison and change of drying mode

The heat and mass exchange process for each drying mode will be considered separately, as they have their own characteristics.

For the drying mode of 60°C (curve 1), at the beginning of the process, the material is heated (to 75% moisture content), then moisture evaporates from the material (to 14% moisture content and then the material begins to warm up, which is not efficient and indicates economic feasibility of completion of the drying process at 14% moisture content at point A.

For the multi-stage convective mode of 80/60°C (curve 2), at the beginning of the process, the material is actively heated (up to 82% moisture content), then moisture evaporates from the material (up to 18% moisture content), the first stage of drying is completed at a coolant temperature of 80°C, then the material heating temperature decreases to point B. After point B, the material is heated again and the process changes from effective to ineffective. In this mode, effective drying of apple slices (close to zero) can be carried out to a moisture content of 8.8%.

For the multi-stage combined infrared-convective drying mode (curve 3), at the beginning of the process, the material is actively heated (up to 77% moisture content), then moisture evaporates from the material (up to 23% moisture content), then the first stage of drying in the IR mode (100 W) +60°C, the temperature and the Rebinder criterion drop sharply to point C. This is due to the shutdown of IR radiation. Then the heating of the material begins again at a coolant temperature of 60°C. It is economically expedient to carry out drying to point A, as in the 60°C mode, to a final moisture content of 14%.

Investigation of quality characteristics of apples

Swelling capacity is one of the quality criteria of dried products.

The complete recovery of dried apples is not observed, due to the fact that during drying the material shrinks, the structure of parenchymal tissues is deformed, and free intercellular spaces through which water is absorbed are compressed. As a result of heat exposure, substances that normally bind water and swell are subjected to irreversible denaturation *(Husarova, 2018; Husarova, 2020; Husarova et al., 2020).*

The highest value of recoverability is observed under multi-stage drying modes 78-80% (Fig.8).

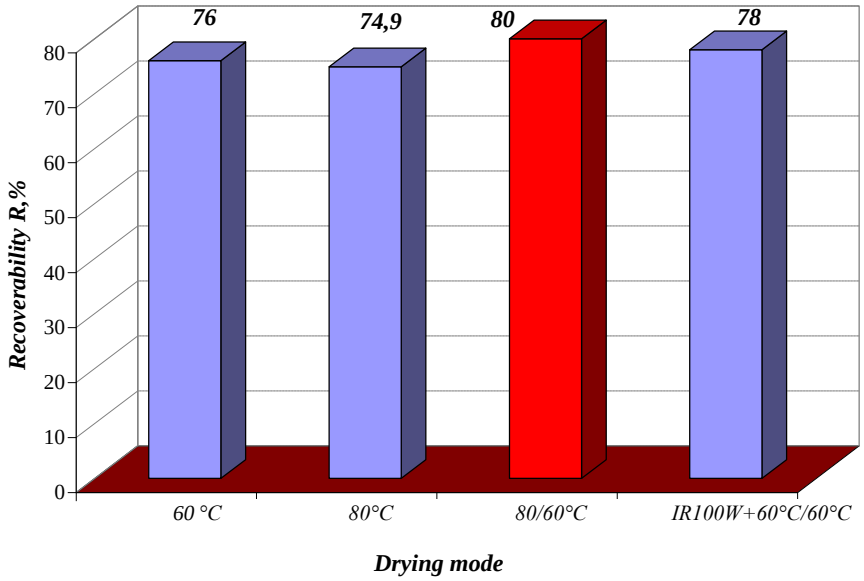

Fig. 8 - Dynamics of changes in the recovery of dried apple slices with dimensions of 5×10×65 mm under different drying modes, *V* = 1.5 m/s, *d* = 10 g/kg of dry air

Organoleptic indicators of the dried slices obtained under a dehydration mode of 80/60 °C and combined IR (100 W) + 60°C / 60°C were as follows: balanced taste, natural aroma, and light cream color inherent to the raw material. Apple slices obtained under a stationary mode of 60 °C had a less pronounced aroma of fresh apples and acquired a yellowish color. This is explained by the long process of dehydration, which leads to reactions of enzymatic darkening of samples and destruction of biologically active substances present in the raw material.

CONCLUSIONS

Summarizing the research results, it can be concluded that a high temperature of the coolant ensures an insignificant duration of the dehydration process, but organoleptic indicators of the finished product are unacceptable.

Drying at low temperatures leads to an increase in dehydration time, and as a result, to an increase in energy consumption and deterioration of organoleptic characteristics and recoverability.

The following results were obtained during the accomplishment of the assigned tasks:

1. To intensify dehydration, reduce energy costs, and ensure a reduction in the duration of drying, the process must be carried out according to the developed modes of convective drying 80/60 °C and combined infrared-convective drying IR (100 W) + 60°C / 60°C.

2. The intensity of the proposed multi-stage drying modes is confirmed by a 1.9-fold reduction in the duration of the process compared to the stationary mode at a coolant temperature of 60°C.

3. Based on the studies of the kinetics of moisture exchange in the combined mode of drying apples, a formula for calculating the total duration of the process was obtained. The difference between the experimental and theoretical values of the drying time does not exceed 3%.

4. Dependencies of the Rebinder number for different modes are constructed, which prove the expediency and effectiveness of using the developed multi-stage dehydration modes.

5. Under the developed multi-stage drying modes, the obtained product had high recoverability (78-80%) and organoleptic indicators, namely, balanced taste, natural aroma, and light cream color inherent to the raw material.

REFERENCES

[1] Bandura V., Kalinichenko R., Kotov B., Spirin A., (2018), Theoretical rationale and identification of heat and mass transfer processes in vibration dryers with IR-energy supply, *Eastern-European Journal of Enterprise Technologies*, 4(8 (94), pp. 50–58. https://doi.org/10.15587/1729-4061.2018.139314

[2] Bandura, V., Bezbah, I., Kupchuk, I., Fialkovsra, L., (2023), Innovative methods of drying rapeseeds using microware energy. *Polityka energetyczna*, 26(2), 217–230. https://doi.org/10.33223/epj/163328

[3] Bessarab O.S, Shutiuk V.V. *Technology of fruit and vegetable drying (Технологія сушіння плодів та овочів),* (2002). Kyiv: NUFT, 84 p.

[4] Bulgakov, V., Bandura, V., Arak, Margus, Olt, Jüri, (2018), Intensification of rapeseed drying process through the use of infrared emitters, *Agronomy Research,* 16(2), pp. 349–356 http://dx.doi.org/10.15159/ar.18.054

[5] Burdo O., Bezbakh I., Kepin N., Zykov A., Yarovyi I., Gavrilov A., Bandura V., Mazurenko I., (2019), Studying the operation of innovative equipment for thermomechanical treatment and dehydration of food raw materials, *Eastern-European Journal of Enterprise Technologies,* 5 (101), pp. 24–32. https://doi.org/10.15587/1729-4061.2019.17893714-157X, https://doi.org/10.1016/j.csite.2023.103676.

[6] Campeanu, G., Neata, G., Darjanschi, G., (2009), Chemical Composition of the Fruits of Several Apple Cultivars Growth as Biological Crop, *Notulae Botanicae Horti Agrobotanici Cluj-Napoca,* 37 (2). pp. 161 – 164. https://doi.org/10.15835/nbha3723465

[7] Hany S. EL-Mesery, Ahmed I. EL-Seesy, Zicheng Hu, Yang Li, (2022), Recent developments in solar drying technology of food and agricultural products, *A review, Renewable and Sustainable Energy Reviews,* Volume 157,112070, ISSN 1364-0321, https://doi.org/10.1016/j.rser.2021.112070

[8] Hany S. El-Mesery, Kwami Ashiagbor, Zicheng Hu, W.G. Alshaer, (2023), A novel infrared drying technique for processing of apple slices: Drying characteristics and quality attributes, *Case Studies in Thermal Engineering,* Volume 52, 103676, ISSN 226.

[9] Husarova O.V. (2020). *Intensification of heat and mass transfer during the production of chips from apples (Інтенсифікація тепломасопереносу під час одержання чипсів з яблук)* (PhD thesis, Technical Sciences, 05.14.06), Kyiv, ITTF of NAN of Ukraine, 241 p.

[10] Husarova O.V., (2018), The influence of the types of apple blanching on the dehydration process during the production of chips (Вплив видів бланшування яблук на процес зневоднення під час виробництва чипсів), *Collection of scientific papers "Progressive equipment and technologies of food production, restaurant industry and trade"* (*Збірник наукових праць „Прогресивні техніка та технології харчових виробництв ресторанного господарства і торгівлі")*, Kharkiv, No 1 (27). pp. 147–156. http://doi:10.5281/zenodo.1306519.

[11] Husarova O., Shapar R., Sorokova N., (2020), *Intensification of heat and mass transfer during the convective drying of apple to low final moisture. Theoretical and practical aspects of the development of the European Research Area (*collective monograph). 4th ed. Riga, Latvia: "Baltija Publishing", pp.191-211. ISBN: 978-9934-588-53-2. https://doi.org/10.30525/978-9934-588-53-2

[12] Paziuk V.M., Liubin M.V., Yaropud V.M., Tokarchuk O.A., Tokarchuk D.M. (2018), Research on the rational regimes of wheat seeds drying, *INMATEH - Agricultural Engineering*, Vol. 56, No 3, pp. 39–48.

[13] Paziuk V.M., Petrova Zh. O., Tokarchuk O.A., Polievoda Yu. (2021), Special aspects of soybean drying with high seedling vigor, *University Politehnica of Bucharest Scientific Bulletin,* Series D, Vol. 83, Issue 2, pp. 327–336.

[14] Snezhkin Yu.F., Boriak L.A., Izbasarov D.S., (2001), Energy saving and intensification of the drying process by pulsed IR irradiation (Энергосбережение и интенсификация процесса сушки импульсным ИК-облучением), *Industrial Heat Engineering (Промышленная теплотехника),* 23 (4-5), pp. 90–96.

APPLE DETECTION METHOD IN THE NATURAL ENVIRONMENT BASED ON IMPROVED YOLOv5

/

基于改进 YOLOv5 的自然环境下苹果检测方法

Yongpeng CHEN, Yi NIU, Weidong CHENG*), Laining ZHENG, Dongchao SUN [1]
School of Agricultural Engineering and Food Science, Shandong University of Technology, Zibo 255091, China
Tel: +86-13589596562; E-mail: 45035828 @qq.com
DOI: https://doi.org/10.35633/inmateh-72-17

Keywords: *Apple; target detection; YOLOv5; natural environment; deep learning*

ABSTRACT

To improve the accuracy of apple fruit recognition, enhance the efficiency of automatic picking robots in orchards, and provide effective visual guidance for the picking robot, a target recognition network model based on improved YOLOv5 is proposed. Firstly, the original apple images collected and the data images obtained by different data enhancement methods are used to establish a dataset of 1,879 images, and the dataset is divided into the training set and the test set under 8:2; then for the problem of low detection accuracy of apple fruits in the natural environment due to the mutual obstruction of apple fruits, this paper modifies the backbone network of YOLOv5 by adding the attention mechanism of the Transformer module, the Neck structure is changed from the original PAFPN to BiFPN that can perform two-way weighted fusion, and the Head structure adds the P2 module for shallow down sampling; finally, the recognition test is performed on the dataset, and a comparative analysis is performed according to different evaluation indexes to verify the superiority of the proposed model. The experimental results show that: compared with other existing models and the single-structure improved YOLOv5 model, the comprehensive improved model proposed in this paper has higher detection accuracy, resulting in an increase of 3.7% in accuracy.

摘要

为提高对苹果果实识别的准确率，提升果园自动采摘机器人的工作效率，为给采摘机械手提供有效的视觉引导，提出了一种基于改进 YOLOv5 目标识别网络模型。首先使用采集到的苹果原始图像以及其搭配不同数据增强方式得到的数据图像共 1879 幅建立数据集，按照 8:2 将数据集划分成训练集与测试集；然后针对苹果果实之间相互遮挡导致自然环境下苹果果实检测精度低的问题，本文将 YOLOv5 的骨干网络进行改动，增添具有注意力机制的 Transformer 模块，Neck 结构由原来的 PAFPN 改成可以进行双向加权融合的 BiFPN，Head 结构增加了浅层下采样的 P2 模块；最后，对数据集进行识别测试,并根据不同评价指标进行对比分析,验证所建模型的优越性。实验结果表明：相比于其他已有模型以及单一结构改进后的 YOLOv5 模型，本文提出的综合改进模型具有更高的检测精度，使识别精确率提升了 3.7%。

INTRODUCTION

The orchard environment is more complex, branch and leaf shading, fruit overlap, light changes, etc. will affect the detection accuracy of the model, resulting in misdetection, leakage, and other problems; in addition, due to the limited arithmetic resources of the embedded platform carried by the picking robot, the detection speed of the complex model cannot meet the task real-time demand, and it is difficult to deploy. Improving the detection speed while ensuring the detection accuracy becomes the main difficult problem and research point of Apple detection in an unstructured environment.

The actual harvest situation faced by the picking robot in the apple orchard is shown in Figure 1. This robot can pick apples that are not obstructed or only covered by leaves. However, apples that are obstructed by branches or other fruits cannot be harvested by the picking robot, because in these situations, if apples are picked directly without accurate recognition, the robot's apples, grasping end effectors, and mechanical picking arms may be damaged, leading to the failure of the picking operation. Therefore, it is crucial for harvesting robots to automatically recognize apple targets that can be grabbed.

[1] *Yongpeng Chen,M.S. Stud. Eng.;Weidong Cheng, As. Ph.D. Eng.; Niu Yi,M.S. Stud. Eng.; Laining Zheng, M.S. Stud. Eng.; Dongchao Sun, M.S. Stud. Eng.*

Fig. 1 - Five-degree-of-freedom apple picking robot

With the development of artificial intelligence, artificial neural networks have been widely used in many research fields in recent years. For example, in the field of economy, stacking and deep neural network models are deployed separately on feature engineered and bootstrapped samples for estimating trends in prices of underlying stocks during pre- and post-COVID-19 period (*Ghosh I. et al., 2020*). Grey relational analysis (GRA) and artificial neural network model are used for the prediction of consumer exchange traded funds (ETFs) (*Malinda M. et al., 2020*). In the field of industry, a relatively simple network control system solution based on fuzzy logic is proposed by using the relevant ideas of neural network (*Precup R. et al., 2020*). A prediction model of maximum power generation of photovoltaic modules based on fuzzy logic principle and artificial neural network is developed (*Mirko S. et al., 2019*). In the field of agriculture, a new deep learning architecture, called VddNet (Vine Disease Detection Net, is proposed for the detection of grape diseases (*Kerkech M. et al., 2020*). Using the combination of machine vision and deep learning, the early Fusarium wilt disease was identified in real time in the potato production system (*Afzaal, H. et al., 2021*).

Up till now, many deep learning network architectures, such as YOLOv2 (*Bresilla K. et al., 2019*), YOLOv3 (*Wu X. et al., 2020, Zhao H. et al., 2021*), Faster R-CNN (*Gao F. et al., 2020, Gene-Mola J. et al., 2019*), DaSNet v2 (*Wang D. et al., 2019*), R-FCN (*Kang H. et al., 2020*), LedNet (*Kang H. et al., 2021*), FCOS (*Long Y. et al., 2021*), DaSNet (*Kang H. et al., 2019*), and Mask R-CNN (*Gene-Mola J. et al., 2020*), have been successfully applied in apple target recognition based on deep learning, and have been successfully applied in the detection of fruit targets on apple trees. The relevant study status is shown in Table 1.

Table 1

Research on apple target recognition, based on deep learning technology

Networks Model	Precision (%)	Recall (%)	mAP (%)	Average Detection Speed (s/pic)
YOLOv2	—	—	90	0.333
YOLOv3	97	90	87.71	0.016
Faster R-CNN	—	—	89.3	0.181
DaSNet-v2	87.3	86.8	88	0.437
R-FCN	95.1	85.7		0.187
LedNet	85.3	82.1	82.6	0.028
FCOS	86.3	84.2	84.5	0.256
DaSNet	87.3	86.8	88	0.437
Mask R-CNN	85.7	90.6	—	—

However, throughout the studies of apple target recognition based on deep learning, although the recognition accuracy of most existing apple detection models was high, the real-time performance of many of them was insufficient, due to its high complexity, large number of parameters, and large size.

In this study, the apple tree fruit is used as the research object. A lightweight apple target real-time recognition algorithm based on improved YOLOv5 for picking robots is proposed, and the goal of this algorithm is to realize the real-time recognition of fruits in different branch shading situations on apple trees and to reduce the loss of apple picking.

MATERIALS AND METHODS

Data set preparation

The image data used in this experiment are obtained from the field shooting in the orchard, the location is the apple orchard in Beibuhou Village, Malianzhuang Town, Laixi City, Shandong Province. The equipment is a Hikvision color industrial camera, and the shooting distance from the apple is 20-80 cm. The shooting angles are the left side, the right side, the top side, the back side, and the front side with five directions. The image saving format is JPEG, and the resolution is 2400×1600. The color of the apples is slightly different depending on the natural light intensity, with the lighted fruits showing bright red and the backlit fruits showing dark red. To adapt to different working environments, image data acquisition was carried out in the morning, afternoon, and evening, and a total of 1281 original Apple images were collected. Including strong light, low light, and artificial supplemental light fruit images, etc. Figure 2 shows some of the acquired images.

Fig. 2 - Some of the collected apple images

Image data preprocessing

The rectangle function in Labelling is used to label the apple fruits in the image. For the marking process, the completely exposed apples are marked on the inside of the rectangle, the exposed parts of apple fruits that are obstructed or placed together are marked in the rectangle, and the apple fruits with less than 10% unobstructed parts appearing at the image boundary will not be marked. Therefore, the .xml file is obtained. Then the dataset is divided in an 8:2 ratio, with 80% being the training set and the remaining 20% being the testing set. The final number of samples for the training and testing sets is 1632 and 207, respectively.

Introduction to YOLO v5

YOLO v5 is a single-stage target detection algorithm, which adds some new improvement ideas based on YOLO v4 so that its speed and accuracy have greatly improved performance. The main improvement ideas are shown below:

- Input side: In the model training stage, some improvement ideas are proposed, mainly including Mosaic data enhancement, adaptive anchor frame calculation, and adaptive image scaling;
- Benchmark network: fusing some new ideas from other detection algorithms, mainly including the Focus structure and the CSP structure;
- Neck Networks: target detection networks tend to insert layers between the Backbone and the final Head output layer. The FPN+PAN structure was added in Yolov5 ;
- Head Output Layer: the anchor frame mechanism of the output layer is the same as YOLO v4. The main improvements are the loss function GIOU_Loss for training, and DIOU_nms for prediction frame screening.

The original Yolov5 network architecture is as follows:

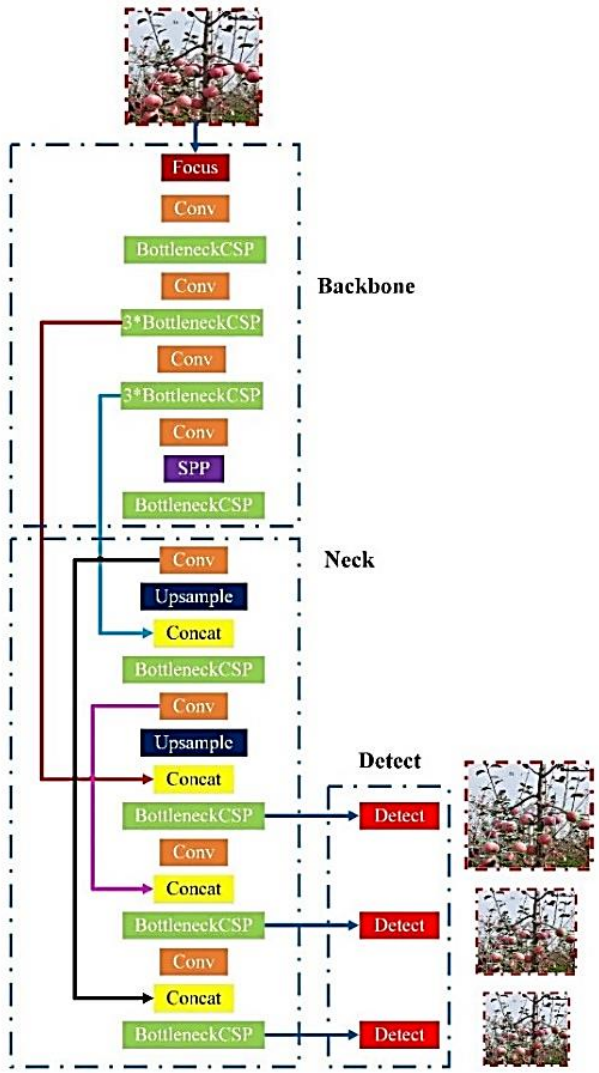

Fig. 3 - The architecture of the original YOLOv5s network

Backbone network optimization

Firstly, the Yolo v5 model backbone network is improved, the biggest drawback of the convolution module is that the convolution parameters need to be set manually, such as the number of convolution kernels (i.e., the number of output channels), the convolution kernel size, the step size, the number of groups, and so on.

In this study, the CSPDDarknet53 backbone network of Yolo v5 is optimized and improved by drawing on the Transform idea. Figure 4 shows the original backbone network of the Yolo v5 model as well as the schematic structure of the improved backbone network.

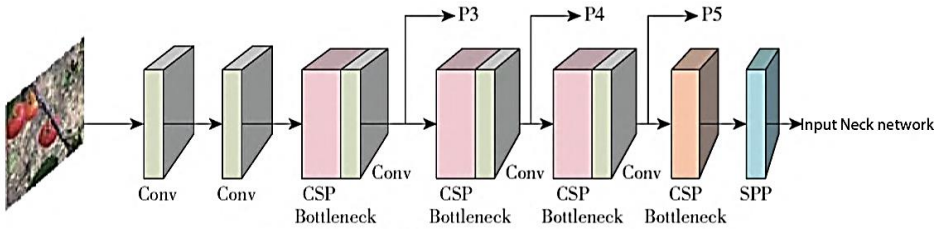

(b)YOLOv5 original backbone network

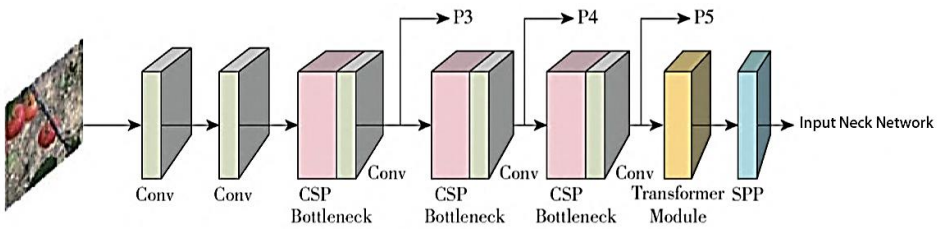

(b) Improved backbone network

Fig. 4 - Comparison between improved backbone network and original network

As can be seen from Fig.3, the improved network replaces the pre-CSPD-Darknet module of the pooled pyramid network used for sensory field feature fusion with the Transformer module, whose outputs are fed into the next level of the Neck network together with the P3, P4, and P5 feature outputs.

Compared to the CSP Bottleneck module, the Transformer module has an attentional mechanism that allows focused extraction of global features. This point can help the detection system to consciously extract the feature points belonging to the apples, to realize better detection effect as well as higher detection accuracy.

Neck Network Optimization

The proposal of PANet proves the effectiveness of bidirectional fusion *(Zhao Y. et al., 2016)*, while the bidirectional fusion of PANet is simpler, this paper introduces the BiFPN structure to improve it, as shown in Fig. 5.

For the current research on apple recognition, the following problems are mainly solved by using BiFPN structure as a Neck network for feature fusion:

(1) Apple Small Target Detection Problem: BiFPN, as a modular repeating feature network layer, can obtain a more advanced feature fusion approach compared to PAFPN, increasing the coupling of features at various scales, especially the shallow features that contribute to small target detection.

(2) Apple target overlap problem: Since BiFPN adopts cross-scale connectivity, different detection features can be suppressed or feature expression can be enhanced according to cross-scale weights, thus alleviating the recognition inaccuracy caused by detection target overlap.

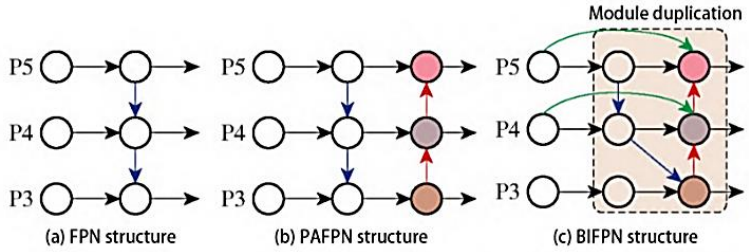

Fig. 5 - Comparison diagram of different neck network structures

Head network optimization

In the Yolo v5 algorithm, the input features of the Head network*(Xia Y et al., 2013)* are selected as the convolution outputs with a down sampling of 32, 16, and 8, i.e., corresponding to P5, P4, and P3 in Fig. The larger the down sampling, the deeper the convolution, and the stronger the semantic expression of the features, which is better for classification in general, but loses more positional information, while the shallower features with smaller down sampling contain more positional information, which is beneficial for the position detection of small objects *(Fan C. et al., 2020)*. According to this feature of the neural network, this paper optimizes the Head output network as follows: the shallow feature output P2 (4 times down sampling rate) is used as an input feature of the Neck network, which jointly fuses the P3, P4, and P5 features, and the Neck network outputs four features with different scales *(Zhang Q. et al., 2021)* as inputs to the Head branch, to improve the position detection accuracy of small targets. The optimization results are shown in Fig. 6.

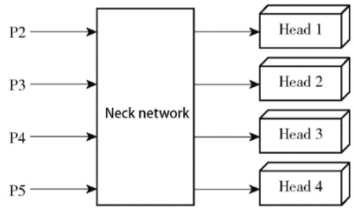

Fig. 6 - Head network optimization

Network Loss Function Optimization

The loss function L of the YOLOv5 network mainly consists of regression frame prediction loss Lloc, confidence loss $Lconf$, and target classification loss $Lclass$, which is calculated *(Yan B. et al., 2021, Yan B. et al., 2022)*.

$$L = L_{conf} + L_{class} + L_{loc} \quad (1)$$

Among them, the confidence loss and the target classification loss are calculated using the binary cross-entropy loss function (BCELoss), calculated as:

$$BCELoss = \begin{cases} -logp' & (y = 1) \\ -log(1 - p') & (y = 0) \end{cases} \quad (2)$$

where $BCELoss$ denotes the BCE loss function, p' denotes the predicted value of the sample, y denotes the true category of the sample, y=1 means it belongs to the target of the category, and y=0 means it does not belong to the target of the category.

The GIoU Loss function is used for the regression box prediction loss. The GIoU loss not only takes into account the overlapping region between the real box and the predicted box but also pays attention to the non-overlapping region. This better reflects the distance between the two frames, and thus the regression of the target frame will be more stable, avoiding the target frame regression dispersion problem that occurs when using IOU for model training.

Network training

Based on a Lenovo Legion Y7000P computer (Intel(R) Core(TM) i5-11400H CPU, 2.6GHz, 16GB RAM; NVIDIA GeForce RTX 3050 GPU, 6GB video memory), the Pytorch deep learning framework was built under the Windows 10 operating system, using the Python language to write the program and call the required libraries, such as CUDA, Cudnn and OpenCV, to achieve the training and testing of the fruit picking method recognition model for picking robots.

A stochastic gradient descent (SGD) method was used to train the modified YOLOv5 network in an end-to-end joint approach. Four samples were used as a batch size for model training, and the BN layer was used for regularization each time the weights were updated, with Momentum set to 0.937, Decay set to 0.000 5, Initial Learning Rate (ILP) set to 0.01, IOU threshold set to 0.01, and Hue, Saturation, and Brightness set to 0.01. The model was trained using the stochastic gradient descent (SGD) method in an end-to-end joint approach. (H), saturation (S) and brightness (V) enhancement factors were set to 0.015, 0.7, and 0.4, respectively, and a total of 300 rounds of training (Epochs) were performed. The obtained weight files are saved after the model training and the performance of the recognition model is evaluated on the test set. After eliminating a large number of redundant prediction frames by post-processing operations such as Non-maximum suppression (NMS), the final output of the network is the prediction category of the apple picking method with the highest confidence score and the coordinates of the fruit location prediction frames are returned.

From the training results, it can be seen that with the increase in the number of training times, the precision and recall as well as the mAP of the improved YOLO v5s network model are relatively significantly improved compared with the YOLO v5s network model. It can be seen that the network model proposed in this paper can effectively carry out the study of multi-target detection problems and meet the requirements of fruit image recognition by picking robots.

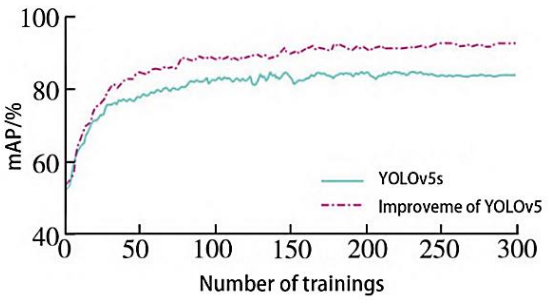

Fig. 7 - mAP curve

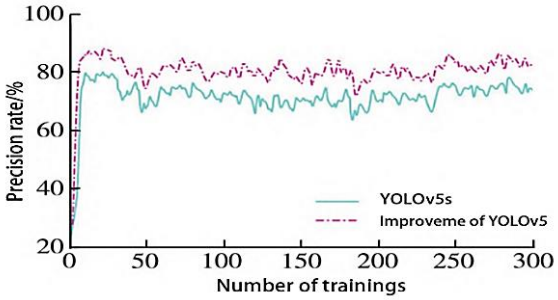

Fig. 8 - Precision rate curve

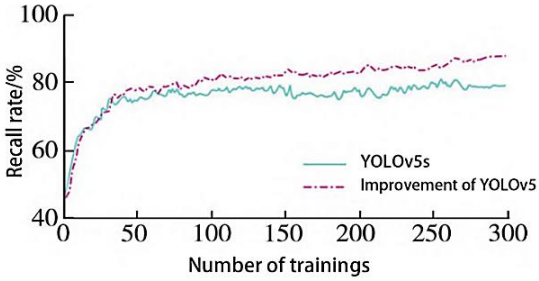

Fig. 9 - Recall rate curve

RESULTS

Target identification result

To verify the performance of the fruit, this study further analyzed the recognition results of the model for 200 test set images based on the real-time recognition model of the apple picking robot with improved design of YOLOv5s. In the 200 test set images, there are 2336 apple targets, of which the number of fruit-grabbable targets is 1007 and the number of non-fruit-grabbable targets is 1329.

Examples of the recognition results of the three network models are shown in Fig. 10, which are the recognition results of the apple target under cloudy and sunny conditions.

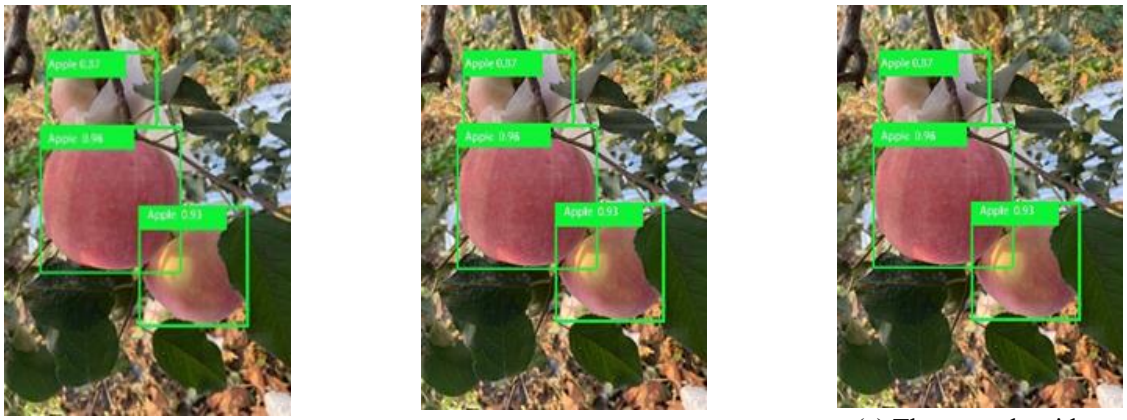

(a) YOLOv3 (b) YOLOv5s (c) The new algorithm

(1) Recognition under sunny and smooth light conditions

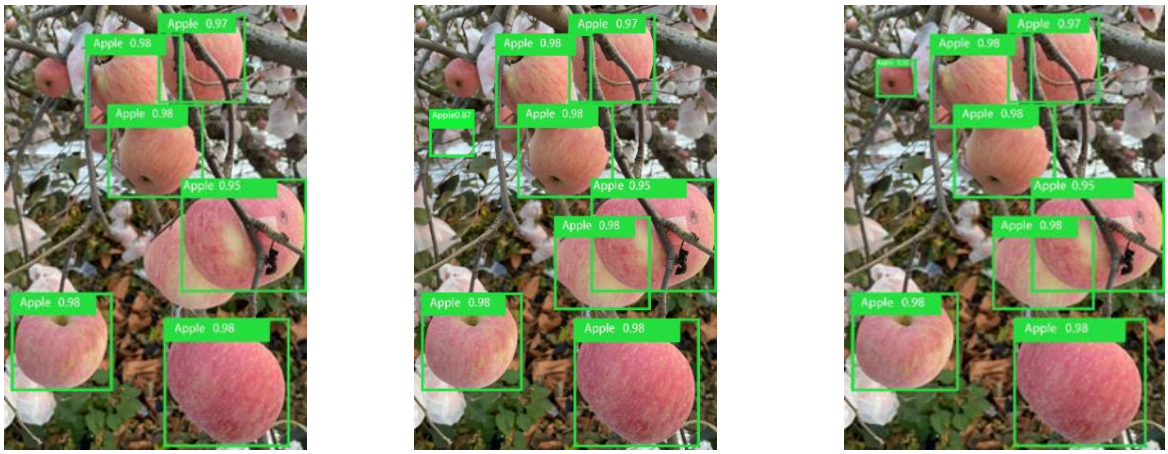

(a) YOLOv3 (b) YOLOv5s (c) The new algorithm

(2) Recognition under cloudy conditions

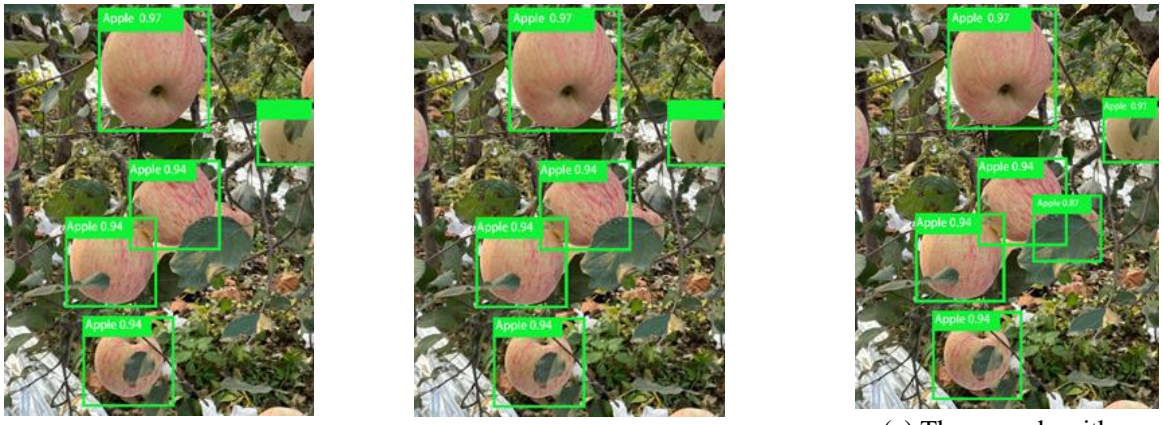

(a) YOLOv3 (b) YOLOv5s (c) The new algorithm

(3) Recognition in leaf-shaded conditions

Fig. 10 - Apple recognition in different conditions

The recognition results of the improved YOLOv5 network, YOLOv5s, and YOLOv3 proposed in the study are accurate under sunny skies and smooth light conditions, with no missed recognition. It can be seen that under cloudy conditions, wrong recognition occurs in YOLOv5s and YOLOv3 networks. Under insufficient light, YOLOv3 does not recognize overlapping fruits and smaller fruits in the photos. YOLOv5s only recognizes overlapping fruits but does not recognize smaller fruits. At the same time, YOLOv5s has multiple detections. In the case of leaf occlusion, error recognition occurs in YOLOv5s and YOLOv3 networks. In the case that most of the apple fruits are occluded by leaves, existing algorithms make it difficult to identify apples.

In conclusion, the model obtained after algorithm optimization in this paper can achieve the best detection effect in apple detection, and can effectively prevent false detection and missing detection under the premise of ensuring the recognition accuracy.

Comparison of different detection algorithms

To further analyze the recognition performance of the proposed algorithm for Apple targets, this study compares the improved YOLOv5 network with the original YOLOv5s, YOLOv3, and YOLOv4-tiny network models on 200 test set images. The model's mAP value and average recognition speed were used as evaluation metrics. The recognition results, size, and number of parameters for each network model are shown in Table 2.

Table 2

Comparison of test indicators of different models

Model	Accuracy / %	recall rate / %	mAP / %	Average Detection Speed (s/pic)
The algorithms in this paper	94.37	96.21	96.73	0.028
YOLOv5s	90.67	93.59	94.32	0.033
YOLOv4—Tiny	89.64	91.58	90.28	0.034
YOLOv3	87.06	92.11	87.69	0.039

As can be seen from Table 2, the improved YOLOv5 network model proposed in this paper has a detection accuracy of 94.37%, a recall of 96.21%, a mAP of 96.73%, and an average single-image detection speed of 0.028 s. Compared with the YOLOv5s, YOLOv4 - Tiny, and YOLOv3 models, the accuracy has been improved by 3.7%, 4.7%, 7.3%, the recall rate increased by 2.6%, 4.6%, and 4.1%, the mAP increased by 2.4%, 6.5% and 9.1%, and the average detection speed of a single image was shortened by 15.2%, 17.6% and 28.2%, respectively. Although the recognition accuracy of the model is slightly affected by the light conditions, branch occlusion, and fruit overlapping, on the whole, compared with other network models, the improved YOLOv5 can effectively recognize the target with strong anti-interference ability, high detection accuracy, and fast recognition speed. Overall, the model proposed in the study is the lightest among the five network models with the highest mAP value. The recognition speed of this model is faster than YOLOv3, YOLOv4, and YOLOv5s networks and can satisfy the requirement of real-time Apple recognition.

CONCLUSIONS

This study aimed at the detection task of small targets and easily occluded overlapping objects, and improved the traditional YOLOv5 model from three aspects, respectively, by adding the Transformer with attention to the backbone network of YOLOv5, which could form a complementary module with convolution, and the attention mechanism could help the model to better detect apples and such small targets; the neck structure could effectively alleviate the problem of overlap between small targets and targets; the shallow feature P2 with smaller down sampling was added to the head structure for feature output, which was therefore helpful for the positional detection of small target objects. The experimental results showed that the advantages of the apple detection algorithm proposed in this paper were shown in the following two points: first, the detection performance, especially the detection speed of the improved YOLOv5s model was excellent, which was suitable for real-time apple recognition of picking robots; Secondly, the recognition success rate of obscured fruits was also relatively high, 3.7% higher than the original model, and there would be no omission or incorrect recognition.

On the other hand, the apple picking robot can work at night, while the algorithm proposed in the study is designed for fruit recognition in the daytime. Therefore, it may not be suitable for apple target recognition at night, which is the limitation of our detection algorithm.

REFERENCES

[1] Afzaal H., Farooque A.A., Schumann A.W., Hussain N., McKenzie-Gopsill A., Esau T., Abbas F., Acharya B. (2021). Detection of a potato disease (early blight) using artificial intelligence. *Remote Sens.*, 13, 411.

[2] Bresilla K, Perulli G.D., Boini A., et al. (2019). Single-shot convolution neural networks for real-time fruit detection within the tree. *Frontiers in Plant Science*, Vol. 10, 1-12.

[3] Fan Cheng, LI Jianian, et al. (2020). Identification method of strawberry based on convolutional neural network (基于卷积神经网络的草莓识别方法). *Transaction of the Chinese Society for Agricultural Machinery*, Vol. 51, No. 2, 237-244.

[4] Gao F., Fu L., Zhang X. et al. (2020). Multi-class fruit-on-plant detection for apple in SNAP system using Faster R-CNN. *Computers and Electronics in Agriculture*, Vol. 176, 1-10.

[5] Gene-Mola J., Sanz-Cortiella R., Rosell-Polo J.R., et al. (2020). Fruit detection and 3D location using instance segmentation neural networks and structure-from-motion photogrammetry. *Computers and Electronics in Agriculture*, Vol. 169, 1-11.

[6] Gene-Mola J., Vilaplana V., Rosell-Polo J.R., et al. (2019). Multi-modal deep learning for Fuji Apple detection using RGB D cameras and their radiometric capabilities. *Computers and Electronics in Agriculture*, Vol. 162, 689-698.

[7] Ghosh, I., Datta Chaudhuri, T. FEB-Stacking and FEB-DNN models for stock trend prediction: A performance analysis for pre and post Covid-19 periods. Decis. Mak. Appl. Manag. Eng. 2020, 4.

[8] Kang H., Chen C., (2019). Fruit detection and segmentation for apple harvesting using visual sensor in orchards. *Sensors*, Vol. 19, No. 20, 45-99.

[9] Kang H., Chen C., (2020). Fast implementation of real-time fruit detection in apple orchards using deep learning. *Computers and Electronics in Agriculture*, Vol. 168, 1-10.

[10] Kang H., Chen C., (2020). Fruit detection, segmentation, and 3D visualisation of environments in apple orchards. *Computers and Electronics in Agriculture*, Vol. 171, 1-10.

[11] Kerkech, M., Hafiane, A.; Canals, R. VddNet: Vine disease detection network based on multispectral images and depth map. Remote Sens. 2020, 12, 3305.

[12] Liu Mochen, Gao Tiantian, Ma Zongxu, et al. (2021). Target detection model of corn weeds in field environment based on MSRCR algorithm and YOLOv4 tiny (基于 MSRCR YOLOv4 tiny 的田间环境玉米杂草检测模型). *Transactions of the Chinese Society for Agricultural Machinery*, Vol. 53, No. 2, 246-255, 335.

[13] Long Yan, Li Nannan, Gao Yan, et al. (2021). Apple fruit detection under natural condition using improved FCOS network (基于改进 FCOS 网络的自然环境下苹果检测). *Transactions of the CSAE*, Vol. 37, No. 12, 307-313.

[14] Malinda, M., Chen, J. The forecasting of consumer exchange-traded funds (ETFs) via grey relational analysis (GRA) and artificial neural network (ANN). Empir. Econ. 2020, 3.

[15] Mirko, S., Aleksandar, S., Đorde, S. ANFIS model for the prediction of generated electricity of photovoltaic modules. Decis. Mak. Appl. Manag. Eng. 2019, 2.

[16] Precup, R., Preitl, S.; Petriu, E.; Bojan-Dragos, C.; Szedlak-Stinean, A.; Roman, R.; Hedrea, E. Model-Based fuzzy control results for networked control systems. Rep. Mech. Eng. 2020, 1.

[17] Wang Dandan, He Dongjian, (2019). Recognition of apple targets before fruits thinning by the robot based on R-FCN deep convolution neural network (基于 R-FCN 深度卷积神经网络的机器人疏果前苹果目标的识别). *Transactions of the CSAE*, Vol. 35, No. 3, 156-163.

[18] Wu Xing, Qi Zeyu, Wang Longjun, et al. (2020). Apple detection method based on light-YOLO v3 convolutional neural network (基于轻量化 YOLO v3 卷积神经网络的苹果检测方法). *Transactions of the Chinese Society for Agricultural Machinery*, Vol. 51, No. 8, 17-25.

[19] Xia Ye, Xiaohui Lei, Andreas Herbst, Xiaolan Lyu, (2023). Research On Pear Inflorescence Recognition Based on Fusion Attention Mechanism With Yolov5. *INMATEH-Agricultural Engineering*, Vol. 69, No. 1, 11-20. https://doi.org/10.35633/inmateh-69-01

[20] Yan B., Fan P., Lei X. Y., et al. (2021). A real-time Apple targets detection method for picking robots based on improved YOLOv5. *Remote Sensing*, Vol. 13 No. 9, 16-19.

[21] Yan Bin, Fan Pan, Wang Meirong, et al. (2022). Real-time apple-picking pattern recognition for picking robot based onimprovedYOLOv5m (基于改进 YOLOv5m 的采摘机器人苹果采摘方式实时识别). *Transaction of the Chinese Society for Agricultural Machinery*, Vol. 53, No. 9, 28-38.

[22] Zhang Lu, Huang Lin, Li Beibei, et al. (2021). Fish school counting method based on multi-scale fusion and no anchor YOLO v3 (基于多尺度融合与无锚点 YOLO v3 的鱼群计数方法). *Transactions of the Chinese Society for Agricultural Machinery*, Vol. 52, 237-244.

[23] Zhang Qinghui, Kong Dexiao, Liu Junqiu, et al. (2021). Design of fruit picking system based on inverse kinematics dimension reduction and YOLO v4 (基于逆运动学降维求解与 YOLO v4 的果实采摘系统研究). *Transaction of the Chinese Society for Agricultural Machinery*, Vol. 52k, No. 9, 15-23.

[24] Zhao Hui, Qiao Yanjun, Wang Hongjun, et al. (2021). Apple fruit recognition in complex orchard environment based on improved YOLO v3 （基于改进 YOLO v3 的果园复杂环境下苹果果实识别）. *Transactions of the CSAE*, Vol. 37, No. 16， 127-135.

[25] Zhao Y., Gong L., Zhou B., et al. (2016). Detecting tomatoes in greenhouse scenes by combining AdaBoost classifier and color analysis, *Biosystems Engineering*, Vol. 148, 127-137.

DESIGN AND EXPERIMENT OF NO-TILLAGE PRECISION PLANTERS WITH STAGGERED SEEDLING BELTS FOR SOYBEAN
/
交错苗带式大豆精量免耕播种机设计与试验

Chuang MA, Weipeng CHEN, Shandong YANG*, Peisong DIAO, Yinping ZHANG, Zengjia LUO, Zhanyang WANG
Shandong University of Technology, Collage of Agricultural Engineering and Food Science, ZiBo (255000), China
*Tel: +86 13864413367 *) Corresponding author E-mail: muren9663@163.com*
DOI: https://doi.org/10.35633/inmateh-72-18

Keywords: *Soybean planter; staggered seedling belt; precision seeding; seedling belt cleaning and preparation; discrete element simulation*

ABSTRACT
According to the requirements of soybean stripping planting in the Huang-Huai-Hai region, a new planting mode was proposed, and a no-tillage staggered seedling belt soybean precision planter was designed. A seed-metering device with staggered distribution of sockets was designed. The optimal parameter combination was obtained through simulation analysis, and its structural rationality was verified through bench experiments. It achieved staggered seedling belt seeding; a retractable top rod seeding device was designed to improve seeding efficiency; the arrangement of the rotary cutter for the seedling belt cleaning and preparation device was designed to reduce work energy consumption. The field experiment results showed that when the forward speed was 8 km/h, the reliability and trafficability of the no-tillage staggered seedling belt soybean precision planter were qualified. The qualified rate of sowing depth was 92.6%, the qualified rate of grain spacing was 94.4%, the leak sowing rate was 1.8%, the repeat sowing rate was 38%, the seed exposure rate was 0.74%, and the operation efficiency was 1.92 hm²/h.

摘要
针对黄淮海地区的大豆带状种植要求，本文提出一种新的种植模式，并设计了一种交错苗带式大豆免耕精量播种机。设计了一种窝眼交错分布的排种器，仿真分析得出最佳参数组合，并通过台架试验验证了其结构合理性，实现了交错苗带播种；对苗带清理整备装置的旋刀的排布进行设计，减少了工作能耗。田间试验结果表明：当前进速度为 8km/h 时，交错苗带式大豆免耕精量播种机可靠性合格，通过性良好。播深合格率为 92.6%,粒距合格率为 94.4%,漏播率为 1.8%,重播率为 3.8%,晾籽率为 0.74%,作业效率为 1.92hm²/h。

INTRODUCTION
Narrow-row-dense-planting, as a soybean planting technique, has a large application area in soybean cultivation internationally *(Chian Statistic Press, 2022; Yao, 2015; Ding et al., 2005)*. The practice has shown that compared to traditional planting techniques, narrow-row-dense-planting techniques can increase yield by more than 15% *(Zhang et al., 1995)*. China proposes to demonstrate and promote soybean strip planting technology in the Huang-Huai-Hai region. At present, the Huang-Huai-Hai region is mostly characterized by equal-width-row-planting and narrow-row-dense-planting. It lacks a unified planting mode that combines dense-planting and strip-planting, as well as corresponding planting machine models *(Zhang et al., 2011)*.

Regarding the soybean planting mode, foreign scholars have conducted research for a long time. Cooper *(Cooper, 1977)*, from the United States, proposed a high-yield "SSS" model for soybeans by reducing row spacing to achieve narrow-row-dense-planting. And the theoretical level and technology of soybean planters in European and American countries are already relatively mature. Foreign planters generally integrate machinery, electricity, fluid, and gas, and combine algorithms to achieve intelligent control of seeding, improving the quality of seeding operations and achieving large-scale operations *(Ale et al., 2023; Karayel et al., 2022; Zavrazhnov et al., 2023)*. A lot of research and exploration have also been conducted on precision seed-metering device. Wright F. S *(Wright et al., 1995).* designed and invented a seeding mechanism with variable particle spacing, and the seeds discharged from it are distributed in a zigzag shape on the seedbed. The Pro Max 40 suction seed-metering device developed by John Deer can adapt to various sizes of seeds by improving the shape of the mold hole, while reducing the vacuum required for the air chamber *(Giannini et al., 1995)*.

Domestic scholars have also conducted related explorations. Chen Wei et al. *(Chen et al., 2019).* designed an air-blown anti-blocking soybean no-tillage planter, which uses a blower fan to blow straw onto the back ridge to achieve no-tillage in a clean area. However, the cleaning effect is not good when the soil moisture is high; Wang Chaoqun et al. *(Wang et al., 2018).* designed a crop removal and no-tillage soybean planter, which uses a combination of moving and fixed blades to clean the straw in the sowing area. However, this machine has high vibration, high energy consumption, and certain safety hazards. Chen Meizhou et al. *(Chen et al., 2018).* designed a single-disc double-row air suction seed-metering device for soybean narrow-row-dense-planting. It uses a seed-metering device with inner and outer double-ring suction holes and a seed splitter to achieve double-row seeding. However, the air suction seed-metering device is expensive and prone to blockage caused by the suction of floating debris during operation, making it unable to work properly.

In response to the lack of a planting mode that combines dense planting and strip sowing in the Huang-Huai-Hai region, this article proposes a staggered seedling belt planting mode. As shown in Figure 1, the width of the seedling belt in this planting mode is 150 mm, and the seeds on the same seedling belt are arranged in a staggered manner. The distance between the two seedling belts is 450 mm, and the distance between two adjacent seeds on the same side of the seedling belt is 140 mm. This planting mode improves ventilation and lighting effects, facilitates plant absorption of nutrients such as water and fertilizer, and increases soybean yield *(Liu et al., 2011; Qi et al., 2013; Yao et al., 2020)*. At the same time, the row spacing is the same as the required row spacing for corn sowing, which can achieve universal use for corn and soybeans. In response to the planting mode and the existing problems of the soybean planters, a staggered seedling belt-type soybean no-tillage precision planter was designed. Its key components were theoretically studied and structurally designed. The working performance of the planter was verified through field experiments, achieving the combination of agronomy and agricultural machinery.

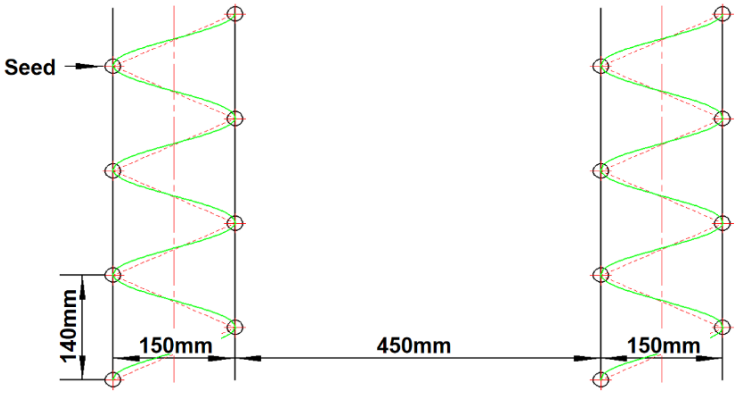

Fig. 1 - Staggered seedling belt planting pattern

MATERIALS AND METHODS

The structure and working principle

The staggered seedling belt type soybean no-tillage precision planter mainly consists of a suspension device, a frame, a depth limiting wheel, a seedling belt cleaning and preparation device, a fertilizer colter, a fertilizer box, a seedbox, a seed opener, a staggered seedling belt type seed-metering device, a cage-type earth covering pressing wheel, etc. The planter is equipped with four sowing units, with a distance of 600 mm between each sowing unit. Its structure is shown in Figure 2.

During operation, the planter is connected to the tractor through a suspension device and moves forward under the traction of the tractor. The ground wheel plays a depth-limiting role, limiting the depth of the operation. The fertilizer ditch is opened by the fertilizer colter. At the same time, the power output of the tractor provides power to the seedling belt cleaning and preparation device, driving it to clean and prepare the seedling belt. After the seedling belt cleaning and preparation are completed, the seed opener opens the seed ditch. The planter drives the cage-type earth-covering pressing wheel to rotate forward while providing power to the staggered seedling belt metering device and fertilizer applicator through the transmission mechanism to complete the seeding and fertilization. Finally, the cage-type earth-covering pressing wheel is used for soil covering and compaction. The main technical parameters of this planter are shown in Table 1.

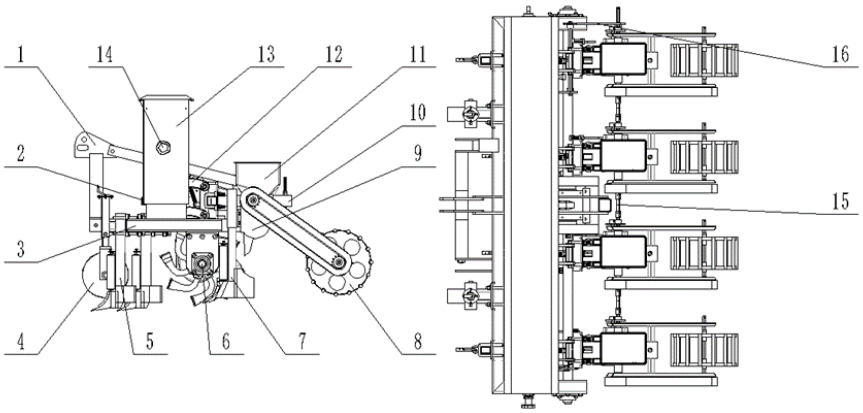

Fig. 2 - Schematic diagram of the structure of the staggered seedling belt type soybean no-tillage precision planter

1. Suspension device; 2. Gearbox; 3. Frame; 4. Depth-limiting wheel; 5. Fertilizer colter; 6. Seedling belt cleaning and preparation device; 7. Seed opener; 8. Cage-type earth-covering pressing wheel; 9. Staggered seedling belts seed-metering device; 10. Planting unit rack; 11. Seedbox; 12. Profiling mechanism; 13. Fertilizer box;14. Fertilization adjustment device; 15. Card gear; 16. Chain transmission gearing.

Table 1

Primary technical parameters

Parameters	Numerical value
Dimensions（length×width×height）/（mm×mm×mm）	1800×2400×1430
Auxiliary power / kW	88~103
Hang	Three-point linkage
Rows	4
Working width / m	2.4
Sowing depth / mm	20~40
Width of staggered seedling belt / mm	150
Qualified rate of seed spacing / %	≥90
Seed interlocking qualification rate / %	≥90

Critical Component Design

Structure and working principle of the seed-metering device

The seed-metering device, as the core component of the planter *(Zhang et al., 2004).*, is the key to achieving staggered seedling belts. To achieve staggered seedling belt planting, a staggered seedling belt metering device is designed, mainly composed of a seed-metering device shell, a socket wheel, a telescopic ejector rod, an ejector rod installation wheel, a seed feeding block, a seed removal brush, a seed protection belt shaft, a flexible seed protection belt, a seed splitter, etc. Its structure is shown in Figure 3.

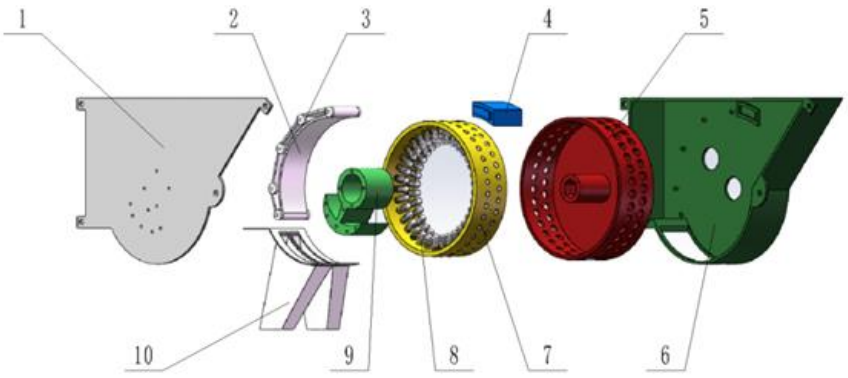

Fig. 3 - Structure diagram of staggered seedling belt seed-metering device

1. Upper shell of seed-metering device; 2. Flexible seed protection belt; 3. Seed protection belt shaft; 4. Seed removal brush; 5. Socket wheel; 6. Lower shell of the seed-metering device;7. Ejector rod installation wheel; 8. Telescopic ejector rod; 9. Seed feeding block;10. Seed splitter;

As shown in Figure 4, the staggered seedling belt metering device consists of a seed filling area, a seed cleaning area, a seed protection area, a seed discharge area, and a reset area. When the seed-metering device is working, the seeds enter the seed chamber from above. Then they are squeezed into the socket by their gravity and the pressure between the seeds. As the socket wheel rotates, the excess seeds in the socket are brushed off by the seed removal brush, and one seed is retained in the socket. Then, the seeds come to the seed discharge area under the protection of the flexible seed protection belt. The seeds in the seed discharge area are thrown out of the socket due to their gravity and the push of the telescopic ejector rod, completing the seeding process.

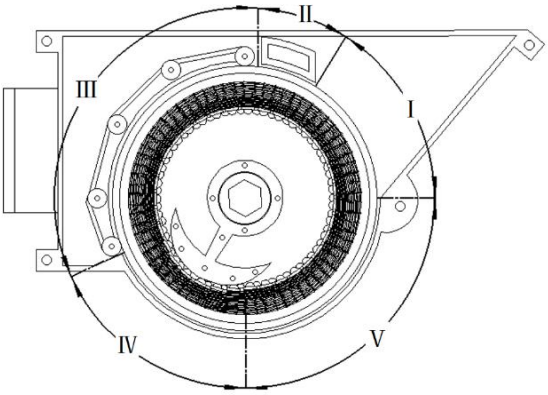

Fig. 4 - Zoning diagram of seed metering device

Ⅰ. Seed filling area; Ⅱ. Seed clearing area; Ⅲ. Seed protection area; IV. Seed discharge area; V. Reset area;

Design of socket wheel

The socket wheel is a key component of the seed-metering device to achieve precision seeding. It was designed because it has a significant impact on the repeat sowing index, leak sowing index, and other factors of the seed-metering device. There are two rows of sockets on the socket wheel, with 35 in each row. The sockets are arranged in a staggered manner to ensure that the seeds are distributed in a staggered manner on the seedling belt. Related studies have shown that the best filling effect is achieved when the diameter of the socket is 1.64 times the average seed diameter *(Dun et al., 2016)*. Therefore, the diameter of the socket is determined to be 12.8 mm and the depth of the socket is 9 mm. The diameter of the socket wheel is designed to be 280 mm. To facilitate seed filling, the chamfer angle of the socket is designed to be 45°. Based on experience, take 35 sockets.

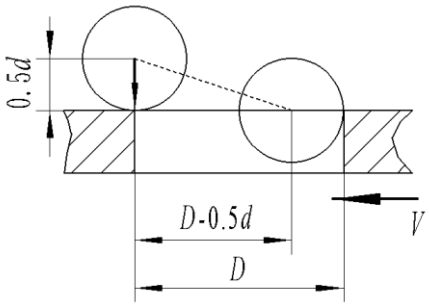

Fig. 5 - Soybean filling process

D - Socket diameter; d - Seed average diameter; V - The relative velocity between the socket and the seed

As shown in Figure 5, analyze the movement between the seed and the socket. When the socket rotates, the center of mass of the seed is on the outer circumference of the socket wheel. When the socket speed reaches a certain value, the seed will slide over the socket, causing missed seeding. At this time, the socket speed is called the limit speed. The necessary condition for smooth seeding is that the socket speed does not exceed the limit speed. The vertical displacement of the seed is 0.5d, the time is t. There is the following relationship:

$$\frac{d}{2} = \frac{gt^2}{2} \tag{1}$$

When the seed can be smoothly filled, the maximum linear velocity at the socket is V_{max}, and the displacement of the seed in the horizontal direction is:

$$D-\frac{d}{2}=V_{\max}t \tag{2}$$

According to equations (1) and (2):

$$V_{\max}=\left(D-\frac{d}{2}\right)\sqrt{\frac{g}{d}} \tag{3}$$

The condition for successfully completing seed filling is (4). Substitute it into (3):

$$v_1 \le V_{\max} \tag{4}$$

$$\frac{2\pi rn}{60}\le\left(D-\frac{d}{2}\right)\sqrt{\frac{g}{d}} \tag{5}$$

It can be concluded that:

$$n\le\frac{60}{2\pi r_w}\left(D-\frac{d}{2}\right)\sqrt{\frac{g}{d}} \tag{6}$$

where:

v_1 - Linear speed of socket wheel, (m/s);

D - Socket diameter, (mm);

D - Seed average diameter, (mm);

G - Gravitational acceleration, (m/s^2);

r_w - Socket wheel radius, (mm);

n - Socket wheel speed, (r/min);

According to equation (6), it can be seen that when the average diameter of seeds and the radius of the socket wheel are constant, the speed of the socket wheel is proportional to the diameter of the socket. To ensure that seeds can be filled smoothly under all socket diameters, the minimum socket diameter is selected to calculate the maximum speed of the socket wheel. When the radius of the socket wheel is 120 mm, the diameter of the socket is 12 mm. When the average seed diameter is 7.31 mm, the rotational speed of the socket wheel calculated according to equation (6) should not exceed 24.3 r/min. Based on practical experience, the distance between the two rows of sockets on the designed socket wheel is 27 mm, and the thickness of the socket wheel is 70 mm. Based on the above data, the structure of the socket wheel is shown in Figure 6.

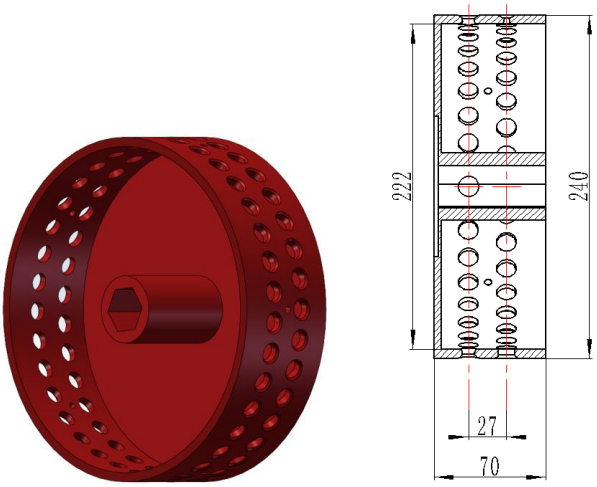

Fig. 6 - Structure diagram of socket wheel

Simulation test

Select the diameter of the socket, the length of the chamfered edge of the socket, and the rotational speed of the socket wheel as the experimental factors. Select the qualified index, repeat sowing index, and leak sowing index as performance evaluation indicators. The simulation experiment was conducted using a three-factor five-level quadratic regression orthogonal rotation combination design method *(Yu et al., 2011)*, and the experimental code is shown in Table 2.

During the simulation experiment, a total of 23 sets of experiments were conducted, including 14 sets of analysis points and 9 sets of zero points. Each set of experiments was repeated 3 times, and the average value was taken as the experimental result.

Table 2

Test factor coding table

Numbers	Factors		
	Socket wheel speed X1 (r/min)	The chamfer edge length of socket X2 (mm)	Socket diameter X3 (mm)
1.682	23.8	2.5	14
1	22.5	2.21	13.6
0	20.4	1.5	13
-1	18.3	0.79	12.4
-1.682	17	0.5	12

Experimental results were obtained through experiments. The experimental results were input into Design-Expert for data analysis and regression fitting *(Jia et al., 2021*). By conducting variance analysis on the qualified index, repeat sowing index, and leak sowing index, and removing insignificant factors, the regression equations between each indicator and each factor are obtained as follows:

$$Y_1 = 93.72 - 0.79X_1 + 0.78X_2 - 0.44X_3 - 0.62X_1X_2 - 1.48X_1^2 - 1.84X_2^2 - 1.00X_3^2 \quad (7)$$

$$Y_2 = 3.56 - 1.43X_1 + 0.82X_2 + 1.42X_3 + 0.64X_2^2 + 0.76X_3^2 \quad (8)$$

$$Y_3 = 2.83 + 2.22X_1 - 1.60X_2 - 0.99X_3 + 1.21X_1^2 + 1.22X_2^2 \quad (9)$$

By using the dimensionality reduction method, one of the parameters of the socket wheel speed, socket chamfer edge length, and socket diameter was adjusted to zero. A response surface graph was drawn to show the interaction between the other two factors on each indicator. Through response surface analysis, it was found that within the range of socket chamfer edge length of 0.5~2.5 mm, socket wheel rotation speed of 17~23.8 r/min, and socket diameter of 12~14 mm, optimization solution is carried out under the condition of maximizing the qualified index and minimizing the repeat sowing index and leak index. The optimal parameter combination of the seed-metering device is obtained as follows: the chamfer length of the socket is 1.5 mm, the socket wheel speed is 20.2 r/min, and the socket diameter is 12.8 mm. At this time, the qualified index is 93.92%, the repeat sowing index is 3.57%, and the leak sowing index is 2.51%.

Design of seedling belt cleaning and preparation device

To ensure the quality of soybean sowing, it is necessary to clean and prepare the operating area. To reduce work resistance, reduce energy consumption, and improve the stability of the machine body during operation, a seedling belt cleaning and preparation device was designed. The device is composed of a knife shaft, a tool magazine, a curved knife, and a straight-faced curved knife. Its structure is shown in Figure 7. The seedling cleaning and preparation device is divided into four knife groups, each corresponding to a seedling belt. The width of the knife group is greater than the width of the seedling belt, and 200 mm is taken. Each knife set includes two straight-faced curved knives on both sides and two curved knives in the middle. The two curved knives in the middle clean and prepare the seedling belt while also cleaning the middle area of the seed opener to prevent blockage. Straight-faced curved knives and curved knives are arranged in a staggered manner. The angle between two straight-faced curved knives in the same cutting group is 180°, and the angle between two curved knives is 180°. The specifications of the rotary knives are all IT245, and their arrangement is shown in Figure 8. Through kinematic analysis, it is determined that the rotational speed of the rotary cutter should be greater than or equal to 379 r/min;

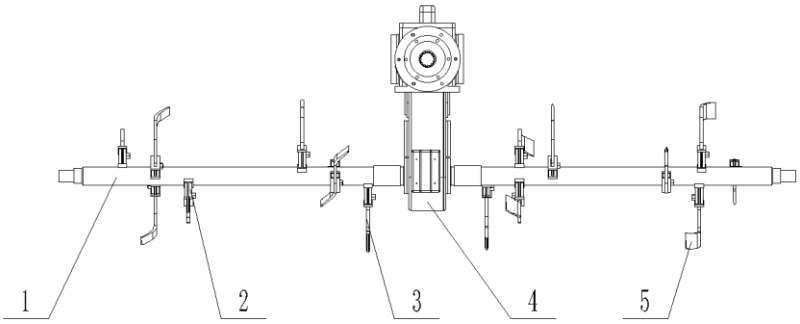

Fig. 7 - Seedling belt cleaning and preparation device

1. Knife shaft; 2. Tool magazine; 3. Straight-faced curved knife; 4. Transmission; 5. Curved knife

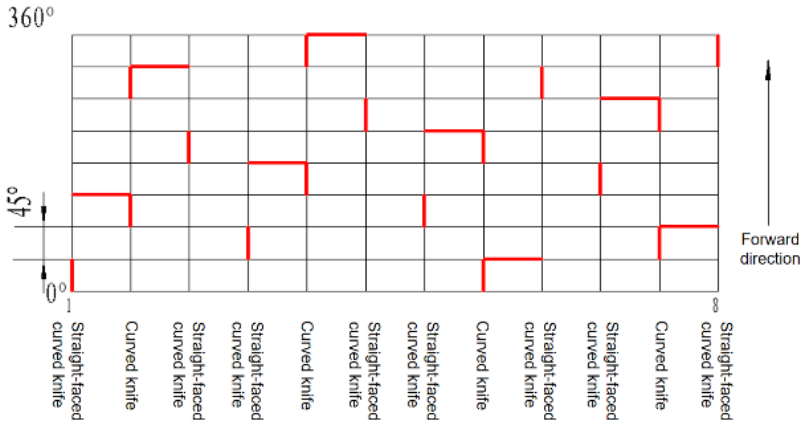

Fig. 8 - Rotary knife arrangement

RESULTS

Bench experiment

To verify the simulation test results, a prototype of the seed-metering device was manufactured according to the optimal parameters obtained from the simulation test, and the seed-metering device bench experiment was carried out, as shown in Figure 9.

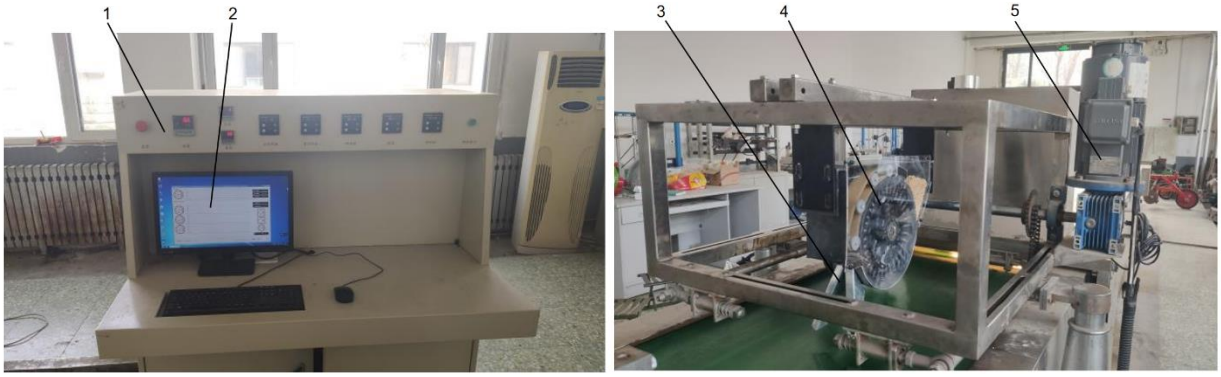

Fig. 9 - Bench test of seed metering device

1. JPS-12 electrical control cabinet; 2. Monitoring and detection software; 3. Staggered seedling belts metering device; 4. Seed splitter; 5. Drive motor

The experiment was conducted on the JPS-12 type seed-metering device performance testing platform, selecting Zhong-Huang13 soybean seeds as the experimental seeds. Before the experiment, the seed-metering device speed was set to 20.2 r/min. Based on the relationship between the theoretical grain spacing, the number of plants per mu, and the number of sockets, the corresponding conveyor belt speed was calculated to be 1.65 m/s. In the experiment, seeds on the conveyor belt after stable seeding were selected for measurement, and their qualified index, repeat sowing index, and leak sowing index were calculated. The experiment was repeated for 5 groups, and the average value was taken as the final result. The experimental results are shown in Table 3.

Table 3

Bench test results

Numbers	Qualified index（%）	Repeat sowing index（%）	Leak sowing index（%）
1	94.02	3.66	2.32
2	93.28	4.13	2.59
3	93.66	3.33	3.01
4	93.37	3.59	3.04
5	93.89	3.57	2.54
Average value	93.64	3.66	2.70

The experimental results showed that the qualified index of the seed-metering device was 93.64%, the repeat sowing index was 3.66%, and the leak sowing index was 2.70%. The difference between the experimental results and the theoretical results was within a reasonable range, proving the reliability of the simulation test data. All indices in the experiment meet the industry standard requirements, indicating that the structure of the staggered seedling belt seed-metering device is reasonable.

Field experiment

The experiment was conducted on June 21, 2021, in Linzi, Shandong Province, as shown in Figure 10. The previous crop in the experimental field was wheat, and the height of machine-harvested stubble was 190 mm. The tractor model was KAT-1404, and the operating speed of the prototype was 8 km/h. The soybean variety selected for the experiment was Zhong-Huang 34. Refer to GB/T6973-2005 "Test Methods for Single Seed (Precision) Planter " for the experiment.

Fig. 10 - Field test diagram

The experimental prototype did not experience any malfunctions or blockages during the operation process. The reliability of the equipment is qualified. Calculate the various data of field experiments on the experimental prototype, and the experimental results are shown in Table 4

Table 4

Test results

Numbers	Sowing depth qualification rate (%)	Grain spacing qualification rate (%)	Leak sowing rate (%)	Repeat sowing rate (%)	Seed exposure rate (%)
1	91.8	94.5	1.6	3.9	0
2	93.1	92.8	2.5	4.7	1.2
3	92.7	94.1	2.2	3.7	0
4	92.9	95.2	1.3	3.5	0.9

Numbers	Sowing depth qualification rate (%)	Grain spacing qualification rate (%)	Leak sowing rate (%)	Repeat sowing rate (%)	Seed exposure rate (%)
5	92.5	95.4	1.4	3.2	1.6
Average value	92.6	94.4	1.8	3.8	0.74
Standard value	80.0	75.0	10.0	20.0	2.0
Conclusion	Qualified	Qualified	Qualified	Qualified	Qualified

From Table 4, it can be seen that at a forward speed of 8 km/h, the sowing depth qualification rate is 92.6%, the grain spacing qualification rate is 94.4%, the leak sowing rate is 1.8%, the repeat sowing rate is 3.8%, the seed exposure rate is 0.74%. The experimental indicators are all better than the industry standard requirements. The forward speed of the experimental prototype during operation is 8 km/h, the operating width is 2.4 m, the operating length is 24 km, and the operating efficiency is 1.92 hm^2/h, which meets the operating requirements.

CONCLUSIONS

(1) A new soybean planting model suitable for the Huang-Huai-Hai region has been proposed. The theoretical spacing of this model is 140 mm, and the width of the seedling belt is 150 mm. The seeds on the same seedling belt are arranged in a staggered manner, and the distance between the two seedling belts is 450 mm, which improves the growth conditions of crops. A staggered seedling belt type soybean no-tillage precision planter was designed, and its structural layout was designed. Based on the planting mode, the operating row spacing was determined to be 600 mm, the operating width to be 2.4 m, the seedling belt width to be 150 mm, and the sowing depth to be 20-40 mm.

(2) A staggered seedling belt metering device was designed, and simulation experiments on the seeding process were conducted. The optimal parameters after data processing were obtained: the diameter of the socket was 12.8 mm, the chamfered edge length of the socket was 1.5 mm, the depth of the socket was 9 mm, the diameter of the socket wheel was 280 mm, and the speed of the socket wheel was 20.2 r/min. Its structural rationality was verified through bench tests, achieving staggered seedling belt seeding. The seedling belt cleaning and preparation device has been designed, and the distribution mode of the rotary blade has been determined to be a staggered arrangement of straight-faced curved blades and curved blades. It was been determined that the blade shaft speed needed to be greater than 379 r/min.

(3) Through field experiments on the planter, the reliability of the staggered seedling belt soybean no-tillage precision planter is qualified, the machine passability is qualified, and meets the industry standard requirements.

REFERENCES

[1] Ale L.P., de Souza C.M.A., da Silva Ferreira F. et al., (2023). Power performance of a tractor-seeder-fertilizer system as a function of furrower depth in no-till [J] (Power performance of a tractor-seeder-fertilizer system as a function of furrower depth in no-till). *Observatório de la Economía LatinoAmericana*, vol.21, no.9, pp.11067-11086;

[2] Chen Meizhou, Diao Peisong, Zhang Yinping et al., (2018). Design of pneumatic seed-metering device with single seed-metering plate for double-row in soybean narrow-row-dense-planting seeder [J] (大豆窄行密植播种机单盘双行气吸式排种器设计). *Transactions of the Chinese Society of Agricultural Engineering*, vol.34, no.21, pp. 8-16;

[3] Chen Wei, Cao Chengmao, Zhao Zhengtao et al., (2019). Design and experiment of air-blowing anti-blocking soybean no-tillage seedling machine [J] (气吹式防堵大豆免耕播种机设计与试验). *Journal of Northeast Agricultural University*, vol.50, no.10, pp. 71-79;

[4] *China Statistical Yearbook* (中国统计年鉴) (2022). Beijing: China Statistical Press. (in Chinese)

[5] Cooper R.L., (1997). Response of soybean cultivars to narrow rows and planting rates under weed-free conditions [J] (Response of soybean cultivars to narrow rows and planting rates under weed-free conditions). *Agronomy Journal*, vol.69, no.1, pp. 89-92;

[6] Ding Qiao, Yang Guanglin, Yang Yueqian et al., (2005). Research on narrow path horizontal seed close planting mode and whole mechanize production system of soybean [J] (大豆窄行平播密植栽培模式及配套机器系统的研究). *Journal of Northeast Agricultural University*, vol.36 no.2, pp. 222-224;

[7] Dun Guoqiang, Chen Haitao, Cha Shaohui., (2016). Parameter optimization and validation of soybean cell wheel seeding plate type-hole based on EDEM [J] (基于 EDEM 的大豆窝眼轮式排种盘型孔参数优化与验证). *Soybean Science*, vol.35, no.5, pp. 830-839;

[8] Giannini G.R., Chancellor W.J., Garrett A.R.E., (1967). Precision Planter Using Vacuum for Seed Pickup [J] (Precision Planter Using Vacuum for Seed Pickup). *Transactions of the Asae*, vol.10, no.5, pp. 0607-0610;

[9] Jia Shuanglin, Yu Jianqun, Torsten Ghayekhloo., (2021). Simulation analysis and construction of maize seeder model based on EDEM [J] (基于 EDEM 的玉米排种器模型构建与仿真分析). *INMATEH-Agricultural Engineering*, vol.63, no.1, pp. 365-374;

[10] Karayel D., Güngör O., Šarauskis E., (2022). Estimation of optimum vacuum pressure of air-suction seed-metering device of precision seeders using artificial neural network models [J] (Estimation of optimum vacuum pressure of air-suction seed-metering device of precision seeders using artificial neural network models). *Agronomy*, vol.12, no.7, pp. 1600.

[11] Liu Jia, Cui Tao, Zhang Dongxing, et al., (2011). Experimental study on pressure of air-blowing precision seed-metering device [J] (气吹式精密排种器工作压力试验研究). *Transactions of the Chinese Society of Agricultural Engineering*, vol.27, no.12, pp. 18-22;

[12] Qi Bing, Zhang Dongxing, Cui Tao, et al., (2013). Design and experiment of centralized pneumatic metering device for maize [J] (中央集排气送式玉米精量排种器设计与试验). *Transactions of the Chinese Society of Agricultural Engineering*, vol.29, no.18, pp. 8-15;

[13] Wang Chaoqun, Cao Chengmao, Qin Kuan et al., (2018). Design and experiment of no-tillage soybean planter with stubble cleaning [J] (灭茬免耕大豆播种机的设计与试验). *Journal of Northeast Agricultural University*, vol.49, no.10, pp. 89-96;

[14] Wang Hanyang, (2013). Study on 2BMFJ-3 type no-till soybean precision planter with straw-covering in wheat stubble fields [D] (2BMFJ-3 型麦茬地免耕覆秸大豆精密播种机的研究). *Harbin: Northeast Agricultural University*;

[15] Wright F.S., Mozingo R.W., (1995). Device for Precision Peanut Seed Placement [J] (Device for Precision Peanut Seed Placement). *Agronomy Journal*, vol.87, no.2;

[16] Yao Qiaoqian, Cao Baoming., (2015). Research on the price of soybean affected by its volumes of China's export and import [J] (中国大豆进出口量与大豆价格关系的分析). *Journal of Chuzhou University*, vol.17, no.1, pp. 32-35;

[17] Yao Wenyan, Zhao Dianbao, Xu Guangfei, et al., (2020). Design and experiment of anti-blocking device for strip-to-row active corn no-tillage seeding [J] (条带对行主动式玉米免耕播种防堵装置设计与试验). *Transactions of the Chinese Society for Agricultural Machinery*, vol.51, no. s2, pp. 55-62,71;

[18] Yu Yaowei, Henrik Saxén, (2011). Discrete element method simulation of properties of a 3D conical hopper with mono-sized spheres [J] (Discrete element method simulation of properties of a 3D conical hopper with mono-sized spheres). *Advanced Powder Technology*, vol.22, pp. 324-331;

[19] Zavrazhnov A.I., Balashov A.V., Zavrazhnov A.A. et al., (2023). Control of Sowing Seeds of Row Crops by Electrified Seeders [J] (Control of Sowing Seeds of Row Crops by Electrified Seeders). *Russian Agricultural Sciences*, vol.49, no.4, pp. 448-453;

[20] Zhang Bing, Li Dan, Zhang Ning., (2011). Soybean planting patterns and benefit analysis of Huang-Huai-Hai region [J] (黄淮海地区大豆主要种植模式及效益分析). *Soybean Science*, vol.30, no.6, pp. 987-992;

[21] Zhang Xiuhua, Xia Ling, Ma Hongliang, et al., (2004). Reliability improvement of a precision planter [J] (精密播种机的可靠性研究). *Transactions of the Chinese Society for Agricultural Machinery*, vol.35, no.2, pp. 62-64;

[22] Zhang Zeping, Ma Chenglin, Wang Chuncheng., (1995). The development of the seed-metering device for precision planter and its theoretical study [J] (精播排种器及排种理论研究进展). *Journal of Jilin University of Technology*, vol.25, no.4, pp. 112-117;

STUDY ON HIGH-TEMPERATURE AEROBIC FERMENTATION TECHNOLOGY OF KITCHEN WASTE
/
餐厨垃圾高温好氧发酵工艺的研究

Yupeng JIANG [1]; Aiping SHI*[1]; Feng LIANG[1]; Jun YANG [1]
[1] College of Agricultural Engineering, Jiangsu University, Zhenjiang 212000, China
Tel: +86-15952866677; E-mail: shap@ujs.edu.cn
Correspondent author: Aiping Shi
DOI: https://doi.org/10.35633/inmateh-72-19

Keywords: *kitchen waste, high-temperature aerobic fermentation, optimum craft, response surface optimization experiment.*

ABSTRACT
With the rapid urbanization in China, there has been a gradual increase in the production of kitchen waste, which poses significant environmental challenges. High-temperature aerobic fermentation is an effective method for recycling kitchen waste. This study focuses on utilizing kitchen waste, wood chips, and compound microbial agents as the main raw materials for fermentation. Various parameters such as temperature, moisture content, and amount of compound microbial agent were selected to conduct experiments on the high-temperature stage of the aerobic fermentation process for kitchen waste. Through response surface optimization experiments, it was determined that the optimal conditions for achieving fast high-temperature fermentation of kitchen waste are as follows: temperature at 60°C, moisture content at 60%, and amount of compound microbial agent at 10%. The order of influence on the reduction rate of kitchen waste is found to be temperature followed by the amount of compound microbial agent and moisture content. These findings provide valuable insights into resource utilization strategies for managing kitchen waste.

摘要
随着我国城市化进程的加快,餐厨垃圾的产量也在逐渐增加,对环境产生了极大影响。将餐厨垃圾进行高温好氧发酵是其资源化利用的有效途径。本文主要发酵原料是餐厨垃圾、木屑和复合发酵菌剂,选取了发酵工艺的主要参数：温度、含水率和复合菌剂添加量进行试验,对餐厨垃圾高温好氧发酵工艺的高温阶段开展实验研究,通过响应曲面优化实验,得出餐厨垃圾高温快速发酵最优工艺条件为：温度 60℃、含水率 60%、菌剂添加量 10%,各因素影对餐厨垃圾减量率的影响顺序为温度、菌剂添加量、含水率。为餐厨垃圾资源化利用提供了依据。

INTRODUCTION
Kitchen waste primarily refers to the waste generated during household, hotel, school canteen, and food processing activities *(Huang et al., 2016)*. According to statistics, the United States, Japan, India, and South Korea discard between 624 – 3500×10^4 t/year of food waste, while developing countries such as Thailand, Vietnam, and Malaysia generate about 440 – 712×104 t/year of food waste. China alone produces an enormous amount of approximately 19,500×10^4 t/year of food waste (*Hafid et al., 2017*). In 2017, the United States produced over 41 million US tons of total food waste, of which only 6% were composted (*Thiel et al., 2021*). According to EUROSTAT, the annual municipal solid waste production per capita in the European Union is 481 kg *(Vakalis et al., 2017)*. The inadequate timely treatment of substantial amounts of food and kitchen waste not only leads to resource wastage but also imposes significant environmental burdens while hindering the establishment of zero-waste cities *(Uçkun et al, 2014*; *Melikoglu, 2020)*. Therefore, high-temperature aerobic fermentation represents an efficacious approach to the safe and sustainable recycling of kitchen waste *(Padoan et al., 2023; Liu, 2021).* Consequently, it holds immense potential for broad application prospects. Both domestic and international researchers have turned their attention towards investigating the speed, quality, and in-situ reduction of kitchen waste. *Yu et al. (2009)* discovered that precise temperature control at approximately 50°C can enhance the degradation of organic matter by microorganisms, thereby accelerating the fermentation process.

[1] *Yupeng Jiang, M.S. Stud; Aiping Shi, Prof; Feng Liang, M.S. Stud; Jun YanG, M.S. Stud*

Liu Minru et al.'s research demonstrated that collaborative fermentation of kitchen waste and other organic waste exhibits superior fermentation quality and efficiency compared to sole utilization of kitchen waste alone *(Liu et al., 2016)*. The addition of auxiliary materials (such as wood chips, straw, and bamboo charcoal) and the inoculation of microbial inoculants not only reduce the fermentation cycle but also enhance the fermentation quality *(Li et al., 2013; Khan et al., 2016).* Li Yun et al. investigated the impact of different auxiliary materials on kitchen waste fermentation and observed that their addition significantly reduced the fermentation cycle duration. Furthermore, sawdust incorporation effectively absorbed H_2S (*Li et al., 2017*). Ravindran et al. explored the effects of bamboo charcoal and biochar supplementation on aerobic kitchen waste fermentation, revealing that both additives extended the high-temperature phase, enhanced organic matter degradation rate, and improved overall fermentation efficiency *(Ravindran B. et al., 2022).* Wang Y et al. introduced mature fermentation products into kitchen waste to expedite degradation by leveraging their rich microbial content for rapid adaptation to the environment, thereby shortening the overall cycle *(Wang et al., 2022)*. Rosik et al.'s research demonstrated that adding 5–10% of compost biochar to kitchen waste significantly reduced the emissions in 70% of the detected volatile organic compounds *(Rosik et al., 2023)*.

Addressing the prevailing issues in aerobic fermentation of kitchen waste, this study focused on utilizing kitchen waste as the primary substrate and supplemented it with wood chips and a composite microbial agent. The key influencing factors, namely temperature, moisture content, and compound microbial agent were carefully selected for comparative experiments to develop an optimized high-temperature aerobic fermentation process. This research holds significant implications for enhancing urban ecological environments, improving the utilization efficiency of kitchen waste resources, establishing zero-waste cities, and promoting sustainable ecological development.

MATERIALS AND METHODS

Experimental equipment

The experimental setup employs a self-designed vertical fermenter, as depicted in the figure below, comprising four main components: the fermenter tank, heating system, stirring system, and ventilation system. The effective fermentation volume of the fermenter is 40 litres (D=360 mm, H=540 mm). The stirring system incorporates a double-layer three-blade propulsion agitator *(Lane, 2017)*. The insulation layer is composed of perlite particles *(Qian et al., 2009)*. Due to the compact size of the fermenter in this study, direct ventilation is achieved using a fan *(Feng et al., 2019).*

The overall experimental platform design is illustrated in Figure 1. Oxygen is a crucial prerequisite for high-temperature aerobic fermentation. Insufficient oxygen supply leads to increased proliferation of anaerobic bacteria in the fermentation product, resulting in anaerobic fermentation and the generation of abundant malodorous gases such as hydrogen sulfide *(Cummins, 2022)*. To ensure sufficient oxygen content during high-temperature aerobic fermentation, the air intake is connected via a silicone hose, with the other end of the hose linked to a 74.4 W small blower. The ventilation mode employed is interstitial-type ventilation (30 minutes of ventilation followed by 30 minutes without), with a ventilation rate set at 0.1 m^3 of air per cubic meter of fermentation per minute, thereby meeting the oxygen requirements for fermentation *(Shen et al., 2011).* Additionally, to maintain the fermentation temperature within a narrow fluctuation range around a specific value, a PID temperature controller and five-chip sensors are utilized. These sensors are strategically placed at the bottom and sides of the fermentation device, and their average reading determines the fermentation temperature of the experiment. Given that heating power reaches up to 4 kW, a solid-state relay is chosen as well as an added heat sink beneath it to ensure experimental safety.

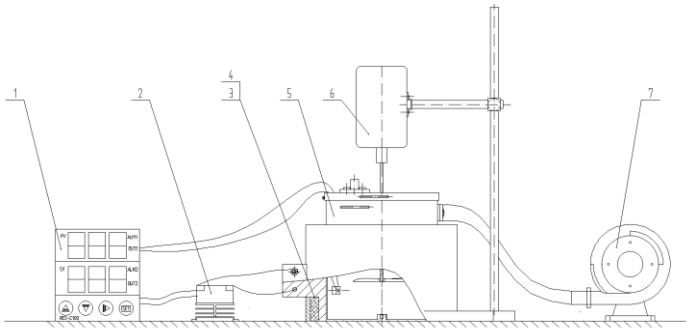

Fig. 1 - Fermentation platform diagram

1 - temperature controller; 2 - solid-state relay; 3 - heating ring; 4 - insulating layer; 5 - fermentation tank; 6 - motors and agitators; 7 - air blower

Experimental material

The primary experimental materials utilized in this study include kitchen waste, wood chips, and compound microbial agents *(Rong et al., 2021; Lanno et al., 2022)*. The kitchen waste was sourced from the school canteen and primarily consisted of vegetables, meat, and rice. Non-fermentable materials such as bone and plastic were meticulously removed and subsequently crushed into particles with a diameter of 5 mm. The wood chips employed were derived from pine wood with a water content below 9% and an approximate diameter ranging between 1-5 mm. For the experiment, a high temperature-resistant composite microbial agent comprising *Aspergillus usamii, Trichoderma longibrachiatum, Candida tropicalis, Aspergillus fumigatus, Chaetomium globosum, Paenibacillus curdlanolyticus, Bacillus thermoliquefaciens, Bacillus subtilis, Thermus thermophilus,* and *Alcaligenes faecalis* was used *(Zhu et al., 2018)*. These bacterial strains are known for their ability to withstand high temperatures up to 80℃ while maintaining excellent survival rates due to their remarkable thermal stability. Moreover, this microbial consortium effectively degrades organic matter present in kitchen waste under elevated temperatures. The fundamental physical and chemical properties of both kitchen waste and wood chips are summarized in Table 1.

Table 1

Basic physicochemical parameters of materials

Material	Moisture content/%	pH	Volatile solid/%	C/N
Kitchen waste	72.4	5.81	17.45	8.86
Wood chip	8.35	5.72	91.05	130.61

Single factor experiment

The effects of temperature, water content, and compound microbial agent on the substrate decrement rate were investigated through a single-factor experiment using a self-designed experimental fermenter.

- **Temperature**

The moisture content was adjusted to 60%, the amount of compound microbial agent was set at 10% of the fermentation substrate, and the fermenter temperature was controlled at 50°C, 55 °C, 60 °C, 65 °C, and 70 °C, respectively. The electric stirring speed was maintained at a constant rate of 15 r/min (stirring every half hour for 4~6 minutes), while intermittent ventilation was achieved using a small blower. Aerobic fermentation experiments were conducted at different temperatures for 24 hours *(Zhang et al., 2021).*

- **Moisture content**

The temperature was set at 60℃, with a composite microbial agent addition rate of 10%. The water content was adjusted to 45%, 50%, 55%, 60%, and 65% respectively while maintaining a rotational speed of 15 r/min (stirring every half hour for 4~6 minutes). Intermittent ventilation was implemented using small blowers, and the fermentation substrate underwent 24-hour aerobic fermentation under varying water contents.

- **Compound microbial agent**

The temperature was set at 60°C, while the moisture content was adjusted to 60%. The amount of compound microbial agent varied as follows: 5%, 10%, 15%, and 20% respectively *(Zhou et al., 2020)*. Electric stirring was conducted at a speed of 15 r/min, intermittent ventilation was achieved using a small blower, and the fermentation substrate underwent aerobic fermentation for 24 hours under different moisture contents *(Liu et al., 2022).*

Response optimization experimental design

The response surface method effectively analyses the interaction between multiple factors, addressing the limitations of single-factor experiments. It enhances and optimizes statistical and mathematical techniques, ultimately achieving the optimal response value through the establishment of a functional model. Following the principles of the BBD method in Design-Expert software, a three-factor, three-level response surface experiment was designed to investigate its impact on temperature, moisture content, compound microbial agent, and the 24-hour decrement rate of food waste aerobic fermentation as the response variable. The level values and codes for each factor are presented in Table 2.

Table 2

BBD experimental factors and levels

Level	Influencing factor		
	Fermentation temperature / ℃	Moisture content / %	compound microbial agent / %
-1	55	55	5
0	60	60	10
1	65	65	15

Detection method

- **Temperature detection**

The temperature is determined using a thermometer. By precisely measuring the positions of the material both near and far from the centre within the tank, the depth at each position is recorded once, resulting in four averaged temperature measurements for accurate determination of the material temperature. Additionally, ambient room temperature is also documented.

- **Moisture content detection**

The moisture content was determined using the drying method by standard CJ/T 313-2009. Firstly, the ceramic crucible was thoroughly cleaned and placed in an electric blast drying oven for 30 minutes to ensure complete dryness before being weighed. Subsequently, 5 g samples were carefully transferred into the prepared crucible and subjected to drying at a temperature of 110 ºC for 6 hours. After cooling for half an hour, the samples were weighed again and underwent additional cycles of drying (1 hour) followed by cooling and weighing until the weight difference between consecutive measurements was less than 1% of the sample volume. The moisture content of each sample was then calculated using the following formula:

$$W = \frac{M_2 - M_1}{M_1 - M} \times 100\% \quad (1)$$

where:

W is the moisture content of the sample, (%); M is the mass of the ceramic crucible, (g);

M_1 is the mass of the sample crucible after drying, (g);

M_2 is the mass of the crucible with the sample, (g).

- **Decrement rate**

According to the single-factor experiment, specific parameters including temperature, moisture content, and the quantity of compound microbial agent added were carefully controlled. The reduction rate of the fermentation substrate was determined by weighing at 2-hour intervals *(Li et al., 2013)*. Each experimental condition was replicated twice to ensure accuracy, and the average value was calculated accordingly. The reduction rate of fermentation substrate is expressed as the ratio between the decrease in material weight after fermentation and its initial weight.

The weight reduction rate is computed using the following formula:

$$Decrement\ rate = \frac{A + B - C}{B} \times 100\% \quad (2)$$

where:

A is the additive amount of compound microbial agent, (g); B is the mass of the fermentation substrate, (g); C is the mass of the material after fermentation, (g).

The experimental results and analysis

Single factor experimental results and analysis

- **Temperature**

Controlling temperature is a crucial factor in enhancing the efficiency of high-temperature and rapid fermentation of kitchen waste. To determine the optimal temperature for the aerobic fermentation process of kitchen waste, a 24-hour fermentation treatment was conducted. The change curve depicting the reduction rate of kitchen waste at different temperatures is illustrated in Figure 2.

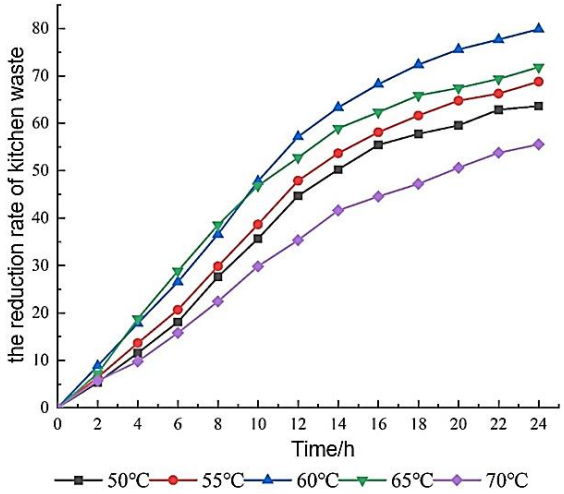

Fig. 2 - Reduction rate profiles of kitchen waste fermentation at varying temperatures

As depicted in the figure, the reduction rate of kitchen waste exhibited an upward trend after 24 hours of fermentation treatment, with the highest reduction rate recorded at 79.86% when maintained at a temperature of 60°C. Within the range of 50°C to 60°C, an increase in temperature resulted in an elevated reduction rate for kitchen waste. However, as the temperature continued to rise beyond this range, during the initial ten hours, there was a higher decrement rate below 65℃ compared to that observed at 60℃; however, during later stages, it became lower than that observed at 60°C. Even under conditions where a temperature as high as 70°C was applied, only a minimal reduction rate (55.56%) for kitchen waste was achieved due to potential adverse effects on microbial activity caused by exceeding their optimum operating range. Considering both reduction effectiveness and compound microbial agent activity levels, it was ultimately determined that maintaining a temperature of 60℃ would be most suitable for achieving optimal results in high-temperature aerobic fermentation processes.

- **Moisture content**

Moisture content plays two crucial roles in the fermentation process: it provides an optimal environment for microbial reproduction and metabolism and facilitates temperature regulation through water evaporation. To determine the optimal moisture content for high-temperature aerobic fermentation of kitchen waste, a 24-hour fermentation treatment was conducted. The reduction rate of kitchen waste under different moisture contents is depicted in Figure 3. As shown in the figure, a water content of 65% resulted in the lowest reduction rate (60.89%) among all treatments. This could be attributed to excessive water content occupying material gaps, creating anaerobic conditions that hinder aerobic bacteria activity and causing temperature loss, thereby affecting waste reduction efficiency. Reduction rates increased with increasing water content between 45% and 60%, reaching a maximum of 79.67% at a water content of 60%. Considering both reduction effectiveness and compound microbial agent activity, a final optimal moisture content of 60% was selected for the high-temperature aerobic fermentation process.

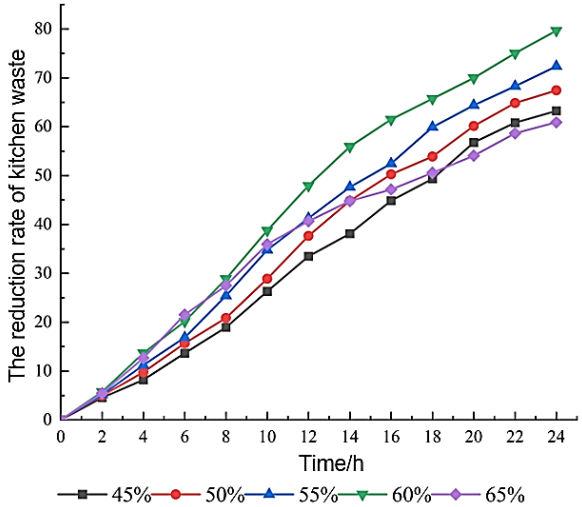

Fig. 3 - Reduction rate profiles of kitchen waste fermentation at varying moisture contents

- **Compound microbial agent**

The addition of a compound microbial agent during high-temperature rapid fermentation of kitchen waste can enhance its reduction efficiency. To determine the optimal dosage of bactericide in the high-temperature aerobic fermentation process, a 24-hour fermentation treatment was conducted on kitchen waste. The change curve depicting the reduction rate of kitchen waste under different dosages of compound microbial agents is presented in Figure 4. As observed from the figure, the reduction rate initially increased and then stabilized for each group. When using a 5% dosage of the compound microbial agent, the reduction rate was found to be minimal at only 62.29%. This could be attributed to insufficient microorganism population resulting in poor reduction efficiency. With an increase in compound microbial agent dosage from 10% to 20%, there was a gradual decrease in the reduction rate after 24 hours, with values recorded as follows: 79.34%, 77.84%, and 74.86% respectively. Considering both cost-effectiveness and reduction efficiency, an optimal inoculant addition amount of 10% was selected for the fermentation process.

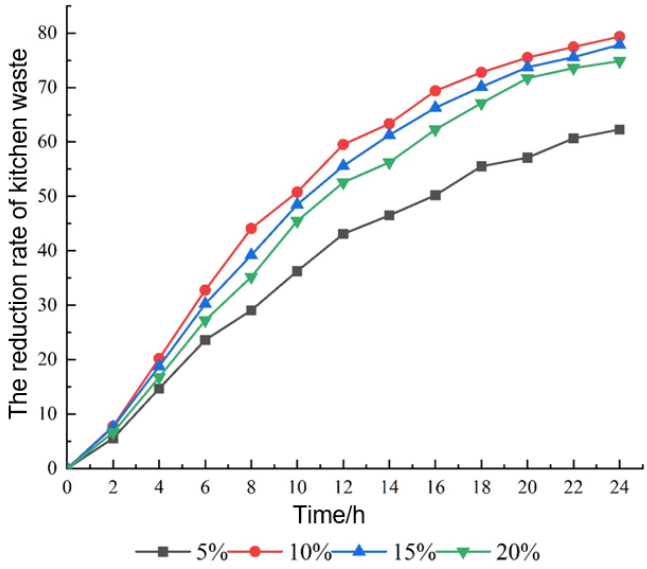

Fig. 4 - Reduction rate profiles of kitchen waste fermentation at varying compound microbial agent

RESULTS

Experimental results and analysis of response surface optimization

The three-factor and three-level experimental scheme was designed using Design-Expert 13 software based on the results of the single-factor experiments, and a mathematical regression model was constructed. The experimental design and results are presented in Table 3.

- **Regression model, equation, and analysis**

The regression analysis of the data presented in Table 3 was performed using Design-Expert 13 software, resulting in the derivation of a quadratic polynomial regression equation with the objective function being the reduction rate of kitchen waste after 24 hours of fermentation:

$$Y = 79.91 + 1.56A - 1.47B - 2.11C + 0.8675AB + 1.08AC - 0.1925BC - 8.73A^2 - 5.79B^2 - 7.56C^2 \quad (3)$$

where: Y is the reduction rate of kitchen waste, (%); A is the variable of temperature, (°C); B is the variable of moisture content, (%); C is the amount of compound microbial agent, (%).

The model underwent error statistical analysis and variance analysis, with the corresponding results presented in Table 4 and Table 5.

Table 3

Experimental scheme and results

Number No.	A / °C	B / %	C / %	Y / %
1	-1	-1	0	65.28
2	1	-1	0	68.29
3	-1	1	0	60.76
4	0	0	0	79.34
5	1	1	0	67.24

Number No.	A / °C	B / %	C / %	Y / %
6	-1	0	0	65.54
7	1	0	0	64.87
8	0	0	-1	79.67
9	-1	0	-1	60.23
10	1	0	0	63.86
11	0	-1	1	70.56
12	0	0	1	81.91
13	0	1	-1	67.84
14	0	-1	0	65.67
15	0	0	-1	78.98
16	0	1	1	62.18
17	0	0	1	79.67

Table 4

Error statistical analysis table

Statistical item	C.V.	R^2	Adjusted R^2	Predicted R^2	Adeq Precision
Value	1.95	0.9852	0.9663	0.8513	20.1796

Table 5

Regression model analysis of variance

Parameter	Sum of squares	Degree of freedom	Mean square	F	P	Significance (<0.05)
model	862.39	9	95.82	51.90	<0.0001	*
A	35.57	1	35.57	19.27	0.0032	*
B	17.35	1	17.35	9.40	0.0182	*
C	19.38	1	19.38	10.50	0.0143	*
AB	5.52	1	5.52	7.45	0.2423	
AC	4.62	1	4.62	2.50	0.1576	
BC	0.15	1	0.1482	0.08	0.7851	
A^2	320.86	1	320.86	173.80	<0.0001	*
B^2	141.25	1	141.25	76.51	<0.0001	*
C^2	260.61	1	240.61	130.34	<0.0001	*
Residual	12.92	7	1.85			
Lack of Fit	7.62	3	2.54	1.91	0.2687	
Pure Error	5.30	4	1.33			
Cor Total	875.31	16				

According to **F** of each factor in the variance analysis table, it can be seen that the order of the influence of each factor on the reduction rate of kitchen garbage is temperature, compound microbial agent, and moisture content.

- **Regression model, equation, and analysis**

The software generates contour maps and three-dimensional response surfaces based on the analysis data, vividly illustrating the pairwise interaction of various factors on the response value. Moreover, it identifies extreme value points in the model and determines corresponding optimal process parameters.

The contours and three-dimensional response surfaces of the interaction between temperature and moisture content on the reduction rate of kitchen waste are depicted in Figure 5. As illustrated in the figure, the interaction between temperature and moisture content exhibits an initial increase followed by a subsequent decrease in kitchen waste reduction. Under constant moisture content, the reduction rate of kitchen waste initially rises with increasing temperature but then declines due to potential deactivation or reduced activity of microbial agents at excessive temperatures, leading to diminished reduction efficacy. Similarly, at a fixed temperature, the influence of moisture content on kitchen waste reduction also follows a pattern of initial increase followed by eventual decrease. Based on the peak position shown in the figure, when keeping compound microbial agents, optimal conditions for achieving maximum reduction rate of kitchen waste are observed at 60 °C temperature and 60% water content.

The contours and three-dimensional response surfaces of the temperature-compound microbial agents' interaction on the reduction rate of kitchen waste are depicted in Figure 6. It is evident from the figure that the interaction between temperature and microbial agents exhibits an initial increase followed by a subsequent decrease in kitchen waste reduction. At constant temperature, the addition of microbial agents leads to an enhanced reduction rate of kitchen waste; however, when the amount of microbial agents exceeds 11%, a gradual decline in reduction rate is observed, possibly due to excessive bactericide concentration inhibiting growth and impeding kitchen waste reduction efficacy. Under identical amounts of microbial agents, the reduction effect initially increases with rising temperatures but eventually diminishes. Based on pole position analysis, at equivalent moisture content levels, optimal reductions in kitchen waste occur at 60℃ with the compound microbial agent of 10%.

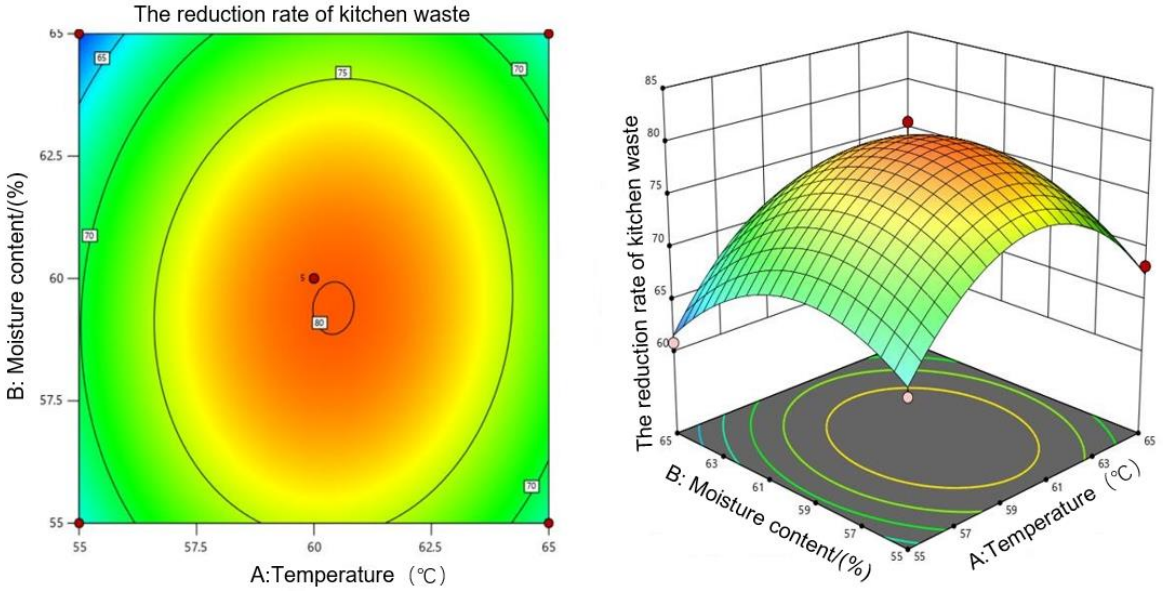

Fig. 5 -The contour and 3D response surface of the temperature-moisture content interaction

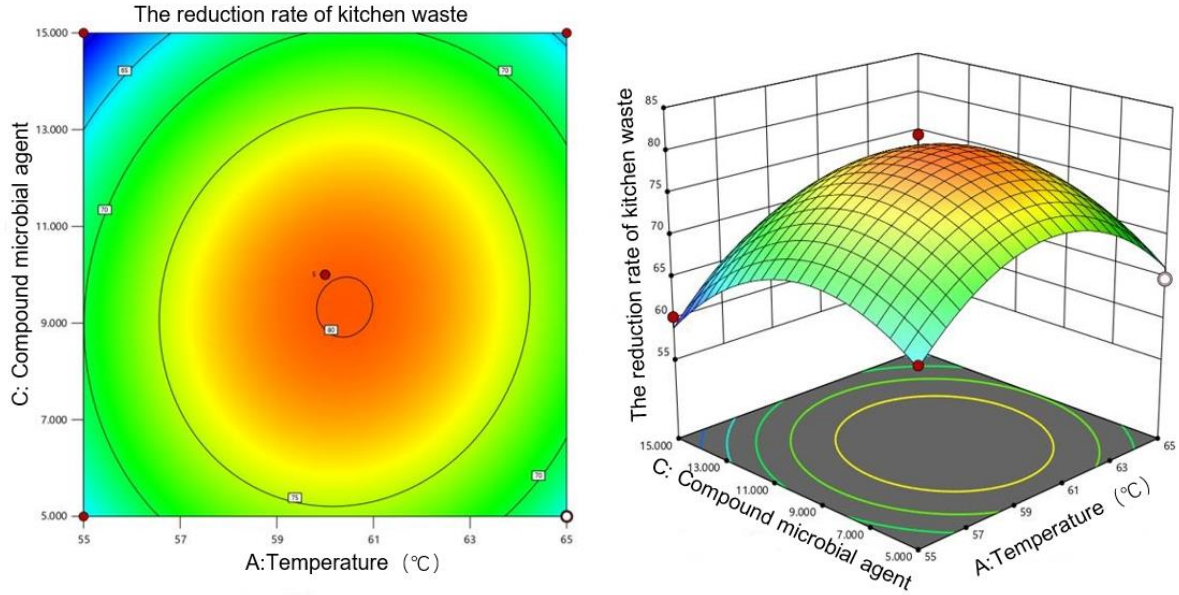

Fig. 6 -The contour and 3D response surface of the temperature-microbial agent interaction

The contours and three-dimensional response surfaces illustrating the interaction between moisture content and bactericide addition on the reduction rate of kitchen waste are depicted in Figure 7. It is evident from the figure that the reduction of kitchen waste initially increases and then decreases with the interaction between moisture content and the amount of bactericide added. When the temperature remains constant, under a fixed dosage of bactericide, the reduction rate of kitchen waste exhibits an initial increase followed by a decrease as material moisture content increases.

Similarly, for a given moisture content, altering the amount of bactericide also follows an initial increase, followed by a decrease in its impact on the decrement rate. Based on analysis from Figure 7, it can be concluded that under identical temperature conditions, optimal conditions for achieving maximum reduction rate of kitchen waste are observed at 10% moisture content and 10% microbial agent addition.

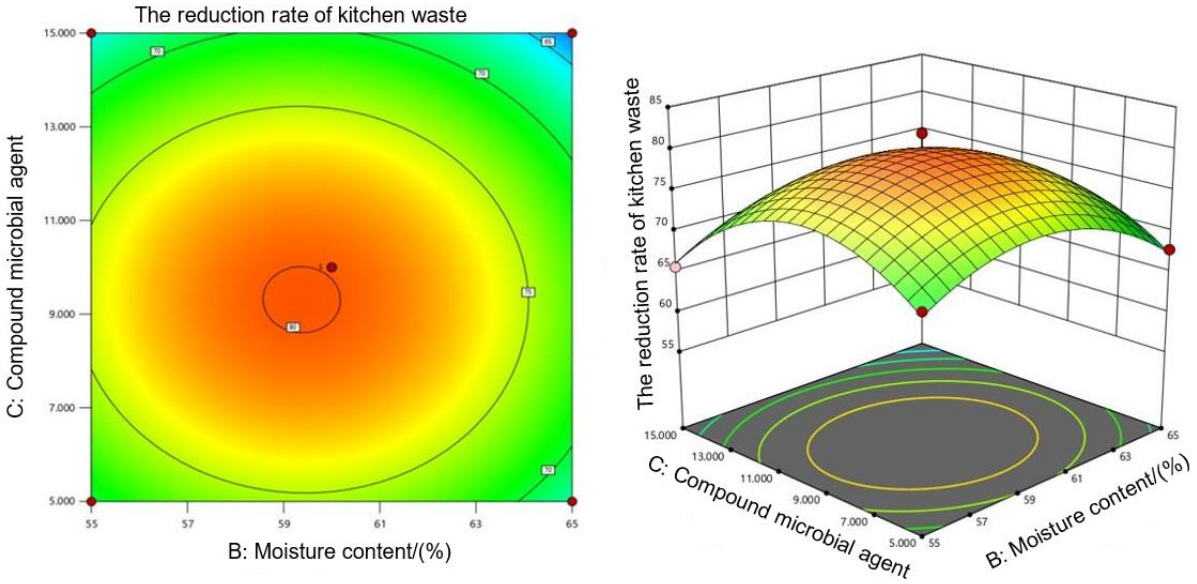

Fig. 7 -The contour and 3D response surface of the microbial agent-moisture content interaction

- **Optimal combination of optimization and verification testing**

According to the Design-Expert software, a combination optimization approach was employed to determine the range of influencing factors and select the maximum reduction rate of kitchen waste as the response value. Consequently, optimal process conditions for high-temperature rapid fermentation of kitchen waste were obtained. The main parameters included a temperature of 60.38℃, material moisture content of 59.40%, and microbial agent amount of 9.83%. The predicted reduction rate of kitchen waste after 24 hours of high-temperature rapid fermentation was found to be 80.20%. Considering practical constraints and limitations in process parameters, the optimal conditions for high-temperature rapid fermentation were determined as follows: a temperature of 60℃, moisture content at 60%, and compound microbial agent addition amount at 10%. To validate the reliability and validity of the response surface model, three experiments were conducted based on these process conditions. The observed decrement rates in these experiments were respectively found to be 79.98%, 80.12%, and 80.08%, with an average value close to that predicted by the model (80.06%). This indicates that the model can effectively predict kitchen waste reduction after high-temperature rapid fermentation and confirms that reliable process conditions have been obtained.

CONCLUSIONS

The present study investigates the impact of temperature, moisture content, and bacterial quantity on the reduction of kitchen waste, followed by the optimization of a high-temperature rapid fermentation process for kitchen waste. The following conclusions can be drawn from this research:

The optimal process conditions and their influencing sequence are as follows, based on the experimental results: a temperature of 60 °C, an additional amount of compound microbial agent at 10%, and a water content of 60%.

Verification experiment results demonstrate that the actual reduction rate of kitchen waste after 24-hour rapid fermentation at high temperatures is consistent with the predicted value obtained through response surface analysis. This indicates that the process conditions optimized using response surface methodology are accurate and reliable.

ACKNOWLEDGEMENT

This work was supported by the National Key Research and Development Program of China (2019YFD1002500).

REFERENCES

[1] Cummins E.M., (2022). *A Whole Systems Evaluation of Food Waste Disposal at Villanova University Utilizing Life Cycle Assessment,* MSc dissertation, Villanova University, College of Engineering, Pennsylvania, United States.

[2] Feng L., Gao T., Zhen X., (2019). Influence Mechanism of Micro-Oxygenation Treatment on Dry Fermentation of Food Waste. *Journal of Biobased Materials and Bioenergy*, 13(1): 149-154.

[3] Hafid H. S., Rahman N. A. A., Shah U. K. M., et al., (2017). Feasibility of using kitchen waste as future substrate for bioethanol production: A review. *Renewable and Sustainable Energy Reviews*, 74: 671-686.

[4] Huang X.Y., Zhang J.T., Wang F., He W.Z., Li G.M., (2016). Research progress in resource utilization of kitchen waste and its process pollution control, *Chemical Industry, and Engineering Progress*, 35(9): 2945-2951.

[5] Lane G.L., (2017). Improving the accuracy of CFD predictions of turbulence in a tank stirred by a hydrofoil impeller. *Chemical Engineering Science*, 169: 188-211.

[6] Lanno M., Klavin M., Purmalis O., Shanskiy M., Kisand A., Kriipsalu M., (2022). Properties of Humic Substances in Composts Comprised of Different Organic Source Material. *Agriculture*, 12, 1797.

[7] Li Y., Yuan J., Li G.X. et al., (2017). Use of additive to control odors and promote the maturity of municipal kitchen waste during aerobic composting (辅料添加对厨余垃圾快速堆肥腐熟度和臭气排放的影响), *China Environmental Science*, 37(3): 1031-1039.

[8] Li Z., Lu H., Ren L., et al., (2013). Experimental and modeling approaches for food waste composting: A review. *Chemosphere*, 93(7): 1247-1257.

[9] Liu D., Ma X., Huang J., et al., (2022). Enhancing the fermentation of acidified food waste using a self-formulated thermophilic and acid-resistant bacterial agent, *Journal of Environmental Chemical Engineering*, 10(3): 107350.

[10] Liu J.H., (2021). *Characteristics and influencing mechanism of heavy metals form transformation during high-temperature aerobic rapid fermentation of food waste (餐厨垃圾高温好氧快速发酵过程中重金属形态转化特征及影响机制)*, MSc dissertation, East China Normal University.

[11] Khan N., Clark I., Sánchez-Monedero M. A., et al., (2016). Physical and chemical properties of biochars co-composted with biowastes and incubated with a chicken litter compost. *Chemosphere*, 142: 14-23.

[12] Melikoglu M., (2020). Reutilisation of food wastes for generating fuels and value added products: a global review. *Environmental Technology & Innovation,* 19:101040.

[13] Padoan E., Montoneri E., Baglieri A., Francavilla M., Negre M., (2023). Mild chemical treatment of unsorted urban food wastes. *Molecules*, 28, 7670.

[14] Prepilkova V., Ponist J., Schwarz M., Samesova D., (2023). Challenges and opportunities for kitchen waste treatment—a review. *Environmental Reviews*, 10.1139/er-2023-0005.

[15] Qian B.Z., Zhu J.F., (2009). Technology Progress of Thermal Insulation Materials of Building Energy Efficiency(建筑节能保温材料技术进展), *Energy-saving Technology & Measure*, 37(02):56-60.

[16] Ravindran B., Karmegam N., Awasthi M.K., et al., (2022). Valorization of food waste and poultry manure through co-composting amending saw dust, biochar, and mineral salts for value-added compost production. *Bioresource Technology*, 346: 126442.

[17] Rong L, Yu F, Huang Y, et al., (2021). An intelligently controlled tilting drum type kitchen waste in-situ processing device. *Journal of Physics: Conference Series*, 2029(1): 012069.

[18] Rosik J., Lyczko J., Marzec L., Stegenta-Dąbrowska S., (2023). Application of Composts' Biochar as Potential Sorbent to Reduce VOCs Emission during Kitchen Waste Storage. *Materials*, 16, 6413.

[19] Shen Y.J., Ren L.M., Li G.X., Chen T.B., Guo R., (2011). Influence of aeration on CH_4, N_2O, and NH_3 emissions during aerobic composting of a chicken manure and high C/N waste mixture. *Waste management (New York, N.Y.)*, 31(1).

[20] Thiel C.L., Park S., Musicus A.A., Agins J., Gan J., Held, J., et al., (2021). Waste generation and carbon emissions of a hospital kitchen in the US: potential for waste diversion and carbon reductions. *PLoS One.* 16:e0247616.

[21] Uçkun Kiran E, Trzcinski A.P., Ng W.J., et al., (2014). Bioconversion of food waste to energy: A review. *Fuel*, 134: 389-399.

[22] Vakalis S., Sotiropoulos A., Moustakas K., Malamis D., Vekkos K., Baratieri M., (2017). Thermochemical valorization and characterization of household biowaste. *Journal of Environmental Management*, 203, pp. 648-654.
[23] Wan L.B., Wang X.T., Cong C., Li J.B., et al., (2020). Effect of inoculating microorganisms in chicken manure composting with maize straw. *Bioresource Technology,* 301, 122730.
[24] Wang F., Chen C., Fu D., Singh R.P., (2024). Effect of reactor temperature and feeding ratio on fed-batch composting of household food waste and green wastes. *Biomass Bioenergy*, 18, 107040.
[25] Wang H., Yao D., Xu J., Liu X., Sheng L., (2021). Investigation of technology for composting mixed deer manure and straw. *Environmental Science and Pollution Research,* 28 (33) pp. 45805-45825.
[26] Wang S.P., Gao Y., Sun Z.Y., Peng X.Y., Xie C.Y., Tang Y.Q., (2022). Thermophilic semi-continuous composting of kitchen waste: performance evaluation and microbial community characteristics *Bioresource Technology*, 363, 127952.
[27] Wang Y., Tang Y., Yuan Z., (2022). Improving food waste composting efficiency with mature compost addition. *Bioresource Technology*, 349: 126830.
[28] Yu H., Huang G.H., (2009). Effects of sodium acetate as a pH control amendment on the composting of food waste. *Bioresource Technology*, 100(6): 2005-2011.
[29] Zhang B., Fan F., Guo C., et al., (2021). Evaluation of Maturity and Odor Emissions in the Process of Combined Composting of Kitchen Waste and Garden Waste. *Applied Sciences*, 11(12): 5500.
[30] Zhou X., Yang J., Xu S., et al., (2020). Rapid in-situ composting of household food waste. *Process Safety and Environmental Protection*, 141: 259-266.
[31] Zhu L., Zhen C.L., Gao F., et al., (2018). Characteristic Analysis of Microbial Diversity in Crud Fertilizer from Compost of Rice Straw (水稻秸秆堆肥发酵粗制肥料中微生物多样性研究). *Transactions of the Chinese Society for Agricultural Machinery*, 49(07):228-234.

EFFECT OF NOZZLE ANGLE OF PLANT PROTECTION UNMANNED AERIAL VEHICLE ON DROPLET DEPOSITION DISTRIBUTION

/

植保无人机喷头角度对雾滴沉积分布的影响

Zhihao BIAN [1,3], Yubin LAN *[1,2,3], Meng WANG [1,3], Changfeng SHAN [1,3], Haozheng GU [1,3], Jingang HAN [1,3]

[1] School of Agricultural Engineering and Food Science, Shandong University of Technology, Zibo / China;

[2] College of Electronic Engineering, College of Artificial Intelligence, South China Agricultural University, Guangzhou / China;

[3] National Key Laboratory of Green Pesticide, Guangzhou / China;

Tel: 8615689316561; E-mail: ylan@sdut.edu.cn

DOI: https://doi.org/10.35633/inmateh-72-20

Keywords: *UAV, flat-fan nozzle, spraying deposition test, droplet distribution*

ABSTRACT

During the field application of pesticides by plant protection UAV, due to the interference of meteorological factors or operating parameters, the deposition effect of droplets is poor. In order to explore the impact of the nozzle angle of plant protection UAV on droplet deposition distribution, this article is based on field experiments and collects data on different flight speeds (1, 3, 5 m/s) and nozzle angles (±60°, ±45°, ±30°, 0°), and performs variance analysis and regression analysis on the test results. The results showed that adjusting the nozzle angle had a significant effect on the amount of droplet deposition and deposition uniformity. Compared with 0°, the nozzle angle of -30° increased the amount of deposition by 76.94% and 61.04% at flight speeds of 1.2 m/s and 3 m/s, respectively. The flight speed had a significant effect on the amount of droplet deposition, and the increase in flight speed decreased the amount of droplet deposition by 55.97%-77.06% and had no significant effect on the uniformity of droplet deposition. This study provides a reference for improving the droplet deposition effect of plant protection UAV field pesticide application operations.

摘要

植保无人机在田间施药过程中，由于气象因素或作业参数的干扰，导致雾滴的沉积效果较差。为了探究植保无人机的喷头角度对雾滴沉积分布的影响，本文基于田间试验，采集不同飞行速度(1、3、5m/s)与喷头角度(±60°、±45°、±30°、0°)下的雾滴沉积分布情况，并对试验结果进行方差分析和回归分析。结果表明，调节喷头角度对雾滴沉积量与沉积均匀性影响显著。与0°相比，喷头角度-30°在飞行速度1.2m/s与3m/s下的沉积量分别增加了76.94%与61.04%。飞行速度对雾滴沉积量影响显著，飞行速度增加雾滴沉积量降低了55.97%-77.06%，并且对雾滴沉积均匀性影响不显著。该研究对提高植保无人机田间施药作业的雾滴沉积效果提供参考。

INTRODUCTION

In recent years, the rapid development of plant protection UAV aerial pesticide application operations has received widespread attention *(Wang et al., 2023)*. As a new method of plant protection operations, plant protection UAV pesticide application has the advantages of high operating efficiency, low operating costs, and small geographical restrictions *(Wang et al., 2020)*. However, due to interference from environmental factors or operating parameters during actual field spraying operations, the droplet deposition distribution is affected, reducing the spray quality and the control effect of pests and diseases *(Sun et al., 2021).*

The factors that affect the droplet deposition distribution of plant protection UAVs mainly include droplet size, drone operating parameters (flight height, flight speed), spraying amount, and rotor downwash wind field (*Xiao et al., 2019*). Relevant studies have shown that the smaller the droplet size, the greater the amount of liquid deposited per unit area, and the better the distribution uniformity and droplet penetration (*Li et al., 2018a*). During the field spraying operation of plant protection UAVs, the flight operation parameters will have a significant impact on the deposition amount of the chemical solution.

[1] *Zhihao BIAN, MS candidate, Student;* *[2] *Yubin LAN, PhD, Professor;* [3] *Meng WANG, MS candidate, Student;*

[4] *Changfeng SHAN, PhD candidate, Student;* [5] *Haozheng Gu, MS candidate, Student;* [6] *Jingang HAN, MS candidate, Student;*

The appropriate flight height and flight speed are reduced, and the droplet deposition amount increases (*Chen et al., 2016; Wang et al., 2017*). Different spraying amounts have significant effects on the deposition and efficacy of the liquid. Appropriately increasing the amount of spraying will increase the amount of deposition, but excessive amounts will lead to an increase in the residual amount of the liquid (*Xin et al., 2018*). The rotor movement of plant protection UAV will produce a downwash wind field, which will enhance the amount and penetration of droplet deposition, and the distribution and strength of the wind field will affect the droplet deposition distribution characteristics (*Chen et al., 2017*). During the actual field application process, the downwash wind field of the plant protection UAV will produce canopy vortices on the crops, and the canopy vortices will promote the deposition and distribution of droplets *(Li et al., 2018b*). The nozzle type and structure can also affect the distribution of droplet deposition. The hydrodynamic ultrasonic atomizing nozzle has a great advantage in generating small droplet sizes and performs well in deposition effect (*Song et al., 2023*). Increasing the conical airflow field on the outside of the nozzle can accelerate the initial speed of droplet movement and improve the effect of droplet deposition (*Liu et al., 2023*). In addition to the above factors, adding adjuvant to agricultural spray on the deposited spray quality is also significant (*Milanowski et al., 2023*).

Regarding the study of how changing the nozzle angle affects the droplet deposition distribution, some scholars conducted spray experiments on the amount of liquid deposited at different nozzle angles of a boom sprayer. The results found that the horizontal direction will increase when the nozzle angle is consistent with the forward direction of the spray boom. When the spraying amount increases, the deposition amount and penetration of the liquid in the vertical direction are enhanced, and the optimal nozzle angle is 30° (*Song et al., 2006*). An experiment on the influence of nozzle angle on droplet drift was carried out under wind tunnel conditions. It was found that when the wind speed increased from 0m/s to 5.92m/s, the nozzle angle in the windward direction increased, the amount of deposition increased, and the droplet drift distance decreased by 33.7% (*Chen et al., 2019*). Taking the downwind direction as the positive direction of the nozzle angle and the nozzle angle 0° as a comparison reference, when the wind speed is 3m/s, the nozzle angles of 15° and -15° can reduce drift, the drift distance is reduced, and -15° has a better deposition effect (*Ding et al., 2019*). Through the study of the downwash wind field of plant protection UAVs, it was found that the canopy vortex and droplet deposition generated during pesticide application at different flight speeds are shifted in position. The canopy vortex area is shifted backward. Adjusting the angle of the centrifugal nozzle can increase the amount of droplet. Regarding droplet deposition amount and penetration, the number of droplets deposited on the leaves increased by 21.58%, and the number of droplets deposited on the back of the leaves increased by 66.05% (*Tian et al., 2022*). At present, there are few studies on the influence of adjusting the angle of the nozzle on the droplet deposition and distribution characteristics, and the relevant research is not comprehensive enough. This paper takes the commonly used fan-shaped nozzles of plant protection UAVs as the research object to explore the droplet deposition distribution characteristics under the influence of different flight speeds and nozzle angles and obtains the regression equation of nozzle angle, flight speed, and droplet deposition. It provides a theoretical reference for increasing spray droplet deposition in field pesticide application operations.

MATERIALS AND METHODS

Equipment

This experiment uses a self-designed X4 four-rotor plant protection UAV. Solidworks is used for 3D structural design. The entire body is made of carbon fiber material. The actual object of the drone are shown in Figure 1. The plant protection UAV flight control system uses the DJI A3 series, including the main control module, power module, LED module, GPS module, and wires. The control system adopts the DJI Lightbridge series, including an image transmission module and remote control. The rotor and motor adopt the DJI E5000 series, with a single-axis pulling force of 7kg, a maximum continuous current of 80A, and a 12S power supply. The weight of the whole machine is 8.5kg, the wheelbase is 1431mm, the arms can be folded laterally, and the drug loading capacity is 10L.

The spray system consists of a spray solution tank, a brushless water pump, a nozzle angle adjustment structure, pipelines, a nozzle body, a nozzle head, etc. The nozzle is a fan-shaped nozzle with 4 nozzles, a nozzle spacing of 1m, the nozzle number is SX110015VS, the spray pressure is 0.3MPa, and the working flow rate is 2.44L/min.

Fig. 1 - Plant protection UAV actual object

The structure and angle adjustment diagram of the nozzle angle control unit is shown in figure 2. The structural parts of the control unit are obtained by 3D printing. Two servos are assembled on the structural parts and control the moment of inertia in two directions. The structural unit is fixed directly below the motor. In this test, the nozzle angle adjustment is consistent with the direction of the flight path. The forward direction of the aircraft body is the negative direction of the angle, and the nozzle angles of the four control units are consistent.

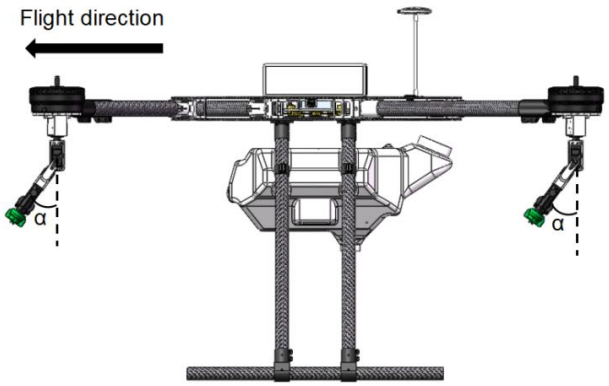

Fig. 2 - Nozzle angle adjustment structural unit and assembly

Figure 3 shows the nozzle angle adjustment controlling system. The controller adopted the STM32F103C8T6 microcontroller. The IO port was programmed to output PWM signals. The PWM signals with different duty cycles controlled the rotation of the servo to control the nozzle angle. In this test, the nozzle angles choosed ±60°, ±45°, ±30°, and 0°. And 0° was used as the reference control group for analysis and comparison. The nozzle angle adjusted by the controlling system is measured by the deLi DL294001 angle measuring instrument, and the program was modified to reduce the angle error.

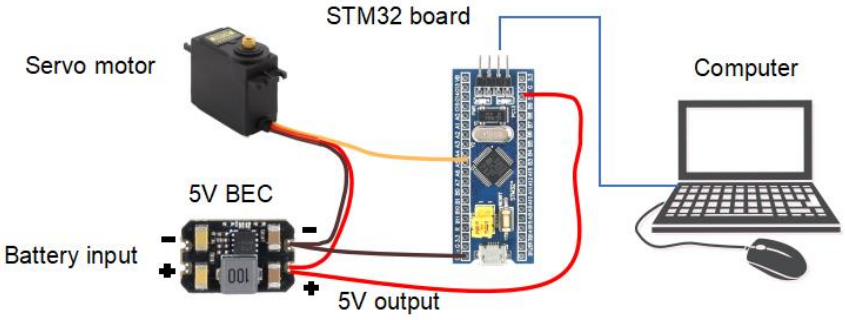

Fig. 3 - Nozzle angle adjustment control system

Meteorological parameter monitoring uses the American Kestrella 5500 wind speed meteorological instrument, which can measure five meteorological parameters: wind speed, wind direction, temperature, humidity, and atmospheric pressure.

Method

The experiments were carried out at the Shandong University of Technology in Zibo City, Shandong Province and between 10:00-16:00. The environmental temperature was about 10°C and the environmental humidity was about 30%. The wind speed was within 2 m/s. The liquid volume of each test used Allura Red solution with a ratio of 5g/L, and a white paper card was used as a droplet collection card. The card size is 60mm × 30mm, and the card sampling height is 0.3m. The card is fixed horizontally to the plastic water pipe with a clip.

In this test, the effective spraying swath adopts the 50% effective deposition determination method. According to ASAE standard S341.3, the sampling point positions on both sides of the aircraft route that can reach 50% of the maximum deposition amount of the droplet collection zone are regarded as the effective spraying swath area. The distance between the starting and ending points is regarded as the effective spraying swath at this working height. According to the test, it could be seen that the effective spraying swath under the flight height of 4m was 2-3m.

Figure 4 shows the layout of the test site. The plant protection UAV route was located on the center line of the test site. The test was arranged with three droplet collection belts (the distance between collection belt A and sampling belt B was 5m, and the distance between collection belt B and collection belt C was 15m). There were 16 sampling points arranged in each collection belt, and the sampling points were numbered X-1~X-16 from left to right (X represented the labels of the three collection belts: A, B, and C).

The droplet sampling zone was divided into a deposition area and two drift areas. The width of the deposition area was set to 5m. The width of the drift area was also set to 5m. The intervals between each sampling point were 1m.

This test aims to explore the droplet deposition distribution rules of plant protection UAV's nozzle angles at different flight speeds. The nozzle angles were ±60°, ±45°, ±30°, and 0°. Under the flight speed of 1 m/s, the droplets would be too large to use. After the test, the flight speeds were 1.2, and 3 m/s, the flight height was 4m as the operating height. After each group of tests was completed, waited until the droplets on the collection card were completely dry, collected them according to the serial numbers and put them into corresponding sealed bags respectively.

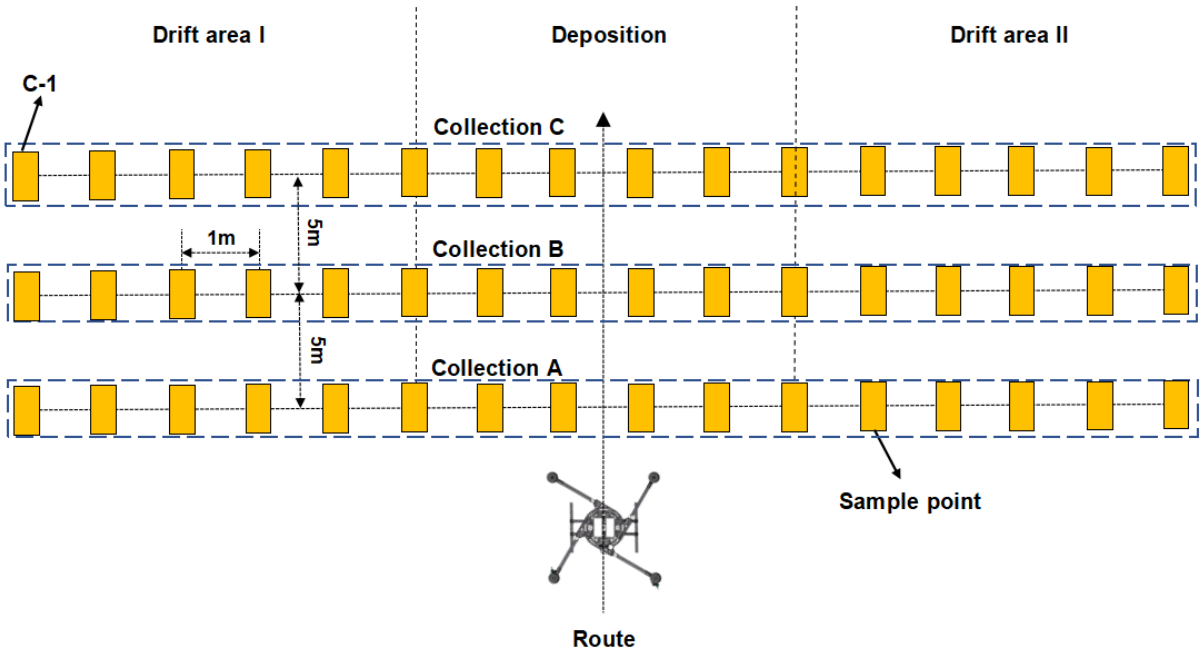

Fig. 4 - Deposition test

Data processing and analysis

Figure 5 shows the results of scanning paper cards and droplet deposition analysis. The paper card was scanned with a scanner. The scanned image was used through the image analysing software DepositScan to obtain parameters such as droplet size, deposition amount, deposition density, and coverage rate of each paper card, and then the data is analyzed.

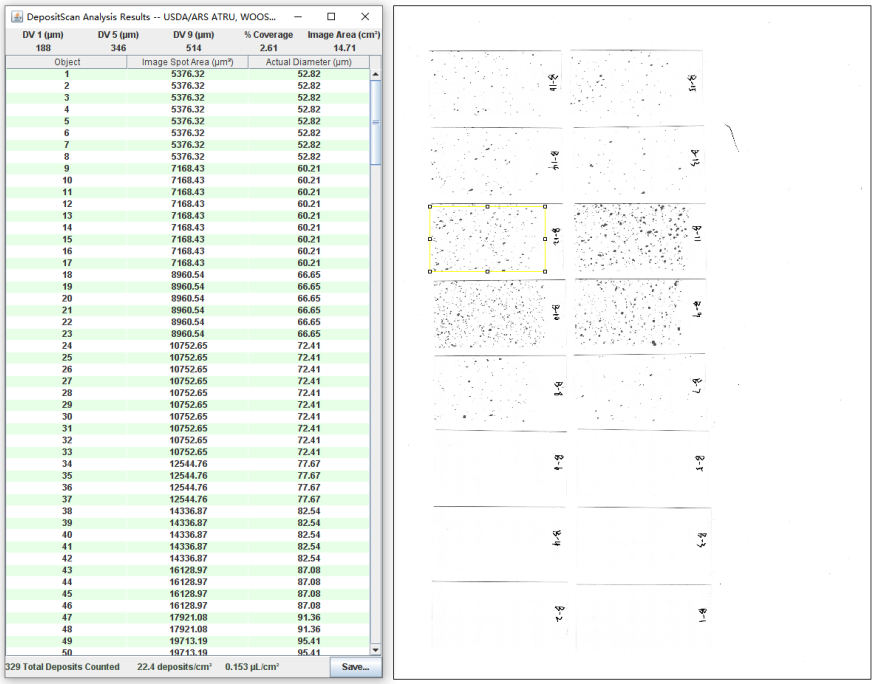

Fig. 5 - Paper card scanning and data analysis

In order to measure the uniformity of droplet deposition distribution between each collection point, this article uses the coefficient of variation (CV) for calculation and analysis. The calculation method of the coefficient of variation (CV) is as follows:

$$CV = \frac{S}{X} \times 100\% \quad (1)$$

$$S = \sqrt{\sum_{i=1}^{n} (X_i - \overline{X})^2 / (n-1)} \quad (2)$$

Where, S is the standard deviation of the samples collected in the same test group; X_i is the deposition rate of each collection point, μL/cm²; $\overline{X}$ is the mean value of deposition rate in each test group, μL/cm²; n is the number of collection points in each test group.

To analyze the droplet deposition distribution of plant protection UAV's nozzle angles at different flight speeds, the experimental data were analyzed using multiple linear stepwise regression methods using SPSS V25.0 software for variance analysis and regression analysis to establish the relationship between droplet deposition distribution and different nozzle angles. The regression model with flight speed was used to test the fitting degree of the regression model and the sample data. The test results were charted using OriginPro 2021 software.

RESULTS

Droplet deposition distribution

Figures 6 and 7 show the distribution of droplet deposition at flight speeds of 1.2 m/s and 3 m/s by adjusting the nozzle angles for the spraying test respectively.

From the distribution of droplet deposition in Figure 6, it can be seen that the trend of droplet deposition under each nozzle angles were basically the same, and the droplet deposition first increased and then decreased. With the increase of the nozzle angle, the droplet deposition increased, then decreased, and then increased. Among them, the amount of droplet deposition at -30° and 60° was larger than that at 0°, and the amount of deposition at -30° was the largest. The droplets were mainly deposited in sampling points from 6# to 10#, but -60°, -45°, and 0° were slightly shifted to the left area, which might be due to the lateral wind that caused the droplets to be shifted to the left area during spraying by the plant protection UAV.

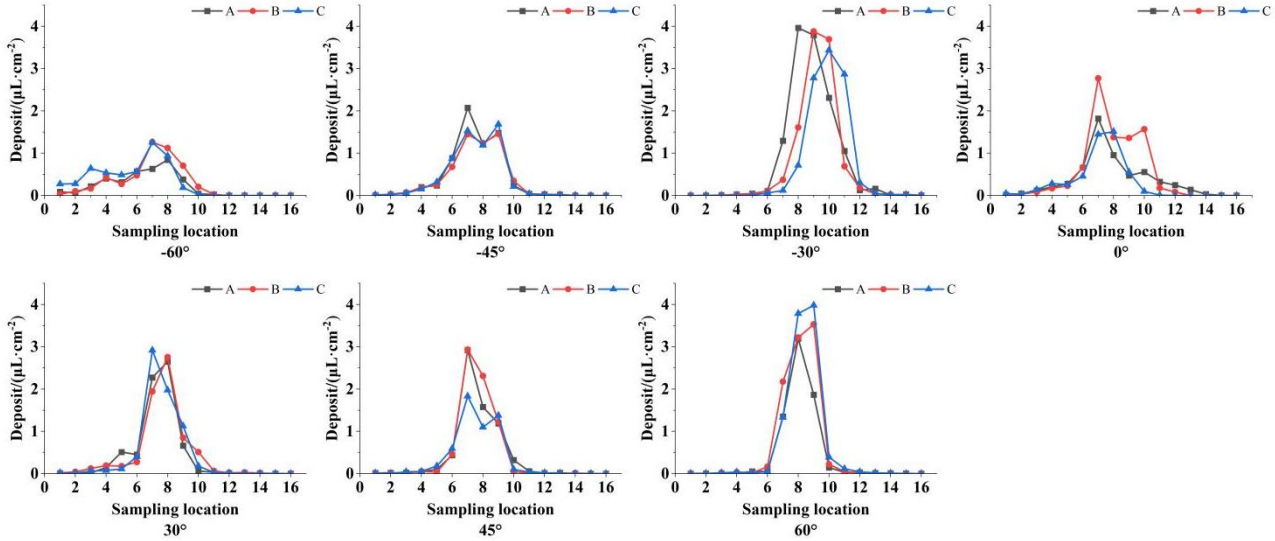

Fig. 6 - Droplet deposition at flight speed of 1.2 m/s

From the distribution of droplet deposition in Figure 7, it can be seen that the trend of droplet deposition under each nozzle angles at a flight speed of 3 m/s were basically the same as that at 1.2 m/s, and the amount of droplet deposition increased first and then decreased. With the increase of the nozzle angle, the amount of droplet deposition first increased and then decreased before increasing. Among them, the amount of droplet deposition at -30°, 45°, and 60° was slightly larger than that at 0°, and the difference was small. The droplets were mainly deposited in sampling points from 6# to 10#, but the deposition at -45° was slightly shifted to the side area, which might be caused by the course shifting to the right area during the application of the plant protection drone.

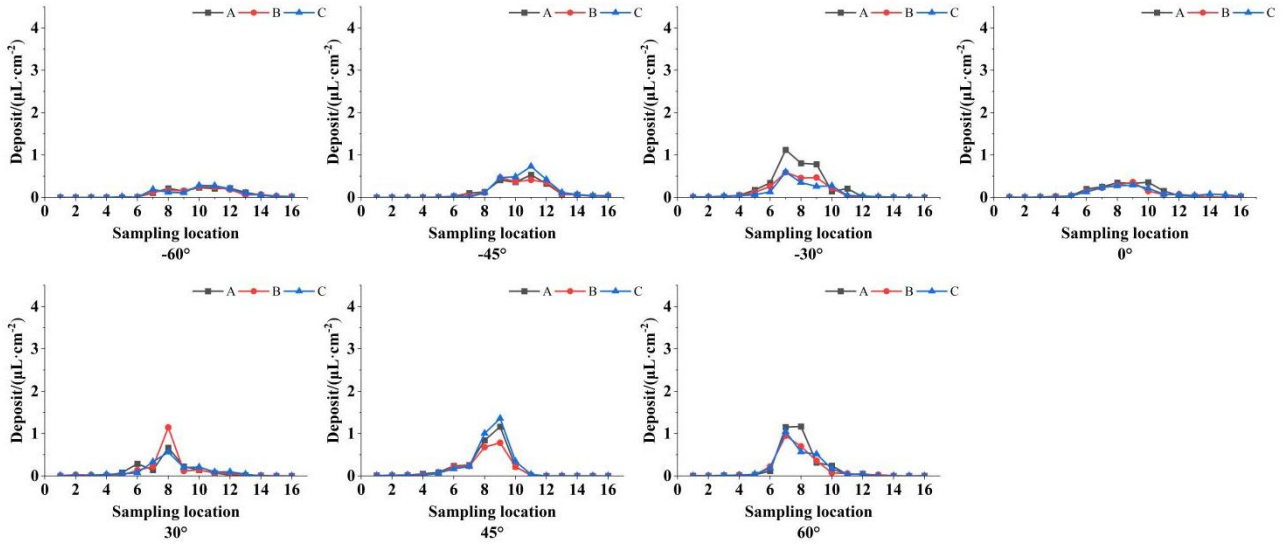

Fig. 7 - Droplet deposition at flight speed of 3 m/s

Figure 8 compares the total droplet deposition amount for each nozzle angle at different flight speeds. The total amount of droplet deposition is obtained by averaging the total deposition for each row of collection belts A, B and C. It can be seen from the results that at a flight speed of 1.2 m/s, there is a large difference in the total amount of droplet deposition for each nozzle angle. Taking the nozzle angle of 0° as a comparison, the total amount of droplet deposition for -30° and 60° increased by 76.94% and 35.28%, respectively. At a flight speed of 3 m/s, the difference in the total amount of droplet deposition for each nozzle angle is smaller, and the total droplet deposition decreases. Taking the nozzle angle 0° as a comparison, the total amount of droplet deposition increased by 61.04%, 74.4%, and 70.32% for -30°, 45° and 60°, respectively.

From the analysis of the results of the distribution of droplet deposition, it can be seen that the speed of flight is increased and the droplet deposition is reduced by about 55.97%-77.06%. Changing the nozzle angle changes the initial position of droplet deposition. When the nozzle angle is -45° and -60°, we found that the droplets had a “rolling-up effect” during flight, causing in some of the droplets being deposited on the fuselage surface. When the plant protection UAV flied forward, there was an attitude angle between the drone and the horizontal plane, and the droplets would produce backward inertia under the influence of the flight speed, and the nozzle angle of 0° tilted backward would lead to droplet drift. The nozzle angle of -30° would offset part of the force, so the amount of droplet deposition increased. The forward flight of the airframe would also cause the downwash wind field to be shifted backward, and when the nozzle angle was 45° or 60°, the droplets were accelerated to be deposited under the coercion of the downwash wind field after being sprayed, thus increasing the amount of droplet deposition.

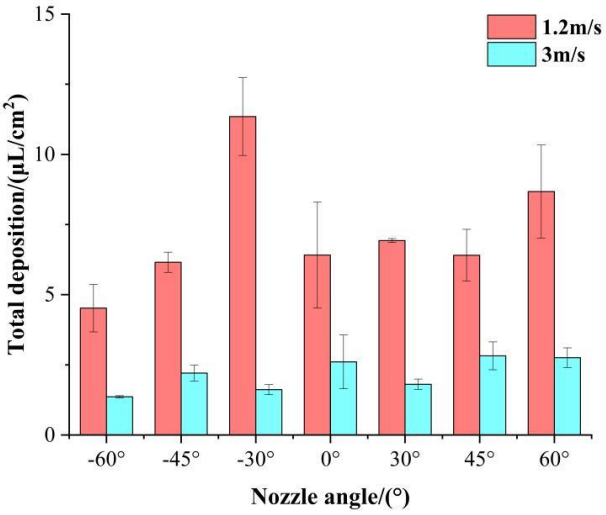

Fig. 8 - Comparison of total deposition at different flight speeds

Droplet deposition uniformity

Tables 1 and 2 show the uniformity of droplet deposition distribution at different flight speeds. It can be seen from the tables, the uniformity of droplet deposition on each collection point under different nozzle angles at the same flight speed is different.

When the flight speed was 1.2 m/s, the uniformity of droplet deposition on collection belt B was different from that on collection belts A and C, and the uniformity of droplet deposition on collection belts A and C was poor. Among them, the variance of droplet deposition reached 71.5% and 79.86% among the collection points on collection belt A at the nozzle angles of -30° and 60°, and the variance of droplet deposition reached 84.14% and 81.11% among the collection points on collection belt C at the nozzle angles of -30° and 0°. The reason for this phenomenon might be due to the uneven distribution of droplet deposition caused by the poor positioning accuracy of the plant protection UAV at the take-off and landing points. The droplet deposition uniformity was best on collection belt B, in which the droplet deposition uniformity was better than 0° at other nozzle angles compared to 0°. The experimental results showed that adjusting the nozzle angle improved the droplet deposition uniformity when the flight speed was low.

Table 1

Droplets deposition uniformity (CV %) at flight speed of 1.2 m/s

Collection belt	CV (%)						
	-60°	-45°	-30°	0°	30°	45°	60°
A	54.96	25.61	71.5	40.77	26.76	25.68	79.86
B	39.88	21.08	46.77	61.26	35.84	44.09	31.31
C	40.25	15.71	84.14	81.11	47.1	72.43	41.88

When the flight speed was 3m/s, the uniformity of droplet deposition on collection belt B and collection belts A and C was different, and the variance of droplet deposition of each collection point on collecting belt C reached 84.28% at the nozzle angle of -30°, and the variance of droplet deposition of each sampling point on collecting belt B reached 74.41% at the nozzle angle of 30°. The reason for this phenomenon might be due to the lateral wind during aerial application by the plant protection UAV, which caused the droplet drift and made the distribution of droplet deposition uneven. The best droplet deposition uniformity was found on collection belt B, where the difference in droplet deposition uniformity at other nozzle angles was smaller compared to nozzle angle 0°. The experimental results showed that when the flight speed increased, adjusting the nozzle angle had less effect on the droplet deposition uniformity.

Table 2

Droplets deposition uniformity (CV %) at flight speed of 3 m/s

Collection belt	CV (%)						
	-60°	-45°	-30°	0°	30°	45°	60°
A	23.91	19.41	61.74	33.66	52.92	12.2	51.3
B	15.42	31.65	38.76	30.63	74.41	65.6	30.92
C	25.32	33.84	84.28	24.26	65.97	40.28	43.4

Table 3 shows the results of variance analysis of the above experimental results. It indicates the effect of flight speed and nozzle angle on the uniformity of droplet deposition distribution at the collection point during the application operation. According to the analysis results, the influence of flight speed on the uniformity of droplet deposition was not significant, and the value of significance level was 0.24. The influence on the amount of droplet deposition was significant, and the value of significance level was less than 0.01. Adjusting the nozzle angle had a significant effect on the uniformity of droplet deposition distribution and deposition amount, and adjusting the nozzle angle had a large effect on the change of droplet deposition amount.

Table 3

Results of deposition rate variance analysis

Source difference	CV (%)	Total deposition (μL/cm²)
	Sig.-value	Sig.-value
Flight speed (m/s)	0.237	0.000
Nozzle angle (°)	0.009	0.000

Note: This article took the significance level α=0.05

CONCLUSIONS

This paper explores the droplet deposition under different flight speeds and nozzle angles of plant protection UAVs through spray deposition test and obtains the distribution of droplet deposition amount and the uniformity of droplet deposition under different flight speeds and nozzle angles. According to the results of variance analysis, the following results can be obtained:

1) Flight speed has a significant effect on the amount of droplet deposition, but flight speed does not have a significant effect on the uniformity of droplet deposition. The increase in flight speed decreases the amount of droplet deposition and has less effect on the uniformity of droplet deposition.

2) The nozzle angle has a significant effect on the amount of droplet deposition and the uniformity of droplet deposition. When the flight speed was 1.2m/s, the deposition amount of nozzle angle -30° and 60° increased by 76.94% and 35.28% respectively with 0° as a comparison. When the flight speed was 3m/s, the deposition amount of nozzle angle -30°, 45°, and 60° increased by 61.04%, 74.4% and 70.32%, respectively, using 0° as a comparison. Adjusting the nozzle angle can improve the uniformity of droplet deposition, when the flight speed is low, adjusting the nozzle angle will improve the uniformity of droplet deposition, when the flight speed is increased, the uniformity of droplet deposition under each nozzle angle is not much different.

3) In the actual field spraying process, to increase the droplet deposition effect on the crop, you can adjust the nozzle angle or reduce the flight speed to increase the amount of deposition and improve the uniformity of droplet deposition. However, the lateral wind will affect the distribution of droplet deposition during the test, and droplet drift will affect the amount of deposition and the uniformity of droplet deposition on the target. Therefore, in the actual application process, it is necessary to consider the impact of wind speed and direction and other environmental parameters on the effect of droplet deposition to improve the effectiveness of the application operation.

ACKNOWLEDGEMENT

The authors thank the experts for editing our paper.This research was funded by the Ningxia Key Research and Development Plan Project (2023BCF01051); National Natural Science Foundation of China (32302410); Shandong Province Natural Science Foundation (ZR2021QC154). We also thank anonymous reviewers for their critical comments and suggestions to improve the manuscript.

REFERENCES

[1] Chen, S., Lan, Y., Li, J., Zhou, Z., Jin, J., and Liu, A. (2016). Effect of spray parameters of small unmanned helicopter on distribution regularity of droplet deposition in hybrid rice canopy. *Transactions of the CSAE* 32, 40-46.

[2] Chen, Y.Y., Hou, C.J., Tang, Y., Zhuang, J.J., Lin, J.T., and Luo, S.M. (2019). An effective spray drift-reducing method for a plant-protection unmanned aerial vehicle. *Int. J. Agric. Biol. Eng*. 12, 14-20. doi:10.25165/j.ijabe.20191205.4289.

[3] Ding, S.M., Xue, X.Y., Qin, W.C., Gu, W., Cai, C., and Cui, L.F. (2019). Influencing factors research and performance experiment on droplets deposition at low wind speed. *Int. J. Precis. Agric. Aviat*. 2. doi:10.33440/j.ijpaa.20190201.0017.

[4] Li, J., Lan, Y., and Peng, J. (2018a). Effect of droplet size spraying by unmanned aerial vehicle on droplet deposition in rice canopy. *Journal of Hunan Agricultural University (Natural Sciences)* 44, 442-446.

[5] Li, J., Lan, Y., and Shi, Y. (2018b). Research progress on airflow characteristics and field pesticide application system of rotary-wing UAV. *Transactions of the CSAE* 34, 104-118.

[6] Liu C., Hu J., Li Y., Zhang W., Li Q. (2023). Experiment on spray flow field characteristics and deposition performance of conical wind field anti-drift spray. *INMATEH - Agricultural Engineering*, Vol.69(1), pp. 559–568.

[7] Milanowski, M.; Subr, A.; Combrzyński, M.; Różańska-Boczula, M.; Parafiniuk, S. (2022). Effect of Adjuvant, Concentration and Water Type on the Droplet Size Characteristics in Agricultural Nozzles. *Appl. Sci*. 12, 5821.

[8] Shengde, C., Yubin, L., Bradley, K., Jiyu, L., Aimin, L., and Yuedong, M. (2017). Effect of wind field below rotor on distribution of aerial spraying droplet deposition by using multi-rotor UAV. Nongye Jixie Xuebao / *Transactions of the Chinese Society of Agricultural Machinery* 48.

[9] Song, J., He, X., and Yang, X. (2006). Influence of nozzle orientation on spray deposits. *Transactions of the CSAE* 22, 96-99. doi:10.3321/j.issn:1002-6819.2006.06.019.

[10] Song, Z.Q., Gong, J.L., Zhang, Y.F. (2023). Deposition performance of hydrodynamic ultrasonic atomizing nozzles with different spray parameters. *INMATEH - Agricultural Engineering*, Vol.71(3), pp. 185–193.

[11] Sun, D.Z., Zhan, X.R., Liu, W.K., Xue, X.Y., Xie, J.X., Li, Z., Song, S., and Wang, W. (2021). Compensation of spray angle to droplet drift under crosswind. *Transactions of the CSAE* 37, 80-89. doi:10.11975/j.issn.1002-6819.2021.21.010.

[12] Tian, Z.W., Xue, X.Y., Duan, F.M., Yao, S., and Ma, W. (2022). Automatic system and method for improving aerial spray droplet penetration. *INMATEH-Agricultural Engineering*, Vol.68(3), pp.265–274.

[13] Wang, C., Song, J., He, X., Wang, Z., Wang, S., and Meng, Y. (2017). Effect of flight parameters on distribution characteristics of pesticide spraying droplets deposition of plant-protection unmanned aerial vehicle. *Transactions of the CSAE* 33, 109-116.

[14] Wang, G., Han, Y., Li, X., Andaloro, J., Chen, P., Hoffmann, W.C., Han, X., Chen, S., and Lan, Y. (2020). Field evaluation of spray drift and environmental impact using an agricultural unmanned aerial vehicle (UAV) sprayer. *Sci. Total Environ*. 737, 139793. doi:10.1016/j.scitotenv.2020.139793.

[15] Wang, J., Ma, C., Chen, P., Yao, W., Yan, Y., Zeng, T., Chen, S., and Lan, Y. (2023). Evaluation of aerial spraying application of multi-rotor unmanned aerial vehicle for Areca catechu protection. *Front. Plant Sci*. 14, 1093912.

[16] Xiao, Q., Xin, F., Lou, Z., Zhou, T., Wang, G., Han, X., Lan, Y., and Fu, W. (2019). Effect of aviation spray adjuvants on defoliant droplet deposition and cotton defoliation efficacy sprayed by unmanned aerial vehicles. *Agronomy* 9, 217.

[17] Xin, F., Zhao, J., Zhou, Y., Wang, G., Han, X., Fu, W., Deng, J., and Lan, Y. (2018). Effects of dosage and spraying volume on cotton defoliants efficacy: a case study based on application of unmanned aerial vehicles. *Agronomy* 8, 85.

3D MULTI-OBJECTIVE FLIGHT PATH OPTIMIZATION OF AGRICULTURAL PLANT PROTECTION UAVS BASED ON EMSDBO ALGORITHM

/

基于EMSDBO算法农业植保无人机三维航迹多目标优化研究

Hexia CHU*[1)]; Hongxing LIU[2)]

[1)] Department of Mathematics Education, Zhumadian Preschool Education College, Zhumadian, Henan, China

[2)] School of Mathematics and Statistics, Henan University, Kaifeng, Henan, China

*E-mail: hexia_chu@163.com

Corresponding author: Hexia Chu

DOI: https://doi.org/10.35633/inmateh-72-21

Keywords: agricultural UAV, patrol inspection, 3D path, multi-objective optimization

ABSTRACT

Both cruising ability and safety should be considered in the 3D inspection path planning of agricultural unmanned aerial vehicles (UAVs). Specific to a complex working environment, the 3D inspection environment of agricultural UAVs was simulated through terrain modeling and threat modeling. First, the dynamic constraints of flight approaching rate and response time were added to the threat cost, and the 3D mission space model and flight path cost function were constructed considering the influence of UAVs' turning performance. Second, the offset estimation strategy, variable spiral search strategy, quasi-reverse learning strategy and dimension-by-dimension mutation strategy were introduced into the dung beetle optimizer (DBO) algorithm to improve the global optimization ability and convergence rate of the algorithm. By establishing a three-dimensional trajectory planning model for unmanned aerial vehicles, the trajectory planning is transformed into a multi-objective function optimization problem, and an improved algorithm is used to solve the three-dimensional trajectory planning of unmanned aerial vehicles. The fitness is evaluated by considering the objective function of trajectory cost, terrain cost, and danger level, and the trajectory planning is iteratively optimized. The results indicate that the proposed improved dung beetle algorithm for trajectory planning has lower overall cost and stability in adapting to different complex terrain environments.

摘要

农业无人机的三维巡检路径规划不仅要考虑续航能力，还要考虑安全性。针对复杂的作业环境，通过地形建模和威胁建模来模拟农业无人机的三维巡检环境。首先，将飞行接近率和响应时间的动态约束添加到威胁成本代价中，并考虑无人机转弯性能的影响，建立三维任务空间模型与航迹代价函数；其次，在蜣螂算法中引入偏移估计策略、变螺旋搜索策略、准反向学习策略和逐维变异策略，提高算法的全局寻优能力和收敛速度。通过建立无人机三维航迹规划模型，将航迹规划转化为多目标函数优化问题，并利用改进算法求解无人机三维航迹规划，以综合考虑航迹代价、地形代价和危险程度的目标函数评估适应度，对航迹规划迭代寻优。结果表明，所提改进蜣螂算法规划的航迹具有更低的总代价和适应不同复杂地形环境的稳定性。

INTRODUCTION

With the development of communication technology, automatic control technology, sensing technology and artificial intelligence, the functions of unmanned aerial vehicles (UAVs) are becoming increasingly perfect. How to improve the working efficiency of UAVs and reduce their energy consumption has become a research hotspot in the field of plant protection UAVs *(Gao et al.,2023)*. UAV route planning refers to designing a UAV flight path according to the purpose of work under the specified constraints, and the quality of the flight path is determined as per the specific purpose of work. In the military application field, military UAVs can perform various tasks such as reconnaissance and early warning, relay communication, battlefield search and rescue, and tracking and positioning. Designing a better UAV flight path can effectively avoid radar detection and improve the success rate of missions *(Ling et al., 2023)*. In addition, UAVs have been widely used in civil applications *(Xu et al., 2020)*.

[1] *Chu Hexia, M.S. Stud. Eng.;*[2] *Liu Hongxing, Associate Professor. Eng.*

In the logistics industry, for example, UAVs-aided autonomous distribution can effectively reduce the labour cost of logistics transportation, and the logistics transportation efficiency can be effectively improved by designing a better flight path of UAVs based on the position information of distribution sites. In the agricultural field, plant protection UAVs have exhibited such advantages as high efficiency and fast speed in the operation of mist spraying, and moreover, UAVs are capable of vertical take-off and landing in small areas and convenient spraying operations on all kinds of terrains *(Qi et al., 2020)*.

Agricultural plant protection is an important part of the modernized agricultural development, and the introduction of UAVs into agricultural plant protection can effectively meet the high-efficiency and low-cost needs in agricultural operations. The UAV technology promoted in the field of agricultural plant protection should be applied on basis of network information technology, and meanwhile, the high-efficiency, convenient and intelligent R & D concept should be adhered to, thus significantly elevating the application value of agricultural plant protection UAVs *(Charalampous et al., 2017)*. In China with a vast territory, the crop characteristics and planting patterns vary from region to region, accompanied by certain limitations in the application of traditional ground machines and tools. Under this background, the promotion of plant protection UAVs can facilitate the mechanization development of China's agriculture and elevate the overall agricultural development level of China in addition to reducing the workload of peasant households and promoting the reconstruction of the modern agricultural system.

State of the art

The flight route design of plant protection UAVs belongs to the category of full-coverage route planning. According to the time point of route design, the full-coverage route planning algorithm is divided into two types *(Zhen et al., 2017)*. First, according to the existing environmental information including the shape and size of the target area and the distribution of obstacles in the area, a UAV flight route is designed before the UAV takes off so that the UAV can fly along the designed route. This method is referred to as the off-line route planning method. Secondly, during the flight of UAVs, the target area is scanned in real time by sensors, and the flight path of UAVs is calculated in real time based on the scanning results. This method is called the online route planning method.

Boysen et al. (2021) put forward a route design method for plant protection UAVs based on genetic algorithm (GA), taking route length, redundant coverage and repeated coverage as the criteria to evaluate the advantages and disadvantages of UAV routes. In addition, they put forward an operation route planning algorithm for irregular areas based on the operation direction, which could quickly plan the UAV operation route according to the specified operation direction. In the actual operation process of plant protection UAVs, the UAVs need to return to the target area several times to complete the spraying operation due to the influence of factors such as the too large target operation area and the limited drug loading and endurance of UAVs. Considering this actual situation, *Zhen et al. (2015)* proposed a path planning method of plant protection UAVs based on grid method and gravity search algorithm, taking the time spent by UAV operation as the criterion to evaluate the quality of the path, and realized the optimization of the number and position of return points. *Kim et al. (2017)* proposed an online route planning algorithm Spiral-STC based on Spanning Tree Coverage (STC), which obtained the surrounding environment information through sensors and generated local maps, and obtained effective grids and obstacle grids through grid division of local maps. This method can ensure that all effective grids are covered, without repeated coverage. Due to too many turns of the designed route, however, the energy consumption cost is increased, and in addition, missing coverage results from the inaccurate grid division. *Ham et al. (2018)* put forward an improved Spiral-STC algorithm, which added outer ring routes to the original Spiral-STC algorithm, which can effectively improve the coverage of routes. *Choi et al. (2021)* added a new map coordinate allocation method on this basis, and redistributed the coordinates by analysing the historical coordinate data of sensors, which can effectively reduce the number of turns of the route. Common path planning algorithms include A* algorithm *(Ha et al., 2016)*, Probabilistic Roadmap (PRM) algorithm *(Lu et al., 2016)*, rapidly expanding random tree (RRT) algorithm *(Agatz et al., 2018)*, artificial potential field method *(Carlsson et al., 2018)*, Dijkstra method *(Kitjacharoenchai et al., 2019)* and so on. Despite the quite mature mathematical theories, the traditional path planning methods can easily fall into the local optimal solution when solving the multi-objective 3D path planning problem of UAVs. With the development of random search theory, many emerging swarm intelligence algorithms have been successfully applied to path planning problems in recent years, such as traditional particle swarm optimization *(Das et al., 2021)*, as well as newly proposed artificial bee colony algorithm, grey wolf algorithm *(Roberti et al., 2021)*.

At present, the main problems of UAVs' 3D path planning lie in the rationality and safety of modeling and the solving accuracy and global optimization ability of algorithms in complex geographical environments.

In terms of modeling improvement, *Kim et al. (2019)* divided sub-paths according to the number of hazard sources and the distance from the hazard sources, and respectively calculated the threat cost of the sub-paths by threat weight factors. *Wang et al. (2017)* adopted a two-level path planning method, established a Markov decision process at the bottom to control the movement of the UAV along the route, divided the UAV control into different discrete actions, and set a reward function to reduce the risk of collision. In the modeling process of the above research, when considering obstacle avoidance, the distance from the obstacle is often used as the judgment condition *(Ulmer et al., 2018)*, but in practice, the manoeuvrability and turning performance of UAVs should be considered comprehensively, so as to plan a safer and more practical path *(Zhang et al., 2021)*. In terms of algorithm improvement, *Otto et al. (2018)* proposed a particle swarm optimization algorithm with spherical vectors, which introduced the elevation angle and azimuth angle of spherical coordinate vectors to achieve performance constraints on the pitch angle and steering angle of UAVs, significantly reducing the search space. Given the large search space and many constraints in the 3D path planning problem and despite the ability to help improve the path planning quality of algorithms to some extent, the above improvement is restricted by the characteristics of traditional algorithms themselves.

To sum up, although the multi-objective path planning problem of UAVs has been investigated by many scholars, the multi-modal and multi-objective characteristics of UAV paths have not been considered in most cases. To solve the above problems, a 3D UAV path planning model under complex environments was established in this study with UAVs' fuel consumption and threat as the optimization objectives. In the aspect of algorithm improvement, the strategy improvement was performed based on the dung beetle optimizer (DBO), and an enhanced multi-strategy dung beetle optimizer (EMSDBO) was proposed, followed by simulation verification on the standard function and the established 3D flight path model of agricultural plant protection UAVs. The experimental results reveal that the improved algorithm can plan the better UAV flight path on the premise of ensuring the rapid and safe optimization.

MATERIALS AND METHODS

Environment Modeling

Environment modeling is the first step of UAV path planning, which usually includes terrain modeling and threat modeling. Obstacles are a key factor affecting the safe flight of agricultural drones. When performing inspection tasks, in addition to avoiding terrain obstacle, it is also necessary to consider detecting obstacle. This article mainly considers the obstacle caused by signal interference in reconnaissance environments, which generally involve obstacle such as radar, electromagnetic, and artillery. These obstacles are simulated using cylinders. Different from the function-based simulation, different elevation values were assigned to different positions in the 2D plane using digital elevation information so as to realize the terrain undulation. In addition, digital elevation model (DEM) has been commonly used to establish 3D environments. After the DEM data of a region was acquired, the simulation modeling of 3D terrains could be implemented via MATLAB to realize the digital simulation of terrain surfaces. When executing a reconnaissance mission, UAVs need to consider the detection threat in addition to evading the terrain threat. In this study, the threat brought by signal interference under the flight environment of agricultural plant protection UAVs was mainly considered. For the sake of simplification, the threatened area was simplified into a cylinder *(Chen et al., 2023)*, expressed by the following formula:

$$\mathrm{E}(\varepsilon)=\left(\frac{x-x_0}{a}\right)^{2d}+\left(\frac{y-y_0}{b}\right)^{2e}+\left(\frac{z-z_0}{c}\right)^{2f} \tag{1}$$

In Equation (1), (x_0,y_0,z_0) represents the coordinates of the interference enter, $a=b$, $d=e=1$, $f>1$; $E(\mathcal{E})=1$ stands for the surface of the cylinder.

Path Planning Model

The path of UAVs can be regarded as a line segment connected by a series of coordinate points. Therefore, the path is coded by means of real number coding, as follows:

$$\left(x_1,x_2,...,x_n,y_1,y_2,...,y_n,z_1,z_2,...,z_n\right) \tag{2}$$

where x_i $(i=1, 2, ..., n)$ represents the x-coordinate of the i-th flight path point; y_i $(i=1, 2, ..., n)$ and z_i $(i=1, 2, ..., n)$ stand for the y-coordinate and z-coordinate of the i-th flight path point, respectively; n denotes the number

of path nodes. The path planning model of UAVs contains terrain constraints and turning angle constraints. Terrain constraints are expressed as follows:

$$h(x_i, y_i) + z_{\min} < z_i < z_{\max}, i = 1,2,...,n \tag{3}$$

where $h(x_i,y_i)$ is the terrain height corresponding to 2D terrain coordinates; Z_{min} and Z_{max} represent the minimum and maximum safety flight heights of UAVs, respectively. According to reference *Radmanesh et al. (2015)* Other constraints such as the minimum and maximum path lengths and the maximum turning angle can be expressed as follows:

$$\theta_i \le \theta_{max}, i = 1,2,...n \tag{4}$$

$$L_i \geqslant L_{min}, i = 1,2,...n \tag{5}$$

$$\sum_{i=1}^{n} L_i < L_{\max}, i = 1,2,...,n \tag{6}$$

where θ_i is the turning angle of the i-th path point; θ_{max} stands for the maximum turning angle; L_i is the length of the i-th path segment; L_{min} is the minimum path length; L_{max} is the maximum path length.

In this study, fuel consumption and threat were taken as two optimization objectives, which were in conflict under some circumstances, e.g., the shorter the path, the greater the threat.

(1) Fuel consumption. Generally speaking, a short path length means short flight time and less fuel consumption. In this study, fuel consumption refers to the fuel consumed by the UAV during the flight from the starting point to the target point. f_{oil} was set as the fuel consumption cost. Assuming that the UAV flied at a constant speed, the fuel consumption was then directly proportional to the path length. Hence, the fuel consumption f_{oil} could be calculated as below:

$$f_{oil} = \alpha \sum_{i=1}^{n} L_i = \alpha \sum_{i=1}^{n} \sqrt{(x_i - x_{i-1})^2 + (y_i - y_{i-1})^2 + (z_i - z_{i-1})^2} \tag{7}$$

where α is the fuel consumption coefficient.

(2) Obstacles. In this study, detection obstacle and height obstacle were mainly considered *(Chen et al., 2023; Lebedeva et al., 2022; Liu et al., 2021)*. A total of m detection obstacles are set, the protection centre coordinate of the k (k=1,2...,m)-th detection threat is C_k, and the radius of the threat is R_k; when the UAV flies from the path node W_i to node W_{i+1}, the straight-line distance from C_k to W_i, W_{i+1} is d_k, as shown in Fig. 1.

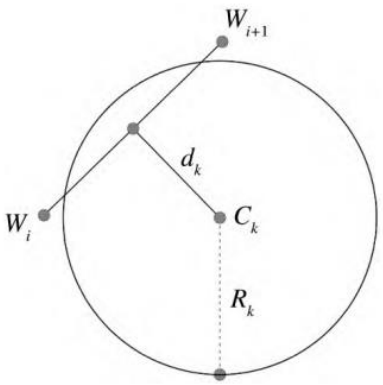

Fig. 1- Definition of detection obstacle

In this case, the detection threat value of UAVs is inversely proportional to its distance d_k. Therefore, the detection threat f_{detect} can be calculated as follows:

$$f_{detect} = \sum_{i=1}^{n} \sum_{k=1}^{m} T_{i,k} \tag{8}$$

$$T_{i,k} = \begin{cases} 0, d_k \geqslant R_k \\ R_k / d_k, 0 < d_k < R_k \\ \infty, d_k = 0 \end{cases} \tag{9}$$

where $T_{i,k}$ denotes the detection threat value borne by the UAV from the k-th interference centre on the i-th path segment. The greater the flight height of the UAV, the higher the probability for the UAV to be discovered by the enemy. Hence, the flight height is also one of the obstacle to be considered in this study. In 3D maps, the UAV should keep flying at an average safety height as much as possible, and meanwhile, prevent the collision with the terrain environment. Hence, the height threat f_{high} can be calculated as below:

$$f_{high} = \sum_{i=1}^{n} H_i \tag{10}$$

$$H_i = \begin{cases} \left| z_i - \frac{z_{\max} + z_{\min}}{2} \right|, h(x_i, y_i) + z_{\min} < z_i < z_{\max} \\ \infty, else \end{cases} \tag{11}$$

where H_i stands for the height threat of the UAV in the *i*-th path segment. Therefore, the threat f_{threat} of the UAV can be expressed as follows:

$$f_{threat} = f_{dctcct} + f_{high} \tag{12}$$

According to the above analysis, the 3D path planning model for the UAV can be expressed as below:

$$F = [\min(f_{oil}), \min(f_{threat})]^T \tag{13}$$

$$s.t. \begin{cases} h(x_i, y_i) + z_{\min} < z_i < z_{\max}, i = 1,2,...,n \\ \theta_i \leqslant \theta_{\max}, i = 1,2,...,n \\ L_i \geqslant L_{\min}, i = 1,2,...,n \\ \sum_{i=1}^{n} L_i \geqslant L_{\max}, i = 1,2,...,n \end{cases} \tag{14}$$

where *F* is the objective vector, which is a constrained double-objective minimization-type optimization problem. In this study, two objective functions—fuel consumption cost and threat cost—were designed when establishing the multi-objective 3D path optimization model of agricultural plant protection UAVs, aiming to realize the optimal overall inspection path. By fully considering the advantages and disadvantages of agricultural plant protection UAVs in patrol inspection, the relationship between the two objective functions was coordinated, and the 3D path optimization of such UAVs was, in essence, the trade-off selection process of participants. Different 3D paths of agricultural plant protection UAVs were selected by assigning different weights to different optimization objectives. In the solving process based on heuristic algorithms, the values of the two objective functions for each generation of individuals could be acquired, and the two objective functions were respectively subjected to uniform dimensionality and quantification as per the following formulas:

$$F_{oil}^{*} = \frac{f_{\text{oil}} - \min f_{\text{oil}}}{\max f_{\text{oil}} - \min f_{\text{oil}}} \tag{15}$$

$$F_{\text{threat}}^{*} = \frac{f_{\text{threat}} - \min f_{\text{threat}}}{\max f_{\text{threat}} - \min f_{\text{threat}}} \tag{16}$$

The two objective functions with the unified dimension were weighted and summed according to the specified weights and transformed into a single-objective model for solving. The single-objective function is expressed as below:

$$\min F^{*} = \alpha_1 F_{oil}^{*} + \alpha_2 F_{threat}^{*} \tag{17}$$

where α_i is the weight of the objective function, $\alpha_i \in [0,1]$ and $\alpha_1 + \alpha_2 = 1$.

Algorithm Design

In this study, the DBO algorithm was improved and the improved algorithm was applied to the established simulation scenario for path planning. The idea of the DBO algorithm is mainly based on four behaviours of dung beetles, namely, ball rolling, reproduction, foraging and stealing. Among them, the ball rolling behaviour is divided into two modes: with and without obstacles *(Sui et al., 2023)*, and the position updating in case of no obstacles in the forward direction is displayed in the following formula:

$$x_i^{t+1} = x_i^t + \alpha \times k \times x_i^{t-1} + b \times \Delta x \tag{18}$$

$$\Delta x = \left| x_i^t - X^w \right| \tag{19}$$

where *t* represents the current iteration number, x_i^t is the position of the *i*-th dung beetle at the *t*-th iteration, *k* is the deflection factor, *b* is a constant value within (0,1), and α is a natural coefficient with a value of -1 or 1, where 1 means no deviation and -1 means the deviation from the original direction. x^W is the worst position of dung beetle in all the solutions and Δx is used to simulate the intensity change of light. When there is an obstacle in the forward direction, the position updating formula is shown in the following Formula (20):

$$x_i^{t+1} = x_i^t + \tan(\theta) \left| x_i^t - x_i^{t-1} \right| \tag{20}$$

The rolling direction is only considered within [0, π]. If θ is equal to 0, $\pi/2$ or π, the position will not be updated. In the breeding behaviour, a dynamic boundary selection strategy is proposed to represent the spawning area, as shown in the following Formulas (21) and (22):

$$Lb^* = \max(X^* \times (1-R), Lb) \quad (21)$$

$$Ub^* = \min(X^* \times (1+R), Ub) \quad (22)$$

Among them: X^* represents the current local optimal position, Lb^* and Ub^*respectively stand for the upper and lower bounds of the breeding area, and R=1-t/T_{max}, in which T_{max} means the maximum number of iterations, and Lb and Ub denote the upper and lower bounds of the optimization problem, respectively. The spawning position will change dynamically, as seen in the following Formula (23):

$$B_i^{t+1} = X^* + b_1 \times (B_i^t - Lb^*) + b_2 \times (B_i^t - Ub^*) \quad (23)$$

Among them: B_i^t is the spawning position of the i-th female dung beetle at the t-th iteration, b_1 and b_2 represent two independent random vectors with a size of 1×D, and D is the dimension of the optimization problem. The optimal foraging area in the foraging behaviour is also dynamically updated, expressed by the following Formulas (24) and (25).

$$Lb^b = \max(X^b \times (1-R), Lb) \quad (24)$$

$$Ub^b = \min(X^b \times (1+R), Ub) \quad (25)$$

where X^b represents the global optimal position, and Lb^b and Ub^b respectively represent the lower and upper limits of the optimal foraging area. The individual position updating is shown in the following Formula (26):

$$x_i^{t+1} = x_i^t + C_1 \times (x_i^t - Lb^b) + C_2 \times (x_i^t - Ub^b) \quad (26)$$

Where C_1 represents a random number that obeys a normal distribution and C_2 represents a random vector within (0,1). The individual position update of stealing behaviour is shown in the following Formula (27):

$$x_i^{t+1} = X^b + S \times g \times (\left|x_i^t - X^*\right| + \left|x_i^t - X^b\right|) \quad (27)$$

Where X^b is the best food source, g is a random vector with a size of 1×D, which follows a normal distribution, and S represents a constant value.

Improved Optimization Strategy

In order to further improve the performance in 3D path planning of UAVs, the following improvement strategy was designed for the DBO algorithm.

(1) Offset estimation strategy. In this study, an offset estimation strategy *(Chen et al., 2023)* was proposed, the mutual relationship between individuals was expressed via a probability model, the probability distribution model was calculated using the current dominant population, the evolutionary direction of the population was led, and new sub-populations were generated based on the sampling of the probability distribution model, followed by continuous iterations until obtaining the optimal solution. The mathematical models for the offset estimation strategy are displayed in Formulas (28), (29), (30) and (31):

$$x_i^{t+1} = \frac{\left(x^b + x_{mean}^t + x_i^t\right)}{3} + y, y \sim N(0, Cov(i)) \quad (28)$$

$$Cov(i) = \frac{1}{pop/2} \sum_{i=1}^{pop/2} \left(x_i^{t+1} - x_{mean}^t\right) \times \left(x_i^t - x_{mean}^t\right)^T \quad (29)$$

$$x_{mean}^t = \sum_{i=1}^{pop/2} \omega_i \times x_i^t \quad (30)$$

$$\theta_i = \frac{\ln\left(pop/2 + 0.5\right) - \ln\left(i\right)}{\sum_{i=1}^{pop/2} \left(\ln(pop/2 + 0.5) - \ln\left(i\right)\right)} \quad (31)$$

where x_{mean}^t represents the weighted average of the dominant population, pop is the population size, θ_i stands for the weight coefficient arranged according to the descending order of the fitness value in the dominant population, and $Cov(i)$ is the weighted covariance matrix. In the process of updating, both the global optimal individual information and the population position and its own information are considered, which is helpful to keep the population diversity of the algorithm.

(2) The spiral search formula of the traditional whale optimization algorithm is a fixed spiral line. In order to dynamically adjust the spiral shape during the search with the iteration and strengthen the ability of the

algorithm to explore unknown areas, an improved variable spiral search strategy was proposed in this study, with the specific mathematical formulas shown in (32) and (33):

$$\beta = e^{Bl} \times \cos(2\pi B) \tag{32}$$

$$l = e^{4\cos((\frac{1-t}{t_{\max}}+1)\pi)} \tag{33}$$

Where *B* is a random number evenly distributed from 0 to 1, *l* changes gradually with the increase in the number of iterations, and the change in the spiral line is controlled by a cosine function. As iterations proceed, the spiral line gradually changes from a large one to a small one. In the early stage, the algorithm searches the target in a large spiral shape, trying to find better individuals as much as possible and enhance the algorithm's global search ability (according to reference *Li et al. 2023)*. In the later stage, ineffective search is reduced, and the target is searched in a small spiral shape to improve the algorithm optimization accuracy and convergence efficiency. The modified foraging, reproduction and stealing formulas for dung beetles are displayed in the following Formulas (34), (35) and (36):

$$x_i^{t+1} = x^* + \beta_1 \times (x_i^t - Lb^*) + \beta_2 \times (x_i^t - Ub^*) \tag{34}$$

$$x_i^{t+1} = x_i^t + \beta_3 \times (x_i^t - Lb^b) + \beta_4 \times (x_i^t - Ub^b) \tag{35}$$

$$x_i^{t+1} = x^b + \beta_5 \times g \times (|x_i^t - x^*| + |x_i^t - x^b|) \tag{36}$$

Lb^b and Ub^b represent the lower limit and upper limit of the optimal feeding area, respectively. Lb^* and Ub^* represent the lower and upper limits of the spawning area, respectively. β_1 and β_2 represent two independent random vectors of size $1\times D$, and D represents the dimension of the optimization problem. β_3 represents a random number that follows a normal distribution, β_4 represents a random vector belonging to (0,1), and β_5 represents a constant value.

(3) Quasi-reverse learning strategy. In the DBO algorithm, the position updating process depends too much on the dominant individuals, which leads to the prematurity of the population. To solve this problem, an adaptive quasi-reverse learning strategy was put forward in this study. The quasi-reverse learning strategy is a variant of the reverse learning strategy, which can evade the low accuracy caused by the excessive position conversion of traditional reverse learning, and meanwhile, can relatively expand the search space and accelerate population convergence, as shown in Formula (37):

$$x_i^{qo} = rand\left(\frac{Lb+Ub}{2}, Lb+Ub-x_i\right), \quad i = 1,2,\ldots,pop \tag{37}$$

In addition, the quasi-reverse learning strategy is used for all individuals as iterations proceed, and many useless searches will appear, which increases the calculation cost and is not good for algorithm convergence. Hence, the linear population reduction strategy was proposed in this study to gradually reduce the number of individuals adopting the quasi-reverse learning strategy with the proceeding of iterations, specifically as seen in Formula (38):

$$pop' = round(\frac{(pop_{\min} - pop_{\max})\cdot t}{M} + pop_{\max}) \tag{38}$$

where *pop*' represents the population size adopting the quasi-reverse learning strategy, and pop_{min} and pop_{max} stand for the maximum and minimum population sizes, respectively.

(4) Dimension-by-dimension mutation strategy

In order to enhance the ability of the algorithm to get rid of the local optimum, the dimension-by-dimension mutation strategy was adopted for the obtained optimal individuals after the ending of each iteration, and the best individual was retained by using the greedy strategy. In this stage, Gaussian mutation or Cauchy strategy was applied to each dimension of the optimal individual, specifically as seen in Formulas (39) and (40):

$$x_{new}^b(j) = \begin{cases} x^b(j) + randn \times \cos(\frac{\pi t}{2t_{\max}}) \times (x^b(j) - x^{random'}(j)), if \quad rand < 0.5 \\ x^b(j) + cauchy \times x^b(j), else \end{cases} \tag{39}$$

$$x^b(j) = \begin{cases} x_{new}^b(j), if \quad f(x_{new}^b) < f(x^b) \\ x^b(j), if \quad f(x_{new}^b) \geq f(x^b) \end{cases} \tag{40}$$

where $x^b(j)$ is the *j*-th dimension of the optimal individual.

Simulation Experiment

First, the improved EMSDBO algorithm was compared with other optimization algorithms to verify the superiority of the improved algorithm; then, different improvement strategies were compared, and the effectiveness of different improvement strategies was analysed; finally, the EMSDBO algorithm was subjected to 3D path planning simulation with other path planning algorithms in the established path planning model of agricultural plant protection UAVs under the same conditions, aiming to verify the effectiveness of this algorithm in path planning.

The real terrain data were acquired by reading DEM maps, which corresponded to the mountainous terrain in real environments. In this study, the DEM data were obtained from ALOSPALSAR database, and elevation points were acquired according to DEM and evenly discretized in the 100*100 coordinate space. *X*-coordinate represents the east longitude, $x \in [0,100]$, y-coordinate stands for the north latitude, $y \in [0,100]$, and z-coordinate denotes the real height of each coordinate point. The simulation experimental parameters and constraints are set as seen in Table 1.

Table 1

Settings of simulation experimental parameters

Experimental parameter	Set value	Experimental parameter	Set value	Experimental parameter	Set value
m	15	T	10	ganum	100
ϕ_{max}	45°	φ_{max}	45°	h_{max}	1000 m
l_{min}	30m	h_{min}	0 m	t_{min}	2s
v_1	15m/s	v_2	10 m/s	v_3	5 m/s
ϕ_0	30°	φ_0	30°	safth	1000 m
α_1	0.6	α_2	0.4	w_1	0.4
w_2	0.2	w_3	0.2	w_4	0.2

RESULTS

In the experiment, the coordinates of the starting point and the target point of the planned path for agricultural plant protection UAVs were (1,1,100) and (100,100,100), respectively. In order to display the planned 3D path for agricultural plant protection UAVs more intuitively and accurately, in the above calculation example, the 3D flight path of the UAVs was displayed through a 3D coordinate system in MATLAB 2014b. Then, the model was solved respectively using the DBO algorithm, the variable spiral search strategy-based DBO (SDBO) algorithm and the enhanced multi-strategy DBO (EMSDBO) algorithm. The convergence curves of the three algorithms are exhibited in Fig. 2, and the paths of agricultural plant protection UAVs obtained by the three algorithms are as shown in Fig. 3.

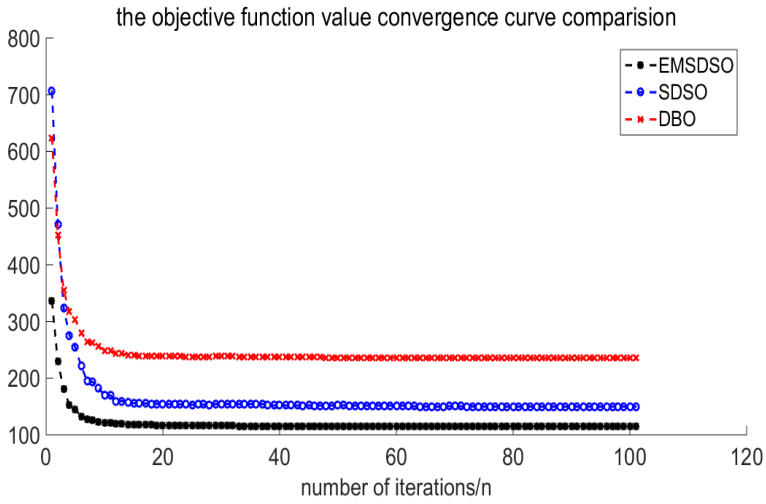

Fig. 2 - Convergence curves of three algorithms

It could be known from Fig. 2 that both the convergence rate and the objective function value of the EMSDBO algorithm were better than those of the DBO algorithm and SDBO algorithm.

The concepts of flight approaching rate and response time were introduced in the EMSDBO algorithm. Compared with the DBO and SDBO algorithms, the average minimum response time of the EMSDBO algorithm was 3.27 s, which was sufficient and reasonable, accompanied by relatively moderate flight distance and threat cost. This reflects that the influence of the flight approaching rate is taken into account and the planned path will be more reasonable and safer and accord with the actual situation by setting the suitable minimum response time, adding the dynamic constraint to the approaching distance and fully considering the manoeuvrability and turning performance of UAVs.

Therefore, it could be seen by comparing the experimental results that the EMSDBO algorithm proposed in this study can effectively avoid obstacle and plan the actually optimal flight path when applied to 3D path planning of plant protection UAVs. This process successfully shortens the search time during path planning using the algorithm and the length of the planned path, thus verifying the effectiveness and progressiveness of the EMSDBO algorithm.

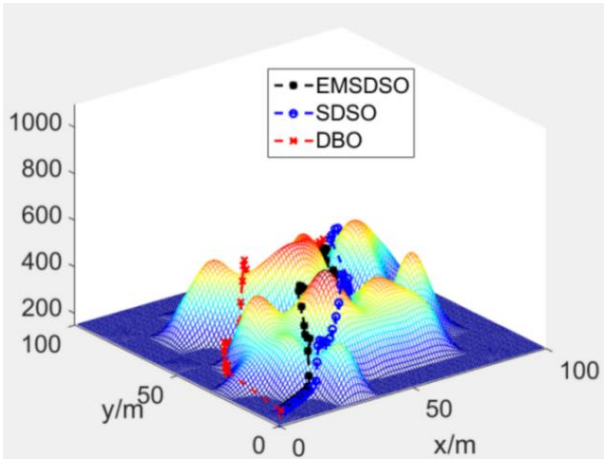

Fig. 3 - Paths of agricultural plant protection UAVs obtained by three algorithms

CONCLUSIONS

In order to effectively solve the 3D path planning problem of UAVs, the 3D UAV path planning models of two different scenarios were proposed first; second, the fuel consumption and threat of UAVs were set as the optimization objectives; finally, the EMSDBO algorithm was proposed. Specifically, multiple improvement strategies such as the offset estimation strategy, variable spiral search strategy, adaptive quasi-reverse learning strategy and hybrid mutation strategy were introduced based on DBO to enhance the population diversity and increase the algorithm global optimization ability and convergence rate. The simulation experimental results manifest that compared with the situation only considering the distance from the hazard source, the generated flight path will be safer and reasonable if the influence of the flight approaching rate and turning rate is taken into account; the improved algorithm exhibits stronger global search ability and can stably plan a feasible and safe flight path. The follow-up study will be carried out from two aspects: the real-time 3D path replanning of UAVs under dynamic environments will be implemented on basis of this study, and meanwhile, the collaborative path planning method under the condition of UAV groups will be explored.

REFERENCES

[1] Agatz N, Bouman P, Schmidt M., (2018), Optimization approaches for the traveling salesman problem with drone, *Transportation Science*, vol. 52, no. 4, ISSN 0041-1655, pp. 965-981, United States;

[2] Boysen N, Fedtke S, Schwerdfeger S., (2021), Last-mile delivery concepts: a survey from an operational research perspective, *OR Spectrum*, vol. 43, ISSN 0171-6468, pp. 1-58, Germany;

[3] Carlsson J G, Song S., (2018), Coordinated logistics with a truck and a drone, *Management Science*, vol. 64, no. 9, ISSN 0025-1909, pp. 4052-4069, United States;

[4] Charalampous K., Kostavelis I., and Gasteratos A., “Thorough robot navigation based on SVM local planning,” Robotics and Autonomous Systems, vol. 70, pp. 166–180, 2017.

[5] Chen X, Huang Y, Fan Q., (2023), Three-dimensional Path Planning of UAV Based on Multimodal Multi-objective Evolutionary Algorithm (基于多模态多目标进化算法的无人机三维路径规划), *Fire Control & Command Control*, vol. 48, no. 11, ISSN 1002-0640, pp. 32-40, China;

[6] Choi Y, Schonfeld P M., (2021), A Comparison of optimized deliveries by drone and truck, *Transportation Planning and Technology*, vol. 44, no. 3, ISSN 0308-1060, pp. 319-336, England;

[7] Das D, Sewani R, Wang J, Tiwari M., (2021), Synchronized truck and drone routing in package delivery logistics, *IEEE Transactions on Intelligent Transportation Systems*, vol. 22, no. 9, ISSN 1524-9050, pp. 5772-5782, United States;

[8] Deng, L.; Chen, H.; Zhang, X.; Liu, H. Three-Dimensional Path Planning of UAV Based on Improved Particle Swarm Optimization. Mathematics 2023, 11, 1987. https://doi.org/10.3390/math11091987

[9] Gao M, Han J, Feng X., (2023), Task allocation and service path optimization for plant protection drone based on agricultural service platforms (基于农服平台的植保无人机任务分配与路径优化), *Journal of Huazhong Agricultural University*, vol. 42, no. 3, ISSN 1000-2421, pp. 250-259, China;

[10] Ham A M., (2018), Integrated scheduling of m-truck, m-drone, and m-depot constrained by time-window, drop-pickup, and m-visit using constraint programming, *Transportation Research Part C: Emerging Technologies*, vol. 91, ISSN 0968-090X, pp. 1-14, England;

[11] Kitjacharoenchai P, Ventresca M, Moshref M, Lee S, Tanchoco J, and Brunese P., (2019), Multiple traveling salesman problem with drones: mathematical model and heuristic approach, *Computers & Industrial Engineering*, vol. 129, ISSN 0360-8352, pp. 14-30, England;

[12] Kim S, Moon I., (2019), Traveling salesman problem with a drone station, *IEEE Transactions on Systems, Man, and Cybernetics: Systems*, vol. 49, no. 1, ISSN 2168-2216, pp. 42-52, United States;

[13] Kim S J, Lim G J, Cho J, Côté M J., (2017), Drone-aided healthcare services for patients with chronic diseases in rural areas, *Journal of Intelligent and Robotic Systems*, vol. 88, no. 1, ISSN 0921-0296, pp. 163-180, Netherlands;

[14] Lebedeva V.V., Lebedev I.V., Algorithms for Calculating the Trajectory of Unmanned Aerial Vehicles for Solving Agricultural Problems, Agricultural Machinery and Technologies, vol. 16, No. 3, 2022

[15] Ling B, Zhang S., (2023), Application Status and development suggestions of UAV for agricultural plant protection in Xinjiang (新疆农业植保无人机的应用现状及发展建议), *China Plant Protection*, vol. 43, no. 4, ISSN 1672-6820, pp. 87-89, China;

[16] Li Y, Sun K, Yao Q, et al. (2023), A dual-optimization wind speed forecasting model based on deep learning and improved dung beetle optimization algorithm [J]. Energy: 129604.

[17] Lu Z., (2016), Modeling of yard congestion and optimization of yard template in container ports, *Transportation Research Part B: Methodological*, vol. 90, ISSN 0191-2615, pp. 83-104, England;

[18] Otto A, Agatz N, Campbell J, Golden B, Pesch E., (2018), Optimization approaches for civil applications of unmanned aerial vehicles (UAVs) or aerial drones: a survey, *Networks*, vol. 72, no. 4, ISSN 1097-0037, pp. 411-458, England;

[19] Panagiotis Radoglou-Grammatikis, Panagiotis Sarigiannidis,Thomas Lagkas, Ioannis Moscholios, A compilation of UAV applications for precision agriculture, Computer Networks, Volume 172, 2020, 107148, ISSN 1389-1286, https://doi.org/10.1016/j.comnet.2020.107148.

[20] Roberti R, Ruthmair M., (2021), Exact methods for the traveling salesman problem with drone, *Transportation Science*, vol. 55, no. 2, ISSN 0041-1655, pp. 315–335, United States;

[21] Radmanesh, Mohammadreza & Kumar, Manish & Nemati, Alireza & Sarim, Mohammad. (2015). Dynamic optimal UAV trajectory planning in the National Airspace System via mixed integer linear programming. Proceedings of the Institution of Mechanical Engineers Part G Journal of Aerospace Engineering. 230. 10.1177/0954410015609361.

[22] Samaniego F, Sanchis J, Rodriguez S G-N, Simarro R., (2019). Smooth 3D Path Planning by Means of Multiobjective Optimization for Fixed-Wing UAVs, Electronics 9(1): 51.

[23] Shubhani Aggarwal, Neeraj Kumar, (2020). Path planning techniques for unmanned aerial vehicles: A review, solutions, and challenges, Computer Communications, Volume 149, Pages 270-299, ISSN 0140-3664, https://doi.org/10.1016/j.comcom.2019.10.014.

[24] Sui D, Yang Z, Ding S, Zhou B., (2023), Three-dimensional path planning of UAV based on EMSDBO algorithm(基于 EMSDBO 算法的无人机三维航迹规划), *Systems Engineering and Electronics*, ISSN 1001-506X, https://link.cnki.net/urlid/11.2422.TN.20231205.1202.016, China;

[25] Tsouros, D.C.; Bibi, S.; Sarigiannidis, P.G. A Review on UAV-Based Applications for Precision Agriculture. Information 2019, 10, 349. https://doi.org/10.3390/info10110349

[26] Ulmer M W, Thomas B W., (2018), Same-day delivery with heterogeneous fleets of drones and vehicles, *Networks*, vol. 72, no. 4, ISSN 1097-0037, pp. 475-505, England;

[27] Wang X, Poikonen S, Golden B., (2017), The vehicle routing problem with drones: several worst-case results, *Optimization Letters*, vol. 11, no. 4, ISSN 1862-4472, pp. 679-697, Germany;

[28] Wang Y, Wang S. (2020). UAV path planning based on improved particle swarm optimization[J]. Computer Engineering & Science, 42(09): 1690.

[29] Xu L, Yang Z, Huang Z, Ding W., (2020), Route planning method for plant protection Unmanned Aerial Vehicles combined with hybrid particle swarm optimization(结合混合粒子群算法的植保无人机航线设计方法), *Journal of Chinese Computer Systems*, 1000-1220, vol. 41, no. 9, ISSN 1000-1220, pp. 1826-1832, China;

[30] Yang, Y.; Xiong, X.; Yan, Y. UAV Formation Trajectory Planning Algorithms: A Review. Drones 2023, 7, 62. https://doi.org/10.3390/drones7010062

[31] Yiheng Liu, Honglun Wang, Jiaxuan Fan, Jianfa Wu, Tiancai Wu, Control-oriented UAV highly feasible trajectory planning: A deep learning method, Aerospace Science and Technology, Volume 110,2021, 106435, ISSN 1270-9638, https://doi.org/10.1016/j.ast.2020.106435.

[32] Yongqiang Qi, Shuai Li, Yi Ke, "Three-Dimensional Path Planning of Constant Thrust Unmanned Aerial Vehicle Based on Artificial Fluid Method", Discrete Dynamics in Nature and Society, vol. 2020, Article ID 4269193, 13 pages, 2020.

[33] Zhang G, Zhu N, Ma S, Xia J., (2021), Humanitarian relief network assessment using collaborative truck-and-drone system, *Transportation Research Part E: Logistics and Transportation Review*, vol. 152, ISSN 1366-5545, pp. 102417, England;

[34] Zhen L., (2015), Tactical berth allocation under uncertainty, *European Journal of Operational Research*, vol. 247, no. 3, ISSN 0377-2217, pp. 928-944, Netherlands;

[35] Zhen L, Zhuge D, Wang S, Wang K., (2017), Daily berth planning in a tidal port with channel flow control, *Transportation Research Part B: Methodological*, vol. 106, ISSN 0191-2615, pp. 193–217.

KINEMATIC SIMULATION AND EXPERIMENTAL ANALYSIS OF A ROLLER BRANCH PICKING MECHANISM
/
辊式枝条捡拾机构运动学仿真与试验分析

Aiqian YANG[1)], Hui LI[1*)], Junfang ZHANG[1)], Xin YANG[2)]
[1)] Hengshui University, Hengshui 053000, China;
[2)] College of Mechanical and Electrical Engineering, Hebei Agricultural University, Baoding, 071000, China;
**E-mail: lihui12345689@163.com*
DOI: https://doi.org/10.35633/inmateh-72-22

Keywords: *apple; branches; counter-roller; picking; model; trajectory*

ABSTRACT
Apple tree branches have the physical characteristics of high cellulose content and high elasticity, and the use of traditional soft straw pickers will miss a large number of branches. It is necessary to design a picking mechanism that adapts to the physical characteristics of fruit tree branches. In the treatment of branches in modern orchards, the picking mechanism is an important part of the picking device. The success rate of picking directly affects the processing performance of the whole machine. To improve the picking rate, the roller branch picking mechanism is studied. The trajectory of the roller picking and the stress state of the branches are analyzed, and five main factors affecting the picking effect are obtained, i.e. the position relationship between the rotation center of the picking roller and the feeding roller, inclination angle of the steel teeth, the effective working length, the speed and the forward speed of the machine. A mathematical model is established to obtain the static and dynamic motion trajectories of the roller picking mechanism are obtained by using Matlab. Taking the analysis results of influencing factors as the optimization goal, the picking trajectory of the mechanism is simulated to obtain a set of non-inferior solutions. A roller branch picker is manufactured according to the parameter values and tested in the field, and the picking rate can reach 91%.

摘要
苹果树枝条具有纤维素含量高、弹性大的物理特性，使用传统的软秸秆类捡拾器进行作业会造成大量枝条漏捡的现象，因此需要设计一种适应果树枝条物理特性的捡拾机构。在现代果园枝条处理过程中，捡拾机构是机器捡拾装置中的重要组成部分。捡拾成功率直接影响着整机的处理性能。为了提高捡拾率，对辊式枝条捡拾机构展开研究。分析了对辊式捡拾运动轨迹以及枝条受力状态，得到 5 项影响捡拾效果的主要因素，分别是捡拾辊与喂入辊的旋转中心相互位置关系、刚性齿的倾斜角度、有效作业长度、转速和机器前进速度。建立数学模型，使用计算机编制 Matlab 程序获得对辊式捡拾机构的静态运动轨迹和动态运动轨迹。以影响因素分析结果作为优化目标，对机构的捡拾轨迹进行了仿真试验，获得一组非劣性解。按照参数值制造出一款对辊式枝条捡拾器并进行了田间试验，捡拾率达 91%。

INTRODUCTION
China has long been the forefront of fruit production in the world. According to incomplete statistics, only in 2020, the apple planting area exceeded 2 million hectares, and the output was as high as 41 million tons, accounting for more than 50% of the world's total output *(Georges et al., 2014)*. With the decline of traditional apple orchard planting modes, China's modern apple orchard cultivation modes have developed rapidly, and the technical means applied are becoming more and more advanced. To ensure apple quality, apple trees need to be pruned several times throughout the year. Pruning has always been a time-consuming, laborious and high-intensity labor process, resulting in about 20% of the management cost of human, material and financial resources *(He et al., 2017)*. Mechanization of pruned branches can reduce investment costs. Picking the scattered branches on the ground and centralizing them is an important step for mechanization.

[1]*Aiqian Yang, Lecture; Hui Li, Assistant Researcher; Junfang Zhang, Lecture; Xin Yang, Professor*

In the harvesting process of ordinary straw crops, the performance of the picking and feeding device directly affects the operational efficiency and quality of the entire machine *(Flick et al., 2019)*.

According to the differences in the biological form and physical characteristics of different crops, different picking methods are the basis of research *(Mou, 2015)*. The key influencing factors, such as the height, position, angle, movement speed and rotation speed of picking, involved in the mechanized treatment of branches are mainly studied. To evaluate the impact of different factors on the picking process of apple branches, its motion trajectory is simulated. A branch picking test platform similar to a sport equipment ball picking mechanism is developed that can adjust the specific parameters of the influencing factors and implement uninterrupted adjustable functions.

Many international agricultural equipment companies have developed picking mechanisms for different crops, with roller picking mechanisms being the majority. For example, the Panther suspended single-roll picking crusher produced by the Niubo manufacturing company in Spain is capable of picking most of the branches. The picking structure of the Super Max suspended roll picking crusher produced by the Niubo Manufacturing Company in Spain consists of the upper and lower rollers. From the axial point of view, the upper roller is forward. During operation, the upper and lower rollers rotate to each other. The lower roller realizes the picking function, and the upper roller realizes the auxiliary feeding function, which greatly reduces the phenomenon of flying out to the outside after the single roller collides with branches *(Velázquez-Martí and Fernández-González, 2019)*. The suspended single-roll picking crusher from the Mirco Bros Pty Company in Australia has added a "steel fork" structure. Its function is to stack the branches on the ground forward, and after reaching the height of single-roll picking, the branches are fed into the crushing chamber.

The TR200 traction branch crushing and collection integrated machine produced by Facma Company in Italy has spiral arrangement of picking teeth, which makes the branch picking movement concentrate towards the center of the spiral *(Amirante et al., 2016)*.

The EDY CHIPPER branch crushing and collection integrated machine produced by the CAEB International Manufacturing Company in Italy was equipped with the gathering device on both sides of the body, increasing the picking width of the machine. This device can concentrate scattered branches on the ground to the center of the orchard rows, making them staggered and intertwined, and the involvement of each other is more conducive to picking *(Adamczyk et al., 2014)*.

The PRB 1.75 circular branch packaging machine jointly developed by the agricultural engineering industry organization in Poland, the orchard farm in Przybroda and the Polish Agricultural University, also applied a roller picking structure *(Frąckowiak et al., 2016)*.

The self-propelled branch crusher jointly developed by IHI Shibaura Co., Ltd., Uji Manufacturing Co., Ltd. and Civil Agricultural Machinery Co., Ltd. in Japan, has its picking part composed of screw augers, which can collect pruned branches to the center in advance.

The main purpose of this study is to design a roller structure picking device suitable for branches, aiming to establish a simulation platform for multi-factor influence on the picking motion of roller. Under the design requirements considering the physical characteristics of apple branches, the influence of the main influencing factors on the picking motion trajectory can be tested to obtain an optimal set of design parameters.

MATERIALS AND METHODS

Characteristics and formation mechanism of the double roller picking and feeding trajectory

Characteristics and posture of picking and feeding trajectories

The double-roller picking and feeding mechanism needs to meet the conditions of continuous conversion of picking, feeding and separating in the picking process of branches. It also needs to be designed taking into account the physical characteristics of apple branches. Generally, the roller picking and feeding mechanism adopts a structure of rotatory roller welded steel teeth, and is composed of the upper part and the lower part. The upper rotatory roller structure is the auxiliary feeding roller, and the lower is the picking roller. Observing the picking of the machine, first, the steel teeth pile up the scattered branches on the ground towards the forward direction of the machine. When the height is higher than the center position of the rotary roller, the branches begin to be lifted off the ground and transit to feeding. During the picking process, a small part of the branches slips off due to being close to the top of the teeth. Some of the branches are assisted by the feeding roller for feeding, as shown in the trajectory 1 in Fig.1.

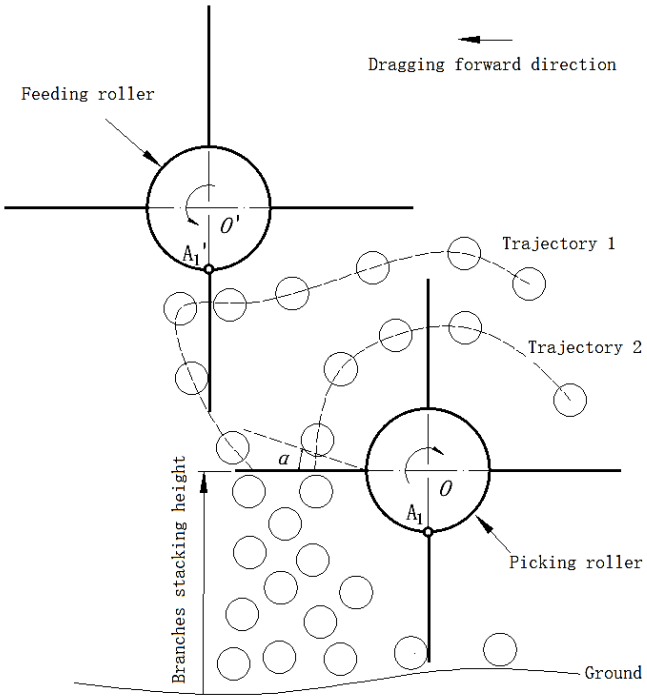

Fig. 1 - The motion trajectory of the double-roller picking and feeding mechanism

Compared with the single-roll picking and feeding mechanism, the double-roll picking and feeding mechanism has added an auxiliary feeding roller to improve the feeding performance and the picking and feeding rate *(Dyjakon et al., 2018)*. The trajectory of the roller steel teeth maintains a perfectly circular shape, showing a regular transverse spiral with different speeds. The picking postures are determined by the spatial angle of the steel teeth. The angle size should comprehensively consider the field obstacle avoidance performance, picking performance and separating performance, shown as α in Fig. 1. The comprehensive analysis shows that the main factors that affect the characteristics of static and dynamic motion trajectories are the position relationship between the rotation centers of the picking roller and the feeding roller, inclination angle of steel teeth, effective working length, speed and machine forward speed. The analysis is as follows:

(1) The position relationship between the rotation centers of the picking roller and the feeding roller

The position between the picking roller and the feeding roller has direct effect on the feeding of branches. When the picking roller mechanism picks up the branches and lifts them off the ground, some branches slip off the tooth tips due to high rotational speed, forming a parabolic trajectory in space and being thrown out. The feeding roller will assist the picking roller in preventing the slipping branches from moving in a parabolic manner, and then feed the branches to the inlet of the crusher. The position between the picking roller and the feeding roller should pay attention to the following points: ① The center position of the feeding roller mechanism should not be too high, and it is best to have the steel tooth tips staggered and "engaged"; ② The center position of the feeding roller should not be too forward or backward relative to the center position of the picking roller mechanism. Excessive forward will effectively prevent the phenomenon of "throwing branches", but will affect the feeding effect. Excessive backward will improve the feeding performance, but will not effectively prevent the phenomenon of “throwing branches".

(2) Inclination angle of the steel teeth

The steel tooth angle of the picking roller is deflected upwards, while that of the feeding roller is deflected downwards. The steel teeth rotate with the roller. The double-roller rotates oppositely in the direction shown in Fig. 1. The steel teeth are arranged axially to form an effective bite angle to feed the branches to the inlet of the crusher. If the inclination angle of the steel teeth is too large, the bite angle formed will be greater, which will affect the separation between the branches and the steel teeth, and may lead to mandatory "cutting" of the branches, causing the machine to instantly overload and stop.

(3) Effective operating length of the steel teeth

The steel teeth are welded onto the roller, and the protective plate is placed on the surface of the roller, but does not contact with the roller and affect its rotation. The length of the steel teeth beyond the radius of the protective plate is the effective operating length.

The effective operating length of the steel teeth is related to the workload, including the rotation radius during picking and feeding operations, as well as the size of machine energy consumption. If the rotation radius is too large, it will raise the picking height, increase the difficulty of picking and increase energy consumption; if the rotation radius is too small, it will directly lead to a narrowing of the feeding window and a decrease in the ability to treat branches.

(4) Rotation speed of the picking and feeding rollers

Since the center position of the picking roller and that of the feeding roller are not on the same vertical coordinate, it is difficult to ensure that each pair of steel teeth is always in the "bite" state during operation in terms of their rotation speed ratio. In the motion simulation trajectory, only when the steel tooth tip of the picking roller and that of the feeding roller intersect in motion can the feeding performance be effectively improved. The solution is to set the initial installation position, so that after a pair of teeth is engaged, the relative position of the power end is fixed for installation. The ratio of the rotation speed of the feeding roller to that of the feeding roller is adjusted to (1.1-1.2):1.

(5) Forward speed

The forward speed of the double-roller picking mechanism should match the processing capacity of branches, and it is also directly affected by the driving force. The forward speed during operation is adjusted based on the branches in the orchards. If the branches are large, the forward speed is reduced; otherwise, the forward speed is increased. If the amount consumed in an instant is large or the diameter of branches is too thick, it is likely to overload and stop.

Dynamic analysis during the picking and feeding process

The double-roller branch picking and feeding mechanism mainly consists of two parts: the picking roller and the feeding roller, which cooperate with each other to complete the picking. Dynamic analysis of the entire mechanism helps to design and optimize the parameters of the mechanism. Fig. 2 shows that the mechanism is roughly up and down, with the feeding roller located in front and above the picking roller. The picking roller rotates clockwise and the feeding roller rotates counterclockwise. Among them, A_1B_1, A_2B_2, $A_3B_3$and A_4B_4 represent four different positions during the movement of the steel teeth on the picking roller. Similarly, $A_1'B_1'$, $A_2'B_2'$, $A_3'B_3'$ and $A_4'B_4'$ represent four different positions during the movement of the steel teeth on the feeding roller. The speed of the two is set according to the kinetic simulation analysis involved later in the design. During operation, the steel teeth on the picking roller rotate at high speed and contact with the scattered branches on the ground. The branches are pushed forward and begin to move forward, pile up, and finally interlace to form a cluster of branches. When the pile reaches a certain height, it will be lifted off the ground by the steel teeth. When leaving the ground, the branches are subjected to the external force exerted by the steel teeth. At the same time, other branches in the stacked state, like the piled rice stalks, have a greater implicated effect, moving forward and upwards *(Lei et al., 2015)*. At this time, the feeding roller rotates counterclockwise, and the steel teeth on the central axis begin to contact the branches, applying backward and downward forces to the branches, making them move towards the entrance of the crushing chamber. After reaching the entrance, they are simultaneously subjected to the dual action of the steel teeth on the feeding roller and the picking roller, moving towards the inside of the crushing chamber. Then the branches are fed into the chamber for crushing, so as to realize picking and feeding.

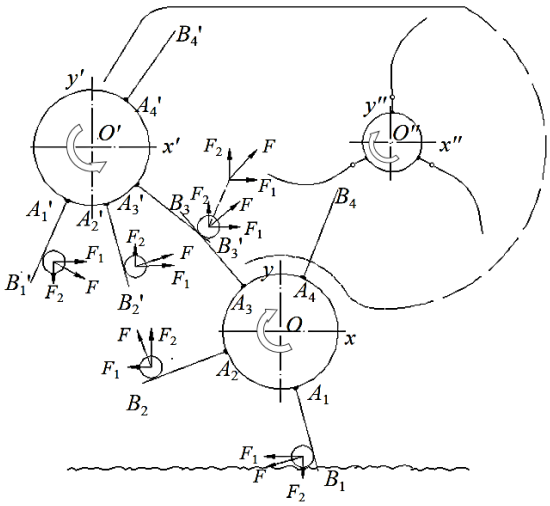

Fig. 2 - Kinetic analysis of the double-roller picking device

In the picking process of branches, the picking roller mainly completes stacking branches, lifting off the ground, conveying backwards, separating branches and returning to the initial state. The feeding roller mainly assists in completing feeding, conveying backwards, separating branches, and returning to the initial state. Under the simultaneous actions, a trajectory is formed from the ground to the air, moving towards the direction of the crushing chamber. As shown in Table. 1.

Table 1

Kinetic analysis during the picking process of branches

Operating parts	Actions	Stress analysis of branches		Space position of the spring teeth
		Horizontal direction F_1	Vertical direction F_2	
Picking roller (Coordinate System *xOy*)	Gather branches	"-"gradually↓	From"-" to"+" gradually↑	A_1B_1~A_2B_2
	Lift off the ground	From"-"to "+"gradually↑	"+"gradually↑	A_2B_2~A_3B_3
	Convey backwards	"+"gradually↑	"+"gradually↓	A_3B_3~A_4B_4
	Branch separating	None	None	A_4B_4~A_1B_1
Feeding roller (Coordinate System*x'Oy'*)	Auxiliary feeding	"+"gradually↑	"+"gradually↑	$A_1'B_1'$~$A_3'B_3'$
	Convey backwards	"+"gradually↓	"+"gradually↑	$A_3'B_3'$~$A_4'B_4'$
	Separating branches	None	None	$A_4'B_4'$~$A_1'B_1'$

Note: "↑" indicates increase; "↓" indicates decrease; "-" indicates the negative direction of the coordinate system axis; "+" indicates the positive direction of the coordinate system axis, and "none" indicates no change.

MATHEMATICAL MODEL OF THE DOUBLE-ROLLER PICKING AND FEEDING MECHANISM

Most fruit tree branches have a high content of wood fiber, a large number of branches, and a certain degree of elasticity *(Nona et al., 2014; Zeng and Chen, 2019)*. Compared with soft straw crops, it is less prone to bending under impact and plastic deformation in compression *(Lei et al., 2022; Yuan et al., 2002)*. In view of these common physical characteristics, a branch picking device with a rigid structure is designed, that is, a double-roller picking and feeding device. It has two parts, the picking roller and the feeding roller, which are installed up and down, and each has irregular shaped steel teeth. The picking roller is located at the lower part of the device, mainly completing the picking, lifting the branches from the ground. The feeding roller is located on the upper part of the device, mainly realizing the function of auxiliary feeding, i.e. feeding the branches to the inlet of the crushing chamber. The entire process is simulated using Matlab software. In the design process of the seedling retrieval mechanism of the automatic transplanting machine, Chen *et al (2013)* used Matlab to optimize the structural parameters to achieve precise clamping. *Mao et al (2013)* and *Liao et al (2015)* studied the kinematic analysis of seven-pole and double-five-pole planting mechanisms respectively, and also solved the mathematical model with the help of Matlab to simulate the motion trajectory and structural optimization. Based on Matlab simulation technology, the structure and working principle of the double-roller picking and feeding device are studied, and a mathematical model is established. Based on Matlab, the software is simulated and analyzed dynamically.

According to the analysis results, the main factors affecting the picking effect are determined, and the main influencing parameters are analyzed by single-factor. Establishing a simulation design platform for branch picking, the main factors are optimized to obtain a set of non-inferior solution combinations. The picking and crushing part of the double-roller branch crusher mainly consists of a frame, a power system, a picking and feeding device, a crushing device, auxiliary support wheel assembly, and a suspension system. Among them, the picking and feeding device mainly includes the transmission end, picking and feeding mechanism, frame, etc. The picking and feeding mechanism is mainly composed of the picking roller, feeding roller, separating assembly, and supporting assembly. The roller is equipped with rigid teeth arranged in a spiral shape, with the axis as the distribution center axis, uniformly distributed, and rotating in opposite directions with *O* and *O'* as the rotation centers, as shown in Fig. 3. The rigid teeth are welded to the central axis. The separation of rigid teeth and branches is accomplished by the separating assembly. The functions of the double-roller picking and feeding device are to accumulate the branches scattered between the rows of orchards, lift the branches off the ground and convey them backwards. During the conveying process, the central axis of the feeding roller rotates oppositely with that of the picking roller. After the rigid teeth of the feeding mechanism contact the branches, it assists it to convey backwards until it enters the crushing chamber for auxiliary feeding.

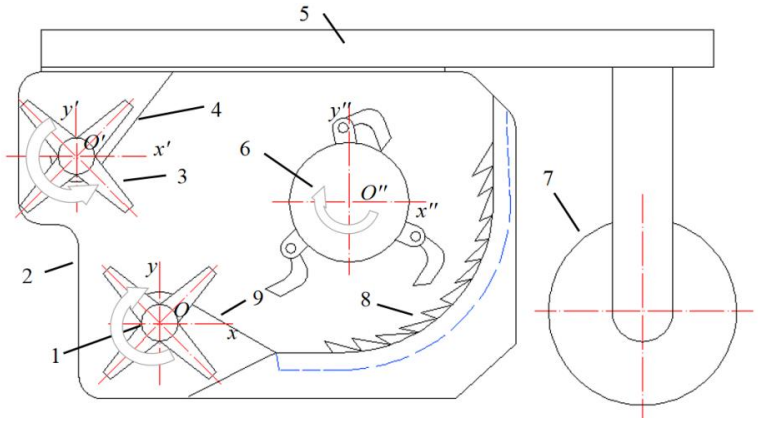

Fig. 3 - Simplified diagram of the branch crusher of the double-roller picking and feeding mechanism

1. Picking roller; 2. Shell; 3. Feeding roller; 4. The feeding roller assembly; 5. Frame; 6. The crusher; 7. Supporting wheel; 8. Serrated blades and filter assembly; 9. The picking roller assembly

(1) The picking roller

The force analysis during the picking process of branches: the picking mechanism rotates clockwise with point *O* as the rotation center. Taking point *O* as the dot, the coordinate system *xOy* is established. A_1, A_2, A_3 and A_4 are four different locations in the operation of point *A*. The coordinates of point *A* are (x_{JA}, y_{JA}); ω_A represents the angular velocity; *t* represents time, and R_{JA} represents the radius of rotation at point *A*. The relationship between ω_A, *t*, and α_A is as follows:

$$\alpha_A = \omega_A \times t \tag{1}$$

The location of point *A*is as follows:

$$x_{JA} = x_{J1} + R_{JA} \times \cos(\alpha_A)$$
$$y_{JA} = y_{J1} + R_{JA} \times \sin(\alpha_A) \tag{2}$$

B_1, B_2, B_3 and B_4 are four different locations in the operation of point B. The coordinates of point B are (x_{JB}, y_{JB}); N_A is the rotation speed, rad/s, and R_{JAB} is the distance from point A to point B, shown as follows:

$$\alpha_B = \alpha_A + N_A \times \frac{\pi}{180} \tag{3}$$
$$x_{JB} = x_{JA} + R_{JAB} \times \cos(\alpha_B)$$
$$y_{JB} = y_{JA} + R_{JAB} \times \sin(\alpha_B) \tag{4}$$

When the tractor runs forward, V_A represents the speed; L_A represents the running distance, and the dynamic coordinates of point A are as follows:

$$x_{DA} = x_{JA} - L_A$$
$$y_{DA} = y_{JA} \tag{5}$$

The dynamic coordinates of point B are as follows:

$$x_{DB} = x_{JB} - L_A$$
$$y_{DB} = y_{JB} \tag{6}$$

(2) The feeding roller

The feeding roller mechanism takes point *O'* as the center of rotation and counterclockwise rotation as the positive direction. Then the coordinates of point *O'* in the *xOy* coordinate system are (x_{w1}, y_{w1}). A_1', A_2', A_3' and A_4' are four different locations in the operation of point A'. The coordinates of point A' are (x_{wA}', y_{wA}'); ω_A' is the angular velocity, and t is the time, shown as follows:

$$\alpha_A' = \omega_A' \times t \tag{7}$$
$$x_{WA}' = x_{W1} + R_{WA'} \times \cos(\alpha_A')$$
$$y_{WA}' = y_{W1} + R_{WA'} \times \sin(\alpha_A') \tag{8}$$

B_1', B_2', B_3' and B_4' are the positions in the operation of point B'. The coordinate of point B' are (x_{wB}', y_{wB}'); N_A' is the rotation speed, rad/s; R_{wA}'$_B$' is the distance from point A' to point B', shown as follows:

$$\alpha_{B'} = \alpha_{A'} + N_{A'} \times \frac{\pi}{180} \tag{9}$$
$$x_{WB}' = x_{WA'} + R_{WA'B'} \times \cos(\alpha_B')$$
$$y_{WB}' = y_{WA'} + R_{WA'B'} \times \sin(\alpha_B') \tag{10}$$

When the tractor is running forward, V_A' represents the speed; L_A' represents the running distance, and the dynamic coordinates of point A' are as follows:

$$x_{DA}' = x_{WA}' - L_A'$$
$$y_{DA}' = y_{wA}' \quad (11)$$

The dynamic coordinates of point B' is as follows:

$$x_{DB}' = x_{WB}' - L_A$$
$$y_{DB}' = y_{WB}' \quad (12)$$

RESULTS AND ANALYSIS

Computer Virtual Simulation of Motion and Parameter Optimization

Based on the kinematic analysis of the double-roller picking and feeding mechanism, and considering the changes in the motion trajectory of the rigid teeth in space in actual operation, a computer program is developed using Matlab to simulate the motion, as shown in Fig. 4.

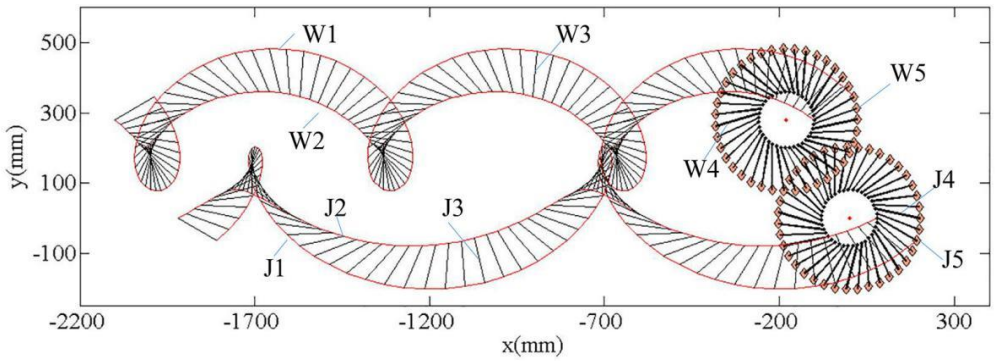

Fig. 4 - Static and dynamic trajectories of the double-roller picking and feeding mechanism

J represents the picking roller mechanism, where *J1* is the dynamic motion trajectory of the steel teeth tip; *J2* is the dynamic motion trajectory of the top of the central rotation axis; *J3* is the space posture of the dynamic motion trajectory of the steel teeth; *J4* is the space posture of the static motion trajectory of the steel teeth; *J5* is the static motion trajectory of the steel tooth tip. *W* represents the feeding roller mechanism, where *W1* is the dynamic motion trajectory of the steel tooth tip; *W2* is the dynamic motion trajectory of the top of the central rotation axis; *W3* is the space posture of the dynamic motion trajectory of the steel teeth; *W4* is the space posture of the static motion trajectory of the steel teeth; W5 is the static motion trajectory of steel tooth tip.

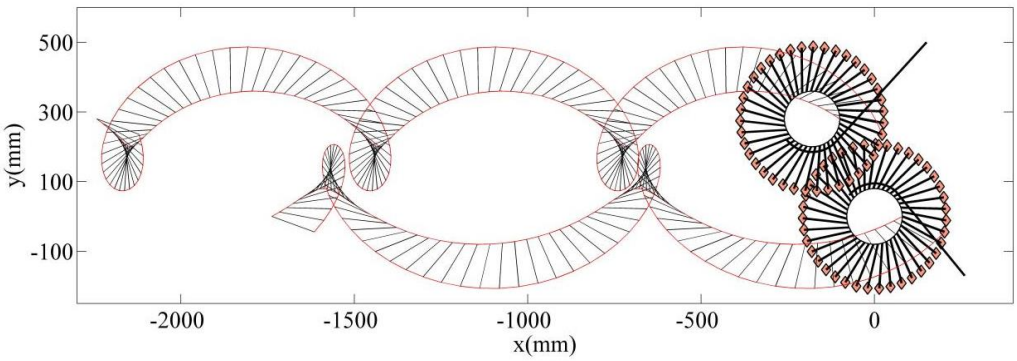

Fig. 5 - Simulation and optimization results of the double-roller picking and feeding mechanism

1. The protective plate of the picking roller; 2. The protective plate of the feeding roller

The dynamic and static motion trajectories of the double-roller picking and feeding mechanism are optimized. The operating posture of the rigid teeth in the picking and feeding roller mechanisms in operation is shown in Fig. 5. The combination of optimized parameters is shown in Table 2. When the inclination angle of the rigid teeth of the picking roller is -20°, it is beneficial for branch picking. At the same time, it forms an angle between it and the protective plate of the picking roller that is conducive to separating branches, reducing the loss of forced cutting of branches. Similarly, when the inclination angle of the rigid teeth of the feeding roller is -20°, the action of auxiliary feeding of branches can be completed. At the same time, the angle conducive to separating branches is formed between the protective plates of the feeding roller. When the rigid teeth are in a horizontal position, the branches basically complete separation under the action of the protective plate.

Table 2

Parameter optimization results of the double-roller picking and feeding mechanism

Parameters	Units	Picking roller	Feeding roller
Rotation center position	(*x*, *y*)	*x*= 0, *y*= 0	*x*= -180, *y*= 280
Radius of the rotation center position	(mm)	80	80
Length of the steel picking teeth	(mm)	130	130
Inclination of the steel picking teeth	(°)	-20	-20
Angle of the protective plate	(°)	-44	50
Rotation speed	(r/min)	33	42
Forward speed	(m/s)	0.5	0.5

Note: The inclination angle of the rigid picking teeth is the angle between the rigid teeth and the horizontal axis; The inclination angle of the rigid picking teeth is the angle between the deviation of the rigid picking from the center of the rotation axis to the root of the rigid teeth. The above direction is negative with clockwise inclination, and vice versa.

Test

Fig. 6 shows the performance test of picking in a rural and mechanical field in Shijiazhuang. First, the branches prepared in advance were weighed, and basically arranged according to the pruning amount of orchard branches of 5-7 years old. The weighed branches were then scattered on a 1.5 m wide and 10 m long channel. The laser tachometer was mounted on the side of the drive shaft to monitor the rotational speed. Finally, the time of passing through the position of the beginning and ending lines was recorded.

Fig. 7 shows that some branches are not treated and there is a phenomenon of "missing picking". Branches that have not been picked up are picked out of the crushed area to record. The method is as follows: the success rate of branch residue collection is defined as the percentage of the total weight of the successfully collected residues *(Xie et al., 2019)*. The picking success rate of branches *(Yu et al., 2018; Li et al., 2019; Popa et al., 2022)* is determined as follows:

Fig. 6 - Ground test of the picking roller

Fig. 7 - The missing branches

$$\eta_2 = \frac{W - W_r}{W} \times 100 \quad (13)$$

where η_2 is the picking success rate; W_r is the lost weight of branches, and W is the weight of the branches scattered on the ground during each test.

According to the data in Table 3, the success rate of picking is 91%. It can be seen that the collection data of this group meets the agricultural technical requirements of picking branches.

Table 3

Statistics of processing data of grapevine and pear branches by the crusher

Items	Branch length (branch)			Branch weight (g)		
	10~20(mm)	20~30(mm)	≥30(mm)	10~20(mm)	20~30(mm)	≥30(mm)
Branches	22	6	2	2678.4	316.2	189.3

CONCLUSIONS

(1) A theoretical model of the double-roller picking and feeding mechanism is established. Based on mathematical models, computer software is used to compile simulation programs. The static and dynamic picking and feeding trajectories of the execution part are simulated by human-machine window interaction. Computer simulation of the picking motion verifies the correctness of the theoretical model. According to the computer simulation, the spatial postures of the execution parts are presented to determine the main factors affecting the simulation motion, including the relative position of the picking roller and the feeding roller, roller speed, forward speed, inclination angle of rigid teeth and effective operating length. Univariate analysis is carried out on the main influencing factors to determine the optimization scope of individual factors. Finally, a set of non-inferior solution parameters are combined as follows: the picking roller, with a rotation center position of (0,0), a rotation center shaft radius of 80 mm, a rigid tooth length of 130 mm, an inclination angle of -20°, a protective plate angle of -44°, a rotation speed of 33 r/min, and a forward speed of 0.5 m/s; the feeding roller, with a rotation center position of (-180, 280), a rotation center shaft radius of 80 mm, a rigid tooth length of 130 mm, an inclination angle of -20°, a protective plate angle of 50°, a rotation speed of 42 r/min, and a forward speed of 0.5 m/s.

(2) The problems and causes of the double-roller picking and feeding mechanism during operation are analyzed as follows: the larger the inclination angle of the rigid teeth, the more the picking performance is enhanced. However, the separating process is not smooth, and even completely relies on the way of cutting the branches. When encountering large tree forks or large swallowing of branches, it is easy to cause stagnation and overload, which is not conducive to the smoothness of machine swallowing branches.

The results of the double-roller branch picking mechanism can provide data support for subsequent research on similar picking mechanisms, making the picking process be smoother. For example, it is applied to institutions for salvaging waste in wetland river basins.

ACKNOWLEDGMENTS

This work was funded by Science Research Project of Hebei Education Department (ZC2023031), Scientific Research Project of Hengshui University (2022GC09), Scientific Research Project of Hengshui University (2023XJZX21), Scientific Research Project of Hengshui University (2022XJZX23), Hengshui Science and Technology Plan Project (2022014024Z), Funding projects for the introduction of overseas students in Hebei Province (C20200355). This research was partially supported in part by Special project for the construction of modern agricultural industrial technology system in China (CARS-27).

REFERENCES

1. Adamczyk, F., Dyjakon, A., Frackowiak, P., Romański, L. (2014). Conception of Machine for Pressing Branches with Pruning Fruit Tree. *Journal of Research and Applications in Agricultural Engineering*, Vol. 59(2), pp. 5-9. (in Poland)
2. Amirante R., Clodoveo M.L., Ruggiero, E.D.F., Tamburrano P. (2016). A tri-generation plant fueled with olive tree pruning residues in Apulia: An energetic and economic analysis. *Renewable Energy*, Vol. 89, pp. 411-421. https://doi.org/10.1016/j.renene.2015.11.085
3. Chen K., Yang X., Yan H., Guo Y., Wu J., Liu J. (2013). Design and Parameter Optimization of the Seedling Picking Mechanism of a Fully Automatic Transplanter Based on Matlab (基于 Matlab 的全自动移栽机取苗机构设计与参数优化). *Chinese Society of Agricultural Machinery*, Vol. 44, pp. 8-11. Doi: 10.6041/j.issn.1000-1298.2013.S1.005 (in Chinese)
4. Dyjakon A., Adamczyk F., Szaroleta M., Pari L., Suardi A., Germer S. (2018). Harvesting of agricultural wood residues from apple orchards using a pruning round baler. *Drewno*, Vol. 61(202), pp. 53-68. DOI:10.12841/wood.1644-3985.04.269.
5. Flick D.E., Nigon C.M., Shinners K.J., Friede J.C. (2019). Control system for a continuous compaction large square baler. *Computers and Electronics in Agriculture*, Vol. 165(June): 104969. https://doi.org/10.1016/j.compag.2019.104969.
6. Frąckowiak P., Adamczyk F., Wąchalski G., Szaroleta M., Dyjakon A., Pari L., Suardi A. (2016). A prototype machine for harvesting and baling of pruning residues in orchards: first test on apple orchard (Malus Mill.) in Poland. *Journal of Research and Applications in Agricultural Engineering*, Vol. 61(3), pp. 88-93.

7. Georges R., Auchet S., Méausoone P.J. (2014). A dynamic measurement of a disc chipper cutting forces. *Biomass and Bioenergy*, Vol. 64, pp: 269-275. https://doi.org/10.1016/j.biombioe.2014.02.033
8. He L., Fu, H., Karkee M., Zhang, Q. (2017). Effect of fruit location on apple detachment with mechanical shaking. *Biosystems Engineering*, Vol. 157, pp. 63-71. http://dx.doi.org/10.1016/j.biosystemseng.2017.02.009.
9. Lei J., Wang D., Li D., Zhang Q., Yang X., Na M. (2015). Analysis and Optimization of Factors Influencing the Formation of Rotating Grass Core in Steel Roller Round Bundling Machine (钢辊式圆捆机旋转草芯形成影响因素分析与优化). *Chinese Society of Agricultural Machinery*, Vol. 46(12), pp. 18-25. DOI:10.6041/j.issn.1000-1298.2015.12.003. (in Chinese)
10. Lei S., Ding L., Li J., Aiken Y. (2022). Study on Bending and Compression Characteristics of Pruning Branches of Jujube (枣树修剪枝条弯曲及压缩特性研究). *Journal of Agricultural Mechanization Research*, Vol. (5), pp. 198-203. DOI: 10.13427/j.cnki.njyi.2022.05.036 (in Chinese)
11. Li H., Yang A.Q., Li J.P. (2019). Subsection Curve Fitting Parameter of Spring-finger Cylinder on Branch Pickup Mechanism Calculated by Reverse Method (多段曲线拟合弹齿式枝条捡拾参数反求法求). *Journal of Agricultural Mechanization Research,* Vol. 41, 34-39. DOI: 10.13427/j.cnki.njyi.2019.09.006 (in Chinese)
12. Liao Q., Liu M., Zhang Z., Hu X. (2015). Multi-objective Optimization Design of Double Five-bar Transplanting Mechanism for Rape Pot Seedling (油菜钵苗移栽机双五杆栽植机构多目标优化设计). *Transactions of the Chinese Society of Agricultural Machinery*, Vol. 46(11), pp. 49-56. (in Chinese)
13. Mao P., Li J., Zhang S., Xu R. (2013). Kinematic Analysis of Seven-rod Planting Mechanism of Seedling Transplanter - Based on MATLAB (七杆式移栽机栽植机构运动学分析——基于 MATLAB). *Journal of Agricultural Mechanization Research,* Vol.12, pp. 59-62. DOI: 10.13427/j.cnki.njyi.2013.12.030 (in Chinese)
14. Mou X. (2015). Design of a Tracked Potato Harvesting and Plastic Film Recycling Compound Machine (履带式马铃薯收获与地膜回收复合作业机的设计), *Shandong Agriculture University*, 2015. (in Chinese)
15. Nona K.D., Lenaerts B., Kayacan E., Saeys W. (2014). Bulk compression characteristics of straw and hay. *Biosystems Engineering,* Vol. 118(1), pp.194-202. https://doi.org/10.1016/j.biosystemseng.2013.12.005
16. Popa L., Trokhaniak V., Constantin, A.M. (2022). Experimental research regarding the realization of an equipment intended for chopping woody waste. *INMATEH Agricultural Engineering*, Vol. 68(3), pp.757-766. https://doi.org/10.35633/inmateh-68-75
17. Velázquez-Martí B., Fernández-González E. (2009). Analysis of the process of biomass harvesting with collecting-chippers fed by pick up headers in plantations of olive trees. *Biosystems Engineering*, Vol. 104(2), pp. 184-190. https://doi.org/10.1016/j.biosystemseng.2009.06.017
18. Xie W., Li X., Fang Z., Quan Wei, Luo H., Wu M. (2019). Design of compound machine for rice straw collecting and continuous baling (水稻秸秆收集与连续打捆复式作业机设计). *Transactions of the Chinese Society of Agricultural Engineering*, Vol. 35(11), pp. 19-25. (in Chinese)
19. Yu Z., Huai S., Wang W. (2018). Optimization of Omission Rate and Working Parameters of Roller Grass Picking Based on the Trajectory of Spring Teeth (基于弹齿轨迹的滚筒式牧草捡拾器遗漏率及工作参数优化).*Transactions of the Chinese Society of Agricultural Engineering*, Vol. 34, pp. 37-43. DOI:10.11975/j.issn.1002-6819.2018.04.005.
20. Yuan Z., Feng B., Zhao A., Liang A. (2002). Dynamic Analysis and Comprehensive Evaluation of Crop-Stem Lodging Resistance (作物茎秆抗倒伏的力学分析及综合评价探讨). *Transactions of the Chinese Society of Agricultural Engineering*, Vol. 18(6), PP. 30-31. (in Chinese)
21. Zeng Z., Chen Y. (2019). Simulation of straw movement by discrete element modelling of straw-sweep-soil interaction. *Biosystems Engineering*, Vol. 180, pp. 25-35. https://doi.org/10.1016/j.biosystemseng.2019.01.009

DESIGNING AND CALIBRATION OF A LOW-COST MULTI-POINT SOIL MOISTURE MONITORING SYSTEM FOR PRECISION AGRICULTURE

/

REALIZAREA ȘI CALIBRAREA UNUI SISTEM, CU COSTURI REDUSE, DE MONITORIZAREA UMIDITĂȚII SOLULUI IN MAI MULTE PUNCTE PENTRU AGRICULTURĂ DE PRECIZIE

Ioan Aurel CHERECHES [1]; Ferenc GASPAR *[1]; Ioan Alin DANCI [2]

[1] Department of Automotive Engineering and Transports, Faculty of Automotive, Mechatronics and Mechanical Engineering, Technical University of Cluj-Napoca, 103-105 Muncii Blvd., Cluj-Napoca / Romania,

[2] Department of Engineering Design and Robotics, Technical University of Cluj-Napoca, 103-105 Muncii Blvd., Cluj-Napoca / Romania

Tel: +40 0264 401 779; E-mail: ferenc.gaspar@auto.utcluj.ro

DOI: https://doi.org/10.35633/inmateh-72-23

Keywords: *soil moisture; data acquisition system; capacitive moisture sensors; Arduino-based system*

ABSTRACT

Soil moisture monitoring and control are essential aspects for precision agriculture. The paper presents the designing and calibration of a low-cost soil moisture monitoring system. The system includes 28 capacitive sensors, connected to an Arduino based data acquisition system, allowing simultaneous multi-point measurements. The calibration process was conducted on six reference points within the moisture content range of 0–25%. The calibration results indicate a non-linear variation and reveal a significant deviation between the sensors leading to the determination of individual variation curves for each sensor.

REZUMAT

Monitorizarea și controlul umidității solului sunt aspecte esențiale pentru agricultura de precizie. Lucrarea prezintă dezvoltarea și calibrarea unui sistem ieftin de monitorizare a umidității solului. Sistemul include 28 de senzori capacitivi, conectați la un sistem de achiziție de date bazat pe placă Arduino, permițând măsurători simultane în mai multe puncte. Procesul de calibrare a fost realizat pe șase puncte de referință în intervalul de umiditate de 0-25%. Rezultatele calibrării indică o variație neliniară și arată o abatere semnificativă între senzori, ceea ce a condus la determinarea unor curbe de variație individuale pentru fiecare senzor.

INTRODUCTION

In recent decades, concern for sustainable agriculture, social sustainability, environmental protection, and sustainable utilization of natural resources has grown in importance over time. Irrigation is an important aspect of agriculture (*Chartzoulakis et al., 2015*) as it provides a reliable source of water for crops, ensuring their growth and productivity. Irrigation helps to mitigate the effects of drought (*Wang et al., 2021*) and ensure crop yields even during periods of limited rainfall.

Efficient irrigation systems can also help to reduce water (*Umair et al., 2019*) waste and prevent soil erosion, preserving the land and water re-sources for future generations. Energy-efficient irrigation systems can help reduce energy consumption and protect the environment. Also, energy production releases an important amount of air polluting gasses, which, law makers are trying to reduce (*Chereches et al., 2018*).

Soil moisture is one of the most important characteristics of total soil fertility, as it directly affects plant growth and crop yield and quality (*Sharma et al., 2018*). Optimum soil moisture can improve crop yields and reduce irrigation costs, while low water content can lead to crop loss and considerable damage to farmers. Therefore, it is essential to monitor soil moisture levels and make well-informed choices regarding irrigation control and crop management as well for researching new irrigation systems (*Mircea et al., 2019*).

Overall, a soil moisture sensor integrated in monitoring system (*Shamshiri et al., 2022*) provides valuable information about soil conditions and helps to optimize water usage in various applications. There are several methods for determining soil moisture content: gravimetric, nuclear, electromagnetic, tensiometric, hygrometric, remote sensing, satellite technology and aerial image processing (*Gheorghe et al., 2019; Susha et al., 2014*) enable indirect quantitative and qualitative soil moisture evaluation.

Literature shows a high interest in developing, testing and calibration of low-cost soil capacitive (*Aringo et al., 2022*), resistive (*Kandwal et al., 2021*) or newly designed, innovative (*Segundo et al., 2011*) moisture sensors usually combined with Arduino-based data acquisition systems. These low budget sensors can be easily integrated in IoT based (*Placidi et al., 2020; Wu et al., 2023; Marino et al., 2023; Ndjuluwa et al., 2023*), wireless (*Schubert et al., 2017*) networks for automated soil moister monitoring (*Nagahage et al., 2019*) or irrigation control (*Dhatri et al., 2019; Sarmphim et al., 2022*) in agriculture or animal husbandry (*Micle et al., 2021*). Due to low energy consumption (*Dhatri et al., 2019*) this monitoring system are suitable for solar powered solutions (*De Melo et al., 2023*). Measurements with low-cost sensor provide a medium accuracy, in some cases show good correlation with traditional soil testing, usually being compared with high end commercial sensor (*Aringo et al., 2022; Schwamback et al., 2023*). However, to provide more accurate measurements (*Domínguez-Niño et al., 2019*), calibration and laboratory or field testing (*Hrisko, 2020*) at different depth and positions for specific soil types (*Kulmány et al., 2022; Adla et al., 2020*) from different geographic areas is mandatory for low-cost sensors (*Bovolenta et al., 2020*). Also, individual calibration (*Bogena et al., 2017*) is recommended as significant deviation and sensor to sensor variability (*Nolz et al., 2013; Nieberding et al., 2023*) has been reported in the same testing conditions. The gravimetric procedure is the most used calibration method to obtain specific linear (*Souza et al., 2020*) or polynomial regression equations.

In this paper, the design and calibration of a data acquisition system based on capacitive soil moister sensors and an Arduino board will be presented.

The proposed system can make determinations of soil moisture content, over a wide range of moisture levels, even outside the range normally encountered in agriculture, using a single acquisition board and 28 sensors arranged in the same plane.

This type of data acquisition system and sensors positioning aims to provide valuable information regarding the efficiency of different irrigation systems in combination with diverse types of soils. It can be used to determine the propagation of water in the soil following irrigation with any type of irrigation system.

MATERIALS AND METHODS

The experiment design consists of two major steps: the system development (design and realization of data acquisition system) and system calibration.

The soil sample used consists of a total of 5000 g of sand (with determined initial moisture content of 0.31%, bulk density 1556 kg/m3, granulometric fractions clay 3.9%, silt 1.4%, fine sand 87.3%, coarse sand 7.3%, other physical characterizations described in (*Fechete-Tutunaru et al., 2019*).

Water used for the experiment was tap water with electric conductivity varied between 70 and 100 µS/cm, the maximum legal limit being <2500 µS/cm.

The capacitive soil moisture sensors used: SKU: CE09640 (Figure 1) are made of a corrosion-resistant material and have the following characteristics: operating voltage: 3.3 ~ 5.5 VDC, output voltage: 0~3.0 VDC, operating current: 5 mA, weight: 15 g, Interface: PH2.0-3P, size: 98mm x 23mm, operating voltage 3.3 - 5.5 V. It has 3 connecting pins. The electronic circuit was manually protected with two-layer sprayed rubber films.

Fig. 1 - Capacitive soil moisture sensor

The moisture content of soil can be assessed by measuring the capacitance between two electrodes inserted in the soil and observing its impact on the dielectric constant. The probe is stimulated with a frequency to facilitate the measurement of the dielectric constant. However, the probe's readout is affected by the soil's type and temperature, and the relationship between water content and the readout is not linear.

The data acquisition system for soil moisture is composed of an Arduino Mega 2560 board, 2 analogue multiplexers with 16 channels CD74HC4067 *(*** Datasheet, 2003*), the 28 capacitive analogue soil moisture 2 electrical strips (one for each polarity), connection cables and the power supply provided via the USB cable connected to a laptop (5V). The system diagram is presented in Figure 2.

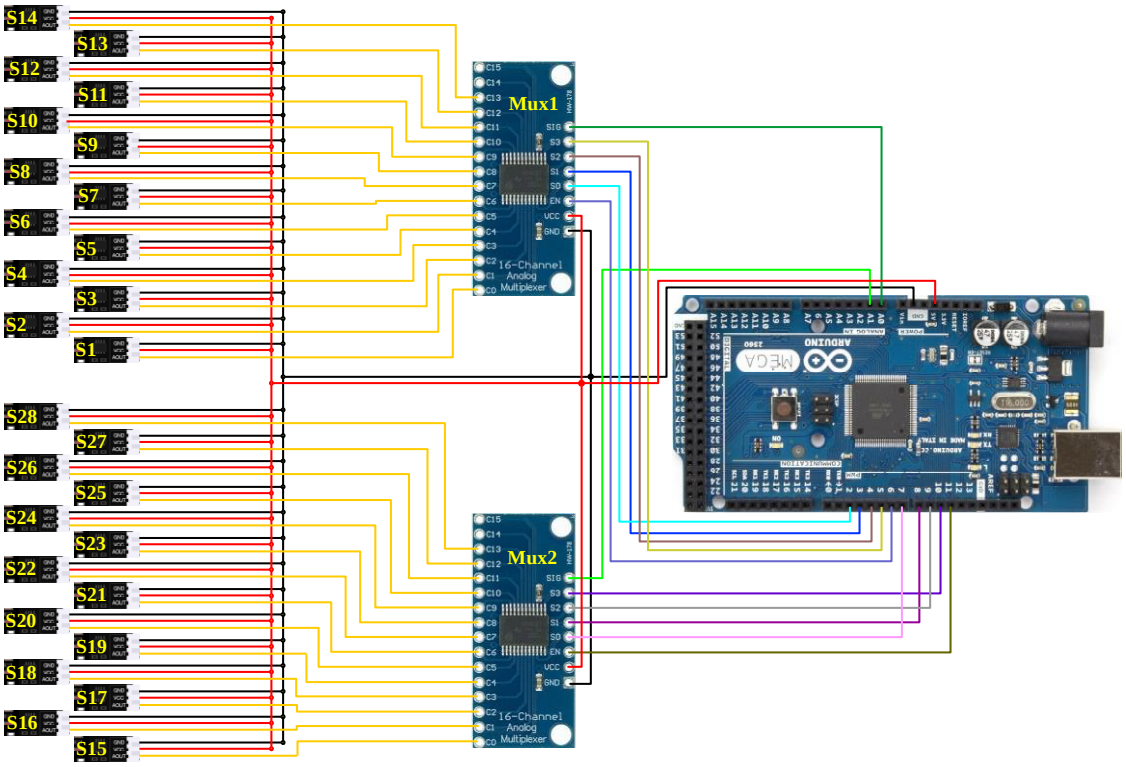

Fig. 2 - The connection diagram of the data acquisition system: S1…S28 – sensors; Mux1, Mux2 - multiplexers

The code for this data acquisition system was written in C++ programming language, which is commonly used for programming microcontrollers like the Arduino, connected to 28 capacitive moisture sensors through two 16 channels multiplexers to increase the number of sensors that can be read by the microcontroller.

The first code lines define the pins that are used to connect to the two multiplexers and the various sensor inputs. The first multiplexer is connected to pins 2-5, and the second multiplexer is connected to pins 7-10. The output enabled pins for the two multiplexers are connected to pins 6 and 11. The moisturePin and moisturePin2 correspond to the analogue inputs connected to the two multiplexers, which read the moisture levels from the sensors.

It is important to multiplex the signals from the soil moisture sensors to reduce the number of input pins needed on the Arduino board. In this code, two 16-channel multiplexers are used to multiplex the signals from the 28 soil moisture sensors.

In the loop function, the code first reads the current time using the getCurrentTime function and prints it to the serial monitor. Then, it loops through each sensor index and reads the moisture value using the selectSensorInput function to select the appropriate input on the multiplexer.

Soil moisture values are stored in a .xls file by using a dedicated software. This allows us to track soil moisture levels over time and have a better understanding of its evolution. Alternatively, a network connection can be used to access data from the real-time soil moisture monitoring system.

After all the sensors have been read, the code loops through each sensor again, with a 1 Hz frequency.

Finally, the code waits for a specified delay using the delay function before starting the loop again.

After the data is collected and stored, specialized software may be used to analyse the data. This allows us to identify patterns in the data and make informed decisions about land management and water resource use.

Overall, this code provides a simple and efficient way to read moisture values from multiple sensors using an Arduino board and to detect moisture distribution.

Analogue capacitive soil moisture sensors produce an electrical voltage between 0 and 5 volts that is proportional to the capacitance of the sensor. This electrical voltage is then measured by an analogue-to-digital converter (ADC) built into the Arduino board, which converts it into a digital value.

All the experimental part took place at room temperature ranging from 20 to 23 ^{0}C.

As a first step a two-reference point calibration step was considered by determining the raw values for dry (in air calibration) and wet conditions (in water calibration, tap water – with conductivity between 70 and 100 µS/cm).

The next step for calibration was to define these values for each sensor, individually, in the written code. Thus, the initial values are transformed into soil moisture percentages and displayed as such.

Aiming for mor precise results, a different, more complex calibration was employed. There are several standards for determining soil moisture, the most common standards for determining soil moisture are ISO 11465:1993 - Soil quality - Determination of dry matter and water content on a mass basis - Gravimetric method. This method involves drying a soil sample at a specific temperature in an oven and measuring the mass of the dry and wet soil to calculate the moisture content; ASTM D2216 - Standard Test Methods for Laboratory Determination of Water (Moisture) Content of Soil and Rock by Mas; ASTM D4643 - Standard Test Method for Determination of Water (Moisture) Content of Soil by Microwave Oven Heating, ISO 11461 - for the determination of soil water content on a volume basis. The authors went on using the procedure described in ISO 11465:1993 - Soil quality standard (*** *ISO-11465-1993, 2016*).

The sand was dried in a thermostatically controlled oven at a temperature of 105 ^{0}C. The procedure consisted in drying a container with lid at 105 ^{0}C and then cooling it, in a desiccator for 60 minutes (Figure 3). Determination of the mass of the wet soil m_{wet} with an accuracy of 10 mg. Then, the container and soil are put in an oven at 105 ^{0}C until constant mass is reached. When constant mass was achieved, the container is cooled with the lid closed, in a desiccator for 60 minutes. The cooled container is immediately measured to determine the mass of the dried soil m_{dry}, with an accuracy of 10 mg.

Fig. 3 – Soil samples in the oven and exicator

During the soil drying procedure and after the procedure was completed, according to (*** *ISO-11465-1993, 2016*), the moisture content of the soil was verified using the AXIS AG120 (*** *Datasheet AGS*) high precision moisture analyser (0.01% moisture and 0.001g mass resolution). The result presented in Figure 4, 0.05%, show that the moisture level was even less than 0.1% mentioned in soil quality standard.

The formula used for determination of water content on a dry mass basis (w_{H2O}), expressed as percentages by mass, to an accuracy of 0.1% (m/m):

$$w_{H_2O} = \frac{m_{wet} - m_{dry}}{m_{dry}} * 100 \quad (1)$$

where:

m_{wet}- represents the mass, in grams, of the wet soil,

m_{dry}- represents the mass, in grams, of the dry soil.

Fig. 4 – AXIS AG120 high precision moisture analyser

Calibration procedure steps include preparing 5000 g of dry soil, preparing soil samples (Figure 5) with soil moisture to 5, 10 … 25% reference values and taking calibration measurements.

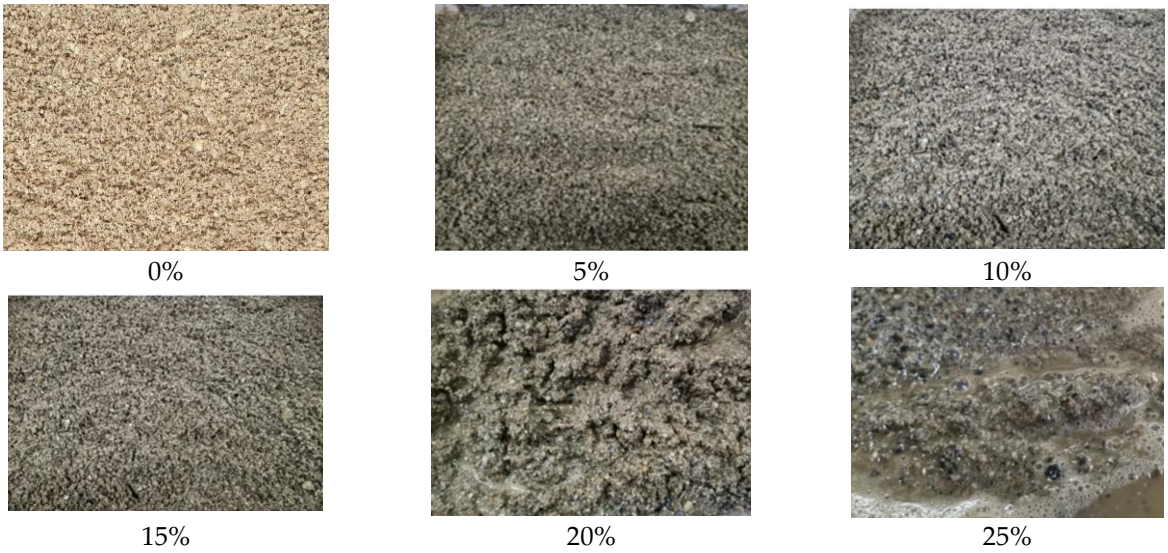

Fig. 5 – Sand samples - different moisture levels

All sensors were calibrated at the same time in the same container at distinct levels of soil moisture and placed at a dept of 70 mm, as can be seen in Figure 6.

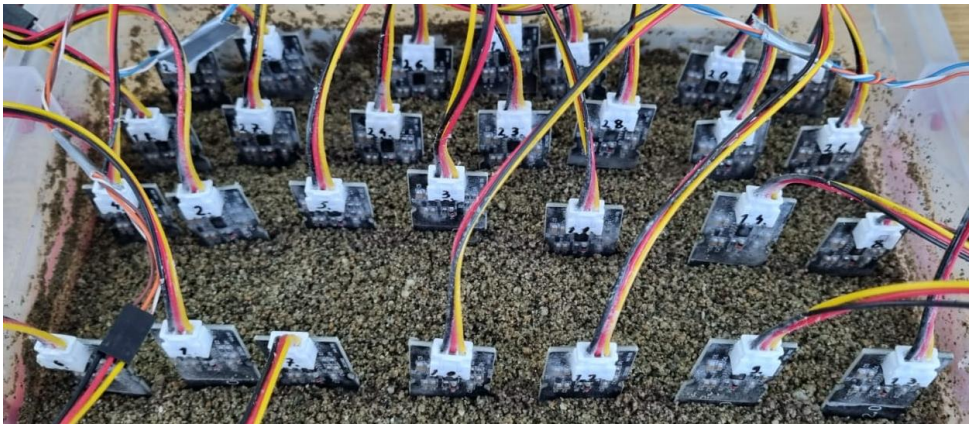

Fig. 6 – Simultaneous sensor calibration step

It is important to specify that the positioning of the sensors and the contact between them and the soil to be analysed required increased attention, because a less good contact between the sensors and the sand produced large variations in the values generated by the sensors.

RESULTS

The values obtained from the 28 capacitive sensors, in all calibration conditions (air, water, and sand at different moisture levels) are plotted in Figure 7. All measurements took place with all 28 sensors inserted in soil (sand) at once and placed at a dept of 70 mm. An average of ten sessions of measurements were produced for each situation (air, water, and sand at different moisture levels), at room temperature (22 ^{0}C). Each session generated at least 15 values for each sensor in every situation (different moisture levels – one measurement per second).

The results of soil moisture sensors calibration measurements, statistically processed, (average, minimum, maximum, standard deviation) are presented in Table 1. The results show a maximum value of 514 Hz for dry and 216 Hz for wet, a minimum of 483 Hz for dry and 190 Hz for wet, an average of 500.35 Hz for dry and 204.71 Hz for wet. The maximum and minimum values are obtained after the stabilization of the measurements. The standard deviation is 9.30 Hz for dry conditions and 6.13 Hz for completely wet conditions.

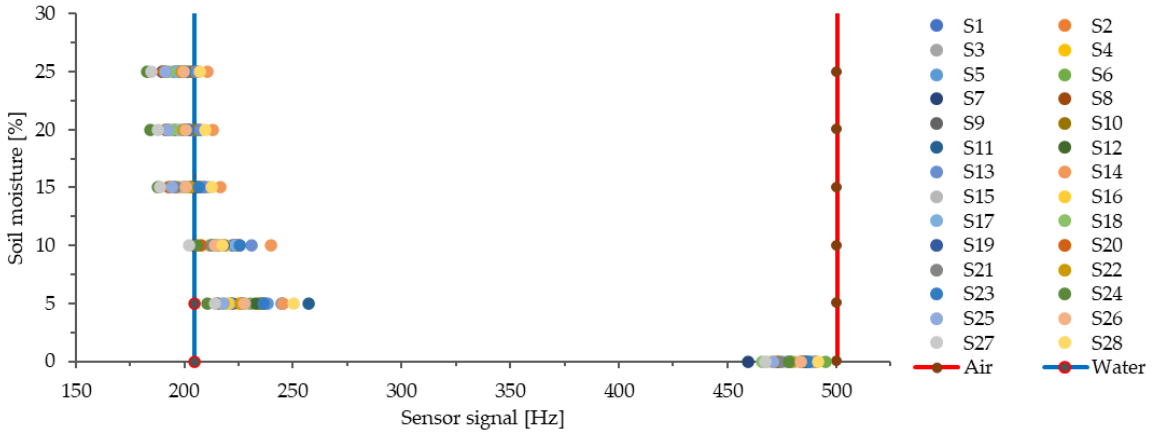

Fig. 7 – Correlation for calibration mean values from 28 sensors – in water, air, and sand (0, 5, … 25% water content)

Table 1

Statistical analysis of calibration results – all sensors average

Analysis	Moisture – signal output [Hz]							
	air	water	0%	5%	10%	15%	20%	25%
Minimum	483	190	459.72	210.90	202.15	187.91	184.43	182.78
Maximum	514	216	495.14	257.17	239.00	216.50	213.08	210.52
Average	500.35	204.71	480.58	230.02	217.65	201.10	198.52	196.45
Standard deviation	9.302	6.133	9.26	11.81	9.48	7.11	6.86	6.68

As can be seen, the initial calibration produces high deviations compared to the precision calibration, thus the values obtained for the initial calibration in air are even higher than in the case of the precision calibration using sand with 0% moisture and in the case of full immersion in water the values obtained are approximately equal to the values obtained in the case of precision calibration at a moisture content of about 15%. This is the reason only on the data obtained by the more accurate method will be relied on.

To assess whether significant differences exist between the mean values of sensors at various soil moisture levels, statistical processing using Analysis of Variance (ANOVA) was employed. The ANOVA test results are presented in Table 2, wherein it is observed that the p-value corresponding to the F-statistic of the one-way ANOVA is less than the standard 0.05 value, indicating that one or more treatments exhibit statistically significant differences.

Table 2

ANOVA test results – only sand samples (0, 5, … 25% soil moisture).

Source of Variation	*SS*	*df*	*MS*	*F*	*P-value*	*F crit*
Between Groups	1737505	5	347501	4763.085	8.9E-174	2.26996
Within Groups	11819.05	162	72.95712			
Total	1749324	167				

The p-value corresponding to the F-statistic of one-way ANOVA is lower than 0.01 which strongly suggests that one or more pairs of treatments are significantly different. For the six levels of moister levels the post hoc Tukey test was applied to pinpoint the statistically significant difference of the 15 pairs of soil moisture samples, Table 3.

The results of the Tukey test indicate that significant differences are observed in most cases, except for pairs corresponding to high soil moisture levels (15–25%). In these cases, sensor sensitivity is reduced, and the recorded signal values for this range of soil moisture are less accurate. Nonetheless, situations where soil moisture exceeds 15% in the case of sandy soil are uncommon and less suitable for agricultural purposes.

Table 3

Tukey test results - only sand samples (0… 25% soil moisture).

Treatments pair	Tukey Q statistic	Tukey p-value	Tukey interference (p<0.01)
0% vs 5%	155.0361	0.001005	significant
0% vs 10%	162.6855	0.001005	significant
0% vs 15%	172.4872	0.001005	significant
0% vs 20%	174.2527	0.001005	significant
0% vs 25%	175.2995	0.001005	significant
5% vs 10%	7.6493	0.001005	significant
5% vs 15%	17.451	0.001005	significant
5% vs 20%	19.2166	0.001005	significant
5% vs 25%	20.2634	0.001005	significant
10% vs 15%	9.8017	0.001005	significant
10% vs 20%	11.5673	0.001005	significant
10% vs 25%	12.614	0.001005	significant
15% vs 20%	1.7656	0.787353	insignificant
15% vs 25%	2.8123	0.353876	insignificant
20% vs 25%	1.0467	0.899995	insignificant

In the pursuit of regression equations several types of variation curves were explored, in Figure 8 the exponential – Asymptotic fit is plotted.

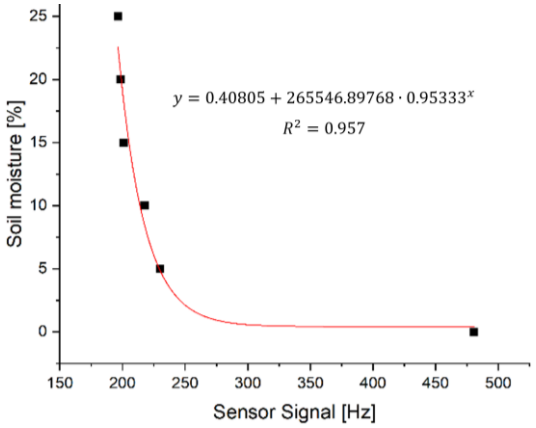

Fig. 8 – General calibration regression curve: Exponential – Asymptotic fit

However, upon the implementation of these equations within certain analysis intervals, substantial deviations were observed as presented in Table 4, where "x" represents signal values and "y" represents the soil moisture. These discrepancies were primarily driven by the elevated variability in sensor-generated data, even though the sensors were procured in a single acquisition. It is worth noting that the batch from which these sensors originate displayed increased variability. Consequently, the analytical domain was partitioned into three distinct intervals: 0–5%, 5–15%, and 15–25%. As a result, the general regression curve obtained across the entire calibration domain was divided into three segments corresponding to the three value intervals, as depicted in Figure 9 along with the corresponding average linear equations.

Table 4

Regression equations analysis

Function	Equations	R^2	Deviation from reference values (predicted values [%] - reference values [%])					
			0 %	5 %	10 %	15 %	20 %	25 %
Linear	$y = 28.08446 - 0.061343 \cdot x$	0.537	1.40	8.97	4.73	0.75	4.09	8.97
Polynomial	$y = 1237.055885 - 13.1996257 \cdot x + +0.04512982 \cdot x^2 - 4.790 \cdot 10^{-5} \cdot x^3$	0.953	0.01	0.70	1.84	3.15	0.48	2.49
Exponential	$y = 0.40805 + 265546.89768 \cdot 0.95333^x$	0.957	0.41	0.13	1.54	3.17	0.50	2.41
Linear: three intervals	$y = 449.91 - 2.1561 \cdot x, x \in [480.3, 230]$	0.978						
	$y = 86.284 - 0.3518 \cdot x, x \in (230, 201.9]$	0.991	0.01	0.01	0.53	0.31	0.83	0.53
	$y = 9.5955 - 0.02 \cdot x, x \in (201.9, 197.3]$	1.000						

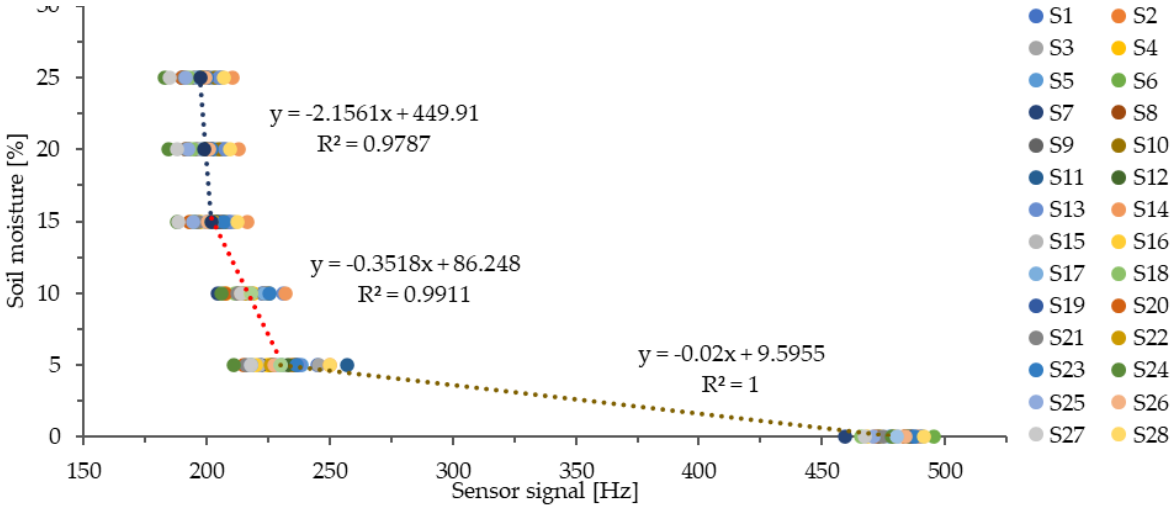

Fig. 9 – General regression curve defined by three linear segments with specific regression equations

However, after subjecting the general linear regression equations to testing for each sensor, a significant deviation from the values obtained during calibration became evident. For these reasons, linear regression equations were determined individually, for each sensor.

The linear regression equations were individually applied to transform the signal values read by each sensor into soil moisture values.

Due to the variation in values generated by different sensors for the same situation (high variability), also proven by the ANOVA test, the p-value corresponding to the F-statistic of one-way ANOVA is lower than 0.01 which strongly suggests that one or more pairs of calibration point references are significantly different.

For the six levels of moisture levels the post hoc Tukey test was applied to pinpoint the statistically significant difference of the 15 pairs of soil moisture samples. The results of the Tukey test show significant differences in most cases, except for calibration point references corresponding to high soil moisture levels (15–25%). In these cases, sensor sensitivity is reduced, and the recorded signal values for this range of soil moisture are less appropriate. Nonetheless, situations where soil moisture exceeds 15% in the case of sandy soil are uncommon and less suitable for agricultural purposes.

The application of a single regression equation results in significant deviations within certain intervals. For these reasons, it was chosen to divide the entire measurement range into three segments (0–5%, 5–15%, and 15–25%) and then calculate individual regression equations for each of the 28 soil moisture sensors, resulting in a total of 74 regression equations. The variation in measured values within the 0–5% range is notably high, leading to significant deviations when applying linear regression across the entire measurement interval (0–25%).

CONCLUSIONS

The paper presents the development and calibration of a multi-point, low cost, soil moisture monitoring system based on 28 capacitive soil moisture sensors connected to a single Arduino board.

Implementing a system like the one presented in the current article requires a heightened degree of attention on calibration. Opting for an expedited calibration will strongly impact the accuracy of measurements, as has been observed. For the best results, it is desirable to conduct an individual calibration process for each sensor, thus minimizing deviations, although it is a time-consuming process.

The available technical equipment and the desire to perform precision calibration directed us towards the mass determination of soil moisture, managing to fit very well within the limits provided by the standards. The use of a quick calibration method, using two extreme environments such as atmospheric air and water, is fast but generates significant deviations, which is why it is not recommended. In line with the water retention capacity of sand, it has been decided that the analysis range should be set between 0% and a maximum of 20% soil moisture, as above 20% the water retention in sand is not possible.

Based on calibration test a polynomial regression curve of the 3rd order or an exponential curve can, in general, produce quite precise values (maximum deviations 3.17%); to have an even higher precision (maximum deviation 0.83%), the 0-25% interval was divided into 3 segments and the linear regression was applied on each of these segments.

This monitoring system should be used to investigate subsurface drip irrigation systems (*Montoya et al., 2022*) and in future articles, the water distribution method for irrigation through several types of soil will be explored and recommendations regarding the suitable irrigation system for different situations will be provided.

REFERENCES

[1] Adla, S., Rai, N.K., Karumanchi, S.H., Tripathi, S., Disse, M., Pande, S. (2020). Laboratory Calibration and Performance Evaluation of Low-Cost Capacitive and Very Low-Cost Resistive Soil Moisture Sensors. *Sensors*, 20, 363, doi:10.3390/s20020363.

[2] Aringo, M.Q., Martinez, C.G., Martinez, O.G., Ella, V.B. (2022). Development of Low-Cost Soil Moisture Monitoring System for Efficient Irrigation Water Management of Upland Crops. *IOP Conf. Ser. Earth Environ. Sci.,* 1038, 012029, doi:10.1088/1755-1315/1038/1/012029.

[3] Bogena, H., Huisman, J., Schilling, B., Weuthen, A., Vereecken, H. (2017). Effective Calibration of Low-Cost Soil Water Content Sensors. *Sensors*, 17, 208, doi:10.3390/s17010208.

[4] Bovolenta, R., Iacopino, A., Passalacqua, R., Federici, B. (2020). Field Measurements of Soil Water Content at Shallow Depths for Landslide Monitoring. *Geosciences*, 10, 409, doi:10.3390/geosciences10100409.

[5] Chartzoulakis, K., Bertaki, M. (2015). Sustainable Water Management in Agriculture under Climate Change. *Agric. Agric. Sci. Procedia*, 4, 88–98, doi:10.1016/j.aaspro.2015.03.011.

[6] Chereches, I.A., Petean, I., Paltinean, G.-A., Mocanu, A., Muresan, L., Arghir, G., Tomoaia-Cotisel, M. (2018). Airborne Particles Pollution in Dej City. *Stud. Univ. Babeş-Bolyai Chem.*, 63, 159–166, doi:10.24193/subbchem.2018.4.13.

[7] De Melo, D.A., Silva, P.C., Da Costa, A.R., Delmond, J.G., Ferreira, A.F.A., De Souza, J.A., De Oliveira-Júnior, J.F., Da Silva, J.L.B., Da Rosa Ferraz Jardim, A.M., Giongo, P.R., et al. (2023). Development and Automation of a Photovoltaic-Powered Soil Moisture Sensor for Water Management. *Hydrology*, 10, 166, doi:10.3390/hydrology10080166.

[8] Dhatri P. V. S. D., Pachiyannan, M., Swaroopa Rani K, J., Pravallika, G. (2019). A Low-Cost Arduino Based Automatic Irrigation System Using Soil Moisture Sensor: Design and Analysis. *In Proceedings of the 2019 2nd International Conference on Signal Processing and Communication (ICSPC);* IEEE: Coimbatore, India, March; pp. 104–108.

[9] Domínguez-Niño, J.M., Bogena, H.R., Huisman, J.A., Schilling, B., Casadesús, J. (2019). On the Accuracy of Factory-Calibrated Low-Cost Soil Water Content Sensors. *Sensors*, 19, 3101, doi:10.3390/s19143101.

[10] Fechete-Tutunaru, L.V., Gaspar, F., Gyorgy, Z. (2019). Soil-Tool Interaction of a Simple Tillage Tool in Sand. *E3S Web Conf.,* 85, 08007, doi:10.1051/e3sconf/20198508007.

[11] Gheorghe, C., Deac, TA., Filip, N. (2019). Image Processing Techniques Used in Soil Moisture Analysis. *INMATEH Agric. Eng.,* 58, 147–154, doi:DOI10.35633/INMATEH-58-16.

[12] Hrisko, J. (2020). Capacitive Soil Moisture Sensor Theory, Calibration, and Testing.

[13] Kandwal, A., Shakya, A., Ramola, A., Vidhyarthi, A. (2021). Development and Analysis of Novel IoT Based Resistive Soil Moisture Sensor Using Arduino UNO. *In Proceedings of the Proceedings of the 2nd International Conference on ICT for Digital, Smart, and Sustainable Development*, ICIDSSD 2020, 27-28 February 2020, Jamia Hamdard, New Delhi, India; EAI: New Delhi, India.

[14] Kulmány, I.M., Bede-Fazekas, Á., Beslin, A., Giczi, Z., Milics, G., Kovács, B., Kovács, M., Ambrus, B., Bede, L., Vona, V. (2022). Calibration of an Arduino-Based Low-Cost Capacitive Soil Moisture Sensor for Smart Agriculture. *J. Hydrol. Hydromech.,* 70, 330–340, doi:10.2478/johh-2022-0014.

[15] Marino, P., Roman Quintero, D.C., Santonastaso, G.F., Greco, R. (2023). Prototype of an IoT-Based Low-Cost Sensor Network for the Hydrological Monitoring of Landslide-Prone Areas. *Sensors*, 23, 2299, doi:10.3390/s23042299.

[16] Micle, D.E., Deiac, F., Olar, A., Drența, R.F., Florean, C., Coman, I.G., Arion, F.H. (2021). Research on Innovative Business Plan. Smart Cattle Farming Using Artificial Intelligent Robotic Process Automation. *Agriculture*, 11, 430, doi:10.3390/agriculture11050430.

[17] Mircea, C., Manea, D., Marin, E., Mateescu, M. (2019). Experimental research in irrigation by condensation in solarium. *Engineering for Rural Development*, 18th International Scientific Conference Engineering for Rural Development, Jelgava, 94-99, DOI: 10.22616/ERDev2019.18. N109.

[18] Montoya, F., Sánchez, J.M., González-Piqueras, J., López-Urrea, R. (2022). Is the Subsurface Drip the Most Sustainable Irrigation System for Almond Orchards in Water-Scarce Areas? *Agronomy*, 12, 1778, doi:10.3390/agronomy12081778.
[19] Nagahage, E.A.A.D., Nagahage, I.S.P., Fujino, T. (2019). Calibration and Validation of a Low-Cost Capacitive Moisture Sensor to Integrate the Automated Soil Moisture Monitoring System. *Agriculture*, 9, 141, doi:10.3390/agriculture9070141.
[20] Ndjuluwa, L.N.P., Adebisi, J.A., Dayoub, M. (2023). Internet of Things for Crop Farming: A Review of Technologies and Applications. *Commodities*, 2, 367–381, doi:10.3390/commodities2040021.
[21] Nieberding, F., Huisman, J.A., Huebner, C., Schilling, B., Weuthen, A., Bogena, H.R. (2023). Evaluation of Three Soil Moisture Profile Sensors Using Laboratory and Field Experiments. *Sensors*, 23, 6581, doi:10.3390/s23146581.
[22] Nolz, R., Kammerer, G., Cepuder, P. (2013). Calibrating Soil Water Potential Sensors Integrated into a Wireless Monitoring Network. *Agric. Water Manag.*, 116, 12–20, doi:10.1016/j.agwat.2012.10.002.
[23] Placidi, P., Gasperini, L., Grassi, A., Cecconi, M., Scorzoni, A. (2020). Characterization of Low-Cost Capacitive Soil Moisture Sensors for IoT Networks. *Sensors*, 20, 3585, doi:10.3390/s20123585.
[24] R. Shamshiri, R., K. Balasundram, S., Kaviani Rad, A., Sultan, M., A. Hameed, I. (2022). *An Overview of Soil Moisture and Salinity Sensors for Digital Agriculture Applications. In Digital Agriculture, Methods and Applications*. R. Shamshiri, R., Shafian, S., Eds.; IntechOpen, ISBN 978-1-80355-462-4.
[25] Susha Lekshmi, S.U., Singh, D.N., Shojaei Baghini, M. A (2014). Critical Review of Soil Moisture Measurement. *Measurement*, 54, 92–105, doi:10.1016/j.measurement.2014.04.007.
[26] Sarmphim, P., Sutthiphon, N., Jaroensong, P., Sirisathitkul, C., Sirisathitkul, Y. (2022). IoT Based Soil Moisture Management Using Capacitive Sensor and User-Friendly Smartphone Application. *INMATEH Agric. Eng.,* 159–166, doi:10.35633/inmateh-66-16.
[27] Schubert, M.J.W., Seign, S., Dai, Q., Hinterseer, S., Pielmeier, F., Pietsch, A., Seebauer, C., Weis, J., Yu, C., Zenger, S. (2017). Capacitive Sensor Technology for Soil Moisture Monitoring Networks. *In Proceedings of the 2017 24th IEEE International Conference on Electronics, Circuits and Systems (ICECS)*, IEEE: Batumi, December, 190–193.
[28] Schwamback, D., Persson, M., Berndtsson, R., Bertotto, L.E., Kobayashi, A.N.A., Wendland, E.C. (2023). Automated Low-Cost Soil Moisture Sensors: Trade-Off between Cost and Accuracy. *Sensors*, 23, 2451, doi:10.3390/s23052451.
[29] Segundo, A.K.R., Martins, J.H., Monteiro, P.M.D.B., Oliveira, R.A.D., Oliveira Filho, D. (2011). Development of Capacitive Sensor for Measuring Soil Water Content. *Eng. Agríc.* 31, 260–268, doi:10.1590/S0100-69162011000200006.
[30] Sharma, M., Singh, A., Mushtaq, R., Nazir, N., Kumar, A., Simnani, S., Khalil, A., Bhat, R. (2018). Effect of Soil Moisture on Temperate Fruit Crops. *A Review. J. pharmacogn. phytochem*, 7(6): 2277-2282.
[31] Souza, G., De Faria, B.T., Gomes Alves, R., Lima, F., Aquino, P.T., Soininen, J.-P. (2020). Calibration Equation and Field Test of a Capacitive Soil Moisture Sensor. In Proceedings of the 2020 IEEE International Workshop on Metrology for Agriculture and Forestry (MetroAgriFor); IEEE: Trento, Italy, November 4; pp. 180–184.
[32] Umair, M., Hussain, T., Jiang, H., Ahmad, A., Yao, J., Qi, Y., Zhang, Y., Min, L., Shen, Y. (2019). Water-Saving Potential of Subsurface Drip Irrigation for Winter Wheat. *Sustainability*, 11, 2978, doi:10.3390/su11102978.
[33] Wang, Y., Li, S., Cui, Y., Qin, S., Guo, H., Yang, D., Wang, C. (2021). Effect of Drip Irrigation on Soil Water Balance and Water Use Efficiency of Maize in Northwest China. *Water*, 13, 217, doi:10.3390/w13020217.
[34] Wu, Y., Yang, Z., Liu, Y. (2023). Internet-of-Things-Based Multiple-Sensor Monitoring System for Soil Information Diagnosis Using a Smartphone. *Micromachines*, 14, 1395, doi:10.3390/mi14071395.
[35] *** Datasheet AGS. AGS Series Moisture Analyzer Datasheet 0318 AGS GB.
[36] *** Datasheet (2003). High-Speed CMOS Logic 16-Channel Analog Multiplexer/Demultiplexer: CD74HC4067, CD74HCT4067 Data Sheet 2003.
[37] *** ISO-11465-1993. (2016). Soil Quality - Determination of Dry Matter and Water Content on a Mass Basis - Gravimetric Method. Zambrano-Vazquez, L.

DESIGN AND PERFORMANCE TEST OF REMOTE DRIVING CONTROL SYSTEM OF SMALL AGRICULTURAL HYDRAULIC CHASSIS
/
小型农用液压底盘远程驾驶控制系统的设计与试验

Xiaorong LÜ[#1)], Yuan FU[#1)], Xinping CHENG[2)], Fugui ZHANG[1)], Yuancai LEN[1)], Dandan HAN[1*)]
[1)] College of Machinery & Electronics, Sichuan Agricultural University, Yaan, Sichuan, 625014, China
[2)]Chengdu Wenjiang Science and Technology Industrial Development Park, Chengdu, Sichuan, 611130, China
[*]*Corresponding author's Email: handan1988@126.com*
DOI: https://doi.org/10.35633/inmateh-72-24

Keywords: *Agricultural chassis, Remote control, Mathematical model, System design, Test.*

ABSTRACT
Aiming at the adaptability and safety problems of agricultural machinery in hilly and mountainous areas, the remote driving control system of agricultural full hydraulic chassis is designed based on ARM-Linux platform. The whole remote driving system is composed of Web upper computer, server system and chassis drive system. According to the requirements of chassis operation, the STM32F407 is used as the lower computer to realize the running control and motion status monitoring of the chassis. Taking the I.MX6ULL as the hardware platform, the Linux as the software platform, and 4G communications as the Web Server, the remote driving of the chassis is realized through Web pages on the computer. It can be seen from the test results that the minimum RTT delay from the Web page driving to the lower computer is 170 ms; the maximum RTT delay is 1310 ms, and the average RTT delay is 222.75 ms. The real-time interactivity of the control system meets the needs of remote driving of the agricultural machinery. The research provides a theoretical basis and technical reference for the development of the remote driving system of the agricultural machinery.

摘要
针对丘陵山区农机具作业适应性、安全性存在的问题，基于 ARM-Linux 平台设计了农用全液压底盘的远程驾驶控制系统。整个远程驾驶系统由 Web 上位机、服务器系统和底盘驱动系统组成。根据底盘作业需求，以 STM32F407 为下位机，实现底盘的行走控制和运行状态监测；以 I.MX6ULL 为硬件平台、以 Linux 为软件平台、基于 4G 通信搭建 Web 服务器，实现在计算机上通过 Web 网页远程驾驶底盘。由测试结果可知，Web 网页驾驶端到下位机的最小 RTT 延时为 170ms，最大 RTT 延时为 1310ms，平均 RTT 延时为 222.75ms，控制系统的实时交互性满足远程驾驶农机具的需要，研究为农用底盘远程驾驶系统的开发提供了理论依据与技术参考。

INTRODUCTION
Due to complex ground conditions, small and micro agricultural machines are more suitable for hilly and mountainous areas *(Wang et al.,2022; Liu, 2018)*. But these agricultural machines have the problems such as poor operation adaptability and manned driving safety. These have resulted in low agricultural mechanization and high agricultural labor costs, restricting the agricultural economic developments in these areas *(Liu et al., 2020; Zheng et al., 2020; Wu et al., 2022)*. Autonomous driving can engage in agricultural production all day to solve these problems of agricultural machinery in hilly and mountainous areas *(Roshanianfard et al., 2020; Zhang et al., 2018; Yang et al., 2021)*. Remote driving can indirectly control the agricultural machinery through the network, improve driving safety, and reduce the demand for labor. Many researches on vehicle remote driving have been carried out to improve vehicle adaptability and controllability *(Alinaghi Hosseinabadi et al., 2020; Zhou et al., 2019; Geetha et al., 2020; Wang et al., 2020; Kim, 2019; Aliff et al., 2019; Cuenca et al., 2019; Han et al., 2022)*. Taking the radio technology as a communication means and a hand-held remote controller as a remote control terminal, *Gázquez et al. (2016)* designed and implemented a remote driving system for agricultural machinery. *Chu et al. (2018)* developed a WIFI based-remote driving intelligent agricultural mobile robot. *Wang et al. (2018)* designed a remote control system for tracked vehicles based on LAN and machine vision. The control system cannot transmit images and has short controllable distance.

Xiaorong LÜ, Professor; Yuan FU, M.S. Student; Xinping CHENG, Engineer; Fugui ZHANG, M.S. Student; Yuancai LEN, M.S. Student; Dandan HAN, Associate Professor.
(#Theses authors contributed to the work equally and should be regarded as co-first authors.)

Heikkilä et al. (2021) designed a remote driving control system on a driving Simulator, which increased the cost and reduced the portability of operation. Based on the Web page and the 4G network, the remote driving control system of agricultural full hydraulic chassis is developed. The study provides a theoretical and technical basis for the development of agricultural machines in hilly and mountainous areas.

MATERIALS AND METHODS

Design of The Hydraulic Drive System

The structure of the chassis hydraulic drive system is shown in Figure 1.

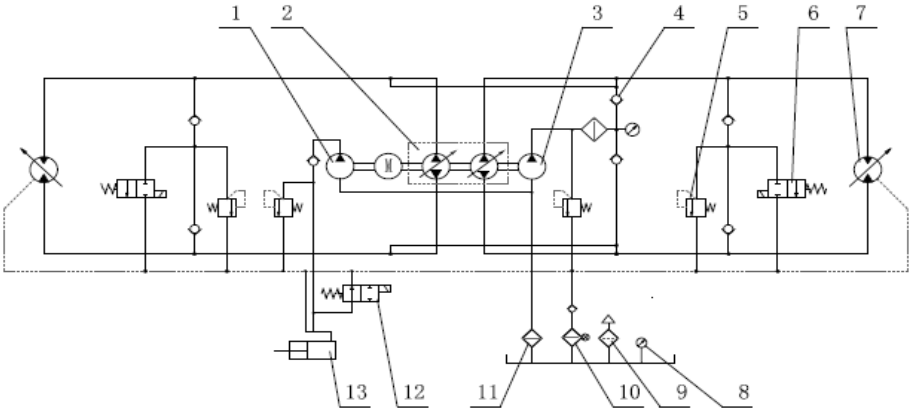

Fig. 1 - Hydraulic drive system diagram of the chassis

1, 3.- Gear pump; 2 - Double-pump; 4 - One-way valve; 5 - Overflow valve; 6, 12 - Electromagnetism reversing valve; 7 - Hydraulic motor; 8 - Pressure gauge; 9 - Air filter; 10, 11 - Oil filter; 13 – Cylinder

When the engine rotates, the transfer case outputs the power to drive the double-pump and gear pump. The power output of the hydraulic system is divided into two routes. When the handle of the double-pump rotates, the valve of the double-pump opens to control the flow of hydraulic oil. Then the hydraulic oil enters the hydraulic motor through the double-pump, and the output shafts of the motor drives the wheels on the chassis to achieve walking. When the handle of the hydraulic control valve is pressed, the gear pump opens and the hydraulic oil enters the hydraulic cylinder through the hydraulic control valve. The hydraulic control valve controls the motion parameters of the cylinder through its flow rate, driving the movement of small agricultural machinery behind the chassis.

Establishment of Control Mathematical Model

The controlled object is a hydraulic chassis powered by a diesel engine. The valve handle of the double-pump is connected to the output shaft of the electric steering gear. Through changing the angle of the steering gear, the opening of the double-pump valve can be changed to control the output speed of the motor. The motor changes the track speed and motion state of the chassis through the drive wheels. The control process of the chassis is shown in Figure 2.

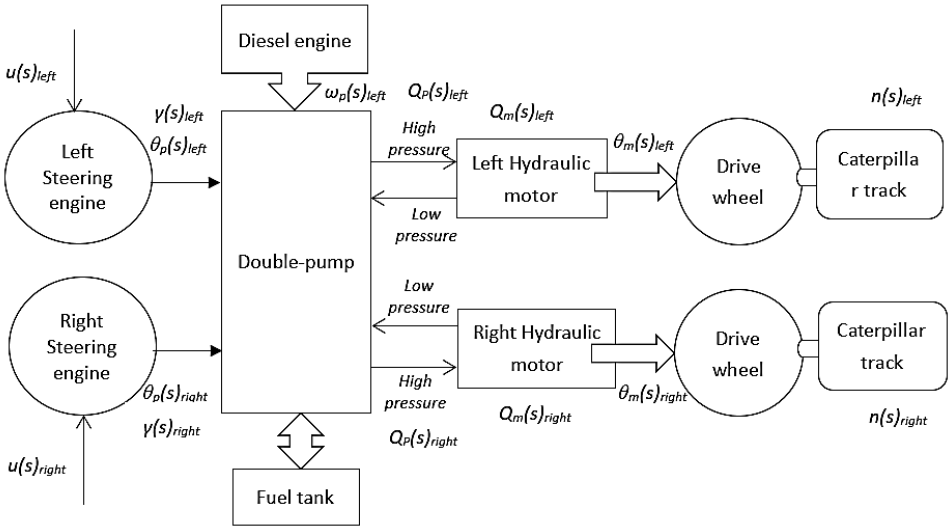

Fig. 2 - Structure of the chassis control

The driving system controls the output speed of the hydraulic motor through an electric steering gear to control the output displacement of the dual pump, realizing the stepless speed regulation of the chassis. Under the action of the controller, the steering gear outputs the angle through the DC motor and the reduction gear. The relationship between the parameters in the dynamic process is analyzed, and the mathematical model of system control is established. The voltage balance of the DC motor is calculated as follows:

$$u(t) = Li'(t) + Ri(t) + K_e\theta_m'(t) \tag{1}$$

where u is the DC motor circuit voltage, V; L is the DC motor inductance, H; R is the DC motor resistance, Ω; I is the DC motor current, A; K_e is the back EMF Constant, V.s/rad, and θ_m is the output angle of DC motor, rad.

The relationship between the DC motor current and output torque is as follows:

$$T = K_T i \tag{2}$$

where T is the DC motor torque, N. m, and K_T is the torque coefficient of DC motor, N· m/A.

The torque balance of the DC motor is calculated as follows:

$$T(t) = J\theta_m''(t) + B_v\theta_m'(t) + M_L \tag{3}$$

where J is the moment of inertia, kg·m^2; B_v is the DC motor damping coefficient, N·s/m; M_L is the equivalent load torque on output shaft of DC motor, N·m.

Through the Laplace transformation of Eqs. (1), (2) and (3), the transfer function of voltage and output angle of the DC motor is as follows:

$$\frac{\theta_m(s)}{u(s)} = \frac{1}{K_e\left(T_m s^2 + s\right)} \tag{4}$$

where T_e is the electrical time constant, s.

The transfer function of the motor output angle and steering gear angle is:

$$\theta_p(s) = K_i\theta_m(s) \tag{5}$$

where K_i -transmission ratio of reduction gear set.

Combined with Eqs.(4) and (5), the transfer function of the DC motor input voltage and the steering gear output angle is as follows:

$$\frac{\theta_p(s)}{u(s)} = \frac{K_i}{K_e\left(T_m s^2 + s\right)} \tag{6}$$

To simplify the modeling process, it is assumed to model under ideal conditions. Setting the speed ω_p of the engine to the variable displacement pump is constant, and ignoring the oil pressure $p_r$of low pressure side, the flow continuity of the hydraulic pump is as follows:

$$Q_p(s) = k_p\omega_p\gamma(s) - C_{tp}p_l(s) \tag{7}$$

where Q_p is the output flow of variable displacement pump, m^3/s; k_p is the displacement gradient of variable displacement pump, m^3/rad^2; γ is the swashplate swing angle of variable displacement pump, rad; ω_p is the operating speed of variable displacement pump, rad/s; p_l is the oil pressure of high-pressure side, Pa; C_{tp} is the total leakage coefficient of the variable displacement pump.

Similarly, ignoring the oil pressure of the low-pressure side, the flow of the high-pressure side of the hydraulic motor is:

$$Q_p(s) = C_{tm}p_l(s) + D_m(s)\theta(s)s + \frac{V_0}{\beta_e}p_l(s)s \tag{8}$$

where C_{tm} is the total leakage coefficient of hydraulic motor, m^5/(N·s); D_m is the hydraulic motor displacement, m^3/rad; V_0 is the total volume of pump control system working chamber and loop connecting pipe, m^3; θ is the output angle of the hydraulic motor, rad.

The torque dynamics of the hydraulic motor and load is as follows:

$$D_m(s)p_l(s) = J_t\theta(s)s^2 + B_m\theta(s)s + G\theta(s) + T_L \tag{9}$$

where J_t - total moment of inertia of hydraulic motor and load, N·m·s^2; B_m -total viscous damping coefficient of hydraulic motor and load, N·m·s/rad; G - Stiffness of load, N·m/rad; T_L - Load torque, N·m.

Assuming the system is a rigid load (G=0) and combined with Eqs. (7), (8) and (9), the transfer function between the swashplate swing angle γ of the variable displacement pump and the output angle θ of the hydraulic motor is as follows:

$$\frac{\theta(s)}{\gamma(s)} = \frac{k_p w_p \omega_h^2}{D_m\left(s^2 + 2\omega_h \xi s + \omega_h^2\right)} \tag{10}$$

where ω_h is the natural frequency of the motor, and ξ is the damping ratio.

The relationship between the two is simplified linearly, as follows:

$$\gamma(s) = K_p \theta_p(s) \tag{11}$$

In actual operation, there will be a certain delay when the output shaft of the steering gear reaches the required angle. There will also be a certain delay when the controlled hydraulic motor pressure by the hydraulic pump reaches the required pressure. Therefore, considering the time-delay link of the system and combined with Eqs. (6), (10) and (11), the transfer function between the input voltage u of the steering gear and the output angle θ of the hydraulic motor is as follows:

$$\frac{\theta(s)}{u(s)} = \frac{K_p k_p \omega_p \omega_h^2 K_e\left(T_m s^2 + s\right)}{D_m K_i\left(s^2 + 2\omega_h \xi s + \omega_h^2\right)} e^{-l} \tag{12}$$

where l -system delay, s.

Since many constant coefficients of the above transfer function are difficult to determine, the identification box of the MATLAB system is used to fit the specific transfer function. Considering that the drive system of the chassis is a large time-delay and nonlinear system, and the maximum time-delay of the system is 150 ms, the transfer function is as follows:

$$\frac{\theta(s)}{u(s)} = \frac{-4.32s^2 + 0.64s}{2250s^2 + 6.4s + 0.0034} e^{-0.15s} \tag{13}$$

Design and Selection of System Hardware

The remote driving system consists of the Web upper computer, the server system and the chassis drive system, as shown in Figure 3. The upper computer is mainly composed of computer equipment that can connect to the internet. The server system consists of the main controller, camera and 4G module. The chassis drive system consists of the lower computer, chassis starting elements, chassis traveling elements, detection elements and PTZ. The starting elements of the chassis include relays, fuel spray nozzle and starter. The chassis traveling elements include the steering engine, double pump and hydraulic motor. The detection elements include speed sensor and inertial measurement unit.

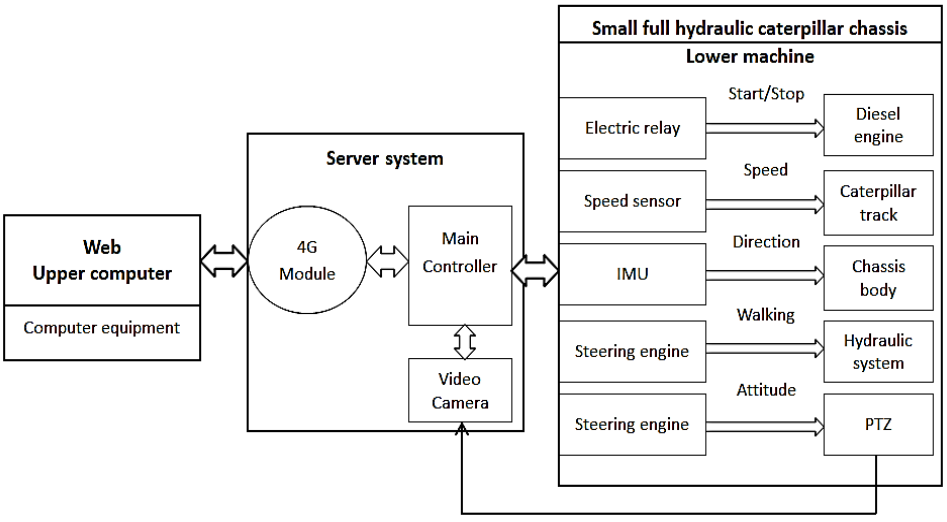

Fig. 3 - Composition and relationship chart of control system

In operation, the main controller sends the image information to the upper computer through the 4G module, and then receives the control command from the upper computer and transmits it to the lower computer. The lower machine controls the start and stop of the diesel engine through ON/OFF of the relay.

The oil pressure of the double-pump and hydraulic motor circuit are controlled by the valve opening of the dual pump controlled by the chassis steering engine, therefore controlling the speed of the hydraulic motor. The traveling speed and direction information of the chassis is obtained by reading the detected data of the encoder and the inertial measurement unit, and the information is uploaded to the upper computer for real-time display. The main controller is mainly used to build the server system, which requires high-speed, multi-transaction processing capabilities and much peripheral interfaces. As shown in Figure 4, the I.MX6U-ALPHA development board is determined to be the main controller. The development board uses I.MX6ULL with Cortex-A7 architecture as the main control chip, the main frequency is 729MHz. The camera provides the video data for the remote control chassis, which requires a certain vision range and good transmission effect. As shown in Figure 5, the HBV-1780-2S2.0 camera is selected. Considering the cost, stability and other factors, EC20 is selected as the 4G network module.

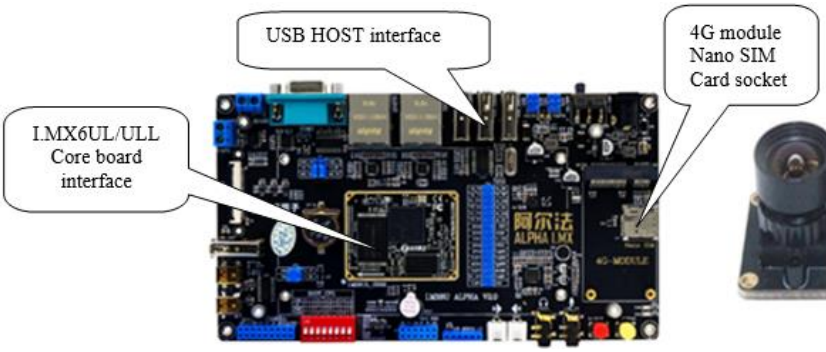

Fig. 4 - I.MX6U-ALPHA development board

Fig. 5 - USB Camera

Considering the requirements of the system for real-time and multitask processing capability, the STM32 core board of ARM architecture is selected as the lower computer. According to the structural characteristics and operating conditions of the chassis, Omron E6B2-CWZ6C is used as the encoder to measure the speed of the chassis. The resolution is 1000P/R, and the input voltage is DC5V-24V. It is installed at the coaxial position of the caterpillar and drive wheel, as shown in Figure 6.

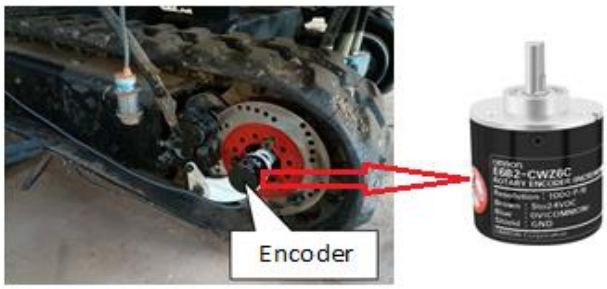

Fig. 6 - Encoder object and installation position

Inertial Measurement Unit (IMU) is used to measure the deflection angle of the chassis. As shown in Figure 7, the six-axis sensor with the chip MPU6050 is selected. It communicates with the main controller through the IIC interface, and the communication rate is 400 kHz. It has an ADC with 16-bit resolution and a DMP digital motion processor. The solution frequency is up to 200 Hz, which can greatly reduce the calculation pressure of the microcontroller.

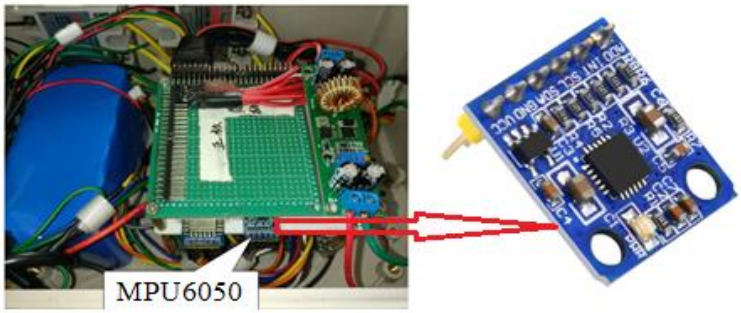

Fig. 7 - Six - axis Sensor and Installation Position

The design and installation of the PTZ should ensure the breadth and depth of the camera's field of view. The PTZ is designed as a 2 DOF mechanism, which can rotate around the x-axis and z-axis by two small steering engines. The top steering engine is used to change the line of sight, and the bottom one is used to change the acquisition range. Therefore, the top steering engine that can rotate 180° is selected, and the bottom steering engine that can rotate 360° is selected. The MG90S is selected as the top steering engine and the SG90 9G is selected as the bottom steering engine. The two steering engine are driven by PWM pulse; the effective high level of the pulse is 0.5 ms-2.5 ms; the response speed of the steering engine is 0.12 sec/60°, and the maximum torque is 1.6 KG/cm. To more comprehensively collect the environmental information, the PTZ is installed in the front of the chassis bridge, as shown in Figure 8.

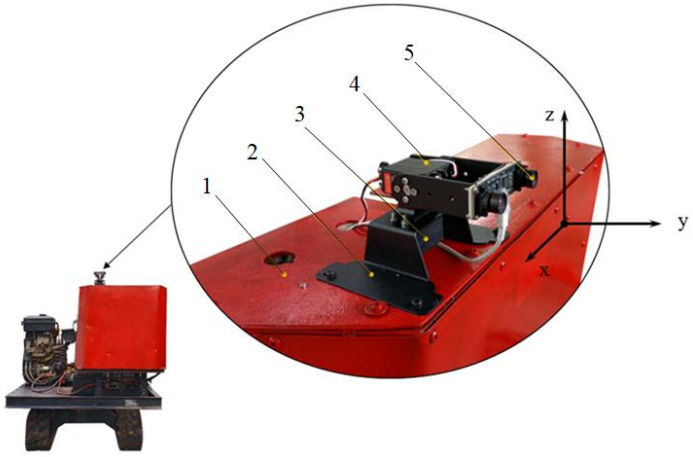

Fig. 8 - Figures of physical objects and installation positions of the pan tilt
1 - Installation platform; 2 – PTZ; 3 - Bottom steering engine; 4 -Top steering engine; 5 -Camera

Design of System Software

The system software is composed of the Web upper computer software, the server system software and the chassis drive system software. The interrelationships and processes are shown in Figure 9.

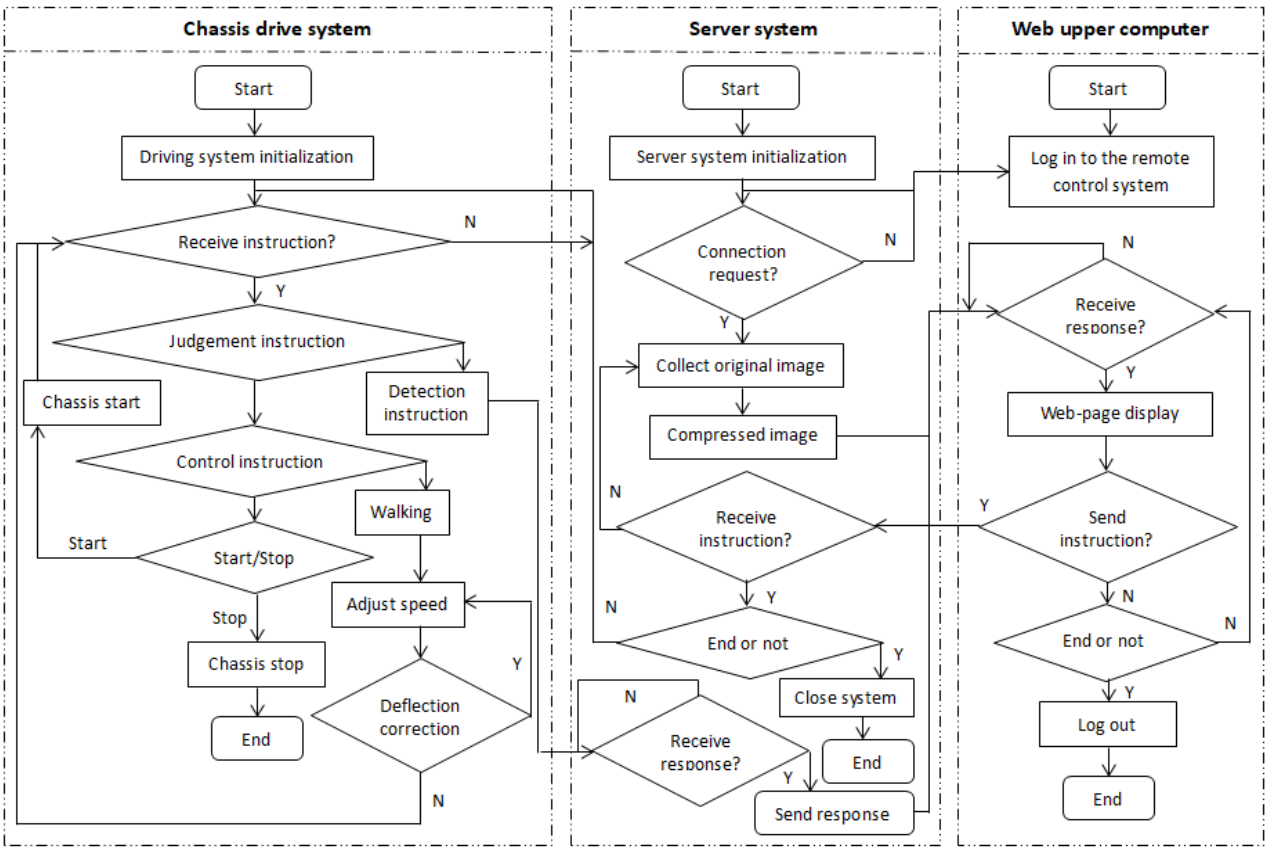

Fig. 9 - Flow chart of software system

The software of the Web upper computer is used to realize the communication function between the remote driving panel and the upper computer. The control commands are sent to the monitoring video through the remote driving panel.

The remote driving Web interface is designed with Bootstrap 3.0 and Ajax technology. The server system software is used to realize the functions of distribution network, video capture, video coding and connection processing. It provides network connection for upper computer and lower computer through Linux operating system.

The network information transmission function of the server system is realized through 4G network. The network channel of the remote control chassis is provided by building a TCP network server. The software of the drive system is used to realize the functions of lower computer communication, chassis drive and detection. With STM32F407 as the control core and MDK5 as the software development platform, the walking control and status detection of the chassis are realized. The lower computer communication is responsible for the data interaction between the upper computer and the lower computer. The timer is used to drive the steering engine to control the movement of the chassis and PTZ. The detection function is used to realize real-time detection of the chassis posture and network status. In this study, the chassis speed is controlled in 0-8 km/h, and the timer is used to measure respectively the output pulses numerical value of (M_{left}, M_{right}) of the left and right encoders. The numerical value of output high-frequency clock pulses is M_{high}, and the output frequency f_{high} is 20 Hz. The basic timer is used to output the sampling pulse, and the data is read once every 50 ms. The M/T method is used to calculate the measured chassis speed v (m/s) by the encoder *(Akkaya et al., 2020; Jia et al., 2018)*.

The calculation is as follows:

$$v = \frac{v_{right} + v_{lift}}{2} = \frac{2\pi r f_{high}}{Z M_{high}} \left(M_{right} + M_{lift} \right) \tag{14}$$

where:

r is the radius of the drive wheel of the chassis, 0.12 m, and z is the solution of the encoder, z=4000P/R.

The six-axis sensor MPU6050 is used as the inertial measurement unit to measure the travel direction angle of the chassis. The lower computer converts the quaternion output by the sensor into Euler angle.

The deflection angle of the chassis is as follows:

$$\emptyset = \tan^{-1}\left(\frac{2wz - 2xy}{w^2 - x^2 + y^2 - z^2}\right) \tag{15}$$

where:

ϕ is the driving deflection angle, and w, x, y, *and* z are the quaternion.

The timer is used to detect the RTT delay between the upper computer and the lower computer. When the time of two adjacent "GET" instructions exceeds the delay threshold, the lower computer reports an exception reminder to ensure the real-time interaction of the system. When the network delay is less than 170 ms, there is little impact on the remote driving. When the network delay is greater than 700 ms, the operability of remote delay will be significantly affected. When the network delay is greater than 1 s, the real-time interactivity of the remote driving can hardly be guaranteed *(Chu et al., 2018; Wang et al., 2018)*. To ensure the smoothness and safety of the remote driving, the delay threshold is set as 1 s.

RESULTS AND ANALYSIS

Steering Performance Test

The real-time interactivity of the remote control system is tested through information transmission during driving and real-time detection of RTT delay. The self-designed hydraulic chassis with a remote driving control system is selected, where the 4G wireless network is used to access the Internet, and the designed software platform is used for remote driving. In the test, the chassis was driven along the specified route at 0.6 m/s. The total travel was about 900 m. The image dates of the surrounding environment and the movement status of the chassis were observed in real time, and the network delay was recorded. The driving route is shown in Figure 10.

Fig. 10 - Roadmap of remote driving

During the chassis driving, the remote control terminal sends the control commands to rotate the PTZ on the chassis, and the surrounding environment images is real-time collected in the front, left, right and rear of the chassis. The real-time test results are shown in Figure 11.

(a) Front environment image (b) Left environment image

(c) Right environment image (d) Rear environment image

Fig. 11 - Image acquisition of the surrounding environment of the chassis

The whole remote driving process takes 28 minutes. During the chassis driving, the RTT delay data is recorded by the upper computer, and the delay data is graphed by MATLAB software. The results are shown in Figure 12.

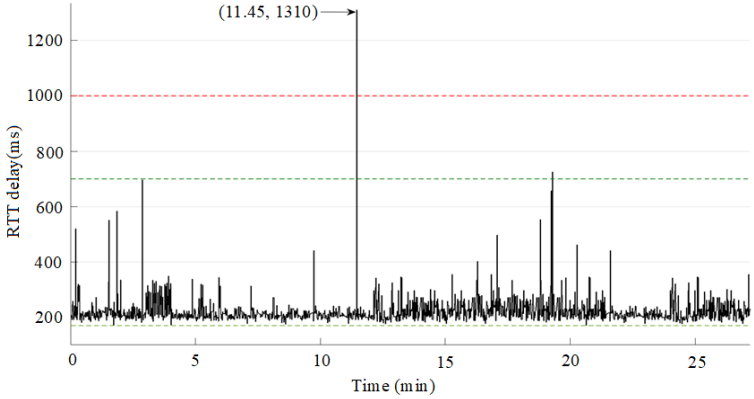

Fig. 12 - RTT delay graph from the upper computer to the lower computer

The test results show that the remote control system can achieve real-time data transmission by the 4G network. The collection for real-time information is flexible; the collected images are complete and accurate, and the image display is stable and smooth, meeting the requirements of the control system for the image collection and transmission of the surrounding environment of the chassis. The remote control system can timely and accurately collect the parameter information in the traveling process of the chassis, and real-time control the chassis for traveling through the instructions. Therefore, the control process is safe and reliable. The delay performance of the control system in Figure 12 shows that the maximum delay time is 1310 ms, which occurs in 11.45 min. At this time, the chassis waits for the network delay to recover within 1000 ms. The minimum delay is 170 ms, occurring at 1.76 min. The delay time occurs twice between 700 m/s and 1000 ms. In this state, the network delay has a significant impact on remote driving. Through calculation, the average RTT delay is 222.75 ms.

CONCLUSIONS

(1) To improve the controllability and safety of the chassis in hilly and mountainous areas, the remote driving control system is designed. The control system can better realize the real-time collection and transmission of the environment images and motion parameters of the chassis through the 4G network. The remote driving control system can realize the remote control of the chassis through human-computer interaction, which is flexible, safe and reliable.

(2) The real-time interaction of the remote driving control system is tested. The test results show that the average delay of data transmission from the upper computer to the lower computer is 222.75 m/s, meeting the requirements of remote driving for real-time interactivity.

(3) The designed control chassis has a certain mechanical delay. Based on the test, the maximum mechanical delay of the chassis is about 100 ms, and the response time of the human brain to sudden situations is about 200 m/s. It can be seen that in case of an emergency, the average delay from the sending of instructions from the upper computer to the execution completion is about 522 ms. When the speed of remote driving chassis is 0.6 m/s, the reaction distance is 0.31 m, meeting the setting requirements of remote control machines.

ACKNOWLEDGEMENT

The study was supported by the National Key Research and Development Program, Key Technologies of Industrialized Agriculture and Intelligent Agricultural Machinery Equipment (2023YFD200050502) and Sichuan Innovation Team of Chinese National Modern Agricultural Industry Technology System (SCCXTD-2024-20).

REFERENCES

[1] Akkaya, R., & Kazan, F. A. (2020). A new method for angular speed measurement with absolute encoder. *Elektronika ir Elektrotechnika*, 26(1), 18-22. https://doi.org/10.5755/j01.eie.26.1.25307

[2] Aliff, M., Raihan, N., Yusof, I., & Samsiah, N. (2019). Development of Remote Operated Vehicle (ROV) Control System using Twincat at Main Control Pod (MCP). *International Journal of Innovative Technology and Exploring Engineering (IJITEE)*, 8(12), 5606-5610. https://doi.org/10.35940/ijitee.L4019.1081219

[3] Alinaghi Hosseinabadi, P., Soltani Sharif Abadi, A., Mekhilef, S., & Pota, H. R. (2020). Chattering-Free Trajectory Tracking Robust Predefined-Time Sliding Mode Control for a Remotely Operated Vehicle. *Journal of Control, Automation and Electrical Systems*, 31, 1177-1195. https://doi.org/10.1007/s40313-020-00599-4

[4] Chu, L. Z., Bai, H. R., Li, J., Wang, F. Y., Guo, R. H., & Sun, Y. (2018). Design of Mobile Robot System Based on the Android System (基于安卓系统农业智能移动机器人的系统设计). *Journal of Agricultural Mechanization Research*, 40(10), 239-242+256. China. https://doi.org/10.13427/j.cnki.njyi.2018.10.046

[5] Cuenca, Á., Zhan, W., Salt, J., Alcaina, J., Tang, C., &Tomizuka, M. (2019). A Remote Control Strategy for an Autonomous Vehicle with Slow Sensor Using Kalman Filtering and Dual-Rate Control. *Sensors*, 19(13), 2983. https://doi.org/10.3390/s19132983

[6] Gázquez, J. A., Castellano, N. N., & Manzano-Agugliaro, F. (2016). Intelligent low cost telecontrol system for agricultural vehicles in harmful environments. *Journal of Cleaner Production*, 113, 204-215. https://doi.org/10.1016/j.jclepro.2015.11.015

[7] Geetha, G., Saranya, G., Meenakshi, K., &Safa, M. (2020). Internet Controlled Remote Vehicle with Live Video Relay and Local Memory. *International Journal of Recent Technology and Engineering (IJRTE)*, 8(5), 4912-4917. https://doi.org/10.35940/ijrte.E5775.018520

[8] Han, K., & Lee, H. (2022). Speed Control of Remotely Operated Multi-Wheel Motor-Driven Vehicles for Unpaved Roads and Obstacles. *International Journal of Automotive Technology*, *23(5)*, 1197-1212. https://doi.org/10.1007/s12239-022-0106-y

[9] Heikkilä, M., Suomalainen, J., Saukko, O., Kippola, T., Lähetkangas, K., Koskela, P., &Posti, H. (2021). Unmanned Agricultural Tractors in Private Mobile Networks. *Network*, 2(1), 1-20. https://doi.org/10.3390/network2010001

[10] Jia, X. D., Wan, Q. H., Zhao, C. H., Du, Y. C., & Yu, H. (2018). Status and Prospect of Velocity Measurement Method with Optical Encoder (光电编码器测速方法现状与展望). *Instrument Technique and Sensor*, (3), 102-107. China.

[11] Kim, J. Y. (2019). A Study of Artificial Intelligence Platform for Vehicle Remote Control: AI Speaker-Based Service Case. *The Journal of Korean Institute of Communications and Information Sciences*, 44(12), 2362-2373. https://doi.org/10.7840/kics.2019.44.12.2362

[12] Liu, C. L., Lin, H. Z., Li, Y. M., Gong, L., & Miao, Z. H. (2020). Analysis on Status and Development Trend of Intelligent Control Technology for Agricultural Equipment(农业装备智能控制技术研究现状与发展趋势分析). *Transactions of the Chinese Society for Agricultural Machinery*, 51(1), 1-18. China.

[13] Liu, X. W. (2018). The path choice of agricultural mechanization development in hilly and mountainous areas (丘陵山区农业机械化发展路径选择). *Modern Agricultural Equipment*, (1), 13-17. China.

[14] Roshanianfard, A., Noguchi, N., Okamoto, H., & Ishii, K. (2020). A review of autonomous agricultural vehicles (The experience of Hokkaido University). *Journal of Terramechanics*, 91, 155-183. https://doi.org/10.1016/j.jterra.2020.06.006

[15] Wang, S., Zhang, S., Ma, R., Jin, E., Liu, X., Tian, H., & Yang, R. (2018). Remote control system based on the Internet and machine vision for tracked vehicles. *Journal of Mechanical Science and Technology*, 32(3), 1317-1331. https://doi.org/10.1007/s12206-018-0236-3

[16] Wang, X.W., Yuan, S.Q., & Jia, W.D. (2022). Current situation and development of agricultural mechanization in hilly and mountainous areas(丘陵山区农业机械化现状与发展). *Journal of Drainage and Irrigation Machinery Engineering*, *40(5)*, 535-540. https://doi.org/10.3969/j.issn.1674-8530.21.0351

[17] Wang, Z., Yang, S., Xiang, X., Vasilijević, A., Mišković, N., & Nađ, Đ. (2020). Cloud-based remote control framework for unmanned surface vehicles. *IFAC-PapersOnLine*, 53(2), 14564-14569. https://doi.org/10.1016/j.ifacol.2020.12.1462

[18] Wu, H.Z., Niu, P., Xie, Y.J., Xia, F., & Wang, M. M. (2022). Present Situation and Suggestions of Agricultural Mechanization in Southwest Hilly and Mountainous Areas (西南丘陵山区农业机械化发展现状及建议). *Agriculture and Technology*, 42(13), 68-70. https://doi.org/10.19754/j.nyyjs.20220715016

[19] Yang, T., & Li, X.X. (2021). Research progress of agricultural machinery autopilot system and analysis of industry competition environment(农机自动驾驶系统研究进展与行业竞争环境分析). *Journal of Chinese Agricultural Mechanization*, 42(11), 222-231.

[20] https://doi.org/ 10.13733/j.jcam.issn.2095-5553.2021.11.33

[21] Zhang, Z.G., Wang, J., Zhu, J.G., Hu, L., & Luo, X.W. (2018). Research progress of auto drive system of agricultural machinery in China. (我国农业机械自动驾驶系统研究进展). *Agriculture Engineering Technology, 38(18),* 23-27. https://doi.org/10.16815/j.cnki.11-5436/s.2018.18.004

[22] Zheng, Y.J., Jiang, S.J., Chen, B.T., Lv, H.T., Wan, C., & Kang, F. (2020). Review on Technology and Equipment of Mechanization in Hilly Orchard (丘陵山区果园机械化技术与装备研究进展). *Transactions of the Chinese Society for Agricultural Machinery*, *51(11)*, 2020, 1-20.

[23] Zhou, L., Wang, G., Sun, K., & Li, X. (2019). Trajectory Tracking Study of Track Vehicles Based on Model Predictive Control. *StrojniškiVestnik - Journal of Mechanical Engineering*, 65(6), 329-342. https://doi.org/10.5545/sv-jme.2019.5980

ANALYSIS AND MANAGEMENT OF ORGANIC AGRICULTURE DEVELOPMENT IN EASTERN EUROPEAN COUNTRIES
/
ANALIZA I ZARZĄDZANIE ROZWOJEM ORGANICZNEGO ROLNICTWA W KRAJACH EUROPY WSCHODNIEJ

Nadiia SHMYGOL[1)], Władysława ŁUCZKA[2)], Nataliia GAVKALOVA[3)], Zhanna HARBAR [4)], Viktor KOVAL [5)] and Lucian-Ionel CIOCA[6,7,*)]

[1] Warsaw University of Technology, Warsaw; nadiia.shmygol@pw.edu.pl
[2] University of Life Sciences in Poznań; wladyslawa.luczka@up.poznan.pl
[3] Warsaw University of Technology, Warsaw; nataliia.gavkalova@pw.edu.pl
[4] Vinnytsia National Agrarian University, 21000 Vinnytsia, Ukraine; garbar_janna@ukr.net
[5] Izmail State University of Humanities, 68601 Izmail, Ukraine; victor-koval@ukr.net
[6] Lucian Blaga University of Sibiu, Sibiu, Romania; lucian.cioca@ulbsibiu.ro
[7] Academy of Romanian Scientists, 3 Ilfov, 050044, Bucharest, Romania

Tel: 004 0745110855; E-mail: lucian.cioca@ulbsibiu.ro
DOI: https://doi.org/10.35633/inmateh-72-25

Keywords: *organic products, risk, agricultural land, agriculture, production*

ABSTRACT

The study analyses trends in domestic markets and international trade in organic products in some Eastern European countries based on a multifactorial comparative analysis in the regional context and estimates of yield losses about traditional agricultural land processing technologies. Prospects for the development of organic farming by region and in general are determined based on unused reserves of agricultural land suitable for this. The study assessed the organic production development in different regions of Poland and Ukraine: the annual growth rate of transitional and organic lands should be at least +13.3% to meet the strategic goal of reaching 3% of the total agricultural land by 2030.

STRESZCZENIE

W badaniu są analizowane trendy handlu na wewnętrznych i międzynarodowych rynkach produktami organicznymi w niektórych krajach Europy Wschodniej na podstawie wieloczynnikowej analizy porównawczej w kontekście regionalnym oraz oceny strat plonów związanych z tradycyjnymi technologiami uprawy rolniczych gruntów. Perspektywy rozwoju rolnictwa organicznego w poszczególnych regionach i ogólnie określane są na podstawie nieużytkowanych zasobów gruntów rolniczych nadających się do tego celu. Badanie ocenia rozwój produkcji organicznej w różnych regionach Polski i Ukrainy: roczny wskaźnik wzrostu obszarów przejściowych i organicznych powierzchni rolnych powinien wynosić co najmniej +13,3%, aby osiągnąć strategiczny cel osiągnięcia 3% ogólnej powierzchni gruntów rolniczych do 2030 roku.

INTRODUCTION

The global agricultural landscape is undergoing a paradigm shift towards sustainability and eco-friendly practices. Increasing food security is one of the key strategic goals of national development in many countries, including the European Union. This contributes to the gradual transformation of the population's consciousness towards the consumption of safe and environmentally friendly food products. This, in turn, has led to an increase in the demand for organic products grown by agricultural enterprises without the use of mineral fertilizers and pesticides. However, the mass introduction of organic farming is associated with certain technological difficulties and limitations, which determine the relevance of this study. Ukraine and Poland, as significant contributors to European agriculture, find themselves at a critical juncture. The urgency arises from environmental concerns, changing consumer preferences favoring sustainable food, and the need for resilient agricultural systems in the face of climate change. The study's relevance is further underscored by the potential environmental impact of conventional farming practices, the growing demand for organic products among consumers, and the delicate balance required for economic viability in organic farming. Examining how Ukraine and Poland navigate these challenges is crucial not only for their agricultural sectors but also for setting global precedents in sustainable agriculture policy.

The purpose of the study is to analyze the prospects of organic farming development in cases of Eastern European countries: Ukraine and Poland.

This study addresses the pressing issues these nations face and explores recent initiatives fostering organic agriculture. In the Literature Review Section, the results of synthesizing contemporary scientific research of organic agriculture current state and future prospects in Ukraine and Poland are presented.

In the Methodology Section, the study presents a methodology for analyzing the prospects of organic farming development in Ukraine and Poland. This approach is designed to address common challenges faced by both countries in sustainable organic production. The study delves into an analysis of trends in domestic markets and international trade of organic products within the contexts of Ukraine and Poland. In the Conclusion, the analysis of the current state and future prospects of organic agriculture in Ukraine and Poland leads to several key recommendations for regulatory policy.

Literary review

The problem of studying the prospects of organic farming has become widespread in various scientific circles (*Galat, 2021; Wojciechowska-Solis et al., 2022)*. Thus, according to the results of research, the development of organic production in Ukraine is connected, first of all, with the growth of demand for its products in the countries of the EU and North America (*Senyshyn et al., 2023; Stupnytskyi et al., 2023*). However, currently, the domestic market is not capable of performing a stimulating function, as it is only in its stage of formation (*Galat, 2021)*. To accelerate this process, the authors emphasize the need to improve the legal framework, the importance of information exchange between organic market operators, the promotion of a healthy lifestyle among the population, and further liberalization of international trade.

Evaluating the prospects of organic farming for producers, *Garazha (2021)* and *Ohorodnyk (2023)* pay attention to the additional competitive advantages they receive, which are the following: significant savings due to the rejection of mineral fertilizers and agrochemicals, as well as high prices for final products, which allow them to compensate for a decrease in productivity and increase profits. Despite this, the concept of organic production as a strategic direction for the development of the agricultural industry in Ukraine has been established among Ukrainian scientists in recent years. The main prerequisites for this are: the rapidly growing market for ecological food products, in combination with limited reserves of increasing organic land in the EU; and the high quality and fertility of Ukrainian chernozem (soil) (*Ohorodnyk, 2023*).

It should be highlighted that scientists have encouraged the growth of organic agriculture if the study of this topic is considered in Poland, specifically, where the active development of organic farming began earlier. For example, *Golik and Żmija (2017)* studied ecological agriculture and the foundations of sustainable development in villages and territorial communities. *Iagaru et al. (2016)* study the process of developing strategic options for the development and diversification of the rural economy based on the principles of environmental protection.

Jasiński et al. (2014) emphasize that organic agriculture is one of the powerful clusters of regional development, as it accumulates significant amounts of labor resources and a highly educated agrarian elite open to innovation. In their study, the authors started with the concept of "zakorzeniony" of the market, which implies a high concentration of certain endogenous resources in a certain area. In the case of organic production, such a market is based on the close cooperation of organic farming operators, processing enterprises, and local government institutions. *Łuczka (2016)* draws attention to the lack of such communication at an appropriate level. In her opinion, the inconsistency of supplies of organic raw materials from producers negatively affects the rhythm and stability of the work of processing enterprises. As a result, there is a shortage of ecological products in the domestic market, even in conditions of high demand. The considered studies of Polish scientists are a theoretical generalization of existing trends, where, along with the obvious advantages and potential of ecological production, there is an understanding that the economic justification of such activity is currently an unresolved issue. In this context, to ensure the balance between the pillars of sustainable development, *Iagău et al (2023)* highlight the implications of strategic thinking, in the development and promotion of the circular economy, including the concept of sustainability, in the agri-food sector.

Marszałek (2018) and *Groszyk (2022)* consider the prospects of this field of activity in the existing European Union strategy. Special attention is paid to the non-alternativeness of this strategy, since only it can ensure the permanent preservation of the balance between ecological, economic, and social systems.

Marszałek (2018) separately notes that the level of social responsibility of society has reached the level where agriculture must ensure not only economic viability but also environmental acceptability. Both studies are characterized by a generalizing theoretical character and practically do not use the economic-mathematical apparatus, which is a significant shortcoming.

Recent studies attest to the role of economic education in the sustainability of agricultural businesses, emphasizing that brand image and loyalty is relevant and directly proportional to it (*Nuanphromsakul et al., 2022*). There are studies that offer optimal solutions for the environment and agriculture in the sense of using sludge from sewage treatment plants (after applying optimal solutions to prevent contamination with metals) for restoring acidic soils (with pH < 6) and reintegrating them into agriculture, respectively in organic agriculture (*Iticescu et al., 2021*).

Continuing the development of this concept, *Zielińska (2015)* considered the indirect benefits of organic production. Based on the results of the research, the author concludes that it is inappropriate to assess the effectiveness of agriculture-based only on economic indicators of activity and offers his own approach to managing the natural value of territories. The theoretical significance of this approach, in our opinion, is beyond doubt. However, its practical application is significantly limited by the lack of any methodology for the quantitative assessment of target indicators.

The results of the generalization of modern scientific experience regarding the state and prospects for the organic agriculture development in Ukraine and Poland are shown in Table 1.

Table 1

Analysis of modern scientific experience of organic farming development.

Research goals	Results and disadvantages	Quantitative assessment methods	Sources
Study of the processes of formation of the internal organic products market in Ukraine	The system of factors restraining of the organic production in Ukraine has been improved: the domestic development market does not perform a stimulating function; insufficient attention of researchers to certain segments of organic production; imperfection of the regulatory framework. The proposed model of the transformation of traditional agriculture underestimates the role of modern world experience regarding the significant increase in costs over income, especially in the transition stage	Summary and grouping, comparison, absolute, relative and average values, index, graph-analytical	*Galat, L. (2021); Wojciechowska-Solis et al. (2022); Senyshyn et al. (2023)*
Approval of the concept of organic production as a strategic direction for the development of the agricultural industry of Ukraine	An economic justification of the need for state financial support of organic producers was carried out. The budget system of Ukraine does not have the financial resources to implement the specified recommendations, following the example of the EU countries	Cost calculation in the analysis of economic activity, rating method of interstate comparisons	*Garazha (2021)*
Implementation of ecological agriculture for sustainable development basis of villages and territorial communities in Poland	The concept of "zakorzeniony" of the market, as a cluster of regional development based on the concentration of certain endogenous resources, received further development. The study requires further development of the mechanisms for realizing competitive advantages in this sector of the economy	Assessment of the dynamics of time series, relative indicators of the structure, interstate comparative analysis, methods of expert assessment, SWOT analysis	*Jasiński et al. (2014); Golikand Żmija, (2017)*
Study of factors promoting organic farming in Poland	Stimulating measures were further developed: provision of communications between producers of agricultural raw materials, processing enterprises and sales channels; the need for state financial support. Economic substantiation of organic activity was not conducted	Combinational grouping	*Luczka (2016)*
A study of the prospects of organic farming in Poland in the context of the EU development strategy	Received further development of the basis of the strategic development of rural areas: the constant preservation of the balance between the economic and ecological systems. The theoretical analysis is not supported by a quantitative assessment methodology	-	*Marszałek (2018);* *Groszyk (2022)*

Research goals	Results and disadvantages	Quantitative assessment methods	Sources
Increasing the economic efficiency of organic production in Poland	An approach to managing the natural value of territories is proposed. Its practical value is leveled by the lack of a methodology and a system of indicators	-	*Zielińska (2015)*

Comparative Table 1 showed the presence of a complex of unsolved scientific tasks, which confirm the relevance and timeliness of this study.

MATERIALS AND METHODS

The analysis of scientific studies both in Ukraine and in Poland showed that the practical measures proposed by the authors are most often based on the generalization of existing developments and the analysis of data from open sources. Moreover, the given recommendations are, in most cases, based on our own expert experience, which is not confirmed by any practical calculations. Taking into account these shortcomings, the actual study proposed a methodology for analyzing the prospects of regional development of organic agriculture, in which the main attention was paid to the use of economic and statistical methods of data processing.

The methodology involved several stages, each with specific tools and techniques:

1 Economic and statistical analyses of organic production trends – utilizes statistical analysis methods for dynamic series and average values.
2 Assessment of the role of state support – deterministic factor analysis and the absolute differences method.
3 Analysis of organic land disposal after state support – economic risk assessment methods.
4 Assessment of the impact of organic production on crop development – relies on statistical methods to evaluate the effectiveness of crop production.
5 Formulation of conclusions and recommendations – draws from expert generalization methods based on ordinal measurement scales.

Each stage is explained in detail with a focus on environmental payments as a key incentive in organic production. These payments are tied to fulfilling specific environmental obligations, and this article highlights the impact of various factors, such as land status, agricultural use, and adjustment factors, on the base rate of organic payments per hectare. This methodology aims to quantify the effects of these factors on organic farming development, whether intensive or extensive, providing valuable insights into the sustainability of organic agriculture in both countries.

This comprehensive analysis draws on statistical and economic methodologies to quantitatively assess the prospects for regional organic farming development in both countries. The evaluation of regional organic farming prospects considers untapped opportunities to expand organic agriculture by utilizing available agricultural land.

The economic and statistical analysis of trends in organic production is based on the methods of analysis of dynamic series and average values: the dynamics of time series were measured using average growth rates; bringing value indicators to the prices of the base period using discounting methods; and the study of a certain phenomenon in a certain period using relative indicators of intensity and structure. At the end of this stage, an idea of the current state of organic production development in the country and the nature of existing trends is obtained.

The practice of producing ecological food products in the EU shows a high dependence of this activity on the amount and duration of state support. Therefore, to assess its role in the development of organic agriculture in different regions, it is suggested to use deterministic factor analysis, namely, the method of absolute differences. Factor analysis makes it possible to obtain a quantitative assessment of the directions for the use of state funds: the expansion of the area of organic land, the growth of the share of small and medium-sized enterprises, changes in agricultural specialization, etc.

The regional analysis of the disposal of organic land after the end of the term of environmental obligations is carried out using economic risk assessment methods, in particular, the risk of uncertainty based on the coefficients of variation of target indicators and the risk of disposal based on the relative indicators of the distribution of the studied phenomenon in a certain environment. Not all natural and climatic conditions

allow effective agricultural activity under the conditions of ensuring its economic payback. Therefore, the purpose of the appropriate stage of the methodology is to determine those regions where state stimulation of agricultural producers of ecological products is more appropriate from this point of view.

Assessment of the impact of organic production on the development of agriculture as a whole is proposed to be carried out with the help of statistical methods of analyzing the effectiveness of activities in crop production. A relative comparison of the productivity of certain crops in relation to traditional farming methods allows us to determine the amount of cumulative losses to the gross harvest from the introduction of new technologies. In this case, it is advisable to replace traditional farming methods where the relative loss of productivity is the smallest.

According to the results of the preliminary multifactorial analysis and using expert generalization methods based on ordinal measurement scales, the regions are ranked. On its basis, conclusions and recommendations are formed regarding the prioritization of territories for the development of organic farming.

The practical implementation of this methodology requires appropriate statistical support. To date, the State Statistics Service of Ukraine does not carry out appropriate accounting, with reporting being publicly available. The sources of information are the Ministry of Agrarian Policy and Food of Ukraine, as well as the Federation of the Organic Movement in Ukraine. However, their data are general and do not allow them to fully implement the proposed methodology. As for Poland, regular reports on the state of organic crop production by voivodeship, according to certain indicators, are published here.

Comparing the experience of implementing organic farming in Ukraine and Poland, common problems for both countries can be observed. Although, according to its duration, ecological production of food products in Poland has existed much longer, the areas of the relevant lands are comparable to each other today. Also, despite the low share of organic land, compared to the average level for EU countries, the development of ecological production in Ukraine and Poland is not sustainable. Therefore, there is a need to develop an appropriate methodology for further research on its prospects (Fig. 1).

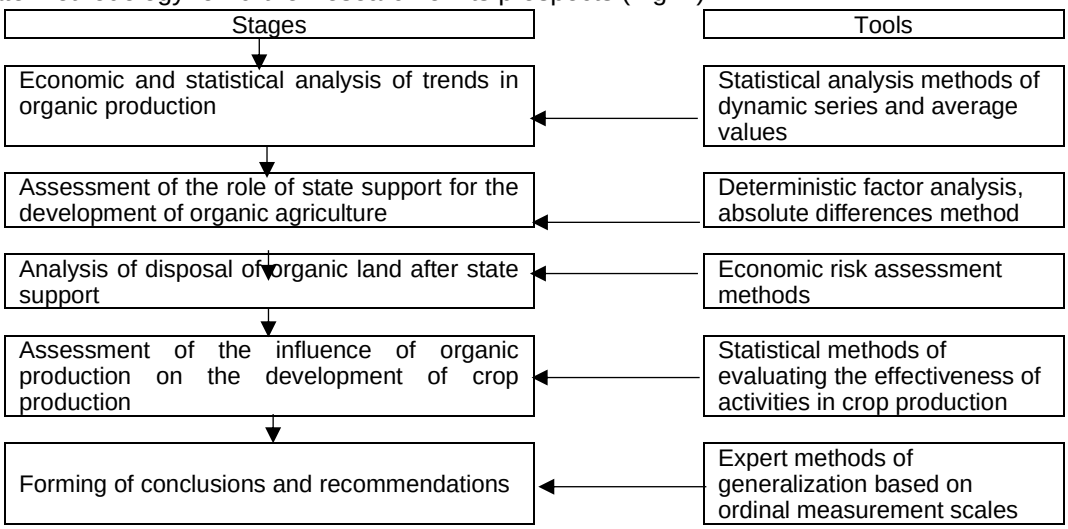

Fig. 1 - Methodology for the analysis of prospects for the development of organic farming.

Let's consider each of the stages of this methodology in detail. To stimulate organic production, appropriate environmental payments have existed in Poland for a long time. To receive them, farms must fulfill certain environmental obligations. Until May 2021, the term of these obligations was 5 years, and after that, 3 years. During this period, the operator of organic production has the right to receive a state subsidy. Such a system of incentives is used as part of the implementation of the Program for the Development of Rural Regions, with the participation of the European Agricultural Fund.

The number of relevant subsidies has a direct correlation with the development of organic production in the country. However, the factors of this development may indicate its different nature: intensive or extensive. That is why their systematization and quantitative assessment of the impact are important scientific tasks.

The basic rate of organic payment, calculated per 1 ha of area, depends on the following:

1 transitional or organic status of agricultural lands;
2 agricultural use of organic land, which includes: cultivation of agricultural, vegetable and herb crops, berries, basic and extensive horticulture, fodder crops and pastures;

3 areas of transitional or organic lands for which a regression scale is introduced. Farms with an area of up to 50 hectares receive up to 100% of environmental payments from the base rate; 75% – with a residual area of up to 100 hectares; 60% – more than 100 hectares;

4 individual adjustment factors of the base rate, which depend on the specificity and intensity of activity. For example, in animal husbandry - from the number of livestock per unit area, in horticulture - from the minimum density of fruit trees, etc.

Aggregate state expenditures to support organic production are formed on the basis of:

$$VOP_i = AOL_i \times SOL_i \times \overline{OP_i}, \quad (1)$$

$$\overline{OP_i} = \sum_{j=1}^{m} (AB_{ij} \times OP_{ij}), \quad for\ all\ \ i=1...n, \quad (2)$$

where: VOP_i – the volume of regional organic payments (subsidies) paid by the state to farms in the i^{-th} voivodship (province), PLN; AOL_i – the area of organic land in the i^{-th} voivodeship (province), ha; SOL_i – share of organic lands of the i^{-th} voivodeship (province) covered by subsidies, %; $\overline{OP_i}$ – the average volume of organic payments per 1 ha in the i^{-th} voivodeship, PLN; AB_{ij} – the specific weight of the area of the j^{-th} type of organic farming for which the subsidy was paid in the i^{-th} voivodeship (province), %; OP_{ij} – the amount of organic payments per hectare in the i^{-th} voivodeship for the j^{-th} type of agriculture, PLN; n, m – respectively, the number of voivodeships (provinces) and types of organic farming. Then, the generalizing factor model will have the form:

$$VOP_i = AOL_i \times SOL_i \times \sum_{j=1}^{m} (AB_{ij} \times OP_{ij}), \quad for\ all \quad i=1...n, \quad (3)$$

RESULTS

Considering the temporarily occupied territories, Ukraine's total area is 60.3 million hectares. Of these, 41.4 million hectares (68.7%) are agricultural land (Verkhovna Rada of Ukraine, 2018), including:

– arable land that is systematically cultivated and used in crop production, the area of which in 2020 in Ukraine was 32.7 million hectares. Considering crop rotation, only 82% of arable land, or 27.7 million hectares, was used as sown area. Accordingly, 5 million hectares were fallow. Thus, the average level of ploughed land in Ukraine today is 54%. The highest level of this indicator is observed in Kirovohrad (71.9%), Zaporizhzhya (69.9%), and Mykolaiv (69.5%) regions; the lowest is in Transcarpathian (15.6%), Ivano-Frankivsk (28.8%), and Rivne (32.8%). In European countries, the average plowing of land is about 35%.

– perennial plantings or orchards and vineyards occupy 0.9 million hectares, or 2.2% of agricultural land; pastures and hayfields are used in animal husbandry for grazing agricultural livestock during the year and occupy an area of 5.3 million hectares and 2.3 million hectares, respectively; fallows are agricultural lands (of 0.2 million hectares), not cultivated for a long time and are a reserve for increasing arable land.

The principles of the organic production in Ukraine are identified by the relevant regulatory acts, which are based on the Law of Ukraine "On the basic principles and requirements for organic production, handling and labeling of organic products" (*Verkhovna Rada of Ukraine, 2018*). According to this, organic production refers to all stages of agricultural activity, including cultivation and harvesting, its processing, mixing and packaging, as well as labeling of finished products.

Each stage is regulated by the relevant rules, and the activity itself undergoes mandatory systematic certification. The dynamics of the number of operators and the corresponding areas of agricultural land in Ukraine during 2016-2020 are shown in Fig. 2 (*Federation of the Organic Movement in Ukraine, 2021*).

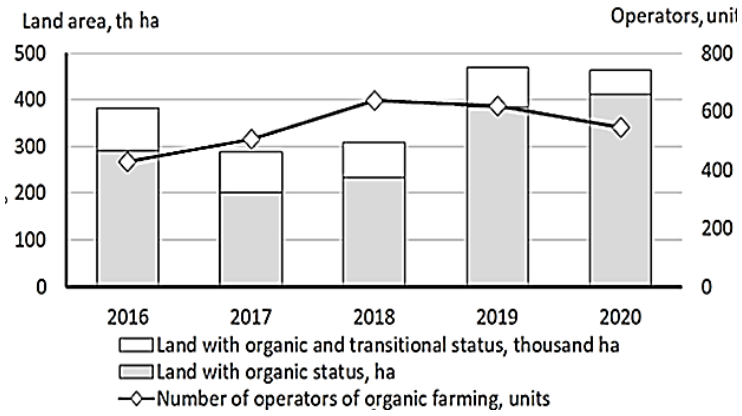

Fig. 2 - Organic farming operators and organic land area in Ukraine from 2016 to 2020

One of the main features of organic production around the world is the need for a transitional period for agricultural land to obtain organic status. On average, its duration is 3 years, and in exceptional cases it can be reduced to two.

During the transition period, organic production methods are used on the relevant lands in order to bring the indicators of soil pollution to a dangerous level, as well as its gradual saturation with organic substances and reproduction of natural fertility. In this regard, in the first years after the abandonment of mineral fertilizers, the yield of these soils drops significantly, and then gradually recovers.

As shown in Figure 1, since 2018, the number of organic farming operators in Ukraine has decreased from 635 to 544 units, or by -14.3%. At the same time, the growth of the areas of the corresponding lands slowed down in 2019, and by the beginning of 2021, it amounted to 462.2 thousand hectares, or only 1.1% of all farmland. It should also be observed that there is a negative tendency to reduce the land area in a transitional state, both in absolute and relative terms.

If, at the beginning of the study period, their areas accounted for up to 40% of land with organic status, then according to 2020, it will be only 12.6%. This means that in the coming years, the reserves for growing lands with organic status due to existing transitional lands will be minimal. According to different regions of Ukraine, the situation in 2020 is heterogeneous, as evidenced by the data in Table 2.

Table 2

The extent of organic and transitional lands in Ukraine in 2020

Regions	Area of land with organic status, thousand ha	Area of transitional lands, thousand ha	The proportion of organic and transitional land in the total area of agricultural land, %
Vinnytsia	4.3	0.4	0.2%
Volynsk	4.7	0.1	0.5%
Dnipropetrovsk	14.6	4.0	0.7%
Zhytomyr	28.1	1.2	1.9%
Zakarpattia	1.1	–	0.2%
Zaporizhzhia	17.1	27.5	2.0%
Ivano-Frankivsk	0.8	–	0.1%
Kyivska	8.6	0.2	0.5%
Kirovohradsk	13.4	0.1	0.7%
Lviv	11.8	0.7	1.0%
Mykolayivska	0.1	0.1	0.0%
Odesa	55.0	3.1	2.2%
Poltava	29.5	0.1	1.4%
Rivne	19.9	0.7	2.2%
Sumy	0.1	0.3	0.0%
Ternopilsk	62.0	0.1	6.0%
Kharkivska	3.3	0.6	0.2%
Khersonsk	70.6	11.1	4.2%
Khmelnytska	16.9	0.1	1.1%
Cherkassy	40.0	–	2.8%
Chernivtsi	0.2	–	0.0%
Chernihivska	8.5	1.2	0.5%
Together in Ukraine	410.7	51.5	1.1%

Based on the data in Table 2, the most common organic production is in the Kherson, Ternopil, Odessa and Cherkasy regions. In total, they account for more than 55% of all organic land in Ukraine. The worst situation took place in the Mykolaiv, Sumy and Chernivtsi regions, and there was no such activity on the territory of Donetsk and Luhansk.

Taking into account the temporary occupation of the Kherson and Zaporizhzhia regions, as of June 2022, Ukraine lost 126.2 thousand hectares of land with organic and transitional status, or 27.3% of their total area. The agricultural specialization of the Kherson region is vegetables, melons, oilseeds and cereals, as well as perennial plantings; the Zaporizhzhia region is grain and oilseeds, as well as vegetables and gardening.

In addition to this, 40% of Kharkiv communities are also occupied. Thus, the total loss of agricultural land in Ukraine is at least 22%.

According to the National Economic Development Strategy until 2030 (Cabinet of Ministers of Ukraine, 2021), percentage of organic and transitional lands in Ukraine should grow from 1.1% to 3.0% or more. Accordingly, the export of organic products should increase from $ 204 million in 2020 to $1 billion.

In 2020, the European Union countries collectively possessed an organic land area of 16.5 million hectares. Spain led with 2.4 million hectares, followed by France with 2.2 million hectares and Italy with 2 million hectares. The average proportion of organic land in relation to the total available agricultural areas was approximately 8.1%. The EU aspired to elevate this ratio to 25% by 2030, as outlined in the EU Biodiversity Strategy. Notably, Austria had already achieved a 26% share, while Estonia and Sweden reached 22% and 20%, respectively, underscoring significant progress towards the EU's biodiversity objectives (*Cabinet of Ministers of Ukraine, 2021*).

In 2021, the agricultural landscape of Europe witnessed notable changes in the realm of organic farming, with key countries in the region demonstrating diverse trends in the expansion of areas, market dynamics, and consumer behavior. France stands out as a leader in expanding organic areas, contributing nearly 2.8 million hectares in 2021, making a significant contribution to the 4.4% growth of organic areas in Europe. Germany, holding the largest market in Europe with 15.9 billion euros in retail sales, experienced moderate growth in 2021 after a substantial surge in 2020.

Austria distinguishes itself with the highest share of organic areas in the EU, encompassing 26.5% of agricultural land, highlighting its robust position in the domestic market. Sweden, with over 20% of agricultural land under organic management, demonstrates a strong organic farming sector with a substantial number of producers and processors. Estonia is making significant strides, approaching EU targets for 2030, with 23.0% of agricultural land dedicated to organic practices and the highest growth rate in organic markets in 2021 (+21%).

Liechtenstein leads the global list with 40.2% of agricultural land under organic management, pioneering dedication to organic practices. Italy contributed to the overall growth of Europe with 2.2 million hectares of organic areas and leads in the number of organic processors. Denmark claims global leadership with a 13.0% share of organic product sales, reflecting high per capita spending on organic produce. The Netherlands play a crucial role as a re-exporter, significantly influencing the import of organic products and demonstrating volume growth. Spain, with 2.6 million hectares of organic areas, adds diversity to the landscape of organic farming in Europe.

This scientific narrative unveils the intricate tapestry of organic farming in selected European countries, elucidating their contributions to the expansion of areas, market dynamics, and consumer preferences in 2021.

Taking into account the geographical characteristics of Poland, the overall extent of the region is 31.3 million hectares, with agricultural territory covering 18.7 million hectares, equivalent to 59.9%. As per the 2020 statistics, the expanse of transitional and organic lands within this framework comprised 509.3 thousand hectares, constituting 2.7% (*Agricultural and Food Quality Inspection, 2021*).

Thus, Ukraine is significantly inferior to the progress that has been achieved in the EU, but from a resource point of view it has significant potential to expand its activities.

Regarding organic and transitional resources, the extent in Poland has, on average, remained nearly constant in recent years, hovering around 500-510 thousand hectares. Compared with Ukraine, according to 2020 data, this area is only 1.1 times larger. Therefore, it can be talked about relative parity between countries on this indicator. The most dynamic development of this sector of the Polish economy took place during 2004-2013, when organic and transitional lands grew from 82.7 thousand hectares to 670.0 thousand hectares, or 8.1 times. After that, business activity began to decline, which lasted until 2017. Thus, it can be assumed that the economic system has come to a state of continuing equilibrium to this day.

In terms of the number of organic farming operators, a similar pattern of dynamics was observed. In 2004-2013, their number increased from 3760 to 27093 units. Among these, 26,598 establishments were involved in the direct manufacturing of organic agricultural goods, while 407 entities, constituting 1.8%, were dedicated to producing items for end consumers using organic raw materials.

In the following years, the number of operators began to decline rapidly. In 2020, their number was 20,274 units. Of these, 5.4% of enterprises have already been engaged in the production of products from organic raw materials.

The fundamental difference between Poland and Ukraine is a large number of small agricultural enterprises, with an average area of organic land of about 27.4 hectares. At the same time, in Ukraine, each such enterprise accounted for up to 850 hectares on average.

This situation in Ukraine has developed for certain objective reasons. Firstly, the lack of a working agricultural land market. Secondly, there is a high threshold for entering the industry due to the lack of state financial support, which is the main direction of spending of the budget of the European Union.

The proportion of Poland's transitional lands during 2016-2020 ranged from 25% to 33% of their overall quantity. This was anticipated to contribute to an annual increase of up to +10% in organic lands. Nonetheless, this expectation was not fulfilled due to the concurrent phenomenon of their gradual conversion into agricultural land (*Rozkrut, 2021*).

During 2016-2020, significant shifts that took place in the structure of organic acreage can be mentioned:

- the share of cereals increased by +10.3% to 29.2%;
- the share of forage plants decreased by -9.1% to 23.1%, and onions and pastures – by -8.7% to 16.9%;
- the share of fruit and berry crops increased by +2.6% to 9.2%, and legumes - by +5.1% to 7.4%; the latter, in turn, contribute to the accumulation of humus in the soil and the development of beneficial microorganisms, enrich it with nitrogen and are good precursors for crop rotation;
- the share of vegetables and potatoes decreased by -4.1% to 5.9%.

In total, these crops in 2020 occupied about 90% of the areas, of which 40% are hayfields and pastures for the needs of organic livestock, and only 15.1% are fruit and berry crops and vegetables directly intended for consumers. This structure is due to the complexity of growing cultivated plants using ecological technologies and low yields. For comparison, the share of hayfields and pastures in total agricultural land in Poland is only 21.7%, and in Ukraine – 20.8%.

In this case, it is advisable to evaluate the impact of each factor on the performance indicator using the method of chain differences. The specified model will be used to determine the nature of the changes that took place in Poland during 2019-2020. During this period, the total volume of organic payments for transitional lands decreased by -6.5%, or by -5104.7 thousand PLN; for lands with organic status increased by +2.7%, or by PLN +6999.1 thousand. Taking into account these data, a conclusion can be drawn about the redistribution of funds, which in the future will lead to a slowdown in the rate of expansion of the organic land area. Simultaneously, the growth of the total volume of financing indicates the gradual development of this sector of agriculture. However, the results of the factor analysis allow detailing and revealing the essence of the specified trends. For transitional lands there will be:

$$-\Delta VOP_{AOL} = \Delta AOL \times SOL_{2019} \times \sum(AB_{2019} \times OP_{2019}) = -6013{,}3 \text{ th. PLN} \quad (4)$$

The growth of the effective indicator due to the first factor $\Delta \mathrm{VOP}_{\mathrm{AOL}}$ will result in an actual expansion of the overall land extent of transitional lands, which is a call sign and vice versa. In our case, the reduction of expenses by -6013.3 thousand PLN was due to the reduction of the area of the relevant land by 8924.1 hectares, which indicates a slowdown in business activity.

$$-\Delta VOP_{SOL} = AOL_{2020} \times \Delta SOL \times \sum(AB_{2019} \times OP_{2019}) = +648{,}4 \text{ th. PLN} \quad (5)$$

The second factor determines the change in government expenditures due to the share of land covered by subsidies ΔVOP_{SOL}. In 2019-2020, it increased from 64.3% to 64.9%, which led to additional expenses in the amount of +648.4 thousand PLN. This growth is positive because it increases economic incentives for farms and has significant untapped reserves for further growth.

$$-\Delta VOP_{AB} = AOL_{2020} \times SOL_{2020} \times \sum(\Delta AB \times OP_{2019}) = -996{,}6 \text{ th. PLN} \quad (6)$$

The third factor indicates structural shifts in the agricultural specialization of farms ΔVOP_{AB}. A positive value of this indicator means redistribution of production in favor of those activities where the basic rate of organic payment per 1 ha is higher, and vice versa. Therefore, this factor does not directly characterize the general development trends in organic production, but reveals its inner essence.

$$-\Delta VOP_{OP} = AOL_{2020} \times SOL_{2020} \times \sum(AB_{2020} \times \Delta OP) = +1256{,}8 \text{ th. PLN} \quad (7)$$

The last factor reveals the change in the volume of organic payments due to adjustments in base rates. The average level of payments per hectare will decrease if large agricultural producers crowd out small businesses, which is undesirable. On the contrary, the mass development of small businesses, according to the accepted regression scale, will increase the average costs per 1 ha for each type of agricultural activity. In our case, this increased the total organic payments by +1256.8 thousand PLN. At the same time, a positive

value of ΔVOP_{OP} with a simultaneous negativeΔVOP_{AOL} means that the increase in the share of small businesses in transitional lands occurred due to the mass exit of large organic producers from the market.

As for the state subsidization of lands with organic status, the results of the factor analysis look like this: $\Delta VOP_{AOL} = +7129{,}6\ \text{th. PLN};\ \Delta VOP_{SOL} = -10656{,}1\ \text{th. PLN};\ \Delta VOP_{OP} = +5219{,}3\ \text{th. PLN}$. This means that the expansion of the area of organic land took place against the background of the growth of the share of small enterprises, which is positive. At the same time, in 2020, subsidies were paid for 78.9% of areas. This means that less than 21% of existing organic land was not covered by the 5-year environmental commitment program. Therefore, this business was characterized by high turnover: after the end of the period of state aid, the vast majority of agricultural enterprises left this market due to high costs and low crop productivity. Thus, today, organic production cannot exist without a subsidy policy. Within the second block of the methodology, an assessment of relevant costs was carried out for each voivodeship (province), followed by a ranking of regions by each factor.

It was mentioned above that the main reason for the lack of progress in the development of organic production in Poland is the high loss of land with organic status, due to the massive reduction of business after the end of the period of state support. From the point of view of public administration, it is important to assess the relevant risks, in terms of regions. For this, let's introduce conventional signs. Let's assume, that $AOL_{B,i}(t)$ is the area of lands of the $i^{\text{-th}}$ voivodeship (province), which were eliminated from the composition of organic during the $t^{\text{-th}}$ year. Then, the risk of uncertainty PH_i will depend on the variation of this indicator during the reporting period, lasting k years, and will be calculated according to the formulas:

$$\text{PH}_\text{i} = \left(\sqrt{\frac{\sum_{t=1}^{k} \left(AOL_{B,i}(t) - \overline{AOL_{B,i}}\right)^2}{k}} \Big/ \overline{AOL_i} \right) \times 100\% \ \rightarrow \ min, \tag{8}$$

$$\overline{AOL_i} = \frac{\sum_{t=1}^{k} AOL_i(t)}{k}, \quad \overline{AOL_{B,i}} = \frac{\sum_{t=1}^{k} AOL_{B,i}(t)}{k} \tag{9}$$

where:

$\overline{AOL_\text{i}}$ – average annual area of organic land in the $i^{\text{-th}}$ voivodship (province), for k years; $\overline{AOL_{\text{B,i}}}$ – the average annual land area of the $i^{\text{-th}}$ voivodeship (province), which was eliminated from the organic composition.

Evaluating the variation of the disposal of organic lands relative to their average area, the indicator of the risk of uncertainty should be minimized. If $\text{PH}_\text{i} \rightarrow 0$, this means that the disposal of organic land is permanent, and its dynamics are constant and predictable. On the other hand, minimizing uncertainty does not guarantee a slow rate of elimination of agricultural land from the composition of organic.

For this purpose, the risk of release PB_i is calculated as a relative indicator of the spread of the studied phenomenon in a certain environment:

$$\text{PB}_\text{i} = \frac{\overline{AOL_{\text{B,i}}}}{\overline{AOL_\text{i}}} \times 100\% \ \rightarrow \ min \tag{6}$$

The simultaneous fulfillment of both target conditions (3) and (5) will be characteristic of regions with minimum areas of disposal of organic land and sustainable trends. In the long term, this will lead to a decrease in the level of SOL_i, which in this case is positive. The results of the corresponding assessment by regional characteristic based on the data of 2015-2020 are shown in Fig. 3.

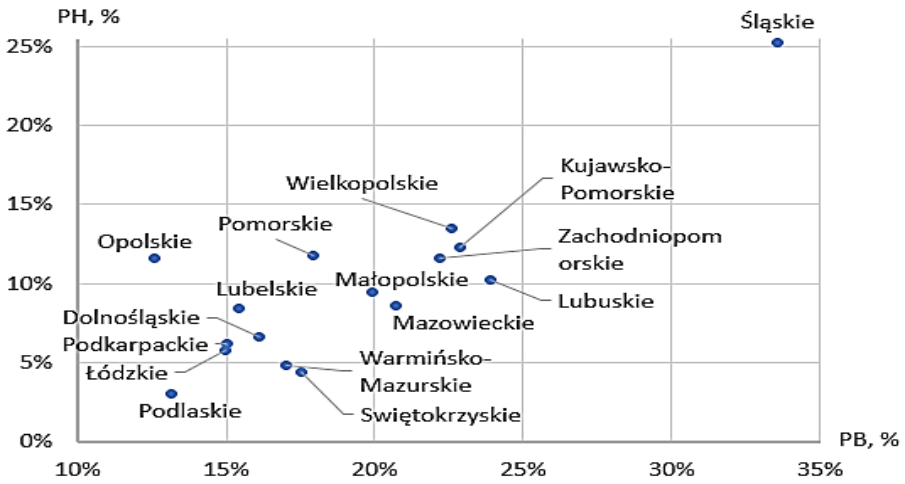

Fig. 3 - Risk indicators of organic production by voivodeship (province) in Poland according to data from 2015-2020

As shown in Fig. 3, according to both criteria, the lowest activity risk occurred in Podlaskie Voivodeship (Province) and the highest in Śląskie. Wielkopolskie, Kujawsko-Pomorskie, Zachodniopomorskie and Lubuskie were also in the high risk zone. Indicators (3) and (5) were also used to rank the regions. The next stage of the methodology provided for an assessment of the impact of organic production on the development of crop production. Several factors complicate such an analysis. Firstly, there is a lack of reliable and detailed information on the planted acreage and gross collection for certain types of crops, especially in organic production. Secondly, the assessment by groups of crops eliminates the factor of the structure of individual crops in the group. For example, the structure of cereals in organic and traditional agriculture may differ in composition. Summary statistical data (*Rozkrut, 2021*) made it possible to compare the yields of certain groups of crops for organic and traditional agriculture in Poland in 2020 (Fig. 4).

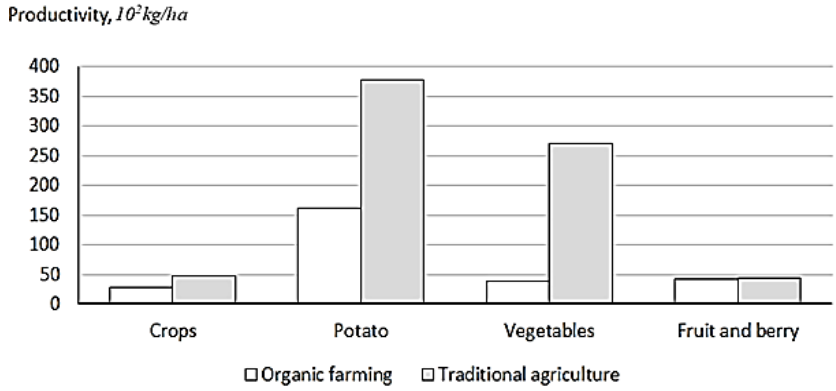

Fig. 4 - Comparison of crop yields for organic and traditional agriculture in Poland in 2020

Despite the indicated shortcomings, the comparative analysis allows us to form an idea of how the gross output of crop production will change as a whole, if part of the agricultural land will be converted to organic, or vice versa. At the same time, the structure of each group must remain stable.

As shown in Fig. 4, organic grain production in 2020 had a national average yield of 27.7x 10^2 kg/ha. This indicator's variation range by region was from 22.3 x 10^2 kg/ha in Lubelskie Voivodeship to 58.4 x 10^2 kg/ha in Małopolskie. At the same time, the average grain yield under traditional farming was 47.9 x 10^2 kg/ha, or 1.7 times higher. Thus, an increase in the organic land area will lead to a loss of 20.2 tons of grain from each hectare. In order to minimize these losses, in our opinion, it is advisable to encourage the development of organic grain production in those voivodships where the difference between its yield and traditional farming is the smallest. These voivodeships include Małopolskie, Swiętokrzyskie, Podkarpackie and Opolskie. On the contrary, the most significant total losses of the crop due to the spread of organic farming occurred in the Pomorskie, Zachodniopomorskie and Łódzkie voivodships.

Potato cultivation on organic lands had an average yield of 162.2 x 10^2 kg/ha, and for agriculture as a whole – 378.2 x 10^2 kg/ha or 2.33 times higher. Taking into account the criterion of minimizing losses of gross potato harvest, it is advisable to stimulate its organic production in the Małopolskie and Podkarpackie voivodeships. At the same time, it is advisable to engage in traditional farming in Opolskie, Zachodniopomorskie and Pomorskie voivodeships.

The situation with vegetables is not so clear, since this group of crops consists of a wide range of products. The largest share of total sown vegetable areas in 2020 was occupied by onions (15.9%), carrots (12.2%), cabbage (9.5%), beets (5.0%) and tomatoes (4.1%). As for organic production, the corresponding structure of acreage is unknown. Thus, only a significant difference in yield of 7.1 times between different farming technologies and the obvious complexity of organic production can be stated in this case.

The last group of crops is fruits. Traditional agriculture includes perennial plantings of orchards and fruit and berry. The latter in 2020 had the following structure of acreage: strawberries – 25.6%, raspberries – 13.6%, currants – 32.5%, gooseberries – 1.1% and others. In organic farming, there is statistical data only on the total cultivation of fruit and berry crops. As a result of comparing yields for different types of agriculture, a relative parity between them can be noted: 41.7 x 10^2 kg/ha in organic and 43.9 x 10^2 kg/ha in traditional production.

Summing up, it can be noted that the overall low level of yield is indeed a significant factor directly affecting the economic feasibility of organic production.

In Poland in 2020, with the help of organic crop production, the following were grown: 315.3 thousand tons of cereals, which is 0.9% of the gross harvest of cereals throughout the country; 22.6 thousand tons of potatoes, or 0.3% of the gross collection; 89,000 tons of vegetables, or 2.3%; 164.3 thousand tons of fruit and berry crops, or 29.7%. As it can be seen, the level of organic production of grains, potatoes and other vegetables was at a low level. Also, operators of organic production were engaged in the cultivation of fodder crops to meet the needs of animal husbandry, the livestock of which included: cattle for meat - 8341 heads, dairy cows - 12061 heads, other cattle - 10700, poultry - 696153, pigs - 3253, sheep - 15803 and goats - 3645 heads. At this stage of the methodology, the following relative indicators were calculated to assess the regional effectiveness of organic activities:

$$RY_{ij} = \frac{Y_{OPГ,ij}}{Y_{ij}} \quad \rightarrow \quad max, \tag{7}$$

where: RY_{ij} – the yield level of organic crops of the j-th species in the $i^{\text{-th}}$ voivodship, relative to traditional agriculture; $Y_{\text{ОРГ,i}j}$ – yield of organic crops of the $i^{\text{-th}}$ species in the $i^{\text{-th}}$ voivodeship, 10^2 kg/ha; Y_{ij} – yield of crops of the $j^{\text{-th}}$ species in the $i^{\text{-th}}$ voivodeship in traditional agriculture, tons/ha.

The calculated indicators $РУ_{ij}$ show how many times the yield in organic production for certain crops is inferior to traditional agriculture. A smaller value of this indicator corresponds to greater losses of the gross harvest when switching from traditional to organic agriculture. Then, summarizing the relative level of productivity by region, it will be calculated according to the arithmetic weighted average formula.

$$RY_{i} = \sum_{j=1}^{p} \left(RY_{ij} \times \frac{AOL_{ij}}{AOL_{i}} \right) \quad \rightarrow \quad max \tag{8}$$

where: RY_{i} – summarizing the relative yield level of organic crops in the $i^{\text{-th}}$ voivodeship (province); AOL_{ij} – area of land under organic crops of the $j^{\text{-th}}$ type in the $i^{\text{-th}}$ voivodeship (province), ha.

In order to generalize the results of the deterministic factor analysis of regional organic payments and the risk of a decrease in business activity after the end of the period of state support for producers and productivity, it is necessary to solve the problem of multidimensional comparison. In the theory of decision-making, various matching methods for quantitative and ordinal scales of measurement are used for this purpose. In this case, a ranking assessment was conducted for each indicator, where a lower rank corresponds to a better value. The generalized ranking was performed using the method of average arithmetic ranks. As a result, each of the regions received the following assessment (Table 3).

Table 3

The results of the rating assessment of voivodships in according (Poland, 2015-2020)

Voivodeships	Overall Ranking
Podlaskie	1
Swiętokrzyskie	2
Dolnośląskie	3
Warmińsko-Mazurskie	4
Podkarpackie	5
Łódzkie	6.5
Małopolskie	6.5
Opolskie	8
Wielkopolskie	9
Mazowieckie	10
Lubuskie	11
Zachodniopomorskie	12
Pomorskie	13
Lubelskie	14
Kujawsko-Pomorskie	15
Śląskie	16

According to the general ranking, the best situation occurred in such voivodships as: Podlaskie, Swiętokrzyskie and Dolnośląskie. According to the analysis, the least favorable situation can be observed in the Śląsk, Kuyavian-Pomeranian and Lublin voivodeships.

Currently in Poland, the progress of organic production falls well below the average in the European Union. Achieving improvement, especially considering the notably low productivity, necessitates government backing and the establishment of supplementary financial motivators.

As for the prospects for the development of organic production in Ukraine, as mentioned above, by 2030, the planned share of organic and transitional land should reach at least 3% of the total area of agricultural land. Taking into account the current situation at the beginning of 2022, the total agricultural area in Ukraine amounted to 41,329 thousand hectares. Then, according to the adopted state development strategy, by the end of 2030, organic and transitional lands should occupy at least 1,233 thousand hectares. For this, the average annual growth of their areas, according to the results of calculations, should be equal to +9.4% and higher.

DISCUSSION

According to the results of the analysis, it can be noted that all the studies and works are the result of the generalization of the modern experience of organic production, in which the proposed proposals are formed based on the expert experience (*Kvasha et al., 2019; Popova et al., 2022*). At the same time, the scope of application of modern economic-mathematical tools is limited to the grapho-analytical method, as well as statistical indicators of dynamics and structure (*Nesenenko, 2022*). The total area of Ukraine, taking into account the temporarily occupied territories, is 60.3 million hectares. Of these, 41.4 million hectares, or 68.7% are agricultural land.

In our opinion, this is a significant drawback as it introduces subjectivity into the decision-making process. One of the reasons for this is the imperfections and the limited amount of available statistical data. In particular, the State Statistics Service of Ukraine, as of mid-2022, does not carry out separate accounting of organic farming in the country. This limits the available methodological apparatus for the analysis of economic activity, mathematical statistics, and modelling in the economy, which, in our opinion, is a significant drawback as it introduces subjectivity into the decision-making process (*Soloviova et al., 2022*).

Ukraine possesses competitive advantages over Poland, including abundant agricultural land and lower labor costs. However, organic agriculture in Ukraine has yet to gain widespread adoption owing to underdeveloped domestic markets and limited profitability. The following recommendations are proposed to foster growth (*Iermakova et al., 2022*):

- Promote awareness of eco-friendly and safe food products in the population.
- Simplifying market entry for producers, especially small and medium-sized farms, subsidizes part of their expenses during the transition period.
- Support small agricultural enterprises as they transition to organic crop production by subsidizing costs and helping them meet ecological standards while selling products at conventional prices.
- In Poland, the analysis revealed that a uniform policy of fixed tariffs, irrespective of regional specifics, hampers the balanced development of organic production. It is evident that the duration of state support significantly influences the life cycle of organic farming in most farms. To address this, a region-based differentiation approach is recommended.
- Group regions based on their performance, with the most successful regions receiving continued state support at the current levels.
- Distribute State aid within the second and third groups to regions with average positions, extending the duration of State support for organic production.
- Provide transitional support to regions facing the most challenging conditions for organic activities, helping maintain organic production in larger agricultural enterprises.

These recommendations aim to optimize organic agriculture development by tailoring strategies to each country's unique circumstances and needs.

CONCLUSIONS

The analysis of the state current status and future outlook of organic farming in Ukraine and Poland, based on the proposed methodology, allows us to offer the following recommendations regarding regulatory policy in this direction.

The competitive advantages of Ukraine over Poland are, firstly, the quantitative and qualitative composition of agricultural land and a lower level of costs, in particular, for labor. As a result, the organic agriculture development in Ukraine took place without direct state intervention in the form of centralized subsidization of producers. Despite this, organic production in Ukraine has not yet become widespread due to the underdevelopment of the domestic market. In addition, low profitability slows the pace of development. Therefore, when formulating recommendations, it is important to consider Poland’s experiences. First, it is

necessary to pay attention to the popularization of ecological and safe food products among the population. Also, it is necessary to simplify the entry threshold to this market as much as possible for producers, particularly, small and medium-sized farms. For this purpose, it is advisable to cover part of the expenses for such enterprises during the transition period at the expense of state subsidies. In the opposite case, small agricultural enterprises do not have the opportunity to engage in organic crop production beyond the break-even point, when the production process must meet ecological standards, while the products are sold at conventional prices.

As for Poland, the analysis of the effectiveness of public spending, the risks of disposal of organic land and the yield of crops proved that the centralized policy of uniform tariffs, without taking into account the specifics of specific regions, does not ensure the uniform development of organic production. As it was shown above, for the vast majority of farms, the life cycle duration of such activities directly depends on the term of state support.

That is why it is necessary to differentiate between the regions. The first group includes the most successful regions according to these criteria, for which state support should remain at the current level. Within the second and third groups, state aid must be distributed in favor of regions that have average positions. Such assistance should include an increase in the duration of state support for organic production. These regions represent the largest untapped reserves of future growth. At the same time, regions with the most difficult conditions for conducting such activities should receive state aid during the transition period. This will allow for the preservation of organic production by large agricultural enterprises.

ACKNOWLEDGEMENTS

This work was supported by a grant of Ministry of Research, Innovation and Digitization, CCCDI - UEFISCDI, project number PN-III-P2-2.1-PED-2021-3678, within PNCDI III.

REFERENCES

[1] Agricultural and Food Quality Inspection. (2021). *The report on organic farming in Poland in 2019–2020*. Redakcja I. Zdrojewska. Warszawa. http://www.ijhars.gov.pl/

[2] Cabinet of Ministers of Ukraine. (2021). *On approval of the National Economic Strategy for the period until 2030*. https://zakon.rada.gov.ua/laws/show/179-2021-%D0%BF#n25

[3] Federation of the Organic Movement in Ukraine. (2021). *Organic in Ukraine*. https://organic.com.ua/organic-v-ukraini

[4] Galat, L. (2021). Trends of development of the organic fruit and vegetable market of Ukraine in the world context. *Agrosvit*, 12, 22. https://doi.org/10.32702/2306-6792.2021.12.22

[5] Garazha, O. (2021). Prospects for the organic agriculture development of Ukraine. *Modern Economics*, 27(1), 29–34. https://doi.org/10.31521/modecon.v27(2021)-04.

[6] Golik, D., & Żmija, D. (2017). Rolnictwo ekologiczne i perspektywy jego rozwoju w Polsce w świetle doświadczeń unijnych. *Zeszyty Naukowe Uniwersytetu Ekonomicznego w Krakowie*, 1(961), 117–129. https://doi.org/10.15678/znuek.2017.0961.0108

[7] Groszyk, J. (2022). Rolnictwo ekologiczne w Polsce w kontekście strategii unijnych. *Infos*, 4(296).

[8] Belinska, Y., Matvejciuk, L., Shmygol, N., Pulina, T., & Antoniuk, D. (2021). EU agricultural policy and its role in smoothing the sustainable development of the EU's agricultural areas. In IOP Conference Series: Earth and Environmental Science (Vol. 628, No. 1, p. 012030). IOP Publishing.

[9] Iagăru, R., Șipoș, A., & Iagăru, P. (2023). Strategic Thinking and Its Role in Accelerating the Transition from the Linear to the Circular Economic Model—Case Study of the Agri-Food Sector in the Sibiu Depression Microregion, Romania. *Sustainability*, *15*(4), 3109.

[10] Iermakova, O., Sedikova, I., & Dashian, A. (2022). Prospects of implementation of blockchain technology into aquaculture sector of Ukraine. *Economics Ecology Socium*, 6(2), 29–37. https://doi.org/10.31520/2616-7107/2022.6.2-3

[11] Iticescu, C., Georgescu, P. L., Arseni, M., Rosu, A., Timofti, M., Carp, G., & Cioca, L. I. (2021). Optimal solutions for the use of sewage sludge on agricultural lands. *Water*, *13*(5), 585.

[12] Jasiński, J., Michalska, S., & Śpiewak, R. (2014). Rolnictwo ekologiczne jako czynnik rozwoju lokalnego. *Wieś i Rolnictwo*, 145–158.

[13] Kvasha, S., Pankratova, L., Koval, V., & Tamošiūnienė, R. (2019). Illicit financial flows in export operations with agricultural products. *Intellectual Economics*, 13(2), 195-209. https://doi.org/10.13165/IE-19-13-2-10

[14] Luczka, W. (2016). Mocne i słabe strony przetwórstwa ekologicznego. *Naukowe Stowarzyszenia Ekonomistów Rolnictwa i Agrobiznesu*, 18, 143-148.
[15] Marszałek, A. (2018). Organic farming and organic food as an opportunity for sustainable development of rural areas. *Problems of Small Agricultural Holdings*, 4, 51–68. https://doi.org/10.15576/pdgr/2018.4.51
[16] Nesenenko, P. (2022). Taxation of the Agricultural Sector in the System of Ukraine's Economic Policy Implementation and Its Digitalization. *Economics Ecology Socium*, 6(3), 10-21. https://doi.org/10.31520/2616-7107/2022.6.3-2
[17] Nuanphromsakul, K., Cioca, L. I., Chaveesuk, S., & Chaiyasoonthorn, W. (2022). Exploring the social sustainability of rubber farmers-individual farmers perspective. *INMATEH-Agricultural Engineering*, *68*(3).
[18] Popova, O., Koval, V., Vdovenko, N., Sedikova, I., Nesenenko, P., & Mikhno, I. (2022). Environmental footprinting of agri-food products traded in the European market. *Frontiers in Environmental Science*, 10, 1036970. https://doi.org/10.3389/fenvs.2022.1036970
[19] Rozkrut, D. (2021). Statistical Yearbook of Agriculture. Warszawa.
[20] Senyshyn, O., Kundytskyj, O., Mayovets, Y., Horodniak, I., & Zhuk, O. (2023). Organic potential of Ukraine in the system of organic production of the European countries. *Management Theory and Studies for Rural Business and Infrastructure Development*, 45(1), 79–93. https://doi.org/10.15544/mts.2023.09
[21] Soloviova, O., Krasnyak, O., Cherkaska, V., & Revkova, A. (2022). Strategic development of international corporate social responsibility in agribusiness. *Economics Ecology Socium*, 6(4), 51-64. https://doi.org/10.31520/2616-7107/2022.6.4-5
[22] Stupnytskyi, V., Filipishyna, L., Chumak, O., Gonchar, V., Komandrovska, V., & Iefimova, G. (2023). Environmental compliance and business strategies practices of entrepreneurial ventures. *E3S Web of Conferences*, 408, 01025. https://doi.org/10.1051/e3sconf/202340801025
[23] Verkhovna Rada of Ukraine. (2018). Law of Ukraine on basic principles and requirements for organic production, circulation and labeling of organic products. https://zakon.rada.gov.ua/laws/show/2496-19#Text (May 9, 2020).
[24] Wojciechowska-Solis, J., Kowalska, A., Bieniek, M., Ratajczyk, M., & Manning, L. (2022). Comparison of the purchasing behaviour of polish and United Kingdom consumers in the organic food market during the COVID-19 pandemic. *International Journal of Environmental Research and Public Health*, 19(3), 1137. https://doi.org/10.3390/ijerph19031137
[25] Zielińska, A. (2015). Rozwój rolnictwa ekologicznego na obszarach przyrodniczo cennych. *Prace Naukowe Uniwersytetu Ekonomicznego We Wrocławiu*, 409, 195-203. https://doi.org/10.15611/pn.2015.409.14
[26] Ohorodnyk, N. (2023). Main aspects of the manufacturer of organic products in Ukraine. *Biotechnologia Acta*, 16(1), 40–50. https://doi.org/10.15407/biotech16.01.040

DETECTION OF APPLE LEAF DISEASES TARGET BASED ON IMPROVED YOLOv7
/
基于改进 YOLOv7 的苹果叶病害目标检测

Lingqing FENG, Yujing LIU*), Hua YANG, Zongwei JIA, Jiaxiong GUAN, Huiru Zhu,Yiming HOU
College of Information Science and Engineering, Shanxi Agricultural University, Taigu/China
Tel: +86-13834837537; E-mail: sxauxky@sxau.edu.cn
DOI: https://doi.org/10.35633/inmateh-72-26

Keywords: *apple leaf, disease detection, YOLOv7, SimAM attention mechanism, SIoU*

ABSTRACT

Apple leaf diseases significantly threaten the yield and quality of apples. In order to detect apple leaf diseases in a timely and accurate manner, this study proposed a detection method for apple leaf diseases based on an improved YOLOv7 model. The method integrated a Similarity-based Attention Mechanism (SimAM) into the traditional YOLOv7 model. Additionally, the regression loss function is modified from Complete Intersection over Union (CIoU) to Structured Intersection over Union (SIoU). Experimental results demonstrates that the improved model exhibits an overall recognition precision of 92%, a recall rate of 99%, and a mean average precision (mAP) of 96.1%. These metrics show a respective improvement of 14.4%, 38.85%, and 18.69% compared to the pre-improved YOLOv7. When compared with seven other target detection models in comparative experiments, the improved YOLOv7 model achieves higher accuracy, lower rates of missed and false detections in disease target detection. The model excels in detecting disease categories in complex environments and identifying small targets at early disease stages. It can provide technical support for effective detection of apple leaf diseases.

摘要

苹果叶部病害严重危害苹果的产量和品质，为了实现及时且准确地对苹果叶病害进行检测，提出了一种基于改进 YOLOv7 模型的苹果叶部病害检测方法，在传统的 YOLOv7 模型基础上融合了无参数注意力机制 SimAM；并将回归损失函数由 CIoU(Complete Intersection over Union）改进为 SIoU(Structured Intersection over Union)。试验结果表明，改进后的模型整体识别精准度、召回率、平均精度均值 mAP（Mean average precision）分别为 92%，99%，96.1%；与改进前 YOLOv7 相比，分别提升 14.4%，38.85%，18.69%，与对比实验中的其他 7 种目标检测模型相比，改进模型检测精度更高、漏检和错检率低、在复杂环境以及病害初期小目标检测中表现优良。可以为苹果叶病害有效检测提供技术支持。

INTRODUCTION

Apples are among the world's most significant economic crops due to their rich nutritional content, high yield, and survival rate, and are widely cultivated in many countries globally *(Zhong & Zhao, 2020).* The prevalent diseases in apple cultivation include Alternaria Blotch, Brown Spot, Grey spot, Rust and mosaic diseases, which pose a severe threat to young fruits, new shoots, petioles, and young leaves *(Chao et al., 2020).* Traditionally, the detection of apple leaf diseases has been performed by experts through visual inspection of the leaves, relying on experience *(Khan et al., 2022).* This method is not only time-consuming and laborious but also prone to misjudgement due to subjective human factors *(Bansal et al., 2021).* However, the spread and development of apple diseases are very rapid; if not identified and addressed promptly, diseases can quickly escalate, greatly impacting the quality and yield of apples and directly affecting their economic benefits *(Bi et al., 2022; Wang & Zhao, 2022).* Therefore, timely and accurate identification of the types of apple leaf diseases is of great significance and practical value for the prevention and control of these diseases.

With the advancement of computer science and technology, computer vision technology has been widely applied in the agriculture sector, and many models utilizing machine learning methods for plant disease identification have been developed for the detection and classification of plant diseases *(Pathan et al., 2020)*. Singh et al. proposed a new segmentation algorithm for diseased parts of apple leaf images, and then extracted colour and texture features from the segmented apple leaves, achieving the best accuracy of 96.4% using a K nearest neighbour classifier *(Singh et al., 2022)*. Sahu et al. proposes a novel hybrid random forest Multiclass SVM (HRF-MCSVM) design for plant foliar disease detection *(Sahu & Pandey, 2023)*.

Although traditional machine learning can reduce identification time, there are obvious limitations in handling large-scale, high-dimensional, nonlinear, and sequential data.

In recent years, with the development of deep learning, many researchers have begun to apply deep learning to plant disease identification. G. Priyadharshini conducted comparative research on the use of CNN, R-CNN, Fast R-CNN, and Faster R-CNN for the detection and classification of tomato leaf diseases *(Priyadharshini et al., 2023)*. He et al. proposed the MFaster R-CNN algorithm based on the Faster R-CNN algorithm, which achieved intelligent diagnosis of complex background and similar disease spot features in corn diseases in field environments, with an overall average accuracy rate of 97.23% *(He et al., 2023)*. Although these two-stage target detection algorithms generally have higher detection accuracy but suffer from long parameter extraction times and slow speeds, they are suitable for large-scale and complex scenarios. Sajitha.et al. presented a leaf disease detection and classification system utilizing YOLO v7, the system achieved high accuracy (96%) in identifying various leaf diseases *(Sajitha et al., 2023)*. Mathew et al. applied the YOLOv5 algorithm to detect bacterial spot disease in pepper plants based on symptoms on the leaves *(Mathew & Mahesh, 2022)*. Li et al. proposed an apple leaf disease detection method based on the BTC-YOLOv5s model for accurate localization and recognition of multiscale and different-shaped apple leaf diseases against complex backgrounds, offering higher detection precision and accuracy *(Li et al., 2023)*. These One-stage target detection methods have relatively faster detection speeds and accuracy.

The above research shows that deep learning has achieved certain effects in crop and plant disease detection methods. However, there is a lack of studies on small targets with less apparent features in the early stages of diseases. Additionally, there are challenges with high rates of missed and false detections when detecting targets against complex backgrounds and identifying multiple disease categories. To address the current challenges faced by apple leaf disease detection methods, this paper presents an efficient and accurate apple leaf disease target detection algorithm based on YOLOv7. The SimAM attention mechanism was introduced in YOLOv7 and SIoU Loss was used to replace the original CIoU loss to improve the detection speed and accuracy of small targets in the early stages of apple leaf disease in various environments.

MATERIALS AND METHODS

Data Acquisition and Preprocessing

Some data used in the experiments in this paper were sourced from AI Studio. In order to collect images of apple diseases from different periods and environments, many early disease images captured using smartphones, and additional images were obtained using web crawlers and Google searches. All images were collected directly from fields under natural light. To ensure the diversity of the dataset, samples of each disease category were selected based on background, severity, and the growth stage of the leaves. The resulting dataset includes images of the four most common apple leaf diseases: Alternaria Blotch, Brown Spot, Grey Spot, and Rust, totalling 1643 pictures as shown in Figure 1.

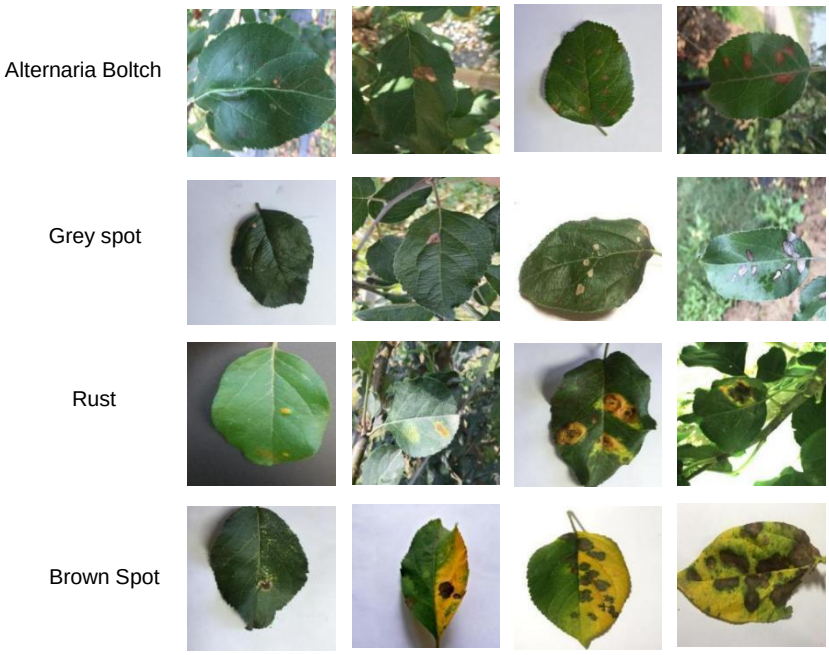

Fig. 1 - Partial data collection

The LabelImg tool was used to mark diseases in the dataset. Each disease in the images is completely enclosed by a rectangular box, with efforts made to minimize the inclusion of unnecessary background within the box. The position of the box is determined by the coordinates of the top-left and bottom-right vertices. After all diseases in the images were annotated, corresponding XML files were generated, containing information such as the size of the images, the names of the labels, and the positions of the labels. The annotation work was carried out by four researchers with relevant expertise.

To ensure the accuracy of model training, improve the robustness of the model, and enhance its ability to recognize apple leaf diseases from different periods and environments, and to avoid model overfitting due to insufficient data, the images were pre-processed to simulate variations in lighting, exposure and angles. The dataset was augmented with operations such as increasing and decreasing brightness, saturation, and contrast, as well as rotation and flipping. A total of 16,430 enhanced images was divided into training, validation, and test sets in an 8:1:1 ratio. with the statistical results of the dataset samples as shown in Table 1.

Table 1

Apple leaf disease dataset

Class name	Original image	Augmented			
		Training set	Validation set	Test set	Total
Alternaria Boltch	400	3200	400	400	4000
Grey spot	370	2960	370	370	3700
Rust	438	3504	438	438	4380
Brown Spot	435	3480	435	435	4350
Total	1643	13144	1643	1643	16430

YOLOv7 Model

YOLOv7*(Wang et al., 2022)* is the seventh generation of the YOLO series, and comparative experiments conducted on public datasets demonstrate that the performance of this version has improved significantly over previous iterations, with detection speed and accuracy surpassing other object detection algorithms. As a single-stage object detection algorithm, YOLOv7 is widely applied in real-time detection due to its superior performance. In this paper, YOLOv7 was utilized as the benchmark model, and its network structure is depicted in Figure 2.

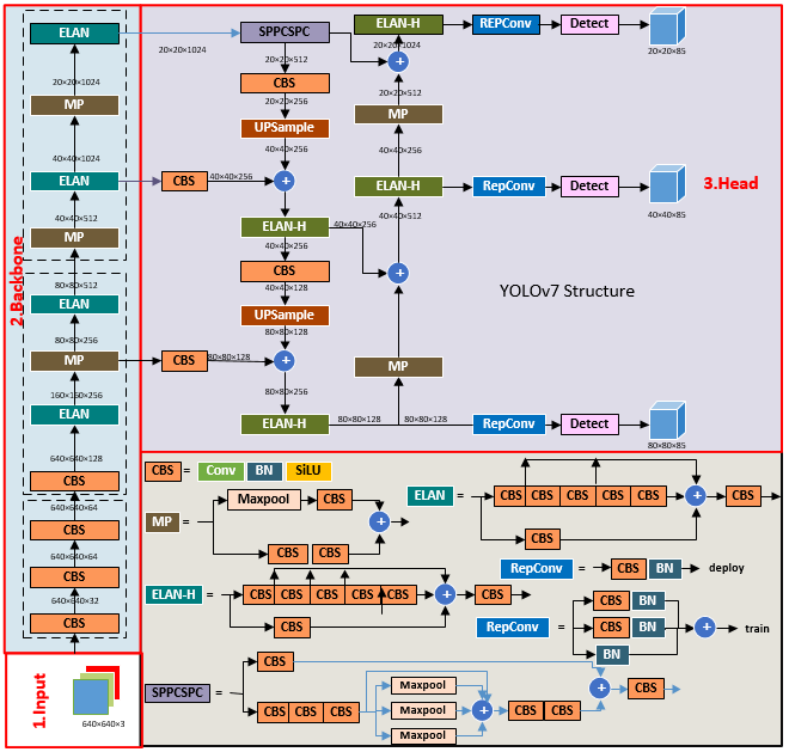

Fig. 2 - Architecture of YOLOv7

The YOLOv7 network structure primarily comprises an Input layer, Backbone layer, and Head layer. The Input layer serves as the initial layer, mainly processing the input images and directing them to the Backbone layer; the Backbone layer, also referred to as the feature extraction layer, is responsible for

extracting features of targets of varying sizes and consists of several CBS modules, MaxPool(MP), and efficient layer aggregation network(ELAN) structures. The Head layer's primary function is to integrate the features provided by the Backbone layer to generate bounding boxes and predict classes, which includes SPPCSPC(Spatial Pyramid Pooling, Cross Stage Partial Channel) layers, several ELAN-H layers, MP layers, and RepConv layers.

Addition of the SimAM Attention Module

Early-stage apple leaf diseases often present as light-coloured and small areas, similar to the colour of the leaves, and can be difficult to distinguish in complex, blurry, or poorly lit environments. As a result, the key information of the targets may become obscured by noise and other interfering factors, leading to lower accuracy. To address this issue, the SimAM attention mechanism was chosen for its lightweight design and strong capability for feature enhancement and representation, coupled with efficient computational performance.

The SimAM attention module was proposed by Yang et al., inspired by the attention mechanisms of the human brain *(Yang et al., 2021)*. It calculates attention weights by exploring the significance of each neuron and assesses the importance of each neuron based on the linear separability between the target neuron and other neurons, as informed by neuroscientific theory. The energy function is defined by Equation (1) as follows:

$$e_t\left(w_t,b_t,y,x_i\right)=\frac{1}{M-1}\sum_{i=1}^{M-1}\left(-1-\left(w_t x_i+b_t\right)\right)^2+\left(1-\left(w_t t+b_t\right)\right)^2+\lambda w_t^2 \quad (1)$$

Where t and x_i represent the target neuron and other neurons of the input feature X, i indexes the spatial dimension, M is the number of neurons in a given channel, y is the label indicating the significance of the neuron, w_t and b_t are the weights and biases, and λ is the regularization coefficient. Simplifying this equation leads to a minimal energy function, expressed as Equation (2):

$$e_t^*=\frac{4\left(\hat{\sigma}^2+\lambda\right)}{(t-\hat{\mu})^2+2\hat{\sigma}^2+2\lambda} \quad (2)$$

Where *t* is the target neuron, *x* represents adjacent neurons, and λ is a hyperparameter, $\hat{\mu}=\frac{1}{M}\sum_{i=1}^{M}x_i$, $\hat{\sigma}^2=\frac{1}{M}\sum_{i=1}^{M}\left(x_i-\hat{\mu}\right)^2$.

Finally, features are enhanced as indicated by Equation (3).

$$\tilde{X}=\text{sigmoid}\left(\frac{1}{E}\right)\odot X \quad (3)$$

This research embeds SimAM within the feature extraction layer of YOLOv7 to identify important neurons while suppressing surrounding ones, enhancing relevant features without increasing the parameter count of the model. This is particularly beneficial for recognizing features of apple leaf disease targets.

Loss Function Improvement: SIoU Loss Function

The quality of the loss function directly impacts the training speed and model detection performance. YOLOv7 incorporates three types of losses: Localization loss, Confidence loss, and Classification loss. Among these, the Localization loss function utilizes Complete Intersection over Union(CIoU). CIoU primarily considers the overlapping area, distance, and aspect ratio between the predicted and ground-truth bounding boxes but does not account for the mismatched orientation between them. This deficiency can lead to slower convergence and low efficiency. To address this, Gevorgyan proposed the SIoU loss function, to further improve the model recognition accuracy *(Gevorgyan, 2022).* SIoU loss was used to replace the CIoU loss in this paper.

The SIoU loss includes four components: angle cost, distance cost, shape cost, and IoU cost. The parameters used in the SIoU loss function are illustrated in Figure 3.

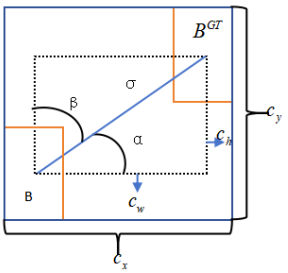

Fig. 3 - Calculation of SIoU loss function

Angle cost:

The calculation of the angle cost is shown in Equation (4):

$$\Lambda = 1 - 2 * \sin^2\left(\arcsin(x) - \frac{\pi}{4}\right) \tag{4}$$

where:

$x = \frac{c_h}{\sigma} = \sin(\alpha), c_h = \max\left(b_{cy}^{gt}, b_{cy}\right) - \min\left(b_{cy}^{gt}, b_{cy}\right)$ is the height difference between the centres of the two boxes and $\sigma = \sqrt{(b_{cx}^{gt} - b_{cx})^2 + (b_{cy}^{gt} - b_{cy})^2}$ is the width difference. If the angle α is greater than 45°, its complementary angle β is used, considering the angle from the y-axis rather than the x-axis.

Distance cost:

The distance cost represents the distance between the centre points of the predicted and ground-truth bounding boxes. Combining the angle cost defined above, SIoU redefines the distance cost as shown in Equation (5):

$$\Delta = \sum_{t=x,y} (1 - e^{-\gamma \rho t}) \tag{5}$$

where:

$\rho_x = (\frac{b_{cx}^{gt} - b_{cx}}{c_w})^2$, $\rho_y = (\frac{b_{cy}^{gt} - b_{cy}}{c_H})^2$, $\gamma = 2 - \Lambda$, and the terms involving c_w and c_H represent the widths and heights of the smallest enclosing boxes for the ground-truth and predicted boxes. When α approaches 0, the contribution of the distance cost significantly decreases. Conversely, as α approaches π/4, the contribution of the distance cost increases. With increasing angle, γ is assigned a time-priority distance value.

Shape cost:

The definition of the shape cost Ω is shown in Equation (6):

$$\Omega = \sum_{t=w,h} (1 - e^{-w_t})^{\theta} \tag{6}$$

where:

$w_w = \frac{|w - w^{gt}|}{\max(w, w, ^{gt})}$, $w_h = \frac{|h - h^{gt}|}{\max(h, h^{gt})}$, and θ represent the attention of the network to shape.

The SIoU loss function is shown in Equation (7):

$$L_{SIoU} = 1 - IoU + \frac{\Delta + \Omega}{2} \tag{7}$$

Model Evaluation Metrics

Model performance is assessed by comparing the detection results of pre- and post-improvement network models on various types of images under the same experimental conditions, focusing on missed and false detections. The study employs precision (P), recall (R), the precision-recall (P-R) curve, and mean average precision (mAP) as evaluation metrics.

The equations for these metrics are as follows:

$$P = \frac{TP}{TP + FP} \tag{8}$$

$$R = \frac{TP}{TP + FN} \tag{9}$$

$$mAP = \frac{\sum_{i=1}^{C} AP(i)}{C} \tag{10}$$

Where:

TP (true positive) represents correct positive predictions, FP (false positive) incorrect positive predictions, and FN (false negative) incorrect negative predictions; C is the number of classes detected. AP represents the area under the P-R curve, measuring the detection precision for a specific class. AP(i) indicates the AP value for the detection of the i-th class. The mAP is the arithmetic mean of the APs for all classes, assessing the overall detection performance of the model. The higher the mAP, the better the detection performance. Typically, mAP is used to evaluate the performance of the entire object detection network model.

RESULTS AND ANALYSIS

The experimental setup utilized the Windows 10 operating system with the deep learning framework PyTorch 1.7.1 and the programming language Python 3.8. The CPU model is Intel(R) Core(TM) i7-13700F @2.10GHz. The GPU model is NVIDIA GeForce RTX 3070.GPU acceleration libraries used are CUDA 10.2 and CUDNN 8.3.3. During training, the input image size was set to 640*640 pixels, initial learning rate was set to 0.001, momentum was set to 0.9, the batch size was set to 4, and the epoch was set to 100. The Adam optimizer was used to optimize the network parameters.

Dataset Analysis

The characteristics of apple leaf disease spots change noticeably over different periods. For instance, early-stage spots of Alternaria Blotch and Grey Spot are small and sparse, taking on circular or oval shapes. In later stages, the spots become larger, darker, and more densely distributed. Rust and Brown Spot typically start as light-coloured circular spots on apple leaves. To prevent issues of overfitting and poor generalization due to imbalanced dataset distribution or insufficient samples in certain categories, an initial data analysis was conducted, focusing on the distribution of target quantities, the number of disease categories, and the distribution of small targets.

Analysing by the number of disease categories in the dataset, 1378 images contain only one category of disease, while 265 images contain more than one. By target quantity in the images, 642 images have only one detection target, and 1001 images have more than one target. The distribution of target quantities across different disease categories is as follows: 996 targets for Alternaria Blotch, 1935 for Brown Spot, 885 for Grey Spot, and 843 for Rust. Brown Spot has the most targets, while the other three diseases have a similar number of targets.

In the dataset of apple leaf diseases, a total of 4659 targets were identified among the four disease categories. After annotating the targets, XML files were generated. The ratio of the area of the target to be predicted in the image to the image was calculated, based on the equation (11) provided:

$$P = \frac{area_t}{area_i} * 100\% \tag{11}$$

where $area_t = width * height$, it is the area of the target, $area_i$ is the area of the image, and the P is the ratio of the target area to the image area. $width = x\max - x\min + 1$, $heigh = y\max - y\min + 1$, width and height are expressed in pixel units. xmin and ymin are the x and y coordinate values of the top-left corner of the bounding box, while xmax and ymax are the x and y coordinate values of the bottom-right corner.

All P values were calculated using the above equation, a threshold of P was set, the data of the disease area proportion of all targets were analysed using Python, and then a histogram was output, as shown in Figure 4. As seen in Figure 4, there are 2352 small targets with p-value less than 6%, accounting for 50.5% of all targets. Since early-stage apple leaf spots are often small, the dataset used in this experiment provides a sufficient data foundation for the detection of early-stage small targets. The experimental results also provide a strong basis for the detection and prevention of early-stage small targets.

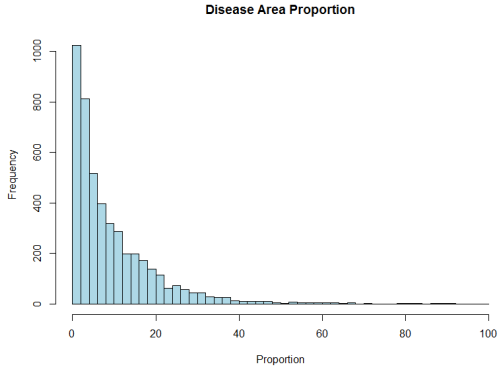

Fig. 4 - Histogram of disease area proportion

Ablation Study and Data Analysis

To verify the effectiveness of the improvements proposed in this study, ablation experiments were conducted on the dataset. Improvements are denoted by "√", while the absence of improvements is indicated by "–". The impact of detecting different models on the performance of apple leaf disease target detection is shown in Table 2.

Table 2

Results of the ablation study for different improvements

Baseline	Order	ECA	CBAM	SE	SimAM	Focal-EIOU	SIOU	Precision (%)	Recall (%)	mAP (%)
YOLOv7	1	—	—	—	—	—	—	77.86	68.15	77.41
	2	√	—	—	—	—	—	80.74	67.98	79.21
	3	—	√	—	—	—	—	80.90	71.87	81.35
	4	—	—	√	—	—	—	84.27	67.46	79.06
	5	—	—	—	√	—	—	87.80	99.00	94.30
	6	—	—	√	—	√	—	80.21	72.32	84.50
	7	—	—	√	—	—	√	78.00	97.00	82.00
	8	—	—	—	√	√	—	77.00	98.00	81.70
	9	—	—	—	√	—	√	92.00	99.00	96.10

Note: "√" represents the use of improvements, while "–" indicates no improvements used.

To validate the effectiveness of incorporating the SimAM attention mechanism into the model and to further analyse the impact of different attention mechanisms on the detection performance of apple tree leaf diseases under varying periods and environmental conditions, this study compared the introduction of ECA, CBAM, SE, and SimAM attention modules into the YOLOv7 network structure. By analysing and comparing the results, the strengths and weaknesses of each attention mechanism can be identified, establishing the effectiveness of SimAM in object detection tasks.

From Table 2, the following conclusions can be drawn:

(1) The YOLOv7 model without the introduction of an attention mechanism achieved a mean average precision (mAP) of 77.41%. The introduction of attention mechanisms significantly improved the mAP value, with the SimAM attention mechanism reaching 94.3%. Compared to the ECA, CBAM, and SE attention modules, the mAP values increased by approximately 15.09%, 12.95%, and 15.24%, respectively, further confirming the accuracy of SimAM in target detection under different periods and environments.

(2) The introduction of the SE attention mechanism with the Focal-EIOU loss function achieved an mAP of 84.5%, while using the SIoU loss function resulted in an mAP of 82%, indicating a slight decrease in detection performance. Introducing the SimAM attention mechanism with the Focal-EIOU loss function resulted in an mAP of 81.7%, and using the SIoU loss function increased the mAP to 96.1%, showing a marked improvement in detection performance.

(3) Implementing both SimAM and SIoU improvements increased the mAP value for apple leaf disease detection from 77.41% to 96.1%, an enhancement of 18.69%, indicating a significant improvement in detection performance. Compared to other models in the experiment, the combination of YOLOv7, SimAM, and SIoU yielded the best results in all three evaluative measures: Precision, Recall, and mAP.

The research demonstrates that the improved YOLOv7 algorithm significantly outperforms the baseline YOLOv7 algorithm, with a 14.4% increase in Precision, a 38.85% increase in Recall, and an 18.69% increase in mAP. It also surpasses the other seven comparative models, indicating that the improved YOLOv7 model performs exceptionally well and can achieve rapid and accurate identification of apple leaf disease targets in natural environments. To provide a more intuitive analysis of the improvements of the YOLOv7 model over the original, the experiment draws a PR curves to reflect changes in Precision and Recall for different disease detections using different schemes, as shown in Figure 5.

Observation of Figure 5 reveals that the experiments using eight improvement schemes for the four diseases show many similarities: The four improvement schemes YOLOv7+ECA, YOLOv7+CBAM, YOLOv7+SE, YOLOv7+SimAM+FocalEIoU did not exhibit significant improvements in detection precision compared to the YOLOv7 model. The improvement schemes YOLOv7+SE+SIoU and YOLOv7+SE+FocalEIoU showed clear advantages over the aforementioned four schemes in detecting Alternaria Boltch, Brown Spot, and Grey spot, but not as much in detecting Rust. The schemes YOLOv7+SimAM and YOLOv7+SimAM+SIoU demonstrated markedly superior performance in Precision and Recall over the others, with a very significant improvement in detection performance compared to the YOLOv7 model. According to the information reflected in Figure 5, considering the detection performance of the model, it can be observed that YOLOv7+SimAM+SIoU has the best detection performance for apple leaf disease in this paper.

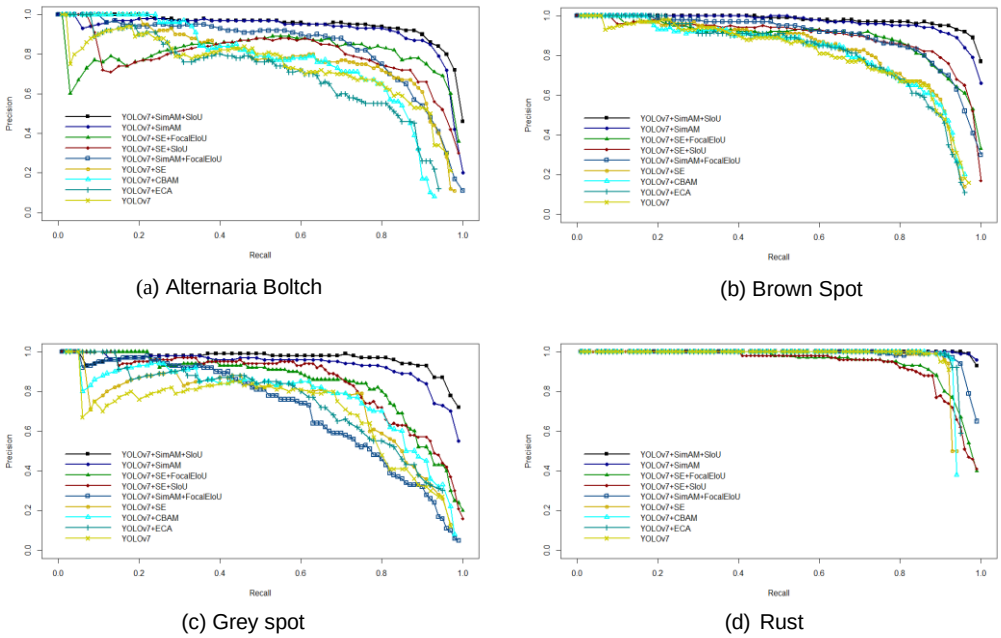

(a) Alternaria Boltch (b) Brown Spot

(c) Grey spot (d) Rust

Fig. 5 - P-R curve

Visualization Analysis of Detection Results

Figure 6 shows the detection results of various models for different classes of apple leaf disease targets against a simple background.

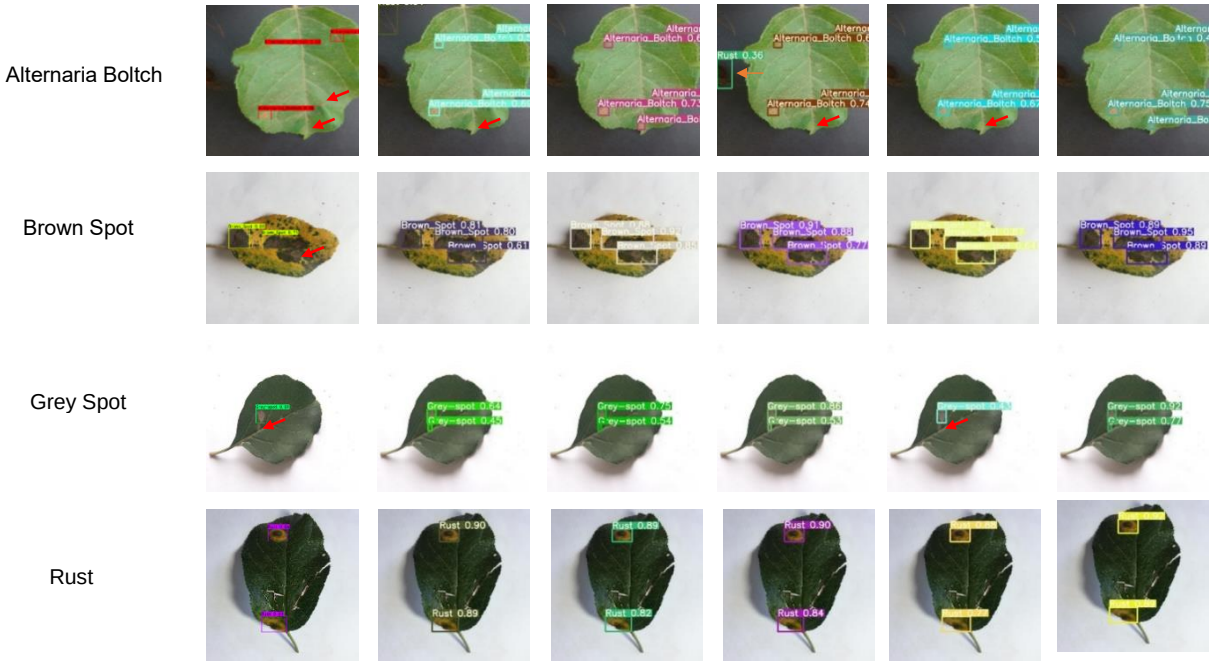

Note: ← Points to a missed target ← Points to a false detection

Fig. 6 - Prediction results of six models against a simple background

The first row shows the detection results for Alternaria Boltch; the original image had 5 targets, the YOLOv7 model detected 3, YOLOv7-SE-Focal-EIOU, YOLOv7-SimAM, and YOLOv7-SimAM-Focal-EIoU detected 4, missing one, and YOLOv7-SimAM had one false positive. YOLOv7-SE-SIOU and YOLOv7-SimAM-SIOU detected all 5 targets. The second row shows the detection results for Brown Spot; the original image had 3 targets, and apart from the YOLOv7 model missing one target, the other models detected all 3. The third row is for Grey spot detection results; YOLOv7 and YOLOv7-SimAM-Focal-EIoU missed one target, while the others detected all. The fourth row shows the detection results for Rust, all models detected all targets.

By comparing the detection results, it is found that the proposed model YOLOv7-SimAM-SIOU can fully detect all targets for the four diseases, and YOLOv7-SimAM-SIOU has the highest corresponding location (bounding box) and confidence values.

Figure 7 displays the detection results for apple leaf disease targets by various models against a complex background. In the original image, there is a small target of Grey spot, which due to its diminutive size and the complex background where the colour of the gaps between leaves closely resembles that of the Grey spot, poses a challenge for detection. As a result, YOLOv7 failed to detect Grey spot, and models such as YOLOv7-SE-Focal-EIOU, YOLOv7-SE-SIOU, YOLOv7-SimAM and YOLOv7-SimAM-Focal-EIoU mistook similar patterns in the background for the target, leading to false positives. YOLOv7-SimAM–SIOU did not suffer from missed or false detections.

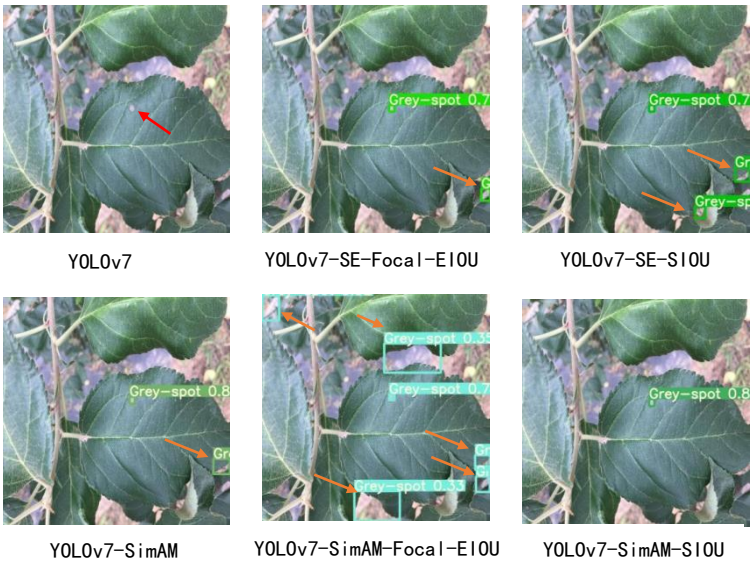

Note: ←Points to a missed target ←Points to a false detection

Fig. 7 - Prediction results of six models against a complex background

Figure 8 shows the detection results of YOLOv7 and YOLOv7-SimAM–SIOU for early-stage apple leaf disease targets. In the early stages of infection on apple leaves, the disease spots appear lighter in colour and smaller in size. For such targets, YOLOv7 had a high rate of missed detections, while the model proposed in this paper, YOLOv7-SimAM-SIOU, detected all early-stage disease targets. This demonstrates that the algorithm proposed in this paper clearly outperforms the YOLOv7 algorithm in detecting small targets in the initial stages of the disease.

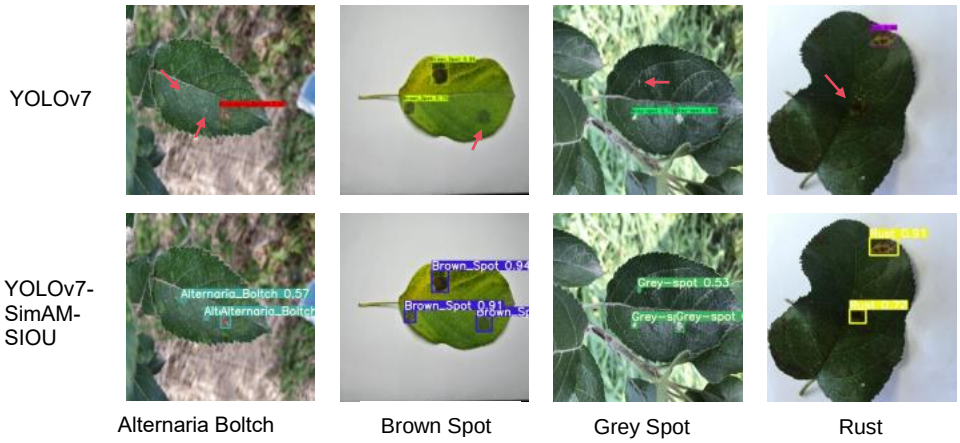

Note: ← Points to a missed target.

Fig. 8 - Prediction results of YOLOv7 and YOLOv7-SimAM-SIOU

CONCLUSIONS

To achieve accurate detection of apple leaf disease targets at different stages and in various environments, this study improved the YOLOv7 model by integrating SimAM and SIoU with YOLOv7, achieved a mAP of 96.1%, a precision of 92%, and a recall of 99% for apple leaf disease detection. Comparative experiments show that the performance of this model is clearly superior to the original YOLOv7 network. Comparison tests with seven other target detection models that the improved model is also superior, further verifying the effectiveness of the improved method for recognizing apple leaf diseases at different stages and in different environments. Through visual analysis, the improved YOLOv7 model shows its good performance in detecting apple leaf diseases in various aspects such as reducing false negatives, false positives, multi-category disease detection, and detection of small disease spots in the early stages of infection. Additionally, the model is minimally affected by factors such as light intensity, weather changes, indicating that the model has good robustness. The optimized YOLOv7 model achieves higher accuracy in apple leaf disease detection and can provide a technical reference for the prevention and diagnosis of plant diseases. In subsequent research, the focus will be on further optimizing YOLOv7-SimAM-SIOU and transferring it to more crop disease detection tasks.

ACKNOWLEDGEMENT

This research was financed by the Science and Technology Innovation Project of Colleges and Universities in Shanxi Province, China (No. 2022L085).

This research was financed by the Basic Research Program of Shanxi Province, China (No.202303021222058).

REFERENCES

[1] Bansal, P., Kumar, R., & Kumar, S. (2021). Disease detection in apple leaves using deep convolutional neural network. *Agriculture*, *11*(7), 617. https://doi.org/10.3390/agriculture11070617

[2] Bi, C., Wang, J., Duan, Y., Fu, B., Kang, J.-R., & Shi, Y. (2022). MobileNet Based Apple Leaf Diseases Identification. *Mobile Networks and Applications*, *27*(1), 172–180. https://doi.org/10.1007/s11036-020-01640-1

[3] Chao, X., Sun, G., Zhao, H., Li, M., & He, D. (2020). Identification of apple tree leaf diseases based on deep learning models. *Symmetry*, *12*(7), 1065. https://doi.org/10.3390/sym12071065

[4] Gevorgyan, Z. (2022). *SIoU Loss: More Powerful Learning for Bounding Box Regression* (arXiv:2205.12740). arXiv. http://arxiv.org/abs/2205.12740

[5] He, J., Liu, T., Li, L., Hu, Y., & Zhou, G. (2023). MFaster R-CNN for Maize Leaf Diseases Detection Based on Machine Vision. *Arabian Journal for Science and Engineering*, *48*(2), 1437–1449. https://doi.org/10.1007/s13369-022-06851-0

[6] Khan, A. I., Quadri, S. M. K., Banday, S., & Shah, J. L. (2022). Deep diagnosis: A real-time apple leaf disease detection system based on deep learning. *Computers and Electronics in Agriculture*, *198*, 107093. https://doi.org/10.1016/j.compag.2022.107093

[7] Li, H., Shi, L., Fang, S., & Yin, F. (2023). Real-Time Detection of Apple Leaf Diseases in Natural Scenes Based on YOLOv5. *Agriculture*, *13*(4), 878. https://doi.org/10.3390/agriculture13040878

[8] Mathew, M. P., & Mahesh, T. Y. (2022). Leaf-based disease detection in bell pepper plant using YOLO v5. *Signal, Image and Video Processing*, *16*(3), 841–847. https://doi.org/10.1007/s11760-021-02024-y

[9] Pathan, M., Patel, N., Yagnik, H., & Shah, M. (2020). Artificial cognition for applications in smart agriculture: A comprehensive review. *Artificial Intelligence in Agriculture*, *4*, 81–95. https://doi.org/10.1016/j.aiia.2020.06.001

[10] Priyadharshini, G., & Judie Dolly, D. R. (2023). Comparative Investigations on Tomato Leaf Disease Detection and Classification Using CNN, R-CNN, Fast R-CNN and Faster R-CNN. *2023 9th International Conference on Advanced Computing and Communication Systems (ICACCS)*, 1540–1545. https://doi.org/10.1109/ICACCS57279.2023.10112860

[11] Sahu, S. K., & Pandey, M. (2023). An optimal hybrid multiclass SVM for plant leaf disease detection using spatial Fuzzy C-Means model. *Expert Systems with Applications*, *214*, 118989. https://doi.org/10.1016/j.eswa.2022.118989

[12] Sajitha, P., Andrushia, D. A., & Suni, S. S. (2023). Multi-class Plant Leaf Disease Classification on Real-Time Images Using YOLO V7. *International Conference on Image Processing and Capsule Networks*, 475–489. https://doi.org/10.1007/978-981-99-7093-3_32

[13] Singh, S., Gupta, S., Tanta, A., & Gupta, R. (2022). Extraction of Multiple Diseases in Apple Leaf Using Machine Learning. *International Journal of Image and Graphics*, *22*(03), 2140009. https://doi.org/10.1142/S021946782140009X

[14] Wang, C.-Y., Bochkovskiy, A., & Liao, H.-Y. M. (2022). *YOLOv7: Trainable bag-of-freebies sets new state-of-the-art for real-time object detectors* (arXiv:2207.02696). arXiv. http://arxiv.org/abs/2207.02696

[15] Wang, Y., & Zhao, J. (2022). MGA-YOLO: A lightweight one-stage network for apple leaf disease detection. *Frontiers in Plant Science*, *13*, 927424. https://doi.org/10.3389/fpls.2022.927424

[16] Yang, L., Zhang, R.-Y., Li, L., & Xie, X. (2021). SimAM: A Simple, Parameter-Free Attention Module for Convolutional Neural Networks. In M. Meila & T. Zhang (Eds.), *Proceedings of the 38th International Conference on Machine Learning* (Vol. 139, pp. 11863–11874). PMLR. https://proceedings.mlr.press/v139/yang21o.html

[17] Zhong, Y., & Zhao, M. (2020). Research on deep learning in apple leaf disease recognition. *Computers and Electronics in Agriculture*, *168*, 105146. https://doi.org/10.1016/j.compag.2019.105146

ONLINE DETECTION OF SOLUBLE SOLID CONTENT IN FRESH JUJUBE BASED ON VISIBLE / NEAR-INFRARED SPECTROSCOPY
/
基于可见/近红外光谱的鲜枣可溶性固形物在线检测

Bin WANG [1]; Lili LI [*1] [1]
[1] College of Information Science and Engineering, Shanxi Agricultural University, Taigu 030800/China
Tel: 18306832356; E-mail: lilycqdxyjs@163.com
DOI: https://doi.org/10.35633/inmateh-72-27

Keywords: *near infrared spectroscopy, soluble solid content, characteristic wavelengths, partial least squares regression, nondestructive testing*

ABSTRACT
Soluble solid content (SSC) is one of the important evaluation indexes of the internal quality and taste of fresh jujube. In order to realize the online nondestructive detection of SSC of fresh jujube, this paper took Huping jujube as the research object, adopted self-constructed nondestructive online testing system to collect the spectral information of jujubes (350~2500 nm), and studied the influence of the rotational speed of 4 r/min on the online prediction model of SSC of jujube. Kennard-Stone (KS) algorithm was used to divide the sample into correction set and prediction set. Six commonly used preprocessing methods such as SG smoothing (S-G), multiplicative scatter correction (MSC), standard normal variate (SNV), orthogonal signal correction (OSC), first derivative (FD), and second derivative (SD) were applied to the spectral data, and the regression coefficient (RC) algorithm and the successive projections algorithm (SPA) were utilized to select informative wavelengths, and a quantitative prediction model for the SSC of Huping jujube was established using partial least squares regression (PLSR). The results indicate that the PLSR prediction model established by preprocessing the original spectrum with OSC and combining it with RC algorithm to select characteristic wavelengths was optimal. Therefore, when predicting the SSC of Huping jujube, the optimal model was OSC-RC-PLSR, and the correlation coefficients of the correction set and prediction set were 0.846 and 0.782, respectively, and the corrected root mean square error (RMSEC) and predicted root mean square error (RMSEP) were 1.962 and 2.247, respectively. The results show that non-destructive detection of soluble solid content of jujube can be achieved by combining visible-near-infrared spectroscopy and appropriate regression model, which provides an innovative way for online sorting and identifying fresh jujube.

摘要
可溶性固形物(Soluble Solid Content, SSC)是鲜枣内部品质与口感的重要评价指标之一。为实现鲜枣SSC的在线无损检测，本文以壶瓶枣为研究对象，采用自行搭建的无损在线检测系统采集壶瓶枣的光谱信息（350～2500nm），研究了旋转速度为4 r/min条件下对壶瓶枣SSC在线预测模型的影响。采用Kennard-Stone (KS)算法将样本划分为校正集和预测集，对原始光谱使用SG平滑(S-G)、乘多元散射校正(MSC)、标准正态变量(SNV)、正交信号校正(OSC)、一阶导数(FD)和二阶导数(SD)等6种方法进行预处理，采用RC回归系数法和连续投影算法对原始光谱降维，结合偏最小二乘回归（PLSR）建立壶瓶枣SSC的定量预测模型。结果表明，原始光谱经OSC预处理，再结合RC算法筛选特征波长建立的PLSR预测模型最优。因此在预测壶瓶枣SSC时，最优模型为OSC-RC-PLSR，其校正集和预测集相关系数分别为0.846和0.782，均方根误差分别为1.962和2.247。该研究表明，结合可见-近红外光谱和合适的回归模型，可实现对壶瓶枣可溶性固形物含量的无损检测，为鲜枣品质在线检测提供新的途径。

INTRODUCTION
Huping jujube is not only a nutritious food, but also a natural health product. Its meat is crispy, its taste is sweet, and its flavor is unique, which is deeply loved by consumers *(Fan et al., 2003)*. The soluble solid content (SSC) is an important indicator of the quality of Huping jujube, and the rapid non-destructive testing of SSC helps to detect and classify the quality of Huping jujube *(Fan et al., 2015)*.

[1] *Bin Wang, Lec. Ph.D.; Lili Li*, Lec. Ph.D.*

The traditional methods for measuring SSC content have drawbacks such as destructive, inefficient, and time-consuming, and are difficult to meet the needs of online detection of large batches of samples. The classification of fresh jujube according to quality is indispensable in the post-production process of fresh jujube, which has important significance for the storage of fresh jujube products and the "price according to quality" in the sales process. Therefore, how to realize the fast and nondestructive online detection of fresh jujube SSC is particularly important.

In recent years, near infrared spectroscopy has been used to detect the quality of apples, strawberries, oranges, pears, watermelons, which is a very effective and economical sorting method *(Agulheiro et al., 2022; Song et al., 2020; Wang et al., 2020)*. Scholars at home and abroad have conducted many studies on online detection of near-infrared red spectroscopy. *Jiang et al. (2023)* studied the influence of different parameters (motion speed, integration time, and light intensity) on the prediction of the apple SSC model by near infrared spectrum based on the online device of near infrared. The study showed that the standard normal variate (SNV) and competitive adaptive reweighting sampling (CARS) and partial least squares (PLS)
(SNV-CARS-PLS) model established had the best performance when the motion speed of the device was 0.5 m/s, integration time was 120 ms, and light intensity was 6.5 A. Its predicted correlation coefficient (Rp) and the prediction root mean square error (RMSEP) were 0.991 and 0.149, respectively. *Liu et al. (2022)* established an online non-destructive testing equipment for apples using near-infrared spectroscopy and established a prediction model for apple SSC. When the detection speed and integration time were 0.5 m/s and 100 ms, respectively, the Rp reached 0.919 and the RMSEP was 0.477. *Ding et al. (2020)* established a non-destructive online detection system for potatoes using visible/near-infrared diffuse transmission spectroscopy (with a detection speed of approximately 4 per second). The correlation coefficient between the predicted starch value and the standard physicochemical value was 0.893, and the partial least squares regression (RMSE) was 0.713%. *Jiang et al. (2023)* established an online detection system for navel orange SSC using near-infrared transmission method. The research results showed that when the detection speed was 0.5 m/s, the partial least squares regression (PLSR) prediction model established had the best performance, with RMSEP and residual prediction error (RPD) of 0.442% and 2.77%, respectively. However, there are few reports on establishing an online detection model using visible/near-infrared spectroscopy technology to detect the internal quality of Huping jujube.

This study selected Huping jujube in Jinzhong City as the research object, dynamically collected its visible/near-infrared spectral data, and the actual SSC values were obtained by handheld refractometer. Comparing the optimal selection of modeling results of different pretreatment methods, the regression coefficient (RC) and successive projections algorithm (SPA) algorithms were used to reduce the dimensionality of the pre-treated full-band spectral data, further discussing the influence of spectral variable selection methods on the accuracy of SSC online detection model, and evaluating the corresponding model prediction effect. The feasibility of applying RC-PLSR model to the prediction of SSC of Jujube was verified, and the reference was provided for the realization of fast, scientific and accurate online SSC detection of fresh jujube.

MATERIALS AND METHODS

Experimental Sample

The experimental samples selected for this study were picked from a jujube garden in Beizhan Village, Taigu County on October 4, 2023, and 120 jujube dates were picked and shipped to the laboratory on the same day, as shown in Fig. 1. The samples with no external defects, rot and injury, and basically the same physical properties were selected as the research objects.

Fig. 1 - Intact samples of Huping jujube

Experimental System and Data Acquisition

This study used the Field Spec3 spectrometer produced by ASD (Analytical Spectral Device) in the United States and a self-developed dynamic spectral collection system to achieve spectral collection of fresh jujube samples. The schematic diagram of the dynamic spectrum acquisition system is shown in Fig. 2. The spectral data collection interval is 1 nm, the wavelength range is 350-2500 nm, the resolution is 3.5 nm, the probe field of view angle is 20°, and the light source is a 14.5 V halogen lamp. The probe of the spectrometer is perpendicular to the upper surface of the sample, 90 mm away from the upper surface of the sample, and the sample is placed between two rollers. To minimize errors, the system configuration optimization and whiteboard calibration were performed 0.5 hours after the spectrometer was turned on. After passing the performance test, the sample spectrum was sampled using diffuse reflection method. During data collection, the fresh jujube sample was rotated at the speed of 4 r/min, and the spectral data of the sample was collected once every 120°, for a total of 3 times, and the average value was obtained as the final spectral data of the test sample.

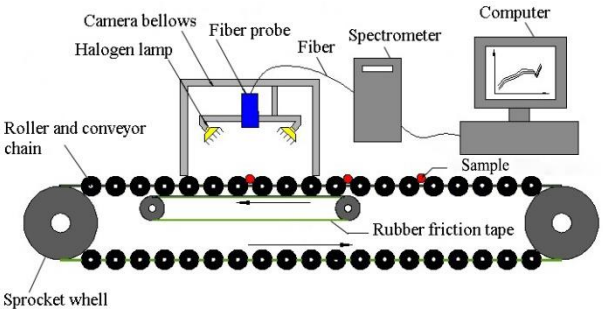

Fig. 2 - Schematic diagram of online Vis-NIR spectroscopy detection device

Determination of Soluble Solid Content

A handheld digital refractometer was used to measure the SSC value of the sample immediately after the collection of the visible/near infrared spectrum. A piece of flesh with skin was cut from the spectral scanning position, and the juice was manually squeezed and filtered to the center of the mirror of the refractometer to read the SSC value. The refractometer needs to be calibrated with distilled water for each measurement, and the average value of each sample was repeated 3 times as the true value of SSC.

Kennard-Stone (KS) method can ensure the uniform distribution of the samples in the training set according to the spatial distance, and improve the stability and accuracy of the prediction model *(Galvao et al., 2005)*. The K-S method was used to divide the correction set and prediction set according to the ratio of 3:1, and the results of sample set division was shown in Table 1.

Table 1

True value tables of intact Huping jujube sample soluble solids for calibration and prediction sets

Sample set	No. of sample	Min. value	Max. value	Average value	Standard deviation	Coefficient of variation (%)
Correction set	90	17.3	37.2	22.15	2.21	9.98
Prediction set	30	18.6	34.6	21.82	1.85	8.48

From Table 1, it can be seen that the SSC range of the correction set was 17.3~37.2, and the SSC range of the prediction set was 18.6~34.6. The SSC range of the correction set covers the prediction set well, which was helpful to establish a stable and effective prediction model.

Data Analysis and Processing Methods

Spectral Pretreatment

In addition to the internal structure and component information of the measured sample, the original NIR spectral data contains interference information caused by light scattering, sample heterogeneity, temperature change, instrument noise and other factors. Therefore, it is necessary to preprocess the original spectrum to improve the stability of the prediction model. In the present work, six spectral pre-processing methods, including S-G smoothing (S-G), multiplicative scatter correction (MSC), standard normal variate (SNV), orthogonal signal correction (OSC), first derivative (FD), and second Derivative (SD) to preprocess the

original spectra *(Liu et al., 2022)*, and PLSR was used to evaluate the performance of different spectral pre-processing data.

Method for Selecting Characteristic Wavelengths

Due to the large amount of wavelength information, continuous information and redundant information contained in the original full spectrum data collected, the correlation between adjacent bands is very strong. The optimal selection of effective wavelength can eliminate redundant information in spectral data, simplify the calculation of spectral data, and improve the efficiency and stability of modeling. In this study, the RC and SPA algorithm were used to reduce the dimensionality of the data to simplify the model.

The PLSR method is based on the PLS algorithm principle and selects the best sensitive band by selecting the local extreme value in the RC *(Wang et al., 2023)*. The greater the absolute value of the regression coefficient corresponding to each wavelength point, the greater the influence of the wavelength on the prediction performance of the model. Therefore, the characteristic wavelength can be extracted according to the local extreme value of the regression coefficient corresponding to the wavelength.

The SPA algorithm is a forward variable selection algorithm that can eliminate the collinearity effect between wavelength data, extract wavelength subsets with the lowest redundancy and collinearity, select a small number of SSC sensitive information variable groups from a large amount of spectral information, reduce model input, and improve modeling speed and efficiency *(Wang et al., 2021)*.

Modeling Methods

PLSR is the most commonly used multivariate statistical method in stoichiometric modeling, which is based on principal component regression. The main idea of PLSR algorithm is to first perform principal component operations on the spectral data matrix, obtain principal factors or hidden variables, eliminate non-useful information in the data matrix, and select useful spectral data information for parameter regression operations.

Model Evaluation

Corrected correlation coefficient (Rc), predicted correlation coefficient (Rp), corrected root mean square error (RMSEC), and predicted root mean square error (RMSEP) were selected as the evaluation criteria. A model with excellent performance has Rc and Rp closer to 1, and RMSEC and RMSEP closer *(Cozzolino et al., 2007)*.

RESULTS AND DISCUSSION

Spectral Characteristics and Analysis

Due to the influence of external adverse factors in the process of collecting NIR spectral data, there will be large noise, baseline drift and other irrelevant information at both ends of the spectral curve, which will directly affect the stability and prediction ability of the built model. Therefore, only the spectral data in the range of 400~2450 nm spectral band were used for analysis in this experiment, with a total of 2051 spectral bands. Fig. 3 shows the spectral diagram of Huping jujube samples with a rotation speed of 1.5 r/min.

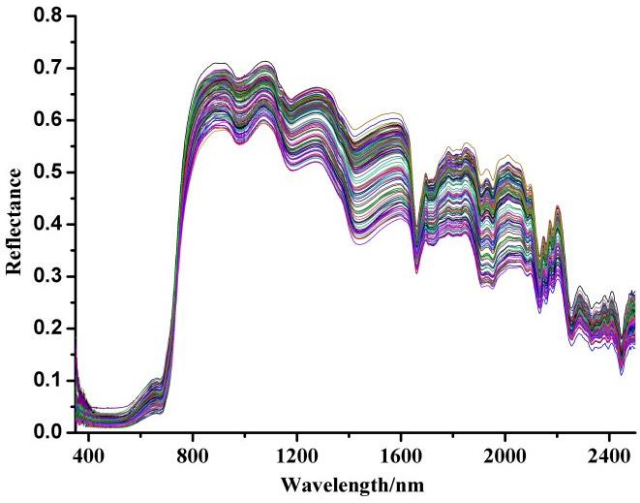

Fig. 3 - Vis-NIR spectral curves of Huping jujube at 1.5 r/min

As can be seen from Fig. 3, the trend of NIR spectral curves of 120 exact jujube samples was basically similar, with no significant differences. From the figure, it can be seen that the absorption peaks at the wavelengths of 960 nm, 1180 nm, 1300 nm, 1590 nm, and 2000 nm, and these absorption peaks at these wavelengths were caused by the absorption of the water contained inside the fresh dates. Among them, the wavelength of 2000 nm was the combined frequency absorption peak of O-H bond, the wavelength of 1300 nm was the primary frequency doubling peak of O-H bond, and the wavelengths of 960 nm and 1180 nm were the secondary frequency doubling peaks of O-H bond *(Liu et al., 2010)*. The wavelength of 2000~2500 nm was the near infrared spectral band of C-H, N-H, and O-H bonds in the soluble solids molecules within the sample of fresh dates, and there was an obvious absorption peak at 680 nm for jujube, which was caused by the spectral absorption of chlorophyll in the fruit pulp cells of jujube.

Spectral Data Preprocessing

From Table 2, it can be seen that the original spectrum uses 13 principal factor numbers, with Rc of 0.647, RMSEC of 2.176, Rp of 0.578, and RMSEP of 1.878. After using OSC processing on the original spectrum, compared with other preprocessing methods, the Rc value of the modeling set using this preprocessing method was 0.876, and the RMSEC was 1.846, which is the smallest. The Rp was 0.763, and the difference between RMSEC and RMSEP was the smallest. The model had good predictive performance and stability, and the OSC was selected as the optimal preprocessing method for comprehensive comparison.

Table 2

Calibration results of PLSR model based on different preprocessing methods

Pretreatment methods	Calibration set		Prediction set		Factors
	Rc	RMSEC	Rp	RMSEP	
Original spectra	0.647	2.176	0.578	1.878	13
S-G	0.742	2.136	0.622	1.864	13
SNV	0.726	2.009	0.584	1.910	9
MSC	0.840	2.068	0.694	2.003	7
OSC	0.876	1.846	0.763	1.792	9
FD	0.752	2.183	0.698	2.013	7
SD	0.801	2.106	0.652	1.896	7

Characteristic Wavelength Extraction

For the full spectral data preprocessed by OSC, the RC and SPA algorithm were used to select the characteristic wavelength, and corresponding 13 characteristic wavelengths (796 nm, 915 nm, 993 nm, 1362 nm, 1463 nm, 1662 nm, 1816 nm, 1953 nm, 1984 nm, 2134 nm, 2198 nm, 2255 nm, and 2415 nm) and 3 characteristic wavelengths (416 nm, 1362 nm, and 2323 nm) were obtained. The analysis results were shown in Fig. 4 and Fig. 5.

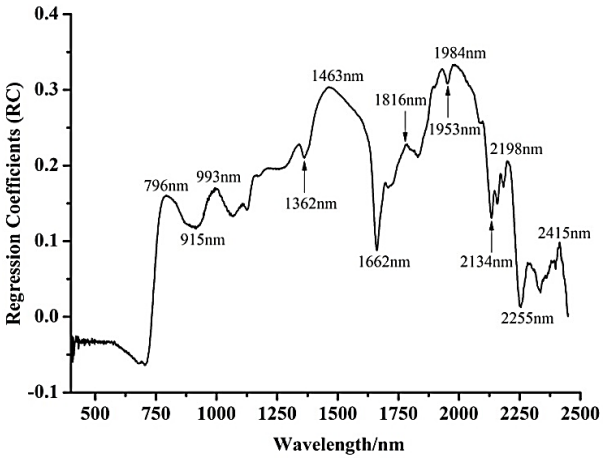

Fig. 4 - Regression coefficients of PLSR model and selected effective wavelength

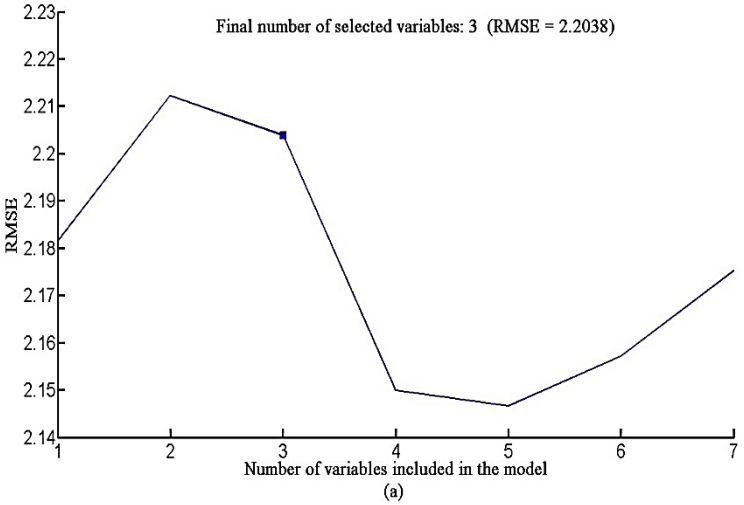

(a) RMSE distribution of SPA with different variables

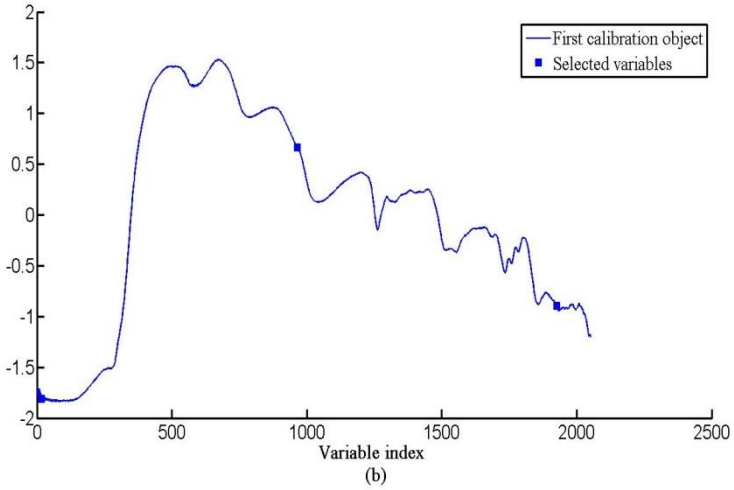

(b) Distribution of preferable characteristic wavenumber for SPA

Fig. 5 - Characteristic wavelengths selected by SPA algorithm

Regression model

The characteristic wavelength spectral data optimized by the RC and SPA algorithm were used as input for establishing the PLSR quantitative analysis model, respectively. And obtain the RC-PLSR and SPA-PLSR prediction models. The relevant parameters of the two established prediction models were shown in Table 3.

Table 3

Results of PLSR models based on different characteristic wavelengths

Model	Calibration set		Prediction set		Factors	No. of variables
	Rc	RMSEC	Rp	RMSEP		
RC-PLSR	0.846	1.962	0.782	2.247	11	13
SPA-PLSR	0.739	2.136	0.673	1.762	3	3

As can be seen from Table 3, the number of factors for the RC-PLSR and SPA-PLSR models were 11 and 3, respectively. According to the evaluation of the merits and stability of the model, compared to the SPA-PLSR model with the corrected set (Rc=0.739, RMSEC=2.136) and predicted set (Rp=0.673, RMSEP=1.762), the RC-PLSR model with the corrected set (Rc=0.846, RMSEC=1.962) and predicted set (Rp=0.782, the RMSEP=2.247) had better performance. This may be due to the fact that important spectral information contained in the original spectrum was removed by SPA. Therefore, the prediction performance of the proposed RC-PLSR prediction model for unknown samples was better than the SPA-PLSR prediction model. Fig. 6 shows the scatter plots of SSC predicted and true values of the optimal RC-PLSR prediction model for 30 samples of the prediction set.

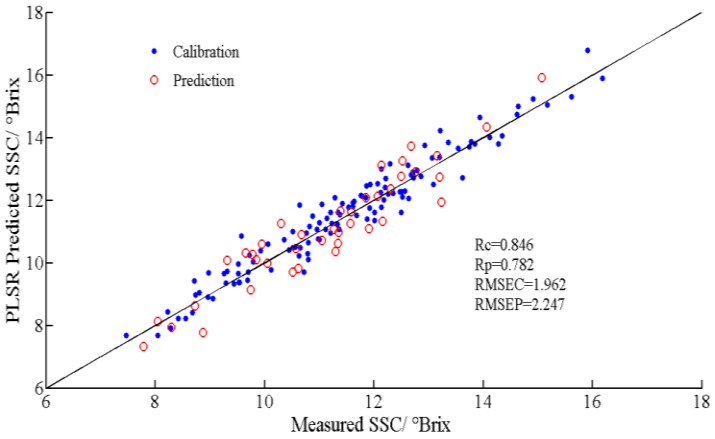

Fig. 6 - Scatter plot of measured and predicted values of SSC index based on the optimal model

CONCLUSIONS

This study used visible/near-infrared spectroscopy combined with RC-PLSR to establish an online detection model for SSC indicators of Huping jujube. By combining multiple preprocessing methods with band selection methods, the prediction accuracy of the model can be effectively improved, and accurate prediction of fresh jujube SSC indicators can be achieved. The results indicate that:

(1) The evaluation of different preprocessing results (Original spectra, S-G, SNV, MSC, OSC, FD, and SD) using PLSR showed that the preprocessed data had higher model accuracy than those directly using raw spectral data as input, and using OSC for preprocessing had the most ideal effect.

(2) Compared with the results of full band modeling, extracting feature wavelengths and establishing a prediction model could reduce computational complexity and improve the prediction accuracy of the model to a certain extent. The RC-PLSR model achieved the optimal prediction performance, with Rp and RMSEP of 0.782 and 2.247, respectively. Research has shown that the RC method can effectively enhance the stability and accuracy of feature wavelength selection in Huping jujube spectral data, improve the prediction accuracy of the model, and dynamically detect the SSC index of fresh jujube based on PLSR and visible/near-infrared spectroscopy was an effective method. At the same time, this study has a reference for the development of more accurate visible/near infrared online nondestructive testing equipment.

ACKNOWLEDGEMENT

This work was funded by Basic Research Project of Shanxi Province (Free Exploration) (Project No. 202203021212426, No. 202303021212120), "Introduction of Talents and Scientific Research Initiation Project" of Shanxi Agricultural University (Project No. 2023BQ42, No. 2023BQ114).

REFERENCES

[1] Agulheiro-Santos, A. C., Ricardo-Rodrigues, S., Laranjo, M., Melgão, C., & Velázquez, R. (2022). Non-destructive prediction of total soluble solids in strawberry using near infrared spectroscopy. *Journal of the Science of Food and Agriculture*, 102(11), 4866-4872.

[2] Cozzolino, D., Kwiatkowski, M. J., Waters, E. J., & Gishen, M. (2007). A feasibility study on the use of visible and short wavelengths in the near-infrared region for the non-destructive measurement of wine composition. *Analytical and bioanalytical chemistry*, *387*(6), 2289-2295.

[3] Ding, J., Han, D., Li, Y., Qi, W., & Xi, H. (2020). Simultaneous non-destructive on-line detection of potato black-heart disease and starch content based on visible/near infrared diffuse transmission spectroscopy. *Spectroscopy and Spectral Analysis*, 40(6), 1909-1915.

[4] Fan, J., Lv, L., & Shang, H. (2003). Progress in research and development of jujube. *Food Science*, *4*(1), 161-163.

[5] Fan, S., Huang, W., Guo, Z., Zhang, B., Zhao, C., & Qian, M. (2015). Assessment of influence of origin variability on robustness of near infrared models for soluble solid content of apple. *Chinese Journal of Analytical Chemistry*, 43(2), 239-244.

[6] Galvao, R. K. H., Araujo, M. C. U., José, G. E., Pontes, M. J. C., Silva, E. C., & Saldanha, T. C. B. (2005). A method for calibration and validation subset partitioning. *Talanta*, 67(4), 736-740.

[7] Jiang, X., Zhu, M., Yao, J., Li, B., & Liao, J. (2023). Research on parameter optimization of apple sugar model based on near-infrared on-line device. *Spectroscopy and Spectral Analysis*, 43(1), 116-121.

[8] Jiang, Z., Ying, J., Wan, Y., Wang, C., Lin, X., & Liu, B. (2023). Non-destructive evaluation of soluble solids content in navel orange by an on-line visible near-infrared system with four parallel spectrometers. *Journal of Food Measurement and Characterization*, 1-11.

[9] Liu, Y., Hu, X., Zhu, M., Yao, J., & Jing, H. (2022). Influence of near-infrared on-line detection device parameters on the applicability of apple soluble solid content model. *Journal of South China Agricultural University*, 43(5), 108-114.

[10] Liu, Y., Sun, X., Zhang, H., & Aiguo, O. (2010). Nondestructive measurement of internal quality of Nanfeng mandarin fruit by charge coupled device near infrared spectroscopy. *Computers and Electronics in Agriculture*, *71*, S10-S14.

[11] Liu, Z., Zhang, R., Yang, C., Hu, B., Luo, X., Li, Y., & Dong, C. (2022). Research on moisture content detection method during green tea processing based on machine vision and near-infrared spectroscopy technology. *Spectrochimica Acta Part A: Molecular and Biomolecular Spectroscopy*, 271, 120921.

[12] Song, J., Li, G., Yang, X., Liu, X., & Xie, L. (2020). Rapid analysis of soluble solid content in navel orange based on visible-near infrared spectroscopy combined with a swarm intelligence optimization method. *Spectrochimica Acta Part A: Molecular and Biomolecular Spectroscopy*, 228, 117815.

[13] Wang, B., He, J. L., Zhang, S. J., & Li, L. L. (2020). Non-destructive testing of soluble solids content in cerasus humilis using visible/near-infrared spectroscopy coupled with wavelength selection algorithm. *INMATEH Agricultural Engineering*, 61(2), 251-262.

[14] Wang, B., He, J., Zhang, S., & Li, L. (2021). Nondestructive prediction and visualization of total flavonoids content in Cerasus Humilis fruit during storage periods based on hyperspectral imaging technique. *Journal of Food Process Engineering*, 44(10), e13807.

[15] Wang, B., Yang, H., Zhang, S., & Li, L. (2023). Detection of Defective Features in Cerasus Humilis Fruit Based on Hyperspectral Imaging Technology. *Applied Sciences*, 13(5), 3279.

OPTIMIZATION DESIGN ANALYSIS OF MOVABLE ROTATING PLATE TYPE GRADING DEVICE FOR POTATO
/
活动转板式马铃薯分级装置优化设计分析

Haohao ZHAO, Weigang DENG*, Zhiqi REN, Chenglong LIU, Dong YAN, Yansong CAI, Zexin ZHAO [1]
College of Mechanical and Electrical Engineering, Inner Mongolia Agricultural University, Hohhot 010018, China
Tel: 0471-6530905; E-mail: wg_deng@126.com
DOI: https://doi.org/10.35633/inmateh-72-28

Keywords: *movable rotating plate, potato, grading, optimization, ANSYS Workbench*

ABSTRACT
The study focused on enhancing a movable rotating plate type grading device for potatoes, prioritizing safety and weight reduction. By optimizing the body frame and movable rotating plate using ANSYS Workbench 2022, a static analysis was conducted to confirm compliance with design requirements for strength and deformation. The optimized frame experienced a remarkable 32.3% weight reduction. Additionally, the direct optimization module of ANSYS Workbench 2022 was employed to lighten the movable rotating plate, resulting in a 22.86% reduction in the total mass of the device. This research serves as an invaluable reference for the structural design and optimization analysis of potato grading devices.

摘 要
本研究针对活动转板式马铃薯分级装置进行了优化设计，注重其安全性和减轻重量。利用 ANSYS Workbench 2022 对机架和活动转板板进行了优化，并进行了静态分析以确认其满足强度和变形要求。通过优化，机架的重量减轻了 32.3%。此外，利用 ANSYS Workbench 2022 的直接优化模块，轻量化了活动转板，使整个装置的总质量较之前状态减少了 22.86%。该研究为马铃薯分级装置的结构设计和优化分析提供了重要的参考。

INTRODUCTION
Potatoes are one of the most important food crops globally. Although China has the largest potato cultivation area in the world, the level of mechanized potato production is relatively low. Therefore, there is an urgent need for research and development in potato mechanization, especially considering the promotion of potato as a staple food strategy *(Kang, H.B. et al., 2022; Liu, P.L. et al., 2021; Ding, Q.L. et al., 2022)*. Potato grading devices play a crucial role in potato harvesting, and researchers in the field have conducted extensive studies on this topic. Currently, there are various types of potato grading devices available, including roller shaft-type, screen-type, and drum-type devices *(Liu, X., 2022)*. These three grading devices often cause damage to the potatoes during the grading process. Moreover, they have limited grading accuracy and require complex adjustments for different grades, which significantly affects the efficiency of potato grading *(Zhou, J.G., 2022; Yu, J.Y., 2022; Lv, J.Q., 2020)*. Therefore, research was conducted and a potato grading device was designed based on the movable rotating plate principle. This grading device utilizes a movable rotary plate with an adjustable gap, resulting in high grading efficiency and the ability to classify potatoes into three different grades. However, the grading device possesses a high safety factor and is relatively heavy, requiring optimization and improvement measures to address these issues.

The traditional optimization approach, which involves making physical modifications, is time-consuming and expensive. In contrast, the virtual simulation optimization design method can significantly reduce the design cycle and save costs to a great extent *(Gu, L.X., 2019)*. There have been numerous reports on virtual simulation optimization both in China and internationally. *Krasyuk A.M. et al*., *(2021)* utilized an optimality criterion based on ANSYS software for the topology-optimized design of axial fan blades, resulting in a significant 60% reduction in blade mass. *Yan, (2022)* performed the lightweight design of the frame of a tensile machine using ANSYS Workbench. As a result, the equivalent force and total deformation of the optimized model were reduced, leading to a weight reduction of 7.11%. *Ma et al., (2012)* optimized the frame of a light truck using ANSYS and the homogenization method.

[1] *Haohao Zhao, Master Candidate; Weigang Deng, Associate Professor; Zhiqi Ren, Master Candidate; Chenglong Liu, Master Candidate; Dong Yan, Master Candidate; Yansong Cai , Master Candidate; Zexin Zhao, Master Candidate*

This approach resulted in an optimized frame topology that met the volume constraint requirements and minimized total flexibility. *Gadwala William Kery et al., (2022),* conducted the optimization of a sports car rim using ANSYS Workbench finite element analysis. The study identified carbon fiber as a viable material for manufacturing the sports car rim. *Jackis Aukah et al., (2020),* optimized a husked corn dryer using ANSYS Workbench and determined that the air velocity at the collector inlet should be increased to 3 m/s, while the air velocity at the biomass heat exchanger outlet should be increased to 2.8 m/s. *Muhammad Aisha et al., (2019),* employed the finite element method in ANSYS Workbench to optimize the topology of a steering knuckle. The optimization process determined the specific mass that needed to be removed to achieve the desired design. Similarly, *Sharma M.P. et al., (2014)* utilized CREO 2.0 in conjunction with ANSYS Workbench to optimize the shape of the automotive steering knuckle.

Jha et al., (2022) utilized CATIA in conjunction with ANSYS Workbench to optimize and enhance the steering knuckle. *Li et al., (2022)* improved and optimized the base structure of the welding robot using ANSYS Workbench. The original model was analyzed and compared to the improved and optimized solution, successfully achieving the desired optimization objectives. *Feng et al., (2022),* utilized ANSYS Workbench to optimize the design of the fan base of the motor. The structural stresses under various operating conditions were simulated and verified. *Li et al., (2023),* employed the response surface optimization of ANSYS Workbench for the lightweight design of an on-board lens in a specific vehicle. The optimization process resulted in a 20.69% reduction in the total mass of the lens. *Li et al., (2017),* optimized the suspension of the potato excavator using ANSYS Workbench and the response surface method. Through the optimization process, the optimal suspension thickness was determined, effectively reducing deformation.

Analysis of existing studies reveals that the virtual simulation optimization design method, known for its cost-saving and high efficiency advantages, has been rarely reported for the optimization design of potato grading devices. Therefore, considering the issues of a high safety factor and heavy mass in the existing movable rotating plate type grading device for potatoes, in this paper, a virtual simulation optimization method based on ANSYS Workbench 2022 is employed to optimize the design of the body frame and movable rotating plate. In line with the optimization requirements of multiple independent variables and multiple objective functions, the MOGA algorithm was utilized for conducting optimization analysis. This led to the identification of an optimal parameter combination that significantly reduced the weight of both the body frame and the movable rotating plate, while ensuring the desired levels of strength and stiffness are met.

MATERIALS AND METHODS

Movable rotating plate type grading device for potato

A movable rotating plate type grading device for potatoes (as shown in Fig. 1) utilizes the gap size of the movable rotating plate to grade potatoes. The grading principle is depicted in the schematic diagram shown in Fig. 2. The movable rotating plate moves cyclically with the conveying chain, with its bottom in contact with the slide rails on both sides. As the tilting angle of the slide rails changes, the gap between adjacent rotating plates gradually widens. Potatoes of different sizes fall into the potato-collecting device through different gaps.

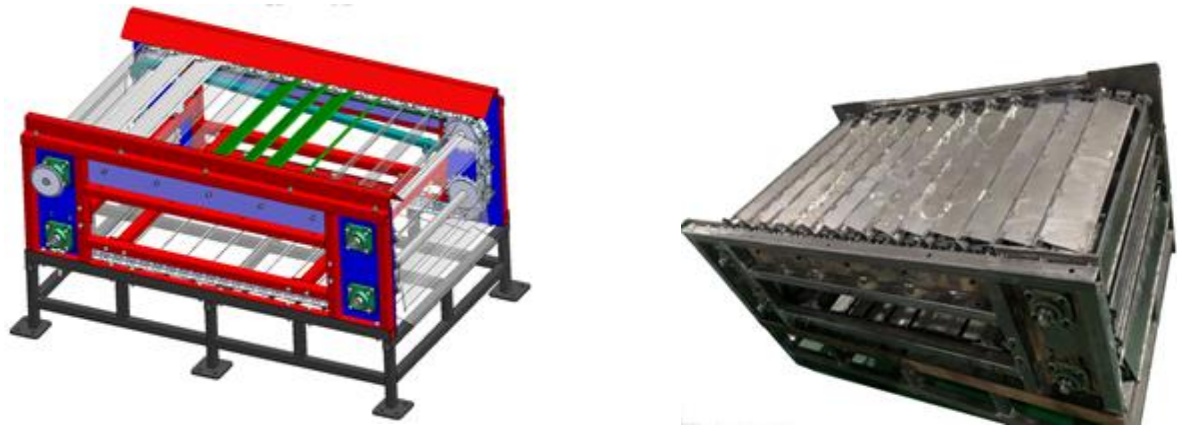

(a) Three-dimensional model diagram (b) Physical diagram

Fig. 1 - Movable rotating plate type grading device for potato

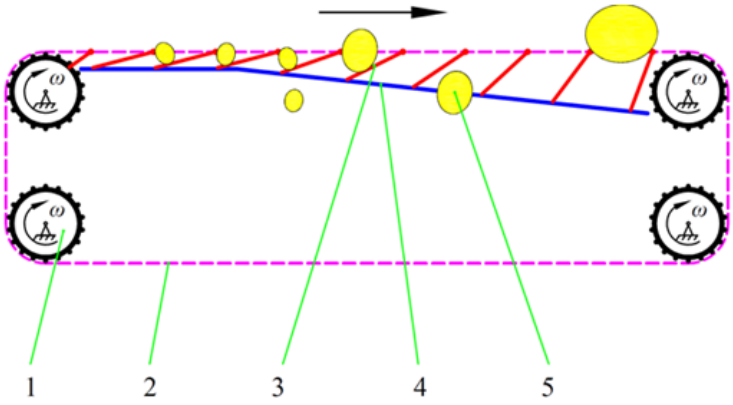

Fig. 2 - Schematic diagram of potato grading principle

1. Sprocket; 2. Chain; 3. Movable rotating plate; 4. Slide; 5. Potato

The body frame (depicted in Fig. 3) consists of the chain fixing part and the base. The chain fixing part primarily serves to secure the chain and the assembly of the movable rotating plate. It is constructed by welding together square steel pipes, with steel plates welded onto the steel pipes to fix the bearing seat. The dimensions of the square steel pipe are 40×40×4 (mm), and the steel plate has a thickness of 8mm. The base is formed by welding together rectangular steel pipes measuring 40×30×3 (mm).

The size of the body frame is 1400×896×780 (mm), and the total mass is 157.82 kg. Due to its high safety factor and large overall mass, the economic performance is below par.

The movable rotating plate (illustrated in Fig. 4) comprises a rotating plate movable shaft, rotating plate, and rotating plate friction shaft, all connected through welding. The rotating plate movable shaft serves as the central component that links the rotating plate to the chain. It is connected to the bracket on the chain section and drives the movement of the rotating plate. The rotating plate friction shaft is in contact with the slide rail and its primary purpose is to prevent direct contact between the rotating plate and the slide rail, thereby minimizing wear and deformation of the rotating plate.

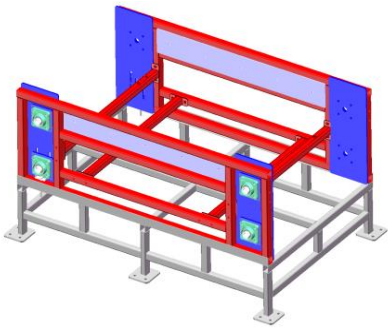

Fig. 3 - Grading device frame

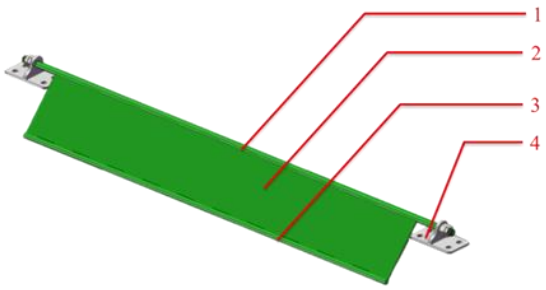

Fig. 4 - Movable rotating plate

1. Rotating plate movable shaft; 2. Rotating plate; 3. Rotating plate friction shaft; 4. Bracket

The dimensions of the existing rotating plate are 640×95×2 (mm) in length, width, and thickness, respectively. The total mass of a single movable rotating plate is 1.7449 kg. With a total of 32 groups of movable rotating plates in the machine, the resulting heavy mass becomes inconvenient for operation.

Static analysis of existing body frame and movable rotating plate

Static analysis of existing body frame

Analysis of load on the body frame

The combined mass of the chain and movable rotating plate assembly (depicted in Fig. 5) amounts to 134.23 kg, while the total mass of the potatoes when the grading device is fully loaded (shown in Fig. 6) is 16.153 kg.

Consequently, the forces exerted on the body frame are as follows.

$$F=(134.23+16.153)\times 9.8=1473.75N \quad (1)$$

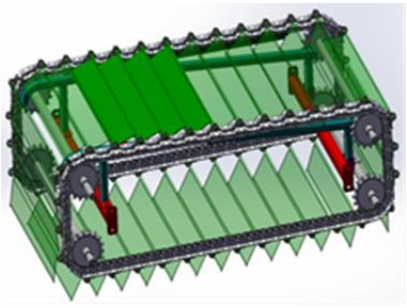

Fig. 5 - Diagram of chain and movable rotating plate assembly

Fig. 6 - A full load of grading device

Pre-processing of the static Analysis of the body frame

According to the design specifications, the body frame is made of Q235 material, and the corresponding material properties are listed in Tab. 1.

Table 1

Material properties

Materials	Density (kg/m^3)	Young's Modulus/Pa	Poisson's Ratio	Yield Strength/Pa	Tangential Modulus/Pa
Q235	7850	2.12×10^{11}	0.288	2.35×10^{8}	6.1×10^{9}

The components of the body frame are joined through a combination of welding and bolting, resulting in a "binding" contact configuration.

When performing an analysis in ANSYS, the size and quality of the mesh divisions at critical locations have a direct impact on the accuracy of the analysis results *(Zhang et al., 2020)*. The denser the mesh divisions, the more accurate the calculation results will be. However, it is important to note that this will also increase the computational volume required for the analysis *(Zhao et al., 2023)*. The frame utilizes an overall tetrahedral meshing method with second-order element ordering, and the mesh cell size is set at 8 mm. However, at the critical force contact position in the bearing seat, a smaller mesh cell size of 3 mm is applied. The completed meshing process yields a total of 1,628,000 nodes and 888,646 cells.

Fixed supports are positioned on the bottom surface of the six foot seats of the body frame, while a combined force of 1473.75 N is applied to the eight bearing surfaces. This results in an equal force of 184.21875 N acting vertically downward on each surface.

The total deformation and equivalent von Mises stress of the body frame were computed, and Fig.7 illustrates the visual representation of the deformation and stress distribution.

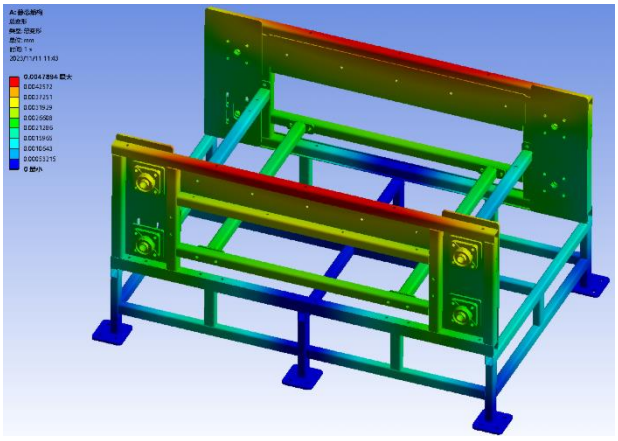

(a) Total Deformation

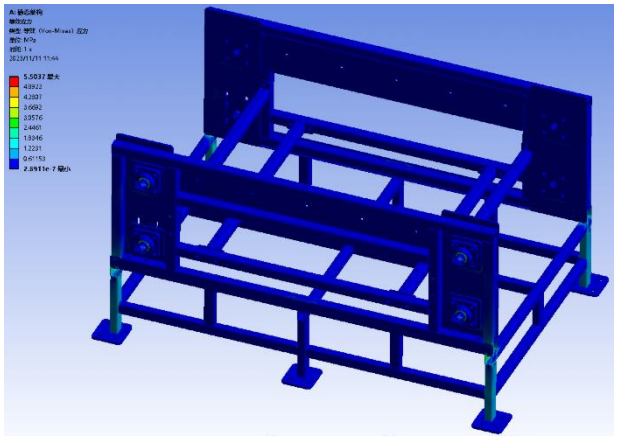

(b) Equivalent von Mises Stress

Fig. 7 - Analysis diagram of the rack before optimization

The cloud diagram of total deformation reveals that the upper steel tube of the body frame experiences more significant deformation. Overall, the deformation gradually decreases from top to bottom, with a maximum deformation of 0.0047894 mm. On the other hand, the cloud diagram of equivalent stress demonstrates that stress is primarily concentrated at the eight bearing positions and the four vertical beams of the base. The maximum stress value recorded is 5.5037 MPa.

In the realm of static analysis in ANSYS, the convergence of forces and displacements serves as pivotal metrics for assessing the convergence and stability of the analysis. They enable the determination of whether the model converged to a stable solution, pinpointing potential issues or errors. The efficacy of force convergence can be evaluated through convergence criteria or residual values, typically requiring force residual values to approach zero, indicative of a reasonable force distribution. A small or gradually stabilizing displacement residual value can suggest that the model is gradually reaching equilibrium. The force convergence and displacement convergence charts are depicted in Fig. 8.

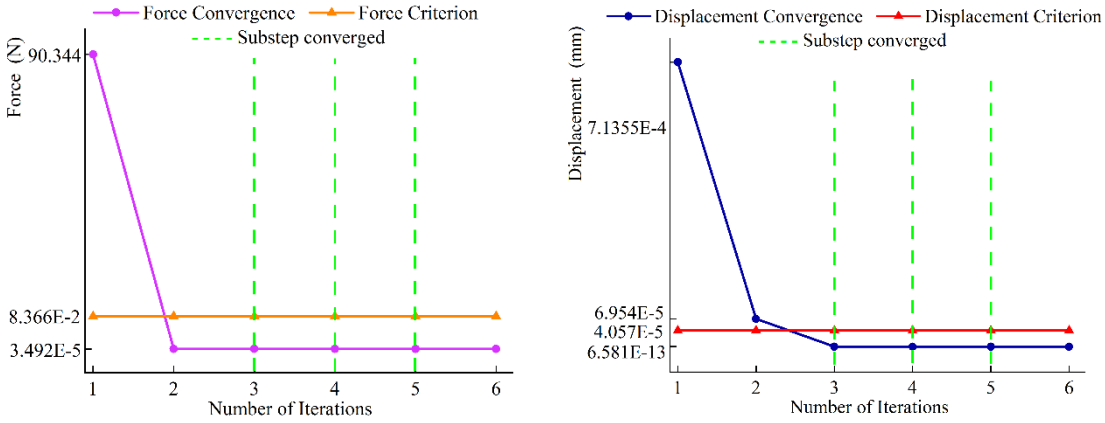

(a) Force convergence (b) Displacement convergence

Fig. 8 - Convergence plot of residual values for the body frame

Based on the analysis results above, it is evident that the current vehicle body frame meets the strength requirements, with a relatively high safety factor, the minimum safety factor being 15, and it possesses sufficient redundancy, as shown in Fig 9. Therefore, there is significant potential for lightweight optimization of the vehicle body frame, providing ample room for improvement.

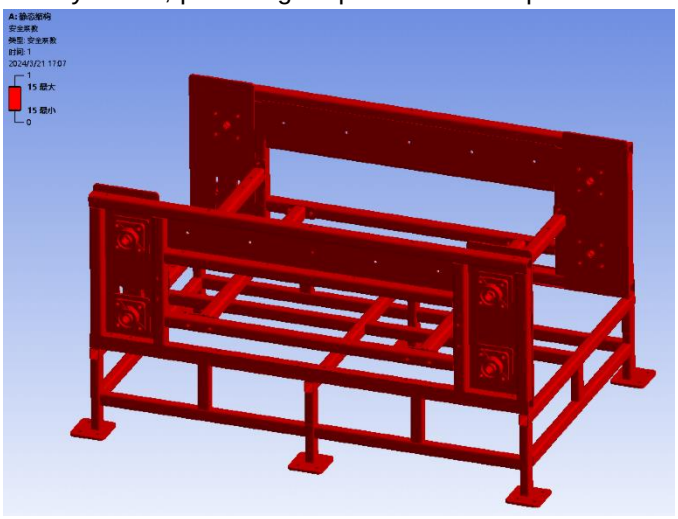

Fig. 9 - Safety factor diagram

Static Analysis of existing movable rotating plate

Calculation of the Load on the movable rotating plate

During the movement of the movable rotating plate, the angle between the plate and the horizontal plane continuously changes from 0 to 90 degrees. When the plate is parallel to the horizontal plane, the maximum load is applied. In order to achieve this maximum load, the entire surface of the rotating plate is covered with potatoes, as depicted in Fig. 10. The total mass of the potatoes is 2.63 kg, equivalent to a force of 25.8 N.

Fig. 10 - Single movable rotating plate covered with potatoes

Statics analysis pre-processing of movable rotating plate

In accordance with the design requirements, the movable rotating plate is made of Q235 material, and its material-related parameters are identical to those of the body frame.

The movable shaft, friction shaft, and rotating plate are welded together, establishing a "fixed" connection between them. The mesh division method employed is "automatic," with a mesh cell size set at 2 mm. This mesh division process generates a total of 426,133 nodes and 250,562 cells.

During the static analysis, fixed constraints are applied to the connection between the rotating plate and the chain, as well as at the contact position with the slide rail. The movable rotating plate is subjected to a downward force of 25.8 N, perpendicular to its surface.

The solution option involved analyzing the total deformation and equivalent von Mises stress. The resulting cloud diagrams illustrating the total deformation and equivalent von Mises stress are presented in Fig. 11. The graphs depicting the convergence of action transfer and displacement transfer are shown in Fig. 12.

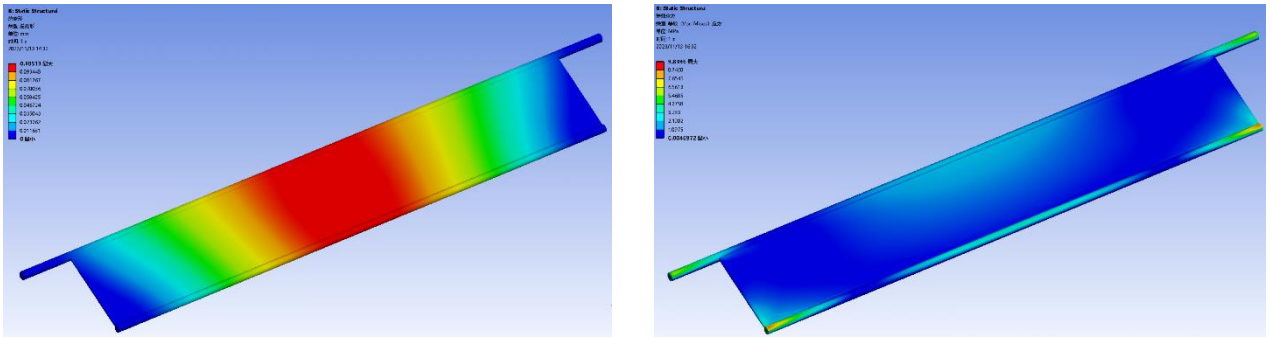

(a) Total Deformation (b) Equivalent von Mises Stress

Fig. 11 - Analysis clouds of the rotating plate before optimization

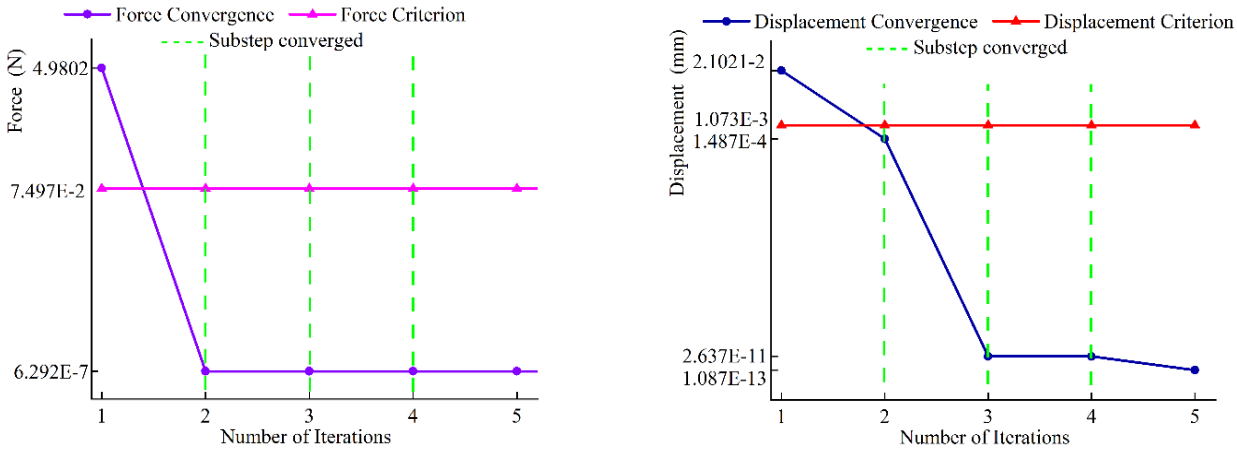

(a) Force convergence (b) Displacement convergence

Fig. 12 - Convergence plot of residual values for the movable rotating plate

The simulation results revealed that the total deformation primarily occurred in the middle section of the rotating shaft, rotating plate, and friction shaft. The overall deformation exhibited a gradual increase from the two ends of the movable rotating plate towards the middle section, reaching a maximum deformation of 0.10513 mm at the central part.

The analysis of the equivalent von Mises stress diagram revealed that the stress concentration was primarily observed at the two ends of the rotating shaft and the friction shaft. This can be attributed to the connection between the bracket and the movable rotating plate shaft at the two ends, causing stress concentration during movement. Additionally, stress concentration was observed at the friction shaft due to contact with the sliding rail. The maximum stress recorded was 9.8396 MPa, which is lower than the material yield strength of 235 MPa.

Based on the aforementioned analysis results, it is evident that the movable rotating plate meets the strength requirements. Therefore, the design can be further optimized by focusing on dimensional parameters.

Optimized design of body frame and movable rotating plate

Body frame optimization design

The wall thickness of the square steel pipe, which forms the body frame, is a critical factor that impacts the structural integrity. Therefore, the wall thickness is reduced from 4 mm to 2 mm. Additionally, the body frame consists of six side plates, each with a thickness of 8 mm, primarily used for fixing the bearing seat and chain brace. Taking into account the high safety factor, the thickness of the side plates is increased to 5 mm. Moreover, the base, being a crucial component that supports the entire machine, undergoes structural improvements as part of the optimization process. The optimized body frame is depicted in Fig. 13, with a total mass of 106.84 kg.

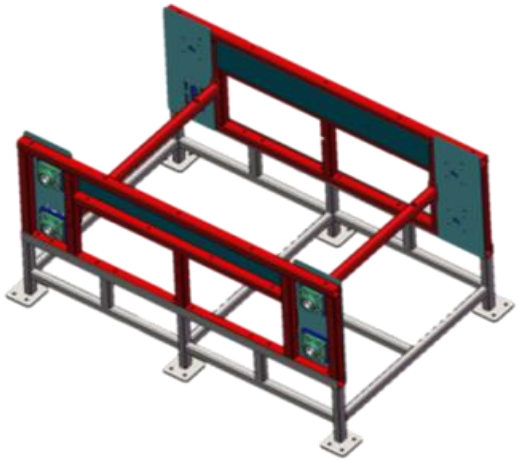

Fig. 13 - Optimized body frame

Optimized design of the movable rotating plate

Rotating plate friction shaft improvement

The current friction shaft for the rotating plate has a diameter of Φ9 mm and a length of 640 mm. Considering its contact position with the slide rail only at the two ends, the friction shaft can be divided into two sections, each measuring 50 mm in length. The schematic diagram of the enhanced friction shaft is depicted in Fig. 14.

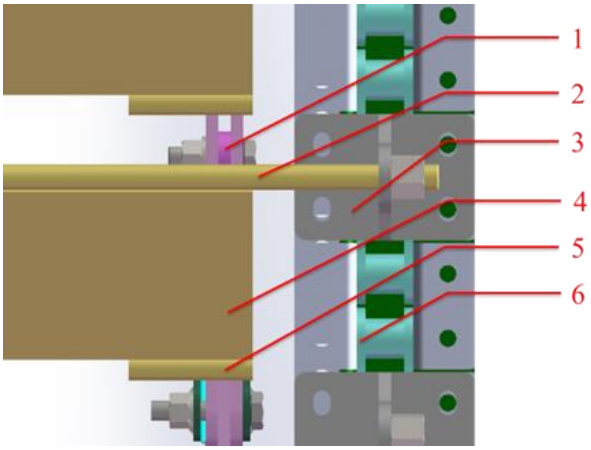

Fig. 14 - Schematic diagram of the improved friction shaft of the rotating plate

1. Slide rail; 2. Rotating plate movable shaft; 3. Bracket; 4. Rotating plate; 5. Rotating plate friction shaft; 6. Chain

Size optimization of rotating plate

For the purpose of optimizing and simplifying the model, the rotating plate friction shaft for the rotary plate was temporarily excluded from the current modelling. Instead, an improved model of the movable rotating plate was created in SolidWorks. The length, width, and thickness of the rotating plate were

defined as the design variables, taking into account the configuration requirements of the Workbench optimization module *(Zhang, 2017; Ren, 2022)*, as shown in Tab. 2.

Table 2

Comparison of relevant parameters before and after frame optimization

Design variable name	Size / mm	Meaning of variables
DS_D1@ thin-stretch1	640	the length of the rotating plate
DS_D2@ sketch2	95	the width of the rotating plate
DS_D3@thin-stretch1	2	the thickness of the rotating plate

The improved model can be seamlessly imported into Workbench using the inter-face between SolidWorks and Workbench, enabling static structural analysis. As per the design requirements, Q235 was chosen as the material for the movable rotating plate. The design variables were selected within the Design Modeler, rendering the model prepared for static structural analysis.

The rotating shaft and rotating plate were welded together, resulting in a "bonded" contact. The mesh division method employed was "Automatic." A mesh cell size of 2 mm was selected, generating a total of 211,015 nodes and 80,593 cells through the grid division process. The grid quality of the movable rotating plate met the requirements, as confirmed by the grid evaluation statistics provided by Workbench.

The fixed restraints and applied loads on the movable rotating plate remained the same as described in the previous section.

The total deformation and equivalent von Mises stress of the model were analyzed in the solution option, resulting in the generation of cloud diagrams illustrating the total deformation and equivalent von Mises stress. These diagrams are presented in Fig. 15.

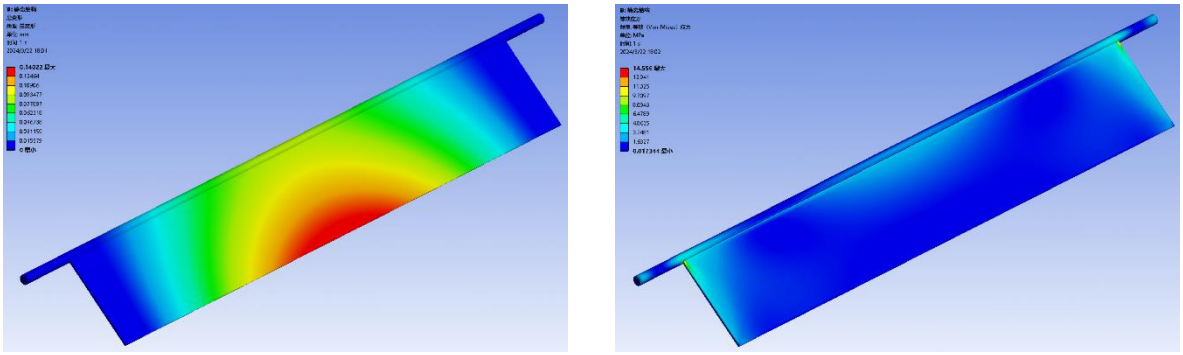

(a) Total Deformation (b) Equivalent von Mises Stress

Fig. 15 - Analysis clouds of the movable rotating plate before optimization

The cloud diagram depicting the total deformation, derived from the simulation results, revealed that the primary deformation occurred in the middle section of the rotating plate and the central part of the rotating shaft. The maximum deformation recorded was 0.14022 mm. On the other hand, the equivalent von Mises stress analysis indicated a maximum stress value of 14.556 MPa.

Structural optimization typically involves adjusting the design variables to enhance the performance of the structure without compromising its functionality, while ensuring compliance with any imposed constraints *(Cha, 2015)*. By modifying the dimensional parameters of the rotating plate, the objective is to minimize its mass while ensuring that both deformation and stresses remain within acceptable limits and maintain a satisfactory safety factor.

This optimization design employs the direct optimization module within Work-bench to seek the optimal combination of dimensional parameters for the rotating plate. As such, the length P_1, width P_2, and thickness P_3 of the rotating plate are treated as design variables. The selection of size ranges is primarily determined by usage and manufacturing requirements. The optimization objectives include maximizing the maximum deformation P_4, maximizing the maximum equivalent force P_5, and minimizing the mass P_6 of the rotating plate. The stress is considered as a safety factor with a value of 1.5, resulting in an allowable stress of 156 MPa. Hence, the minimum stress must not exceed 156 MPa. The optimization design problem can be mathematically formulated as follows:

$$\begin{cases} \min \begin{cases} p_4 = f_1(p_1, p_2, p_3) \\ p_5 = f_2(p_1, p_2, p_3) \leq 156MPa \\ p_6 = f_3(p_1, p_2, p_3) \end{cases} \\ s.t. \begin{cases} p_1 \in (610, 616, 620, 640) \\ p_2 \in (95, 98, 100) \\ p_3 \in (1, 1.2, 1.5, 1.8, 2) \end{cases} \end{cases} \quad (2)$$

Building a direct optimization model

To establish a direct optimization model, the optimization algorithm must first be defined. In the field of multivariate and multi-objective optimization algorithms, two commonly used methods are the Screening algorithm and the MOGA algorithm. These algorithms differ in their objectives and application domains. The Screening algorithm is primarily used for feature selection and dimensionality reduction, aiming to improve model interpretability and computational efficiency. On the other hand, the MOGA algorithm is specifically designed to tackle multi-objective optimization problems by identifying a set of non-dominated solutions, providing decision-makers with a range of choices across multiple objectives. Considering the optimization requirements of multiple independent variables and multiple objective functions in this article, the MOGA algorithm was chosen for the optimization analysis. The MOGA algorithm excels in handling multiple objectives and constraints, and it requires continuous input parameters. It is particularly effective in calculating global maxima or minima, enabling the identification of the global optimum while mitigating the limitations associated with local optima *(Zuo, 2023; Chen, 2015)* In the configuration of the MOGA algorithm, the initial sample capacity was set to 100, generating 50 samples per iteration. The maximum number of iterations was defined as 20, and the restriction of a maximum of 3 candidates was applied.

The objectives and constraints for the rotating plate length P_1, width P_2, and thickness P_3 were established based on the aforementioned mathematical model. Following the parameter settings, the optimization scheme was updated, and subsequently, the solution was initiated.

The total deformation, equivalent von Mises stress, and mass of the model were obtained for various cases of the rotating plate length, width, and thickness by analyzing the 60 sets of design solutions. The results are presented in Tab. 3.

Table 3

Raw optimization data

Serial number	P_1 / mm	P_2 / mm	P_3 / mm	P_4 / mm	P_5 / MPa	P_6 / kg
1	610	95	1	0.335376	31.37097	0.924593
2	616	95	1	0.33314	31.54316	0.929073
3	620	95	1	0.338713	31.4189	0.93206
4	640	95	1	0.343188	33.55511	0.946994
5	610	98	1	0.353951	31.02046	0.938977
6	616	98	1	0.351401	31.18514	0.943598
7	620	98	1	0.357154	31.05804	0.946679
8	640	98	1	0.36119	33.17132	0.962085
9	610	100	1	0.366924	30.81309	0.948566
10	616	100	1	0.364175	30.97273	0.953282
11	620	100	1	0.370046	30.84402	0.956426
12	640	100	1	0.373807	32.94609	0.972146
13	610	95	1.2	0.247201	26.80225	1.01569
14	616	95	1.2	0.246619	26.99724	1.021066
15	620	95	1.2	0.250821	26.8091	1.024651

Serial number	P_1 / mm	P_2 / mm	P_3 / mm	P_4 / mm	P_5 / MPa	P_6 / kg
16	640	95	1.2	0.25723	28.43592	1.042571
17	610	98	1.2	0.258042	26.48829	1.032951
18	616	98	1.2	0.257254	26.67827	1.038497
19	620	98	1.2	0.261565	26.4883	1.042194
20	640	98	1.2	0.267701	28.09787	1.060681
21	610	100	1.2	0.265646	26.29697	1.044458
22	616	100	1.2	0.26473	26.48342	1.050117
23	620	100	1.2	0.269111	26.29202	1.05389
24	640	100	1.2	0.275079	27.8929	1.072754
25	610	95	1.5	0.178684	21.59502	1.152336
26	616	95	1.5	0.179551	21.69055	1.159057
27	620	95	1.5	0.1823	21.58057	1.163537
28	640	95	1.5	0.189913	22.48546	1.185938
29	610	98	1.5	0.184138	21.33209	1.173912
30	616	98	1.5	0.184898	21.4249	1.180844
31	620	98	1.5	0.187684	21.31408	1.185466
32	640	98	1.5	0.195152	22.20793	1.208575
33	610	100	1.5	0.188006	21.16695	1.188296
34	616	100	1.5	0.1887	21.25752	1.19537
35	620	100	1.5	0.19151	21.14581	1.200086
36	640	100	1.5	0.198891	22.03336	1.223666
37	610	95	1.8	0.140836	17.79926	1.288982
38	616	95	1.8	0.142329	17.86102	1.297047
39	620	95	1.8	0.14429	17.78071	1.302423
40	640	95	1.8	0.15203	18.18255	1.329304
41	610	98	1.8	0.143799	17.57471	1.314873
42	616	98	1.8	0.145232	17.63877	1.323192
43	620	98	1.8	0.147198	17.55431	1.328738
44	640	98	1.8	0.154848	17.94952	1.356468
45	610	100	1.8	0.145937	17.43167	1.332134
46	616	100	1.8	0.147335	17.49638	1.340623
47	620	100	1.8	0.149304	17.40931	1.346282
48	640	100	1.8	0.156902	17.80011	1.374578
49	610	95	2	0.129303	14.27097	1.38008
50	616	95	2	0.131227	14.31895	1.38904
51	620	95	2	0.132632	14.2965	1.395014
52	640	95	2	0.140215	14.55594	1.424882
53	610	98	2	0.131863	14.06587	1.408847

Serial number	P_1 / mm	P_2 / mm	P_3 / mm	P_4 / mm	P_5 / MPa	P_6 / kg
54	616	98	2	0.133774	14.11403	1.418091
55	620	98	2	0.135171	14.08991	1.424253
56	640	98	2	0.142727	14.34426	1.455064
57	610	100	2	0.133604	13.93621	1.428026
58	616	100	2	0.135506	13.9844	1.437458
59	620	100	2	0.1369	13.95889	1.443746
60	640	100	2	0.14444	14.20926	1.475186

RESULTS

Static analysis of optimized body frame

The optimized body frame underwent a static structural analysis using the same mesh division, fixed supports, and load constraints as the original body frame. The analysis yielded results for total deformation and equivalent von Mises stress, which are illustrated in Fig. 16.

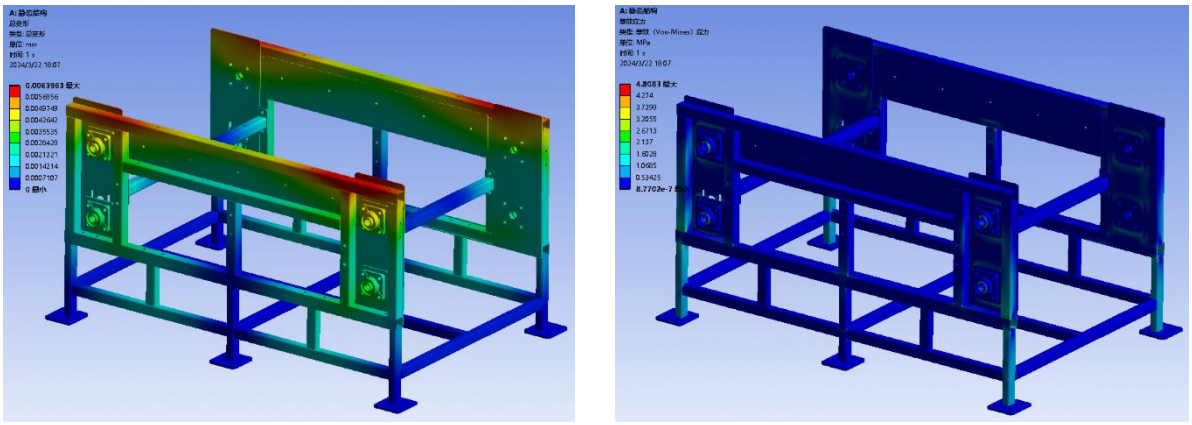

(a) Total Deformation (b) Equivalent von Mises Stress

Fig. 16 - Clouds of optimized body frame analysis results

The final optimized body frame exhibits a maximum total deformation of 0.0063963 mm and a maximum equivalent von Mises stress of 4.8083 MPa. The deformation primarily occurs in the middle section of the steel tube above the frame, but the overall deformation is minimal. Stress concentration is observed at the bearing positions and the vertical beams of the frame base, but the stress levels remain significantly lower than the yield stress.

In conclusion, the optimized body frame successfully meets the strength requirements while significantly reducing the total mass of the machine. A comparison of the relevant parameters before and after the body frame optimization is presented in Tab. 4, demonstrating a remarkable 32.3% reduction in total mass compared to the pre-optimized frame.

Table 4

Comparison of relevant parameters before and after frame optimization

Projects	Steel pipe wall thickness/mm	Side plate thickness/mm	The total mass of frame/kg
Before optimization	4	8	157.82
After optimization	2	5	106.84

Analysis of optimized results from movable rotating plate

The optimization process reached convergence after 1 iteration without any failure points, resulting in three sets of optimal solutions. These solutions are presented in Tab. 5.

Table 5

Optimized design points

Candidate points	P_1 / mm	P_2 / mm	P_3 / mm	P_4 / mm	P_5 / MPa	P_6 / kg
1	610	95	1.2	0.2472	26.802	1.0157
2	616	95	1.2	0.24662	26.997	1.0211
3	620	95	1.2	0.25082	26.809	1.0247

Candidate point 1 was chosen as the ultimate optimization solution. By comparing the design variables and target variables before and after optimization, it is evident that the mass has been reduced by 28.7%. However, there is a slight increase of 0.1 mm in deformation and a 12 MPa increase in stress. Nevertheless, these values remain within the allowable limits, satisfying the strength requirements for the movable rotating plate. The reliability and safety aspects are in accordance with the specified requirements. A comparison of the parameters before and after the optimization of the rotating plate is presented in Tab. 6.

Table 6

Comparison of the parameters before and after the optimization of the rotating plate

Projects	P_1 / mm	P_2 / mm	P_3 / mm	P_4 / mm	P_5 / MPa	P_6 / kg
Before optimization	640	95	2	0.140215	14.55594	1.424882
After optimization	610	95	1.2	0.2472	26.802	1.0157

As mentioned in the previous section, the ANSYS Workbench was utilized for the optimized design of the movable rotating plate. In this design process, the rotating plate friction shaft was not explicitly modelled or optimized. However, after the optimization of the rotating plate structure, the rotating plate friction shaft was included for finite element analysis. By considering the combined effects of the optimized rotating plate and the friction shaft, the final optimized results for the movable rotating plate were obtained. These results are illustrated in Fig. 17.

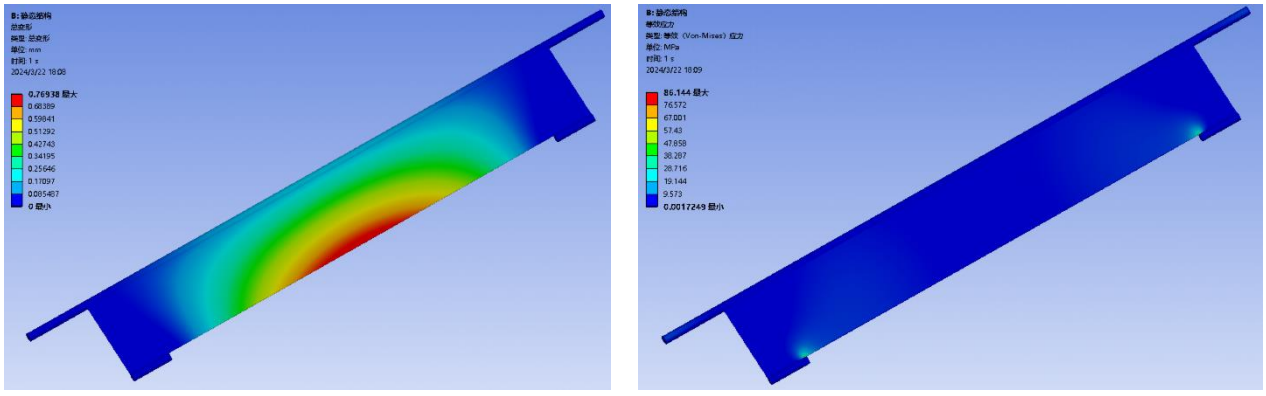

(a) Total Deformation (b) Equivalent von Mises Stress

Fig. 17 - Analysis clouds of the movable rotating plate after optimization

Based on the results of static analysis, the final optimized movable rotating plate demonstrated a maximum deformation of 0.76938 mm, a maximum stress value of 86.144 MPa, and a minimum safety factor of 2.9718. Although the most significant deformation still occurs in the middle section of the rotating plate, it still satisfies the safety and strength requirements. The stress concentration primarily occurs in the movable shaft and friction shafts of the rotating plate. Taking real-world considerations into account, it is necessary to bolt the movable shaft of the rotating plate, and the friction shaft of the rotating plate experiences friction with the slide rail. Nevertheless, the maximum stress remains below the allowable stress of the material.

CONCLUSIONS

The comparison of static structural analysis between the frame and movable rotating plate before and after optimization is presented in Tab. 7.

Table 7

Comparison of the parameters before and after the optimization of the rotating plate

Optimization Project		Mass / kg	Total deformation / mm	Equivalent Stress / MPa
Body frame	Before optimization	157.82	0.0047894	5.5037
	After optimization	106.84	0.0063963	4.8083
Movable rotating plate	Before optimization	1.7449	0.10513	9.8396
	After optimization	1.0657	0.76938	86.144

The original mass of the movable rotating plate was 1.7449 kg, which was reduced to 1.0657 kilograms after optimization, reduction of 38.9% being achieved through the implementation of a lightweight design. The maximum total deformation post-optimization was 0.76938 mm, staying within the acceptable deformation range. The maximum equivalent stress in the optimized movable rotating plate is 86.144 MPa, remaining below the material's yield limit and meeting the strength criteria.

Before the optimization, the mass of the classifier was 320 kg. However, after optimizing the body frame and the movable rotating plate, the mass of the classifier reduced to 246.8456kg. This represents a significant decrease of 22.86% compared to the overall machine mass.

This article utilized the direct optimization module available in ANSYS Workbench to establish a finite element model of the movable rotating plate. Through finite element calculation, simulation, and verification, the optimal combination of dimensional parameters was derived. However, further theoretical and practical validation is necessary to assess the accuracy, reliability, and applicability of the optimization method proposed in this article. The methodology presented in this study offers valuable theoretical guidance for engineering design and structural optimization, effectively mitigating inaccuracies resulting from practical design and saving design time.

ACKNOWLEDGEMENT

This research was funded by the Natural Science Foundation of Inner Mongolia Autonomous Region of China (2022MS05027), Program for improving the Scientific Research Ability of Youth Teachers of Inner Mongolia Agricultural University (BR220127), Scientific Research Start-up Foundation for importing the high level/excellent doctoral talents of Inner Mongolia Agricultural University (NDYB2021-12) and Science and Technology Plan Project of Hohhot (2023-Nong-11).

REFERENCES

[1] Cha, S.; Shang, X. J.; Gang, X. Y. (2015). *Engineering structure optimization design methods and applications (工程结构优化设计方法与应用)*, 1st ed.; China Railway Press: Beijing, China; pp. 1-15.

[2] Chen, X. L.; Liu, Y. J. (2015). *Finite Element Modeling and Simulation with ANSYS Workbench*, 1st ed.; Taylor & Francis Group: Boca Raton, London, New York; pp. 331-356.

[3] Ding, Q.L.; Guo, F.Y. (2022). Key Technologies and Development Trend of Potato Mechanized Harvest (马铃薯机械化收获关键技术及发展趋势), *Agricultural Mechanization Using ＆ Maintenance*, 11, 44–46.

[4] Feng, Y.; Miao, J.; Zheng, L. B.; Wang, X. R. (2022). Optimal Design of Multi-Objective Parameters for Interference Fit of Motor Fan Pedestal based on ANSYS. *Journal of Physics: Conference* Series. 2202, 012044.

[5] Gu, L.X.; Wang, C.G.; Hu. (2019). *Finite Element Analysis and Virtual Simulation of Potato Motion on Oscillating Separation Sieve (马铃薯在摆动分离筛上运动的有限元分析与虚拟仿真研究)*. *The Second Sino-German Symposium on Electromechanical Integration Vocational Education and the Third National Symposium on Electromechanical Integration Professional Teaching Experience Exchange*. pp.48-51, Shandong / China.

[6] Gadwala William Kery; Babu G Raghu. (2022). Modeling and analysis of car wheel rim for weight optimization to use additive manufacturing process. *Materials Today: Proceedings*. 62, 336-345.

[7] Jackis Aukah; Mutuku Muvengei; Hiram Ndiritu; Calvin Onyango. (2020). Optimization of the Performance of Hybrid Solar Biomass Dryer for Drying Maize Using ANSYS Workbench. *Journal of Energy Research and Reviews*. 4. 50-69.

[8] Jha, A.R.; Jaiswal, R.; Karki, A.; Basnet, A.; Jaiswal, S.; Jaiswal. P.; Rajgadia, D. (2016). Design and Finite Element Analysis of Knuckle Joint Using CATIA and ANSYS Workbench. *International Journal of Research in Mechanical Engineering*. 4, 01-05.

[9] Kang, H.B.; Liu, M.; Wang, L.; Wei, M.Y.; Liu, J.C.; Zhou, J.D.; Zhang, S.Q. (2022). Simulation Analysis of Separating and Conveying Device of Potato Harvester Based on EDEM (基于 EDEM 的马铃薯收获机分离输送装置仿真分析). *Journal of Agricultural Mechanization Research*. 44, 1-8.

[10] Krasyuk A. M.; Russky E. Yu. (2021). Optimizing design of blades for high-speed axial fans. *Journal of Mining Science*. 56, 1024–1031.

[11] Liu, P.L.; Zhou, Y.; Zhang, W.J. (2021). Study on production efficiency and its influencing factor of potato production areas in China under the background of main grain production (主粮化背景下中国马铃薯主产区生产效率及其影响因素研究). *Journal of Agricultural Science Yanbian University*. 43, 93–100.

[12] Liu, X. (2022). *Design and Experimental Research on Potato Conveying and Grading Device (马铃薯输送分级装置设计与试验研究)*. Northwest A&F University, Xianyang, Shaanxi, China, May.

[13] Lv, J.Q. (Northeast Agricultural University, Harbin, Heilongjiang, China); Wen, X.Y. (Northeast Agricultural University, Harbin, Heilongjiang, China); Yang, X.H (Northeast Agricultural University, Harbin, Heilongjiang, China). (2020). *Research Status and Prospect of Potato Grader Grading Adjustment Device (马铃薯分级机分级调节装置的研究现状及展望)*. 423-438.

[14] Li, X.J.; Liang, J. (2022). Optimization design and finite element analysis of welding robot base based on ANSYS Workbench. *Journal of Physics: Conference Series*. 2383, 012073.

[15] Li, C. C.; Li, S. Li, M. Z.; Mao, K. (2023). Structural optimization design of vehicle mounted lens for special vehicles (特种车辆的车载镜头轻量化设计). *Agricultural Equipment & Vehicle Engineering*. 61, 144-149.

[16] Li, X.; Wang, C. G.; Deng, W. G.; Xie, S. S.; Wang, X. R. (2017). Static analysis and optimization design of the suspension frame of potato digger (马铃薯挖掘机悬挂架的静力学分析与优化设计). *Chinese Journal of Construction Machinery*. 2017, 15, 42-46.

[17] Ma, C.B.; Wu, Y.H. (2012). Optimize Design of a Light Truck Frame. *Advanced Materials Research*. 590, 346-351.

[18] Muhammad Aisha; Shanono Ibrahim Haruna. (2019). Transient Analysis and Optimization of a Knuckle Joint. *Kinetik: Game Technology, Information System, Computer Network, Computing, Electronics, and Control*. 4, (2).

[19] Ren, J.W.; Shu, S.R.; Deng, F.F. (2022). *ANSYS Workbench modern mechanical design practical tutorial: finite element analysis - optimization design - reliability design (ANSYS Workbench 现代机械设计实用教程：有限元分析•优化设计•可靠性设计)*, 1st ed.; Chemical Industry Press: Beijing, China, pp. 235-264.

[20] Sharma M P; Mevawala D S; Joshi H; et al. (2014). Static Analysis of Steering Knuckle and Its Shape Optimization. *IOSR Journal of Mechanical and Civil Engineering*, 8, 34-38.

[21] Yu, J.Y. (2022). *Design and Experiment Research of Roller Potato Grading Device (辊式马铃薯分级机设计与试验研究)*. Northeast Agricultural University, Harbin, Heilongjiang, China, June.

[22] Yan, H.D. (2022). Optimization Design of Tension Machine Frame Based on Solidworks and ANSYS Workbench. *Journal of Engineering Research and Reports*. 23, 11-17.

[23] Zhang, X. M.; Zhang, Y. B.; Wang, Y. C. (2020). Improved Design of Three-wheeled Vehicle Headlamp Fixing Bracket Based on UG (基于 UG 的三轮汽车前照灯固定支架改进设计). *Agricultural Equipment & Vehicle Engineering*. 58, 119-124.

[24] Zhang, Y. (2017). *ANSYS Workbench 17.0 Finite Element Analysis from beginner to master (ANSYS Workbench 17.0 有限元分析从入门到精通)*, 2nd ed.; China Machine Press: Beijing, China; pp. 403-425.

[25] Zhao, W. Y.; Yang, J. P.; Dong, X. H.; Huang, B. (2023). Simulation Analysis and Research of Subsoiler Shovel Seat Based on ANSYS Workbench (基于 ANSYS Workbench 的深松机铲座的仿真分析与研究). *China Southern Agricultural Machinery*. 54, 10-14.

[26] Zhou, J.G. (2022). *Study on Key Technologies of Potato Joint Harvest and Primary Classification in Hilly Mountainous Areas (丘陵山区马铃薯联合收获与初选分级关键技术研究)*. Northwest A&F University, Xianyang, Shaanxi, China, May.

[27] Zuo, A. D.; Zhao, Y. Y. (2023). Application of Ansys_Workbench Optimization Module Combined with Limit Load Analysis in Engineering Design (Ansys_Workbench 优化模块结合极限载荷分析在工程设计中的应用). *China Special Equipment Safety*. 39, 19-25.

SIMULATION AND TEST OF FILLING PERFORMANCE OF PNEUMATIC PRECISION SEED METERING DEVICE BASED ON EDEM SOFTWARE
/
基于EDEM 软件的气压式精量排种器充种性能模拟与试验

Wenqi GUO, Wenyi ZHANG, Yunxia WANG, Youqiang DING, Bing QI*[1]
Nanjing Institute of Agricultural Mechanization, Ministry of Agriculture and Rural Affairs, Nanjing, 210014/China
Tel: 15366092903; E-mail: qb0823521@163.com
DOI: https://doi.org/10.35633/inmateh-72-29

Keywords: *Precision seed metering device; Pneumatic type; Seed filling performance; EDEM*

ABSTRACT
In order to study the effect of population disturbance on the filling performance of the seed metering device, this paper uses the pneumatic precision seed metering device as the model, and uses EDEM software to simulate the population movement of three different seed metering devices. The bench test was carried out at different pressures at 12 km/h and at different speeds at 3.5 kPa. The results show that the designed seed disk with grooves has the most intense disturbance and the highest qualified rate. In order to verify the performance of the disk, full factor tests are carried out on the air pressure and speed, The test results show that when the operating speed is 10~12 km/h and the positive pressure is 3~3.5 kPa, the leakage rate is no higher than 5.42%, the replay rate is no higher than 0.42%, and the qualified rate is no lower than 94.58%. When the operating speed is 14 ~ 16 km/h and the positive pressure is 3.5~4 kPa, the leakage rate is not higher than 6.7%, the replay rate is not higher than 1.04%, and the pass rate is not lower than 93.12%. All the indicators are better than the national standard.

摘要
为研究种群扰动对排种器充种性能的影响，本文以气压式精量排种器为模型，运用 EDEM 软件对 3 种不同的排种盘进行种群运动仿真，以种层上方颗粒数目和种群平均运动速度作为指标，分析了各排种盘在不同转速下的种群平均运动速度和种层上方区域数量，仿真结果表明转速越快，种群运动越明显。通过台架试验对 12km/h 速度下不同气压和 3.5kPa 气压下不同速度进行试验，结果表明设计的带凹槽的排种盘扰动最激烈，合格率最高。为了验证该盘的性能对气压和转速进行全因素试验，试验结果表明针对当作业速度 10～12km/h，给定正压 3～3.5kpa 时，漏播率不高于 5.42%，重播率不高于 0.42%，合格率不低于 94.58%；当作业速度在 14～16km/h，给定正压 3.5～4kpa 时，漏播率不高于 6.7%，重播率不高于 1.04%，合格率不低于 93.12%，各项指标均优于国家标准。

INTRODUCTION
At present, high speed, high density and high efficiency are the development trend of precision seeding technology. "Quantitative and targeted" precision seeding technology has been widely used in corn, soybean and other crops in China. Single grain precision seeding is the main sowing method of corn planting in China, and the seed discharging device is the core component of the seeder, whose performance determines the efficiency and quality of seeding operation. According to its structure and working principle, it can be divided into pneumatic type and mechanical type. Pneumatic type has the characteristics of good seed adaptability and no seed damage. Pneumatic seeding has become the focus of current research.

Pneumatic precision seed metering device includes pneumatic type, air suction type, air blowing type, central collection type and so on (*Yang et al., 2016*), It has been noted that the state of seed population has a significant effect on the filling performance (*Yang et al., 2010*). The filling process of pneumatic seed metering device is the process of separating seeds from disordered groups into ordered individuals under the action of adsorption force. During this period, it is necessary to overcome the resistance of seed population to individual movement, and the filling process determines the seed placement performance. In the case of Maxima series of suction seed metering device, produced by Kuhn company of France, the disturbing button is used above the mold hole to increase the disturbance. Seed adaptability is related to seed filling performance. *Yazgi and Degirmenioglu, (2007)*, found that the diameter of the suction hole is the main factor affecting the performance of the seeder, followed by the vacuum degree and the linear speed of the seeding disk.

Among them, the diameter of the suction hole and the required vacuum degree are mainly related to the physical characteristics of the seed (*Yazgi et al., 2005*). Singh conducted a study on the linear speed of the seed disk and the shape of the suction hole inlet for cotton seeds. The experiment showed that the seeding performance was inversely proportional to the rotation speed of the seed disk. The suction hole inlet with a 120 ° chamfer had better seeding performance and required lower vacuum degree (*Singh et al., 2007*). The shape of the hole has an impact on the seeding performance.

Zhang Kaxing et al, (2021), used the CFD-DEM coupling method to obtain the optimal combination hole structure and obtained the optimal working parameters under the hole through experiments. *Zhang Xiaoshuang et al, (2021)*, conducted experiments on different hole shapes and sizes to determine the optimal hole shape, providing a basis for improving the performance of the seeder. *Wang Fenghua et al, (2020)*, designed a single row air-suction micro-potato planter to increase population disturbance by vibrating seed feeding mechanism. The air-suction seed metering device developed by Horsch, Germany, uses the chamfered asymptote hole to improve the seed adsorption capacity, and the maximum operation reaches 15 km/h. *Chen Yulong et al, (2021)*, designed a vertical disk seeding device with a seed mixer to increase the seeding probability.

Zhao Zhan et al, (2018), obtained the relationship between expansion coefficient and vibration intensity by letting the seed disk vibrate to separate the population. When the vibration intensity is 5.65, the motion state is the most ideal. *Chen and Li, (2002)*, concluded through the study of the law of seed movement that the introduction of mechanical vibration can make the seeds reach the "boiling" state and improve the seed absorption rate. *Xie Dongbo et al, (2022)*, designed a garlic seed metering device assisted by air suction with disturbed teeth, constructed the curved surface equation of disturbed teeth, and explored the influence of different disturbed teeth on the qualification rate.

Su Wei et al, (2023), designed a kind of gas-suction broad bean precision seed metering device with flat belt auxiliary seed filling device, and carried out dynamic analysis on its working state. The flat belt auxiliary seed filling device transformed the population resistance to the adsorbed seeds into a favorable supporting force for seed filling, so as to improve the seed filling performance. *Ding Li et al, (2018)*, designed the disturbance population of the shaped hole head according to the size of corn, which played an auxiliary role in seed filling. The average distance between the population particles and the seed disk, the average speed of the population and the average speed under different angular speeds were selected as indicators.

In this paper, the pneumatic precision seed metering device was used as the research carrier, and the EDEM simulation software was used to test the disturbed species of different seed metering devices. The indexes of population disturbance degree were established with different rotational speed and the number of seeds generated as variables, and the effects of different disturbed seed metering devices on population disturbance size and disturbance degree on filling performance were obtained through bench verification.

MATERIALS AND METHODS

Population index analysis

Although existing studies have proposed that seed population state has a significant impact on seed filling performance, and developed a variety of mechanisms to improve seed population state, the research on the mechanism of seed population state impact on seed filling performance is not deep enough, and most of them remain in the stage of experimental research and qualitative description, lacking a clear quantitative model to accurately describe the characteristics of reasonable seed population state. The guidance for the design and optimization of seed metering device is limited.

In this paper, two indicators are created according to the obvious degree of seed disturbance. In the display option function of the data analysis interface, the transparency of the geometry is changed to make the particles appear. The target particles are selected, and the particle display type is adopted as default. The speed is colored by the attribute coloring in the color identification TAB, which can distinguish the speed of different particles. The more intense the disturbance, the larger the particle motion speed, and the more obvious the filling effect.

The function of grid cell group is to divide the entire model area into grid cells with the same volume. Right-click on the setting options in the data analysis interface and select Add option, select Grid Bin Group, set the center position of the cell group and the dimensions in three directions XYZ, set the grid cell group to 1, and the bottom of the grid cell region just exceeds the layer. The number of seeds in the cell reflects the degree of disturbance. The more intense the disturbance, the more the number of seeds will be driven to the cell, and the less intense the disturbance, the less the number of seeds.

Structure principle of Seeding device

On the basis of the previous research conducted by Nanjing Institute of Agricultural Mechanization, Ministry of Agriculture and Rural Affairs, this paper adopted the pneumatic precision seed metering device developed in the earlier stage to carry out the research. The structure of the seed metering device is shown in Figure 1.

The working process of the seed metering device includes seed filling, seed clearing, seed carrying and seed casting. During operation, the air flow enters the inside of the seed metering device through the air inlet, and seed filling is carried out under positive pressure. When the seed disk rotates, the internal and external pressure difference makes the seeds press to the mold hole, and then reach the position of the seed drop mouth. The air pressure difference is eliminated under the air blocking device, and the seeds fall into the seed drop tube.

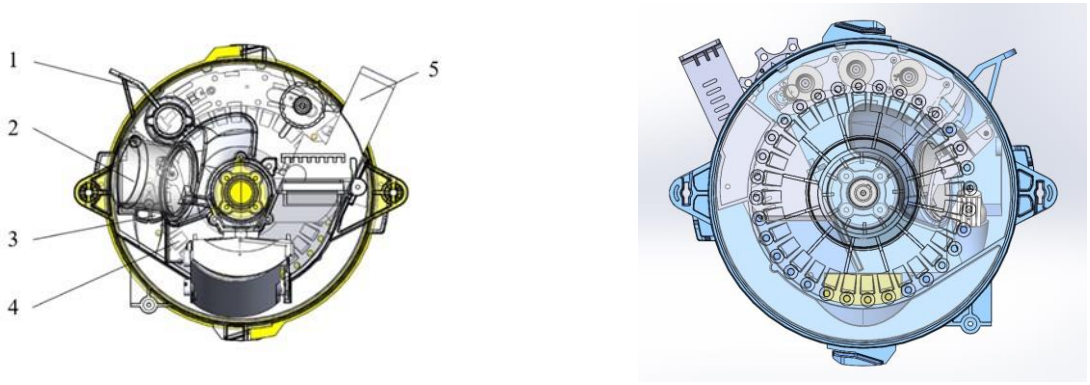

a. Front view of the seed metering device b. Rear view of seed metering device

Fig. 1 - Schematic diagram of seed metering device structure

1. Front housing;2. Air inlet;3. Seed port;4. Feed disk;5. Baffle plate.

Disturbance comparison and mechanical analysis

As shown in Fig. 2a, in the case of grooves, seeds were disturbed and showed a discrete state in the seed filling area of the seed layer with the rotation of the seed disk, while populations without grooves showed a stacked state, as shown in Fig. 2b.

a. Grooved population disturbed state b. Ungrooved population state

Fig. 2 - Effects of different types of disks on populations

The filling process of seeds is actually a process in which the air drag overcomes the population movement resistance (*Qi et al., 2013*). With the rotation of the seed disk during filling, the seeds were separated from the population by the disturbed seed disk, and the seeds were only affected by their own gravity and air compression force, as shown in Fig. 2a.

a. Disturbance force analysis b. Undisturbed force analysis

Fig. 3 - Comparison of force analysis under two different states

Therefore, when disturbed, seeds that do not come into contact with the population only need to meet the airflow pressure greater than their own gravity to be adsorbed, as shown in equation 1.

$$F_d \geq G \tag{1}$$

In Equation (1): F_d is the Airflow pressure, N. G is seed's own gravity, N.

When there is no disturbance, seeds come into contact with other seeds on the surface of the seeds, the seed is subjected to the horizontal component of population movement resistance and the vertical component of population movement resistance. At this point, the seed filling condition is reached as shown in equation 2.

$$F_d \geq G + F_{fi} + F_{fj} \tag{2}$$

In Equation (2): F_d is the airflow pressure, N. F_{fi} is the horizontal component of group movement resistance; F_{fj} is the vertical component of population movement resistance.

Through the comparison of whether there is disturbance or not, it can be concluded that when there is disturbance, the seed can be pressed to the mold hole by overcoming its own gravity, and the air compression force is smaller than that when there is no disturbance, the required pressure value is also small, and the efficiency is high.

Seed disk structure

According to the working principle, the seed disk is the key structure responsible for seed carrying in the seed disk, and its important parameters include the size of the mold hole, the number of the mold hole and the distance from the center hole of the disk. The friction in the population increases when the seed layer accumulates, and the rotation of the seed disk causes the disturbed seed groove to disturb the population and reduce the friction, which is conducive to seed adsorption during the filling. In this paper, three kinds of seed disks are compared. The hole size of all disks is 5.5 mm, the number of holes is 32, and the distance from hole center to disk center is 90 mm. Disk A is designed as a trapezoidal inclined groove, disk B has a circular groove with a diameter of 9.5 mm and a depth of 1 mm around the hole, and disk C has no groove. The three types of seed rows are shown in Figure 4.

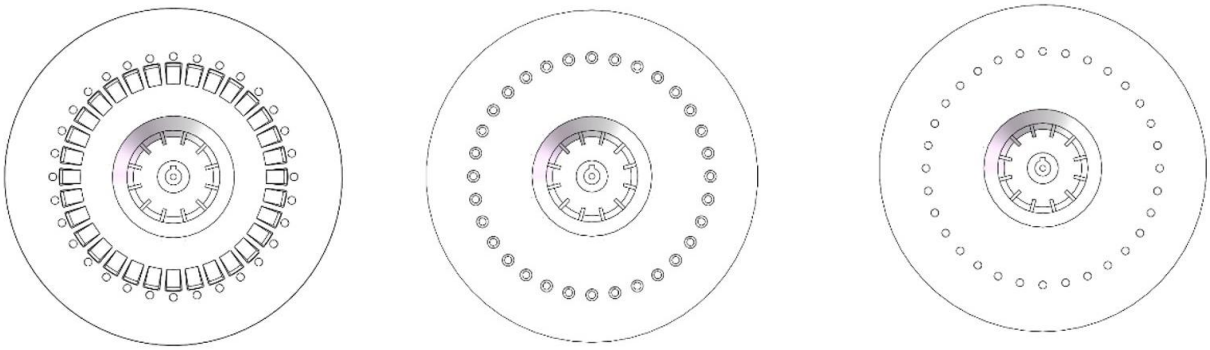

a. Disk A b. Disk B c. Disk C

Fig. 4 - Three types of seed disk structure

According to the literature, the maximum length and width of Zhengdan 958 corn seeds are 14 mm, 11.3 mm, and the minimum thickness is 3.3 mm, respectively. The size of corn seeds should be considered when designing the disturbed seed tank, and the length and width of the tank should be greater than the maximum size of corn, so that the seeds can completely enter the disturbed seed tank, and the length and width of the tank are 16 mm and 11.5 mm, respectively. The depth of the groove is smaller than the minimum seed thickness to prevent the seeds from being completely trapped in the groove affecting the disturbance performance, and the groove depth is 2.5 mm, as shown in the Figure 5.

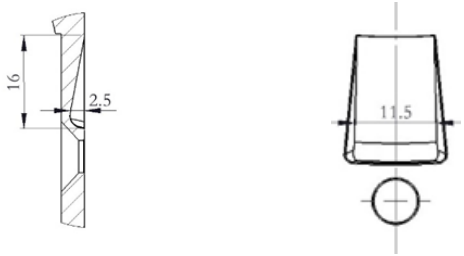

a. Left view profile of A-type slot b. A-slot main view

Fig. 5 - Partial schematic diagram

As shown in Figure 6, the disturbed seed slot has a certain slope. When the seeds are in contact with the seed disk, they slide into the slot and close to the shaped hole under the influence of centrifugal force and gravity, and a certain slope can guide the seed flow.

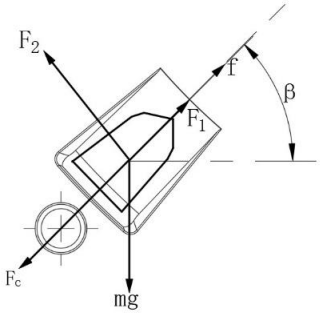

Fig. 6 - The seeds are subjected to force in the groove

$$\begin{cases} F_c = f + F_1 \\ mg = \dfrac{F_2}{\cos\beta} \end{cases} \quad (3)$$

In Equation (3): F_c is the centrifugal force on the seeds in the tank, N. F_1 is the supporting force of the bottom of the tank on the seed, N; F_2 is the supporting force of the groove side to the seed, N; β is the angle between the groove and the center of the disk and the horizontal line, (°); f is the friction between seed and tank, N; m is the quality of the seed, kg; g is the gravitational acceleration, m/s^2.

Among them, the centrifugal force F_c is affected by the speed and centrifugal radius, and the centrifugal radius is 90 mm, the centrifugal force can be shown in equation (4).

$$F_c = 0.36\pi^2 n^2 \quad (4)$$

In Equation (4): n is the rotational speed of the seed disk, r/min.

As shown in Figure 7, when seeds enter the tank, the population will have a vertical and disk pressure on the seeds in the tank, and the positive pressure of the population on the seeds can be found as shown in equation (5).

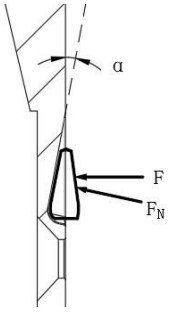

Fig. 7 - Left view of seeds under force in the groove

$$F_N = F\cos\alpha \quad (5)$$

In Equation (5): F_N is the positive population pressure, N; F is the Total population pressure, N; α is the angle between the groove bevel and the disk surface (°)

The friction force is shown by equation (6):

$$f = \mu F\cos\alpha \quad (6)$$

In Equation (6): μ is the Friction coefficient.

Substitute formula (4)(5)(6) into formula (3), it is obtained:

$$\begin{cases} 0.36m\pi^2 n^2 = \mu F\cos\alpha + F_1 \\ mg = \dfrac{F_2}{\cos\beta} \end{cases} \quad (7)$$

Force analysis through formula (7), the seeds in the tank are mainly affected by the rotation speed of the seed disk itself. When the height of the seed baffle is adjusted, the seeds move from the bottom to the surface when the height of the seed layer is fixed, the total pressure of the population on the seeds in the tank becomes smaller, the angle β becomes smaller, the seeds are subjected to greater force by the wall of the tank, the surface velocity of the seed layer increases, the number of seeds in the set area increases, and the disturbance becomes more obvious.

Particle seed modeling and motion simulation

In this paper, Zhengdan 958 corn seed was used for simulation. After preliminary screening, the seed was divided into four shapes: big circle, big flat, small circle and small flat. After modeling in SolidWorks, the seed was imported into EDEM for multi-spherical particle filling, the modeling and filling effects are shown in the figure 8.

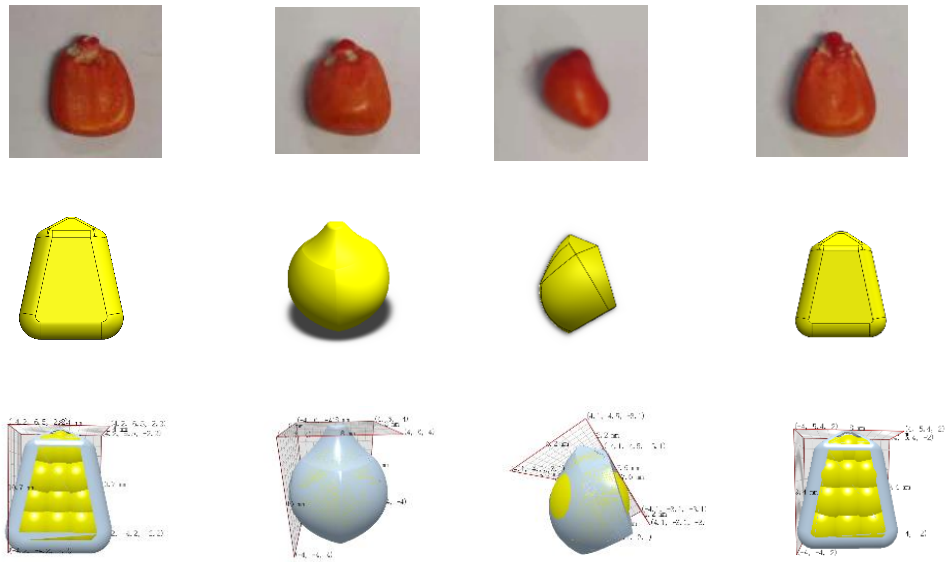

a. Large flat b. Large circle c. Small circle d. Small flat

Fig. 8 - Zhengdan 958 maize seed model

The relevant mechanical properties and characteristic parameters of corn seeds and seed disks are shown in Table 1 with reference to relevant literatures (*Liu et al., 2015*).

Table 1

Physical characteristics and contact parameters of maize seed and seed disk

Contact form	Collision recovery coefficient	Coefficient of static friction	Coefficient of dynamic friction
Seed and seed	0.182	0.431	0.0782
Seed disk and seeds	0.621	0.459	0.178

Due to the irregular shape of corn seeds and the lack of adhesion on the surface of grains, the Hertz-Mindlin (no slip) model was chosen (*Shi et al., 2015*).

The particle size distribution was normal, and the mean value of the normal size distribution parameter was 1 and the standard deviation was 0.05. The particle factory was set to generate four kinds of particles respectively. In order to improve the solving calculation speed, the model was simplified when imported, the redundant parts were deleted, and key contact parts such as shell and seed disk were retained. Set the rotation speed of the seed disk to 20.7, 24.9, 29.1 and 33.3 r/min respectively.

Set the number of corn seeds in Figure 2 according to the total number of 800 and the ratio of 5:3:1:1, respectively, and generate them according to the total number of 500 per second, ensuring that the number of seeds generated can fill the seed inlet, as shown in Figure 9.

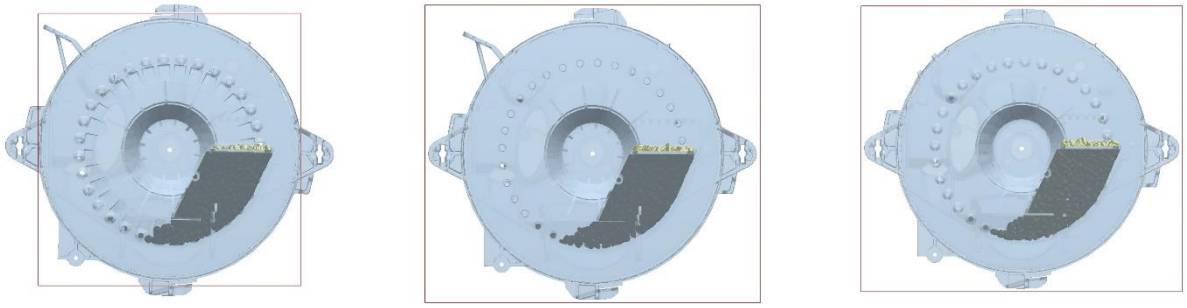

a. disk A b. disk B c. disk C

Fig. 9 - The simulation process of each seed disk

The solution setting adopts Euler time integration, with a Rayleigh time step of 2×10^{-6} seconds, the total simulation time is 7 seconds, and the particle generation time is less than 1 second. The generation is completed, and the seeding disk is set to start rotating at 1 second. Therefore, in the analysis interface, only the particle motion speed of 1 to 7 seconds and the number of seeds in the divided area need to be extracted.

Summary of simulation results

The disturbed seed tank can break the static state of population accumulation, and the seeds at the bottom can be moved upward in the process of movement, and the seeds near the seed layer can leave the surface of the seed layer through the disturbed seed tank, increasing the degree of seed dispersion. Therefore, the average velocity of seeds and the number of seeds entering the area above the seed layer were used as indicators to reflect the degree of species disturbance of the population. As shown in Figure 10, this article analyzes each disk at a speed of 19 r/min when the forward speed of the implement is 12 km/h.

In the post-processing, the simulation data of 1~7 s is extracted at a time interval of 0.4 s. The results show that the average speed of different kinds of disks fluctuates greatly, and the average speed of A disk mainly ranges from 0.005 to 0.02 m/s, while the average speed of B and C disks does not fluctuate.

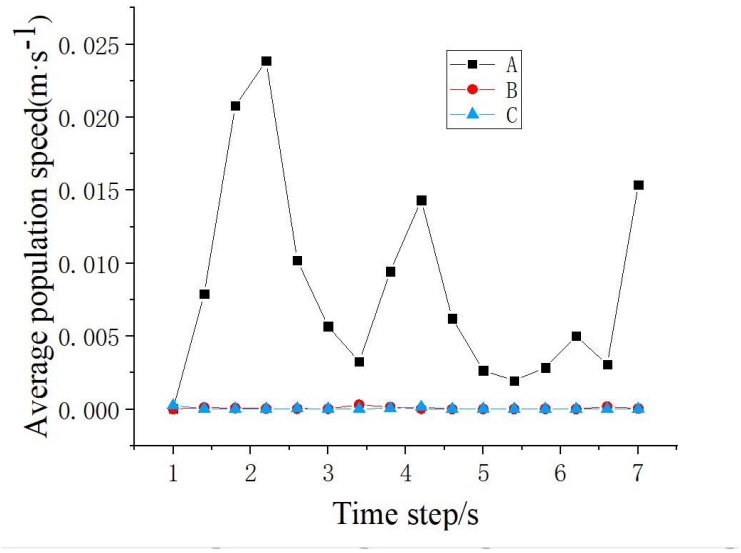

Fig. 10 - The fluctuation of the average velocity of the population of each seed disk with time

As time changes, it can be seen that the number in disk B and disk C is 0, indicating that the seed disk cannot bring the seeds into the area above the seed layer, and there is no obvious disturbance. As shown in Figure 11, the number of seeds above the seed layer of disk A fluctuated from 18 to 24, and there was obvious disturbance above the seed layer and the number was relatively stable, maintaining a stable filling state in the filling area.

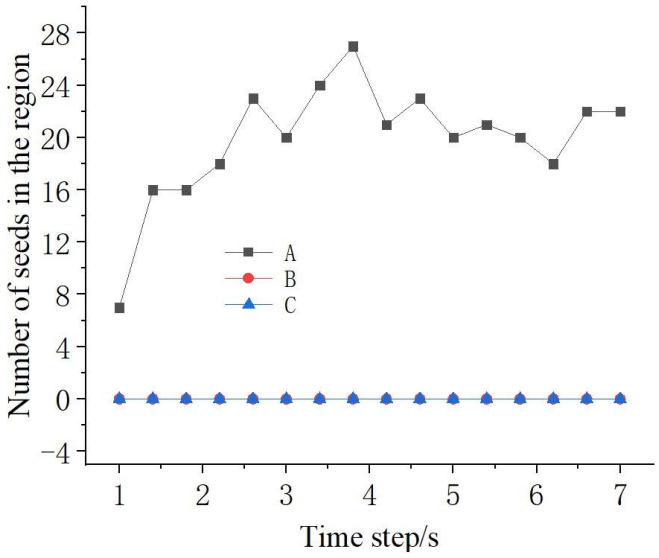

Fig. 11 - Number of seeds in each disk area at a speed of 12km/h

In general, with the increase of the rotation speed of the seeding disk, the average speed of the overall population increased. As shown in Figure 12, the average speed of the population of disk A was greater than 5×10^{-3}m·s^{-1}at each rotation speed, and could reach more than 0.01 m/s at high speed, and the population speed increased gently, while the speed of disk B was not much higher than that of disk C. Compared with disk A, it is found that the disturbance condition is disk A > disk B > disk C.

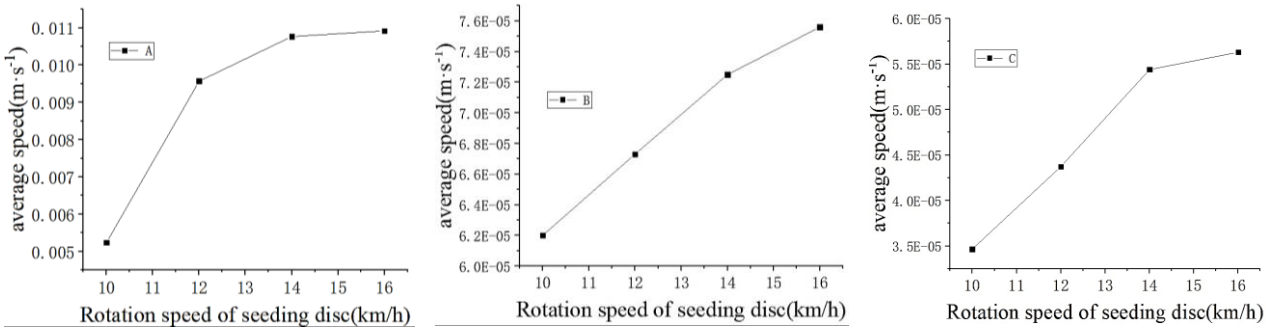

Fig. 12 - The average speed of the population at different seed disk speeds

In summary, the seed disturbing tank of disk A has a large disturbance ability, which can significantly increase the average speed of the population, reduce the internal friction of the seeds, drive the seeds away from the seed layer, and the seed disturbing effect is stable, which is conducive to the seed adsorption on the mold hole, and the seed filling performance of disk A is the best.

RESULTS

Bench test

Test materials and equipment

The selected seed was ungraded Zhengdan 958 corn seed with a 1000-grain weight of 330 g and a water content of 12%. In order to facilitate observation, the seed metering device is processed with a transparent shell, and the trial-produced seed metering disk is installed on the pneumatic high-speed precision seed metering device. The seed metering device is installed on the seed metering test bench of JPS-12, Nanjing Institute of Agricultural Mechanization, Ministry of Agriculture and Rural Areas. The plant distance and forward speed are set by the self-developed intelligent monitoring system of the seeder, and the speed is adjusted by the motor, The device is shown in the figure 13.

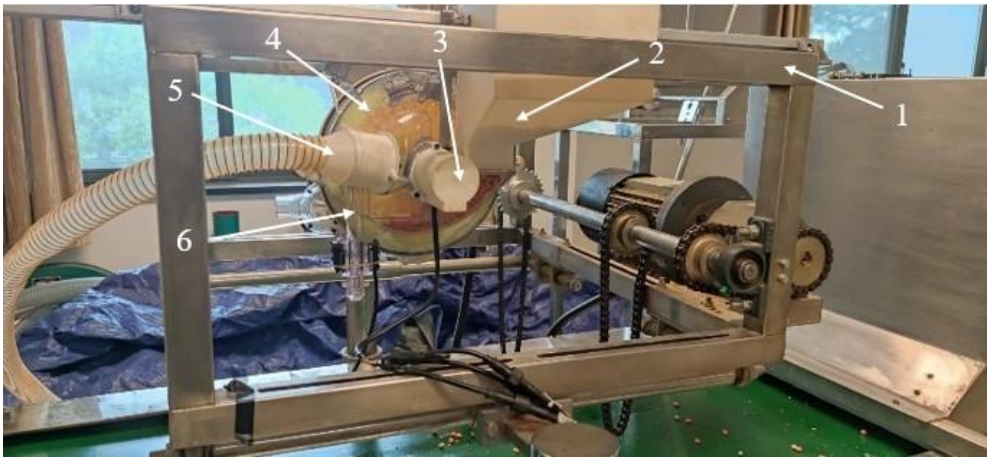

Fig. 13 - Seeding test bench

1. Profile racks; 2. Seed box; 3. Electrical machinery; 4. Seed metering device; 5. Air inlet port; 6. Seed feeding port

Test method

In the performance test of the seeding disk, Operation forward speed setting 10, 12, 14, 16km/h, and the working positive pressure was set to 3, 3.5, 4kPa. Marks were marked on the seeding disk to record the number of laps. The recording area started when the mold hole left the seed layer and ended at the highest position of the seeding position. The average value was repeated for 3 times as the test result.

Analysis of test results

It can be seen from Figure 14(a) that at the speed of 12km/h, the pass rate of disk A increases with the increase of air pressure, while the leakage rate of disk A decreases with the increase of air pressure in Figure 14(b). There is little difference between disk A and disk B within the range of 3.5~4 kPa, and the performance of disk A is higher than that of disk B, and the leakage rate of disk C is the largest. It can be seen from Figure 15(b) and (c) that with the increase of speed, the leak rate of disk C is the largest. When the rotation speed is 16 km/h, the leak rate of disk C is more than 8 percentage points higher than that of other disks, while the replay rate is the smallest. The reason for the above test results is that the groove disturbance performance of disk A is the best, which is conducive to the seed filling of mold holes.

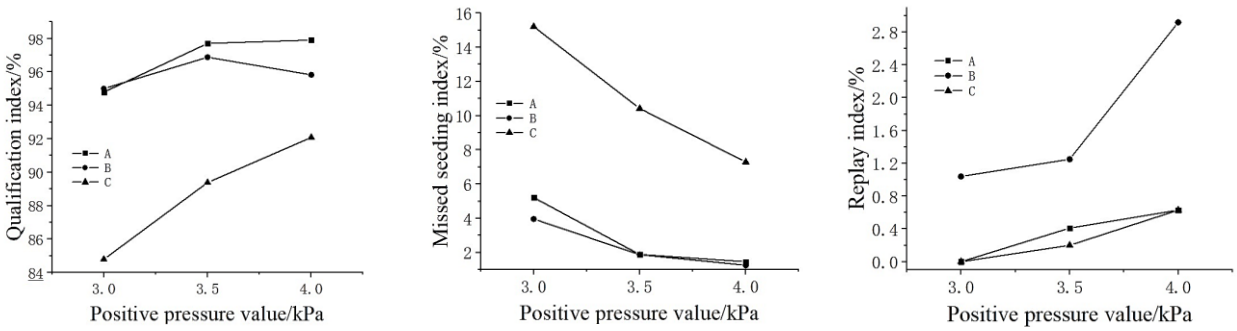

a. Qualification index b. Missed seeding index c. Replay index

Fig. 14 - Filling performance under different positive pressure at speed of 12 km/h

It can be seen from Figure 15(a) that the pass rate of disk A increases at the speed of 10~12 km/h, while the pass rate of disk C decreases at the speed of 12~16 km/h, among which the pass rate of disk C is the least. The result is that in a certain speed range, the appropriate increase of the speed makes the disturbance larger, and the seed disk can be better filled, so the pass rate is higher. Under high-speed operation, the centrifugal force on the seeds becomes larger, and it is easy to miss sowing, resulting in an increase in the miss sowing rate and a decrease in the qualified rate. Because there is no seed disturbing effect, the seeds are immovable under high-speed operation, and the interaction force between the populations is greater, and the seeds are difficult to adsorb. Therefore, the qualified rates of the seeds are much different from those of disk A and disk B.

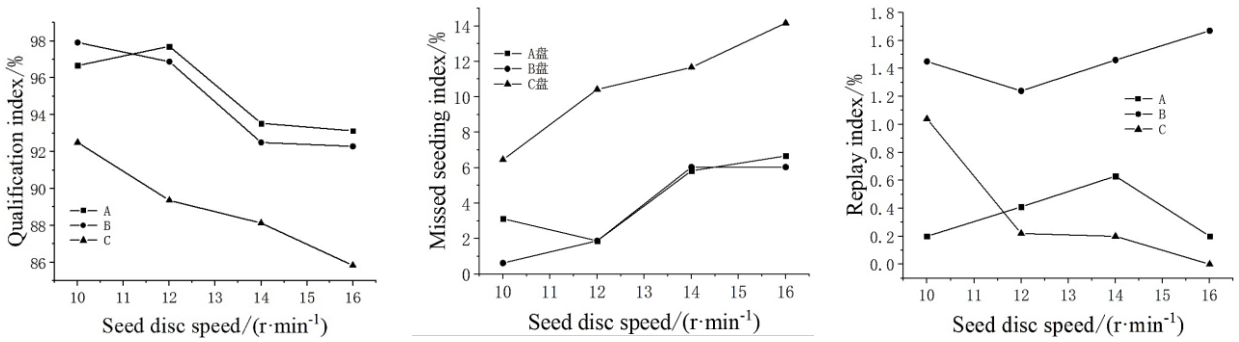

a. Qualification index b. Missed seeding index c. Replay index

Fig. 15 - Seed filling performance under different seed disk rotation speed of 3.5kPa

Validation test

In order to verify the seeding performance of the installation of A disk seeding device, according to GB/T6973-2005 "Test Method for Seeder", the qualified rate, missing seeding rate and reseeding rate of seeds were taken as test indexes, and the full factor test of the rotation speed of the seed disk and the given positive pressure were carried out. The test results are shown in Table 2.

Table 2

Full factor test results

Operating speed km/h	Barotropic value /kPa	Miss seeding rate/%	Replay rate/%	Pass rate/%
10	3	5.42	0	94.58
10	3.5	5.13	0.21	96.66
10	4	1.25	0.63	98.12
12	3	5.21	0	94.79
12	3.5	1.88	0.42	97.7
12	4	1.46	0.63	97.91
14	3	11.25	0.21	88.54
14	3.5	5.83	0.63	93.54
14	4	3.96	1.04	95
16	3	11.88	0	88.12
16	3.5	6.67	0.21	93.12
16	4	4.17	0.42	95.41

According to the test results of the A-type seed disk, when the operating speed is 10~12 km/h and the positive pressure is 33.5 kPa, the leakage rate is no higher than 5.42%, the replay rate is no higher than 0.42%, and the qualified rate is no less than 94.58%. When the operating speed is 14~16 km/h and the positive pressure is 3.5~4 kPa, the leakage rate is not higher than 6.7%, the replay rate is not higher than 1.04%, and the pass rate is not lower than 93.12%. All the indicators are better than the national standard.

CONCLUSIONS

(1) In order to investigate the effect of population disturbance on the leakage of seed metering device, two indexes were established for population disturbance. Through simulation, it was found that the population velocity of disk A was the largest, the number of seeds entering the area above the seed layer was the largest, and the degree of disturbance was the largest.

(2) The comparative test of the three seed arrangement disks used in the simulation with the same speed and different pressures and the same pressure and different speeds found that the seed disturbing performance of disk A was the best, which made the seeds more easily pressed on the mold hole, and the disturbance performance of disk A > disk B > disk C.

(3) The full factor test of speed and pressure was carried out on the best designed seed disk. At the operating speed of 16 km/h, by adding grooves to increase the disturbance, the leakage rate was reduced by 8 percentage points compared with the smooth disk without any disturbance. When the operating speed is 10~12 km/h and the positive pressure is 3~3.5 kPa, the leakage rate is no higher than 5.42%, the replay rate is no higher than 0.42%, and the qualified rate is no lower than 94.58%. When the operating speed is 14~16 km/h and the positive pressure is 3.5~4 kPa, the leakage rate is not higher than 6.7%, the replay rate is not higher than 1.04%, and the pass rate is not lower than 93.12%. All the indicators are better than the national standard.

ACKNOWLEDGEMENT

We greatly appreciate the careful and precise reviews by the anonymous reviewers and editors. This research was funded by the Jiangsu Provincial Natural Science Foundation of China (Grant No. BK20211021), the Jiangsu Province Agricultural Science and Technology Independent Innovation Fund (Grant No. CX(21)3143), and the Innovation Program of Chinese Academy of Agricultural Sciences (CAAS-SAE-202301).

REFERENCES

[1] Chen Jin, Li Yao Ming, (2002). Study on Seeds Movement Lawin Sowing Test Stand with Suction and Vibration (气吸振动式播种试验台内种子运动规律的研究). *Transactions of the Chinese Society for Agricultural Machinery*, Vol.(01), pp. 47-50.

[2] Chen Yulong, Zhang Meng, Liu Zeqi, et al., (2021). Design and experiment of seed agitator for vertical disk seed metering device. *INMATEH-Agricultural Engineering*, Vol.63(01), pp.178-188.

[3] Ding Li, Yang Li, Liu Shourong, et al., (2018). Design of air suction high speed precision maize seed metering device with assistant seed filling plate (辅助充种种盘玉米气吸式高速精量排种器设计). *Transactions of the Chinese Society of Agricultural Engineering*, Vol.34(22), pp.1-11.

[4] Liu Rui, Liu Zhongjun, Liu Lijing et al., (2022). Design and Experiment of Corn High Speed Air Suction Seed Metering Device with Disturbance Assisted Seed-filling (玉米扰动辅助充种高速气吸式排种器设计与试验). *Transactions of the Chinese Society for Agricultural Machinery*, Vol.53(09), pp.50-59.

[5] Qi Bing, Zhang Dongxing, Cui Tao, et al., (2013). Design and experiment of centralized pneumatic seed metering device for maize (中央集排气送式玉米精量排种器设计与试验). *Transactions of the Chinese Society of Agricultural Engineering*, Vol.29(18), pp.8-15.

[6] Singh R.C., Singh, G., Saraswat D.C., (2005). Optimisation of design and operational parameters of a pneumatic seed metering device for planting cottonseeds. *Biosystems Engineering*, Vol.92(4), pp.429-438.

[7] Shi Song, Zhang Dongxing, Yang Li, et al., (2015). Simulation and verification of seed-filling performance of pneumatic-combined holes maize precision seed-metering device based on EDEM (基于 EDEM 软件的气压组合孔式排种器充种性能模拟与验证). *Transactions of the Chinese Society of Agricultural Engineering*, Vol.31(03), pp. 62-69.

[8] Su Wei, Zhao Qinghui, Lai Qinghui, et al., (2023). Design and Experiment of Air-suction Broad Bean Seed Metering Device with Flat Belt Auxiliary Seed-filing (辅助充种带气吸式蚕豆精量排种器设计与试验). *Transactions of the Chinese Society of Agricultural Engineering*, Vol.54(07), pp.144-155.

[9] Wang Fenghua, Sun Kai Lai, Qinghui, et al., (2020). Design and Experiment of Minituber Precision Single-row Air-suction Planter (单行气吸式微型薯精密播种机设计与试验). *Transactions of the Chinese Society for Agricultural Machinery*, Vol.51(01), pp.66-76.

[10] Xie Dongbo, Zhang Chunling, Wu Xiaoqing et al. (2022). Design and Test of Garlic Seed Placer with Seed Disturbing Tooth Assisted Air Suction (扰种齿辅助气吸式大蒜排种器设计与试验). *Transactions of the Chinese Society for Agricultural Machinery*, Vol.53(02), pp.47-57.

[11] Yang Li, Yan Bingxin, Zhang Dongxing, et al., (2016). Research Progress on Precision Planting Technology of Maize (玉米精密播种技术研究进展). *Transactions of the Chinese Society for Agricultural Machinery*, Vol.47(11), pp. 38-48.

[12] Yang Mingjin, Qiu Bing, Yang Ling, et al., (2020). Metering performance of the vibrational vacuum precision tray seeder (振动气吸式精密穴播机的排种性能). *Transactions of the CSAE*, Vol.26(9), pp.139-143.

[13] Yazgi A., Degirmencioglu A., (2007). Optimisation of the seed spacing uniformity performance of a vacuum-type precision seeder using response surface methodology. *Biosystems engineering*, Vol.97(3), pp. 347-356.

[14] Zhang Kaixing, Zhang Lan, Ding Yang, et al., (2021). Design and experiment of seed agitatro for vertical disk seed metering device. *INMATEH-Agricultural Engineering*, Vol.64(02), pp.345-354.

[15] Zhang Xiaoshuang, Zhu Dequan, Xue Kang, et al., (2021). Parameter optimization and experiment of slider-hole-wheel seed-metering device based on discrete element method. INMATEH-Agricultural Engineering, Vol.65(03), pp.410-420.

[16] Zhao Zhan,Tian Chunjie, Wu Yafang, et al. (2018). Dynamic simulation of seed pick-up process and parameter optimization on vacuum plate seeder for rice (盘吸式水稻排种器吸种动力学过程模拟及参数优化). *Transactions of the Chinese Society of Agricultural Engineering*, Vol.37(07), pp.38-44.

EXPERIMENTAL STUDY ON THE SEEDING PERFORMANCE OF THE SPOON-WHEEL MAIZE SEED-METERING DEVICE UNDER VIBRATION CONDITIONS
/
勺轮式排种器在振动条件下的排种性能试验研究

Qing WANG, Dandan HAN*, You XU, Yuxia HUANG, Chao TANG, Wei LI [1]
College of Mechanical and Electrical Engineering, Sichuan Agricultural University, Ya'an 625014, China
Tel: 08352883018; E-mail: handd1988@126.com
Corresponding author: Dandan Han
DOI: https://doi.org/10.35633/inmateh-72-30

Keywords: *maize, spoon-wheel type, seed-metering device, vibration, seeding performance*

ABSTRACT
The seeder was tested and evaluated for field operations vibration characteristics in light of the issue that the spoon-wheel maize precision seeder vibrates due to the field operating conditions, which impairs the performance of the seed-metering device. During field testing, it was discovered that the seed-metering device vibrated greater as the forward speed increased, resulting in a higher peak vibration acceleration. However, fluctuations in forward speed did not affect the frequency distribution of the peak vibration acceleration. Time-domain and spectrogram investigations revealed that the vibration frequency of the seed-metering device was predominantly within 0~10 Hz for seeder operating speeds ranging from 2~6 km/h, with acceleration values spanning from 0.85~1.86 m/s². An electromagnetic seeding test stand was established in response to the discoveries. The essential variables governing the seeding performance of the spoon-wheel seed-metering device were then investigated using orthogonal tests, such as forward speed, vibration frequency, and vibration acceleration. The empirical results elucidated a hierarchical relationship between these factors and seeding quality. Specifically, vibration frequency emerged to be the predominant factor, followed by vibration acceleration, and forward speed. The seeding quality of the seed-metering device was negatively correlated with increases in forward speed and vibration acceleration, which led to a lower qualified rate, higher leakage rate, and variation coefficient. Overall, the qualified rate, leakage rate, and variation coefficient were all significantly influenced by the three factors.

摘要
针对勺轮式玉米精量播种机受田间作业工况的影响而产生振动，从而影响排种器排种性能的问题，对播种机进行田间作业振动特性测试与分析。田间试验结果表明，随着前进速度的增加，排种器受到的振动越剧烈，振动加速度峰值越大。但是振动加速度峰值的频率分布不受前进速度影响。当播种机的田间作业速度为 2~6 km/h 时，通过时域和频谱图分析，发现排种器的振动主频集中在 0~10 Hz，加速度范围为 0.85~1.86 m/s²。搭建振动排种试验台，通过正交试验对影响勺轮式排种器排种性能的前进速度、振动频率、振动加速度三个因素进行试验研究。结果表明：影响合格指数的因素主次关系为振动频率、振动加速度、前进速度；随着前进速度和振动加速度的增加，会导致排种器的合格指数降低、漏播指数及变异系数上升；三个因素对合格指数、漏播指数和变异系数均有显著性影响。

INTRODUCTION
Crop productivity is largely dependent on the efficiency with which seeding gear operates, making it a crucial component of agricultural production *(Yang et al., 2016)*. One of China's four major grain-producing regions, the hilly and mountainous areas of Southwest China are distinguished by the complex terrain, heavy soil, and uneven soil surface in their agricultural production land *(Han et al., 2023)*. The capability of the seeder to effectively seed will be adversely affected by its high vibration when operating in the field *(Zheng et al., 2020; Zhai et al., 2019)*. To strengthen seeding performance, vibration technology is currently mostly deployed in seeding machinery through the design and testing of vibration parts and vibration reduction devices, such as vibration seeding plates *(Wang et al., 2013; Chen et al., 2012; Liu et al., 2014)*.

[1] *Qing Wang, M.S. Stud. Agr.; Dandan Han, Lecturer. Ph.D. Eng.; You Xu, M.S. Stud. Agr.; Yuxia Huang, M.S. Stud. Agr.; Chao Tang, M.S. Stud. Agr.; Wei Li M.S. Stud. Eng.*

The seed metering device is the core component of the seeder *(Han et al., 2018; Su et al., 2022)*, whose capability is directly impacted by the working environment of the seeder *(Zhang et al., 2023)*. Based on how it operates, the seed-metering device can be classified into two categories: mechanical and pneumatic *(Gao et al., 2021; Han et al., 2023)*. The spoon-wheel seed-metering device is mechanical, mainly relying on gravity to facilitate seed cleaning and distribution, with the advantages of not easily injured seeds, good seeding quality, and adaptability to the shapes of the seeds, and is widely utilized in the production practices of the hilly and mountainous areas in southwest China *(Zhang et al., 2016; Zhang et al., 2023; Huang et al., 2021)*.

Scholars both at home and abroad have been focusing more on how vibration affects the performance of the seed-metering device in recent years. Liao et al. donned the 2BFQ-6 rape precision combined direct seeding machine as the research object, the vibration tester was utilized to assess the vibration of the direct seeding machine. They also constructed a vibration simulation seeding test bench to conduct the bench test and investigate the impact of mechanical vibration on the seeding performance *(Liao et al., 2022; Zheng et al., 2023)*. The target seeding rate of a rapeseed centralized seed-metering device at various vibration frequencies was elevated by Wu et al. by adjusting the longitudinal distance *(Wu et al., 2022)*. Boydas et al. explored the repercussions of four distinct vibration levels on the homogeneity of flow uniformity of grains like wheat and barley, the findings indicated that the vibration intensity had an enormous impact on the barley flow consistency while not affecting all of the wheat flow *(Boydas et al., 2007)*. Vishnyakov et al. studied the main factors influencing the quality of seeding by vibration device and, according to research results, a graph of their influence on estimates of seeding was constructed *(Vishnyakov et al., 2015).* Emrah's research indicates that planter vibration greatly interferes with the seed discharging process of the planter and reduces the uniformity of seed discharging, thus affecting the quality of the planter *(Emrah, 2021).* The study by Min et al. aimed to investigate the optimum vibration condition of the seed hopper on the vacuum suction nozzle seeder for improving seeding performance *(Min et al., 2008).* Based on a theoretical analysis of the working process of sowing winter-wheat seeds using a vibrating sowing apparatus, analytical dependences of the actual and calculated specific weight costs on the acceleration of vertical and horizontal oscillations of the apparatus trough were obtained, which graphically illustrated the uniformity of the distribution of winter wheat seeds by Alexander et al *(Alexander et al., 2021).* To address the issue of the existing sugarcane seed-metering device having a high percentage of damaged seeds and an omission rate, an electromagnetic vibration-type single-bud sugarcane seed-metering device availed itself of the automatic vibrating metering feature to avoid ruining the buds *(He et al., 2019; Wu et al., 2023)*.

To inspect whether the seed-metering device would resonate with the working process, an approach that consisted of modal analysis and vibration testing was employed by Liu et al. to examine the vibration properties of the air-suction seed-metering device, and its vibration response under the excitation of the tillage surface during the seeding operation *(Liu et al., 2019; Liu et al., 2021)*. To survey the influence of the vibration of the air-suction no-tillage planter on the seeding performance, the spectrum map was obtained through MATLAB processing and analysis, the greatest vibration point was identified, and the major parameter model influencing the vibration of the no-tillage planter was established by Zhao et al *(Zhao et al., 2012; Zhang et al., 2015; Dong et al., 2015;)*. To cope with the matter of the low level of intelligence of the air-suction vibrating disc seed meter, Cheng et al. proposed an online monitoring system scheme for the air-suction vibrating disc seed meter based on the Internet of Things and configuration software *(Cheng et al., 2022)*.

To attempt to perform the seeding performance of the mechanical seed-metering device in vibration conditions, a vibration seed-metering simulation test bench was erected by Huang et al. The seeding test was carried out for the pick-up finger seed-metering device based on the two distinct factors of vibration frequency and amplitude, and the results showed that the qualified rate gradually decreased with the increase of the two factors. *(Huang et al., 2019; Wang et al., 2019)*. Wang et al. conducted an experimental study to investigate the implication of vibration on the sowing quality of a shovel-type precision seeder and explored the vibration characteristics of the seeder. The results advocated that the vibration frequency of the seeder was concentrated in the low-frequency region, the vibration intensity increased with speed, and an increase in vibration intensity would lead to a reduction in seeding performance *(Wang et al., 2008; Zhang et al., 2014)*.

The spoon-wheel type maize precision seeder, which is prevalently employed in hilly and mountainous areas of Southwest China, is the subject of this study. The field vibration signals of the seeder in the time and frequency domains under various speed settings were systematically analyzed.

A vibration seeding test intermediary was constructed for controlled testing to facilitate extensive wisdom. The primary objective was to discern the impact of the field vibration characteristics of the seeder on the seeding performance of the seed-metering device. The findings derived from this study are intended to provide insightful recommendations for the refinement and enhancement of the spoon-wheel seed-metering device, ultimately elevating the operational quality of the seeder amidst field vibration scenarios.

MATERIALS AND METHODS

Theoretical analysis of vibration characteristics of the spoon-wheel maize precision seeder

Structure and working principle of the seeder

The field vibration characteristics of the spoon-wheel seed-metering device were tested and analyzed in this study employing the maize spoon-wheel seeder produced cooperatively with Sichuan Agricultural University and Hebei Nonghaha Machinery Group Co. The tractor and seeder were joined via a three-point hitch. The essential technical aspects of the seeder are listed in Table 1.

Table 1

Main parameters of the maize spoon-wheel seeder

Parameters	Unit	Values
Overall size	[mm]	1595×1590×1200
Furrowing depth	[mm]	≤280
Maximum fertilization	[kg/hm^2]	1050
Rows	/	3
Row spacing	[mm]	500-700
Plant spacing	[mm]	120-310

The planting unit, ground wheel, three-point hitch, fertilizer tank, and fertilizer applicator are some of the essential parts that collectively make up the seeder assembly. Wherein, the planting unit is mainly composed of a spoon-wheel seed-metering device, a parallel four-link mechanism, a packer wheel, a seeds case, and a seed-furrow opener. The parallel four-link mechanism is tightly fastened to the three-point hitch by a tension spring. Additionally, the two ground wheels of the seeder are symmetrically affixed on the three-point hitch. The operating power of the spoon-wheel seed-metering device is mainly transmitted by the ground wheels through the chain drive. The general structure of the seeder is depicted in Fig. 1.

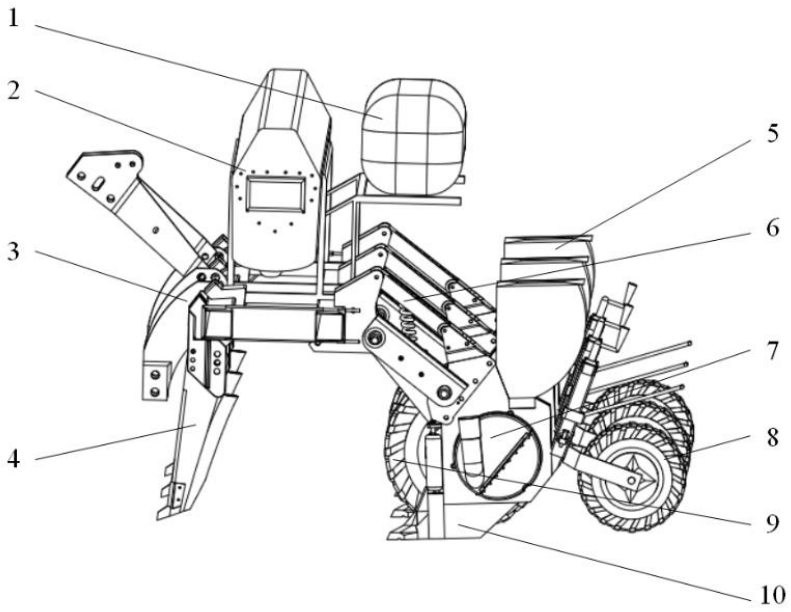

Fig. 1 - The structural diagram of the spoon-wheel maize seeder

1. Reservoir; 2. Fertilizer tank; 3. Three-point hitch; 4. Fertilizer applicator; 5. Seeds case; 6. Parallel four-link mechanism; 7. Spoon-wheel seed-metering device; 8. Packer wheel; 9. Ground wheel; 10. Seed-furrow opener

The seed-metering device is the core component of the seeder, and its structural parameters directly determine the sowing quality. The spoon-wheel type seed-metering device, which is more commonly adopted on seeders in southwest China, consists of a rear shell, seed-guiding wheel, spacer plate, spoon-wheel disc, front shell, and other components. The concrete structure of the seed-metering device is displayed in Fig. 2. The rear shell mainly serves as a fixation and support for the seed-metering device. The scoop-wheel disc utilizes the scoop to ladle up the seeds and deliver them to the seed-guiding wheel. The spacer plate separates the spoon-wheel disc from the seed-guiding wheel, and its opening location dictates the initial position of the seed delivery from the spoon to the seed-guiding wheel. The seed-guiding wheel receives the seed delivered by the spoon-wheel disc and releases it smoothly from the seed-metering device. The movement of the seeds in the seed-metering device will be easily observed through the transparent front shell.

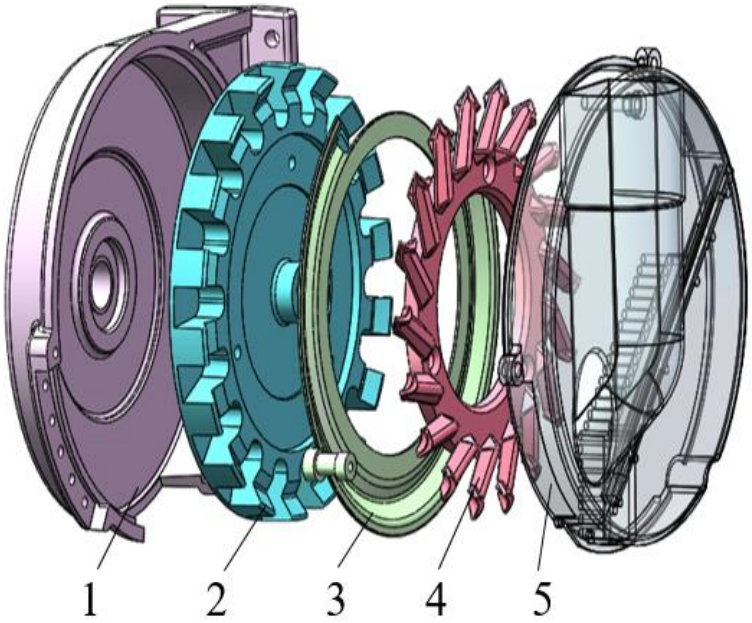

Fig. 2 - Schematic diagram of the spoon-wheel seed-metering device

1. Rear shell; 2. Seed-guiding wheel; 3. Spacer plate; 4. Spoon-wheel disc; 5. Front shell

The fertilizer pipe uniformly distributes the fertilizer into the ditch to finalize the fertilization after the seeder goes on the field. Meanwhile, the trench is initially created by the seed-furrow opener, the ground wheels rotate with the advance of the tractor and transmit the power to the spindle of the seed-metering device through the chain drive to actuate its operation. The single seed in the spoon falls into the trench regularly from the seed-metering device. The packer wheel, which can be contoured following the undulation of the field terrain, is followed by a parallel four-bar mechanism with a tension spring. To guarantee optimal soil-seed contact, the packer wheel could cover and annihilate the seeds in the trench. Moreover, contingent upon demand, the seeder can also irrigate the seeds to offset the soil drought triggered by an absence of irrigation in southwest China during the sowing season.

Theoretical model of the seeder vibration characteristics

Regardless of the adjustable connection between the seeder and the three-point hitch, the undulation of the field surface will cause varying degrees of vibration to be enacted to the seeder, which will ultimately result in a vertical displacement modification of the seed-metering device. To legitimately simplify the vibration system model of the seeder, the secondary factors affecting the vibration characteristics of the seeder field operation and lateral vibration are disregarded. Each component of the seeder is assumed to be a rigid body. The stiffness of the fertilizer applicator, seed-furrow opener, and depth-limiting wheel, which are in direct contact with the soil, is a linear function of displacement, while the damping force generated by the interaction with the soil is a linear function of velocity *(Zhang et al., 2014; Liu et al., 2016; Gao et al., 2022)*. The field soil profile can be converted to a sine function while the seeder is running. The mass of the seeder is set to M, the amplitude to H, and the length in the forward direction to L. The simplified vibration system model of the seeder is portrayed in Fig. 3.

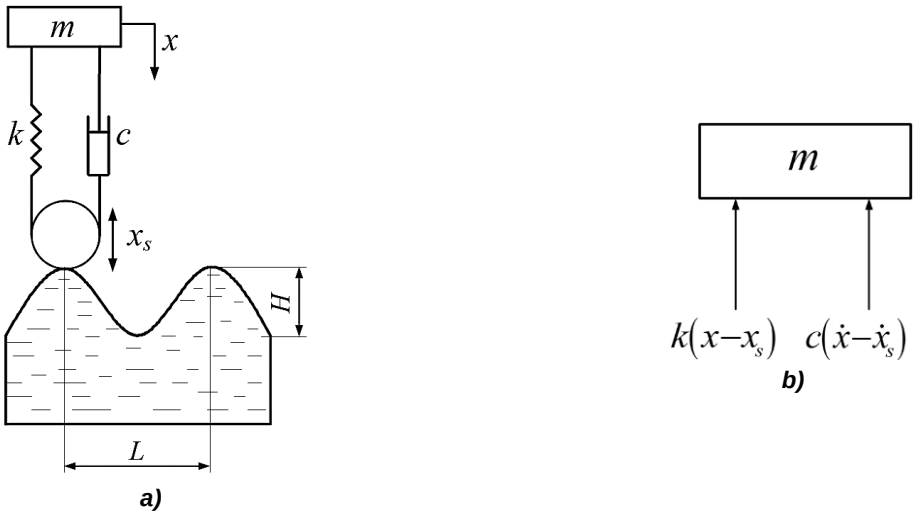

Fig. 3 - The vibration system model of the spoon-wheel maize planter

a) Vibration system model; b) Mass block

The seeder exhibits simple harmonic motion at the supporting point with the following equation of motion:

$$x_s = H \sin \omega t \tag{1}$$

In which:

$$\omega = 2\pi \frac{v}{L} \tag{2}$$

The displacement of the seeder mass block (m) was considered to be the generalized coordinates, and the direction of descent was specified to be positive. When the distance between the mass block (m) and the static equilibrium position is x, the spring deformation should be x-x_s, and the relative velocity between the mass block and the supporting point is $\dot{x} - \dot{x}_s$. Consequently, the mass block was susceptible to the elastic resilience $k(x\text{-}x_s)$, and the damping force $c\left(\dot{x} - \dot{x}_s\right)$, as illustrated in Fig.2 (b). The differential equation of motion for the seeder vibration can be expressed as follows using Newton's law of motion:

$$m\ddot{x} = -k\left(x - x_s\right) - c\left(\dot{x} - \dot{x}_s\right) \tag{3}$$

Combining Eq. (1) with Eq. (3) produces the following results:

$$m\ddot{x} + c\dot{x} + kx = H\sqrt{k^2 + (c\omega)^2} \sin\left(\omega t + \arctan\frac{c\omega}{k}\right) \tag{4}$$

Where in Eq. (4),

$$\begin{cases} F_d = H\sqrt{k^2 + (c\omega)^2} \\ \psi = \arctan\dfrac{c\omega}{k} \end{cases} \tag{5}$$

Consolidating the above equations and introducing Eq. (6):

$$\begin{cases} \omega_n = \sqrt{\dfrac{k}{m}} \\ \zeta = \dfrac{c}{2\sqrt{mk}} \\ \Delta_{st,d} = \dfrac{F_d}{m\omega_n^2} \end{cases} \tag{6}$$

Eventually, the vibration equation for the field operation of the seeder was estimated to be:

$$\ddot{x} + 2\omega_n \zeta \dot{x} + \omega_n^2 x = \Delta_{st,d}\omega_n^2 \sin\left(\omega t + \psi\right) \tag{7}$$

where: F_d is the amplitude of the excitation force in N, ψ is the phase difference of the excitation in rad, ω_n is the natural frequency of the seeder in Hz, ζ is the damping coefficient of the seeder, and $\Delta_{st,d}$ is the net displacement in m.

As demonstrated in Eq. (7), the majority of vibration-causing factors during field operation are the structure, forward speed of the seeder, and soil flatness.

Test and analysis of the field operation vibration characteristics

An empirical study was carried out on the vibration characteristics of the spoon-wheel seed-metering device used in the seeder. Conforming to the vibration frequency and acceleration of the seeder during field operation as estimated by the preparatory test, the UT6819A vibration tester and CA-YD-103 piezoelectric transducer were identified to construct a vibration seeding test stand.

Experimental conditions and schematic design

A three-row spoon-wheel maize precision seeder was adopted for the vibration characteristic test trials. The supporting power was provided by a Kubota M704 tractor, and the previous crop at the test was oilseed rape. The plots were rototilled in preparation for the execution of the study. The parameters of the traits of the field blocks and tractors employed in the test are listed in Table 2.

Table 2

Field vibration test equipment and parameters relevant to field characteristics

Categories	Parameters	Values
Tractor	Calibrated engine rotational speed [r/min]	2500
	Overall size (*L*×*W*×*H*) [mm]	4110×1950×2560
Field characteristic parameters	Average soil moisture content [%]	32.28
	Average soil firmness [kPa]	718.89
	Capacity [g·cm^3]	1.26

The forward speed has an immense impact on the vibration characteristics of the seeder, as can be recognized by the preceding analysis of the theoretical model of those characteristics. To conduct the single-factor test of the effect of the forward speed on the vibration characteristics of the seeder, the various forward speeds were first identified as test factors in this study. Since restrictions on the field plot area and soil viscosity in the hilly and mountainous areas of southwest China, the seeder can't run at a speedy pace to guarantee the quality of seeding. To perform the vibration characteristic test of the seed-metering device at various operating speeds, the forward speed will be adjusted to ranged working conditions, such as 2~6 km/h.

The seeder was suspended over the tractor at three points, as indicated in Fig. 4(a). The vibration sensor was mounted horizontally on the anti-tangle roller bracket, as noted in Fig. 4(b). Real-time monitoring of the tractor's forward speed was attempted with GPS. Since the seeder vibration during field operation was primarily in the vertical direction, the vibration data of the seed-metering device in the vertical direction within 10 seconds after the seeder operates smoothly are predominantly captured. Three replicate tests were performed for each forward speed, and the average value was taken as the ultimate measurement of what would occur.

a) ***b)***

Fig. 4 - Field Experiment

a) Experimental seeder; b) Sensor mounting position

Seeding performance test of the spoon-wheel seed-metering device under vibration condition

Construction of the vibratory seeding test stand

A test table for the vibration characteristics of the spoon-wheel seed-metering device test was erected based on the field vibration characteristic of the seeder, as shown in Fig. 5. The main components of the test bench include a JPS-12 type seed-metering device performance test bench, a computer, an acceleration sensor, a vibration tester, a shaker, a spoon-wheel seed-metering device, and other pieces. By altering the speed of the conveyor belt motor on the JPS-12 seed metering test stand, the forward speed of the seeder in the field was simulated. The spoon-wheel seed-metering device was positioned in the center of the metal plate, and the top rod of the exciter acted on the metal plate to secure the entire exciter to the top of the bench. The metal plate was fastened to the bench by four springs, and the vibration load was applied to the metal plate via an exciter. To validate that the seed-metering device runs at a specific vibration frequency and vibration acceleration, the vibration characteristics of the seed-metering device were continuously monitored using the vibration test equipment. When the seed-metering device was in application, the seeds fell from the seed-voting port onto the seedbed belt, which was sprayed with a layer of oil to simulate soil to minimize seed bounce. Lastly, the seeding data was monitored and collected in real-time by the image processing unit of the seed-metering device performance test bench.

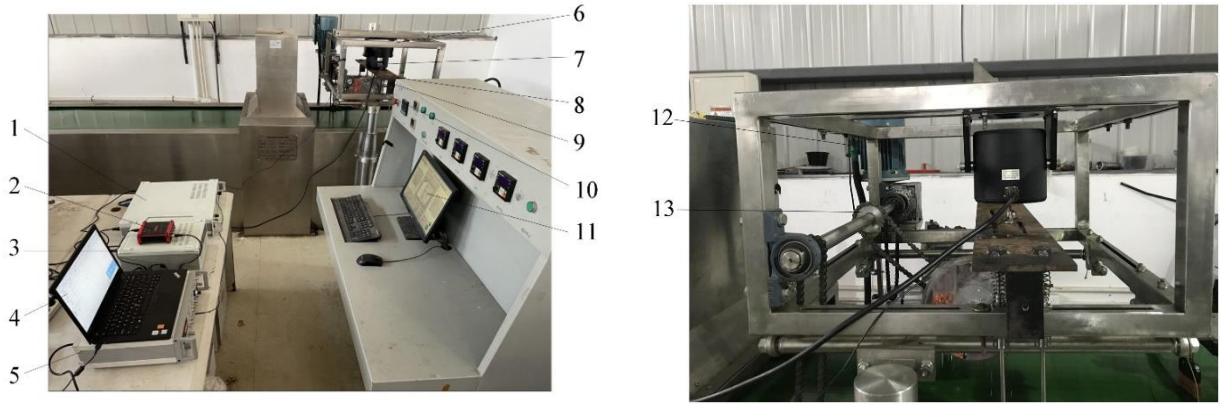

Fig. 5 - Vibration testing stand for the seed-metering device

1. Power amplifier; 2. Data collector; 3. Sweep signal generator; 4. Computer; 5. Vibration tester; 6. Metal bench; 7. Exciter; 8. The metal plate; 9. Vibration acceleration sensor; 10. Spoon-wheel seed-metering device; 11. Operation monitor; 12. Motor; 13. Gearing

Orthogonal Experimental Design

According to the theoretical analysis model and vibration test results, the working performance of the seed-metering device under vibration conditions is associated with the forward speed, vibration frequency, and vibration acceleration. To comprehend the effect of vibration on the seeding performance of the spoon-wheel seed-metering device, measurements were conducted on the impacts of various forward speeds, vibration frequencies, and vibration accelerations. The qualified rate, multiple rate, leakage rate, and variation coefficient served as evaluation indicators, paired with the three-factor and five-level orthogonal test design approach. Under the agronomic requirements for planting maize net crops in the hilly and mountainous areas of southwest China, the theoretical plant spacing was fixed at 20 cm. The orthogonal test design is listed in Table 3.

Table 3

Three factors five levels orthogonal test factor level table

Levels	Factors		
	A Forward speed [km/h]	B Vibration frequency [Hz]	C Vibration acceleration [m/s^2]
1	2	2	0.8
2	3	4	1.1
3	4	6	1.4
4	5	8	1.7
5	6	10	2

RESULTS

Experiment results and analysis of field operation

The root-mean-square (RMS) of vibration acceleration was used as an evaluation indicator of the seeder vibration amplitude in field operations. The vibration time domain analysis of the seeder in the vertical direction at various forward speeds is depicted in Fig. 6. The time-domain graphic demonstrated that the seeder's vertical vibration acceleration rises with the forward speed, intensifying the vibration effect.

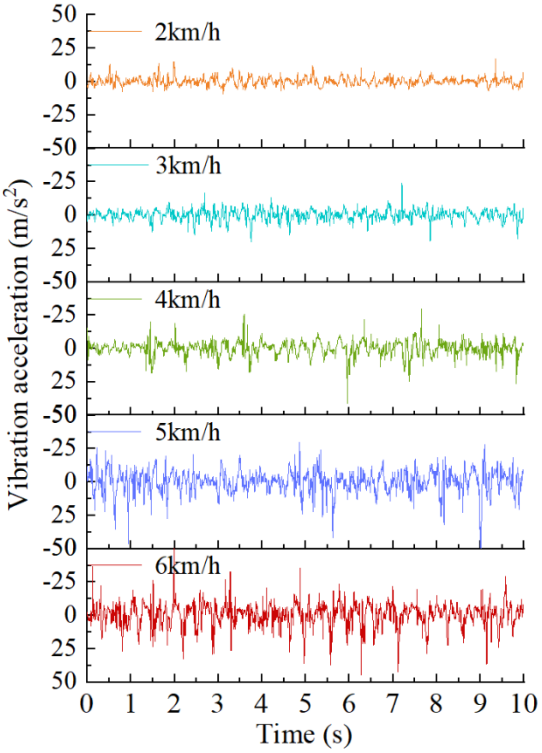

Fig. 6 - Time domain diagram

The spectrum analysis of the seeder's vertical direction at various forward speeds is exhibited in Fig. 7. The spectrogram analysis revealed that the seeder was mostly vibrated at low frequencies around forward speeds of 2~6 km/h. The foremost vibration acceleration was generated in this frequency range, where the stronger vibration was predominantly focused at 0~10 Hz. The maximum value of vibration acceleration evolves in lockstep with the forward speed.

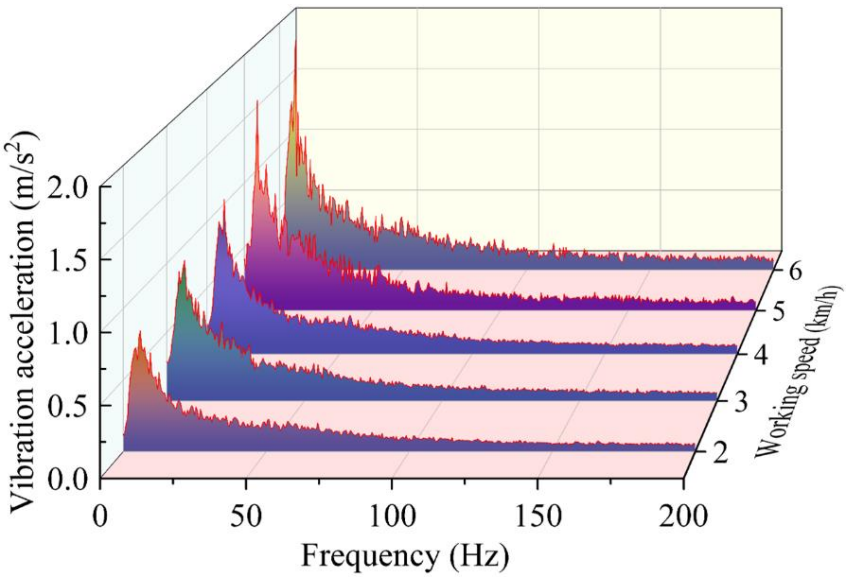

Fig. 7 - Spectrogram

The vibration characteristic parameters corresponding to various forward speeds were identified leveraging spectrum analysis, as stated in Table 4. The peak vibration acceleration ascends along with rising forward speed as well as the seeder vibration intensity. Nevertheless, the frequency distribution of the peak vibration acceleration is independent of the forward speed.

Table 4

Vibration characteristics at various forward speeds

Working speed [km/h]	Vibration frequency [Hz]	Vibration acceleration [m/s^2]
2	6.0	0.85
3	6.5	1.02
4	6.5	1.17
5	5.0	1.65
6	6.5	1.86

Results and range analysis of the orthogonal test

The results of the test conducted per the orthogonal test design scheme are exhibited in Table 5.

Table 5

Results of the three-factor and five-level orthogonal test

No.	*A*	*B*	*C*	Qualified rate [%]	Multiple rate [%]	Leakage rate [%]	Variation coefficient [%]
1	1	1	1	93.0	0.3	6.7	24.3
2	1	2	2	92.5	1.5	6.0	23.5
3	1	3	3	92.6	2.3	5.1	22.6
4	1	4	4	92.3	2.4	5.3	23.7
5	1	5	5	90.8	3.6	5.6	24.8
6	2	1	2	89.6	2.7	7.7	34.2
7	2	2	3	90.8	2.4	6.8	26.1
8	2	3	4	91.1	3.6	5.3	24.3
9	2	4	5	90.9	2.8	6.3	28.5
10	2	5	1	93.3	3.1	3.6	24.9
11	3	1	3	80.1	5.6	14.3	43.2
12	3	2	4	88.2	1.7	10.1	28.9
13	3	3	5	88.5	0.4	11.1	36.2
14	3	4	1	91.0	4.1	4.9	26.9
15	3	5	2	92.4	0.7	6.9	26.7
16	4	1	4	75.0	5.3	19.7	49.4
17	4	2	5	83.0	8.1	8.9	38.1
18	4	3	1	93.0	0.7	6.3	28.2
19	4	4	2	91.2	2.4	6.4	27.3
20	4	5	3	90.0	2.9	7.1	24.6
21	5	1	5	70.0	7.6	22.4	46.7
22	5	2	1	92.2	2.1	5.7	29.4
23	5	3	2	86.3	5.3	8.4	31.4
24	5	4	3	86.9	4.0	9.1	31.0
25	5	5	4	90.4	2.7	6.9	32.9

The range analysis of the orthogonal test results is illustrated in Table 6.

Table 6

Range analysis of the orthogonal test results

Evaluation indicators	Factors	Levels					Extreme Difference	Optimal level	Optimal combination
		k_1	k_2	k_3	k_4	k_5			
Qualified rate	*A*	92.24	91.14	88.04	86.44	85.16	7.08	1	$A_1B_5C_1$
	B	81.54	89.34	90.30	90.46	91.38	9.84	5	
	C	92.50	90.40	88.08	87.40	84.64	7.86	1	
Multiple rate	*A*	2.02	2.92	2.50	3.88	4.34	2.32	1	$A_1C_1B_2$
	B	4.30	3.16	2.46	3.14	2.60	1.84	3	
	C	2.06	2.52	3.44	3.14	4.50	2.44	1	
Leakage rate	*A*	5.74	5.94	9.46	9.68	10.50	4.76	1	$A_1C_1B_5$
	B	14.16	7.50	7.24	6.40	6.02	8.14	5	
	C	5.44	7.08	8.48	9.46	10.86	5.42	1	
Variation coefficient	*A*	23.78	27.60	32.38	33.52	34.28	10.5	1	$A_1B_5C_1$
	B	39.56	29.20	28.54	27.48	26.78	12.78	5	
	C	26.74	28.62	29.50	31.84	34.86	8.12	1	

According to the range analysis results shown in Table 6, the primary and secondary factors that determine the qualified rate of the spoon-wheel type seed-metering device are *B*>*C*>*A*, and the ideal combination is $A_1B_5C_3$. The major and secondary factors that affect the multiple rate are *C*>*A*>*B*, and the optimal combination is $A_1C_1B_2$. The main and auxiliary factors affecting the leakage rate are *B*>*C*>*A*, and the best combination is $A_1C_1B_5$. The initial and subsequent factors influencing the variation coefficient are *B*>*A*>*C*, with $A_1B_5C_1$ being an excellent combination. The results of the extreme difference analysis results also demonstrated that all evaluation indicators had the same desired levels for forward speed (*A*) and vibration acceleration (*C*), which are A_1 and C_1, respectively. The appropriate level of vibration frequency (*B*) is B_2 for the multiple rate, while B_5 is the preferred level for the other three evaluation indicators. When the acceleration of vibration remains constant, the vertical displacement of the seed-metering device will decrease as the vibration frequency increases. Consequently, whilst the vibration frequency is fixed, the seed-metering device behaves reasonably smoothly and the seeding performance is more stable under lower forward speed and vibration acceleration conditions.

Based on the detailed investigation, the ideal forward speed of the spoon-wheel maize seeder in the hilly and mountainous areas of southwest China is 2 km/h. At this particular time, the seeder is vibrating at a frequency of 10 Hz and an acceleration of 0.8 m/s^2.

Effect of forward speed, vibration frequency, and acceleration on the qualified rate

As observed in Fig. 8, the qualified rate of the spoon-wheel seed-metering device significantly decreased as the forward speed increased, attending from 92.24% to 85.16%, while the qualified rate progressively evolved from 81.54% to 91.38% as the vibration frequency increased. When the vibration acceleration increases, there is a notable decline in the qualified rate from 92.5% to 84.64%.

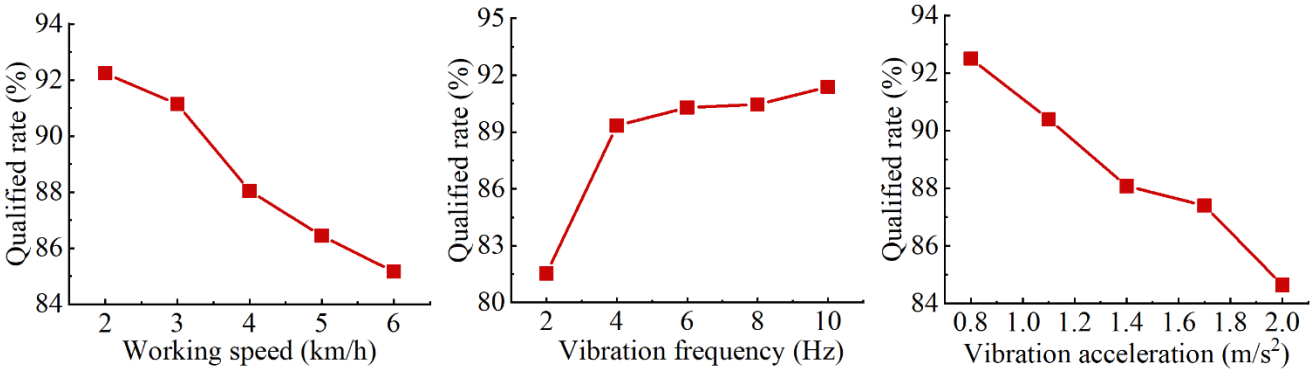

Fig. 8 - Effect of the working speed, vibration frequency, and acceleration on the qualified rate

Effect of forward speed, vibration frequency, and acceleration on the multiple rate

As illustrated in Fig. 9, the multiple rate exhibited an overarching increasing tendency with an increase in forward speed and vibration acceleration. With the increase in forward speed, the multiple rate jumped from 2.02% to 4.34%, accompanied by an increase in vibration acceleration from 2.06% to 4.50%. As the vibration frequency increased, the multiple rate generally trended lessened dropping from 4.30% to 2.60%.

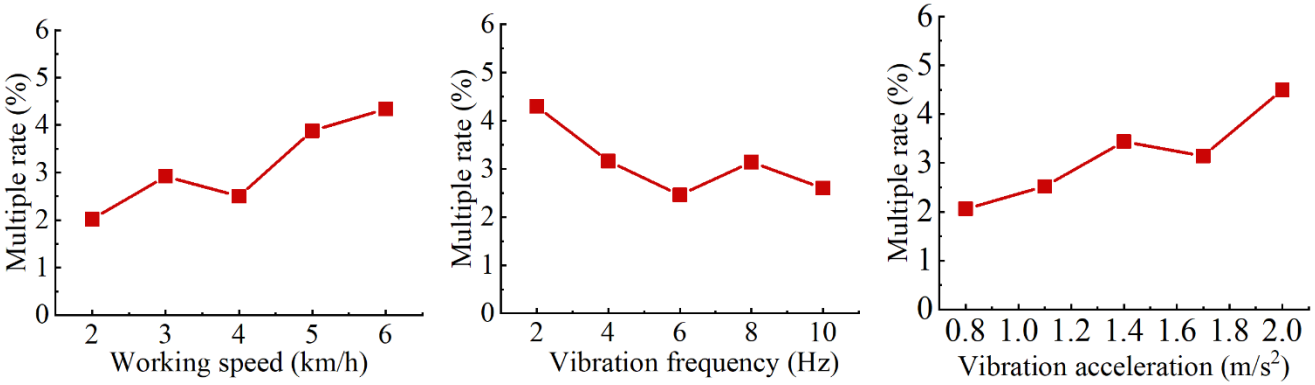

Fig. 9 - Effect of the working speed, vibration frequency, and acceleration on multiple rate

Effect of forward speed, vibration frequency, and acceleration on the leakage rate

The leakage rate of the spoon-wheel seed-metering device exhibits an increasing trend given that the forward speed and vibration acceleration increase, as indicated in Fig. 10. There was a significant fluctuation in the leakage rate, which went from 5.74% to 10.5% with an increase in forward speed, and from 5.44% to 10.86% with a vibration acceleration increase. There was a discernible reduction in the leakage rate as vibration frequency increased from 14.16% to 6.02%.

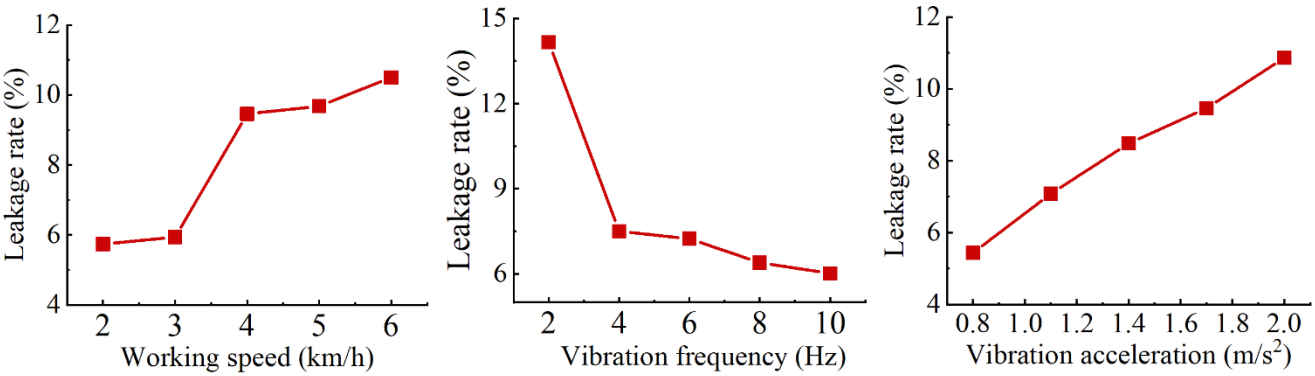

Fig. 10 - Effect of the working speed, vibration frequency, and acceleration on leakage rate

Effect of forward speed, vibration frequency, and acceleration on the variation coefficient

The variation coefficient of the spoon-wheel seed-metering device exhibits an increasing trend when the forward speed and vibration acceleration increase as stated in Fig. 11. With an increase in forward speed, the variation coefficient increases from 23.78% to 34.28%, and from 26.74% to 34.86% with an increase in vibration acceleration, while it decreases from 39.56% to 26.78% with an increment in vibration frequency.

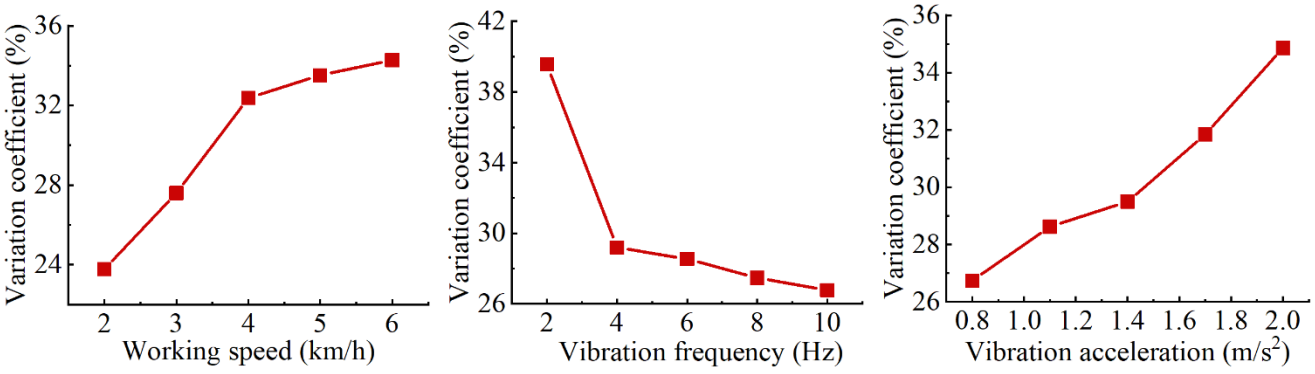

Fig. 11 - Effect of the working speed, vibration frequency, and acceleration on variation coefficient

An extensive assessment of the orthogonal test results revealed that the seeding performance of the spoon-wheel seed-metering device drastically deteriorated with rising forward speed. Which stipulates that the seeds in the spoon hole have a shorter seed-filling and cleaning duration. As a result, the seeds are filled and cleared earlier than they should, thereby boosting the probability of the multiple and leakage seeding. When the vibration acceleration serves as constant, the vertical displacement of the seed-metering device will decrease as the vibration frequency increases since the vibration frequency and acceleration manifest simultaneously. Consequently, the qualified rate increased and the leakage rate dropped as the vibration frequency increased. Leakage seeding occurs when the vibration acceleration increases and the vertical displacement of the seed-metering device increases, the seeds effortlessly break away from the spoon hole during the seed-filling and seed-cleaning processes and fall back to the seed-filling area again. The qualified rate, multiple rate, and leakage rate are strongly related to the variation coefficient. Hence, the variation coefficient will increase with advancements in forward speed and vibration acceleration.

Variance analysis of the orthogonal test

To identify the major and secondary relationships between the contribution of the test factor to the evaluation indicators and the best level, the range analysis of the orthogonal test results is frequently utilized. The results of the orthogonal test were further subjected to variance analysis to ascertain the significance of the impact of the experimental variables on the evaluation indicator. The results of the variance analysis are presented in Table 7.

Table 7

Variance analysis of the three-factor and five-level orthogonal test

Variables	Source of variance	Sum of squares	Df	Mean square	*F*-value	*P*-value	Significance
Qualified rate	*A*	182.57	4	45.64	4.16	0.0024	*
	B	322.35	4	80.59	7.34	0.003	**
	C	179.21	4	44.80	4.08	0.026	*
	Error	131.80	12	10.98			
Multiple rate	*A*	18.498	4	4.625	1.07	0.412	-
	B	10.498	4	2.625	0.61	0.664	-
	C	17.450	4	4.363	1.01	0.440	-
	Error	51.747	12	4.312			
Leakage rate	*A*	101.034	4	25.258	4.55	0.018	*
	B	224.526	4	56.131	10.10	0.001	**
	C	87.966	4	21.991	3.96	0.028	*
	Error	66.673	12	5.556			
Variation coefficient	*A*	401.67	4	100.42	8.37	0.002	**
	B	551.99	4	138.00	11.51	0.000	**
	C	196.50	4	49.13	4.10	0.025	*
	Error	143.90	12	11.99			

**Note: * means significant influence in 95% confidence interval, ** means significant influence in 99% confidence interval, - means no significant influence.*

The deductions of the variance analysis indicated that forward speed had a generally significant influence on the qualified rate and leakage rate, as well as an exceedingly significant influence on the variation coefficient. Vibration frequency had an especially substantial effect on the qualified rate, leakage rate, and variation coefficient, while vibration acceleration typically had a general impact on these three evaluation indicators. There was no discernible influence of the three factors on the multiple rate. Thus, the seed-metering device has to conserve the qualified rate during the actual seeding operation, while minimizing the leakage rate.

CONCLUSIONS

The vibration system model of the seeder in field operation was constructed and theoretically investigated by employing the spoon-wheel seeder as the study object. It is concluded that the quality of the seeding is affected by the construction of the seeder, forward speed, ground roughness, and other variables. The vibration characteristics of the seeder were tested and analyzed at a field speed of around 2 to 6 km/h.

The main conclusions are as follows:

(1) The time-domain investigation implies that the vibration accelerates with the forward speed and that the higher the forward speed, the more vibration it renders with increasing forward speed. The vibration properties of the seed-metering device at various operating speeds were determined through spectrum analysis.

(2) A three-factor and five-level orthogonal test was conducted with the development of a vibration seeding test stand, and the forward speed, vibration frequency, and vibration acceleration as test factors. The results concluded that the forward speed, vibration acceleration, and vibration frequency are the primary and secondary factors influencing the qualified rate of the spoon-wheel seed-metering device.

(3) The qualified rate increased regardless of the vibration frequency and decreased with increasing the forward speed and vibration acceleration. The leakage rate and variation coefficient increased with forward speed and decreased as the vibration frequency improved. The fluctuating trend of the multiple rate is generally consistent with the variation coefficient and the leakage rate.

(4) Both the qualified rate and the leakage rate are significantly impacted by the forward speed, which also has a highly substantial influence on the variation coefficient. The vibration frequency and vibration acceleration exhibited high and general effects on the qualified rate, leakage rate, and variation coefficient, respectively. Concerning the multiple rate, there was no substantial effect of any of the three factors on it. In the event of field vibration, the research in this paper can serve as a reference basis for optimizing and enhancing the spoon-wheel seed-metering device, as well as the seeding quality of the seeder.

ACKNOWLEDGEMENTS

The authors acknowledge the support from the Natural Science Foundation of Sichuan Province (2022NSFSC0138), technological Innovation R&D Projects of Chengdu Science and Technology Bureau (2022YF0501141SN), and the Listing Project of Rural Revitalization Research Institute of Sichuan Tianfu District (XZY1-11).

REFERENCES

[1] Boydas, M. G., Turgut, N. (2007). Effect of vibration, roller design, and seed rates on the seed flow evenness of a studded feed roller. *Applied Engineering in Agriculture*, Vol.23, No.4, pp.413-418. Erzurum/Turkey.

[2] Chen, S., Hou, L., Zhang, S. (2012). Dynamic characteristic analysis and experiment of piezoelectric vibration table of industrialized precision seeding device. *Applied Mechanics and Materials*, Vol.249-250, pp.604-609. Lianyungang/China.

[3] Cheng, J., Li, Y., Chen, J., Liu, Y., Ji, K., Chen, T. (2022). Design and realization of seeding quality monitoring system for air-suction vibrating disc type seed meter. *Processes*, Vol.10, No.9, pp.1745. Zhenjiang/China.

[4] Dong, S., Zhao, M., Zhang, X., Liu, F., Liu, Y. (2015). Air-suction tillage seeder vibration testing and analysis of arable land under corn stock job (气吸式免耕播种机排种装置振动测试及分析). *Journal of Agricultural Mechanization Research*, Vol.37, No.6, pp.181-184. Huhehaote/China.

[5] Emrah, K. (2021). Field-scale evaluation of parameters affecting planter vibration in single seed planting. *Measurement*, Vol.184. lgdir/Turkey.

[6] Gao, W., Lin, J., Li, B., Wang, W., Gu, S. (2022). Vibration characteristics analysis and structural optimization of straw deep bury and returning machine (秸秆深埋还田机振动特性分析与结构优化). *Journal of Jilin University (Engineering and Technology Edition)*, Vol.52, No.4, pp.970-980. Shenyang/China.

[7] Gao, X., Cui, T., Zhou, Z., Yu, Y., Xu, Y., Zhang, D., Song, W. (2021). DEM study of particle motion in novel high-speed seed metering device. *Advanced Powder Technology*, Vol.32, No.5, pp.1438-1449. Beijing/China.

[8] Han, D., He, B., Yang, W., Xu, Y., Lv, X., Zhang, L. (2023). Design and experiment of an integrated air-suction soybean-corn strip intercropping planter (气吸式大豆-玉米带状间作播种机的设计与试验). *Journal of Gansu Agricultural University*, Vol.58, No.4, pp.260-268. Yaan/China.

[9] Han, D., He, B., Zhou, Y., Yang, W., Xu, Y., Zhang, L. (2023). Design and experiment of air suction type dense planting precision seed metering device (气吸式密植精量排种器的设计与试验). *Journal of Huazhong Agricultural University*, Vol.42, No.1, pp.237-247. Yaan/China.

[10] Han, D., Zhang, D., Jing, H., Yang, L., Cui, T., Ding, Y., Wang, Z., Wang, Y., Zhang, T. (2018). DEM-CFD coupling simulation and optimization of an inside-filling air blowing maize precision seed-metering device. *Computers and Electronics in Agriculture*, Vol.150, pp.426-438. Beijing/China.

[11] He, F., Deng, G., Li, M., Niu, Z., You, X. (2019). Design of electromagnetic vibration-type single-bud sugarcane seed metering device. *Sugar Tech*, Vol.21, No.5, pp.815-824. Zhanjiang/China.

[12] Huang, X., Wang, Z., Jiang, X., Zhu, L., Wang, Q., Huang, D. (2019). Vibration Simulation and Experimental Analysis of Picker Finger Seed meter (指夹式排种器振动模拟与试验分析). *Journal of Agricultural Mechanization Research*, Vol.41, No.4, pp.149-153. Changchun/China.

[13] Huang, Y., Han, D., Han, Z, Huang, J., Chen, P., He, B., Zhang, L. (2021). Experiment on the influence of vibration on the seeding performance of the scoop-wheel seed mete (振动对勺轮式排种器排种性能的影响试验). *Journal of Henan Agricultural University*, Vol.55, Vol.5, pp. 896-905. Yaan/China.

[14] Liao, Y., Qi, T., Liao, Q., Zeng, R., Li, C., Gao, L. (2022). Vibration characteristics of pneumatic combined precision rapeseed seeder and its effect on seeding performance (气力式油菜精量联合直播机振动特性及对排种性能影响). *Journal of Jilin University (Engineering and Technology Edition)*, Vol.52, No.4, pp.970-980. Wuhan/China.

[15] Liu, H., Zhou, J., Fang, H., Shi, S., Jian, S., Xu, G . (2019). Vibration analysis of high speed corn seeding machine based on modal analysis (基于模态的玉米高速精密排种器振动特性分析). *Journal of Agricultural Mechanization Research*, Vol.41, No.7, pp.47-52. Jinan/China.

[16] Liu, H., Zhou, J., Zhang, R., Shi, S., Wei, G. (2021). Reliability analysis and verification of vibration test bench for seed meter under vertical vibration excitation (垂直振动激励下排种器振动试验台可靠性分析和验证). *Journal of Agricultural Mechanization Research*, Vol.43, No.8, pp.158-163. Jinan/China.

[17] Liu, Y., Liu, F., Zhao, M., Dong, S., Zhang, X. (2016). Analysis of vibration test and vibration theory of air-suction no-tillage planter (气吸式免耕播种机的振动测试与振动理论分析). *Journal of China Agricultural University*, Vol.21, No.10, pp.109-116. Huhehaote/China.

[18] Liu, Y., Zhao, M., Liu, F., Dong, S., Zhang, X. (2014). Vibration test and analysis of no-tillage planter on the maize stubble surface. *Advanced Materials Research*, Vol.1061-1062, pp.788-793. Huhehaote/China.

[19] Machkarin, A., Ryzhkov, A., Chehunov, O., Makareenko A. (2021) Justification of constructive and technological parameters of vibrating seeding unit. *Engineering for Rural Development*, Vol.20, No.5, pp.26-28. Jelgava/Latvia.

[20] Min, Y. B., Kim, S. T., Kwon, H. D., Moon, S. W., Kang, D. H. (2008). Effect of the seed hopper vibration on the seeding performance of the vacuum suction nozzle seeder. *Journal of Biosystems Engineering*, Vol.33, No.3, pp. 179-185. Gyeongsang/Korea.

[21] Su, W., Chen, Z., Lai, Q., Jia, G., Lv, Q., Tian, B. (2022). Design and test of wheel-spoon type precision seed-metering device for Chinese herbal medicine pinellia ternate (轮勺式半夏精密排种器设计与试验). *Transactions of the Chinese Society for Agricultural Machinery*, Vol.53, No.9, pp.60-71. Kunming/China.

[22] Vishnyakov, A. A., Vishnyakov, A. S., Klak, A. I. (2015). Seeding of rapeseed by the use of vibration sowing device of a seeder. *Tractors and Agricultural Machinery*, Vol.82, No.10, pp.36-39. Krasnoyarsk/Russia.

[23] Wang, Q., Zhu, L., Li, M., Huang, D., Jia, H., Zhuang, J. (2019). Vibration characteristics of corn no-tillage finger-type precision planter and its effect on seeding performance (指夹式玉米免耕精密播种机振动特性及对排种性能的影响). *Transactions of the Chinese Society of Agricultural Engineering*, Vol.35, No.9, pp.9-18. Changchun/China.

[24] Wang, Y., Li, C., Wang, H. (2008). Experimental study on influence of vibration of precision spade punch planter of maize on sowing quality (铲式玉米精密播种机振动对播种质量影响的试验). *Journal of Agricultural Mechanization Research*, No.8, pp.124-126. Shenyang/China.

[25] Wang, Y., Zhao, X., Xu, L., Hou, X. (2013). Application progress of vibration technology in agricultural production (振动技术在农业生产中的应用进展). *Journal of China Agricultural University*, Vol18, No.6, pp. 231-236. Beijing/China.

[26] Wu, F., Li, S., He, Y., Song, M., Ma, F., Teng, X., Liang, Y. (2023). Optimized design and performance of pre-cutting vibrating sugarcane sett metering device. *Sugar Tech*, Vol.25, No.1, pp.210-222. Qinzhou/China.

[27] Wu, W., Chang, C., Li, T, Hu, H., Zhou, Z., Yang, W., Guo, J., Zhu, P., Li, J., Hu, J., Cheng, H., Tao, Y., Zhou W., Deng, F., Chen, Y., Ren, W., Lei, X., (2022). Seed-filling characteristics of a centralized seed-metering device for rapeseed caused by vibration. *Agriculture*, Vol.12, No.7, pp.965. Yaan/China.

[28] Yang, L., Yan, B., Cui, T., Yu, Y., He, X., Liu, Q., Liang, Z., Yin, X., Zhang, D. (2016). Global overview of research progress and development of precision maize planters. *International Journal of Agricultural and Biological Engineering*, Vol.9, No.1, pp.9-26. Beijing/China.

[29] Zhai, C., Long, J., Taylor, R., Weckler, P., Wang, N. (2020). Field scale row unit vibration affecting planting quality. Precision Agriculture, Vol.21, No.3, pp. 589-602. Beijing/China.

[30] Zhang, C., Chen, L., Wu, R. (2016). Simulation analysis of seeding performance of spoon-wheel seed metering device based on the discrete element method (基于离散元法的勺轮式排种器性能仿真分析). *Journal of Anhui Agricultural University*, Vol.43, No.5, pp.848-852. Hefei/China.

[31] Zhang, R., Liu, H., Wei, G., Zhou, J., Shi, S., Li, H., He, T. (2023). Design and test of key components of scoop type precision sorghum seed metering device (勺式高粱精量排种器关键部件设计与试验). *Journal of Agricultural Mechanization Research*, Vol.45, No.12, pp.215-219. Jinan/China.

[32] Zhang, X., Cheng, J., Shi, Z., Wang, M., Fu, H., Wu, H. (2023). Simulation and experiment of seed taking performance of sowing clamp type maize precision seed-metering device (摆动夹取式玉米精量排种器设计与试验). *Transactions of the Chinese Society for Agricultural Machinery*, Vol.54, No.4, pp.38-50. Wulumuqi/China.

[33] Zhang, X., Li, C., Li, J., Zhou, M. (2014). Mathematic vibration model of spade punch planter of maize (铲式玉米精密播种机振动特性模型建立与试验). *Transactions of the Chinese Society for Agricultural Machinery*, Vol.45, No.2, pp.88-93. Changchun/China.

[34] Zhang, X., Liu, F., Dong, S., Liu, Y., Zhao, M. (2015). Experimental study on the vibration air-suction no tillage planter metering device (基于 MATLAB 对免耕播种机排种装置振动的试验研究). *Journal of Chinese Agricultural Mechanization*, Vol.36, No.6, pp19-21+31. Huhehaote/China.

[35] Zhang, X., Zhao, M., Liu, F., Dong, S., Liu, Y. (2014). Vibration analysis based on the mathematical model of the air-suction device tillage seeder seeding. *Advanced Materials Research*, Vol.1061-1062, pp.794-798. Huhehaote/China.

[36] Zhao, M., Hu, Y., Liu, Y. (2012). Measurement and analysis on vibration characteristics of pneumatic seed metering device of no-till seeder. *Transactions of the Chinese Society of Agricultural Engineering*, Vol.28, No.S2, pp.78-83. Huhehaote/China.

[37] Zheng, J., Liao, Y., Qi, T., Liao, Y., Gao, L., Liu, J. (2023). Effect of vibration on performance of pneumatic rapeseed precision metering device (振动对气力式油菜精量排种器性能影响). *Journal of Huazhong Agricultural University*, Vol.42, No.2, pp.233-242. Wuhan/China.

[38] Zheng, K., Liu, G., Xia, J., Liu, B., Xu, L., Cheng, J., Li, D. (2020). Application of vibration technology in tillage, seeding and harvesting machinery: a review (振动技术在耕种收机械中的应用研究进展与展望). *Acta Agriculturae Universitatis Jiangxiensis*, Vol.42, No.5, pp.1067-1077. Wuhan/China.

PARAMETER CALIBRATION FOR DISCRETE ELEMENT SIMULATION OF CUTTING DECK CLEANING IN SMALL PLOT WHEAT COMBINE HARVESTER
/
小区小麦联合收获机割台清理离散元仿真参数标定

Jian ZHANG[1,2], Yong DING[1], Ranbing YANG[1,2], Zhiguo PAN*[1], Jie MU[1], Weijing WANG[1], Qi LIU[1], Shuai WANG[1]
[1] College of Mechanical and Electrical Engineering, Qingdao Agricultural University, Qingdao 266109, China
[2] College of Mechanical and Electrical Engineering, Hainan University, Haikou 570228, China.
Tel: +8613963922295; E-mail: 13963922295@163.com
DOI: https://doi.org/10.35633/inmateh-72-31

Keywords: *Plot harvesting; Stacking corners; Parameter optimization; Regression equations; Stiffness factor;*

ABSTRACT
The analysis of the clearing process of the cutting deck of a small plot wheat combine harvester requires the use of discrete element simulation methods. However, the current simulation test lacks the contact parameters such as wheat stalk and stalk-seed. In this paper, the wheat stalks and seeds at harvest time were taken as the research objects, and the calibration study of the discrete element simulation model parameters of stalks and stalk-seeds was carried out by means of mechanical test determination and EDEM software simulation. The stiffness coefficients of wheat stalks were determined by mechanical tests; the average values of wheat stalk stacking angle of 39.22° and wheat stalk-seed stacking angle of 44.41° were obtained by stacking angle tests. By the steepest climb test and binary regression test, the stalk normal stiffness coefficient was determined to be 5e+08N/m2 and tangential stiffness was determined to be 6.35e+08N/m2; the stalk-stalk collision recovery coefficient was obtained to be 0.551, static friction coefficient was obtained to be 0.797, and rolling friction coefficient was obtained to be 0.079 by the two-level analytical factorization test, the steepest climb test, and the three-factor response surface test. Based on this, the average value of wheat stalk-seed stacking angle was obtained to be 39.22° and the average value of wheat stalk-seed stacking angle was obtained to be 44.41° by the stacking angle test. On this basis, the coefficient of recovery of stalk-stalk collision was 0.434, the coefficient of static friction was 0.884, and the coefficient of rolling friction was 0.339 obtained by the three-factor response surface test. Three validation experiments were carried out by substituting the obtained parameters into the simulation test, and the error values were close to the error value %0.255 in the model, which proved that the experimental data were reliable.

摘 要
小区小麦联合收获机割台清理过程的分析需要使用离散元仿真方法。但目前仿真试验缺乏小麦茎秆、茎秆-籽粒等接触参数。本文以收获期的小麦茎秆、籽粒为研究对象，通过力学试验测定和EDEM软件仿真的方式对茎秆和茎秆-籽粒的离散元仿真模型参数展开标定研究。通过力学试验测定了小麦茎秆的刚度系数；通过堆积角试验，得到小麦茎秆堆积角的平均值为 39.22°及小麦茎秆-籽粒堆积角的平均值为 44.41°。通过最陡爬坡试验和二元回归试验，确定了茎秆法向刚度系数为 5e+08N/m2 和切向刚度为 6.35e+08N/m2；通过二水平析因试验、最陡爬坡试验和三因素响应曲面试验获得了茎秆-茎秆的碰撞恢复系数为 0.551、静摩擦系数为 0.797、滚动摩擦系数为 0.079；在此基础上，通过三因素曲面响应试验获得了茎秆-籽粒的碰撞恢复系数为 0.434、静摩擦系数为 0.884、滚动摩擦系数为 0.339。将得到参数代入仿真试验中进行三次验证实验，误差值接近模型中的误差值%0.255，证明试验数据可靠。

INTRODUCTION
When the small plot wheat combine harvester works, it is required to realize no material residue, and to solve the problem of material residue on the cutting platform of the combine harvester, it is necessary to study the movement law of wheat harvesting material in the combine harvester *(Li., 2022)*, and to establish a more accurate discrete element simulation model.

[1] *Jian ZHANG, Prof.Ph.D.Eng; Yong DING, Ph.D.Stud.Eng; Ranbing YANG, Prof.Ph.D.Eng, Zhiguo PAN*, Prof.Ph.D.Eng; Jie MU, Ph.D. Stud.Eng; Weijing WANG, Ph.D. Stud.Eng; Qi LIU, Ph.D. Stud.Eng; Shuai WANG, Ph.D. Stud.Eng;*

The discrete element method is a numerical simulation method that can accurately describe the discontinuous nature of the flow of material particles *(Carr et al., 2023)*, so as to reveal the internal mechanism of action and shorten the research period. When discrete element simulation is carried out, the relevant parameters are usually obtained by means of direct measurement method and virtual calibration, and for some parameters that are difficult to be measured directly, they need to be obtained by means of calibration *(Liu et al., 2021).* The soybean intrinsic parameters as well as the contact parameters between soybean and seed expeller were calibrated by Tao Zhang et al. *Li Jinguang et al*. obtained the mechanical property parameters of the main root system of spinach by compression test, and derived the normal and tangential stiffness coefficients of the root system *(Dai et al., 2023)*. Ucgul et al. integrated the linear adhesion cohesive model into the linear Hysteretic Spring model to obtain the soil static friction factor, rolling friction factor and recovery coefficient similar to the actual angle of repose *(Ucgul et al., 2014)*. Fanyi et al. proposed a nonlinear contact model based on DEMeter++ software to characterize the plastic characteristics between stems, but it could not characterize the viscosity effects of stems with different compression degrees *(Fanyi et al., 2018)*. Thakur et al. proposed the Edinburgh Elasto-Plastic Adhesion (EEPA) contact model, which is based on Hertz's contact theory and extends to include the elastoplastic and viscous properties of the particle contact model *(Thakur et al., 2014)*. Park et al. measured the angle of repose and the number of remaining particles of garlic particles experimentally, and derived the friction factor between particles by using the swing arm method *(Park et al., 2021)*.

In this paper, the wheat stalks in harvest season were taken as the research object, and EDEM simulation software was used as the test platform. By using the loading force obtained in the three-point bending physical test of the stalk as the reference value, the test was conducted in EDEM with the loading force in the three-point bending simulation as the target value *(Wang et al., 2021)*. The factor intervals were narrowed down by the steepest climb test, and then the normal/tangential stiffness coefficients of the stalks were obtained by binary regression test *(Ni et al., 2022)*; the stacking angle of the stalk particles was obtained by the stalk particle cylinder lifting test, and with this as the target value the two-level analytical factorization test based on the cylinder lifting test, the steepest climb test, and the three-factor response surface test were carried out in the EDEM, and the factors influencing the stacking angle and the contact parameters between the stalks; the stacking angle of the mixture was obtained by performing cylinder lifting test on the stalk and seed mixture *(Li et al., 2021)*, and a three-factor surface response test was conducted with this objective value to obtain the contact parameters between the stalks and the seeds. This study provides basic parameters for the discrete element simulation study of wheat harvesting, and provides a modelling method and parameter calibration method for the discrete element simulation analysis of the material motion process of the cutting platform.

MATERIALS AND METHODS

Determination of parameters

- **Wheat stem eigen parameters**

Selected the wheat at the crown of the year as the experimental subject, and volume of leaves shrinked due to lossing of water during the harvesting process but this shrinkage had litte impact on the experiment results, so leaves were removed during the experiment. After measuring 300 stalks by vernier callipers, the mean length was 632.32 mm, the standard deviation of length was 8.23, the mean diameter was 4.45 mm, the standard deviation of diameter was 1.07; and the mean density of stalks was 1.642 g/cm by overflow method.

- **Three-point bending physical tests**

The mechanical properties of wheat stalks have a large impact on the operational performance of harvesting machinery. In order to establish the discrete elemental model of the wheat cutter harvester at a later stage, it is necessary to know the normal and tangential stiffness of the wheat stalk. Therefore, the three-point bending test was chosen to determine the loading pressure of the stalk under 0.5 mm bending deflection, and then the three-point bending test was simulated in EDEM at a later stage to explore the loading force under the same bending deflection, and when the loading force is the same, the normal and tangential stiffness of the wheat stalks can be obtained.

In order to generalize the data collected to represent the relevant physical characteristics of the wheat plant, a sample of 10 wheat stalks with strong growth was used for the selection prior to the three-point bending test. The stalks were measured and the diameter and cross-sectional area were calculated.

Test process: the three-point bending device support frame is fixed to the universal test bench under the fixture, the indenter is fixed to the fixture on the test bench, adjust the spacing of the support frame for 150mm, the upper indenter will be lowered to the lower fixture above the 5 mm (leaving the width occupied by the diameter of the stalks) .The stalks are loaded at a speed of 10mm/min for 2min, and the computer will record the experimental data automatically. The experiment is conducted ten times and get the average loading force 6.91N.

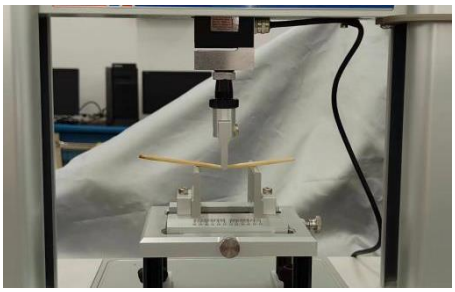

Fig. 1 - Three-point bending physical test

- **Angle of accumulation of stalks**

Wheat stalk stacking angle is the cone of stacking of stalk segments of 20 mm length in the natural state, which is an important indicator of the friction between materials and provides basic data for stalk discrete element modelling *(Tong et al., 2023)*.

The cylinder lifting method was used to measure the stacking angle of the stem samples in this study. Test method: a hollow cylinder with the top and bottom removed was placed on the test bench, the stalk sample was slowly injected into the cylinder from the top of the cylinder, and then the cylinder was rapidly lifted vertically upward so that the stalks naturally collapsed into a conical shape under the action of gravity to form the stacking angle, which was then measured using a protractor *(Liao et al., 2020)*. The test was carried out 10 times, and the average value of the particle stacking angle of stalks and seeds was obtained as 39.08°.

- **Angle of accumulation of stalk-seed mixtures**

The stacking angle of stalk-seed was obtained by using a mixed stacking of stalk particles and seeds, and the stalk-seed contact parameters were solved using the stacking angle as the target value. Test: The stalks were cut into small segments of 20 mm in length, and the number of samples of small segments of stalks was 100. Bran and impurities were removed from the seeds and 200 g of wheat seeds were weighed. The seeds and stalks were thoroughly mixed in a dry beaker and poured into a hollow cylinder, which was quickly lifted vertically upwards, and the mixed pile rapidly collapsed into a cone *(Gao., 2019)*. The test was conducted 10 times and the average value of stacking angle was obtained as 44.63°. The test procedure is shown in Fig.2.

(a) Angle of wheat stalk accumulation

(b) Accumulation angle of mixed materials between wheat grains and wheat straw

Fig. 2 - Material accumulation angle test

SIMULATION MODEL

Simulation model of three-point bending of stem

Due to the bending deformation of the wheat stalk during the downward pressure by the pivot wheel during harvesting, it is necessary to model the wheat stalk as a flexible body by adopting the Hertz-Mindlin (no slip) and Bonding model, and the particles in the model of the wheat stalk are connected by Bonding bonds, which gives the model flexible body qualities by inputting the appropriate normal and tangential stiffness coefficients. The model is made flexible by inputting appropriate normal and tangential stiffness coefficients.

Create a three-point bracket model in Solid Works, export it to *stl* format and then import it into EDEM software *(Liu., 2021)*, set the particle radius to 0.5 mm, the contact radius to 0.62 mm, the stem length to 250 mm, and the stem radius to 4.25 mm. Set up the particle factory on the left side of the cylinder's circular surface, adjust the gravity to the negative direction of the lateral X-axis so that the particles are moving to the right side, and fill the particles as 5000, generating 2500 particles per second, and the generation is completed in 1 second. Set the bond key to be generated at 1.1 s, and make the loading column move downward at a uniform speed at 1.2 s, the loading speed of the loading column is 10 mm/s, the loading time is 4 s, and the total time of simulation is 5.2 s.

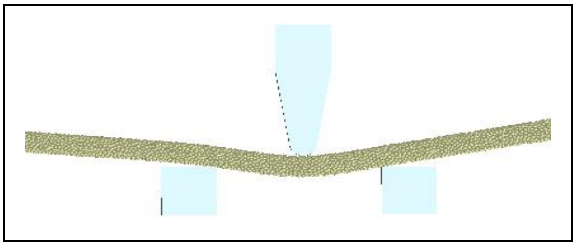

Fig. 3 - Three-point bending simulation test process

Simulation modelling of stem particle stacking angle

In EDEM, the Hertz-Mindlin model is selected for the wheat stalk cylinder lifting simulation test, as a way to calculate the force and motion process between wheat stalk and stalk, and decompose the force and motion process between wheat stalk particles into normal motion, tangential motion and rolling motion *(Wang et al., 2021)*. The wheat stalks are in cylinder shape, so several spherical particles were put together in one direction to get the closest physical experiment situation, see fig 5, and radius of the spherical particle is set to 2.15mm, so that nine combined spherical particles could become a 20mm approximate cylinder and then use this kind of combined spherical particles to conduct pile angle simulation experiment and simulate how the wheat stalks pile under cylinder lifting experiment. Combined with the simulation parameters of the wheat material in the discrete element simulation, the range of variation of the simulation parameters in this study was determined as shown in Table 1.

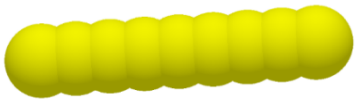

Fig. 4 - Wheat stalk granular pattern

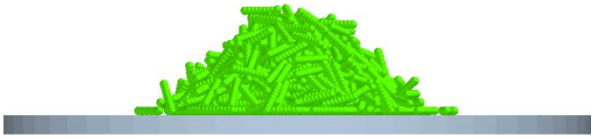

Fig. 5 - Simulation test of stem particle cylinder lifting

Table 1

Simulation parameter value list

Simulation parameters	numerical value
Stem density/(kg/m^3)	1642a
Stem Poisson's ratio	0.4b
Stem shear modulus/MPa	5.52e+06a
Density of steel/(kg/m^3)	7810b
Poisson's ratio of steel	0.3b
Steel shear modulus/MPa	2.07e+11b
Stalk-stalk collision recovery coefficient x_1	0.1-0.4c
Coefficient of static friction of stalk-stalk x_2	0.3-0.5c
Coefficient of rolling friction of stalk-stalk x_3	0.05-0.15c
Stem-steel collision recovery coefficient x_4	0.3-0.7c
Static friction coefficient of stem-steel x_5	0.14-0.20c
Rolling friction coefficient of stem-steel x_6	0.05-0.15c

Note: Item a is determined experimentally, item b is obtained from the literature, and item c is the experimental variable, the range of which is the upper and lower limits of the value of the variable, the same as below.

Simulation model of stalk-seed mixture stacking angle

The Hertz-Mindlin model was used to model the seed particles. As shown in Fig.6, the seed grain models were all simplified to elliptical shapes to improve the simulation efficiency.

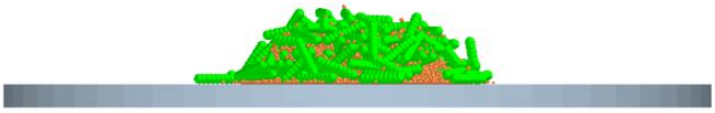

Fig. 6 - Cylinder lifting test of soil and stem mixed materials

Table 2

Parameter List of Cylinder Lifting Simulation Test for Straw and grains Mixed Materials

Simulation parameters	Numerical value
Stalk density/(kg/m^3)	1642
stem Poisson's ratio	0.4
Stem shear modulus/MPa	5.52e+06
Density of steel/(kg/m^3)	7810
Poisson's ratio of steel	0.3
Steel shear modulus/MPa	2.07e+11
Stalk-stalk collision recovery coefficients	0.551
Coefficient of static friction of stalk-stalk	0.797
Coefficient of rolling friction of stalk-stalk	0.079
Collision recovery coefficients for stalk-steel	0.5
Static friction coefficient of stalk-steel	0.7
Rolling friction coefficient of stalk-steel	0.1
Stalk-seed collision recovery coefficient x_7	0.3-0.7
Static friction coefficient of stalk-seed x_8	0.5-0.9
Rolling friction coefficient of stalk-seed x_9	0.3-0.6

Some of the parameters in the table have been obtained by investigating the literature, physical tests, and stalk stacking calibration tests, but the collision recovery coefficients of stalk-seed x_7, static friction coefficients of stalk-seed x_8, and rolling friction coefficients of stalk-seed x_9 are still lacking, so the range intervals in which the values are located were determined by reviewing the literature, and then the specific values were obtained by calibrating them.

RESULTS

Stem stiffness coefficient calibration

(1) Selection of test factor level range: According to the existing research on wheat stalks, there is no exact value for the stiffness coefficient of wheat stalks, which is due to the different varieties of the samples used and the differences between the individuals of the samples used; therefore, this study combines the data of the previous researchers, and determines the normal stiffness value of wheat stalks, x_{10} , and the tangential stiffness value of wheat stalks, x_{11} , between 1e+ 08N/m2 to 1.1e+09N/m2 .

Table 3

Test factor level

level (of	1	2	3	4	5	6
numerical	1e+08	3e+08	5e+08	7e+08	9e+08	1.1e+09

(2) Steepest Climbing Test: Since x_{10} and x_{11} are stiffness coefficients, the loading force is bound to increase with the increase of stiffness coefficients, so design the stiffness coefficients incrementally, and record and observe the error value between the loading force and the loading force in the physical test *(Yuan et al., 2020)*.

The steepest climb test design and results are shown in Table 4, from which it can be seen that as the stiffness factor increases, the relative error value of the loading force compared to the physical test results decreases and then increases, so the optimum value of the stiffness factor should be between the test parameters of the 3rd and 4th sets of tests.

Table 4

Design and results of the steepest climbing test

serial number	x10	x11	Loading force (N)	relative error
1	1e+08	1e+08	0.493	27.82%
2	3e+08	3e+08	0.567	16.98%
3	5e+08	5e+08	0.635	7.03%
4	7e+08	7e+08	0.712	4.25%
5	9e+08	9e+08	0.793	16.11%
6	1.1e+09	1.1e+09	0.879	28.7%

(3) Binary regression test: from the results of the steepest climbing test data, the range of stiffness coefficient is narrowed from 1e+08N/m^2 to 1.1e+0.9N/m2 to 5e+08N/m^2 to 7e+08N/m^2, in order to obtain the specific value of the stiffness coefficient, the corresponding functional relationship between the stiffness coefficient and loading force is obtained through the two-factor, three-level binary regression test and then the specific value is obtained through the inverse function. In order to obtain the specific value of the stiffness coefficient, the corresponding functional relationship between the stiffness coefficient and loading force was obtained by two-factor three-level binary regression test. The test design and results are shown in Table 5.

Table 5

Design and results of a binary regression experiment

Test number	x_{10}	x_{11}	error value
1	-1	-1	3.03
2	1	-1	1.28
3	-1	1	0.3
4	1	1	7.03
5	-r	0	1.11
6	r	0	3.93
7	0	-r	2.24
8	0	r	3.67
9	0	0	0.18
10	0	0	0.19
11	0	0	0.2
12	0	0	0.19
13	0	0	0.19

The two-factor, three-level binary regression simulation test conducted to solve the wheat stem stiffness coefficient was analysed by ANOVA as shown in Table 6, and the P-value of the model was <0.0001, indicating that the model had a good fit. The P-values of the two main terms x_{10} and x_{11} are <0.0001, indicating that the two main terms are significant. The interaction term $x_{10}x_{11}$ has a p-value <0.0001 and the interaction term is significant. P-value for both squared terms x_{10}^2 and x_{11}^2 < 0.0001 indicating that both squared terms are significant.

Table 6

Analysis of variance in binary regression tests

items	square sum (e.g. equation of squares)	(number of) degrees of freedom (physics)	mean square and	P-value	F-value
mould	52.74	5	10.55	240.42	<0.0001
x_{10}	10.05	1	10.05	229.14	<0.0001
x_{11}	3.18	1	3.18	72.44	<0.0001
$x_{11}x_{12}$	17.98	1	17.98	409.75	<0.0001
x_{10}^2	10.15	1	10.15	231.42	<0.0001
x_{11}^2	14.14	1	14.14	322.25	<0.0001
pure error	0.0002	4	0.0001		

The regression equation for the actual value was obtained through a binary regression test:

$$R_1 = 160.8172 - 2.6097x_{10} - 2.9197x_{11} + 2.12x_{10}x_{11} + 1.2081x_{10}^{\ 2} + 1.4256x_{11}^{\ 2} \quad (1)$$

The minimum value of the function is found to be 0.07, when x10 is 5e+08N/m^2 and x11 is 6.35e+08N/m^2.

Calibration of stalk-stalk contact parameters

For discrete element simulation of wheat harvesting, the stalk-seed contact parameter needs to be input, but this parameter is difficult to obtain directly, and the stalk-seed contact parameter can be obtained by subjecting the mixture material of stalks and seeds to a calibration test based on the lifting of discrete element cylinders. However, the stalk-to-stalk contact parameter is needed for the stacking simulation test of the mixture material, so the stacking calibration test of the stalk particles needs to be performed first. The test index is the stacking angle, the value of the angle is measured by physical test and the angle measured by physical test is used as the target value in the calibration test *(Zhang et al., 2023)*.

(1) Two level factorial test: the basic contact parameters affecting the stacking angle of stalk particles in the test included six factors: collision recovery coefficient of stalk-stalk x_1 , static friction coefficient of stalk-stalk x_2 , rolling friction coefficient of stalk-stalk x_3 , collision recovery coefficient of stalk-steel x_4 , static friction coefficient of stalk-steel x_5 , rolling friction coefficient of stalk-steel x_6 , and the factors were ranked in order of significance by the two-level factorial test.

The contribution of the factors and whether they were significant or not was determined by a two-level analytic factorization test. The simulation test factors and levels are shown in Table 7 and the simulation test design and results are shown in Table 8.

Table 7

Factors and level selection of two-level factorial test

Considerations	Level (of achievement etc.)	
	-1	1
Stalk-stalk collision recovery coefficient x_1	0.3	0.7
Coefficient of static friction of stalk-stalk x_2	0.5	0.9
Coefficient of rolling friction of stalk-stalk x_3	0.05	0.15
Stem-steel collision recovery coefficient x_4	0.3	0.7
Static friction coefficient of stem-steel x_5	0.5	0.9
Rolling friction coefficient of stem-steel x_6	0.05	0.15

Table 8

Two-level factorial experimental design and results

Serial number	x_1	x_2	x_3	x_4	x_5	x_6	Stacking angle (°)
1	0.3	0.5	0.05	0.3	0.5	0.05	39.43
2	0.7	0.5	0.05	0.3	0.9	0.05	36.09
3	0.3	0.9	0.05	0.3	0.9	0.15	43.31
4	0.7	0.9	0.05	0.3	0.5	0.15	42.71
5	0.3	0.5	0.15	0.3	0.9	0.15	42.21
6	0.7	0.5	0.15	0.3	0.5	0.15	42.4
7	0.3	0.9	0.15	0.3	0.5	0.05	46.93
8	0.7	0.9	0.15	0.3	0.9	0.05	41.16
9	0.3	0.5	0.05	0.7	0.5	0.15	38.01
10	0.7	0.5	0.05	0.7	0.9	0.15	33.69
11	0.3	0.9	0.05	0.7	0.9	0.05	51.80
12	0.7	0.9	0.05	0.7	0.5	0.05	36.12
13	0.3	0.5	0.15	0.7	0.9	0.05	45.47
14	0.7	0.5	0.15	0.7	0.5	0.05	47.46
15	0.3	0.9	0.15	0.7	0.5	0.15	44.40
16	0.7	0.9	0.15	0.7	0.9	0.15	48.01

Table 9 was obtained through the analysis function that comes with the Design-Expert software, from which the significant degree of the effect of each test factor on the stalk accumulation angle can be obtained, and the order of the influence of each factor on the wheat stalk accumulation angle from the largest to the smallest is as follows: the rolling friction coefficient of stalk-stalk x_3, the static friction coefficient of stalk-stalk x_2, the collision recovery coefficient of stalk-stalk x_1 , collision recovery coefficient of stalk-steel x_4, rolling friction coefficient of stalk-steel x_6, and static friction coefficient of stalk-steel x_5, among which, collision recovery coefficient of stalk-steel x_4, rolling friction coefficient of stalk-steel x_6, and static friction coefficient of stalk-steel x_5 had lower influence rates of 1.97%, 1.62%, and 0.31%, respectively.

Table 9

Significance Analysis of Parameters in Two Level Factorial Test

Parameters	Effect	Mean square	Impact rate / %	Order of significance
x1	-2.99	35.76	9.8	3
x2	3.71	55.06	15.08	2
x3	4.61	85.01	23.29	1
x4	1.34	7.18	1.97	4
x5	0.54	1.14	0.31	6
x6	-1.22	5.9	1.62	5

(2) Steepest-climbing test: the steepest-climbing test can quickly narrow down the range of values of the test factors and improve the accuracy of the regression model established by the response surface test *(Zhang et al., 2023)*. The significant factors affecting the stacking angle of wheat stalks were rolling friction coefficient of stalk-stalk x_3, static friction coefficient of stalk-stalk x_2, and collision recovery coefficient of stalk-stalk x_1, with the value ranges of 0.05-0.15, 0.5-0.9, and 0.3-0.7, respectively, and equated to five gradients for the steepest-climbing test, whereas the collision recovery coefficient of stalk-steel x_4, the stalk-steel static friction coefficient x_5, and rolling friction coefficient x_6 of stalk-steel do not have a significant effect on the test results, so the intermediate values are taken directly during the test *(Hongcheng et al., 2022)*, which are x_4 (0.5), x_5 (0.7), and x_6 (0.1), respectively.

The design of the steepest climb test and the results of the test are shown in Table 10, the optimum value should be in the vicinity of the 3rd group of tests, and the range of the selection of the factors was set between the 2nd and 4th groups, x_1 (0.4 to 0.6), x_2 (0.6 to 0.8), and x_3 (0.075 to 0.125).

Table 10

Design and results of the steepest climbing test

Serial number	1	x2	x3	Stacking angle θ_{stalk} / (°)	Relative error $\delta_{\theta stalk}$ / %
1	0.3	0.5	0.05	45.19	15.63%
2	0.4	0.6	0.075	34.24	12.38%
3	0.5	0.7	0.1	37.12	5.02%
4	0.6	0.8	0.125	43.05	10.24%
5	0.7	0.9	0.15	45.79	17.17%

(3) Three-factor surface response test: According to the two-level analytical factorization test, the significant factors affecting the stalk-stalk stacking angle were determined to be the collision recovery coefficient of stalk-steel x_4 , the static friction coefficient of stalk-steel x_5 , and the rolling friction coefficient of stalk-steel x_6 , and the range of values of the factors were determined to be based on the results of the steepest-climbing test), x_2 (low level 0.6, zero level 0.7, high level 0.8), x_3 (low level 0.075, zero level 0.1, high level 0.125). The experiment was conducted 17 times and the experimental design and results are shown in Table 11.

Table 11

Three factor response surface experimental design and results

Serial number	x1	x2	x3	Stacking angle θ_{stalk}/°	Relative error $\delta_{\theta stalk}$ / %
1	0.4	0.6	0.1	42.18	7.93
2	0.6	0.6	0.1	46.85	19.88
3	0.4	0.8	0.1	43.57	11.49
4	0.6	0.8	0.1	40.12	2.66

Serial number	x1	x2	x3	Stacking angle θ stalk/°	Relative error δθstalk / %
5	0.4	0.7	0.075	41.56	6.35
6	0.6	0.7	0.075	41.59	6.42
7	0.4	0.7	0.125	44.23	13.18
8	0.6	0.7	0.125	44.59	14.1
9	0.5	0.6	0.075	45.93	17.53
10	0.5	0.8	0.075	37.63	3.71
11	0.5	0.6	0.125	42.65	9.14
12	0.5	0.8	0.125	45.66	16.84
13	0.5	0.7	0.1	42.96	9.93
14	0.5	0.7	0.1	43.10	10.29
15	0.5	0.7	0.1	43.36	10.95
16	0.5	0.7	0.1	42.86	9.67
17	0.5	0.7	0.1	43.02	10.08

The ANOVA of the simulation test is shown in Table 12, the P-value of the model <0.0001 indicates that the model has a good fit; the P-value of x_1 is 0.04, the P-value of both x_2 and x_3 is <0.0001, and the P-values of the three main terms are less than 0.05, which indicates that the three main terms are significant; the P-values of the interaction terms, x_1x_2, and x_2x_3 are less than 0.05, which indicates that they are significant, and the P-value of the squared term, x_1x_3 P-value of x_1x_3 is 0.4756 indicating that it is not significant; P-value of squared terms x_{12} and x_{22} is more than 0.5 indicating that it is not significant and P-value of squared term x_{32} is less than 0.5 indicating that it is significant.

Table 12

Analysis of variance in three factor response surface test

Source of variance	degrees of freedom	mean square	F	P
mould	9	8.51	177.66	<0.0001
x_1	1	0.32	6.76	0.04
x_2	1	14.12	294.77	<0.0001
x_3	1	13.57	238.24	<0.0001
x_1x_2	1	16.48	344.00	<0.0001
x_1x_3	1	0.03	0.57	0.4756
x_2x_3	1	31.98	667.37	<0.0001
x_{12}	1	0.02	0.46	0.5186
x_{22}	1	0.01	0.20	0.6696
x_{32}	1	0.08	1.72	0.2308
residual	7	0.05		
lost proposal	3	0.06	1.79	0.2883
pure error	4	0.04		
aggregate	16			

The optimized regression equation is based on ensuring that the model is significant and the out-of-fit term is not significant, and removing the insignificant terms:

$$\theta_{stalk} = 52.19 + 144.11x_1 - 24.89x_2 - 696.93x_3 - 203x_1x_2 + 1131x_2x_3 - 213.33x_3^2 \quad (2)$$

Through the regression equation obtained from the above test, it is difficult to get directly the values of x_1, x_2, x_3 respectively under the target value obtained from the physical test, so the stacking angle error value for the target value is analysed for the corresponding surface analysis, and the equation obtained is as follows:

$$\delta_{\theta stalk} = 30.34 + 434.61x_1 - 127.07x_2 - 1635.61x_3 - 519.5x_1x_2 + 85x_1x_3 + 2152x_2x_3 - 74.33x_1^2 + 104.93x_2^2 + 914.8x_3^2 \quad (3)$$

Taking the stacking angle as a function of 39.08°, the stalk-stalk contact parameters were obtained as: x_1 =0.551, x_2 =0.797, x_3 =0.079, at which time the error δ_θ was 0.255%.

Stem stacking angle validation test

The optimal parameter solutions obtained after optimization of the three-factor surface response design test were substituted into the EDEM simulation model for simulation validation test. The simulation parameters were set as follows: the collision recovery coefficient of stalk-stalk was 0.551, the static friction coefficient of stalk-stalk was 0.797, and the rolling friction coefficient of stalk-stalk was 0.079, and all other non-significant factors were taken to be the middle of the corresponding range of factors. The validation test was conducted three times and the mean value of stacking angle was obtained as 39.22°, at which point the error value was 0.358%. It is close to the error value of 0.255% in the model, indicating that the test data are reliable.

Calibration of stalk-seed contact parameters

(1) Parameter setting: the contact parameters between the stalks have been obtained through the study in the previous section and hence the parameters have been set in the table below for the cylinder lifting simulation tests on the stalk-seed mixtures:

Table 13

Parameter List of Cylinder Lifting Simulation Test for Straw and Soil Mixed Materials

Simulation parameters	Numerical value
Stalk density/(kg/m^3)	1642
Stem Poisson's ratio	0.4
Stem shear modulus/MPa	5.52e+06
Density of steel/(kg/m^3)	7810
Poisson's ratio of steel	0.3
Steel shear modulus/MPa	2.07e+11
Stalk-stalk collision recovery coefficients	0.551
Coefficient of static friction of stalk-stalk	0.797
Coefficient of rolling friction of stalk-stalk	0.079
Collision recovery coefficients for stalk-steel	0.5
Static friction coefficient of stalk-steel	0.7
Rolling friction coefficient of stalk-steel	0.1
Stalk-seed collision recovery coefficient x_7	0.3-0.7
Static friction coefficient of stalk-seed x_8	0.5-0.9
Rolling friction coefficient of stalk-seed x_9	0.3-0.6

Some of the parameters in the table have been obtained by investigating the literature, physical tests, and stalk stacking calibration tests, but the collision recovery coefficient of stalk-seed x_7 , the static friction coefficient of stalk-seed x_8 , and the rolling friction coefficient of stalk-seed x_9 are still lacking, therefore, in combination with the relevant parameters obtained in the previous section, the range interval in which the values are located is determined by consulting the literature, and then the specific values are obtained by calibration.

(2) Three-factor surface response test: Design-Expert software was used to design the three-factor surface response test and establish the regression model, and the test design and results are shown in Table 14.

Table 14

Three factor and three level experimental design and results

Serial number	x_7	x_8	x_9	stacking angle $\theta_{Stalks\ -\ Seeds}$/°	relative error $\delta_{\theta Stalks\ -\ Seeds}$ / %
1	0.3	0.7	0.6	44.82	0.43
2	0.5	0.7	0.45	43.63	2.24

Serial number	x_7	x_8	x_9	stacking angle $\theta_{Stalks - Seeds}$/°	relative error $\delta_{\theta Stalks - Seeds}$ / %
3	0.5	0.9	0.6	45.47	1.88
4	0.3	0.5	0.45	43.03	3.59
5	0.5	0.7	0.45	43.66	2.17
6	0.7	0.5	0.45	41.53	6.95
7	0.5	0.5	0.3	41.85	6.23
8	0.5	0.7	0.45	43.81	1.84
9	0.7	0.9	0.45	44.19	0.99
10	0.5	0.9	0.3	44.23	0.9
11	0.3	0.7	0.3	43.83	1.79
12	0.7	0.7	0.3	42.19	5.47
13	0.5	0.7	0.45	43.81	1.84
14	0.7	0.7	0.6	43.42	2.71
15	0.3	0.9	0.45	45.68	2.35
16	0.5	0.5	0.6	42.78	4.15
17	0.5	0.7	0.45	43.81	1.84

The response surface test was conducted and the test results were fitted by Design-Expert software, and the coefficient of determination R^2 of the model was obtained to be 0.9980, which indicated a high degree of fit; the fitted regression model was:

$$\theta_{stalk\text{-}seed} = 43.74 - 0.7538x_7 + 1.3x_8 + 0.5488x_9 + 0.0025x_7x_8 + 0.06x_7x_9 + 0.0775x_8x_9 - 0.077x_7^2 - 0.0595x_8^2 - 0.102x_9^2 \quad (4)$$

The analysis of variance (ANOVA) of the simulation test is shown in Table 14, the P-values of x_7 , x_8 , and x_9 are <0.0001, indicating that the three main terms are significant; the P-values of the interaction terms x_7 x_8 , x_7 x_9 , and x_8 x_9 are greater than 0.05, indicating that the interaction terms are insignificant; the P-values of the squared terms x_8^2 and x_9^2 are greater than 0.05, indicating that the two squared terms are insignificant, and the P-values of the squared term x_7^2 are smaller than 0.05, indicating that it is significant; after removing the insignificant terms the regression equation of the optimized model is obtained as:

$$\theta_{stalk\text{-}seed} = 43.68 - 0.7538x_7 + 1.3x_8 + 0.5488x_9 - 0.1096x_9^2 \quad (5)$$

Table 14

Analysis of variance in three factor and three level experiments

Source of variance	Degrees of freedom	Mean square	F	P
mould	9	2.28	390.43	<0.0001
x_7	1	4.55	777.04	<0.0001
x_8	1	13.47	2302.51	<0.0001
x_9	1	2.41	411.85	<0.0001
x_7x_8	1	0	0.0043	0.9497
x_7x_9	1	0.0144	2.46	0.1606
x_8x_9	1	0.024	4.11	0.0823
x_7^2	1	0.025	4.27	0.0777
x_8^2	1	0.0149	2.55	0.1544
x_9^2	1	0.0438	7.49	0.0291
residual	7	0.0058		
lost proposal	3	0.0026	0.3150	0.8151
pure error	4	0.0083		
aggregate	16			

Through the regression equation obtained from the above test, it is difficult to get directly what values of x_7, x_8, x_9 respectively under the target value obtained from the physical test, so the stacking angle error value for the target value is analysed for the corresponding surface analysis, and the equation obtained is as follows:

$$\delta_{\theta stalk\text{-}seed} = 38.6 - 2.79x_7 + 7.38x_8 + 4.93x_9 + 0.06x_7x_8 + 2x_7x_9 + 2.58x_8x_9 - 1.93x_7^2 - 1.49x_8^2 - 4.53x_9^2 \quad (6)$$

Taking the stacking angle as a function of 44.63°, the stem-seed contact parameters were obtained as follows: x_7 =0.434, x_8 =0.884, x_9 =0.339, at which point the error was 0.255%.

Stalk-seed stacking angle validation test

The optimal parameter solutions obtained from the optimization of the three-factor surface response design test were substituted into the simulation model for the simulation verification test. The simulation parameters were set as follows: the collision recovery coefficient of stalk-seed was 0.434, the static friction coefficient of stalk-seed was 0.884, the rolling friction coefficient of stalk-seed was 0.339, and the other insignificant factors were taken to be the middle of the corresponding range. The validation test was carried out three times and the mean value of the stacking angle of the stalk-seed mixture was obtained as 44.41°, at which point the error value was 0.493%. It is close to the error value of 0.255% in the model, indicating that the experimental data are reliable.

CONCLUSIONS

(1) The intrinsic parameters of wheat stalks were measured using harvested wheat plants as the study object. The intrinsic parameters of wheat stalks were obtained. The discrete elemental model of wheat stalk and seed was developed based on the combination of literature review and measured eigen-parameters using Hertz-Mindlin model and Hertz-Mindlin with bonding model.

(2) Physical tests were carried out on wheat stalks and seeds and by calibrating these parameters, normal stiffness of 5e+08N/m2 and tangential stiffness of 6.35e+08N/m2 were obtained for wheat stalks.

(3) The average value of the stacking angle obtained from the physical test in the stalk-stalk stacking angle validation test is 39.22°, and the simulation parameters of stalk-stalk are determined after the validation of the simulation test, the collision recovery coefficient is 0.551, the static friction coefficient is 0.797, and the rolling friction coefficient is 0.079, and the average value of the stacking angle of the stalk-seed cylindrical lifting simulation experiment is 44.41°. With these parameters, it can be verified that the collision recovery coefficient of stalk-seed grain is 0.434, static friction coefficient is 0.884 and rolling friction coefficient is 0.339.

ACKNOWLEDGEMENT

This work was supported by the National Key Research and Development Program of China (Project No. 2023YFD2000400).

REFERENCES

[1] Carr, M. J., Roessler, T., Robinson P. W., Otto, H., Richter, C., Katterfeld, A., & Wheeler, C. A., (2023). Calibration procedure of Discrete Element Method (DEM) parameters for wet and sticky bulk materials. *Powder Technology*, Vol. 429, pp. 118919, Switzerland.

[2] Dai, F., Song, X., Shi, R., Guo, W., Wang, F., Zhao, W., (2023). Migration law of threshing material in wheat threshing and cleaning machine of small plot breeding (小区育种小麦脱粒清选机内脱粒物料迁移运动规律). *Agricultural Engineering Technology*, Vol. 43, pp. 134, China

[3] Fanyi, L., Jian, Z., Jun, C., (2018). Modeling of flexible wheat straw by discrete element method and its parameters calibration (基于离散元法的柔性小麦秸秆建模及其参数标定). *International Journal of Agricultural and Biological Engineering*, Vol. 11, pp. 42-46, China.

[4] Gao, Y., (2019). *Simulation optimization and experimental research on counter-rotating stalk return machine based on discrete element method (基于高散元法的反旋秸秆还田机仿真优化及试验研究)*. MSc Thesis, Anhui Agricultural University, Anhui/China

[5] Hongcheng, L., Rong, Z., Zhiyou, N., Junqi, Z., (2022). A Calibration Method for Contact Parameters of Maize Kernels Based on the Discrete Element Method. *Agriculture,* Vol. 12, pp. 664-664, Switzerland.

[6] Liao, Y., Liao, Q., Zhou, Y., Wang, Z., Jiang, Y., Liang, F., (2020). Parameter calibration of discrete element simulation for stalk crushing in fodder rape harvest at shoot stage (饲料油菜莹期收获茎秆破碎高散元仿真参数标定). *Journal of Agricultural Machinery*, Vol. 51, pp. 73-82, China.

[7] Li, K., (2022). *Research on key technology of flexible plucking for wheat harvester (小麦收获机柔性拨禾关键技术研究)*. MSc Thesis, Shandong Agricultural University, Shandong/China

[8] Li, J., Liu, X., Zou, L., Yin, R., Yang, K., Yun, J., (2021). Discrete elemental modeling method and experimental validation of spinach primary root (菠菜主根高散元建模方法与试验验证). *Agricultural Mechanization Research*, Vol. 43, pp. 181-185, 191, China.

[9] Liu, W., (2021). *Wheat plant modeling and single longitudinal axial flow wheat combine harvester material conveyance detection test (小麦植株建模与单纵轴流小麦联合收获机物料输送检测试验)*. MSc Thesis, Henan Agricultural University, Henan /China

[10] Liu, Y., Yang, R., Wu, X., Yang, X., (2021). Design of ear picking device for small plot corn harvester (小区玉米收获机摘穗装置的设计). *Agricultural Mechanization Research*, Vol. 43, pp. 103-106, 138, China.

[11] NI, Y., Jin, C., Wang, T., Zhou, L., Liu, Z (2022). Design and test of 4LZ-1.5 soybean combine harvester (4LZ-1.5 型大豆联合收获机设计与试验). *Journal of Agricultural Engineering*, Vol. 38, pp. 1-11, China.

[12] Park, D., Lee, C.G, Yang, D., Kim, D., Kim, J. Y, & Rhee, J.Y., (2021). Analysis of inter-particle contact parameters of garlic cloves using discrete element method. *Journal of Biosystems Engineering*, Vol. 46, pp. 1-14, South Korea.

[13] Tong, S., Shao, M., Cao, M., Zhao, J., (2023). Parameter calibration of discrete element model of corn straw based on DEM (基于 DEM 的玉米秸秆离散元模型参数标定). *Chinese Journal of Agricultural Mechanization*, Vol. 44, pp. 69-75, China.

[14] Thakur, S. C., Morrissey, J. P., Sun, J., Chen, J. F, & Ooi, J. Y., (2014). Micromechanical analysis of cohesive granular materials using the discrete element method with an adhesive elasto-plastic contact model. *Granular Matter,* Vol.16, pp. 383-400, Germany.

[15] Ucgul, M., Fielke, J.M., and Saunders, C., (2014). Three-dimensional discrete element modelling of tillage: Determination of a suitable contact model and parameters for a cohesionless soil. *Biosystems Engineering*, Vol.121, pp. 105-117, United Kingdom.

[16] Wang, Y., Xu, Z., Li, G., Yang, C., Sun, Q., Li, G., (2021). Research history and prospect of precision sowing mechanization equipment in wheat community (小麦小区精密播种机械化装备研究历程及展望). *Agricultural Engineering*, Vol. 11, pp. 20-24, China.

[17] Wang, Z., Cui, T., Zhang, D., Yang, L., He, X., Zhang, Z., (2021). Design and test of ripple threshing element for corn combine harvester (玉米联合收获机纹杆式脱粒元件设计与试验). *Journal of Agricultural Machinery*, Vol. 52, pp. 115-123, China.

[18] Yuan, J., Li, J., Zou, L., LI, X., (2020). Optimization design and test of spinach harvester root cutting shovel based on discrete elements (基于高散元的菠菜收获机根切铲优化设计与试验). *Journal of Agricultural Machinery*, Vol.51, pp. 85-98, China.

[19] Zhang, S., Zhang, R., Cao, Q., Zhang, Y., Fu, J., Wen, X., &Yuan, H., (2023). A calibration method for contact parameters of agricultural particle mixtures inspired by the Brazil nut effect (BNE): The case of tiger nut tuber-stem-soil mixture. *Computers and Electronics in Agriculture*, Vol. 212, pp. 108112, Netherlands.

[20] Zhang, H., Zhang, C., Li, Z., Ding, L., Zhu, C., Zhang, J., (2023). Analysis and optimization of vibration characteristics of maize finger-clamped seed discharger based on EDEM-RecurDyn (基于 EDEM-RecurDyn 的玉米指夹式排种器振动特性分析与优化). *Journal of Agricultural Machinery*, Vol. 54, pp. 36-46, China.

INVESTIGATION OF THE MICROSCOPIC DAMAGE MECHANISM OF BAIJIU YEAST SPRAY DRYING
/
白酒酵母喷雾干燥微观损伤机制探究

Feng-Kui XIONG[1, 2)], Jing-Yu LI[1)], Yue-Jin YUAN[2*)], Ying-Ying XU[2)], Guang-Zhong HU[1)]
[1)] College of Mechanical Engineering, Library, Sichuan University of Science & Engineering, Yibin, Sichuan / China;
[2)] College of mechanical & Electrical Engineering, Shaanxi University of Science & Technology, Xian, Shaanxi / China
Corresponding author: Yue-jin Yuan. Tel: +86-029-86168810. E-mail: yyjyuan1@163.com
DOI: https://doi.org/10.35633/inmateh-72-32

Keywords: *Modified Sporidiobolus johnsonii A (MSJA); microscopic damage mechanism by spray drying; Combined drying; equipment design*

ABSTRACT
In this paper, the microscopic damage mechanism of Modified Sporidiobolus johnsonii A (MSJA) in spray drying was investigated. The results showed that at a water content of 0.21 or a temperature of 52 °C and at a water content of 0.07 or a temperature of 71°C, irreversible damage such as selective-permeable damage and collapse due to the transformation of the gel phase and the inverse-hexagonal phase of the phospholipid molecular layer of the cell membrane bilayer were the main reasons for the beginning of inactivation and large amount of inactivation of MSJA, respectively, in the spray-drying process.

摘要
本文对喷雾干燥中改性约氏掷孢 A(MSJA)的微观损伤机制进行了探究。结果表明：在含水率为 0.21 或温度达到 52 ℃时和含水率为 0.07 或温度达到 71 ℃时，细胞膜双层磷脂分子层的凝胶相和反六角相转变导致的选择透过性损伤和坍塌等非可逆性损伤分别是喷雾干燥过程中 MSJA 开始失活和大量失活的主要原因。

INTRODUCTION
As a culture throughout the Chinese civilization, baijiu is not only a treasure of the Chinese culture (*Liu Z. et al., 2023*), but also one of the pillars of the national economy, which has formed a trend of "blossoming" in the country *(Wang et al., 2021*). However, high-quality liquid active liquor yeasts (such as Modified *Sporidiobolus johnsonii A*, MSJA) are difficult to store and transport due to weak vitality, which seriously restricts the promotion and development of high-end baijiu in China (*Cheng, et al., 2022*). Current research generally agrees that drying the yeast to reduce its moisture content (*Cheng et al., 2021*), so that it is in a dormant state, is the optimal method to achieve its convenient transportation, long-term storage and promotion of the using (*Uki et al., 2021*). Meanwhile, spray drying has been occupying a dominant position in the field of drying microorganisms, such as yeast, by virtue of both high drying efficiency and low cost (*Gong P., et al. 2018*). Therefore, it is particularly important to investigate the microscopic damage mechanism of MSJA during the spray drying process to provide theoretical guidance for the subsequent design of the combined drying process with high efficiency and high survival rate of MSJA. (*Yuan et al., 2022*).

Regarding the investigation of damage mechanisms during spray drying of microorganisms: *Izu H. et al (2023)* investigated the hot air drying of sake cake containing Aspergillus niger and Saccharomyces cerevisiae and observed many free amino acids and a large amount of S-adenosylmethionine (SAM), which indicated that ribosomes of either *Aspergillus niger or Saccharomyces cerevisiae* were damaged during the hot air drying process. However, the critical temperature and mechanism of ribosome damage were not explored. *Yang H., et al (2023)* investigated the physical and thermal damage of Tetrahymena halophila during spray drying using flow cytometry, and obtained that heat-excited treatment prior to drying better maintains the integrity of the cell membrane, thus improving its survival rate in drying. However, the mechanism of cell membrane damage was not explored, and the critical temperature at which cell membrane integrity was damaged was not derived.

Therefore, the *MSJA*, which was jointly developed by the China Academy of Baijiu, was taken as the research object. Our team, carried out spray drying real-time sampling experiments, combined with Fourier Transform Infrared Scanning (FTIR), differential incubation, Scanning Electron Microscopy (SEM) and other microscopic detection means to explore the real damage mechanism of *MSJA* in the spray drying process.

MATERIALS AND METHODS

Experimental materials and experimental program design

The *MSJA* developed by the China Academy of Baijiu was used as the drying object in this experiment, and a small experimental spray dryer of Beicheng brand was used to carry out the spray drying experiment (*Al Zaitone, et al., 2022*). Spray dryer main drying tower height was h = 1.65 m, cylinder height h_1 = 1.14 m, diameter D = 800 mm, of which the effective drying section height was h_2 = 1 m, the bottom of the cone taper a = 60°, the bottom of the tower outlet aperture d = 150 mm. And set the material flow rate of 700 mL/h, hot air flow rate of 70 m³/h, and experimental variables inlet hot air temperature of 80, 100, 120℃ and 140℃, respectively. The experimental process and experimental equipment are shown in Fig. 1 (*Xiong, et al., 2022*).

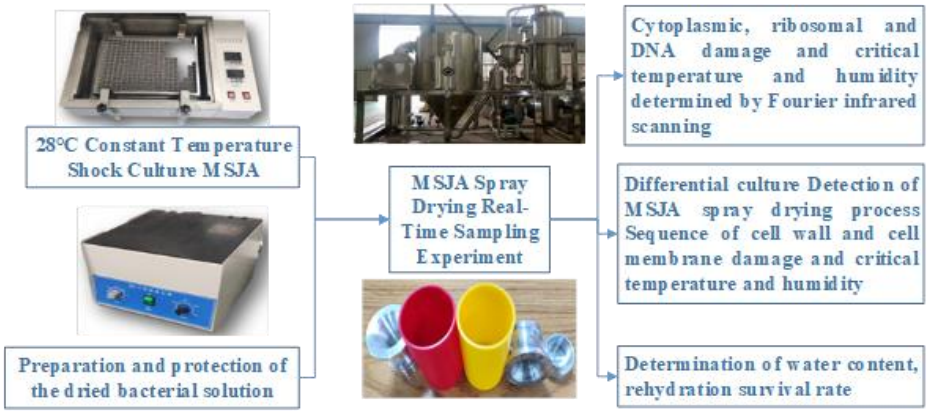

Fig. 1 - Experimental flow chart

Aiming at the difficulty of real-time sampling and nondestructive preservation of the spray drying process, this study developed a step-type double-cup body curved sampling cup with real-time efficient sampling and low-temperature nondestructive preservation system. In this system, firstly, the strong magnet at the bottom of the outer cup and the heat-insulating magnetic sticker on the outer surface work together to form a directional strong magnetic field at the mouth of the cup, which attracts the dry particles coated with carboxy iron powder (CIP) to enter into the inner cup, realizing high-efficiency sampling.

The first 20 cm of the curved inner cup is then formed by rotating a Bezier cubic curve (Eqs 1-3 below) with control points A, B, C, and D.

$$P(\mu)=\sum_{i=0}^{n} B_i^n(\mu)P_i \tag{1}$$

$$B_i^n(\mu)=\frac{n!}{i!(n-1)!}\mu^i(1-\mu)^{n-i} \tag{2}$$

$$P(\mu)=\mu^0(1-\mu)^3P_0+3\mu(1-\mu)^2P_1+3\mu^2(1-\mu)P_2+\mu^3(1-\mu)^0P_3=(1-\mu)^3P_0+3\mu(1-\mu)^2P_1+3\mu^2(1-\mu)P_2+\mu^3P_3 \tag{3}$$

This curved inner cup is used to optimize the hot air flow field at the cup mouth to achieve the goal of reducing hot air inflow into the sampling cup. The curved inner cup optimizes the hot air flow field at the mouth of the cup to achieve the goal of reducing the flow of hot air into the sampling cup under the premise of ensuring the stability of sampling. Together with the freezing layer filled with -40℃ antifreeze and the low-temperature and heat-insulating effect of the outer cup thermal insulation stickers, the samples can be stored at low temperatures (T≤4℃) without damage. Eventually, the step arrangement scheme and the cup mouth baffle were combined with the non-destructive installation of connecting magnets to achieve the goal of both real-time stable sampling and non-destructive cryopreservation of samples. The newly developed curved sampling cups and the pre-designed straight sampling cups are shown in Fig. 2.

A comparison of the bottom temperature (cryostat capability) and sampling quality (sampling stability) of the straight and curved sampling cups is shown in Fig. 3. The specific dimensions of the curved sampling cups were: the upper curved surface of the inner cup was 20 mm high with a minimum inner diameter of 18 mm; the lower part of the inner cup was 10 mm high with an inner diameter of 24 mm; the outer cup was 65 mm high with an outer diameter of 42 mm; and the wall thicknesses were all 2 mm. The dried particles were rehydrated in real-time by filling the cups with saline to constitute rehydrated sample sampling cups for microscopic observation of their drying damage.

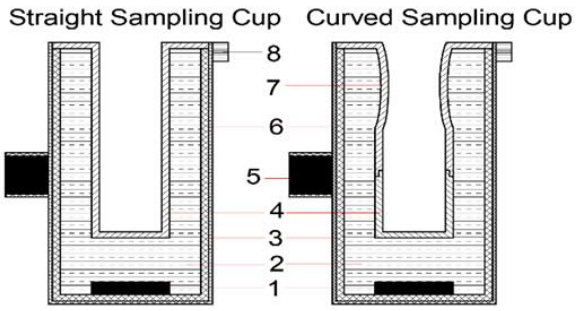

Fig. 2 - Schematic diagrams of curved and straight sampling cups with double cups

1-Connecting magnet; 2-Frozen layer; 3-Outer cup; 4-Lower part of inner cup; 5-Powerful magnets; 6-Heat and magnetic insulation tape; 7-Upper part of inner cup; 8-Wireless temperature and humidity sensors.

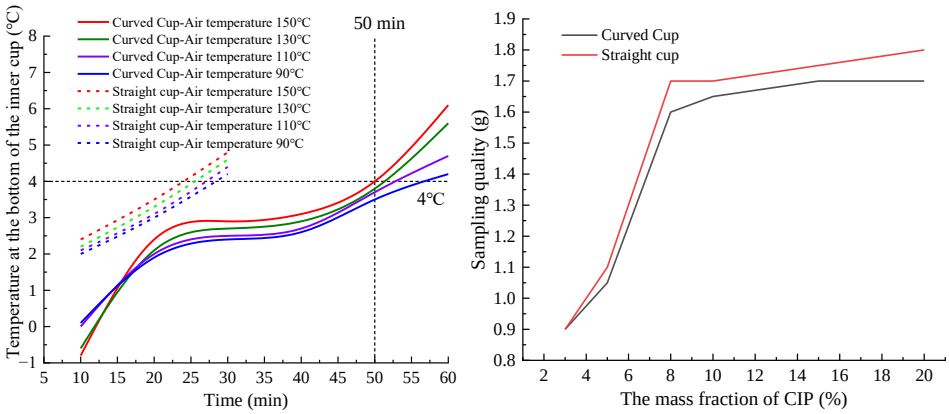

Fig. 3 - Comparison of bottom temperature and sampling quality of different types of sampling cups

The arrangement scheme is shown in Fig. 4, where the cups' rounded baffles together with the stepped arrangement scheme eliminate the sampling interference among the sampling cups (*Xiong et al., 2022*).

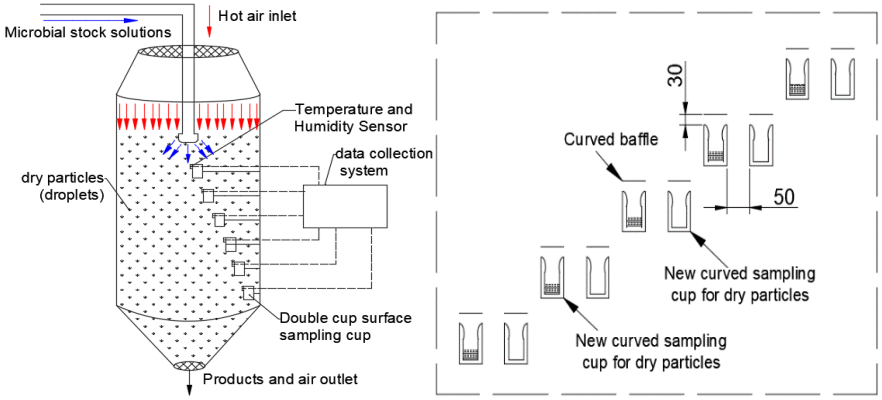

Fig. 4 - Schematic diagram of sampling experiment

Determination of experimental parameters

First, the temperature and humidity sensors arranged at the mouth of the sampling cups together with the data acquisition system collected and recorded the air temperature and humidity at each sampling point. Then, the samples in the sampling cups were removed and placed in a refrigerator at 4°C. Finally, the moisture content, rehydration survival rate, cell wall morphology, cell membrane, cell wall, protein and DNA damage and the order of damage were determined after the experiment was performed.

Determination of moisture content is as follows: preheat the moisture meter for 20 min→put the sample in the crucible→click the measurement button→read and record (*Spreutels et al., 2014*).

The rehydration survival rate of rehydrated samples was determined by the hypomethylated orchid staining + hemocyte counting method; and the formula for rehydration survival rate was (*Gomez-Narvaez F. et al., 2023*).

$$Q_v = \left\langle \frac{N_{us}}{N_T} \right\rangle \Big|_{three\text{-}fields} \times 100\% \quad (4)$$

Q_v - survival rate of rehydrated water; N_{us} - number of live bacteria (number of colourless organisms); N_T - total number of bacteria.

Determination of cell wall and cell mould damage

The MIC assay is a key step in the preparation (determining the amount of experiment reagents to be added) for the determination of *MSJA* cell membrane and cell wall damage. The steps of the assay are as follows: ① Prepare a sterile solution (20 groups in total) with deionized water according to Table 1, and filter it with a sterile membrane to remove bacteria, and at the same time, put YEPD medium into an autoclave at 120 ℃ for 15 min for spare, and finally prepare 24 triangular flasks numbered (labelled with the name of the additives and concentration) for spare. ② Add 10 ml of sterilized YEPD medium to each triangular flask according to the number, then add 10 ml of sterile solution prepared according to Table 1, and finally inoculate the dried *MSJA* particles in the triangular flasks at the ratio of 2% (v/v). ③ Firstly, the triangular flasks were placed in a constant temperature and humidity shaking incubator at 30°C and 70% humidity at 150 r/min for 12 h. Then, the absorbance of the culture solution in the well plates at 600 nm (OD600) was measured by UV spectrophotometer. Finally, the value of the minimum added concentration that significantly inhibits the growth of MSJA, obtained by graphing the data with Origin, is the MIC of the MSJA culture.

Table 1

Concentration for each component of the solution

Number	1	2	3	4	5	6
Penicillin (ug/ml)	0	0.156	0.312	0.624	1.248	2.496
Lysozyme (mg/ml)	0	0.156	0.312	0.624	1.248	2.496
Bovine bile salt (%)	0	0.032	0.064	0.128	0.256	0.512
NaCl (%)	0	0.25	0.5	1	2	4

In order to exclude the inhibitory effect of the four additives on the growth of healthy bacteria, and at the same time to use the sensitivity of *MSJA* bacteria to the four additives to determine the damage or collapse of the cell wall (membrane), the present study used the addition of 1/2 MIC concentration of the four additives to carry out the experiment. Specific experimental steps were as follows: ① YEDP medium containing the four additives was prepared according to 1/2 of the minimum inhibitory concentration obtained by MIC determination, and dried *MSJA* particles were inoculated into the newly made medium at the ratio of 2% (v/v) and incubated for 12 h. ② The number of viable bacteria and survival rate of *MSJA* were measured. ③ According to the change of *MSJA* sensitivity to penicillin, lysozyme, bovine bile salt and NaCl, the order of cell membrane and cell wall damage can be determined.

SEM observation of bacterial morphology and cell wall damage

Rehydrated samples were used: ① Bacteriophage was washed twice with PBS buffer, then fixed overnight with 4% (v/v) glutaraldehyde solution and washed again with PBS buffer. ② Sequentially dehydrated with alcohol at concentrations of 50%, 70%, 90% and 100% for 20 min. ③ Replaced ethanol by isoamyl acetate 2 times for 30 min each time (Note: before each washing or replacement of liquid, it was separated by centrifugation at 4000 rpm for 10 min, and the supernatant was discarded to take the precipitated bacterial bodies). ④ Put the bacteria obtained by centrifugation into a refrigerator at -40 ℃ for 8 h, and then remove the excess water and isoamyl acetate by freeze-drying. ⑤ The above-dehydrated samples were pasted onto specific copper plates with conductive double-sided tape. ⑥ The dehydrated samples were pasted onto specific copper plates with conductive double-sided tape. ⑦ The copper plates were sprayed with gold using an ion sputtering coater, and then the changes in the morphology of the bacteria were observed on the scanning electron microscope (SEM).

Dry pellet samples are used: ① Directly fix the dry pellet samples on the aluminium plate with conductive double-sided tape. ② Gold spraying treatment. ③ The damage of the *MSJA* cell wall can be obtained by observation under SEM.

Finally, the temperature and moisture content of each sampling point can be combined to obtain the critical temperature and moisture content of *MSJA* cell wall and cell membrane damage during spray drying, and then combined with SEM images can be analysed to obtain the kind of morphology that *MSJA* is less susceptible to be damaged during drying.

Determination of cytoplasmic, ribosome and DNA damage

Fourier transform infrared (FTIR) was used to determine the damage of *MSJA* cytoplasm, ribosomes and DNA (*Kandasamy, et al., 2022*). Firstly, the FTIR spectra of MSJA particles with different moisture contents during spray-drying were determined in the 3000-2700 cm^{-1} band associated with the C-H stretching of cell membrane lipids, the 1750-1500 cm^{-1} band associated with proteamides and the 1300-900 cm^{-1} band

associated with ribosomes (*Noghabi, et al., 2020*), respectively. Then, the second-order derivatives of the FTIR spectra were derived to obtain the corresponding FTIR second-order derivative maps. Finally, each FTIR second-order derivative profile was analysed in conjunction with microbiology to investigate the damage of cell membrane fatty acids, proteins and DNA in MSJA bacteria during spray drying.

The steps were as follows, ① Take the rehydrated sample and resuspend the bacteria in saline to make a resuspension solution. ② Take 0.03 mL of resuspended bacterial solution and evenly coat it on the zinc selenide window slice. ③ Put the window slice into a 40 ℃ hot air drying oven to dry for 1 h to remove the residual moisture, in order to avoid the interference of moisture on the spectrum during the experimenting process. ④ The infrared spectrometer was adjusted to the ATR reflectance mode, and the scanning was repeated 390 times at a resolution of 10 cm^{-1} in the range of 100~4000 cm^{-1} to obtain the Fourier infrared spectra of the samples. ⑤ The image data were processed with OMINIC 8.0 software, based on which the relevant absorption peaks were analysed and identified (the processing method was, firstly, 5-point smoothing of the spectral curves using the Savitzky-Golay equation, and then normalizing the spectrograms using the second-order derivatives).

RESULTS

Analysis of temperature, yeast moisture content and survival at sampling sites

Spray drying experiments of baijiu brewer's yeast were carried out according to the above experimental scheme, and then analysed graphically by Origin, and the resulting temperature of the mouth of each sampling cup, moisture content of dried particles and rehydration survival rate are shown in Fig. 5.

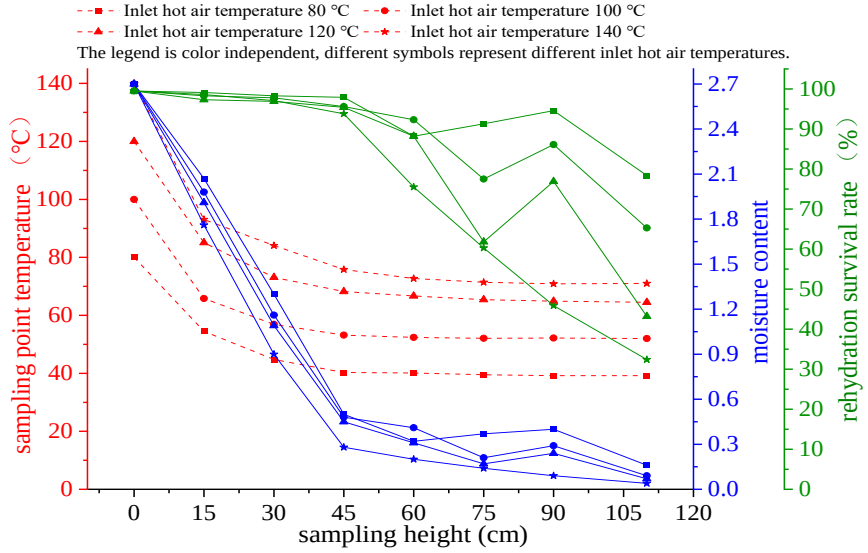

Fig. 5 - Temperature, moisture content and survival of yeast particles as a function of sampling altitude

From the temperature change curve in Fig. 5, it can be seen that the temperature in the drying tower generally decreases from top to bottom, but the rate of decrease decreases rapidly at the sampling heights of 15 cm and 45 cm, and stabilizes at 45 cm near the outlet temperature.

Combined with the moisture content curve and rehydration survival rate curve, it is easy to find that before the sampling height of 45 cm, the moisture content and temperature of the dried particles decreased sharply while the rehydration survival rate of the yeast in the particles almost did not decrease. This may be due to the fact that in the initial stage of downflow spray drying, the free water in the particles evaporates quickly and absorbs a large amount of heat from the hot air, and at the same time, it can also make the surface of the particles reach the equilibrium of the two gas-liquid species, which ensures that the yeast is in the "wet bulb temperature" environment and is almost not subject to thermal damage. The initial stage of microbial spray drying was called the "constant speed drying stage" (*Samborska et al., 2021*). After the sampling height of 45 cm, the free water in the pellet evaporates and the gas-liquid equilibrium on the surface of the pellet cannot be ensured, and the bacteria are exposed to the air temperature; at the same time, the bound water starts to evaporate, which leads to a gradual slowing down of the decrease of the moisture content of the pellet (reduced-rate drying stage) and a rapid decrease in the rehydration survival rate of *MSJA*. With the decelerated loss of bound water and the exposure of the bacteria to higher exit air temperatures, the *MSJA* bacteria were rapidly inactivated by both dehydration damage and thermal damage (*Hanae et al., 2018*).

Combined with the analysis of the moisture content and rehydration survival rate curves of spray-dried particles in Fig. 5, it is not difficult to conclude that the yeast particles are not completely top-down movement. Rather, the undried yeast particles will rise along the wall of the drying tower under the sheer force of the rising airflow along the wall to extend the drying time, and the specific trajectory is shown in Fig. 6 below.

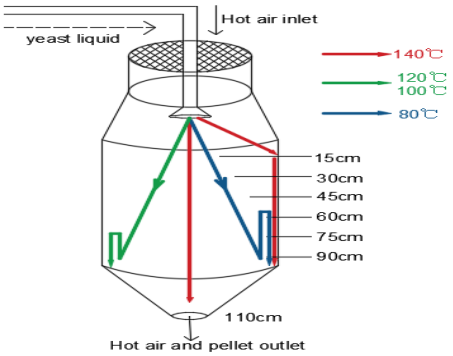

Fig. 6 - Trajectory of MSJA particles at each t air temperature

It is not difficult to find that the moisture content of the particles corresponding to the beginning of rapid inactivation of *MSJA* is between 0.2-0.32.

The order of cell wall (membrane) damage and temperature and moisture content determination

The effects of the four additives on *MSJA* growth at different concentrations as measured by the MIC experiment are shown in Fig. 7

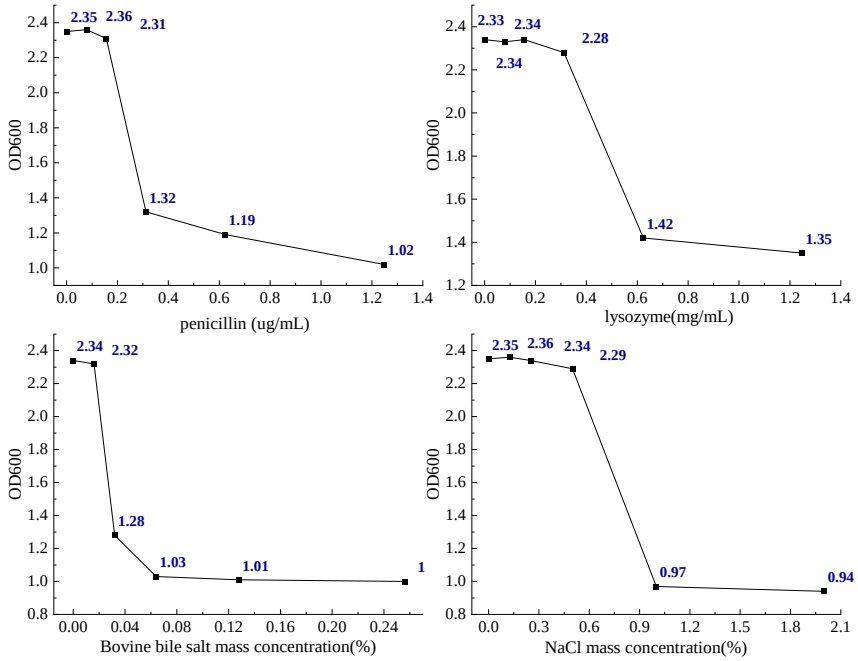

Fig. 7 - Effect of each concentration on yeast growth

From the analysis of Fig. 7, it could be seen that the OD600 value decreased rapidly and then approached to stabilization when penicillin, lysozyme, bovine bile salt and NaCl were added at the concentrations of 0.312 ug/mL, 0.624 mg/mL, 0.032% and 1%, respectively. This further indicates that the MIC values of penicillin, lysozyme, bovine bile salt and NaCl on *MSJA* growth were 0.312 ug/mL, 0.624 mg/mL, 0.032% and 1%, respectively.

NaCl can enter the cytoplasm through the cell membrane, which has lost its selective permeability, and inactivate *MSJA* due to the imbalance of osmotic pressure between the inside and outside of *MSJA*. Meanwhile, taurocholate can cross the collapsed cell membrane into the cytoplasm and cause DNA damage and *MSJA* inactivation. Therefore, the sensitivity of *MSJA* to NaCl and bile salts is related to the selectivity and integrity of *MSJA* cell membrane, respectively.

The sensitivity of *MSJA* organisms to the four additives can be measured by calculating the loss ratios after the addition of the four additives to the culture, using the blank group as a control, where the loss ratios are calculated as shown in Eq. 5 below.

$$D_s = \frac{Q_{vCK} - Q_{vT}}{Q_{vCK}} \quad (5)$$

where:

D_S - loss ratio; Q_{vCK} - survival rate of the control group, %; Q_{vT} - survival rate of treatment group, %. The calculations lead to the following: the loss ratio of *MSJA* at different moisture contents and temperatures are shown in Tables 2 and 3.

Table 2

Loss ratios of MSJA with different moisture content cultured on four additive media

Moisture content	Penicillin	Lysozyme	Bovine bile salt	NaCl
0.65	0.03±0.003 c	0.02±0.003 c	0.04±0.010 c	0.03±0.005 c
0.37	0.05±0.003 c	0.03±0.013 c	0.03±0.007 c	0.04±0.007 c
0.31	0.46±0.015 a	0.34±0.031 b	0.04±0.005 c	0.04±0.03 b
0.24	0.44±0.031 a	0.38±0.027 b	0.07±0.013 c	0.35±0.022 b
0.21	0.49±0.018 a	0.41±0.029 b	0.06±0.004 c	0.64±0.028 b
0.14	0.54±0.021 a	0.44±0.033 b	0.05±0.007 c	0.73±0.025 b
0.09	0.30±0.025 b	0.65±0.027 a	0.06±0.007 c	0.79±0.041 b
0.07	0.23±0.021 b	0.78±0.042 a	0.56±0.034 b	0.94±0.078 a
0.04	0.20±0.018 b	0.81±0.031 a	0.91±0.038 a	0.60±0.058 b

Note: The letters a, b and c in the table characterize the significant differences between the loss rates of MSJA pellets incubated with the same additive at different moisture contents.

As shown in Table 2, *MSJA* organisms were not susceptible to either penicillin or lysozyme until the moisture content was greater than 0.37, were sensitive to penicillin but not to lysozyme between moisture contents of 0.31-0.14, and were sensitive to lysozyme but not to penicillin between moisture contents of 0.09-0.04. Penicillin, as an inhibitor of peptidoglycan synthesis, inhibits synthetic repair of the cell wall and is associated with the presence or absence of reversible cell wall damage. Lysozyme can dissolve the cell wall structure of *MSJA* by hydrolysing the β-1,4-glycosidic bond of the *MSJA* broken cell wall, which is related to whether there is irreversible damage or even collapse of the cell wall. So, it can be concluded that the cell wall of *MSJA* showed reversible damage between moisture content of 0.37-0.31 and irreversible damage or even collapse between moisture content of 0.14-0.09.

MSJA was extremely insensitive to both NaCl and taurocholate when the moisture content was 0.65-0.31, more sensitive to NaCl and insensitive to taurocholate when the moisture content was 0.24-0.09, extremely sensitive to both NaCl and taurocholate when the moisture content was 0.07, insensitive to NaCl and extremely insensitive to taurocholate when the moisture content was 0.04. The inactivation of *MSJA* was caused by the fact that NaCl could enter the cytoplasm through the cell membrane which lost its selectivity. NaCl can enter the cytoplasm through the cell membrane which has lost its selectivity, so that the osmotic pressure inside and outside the bacterium is imbalanced and *MSJA* is inactivated; at the same time, taurocholate can enter the cytoplasm through the cell membrane which has collapsed, and cause damage to the DNA which is inactivated by *MSJA*; therefore, the sensitivities of *MSJA* to NaCl and taurocholate are respectively related to the selectivity and the integrity of the cell membrane of *MSJA*. Therefore, it can be concluded that the selective permeability of the *MSJA* cell membrane began to be impaired when the moisture content was between 0.31-0.24, and collapsed when the moisture content was between 0.09-0.07, and the cell membrane collapsed in a wide range when the moisture content reached 0.04.

Table 3

Loss ratio of MSJA cultured on four additive media at different temperatures

Temperature℃	Penicillin	Lysozyme	Bovine bile salt	NaCl
71	0.20±0.018 b	0.81±0.031 a	0.91±0.038 a	0.60±0.058 b
64.5	0.23±0.021 b	0.78±0.042 a	0.56±0.034 b	0.94±0.078 a
52	0.30±0.025 b	0.65±0.027 b	0.06±0.007 b	0.79±0.041 a
39.2	0.94±0.021 a	0.03±0.003 c	0.02±0.007 c	0.04±0.011 c

Note: The letters a, b and c in the table characterize the significant differences between the loss rates of MSJA pellets incubated with the same additive at different temperatures.

As shown in Table 3, *MSJA* organisms were extremely sensitive to penicillin and insensitive to lysozyme at 39.2℃, insensitive to both penicillin and lysozyme at 52℃, and insensitive to penicillin but extremely sensitive to lysozyme at 64.5℃ and 71℃. It can be deduced that the cell wall of *MSJA* bacteriophage began to suffer reversible damage near 39.2℃, and irreversible damage, such as collapse, began to 64.5℃.

MSJA organisms were extremely insensitive to both NaCl and bovine bile salts at 39.2℃, insensitive to penicillin and lysozyme at 52℃ and 64.5℃, extremely sensitive to NaCl but more sensitive to bovine bile salts at 64.5℃ and 71℃, and more sensitive to NaCl but extremely sensitive to bovine bile salts at 71℃. From this, it can be inferred that the cell membrane of *MSJA* bacteriophage began to be impaired in selective permeability near 52℃, and irreversible damage such as collapse began to occur near 71℃.

In summary, it can be concluded that the damage process of MSJA organisms during spray drying is as follows: first, reversible damage begins to occur at a water content of between 0.31-0.24 or at a temperature of 39.2°C. Subsequently, the selective permeability of the cell membrane began to be impaired at a water content of between 0.31-0.24 or a temperature of 52°C. Then, irreversible damage or even partial collapse of the cell wall began to occur at a water content of between 0.14-0.09 or a temperature of 64.5°C. Finally, irreversible damage, such as cell membrane collapse, began to occur at water contents between 0.09-0.07 or at a temperature of 71°C.

Observation of the morphology of the bacterium and cell wall damage mechanism

Using SEM at a magnification of 20,000 times, observations were made on rehydrated samples in rehydrated sample sampling cups at a sampling height of 45 cm under the four processes to investigate the effect of the size and morphology of the *MSJA* organisms on their survival rate. Dried particles with moisture content of 0.81, 0.34, 0.21, 0.09, 0.07 and 0.04 were observed in dried sample sampling cups to investigate the process of *MSJA* cell wall damage as shown in Fig. 8 and Fig. 9, respectively.

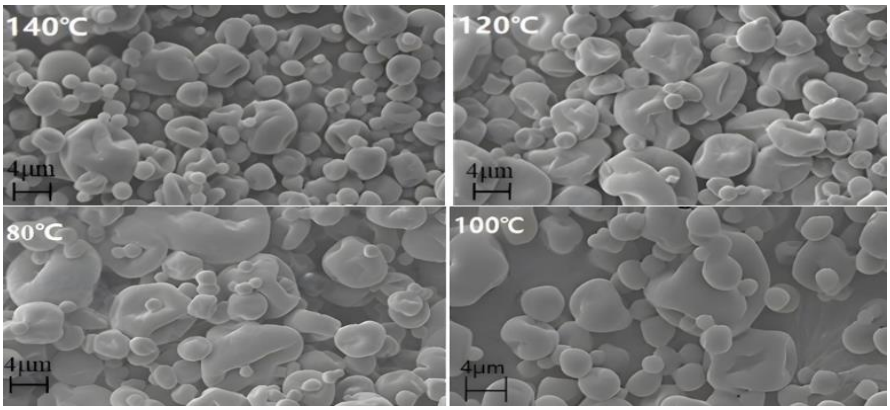

Fig. 8 - SEM scans of samples at 45 cm at each inlet temperature

As shown in Fig. 8, on the one hand, from the point of view of the average size of the bacterium, after the end of the descending-rate drying stage of spray drying, the size of the *MSJA* bacterium at different inlet temperatures was ranked as 80°C>100°C>120°C>140°C. The reason for this situation may be that the higher the hot air temperature is, the faster the water loss rate is. This may be due to the fact that, under the condition of certain material flow rate and hot air velocity, the higher the hot air temperature, the faster the water loss rate in the descending drying stage, and if the water loss rate is too fast, the more serious the dehydration damage is, which ultimately leads to the rapid contraction or even collapse of the cell wall of some bacteria. Therefore, from the point of view of the size of the bacterium (cell wall damage), the maximum inlet air temperature of spray drying should be limited to reduce the dehydration damage in the drying process of *MSJA*.

On the other hand, from the point of view of morphology and size uniformity, it is not difficult to find that with the increase of inlet temperature, the morphology of the bacterium is more similar while the size is more uniform. It may be due to the low inlet temperature, resulting in the uneven heating of the bacterial particles during atomization and descent, which ultimately led to the inconsistency of the morphology and size of the bacteria within the particles. Therefore, from the morphology and size uniformity of the bacteria, the minimum inlet temperature of spray drying should be limited. In summary, the inlet air temperature should be 100-120℃.

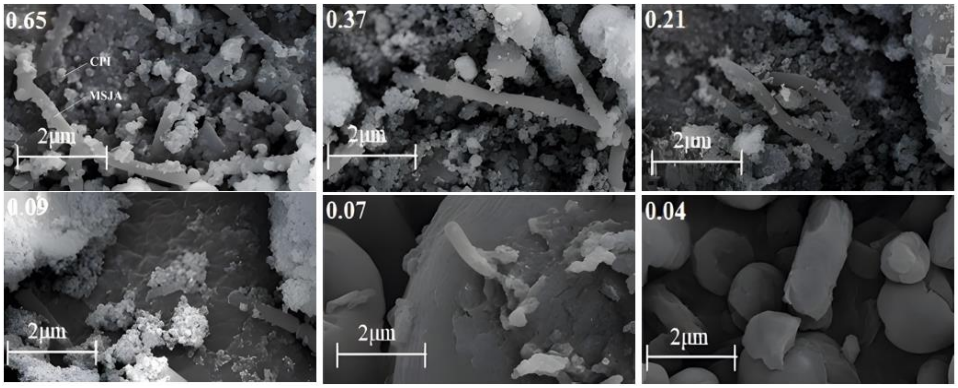

Fig. 9 - SEM scanning images of dried particles with different moisture content during the spray drying process

Observing Fig. 9, it is easy to see that the cell walls of the majority of *MSJA* organisms can remain intact and smooth before the moisture content is higher than 0.21, but as the moisture content drops to 0.07, the cell walls of the *MSJA* organisms gradually begin to shrink or even rupture. Because the rapid inactivation of *MSJA* occurs between 0.21-0.34 moisture content, it can be concluded that the cell wall is one of the sites of inactivation of *MSJA* organisms, but it is not the key site.

Analysis of damage to cell membrane fatty acids, proteins and DNA

The FTIR second-order derivative profiles at three bands are shown in Fig. 10 (a) - (c), respectively.

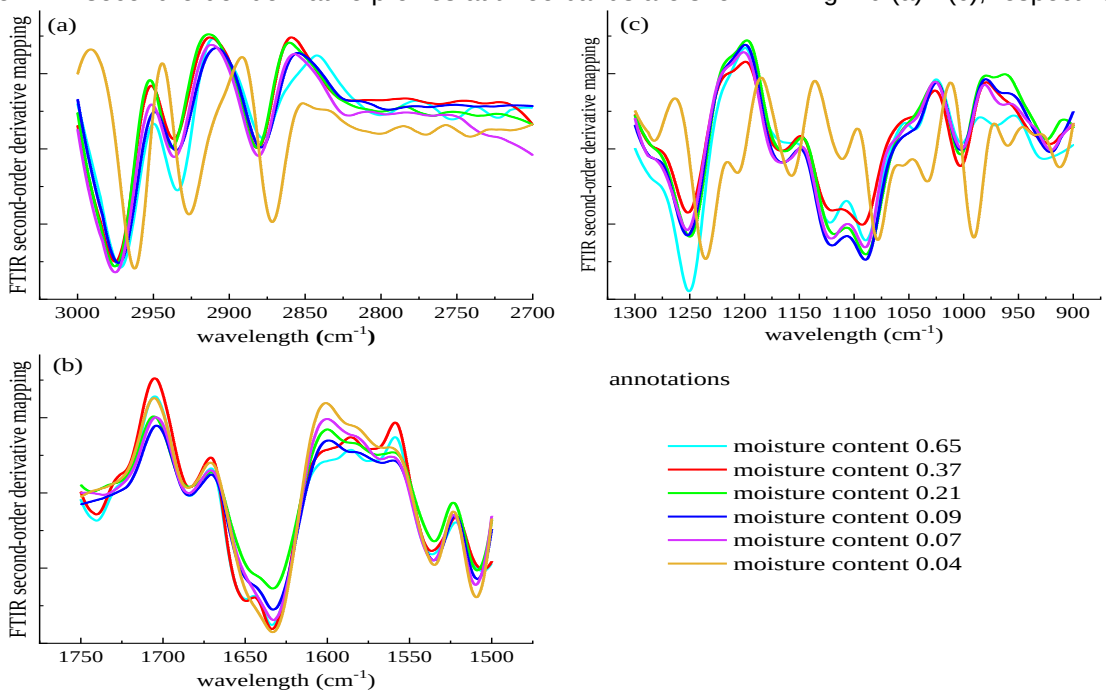

Fig. 10 - FTIR second-order derivative mapping

As shown in Fig. 10 (a), the FTIR second-order derivative patterns of *MSJA* particles with different moisture contents all showed obvious absorption peaks in the regions near the wavelengths of 2950 cm^{-1}, 2900 cm^{-1} and 2850 cm^{-1}, which were closely related to the composition and phase transition of the cell membrane lipids of the *MSJA* organisms. The absorption peaks near 2950 cm^{-1} and 2900 cm^{-1} were related to the symmetric expansion and contraction of CH_3 and CH_2 in the lipid acyl groups of the cell membrane, i.e., the gel phase transition of the cell membrane, and the absorption peaks near 2850 cm^{-1} were related to the asymmetric expansion and contraction of CH_3 and CH_2 in the lipid acyl groups of the cell membrane, i.e., the anti-hexagonal phase transition of the cell membrane. At the wavelengths of 2950 cm^{-1} and 2900 cm^{-1}, the absorption peaks gradually shifted to 2935 cm^{-1} and 2875 cm^{-1} when the moisture content was lower than 0.21, and the peak heights were also gradually increased. This indicates that the van der Waals force between the bilayer phospholipid molecules of the *MSJA* cell membrane increases at moisture content of 0.21, and the gel phase transition occurs, and the selective permeability of the cell membrane is also damaged.

At the wavelength of 2850 cm^{-1}, the peak height of the absorption peak was dramatically lowered when the moisture content was lower than 0.07. This indicates that at moisture content of 0.04, the cell membrane of *MSJA* bacteriophage begins to undergo an anti-hexagonal phase transition and thus begins to collapse. This is consistent with the two critical moisture content points for the massive death of *MSJA*, indicating that the gel phase transition and the anti-hexagonal phase transition of the cell membrane at moisture content of 0.21 and 0.07, respectively, are the key causes of the death of *MSJA* during the spray-drying process.

As shown in Fig. 10 (b), the FTIR second-order derivative patterns of *MSJA* particles with moisture contents of 0.065 and 0.037 both showed fluctuation peaks at wavelengths ranging from 1660 cm^{-1} to 1635 cm^{-1} associated with protein β-turns and α-helices, respectively. And the fluctuation peaks were obviously weakened as the moisture content decreased to 0.21 and 0.09, and the fluctuation peaks completely disappeared as the moisture content decreased to 0.07. The α-helix and β-rotor are an ordered structural component of proteins, and the disappearance of the α-helix and β-rotor implies that the protein structure in the bacterium has been irreversibly damaged. It means that the proteins in the bacterium begin to suffer reversible damage when the moisture content is 0.21, and the proteins in the bacterium begin to suffer irreversible damage when the moisture content is 0.07.

As shown in Fig. 10 (c), the FTIR second-order derivative patterns of *MSJA* particles at each moisture content all showed distinct absorption peaks closely related to the symmetric and asymmetric scaling of PO^{2-} in the DNA ribosome in the region near the wavelengths of 1200 cm^{-1} and 1040 cm^{-1}, respectively. The symmetric expansion of PO^{2-} in DNA started to move slowly to the right to 1195 cm^{-1} when the moisture content reached 0.07, and finally moved rapidly to 1180 cm^{-1} when the moisture content was 0.04. The asymmetric expansion of PO^{2-} in DNA suddenly moved rapidly to 1010 cm^{-1} when the moisture content reached 0.04. The symmetric expansion of PO^{2-} in DNA was also found in the region near 1200 cm^{-1} and 1040 cm^{-1}. It indicates that the DNA of *MSJA* bacteriophage started to suffer reversible and non-lethal damage at moisture content of 0.07, and started to suffer greater damage only at moisture content lower than 0.04.

CONCLUSIONS

During the spray-drying process of *MSJA*, although the cell wall was damaged first, this damage did not directly lead to the death of MSJA; it was the immediately following cell membrane damage that was the most critical to directly cause the death of *MSAJ*. The critical temperature and moisture content for the cell membrane phospholipid bilayer to undergo gel phase transition, leading to the death of MSJA, were 52℃ and 0.21℃, respectively, while the critical temperature and moisture content for the cell membrane phospholipid bilayer to undergo anti-hexagonal phase transition or even disintegration, leading to the death of a large number of MSJA, were 71℃ and 0.07℃, respectively.

When the drying water content was lower than 0.21, the phase transition of the phospholipid bilayer resulted in the loss of selective permeability of the cell membrane, which was the key factor leading to the death of MSJA. Only when the water content was lower than 0.04, protein damage in the bacterium caused MSJA death, and the effect of DNA damage on MSJA death was almost negligible.

The hot air inlet temperature and outlet temperature of spray drying should be limited to 100-120℃ and 48-52℃ respectively.

ACKNOWLEDGEMENT

This work was supported by the National Natural Science Foundation of China [grant number 51876109]; the key R&D Program Project of Shaanxi Provincial [grant number 2021NY-129]; and the Scientific research plan project of youth innovation team of Shaanxi Provincial Department of Education [grant number 22JP012].

REFERENCES

[1] Al Zaitone, B.; Al-Zahrani, A.; Ahmed, O.; Saeed, U.; Taimoor, A.A. (2022). Spray Drying of PEG6000 Suspension: Reaction Engineering Approach (REA) Modeling of Single Droplet Drying Kinetics. *Processes*. 10, 1365. https://doi.org/10.3390/pr10071365.

[2] Cheng, S.S.; Su, W.T.; Yuan, L.; Tan, M.Q. (2021). Recent developments of drying techniques for aquatic products: With emphasis on drying process monitoring with innovative methods. *Drying Technology*. 39(11), 1577-1594. https://doi.org/10.1080/07373937.2021.1895205.

[3] Cheng, W.; Chen, X.F.; Zhou, D.; Xiong, F.K. (2022). Applications and prospects of the automation of compound flavor baijiu production by solid-state fermentation. *International journal of food engineering*. 12(18), 737–749. https://doi.org/10.1515/ijfe-2022-0200.

[4] Dukic, N.; Radonjic, A.; Popovic, B.; Andric, G. (2021). Development and progeny performance of Tribolium castaneum (Herbst) in brewer's yeast and wheat (patent) flour at different population densities. Journal of Stored Products Research. 94, 101886. https://doi.org/10.1016/j.jspr.2021.101886.

[5] Fang, L.; Yang, W.; Hou, J.H; Zheng, K.W.; Hussain, A.; Zhang, Y.C.; Hou, Z.H.; Wang, X.Z. (2023). Tofukasu-derived biochar with interconnected and hierarchical pores for high efficient removal of Cr (VI). *Biochar*. 5(1), 69. https://doi.org/10.1007/s42773-023-00268-0.

[6] Gong, P.M.; Sun, J.L.; Lin, K.; Di, W.; Zhang, L.W.; Han, X. (2018). Changes process in the cellular structures and constituents of Lactoba-cillus bulgaricus sp1.1 during spray drying. *LWT- Food Sci. Technol*. 102, 30–36. https://doi.org/10.1016/j.lwt.2018.12.005.

[7] Gómez-Narváez, F.; Díaz-Osorio, A.; Gómez-Narváez, S.; Simpson, R.; Contreras-Calderón, J. (2023). Modeling the impact of spray drying conditions on some Maillard reaction indicators in nano-filtered whey. *Journal of food process engineering*. 46(1), 14212. https://doi.org/10.1111/jfpe.14212.

[8] Kandasamy, S.; Naveen, R. (2022). A review on the encapsulation of bioactive components using spray-drying and freeze-drying techniques. Journal of food process engineering. 45(8), 14059. https://doi.org/10.1111/jfpe.14059.

[9] Izu, H.; Yamashita, S.; Arima, H.; Fujii, T. (2018). Nutritional characterization of sake cake (sake-kasu) after heat-drying and freeze-drying. *Bioscience Biotechnology & Biochemistry*. 83(8), 1-7. https://doi.org/10.1080/09168451.2018.1559723.

[10] Liu, Z.; Xu, L.; Wang, J.; Duan, C. (2023). Research progress of protein haze in baijius. Food Science and Human Wellness. 12(5), 1427-1438. https://doi.org/10.1016/j.fshw.2023.02.004.

[11] Noghabi, M.S.; Molaveisi, M. (2020). Microencapsulation optimization of cinnamon essential oil in the matrices of gum Arabic, maltodextrin, and inulin by spray-drying using mixture design. *Journal of Food Process Engineering*. 43, 13341. https://doi.org/10.1111/jfpe.13341.

[12] Paup, V.D.; Barton, T.L.; Edwards, C.G.; Lange, I.; Lange, B.M.; Lee, J.; Ross, C.F. (2016). Influence of polysaccharides on the taste and mouthfeel of white wine. *Australian Journal of Grape and Wine Research*. 22(3):350-357. https://doi.org/10.1111/1750-3841.16371.

[13] Samborska, K.; Edris, A.; Jedlinska, A.; Baranska, A. (2021). The production of white mulberry molasses powders with prebiotic carrier by dehumidified air-assisted spray drying. *Journal of Food Process Engineering*. 45, 13928. https://doi.org/10.1111/jfpe.13928.

[14] Spreutels, L.; Haut, B.; Chaouki, J.; Bertrand, F. (2014). Conical spouted bed drying of Baker's yeast: Experimentation and multi-modeling. *Food Res. Int.* 62, 137–150. https://doi.org/10.1016/j.foodres.2014.02.02.

[15] Wang, Y.; Huang, X.Y.; Aheto J.; Ren, Y.; Zhang, X.; Wang, L. (2021). Novel colorimetric sensor array for Chinese rice wine evaluation based on color reactions of flavor compounds. *Journal of food process engineering*. 44(12), e13889. https://doi.org/10.1111/jfpe.13889.

[16] Xiong, F.K.; Yuan, Y.J.; Xu, Y.Y.; Li, J.Y.; Zhao, Z.; Tan, L.B. (2022). Modeling Study of a Microbial Spray-Drying Process Based on Real-Time Sampling. *Processes*. 10, 1789. https://doi.org/10.3390/pr10091789.

[17] Yang, H.; Huang, P.; Hao, L.Y.; Che, Y.L.; Dong, S.R.; Wang, Z.H.; Wu, C.D. (2023). Enhancing viability of dried lactic acid bacteria prepared by freeze drying and spray drying via heat preadaptation. *Food Microbiology*, 112,104239. https://doi.org/10.1016/j.fm.2023.104239.

[18] Yuan, Y.J.; Xiong, F.K.; Li, J.Y.; Xu, Y.Y.; Zhao X.T. (2022). Review on Drying Technology and Damage Protection Mechanism of Liquor Yeast. *INMATEH - Agricultural Engineering*. 68 (3) 735-746. https://doi.org/10.35633/inmateh-68-73.

PARAMETER CALIBRATION AND DISCRETE ELEMENT MODEL OF HIGHLAND BARLEY STEM BASED ON EDEM

/

基于EDEM 的青稞茎秆离散元参数标定

Fan JIN[1)], Dejiang LIU*[1)], Chengyi ZHONG[1*)], Keheng YAO[1)], Jian TONG[2)], Zhibing JIANG[2)]
[1)]Nanjing Institute of Agriculture Mechanization, Ministry of Agriculture and Rural Affairs, Nanjing 210014, China
[2)]Tibet Academy of Agricultural and Animal Husbandry Sciences, Lhasa 850000, China
Tel: 025-84346278; Corresponding author E-mail: zhongchengyi@caas.cn; liudejiang@caas.cn
DOI: https://doi.org/10.35633/inmateh-72-33

Keywords: *Stem; Simulation parameters; Response surface methodology; Simulation; Repose Angle*

ABSTRACT

In view of the lack of accurate contact parameters and the difficulty of measuring contact parameters in the discrete element simulation of mechanized harvesting of highland barley, this study took the wax-ripening highland barley as the object, carried out the discrete element simulation of highland barley stem based on EDEM, and calibrated the discrete element simulation parameters of highland barley stem by response surface optimization. In this paper, Plackett-Burman test was used to screen 8 initial parameters. It was found that the static friction coefficient between highland barley stems, the rolling friction coefficient between highland barley stems, and the rolling friction coefficient between highland barley stems and steel plates have significant effects on the particle angle of repose. Based on the optimal value range of significant factors determined by the steepest ascent test, a second-order regression model of the angle of repose and significant parameters was established and optimized based on the results of Box-Behnken test. The optimal parameter combination of significant parameters was obtained as follows: static friction coefficient between highland barley stems is 0.27, rolling friction coefficient between highland barley stems is 0.07, and rolling friction coefficient between highland barley stems and steel is 0.26. Finally, the simulation results under the optimal parameter combination are compared with the actual test angle of repose. The relative error is 0.52 %. That indicates that the parameters of the simulation calibration are credible, which can provide a reference for the future research on the cleaning device in the mechanized harvesting of highland barley.

摘要

针对目前青稞机械化收获离散元仿真缺乏准确的接触参数、接触参数测量难度大的问题，本研究以蜡熟期的青稞为对象，基于EDEM 开展青稞茎秆离散元仿真，通过响应面优化标定了青稞茎秆离散元仿真参数。研究应用Plackett-Burman 试验对8 个初始参数进行筛选，发现青稞茎秆间静摩擦系数、青稞茎秆间滚动摩擦系数与青稞茎秆-钢板滚动摩擦系数对颗粒堆积角有显著影响。以最陡爬坡试验确定的显著性因素最优取值区间为基础，基于Box-Behnken 试验结果建立堆积角与显著性参数的二阶回归模型并对其进行优化，得到显著性参数的最佳参数组合为青稞茎秆间静摩擦系数 0.27、青稞茎秆间滚动摩擦系数 0.07、青稞茎秆-钢板滚动摩擦系数 0.26。最后将最佳参数组合下的仿真结果与真实试验堆积角对比，二者相对误差为 0.52%，误差很小表明仿真标定的参数是可信的，可以为以后的青稞机械化收获中清选装置的研究提供参考。

INTRODUCTION

As the largest food crop in the Qinghai-Tibet Plateau, highland barley is also an agricultural characteristic industry in the plateau area, which can provide an important driving force for local agricultural development (*Xu et al., 2020*). At present, an important problem is that the mechanized harvesting level of highland barley is not high, which restricts the good development of highland barley related industries to a certain extent (*Bian et al., 2015; Zhang et al., 2022*). Due to the similarity with rice and wheat plants, the mechanized harvesting of highland barley is mainly carried out by improving the grain combine harvester, but a large amount of grain is often lost in the cleaning process and the impurity content is high. In order to solve the problem of cleaning loss and high impurity content during the harvesting process, it is crucial to establish a more accurate stem model and contact parameters (*Wang et al., 2017; Wang et al., 2021*).

[1] *Fan Jin, M.S. Stud; Chengyi Zhong, Prof.; Dejiang Liu, Ph.D.*

As a numerical simulation method to solve the problem of discontinuous media, discrete element method has been widely used in the field of agricultural engineering (*Wang et al., 2018*). Parametric simulation of the operation process of agricultural machinery is carried out. Parameter calibration is one of the key problems in discrete element simulation (*Su et al., 2020*). Among them, Hertz Mindlin (no slip) contact model and Hertz Mindlin with Bonding bond contact model in EDEM are widely used in material modeling, and a series of important progress has been made in parameter calibration of rice, wheat, corn and other crops (*Liao et al., 2020; Hou et al., 2022; Chen et al., 2023*). Many scholars have provided effective research methods for the calibration of discrete element parameters of stems (*Zeng et al., 2021*), but there are few studies on the parameter calibration of highland barley stems. In this study, the highland barley stems are short stems after threshing, so the multi-sphere aggregation model is used to establish the stem geometric model (*Zhang et al., 2020*).

When EDEM is used to simulate the grain cleaning process, the parameter setting of the stem directly affects the accuracy of the simulation results (*Wang et al., 2020*). The model parameters mainly include material intrinsic parameters and basic contact parameters. The intrinsic parameters such as material density, geometric size, shear modulus and Poisson's ratio are obtained by physical measurement (*Wang et al., 2017*). The static friction factor, rolling friction factor and collision recovery coefficient between the material and the contact material are obtained by physical test (*Wang et al., 2022; Liu et al., 2016*). In this paper, the highland barley stem harvested at wax ripening stage was used as the test object, and the basic parameter test was carried out. Based on the EDEM and Hertz Minding (no slip) contact model, the discrete element simulation parameters were calibrated by Plackett-Burman, steepest ascent and Box-Behnken tests, and the results of the short stem angle of repose real test and the simulation test were compared and verified, in order to provide basic parameters for the simulation study of the highland barley harvesting process.

MATERIALS AND METHODS

Intrinsic characteristics of the material

The stem of highland barley Zangqing-2000 used in the experiment was selected from the experimental field of Gannan Institute of Agricultural Sciences. The collected highland barley was in the state of wax ripening, no pests and diseases, no mechanical damage, and the spikes and leaves were removed. The moisture content of 50 g treated highland barley stems was 22.45 %, and the true density of the test stems was 757 kg/m^3. The outer diameter and wall thickness of 20 highland barley stems were measured by vernier caliper. The average outer diameter was 5.1 mm and the wall thickness was 0.52 mm.

Physical parameter measurements

The physical parameters required for the calibration of discrete element parameters of highland barley stalk include Poisson's ratio, shear modulus, static friction coefficient, rolling friction coefficient and collision recovery coefficient, etc. The test equipment required for the test includes material characteristics test bench and SUNS universal mechanical testing machine.

Coefficient of static friction

The static friction coefficient is the ratio of the maximum static friction force to the normal pressure on the object (*Wang et al., 2020*). During the measurement, the highland barley stem to be measured is placed axially on the horizontal steel plate, and the angle meter is placed in a suitable position. The handle is rotated to make the steel plate rise slowly. When the highland barley stem slides on the surface of the steel plate, it stops, and the angle α of the angle meter is recorded at this time. The static friction coefficient is calculated according to Equation (1). The measurement process and force analysis are shown in Fig. 1.

$$f_s = tan\ \alpha \quad (1)$$

where: f_s is the coefficient of static friction and α is the critical angle of static friction (°).

When measuring the static friction coefficient of highland barley stem-highland barley stem, the uniform arrangement of highland barley stem plate can replace the steel plate. Repeat the test for 20 times, the range of static friction coefficient between highland barley stems is 0.2 ~ 0.6, and the range of static friction coefficient between highland barley stems and steel plate is 0.3 ~ 0.6.

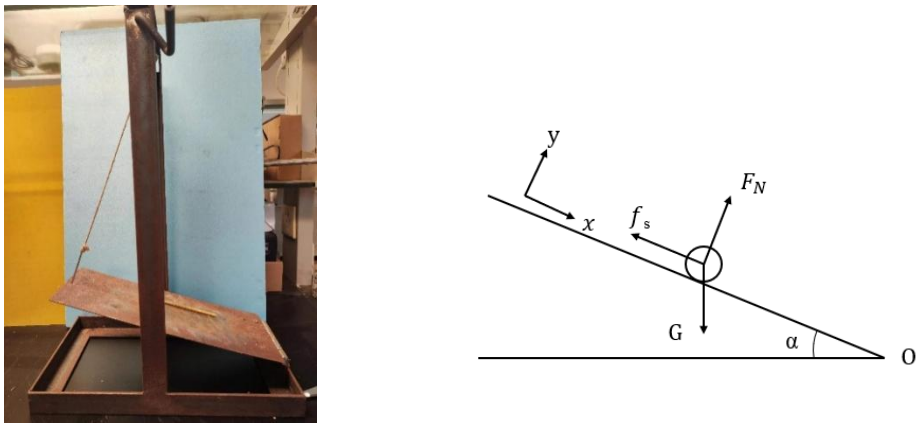

a) b)

Fig. 1 – Barley stem static friction coefficient measurement device and force analysis diagram

a) Measurement device; b) Force analysis diagram

Rolling friction coefficient

Rolling friction refers to the blocking effect of the deformation of the object on the contact surface on rolling when an object rolls without sliding or has a rolling trend on the surface of another object (*Chen et al., 2023*). Similar to the static friction coefficient measurement method, the stem was placed horizontally on the horizontal steel plate, and the handle was shaken to slowly raise the steel plate. When it was observed that the highland barley stems had just rolled purely on the steel plate, stop shaking the handle. The tilt angle θ of the plane at this time was measured by the angle meter. The measuring device and force analysis are shown in Fig. 2.

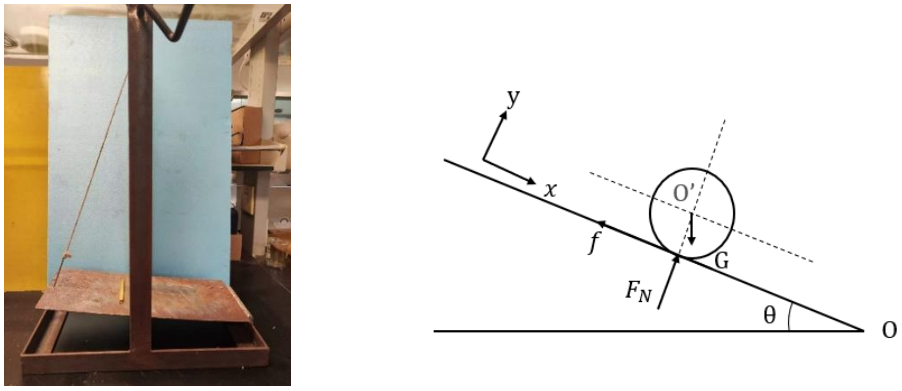

a) b)

Fig. 2 – Barley stem rolling friction coefficient measurement device and force analysis diagram

a) Measurement device; b) Force analysis diagram

During the rolling process of highland barley, the rolling friction moment M is proportional to the positive pressure F_N of the support surface. As the inclination angle of the slope increases, the highland barley stem rolls. From the force analysis:

$$M = fF_N \quad (2)$$

$$F_N - Gcos\theta = 0 \quad (3)$$

$$Grsin\theta - M = 0 \quad (4)$$

$$f = \frac{M}{F_N} = rtan\theta \quad (5)$$

Where:

M - rolling friction moment, [N•m];

f - coefficient of rolling friction;

F_N - the support force of the bevel to the stem, [N];

G - gravity of barley stems, [N];

θ - critical angle of rolling friction of barley stems, [°];

r - radius of barley stems, [mm].

When measuring the rolling friction coefficient between highland barley stems, the steel plate can be replaced by the evenly arranged highland barley stem plate. The range of rolling friction coefficient between highland barley stem was 0.05 ~ 0.15, and the range of rolling friction coefficient between highland barley stem and steel plate was 0.2 ~ 0.4.

Collision restitution coefficient

The collision recovery coefficient is the ratio of the normal velocity of the center of mass at the end of the collision to the normal velocity of the center of mass before the collision. It is a parameter to measure the recovery ability of the object after deformation (*Xiao et al., 2019*). The test device and principle are shown in Fig. 3.

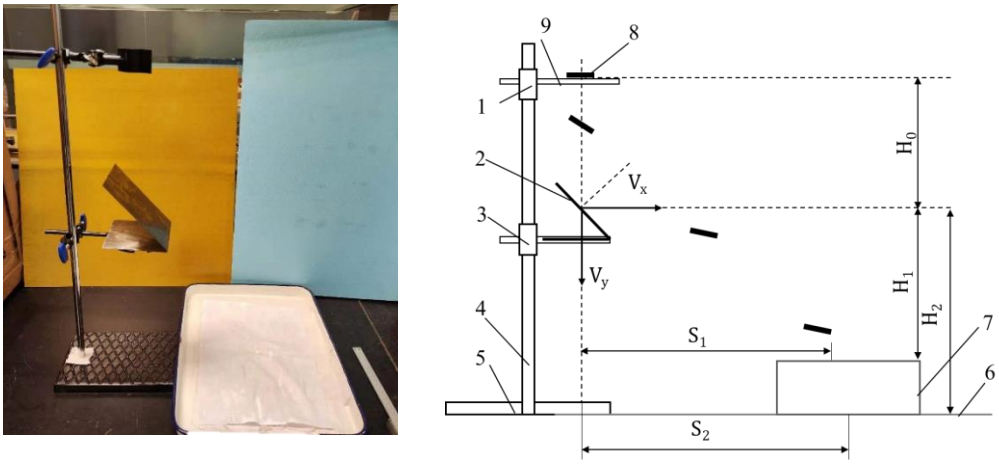

a) *b)*

Fig. 3 - Measurement device and motion analysis of barley stem collision restitution coefficient

a) Measurement device; b) Motion analysis of barley stem collision restitution coefficient

During the experiment, the short stem of highland barley fell freely from a certain height H without initial velocity, and collided with the inclined plate (steel plate and stem inclined plane) placed at 45° directly below, and the stem made a flat parabolic motion, and finally fell on the receiving plate. The relative height of the receiving plate and the collision point O is H_1, and the horizontal displacement of the stem is S_1. Changing the relative height H_2 between the blanking plate and the collision point obtains the horizontal displacement of the stem as S_2, and the collision recovery coefficient e between the stem and the inclined plate can be calculated by kinematic Equation (6). The test was repeated for 20 times, and the collision recovery coefficient between barley stem and barley stem was 0.1~0.6, and the collision recovery coefficient between barley stem and steel plate was 0.4~0.8.

$$e = \frac{\sqrt{\left(v_x{}^2 + v_y{}^2\right)} \cdot cos\left[45° + arctan\left(\frac{v_x}{v_y}\right)\right]}{v_0 \cdot sin45°} \tag{6}$$

Among them, v_0 is the vertical velocity component before stem collision, which can be calculated by falling height, [mm/s]. The horizontal velocity component v_x and the vertical velocity component v_y after stem collision can be obtained by Equation (7):

$$\begin{cases} v_x = \sqrt{\dfrac{gS_1S_1(S_1 - S_2)}{2(H_1S_2 - H_2S_1)}} \\ v_y = \dfrac{H_1 v_x}{S_1} - \dfrac{gS_1}{2v_x} \end{cases} \tag{7}$$

Physical experiment on the angle of repose of highland barley stem

This research adopts a steel plate (Q235) cylinder, according to the length of the highland barley stem particles, the inner diameter and height were determined to be 100 and 180 mm respectively. During the measurement, the cylinder is placed on the plane of the steel plate and filled with the test sample, and then the universal testing machine is used to raise it at a constant speed of 0.05 m/s to form a stable stack of test sample and measure the angle of repose, as shown in Fig. 4. The test was repeated 10 times, and the average angle of repose was 30.82°.

Fig. 4 - Physical test of the angle of repose by cylinder lifting method

Model of simulation test and parameters

Discrete element model of highland barley

The short stem model of highland barley was established by software EDEM2021 as shown in Fig. 5. Since the stem wall was very thin, the calculation amount of the real value was too large, so the stem wall thickness was enlarged in the simulation. According to the test in Reference (Liu., 2018), it was proved that the enlarged wall thickness had no significant effect on the test results during the simulation. Therefore, the stem wall thickness of the simulation model was set to 1 mm, the outer diameter was 5.20 mm, and the length was 25 mm.

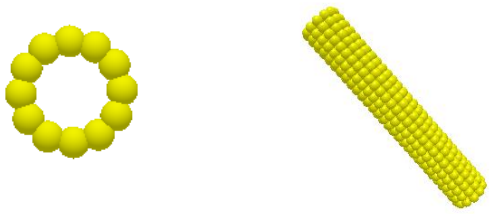

Fig. 5 - Particle model of highland barley stem

Simulation parameters

In order to improve the accuracy of calibration parameters, the multi-sphere aggregation model in EDEM2021 was used in the simulation test of highland barley stem particle accumulation (*Ding et al., 2021*). In order to be the same as the actual accumulation test stem particle length, the stem particle length is 25 mm. Combined with the previous physical experiment of stem intrinsic parameters and the related literatures (*Shu et al., 2022; Wang et al., 2012*) of discrete element simulation of agricultural materials, the numerical range of each simulation parameter in this study is shown in Table 1.

Table 1

Parameters required in DEM simulation

Parameter	Value
The Poisson's ratio of barley stem	0.2~0.5
The Poisson's ratio of the steel plate	0.3
Shear modulus of barley stem / MPa	50~90
Shear modulus of steel plate / MPa	7.9×10^{4}
Density of barley stem / ($kg\cdot m^{-3}$)	758
Density of steel / ($kg\cdot m^{-3}$)	7800
Restitution coefficient between barley stems	0.1~0.6
Static friction coefficient between barley stem and barley stem	0.2~0.6
Rolling friction coefficient between barley stem and barley stem	0.05~0.15
Restitution coefficient between barley stem and steel	0.4~0.8
Static friction coefficient between barley stem and steel	0.3~0.6
Rolling friction coefficient between barley stem and steel	0.2~0.4

Cylinder lifting experiment

The inner diameter and height of the cylinder in the simulation are the same as those in the experiment. The dynamic particle generation method was used to freely fall in the particle factory and fill the cylinder. The generation rate was 5000/s, the generation time was 1s, and a total of 500 particles were generated. After the particle state was stable, the cylinder was lifted vertically at a speed of 0.05 m/s. The stem particles slowly flowed out from the bottom of the cylinder, and finally formed a stable particle pile on the bottom plate. Combined with the mechanical characteristics of highland barley stem and the calculation accuracy of the model, the Hertz-Mindlin (no slip) contact model built in EDEM software was adopted. All simulation time steps select 20 % Rayleigh time step. In the simulation, the mesh size is 2.5 times of the spherical unit size, and the simulation time is 6 s.

RESULTS

Plackett-Burman test and result

R4.2.3 was used for experimental design and data analysis. In order to screen out the parameters that have a significant effect on the angle of repose of highland barley stem particles, 8 real parameters and 3 virtual parameters were selected for the Plackett-Burman test with a design level of 2. The factor levels are expressed in the form of -1 and +1, as shown in Table 2.

There is only one central point in this experiment. A total of 13 experiments were conducted. The experimental design and results are shown in Table 3.

Table 2

Parameters of Plackett-Burman test

Symbol	Parameters	Low level (-1)	High level (+1)
X_1	The Poisson's ratio of barley stem	0.2	0.5
X_2	Shear modulus of barley stem /MPa	50	90
X_3	Barley stem-barley stem restitution coefficient	0.1	0.6
X_4	Barley stem-barley stem static friction coefficient	0.2	0.6
X_5	Barley stem-barley stem rolling friction coefficient	0.05	0.15
X_6	Barley stem -steel restitution coefficient	0.4	0.8
X_7	Barley stem -steel static friction coefficient	0.3	0.6
X_8	Barley stem -steel rolling friction coefficient	0.2	0.4
X_9、X_{10}、X_{11}	Virtual parameters	-	-

Table 3

Design and results of Plackett-Burman test

No.	X1	X2	X3	X4	X5	X6	X7	X8	X9	X10	X11	Angle of repose/ [°]
1	-1	1	1	-1	1	1	1	-1	-1	-1	1	30.65
2	-1	-1	-1	-1	-1	-1	-1	-1	-1	-1	-1	28.9
3	-1	1	-1	1	1	-1	1	1	1	-1	-1	38.71
4	1	1	-1	-1	-1	1	-1	1	1	-1	1	32.38
5	-1	1	1	1	-1	-1	-1	1	-1	1	1	37.54
6	1	1	1	-1	-1	-1	1	-1	1	1	-1	30.96
7	1	-1	-1	-1	1	-1	1	1	-1	1	1	34.15
8	-1	-1	-1	1	-1	1	1	-1	1	1	1	31.44
9	1	-1	1	1	-1	1	1	1	-1	-1	-1	33.63
10	1	1	-1	1	1	1	-1	-1	-1	1	-1	38.44
11	1	-1	1	1	1	-1	-1	-1	1	-1	1	36.36
12	-1	-1	1	-1	1	1	-1	1	1	1	-1	33.69
13	0	0	0	0	0	0	0	0	0	0	0	38.29

R4.2.3 was used to analyze the variance of the Plackett-Burman test results, and the influence of each parameter was shown in Table 4 below. From the variance results, the P values of the static friction coefficient between barley stems (X_4), the rolling friction coefficient between barley stems (X_5) and the rolling friction coefficient between barley stems and steel plate (X_8) were all less than 0.05, indicating that the impact on the angle of repose was significant, and other factors had no significant effect on the experimental results. Therefore, these three factors can be used directly as test factors for the steepest ascent test and the Box-Behnken test.

Table 4

Analysis of significance of parameters in Plackett-Burman test

Source of variation	Quadratic sum	Freedom	Mean square	F	P value
Model	112.91	8	14.11	14.7	0.0246*
X1	2.08	1	2.08	2.16	0.238
X2	9.21	1	9.21	9.58	0.0535
X3	0.12	1	0.12	0.12	0.7491
X4	53.72	1	53.72	55.93	0.0050**
X5	24.51	1	24.51	25.52	0.0150*
X6	3.4	1	3.4	3.54	0.1564
X7	5.03	1	5.03	5.24	0.1061
X8	14.85	1	14.85	15.46	0.0293*
Residual	112.91	3	14.11		

*Note: * shows the term is significant (P<0.05), ** shows the term is significant (P<0.01).*

Steepest ascent test and result

In order to quickly approach the optimal value, the steepest ascent test was carried out based on the significant influencing factors screened by Plackett-Burman test. The static friction coefficient between highland barley stems, the rolling friction coefficient between highland barley stems, and the rolling friction coefficient between highland barley stems and steel plates gradually increase according to the fixed steps. The non-significant factors take the intermediate level of the Plackett-Burman test. The relative error of the angle of repose between the simulation results and the actual test is the test index. The design and results of test is shown in Table 5.

Table 5

Design and results of steepest ascent test

No.	Barley stem- barley stem static friction coefficient A	Barley stem- barley stem rolling friction coefficient B	Barley stem-steel rolling friction coefficient C	Angle of repose [°]	Relative error [%]
1	0.2	0.05	0.2	29.16	5.39
2	0.28	0.07	0.24	31.66	2.73
3	0.36	0.09	0.28	34.95	13.40
4	0.44	0.11	0.32	36.15	17.29
5	0.52	0.13	0.36	41.63	35.07
6	0.6	0.15	0.4	52.27	69.60

It can be seen from the table that the angle of repose increases with the increase of the test factor value, and the relative error can show a trend of decreasing first and then increasing. When the values of A, B and C are 0.28, 0.07 and 0.24 respectively, the relative error of the angle of repose is the smallest. Therefore, the optimal value interval is near the level 2. The level 2 is set as the center point of the response surface test, and the levels 1 and 3 are taken as the low level and high level of the response surface test.

Box-Behnken test and regression model

According to the screening results, the three contact parameters of the static friction coefficient A between highland barley stems, the rolling friction coefficient B between highland barley stems, and the rolling friction coefficient C between highland barley stems and steel plates were taken as test factors, and the design of Box-Behnken test with three-factor and three-level was carried out. The number of repetitions of the center point was 4, and a total of 16 sets of simulation tests were carried out. The experimental design and results are shown in Table 6.

Table 6

Design and results of Box-Behnken test

No.	Barley stem- barley stem static friction coefficient A	Barley stem- barley stem rolling friction coefficient B	Barley stem-steel rolling friction coefficient C	Angle of repose [°]
1	-1 (0.2)	-1 (0.05)	0 (0.24)	26.79
2	1 (0.36)	-1	0	31.89
3	-1	1 (0.09)	0	32.8
4	1	1	0	33.3
5	-1	0 (0.07)	-1 (0.2)	28.02
6	1	0	-1	33.82
7	-1	0	1 (0.28)	32.55
8	1	0	1	32.32
9	0 (0.28)	-1	-1	27.8
10	0	1	-1	33.88
11	0	-1	1	30.28
12	0	1	1	32.89
13	0	0	0	32.02
14	0	0	0	32.12
15	0	0	0	32.61
16	0	0	0	32.25

The regression model was established based on the response surface regression test results. The quadratic regression model between the angle of repose θ and static friction coefficient A between barley stem, rolling friction coefficient B between barley stem and rolling friction coefficient C between barley stem - steel was obtained as follows:

$$\theta = -72.145 + 209.92A + 841.31B + 316.43C - 718.75AB - 471.1AC - 1084.4BC - 51.95A^2 - 1993.75B^2 - 196.88C^2 \quad (8)$$

According to the variance analysis results of the model, the static friction coefficient A between the highland barley stems, the rolling friction coefficient B between the highland barley stems, and the rolling friction coefficient C between the highland barley stems and the steel plate have extremely significant effects on the accumulation angle. The interaction terms AB, BC, AC and quadratic term B^2 also have extremely significant effects on the angle of repose. The response surface of the interaction between the factors on the angle of repose is shown in Fig. 6.

The P value ($P<0.0001$) of the fitting regression model shows that the regression relationship reaches extremely significant, and the regression model can describe the quantitative relationship of most experimental data. The P value of the lack of fit is 0.49230, and there is no lack of fit, indicating that the regression equation fits well. The determination coefficient R^2 is equal to 0.9868, adjusted R^2_{adj} is equal to 0.9669, both are close to 1, indicating that the fitting equation has high reliability. The variance test results are shown in Table 7 below.

In the case of ensuring that the model is significant and the lack of fit is not significant, the items with insignificant effects are eliminated, and the quadratic regression model is optimized to obtain a new regression Equation (9):

$$\theta = -58.649 + 180.83A + 866.31B + 226.94C - 718.75AB - 471.1AC - 1146.88BC - 2056.25B^2 \quad (9)$$

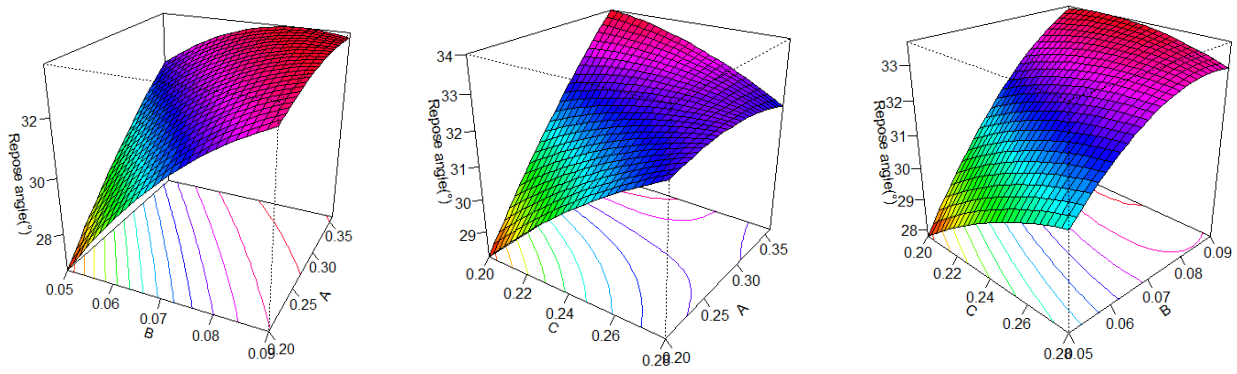

a) b) c)

Fig. 6 - Response surfaces for angle of repose

Table 7

ANOVA of quadratic polynomial model of Box-Behnken test

Source of variation	Quadratic sum	Freedom	Mean square	F	P value
Model	71.365	9	7.929	49.73	<.0001***
A	15.596	1	15.596	95.7233	<.0001***
B	33.252	1	33.252	204.0888	<.0001***
C	2.785	1	2.785	17.0921	0.0061**
AB	5.29	1	5.29	32.4681	0.0013**
AC	9.09	1	9.09	55.7925	0.0003 ***
BC	3.367	1	3.367	20.6668	0.0039**
A2	0.378	1	0.378	2.3214	0.1784
B2	2.706	1	2.706	16.6086	0.0065 **
C2	0.462	1	0.462	2.838	0.143
Residual	0.978	6	0.1629		
Lack of fit	0.495	3	1649	1.0244	0.4923
Pure error	0.483	3	0.161		
Sum	72.343	15			

*Note: * shows the term is significant (P<0.05), ** shows the term is significant (P<0.01), *** shows the term is significant (P<0.001)*

The variance analysis of the optimized regression model is shown in Table 8. The coefficient of determination R^2 of the model is equal to 0.9754, and the adjusted R^2_{adj} is equal to 0.9539, both of which are close to 1, indicating that the fitting reliability of the optimized equation is still high. The standard error of the residual is 0.4767, and a smaller value indicates that the higher the prediction accuracy of the model, the better the fit of the model. It is explained that the optimization model can be used to predict the accumulation angle of the particle pile.

Table 8

ANOVA of modified model of Box-Behnken test

Source of variation	Quadratic sum	Freedom	Mean square	F	P value
Model	72.081	7	10.297	45.31	<0.0001***
A	15.596	1	15.596	68.622	<0.0001***
B	33.252	1	33.252	146.307	0.008**
C	2.78	1	2.78	12.253	0.008**
AB	2.706	1	2.706	11.906	0.001**
AC	5.29	1	5.29	23.276	<0.0001***

Source of variation	Quadratic sum	Freedom	Mean square	F	P value
BC	9.09	1	9.09	39.997	0.005**
B2	3.367	1	3.367	14.816	0.008**
Residual	1.81	8	0.228		
Sum	73.891	15			

Optimal parameter combination and simulation verification

The ridge analysis of software R was used to obtain the parameter combination closest to the true value in the regression model. The static friction coefficient between barley stem was 0.27, the rolling friction coefficient between barley stem was 0.07, and the rolling friction coefficient between barley stem and steel should be 0.26. The other non-significant parameters take the intermediate level (the Poisson's ratio of highland barley stem is 0.35, the shear modulus of highland barley stem is 70 MPa, restitution coefficient between barley stem is 0.35, restitution coefficient between barley stem and steel is 0.6, and the static friction coefficient between barley stem and steel is 0.45). The numerical simulation of the above parameters is used to verify the accuracy of the optimal parameter combination. The particle accumulation morphology is simulated by using the above parameter values as shown in Fig. 7. The angles of repose of highland barley stem particles obtained by repeated three experiments were 30.26 °, 31.04 ° and 30.68 °, respectively, with an average value of 30.66 °. The relative error between the simulated and experimental values was 0.52 %. The small relative error indicates that there is no significant difference between the simulation results and the actual test results, indicating that the calibrated parameters are credible. It can be used for discrete element simulation of highland barley and provide reference for subsequent research on highland barley screening.

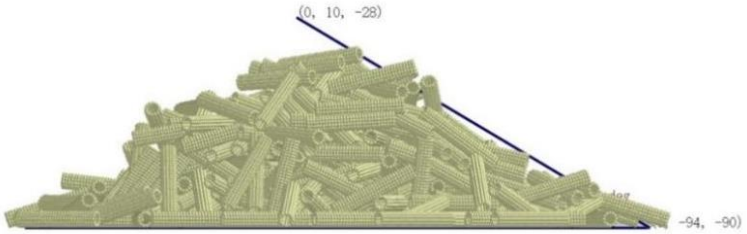

Fig. 7 - Simulation model of highland barley stem angle of repose

CONCLUSIONS

1) Through the Plackett-Burman test results, three factors that had significant effects on the accumulation angle of highland barley stem particles were screened out: static friction coefficient between barley stems, rolling friction coefficient between barley stems and rolling friction coefficient between barley stem and steel; the Poisson's ratio, shear modulus and collision recovery coefficient of highland barley stem had no significant effect on the stacking angle.

2) According to the results of the Box-Behnken experiment, a quadratic regression model between the significance parameters and the accumulation angle was established and optimized, and the primary terms of the three significance parameters (static friction coefficient between barley stems, rolling friction coefficient between barley stems, rolling friction coefficient between barley stems and steel) and the quadratic terms of the rolling friction coefficients between barley stems had significant effects on the calibration of barley parameters, and a quadratic regression model between the angle of repose θ and the three significance parameters was established.

3) By solving the optimized regression model, it is found that when the static friction coefficient between barley stems is 0.27, the rolling friction coefficient between barley stems is 0.07, the rolling friction coefficient between barley stems and steel should be 0.26, and the other non-significant parameters are at the intermediate level (the Poisson's ratio of highland barley stems is 0.35, the shear modulus of highland barley stems is 70 MPa, restitution coefficient between barley stems is 0.35, restitution coefficient between barley stems and steel is 0.6, and the static friction coefficient between barley stems and steel is 0.45), the relative error between the simulation and the actual test is 0.52 %. It shows that the calibrated contact parameters are effective and feasible.

ACKNOWLEDGEMENT

This research was supported by the Science and Technology plan project of Tibet Autonomous Region - Research and development and application of equipment for key links of highland barley mechanized production（XZ202301ZY0015N), the National technical system of barley and highland barley industry (CRAS-05-04A-01).

REFERENCES

[1] Bian B., (2015), The production status and countermeasures of mechanization of highland barley (浅议青稞机械化生产现状及对策). *Tibet journal agricultural sciences*, Vol. 37, Issue 02, pp. 46-48, Tibet/China.

[2] Chen T., Yi S., Li Y., (2023), Establishment of Discrete Element Model and Parameter Calibration of Alfalfa Stem in Budding Stage (苜蓿现蕾期茎秆离散元模型建立与参数标定). *Transactions of the Chinese Society for Agricultural Machinery*. Vol. 54, Issue 5, pp. 91-100, Beijing/China.

[3] Ding W., Zhu J., Chen W., (2021), Simulation calibration of highland barley contact parameters based on EDEM (基于 EDEM 的青稞接触参数仿真标定). *Journal of Chinese Agricultural Mechanization*, Vol. 42, Issue 9, pp. 114-121, Beijing/China.

[4] Hou J.， Xie F., Wang X., (2022), Measurement of contact physical parameters of flexible rice straw and discrete element simulation calibration (水稻茎秆接触物理参数测定与离散元仿真标定). *Acta Agriculturae Universitatis Jiangxiensis*. Vol. 44, Issue 3, pp. 747-758, Jiangxi/China.

[5] Liao Y. Wang Z., Liao Q., (2020), Calibration of Discrete Element Model Parameters of Forage Rape Stalk at Early Pod Stage (果荚初期饲料油菜茎秆离散元接触模型参数标定). *Transactions of the Chinese Society for Agricultural Machinery*. Vol. 51, Issue S1, pp. 236-243, Beijing/China.

[6] Liu F., Zhang J., Li B., Chen J., (2016), Calibration of parameters of wheat required in discrete element method simulation based on repose angle of particle heap (基于堆积试验的小麦离散元参数分析及标定). *Transactions of the Chinese Society of Agricultural Engineering*, Vol. 32, Issue 12, pp. 247-253, Beijing/China.

[7] Liu F., (2018), Discrete element modelling of the wheat particles and short straw in cleaning devices (清选装置中小麦颗粒和短茎秆离散元建模研究). MSc Thesis, Northwest A＆F University, Shaanxi/China.

[8] Shu C., Yang J., Wan X., (2022), Calibration and experiment of the discrete element simulation parameters of rape threshing mixture in combine harvester (联合收获油菜脱出物离散元仿真参数标定与试验). *Transactions of the Chinese Society of Agricultural Engineering*, Vol. 38, Issue 9, pp. 34-43, Beijing/China.

[9] Su Z.， Li Y.， Dong Y.， et al. (2020), Simulation of rice threshing performance with concentric and non-concentric threshing gaps. *Biosystems engineering*, 197, pp. 273-276, England.

[10] Wang J., (2017), Development status and problems of agricultural mechanization in Tibet (西藏农业机械化发展的现状及问题). *Tibet Science and Technology*, Vol.11, pp. 10-11, Tibet/China.

[11] Wang B., Zhang Q., Ding X., (2021), Current Situation and Existing Problems of Highland Barley Mechanized Harvest (青稞机械化收获现状及存在问题). *Guangdong Sericulture*, Vol.55, Issue 01, pp.55-57, Guangdong/China.

[12] Wang M., Wang W., Yang L., (2018), Research of discrete element modeling method of maize kernel based on EDEM (基于 EDEM 的玉米子粒建模方法的研究). *Journal of Henan Agricultural University*, Vol. 52, Issue 01, pp. 80-84+103, Henan/China.

[13] Xu Y., Jiang H., Wei D., (2020), Current situation and countermeasures of mechanized production of highland barley under the integration of “Five Good” (“五良”融合下青稞机械化生产现状及对策浅析). *Agricultural Technology& Equipment*, Vol. 371, Issue 11, pp. 63-64, Shanxi/China.

[14] Zeng Z., Ma X., Cao X., (2021), Critical review of applications of discrete element method in agricultural engineering (离散元法在农业工程研究中的应用现状和展望). *Transactions of the Chinese Society for Agricultural Machinery*. Vol. 52, Issue 4, pp. 1-20, Beijing/China.

[15] Zhang R., Jiao W., Zhou J., (2020), Parameter calibration and experiment of rice seeds discrete element model with different filling particle radius (不同填充颗粒半径水稻种子离散元模型参数标定). *Transactions of the Chinese Society for Agricultural Machinery*. Vol. 51, Issue S1, pp. 227-235, Beijing/China.

[16] Zhang Y., (2022), Development Status and Countermeasures of Agricultural Mechanization in Tibet (西藏农业机械化发展现状及对策). *Co-Operative Economy & Science*, Vol. 24, Issue 59, pp. 40-42.

[17] Wang C., Li Y., Ma L., (2012), Experimental study on measurement of restitution coefficient of wheat seeds in collision models (小麦籽粒碰撞模型中恢复系数的测定). *Transactions of the Chinese Society of Agricultural Engineering*, Vol. 28, Issue 11, pp. 274-278, Beijing/China.

[18] Wang W., Liu W., Yuan L., (2020), Simulation and experiment of single longitudinal axial material movement and establishment of wheat plants model (小麦植株建模与单纵轴流物料运动仿真与试验). *Transactions of the Chinese Society for Agricultural Machinery*. Vol. 51, Issue S2, pp. 170-180, Beijing/China.

[19] Wang X., Hu H., Wang Q., (2017), Calibration method of soil contact characteristic parameters based on DEM theory (基于离散元的土壤模型参数标定方法). *Transactions of the Chinese Society for Agricultural Machinery*. Vol. 48, Issue 12, pp. 78-85, Beijing/China.

[20] Wang R., Li P., Wang T., (2022), Discrete element parameter calibration for round bales of corn stalks (圆捆玉米秸秆离散元参数标定). *Journal of Shenyang Agricultural University*. Vol. 53, Issue 3, pp. 319-326, Liaoning/China.

[21] Xiao J., Liu G., Liu J., et al. (2019), Parameters of a discrete element ballasted bed model based on a response surface method. *Journal of Zhejiang University-SCIENCE A*, Vol. 20, Issue 9, pp.685-700, *Zhejiang/China.*

PARTICLE MOTION OF COATED CORN SEED ACCUMULATION PROCESS BASED ON DISCRETE ELEMENT METHOD
/
基于离散元法的包衣玉米种子堆积过程颗粒运动研究

Shihao WANG [1)], Shouhao XIA [1)], Yongxin CHEN [1)], Chao LOU [1)], Dinglin REN [1)], Zhaodong LI*[1, 2)]
[1)] College of Engineering, Anhui Agricultural University, Hefei, Anhui, 230036, China
[2)] Engineering Laboratory of Intelligent Agricultural Machinery Equipment, Anhui, Hefei, 230036, China
Tel: +86 13675606219; E-mail addresses: Lizd@ahau.edu.cn
DOI: https://doi.org/10.35633/inmateh-72-34

Keywords: *model of particles; corn; angle of repose; liquidity; discrete element method*

ABSTRACT
The rolling friction coefficient was a fundamental parameter for particle modeling, but it was challenging to quantify for unevenly shaped corn seeds. If the rolling friction coefficients of corn with different guiding seeds and different shapes were not believed to be significantly different, direct simulation in EDEM would produce simulation distortion. This paper began by selecting three models with a relatively high proportion from five corn samples with various shapes (such as horse-tooth shape, spherical shape, oblate shape, and irregular shape, etc.) and modeling them according to the actual seeds. Due to the large disparity between seed models with different shapes, the study adopted the method of combining physical experiment and discrete element simulation, took the rolling friction coefficient as the independent variable and the angle of repose in the simulation test as the target value, and calibrated the rolling friction of various shapes of corn seed particles separately. Coated corn seeds' rolling friction coefficients were accurately predicted (0.0047 for horse tooth, 0.0058 for pyramid, and 0.049 for spherical shape). During the validation test, the calibrated simulation parameters were entered into EDEM for simulation, and the distribution of seeds on the seed platter was compared between the actual test and the simulation test. The results demonstrated that the difference in the sizes of key features was less than 5.60 percent, and the population boundary in the seed platter after calibration was closer to the actual situation, which improved the accuracy of the simulation.

摘要
滚动摩擦系数是进行颗粒模拟的基础参数，但对于形状不规则的玉米种子，滚动摩擦系数难以测量。如果不考虑模型形状的不同导种不同形状玉米之间的滚动摩擦系数有较大差异，直接在 EDEM 中进行仿真，会出现仿真失真的情况。针对此问题，本文首先从五种不同形状的玉米样品（如马齿形、球形、扁球形和不规则形状等）选出三种较为典型且占比较高的模型，根据实际种子进行建模。由于不同形状种子模型的差距较大，本文采用物理实验和离散元仿真结合的方法，以滚动摩擦系数为自变量，以仿真试验的休止角为目标值，将几种不同形状玉米种子颗粒的滚动摩擦进行了单独标定，详细预测包衣玉米种子的滚动摩擦系数(马齿形为 0.0047、棱锥形为 0.0058、类球形为 0.049）。同时研究了包衣玉米种子滚动摩擦系数和颗粒形状对休止角形成过程的影响，提取了种群势能和平均速度，结果表明滚动摩擦系数可以改变种群流动性，增加玉米种子休止角形成的时间；玉米形状不同对休止角形成过程的作用不同，流动性较差马齿状可以很好的增加种子堆的高度和休止角，流动性较好的类球形则会增大堆积范围。在验证试验中，将标定的仿真参数输入 EDEM 中进行仿真，对比实际试验与仿真试验排种器内种子的分布情况，结果表明：关键特征尺寸数值差异在 5.6%以内标定后的排种器内种群的边界与实际情况更接近，提高了仿真的可靠性，为气力式玉米排种器离散元研究提供了理论依据。

INTRODUCTION
Corn is an important grain, oil, and feed crop that plays a significant role in agricultural output (*Shi et al., 2014*). The quality of the seeds ensures a stable and abundant harvest. In order to ensure the quality of seeds, researchers need to do a lot of analysis of the seeding process.

Shihao Wang, U.G. Stud.; Shouhao Xia, M.S. Stud.; Yongxin Chen, Prof.;
Chao Lou, M.S. Stud.; Dinglin Ren, M.S. Stud.; Zhaodong Li, Assoc. Prof

The processes of seed filling, seed clearing, seed carrying, and seed casting of the corn seed in the seeding process through the seeder were all discrete particle movements (*Ding et al., 2019*). The contact movement process between seeds and seeds, as well as between seeds and the seed-metering device, was rather complicated in the preceding procedure. Using the discrete element method (DEM) to examine the migration law of the seed-metering device in the seed drainer during the seed drainage process (*Owen and Cleary, 2012*).

Establishing a more precise seed particle model is necessary for discrete element simulation (*Chen et al., 2018*). Using the polyhedron filling approach (*Wang et al., 2022),* they created six sunflower seed multi-sphere models with varying accuracy (25, 28, 31, 34, 37, and 40 subspheres), and the results indicate that the 31-sphere model is more consistent with the real test results. Using the multi-sphere technique, *Zhou et al., (2020),* created four seed particle models of differing precision. The multi-ball model employs artificial roughness to assess its filling precision. On the basis of the combined spherical technique, *Li et al., (2020*), created a discrete elementary particle model for buckwheat seeds. *Wang et al., (2018)* established the discrete fundamental model of corn seeds and *Xu et al., (2020)*, constructed the discrete elementary model of soybean seeds, while *Zhang et al., (2022)*, got the shape of rice seeds using 3D scanning and reverse fitting. They constructed different rice seed particle radius models (0.30, 0.21, 0.18, 0.16, and 0.15 mm). Based on the volume distribution of peanuts, *Wu et al., (2020)*, built a simulation model of peanut seeds. *Ma et al., (2020)*, constructed the discrete element model of alfalfa seed and calibrated the discrete element parameters based on the actual shape of alfalfa seed.

The correct calibration of particle model parameters has a direct impact on the accuracy of discrete element simulation results (*Zhou et al., 2020*). Among these, the rolling friction coefficient is an essential parameter in the discrete element modeling of coated corn seed particles, the foundation of DEM particle simulation, and the foundation for building and enhancing particle processing machines. The coefficient of rolling friction is an essential physical property of corn particles. In the process of motion, the relative rolling of two objects generates rolling friction. Due to the uneven form of corn particles, it is difficult to determine the value of this coefficient (*Wang et al., (2018)*. It has been discovered that particle form and interparticle friction have a significant influence on the uniaxial compression behavior of materials. When rolling friction is applied, simulations of single-nozzle fluidized beds can be greatly enhanced *Goniva et al., (2012)*. The rolling friction force can lower the velocity of particles leaving a flat-bottom bin and influence particle accumulation (*Balevičius et al., 2012*). According to previous research, the relationship between rolling friction and rolling speed of a soft ball on a hard plane is nonlinear (*Yung and Xu, 2003),* and the friction coefficient grows linearly with the increase in average contact pressure until the maximum limit of the constant friction coefficient. (*Xiao et al., 2007*)

According to the aforementioned research, the quality of seed particle modeling and the calibration of seed parameters are the primary factors influencing the accuracy of simulation findings when discrete element simulation of corn seed particles is performed. Few studies, however, have used the discrete element method to investigate the effect of the interplay between seed particle morphologies and rolling friction coefficients on the angle of repose. Angle of repose is a macroscopic quantity that characterizes the flow, friction, and other properties of granular materials; it is related to the physical properties of contact materials and the materials themselves (*Boac et al., 2010)*. In agricultural engineering, it is typically used to calibrate material parameters, such as seeds and soil (*Wang et al., 2017*). In this study, the characteristic sizes of three distinct corn seed shapes were measured, and a strategy for establishing reliable seed models based on the positive distribution of the characteristic sizes was provided. The method ensured the precision of model construction and the efficiency of simulation time. The effects of various corn seed shapes and rolling friction coefficients on population migration were then investigated. It provided a theoretical basis for the design of a corn precision seed-metering device and the discrete element research of the law of orderly transport of corn seed particles in the corn precision seed-metering device.

MATERIALS AND METHODS

Establish particle contact mechanics model

Zhengdan 958, a commonly planted variety, was chosen for this investigation, and the drying process evaluated its moisture content, which was 12.7%. The moisture concentration of corn seed particles was lower; therefore, particle adhesion could be disregarded. To simulate the accumulation process of corn seeds, the rolling friction model related to relative velocity, namely the Hertz-Mindlin (no slip) contact model in EDEM software, was chosen (*Peng et al., 2018*).

Density, Poisson ratio, shear modulus, recovery coefficient, static friction coefficient, and rolling friction coefficient are the parameters of the Hertz-Mindlin model. The discrete element method simulates the propagation process of moving particles, and the movement of particles will inevitably result in collisions and force generation between particles. According to the different contact modes, the discrete element can be subdivided into hard ball contact and soft ball contact, and the soft particle contact model permits overlap between the contact points of two particles. The contact force can be calculated based on the amount of normal phase overlap and tangential displacement between particles, and the normal phase and tangential forces are closely related to the friction between particles. Therefore, this study employs the soft particle contact model, as illustrated in Fig. 1.

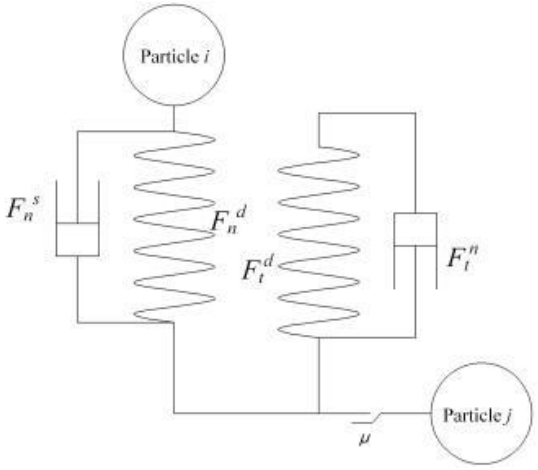

Fig. 1 - Particle-contact model

The definitions of normal contact force and tangential contact force are as follows:

$$F_n = F_n^s + F_n^d \quad (1)$$

$$F_t = F_t^s + F_t^d \quad (2)$$

where:

F_n is the normal contact force; F_t is the tangential contact force [N]; F_n^s is the elastic and viscous damping forces of vertical; F_n^d is the contact surface [N]; F_t^s is the static friction force; F_t^d is the dynamic friction force in the tangent direction of the contact surface [N].

$$F = \begin{cases} F_t \cdot if \cdot F_t < \mu \cdot F_n \\ \mu \cdot F_n^s \cdot if \cdot F_t < \mu \cdot F_n \end{cases} \quad (3)$$

where:

μ is the friction coefficient; F is the tangential total contact force.

After calculating F_n and F_t, the gravitational force is applied to these two forces to determine the resultant force. The resultant force F_{res} is calculated as follows:

$$F_{res} = F_n + F_t + mg \quad (4)$$

where:

m is the mass [g]; g is the gravitational acceleration of particles [m/s^2]; F_{res} is the resultant force on the particle [N].

Due to the fact that the tangential component of the contact force causes the torque effect M, the magnitude of the torque effect is calculated as the product of the tangential force F_t and the vertical distance between the contact point and the center of mass r (*Tanaka et al., 2000*). Consequently, the torque effect is determined as follows:

$$M = r \cdot F_t \quad (5)$$

$$r_{ij} = \frac{r_i \cdot r_j}{r_i + r_j} \quad (6)$$

where:

M is the torque generated by the tangential component of the contact force [N·m]; r_i, r_j are the equivalent diameters of particles i and j [mm].

In granular systems, rolling frictional drag consumes energy during relative rotation and provides packing support that stabilizes the granular system. Therefore, additional torques are applied to the contact surface.

$$M_r = -\mu_r \cdot F_n^s \cdot r \cdot \lambda_\theta \tag{7}$$

where:

M_r is the torque due to rolling friction [N·m]; μ_r is the coefficient of rolling friction; $\lambda_{\dot{\theta}}$ is the vector of angular velocity per unit time; $\dot{\theta}$ is the contact point angle [°].

The resultant torque M_{res} is as follows:

$$M_{res} = M + M_r \tag{8}$$

Newton's second law of motion is used to calculate the particle's acceleration in order to update its position. The particle's translational and rotational accelerations are as follows:

$$\ddot{a} = \frac{F_{res}}{m} \tag{9}$$

$$\ddot{\omega} = \frac{M_{res}}{I} \tag{10}$$

where:

$\ddot{a}$ is the particle translational acceleration [m/s²]; $\ddot{\omega}$ is the particle rotational acceleration [m/s²]; I is the moment of inertia of the particle [mm⁴].

After calculating the velocity, the new particle localization is determined by integrating the velocity over the time interval. The following are the definitions of normal and tangential contact forces and damping forces between two particles:

$$F_n^s = -K_n h^{\frac{3}{2}} \tag{11}$$

$$K_n = 2 \cdot E_{ij} \cdot \sqrt{r_{ij} \cdot a_{ijn}} \tag{12}$$

$$\frac{1}{E_{ij}} = \frac{(1-v_i^2)}{E_i} + \frac{(1-v_j^2)}{E_j} \tag{13}$$

where:

K_n is the normal stiffness; h is the normal component of relative displacement [mm]; E is the Young's modulus of the corresponding particle; v is the Poisson ratio of corresponding particles i and j.

Mindlin's definition of tangential contact forces:

$$F_s^t = -K_t \cdot h \tag{14}$$

$$K_t = 8 \cdot G_{ij} \sqrt{r_{ij} \cdot h} \tag{15}$$

$$\frac{1}{G_{ij}} = \frac{2-v_i}{G_i} + \frac{2-v_j}{G_j} \tag{16}$$

where:

K_t is the tangential stiffness defined by Mindlin; G is the shear modulus of particles i and j [g].

Then the normal damping and tangential damping forces are:

$$F_n^d = -2 \cdot \sqrt{\frac{5}{6}} \cdot \psi \cdot \sqrt{K_n \cdot m_{ij}} \cdot \dot{a}_{ijn} \tag{17}$$

$$F_t^d = -2 \cdot \sqrt{\frac{5}{6}} \cdot \psi \sqrt{K_n \cdot m_{ij}} \cdot \dot{a}_{ijt} \tag{18}$$

$$m_{ij} = \frac{m_i + m_j}{m_i \cdot m_j} \tag{19}$$

where:

ψ is the corresponds to the viscous damping coefficient in tangential and normal directions [N·m/s]; m is the mass of particles i and j [g].

When DEM is used to simulate the motion law of coated corn seeds, the rolling friction coefficient and restoration coefficient of the particle model are important parameters that affect the accuracy of different corn simulation models, and the rolling friction coefficient is an important parameter for studying the fluidity of different corn seed particle model shapes.

Analysis of the geometric shape of corn

Multi-contrast observation was used to classify Zheng-dan 958 corn seeds into horse-tooth shape, prism shape, spherical shape, spherical-cone and irregular shape. As depicted in Fig. 2. The upper and lower profiles of the horse tooth seed particles are trapezoidal, the overall thickness varies little, the width is significantly greater than its thickness, and the shape resembles horse teeth. The prism edge has four distinct edges and has the general shape of a cone; its thickness decreases gradually from base to apex, and its width is slightly greater than its thickness. The quasi-sphere can be represented as a sphere with a circle-like surface. The base of the cone is circular, while the upper portion is conical. Other than the aforementioned four, irregular shapes consist of all other shapes.

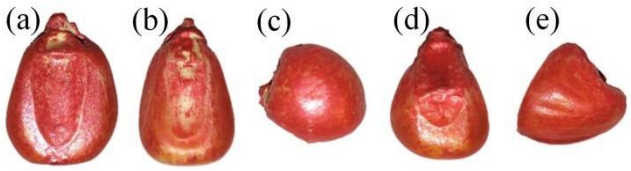

Fig. 2 - Geometrical shape classification of corn seeds of the same variety

(a) horse-tooth, (b)prism, (c) spherical, (d) spherical-cone, and (e) irregular shape.

One thousand seeds were selected at random and categorized according to their respective shapes. As illustrated in Fig. 3, the percentage of equine tooth-shape, prism shape, spherical shape, and irregular shape were 62.2%, 17.2%, 13.8%, 3.8%, and 3%, respectively, and the sum of equine tooth shape, prism shape, and spherical shape comprised approximately 93.2% of the total number of corn grains. The proportion of irregular and spherical conical seeds does not exceed 7%. Since the percentage of these two types of seeds is much lower than the percentage of the other three types of seeds, they are disregarded to simplify the modeling of corn seed particles in this paper.

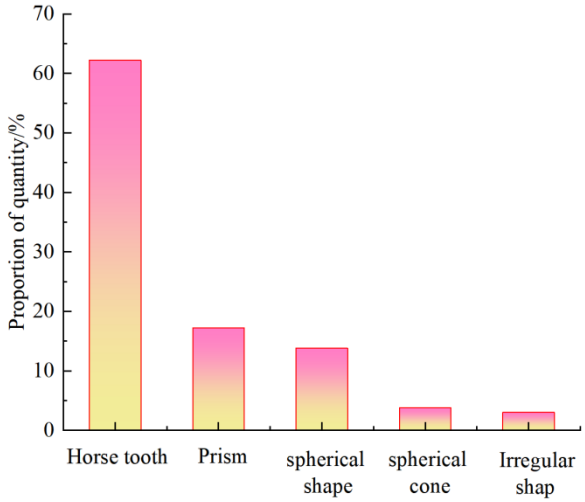

Fig. 3 - Percentage of each shape of corn seeds for Zheng-dan 958

Process for modeling corn seed particle and related analysis

Currently, numerous scientists establish the particle model of corn seeds using the sphere filling method (*Pasha et al., 2016*). In the model presented above, the arrangement and quantity of marbles are distinct. The calculation time increases as the number of marbles increases. However, this does not necessarily increase the accuracy of the model for corn seeds (*Urtė et al., 2016*). When the number of marbles reaches a certain threshold in practical applications, model accuracy and calculation time will converge to an acceptable level (*Wang et al., 2017*). There is currently no consensus on the arrangement and number of subfields, and the topic requires additional research. In addition, when establishing its particle model, some studies as for example *Wang et al., (2017)*, only select the triaxial size of corn seeds as the characteristic size. It is difficult to represent the physical characteristics of actual corn seeds.

This study examines coated corn as its research object. The various seed particle morphologies of coated corn were modeled. The size and distribution of corn particles are significant parameters because they affect the modeling basis. Through comparative observation, the corn seeds were divided into three representative shapes: horse-tooth shape, prism shape, and spherical shape. To more accurately model corn seed particles, the size and shape of the actual seed particles were determined.

In order to create a more precise corn model, the characteristic sizes of three distinct corn seed shapes were specified and measured. As illustrated in Fig. 4, the upper width W_1, lower width W_2, thickness T, and height H of horse tooth seeds were primarily measured. Compared to horse tooth seeds, the thickness of prism seeds was significantly altered; however, the overall thickness of horse tooth seeds remained the same, whereas prism seeds had a conical shape with a thicker base and a progressively thinner top. Therefore, the primary dimensions of prism seeds are the upper width W_1, the lower width W_2, the upper thickness T_1, the lower thickness T_2, and the height H, whereas the primary dimensions of spherical seeds are the vertical and horizontal diameters D_1 and D_2. The measurement histogram of the size distribution of three different types of corn seeds is shown in Fig. 5. Origin software is utilized during the fitting process. The fitting curve follows the normal distribution approximately, and the fitting equation is as follows:

$$f(x)=\frac{1}{\sqrt{2\pi}\sigma}e^{-\frac{(x-\mu)^2}{2\sigma^2}} \quad (20)$$

It is symbolized by the symbol N (μ,σ^2), where the horse tooth is W_2 *(9.42, 0.42)*, T *(6.34, 0.55)*, prism W_2 *(8.47, 0.47)*, T_2 *(6.36, 0.51)*, and spherical D_1 *(8.82, 0.51)*, D_2 *(9.08, 0.81)*.

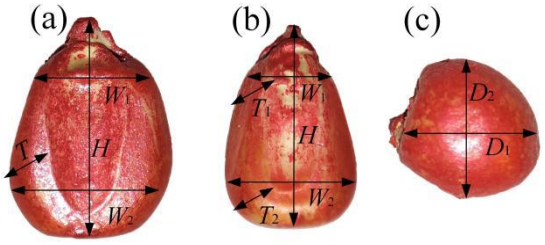

Fig.4 - Corn seed size and discrete element mode
(a) horse-tooth, (b) prism, and (c) spherical.

In the modeling process, pellets are used to determine the number of spheres required within the component to construct the simulated corn. Consequently, the issue is determining the size of each particle within the component used to simulate coated corn seed particles. Currently, some researchers are establishing the particle model of corn seeds via the sphere filling method, using 5, 10, 15, and 20 spheres, respectively, to establish their analysis models. In theory, as the number of spheres increases, the seed model will become closer to the actual seed. However, the study found that the calculation time increased as the number of spheres increased. This does not necessarily enhance the model accuracy of corn seeds, though. In practice, when a certain number of child spheres is reached, model accuracy and calculation time will converge to an acceptable level. In this study, a small number of spheres will be used to establish the seed simulation model so that it closely resembles the actual seed size.

Table 1

Modeling parameters of corn seed morphology

Seed shape	Mean of characteristic sizes						
	W_1	W_2	T_1	T_2	D_1	D_2	H
	[mm]	[mm]	[mm]	[mm]	[mm]	[mm]	[mm]
Horse-tooth	6.9	9.5	5.2	5.2			13.3
Prism	4.8	8.2	4.6	5.6			12.5
Spheroid					8.8	8.6	

The characteristic diameters of three types of seed model particles are displayed in Table 1. The multi-ball filling method of three-shaped corn seed particle models is produced according to the dimensions in Table 1, as depicted in Fig. 6 where (a) is a horse-tooth shape, (b) is a spherical shape, (c_1) is a prism shaped front view, and (c_2) is a prism shaped side view. The thickness of horse tooth seed is comparable to that of the diameter d_1 of the balls in the lower three rows of the horse-tooth shape, which was equal to the thickness of the horse tooth shape, which was 5.2 mm. The diameters of the balls in the upper two rows were d_2 = 4 mm and d_3 = 2 mm. Prism corn seeds were filled with small balls with a d_4 diameter of 4 mm and a d_5 diameter of 8.4 mm. As the thickness decreases gradually from bottom to top, the bottom two layers are filled with 3 mm d_6 balls. Because the thickness and width of the prism base differ, so does the distance between the corresponding balls. The upper width and depth of the prism corn seeds are comparable, so the upper layer is filled with d_8-diameter balls. In the middle, a d_7 = 4.6 mm ball is used for transition, while d_9 = 4.5 mm and d_{10} = 2.3 mm balls are used in the upper portion.

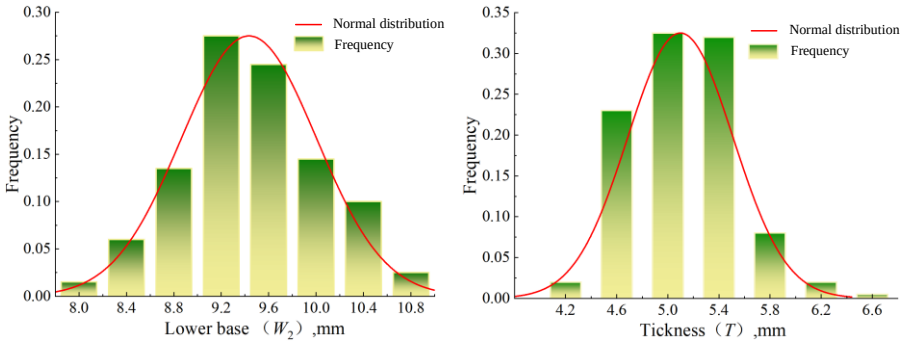

(a) horse-tooth shape

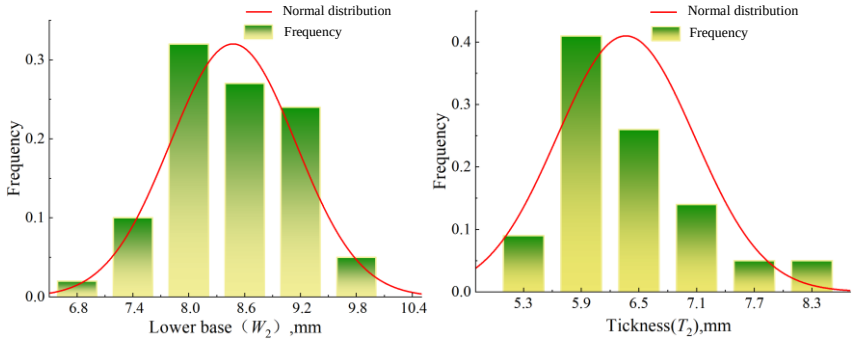

(b) prism shape

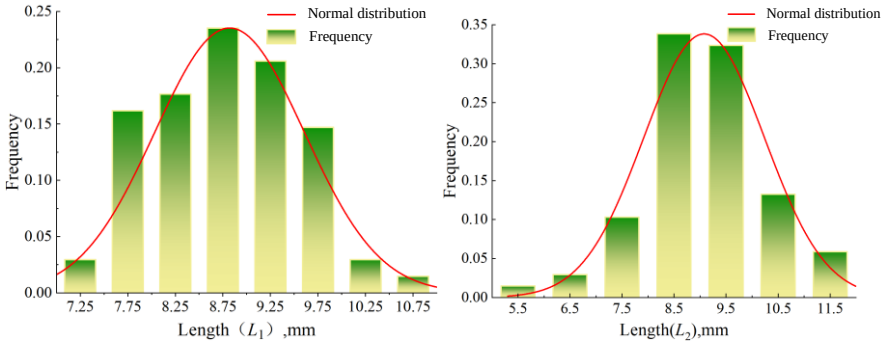

(c) spherical shape

Fig. 5 - Corn seed size and discrete element mode

(a) horse-tooth, (b) prism, (c) spherical

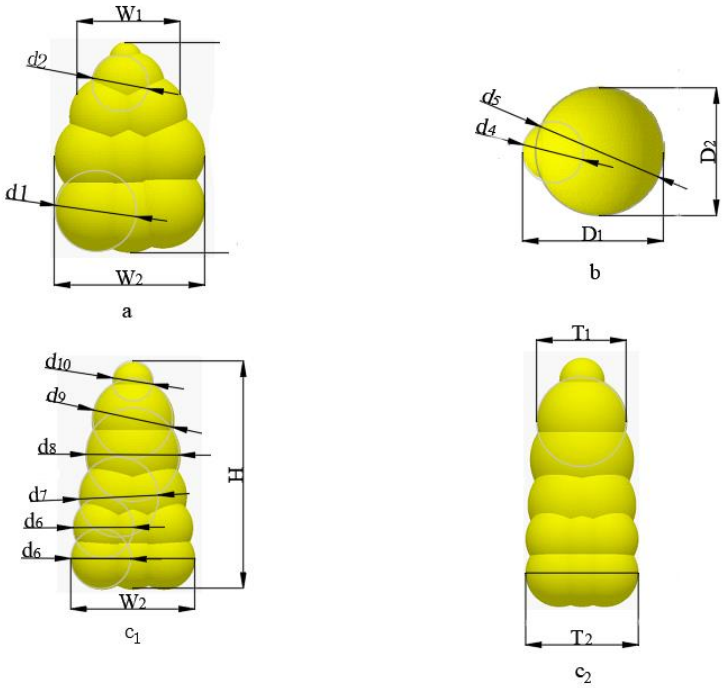

Fig. 6 - A multi-ball filling method for horse-tooth, prism and spherical coated corn seed particle model

(a) Horse-tooth shape; (b) Spherical shape; (c_1) Frontal view of the prism shape; (c_2) The side view of Prism shape.

Formation of the actual angle of repose

The formation process of the plexiglass angle of repose is shown in Fig. 7. 1000 Zhengdan-958 corn seeds are randomly placed into a plexiglass cylinder with an inner diameter of 50 mm. The lower portion of the cylinder tube is attached to the tabletop, and the plexiglass cylinder tube is then lifted vertically and steadily at a rate of 3 mm/s. The angle of repose is the angle between the inclined plane and the horizontal plane of the seed pile. As shown in Fig. 8, the actual seed drop test value is made more precise using computer image processing technology and Matlab software to read the seed drop test image, followed by grayscale and binarization processing to obtain a more precise population accumulation boundary line. Then, in Matlab, invoke cftool to fit the stacked boundary line. As shown in Table 2, the correct value of the angle of repose is the slope of the fitted line; this value is then averaged over the 5 test groups. The angle of repose for the horse tooth is 25.3 °, the angle of repose for the prism is 23.5 °, and the angle of repose for the spherical object is 22.2 °.

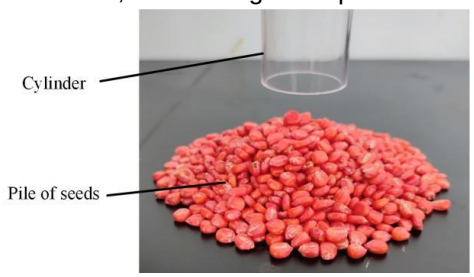

Fig. 7 - Experimental angle of repose of corn seeds

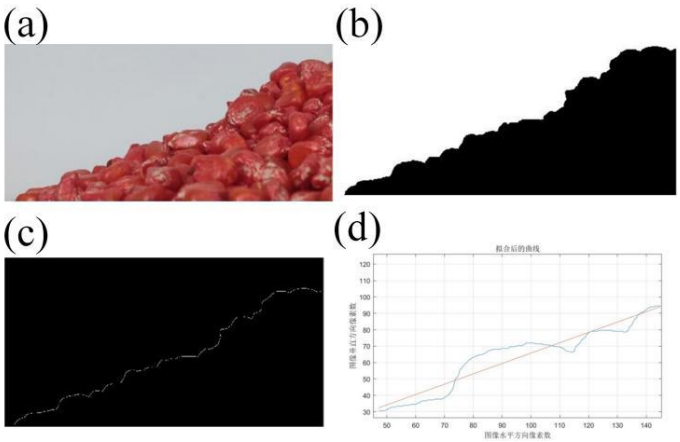

Fig. 8 - The measured value of actual seed dropping test

(a) Original image; (b) Boundary image; (c) Binarized image; (d) Repose angle curve after fitting.

Table 2

Measured repose angles of seed particles with different shapes of coated corn

Material	Angle of repose [°]					Average value [°]	STDEV
Horse-tooth shape	24.7	25.9	26.2	24.7	25.2	25.3	0.62
Prism	24.1	23.7	24.2	22.9	22.7	23.5	0.62
Spherical shape	22.0	22.7	21.9	21.7	22.6	22.2	0.40

Simulation numerical of angle of repose

Angle of repose is a macroscopic quantity that characterizes the flow, friction, and other properties of granular materials. It is related to the physical properties of contact materials and the materials themselves. Before discrete element simulation, it is necessary to identify material characteristic parameters and interaction parameters. Material characteristics include seed size, density, Poisson's ratio, and shear modulus. The form and size of seeds were determined by measuring their triaxial size, and their density was determined by the drainage method to be 1197 kg/m^3. The interaction parameters are the restitution coefficient, the static friction coefficient, and the rolling friction coefficient. The reference contains additional parameters that are required (*Liu et al., 2021*). Among these, measuring methods and theories for the coefficient of restitution of corn seeds and the static friction coefficient of irregularly shaped materials are substantially developed.

The coefficient of restitution between corn seeds, which is 0.37 (*Gonzá et al., 2012*) is one of the important corn seed characteristics required for numerical modeling. Corn seeds of static friction coefficient is 0.2, (*Wang et al., 2017*). Due to the irregular shape of corn, it is difficult to measure the rolling friction coefficient,

and the rolling friction coefficient is the basis of the improved interaction between particles, requiring calibration prior to simulation. Therefore, the study is centered on the rolling friction coefficient across different types of maize species. Table 3 provides a comprehensive list of other attribute settings and interaction parameters.

Table 3

Other parameters required for DEM simulation

Simulation condition	Parameters	Value
Corn seeds	Poisson ratio	0.4
	Shear modulus [Pa]	1.37×108
	Density [kg·m^{-3}]	1197
Organic glass	Poisson ratio	0.4
	Shear modulus [Pa]	2.5×1010
	Density [kg·m^{-3}]	2700
Corn seeds and organic glass	Coefficient of restitution	0.709
	Coefficient of static friction	0.459
	Coefficient of dynamic friction	0.0931

The simulation angle of repose is depicted in Fig. 9, 1000 corn seeds are produced in a tube with a diameter of 50 mm, a radius of 25 mm, a distance of 300 mm between the seed factory and the bottom plate, and a generation rate of 500 seeds per second. Within 2 s, corn seeds are produced, and within 2.1 s, the cylinder begins to rise at a rate of 0.3 mm/s. Due to the lack of restraint provided by the tube wall, the corn at the bottom of the cylinder began to disperse upon lifting the cylinder. After the corn particles had stabilized, the angle of repose was determined.

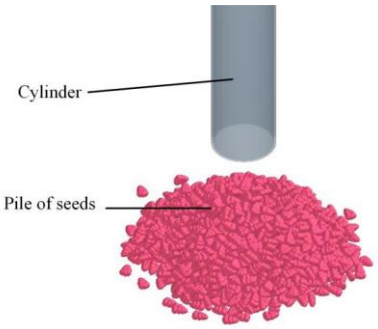

Fig. 9 - Simulation angle of repose test

RESULTS AND DISCUSSION

Interspecific rolling friction coefficient of each corn seed

In order to acquire the interspecific rolling friction coefficient of coated corn seed particles of various shapes, the simulation angles of restate of horse tooth, prism, and spherical corn seed models were determined by varying the rolling friction coefficient in a DEM simulation test. Horse tooth and prism rolling friction coefficients were chosen at 0.001, 0.003, 0.005, and 0.007. The friction coefficients for spherical rolling are set to 0.01, 0.03, 0.05, and 0.07, respectively. Under various rolling friction coefficients, the angles of repose for horse-toothed, prism, and spherical coated corn seed models were measured. By comparing the DEM simulation angle of repose to the actual test angle of repose, more accurate predictions of the interspecific friction coefficients of horse toothed, prism, and spherical corn seeds were made, as depicted in Fig. 10. The projected interspecific rolling friction coefficient for horse-toothed corn seeds was 0.0042, for prism corn seeds it was 0.0032, and for spheroidal corn seeds it was 0.047.

Interspecific rolling friction coefficient of mixed corn seed particles

In order to obtain the interspecific rolling friction coefficient between different corn seed particles, the rolling friction coefficient model of horse tooth and prism corn, horse tooth and spherical corn, prism and spherical corn were mixed with 500 samples each in a DEM simulation test. The rolling friction coefficients of horse tooth shape and prism shape, horse tooth shape, and spherical shape were set to 0.001, 0.005, 0.009, and 0.013, respectively, while the rolling friction coefficients of prism and quasi-circle were set to 0.005, 0.010, 0.015, and 0.02. By comparing the simulation angle of repose obtained by setting different rolling friction coefficients with the simulation angle of repose obtained by the actual experiment, more accurate inter-specific rolling friction coefficients between different shapes of coated corn seed particles were deduced. As shown in Fig. 10, it was predicted that the rolling friction coefficient of horse-toothed and prism corn was 0.0097, that of horse-toothed and spherical corn was 0.0086, and that of prism and spherical corn was 0.0135.

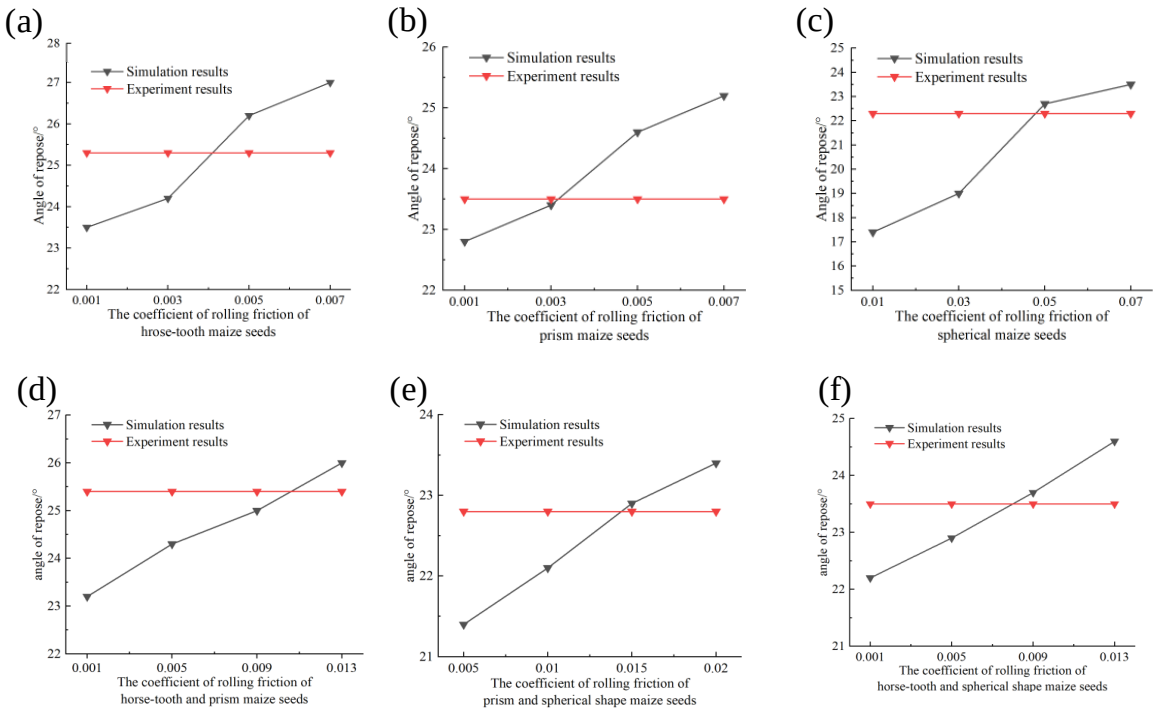

Fig. 10 - Relationship between the coefficient of rolling friction and the repose angle

(a) Horse-tooth shape; (b) Prism shape; (c) Spherical shape.

The effect of seed particle form and rolling friction coefficient on the flow behavior of particles

To investigate the effect of the population flow behavior of corn particles with different shapes on the accumulation process, three distinct types of corn seed particles (horse-tooth shape, prism shape, and spherical shape) were generated above the cylinder and subsequently deposited within it. After filling the cylinder with seed particles, the cylinder began to ascend. As the cylinder was raised upward, the lower seeds lost support from the cylinder wall and began to slip out of the cylinder. During sliding and rolling, particles came into contact with the packing.

The results were shown in Fig. 11 (a), (b), (c) of the horse tooth, respectively, prism and spherical corn under different rolling friction coefficients. At a time of 3.2 s population average velocity diagram, a cylinder at the bottom of the corn, due to the lack of constraints, began to spread around the wall, above and below the corn due to a lack of corn support. Under the influence of gravity, the corn began to descend, and as a result, its gravitational potential energy transformed into kinetic energy and rolled downward. The overall corn height continued to drop, while the spread area continued to grow. The cylinder at the bottom of the corn accumulation had formed a stable state, while at the top, the corn seed particles had greater speed. The horse-tooth shaped maize seed particles were flat, which hindered the movement of the lower group of particles. The corn seed particles on top of the downward movement along the circular pile formed by the corn below the downward slope remain stable. The maize seed particles, which had a high level of sphericity, had good fluidity, resulting in slower speed attenuation compared to particles with a horse tooth shape or pyramid shape. While the upper seeds exhibited a continuous downward flow, the lower group of particles remained unstable and exhibited a specific velocity. As a result, the majority of the corn seed particles located on the upper surface were going to exert pressure on the corn seed particles located beneath them, causing them to disperse. A small portion of it rolls along the circular slope formed below. In the process of forming the angle of repose, the shape of the corn seed particles played a significant role in determining the fluidity of the corn seed particles. Irregular seed particles (horse-tooth-shaped and prism) limited the flow of particle groups, and the more irregular the seed particles in the accumulation process, the more likely it was that a stable state would be formed, which was advantageous to the angle of repose.

As the simulation progressed, the influence of the rolling friction coefficient on the number of falling particles increased; the greater the rolling friction, the lower the population mobility and accumulation rate; conversely, the greater the rolling friction of corn seed particles, the faster the accumulation of particles when there were more seeds in the cylinder and longer distances between the seeds and the cylinder. The longer it took for the seed particles to fall through the stuffing hole and onto the corn bed, the larger the stuffing hole must have been. Spheroidal corn seed particles were the most susceptible to changes in rolling friction coefficient.

Fig. 12 depicted the top view of the seed pile at the time of Fig. 11, where (a), (b), and (c) correspondingly revealed that the horse teeth type seeds had the best fluidity, and the seed diffusion range was the largest in the top view. During the accumulation phase, the flat shape of the horse tooth-shaped corn seed restricted the movement of the corn seed group, resulting in the smallest diffusion area for the horse tooth-shaped corn seed. From largest to smallest, the diffusing areas of diverse corn seed types were spherical, prism, and horse-tooth shaped. The degree of dispersion of corn grains was significantly affected by the varying forms of corn seeds. The angle of repose increased as the rolling friction coefficient increased. This effect occurred because when the corn particles interacted with the contact surface, the coefficient of rolling friction increased, resulting in an increase in rolling resistance. On a flat surface, corn grains did not disperse easily. Consequently, the accumulation area was diminished. Additionally, the greater friction between corn grains made it less likely that the grains would slide down the hill and more likely that they would accumulate.

Influence of particle shape on energy change in accumulation process

The angle of repose test was actually a process of energy conversion. In this process, the potential energy of the kernels would be turned into kinetic energy, and the seeds with kinetic energy would disperse and come to rest gradually, resulting in a larger area of accumulation. Fig.11 depicts the change in potential energy over time for three types of seed particle shapes: horse tooth, prism, and spherical.

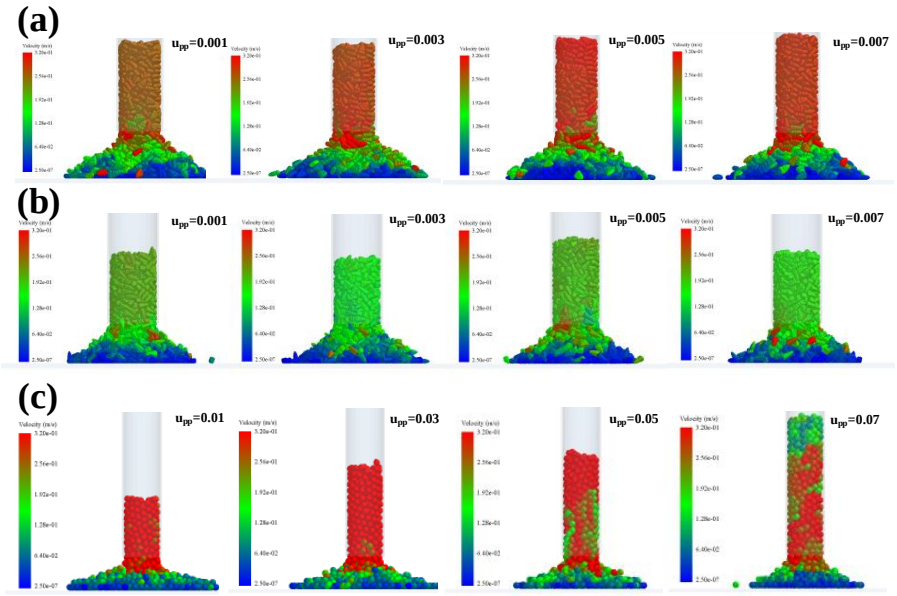

Fig. 11 - Front view of the motion velocity

(a) horse tooth shaped; (b) prism and (c) spherical seed particles under different rolling friction coefficients.

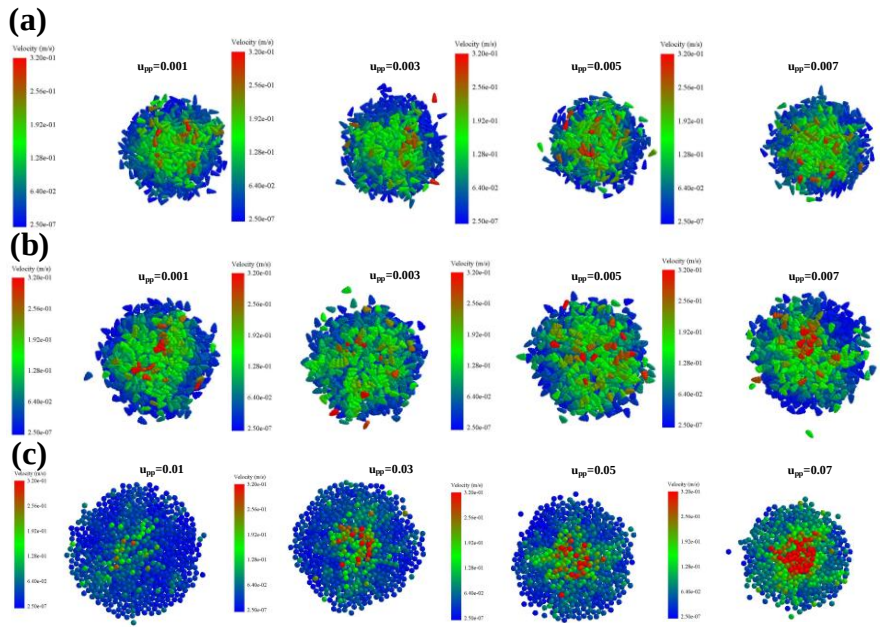

Fig. 12 - Attached view of the motion velocity

(a) horse tooth shaped; (b) prism and (c) spherical seed particles under different rolling friction coefficients.

During the simulation period from 0 s to 1.5 s, as depicted in Fig. 13, three morphologies of corn kernels gradually form while the total potential energy of corn seed particles increases linearly. At 1.5 s, 1000 corn seeds were loaded into the barrel, and between 1.5 s and 2.2 s, the potential energy of seed particles reached an inflection point. Due to the upward movement of the cylinder, the corn seeds in the cylinder would be lifted by the friction of the cylinder wall. At this time, the cylinder lifting height was low. The lower seeds were subject to interspecific friction. The seeds of corn seed particles did not collapse; potential energy had a small improvement in seeds until around 2.5 s, when the constraints completely out of the wall below the seed caused the seed to begin to collapse. Without the support of the seeds below, the top population started to diminish, and the corn fragments kept falling out of the stuffing mouth.

As the corn grain outflows, the total potential energy decreases gradually, especially with the horse tooth shape and type of spherical kernels falling rapidly, reducing the potential energy of the seed. The rolling friction coefficient of corn seed particles with different shapes was different. The descending rate of potential energy was not the same, and the descending rate of potential energy of the spherical seed was the fastest, the potential energy decline rate of the prism seed was much slower than that of the other two shapes of corn seeds. The horse tooth shape had a potential energy of approximately 3.5 s, the prism shape had a potential energy of approximately 3 s, and the spherical shape had a potential energy of approximately 3.2 s, indicating that all the corn seed particles had left the packing and accumulated in the corn pile. The sliding and rolling of corn particles on the corn pile progressively cease due to friction, and the potential energy approaches its stable value.

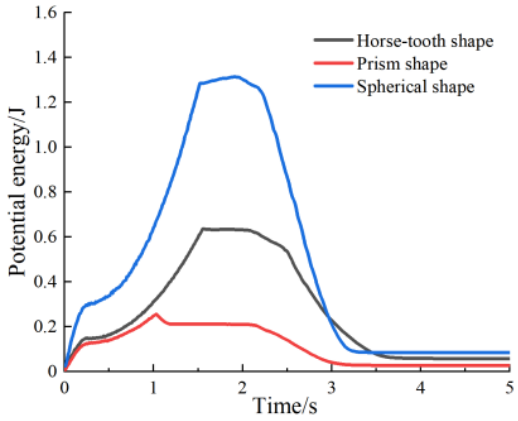

Fig. 13 - Potential energy variation of corn seeds with three shapes during accumulation

Fig.14 depicts the evolution of the average population velocity of three different-shaped corn seeds during the accumulation process. Fig.12 demonstrated that the average velocity of different-shaped corn seed particles first increased, then declined, and finally became static. The average speed of the population swung within 1.5 s-2 s, however, the variation amplitude was minor, as depicted in the graph. After 2 s, the population speed of the three types of corn seeds continued to increase, with spherical, horse-tooth, and prism having the highest average population speed, respectively. The results are shown in Fig.14. The average velocity attenuation rate of corn seed particles with different shapes was distinct, with spherical seed particles having the highest attenuation rate and horse teeth seed particles having the lowest. It was evident that the form of corn kernels was a significant element in preventing their flow.

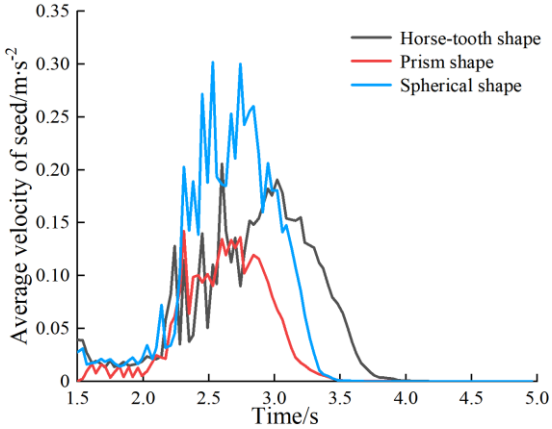

Fig.14 - Plot of average velocity variation of corn seeds of three shapes during accumulation

Influence of seed particle mixing with different shapes on accumulation process

To examine the role of three typical shapes of coated corn seeds in the creation of the angle of repose, the distribution positions of various shapes of corn kernels in the angle of repose are examined. The horse tooth, prism, and spherical corn seeds were mixed with 1000 seeds in a ratio of 43:12:10. In order to make the accumulation process more realistic, three kinds of corn seed particles must be mixed inside the cylinder so that each shape of corn seed particle has good dispersal. Fig.15 depicts the angle of process for three kinds of shapes of corn seed particles.

Starting from 0 s, seed particles of three shapes continued to form and gradually fall and fill the cylinder. At 2 s, the seed particles finished filling the cylinder and began to rise. During the lifting of the cylinder, the seeds began to disperse without the confinement of the cylinder wall. At 5.0 s, the seeds ceased to disperse and accumulated into a seed pile. For better research on the formation of the angle of repose, which played a different role in different shapes of corn seeds, respectively from the seeds of intermediated middle distance and distance of 30 mm thickness for 5 mm slices, as shown in Fig. 16 for the seeds of the slicing process, by examining three different locations of slice, because the horse tooth shape of corn seed particles was more prevalent, the angle of repose played a different role in the formation of these seeds. Therefore, the majority of the section surface was formed of horse tooth-shaped corn seeds, with a few round and prism-shaped corn seeds filling in the gaps. It could be shown that horse tooth-shaped corn grains played a significant role in the height direction of the angle of repose, but prism and spherical corn seed particles played just a little role. Observing the front view and top view of the seed heap between 4.4-5 s in the stacking process of Fig. 15 revealed that the diffusion amplitude of the horse-tooth seed, which occupies a large proportion, was smaller than that of the spherical seed particles in the circumferential direction of the seed heap during the final stacking process. The circumferential direction of the seed pile could be attributed primarily to the spherical corn seeds. Horse tooth and prism corn seed particles performed a supporting role, showing that the sphericity of horse tooth and prism seed was lower and the population mobility effect was bad, whereas the sphericity of quasi-spherical seed was higher and the population mobility effect was better.

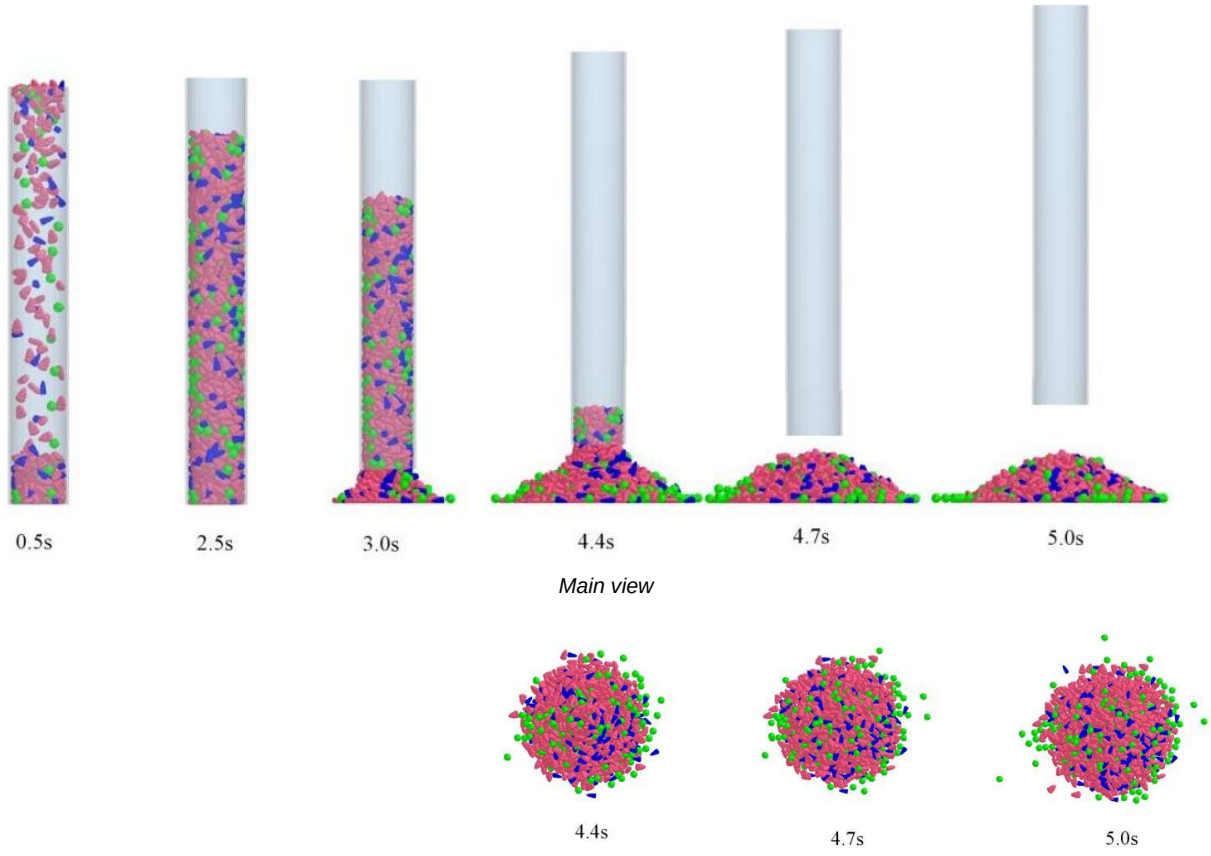

Main view

Top view

Note: Red is horse tooth shape; blue is prism shape; green is spherical

Fig. 15 - Mixed accumulation process of corn grains with different shapes

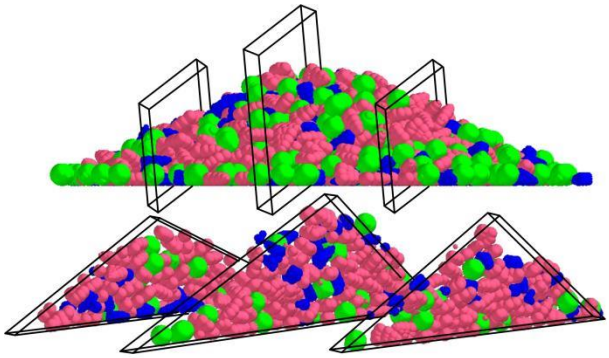

Fig. 16 - Model of slice

Verification test

In this study, the rolling friction coefficient between different corn seed particles was estimated using a combination of practical and simulated testing to validate the rolling friction coefficient approach. 1000 seeds were combined in a proportion of 43:12:10 for horse tooth shape, pyramid shape, and quasi-circle shape under the same conditions. The coefficient for predicting the rolling friction of horse tooth-shaped corn seed was fixed at 0.0042. The prediction coefficient for rolling friction was 0.0032 for the pyramidal corn model and 0.047 for the spherical corn model. The coefficient of rolling friction prediction for horse tooth and pyramid corn seeds was 0.0092, for horse tooth and round corn seeds it was 0.0086, and for pyramid and round corn seeds it was 0.014. After the model was stabilized, 1000 seeds were dropped from above the seed box of the pneumatic corn seed feeder into the seed feeder. The real measurement and simulation tests were done three times, respectively, to observe the seed distribution (Figure 17). The essential feature sizes of the distributions of two major populations were chosen for comparison, as depicted in Figure 17c, and the measured values were presented in Table 3.

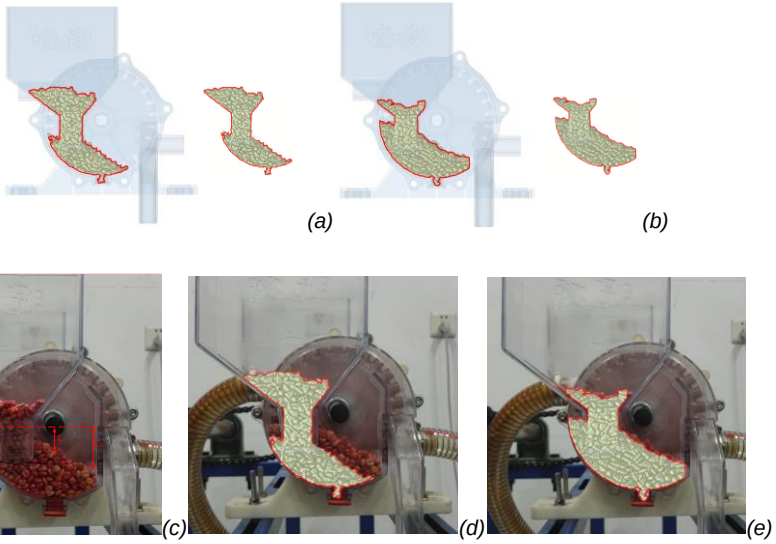

Fig.17 - Comparison of simulation and actual tests

(a) Before calibration; (b) After calibration; (c) Actual measurement; (d) Compare with the actual measurement before calibration; (e) Compare with the actual measurement after calibration.

The measured data indicated that the key size of the population determined by the simulated test with calibrated contact parameters and the measured value differ by less than 5.6%. The calibrated contacted parameters increase the fluidity of the corn coupling model and restore its physical properties to those of actual corn particles. This would ensure the authenticity of the coupling simulation that follows.

Table 4

Comparison of key feature sizes for simulation and actual results

Key feature sizes	Simulation value	Actual measurement value	Difference value
	[mm]	[mm]	[%]
L_1	29.47	31.12	5.60
L_2	47.76	50.02	4.73

CONCLUSIONS

In the study, comparative observation was used to pick three typical corn models (including horse teeth shape, prism shape, and spherical shape) with a large proportion of irregularly shaped corn. Three more accurate corn particle models were developed after measuring the real characteristic size of each corn shape and obtaining its positive distribution. The angle of repose of the plexiglass cylinder container was simulated using the rolling friction coefficient of the particle model as the independent variable and the desired value of the simulated angle of repose. The rolling friction prediction coefficients for horse tooth, prism shape, and spherical corn seeds were 0.0042, 0.0032, and 0.047, respectively. The rolling friction prediction coefficients between horse teeth and prism, horse tooth and spherical, and prism and spherical seed were 0.0092, 0.0086, and 0.014, respectively.

To examine the effects of seed particle shape and rolling friction coefficient on seed flow behavior, the motion velocities of three types of corn under different rolling friction coefficients and the potential energy and average velocity of seed particles with different shapes under the same rolling friction coefficient were extracted. In stacking tests with different rolling friction coefficients, the three shapes of corn showed that as the rolling friction coefficient went up, the stacking rate went down, the seed flow got worse, and the time it took for the seeds to leave the cylinder went up. The sensitivity of the spherical form to changes in the rolling friction coefficient was significantly greater than that of the horse teeth and prism shapes.

The three corn models had very different shapes. When the rolling friction coefficient was the same, the spheroidal seed particles with higher sphericity moved more easily than the horse tooth shape and the prism shape of the non-spherical model. Also, the spherical seed particles with better fluidity had a smaller resting angle than the horse tooth shape and the prism shape.

ACKNOWLEDGEMENT

This work was supported by the National Natural Science Foundation of China, China (Grant numbers 52275229), Natural Science Foundation Project of Anhui Province (Grant numbers 1908085MC91).

REFERENCES

[1] Balevičius R., Sielamowicz I., Mróz Z., Kačianauskas R. (2012). Effect of rolling friction on wall pressure, discharge velocity and outflow of granular material from a flat-bottomed bin. *Particuology*, 10(6), 672–682.

[2] Boac J., Casada M., Maghirang R., Harner J. (2010). Material and interaction properties of selected grains and oilseeds for modeling discrete particles. *ASABE*, 53(4): 1201–1216.

[3] Chen H., Zhao S., Zhou X. (2020). DEM investigation of angle of repose for super-ellipsoidal particles. *Particuology*, 50, 53–66.

[4] Chen Z., Yu J., Xue D., Wang Y., Zhang Q., Ren L. (2018). An approach to and validation of corn-seed-assembly modelling based on the discrete element method. *Powder Technology*, 328, 167-183.

[5] Ding L., Yang L., Zhang D., Cui T. (2019). Parametric Design and Test of Seed Cleaning Mechanism of Air-suction Corn Seed-metering Device (气吸式玉米排种器清种机构参数化设计与实验). *Transaction of the Chinese Society Agricultural Machinery*, 50(09):47-56. (in Chinese)

[6] Goniva C., Kloss C., Deen N., Kuipers J., Pirker, S. (2012). Influence of rolling friction on single spout fluidized bed simulation. *Particuology*, 10(5), 582–591.

[7] Gonzá M., Fuentes J., Ayuga-Té L., Ayuga F., (2012). Determination of the mechanical properties of corn grains and olives required for use in DEM simulations. *Journal of Food Engineering*,111(4): 553–562.

[8] Li M., Mitsuoka M., Inoue E., Ye J., Liu J., Yang S., Zeng B., Song X., Okayasu T., Hirai Y. (2020). Design and performance analysis of a seed metering device for a buckwheat seeder adopting discrete element analysis. *J. Fac. Agric. Kyushu Univ*, 65(1), 123–129.

[9] Liu R., Li Y., Liu Z., Liu L., Lv H., (2021). Analysis and Calibration of Discrete Element Parameters of Coated Corn Seed（包衣玉米种子离散元参数分析与标定）.*Transactions of the Chinese Society for Agricultural Machinery*, 52(S0), 1-8. (in Chinese)

[10] Ma W., You Y., Wang D., Yin S., Huan X., (2020). Parameter Calibration of Alfalfa Seed Discrete Element Model Based on RSM and NSGA-Ⅱ（基于 RSM 和 NSGA-Ⅱ的苜蓿种子离散元模型参数标定）. *Transactions of the Chinese Society of Agricultural Engineering (Transactions of the CSAE)*, 51(08): 136-144. (in Chinese)

[11] Owen P., Cleary P., (2012). Prediction of screw conveyor performance using the discrete element method (DEM). *Powder Technology*, 193(3): 269–282
[12] Pasha M., Hare C., Ghadiri M., Gunadi A., Piccione M., (2016). Effect of particle shape on flow in discrete element method simulation of a rotary batch seed coater. *Powder Technology*, 296, 29–36.
[13] Peng F., Wang H., Fang F., Liu Y., (2018). Calibration of discrete element model parameters for pellet feed based on injected section method（基于注入截面法的颗粒饲料离散元模型参数标定）. *Transactions of the CSAM*,49(4), 140–147. (in Chinese)
[14] Shi S., Zhang D., Yang L., Cui T., Zhang R., Yin X., (2014) Design and experiment of pneumatic corn precision seed-metering device with combined holes [J]. *Transactions of the Chinese Society of Agricultural Engineering (Transactions of the CSAE)*, 30(5): 10-18.
[15] Tanaka H., Momozo M., Oida A., Yamazaki M. (2000). Simulation of soil deformation and resistance at bar penetration by distinct element method. *Journal of Terramechanics*, 37(1), 41–56.
[16] Urtė R., Álvaro R., Rimantas K. (2016). Determining the shape of agricultural materials using spherical harmonics. *Comput Electron Agric*, 128, 160–171.
[17] Wang J., Tang H., Wang J., Li X., Huang H., (2017). Optimization design and experiment on ripple surface type pickup finger of precision corn seed metering device. *Int. J. Agric. & Biol. Eng*, 10, 61–71.
[18] Wang L., Li R., Wu B., Wu, Z., Ding Z., (2017). Determination of the coefficient of rolling friction of an irregularly shaped corn particle group using physical experiment and simulations. *Particuology*, 38(6): 185–195.
[19] Wang L., Li R., Wu B., Wu Z., Ding Z., (2018). Determination of the coefficient of rolling friction of an irregularly shaped corn particle group using physical experiment and simulations. *Particuology*, 38, 185-195.
[20] Wang S., Yu Z., Aorigele, Zhang W., (2022). Study on the modeling method of sunflower seed particles based on the discrete element method. *Computers and Electronics in Agriculture*, 198, 107012, ISSN 0168-1699.
[21] Wang X., Yu J., Lv F., Wang Y., Fu H., (2017). A multi-sphere-based modelling method for corn grain assemblies. *Powder Technol*, 28, 584–595.
[22] Wang Y., Lv F., Xu T., Yu J., (2018). Soybean seed shape and size analysis and its modelling (大豆籽粒形状和尺寸分析及其建模). *J. Jilin University. Engineering and Technology Edition*, 48 (02), 507–517.
[23] Wang Y., Wang X., Chen Z., Yu J., (2018). Corn seed modeling based on discrete element method (基于离散元法的玉米籽粒建模). *J. Jilin University. Engineering and Technology Edition*, 48 (05), 1537–1547. (in Chinese)
[24] Wu M., Cong J., Yan Q., Zhu T., Peng X., Wang Y., (2020). Calibration and experiments for discrete element simulation parameters of peanut seed particles（花生种子颗粒离散元仿真参数标定与试验）. *Transactions of the Chinese Society of Agricultural Engineering (Transactions of the CSAE)*,36(23): 30-38. (in Chinese)
[25] Xiao L., Björklund S., Rosén B., (2007). The influence of surface roughness and the contact pressure distribution on friction in rolling/sliding contacts. *Tribology International*, 40(4), 694–698.
[26] Xu J., Wang X., Zhang Z., Wu W., (2020). Discrete element modeling and simulation of soybean seed using multi-spheres and super-ellipsoids. *IEEE Access*, 8, 222672–222683.
[27] Yung K., Xu Y., (2003). Non-linear expressions for rolling friction of a soft ball on a hard plane. *Nonlinear Dynamics*, 33(1), 33–41.
[28] Zhang S., Zhang R., Chen T., Fu J., Yuan H., (2022). Calibration of Simulation Parameters of Mung Bean Seeds Using Discrete Element Method and Verification of Seed-metering Test（绿豆种子离散元仿真参数标定与排种试验）. *Transaction of the Chinese Society Agricultural Machinery*, 53(03): 71-79. (in Chinese)
[29] Zhou L., Yu, J., Wang Y., Yan D., Yu Y., (2020). A study on the modelling method of corn-seed particles based on the discrete element method. *Powder Technology*, 374, 353-376.

RESEARCH ON THE CONSTRUCTION METHOD OF HIGH PRECISION 3D POINT CLOUD MAP FOR AGRICULTURAL ENVIRONMENTS
/
农业环境高精度三维点云地图构建方法研究

Bo ZHAO[1)], Suchun LIU[1)], Xiufeng Zhao[2)], Licheng ZHU[1*)], Tianfu ZHANG[1)], Zhenhao HAN[1)], Weipeng ZHANG[1)]
[1)] National Key Laboratory of Agricultural Equipment Technology, China Academy of Agricultural Mechanization Science Group Co., Ltd, Beijing 100083, China;
[2)] Nong'an County Agricultural Mechanization Technology Promotion Station, Changchun, Jilin 130200, China
Tel: +86-13601287800; E-mail: zhulicheng@caams.org.cn; Correspondent author: Licheng ZHU
DOI: https://doi.org/10.35633/inmateh-72-35

Keywords: *Point cloud high-definition map; driverless; semantic segmentation*

ABSTRACT

In agricultural operation scenarios, the diversity of farmland terrain, crops and other forms, as well as uncertain factors such as weather changes and crop growth during agricultural operation, can have an impact on the construction of high-precision maps. To address these challenges and analyze operational scenarios based on the characteristics of agricultural scenarios, this paper proposes a point cloud map construction algorithm for plant point removal and locatability estimation. Based on the existing Simultaneous Localization and Mapping (SLAM) framework, plant point removal and locatability estimation are improved. Firstly, Red, Green, Blue (RGB) images and Near Infrared (NIR) images are fused to identify and remove plant point clouds, preserving effective inter frame matching information, reducing the impact of dynamic points on inter frame matching, and achieving high front-end motion estimation accuracy. Then, the localization estimation method based on learning is used to determine the motion estimation status and determine whether to execute the backend optimization algorithm. Finally, the back-end optimization algorithm based on Factor graph is designed, and the Factor graph, constraint relationship and optimization function are constructed to optimize the pose of all frames. The optimized map construction algorithm reduces the re projection errors between field roads, paths, and crop rows by 10.27%, 20.76%, and 14.36% compared to before optimization. To verify the actual operational effectiveness of the point cloud map construction algorithm, the hardware part of the multi-sensor information collection system was designed, and sensor internal and external parameter calibration were also carried out. A map information collection vehicle was built and field experiments were conducted. The results showed that the positioning error of the point cloud map construction method proposed in this paper is less than 0.5°, and the cumulative error of 30 m translation is less than 12 cm, which meets the actual operational requirements.

摘要

在农业作业场景中，农田地形、作物等形态的多样性，以及农业作业过程中的天气变化、作物生长等不确定因素，都会对高精度地图的构建产生影响。为了应对这些挑战，并根据农业场景的特点分析操作场景，本文提出了一种用于植物点去除和定位估计的点云地图构建算法。在现有 SLAM 框架的基础上，对植物点去除和可定位性估计进行了改进。首先，将 RGB 图像和近红外图像融合，识别和去除植物点云，保留了有效的帧间匹配信息，减少了动态点对帧间匹配的影响，实现了较高的前端运动估计精度。然后，使用基于学习的局部估计方法来确定运动估计状态，并确定是否执行后端优化算法。最后，设计了基于因子图的后端优化算法，构造了因子图、约束关系和优化函数，对所有帧的姿态进行优化。与优化前相比，优化后的地图构建算法将田间道路、路径和作物行之间的重新投影误差分别降低了 10.27%、20.76%和 14.36%。为了验证点云地图构建算法的实际操作有效性，设计了多传感器信息采集系统的硬件部分，并进行了传感器内外参数校准。建造了地图信息采集车，并进行了野外试验。结果表明，本文提出的点云地图构建方法定位误差小于 0.5°，30m 平移累积误差小于 12cm，满足实际操作要求。

INTRODUCTION

The need for unmanned and refined agriculture has promoted the development of intelligent technologies such as driverless, robots and sensors (*Kim et al., 2022*). The use of unmanned technology in agricultural fields requires high-precision maps to provide vehicles with relevant information about the

environment and this information helps self-driving vehicles perceive their surroundings and make navigation decisions. The highly unstructured nature of agricultural scenarios and the complexity of semantic information bring great challenges to the construction of high-precision maps. To cope with these challenges, agricultural high-precision point cloud map construction is needed, i.e., to construct a map containing environmental information through multiple point cloud datasets. The point cloud data in the map can provide useful semantic information for robots or other intelligent devices to support their autonomous localization and navigation in unknown environments (*Qi et al., 2017; Wang et al., 2022*).

Numerous scholars have carried out research in various aspects of point cloud map construction. Ji et al. developed a LiDAR-based point cloud acquisition system for farmland environment (*Ji et al., 2019*), aiming to realize the stable and reliable information acquisition of farmland environment point cloud and positional attitude of farm machinery. The system employs multi-sensor data acquisition software to achieve accurate and consistent global point cloud data acquisition. Chris et al. proposed a methodology using high-resolution LiDAR point cloud data for classification and segmentation to detect linear vegetation elements in agricultural landscapes (*Lucas et al., 2019*). Due to the ground and trees are surrounded by foliage, thorns, and vines, and sensors often experience extreme motion, Guilherme et al. proposed an end-to-end trunk diameter estimation method that is based on semantic segmentation and LiDAR odometry with map building (*Chen et al., 2020*). Poor feature descriptiveness and insufficient point cloud alignment accuracy due to the lack of highly distinguishable high-level structures of points, lines, and surfaces, therefore, Dong et al. proposed a point cloud method based on rotated surface contour features for farmland surface point clouds (*Dong et al., 2020*).

Aiming at the problems of highly unstructured scene and complex environment semantic information in the construction of high-precision point cloud semantic map for agriculture, this paper proposes a method of multimodal map construction based on multi-sensors. By designing a multi-sensor information acquisition device and proposing a point cloud map construction algorithm and a multi-modal semantic segmentation algorithm, high-precision point cloud semantic maps are established to provide accurate data support for unmanned operation of agricultural machines.

MATERIALS AND METHODS

Data Acquisition Vehicle Construction

The overall design of the data acquisition vehicle is shown in Figure. 1, which consists of the information acquisition device, the modified bracket and the vehicle underpan, respectively. The Livox-mid70 non-repeating scanning lidar, Intel RealSense D455 depth camera and MER2-507-23GM NIR near-infrared optical camera are used for data acquisition, respectively. The collection vehicle uses the Agile HUNTER2.0 chassis, which features a wheel drive system, Ackermann turning mode, and independent suspension system. This setup provides a reliable platform with precise control and smooth movement.

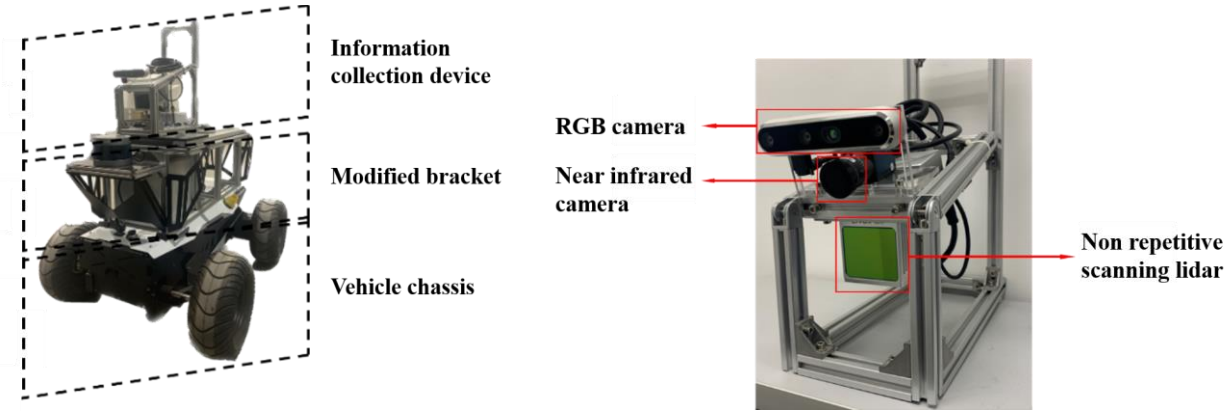

Fig. 1 - The information collection vehicle

Principle of Point Cloud Map Construction

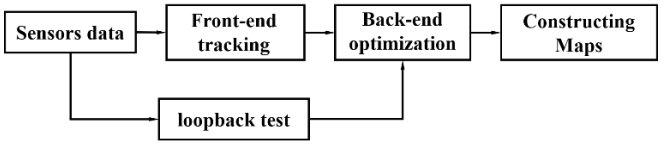

Fig. 2 - Process of the classic SLAM algorithm

The construction of a point cloud map relies heavily on the use of the SLAM (Simultaneous Localization and Mapping) technique (*Zeng et al., 2022; Johnson et al., 1999; Li et al., 2021*). Its algorithmic process is exemplified in Figure. 2 and is employed to achieve simultaneous localization and map construction by continually estimating and updating the robot movements and surroundings for independent localization and navigation. The key stages of the SLAM technology used during point cloud map creation encompass point cloud data acquisition, motion estimation, point cloud alignment, point cloud feature extraction, point cloud filtering and optimization, and map construction.

During point cloud data acquisition, several sensors are employed to gather point cloud data within the environment and then process and fuse it to enhance the completeness of environmental information. Front-end tracking utilizes camera acquired image frames captured during motion at distinct times to solve the camera position transformation between neighboring domains through feature matching. This facilitates image frame fusion to reconstruct the map (*Tombar et al., 2010; Johnson et al., 1999*). However, the estimation of the position at the frontend over an extended period will lead to error accumulation during the moving process, leading to offset phenomenon. To decrease the accumulation of mistakes, loopback detection and backend optimization techniques are introduced. Loopback detection aims to establish whether the same position is achieved again, whereas backend optimization improves the noise problem in the position estimation (*Han et al., 2022; Han et al., 2022; Xu et al., 2022*). After detecting feedback loops and optimizing the camera positions obtained from motion estimation, it is possible to generate globally consistent trajectories and their corresponding map forms.

POINT CLOUD MAP CONSTRUCTION ALGORITHM

Algorithm Framework

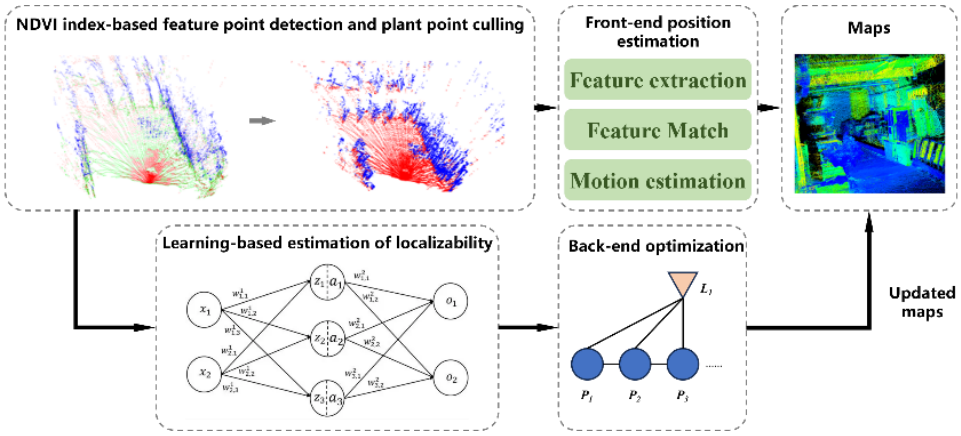

Fig. 3 - Point cloud map construction algorithm framework

In the frontend part of the algorithm, edge and feature points are first extracted by extracting scene information such as non-vegetation points (e.g. ground, obstacles and debris). Feature point matching is performed using the nearest neighbor method, whilst the Iterative Closest Point (ICP) algorithm estimates motion to determine the interframe locality matching. During the backend optimization phase is utilized the optimization algorithm that is rooted in factor graph (*Vizzo et al., 2022; Wang et al., 2021*). This optimization algorithm is used to enhance the position and feature points of all frames by constructing factor graph, constraint relationships and optimization functions, thereby improving the accuracy of the map. Following the generation of a high-precision 3D map, execution of the map building algorithm results in an accurate map being created. The complete algorithm framework is depicted in Figure 3.

Plant Point Culling Based on Image Information

This paper utilizes the Normalized Difference Vegetation Index (NDVI) to separate plant and non-plant regions (*Ao et al., 2021; Tian et al., 2021*). By combining the RGB and NIR images, a multispectral image with red, green, blue, and near-infrared band information can be obtained. Segregation of plant and non-plant regions can be accomplished through the use of the $NDVI$. The normalized vegetation index, calculated using the NIR and red bands in a multispectral image, can be expressed through Equation (1).

$$NDVI = \frac{NIR - Red}{NIR - Red} \quad (1)$$

where NIR denotes the pixel value in the near-infrared band and Red denotes the pixel value in the red band. As shown in Figure 4, the non-vegetative points can be segmented by extracting non-vegetative data from the camera image and mapping it onto the point cloud.

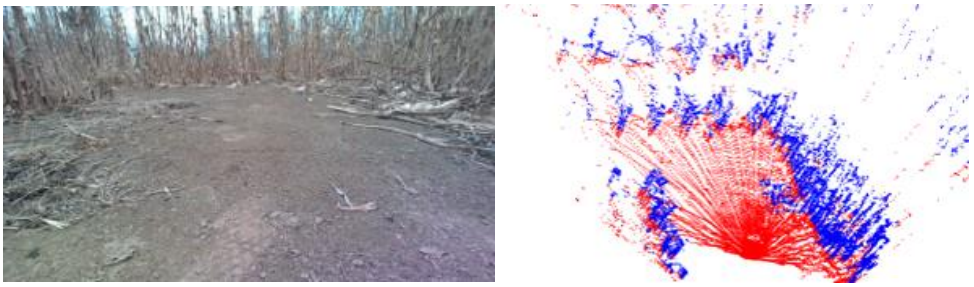

Fig. 4 - Plant spot removal in field experiments

Learning-Based Estimation of Localizability

Conventional algorithms may degrade, which can result in a significant deviation from the estimated bit position. To detect such a situation, an end-to-end method for estimating bit position is proposed. This method helps identify whether the conventional approach is degraded or not.

- *Mathematical modeling*

3D LIDAR point cloud scanning data is analyzed to forecast the feasibility of accomplishing localizations in the existing surroundings by employing scan matching methods. The LiDAR point cloud data is exploited to supply an approximation of localization, which is described as the identification across six degrees of freedom. The LiDAR point cloud data is exploited to supply an approximation of localization, which is described as the identification across six degrees of freedom. Abbreviations will be clarified whenever initially employed.

$$D_k = (d_x, d_y, d_z, d_\varphi, d_\theta, d_\psi)^T \quad (2)$$

x, y, z – the translation coordinate;

φ, θ, ψ – the Euler angles for roll, pitch, and yaw; [°]

For practical purposes, the localization of orientation is considered in binary terms. Therefore, for all $i \in \{x, y, z, \varphi, \theta, \psi\}$, there exists $d_i \in \{0,1\}$, where 0 indicates successful localization and 1 indicates unsuccessful localization. Localization is accomplished through interframe matching of the current and previous frame point clouds.

The ability to localize at time k is determined by scanning data from the current point cloud $s_k \in R^{n_k \times 3}$. Therefore, the function $sk \to dk$ can be approximated $\widetilde{D}_k(\Theta, s_k)$, where $\Theta \in R^p$ is the P trainable parameters in the network. These parameters are obtained by minimizing the supervised classification loss $\underset{\theta}{\operatorname{argmin}}(\widetilde{D}(\Theta, S), T)$ in the training set S, which includes the point cloud frames $s_i \in S$ and corresponding labels $t_i \in T$.

- *Training set generation: sampling and alignment*

Generating the data for training occurs in two stages: initially, the alignment error e_k is calculated; subsequently, this error is mapped to d_k through the implementation of a thresholding operation.

- Alignment Error

Obtain a set of child point clouds adjacent to the parent point cloud s_p through Monte Carlo sampling to calculate the expected alignment error. Align the child point clouds with the parent point cloud to obtain the average alignment residuals of the point cloud distribution. The mean absolute error is then calculated to obtain the alignment error e_p of the s_p.

A group of M sub-point clouds s_p are randomly sampled using Monte Carlo within the vicinity of $s_{c,j} \in \{1, \ldots, M\}$. To determine its positional attitude $T_{p,c,j}$ relative to the main point cloud, each sub-point cloud requires six perturbations in the direction $i \in \{x, y, z, \varphi, \theta, \psi\}$ using a Gaussian function $N(0, \sigma 2i)$. The alignment of each sub-point cloud with the main point cloud is achieved using the ICP algorithm with point-to-plane implementation, resulting in the transform matrix $T_{p,c,j}$. The sub-point cloud's alignment quality to the parent point cloud is assessed by computing the mean absolute error between each sub-point cloud and its aligned point cloud on the parent point cloud. Subsequently, the mean absolute error of all child point clouds is averaged to obtain the alignment error e_p of the parent point cloud s_p.

$$e_p = \frac{1}{M} \sum_{j=1}^{M} \left| \gamma(\tilde{T}_{p,c,j}{}^{-1} - T_{p,c,j}) \right| \quad (3)$$

The alignment error γ for each sub point cloud is determined by aligning it with the parent point cloud using ICP. The $T_{p,c,j}$ attitude of each sub point cloud is converted to $\tilde{T}_{p,c,j}$ in relation to the parent point cloud, as indicated in Equation (3), and is then utilized as input for the ICP to compute the alignment error γ.

- *Localizability estimation*

Once the 6D alignment error has been calculated, it must be compared with a preset threshold to determine whether localization can be successful in a particular direction. If the alignment error exceeds the preset threshold, positioning in that direction is considered to have failed and the corresponding Localizability label is set to 1. Conversely, it is set to 0. Positioning is considered successful if the translation error is less than 10 cm and the rotation error is less than 2°.

Frontend position estimation

Frontend pose estimation consists of three stages: feature extraction, feature matching and motion estimation.

- *Feature extraction*

A 3D curvature based feature extraction method is used to extract points with distinct geometric features. The point cloud is meshed and divided into a number of small cubes, and the center point pi within each small cube is computed. For each point p_i, its normal vector n_i is computed. the curvature tensor C_i of each point p_i is computed, where C_i is computed from the normal vectors of all points in its neighborhood, and the calculation formula is as Equation (4).

$$C_i = \frac{1}{N}\sum_{j=1}^{N}(n_j - n_i)(n_j - n_i)^T \tag{4}$$

N – the number of points in the neighborhood of p_i;

n_j – the normal vector of the j^{th} neighborhood point.

For every p_i, determine the eigenvalues λ_1 and λ_2 of its curvature. These eigenvalues are accessible from the eigenequations of the curvature tensor C_i as shown in Equation (5). In the equation for the unit matrix, the symbol I represents the unit matrix.

$$\det(C_i - \lambda I) = 0 \tag{5}$$

To calculate the curvature index K_i of a point p_i, λ_1 and λ_2 are used in the following manner.

$$K_i = \frac{\lambda_i}{\lambda_1 - \lambda_2} \tag{6}$$

By defining K_e and K_f thresholds, it is possible to filter the feature information contained in the point cloud. This filtering process includes both edge points and feature points.

$$f(k) = \begin{cases} Edge\ points & K_i > K_e \\ Feature\ points & K_f < K_i < K_e \\ Noise\ points & other \end{cases} \tag{7}$$

- *Feature match*

The matching of feature points utilizes the nearest neighbor algorithm. p_i^1 in the first frame point cloud represents the i^{th} feature point and p_j^2 in the second frame refers to the j^{th} feature point. The Euclidean distance serves as the distance metric between these points, and it is computed by measuring the distance between the two point cloud frames, as illustrated in Equation (8).

$$d_{i,j} = \left|p_i^1 - p_j^2\right| \tag{8}$$

where $|\cdot|$ denotes the Euclidean paradigm. Find the feature point p_i^1 that is closest to p_i^2 in the second frame of the point cloud.

$$k = \mathrm{argmin} j d_{i,j} \tag{9}$$

If the square of p_k^2 is too distant from p_i^2, it will be removed. The ultimate matching of feature points obtained can be presented as a set $M = \{(i,k)|i = 1,\ldots,n_1, k = 1,\ldots,n_2\}$, where (i,k) indicates that the first frame point cloud's ith feature point has been successfully matched with the second frame point cloud's kth feature point.

- *Motion estimation*

After preprocessing the point cloud frames through feature extraction, dynamic objects are excluded, and static point features are simultaneously acquired. These characteristics facilitate interframe matching with ICP algorithm, leading to improved results by removing dynamic objects and higher efficacy for real-time applications.

Assume that frame point clouds P and Q are given, and let M be the set of feature points obtained by feature matching. The objective of the ICP algorithm is to transform point cloud P to Q in the same coordinate system. Define the transformation matrix T as shown in Equation (10), which transforms the point cloud P into the coordinate system.

$$P' = TP \tag{10}$$

P' – the transformed point cloud P.

The objective of the ICP algorithm is to minimize the distance between P' and Q by iteratively refining the transformation matrix T. The average distance between P' and Q serves as the basis for the ICP algorithm. The least squares method is utilized to solve T such that the average distance between P' and Q is minimized. Technical term abbreviations are explained upon their first usage. The equation used to calculate the transformation matrix T is as follows:

$$T = (Q_M^T P_M)^T (Q_M^T P_M)^{-1} \tag{11}$$

Q_M, P_M – the feature point sets after feature matching in point clouds Q and P, respectively;

$Q_M^T P_M$ – the correspondence between feature points;

$Q_M^T P_M$ – the covariance matrix between feature points.

The optimal rigid body transformation matrix T between point clouds P and Q is obtained by solving the least squares solution.

Back-end optimization

The graph optimization algorithm is a highly effective back-end optimization approach for the issue of creating precise point cloud maps utilizing LiDAR in agricultural settings. This approach involves modeling successive frames of LiDAR-obtained point clouds and incorporating landmark extraction from point cloud frames where localization fails, thereby constraining pose estimation. In the factor graph represented in Figure 5, nodes portray each frame replete with landmarks, while edges depict the constraint relationships between them. The nodes symbolize the state variables of the LiDAR point cloud frames and landmarks.

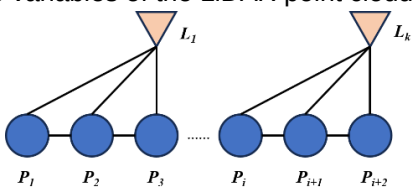

Fig. 5 - Factor diagram

The motion constraint relationship between neighboring frames and the previous frame of landmarks is established through the motion relationship. Equation (12) illustrates the motion constraint relation between neighboring frames, where $T_{i.j}$ represents the motion relation between frame *i* and frame *j* and T_k represents the motion relation between the signpost and frame *k*.

$$z_{i,j} = \begin{bmatrix} R_{i,j} & t_{i,j} \\ 0^T & 1 \end{bmatrix} = \begin{bmatrix} T_{i,j} & 0 \\ 0^T & 1 \end{bmatrix} \tag{12}$$

where the rotation and translation of the i^{th} frame with respect to the j^{th} frame are represented by $R_{k,i}$ and $t_{i,j}$, respectively. Additionally, the bit-position transformation matrix of the i^{th} frame with respect to the j^{th} frame is denoted as $T_{i,j}$. Similarly, the motion relationship between the road sign and the first three frames can be expressed in the same manner as shown in Equation (13), where $R_{k,i}$ and $t_{k,j}$ are the rotation and translation of the roadmap with respect to frame i, respectively, and T_k is the bit-pose transformation matrix of the roadmap.

$$z_{k,j} = \begin{bmatrix} R_{k,i} & t_{k,i} \\ 0^T & 1 \end{bmatrix} = \begin{bmatrix} T_k & 0 \\ 0^T & 1 \end{bmatrix} \tag{13}$$

With this factor graph, a function to be optimized is defined that represents the state of each node as a vector and optimizes the minimization error over all constraint relations. This optimization problem can be expressed as minimizing the objective function $f(x)$ as follow:

$$f(x) = \sum_{k=1}^{N} \sum_{i,j \in N_k} e_{ij}^k(x)^T \Omega_{ij}^k e_{ij}^k(x) + \sum_{m=1}^{M} \sum_{i,j \in N_m} e_{ij}^m(x)^T \Omega_{ij}^m e_{ij}^m(x) \tag{14}$$

N_k – the set of the k^{th} node and its adjacent nodes;

N_m – the set of the m^{th} signpost and its associated nodes;

$e_{ij}^k(x)$, $e_{ij}^m(x)$ – the error vectors between nodes i and j;

Ω_{ij}^k, Ω_{ij}^m – the corresponding information matrices.

Analysis of point cloud map construction algorithms

To assess the dependability of the point cloud mapping algorithm put forward in this paper, front-end position estimation comparison experiments and back-end optimization comparison experiments were conducted on field roads, paths, and crop rows. The algorithm's performance is evaluated using the reprojection error as the index, where a smaller error indicates a position estimation that is closer to the actual position and hence a higher accuracy.

The reprojection error is calculated using the following formula:

$$ereproj = \frac{1}{n}\sum_{i=1}^{n}\frac{|p_i' - p_i|_2}{\sqrt{w^2+h^2}} \quad (15)$$

p_i – the location of the *ith* point in the actual world;

p_i' – the position of the reprojected point;

w, h – the dimensions of the image;

n – the count of points within the point cloud.

- *Analysis of point cloud map construction algorithms*

To evaluate the effectiveness of the Plant Point Rejection method in estimating motion, this experiment compares it with the ground extraction-based algorithm. The positioning accuracies of the motion estimation method based on ground extraction and the method based on plant point rejection are compared in three scenarios: a large field road, a small field road and a crop row. This is done by comparing the reprojection errors of both methods.

Figure 6 shows the accuracy control plot of the experiments. The plant point culling method (A) has a significantly reduced reprojection error compared to the ground extraction-based method (B) for the three experimental scenarios (1, 2, 3) by 10.27%, 20.76% and 14.36% respectively. This suggests that the method based on plant point culling is more precise and reliable in motion estimation.

The experiments simulated different pavement conditions such as flat pavement, raised pavement and pothole pavement. The results show that the vegetation point rejection-based method is better able to adapt to the variations of different pavement conditions with greater robustness and reliability than the ground extraction-based method. This is because the method is better able to remove non-ground points, including raised objects and low-lying areas with large height variations.

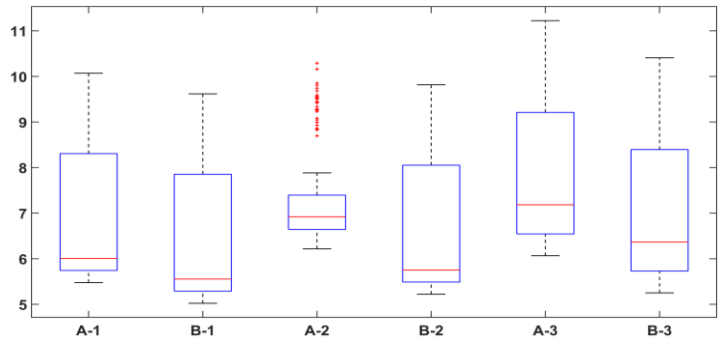

Fig. 6 - Comparison of motion estimation accuracy

- *Experiment of back-end optimization comparison*

To evaluate the effectiveness of the loanability estimation inspired back-end optimization algorithm, this experiment compares it with the distance and time based back-end optimization algorithm. The sensor data were collected in three scenarios: field road, field path and crop row, and the collected data were fed into the loanability estimation inspired back-end optimization algorithm and the distance and time based back-end optimization algorithm respectively for processing, and their accuracy and robustness were compared by comparing the reprojection errors of the two methods.

The experimental results showed that the reprojection error of the loanability estimation-inspired back-end optimization compared to the distance and time-inspired back-end optimization was reduced by 19.3%, 15.53% and 10.95% for three scenarios: large field roads, small field roads and crop rows. The results show that the heuristic back-end optimization algorithm based on localization estimation can significantly improve the localization accuracy and trajectory accuracy of the robot.

RESULTS

Example of Map Construction

To evaluate the performance of the proposed point cloud map construction approach, a test was conducted at the Xiaowangzhuang Agricultural Machinery Experimental Station of the China Agricultural Machinery Institute.

The point cloud map for the experimental field is shown in Figure 7(a). The green dots signify non-vegetative points, which include open areas, rocks on the land surface, and other comparable features. Meanwhile, blue dots indicate obstacles surrounding them, such as cornstalks or weeds. Figure 7(b) shows the performance of the point cloud map construction algorithm between crops rows in the experimental field. The algorithm has the function of localization estimation and can detect the failure of front-end pose tracking. Once tracking failure is detected, the localization estimation algorithm will be modified to improve the robustness and stability of the algorithm. Figure 7(c) illustrates an instance of point cloud map construction for field edges and field tracks. In this scenario, the luxuriant vegetation may lead to occlusion and increased noise in the point cloud data, thereby complicating the construction and localization of the point cloud map. Within the point cloud map, the geometric shape of the pathway and the distribution of surrounding vegetation are distinctly observable. The width and curvature of the pathway, as well as the potential presence of obstacles, are clearly discernible. Figure 7(d) illustrates a field pathways where point cloud mapping has been employed. The road is characterized by street trees situated on either side and a tarmac surface. The point cloud map provides clear visualization of the geometry and features of road, while also presenting the distribution and structure of the street trees as point clouds in space.

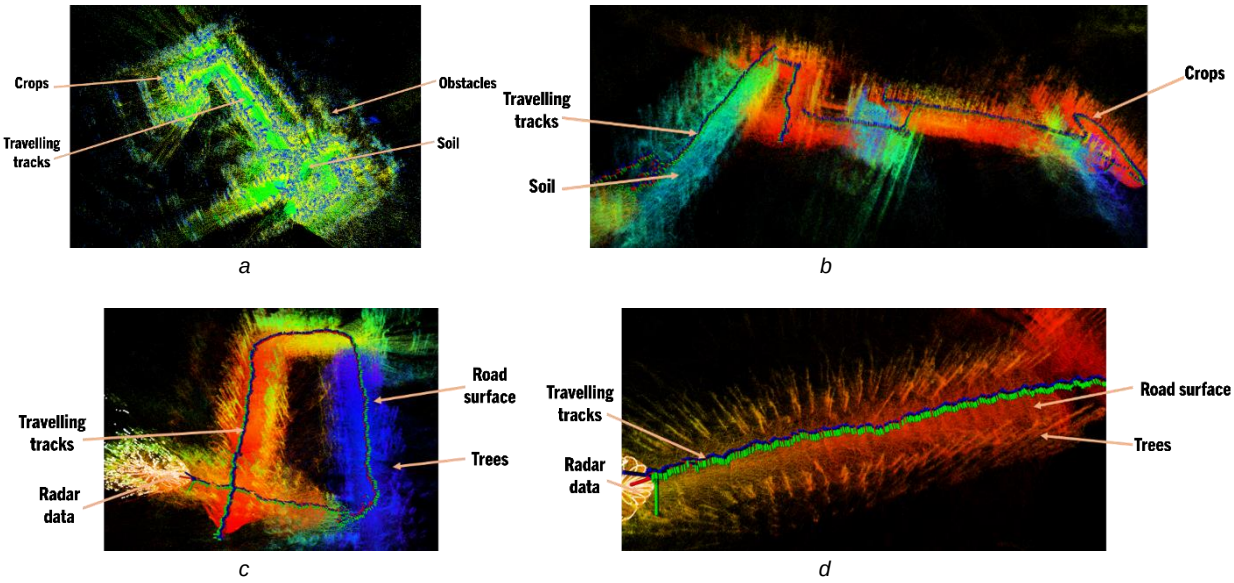

Fig. 7 - Example of point cloud map construction

a - example of point cloud mapping in experimental fields; b - example of point cloud mapping between crop row; c - example of point cloud mapping along field edges and field tracks; d - example of point cloud mapping on field pathway

Localization Accuracy Evaluation

In this experiment, the localization error in point cloud maps serves as the evaluation metric. The point cloud map localization error specifically signifies the distance difference between the algorithmically obtained localization result (P_{pos}) and the true position (P_{gt}) during the localization process. This difference is quantified using the Euclidean distance. Given the point cloud map localization result as P_{pos} and the true position as P_{gt}, the point cloud map localization error (E) is calculated as follows:

$$E_{pos} = \left\| P_{pos} - P_{gt} \right\| \tag{16}$$

Point cloud map localization accuracy refers to the statistical properties of localization errors, typically quantified using Root Mean Square Error (RMSE). RMSE represents the square root of the average of the squared values of all localization errors. Let n be the number of localization error samples, $E_{pos,i}$ and be the localization error of the i^{th} sample. The calculation formula for point cloud map localization accuracy is given:

$$RMSE = \sqrt{\frac{1}{n}\sum_{i=1}^{n}\left(E_{pos,i}\right)^2} \tag{17}$$

In assessing the performance of the mapping algorithm in terms of rotation and translation, high-precision gyroscope data and Global Navigation Satellite System (GNSS) data were employed to obtain accurate rotation and translation information. The gyroscope recorded acceleration data, allowing for the derivation of rotation angles, which were then compared with the pose transformations calculated by the mapping algorithm to assess rotational accuracy. Positional information obtained through GNSS, and the translation vectors calculated by the mapping algorithm were compared to evaluate the algorithm's precision in translation. The data collection vehicle traversed along predefined paths, collecting three-dimensional point cloud data. Simultaneously, the gyroscope recorded the vehicle's rotational information, while GNSS captured the vehicle's positional data.

Table 1

Rotating positioning accuracy.

Localization Accuracy / °	Between Crop Rows	Field Edges	Field Tracks	Field Pathways
Roll Angle	0.429	0.405	0.284	0.261
Pitch Angle	0.249	0.250	0.206	0.175
Yaw Angle	0.179	0.155	0.149	0.151

The gyroscope was mounted at the central position of the vehicle, maintaining a fixed relative orientation to the vehicle body. In this gyroscope setup, the x-axis pointed in the vehicle's forward direction, the y-axis pointed to the right, and the z-axis pointed upward. Thus, the rotation angle of the vehicle's front around the x-axis was referred to as the Roll Angle (θ_x), rotation around the y-axis as the Pitch Angle (θ_y), and rotation around the z-axis as the Yaw Angle (θ_z). These angles were used to describe the vehicle's orientation and pose information. A detailed presentation of the positioning accuracy data is provided in Table 1.

In the experiments, it is observed that in densely populated areas such as field edges and between crop rows, the accuracy is relatively lower, yet it remains within an error margin of approximately 0.5°. This discrepancy can be attributed to increased interference in motion estimation as the density of plants rises. Despite the removal of a significant portion of plant points during initial data processing, the presence of dense vegetation introduces more occlusion. Consequently, the availability of feature points for accurate estimation diminishes, making feature matching more challenging. In contrast, relatively open areas such as field pathways and large field pathways exhibit higher positioning accuracy due to reduced interference in motion estimation caused by limited occlusion.

Following the validation of the algorithm's rotational accuracy, the subsequent step involves evaluating its translational precision. The GNSS positioning is employed as the ground truth in the experiment, with each scenario involving a 30-meter drive and error calculation performed every ten meters. The vehicle's position information is compared with GNSS positioning data, and translational errors are calculated. By comparing the differences between the vehicle's positioning and the actual GNSS positioning, the accuracy and precision of point cloud pose estimation are assessed. Detailed experimental results are presented in Table 2.

Table 2

Cumulative error.

Error (cm)	Orientation	10 m	20 m	30 m
Field Pathways	x	1.98	3.96	5.03
	y	1.95	2.83	4.85
Field Tracks	x	3.31	5.87	8.25
	y	1.93	3.85	6.87
Field Edges	x	3.84	7.73	11.45
	y	2.76	5.68	8.13
Between Crop Rows	x	4.15	7.53	11.68
	y	2.87	5.63	8.73

In the scenarios of field pathways and field tracks, relative to the more complex terrains of field edges and between crop rows, the topography is relatively flat and open. Additionally, there is comparatively less vegetation obstruction and reflection interference. Therefore, in these two scenarios, the mapping algorithm exhibits higher translational accuracy, with cumulative errors over a 30 m travel distance measuring 5.03 cm and 8.25 cm, respectively. In contrast, in the scenarios of field edges and between crop rows, the distribution density of plants is higher, and the height and morphology of vegetation are more complex. This complexity results in more noise and errors in the point cloud data detected by the lidar sensor. Cumulative errors over a 30 m distance in these scenarios are 11.45 cm and 11.68 cm, respectively. Despite the challenges posed by higher vegetation density and complexity, the cumulative errors in these scenarios remain within 12 cm.

CONCLUSIONS

(1) Considering the environmental characteristics of typical agricultural machinery operation scenes, a comprehensive plan for semantic point cloud map construction was devised. In hardware design, a data acquisition device incorporating Lidar, RGB, and NIR sensors was designed. Furthermore, a calibration board was created for calibrating both visible and non-visible light cameras, and an algorithmic workflow for multi-sensor joint intrinsic and extrinsic parameter calibration was established. In terms of algorithmic design, an advanced algorithm for high-precision point cloud map construction within the SLAM framework was proposed. Additionally, a Transformer-based semantic segmentation algorithm was introduced.

(2) The algorithm, built upon the SLAM framework, addresses the challenges posed by dynamic points interference in agricultural machinery operation scenes through a plant point removal preprocessing method. An optimization algorithm inspired by locatability estimation was proposed for the backend, addressing the limitations of time or distance-based heuristics. Experimental evaluations conducted in field pathways, small pathways, and between crop rows showcased the effectiveness of the optimized mapping algorithm, with the median reprojection error Euclidean distances reduced by 10.27%, 20.76%, and 14.36%, respectively.

(3) A high-precision map information collection vehicle was assembled, equipped with field information collection devices and deployed with mapping and semantic segmentation algorithms. Experimental trials conducted in field pathways, small pathways, field edges, and between crop rows demonstrated favorable results. At 30 meters, the average rotational localization errors were 0.429°, 0.405°, 0.284°, and 0.261°, with minimum cumulative errors ranging from 1.93 cm to 4.15 cm at 10 meters, 2.83 cm to 7.73 cm at 20 meters, and 4.85 cm to 11.68 cm at 30 meters.

ACKNOWLEDGEMENT

The work was sponsored by the National Key R&D Program Project of China (2021YFD2000105).

REFERENCES

[1] Ao, Z., Sun, Y., Xin, Q. (2021). Constructing 10-m NDVI Time Series from Landsat 8 and Sentinel 2 Images Using Convolutional Neural Networks. *IEEE Geoscience and Remote Sensing Letters*, Vol. 18, pp. 1461-1465, Guangzhou/China.

[2] Chen, S., Nardari, G., Lee, E., Chao, Q., Xu, L., Roseli, A., Vijay, Kumar. (2020). SLOAM: Semantic Lidar Odometry and Mapping for Forest Inventory. *IEEE Robotics and Automation Letters*, Vol. 5, pp. 612-619, United States.

[3] Dong, N., Chi, R., Du, Y., Wen, C., Zhang, Z. (2020). Research on field surface point cloud Registration based on rotary Surface profile (基于旋转曲面轮廓特征的农田地表点云配准研究). *Transactions of the Chinese Society for Agricultural Machinery*, Vol. 51, pp. 325-332, Beijing/China.

[4] Han, B., Luo, L., Liu, X., Shen, H. (2022). Feature Descriptor Enhancement for Loop Detection Based on Metric Learning (基于度量学习的回环检测描述子提升算法). *Pattern Recognition and Artificial Intelligence*, Vol. 35, pp. 51-61, Zhejiang/China.

[5] Han, C., Chen, M., Huang, Y., Zhao, M., Du, Q., Liang, Q. (2022). Laser SLAM loopback detection based on global feature descriptor (基于全局特征描述子的激光 SLAM 回环检测方法). *Journal of Shanghai Jiao Tong University*, Vol. 10, pp. 1379-1387, Shanghai/China.

[6] Ji, Y., Xu, H., Zhang, M, Li, S., Cao, R., Li, H. (2019). Design of farmland environment point cloud acquisition system based on laser radar (基于激光雷达的农田环境点云采集系统设计). *Transactions of the Chinese Society for Agricultural Machinery*, Vol. 50, pp. 1, Beijing/China.

[7] Johnson, A. E., Hebert, M. (1999). Using spin images for efficient object recognition in cluttered 3D scenes. *IEEE transactions on pattern analysis and machine intelligence*, Vol. 21, pp. 433-449, USA.

[8] Kim, L., Wu, Z. (2022). Practice path of Promoting Agricultural Modernization with Agricultural Science and technology Modernization (以农业科技现代化促进农业现代化的实践路径). *Journal of Drainage and Irrigation Machinery Engineering*, Vol. 40(10), pp. 1056-1064, Jiangsu/China.

[9] Li, X., Wei, P., He J., Li, M., Zhang, M., Wen, B. (2021). Field plant point cloud registration method based on Kinect V3 depth sensor (基于 Kinect V3 深度传感器的田间植株点云配准方法). *Transactions of the Chinese Society of Agricultural Engineering*, Vol. 37, pp. 45-52, Guangxi/China.

[10] Li, X., He, W., Zhu, S., Li, Y., Xie, T. (2021). A review of synchronous localization and map construction methods based on environmental semantic information (基于环境语义信息的同步定位与地图构建方法综述). *Chinese Journal of Engineering Science*, Vol. 43, pp. 754-767, Zhejiang/China.

[11] Lucas, C., Bouten, W., Koma, Z., Kissling, W., Seijmonsbergen, A. (2019). Identification of Linear Vegetation Elements in a Rural Landscape Using LiDAR Point Clouds. *Remote Sensing*, Vol. 11, pp. 292, Netherlands.

[12] Newcombe, R. A., Lovegrove, S. J., Davison, A. J. (2011). DTAM: Dense tracking and mapping in real-time. *IEEE Conference on Computer Vision and Pattern Recognition*, pp. 2320-2327, United Kingdom.

[13] Qi, F., Zhou, X., Wu, Z., Zhang, X. (2017). Path and method of infrastructure engineering in the process of agricultural modernization (农业现代化过程中基础设施工程化路径与方法). *Transactions of the Chinese Society of Agricultural Engineering*, Vol.33, pp. 16-25, Beijing/China.

[14] Tian, X., Zhang, M., Yang, C., Ma, J. (2021). FusionNDVI: A Computational Fusion Approach for High-Resolution Normalized Difference Vegetation Index [J]. *IEEE Transactions on Geoscience and Remote Sensing*, Vol. 59, pp. 5258-5271, Hubei/China.

[15] Tombari, F., Salti, S., Di, S. L. (2010). Unique Signatures of Histograms for Local Surface Description. *European Conference on Computer Vision*, Vol. 11, pp. 356-369, Italian.

[16] Vizzo, I., Guadagnino, T., Mersch, B., Wiesmann, L., Behley, J., Stachniss, C. (2023). KISS-ICP: In Defense of Point-to-Point ICP – Simple, Accurate, and Robust Registration If Done the Right Way[J]. *IEEE Robotics and automation letters*, Vol. 8, pp. 1029-1036, Germany.

[17] Wang, X., Yuan, S., Jia, W. (2022). Current situation and development of agricultural mechanization in hilly and mountainous areas (丘陵山区农业机械化现状与发展). *Journal of Drainage and Irrigation Machinery Engineering*, Vol. 5, pp. 535-540, Jiangsu/China.

[18] Wang, Y., Lou, Y., Zhang, Y., Song, W., Huang, F., Tu, Z. (2021). A Robust Framework for Simultaneous Localization and Mapping with Multiple Non-Repetitive Scanning Lidars. *Remote Sensing*, Vol. 13, pp. 2015, Hubei/China.

[19] Xu, X., Li, N., Yao, Y. (2022) Laser Radar SLAM Algorithm Based on fast loopback detection in Outdoor environment (基于深度学习的室内动态场景下的 VSLAM 方法). *Journal of Chinese Inertial Technology*, Vol. 30 pp. 716-722, Jiangsu/China.

[20] Zeng, Q., Luo, Y., Sun, K., Li, Y., Liu, J. (2022). Review on the development of SLAM technology based on vision and its integration with inertia (视觉及其融合惯性的 SLAM 技术发展综述). *Journal of Nanjing University of Aeronautics and Astronautics*, Vol. 54, pp. 1007-1020, Jiangsu/China.

ACCURATE NON-DESTRUCTIVE TESTING METHOD FOR POTATO SPROUTS FOCUSING ON DEFORMABLE ATTENTION
/
聚焦可变形注意力的马铃薯芽苗精确无损检测方法

Binxuan GENG[1)], Guowei DAI[2)], Huan ZHANG[1,*)], Shengchun QI[1)], Christine DEWI[3)]
[1)] Faculty of Mechanical and Electrical Engineering, Qingdao Agricultural University, Qingdao 266000 / China;
[2)] Agricultural Information Institute of CAAS, Beijing 100081 / China;
[3)] Faculty of Information Technology, Satya Wacana Christian University Salatiga / Indonesia
Tel: 13864215762; E-mail: huan0804@163.com Corresponding author: Zhang Huan
DOI: https://doi.org/10.35633/inmateh-72-36

Keywords: *deep learning, non-destructive inspection, YOLOv8, DAS Attention Mechanism, potato sprouts*

ABSTRACT

Accurate potato sprout detection is the key to automatic seed potato cutting, which is important for potato quality and yield. In this paper, a lightweight DAS-YOLOv8 model is proposed for the potato sprout detection task. By embedding DAS deformable attention in the feature extraction network and the feature fusion network, the global feature context can be efficiently represented and the attention increased to the relevant pixel image region; then, the C2f_Atten module fusing Shuffle attention is designed based on the C2f module to satisfy the attention to the key feature information of the high-level abstract semantics of the feature extraction network. At the same time, the ghost convolution is introduced to improve the C2f module and convolutional module to realize the decomposition of the redundant features to extract the key features. Verified on the collected potato sprout image data set, the average accuracy of the proposed DAS-YOLOv8 model is 94.25%, and the calculation amount is only 7.66 G. Compared with the YOLOv8n model, the accuracy is 2.13% higher, and the average accuracy is 1.55% higher. In comparison to advanced state-of-the-art (SOTA) target detection algorithms, the method in this paper offers a better balance between comprehensive performance and lightweight model design. The improved and optimized DAS-YOLOv8 model can realize the effective detection of potato sprouts, meet the requirements of real-time processing, and can provide theoretical support for the non-destructive detection of sprouts in automatic seed potato cutting.

摘要

马铃薯芽苗准确检测是马铃薯种薯自动切块的关键，对马铃薯的品质和产量具有重要意义。本文提出一种轻量级的DAS-YOLOv8 模型用于马铃薯芽苗检测任务。通过在特征提取网络与特征融合网络嵌入 DAS 可变形注意力，以高效表示全局特征上下文和增加对相关像素图像区域的关注度；然后，基于 C2f 模块设计融合 Shuffle 注意力的 C2f_Atten 模块，以满足特征提取网络高层抽象语义关键特征信息的关注，同时引入幽灵卷积改进 C2f 模块和卷积模块，实现分解冗余特征提取关键特征。在采集到的马铃薯芽苗图像数据集进行验证，拟议 DAS-YOLOv8 模型的平均精度均值为 94.25%，计算量仅为 7.66 G，相比 YOLOv8n 模型，精准率提高 2.13%，平均精度均值提高 1.55%。在先进 SOTA 目标检测算法比较中，本文方法的综合性能更好模型更轻量化。改进优化后的 DAS-YOLOv8 模型能够实现马铃薯芽苗的有效检测，满足实时处理的要求，可为种薯自动切块中的芽苗无损检测提供理论支撑。

INTRODUCTION

Potato is one of the world's major food crops and plays an important role in ensuring global food security and stability. China is the country with the largest area under potato cultivation (31.89% of the global cultivated area) and also the country with the highest potato production (25.09% of the global total production) *(Lun et al., 2023)*. In the potato industry, the level of mechanization has been increasing, including the mechanization of seeding, harvesting, cultivation, and grading of potatoes. However, at present, the cutting of seed potatoes still relies mainly on manual operation, with problems such as high labor intensity, low efficiency, and high costs. With the rise of labor costs and the reduction of the labor force, there is an urgent need to solve the problem of automatic seed potato cutting *(Danielak et al., 2023)*. Among them, accurate detection of potato sprouts is the key to realizing automatic seed potato cutting.

With the continuous progress and development of computer technology, computer vision technology has gradually been widely used in the field of agriculture. However, the research on potato sprout recognition is more limited.

Non-destructive testing (NDT) is usually based on RGB imaging systems and hyperspectral/multispectral imaging systems is used to obtain images of the surface of agricultural products. In terms of traditional machine vision methods, *Li et al., (2018),* proposed a potato sprout eye recognition method based on three-dimensional geometric features of color saturation. This method has a sprout eye recognition rate of 91.48% and takes an average of 2.68 seconds to identify a single image. Gao et al. *(Gao, 2022)* trained SVM classifiers based on extracting B and H components in RGB color space and HSV color space and used weighted Euclidean distance and morphological methods to detect and label potato sprouting loci with an average recognition rate of 90.6%. *Lu et al., (2021),* performed potato image filtering based on Gabor features and selected filtered images under orientation two and scale four for morphological image processing, and the proposed algorithm's bud eye recognition rate was 93.4%. *Dhulipalla Ravindra Babu et al., (2023)* calculated four parameters of variance, correlation, homogeneity, and uniformity using gray level co-occurrence matrix on the collected potato dataset, and the classification accuracy by support vector machine was 99.5%.

The above methods need to design and extract image features manually and usually use low-level features such as edges, textures, colors, etc.; feature extraction has blindness and uncertainty and is less adaptable to complex scenes *(Su & Xue, 2021)*. With the rapid development of computer technology, especially deep learning, in recent years, the related technology has been successfully applied to the field of agriculture. Compared with the traditional methods, deep learning methods have more powerful feature learning and modeling capabilities in the target detection task, and can deal with more complex scenes and target variations, as well as possessing higher accuracy and generalization capabilities. *Zhang et al., (2022),* achieved an accuracy rate of 88.33% for seed potato sprout eye detection based on the YOLOv3-tiny network using the CIoU border regression loss function with the K-means clustering method. *Yang et al., (2021),* based on multispectral images combined with a Supervised Multi-Threshold Segmentation Model (SMTSM) and Canny edge detector in order to achieve 89.67% accuracy in seed potato sprout detection. Wang et al. *(Wang C. & Xiao, 2021)* used the convolutional layer of ResNet101 as the base network structure to improve Faster RCNN, which achieved 98.7% accuracy in detecting surface defects on potatoes. *Dai et al., (2022),* enhanced the feature similarity problem of the feature representation fusion process by replacing the Conv of the C3 module in YOLOv5 with CrossConv. They used the 9-Mosaic data augmentation algorithm to improve the model generalization ability, and the accuracy of the improved model for potato germination recognition in complex scenarios was 90.14%.

For these reasons, this work proposes a lightweight method for potato sprout detection. By collecting potato sprout-related picture information, using DAS deformable attention in the backbone network and neck network to deepen the information interaction of semantic features at the abstraction level, and designing a C2f module incorporating Shuffle Attention for automatic feature extraction in the backbone network, and secondly, using Ghost Convolution to simplify the model computation and ensure the model's detection accuracy and lightness, a better sprout detection accuracy was obtained in the potato sprouts dataset.

MATERIALS AND METHODS

Image Acquisition Platform

The image acquisition system is shown in Fig. 1 and includes a cell phone, LED ring light, stepper motor, potato base, shade cloth, reflector, and computer.

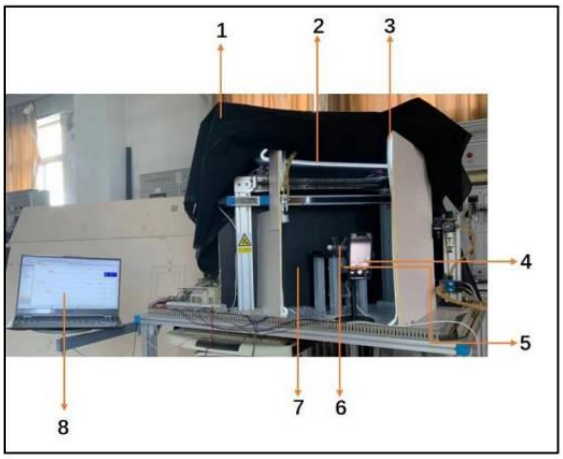

Fig. 1 - Image Acquisition Platform for Potato Sprouts

1. Shade cloth; 2,3. LED strip light; 4. Shooting phone; 5. Stepping motor; 6. Potato base; 7. Reflector; 8. Computer

The stepper motor step angle was 0.9 degrees. The sprouted potato seed potato was placed into the potato base located above the stepper motor, after which the stepper motor began to rotate. Image acquisition was performed at every 120° of rotation so that a complete sprouted potato was identified from three images. In addition, the position of the camera used for image acquisition must be at the same horizontal height as the sprouted potatoes in order to prevent the emergence of the situation of top-down or upward view angle, which may cause visual difference and, thus, data errors in the subsequent work.

Dataset Construction

The experimental sample is 200 potatoes, and a total of 600 images are collected. In the deep learning task, in order to improve the generalization ability of the model, prevent overfitting, enhance the robustness of the model, and at the same time simulate the various changes in the real world to adapt to different scenarios, it is necessary to augment the collected images with data. By applying various transformations to the image, the dataset used for training can be expanded so that the model can recognize more features and patterns during the learning process, resulting in higher accuracy and stability in practical applications. In this deep learning task, it was performed image vertical flip and horizontal flip, increased image contrast, increased image brightness, added motion blur noise, splash transform, and pixel transform to the image, and added digital noise to the acquired potato images, using all of the above for data augmentation. The results of the data augmentation are detailed in Fig. 2.

After data augmentation, the dataset contains a total of 2000 images. The images were labeled using the automatic labeling X-AnyLabeling tool and using the standard format of the YOLO dataset, which is suitable for the YOLO family of neural network detection models. From these 2000 images, 1500 images were randomly selected as the training set, 300 images as the validation set, and 200 images as the test set, with no overlap between the three. The potato sprout dataset (PSD) included in this paper is divided into the dataset PSD-One of the original 600 images and the dataset PSD-Two of 2000 images.

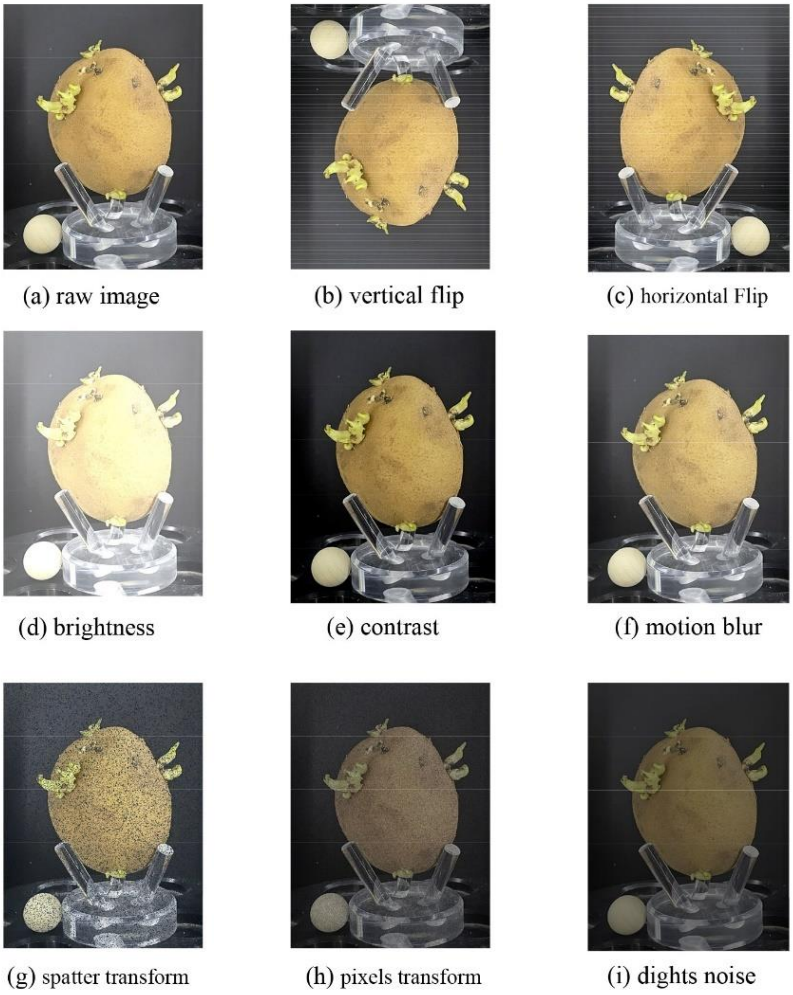

Fig. 2 - Results of image data augmentation of potato sprouts

DAS Attention Mechanism

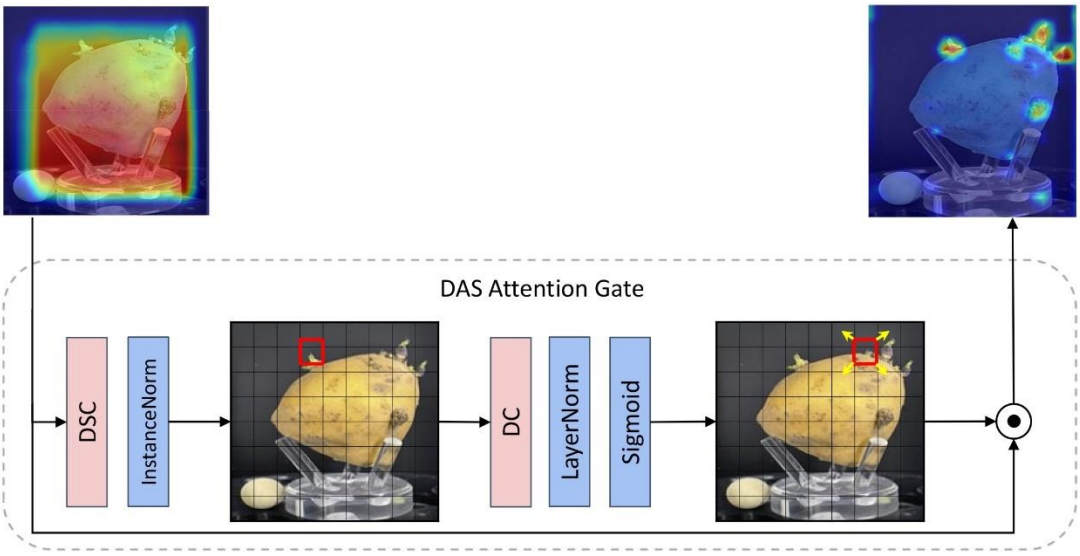

Fig. 3 - The heatmap shows the comparison results of saliency maps with the addition of the DAS attention mechanism, which integrates deeply separable convolution (DSC) with deformable convolution (DC) to focus attention on salient regions

Deformable Attention DAS is a fast and simple fully convolutional method that helps to focus attention on relevant information (Fig. 3). The DAS consists of depth separable convolution (DSC) with deformable convolution (DC). DSC operations are used in the bottleneck layer to improve computational efficiency by reducing the number of channels in the feature map. The channel is reduced from c to $a \times c$, the only hyperparameter ranges from 0 < α < 1 and is insensitive for 0.1 < α. The instance normalization InstanceNorm process is performed after the bottleneck layer to achieve the removal of instance-specific contrast information from the image, thus improving the robustness of the DAS model during training, followed by the addition of a nonlinear activation function, GELU, to enhance the representation of the features as shown in equation (1), where $\mathbf{X}$ is the input feature, $\mathbf{W}_1$ is the depth-separable convolution, and $\mathbf{X}_c$ denotes the feature context.

$$\mathbf{X}_c = \text{GELU}(\text{InstanceNorm}(\mathbf{X}\mathbf{W}_1)) \tag{1}$$

The above feature context is compressed; equation (2) uses deformable convolution of a dynamic grid to focus on the image region of interest, K is the size of the convolution kernel, w_k is the weight parameter, $p_{ref,k}$ is a fixed reference point, and the trainable parameters, w_p and Δp_k, depend on the specific features of the kernel function being applied. Next, as in equation (3), the number of channels of the feature map is converted to the original input c, using the layer normalized LayerNorm with Sigmoid activation function σ operation. The information flow of the feature map is controlled, and it is decided that part of the feature map is emphasized or filtered. The output of equation (4) is the input of the next layer of the CNN model, $\mathbf{X}$ is the upper layer feature, and $\odot$ denotes the dot product.

$$deform(p) = \sum_{k=1}^{K} w_k \cdot w_p \cdot \mathbf{X}(p_{ref,k} + \Delta p_k) \tag{2}$$

$$\mathbf{A} = \sigma\left(\text{LayerNorm}\left(deform(\mathbf{X}_c)\right)\right) \tag{3}$$

$$\mathbf{X}_{\mathbf{out}} = \mathbf{X} \odot \mathbf{A} \tag{4}$$

C2f_Atten Module

The Shuffle Attention (SA) module combines group convolution, spatial attention mechanisms, and channel attention mechanisms *(Hao et al., 2023; Song et al., 2024)*. Not only is it possible to take the information between different channels, but the amount of computation is also reduced, which helps to achieve the precise location and recognition of the target. Shuffle Attention contrasts with the traditional attention mechanism by disrupting and reordering the input sequence, thereby enhancing the model's ability to generalize while maintaining computational efficiency. Additionally, the importance of each position is determined within this process. SA Attention Module is shown in Fig. 4.

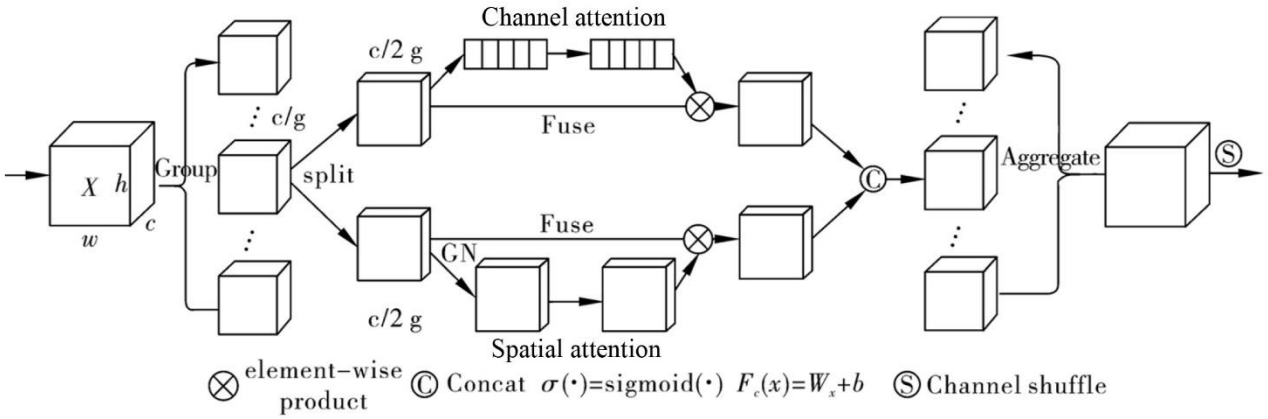

Fig. 4 - General Architecture of the Shuffle-Attention Module

The main process is that for the input feature map as $X \in R^{C\times H\times W}$ divided into g groups $X = 2[X_1,\cdots,X_G], R^{C/G\times H\times W}$, along the channel dimensions, the feature X will be split into two branches as $X_{k1}, X_{k2} \in R^{C/2G\times H\times W}$, which will be used to learn the channel attention features and spatial attention features respectively. For each group of features, the information within the group is fused by means of Concat to generate different importance coefficients. The upper branch channel attention mechanism uses GAP, a combination of scaling factor and Sigmoid function; W_1 and b_1 are two dynamic parameters of the scaled feature map; the specific process is described as follows:

$$s = F_{gp}(X_{k1}) = \frac{1}{H\times W}\sum_{i=1}^{H}\sum_{j=1}^{W} X_{k1}(i,j), \tag{5}$$

$$X'_{k1} = \sigma(F_c(s)) \times X_{k1} = \sigma(W_1 s + b_1) \times X_{k1}, \tag{6}$$

The branch below SA is the spatial attention mechanism, as shown in equation (7).

GroupNorm (GN) is used to process X_{k2} to get the statistical information at the spatial domain level, and then the $F_c(\ )$ operation is used. The Channel Shuffle operation is used to enhance the interaction and information transfer to the group's features. The Concat fusion is used to get $X_k = concat[X'_{k1}, X'_{k2}]$ to realize the information circulation between different groups.

$$X'_{k2} = \sigma(W_2 \times GN(X_{k2}) + b_2) \times X_{k2}, \tag{7}$$

The C2f_Atten module integrates the SA module on top of the C2f module, i.e., it realizes the addition of the attention mechanism to the C2f module. SA is located after the second Conv module, which makes the model more concerned about the location information of the target region in order to improve the accuracy of the detection of the target region, and the details of the code implementation are shown in Table 1.

Table 1

C2f_Atten module specific algorithm implementation details

```
class C2f_Attention(nn.Module):
  def __init__(self, c1, c2, n=1, shortcut=False, g=1, e=0.5):
    super().__init__()
    self.c = int(c2 * e)
    self.cv1 = Conv(c1, 2 * self.c, 1, 1)
    self.cv2 = Conv((2 + n) * self.c, c2, 1)
    self.attention = ShuffleAttention(c2)
    self.m = nn.ModuleList(Bottleneck(self.c, self.c, shortcut, g,
k=((3, 3), (3, 3)), e=1.0) for _ in range(n))
  def forward(self, x):
    y = list(self.cv1(x).chunk(2, 1))
    y.extend(m(y[-1]) for m in self.m)
```

```
    return self.attention(self.cv2(torch.cat(y, 1)))
  def forward_split(self, x):
    y = list(self.cv1(x).split((self.c, self.c), 1))
    y.extend(m(y[-1]) for m in self.m)
    return self.cv2(torch.cat(y, 1))
```

DAS-YOLOv8 potato sprout detection model

YOLOv8 is the SOTA target detection model of the current YOLO series of networks, which has the characteristics of a lightweight and wide adaptation range *(Ma et al., 2023; Z. Wang et al., 2024)*. In this paper, the YOLOv8n network model was taken as the basic framework, and the structure of the improved model is shown in Fig. 5, which mainly includes the input, backbone network, neck network, and head module.

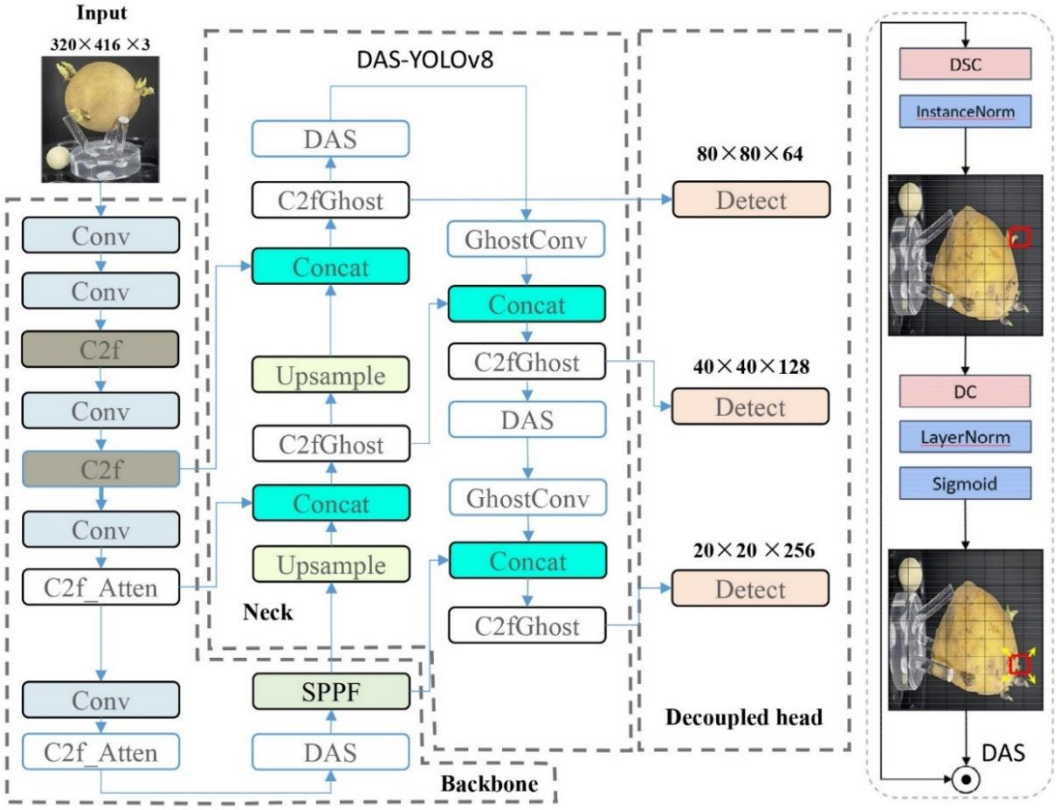

Fig. 5 - The general architecture of DAS-YOLOv8, consists of three components: the Backbone for feature extraction, the Neck for feature connectivity and the Head for output

Input side: By using Mosaic data augmentation to perform operations such as flipping (flipping left and right of the original picture), scaling (scaling the size of the original picture), and color gamut transformation (changing the brightness, saturation, and hue of the original picture) on the random pictures, and then combining the pictures, the model can be better adapted to the complex scenes in the real world, so that it has better robustness and generalization ability, and then improve the model's ability to detect markers in complex backgrounds. Note that by default 10 Epochs before the end of training will automatically turn off Mosaic data augmentation.

Backbone network: The backbone network in YOLOv8 acts as a feature extractor, which mainly consists of the Conv module, C2f module, and SPPF module. Its main function is to extract features from the input image, which are used for subsequent tasks. In this paper, the penultimate two C2f modules of the backbone network are replaced with C2f_Atten to obtain the key factor information of highly abstract semantic features in the feature extraction layer. DAS-intensive attention is applied before the SPPF module, and the feature context is considered comprehensively. Through a series of convolution and pooling operations, the backbone network gradually reduces the spatial dimensions of the feature maps while increasing the depth of these feature maps. This process allows the neural network to capture and represent features of varying complexity and scale in the input image.

Neck network: used to process further the feature maps extracted by the backbone network. Its main purpose is to integrate different levels of feature information to improve the performance of target detection. The main improvements in designing the model include reducing the number of parameters of the model by replacing the Conv module with GhostConv to share parameters between channels. C2fGhost, on the other hand, changes the structure of the C2f module by replacing all of the Convs contained in the C2f module with GhostConvs, and by combining a small number of actual filters with linear combinations of these filters, this helps to reduce model complexity without sacrificing accuracy *(Wang Y. et al., 2024)*. The introduction of GhostConv with C2fGhost aims to achieve a balance between model performance and efficiency. DAS is adopted after the second upsampling to solve the problem of the possible loss of primary semantic features of the backbone network. The subsequent DAS can take over the mixed semantic feature information from the C2f_Atten module and the DAS of the backbone network to better utilize, in addition to the basic feature information of the backbone network attention information.

Head module: plays a crucial role in the target detection task, and its main responsibility is to generate bounding boxes, classification probabilities, and target attributes. This module is designed to extract information related to detected object location and classification labels from the feature map. The generated bounding boxes are processed with non-extremely large value suppression to obtain the final target detection results. In the design phase, the feature information sources of multiple Detect modules are decentralized in order to avoid focusing all the attention on single-scale feature information.

Experimental platforms and performance indicators

The desktop computer used for the experiment has an Intel Core i7-12700F processor, 32GB of RAM, and is equipped with an NVIDIA GeForce RTX 3090 GPU to accelerate the experimental process, which has 24G of video memory.

The experiments were run on Windows 11 (64-bit) operating system, VS2015 version, Python version 3.9.13, using PyTorch (version 1.13.1) as the framework for deep learning, equipped with CUDA version 11.7 parallel computer architecture with cuDNN version 8.6 deep neural network acceleration library. The batch size for network training is 32, and the optimizer selects SGD. By default, the input size of the original image is resized to 320 × 416. In addition, the training process supervises the model outputs using early stopping, which is effective in preventing overfitting.

In order to evaluate the detection performance of the proposed model for potato sprouts, equations (8-11), i.e., Precision, Recall with mean average precision mean (mAP, IoU threshold is taken as 0.5), were used to evaluate the complexity of the algorithm using the model's floating point calculations (FLOPs) as an important indicator of the complexity of the algorithm.

Where TP (True Positive): predicted to be a sprout and actually a sprout, i.e., the number of correctly identified potato sprouts; FP (False Positive): predicted to be a sprout and actually not a sprout, i.e., the number of incorrectly identified potato sprouts; FN (False Negative): predicted not to be a sprout and actually a sprout, i.e., the number of omitted potato sprouts; and TN (True Negative): predicted to be not a sprout and actually not a sprout, i.e., the number of correctly identified non-potato sprouts.

$$\text{Precision} = \frac{TP}{TP + FP} \tag{8}$$

$$\text{Recall} = \frac{TP}{TP + FN} \tag{9}$$

$$\text{AP} = \frac{1}{n}\sum_{i=1}^{n} \text{Precision}_i \tag{10}$$

$$= \frac{1}{n}\text{Precision}_1 + \frac{1}{n}\text{Precision}_2 + \cdots + \frac{1}{n}\text{Precision}_n$$

$$\text{mAP} = \frac{\sum_{i=1}^{Q} AP_i}{Q} \tag{11}$$

RESULTS

Analysis of potato sprout detection performance

In this section, the performance of the proposed DAS-YOLOv8 model will be validated from various aspects. As shown in Table 2, the DAS-YOLOv8 model improves the precision rate by 2.13%, the recall rate by 2.55%, and the average precision mean by 1.55% compared to the unimproved YOLOv8n model. Notably, the FLOPs of the DAS-YOLOv8 model are only 7.66, which is 0.94% lower compared to YOLOv8n, proving the property of model lightness.

As shown in Fig. 6, 60 images were randomly selected from the potato sprout test set of 200 images for testing, and the random image selection process was performed four times.

Table 2

Comparative results of DAS-YOLOv8 model improvement experiments

#	Model	Datasets	Precision (%)	Recall (%)	mAP (%)	FLOPs (G)
1	YOLOv8n	PSD-Two	91.11	84.45	92.70	8.60
2	DAS-YOLOv8	PSD-Two	93.24	87.68	94.25	7.66

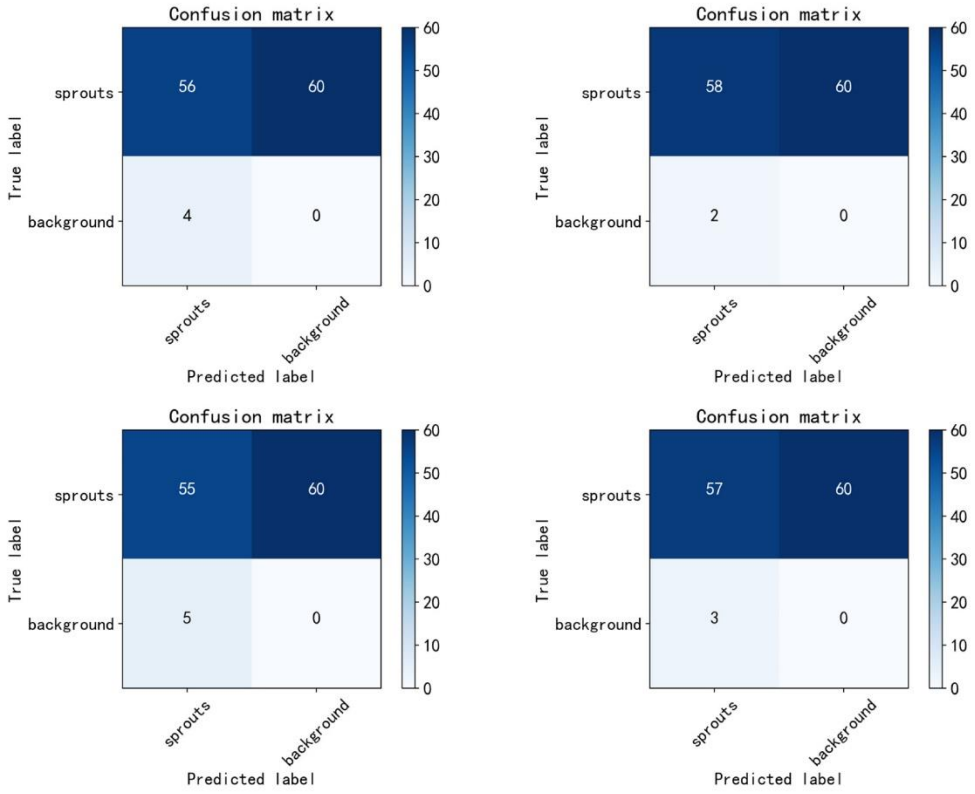

Fig. 6 - Confusion Matrix for Test Results of Randomly Selected Samples from the Potato Sprout Test Set

C2f_Atten module ablation experiment

In this section, the performance of the proposed C2f_Atten module will be verified for potato sprout detection in the DAS-YOLOv8 model. The C2f_Atten module is employed in the backbone network of the DAS-YOLOv8 model, which improves the C2f module. Based on the original C2f module code, any intrusive code revisions were divided into three main parts. As shown in Table 1, part 1 (SA-1) uses the SA attention mechanism at the C2f module code cv1, part 2 (SA-2) uses the SA attention mechanism at the C2f module code cv2, and part 3 (SA-3) uses the SA attention mechanism at the C2f module code m (bottleneck network). The experimental results, shown in Table 3, show that the SA-2 attention combination used in the proposed DAS-YOLOv8 model achieves the best performance, with an average precision mean of 94.25%, and precision and recall rates of 93.24% and 87.68%, respectively. SA-3 improved the accuracy rate by 0.12% compared to SA-2, but the FLOPs increased by 0.04%. The mean average precision value of SA-3 was lower than that of SA-2, which was 94.12%. The mean average precision value of SA-1 was 93.98%, and it had the worst performance in the performance of the ablation test of the C2f_Atten module, but the model complexity was the same. In summary, the DAS-YOLOv8 modeling submodule for intrusive code improvement can effectively improve the model detection performance.

Table 3

Results of the C2f_Atten module ablation experiment

#	Model	C2f_Atten	Datasets	Precision (%)	Recall (%)	mAP (%)	FLOPs (G)
1	DAS-YOLOv8	SA-1	PSD-Two	92.59	87.24	93.98	7.66
2	DAS-YOLOv8	SA-2	PSD-Two	93.24	87.68	94.25	7.66
4	DAS-YOLOv8	SA-3	PSD-Two	93.36	86.53	94.12	7.70

DAS-YOLOv8 ablation experiment

In this section, the performance differences between the C2f_Atten, DAS, C2fChost, and GhostConv modules for the DAS-YOLOv8 model are analyzed. Table 4 shows that the mean average precision value of the C2f_Atten module embedded in the backbone network is 93.15%, the mean average precision value of the DAS module embedded in the backbone network with a necking network is 94.58%, and the performance enhancement advantage of the DAS module is some obvious. C2f_Atten was used in fusion with the DAS module for a mean average precision of 94.67%. The C2fChost and GhostConv modules were mainly used to lighten the DAS-YOLOv8 model, and as can be seen in Table 4, test numbers 4-6, the C2fChost and GhostConv modules resulted in a reduction of the mean average precision by 0.42%. However, model complexity FLOPs were reduced by 16.19%. Compared to Trial No. 1, Trial No. 7 used C2f_Atten with DAS module for model lightening, and as a result, the mean average accuracy was reduced by 1.48%, which is a significant advantage over not using C2f_Atten with DAS module. From the point of view of analyzing the dataset, the DAS module and the C2f_Atten module, which contains the SA attention mechanism, demonstrate the sophistication of the DAS-YOLOv8 model.

Table 4

Ablation experiments

No.	Embedded model method				mAP (%)	FLOPs (G)
	C2f_Atten	DAS	C2fChost	ChostConv		
1	-	-	-	-	92.70	8.60
2	+	-	-	-	93.15	8.68
3	-	+	-	-	94.58	8.96
4	+	+	-	-	94.67	9.14
5	+	+	+	-	94.31	7.92
6	+	+	+	+	94.25	7.66
7	-	-	+	+	91.22	7.20

SOTA algorithm comparison experiment

In order to further verify the effectiveness and advancement of improving the potato sprout detection algorithm proposed in this paper, current mainstream target detection algorithms such as YOLOv6n (*Bist et al., 2023*), YOLOv5s (*Khalid et al., 2023*) YOLOv7 (*Guo et al., 2023*), and YOLOv8s are used to train and test the model under the same conditions. The experimental results are shown in Table 5. From the data in the table, compared with YOLOv8s, this paper's method is 0.44% behind in mAP. However, the model complexity is 70.40% lower than it, indicating that the comprehensive performance of this paper's method is better. The model is more lightweight, which is suitable for the practical application of agricultural equipment engineering. Compared to other algorithms, there are different degrees of advantages in terms of detection accuracy, mean average precision, and computation. In addition, the mean average precision value of the proposed model in the PSD-One dataset is 82.69%, which is lower than the mean average precision value of 94.25% in the PSD-Two dataset. The accuracy gap of the same model illustrates the practical value of employing data augmentation for potato sprout images, which better improves the performance of the model.

To further illustrate the effectiveness of the method in this paper, 16 test result visualizations were randomly extracted from the PSD-Two test set for subjective analysis, and the test results are shown in Fig. 7. From the figure, it can be seen that the proposed DAS-YOLOv8 model accurately detects potato sprouts at different types of locations with the ability to detect potato sprouts under certain disturbing conditions because of better robustness due to the pre-processing of the dataset that innately takes into account the instability of the environmental factors under the Agricultural Equipment Engineering.

Table 5

Performance comparison results of different SOTA algorithms

Algorithm	Backbone	Datasets	Precision (%)	Recall (%)	mAP (%)	FLOPs (G)
YOLOv6n	CSPDarknet53	PSD-Two	93.32	87.77	94.11	11.35
YOLOv5s	CSPDarknet53	PSD-Two	91.74	86.36	92.88	15.80
YOLOv7	CSPDarknet53	PSD-Two	92.98	87.55	93.42	13.32
YOLOv8s	CSPDarknet53	PSD-Two	94.26	89.13	94.69	26.6
YOLOv8n	CSPDarknet53	PSD-Two	91.11	84.45	92.70	8.60
DAS-YOLOv8	Ours	PSD-Two	93.24	87.68	94.25	7.66
DAS-YOLOv8	Ours	PSD-One	78.43	69.11	82.69	7.66

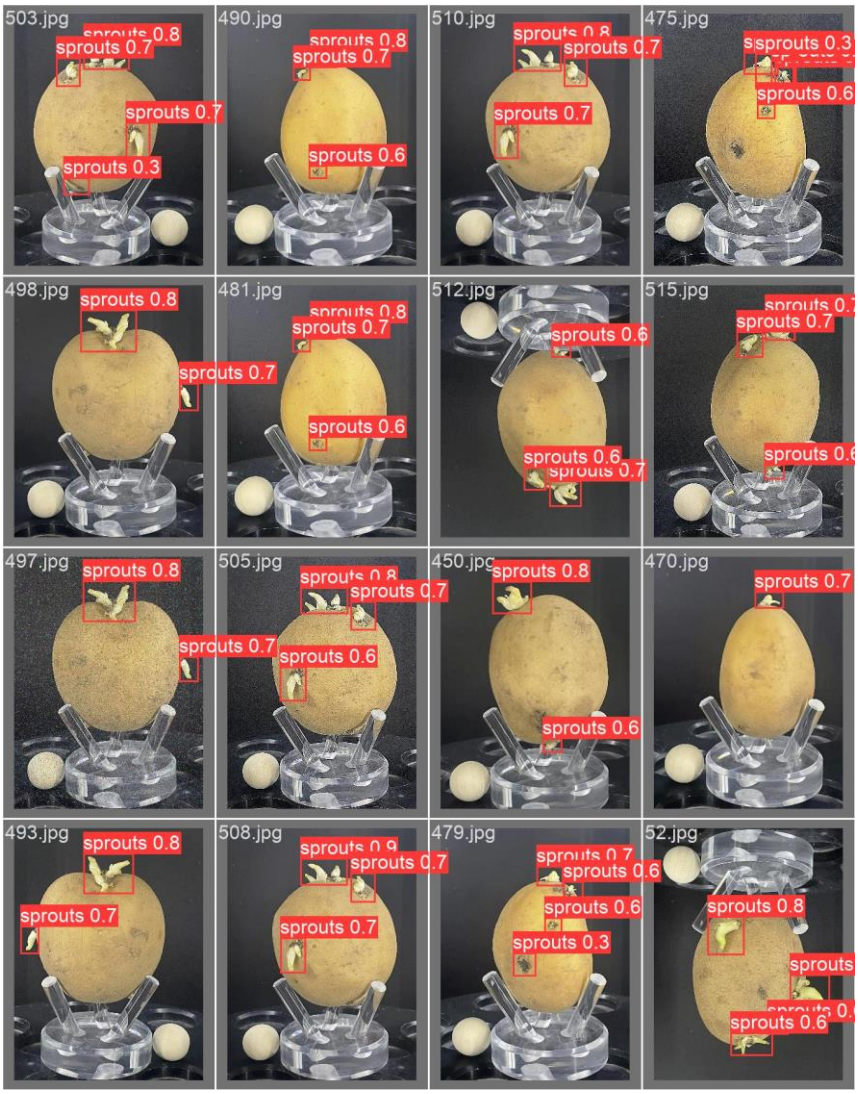

Fig. 7 - Plot of detection results of potato sprout test set in DAS-YOLOv8 network

CONCLUSIONS

In this paper, a target detection model based on deformable attention DAS fusion backbone network SA attention mechanism, called DAS-YOLOv8, is proposed based on YOLOv8 algorithm, which is mainly used for the target detection task of potato sprout images in agricultural scenarios. By designing the DAS attention mechanism embedded after the C2f module of the backbone network and the neck network to avoid the loss of accuracy caused by the loss of feature information about the feature maps of the model during the down sampling process, the context-aware attention mechanism delivered by the neck network taking over from the backbone network is upgraded by one level in terms of the degree of attention to the relevant information. In addition, the design and replacement of the C2f module of the backbone network embed the SA attention mechanism to make the model more focused and further improve the model performance by concentrating on

key information as the feature abstraction level increases with the increase of convolution depth. Meanwhile, the C2fChost convolution module and GhostConv module are introduced to construct a lightweight neck feature fusion module, which reduces the number of parameters and computation of the model while ensuring accuracy. The experiment was tested and compared on the potato sprout PSD-Two dataset, and the feasibility of each advanced improvement was demonstrated through experimental analysis. Compared to the original YOLOv8n model, the proposed model has a mean increase in average accuracy of 1.55%, an increase in precision rate of 2.13%, and FLOPs of only 7.66, which is a reduction of 0.94% compared to YOLOv8n, and has a significant advantage compared to the other mainstream target detection algorithms in all aspects.

The DAS-YOLOv8 model proposed in this paper updates the industry challenge of potato sprout detection and identification in the field of agricultural information engineering and is particularly informative in dealing with the need for lightweight target detection models and intensive detection tasks in the agricultural field. The next plan is how to maintain the accuracy while further reducing the model computation and deploying it in embedded devices to allocate and utilize the resources more efficiently.

ACKNOWLEDGEMENT

This work was supported by the National Agriculture Science Data Center. The authors would also like to thank all authors and anonymous reviewers cited in this paper for their helpful comments and suggestions.

REFERENCES

[1] Bist, R. B., Subedi, S., Yang, X., & Chai, L. (2023). A Novel YOLOv6 Object Detector for Monitoring Piling Behavior of Cage-Free Laying Hens. *AgriEngineering*, *5*(2), Article 2. https://doi.org/10.3390/agriengineering5020056

[2] Dai, G., Hu, L., Fan, J., Yan, S., & Li, R. (2022). A Deep Learning-Based Object Detection Scheme by Improving YOLOv5 for Sprouted Potatoes Datasets. *IEEE Access*, 10, 85416–85428. https://doi.org/10.1109/ACCESS.2022.3192406

[3] Danielak, M., Przybył, K., & Koszela, K. (2023). The Need for Machines for the Nondestructive Quality Assessment of Potatoes with the Use of Artificial Intelligence Methods and Imaging Techniques. *Sensors*, 23(4), Article 4. https://doi.org/10.3390/s23041787

[4] Dhulipalla Ravindra Babu, R. C. Verma, Navneet Kumar Agrawal, & Isha Suwalk. (2023). Classification of Defects in Potato Using Grey Level Co-Occurrence Matrix and Support Vector Machine. Journal of Agricultural Engineering (India), 60(2), 165–177. https://doi.org/10.52151/jae2023602.1805

[5] Gao, S. (2022). Research on detection method of sprouted potato based on SVM and weighted Euclidean distance. *6th International Conference on Mechatronics and Intelligent Robotics (ICMIR2022)*, 12301, 719–725. https://doi.org/10.1117/12.2644666

[6] Guo, J., Yang, Y., Lin, X., Memon, M. S., Liu, W., Zhang, M., & Sun, E. (2023). Revolutionizing Agriculture: Real-Time Ripe Tomato Detection With the Enhanced Tomato-YOLOv7 System. *IEEE Access*, 11, 133086–133098. https://doi.org/10.1109/ACCESS.2023.3336562

[7] Hao, W., Zhang, L., Han, M., Zhang, K., Li, F., Yang, G., & Liu, Z. (2023). YOLOv5-SA-FC: A Novel Pig Detection and Counting Method Based on Shuffle Attention and Focal Complete Intersection over Union. *Animals*, *13*(20), Article 20. https://doi.org/10.3390/ani13203201

[8] Khalid, M., Sarfraz, M. S., Iqbal, U., Aftab, M. U., Niedbała, G., & Rauf, H. T. (2023). Real-Time Plant Health Detection Using Deep Convolutional Neural Networks. *Agriculture*, *13*(2), Article 2. https://doi.org/10.3390/agriculture13020510

[9] Lun, R., Luo, Q., Gao, M., Li, G., & Wei, T. (2023). How to Break the Bottleneck of Potato Production Sustainable Growth—A Survey from Potato Main Producing Areas in China. *Sustainability*, *15*(16), Article 16. https://doi.org/10.3390/su151612416

[10] Li Y., Li T., Niu Z. Wu Y., Zhang Z., Hou J. (2018). Potato bud eyes recognition based on three-dimensional geometric features of color saturation (基于色饱和度三维几何特征的马铃薯芽眼识别). *Transactions of the Chinese Society of Agricultural Engineering (Transactions of the CSAE)*, 34(24): 158-164, Taian / China https://doi.org/10.11975/j.issn.1002-6819.2018.24.019

[11] Lu Z., Qi X., Zhang W., Liu Z., Zheng W., Mu G. (2021). Study on Mechanical Properties and Finite Element Analysis of Seed Cucurbita (基于 Gabor 特征的马铃薯图像芽眼识别). *Journal of Agricultural Mechanization Research*, 43(02), 203–207, Taian / China. https://doi.org/10.13427/j.cnki.njyi.2021.02.036

[12] Ma, N., Li, Y., Xu, M., & Yan, H. (2023). IMPROVED YOLOv8-BASED AUTOMATED DETECTION OF WHEAT LEAF DISEASES. *INMATEH Agricultural Engineering*, 499–510. https://doi.org/10.35633/inmateh-71-43

[13] Su, W.-H., & Xue, H. (2021). Imaging Spectroscopy and Machine Learning for Intelligent Determination of Potato and Sweet Potato Quality. Foods, 10(9), Article 9. https://doi.org/10.3390/foods10092146

[14] Song, X., Li, H., Liang, L., Shi, W., Xie, G., Lu, X., & Hei, X. (2024). TransBoNet: Learning camera localization with Transformer Bottleneck and Attention. *Pattern Recognition*, *146*, 109975. https://doi.org/10.1016/j.patcog.2023.109975

[15] Wang, C., & Xiao, Z. (2021). Potato Surface Defect Detection Based on Deep Transfer Learning. *Agriculture*, *11*(9), Article 9. https://doi.org/10.3390/agriculture11090863

[16] Wang, Y., Zhang, C., Wang, Z., Liu, M., Zhou, D., & Li, J. (2024). Application of lightweight YOLOv5 for walnut kernel grade classification and endogenous foreign body detection. *Journal of Food Composition and Analysis*, *127*, 105964. https://doi.org/10.1016/j.jfca.2023.105964

[17] Wang, Z., Hua, Z., Wen, Y., Zhang, S., Xu, X., & Song, H. (2024). E-YOLO: Recognition of estrus cow based on improved YOLOv8n model. *Expert Systems with Applications*, *238*, 122212. https://doi.org/10.1016/j.eswa.2023.122212

[18] Yang, Y., Zhao, X., Huang, M., Wang, X., & Zhu, Q. (2021). Multispectral image based germination detection of potato by using supervised multiple threshold segmentation model and Canny edge detector. *Computers and Electronics in Agriculture*, *182*, 106041. https://doi.org/10.1016/j.compag.2021.106041

[19] Zhang, W., Han, Y., Huang, C., & Chen, Z. (2022). Recognition method for seed potato buds based on improved YOLOv3-TINY. *INMATEH Agricultural Engineering*, 364–373. https://doi.org/10.35633/inmateh-67-37

DESIGN AND TEST OF DOUBLE-SHAFT TYPE SWEET POTATO HAULM CUTTING RETURN MACHINE
/
双轴式甘薯打秧还田机设计与试验

Kuan QIN*), Yun ZHAO, Rui YANG
College of Engineering, Anhui Agricultural University, Anhui, Hefei, 230036 / China;
Tel: +86 18855102551; E-mail:qinkuan@ahau.edu.cn
DOI: https://doi.org/10.35633/inmateh-72-37

Keywords: *Design, Double-shaft type sweet potato haulm cutting return machine, Orthogonal test, Response surface*

ABSTRACT
In this study, a double-shaft type sweet potato haulm cutting return machine was designed. The structure of the whole machine as well as the key components were analyzed, and the influence of each factor on the operation quality was studied. The results of the study showed that the order of the influence of each factor on the length of broken stems and leaves and the rate of checking was as follows: roller speed > toggle ground clearance > toggle spacing; the order of the influence on the stubble height was as follows: toggle clearance > roller speed > toggle spacing; and the order of the influence on the rate of injury to potatoes was as follows: roller speed = toggle clearance = toggle spacing. The optimal combination of working parameters in the field test was 1944 r/min for roll speed, 132 mm for toggle spacing, and 20 mm for toggle clearance, at which the qualification rate of stem and leaf breaking length was 94.32%, stubble height was 33.61 mm, and potato injury rate was 0.26%. The relative error with the theoretical optimization value is between 0.13% and 7.14%, which meets the operational requirements of sweet potato rice transplanter.

摘要
本研究设计了双轴式甘薯打秧还田机。分析了整机结构以及关键部件，并研究了各因素对作业质量的影响。研究结果表明:各因素对茎叶打碎长度及格率的影响顺序为杆辊转速>拨杆离地间隙>拨杆间距，对留茬高度的影响顺序为拨杆离地间隙>杆辊转速>拨杆间距，对伤薯率的影响顺序为杆辊转速=拨杆离地间隙=拨杆间距。田间试验最优工作参数组合为杆辊转速 1944 r/min、拨杆间距 132 mm、拨杆离地间隙 20 mm，此时茎叶打碎长度合格率为 94.32%、留茬高度为 33.61 mm、伤薯率 0.26%。与理论优化值的相对误差在 0.13%~7.14%之间，满足甘薯打秧机的作业需求。

INTRODUCTION
Sweet potatoes belong to the sweet potato genus of the family Cyclophyllaceae and are also known as sweet potatoes, groundnuts, etc., which varies from place to place (*Gao et al., 2018*). Sweet potato contains a variety of beneficial substances for human health and high content of purple potato anthocyanins, with good health effects (*Lian et al., 2009*; *Wang et al., 2012; He et al., 2013; Hu et al., 2016; Xie et al., 2022*). China is the world's largest sweet potato producer (*Phesatcha et al., 2013; Yuan et al., 2016*). According to the statistics of the Food and Agriculture Organization of the United Nations (FAO), it can be seen that China's total sweet potato production in 2019 was 5.2×107 t, accounting for 56.62% of the total global sweet potato production (*Chen et al., 2022*).

Before harvesting sweet potatoes, haulm must be removed. Earlier haulm removal prevents the loss of sweet potato nutrients and reduces the rate of potato injury during harvest. However, sweet potato haulm have long vines and luxuriant growth, and the vines are too long and may even cover several sweet potato ridges, resulting in the entanglement of several sweet potato haulm. Manual haulm removal is time-consuming, labor-intensive and not economically efficient (*Xia et al., 2011*), and sweet potato haulm cutting machinery can improve productivity and reduce costs.

Kuan Qin, A.P. Ph.D. Eng.; Yun Zhao, M.S. Stud. Eng.; Rui Yang M.S. Stud. Eng.

The development of foreign sweet potato haulm and vine handling machinery started earlier, and its related technology is relatively mature, while having a high degree of automation (*Amer et al., 2012; Amer et al., 2013*). Sweet potato haulm cutting machinery can be divided into two main types: the first is a joint harvest, the haulm and vine crushing, digging sweet potato, potato and haulm separation, haulm and vine cleaning, harvesting and other aspects of a one-time completion. Relevant representative machines are: the United States Model 674 sweet potato direct harvesting combined harvesting machinery and the TSP series of towed sweet potato combined harvesting equipment produced by Standen Agricultural Machinery Company in the United Kingdom. The second is segmented harvesting, in which sweet potato haulm and vines are first crushed by haulm cutting machinery during digging and harvesting of sweet potato. Relevant representative machine: Germany Grimme (GRIMME) Company developed the KS75-4 type four rows of haulm cutting machine. Due to the foreign sweet potato planting model, resulting in the related machinery large size, power demand, agronomy and agro-mechanical requirements are strict (Wu et al., 2018), China has not yet been able to adopt the model, so it is difficult to promote it domestically. China's sweet potato haulm and vine handling machinery development is relatively lagging behind, in recent years the machinery is mostly based on potato rice transplanter and straw crushing machine developed. Relevant representative machines include the 4US-1 haulm cutting developed and manufactured by Tengzhou Golden Potato King, and the 4UL-80 potato haulm cutting developed and manufactured by Fuyang Agricultural Machinery Institute. Most of the domestic research and development of sweet potato haulm and vine processing machinery is only crushing shaft of the one shaft haulm cutting machine, a number of problems such as poorly qualified stem and leaf breaking lengths and high stubble heights were prevalent.

In this paper, for the current domestic one shaft haulm cutting machine existing general problems, combined with sweet potato planting mode and physical characteristics of haulm, a double-shaft type sweet potato haulm cutting machine was researched and designed.

MATERIALS AND METHODS

Structure and working principle of the whole machine

Double-shaft type sweet potato haulm cutting return machine is mainly composed of flail knife, transmission system, haulm picking device, haulm cutting device and other components. The basic structure is shown in Figure 1.

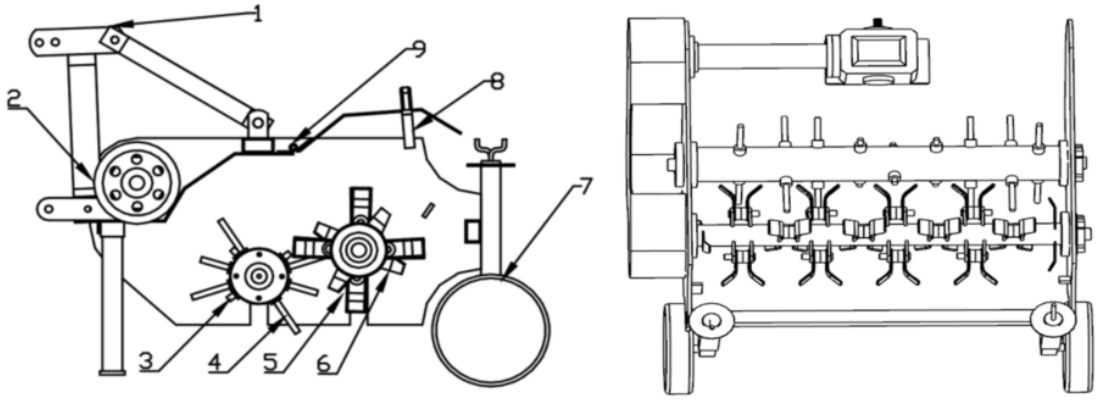

Fig. 1 - Schematic diagram of the structure of double-shaft type sweet potato haulm cutting return machine

1-suspension frame; 2-gear box; 3-haulm picking device; 4-toggle lever; 5-haulm cutting device; 6-flail knife; 7-depth limiting wheel; 8-row of fixed knife device; 9-cover of the whole machine.

When the double shaft type sweet potato haulm cutting return machine works, the power generated by its traction tractor engine is input to the gearbox through the transmission shaft, and then the power is transmitted to the main pulley through the gear shaft. The main belt pulley then conveys the power to the haulm picking device belt pulley and the haulm cutting device belt pulley respectively, and the haulm picking device belt pulley drives the rod shaft to rotate at a high speed, and picks up the haulm stalks creeping on the surface of the sweet potato ridge and throws them backward and upward. Once the upper haulm cutting device with the flail knife cuts and crushes the sweet potato vines and haulm, simultaneously, a row of fixed knives on the cover shell wall performs secondary crushing on the already crushed haulm and vine. Ultimately, the crushed haulm and vine stalks are thrown in a high-speed manner, sliding uniformly along the cover shell wall to the surface of the ridge. The structural and operating parameters of the machine are shown in Table 1.

Table 1

Structural parameters of the double-shaft type potato haulm cutting return machine

Serial number	Project name	Unit	Design specification
01	Overall dimensions (L*W*H)	mm	1200*1300*800
02	Auxiliary power	kw	36.8
03	Working width	mm	900
04	Number of rows	line	1
05	Traveling speed	km/h	5~10
06	Rotation speed of haulm picking device	r/min	≥1500
07	Rotation speed of seeding device	r/min	≥1500
08	Pure hourly production efficiency	hm^2/h	1±0.2
09	Overall quality	kg	220±10

Design and calculation of key components

Design of haulm picking device

Double-shaft type potato haulm cutting return machine compared to the traditional one shaft sweet potato haulm cutting machine increased picking device, the device reduces the power of the knife in the haulm cutting device, reduces the rate of injury to the potato and solves the traditional one-shaft haulm cutting machinery field operation when the vines entangled the equipment. The haulm picking device is mainly composed of rod roller shaft, rod holder, toggle rod and other components, as shown in Figure 2.

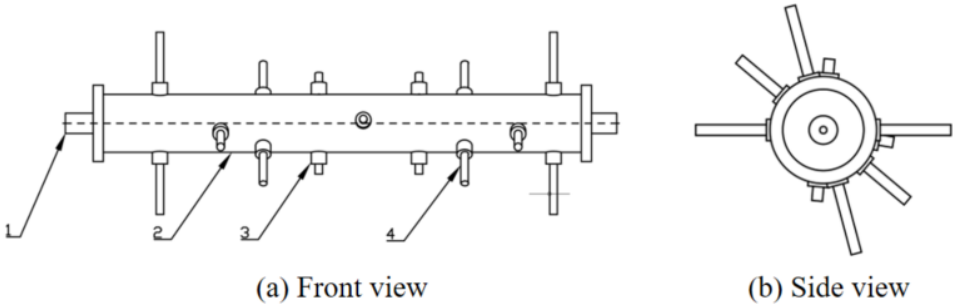

Fig. 2 - Structure of haulm picking device

1 - shaft head; 2 - rod roller shaft; 3 - rod holder; 4 - toggle rod.

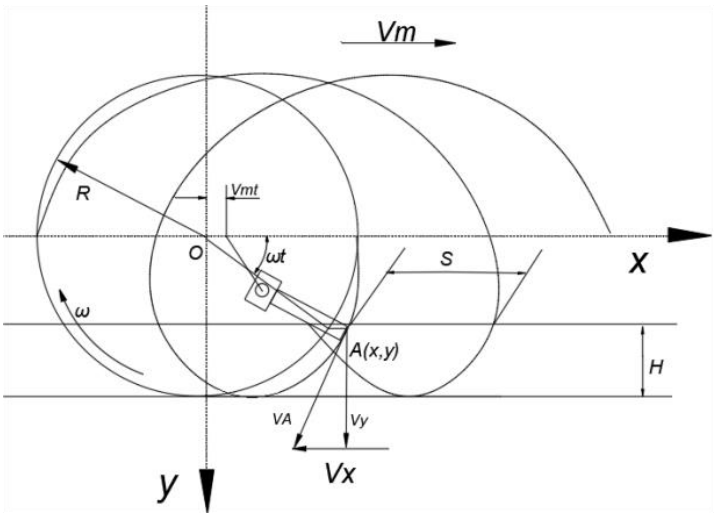

Fig. 3 - Toggle rod movement trajectory diagram

The toggle rod is the key component of the haulm picking device, and its shape, material, quantity and arrangement will affect the haulm cutting effect after operation. After a number of prototype tests, in order to pick up the haulm and not to cut the stalks of the haulm to affect the efficiency of the subsequent haulm cutting stage, the toggle rod adopts a cylinder with a diameter of 15 mm, and the material chosen is 65 Mn steel sheet, the hardness of which can reach 48~56 HRC after heat treatment. The number of toggle rods is 18 and the arrangement is a double helix arrangement structure (*Zhang et al., 2007*).

The rotation speed of the rod roller of the toggle rod is one of the main parameters of the haulm picking device. When the machine is in operation, the toggle rod produces both linear and circular motions at the same time, and the absolute motion of the toggle rod is synthesized from the above two motions. It can be concluded that the trajectory of any point on the toggle rod is a regular curve, i.e., a pendulum. When the radius of motion of the toggle rod is R, the forward speed of the whole machine is v_m, and the angular velocity of the rotation is ω, the coordinate system O point is used as the origin coordinate system, as shown in Fig. 3.

The initial rotation center of the toggle rod shaft is set as the origin of the coordinate system, the forward direction of the haulm cutting machine is set as the x-axis, the direction perpendicular to the downward direction of the forward direction is set as the y-axis, and the radius of rotation of the toggle rod movement is R. The relationship between the time t and the coordinates of the toggle rod tip is shown in Equation 1:

$$\begin{cases} x = R\cos\omega t + v_m t \\ y = R\sin\omega t \end{cases} \quad (1)$$

where: v_m is the forward speed of the whole machine, [m/s]; R is the radius of the toggle rod roll circumference, [m].

The expression for the velocity of motion at the endpoint of the toggle rod is Equation 2:

$$\begin{cases} v_x = \dfrac{d_x}{d_t} = v_m - R\cdot\omega\cdot\sin\omega t \\ v_y = \dfrac{d_y}{d_t} = R\cdot\omega\cdot\cos\omega t \end{cases} \quad (2)$$

where: v_x is the horizontal partial velocity at the endpoint of the toggle rod, [m/s]; v_y is the vertical partial velocity at which the toggle rod is disconnected, [m/s].

The expression for the absolute velocity of motion at the endpoint of the toggle rod is Equation 3:

$$v = \sqrt{v_x^2 + v_y^2} = \sqrt{v_m^2 + R^2\omega^2 - 2v_m R\omega\sin\omega t} \quad (3)$$

The circular velocity of the end point of the toggle rod $v_p = R\omega$, so that $\lambda = v_p/v_m = R\omega/v_m$, where λ is the rotational speed ratio, and the size of the λ value has a direct impact on the trajectory of the toggle rod and the operational efficiency. Therefore, substituting $\lambda = R\omega/v_m$ into Equation 2 leads to Equation 4:

$$v_x = v_m - R\cdot\omega\cdot\sin\omega t = v_m(1 - \lambda\cdot\sin\omega t) \quad (4)$$

When λ < 1, there must be v_x>0 regardless of any position of the toggle rod motion. That is, the horizontal partial velocity of the end point of the toggle rod is always the same as the forward direction of the whole haulm cutting machine, and its trajectory is a pendulum line, at which time the toggle rod throws backward sweet potato haulm and vines. When λ>1, the toggle rod moves to a certain position, v_x<0, i.e., the horizontal partial velocity at the end point of the toggle rod is opposite to the forward direction of the whole machine, and its trajectory is a trochoid. The machine works properly when the trajectory of any point of the toggle rod endpoint is a trochoid. The design study of the double-shaft type sweet potato haulm cutting return machine takes λ>1. Therefore, to ensure that v_x<0, at this time $\sin\omega = (R-H)/R$, which leads to Equation 5:

$$n \geq 30(v_c + v_m)/[\pi(R - H)] \quad (5)$$

where: v_c is the picking speed of the toggle rod, [m/s]; n is the rotational speed of the toggle rod, [r/min]; H is the picked haulm thickness, [m].

When picking haulm, v_m = 0.55m/s, v_c = 23m/s, H = 0.15m, R = 0.303m (the maximum radius of rotation of the toggle rod lever) is substituted into Equation 5, and n≥1469 can be obtained, so the rotation speed of the toggle rod lever roller should be not less than 1469 r/min.

Design of haulm cutting device

The haulm cutting device is the key component of the double-shaft type sweet potato haulm cutting return machine, which mainly destroys and crushes the haulm vines thrown by the picking device when the machine is in operation. The haulm cutting device mainly consists of a flail knife, a knife holder, a knife roller shaft, and pin shaft, as shown in Fig. 4. In order to minimize the weight of the whole machine and thus reduce energy consumption, the knife roller shaft adopts a hollow shaft (*Du et al., 2015*).

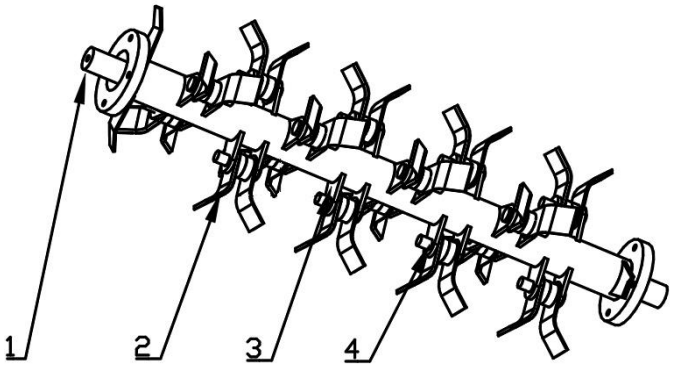

Fig. 4 - Structure of seeding device

1-shaft head; 2-flail knife; 3-knife holder; 4-knife roller shaft.

As a key component of the haulm cutting device of the double-shaft type sweet potato haulm cutting return machine, the flail knife plays a very important role in the operation of the machine. At present, the Y-type flail knife is the most widely used knife type, with strong shear force, double-sided open edge, and high qualified rate of stem and leaf breaking. In this study, an improved Y-type flail knife was designed as shown in Fig. 5. Since the flail knife is a wear part, 65 Mn steel sheet was chosen for its material (*Li et al., 2014*). After heat treatment, the hardness of the knife reaches 48~56 HRC and the hardness of the shank reaches 33~40 HRC.

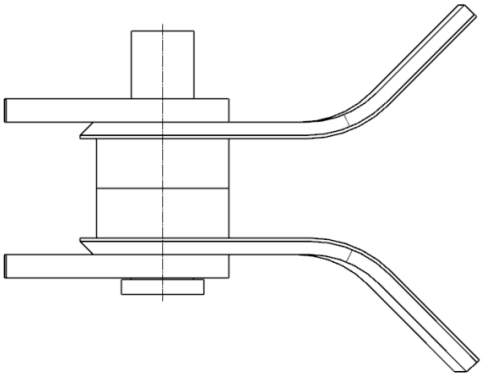

Fig. 5 - Schematic diagram of the improved Y-type flail knife

The number and arrangement of flail knives have a great impact on the machine's operating performance. The design of the number of flail knives should be reasonable, if the number is too small, the leakage rate increases, and the operation effect is unqualified. If the number is too big, it is easy to produce clogging phenomenon during operation, and the power consumed will increase (*Pan et al., 2015*).

Equation 6 can be used to calculate the number of flail knives:

$$N_1 = C_1 \times L_1 \tag{6}$$

where:

N_1 is the total number of knives, [roots]; C_1 is the density of knives, [roots/mm]; L_1 is the working width of the machine, [mm].

The density of the Y-shaped flail knife was taken as 0.02-0.04 pieces/mm (*Gu et al., 2016*). In designing the double-shaft type sweet potato haulm cutting machine, the operating width of the machine was designed to be 900 mm, i.e., L_1 was 900 mm. Substituting the data obtained above into Equation 6, it can be obtained that the number of improved Y-type flail knives should be 16 by removing the L-type flail knives at both ends of the four-piece knife roller shaft.

In order to ensure the stability of the machine during operation and the uniform loading of the knife rollers, the axial distance between the flail knives should be as large as possible to avoid clogging (*Lv et al., 2016*). To synthesize the advantages and disadvantages of various arrangements, the machine adopts a staggered and balanced arrangement, as shown in Figure 6.

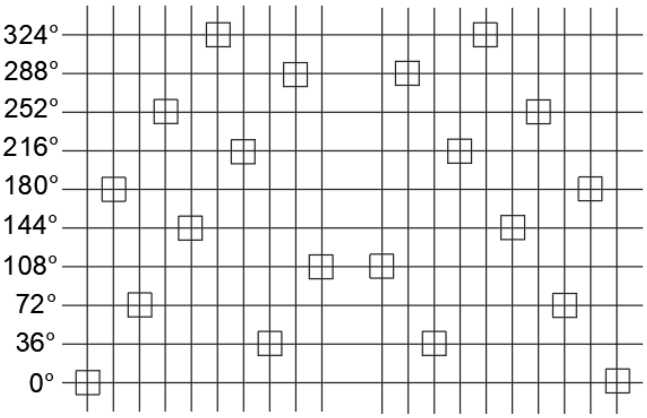

Fig. 6 - Schematic diagram of the improved Y-type flail knife

The cutter shaft is usually considered to be a homogeneous rotating body, i.e. the centrifugal force of the cutter shaft is close to zero. The vibrations to which the machine is subjected during operation come from the centrifugal force generated by the high speed rotation of the knife rollers and transmitted through the bearings. The centrifugal force generated by the knife and attachments is the cause of the moment on the pivot point of the knife roll and the cause of vibration. If the degree of vibration of the whole machine is to be minimized, the moment generated by the centrifugal force of the flail knife on the pivot point should be reduced to zero (*Li et al., 2020*). The centrifugal force of the knife roller shaft is analyzed as shown in Fig. 7.

From Fig. 7, the plane of symmetry of the first leftmost flail knife position is set as a, and the plane of symmetry of the first rightmost flail knife positionis set as b. According to the equilibrium equations (*Ji et al., 2003; Mu, 2021*), all the centrifugal forces are decomposed to the x,y-axis, and Equations 7 and 8 are obtained:

$$\begin{cases} F_{ax} = \sum_{N}^{N} N-1 \frac{N-i}{N-1} F\cos\theta \\ F_{ay} = \sum_{N}^{N} N-1 \frac{N-i}{N-1} F\sin\theta \end{cases} \quad (7)$$

$$\begin{cases} F_{bx} = \sum_{N}^{N} N-1 \frac{N-i}{N-1} F\cos\theta \\ F_{by} = \sum_{N}^{N} N-1 \frac{N-i}{N-1} F\sin\theta \end{cases} \quad (8)$$

where:

F is the centrifugal force on the flail knives and their holders, [N]; N is the number of flail knives, [pieces]; i is the order of the flail knives; and θ is the angle between adjacent flail knives, [°].

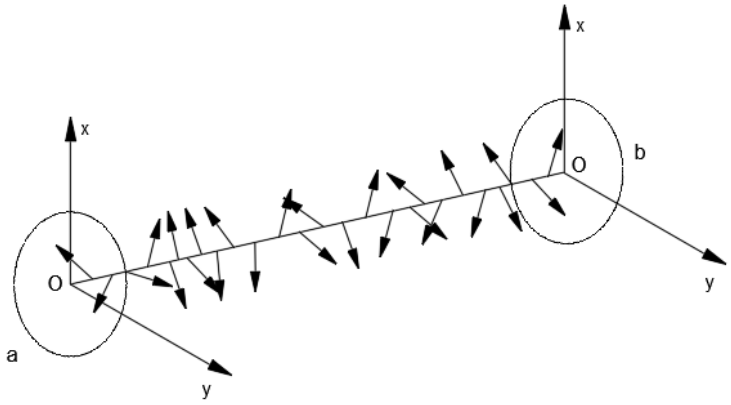

Fig. 7 - Knife roller shaft centrifugal force analysis diagram

The values obtained for the knife arrangement are substituted into Equations 7 and 8 for calibration calculations, and the results obtained show that the number and arrangement of knife designs are reasonable.

Drive train design

The traction power was selected from a Changchai 4L68 diesel tractor with a power output speed n1 of 1200 r/min. A schematic diagram of the drive train is shown in Figure 8.

With the known diameter and number of teeth of the gearbox gears, the total transmission ratio of the haulm cutting machine can be calculated, Equation 9:

$$i = \frac{z_1}{z_2} \times \frac{p_1}{p_2} = 1.87 \quad (9)$$

where: z_1, z_2 is the number of teeth of the gearbox gear, [pcs]; p_1, p_2 is the diameter of the gearbox gear, [mm].

Substituting the known tractor power output speed n_1=1200 r/min and the total transmission ratio of the haulm cutting machine. i =1.87 into Equation 9, it can be concluded that the rotational speed of rod roller and knife roller of the double-shaft type sweet potato haulm cutting return machine n_{max}=2244 r/min, which is in line with the operational requirements of the haulm cutting machine.

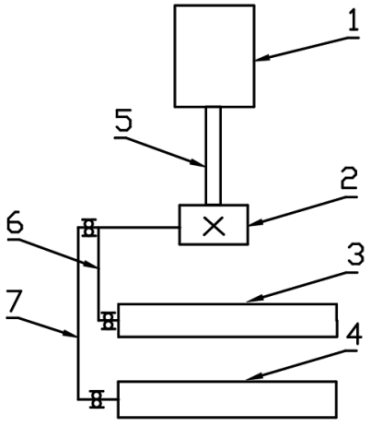

Fig. 8 - Schematic diagram of transmission system of double shaft type sweet potato haulm cutting return machine

1-engine; 2-gearbox; 3-haulm picking device; 4-haulm cutting device; 5-drive shaft; 6-pulley 1; 7-pulley 2

Parameter optimization test

The location of this experiment was in the sweet potato planting base in Dailukou Township, Si County, Suzhou City, Anhui Province, where the local soil type is sandy loam. The average water content was 16.2%, and the soil had good air and water permeability and loose texture, which was suitable for sweet potato cultivation. The average width of the rows was 900 mm and the average spacing of the rows was 200 mm. The sweet potatoes were harvested at the time of the experiment, and the stalks of the sweet potato haulm were 150 mm from the roots and about 60 mm in length.

The test equipment and instruments mainly include: 4L68 diesel tractor, double-shaft type sweet potato haulm cutting return machine, moisture meter, tape measure, electronic balance, stopwatch, tachometer, marker, scissors and so on.

The experiments were conducted to determine the length and percentage of broken stems and leaves Z_1, the average stubble height Z_2, and the injury rate Z_3 of the double-shaft type sweet potato haulm cutting return machine under different working parameters as their evaluation indexes. There are many factors affecting the evaluation indexes of the twin-axle sweet potato rice-planting and field-returning machine, and it was determined on the basis of the previous test that the rod roller speed A (the same speed of the rod roller and the knife roller), the toggle rod spacing B, and the toggle rod clearance C were taken as the main factors affecting the operational performance, and the test factors and levels were shown in Table 2.

Before operation, 2 round trips were measured, and 5 equally spaced 1 m square performance measurement points were selected within each trip, as shown in Figure 9. All broken stalks within each performance measurement point were collected and weighed, and then stalks with a length greater than 100 mm were singled out from them and weighed, and the length of broken stalks within each performance measurement point and the pass rate were calculated according to Equation 10, and the average of 10 measurement points in 2 round-trip journeys was randomly selected.

$$Z_1 = \frac{m_y - m_b}{m_y} \times 100 \quad (10)$$

where:

Z_1 is the pass rate for broken stem length, [%]; m_b is the mass of broken stems, [kg]; m_y is the mass of broken stems >100 mm, [kg].

Table 2

Test factors and level

Level	Factor		
	Rod roller speed A / (r/min)	Toggle rod spacing B / (mm)	Toggle rod ground clearance C / (mm)
1	2200	150	25
0	1850	125	20
-1	1500	100	15

Fig. 9 - Performance test sample point

The length of 10 stubble stubs was randomly selected at the performance measurement points after the seeding operation, and the average of the 10 measurement points in 2 round trip trips was randomly selected.

$$Z_2 = \frac{L_N}{N} \quad (11)$$

where:

Z_2 is the average stubble height on the ridge, [mm]; L_N is the sum of stubble heights, [mm]; N is the number of plants measured, [n].

All sweet potatoes in the area of each measurement point were dug out and weighed, and then the wounded potatoes among them were picked out and weighed, and the rate of wounded potatoes within each measurement point was calculated according to Equation 12, and the average of the 10 measurement points in the 2 round-trip journeys was randomly selected.

$$Z_3 = \frac{M_s}{M} \times 100 \quad (12)$$

where:

Z_3 is the rate of injury, [%]; M_s is the mass of injured potatoes, [kg].; M is the total mass of sweet potatoes in each performance point, [kg].

RESULTS

Test results

Box-Behnken principle was used to design a three-factor, three-level quadratic regression orthogonal test (*Zhang et al., 2015*), and the test protocol and response values are shown in Table 3.

Table 3

Test scheme and results

Test serial number	Level of factors			Response value		
	A	B	C	Z_1	Z_2	Z_3
1	2200	125	25	90.35	58	0.3
2	1500	125	25	61.87	84	0.02
3	1850	150	15	86.61	48	0.42
4	1500	125	15	85.06	50	0.47
5	2200	100	20	81.04	42	0.55
6	1850	150	25	75.07	63	0.05
7	1850	125	20	94.45	30	0.24
8	1850	100	15	82.43	40	0.49
9	2200	125	15	98.49	18	0.57
10	1500	150	20	65.44	69	0.11
11	1850	125	20	92.93	34	0.22
12	1850	125	20	90.06	35	0.25
13	1850	125	20	94.16	39	0.22
14	1500	100	20	65.82	64	0.3
15	2200	150	20	87.95	40	0.31
16	1850	125	20	92.98	31	0.26
17	1850	100	25	76.64	66	0.32

Regression modeling and significance test analysis

Combining the experimental and resultant data obtained from Table 3, the results obtained from this experiment were analytically optimized and fitted with multiple regression using Design-Expert 11.0 analysis software (*Shi et al., 2017; Wu et al., 2017*). A quadratic polynomial response surface regression model was developed for Z_1, Z_2, and Z_3 on the three independent variables A, B, and C.

After analyzing the data with Design-Expert software, the regression equations for Z_1, Z_2, Z_3 were fitted as shown in Equation 13.

$$\begin{cases} Z_1 = 92.92 + 9.96A - 6.08B + 1.14C + 3.76AB + 1.82AC - \\ 1.44BC - 7.05A^2 - 1.92B^2 - 10.80C^2 \\ Z_2 = 33.80 - 13.62A + 14.38B + 1.00C + 1.50AB - 1.75AC - \\ 2.75BC + 9.10A^2 + 9.60B^2 + 10.85C^2 \\ Z_3 = 0.2380 + 0.1037A - 0.1575B - 0.0963C + 0.0450AB - \\ 0.0125AC - 0.050BC + 0.0498A^2 + 0.0522B^2 + 0.0298C^2 \end{cases} \quad (13)$$

Table 4

Analysis of variance of Z_1 regression equation for stem and leaf fragmentation length

Source of variation	Z_1				
	Square sum	Degrees of freedom	Mean square	*F-value*	*P-value*
Model	1949.95	9	216.66	37.29	< 0.0001
A	792.82	1	792.82	136.47	< 0.0001
B	10.44	1	10.44	1.80	0.2219
C	295.97	1	295.97	50.95	0.0002
AB	56.63	1	56.63	9.75	0.0168
AC	13.29	1	13.29	2.29	0.1742
BC	8.27	1	8.27	1.42	0.2718
A^2	209.23	1	209.23	36.01	0.0005
B^2	15.59	1	15.59	2.68	0.1454
C^2	491.50	1	491.50	84.60	< 0.0001
Residual	40.67	7	5.81		
Incoherent	28.60	3	9.53	3.16	0.1476
Inaccuracies	12.06	4	3.02		
Aggregate	1990.62	16			

As can be seen from Table 4, the four regression terms A, B, A^2, and C^2 had extremely significant effects on Z_1 ($P < 0.01$). AB had a more significant effect on Z_1 ($0.01 < P < 0.05$).C, AC, BC, and B^2 did not have a significant effect on Z_1 ($P > 0.1$). Since the value of misfit P = 0.1476 is greater than 0.05, the model does not have to take into account any interaction term between the factors, i.e., the effect of the other factors on the length of stem and leaf breaking is not significant. Some of the factors whose effects were not significant were removed and then their models were optimized to arrive at the regression Equation 14 (*Yan et al., 2017*).

$$Z_1 = 92.92 + 9.96A - 6.08B + 3.76AB - 7.05A^2 - 10.80C^2 \quad (14)$$

As can be seen from Table 5, A, B, A^2, B^2, and C^2 were extremely significant ($P < 0.01$) on Z_2. C, AB, AC, and BC were not significant ($P > 0.1$) on Z_2. Since the value of misfit P = 0.1172 is greater than 0.05, the model does not have to take into account any interaction term between the factors, i.e., the effect of other factors on stubble height is not significant. Some of the factors with insignificant effects were removed and then their models were optimized to obtain regression equation 15.

$$Z_2 = 33.80 - 13.62A + 14.38B + 9.10A^2 + 9.60B^2 + 10.85C^2 \quad (15)$$

Table 5

Analysis of variance of the Z2 regression equation for stubble retention height

Source of variation	Z_2				
	Square sum	**Degrees of freedom**	**Mean square**	***F-value***	***P-value***
Model	4573.98	9	508.22	18.38	0.0004
A	1485.12	1	1485.12	53.71	0.0002
B	8.00	1	8.00	0.2893	0.6073
C	1653.13	1	1653.13	59.79	0.0001
AB	9.00	1	9.00	0.3255	0.5862
AC	12.25	1	12.25	0.4430	0.5270
BC	30.25	1	30.25	1.09	0.3303
A^2	348.67	1	348.67	12.61	0.0093
B^2	388.04	1	388.04	14.03	0.0072
C^2	495.67	1	495.67	17.93	0.0039
Residual	193.55	7	27.65		
Incoherent	142.75	3	47.58	3.75	0.1172
Inaccuracies	50.80	4	12.70		
Aggregate	4767.53	16			

As can be seen from Table 6, A, B, and C had extremely significant effects on Z_3 ($P < 0.01$). AB, BC, A^2, and B^2 had more significant effects on Z_3 ($0.01 < P$ less than 0.05).C^2 had significant effects on Z_3 ($0.05 < P < 0.1$). AC had no significant effect on Z_3 ($P > 0.1$). Since the value of misfit P = 0.0595 is greater than 0.05, the model does not have to take into account any interaction term between the factors, i.e., the effect of other factors on stubble height is not significant. Some of the factors with insignificant effects were removed and then their models were optimized to obtain regression equation 16.

$$Z_3 = 0.2380 + 0.1037A - 0.1575B - 0.0963C + 0.0450AB - 0.050BC + 0.0498A^2 + 0.0522B^2 + 0.0298C^2 \quad (16)$$

Table 6

Analysis of variance in the Z3 regression equation for the rate of wounded potatoes

Source of variation	Z_3				
	Square sum	**Degrees of freedom**	**Mean square**	***F-value***	***P-value***
Model	0.4058	9	0.0451	45.39	< 0.0001
A	0.0861	1	0.0861	86.67	< 0.0001
B	0.0741	1	0.0741	74.59	< 0.0001
C	0.1984	1	0.1984	199.73	< 0.0001
AB	0.0081	1	0.0081	8.15	0.0245
AC	0.0006	1	0.0006	0.6290	0.4537
BC	0.0100	1	0.0100	10.06	0.0157
A^2	0.0104	1	0.0104	10.49	0.0143
B^2	0.0115	1	0.0115	11.57	0.0114
C^2	0.0037	1	0.0037	3.75	0.0940
Residual	0.0070	7	0.0010		
Incoherent	0.0057	3	0.0019	5.91	0.0595
Inaccuracies	0.0013	4	0.0003		
Aggregate	0.4128	16			

As shown in Tables 4, 5, and 6, the P-values of the response surface models for stem and leaf breaking length and qualification rate Z1, stubble height Z2, and potato injury rate Z3 were less than 0.01, indicating that the regression models were extremely significant (*Yu et al., 2015*). The P-values of the misfit terms were 0.1476, 0.1172, and 0.0595 were all greater than 0.05, indicating that the regression equation was highly fitted.

Response surface analysis

With the results obtained above, the response surface was plotted for the model using Design-expert 11.0 software, and the effects of the interaction terms between factors A, B, and C on Z_1, Z_2, and Z_3, respectively, were analyzed based on the response surface.

The interaction terms with more significant effect on Z_1 were selected for response surface analysis. Table 4 shows that the factor interaction term with the smallest p-value is AB and therefore has a more significant effect on Z_1. When B is 125 mm, the response surface is shown in Fig. 10. It can be seen that when A is fixed, Z_1 increases and then decreases with the increase of C. The optimal C is between 19 and 21 mm. When C was fixed, Z_1 first increased and then decreased with increasing A. The optimal A was between 1800 and 1900 r/min. In the interaction between both A and C, the magnitude of A is the main factor affecting the length of stem and leaf breaking and Z_1 (Zhao et al., 2018).

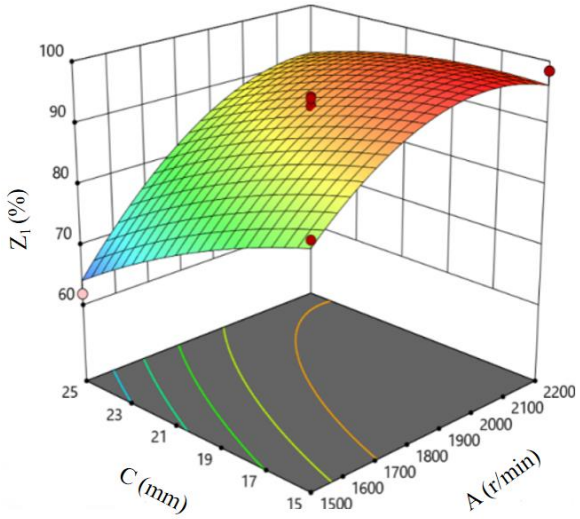

Fig. 10 - Interaction of rod-roller speed and toggle rod clearance C=125 mm

The interaction terms with more significant effects on Z_2 were selected for response surface analysis. Table 5 shows that the factor interaction term with the smallest p-value is the interaction term BC between C and B. Therefore, the effect on Z_2 is more significant. When A is 1850 r/min, the response surface is shown in Fig. 11. It can be seen that when B is fixed, Z_2 increases as C increases and the optimum C is between 19 and 21 mm. When C is fixed, Z_2 decreases and then increases with increasing B. The optimal B is between 120 and 130 mm. In the interaction between C and B, the size of B is the main factor affecting Z_2.

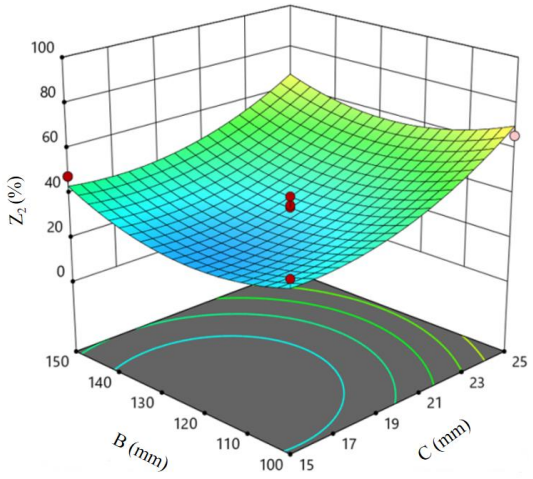

Fig. 11 - Interaction of toggle rod spacing and toggle rod ground clearance A = 1850 r/min

The interaction terms with more significant effects on Z_3 were selected for response surface analysis. As can be seen from Table 6, the interaction term BC of C and B, which has the smallest p-value among the factor interaction terms, therefore has a more significant effect on Z_3. When A is 1850 r/min, the response surface is shown in Fig. 12. It can be seen that when C is fixed, Z_3 decreases as B increases and the optimal B is between 120 and 130 mm. When B is fixed, Z_3 decreases and then increases with the increase of C, and the optimal C is between 19~21 mm. In the interaction between C and B, the size of C is the main factor affecting Z_3.

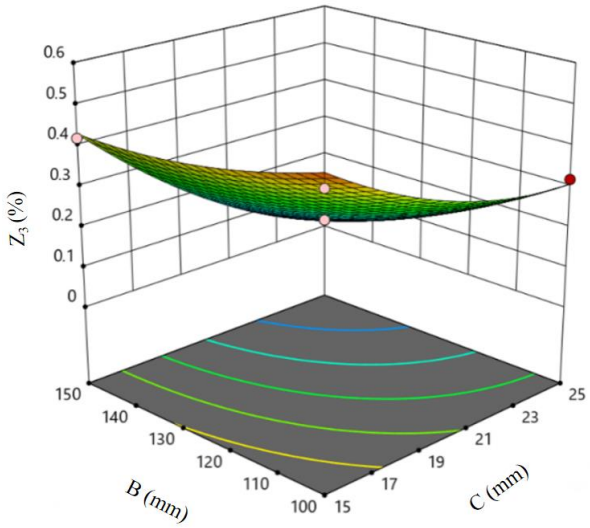

Fig. 12 - Interaction of toggle rod spacing and toggle rod ground clearance A = 1850 r/min

Parameter optimization and experimental validation

Through the analysis of the above three response surfaces, the regression models of Z_1, Z_2 and Z_3 were optimized and solved using the optimization module in the Design-Expert11.0 analysis software, and the optimization constraints were finally determined according to the actual operating conditions of rice-planting machine and the relevant group standards of rice-planting machinery class to meet the operating requirements of high pass rate of stem and leaf breaking length, low stubble height and low rate of injury to potatoes, as in Equation 17.

$$\begin{cases} \max Z_1(A,B,C) \\ \min Z_2(A,B,C) \\ \min Z_3(A,B,C) \\ A、B、C>0 \\ -1 \leqslant Z_f \leqslant 1 \end{cases} \quad (17)$$

(a) Before operation (b) After operation

Fig. 13 - Comparison of the effect of haulm cutting machine before and after field operation

The optimization solution using Design-Expert 11.0 analysis software yields optimal results of 94.45% for Z_1, 32.44 mm for Z_2 and 0.28% for Z_3 when A is 1943.87 r/min, B is 131.85 mm and C is 20.24 mm.

To further validate the optimization results, a field validation test was carried out using a double-shaft type sweet potato haulm cutting return machine at the sweet potato planting base in Dailukou Township, Siachen County, Anhui Province, as shown in Fig. 13. The rice-planting machines A, B, and C were set at 1944 r/min, 132 mm, and 20 mm, respectively, and the average values of 10 measurement points were randomly selected for 2 round trips. At this time, Z_1 is 94.32%, Z_2 is 33.61 mm, and Z_3 is 0.26%. As shown in Table 7, it can be concluded that the results of the comparison experiments are consistent with the results of the optimal parameter combinations derived from theoretical analysis, and also satisfy the industry standard of the double-shaft type sweet potato haulm cutting return machine.

Table 7

Theoretical analysis results, comparative test results and reference indicators are compared

Serial number	Z_1	Z_2	Z_3
Optimizing the average	94.45	32.44	0.28
Test Mean	94.32	33.61	0.26
Relative error/%	0.13	2.03	7.14

CONCLUSIONS

(1) The main influencing factors for the test of a double-shaft type sweet potato haulm cutting return machine were analyzed and determined: rod-roller speed, toggle rod clearance from the ground, and toggle rod spacing. The three-factor, three-level quadratic regression orthogonal test was designed using Box-Behnken principle with stem and leaf breaking length and qualification rate, stubble height, and potato injury rate as test indexes, respectively. The effects of rod roller rotational speed, toggle rod spacing, and toggle ground clearance from the ground on the length of stem and leaf breaking, stubble height, and potato injury rate were analyzed and parameter optimization was carried out. The relative errors between the actual measured values and the theoretical optimized values were obtained between 0.13% and 7.14% through the validation test, which indicated that the model was highly reliable.

(2) The order of the effect of each factor on the length of broken stems and leaves and the rate of grams is the speed of the rod roller > toggle rod clearance > toggle rod spacing. The order of influence of each factor on stubble height is toggle ground clearance>roller speed>toggle rod spacing. The order of the influence of each factor on the rate of potato injury is roller speed = toggle rod clearance = toggle rod spacing.

(3) The optimal working parameters of the double-shaft type sweet potato haulm cutting return machine were 1944 r/min for the rotational speed of the rod rollers, 132 mm for the spacing of the toggle rod bars, and 20 mm for the clearance of the toggle rod bars from the ground, and at this time, the qualification rate of the length of the broken stems and leaves was 94.32%, and the stubble height was 33.61 mm, and the rate of injury to the potatoes was 0.26%.

ACKNOWLEDGEMENT

This work was supported by the National Natural Science Foundation of China (Grant No. 52105239), the Anhui Provincial Agricultural Material Technology Equipment Field Project (S202320230906020015) for the Development and Application of Yam Planting Machines (Line Type Automatic Yam Transplanter), and the Suzhou City Science and Technology Plan Project (SZKJXM202209) for the Key Technology Research and Equipment Development of Mechanized Production of Sweet Potatoes.

REFERENCES

[1] Amer, N., Kakahy, D., Ahmad, M. et al. (2012). Design and development of an Integrated Slasher (Pulverizer) for Sweet Potato Harvester: A Review. *IOP Conference Series: Materials Science and Engineering* (1). https://doi.org/10.1088/1757-899X/36/1/012007.

[2] Amer, N., Kakahy, D., Ahmad, M. et al. (2013). Effects of Knife Shapes and Cutting Speeds of a Mower on the Percentage Pulverization of Sweet Potato Vine. *Applied Mechanics and Materials* (421-421). https://doi.org/10.4028/www.scientific.net/AMM.421.29.

[3] Chen, X., Lu, J., Wang, X. et al. (2022). Analysis of Changes in Production Layout and Drivers of Sweet Potato in China (中国甘薯生产布局变迁及动因分析). *Chinese Journal of Agricultural Resources and Regional Planning,* 43(02):1-12. https://doi.org/10.7621/cjarrp.1005-9121.20220201.

[4] Du, H., (2015). Development of Sweet Potato Rice Stem Crushing and Returning Machine (红薯秧茎破碎还田机的研制). *Research on agricultural mechanization*, 37(11):113-116. https://doi.org/10.13427/j.cnki.njyi.2015.11.025.

[5] Gao, H., Sun, S., Chen, Y. et al. (2018). Theory and practice of sustainable development of sweet potato industry (甘薯产业可持续发展的理论与实践). *Journal of Hebei Normal University of Science&Technology*, (03), 65-70. https://doi.org/10.3969/J.ISSN.1672-7983.2018.03.012.

[6] Gu, F., Hu, Z., Chen, Y., et al. (2016). Development and experiment of peanut no-till planter under full wheat straw mulching based on “clean area planting” (“洁区播种”思路下麦茬全秸秆覆盖地花生免耕播种机研制). *Transactions of the Chinese Society of Agricultural Engineering*, 32(20):15-23. https://doi.org/10.11975/j.issn.1002-6819.2016.20.002.

[7] He, J., Cheng, L., Hong, Y., et al. (2013). Optimization of compound color fixative without sulfur during sweet potato flour processing (甘薯全粉加工中无硫复合护色工艺优化). *Transactions of the Chinese Society of Agricultural Engineering*, 29(9): 275-284. https://doi.org/10.3969/j.issn.1002-6819.2013.09.035.

[8] Hu, L., Wang, B., Wang, G., et al. (2016). Design and experiment of type 2ZGF-2 duplex sweet potato transplanter (2ZGF-2 型甘薯复式栽植机的设计与试验). *Transactions of the Chinese Society of Agricultural Engineering*, 32(10):8-16. https://doi.org/10.11975/j.issn.1002-6819.2016.10.002.

[9] Ji, J., Li, Q., Cai, Wei., (2003). Analysis of the effect of tool arrangement on the vibration of a stalk chopping and returning machine (刀具布置对茎秆切碎还田机振动的影响分析). *Research on agricultural mechanization*, (04):63-64. https://doi.org/10.13427/j.cnki.njyi.2003.04.025.

[10] Li, G., Li, Y., Zhang, X. et al. (2014). Design of the flail knife for the straw chopper and returning machine. (秸秆粉碎还田机甩刀的设计). *Research on agricultural mechanization*, 36(08):122-125. https://doi.org/10.13427/j.cnki.njyi.2014.08.031.

[11] Li, B., Liu, Y., Niu, G. et al. (2020). Analysis of the Research Dynamics of Straw Crushing and Returning Machine and Key Components (秸秆粉碎还田机及关键部件的研究动态分析). *Agricultural Mechanization in Xinjiang*, No.203 (05): 10-13. https://doi.org/10.13620/j.cnki.issn1007-7782.2020.05.003.

[12] Lian, X. J., Li, J., Wang, H., et al. (2009). Regularity for change of respiration intensity of different sweet potato varieties at normal atmospheric temperature (不同品种甘薯常温贮藏期间呼吸强度变化规律). *Transactions of the Chinese Society of Agricultural Engineering*, 25(6): 310-313. 10.3969/j.issn. https://doi.org/1002-6819.2009.06.058.

[13] Lv, J., Shang, Q., Yang, Y. et al. (2016). Design Optimization and Experiment on Potato Haulm Cutter (马铃薯杀秧机设计优化与试验). *Journal of Agricultural Machinery*, 47(05):106-114+98. https://doi.org/10.6041/ j.issn.1000-1298.2016.05.015.

[14] Mu, G., (2021). Research on the key technology and device of crushing and throwing of sweet potato seedling recycling machine imitating the ridge type (仿垄式甘薯秧回收机粉碎抛送关键技术与装置研究). *Shandong Agricultural University*. https://doi.org/10.27277/d.cnki.gsdnu.2021.000973.

[15] Pan, F., Kang, J., Yan, L. (2015). Design and experiment to key components of Y type cutting device of smashed straw machine (Y 型甩刀式秸秆粉碎还田机关键部件的设计与性能试验). *Research of agricultural modernization*, 36(05):912-915. https://doi.org/10.13872/j.1000-0275.2015.0090.

[16] Phesatcha, K., & Wanapat, M. (2013). Performance of lactating dairy cows fed a diet based on treated rice straw and supplemented with pelleted sweet potato vines. *Tropical animal health and production* (2). https://doi.org/10.1007/s11250-012-0255-5.

[17] Shi, L., Hu, Z., Gu, F. et al. (2017). Sign and parameter optimization on teeth residue plastic film collector of ridged peanut (耙齿式垄作花生残膜回收机设计及参数优化). *Transactions of the Chinese Society of Agricultural Engineering*, 33(02):8-15. https://doi.org/10.11975/j.issn.1002-6819.2017.02.002.

[18] Wang, X., Zhang, M., Mu, T. (2012). Process optimization on alcohol production using sweet potato residue by simultaneous saccharification and fermentation method (甘薯渣同步糖化发酵生产酒精的工艺优化). *Transactions of the Chinese Society of Agricultural Engineering*, 28(14): 256-261. https://doi.org/10.3969/j.issn.1002-6819.2012.14.039.

[19] Wu, F., Xu, H., Gu, F. et al. (2017). Improvement of straw transport device for straw-smashing back-throwing type multi-function no-tillage planter (秸秆粉碎后抛式多功能免耕播种机秸秆输送装置改进). *Transactions of the Chinese Society of Agricultural Engineering*, 33(24):18-26. https://doi.org/10.11975/j.issn.1002-6819.2017.24.003.

[20] Wu, T., Wang, G., Hu, L., et al. (2018). Modal analysis of the knife roller of walking type sweet potato chopper-returning machine (步行式甘薯碎蔓还田机刀辊模态分析). *Journal of Jiangsu Normal University (Natural Science Edition)*, 36(03):47-49+53. https://doi.org/10.3969/j ISSN. 2095-4298.2018.03.009.

[21] Xia, Y., He, Y., Wang, W. et al. (2011). Experimental research on mechanized harvesting pattern of sweet potato in sections (分段红薯机械化收获模式实验研究). *Chinese Agricultural Mechanization*, No.238(06):70-72+69. https://doi.org/10.3969/j.issn.1006-7205. 2011.06.017.

[22] Xie, Y., Bian, X., Jia, Z. et al. (2022). Development status and prospect of fresh sweet potato industry in China (中国鲜食甘薯产业发展现状及其发展前景). *Jiangsu J. of Agr. Sci*, 38(06):1694-1701. https://doi.org/10.3969/j.issn.1000-4440.2022.06.028.

[23] Yan, W., Hu, Z., Wu, N. et al. (2017). Parameter optimization and experiment for plastic film transport mechanism of shovel screen type plastic film residue collector (铲筛式残膜回收机输膜机构参数优化与试验). *Transactions of the Chinese Society of Agricultural Engineering*, 33(01):17-24. https://doi.org/10.11975/j.issn.1002-6819.2017.01.003.

[24] Yu, Z., Hu Z., Wang, H., et al. (2015). Parameter optimization and experiment of garlic picking mechanism (大蒜果秧分离机构参数优化及试验). *Transactions of the Chinese Society of Agricultural Engineering*, 31(01):40-46. https://doi.org/10.3969/j.issn.1002-6819.2015.01.006.

[25] Yuan, B., Xue, L., Zhang, Q., et al. (2016). Essential Oil from Sweet Potato Vines, a Potential New Natural Preservative, and an Antioxidant on Sweet Potato Tubers: Assessment of the Activity and the Constitution. *Journal of agricultural and food chemistry* (40). https://doi.org/10.1021/acs.jafc.6b03175.

[26] Zhang, J., Wang, X., Chen, F. et al. (2007). Design of new multifunctional straw crushing and returning recycling machine (新型多功能秸秆粉碎还田回收机的设计). *Research on agricultural mechanization*, No.150(10):65-67. https://doi.org/10.13427/j.cnki.njyi.2007.10.030.

[27] Zhang, M., Jin, C., Liang, S. et al. (2015). Parameter optimization and experiment on air-screen cleaning device of rapeseed combine harvester (风筛选式油菜联合收割机清选机构参数优化与试验). *Transactions of the Chinese Society of Agricultural Engineering*, 31(24):8-15. https://doi.org/10.11975/j.issn.1002-6819.2015.24.002.

[28] Zhao, Y., Wang, Y., Liu, H. et al. (2018). Design and Test of Stubble-breaking Components on Strip Subsoiling and Stubble-breaking Machine (带状深松灭茬机灭茬部件设计与试验). *Journal of Agricultural Machinery*, 49(03):94-103. https://doi.org/10.6041/j.issn.1000-1298.2018.03.011.

DESIGN OF ENERGY MANAGEMENT STRATEGY FOR DUAL-MOTOR-DRIVEN ELECTRIC TRACTORS
/
双电机驱动电动拖拉机能量管理策略的研究

Jun YANG[1)], Aiping SHI*[1)], Yupeng JIANG[1)], Bochuan DING[1)]
[1)] College of Agricultural Engineering, Jiangsu University, Zhenjiang 212000, China
Tel: +86-15952866677; E-mail: shap@ujs.edu.cn
Correspondent author: Aiping Shi
DOI: https://doi.org/10.35633/inmateh-72-38

Keywords: *dual-motor driving, electric tractor, dynamic programming, energy management*

ABSTRACT
At present, electric tractors experience significant battery energy loss during operation, resulting in a short continuous running time. Therefore, in order to reduce the power consumption of the tractor drive system, minimize battery energy loss, and extend the operating time under various conditions, this paper presents a method for driving an electric tractor based on dual-motor coupling. Based on the characteristics of the transmission structure, an online torque distribution strategy for dual-motor coupling-driven electric tractors using a fuzzy control approach is proposed. First, an enhanced genetic algorithm is utilized to optimize the fuzzy rule table. Simultaneously, it is compared with the offline optimization strategy of dynamic programming. Subsequently, a method that integrates test data models and theoretical models is employed to establish an efficiency model of key components of the electric tractor drive system and a longitudinal dynamics model of the entire machine. The performance of the entire vehicle was simulated and analyzed under plowing conditions. Finally, on the experimental bench, conduct steady-state load tests and dynamic performance tests on the dual-motor coupled drive system. The results show that the State of Charge (SOC) change trends of the fuzzy control strategy based on the improved genetic algorithm and the dynamic programming strategy are similar. The SOC change values are close, which enhances the adaptability of the electric tractor in various operating conditions. Compared with the fuzzy control strategy, the improved strategy reduced average power consumption by 8.8%, demonstrating that the fuzzy control energy management strategy based on the enhanced genetic algorithm is both economical and superior. The bench experiment demonstrated that the dual-motor drive system can adapt to load changes to achieve power distribution between the two motors, meeting the required workload while reducing power consumption.

摘要
目前电动拖拉机在在工作时电池能量损耗较大，持续运行时间较短，因此，本文为降低拖拉机驱动系统功率消耗，减少电池能量的损耗，延长工况运行时间，根据双电机耦合驱动电动拖拉机的传动结构特性，提出了一种基于模糊控制策略的双电机耦合驱动电动拖拉机的在线转矩分配策略，首先采用改进遗传算法对模糊规则表进行优化，同时与动态规划的离线优化策略进行对照，随后采用试验数据模型和理论模型相结合的方法，建立了电动拖拉机驱动系统关键部件效率模型和整机纵向动力学模型，在犁耕下对整车性能进行仿真分析，最后在搭建的实验台架上对双电机耦合驱动系统进行稳态负载试验和动态性能试验。结果表明：基于改进遗传算法的模糊控制策略与动态规划策略的 SOC 变化趋势相似，SOC 变化值接近，改善了电动拖拉机不同作业工况的适应性，且改进后的策略与模糊控制策略相比，平均耗电量降低了 8.8%，证明了基于改进遗传算法的模糊控制能量管理策略具有良好的经济性和优越性，台架实验表明双电机驱动系统能够跟随负载变化实现两电机的功率分配，满足作业负载的同时降低了功率损耗。

INTRODUCTION
In the midst of the current global energy crisis and the increasingly severe environmental pollution problems, the use of electric tractors in agriculture has become an unavoidable trend (*Cao, 2013*). As a novel form of agricultural machinery that emphasizes environmental protection, energy efficiency, and high performance, the electric tractor presents clear advantages.

[1] Jun Yang, *M.S. Stud; Aiping Shi, Prof; Yupeng Jiang, M.S. Stud; Bochuan Ding, M.S. Stud*

Traditional tractors produce a significant amount of harmful gases in the field due to the use of diesel generators. They also contribute to high noise levels and low efficiency. Pure electric tractors can effectively address these limitations. Currently, pure electric tractors are mainly powered by a single motor, which often results in insufficient power when encountering complex operating conditions in the field with high power requirements (*Volpato et al., 2016; Chen, 2018*). Therefore, to improve the efficiency and performance of pure electric tractors, the dual-motor driving system is a promising solution. In cases where low speed and power requirements are needed, small motors are used to drive tractors. However, an effective energy management strategy is crucial for the advancement of dual-motor driving electric tractors (*Wang et al., 2022*).

Currently, the majority of research on dual-motor driving systems is focused on electric vehicles, with relatively limited research conducted on dual-motor-driven pure electric tractors. *Zhang et al.* (*2015*) proposed a rule-based power distribution control strategy based on Pontryagin's Minimum Principle (PMP) control strategy through six cycle conditions to enhance the operating efficiency of dual-motor-driven electric buses. *Chen et al.* (*2023*) developed a torque allocation strategy aimed at minimizing losses in a real-time electric drive system. This strategy is based on the loss mechanism of the electric drive system and has been shown to enhance the economic performance and adaptability of the vehicle under various working conditions. *Chen* (*2021*) from Jiangsu University proposed a torque allocation system for a dual-motor coupling driving electric tractor based on the linear diminishing weights particle swarm algorithm. *Wen et al.* (*2022*) proposed a set of innovative design and verification methods for the dual-motor power coupling drive system of electric tractors. The aim was to address the issues of excessive focus on static indicators, neglect of the distribution of high-efficiency power source areas, and incomplete simulation and test verification systems in the design and parameter optimization of multi-power source tractors.

In a detailed study of the transmission system of electric tractors, *Zhang et al.* (*2023*) proposed a dynamic optimization method for the speed ratio of the transmission system based on motor coupling characteristics. This innovative method utilized a simulation environment and the advanced Deep Deterministic Policy Gradient (DDPG) algorithm of reinforcement learning for iterative solutions. It significantly improved the power performance and overall work efficiency of electric tractors. *Wang et al.* (*2023*) focused on the rotary tillage unit of extended-range electric tractors. Based on the background of dual-motor independent electric drive, they pioneered the use of dual-input variable inverse modeling technology. By combining actual measurement data and empirical formulas, they successfully established an accurate model that reflects the periodic characteristics of rotary tillage conditions. *Liu* (*2023*) designed a dual-motor power-coupled drive system for electric tractors. They conducted in-depth discussions and experimental verification on structural design and key parameter optimization using a method that combines the particle swarm optimization algorithm and dynamic programming. *Chen et al.* (*2019*) proposed a parameter matching and optimization design method for the electric tractor powertrain based on a dual-motor coupling drive approach. They utilized a particle swarm optimization algorithm incorporating a hybrid penalty function to address the optimization of the traction performance of the electric tractor.

Therefore, for the dual-motor-driven electric tractor, improving system efficiency is the top priority, making a well-planned energy management strategy essential.

This paper uses dynamic programming to globally optimize the power system. By analyzing the results of dynamic programming, a fuzzy control strategy is designed based on the characteristics of the power system. The fuzzy rule table is optimized, and finally, through simulation experiments and comparison with the dynamic programming strategy, the effectiveness of the energy management strategy is verified.

MATERIALS AND METHODS

Main Component Parameters and Power System Composition

The reason for choosing to use two low-power motors instead of a single high-power motor is that a dual-motor coupled drive is more energy-efficient than a single-motor drive. A dual-motor coupled drive can meet different requirements while still satisfying the power needs of the electric tractor. Through reasonable energy management strategies, the driving efficiency of the two motors can be improved to achieve energy-saving effects under load conditions. When the electric tractor is working with a low load, the single-motor drive mode is used. To improve the working efficiency of the motor and achieve energy saving under the same torque demand, increasing the motor load rate is the key. When the electric tractor needs to work at high speeds with loads in the field, the main motor and the auxiliary motor are coupled to drive.

The dual-motor coupled drive system has the advantage of having a high-efficiency area. Due to the increase in the high-efficiency area, the motor can run in the high-efficiency area more frequently, thereby

achieving the goal of energy saving. The purpose of this research is to further optimize the energy management strategy of the dual-motor electric tractor designed by the team. Figure 1 shows the actual picture of the designed dual-drive electric tractor, and Figure 2 shows the schematic diagram of the high-efficiency range of the dual motors.

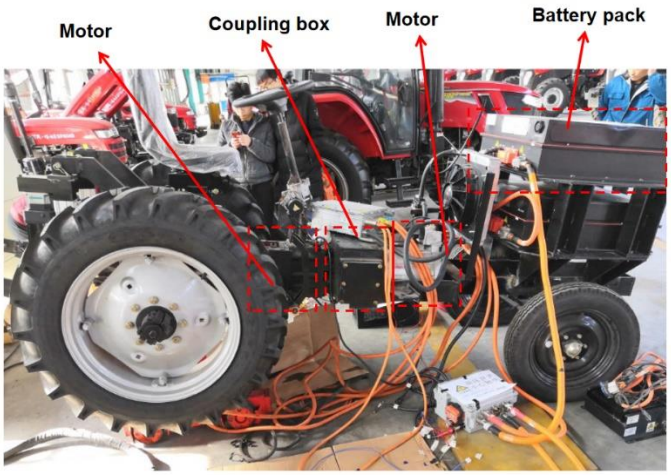

Fig. 1 - Actual picture of electric tractor

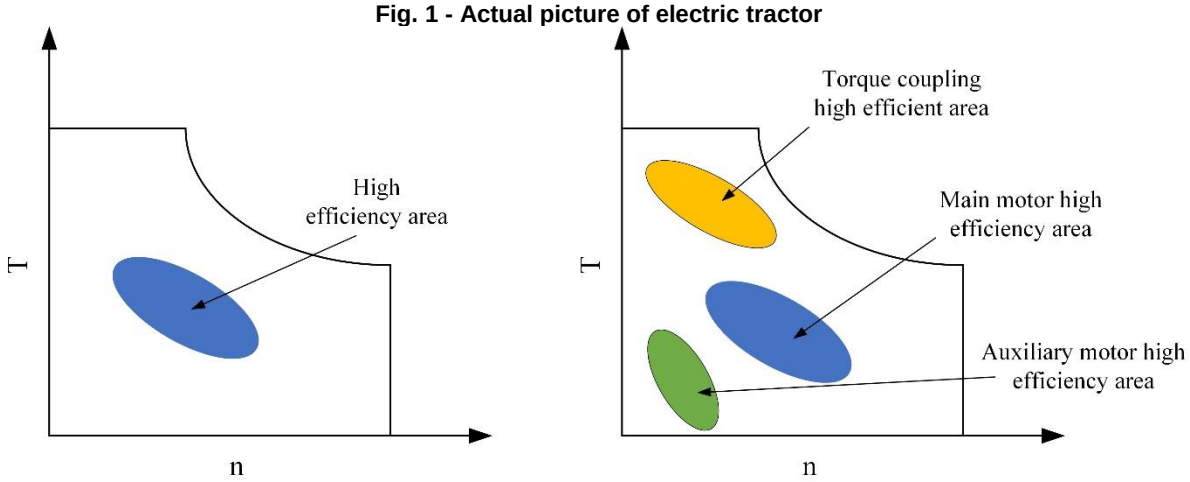

Fig. 2 - Comparison diagram of high efficiency area between single motor and dual motor

The power source of the electric tractor driven by two motors is the main motor and the auxiliary motor. The two motors are connected through the coupling device to realize the dynamic coupling of the two motors, and then the power is transmitted to the driving wheel through the components such as the gearbox and the differential (*Hu 2018; Enang and Bannister, 2017*), as shown in Fig. 3, and the main parameters are shown in Table 1.

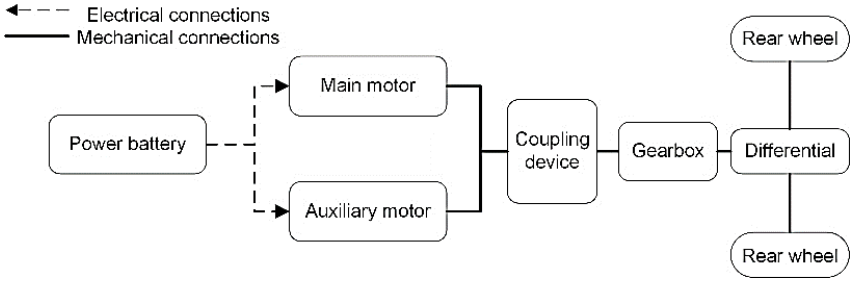

Fig. 3 - Schematic diagram of a dual-motor-driven electric tractor

Table 1

Basic parameters of tractor

Parameter	Value
Tractor mass/kg	2100
Drive wheel radius/m	0.51
Rolling resistance coefficient	0.07(Field) 0.016(Road)

Establishment of Theoretical Model

- **Vehicle Longitudinal Dynamics Model**

The wheeled electric tractor needs to overcome the resistance to carry out the working condition operation. The main resistances include rolling resistance, acceleration resistance, slope resistance, and traction resistance. The speed of the tractor is slow and the air resistance is ignored. The longitudinal dynamic model of the electric tractor is as follows.

$$T_w = (mgf\cos\theta + mg\sin\theta + \delta m\frac{dv}{dt} + F_t)\cdot r_w \quad (1)$$

where:

T_ω is the driving wheel torque, (N·m); m is the mass of the tractor, (kg); g is the acceleration of gravity, (m/s²); f is the rolling resistance coefficient; θ is the slope, (°); δ is rotation mass conversion coefficient; F_t is the hook traction force, (N); r_ω is the radius of the driving wheel, (m).

- **Battery Model**

The battery is a critical component of the electric tractor. The lithium battery undergoes a complex chemical reaction during the charging and discharging processes. It is difficult to establish a reliable working model without an accurate model. As a result, this paper does not discuss the thermal temperature effect and transient response of the battery. The influence of state of charge on electromotive force and internal resistance is the main focus, and the Rint model is selected (*Onori et al., 2016*), as shown in Fig. 4.

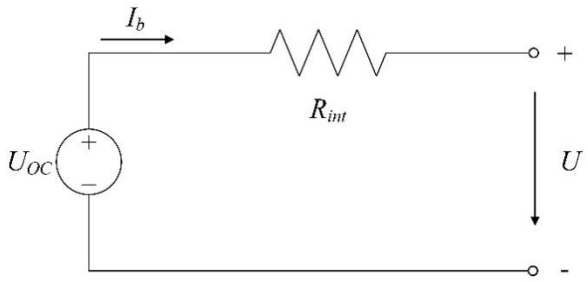

Fig. 4 - Battery Equivalent Circuit Model

For the battery internal resistance model, there are:

$$U = U_{OC} - I_b R_{\text{int}} \quad (2)$$

The calculation formula of battery power output and current module is:

$$P_m = U\cdot I_b \quad (3)$$

$$I_b = \frac{U_{OC} - \sqrt{U_{OC}^{\ 2} - 4P_m R_{\text{int}}}}{2R_{\text{int}}} \quad (4)$$

where:

U_{OC} is the open-circuit voltage of the battery, (V); P_m is battery output power, (W); R is the equivalent internal resistance of the battery, (Ω); I_b is battery charge and discharge current, (A).

The battery state of charge equation is:

$$SOC(t) = SOC_0 - \frac{1}{Q_b}\int_0^t \eta I_b(t)dt \quad (5)$$

where:

$SOC(t)$ is the SOC of t at that moment in time, (%); Q_b is the rated capacity of the battery, (Ah); η is the battery discharge efficiency, (%).

- **Motor Model**

This paper utilizes a brushless DC motor and employs experimental modeling to measure the motor's experimental data using a built test bench. It also utilizes the spline interpolation method to establish the motor's efficiency model (*Rizzoni et al., 1999*). The parameters of the motor are shown in Table 2.

Most of the working conditions for electric tractors involve towing agricultural tools in the field, where the vehicle typically travels at a relatively slow speed. Hence, there is no need to consider the effects of acceleration resistance and wind speed resistance. The main consideration is the effect of traction resistance on the tractor's field operations. When the main motor is working, it directs the majority of power to the output shaft to enhance the tractor's power output during rotary tillage operations. Therefore, initially calculate the power requirements of the main motor to meet the rotary tillage conditions. The average power consumed by a tractor during rotary tillage work is typically calculated using the soil-specific resistance method.

$$P_X = 0.1K_\lambda h_k v B \tag{6}$$

where:

P_X is the average power consumed by the main motor of an electric tractor during rotary tillage operations, (kW); K_λ is rotary tillage specific resistance, (N/cm^2); h_k is tillage depth, (cm); v is the driving speed of electric tractor during rotary tillage, (m/s); B is the ploughing width, (m)。

While the main motor drives the power output shaft, a portion of the power is transmitted to the driving wheels and the auxiliary motor to propel the vehicle. In order to ensure that the tractor can operate stably in various working environments, the traction capacity of the main motor should be increased by 20-30%. Therefore, the formula for calculating the rated power of the main motor is:

$$P_{m1} = (1.2 \sim 1.3)P_X \tag{7}$$

The sum of the power of the main motor and the power of the auxiliary motor is equal to the traction power, so the rated power of the speed-regulating motor can be determined as:

$$P_{m2} = \frac{P_{Tn}}{\eta_T} - P_{m1} \tag{8}$$

where:

P_{Tn} is the rated driving power of tractor, (kW); η_T is the traction efficiency.

Table 2

Basic parameters of motor

Parameter	Value
The rated power of the main motor/kW	20
The rated speed of the main motor/r·min^{-1}	3000
The rated torque of the main motor/N·M	70
The rated power of the auxiliary motor/kW	10
The rated speed of the auxiliary motor/r·min^{-1}	3400
The rated torque of the auxiliary motor/N·M	28

- **Driver Model**

The driver model is an essential component of the simulation platform, used to replicate driver behavior in real driving scenarios. The input signal of the model comprises the desired vehicle speed and the actual vehicle speed of the driving cycle, while the output signal is the command for the accelerator/brake pedal. The driver model uses PID control (Proportional-Integral-Derivative Control) to provide feedback on the accelerator/brake pedal opening based on the difference (e) between the target vehicle speed and the actual vehicle speed.

$$acc = K_P e + K_I \int e dt + K_D \frac{de}{dt} \tag{9}$$

where:

acc is the pedal opening degree; e is the difference between the target speed and the actual speed, (m/s); K_P is the proportional coefficient of the driver model; K_I is the integral coefficient of the driver model; K_D is the differential coefficient of the driver model.

Based on the MATLAB/Simulink environment, the vehicle longitudinal dynamics model and driver model were built, as well as the key components of the power system, the battery, and the motor, for focused modeling. The final simulation model diagram is as follows.

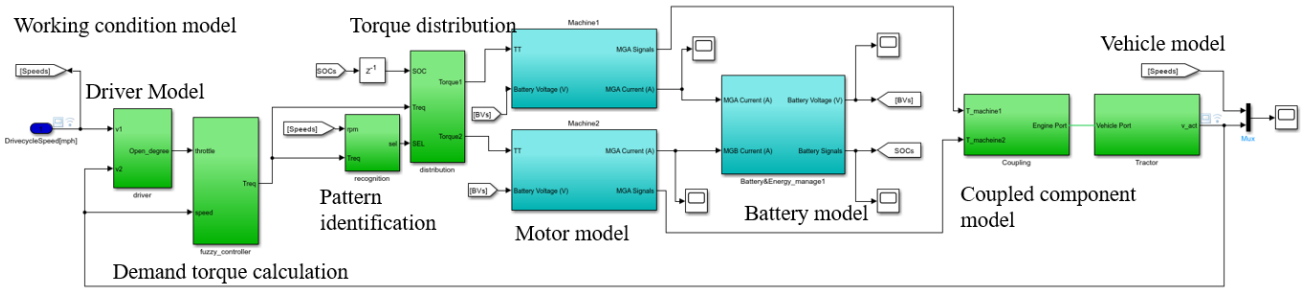

Fig. 5 - Schematic diagram of simulation model of electric tractor

Pattern Analysis

Based on the performance indicators and evaluation standards of the electric tractor, the power coupling mechanism is designed to achieve different drive modes, specifically the torque coupling drive mode and the main motor-independent drive mode.

Offline Optimization Strategy based on Dynamic Programming

The essence of energy management for electric tractors driven by dual-motor coupling is to optimally distribute the output power between the two motors to achieve optimal driving costs for the entire vehicle. Therefore, the process of power allocation can be regarded as a multi-stage decision-making problem with time as a step. Dynamic programming is an idea or approach to solving multi-stage decision-making optimization problems (*Wang et al., 2018*; *Bertsekas, 2012*). Its main idea is to divide the problem into multiple interconnected sub-stages. After the decision-making in one stage is determined, it often affects the next stage. Finally, the optimal solutions of the sub-stages are combined to obtain the optimal solution of the original problem.

The global optimal solution can be found using the DP algorithm. However, this method can only be utilized when the operational cycle is known, and the computational cost is exceedingly high. Therefore, the optimization results of DP can serve as a benchmark for evaluating the performance of various energy management strategies.

It can be seen from the evolution of the dual-motor coupling drive system that the power battery SOC fluctuates with the operation of the vehicle, and the SOC can reflect the status of the tractor system. Therefore, the battery SOC is defined as the state variable of the optimal control system of the electric tractor. As shown in the following equation (7):

$$x(k) = SOC(k) \tag{10}$$

During the driving process of an electric tractor driven by dual motor coupling, the output power of the tractor determines the change of the control variable, so the torques T_{m1} and T_{m2} of the two motors of the vehicle are selected as the control variables of the system. As shown in the following equation (8):

$$u(k) = [T_{m1}(k), T_{m2}(k)] \tag{11}$$

At the same time, the cyclic working conditions are discretized according to time, the discretization accuracy is selected to be 1 s, and the following model is established in the time discrete state space:

$$x(k+1) = f(x(k), u(k)) \tag{12}$$

where: $x(k)$ is the state vector of the system; $u(k)$ is the control vector; f is the state transition function.

Set the initial value of SOC to 0.9, △SOC to 0.025, and △Tm to 1 N·m. At the same time, according to the battery equivalent model established in the previous section, it is known that the state quantities of the two adjacent sub-stages satisfy the following relationship.

$$SOC(k+1) = SOC(k) - \frac{(V_{oc} - \sqrt{V_{oc}^{\ 2} - 4RP})\Delta t}{2R \cdot Q} \tag{13}$$

In order to ensure normal decision-making, the actual situation of the variables related to the battery and motor needs to be reasonably constrained.

The specific constraint functions are as follows:

$$\begin{cases} SOC_{\min} \le SOC(k) \le SOC_{\max} \\ T_{\min\_m1} \le T_{m1}(k) \le T_{\max\_m1} \\ T_{\min\_m2} \le T_{m2}(k) \le T_{\max\_m2} \\ n_{\min\_m1} \le n_{m1}(k) \le n_{\max\_m1} \\ n_{\min\_m2} \le n_{m2}(k) \le n_{\max\_m2} \end{cases} \quad (14)$$

where:

SOC_{min} and SOC_{max} represent the minimum and maximum SOC of the battery, respectively, (%); T_{min_m1}, T_{max_m1}, T_{min_m2} and T_{max_m2} represent the minimum and maximum output torque of the main motor and the auxiliary motor, respectively, (N·m); n_{min_m1}, n_{max_m1}, n_{min_m2} and n_{max_m2} represent the minimum and maximum speed of the main motor, respectively, (rpm).

For a dual-motor-driven electric tractor, the focus of the strategy is mainly on the vehicle's economy. Therefore, the objective is to minimize the power consumption of the drive system of the electric tractor during working conditions. The cost function for the entire operating time from 0 to N is established as follows:

$$J = \sum_{k=0}^{N} L_k(x(k), u(k)), k = 0,1,...,N-1 \quad (15)$$

$$L = \frac{P_{m1}}{\eta_{m1}} + \frac{P_{m2}}{\eta_{m2}} \quad (16)$$

where: L is the instantaneous transfer cost; N is the total number of stages after the discrete driving cycle time domain; J is the cost function value accumulated during the iteration process; P_{m1} and P_{m2} represent the output power of main motor and auxiliary motor, respectively, (kW); η_{m1} and η_{m2} represent the efficiency value of main motor and auxiliary motor, respectively.

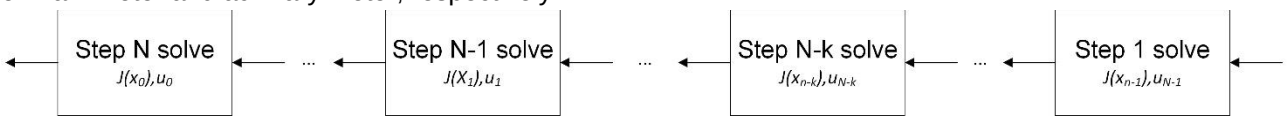

Fig. 6 - Schematic diagram of the reverse solution process

As depicted in Fig. 6, during dynamic programming, the entire operational time needs to be traversed, and the state and control quantities are calculated simultaneously. The dynamic programming reverse solution starts from the final stage N, and calculates and saves the optimal cumulative objective function and control quantity for each step. At this point, the reverse solution concludes. At this time, the initial quantity of the state is known. In the reverse solution process, the optimal control solution for each stage is used to perform the forward solution sequentially. This process yields the optimal control variables in different states, representing the optimal distribution under cycle conditions.

Energy management that relies on dynamic programming can obtain solutions. However, it heavily depends on accurate predictions of cycle conditions and has poor real-time which makes it unsuitable for direct application. Therefore, the optimal results obtained from the dynamic programming strategy serve as a benchmark for comparing the effects of the following energy management strategies and for guiding the selection of rules for energy management strategies based on fuzzy control (*Wang et al., 2022*).

Online Energy Management Strategy based on Fuzzy Logic Control

- **Establishment of Fuzzy Logic Control Strategy**

Fuzzy control does not require an accurate mathematical model of the controlled object and offers robustness and fault tolerance. It can also address dynamic control problems in nonlinear systems and is highly suitable for the control system of electric tractors (*Zhu et al., 2022*).

The fuzzy controller described in this paper takes the tractor's required torque (T_{req}) and the battery SOC as inputs and produces the torque distribution coefficient (λ) as the output variable. The fuzzy inference method utilizes the Mamdani direct inference method and employs triangular membership functions as the primary form, as shown in Fig. 7.

Among them, the fuzzy subsets of the input variable demand torque T_{req} are {NB, NS, M, PS, PB}, representing very small, small, medium, high, and very high, respectively. The fuzzy subsets corresponding to

the battery SOC are {VL, L, M, H, VH}, representing very low, low, medium, high, and very high, respectively. The fuzzy subsets of the output variable are {VS, S, M, B, VB}, representing very small, small, medium, big, and very big (*Ji et al., 2022; Ji et al., 2022*).

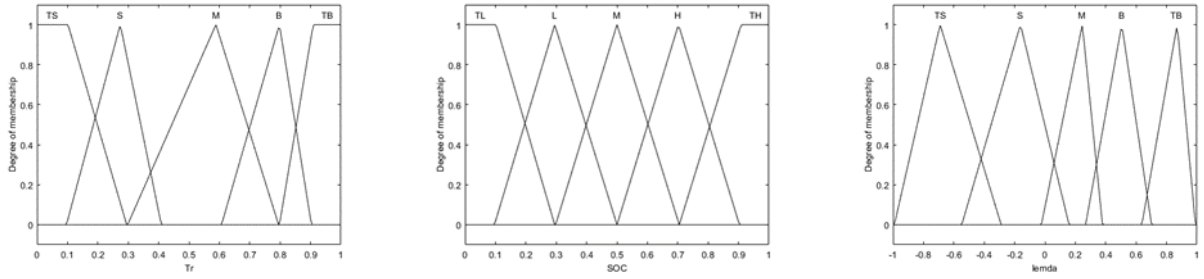

(a) Demand torque membership function *(b) Battery SOC membership function* *(c) λ membership function*

Fig. 7 - Membership function

For fully electric tractors, the working conditions primarily involve field operations. Therefore, ensuring that the tractor meets the power performance requirements is essential without significantly depleting the battery energy. Based on this principle, the following fuzzy rule table is established using the output results of dynamic programming (*Zhou et al., 2023*).

Table 3

Fuzzy rule table

λ		SOC				
		VL	L	M	H	VH
T_{req}	NB	VS	S	B	VB	VB
	NS	VS	VS	M	VB	B
	M	VS	VS	S	M	M
	PS	VS	VS	VS	M	S
	PB	VS	VS	VS	S	VS

- **Genetic Algorithm Optimization Fuzzy Logic Control**

Fuzzy control is a type of intelligent control that utilizes expert knowledge to regulate the control strategy and behavior of the controlled object (*Ding et al., 2021; Lü et al., 2020*). Professional knowledge plays a crucial role in the implementation of the control strategy. Therefore, genetic algorithms need to be implemented to optimize it. The genetic algorithm is an optimization technique that simulates the process of natural evolution and is employed to solve complex optimization problems. It is based on the principles of genetics and evolution and enhances the quality of solutions from one generation to the next by simulating operations such as natural selection, crossover, and mutation to identify optimal or near-optimal solutions. Given the subjective nature of professional knowledge, this paper aims to enhance the fuzzy control table using a genetic algorithm. The flow of the optimization algorithm is depicted in the Fig. 8 below.

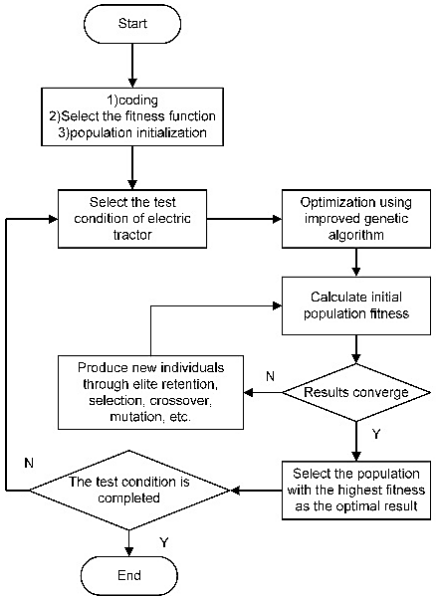

Fig. 8 - Optimized fuzzy control process

- **Genetic Algorithm Parameter Selection**

When using genetic algorithms, selecting the appropriate parameters is crucial for the performance and convergence of the algorithm.

The choice of the initial population size will impact the evolutionary efficiency and the optimization results of the algorithm. In general, the population size should be large enough to thoroughly explore the search space, but it must also take into account the limitations of computing resources. Therefore, the population size is set to 100. At the same time, the coding of the genetic algorithm selects 120 binary numbers. The crossover rate determines the probability of executing a crossover operation. A higher crossover rate can facilitate the exchange of genetic information and preserve diversity. However, an excessively high crossover rate may result in premature convergence and loss of diversity. Choose 0.6 according to the actual situation. The mutation rate determines the likelihood of a mutation operation occurring. The mutation operation helps introduce new gene combinations and explore new solutions in the search space. It is determined to occur with a probability of 0.05, based on the actual situation. The termination condition determines when the algorithm stops iterating, and 80 is chosen based on comprehensive considerations.

- **Improved Traditional Genetic Algorithm**

The traditional genetic algorithm is a heuristic search algorithm that relies on individuals within the population to conduct the search. In some instances, the genetic algorithm may converge to a local optimal solution and fail to identify the global optimal solution.

Therefore, this proposes some improvements to the traditional genetic algorithm and incorporates the adoption of an elite retention strategy (*Yu et al., 2023*). The basic idea is to directly copy the best-fit individuals in the current population into the next generation to ensure that these excellent individuals will not be eliminated due to selection, crossover, and mutation operations. It addresses the limitations of genetic algorithms, such as getting stuck in local optimal solutions, slow convergence speed, and loss of excellent solutions, by preserving excellent solutions, speeding up convergence, safeguarding genetic information of excellent solutions, and enhancing the stability of the algorithm. Finally, an improved algorithm is used to reoptimize the fuzzy control table.

Establishment of Theoretical Model

This paper presents a design for a test platform that aims to achieve precise control of the dual-motor power system of an electric tractor. The platform also aims to optimize performance, verify and improve energy management strategies, and ensure system safety under simulated conditions.

Test platforms offer several advantages, such as improved control accuracy, enhanced dynamic response, and efficient energy management. They also increase system flexibility and adaptability while reducing development risks and costs. Different power coupling and motor combination methods can be adapted to cope with various working conditions. The motor drive is controlled through the motor drive controller, and the power is output to the load through the coupling box. The platform obtains optimal key and operating parameters through testing, meeting the power requirements of different workloads while reducing energy consumption, improving the efficiency of the drive system, and extending the reliable working time. The actual picture of the bench is shown in Figure 9.

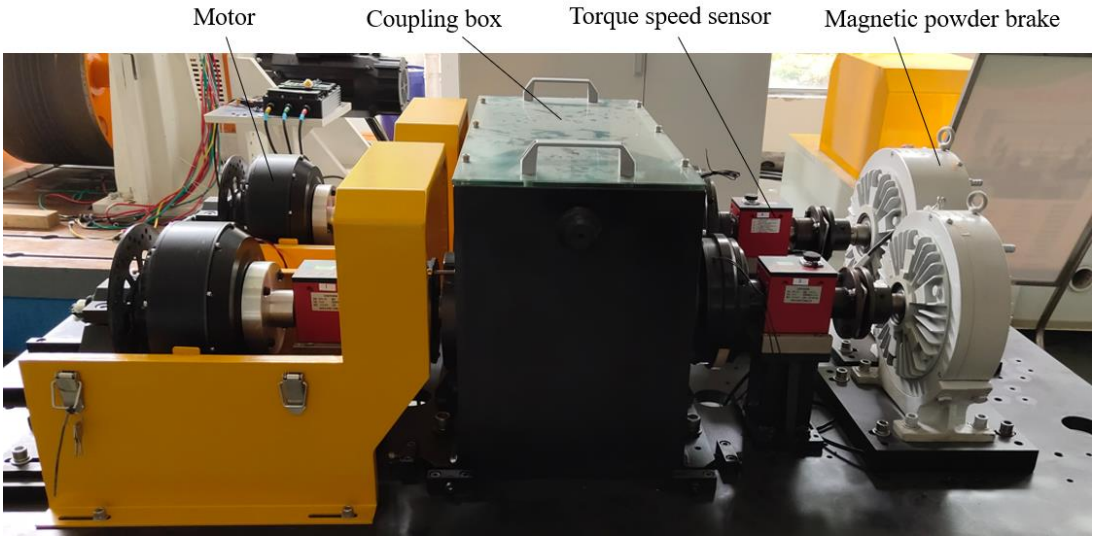

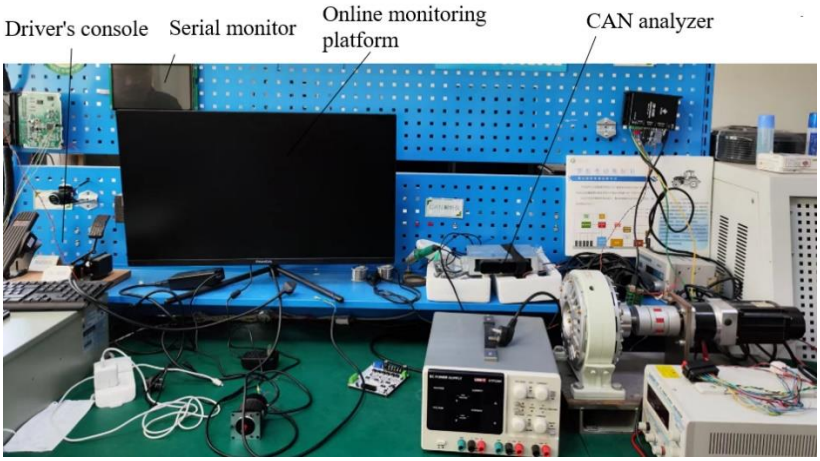

Fig. 9 - Actual picture of the bench

In order to verify the effectiveness of the electric tractor control system and the transmission performance of the dual-motor drive system, through the above experimental bench, the bench test was carried out. According to the above, the bench test is only for the dual-motor coupled-drive electric tractor under the coupling box for the torque coupling mode.

- **Steady state load experiment**

To check the functional status of the complete machine controller, first power on the complete machine test system. Then, turn the key switch and adjust it to the forward gear to start the main motor and auxiliary motor. After that, adjust the magnetic powder brake to ensure its simulated load torque stays stable at 500 N·m. During this process, the operator needs to depress the accelerator pedal. At this moment, the system will collect and calculate the signals of the pedal opening and its change rate, convert these signals into speed and torque signals, and transmit them to the motor controller. The power is then transferred to the output shaft via the coupling box. As the speed of the output shaft gradually increases from zero, the data will be collected after stable operation, and the speed curve and power curve will be obtained by fitting the data.

- **Dynamic load experiment**

In order to simulate and test large load changes in field operations, the load of an electric tractor's working environment must be limited to a range with upper and lower limits. The experiment begins with powering on and detecting the entire test system to confirm the normal operation of the entire machine controller. The main motor and auxiliary motor are then started by turning the key switch and adjusting the gear to the forward position. The magnetic powder brake is adjusted to simulate a load torque of 450 N·m and manually adjusted to achieve a load variation range of approximately 200 N·m. As the accelerator pedal is depressed, the whole machine controller begins to collect and calculate signals of the pedal opening and its rate of change. These signals are then converted into speed and torque signals and sent to the motor controller through the coupling box. The power is transmitted to the output shaft and the rotation speed of the output shaft gradually increases from zero, while data collection begins. Finally, the rotation speed and power curves are obtained.

RESULTS AND DISCUSSION

Model Validation

There are two primary transportation conditions for tractors: field transfer and suburban road transportation. Therefore, the suburban low-speed working condition EUDC (Extra Urban Driving Cycle) is referred to as the test condition for tractor transportation, as shown below:

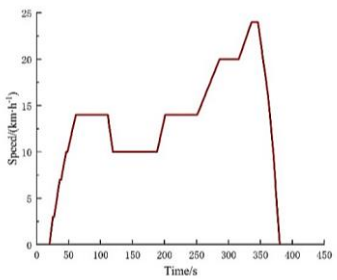

Fig. 10 - Tractor speed under road transport condition

The simulation time for the working condition is set to 400 seconds, with a maximum vehicle speed of 24 km/h during operation and an average vehicle speed of 12.49 km/h.

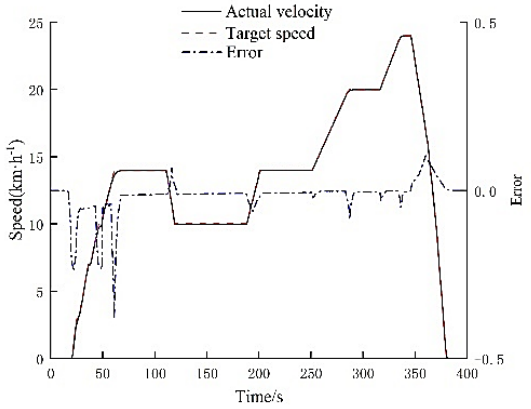

Fig. 11 - Speed tracking under road transport condition

Fig. 11 illustrates that the simulated vehicle speed of the tractor has a high degree of followability with the set target operating speed. The absolute maximum deviation between the simulated vehicle speed and the target operating speed is 0.391, while the absolute mean deviation is 0.021. The error is minor and does not affect the actual transportation situation, so it can be ignored. Therefore, it can be demonstrated that the construction of the entire vehicle model is highly accurate and can genuinely and effectively reflect the actual working conditions of the tractor.

Analysis of Simulation Results of Ploughing Test Conditions

The theoretical value can be obtained from the tractor's traction resistance calculation formula. However, in real-world conditions, ploughing is influenced by various factors, including soil conditions, ploughing depth and width, and driver's operation. As a result, the traction resistance experienced by the tractor is not constant. Therefore, the ploughing test condition depicted in the figure is established. In this scenario, the average traction resistance is 3657.64 N, the average vehicle speed is 6.11 km/h, and the simulation time is 1200 s. The specific working conditions are shown in the Fig. 12.

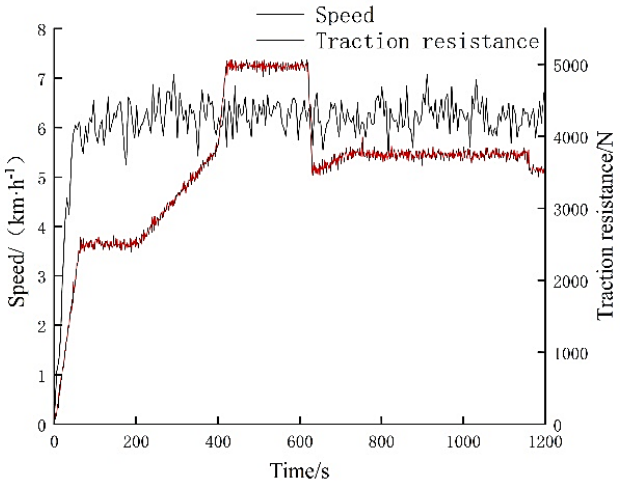

Fig. 12 - Tractor speed and traction in ploughing test conditions

- **Results of Dynamic Programming**

The SOC of the battery indicates the remaining capacity of the battery, while its magnitude indicates the amount of energy stored in the battery. The Fig. 13(a) illustrates the battery SOC change curve for the energy management strategy under ploughing cycle conditions. It is evident from the figure that the SOC change curve of the dynamic programming algorithm changes relatively smoothly. At the conclusion of the final operating cycle, the battery SOC termination value, determined using the dynamic programming algorithm, is 84.06%.

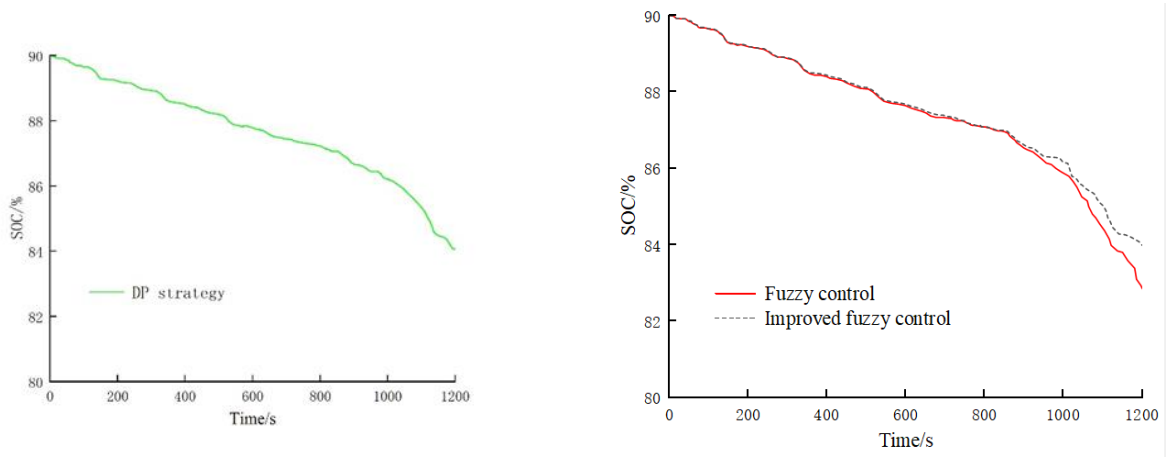

(a) Soc change curve 1 *(b) Soc change curve 2*

Fig. 13 - Soc change curve

- **Results of Fuzzy Logic Control**

The fuzzy control strategy was simulated under test conditions. The battery SOC change curve is shown in Fig. 13(b) above and compared with the improved fuzzy control strategy.

It is evident from the figure that in the early 400 s of the working condition, the variance in battery power consumption between the two energy management strategies is relatively small. However, as the operating time of the working condition increases, the disparity between the two gradually becomes larger. After the final operating cycle, the battery SOC termination value using the fuzzy control algorithm was 83.31%, whereas the SOC termination value based on the control strategy optimized by the improved genetic algorithm was 83.73%. The improved control strategy was compared with the SOC of the fuzzy control strategy. It has been improved, and the fluctuation of SOC is also smaller. Therefore, it distributes the output of the two motors more reasonably, also better improves the economic performance of the tractor, and is more adaptable to the tractor's working conditions.

Compared with the fuzzy control strategy, the average power consumption based on the improved fuzzy control strategy is reduced by 8.8%, and the average power consumption based on the dynamic programming strategy is reduced by 10.5%. The entire test condition is based on the improved fuzzy control strategy and shows a SOC change trend similar to the dynamic programming strategy, and the change range is less than 2%. Therefore, compared with the fuzzy control strategy, the other two distribute the output of the two motors more reasonably and better improve the economic performance of the tractor. This further demonstrates that the fuzzy control strategy based on improved genetic algorithm optimization has a better economy and working condition adaptability.

Table 4

Comparison of the simulation results

	Fuzzy Control	Improved Fuzzy Control	DP
SOC termination value/%	83.31	83.98	84.06
SOC change value/%	6.69	6.02	5.94
Power consumption per kilometer	1.60	1.46	1.43
Energy consumption reduction ratio/%	—	8.8	10.5

After analyzing the simulation results of three different working conditions, it was found that the energy management strategy based on improved fuzzy control is as effective as the strategy based on dynamic programming, while also making up for the flaw of poor real-time performance that the latter has. Moreover, compared to the fuzzy control strategy, the improved fuzzy control-based strategy is more efficient in reducing the energy consumption of the vehicle and is better suited to adapt to various working conditions.

Analysis of Bench Test

- **Results of Steady State Load Experiment**

In Figure 14(a), the output speeds of the two motors under steady load are displayed. As the main motor's output speed increases, the output torque of the auxiliary motor also increases steadily. The maximum speeds for the main motor and the auxiliary motor are 5432.6 r/min and 4667.7 r/min, respectively.

Figure 14(b) shows the power variation curve, and by analyzing this data the system efficiency can be derived by calculating the ratio of input power to output power. Upon observing this curve, it can be seen that at around 200 seconds, the ratio of output power to input power reaches its peak value. At this time, the efficiency of the entire system is at its maximum, which is about 70%.

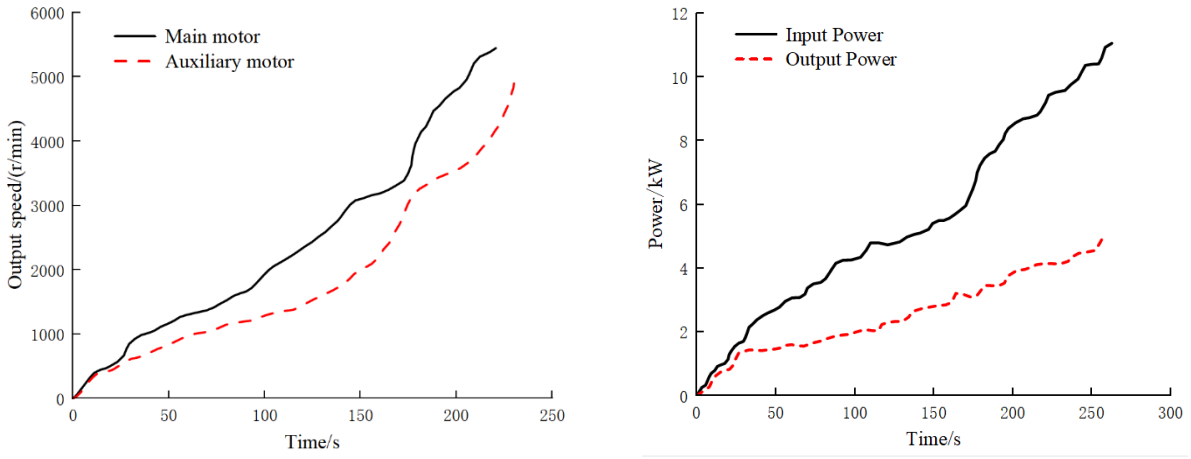

(a) Speed curve under constant load *(b) Power curve under constant load*

Fig. 14 - Results of steady state load experiment

- **Results of Dynamic Load Experiment**

Figure 15(a) shows that the output speeds of the main motor and auxiliary motor fluctuate within a range of 120 r/min due to load changes. The two motors' rotational speeds increase from 0 to 16 seconds and then stabilize, maintaining a relatively fixed range. After 16 seconds, the output speed of the entire drive system remains stable.

Figure 15(b) shows that load changes significantly impact the input and output power of the complete machine drive system, resulting in obvious fluctuations. By calculating the ratio of input power to output power, the overall system efficiency changes can be observed. When the load of the whole machine increases, the power of the main motor and the auxiliary motor increases simultaneously, improving the efficiency of the entire machine. Conversely, when the load of the whole machine decreases, the power of the main motor and the auxiliary motor decreases, reducing the overall machine efficiency.

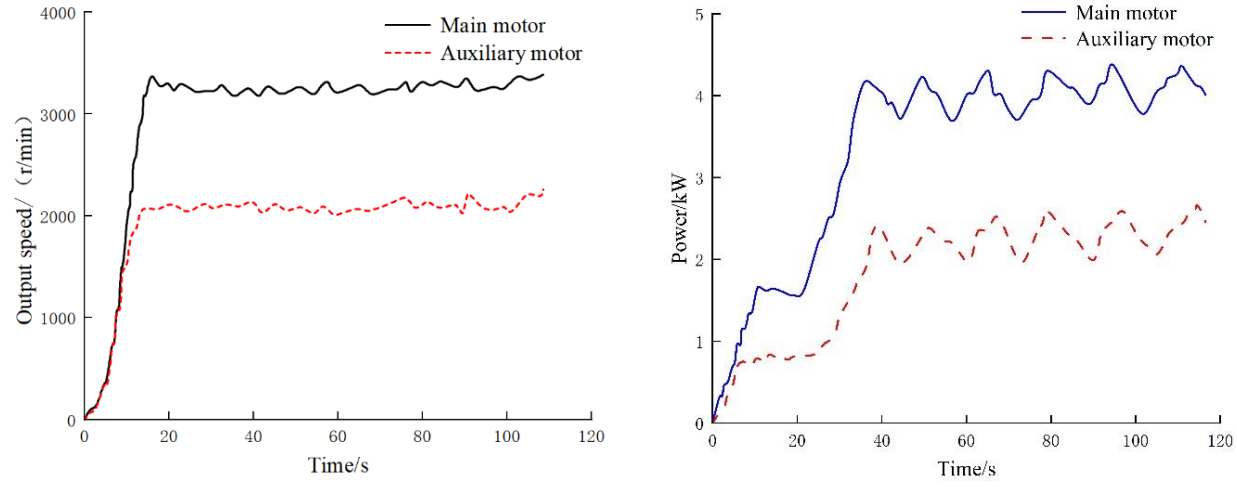

(a) Output torque curve under dynamic load *(b) Input power curve under dynamic load*

Fig. 15 - Results of dynamic load experiment

The fluctuation range of the two motors is around 1 kW, and the power ratio of the two motors fluctuates between 1.11 and 2.79. The input power of the two motors can be distributed according to the control strategy following the load fluctuation. The highest efficiency is 79%, with a load torque of 405 N·m, main motor power of 3.5 kW, and auxiliary motor power of 1.91 kW.

CONCLUSIONS

This paper aims at the issue of inadequate power in single-motor-driven electric tractors when faced with complex working conditions and high power demands. Based on the dual-motor coupling drive system scheme, a simulation model is constructed, and detailed simulation verification of road transportation cycle conditions is carried out. The results indicate that the established vehicle, battery, and motor models demonstrate good accuracy and rationality. They can effectively simulate energy flow and power transmission under actual working conditions.

The dynamic programming strategy is capable of achieving globally optimal energy management effects in theory. However, it relies on preset settings and offline calculations, which limit its application in real-time changing working environments and its ability to adapt to real-time adjustments to working conditions. On the other hand, the fuzzy control strategy, based on an improved genetic algorithm optimization proposed in this article, has demonstrated significant practical value in simulation experiments. Simulation data shows that this strategy exhibits similar SOC curve trends and a smaller gap compared to the dynamic programming method. In comparison to the original fuzzy control strategy, this strategy reduces the average energy consumption by 5.6%, significantly enhancing the efficiency of the drive system. The enhanced endurance of the electric tractor directly reflects the effectiveness of the fuzzy control energy management strategy optimized by the improved genetic algorithm. This optimization demonstrates clear advantages in economic performance and superior real-time adaptation to changes in working conditions. It is feasible and superior. In future research, the potential loss mechanisms in dual-motor coupled-drive electric tractor systems will be further explored and efforts will be made to develop a comprehensive and accurate loss model to quantitatively analyze the interaction between mechanical coupling devices, transmission components, and motors. The focus will not only be on the direct physical losses during the power transmission process, such as friction losses, energy dissipation caused by torque fluctuations, and the efficiency of the coupling equipment itself but also the energy interactions that may occur when motors work together under different working conditions, leading to low conversion efficiency, will be considered.

Simulation and bench test results show that the power coupling gearbox designed in this paper can meet the functional requirements of the electric tractor dual-motor drive system; the designed drive control strategy can achieve power distribution and control effects of the two motors under different working conditions. The response speed is good and can meet the power needs of the real drive system.

ACKNOWLEDGEMENT

This work was supported by the "Thirteenth Five-Year Plan" National Key Research and Development Plan Project (2016YFD0701002) and the National Key Research and Development Program of China (2019YFD1002500).

REFERENCES

[1] Bertsekas D., (2012). *Dynamic programming and optimal control*, vol. 4, Athena scientific.

[2] Cao Z., (2013). Future Orientation of Ecological Agriculture （生态农业未来的发展方向）. *Chinese Journal of Eco-Agriculture*, 21(1), 29–38.

[3] Chen Y., (2018). *Study on Design and Drive Control Methods of Powertrain for Electric Tractor* （*电动拖拉机动力系统设计与驱动控制方法研究*）, PhD dissertation, China Agricultural University, Beijing/China.

[4] Chen A., Chen S., Shi A., Xu L., & Zhang H., (2021). Design of Torque Distribution Strategy for Dual-Motor Variable-Speed Drive Electric Tractor (双电机耦合驱动电动拖拉机转矩分配策略设计). *Journal of Agricultural Mechanization Research*, 43(11), 1–6.

[5] Chen S., Hu M., & Zhao J., (2023). Real-Time Torque Distribution Strategy for Dual-Motor Pure Electric Vehicle with Minimum System Loss (系统损耗最小的双电机纯电动汽车实时转矩分配策略). *Chinese Journal of Mechanical Engineering*, 1–13.

[6] Chen Y., Xie B., Du Y., & Mao E. (2019). Powertrain parameter matching and optimal design of dual-motor driven electric tractor. *International Journal of Agricultural and Biological Engineering*, 12(1), 33-41.

[7] Ding N., Prasad K., & Lie T., (2021). Design of a hybrid energy management system using designed rule-based control strategy and genetic algorithm for the series-parallel plug-in hybrid electric vehicle. *International Journal of Energy Research*, 45(2), 1627-1644.

[8] Enang W., Bannister C., (2017). Modelling and control of hybrid electric vehicles (A comprehensive review). *Renewable and Sustainable Energy Reviews*, 74, 1210-1239.

[9] Hu Z., (2018). *Research on Energy Management Strategy of Dual Motor Driving Electric Vehicle* (*双电机构型电动汽车的能量管理策略研究*). MSc dissertation, Beijing University of Technology, Beijing/China.

[10] Ji K., Li Y., Liang Z., Liu Y., Cheng J., Wang H., & Zheng G., (2022). Device and Method Suitable for Matching and Adjusting Reel Speed and Forward Speed of Multi-Crop Harvesting. *Agriculture*, 12(2), 213.

[11] Ji K., Li Y., Zhang T., Xia S., & Cheng J., (2022). Technology of Adjusting the Header Height of the Harvester by Multi-Sensor Data Fusion Based on Bp Neural Network. *INMATEH - Agricultural Engineering*, 68(3), 91–98.

[12] Lü X., Wu Y., Lian J., Zhang Y., Chen C., Wang P., & Meng L., (2020). Energy management of hybrid electric vehicles: A review of energy optimization of fuel cell hybrid power system based on genetic algorithm. *Energy Conversion and Management*, 205, 112474.

[13] Liu Y., (2023). Design and Experimental Study of Dual Motor Drive System for Electric Tractor (电动拖拉机双电机驱动系统的设计及试验研究). *Journal of Agricultural Mechanization Research*, 45(11), 247–252.

[14] Onori S., Serrao L., & Rizzoni G., (2016). *Hybrid electric vehicles: Energy management strategies*.

[15] Rizzoni G., Guzzella L., & Baumann B., (1999). Unified modeling of hybrid electric vehicle drivetrains. *IEEE/ASME transactions on mechatronics*, 4(3), 246-257.

[16] Wang W., Shi J., Zhang Z., & Lin C., (2018). Optimization of a dual-motor coupled powertrain energy management strategy for a battery electric bus. *Energy Procedia*, 145, 20-25.

[17] Wang Z., Xu S., & Luo W., (2022). Research on Energy Management Strategy of Fuel Cell Vehicle Based on Dynamic Programming (基于动态规划的燃料电池车能量管理策略研究). *Acta Energiae Solaris Sinica*, 52(09), 2077–2084.

[18] Volpato C. E. S., de Paula V. R., Barbosa J. A., & Volpato, E. L., (2016). Evaluation of the operational viability of the use of electricity as a source of power in agricultural tractors. *In 2016 ASABE Annual International Meeting (p. 1).* American Society of Agricultural and Biological Engineers.

[19] Wang Z., Zhou J., & Rizzoni G., (2022). A review of architectures and control strategies of dual-motor coupling powertrain systems for battery electric vehicles. *Renewable and Sustainable Energy Reviews*, 162, 112455.

[20] Wang Z., Zhou J., & Wang X., (2023). Research on Energy Management Model for Extended-range Electric Rotary-tilling Tractor (增程式电动拖拉机旋耕机组能量管理模型研究). *Transactions of the Chinese Society for Agricultural Machinery*, 54(4), 428-438.

[21] Wen C., Zhang S., Xie B., Song Z., Li T., Jia F., & Han J., (2022). Design and verification innovative approach of dual-motor power coupling drive systems for electric tractors. *Energy*, 247, 123538.

[22] Yu Q., Li X., Pan X., He X., Fan W., Wang F., & Wang Y., (2023). Research on the Energy Control Optimized Strategy of Electric Tractor Composite Power Supply Based on Improved Genetic Algorithm (基于改进遗传算法的电动拖拉机复合电源优化控制策略研究). *Journal of Intelligent Agricultural Mechanization*, 4(3), 14–23.

[23] Zhang S., Xiong R., & Zhang C., (2015). *Pontryagin's minimum principle-based power management of a dual-motor-driven electric bus*. *Applied energy*, 159, 370-380.

[24] Zhang Y., Liu M., Xu W., & Xu L., (2023). Parameter Optimization of Electric Tractor Dual Motor Coupling Drive Based on DDPG Algorithm (基于 DDPG 算法的电动拖拉机双电机耦合传动参数优化). *Journal of Chinese Agricultural Mechanization*, 44(10), 129–136.

[25] Zhu Z., Zeng L., Chen L., Zou R., & Cai Y., (2022). Fuzzy Adaptive Energy Management Strategy for a Hybrid Agricultural Tractor Equipped with HMCVT. *Agriculture*, 12(12), 1986.

[26] Zhou H., Yu Z., Wu X., Fan Z., Yin X., & Zhou L., (2023). Dynamic programming improved online fuzzy power distribution in a demonstration fuel cell hybrid bus. *Energy*, 284, 128549.

MEASUREMENT OF THE PHYSICAL PARAMETERS OF PEANUT SEEDS AND CALIBRATION OF THE DISCRETE ELEMENT PARAMETERS
/
花生籽粒物理参数测定与离散元参数标定

Hongwei DIAO[1)], Wenlong YE[2)], Zhicheng ZHANG[1)], Xin LIU[1)], Zhihuan ZHAO[*1)], Xuying LI[*2)], Ji CUI[2)], Fandi ZENG[1)], Yinzeng LIU[1)]

[1)] Shandong Agriculture and Engineering University, College of Mechanical and Electronic Engineering, Jinan, China;
[2)] Inner Mongolia Agricultural University, College of Mechanical and Electrical Engineering, Hohhot, China.
Tel: +86 18447072749; E-mail addresses: zhaozhihuan@sdaeu.edu.cn; lixuy2000@imau.edu.cn
DOI: https://doi.org/10.35633/inmateh-72-39

Keywords: *peanut seeds, angle of repose, discrete element method, number of filled balls*

ABSTRACT

This study measured the intrinsic and contact parameters through physical experiments to improve the accuracy of discrete element simulation analysis of peanut seeds. Discrete element models for five different peanut seed filling ball numbers were established. The simulation parameters were calibrated through a combination of physical and simulation experiments. Firstly, the Plackett-Burman test was used to screen the significance of simulation parameters. Then, the steepest climbing test was conducted to determine the optimal range of significance parameters using the relative error between the simulated and the physical experimental as the evaluation index. Finally, a response surface experiment with three factors and three levels was conducted using the angle of repose as the response value. The static and rolling friction coefficients among peanut seeds were set as 0.43 and 0.50 separately, and the rolling coefficient between peanut seeds and steel plate was set as 0.12. During verification experiments, the simulated angle of repose was 25.18°, with a relative error of 2.42% compared to the physical angle of repose, further verifying the reliability of the simulation model. The research group used different numbers of filling balls with optimal parameters in the angle of repose experiment. Then they evaluated the simulation time and the error value of the angle of repose between the simulated and physical experiment. The optimal number of filled balls was the Sphere 1178. The research results indicate that discrete element model of peanut seeds and calibration parameters are reliable. Based on the results of this research, an intelligent peanut precision sowing machine can be developed.

摘要

为了提高花生籽粒离散元仿真分析过程中的仿真精度，该研究通过物理试验测定了花生籽粒的本征参数和接触参数，建立了五种不同填充球数的花生籽粒的离散元模型，通过物理试验与仿真试验相结合的方式对仿真参数进行了标定。首先，采用 Plackett–Burman 试验对仿真参数进行显著性筛选。然后，以仿真堆积角与物理试验堆积角之间的相对误差为评价指标，进行最陡爬坡试验，确定了显著性参数的最优取值范围。最后，以堆积角为响应值，进行了三因素三水平的响应面试验，得到最优参数组合为：花生籽粒间的静摩擦系数 0.43、花生籽粒间滚动摩擦系数 0.50、花生籽粒-钢板滚动摩擦系数 0.12。并进行验证试验，得出仿真堆积角为 25.18，与物理堆积角之间的相对误差为 2.42%，进一步验证了仿真模型的可靠性。以最优参数进行不同填充球数的堆积试验，以仿真堆积角与物理实验堆积角的误差值和仿真时间为评价指标，得到最佳填充球数为 1178。研究结果表明该花生籽粒离散元模型及标定参数可靠，可为智能花生精量播种机具的研制提供依据。

INTRODUCTION

Peanut is a kind of important economic and oil crops and it has been widely cultivated in many countries and regions *(Chen et al., 2020; Wang et al., 2021; Wang et al., 2018; Xu et al., 2023)*. Peanut seeds have an oil content of 44% to 56% and are rich in protein and various vitamins, with high nutritional value. The core component of a peanut precision seeder is the seeder, which directly affects its performance *(Ding et al., 2022; Zhang et al., 2023)*. The influence of the physical parameters and distribution of agricultural materials on particle flow was fully considered in discrete element analysis *(Hao et al., 2023; Hou et al., 2020; Peng et al., 2018)*. It is particularly suitable for studying nonlinear problems such as the motion laws and mechanical characteristics changes of peanut seeds during seeding.

Qian et al., (2023), used the discrete element method to model different varieties of peanut seeds and obtained the differences between different types of peanuts, as well as the effects of variety differences and seeder speed on the seeding process.

Zhang et al., (2023), designed a seed tray for an air suction drum type hole seeder and simulated the suction and primary seeding processes using the DEM-CFD gas-solid coupling calculation method. They analyzed the seed movement trajectory and seeding performance in the seed-carrying area. Based on the adhesive particle model, *Yu et al., (2020)*, used the discrete element method to model and calibrate the parameters of the seeds of medicinal herbs. The precision seeder of the seeds of medicinal herbs was validated using the pass rate, miss rate, and replay rate of the seeder as experimental indicators. *Zhang et al., (2022)*, calibrated the discrete element parameters of mung bean seeds. They conducted simulation experiments on the seeder's performance with the seeding shaft's rotation speed as the experimental factor. *Shi et al., (2019)*, used the discrete element method to calibrate the discrete element parameters of sesame seeds and conducted simulation experiments on irregular hole seeders and field experiments. *Zhu et al., (2019)*, built a discrete element simulation platform for a wide seedling belt wheat spreader. They used the coefficient of variation of wheat grain lateral uniformity as an indicator to simulate and optimize the design of the spring seed board for the wheat-wide seedling belt spreader. *Chen et al., (2022)*, established a simulation model of the seed tube body of a precision seeder based on the discrete element method. They conducted seed-guiding performance simulation experiments with factors such as operating speed and the inclination angle of the delivery section end. *Li et al., (2020)*, performed discrete element modeling and parameter calibration on cotton seeds, established a simulation model of a rotary hole precision seeder and obtained the effects of the motion parameters of the seed wheel and the speed of the seeder on the seeding performance of the seeder. Some scholars have studied the flow performance of seeds during the seeding process *(Lu et al., 1997; Vu-Quoc et al., 2000; Wang et al., 1999)*. *Zhang et al., (2023)*, established a compacted straw cube discrete element model that includes flexible straw's elastic, plastic, and viscous mechanical properties. *Bembenek et al.,(2022)* found a discrete element model for material compaction in a roller press. Compared with the finite element method, the model established by the discrete element method is more applicable.

This research group chose Yiyuan peanut seeds as the research object because it is widely planted in Yiyuan County, Zibo, Shandong Province, China. Five different peanut seed models with other filling ball numbers were established by using the discrete element method. Besides, the group calibrated the simulation parameters of peanut seeds utilizing a combination of simulation and physical experiments. The Plackett−Burman experiment, steepest climbing experiment, and response surface experiment were carried sequentially to determine the simulation parameters of the optimal filling ball number peanut seed model. This study aims to provide a basis for the development of intelligent peanut precision sowing machines.

MATERIALS AND METHODS

A five-point sampling method was used to sample Yiyuan peanuts in the peanut planting area of Yiyuan to establish a three-dimensional model of peanut seeds accurately. After shelling treatment, 200 peanut seeds were randomly selected for triaxial size measurement. The experimental equipment is set with a digital vernier caliper with an accuracy of 0.01 mm, and the three-axis dimensions (length *L* × Wide *B* × Thick *W*), as shown in Fig. 1. By using an electronic balance with an accuracy of 0.01 g, the mass of each peanut seed was measured. The volume of peanut seeds was measured with a cylinder, whose accuracy is 0.2 mL. The moisture content of peanut seeds was collected by using oven drying method. Take the average of the measurement results and the data is shown in Table 1.

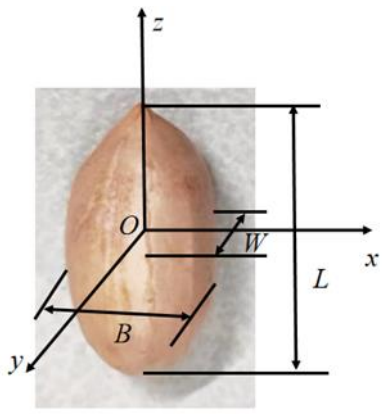

Fig. 1 - Three axis dimensions of the peanut seed

Table 1

Three axis dimensions of peanut seeds

Physical parameters	Value
Three axis dimensions (length *L* × Wide *B* × Thickness *W*)/mm	17.16×8.09×7.41
Mass/g	1.39
Density/(kg/cm^3)	1390
Moisture content/%	32.37

This study used a CNY-1 inclined plane instrument to measure the friction coefficient between peanut and peanut seeds (the steel plate). When calculating the static friction coefficient between peanut seeds, 30 were bonded to form a peanut seed plate Fig. (2a) and connected to the testing plane. The inclined plane meter was rotated until the peanut seeds were observed to slide. The angle on the digital inclinometer was recorded Fig. (2b), and the static friction coefficient between peanut seeds was calculated with Formula (1). When the peanut seeds start rolling, stop rotating and record the angle on the digital inclinometer. Formula (2) helped to calculate the rolling friction coefficient between the peanut seeds. Each experiment was repeated ten times, and the average value was taken as the final value. According to Formula (1), the static friction coefficient between peanut seeds is 0.39~0.61, and the static friction coefficient between peanut seeds and steel plate is 0.43~0.63. According to Formula (2), the rolling friction coefficient between peanut seeds is 0.42~0.60, and the rolling friction coefficient between peanut seeds and steel plate is 0.11~0.32.

$$\mu_1 = \tan\alpha_1 \quad (1)$$

In the Formula: μ_1 is the static friction coefficient, α_1 is the critical angle for the static friction coefficient, (°).

$$\mu_2 = \tan\alpha_2 \quad (2)$$

In the Formula: μ_2 is the static friction coefficient, α_2 is the critical angle for the static friction coefficient, (°).

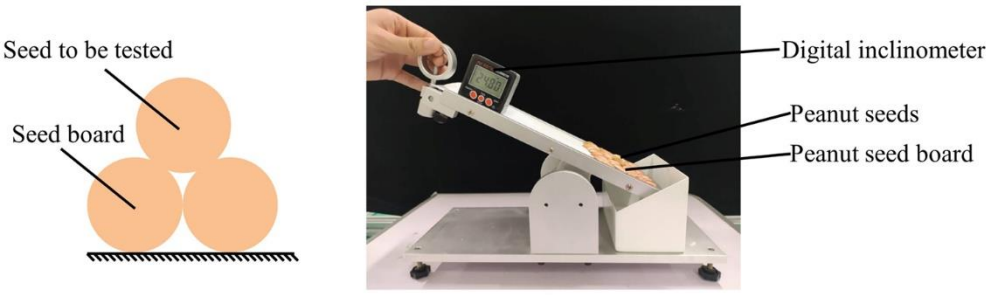

Fig. 2 - Sketch for measuring friction coefficient of peanut seeds
(a) Seed board; (b) Friction coefficient testing device

The angle of repose is an essential parameter for testing the accuracy of parameters. The angle of repose of peanut seeds was determined by the hollow cylinder method. During the experiment, a hollow cylinder with an inner diameter of 80 mm and a height of 150 mm was used. After all peanut seeds were utterly stationary on the bottom plate, a high-definition camera was used to take a frontal image of the seed pile. Fig. 3 is the sketch of angle of repose physical test. Matlab was used to grayscale and binarize seed stacking images, extract image boundary pixels, and fit boundary pixels. Through multiple repeated experiments, the average angle of repose of peanut seeds was obtained to be 24.57°.

Fig. 3 - Angle of repose physical test

There is no slip contact force among particles or between particles and surfaces. Mutual forces control the behavior between particles. Therefore, the Hertz-Mindlin (no slip) model *(Lei et al., 2023; Wang et al., 2023)* was chosen as the particle contact model using Altair EDEM 2022 Software, as shown in Fig. 4.

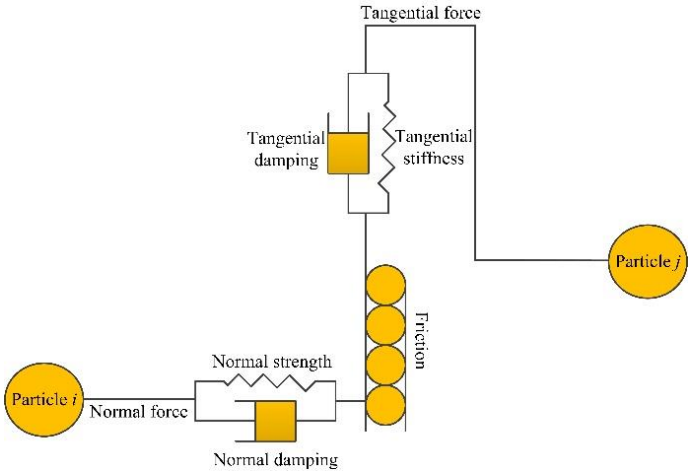

Fig. 4 - Particle to particle contact model

In the Formula, the particle dynamics equations define the translational and rotational motion of particles, which can be expressed as:

$$m_i \ddot{v} = m_i g + \sum_{j=1}^{n} F_n + F_n{}^d + F_t + F_t^d \tag{3}$$

In the Formula: m_i is the mass of particle *i*, $\ddot{v}$ is the acceleration of the particle center of mass, g is the acceleration of gravity, F_n, F_t are the normal force and tangential force, respectively, $F_n{}^d, F_t^d$ are the normal damping and tangential damping. The definition of normal force is as follows:

$$F_n = \frac{4}{3} E^* (R^*)^{\frac{1}{2}} \delta_n^{\frac{3}{2}} \tag{4}$$

In the Formula: E^* is the equivalent elastic modulus, R^* is the equivalent radius, and δ_n is the normal overlap.

$$F_n{}^d = -2\sqrt{\frac{5}{6}} \frac{\ln\gamma}{\sqrt{(\ln\gamma)^2 + \pi^2}} \sqrt{S_n m^*} v_n' \tag{5}$$

In the Formula: γ is the recovery coefficient, S_n is the normal stiffness, m^* is the equivalent mass, and v_n' is the relative normal velocity.

$$F_t = -S_n \delta_t \tag{6}$$

In the Formula: δ_t is the tangential overlap.

$$F_t{}^d = -2\sqrt{\frac{5}{6}} \frac{\ln\gamma}{\sqrt{(\ln\gamma)^2 + \pi^2}} \sqrt{S_t m^*} v_t' \tag{7}$$

In the Formula: S_t is the tangential stiffness, v_t' is the relative tangential velocity.

$$I_i \dot{\omega} = \sum_{j=1}^{n} T_t + T_r \tag{8}$$

$$T_t = R_i (F_t + F_t^d) \tag{9}$$

In the Formula: I_i is the moment of inertia of particle *i*, $\dot{\omega}$ is the angular acceleration, T_t is the tangential moment, T_r is the rolling friction torque, and R_i is the distance from the center of mass *i* to the contact point.

$$T_r = -\beta R_r |F_n| \frac{\omega'}{|\omega'|} \tag{10}$$

In the Formula: β is the dynamic friction coefficient, R_r is the effective rolling contact radius, and ω' is the relative angular velocity of two contact particles.

This research established a geometric model of peanut seeds by using 3D modeling software, and then converted the peanut seed model into. * stp format. Next, the files were imported into Altair EDEM 2022. To make the surface of peanut seeds smoother, multiple sets of particles were simulated and modeled, with the number of filled spheres set to five types: Sphere 368, Sphere 607, Sphere 1176, Sphere 2823, and Sphere 9772, as shown in Fig. 5.

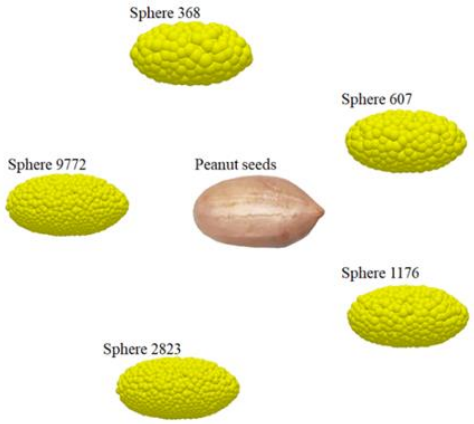

Fig. 5 - Peanut grain combination model

The Hertz-Mindlin (no slip) model was selected for peanut seeds in the simulation experiment. The research group established a virtual particle factory above the hollow cylinder to generate peanut seeds. The seed particles were generated dynamically at a rate of 2000/s, resulting in 450 peanuts. To consider both the reliability and efficiency of the simulation results, the size of the generated seed particles was fixed. The total simulation time is 2 seconds, the Rayleigh time step is 25%, the data storage interval is 0.01 seconds, and the grid size is three times the minimum particle radius. The simulation process is shown in Fig. 6.

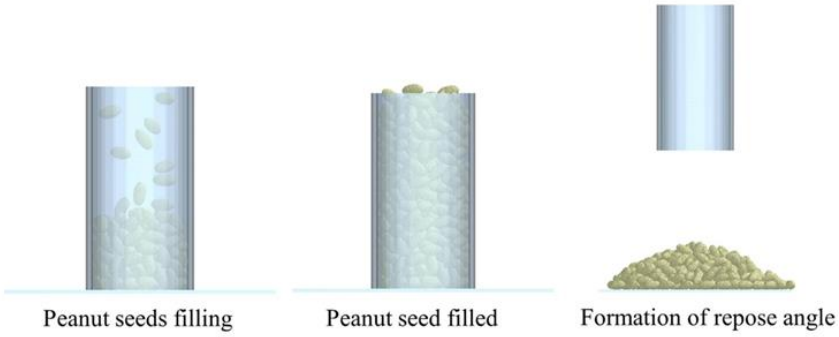

Fig. 6 - Discrete element simulation of the hollow cylinder method

There are numerous discrete element simulation parameters for peanut seeds. To accurately identify parameters and ranges with significant effects in simulation parameters, take the peanut grain model of the Sphere 607 as an example. The significance of each parameter was obtained using the Plackett-Burman test. The optimum of significant influence parameters was determined by the steepest climb test. The optimal parameter combination was determined by the Box-Behnken test. The experimental results were performed response surface analysis, using the angle of repose obtained from physical experiments as the experimental indicator to determine the optimal parameter combination.

The parameter range of the Plackett-Burman test is based on the results of physical experiments, with the simulated angle of repose of peanut seeds as the response value. The Plackett-Burman test is used to screen out parameters that have a significant impact on the response value. The range of values for the experimental parameters, including Poisson's ratio and shear modulus of peanut seeds, collision recovery coefficient between peanut seeds, and collision recovery coefficient between peanut seeds and steel plates, were determined by referring to relevant literature *(Hao et al., 2021; Lu et al., 2016; Wan et al., 2022; Wang. 2017; Zhang et al., 2018)*. The remaining parameters were measured through physical experiments. Encode the minimum and maximum values of the experimental parameters in Table 2 as -1 and+1, respectively. The encoded value of -1 represents the low level of the parameter, and +1 represents the high level of the parameter. After each set of simulation experiments, the angle of repose of peanut seed was measured by using the same method as measuring the angle of repose in physical experiments.

Table 2

Plackett-Burman test parameters table

No.	Test parameters	Levels		
		Low(-1)	Middle (0)	High(+1)
A	Peanut seeds Poisson's ratio	0.3	0.4	0.5
B	Shear modulus of peanut seeds/MPa	5.0	6.0	7.0
C	The collision recovery coefficient between peanut seeds	0.45	0.6	0.75
D	Peanut seeds steel plate collision recovery coefficient	0.470	0.485	0.500
E	Static friction coefficient between peanut seeds	0.39	0.5	0.61
F	Peanut seeds steel plate static friction coefficient	0.43	0.53	0.63
G	Rolling friction coefficient between peanut seeds	0.42	0.51	0.6
H	Rolling friction coefficient between peanut seeds and steel plate	0.11	0.22	0.32

Based on the Plackett-Burman experiment, perform the steepest climb test on the selected significance parameters. The relative error between the simulation experiment angle of repose and the physical experiment angle of repose was used as the evaluation index, the optimal range of simulation experiment parameters was determined. Other non-significant parameters were measured by using physical experiments to determine the average values.

In the steepest climbing test of peanut seeds, the 3rd level was taken as the center point (0), while the 2nd and 4th levels were taken as the low level (-1) and high level (1), respectively. The angle of repose was used as the response value and a Box-Behnken experiment with significance parameters was conducted to determine the optimal parameters for peanut seeds. The horizontal coding of peanut seeds is shown in Table 3.

Table 3

Levels coding table of factor

Levels	Parameters		
	E	***G***	***H***
-1	0.39	0.42	0.11
0	0.45	0.47	0.17
+1	0.5	0.51	0.22

In order to verify the accuracy of the contact parameters obtained from calibration experiments, it is necessary to further analyze the impact of different particle filling numbers on simulation accuracy (angle of repose, simulation time) and use the relative error between simulation experiment angle of repose and physical experiment angle of repose as the evaluation index to determine the optimal filling number.

RESULTS

Due to the multiple influencing factors of the angle of repose test, it is necessary to determine the significance of each factor's impact on the angle of repose test through the Plackett-Burman test. This research used the Plackett-Burman module to screen the contact parameters of peanut seeds (collision recovery coefficient between peanut seeds, static friction coefficient, rolling friction coefficient, collision recovery coefficient between peanut seeds and steel plate, static friction coefficient, rolling friction coefficient, Poisson's ratio and density of peanut seeds) based on the response value of peanut seed stacking angle. Each parameter is set at three levels, high (1) and low (-1), for 12 experiments. Each experiment was repeated three times, and the average value was taken. The experimental plan and results are shown in Table 4.

Table 4

Plackett−Burman trial protocol and results

No.	*A*	*B*	*C*	*D*	*E*	*F*	*G*	*H*	Angle of repose *θ* / °
1	-1	-1	-1	-1	-1	-1	-1	-1	24.47
2	-1	-1	-1	1	-1	1	1	-1	25.32
3	1	-1	-1	-1	1	-1	1	1	29.58
4	1	1	-1	1	1	1	-1	-1	28.54
5	-1	1	1	1	-1	-1	-1	1	26.51
6	1	-1	1	1	1	-1	-1	-1	26.83
7	1	1	-1	-1	-1	1	-1	1	25.04
8	1	-1	1	1	-1	1	1	1	27.11

No.	A	B	C	D	E	F	G	H	Angle of repose θ / °
9	-1	1	1	-1	1	1	1	-1	28.15
10	-1	1	-1	1	1	-1	1	1	27.69
11	1	1	1	-1	-1	-1	1	-1	24.62
12	-1	-1	1	-1	1	1	-1	1	27.78

Table 5

Significance analysis of Plackett-Burman test parameters

Parameter	Effect	Mean square sum	Influence ratio / %	Significance order
A	0.32	0.30	1.00	6
B	-0.11	0.034	0.11	7
C	0.077	0.018	0.059	8
D	0.41	0.50	1.68	4
E	2.60	20.28	67.61	1
F	0.36	0.38	1.27	5
G	0.53	0.85	2.84	3
H	0.95	2.69	8.96	2

According to Table 5, after conducting significance screening through the Plackett -Burman test, it can be concluded that E, G, and H have a significant impact on the peanut grain stacking angle test, with the significance order being E>H>G, A, B, C, D, and F have a relatively low contribution rate to the peanut grain angle of repose experiment, so E, G, and H are selected as the experimental factors for the steepest climbing experiment.

After completing the Plackett-Burman test screening, the steepest climbing test was conducted, and the test results are shown in Table 6. As E, G, and H increase, the stacking angle of peanut seeds in the simulation experiment gradually increases. Comparing the simulation stacking test results with the physical ones, the error shows a trend of first decreasing and then increasing. Due to the relative minimum mistake in Experiment 2, Experiment 2 was chosen as the center level, and Experiment 1 and Experiment 3 are considered low and high levels, respectively.

Table 6

Results of steepest climbing test

No.	E	G	H	Angle of repose θ/ °	Relative error S / %
1	0.39	0.42	0.11	23.15	5.78
2	0.45	0.47	0.17	25.42	3.46
3	0.50	0.51	0.22	27.53	10.75
4	0.56	0.56	0.27	28.59	14.06
5	0.61	0.60	0.32	30.48	19.39

The static friction coefficient E, rolling friction coefficient G, and rolling friction coefficient between peanut seeds and steel plate H were used as experimental factors, and the simulated angle of repose was used as an indicator to conduct a response surface experiment with three factors and three levels. The investigation was performed 17 times, and the design and results of the response surface experiment are shown in Table 7.

Table 7

Test design and results

No.	E	F	G	Angle of repose θ / °
1	-1	0	1	32.47
2	0	-1	-1	21.15
3	-1	0	-1	27.22
4	0	0	0	29.13
5	0	-1	1	25.36
6	0	0	0	27.84
7	0	0	0	28.92
8	1	0	-1	26.88
9	0	1	-1	24.85
10	-1	1	0	31.23
11	-1	-1	0	33.95

No.	*E*	*F*	*G*	Angle of repose *θ* / °
12	1	-1	0	28.11
13	0	1	1	26.27
14	0	0	0	29.74
15	1	0	1	27.86
16	1	-1	0	31.41
17	0	0	0	29.89

Table 8

Analysis of variance of the angle of repose

Source	Freedom	Mean square	*F* value	*P* value
Model	9	16.42	23.98	0.0002**
E	1	14.07	20.55	0.0027**
G	1	3.37	4.92	0.0621
H	1	17.58	25.68	0.0015**
EG	1	9.06	13.23	0.0083**
EH	1	4.56	6.66	0.0365*
GH	1	1.95	2.84	0.1357
E^2	1	41.40	60.46	0.0001**
G^2	1	4.77	6.97	0.0334*
H^2	1	55.54	81.12	<0.0001**
Residual	7	0.68		
Lack of fit	3	0.71	1.07	0.4545
Pure error	4	0.66		
Cor Total	16			

*Notes: * indicates significant (P<0.05), ** indicates highly significant (P<0.01)*

The analysis of variance and significance of the experimental results is shown in Table 8, and the determination coefficient R^2 is 0.9686. The variance model is close to 1, indicating that the regression model is highly significant, and the loss of fit term P is greater than 0.05. The coefficient of variation is 2.92%, meaning that the experiment has good reliability. The binary regression equation is:

$$\theta = 29.10 - 1.33E + 0.65G + 1.48H + 1.50EG - 1.07EH - 0.70GH + 3.14E^2 - 1.06G^2 - 3.63H^2 \quad (11)$$

The optimal value parameters were found by optimizing Equation (11) with the physical experiment angle of repose as the objective. The static friction coefficient E between peanut seeds, rolling friction coefficient G between peanut seeds, and rolling friction coefficient H between peanut seeds and steel plate were 0.43, 0.50, and 0.12, respectively. By reintroducing the parameters into the discrete element method for repose angle simulation experiments, it was found that the simulated angle of repose was 25.18°, with a relative error of 2.42% compared to the physical angle of repose test. The relative error is relatively small, and the experiment shows that the established peanut seeds angle of repose and regression model are better.

Angle of repose simulation experiments were carried out for five models with Sphere 368, Sphere 607, Sphere 1176, Sphere 2823 and Sphere 9772 filled balls based on the optimal value parameters. Compare the simulation test results with the physical angle of repose and obtain the relative error. The test results are shown in Table 9.

Table 9

Simulation test results of angle of repose with different ball numbers

Number of balls / piece	Simulation time / min	Simulated angle of repose *θ* / °	Relative error S_1 / %
Sphere 368	30	27.08	10.21
Sphere 607	50	26.15	6.43
Sphere 1176	80	25.43	3.50
Sphere 2823	260	25.11	2.20
Sphere 9772	530	24.87	1.22

As the number of the balls increases, the relative error between simulated and physical angles of repose gradually decreases, and the simulation time gradually increases. When the number of hops is between Sphere 607 and Sphere 1176, the angle of repose error is 6.43% and 3.50%, respectively. The accuracy of the angle of repose slowly decreases with the number of balls, and the simulation time gradually increases with the number of hops. Therefore, after careful consideration, it is more reasonable to choose a model with Sphere 1176 balls as the simulation model.

CONCLUSIONS

1) The basic physical parameters of peanut seeds, including external dimensions, mass, density, and moisture content, were determined through physical experiments. The static friction coefficient and rolling friction coefficient between peanut seeds and steel plate were measured using the CNY-1 inclined plane instrument. From this research, several conclusions can be gotten.

2) Based on the intrinsic and contact parameters of peanut seeds determined by physical experiments and references to relevant literature, the Plackett-Burman experiment was conducted to screen out parameters that significantly impact the angle of repose. Conduct the steepest climbing test using the relative error between the simulated angle of repose and the physical testing angle of repose as the evaluation index. The optimal range of significance parameters has been determined: the static friction coefficient between peanut seeds is 0.39~0.61, the rolling friction coefficient between peanut seeds is 0.42~0.60, and the rolling friction coefficient between peanut seeds and steel plate is 0.11~0.32. Then, the response surface experiment was conducted with the angle of repose as the response value. The experimental results showed the optimal parameter combination: the static friction coefficient between peanut seeds was 0.43, the rolling friction coefficient between peanut seeds was 0.50, and the rolling friction coefficient between peanut seeds and steel plate was 0.12. Besides, by using the optimal parameter combination as the experimental parameters, simulation angle of repose tests were conducted on five models with a filling ball number of the Sphere 368, Sphere 607, Sphere 1176, Sphere 2823, and Sphere 9772, and the model with a filling ball number of the Sphere 1176 was determined as the optimal simulation model.

REFERENCES

[1] Bembenek M., Buczak M. &Baiul K. (2022). Modelling of the Fine-Grained Materials Briquetting Process in a Roller Press with the Discrete Element Method. *Materials*, 15(14), 4901.

[2] Chen Y.L., Han J., Lan Y. B., Zhang M., Jin Y. C., Zhang Z. &Wang W. J. (2022). Design and experiment of the combined seed guiding tube for precision metering device. *Transactions of the Chinese Society of Agricultural Engineering*, 38(24), 14-24.

[3] Chen Y. Q., Hu Z. C., Wang S. Y., Cao M. Z., Xu H. B., Wang G. P. &Yan J. C. (2020). Design and experiments of pickup device of peanut harvester after cutting peanut straws. *Transactions of the Chinese Society of Agricultural Engineering*, 36(16), 1-8.

[4] Ding L., Dou Y. F., Wang W.Z., Xu Y.F., He X. & Qu Z. (2022). Design and Experiment of Seed Metering Device with Combination Hole and Inner Filling for Cyperus esculentus. *Transactions of the Chinese society for agricultural machinery*, 53(12), 100-115.

[5] Hao J.J., Qin J.H., Yang S.H., Ai Q.H. & Ma Z.K. (2023). Design and experiments of a precision sowing unit with the spoon clip for single peanut seed planting in plot. *Transactions of the Chinese Society of Agricultural Engineering*, 39(03), 33-41.

[6] Hao J.J., Wei W.B., Huang P.C., Qin J.H. & Zhao J.G. (2021). Calibration and experimental verification of discrete element parameters of oil sunflower seeds. *Transactions of the Chinese Society of Agricultural Engineering*, 37(12), 36-44.

[7] Hou Z. F., Dai N.Z., Chen Z., Qiu Y. & Zhang X. W. (2020). Measurement and calibration of physical property parameters for Agropyron seeds in a discrete element simulation. *Transactions of the Chinese Society of Agricultural Engineering*, 36(24), 46-54.

[8] Lei X.L., Wu W.C., Deng X., Li T., Liu H.N., Guo J.Y., Li J., Zhu P.X. & Yang K. (2023). Determination of Material and Interaction Properties of Granular Fertilizer Particles Using DEM Simulation and Bench Testing. *Agriculture*, 13(9), 1704.

[9] Li J.J., Zhang H.P., Bi X.S., Wang J., Hu B. & Li S.Z. (2020). Simulation analysis and test on the filling performance of rotary type-hole precision seed-metering device for cotton. *Transactions of the Chinese Society of Agricultural Engineering*, 36(05), 38-49.

[10] Lu Z., Negi S. & Jofriet J. (1997). A numerical model for flow of granular materials in silos. Part 1: model development. *Journal of Agricultural Engineering Research*, 68(3), 223-229.

[11] Lu Y.G., Wu N., Wang B., Yu Z.Y., Lin D.Z. & Hu Z.C. (2016). Measurement and analysis of peanuts restitution coefficient in point-to-plate collision model. *Journal of China Agricultural University*, 21(08), 111-118.

[12] Peanut Picking and Harvesting Machine. *Transactions of the Chinese society for agricultural machinery*, 52(01), 109-118+198.

[13] Peng F., Wang H.Y., Fang F. & Liu Y.D. (2018). Calibration of Discrete Element Model Parameters for Pellet Feed Based on Injected Section Method. *Transactions of the chinese society for agricultural machinery*, 49(04), 140-147.
[14] Qian K., Liu L., Liu D.Q., Sun Q.T., Wang D.W., Chen K. Y., Wang J.W. & Li X. J. (2023). Simulation and experiment of seed filling characteristics of different peanut varieties based on EDEM. *Agricultural Engineering*, 13(05), 97-104.
[15] Shi L.R., Ma Z.T., Zhao W.Y., Yang X.P., Sun B.G. &Zhang J.P. (2019). Calibration of simulation parameters of flaxed seeds using discrete element method and verification of seed-metering test. *Transactions of the Chinese Society of Agricultural Engineering*, 35(20), 25-33.
[16] Vu-Quoc L., Zhang X. &Walton O.R. (2000). A 3-D discrete-element method for dry granular flows of ellipsoidal particles. *Computer methods in applied mechanics and engineering*, 187(3-4), 483-528.
[17] Wan X.Y., Liao Q.X., Jiang Y.J., Shan Y.Y., Zhou Y. & Liao Y.T. (2022). Discrete element simulation and experiment of mechanized harvesting and chopping process of forage rape. *Journal of Jilin University (Engineering Edition)*, 52(11), 2735-2745.
[18] Wang B.K., Hu Z.C, Cao M.Z, Zhang P., Yu Z.Y. & Zhang C. (2021). Design and test of axial-flow peanut picking and harvesting machine. *Trans. CSAM*, 52(98), 109-118.
[19] Wang C.Y., Wang C.F. & Sheng J. (1999). A packing generation scheme for the granular assemblies with 3D ellipsoidal particles. *International Journal for Numerical and Analytical Methods in Geomechanics*, 23(8), 815-828.
[20] Wang J.N., Liu M.J., Hu Z.C., Xie H.X., Peng B.L., Yan J.C. &Chen Y.Q. (2018). Optimization of key working parameters of belt separator for peanut seeds. *Transactions of the Chinese Society of Agricultural Engineering*, 34(23), 33-41.
[21] Wang Z.P., Zhu T., Wang Y.Z., Ma F., Zhao C.Y. & Li X. (2023). Optimal discrete element parameters for black soil based on Multi-objective total evaluation normalized-response surface method. *Processes*, 11(8), 2422.
[22] Wang X.M. (2017). *A Multi-sphere Based Modelling Method for Maize Grain Assemblies* [Master dissertation], Jilin University.
[23] Xu H.B., Zhang P., Zhang Y.H., Wang S.Y., Yu Z.Y. & Gu F.W. (2023). Design and Experiment of Peanut Pod-picking and Conveying Device of Multistage Tangential Flow Type Peanut Combine. *Transactions of the chinese society for agricultural machinery*, 54(S2), 52-60.
[24] Yu Q.X., Liu Y., Chen X.B., Sun K. & Lai Q.H. (2020). Calibration and Experiment of Simulation Parameters for Panax notoginseng Seeds Based on DEM. *Transactions of the chinese society for agricultural machinery*, 51(02), 123-132.
[25] Zhang X.J., Chen J.P., Shi Z.L., Wang M.J., Fu H. & Wu H.F. (2023). Simulation and Experiment of Seed Taking Performance of Swing-clamp Type Maize Precision Seed-metering Device. *Transactions of the chinese society for agricultural machinery*, 54(04), 38-50.
[26] Zhang C.Y., Kang J.M., Zhang N.N., Peng Q.J., Zhang H. & Wang X.Y. (2023). Design and experiment of seed separation tray of air-suction roller dibbler for peanut. *Transactions of the Chinese society for agricultural machinery*, 54(06), 28-37.
[27] Zhang S.W., Zhang R.Y., Chen T.Y., Fu J. & Yuan H.F. (2022). Calibration of Simulation Parameters of Mung Bean Seeds Using Discrete Element Method and Verification of Seed-metering Test. *Transactions of the Chinese society for agricultural machinery*, 53(03), 71-79.
[28] Zhu Q.Z., Wu G.W., Chen L.P., Zhao C.J., Meng Z.J. & Shi J.T. (2019). Structural design and optimization of seed separated plate of wheat wide-boundary sowing device. *Transactions of the Chinese Society of Agricultural Engineering*, 35(01), 1-11.
[29] Zhang Z.Y., Mei F.W., Xiao P.J., Zhao W. & Zhu X.H. (2023). Discrete element modelling and simulation parameters calibration for the compacted straw cube. *Biosystems Engineering*, 230(301-312.
[30] Zhang T., Liu F., Zhao M.Q., Ma Q., Wang W., Fan Q. &Yan P. (2018). Determination of corn stalk contact parameters and calibration of DEM simulation. Journal of China Agricultural University, 23(04), 120-127.

FORCE ANALYSIS OF A ROTARY TILLER WITH A VERTICAL ROTATION AXIS

ՈՒՂՂԱՁԻԳ ՊՏՏՄԱՆ ԱՌԱՆՑՔՈՎ ՀՈՂԱՄՇԱԿ ՖՐԵԶԻ ՈՒԺԱՅԻՆ ՎԵՐԼՈՒԾՈՒԹՅՈՒՆ

Arshaluys TARVERDYAN, **Artur ALTUNYAN*)**, **Albert GRIGORYAN**
Scientific Research Institute for Agricultural Mechanization and Automation, Armenian National Agrarian University, Yerevan, Armenia
Tel: +37455327325; E-mail: arturaltunyan@gmail.com
Corresponding author: Artur Altunyan
DOI: https://doi.org/10.35633/inmateh-72-40

Keywords: *rotary tiller, driving mechanism, blade trajectory, kinematic and dynamic parameters*

ABSTRACT

The article considers the issue of updating the machines designed for the cultivation of near-trunk and near-vine spaces. From the prospect of complete satisfaction of the agrotechnological and technical requirements of the mentioned machines, the rotary tillers with vertical rotation axis are preferable, which, however, need to get structurally developed. On this account, it is recommended to select planetary mechanism with external gear as a driving mechanism, which enables to ensure high rotation numbers of the tiller in case of relatively low rotation numbers of the rotor. The kinematic analysis of the driving mechanisms has been conducted, analytical expressions have been derived, which enable to determine the trajectory, speeds and accelerations of the tiller's blades depending on the frequency of rotor's rotation and the gear ratio of the mechanism. Based on the analytical expressions resulted from the kinematic research of the mechanism force analysis of the rotary tiller has been conducted. The estimated expressions of the general resistance moment value applied to the shaft of the moving rotor of the machine, as well as the value of resistance moments generated on the planet gear (satellite) rotors have been derived, which enable to identify the optimal kinematic and geometric parameters for the mechanism and rotary through the theoretical calculation method ensuring the optimal values of traction resistance force and other force factors in conditions of the stated working rules.

ԱՄՓՈՓԱԳԻՐ

Հոդվածը նվիրված է պտղատու և խաղողի այգիների մերձբնային և մերձվազային տարածքների մշակման մեքենաների կատարելագործման հիմնախնդրին: Այդ մեքենաներին ներկայացվող ագրոտեխնոլոգիական և տեխնիկական պահանջների լիակատար բավարարման տեսանկյունից, գերադասելի են ուղղաձիգ պտտման առանցքով հողամշակ ֆրեզները, որոնք, սակայն կառուցվածքային կատարելագործման կարիք ունեն: Այդ նկատառումներից ելնելով առաջարկվել է հողամշակ ֆրեզի համար, որպես հաղորդակ ընտրել արտաքին կառչմամբ պլանետարային մեխանիզմ, որը հնարավորություն է տալիս ռոտորի համեմատաբար փոքր պտուտաթվերի դեպքում ապահովել ֆրեզի մեծ պտուտաթվեր: Կատարվել է հաղորդակային մեխանիզմի կինեմատիկական վերլուծություն, ստացվել են անալիտիկ արտահայտություններ, որոնք հնարավորություն են տալիս որոշելու ֆրեզի դանակների հետագիծը, արագությունները և արագացումները կախված ռոտորի պտտման հաճախությունից և մեխանիզմի փոխանցման թվից: Մեխանիզմի կինեմատիկական հետազոտության արդյունքում ստացված անալիտիկ արտահայտությունների հիման վրա կատարվել է հողամշակ ֆրեզի ուժային վերլուծություն: Ստացվել են ինչպես սատելիտ-ֆրեզների վրա առաջացող դիմադրության մոմենտների, այնպես էլ մեքենայի տարիչ-ռոտորի լիսեռին կիրառվող ընդհանուր դիմադրության մոմենտի մեծության հաշվարկային արտահայտություններ, որոնք հնարավորություն են տալիս տեսական հաշվարկային եղանակով սահմանելու մեխանիզմի, ինչպես նաև ֆրեզի կինեմատիկական ու երկրաչափական օպտիմալ պարամետրերը՝ ապահովելով քարշային դիմադրության ուժի և այլ ուժային գործոնների օպտիմալ արժեքներ՝ սահմանված բանելակարգի պայմաններում:

INTRODUCTION

Cultivation of inter-row and inter-trunk spaces is very important from the prospect of mechanization of agro-technical activities taken for the orchards and vineyards treatment. By its specific volume it takes up 40% of the implemented overall activities.

The mentioned works are of priority activities among the agro-technical requirements, since due to their accurate and timely implementation soil moisture, thermal and air regimes are ensured, its physico-mechanical and chemical properties get improved, biological processes in plants and soil get activated, efficient weed and pest control is carried out and last, but not the least, the orchard yield capacity and quality is increased *(Monaenkov K.A., 2017; Zhilitsky Ya. Z. Gerasimov N.I., 1973)*.

From technical standpoint, cultivation of inter-trunk and near-trunk spaces is related to a number of difficulties *(Gerasimov N.I., 1979; Dmitriy Khort et al., 2020)*, particularly the centrifugal installation of the tree inter-trunk and near-trunk cultivation device against the tractor's longitudinal axis, the periodic changes of longitudinal and latitudinal components in soil resistance during the cultivation process, especially under soil and relief conditions of orchards and vineyards of the Republic of Armenia, entail to instability of tractor's operation, which in its turn causes breakdown in technological procedures. And this ends up with either uncultivated area or tree trunk damage.

The above stated circumstances indicate that when developing such kind of machines all agro-technical, technological and technical factors and requirements should be taken into account.

The operational practice of such machines has enabled to develop the main agrotechnical requirements and it has been figured out that the machines with active working parts are more effective *(Gerasimov N.I., 1979; Parkhomenko G.G., 2012; Matin M.A. et al., 2014, 2015)*. They are mostly rotary tillers with horizontal or vertical rotation axes and with mechanical or hydraulic gears *(Panov I.M., 1963; Tarverdyan A.P. et al., 2017; Dmitriy Khort et al., 2020)*.

Structural peculiarities of the rotary tillers with vertical rotation axis enable to maximally adjust the machine to the cultivation conditions of the trees inter-trunk spaces ensuring the observance of agro-technical requirements. The remarkable advantages of the machines belonging to this category are reported in multiple research works, nevertheless, the operational practice of the tillers with vertical axis and the analysis of the literature data show that they are not void of shortcomings either *(Panov I.M., 1963; Byshov N.V., 2017; Chudak S.V., 1975; Mosatovskiy V.B., 1980)*. This made us consider the rotary tiller with vertical rotation axis as the research object.

Considering that rotary tillers with vertical axis have more perspective in view of updating and technical-technological improvements, long-term efforts have been exerted to study the operational indices of the existing tillers, to analyze the literature sources and data and to disclose their shortcomings *(Tarverdyan A.P. et al., 2017; Matin M.A. et al., 2014; Yiwen Tarverdyan A.P. et al, 2022)*.

Taking into account the circumstance that the operational reliability of the existing machines is rather low, particularly in the soil types containing huge amount of rocks and ballast, such as most horticultural areas of the Republic of Armenia, an attempt has been made to develop a rotary tiller with vertical rotation axis, possibly free from the above mentioned flaws, for the cultivation of inter-tree, inter-trunk and inter-vine spaces in orchards and vineyards *(Tarverdyan A.P. et al, 2020; Tarverdyan A.P. et al, 2022; Tarverdyan A.P. et al, 2024).*

The efforts, aimed at the solution of the current problem through the optimization of the blade form and profile in the existing rotary tillers with vertical axis, haven't provided the expected outcomes *(Byshov N.V., 2017; Mosatovskiy V.B., 1980; Yiwen Yuan et al., 2023)*. Thus, the only way of problem solving is to make fundamental changes in the tiller's structure.

The aim of the current work is to identify the kinematic and force descriptors of the active working parts driven through the structurally new planetary mechanism via analysis and theoretical research, to determine the effect of the main factors on such technically vital parameters, as the values of the main moment and main vector of resistance forces of the tiller's moving shaft in order to set up the optimal working and structural parameters.

MATERIALS AND METHODS

Based on the results of previous research *(Matin M.A. et al., 2015; Tarverdyan A.P. et al., 2019; Tarverdyan A.P. et al., 2017; Iman Ahmadi, 2017)* it was initiated to develop a gear for a tiller with vertical axis, which would be able to ensure high rotation numbers (200 -250 rpm) of the working tiller in case of rotor's relatively lower rotation numbers (e.g. 50-80 rpm); as a matter of fact, it is a planetary mechanism with external gear and with a fixed sun gear (Figure 1).

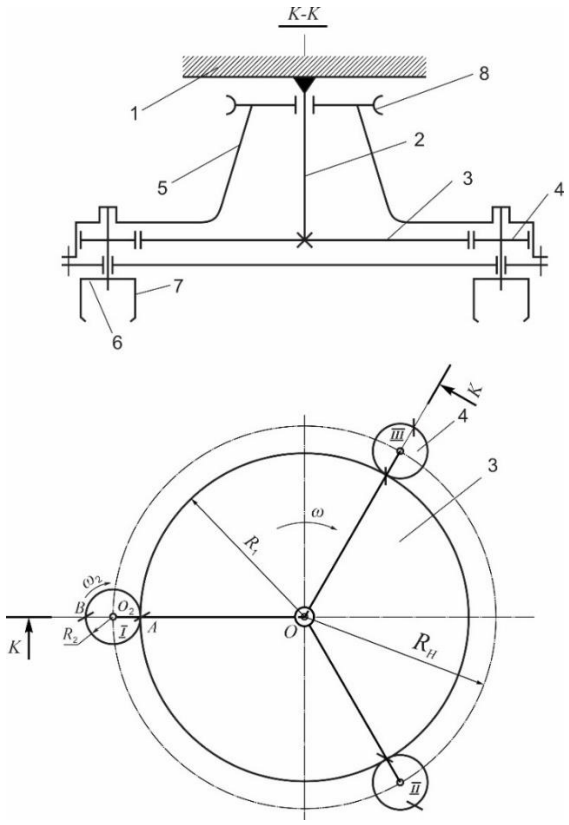

Fig. 1 - The basic diagram of the rotary tiller with planetary gear designed for the cultivation of inter-trunk and near-trunk spaces in orchards and vineyards

The rotary tiller with planetary gear and vertical rotation axis designed for the cultivation of inter-trunk and near-vine spaces of orchards and vineyards consists of a fixed sun gear (3), mounted to the support (2) attached to the rotor's frame (5), planet gears (4) rolled thereto, the rotation axis of which is installed in the grooves of rotor housing/casing. The tillers discs (6) are rigidly attached to the free ends of the rotation axes of the planet gears (4), on which the tiller's blades (7) are mounted in a symmetrical pattern.

The rotor (5) of the tilling machine receives the rotational movement from the hydraulic motor or through the chain transmission (8). The rotational motion is transmitted from the power take-off shaft of the tractor or hydraulic motor to the rotor of the rotary tiller, which in this case acts as a driver of planetary mechanism; due to the rotor's rotation the planet gears (4) roll over the ring belt of the fixed sun gear (3) with the multiplied angular velocity of the gear ratio of the mechanism. In terms of qualitative evaluation, the selected mechanism enables to solve the raised problem: to get the large angular, and hence, linear speeds/velocities of the rotary tillers (working parts) with small diameter in case of relatively small rotation numbers of the rotor.

In the discussed work, per the goals and objectives set up, the trajectories of the tillers' blades, the relation between the geometric and kinematic parameters is of primary interest. To reveal the above discussed questions, let's consider the trajectory of any blade in the tiller, mounted to the axis of planetary mechanism planet gear (4) with the account of forward movement of the machine. The calculation scheme of the problem is presented in Figure 2.

It is known that due to the driver's rotation the fixed point of the planet gear circumference of the planetary mechanism with external gear draws a smooth curve – epicycloid. Moreover, depending on the relationship of the fixed sun gear (R_1) and planet gear (satellite) (R_2) radii, the epicycloidal shape and number of arcs are different *(Ossetsky V.M., 1977)*.

In the discussed problem the epicycloid shape is important when the fixed sun gear (3) makes a forward movement with a constant speed, since in that case epicycloid is manifested as trajectories of the tiller's (6) blades (7), which enable the determination of optimal geometric and kinematic parameters of the developed rotary tiller.

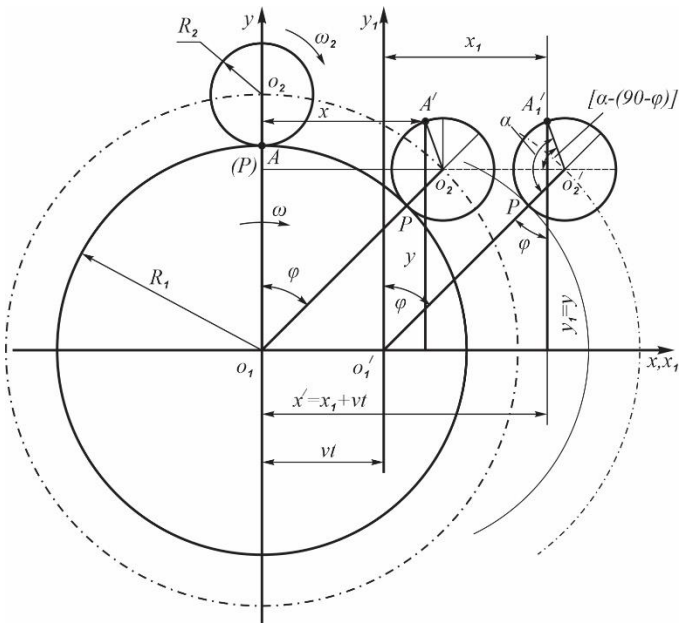

Fig. 2 - The scheme of deriving equations of blade motion in the rotary tiller with planetary driving mechanism

Let's align the initial coordinates point with the center of sun gear (O_1) and assume that in the initial position the center of planet gear (O_2) is on the y axis. O_1O_2 driver gets a rotational motion with ω angular velocity, whereas the planet gear will get a rotational motion with ω_2 angular velocity.

In case of the fixed sun gear, at the *t* moment, when the driver (O_1O_2) rotated with φ angle, the friction A point of sun gear and planet gear would accept $A^{/}$ position, but according to the stated term, the sun gear conducts a forward movement with V constant velocity, hence, A point will take on $A^{//}$ position, since it also shifts through the direction of X axis with V_t value.

The equation of movement of any fixed A point of the planet gear or tiller's blade with parametric description will look as follows (according to the scheme of figure 2):

$$\begin{cases} x = V \cdot t + (R_1 + R_2)sin\varphi - R_2 sin\left(\frac{R_1+R_2}{R_2} \cdot \varphi\right) \\ y = (R_1 + R_2)cos\varphi - R_2 cos\left(\frac{R_1+R_2}{R_2} \cdot \varphi\right) \end{cases} \quad (1)$$

where R_1 is the radius of relatively fixed sun gear, [m], R_2 is the planet gear radius, [m], $(R_1 + R_2 = R_H)$ is the radius of planetary mechanism driver.

The angular ω_2 speed of the planet gear and the rotation α angle of epicycloid-drawing point are determined through the following expressions:

$\alpha = (i+1)\varphi$; $\omega_2 = (i+1)\omega$, where $i = \frac{R_1}{R_2}$ – is the transmission ratio.

RESULTS AND ANALYSIS

To determine the speed and acceleration of the fixed point (A) of the tiller's blade, the Equation (1) is relevant to introduce in the following form:

$$\begin{cases} X = V \cdot t + R_H\, sin\omega t - R_2 sin(i+1)\omega t \\ Y = R_H cos\omega t - R_2 cos(i+1)\omega t \end{cases} \quad (2)$$

When differentiating Eq. (2) per time, the speed components of any fixed (A) point for the tiller's blade will be obtained:

$$\begin{cases} V_x = V + \omega[R_H cos\omega t - R_2(\mathrm{i}+1)cos(\mathrm{i}+1)\omega t] \\ V_y = -\omega[R_H sin\omega t - \mathrm{R}_2(\mathrm{i}+1)sin\,(\mathrm{i}+1)\omega t] \ldots \end{cases} \quad (3)$$

The module of the total velocity for the considered point will be:

$$V_A = \sqrt{V_x^2 + V_y^2} \quad (4)$$

Making respective modifications and considering that $R_H=(i+1)R_2$, for the module of total velocity the following calculated expression will be obtained:

$$V_A = \sqrt{V^2 + 2\omega^2 V R_2^2 (i+1)^2[1 - cos(2+i)\omega t] + 2V\omega R_2(i+1)[cos\omega t - cos(i+1)\omega t)} \quad (5)$$

To determine the acceleration components of the considered A point of the blade, let's differentiate the expression Eq. (3) per (t) time and will be obtained:

$$\begin{cases} \alpha_x = -\omega^2[(R_1 + R_2)sin\omega t - R_2(i+1)^2 sin(i+1)\omega t\,] \\ \alpha_y = -\omega^2[(R_1 + R_2)cos\omega t - R_2(i+1)^2 cos(i+1)\omega t\,] \end{cases} \quad (6)$$

The acceleration module will be determined in the following way:

$$\alpha_A = \sqrt{{\alpha_x}^2 + {\alpha_y}^2}$$

The article considers the option of planetary mechanism, in which the number of planet gears is three, installed at 120^0 (Fig. 1, Fig. 3). The trajectories of the fixed points A_0 and B_0) of random blade of the tiller, which are implementing rotational and forward movements throughout one rotation of the tiller are introduced in Fig. 3.

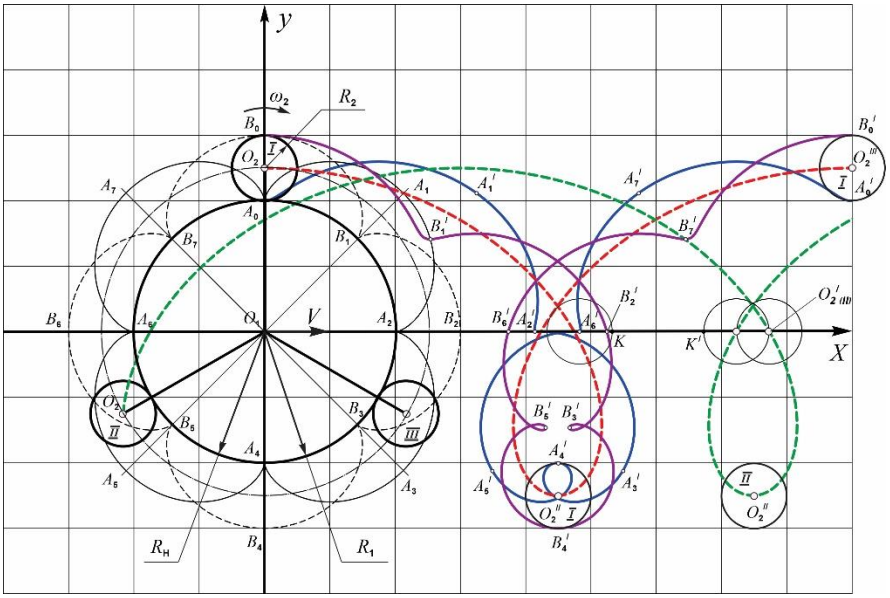

Fig. 3 - The scheme of determining the trajectory of the blades in the rotary tiller with planetary mechanism

The trajectories of the blades attached in the A_0 and B_0 points of the conventional (I) first planet gear without the forward movement of the tiller (V=0) are $A_0\,A_1\,A_2\,A_3\,A_4\,A_5\,A_6\,A_7\,A_0$ ⊔ $B_0\,B_1\,B_2\,B_3\,B_4\,B_5\,B_6\,B_7\,B_0$ epicycloids (Figure 3), whereas in case of forward movement of the machine, they are the curves $A_0\,A_1'\,A_2'\,A_3'\,A_4'\,A_5'\,A_6'\,A_7'\,A_0'$ ⊔ $B_0\,B_1'\,B_2'\,B_3'\,B_4'\,B_5'\,B_6'\,B_7'\,B_0'$, respectively (extended epicycloids), which are wrapped around the shortened cycloid (trochoid) $O_2'O_2''O_2'''O_2''''$ drawn by the O_2 center of the planet gear.

In case of one complete rotation of the tiller's rotor casing, which acts as the driver of the planetary mechanism, the length of the soil layer (a segment is shown with a dashed line) cultivated with a tiller attached to a planet gear, is equivalent to the trajectory trochoid length of O_2-center, while the width is equal to the diameter of the tiller attached to the planet gear.

Figure 3 also depicts the trajectory (trochoid) of O_2 center of the second (II) planet gear staying back from the first (I) planet gear by $\frac{\pi}{3}$ phase, which intersects X axis at $O'_{2(II)}$ point. It is obvious that no uncultivated land area will be left if K and K' points coincide ($KK' = 0$). By this term the important kinematic parameter of the machines with rotary working parts is determined, i.e. the relation of forward movement speed (V) and rotor's rotation frequency (ω). In case of 3 planet gear - tillers this relation looks as follows:

$$V \leq 6R_2 \cdot \omega$$

In the problems of kinematic and dynamic analysis of the tiller's blade, as mentioned above, the changing parameters of the velocities and accelerations of its fixed point are of great significance, therefore, it is worthwhile introducing the changing graphs of velocity and acceleration components according to the Eq.(3) and Eq.(6) expressions.

It is relevant to present the graphs through some specific example.

Assuming R_1=0.2m, R_2=0.05m, (R_H=0,25m, i=4): ω=5s^{-1}, V=1m/s, ω_2=25s^{-1}.

The changing graphs for velocity components (V_x and V_y) of fixed point of blade attached to the planet gear disc of the rotary tiller and the module of total velocity (V_A) depending on the rotation angle (φ) of the

rotor-driver, as well as the changing graphs of the given point's regular acceleration (a_A) and its components ($a^n_{A(x)}$ and $a^n_{A(y)}$) are introduced in Figure 4.

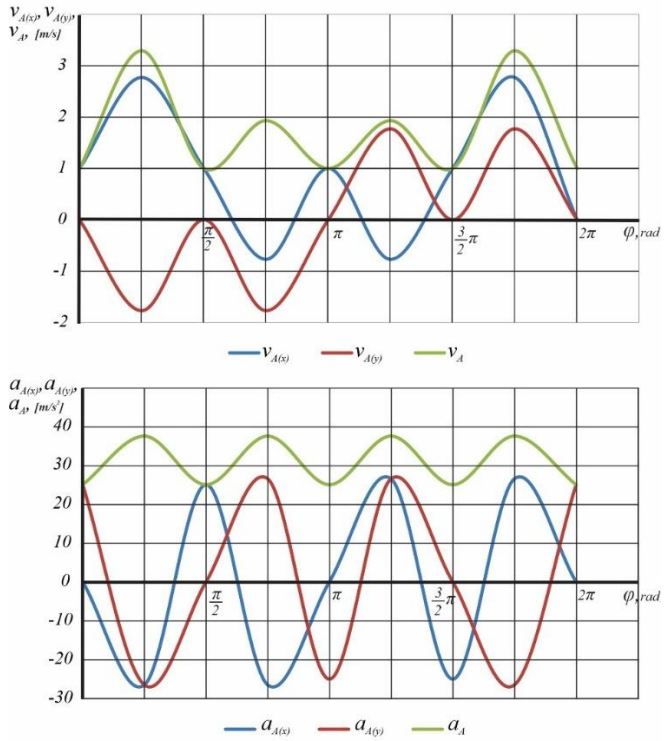

Fig. 4 - The changing graphs of velocities (V_A) and accelerations (a_A) of the fixed point of the tiller blade

From the prospect of the discussed problem, the changing parameters of total velocity module (V_A) and total accelerations module (a_A) are of primary interest. The changing parameters of (V_A) and (a_A) during one rotation period of the driver are related to the rotational or circumferential frequencies of both the driver (ω) and planet gear (ω_2), moreover, the view of their graphs is related to the transmission numbers (i) of the planetary mechanism.

In the phases of $\frac{\pi}{4}$ and $\frac{7}{4}\pi$ V_A gets the maximum value (2.77 m/s), while in those of $\frac{\pi}{2}$, π and $\frac{3}{2}\pi$ – the minimum value (1.0 m/s), which is the speed of forward movement of the aggregate (tractor).

In the intervals of $0 \leq \varphi \leq \frac{\pi}{2}$ and $\frac{3}{2}\pi \leq \varphi \leq 2\pi$ the changing amplitude of (V_A) is 1.145 m/s, while in the interval of $\frac{\pi}{2} \leq \varphi \frac{3}{2}\pi$ it makes 0.465 m/s.

Regarding the changing graph of total acceleration module (a_A) it is presented as a sinusoid of the general view (Figure.4), which is shifted in the direction of y axis to the extent of ω^2, and the amplitude of which in the discussed example is 6.25 m/s^2, while the period is $T = \frac{2\pi}{\omega_2}$.

To ensure possibly maximum uniform rotation moment for the rotor's shaft of the rotary tiller, it is necessary to select such number and location of planet gears of the planetary mechanism, in case of which the amplitude in the general graph of total accelerations could be minimum. It is apparent that this can be achieved by adding the number of planet gears and their symmetric installation considering the term of planet gears vicinity and their optimal number.

To determine the energy indicators of the recommended machine, it is necessary to disclose the nature of force factors (resistance forces) in the interaction of tiller's blades and the cultivated soil mass throughout the working process of the machine, their values and the patterns of directional changes. At this stage of problem discussion, let's assume the value of the resistance force for a tiller's blade as known and approximately constant (they are factually changing values), set up the changing parameters for the direction of that force effect, since the main, momentum force factors generated during the tiller's operation are mostly related to the directions of resistance force effect lines.

In this regard the analysis of the movement trajectory of the tiller's blade is pushed forth, since during the machine operation the interaction force (resistance) of the blade and cultivated medium (soil) is directed to the tangent in the given point of the trajectory and has a direction opposite to the total velocity vector *(Bat*

M.I. et al., 1975). It is obvious that the problem solution leads to the $y'_{(x)}$ function or to the identification of the equation of the tangent for the trajectory (curve) of the blade's fixed point. As in the discussed case the movement equation is presented in the parametric form Eq. (2), hence, it is known that $\frac{dy}{dx} = \frac{y'(t)}{x'(t)}$, where $y'(t)\ and\ x'(t)$ are determined per (2) expressions:

$$y'(x) = -\frac{\omega[(R_1 + R_2) \cdot sin\omega t - R_2(i+1) \cdot sin(i+1)\omega t]}{V\omega[(R_1 + R_2) \cdot cos\omega t - R_2(i+1) \cdot cos(i+1)\omega t]} \quad (7)$$

Anyhow, it is worthwhile mentioning that the trajectories of fixed points (A and B) of the tiller's arbitrary blades in the rotary machine during one rotation of the driver have complex form in case of $i = 4$ and the derived expression Eq. (7) is not applicable along the whole length of the trajectory. In case of one rotation of the driver, A and B points of the conventional planet gear (I) have quadruple reversal points $A_2'A_4'A_6'A_0'$ and $B_1'B_3'B_5'B_7'$ (Figure 3) of epicycloid or extended epicycloid ($A_0A_1'A_2'A_3'A_4'A_5'A_6'A_7'A_0'$ and $B_0B_1'B_2'B_3'B_4'B_5'B_6'B_7'B_0$), which are special points of parametric function, in which the graph of the function breaks and in those points Eq. (2) the expression is not applicable. In the vicinity of those points the behavior of the function is researched with the help of Taylor's formula.

In order to present the changing picture of the blade's resistance forces during the operation of the rotary machine, let's consider the trajectories of A and B fixed points of the two symmetric blades in *I* planet gear in the rotation domain of $0 \le \varphi \le \frac{\pi}{2}$ for the planetary mechanism driver - $O_1O_2 = R_1 + R_2$ (Figure 5).

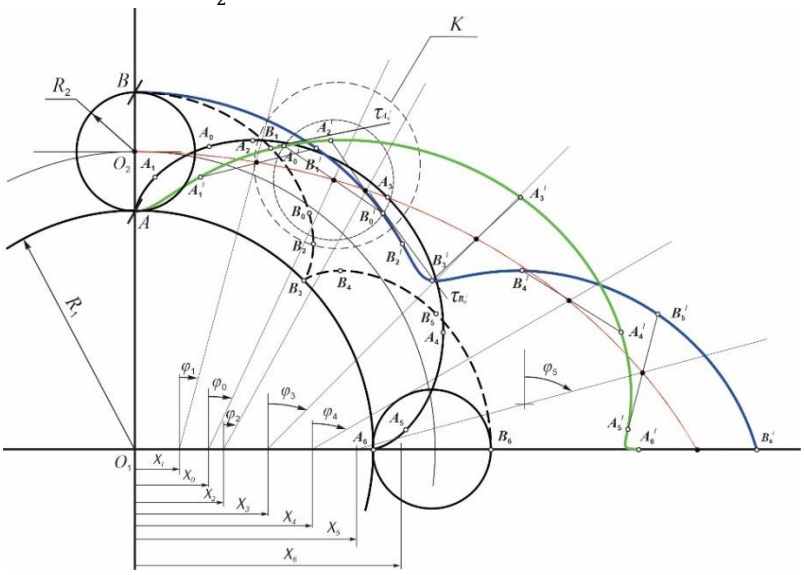

Fig. 5 - **Synchronous scheme of the trajectory of fixed symmetric points in A and B blades attached to the planet gear of the rotary tiller in $0 \le \varphi \le \frac{\pi}{2}$ domain**

The trajectory of A blade is $A\,A_0'A_1'A_2'A_3'\ldots A_6'$, and for the B blade - $B\,B_0'B_2'\ldots B_6'$; besides, in the mentioned domain B blade has a reversal point - B_3', the consecutive positions of the blades' attachment diameter (AB) are $A_1'B_1'$, $A_2'B_2'$, $A_3'B_3'$, $A_4'B_4'$, $A_5'B_5'$ and $A_6'B_6'$, which correspond to the driver's rotation angles $\varphi_1;\ \varphi_2;\ldots\frac{\pi}{2}$. The problem of determining the direction of interaction forces in the blades and cultivated soil is relevant to consider in the domain, where the trajectories of the A and B blades (points) are simultaneously missing the reversal points, e.g. when the driver rotated at φ_0 angle which is conformed to $A_0'B_0'$ position of the blades attachment diameter.

The tangent drawn to the trajectory of A blade at A_0' point is $\tau_{A_0'}$, that of the trajectory of B blade at B_0' point is $\tau_{B_0'}$, and to determine their direction it can be used the Eq. (7) expression, but it should be taken into account that this expression has been derived from *I* planet gear for A blade (point). To use this expression for B point its phasal deviation from A point should be considered.

To present the calculated scheme more clearly, the mentioned sector of Figure 5 (K circle) is depicted in Figure 6 with augmented form, besides, the speeds of A_0 and B_0 points $\left(V_{A_0}\text{and}\,V_{B_0}\right)$ are introduced without the forward movement of the unit ($V = 0$, Figure 6a) and with the presence of forward movement $\left(V_{A_0'}\text{ and }V_{B_0'}\right)$

(Figure 6b). In the former case, the total velocity of A point $\bar{V}_{A_0} = \bar{V}_{A_0O_2} + \bar{V}_{O_2}$ is directed towards the length of τ_{A_0} tangent at the A_0 point of the A_1A_2 fragment in the epicycloid, the total velocity of B point $\bar{V}_{B_0} = \bar{V}_{B_0O_2} + \bar{V}_{O_2}$ is directed towards the length of τ_{B_0} tangent at the B_0 point of $B_1'B_2'$ fragment in the extended epicycloid. In the second case (Figure 6b) A_0' total velocity $\bar{V}_{A_0'} = \bar{V}_{A_0} + \bar{V}$ is directed towards the length of tangent $\tau_{A_0'}$ at the A_0' point of $A_1'A_2'$ fragment in the extended epicycloid, the total velocity of B_0' point $\bar{V}_{B_0'} = \bar{V}_{B_0} + \bar{V}$ - towards the length of tangent $\tau_{B_0'}$ at the B_0' point of $B_1'B_2'$ fragment in the extended epicycloid.

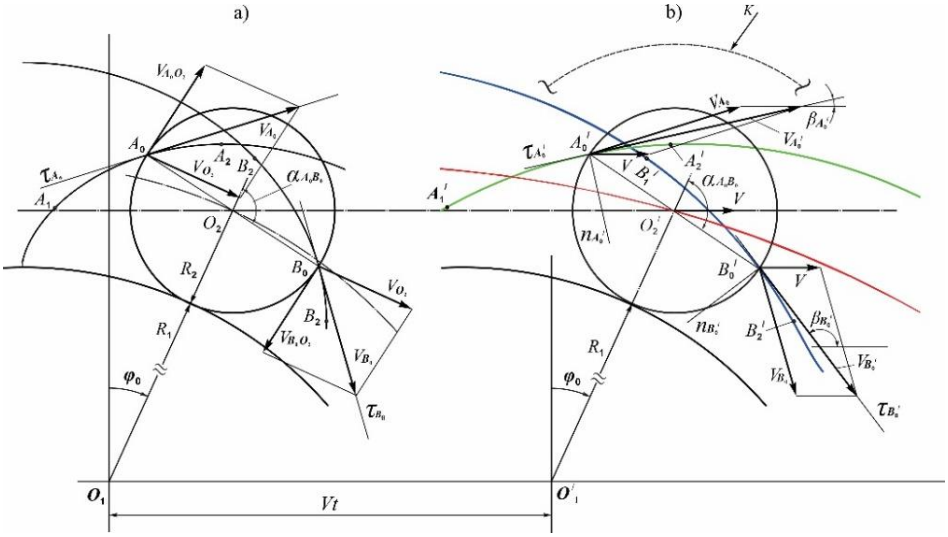

Fig. 6 - The scheme of determination of the velocities of A and B blades attached to the planet gear of the rotary tiller without forward movement (a), with forward movement (b).

Taking into account that during the soil cultivation the total resistance force of the medium affects the tiller's blade in the direction of total velocity vector and has an opposite direction, the scheme of force affecting a planet gear of rotary machine will have the following view (Figure 7). At the observation moment ($\varphi = \varphi_0$) the line affecting the A blade force $\left(P_{A_0'}\right)$ coincides with the direction of the total velocity $\left(V_{A_0'}\right)$ vector of the fixed point of that blade, has an opposite direction and forms $\beta_{A'_0}$ angle with x axis. The force $P_{B_0'}$ affecting B blade has a direction opposite to $V_{B_0'}$ and forms $\beta_{B'_0}$ angle with x axis.

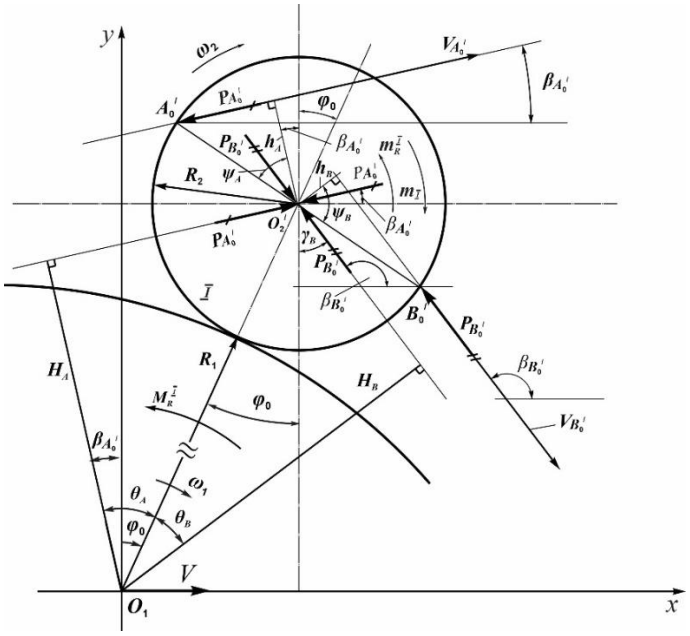

Fig. 7 - The scheme for determining the resistance force factors of the blades attached to the tiller's planet gear

Considering the force system acting on the tiller attached to the planet gear as flat, based on the well-known principles of mechanics *(Loytsyansky L.G., Lurie A.I., 2006)*, it can be stated that the mentioned forces generate force couples, the sum of moments of which will come forth as the resistance moment with respect to the planet gear axis (O′$_2$) and the forces $P_{A_0'}$ and $P_{B_0'}$ affecting that axis with their respective directions and values. The moment of resistance forces towards the planet gear axis will be:

$$m_R^I = \left(m_{P_{A_0'}}\right) + \left(m_{P_{B_0'}}\right) = P_{A_0'} \cdot h_A + P_{B_0'} \cdot h_B \quad (8)$$

The schemes indicate (Figure 6 and Figure 7) that $h_A = R_2 \cdot cos\psi_A,\ h_B = R_2 \cdot cos\psi_B$ where $\psi_A = \pi - \alpha - \beta_{A_0'} - \varphi_0;\ \ \psi_B = -\pi + \beta_{B_0'} + \alpha + \varphi_0$.

Considering that $\alpha = i\varphi$, by placing the values in (8), there will be:

$$m_R^I = -P_{A_0'} \cdot R_2 cos\left[(i+1)\varphi_0 + \beta_{A_0'}\right] - P_{B_0'} \cdot R_2 cos\left[(i+1)\varphi_0 + \beta_{B_0'}\right] \quad (9)$$

At this stage of problem solution, when assuming that the resistance forces are known, the determination of which depending on the blades geometrical shape and installation parameters, is a matter of individual consideration, the problem of resistance moment identification leads to the determination of $\beta_{A_0'}$ and $\beta_{B_0'}$ angles.

Since the affecting lines of $P_{A_0'} and\ P_{B_0'}$ resistance forces coincide with the direction of tangents drawn towards the specific point of the blades trajectory, hence:

$$tg\beta_{A_0'} = \frac{dy_A}{dx_A}, \qquad tg\beta_{B_0'} = \frac{dy_B}{dx_B}$$

$tg\beta_{A_0'}$ is determined via Eq. (2) expression. $tg\beta_{B_0'}$ is determined with the same logic. Considering the phasal deviation of A and B points, the equation of the fixed point motion of B blade will have the following form:

$$\begin{cases} x_B = Vt(R_1 + R_2) \cdot sin\omega t + R_2 sin(i+1)\omega t \\ y_B = (R_1 + R_2) \cdot cos\omega t + R_2 cos(i+1)\omega t \end{cases} \quad (10)$$

Thus:

$$tg\beta_{B_0'} = \frac{dy_A}{dx_A} = \frac{-\omega[(R_1 + R_2) \cdot sin\omega t + R_2(i+1)sin(i+1)\omega t]}{V\omega[(R_1 + R_2) \cdot cos\omega t + R_2(i+1)cos(i+1)\omega t]} \quad (11)$$

By placing the identified values of $\beta_{A_0'}$ and $\beta_{B_0'}$ in Eq. (9), the resistance moment towards the planet gear axis can be determined. In their turn, $P_{A_0'}$ and $P_{B_0'}$ forces moved towards the parallel of their acting line and applied to the planet gear rotation axis (O′$_2$), generate force couples against the driver's rotation axis with $M^I_{R\left(P_{A_0'}\right)}$ and $M^I_{R\left(P_{B_0'}\right)}$ moments, which are resistance force factors of affected/impact medium; besides, $P_{A_0'} and\ P_{B_0'}$ forces are applied to the driver's rotation axis (O) with their preliminary directions.

According to the scheme presented in Figure 7:

$$M^I_{R\left(P_{A_0'}\right)} = P_{A_0'} \cdot H_A = P_{A_0'} \cdot (R_1 + R_2) \cdot cos\left(\beta_{A_0'} + \varphi_0\right)$$

$$M^I_{R\left(P_{B_0'}\right)} = P_{B_0'} \cdot H_B = -P_{B_0'} \cdot (R_1 + R_2) \cdot cos\left(\beta_{B_0'} + \varphi_0\right)$$

The general resistance moment from the *I* planet gear applied in the driver of planetary mechanism will be:

$$M_R^I = P_{A_0'} \cdot (R_1 + R_2) \cdot cos\left(\beta_{A_0'} + \varphi_0\right) - P_{B_0'} \cdot (R_1 + R_2) \cdot cos\left(\beta_{B_0'} + \varphi_0\right) \quad (12)$$

Similarly for the II and III planet gears, and given that they are shifted against the I planet gear by 120^0 and 240^0, for A and B blades there will respectively be:

II planet gear, A blade:

$$tg\beta_A = \frac{-\omega R_2(i+1)\{cos(60-\varphi) + cos[(i+1)\varphi - 60]\}}{V\omega R_2(i+1)\{sin(60-\varphi) - sin[(i+1)\varphi - 60]\}} \quad (13)$$

B blade:

$$tg\beta_B = \frac{-\omega R_2(i+1)\{cos(60-\varphi) - cos[(i+1)\varphi - 60]\}}{V\omega R_2(i+1)\{sin(60-\varphi) + sin[(i+1)\varphi - 60]\}} \quad (14)$$

III planet gear, A blade:

$$tg\beta_A = \frac{-\omega R_2(i+1)\{cos(\varphi+30) - cos[150-\varphi(i+1)]\}}{V \mp \omega R_2(i+1)\{sin(\varphi+30) + sin[150-\varphi(i+1)]\}}. \quad (15)$$

B blade:

$$tg\beta_B = \frac{-\omega R_2(i+1)\{cos(\varphi+30) + cos[150-\varphi(i+1)]\}}{V \mp \omega R_2(i+1)\{sin(\varphi+30) - sin[150-\varphi(i+1)]\}}. \quad (16)$$

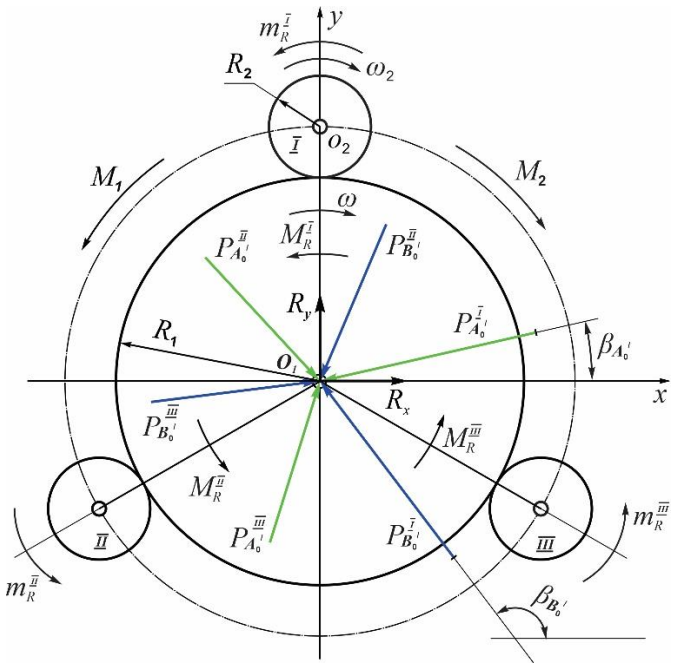

Fig. 8 - The scheme of resistance forces affecting the rotary tiller with planetary mechanism

The resistance moments m_R^{II}; M_R^{II}; m_R^{III} *and* M_R^{III} are determined through Equations (9) and (12) expressions, by placing therein the values of $tg\beta_A$ and $tg\beta_B$ from Equations (13) (14) (15) and (16) expressions, respectively. The scheme of resistance forces affecting the rotary tiller with planetary mechanism equipped with three planet gear arranged at 120^0 looks as follows (Figure 8).

Since the resistance moments (m_R^i and M_R^i) applied to the planet gears and drivers are acting within one plane, thus the total resistance moment or the main resistance moment applied to the driver's shaft will be determined in the following way:

$$M_1 = m_R^I + M_R^I + m_R^{II} + M_R^{II} + m_R^{III} + M_R^{III} \quad (17)$$

Having the value of the resistance moment (M_1) applied to the shaft of the driving rotor in the rotary tiller, it will be possible to determine the required power of the motor and the moment (M_2) applied to the shaft of transmission gear.

Regarding the forces applied to the driver $P_{A_0}^{I}$; $P_{B_0}^{I}$; $P_{A_0}^{II}$; $P_{B_0}^{II}$; $P_{A_0}^{III}$; $P_{B_0}^{III}$, they form a planar convergent force system, the vector sum of which serves as the main vector R applied to the axis of the driver's shaft.

Considering the scheme depicted in Figure 8 and the expressions of Equations (7), (11) and (14), it becomes easily clear that in case of insignificant difference between the resistance forces applied to the tiller's blades, which is empirically approved, the forces applied to the driving rotor are balanced, which practically leads to the abrupt reduction in the traction resistance of the aggregate (tractor).

The aforementioned is one of the most considerable results in the application of the planetary mechanism of the tiller's transmission gear. Thus, the energy indicators of the machine are foremost and mainly related to the resistance moment loading. Taking into account the hypothesis about the equality of the resistance forces applied to the tiller's blade, the resistance moment applied to the rotor's shaft of the rotary machine can be practically determined in the following way per the expression Eq. (17):

$M_1 = (M_R + m_R)$ or by inserting the values of M_R and m_R, it will be obtained:

$$M_1 = 3P \cdot R_2 \left((i+1)\left[cos\left(\beta_{A'_0} + \varphi_0\right) \cdot cos\left(\beta_{B'_0} + \varphi_0\right)\right] - cos\left[(i+1)\varphi_0 + \beta_{A'_0}\right] + cos\left[(i+1)\varphi_0 + \beta_{B'_0}\right]\right). \quad (18)$$

After the identification of the resistance moment applied to the shaft of the driver's rotor, another priority issue is to determine the optimal geometric and kinematic parameters of the transmission chains, in the case of which the uniformity of the mentioned moment under the operational cycle will be maximum or the changing amplitude will be minimum. The solution to this problem will be presented in the next article.

CONCLUSIONS

1. For the rotary tiller with vertical axis developed for the tillage of inter-trunk and near-trunk spaces of orchards and vineyards a planetary mechanism with immobile sun gear, external planet gears and driving rotor (carrier) has been selected as a driving mechanism, which enabled to provide velocities in multiple times higher than the tiller's blades transmission number in case of relatively smaller rotation numbers of the rotor (e.g. in case of 50 rpm rotation number of the rotor 250 rpm of the tiller has been received.

2. In the result of kinematic analysis of the mechanism, analytical expressions have been derived, which enable to establish a relationship between the transmission number of rotation frequency of driving rotor and tiller's blade velocities and accelerations.

3. In the result of kinematic research of planetary transmission mechanism of the rotary tiller analytical expressions have been derived based on which force analysis of working parts have been conducted. Analytical expressions for the determination of the tiller's and rotor's resistance moments have been received, which enable to solve the problem of ensuring their minimum optimal values.

4. The expressions obtained in the result of dynamic research of the recommended mechanism enable to identify the optimal geometric parameters of the tillers disc blades and their mutual arrangements, in case of which the resistance forces of the cultivated medium will be at minimum.

ACKNOWLEDGEMENTS

The work was supported by the Science Committee of MESCS RA, in the frames of the research project № 21APP-2D015

REFERENCES

[1] Bat M.I., Dzhanelidze G.Yu., Kelzom A.S. (1975), *Theoretical mechanics in examples and problems (Теоретическая механика в примерах и задачах)*. "Science", Volume I., Moscow

[2] Byshov N.V., (2017), Modern technical facilities for working in gardens (Современные технические средства для работы в садах). *Scientific journal of Kuban SAU (Научный журнал Куб ГАУ)*, №134.

[3] Chudak S.V., (1975), *Research and development of a vertical tiller for surface tillage in vineyards (Исследование и разработка вертикальной фрезы для поверхностной обработки почвы в виноградниках).* Thesis for the candidate of technical sciences, Chisinau.

[4] Gerasimov N.I., (1979), Treatment of inter-trunk strips/spaces in gardens (Обработка межствольных полос в садах). *Technology, organization and mechanization of intensive gardening. Proceedings, All-Russian Scientific Research Institute of Horticulture named after I.V. Michurin, Michurinsk, (Технология, организация и механизация интенсивного садоводства. Сб. Научн. Тр. ВНИИС им. И. В. Мичурина)* Ed. 28. pp.149-156, Michurinsk

[5] Iman Ahmadi, (2017), A torque calculator for rotary tiller using the laws of classical mechanics, *Soil and Tillage Research*, Volume 165, pp. 137-143, https://doi.org/10.1016/j.still.2016.08.009

[6] Khort D., Filippov R., Smirnov I., Kutyrev A. and Semichev S., (2020), Automated section for milling soil in near-trunk zones of orchard, *E3S Web of Conferences* 161, 01068. https://doi.org/10.1051/e3sconf/20 2016101068

[7] Loytsyansky L.G., Lurie A.I., (2006), *Course of theoretical mechanics (Курс теоретической механики)*, volume 2, Moscow

[8] Matin M.A., Fielke J.M., Desbiolles Jacky M.A., (2014) Furrow parameters in rotary strip-tillage: Effect of blade geometry and rotary speed, *Biosystems Engineering*, Volume 118, pp. 7-15, ISSN 1537-5110, https://doi.org/10.1016/j.biosystemseng.2013.10.015

[9] Matin M.A., Fielke J.M., Desbiolles J.M.A., (2015), Torque and energy characteristics for strip-tillage cultivation when cutting furrows using three designs of rotary blade, *Biosystems Engineering*, Volume 129, pp.329-340, https://doi.org/10.1016/j.biosystemseng.2014.11.008

[10] Monaenkov K.A., (2017), Improving soil cultivation in near- trunk strips of intensive gardens (Совершенствование обработки почвы в приствольных полосах интенсивных садов).

Technologies of food and processing industry. Scientific journal of Mich. SAU (Технологии пищевой и перерабатывающей промышленности. Научн. журнал Мич. ГАУ), №3.

[11] Mosatovskiy V.B., (1980), *Study of the process of near-trunk spaces cultivation in intensive gardens with vertical tillers and justification of the types and parameters of their working parts (Исследование процесса обработки приствольных полос в интенсивных садах вертикальними фрезами и обоснование типов и параметров их рабочих прганов).* Thesis for the candidate of technical sciences, Chisinau.

[12] Ossetsky V.M., (1977), *Kinematics of the satellite of a planetary mechanism with external gearing (Кинематика сателита планетарного механизма с внешным зацеплением).* "Applied Mechanics", "Mechanical Engineering" («Прикладная механика» под общей редакции В.М.Осецкого. Москва, «Машиностроение»), Moscow

[13] Parkhomenko G.G., (2012), *Tillage in rows of orchards and vineyards*. *Processes, devices*. *(Обработка почвы в рядах садов и виноградников. Процесси, устройства)*. LAP LAMBERT Academic Publishing, ISBN 978-3-659-30811-6, p.148, Saarbrücken/Germany

[14] Panov I.M., (1963), *Rotary tillage machines and tools (Ротационные почвообрабативающие машины и орудия)*. Moscow.

[15] Tarverdyan A.P., Altunyan A.V., Grigoryan A.S. et al., (2020), *Inter-trunk zone cultivation machine for orchards*, Patent, №3368A, Armenia.

[16] Tarverdyan A.P., Altunyan A.V., Grigoryan A.S. et al., (2022), *Inter-trunk zone cultivation machine*, Patent, №736Y, Armenia

[17] Tarverdyan A.P., Altunyan A.V., Grigoryan A.S. et al., (2024) *A working body of the tiller machine*, Patent, №862Y, Armenia

[18] Tarverdyan A.P., Hayrapetyan H.H., (2019), Kinematic and dynamic Study of the rotary crusher transmission gear in the potato digger. *Agriscience and Technology*, Armenian National Agrarian University, Yerevan, №4(68):

[19] Tarverdyan A.P., Sargsyan S.F., Altunyan A.V., (2017), Investigation results of kinematic and dynamic indicators of tiller with vertical rotation axis in orchards soil cultivation, *Annals of Agrarian Science, Journal-Elsevier*, Vol.15, N₀ 2, https://doi.org/10.1016/j.aasci.2017.03.004.

[20] Yiwen Yuan, Jiayi Wang, Xin Zhang, Shuhong Zhao, (2023), Study on tillage resistance and energy consumption of a plain straight rotary blade for strip tillage, *Engenharia Agricola* 43(2), http://dx.doi.org/10.1590/1809-4430-Eng.Agric.v43n2e20220127/2023

[21] Zhilitsky Ya.Z., Gerasimov N.I., (1973), *Mechanization of work in gardening (Механизация работ в садоводстве)*, "Kolos", Moscow

JOINT OPTIMIZATION OF COLD-CHAIN PICK-UP VEHICLE ROUTING AND CARGO ALLOCATION FOR FRESH AGRICULTURAL PRODUCTS
/
生鲜农产品冷链集货车辆路径与货物配载联合优化研究

Jingqiong WU*[1,2]; Xuke WU[1]; Jiabo HUANG[1]
[1]School of Traffic Engineering, Kunming University of Science and Technology, Kunming, Yunnan, China;
[2]Yunnan Engineering Research Center of Modern Logistics, Kunming Yunnan, China
Tel: (+86)18787031913; E-mail: mote_1984@163.com
DOI: https://doi.org/10.35633/inmateh-72-41

Keywords: *cold-chain pick-up vehicle routing, cargo allocation, ALNS, HDFS*

ABSTRACT
As a bridge connecting agricultural production and consumption, the circulation of agricultural products has the function of connecting supply and demand, guiding production and promoting consumption. However, the development of rural logistics in China is slow, and most logistics centers still rely on experience to plan the pick-up vehicle routing, resulting in long transport time and high cost. In order to improve the efficiency of pick-up and reduce transportation costs, a joint optimization model of cold-chain pick-up vehicle routing and cargo allocation for fresh agricultural products was proposed in this study. Soft time window constraint and three-dimensional loading constraints were considered, and the lowest pick-up cost was used as optimization goals in this model. In addition, adaptive large neighborhood search algorithm (ALNS) and heuristic depth-first search algorithm (HDFS) were combined to solve the model. A case study of Kunming International Flower Auction Center was conducted to compare the schemes of pick-up vehicle routing before and after optimization. Results demonstrate that the pick-up cost after optimization decreases by 9.6 %, the number of vehicles decreases by one, the total volume utilization rate of vehicles increases by 23 %, and the total load utilization rate of vehicles increases by 15 %. This study provides a model reference and solution method for enterprise operators to formulate schemes of pick-up vehicle routing quickly and reasonably.

摘要
农产品流通作为连接农业生产和消费的桥梁，具有连接供需、引导生产、促进消费的功能。然而，中国农村物流发展缓慢，大多数物流中心仍然依靠经验来规划取货车辆路线，导致运输时间长，成本高。为了提高提货效率，降低运输成本，本文提出了一种生鲜农产品冷链集货车辆路径与货物配载联合优化模型。该模型考虑了软时间窗约束和三维装载约束，以最低集货成本为优化目标。此外，结合自适应大邻域搜索算法(ALNS)和启发式深度优先搜索算法(HDFS)对模型进行求解。以昆明国际花卉拍卖中心为例，对比优化前后的集货车辆路径方案。结果表明，优化后的集货成本降低 9.6%，车辆数量减少 1 辆，车辆总容积利用率提高 23%，车辆总载重利用率提高 15%。本研究为企业运营者快速合理地制定集货车辆路线方案提供了模型参考和解决方法。

INTRODUCTION
The circulation of agricultural products has the function of connecting supply and demand, connecting urban and rural areas, guiding production and promoting consumption *(Takahashi., 2003; Ma et al., 2023)*. As the main way of fresh agricultural products circulation, cold chain logistics can not only greatly reduce the circulation loss of agricultural products and promote the increase of farmers' income, but also effectively improve the international competitiveness of China's agricultural products and comprehensively support and drive the development of agricultural modernization (*Lv et al., 2014; Rahmanifar et al., 2024)*. However, China's cold-chain logistics started late, and there are problems such as large loss, low efficiency and high cost, which cannot meet the current social cold-chain logistics needs. Most agricultural products logistics centers still rely on experience to dispatch transport vehicles, which is easy to cause problems such as excessive consumption of agricultural products, high transportation cost and low transportation efficiency. Based on this, scholars all over the world did many studies on the vehicle routing problem for fresh agricultural products, usually establishing a mathematical model with the lowest transportation cost as the goal, and designing algorithms to solve it. Sun et al. solved the optimization problem of distribution vehicle routing for fresh agricultural products with ant colony algorithm *(Sun et al., 2017)*.

Li et al. were concerned with the impact of the decaying factor on the total distribution cost and proposed a multi-objective VRP optimization model for multiple fresh products *(Li et al., 2019).* Jiang et al. proposed a multi-item packaging strategy that integrates different categories of fresh agricultural products according to food cold-chain temperature, and established an optimization model of vehicle routing that integrates multi-item packaging and sorting distribution *(Jiang et al., 2020).*

Xie pointed out that the exploration of "the first kilometer" is an indispensable step in the circulation of fresh agricultural products *(Xie, 2022)*. At present, on the optimization of cold chain transport path of fresh agricultural products, scholars' research focuses on the "last kilometer" distribution and transportation, and few pay attention to the collection transportation. At present, most scholars focus on the delivery vehicle routing problem for fresh agricultural products, and few pay attention to the pick-up vehicle routing problem. Zhu et al. proposed an optimization model of vehicle routing for agricultural products aiming at minimizing delivery cost, but this model did not include vehicle type variables *(Zhu et al., 2021)*.

Lin et al. used the improved genetic algorithm to solve the vehicle routing problem of agricultural products, but it could not solve the multi-vehicle distribution problem *(Lin et al., 2022)*. Fernando et al. established an optimization model of vehicle routing for agricultural products in the retail mode, but it is not suitable for multi-vehicle distribution *(Fernando et al., 2024)*. Varas et al. built an optimization model of vehicle routing with time window, but did not consider the road traffic conditions in the transportation process *(Varas et al., 2024)*. Lehmann et al. studied the pick-up vehicle routing problem, but did not consider the impact of traffic conditions on actual driving *(Lehmann et al., 2024)*. Ni et al. established an optimization model of vehicle routing for agricultural products based on low-carbon perspective, but set vehicle speed as a fixed value *(Ni et al., 2024)*.

Liu et al. introduced soft time window function and carbon emission parameters to build an optimization model of vehicle routing aiming at the lowest distribution cost and carbon emission, but the model did not conform to the actual driving conditions of vehicles *(Liu et al., 2023)*. Vehicle routing optimization or cargo allocation optimization cannot solve the problems of chaotic cargo handling, high empty driving rate and detour at the same time. Considering vehicle routing problem and vehicle filling problem at the same time is more conducive to improving vehicle space utilization, reducing transportation costs, and avoiding safety problems triggered by overload and other situations. Sbai et al. studied the vehicle routing problem with two-dimensional loading constraints, but did not consider three-dimensional loading constraints *(Sbai et al., 2022)*.

Pinto et al. proposed a multi-starting algorithm to solve the vehicle routing problem with two-dimensional loading constraints, and verified the effectiveness of the algorithm through case tests, but the algorithm could not solve the vehicle routing problem with three-dimensional transfer constraints (*Pinto et al., 2021)*. Ji et al. proposed an optimization model of vehicle delivery routing with two-dimensional loading constraints, but this model could not solve the vehicle routing problem with three-dimensional loading constraints *(Ji et al., 2021)*. Ines et al. introduced two-dimensional loading constraints to construct a dynamic optimization model of vehicle routing, but the model was not completely consistent with the actual loading of cargo *(Ines et al., 2021)*.

Chi et al. studied the vehicle routing problem with three-dimensional loading constraints, but did not consider the gravity center constraints *(Chi et al., 2023)*. Che et al. built an optimization model of vehicle routing with three-dimensional loading constraints, but the model lacked gravity center constraints *(Che et al., 2023)*. Wang et al. established an optimization model of vehicle routing aiming at the lowest operating cost and the least number of vehicles used on the premise of three-dimensional loading constraints, but the proposed loading scheme could not guarantee the safe running of vehicles *(Wang et al., 2021)*. Wei et al. proposed an optimization model of multi-vehicle routing with three-dimensional loading constraints, which aims at minimizing delivery cost, but the proposed model did not meet the requirements of safe vehicle driving *(Wei et al., 2014)*.

In summary, the existing studies did not consider the realistic constraints in detail, and the applicability of the model is not high. Therefore, it is an urgent problem to establish an optimization model of pick-up vehicle routing for fresh agricultural products, which is suitable for the actual situation and has good applicability. Thus, a joint optimization model of pick-up vehicle routing and cargo allocation for fresh agricultural products is proposed in this study. Soft time window constraint and three-dimensional loading constraints are considered in this model. In addition, ALNS algorithm and HDFS (Hadoop Distributed File System) are combined to solve the model.

MATERIALS AND METHODS

Problem Description

In this study, the collection vehicle routing problem for fresh agricultural products can be specifically described as: within one identified production area, a collection center with different models of refrigerated transport vehicles performs collection operations at multiple collection points.

Agricultural products are packaged into cuboids of certain specifications, and consider the loading position and loading sequence of cargo. Under certain practical constraints, a vehicle routing scheme is obtained which minimizes the pick-up cost.

Model Assumptions

Before establishing the optimization model of pick-up vehicle routing for fresh agricultural products, the following assumptions need to be satisfied:

(1) The pick-up center grasps the coordinates of each pick-up point, the quantity of various agricultural products and other data, and the data remains unchanged.

(2) In the process of pick-up, consider road congestion, but do not consider vehicle failure, fuel exhaustion and other situations.

(3) Each pick-up point must be serviced once and only by one vehicle, and the vehicle has reached the best refrigeration temperature when leaving the pick-up center.

(4) The vehicle compartment and each piece of cargo are simplified into cuboids, and all kinds of cargo can be mixed.

Modeling

To make the model closer to the actual situation, the road congestion index is introduced to reflect the actual driving time of vehicles in this study. The actual driving time of vehicle in a certain road section is the product of the time that the vehicle passes the road section at an average speed and the road congestion coefficient corresponding to the period. The actual travel time of vehicle k from point *i* to point *j* is calculated by the following formula.

$$t_{ij}^{k} = \frac{d_{ij}}{v_0^k} \varepsilon_{ij}^{u} \tag{1}$$

where: d_{ij} is the distance between pick-up point *i* and pick-up point *j*, v_0^k is the average travel speed of vehicle *k*, ε_{ij}^{u} is the congestion coefficient of road section (*i*, *j*).

Vehicle fixed cost

Vehicle fixed cost mainly includes the depreciation cost caused by each start-up of the vehicle. Vehicle fixed cost can be expressed as:

$$C_g = \sum_{k=1}^{K} \sum_{j=1}^{n} f_k x_{0j}^{k} \tag{2}$$

where: f_k is the fixed cost for starting vehicle *k*, x_{0j}^{k} is the decision variable, $x_{0j}^{k} = 1$ indicates that vehicle *k* leaves the pick-up center to pick-up point *j*, otherwise $x_{0j}^{k} = 0$.

Vehicle transportation cost

In the actual driving process, there is a very complex nonlinear relationship between fuel consumption and speed, road condition and load, which is difficult to quantify accurately. Therefore, vehicle transportation cost is expressed as the product of the driving cost per unit distance and the driving distance, and the two cases of no-load driving and load driving of the vehicle are considered respectively. Vehicle transportation cost can be expressed as:

$$C_t = \sum_{k=1}^{K} \sum_{i=1}^{n} C_1^k d_{0i} x_{0i}^{k} + \sum_{k=1}^{K} \sum_{j=0}^{n} \sum_{i=1}^{n} C_2^k d_{ij} x_{ij}^{k} \tag{3}$$

where: C_1^k is the transportation cost per kilometer of vehicle *k* when unloaded-driving, C_2^k is the transportation cost per kilometer of vehicle *k* when loaded-driving, d_{0i} is the distance from pick-up center to

pick-up point *i*, d_{ij} is the distance from pick-up point *i* to pick-up point *j*, x_{ij}^k is the decision variable, $x_{ij}^k = 1$ indicates that vehicle *k* goes to pick-up point *j* after serving pick-up point *i*, otherwise $x_{0j}^k = 0$.

Vehicle refrigeration cost

Vehicle refrigeration cost is divided into two parts, one is the refrigeration cost of maintaining the low temperature inside the carriage, and the other is the refrigeration cost caused by opening the door. Vehicle refrigeration cost can be expressed as:

$$C_z = \sum_{k=1}^{K}\sum_{j=0}^{n}\sum_{i=0}^{n} P_k t_{ij}^k x_{ij}^k + \sum_{k=1}^{K}\sum_{i=1}^{n} P_k^{'} y_i^k \tag{4}$$

where: P_k is the refrigeration cost of vehicle *k* per hour, $P_k^{'}$ is the refrigeration cost of vehicle *k* when opening the compartment door one time, t_{ij}^k is the travel time of vehicle k from pick-up point *i* to pick-up point *j*, y_i^k is the decision variable, $y_i^k = 1$ indicates that pick-up point *i* is served by vehicle *k,* otherwise $y_i^k = 0$.

Cargo damage cost

Cargo damage cost is mainly divided into two parts, one is the corruption cost of fresh agricultural products caused by respiration, and the other is the damage cost incurred by loading cargos. Cargo damage cost can be expressed as:

$$C_s = \sum_{k=1}^{K}\sum_{r=1}^{R}\sum_{i=1}^{n} P_r Q_i^r \left(1 - e^{\alpha_r \left(t_k - t_i^k\right)}\right) y_i^k + \sum_{k=1}^{K}\sum_{r=1}^{R}\sum_{j=1}^{n}\sum_{i=1}^{n} P_r Q_i^r \alpha_r^{'} x_{ij}^k \tag{5}$$

where: P_r is the unit price of type *r* agricultural product, Q_i^r is the weight of agricultural product *r* at pick-up point *i*, α_r is the decay rate of type *r* agricultural product, $\alpha_r^{'}$ is the spoilage rate of type *r* agricultural product, t_k is the arriving time of vehicle *k* to the pick-up center, t_i^k is the arriving time of vehicle *k* to pick-up point *i*.

Time window penalty cost

Time window penalty cost can be expressed as:

$$C_f = \sum_{k=1}^{K}\sum_{i=1}^{n} \eta_1 max\left(E_i - t_i^k, 0\right) + \eta_2 max\left(t_i^k - L_i, 0\right) \tag{6}$$

Time window penalty cost function is as follows:

$$C_f(t_i^k) = \begin{cases} M, & t_i^k < e_i \quad or \quad t_i^k > l_i \\ \eta_1(E_i - t_i^k), & e_i < t_i^k < E_i \\ \eta_2(t_i^k - L_i), & L_i < t_i^k < l_i \\ 0, & E_i < t_i^k < L_i \end{cases} \tag{7}$$

where: $[E_i, L_i]$ is the ideal time window of pick-up point *i*, there is no penalty cost for arriving at collection point *i* within this time period. e_i is the earliest time for pick-up point *i* to accept the operation, and l_i is the latest time for point *i* to accept operation. Pick-up operation earlier than the earliest time or later than the latest time will not be allowed. If operation occurs in $[e_i, E_i]$ or $[L_i, l_i]$, there will be a certain penalty cost. η_1 is the penalty coefficient for early arrival, η_2 is the penalty coefficient for late arrival.

Optimization model setting

Based on the above analysis, the following model is established.

$$MinZ_1 = C_g + C_t + C_z + C_s + C_f \tag{8}$$

The constraints are as below:

$$\sum_{t=1}^{T} Q_t z_t^k \le Q_k, \quad k = 1,2,3,\cdots,K \tag{9}$$

$$\sum_{t=1}^{T} V_t z_t^k \le \mathrm{V}_k, \quad k = 1,2,3,\cdots,K \tag{10}$$

$$\sum_{k=1}^{K} y_i^k = 1, \quad i = 1,2,3,\cdots,n \tag{11}$$

$$\sum_{k=1}^{K}\sum_{j=0}^{n} x_{ij}^k = 1, \quad i = 1,2,3,\cdots,n \tag{12}$$

$$\sum_{k=1}^{K}\sum_{i=0}^{n} x_{ij}^k = 1, \quad j = 1,2,3,\cdots,n \tag{13}$$

$$\sum_{k}^{K} z_t^k = 1, \quad t = 1,2,3,\cdots,T \tag{14}$$

$$\sum_{i=1}^{n} x_{0i}^k = \sum_{i=1}^{n} x_{i0}^k \le 1, k = 1,2,3,\cdots,K \tag{15}$$

$$XR_t^k \le L_k, k = 1,2,3,\cdots,K, t = 1,2,3,\cdots,T \tag{16}$$

$$YR_t^k \le W_k, k = 1,2,3,\cdots,K, t = 1,2,3,\cdots,T \tag{17}$$

$$ZR_t^k \le H_k, k = 1,2,3,\cdots,K, t = 1,2,3,\cdots,T \tag{18}$$

$$XL_t^k \ge 0, k = 1,2,3,\cdots,K, t = 1,2,3,\cdots,T \tag{19}$$

$$YL_t^k \ge 0, k = 1,2,3,\cdots,K, t = 1,2,3,\cdots,T \tag{20}$$

$$ZL_t^k \ge 0, k = 1,2,3,\cdots,K, t = 1,2,3,\cdots,T \tag{21}$$

$$\left[\left(XL_t^k - XR_t^k\right) - L_t\right]\left[\left(YL_t^k - YR_t^k\right) - L_t\right] = 0, k = 1,2,3,\cdots,K, t = 1,2,3,\cdots,T \tag{22}$$

$$\left[\left(XL_t^k - XR_t^k\right) - W_t\right]\left[\left(YL_t^k - YR_t^k\right) - W_t\right] = 0, k = 1,2,3,\cdots,K, t = 1,2,3,\cdots,T \tag{23}$$

$$ZL_t^k - ZR_t^k = H_t, k = 1,2,3,\cdots,K, t = 1,2,3,\cdots,T \tag{24}$$

$$\frac{\sum_{t=1}^{T} Q_t GX_t^k z_t^k}{\sum_{t=1}^{T} Q_t z_t^k} \in \left[GX_{k1}, GX_{k2}\right], k = 1,2,3,\cdots,K \tag{25}$$

$$\frac{\sum_{t=1}^{T} Q_t GY_t^k z_t^k}{\sum_{t=1}^{T} Q_t z_t^k} \in \left[GY_{k1}, GY_{k2}\right], k = 1,2,3,\cdots,K \tag{26}$$

$$\frac{\sum_{t=1}^{T} Q_t GZ_t^k z_t^k}{\sum_{t=1}^{T} Q_t z_t^k} \in \left[GZ_{k1}, GZ_{k2}\right], k = 1,2,3,\cdots,K \tag{27}$$

where: Q_t and V_t are the weight and volume of cargo t, Q_k and V_k are the rated load and volume of vehicle k, L_t, W_t and H_t are the length, width and height of cargo t, L_k, W_k and H_k are the length, width and height of vehicle k, $\left[GX_{k1}, GX_{k2}\right]$, $\left[GY_{k1}, GY_{k2}\right]$ and $\left[GZ_{k1}, GZ_{k2}\right]$ are the range of gravity center in length, width and height direction of vehicle k, $\left(GX_t^k, GY_t^k, GZ_t^k\right)$ is the gravity center coordinates of cargo t in compartment of vehicle k, $\left(XL_t^k, YL_t^k, ZL_t^k\right)$ and $\left(XR_t^k, YR_t^k, ZR_t^k\right)$ are the left upper corner coordinates and right rear lower corner coordinates of cargo t in compartment of vehicle k, $z_t^k = 1$ is the decision variable, $y_i^k = 1$ indicates that cargo t is loaded by vehicle k, otherwise $y_i^k = 0$.

Equation (8) is objective functions, indicating the minimum total cargo cost, the maximum vehicle load utilization rate, the maximum vehicle volume utilization rate and the minimum number of vehicles used respectively. Equation (9) indicates that the total weight of agricultural products on each routing shall not exceed the maximum carrying weight of vehicles. Equation (10) indicates that the total volume of agricultural products on each routing shall not exceed the maximum carrying volume of vehicles. Equation (11) indicates that each collection point can be served once. Equation (12) and (13) indicate that each collection point can only be served once by one vehicle. Equation (14) indicates that each cargo is loaded and is only loaded by one vehicle.

Equation (15) indicates that each vehicle must return to the pick-up center after completing operation. Equation (16), (17), (18), (19), (20) and (21) indicate that the cargo shall not exceed the compartment. Equation (22), (23) and (24) indicate that the cargo shall not be placed on a diagonal. Equation (25), (26) and (27) indicate that the total gravity center of the cargo is within the gravity center of the carriage.

Algorithm Design

ANLS and HDFS are combined to solve the model, the former is used to generate the scheme of pick-up vehicle routing, and the latter is used to generate and test the scheme of cargo allocation. The essence of ALNS is to adaptively select a group of better damage operators and repair operators to deal with the current solution by examining the "historical performance" of different neighborhood search operators, and increase the probability of obtaining the optimal solution. The essence of HDFS is to search the current valid space and invalid space of the carriage, merge them according to the space merging rules, generate a larger valid space, and fill the cargo to be filled to the highest matching effective space. Repeat the above operations until the cargo cannot be filled or all cargo is loaded.

Correlation degree damage operator

The principle of the damage operator is to randomly select a pick-up point for destruction, calculate the correlation degree between the pick-up point and the remaining pick-up points, and carry out descending order to destroy the first n pick-up points, and put all the damaged pick-up points into the virtual request library. The correlation degree between pick-up point *i* and *j* is calculated by the following formula.

$$R(i,j)=\varphi_1 d_{ij}+\varphi_2\left(\left|\sum_{r=1}^{R}Q_i^r-\sum_{r=1}^{R}Q_j^r\right|\right)+\varphi_3\left(\left|\sum_{r=1}^{R}V_i^r-\sum_{r=1}^{R}V_j^r\right|\right)+\varphi_4 \quad (28)$$

where φ_1, φ_2, φ_3 and φ_4 respectively are the distance, weight difference, volume difference and weight coefficient of the routing between pick-up point *i* and *j.*

Worst damage operator

The damage operator is designed to destroy the pick-up points that have the greatest impact on the current cost, thus reduce the pick-up cost of the entire transportation network. Its principle is to calculate the added value of the cost after the destruction of each pick-up point, select the point with the largest added value to destroy, and put it into the virtual request library. Repeat the destruction operation until n pick-up points are destroyed.

Random routing damage operator

The damage operator is designed to take into account random factors and reduce the possibility of the algorithm falling into local optimality. The principle is to select a routing with the largest pick-up cost, randomly destroy a pick-up point on the routing, and update the pick-up routing at the same time. Repeat the destruction operation until n pick-up points are destroyed, and place all the damaged pick-up points into the virtual request library.

Longest time damage operator

The principle is to calculate the added value of the pick-up time after each collection point is destroyed, and select the pick-up point with the largest added value into the virtual request library. Repeat until there are no pick-up points in the virtual request library.

Shortest time repair operator

The principle of the repair operator is to randomly select a pick-up point from the virtual request library and insert it into the appropriate position (the incremental travel time before and after the insertion is minimal). Repeat until there are no pick-up points in the virtual request library.

Shortest distance repair operator

The principle of the repair operator is to randomly select a pick-up point from the virtual request library and insert it into the appropriate position (the total mileage incremental before and after insertion is minimal). Repeat until there are no pick-up points in the virtual request library.

Lowest cost repair operator

The principle of the repair operator is to insert the destroyed pick-up points into the routing one by one with the smallest incremental cost until there are no pick-up points in the virtual request library.

Regret repair operator

The principle of the repair operator is to calculate the regret value of all the pick-up points in the virtual request library, and insert the pick-up point with the largest regret value into the appropriate position each time (the increment of the pick-up cost is the smallest before and after insertion). Repeat until there are no pick-up points in the virtual request library. The formula for calculating regret value is as follows:

$$c_i^* = \Delta F_{i,xi2} - \Delta F_{i,xi1} \quad (29)$$

where: $\Delta F_{i,xi1}$ is the cost increment after the pick-up point *i* is inserted into the appropriate position. $\Delta F_{i,xi2}$ is the cost increment after the pick-up point *i* is inserted into the second-appropriate position.

Operator selection mechanism

In each iteration process, the roulette choice method is used to call one damage operator and one repair operator to enhance the robustness of the algorithm. There are *n* damage operators, and the probability of damage operator α being called in the *s*th iteration is calculated as follows:

$$p(\alpha_s) = \frac{w_{\alpha,s-1}}{\sum_{i=1}^{n} w_{i,s-1}} \quad (30)$$

where: $w_{\alpha,s-1}$ is the weight of the damage operator α in the *s*th iteration.

Operator scoring mechanism

The score of the operator directly reflects the "historical performance" of the operator in the algorithm iteration process, and the specific scoring mechanism is as follows:

(1) If the candidate neighborhood solution obtained by a group of operators is better than the current solution, and better than the global optimal solution, then each operator is added *p1* score.

(2) If the candidate neighborhood solution obtained by a group of operators is better than the current solution, but not better than the global optimal solution, then each operator is added *p2* score.

(3) If the candidate neighborhood solution obtained after a group of operators is inferior to the current solution, but accepted by the acceptance criteria, then each operator is added *p3* score.

Operator weight adjustment mechanism

With the increase of the number of algorithm iterations, some operators that are suitable to be called in the early stage may not be suitable in the subsequent stage. Therefore, the operator weights should be dynamically adjusted according to the "historical performance" of operators to guide the operator invocation in the next stage. The weight update formula is as follows:

$$w_{i,s} = (1-\delta) w_{i,s-1} + \delta \frac{s_{i,s}}{t_i} \quad (31)$$

where: $w_{i,s}$ is the weight of the operator *i* in the *s*th iteration. $s_{i,s}$ is the score of operator *i* in the *s*th iteration. t_i is the number of times the operator *i* is called. δ is the reaction coefficient, with values from 0 to 1.

Acceptance criteria

In the process of searching for the global optimal solution, blindly accepting the optimal solution will narrow the neighborhood structure and cause the algorithm to fall into a local loop, and properly accepting the inferior solution will make the algorithm jump out of the local optimal. Therefore, the Metropolis criterion is adopted to accept the inferior solution with a certain probability to improve the searching ability of the algorithm. The probability of accepting the inferior solution is calculated as follows:

$$p = e^{-\frac{|f(x')-f(x)|}{\varphi T_0}} \quad (32)$$

where: $f(x)$ is the objective function value of the current solution. $f(x')$ is the objective function value of the inferior solution. T_0 is the initial temperature of the simulated annealing algorithm. φ is the annealing coefficient.

Basic steps of algorithm

Step 1): Generate the initial solution of the pick-up routing scheme and set the initial parameters.

Step 2): Determine whether the initial solution satisfies the termination condition. If the termination condition is reached, go to step 3; if not, go to step 10.

Step 3): Generate the initial solution of the cargo allocation scheme.

Step 4): Determine whether there is any cargo that are not loaded in the cargo set. If there is cargo that is not loaded, go to step 5; if not, go to step 19.

Step 5): Select a group of cargo from the cargo set for loading.

Step 6): Determine whether there is any cargo that are not unloaded in this cargo group. If there is cargo that is not loaded, go to step 7; if not, go to step 4.

Step 7): Select a cargo from this cargo group for loading.

Step 8): Determine whether the effective space set is empty. If it is empty, go to step 9; if not, go to step 20.

Step 9): Determine whether the invalid space set is empty. If it is empty, go to step 10; if not, go to step 22.

Step 10): Determine whether the weight update condition is met. If it is met, go to step 11; if not, go to to step 12.

Step 11): Update operator weight.

Step 12): Update annealing temperature.

Step 13): Select a repair operator and a damage operator.

Step 14): Determine whether the new solution is accepted. If it is accepted, go to step 15; if not, go to step 18.

Step 15): Set the new solution to the current solution.

Step 16): Determine whether the current solution is better than the optimal solution. If it is better than the optimal solution, go to step 17; if not, go to step 18.

Step 17): Set the current solution to the optimal solution.

Step 18): Update operator score, and go to step 2.

Step 19): Determine whether the loading scheme is feasible. If it is feasible, output loading scheme; if not, go to step 24.

Step 20): Determine whether there is a suitable valid space after merge. If there is a suitable valid space, go to step 21, if not, go to step 10.

Step 21): Place the cargo, and go to step 6.

Step 22): Make space merge.

Step 23): Determine whether there is a suitable valid space after merger. If there is a suitable valid space, go to step 21; if not, go to step 10.

Step 24): Determine whether the adjusted loading scheme is feasible. If it is feasible, output loading scheme; if not, go to step 10.

RESULTS

Case Introduction

Kunming International Flower Auction Center is selected as an example. The enterprise is a comprehensive industrial service platform, which mainly focuses on flower auction and integrates flower market information service, technical service and logistics service. At present, 43 cold chain transportation lines have been established in Yunnan Province, involving more than 460 cargo collection stations, covering the main production areas of Yunnan flowers, and solving the difficult problem of flower farmers' flowers transportation from origin to market.

According to the statistics, the main types of fresh cut flowers in a planting area are Brushed gerbera (R1), Blue demon (R2), Peach snow mountain (R3), Corolla (R4), Maria (R5) and Cappuccino (R6). To facilitate loading, the cargo collection center issues packing boxes for each farmer, and the farmer treats each variety of fresh cut flowers into cuboids cargos of different specifications in advance (10 bundles for one cargo). The relevant information about each variety of fresh cut flowers is shown in Table 1.

The parameters such as rated volume, rated load and size of the three types of refrigerated trucks in the pick-up center are shown in Table 2. The penalty coefficients for early and late arrival are set 1.0 yuan per minute and 1.5 per minute. The locations of pick-up points and center were processed with two-dimensional

coordinates. The time window, location, type and quantity of goods at each collection point are shown in Table 3. Baidu Map intelligent transportation network is used to predict the road traffic congestion index of a certain area throughout the day, and the road congestion index of the area on the same day is shown in Table 4.

Table 1

Information on each variety of fresh cut flowers

	R1	R2	R3	R4	R5	R6
Packing specifications (cm)	100*60*60	100*60*50	100*50*50	100*45*45	100*36*36	100*30*25
Weight of each package (kg)	40	30	25	20	18	16
Volume of each package (m^3)	0.36	0.3	0.25	0.2025	0.1296	0.075
Spoilage rate	3%	2%	3%	4%	2%	3%
Decay rate	4%	5%	6%	5%	7%	4%
Unit price(yuan/kg)	7	12	14	10	13	16

Table 2

Vehicle parameters

	A	B	C
Fixed cost for starting vehicle one time (yuan/time)	20	30	35
Transportation cost per kilometer when unloaded-driving (yuan/km)	2.3	3.4	4.0
Transportation cost per kilometer when loaded-driving (yuan/km)	5.0	5.5	6.2
Refrigeration cost per hour (yuan/h)	20	30	40
Refrigeration cost when opening the compartment door (yuan/time)	30	40	50
Length (m)	4.2	6.2	8.2
Width (m)	1.4	1.8	2.2
Height (m)	1.8	2.0	2.4
Rated load (kg)	2530	3620	6240
Rated volume (m^3)	10.584	22.32	43.296

Table 3

Information on each pick-up point

Points	XY(km)	Type and quantity of cargo	$[E_i, L_i]$	$[e_i, l_i]$
0	(30,35)	/	/	/
1	(30,35)	6*R1+5*R2+2*R3+4*R4+6*R5+10*R6	5:00-8:30	5:00-11:00
2	(44,37)	6*R1+4*R2+2*R3+3*R4+7*R5+9*R6	6:00-9:00	5:30—12:00
3	(40,43)	5*R1+4*R2+0*R3+6*R4+5*R5+11*R6	5:30-9:00	5:00-11:00
4	(35,57)	2*R1+1*R2+1*R3+2*R4+2*R5+4*R6	6:30-10:00	5:30-11:30
5	(29,64)	7*R1+3*R2+3*R3+3*R4+8*R5+12*R6	6:00-9:30	5:00-12:00
6	(61,42)	4*R1+2*R2+3*R3+3*R4+7*R5+6*R6	5:00-8:30	5:00-11:30
7	(53,58)	7*R1+1*R2+0*R3+4*R4+5*R5+12*R6	7:40-10:40	5:40-11:50
8	(42,67)	7*R1+1*R2+0*R3+4*R4+5*R5+12*R6	7:00-9:00	6:00-11:00
9	(39,80)	1*R1+3*R2+0*R3+0*R4+3*R5+4*R6	8:30-10:30	7:00-11:30
10	(37,108)	4*R1+3*R2+1*R3+3*R4+3*R5+4*R6	5:40-8:00	5:40-9:50
11	(90,30)	1*R1+3*R2+0*R3+1*R4+1*R5+4*R6	6:00-9:00	5:00-11:00
12	(93,36)	4*R1+5*R2+1*R3+6*R4+5*R5+8*R6	6:00-9:30	5:00-11:10
13	(80,40)	8*R1+5*R2+0*R3+6*R4+9*R5+11*R6	5:00-8:30	5:00-10:10
14	(80,56)	5*R1+4*R2+3*R3+1*R4+6*R5+8*R6	6:00-9:00	5:00-11:20
15	(70,65)	7*R1+5*R2+1*R3+0*R4+7*R5+6*R6	6:00-10:00	5:00-11:10
16	(60,79)	4*R1+4*R2+1*R3+7*R4+1*R5+7*R6	7:00-9:30	5:30-10:50
17	(59,102)	3*R1+4*R2+2*R3+0*R4+10*R5+11*R6	6:00-10:00	5:00-11:40
18	(121,35)	3*R1+2*R2+1*R3+0*R4+1*R5+3*R6	5:00-8:30	5:00-10:10
19	(115,50)	2*R1+2*R2+1*R3+2*R4+4*R5+6*R6	5:30-9:00	5:00-11:10
20	(110,58)	5*R1+4*R2+3*R3+6*R4+3*R5+10*R6	6:00-8:00	5:00-10:20
21	(92,70)	4*R1+5*R2+0*R3+6*R4+9*R5+7*R6	7:00-9:30	6:00-10:50
22	(76,94)	4*R1+5*R2+0*R3+4*R4+1*R5+10*R6	7:30-10:30	6:30-12:10
23	(57,128)	6*R1+3*R2+1*R3+2*R4+10*R5+8*R6	6:40-8:40	5:40-10:50
24	(41,140)	3*R1+2*R2+1*R3+2*R4+0*R5+4*R6	8:00-11:00	7:00-12:30

Points	XY(km)	Type and quantity of cargo	$[E_i, L_i]$	$[e_i, l_i]$
25	(140,40)	1*R1+0*R2+0*R3+1*R4+2*R5+2*R6	8:50-11:50	7:30-13:00
26	(135,60)	2*R1+3*R2+3*R3+0*R4+6*R5+9*R6	9:00-12:00	7:50-14:00
27	(120,68)	6*R1+2*R2+0*R3+4*R4+6*R5+10*R6	8:00-11:30	7:00-13:30
28	(114,80)	6*R1+2*R2+0*R3+4*R4+5*R5+9*R6	8:20-10:20	7:20-12:10
29	(99,101)	6*R1+0*R2+3*R3+0*R4+8*R5+10*R6	10:40-11:50	8:40-13:40
30	(79,110)	3*R1+2*R2+1*R3+1*R4+3*R5+4*R6	11:00-12:00	9:50-14:00
31	(78,136)	1*R1+3*R2+0*R3+1*R4+5*R5+6*R6	9:30-12:30	8:30-13:20
32	(160,60)	2*R1+6*R2+2*R3+2*R4+4*R5+9*R6	10:00-12:00	8:50-14:10
33	(140,70)	2*R1+5*R2+1*R3+4*R4+8*R5+8*R6	9:00-11:10	8:00-12:50
34	(125,92)	3*R1+5*R2+2*R3+1*R4+6*R5+7*R6	9:00-11:40	7:50-13:10
35	(119,104)	3*R1+2*R2+0*R3+1*R4+3*R5+2*R6	8:00-11:25	6:30-13:30
36	(113,126)	6*R1+7*R2+0*R3+6*R4+5*R5+8*R6	8:50-10:40	7:20-11:50
37	(160,93)	7*R1+6*R2+3*R3+5*R4+5*R5+7*R6	8:30-11:50	6:50-13:40
38	(139,102)	6*R1+7*R2+1*R3+0*R4+6*R5+9*R6	11:40-13:00	9:50-14:20

Table 4

Congestion index predicted by Baidu map intelligent traffic network

Time period	Congestion coefficient	Time period	Congestion coefficient
[5:00-6:00)	1.00	[10:00-11:00)	1.39
[6:00-7:00)	1.25	[11:00-12:00)	1.31
[7:00-8:00)	1.76	[12:00-13:00)	1.42
[8:00-9:00)	1.74	[13:00-14:00)	1.55
[9:00-10:00)	1.49	[14:00-15:00)	1.52

Simulation Results

The original scheme of pick-up vehicle routing is shown in Table 5. Python software was used to complete the algorithm programming. As shown in Fig. 1, the adaptive mechanism in the algorithm guides the entire search direction to converge towards the optimization direction, gradually approaches the optimal solution, and reaches a stable state after about 870 iterations. The optimized vehicle routing scheme is shown in Fig. 2 and Table 6, and the visualization results of each vehicle's three-dimensional packing are shown in Fig. 3.

The original scheme requires seven vehicles to complete the pick-up operation, including three type A vehicle, 2 type B vehicles and 2 type C vehicles. The total cost is 10742 yuan, the total volume utilization rate is 60%, and the total load utilization rate is 55%. After optimization, six vehicles need to be dispatched to complete the pick-up operation, including 1 type A vehicle, 1 type B vehicle and 4 type C vehicles. The total cost is 9714 yuan, the total volume utilization rate is 83%, and the total load utilization rate is 70%.

The calculation results show that the cost of the optimized vehicle routing scheme reduces by 9.6% and the number of vehicles reduces by one compared with the original vehicle routing scheme. In addition, the total volume utilization rate and total load utilization rate of the vehicle increase by 23% and 15%. Three-dimensional diagram of cargo loading shows that cargo loading is not a process of neatly filling the carriage, and many gaps that cannot be utilized will be generated in actual placement. Therefore, it is necessary to consider the three-dimensional loading constraints when modeling. Under the background of market economy, the competition of cold-chain logistics enterprises is increasing day by day. Therefore, the optimization model of pick-up vehicle adopting soft time window constraints and three-dimensional loading constraints is more suitable for the actual situation. The effectiveness of the proposed model and algorithm is verified by comparing the schemes of pick-up vehicle routing before and after optimization.

Table 5

Original pick-up vehicle routing scheme

Routings	Vehicle types	Cost (yuan)	Volume utilization rate	Load utilization rate
0→15→8→3→13→6→7→2→27→20→0	C	1824	79%	62%
0→4→9→29→16→23→22→1→5→12→0	C	1910	76%	60%
0→36→24→10→11→37→17→0	B	1850	74%	62%
0→25→21→14→28→38→0	B	1735	75%	63%
0→18→35→34→0	A	1263	70%	61%
0→30→33→32→0	A	1155	68%	59%
0→19→26→31→0	A	1005	64%	51%

Note: The results in the table are rounded.

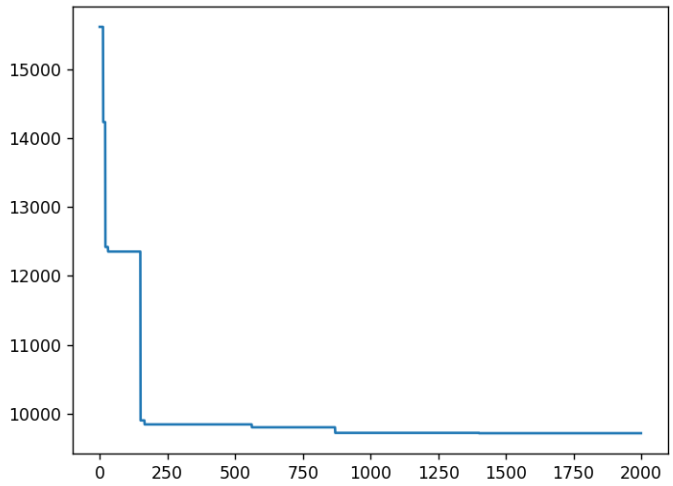

Fig. 1 - Pick-up cost iteration diagram

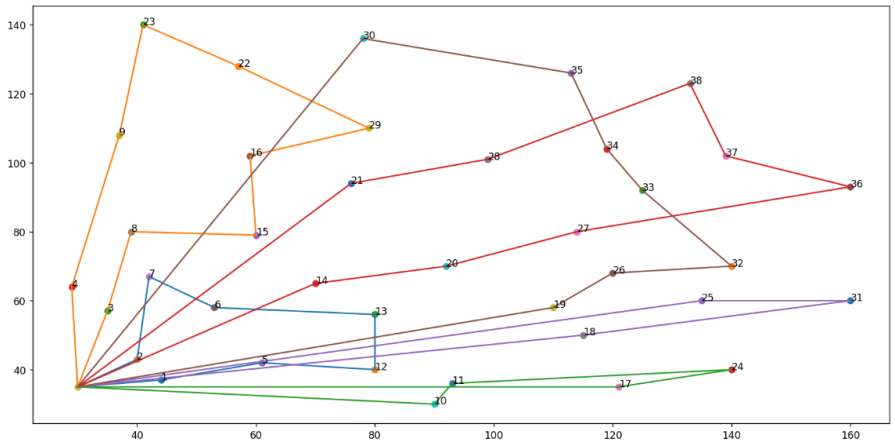

Fig. 2 - Pick-up vehicle routing diagram

Table 6

Optimization scheme of pick-up vehicle routing

Routings	Vehicle types	Cost(yuan)	Volume utilization rate	Load utilization rate
0→1→5→12→13→6→7→2→0	C	1547	84%	73%
0→4→9→23→22→29→16→15→8→3→0	C	1875	82%	72%
0→10→11→24→17→0	B	1796	87%	66%
0→21→28→38→37→36→27→20→14→0	C	1728	85%	72%
0→18→31→25→0	A	1113	78%	67%
0→30→35→34→33→32→26→19→0	C	1655	76%	52%

Note: The results in the table are rounded.

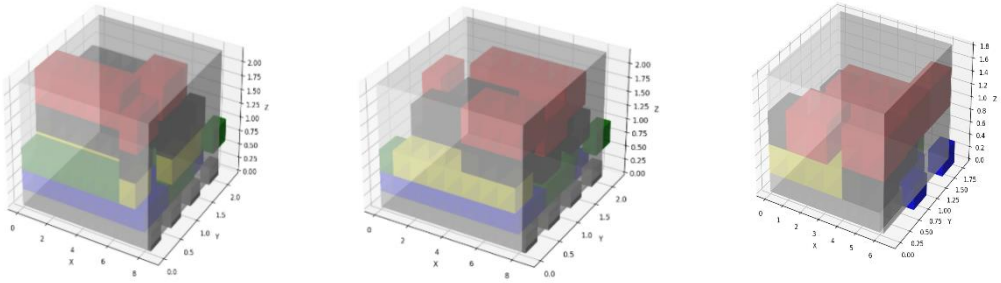

0→1→5→12→13→6→7→2→0 0→4→9→23→22→29→16→15→8→3→0 0→10→11→24→17→0

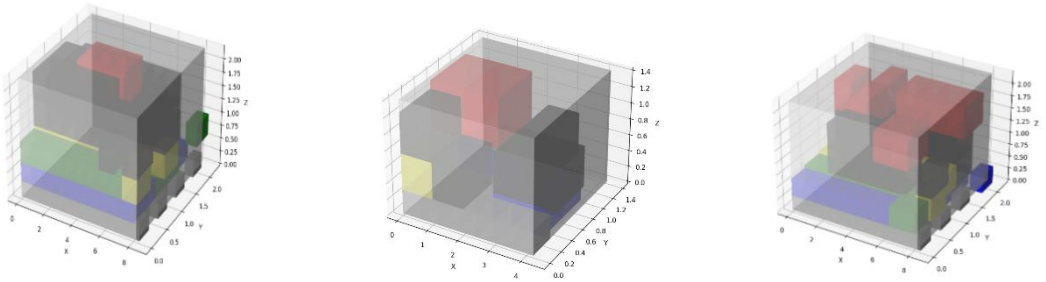

0→21→28→38→37→36→27→20→14→0 0→18→31→25→0 0→30→35→34→33→32→26→19→0

Fig. 3 - Three-dimensional diagram of cargo loading

CONCLUSIONS

To reduce pick-up time and cost, a joint optimization model of pick-up vehicle routing and cargo allocation for fresh agricultural products was constructed. ALNS and HDFS were integrated to solve the model. A case study of Kunming International Flower Auction Center was conducted to compare the schemes of pick-up vehicle routing before and after optimization. The following conclusions could be drawn:

(1) Compared with the original scheme, the total cost of the optimized scheme reduces by 9.6%, the number of vehicles used reduces by one, and the total volume utilization rate and total load utilization rate of the vehicle increase by 23% and 15%. The experimental results show that ALNS combined with HDFS has good sensitivity and can be applied to solve the proposed model in this study.

(2) The damage operators and repair operators are used to process the current solution, which enriches the diversity of the neighborhood structure, enhances the optimization ability of the algorithm, and helps the algorithm to avoid premature convergence and local optimal. A variety of operators designed according to the characteristics of the problem can even further solve the optimization problem of pick-up vehicle routing for large-scale fresh agricultural products, and provide more decision-making basis for enterprise operators.

The joint optimization of vehicle routing and cargo allocation is a very complex and systematic task. In this study, time limits and three-dimensional loading constraints are considered, which provides a reference for cold-chain logistics enterprises to optimize pick-up vehicle routing. However, the proposed model does not consider the impact of traffic accidents and weather conditions on vehicle driving and the change of pick-up point orders. Therefore, it is vital to construct a more realistic dynamic model in the future.

ACKNOWLEDGEMENT

This work was supported by the Natural Science Foundation of China (Grant No. 71904068) and Yunnan Provincial Colleges and Universities Education Cooperation Humanities (Grant No. SYSX202016).

REFERENCES

[1] Chi, J., & He, S. (2023). Pickup capacitated vehicle routing problem with three-dimensional loading constraints: model and algorithms. *Transportation Research Part E*, United Kingdom, *176,* 103208. http://dx.doi.org/10.1016/J.TRE.2023.103208

[2] Che, L., & Yang, Z. (2023). Optimization of cyclic pick-up path for simultaneous pick-up and delivery of auto parts under three-dimensional loading constraints (三维装载约束下汽车零部件同时取送的循环取货路径优化研究). *Journal of Chongqing Normal University (Natural Science)*, China, *40*(1), 61-72.

[3] Fernando, M. W., Thibbotuwawa, A., Perera, N., Nielsen, P., & Kilic, D. K. (2024). An integrated vehicle routing model to optimize agricultural products distribution in retail chains. *Cleaner Logistics and Supply Chain*, United Kingdom, *10*, 100137. http://dx.doi.org/10.1016/J.CLSCN.2023.100137

[4] Ines, S., & Saoussen, K. (2021). A novel adaptive genetic algorithm for dynamic vehicle routing problem with backhaul and two-dimensional loading constraints: a case in Tunisian Posta. *International Journal of Applied Metaheuristic Computing*, United States, *13*(1), 1-34. http://dx.doi.org/10.4018/IJAMC.2022010103

[5] Ji, B., Zhou, S., Samson, S., & Wu, G. (2021). An enhanced neighborhood search algorithm for solving the split delivery vehicle routing problem with two-dimensional loading constraints. *Computers & Industrial Engineering*, United Kingdom, *162,* 107720. http://dx.doi.org/10.1016/J.CIE.2021.107720

[6] Jiang, Y., Bian, Be, & Liu, Y. (2020) Integrated multi-item packaging and vehicle routing with split delivery problem for fresh agri-product emergency supply at large-scale epidemic disease context. *Journal of Traffic and Transportation Engineering (English Edition),* Netherlands, *8*(2), 196-208. http://dx.doi.org/10.1016/J.JTTE.2020.08.003

[7] Lv, D., Zhou, Q., Yang, M., & Chen, Q. (2014). Evaluation of AHP-based agricultural products circulation efficiency index. *BioTechnology: An Indian Journal*, India, *10*(18), 10305-10310.

[8] Li, S., Liu, Z., Fang, H., & Liu, L. (2019). Vehicle routing problem of fresh agricultural products considering decaying factors. *IOP Conference Series: Materials Science and Engineering*, United Kingdom, *688*(4), 044012. http://dx.doi.org/10.1088/1757-899X/688/4/044012

[9] Li, J., Liu, M., & Liu, P. (2021). Route optimization of multi-vehicle cold chain logistics for fresh agricultural products (生鲜农产品多车型冷链物流车辆路径优化). China, *Journal of China Agricultural University*, *26*(7), 115-123.

[10] Lin, Y., Zhao, X., & Shen, H. (2022). Research on route optimization of agricultural products transport vehicles based on improved genetic algorithm (基于改进遗传算法的农产品运输车辆路径优化研究). China, *Automation Application*, *12*, 5-8+14. http://dx.doi.org/10.19769/j.zdhy.2022.12.002

[11] Lehmann, J., & Winkenbach, M. (2024). A matheuristic for the two-echelon multi-trip vehicle routing problem with mixed pickup and delivery demand and time windows. *Transportation Research Part C*, United Kingdom, *160*, 104522. http://dx.doi.org/10.1016/J.TRC.2024.104522

[12] Liu, Z., Niu, Y., Guo, C., & Jia, S. (2023). A vehicle routing optimization model for community group buying considering carbon emissions and total distribution costs. *Energies*, Switzerland, *16*(2), 631. http://dx.doi.org/10.3390/EN16020931

[13] Ma, L., Chen, Z., & Li, Y. (2023). Research on the circulation strategy of agricultural products under extreme weather. *Journal of Physics: Conference Series*, United Kingdom, *2468*(1), 012153. http://dx.doi.org/10.1088/1742-6596/2468/1/012153

[14] Ni, C., & Katarzyna, D. (2024). Research on optimization of agricultural products cold chain logistics distribution system based on low carbon perspective. *International Journal of Information Systems and Supply Chain Management*, United States, *17*(1), 1-14. http://dx.doi.org/10.4018/IJISSCM.338220

[15] Pinto, L. F., Carlos, J. F., Augusto, G. H., Victoria, B. J. L., & Marko, B. (2021). A multi-start algorithm for solving the capacitated vehicle routing problem with two-dimensional loading constraints. *Symmetry*, Switzerland, *13*(9), 1697. http://dx.doi.org/10.3390/SYM13091697

[16] Rahmanifar, G., Mohammadi, M., Golabian, M., Sherafat, A., & Keshteli, M. H. (2024). Integrated location and routing for cold chain logistics networks with heterogeneous customer demand. J*ournal of Industrial Information Integration, Netherlands*, *38*, 100573. http://dx.doi.org/10.1016/J.JII.2024.100573

[17] Sun, M., & Pang, D. (2017). Vehicle routing optimisation algorithm for agricultural products logistics distribution. *International Journal of Applied Decision Sciences*, United Kingdom, *10*(4), 327-334. http://dx.doi.org/10.1504/IJADS.2017.087175

[18] Sbai, I., Krichen, S., & Limam, O. (2022). Solving the capacitated vehicle routing problem with two-dimensional loading constraints using a parallel VNS approach. *International Journal of Metaheuristics*, United Kingdom, *8*(1), 51-78. http://dx.doi.org/10.1504/IJMHEUR.2022.10052727

[19] Takahashi, T. (2003). The social meaning of the organic agricultural produce circulation channel formation by the organic farming management activities. *The Journal of Japan Society for Distributive Sciences*, Japan, *2003*(16), 51-57. http://dx.doi.org/10.14904/jsds1988.2003.51

[20] Varas, M., Baesler, F., Basso, F., Contreras, J. P., & Pezoa, R. (2024). A home hospitalization assignment and routing problem with multiple time windows, mandatory returns and perishable biological samples: a Chilean case study. *Computers & Industrial Engineering*, United Kingdom, *189*, 109951. http://dx.doi.org/10.1016/J.CIE.2024.109951

[21] Wang, Y., We,i Y., Jiang, Q., & Xu, M. (2021). Vehicle routing problem based on transportation resource sharing under three-dimensional loading constraints (三维装载约束下基于运输资源共享的车辆路径问题). *Computer Integrated Manufacturing Systems*, China, *29*(9), 3153-3170. http://dx.doi.org/10.13196/j.cims.2023.09.025

[22] Wei, L., Zhang, Z., & Lim, A. (2014). An adaptive variable neighborhood search for a heterogeneous fleet vehicle routing problem with three-dimensional loading constraints. *IEEE Computational Intelligence Magazine*, United States, *9*(4), 18-30. http://dx.doi.org/10.1109/MCI.2014.2350933

[23] Xie, R. (2022). Discussion on the development of "the first one kilometer" of cold chain logistics of fresh agricultural products in China (中国生鲜农产品冷链物流“最先一公里”发展探讨). *Journal of Commercial Economics*, China, *2*, 114-117.

[24] Zhu, S., Fu, H., & Li, Y. (2021). Optimization research on vehicle routing for fresh agricultural products based on the investment of freshness-keeping cost in the distribution process. *Sustainability*, Switzerland, *13*(14), 8110. http://dx.doi.org/10.3390/SU13148110

FIELD TRAVERSAL PATH PLANNING FOR AGRICULTURAL ROBOTS IN HILLY AREAS BASED ON DISCRETE ARTIFICIAL BEE COLONY ALGORITHM
/
基于离散人工蜂群算法的农业机器人丘陵地区农田遍历路径规划

Xiaodong LOU [1], Zheng LI *[2]
[1] College of Digital Commerce, Zhejiang Business Technology Institute, Ningbo, Zhejiang/ China
[2] School of Teacher Education, Shaoxing University, Shaoxing, Zhejiang/ China
Tel: +8615968035670; E-mail: lizheng@nbu.edu.cn
Corresponding author: Zheng Li
DOI: https://doi.org/10.35633/inmateh-72-42

Keywords: *Hilly area; agricultural robots; traversal path planning; 2-opt; discrete artificial bee colony algorithm*

ABSTRACT
In this study, the discrete artificial bee colony (DABC) algorithm was proposed to plan the path of agricultural robots traversing multiple fields in hilly areas. Based on the basic ABC algorithm as the framework, the path coding method was adopted, and the discrete crossover operator, reverse operator, immune operator, and single/multi-step 2-opt operator were comprehensively used to help hired bees, observing bees, and scout bees to generate new food sources. Finally, the optimized field traversal order and the entrance and exit distribution of each field were obtained. The simulation results showed that compared with the traditional ABC algorithm, the average shortest path of the DABC algorithm proposed in this study was shortened by 1.59%, accompanied by the less iterations contributing to algorithm convergence and good ability to jump out of the local optimal solution. The simulation experiment was carried out using real field data and field operation parameters. The field traversal order and the entrance and exit distribution obtained by the proposed method can effectively reduce the length of the transfer path and its repeatability. This study exhibits superiority and feasibility in the field traversal path planning of agricultural robots in hilly areas, and the trajectory coordinates output by the algorithm can provide a path reference for large-area operations of agricultural machinery drivers or unmanned agricultural machineries.

摘要
本研究针对丘陵地区的农田环境下农业机器人遍历多个田块的遍历路径问题，提出了离散人工蜂群算法对农业机器人丘陵地区农田遍历路径进行规划。以基本人工蜂群算法为框架，采用路径编码的方式，综合运用离散交叉算子，逆转算子，免疫算子和单/多步 2-opt 算子以帮助雇佣蜂，观察蜂和侦察蜂产生新食物源，最终得到优化后的田块遍历顺序以及每个田块的进出口分布。仿真结果表明，与传统人工蜂群算法相比，本研究提出的离散人工蜂群算法平均最短路径缩短 1.59%，算法收敛迭代次数更少，并表现出较好的跳出局部最优解的能力。利用真实的农田数据和田间作业参数进行仿真试验，通过本研究方法得到的田块遍历顺序和进出口的排布能够有效地减少转移路径的长度和路径的重复率。本研究在农业机器人丘陵地区农田遍历路径规划上的优越性和可行性，算法输出的轨迹坐标能为农机驾驶员或无人农机在大面积作业时提供路径参考。

INTRODUCTION
Intelligent agricultural robots are an emerging technology in the field of agriculture, which is gradually being promoted and applied globally. The development of this technology began with the high automation and intelligence requirements of agricultural production. Agricultural technology enterprises from various countries have invested in research and development, and have achieved a series of research results. Intelligent agricultural robots have been widely used in fields such as traversing farmland, monitoring pests and diseases, and fertilizing herbs. It is based on high-precision sensors and advanced image recognition technology, which can autonomously inspect, identify pests and diseases, monitor meteorological data, and achieve big data analysis and decision support through cloud computing. In the field of farmland traversal, intelligent agricultural robots adopt advanced autonomous navigation and path planning algorithms, which can independently complete farmland traversal tasks and accurately cover the entire farmland. Compared to traditional manual traversal methods, robots have a faster traversal speed and can greatly improve the efficiency of agricultural production.

In China, the cultivated area in hilly and mountainous counties accounts for about 34.62% of national cultivated area, and the sown area accounts for 34.20% of the total sown area across China. The agricultural development in such areas is of crucial importance to the supply of agricultural products and facilitating farmers to get rid of poverty and become better off *(Xu et al., 2021)*. However, the field structure in hilly areas is obviously different from that in flat areas. Hilly areas are characterized by small irregularly and densely distributed fields with obstruction by ridges, which brings about a series of challenges to the operation of agricultural machineries and seriously impedes the mechanized and intelligent agricultural development *(Lan et al., 2021)*. Therefore, the development of intelligent agricultural machinery and equipment suitable for hilly areas is an important way to improve working capacity and quality, reduce costs, ensure national food security, and alleviate the shortage of rural labor *(Liu et al., 2020)*. In recent years, with the rapid development of mobile robot technology, intelligent equipment has been widely used in various fields of society, bringing great convenience to people's production and life. As a kind of agricultural robot, mowing robots are not only used for lawn mowing in municipal green spaces, airports, and golf courses but also for weeding in cultivated land and woodland, so they have drawn extensive concerns, and traversal path planning plays a vital role in the application of mowing robots *(Chen et al., 2022)*. Full-coverage traversal path planning is a special type of path planning in two-dimensional environment, which refers to finding a continuous path from the starting point to the end point and passing through all reachable points in a set area on the premise of satisfying some optimal performance indicators *(Zhang et al., 2017*). Up to now, a lot of research results have emerged regarding this technology. Intelligent agricultural robots have enormous development potential and broad application prospects in field traversal. Through efficient traversal ability, precise recognition function, diversified data collection, and intelligent operation interface, intelligent agricultural robots provide comprehensive technical support for agricultural production. With the continuous progress and promotion of technology, it is believed that intelligent agricultural robots will play an increasingly important role in the field of agricultural traversal, further promoting the modernization and intelligence of agricultural production (*Jeddisaravi et al.*, *2016*). In this study, therefore, a discrete artificial bee colony (DABC) traversal algorithm was proposed, which determined the traversal order of sub-areas after the target area was divided, and carried out cross-area transfer path planning to realize the field traversal path planning of agricultural robots in hilly areas.

Literature review

After the 1970s, industrial robots flourished and began to back-feed agriculture, and the most advanced technology in industrial robots was applied to the agricultural field, which resulted in a variety of agricultural robots with varied functions. Advanced technology was put into agricultural production, which significantly improved the efficiency of agricultural production (*Guruji et al.*, *2016*).

Rokbani et al., (2018), designed a double-heuristic ant colony optimization algorithm to solve the traveling salesman problem, which provided a theoretical basis for robot field traversal path optimization. To finish pesticide spraying and insect repellent tasks more accurately and efficiently, *Sun et al. (2017),* proposed an improved algorithm to solve the path optimization problem of mobile robots. *Zhao et al. (2018),* put forward the application of smooth AR (Augmented Reality) algorithm in intelligent vehicle path planning. *Zhao et al. (2018)* developed an autonomous robot that combined a novel obstacle separation algorithm and could continuously pick strawberries in multiple tunnels, making it possible for robots to pick strawberries located in the cluster. The obstacle separation algorithm pushes off the surrounding leaves, strawberries, and other obstacles through the gripper (*Zhao et al., 2018*). *Zeng et al. (2016)* developed a green agricultural robot based on machine vision technology. When conducting experiments on a field farm planed with pineapples, bananas, and apples, the robot collects the surrounding environmental information through cameras, sensors, and other equipment, feeds back the information to the monitoring personnel in real time, and walks freely among crops by using machine vision navigation technology. *Ding et al. (2021)* put forward an algorithm combining fuzzy logic with artificial potential field. When the robot falls into the local minimum, the fuzzy controller will generate an angle to change the current driving direction so that the robot can escape from local minimum and avoid obstacles safely *(Ding et al., 2021). Gu et al. (2021)* developed a new hybrid algorithm, that is, combining PSO with artificial potential field, which is applicable to complex scenarios with multiple obstacles. This algorithm can find the drivable path quickly, with short calculation time and high planning efficiency *(Gu et al., 2021).*

Wang et al. (2019) proposed an improved APF (Artificial Potential Field Method Path Planning Algorithm) method based on the dynamic window method to solve the tendency of robots to fall into the local minimum before reaching the destination. The points around the robot were evaluated in the local minimum through an evaluation function, and the best point was selected as the next path point *(Wang et al., 2019).*

Path planning, a key component of intelligent agricultural systems, can optimize the driving route of agricultural machinery and minimize repetitive work and time waste *(Li et al., 2020)*. Through reasonable path planning, agricultural machineries can cover fields efficiently, ensure that crops are fully cultivated and managed, and improve the crop yield and quality *(Wang et al., 2018)*. In agricultural production, the path covering field and generated by coverage path planning is used for agricultural machinery to perform specific operations, including harvesting, sowing, and fertilizing. The coverage path planning for a single field is mainly divided into two parts. First, a set of parallel straight-line trajectories are generated according to field data and agricultural machinery parameters. Secondly, parallel trajectories are connected to form an optimal trajectory sequence connected by arcs *(Tu et al., 2018). Heidari et al. (2019)* expressed the field coverage trajectory as the main operation area trajectory, the edge passage and the turning trajectory to construct a virtual road network map, and finally planned the coverage path based on the map. It is experimentally proved that this method is universal for all types of fields *(Heidari et al., 2019). Li et al. (2021)* adopted the simulated annealing algorithm to obtain the optimal path set, and solved the full-coverage traversal order through unit disassembly and synthesis. Compared with the traditional rule traversal method, *Li et al. (2021),* effectively dealt with different boundary constraints and greatly reduced the consumption of operations. Considering many warehouses for agricultural machinery replenishment around the field, *Song et al. (2019)* designed the connection paths for connecting warehouses, edge passages, and coverage paths, and used the simulated annealing algorithm to solve the traversal order between coverage paths. The existing research on multiple fields focuses on decomposing large-scale fields with complex shapes into several sub-fields with simple shapes according to certain laws, and then using intelligent algorithms to realize the optimal traversal sorting of sub-fields based on related traversal indexes. *Hu et al. (2021)* proposed a traversal algorithm combining memory simulated annealing with A* algorithm, which is a heuristic search algorithm widely used for path finding and graph traversal. First, the walking order of the optimal target point of the task was searched by memory simulated annealing algorithm, and then the cross-area connection path planning was carried out by A* algorithm. Considering the slope of fields in hilly areas, *Zhang et al.* (*2019*). obtained the optimal driving angle based on the energy consumption model of agricultural machinery, and then used genetic algorithm to obtain the optimal traversal order of multiple fields. The results show that this method can minimize the energy consumption of agricultural machinery to the greatest extent. To sum up, most of the existing studies are aimed at the coverage path planning of a single large field, while in a few studies on the traversal path planning of multiple fields, the linear distance is generally taken as the distance cost. Since the fields in hilly areas are small and densely distributed with obstruction by ridges, there lacks definite connected relations between fields, leading to the failure to form a continuous driving route between them and making it necessary to repeatedly seek for the appropriate position for transfer, which increases the operating time and costs. Given the aforesaid problems, this study aims to discuss the traversal route planning method of agricultural robots applicable to hilly areas. Through field investigation and data collection, the fields in hilly areas were surveyed in detail, and a method establishing the connecting related relations between fields was designed. Meanwhile, the DABC (Improved artificial bee colony algorithm based on differential mutation operator) traversal algorithm was put forward. Based on the road network diagram between fields, this distance was regarded as the distance cost required for inter-field transfer, and the optimal traversal order of multiple fields was obtained by DABC algorithm, thus realizing the multi-field traversal path planning of agricultural robots. This study aims to provide theoretical guidance and technical support for agricultural robots to realize continuous large-scale operations in hilly areas, so as to improve operation efficiency and agricultural production level.

MATERIAL AND METHODS

Search node positioning of intelligent agricultural network equipment

In this study, environment modeling of fields in hilly areas was performed using structural space method. The principle of structural space method is to express the working environment of robot through space modeling. At the same time, the structure space is integrated with the obstacle information and the pose information of the robot during operation. Then, the path search algorithm is used to solve a better safe path.

Voronoi diagram is a typical representative of structural space method. When constructing the model, Voronoi diagram regards the obstacle vertices in the environment as a set composed of multiple points. The trajectory formed by the points with close distance in the set is the edge of the map, and the vertex of the map is formed by the intersection of these trajectories. At the same time, these points are not allowed to penetrate the obstacle directly. This modeling method maximizes the distance between the obstacle and the robot. Therefore, it is difficult to find a better safe path when using this method to build an environment model.

The geometric characteristics of the agricultural robot traversing the environment were mapped into the geometric space for description through points, lines, and planes. In the actual traversal, it is necessary to reserve turning space and edge area according to the parameters of agricultural robots and traversal parameters. Hence, the field was divided into two functional areas: edge area and main traversal area. The edge area was used to meet the needs of agricultural robots to turn around and change lines. The main traversal area consisted of a series of parallel straight-line trajectories, in which agricultural robots carried out farming, sowing and other operations.

The calculation method of the edge area width W_h is shown in Formula (1).

$$W_h = r + \frac{\omega}{2} + r \times |\cos\varphi| \tag{1}$$

where r represents the minimum turning radius of the agricultural robot; ω represents the traversal width; φ indicates the included angle between the traversal direction and the field boundary. According to this calculation method, the edge area and main traversal area of fields were constructed. The edge of the field, which is close to the field boundary, is specially used for agricultural robots to turn. When turning in the field, the agricultural robot will not make a specific traversal. This means that the agricultural robot can move in the edge area after completing the coverage traversal of the field in the main traversal area so that it can smoothly transfer to the next field. Such an arrangement can ensure that the agricultural robot can move between fields more efficiently and smoothly.

Fitness function

The following constraints need to be met in the process of agricultural robot's traversal path planning: the traversal path of the agricultural robot must be limited in the map space and cannot exceed the map boundary; the traversal path length of the robot is the shortest to ensure that the acquired path is the optimal one; the traversal path of the agricultural robot cannot cross the obstacle area of fields to avoid collision; because agricultural robots traverse terraces in hilly areas with a height difference in the traversal path, it is necessary to consider the influence of height change on the fitness function; according to the above constraints, the traversal path planning problem of agricultural robots can be abstracted as a single-objective optimization problem with the minimum fitness, and the fitness function of the problem can be derived as follows:

$$\min f = \sum_{i=1}^{n} L_{\text{path}}(i) + G_{\text{obstacle}}(p_i) \tag{2}$$

Among them: i is the number of algorithm iterations; $L_{\text{path}}(i)$ represents the length of the path planned for the robot upon the i-th iteration, which is specifically defined as below:

Where (x_i, y_i, z_i) stands for the position coordinates of the robot upon the i-th iteration; $(x_{i-1}, y_{i-1}, z_{i-1})$ denotes the position coordinates of the robot upon the i-1-th iteration; the solved $L_{\text{path}}(i)$ is the Euclidean distance between two points.

$$L_{\text{path}}(i) = \sqrt{(x_i - x_{i-1})^2 + (y_i - y_{i-1})^2 + (z_i - z_{i-1})^2} \tag{3}$$

$G_{\text{obstacle}}(p_i)$ is used to judge whether the path point p_i transcends the boundary or its ligature with the previous path point crosses the obstacle upon the i-th iteration. When the path point is feasible, the return value is 0, or otherwise, a relatively large constant $N \times N$ will be returned, which is specifically defined as follows:

$$G_{\text{obstacle}}(p_i) = \begin{cases} N \times N, p_i \text{ infeasible} \\ 0, p_i \text{ feasible} \end{cases} \tag{4}$$

Algorithm design

The DABC algorithm proposed in this study to solve the field traversal problem of agricultural robots in hilly areas included 5 main components, namely, control parameter initialization, bee colony (food source) initialization, hired bee stage, observing bee stage, and scout bee stage.

Control parameter initialization

The DABC algorithm has 3 control parameters, namely colony_Size, abandonment condition $limit$ and termination condition max_Evaluations. In the DABC algorithm, the whole bee colony contains an equal number of hired bees and observing bees, and each hired bee corresponds to a food source (that is, a solution in the solution space). Therefore, the number of food sources food_Number is half the size of the bee colony,

that is, food_Number=colony_Size/2. For each food source S_i, the variable $trial_i$ records the number of times for which the food source has continuously not been improved during the search. If the corresponding *trial* value of a food source exceeds the predetermined *limit*, the food source will be abandoned by the corresponding hired bees and replaced by a new food source randomly searched by the scout bees. The algorithm continuously repeats the hired bee stage, observing bee stage, and scout bee stage until the number of evaluations of the objective function (1) exceeds the allowed maximum value max_Evaluations, and then the algorithm terminates. Before the start of the DABC algorithm, the values of the above three control parameters need to be determined manually, and the algorithm performance is affected by different values of the control parameters (*Li et al., 2020*).

Bee colony initialization

As for bee colony initialization, the DABC algorithm encodes the food source in the order of field traversal. For n fields, each food source is encoded as a complete array from 0 to n-1. This encoding method has the following advantages: The legal constraints for field traversal of agricultural robots in hilly areas are hidden in bee colony initialization, crossover operation, and other operations, i.e., field number will not appear repeatedly. In the initialization stage, the algorithm, randomly generates food_Number food sources (solutions) according to the search space of the problem. Next, the objective function of random solutions is calculated so as to find the optimal (minimum objective function) food source gbest_Solution in the current bee colony is found. In this case, the number of evaluations is food_Number, and the trial of each food source is initialized as 0.

Hired bee stage

In the hired bee stage, for food source S_i, its neighbor is determined first. Here, "Neighbor" is defined as another food source randomly selected by the bee colony (*Han et al., 2019*). Then, one offspring individual of S_i and neighbor is generated using a crossover operator and evaluated after being applied with a reverse operator, an immune operator, and a single-step 2-opt operator. If Off_spring is better than S_i, S_i is replaced by Off_spring and $trial_i$ is set to 0, or otherwise, the value of $trial_i$ will increase by 1. If Off_spring is also better than gbest, gbest will then be updated.

Crossover operator: In this study, a partial matching crossover operator (PMX) was adopted. Specifically, one segment is randomly chosen from the two parent strings. A series of exchanges are defined using the elements of the two parent strings in the selected segment, which can execute respectively in each parent string to generate offspring chromosomes. For parent strings p1= [6 5 1 ,7 4 0 2,3 8 9] and p2= [5 0 6, 3 8 1 7,2 9 4], the sub-strings generated by the exchanges, which are defined by the elements in the selected segment, are q1= [5 2 6,7 4 0 1,3 8 9] and q2= [5 0 6,3 8 4 7,2 9 1], respectively.

Reverse operator: the traversal points between two different random positions in the path string are numbered in reverse order. This operator is beneficial to the small-scale migration of the algorithm.

Immune operator: Immune operator is a common technical means of solving the field traversal problem of agricultural robots in hilly areas. Specifically, a position pos is randomly chosen from the path string, and the nearest field is found around the traversal points corresponding to this position and inserted after pos. For example, p= [6 5 1 ,7 4 0 2,3 8 9], if the field number corresponding to the randomly selected position is 6 and the field number closest to field 6 is 2, then the new individual p'= [6 5 2 ,7 4 0 1,3 8 9] is obtained after the immune operator is executed.

Single-step 2-opt operator: Similar to the reverse operator, this operator numbers the traversal points between two different random positions in the path string in reverse order. Differently, before reverse ordering, it is necessary to judge whether the objective function is improved after reverse ordering. If yes, the reverse ordering will be implemented; if not, the original path string will keep unchanged *(Ding et al., 2021).* The 2-opt operator is a very effective local search technology for solving the TSP problem, which has been widely used in all kinds of evolutionary algorithms. The pseudo-code for the hiring phase looks like this:

For i=1 to foodNumber

1. For each solution S_i, determine its "neighbor"; // Use the crossover operator to generate offspring of S_i and its neighbors

2.Offspring =crossoverOperator(S,neighbor)// Perform the reversal operator on the Offspring

3.Offspring =inverseOperator(Offspring)// Immunizes the Offspring

4.Offspring =immuneOperator(Offspring)// Run the one-step 2-opt operator on the Offspring

5.Offspring =2-opt(Offspring)
6. Assess the Offspring
7.evaluations =evaluations +1
8. If (Offspring is better than S_i) Replace S_i with Offspring
trial[i]=0
else
trial[i]=trial[i]+1
9. Replace If(Offspring is better than gbestSolution) with Offspring
gbestSolution

Observing bee stage

In this stage, the observing bees will select individuals by means of roulette for improvement according to the food source information provided by the hired bees. The probability for the *i*-th food source to be chosen is denoted as $prob_i$, which is calculated as follows:

1) Calculate the objective function T_i of the *i*-th food source;
2) Find the minimum value *min* in all T_i;
3) Calculate $D_i = T_i - min$, $i = 1, 2, \ldots, FN$, in which *FN* denotes food_Number, i.e., the number of food sources;
4) Calculate $sum = \sum_{i=1}^{FN} D_i$;
5) If $sum > 0$, $prob_i = 1 - (0.9 \times \frac{D_i}{sum} + 0.1)$; if $sum = 0$, $prob_i = 1/FN$.

In a specific bee colony, the minimum value *min* of the objective function for all food sources is fixed. If $sum > 0$ (namely, the objective functions of different food sources are not completely equal), $prob_i$ is calculated. In this case, the smaller the objective functions of food sources (the better), the smaller the D_i value, the greater the $prob_i$ value, i.e., outstanding food sources will be chosen at a relatively large probability. If $sum = 0$ (namely, the objective functions of all food sources are equal), the probability for each food source to be chosen is $prob_i = 1/FN$.

After one food source is successfully selected, the observing bees will perform reverse and immune operations for this food source, followed by the execution of the multi-step 2-opt operator. For *n* traversal points, the 2-opt operation is implemented totally $n(n-1)/2$ times *(Huang et al., 2021)*, specifically as follows. The pseudo-code for the watch-bee phase looks like this:

Calculate the selection probability prob
i=0; t=0;
While t < foodNumber
If rand < prob[i]
1.t++; Offspring =S// Perform the reversal operator on Offspring
2.Offspring =nverseOperator(Offspring)// Immunize the Offspring
3. Offspring =immuneOperator(Offspring)// Perform the multi-step 2-opt operator on the Offspring
4.Offspring =exhausted2-opt(Offspring)
5. Assess the Offspring
6.evaluations = evaluations +1
7.I(Offspring is better than Si. Replace Si with Offspring
trial[i] = 0
else
trial[i] = trial[i] + 1
8.If(Offspring is better than gbestSolution)
Replace gbestSolution with Offspring
End If
i=i+1
If(i== foodNumber) i= 0
End While

Scout bee stage

The process of the scout bee stage is as aforesaid. When the trial value of one food sources exceeds the limit, the food source will be abandoned, and the corresponding hired bees will be converted into scout bees. First, the food source with the maximum trial value in the bee colony is found, and whether its trial value is greater than the limit is judged. If yes, a new food source (solution) is randomly generated and improved using the greedy strategy, followed by the implementation of the reverse, immune, and multi-step 2-opt operators. Finally, the new solution is evaluated and used to replace the original food source. In this stage, the greedy strategy is defined as follows: the first traversal point of the old solution is kept unchanged, and the traversal point nearest to the first one is found from the rest ones as the second traversal point, i.e., the traversal point nearest to the previous one is found each time as the next traversal point until all traversal points are traversed. The operation of the other operators resembles that in the hired bee and observing bee stages, which, therefore, will not be repeated hereby. The pseudo-code for the scout bee phase looks like this:

// Determine the food source with the maximum trial value
maxTrialIndex = 0
For(j=l; j<foodNumber; j++)
If (trial[j] > trial[maxTrialIndex])
maxTrialIndex =j;
End For
If trialmaxTrialIndex] > limit
1. Randomly generate a new food source solution
2. Adopt greedy strategy to improve solution// Implement reversal operator on solution
3.solution= inverseOperator(solution)// Applies the immune operator to the solution
4. solution= immuneOperator(solution)// Perform the multi-step 2-opt operator on the solution
5.solution= exhausted2-opt(solution)
6. Evaluate the solution
7.evaluations =evaluations +1
8. Replace the maxTrialIndex food source with solution
9.trial[maxTrialIndex] =0
End If

Example analysis

Simulation experiment

To verify the effect of the multi-field traversal path planning method proposed in this study, the simulation experiment was carried out using real field data and field operation parameters in MATLAB2014a programming environment. The actual operation area was chosen as the simulation object, with its satellite images displayed in Fig.1

Fig. 1 - Field satellite image of traversal path planning simulation test

The working area consisted of 22 groups of fields, the boundary contour of which was irregular. The data parameters of each field are shown in Table 1. The working parameters of the agricultural robots were as follows: the minimum turning radius was 1.5 m, and the working width was 2 m.

In Fig.1, it is assumed that a vertical line at the leftmost endpoint is the Y axis of the coordinate system, and a horizontal line at the bottom endpoint is the x axis of the coordinate system, and the intersection of the x and Y axes is the origin of the coordinates.

Table 1

Traversal path planning simulation test field data parameters

Farmland serial number	Area (m^2)	Circumference (m)	coordinates (X) m	coordinates (Y) m
1	105	48	10.61	43.7
2	99	45	22.8	44.12
3	52	30	29.76	43.78
4	237	71	23.29	38.38
5	110	56	24.63	40.31
6	313	105	34.29	39.08
7	232	169	55.07	33.67
8	241	190	73.94	32.43
9	243	209	76.39	30.01
10	98	52	86.35	32.43
11	89	50	11.4	25.5
12	225	83	35.45	20.57
13	97	32	47.78	27.26
14	93	106	44.7	22.75
15	201	142	79.31	26.76
16	237	162	79.08	27.29
17	87	56	32.11	18.44
18	49	30	40.37	19.26
19	94	54	45.00	24.63
20	102	45	51.11	26.19
21	320	121	80.14	20.07
22	90	48	88.78	18.98

In this section, the DABC algorithm was mainly used to solve some test problems in the field traversal of agricultural robots in hilly areas, and the simulation results were recorded and analyzed. According to the parameter selection experiment in the previous section, the control parameters of the DABC algorithm were set as colony_Size=100, limit=500, and max_Evaluations=1,000,000. The number of independent operations was set toNt and the number of times to successfully find the theoretical optimal value to Ns, and then the success rate was Ns/Nt×100%. Agricultural robots must stop at all monitoring points in the process of traversing fields in hilly areas. The DABC algorithm and traditional ABC algorithm were respectively subjected to simulation tests, and the corresponding calculation results were compared.

RESULTS

To eliminate the influence of various random factors and verify the advantages and disadvantages of the DABC algorithm designed in this study, the DABC algorithm was used to optimize the traversal detection path of agricultural robots for 200 times. The convergence curve of the DABC algorithm is shown in Fig. 2. The optimal path of agricultural robot inspection is shown in Fig. 3

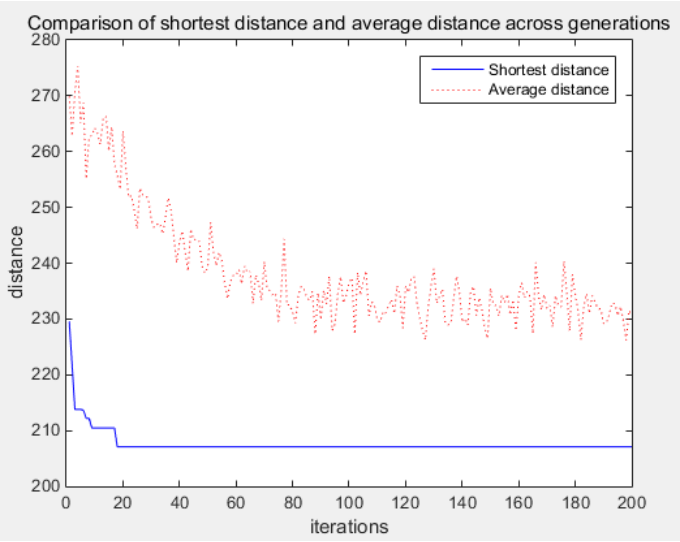

Fig. 2 - Convergence curve of discrete artificial bee colony algorithm

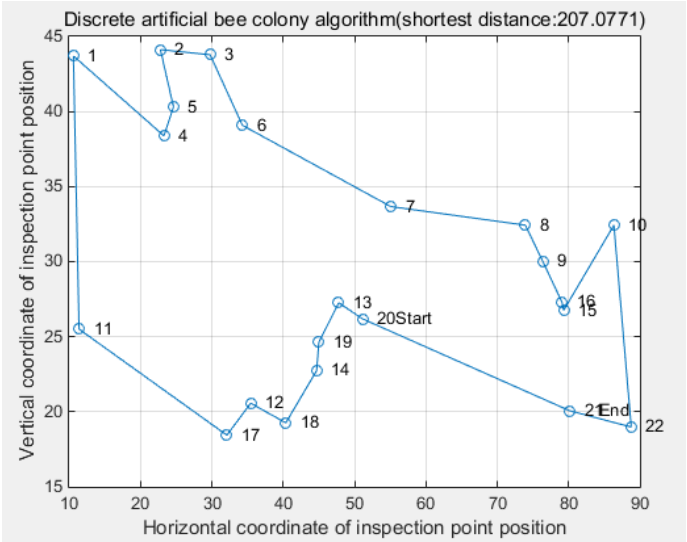

Fig. 3 - Agricultural robot traverses the optimal path(m)

To verify the effectiveness of the model and algorithm, the traditional ABC algorithm was used on the same platform, and the optimization model proposed in this study was solved with the same parameters. For the sake of more scientific and effective experimental results, the maximum number of iterations of the traditional ABC algorithm was also set to 200, and its convergence curve is exhibited in Fig. 4 and the optimal path traversed by agricultural robots is displayed in Fig. 5.

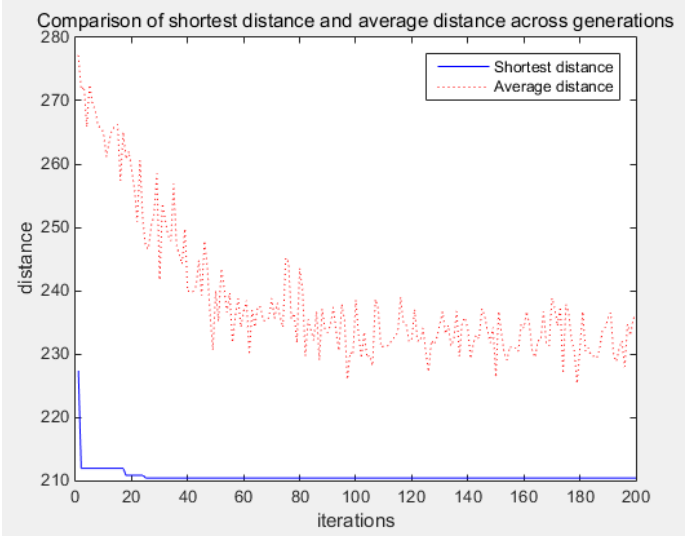

Fig. 4- Convergence curve of traditional artificial bee colony algorithm

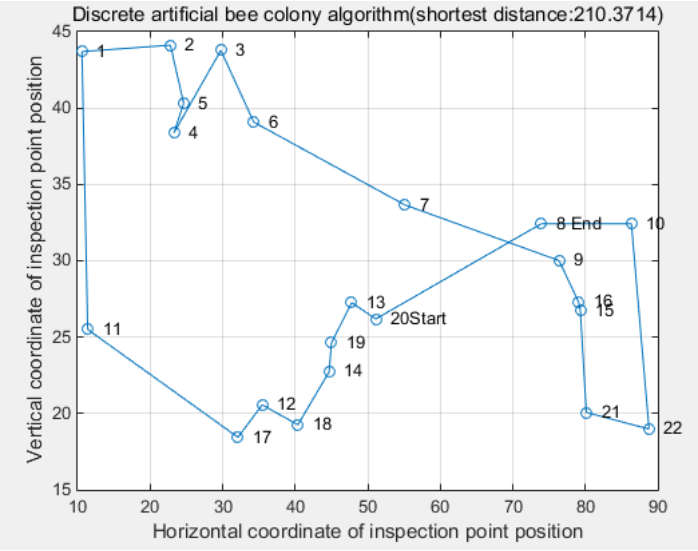

Fig. 5 - Agricultural robot traverses the optimal path

The DABC algorithm was compared with the traditional ABC algorithm in the inspection path, the total traversal travel distance of agricultural robots, and convergence time, as seen in Table 2.

Table 2

Comparison of discrete artificial bee colony algorithm and traditional artificial bee colony algorithm

Algorithm	Inspection path	Distance (m)	Algorithm convergence time (s)
Discrete artificial bee colony algorithm	20→13→19→14→18→12→17→11 →1→4→5→2→3→6→7→8→9→16→15 →10→22→21→20	207.08	56.17
Traditional artificial bee colony algorithm	20→13→19→14→18→12→17→11 →1→2→5→4→3→ 6→7→9→16→15→21→22→10→8→20	210.37	68.11

As seen in Table 2, the optimization ability and convergence of the DABC algorithm were stronger than those of the traditional ABC algorithm. It could be intuitively seen from the convergence curves of algorithms that in terms of the total traversal distance of agricultural robots, the optimal path length acquired by the DABC algorithm was better than that obtained through the traditional ABC algorithm. The total traversal distance of the DABC algorithm was 3.29 m shorter than that of the traditional ABC algorithm with a reduction of 1.59%; in the aspect of convergence time, the convergence time of the traditional ABC algorithm was longer than that of the DABC algorithm. In addition, the convergence time of the DABC algorithm was 11.94 s shorter than that of the traditional genetic algorithm by 21.26%. The experimental results show that this method has better performance in terms of path length and path repetition rate, and the arrangement of field traversal sequence and import and export can effectively reduce the path length and path repetition rate.

By using discrete artificial bee colony algorithm to search for the optimal traversal order of task target points, the agricultural robot can traverse all target points with minimum moving cost. At the same time, the discrete artificial bee colony algorithm is used to plan the cross-region connection path, and the shortest and collision-free walking path between the target points is found. In the traversal process of agricultural robot, the vertex of the zone closest to the end point of the previous farmland is selected as the starting point of this farmland, and then "round-trip" traversal planning is carried out along the long side, and finally the traversal path planning of the entire farmland map is realized.

CONCLUSIONS

In this study, a new DABC algorithm was proposed to effectively solve the field traversal problem of agricultural robots in hilly areas. Then, the effectiveness of the proposed algorithm was verified through simulation experiments. Finally, the main conclusions were drawn as follows:

(1) Given the small and densely distributed fields in hilly areas with obstruction by ridges between fields and no connected relations between fields, a method of establishing the connected relations between fields was proposed in this study, aiming to predict how agricultural robots will transfer to the next field after completing the coverage path of one field.

(2) A DABC algorithm was raised to solve the field traversal order planning problem. Following the idea of the adaptive strategy, the new algorithm transformed feasible solutions into food sources by means of path encoding. In the hired bee, observing bee, and scout bee stages, new food sources were generated by the algorithm based on the discrete crossover operator, reverse operator, and immune operator, and the algorithm performance was improved using the famous single/multi-step 2-opt local search algorithm. The MATLAB simulation experimental results showed that the average traversal path distance obtained by the improved genetic algorithm was reduced by 1.59% than that acquired through the traditional genetic algorithm.

(3) Through the comparative analysis of experiments, the field traversal order and the entrance and exit arrangement obtained by the proposed method can effectively reduce the path length and its repeatability, providing the superiority and feasibility of the proposed method. Meanwhile, the trajectory coordinates output by the algorithm can provide a reference for the large-area operations of agricultural machinery drivers or unmanned agricultural machineries. The follow-up study will focus on solving the challenges faced by intelligent algorithms in practical applications, especially online real-timeliness of navigation systems, Kalman linear filtering, etc.

REFERENCES

[1] Chen, K., Xie, Y.S., Li, Y.M., Liu, C.L., &Mo, J.Q. (2022). A full coverage path planning method for agricultural machinery under multi-constraint conditions (多约束情形下的农机全覆盖路径规划方法). *Transactions of the Chinese Society for Agricultural Machinery*, Vol.53, No.5, pp.17-26, Beijing/China.

[2] Ding, J.H., Mao, Y.L., & Gu, L.B. (2021). Robot path planning based on improved genetic algorithm. *Journal of Henan Science and Technology*, Vol. 40, No. 27, pp. 6-8, Henan/China.

[3] Ding, X. C. & Wang, H.J. (2021). A multiple optimization algorithm based on cuckoo iterative updating strategy. *Computer Engineering and Applications*, vol. 58, pp. 1-8, Beijing/China.

[4] Guruji, A.K., Agarwal, H., & Parsediya, D.K., (2016). Time-efficient Algorithm for Robot Path Planning. *Procedia Technology*, Vol. 23, No. 2, pp. 144-149, Netherlands.

[5] Gu, P., Li, H.C., & Yang, S.Y. (2021). Improvement and implementation of Q-learning algorithm. *Computer Science and Application*, Vol. 11, No. 7, pp. 1994-2007, Wuhan/China.

[6] Han, J., Zhu, K., Liu, Y., & Harris, R. A. (2019). Enforced microglial depletion and repopulation as a promising strategy for the treatment of neurological disorders, *Glia*, Vol. 67, No. 2, pp. 217-231, United States.

[7] Heidari, A.A., Mirjalili, S., Faris, H., Aljarah, I., Mafarja, M., & Chen, H. (2019). Harris hawks optimization: algorithm and applications. *Future Generation Computer Systems*, Vol. 97, pp. 849-872, Netherlands.

[8] Huang, L.W. (2021). Application of principal component analysis based on ideal point in comprehensive evaluation. *Management Decision*, Vol. 37, pp. 184-188, United Kingdom.

[9] Hu, J.B., Wang, X.S., & Zhang, Q. (2021). Optimization of multi-step ant colony algorithm for robot path planning problem. *Sensor and Micro System*, Vol. 40, No. 10, pp. 121-124, Sichuan/China.

[10] Jeddisaravi, K., Alitappeh, R.J., Pimenta, L. C. A., & Guimarães, F.G. (2016). Multi-objective approach for robot motion planning in search tasks. *Applied Intelligence*, Vol. 45, No. 2, pp. 305-321, USA.

[11] Li, S.M., Chen, H.L., Wang, M.J., Heidari, A. A., & Mirjalili, S. (2018). Moth search algorithm: a bio-inspired metaheuristic algorithm for global optimization problems. *Memetic computing*, Vol. 10, No. 2, pp. 151-164, Germany.

[12] Liu, C.L., Lin, H.Z., Li, Y.M., Gong, L. & Miao, Z.H. (2020). Research Status and Development Trend of Intelligent Control Technology for Agricultural Equipment (农业装备智能控制技术研究现状与发展趋势分析). *Transactions of the Chinese Society for Agricultural Machinery*, Vol.51, No.1, pp.1-18, Beijing/China.

[13] Li, Z.K., Huang, Y.Q., & Xu, Y.Q. (2020). Path planning of mobile robot based on improved variable step size ant colony algorithm. *Journal of Electronic Measurement and Instrument,* Vol. 34, pp. 15-21, Beijing/China.

[14] Li, S.M., Chen, H.L., Wang, M.J., & Heidari, A.A., & Mirjalili, S. (2020). Slime mould algorithm: a new method for stochastic optimization. *Future Generation Computer Systems*, Vol. 111, pp. 300-323, Netherlands.

[15] Li, B., Yang, H.Z., & Gan, X.S. (2021). Path planning and design of industrial robot based on improved PSO algorithm and artificial potential field method. *Journal of Systems Science and Mathematics*, Vol. 41, No. 4, pp. 940-952, Beijing/China.

[16] Lan, Y.B., Zhao, D.N., Zhang Y.F., & Zhu J.K. (2021). Exploration and development prospect of eco-unmanned farm modes (生态无人农场模式探索及发展展望). *Transactions of the Chinese Society of Agricultural Engineering*, Vol.37, No.9, pp.312-327, Beijing/China.

[17] Nizar R., Raghvendra K., Ajith A., Adel, M. A., Hoang, V.L., Ishaanj, P., & Le, H.S. (2021). Bi-heuristic antcolony optimization-based approaches for traveling salesman problem. *Soft Computing*, Vol. 25, No. 2, pp. 3775-3794, Germany.

[18] Sun, W., Lu, Y.F., Tang, H.W., & Xu, M. (2017). Path rules for mobile robots based on an improved algorithm. *Journal of Hunan University (Natural Science Edition)*, Vol. 44, No. 4, pp. 94-101, Hunan/China.

[19] Song, Y. & Wang, Z.M., (2019). Path planning for mobile robot based on improved genetic algorithm, *Modern Electronics Technique*, Vol. 42, No. 24, pp. 172-175, Shaanxi/China.

[20] Tu, J., Chen, H.L., Wang, M.J., & Gandomi, A.H. (2021). The colony predation algorithm, *Journal of Bionic Engineering*, Vol. 18, No. 3, pp. 674-710, Jilin/China.

[21] Wang, G.G., Deb, S., & Cui, Z.H. (2018). Monarch butterfly optimization. *Neural Computing & Applications*, Vol. 31, No. 19, pp. 1995-2014, Germany.

[22] Wang, G.G., Deb S., & Cui Z.H., "Monarch butterfly optimization," Neural Computing & Applications, vol. 31, pp. 1995–2014, 2019.

[23] Xu, F., Zhu H.Q., Cheng, S.G., & Peng, J.M. (2021). Development Status and Realization Path of Unmanned Agriculture in Field (大田无人农业发展现状与实现路径). *Agricultural Engineering*, Vol.11, No.3, pp.11-14, Beijing/China.

[24] Zeng, N. Y., Zhang, H., Chen, Y. P., Chen, B., &Liu, Y. (2016). Path planning for intelligent robot based on switching local evolutionary PSO algorithm. *Assembly Automation*, Vol. 36, No. 2, pp. 5144-5154. United Kingdom.

[25] Zhang, W., Liu, Y., Zhang, C.F., Zhang, L., & Xia, Y.W. (2017). Real-time path planning of greenhouse robot based on direction A* algorithm (基于方向 A*算法的温室机器人实时路径规划).*Transactions of the Chinese Society for Agricultural Machinery*, Vol.48, No.7, pp.22-28, Beijing/China.

[26] Zhao, X. & Hu, G.D. (2017). Application of smooth AR algorithm in intelligent vehicle path planning. *Mechanical Science and Technology*, Vol. 36, No. 8, pp. 1272-1275, Korea.

[27] Zhao, X., Wang, W., Huang, C.W., & Zhao, Y.W. (2018). Path planning of mobile robot based on improved algorithm. *Robot*, Vol. 40, No. 6, pp. 903-910, United States.

[28] Zhang, X.M., Wang, D.D., &Chen, H.Y. (2019). Best and worst coyotes strengthened Coyote Optimization Algorithm and its application to quadratic assignment problem. *Computer Applications*, Vol. 39, pp. 2986-2991, Sichuan/China.

STUDY ON THE DETERMINATION OF PHYSICAL AND MECHANICAL PROPERTIES OF LAVENDER
/
薰衣草物理力学特性的测定研究

Yang LI [1)], Yanmin TAO [2)], Yulong CHEN [3)], Yiteng LEI [*1)]
[1)] School of Electronic and Engineering, Yili Normal University, Yining, Yili 835000, China;
[2)] Shandong Kexiang Intelligent Technology Co., Ltd., Jinan 250013, China;
[3)]College of Agricultural Engineering and Food Science, Shandong University of Technology, Zibo 255000, China
Tel: +8615699398577; E-mail: younger1425580067@163.com
DOI: https://doi.org/10.35633/inmateh-72-43

Keywords: *lavender, physical properties, mechanical properties, moisture content, determination and study*

ABSTRACT
The mechanical properties of lavender are the basis for design and study of mechanized equipment for planting and harvesting of lavender. This paper determines and studies the natural width and height of plant and spike length of three kinds of lavender widely planted in the Yili region and obtains the distribution rules of parameters of the basic physical properties of lavender. Meanwhile, the test of the mechanical properties of lavender was done at the moisture content in the harvest period and different moisture contents. The results indicated that the maximum separation force of the flower of three kinds of lavender (111.3N) was much smaller than the minimum breaking force of the stem (201.5N); and the moisture content significantly affected the mechanical properties of lavender, which could provide corresponding design parameters and important theoretical basis for the design of a new lavender harvester based on separation technology.

摘要
薰衣草的机械力学特性是设计研究薰衣草种植、收获机械化装备的基础。本文对伊犁地区广泛种植的三种薰衣草的植株自然宽度、自然高度以及花序长度进行了测定研究，获得了薰衣草基本物理特性参数的分布规律。同时，在收获期含水率和不同含水率条件下，进行了薰衣草的力学特性试验。结果表明，三种薰衣草花脱离力的最大值（111.3N）远小于茎拉断力的最小值（201.5N）;含水率对薰衣草的力学特性有显著影响，可为设计基于脱离技术的新型薰衣草收获机提供相应的设计参数和重要的理论基础。

INTRODUCTION
Lavender is a perennial plant with branched stems, growing to a height of 20-60 cm, with lance-shaped, linear or sessile leaves and flowers that are found at the tops of stems (*Katarzyna et al., 2014*). The branches at the bottom of the plant are tall and ramified, bearing multiple shoots. The flowers have a spiral shape, and the blue-violet corolla has the shape of two lips with a length of approximately 1 cm (*Fakhriddinova et al., 2020*). Lavender flowers play an important role because they contain 2-4.5% essential oils (*Katarzyna et al., 2014; Fakhriddinova et al., 2020; Prusinowska et al., 2014*). The essential oil extracted from its spike is widely used in articles of everyday use, including shampoo, soap, and detergent (*Li et al., 2016*), but they can also be used as pest and insect repellents (*Costea et al., 2019*). It is one of the most important natural essential oils in the perfume industry.

Thanks to its favorable geographical and climatic environments, Xinjiang's Yili region, which shares the same latitude as Provence, France, stands as the world's third-largest planting base of lavender (*Li et al., 2016*). Currently, the planting area of lavender in the Yili region of Xinjiang is up to 4,900 hm^2, accounting for 98% of that in the whole country. It has become the biggest lavender planting base in China (*Kan et al., 2017*). The weather of lavender harvest in Yili region is hot, but the harvest of lavender is mainly artificial, and the harvest efficiency is low, which seriously restricts the large-scale production and development of lavender. Therefore, it is urgently necessary to develop a new efficient lavender harvesting machinery.

The mechanical properties of lavender are the basis for the design and study of mechanized equipment for its planting and harvesting (*Dimitriadis et al., 2014*). Deniz Yilmaz et al. found that with the extension of harvest time, the shear stress of each stem segment of lavender decreased, and the mechanical property

[1)]*Yang LI, lecturer; Yanmin TAO, Engineer; Yulong CHEN, Associate Professor; Yiteng LEI, Associate Professor.*

parameters such as biological yield force, shear force and bending stress of the bottom stem segment of lavender were much greater than those of the top stem segment, so it was recommended to harvest near the top (*Deniz et al., 2016*). The study of Deniz Yilmaz et al. also showed that water content had significant effects on the physical and mechanical properties of lavender, such as flower stem size, flower stem ratio, picking power and essential oil content (*Deniz et al., 2014*). Hassiotis et al. studied lavender in two regions of Greece and found that harvesting at 60% flowering time was the best harvest stage for lavender (*Hassiotis et al., 2014*). Dimitriadis' research has shown that the most cost effective operation was not achieved at maximum yield but at a set up in which the machine was capable of harvesting the maximum flower head with the minimum stem percentage (*Dimitriadis et al., 2016*). Ana Clara Aprotosoaie and Elvira Gille et al. found that lavender essential oil extraction can also use other parts except inflorescence, but the essential oil content is very low, and the content of linalool, camphor and other components are also low (*Aprotosoaie et al., 2017*). Cigdem Sonmez et al. found that the average value of fresh grass yield, hay yield, floating grass yield, essential oil content and essential oil yield of lavender was the highest at 8 am during the lavender harvesting period, while the average value of essential oil content and essential oil yield was the lowest at 14 PM (*Cigdem et al., 2019*). China primarily concentrates on lavender essential oil extraction and industrial development, with limited reports on the physical and mechanical characteristics of lavender.

This paper takes three kinds of lavender widely planted in the Yili region as an example, determines and studies their basic physical properties, and explores the mechanical properties of different kinds of lavender and the effect of moisture content on the mechanical properties of lavender. It can provide corresponding design parameters and an important theoretical basis for the mechanized harvesting and processing equipment of lavender.

MATERIALS AND METHODS

In this test, Princess Jieyou No. 1, French Blue, and High Yield Blue widely planted in the Yili region were considered as the test objects. The test samples were taken from the Wucai River Valley Lavender Base in Huocheng County, Yili Prefecture, Xinjiang Uygur Autonomous Region on July 13th, 2023. The lavender in this base is planted in a single row with a row spacing of 80 cm and a line spacing of 120 cm. All three kinds of lavender are in their growth period of the fourth year and full-blossom period (*50%～70% of them bloom*).

Test devices

Tape measure, steel ruler, electronic universal tensile testing machine (*Xiamen Jinheyuan Technology Co., Ltd., JHY-5000 single-column digital display, with a maximum range of 500 N and test force resolution of 1/300,000*), digital display vernier caliper (*Qinghai Measuring & Cutting Tools Co., Ltd., with an accuracy of 0.02mm*), and halogen moisture meter (*Xiamen Jinheyuan Technology Co., Ltd., JH-150F, with readability of ±0.01%*).

Determination of the basic physical properties of lavender plants

The lavender plant samples were selected with a reference to the provisions of NY/T1133-2006, an agricultural industry standard in China (*The Agricultural Mechanization Sub Technical Committee of the National Agricultural Machinery Standardization Technical Committee, 2016*). The field measurement method was as follows. The test field was a rectangular planting area. Two diagonal lines of the rectangular area were connected. The plot was divided into 4 parts. The central part of the plot was the fifth part. Each part was a sampling area. 20 healthy lavender plants with similar growth were randomly selected from 5 sampling areas and there was a total of 100 samples.

With reference to the Agricultural Machinery Design Manual (*China Academy of Agricultural Mechanization Science, 2017*), combined with the design requirements of the lavender harvesting device, the natural width and height and spike length of the lavender plant in the harvest period were selected as evaluation indicators of the basic physical properties of lavender. After the determination of the parameters of the basic physical properties of lavender, 50 lavender branches were selected from each plot randomly, cut 100 mm below the spike, and immediately put into a sealed and dry plastic box. After the samples were collected, they were sent to the Engineering Training Center of Yili Normal University for subsequent test of the mechanical properties of lavender.

Determination of separation force of lavender flower *at the moisture content in the harvest period*

Researches show that 97.5% of the essential oil of lavender is from flowers when the essential oil is extracted and lavender stems only contain a little essential oil with poor quality (*Petras et al., 1997; Rabotyacov et al., 1980*). Therefore, to get essential oil with good quality, flowers and stems of lavender should be separated. Currently, in the manual harvesting of lavender in the Yili region, stems and flowers are cut off. And then, essential oil is extracted, which not only increases transportation and distillation costs but also hinders

the production of essential oil with good quality. Therefore, an experimental study on the mechanical properties of lavender is necessary to provide corresponding theoretical data for the design of a new lavender harvester.

The separation force of lavender flowers was measured in the Engineering Training Center of Yili Normal University with an indoor temperature of 34°C and a relative humidity of 39% on that day. After sampling, the average moisture content of the lavender samples measured with a moisture meter was 12.1%, which was consistent with the most suitable moisture content for harvesting of medicinal plants and aromatic plants (*Deniz et al., 2014*).

To determine the force required to separate the flower from the stem, a metal plate with a hole was fixed and installed at the lower end of the electronic universal tensile testing machine. The diameter of the hole was 3 mm. Part of the end of the lavender stem without a spike was cut off with scissors. Only the part with a length of 30 mm was kept and fixed in the fixture at the upper end of the testing machine after passing through the small hole. The lavender spike is on the lower side of the hole, as shown in Figure 1a.

The loading speed of the electronic universal tensile testing machine can be adjusted in the range of 0.1～500 mm/min. However, considering that the operating speed of an agricultural harvester is usually 3～8 km/h, if the loading speed is too high, it can also affect the test results (*Ma et al., 2004; Wang et al., 2011*). Therefore, a constant loading speed of 60 mm/min was selected for the separation force test of lavender flowers (*Wang et al., 2015*). When the stem was completely separated from the metal plate, as shown in Figure 1b, the rising stopped and the data was recorded. After an experiment was completed, the remaining spikes in the small hole on the metal plate were removed. And then, the next experiment was done. The experiment was repeated for 15 times for each kind of lavender and the results were averaged.

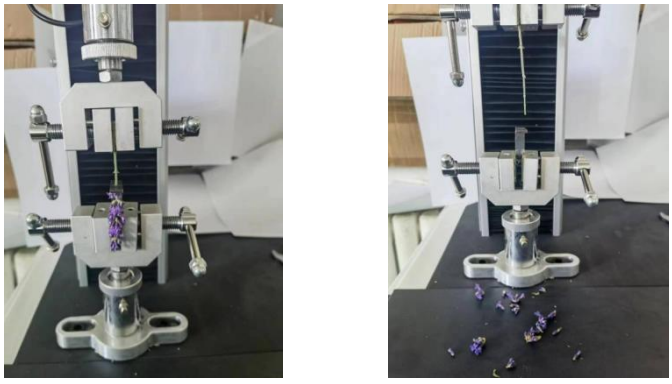

a. Before separation of lavender flower *b. After separation of lavender flower*

Fig. 1 - Measurement of separation force of lavender flower with an electronic universal tensile testing machine

Determination of breaking force and ultimate tensile strength (UTS) of the stem of lavender at the moisture content in the harvest period

With reference to GB/T 1040 Determination Method of the Tensile Strength, Tensile Modulus, and Tensile Stress-Strain Relationship of Plastics and Composite Materials (*GB/T1040.1-2018, 2018*), the breaking force of the stems of lavender was determined. Before the test, the part of the spike of lavender was cut off, both ends of the remaining stem were cut off, and the part with a length of 80 mm in the middle was kept. The cross-section of the stem of lavender is rectangular and the middle part is slightly empty. If the stem is directly clamped on the fixture for a test, it may break or slide. In the test, to ensure that the clamps on both ends could grip the stem without damaging it, the binding wire with a length of 20 mm and diameter of 0.3 mm was inserted into both ends of the stem. Its outside was bonded firmly with medical tape to avoid sliding in the process of the test with a bonding length of 20 mm (*Guo et al., 2019*). The breaking force test of the stem was done with a constant loading speed of 60 mm/min. The test process is as shown in Figure 2.

Fig. 2 - Measure the breaking force of the stem with the universal tensile testing machine

The single-factor and single-level repeated test method was used, the experiment was repeated 15 times, and the results were averaged. As the load increased, the test was considered successful when the breaking part was not on both ends of the stem (*Wang et al., 2016*). When the stem was completely broken, the rising stopped and the data was recorded.

The ultimate tensile strength of the stem of lavender can be obtained from the results of the test of the breaking force of the stem. With the method specified in GB/T24887-2010 Guidelines for Test of the Specificity, Consistency, and Stability of New Varieties of Plants, the vertical and horizontal dimensions of the cross section of the stem of lavender were selected, the ultimate tensile strength in the directions of the maximum and minimum dimensions was measured, and the mean was considered as the final result. The cross-sectional area of the stem was calculated according to its vertical and horizontal dimensions. The ultimate tensile strength (UTS) of the stem could be obtained with Equation (1).

$$R_m = \frac{F}{A} \tag{1}$$

where:

R_m is the ultimate tensile strength, [MPa];

F is the breaking force of the stem of lavender, [N];

A is the cross-sectional area of the stem of lavender, [mm^2].

Test of mechanical properties of lavender at different moisture contents

To verify the effects of moisture content on the separation force of the flower, breaking force of the stem, and ultimate tensile strength of the stem of lavender, 30 plants of lavender samples of each kind at the moisture content in the harvest period were divided into 3 groups with 10 plants in each group and they were numbered. The samples were naturally dried at room temperature for 24, 48, and 72 hours. And then, some samples were taken and placed in the balance of the halogen moisture meter. The temperature was set as 100℃. The moisture content of the sample could be automatically measured. The average moisture content of each group of samples is shown in Table 1.

Table 1

Statistical table of moisture contents of samples

Lavender	Princess Jieyou No. 1/%	French Blue/%	High Yield Blue/%	Mean/%
Group 1 (24 hours)	10.81	11.12	10.63	10.85
Group 2 (48 hours)	8.23	8.42	8.13	8.26
Group 3 (72 hours)	5.94	6.05	5.82	5.94

After drying, the separation force of the lavender flower, the breaking force of the stem, and the ultimate tensile strength of the stem of samples were determined according to the above test steps.

RESULTS

The statistical results of the parameters of the basic physical properties of three kinds of lavender plants are shown in Table 2. The probability distribution of plant samples is shown in Figure 3.

Table 2

Parameters of the basic physical properties of three kinds of lavender

Lavender	Natural width of plant (mean/ cm)	Natural width of plant (max/cm)	Natural width of plant (min/cm)	Natural height of plant (mean/ cm)	Natural height of plant (max/cm)	Natural height of plant (min/cm)	Spike length (mean/ cm)	Spike length (max/cm)	Spike length (min/cm)
Princess Jieyou No.1	102.8	115	91	65.6	80	55	11.2	16.8	7.2
French Blue	113.6	124	101	68.0	80	56	11.9	18.6	7.2
High Yield Blue	141.7	155	131	81.1	95	71	16.9	22.2	11.5

Table 2 shows that the average natural width, height, and spike length of plants of High Yield Blue lavender are the biggest among the three kinds of lavender, while the average natural width, height, and spike length of plants of Princess Jieyou No. 1 are the smallest among three kinds of lavender.

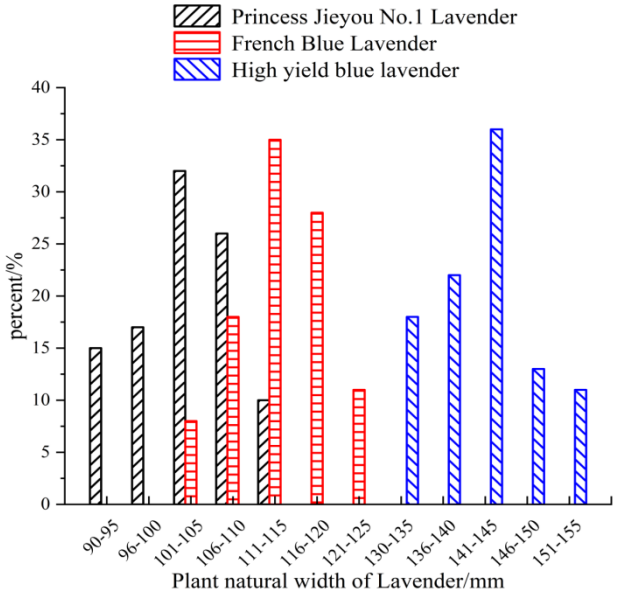

a. Distribution map of natural width of plants of lavender

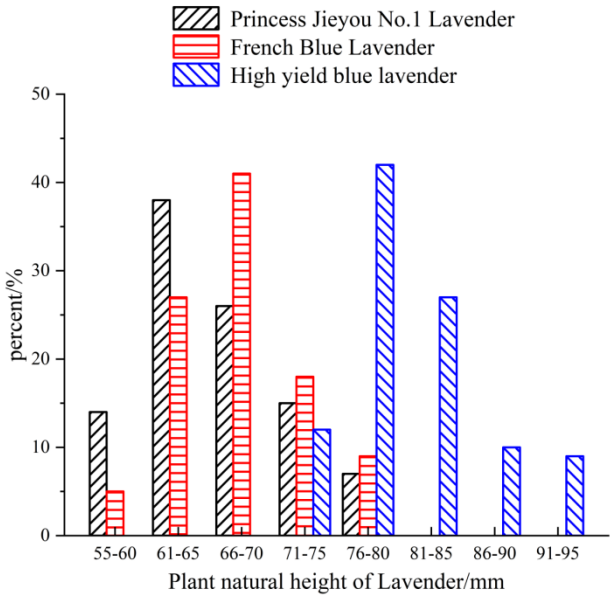

b. Distribution map of natural height of plants of lavender

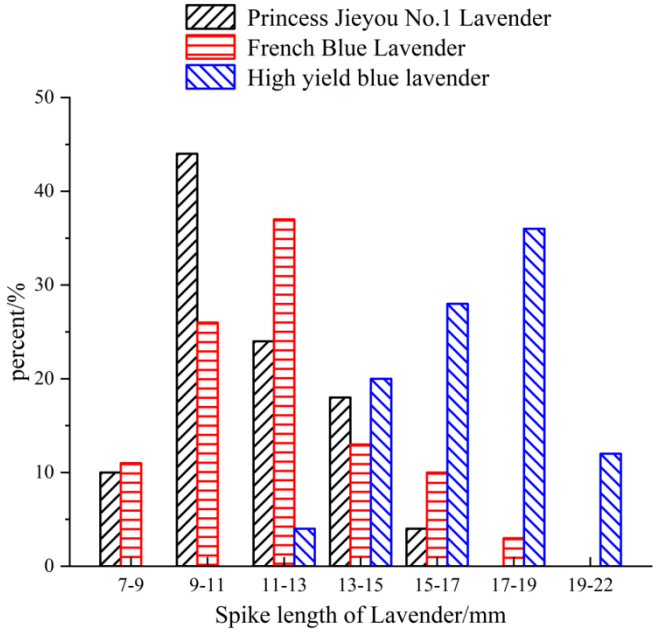

c. Distribution map of spike length of lavender

Fig. 3 - Histogram of the distribution of the basic physical properties of lavender

Figure 3a shows that the natural width of plants of Princess Jieyou No. 1 lavender is mainly in the range of 96～110 cm, accounting for 75% of the total sample size; that of French Blue lavender is mainly in the range of 106～120 cm, accounting for 81% of the total sample size; and that of High Yield Blue lavender is mainly in the range of 130～145 cm, accounting for 76% of the total sample size.

Figure 3b shows that the natural height of plants of Princess Jieyou No. 1 lavender is mainly in the range of 61～75 cm, accounting for 79% of the total sample size; that of French Blue lavender is mainly in the range of 61～75 cm, accounting for 86% of the total sample size; and that of High Yield Blue lavender is mainly in the range of 71～85 cm, accounting for 81% of the total sample size.

Figure 3c shows that the spike length of Princess Jieyou No. 1 lavender is mainly in the range of 9～15 cm, accounting for 86% of the total sample size; that of French Blue lavender is mainly in the range of 9～15 cm, accounting for 76% of the total sample size; and that of High Yield Blue lavender is mainly in the range of 13～19 cm, accounting for 84% of the total sample size.

By combining Table 1 and Figure 3, it can be known that the parameters of the basic physical properties of Princess Jieyou No.1 lavender and French Blue lavender are not quite different. The parameters of the basic physical properties of High Yield Blue lavender are much bigger than those of the other two kinds of lavender, which makes the design of a lavender harvesting device more difficult.

In the process of the test, the TESTER system in the electronic universal tensile testing machine automatically drew a load-time curve and recorded the maximum separation force, as shown in Figure 4.

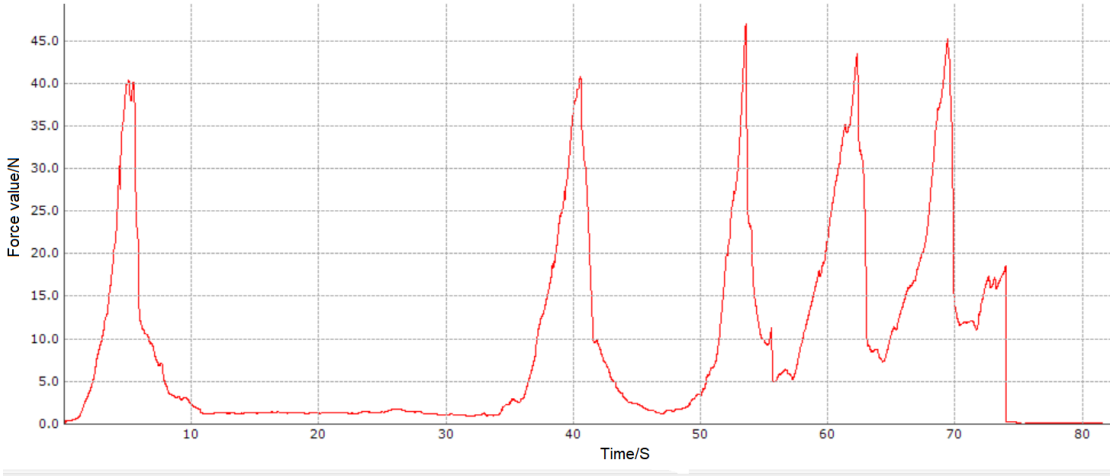

Fig. 4 - Separation force-time curve of lavender flower

Figure 4 shows that the separation force increased fast and the flower was peeled off with the increase of load after the test started. And then, the force decreased fast. At this time, the first spike was separated. After a long time, the separation force increased fast, and then decreased fast. The separation of the second spike started. The number of times of fast increase and decrease of the separation force represents the number of spikes of lavender. In most cases, the first and second spikes are farther than other spikes, so the interval is the biggest.

The statistical results of the separation force of the lavender flower, the breaking force of the stem, and the ultimate tensile strength (UTS) of the stem at the moisture content in the harvest period are shown in Table 3.

Table 3

Statistical table of parameters of mechanical properties of lavender at the moisture content in the harvest period

Lavender	Sepa-ration force of the flower (mean/ N)	Sepa-ration force of the flower (max/N)	Sepa-ration force of the flower (min/N)	Breaking force of the stem (mean/N)	Breakin g force of the stem (max/N)	Break-ing force of the stem (min/N)	Ultimate tensile strength (mean/MPa)	Ultimate tensile strength (max / MPa)	Ultimate tensile strength (min / MPa)
Princess Jieyou No.1	52.8	62.4	45.7	229.3	280.5	201.5	52.5	55.2	50.7
French Blue	59.3	70.3	49.8	231.1	285.7	205.4	52.8	56.7	50.6
High Yield Blue	88.3	111.3	69.8	247.6	287.6	210.6	59.8	63.9	55.4

The data in Table 3 shows that the average separation force of the flower, the breaking force of the stem, and the ultimate tensile strength of the stem of the lavender sample of Princess Jieyou No. 1 at the moisture content in the harvest period are the smallest; the average separation force of the flower, the breaking force

of the stem, and ultimate tensile strength of the stem of the lavender sample of High Yield Blue are the biggest; and the parameters of mechanical properties of the lavender sample of French Blue are slightly higher than those of the Princess Jieyou No. 1 lavender and there is no significant difference between the two lavender samples. The separation force of the flower of samples of three kinds of lavender is 45.7～111.3 N, the breaking force of the stem is 201.5～287.6 N, and the ultimate tensile strength of the stem is 50.7～63.9 MPa.

The determination results of the mechanical properties of three kinds of lavender at different moisture contents are shown in Figure 5-7.

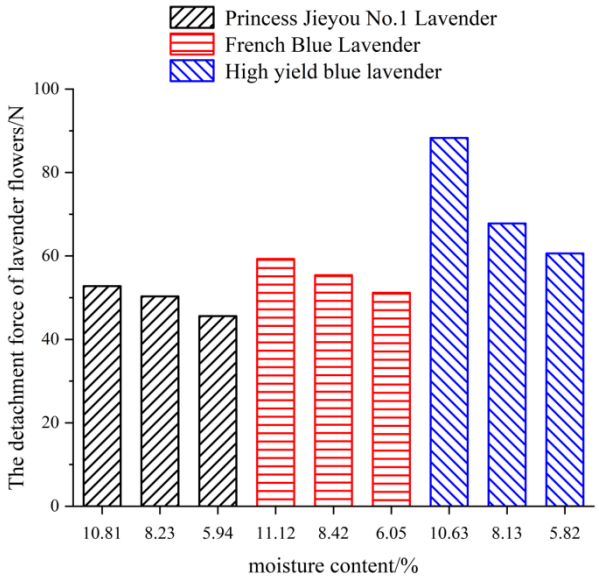

Fig. 5 - Separation force of lavender flower at different moisture contents

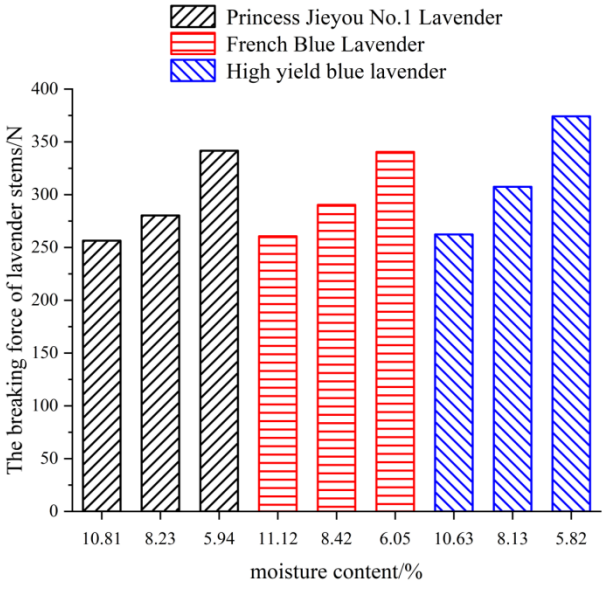

Fig. 6 - Breaking force of lavender stem at different moisture contents

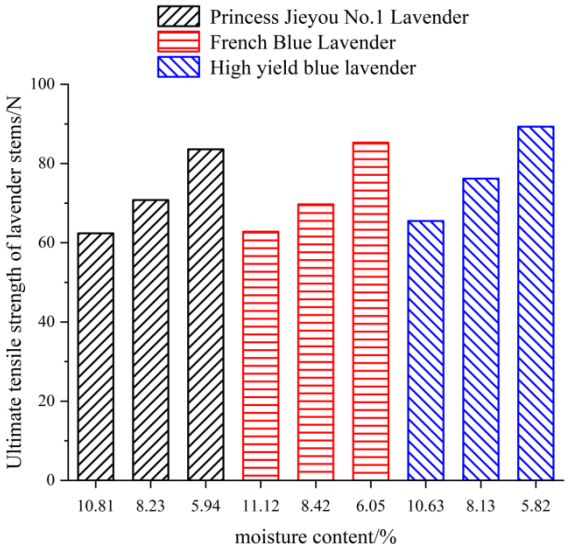

Fig. 7 - Ultimate tensile strength of lavender stem at different moisture contents

As the moisture content decreases, the separation force of the three kinds of lavender flowers also decreases, but the breaking force and ultimate tensile strength of the stems of the three kinds of lavender increase with the decrease of moisture content, because the decrease of moisture content causes the increase of cellulose intensity, thus improving the tensile resistance and tensile strength of the stem of lavender. It can be seen that moisture content has a significant effect on the mechanical properties of lavender.

CONCLUSIONS

1) According to the determination, the natural width of plants of three kinds of lavender is 91～155 cm, the natural height is 55～95 cm, and the spike length is 11.2～22.2 cm.

2) At the moisture content in the harvest period, the average separation force of the flower of three kinds of lavender is much smaller than the average breaking force of the stem. The average breaking force of the stem of Jieyou Princess No.1 lavender and French Blue lavender is 4 times the average separation force of the flower, and the average breaking force of the stem of High Yield Blue lavender is 2.8 times the average separation force of the flower. The maximum separation force of the flowers of three kinds of lavender (111.3 N) is much smaller than the minimum breaking force of the stem (201.5 N). This indicates that the flower can be peeled off from the stem without breaking it when lavender is harvested.

3) The moisture content has a significant effect on the mechanical properties of lavender. As the moisture content decreases, the separation force of the flowers of lavender also decreases. However, the breaking force and ultimate tensile strength of the stem of lavender increase.

4) At the moisture content in the harvest period and different moisture contents, the average separation force of the flower of High Yield Blue lavender is much greater than that of the other two kinds of lavender mainly because the peduncle of High Yield Blue lavender is relatively long. The average breaking force and ultimate tensile strength of the stem of High Yield Blue lavender are not significantly different from those of the other two kinds of lavender and have little effect on the design of a new lavender harvester based on the peeling technology.

ACKNOWLEDGEMENT

This work was financially supported by the university level scientific research project of Yili Normal University (2023YSYB030) and the Yili Prefecture Science and Technology Plan project (YZ2022Y011), as well as the vibration signal capture and intelligent processing laboratory of Yili Normal University.

REFERENCES

[1] Aprotosoaie, A. C., Gille, E., Trifan, A., Luca, V. S., Miron, A. (2017). Essential Oils of Lavandula Genus: A Systematic Review of Their Chemistry. *Phytochem. Rev,* vol.16, pp. 761-799. https://doi 10.1007/s11101-017-9517-1

[2] Costea, T., Strainu, A.-M., Gird, C. E. (2019). Botanical characterization, chemical composition and antioxidant activity of Romanian lavender (*Lavandula angustifolia Mill*.) Flowers, Studia Universitatis“ Vasile Goldis,”. *Stinţele Vieţii Series*, vol.29, pp. 159-167.

[3] China Academy of Agricultural Mechanization Science (2017). *Handbook of Agricultural Machinery Design*. Beijing: China Agricultural Science and Technology Press.

[4] Cigdem, S., Hulya, O. (2019). The Effect of Diurnal Variation on Some Yield and Quality Characteristics of Lavender under Cukurova Ecological Conditions. *Turkish Journal of Agriculture-Food Science and Technology*, vol.3, pp. 531-535.

[5] Dimitriadis, C., Brighton J., O'Dogherty M., Kokkora M., Darras A. (2014). Physical and Aerodynamic Properties of Lavender in relation to Harvest Mechanisation. *International Journal of Agronomy*. https://doi.org/10.1155/2014/276926

[6] Dimitriadis, C. I., Pavloudi, A., Aggelopoulos, S. (2016). Validation in a Novel Lavender Harvester for oil Production. *Journal of Environmental Protection and Ecology*, vol.4, pp. 1504-1513.

[7] Fang, H. M., Ji, C. Y., Zhang, Q. Y., Farman, A. C. (2014). Research on the mechanical properties of wheat straw at home and abroad. *Journal of Chinese Agricultural Mechanization*, vol.35, pp. 304-308. https://doi.org/10.13733/j.jcam.issn.2095-5553.2014.06.074

[8] Fakhriddinova, D.K., Rakhimova, T.R., Dusmuratova, F.M., Duschanova, G.M., Abdinazarov, S.H., Samadov, I.N. (2020). The Anatomical Structure of Vegetative Organs Lavandula officinalis Chaix in the Introduction of Tashkent Botanical Garden. *Am. J. Plant Sci*, vol.11, pp. 578–588.

[9] GB/T1040.1-2018. (2018). *Determination of tensile properties of plastics*. Beijing: China Standards Publishing House.

[10] Guo, Q. H. (2019). Research on the mechanical properties of alfalfa and king grass and development of a flexible cutting test bench. Shandong Agricultural University.

[11] Hassiotis, C.N., Ntana, F., Lazari, D.M., Poulios, S., Vlachonasios, K. E. (2014). Environmental and developmental factors affect essential oil production and quality of Lavandula angustifolia during flowering period. *Ind.Crops Prod,* vol.42, pp. 359-366.

[12] Li, Y. M., Qin, T. D., Chen, J., Zhao, Z. (2011). Experimental study and analysis on mechanical property of corn stalk reciprocating cutting. *Transactions of the CSAE*, vol.27, pp. 160-164. https://doi.org/10.3969/j.issn.1002-6819.2011.01.025

[13] Li, Y. P. (2016). Reasons for Low Yield of Lavender Crops and Solutions. Agricultural Science-Technology and Information, vol.17, pp.68. https://doi.org/10.15979/j.cnki.cn62-1057/s.2016.17.043

[14] Kan, Y. (2017). Research on the Current Situation and Countermeasures of Lavender Tourism Development in the Yili River Valley. Tourism Overview, vol.12, pp. 155-156.

[15] Katarzyna, S.L., Romuald, M., Wojciech, K., Bogdan, K., Jan, B. (2014). Yielding and quality of lavender flowers (Lavandula angustifolia Mill.) from organic cultivation. *Acta Sci. Pol. Hortorum Cultus*, vol.13, pp.173-183.

[16] Ma, H. S., Zhang, Z. J., Cao, L. K. (2004). Experimental study on the biomechanical properties of like vegetables. *Transactions of the CSAE*, vol.20, pp. 74-77.

[17] Petras, R. V., Airidas, D., Marija, B. (1997). Composition of the Essential Oil of Lavender (*Lavandula angustifolia Mill.*) from Lithuania. *Journal of Essential Oil Research*, vol.9, pp.107-110. https://doi.org/10.1080/10412905.1997.9700727

[18] Prusinowska, R., Smigielski, K.B. (2014). Composition, biological properties and therapeutic effects of lavender (*Lavandula angustifolia L.*). A review. Kerba Pol. vol.60, pp. 56-66.

[19] Rabotyacov, V. D., &Yakovlev, L. K. (1980). Study of the variability of the content of essential oil in lavender. Cytology and genetics (USA), vol.14, pp. 33-35.

[20] The Agricultural Mechanization Sub Technical Committee of the National Agricultural Machinery Standardization Technical Committee. (2016). NY/T1133-2006 Cotton Picker Operation Quality. Beijing: China Agricultural Publishing House.

[21] Wang, J., Zhang, K. P., Zhang, F. W., Chai, Q. (2016). Experimental on mechanical properties of pea stalks. *Journal of Chinese Agricultural Mechanization*, vol.37, pp. 103-107. https://doi.org/10.13733/j.jcam.issn.2095-5553.2016.12.021

[22] Wang, P. H., Chen, L. H., Ji, X. D., Zhou, S., Lv, C. J., Jiang, K. Y. (2011). Quantitative study on the mechanical properties of birch root system. *Bulletin of Soil and Water Conservation*, vol.31, pp. 154-158. https://doi.org/10.13961/j.cnki.stbctb.2011.04.049

[23] Wang, X. H., Li, J. B., Kan, Z., Sultan, B., Dong, C.C. (2015). Mechanical determination and analysis of safflower. Jiangsu Agricultural Sciences, vol.43, pp. 352-354. https://doi.org/10.15889/j.issn.1002-1302.2015.03.113

[24] Yan, Y. X., Zhao, S. H., Yang, Y. Q., Tian, B. L. (2012). Study on mechanics properties of soybean stems in mature stage. *Journal of Northeast Agricultural University*, vol.43, pp. 46-49. https://doi.org/10.19720/j.cnki.issn.1005-9369.2012.05.009

[25] Yilmaz, D., Mehmet., Gokuman, M. (2014). Effect of Moisture Contents on Physical-Mechanical Properties of Lavandin. *Journal of Essential Oil Bearing Plants*, vol.17, pp. 1224-1232. https://doi.org/10.1080/0972060X.2014.958565

[26] Yilmaz, D, Y., Jasinskas, A. (2016). Determination of cutting properties of Lavandin (Lavandula x intermedia Emeric ex Loisel.) at different harvesting time. Agricultural Engineering, *Research Papers*, vol.48, pp. 1-5.

REVIEW ON THE DEVELOPMENT OF LAVENDER HARVESTING TECHNIQUES
/
薰衣草收获技术发展综述

Yang LI [1], Yanmin TAO [2], Yulong CHEN [3], Yiteng LEI *[1]
[1] School of Electronic and Engineering, Yili Normal University, Yining, Yili 835000, China;
[2] Shandong Kexiang Intelligent Technology Co., Ltd., Jinan 250013, China;
[3] College of Agricultural Engineering and Food Science, Shandong University of Technology, Zibo 255000, China
Tel: +8615699398577; E-mail: younger1425580067@163.com
DOI: https://doi.org/10.35633/inmateh-72-44

Keywords: *Lavender, mechanical properties, harvesting time, essential oil, harvesting machinery*

ABSTRACT

The harvesting technology of China's lavender industry is in urgent need of improvement, and there is a pressing demand to expedite the development of mechanized collection equipment to facilitate the modernization process and optimize efficiency within the sector. This article adopts a literature review method to introduce the current research status of lavender harvesting techniques, including mechanical properties, harvesting time, and distribution of essential oils in stems and leaves, both domestically and internationally. It is found that there is relatively little research on lavender harvesting techniques in China, and the main research hotspots are focused on industrial development and essential oil extraction. By summarizing the mechanical harvesting equipment and its characteristics of lavender both domestically and internationally, it is analyzed that developed countries have fully achieved mechanical harvesting of lavender, while China's level of mechanical harvesting of lavender lags far behind developed countries. It is proposed to develop diversified lavender harvesting equipment, strengthen the research and cooperation of lavender harvesting machinery, promote the integration of agricultural machinery and agronomy, and combine basic research with equipment development. These development measures have a certain reference and promotion effect on accelerating the process of mechanical harvesting of lavender in China.

摘要

中国薰衣草产业的收获技术亟待提升，迫切需要加快机械化采收装备的研发步伐，以促进产业的现代化进程和效率优化。本文采用文献综诉法，介绍了国内外薰衣草机械力学特性、收获时间、茎叶精油分布等有关收获技术的研究现状，发现中国在薰衣草收获技术方面的研究较少，主要研究热点集中在产业发展、精油萃取等方面。通过总结国内外薰衣草机械化收获装备及其特点，分析出发达国家已全面实现了薰衣草的机械化收获，而我国薰衣草的机械化收获水平远落后于发达国家，提出开发多样化的薰衣草收获装备，加强薰衣草收获机械的研发与合作，促进农机与农艺相融合，基础研究与设备研制相结合等发展措施，对加快中国薰衣草机械化收获进程具有一定的参考和促进作用。

INTRODUCTION

Lavender, a member of the *Labiaceae family*, is a small perennial shrub that is 30-60 (100) cm tall, gray in color, and has a strong odor *(Katarzyna et al., 2014)*. Lavender is a semi-heat-resistant plant with fragrant purple-blue flowers. The spines of lavender consist of rings of 6-10 flowers which are bilabiate, small, 0.8 cm-long. The majority of the oil, extracted from the flowers, is contained in the glands on the calyx *(Raev et al., 2002)*.

Lavender flowers contain 2-4.5% essential oils *(Katarzyna et al.,2014; Fakhriddinova et al., 2020; Prusinowska et al., 2014)*, the main components of which are linalool acetate, linalool and geranyl, but also contain compounds such as flavonoids, anthocyanins, phenolcarboxylic acids, zinc, calcium, magnesium, manganese, etc. *(Costea et al., 2019)*. Extensive research indicates that lavender and its essential oil possess antibacterial, anti-inflammatory, freckle-removing, skin-whitening, sedative, analgesic, and anti-anxiety effects, making them widely used in medical, beauty, aromatherapy, cosmetics, and other areas *(Sha et al., 2021; Guo et al.,2023)*, and could also be used as an insect repellent *(Sabara et al., 2019)*. In addition, lavender is a good honey plant - one hectare of lavender during its flowering period gives more than 100 kg of white, aromatic and tasteful honey *(Zatuchny et al., 1972)*.

[1] *Yang LI, lecturer; Yanmin TAO, Engineer; Yulong CHEN, Associate Professor; Yiteng LEI, Associate Professor.*

Lavender is native to the Mediterranean and southern Europe *(Yao et al., 2002)* and prefers bright, dry conditions *(Zhang et al., 2016)*. The main planting area of lavender is concentrated in France *(Monge et al., 2012),* Bulgaria *(Stanev et al., 2016)*, Italy *(Contino et al., 2020)*, Turkey *(Gul et al., 2016),* Spain *(Fernandez et al., 2020)*, Japan, China and other places, while the main producers of lavender are France and Bulgaria *(Giray et al., 2018)*. Thanks to its favorable geographical and climatic environments, Xinjiang's Yili region, which shares the same latitude as Provence, France, stands as the world's third-largest planting base of lavender *(Li., 2016)*.

Lavender blooms from mid-June to mid-July each year *(Muntean et al., 2016)*, depending on geographic region. Generally, when the flowers are 60% full *(Hassiotis et al., 2014)*, they can be harvested. Because of the backward development level of agricultural mechanization in Yili region, the harvesting of lavender has been mainly artificial, which seriously restricts the large-scale production and development of lavender. In this paper, the development status of lavender harvesting machinery at home and abroad and the basic research affecting lavender harvesting were summarized, the problems existing in domestic lavender harvesting technology were found, and the relevant suggestions were put forward.

Lavender harvesting techniques

Mechanical properties of lavender

Design engineers working with plant material need to know their properties and structures when subjected to cutting, bending, tensile, and compressive forces in order to understand the behavior of the material in conjunction with the machine involved. A designer should therefore be conversant with the physical and mechanical properties of the investigated plant.

Deniz Yilmaz from Suleyman Demirel University in Turkey studied the relationship between the harvesting time of lavender and the mechanical characteristics of different stem segments and the stem. The study reveals that with the extension of time, the shear stress of each stem segment of lavender decreases. The mechanical characteristic parameters such as biological yield strength, shear force, and bending stress of the bottom stem segments are much greater than those of the top stem segments. Consequently, it is advisable to harvest lavender closer to the top during harvesting *(Deniz et al., 2016)*.

Christos I. Dimitriadis and James L. Brighton from the School of Applied Sciences, College of Science and Technology at Cranfield University in the UK used an Instron 1122 tensile testing machine to measure the force required to separate lavender flowers from stems and the ultimate tensile stress (UTS). They also examined the resistance of the flowers in airflow and the terminal velocity of the flowers during free fall. The findings indicate that the force needed to separate lavender flowers from stems is lower than that required to break the stem and it is viable to harvest lavender by only removing the flowers *(Dimitriadis et al., 2014).*

Deniz Yilmaz and Mehmet Emin Gokduman at Suleyman Demirel University in Turkey uncovered through experiments that moisture notably influences the physical and mechanical characteristics of lavender, such as flower stem size, flower-stem ratio, picking force, and essential oil content *(Deniz et al., 2014)*.

Trendafilov and Delchev from Bulgaria, conducted a comparative study on lavender harvesters using arc cutting knives and straight knives. The study results showed that the use of arc cutting tools could significantly reduce the impurity content compared with the straight knife cutting; however, there was almost no difference in the percentage of lavender loss between the two. Therefore, it is recommended to apply arc cutting units in lavender harvesters to effectively improve the quality of harvested materials *(Trendafilov et al., 2006)*.

Lavender harvest time

The distribution of essential oil in the stems and leaves of lavender affects the way lavender is harvested. When harvesting, the flowers are harvested together with the stems and leaves, and the stalks should be cut to a suitable length. If the stem is too long, it will increase the transportation cost and also affect the quality of lavender essential oil extraction. If the lavender flower is stripped from the stem and harvested separately, whether it will affect the yield of essential oil is a question that needs to be discussed.

There are several views on the distribution of essential oil content in lavender. The lavender harvesting starts in the second year of the crop at flowering, which takes place in June-July and continues yearly for 12-15 years in conditions of high productivity. Beyond this time interval, the crop becomes less feasible *(Muntean et al., 2016)*. The crop enters full productive capacity in the second and third years post-establishment *(Giannoulis et al., 2020)*.

The period and duration of flowering varies with geographical region. In Eastern Europe silvosteppe areas, the flowering, with a flowering duration of 15-20 days, occurs earlier than in colder temperate regions, where flowering can occur later and lasts about 25-30 days *(Muntean et al., 2016)*.

Goncearіuc, M. and Zbanc, A. et al., in their Practical Guide to Lavender Cultivation and Commercial Management, Lavender harvesting differs depending on the plant variety - it can have an early, medium or late flowering period. As a rule, small crops can be harvested when the flowers are 75-80% open. While for the extended crops, which are harvested within 10-15 days, the picking process can be initiated when the plants are 50-60% open and ends when they reach a threshold of 95-100% flowering *(Goncearіuc et al., 2019)*. The best time to harvest lavender during the day is from 10 a.m. to noon or after noon *(Muntean et al., 2016)*.

Baydar and Erbaku of Lyman Demirel University studied lavender harvested on four different dates and dried at four different temperatures to assess the effects of harvesting time and drying temperature on its essential oil content and composition. The results showed that both harvesting time and drying temperature had an impact on the essential oil content. The highest linalool content was harvested in the middle of flowering period (mid-July), and the drying temperature was recommended between 30-40°C to maintain the high quality of dried lavender *(Baydar et al., 2009)*.

Hassiotis et al, from the Aristotle University of Thessaloniki in Greece, tapped into how the quality and quantity of lavender essential oil (EO) change during the flowering period in two regions of Greece. They unveiled that the best time to harvest lavender is when 60% of the flowers are in bloom *(Hassiotis et al., 2014)*.

Çiğdem Sönmez and Hülya Okkaoğlu from the Faculty of Agriculture at Izmir Ege University in Turkey carried out a random allocation experiment to study the effects of different harvesting times on the fresh flower yield and essential oil yield of lavender. The findings suggest that at 8:00 in the morning during the lavender harvest time, the average of fresh forage yield, dry forage yield, floating forage yield, essential oil content, and essential oil yield are highest, while the average is lowest at 14:00 in the afternoon *(Çiğdem et al., 2019)*.

Jiang Xinming and Guo Danli from the Institute of Agricultural Science, the Fourth Division of Xinjiang Production and Construction Corps utilized gas chromatography-mass spectrometry and steam distillation to measure and analyze the components of lavender essential oil harvested at different flowering periods and different times. They found that the flowering periods and varieties of lavender weigh heavily on essential oil quality, while the harvest time exerts a minor impact. This provides a theoretical basis for determining the harvest time of different lavender varieties *(Jiang et al., 2016)*.

Distribution of essential oil in stems and leaves of lavender

The distribution of essential oil in the stems and leaves of lavender affects the way lavender is harvested. When harvesting, the flowers are harvested together with the stems and leaves, and the stalks should be cut to a suitable length. If the stem is too long, it will increase the transportation cost and also affect the quality of lavender essential oil extraction. If the lavender flower is stripped from the stem and harvested separately, whether it will affect the yield of essential oil is a question that needs to be discussed when harvesting lavender.

There are several views on the distribution of essential oil content in lavender. Lavender essential oil is found in the upper part of the calyx, more precisely in the oil glands on the surface of the calyx, but also in the leaves or dried flowers of the plant. Fresh lavender flowers contain about 0.7-1.4% of volatile oils. When plant material dries, it loses some of its volatile oils. On average, one ton of fresh inflorescence produces about 10 kilograms of volatile oils *(Muntean et al., 2016)*.

Wilson T.M. et al., reconfirmed in a recent study that the calyx is the main part of lavender that accumulates volatile oil, with the calyx alone producing 1.3%, followed by the corolla (0.1%) and leaves (0.05%), and the entire flowering top producing 0.7% *(Wilson et al., 2021)*. Blinova et al showed in their experimental results that all parts of the plant contain essential oils (lavender): leaves - up to 0.4%, stems - up to 0.2%, and large amounts of essential oils accumulate in the inflorescence (3.5-4.5%) (*Blinova et al., 1990*).

Rabotyacov and Yakovlev, from the US, explored the variability of lavender volatile oil. They found that during harvest time, lavender essential oil is mainly concentrated in glands, which are primarily located on sepals and petals. The yield of extracted oil is proportional to the number and size of essential oil glands *(Rabotyacov et al., 1980)*. In 1997, Petras Rimantas Venskutonis et al, from the Department of Food Technology at Kaunas University of Technology in Lithuania, analyzed the volatile oils in lavender flowers and stems using capillary gas chromatography and gel chromatography. They discovered that the oil content in lavender stems is more than 30 times lower than that in lavender flowers, providing the correct direction for efficient mechanical harvesting of lavender *(Petras et al., 1997)*. A report from the Department of Agriculture in Western Australia in 2000 pointed out that the mass of dry matter during distillation affects that of the oil. Therefore, it is recommended to harvest lavender stems not exceeding 15 centimeters in length under minimal wind conditions with temperatures below 28°C. Otherwise, oil yield will be impacted *(Bulletin, 2000)*.

Dimitriadis from the Alexander Technological Educational Institute of Thessaloniki, Greece, found that the most economically efficient lavender harvesting operation does not occur at maximum yield. Instead, it is attained by setting machines to harvest the largest flower heads with the minimum percentage of stems *Dimitriadis et al., 2016)*.

Ana Clara Aprotosoaie and Elvira Gille, from the Carol Davila University of Medicine and Pharmacy of Romania, conducted a systematic study of the chemical composition of lavender essential oil based on research from the past 15 years. The findings show that lavender essential oil can be extracted from parts other than the inflorescence; however, the oil content is low, and the quantity of components such as linalool and camphor is also meager *(Aprotosoaie et al., 2017)*.

Détár Enikő and Éva Zámboriné Német from St. Stephen University in Hungary evaluated the essential oil characteristics of six narrow-leaved lavender and two intermediate lavender varieties to verify the influence of varieties and growth years on lavender and lavender essential oil characteristics. According to the experiments, intermediate lavender possesses a lower ratio of acetic linalool ester to total esters than narrow-leaved lavender, and the growth year does not notably influence the characteristics of lavender essential oil *(Détár et al., 2020)*.

Shiyuge from Xinjiang University employed two extraction techniques, steam distillation and headspace solid-phase micro-extraction, to analyze the volatile chemical components of narrow-leaved lavender, toothed lavender, and different parts of narrow-leaved lavender utilizing gas chromatography and gas chromatography-mass spectrometry. The analysis shows that in narrow-leaved lavender, the flowers contain the most volatile components, followed by the leaves, with the stems harboring the least quantity. The quality of narrow-leaved lavender surpasses that of toothed lavender *(Shi et al., 2012)*.

In summary, research on lavender harvesting technology was conducted earlier and more comprehensively abroad, involving various aspects such as lavender mechanical properties, harvesting time, and essential oil distribution in stems and leaves. Research on lavender in China mainly focuses on essential oil extraction, industrial development, and other aspects. For example, Zhao Wenbin and Chen Hanying selected extraction pressure, extraction temperature, CO2 flow rate, and extraction time as influencing factors, and determined the optimal extraction process conditions for supercritical fluid extraction of lavender volatile oil using orthogonal tests *(Zhao et al., 2009)*. Huang Xiaode and Yang Jianxin et al. improved the traditional water vapor oil extraction device. The improved integrated lavender essential oil extraction device can significantly reduce the amount of distillation water used and increase the extraction rate of lavender essential oil *(Huang et al., 2022)*. Liu Ying delved into the industrial development of lavender in Huocheng County, Xinjiang, summarized the advantageous conditions and industrial foundation, and proposed countermeasures and suggestions for the issues that arose during the development of the industry in the county *(Liu et al., 2019)*. Ding Lijuan studied the historical development of the lavender industry in the Yili region and put forth that cooperation between operating entities represents the most effective developmental trajectory for the local lavender industry *(Ding et al., 2019)*.

Lavender harvesting machinery

Foreign lavender harvesting machinery

Foreign research started rather early on lavender harvesting machinery. In the late 1940s, foreign lavender producers, entrepreneurs, and engineers attempted to mechanize lavender harvesting. In 1949, the world's first lavender harvester was developed and put into use at the Bridestowe Lavender Farm in Australia. The operational principle of the lavender harvester resembles that of a forage harvester, employing blades to cut lavender stems. Then the cut lavender is conveyed to a collection box at the machine's rear through a conveying device (Fig. 1) *(Mcleod, 1994)*.

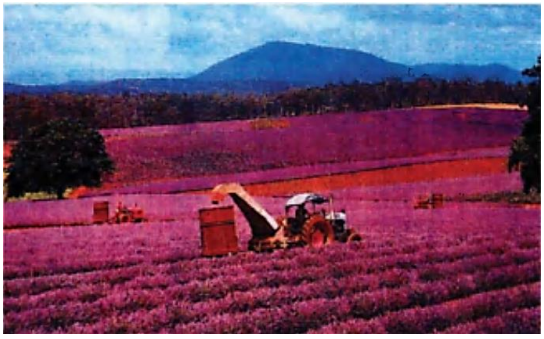

Fig. 1 - The first lavender harvester at the Australian farm

In 2005, Dimitriadis, Pavloudi and others from the Alexander Technological Educational Institute of Thessaloniki, Greece, designed and manufactured a small lavender harvester (Fig. 2), which deploys a rotating drum with a stripping component to harvest lavender. While in operation, the machine can selectively remove lavender flower heads and preserve the majority of stems. The separated lavender flower heads are conveyed to the rear collection box by the airflow generated from the rotating drum *(Dimitriadis, 2005)*. This new lavender harvester can be used to produce high-quality lavender essential oil, reducing transport and distillation costs, but is not commercially available due to harvesting efficiency.

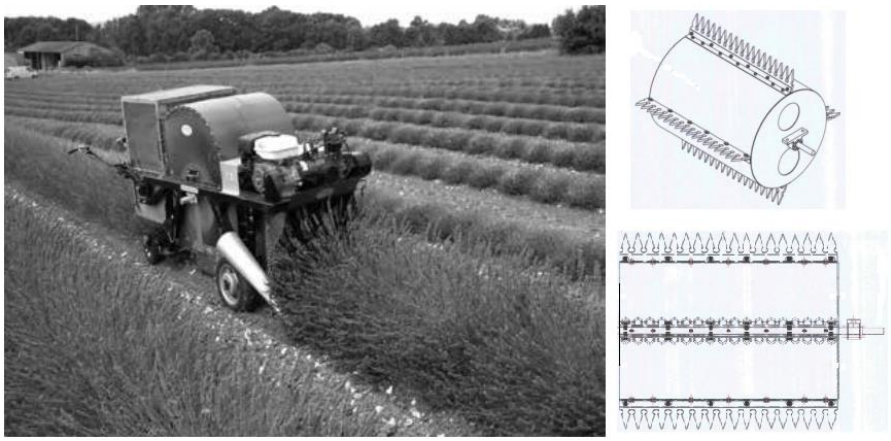

Fig. 2 - Small lavender harvester

Since the beginning of the 21st century, developed countries such as Japan, France, the Netherlands, Italy, and Bulgaria have successively achieved the mechanical harvesting of lavender. At present, mainstream foreign lavender harvester manufacturers include Germany's CLAAS and RIBERI, France's CLIER, and Italy's BONION. There are self-propelled harvesters capable of harvesting three rows at once, without being restricted by planting patterns or row spacing. There are also small, traction single-row harvesters that offer flexibility, convenience, low maintenance costs, and ease of operation. Additionally, there are small handheld lavender harvesters that cater to the diverse needs of lavender growers.

The German CLAAS JAGUAR 950 self-propelled forage harvester can be used for lavender harvesting (Fig. 3). The machine is equipped with a powerful Mercedes OM520 engine, a 3m-wide variable header drive, and can harvest a maximum of four rows of lavender concurrently. It allows for precise adjustment of the cutting length, ensuring a high level of automation. The series of models provides users with two harvesting methods to choose from. One option involves employing a single harvester to complete lavender harvesting, collecting, bundling, and unloading. The other option necessitates a transport vehicle during the harvesting process. The harvester first cuts the lavender along the neck position, then shreds the lavender with blades, and finally transfers it to the discharge spout for conveyance to the transport vehicle traveling side by side.

Fig. 3 - German CLAAS JAGUAR 950 forage harvester

The Italian BONINO BE series traction lavender harvester, as shown in Fig. 4, can be used with tractors with a power of 70 kW or more. The two V-shaped toothed brushes at the front of the machine can lift fallen lavender, convey it to the cutting system, and cut it with a rotating cutter bar with a cutting width of up to 1m. The cut lavender is then transported to a 17m^3 hopper via a loading ladder. After being filled with lavender, the hopper can be unloaded using the hydraulic device.

Fig. 4 - Italian BONINO BE400 lavender harvester

The SALIUNCA model lavender harvester from Italy's RIBERI (Fig. 5) is affixed to the right side of a tractor for operation. During operation, the front-mounted crop lifter straightens fallen lavender and transports it to the cutting system by the undulating comb teeth. The cut lavender is subsequently conveyed to the rear hopper using the lifting device.

Fig. 5 - Italy RIBERI SALIUNCA lavender harvester

The Dutch EazyCut 1200 hand-pushed small harvester, shown in Fig. 6, was originally used mainly for tea harvesting, but in recent years has also been used for lavender harvesting. The harvesting device is mainly composed of vertical arranged comb teeth and transverse curved serrated blades, which can not only harvest lavender, but also prune it, and the height can be adjusted. In addition, the machine's supporting blower and collection bag can realize the automatic bagging of lavender after harvest.

Fig. 6 - Dutch EazyCut 1200 hand-push lavender harvester

Chinese lavender harvesting machinery

In the 1950s, lavender was introduced into China for trial planting in regions such as Xinjiang, Henan, and Shaanxi, with the Yili region proving to be the most suitable natural environment for growing lavender (*Zhang et al., 2016*). Currently, the lavender planting area in the region has reached 4900 hm^2, but the mechanical harvesting of lavender is still in the initial development stage. From 1955 to 2010, all domestic lavender was harvested manually. After 2010, some domestic experts and scholars began the design and research of lavender harvesting machinery.

In 2013, Li Lujun, a farmer at Telehala Ranch in Xinyuan County, Xinjiang, designed a lavender harvesting machine, which became the first self-developed lavender harvesting machine in China. The aircraft began testing at the Lavender Base of Yining Airport on June 18 of that year (Fig. 7). The harvester is a single-row, self-propelled type, with the cutter on the header swinging and cutting under the action of the swing axle. The cut lavender is conveyed to the rear charging box by a fan and suction pipe. Operating at an efficiency of two hectares/day, the harvesting rate is 85%, essentially meeting the technical requirements for lavender mechanical harvesting *(Li., 2013)*. However, due to the harvesting quality, efficiency and the existence of damaged seedlings in the later period, there was no commercial mass production for promotion and use.

Fig. 7 - First domestic lavender harvester

The rest of the domestic research on lavender harvesting machinery is mostly recorded in patent literature, only theoretical design, and has not been produced.

Guo Jing from Urumqi, Xinjiang invented a traction type lavender harvester, which was composed of a shifting fork, a holding cylinder, a baling machine, a straw bale flatbed truck, a compression chamber, etc., as shown in Fig. 8. During operation, the rotating lifting cylinder at the front end of the machine can erect the falling lavender stalk and cut it by the rotating cutting cutter. After cutting, the lavender is driven by the gearbox to push the crank, connecting rod and fork into the feeding port of the compression chamber. In the compression chamber, the lavender is pressed into a rectangular grass block with a certain density (the length of the grass block is 300~1200 mm and the weight is about 8~18 kg). Then the square grass blocks formed by compression are bundled with plastic rope by the baling machine, and finally transported to the straw bale flat truck. Its advantages are that it can adapt to small plots and irregular plots, can maintain a consistent cutting height, and can automatically compact and bundle lavender *(Guo, 2012)*.

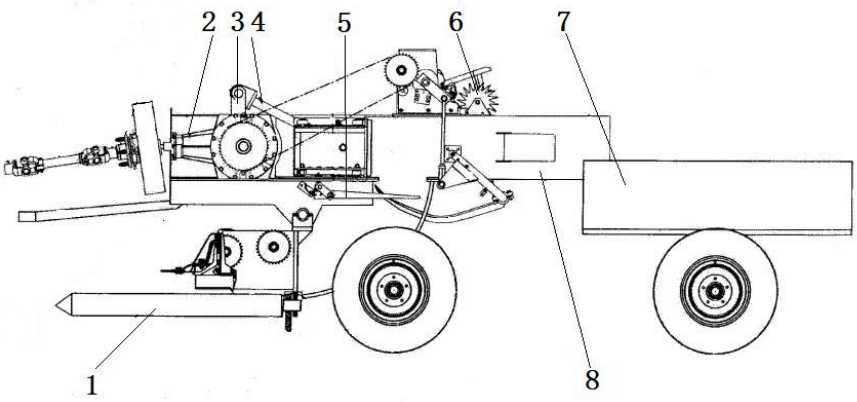

Fig. 8 - Traction lavender harvester

1. Crop lifter 2. Gearbox 3. Crank 4. Connecting rod 5. Fork 6. Bander 7. Bundle transporter 8. Compression chamber

Liu Jiaodi and Tian Dongyang from Shihezi University devised a lavender cutting device suspended on the side of a tractor, as shown in Fig. 9. Before operation, manually adjust the adjusting screw assembly to determine the opening angle of the feeding assembly. At the beginning of harvesting, the divider in front of the lavender is righted, the hydraulic motor provides power to the drive sprocket, drives the wave conveyor belt movement, the righted lavender is gathered and tightened, and then evenly and stably sent to the cutting assembly, and then the cutting assembly is driven by the crank connecting rod mechanism to cut the lavender *(Liu et al., 2016)*. The advantages of this device are fast harvesting speed and consistent cutting height, which can adapt to a variety of cultivation modes of lavender.

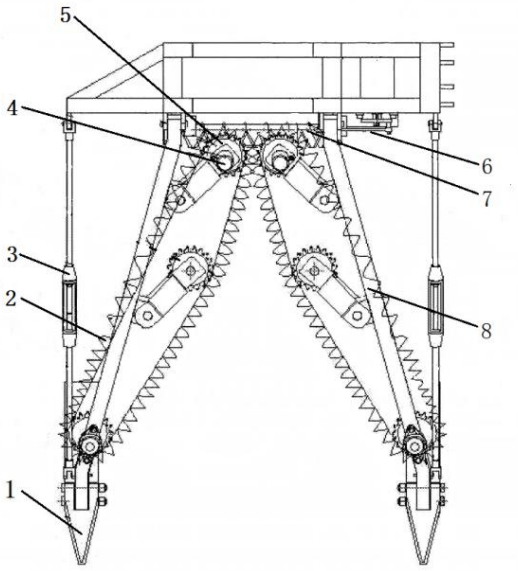

Fig. 9 - Lavender cutting device

1. Divider; 2. Undulating conveyor belt; 3. Regulating screw; 4. Hydraulic motor; 5. Drive sprocket; 6. Crank linkage mechanism; 7. Cutting assembly 8. Feeding assembly

Li Lin and others from Xinjiang Zhongzhi Agricultural and Animal Husbandry Machinery Co., Ltd. invented a new type of trailed lavender harvester, as shown in Fig. 10. When working, first connect the suction equipment outside the negative pressure mouth to make the middle of the negative pressure mouth produce negative pressure. The divider straightens the lavender, and the moving belt can send the lavender to the rotating cutter for cutting, and the cut lavender is collected into the negative pressure mouth under the action of negative pressure. The ground is not normal, the left end of the divider guide rod can be supported on the ground, driving the angle of the mounting plate to change, so that the harvesting process is smoother and the working stability is better. In addition, the machine uses only one motor as a power source, which can effectively save energy *(Li et al., 2020)*.

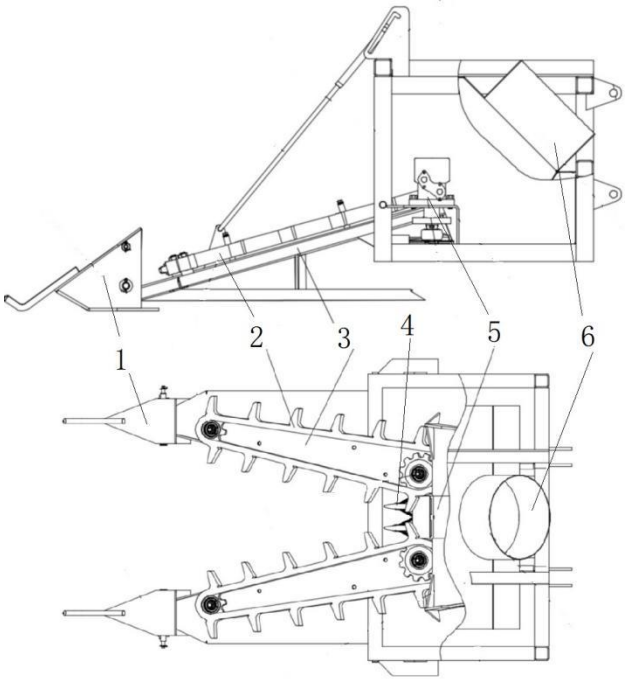

Fig. 10 - A new lavender harvester

1. Divider; 2. Conveyor belt; 3. Mounting plate; 4. Cutting tool; 5. Motor; 6. Negative pressure port

Ni Zhiming and Ni Shengdao of Yancheng Xinmingyue Machinery Manufacturing Co., Ltd. invented a small self-propelled lavender harvester, as shown in Fig. 11.

The machine includes a harvesting device, a cutting table, a conveyor belt, a storage hopper, etc. In the process of operation, the lavender is guided to the cutting table after being righted by the grass holding device in front of the machine, and the cut lavender is transported to the storage hopper by the conveyor belt, which can realize the integrated operation of cutting, conveying and storage. It has the advantages of simple structure and small volume, and can adjust the tilt of the conveyor belt and the height of the cutting device by using the lifting cylinder, and the operation is flexible *(Ni et al., 2023)*.

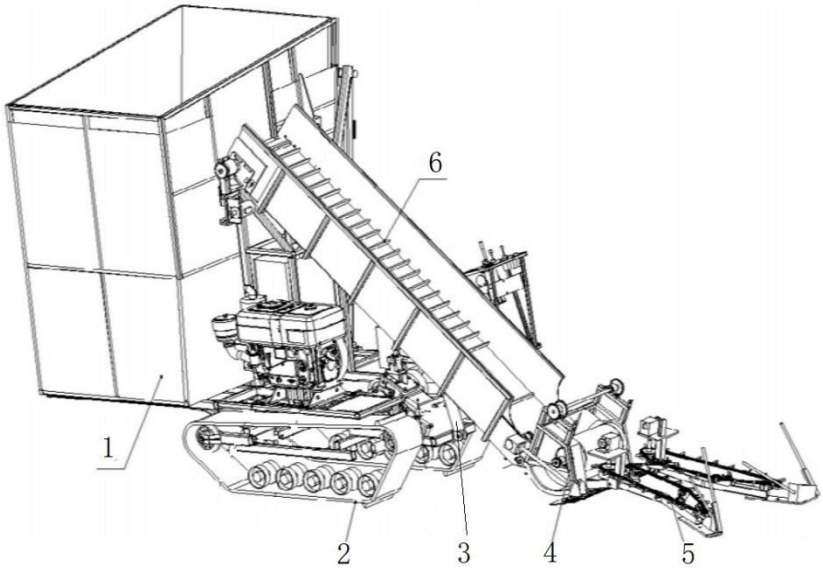

Fig. 11 - Small self-propelled lavender harvester

1. Storage hopper 2. Traveling crawler 3. Lifting cylinder 4. Header 5. Divider 6. Conveyor belt

In recent years, some areas in Chabuchaer County, Yili Kazakh Autonomous Prefecture, have started using foreign side-hanging lavender harvesters to harvest lavender. However, due to compatibility issues between foreign models and local lavender planting patterns, the usage area is limited. In Huocheng County, Yili Kazakh Autonomous Prefecture, some farmers have modified the headers of combine harvesters, originally used for wheat harvesting, for harvesting lavender. This modification has significantly increased harvesting efficiency. However, this harvesting method has not gained widespread adoption due to the substantial loss of lavender flower spikes during harvesting and the longer stems post-harvest compared to manual harvesting, which hinders essential oil extraction and greatly impacts the essential oil's quality.

Problems with lavender harvesting techniques

(1) The level of mechanical harvesting lags far behind that of developed countries. Foreign research on lavender harvesting machinery started rather early and has developed rapidly, resulting in comprehensive mechanical lavender harvesting at present. More than 98% of China's lavender planting area is concentrated in the remote Xinjiang Yili area, human resources and scientific research level is relatively backward, agricultural machinery research and development level is insufficient. So far, the domestic research on lavender harvesting machinery is only documented in patent literature, there is no independent research and development of commercial lavender harvesting machine, lavender harvest is still mainly artificial, mechanized harvest rate is less than 10%.

(2) The integration of agricultural machinery and agronomy is insufficient. During manual lavender harvesting, there is no strict requirement for plant spacing. To maximize per-acre yield while ensuring sufficient photosynthesis, farmers tend to densely plant lavender. During mechanical harvesting, factors such as tractor wheel spacing, width, and turning present substantial requirements for lavender plant spacing and field plot configuration. However, current lavender planting in China adheres to manual harvesting. Directly employing existing harvesting machinery for cutting may lead to plant damage and pressurizing, thus posing more challenges to mechanical harvesting. Moreover, lavender planting in the Yili region is dispersed. Besides major zones like Tianshan Huahai in Yining County and Jieyou Gongzhu in Huocheng County, the remaining planting areas are scattered. Some areas are even situated on slopes, making it difficult for large-scale mechanical operations. Consequently, only small single-row harvesters are utilized, resulting in low efficiency and high labor intensity.

(3) There is little research on lavender harvesting techniques. The mechanical and physical characteristics of lavender are fundamental for designing and researching mechanical equipment for lavender planting and harvesting *(Deniz et al., 2016)*. The study of lavender harvesting time and essential oil distribution in stems and leaves is also an important factor to improve the yield and essential oil quality of lavender. Foreign research on lavender harvesting began early and encompasses a wide range of aspects, including lavender essential oil, the physical and mechanical characteristics of lavender, and mechanical harvesting. In contrast, China primarily concentrates on lavender essential oil extraction and industrial development, with limited reports on the physical and mechanical characteristics of lavender.

Suggestions for the development of lavender harvesting techniques

(1) Attach importance to the research of key technologies of lavender harvesting, and develop diversified lavender harvesting equipment. China should start from the physical and mechanical characteristics of lavender, essential oil distribution and other aspects affecting mechanized harvesting, pay attention to the basic research of harvesting technology, can accelerate the development process of mechanized harvesting equipment of lavender, and promote the development of lavender industry.

If the quality of lavender essential oil is not high, or only used to make incense bags, pillows and other derivatives after harvest, you can use conventional harvesting machinery, together with the stem and flower piece cut to harvest lavender. For lavender that needs to process high-quality essential oils, it can be done by harvesting only lavender flowers, which requires more diverse lavender harvesting equipment.

Optimize lavender planting patterns and facilitate the integration of agricultural machinery and agronomy. First, following the requirements of "increasing areas of small fields, squaring angled fields, and leveling sloped fields", it is essential to reorganize scattered and fragmented farmlands, create farmlands suitable for machinery (Zheng et al.,2023), and encourage farmers to adopt lavender planting in line with mechanical harvesting patterns. Second, it is essential to develop lavender harvesting machinery with strong adaptability, thus meeting the requirements of self-propelled combined harvesting by large planting enterprises, as well as the models suitable for small planters. Meanwhile, lavender harvesters should integrate adaptive profiling technology to cater to the applications in diverse terrains and farmlands.

(3) Improve the utilization rate of lavender harvesting machinery. The flowering period of lavender is short, the annual flowering duration is 20-30 days, and the harvesting time is more concentrated. Large self-propelled lavender harvester prices up to several million yuan, only 20-30 days a year, idle the rest of the time, is obviously not conducive to the improvement of lavender economic benefits. If during the harvesting, the cutting table of the combine harvester is replaced by a lavender harvesting table, such problems can be effectively solved. In addition, the hanging lavender harvesting device used in conjunction with the tractor has low manufacturing costs, and should also be the focus of domestic lavender harvesting machinery research and development.

CONCLUSIONS

This paper describes the development status of lavender harvesting machinery at home and abroad, introduces the types and characteristics of lavender mechanized harvesting equipment. The research status of lavender harvesting technology at home and abroad was summarized from the aspects of mechanical characteristics of lavender, harvesting time, essential oil distribution in stems and leaves, etc. It was found that the mechanized harvesting level of lavender in China was far behind that in developed countries. The reason is that in addition to the concentration of planting area in remote areas with relatively backward human resources and scientific research level, it is also related to the lack of integration of agricultural machinery and agronomy, and less research on lavender harvesting technology. Finally, according to the actual situation of lavender in China, the relevant suggestions were put forward, which has important reference significance for speeding up the mechanized harvesting process of lavender in China.

ACKNOWLEDGEMENT

This work was financially supported by the Yili Prefecture Science and Technology Plan project (YZ2022Y011) and the university level scientific research project of Yili Normal University (2023YSYB030), as well as the vibration signal capture and intelligent processing laboratory of Yili Normal University.

REFERENCES

[1] Aprotosoaie, A. C., Gille, E., Trifan, A., Luca, V. S., Miron, A. (2017). Essential Oils of Lavandula Genus: A Systematic Review of Their Chemistry. *Phytochem. Rev,* vol.16, pp.761-799.

[2] Baydar H., Erbaku S. (2009). Effects of Harvest Time and Drying on Essential Oil Properties in Lavandin (*Lavandula×intermedia Emeric ex Loisel*.). *Acta Hort,* pp.377-381.

[3] Blinova, K. F., Yakovlev, G. P. (1990). Botanical and Pharmacognostic Dictionary: Ref. Allowance. *Higher School, Moscow,* p.202.

[4] Bulletin. (2000). Growing lavender in Western Australia. *Department of Agriculture-West Australia,* pp.4-18.

[5] Colt, U.M. (2016). Step-by-Step Creation of a Lavender Plantation. *J. Bot,* vol.8, pp.76-80.

[6] Dimitriadis C.I., Brighton J., O'Dogherty M., Kokkora M., Darras A. (2014). Physical and Aerodynamic Properties of Lavender in relation to Harvest Mechanisation. *International Journal of Agronomy.* https://doi.org/10.1155/2014/276926

[7] Dimitriadis C.I. (2005). The Design of an Improved Efficiency Lavender Harvester. *Silsoe Cranfield Bedford of UK: Cranfield University.*

[8] Dimitriadis C.I., Pavloudi A., Aggelopoulos S. (2016). Validation in a Novel Lavender Harvester for oil Production. *Journal of Environmental Protection and Ecology,* vol.4, pp.1504–1513.

[9] Hassiotis C.N. (2014). Environmental and developmental factors affect essential oil production and quality of Lavandula angustifolia during flowering period. *Ind.Crops Prod,* vol.62, pp.359-366. https://doi.org/10.1016/j.indcrop.2014.08.048

[10] Çiğdem, S., Hülya, O. (2019). The Effect of Diurnal Variation on Some Yield and Quality Characteristics of Lavender under Çukurova Ecological Conditions. *Turkish Journal of Agriculture-Food Science and Technology,* vol.7, pp.531-535. https://doi.org/10.26919/d.cnki.gannu.2019.000531

[11] Costea, T., Străinu, A.M., Gîrd, C.E. (2019). Botanical characterization, chemical composition and antioxidant activity of Romanian lavender (*Lavandula angustifolia Mill*.) Flowers, Studia Universitatis "Vasile Goldis". Ser. *Stiintele Vietii,* vol.29, pp.159-167.

[12] Contino, M. (2020). Lavender Fields in Tuscany: *Provence in Pisa.* https://magazine.dooid.it/en/destinations/lavender-fields-in-tuscany-provence-in-pisa/.

[13] Détár, E., Éva, Z. N., Gosztola, B. (2020). Effects of variety and growth year on the essential oil properties of lavender (Lavandula angustifolia Mill.) and lavandin (Lavandula x intermedia Emeric ex Loisel.). *Biochemical Systematics and Ecology, v*ol.90, pp.104020. https://doi.org/10.1016/j.bse.2020.104020

[14] Ding, L. J. (2019). Research on the Development Path of Lavender Characteristic Industry in Yili, Xinjiang. *Hefei: Anhui Agricultural University.* https://doi.org/10.26919/d.cnki.gannu.2019.000531

[15] Fakhriddinova, D. K., Rakhimova, T. R., Dusmuratova, F. M., Duschanova, G. M., Abdinazarov, S. H., Samadov, I. N. (2020). The Anatomical Structure of Vegetative Organs Lavandula officinalis Chaix in the Introduction of Tashkent Botanical Garden. *Am. J. Plant Sci,* vol.11, pp.578-588. https://10.4236/ajps.2020.114043

[16] Fernández, S. M., Carrillo, J. M. (2020). Environmental Effects on Yield and Composition of Essential Oil in Wild Populations of Spike Lavender (Lavandula latifolia Medik.). *Agriculture,* vol.10, pp.626. https://doi.org/10.3390/agriculture10120626

[17] Guo, F. J., Liu, F., Yang, S. Z. (2023). Research progress on skin care effect of lavender essential oil. *Detergent & Cosmetics,* vol.01, pp. 35-40.

[18] Giray, F.H. (2018). An Analysis of World Lavender Oil Markets and Lessons for Turkey. J. Essent. Oil Bear. *Plants,* vol.21, pp.1612-1623. https://doi.org/10.1080/0972060X.2019.1574612

[19] Geng, Q. T. (2012). Research on the Development Status, Problems and Countermeasures of Lavender Industry in Yili. *Xinjiang State Farms Economy,* vol.03, pp. 46-51.

[20] Guo, J. (2012). Lavender Harvester. *China Utility Model Patent:* CN202310592U.

[21] Gül, M., Kart, M. C., Sirikci, S. S. (2016). Determining Costs and Profitability of Lavender Farms in Isparta Province of Turkey. *J. Essent. Oil Bear. Plants,* vol.19, pp.686-692.

[22] Giray, F.H. (2018). An Analysis of World Lavender Oil Markets and Lessons for Turkey. *J. Essent. Oil Bear. Plants,* vol.21, pp.1612-1623. https://doi.org/10.1080/0972060X.2019.1574612

[23] Giannoulis, K.D., Evangelopoulos, V., Gougoulias, N., Wogiatzi, E. (2020). Lavender Organic Cultivation Yield and Essential Oil Can Be Improved by Using Bio-Stimulants. *Acta Agric. Scand. Sect. B-Soil Plant Sci,* vol.70, pp. 648-656. https://doi.org/10.1080/09064710.2020.1833974

[24] Goncearіuc, M., Zbancă, A., Panut, A.S. (2019). A Practical Guide to Growing Lavender and Managing the Business/Ghid Practic Privind Cultivarea Lavandei si Administrarea Afacerii. Lavanda. *MD: Chisinău, Moldova,* pp.128. ISBN 978-9975-56-687-2. https://doi.org/10.17660/ActaHortic.2009.826.53

[25] Hassiotis, C. N., Ntana, F., Lazari, D. M., Poulios, S., Vlachonasios, K.E. (2014). Environmental and Developmental Factors Affect Essential Oil Production and Quality of Lavandula angustifolia during Flowering Period. *Ind. Crops Prod,* vol.62, pp.359-366. https://doi.org/10.1016/j.indcrop.2014.08.048

[26] Huang, X.D., Yang, J.X., Luo, W.K. (2022). Research and Application of Integrated Lavender Essential Oil Extraction Device. *Journal of Suihua University,* vol.42, pp. 149-152.

[27] Han, K.L., Zhang, W.M, Yang, J.X. (2013). Cultivation Techniques of Organic Lavandula angusitifolia in Ili River Valley. *Chinese Wild Plant Resources, vol*.32, pp. 59-61.

[28] Hassiotis, C. N., Lazari, D., Vlachonasios, K. (2010). The Effects of Habitat Type and Diurnal Harvest on Essential Oil Yield and Composition of Lavandula angustifolia Mill. *Fresenius Environ, v*ol.19, pp.1491-1498.

[29] Jiang, X.M., Guo, D.L., Lu, Z. (2016). Study on the Change of Lavender Essential Oil Composition in Different Cultivars, Florescence and Harvest Time. *Journal of Anhui Agricultural Sciences*, vol.27, pp.22-24. https://doi.org/10.13989/j.cnki.0517-6611.2016.27.007

[30] Katarzyna, S.-L., Romuald, M., Wojciech, K., Bogdan, K.; Jan, B. (2014). Yielding and quality of lavender flowers (Lavandula angustifolia Mill.) from organic cultivation. *Acta Sci. Pol. Hortorum Cultus*, vol.13, pp.173-183.

[31] Liu, Y. (2019). *Research on the Development Issues and Countermeasures of Lavender Industry in Huocheng County*. Chengdu: Sichuan Agricultural University. https://doi.org/10.27345/d.cnki.gsnyu.2019.000221

[32] Li, Y.P. (2016). Reasons for Low Yield of Lavender Crops and Solutions. *Agricultural Science-Technology and Information*, vol.17, pp. 68. https://doi.org/10.15979/j.cnki.cn62-1057/s.2016.17.043

[33] Li, L.J. (2013). Lavender Harvester. China Utility Model Patent: CN202857323U

[34] Liu, J. D., Xu, H. Z., Cao, W. B (2016). A lavender harvesting device. Chinese Invention Patent: CN105766204A.

[35] Li, L., Gao, J., Liu, Y.L. (2020). *A New Lavender Harvester*. China Utility Model Patent: CN211210549U.

[36] Monge, R. (2012). Les Routes de la Lavande: Au Carrefour du Développement Culturel et de la Valorisation de la Ressource. *Routes Touristiqueset Itinéraires Culturels, entre Mémoire et Développement: Québec*, QC, Canada, vol, pp.139-147.

[37] Muntean, L.S., Tămas, M., Muntean, S. (2016). *Treatise of Cultivated and Spontaneous Medicinal Plants*. Risoprint: Cluj-Napoca, Romania, ISBN: 978-973-53-1873-4.

[38] Mcleod, J. (1994). *Lavender sweet lavender*. Kenthurst NSW: Kangaroo Press.

[39] Ni, Z.M., Ni, S.D. (2023). *A small lavender harvester and its working method*. Chinese Invention Patent: CN116195428A.

[40] Petras, R.V., Airidas, D., Marija, B. (1997). Composition of the Essential Oil of Lavender (Lavandula angustifolia Mill.) from Lithuania. *Journal of Essential Oil Research*, vol.9, pp.107-110. https://doi.org/10.1080/10412905.1997.9700727

[41] Prusinowska, R., Smigielski, K. B. (2014). Composition, biological properties and therapeutic effects of lavender (Lavandula angustifolia L.). A review. *Herba Polonica*, vol.60, pp. 56-66. https://doi.org/10.2478/hepo-2014-0010

[42] Raev, R., Jordanov, R., Zheljazkov, V., Rabotyagov, V., Craker, L., Nolan, L., Shetty, K. (1996). Induced polyploidy in lavender. *Acta Horticult*, vol.426, pp. 561-572. https://doi.org/10.17660/ActaHortic.1996.426.61

[43] Rabotyacov, V.D., Yakovlev, L.K. (1980). Study of the variability of the content of essential oil in lavender. *Cytology and genetics* (USA), vol.14, pp. 33-35.

[44] Sabara, D., Kunicka-Styczyńska, A. (2009). Lavender oil - Flavouring or active cosmetic ingredient? *Scientific bulletin of the technical university of Lodz*, vol.73, pp. 33-40.

[45] Sha, W., Li, J., Zhang, M.J. (2021). Research Progress of Lavender and its Essential Oil in Medical Treatments. *Molecular Plant Breeding,* vol.8, pp. 8.

[46] Shi, Y.G. (2012). *Analysis of volatile components and quality control of lavender*. Urumqi: Xinjiang University.
[47] Stanev, S., Zagorcheva, T., Atanassov, I. (2016). Lavender cultivation in Bulgaria-21st century developments, breeding challenges and opportunities. *Bulg. J. Agric. Sci*, vol.22, pp. 584-590.
[48] Trendafilov, K., Delchev, N. (2006). Study on impurities and losses during lavender harvesting with arc-shaped cutting unit. *Agricultural Engineering (Bulgaria),* vol.43, pp. 2-7.
[49] Wilson, T.M., Poulson, A., Packer, C., Carlson, R. E., Buch, R.M. (2021). Essential Oil Profile and Yield of Corolla, Calyx, Leaf, and Whole Flowering Top of Cultivated Lavandula angustifolia Mill. *Molecules,* vol.26, pp. 2343. https://doi.org/10.3390/molecules26082343
[50] Yao, L., Zhang, S. L. (2002). *Aromatic Plants. Shanghai Education Press.*
[51] Yilmaz, D., Jasinskas A. (2016). Determination of cutting properties of Lavandin (*Lavandula x intermedia Emeric ex Loisel*) at different harvesting time. *Agricultural Engineering, Research Papers,* vol.48, pp.1-5.
[52] Yilmaz, D., Gökduman, M.E. (2014). Effect of Moisture Contents on Physical-Mechanical Properties of Lavandin. *Journal of Essential Oil Bearing Plants,* vol.17, pp.1224-1232. https://doi.org/10.1080/0972060X.2014.958565
[53] Zhang, Y.X., Du, L.L. (2016). Cultivation techniques of lavender in Yili Valley. Rural Science& Technology, vol.09, pp.45-46.
[54] Zhao, W.B., Chen, H.Y., Xu, Y.H. (2009). A Study on Extraction Technology of Essential Oil from Lavender with Supercritical Carbon Dioxide Fluid. *Journal of Shihezi University* (Natural Science), vol.27, pp. 634-636. https://doi.org/10.13880/j.cnki.65-1174/n.2009.05.003
[55] Zheng, H., Fu, T., Xue, X.L. (2023). Research status and prospect of tea mechanized picking technology. *Journal of Chinese Agricultural Mechanization*, vol.44, pp. 28-35. https://doi.org/10.13733/j.jcam.issn.2095-5553.2023.09.005
[56] Zatuchny, V. L., Kigelman, M. Kh. (1972). Biology and Features of Agricultural Technology of Lavender in the USSR. Essential Oil Crops of Moldova and Essential Oils: Collection. *Scientific TR*, pp.24-39.

TRAJECTORY PLANNING FOR COLLABORATIVE OPERATION OF MULTIPLE AGRICULTURAL HANDLING ROBOTS BASED ON IMPROVED WHALE OPTIMIZATION ALGORITHM
/
基于改进鲸鱼优化算法的多农业搬运机器人协同作业轨迹规划研究

Jiahao LAN, Yunjie MA *)
School of Economics and Management, Ningbo University of Technology, Ningbo, Ningbo/ China
Tel: +8619157501635; E-mail: flmyj123@163.com
Corresponding author: Ma Yunjie
DOI: https://doi.org/10.35633/inmateh-72-45

Keywords: *Agricultural robot; trajectory planning; collaborative operation; job path; whale optimization algorithm (WOA)*

ABSTRACT
To solve the problem that the moving trajectory and operating trajectory are relatively independent and time-consuming when robots transfer agricultural products from harvesting fields to warehouses or transport vehicles, a type of agricultural materials handling robot was designed, the optimal trajectory planning method for the collaborative operating time of agricultural materials handling robots was proposed, and the time optimal trajectory under the collaborative operation of robot operating system and traveling system was acquired. Specifically, the kinematic model and dynamic model for the collaborative operation of robots were established to perform time optimal trajectory planning for materials handling robots, the Beta distribution was then applied to the Whale Optimization Algorithm (WOA) for population initialization, and a nonlinear convergence factor was introduced to prevent local optimum in the later stage of iterations. Finally, WOA was improved combining the variable neighborhood algorithm to enhance the diversity of the neighborhood structure, and this improved algorithm was applied to model solving. The results reveal that the proposed trajectory planning method can facilitate robots to obtain a smooth and time optical moving trajectory in collaborative operations of materials grabbing and discharging and obstacle avoidance. The displacement, speed, acceleration, and force/torque curves of each joint of the robots change gently, and the double-crawler traction can meet the requirements of the robots and rapidly stabilize and track the time optical trajectory.

摘要
为了解决机器人将农产品从收获场所转移到仓库或运输车辆存在的移动轨迹和作业轨迹相对独立且耗时长的问题，本文设计一种农业物料移运机器人，并提出一种农业物料移运机器人协同作业时间最优轨迹规划方法，获得机器人作业系统和行驶系统协同作业的时间最优轨迹。该方法建立机器人协同作业的运动学模型和动力学模型，对物料移运机器人开展时间最优轨迹规划，并将 Beta 分布应用于鲸鱼优化算法(Whale Optimization Algorithm，WOA)进行种群初始化，再引入非线性收敛因子改善迭代后期陷入局部最优的情况，最后结合变邻域算法改进了鲸鱼优化算法来增加邻域结构的多样性，并将此算法应用于该模型求解。结果表明，提出的轨迹规划方法可使机器人在抓放料协同作业和避障协同作业中取得平滑且时间最优的运动轨迹，机器人各关节的位移、速度、加速度、力/力矩曲线变化平缓，两履带牵引力满足机器人的要求且可快速稳定跟踪时间最优路径。

INTRODUCTION
As an important starting point to promote agricultural modernization, the development of agricultural robots is of great significance for improving agricultural production efficiency, popularizing new agricultural technologies, protecting farmland environment, and reducing dependence on human resources. Agricultural robots will contribute to agricultural automation, informatization and intelligence, thus changing the operation mode of traditional agriculture (*Wang et al., 2022*). Under the increasing pressure of environmental protection, agricultural robots, if applied, will also help protect the farmland environment and avoid the pollution of soil and groundwater caused by the excessive use of chemical fertilizers and pesticides (*Huo et al., 2018*). Nowadays agricultural robots can complete some heavy and trivial agricultural tasks, such as sowing, spraying, fertilizing, harvesting, and weeding so as to reduce the labor intensity of farmers and relieve their dependence on human resources. Meanwhile, handling robots, which have been widely used in such fields as industry, storage,

manufacturing, and service, are usually divided into fixed and mobile types (*Long et al., 2017*). Usually installed in production lines, machine tools, etc., agricultural handling robots can automatically perform assembly and handling tasks through programming, maintaining high working accuracy and efficiency (*Yin et al., 2023*). When facing the unknown environment, agricultural handling robots first collect environmental information through Lidar or depth cameras to build a map. Secondly, they can run autonomously in the workspace with obstacles through preset commands or real-time control of the upper computer; finally, the user can use the mouse, keyboard or program to complete the handling task (*Zhang et al., 2020*). Therefore, the collaborative system of multiple agricultural handling robots is an important development direction of robot application at present. Compared with the single agricultural robot system, the collaborative system of multiple agricultural robots can not only solve complex tasks and improve the robustness and reliability of the system but also has been successfully applied to logistics warehouse handling and agricultural handling. At present, however, most of these tasks are realized by manual teaching, lacking the ability of independent motion planning. As the requirement for intelligent production is put forward in China, the multi-agricultural-robot collaborative system should have the ability to plan the motion independently, making it very necessary to study the motion planning of the multi-agricultural-robot collaborative system.

Literature review

At present, many algorithms have been used in robot path planning. *Wang et al. (2019)* proposed a wireless positioning system based on ZigBee, which can locate the handling robot in real time and give instructions for cargo handling. *Chen et al. (2019)* came up with a method based on greedy algorithm to meet the needs of temporary route adjustment of handling robots. *Božek et al. (2016)* raised a method to identify and judge the medical garbage bin based on machine vision, and the robot Lidar can navigate to the target garbage bin when receiving the start signal. *Palleschi et al. (2020)* implemented a map construction method based on laser SLAM, which exhibits higher mapping accuracy and serves as the suitable map construction method for handling robot path planning. *Abu-Dakka et al. (2017)* proposed an improved artificial potential field method for path planning of handling robots, which solved the failure of traditional algorithms to reach the target point. *Daniel et al. (2019)* put forward an improved ant colony algorithm to plan the path of handling robots, which can elevate the speed of the handling robots and reduce the loss. Among many algorithms, A* algorithm is considered a common and appropriate algorithm to solve the path planning problem of handling robots by virtue of its rapid response to the environment and direct path search. In some literature, A* algorithm has been used to solve the path planning problem of robots. *Sathiya et al. (2019)* proposed an improved A* algorithm, which introduced a "reward and punishment mechanism" on the basis of single handling robot and obstacle prediction, thus reducing the number of turns of the handling robot in the moving process. *Amruta et al. (2020)* proposed a robot path planning method combining A* algorithm with dynamic window method, and improved the smoothness of the path. *Park et al. (2020)* proposed an improved A* algorithm, which improved the actual operation efficiency of robots, reduced their energy consumption, and shortened the time of path search planning. Although A* algorithm has been used to plan the motion path of handling robots so that they can avoid all obstacles and safely deliver the goods to the destination, the efficiency of A* algorithm will significantly decline if handling robots work under large environments, and the planned path is usually not the optimal one.

The research on path planning of robots mainly includes path generation and path tracking. First of all, path generation refers to the path with the shortest generation time or the least energy consumption, which is mainly solved by particle swarm optimization algorithm, ant colony algorithm, firefly algorithm, and genetic algorithm. *Seyedali et al. (2016)* could generate motion paths in complex areas by setting constraints and collision models and discretizing variables at equal intervals. *Elhosseini et al. (2019)* proposed a path generation algorithm based on obstacle cost potential field to dynamically adjust the path, contributing to the smooth motion path of robots and keeping them at a safe distance from obstacles. *Chen et al. (2019)* put forward a double-optimized ant colony algorithm to adaptively adjust the probability transfer function and re-optimize the path to solve the low convergence path quality in path planning. *Ahmed et al. (2019)* proposed an improved potential field ant colony algorithm, constructed a negative feedback channel through the convergence times of the algorithm, and dynamically adjusted the update speed of parameters to obtain the optimal path. *Gu et al. (2021)* used ant colony algorithm and geometric method to optimize the path, and combined pheromone diffusion with geometric local optimization to generate a global optimal path. Path tracking refers to controlling the robot to follow a specified path. For instance, *Li et al. (2020)* established the dynamic model of tracked vehicles based on the principle of spherical contact, and designed a tracking

controller by using deep reinforcement learning, which can accurately track the path. *Tu et al. (2021)* came up with a path tracking method based on heuristic dynamic programming, which integrated the tracking error and tracking stability of the path to design a return function to enhance the environmental adaptability of path tracking. *Heidari et al. (2019)* raised a fuzzy predictive control algorithm combining the dynamics characteristics of the robot to track the path, so as to solve the high time delay in high-speed trajectory tracking control. *Li et al. (2021)* could generate a better path in the target space by combining various algorithms, but the calculated quantity was large, which degraded the efficiency and real-time performance of path generation to some extent; the tracking control law stated by *Hu et al. (2021)* is complex, and it is difficult to determine the optimal control law parameters. In face of the requirements for the efficient operation of agricultural robots, studying the coordination between robot operating system and traveling system is an important development opportunity and challenge for agricultural robots *(Hu et al., 2021)*. Some problems have been found in the existing research. For example, the research on path planning of robots needs to be determined in advance and the action completed by the collaborative operation of the traveling system and operating system is relatively simple, making it difficult to realize real-time trajectory planning under complex scenarios.

To sum up, the research on the handling path of robots mainly focuses on single-robot handling path planning, while the trajectory planning through the collaborative operation of multiple agricultural handling robots has been less investigated. Based on the abovementioned research results, a trajectory planning model for the collaborative operation of multiple agricultural handling robots was constructed in this study. Then, the population was initialized using Beta distribution based on the basic Whale Optimization Algorithm (WOA), a nonlinear convergence factor was added to prevent the algorithm from local optimum in the later stage of iterations, and the diversity of the neighborhood structure was enhanced by introducing the variable neighborhood algorithm. As revealed by the comparison results with basic WOA, the improved algorithm can effectively improve the model solving efficiency.

MATERIALS AND METHODS

Collaborative kinematics analysis of agricultural handling robots

When a rigid body is collaboratively handled by 2 agricultural handling robots, the base of each robot is fixed, and then the homogeneous transformation (BWT) from the base coordinate system {B} of each robot to the world coordinate system {W} is fixed. The two handling robots are set to jointly hold the workpiece and do linear motion with an unchanged pose, so the coordinate system {U} of the workpiece will change constantly. Taking the world coordinate system {W} as a reference, the initial pose and the target pose of the workpiece are expressed as Formulas (1) and (2) respectively:

$$ {}^{\mathrm{W}}_{\mathrm{U}}\mathrm{T}^{\mathrm{start}} = \begin{bmatrix} {}^{\mathrm{W}}_{\mathrm{U}}\mathrm{R} & {}^{\mathrm{W}}_{\mathrm{U}}\mathrm{P}^{\mathrm{start}} \\ 0 & 1 \end{bmatrix} \quad (1) $$

$$ {}^{W}_{U}T^{\mathrm{goal}} = \begin{bmatrix} {}^{W}_{U}R & {}^{W}_{U}P^{\mathrm{goal}} \\ 0 & 1 \end{bmatrix} \quad (2) $$

Hence, the straight path is $L = \sqrt{(P^{\mathrm{start}} - P^{\mathrm{goal}})^2}$ in length, which is equally divided into N portions, and then N+1 path points are generated. Therefore, the N+1 pose sequence of {U} about {W} is displayed in Formula (3):

$$ \left\{ {}^{W}_{U}T(k) = \begin{pmatrix} {}^{W}_{U}R & P(k) \\ 0_{1\times 3} & 1 \end{pmatrix} \right\}, 0 \leqslant k \leqslant N \quad (3) $$

The motion at the ends of the two handling robots about the base coordinate system is respectively calculated as per Formulas (4) and (5):

$$ {}^{B_1}_{E_1}T(k) = \begin{pmatrix} W \\ B_1 \end{pmatrix} T^{-1} \begin{pmatrix} W \\ U \end{pmatrix} T(k) \begin{pmatrix} U \\ E_1 \end{pmatrix} \quad (4) $$

$$ {}^{B_2}_{E_2}T(k) = \begin{pmatrix} W \\ B_2 \end{pmatrix} T^{-1} \begin{pmatrix} W \\ U \end{pmatrix} T(k) \begin{pmatrix} U \\ E_2 \end{pmatrix} \quad (5) $$

Given the fixed values of WBT and UET, it is only necessary to solve the pose $({}^{W}_{U}T(k))$ of {U} relative to {W}, and then the motion at the ends of the two handling robots about their base coordinate system is solved. Furthermore, the change $\{{}^{1}q_n\}(1 \le n \le 6)$ in each joint of Robot 1 and that $(\{{}^{2}q_n\}(1 \le n \le 6))$ of Robot 2 can be solved through inverse solutions.

In this section, the changes in the joints of the 2 robots can be solved through the collaboration model of multiple agricultural handling robots established, thus laying a foundation for establishing the path optimization function subsequently.

Modeling

The path selection function for agricultural handling robots is established with their operating length fr_1, operating difficulty index fr_2, and operating time fr_3 as the objective functions. For the objective function fr_1, the available motion path of agricultural handling robots is assumed to be R={ $r_1, r_2, \ldots, r_n$} and the number of nodes on the available motion path to be n. fr_1 is calculated through the following formula:

$$fr_1 = \sum_{i,j=1;i\neq j} d(r_i, r_j) \tag{6}$$

Where r_1, r_j represent the i-th and j-th nodes on the available path; $d(r_1, r_i)$ denotes the distance between r_1 and r_j.

The total difficulty index fr_2 of each node in the path passed by agricultural handling robots is calculated as follows:

$$fr_2 = \sum_{i=1}^{n} z_i g(r_i) \tag{7}$$

Where $g(r_i)$ is the difficulty index when the handling robot passes r_i; z_i denotes the number of robots passing any node within a designated time window.

The objective function fr_3 is calculated as below:

$$fr_3 = \sum_{i,j=1}^{n} \sum_{a=1}^{A} x_{ar_{ij}} \left(t_{ij}^{s} \cdot w_{ij} + t_{ij}^{c} + t_w \right) \tag{8}$$

Where A is the number of agricultural handling robots; $x_{ar_{ij}}$ stands for the number of handling tasks; t_{ij}^{s} is the time needed by the agricultural handling robot to pass the straight road section from node i to j; t_{ij}^{c} represents the time needed to pass the turning road segment from node i to j; w_{ij} is the weight of the road segment from node i to j; t_w is the time window.

t_{ij}^{s} is calculated as follows:

$$t_{ij}^{s} = \frac{L(i,j)}{v_s} - \frac{L_v}{v_s} \tag{9}$$

Where v_s represents the uniform running speed of agricultural handling robots; $L(i,j)$ is the distance between i and j; L_v is the length of agricultural handling robots.

$$t_{ij}^{c} = \frac{L_v}{v_c} + \frac{\pi R_{tc}}{v_c} \tag{10}$$

Where v_c is the running speed of agricultural handling robots at the turning; R_{tc} represents the turning radius of robots.

In this study, three objective functions, operating length, operating difficulty index, and operating time, were designed when constructing the trajectory planning model of multiple agricultural handling robots, aiming to achieve the optimal trajectory for the collaborative operation of multiple agricultural handling robots. By assigning different weights to different optimization objectives, the objective functions were subjected to dimensionless processing uniformly through the following formula.

$$fr_1^{*} = \frac{fr_1 - \min fr_1}{\max fr_1 - \min fr_1} \tag{11}$$

$$fr_2^* = \frac{fr_2 - \min fr_2}{\max fr_2 - \min fr_2} \quad (12)$$

$$fr_3^* = \frac{fr_3 - \min fr_3}{\max fr_3 - \min fr_3} \quad (13)$$

The three objective functions of the unified dimension were weighted and summed according to the specified weights and transformed into a single-objective model for solving. The expression of the single-objective function is:

$$\min fr^* = \alpha_1 fr_1^* + \alpha_2 fr_2^* + \alpha_3 fr_3^* \quad (14)$$

Where α_i is the weight of the objective function and $\alpha_i \in [0,1]$, $\alpha_1 + \alpha_2 + \alpha_3 = 1$.

Constraints

The multiple constraints for the established motion path selection function of handling robots are expressed as follows:

$$x_{ar_{ij}} = 1 \quad (15)$$

$$t_w = t_{r_{ij}}^{a,\text{end}} - t_{r_{ij}}^{a,\text{start}} \quad (16)$$

$$\begin{cases} N_{r_{ij}}^{t_{r_{ij}}^a} = r_{ij} \cdot \sum_{a=1}^{A} x_a^{t_{r_{ij}}^a} \\ N_{r_{ji}}^{t_{r_{ji}}^a} = r_{ji} \cdot \sum_{a=1}^{A} x_a^{t_{r_{ji}}^a} \end{cases} \quad (17)$$

$$z_i \geqslant N_{r_{ij}}^{t_{r_{ij}}^a} + N_{r_{ji}}^{t_{r_{ji}}^a} \quad (18)$$

Formula (15) is the handling task constraint of handling robots, i.e., any handling robot can only execute one task in intelligent storage; Formula (16) is the time window constraint, namely, the time window t_w constraint of Robot a on path r_{ij}. Formula (17) constrains the number of handling robots within the time window, namely, it is the constraint for the number of handling robots within a designated time window; Formula (18) constrains the number of handling robots on the path within the designated time window, i.e., the constraint for the number of handling robots on r_{ij} within $t_{r_{ij}}^a$.

ALGORITHM DESIGN

How to solve the path optimization problem accurately and efficiently has always been a major problem. In the existing studies, heuristic algorithms have often been used to solve similar problems. As a type of heuristic algorithm, WOA has enjoyed extensive development and application because of simple mechanism, few parameters, and strong optimization ability. Model solving can be achieved more rapidly and effectively by improving the standard WOA.

WOA

WOA is a meta-heuristic optimization algorithm proposed in 2016, which is inspired by the hunting behavior of humpback whales. By simulating the hunting behavior of random or optimal individuals, researchers have found that there are two kinds of bubble net hunting methods for whales, i.e., "upward spiral strategy" and "double spiral strategy". In the "upward spiral strategy", the humpback whale will dive by about 12 m first, then start making bubbles in the spiral, and swim to the surface. The "double spiral strategy" includes three different links: coral link, whale tail flapping on the water surface link, and capture link. The above predation process can be applied to solving WOA, that is, one solution can be expressed by one whale individual, and multiple solutions can be expressed by multiple whale individuals. The idea of solving WOA can be equivalent to the fact that many whales are constantly changing their positions until searching a satisfactory solution.

(1) Prey encirclement

It is assumed that in a d-dimensional space, the position of the optimal whale individual X^* is $(X_1^*, X_2^*, ..., X_d^*)$, and the position of the whale individual X^j is $(X_1^j, X_2^j, ..., X_d^j)$. The next position X^{j+1}

$(X_1^{j+1}, X_2^{j+1}, ..., X_d^{j+1})$ of the whale individual X^j under the influence of the optimal whale individual is calculated as follows:

$$X_k^{j+1} = X_k^* - A_1 D_k \quad (19)$$

$$D_k = | C_1 X_k^* - X_k^j | \quad (20)$$

$$C_1 = 2r_2 \quad (21)$$

$$A_1 = 2ar_1 - a \quad (22)$$

$$a = 2 - 2t / t_{max} \quad (23)$$

Where X_k^{j+1} is the *k*-th component of the space coordinate X^{j+1}; the convergence factor a linearly declines from 2 to 0 with the increase in the number of iterations; t is the current number of iterations; both r_1 and r_2 are random numbers within [0,1].

(2) Prey capturing

When the whale individuals approach the current best whale individual in a spiral way to catch their prey, half of them will choose to shrink the ring of encirclement, while the other half will choose to run to the prey in a spiral way.

$$D_k = | X_k^* - X_k^j | \quad (24)$$

When p < 0.5,

$$X_k^{j+1} = X_k^* - A_1 D_k \quad (25)$$

When p≥0.5,

$$X_k^{j+1} = X_k^* + D_k \exp(bl) cos(2\pi l) \quad (26)$$

Where *b* is the logarithmic spiral shape constant and l is a random number within [-1, 1].

(3) Prey search

In the mathematical model for prey capturing behavior, the value of A_1 is restricted within [-1, 1]. If the value does not fall into this range, whale individuals will randomly select a whale individual to approach from the current whale individuals. It is assumed that the spatial position of a random whale individual X^s in the whale population is $(X_1^s, X_2^s, ..., X_d^s)$, and then the mathematical model for prey search behavior is displayed as below:

$$X_k^{j+1} = X_k^s - A_1 D_k \quad (27)$$

$$D_k = | C_1 X_k^s - X_k^j | \quad (28)$$

Improved WOA

Generally, when the NPL problem is solved using swarm intelligence algorithms, the algorithm performance is mainly affected by premature convergence and convergence speed, and it is especially important to balance the exploration and development abilities of algorithms in search space (*Zhang et al., 2019*). Particle Swarm Optimization (PSO) has fast convergence speed but weak global exploration ability. WOA displays good exploration ability, but its development ability is mainly restricted by the distance between the current position and the optimal position. In PSO, if the global optimal solution of the population falls into a local optimum, other particles will stop searching and follow the global optimal solution into the local optimum. To sum up, the PSO algorithm has strong optimization ability but weak space exploration ability, and WOA is characterized by strong space exploration ability, but its optimization ability is restricted by the convergence speed. Therefore, PSO can be applied to the development stage of WOA to improve the ability of the algorithm to get the global optimal solution.

Hybrid PSO-AWOA is a combination of PSO algorithm and WOA. By introducing nonlinear weight factors into PSO algorithm and WOA, the shortcoming of PSO algorithm, namely, the restriction of a constant inertia weight, which results in a small scope of search space, is overcome. Meanwhile, in WOA, a nonlinear inertia weight is introduced to shrink the ring of encirclement and update the spiral migration position, which accelerates the algorithm convergence and enhances its optimization ability (Li et al., 2020). Hybrid PSO-AWOA absorbs the respective advantages of the two, thus showing more prominent optimization performance

(*Ding et al., 2021*). The inertia weight factor is the dominant factor balancing the global search ability and local development ability of the algorithm. In this study, the adaptive inertia weight strategy was adopted and the nonlinear weight w was introduced. As the number of iterations grew, the value of w changed dynamically. In the initial stage of iterations, a large weight could improve the global exploration ability of the algorithm. In the later stage, however, a small weight could facilitate the refined local optimization of the algorithm.

W is updated through the following formula:

$$w = \left[1 - \sin\left(\frac{\pi}{2} \times \frac{t}{\text{Max\_iter}}\right)\right]^k \tag{29}$$

Where: k is the adjustment coefficient, and the weight w changes with the k value. In addition, the change rate of weight w varies with the k value. PSO-AWOS expects a relatively large weight value in the initial stage of iterations so that the algorithm can possess strong global search ability and a high convergence speed. With the increase in the number of iterations, the weight declines sharply in the middle stage of iterations and approaches 0 slowly in the later stage, which improves the convergence speed and solving accuracy of the algorithm. Through repeated experiments, k=1.8 was taken in this study (*Huang et al., 2021*).

After the nonlinear weight is introduced into the hybrid algorithm, the position update formula of WOA algorithm is as follows:

$$X(t+1) = w \times X^*(t) - A \times D \tag{30}$$

$$X(t+1) = D' \times e^{bl} \times \cos(2\pi l) + w \times X^*(t) \tag{31}$$

$$X(t+1) = w \times X_{\text{rand}} - A \times D \tag{32}$$

The particle movement speed and position of the PSO algorithm are updated as per the following formula:

$$V_{id}(t+1) = w \times V_{id}(t) + c_1 r_1 \times \left[X^*(t) - X_{id}(t)\right] \tag{33}$$

$$X(t+1) = X_{id}(t) + V_{id}(t) \tag{34}$$

Steps of improved WOA

The specific implementation steps of improved WOA are described as below:

Step 1: population and algorithm parameter initialization. The position of the whale population and particle swarm is randomly initialized as $X_i = (X_{i1}, X_{i2}, \cdots, X_{id})$ and the movement speed as $V_i = (V_{i1}, V_{i2}, \cdots, V_{id})$, where $i = 1,2,3,\cdots,M$. Meanwhile, the population size M, the maximum number of iterations Max_pop, the dimension d of search space, and the initial number t of iterations should be initialized to calculate the fitness value of each individual in the population. Next, the position X_best of the optimal individual is found through comparisons:

Step 2: The values of coefficients A and C are updated as per Formulas (22) and (23), so are the values of b, l, c_1, and r_1, generating a random number p within [0,1];

Step 3: Position updating based on the values of p and $|A|$. If $p < 0.5$ and $|A| \geq 1$, the whale individual X_{rand} is randomly selected from the population, followed by position updating as per Formulas (17) and (30); if $p < 0.5$ and $|A| < 1$, position updating is then implemented according to Formulas (17) and (30); if $p \geq 0.5$, position updating is performed through Formula (31);

Step 4: The movement speed of individuals in the particle swarm is updated according to Formula (33), and the position X of the particle swarm is updated through Formula (34);

Step 5: Return to Step 2 for iterative updating and judge whether the maximum number of iterations is reached. If iterations of the algorithm are completed, the implementation of the algorithm is terminated;

Step 6: The algorithm iteration is completed. Return to the finally calculated optimal position X_best and solve the individual position of the population in case of the optimal value. Thereby, solving is completed.

RESULTS

To further verify the practicability and feasibility of the hybrid PSO-AWOA proposed in this study, the working environment of robots was simulated using the traditional grid map. Obstacles exist in the black region and the black region is a feasible region, where the starting point and endpoint of robots are (1,1) and (100,100), respectively; the boundary of the map is the outermost area of the whole path planning, which is regarded as an obstacle.

Hardware environment and parameter settings

The hardware platform of the experiment is Windows, the processor is Intel Core i5-14600K, the memory is 8 GB, and the software platform is Matlab2014b. The relevant parameter settings of each compared algorithm are listed in Table 1.

Table 1

Parameter settings of each algorithm

Algorithm	Parameter
WOA	b=1
PSO-AWOA	$b=1, c_1=2, w=1-\sin\left(\frac{\pi}{2}\times\frac{t}{Max\_iter}\right)^k, k=2.2$

Path planning simulation experiment

The experimental environment was a 100 m×100 m grid map, the agricultural handling robot moved from the starting point to the target point, and obstacles existed in the black region. In the simulation experiment, the same parameters were adopted for the 2 algorithms, for example, the initial population size was 50, the maximum number of iterations was 200, and the scope of search space was [-100,100] for both. To ensure the optimality of the generated path, the generation direction of the path was further defined in the path generation stage, that is, the path would not be "turned back" or "looped back", and the barrier-free region of the generated path point was simply optimized by interpolation or direct connection, thus ensuring the optimality of the path. Finally, the performance of the algorithm was assessed by statistically analyzing the length of the planned path, time consumption, and the number of inflection points generated by the algorithm. The planned path obtained through the simulation experiment is exhibited in Fig. 1. The length of the optimal path found by the PSO-AWOA algorithm under the 100 m ×100 m complex environment was 140.67 m, the algorithm converged at 1.77 s, and the optimal path was achieved after 114 iterations.

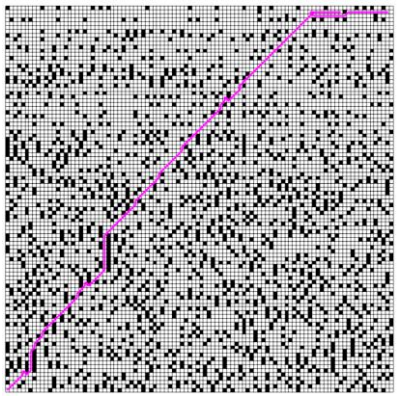

Fig. 1 - PSO-AWOA path planning

To verify the effectiveness of hybrid PSO-AWOA in solving the path planning problem of robots, standard WOS and hybrid PSO-AWOA established in this study were subjected to the comparative simulation experiment under a complex multi-obstacle simulation experimental environment. The handling path of agricultural robots obtained by standard WOA is displayed in Fig. 2. The length of the optimal path found by WOA under the 100 m×100 m complex environment was 179.94 m, the algorithm converged at 2.38 s, and the optimal path was harvested after 168 iterations.

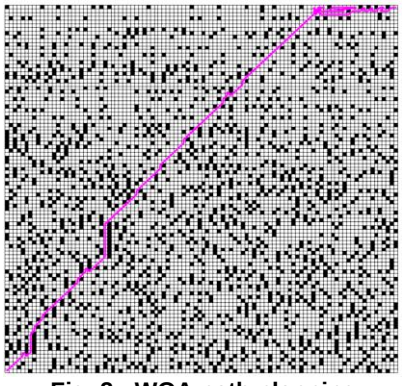

Fig. 2 - WOA path planning

Finally, the performance of the algorithm was evaluated by statistically analyzing the length of the planned path, time consumption, and the number of inflection points generated by the algorithm. The comparative data on the time consumption, number of iterations leading to convergence, the path length, and the number of inflection points on the path planned by PSO-AWOA and WOA are listed in Table 3.

Table 3

Experimental results of complex scene simulation

Algorithm	Time-consuming / s	Convergence algebras (algebras)	Path length / m	Number of inflection points (number)
PSO-AWOA	1.77s	114	140.67m	27
WOA	2.38s	168	179.94m	39

By comparing the time consumption, the number of iterations leading to convergence, the path length, and the number of inflection points on the path obtained by the two algorithms, it could be known that PSO-AWOA averagely spent 1.77 s, which was 0.61 s shorter than that of WOA, and the efficiency was improved by 34.46%. In the complex environment with many obstacles, PSO-AWOA algorithm acquired the optimal path after 114 iterations, and the length was 140.67 m; WOA achieved the optimal path after 168 iterations, and the length was 179.94 m; the number of inflection points on the path obtained by PSO-AWOA was 27 while that by WOA was 39, indicating that the robot path solved by PSO-AWOA was smoother. The above data and analysis manifest that PSO-AWOA can be successfully applied to the path planning problem of robots, and its convergence accuracy and convergence speed are both improved no matter under simple scenarios or complex scenarios.

CONCLUSIONS

In this study, the time optimal trajectory planning method for the collaborative operation of multiple agricultural handling robots was proposed to solve the relatively independent moving trajectory and great time consumption in the collaborative operation of multiple agricultural handling robots and the collaborative operation of obstacle avoidance. Then, three objective functions, operating length, operating difficulty, and operating time, were established and the multi-objective function was transformed into a single-objective function through the weighting method, aiming to achieve the optimal trajectory of multiple agricultural handling robots in collaborative operation. Moreover, an improved WOA based on PSO and adaptive inertia weight was proposed. Next, PSO with relatively strong optimization ability was introduced into the development stage of WOA to balance the exploration and development abilities of the algorithm. Meanwhile, adaptive weight factors were introduced so that the improved algorithm could possess a relatively large weight in the initial stage of iterations and fully explore the unknown space. In the later stage of iterations, the algorithm weight presented a nonlinear reduction, and the algorithm could realize refined search within a local scope. Finally, the improved algorithm was used to solve the path planning problem of robots in a grid map environment, verifying that the algorithm can solve the optimal collision-free motion path of multiple agricultural handling robots faster. In the follow-up study, the improvement room for the algorithm performance will be further explored in real environments and dynamic obstacle-containing environments.

REFERENCES

[1] Abu-Dakka, F.J., Assad, I. F., Alkhdour, R. M., & Abderahim, M. (2017). Statistical evaluation of an evolutionary algorithm for minimum time trajectory planning problem for industrial robots. *The International Journal of Advanced Manufacturing Technology*, Vol. 89, No. 1-4, pp. 389-406. Germany.

[2] Ahmed, M. M., Mahmoud, A. A., & Almoataz, Y. A. (2019). Whale optimization algorithm to tune PID and PIDA controllers on AVR system. *Ain Shams Engineering Journal*, Vol. 71, pp. 1-13, Egypt.

[3] Božek, P., Ivandić, Ž., Alexander, L., Lyalin, V., & Tarasov, V. (2016). Solutions to the characteristic equation for industrial robot's elliptic trajectories. *Tehnički Vjesnik*, Vol.23, No.4, pp.1017-1023. Croatia.

[4] Chen, G., Yuan, B., Jia, Q., Fu, Y., & Tan, J. (2019). Trajectory optimization for inhibiting the joint parameter jump of a space manipulator with a load-carrying task. *Mechanism and Machine Theory*, Vol.140, pp.59-82. Netherlands.

[5] Chen, H., Xu, Y., Wang, M., & Zhao, X. (2019). A balanced whale optimization algorithm for constrained engineering design problems. *Applied Mathematical Modelling*, Vol. 71, pp. 45–59. United States.

[6] Daniel, S. and Kevin, D. (2019). Smooth cubic polynomial trajectories for human-robot interactions. Journal of Intelligent & Robotic Systems, Vol. 95, No. 3-4, pp. 851–869. Germany.
[7] Ding, X. C. and Wang, H. J. (2021). A multiple optimization algorithm based on cuckoo iterative updating strategy. *Computer Engineering and Applications*, Vol. 58, pp. 1-8. Beijing/China
[8] Fu, L. Y., Li, S. W., Zhang, L., & Meng, Y. Y. (2021). Research Progress on Field Weeding Robots: A Review (田间除草机器人研究进展综述). *Robot,* Vol. 43, No.6, pp.751-768, Shenyang/China
[9] Gu, P., Li, H. C., & Yang, S. Y. (2021). Improvement and implementation of Q-learning algorithm. *Computer Science and Application*, Vol. 11, No. 7, pp. 1994-2007. Wuhan/China.
[10] Heidari, A. A., Mirjalili, S., Faris, H., Aljarah, I., Mafarja, M., & Chen, H. (2019). Harris hawks optimization: algorithm and applications. *Future Generation Computer Systems*, Vol. 97, pp. 849–872. Netherlands.
[11] Hu, J. B., Wang, X. S., & Zhang, Q. (2021). Optimization of multi-step ant colony algorithm for robot path planning problem. *Sensor and Micro System*, Vol. 40, No. 10, pp. 121-124. Heilongjiang/China.
[12] Huang, L. W. (2021). Application of principal component analysis based on ideal point in comprehensive evaluation. *Management Decision*, Vol. 37, pp. 184-188. United Kingdom.
[13] Huo, F. C., Chi, J., Huang, Z. J., Ren, L., Sun, Q. J., & Chen, J. L. (2018). Review of Path Planning for Mobile Robots (移动机器人路径规划算法综述). *Journal of Jilin University (Information Science Edition)*, Vol. 36, No.06, PP.639-647. Jilin/China.
[14] Khashan, N., Elhosseini, M. A., Haikal, A. Y., & Badawy, M. (2019). Biped robot stability based on an A-C parametric Whale Optimization Algorithm. *Journal of Computational Science*, vol.31, pp.17-32. Netherlands.
[15] Li, B., Yang, H. Z., & Gan, X. S. (2021). Path planning and design of industrial robot based on improved PSO algorithm and artificial potential field method. *Journal of Systems Science and Mathematics*, Vol. 41, No. 4, pp. 940-952. Beijing/China.
[16] Li, S. M., Chen, H. L., Wang, M. J., Heidari, A. A., & Mirjalili, S. (2020). Slime mould algorithm: a new method for stochastic optimization. *Future Generation Computer Systems*, Vol.111, pp.300-323. Netherlands.
[17] Li, Z. K., Huang, Y. Q, & Xu, Y. Q. (2020). Path planning of mobile robot based on improved variable step size ant colony algorithm. *Journal of Electronic Measurement and Instrument*, Vol. 34, pp. 15–21. Beijing/China.
[18] Long, W., Cai, S. H., Jiao, J. J., Tang, M. Z., & Wu, T. B. (2017). Improved whale optimization algorithm for large scale optimization problems (求解大规模优化问题的改进鲸鱼优化算法). *Systems Engineering-Theory & Practice,* Vol.37, No.11, PP.2983-2994. Beijing/China.
[19] Palleschi, A., Mengacci, R., Angelini, F., Caporale, D., Pallottino, L., Luca, D. A., & Garabini, M. (2020). Time-optimal trajectory planning for flexible joint robots. *IEEE Robotics and Automation Letters*, Vol.5, No.2, pp. 938-945. Germany.
[20] Park, S. O., Lee, M. C., & Kim, J. (2020). Trajectory planning with collision avoidance for redundant robots using Jacobian and artificial potential field-based real-time inverse kinematics. International Journal of Control, *Automation and Systems*, Vol. 18, No. 8, pp. 2095–2107. Korean.
[21] Rout, A., Bbvl, D., & Biswal, B. B. (2020). Optimal trajectory generation of an industrial welding robot with kinematic and dynamic constraints. *Industrial Robot-The International Journal of Robotics Research and Application*, Vol. 47, No.1, pp. 68-75. United Kingdom.
[22] Sathiya, V. and Chinnadurai, M. (2019). Evolutionary algorithms-based multi-objective optimal mobile robot trajectory planning. *Robotica*, Vol. 37, No. 8, pp. 1363–1382. United Kingdom.
[23] Seyedali, M. Andrew, L. (2016). The whale optimization algorithm. *Advances in Engineering Software*, Vol. 95, pp. 51-67. United Kingdom.
[24] Tu, J., Chen, H. L., Wang, M. J., & Gandomi, A. H. (2021). The colony predation algorithm. *Journal of Bionic Engineering*, Vol. 18, no. 3, pp. 674-710. Jilin/China.
[25] Wang, H., Wang, H., Huang, J., Zhao, B., & Quan, L. (2019). Smooth point-to-point trajectory planning for industrial robots with kinematical constraints based on high-order polynomial curve. *Mechanism and Machine Theory*, Vol.139, pp. 284-293. Netherlands.
[26] Wang, N., Han, Y. X., Wang, Y. X., Wang, T. H., Zhang, M., & Li, H. (2022). Research Progress of Agricultural Robot Full Coverage Operation Planning (农业机器人全覆盖作业规划研究进展). *Transactions of the Chinese Society for Agricultural Machinery*, Vol. 53, No.S1, pp.1-19. Beijing/China.

[27] Yin, M., Ke, P., & Zhang, C. R. (2023). An improved whale optimization algorithm with multiple strategies (一种融合多种策略的改进鲸鱼优化算法). *Journal of Wuhan University of Science and Technology*, Vol. 46, No.02, pp.145-152. Wuhan/China.

[28] Zhang, S., Zanchettin, M. A., Villa, R., & Dai, S. (2020). Real-time trajectory planning based on joint-decoupled optimization in human-robot interaction. *Mechanism and Machine Theory*, Vol.144, pp.103664. Netherlands.

[29] Zhang, X. M., Wang, D. D., & Chen., H. Y. (2019). Best and worst coyotes strengthened Coyote Optimization Algorithm and its application to quadratic assignment problem. *Computer Applications*, Vol. 39, pp. 2986–2991. Sichuan/China.

EXPERIMENTAL RESEARCH ON THE STABILITY OF A SPRAY BOOM WITH AN ACTIVE AND PASSIVE PENDULUM SUSPENSION
/
摆式主被动悬架喷雾机喷杆稳定性试验研究

Fang LI[1], Xiaohu BAI*[2]
[1] School of Information and Control Engineering, Liaoning Petrochemical University, Fushun/China;
[2] College of Engineering, Shenyang Agricultural University, Shenyang/China
E-mail: baixiaohu@syau.edu.cn
DOI: https://doi.org/10.35633/inmateh-72-46

Keywords: *Transient response, Dynamic response, Boom stability, Response surface method, Pendulum suspension*

ABSTRACT
When a sprayer is operating in the field, the uneven ground excitation causes the spray boom to move irregularly, significantly affecting the spray distribution uniformity and reducing the effectiveness of pesticide application. Installing a suspension between the vehicle and the boom is a crucial method to improve the boom stability. In this paper, experimental research on the stability of a boom with an active and passive pendulum suspension was carried out. The results of the transient response test of the passive suspension demonstrate that an increase in the suspension rotation damping coefficient reduces the overshoot of the system but slows down the response speed. Conversely, an increase in the suspension rotation stiffness coefficient speeds up the response speed. The results of the dynamic response test of the active suspension indicate that a smaller adjustment threshold of the control system for the boom inclination angle results in higher control accuracy. However, when the threshold is less than 1 cm, the boom becomes challenging to balance. The results of the combination experiments based on the response surface method reveal that the rotation stiffness coefficient, rotation damping coefficient, unit forward speed, and their interactions significantly impact the adjustment time of the boom and the variation coefficient of the boom inclination angle. Through contribution rate analysis, the influence order of each factor on the adjustment time and variation coefficient was obtained. Additionally, the analysis of variance results show that the established regression model fits the actual situation well, and has reference significance for the design and application of the suspension.

摘要
喷杆喷雾机田间作业时，田间不平地面的激励导致喷杆产生不规律运动，极大地影响雾滴分布均匀性，降低农药的施用效果。在车体与喷杆之间安装悬架是提高喷杆稳定性的重要途径。本文对安装摆式主被动悬架的喷杆稳定性进行了试验研究。被动悬架瞬态响应试验结果表明，悬架旋转阻尼系数增大，系统超调量减小，但响应速度变慢。悬架旋转刚度系数增加，系统响应速度加快。主动悬架动态响应试验结果表明，喷杆倾角控制系统调节阈值越小，控制精度越高。但当阈值小于1cm时，喷杆难以平衡。基于响应面法的组合试验结果表明，旋转刚度系数、旋转阻尼系数、机组前进速度及其交互作用对喷杆调节时间、喷杆倾角变异系数影响显著。通过因素贡献率分析，得到了各因素对调节时间和变异系数的影响顺序。方差分析结果表明，建立的回归模型与实际情况高度拟合，对悬架的设计和应用具有参考意义。

INTRODUCTION
Plant protection equipment is one of the most important aspects influencing the chemicals spraying effect and utilization efficiency (*He, 2020*). Boom sprayers are widely used in agriculture for the application of chemical materials such as pesticides, herbicides and fertilizers due to their large widths and high efficiency (*He, 2022; Qiu et al., 2015*). When a sprayer runs over obstacles or uneven terrains, the spray boom oscillates both vertically and horizontally, impacting the spray distribution pattern. Previous research has shown that spray deposit distribution ranges between 0 and 800% as a result of spray boom vibrations (*Ooms et al., 2002*). Therefore, the stability of the boom has significant influence on spraying quality (*Lipinski et al.*, 2022). A stable boom can result in more uniform spray coverage and prevent the boom tips from touching the ground.

Fang Li, Lecturer, Ph.D.; Xiaohu Bai, Associate Prof., Ph.D.,Corresponding Author.

To address boom instability and enhance spray uniformity, manufacturers have equipped sprayers with various types of suspensions (*Cui et al., 2019*). The most commonly used suspension is the double-pendulum suspension, with the first pendulum serving as a passive suspension and the second pendulum functioning as an active suspension (*Tahmasebi et al., 2013*).

Theoretical investigations and practical experiments have been conducted for improving the stability of a spray boom. To optimize the vertical suspension for a 39 m wide sprayer of John Deere, Anthonis et al. established a mathematical model of the suspension with an existing nonlinear damper. The standard deviation of the absolute boom rotation around the horizontal axis was minimized by applying several tracks based on power spectral densities of measurements in field conditions. The distance to the rotation point of the damper and the appropriate damping value were obtained (*Anthonis et al., 2005*). In order to investigate boom movements under excitation signals, Wu and Miao set up a model with four spring-damper modules between the boom and the frame, and obtained the ideal stiffness coefficient and damping coefficient (*Wu et al., 2012*). To acquire good responsiveness, stability and accuracy of the active suspension, Xue et al. developed a control algorithm based on adaptive fuzzy sliding model with the spray boom inclination angel as the control object. The test results indicated that the active suspension can effectively isolate the disturbing swing of the vehicle body and keep the spray boom stable (*Xue et al., 2018*). Aiming at the problem of poor stability caused by parameter uncertainties and random disturbances in the passive and active pendulum suspension, Cui et al. designed an adaptive robust controller, taking into account damping, stiffness, uncertain disturbances, Coulomb friction, and other parameters of the suspension (*Cui et al., 2020*). Zhuang carried out the performance test of cable-stayed spring, vertical spring, horizontal damper, and vertical damper. The results of transient response tests and field tests showed that the spring and damper had significant impacts on the transient vibration and the low-frequency vibration of the boom (*Zhuang, 2020*). Yan et al. studied the dynamic behaviour of the spray boom under step excitation, and analysed the effects of sprayer speed, boom length, and boom cross-section shape on boom vibration (*Yan, 2021*).

In this paper, experiments were conducted to test the transient response of the passive suspension and the dynamic response of the active suspension. The impacts of spring, damper, sprayer speed and their interactions on the adjustment time of the boom and the variation coefficient of the boom inclination angle were investigated by response surface analysis. The objective of this research is to provide references for the design and application of boom suspensions.

MATERIALS AND METHODS

Experimental setup

Figure 1 illustrates a schematic representation of the experimental setup. The spray boom, constructed from welded steel section, had a mass of 49 kg and a moment of inertia around the centre of mass of 93 kgm^2. The first pendulum rod of the suspension system was 0.45 m long, and the second one was 0.25 m long. A spring and a damper were connected between the first pendulum rod and the frame to inhibit boom oscillation. The damping coefficient of the damper was 1875 Ns/m. The stiffness coefficient of the spring was 730 N/m. The spring was installed inside a guide sleeve to ensure stability when compressed. An actuator, a 24V DC electric linear push rod, was used to adjust its length in response to signals from the control system. Additionally, two ultrasonic sensors were employed to measure the distance between the boom end and the ground surface. The prototype of the experimental setup is shown in Figure 2.

To generate the required excitation signal, wooden boards of varying heights were placed on the ground to simulate a field slope, as shown in Figure 3. Considering the boom length and the wheel-track of the tractor, the angle of the simulated slope was set at 1.5° (*Qiu et al., 2012, Wei et al., 2015*).

Method of transient response tests of the passive pendulum suspension

Attach the frame to the three-point hitch linkage of the tractor, and unfold the spray boom. Then lift one side of the boom to a position with an inclination angle of about 5°. Turn off the control system for the boom inclination angle and release the boom. Subsequently, record the distance from the ultrasonic sensors at the left and right ends of the boom to the ground, and then calculate the inclination angle of the boom during oscillation.

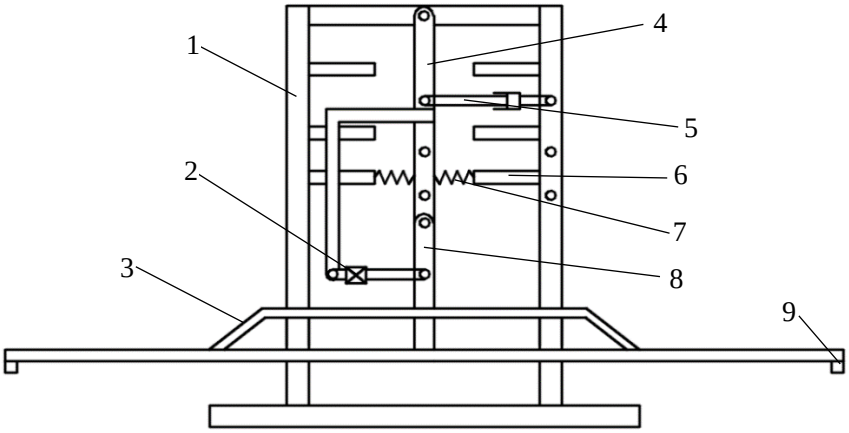

Fig. 1 - Schematic of the experimental setup

1- frame; 2- actuator; 3- spray boom; 4- first pendulum rod; 5- damper; 6- guide sleeve; 7- spring; 8- second pendulum rod 9- ultrasonic sensor

Fig. 2 - Prototype of the experimental setup

Fig. 3 - Simulated slope for experiments

Method of dynamic response tests of the active pendulum suspension

Level the spray boom to a height of 80 cm from the ground. Then place a box with a height of 40 cm beneath the right ultrasonic sensor to mimic a sloped terrain (*Herbst et al., 2018*). Activate the control system for the boom inclination angle, which adopts a fuzzy PID control algorithm based PSO (*Li et al., 2023)*. Record the distance from the ultrasonic sensors at the left and right ends of the boom to the ground.

Method of experiments of the boom stability

Based on the structure and working principle of the pendulum suspension, three main factors affecting the boom stability were selected: unit forward speed, suspension rotational damping coefficient, and suspension rotational stiffness coefficient. The suspension rotational damping coefficient can be calculated from the damping coefficient and the damper's installation position, while the suspension rotational stiffness coefficient can be determined from the stiffness coefficient and the spring's installation position (*Cui et al.,2017a*, *Cui et al.,2017b*). According to the working requirements of the sprayer, the unit forward speed was set at 2~4 km·h^{-1}, the suspension rotational damping coefficient at 100~300 Nms·rad^{-1}, and the suspension rotational stiffness coefficient at 20~100 Nm·rad^{-1}. Factors and levels of the experiments are presented in Table 1.

Table 1

Factors and levels

Factors / Levels	Unit forward speed	Suspension rotational damping coefficient	Suspension rotational stiffness coefficient
	[km·h^{-1}]	[Nms·rad^{-1}]	[Nm·rad^{-1}]
-1	2	100	20
0	3	200	60
1	4	300	100

To evaluate the speed of the spray boom in tracking the ground slope and its stability after reaching steady state, the adjustment time of the boom and the variation coefficient of the boom inclination angle were chosen as experimental indicators. The adjustment time of the boom is the time from when the tractor begins to drive up a slope to when the boom reaches a steady state. The variation coefficient of the boom inclination angle is the ratio of its standard deviation to the average value after the boom achieves a steady state.

Since many nonlinear factors affect the boom inclination angle, quadratic or higher-order models are commonly used to estimate the boom response (*Jeon et al., 2004*). The Box-Behnken combination experimental design based on response surface method was employed. A three-factor and three-level scheme was designed, with 5 replicates of the central point, resulting in a total of 17 experiments.

RESULTS

Transient response of the passive pendulum suspension

Maintain the initial angle of the boom and change the damping effect by adjusting the installation position of the damper. When the damper was placed at positions 0.23 m, 0.326 m, and 0.4 m away from the hinge point of the first pendulum rod and the frame, the corresponding suspension rotational damping coefficients were 100 Nms·rad^{-1}, 200 Nms·rad^{-1}, and 300 Nms·rad^{-1}, respectively.

The impact of three different rotational damping coefficients on the inclination angle changes of the boom is demonstrated in Figure 4. It reveals that the rotational damping coefficient notably influences the peak value of the transient response of the boom. When *C* is 100 Nms·rad^{-1}, the peak time is approximately 2 s, with a 50% overshoot, and the boom angle stabilizes within 10% of the initial value at around 6.5 s. For *C* at 200 Nms·rad^{-1}, the peak time is roughly 2.1 s, with an 18.37% overshoot, and the boom angle stabilizes within 10% of the initial value at approximate 3.2 s. With *C* at 300 Nms·rad^{-1}, the peak time extends to about 3.1 s, and the overshoot is 3.7%. It is obvious that increasing the damping coefficient decreases the overshoot, but if the damping coefficient is too large, the peak time will increase, leading to a slower system response.

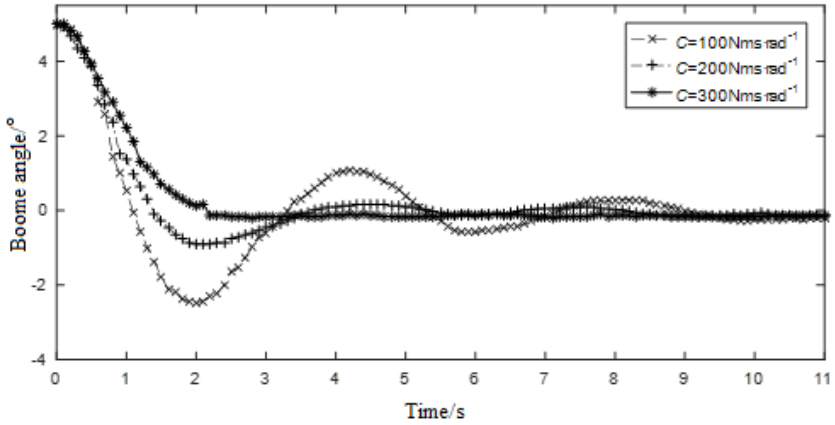

Fig. 4 – Transient response of the boom with different rotational damping coefficients

The variations in the inclination angle of the boom with three different rotational stiffness coefficients are shown in Figure 5. When *K* is 20 Nm·rad^{-1}, 60 Nm·rad^{-1}, and 100 Nm·rad^{-1}, the peak time is approximately 1.6 s, 1.9 s, and 2.0 s, respectively. It can be inferred that the peak time of transient response of the suspension decreases with a larger rotational stiffness coefficient, indicating a faster response speed.

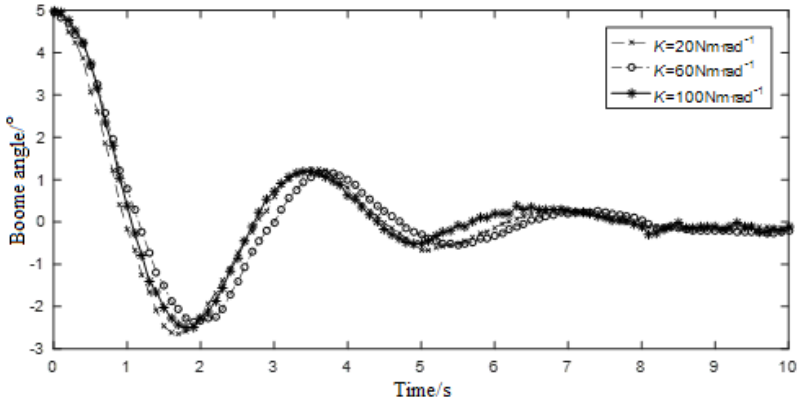

Fig. 5 – Transient response of the boom with different rotational stiffness coefficients

Dynamic response of the active pendulum suspension

When the boom is in a horizontal position, the distance between the left sensor and the ground is 80 cm, and the distance between the right sensor and the box is 40 cm. This results in a 40 cm difference between the two sensors and the target, prompting the control system to decrease the distance difference. The adjustment process is shown in Figure 6 and Figure 7. At the outset, with the distance difference at 40 cm and a zero-distance change rate, the control system outputs a 20% duty cycle for the electric push rod. As the distance difference and the distance change rate alter, the duty cycle is consistently modified, reaching 30% at 0.3 s. At the same time, the right end of the boom rises while the left end descends. By 2 s, the boom reaches its initial equilibrium position, and the duty cycle is reduced to zero. However, due to the change in the position of the gravity centre, the boom continuous to swing, and the duty cycle becomes relatively small. After 5.6 s, the boom reaches its final equilibrium position, with the distance between the left sensor and the ground at 61 cm, and the distance between the right sensor and the box at 59 cm. The steady-state error of the control system is 1 cm.

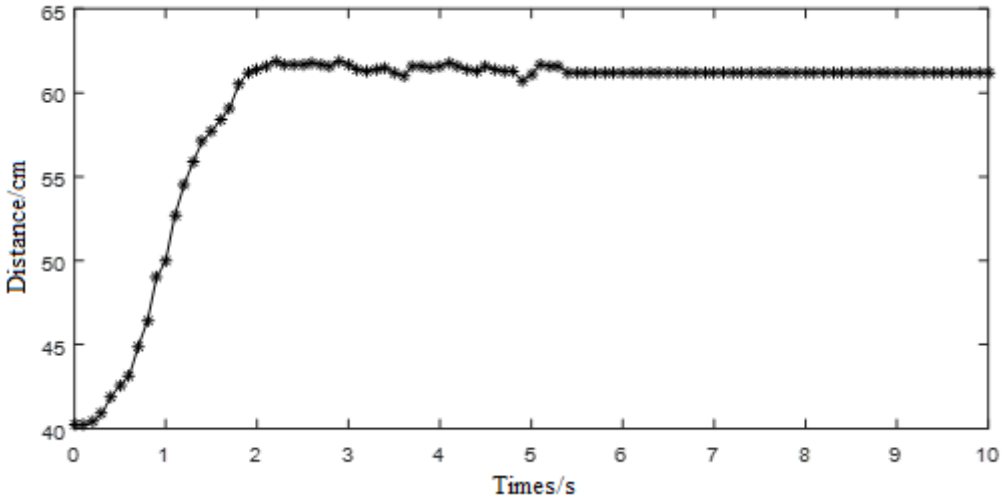

Fig. 6 – Distance between the right sensor and the target

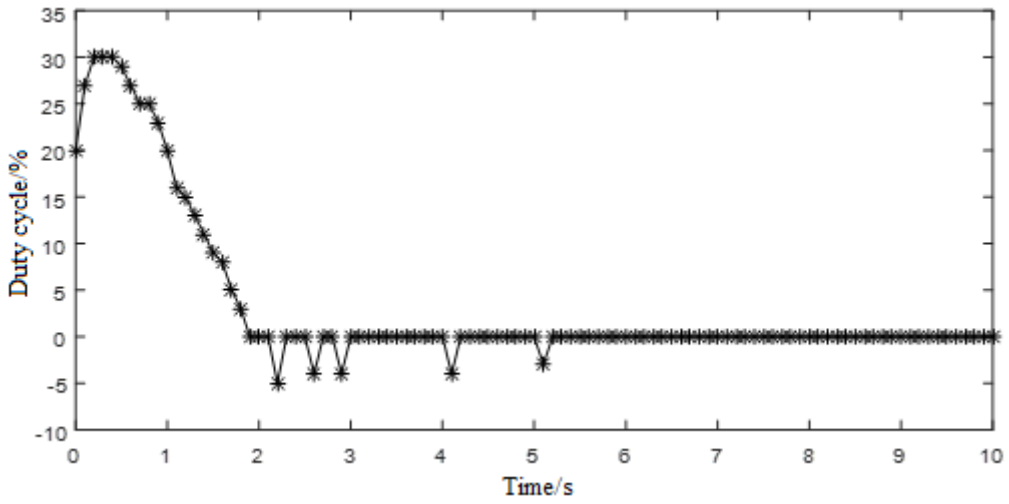

Fig. 7 – Duty cycle output by the control system

To test the effect of the boom height threshold on control performance, various thresholds of 10 cm, 7 cm, 5 cm, 3 cm, 2 cm, and 1 cm were set. The results are presented in Table 2. Upon setting the threshold above 2 cm, the control system can effectively adjust the boom height at both ends to the ground, and successfully confine the height error within the prescribed threshold for both ends. However, with the threshold set at 1 cm, the electric push rod continues to be active, preventing the boom from achieving equilibrium.

Table 2

Results of threshold test

Boom height before balance [cm]		Threshold [cm]	Boom height after balance [cm]	
Left end	Right end		Left end	Right end
80	40	10	63.8	56.2
		7	62.0	57.2
		5	57.5	62.1
		3	61.0	58.5
		2	59.5	61.2
		1	—	—

Stability of the spray boom

The experimental scheme and results are shown in Table 3.

Table 3

Experimental scheme and results

No.	Factors and levels			Experimental indicators	
	Rotational stiffness coefficient	Rotational damping coefficient	Unit forward speed	Adjustment time	Variation coefficient
	X_1	X_2	X_3	Y_1/s	Y_2/%
1	0	-1	-1	6.6	10.71
2	0	0	0	5.4	10.29
3	1	0	1	5.9	11.86
4	1	1	0	7.4	11.45
5	1	-1	0	7.1	11.43
6	0	0	0	5.3	10.27
7	0	1	-1	7.0	10.63
8	-1	1	0	7.7	11.36
9	0	-1	1	6.8	10.86
10	0	0	0	5.4	10.19
11	1	0	-1	5.9	11.29
12	-1	0	-1	5.2	11.28
13	0	0	0	5.4	10.28
14	-1	0	1	5.6	11.41
15	-1	-1	0	6.3	11.12
16	0	1	1	7.6	11.15
17	0	0	0	5.5	10.18

Regression Model Establishment and Significance Test

The statistical analysis software Design Expert 8.0.5 was applied to process the data in Table 3, and the results are shown in Table 4.

The *P* values of the model terms related to the adjusting time Y_1 and variation coefficient Y_2 are all less than 0.0001, indicating a high degree of significance for the regression model. Furthermore, the *P* values of the lack of fit terms corresponding to these two indicators are 0.2564 and 0.9527, both greater than 0.05, suggesting a strong fit of the regression model to the actual circumstances. The significance of the quadratic terms X_1^2、X_2^2、X_3^2, and interaction terms X_1X_2、X_1X_3、X_2X_3 indicates that there is a quadratic nonlinear relationship and interaction among the three factors and the experimental indicators.

Consequently, response surface quadratic polynomial regression models for the adjusting time Y_1 and variation coefficient Y_2 were established, as depicted in equations (1) and (2).

$$Y_1=5.4+0.23X_1+0.33X_2+0.15X_3-0.2X_1X_2-0.1X_1X_3+0.1X_2X_3+0.15X_1^2+1.5X_2^2+0.1X_3^2 \quad (1)$$

$$Y_2=10.24+0.11X_1+0.059X_2+0.17X_3-0.055X_1X_2+0.11X_1X_3+0.093X_2X_3+0.86X_1^2+0.24X_2^2+0.36X_3^2 \quad (2)$$

Table 4

Results of analysis of variance

Variance source	Adjustment time Y_1				Variation coefficient Y_2			
	Square sum	Degree of freedom	*F* value	*P* value	Square sum	Degree of freedom	*F* value	*P* value
Model	11.52	9	179.21	<0.0001**		4.65	9	302.28
X_1	0.41	1	56.70	0.0001**		0.092	1	54.13
X_2	0.85	1	118.30	<0.0001**		0.028	1	16.17
X_3	0.18	1	25.20	0.0015**		0.23	1	137.37
X_1X_2	0.16	1	22.40	0.0021**		0.012	1	7.08
X_1X_3	0.04	1	5.60	0.0499*		0.048	1	28.34
X_2X_3	0.04	1	5.60	0.0499*		0.034	1	20.04
X_1^2	0.095	1	13.26	0.0083**		3.12	1	1824.5
X_2^2	9.47	1	1326.3	<0.0001**		0.24	1	139.36
X_3^2	0.042	1	5.89	0.0456*		0.54	1	315.53
Residual	0.05	7				0.012	7	
Lack of fit	0.03	3	2.00	0.2564		0.001	3	0.11
Error	0.02	4				0.011	4	
Sum	11.57	16				4.66	16	

Note: $P<0.01$ means highly significant (**), and $P<0.05$ means significant (*).

Impact of Factors on Response Values

The impact of each factor on the model can be compared using the contribution rate *K* (*Xie et al., 2019, Shen et al., 2019*). A larger *K* value indicates a greater impact. The calculation method for the contribution rate is shown in equations (3) and (4), and the results are presented in Table 5.

$$\delta=\begin{cases}0, & F\leqslant 1\\ 1-\dfrac{1}{F}, & F>1\end{cases} \quad (3)$$

$$K_{X_i}=\delta_{X_i}+0.5\sum\delta_{X_iX_j}+\delta_{X_i^2} \qquad i,j=1,2,3 \;\; i\neq j \quad (4)$$

Where:

K_{Xi} is the contribution rate of the factor X_i, *F* is the *F*-value of each regression term in the model, δ is the assessment value corresponding to the *F*-value.

Table 5

Analysis of contribution rate of factors

Indicators	Contribution rate			Order of contribution rate
	Rotational stiffness coefficient X_1	Rotational damping coefficient X_2	Unit forward speed X_3	
Adjustment time	2.795	2.879	2.612	$X_2>X_1>X_3$
Variation coefficient	2.893	2.835	2.947	$X_3>X_1>X_2$

Impact of Interactions on Response Values

The software Design Expert 8.0.5 was utilized to create response surfaces and analyse the impact of interactions on the adjustment time and variation coefficient, as shown in Figure 8.

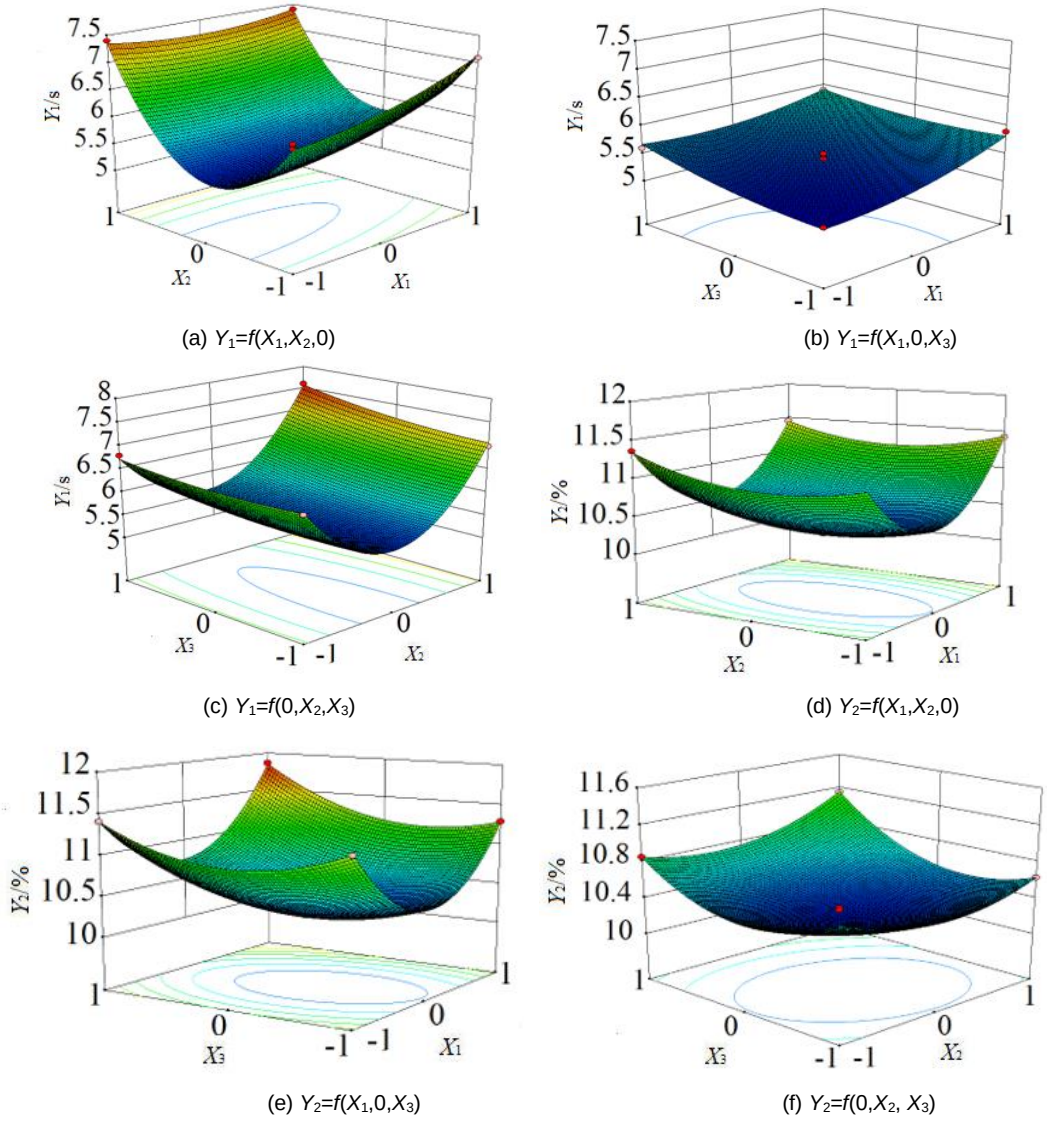

(a) $Y_1=f(X_1,X_2,0)$ (b) $Y_1=f(X_1,0,X_3)$

(c) $Y_1=f(0,X_2,X_3)$ (d) $Y_2=f(X_1,X_2,0)$

(e) $Y_2=f(X_1,0,X_3)$ (f) $Y_2=f(0,X_2,X_3)$

Fig. 8 – Impact of interactions on the adjustment time and variation coefficient

When the unit forward speed is set to zero level, at all levels of the rotational stiffness coefficient, the adjustment time initially decreases and then increases as the rotational damping coefficient increases. This indicates that under damping causes the overshoot of the boom angle to be too large and slows down the transient component attenuation when the damping coefficient is too low. Conversely, an excessively high damping ratio makes the connection between the pendulum and the frame almost rigid, making it easy for high-frequency excitation signals to be transmitted to the boom. When the rotational stiffness coefficient is set to zero level, at a lower level of the rotational stiffness coefficient, the adjustment time gradually increases as the unit forward speed increases. This suggests that excessive forward speed generates stronger excitation on the boom, and the reaction force generated by the spring intensifies the oscillation of the boom.

When the unit forward speed and rotational damping coefficient are each set to zero level, the variation coefficient demonstrates a trend of initially decreasing and then increasing as the rotational stiffness coefficient increases. This indicates that a spring with too low stiffness exerts a weak inhibitory effect on boom vibration. However, if the spring stiffness is excessive, it leads to a higher resonance frequency in the suspension, allowing disturbances in a wider frequency range to be transmitted to the boom, thus resulting in poor stability. The influence of the rotational damping coefficient on the variation coefficient is generally consistent with its impact on the adjustment time, albeit changing at a slower rate.

CONCLUSIONS

The results of transient response tests of the passive suspension indicate that increasing the rotational damping coefficient leads to a decrease in system overshoot. However, if the damping coefficient is excessively large, the system response becomes slower. Furthermore, a higher rotational stiffness coefficient results in a shorter peak time and faster response speed.

The results of dynamic response tests of the active suspension reveal that the control system for the boom inclination angle can effectively respond and adjust the height difference on both ends of the boom, with a short response time and small steady-state error. Moreover, reducing the threshold enhances control accuracy. However, if the threshold is excessively small, the boom may fail to achieve balance.

The effects of the rotational stiffness coefficient, rotational damping coefficient, and unit forward speed on the boom adjustment time and the boom angle variation coefficient were investigated using the Box-Behnken combination experimental design based on response surface. A quadratic regression model was established and analysis of variance was conducted. The contribution rate analysis revealed that the order of the effects of all factors on the adjustment time as follows: rotational damping coefficient, rotational stiffness coefficient, and unit forward speed. Similarly, the order of the effects of all factors on the variation coefficient was determined as: unit forward speed, rotational stiffness coefficient, and rotational damping coefficient. Through analysis of the response surfaces, the impacts of all factors and their interactions on the experimental indicators were studied.

ACKNOWLEDGEMENT

This research was supported by talent scientific research fund of Liaoning Petrochemical University (No.2021XJJL-024).

REFERENCES

[1] Anthonis, J., Audenaert, J., Ramon, H. (2005). Design optimization for the vertical suspension of a crop sprayer boom. *Biosystem Engineering*, 90(2), 153–160.

[2] Cui, L., Xue, X., Ding, S., Qiao, B., Le, F. (2017a). Analysis and test of dynamic characteristics of large spraying boom and pendulum suspension damping system (大型喷杆及其摆式悬架减振系统动力学特性分析与试验). *Transactions of the Chinese Society of Agricultural Engineering*, 33(9), 69–76.

[3] Cui, L., Xue, X., Ding, S., Gu, W., Chen, C, Le, F. (2017b). Modeling and simulation of dynamic behavior of large spray boom with active and passive pendulum suspension (双钟摆主被动悬架式大型喷雾机喷杆动力学仿真与试验). *Transactions of the Chinese Society of Agricultural Machinery*, 48(2), 82–90.

[4] Cui, L., Xue, X., Le, F., Mao, H., Ding, S. (2019). Design and experiment of electro hydraulic active suspension for controlling the rolling motion of spray boom. International *Journal of Agricultural and Biological Engineering*, 12(4), 72–81.

[5] Cui, L., Xue, X., Le, F., Ding, S. (2020). Adaptive robust control of active and passive pendulum suspension for large boom sprayer (大型喷杆喷雾机钟摆式主被动悬架自适应鲁棒控制研究). *Transactions of the Chinese Society of Agricultural Machinery*, 51(12), 130–141.

[6] Herbst, A., Osteroth, H., Stendel, H. (2018). A novel method for testing automatic systems for controlling the spray boom height. *Biosystems Engineering*, 174(8), 115–125.

[7] He, X. (2020). Research progress and developmental recommendations on precision spraying technology and equipment in China (中国精准施药技术和装备研究现状及发展建议). *Smart Agriculture*, 2(1), 133–146.

[8] He, X. (2022). Research and development of efficient plant protection equipment and precision spraying technology in China: a review (高效植保机械与精准施药技术进展). *Journal of Plant Protection*, 49(1), 389–397.

[9] Jeon, H.Y., Womac, A.R., Gunn, J. (2004). Sprayer boom dynamic effects on application uniformity. *Transactions of the American Society of Agricultural Engineers*, 47(3), 647–658.

[10] Lipinski, A.J., Lipinski, S., Burg, P., Sobotka, M. S. (2022). Influence of the instability of the field crop sprayer boom on the spraying uniformity. *Journal of Agriculture and Food Research*, 10, 1–4.

[11] Li, F., Bai, X., Su, Z., Tang, S., Wang, Z., Li, F., Yu, H. (2023). Development of a control system for double-pendulum active spray boom suspension based on PSO and fuzzy PID. *Agriculture-Basel*, 13(9), 1660.

[12] Ooms, D., Lebeau, F., Ruter, R., Destain, M.F. (2002) Measurements of the horizontal sprayer boom movements by sensor data fusion. *Computers and Electronics in Agriculture*, 33, 139-162

[13] Qiu, B., Yang, N., Xu, X., Guan, X., Wu, C. (2012). Ideal spray Boom response extraction with front and rear tires excited by step track (喷雾机前后轮相继激励下喷杆理想运动响应提取). *Transactions of the Chinese Society of Agricultural Machinery*, 43(2), 55–60.

[14] Qiu, B., Yan, R., Ma, J., Guan, X., Ou, M. (2015). Research progress analysis of variable rate sprayer technology (变量喷雾技术研究进展分析). *Transactions of the Chinese Society of Agricultural Machinery*, 46(3), 59–72.

[15] Shen, G., Wang, G., Hu, L., Yuan, J., Wang, Y. (2019). Development of harvesting mechanism for stem tips of sweet potatoes (甘薯茎尖收获机研制). *Transactions of the Chinese Society of Agricultural Engineering,* 35(9), 46–55.

[16] Tahmasebi, M., Rahman, R.A., Mailah, M., Gohari, M. (2013). Active force control applied to spray boom structure. *Applied Mechanical Material*, 315, 616–620.

[17] Wu, J., Miao, Y. (2012). Dynamic characteristic analysis of boom for wide sprayer with different exciting sources (不同激励源下宽幅喷雾机喷杆的动态特性分析). *Transactions of the Chinese Society of Agricultural Engineering*, 28(4), 39–44.

[18] Wei, X., Shao, J., Miao, D., Li, L., Xie, X. (2015). Online control system of spray boom height and balance (喷杆式喷雾机喷杆高度及平衡在线调控系统). *Transactions of the Chinese Society of Agricultural Machinery*, 46(8), 66–71.

[19] Xie, J., Zhang, F., Chen,X., Han, Y. Tang, W. (2019). Design and parameter optimization of arc tooth and rolling bundle type plastic film residue collector (弧形齿滚扎式残膜回收机的设计及参数优化). *Transactions of the Chinese Society of Agricultural Engineering,* 35(11), 26–37.

[20] Xue, T., Li, W., Du, W., Mao, E. Wen, H. (2018). Adaptive fuzzy sliding mode control of spray boom active suspension for large high clearance sprayer (大型高地隙喷雾机喷杆主动悬架自适应模糊滑模控制). *Transactions of the Chinese Society of Agricultural Engineering,* 34(21), 47–56.

[21] Yan, J., Xue, X., Cui, L., Ding, S., Gu, W., et al. (2021). Analysis of dynamic behavior of spray boom under step excitation. *Applied Science*, 11(21), 10129.

[22] Zhuang, T. (2020). *Theoretical analysis and experimental research on boom vibration of large-scale high clearance sprayer* (大型高地隙喷雾机喷杆振动理论分析与试验研究) [Doctoral dissertation, Chinese Academy of Agricultural Mechanization Sciences).

DESIGN AND EXPERIMENTAL STUDY OF HORIZONTAL-SHAFT ROLLER-TYPE COTTON STALK PULLER BASED ON RESPONSE SURFACE METHOD
/
基于响应曲面法的横轴对辊式棉花拔秆机的设计与试验研究

Dangqin XUE[1)]*, Zhouming GAO[2)], Jiaxi ZHANG[2)]
[1)] Nanyang Institute of Technology, Nanyang, Henan, China;
[2)] Xinjiang Agricultural University, Urumqi, Xinjiang, China.
Tel: +86037763121567; E-mail: 286409568@qq.com
Corresponding author: Dr. Dangqin Xue
DOI: https://doi.org/10.35633/inmateh-72-47

Keywords: *agricultural machinery, horizontal-shaft roller type, response surface method, cotton stalk*

ABSTRACT

In this paper, a new horizontal-shaft roller-type cotton stalk puller was designed to address the problems of weak research on cotton stalk pulling and harvesting machines, poor agronomic adaptability, and insufficient research. First, the physical and mechanical properties of cotton stalk were experimentally studied, the cotton stalk pulling force test was conducted and the moisture content and the bending characteristics of cotton stalk were evaluated. The test results showed that cotton stalk pulling force was positively correlated with the cotton stalk diameter and the bending characteristics were positively correlated with the moisture content but were not evidently influenced by the diameter. Second, with the missed pulling rate and pull-off rate as the evaluation indexes and three independent variables, namely, forward speed, linear speed of stalk pulling rod, and rotation speed of stalk pulling roller, as the influencing factors, a 3D response surface model was established. On this basis, the lack-of-fit term P (p = 0.3650) > 0.05 of the evaluation index—missed pulling rate P1—was acquired, and the P value of pull-off rate P2 was always smaller than 0.0001. Finally, the results demonstrated that the influence of various factors on the missed pulling rate of cotton stalk is significant and followed the order forward speed > linear speed of stalk pulling rod > rotation speed of stalk pulling roller; the significance level regarding the influence on the pull-off rate followed the order rotation speed of stalk pulling roller > linear speed of stalk pulling rod > forward speed. Through the parameter optimization analysis, the optimal parameter combination was obtained which coincide with the model optimization and prediction result. The proposed method provides a basis and experimental reference for studying cotton stalk harvesting machineries.

摘要

针对棉秆起拔收获机研究薄弱，农艺适应性差，研究不足等问题，本文设计了一种新型横轴对辊式棉花拔秆机。首行进行了物理力学特性和棉秆起拔力试验，开展棉秆含水率和棉秆抗弯特性试验，结果显示棉秆起拔力与棉秆直径呈正相关关系，抗弯特性与含水率呈正相关，棉秆直径对抗弯特性影响并不明显。其次以漏拔率、拔断率作为评价响应指标，选取前进速度、拨禾杆线速度、拔秆辊转速 3 个自变量为影响因素，建立起响应面三维模型，得出评价指标棉秆漏拔率 P1 的失拟项 P（P=0.3650）>0.05，拔断率 P2 的 P 值均小于 0.0001；开展试验结果显示各因素对棉秆漏拔率的影响显著性顺序为前进速度>拨禾杆线速度>拔秆辊转速；对拔断率的影响显著性为拔秆辊转速>拨禾杆线速度>前进速度。通过参数优化得到最佳组合，与模型优化预测结果基本吻合。该装置为棉花秸秆收获机械的研究提供依据及实验参考。

INTRODUCTION

Cotton stalk is an important renewable biomass resource, which can be used as feed for poultry and are also applicable to fields such as papermaking, edible fungus cultivation, environmental protection materials, and biomass briquette fuel *(Uzair et al., 2020; Raju et al., 2019; Jinesh et al., 2022; Fawzy et al., 2021)*. If cotton stalk can be recycled, substantial economic benefits will be achieved *(Pandirwar et al., 2023)*. The current research on complete cotton stalk harvesting technology in China remains in the starting stage, without mature, efficient cotton stalk harvesting machineries in the market. Treatment methods like arbitrary discarding or incineration seriously destroy the ecological environment *(Ding et al., 2021)*.

Dangqin Xue, Prof. Ph.D. Eng.; Zhouming Gao, M.S. Stud. Eng.; Jiaxi Zhang, Prof. Ph.D. Eng

Therefore, developing stable, efficient cotton stalk harvesting machinery and equipment is the research focus of agricultural machinery.

Among the cutting-type cotton stalk harvesting machinery in China, the 4JSM-1800 cotton stalk returning to field and plastic film residue recovery combined machine designed by Wang X.N. et al. *(Wang et al., 2003)* is a representative machine type of flail cotton stalk harvester. The cutter shaft of the machine drives the movable cutter to rotate at high speed and cooperates with the fixed cutter to crush cotton stalks and scatter them into cotton fields. The disadvantage is that the stubbles less than 5 cm are flipped into the earth, hindering their rotting. In addition, the film hanging problem exists in the recovery of plastic film residue, which aggravates the operation difficulty, results in earth hanging by plow, and seriously affects the working efficiency. The representative shear-type cotton stalk harvesting machinery is the 4MG-275 self-propelled combined harvester developed by Sun Y.F. et al. *(Sun et al., 2012)*, which is not restricted by the row spacing of cotton with strong adaptability yet accompanied by stubble remaining on the ground and easy wear of the cutting knife. The operation of the machine is greatly affected by ground flatness. A representative pulling and shovel cutting-type cotton stalk harvesting machinery is the 4MB-6 row-aligned shovel pulling and laying machine for densely planted cotton designed by He X.W. et al. *(He et al., 2020)*. In the operation, this machine needs to be strictly buried in soil in a row-aligned way with a satisfactory pulling effect, but the power consumption is large, which seriously damages the mulching film. Moreover, the plastic film residue cannot be easily recovered, and the shovel cutting device is subjected to heap soil problem, failing to operate continuously for a long time and needing timely manual clearing. A toothed disc-type cotton stalk harvesting machinery *(Chen et al., 2019)* is pulling-type cotton stalk harvesting machinery, which is mainly characterized by multirow cotton stalk pulling and strict requirement for row alignment, but the missed pulling rate and the power consumption are small along with cotton stalk blocking between two toothed discs. Hence, this machine fails to operate continuously for a long time, and it is only applicable to the large single-row cotton planting mode. The 4MGB-210 self-propelled combined cotton stalk harvesting and binding machine *(Liao et al., 2021)* is toothed roller-type cotton stalk harvesting machinery, which features low energy consumption, high cotton stalk harvesting efficiency, no requirement for row alignment, and strong adaptability to row spacing, but grass may be entangled on the toothed roller, the film may be tangled, the cotton stalk cannot fall off from the toothed roller, and the conveyer device may be blocked. The 4JB-2200 suspension-type cotton stalk puller *(Shi et al., 2015) is* roller-type cotton stalk harvesting machinery, which is applicable to the planting mode with a wide row spacing but fails in large-area promotion; this machine is of high energy consumption and serious roller wear.

To sum up, cotton stalk harvesters have many kinds, all of which need row alignment. The toothed disc-type cotton stalk harvester is suitable for cotton stalk harvesting under the large single-row planting mode. Although the shovel cutting-type cotton stalk harvester works well, it needs to be buried in the soil, which has high power consumption and damages the plastic film. The roller-type cotton stalk harvester needs to work strictly under the row alignment mode, with poor adaptability to the row spacing. The mature machine type not needing row alignment smashes and returns the cotton stalk to the field or harvests cotton stalk by means of shear, but the stubbles may be left on the ground, which is not favorable for the subsequent cultivation and plastic film residue recovery. In China, diversified cotton planting modes are adopted, row spacing and plant spacing are not standard, row alignment-type operation machineries cannot be promoted in a large area, and the subsequent plastic film residue recovery is difficult in most film mulch planting modes. Thus, the physical and mechanical property test, bending resistance test, and cotton stalk pulling force test of cotton stalk were implemented. With the cotton stalk under the dense planting mode of machine-harvested cotton as the study object, a cotton stalk puller not needing row alignment and soil burying operations and not leaving stubbles was developed in this paper to solve the problems of the existing machines and tools, such as poor adaptability to row spacing, damage of mulching film, and stubble remaining on the ground.

State of the art

Chinese and foreign scholars have made some achievements in cotton stalk harvesting technology and equipment *(Mostofi , 2018; Srinidhi and Sushilendra, 2023; Fiaz et al., 2020)*. Cotton stalk harvesting machines in Australia, India, Russia, the United States, and other cotton-growing countries are relatively mature.

The KV-3.6 and KV-4 shovel cutting-type cotton stalk harvesting machines *(Ding, 2018)* produced in Uzbekistan have similar structures, and both adopt traction-type hooks; shovel-cutting devices dig into the soil to break the roots of the cotton stalks. This kind of cotton stalk harvesting method needs row alignment, the root is thoroughly shoveled, and the net yield is high, but some problems such as serious wear and tear of digging shovel and high energy consumption also exist. The Australian multi-stalk puller and the American AMADAS cotton stalk harvesting chopper use several pairs of rubber rollers installed at a certain inclination angle to rotate toward one another and then clamp cotton stalks to complete the pulling operation *(Jiang, 2016)*. Both machines adopt the rear suspension mode, and the rubber roller is driven by hydraulic pressure to rotate. The former has a wide working width and can pull out eight rows of cotton stalks simultaneously, whereas the latter can pull out three rows of cotton stalks, and the pulled cotton stalks are chopped and returned to the field by the crushing device arranged at the rear. This kind of cotton stalk harvesting method is affected by the size of the rubber roller, which has certain requirements for the row spacing of cotton in agronomy.

Dave Koenig's cotton stalk planer and Orthman's cotton stalk planer from the United States *(Li et al., 2008)* adopted a pair of symmetrically installed inclined disks to excavate cotton stalks. Dave Koenig's cotton stalk planer can adjust the number of discs according to the actual needs and harvest different rows of cotton stalks. Orthman's cotton stalk planer and digger are equipped with a chopping device, which can crush and return cotton stalks to the field after pulling out. Compared with shovel cutting, this digging-type cotton stalk harvesting has reduced energy consumption but still has strict requirements for row alignment. The cotton stalk harvesting machinery in the above countries is mature, the planting agronomic standards are normative, and the cotton stalk harvesting methods all have requirements for row alignment, which is not applicable to China. *Zhang J.X. et al. (2019)* studied the toothed disc-type cotton stalk harvester by using the Box–Behnken central composite test method and taking the missed pulling rate and pull-off rate as the evaluation indexes. At the pulling height of 66.2 mm, toothed disc diameter of 627.59 mm, and toothed disc speed ratio of 0.57, the pulling height and toothed disc speed ratio exerted significant effects on the pull-off rate and missed pulling rate of cotton stalk.

Chen et al., (2019), studied the effects of the circumferential linear speed of the toothed disc, the forward speed of the tractor, and the ratio of the circumferential linear speed of the toothed disc to the forward speed of the tractor on the cotton stalk pulling rate, the pull-off rate, and the missed pulling rate through single- and multi-factor experiments. At the constant forward speed of the tractor, the increase in the linear speed of the toothed disc helps improve the stalk pulling efficiency, and the speed ratio is the key factor affecting the stalk pulling effect. However, these two kinds of toothed disc-type cotton stalk harvesters easily cut off cotton stalks, and cotton stalks need to be pulled in a row-aligned way. *Xie J.H. et al. (2023)* determined the structural and working parameters of each part through the dynamic analysis of the cotton stalk pulling mechanism; they found that the factors of the cotton stalk pulling rate are mainly the rotation speed of the upper pulling roller, the forward speed of the machine, and the speed ratio; the factors of the missed pulling rate of cotton stalks are the speed ratio, the forward speed of the machine, and the rotation speed of the upper stalk pulling roller. However, some cotton stalks may be missed during the pulling operation.

Based on the above analysis, three-factor and three-level experiments were designed through the response surface analysis method in Design Expert software with the missed pulling rate and the pull-off rate as the evaluation indexes. Then, a 3D response surface model was constructed by taking three independent variables—forward speed, linear speed of stalk pulling rod, and rotation speed of stalk pulling roller—as the influencing factors. Next, the optimal parameter combination was found, providing a basis and experimental reference for studying cotton stalk harvesting machineries.

The remainder of this paper is organized as follows: In Section III, the mechanical and physical properties of cotton stalks are studied, the main test content includes the measurement of moisture content and bending strength of cotton stalks, and the test results render a basis for the subsequent cotton stalk puller design. In Section IV, the prototype is designed and subjected to the field experiment to investigate its operation performance. The significance of the influence of each factor on the operation performance of the machine is determined according to the experimental results. Combining the field experiment, the reasons for the experimental phenomena are analyzed, the optimal combination of working parameters for key parts is sought, the prototype is optimized, and a verification test is performed to achieve the best operation effect, providing a reference for the follow-up cotton stalk puller design. In Section V, the study results are summarized, and relevant conclusions are presented.

MATERIALS AND METHODS

Experimental study on cotton stalk pulling force

Cotton stalk pulling force is an important index parameter in the design of the cotton stalk puller. To obtain the value of the cotton stalk pulling force needed for harvesting after mechanical cotton harvesting, the measurement experiment of cotton stalk pulling force was conducted. In the entire process of completing pulling the roots of cotton stalks out of the ground, the maximum tensile force borne by cotton stalks is the cotton stalk pulling force. To reduce the test errors and acquire more real, effective test data, the cotton stalks in the test cotton field were subjected to the pulling force test through the double-diagonal five-point sampling method. Following the rules of double-diagonal five-point sampling, the test cotton field was divided into five test plots; in each test plot, 10 groups of cotton stalk pulling force tests were implemented, and the tensile force value needed to pull each cotton stalk out successfully was recorded.

The experiment was conducted by using a mobile cotton stalk pulling force measuring device *(Xue et al., 2021)* self-developed by the research group, as shown in Figure 1. The device was composed of a traveling wheel, a transmission system, a storage battery, a motor, a stalk pulling device, and a tension sensor. The device can pull cotton stalks out in a static state, and the tensile force required for pulling cotton stalks was measured by the tension sensor. In addition, the test instruments included a TJSD-750-II digital soil compactness tester, a notebook computer, a QS-WT soil moisture temperature tester, a vernier caliper, a meter ruler, and a tool set.

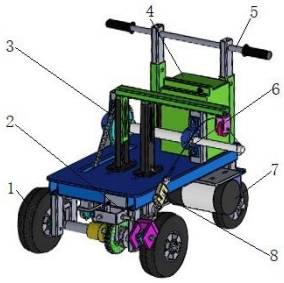

Fig. 1 - Schematic of the mobile cotton stalk pulling force measuring device
1. Traveling wheel; 2. Cotton stalk clamping device; 3. Transmission system; 4. Storage battery; 5. Handle; 6. Drag rope; 7. Motor; 8. Tension sensor

To find the relationship between cotton stalk pulling force and cotton stalk diameter, the measurement data of cotton stalk pulling force in five experimental plots were processed by Origin2018 software, and the scatter diagram of the relationship between cotton stalk diameter and cotton stalk pulling force was established, as shown in Figure 2. The cotton stalk pulling force increased with the increase of cotton stalk diameter, indicating a positive correlation between cotton stalk pulling force and cotton stalk diameter. Among 50 cotton stalks pulled out from five experimental plots, the maximum pulling force was 821N.

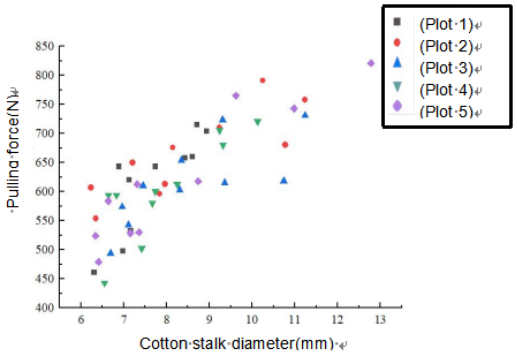

Fig. 2 - Cotton stalk pulling force–cotton stalk diameter correlation diagram

Experimental study on cotton stalk moisture content

The moisture content of cotton stalks directly affects their tensile, compressive, and bending mechanical properties *(Zhang et al., 2022)*. The experimental results can provide a theoretical basis for the follow-up experimental study on bending characteristics of cotton stalks.

The first batch of moisture content test was conducted on the day when the cotton stalk test samples were brought to the laboratory.

The moisture content was measured through the oven drying method using a PC-16A Shanghai Puchun moisture content tester, which can directly read and record the measurement results of cotton stalk moisture content. The experimental site is displayed in Figure 3-b. The second batch of cotton stalk moisture content test was performed 15 days after the first batch of test, during which natural drying was implemented. Then, the influence of the natural moisture loss state of cotton stalks on their moisture content was explored.

The cotton stalk sample variety was “XLZ No. 45”, branches were manually removed from cotton stalks with good growth momentum and without stalk damage or evident defects after harvesting with a puller. Only the main stems of the cotton stalks were reserved and manually intercepted into segments with equal length, as shown in Figure 3-a. The main instruments and equipment used in the experiment were a PC-16A Shanghai Puchun moisture content tester, a vernier caliper, a woodworking saw, scissors, stickers, a ballpoint pen, and A4 paper.

a- Cotton stalk samples

b- Cotton stalk moisture content measurement

Fig. 3 - Field experiment photos

The two batches of cotton stalk moisture content test results are listed in Table 2. The average cotton stalk moisture contents in the first and second batches are 33.7% and 25.4%, respectively. Within 15 days of natural drying, the cotton stalks experienced certain moisture loss.

Experimental study on cotton stalk bending properties

The test result of cotton stalk bending properties is an important parameter in the design of cotton stalk pullers. The maximum bending angle bearable by cotton stalks before breakage was measured combining the bending effect on the cotton stalks during the field test of the machines and tools. The bending property parameters of the cotton stalks acquired in this manner were of direct reference values to machine and tool design, providing data support for designing cotton stalk pullers.

The bending property test results of the first batch of cotton stalks are listed in Table 1. The average moisture content of this batch of cotton stalks is 33.7%, and the maximum and minimum bending angles measured for this batch are 142.58° and 64.94°, respectively.

Table 1

Bending test results of first batch of cotton stalks

S/N	Root diameter (mm)	Bending angle (°)	S/N	Root diameter (mm)	Bending angle (°)
1	7.82	105.06	7	10.04	101.55
2	9.14	76.76	8	8.32	64.94
3	7.08	100.64	9	9.10	104.58
4	9.18	142.58	10	8.28	92.45
5	6.82	91.36	11	8.26	87.48
6	7.86	97.49	12	9.98	107.37

The bending property test results of the second batch of cotton stalks are exhibited in Table 2.

Table 2

Bending test results of second batch of cotton stalks

S/N	Root diameter (mm)	Bending angle (°)	S/N	Root diameter (mm)	Bending angle (°)
1	7.98	69.88	7	9.12	69.23
2	8.02	64.88	8	10.14	87.85
3	8.70	65.97	9	10.02	98.82
4	8.34	70.31	10	9.52	101.29
5	7.78	89.88	11	8.96	89.30
6	7.76	79.66	12	9.08	80.97

The previous section presented that the average moisture content of this batch is 25.4%, and the maximum and minimum bending angles measured for this batch are 101.29° and 64.88°, respectively.

Comparing the bending property test results of two batches of cotton stalks finds that the maximum and minimum bending angles of the second batch are smaller than those of the first batch. Only judging from the changes in the maximum and minimum bending angles of cotton stalks measures through the two tests, the bending resistance of cotton stalks weakened after moisture loss.

To explore further the relationship between the bending properties of cotton stalks and their own moisture content as well as the relationship between the bending properties and the diameter of cotton stalks, the two bending test results of cotton stalks were processed via Origin2018, and the correlation scatter diagram between the diameter and tensile strength of cotton stalks was established, as shown in Figure 4. After the second batch of cotton stalks were naturally aired for 15 days, the bending angle of cotton stalks was generally smaller than that of the first batch, once again reflecting that the bending resistance of cotton stalks would decline with the reduction of moisture content, and the bending resistance is positively correlated with the moisture content of cotton stalks. In addition, as the diameter of cotton stalks increased, the increase in the bending angle of cotton stalks displayed by the two bending property test results was not evident, manifesting that the diameter of cotton stalks is not directly related to their bending resistance.

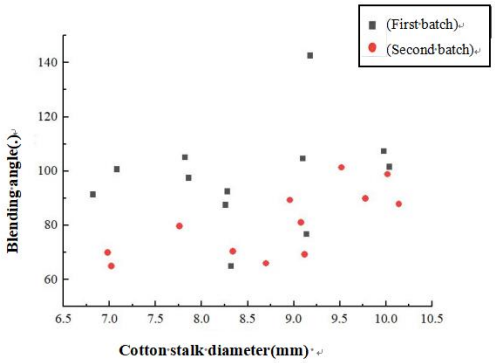

Fig. 4 - Schematic of measuring device for cotton stalk pulling force

RESULTS

Complete machine structure and working principle

The cotton stalks under the dense planting mode of machine-harvested cotton were taken as the study objects. The early-stage field survey of the cotton field revealed that the “one film for four rows” cotton planting mode is a dominant dense planting mode, the row spacing is 660 ±100 mm, and the plant spacing is about 50 mm.

Based on the above design requirements, a horizontal-shaft roller-type cotton stalk puller was developed, and the structure of the complete machine is shown in Figure 5. The device was composed of a traction frame, a stalk feeding device, a roller spacing adjusting structure, a stalk pulling device, and a transmission system. The stalk feeding device was composed of a stalk pulling rod, a toothed belt, and a pulley. The stalk pulling device mainly consisted of a pair of pulling rollers. The key working parts of the horizontal-shaft roller-type cotton stalk puller included the stalk feeding device, the pulling device, and the roller pressing mechanism.

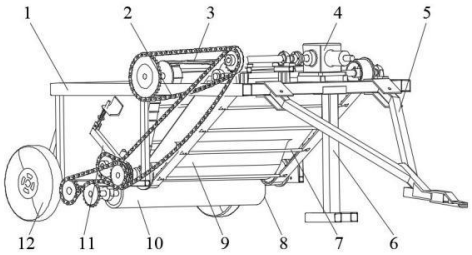

Fig. 5 - Schematic of the horizontal-shaft roller-type cotton stalk puller structure

1- Rack; 2- Transmission system; 3- Stalk feeding device; 4- Gearbox; 5- Traction frame; 6- Support frame; 7- Stalk pulling rod; 8- Stalk pulling roller; 9- Baffle; 10- Stalk pulling device; 11- Roller spacing adjusting device; 12- Traveling wheel

The horizontal-shaft roller-type cotton stalk pulling device was hung on the tractor in a traction mode of the rear suspension, and power was provided by the rear power take-off shaft of the tractor. The hanging device at the rear end of the tractor not only provided traction for the cotton stalk pulling machine but also could adjust the working heights of the stalk feeding device and the stalk pulling device.

The working process of the machine can be divided into five stages, namely, initial contact stage between cotton stalks and stalk pulling rod, stalk feeding stage, feeding stage, stalk pulling stage, and throwing stage, as shown in Figure 6.

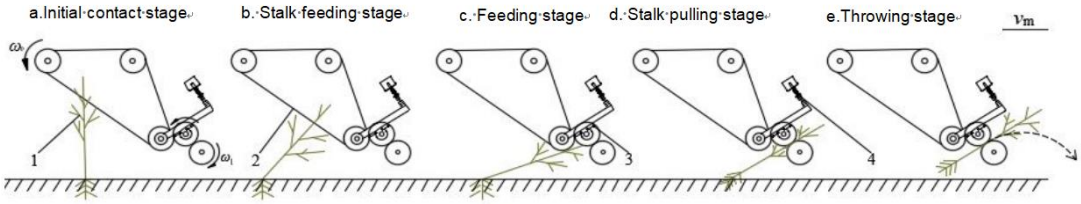

Fig. 6 - Schematic of working principles

1. Cotton stalks; 2. Stalk feeding device; 3. Stalk pulling device; 4. Roller pressing mechanism

Determination of response indexes

The test was implemented with reference to the Equipment for Harvesting-Combine Harvesters-Test Procedure (GB/T 8097-2008). In each group, the test length was 10 m, the test was implemented three times, and the average value of the three tests was taken. A test plot 300 m in length and 150 m in width was divided, and the evaluation indicators were calculated as follows:

The calculation formula for the missed pulling rate P_1 of cotton stalks is shown in equation 1:

$$P_1 = \frac{Z_1}{Z} \times 100\% \quad (1)$$

where Z_1—number of cotton stalks going through missed pulling in each group of test plot, and Z—total number of cotton stalks in each group of test plot.

The formula for the missed pulling rate P_2 of cotton stalks is shown in equation 2:

$$P_2 = \frac{Z_2}{Z} \times 100\% \quad (2)$$

where Z_2—number of pull-off cotton stalks in each group of test plot.

Determination of structural parameters and working parameters

The main factors of the working performance of the horizontal-shaft roller-type cotton stalk puller included the forward speed, the linear speed of stalk pulling rod, and the rotation speed of the stalk pulling roller, so they were taken as the influencing factors in the test. The forward speed depends on the gear adjustment of the test prototype equipped with a Changfa CFD604A wheeled tractor. According to the field test, the forward speed was about 0.56 m/s in the slow first gear, 0.78 m/s in the slow second gear, and 1 m/s in the fast first gear. The linear speed of the stalk pulling rod and the rotation speed of the stalk pulling roller were adjusted by changing the sprocket in the chain transmission system.

The Box–Behnken central composite design method was adopted in the test, and a three-factor three-level quadratic regression orthogonal test scheme was used *(Bano and Irfan, 2019)*, followed by analysis through the response surface method *(Oznur et al., 2023; Zhang and Wu, 2023)*. Moreover, a mathematical model indicating the relationship between pulling force and each factor was established to obtain the optimal combination of working parameters *(Zhu et al., 2023)*. The test factors and levels are listed in Table 3.

Table 3

Test factors and levels

Level	Forward speed *A* (m·s^{-1})	Linear speed of stalk pulling rod *B* / (m·s^{-1})	Rotation speed of stalk pulling roller *C* / (r·min^{-1})
-1	0.56	1.5	191
0	0.78	1.75	239
1	1	2	287

Results and significance analysis

(1) Regression analysis of missed pulling rate and pull-off rate

The test scheme and results are listed in Table 4. The test results were subjected to quadratic regression analysis by using Design Expert 8.0.6 *(Zhang et al., 2018)*, and the quadratic polynomial response surface regression models of missed pulling rate and pull-off rate for three independent variables—forward speed, linear speed of stalk pulling rod, and rotation speed of stalk pulling roller-were established, as displayed in Equations 3 and 4. Subsequently, the analysis of variance of the regression models was performed *(Esmailzadeh et al., 2021)*, and the results are shown in Table 4.

$$P_1 = 5.84 + 5.49A - 1.40B - 1.22C - 0.78AB + 0.99AC - 1.46BC + 3.92A^2 + 1.75B^2 + 1.94C^2 \quad (3)$$

$$P_2 = 132.37 - 98.86A - 63.25B - 0.29C - 14.23AB + 0.09AC - 0.12BC + 80.96A^2 + 27.94B^2 + 8.41C^2 \quad (4)$$

A - Forward speed;

B - Linear speed of stalk pulling rod;

C - Rotation speed of stalk pulling roller.

Table 4

Response surface test scheme and results

Test No.	Factor			Missed pulling rate P_1 / %	Pull-off rate P_2 / %
	A	*B*	*C*		
1	1	0	1	16.74	13.73
2	0	0	0	5.67	5.28
3	0	0	0	5.03	5.2
4	0	-1	1	11.62	10.28
5	0	0	0	5.49	4.91
6	1	1	0	14.64	9.13
7	0	1	1	5.83	15.63
8	-1	0	1	3.37	11.73
9	-1	-1	0	6.8	6.57
10	0	0	0	6.44	5.08
11	1	0	-1	18.04	3.6
12	0	0	0	6.56	4.31
13	0	-1	-1	10.3	2.35
14	-1	0	-1	8.63	4.6
15	1	-1	0	18.93	5.43
16	-1	1	0	5.64	7.6
17	0	1	-1	10.34	4.41

The analysis of variance in Table 5 presents that the values of P1 and P2 were smaller than 0.0001, indicating the high significance level of this regression model. The lack-of-fit term of P1 was P (P = 0.3650) > 0.05, also manifesting its high fitting degree, and its coefficient of determination was R2 = 0.9900, reflecting that the two models could explain over 98% of the evaluation indexes. Hence, the two models could optimize the working parameters of this device.

Table 5

Analysis of variance of regression equations

Source of variance	Missed pulling rate / P_1				Pull-off rate P_2			
	Quadratic sum	Degree of freedom	*F* value	*P* value	Quadratic sum	Degree of freedom	*F* value	*P* value
Model	385.69	9	86.77	<0.0001	225.56	9	88.15	<0.0001
A	241.01	1	488.01	<0.0001	0.24	1	0.85	0.3874
B	15.68	1	31.75	0.0008	18.42	1	64.80	<0.0001
C	11.88	1	24.06	0.0017	165.71	1	582.86	<0.0001
AB	2.45	1	4.96	0.0612	1.78	1	6.27	0.0408
AC	3.92	1	7.94	0.0259	2.25	1	7.91	0.0260
BC	8.50	1	17.21	0.0043	2.71	1	9.52	0.0177
A^2	64.65	1	130.91	<0.0001	6.44	1	22.66	0.0021
B^2	12.84	1	25.99	0.0014	4.12	1	14.50	0.0066
C^2	15.82	1	32.04	0.0008	20.79	1	73.12	<0.0001
Residual error	3.46	7			1.99	7		
Lack-of-fit term	1.77	3	1.40	0.3650	1.39	3	3.09	0.1519
Variance	1.69	4			0.60	4		
Sum	389.14	16			227.55	16		

(Remarks: p < 0.01 indicates extremely significant; 0.01 < p <0.05 reflects significant; p > 0.05 means insignificant)

The magnitude of P value reflected the influence degree of each parameter on the regression models. According to the P value of each factor in Table 5, all the other regression terms except AB in the P_1 model produced significant influences, among which the seven regression terms A, B, C, BC, A^2, B^2, and C^2 showed extremely significant influences; in the P_2 model, the other regression terms except A generated significant influences, among which B, C, A^2, B^2, and C^2 exhibited extremely significant influences. The F value of each factor in Table 5 shows that the significance of the influence of each factor on P_1 in descending order was A, B and C; that on P_2 in descending order was C, B and A.

(2) Response surface analysis of missed pulling rate and pull-off rate

To express vividly the significance of the influence of each test factor on the working performance of the machine, a 3D response surface model *(Shi et al., 2023)* was established, and the consistency between the influencing trend of each factor on evaluation indexes and the analysis result of variance was assessed *(Jiang et al., 2024)*, as shown in Figure 7.

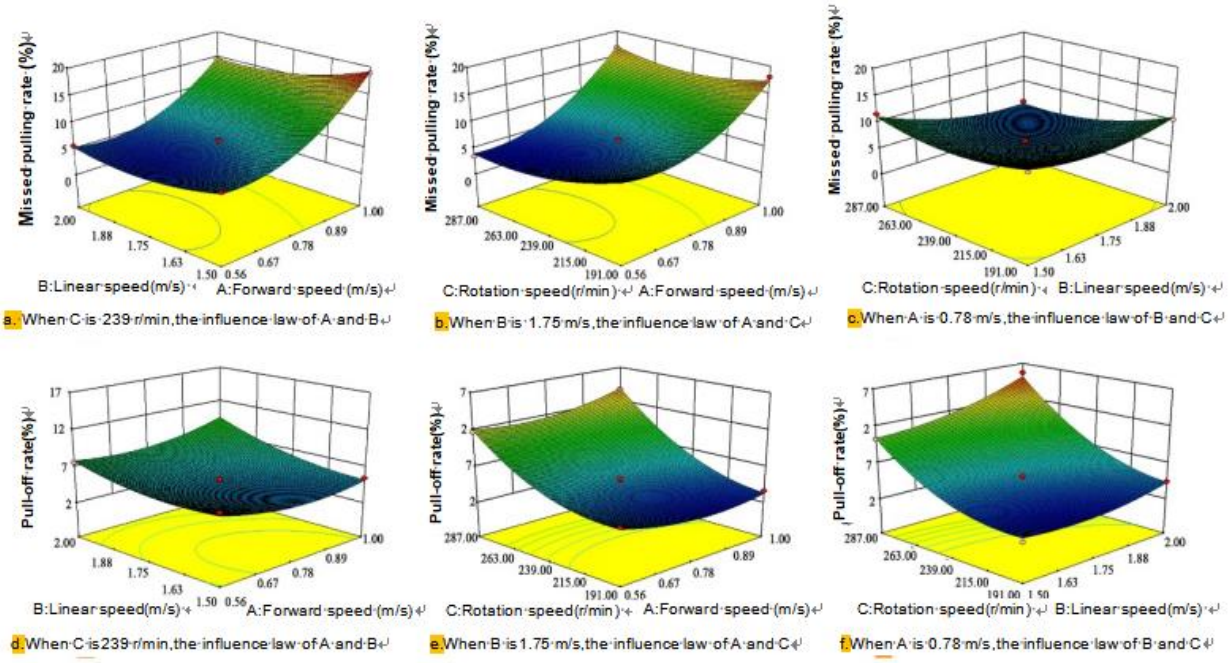

Fig. 7 - Interactive influence of test factors on missed pulling rate and pull-off rate of cotton stalks

According to the variation trend of response surface, the significance of the influence of each test factor on the missed pulling rate of cotton stalks in descending order was A > B > C, and that on the pull-off rate was C > B > A; both were consistent with the analysis results of variance. Combining the concrete field test, the reasons for missed pulling and pull-off phenomena of cotton stalks were mainly considered as follows: after machine-aided cotton harvesting, the working conditions were complicated, some cotton stalks fell over seriously, preventing the machine from completing stalk feeding; this resulted in missed pulling. At an excessively high forward speed, the machine failed to convey cotton stalks to the bottom end to complete feeding, so the stalk feeding effect was poor, leading to missed pulling; cotton stalks would be damaged to some extent by the spindle part of the cotton harvester and could be easily broken when pulled up.

Parameter optimization and test verification

To achieve the best pulling effect of the horizontal-shaft roller-type cotton stalk puller, the experimental factors that affect its operation effect need to be optimized. The table of the analysis of variance and the response surface model shows that the machine generated a good pulling effect under a slow forward speed, a medium linear speed of the stalk pulling rod, and a medium rotation speed of the stalk pulling roller. The results obtained through Design-Expert 8.0.6 show that when forward speed = 0.68 m/s, linear speed of stalk pulling rod = 1.73 m/s, and rotation speed of stalk pulling roller = 221.54 r/min, the predicted missed pulling rate of cotton stalks reached 5.06% and the predicted pull-off rate reached 3.83%, indicating that theoretically, the horizontal-shaft roller-type cotton stalk puller achieved the best pulling effect under this working state.

To verify the accuracy of the parameter combination optimized by the software, a field verification test was conducted, and the test site is shown in Figure 8. Before the test, the working parameters of the device were set to be 1.75 m/s for the linear speed of the stalk pulling rod, 221 r/min for the rotation speed of the stalk pulling roller, and 0.68 m/s for the forward speed of the unit. The test was repeated three times, and the average value of the three tests was taken as the verification value, as listed in Table 6. Under the optimal parameter combination, the missed pulling rate was 5.24%, the pull-off rate was 3.75%, and the relative error of theoretically predicted values from the average value of the three tests was always smaller than 4%, thus meeting the design requirements and proving that the parameter optimization model was reasonable.

Table 6

Optimized value and test verification value

Item	Missed pulling rate of cotton stalks P_1 / %	Pull-off rate of cotton stalks P_2 / %
Average value in the field experiment	5.24	3.75
Software optimized value	5.06	3.83
Relative error	3.44	2.13

a- Before operation *b- After operation*

Fig. 8 - Effect comparison before and after operation at the test site

CONCLUSIONS

Based on the current research status of cotton stalk pulling and harvesting machines, a new type of cotton stalk pulling machine, which could pull up the whole cotton stalk, was designed. The physical and mechanical properties of cotton stalks were studied to provide a theoretical basis for machine design. Moreover, the structural parameters and working parameters were determined, and the factors influencing the working performance of the machine were acquired. Then, the prototype was subjected to the field experiment to obtain the optimal parameter combination. Finally, the following main conclusions were drawn:

(1) According to the cotton stalk pulling force test results, the cotton stalk pulling force is positively correlated with the diameter of cotton stalks, and the maximum pulling force is 821 N. As revealed by the bending property test, the bending resistance of cotton stalks is positively correlated with their moisture content, and the diameter of cotton stalks exerts an insignificant influence on their bending resistance, with the minimum bending angle of 64.88°.

(2) The interactive influence between the response curve and influencing factors on the model, the change laws of the cotton stalk pulling force and pull-off rate under the influences of the forward speed, the linear speed of the stalk pulling rod, and the rotation speed of the stalk pulling roller were analyzed. The significance of the influence on the missed pulling rate followed the order forward speed > linear speed of stalk pulling rod > rotation speed of stalk pulling roller; the significance of the influence on the pull-off rate followed the order rotation speed of stalk pulling roller > linear speed of stalk pulling rod > forward speed.

(3) The working parameters for the horizontal-shaft roller-type cotton stalk puller were optimized by the response surface combination test method, and the regression equations for the missed pulling rate and pull-off rate of cotton stalks were optimally solved. The results show that when linear speed of stalk pulling rod = 1.75 m/s, the rotation speed of stalk pulling roller = 221 r/min, and the forward speed of the unit=0.68 m/s, the missed pulling rate and pull-off rate of cotton stalks were 5.24% and 3.75%, respectively, and the relative error of predicted values from the average value of the three tests remained smaller than 4%, thus meeting the design requirements and indicating the reasonability of the optimization model. Then, the horizontal-shaft roller-type cotton stalk puller prototype was subjected to a field experiment, and the error of the test result was smaller than 4%, indicating that the response surface method is capable of intuitive prediction and improving and optimizing equipment parameters, providing reference significance for the parameter optimization of cotton stalk pulling machines.

REFERENCES

[1] Bano A., Irfan M., (2019), Alkali pretreatment of cotton stalk for bioethanol, *Bangladesh Journal of Scientific and Industrial Research*, vol.54, no.1, pp.73-82, Bangladesh;

[2] Chen M.J., Zhao W.S., Wang Z.W., (2019), Operation Process Analysis and Parameter Optimization of Dentate Disc Cotton-stalk Uprooting Mechanism (齿盘式多行拔棉秆装置拔秆过程分析与参数优化), *Transactions of the Chinese Society for Agricultural Machinery*, vol.50, no.03, pp.109-120, Beijing / China;

[3] Ding F., Lu J., Liu Q., (2021), Migration of cotton planting regions and residual pollution of mulch film in China (我国棉花主产区变化与地膜残留污染研究), *Journal of Huazhong Agricultural University*, vol. 40, no. 06, pp. 60-67, Hubei / China;

[4] Ding Z.X., (2018), Research on Development Status of Puller Technology (棉秆收获技术的发展现状研究), *Xinjiang Agricultural Mechanization*, no.03, pp. 24-25+34, Xinjiang/China;

[5] Esmailzadeh S., Shahrabi T., Yaghoubinezhad Y., (2021), Optimization of nickel selenide for hydrogen and oxygen evolution reactions by response surface methodology, *Journal of Colloid and Interface Science*, vol. 600, pp. 324-337, United States;

[6] Fawzy S., Osman AI., Farrell C., (2021), Characterization and kinetic modeling for pyrolytic conversion of cotton stalks, *Energy Science & Engineering*, vol.9, no.10, pp.1908-1918, England;

[7] Fiaz A., Muhammad T.J., Alamgir A.K., (2020), Field Performance Evaluation and Finite Element Simulation of Cotton Stalk Puller-Shredder: A Sustainable Mechanical Solution to Control Pink Bollworm (Pectinophora Gossypiella), *Sustainability*, vol. 12, pp. 3407, Switzerland;

[8] He X.W., Liu J.X., Xu Y., (2020), Improvement Design of 4MB-6Row-controlled Shoveling and Drawing Placement Machine for Cotton-stalks in Close Planting (4MB-6 型密植秆对行铲拔铺放机改进设计), *Transactions of the Chinese Society for Agricultural Machinery*, vol. 51, no.2, pp. 21-30, Beijing/China;

[9] Jiang B., Shi Z. L., Chen H., (2024), Parameter Optimization and Experiment of Precision Hole-seeding Wheel on Clamped Corn Film (夹持式玉米膜精密穴播轮的参数优及试验), J*ournal of Agricultural Mechanization Research*, vol. 46. no. 2, pp.184-188, Heilongjiang/China;

[10] Jiang L., (2016), *Research on farmers behaviors in the resource utilization of straw and its optimization strategies* (农户对秸秆的资源化利用行为及其优化策略研究), Doctoral dissertation, Hua Zhong Agricultural University, Hubei/China;

[11] Jinesh B., Shah Janak B., (2022), Valaki Techno Economic Analysis of Cotton Stalk Biomass Based Bio-Oil Production Using Slow Pyrolysis Process, *Jurnal kejuruteraan*, vol. 34, no.3, pp.16, Malaysia;

[12] Li S.J., Yang B.N., Wang J.Y., Lv H.Z., Yan X.H., (2008), Development of straw collection technology for major crops (主要农作物秸秆收集技术发展), *Farm Machinery,* no. 16, pp. 23-26, Beijing/China;

[13] Liao P.W., Zhuo D.L., Fu C.X., (2021), Improve design and test of self-propelled cotton stalk combine harvest bale (自走式棉秆联合收获打捆机改进设计与试验), *Journal of Chinese Agricultural Mechanization*, vol. 42, nol. 7, pp.19-25, Jiangsu/China;

[14] Mostofi M. R., (2008), Evaluation of a cotton stalk puller performance, *American- Eurasian Journal of sustainable agriculture*, vol. 2, no.1, pp.19-24, United States;

[15] Oznur Y., Dogukan T., Bestami O., (2023), Optimization of enzymatic hydrolysis conditions of chemical pretreated cotton stalk using response surface methodology for enhanced bioethanol production yield, *Biomass Conversion and Biorefinery*, vol.13, pp.6623-6634, Germany;

[16] Pandey S. N., (1987), Shaikh A. J. Utilization of cotton plant stalk for production of pulp and paper, *Biological Wastes*, vol. 21, no.1, pp. 63-70, Netherlands;

[17] Pandirwar A. P., Khadatkar A., Mehta C.R., Majumdar G., Idapuganti R., Mageshwaran V., Shirale A. O., (2023), Technological advancement in harvesting of cotton stalks to establish sustainable raw material supply chain for industrial applications: a Review, *Bio Energy Research*, vol. 16, pp. 741-760, United States;

[18] Raju N.P., Raju M., (2019), Experimental Study of Cotton Stalk Pellet Renewable Energy Potential from Agricultural Residue Woody Biomass as an Alternate Fuel for fossil fuels to Internal Combustion Engines, *IJERT-International Journal of Engineering Research & Technology*, vol. 9, pp. 49-54, India;

[19] Shi X., Niu C. H., Zhang J. X., (2015), Developing of 4JB-2200 direct-connected cotton straw pulling machine (4JB-2200 型悬挂式棉秸秆拔取机的研制), *Xinjiang Agricultural Mechanization*, no. 06, pp.5-7, Xinjiang/China;

[20] Shi Y.S, Du K., Li S., (2023), Optimization of strength of safety box buckle based on response surface model (基于响应面模型的安全箱卡扣强度优化), *Journal of Civil Aviation University of China*, vol. 41, no. 3, pp. 59-64, Tianjin/China;

[21] Srinidhi G., Sushilendra S.S., (2023), Performance Evaluation of Tractor Operated Cotton Stalk Shredder Cum Uprooter, *British Journal of Environment & Climate Change*, vol.13, no.11, pp. 185-195, England;

[22] Sun Y. F., Chen Z., Dong S. P., (2012), Study on Cutter Mechanism of 4MG-275 Self-walking Cotton-stalk Combine Harvester (4MG-275 型自走式棉秆联合收获机切碎装置的研究), *Journal of Agricultural Mechanization Research*, vol. 34, no. 6, pp.13-16+21, Heilongjiang/China;

[23] Uzair A., Sohail S., Shaikh NU., Shan A., (2020), Agricultural residue as an alternate energy source: A case study of Punjab province, Pakistan-Science Direct*, Renewable Energy*, no. 162, pp.2066-2074, England;

[24] Wang X.N., Feng B., Chen F., (2003), Development of 4JSM-1800 cotton straw returning to the field and residual film recovery (4JSM-1800 棉秸秆还田及残膜回收联合作业机研制), *Xinjiang agricultural mechanization*, no. 04, pp. 53-54, Xinjiang/China;

[25] Xie J.H., Wu S.H., Cao S.L., (2023), Design and Test of Clamping-roller Cotton Stalk Pulling Device (夹持辊式棉杆拔取装置设计与实验), *Transactions of the Chinese Society for Agricultural Machinery*, vol. 54, no. 5, pp. 101-111, Beijing/China;

[26] Xue D.Q., Zhang L.H., Zhang J.X., (2021), Design and experimental research of mobile cotton stalk pulling resistance test device based on response surface method (基于响应曲面法的移动式棉秆拔取力测试装置设计与实验研究), *Journal of Chinese Agricultural Mechanization*, vol.42, no.5, pp. 06-12, Jiangsu/China;

[27] Zhang B., Chen X., Liang R., (2022), Cotton stalk restitution coefficient determination tests based on the binocular high-speed camera technology, *International Journal of Agricultural and Biological Engineering*, no. 04, pp. 015, China;

[28] Zhang H., Wu J.H., (2023), Statistical optimization of sodium hydroxide pretreatment and enzymatic hydrolysis of corn stover powder for enhancing sugar production using response surface methodology, *Biomass Conversion and Biorefinery*, vol. 13, pp: 7111-7125, Germany;

[29] Zhang J.X., Wang T.J., Chen M.J., (2019), Design of toothed disc cotton stalk harvester (齿盘式棉杆收获机的设计), *Transactions of the Chinese Society of Agricultural Engineering*, vol. 35, no. 15, pp.1-8, Beijing/China;

[30] Zhang J.X, Yang C., Guo J.X., (2018), Design and experiment of hob-type joint operation machine for silage corn root stubble plucking and residual plastic film collecting (滚刀式青贮玉米起茬及残膜回收联合作业机的设计与试验), *Transactions of the Chinese Society of Agricultural Engineering*, vol. 34, no. 6, pp. 25-34, Beijing/China;

[31] Zhu H.B., Zhang X., Qian C., (2023), Design and experimental study on pruning machine of Yunnan edible rose, *Scientific reports*, vol.13, pp. 4118, England.

PRELIMINARY RESEARCHES ON SOME TECHNICAL-FUNCTIONAL PARAMETERS OF AN EXPERIMENTAL MODEL OF CONVECTIVE DRYER WITH TOTAL ENERGY INDEPENDENCE

/

CERCETĂRI PRELIMINARE ASUPRA UNOR PARAMETRI TEHNICO-FUNCȚIONALI AI UNUI MODEL EXPERIMENTAL DE USCĂTOR CONVECTIV CU INDEPENDENȚĂ ENERGETICĂ TOTALĂ

Cristian SORICĂ[1*)], Andrei PĂTRUȚ[2)], Gheorghe ȘOVĂIALĂ[3)], Elena SORICĂ[1)], Laurențiu VLĂDUȚOIU[1)], Mario CRISTEA[1)], Gabriela MATACHE[3)] , Ioan PAVEL[3)]

[1)]INMA Bucharest, No. 6 Ion Ionescu de la Brad Blvd., Bucharest, Romania

[2)]CALORIS GROUP S.R.L., No. 8A Berceni Road, Bucharest, Romania

[3)]INOE 2000-IHP, No.14 Cuțitul de Argint Street, Bucharest, Romania

**E-mail: cri_sor2002@yahoo.com*

DOI: https://doi.org/10.35633/inmateh-72-48

Keywords: *biomass gasification, convective drying, energy independence, isolated areas*

ABSTRACT

In order to be consumed whole year at a nutritional value close to the freshly picked product, seasonal vegetal products (vegetables, fruits, aromatic and medicinal plants, seeds, berries, mushrooms etc.) are preserved by artificial dehydration. Unlike other preservation methods and techniques, dehydration leads to obtaining products with a weight 8-10 times reduced and a volume 3-4 times smaller, a fact that contributes to the reduction of the spaces required for storage and the substantial reduction of handling and transport costs, compared to those for fresh vegetal products. Taking into account the general context related to global warming, as well as the need to reduce energy consumption from fossil fuels, the paper approaches the preliminary experimental research of a small capacity convective dryer, with total energy independence from the electricity network, intended for small agricultural producers from isolated hill and mountain areas. The technical equipment consists of a thermal generator operating on TLUD principle, which utilizes existing biomass at the local level, a high-efficiency air-air heat exchanger and a drying room with trays. The aim was to determine some important technical-functional parameters in the working process of the equipment, such as: the temperature of the burnt gases, the biomass loading capacity of the gasification reactor, the capacity to regulate the air flow required for the thermo-chemical processes, the temperature at various keypoints inside equipment etc. Following the analysis of the experimental data, there were highlighted quantitative values useful for estimating the inputs required for a normal operation of the equipment.

REZUMAT

Pentru a putea fi consumate tot timpul anului la o valoare nutritivă apropiată de produsul proaspăt cules, produsele vegetale sezoniere (legume, fructe, plante aromatice și medicinale, semințe, fructe de pădure, ciuperci etc.) sunt conservate prin deshidratare artificială. Spre deosebire de alte metode și tehnici de conservare, deshidratarea conduce la obținerea unor produse având o greutate redusă de 8-10 ori și un volumul de 3-4 ori mai mic, fapt care contribuie la reducerea spațiilor necesare pentru depozitare și diminuarea substanțială a costurilor de manipulare și transport, comparativ cu cele pentru produsele vegetale proaspete. Ținând cont de contextul general referitor la încălzirea globală, precum și de necesitatea reducerii consumului de energie provenită din combustibili fosili, lucrarea abordează cercetarea experimentală preliminară a unui uscator convectiv de capacitate mică, cu independență energetică totală față de rețeaua de energie electrică, destinat micilor producători agricoli din zonele izolate de deal și de munte. Echipamentul tehnic are în componență un generator termic cu funcționare pe principiul TLUD, care valorifică biomasa existentă la nivel local, un schimbător de căldură aer-aer cu eficiență ridicată și o incintă de uscare cu tăvițe. S-a urmărit determinarea unor parametri tehnico-funcționali importanți în procesul de lucru al echipamentului, precum: temperatura gazelor arse, capacitatea de încărcare cu biomasă a reactorului de gazeificare, capacitatea de reglare a debitului de aer necesar desfășurării proceselor termo-chimice, temperatura în diverse puncte cheie din interiorul echipamentului etc. În urma analizei datelor experimentale s-au evidențiat valori cantitative utile pentru estimarea input-urilor necesare unei funcționări normale a echipamentului.

INTRODUCTION

Fruits and vegetables have always represented basic elements in human nutrition, due to the intake of proteins, carbohydrates, lipids, as well as vitamins, minerals, fibers, enzymes, volatile aromatic substances etc., their consumption throughout the year being beneficial for health (*Muscalu et al., 2022*). Also, the spontaneous flora offers an extremely rich range of berries, mushrooms, medicinal and aromatic plants, which complete the supply of substances necessary for a rational and balanced human diet.

These products are seasonal, the harvest periods are relatively short, and for most of them the perishability is very high or average, which makes their fresh use possible only after demanding storage, which considerably increases its costs.

The large volume of vegetal products necessary to satisfy consumption needs and their high degree of perishability constitute a problem of great importance in maintaining the quality for food throughout the year.

The main causes for the quality deterioration of these products are represented by mechanical actions (degradation of structure by crushing), aging processes (especially in the case of fruits) and degrading actions of pests (microflora existing on the surface of the products, rodents, birds etc.). The metabolic activity of the microflora is decisively dependent on the available water. A decrease in water activity has important influences on the development of microorganisms (*Murugan and Saji Raveendran, 2021*). In this context, the dehydration of vegetal products is the technological process by which the natural water content is reduced to a level that prevents the activity of microorganisms, without destroying the tissues or depreciating the food value of these products (*Calín-Sánchez et al., 2020; Jambh et al., 2021; Kamiloglu et al., 2016*). Dehydration leads to obtaining products that are 8-10 times lighter in weight and 3-4 times smaller in volume, a fact that contributes to reducing the space required for storage and substantially reducing handling and transport costs, compared to those for fresh vegetal products.

The ensemble of phenomena that occur during dehydration leads to the concentration of valuable principles, to volume reduction of the raw material used and to the increase of the food value and therefore commercial value of the finished product. The raw materials must keep its qualitative characteristics, especially the taste, appearance and nutritional components, and undergo as few changes as possible during dehydration. In general, fresh fruits and vegetables contain approximately 85 – 90 % water, while the maximum moisture content of dehydrated fruits is approx. 20 – 25 %, and of vegetables approx. 5 – 7 %. The excess water that must be removed by dehydration varies depending on the raw material used, as well as depending on the storage time of the finished product.

The removal of excess water through the classical dehydration of vegetal products can be done either with the help of solar heat - natural drying, or with the help of artificially produced heat (combustion gases, hot air, heated surfaces etc.) - artificial drying or dehydration. In recent years, a series of emerging dehydration methods, based on non-thermal processes, have gained increased attention (Heat Pump Drying - *Moses at al., 2014; Rahman, 2020*, Microwave Drying - *Joardder et al., 2013*, Infrared Drying - *Boudhrioua et al., 2009*, Radio Frequency Drying - *Babu et al., 2018; Boudhrioua et al. 2009* etc.) or their combinations with classical processes (Microwave-Assisted Convective Drying - *Kumar and Karim, 2017*, Vacuum-Microwave Drying – *Calín-Sánchez et al., 2012; Figiel, 2009a; Figiel and Michalska-Ciechanowska, 2016; Szychowski et al., 2018; Zielinska and Michalska-Ciechanowska, 2016*, Convective Drying Followed by Vacuum Microwave Drying - *Figiel, 2010b; Kwasnica et al., 2020; Nowicka et al., 2015; Szychowski et al., 2018*, Intermittent Drying of Food Products Assisted by Temperature, Pressure, Humidity, Convection, Radiation, and Microwave – *Kumar et al., 2014; Pham et al. al., 2017a, Pham et al., 2018b*, Ultrasound-Assisted Convective Drying - *Santacatalina et al., 2016; Witrowa-Rajchert et al., 2014*, Pulse electric field-Assisted Convective Drying - *Barbosa de Lima et al., 2015; Wiktor et al., 2015* etc.), which have been reported to enhance the quality attributes of dried products, reduce drying time and energy demand, and increase the overall drying efficiency.

Although these emerging methods have the potential to replace, at an industrial and commercial level, in the future, the classic dehydration methods, however, they are very expensive and some of them have demonstrated results only at the research level.

In the context of the deepening of the energy and food crisis worldwide, the use of clean energy in agricultural production processes, the increase of energy independence in relation to the national energy system and the energy efficiency of processing equipment have become major concerns of the stakeholders in the field.

An important direction addressed in research on the preservation of vegetal products by dehydration refers to the use within this process of solar energy or that obtained from other renewable sources (*Murugan and Saji Raveendran, 2021*).

Taking into account the general context related to global warming, as well as the need to reduce energy consumption from fossil fuels, the paper addresses the preliminary experimental research of a small capacity convective dryer, with total energy independence from the electricity grid, intended for small farmers from hill and mountain isolated areas. The use of improved burn technology, such as the TLUD gasification process, produces thermal energy and biochar which can be used as a basic material for the improvement of degraded soils, and to sequester carbon in the soil over a long period of time, contributing to the reduction of greenhouse gas emissions, to the achievement of an efficient protection of the environment and to the achievement of a sustainable energy development.

MATERIALS AND METHODS

The experimental research was carried out using an experimental model of a convective dryer with total energy independence, fig. 1 – left side, consisting of a hot air generator operating on the TLUD principle (top-lit updraft gasifier) (1), which utilizes locally existing biomass, a high-efficiency air-to-air heat exchanger (2) and a drying chamber with trays (3). The functional diagram of a TLUD energy module (*Maican et al., 2017*) is presented in fig. 1 – right side. The experimental model was developed within a research project carried out in a partnership formed by an SME and two research institutes.

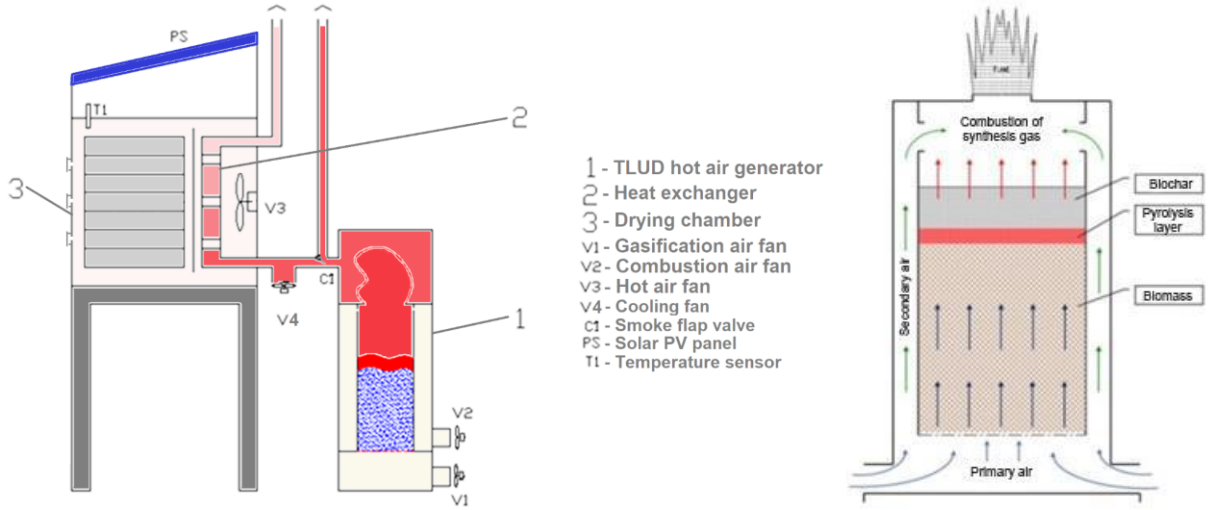

Fig. 1. Experimental model of convective dryer with total energy independence and the TLUD functional diagram

The biomass is introduced into the reactor and rests on a grate through which the primary air for gasification passes, from bottom to top. The process starts with the ignition of the top layer of biomass. Primary air flows upward, through the biomass bed. Partial oxidation of biomass takes place in the presence of oxygen from the primary air. Due to the heat generated by the oxidation process, the biomass in the proximity will decompose through pyrolysis resulting in synthesis gas, tar and coal. The tars pass through the layer of incandescent coal, are cracked and completely reduced due to the heat radiated by the pyrolysis front and the flame in the upper part, the pyrolysis layer progressively moving downward (*Maican et al., 2017*).

Within the experimental model of a convective dryer with total energy independence, the temperature in the drying chamber is monitored by means of a temperature sensor (T1) which influences the manual modification of the smoke flap valve position (C1) and the direction of the flow of hot burnt gases to the heat exchanger (2) from the drying chamber (3) or to the atmosphere through the natural draft tubing, depending on the temperature requirements of the specific drying technology. If the drying temperature is accidentally exceeded or the drying process requires reducing the temperature in the drying chamber, then it is manually operated the smoke flap valve (C1) in order to block the route to the heat exchanger and the cooling fan (V4) will be operated in order to introduce cold atmospheric air into exchanger, cooling it. The electrical energy required for the operation of the equipment is provided by a pack of solar batteries charged from the photovoltaic panel (PS). In the experimental model version of the dryer, the actuation of the execution elements is done manually in order to be able to independently control the operation of each one and observe their influence on the drying process. Also, the heat exchanger was executed in two versions: with location inside

the drying chamber and outside it. In order to be able to efficiently monitor the temperature of the thermal agent at the exit from the heat exchanger, the heat exchanger variant located outside the drying chamber was used, and to monitor the temperature variation in the drying chamber, the heat exchanger variant located inside the drying chamber was used.

The preliminary testing of the experimental model of convective dryer with total energy independence was carried out using a data acquisition system equipped with sensors and automatic systems. The diagram of the experimental data acquisition system is presented in figure 2.

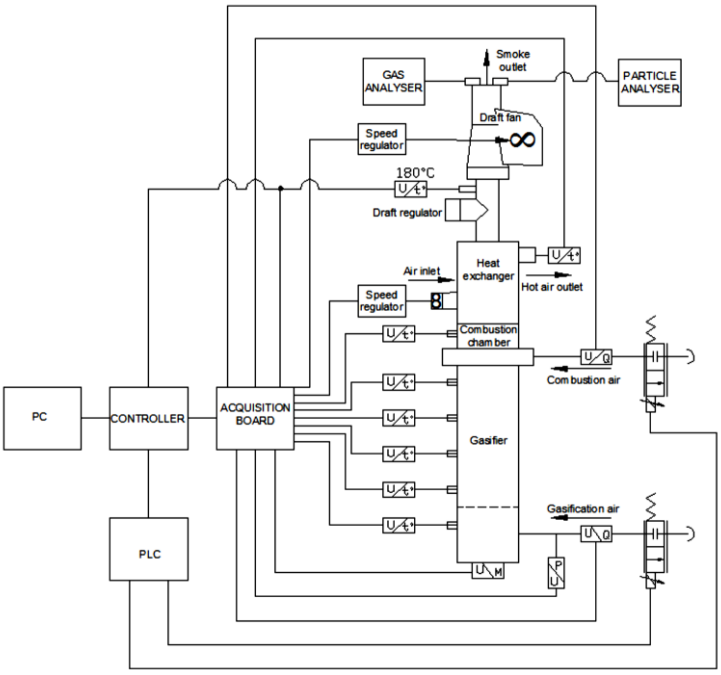

Fig. 2. Data acquisition system equipped with sensors and automatic systems

In order to test the experimental model of the convective dryer, a virtual instrument type application was created in the LabView environment and also the temperature regulator developed as an IoT device, using the REST architecture to transmit data via the Internet to other terminals.

For the experimental data collection there are used 8 temperature transducers, 2 air flow transducers, a weighing dose (load cell), a pressure transducer and gas and particle analyzers. The application panel, fig. 3, contains the sketch of the TLUD hot air generator with numerical indicators for viewing the parameters during operation. On the panel there are also thermometer-type indicators, graphical display blocks of parameter variation and a cursor-type button for adjusting the air flow with the help of a proportional valve.

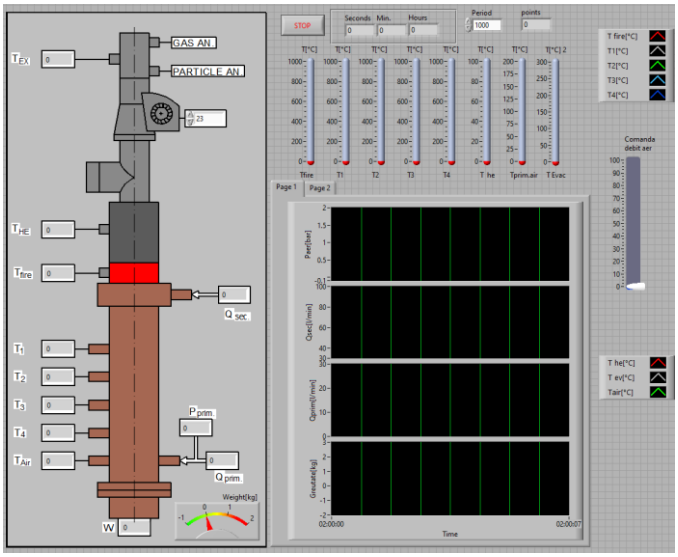

Fig. 3. The panel of the virtual instrument type application made within the LabView environment for the preliminary testing of the experimental model of the convective dryer

The meaning of the numerical indicators on the TLUD installation diagram is as follows:

-T_1, T_2, T_3, T_4 - the temperature values indicated by the temperature sensors of the installation, positioned equidistantly on the height of the gasification reactor, between the primary and secondary air intake points, °C;

- T_{air} - primary air temperature (gasification), [°C];
- p_{prim} - primary air pressure, [bar];
- Q_{prim} - primary air flow, [l/min];
- Q_{sec} - secondary air flow rate (combustion of syngas), [l/min];
- T_{fire} - flame temperature, at the level of the combustion chamber, [°C];
- T_{HE}- temperature at the exit from the air-air heat exchanger, [°C];
- T_{EX} - the temperature of the flue gas-smoke mixture on the chimney, [°C];
- PARTICLE AN - plug for the particle analyzer;
- GAS AN - plug for the gas analyzer;
- W - the load cell, which indicates the loss of mass through the gasification process over time, during the operating cycle (compared to time T_0 - start of the gasification process).

Within the experimentation, the temperature control on the chimney was achieved through the loop created with the temperature regulator developed as an IoT device, using the REST architecture for transmitting data via the Internet to other terminals. Fig. 4 shows the block diagram of the regulator. The value of the temperature of the chimney exhaust gases is measured using a thermoresistance type temperature transducer with a current output signal of 4...20 mA, two-wire connection and the measuring range 0...200 °C. The temperature of the combustion gases is controlled by the flow of air introduced into the combustion chamber, flow varied by means of a proportional valve having the role of an air intake valve. The gasification air flow, which also controls the temperature on the chimney, is proportional to the control signal of the air inlet valve, unified current signal 4...20 mA. The temperature regulator function is provided by the temperature controller that uses a proportional-integral-derivative regulation law (PID controller). The temperature controller integrates an RS485 serial data communication line, which allows the monitoring and control of process variables, namely the desired temperature, the flue gas temperature and the control of the air inlet valve. The communication protocol implemented on the serial line is MODBUS-RTU.

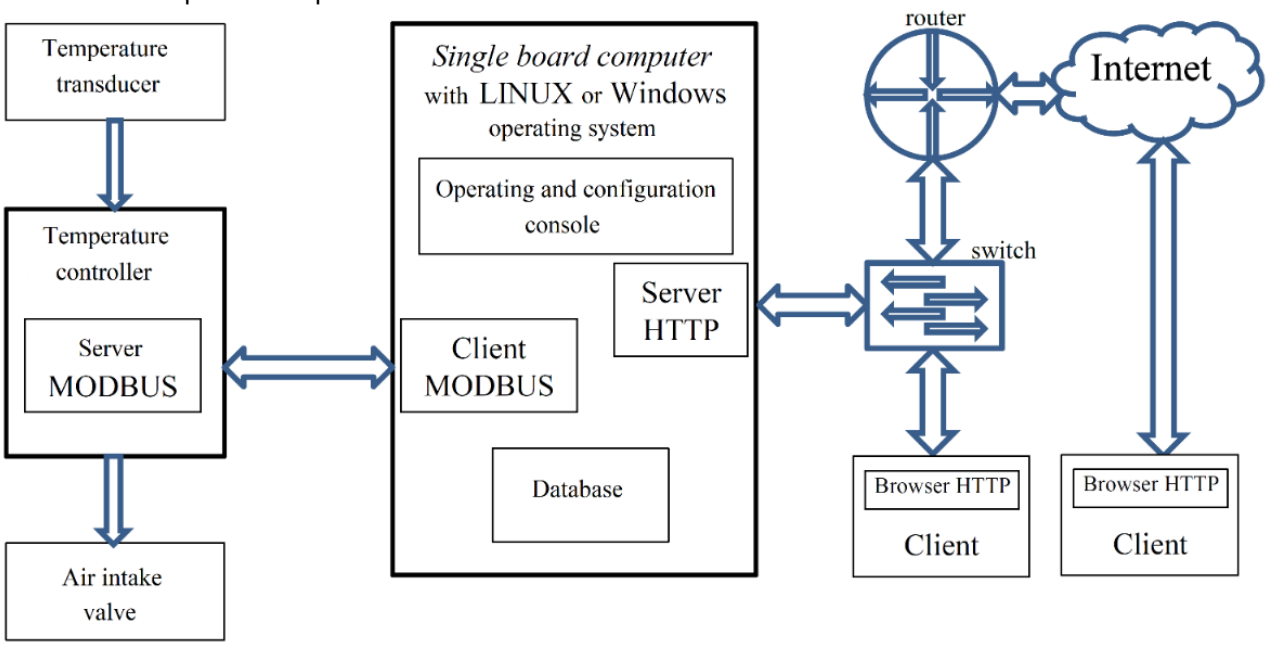

Fig. 4. Block diagram of the temperature controller developed as an IoT device, using the REST architecture

The preliminary experimentation of the equipment aimed to determine some technical-functional parameters important within the working process, such as:

- biomass loading capacity of the gasification reactor;
- the ability to regulate the flow of air necessary for the development of thermo-chemical processes;
- the temperature of the burnt gases as well as the temperature in various key points inside the equipment.

RESULTS

Following the processing and interpretation of the experimental results, a series of useful information was obtained for the estimation of the inputs necessary for a normal operation of the equipment.

The duration of operation is measured from the initiation of the combustion process until the completion of the combustion. The entire period includes an initiation phase (10-15 min), a phase of operation in stabilized gasification mode (60-90 min, depending on the size of the gasifier and the amount of biomass introduced) and a phase of total combustion of the biochar (10-25 min). In the end, a small amount of ash will be obtained. It is obvious that the combustion process continues even after the completion of the gasification, by burning the biochar, but it must be monitorized very carefully so that the process is not accompanied by emissions of smoke or unburned gases. When the pyrolytic front has moved to the base of the reactor, and the thickness of the biochar layer has decreased under the conditions of maintaining the gasification air flow, the combustion process accelerates and the time is shortened. Even after reducing the combustion process, the generator will provide warm air, due to thermal inertia. Completion of the biomass gasification process and the beginning of biochar combustion (gasification) is also determined by the change in the color of the flame, which becomes bluish when the biochar burns. The further burning of biochar is a purely economic choice of the user. The amount of biochar is, under normal conditions, between 15 and 25 percent of the biomass used, depending on the type of biomass. Experiments have shown that by stopping the gasification process when the biochar starts burning, the amount left on the sieve is approx. 2 kg, representing a percentage of 18% of the mass of the pellets introduced into the solid fuel basket of the reactor.

The operating period in stabilized mode of the reactor, when using spruce pellets as solid fuel, until the completion of the biomass gasification process and the start of combustion (gasification) of the biochar was 96 min and the operating period in stabilized mode of the reactor until the complete combustion of the biochar was 108 min.

Regarding the ***verification of the biomass loading capacity***, it was determined theoretically, by calculation, depending on the useful geometric volume of the reactor and the density of the biomass. Taking into account the geometric characteristics of the fuel basket, respectively the position of the sieve and the holes for burning the syngas, the volume of biomass loaded into the gasification reactor, determined by calculation, was 16.73 dm^3, the equivalent of 11.04 kg pellets, respectively 7.20 kg biomass chopped wood (the specific weight of pellets is 0.66 kg/dm^3, and of chopped biomass with dimensions 30...50 mm and 18 % humidity is 0.43 kg/dm^3).

To ensure the good functioning of the generator, it is necessary for the equipment to enter a stabilized gasification regime as quickly as possible. This period lasts from the ignition of the flame at the level of the oxidizing material in the reactor to its passage to the burner, where the combustion of the syngas takes place through the turbulent mixing with the secondary air flow that brings in oxygen for complete combustion. The period until entering the stabilized regime is also influenced by the type and amount of fuel used for ignition. The period between the ignition of the biomass and the entry of the reactor into the stabilized gasification regime was approximately 10...15 min.

For the efficient management of the gasification process, the ***air flows necessary for the proper development of the thermo-chemical processes*** must be ensured. In a TLUD type gasifier, part of the air is used in the biomass gasification process and part in the combustion process of the synthesis gas obtained. In both situations, the amount of air has an essential role because the combustion of the resulting gas can only be achieved in the presence of combustion air. It is very important that the gasification air is well separated (isolated) from the combustion air.

The volume of oxygen required for complete combustion of one fuel unit (minimum oxygen required for combustion) is O_{min}:

$$O_{min} = 22.414 \cdot \left(\frac{c}{12} + \frac{h}{4} + \frac{s}{32} - \frac{o}{32}\right), \left[\frac{m_N^3\, O_2}{kg_{fuel}}\right] \quad (1)$$

where ”c”, ”h”, ”s” and ”o” are the mass shares of the main combustible chemical elements specific to the type of biomass used, [kg component / kg fuel].

For spruce, the percentage content of chemical components is as follows: C=49.9%, H=8.2%, S=0.03% si O=38.1%, and their mass participation for 1 kg of solid fuel is: c=0.499 kg C, h=0.082 kg H, s=0.0003 kg S si o=0.381 kg O. Substituting in relation (1), the following is obtained:

$$O_{min} = 22.414 \cdot \left(\frac{0.499}{12} + \frac{0.082}{4} + \frac{0.0003}{32} - \frac{0.381}{32}\right) = 1.1207, \left[\frac{m_N^3\, O_2}{kg_{fuel}}\right] \quad (2)$$

Considering that the minimum oxygen required for combustion is procured from the air that is wet, containing an amount of moisture x [kg water vapor / kg air] and as the volume participation of oxygen within the air is 21 %, it can be calculated the minimum volume of air required for combustion. It was considered that the air has a temperature of 25 °C and a relative humidity of 45 % and the moisture content is 0.009 kg water vapor / kg air. In this situation, the minimum volume of air required for burning 1 kg of fuel is L_{min}:

$$L_{min} = \frac{O_{min}}{0.21} \cdot (1 + 1.61 \cdot x) = \frac{1.1207}{0.21} \cdot (1 + 1.61 \cdot 0.009) = 5.41, \left[\frac{m_N^3\ air}{kg_{fuel}}\right] \quad (3)$$

where:

L_{min} is the minimum volume of air required for burning 1 kg of fuel, $\left[\frac{m_N^3\ air}{kg_{fuel}}\right]$;

O_{min} – the minimum volume of oxygen required for combustion, $\left[\frac{m_N^3\ O_2}{kg_{fuel}}\right]$;

x - the amount of moisture contained within the air, [kg water vapor / kg air].

The total volume of air for the complete gasification of a load of pellets (11.04 kg, which is the capacity of the fuel basket) is 59.73 m_N^3. Taking into account the time recorded for the gasification of the load (108 min), it results by calculation an air flow rate of 553.06 l/min (138.27 l/min for gasification, respectively 414.79 l/min for syngas combustion).

If it is desired to obtain biochar (18 % of the mass of the load), the volume of air for the gasification of 9.05 kg of biomass is 48.96 m_N^3. The process lasted 96 min, the required air flow being 510 l/min (127.50 l/min for gasification, respectively 382.50 l/min for syngas combustion).

Experimental research in the field of TLUD biomass gasification reactors led to the conclusion that the optimal ratio between primary air (gasification) and secondary air (combustion) is 1:3. Depending on the construction of the gasification reactor and the type of biomass, this ratio can be different and can only be established experimentally, aiming to reach the predetermined power with a clean combustion.

The monitoring of temperatures in various key points, during the preliminary experiments, highlights the thermal inertia of the equipment and provides useful information for choosing the proportionality constants involved in the automatic management of the drying process for the prototype phase of the equipment. The test conditions were the following:

- The solid fuel used into the gasification reactor: spruce pellets with a specific weight of 0.66 kg/dm^3 and humidity 15 %;
- Ambient air temperature: 4...30 °C;
- The initial temperature of the air in the drying chamber: 8.6 °C;
- Pre-set temperature in the drying chamber: 80 °C.

The temperature values obtained at various key points during the experimentation are presented within table 1:

Table 1

Temperatures recorded at various key points of the equipment

No.	Characteristic	UM	Value
1	Flame temperature in the combustion chamber	°C	450-600
2	The maximum temperature in the combustion chamber when establishing a ratio of 1:3 between gasification air and syngas combustion air		576.9
3	The temperature of the burnt gases at the chimney output		80-180
4	Hot air temperature at the exit from the heat exchanger		40-90
5	The temperature in the drying chamber after the total closure of the exchanger flue gas intake circuit		85

Aspects during temperature monitoring in various key points, in the version with a heat exchanger located outside the drying chamber, are presented in figure 5:

Fig. 5. Images during testing in the version with a heat exchanger located outside the drying chamber, using sensors and automatic systems

Figure 6 shows the graphic interface of the virtual instrument type application made in LabView:

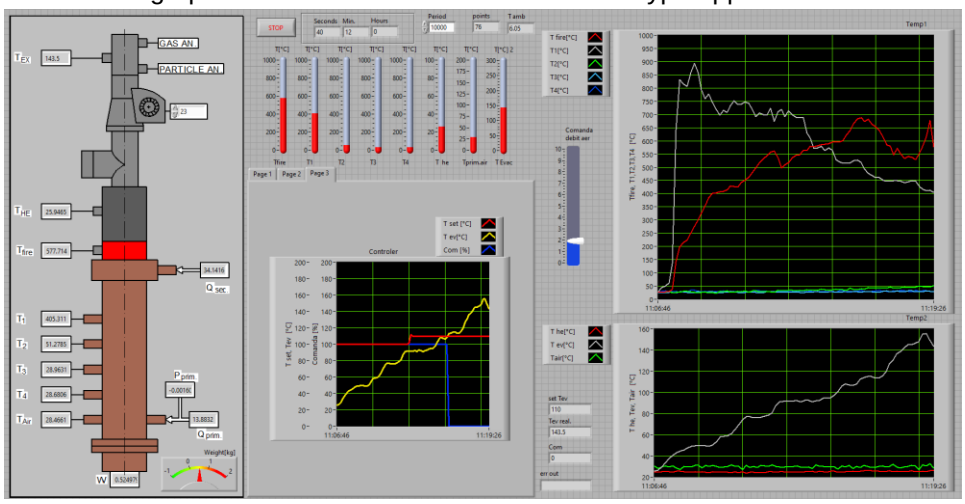

Fig. 6. The panel of the virtual instrument type application made within the LabView environment - during equipment testing

When actuating the valve regulating the flow of thermal agent (burnt gases) through the air-air heat exchanger, the system reacts with a certain delay due to thermal inertia. The periods that have passed since the command was sent and until the target values for the temperature in the drying room are reached, are presented in table 2:

Table 2

The periods of time until reaching some target values for the temperature in the drying chamber

No.	Characteristic	UM	Value
1	The period of time until the temperature in the drying chamber increases within the interval ΔT=80-8.6=71.4 °C	min	15
2	The period of time until the temperature in the drying chamber increases within the interval ΔT=85-80=5 °C		5
3	The period of time until the temperature in the drying chamber returns from the maximum value (85 °C) to the preset value (80 °C)		6

Aspects during the monitoring of the temperature variation in the drying room, in the version with a heat exchanger located inside the room, are presented in figure 7:

Fig. 7. Images from testing in the version with a heat exchanger located inside the drying chamber

CONCLUSIONS

In order to be consumed whole year at a nutritional value close to the freshly picked product, seasonal vegetal products (vegetables, fruits, aromatic and medicinal plants, seeds, berries, mushrooms etc.) are preserved by artificial dehydration.

Unlike other preservation methods and techniques, dehydration leads to obtaining products with a weight 8-10 times reduced and a volume 3-4 times smaller, a fact that contributes to the reduction of the spaces required for storage and the substantial reduction of handling and transport costs, compared to those for fresh vegetal products.

The removal of excess water through the classical dehydration of vegetal products can be done either with the help of solar heat - natural drying, or with the help of artificially produced heat (combustion gases, hot air, heated surfaces etc.) - artificial drying or dehydration.

In recent years, a series of emerging dehydration methods based on non-thermal processes or their combinations with classical processes have gained increased attention, reporting that they enhance the quality attributes of dried products, reduce drying time and energy demand, and increase the overall drying efficiency.

Although these emerging methods have the potential to replace, at an industrial and commercial level, in the future, the classic dehydration methods, however, they are very expensive and some of them have demonstrated results only at the research level.

Taking into account the general context related to global warming, as well as the need to reduce energy consumption from fossil fuels, the paper addresses the preliminary experimental research of a small capacity convective dryer, with total energy independence from the electricity grid, intended for small farmers from hill and mountain isolated areas.

The preliminary tests carried out on the experimental model of the convective dryer demonstrated the functionality of the product, the possibility of adjusting within wide limits the main process parameters, in accordance with the dehydration technologies of different plant species, as well as the possibility of automatic management of the working process for the prototype phase of equipment. Also, the thermal power of the gasification reactor can be adjusted around the optimal operating point which stabilizes when the ratio between primary air (gasification) and secondary air (combustion) is 1:3.

ACKNOWLEDGEMENT

This work was supported by a grant of the Romanian Ministry of Research, Innovation and Digitization, project code PN-III-P2-2.1-PTE-2021-0306, contract no. 87PTE/21.06.2022 and through the NUCLEU Programme, Contract no. 9N/01.01.2023, Project code PN 23 04 02 04.

REFERENCES

[1] Babu A., Kumaresan G., Raj V.A.A., Velraj R., (2018), Review of leaf drying: mechanism and influencing parameters, drying methods, nutrient preservation, and mathematical models*, Renew. Sustain. Energy Rev.,* 90, 536–556;

[2] Barbosa de Lima A. G., da Silva J. V., Pereira E. M. A., dos Santos I. B., Barbosa de Lima W. M. P., (2015), Drying of bioproducts: quality and energy aspects*, Drying and Energy Technologies*, pp. 1– 18, Switzerland: Springer International Publishing, http://doi.org/10.1007/978-3-319- 19767-8;

[3] Boudhrioua N., Bahloul N., Ben Slimen I., Kechaou N., (2009), Comparison on the total phenol contents and the color of fresh and infrared dried olive leaves*, Ind. Crop. Prod.,* 29, pp. 412–419;

[4] Calín-Sánchez Á., Figiel A., Hernández F., Melgarejo P., Lech K., Carbonell-Barrachina Á., (2012), Chemical composition, antioxidant capacity, and sensory quality of pomegranate (Punica granatum L.) arils and rind as affected by drying method*, Food Bioprocess Technol.,* 6, 1644–1654;

[5] Calín-Sánchez Á., Lipan L., Cano-Lamadrid M., Kharaghani A., Masztalerz K., Carbonell-Barrachina Á., Figiel A., (2020), Comparison of traditional and novel drying techniques and its effect on quality of fruits, vegetables and aromatic herbs, *Foods*, vol. 9, ISSN 2304-815, DOI 10.3390/foods9091261;

[6] Figiel A., (2009), Drying kinetics and quality of vacuum-microwave dehydrated garlic cloves and slices, *J. Food Eng.*, 94, 98–104;

[7] Figiel A., (2010), Drying kinetics and quality of beetroots dehydrated by combination of convective and vacuum-microwave methods, *J. Food Eng.*, 98, 461–470;

[8] Figiel A., Michalska-Ciechanowska A., (2016), Overall quality of fruits and vegetables products affected by the drying processes with the assistance of vacuum-microwaves, *Int. J. Mol. Sci.*, 18, 71;

[9] Jambh H.K., Singh R., Kumar K., (2021), Review of industrial drying of fruits and vegetables, *Journal of Food Safety and Food Quality-Archiv Fur Lebensmittelhygiene*, Volume72, Issue3, Page76-88, DOI10.2376/0003-925X-71-XX;
[10] Joardder M.U.H., Karim A., Kumar C., (2013), Effect of temperature distribution on predicting quality of microwave dehydrated food, *J. Mech. Eng. Sci.*, 5, 562–568;
[11] Kamiloglu S., Toydemir G., Boyacioglu D., Beekwilder J., Hall R.D., Capanoglu E., (2016), A review on the effect of drying on antioxidant potential of fruits and vegetables, *Critical Reviews in Food Science and Nutrition*, Volume56, Page: S110-S129, Supplement1, DOI10.1080/10408398.2015.1045969;
[12] Kumar C., Karim M.A., (2017), Microwave-convective drying of food materials: A critical review, *Crit. Rev. Food Sci. Nutr.*, 59, 379–394;
[13] Kumar C., Karim M.A., Joardder M.U.H., (2014), Intermittent drying of food products: A critical review, *J. Food Eng.*, 121, 48–57;
[14] Kwasnica A., Pachura N., Masztalerz K., Figiel A., Zimmer A., Kupczynski R., Wujcikowska K., Carbonell-Barrachina Á., Szumny A., Rózanski H., (2020), Volatile composition and sensory properties as quality attributes of fresh and dried hemp flowers (Cannabis sativa L.), *Foods*, 9, 1118;
[15] Maican E., Duţu I.C., Matache G., Dumitrescu C., Pavel I., (2017), CFD analysis of an improved TLUD based equipment for heating small greenhouses and hothouses, *INMATEH - Agricultural Engineering*, vol. 53, no. 3, 5-12;
[16] Moses J.A., Norton T., Alagusundaram K., Tiwari B., (2014), Novel drying techniques for the food industry, *Food Eng. Rev.*, 6, 43–55;
[17] Murugan P.C., Saji Raveendran P., (2021), Experimental studies on the application of biomass gasifier for drying tapioca in remote areas, *IOP Conf. Ser.: Mater. Sci. Eng.,* 1084 012107, DOI 10.1088/1757-899X/1084/1/012107;
[18] Muscalu A., Vintilă M., Tudora C., Sorica C., Petre A., Pruteanu A., (2022), The use of DIC technology (instant controlled pressure drop) in fruit deshydratation (Utilizarea tehnologiei DIC (detentă instantanee controlată) la deshidratarea fructelor), *Fruit Growing Research*, Vol. XXXVIII, ISSN 2286 - 0304, ISSN-L 2286 – 0304, ONLINE ISSN 2344 – 3723, ISSN-L 2286 – 0304, pp. 215-220, DOI 10.33045/fgr.v38.2022.31, https://publications.icdp.ro/index.php;
[19] Nowicka P., Wojdyło A., Lech K., Figiel A., (2015), Chemical composition, antioxidant capacity, and sensory quality of dried sour cherry fruits pre-dehydrated in fruit concentrates, *Food Bioprocess Technol.*, 8, 2076–2095;
[20] Pham N.D., Khan I.H., Joardder M.U.H., Rahman M.M., Mahiuddin Abesinghe A.N., Karim M.A., (2017), Quality of plant-based food materials and its prediction during intermittent drying, *Crit. Rev. Food Sci. Nutr.*, 59, 1197–1211;
[21] Pham N.D., Martens W., Karim M.A., Joardder M.U.H., (2018), Nutritional quality of heat-sensitive food materials in intermittent microwave convective drying, *Food Nutr. Res.*, 62, 62;
[22] Rahman, M.S., (2020), *Handbook of Food Preservation*, Informa UK Limited: Colchester, UK;
[23] Santacatalina J.V., Contreras M., Simal S., Cárcel J.A., Garcia-Perez J.V., (2016), Impact of applied ultrasonic power on the low temperature drying of apple, *Ultrasonics Sonochemistry*, 28, 100–109, http://doi.org/10.1016/j.ultsonch.2015.06.027;
[24] Szychowski P.J., Lech K., Sendra E., Hernández F., Figiel A., Wojdyło A., Carbonell-Barrachina Á., (2018), Kinetics, biocompounds, antioxidant activity, and sensory attributes of quinces as affected by drying method, *Food Chem.*, 255, 157–164;
[25] Witrowa-Rajchert D., Wiktor A., Sledz M., Nowacka M., (2014), Selected emerging technologies to enhance the drying process: A review, *Drying Technology: An International Journal*, 32(11), 1386–1396, http://doi.org/10.1080/07373937.2014.903412;
[26] Wiktor A., Nowacka M., Sledz M., Rybak K., Lojkowski W., Chudoba T., Witrowa - Rajchert D., (2015), The effect of pulsed electric field (PEF) on drying kinetics, color and microstructure of carrot, *Drying Technology*, 3937, 07373937.2015.1105813, http://doi.org/10.1080/07373937.2015.1105813;
[27] Zielinska D., Michalska-Ciechanowska A., (2016), Microwave-assisted drying of blueberry (Vaccinium corymbosum L.) fruits: Drying kinetics, polyphenols, anthocyanins, antioxidant capacity, colour and texture, *Food Chem.*, 212, 671–680.

OPTIMIZATION AND EXPERIMENT ON MECHANICAL VIBRATION HARVESTING PROCESS PARAMETERS OF MULBERRY

/

桑葚机械振动收获参数优化与试验研究

Junming Hou, Yachen Yu, Ziyuan Tang, Liang Zhang, Jiuyu Jin, Wei Wang
Shenyang Agricultural University, College of Engineering / China;
Tel: +86024-88487663; E-mail: syndhjm@syau.edu.cn
DOI: https://doi.org/10.35633/inmateh-72-49

***Keywords**: Mulberry vibration, modal analysis, harmonic response analysis, triaxial acceleration*

ABSTRACT

The mechanized harvesting of mulberry is important for its production. In the process of harvesting, it is considered not only the mechanical damage of mulberry fruit but also its harvesting efficiency. It is very important to improve the vibration harvesting efficiency of mulberry. In this study, modal analysis of mulberry trees and harmonic response analysis of branches were carried out to determine the harvesting frequency of the branch's vibration and other parameters. The effects of excitation frequency and vibration position on the triaxial acceleration of the mulberry branch at different positions were analyzed by vibration test. Then the triaxial acceleration of branches at different positions was analyzed. The conditions of the mulberry fruit shedding were obtained through theoretical analysis. Through the 20-order modal analysis of mulberry, it is concluded that a better vibration effect can be achieved when the vibration frequency is controlled at 4-16 Hz. According to the harmonic response analysis, the best excitation frequencies are 5-6 Hz, 10-13 Hz, and 14-16 Hz. The harmonic response analysis of fruit branches was carried out, and the stress of fruit stalks at 5 Hz, 10 Hz, and 15 Hz were analyzed. The result shows that the maximum stress is 2.9252×107 Pa, the excitation position is the first-order branch, and the excitation frequency is 15 Hz. The frequencies obtained from modal analysis and harmonious response analysis were used to conduct experiments. When the excitation frequency was 15 Hz, the triaxial accelerations a_X, a_Y, and a_Z were 2.12 g, 4.16 g, and 3.99 g, respectively, which were more conducive to the shedding of mulberry fruits.

摘要

桑树机械化采收是桑树生产的重要环节。在采收过程中，既要考虑桑树果实的机械损伤，又要考虑桑树果实的采收效率。提高桑树振动采收效率具有十分重要的意义。本研究通过对桑树进行模态分析和对树枝进行谐波响应分析，确定树枝振动的收获频率等参数。通过振动试验，分析了激励频率和振动位置对桑树枝条不同位置三轴加速度的影响。然后对不同位置支路的三轴加速度进行分析。通过理论分析，得出了桑树果实脱落的条件。通过对桑树的 20 阶模态分析，得出当振动频率控制在 4-16hz 时，可以获得较好的振动效果。根据谐波响应分析，最佳激励频率为 5-6Hz、10-13Hz 和 14-16Hz。对果枝进行谐波响应分析，对果柄在 5Hz、10Hz 和 15Hz 下的应力进行分析。结果表明:最大应力为 2.9252x107Pa，激励位置为一阶枝干，激励频率为 15Hz。利用模态分析和协调响应分析得到的频率进行试验。当激励频率为 15Hz 时，三轴加速度 a_x 为 2.12g, a_y 为 4.16g, a_z 为 3.99g。更有利于桑树果实的脱落。

INTRODUCTION

Mulberry trees can adapt to various complex and harsh environments, which plays an important role in improving the environment of sandstorm areas. It is known as the most suitable "factory" for sustainable development (*Gulab et al., 2020*). The products of mulberry trees such as mulberry leaves and mulberries are applied in food, pharmaceutical, cosmetics, and various industries. Mulberries are the fruits of mulberry trees, which have rich nutrition and physiological health functions. It is one of the first agricultural products with both food and medicine approved (*Zheng et al., 2016; Xue et al., 2013; Zeng et al., 2019; Xu et al., 2017*). With the planting area of mulberry increased, the mulberry planting area of China reached 796,700 hectares in 2021. The problem of mulberry harvest becomes very important. Therefore, the mechanization of mulberry fresh fruit production becomes very important.

Fruit harvesting is the most critical part of the fruit production process. It is a very seasonal and labor-intensive work. Labor forces account for 30-45% of the fruit production (*Du et al., 2011*). At present, compared with other crops, the mechanization of mulberry fruit harvesting progress is slow. In the process of mulberry harvesting, too low harvest efficiency will cause the large number of fruit to decay, then cause serious economic losses. Therefore, the factors affecting mechanical harvesting efficiency play an important role in the mulberry harvest, which include vibration frequency, amplitude, and excitation position.

Many studies have been done on cherry harvesting, which includes the analysis of energy transfer efficiency with different vibration frequencies. *Liu et al. (2018)* improved the efficiency of mechanical apple harvesting by designing a suitable harvesting mode. They found that a higher harvest rate could be achieved when the change rate of vibration frequency was 8 Hz/s. *Peng et al. (2017)* studied the harvest process of winter jujube by applying the FEM to analyze its dynamic response under vibration excitation at different frequencies. They found out the relationship between acceleration and frequency. *Sergio et al. (2020)* conducted experiments on 22 secondary branches of Valencia orange. They studied the effects of fruit and leaves on the dynamic response of the secondary branches. *Wang et al. (2019)* studied the vibration harvesting efficiency of litchi and concluded that 90% of fruits were defruiting at different speed.

Fu et al. (2019) designed a vibrating screen with adjustable vibration amplitude for harvesting apples. The results show that the vibration amplitude at 30 mm was enough to make fruits fall off and obtain high quality fruits. *Yang et al. (2019)* studied the influence of vibration time, vibration frequency, and vibration excitation point amplitude on apricot tree vibration acceleration and dynamic response in the apricot shedding process. *San et al. (2018)* studied the effect of vibration mode and frequency on the vibration harvesting response of apricot trees. They obtained the acceleration vibration response curves of different positions through vibration transmission from the clamping position.

Ding et al. (2017) studied the dropping characteristics of mulberry fruit, analyzed the main factors affecting the inertia force in the process of vibration harvesting, and obtained the vibration parameters of the vibration harvesting device when the mulberry fell off. *Sun et al. (2023)* proposed a branch stalk fruit of apple as a base system. They investigated the vibration mechanism and separation deformation law of apple tree branches through dynamic tests and simulation.

Alberto et al. (2019) evaluated an innovative system for mulberry fruit harvesting, which increases per capita hourly productivity by three times, but requires at least four workers. *Zhou et al. (2022)* designed a new vibrator for fruit-picking machines with adjustable amplitude. Moreover, the kinematic and dynamic models were set up through theoretical analysis and simulation.

Wang et al. (2023) designed the vibration clamping head of a harvesting machine and conducted vibration shedding tests on mulberry branches at different locations. In conclusion, the research on vibration parameters and dynamic response of various fruit trees is not very perfect, which is difficult to apply to mechanical design and actual production. Moreover, the study on the vibration of mulberry fruit trees is less.

In this study, a mulberry tree model was established to determine the harvesting frequency and other parameters of branch vibration. The effects of excitation frequency and vibration position on the triaxial acceleration of the mulberry tree branch at different positions were analyzed by experiment. Through the comparison of different locations, excitation frequencies, and monitoring points, the influence on mulberry branch acceleration was obtained. Then the influence on mulberry harvest efficiency was analyzed.

MATERIALS AND METHODS

Properties test of mulberry branch

The properties of mulberry branches, including their density and elastic modulus, are the necessary parameters for simulation. Therefore, the bending method was applied to measure the elastic modulus of mulberry branches. The drainage method was applied to measure the density of mulberry branches, which provided the basis for the material properties of the mulberry model. The bending elastic modulus of the mulberry branch was measured based on the three-point bending method. Five periods of mulberry branches were selected. The TMS-Pro professional food property machine was applied for the three-point bending test. The distance between two points is set at 80 mm. To measure the displacement situation of middle position, two different displacement points of each branch were chosen. Then the bending elastic modulus of the mulberry branches was calculated. The determination of bending elastic modulus is shown in Fig. 1.

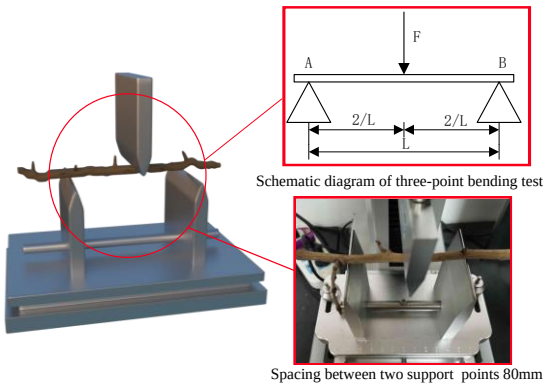

Fig. 1 – Measurement of bending elastic modulus of mulberry branches

The equation for calculating the bending elastic modulus of mulberry branches is shown in Eqs. (1), (2) and (3) (*Feng et al., 2020*).

$$W = \frac{FL^3}{48EI} \tag{1}$$

where: W is the deformation of the mulberry branch, mm; F is the external force applied, N; L is the distance between two support points, mm; E is the bending elastic modulus of mulberry branch MPa; I is the moment of inertia of mulberry branch section, mm^4.

$$I = \frac{\pi d^4}{64} \tag{2}$$

where: d is the cross-section diameter of the mulberry branch, mm.

$$E = \frac{4FL^3}{3W\pi d^4} \tag{3}$$

The three-point bending test was carried out on five different diameters of mulberry branches. Two different dislocations were selected for each branch to measure the elastic modulus. The result is shown in Table 1. It can be drawn that the average bending elastic modulus of mulberry branches is 1981.40 MPa. The maximum flexural elastic modulus is 2189.19 MPa, and the minimum flexural elastic modulus is 1575.87 MPa. The mulberry branches were divided into five sections, then their density values were measured respectively. The average value was taken as the final result of the experiment. Then the branches were put into a measuring cup with a certain scale to calculate the density value of the mulberry tree. The average density of mulberry branches was 804.38 kg/m^3. The test results are shown in Table 2.

Table 1

Bending elastic modulus of mulberry branches

Number	Diameter [mm]	Displacement 1: flexural modulus of elasticity [MPa]	Displacement 2: flexural modulus of elasticity [MPa]	Average value [MPa]
1	3.75	2117.48	2086.03	2101.76
2	3.59	2000.35	1993.29	1996.82
3	4.9	2091.73	2031.88	2061.80
4	4.83	2118.28	2189.19	2153.73
5	6.52	1609.95	1575.87	1592.91
Average value				1981.40

Table 2

Determination of fresh mulberry fruit density

Number	1	2	3	4	5	Mean value
Mulberry fruit density [kg/m^3]	870.00	596.25	958.72	869.44	727.50	804.38

Fruit separation conditions test

Connecting force between the stalk and fruit

The connection of the fruit with the stalk was measured by the TMS-PRO food physical property analyzer. Shensang's No. 1 mulberry variety was selected as the test material. Firstly, the pulp of mulberry fruit was removed, and the branches connected with the stalk and the fruit were respectively fixed on the base and held on the upper clamp head. Then the stalk was stretched. The connecting relay was measured at the stalk and branch. The connection of the fruit stalk is shown in Fig.2.

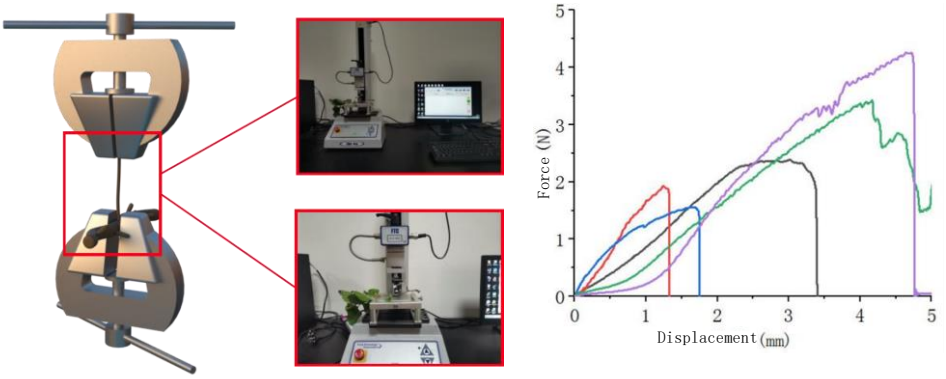

Measurement of the connecting force of fruit stalk Force displacement curve

Fig. 2 – Determination of connection of fruit stalk

The fruits were selected for the test, and then the results for the stem connection of mature fruits were obtained, as shown in Table 3. The maximum stem connection of mature fruits is 1.529 N, and the average stem connection of mature fruits is 1.238 N. The immature fruits were selected for the determination of stem connection, as shown in Table 4. The maximum stem connection of immature fruits is 4.715 N, and the average of immature fruits is 3.677 N.

Table 3

Connecting force of fruit stalk of mature fruit

Number	1	2	3	4	5	6	7	8	9	10	Mean value
Fruit stalk connecting force [N]	1.529	1.386	0.925	1.541	1.766	1.030	1.207	1.086	0.965	0.943	1.238

Table 4

Connecting force of immature fruit stalk

Number	1	2	3	4	5	6	7	8	9	10	Mean value
Fruit stalk connecting force [N]	3.407	4.241	4.715	4.256	3.872	4.098	2.875	3.375	2.180	3.749	3.677

Principle of fruit shedding

The stalk connection of mulberry fruits at different growth stages is significantly different. The stalk connection decreases gradually with fruit ripening. The excitation force is applied to the branches of the mulberry tree through the excitation device. The excitation force will be transferred to the mulberry fruit through the branches in the process of vibration. The acceleration generated by the mulberry fruit and the fruit's gravity has an inertial effect, so it will lead to the falling off of the mulberry fruit (*San et al., 2018*).

The spatial stress analysis of mulberry fruits was carried out to analyze the shedding conditions of mulberry fruits. Fig. 3 shows the stress analysis diagram of mulberry fruits. When the combined force of the inertia force along the stem direction (F_n) and the component force of the gravity of the mulberry fruit along the stem direction (F_g) is greater than that of the mature fruit (F_L), mature mulberry fruit falls off. Similarly, F_n and F_g less than immature mulberry fruit peduncle relay (F_W), immature mulberry fruit does not fall off.

$$F_W \geq F_n + F_g \geq F_L \quad (4)$$

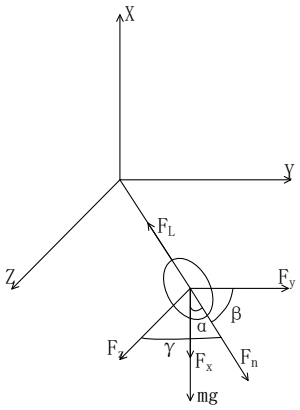

Fig. 3 – Stress analysis of mulberry

where: F_x is the inertia force of Mulberry fruit along the X axis, N; F_y is the inertia force of mulberry fruit along the Y-axis direction, N; F_z is the inertia force of mulberry fruit along the Z axis, N; F_n is the inertia force of mulberry fruit along the X-axis direction, N; F_g is the force of the gravity of mulberry fruit along the stem direction; F_L is the stalk connecting relay of mature mulberry fruit; F_W is connected to the stalk of mature fruit.

The inertia force generated by the acceleration in the X, Y, and Z directions of mulberry fruit caused by vibration is F_x, F_y, and F_z; the acceleration in the three directions is a_X, a_Y, and a_Z respectively; the combined force of the three directions along the stalk direction is F_n.

$$\begin{aligned} F_X &= ma_X \\ F_Y &= ma_Y \\ F_Z &= ma_Z \end{aligned} \quad (5)$$

$$F_n = F_X \cos\alpha + F_Y \cos\beta + F_Z\gamma \quad (6)$$

where: α is the included angle between the fruit stalk and X-axis; β is the angle between the fruit stalk and Y-axis; γ is the angle between the stalk and Z-axis.

In the vibration harvesting process of mulberry fruit, fruit shedding depends mainly on the inertia force F_n along the stem direction, and the component force of fruit gravity along the stem direction can be ignored. Therefore, the shedding of mature fruits and the non-shedding of immature fruits must ensure that F_n is greater than F_L and less than F_W.

$$F_L \leq ma_X \cos\alpha + ma_Y \cos\beta + ma_Z \cos\gamma \leq F_W \quad (7)$$

Simulation setup procedure

It is established as a three-dimensional model of mulberry according to the measured diameter of mulberry branches. The diameter of the trunk is 80±3 mm, the diameter of the first branch is 45±2 mm, and the diameter of the second branch is 30±2 mm. The selection of mulberry plants is shown in Fig. 4(a). The trunk, primary, and secondary branches of the selected mulberry plants are close to the average diameter measured, and then the height of each branch is appropriate. The material characteristics of mulberry are shown in Table 5. The mulberry model was simplified and established as a secondary branch. The established mulberry tree model is shown in Fig. 4(b).

Table 5

Mulberry parameters

Trunk [mm]	Primary branch [mm]	Secondary branch [mm]	Density [kg/m³]	Flexural modulus of elasticity [MPa]	Poisson's ratio
80±3	45±2	30±2	804.38	1981.40	0.3

The established model was imported into ANSYS 12.0 software for grid division. To ensure calculation accuracy and avoid excessive computation, the grid size was set to 0.01 m, the number of grids was 19629, and the number of nodes was 32901. Constraints were added to the mulberry tree model, and the bottom and ground of the mulberry trunk were regarded as fixed constraints, so fixed constraints were added to the bottom of the trunk.

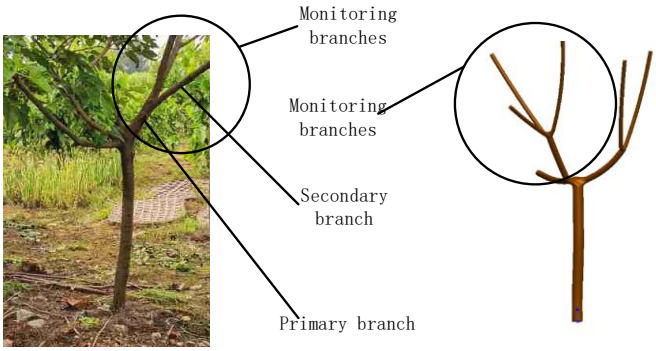

(a) Mulberry material object *(b) Mulberry model*

Fig. 4 – Mulberry model and real object

Vibration test of mulberry branches

The mulberry plant of Shenyang No. 1 was selected as experimental material. The main trunk, primary branch (the primary branch is the branch branching upward from the main trunk), and the secondary branch (the second branch is the branch branching from the primary branch) were analyzed respectively.

The instruments and equipment include that TCH adjustable electric reciprocating saw modified vibrator with adjustable frequency, maximum reciprocating frequency is 46.7 Hz, reciprocating stroke is 15 mm, saw blade chuck is applied as vibration head, which is fixed to vibrate fruit trees. The six-axis acceleration sensor can measure the acceleration in X, Y, and Z directions, which is shown in Fig. 5. The vibration frequency, location of the excitation point, and different positions of the three branches were selected as test factors. The branch acceleration in X, Y, and Z directions was selected as test indexes. According to the results, the excitation frequencies of 5, 10, and 15 Hz were selected. The starting end of the first-order branch and the beginning end of the second-order branch were selected as the locations of excitation points. The location of excitation points is shown in Fig. 6. The sensors were placed on the secondary branch, which is shown in Fig. 7. The X-axis is perpendicular to the ground direction upward, the Y-axis is parallel to the ground directly to the direction of branch growth, and the Z-axis is perpendicular to the branch direction. The experimental design is shown in Table 6.

(a) Acceleration sensor *(b) Sensor installation method*

Fig. 5 – BWT61CL six-axis Bluetooth acceleration sensor

(a)Beginning of primary branch *(b) beginning of secondary branch*

Fig. 6 – Location of excitation point

(a)Sensor leveling *(b) sensor layout*

Fig. 7 – Placement mode of the acceleration sensor

Table 6

Experimental design

A: Excitation position	B:(monitoring position) from the starting point of secondary branch[mm]	C: Excitation frequency [Hz]
Primary branch	200, 400, 600	5, 10, 15
Secondary branch	200, 400, 600	5, 10, 15

RESULTS

Modal analysis for vibration

Because the most influential modes are the first several modes, in which the frequency is in the middle and low period, therefore, the first 20 modes of the mulberry model are selected for analysis. The natural frequencies of the 20 modes are obtained. The natural frequencies of mode 20 are shown in Table 7.

Table 7

Natural frequencies of 20th order modes

Order	Natural frequency [Hz]	Order	Natural frequency [Hz]
1	4.1188	11	14.921
2	4.188	12	16.951
3	6.5182	13	20.945
4	7.2701	14	21.603
5	9.7037	15	32.192
6	11.303	16	32.785
7	11.504	17	40.019
8	11.685	18	40.471
9	11.935	19	58.876
10	12.19	20	62.999

From the 14th order, the natural frequency changes significantly. So, the first 14 modal formations were analyzed. The modal response analysis of the mulberry tree is shown in Fig. 8.

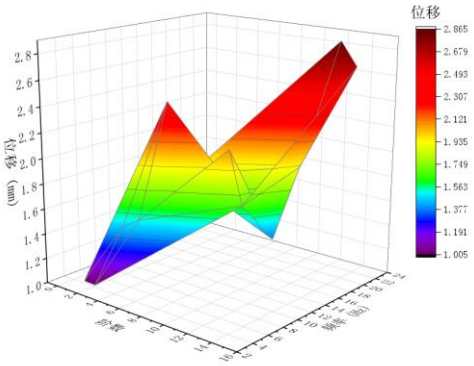

Fig. 8 – Modal response analysis of mulberry

According to the results in Fig. 8, the natural frequency of mulberry at the first order is 4.118 Hz and the deformation is 1.0153 m. The deformation of the mulberry tree was the largest at the 5th, 9th, and 13th steps, which were 2.4277 m, 2.0925 m, and 2.8614 m, respectively. The deformation of mulberry trees at the 6th, 8th, and 12th steps was 1.8555 mm, 1.9471 mm, and 1.9230 mm, respectively. The modal cloud diagram of the mulberry tree is shown in Fig. 9.

With the increase in frequency, the deformation of the tree body increases gradually. According to the typical modal shapes, the trunk and branches wobble slightly in mode 1. The second branch oscillates up and down in the third mode. The first and second branches oscillate up and down in the fifth mode. Most of the secondary branches oscillate from side to side in mode 7. The secondary branch oscillates greatly in mode 9. The main trunk and the first and second branches of the tree oscillate from side to side in mode 11. So, the vibration harvesting frequency of mulberry is controlled within the range of 4-16 Hz.

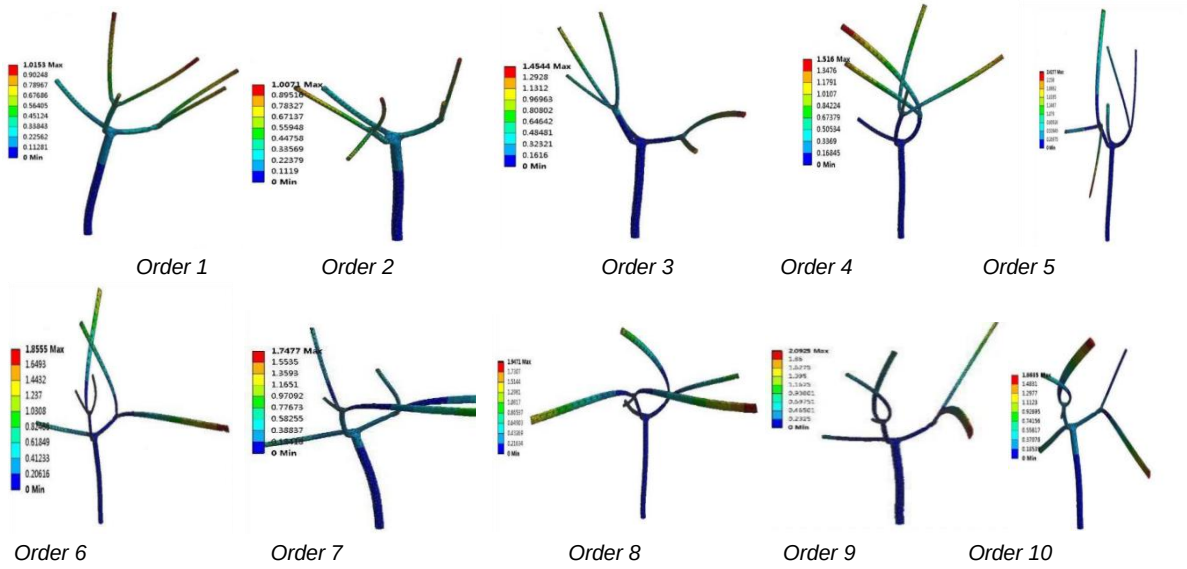

Fig. 9 – Cloud diagram of mulberry modal analysis

Harmonic response analysis

The dynamic response of the mulberry tree under sinusoidal excitation was determined by analyzing the harmonic response of the mulberry tree. If the mulberry fruit is connected to monitoring point 1, the elastic modulus of the fruit stalk can be approximately considered as 80% of the elastic modulus of the branch (Luo et al., 2016). The mulberry branch model is shown in Fig. 10.

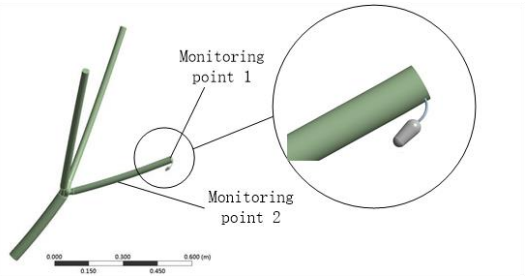

Fig. 10 – Stem model with fruit branch

The excitation point was set at the tail end of the first branch, and the displacement load was set at 15 mm. The frequency range is from 0 to 16 Hz. By analysis, the acceleration curves of the monitoring points can be obtained.

The acceleration curve of monitoring point 1 is shown as Fig. 11. The acceleration curve of monitoring point 2 is shown as Fig. 12.

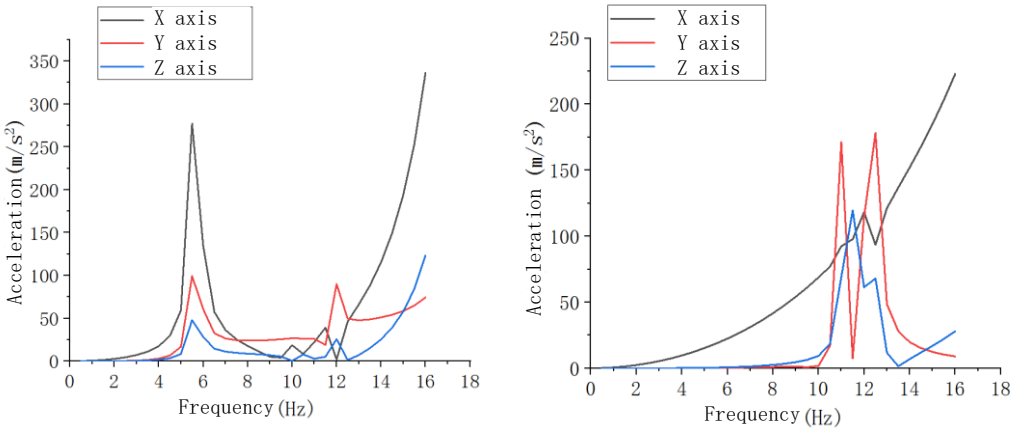

(a)Loading position primary branch start; (b) Loading position secondary branch start

Fig. 11 – Acceleration change curve of monitoring point 1

It is defined that the X-axis direction is consistent with the loading direction, Y-axis is vertical to the ground, and the z-axis direction is vertical to the loading direction and horizontal to the ground. When the test begins at the primary branch, the three-axis acceleration of the monitoring point in the set frequency interval has a typical peak acceleration at 5.5 Hz, the X-axis acceleration has a typical peak acceleration at 10 Hz and 11.5 Hz, and the Y-axis acceleration has a typical peak acceleration at 12 Hz. The Z-axis acceleration has typical velocity peak values at 10.5 Hz and 12 Hz. When the excitation point is the beginning of the secondary branch, the X-axis acceleration has a typical velocity peak at 12 Hz, the Y-axis acceleration has a typical velocity peak at 11 Hz and 12.5 Hz, and the Z-axis acceleration has a typical velocity peak at 11.5 Hz and 12.5 Hz. Moreover, the triaxial acceleration speed increases with the increase of frequency to 16 Hz after the peak.

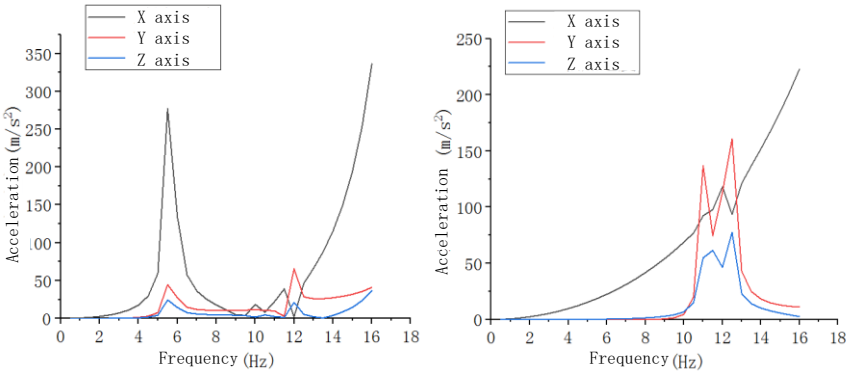

(a)Loading position primary branch start; (b) Loading position secondary branch start

Fig. 12 – Acceleration change curve of monitoring point 2

The acceleration curve of the mulberry fruit is shown in Fig.13. It can be seen from Fig. 13 (a) that when the excitation frequency is 8 Hz, the Y-axis acceleration has a typical peak acceleration. When the excitation frequency is 12 Hz, the z-axis acceleration has a typical peak value. The X-axis acceleration increases as the frequency increases. It can be seen from Figure 13(b) that when the excitation frequency is 6 Hz, the three-axis accelerations all have typical peak accelerations. The triaxial acceleration is at the peak at 12-13 Hz, but it is not obvious. When the vibration frequency is more than 13 Hz, the triaxial acceleration increases with the increase of vibration frequency.

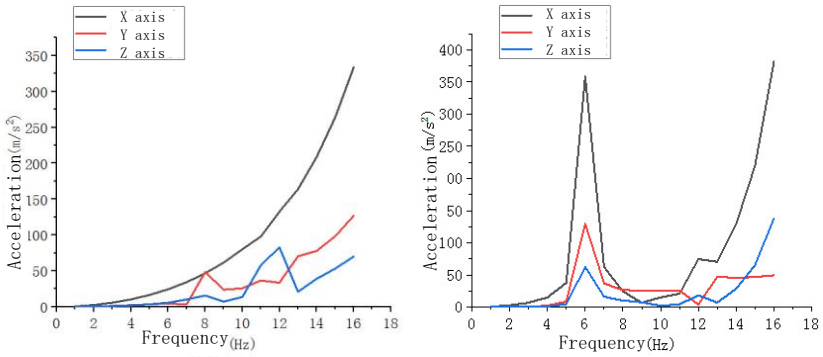

(a)Loading position primary branch start; (b) Loading position secondary branch start

Fig. 13 – Acceleration curve of mulberry fruit

The response analysis shows that the peak point and the high point of acceleration mostly exist in the period of 5-6 Hz, 10-13 Hz, and 14-16 Hz. Therefore, the vibration test adopts 5 Hz, 10 Hz, and 15 Hz to experiment.

The initial end of the primary branch and the secondary branch were stimulated respectively to analyze the stress of the fruit stalk when the excitation frequency was 5 Hz, 10 Hz, and 15 Hz. The stress cloud of the fruit stalk of the excited primary branch is shown in Fig. 14. The stress cloud of the fruit stalk of the excited secondary branch is shown in Fig. 15.

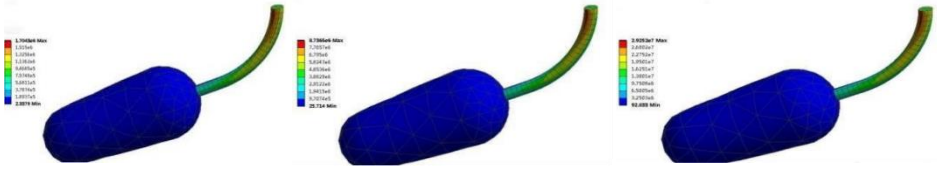

(a) 5Hz (b) 10Hz (c) 15Hz

Fig. 14 – Stress nephogram of fruit stalk of primary branch excited by vibration

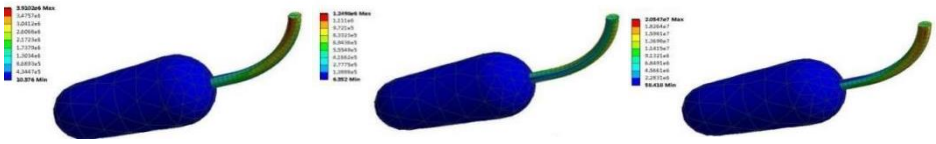

(a) 5Hz (b) 10Hz (c) 15Hz

Fig. 15 – Stress nephogram of secondary branch fruit stalk excited by vibration

The stress concentration area at the fruit stalk is the connection area between the fruit stalk and the branches. When the mulberry fruit falls off with vibration, the connection area between the fruit stalk and the branches is broken. The fruit shedding stress is 394267.52 Pa according to the ratio of cloud pulling force to fruit stalk cross-sectional area. When the excitation frequency is 5, 10, and 15 Hz, the maximum stress is 1.7043×10^6, 8.7365×10^6, and 2.9252×10^7 Pa. When the excitation frequency is 5, 10, and 15 Hz, the maximum stress is 3.9102×10^6, 1.2796×10^6, and 2.0547×10^7 Pa respectively. The result shows that the maximum stress is 2.9252×10^7 Pa. The result shows that when the excitation frequency is 15 Hz, the fruit is easier to fall off and the vibration harvesting efficiency can be improved.

Vibration experiment results and analysis

In the process of vibration harvesting of mulberry fruit, different excitation frequencies and locations have an impact on fruit shedding. Moreover, the triaxial branching acceleration will be different in condition of different excitation frequencies and locations. The triaxial acceleration at different excitation frequencies and different excitation positions was analyzed. The influence of different excitation positions on triaxial acceleration is shown in Fig. 16. The influence of different excitation frequencies on the triaxial acceleration is shown in Fig. 17.

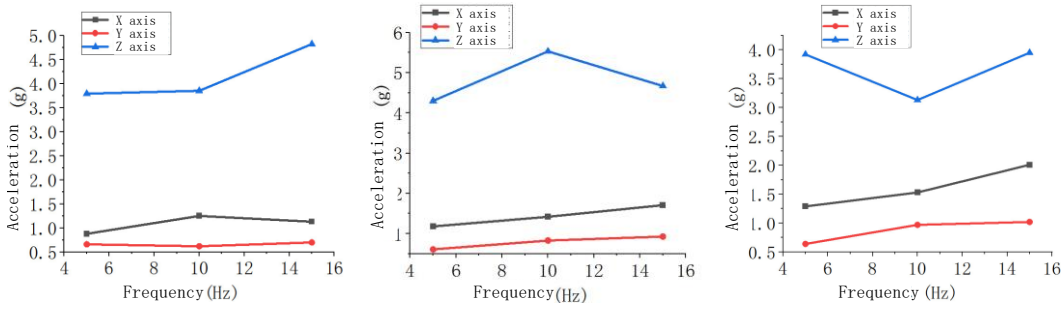

(a) 200mm *(b) 400mm* *(c) 600mm*

Fig. 16 – Triaxial acceleration of exciting primary branch

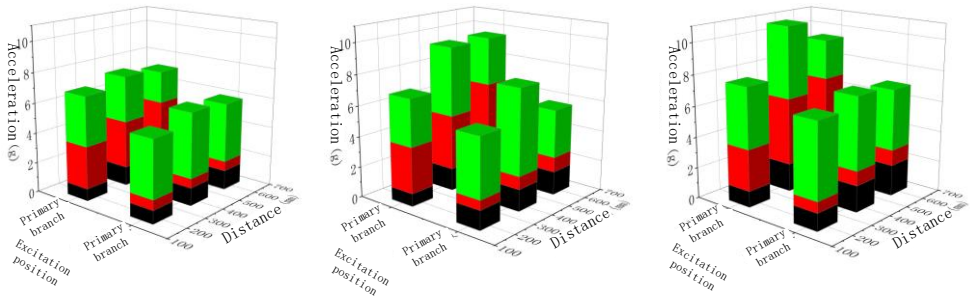

(a) 5Hz *(b) 10Hz* *(c) 15Hz*

Fig. 17 – Shows the triaxial acceleration at different excitation positions

The significance analysis shows that the excitation frequency has a significant effect on the branch acceleration of the X-axis (P<0.01), the branch acceleration of the Y-axis (P=0.0035<0.01), and has no significant effect on the branch acceleration of the Z-axis (P=0.056>0.05). The vibration position had no significant effect on the branch acceleration of the X-axis (P=0.054), had a very significant effect on the branch acceleration of the Y-axis (P<0.01), and had a very significant effect on the branch acceleration of the Z axis (P=0.009<0.01). The monitoring position had a significant influence on the branch acceleration of the X-axis (P<0.01), Y-axis (P<0.01), and Z-axis (P=0.065>0.05).

When the excitation frequency is 15 Hz and the position is 600 mm away from the starting point of the secondary branch, the acceleration on the X-axis is the largest, which is 2.43 g. When the excitation frequency is 15 Hz, the maximum Y-axis acceleration is 4.41 g at the position 600 mm away from the starting point of secondary branching. When the excitation frequency is 10 Hz, the maximum z-axis acceleration is 5.53 g at 400 mm from the starting point of the secondary branch.

A hybrid optimization of three indexes was carried out for three-axis acceleration. Optimization conditions are as follows:

$$\begin{cases} max a_X\ (\mathrm{A},\ \mathrm{B},\ \mathrm{C}) \\ max a_Y\ (\mathrm{A},\ \mathrm{B},\ \mathrm{C}), \mathrm{in}, \\ max a_Z\ (\mathrm{A},\ \mathrm{B},\ \mathrm{C}) \end{cases} \quad \begin{matrix} \mathrm{A}: \ \text{Primary branches, secondary branch} \\ 200 \le \mathrm{B} \le 600 \\ 5 \le \mathrm{C} \le 15 \end{matrix} \tag{8}$$

When the excitation frequency is 15 Hz, the triaxial maximum accelerations a_X, a_Y, and a_Z of the branch are 2.12 g, 4.16 g, and 3.99 g, respectively. Therefore, when the excitation frequency is 15 Hz, it is more conducive to the shedding of mulberry fruits.

CONCLUSIONS

The principle of fruit shedding of mulberry was analyzed. The effects of excitation frequency, vibration position, and detection position on the triaxial branch acceleration of the mulberry branch were studied. The triaxial acceleration of the branch was measured by a six-axis acceleration sensor. By comparing the influence of different excitation positions, vibration frequencies, and detection points on mulberry branch acceleration, the acceleration influence law under different factors in the mulberry mechanized vibration harvesting process was obtained. Through theoretical analysis, it is found that the peak acceleration of the X, Y, and Z axes of mulberry fruit is easier to harvest when the frequency is 5-6 Hz, 10-13 Hz, and 14-16 Hz respectively.

The mean value of stem to trunk connection relay in mature mulberry fruits is 1.238 N, while in immature mulberry fruits it is 3.677 N. Through the modal analysis of mulberry trees, it can be seen that the best vibration effect can be achieved by controlling the vibration frequency within the range of 4-16 Hz. According to the harmonic response analysis, the best excitation frequencies are 5-6 Hz, 10-13 Hz, and 14-16 Hz. The harmonic response analysis of fruit branches was carried out, and the stress of fruit stalks at 5 Hz, 10 Hz, and 15 Hz were analyzed. The maximum stress was 2.9252×10^7 Pa, the excitation position was the first-order branch, the excitation frequency of which was 15 Hz.

When the excitation frequency was 15 Hz, the triaxial accelerations a_X, a_Y, and a_Z of branches were 2.12 g, 4.16 g, and 3.99 g respectively. The position from the starting point of the secondary branches was 488.25 mm. Therefore, when the excitation frequency is 15 Hz, it is more conducive to the shedding of mulberry fruits.

ACKNOWLEDGMENTS

This research was supported by the Educational Commission of Liaoning Province of China (LJKMZ20221002), the authors thank relevant scholars for their assistance in the literature.

REFERENCES

[1] Assirelli, A., Stagno, F., Cocchi, A., Sirri, S., Saviane, A., Giovannini, D., & Cappellozza, S. (2019). Innovative system for mulberry fruit harvesting. *Journal of Berry Research*, 9(4), 615-630. https://doi.org/10.3233/JBR-190411

[2] Castro-Garcia, S., Aragon-Rodriguez, F., Arias-Calderón, R., Sola-Guirado, R. R., & Gil-Ribes, J. A. (2020). The contribution of fruit and leaves to the dynamic response of secondary branches of orange trees. *Biosystems Engineering*, 193, 149-156. https://doi.org/10.1016/j.biosystemseng.2020.02.019

[3] Chen, D., Du, X., & Zhang, Q. (2011). Mechanism of vibratory fruit harvest and review of current advance. *Transactions of the Chinese Society of Agricultural Engineering*, 27(8), 195-200. https://doi.org/10.3969/j.issn.1002-6819.2011.08.033.

[4] Ding, H. X., Li, M. T. & Xue, Z. M. (2017). The test device design and vibration of main low order resonance frequency of picking mulberry. *Journal of Agricultural Mechanization Research*, Vol.39, Issue 08: 159-164. https://doi.org/10.3969/j.issn.1003-188X.2017.08.032.

[5] Fu, H., Duan, J., Karkee, M., He, L., Xia, H., Li, J., & Zhang, Q. (2019). Effect of shaking amplitude and capturing height on mechanical harvesting of fresh market apples. *IFAC-PapersOnLine*, 52(30), 306-311. https://doi.org/10.1016/j.ifacol.2019.12.553

[6] Ghosh, A., Gangopadhyay, D., & Chowdhury, T. (2017). Economical and environmental importance of mulberry: a review. *International Journal of Plant and Environment*, 3(2), 51-58. https://doi.org/10.18811/ijpen.v3i02.10437

[7] He, L., Zhou, J., Du, X., Chen, D., Zhang, Q., & Karkee, M. (2013). Energy efficacy analysis of a mechanical shaker in sweet cherry harvesting. *Biosystems Engineering*, 116(4), 309-315. https://doi.org/10.1016/j.biosystemseng.2013.08.013

[8] Liu, M., Wang, F., Xing, H., Ke, W., & Ma, S. (2018). The experimental study on apple vibration harvester in tall-spindle orchard. *IFAC-PapersOnLine*, 51(17), 152-156. https://doi.org/10.1016/j.ifacol.2018.08.079

[9] Peng, J., Xie, H., Feng, Y., Fu, L., Sun, S., & Cui, Y. (2017). Simulation study of vibratory harvesting of Chinese winter jujube (Zizyphus jujuba Mill. cv. Dongzao). *Computers and Electronics in Agriculture*, 143, 57-65. https://doi.org/10.1016/j.compag.2017.09.036

[10] San, Y. L., Yang, H. M., Wang, X. N., Guo, W. S., & Hou, S. L. (2018). Dynamic response analysis of apricot fruit dropping during vibration harvesting. *Trans. Chin. Soc. Agric. Eng*, 34, 68-75. https://doi.org/10.11975/j.issn.1002-6819.2018.18.009

[11] San, Y. L., Yang, H. M., Wang, X. N., Niu, C. H., & Guo, W. S. (2018). Effects of vibration mode and frequency on vibration harvesting of apricot trees. *Journal of Agricultural Engineering*, 34(8), 10-17. https://doi.org/10.11975/j.issn.1002-6819.2018.08.002

[12] Sun, X., Wu, W., Cao, C., Xu, L., Jiang, R., Fang, L., ... & Lu, X. (2023). Research on vibration response characteristics and separation deformation law of fruit-branch system. AIP *Advances*, 13(6). https://doi.org/10.1063/5.0153355

[13] Torregrosa, A., Albert, F., Aleixos, N., Ortiz, C., & Blasco, J. (2014). Analysis of the detachment of citrus fruits by vibration using artificial vision. *Biosystems Engineering*, 119, 1-12. https://doi.org/10.1016/j.biosystemseng.2013.12.010

[14] Wang, C., Li, C J., Lin, W L., & Lin, J L. (2023). Low frequency resonance clamping and fruit picking: A case study of mulberry picking. *Southern Agricultural Machinery* (23),86-87+128. https://doi.org/10.3969/j.issn.1672-3872.2023.23.021

[15] Wang, W., Lu, H., Zhang, S., & Yang, Z. (2019). Damage caused by multiple impacts of litchi fruits during vibration harvesting. *Computers and Electronics in Agriculture*, 162, 732-738. https://doi.org/10.1016/j.compag.2019.04.037

[16] Xu, Y., Zhang, C., Chen Z. H., & Xu, H. (2017). The development of fruit mulberry researching, processing and utilizations. *Food Research and Development*. 38(16), 209-213. https://doi.org/10.3969/j.issn.1005-6521.2017.16.045

[17] Yang, H. M., San, Y. L., Chen, Y. F., Wang, X. N., Niu, C. H., & Hou, S. L. (2019). Influence of different vibration characteristic parameters on vibration response of apricot trees. *Transactions of the CSAE*, 35(2), 10-16. https://doi.org/10.11975/j.issn.1002-6819.2019.02.002

[18] Zheng, D., Li, H., Lin, X., & Zhang, X. (2016). Application prospect of developing mulberry silkworm on soil desertification area of the northwest of Liaoning province. *Journal of Shenyang Normal University (Natural Science Edition)*, 28(4), 268-271. https://doi.org/10.3969/j.issn.2095-5456.2016.04.004

[19] Zhou, J., He, L., Zhang, Q., & Karkee, M. (2014). Effect of excitation position of a handheld shaker on fruit removal efficiency and damage in mechanical harvesting of sweet cherry. *Biosystems engineering*, 125, 36-44. https://doi.org/10.1016/j.biosystemseng.2014.06.016

[20] Zhou, X., & He, Z. (2022). Analysis and simulation of excitation mechanism of variable amplitude vibration type forest fruit picker. *Mechanical design* (10), 105-113. The doi: 10.13841 / j.carol carroll nki JXSJ. 2022.10.015. https://doi.org/10.13841/j.cnki.jxsj.2022.10.015

DESIGN AND EXPERIMENT OF SWING TYPE SYNCHRONOUS MULCHING FOR RICE DIRECT SEEDER
/
悬摆式同步覆土水稻直播机的设计与试验

Jiajia YU[1,2], Zhongyan TAO[1,2], Liping XIAO[1,2], Jun'an LIU[1,2], Xiongfei CHEN[1,2*], Muhua LIU[1,2], Nan HUANG[1,2], Wei DONG[1,2]
[1] College of Engineering, Jiangxi Agricultural University, Nanchang 330045, China
[2] Key Laboratory of Modern Agricultural Equipment library, Nanchang 330045, China
*Corresponding authors: Xiongfei Chen, Email: 121686212@qq.com
DOI: https://doi.org/10.35633/inmateh-72-50

Keywords: rice, mechanical direct seeding, swing type, mulching coefficient, mulching depth

ABSTRACT
In order to solve the problem of mechanical direct seeding of rice seeds on the exposed soil surface, which is affected by bird and mouse damage, rain and sun exposure, etc., a pendulum-type synchronous soil-covered rice direct seeding machine was developed. In order to clarify the leakage and anti-entanglement performance of the mulching plate, linear function type, quadratic function type and exponential function of the sliding blade mulching plate were designed, and the mulching plate structure, straw distribution spacing and suspension rotation speed were used as independent variables. Using straw entanglement rate and straw interference rate as evaluation indicators, a full-factor experimental study was carried out to determine the optimal structure of the mulching plate; a pendulum-type synchronous soil covering live broadcast EDEM simulation model was established, and field experiments were conducted to verify its synchronous soil covering performance. The test results show that the exponential function of the sliding blade mulching plate has the best performance, and the soil covering rate of the three soil covering plate structures is 87.37~98.54 under the conditions of forward speed 0.6~1.0 m/s and suspension rotation speed 90~150 r/min. %, the covering soil thickness is 5.08~5.84 mm. This research can provide reference for rice mechanical direct seeding technology and equipment.

摘要
水稻机械直播稻种裸露土壤表面，易受周围环境和气候等影响，造成出苗率降低，针对此问题，研制了一种悬摆式同步覆土水稻直播机。为了明确覆土板的漏覆和防缠性能，设计了一次函数型、二次函数型和指数函数型滑刃式覆土板，并以覆土板结构、秸秆分布间距和悬摆转速为自变量，将秸秆缠挂率和秸秆干扰率为评价指标，开展了全因素试验研究，确定最优覆土板结构；为了分析覆土板与土壤之间的相互作用，建立悬摆式同步覆土直播 EDEM 仿真模型，并通过开展田间试验验证其同步覆土性能。试验结果表明：指数函数型滑刃式覆土板性能最佳，且三种覆土板结构在前进速度为 0.6~1.0m/s 和悬摆转速 90~150r/min 条件下，覆土率为 87.37~98.54%，覆土厚度为 5.08~5.84mm。该研究可为水稻机械直播技术与装备设计提供参考。

INTRODUCTION
Rice is an important crop in the world, and mechanical direct seeding technology was a simple and effective cultivation method for saving labor, time and seeds (*Wan et al., 2021; Wang et al., 2020)*. In particular, the advantage of row sowing and hole sowing could improve the yield *(Jang et al., 2021; Sansen et al., 2019; Sugirbay et al., 2020)*, and planting trenches and ditches could promote lodging resistance and population quality of rice (*Shu et al.,2010; Chen et al., 2021*). With the development of rice mechanical seeding technology, the advantages had been accepted by most farmers (*Pitoyo et al., 2021*). *Luoet al. (2007)* firstly developed mechanical direct seeding technology for ditching furrows and building ridges, and designed the direct seeder. Studies had shown that the yield of rice mechanical direct seeding was higher than manual sowing and UAV sowing *(Zhang et al., 2017; Singh et al., 2023)*. The direct seeder was sowing in furrows without mulching. The environment and climate would affect the seedling emergence and uniformity of double-cropping rice at low temperatures (*Hiroei et al., 2021, Yu et al., 2020*). Synchronous mulching technology could improve the emergence rate of basic seedlings and effective spikes in the field by using the rice dry direct seeding technology *(Youichi et al., 2019; Xu et al., 2014; Wang et al., 2016)*.

Liet al. (2020) developed a no-till seeding method of mulching rice stubble with a drill seeder, and *Zeng (2019*) used a precision hole drill of rice furrow fertilization in a dry drill. *Makangeet al. (2020)* and *Mudarisovet al.* (*2022*) predicted the cutting force and soil characteristics through discrete element simulation. They also studied the discrete element modeling of contact model particle parameters in wet soil. In addition, the element model of mulching equipment and ditching soil was established (*Pue et al., 2019; Lu et al., 2023*). Direct seeding fields had a high water content and fluidity, and wet direct seeding was generally adopted in southern China. However, there were few technologies and equipment for synchronous mulching *(Cheng et al., 2021; Zhang et al., 2023)*. To improve the anti-risk ability of rice, a synchronous mulching technology of wet direct seeding was studied. The results showed that different mulching depths and rice varieties had a great influence for seedling emergence, and the depth of seeds mulching with 5~10 mm soil was great (*Yu et al., 2020*). Then the sliding blade structures of mulching plates were introduced to reduce the twisting and interference of rice stubble. Finally, the swing synchronous mulching for rice direct seeder was designed and its performance was verified in the field.

MATERIALS AND METHODS

Swing type synchronous mulching direct seeder

Swing synchronous mulching of rice direct seeder was designed based on the power chassis of high speed seedling transplanter, the precision metering device of rice, the ditching and ridging equipment, the transmission system, and the swing synchronous mulching of equipment. The power of the high-speed seedling transplanter is provided to the measuring device and covering equipment by the transmission shaft, gear head, chain and axle sleeve as shown in Fig.1.

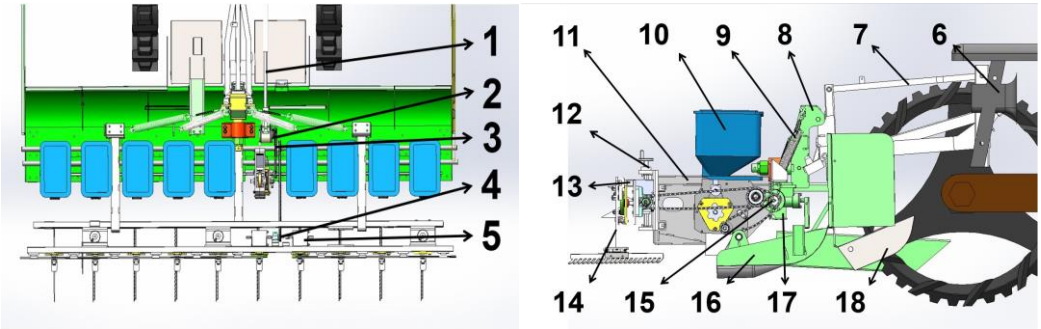

Fig.1 - Structure diagram of the synchronous mulching of rice direct seeder

1 - Transmission shaft; 2 - Gear box; 3 - Double row chain wheel; 4 - Driven sprocket; 5 - Bevel gearbox; 6 - Power chassis of high speed seedling transplanter; 7 - Hydraulic power lift; 8 - Hookup mechanism; 9 -Horizontal profiling mechanism; 10 -Metering device; 11 - Mounting rack; 12 - Slides; 13 - Horizontal mounting rack; 14 - Swing type synchronous mulching equipment; 15 - Transmission system; 16 - Ditching and ridging device 17 - Main horizontal beam; 18 - Profiling mechanism;

The placement of mulching equipment was adjusted to keep 10 mm between the soil surfaces, and the seeder was preceded by ditching and ridging device to open the water furrow and seed furrow. At the same time, the transmission system would support the power to the metering device and the swing synchronous mulching equipment. The mulching plate would break the ridge of the seed furrow to mulch the seeds, and then the direct seeder can sow and mulch at all once.

Build EDEM simulation model

The studies showed the soil diameter was less than 2 mm before seeding in the Poyang Lake region (*Zhu et al., 2020*). To study the interaction between the mulching plate and soil, the discrete element method was introduced to build the simulation model, shown in Fig. 2 (*Peng et al., 2023*). The high moisture of soil model used Hertz-Mindlin simulation model with JKR, and simulation parameters were shown as Table1 *(Zhu et al., 2020; Deng et al., 2022)*. To calculate the soil movement 20-30 mm below the surface in the seed furrow, two soil layers of different colors were established, that is, a 20 mm deep gray surface layer and a 40 mm deep red subsoil layer *(Zhang et al., 2022)*. To promote the accuracy and efficiency of the simulation (*Liu et al., 2021*), the particle size of the topsoil was 2 mm, and the diameter of the subsoil layer was 5 mm. The rice seed diameter was filled with 2 mm particles.

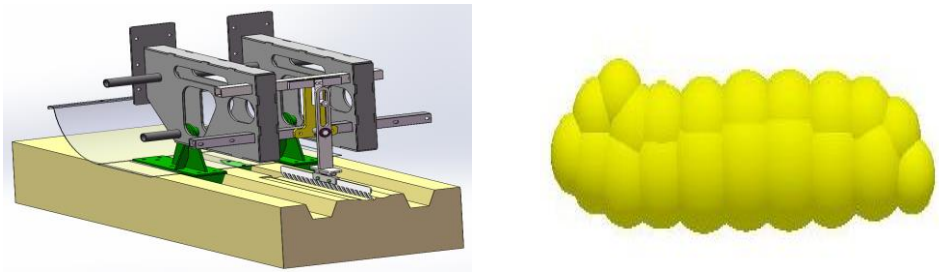

Fig. 2 - Drawings of synchronous mulching equipment and rice seed model in EDEM

Table 1

Parameters of the discrete element simulation model of soil, seed and ABS

Simulation parameters	Values
Density of ABS, g/cm^3	1.661
Poisson ratio of ABS	0.394
Shear modulus of ABS, Pa	8.9×10^8
Bulk density of soil, g/cm^3	1.650
Poisson ratio of soil	0.308
Shear modulus of soil, Pa	1.2×10^5
Bulk density of rice seed, g/cm^3	0.946
Poisson ratio of rice seed	0.3
Shear modulus of rice seed, Pa	1.08×10^8
Coefficient of static friction between soil and soil	0.3
Coefficient of kinetic friction between soil and soil	0.2
Coefficient of restitution between soil and soil	0.3
Surface energy between soil and soil, J/m^2	1.5
Coefficient of static friction between soil and ABS	0.15
Coefficient of kinetic friction between soil and ABS	0.152
Coefficient of restitution between soil and ABS	0.145
Coefficient of static friction between rice seed and rice seed	0.390
Coefficient of kinetic friction between rice seed and rice seed	0.037
Coefficient of restitution between rice seed and rice seed	0.086
Coefficient of static friction between rice seed and ABS	0.592
Coefficient of kinetic friction between rice seed and ABS	0.001
Coefficient of restitution between rice seed and ABS	0.600
Coefficient of static friction between soil and rice seed	1
Coefficient of kinetic friction between soil and rice seed	1
Coefficient of restitution between soil and rice seed	0.001

The number of soil particles in the surface layer and subsoil layer was respectively 3×10^5 and 5×10^5, and the number of rice seeds was 500. The forward speed and rotating speed were set as before. The simulation time was 3 s, and the length of simulation sample was 1000 mm. The mulching coefficient and mulching depth were used as the evaluation index (*Chen et al., 2021*).

The simulation of synchronous mulching is shown in Fig. 3, and the mulching coefficient is calculated as follows:

$$A_1 = \frac{B_1}{C_1} x100\% \quad (1)$$

where A_1 is the mulching coefficient, %; B_1 is the mulching area in the seed furrow, m^2, and C_1 is the total area of the seed furrow, m^2.

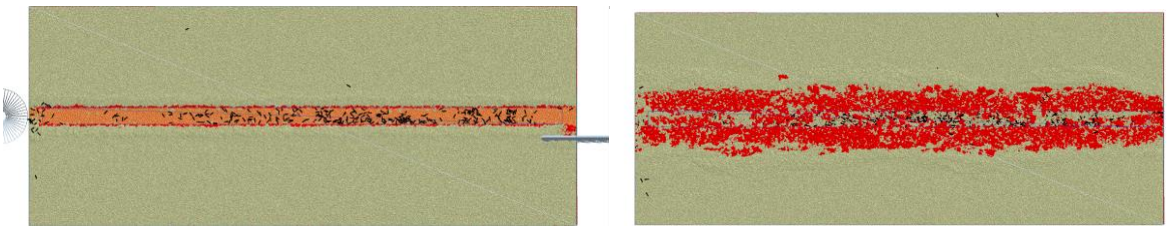

(a) Ditching (b) Mulching

Fig. 3 - Sampling diagram of the mulching coefficient

Full factor experiment of the mulching plate

The mulching plate can directly break the ridge and move the soil to the seed furrow, and the seeds are mulched with soil after the direct seeder works. The field conditions would influence the mulching performance of rice stubble, and three different sliding blade structures of the mulching plate were designed with linear function type *(Zhang et al., 2020)*, quadratic function type and exponential function type, as shown in Fig. 4.

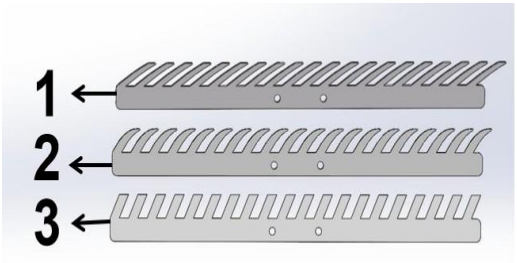

Fig. 4 - Three types of mulching plates

1 - Quadratic function type; 2 - Exponential function type; 3 - Linear function type

To study the performance of mulching plates, rotating speeds and distance of rice stubble were used in a full factor experiment, with a forward speed of 0.8 m/s, and the twisting index and interference of rice stubble were evaluated. The rice stubble is easily twisted by the plate, and the seeds and ridge are also affected by the stubble. Therefore, the twisting index and interference of rice stubble are calculated as Eq. (2) and Eq. (3), as shown in Fig. 5 and Table 2.

(a) 10 cm (b) 30 cm (c) 50 cm

Fig. 5 - Density of rice stubble

Table 2

Full factor experiment

No.	Rotating speed /r·min^{-1}	Mulching plate	Distance of rice stubble/cm
1	70	quadratic function type	10
2	95	exponential function type	30
3	120	linear function type	50

$$D_1=\frac{E_1}{F_1} \quad (2)$$

where:

D_1 is the twisting index, %; E_1 is the twisting number of stubble, and F_1 is the total number of stubble/meter.

$$G_1=\frac{H_1}{M_1} \quad (3)$$

where: G_1 is the interference index of rice stubble, %; H_1 is the interference length/meter, m, and M_1 is the total length of the seed furrow, m.

RESULTS

Effect of the twisting index and interference index of rice stubble

As shown in Fig. 6, when the distance of rice stubble is 10 cm, the rotating speed increases, and the twisting index of the exponential function type mulching plates increases from 0 to 0.98%, and that of linear function type decreases from 32.29% to 3.92%. When the distance increases to 30 cm, the twisting index of the quadratic function type decreases from 2.38% to 0, and that of the linear function type decreases from 23.81% to 4.17%. Once the distance remains at 30 cm, only exponential function type mulching plate has a twisting index, and more rice stubble is left in the field. Therefore, the exponential function type mulching plate has optimal structure for preventing twisting.

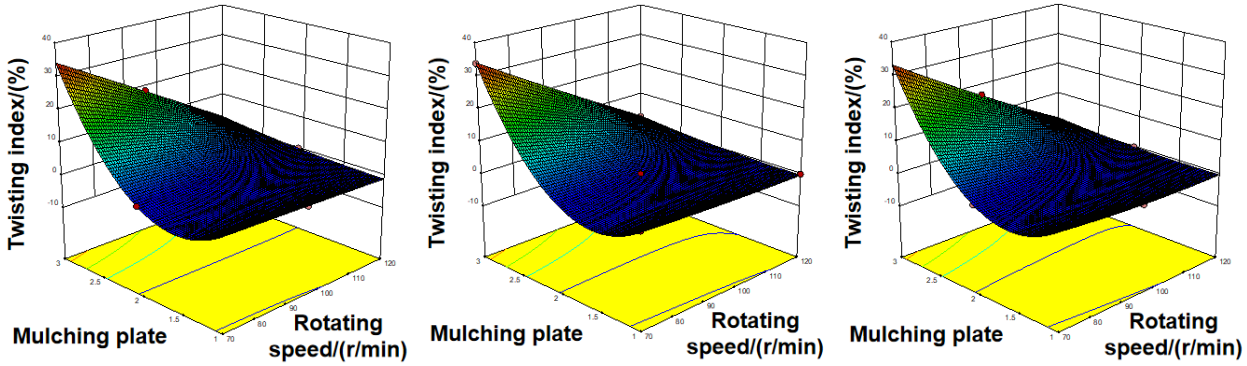

Distance of rice stubble: 10 cm *Distance of rice stubble: 30 cm* *Distance of rice stubble: 50 cm*

Fig. 6- Response surface diagram of the twisting index

The interference index of rice stubble is shown in Fig. 7. When the distance of rice stubble is 10 cm, the lower the rotating speed, the greater the interference index, especially for the exponential function type mulching plate with a rotating speed of 95 r·min^{-1} and 20.84%. When the distance increases to 30 cm, the exponential function type and linear function type respectively decrease to 10.42% and 17.92%, with the rotating speed increasing from 70 to 120 r·min^{-1}. When the distance of rice stubble reaches 50 cm, these three mulching plates decrease, and the minimum value of the exponential function type is 1.43%. It is smaller than 3.12% and 21.84% respectively compared to the quadratic function type and the linear function type. Therefore, the exponential function type mulching plate is an optimal structure for interference.

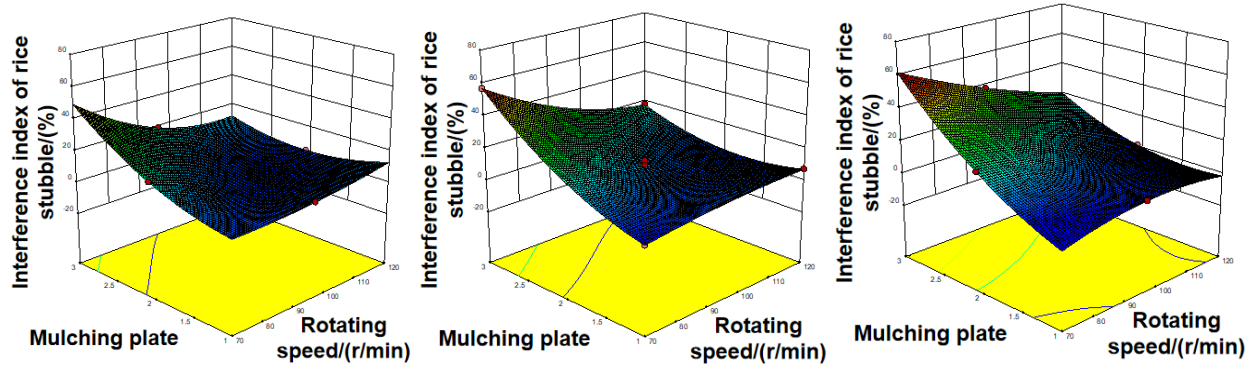

Distance of rice stubble: 10 cm *Distance of rice stubble: 30 cm* *Distance of rice stubble: 50 cm*

Fig. 7- Response surface diagram of the interference index of rice stubble

The results indicate that the optimized structure of mulching plates could reduce the twisting index and interference index of rice stubble. The higher the rotating speed, the lower the twisting index and the interference.

Regression analysis

To find the influence relationship of the swing synchronous mulching direct seeder, the mathematical models of regression analysis in the twisting index and interference index are analyzed, shown as Table 3 and Table 4.

Table 3

Variance analysis of the twisting index regression model

Source of variance	III sum of square	Degree of freedom	Mean square	F	p	Significance
Modify model	1469.63	11	133.6	1419.94	< 0.0001	**
Rotating speed/r·min^{-1}	0	1	0	0	1	
Covering plate	604.82	1	604.82	6428.15	< 0.0001	**
Distance of stubble/cm	0.77	1	0.77	8.14	0.0357	*
Rotating speed*Covering plate	210.98	1	210.98	2242.27	< 0.0001	**
Rotating speed*Distance of stubble	0	1	0	0	1	
Covering plate*Distance of stubble	0.77	1	0.77	8.14	0.0357	*
Rotating speed*Rotating speed	0.52	1	0.52	5.56	0.0649	
Covering plate*Covering plate	363.39	1	363.39	3862.11	< 0.0001	**
Distance of stubble*Distance of stubble	0.52	1	0.52	5.56	0.0649	
Rotating speed*Covering plate*Covering plate	0.38	1	0.38	4.07	0.0997	
Residual	142.89	1	142.89	1518.65	< 0.0001	**
Lack of Fit	0.47	5	0.094			
Pure Error	0.47	1	0.47			
Cor Total	0	4	0			
Cor Total	1470.1	16				

Note: *indicates significance, i.e. (p<0.05); **indicates extreme significance, i.e. (p<0.001).

Table 3 shows that the regression model of the twisting index of mulching plate is significant (p<0.0001), mulching plate structure, the interaction between the rotating speed and the mulching plate structure, the interaction between mulching plate structures have significant influence. The stubble distance, the interaction between the mulching plate structure and stubble distance also has significant influence. In this way, the regression mathematical model Y_1 is established as (3), and the determination coefficient R^2 is 0.99.

$$Y_1 = 87.22 - 128.69B_2 + 0.39C_2 + 1.06A_2B_2 - 0.02B_2C_2 + 41.41B_2^2 + 0.35*10^{-4}A_2^2C_2 \quad (4)$$

where: Y_1 is the twisting index, %; A_2 is rotating speed, r/min^{-1}, B_2 is the structure of mulching plate, and C_2 is the distance of stubble, cm.

Table 4

Variance analysis of the interference index in the regression model of rice stubble

Source of variance	III sum of square	Degree of freedom	Mean square	F	p	Significance
Modify model	3337.42	11	303.4	77.42	< 0.0001	**
Rotating speed/r·min^{-1}	516.65	1	516.65	131.84	< 0.0001	**
Covering plate	604.67	1	604.67	154.3	< 0.0001	**
Distance of stubble/cm	53.14	1	53.14	13.56	0.0143	*
Rotating speed*Covering plate	537.54	1	537.54	137.17	< 0.0001	**
Rotating speed*Distance of stubble	3.53	1	3.53	0.9	0.3859	
Covering plate*Distance of stubble	131.33	1	131.33	33.51	0.0022	*
Rotating speed*Rotating speed	31.2	1	31.2	7.96	0.037	*
Covering plate*Covering plate	300.8	1	300.8	76.76	0.0003	**
Distance of stubble*Distance of stubble	7.91	1	7.91	2.02	0.2148	
Rotating speed*Rotating	42.55	1	42.55	10.86	0.0216	*

Source of variance	Ill sum of square	Degree of freedom	Mean square	F	p	Significance
speed*Covering plate						
Rotating speed*Covering plate*Covering plate	36.47	1	36.47	9.31	0.0284	*
Residual	19.59	5	3.92			
Lack of Fit	0.063	1	0.063	0.013	0.915	not significant
Pure Error	19.53	4	4.88			
Cor Total	3357.02	16				

Note: *indicates significance, i.e. (p<0.05); **indicates extreme significance, i.e. (p<0.001).

Table 4 shows that the interference index of the regression model for rice stubble with mulching plate is significant (p<0.0001). The rotating speed, and the mulching plate structure, the interaction between the rotating speed and the mulching plate structure, the interaction between the mulching plate structures have significant influence. The stubble distance, the interaction between the mulching plate structure and the stubble distance, the interaction between the rotating speeds, the interaction between the square of rotating speed and the structure of mulching plates, the interaction between the rotating speed and the square of rotating speed are significant. Therefore, the regression mathematical model Y_2 is established as (4), and the determination coefficient R^2 is 0.99.

$$Y_2 = -37.10 + 0.69A_2 + 80.55B_2 - 3.09C_2 - 1.87A_2B_2 + 0.29B_2C_2 - 0.16*10^{-3}A_2^2 + 8.45B_2^2 + 0.74*10^{-2}A_2^2C_2 - 0.34*10^{-3}B_2^2C_2 \quad (5)$$

where Y_2 is the interference index, %; A_2 is the rotating speed, r·min^{-1}; B_2 is the structure of mulching plate, and C_2 is the distance of stubble, cm.

The optimal parameters for exponential function type mulching plate are a rotating speed of 120 r·min^{-1} and a disturbance of 50 cm.

Field experiment

To verify the performance of swing synchronous mulching equipment, the field experiment was conducted, and the field soil was operated with rotating tillage. The water moisture of soil was tested with 32% (DH-190 Automatic Halogen Moisture Analyzer, Shanghai Jiashi Electronics Co., Ltd.), and the bulk density of soil was 1.65 g/cm^3 (Nanjing Soil Instrument Factory). The parameters are the same as the simulation model, with 5-6 rice seeds in each hole, and the mulching coefficient and mulching depth are sampled and tested as shown in Fig. 8. The results are shown in Table 5.

Fig. 8 - Field experimental of synchronous mulching

Table 5

Experiment and simulation results

Forward speed/m·s^{-1}	Rotating speed/r·min^{-1}	mulching coefficient/%		Error	mulching depth/mm		Error
		Simulation value	Experiment value		Simulation value	Experiment value	
0.6	90	93.10	87.37	6.15	6.07	5.56	8.40
0.8	120	93.40	98.54	5.50	6.27	5.08	8.98
1.0	150	94.18	91.67	2.67	6.21	5.84	5.96

The rotating speed matched the forward speed of the seeder. When the forward speed was 0.6 m/s, the rotating speed was 90 r·min^{-1}, and when the mulching coefficient was 87.37%, the mulching depth was 5.56 mm.

When the forward speed increased to 0.8 m/s, the mulching coefficient and mulching depth decreased to 98.54% and 5.08 mm respectively; when the forward speed was 1.0 m/s, the mulching coefficient was 91.67%, and the mulching depth was 5.84 mm. The errors between experimental value and simulation value were 2.67- 6.15% and 5.96 -18.98%, respectively. However, the mulching coefficient can reach more than 87.37%, and the simulation values also have significant values. Although there is a significant error in the mulching depth, the value is in the range of 5 -10 mm, which is consistent with previous study.

CONCLUSIONS

(1) To meet the agronomic requirements of rice direct seeding, a swinging synchronous mulching of rice direct seeding machine was designed, with a coverage depth of 5-10 mm.

(2) Three different sliding blades of mulching plate with linear function type, quadratic function type and exponential function type were designed. The bench superconductive with the rotating speed and the stubble distance as the independence, and the twisting index and interference index of rice stubble were used as dependence. The results showed that the structure of the exponential function type mulching plate was optimal.

(3) To study the interaction between mulching equipment and soil, the EDEM simulation model was established by introducing the discrete element method, and its performance was verified by field experiments. The results showed that the synchronous mulching seeder had a rotating speed of 90-150 r·min^{-1} and a forward speed of 0.6 -1.0 m·s^{-1}. The mulching coefficient was 87.37-98.54% and the mulching depth was 5.08 -5.84 mm and the errors are between 2.67~6.15% and 5.96~18.98% respectively compared with the simulation model.

ACKNOWLEDGEMENTS

This study was sponsored by the National Natural Science Foundation, Grant#51965024 and Jiangxi Provincial Agricultural machinery equipment application industrial Technology Research Systems, Grant#JXARS-21.

REFERENCES

[1] Chen, L. M., Wang, W. X., Xiong, R. Y., Xie, J. X., Wu, Z. M., Tan, X. M, Zeng, Y. J., Chen, X. F., Shi, Q. H., &Pan, X. H. (2021). Effects of simultaneous furrow ridging and precision hill-direct-seeding on grain yield and quality of double-cropping indica rice in South China (同步开沟起垄精量穴直播对南方双季籼稻产量和稻米品质的影响). *Transactions of the Chinese Society of Agricultural Engineering, 37(01)*, 28-35. DOI:10.11975/j.issn.1002-6819.2021.01.004

[2] Chen, Q. T. (2021). Design and experiment of rice mechanical direct seeding synchronous pendulum type mulching device (水稻机械直播同步悬摆式覆土装置的设计与试验). *Jiangxi Agricultural University, Jiangxi, China*. DOI:10.27177/d.cnki.gjxnu.2019.000375

[3] Cheng, J., Zheng, K., Xia, J. F., Liu, G. Y., Jiang, L., & Li. D. (2021). Analysis of Adhesion between Wet Clay Soil and Rotary Tillage Part in Paddy Field Based on Discrete Element Method. *Processes*, *9(5)*, 845. Doi:10.3390/pr9050845

[4] Deng, H. (2022). Design and experiment research of rice spreading device based on unmanned aerial vehicle wind field (基于无人机运动风场的水稻撒播装置设计与试验). *Sichuan Agricultural University, Sichuan, China.* DOI:10.27345/d.cnki.gsnyu.2022.000493

[5] Hiroei, K., Satoshi, S., Hisashi, S., Kazuya O. (2021). Control of Bird Damage of Rice Direct Seeding Under Flooding. *Tohoku Journal of Crop Science*, *64*, 33-34. DOI:10.20725/TJCS.64.0_33

[6] Jang, S. G., Park, S. Y., Lar, S. M., Zhang, H. J., Lee, A. R., Cao, F. Y., Seo, J., Ham, T. H., Lee, J., & Kwon, S. W. (2021). Genome-Wide Association Study (GWAS) of Mesocotyl Length for Direct Seeding in Rice.*Agronomy*,*11(12)*, 2527-2527.DOI:10.3390/AGRONOMY11122527

[7] Li, C. S., Tang, Y. L., McHugh, A. D., Wu, X. L., Liu, M., Li, M., Xiong, T.,Ling, D., Tang, Q., Liao, M.,Du, S. Z., Zhu, J., &Huang, Y. (2020). Development and performance evaluation of a wet-resistant strip-till seeder for sowing wheat following rice. *Biosystems Engineering*, *220*, 146-158. DOI:10.1016/J.BIOSYSTEMSENG.2022.05.019

[8] Liu, Y. G., Zhao, J. G., Qi, H. K., Ma, Z. K., Li, H., &Hao, J. J. (2021). Parameters calibration of discrete element of clay soil in yam planting area (麻山药种植区黏质土壤离散元参数标定与试验). *Journal of Agricultural University of Hebei*, *44(06)*, 99-105. DOI:10.13320/j.cnki.jauh.2021.0108

[9] Lu, Q., Liu, F. J., Liu, L. J., Liu, Z. J., & Liu, Y. Q. (2023). Establishment and Verification of Discrete Element Model for Seed Furrow Soil—Seed-mulching Device (种沟土壤-种子-覆土装置互作离散元模型建立与验证). *Transactions of the Chinese Society for Agricultural Machinery*, *54(10)*, 46-57. Doi:10.6041/j.issn.1000-1298.2023.10.004

[10] Luo, X. W., Liu, T., Jiang, E. C., &Li, Q. (2007). Design and experiment of hill sowing wheel of precision rice direct-seeder (水稻精量穴直播排种轮的设计与试验). *Transactions of the Chinese Society of Agricultural Engineering*, *2007(03)*, 108-112. DOI:10.3321/j.issn:1002-6819.2007.03.022

[11] Makange, N. R., Ji, C., &Torotwa, I. (2020). Prediction of cutting forces and soil behavior with discrete element simulation. *Computers and Electronics in Agriculture*, *179*, 105848. DOI:10.1016/j.compag.2020.105848

[12] Mudarisov, S., Farkhutdinov, I., Khamaletdinov, R., Khasanov, E., Mukhametdinov, A. (2022). Evaluation of the significance of the contact model particle parameters in the modelling of wet soils by the discrete element method. *Soil Tillage Research*, *215*, 105228.DOI:10.1016/J.STILL.2021.105228

[13] Peng, Y. F. (2023). Design and Experiment of Centrifugal Rice Spreader with Double Feeding Points (双落种点供料离心式水稻撒播机的设计与试验). *Jiangxi Agricultural University, Jiangxi, China*. DOI:10.27177/d.cnki.gjxnu.2022.000342

[14] Pitoyo, J., & Idkham, M. (2021). Review of rice transplanter and direct seeder to be applied in Indonesia paddy field. *IOP Conference Series: Earth and Environmental Science*, *922(1)*, 012019. DOI:10.1088/1755-1315/922/1/012019

[15] Pue D. J., & Cornelis M. W. (2019). DEM simulation of stress transmission under agricultural traffic Part 1: Comparison with continuum model and parametric study. *Soil Tillage Research*, 195, 104408. DOI:10.1016/j.still.2019.104408

[16] Sansen, K., Wongboon, W., Jairin, J., & Kato, Y. (2019). Farmer-participatory evaluation of mechanized dry direct-seeding technology for rice in northeastern Thailand. *Plant Production Science*,*22(1)*, 46-53.DOI:10.1080/1343943X.2018.1557530

[17] Shu, S. F., Zheng, T. X., Jia, X. L., Luo, X. W., Li, G. X., Wang, Z. M., Chen W. T., & Tang, X. R. (2010). Yield formation characteristics of precision hill-direct-Seeding Late rice (精量穴直播晚稻的产量形成特性研究). *Journal of South China Agricultural University, 31(01)*, 96-98.

[18] Singh, P. K., Kumar, A., Naresh, R. K., Sisodi, R. S., Hota, R., Halder, N., Das, D., Viviana, P., Tiwari, H., & Kumar, S. (2023). Unmanned Aerial Vehicle Direct Seeding Versus Ground Seeding Mechanization Services in Smallholder Farming Systems of North West IGP on Energy Use Efficiency and Quality of Rice Culture: A Review. *International Journal of Environment and Climate Change*, *13(9)*, 2105-2121.DOI:10.9734/IJECC/2023/V13I92444

[19] Sugirbay, A. M., Zhao, J., Nukeshev, S. O., & Chen, J. (2020). Determination of pin-roller parameters and evaluation of the uniformity of granular fertilizer application metering devices in precision farming. *Computers and Electronics in Agriculture*, *179*, 105835.DOI:10.1016/j.compag.2020.105835

[20] Wan, W. H., Hu, K, &Wang, Y. (2021). Research on intelligent equipment for miniaturized rice precision direct broadcast and synchronous deep fertilization in hilly area (丘陵区小型化水稻精量直播及同步深施肥智能装备研究). *China Southern Agricultural Machinery*, *52 (01)*, 6-7. DOI: 10.3969/j.issn.1672-3872.2021.01.003

[21] Wang, D. Y., Chu, G., Chen, S., Xu, C. M., Chen, L. P., & Zhang, X. F. (2020). Innovation and development of rice mechanical precision wet direct broadcast technology (水稻机械精量湿润直播技术的创新与发展). *China Rice*, *26(05)*, 19-21+25.

[22] Wang, Z. M., Dai, Y. Z., Wang, B. L., Zhang, M. H., Mo, Z. W., & Luo, X. W. (2016). Research on hill-drop drilling and row drilling of rice (水稻机械化穴播和条播的对比研究). *Chinese Rice*, *22(4)*, 19-20.DOI:10.3969/j.issn.1006-8082.2016.04.005

[23] Xu, K., Tang, L., Zhang, H. C., Guo, B. W., Huo, Z. Y., Dai, Q. G., Wei, H. Y., & Wei, H. H. (2014). Effect of different mechanical direct seeding methods on tiller characteristics and yield of rice (不同机械直播方式对水稻分蘖特性及产量的影响). *Transactions of the Chinese Society of Agricultural Engineering*, *30(13)*, 43-52. DOI:10.3969/j.issn.1002-6819.2014.13.006

[24] Youichi, O., Furuhata, M., Akihiro, O., Tsutomu, I., & Masaki O. (2019). Effect of Seed Pretreatment and mulching with Soil in V-furrow No-Till Direct Seeding of Rice on Seedling Establishment, Early Plant Growth and Yield in South Cold Climate Region. *Summary of the lecture of the Japanese Crop Society*,*247*, 119.DOI:10.14829/JCSPROC.247.0_119

[25] Yu, J. J., Liu, J. A., Shu, J. G., Chen, Q. T., Chen, X. F., &Liu, M. H. (2020). Design and Experiment of Synchronous Swing-type mulching Device for Mechanical Direct Seeding of Rice (水稻机械直播同步悬摆式覆土装置设计与试验). *Acta Agriculturae Universitatis Jiangxiensis, 42(06)*, 1250-1259. DOI:10.13836/j.jjau.2020139

[26] Yu, J. J., Liu, J. A., Zhu, B.Y., Chen, X. F., Liu, M. H., Shi, Q. H., &Chen, Q. T., (2020). Effect of mulching thickness on the full stand of direct seeding early rice (覆土厚度对直播早稻全苗的影响). *Acta Agriculturae Universitatis Jiangxiensis*, *42(03)*, 419-428. DOI:10.13836/j.jjau.2020049

[27] Zeng, S. (2019). Research and Application of Rice Precision Direct Seeding Machine for Dry Land (水稻精量旱直播机研究与应用). *Modern Agricultural Equipment*, *40(04)*, 14-18.

[28] Zhang, J., Xia, M., Chen, W., Yuan, D., Wu, C. Y., &Zhu, J. P. (2023). Simulation Analysis and Experiments for Blade-Soil-Straw Interaction under Deep Ploughing Based on the Discrete Element Method. *Agriculture-Basel*, *13(1)*, 136. Doi:10.3390/Agriculture 13010136

[29] Zhang, M. H., Wang, Z. M., Luo, X. W., Yang, W. W., Dai, Y. Z., & Wang, B. L. (2017). Design and experiment of furrowing device of precision hill-drop drilling machine for rice (水稻精量穴直播机开沟装置的设计与试验). *Transactions of the Chinese Society of Agricultural Engineering*, *33(5)*, 10-15. DOI:10.11975/j.issn.1002-6819.2017.05.002

[30] Zhang, W. L., Du, J., Zhang, J. M., Liu, Z. Y., Li, D., Li, Z. Y., Luo, S. C., &Xia, J. F. (2020). Design and test of the plough and rotary burying straw returning combine (犁旋式秸秆还田联合作业机设计与试验). *Journal of Gansu Agricultural University*, *55(02)*, 190-200+208. DOI: 10.13432/j.cnki.jgsau.2020.02.026

[31] Zhang, X. R., Zeng, W. Q., Liu, J. X, Wu, P., Dong, X. H., &Hu, H. N. (2022). Design and Experiment of lateritic Soil Inclined Handle Folding Wing Subsoiling Shovel Based on Discrete Element Method (基于离散元法的砖红壤斜柄折翼式深松铲设计与试验). *Transactions of the Chinese Society for Agricultural Machinery, 53(03)*, 40-49. DOI: 10.6041/j.issn.1000-1298.2022.03.004

[32] Zhu, B. Y., Liu, J. A., Chen, X. F., Yu, J. J., Liu, M. H., &Zhang, Q. S. (2020). Parameter calibration of soil in the Poyang lake region based on discrete element method. *American Journal of Biochemistry and Biotechnology*, *16(4)*, 538-548.DOI:10.3844/ajbbsp.2020.538.548

STUDY OF FIBER DEFORMATION OF ELASTIC BRUSH-LIKE SCREWS DURING GRAIN MATERIAL TRANSPORTATION

/

ДОСЛІДЖЕННЯ ДЕФОРМАЦІЇ ВОЛОКОН ЕЛАСТИЧНИХ ЩІТКОПОДІБНИХ ШНЕКІВ ПРИ ТРАНСПОРТУВАННІ ЗЕРНОВОГО МАТЕРІАЛУ

Andrii DIACHUN, Ivan GEVKO, Oleg LYASHUK, Andrii STANKO, Andrii PIK, Yuri OMELYANSKYI
Ternopil Ivan Puluj National Technical University, Ukraine;
E-mail: oleglashuk@ukr.net
DOI: https://doi.org/10.35633/inmateh-72-51

***Keywords*:** *brush-like screw, grain material, deformation, elastic fiber, differential equation*

ABSTRACT

A new design of an elastic brush-like screw for grain material transportation and mixing by screw conveyors with a lower degree of damage to some particles of the material has been presented in the paper under discussion. The theoretical calculation of the fiber displacement value of an elastic brush-like screw has been carried out on the basis of the deformation analysis of an idealized system with elastic elements. A differential equation of the mean line of deformation of several fibers of an elastic brush-like screw located in the same plane perpendicular to the distributed loading during grain material transportation has been derived. The solution of the differential equation was obtained by the numeric method and on its basis the curves of the middle line of deformed fibers of an elastic brush-like screw for different values of its structural parameters. The results of the experimental study of the maximum deformation value of the elastic fibers of a brush-like screw have been presented.

РЕЗЮМЕ

У статті представлено нову конструкцію еластичного щіткоподібного шнека для транспортування та змішування зернових матеріалів гвинтовими конвеєрами із зниженим ступенем пошкодження окремих частинок матеріалу. Проведено теоретичний розрахунок величини переміщення волокон еластичного щіткоподібного гвинтового шнека на основі аналізу деформацій ідеалізованої системи з пружними елементами. Виведено диференціальне рівняння середньої лінії деформації декількох волокон еластичного щіткоподібного шнека, розміщених в одній площині перпендикулярній розподіленому навантаженню при транспортуванні зернового матеріалу. Розв'язок диференціального рівняння проведено чисельним методом, на основі чого побудовані графіки середньої лінії деформованих волокон еластичного щіткоподібного шнека при різних значеннях його конструктивних параметрів. Представлено результати експериментальних досліджень величини максимальної деформації волокон еластичного щіткоподібного шнека.

INTRODUCTION

Screw conveyors with different types of working bodies have been widely used in technological processes of agricultural and industrial production, namely in the transportation of grain, seed materials, granular mineral fertilizers, and others. Such materials can be badly damaged during transportation in closed casings, both rigid and elastic ones, and this can't meet the agrotechnical requirements. The main reasons for grain material damage involve particles' falling into a gap between the rotating screw surface and the fixed internal surface of the casing.

To avoid this damage, the screw surface is quite often made of elastic section materials *(Hevko R.B. et.al., 2015; Loveikin V. and Rogatynska L., 2011; Zalutskyi S.Z. et.al., 2018;)* or as an elastic brush-like screw *(Tian Y. et.al., 2018; Zaica A. et.al., 2016; Zaica A. et.al., 2020)*. The latter was proposed to use in grain material coating.

Another direction of the screw conveyor improvement is rotating casings use *(Rohatynskyi R. et.al., 2019)* with some extra screw oscillations *(Hevko B.M. et.al., 2015)*, enabling an increase in the grain material transportation and mixing efficiency, though it cannot solve the problem of grain damage completely.

Some papers consider the operation mode of an inclined screw conveyor which has a screw operating element with constant parameters incorporated in it (*Mondal, 2018, Lyashuk et.al, 2019*). The kinematics of

grain loading has been investigated based on the motion equations in a screw conveyor. The analysis of loading movement at constant high-speed mode has been analyzed.

Polymer coatings of screws facilitate the operation resource increase of the mechanisms, though they do not provide any essential reduction of grain material damage. These papers (*Prisyazhnaya et.al.,2020; Prisyazhnaya et.al.,2021; Soldatenko et.al.,2021;*) conclude that the bio based composites constitute a promising field in polymeric composites that increase awareness for applications in various fields ranges to avoid pinching and damage during transportation.

It is very important to study screw deformations during bulk material transportation and to determine the values of screw oscillations *(Rohatynskyi R.M. et.al., 2015; Hevko I.B. et.al., 2015; Zaica A. et.al., 2019; Hou Junming et.al., 2023)*, deformations of separate fibers of a brush-like screw *(Hevko R.B. et.al., 2016; Tian Y. et.al., 2018)* or elastic sections of the screw *(Hevko R.B. et.al., 2019; Trokhaniak et.al., 2020),* under loading action conditions taking place during bulk material transportation. The developed new design of screw conveyors with elastic brush-like screws requires some further study of the impact of their design and kinematic parameters on the value of elastic fibers deformation on brush-like screw enabling us to predict the resistance to loading of the transported material to provide the fiber deformation within the boundaries of the maximum allowable value without reverse motion of the bulk material separate elements.

MATERIALS AND METHODS

One of the directions providing the reduction of grain and seed material damage is using the brush-like elastic elements on the screw spiral peripheral surface, as shown in fig. 1. The developed design of a screw conveyor with a brush-like elastic screw consists of guiding casing *1*, a shaft *2* where cylindrical tubes *3* are fixed with bunches of brush-like elastic elements *5*. The edges *4* of the tubes overhanging above the external surface of shaft *2* are being changed into an elliptical shape to fix the elastic brushes.

In case when some particles of grain material are caught between the internal surface of the guiding casing and the peripheral surface of the elastic brush, the latter sags and lets the material through without any damage.

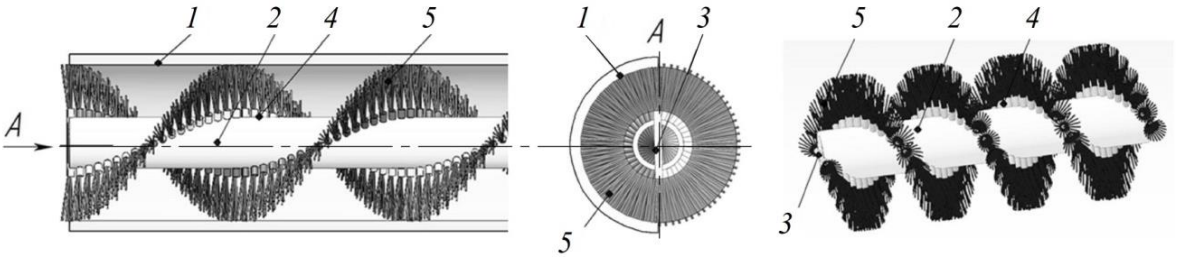

Fig. 1 - Design of a screw conveyor with an elastic brush-like screw

In another version, shown in fig. 2, a combined elastic screw conveyor consists of a bunker *1*, joined with a guiding casing *2*, where a screw *3* is located with an unloading nozzle *4*.

In the material loading zone, a step T_1 of the screw is the smallest one, and the stiffness C_1 of its surface is maximal. In the area of the bunker transition to the casing, the screw step T_2 and stiffness C_2 of its peripheral surface is average. In the material transportation zone, the step T_3 of the screw is the largest one, though its surface stiffness C_3 is minimal.

The above-mentioned design of the screw conveyor provides the guaranteed flow of the material towards the guiding casing, which will enable to provide the material distribution on the casing surface caused by the action of the centrifugal force within the process of its transportation.

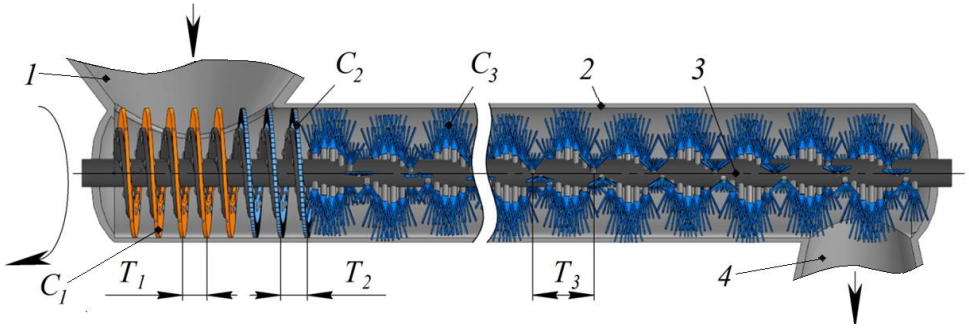

Fig. 2 - Design of a combined elastic screw conveyor

Based on the design shown in fig. 1, an experimental equipment is made to study the screw conveyor with an elastic brush-like screw. A picture of this equipment is given in figure 3.

An elastic brush-like screw, shown in fig. 3 *b* consists of a hollow shaft *1*, where some holes are made along the screw line perpendicular to its central axis, where some hollow cylindrical tubes *2* are fixed, overhanging above the external surface of the hollow shaft on which the bunches of brush-like elastic fibers *3* are fixed. The diameter of the fibers cross-section is from 1.8 mm to 2.6 mm, the length is from 28 mm to 36 mm and they are made from nylon. The external diameter of the brush-like screw is from 96 mm to 106 mm. The operating speed is from 180 to 250 rpm. The inclination angle of the casing is up to 45 degrees.

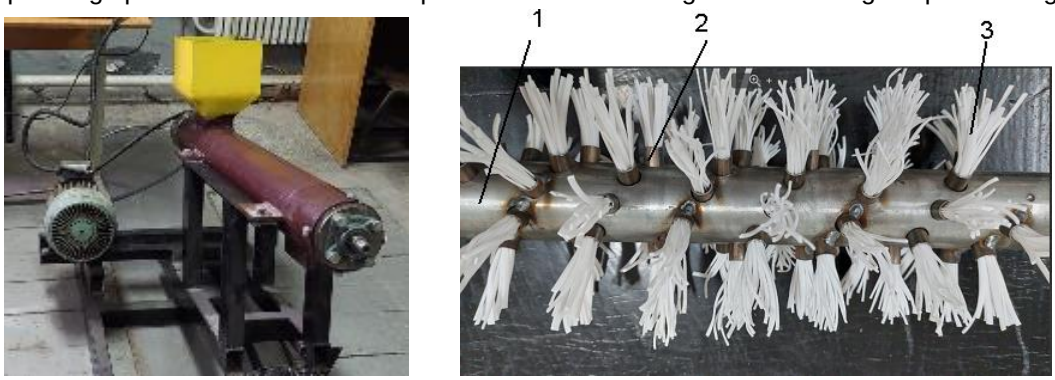

a) b)

Fig. 3 - Picture of a screw conveyor a) with an elastic brush-like screw b)

During the process of calculations, it was found, that the shaft and the casing rigidity is much greater than the rigidity of elastic brush-like screws, so the deformation of these elements was not taken into account in modeling. The displacement of the fibers of an elastic brush-like screw (fig. 4 *a*) has been determined from the analysis of deformations of an idealized system with elastic elements shown in fig. 4 *c*. A brush-like screw while being installed into the casing without any gap is subjected to the initial radial and axial deformation to reduce the damage of grain material and rests on the casing surface (fig. 4 *b*), in this case, the fibers are rigidly fixed on the shaft. Under the conveyor performance and loading increase conditions, the fibers of an elastic brush-like screw are bent in the negative direction of the axis *y*, and in this case, the bulk material transportation is provided (fig. 4 *c*). When the maximum allowable value of the load on the elastic brush-like screw is exceeded (fig. 4 *d*), the fibers are bent to create a gap between the casing and an elastic brush-like screw, whose value is sufficient enough to transport the grain material in the opposite direction. As the stiffness of the fibers of an elastic brush-like screw is lower than the rigidity of separate elements of grain material, the latter cannot be damaged.

Let's carry out the study of fibers static deformations on brush-like screw. The distributed loading $q(x)$ in the screw axial direction during grain material transportation to the fibers of brush-like screw is uneven along the length of the fibers and depends on the load factor q_1, the casing angle of inclination β, and the screw conveyor speed operation mode. In this case, the maximum value of such loading takes place on the screw external diameter, and the minimum one – on its external diameter.

The distributed load on the fibers of the elastic brush-like screw during bulk material transportation at a small load factor of a horizontal and hollow inclined screw conveyor with a small speed operation mode has been approximated by the dependence:

$$q(x) = \frac{(q_{\max} - q_{\min})x}{l} + q_{\min} \tag{1}$$

where l – the length of the working part of the elastic fibers of brush-like screw; $q_{\max}$ - maximum distributed load on the fibers (takes place on the brush-like screw external diameter); $q_{\min}$– minimal distributed load on the fibers.

The equation of the middle line of deformation of several fibers located in the same plane with the distributed load $q(x)$ will look as follows:

$$nEI\frac{d^2y}{dx^2} = M(x) - N_1 \sin\gamma \cdot y + F_i \cdot y + G \cdot y \cdot \cos\beta\cos\theta \tag{2}$$

where n – the number of fibers located in the same plane with the distributed load $q(x)$; E – modulus of elasticity of the fibers material of the elastic brush-like screw; $M(x)$ - the bending moment of a fiber of the

elastic brush-like screw; N_1 – the force of initial deformation of the elastic fibers of brush-like screw at its fixing in the casing; y – inclination angle of the elastic fibers of brush-like screw after initial deformation; N_i– centrifugal force acting on the fibers during the elastic brush-like screw rotation; G – weight force acting on the fibers; $G=mg$; I – the moment of inertia of the fiber cross-section of the elastic brush-like screw; β - inclination angle of the casing; θ – the angle of rotation of the elastic brush-like screw; m– fiber mass; g – free-fall acceleration.

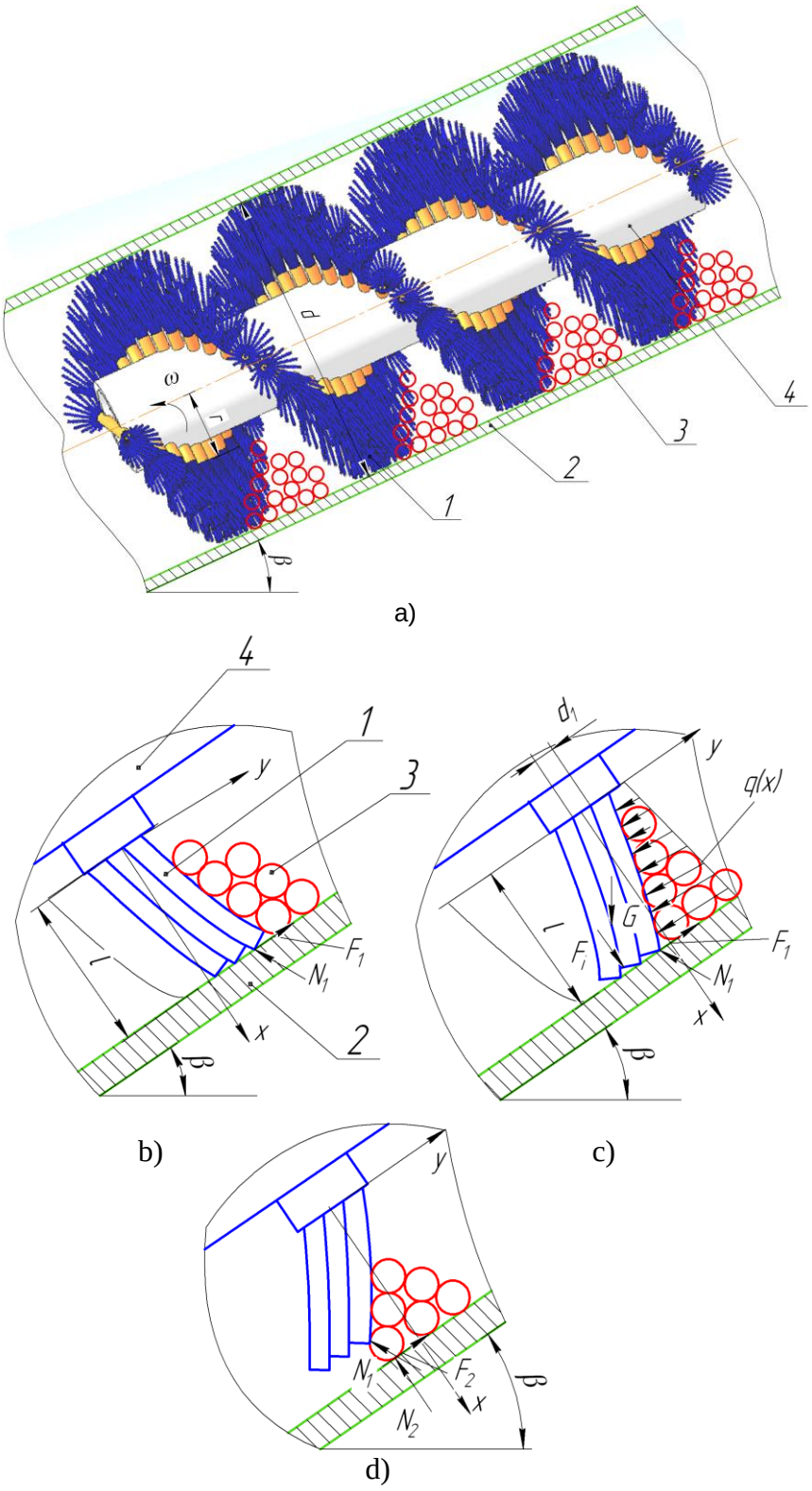

Fig. 4 - Calculation scheme to determine the deformation of an elastic brush-like screw during grain material transportation:

1 – elastic brush-like screw; 2 – casing; 3 - bulk material; 4 – shaft

The bending moment of a fiber of the elastic brush-like screw is found by the formula *(Pysarenko H.S., et.al., 1988)*:

$$M(x) = \int_{x}^{l} Q(x)dx + M(0) \tag{3}$$

where $Q(x)$ - the shear force in the fibers of the elastic brush-like screw; $M(0) = 0$ – the bending moment of a fiber cross-section of the elastic brush-like screw.

The shear force in the fibers of the elastic brush-like screw is calculated in the following way:

$$Q(x) = F_1 + N_1 \cos\gamma - \int_{x}^{l} q(x)dx - G \cdot \sin\beta \tag{4}$$

where F_1 – friction force between the fibers of elastic brush-like screw and the casing.

The force of initial deformation of the fibers of elastic brush-like screw at the moment of its installation in the casing has been found for the case when the fibers are considered as a cantilevered beam *(Pysarenko H.S., et.al., 1988)*:

$$N_1 = \frac{3nfEI}{l^3} \tag{5}$$

where f – is the value of the initial deformation of the elastic fibers of brush-like screw at the moment of its installation in the casing.

The value of initial deformation of the elastic fibers of brush-like screw at the moment of its installation in the casing has been found by the formula:

$$f = \sqrt{l^2 - (l-k)^2} \tag{6}$$

where k – length of the fiber part that is used to remove the gap between the elastic brush-like screw and the casing.

This length has been found on the basis of the conveyor structural parameters:

$$k = \frac{D-d}{4} \tag{7}$$

where D – is the external diameter of the elastic brush-like screw prior to its installation in the casing; d– the casing internal diameter.

The moment of inertia of the fiber round-shaped cross-section:

$$I = \frac{\pi d_1^4}{64} \tag{8}$$

where d_1 – is the diameter of the fiber cross-section.

The angle of inclination of fibers of the elastic brush-like screw after initial deformation:

$$\gamma = \arcsin\frac{\sqrt{l^2 - \left(l - \frac{D-d}{4}\right)^2}}{l} \tag{9}$$

After substituting the formulae Eq. 6, Eq. 7, Eq. 8 in equation Eq. 5, it has been obtained:

$$N_1 = \frac{3n\sqrt{l^2 - \left(l - \frac{D-d}{4}\right)^2}E\pi d_1^4}{64l^3} \tag{10}$$

Centrifugal force acting on the fibers during the elastic brush-like screw rotation:

$$F_i = m\omega^2(r+l) \tag{11}$$

where ω – angular rotation frequency of the elastic brush-like screw; r – radius of the central shaft.

The friction force between the elastic fibers of brush-like screw and the casing:

$$F_1 = N_1\mu_1 \tag{12}$$

where μ_1 – is the friction coefficient between the elastic fibers of brush-like screw and the casing.

RESULTS AND DISCUSSION

After substituting the Eq. 3, Eq. 4, Eq. 11, Eq. 12 in equation Eq. 2, the equations of the middle line of several fibers' deformation of the elastic brush-like screw have been obtained:

$$nEI\frac{d^2y}{dx^2}=\int_x^l N_1\left(\cos\gamma+\mu_1\right)dx-\int_x^l\int_x^l\left(\frac{\left(q_{\max}-q_{\min}\right)x}{l}+q_{\min}\right)dxdx-\int_x^l mg\sin\beta dx- \\ -N_1\sin\gamma\cdot y+m\cdot y\left(\omega^2\left(r+l\right)+g\cos\beta\cos\theta\right) \quad (13)$$

In case when there is a gap between the elastic fibers of brush-like screw and the casing, equation Eq. 13 is written in the simplified form:

$$nEI\frac{d^2y}{dx^2}=-\int_x^l\int_x^l q(x)dxdx-\int_x^l mg\sin\beta dx+m\cdot y\left(\omega^2\left(r+l\right)+g\cos\beta\cos\theta\right) \quad (14)$$

After the integration of the Eq. 13 we have obtained:

$$nEI\frac{d^2y}{dx^2}=N_1\left(\cos\gamma+\mu_1\right)\left(l-x\right)-\frac{1}{2}\left(q_{\max}\left(l^2-x^2\right)+q_{\min}\left(l-x\right)^2\right)\left(1-\frac{x}{l}\right)- \\ -mg\sin\beta\left(l-x\right)-N_1\sin\gamma\cdot y+m\cdot y\left(\omega^2\left(r+l\right)+g\cos\beta\cos\theta\right) \quad (15)$$

Taking into account equation Eq. 10, it has been obtained:

$$\frac{nE\pi d_1^4}{64}\frac{d^2y}{dx^2}=\frac{3n\sqrt{l^2-\left(l-\frac{D-d}{4}\right)^2}E\pi d_1^4}{64l^3}\left(\left(\cos\gamma+\mu_1\right)\left(l-x\right)-\sin\gamma\cdot y\right)- \\ -\frac{1}{2}\left(q_{\max}\left(l^2-x^2\right)+q_{\min}\left(l-x\right)^2\right)\left(1-\frac{x}{l}\right)-mg\sin\beta\left(l-x\right)+m\cdot y\left(\omega^2\left(r+l\right)+g\cos\beta\cos\theta\right) \quad (16)$$

The differential equation Eq. 16 can be used to determine the deformation of the elastic fibers of brush-like screw under static load conditions.

The general solution of the differential equation Eq. 16 looks like this:

$$y=A_1\sin(k_1x)+A_2\cos(k_1x)+y* \quad (17)$$

where A_1 and A_2 – are the coefficients that can be determined from the boundary conditions, mm; y^* - partial solution of the equation; k_1 – frequency characteristics.

The initial conditions for the solution of equation Eq. 16 are as follows: when $x=0$, $y=0$, $dy/dx=0$.

The solution of Eq. 16 has been found using the numerical method and is presented as curves in fig. 5 - 8 for different variable parameters. The view of the mean line of deformed fibers of an elastic brush-like screw at different values of external distributed load on the fibers from the side of the transported material is presented by the curves in fig. 5. The view of the mean line of deformed fibers of an elastic brush-like screw at different values of diameter d_1 of the fiber cross-section is presented by the curves in fig. 6. The view of the mean line of deformed fibers of an elastic brush-like screw at different values of length *k* of the fiber part used to remove the gap between the elastic brush-like screw and the casing is presented by the curves in fig. 7. The view of the mean line of deformed fibers of an elastic brush-like screw at different values of length *l* of the working part of the fibers of elastic brush-like screw is presented by the curves in fig. 8.

To check the adequacy of the differential equation Eq. 16 and its solution by the numerical method, some experimental study was conducted on the maximum deformation value Δy of nylon fibers of the elastic brush-like screw using the technique described in the article (*Hevko R.B. et.al, 2016*). The loading on the elastic fibers of brush-like screw from the side touching the casing was performed by means of some measured cargo in the form of balls, here the angle of inclination of the casing β was equal to 90 degrees. The deformation Δy was measured by a caliper. During the above-mentioned experiments, three main factors have been varied: diameter of the fiber cross-section d_1, length *l* of the working part of the elastic fibers of brush-like screw, and load *P* of the measured cargo.

To find the dependence $\Delta y = f(d_1, l, P)$, the full factorial experiment was used. Taking into account, that the dispersions in each point of the factorial space are homogeneous, it has been decided to apply the system of the experiment implementation scheme with duplication in one point (in the center of the plan) four times. After processing the experimental research results, the regression equation was derived to predict the value of deformation Δy:

$$\Delta y = 3.397 - 9.34d_1 + 0.425l + 3.04P - 0.432d_1 l - 2.696d_1 P + 0.148lP + 5.05d_1^2 + 0.0086l^2 + 0.012P^2 \quad (18)$$

Empirical dependence Eq. 18 adequately shows the parameter under study on the intervals of variable factors: 1.8 mm< d_1 <2.6 mm, 28 mm< l <36 mm, 1.4 N < P <2.6 N.

On the basis of Eq. 18 the response surfaces of the maximum deformation value Δy as a functional are drawn, as shown in fig. 9.

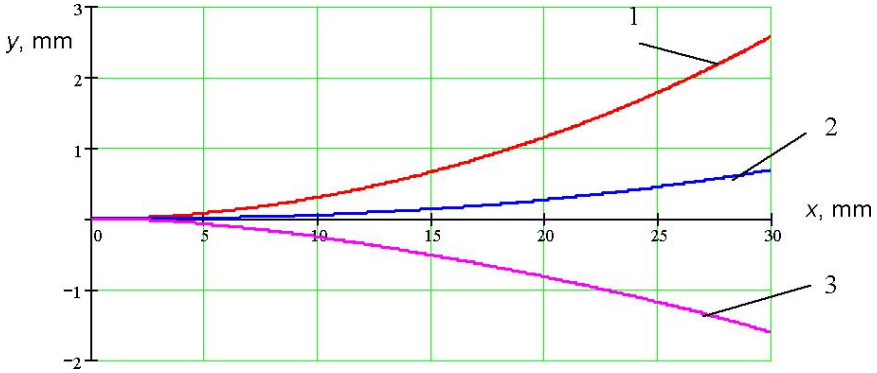

Fig. 5 - Curves of mean line of deformation of four nylon fibers of an elastic brush-like screw located in the same plane with distributed load l =30 mm, k =0.1 mm, d_1 = 0.1 mm, β = 45 degrees:

1) deformation at the initial installation of an elastic brush-like screw in the screw conveyor casing q_{max} =0 N/mm; q_{min} = 0 N/mm; 2) q_{max} =0.05 N/mm; q_{min} = 0.02 N/mm; 3) q_{max} =0.1 N/mm; q_{min} = 0.06 N/mm

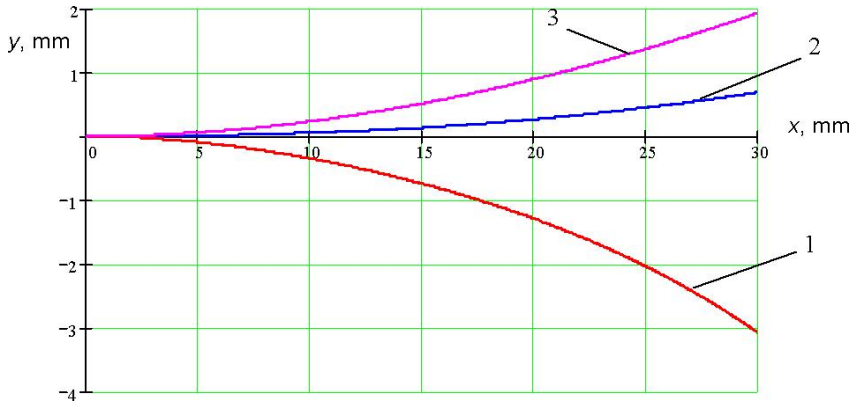

Fig. 6 - Curves of mean line of deformation of four nylon fibers of an elastic brush-like screw located in the same plane with distributed load l =30 mm, k =0.1 mm, β = 45 degrees:

q_{max} =0.05 N/mm; q_{min} = 0.02 N/mm; d_1 = 1.7 mm; 2) d_1 = 2 mm; 3) d_3 = 2.3 mm

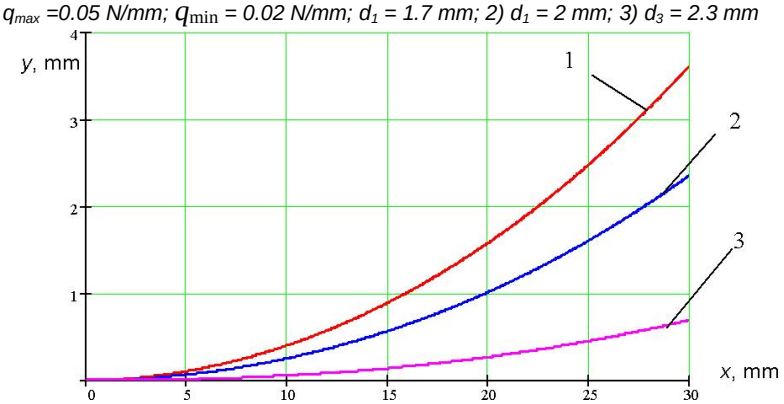

Fig. 7 - Curves of mean line of deformation of four nylon fibers of an elastic brush-like screw located in the same plane with distributed load l =30 mm, d_1 = 2 mm, q_{max} =0.05 N/mm; q_{min} = 0.02 N/mm; β = 45 degrees:

1) k =0.3 mm, 2) k =0.2 mm, 3) k =0.1 mm

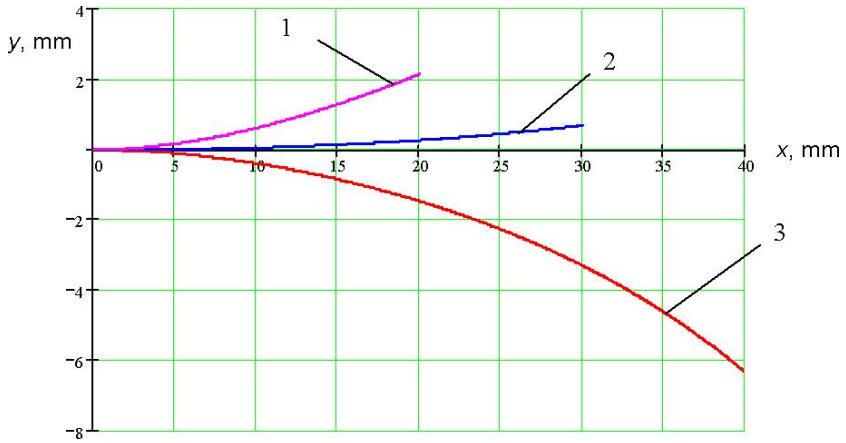

Fig. 8 - Curves of mean line of deformation of four nylon fibers of an elastic brush-like screw located in the same plane with distributed load k =0.1 mm, d_1 = 2 mm, q_{max} =0.05 N/mm; q_{min} = 0.02 N/mm; β = 45 degrees: *1)* l =20 mm; *2)* l =30 mm; *3)* l =40 mm

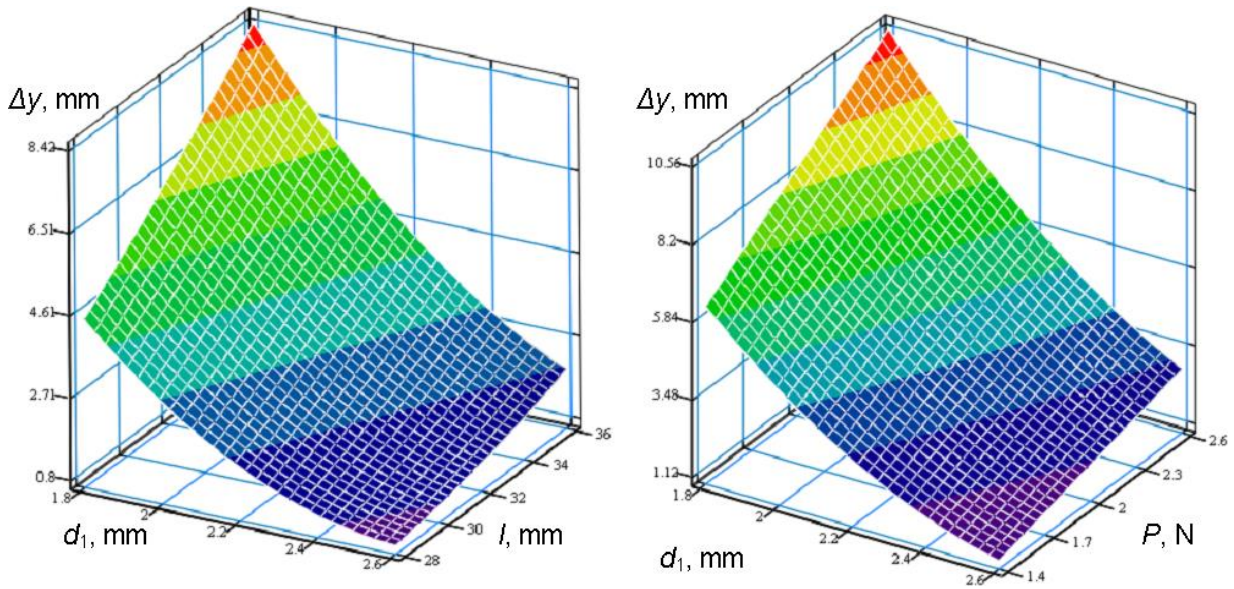

a) b)

Fig. 9 - Response surfaces of the maximum deformation value Δy as a functional

a) $\Delta y = f(d_1;l)$ *at* $P = 2$ *N; b)* $\Delta y = f(d_1;P)$ *at* $l = 36$ *mm*

CONCLUSIONS

Curve 1 in fig. 5 corresponds to fig. 4*b*, for the case when the brush-like screw at the moment of its installation in the casing is initially deformed up to 2.5 mm and rests on the casing surface, here there isn't any external distributed load from the side of the transported material. When the increase of external load q_{min} and q_{max} is up to 0.06 N/mm and 0.1 N/mm respectively the deformation of the fibers of elastic brush-like screw is up to 1.5 mm (curve 3), which corresponds to fig. 4*c,* and the total bending of the fiber is 5 mm.

When the fiber diameter is reduced (fig. 6) from 2.3 mm (curve 3) to 1.7 mm (curve 1) for the same external loads, the fiber deformation takes place in the negative direction of the axis *y* from 2 mm to 3 mm and the total bending of the fiber is 5 mm.

When the value k (fig. 7) increases from 0.1 mm to 0.3 mm, the previous deformation of the fiber also increases (fig. 4 b) from 0.7 mm to 3.5 mm, providing the increase in uploading capacity of the elastic brush-like screw, though the material transportation capacity also gets higher due to the greater force of friction between the fibers of the elastic brush-like screw and the conveyor casing.

When the fiber working part *l* increases (fig. 8) from 20 mm (curve 1) to 40 mm (curve 3), for the same external loads the fiber deformation takes place in the negative direction of the axis *y* from 2.2 mm to 6.4 mm, and the total bending of the fiber is 8.6 mm. Thus, the use of fibers of greater length *l* of the working part can reduce the loading capacity of the elastic brush-like screw, though the transported material damage value is lower.

The real value of the deformation quantity of the fibers of elastic brush-like screw during the bulk material transportation process is higher due to the dynamic load that occurred. As the probability of resonance is inconsiderable, the real value of the deformation quantity of the fibers of elastic brush-like screw during the bulk material transportation process can be determined by the product of the fiber deformation value at static calculations by the dynamism factor: $y_r = y \cdot k_d$.

On the basis of the analysis of the regression Eq.18 and the constructed curves (fig. 9), it has been found, that the smaller diameter of the fiber cross-section d_1 and the bigger length of the working part of the elastic fibers of brush-like screw l is, and the greater load P is, the value of deformation Δy of nylon fibers of the elastic brush-like screw is higher. The maximum value of deformation Δy is 10.5 mm, and the minimum one is 0.7 mm. The increase of the parameter d_1 from 1.8 mm to 2.6 mm results in a 4.4 times reduction of the deformation Δy. The increase of the parameter l from 28 mm to 36 mm causes a 2.4 times increase in deformation Δy and, in this case, the increase of load P from 1.4 H to 2.6 H results in 2.36 times increase in deformation Δy. The deviation of the theoretical results of the study from the experimental ones is not more than 17%.

REFERENCES

[1] Hewko B.M., Popovich P.V., Diachun A.Y., Lyashuk O.L., Liubachivskyi R.O., (2015), The study of bulk material kinematics in a screw conveyor-mixer, *INMATEH: Agricultural Engineering*, vol.47, no.3, pp.156-163, Bucharest/Romania;

[2] Hevko I.B., Dyachun A.Ye., Gud V.Z., Rohatynska L.R., Klendiy V.M., (2015), Investigation of the stability of the torsorial vibrations of a screw conveyer under the influence of pulse forces, *INMATEH: Agricultural Engineering*, vol.45, no.1 pp. 77-86, Bucharest/Romania;

[3] Hevko R.B., Dzyadykevych Y.V., Tkachenko I.G., Zalutskyi S.Z., (2016), Parameter justification for interworking relationship of elastic screw operating element with grain material, *Bulletin of Ternopil Ivan Puluj National Technical University (Вісник ТНТУ ім. І.Пулюя)*, vol.81, no.1, pp. 77-87, Ternopil/Ukraine;

[4] Hevko R.B., Zalutskyi S.Z., Hladyo Y.B., Tkachenko I.G., Lyashuk O.L., Pavlova O.M., Pohrishchuk B.V., Trokhaniak O.M., Dobizha N.V., (2019), Determination of interaction parameters and grain material flow motion on screw conveyor elastic section surface, *INMATEH: Agricultural engineering*, vol.57, no.1, pp.123-134, Bucharest/Romania; https://doi.org/10.35633/INMATEH_57_13

[5] Hevko R.B., Zalutskyi S.Z., Tkachenko I.G., Klendiy O.M., (2015), Development and investigation of reciprocating screw with flexible helical surface, *INMATEH: Agricultural engineering*, vol.46, no.2, pp.133-138, Bucharest/Romania;

[6] Hou Junming, Ren Zhaotan, Zhang Liang, Sun Qijie, Wang Wei (2023), Research on comb brush harvester and damage mechanism to material. A review, *INMATEH: Agricultural engineering*, Vol. 69. no. 1, pp. 74–87, Bucharest/Romania; https://doi.org/10.35633/inmateh-69-07

[7] Loveikin V., Rogatynska L., (2011), A Model of Loose Material Transportation by Means of High-Speed Conveyers with Elastic Operating Devices (Модель транспортування сипкого вантажу швидкохідними гвинтовими конвеєрами з еластичними робочими органами), *Bulletin of Ternopil Ivan Puluj National Technical University (Вісник ТНТУ ім. І. Пулюя)*, vol.16, pp.66-70, Ternopil/Ukraine;

[8] Lyashuk O., Vovk Y., Sokil B., Klendii V., Ivasechko, R., Dovbush T., (2019), Mathematical model of a dynamic process of transporting a bulk material by means of a tube scraping, *Agricultural Engineering International: CIGR Journal*, vol. 21, no.1, pp. 74-81. https://cigrjournal.org/index.php/Ejounral/article/view/4807/2913.

[9] Pysarenko H.S., Yakovlev A.P., Matveev V.V., (1988) - Reference on strength of materials (Справочник по сопротивлению материалов), published by Naukova Dumka (видавництво Наукова думка), 736p. Kyiv/Ukraine;

[10] Prisyazhnaya I., Sinegovskya V., Prisyazhnaya S. and Sinegovskiy M., (2021), Combine harvester improvement for selection and collection of high-quality soybeans, *AGRITECH-V 2020: IOP Conf. Series: Earth and Environmental*, Science 839, 052030; https:// doi:10.1088/1755-1315/839/5/052030

[11] Prisyazhnaya I., Sinegovskya V., Prisyazhnaya S. and Sinegovskiy M., (2020), Harvester and transporting device development for high-quality soybean seeds obtaining, *AGRITECH-III 2020: IOP Conf. Series: Earth and Environmental*, Science 548, 062078; https:// doi:10.1088/1755-1315/548/6/062078

[12] Rohatynskyi R., Gevko I., Diachun A., Lyashuk O., Skyba O., Melnychuk A., (2019), Feasibility study of improving the transport performance by means of screw conveyors with rotary casings, *Acta Technologica Agriculturae*, vol.4/2019, pp.141-146, Nitra/Slovakia;

[13] Rogatynskyi R., Hevko I., Diachun A., Rogatynska O., Melnychuk A., (2019), The cargo movement model by the screw conveyor surfaces with the rotating casing, *Bulletin of Ternopil Ivan Puluj National Technical University,* vol.92, no.4, pp. 34-41, Ternopil/Ukraine;

[14] Rohatynskyi R. M., Hevko Iv. B., Diachun A. Ye., (2015), The research of the torsional vibrations of the screw in terms of impulsive force impacts, *Naukovyi Visnyk Natsionalnoho Hirnychoho Universytetu (Науковий вісник Національного гірничого університету)*, vol.149, no.5, pp.64-68, Dnipropetrovsk/ Ukraine;

[15] Soldatenko L., Shipko A., Shipko I., (2021), Attempt to improve the operating and technological properties of the combined grain washing machine. *Grain products and mixed fodder's*, Vol.21 no.2(82), pp.7-13, Odessa/Ukraine. DOI https://doi.org/10.15673/.

[16] Trokhaniak O. M., Hevko R. B., Lyashuk O. L., Dovbush T. A., Pohrishchuk B. V., Dobizha N. V., (2020), Research of the of bulk material movement process in the inactive zone between screw sections, INMATEH: Agricultural engineering, Vol. 60. no. 1. pp. 261–268, Bucharest/Romania; https://doi.org/10.35633/inmateh-60-29

[17] Tian Y., Yuan P., Yang F., Gu J., Chen M., Tang J., Su Y., Ding T., Zhang K., Cheng Q., (2018), Research on the Principle of a New Flexible Screw Conveyor and Its Power Consumption, *Applied Sciences*, vol.8, no.7.; https://doi.org/10.3390/app8071038

[18] Zaica A., Olan M., Bunduchi G., Zaica A., Gageanu P., Paun A., (2020), Factors that influence coverage degree in seed treatment equipment having brush screw conveyor, *Engineering for rural development*, 20.-22.05.2020, pp.1325-1330, Jelgava/Latvia; https://doi.org/10.22616/ERDev.2020.19.TF331

[19] Zaica A., Visan A., Paun A., Gageanu P., Bunduchi G., Zaica A., Stefan V., Manea D., (2016), The coating process of corn grains using a treatment machine with brush screw conveyor, *Proceedings of the 44th International Symposium on Agricultural Engineering: Actual Tasks on Agricultural Engineering*, 23-26 February 2016, pp.333-345, Opatija/Croatia;

[20] Zaica A., Visan A., Zaica A., Olan M., Bunduchi G., (2019), Coating process of corn grains using treatment machine with brush screw conveyor, *Engineering for rural development*, 22.-24.05.2019, pp.233-238, Jelgava/Latvia; https://doi.org/10.22616/ERDev2019.18.N315

[21] Zalutskyi S.Z., Hevko R.B., Hladio Y.B., Tkachenko I.H., Klendii O.M., (2018), Loose material flow motion on surface of screw with overlapping elastic sections (Рух потоку сипкого матеріалу по поверхні шнека з еластичними секціями, що перекриваються між собою), *Kharkiv P. Vasylenko National Technical University of Agriculture (Харківський національний технічний університет сільського господарства імені Петра Василенка)*, vol.11, pp.81-90, Kharkiv/Ukraine.

DESIGN AND EXPERIMENT ON CUTTING AND CRUSHING DEVICE OF SIDE-SWEEPING STRAW RETURNING MACHINE
/
侧扫式秸秆还田机切割粉碎装置设计与试验

Ruili WANG[1)], Deshuai LI[1)], Shuai LI[1)], Tong REN[1)], Hongbo BAI[2)], Yashuang JIN[2)], Wei WANG[1,*)], Satyanarayan R.S. DEV[3] [1]

[1)] College of Engineering, Shenyang Agricultural University, Shenyang 100866, China
[2)] Yushu City Enyu Township Comprehensive Service Center, Changchun 130408, China
[3)] College of Agriculture and Food Sciences, Florida A&M University, Tallahassee, FL 32307, USA
Corresponding authors. Email: syww@syau.edu.cn
DOI: https://doi.org/10.35633/inmateh-72-52

Keywords: *Straw returning to the field; Cutting and crushing device; Optimization tests*

ABSTRACT
This paper aims to solve the problems of complex structure, poor straw crushing effect and high power consumption of existing straw returning machines. A cutting and crushing device with moving and fixed blades has been developed. The moving blade has collision and automatic retraction functions, which can effectively reduce destructive damage caused by blade obstacles and extend its service life. The double-type single-support cutting method has the advantages of improving the straw crushing effect and reducing the running power consumption. The effects of blade rotational speed, blade offset angle and blade number under the condition of composite single-support cutting were tested according to the uneven ratio of straw throwing and the qualification ratio of straw crushed length. The optimal combination of working parameters of the cutting and crushing device was determined: blade rotational speed of 1968 r/min, blade offset angle of 5°, blade number of 4. The test results show that the uneven ratio of straw throwing is 17.18%, and the qualification ratio of straw crushed length is 92.23%. The operation effect of the side-sweeping straw returning machine was tested on the field. All operating indicators are equipped with cutting and crushing devices, and the results show that all operating indicators meet the technical requirements of straw return.

摘要
本文旨在解决现有秸秆深还机切割粉碎装置结构复杂、秸秆破碎效果差、功耗高等问题。设计了一种侧扫式秸秆深还机切割粉碎装置。该切割粉碎装置采用动定刀结合的设计，动刀片具有碰撞自动回缩功能，可有效降低障碍物对刀片的破坏性伤害，延长其使用寿命。采用复式单支撑的切割方式，具有提高秸秆粉碎效果和降低作业功耗等优点。本文利用自制的玉米秸秆切割粉碎试验台，以秸秆抛洒不均匀率和秸秆切碎长度合格率为目标值，对刀盘转速、偏移角度和刀片数目等影响因素进行了玉米秸秆复式单支撑切割条件下的单因素试验和中心组合试验。试验结果表明：当刀盘转速为 1968r/min、偏移角度为 5°，刀片数目为 4 时，秸秆抛洒不均匀率为 17.18%，秸秆切碎长度合格率为 92.23%。对安装了切割粉碎装置的侧扫式秸秆还田机整机作业效果进行了田间性能试验，结果表明各项作业指标均可达到国家相关标准的技术要求

INTRODUCTION
Northeast China is abundant in straw resources, corn straw is widely distributed, and the potential for use is enormous. Straw recycling is one of the most common methods of treatment and reuse at home and abroad. In some developed countries, the utilization rate of straw resources is very high, which basically solves the problem of straw piles and open burning *(Wang et al., 2017; Yeboah et al., 2017)*. By returning the straw to the field, the soil fertility can be significantly increased *(Liang et al., 2021; Dong et al., 2019; Han et al., 2020; Song et al., 2019)*. Taking straw back to the field can bring other benefits, including curing soil, wind and water erosion resistance, improved permeability, water storage, promoting drought resistance, and increased crop yield *(Liang et al., 2020; Guo et al., 2020; Li and Wang, 2020; Awad et al., 2022; Shao et al., 2023)*. Straw crushing and deep burial operation can reach 30 cm deep *(Wang et al., 2017)*.

[1] *Ruili Wang, Associate professor; Deshuai Li, Postgraduate; Shuai Li: Postgraduate; Tong Ren: Postgraduate; Hongbo Bai: Senior engineer; Yashuang Jin: Senior engineer; Wei Wang: Professor; Satyanarayan R S Dev: Associate professor*

It can effectively break the bottom of the plough, store water, increase the content of nitrogen, phosphorus, potassium, and other organic matter and nutrients in the soil, improve the soil tillage layer structure, promote the absorption of nutrients by crop roots, reduce the dust pollution caused by straw burning, and reduce the destructive damage caused by high temperature caused by combustion to some microorganisms in the soil *(Lin et al., 2019; Tian et al., 2018).*

At present, the corn straw crushing and returning equipment on the market is basically divided into two forms: one is the straw crushing and returning machine matching with the corn combine harvester, and the other is the straw returning machine suspended by the tractor *(Xie et al., 2022; Zheng et al., 2016)*. The analysis of the blade types of the cutting and crushing devices of different straw crushing and returning machines can be roughly divided into hammer claw type, L type or Y type and straight blade type. Hammer-claw type blade has large volume, strong hammer force and good crushing effect. However, its structure is complex, and the working power consumption and high-speed rotation are easy to cause vibration. Type L or Y blades are good for cutting and picking up, but their structure is slender and complex, and processing is more difficult. Straight blade, mostly using a moving blade and fixed blade matching cutting mode, its structure is simple, picking up and scattering effect is better, the material is lightweight, easy to replace, but its working width is small, it needs to increase the density of the blade in order to achieve a good working effect *(Jia et al., 2015; Guo et al., 2014)*. The cutting and crushing device of straw deep returning machine is the key to ensure the qualified rate of straw crushing. There is a pressing need to develop an efficient, low-consumption, simple, and reliable cutting and crushing device.

The straight blade is chosen by comparing the advantages and disadvantages of the straw returning blade in the existing straw returning machine. Based on the principle of sliding cutting, a moving fixed tool composite single support is designed. By optimizing the affecting factors of blade rotational speed, blade offset angle and blade number, the experiment index of crushing effect of the cutting and crushing device on straw is improved, and the working power consumption is reduced. The results serve as a foundation for future development of deep straw buried back in the field.

MATERIALS AND METHODS

The side-sweeping straw returning machine is mainly composed of a frame, three-point suspension device, transmission device, dust proof shell, trenching and mulching plough, depth-limiting device, anti-cutting shell, cutting and crushing device, etc. (Fig. 1). The cutting and crushing devices are mounted on the frame of the designed Side-sweeping straw returning machine and connected to the drive device. Two cutting and crushing devices are arranged from front to back, with the right on the front and the left on the back, with a keyway above the tool shaft that is connected to the pulley in the drive. Table 1 shows the main technical parameters of a straw deep returning machine with a cutting and crushing device.

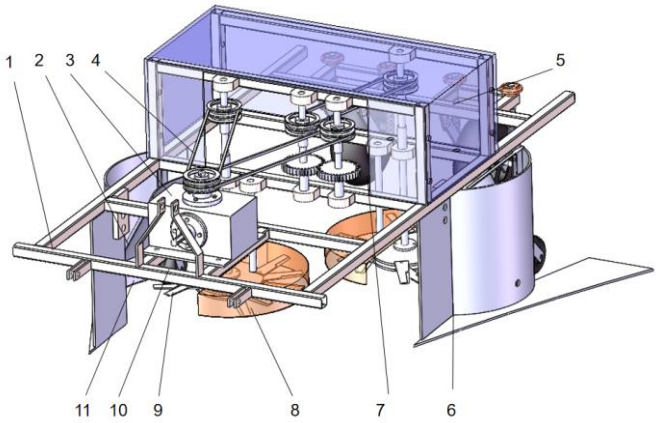

Fig. 1 - Structure of the side-sweeping straw returning machine

(1) frame; (2) three-point suspension device; (3) gearbox; (4) transmission device; (5) dust proof shell; (6) trenching and mulching plough; (7) depth-limiting device; (8) anti-cutting shell; (9) cutting and crushing device; (10) compaction wheel; (11) guide disc.

The side-sweeping straw deep returning machine is attached to the rear of the tractor through the three-point suspension device. The tractor's power output shaft uses a universal coupling to transfer the power to the transmission, which then transfers the power to the pulley and gear inside the transmission device, causing the left and right cutting and crushing devices to rotate in the opposite direction through the power transmission. The high-speed rotation of the cutting and crushing device can crush and smash the straw on the ground and

throw it into the automatic plough chamber. The body of the automatic trenching and mulching plough opens the embedded ditch before the cutting and crushing device can crush the straw. The broken straw flows into the ditch through the rectangular opening of the end of the plough body. The compaction wheel installed at the opening of the plough body will press down the broken straw. Following that, trenching and mulching plough's wing broke the soil, and the soil on both sides of the plough changed the original physical structure and fell into the ditch as a result of shear, extrusion, lifting, and gravity. The broken straw is buried 30 cm underground to realize the whole straw enrichment and returned to the field.

Cutting and crushing device mainly includes cutting plate, moving blade, fixed blade, blade shaft, lock, anti-cutting shell, etc. The moving blade and the blade disc are connected by riveting, and the moving blade can rotate freely around the riveting point, and the cutting range is larger. Dynamic blade for the upper and lower double layer, fixed blade welded in the anti-cutting shell inside, located in the middle of the two layers of dynamic blade, composed of dynamic blade and fixed blade form a single cutting and crushing support.

Table 1

Main technical parameters of the straw returning machine

Items	Technical parameters
Dimension (*L*×*W*×*H*) (mm)	2500×2000×1500
Number of rows	2
Applicable row spacing (mm)	600
Working width (mm)	1200
Type of throwing blade	Straight cut H type
Trenching depth (mm)	300
Trenching width (mm)	300
Matching power (kW)	≥80
Machine mass (kg)	350

Fig. 2 shows the working principle of the cutting and crushing device. The composite single support cutting of the support blade is adopted. The blade serves as a support, the blade rotates at a high speed, and the straw is cut several times. The power of the machine is transmitted to the transmission from the tractor through the universal coupling. Through the way of power transmission, the two cutting and crushing devices are rotated in opposite directions, and the straw on the ground is crushed, thrown to the diversion plate, and transported to the ditch, to realize the deep burial of the straw.

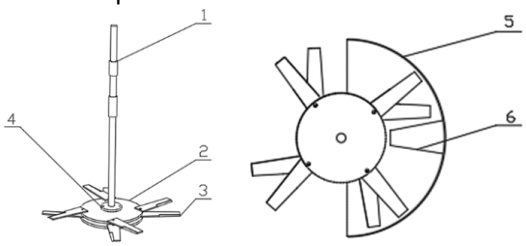

Fig. 2 - Working diagram of moving-fixed blade cutting and crushing device

(1) blade shaft; (2) blade disc; (3) moving blade; (4) lock; (5) anti-cutting shell; (6) fixed blade

Fig. 3 shows the structure of the blade, which is of the sharp H type. Four blades are installed symmetrically on each blade with a radius of 120 mm, length of 220 mm, blade opening of 140 mm and face up for repair and replacement. The upper and lower blades in each set of tools are staggered, and the angle between the upper and lower adjacent blades is 15°-25°; the distance between the disc center and the farthest end of the blade is 305 mm. On the premise that the strength of the crushing blade can be guaranteed, the blade thickness should be designed between 5-10 mm *(Zhang, 2018)*. Existing studies show that in order to ensure the straw crushing quality, the moving blade thickness should be as small as possible, so the blade thickness is designed as 5 mm *(Wang et al., 2021)*. The wider the blade, the greater the resistance of the blade crushing process, and the width of the blade will cause the weight of the straw crushing effect *(Cao et al., 2023; Liu et al., 2020)*, so the narrow end of the blade is 40 mm, and the wide end of the blade is 60 mm. The blade material is made of 65 Mn steel, and the edge of blade is treated by quenching.

The kinematic analysis refers to the qualitative or quantitative analysis of the position change of the mechanism without considering the effect of force. The kinematic analysis method was often used to study the influence of different parameter ratios of the mechanism on the change of its motion trajectory *(Ma et al., 2019)*. Based on this, the following content would use the curve drawing software SolidWorks to establish the motion trajectory model of the cutting and crushing device.

When the cutting and crushing device is working, the blade is centered around the riveting point on the blade plate and around the center of the blade disc. When rotating without load, the cutting and crushing device will experience three states, including start, stability and braking *(Liu et al., 2021; Liu et al., 2019)*. At the beginning of the start, the disc accelerates rapidly with the blade shaft. Due to inertia, the blade will have a stage lagging behind the disc, and the blade's center of mass will be deflected at a certain angle. When the disc speed is stable, the deflection angle is maximum. When the cutting and crushing device is stable, the blade has reached its equilibrium state, and the blade's center of mass is collinear with the riveting point and the center of the disc, as well as the tension of the blade on the riveting point and the centripetal force required for blade movement. When the cutting and crushing device brakes, the speed of the blade disc begins to decrease. Because of the blade's inertia, it will be ahead of the blade disc, and the blade's center will deflect at a certain angle forward. When the disc speed is stable, the deflection angle is maximum. Then the blade gradually deflects in reverse. The stable state is achieved when the blade's center of mass is collinear with the riveting point and the center of the blade disc, as shown in Fig. 4.

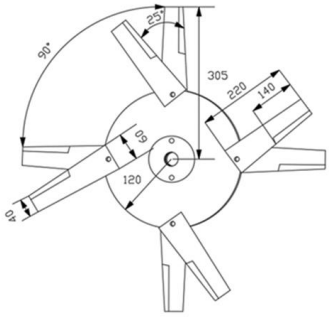

Fig. 3 - The main design parameters of blade

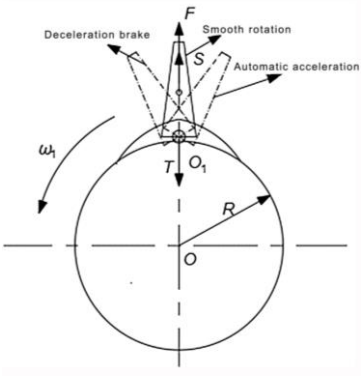

Fig. 4 - Blade motion analysis

This test was carried out on the self-made corn straw cutting and crushing tester, which consists of bench, cutting and crushing device, speed regulating motor, regulating rod, coupling, drive shaft, etc., as shown in Fig. 5. The power is output by the speed regulating motor and transmitted to the cutting and crushing device below through the drive shaft, the rear adjusting rod can adjust the deviation angle of the cutting and crushing device, the rotation speed of the cutting and crushing device can be adjusted within the range of 0 ~ 3250 rad / min, the scale range of the blade offset angle on the adjusting rod is 0°~12°, the test equipment also includes electronic scale, meter ruler, round hole sieve and vernier caliper.

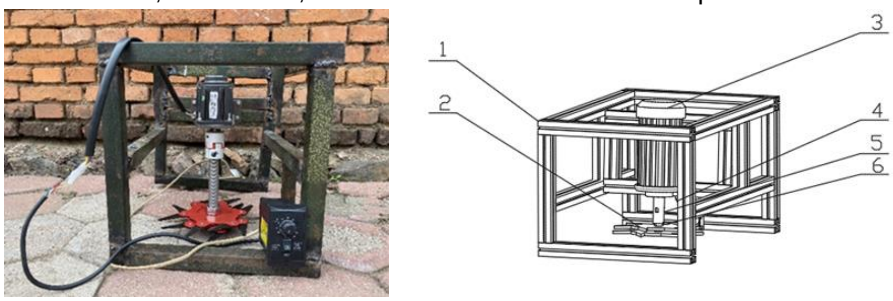

Fig. 5 - Corn straw cutting and crushing tester

(1) bench; (2) cutting and crushing device; (3) speed regulating motor; (4) regulating rod; (5) coupling; (6) drive shaft.

Blade rotational speed, blade offset angle, and blade number are the main factors of straw cutting and crushing performance, based on the principle of support sliding cutting and crushing, as well as blade dynamics analysis and kinematics analysis. Because the blade rotational speed can be controlled by the speed regulating motor, and the speed adjustment is convenient and fast, the blade rotational speed, blade offset angle and blade number are selected as the test factors. Determine the value range of each factors: blade speed 600~3000 rad/min, blade offset angle 2°~18° and blade number 2~10.

The evaluation index of straw returning machine is based on the industry standard NY/T500-2015 Operation Quality of straw returning machine. With the uneven ratio of straw throwing and the qualification ratio of straw crushed length as the test index, the influence of the blade rotational speed, blade offset angle and blade number on the test index is investigated, and the influence law of each factor on the straw cutting and crushing performance is analyzed.

During the single-factor test analysis, two factors were fixed, and the third factor was adjusted to the test. Each group of tests was repeated three times and averaged, and the effect of each factor on uneven ratio of straw throwing and the qualification ratio of straw crushed length was analyzed.

A three-factor Box-Behnken experiment was designed using Design-Expert13 software based on the previous single-factor test, as shown in Table 2, in which the center point test was repeated five times for a total of 17 trials. The relationship between the uneven ratio of straw throwing and qualification ratio of straw crushed length and the three influencing factors are shown in Table 3, where X_1, X_2, and X_3 are the coded values of blade rotational speed, blade offset angle, and the blade number.

Table 2

Factors and codes of test

Coding	Factors		
	Blade rotational speed (X_1/(r/min))	Blade offset angle (X_2/°)	Blade number (X_3)
-1	1800	4	3
0	2100	6	4
1	2400	8	5

Table 3

Experiment protocol and the results

No.	Factor level			Uneven ratio of straw throwing / %	Qualification ratio of straw crushed length / %
	Blade rotational speed / x_1	Blade offset angle / x_2	Blade number / x_3		
1	-1	-1	0	17.6	93.8
2	1	-1	0	17.5	91.2
3	-1	1	0	24.8	85.2
4	1	1	0	18.5	91.9
5	-1	0	-1	19.9	90.4
6	1	0	-1	17.9	90.6
7	-1	0	1	20.4	85.2
8	1	0	1	18.2	92.6
9	0	-1	-1	21.5	90.5
10	0	1	-1	24.7	88.9
11	0	-1	1	18.4	91.1
12	0	1	1	19.2	89.9
13	0	0	0	20.3	90.8
14	0	0	0	18.7	92.8
15	0	0	0	22.8	90.7
16	0	0	0	17.1	93.6
17	0	0	0	17.2	92.9

Straw returning to the field to cultivate fertilizer is the most direct and effective way to use straw resources. According to NY/T500-2015, the field test was carried out on the side-sweeping straw returning machine, and the qualified rate of straw crushing length, average stubble height, leakage rate and uneven ratio of straw throwing were taken as the test indexes. The tractor forward speed was 1.6 m/s, and the measurements were repeated twice.

The qualified rate of straw chopped length at each measured point is calculated according to the following formula:

$$F_h = \frac{\sum(m_z - m_b)}{\sum m_z} \times 100\% \quad (1)$$

where: F_h is qualification ratio of straw crushed length, %; m_z is the mass of straw in the measurement points, g; m_b is the mass of unqualified straw in the measuring points in terms of crushed length, g.

At each point, the stubble height of the left, middle, and right points was measured on the operating width of the straw deeper, and the average value of the three points was recorded as the stubble height of the point. The average value of the three points will be recorded as the stubble height of the point. A total of five points should be measured. The following formula calculates the uneven ratio of straw throwing:

$$\bar{m} = \frac{\sum m_z}{N_j} \quad (2)$$

$$F_b = \frac{(m_{max} - m_{min})}{\bar{m}} \times 100\% \quad (3)$$

where: m is the average mass of straw at each point within the measurement area, g; N_j is the number of measurement points in each measurement area; F_b is uniformity of spreading, %; $m_{\max}$ is maximum mass of straw at each point in the measurement area, g; $m_{\min}$ is the minimum value of straw mass at each point in the measurement area, g.

The ratio of straw missing cut is calculated according to the following formula:

$$F_1 = \frac{m_{s1}}{m_s} \times 100\% \tag{4}$$

where: F_1 is ratio of straw missing cut, %; m_s is the total amount of straw that should be returned per square meter, g; m_{s1} is the amount of straw missing cut per square meter, g.

RESULTS AND DISCUSSION

Assuming that the surface straw density of the corn harvester is certain, the cutting and crushing device of the side sweep straw deep returning machine can be considered as a swing with small deflection angle during the process from steady state rotation under no load to uniform speed movement under load. An external excitation is added to the movement of the blade around the riveting point as a result of straw obstruction, and the blade will appear repeatedly during the straw crushing process. The resistance of the surface straw to the blade f, the positive pressure N of the riveting point on the blade plate to the blade, the centrifugal force S generated by the high-speed rotation of the blade with the riveting point, and the centrifugal inertia force F generated by the high-speed rotation of the blade with the center of the blade disc are all part of the blade's main force. The force of the blade in the cutting and crushing device is shown in Fig. 6.

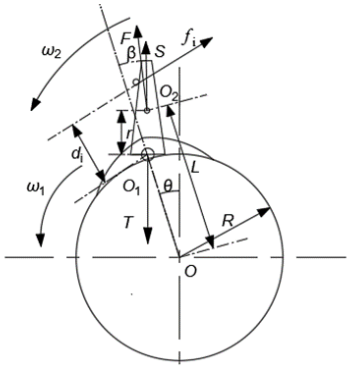

Fig. 6 - Analysis of force on blade

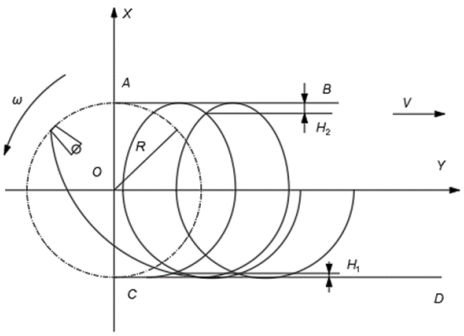

Fig. 7 - Blade motion path

Because the blade swings around the riveting point, the differential equation of the swing is:

$$J_{O1}\frac{d^2\varphi}{dt^2} = -FR\sin\theta + \sum f_i d_i \tag{5}$$

where: J_{O1} is the moment of inertia of the blade around the center O_1 of the riveting point, kg·m²; F is inertia force, N; R - radius of the blade, mm; f_i is the resistance of the straw to the blade, N; d_i is the distance between the straw and the riveting point, mm.

$$F = m\omega_1^2 L \tag{6}$$

$$L = \sqrt{r^2 + R^2 + 2rR\cos\varphi} \tag{7}$$

where: ω_1 is the rotational speed of the blade, rad/s; m is blade mass, kg; L is distance from the center of mass of the blade to the center of the blade disc, mm; r is blade center of mass to the center of the riveting point of rotation radius, mm.

Bring formula (6) -(7) into (5), it is obtained:

$$\sum f_i d_i = J_{O1}\frac{d^2\varphi}{dt^2} + m\omega_1^2 R\sin\theta\sqrt{r^2 + R^2 + 2rR\cos\varphi} \tag{8}$$

Assuming that the density of straw is small and the resistance is small, and the blade swings around the riveting point, sinφ≈φ, cosφ≈1. Equation (7) can be written as:

$$\sum f_i d_i = J_{O1}\frac{d^2\varphi}{dt^2} + m\omega_1^2 (R + r) R\sin\theta \tag{9}$$

When the side-sweeping straw deep returning machine works, the blade needs to overcome the torque of straw to cut and crush. The torque of cutting straw should be equal to the resistance torque of straw. $M=\Sigma f_i d_i$. From formula (8), the torque of cutting straw is:

$$M = J_{O1}\frac{d^2\varphi}{dt^2} + m\omega_1^2\left(R+r\right)R\sin\theta \tag{10}$$

The intersection of the blade trajectory was used to determine the spacing between the left and right blade groups, as shown in Fig. 7. The blade movement mainly consists of rotating motion and linear movement around the center of the blade, where the linear movement of the blade is provided by the tractor.

The trajectory of the blade endpoints is the cycloid. The trajectory curve equation of the blade is as follows: with the center of the blade disc as the coordinate origin, the *y*-axis direction is the forward direction of the blade disc, and the *x*-axis direction is the vertical direction, the trajectory curve equation of the blade is as follows:

$$\begin{cases} x = R\cos\omega t \\ y = R\sin\omega t + vt \end{cases} \tag{11}$$

where: t is time, s; ω is the angular velocity, rad/s; v is forward speed, m/s; R is rotation radius, mm.

The points on the edge of the envelope range of the blade movement trajectory are separated from the common tangent *AB* and *CD* of each blade trajectory, and the distances are H_1 and H_2, respectively, and the maximum values are H_1 and H_2, respectively. The maximum value is connected into a line, and the adjacent blade groups are also overlapped to obtain the appropriate blade overlap distance, reducing the re-cut area and avoiding leakage. Connect the maximum value to a line, so that adjacent tool groups also connect the line to overlap, and get the appropriate blade overlap distance, which can reduce the over-cutting area and avoid missing cutting. The overlapping distance of the leaves was 40mm after the calculation and analysis.

The results of single factor test show that (Fig. 8) when the uneven ratio of straw throwing and the qualification ratio of straw crushed length are better, the range of the blade rotational speed is 1800-2400 r/min, the range of blade offset angle is 4-8°, and the range of blade number is 3-5.

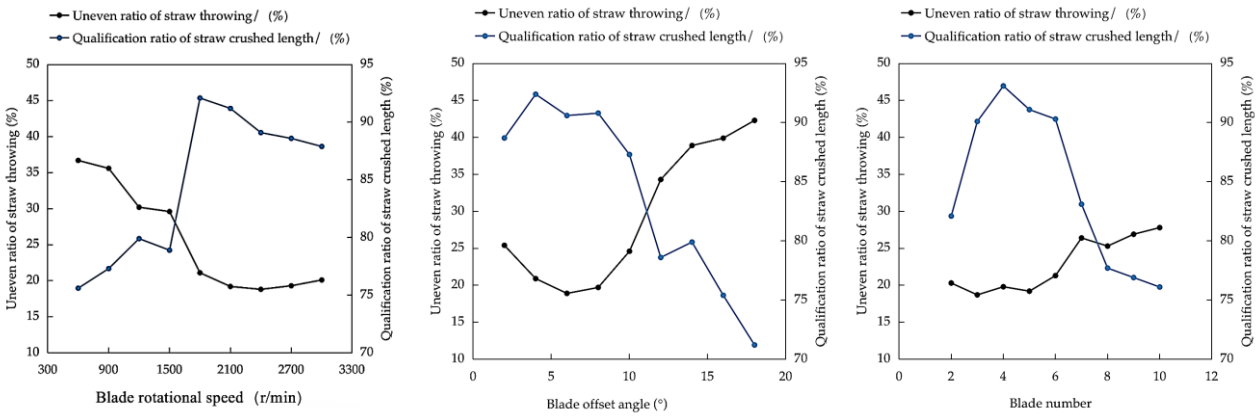

Fig. 8 - Results of single factor tests

The fitting regression analysis of the test results was performed using Design-Expert13 software to derive the regression equations for the uneven ratio of straw throwing W_1 and the qualification ratio of straw crushed length W_2, and the significance test was performed.

(1) Regression model for the uneven ratio of straw throwing W_1.

The results of ANOVA and significance test of regression coefficients for the regression model of the uneven ratio of straw throwing W_1 are shown in Table 4. The regression model's p-value (< 0.0001) for the uneven ratio of straw throwing W_1 was less than 0.01. This regression equation was highly significant. The p-value (0.9849) of the misfit term was more significant than 0. 05. The misfit term was not significant, so the fit could be used to predict the throwing unevenness rate. The regression equation for the throwing unevenness rate W_1 was:

$$\begin{aligned}\hat{W}_1 = {} & 17.72 + 2.45x_1 + 0.61x_2 + 0.89x_3 + 0.7x_1x_3 \\ & - 0.58x_2x_3 + 2.38x_1^2 + 1.25x_2^2 + 0.55x_3^2\end{aligned} \tag{12}$$

Table 4

Variance analysis of uneven ratio of straw throwing

Source	Sum of Squares	*df*	Mean Square	*F*-value	*P*-value
Model	95.32	9	10.59	47.51	< 0.0001**
x_1	48.02	1	48.02	215.41	< 0.0001**
x_2	3.00	1	3.00	13.46	0.0080**
x_3	6.30	1	6.30	28.27	0.0011**
x_1x_2	0.4900	1	0.4900	2.20	0.1818
x_1x_3	1.96	1	1.96	8.79	0.0210*
x_2x_3	1.32	1	1.32	5.93	0.0450*
x_1^2	23.80	1	23.80	106.76	< 0.0001**
x_2^2	6.61	1	6.61	29.63	0.0010**
x_3^2	1.29	1	1.29	5.77	0.0474*
Residual	1.56	7	0.2229		
Lack of Fit	0.0525	3	0.0175	0.0464	0.9849
Pure Error	1.51	4	0.3770		
Cor Total	96.88	16			

Note: ** indicates highly significant difference (P < 0.01), * indicates significant difference (P < 0.05), the same below.

Further analysis of each regression term of this regression equation showed that the regression terms x_1, x_2, x_3, x_1^2, and x_2^2 had a highly significant effect (P<0.01) on the throwing unevenness rate W_1, and x_1x_3, x_2x_3, and x_3^2 had a significant effect (P< 0.05) on the uneven ratio of straw throwing W_1; the effects of the other factors were not significant.

(2) Regression model of qualification ratio of straw crushed length W_2.

The results of ANOVA and significance test of regression coefficients for the regression model of qualification ratio of straw crushed length W_2 are shown in Table 5. The p-value (0.0004) of the regression model of qualification ratio of straw crushed length W_2 was less than 0.01. This regression equation was highly significant. The p-value (0.5390) of the misfit term was more significant than 0.05. The misfit term was not significant, so the fit could be used to predict the qualification ratio of straw crushed length. The regression equation of code for the qualification ratio of straw crushed length W_2 was:

$$\hat{W}_2 = 92.96 - 1.14x_1 - 1.39x_2 - 1.3x_3 - 1.45x_1x_3 - 1.2x_2x_3 - 1.22x_1^2 - 1.17x_2^2 - 2.39x_3^2 \quad (13)$$

Further analysis of each regression term of this regression equation showed that the regression terms x_1, x_2, x_3, x_1x_3, and x_3^2 had a highly significant effect (P < 0.01) on the qualification ratio of straw crushed length W_2, and x_2x_3, x_1^2, and x_2^2 had a significant effect (P < 0.05) on the qualification ratio of straw crushed lengthW_2; the effects of the other factors were not significant.

Response surface analysis method was used to analyze the experiment data and study the relationship between the target value of straw cutting and crushing performance (uneven ratio of straw throwing and qualified rate of straw crushing length) and the influencing factors (blade rotational speed, blade offset angle, blade number) *(Wang et al., 2020; Gapparov and Karshiev, 2020)*. According to the analysis results, the response surface Fig. 9 and Fig. 10 are drawn. The response surface diagram clearly shows the influence of the influencing factors on the performance of straw cutting and crushing performance, as well as the interaction between the influencing factors on the performance.

Table 5

Variance analysis of qualification ratio of straw crushed length

Source	Sum of Squares	*df*	Mean square	*F*-value	*P*-value
Model	93.39	9	10.38	18.80	0.0004**
x_1	10.35	1	10.35	18.75	0.0034**
x_2	15.40	1	15.40	27.90	0.0011**
x_3	13.52	1	13.52	24.49	0.0017**
x_1x_2	0.3025	1	0.3025	0.5479	0.4832
x_1x_3	8.41	1	8.41	15.23	0.0059**
x_2x_3	5.76	1	5.76	10.43	0.0145*
x_1^2	6.24	1	6.24	11.31	0.0120*
x_2^2	5.74	1	5.74	10.40	0.0146*
x_3^2	24.10	1	24.10	43.66	0.0003**
Residual	3.86	7	0.5521		
Lack of Fit	1.49	3	0.4975	0.8390	0.5390
Pure Error	2.37	4	0.5930		
Cor Total	97.26	16			

Blade rotational speed, blade number, and blade offset angle were the most important influencing factors on the uneven ratio of straw throwing. There was a significant (P<0.05) interaction between the three influencing factors on the uneven ratio of straw throwing, and the main order of influencing factors on the qualification ratio of straw crushed length was blade offset angle, blade number, and blade rotational speed. There was a significant (P<0.05) interaction between the three influencing factors on the qualification ratio of straw crushed length interaction. As shown in Fig. 19 (a) and Fig.10 (a), with the increase in the blade number, the uneven ratio of straw throwing tends to decrease and then increase, and the qualification ratio of straw crushed length tends to increase and then decrease. From Fig. 9(b) and Fig.10 (b), with the increase of blade offset angle, the uneven ratio of straw throwing tends to decrease and then increase, and the qualification ratio of straw crushed length tends to increase and then decrease.

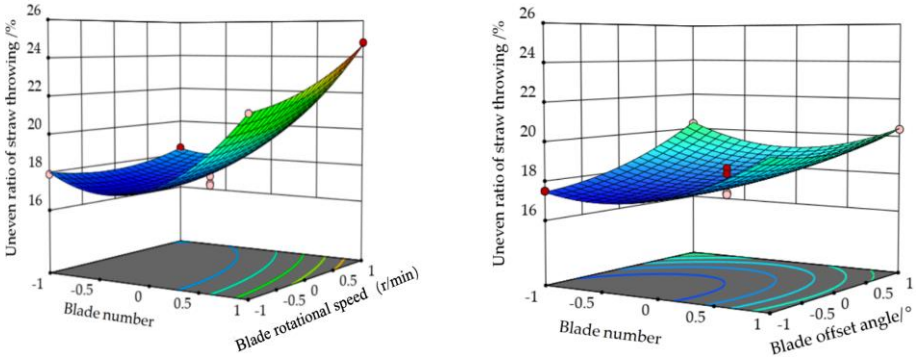

Fig. 9 - Influence of various factors on uneven ratio of straw throwing

(a) Blade rotational speed and blade number *(b) Blade offset angle and blade number*

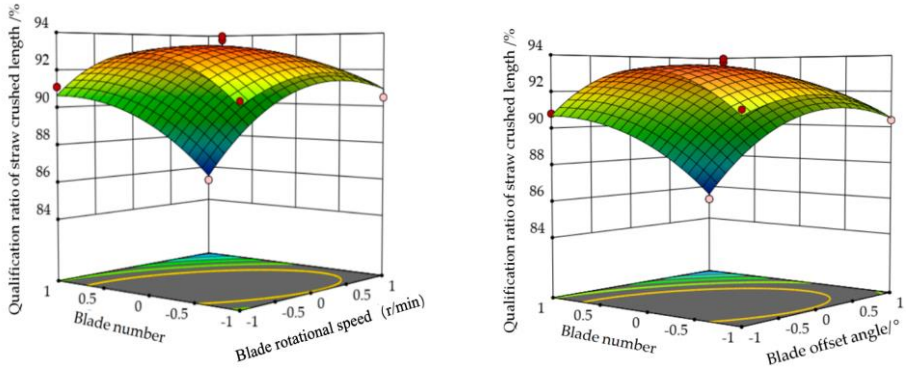

Fig. 10 - Influence of various factors on qualification ratio of straw crushed length

(a) Blade rotational speed and blade number *(b) Blade offset angle and blade number*

Using the Optimization function of Design-Expert13 software, the optimization analysis obtains the optimal parameter combination of the device: the blade speed is 1968 rad/min, the blade offset angle is 5.24° and the blade number is 4. At this time, the uneven ratio of straw throwing is 16.98%, and the qualified rate of straw crushing length is 93.59%. The working parameters of straw cutting and crushing were adjusted to the value of the preferred test factors, and the test was repeated, and the uneven ratio of straw throwing was 17.18%, and the qualification ratio of straw crushed length was 92.23%.

Field test

The field operation effect of the side-sweeping straw returning machine is shown in Fig. 11, and the field test results are shown in Table 6. The machine works well under the condition of low water content of harvested corn field and corn straw, and all the indexes can meet the design requirements.

Fig. 11 - The operation effect of side-sweeping straw returning machine

Table 6

Field test results of side-sweeping straw returning machine

Test item	Standard value	Test results
Qualification ratio of straw crushed length (%)	≥90	94.22
Average stubble height (mm)	≤80	42
Uneven ratio of straw throwing (%)	≤20	17.21
Ratio of straw missing cut (%)	≤1.5	0.81

Discussion

The results show that the optimal results obtained by theoretical calculations are very similar to the field tests, thus verifying the accuracy of simulation model building. According to the blade structure and shape in the cutting and crushing device of straw returning machine, it can be roughly divided into hanging claw type, bending blade type, Y type and straight blade type and combined bending blade type *(Gapparov and Karshiev, 2020; Lin et al., 2017)*. For example, the crushing device of 1 JKL-2 straw deeply buried back to the field is Y-type throwing blade, which rotates at high speed and cuts straw in the field operation *(Lin et al., 2022; Chinese Academy of Agricultural Mechanization Science, 2007)*. Compared with the cutting device designed in this paper, the cutting method is simple, light and easy to replace *(Zhang et al., 2021; Wang, et al., 2019)*. It can significantly improve the cutting efficiency and reduce the power consumption. The side sweeping straw cutting and crushing device designed in this paper significantly improves the blade life, reduces the damage of the obstacles to the blade, and extends the life of the blade. The compound single support cutting method has the advantages of improving the straw crushing rate and reducing the operating power consumption.

The Side-Sweeping Straw Returning Machine designed in this paper meets the design requirements, but there are still some problems worth improving, which makes the operation quality further improved. The coverage rate of the automatic coverage plough is 80.63%, which meets the design requirements, but the impact on the coverage rate can still be studied by adjusting the structural parameters, improving the coverage rate of the automatic coverage plough, using the bionic and surface spraying technology to make the cutting and crushing device more effective and reduce the resistance of the automatic covering plough in the soil, by optimizing the structure of the whole machine.

CONCLUSIONS

(1) Based on the principle of support sliding cutting and crushing, a double single support cutting and crushing device is designed, which realizes the multiple sliding cutting of the blade to the corn straw in the whole cutting and crushing process, and the straw crushing effect is good. The kinematics and dynamics analysis of the blade in the cutting and crushing device are made to ensure the simplification and lightweight of the corn straw returning machine.

(2) Three secondary response surface analysis of the test data by Design-Expert13 software, and the significance of the factors affecting the uneven ratio of straw throwing is the blade rotating speed, the blade number and the blade offset angle. The significant factors affecting the qualified ratio of straw crushing are blade offset angle, blade number and blade rotating speed.

(3) The optimal working parameter combination of the side-sweeping straw returning machine is the blade speed of 1968 rad/min, the blade offset angle of 5.24° and the blade number of 4. At this time, the uneven ratio of straw throwing is 16.98%, and the qualification ratio of straw crushed length is 93.59%. Process the side sweep straw deep returning machine according to the optimal working parameters, and the field performance test was carried out. According to the test results, the uneven ratio of straw throwing is 17.21%, and the qualification ratio of straw crushed length is 94.22%. According to the operation standard of straw returning machine to the field, and the test results meet the operation requirements. This study provides a technical basis for the industrialization of corn straw buried in the field.

ACKNOWLEDGMENTS

The authors would like to thank for Shenyang Agricultural University for providing the test instruments and equipment as well as the test site. This research was funded by the Natural Science Foundation of Liaoning Province (Grant No.2022-NLTS-19-05), and the “Jie Bang Gua Shuai” Science and Technology Program Major Project of Liaoning Province (Grant No.2022JH1/10400017).

REFERENCES

[1] Awad, R., G. M. ElMasry S. A. M. Abd El-Azeem. (2022). Influence of Incorporating Shredded Corn Stover on some Physicochemical Properties of the Soil and Corn Crop Production. *Journal of Soil and Water Sciences*, Vol.7(1), pp. 1-12. United States.

[2] Cao, S, L., Xie, J, H., Yang, Y, X., Liu, Y, R., Lu, Y, T., Sun, B. (2023). Design and experiment of side row cotton straw returning and residual film recovery combined machine (侧排式棉秸秆还田及残地膜回收联合作业机的设计与试验). *Journal of Jilin University (Engineering and Technology Edition)*, Vol. 53 (5), pp. 1514-1528. China.

[3] Chinese Academy of Agricultural Mechanization Science. (2007). Agricultural Machinery Design Manual: First Volume. *Beijing: China Agricultural Science and Technology Press*, China.

[4] Dong, L. L., Wang, H. H., Lu, C. Y., Jin, M. J., Zhu, X. L., Shen, Y., & Shen, M. X. (2019). Effects of straw returning amount and type on soil nitrogen and its composition (秸秆还田量和类型对土壤氮及氮组分构成的影响). *The Journal of Applied Ecology*, Vol. 30(4), pp.1143-1150. China.

[5] Gapparov, S., & Karshiev, F. (2020). Development chopper device that chops baled rough fodders. IOP Conference Series: *Materials Science and Engineering*, Vol. 883(1), pp.12158. England.

[6] Guo, H.Y., Zhao, S.F., Dong, Z.W., Wang, Q., Xia, D.P., Jia, J.B., Yin, X.J., Yu, H.F., (2020). Clean and efficient utilization of coal combined with corn straw by synergistic biodegradation. *Renewable Energy*, Vol.161, pp.701-711. England.

[7] Guo, Q., Zhang, X.L., Xu, Y.F., Li, P.P., Chen, C., Wu, S. (2014). Design and experiment of cutting blade for cane straw (藤茎类秸秆专用切割刀片的设计与试验). *Transactions of the Chinese Society of Agricultural Engineering*, Vol. 30(24), pp. 47-53. China.

[8] Han, Y., Ma, W., Zhou, B., Yang, X., Salah, A., Li, C., Zhao, M. (2020). Effects of Straw-Return Method for the Maize–Rice Rotation System on Soil Properties and Crop Yields. *Agronomy*, Vol. 10(4), pp. 461. Switzerland.

[9] Jia, H.L., Jiang, X.M., Guo, M.Z., Liu, X.L., Wang, L.C. (2015). Design and experiment of V-L shaped smashed straw blade (V-L 型秸秆粉碎还田刀片设计与试验). *Transactions of the Chinese Society of Agricultural Engineering*, Vol. 31(1), pp. 28-33. China.

[10] Li, Y., Wang, Q.B. (2020). Study on potential of straw resource nutrient return to field and application technology in China (我国秸秆资源养分还田利用潜力及技术分析). *Soil and Fertilizer Sciences in China*, Vol. (1), pp. 119-126. China.

[11] Liang, X.X., Shi, Z.L., Wang, J.C., et al. (2020). Review on the crop straw utilization technology of China. *American Journal of Environmental Science and Engineering*, Vol. 4(4), pp. 61-64. American.

[12] Liang, Y., Al-Kaisi, M., Yuan, J., Liu, J., Zhang, H., Wang, L., Ren, J. (2021). Effect of chemical fertilizer and straw-derived organic amendments on continuous maize yield, soil carbon sequestration and soil quality in a Chinese Mollisol. *Agriculture, Ecosystems & Environment*, Vol. 314, pp. 107403. Netherlands.

[13] Lin, H., He, J., Li, H., Wang, Q., Lu, C., Yang, W., Chang, Y. (2022). Design and Experiment of a Reciprocating Intermittent Chopping Device for Maize Straw Returning. *Agriculture*, Vol. 12(2), pp. 220. Switzerland.

[14] Lin, J., Ma, T., Li, B.F. (2017). Design and test of 1JHL-2 type straw deep burying and retuning machine (1JHL-2 型秸秆深埋还田机设计与试验). *Transactions of the Chinese Society of Agricultural Engineering*, Vol. 33(20), pp. 32-40. China.

[15] Lin, J., Zhang, T.J., Chen, B., Han, W., Lv, Q.L., Wang, J.Q. (2019). Design and Test of Subsoiling Rotary Rilling and Rilling Combined Operating Machine (深松灭茬旋耕起垄联合作业机设计与试验). *Transactions of the Chinese Society for Agricultural Machinery*, Vol. 50(2), pp. 28-39. China.

[16] Liu, J. B., Bao, Y., Zheng, W. T., & Hayat, S. (2021). Network coherence analysis on a family of nested weighted n-polygon networks. *Fractals*, Vol. 29(08), pp. 2150260. United States.

[17] Liu, J. B., Zhao, J., Min, J., & Cao, J. (2019). The Hosoya index of graphs formed by a fractal graph. *Fractals*, Vol. 27(08), pp.1950135. United States

[18] Liu, P., He, J., Li, Y.J., Li, H.W., Wang, Q.J., Lu, C.Y., Zhang, Z.G., Li, S.H. (2020). Design and experiment of double rollers maize stalk chopping device with different rotation speeds (异速对辊式玉米秸秆粉碎还田装置设计与试验). *Transactions of the Chinese Society of Agricultural Engineering*, Vol. 36(14), pp. 69-79. China.

[19] Ma, P.Y., Li, S.J., Zhao, C.Q., Zhang, Y.L., Zhang, X.C., Zhang, C.Y. (2019). Design and test of the orange garden profile mower cutter (柑橘园仿形割草机切割器的设计与试验). *Journal of Huazhong Agricultural University*, Vol. 38(06), pp. 156-162. China.

[20] Shao, J., Gao, C., Afi Seglah, P., Xie, J., Zhao, L., Bi, Y., & Wang, Y. (2023). Analysis of the Available Straw Nutrient Resources and Substitution of Chemical Fertilizers with Straw Returned Directly to the Field in China. *Agriculture*, Vol. 13(6), pp.1187. Switzerland.

[21] Song, X., Sun, R., Chen, W., & Wang, M. (2019). Effects of surface straw mulching and buried straw layer on soil water content and salinity dynamics in saline soils. *Canadian Journal of Soil Science*, Vol. 100(1), pp, 58-68. Canada.

[22] Tian, Y., Lin, J., Li, B.F. (2018). Design and test of conveying device of pneumatic straw deep burying and returning machine (气力式秸秆深埋还田机输送装置设计与试验). *Transactions of the Chinese Society for Agricultural Machinery*, Vol. 49(12), pp. 36-44. China.

[23] Wang, J., Wang, X.Y., Li, H.W., He, J., Lu, C.Y., Liu, D. (2021). Design and Experiment of Rice Straw Chopping Device for Agitation Sliding Cutting and Tearing (水稻秸秆激荡滑切与撕裂两级切割粉碎装置设计与试验). *Transactions of the Chinese Society for Agricultural Machinery*, Vol. 52(10), pp. 28-40. China.

[24] Wang, J.W., Tang, H., Wang, J.F. (2017). Comprehensive Utilization Status and Development Analysis of Crop Straw Resource in Northeast China (东北地区作物秸秆资源综合利用现状与发展分析). *Transactions of the Chinese Society for Agricultural Machinery*, Vol. 48(5), pp. 1-21. China.

[25] Wang, R., Yang, P., Rabiu, F., & Dou, S. (2017). Design and experiment of combine machine for deep furrowing, stubble chopping, returning and burying of chopped straw (秸秆深埋还田开沟灭茬机设计与试验). *Transactions of the Chinese Society of Agricultural Engineering*, Vol. 33(5), pp. 40-47. China.

[26] Wang, S.W., Li, S.J., Zhang, Y.L., Wan, Q., Chen, H., Meng, L. (2019). Mole toe bionics and surface heat treatment improving resistance reduction and abrasion resistance performance of toothed ditching blade (鼹鼠趾仿生及表面热处理提高齿形开沟刀减阻耐磨性能). *Transactions of the Chinese Society of Agricultural Engineering*, Vol. 35(12), pp. 10-20.

[27] Wang, X.Y., Zhu, S., Li, X.Q., Li, T.X., Wang, L.L., Hu, Z.X. (2020). Design and Experiment of Directional Arrangement Vertical and Horizontal Cutting of Seed Potato Cutter (定向排列纵横切分马铃薯种薯切块机设计与试验). *Transactions of the Chinese Society for Agricultural Machinery*, Vol. 51(6), pp. 334-345. China.

[28] Xie, R.-Z., Ming, B., Gao, S., Wang, K.-R., Hou, P., Li, S.-K. (2022). Current state and suggestions for mechanical harvesting of corn in China. *Journal of Integrative Agriculture*, Vol.21(3), pp. 892-897. China.

[29] Yeboah, S., Lamptey, S., Zhang, R., & Li, L. (2017). Conservation Tillage Practices Optimizes Root Distribution and Straw Yield of Spring Wheat and Field Pea in Dry Areas. *Journal of Agricultural Science*, Vol. 9(6), pp. 37-48. United States.

[30] Zhang, Y., Qiao, C.X., Wang, T.Q., Cao, J.F., Wang, P.F., Shi, L. (2021). Drag reduction mechanism of the 3D geometry of foreleg's claw toe of the mole cricket (*Gryllotalpa orientalis*) (蝼蛄前足爪趾三维几何构形的减阻机理). *Transactions of the Chinese Society of Agricultural Engineering*, Vol. 37(19), pp. 309-315.

[31] Zhang, Z.Q. (2018). *Research on corn straw chopping and spreading machine design and dynamic characteristic of straw (玉米秸秆粉碎抛撒还田机的设计与秸秆运动特性研究).* Beijing: China Agricultural University. China.

[32] Zheng, Z.Q., He, J., Li, H.W., Xi, P.S., Wang, Q.J., Zhang, X.C. (2016). Design and experiment of straw-chopping device with chopping and fixed knife supported slide cutting (动定刀支撑滑切式秸秆粉碎装置设计与试验). *Transactions of the Chinese Society for Agricultural Machinery*, Vol. 47(S1), pp. 108-116. China.

REAL-TIME WHEAT DETECTION BASED ON LIGHTWEIGHT DEEP LEARNING NETWORK REPYOLO MODEL
/
基于轻量级深度学习网络 RepYOLO 模型的麦穗实时检测

Zhifang BI[1], Yanwen LI[2], Jiaxiong GUAN[2], Xiaoying ZHANG[*3]
[1] Department of Basic Courses, Shanxi Agricultural University, Shanxi / China
[2] College of Information Science and Engineering, Shanxi Agricultural University, Shanxi / China
[3] School of Software, Shanxi Agricultural University, Shanxi / China
Tel: +86-15803449361; E-mail: xiaoyingzhang@sxau.edu.cn
DOI: https://doi.org/10.35633/inmateh-72-53

Keywords: *Real-time detection; Wheat; YOLOv4; RepVGG; CBAM; ATSS Algorithm*

ABSTRACT

Real-time detection has become an essential component in intelligent agriculture and industry. In this paper, a real-time wheat spike detection method based on the lightweight deep learning network RepYOLO is proposed. Addressing the small and densely packed phenotype characteristics of wheat spikes, the channel attention mechanism module CBAM from the traditional YOLOv4 algorithm is introduced and multiple convolutional kernels are merged using a structural reparameterization method. Additionally, the ATSS algorithm is incorporated to enhance the accuracy of object detection. These approaches significantly reduce the model size, improve the inference speed, and lower the memory access cost. To validate the effectiveness of the model, it is trained and tested on a large dataset of diverse wheat spike images representing various phenotypes. The experimental results demonstrate that the RepYOLO algorithm achieves an average accuracy of 98.42% with a detection speed of 8.2 FPS. On the Jetson Nano platform, the inference speed reaches 34.20 ms. Consequently, the proposed model effectively reduces the memory access cost of deep learning networks without compromising accuracy and successfully improves the utilization of CPU/MCU limited performance.

摘要

实时检测已成为智能农业的重要组成部分。本文提出了一种轻量级深度学习网络 RepYOLO 的小麦穗实时检测方法。针对小麦穗小而密的表型特征，从传统的 YOLOv4 算法中引入通道注意机制模块 CBAM，并使用结构重参数化方法合并多个卷积核。此外，结合了 ATSS 算法来提高目标检测的准确性。这些方法显著减小了模型尺寸，提高了推理速度，降低了内存访问成本。为了验证该模型的有效性，本实验在代表不同表型的小麦穗图像的大型数据集上进行了训练和测试。实验结果表明，RepYOLO 算法的平均准确率为 98.42%，检测速度为 8.2fps。在 Jetson nano 平台上，推理速度达到 34.20/ms。因此，本文提出的模型在不影响精度的前提下，有效地降低了深度学习网络的内存访问成本，并成功地提高了 CPU/MCU 有限性能的利用率。

INTRODUCTION

Drones have become an important technology in agriculture due to their advantages, including low cost, high speed, low-altitude flying capability, and efficient operation *(Radoglou-Grammatikis et al., 2020)*. They are equipped with various sensors such as RGB cameras, thermal imaging cameras, and multispectral cameras, which allow for capturing high-resolution images of wheat fields at different spatial scales, unlike remote sensing images from satellites and ground platforms *(Hassan et al., 2019)*.

Deep learning technology combined with drone detection has become the mainstream detection technology. It enables crop growth monitoring, management efficiency improvement, and precision agriculture. In the field of computer vision, deep learning has made tremendous progress. Chen et al.'s research has shown the successful application of deep learning in this field *(Chen et al., 2021)*. Alsalm et al. developed a computer vision-controlled drone monitoring system that can accurately detect crop health and pests *(Jin et al., 2017)*. Khan et al. proposed a new framework based on drones and object detection technology that can be used for precision agriculture, remote sensing, search, and rescue *(Khan et al., 2022)*.

However, methods relying on cloud computing platforms for detection have latency issues in practical applications and cannot meet real-time requirements *(Khalil et al., 2022)*. Additionally, without support from a local area network and large computing devices, application and implementation are impossible. Directly porting the inference detection program to an embedded unmanned aerial vehicle (UAV) chip is the best way to solve this problem.

However, due to the large amount of computing resources required for deep learning during the inference process, current deep learning technology cannot be applied to embedded UAV chips. Therefore, this paper proposes a target detection model suitable for embedded UAV chips - RepYOLO.

The RepYOLO model greatly reduces MAC (memory access cost) *(Ma et al., 2022)* by changing the backbone network to RepBlock *(Ding et al., 2021)* and simplifies the prediction boundary box calculation process by changing the detection head to anchor-free *(Wang et al., 2021)*. In addition, the CBAM attention mechanism (*Woo et al., 2018*) is added to the Neck network structure to further improve the model's accuracy. The ATSS algorithm *(Zhang et al., 2022)* was chosen in the training process to improve the model's inference accuracy. Because wheat data exhibits multi-phenotype characteristics and fields present complex scenes with dense distribution, overlap, and occlusion, the Global Wheat Dataset *(David et al., 2021)* and real UAV-captured wheat images from fields were used for the dataset.

Finally, the experimental results of this paper show that the RepYOLO model can achieve optimal accuracy and speed on UAV devices when detecting wheat data with complex features, and the detection performance and accuracy are higher than the YOLOv4 *(Bochkovskiy et al., 2020)* model directly ported to the UAV chip. Since the proposed model in this paper is universal, it is also suitable for detecting other targets.

MATERIALS AND METHODS

Data Acquisition and Preprocessing

The dataset used in this experiment is based on the Global Wheat Head Detection Dataset. To address the issue of uneven distribution in the sample data, increase the diversity of the dataset and mitigate the risk of trained model errors and biases, both web crawling and field data collection methods were used. With these methods, wheat image data of four phenotypic features were obtained: grain saturation, wheat spike maturity, spike length, and awn features (Fig.1).

Fig. 1 - Four Phenotypic Features

To ensure the statistical properties of the dataset, skewness, kurtosis, standard deviation, and Z-Score are also computed to evaluate whether the sample data conforms to normal distribution. During data preprocessing, multiple measures were taken to improve the convergence speed of training and the quality of the dataset. Firstly, the original images were cropped and adjusted to 416x416 pixels in size to improve the convergence speed of training. In addition, a complex frequency domain Gaussian low-pass filter method was used to eliminate image noise.

In this dataset, wheat image data containing four phenotypic traits were collected and fitted curves were plotted for the quantity distribution of different traits, as shown in Fig.2. The fitted curves reflect the statistical regularities of the quantity distribution of wheat images with different phenotypic traits in the dataset.

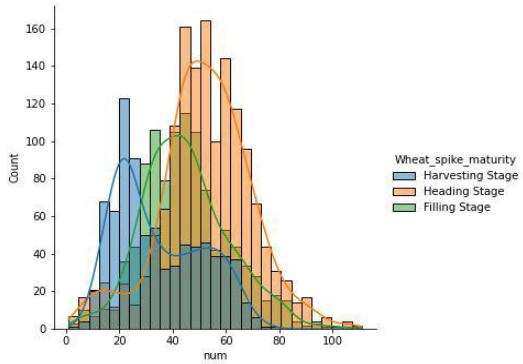

(a) Grain saturation

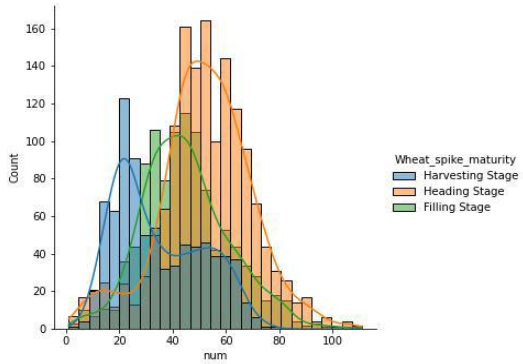

(b) Wheat spike maturity

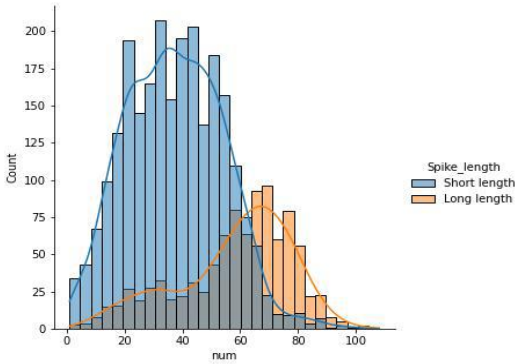

(c) Spike length

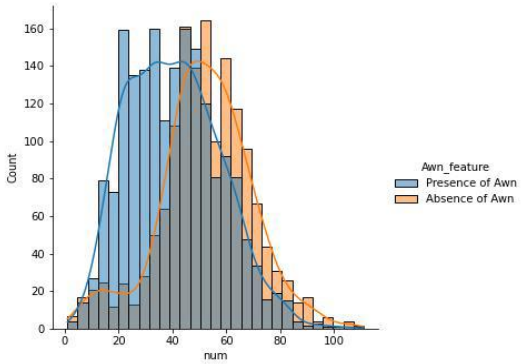

(d) Awn feature

Fig. 2 - Distribution of Sample Data under Different Phenotypic Features

The skewness, kurtosis, standard deviation, Z-Score of four phenotypic features are in Table 1. Skewness is used to describe the degree of deviation from a normal distribution. Kurtosis measures the thickness of the distribution's peak compared to a normal distribution. Standard deviation reflects the dispersion of the distribution, and Z-score is primarily used to determine whether the sample data conforms to a normal distribution. When the value of Z-score is between -1.96 and 1.96, 95% of the data is included in this interval, indicating that it conforms to a normal distribution.

Table 1

Kurtosis, Skewness, Standard Deviation and Z-Score of Different Phenotypic Data

Phenotypic features	Grain saturation		Wheat spike maturity		
	Shriveled type	Saturated type	Heading stage	Filling stage	Harvesting stage
Skewness	0.2694	0.2587	-0.1933	0.4382	0.4672
Kurtosis	0.0559	0.0857	0.6251	0.3949	-0.9842
Standard Deviation	0.4732	0.4007	0.5181	0.5201	0.6903
Z_1-Score	0.5694	0.6457	-0.3732	0.8426	0.6767
Z_2-Score	0.1180	0.2138	1.2066	0.4687	-1.4257
Phenotypic features	**Spike length**		**Awn feature**		
	Short length	**Long length**	**Absence of Awn**	**Presence of Awn**	
Skewness	0.2123	-0.6443	-0.1933	0.3841	
Kurtosis	-0.2248	-0.2099	0.6251	-0.2027	
Standard Deviation	0.4523	0.5127	0.5019	0.3140	
Z_1-Score	0.4694	-1.2568	1.2455	1.2232	
Z_2-Score	-0.4789	-0.4094	1.2045	-0.6457	

Figure 2 shows the bimodal analysis distribution fitting curves of the four feature samples. It can be seen from the figure that the data distribution roughly conforms to the normal distribution. Table 1 provides a quantitative analysis of the sample data, including skewness, kurtosis, standard deviation, and Z-Score calculation. The results of the calculation indicate that the sample distribution of the four phenotypic features conforms to the normal distribution, as the values of Z_1-Score and Z_2-Score are both between -1.96 and 1.96.

In order to enhance the generalization ability of deep learning models and avoid overfitting, data augmentation techniques were utilized, including Gaussian blurring, Random noise, Hue, Exposure, Cutout, and Mosiac (Fig. 3. The aforementioned data augmentation techniques were used to process RGB images with a size of 416x416 pixels, generating a total of 11,541 images. These images were randomly shuffled and divided into training, validation, and testing sets with a ratio of 7:2:1. The training set was used to train the model, the validation set was used to tune the hyperparameters, and the testing set was used to evaluate the performance of the model. The specific parameter settings for data augmentation are shown in Table 2.

(a) Original **(b) Gaussian blurring** **(c) Random noise** **(d) Hue**

(e) Exposure **(f) Cutout** **(g) Mosiac** **(h) Combination**

Fig. 3 - Data Enhancement

Table 2

Data Enhancement Setting

Gaussian blurring	Random noise	Hue
Up to 2px	Up to 1% of pixels	-40° ~ +40°
Exposure	**Cutout**	**Mosiac [1]**
-5% ~ +5%	3 boxes with 5% size	Applied

RepYOLO structure

RepYOLO is a detection algorithm that is improved based on YOLOv4. Similar to other methods in the YOLO series, RepYOLO can output detection boxes containing information such as coordinates, categories, and confidence scores. This study mainly focuses on modifying the backbone, head, and neck of the algorithm to maximize the utilization of limited computing resources on drone chips. Structural reparameterization technology can effectively improve the utilization of computer resources (*Ding et al., 2021, Zagoruyko et al., 2017)*. Inspired by the RepVGG classification network, RepBlock was used instead of the original CSPDarknet in the backbone network to increase detection speed. Previous studies have shown that anchor-based detection heads significantly decrease network speed compared to anchor-free detection heads, but this is due to the uneven distribution of positive and negative samples during training. To further improve the utilization of limited computing resources on drones, an anchor-free detection head was used instead of the original one in the head network and the ATSS algorithm was adopted to replace the original positive and negative sample matching scheme. At the same time, the CBAM attention mechanism module was inserted in the neck network to further integrate advanced semantic features and low-level spatial information, and improve the accuracy of the detection model.

Previous research has indicated that multi-branch networks typically exhibit better classification performance than single-path networks, but this can lead to an increase in inference latency (*Szegedy et al., 2019, He et al., 2016*). In this study, inspired by RepVGG, the limited computing performance of unmanned aerial vehicles was considered. To balance accuracy and speed, an efficient and parameterizable backbone network, known as RepBlock, was utilized. The RepBlock network leverages hardware computing capabilities, and after model training, inference latency was significantly reduced by converting the multi-branch topology to a 3x3 convolution layer (RepConv) with a ReLU activation function. The reparameterization method outlined in the RepVGG paper, which separates the multi-branch topology during training from the single-path network during inference, was employed. Previous studies have shown that the Batch Normalization (BN) layer normalizes data within each mini-batch. This normalization ensures stable means and variances, and reduces the coupling between adjacent layers. Consequently, the BN layer makes network training more stable. In addition, the BN layer acts as a regularization technique to prevent overfitting. As shown in Fig.4, the RepBlock Training Structure introduces the BN layer.

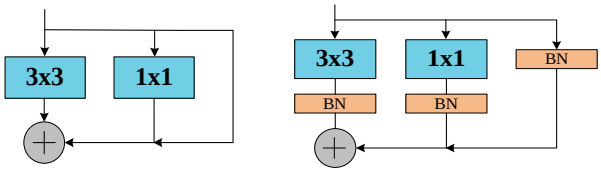

(a) Original Multi-branch (b) Multi-branch with BN

Fig. 4 - Introduction of BN Layer

The YOLOv4 algorithm for object detection traditionally uses an anchor-based detection head. To improve detection performance and reduce computation, this paper proposes the RepYOLO algorithm, which utilizes an anchor-free detection head and the ATSS algorithm to define positive and negative training samples. In contrast to the IoU threshold allocation scheme used in the YOLOv4 algorithm, the RepYOLO method can better adapt to objects of different scales and shapes while also effectively reducing computation.

Previous studies have demonstrated that anchor-free object detection yields lower accuracy compared to anchor-based algorithms. However, recent research has highlighted that the fundamental disparity between anchor-based and anchor-free algorithms lies in how they define positive and negative training samples, leading to a performance gap during the training process. If these algorithms implement identical definitions for positive and negative samples during training, regardless of whether it is based on box or point regression, there will be no conspicuous difference in their final performance *(Ge et al., 2021)*. The latest scientific research has proposed the ATSS algorithm for positive and negative sample matching, which successfully addresses the issue of reduced accuracy in anchor-free object detection algorithms, making its accuracy comparable to that of anchor-based algorithms *(Zhang et al., 2020)*.

To compare the performance of anchor-free and anchor based algorithms, the two algorithms were calculated in terms of detection accuracy, computation speed, and the definition of positive and negative samples used in the training process. In the model performance evaluation section, it will be demonstrated, from the perspectives of detection accuracy and speed, that our RepYOLO algorithm outperforms YOLOv4 in both aspects and is more adaptable to different scenarios. This will prove the practicality and effectiveness of our proposed algorithm for unmanned aerial vehicle object detection.

In order to further enhance the feature extraction and fusion abilities of the PAN layer, the CBAM attention mechanism was integrated into PAN in our study. Traditional convolutional neural networks (CNNs) have limitations in capturing channel and spatial information, which can affect their feature representation ability. The Convolutional Block Attention Module (CBAM) selectively emphasizes important features and suppresses unimportant ones, improving the accuracy of feature representation. Compared to other attention mechanisms, CBAM has relatively smaller computational costs while still preserving limited UAV performance. Therefore, the CBAM attention mechanism was introduced into the PAN layer to further optimize the model's performance.

The CBAM module comprises the Channel Attention Module (CAM) and the Spatial Attention Module (SAM). CAM is responsible for learning the weights of channel attention and computing the attention map between channels to enable the network to selectively emphasize informative channels and suppress uninformative ones. On the other hand, SAM learns the weights of spatial attention and computes the attention map between spatial positions, enabling the network to selectively focus on significant spatial regions and suppress irrelevant ones.

The final attention map is obtained by multiplying the attention maps of the two modules. This final attention map is then applied to the original feature map to obtain the ultimate output. The structure of CBAM is illustrated in Fig.5.

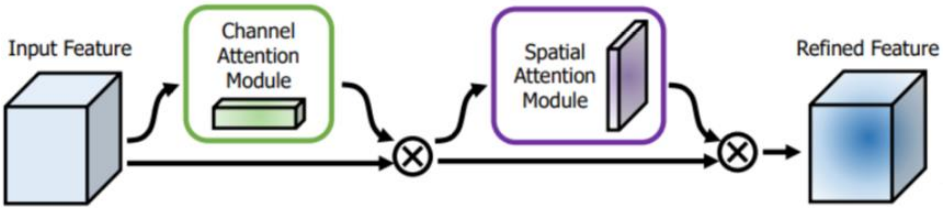

Fig. 5 - The Structure of CBAM

To compare the performance differences between the CBAM-inserted algorithm and the one without CBAM, the focus was on comparing them based on detection accuracy. To further validate the performance differences, the Grad-CAM heatmap visualization method was employed.

Experimental Environment

The experimental training was conducted on a machine equipped with an Intel ® Xeon(R) Platinum 8255C processor and an NVIDIA GeForce RTX 3090 graphics processor (GPU). The operating system used was Ubuntu 20.04. The training framework was CUDAv11.5, cuDNNv8.2.0, and PyTorch 1.6.1.

The training parameters were set as shown in Table 3.

Table 3

Parameters of Training Setting

Optimizer	Momentum	Initial Learning rate	L2 Regularization
SGD/ADMW	0.9	0.01	0.001
Training Epochs	**Warmup Epochs**	T_{max}	**Batch Size**
300	10	290	8

In this study, model transfer experiments were conducted using two unmanned aerial vehicles (UAVs) with different configurations. The first UAV was equipped with a Raspberry Pi 4B processor (ARM Cortex-A72 CPU, 8G Broadcom Video-Core VI DSP (GPU), 8GB LPDDR4-3200 SDRAM RAM), running on Ubuntu 18.04 with the PyTorch v1.7.0 framework. The second UAV was equipped with a Jetson nano processor (ARM Cortex-A57 CPU, 128-core NVIDIA Maxwell GPU, 8GB LPDDR4-3200 SDRAM RAM).

Evaluation indexes of the model

Precision, Recall, F1 value, and mean Average Precision (mAP) were used as evaluative metrics. Precision is the area under the Precision-Recall curve; mAP is the average detection accuracy of the model overall categories of wheat ear targets; and Frames per Second (FPS) is real-time evaluation. The more excellent the value, the better the model's real-time performance.

MAC (Memory Access Cost) and FLOPs (Floating Point Operations) are two metrics used to measure the computational complexity of deep learning models. These metrics have a significant impact on the model inference speed. MAC represents the number of memory accesses when a model performs inference, while FLOPs refer to the total number of floating-point operations during the entire inference process, including matrix multiplication and other mathematical operations.

RESULTS

Grad-CAM is a visualization technique commonly used in convolutional neural networks. It identifies important spatial locations and presents the corresponding attention regions. By analyzing the key focus regions identified by the target detection network, a more intuitive understanding of how the network extracts features and applies them to target detection can be gained.

To evaluate the performance of RepYOLO, its visualization results were compared with the YOLOv4 baseline. Figure 6 displays that the Grad-CAM heatmap mask of RepYOLO more effectively covers the target object region. This indicates that RepYOLO exhibits better detection performance and stronger robustness in wheat with different phenotypic features.

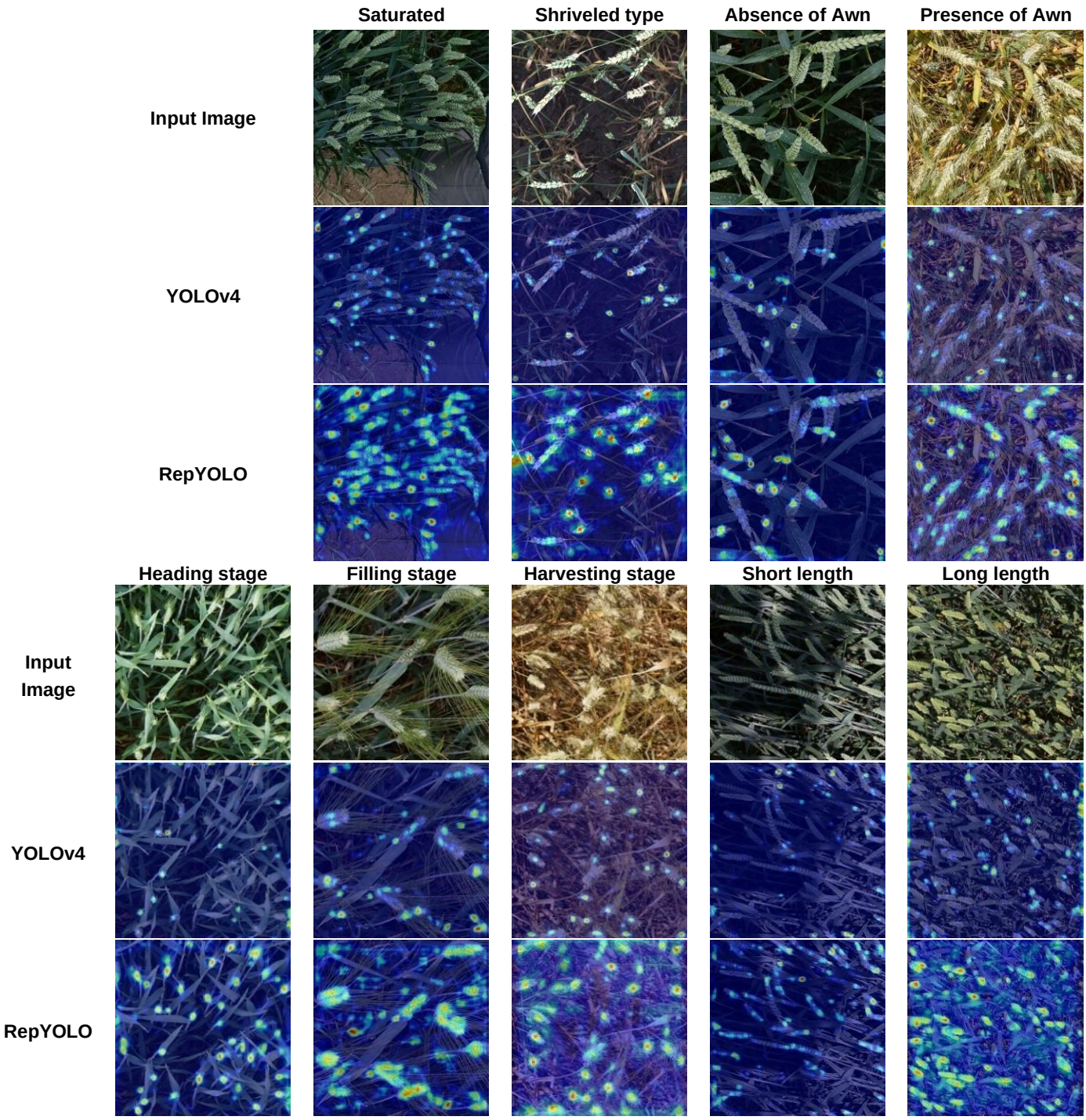

Fig. 6 - Grad-CAM visualization result of different traits

In the analysis of experimental results, Precision was used to evaluate the detection accuracy, while Recall, F1, and mAP were used to evaluate whether the training was sufficient. The small model (with half the standard number of neurons per layer) was represented as "-n", the standard model as "-s", and the large model (with twice the standard number of neurons per layer) as "-l". Through the analysis of the experimental results in Table 4, it was found that the RepYOLO standard model improved by 4.67%, 1.37%, 1.51%, and 1.68% in Precision, Recall, F1, and mAP, respectively, compared to the YOLOv4 standard model. These results suggest that RepYOLO significantly improved in terms of detection accuracy performance, which is consistent with the results of Grad-CAM heatmap visualization.

Based on these findings, it can be speculated that the CBAM feature refinement process in RepYOLO enables the network to better utilize the given features and improve detection performance. In section Ablation Study, the focus is on analyzing the impact of CBAM on the accuracy of RepYOLO. Our goal is to demonstrate the significant improvement in detection performance after integrating CBAM. This section will provide a detailed analysis and exploration of CBAM to verify its effectiveness in RepYOLO.

Table 4

Precision Evaluation Metrics of YOLOv4 and RepYOLO

Base Model	Size	P/%	R/%	F1/%	mAP/%
YOLOv4	-n	91.62	80.69	87.10	80.11
	-s	93.55	82.34	88.88	81.74
	-l	93.89	82.63	89.19	82.03
RepYOLO	-n	96.75	82.45	89.03	82.17
	-s	98.22	83.71	90.39	83.42
	-l	98.71	84.13	90.83	83.84

From the perspective of ShuffleNetV2, the use of FLOPs as an indicator of model speed has limitations. The experimental results reveal that although ShuffleNetV2 has higher FLOPs than MobileNetV2, its MAC is much smaller than MobileNetV2 *(Ma et al., 2018, Sandler et al., 2018)*. Moreover, the inference speed of ShuffleNetV2 is significantly faster than MobileNetV2, suggesting that MAC has a greater impact on inference speed than FLOPs. Therefore, this study focuses on analyzing the MAC issue *(Ma et al, 2018)*.

The aim of this paper is to reduce the impact of Elemwise operations on MAC and further improve speed by adopting the structure reparameterization and multi-branch structure design of RepVGG based on the efficient network criteria proposed by ShuffleNetV2, converting the multi-branch structure into a single path.

Figure 7 illustrates the significant reduction in Elemwise operations of RepVGG compared to YOLOv4 on different inference platforms. On GPU, Raspberry 4B, and Jetson Nano, RepVGG's Elemwise operations cause 50.0%, 40.2%, and 49.2% of the inference delay of YOLOv4, respectively. This indicates that the RepVGG design effectively solves the MAC problem inherent in YOLOv4.

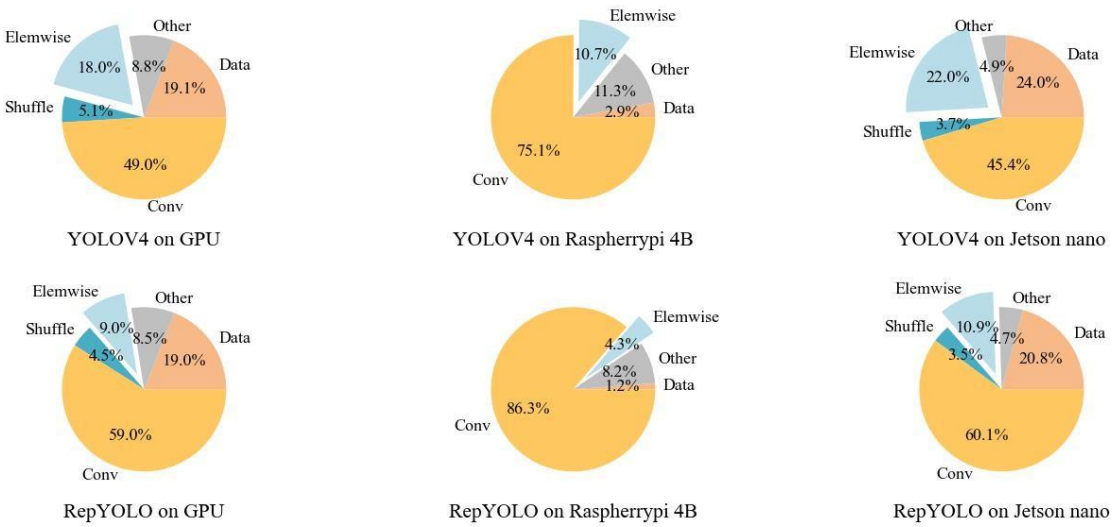

Fig. 7 - Run time decomposition on YOLOv4 and RepYOLO

The analysis of experimental results in Table 5 reveals that the RepYOLO standard model reduces inference time by 35.22%, 37.02%, and 41.44% on GPU, Raspberry 4B, and Jetson Nano, respectively, compared to the YOLOv4 standard model. These results demonstrate that the structures and reparameterization used in RepYOLO effectively reduce MAC and significantly improve inference speed.

Table 5

Speed Evaluation Metrics of YOLOv4 and RepYOLO

Base Model	Size	FLOPs/G	GPU/ms	4B/ms	nano/ms
YOLOv4	-n	8.2	225	126.7	79.2
	-s	16.5	49.0	276.0	126.7
	-l	33.00	112.0	469.2	215.4
RepYOLO	-n	8.2	14.4	81.1	34.2
	-s	16.0	31.7	173.8	74.2
	-l	32.9	72.5	281.5	160.2

In the subsequent Ablation Study section, the contribution of anchor-free to inference speed will be further analyzed. This analysis is necessary due to the influence of various factors on inference speed delay.

In order to enhance our comprehension of the influence of different modules and algorithms on the RepYOLO algorithm, a qualitative analysis was conducted in this section.

Table 6 presents the accuracy metrics of the RepYOLO algorithm with different modules and algorithms removed ((w/o) represents word without). Removing the ATSS algorithm significantly decreased the accuracy indicators of the RepYOLO algorithm with the same scale, even lower than the standard YOLOv4 detection algorithm (refer to table 5). This highlights the crucial importance of the ATSS algorithm in our proposed model and is consistent with previous research showing that anchor-free detection heads with positive and negative sample allocation algorithms have lower accuracy than anchor-based algorithms. Additionally, removing the CBAM algorithm resulted in decreased accuracy indicators. Then, heat maps were generated and compared with the original RepYOLO algorithm. Figure 6 shows that from the heat map visualization, it is evident that the CBAM algorithm plays a crucial role in improving the expression ability of the feature map. Simultaneously removing both algorithms resulted in a significant decrease in model performance, with accuracy much lower than the current model detection results, and even lower than the YOLOv4 detection performance.

Table 6

Ablation Study of RepYOLO Precision

Base Model	Size	P/%	R/%	F1/%	mAP/%
RepYOLO	-n	96.75	82.45	89.03	82.17
	-s	98.22	83.71	90.39	83.42
	-l	98.71	84.13	90.83	83.84
(w/o)CBAM and ATSS	-n	89.40	77.75	83.17	78.48
	-s	91.29	80.36	85.48	80.08
	-l	91.95	80.98	87.11	80.39
(w/o)ATSS	-n	92.53	80.62	86.17	80.03
	-s	94.36	82.18	87.85	81.58
	-l	95.04	82.76	88.48	82.16
(w/o)CBAM	-n	92.28	81.26	86.42	80.67
	-s	93.03	82.75	87.59	82.15
	-l	95.43	83.04	88.80	82.75

Table 7 presents the speed indicators of the RepYOLO algorithm with and without the Anchor-free detection head on various hardware platforms, denoted by (w/o) for the removed algorithm. Removing the Anchor-free detection head and using the Anchor-based detection head led to a significant increase in the inference latency of the RepYOLO algorithm with the same scale, with an approximately 8-12% increase in inference time. This finding suggests that the Anchor-free detection head can simplify the prediction of bounding boxes' calculation process, thereby enhancing computational efficiency and inference speed

Table 7

Ablation Study of RepYOLO Speed

Base Model	Size	FLOPs /G	GPU /ms	4B /ms	nano /ms
RepYOLO	-n	8.2	14.4	81.1	34.2
	-s	16.0	31.7	173.8	74.2
	-l	33.0	72.5	281.5	160.2
(w/o)Anchor-free	-n	8.9	15.7	111.1	38.0
	-s	17.5	34.9	203.8	81.4
	-l	36.6	79.8	310.5	179.4

CONCLUSIONS

In order to fully utilize the arithmetic capability of edge chips, the basic structure of the YOLO algorithm was modified in our work, using structural reparameterization and anchor-free detection head to make RepYOLO suitable for drone-friendly devices. However, changing the structure reintroduces the problem of reduced detection accuracy. Therefore, the CBAM attention mechanism and ATSS training method were adopted to enhance the original structure, enabling our model and structure to ultimately outperform the original YOLOV4 model on edge devices for drones.

In applications, software and hardware jointly limit the development of embedded IoT drones. The same network structure has different inference speeds on different hardware embedded platforms. The storage size of neural network parameter weight files in edge devices, memory sticks, and flash memories, as well as the limited computational performance of CPUs, limit the inference speed of neural network models. MCUNet proposed the inference framework of TinyNAS and TinyEngine, which can be used without relying on the cloud *(Lin et al., 2020)*. MCUNetv2 proposed a new memory bottleneck to solve the problem of memory allocation imbalance in CNN convolutional neural networks *(Lin et al., 2021)*. Compared with TF-lite and CMSIS-NN, MCUNet has achieved a fundamental transformation from mobile CPU inference to microcontrollers in terms of inference speed and accuracy.

ACKNOWLEDGEMENT

This research was supported by Fundamental Research Program of Shanxi Province (No.202203021212450 and No.202303021212115).

REFERENCES

[1] Bochkovskiy, A.; Wang, C.-Y.; Liao, H.-Y.M. (2020). YOLOv4: Optimal speed and accuracy of object detection. *arXiv preprint arXiv:2004*.10934. https://doi.org/10.48550/arXiv.2004.10934

[2] Chen, X.; Luo, X.; Weng, J.; Luo, W.; Li, H.; Tian, Q. (2021). Multi-view gait image generation for cross-view gait recognition. *IEEE Transactions on Image Processing*, 30, 3041-3055.

[3] David, E.; Serouart, M.; Smith, D.; Madec, S.; Velumani, K.; Liu, S.; Wang, X.; Pinto, F.; Shafiee, S.; Tahir, I.S. (2021). Global wheat head detection 2021: An improved dataset for benchmarking wheat head detection methods. *Plant Phenomics*. https://doi.org/10.34133/2021/9846158

[4] Ge, Z.; Liu, S.; Wang, F.; Li, Z.; Sun, J. (2021). Yolox: Exceeding yolo series in 2021. *arXiv preprint arXiv:2107.08430*. https://doi.org/10.48550/arXiv.2107.08430

[5] Hassan, M.A.; Yang, M.; Rasheed, A.; Yang, G.; Reynolds, M.; Xia, X.; Xiao, Y.; He, Z. (2019). A rapid monitoring of NDVI across the wheat growth cycle for grain yield prediction using a multi-spectral UAV platform. *Plant science*, 282, 95-103. https://doi.org/10.1016/j.plantsci.2018.10.022

[6] He, K.; Zhang, X.; Ren, S.; Sun, J. (2016). Deep residual learning for image recognition. In *Proceedings of the IEEE conference on computer vision and pattern recognition*; pp. 770-778.

[7] Jin, X.; Liu, S.; Baret, F.; Hemerlé, M.; Comar, A. (2017). Estimates of plant density of wheat crops at emergence from very low altitude UAV imagery. *Remote Sensing of Environment*, 198, 105-114. https://doi.org/10.1016/j.rse.2017.06.007

[8] Khan, S.; Tufail, M.; Khan, M.T.; Khan, Z.A.; Iqbal, J.; Wasim, A. (2022). A novel framework for multiple ground target detection, recognition and inspection in precision agriculture applications using a UAV. *Unmanned Systems*, 10, 45-56. https://doi.org/10.1142/S2301385022500029

[9] Khalil, M.; Khomonenko, A.; Matushko, M. (2022). Measuring the effect of monitoring on a cloud computing system by estimating the delay time of requests. *Journal of King Saud University-Computer and Information Sciences*, 34, 3968-3972.10.https://doi.org/1016/J.JKSUCI.2021.02.001

[10] Lin, J.; Chen, W.-M.; Lin, Y.; Gan, C.; Han, S. (2020). Mcunet: Tiny deep learning on iot devices. *Advances in Neural Information Processing Systems*, 33, 11711-11722.

[11] Radoglou-Grammatikis, P.; Sarigiannidis, P.; Lagkas, T.; Moscholios, I. (2020). A compilation of UAV applications for precision agriculture. *Computer Networks*, 172, 107148.

[12] Sandler, M.; Howard, A.; Zhu, M.; Zhmoginov, A.; Chen, L.-C. (2018). Mobilenetv2: Inverted residuals and linear bottlenecks. In *Proceedings of the IEEE conference on computer vision and pattern recognition*; pp. 4510-4520. https://doi.org/10.48550/arXiv.1801.04381

[13] Selvaraju, R.R.; Cogswell, M.; Das, A.; Vedantam, R.; Parikh, D.; Batra, D. Grad-cam: Visual explanations from deep networks via gradient-based localization. In *Proceedings of the IEEE international conference on computer vision*, 2017; pp. 618-626. https://doi.org/10.1007/s11263-019-01228-7

[14] Shapiro, S.S.; Wilk, M.B. An analysis of variance test for normality (complete samples). *Biometrika* 1965, 52, 591-611. https://doi.org/10.1080/01621459.1972.10481232

[15] Szegedy, C.; Liu, W.; Jia, Y.; Sermanet, P.; Reed, S.; Anguelov, D.; Erhan, D.; Vanhoucke, V.; Rabinovich, A. (2015). Going deeper with convolutions. In *Proceedings of the IEEE conference on computer vision and pattern recognition*, pp. 1-9. https://doi.org/10.48550/arXiv.1409.4842

[16] Wang, H.; Wu, X.; Liu, J.; Li, J. (2021). Research on Flame Detection Based on Anchor-Free Algorithm FCOS. In Proceedings of the Neural Information Processing: 28th International Conference, ICONIP 2021, Sanur, Bali, Indonesia, *Proceedings*, Part V 28, 2021; pp. 124-131. https://doi.org/10.48550/arXiv.1904.01355

[17] Woo, S.; Park, J.; Lee, J.-Y.; Kweon, I.S. (2018). Cbam: Convolutional block attention module. In *Proceedings of the European conference on computer vision (ECCV)*, pp. 3-19.

[18] Zagoruyko, S.; Komodakis, N. Diracnets: Training very deep neural networks without skip-connections. arXiv preprint arXiv:1706.00388 2017. https://doi.org/10.48550/arXiv.1706.00388

[19] Zhang, S.; Chi, C.; Yao, Y.; Lei, Z.; Li, S.Z. (2020). Bridging the gap between anchor-based and anchor-free detection via adaptive training sample selection. In *Proceedings of the IEEE/CVF conference on computer vision and pattern recognition*, pp. 9759-9768. https://doi.org/10.1109/CVPR42600.2020.00978

NUMERICAL AND EXPERIMENTAL ANALYSIS OF THE ABRASIVE WEAR OF TWO STEELS USED IN TILLAGE TOOLS
/
ANÁLISIS NUMÉRICO Y EXPERIMENTAL DEL DESGASTE ABRASIVO DE DOS ACEROS UTILIZADOS EN APEROS DE LABRANZA

Ángel SÁNCHEZ-IZNAGA[1)], Carlos MONTES-RODRÍGUEZ[2*)], Roberto TORRES-RODRÍGUEZ[3)], Nadia GONZÁLEZ-LÓPEZ[2)], Julio PÉREZ-GUERRERO[3)], Carlos RECAREY-MORFA[4)], Miguel HERRERA-SUÁREZ[3)]

[1)]University of Cienfuegos. Collaboration between the University of Cienfuegos and the Metropolitan University of Ecuador / Ecuador;
[2)] Technical University of Manabi, Faculty of Basic Sciences. Department of Physics / Ecuador;
[3)]Technical University of Manabi, Faculty of Engineering and Applied Sciences, Department of Mechanics / Ecuador;
[4)]Central University of Las Villas, International Centre for Numerical Methods in Engineering / Cuba;
Tel: +593 959086234; E-mail: carlos.montes@utm.edu.ec
DOI: https://doi.org/10.35633/inmateh-72-54

Keywords: *Numerical methods, simulation, distinct elements, wear, tillage tool.*

ABSTRACT

This study combines computer simulation using the Discrete Element Method (DEM) with field experiments to assess the resistance to abrasive wear of AISI 1010 and AISI C1064 steels in tillage tools. It was found that the wear on AISI 1010 was over 50% higher than on AISI C1064. The DEM model accurately predicted wear $(e = 0.005g, R^2 = 99.8\%)$*, regardless of operational conditions and steel characteristics. The mean absolute errors of the simulation compared to field tests were 0.01937 g for AISI C1064 and 0.08619 g for AISI 1010.*

RESUMEN

Este estudio combina simulación computacional con el Método de Elementos Discretos (DEM) y experimentos de campo para evaluar la resistencia al desgaste abrasivo de los aceros AISI 1010 y AISI C1064 en herramientas de labranza. Se encontró que el desgaste en AISI 1010 fue más del 50% mayor que en AISI C1064. El modelo DEM predijo con precisión el desgaste $(e = 0.005g, R^2 = 99.8\%)$*, independientemente de las condiciones operativas y características de los aceros. Los errores absolutos medios de la simulación respecto a las pruebas de campo fueron 0.01937 g para AISI C1064 y 0.08619 g para AISI 1010.*

INTRODUCTION

The development of agriculture worldwide has been achieved due to different characteristics, among which stand out the modification and creation of some tillage tools based on designs that guarantee a higher quality of work, the reduction of energy consumption and the damage to the soil that brings with it the loss of fertility and low levels of agricultural production. In Cuba, among the soils of greatest economic importance are those classified as Yellow Ferrite, according to the New Version of the Genetic Classification of Soils in Cuba *(Hernández et al., 2015)* and as Ultrasol, according to the USDA Soil Taxonomy *(Soil Survey Staff, 2010).* In most cases, these soils are used for the production of tobacco, vegetables, grains, as well as roots and tubers, and for the development of livestock. They are considered to be highly abrasive soils, i.e. they cause considerable wear of tillage tools, due to the presence of iron and quartz particles, whose ratio (SiO_2/F_2O_3) is predominant, reaching values that oscillate between 10 and 15%, constituents that justify their abrasive character. These particles lead to abrasive wear, which increases energy consumption and makes soil preparation, conditioning and cultivation more expensive *(Herrera et al., 2010).*

This phenomenon has been widely studied due to the large losses caused in the mechanised tools used in the different tasks of agricultural processes. It is generally quantified by measuring the loss of material, and currently experimental *(Pérez et al., 2010; López, 2011; González, 2012; Jia y Zhou, 2012; Rojek, 2014; Singh et al., 2017; Obrad et al., 2018; Chen et al., 2018; Bedolla et al., 2018)* and numerical methods have been used for its study. Among the numerical ones, the Distinct or Discrete Element Method (DEM) has the most application for the study of abrasive wear *(Graff, 2010; Rojek, 2014; Perazzo et al., 2016; Hoormazdi et al., 2018; Chen et al., 2018; Ucgul et al., 2017, Graff, 2010, Bedolla et al., 2018; Montes, Herrera, López, Pérez, & Torres, 2023; Zolotarevskiy, Gallo, Pereira, & Barnett, 2022; Zhang, Fu, Ren, Liu, Lin, Zhang & Zhang, 2024).* The advantage of the latter over traditional methods is that it allows predicting the behaviour of a given phenomenon, and also decreases the time required for testing.

The models developed in DEM in the aforementioned research, for the simulation of problems related to geomaterials, take as input data the parameters related to the microstructure of these materials *(Graff, 2010; Rojek, 2014; Perazzo et al., 2016; Hoormazdi et al., 2018; Chen et al., 2018).* Microstructural parameters, as usual, can be estimated by simulation from macrostructural properties, which are determined by conventional tests performed in soil mechanics laboratories, or from tests performed directly in the field *(Pérez et al., 2010; López, 2011; Obrad et al., 2018; Bedolla et al., 2018).* The definition of one or the other microstructural parameter depends on the software to be used. Among the software suitable for DEM simulation is the Yet Another Dynamic Engine (YADE), a non-commercial software available as free software on the Internet that has been applied to the study of soil and its interaction with tillage tools.

Based on the above, the aim of this paper is to determine the abrasive wear resistance of AISI 1010 and AISI C1064 steels used in tillage tools.

MATERIALS AND METHODS

Methodology for the simulation of the abrasive wear of tillage implement parts using the Discrete Element Method (DEM)

Development of the virtual method. For the simulation of abrasive wear under these conditions, a 3D virtual model was developed, which can be found in Sánchez, (2015). In it, the tilling process was idealised from the representation of a homogeneous soil block (1) with which the tools (2) interact; these tools have the same dimensions and geometries as those used in the experimental abrasive wear tests under operating or field conditions *(Sánchez et al., 2018)*. A soil block with the dimensions of $0.3m$ length, $0.12m$ height and $0.12m$ width was generated. It consisted of a total of 22942 randomly distributed spherical particles. The diameter of the particles ranged from 0.002 to $0.0007m$, and the density was $12235\ g/cm^3$ (Sánchez, 2015).

For the case of the tillage tools, 3D sketches with geometries equal to the tools were initially created to be used in the experimental trials and then a particle packing was generated inside the sketch. For this, a hexagonal assembly to gravity deposit the particles inside the sketches was used (Figure 1a). Finally, the lines from the sketches were removed and the virtual model of the tools with particles formed itself (Figure 1b). The rectangular tools were formed with a total of 19800 spherical particles of $0.0005m$ diameter.

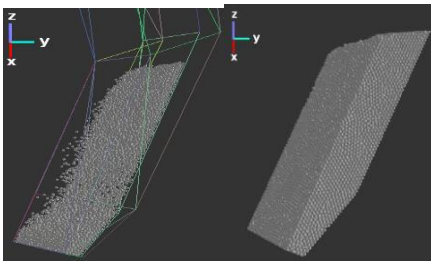

a b

Fig. 1 - Process of elaboration of virtual tool.
a) Process of filling the virtual tool, b) virtual tool after its elaboration

Establishment of boundary conditions. The movement of the soil particles *(Sanchez, 2015)*, is limited in the normal direction of the lateral planes that delimit the block (3); but nevertheless the soil particles could move freely (translation and rotation) in all axes within the blocks. The tool (y-axis) was set to a velocity movement similar to that obtained in experiments under operational or field conditions. The rest of the directions were limited to the tool movement. The simulation was completed in 25 h of the tool in the soil block.

Procedure for DEM simulation of tillage tool wear. The DEM simulation of wear was performed using the method previously developed and validated in laboratory conditions by *Sanchez, (2015)*. Tool wear was simulated through mass or particle loss, in which the effect of the resulting force on the tool particles that originates from the resistance that the soil exerts on the tool during tillage was taken into account. Wear was quantified by integrating mass loss over time (Equation 1).

$$P_{mass} = \int \dot{P}_{mass}\, dt \quad (1)$$

In the simulation the tool was allowed to travel only a distance of $0.25m$ total length of the soil block to avoid the effect of the edge of the container back wall increasing soil pressures on the tools and causing

unnecessary particle removal. In the model a function was programmed to impose a penalty to stop the movement of the tool when it completes the intended path. The simulation results were compared with those obtained in experimental tests under operational or field conditions.

Microstructural parameters of the soil and tool

These parameters used as input data for the simulation were estimated through the simulations of the direct and direct modified cuts trials. (Table 1).

Table 1

Parameters employed as input data for the simulation

Parameters	E_m	$\nu_m(-)$	$c_m\ (kPa)$	$\phi_m\ (°)$
Soil	1796.85	0.36	6	32.24
Parameters	E_{s-mm}	$\nu_m\ (-)$	$c_m\ (kPa)$	$\delta_{s-mm}\ (°)$
Interphase soil-metal				
AISI 1010	2.300	0.36	8.19	30.44
AISI C1064	2.800	0.36	8.19	30.44
Parameters	E_{mm}	$\nu_{mm}\ (-)$	C_N	C_T
AISI 1010	$1{\cdot}10^{+10}$	0.29	$1{\cdot}10^{+20}$	$1{\cdot}10^{+20}$
AISI C1064	$2.1{\cdot}10^{+10}$	0.29	$1{\cdot}10^{+20}$	$1{\cdot}10^{+20}$

Simulation of the wear and tear of tillage implements. The simulations were carried out on a desktop computer with the following characteristics: Processor: Intel Pentium, Hard Disk: 250 GB, RAM: 4 GB and three USB ports. The simulation was completed in five passes of the tools through the soil block, covering a real simulation time of 5 h.

Methodology for the characterisation of the test conditions and determination of the operating conditions of the tractor-crop tillage unit.

This research was carried out in the production areas of the Empresa de Cultivos Varios Manacas *(Sánchez et al., 2018)*, located in Santo Domingo municipality, Villa Clara province, Cuba. In this enterprise, Yellow Ferritic soils predominate, which are considered highly abrasive, causing great wear on tillage tools. For the development of this experiment, the set made up of the Yumz-6m tractor and a Tiller type cultivator with 11 working bodies was used, which can be consulted in *Sánchez et al. (2018)*.

Methodologies for the characterization of operation conditions.

To determine the operating conditions, the following variables were quantified: ambient temperature, soil moisture, soil bulk density, tillage forward speed, mass loss and working time.

Room temperature

This variable was measured using a digital thermometer and the procedure for its determination can be found in Sánchez et al. (2010). Data were taken every 30 minutes, during the duration of the wear experiments in order to know the variation of this variable during its development.

Soil humidity (w).

It was carried out using the gravimetric method, following the procedure established in the Cuban standard NC ISO 67:2000. The samples were weighed with the precision balances indicated in *Sánchez et al. (2010)*. The equipment indicated in *Sánchez et al. (2010)* was used to take the samples, and five points were chosen at random in the diagonal of the test plot as shown in (Figure 2a), three soil samples were taken in each one at three different depth levels (Figure 2b).

Apparent soil density (γd)

The procedure described in the Cuban standard NC ISO 3447:2003, which is based on the Kopecky ring method, was followed, as shown in *Sánchez et al. (2010)*. The determination of the mass of the soil samples was carried out with a balance of $10 \pm 0.01kg$ accuracy, which can be consulted in *Sánchez (2015)*. Sampling was carried out at the same points where the samples were taken for moisture determination (Figure 2), so the number of samples was the same as for the previous test.

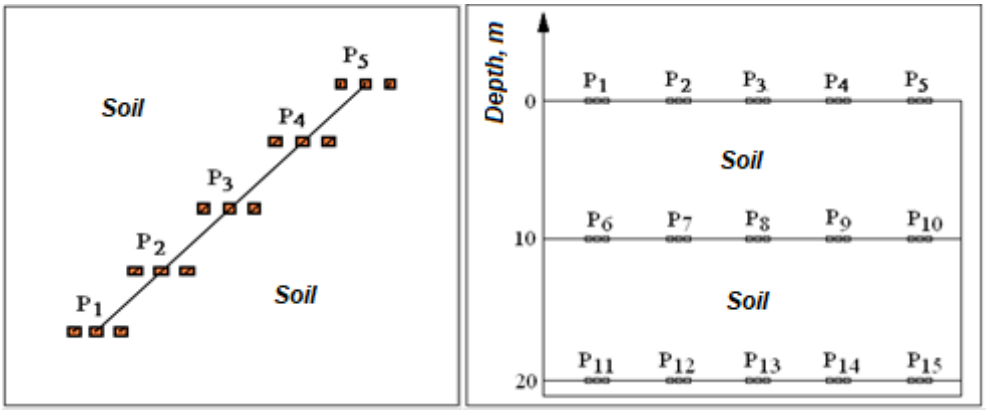

Fig. 2 - Collection of samples for the determination of humidity and soil density.
a) Points for the collection of the humidity and density samples, view in the plant of the parcel;
b) Points for the collection (from P1 to P15), lateral view of the parcel.

Methodologies for determining the operating parameters of the assembly. Determination of the feed rate of the assembly.

As a previous step to the determination of this variable, the length of the experimental plot was measured in order to know the distance travelled by the tool. During the experiment, the time in which the assembly travelled that distance was measured using a stopwatch. The calculation of the forward speed of the tool was carried out using equation 2.

$$V_T = \frac{D_R}{T_E}[m/s] \quad (2)$$

where:

D_R - distance travelled, [m];

T_E - time of the experiment, [s].

Methodology for the experimental determination of the wear under field conditions.

The tillage implements used in the experiments are those of the company where the experiments were carried out. Their geometry is shown in figure 3.

Fig. 3 - Geometry of the tool used in the experiments (Isometric view)

The main characteristics of the used tools or tillage tools are shown in table 2.

Table 2

Characteristics of the tools object of study

Type of part	Type of material	Nominal mass, g	Hardness, HB	Roughness, μm
Rectangular	AISI 1010	802.4	110	12.5
Rectangular	AISI C1064	725.51	165	12.5

Under these conditions, the mass loss of the AISI 1010 and AISI C1064 steel tools was determined with rectangular geometries, moving the assembly at the second speed of the tractor and the duration of the experiment was 24 h. The tools were weighed every 5 h of work. With these objectives in mind, an experimental design was carried out with two randomised treatments (Table 3) and four replicates.

Table 3

Design of experiment for the determination of the wear in field conditions

Treatments	Speed, $km \cdot h^{-1}$	Geometry	Material
T1	Second speed	Rectangular	AISI 1010
T2	Second speed	Rectangular	AISI C1064

Methodology for the statistic processing of results

The statistical processing of the wear determination experimental results under operating or field conditions, the simulation results and the comparison between them was carried out with the statistical processor STATGRAPHICS Centurion XV, using the analysis of simple regressions, comparison of means and Kolmogorov-Smirnov tests, with the purpose of finding the existing relationships between the study variables.

RESULTS AND DISCUSION

Results of the simulation of abrasive wear as a function of the type of material (AISI 1010 and AISI 1046). The results of the simulations show that during the interaction of the tillage tool with the soil, the tool of both materials wears and changes its shape progressively with increasing working time (Figure 4); this has been widely described in scientific literature *(Ucgul et al., 2015; Skirkus and Jankauskas, 2015)*. The wear is due to the loss of mass that results in the deformation over time of the machining tool losing its cutting edge completely. This directly contributes to increased energy demand and decreased quality of workmanship. The trend of increasing wear over working time was previously reported by *(Ucgul et al., 2017; Kostencki et al., 2016; Wang et al., 2016; Sun et al., 2018)*.

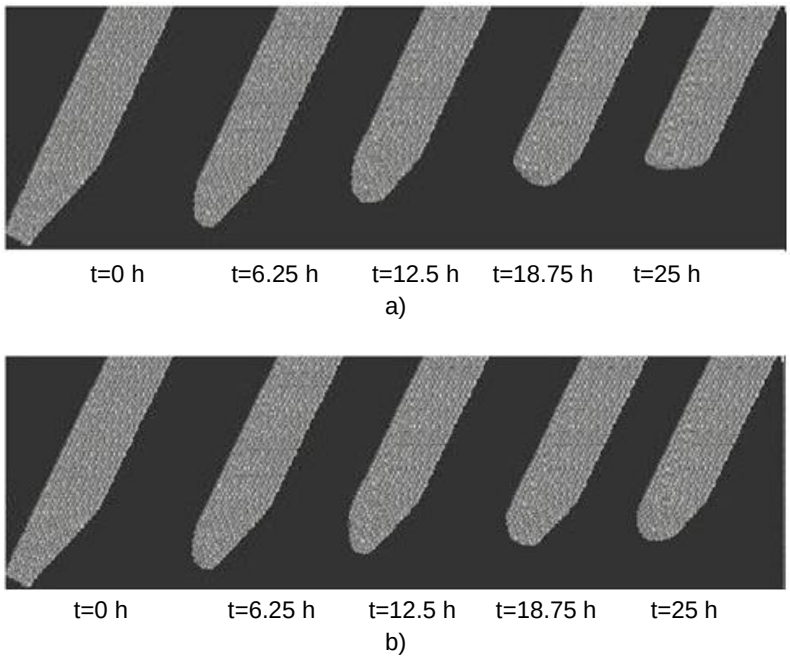

Fig. 4 - Evolution through time of the profiles of the tools during the tillage.
Results of the simulation ($V = 7.38\ km \cdot h^{-1}$). a) Steel AISI 1010; b) AISI C 1064

The comparative analysis of the mass loss obtained in the simulations for each type of steel showed a tendency to increase in magnitude as the clean (uninterrupted) working time increased, reaching total values of 314.03 and $79.08g$, for AISI 1010 and AISI C1064 steel tools, respectively (Figure 5). The trend and values obtained in the simulation were similar to those found by other researchers, either by simulation *(Graff, 2010; Rojek, 2014)* or experimentation in controlled or field conditions directly *(Graff, 2010; Rojek, 2014; Hoormazdi et al., 2018; Chen et al., 2018; Ucgul et al., 2017, Graff, 2010, Bedolla et al., 2018)*.

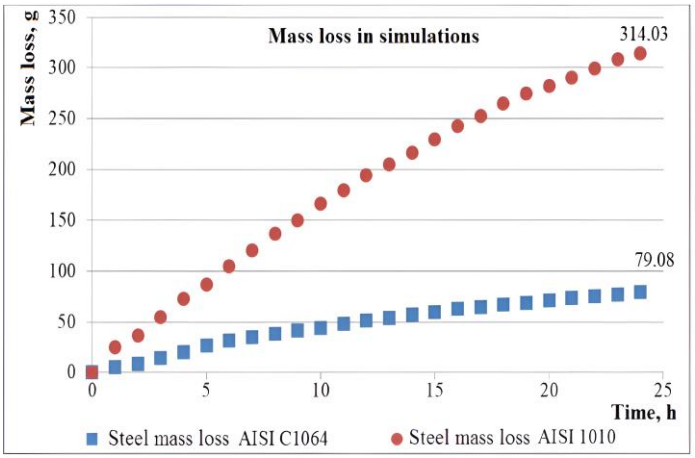

Fig. 5 - Mass loss of the tools depending on the simulation time

Simple regression analysis of the mass loss results in the simulations showed that there is a linear relationship between the mass loss of AISI C1064 steel and the clean working time with $R^2 = 0.9698$ (Figure 6).

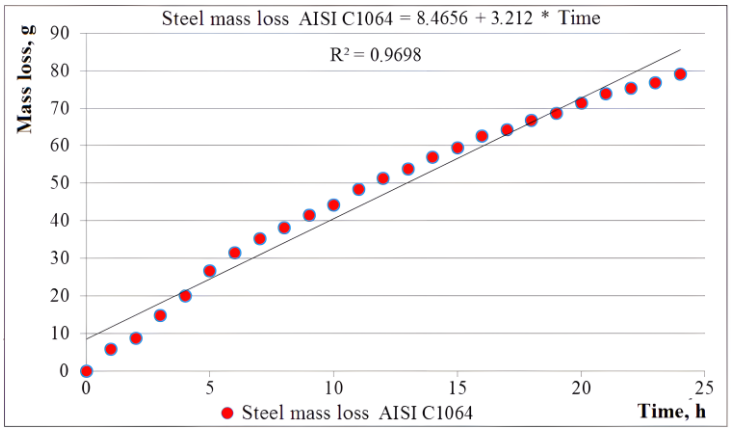

Fig. 6 - Analysis of simple regression of the dependence of the mass loss in the simulation on Steel AISI 1010 in respect to the clean work time

On the other hand, simple regression analysis of the mass loss in the simulations on AISI 1010 steel showed that there is also a linear relationship between its mass loss and the clean working time, with $R^2 = 0{,}9863$ (Figure 7).

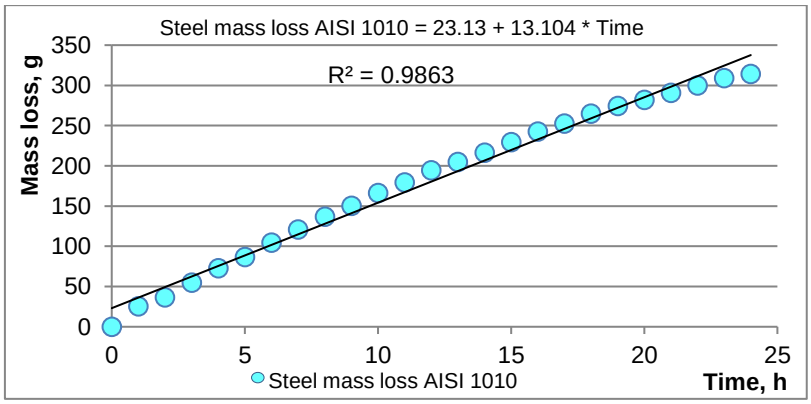

Fig. 7 - Analysis of simple regression of the dependence of the mass loss in the simulation on Steel AISI 1010 in respect to clean work time

The results of experiments in field conditions show that during the interaction of the tillage tool with the soil, the tool of both materials wears and changes the edge geometry progressively with increasing working time (Figure 8), this has been widely described in the scientific literature. *(Graff, 2010; Rojek, 2014; Hoormazdi et al., 2018; Chen et al., 2018(Ucgul et al., 2017, Graff, 2010, Bedolla et al., 2018)*.

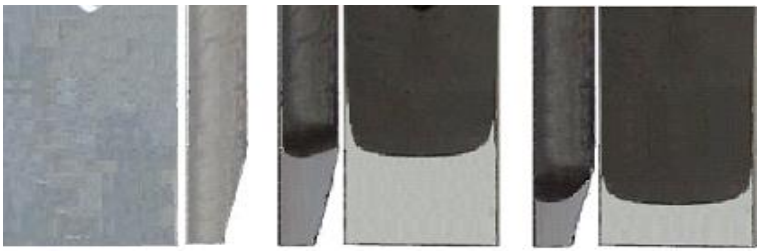

a b c d e f

Fig. 8 - Variation of the geometries of the tools in field experiments.
a) and b) before the trial T=0 h; c) and d) tool after the trial T=24 h (steel AISI 1010);
e) and f) tool after the trial T=24 h (steel AISI C 1064)

The comparative analysis of the mass loss obtained in the experimentation under field conditions for both steels showed a tendency to increase its magnitude as the clean (uninterrupted) working time increased, reaching total values of $304.02g$ for the AISI 1010 tool steel and $79.81g$ for the AISI C 1064 steel (Figure 9). Both the trend and the values obtained in the experimentation under field conditions were similar to those found by other researchers under similar conditions *(Graff, 2010; Rojek, 2014; Hoormazdi et al., 2018; Chen et al., 2018, Ucgul et al., 2017, Graff, 2010, Bedolla et al., 2018)*.

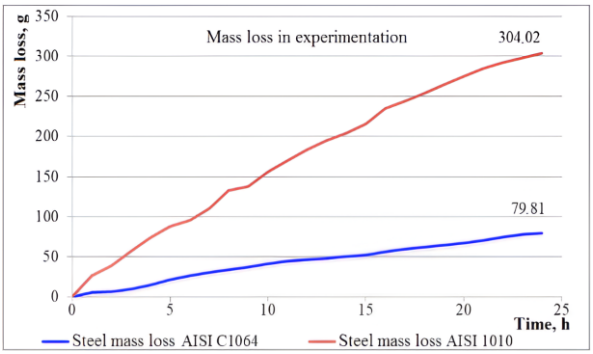

Fig. 9 - Mass loss of the tools depending on the experimentation time

The lowest mass losses were found in the AISI C 1046 steel (Figure 9), this result being consistent with the nature of this type of material which is composed of elements of higher wear resistance, as the carbon content reaches 0.61% and the manganese content 1.06%.

Statistical comparison of the tool wear results obtained in the experiments, using a Kolmogorov-Smirnov test, showed that there are significant differences between the mass loss experienced by both steels during working process, with a reliability level of 95% (Figure 10).

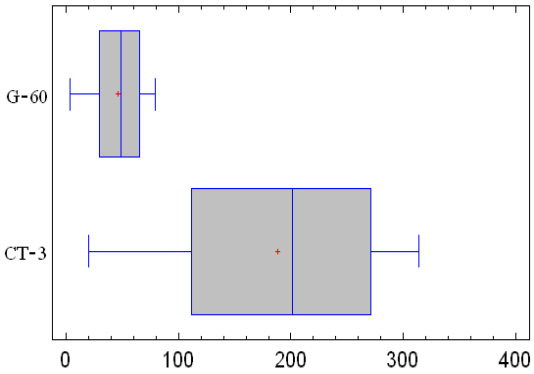

Fig. 10 - Results of the comparison of the mean mass loss of the tools (Kolmogorov-Smirnov), during the tillage in operation conditions

The comparative analysis of the mass loss obtained in the experimental tests and the simulations showed that the wear curves of the simulations follow the same trend shown in the experimental tests, i.e. the mass loss increases with increasing time for the two steels investigated (Figure 11). This same trend was found by *Graff (2010), Rojek (2014), Kostencki et al. (2016), Perazzo et al. (2016), Bedolla et al. (2018)*.

A similarity in the magnitudes of mass loss was also found, being very accurate for the case of AISI C 1064 steel (Figure 11).

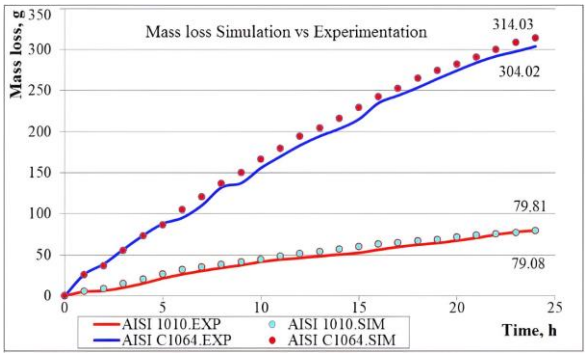

Fig. 11 - Mass loss of the tools in the simulation and experiment according to time function

The simple regression analysis of the mass loss results on AISI C 1064 steel showed a linear relationship between the mass loss obtained in the simulation with respect to the experiment with a reliability level of 95%, with $R^2 = 99.13$ % (Figure 12). Similar results were reported by *Perazzo et al. (2016)*, but on another type of steel.

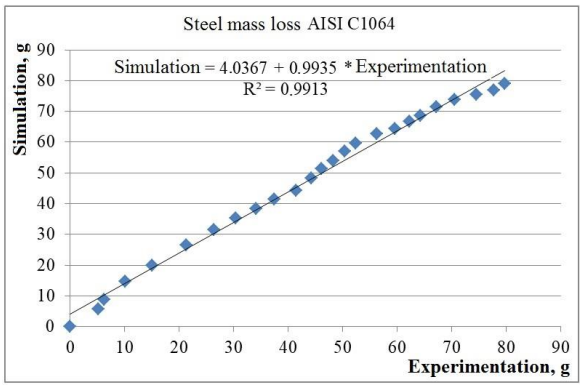

Fig. 12 - Analysis of simple regression of the dependency of the mass loss in the simulation on Steel AISI C1064 regarding the experimental one

On the other hand, the results of the simple regression analysis of mass loss in AISI 1010 steel show a linear dependence of the mass loss obtained in the simulation with respect to that obtained experimentally, with a reliability level of 95% (Figure 13). This same relationship was obtained by *Perazzo et al. (2016)* on steels with different properties.

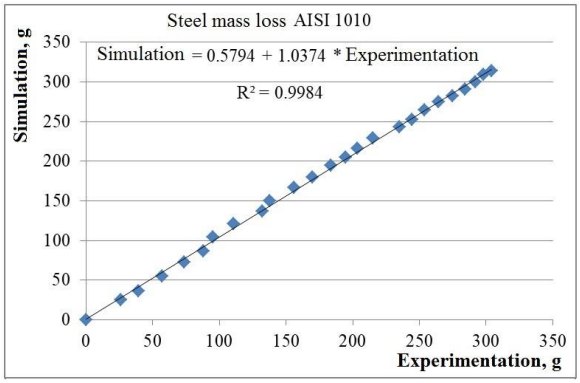

Fig. 13 - Analysis of simple regression of the dependency of the mass loss in the simulation on Steel AISI 1010 regarding the experimental one

Finally, a simple regression analysis of the validation results showed that there are statistically significant relationships between simulation and experimental mass loss for a 95% confidence level (Figure 14). The regression equation showed that there is a linear relationship between simulated and experimental mass loss ($R^2 = 0.998\ and\ e = 0.005g$). Similar results were obtained by *Graff (2010), Rojek (2014) and Kostencki et al. (2016)*.

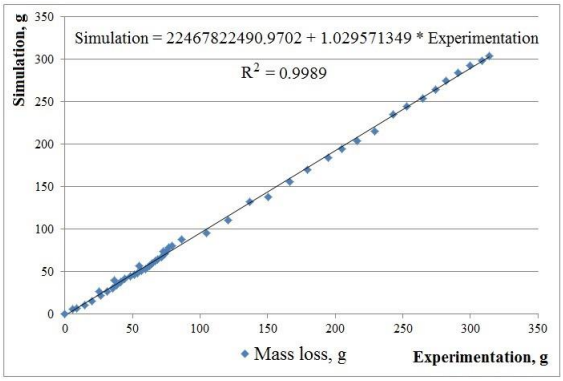

Fig. 14 - Analysis of simple regression of the dependency of the mass loss in the simulation regarding the experimental one

CONCLUSIONS

The results of the simulations, as well as the experiments, showed that the mass loss and geometry changes were much higher than 50% in AISI 1010 steel compared to AISI C1064.

The model developed in DEM is able to accurately predict the wear experienced in the tillage tools, independently of the characteristics of the steels and the operating conditions $(R^2 = 0.998 \; and \; e = 0.005g)$.

The high degree of correlation between the values of mass loss predicted by the abrasive wear model and those determined experimentally under operating or field conditions $(r = 0.99)$, is another indicator of the validity of the model developed for the simulation of the wear of the working parts of the tillage tools under the conditions studied.

The mean absolute errors of the simulation with respect to the field tests reached 0.01937 g for AISI C1064 steel and 0.08619 g for AISI 1010.

REFERENCES

Bedolla, P. O., Vorlaufer, G., Rechberger, C., Bianchi, D., Eder J, S., Polak, R., y otros. (2018). Combined experimental and numerical simulation of abrasive wear and its application to a tillage machine component. *Tribology International*. 127, 122-128, https://doi.org/10.1016/j.triboint.2018.03.019.

Chen, G., Lodewijks , G., & L Schott, D. (2018). Numerical prediction on abrasive wear reduction of bulk solids handling equipment using bionic design. *Particulate Science and Technology*. 1-10, https://doi.org/10.1080/02726351.2018.1480547.

González, S. H. A. (2012). *Development of a model for determining soil abrasiveness with vertic characteristics (Desarrollo de un modelo para determinación de abrasividad de suelos con características vérticas)*. [Doctoral dissertation, Universidad Nacional de Colombia]. UNAL Campus Repository. https://repositorio.unal.edu.co/handle/unal/10237.

Graff, L. (2010). *Discrete element method simulation of wear due to soil-tool interaction*. [Doctoral dissertation, University of Saskatchewan]. USask Campus Repository http://hdl.handle.net/10388/etd-03312010-142510.

Hernández, J. A., Pérez Jiménez, J., Bosch Infante, D., & Castro Speck, N. (2019). The classification of soils in Cuba: emphasis on the 2015 version (La clasificación de suelos de Cuba: énfasis en la versión de 2015). *Cultivos Tropicales*, *40*(1). http://scielo.sld.cu/scielo.php?script=sci_arttext&pid=S0258-59362019000100015&lng=es&tlng=es.

Herrera, S. M., Iglesias C, E., Contreras M, Y., López B, E., & Sánchez I, A. (2010). Analysis of factors influencing the wear of working parts in tillage implements (Análisis de factores que inciden en el desgaste de los órganos de trabajo de los aperos de labranza). *Revista Ciencias Técnicas Agropecuarias, 19*(2), 1-9. http://scielo.sld.cu/scielo.php?script=sci_arttext&pid=S2071-00542010000200001.

Hoormazdi, G., Küpferle, J., Röttger, A., Theisen, W., & Hackl, K. (2018). A Concept for the Estimation of Soil-Tool Abrasive Wear Using ASTM-G65 Test Data. *International Journal of Civil Engineering*. 1-9, https://doi.org/10.1007/s40999-018-0333-9.

Jia, P., & Zhou, M. (2012). Tool wear and its effect on surface roughness in diamond cutting of glass soda-lime. *Chinese Journal of Mechanical Engineering*, *25*(6), 1224-1230, http://doi.org/10.3901/CJME.2012.06.1224.

Kostencki, P., Stawicki, T., & Białobrzeska, B. (2016). Durability and wear geometry of subsoiler shanks provided with sintered carbide plates. *Tribology International*, 104, 19-35. http://doi.org/10.1016/j.triboint.2016.08.020.

López, A. K. (2011). *Design of a wear system for the plough disc test bench (Diseño de un sistema de desgaste para el banco de pruebas de discos de arado)*. [Bachelor thesis, Universidad Autónoma Agraria Antonio Narro]. UAAAN Campus Repository. https://n9.cl/wyscty.

Montes-Rodríguez, C., Herrera-Suárez, M., López-Zamora, M., Pérez-Guerrero, J., & Torres-Rodríguez, R. (2023). Dem Computational Simulation of the polishing of the tagua (Phytelephas Aequatorialis) palm nuts. *Inmateh-Agricultural Engineering*, *70*(2), 299-308. https://doi.org/10.35633/inmateh-70-29.

Obrad, A., Jovic, S., Stanojevic, N., Marsenic, M., Pejovic, B., & Nedic, B. (2018). Estimation of tool wear according to cutting forces during machining procedure. *Sensor Review*, 38(2), 176-180 https://doi.org/10.1108/SR-07-2017-0147.

***Oficina Nacional de Normalización. (2000). Metodología para la determinación del contenido de humedad de los suelos y rocas en el laboratorio. *NC*: 67 2000.Vig. Marzo 2000. La Habana, Cuba.

***Oficina Nacional de Normalización. (2003). Metodología para la determinación de las condiciones de ensayo, Máquinas Agrícolas y Forestales. *NC*: 3447 2003. La Habana, Cuba.

Perazzo, F., Knopa, F., Mascaróa, P., & Placenciaa, G. (2016). Numerical Modeling of the Rate and Pattern of Abrasive Wear Using the Discrete Element Method (Modelación Numérica de la Tasa y El Patrón de Desgaste Abrasivo Mediante el Método de Elementos Discretos). *Mecánica Computacional*, *34*(15), 1013-1026.

Pérez, W. G., González, H., & del Toro, A. (2010). Abrasive Wear of Rotary Plow Blades in a Sandy Loam Soil (Desgaste abrasivo de cuchillas de arado rotativo en un suelo franco arenoso). *Dyna*, *77*(162), 105-114. https://n9.cl/38it9.

Rojek, J. (2014). Discrete element thermomechanical modelling of rock cutting with valuation of tool wear. *Comput Part Mech, 1*(1), 71–84, https://link.springer.com/article/10.1007/s40571-014-0008-5.

Sánchez, I. A. (2015). *Development of a Model Using the Discrete Element Method (DEM) for Computational Simulation of Abrasive Wear on Tillage Implement Working Parts (Desarrollo de un modelo mediante el Método de los Elementos Distintos (MED) para la simulación computacional del desgaste abrasivo de órganos de trabajo de los aperos de labranza)*. [Thesis, Universidad Agraria de La Habana].

Sánchez, I. A., Herrera Suárez, M., López Morfa, J., Socarrás Armenteros, Y., & Machado Guevara, A. (2018). Effect of geometry and type of material in tillage implements wear. *Revista Ciencias Técnicas Agropecuarias*, *27*(1), 36-45, http://scielo.sld.cu/pdf/rcta/v27n1/rcta04118.pdf.

Sánchez, I. A., Herrera Suárez, M., Recarey Morfa, C., López Bravo, E., & González Cueto, O. (2010). Determination of the wear of soil tillage tools under conditions of field (Determinación del desgaste de los aperos de labranzas de suelo en condiciones de campo). *Revista Ciencias Técnicas Agropecuarias, 19*(4), 60-66, http://scielo.sld.cu/pdf/rcta/v19n4/rcta10410.pdf.

Singh, J., Singh Chatha, S., & Singh Sidhu, B. (2017). Influence of soil conditions on abrasion wear behavior of tillage implements. *International Journal of Latest Trends in Engineering and Technology*, 258-263. https://n9.cl/y5twm.

***Soil Survey Staff. (2010). Natural Resources Conservation Service y Agriculture Dept. *Keys to Soil Taxonomy*, 344.

Sun, J., Wang, Y., Ma, Y., Tong, J., & Zhang, Z. (2018). DEM simulation of bionic subsoilers (tillage depth 40 cm) with drag reduction and lower soil disturbance characteristics. *Advances in Engineering Software*, 119, 30-37, http://doi.org/10.1016/j.advengsoft.2018.02.001.

Ucgul, M., Saunders, C., & Fielke J, M. (2017). Discrete element modelling of tillage forces and soil movement of a one-third scale mouldboard plough. *Biosystems Engineering*, 155, 44-54. http://doi.org/10.1016/j.biosystemseng.2016.12.002.

Wang, Z., Gao, K., Sun, Y., Zhang, Z., Zhang, S., Liang, Y., y otros. (2016). Effects of Bionic Units in Different Scales on the Wear Behavior of Bionic Impregnated Diamond Bits. *Bionic Engineering*, *13*(4), 659-668. http://doi.org/10.1016/S1672-6529(16)60337-2.

Zhang, C., Fu, X., Ren, A., Liu, Y., Lin, J., Zhang, H., ... & Zhang, X. (2024). The development of wear characteristics of the picking spindle hook teeth based on the discrete element method. *Wear*, *546*, 205295. https://doi.org/10.1016/j.wear.2024.205295.

Zolotarevskiy, V., Gallo, S. C., Pereira, M. P., & Barnett, M. R. (2022). Modelling of impeller-tumbler wear test with discrete element method. *Wear*, *510*, 204509. https://doi.org/10.1016/j.wear.2022.204509.

THE INFLUENCE OF WORKING SPEED ON THE QUALITY PARAMETERS FOR SPRAYING IN VINEYARDS

/

INFLUENȚA VITEZEI DE LUCRU ASUPRA PARAMETRILOR CALITATIVI LA EFECTUAREA LUCRĂRILOR DE STROPIT ÎN VII

Tibor RITTNER, Alexandru Bogdan GHEȚE*, Ovidiu MARIAN, Ovidiu RANTA, Valentin CRIȘAN, Cătălin BOGDAN, Adrian MOLNAR

Department of Technical Sciences and Soil Sciences, University of Agricultural Sciences and Veterinary Medicine Cluj-Napoca, Calea Mănăștur Street, no. 3-5, 400372, Cluj-Napoca, Romania

Tel: +40374492010; E-mail: alexandru.ghete@usamvcluj.ro

Corresponding author: Alexandru Bogdan Ghețe

DOI: https://doi.org/10.35633/inmateh-72-55

Keywords: *diameter volume; coverage degree; vineyard spraying*

ABSTRACT

In vine cultivation, pests are obstacles to obtaining crops that correspond both qualitatively and quantitatively. In this work, main working qualitative indices were determined. These working qualitative indices were determined under real field conditions using 2 types of nozzles, an air injection nozzle and a standard nozzle. The working qualitative indices determined were DV1, DV5, DV9, coverage degree, number of drops and the amount of solution deposited on target surface. For both speeds of 5 and 7 km/h, DV5 values classified the spray extra and ultra coarse spectrum. The coverage rate was between 55% and 99% regardless of travel speed.

REZUMAT

În culturile viticole, bolile reprezintă obstacole în obținerea culturilor care corespund atât calitativ, cât și cantitativ. În cadrul acestei lucrări, au fost determinați principalii indici calitativi. Acești indici calitativi de lucru au fost determinați în condiții reale folosind 2 duze, cu injecție de aer și o duză standard. Indicii calitativi determinați au fost DV1, DV5, DV9, gradul de acoperire, numărul de picături și cantitatea de soluție depusă. Pentru ambele viteze de 5 și 7 km/h, valorile DV5 clasifică spectrul în extra și ultra grosier. Rata de acoperire a fost între 55% și 99%, indiferent de viteza de deplasare.

INTRODUCTION

Plant viral diseases represent significant hurdles, leading to substantial yield losses globally across agricultural and horticultural crops. Conventional methods often fall short in completely eradicating viral loads from infected plants. Despite the ongoing utilization of unconventional approaches to prevent viral infections, their efficacy is not consistently reliable. Hence, there is an urgent need to identify the most promising and sustainable management strategies for economically significant plant viral diseases *(Manjunatha, et al., 2022; Signorini, et al., 2021).*

Continuous monitoring of the long-term effects of viticultural management practices is crucial, alongside assessing opportunities to enhance the environmental sustainability of vineyard operations. This holds particular significance for the wine industry, given the disruptive challenges posed by climate change, labour shortages, and increasing production costs faced by growers *(Tardaguila, et al., 2021).*

The aim of utilizing an air carrier sprayer for plant spraying is to achieve the deposition of spray material onto the canopy in adequate amounts, with uniform distribution, and minimal off-target loss, all within a timely manner. Spray droplets, formed via hydraulic or air shear atomization, are nevertheless conveyed to and onto the plant canopy by air jets generated by the sprayer. The turbulence of the air and the dispersion of the spray within the airflow are pivotal factors in ensuring optimal spray deposition within the canopy *(Manor, et al., 2002)*.

The effective utilization of crop protection products depends on various variables, including the type of application equipment *(Signorini, et al., 2023),* tank mix specifications *(Dai, et al., 2019)*, canopy porosity *(Diago, et al., 2016)*, operational features *(Sasturain, et al., 2024)* and environmental patterns such as meteorological aspects *(Belyakov, et al., 2021)*.

Research has shown that spray formulations and droplet size significantly determine the success of aerial applications *(Torrent, et al., 2019)*. All these aspects related to the management of the administration of phytosanitary treatments decide the effectiveness of the treatment carried out *(Grella, et al., 2020; He, et al., 2024)*.

Spray drifting represents a primary source of pollution identified during the application of pesticides on crops. So, in order to reduce environmental pollution, the characteristics of the droplets proved to be extremely important, because their size and weight are the most used factors taken into account in reducing the drift *(Creech, et al., 2015; Butler Ellis, et al., 2017; Rad, et al., 2022)*.

Other studies have demonstrated that a significant portion of the applied phytosanitary product is lost with previous studies indicating that only 30–40% of pesticide droplets are effectively deposited on the intended target. Typically, only a small fraction of the sprayed liquid adheres to the plant canopy, while the majority either falls to the ground or drifts away *(Ortiz, et al., 2023; Zhao, et al., 2023)*.

A new method for testing dispersion devices used for pesticide application in crops or orchards and not only has been discovered and was highly debated by other researchers with the same thoughts and aims to make an efficiency in pesticide management. Early researches in pesticide drift monitoring were also made using image analysis technique and LIDAR sensors *(Gheres, et al., 2023; Li, et al., 2023; Kashdan, et al., 2007; Gregorio, et al., 2014)*.

Contemporary vineyards, marked by monoculture and simplified landscapes, confront numerous challenges in pest management. These include increased pest and disease pressure, dependency on agrochemicals, the emergence of pesticide resistance, and susceptibility to the impacts of climate change. Also, the pest management comes with the necessity of access to finance which is a crucial aspect of vineyard development and performance. Several factors influence this access, including financial management capacity, which is closely tied to the level of financial literacy within the vineyard management *(Favor, et al., 2024; Hoxha, et al., 2023)*.

These challenges can find their answer in increasing the “precision” of spraying, that might be able to provide maximum effective coverage while applying lower chemical doses. From economic and environmental standpoints this can be considered the most viable approach. For this purpose, air injection nozzles can be used, capable of reducing drift *(Zande, et al., 2008; Nuyttens, et al., 2006)*, and thus implicitly pollution, while keeping the degree of coverage similar to the classic nozzles, hydraulic, disc–core nozzles *(Derksen, et al., 2000; Ranta, et al., 2021)*.

Checking the quality of the application of pest control products by spraying can be done by applying WPS water-sensitive paper collectors on the target surface, after applying the products, the WPS collectors are scanned, and the results obtained are interpreted. When in contact with water droplets, WPS changes its colour from yellow to blue, so it is not necessary to use colorant in the applied solution *(Sundaram, et al., 1987; Thériault, et al., 2001; Deveau, 2024)*.

The quality of the coverage of the target area is checked considering a series of parameters such as: the degree of coverage and the number of deposits, as well as the size of the drops. Companies producing pest products such as Singenta recommend that for satisfactory results the thresholds should be: minimum 50-70 drops/cm^2 for fungicide, minimum 20-30 drops/cm^2 for insecticides or pre-emergence herbicides and minimum 30-40 drops/cm^2 for contact postemergence herbicides *(Deveau, 2024; Zhu, et al., 2011; Wang, et al., 2019)*.

The aim of this study was to comparatively evaluate the spraying parameters and to measure the quality of the spraying with two types of nozzles used for treatments in vineyards and orchards.

MATERIALS AND METHODS

In order to achieve the proposed objectives an experimental plot with a vineyard was organized near the municipality of Oradea, Bihor County. For this study, 2 types of nozzles were used, a standard set of nozzles and an air injection nozzle (figure 1) at 2 different speeds and the main qualitative parameters of pesticide application were determined.

These nozzles were tested at two working speeds of 5 km/h and 7 km/h, without changing the pressure (9 bar) in three repetitions. The amount of solution varied so that the pressure remained constant. For the standard nozzles the rate/hectare was 890 l for 5 km/h and 640 l for 7 km/h. For injection nozzle the rate/hectare was 660 l for 5 km/h and 470 l for 7 km/h. The rate/hectare was changed according to working speed and constant pressure.

a) b)

Fig. 1 - The types of nozzles used in the experiment
a) standard nozzle; b) air injection nozzle

To achieve these working conditions, a Lombardini brand TUBER 40 tractor, an ATOM 300 pest control application machine (sprayer) (figure 2 a), with the following technical characteristics: main tank 300 L capacity 12 nozzles (6 on each side), a membrane piston pump and a 550 mm fan with an air flowrate of 26.000 m^3/h *(tehnofavorit.ro, 2024)* were used.

The vineyard had a 2.2 m row spacing.

Before performing the experiment, the machine and the nozzles were tested using the HERBST Pflanzenschutztechnik stand *(http://www.herbst-pflanzenschutztechnik.de/, 2024)*. This is a special stand which can determine the flowrate on each nozzle. The sprayer was calibrated according to the data obtained from the stand software.

a) b)

Fig. 2 – Equipment used in research
a) TUBER 40 tractor and Atom 100 equipment used for the treatments: b) and WPS position (at the base of the plant, in the middle of the trellis and at the top of the trellis)

For each data collection point, water sensitive paper WPS was mounted on 3 positions, at the base, in the middle and at the top of the vine plant (figure 2 b). The WPS were scanned with a CANON scanner and later the images were processed using the imaging software ImageJ using the algorithm DepositScan created by USDA ARS *(DepositScan, 2024)*, the program calculates DV 1 (10% of the volume sprayed is in droplets smaller than the expressed value), DV 5 (half of the volume of spray is in droplets either smaller or higher) and DV 9 (indicates that 90% of the volume of spray is in droplets smaller than the given values). The obtained results were analyzed with the Statistica 10 program, interpreted with the help of Whisker Box Plots.

Based on droplet characteristics (volume median diameter) drops can be classified into eight categories as follows: extremely fine (<60 μm), very fine (60–145 μm), fine (146–225 μm), medium (226–325 μm), coarse (326–400 μm), very coarse (401–500 μm), extremely coarse (501–650 μm) and ultra-coarse (>650 μm) *(https://pesticidestewardship.org/, 2024)*.

RESULTS

Results on the influence of working speed on the main qualitative indices in the case of injection nozzle and standard nozzle show a dependence on the speed of work.

For the first indicator DV1 the influence of travel speed is shown in figure 3.

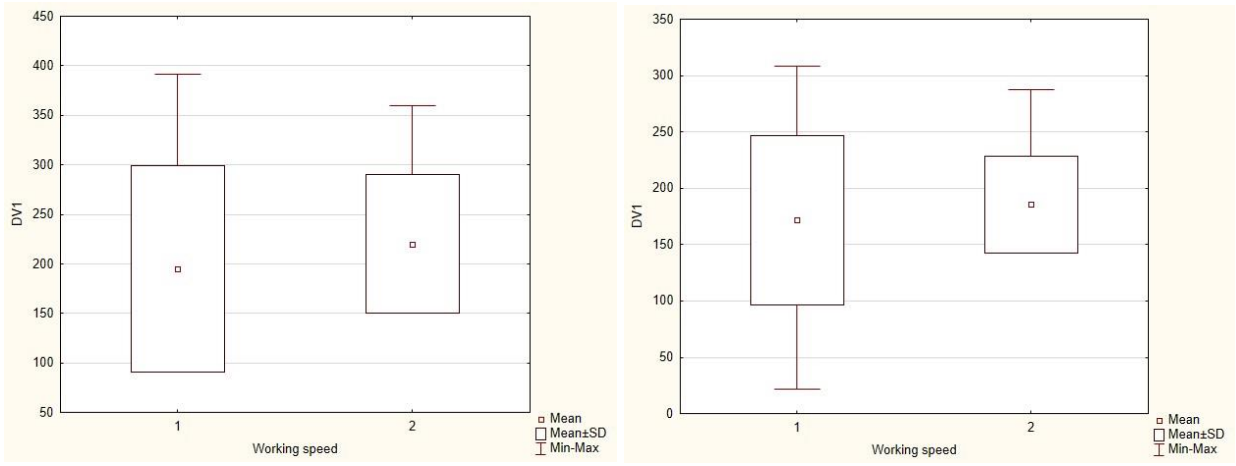

a) b)

Fig. 3 - Influence of the working speed on the DV 1

a) injection nozzle; b) standard nozzle

The DV 1 parameter indicates that 10 % of drops are lower than this value. Thus, in the figure 1 at speed V1 (5 km/h) this parameter varies from the minimum value (103.4 μm) to 391.4 μm in case of the injection nozzle. This indicates a relatively symmetrical distribution of data with the mean at 195 μm. This indicates that 90 % of the droplet spectrum are smaller than 195 μm. In the case of operating speed V2 (7 km/h) the data distribution range is between 154.4 μm and 359.6 μm. The distribution in this case is a symmetric distribution. In this case, the average is 220.2 μm. It can be seen that with increasing speed from 5 km/h to 7 km/h, the droplet size increases.

Standard nozzle at V1 speed (5 km/h) shows that the minimum value of the range is 21.7 μm and the maximum value is 308.3 μm. This indicates a relatively wide distribution of data with the mean at 171.67 μm. This indicates that 90 % of the droplet spectrum is smaller than 171.67 μm. In the case of operating speed V2 (7 km/h) the data distribution range is between 149.1 μm and 287.4 μm. In this case, the average is 220.71 μm.

In the case of the first working speed of 5 km/h the differences between the lower limits of the 2 nozzles are small, about 80 microns. For the upper limits the differences reach around 80 microns. In the case of the nozzle with air injection, the average of 197 microns compared to the standard nozzle whose average is 171.6 microns indicates that it generates droplets of a larger size.

In the case of travel speed of 7 km/h the differences are more pronounced. Thus, for the air injection nozzle, the minimum value of 154.4 microns indicates that with the increase in speed comes another factor that influences the size of the droplets. This factor can be identified as an interaction between the speed of the air current at which the solution is sprayed and the air currents existing in the atmosphere. This interaction causes further fragmentation of droplets. The same trend is observed for the upper limit of this indicator.

The influence of travel speed on the DV5 indicator is shown in figure 4.

In the figure 4 the influence of travel speed on the DV5 parameter is shown. This parameter indicates that 50 % of the droplet spectrum is lower than its value and the volume of 50 % of droplets is greater. This parameter is also the parameter characterizing the spectrum of droplets in terms of droplet size.

For the air injection nozzle at low speed of 5 km/h droplets have a diameter between 233.9 and 731.6 μm. The average droplet value is 419.7 μm. At 7 km/h it can be seen that the droplet spectrum is in the range of 260.4 μm to 718 μm. The average value of DV 5 is 636.8 μm. The increase in speed causes an increase in the DV5 parameter, which indicates an increase in the average diameter of droplets. Both speeds frame the spectrum of droplets in very coarse and extremely coarse spraying.

For the standard nozzle the influence of travel speed on the DV5 parameter is shown in figure 2 b). At low speed of 5 km/h droplets have a diameter between 83.8 and 763 μm. The average droplet volume value is 605.44 μm. At 7 km/h it can be seen that the droplet spectrum is in the range of 596.3 μm and 733.7 μm. The average value of DV 5 is 700 μm.

The increase in speed causes a slight increase in the DV5 parameter, which indicates an increase in the diameter of droplets. Also, as for the injection type, both speeds fit the droplet spectrum into the very ultra-coarse spray type.

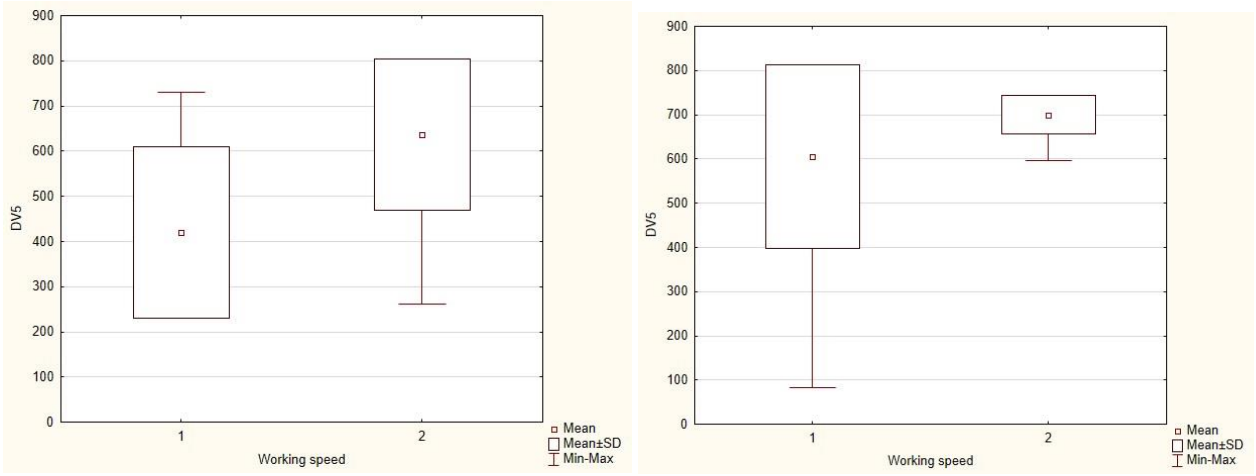

a) b)

Fig. 4 - Influence of the working speed on the DV 5
a) injection nozzle; b) standard nozzle

For the first travel speed of 5 km/h, analyzing the data presented in figure 2, it is found that for the nozzle with air injection the minimum droplet diameter value for the DV5 parameter was 233.9 microns and for the standard nozzle it was 83.8 microns. The maximum recorded values of the 2 nozzles register a difference of about 30 microns. The mean values are close, the difference between the 2 averages being 190 microns, with higher values at the standard dose.

Raising the speed to 7 km/h shows the differences between the 2 nozzles in terms of DV 5. Thus, the difference between the recorded minimums of the 2 nozzles is 330 microns. In the case of maximum recorded values, the difference is much smaller, namely 15 microns. The mean value of DV 5 showed a difference of 64 microns, the higher value being recorded for the standard nozzle.

The DV5 parameter is representative of the overall droplet spectrum. The results indicate that half of the droplets have a diameter greater than or less than 419.7 microns in the case of the air-injected nozzle and a travel speed of 5 km/h. Increasing this speed, the average value drops to 636.8 microns. For both speeds, the mean values of the DV5 parameter frame the droplet spectrum in a very coarse or extremely coarse spray.

The standard nozzle used in phytosanitary treatment machines in vineyards and orchards recorded an average droplet diameter of 605.4 microns at 5 km/h and increased as the speed increased to 700 microns.

Regardless of the speed of travel and the type of nozzles tested, the spray is classified as very coarse or extremely coarse. The large droplet size that characterizes the spray spectrum indicates that many droplets could reach the target surface, thus reducing the risk of drift leading to environmental pollution.

In figure 5, the influence of travel speed on DV 9 for both nozzle is shown.

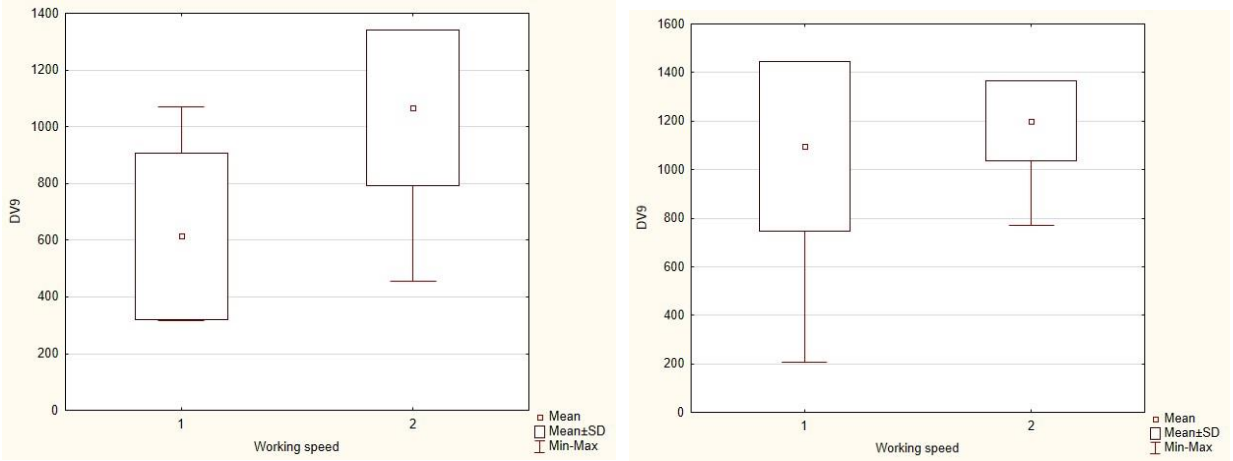

a) b)

Fig. 5 - Influence of the working speed on the DV 9
a) injection nozzle; b) standard nozzle

This parameter indicates that 90 % of the droplet spectrum is lower than this value and the volume of 10 % of droplets is greater.

The injection nozzle registers at a low speed of 5 km/h an average diameter of DV9 of 614.2 μm. The range varies from 315.9 μm to 1071.8 μm. At 7 km/h the mean value of DV9 shows an increase to 1066.22 μm. In contrast, the range in which values are found is greater, from 456.4 μm to 1219.1 μm.

Standard nozzle at a low speed of 5 km/h has the DV9 average diameter of 1094.7 μm. The values range from 204.9 μm to 1363.4 μm. At 7 km/h the average value of DV9 is kept approximately constant with a slight increase of 100 μm. In contrast, the range is smaller, from 769.1 μm to 1292.7 μm.

In the case of parameter DV9, it is observed that the minimum and maximum values differ in the case of the 2 nozzles. Thus, in the case of the nozzle with air injection at the first travel speed of 5 km/h, the maximum value of this parameter is almost double compared to the minimum value, with an average of 614.2 microns. If the speed is increased to 7 km/h, the minimum and maximum values differ by 102 microns for the minimum value and 130 microns for the maximum value. The average value doubles at higher speed, reaching 1066.2.

In the case of the standard nozzle at a low speed of 5 km/h, the maximum value of the parameter DV9 tripled from the minimum value. The average value of this parameter is high, being 1094.7 microns. If the speed is increased to 7 km/h, the standard nozzle registers an increase in limit values of approximately 500 microns for the minimum values, while at the same time recording a slight increase in the maximum value of this parameter. The average value of DV9 is 1292.7 microns, slightly higher than the value recorded at the previous speed.

In figure 6, the influence of working speed on the degree of coverage is shown.

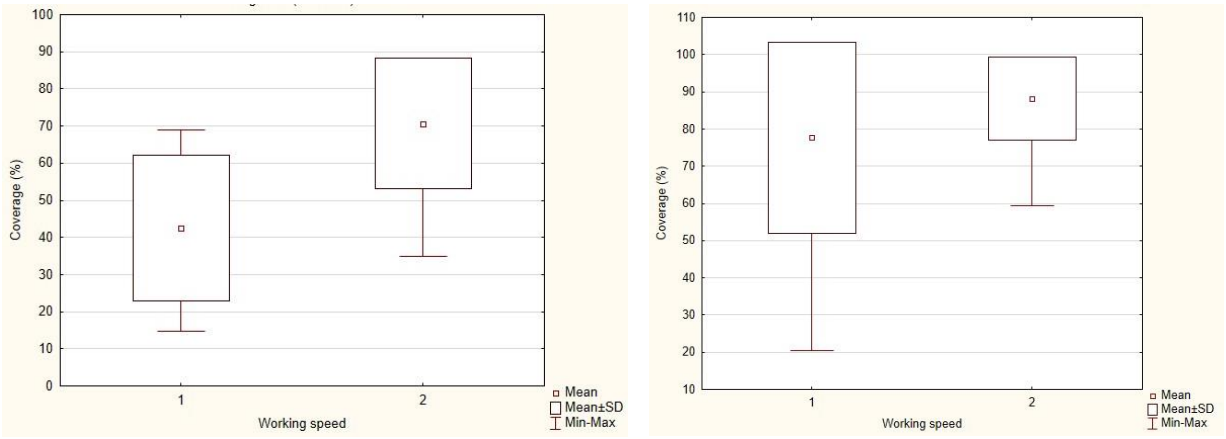

Fig. 6 - Influence of the working speed on the Coverage degree

a) injection nozzle; b) standard nozzle

The degree of coverage is one of the most important indicators of the phytosanitary treatments and is directly associated with its effectiveness. Therefore, a high degree of coverage represents a better efficacy of the phytosanitary treatment. Regardless of the speed of movement of the agricultural aggregate and the nozzle, the coverage was above 55 % lower limit and close to 99 % upper limit.

For the injection nozzle the coverage rate for speeds of 5 km/h is in the range of 14.8-69 percent. The average value recorded for the speed of 5 km/h is 42.5 %. Increasing the speed to 7 km per hour causes increased coverage. The average coverage value recorded at this speed is 70.7 %. The coverage range is between 34.9 % and 85.6 %.

The coverage rate for the standard nozzle at 5 km/h is in the range of 20.3 – 98.4%. The average value recorded for the speed of 5 km/h is 77.6 %. Increasing the speed to 7 km per hour causes increased coverage. The average coverage value recorded at this speed is 88 %. The coverage range is between 59.4 % and above 95 %.

In figure 7, the influence of working speed on the number of drops/cm^2 is shown.

The air-injected nozzle at a working speed of 5 km/h recorded several droplets per unit area between 10.8 and 22.1. The mean number of drops was 18.1 drops/cm^2. At 7 km/h the minimum number of drops increased slightly to 13.1 drops/cm^2. The maximum number of drops recorded per unit area was 49.5 and the mean number of drops per de-termination was 28.7 drops/cm^2.

The standard nozzle for phytosanitary treatments recorded at a speed of 5 km/h a number of droplets between 2 and 281.3 drops per unit area. The mean number of drops was 57.5 drops/cm^2. At 7 km/h the number of droplets recorded was between 1.4 and 110 drops per unit area. The mean number of drops was 18.6 drops/cm^2.

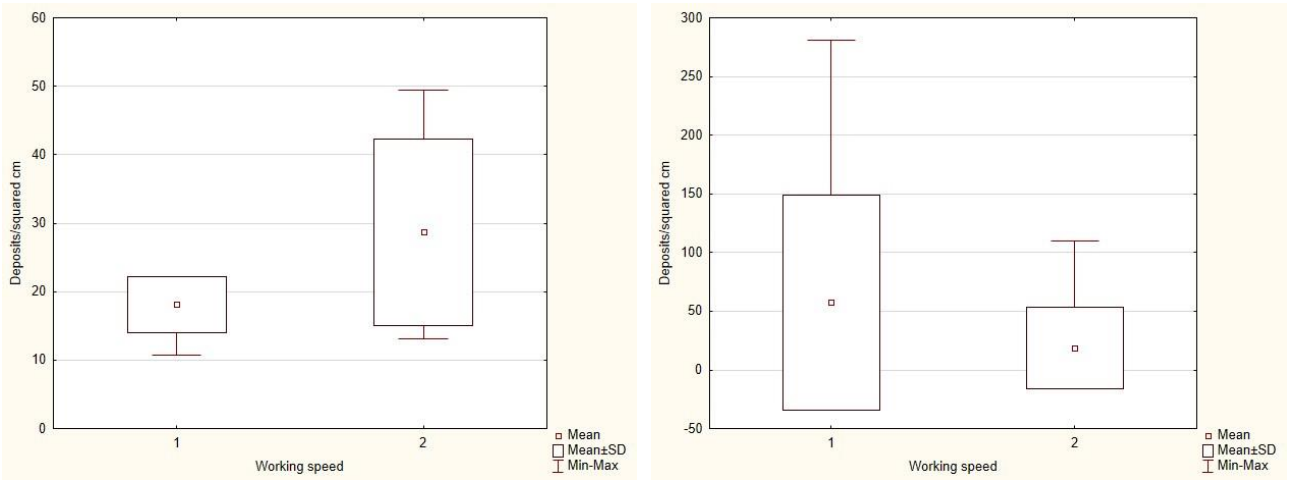

Fig. 7 - Influence of the working speed on the number of droplets/cm^2
a) injection nozzle; b) standard nozzle

In the figure 8 the influence of working speed on the deposition/cm^2 is shown.

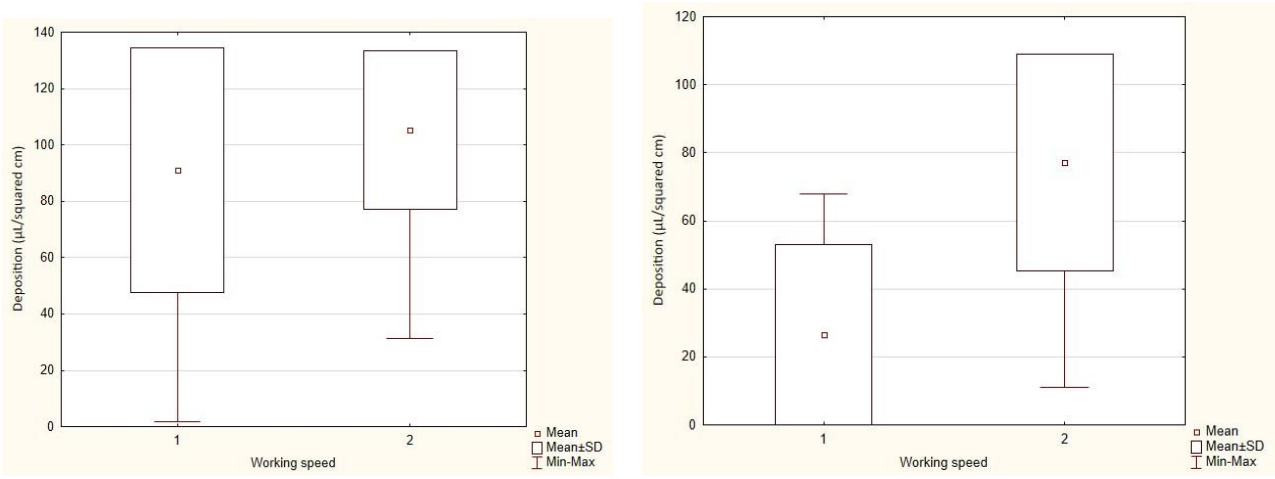

Fig. 8 - Influence of the working speed on the deposition/cm^2
a) injection nozzle; b) standard nozzle

The amount of solution deposited on the target surface is an important indicator of phytosanitary treatment work. The analysis of this parameter was performed using the algorithms of the DepositScan program, and the amount of solution is measured in µL/cm^2.

Thus, for the nozzle with air injection, an average amount per unit area of 26.39 µL was recorded for the speed of 5 km/h. The range of determined values was 3.94 µL/cm^2 and 68.06 µL/cm^2. At 7 km/h, the average amount deposited on the target surface was 77.14 µL/cm^2. The minimum value recorded was 10.94 µL/cm2 and the maximum value was 104.32 µL/cm^2.

The standard nozzle for phytosanitary treatments in vineyards and orchards, recorded at a speed of 5 km/h an average value of the amount of solution of 90.93 µL/cm^2. The minimum value recorded was 1.9 µL/cm^2, the maximum value was 131 µL/cm^2. The mean value of the amount of solution deposited on the target surface at 7 km/h was 105.37 µL/cm^2.

Analysing the data presented in terms of parameters characterizing the droplet spectrum for the two nozzles, it is observed that for parameter DV1, at a speed of 5 km/h the nozzle with air injection generates larger droplets by approximately 20 µm. The increase in speed generated an average droplet size of about 220 µm for both nozzles. The DV5 parameter characterizing the droplet spectrum at 5 km/h recorded a lower value for the air-injected nozzle than for the standard nozzle.

This can be explained on the one hand from the perspective of field conditions, and on the other hand from the perspective of the capabilities of DepositScan algorithms. Under field conditions, droplets carried in the air stream generated by the fan, in the case of standard nozzles, have a higher probability of collision, depositing a slightly higher amount of liquid on the target surface. Air-injected nozzles generate air-filled droplets that have a more stable trajectory. From the perspective of the DepositScan algorithm, the determination of the size of drops is carried out by comparing the fingerprint of the drop with the shade of the background. Thus, if there are overlapping droplets, even if not completely, the imprint of several drops is regarded as a single drop.

The parameters characterizing the quality of the treatment are influenced by the working speed. The coverage degree of air injection nozzles is higher at 7 km/h by approximately 60%. This is also observed in standard nozzles, only the increase is less pronounced (13%). The number of drops increases to 7 km/h in the case of the air-injected nozzle, while in the case of standard nozzles the number of drops decreases. Atmospheric conditions can influence the trajectory of droplets, especially wind gusts, depending on the vector of travel. In the case of air-injected nozzles, the increase in the number of droplets can be explained by the resultant speed of movement of the aggregate of phytosanitary treatments, the distance from the nozzle to the target surface and possible gusts of wind. In the case of standard nozzles, wind gusts have a great influence through the fact that they generate small droplets with a small mass that can deviate from the target surface. The amount of substance deposited on the target surface in the case of air injection nozzles also increases with increasing speed, a phenomenon that is also observed in the droplet count parameter. In contrast, at the standard nozzle, the amount of substance increases, although the number of drops parameter decreases. Swirling effects can affect the amount of the substance, with the likelihood of several drops reaching the same site is high.

CONCLUSIONS

This research conducted in field, determined the qualitative indices for vineyard treatments. The factor which was tested was working speed under two gradients (5 km/h and 7 km/h). Based on the droplets spectra characterization under the volume median diameter (DV1, DV5 and DV9) and the coverage degree, one can draw the following conclusions: for the 5 km/h speed, the average coverage degree was 42.53 % with a droplet DV5 of 419.7 μm for the injection nozzle set and 77.64% with a droplet DV5 of 605.44 μm for the standard nozzle set; for 7 km/h the average coverage degree was 70.72% with a droplet DV5 of 636.81 μm for the injection nozzle set and 88% with a droplet DV5 of 700 μm for the standard nozzle set. Both speeds classify the treatment as extra coarse and ultra coarse.

Both nozzles generated droplets with a high median diameter, but the coverage degree was higher than 40% for both nozzles at 5 km/h, and 70% at 7 km/h. Although the working qualitative indices for the 2 nozzles were close, the air injection nozzle required a smaller amount of substance per hectare for both speeds. Thus, the use of the nozzle with air injection generates larger droplets, a high degree of coverage in general, a smaller number of drops than the standard nozzle. This makes that with a smaller amount of substance per hectare high working qualitative indices are obtained.

The results show that in this experiment, there are several factors that interfere with the droplets spectra and coverage degree which needs further investigation.

Promoting sustainable agriculture and responsible pesticide use requires ongoing research to enhance spraying precision. This includes achieving better coverage and using larger droplets. Effectively treating crops at higher canopy levels remains a significant challenge that warrants attention. This research aims to build upon the existing knowledge and develop more efficient approaches for managing spatial crops.

REFERENCES

[1] Belyakov, N., & Nikolina, N. (2021). Plant Protection Technologies: From Advanced to Innovative. *J. Phys.: Conf. Ser. doi:10.1088/1742-6596/1942/1/012072*.

[2] Butler Ellis, M., Alanis, R., Lane, A., Tuck, C., Nuyttens, D., & van de Zande, J. (2017). Wind Tunnel Measurements and Model Predictions for Estimating Spray Drift Reduction under Field Conditions. *Biosystems Engineering doi:10.1016/j.biosystemseng.2016.08.013*.

[3] Creech, C., Henry, R., Fritz, B., & Kruger, G. (2015). Influence of Herbicide Active Ingredient, Nozzle Type, Orifice Size, Spray Pressure, and Carrier Volume Rate on Spray Droplet Size Characteristics. *Weed technol. doi:10.1614/WT-D-14-00049.1*.

[4] Dai, X., Xu, Y., Zheng, J., & Song, H. (2019). Analysis of the Variability of Pesticide Concentration Downstream of Inline Mixers for Direct 372 Nozzle Injection Systems. *Biosystems Engineering doi:10.1016/j.biosystemseng.2019.01.012*, 59-69.

[5] *DepositScan*. (2024, 03 25). Retrieved from DepositScan: https://www.ars.usda.gov/midwest-area/wooster-oh/application-technology-438 research/engineering/depositscan/

[6] Derksen, R., Zhu, H., Fox, R., Brazee, R., & Krause, C. (2000). Coverage and Drift Produced by Air Induction and Conventional Hydraulic Nozzles Used for Orchard Applications. *Transactions of the ASABE doi:10.13031/2013.23941*.

[7] Deveau, J. (2024, 04 3). *Comparing three brands of water sensitive paper.* Retrieved from sprayer101: https://sprayers101.com/3_wsp/

[8] Diago, M., Krasnow, M., Bubola, M., Millan, B., & Tardaguila, J. (2016). Assessment of Vineyard Canopy Porosity Using Machine Vision. *Am J Enol Vitic doi:10.5344/ajev.2015.15037*, 229-238.

[9] Favor, K., Gold, M., Halsey, S., Hall, M., & Vallone, R. (2024). Agroforestry for Enhanced Arthropod Pest Management in Vineyards. *Agroforest Syst doi:10.1007/s10457-023-00900-9.*

[10] Gheres, M., Scurtu, I.-L., Szabo, I., Gheres, M., & Ionescu, A. (2023). New Method for Testing Dispersion Devices Used for Pesticide 401 Application / O Nouă Metoda Pentru Încercarea Dispozitivelor de Dispersie Utilizate Pentru Aplicarea Pesticidelor. *ISB-INMA-TEH*.

[11] Gregorio, E., Rosell-Polo, J., Sanz, R., Rocadenbosch, F., Solanelles, F., Garcerá, C., . . . al., e. (2014). Alternative to Passive Collectors to Measure Pesticide Spray Drift. doi:10.1016/j.atmosenv.2013.09.028**.** *Atmospheric Environment doi:10.1016/j.atmosenv.2013.09.028.*

[12] Grella, M., Miranda-Fuentes, A., Marucco, P., Balsari, P., & Gioelli, F. (2020). Development of Drift-Reducing Spouts For Vineyard Pneumatic Sprayers: Measurement of Droplet Size Spectra Generated and Their Classification. *Applied Sciences doi:10.3390/app10217826*.

[13] He, M., Qi, P., Han, L., & He, X. (2024). Study on Spray Evaluation: The Key Role of Droplet Collectors. *Agronomy doi:10.3390/agronomy14020305*.

[14] *Herbst-Pflanzenschutztechnik.* (2024, 03 25). Retrieved from Herbst-Pflanzenschutztechnik.: http://www.herbst-pflanzenschutztechnik.de/index-436 Dateien/ED20_900_A4Englisch.pdf

[15] Hoxha, A., Mulliri, J., Shahu, E., Imami, D., Zhllima, E., & Gjokaj, E. (2023). Financial Literacy for Farmers – the Case of Vineyard Farmers in Kosovo. *Die Bodenkultur: Journal of Land Management, Food and Environment doi:10.2478/boku-2023-0002*.

[16] Kashdan, J., Shrimpton, J., & Whybrew, A. (2007). A Digital Image Analysis Technique for Quantitative Characterisation of High-Speed Sprays. *Optics and Lasers in Engineering doi:10.1016/j.optlaseng.2006.03.006*.

[17] Li, S., Li, J., Yu, S., Wang, P., Liu, H., & Yang, X. (2023). Anti-Drift Technology Progress of Plant Protection Applied to Orchards: A Review. *Agronomy doi:10.3390/agronomy13112679*.

[18] Manjunatha, L., Rajashekara, H., Uppala, L., Ambika, D., Patil, B., Shankarappa, K., . . . Mishra, A. (2022). Mechanisms of Microbial Plant Protection and Control of Plant Viruses. *Plants, 11, doi:10.3390/plants11243449*.

[19] Manor, G., & Gal, Y. (2002). Development of an Accurate Vineyard Sprayer. *American Society of Agricultural and Biological Engineers*.

[20] *Masina de stropit in vii si livezi | ATOMIZOR 300*. (2024, 04 5). Retrieved from /tehnofavorit.ro: https://tehnofavorit.ro/produse/atom-300-400/

[21] Nuyttens, D., Schampheleire, M., Steurbaut, W., Baetens, K., Nicolaï, B., Ramon, H., & Sonck, B. (2006). Experimental Study of Factors Influencing the Risk of Drift from Field Sprayers. *Aspects of Applied Biology 77, International Advances in Pesticide Application*.

[22] Ortiz, C., Torregrosa, A., Saiz-Rubio, V., & Rovira-Más, F. (2023). Vibration Analysis of Pulse-Width-Modulated Nozzles in Vineyard 397 Blast Sprayers. *Horticulturae doi:10.3390/horticulturae9060703*.

[23] Rad, S., Ray, A., & Barghi, S. (2022). Water Pollution and Agriculture Pesticide. *Clean Technol doi:10.3390/cleantechnol4040066*.

[24] Ranta, O., Marian, O., Muntean, M., Molnar, A., Ghețe, A., Crișan, V., . Rittner, T. (2021). Quality Analysis of Some Spray Parameters When Performing Treatments in Vineyards in Order to Reduce Environment Pollution. *Sustainability doi:10.3390/su13147780*.

[25] Sasturain, J., Blaschke, U., Stauber, F., Oteyza, T., Huby, J.-P., Adham, S., al., 3. e. (2024). Minimizing Operator Exposure: Field Data Analysis of Three Closed Transfer Systems for Pesticide Mixing and Loading. *J Consum Prot Food Saf doi:10.1007/s00003-023-01472-7*.

[26] Signorini, G., & Lewis Ivey, M. (2023). Comparative Feasibility Analysis of Mechanized Equipment for Vineyard Operations. *Horttech doi:10.21273/HORTTECH05147-22*.

[27] Signorini, G., Smith, M., & Dami, I. (2021). Feasibility Assessment of Grape Vineyards in the Midwest U.S.A. *Horticulturae doi:10.3390/horticulturae8010018*.

[28] Sundaram, K., de Groot, P., & Sundaram, A. (1987). Permethrin Deposits and Airborne Concentrations Downwind from a Single 423 Swath Application Using a Back Pack Mist Blower. *J. of Env. Sc. & Hlth., Part B doi:10.1080/03601238709372552*.

[29] Tardaguila, J., Stoll, M., Gutiérrez, S., Proffitt, T., & Diago, M. (2021). Smart Applications and Digital Technologies in Viticulture: A Review. *Smart Agricultural Technology doi:10.1016/j.atech.2021.100005*.

[30] Thériault, R., Salyani, M., & Panneton, B. (2001). Spray distribution and recovery in citrus application with a recycling sprayer. *Transactions of the ASAE doi:10.13031/2013.6430*.

[31] Torrent, X., Gregorio, E., Douzals, J.-P., Tinet, C., Rosell-Polo, J., & Planas, S. (2019). Assessment of Spray Drift Potential Reduction for Hollow-Cone Nozzles: Part 1. Classification Using Indirect Methods. *Science of The Total Environment doi:10.1016/j.scitotenv.2019.06.121*.

[32] *Understanding Droplet Size*. (2024, 04 10). Retrieved from Pesticide Environmental Stewardship: https://pesticidestewardship.org/pesticide-drift/understanding-droplet-size/

[33] Wang, G., Lan, Y., Yuan, H., Qi, H., Chen, P., Ouyang, F., & Han, Y. (2019). Comparison of Spray Deposition, Control Efficacy on Wheat Aphids and Working Efficiency in the Wheat Field of the Unmanned Aerial Vehicle with Boom Sprayer and Two Conventional Knapsack Sprayers. *Applied Sciences doi:10.3390/app9020218*.

[34] Zande, van de Zande, J., Holterman, H., & Wenneker, M. (2008). Nozzle Classification for Drift Reduction in Orchard Spraying: Identification of Drift Reduction Class Threshold Nozzles. *Agricultural Engineering International X*.

[35] Zhao, G., Zhang, Y., Lan, Y., Deng, J., Zhang, Q., Zhang, Z., Ma, J. (2023). Application Progress of UAV-LARS in Identification of Crop Diseases and Pests. *Agronomy doi:10.3390/agronomy13092232*.

[36] Zhu, H., Salyani, M., & Fox, R. (2011). A Portable Scanning System for Evaluation of Spray Deposit Distribution. *Computers and Electronics in Agriculture doi:10.1016/j.compag.2011.01.003.*

USING SOLAR ENERGY AS NON-CONVENTIONAL ALTERNATIVE ENERGY IN SMALL AND MEDIUM-SIZED FARMS (Part I)
/
UTILIZAREA ENERGIEI SOLARE CA SURSĂ ALATERNATIVĂ NECONVENŢIONALĂ DE ENERGIE ÎN FERMELE DE DIMENSIUNI MICI ŞI MEDII (Partea I)

Mario CRISTEA[1)], Nicolae-Valentin VLĂDUȚ[1*)], Nicoleta UNGUREANU[2*)]
[1)]INMA Bucharest / Romania; [2)]POLITEHNICA Bucharest / Romania
Corresponding authors: valentin_vladut@yahoo.com; nicoletaung@yahoo.com
DOI: https://doi.org/10.35633/inmateh-72-56

Keywords: *farm, solar energy, support, sunshine, rotation*

ABSTRACT
Solar energy represents a future solution for clean, sustainable energy, because the sun generates much more energy every day than it is necessary for daily consumption, unlike fossil fuels. The only limitation related to this renewable resource is the ability to transform this energy into electricity. The paper presents a functional model of equipment that allows the capture of solar energy using special panels, which can rotate according to the sun, so that the incidence of rays with the radiating surface of the panels is maximum, and the yields obtained at different angles of inclination (in the vertical plane: 30° and 45°, and in the horizontal plane: 0° to be maximum.

REZUMAT
Energia solară reprezintă o soluţie de viitor pentru o energie curată, sustenabilă, datorită faptului că soarele generează în fiecare zi mult mai multă energie decât avem nevoie pentru consumul zilnic, spre deosebire de combustibilii fosili. Singura limitare legată de această resursă regenerabilă este capacitatea de a transforma această energie în electricitate. În lucrare se prezintă un model funcţional de echipament care permite captarea energiei solare utilizând panouri speciale, care se pot roti după soare, astfel încât incidenţa razelor cu suprafaţa radiantă a panourilor să fie maximă, iar randamentele obținute la diferite unghiuri de înclinaţie (în plan vertical: 30° şi 45°, iar în plan orizontal: 0° să fie maxime.

INTRODUCTION

The sun provides the majority of the energy consumed by humanity on Earth. "Solar" energy is derived directly from the sun. Renewable energy is also known as environmentally friendly power, green power, sustainable power, or alternative energy. The surrounding stellar environment absorbs the majority of the sun's energy, so very little of it reaches Earth as radiation (*Majeed et al, 2023*).

A square meter on Earth's surface receives an average of 1366 W of solar energy (*Lindsey, 2009*), but this might vary depending on latitude (*Cocks, 2016*). The first stage in capturing solar energy is estimating the quantity of energy available from the sun in a specific area of the Earth. A country's economic and social success is determined by its ability to obtain a consistent and affordable supply of energy (*Fatai et al., 2004; Muneer et al., 2006*).

Renewable energy sources, such as wind and sun, can be used to power farm vehicles in a way that is beneficial to the economy and the environment (*Balasuadhakar et al., 2016*).

Clean energy, also known as renewable energy, is derived from non-anthropogenic sources such as the sun and wind. These sources can be replenished continuously, despite the fact that they are time and weather-dependent. On the other hand, fossil fuel is a collective name given to oil, natural gas, and coal, which are non-renewable energy sources generated from carbon-based dead and buried organisms that disintegrated millions of years ago (*Bhatia and Gupta, 2019; Zekai, 2008*).

Solar energy remains one of the oldest renewable sources of energy in the universe, which is taken in the form of solar radiation from the sun and primarily employed in three ways: a) electricity generation with solar cells in which photovoltaic or photoelectric cells are used; b) the sun heat can be used to warm water in a glass panel of a solar energy system through solar water heating; c) production of high temperatures from the sun through the use of furnaces and mirrors to collect the sun's energy is the primary focus, which may also be utilized in cooking and processing food, enhanced oil recovery, water desalination, chemical production, and mineral processing (*Zekai, 2008; Ihssen et al., 2014; Zhao et al., 2013).*

The global public and private sectors are actively pursuing new solutions to meet the demand for clean energy while lowering greenhouse gas emissions and energy costs in their operations. Consequently, the installation of renewable and sustainable energy systems became a priority (*Mekhilef et al., 2012; Kahraman and Dincer, 2022; Tong et al., 2022; Găgeanu et al., 2011*). Thus, solar energy remains the most viable alternative energy source because it offers a number of advantages over other options (*Ahmed et al., 2022)*. Solar energy is naturally available as an environmentally beneficial energy source supplied by the sun, which may be exploited to directly generate power (*Jahid et al., 2018*). Furthermore, solar energy produces no pollution, requires little maintenance, and the product technology has a long life expectancy of around 20-30 years (*Jahid et al., 2018; Saidur and Mekhilef, 2010*). Solar applications were initially developed for rural electrification, telecommunications, and agriculture sectors, but they are now used in a wide range of applications, such as solar water heating, solar drying, and solar photovoltaics (PVs) (*Saidur, 2010; Mohammed Wazed et al., 2018; Zaharaoui et al., 2021; Xiong et al., 2021; Huang et al., 2022)*. Besides, solar power can supply 100 percent of the world's primary energy demand (*Perez and Perez, 2022*).

Heat transmission (HT) is a branch of heat research that studies the creation, use, modification, and preservation of thermal energy systems. In recent years, there has been a growth in interest in the topic of HT as people become more concerned about climate change and its implications for energy systems. Understanding the concepts of HT has never been more important as the world strives to decrease its carbon footprint and switch to renewable energy sources.

This study seeks to provide an overview of the fundamentals of HT, its uses, and its significance in the context of renewable energy and climate change. The study of HT includes several components, such as heat transfer by conduction, convection, and radiation (*Salawu et al., 2022*). Many academics offer different approaches to explaining heat transfer ideas in engineering challenges (*Hussain et al., 2021; Kartal, 2022*). Some of the applications studied include spaceship design, comets and asteroids, mass transfer preservation, heat exchanger design, and heat piping system development.

The accelerating depletion of fossil fuels, along with increased concerns about climate change, has driven the world to a critical juncture in its energy transition. During this paradigm change, hybrid renewable energy systems (HRES), especially those incorporating solar and wind power technologies, have emerged as key options to meet the difficulties of energy sustainability (*Marks-Bielska et al., 2020; Dincer, 2000*). However, such systems reduce the intermittency difficulties inherent in individual renewable sources, increasing the overall reliability and stability of energy production. Solar power's highest output occurs during daylight hours; however, wind power can be harvested even when solar availability is limited (*Garratt et al., 2023*). Integrating these sources makes the energy supply more consistent, lowering the chance of power outages during inclement weather. Furthermore, energy storage technologies integrated into hybrid systems provide surplus energy storage during peak production periods, allowing its usage during low production phases, enhancing total system efficiency, and lowering waste (*Hassan et al., 2023; Maican et al., 2019*).

MATERIALS AND METHODS

The operating principle of the solar collector is based on the use of the black body effect (achieved by means of the absorbent surface) combined with the greenhouse effect (achieved by the glass plate and the polyester film). The installation is made as an experimental model and uses flat solar collectors with gaseous thermal agent (air). Structurally, it was designed specifically for research. In addition to the basic function of capturing and converting solar energy into thermal energy by heating the air, the installation allows the horizontal and vertical rotation of the solar panels to further expand the scope of investigations depending on the angle of incidence of the sun's rays with the surface of the panel.

The experimental model of the module for capturing and converting solar energy into thermal energy (Figure 1) is located in an area with exposure to the sun throughout the day, at a distance that ensures minimal losses on the thermal agent transport network (air), from solar collectors to potential users such as a fruit drying facility. The main component subassemblies of the module for capturing and converting solar energy into thermal energy are: the support frame, the solar collectors and the air tubes with a low-pressure centrifugal fan. The rotation of the solar collectors around a central pivot by 45° left-right from the initial orientation position to the south and also the orientation of the solar collectors in the vertical plane at fixed angles of 30° and 45° is done manually and checked each time with appropriate measuring instruments. With these facilities, the variation of solar energy can be highlighted throughout the day by orienting the panels according to the position of the sun, and adjustments can be made to optimize the system's operating regime.

Fig. 1 – Module for capturing and converting solar energy

The module for capturing and converting solar energy into thermal energy consists of:

- *The support frame*, is an assembly made up of removable modulated elements, and forms the structure on which the solar collectors are mounted with their connecting elements and air ducts. On the upper part of the frame, two plates are mounted that can rotate with respect to each other and that allow the horizontal rotation of the panel support frame. The support of the solar collectors is mounted on the mobile plate, it supports the solar collectors and through a joint allows their angle to be adjusted in the vertical plane.
- *Solar collectors* transform the captured solar energy into thermal energy that is taken by means of a continuous air current produced by a low-pressure fan and led to a technological line that uses hot air.
- The *air ducts* are each connected by special connections to one solar collector and make the hot air transport circuit to the user (drying room). A centrifugal, low-pressure fan has been interspersed in the air circuit, which ensures counter-current air circulation.

The module for capturing and converting solar energy has as its operating principle the use of the black body effect (realized by means of the absorbing surface) combined with the greenhouse effect (realized by the glass plate and the transparent polyester film).

The sun radiates maximum energy in the visible spectrum, a field in which the glass plate and the polyester film are transparent. Thermal solar radiation has a wavelength between 0.72 and 400 μm, easily passes through the glass plate and foil and reaches the absorbent plate.

- *The absorbent plate* (black body of the collector) absorbs solar radiation, heats up to a temperature of 80÷120°C and radiates in the far infrared. The glass plate, transparent in the visible spectrum, is opaque in the infrared to radiation with a wavelength of over 4.5 μm and thus the collector becomes a trap for electromagnetic waves that once entered cannot leave it. Thus, the glass surface becomes a one-way gate for capturing solar energy. The module also has the possibility to change its position following the movement of the sun throughout the day. The module has a pull-type device (Figure 2) for changing the angle of inclination of the collector in the vertical plane within the limits of 30 and 60° compared to the horizontal plane of the ground.

Fig. 2 – Tie rod for changing the angle of inclination of the collector in the vertical plane

The measurement of the angle of rotation in the horizontal plane is done with an indicator (Figure 3), with a position index from 15 to 15°. Initially, the module is fixed with the zero position of the pointer to the south. From this position, the module can be rotated by 45° towards sunrise or sunset depending on the position of the sun in order to obtain a maximum efficiency of its radiation.

Fig. 3 – Angle indicator in horizontal plane

- The ducts for heated air have transducers along the route to measure the temperature and air flow. In order to benefit from warmer air, one can try to reduce the air flow by interposing a shutter with an adjustable section along the tube route. In order to reduce thermal energy losses, the ducts for hot air conduction will be insulated with a layer of glass wool and the shortest routes will be sought between the installation for capturing and converting solar energy into thermal energy and the technological line benefiting from the intake of hot air.

Main technical characteristics:

- the thermal agent used: air;
- number of collectors: 4;
- type of collectors: plane;
- mode of placement: on the ground, on a metal support frame;
- the capture surface: - on a collector: 1.5 m^2;
  - on the module: 6 m^2;
- the air passage section through the absorbent plate of the collector:
  - variant A……. 288 cm^2;
  - variant B……. 576 cm^2;
  - variant C……. 144 cm^2;
  - variant D……. 288 cm^2;
- the glass window: transparent glass, 4 mm;
- isolation: polyurethane foam;
- max. temperature of the absorbent plate: +130°C;
- max. temperature of air at the outlet of the manifold (in free circulation): +90°C;
- heated air flow rate (per module): approx. 100 m^3/h;
- the angle of inclination to the horizontal: min. 30°, max. 60°;
- the angle of rotation in the horizontal plane: 45° left-right;
- energy capacity: 350-700 Wh/m^2;
- dimensions of the entire module:
  - length (without tubes): 3 m;
  - width: 2.1 m
  - height: 4.15 m
- The panels can rotate both vertically and horizontally, thus:
  - inclination in the vertical plane (fixed angles): 30°, 45°, and 60°;
  - inclination in the horizontal plane (fixed angles): -30°, -15°, 0°, +15°,+30°, 0° representing the orientation to the south).

The experiments aimed at verifying the installation under normal operating conditions and identifying the optimal solution for building and operating the installation for capturing and converting solar energy into thermal energy **at angles of 30° and 45° in the vertical plane** (maintaining at 0° in the horizontal plane).

During the tests, depending on the time of day, was measured for each panel:

- inlet temperature (T_0) and outlet temperature from the panel (T_i);
- the speed of the air current (v_i) at the exit from each solar collector.

To differentiate them, the solar collectors (panels) were numbered as follows:

- panel no. 1, constructively defined as variant A;
- panel no. 2, constructively defined as variant B;
- panel no. 3, constructively defined as variant C;
- panel no. 4, constructively defined as variant D.

RESULTS

Experiments with tilting the collectors in the vertical plane at 30°

The results of measurements for the tilt position of the panels at 30° in the vertical plane and fixed orientation to the south are presented in Table 1 and in the related diagrams. The measurements were carried out with the testovent, an electronic device that measures the instantaneous values of current speed and air temperature.

Figure 4 shows the temperature variation for each panel with measurements taken in increments of 15 minutes, between 10 a.m. and 4 p.m. The graph shows that the temperatures recorded at panel 1 (T1) are the highest.

Figure 5 shows the variation of the air flows resulting from the calculation, depending on the speed of the air current measured in the outlet section of the collector. The flows were denoted by L1, L2, L3, and L4 and resulted by calculation according to the relation:

$$L = v \cdot S \ [m^3/h] \quad (1)$$

where:

$S = 0.12\ m^2$ – represents the area of the exit section of the solar collector where the measurement was made;

v – represents the speed of the air current.

Figures 6 and 7 show the variation of the heat accumulated by solar collectors during the day between 10 a.m. and 4 p.m., respectively the variation of the yields of the solar panels resulting from the calculation. The efficiency of the solar heat storage installation (yield) can be calculated with the relation:

$$\eta = \frac{Q_i}{Q} \quad (2)$$

where:

Q_i - is the heat accumulated by the solar collector (i=1÷4) [Kcal/h];

Q - is the total heat received by the collector [Kcal/h].

The heat accumulated by each collector was calculated using the relation:

$$Q_i = L_I \cdot c \cdot (T_i - T_0) \quad (3)$$

where:

L_i – the flows resulting from the calculation at each solar collector [m^3/h];

c – the specific heat of the working fluid [Kcal/m^3 °C];

T_i – the temperature recorded at the exit from the panel (i=1÷4) [°C];

T_0 – environmental temperature [°C];

The total heat received from the sun was calculated using the relation:

$$Q = I \cdot A \cdot S_c \quad (5)$$

where:

I – average hourly radiation intensity [Kcal/m^2h];

A – absorption coefficient of solar radiation ($A \approx 0.90$);

S_C – the capture surface ($S_C = 1.5\ m^2$).

From Figures 6 and 7 it can be seen that the presented values are relatively close, the solar collector version A being, however, in the highest areas of the diagrams.

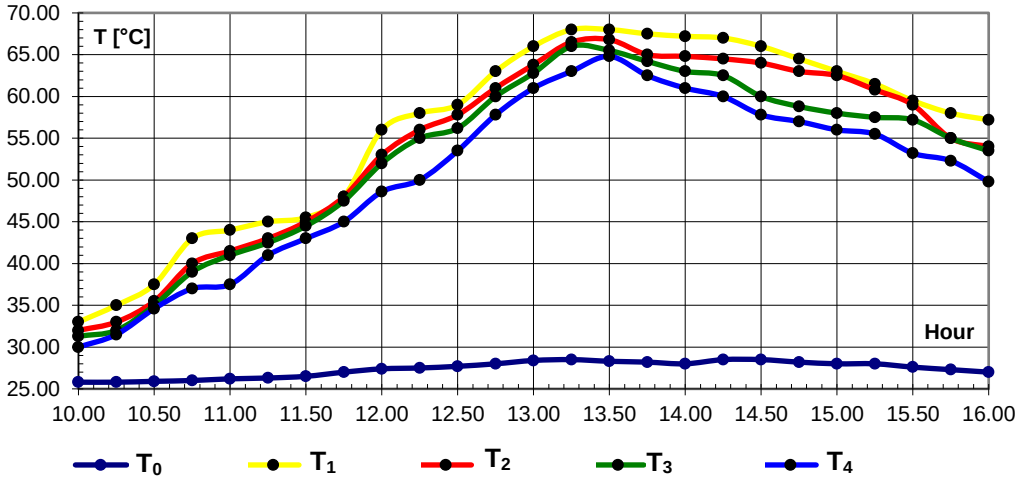

Fig. 4 - Variation of the temperature of the panels for tilting in the vertical plane at 30° from the horizontal plane T_0 – environmental temperature; T_1 - panel 1 temperature; T_2 - panel 2 temperature; T_3 - panel 3 temperature; T_4 - panel 4 temperature

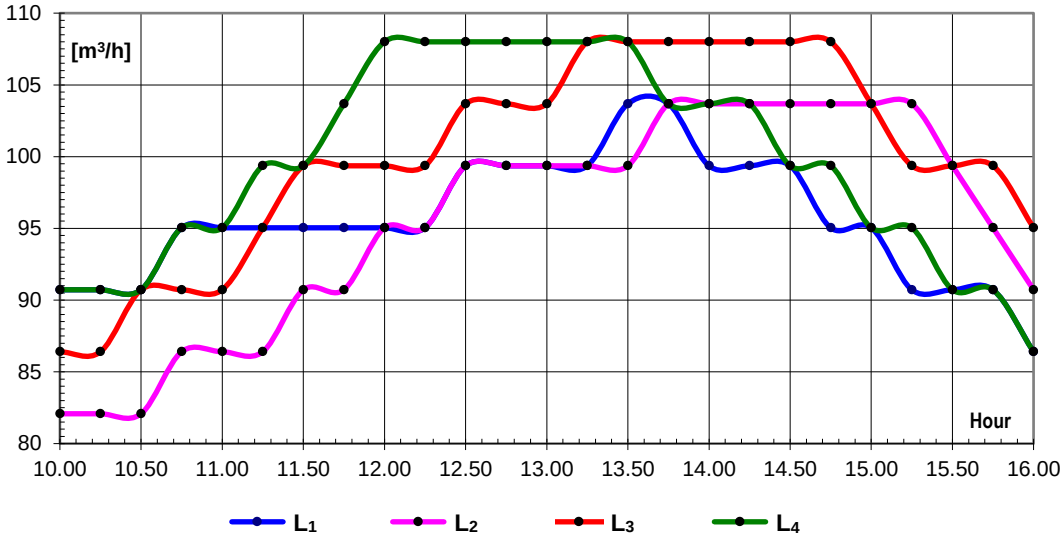

Fig. 5 - Variation of the air flows for tilting in the vertical plane at 30° from the horizontal plane L_1 – air flow to the panel 1; L_2 – air flow to the panel 2; L_3 – air flow to the panel 3; L_4 – air flow to the panel 4

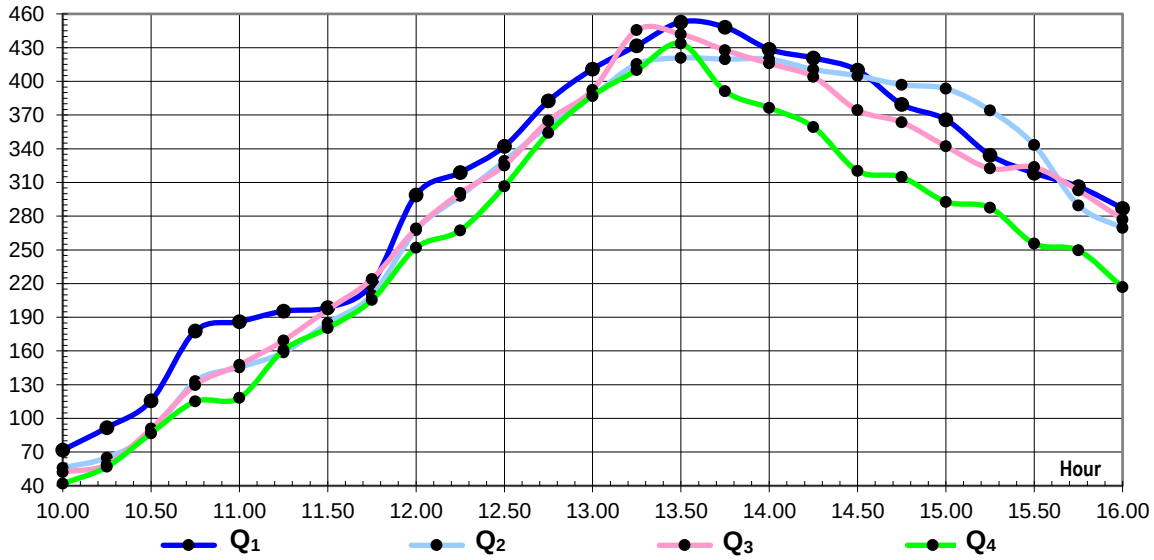

Fig. 6 - Variation of the accumulated heat on the panels for tilting in the vertical plane at 30° from the horizontal plane Q_1 – heat accumulated on panel no. 1; Q_2 – heat accumulated on panel no. 2; Q_3 – heat accumulated on panel no. 3; Q_4 – heat accumulated on panel no. 4

Table 1

Hour	Temperature differences ($T_{panel} - T_{environment}$) [°C]				Air flows [m^3/h]				Accumulated heat [Kcal/h]				Average radiation intensity [$Kcal/m^2$ h]	Heat received [Kcal/h]	Yields [%]			
	Panel 1	Panel 2	Panel 3	Panel 4	Panel 1	Panel 2	Panel 3	Panel 4	Panel 1	Panel 2	Panel 3	Panel 4	-	-	Panel 1	Panel 2	Panel 3	Panel 4
10.00	7.20	6.20	5.50	4.20	90.72	82.08	86.4	90.72	71.850	55.979	52.272	41.913	270	364.5	19.71	15.36	14.34	11.50
10.25	9.20	7.20	6.20	5.70	90.72	82.08	86.4	90.72	91.809	65.007	58.925	56.881	280	378	24.29	17.20	15.59	15.05
10.50	11.60	9.60	9.10	8.70	90.72	82.08	90.72	90.72	115.76	86.676	90.811	86.819	290	391.5	29.57	22.14	23.20	22.18
10.75	17.00	14.00	13.00	11.00	95.04	86.4	90.72	95.04	177.72	133.05	129.73	114.99	320	432	41.14	30.8	30.03	26.62
11.00	17.80	15.30	14.80	11.30	95.04	86.4	90.72	95.04	186.09	145.41	147.69	118.13	325	438.75	42.41	33.14	33.66	26.93
11.25	18.70	16.70	16.20	14.70	95.04	86.4	95.04	99.36	195.50	158.72	169.36	160.67	355	479.25	40.79	33.12	35.39	33.52
11.50	19.00	18.50	18.00	16.50	95.04	90.72	99.36	99.36	198.63	184.62	196.73	180.34	410	553.5	35.89	33.35	35.54	32.58
11.75	21.00	21.00	20.50	18.00	95.04	90.72	99.36	103.68	219.54	209.56	224.06	205.23	450	607.5	36.14	34.50	36.88	33.79
12.00	28.60	25.60	24.60	21.20	95.04	95.04	99.36	108	299	267.64	268.87	251.86	560	756	39.55	35.40	35.56	33.31
12.25	30.50	28.50	27.50	22.50	95.04	95.04	99.36	108	318.86	297.95	300.56	267.3	575	776.25	41.08	38.38	38.72	34.43
12.50	31.30	30.10	28.50	25.80	99.36	99.36	103.68	108	342.10	328.98	325.04	306.50	600	810	42,23	40.61	40.13	37.84
12.75	35.00	33.00	32.00	29.80	99.36	99.36	103.68	108	382.54	360.68	364.95	354.02	610	823.5	46.45	43.80	44.32	42.99
13.00	37.60	35.40	34.40	32.60	99.36	99.36	103.68	108	410.95	386.91	392.33	387.29	625	843.75	48.71	45.86	46.50	45.90
13.25	39.50	38.00	37.50	34.50	99.36	99.36	108	108	431.72	415.32	445.5	409.86	630	850.5	50.76	48.83	52.38	48.19
13.50	39.70	38.50	37.20	36.50	103.68	99.36	108	108	452.77	420.79	441.94	433.62	640	864	52.40	48,70	51.15	50.12
13.75	39.30	36.80	36.00	34.30	103.68	103.68	108	103.68	448.21	419.70	427.68	391.18	650	877.5	51.08	47.83	48.74	44.58
14.00	39.20	36.80	35.00	33.00	99.36	103.68	108	103.68	428.44	419.70	415.8	376.36	600	810	52.89	51.81	51.33	46.46
14.25	38.50	36.00	34.00	31.50	99.36	103.68	108	103.68	420.79	410.57	403.92	359.25	560	756	55.66	54.39	53.43	47.52
14.50	37.50	35.50	31.50	29.30	99.36	103.68	108	99.36	409.86	404.87	374.22	320.24	550	742.5	55.2	54.53	50.4	43.13
14.75	36.30	34.80	30.60	28.80	95.04	103.68	108	99.36	379.49	396.89	363.53	314.77	540	729	52.06	54.44	49.87	43.18
15.00	35.00	34.50	30.00	28.00	95.04	103.68	103.68	95.04	365.90	393.47	342.14	292.72	530	715.5	51.14	54.99	47.82	40.91
15.25	33.50	32.80	29.50	27.50	90.72	103.68	99.36	95.04	334.30	374.08	322.42	287.50	515	695.25	48.08	53.80	46.38	41.35
15.50	31.90	31.40	29.60	25.60	90.72	99.36	99.36	90.72	318.34	343.19	323.52	255.47	510	688.5	46.24	49.85	46.99	37.10
15.75	30.70	27.70	27.70	25.00	90.72	95.04	99.36	90.72	306.36	289.58	302.74	249.48	505	681.75	44.94	42.48	44.41	36.59
16.00	30.20	27.00	26.50	22.80	86.4	90.72	95.04	86.4	287.02	269.44	277.04	216.69	500	675	42.52	39.92	41.04	32.10
														Average yield [%]	**45.59**	**43.21**	**42.69**	**38.83**

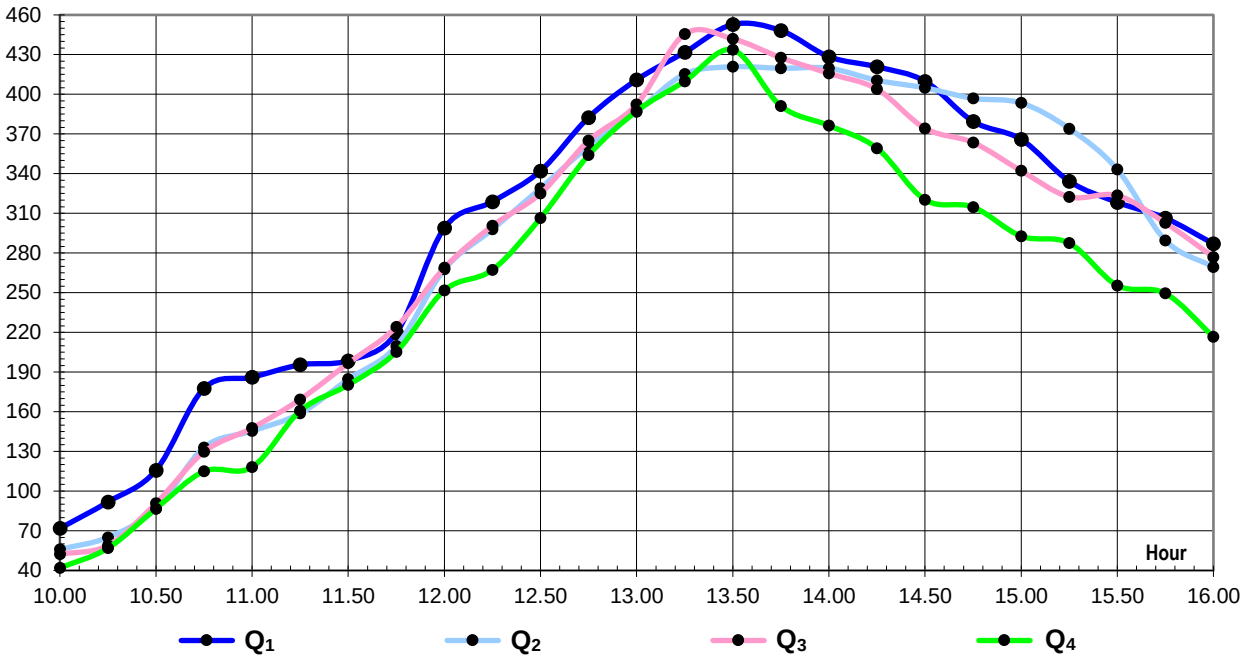

Fig. 6 - Variation of the accumulated heat on the panels for tilting in the vertical plane at 30° from the horizontal plane
Q_1 – heat accumulated on panel no. 1; Q_2 – heat accumulated on panel no. 2;
Q_3 – heat accumulated on panel no. 3; Q_4 – heat accumulated on panel no. 4

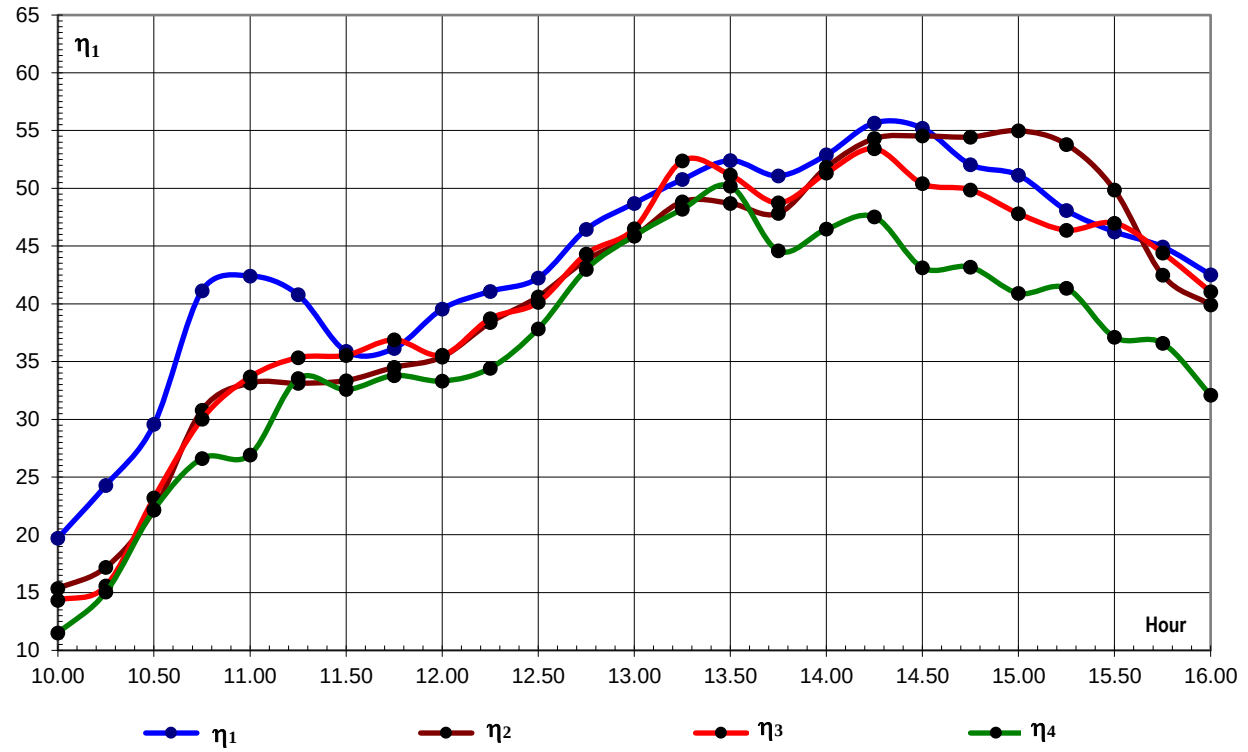

Fig. 7 - Variation of the yield at panels for tilting in the vertical plane at 30° from the horizontal plane
η_1 – yield on panel no. 1; η_2 - yield on panel no. 2; η_3 - yield on panel no. 3; η_4- yield on panel no. 4

Experiments with tilting the collectors in the vertical plane at 45°

The measurement results for the tilt position of the panels at 45° in the vertical plane and fixed orientation to the south are presented in the related diagrams. Figure 8 shows the temperature variation for each panel with measurements taken every 15 minutes between 10 a.m. and 4 p.m. The graph shows that the temperatures recorded at panel 1 (T1) are the highest. Figure 9 shows the variation of the air flows resulting from the calculation depending on the speed of the air current measured in the outlet section of the collector. Figures 10 and 11 show the variation of the heat accumulated by solar collectors during the day between 10 a.m. and 4 p.m., respectively the variation of the yields of the solar collectors resulting from the calculation.

It can be seen that the values of heat accumulated on the collectors inclined at 45° have the highest values for the collector variant "A", as well as the best efficiency.

Table 2 shows the results of the calculations performed for the temperature differences, the air flows, the accumulated heat, the total heat received from the sun and the average daily yields of the solar collectors. The values presented in the Table were processed in EXCEL with the help of relations (1-4). From the diagrams presented in Figures 10 and 11, it can also be seen that the collector variant "A" presents the highest values both for the accumulated heat and for the yield.

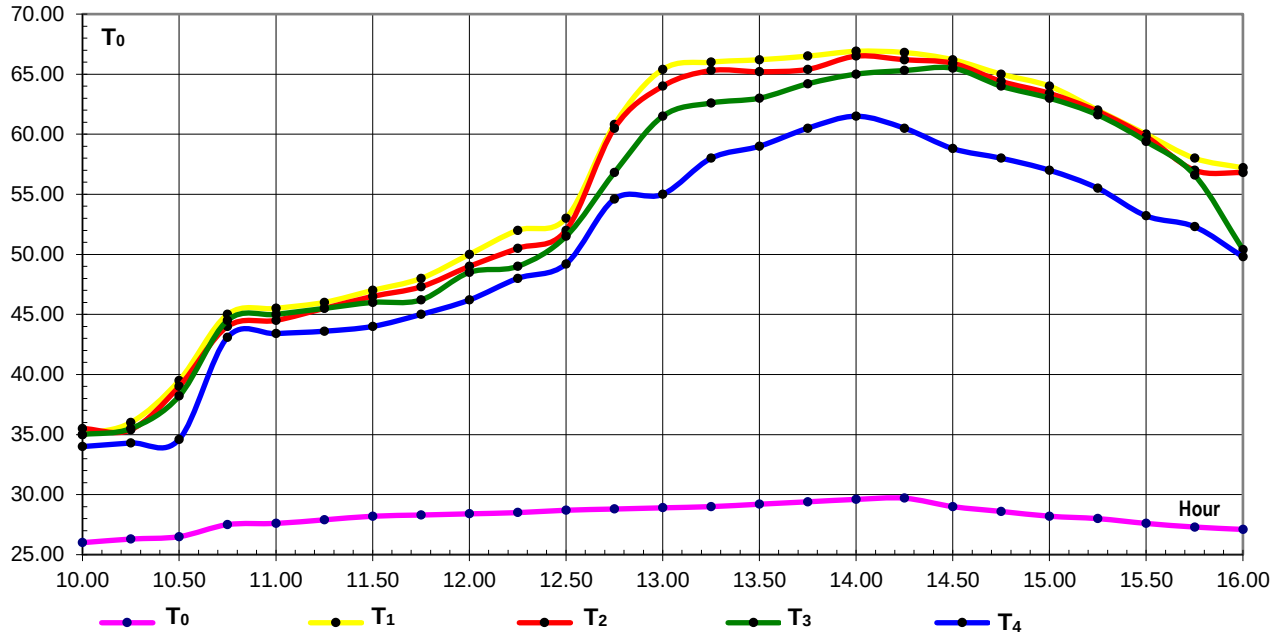

Fig. 8 - Variation of the temperature of the panels for tilting in the vertical plane at 45° from the horizontal plane T_0 – environmental temperature; T_1 - panel no. 1 temperature; T_2 - panel no. 2 temperature; T_3 - panel no. 3 temperature; T_4 - panel no. 4 temperature

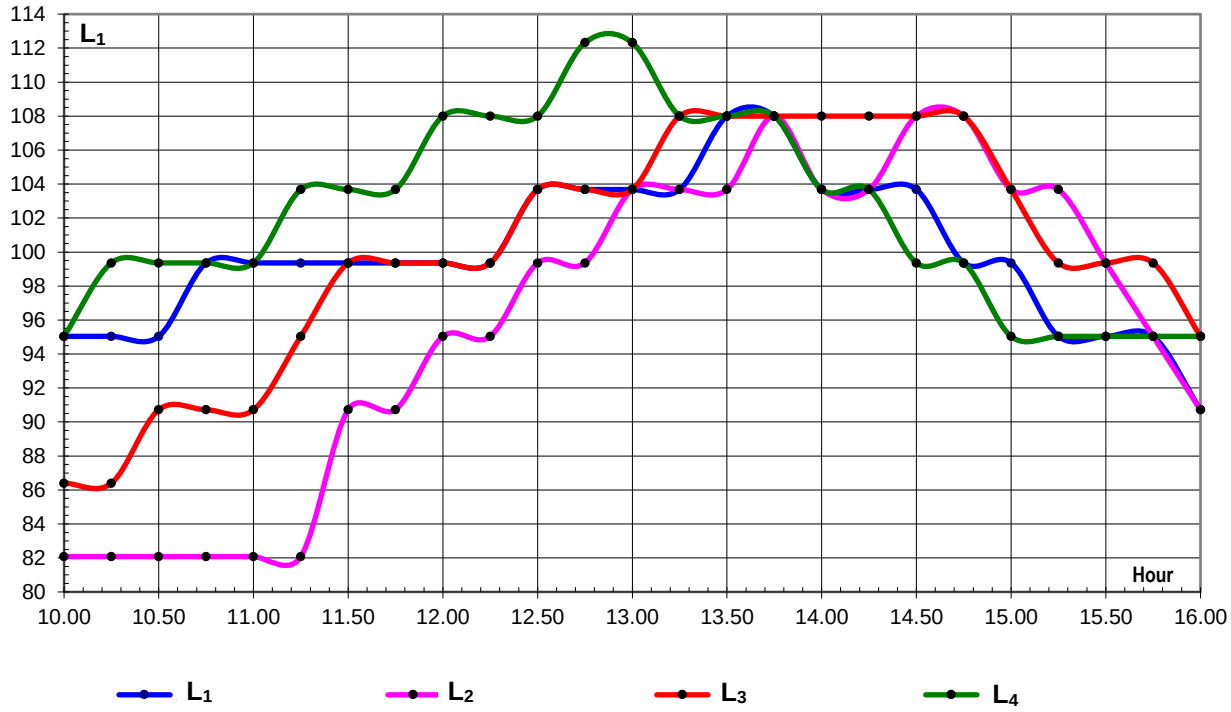

Fig. 9 - Variation of the air flows for tilting in the vertical plane at 45° from the horizontal plane L_1 – air flow to the panel no. 1; L_2 – air flow to the panel no. 2; L_3 – air flow to the panel no. 3; L_4 – air flow to the panel no. 4

Table 2

Hour	Temperature differences ($T_{panel} - T_{environment}$) [°C]				Air flows [m^3/h]				Accumulated heat [Kcal/h]				Average radiation intensity [Kcal/m^2 h]	Heat received [Kcal/h]	Yields [%]			
	Panel 1	Panel 2	Panel 3	Panel 4	Panel 1	Panel 2	Panel 3	Panel 4	Panel 1	Panel 2	Panel 3	Panel 4	-	-	Panel 1	Panel 2	Panel 3	Panel 4
10.00	9.00	9.50	9.00	8.00	95.04	82.08	86.4	95.04	94.09	85.774	85.536	83.635	270	364.5	25.81	23.53	23.47	22.95
10.25	9.70	9.10	9.20	8.00	95.04	82.08	86.4	99.36	101.41	82.162	87.437	87.437	280	378	26.83	21.74	23.13	23.13
10.50	13.00	12.50	11.70	8.10	95.04	82.08	90.72	99.36	135.91	112.86	116.76	88.53	290	391.5	34.71	28.83	29.82	22.61
10.75	17.50	16.50	17.00	15.60	99.36	82.08	90.72	99.36	191.27	148.98	169.65	170.50	300	405	47.23	36.78	41.89	42.10
11.00	17.90	16.90	17.40	15.80	99.36	82.08	90.72	99.36	195.64	152.59	173.64	172.69	325	438.75	44.59	34.78	39.58	39.36
11.25	18.10	17.60	17.60	15.70	99.36	82.08	95.04	103.68	197.83	158.91	184	179.06	355	479.25	41.28	33.16	38.39	37.36
11.50	18.80	18.30	17.80	15.80	99.36	90.72	99.36	103,68	205.48	182.62	194.55	180.20	410	553.5	37.12	32.99	35.15	32.56
11.75	19.70	19.00	17.90	16.70	99.36	90.72	99.36	103.68	215.31	189.60	195.64	190.46	540	729	29.54	26.01	26.84	26.13
12.00	21.60	20.60	20.10	17.80	99.36	95.04	99.36	108	236.08	215.36	219.68	211.46	560	756	31.23	28.49	29.06	27.97
12.25	23.50	22.00	20.50	19.50	99.36	95.04	99.36	108	256.85	230	224.06	231.66	575	776.25	33.09	29.63	28.86	29.84
12.50	24.30	23.30	22.80	20.50	103.68	99.36	103.68	108	277.14	254.66	260.03	243.54	600	810	34.21	31.44	32.10	30.07
12.75	32.00	31.70	28.00	25.80	103.68	99.36	103.68	112.32	364.95	346.46	319.33	318.76	610	823.5	44.32	42.07	38.78	38.71
13.00	36.50	35.10	32.60	26.10	103.68	103.68	103.68	112.32	416.28	400.31	371.80	322.47	625	843.75	49.34	47.44	44.06	38.22
13.25	37.00	36.30	33.60	29.00	103.68	103.68	108	108	421.98	413.99	399.17	344.52	630	850.5	49.62	48.68	46.93	40.51
13.50	37.00	36.00	33.80	29.80	108	103.68	108	108	439.56	410.57	401.54	354.02	640	864	50.88	47.52	46.48	40.98
13.75	37.10	36.00	34.80	31.10	108	108	108	108	440.75	427.68	413.42	369.47	650	877.5	50.23	48.74	47.11	42.10
14.00	37.30	36.90	35.40	31.90	103.68	103.68	108	103.68	425.40	420.84	420.55	363.81	600	810	52.52	51.96	51.92	44.92
14.25	37.10	36.50	35.60	30.80	103.68	103.68	108	103.68	423.12	416.28	422.93	351.27	560	756	55.97	55.06	55.94	46.46
14.50	37.20	36.90	36.50	29.80	103.68	108	108	99.36	424.26	438.37	433.62	325.70	520	702	60.44	62.45	61.77	46.40
14.75	36.40	35.80	35.40	29.40	99.36	108	108	99.36	397.84	425.30	420.55	321.33	500	675	58.94	63.01	62.30	47.60
15.00	35.80	35.20	34.80	28.80	99.36	103.68	103.68	95.04	391.28	401.45	396.89	301.09	475	641.25	61.02	62.60	61.89	46.95
15.25	34.00	33.90	33.60	27.50	95.04	103.68	99.36	95.04	355.45	386.62	367.23	287.50	450	607.5	58.51	63.64	60.45	47.32
15.50	32.40	32.20	31.80	25.60	95.04	99.36	99.36	95.04	338.72	351.93	347.56	267.63	440	594	57.02	59.25	58.51	45.06
15.75	30.70	29.70	29.30	25.00	95.04	95.04	99.36	95.04	320.95	310.50	320.24	261.36	435	587.25	54.65	52.87	54.53	44.51
16.00	30.10	29.70	23.30	22.70	90.72	90.72	95.04	95.04	300.37	296.38	243.59	237.31	430	580.5	51.74	51.06	41.96	40.88
Average yield [%]															**46.07**	**43.78**	**43.61**	**38.14**

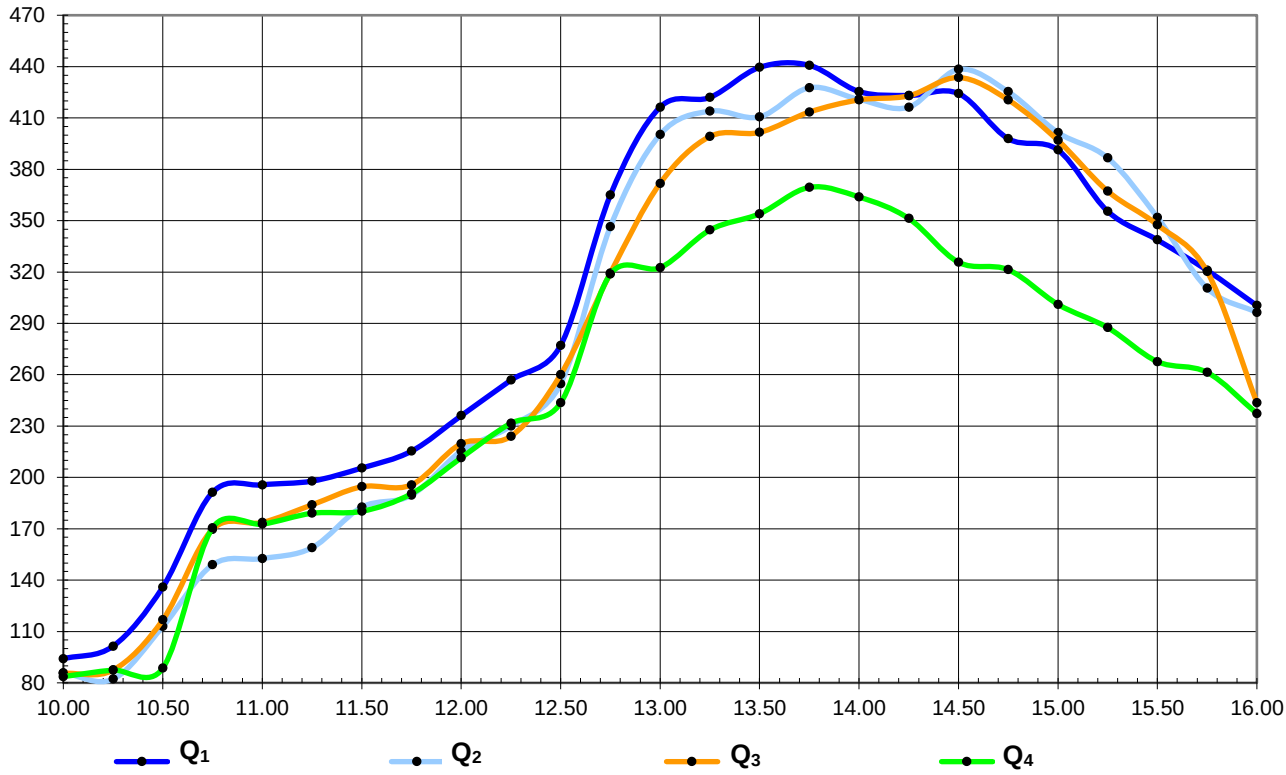

Fig. 10 - Variation of the accumulated heat for tilting in the vertical plane at 45° from the horizontal plane
Q_1 – heat accumulated on panel no. 1; Q_2 – heat accumulated on panel no. 2;
Q_3 – heat accumulated on panel no. 3; Q_4 – heat accumulated on panel no. 4

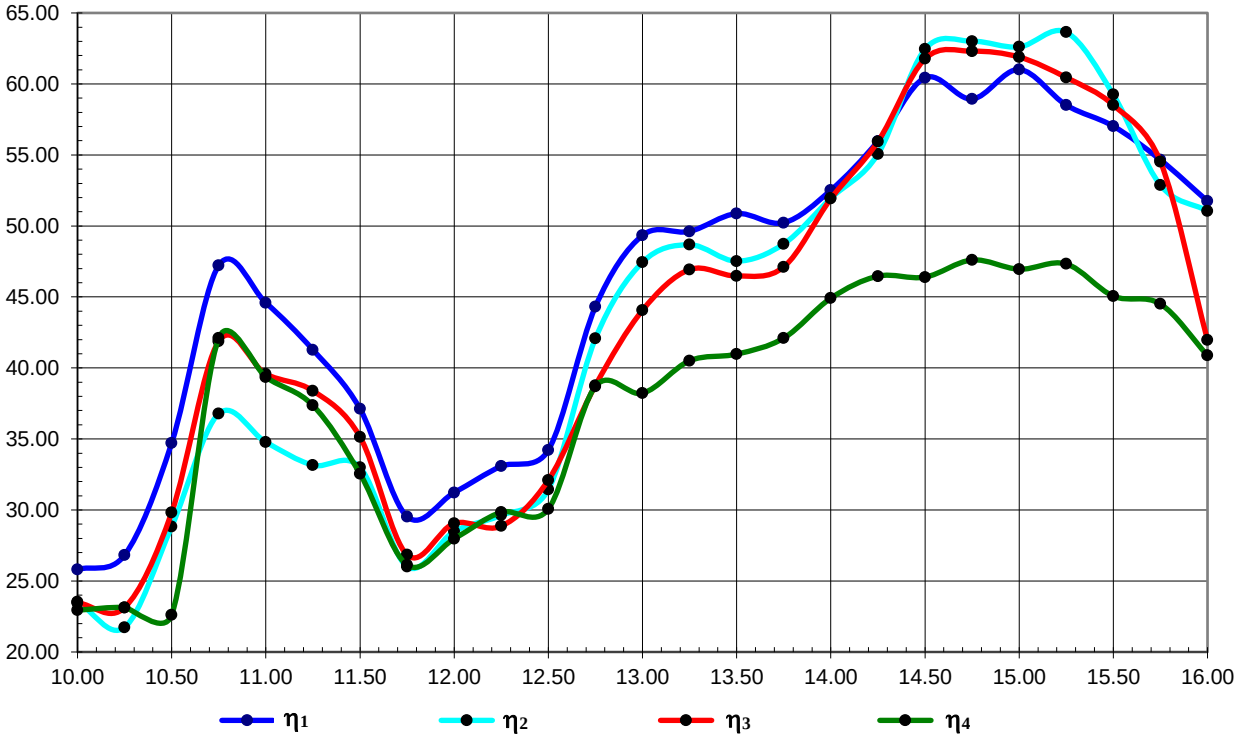

Fig. 11 - Variation of the yield at panels for tilting in the vertical plane at 45° from the horizontal plane
η_1 - yield at panel no. 1; η_2 - yield at panel no. 2;η_3 - yield at panel no. 3; η_4 - yield at panel no. 4

CONCLUSIONS

The experiments highlighted the fact that in the months of May - June in the Bucharest-Ilfov area, the angle of inclination of the solar collectors in the vertical plane is recommended to be 45°, at which the highest values for conversion yields of for solar energy into thermal energy were obtained.

As a result of the experiments carried out, it was found that of the four variants initially tested, variant A was the most efficient in terms of the heat transfer achieved, which recommends expanding the use of the installation in small and medium-sized farms for dehydrating vegetables and fruits, drying cereals and herbal medicine.

ACKNOWLEDGEMENT

This paper was supported by the Romanian Ministry of Education and Research, through the project of the Ministry of Research, Innovation and Digitalization through Program 1 - Development of the national research-development system, Subprogram 1.2 - Institutional performance - Projects for financing excellence in RDI, Contract no. 1PFE/30.12.2021.

REFERENCES

[1] Ahmed F., Sharizal Abdul Aziz M, Palaniandy P., Shaik F. (2022). A review on application of renewable energy for desalination technologies with emphasis on concentrated solar power. *Sustainable Energy Technologies and Assessments*, *53*(D), 102772. DOI: https://doi. org/10.1016/j.seta.2022.102772.

[2] Balasuadhakar A., Fisseha T., Atenafu A., Bino B. (2016). A review on passive solar dryers for agricultural products. *International Journal of Innovative Science and Research Technology, 3*, 64**–**70.

[3] Bhatia S.C., Gupta R.K. (2019). Textbook of Renewable Energy. *Woodhead Publishing India PVT. Limited*, ISBN: 938-505-995-5.

[4] Cook R.M., Torsvik H.T (2016). Climates Past and Present. Chapter 16. *Earth History and Paleogeography, Cambridge University Press*, https://www.cambridge.org/core/books/abs/earth-history-and-palaeogeography/climates-past-and-present/2FC8EE23A3F4622906BDA7DA8A7C856C

[5] Dincer I. (2000). Renewable energy and sustainable development: a crucial review. *Renewable and Sustainable Energy Reviews, 4*(2), 157–175. DOI: https://doi.org/10.1016/S1364-0321(99)00011-8.

[6] Fatai K., Oxley L., Scrimgeour F.G. (2004). Modelling the causal relationship between energy consumption and GDP in New Zealand, Australia, India, Indonesia, The Philippines and Thailand. *Mathematics and Computers in Simulation,* 64(3–4), 431–445. DOI: https://doi.org/10.1016/S0378-4754(03)00109-5.

[7] Garratt A., Petrella I., Zhang Y. (2023). Asymmetry and interdependence when evaluating US energy information administration forecasts. *Energy Economics, 121*, 106620. DOI: https://doi.org/10.1016/j.eneco.2023.106620.

[8] Găgeanu P., Vlăduţ V., Păun A., Chih I., Biriş S. (2011). Pure plant oil – source of alternative energy, Proceedings of the 39th International Symposium on Agricultural Engineering *"Actual Tasks on Agricultural Engineering",* 141**–**152, Opatija, Croatia.

[9] Hassan Q., Sameen A.Z., Salman H.M., Jaszczur M. (2023). A roadmap with strategic policy toward green hydrogen production: the case of Iraq. *Sustainability, 15*(6), 5258. DOI: https://doi.org/10.3390/su15065258.

[10] Huang W., Dai J., Xiong L. (2022). Towards a sustainable energy future: factors affecting solar-hydrogen energy production in China. *Sustainable Energy Technologies and Assessments*, *52*, 102059. DOI: https://doi.org/10.1016/j.seta.2022.102059.

[11] Hussain S.M., Jamshed W., Kumar V., Kumar V., Nisar K.S., Eid M.R., Safdar R., Abdel-Aty A.-H., Yahia I. (2021). Computational analysis of thermal energy distribution of electromagnetic Casson nanofluid across stretched sheet: shape factor effectiveness of solid-particles. *Energy Reports, 7*, 7460–7477. DOI: https://doi.org/10.1016/j.egyr.2021.10.083.

[12] Ihssen J., Braun A., Faccio G., Gajda-Schrantz K., Thony-Meyer L. (2014). Light harvesting proteins for solar fuel generation in bioengineered photoelectrochemical cells. *Current Protein & Peptide Science, 15*(4), 74–384. DOI: https://doi.org/10.2174/1389203715666140327105530.

[13] Jahid A., Monju M.K.H., Hossain M.E., Hossain M.F. (2018). Renewable energy assisted cost aware sustainable off-grid base stations with energy cooperation. *IEEE Access, 6*, 60900–60920. DOI: https://doi.org/10.1109/ ACCESS.2018.2874131.

[14] Kahraman U., Dincer I. (2022). Performance analysis of a solar based waste to energy multigeneration system. *Sustainable Energy Technology and Assessments*, *50*, 101729. DOI: https://doi.org/10.1016/j.seta.2021.101729,.
[15] Kartal M.T. (2022). The role of consumption of energy, fossil sources, nuclear energy, and renewable energy on environmental degradation in top-five carbon producing countries. *Renewable Energy, 184*, 871–880. DOI: https://doi.org/10.1016/j.renene.2021.12.022.
[16] Lindsey R. (2009). Climate and Earth's Energy Budget. *NASA - Earth Observatory*, https://earthobservatory.nasa.gov/features/EnergyBalance.
[17] Maican E., Vlăduţ V., Vilcu C., Sorică C., Dorian M., Mirea D.P., Bogăţeanu R. (2019). Hybrid renewable energy systems for isolated farms. A review. *INMATEH – Agricultural Engineering, 59*(3), 77–92. DOI: 10.35633/INMATEH-59-09.
[18] Majeed Y., Khan M.U., Waseem M., Zahid U., Mahmood F., Majeed F., Sultan M., Raza A. (2023). Renewable energy as an alternative source for energy management in agriculture. *Energy Reports, 10*, 344–359. DOI: https://doi.org/10.1016/j.egyr.2023.06.032.
[19] Marks-Bielska R., Bielski S., Pik K., Kurowska K. (2020). The importance of renewable energy sources in Poland's energy mix. *Energies, 13*(18), 4624. DOI: https://doi.org/10.3390/en13184624.
[20] Mekhilef S., Safari A., Mustaffa W.E.S., Saidur R., Omar R., Younis M.A.A. (2012). Solar energy in Malaysia: current state and prospects. *Renewable and Sustainable Energy Reviews, 16*, 386–396. DOI: https://doi.org/10.1016/j.rser.2011.08.003.
[21] Mohammed Wazed S., Hughes B.R., O'Connor D., Kaiser Calautit J. (2018). A review of sustainable solar irrigation systems for Sub-Saharan Africa. *Renewable and Sustainable Energy Reviews*, *81,* 1206–1225. DOI: https://doi.org/10.1016/j.rser.2017.08.039.
[22] Muehlbauer W. (1986). Present status of solar crop drying. *Energy in Agric*ulture, *5*, 121–138. DOI: 10.1016/0167-5826(86)90013-6.
[23] Muneer T., Maubleu S., Asif M. (2006). Prospects of solar water heating for textile industry in Pakistan. *Renewable and Sustainable Energy Reviews, 10*(1), 1**–**23. DOI: https://doi.org/10.1016/j.rser.2004.07.003.
[24] Perez M., Perez R. (2022). Update 2022 – a fundamental look at supply side energy reserves for the planet. *Solar Energy Advances*, *2*, 100014. DOI: https://doi.org/10.1016/ j.seja.2022.
[25] Saidur R., Mekhilef S. (2010). Energy use, energy savings and emission analysis in the Malaysian rubber producing industries. *Applied Energy, 87*, 2746–2758. DOI: https://doi.org/10.1016/j.apenergy.2009.12.018.
[26] Saidur R. (2010). A review on electrical motors energy use and energy savings. *Renewable and Sustainable Energy Reviews, 14*, 877–898. DOI: https://doi.org/10.1016/j. rser.2009.10.018.
[27] Salawu S., Obalalu A., Fatunmbi E., Oderinu R. (2022). Thermal Prandtl-Eyring hybridized MoS2-SiO2/C3H8O2 and SiO2-C3H8O2 nanofluids for effective solar energy absorber and entropy optimization: a solar water pump implementation. *Journal of Molecular Liquids, 361*, 119608. DOI: https://doi.org/10.1016/j.molliq.2022.119608.
[28] Tong G., Chen Q., Xu H. (2022). Passive solar energy utilization: a review of envelope material selection for Chinese solar greenhouses. *Sustainable Energy Technology and Assessments*, *50*, 101833. DOI: https://doi.org/10.1016/j.seta.2021.101833.
[29] Xiong Q., Altnji S., Tayebi T., Izadi M., Hajjar A., Sunden B., et al. (2021). A comprehensive review on the application of hybrid nanofluids in solar energy collectors. *Sustainable Energy Technology and Assessments*, *47*, 101341. DOI: https://doi.org/ 10.1016/j.seta.2021.101341.
[30] Zahraoui Y., Basir Khan M.R., Alhamrouni I., Mekhilef S., Ahmed M. (2021). Current status, scenario, and prospective of renewable energy in Algeria: a review. *Energies, 14(9),* 2354. DOI: https://doi.org/10.3390/en14092354.
[31] Zekai S. (2008). Solar Energy Fundamentals and Modeling Techniques: Atmosphere, Environment, Climate Change and Renewable Energy. *Springer,* Berlin. DOI: https://doi.org/10.1007/978-1-84800-134-3.
[32] Zhao N., Zeng X., Han S. (2013). Solar radiation estimation using sunshine hour and air pollution index in China. Energy Conversion and Management, *76*, 846–851. DOI: https://doi.org/10.1016/j.enconman.2013.08.037.

USING SOLAR ENERGY AS NON-CONVENTIONAL ALTERNATIVE ENERGY IN SMALL AND MEDIUM-SIZED FARMS
/
UTILIZAREA ENERGIEI SOLARE CA SURSĂ ALATERNATIVĂ NECONVENŢIONALĂ DE ENERGIE ÎN FERMELE DE DIMENSIUNI MICI ŞI MEDII

Mario CRISTEA[1)], Nicolae-Valentin VLĂDUȚ[1*)], Nicoleta UNGUREANU[2*)]
[1)]INMA Bucharest / Romania; [2)]POLITEHNICA Bucharest / Romania
Corresponding authors: valentin_vladut@yahoo.com; nicoletaung@yahoo.com
DOI: https://doi.org/10.35633/inmateh-72-56

Keywords: *farm, solar energy, support, sunshine, rotation*

ABSTRACT
Solar energy represents a future solution for clean, sustainable energy, because the sun generates much more energy every day than it is necessary for daily consumption, unlike fossil fuels. The only limitation related to this renewable resource is the ability to transform this energy into electricity. The paper presents a functional model of equipment that allows the capture of solar energy using special panels, which can rotate according to the sun, so that the incidence of rays with the radiating surface of the panels is maximum, and the yields obtained at different angles of inclination (in the vertical plane: 30° and 45°, and in the horizontal plane: 0° to be maximum.

REZUMAT
Energia solară reprezintă o soluţie de viitor pentru o energie curată, sustenabilă, datorită faptului că soarele generează în fiecare zi mult mai multă energie decât avem nevoie pentru consumul zilnic, spre deosebire de combustibilii fosili. Singura limitare legată de această resursă regenerabilă este capacitatea de a transforma această energie în electricitate. În lucrare se prezintă un model funcţional de echipament care permite captarea energiei solare utilizând panouri speciale, care se pot roti după soare, astfel încât incidenţa razelor cu suprafaţa radiantă a panourilor să fie maximă, iar randamentele obținute la diferite unghiuri de înclinaţie (în plan vertical: 30° şi 45°, iar în plan orizontal: 0° să fie maxime.

INTRODUCTION

The sun provides the majority of the energy consumed by humanity on Earth. "Solar" energy is derived directly from the sun. Renewable energy is also known as environmentally friendly power, green power, sustainable power, or alternative energy. The surrounding stellar environment absorbs the majority of the sun's energy, so very little of it reaches Earth as radiation (*Majeed et al, 2023*).

A square meter on Earth's surface receives an average of 1366 W of solar energy (*Lindsey, 2009*), but this might vary depending on latitude (*Cocks, 2016*). The first stage in capturing solar energy is estimating the quantity of energy available from the sun in a specific area of the Earth. A country's economic and social success is determined by its ability to obtain a consistent and affordable supply of energy (*Fatai et al., 2004; Muneer et al., 2006*).

Renewable energy sources, such as wind and sun, can be used to power farm vehicles in a way that is beneficial to the economy and the environment (*Balasuadhakar et al., 2016*).

Clean energy, also known as renewable energy, is derived from non-anthropogenic sources such as the sun and wind. These sources can be replenished continuously, despite the fact that they are time and weather-dependent. On the other hand, fossil fuel is a collective name given to oil, natural gas, and coal, which are non-renewable energy sources generated from carbon-based dead and buried organisms that disintegrated millions of years ago (*Bhatia and Gupta, 2019; Zekai, 2008*).

Solar energy remains one of the oldest renewable sources of energy in the universe, which is taken in the form of solar radiation from the sun and primarily employed in three ways: a) electricity generation with solar cells in which photovoltaic or photoelectric cells are used; b) the sun heat can be used to warm water in a glass panel of a solar energy system through solar water heating; c) production of high temperatures from the sun through the use of furnaces and mirrors to collect the sun's energy is the primary focus, which may also be utilized in cooking and processing food, enhanced oil recovery, water desalination, chemical production, and mineral processing (*Zekai, 2008; Ihssen et al., 2014; Zhao et al., 2013).*

The global public and private sectors are actively pursuing new solutions to meet the demand for clean energy while lowering greenhouse gas emissions and energy costs in their operations. Consequently, the installation of renewable and sustainable energy systems became a priority (*Mekhilef et al., 2012; Kahraman and Dincer, 2022; Tong et al., 2022; Găgeanu et al., 2011*). Thus, solar energy remains the most viable alternative energy source because it offers a number of advantages over other options (*Ahmed et al., 2022)*. Solar energy is naturally available as an environmentally beneficial energy source supplied by the sun, which may be exploited to directly generate power (*Jahid et al., 2018*). Furthermore, solar energy produces no pollution, requires little maintenance, and the product technology has a long life expectancy of around 20-30 years (*Jahid et al., 2018; Saidur and Mekhilef, 2010*). Solar applications were initially developed for rural electrification, telecommunications, and agriculture sectors, but they are now used in a wide range of applications, such as solar water heating, solar drying, and solar photovoltaics (PVs) (*Saidur, 2010; Mohammed Wazed et al., 2018; Zaharaoui et al., 2021; Xiong et al., 2021; Huang et al., 2022)*. Besides, solar power can supply 100 percent of the world's primary energy demand (*Perez and Perez, 2022*).

Heat transmission (HT) is a branch of heat research that studies the creation, use, modification, and preservation of thermal energy systems. In recent years, there has been a growth in interest in the topic of HT as people become more concerned about climate change and its implications for energy systems. Understanding the concepts of HT has never been more important as the world strives to decrease its carbon footprint and switch to renewable energy sources.

This study seeks to provide an overview of the fundamentals of HT, its uses, and its significance in the context of renewable energy and climate change. The study of HT includes several components, such as heat transfer by conduction, convection, and radiation (*Salawu et al., 2022*). Many academics offer different approaches to explaining heat transfer ideas in engineering challenges (*Hussain et al., 2021; Kartal, 2022*). Some of the applications studied include spaceship design, comets and asteroids, mass transfer preservation, heat exchanger design, and heat piping system development.

The accelerating depletion of fossil fuels, along with increased concerns about climate change, has driven the world to a critical juncture in its energy transition. During this paradigm change, hybrid renewable energy systems (HRES), especially those incorporating solar and wind power technologies, have emerged as key options to meet the difficulties of energy sustainability (*Marks-Bielska et al., 2020; Dincer, 2000*). However, such systems reduce the intermittency difficulties inherent in individual renewable sources, increasing the overall reliability and stability of energy production. Solar power's highest output occurs during daylight hours; however, wind power can be harvested even when solar availability is limited (*Garratt et al., 2023*). Integrating these sources makes the energy supply more consistent, lowering the chance of power outages during inclement weather. Furthermore, energy storage technologies integrated into hybrid systems provide surplus energy storage during peak production periods, allowing its usage during low production phases, enhancing total system efficiency, and lowering waste (*Hassan et al., 2023; Maican et al., 2019*).

MATERIALS AND METHODS

The operating principle of the solar collector is based on the use of the black body effect (achieved by means of the absorbent surface) combined with the greenhouse effect (achieved by the glass plate and the polyester film). The installation is made as an experimental model and uses flat solar collectors with gaseous thermal agent (air). Structurally, it was designed specifically for research. In addition to the basic function of capturing and converting solar energy into thermal energy by heating the air, the installation allows the horizontal and vertical rotation of the solar panels to further expand the scope of investigations depending on the angle of incidence of the sun's rays with the surface of the panel.

The experimental model of the module for capturing and converting solar energy into thermal energy (Figure 1) is located in an area with exposure to the sun throughout the day, at a distance that ensures minimal losses on the thermal agent transport network (air), from solar collectors to potential users such as a fruit drying facility. The main component subassemblies of the module for capturing and converting solar energy into thermal energy are: the support frame, the solar collectors and the air tubes with a low-pressure centrifugal fan. The rotation of the solar collectors around a central pivot by 45° left-right from the initial orientation position to the south and also the orientation of the solar collectors in the vertical plane at fixed angles of 30° and 45° is done manually and checked each time with appropriate measuring instruments. With these facilities, the variation of solar energy can be highlighted throughout the day by orienting the panels according to the position of the sun, and adjustments can be made to optimize the system's operating regime.

Fig. 1 – Module for capturing and converting solar energy

The module for capturing and converting solar energy into thermal energy consists of:

- *The support frame*, is an assembly made up of removable modulated elements, and forms the structure on which the solar collectors are mounted with their connecting elements and air ducts. On the upper part of the frame, two plates are mounted that can rotate with respect to each other and that allow the horizontal rotation of the panel support frame. The support of the solar collectors is mounted on the mobile plate, it supports the solar collectors and through a joint allows their angle to be adjusted in the vertical plane.
- *Solar collectors* transform the captured solar energy into thermal energy that is taken by means of a continuous air current produced by a low-pressure fan and led to a technological line that uses hot air.
- The *air ducts* are each connected by special connections to one solar collector and make the hot air transport circuit to the user (drying room). A centrifugal, low-pressure fan has been interspersed in the air circuit, which ensures counter-current air circulation.

The module for capturing and converting solar energy has as its operating principle the use of the black body effect (realized by means of the absorbing surface) combined with the greenhouse effect (realized by the glass plate and the transparent polyester film).

The sun radiates maximum energy in the visible spectrum, a field in which the glass plate and the polyester film are transparent. Thermal solar radiation has a wavelength between 0.72 and 400 μm, easily passes through the glass plate and foil and reaches the absorbent plate.

- *The absorbent plate* (black body of the collector) absorbs solar radiation, heats up to a temperature of 80÷120°C and radiates in the far infrared. The glass plate, transparent in the visible spectrum, is opaque in the infrared to radiation with a wavelength of over 4.5 μm and thus the collector becomes a trap for electromagnetic waves that once entered cannot leave it. Thus, the glass surface becomes a one-way gate for capturing solar energy. The module also has the possibility to change its position following the movement of the sun throughout the day. The module has a pull-type device (Figure 2) for changing the angle of inclination of the collector in the vertical plane within the limits of 30 and 60° compared to the horizontal plane of the ground.

Fig. 2 – Tie rod for changing the angle of inclination of the collector in the vertical plane

The measurement of the angle of rotation in the horizontal plane is done with an indicator (Figure 3), with a position index from 15 to 15°. Initially, the module is fixed with the zero position of the pointer to the south. From this position, the module can be rotated by 45° towards sunrise or sunset depending on the position of the sun in order to obtain a maximum efficiency of its radiation.

Fig. 3 – Angle indicator in horizontal plane

- The ducts for heated air have transducers along the route to measure the temperature and air flow. In order to benefit from warmer air, one can try to reduce the air flow by interposing a shutter with an adjustable section along the tube route. In order to reduce thermal energy losses, the ducts for hot air conduction will be insulated with a layer of glass wool and the shortest routes will be sought between the installation for capturing and converting solar energy into thermal energy and the technological line benefiting from the intake of hot air.

Main technical characteristics:

- the thermal agent used: air;
- number of collectors: 4;
- type of collectors: plane;
- mode of placement: on the ground, on a metal support frame;
- the capture surface: - on a collector: 1.5 m^2;
  - on the module: 6 m^2;
- the air passage section through the absorbent plate of the collector:
  - variant A……. 288 cm^2;
  - variant B……. 576 cm^2;
  - variant C……. 144 cm^2;
  - variant D……. 288 cm^2;
- the glass window: transparent glass, 4 mm;
- isolation: polyurethane foam;
- max. temperature of the absorbent plate: +130°C;
- max. temperature of air at the outlet of the manifold (in free circulation): +90°C;
- heated air flow rate (per module): approx. 100 m^3/h;
- the angle of inclination to the horizontal: min. 30°, max. 60°;
- the angle of rotation in the horizontal plane: 45° left-right;
- energy capacity: 350-700 Wh/m^2;
- dimensions of the entire module:
  - length (without tubes): 3 m;
  - width: 2.1 m
  - height: 4.15 m
- The panels can rotate both vertically and horizontally, thus:
  - inclination in the vertical plane (fixed angles): 30°, 45°, and 60°;
  - inclination in the horizontal plane (fixed angles): -30°, -15°, 0°, +15°,+30°, 0° representing the orientation to the south).

The experiments aimed at verifying the installation under normal operating conditions and identifying the optimal solution for building and operating the installation for capturing and converting solar energy into thermal energy **at angles of 30° and 45° in the vertical plane** (maintaining at 0° in the horizontal plane).

During the tests, depending on the time of day, was measured for each panel:

- inlet temperature (T_0) and outlet temperature from the panel (T_i);
- the speed of the air current (v_i) at the exit from each solar collector.

To differentiate them, the solar collectors (panels) were numbered as follows:

- panel no. 1, constructively defined as variant A;
- panel no. 2, constructively defined as variant B;
- panel no. 3, constructively defined as variant C;
- panel no. 4, constructively defined as variant D.

RESULTS

Experiments with tilting the collectors in the vertical plane at 30°

The results of measurements for the tilt position of the panels at 30° in the vertical plane and fixed orientation to the south are presented in Table 1 and in the related diagrams. The measurements were carried out with the testovent, an electronic device that measures the instantaneous values of current speed and air temperature.

Figure 4 shows the temperature variation for each panel with measurements taken in increments of 15 minutes, between 10 a.m. and 4 p.m. The graph shows that the temperatures recorded at panel 1 (T1) are the highest.

Figure 5 shows the variation of the air flows resulting from the calculation, depending on the speed of the air current measured in the outlet section of the collector. The flows were denoted by L1, L2, L3, and L4 and resulted by calculation according to the relation:

$$L = v \cdot S \ [m^3/h] \quad (1)$$

where:

$S = 0.12\ m^2$ – represents the area of the exit section of the solar collector where the measurement was made;

v – represents the speed of the air current.

Figures 6 and 7 show the variation of the heat accumulated by solar collectors during the day between 10 a.m. and 4 p.m., respectively the variation of the yields of the solar panels resulting from the calculation. The efficiency of the solar heat storage installation (yield) can be calculated with the relation:

$$\eta = \frac{Q_i}{Q} \quad (2)$$

where:

Q_i - is the heat accumulated by the solar collector (i=1÷4) [Kcal/h];

Q - is the total heat received by the collector [Kcal/h].

The heat accumulated by each collector was calculated using the relation:

$$Q_i = L_I \cdot c \cdot (T_i - T_0) \quad (3)$$

where:

L_i – the flows resulting from the calculation at each solar collector [m^3/h];

c – the specific heat of the working fluid [Kcal/m^3 °C];

T_i – the temperature recorded at the exit from the panel (i=1÷4) [°C];

T_0 – environmental temperature [°C];

The total heat received from the sun was calculated using the relation:

$$Q = I \cdot A \cdot S_c \quad (5)$$

where:

I – average hourly radiation intensity [Kcal/m^2h];

A – absorption coefficient of solar radiation ($A \approx 0.90$);

S_C – the capture surface ($S_C = 1.5\ m^2$).

From Figures 6 and 7 it can be seen that the presented values are relatively close, the solar collector version A being, however, in the highest areas of the diagrams.

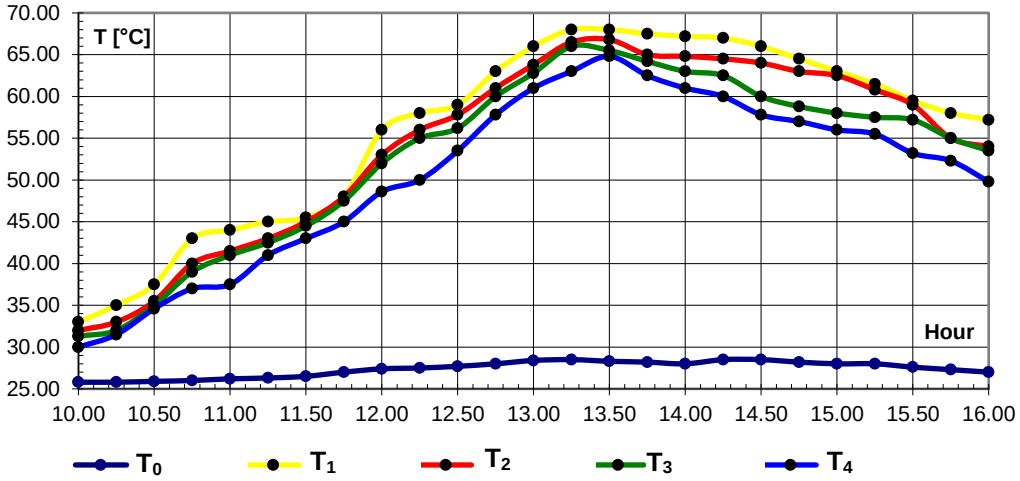

Fig. 4 - Variation of the temperature of the panels for tilting in the vertical plane at 30° from the horizontal plane T_0 – environmental temperature; T_1 - panel 1 temperature; T_2 - panel 2 temperature; T_3 - panel 3 temperature; T_4 - panel 4 temperature

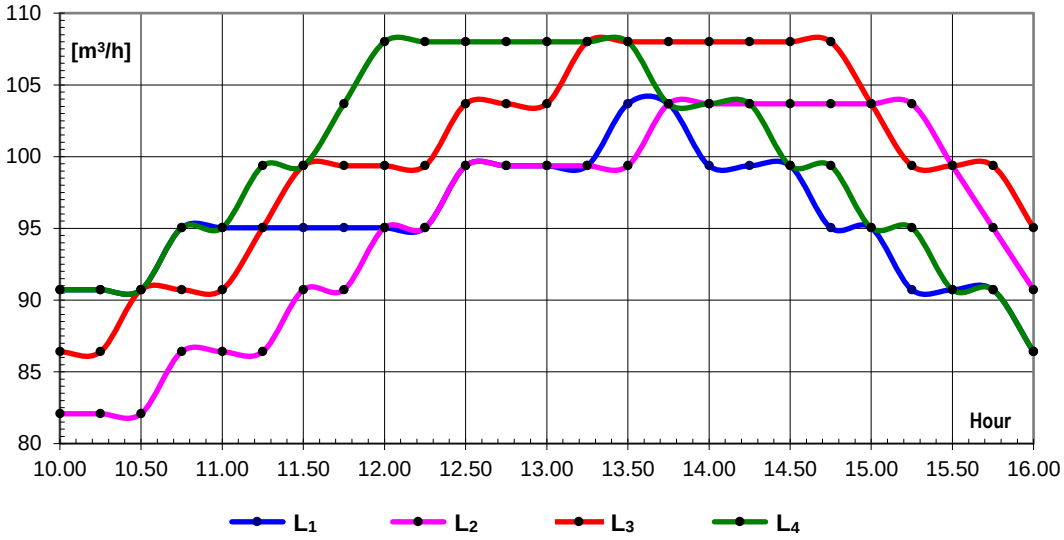

Fig. 5 - Variation of the air flows for tilting in the vertical plane at 30° from the horizontal plane L_1 – air flow to the panel 1; L_2 – air flow to the panel 2; L_3 – air flow to the panel 3; L_4 – air flow to the panel 4

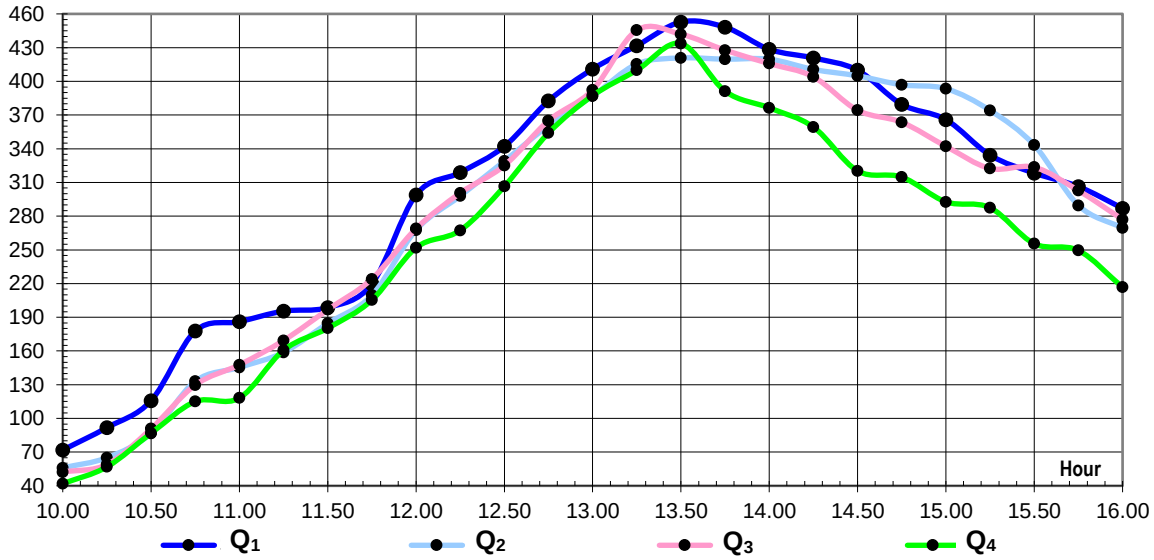

Fig. 6 - Variation of the accumulated heat on the panels for tilting in the vertical plane at 30° from the horizontal plane Q_1 – heat accumulated on panel no. 1; Q_2 – heat accumulated on panel no. 2; Q_3 – heat accumulated on panel no. 3; Q_4 – heat accumulated on panel no. 4

Table 1

Hour	Temperature differences ($T_{panel} - T_{environment}$) [°C]				Air flows [m^3/h]				Accumulated heat [Kcal/h]				Average radiation intensity [$Kcal/m^2$ h]	Heat received [Kcal/h]	Yields [%]			
	Panel 1	Panel 2	Panel 3	Panel 4	Panel 1	Panel 2	Panel 3	Panel 4	Panel 1	Panel 2	Panel 3	Panel 4	-	-	Panel 1	Panel 2	Panel 3	Panel 4
10.00	7.20	6.20	5.50	4.20	90.72	82.08	86.4	90.72	71.850	55.979	52.272	41.913	270	364.5	19.71	15.36	14.34	11.50
10.25	9.20	7.20	6.20	5.70	90.72	82.08	86.4	90.72	91.809	65.007	58.925	56.881	280	378	24.29	17.20	15.59	15.05
10.50	11.60	9.60	9.10	8.70	90.72	82.08	90.72	90.72	115.76	86.676	90.811	86.819	290	391.5	29.57	22.14	23.20	22.18
10.75	17.00	14.00	13.00	11.00	95.04	86.4	90.72	95.04	177.72	133.05	129.73	114.99	320	432	41.14	30.8	30.03	26.62
11.00	17.80	15.30	14.80	11.30	95.04	86.4	90.72	95.04	186.09	145.41	147.69	118.13	325	438.75	42.41	33.14	33.66	26.93
11.25	18.70	16.70	16.20	14.70	95.04	86.4	95.04	99.36	195.50	158.72	169.36	160.67	355	479.25	40.79	33.12	35.39	33.52
11.50	19.00	18.50	18.00	16.50	95.04	90.72	99.36	99.36	198.63	184.62	196.73	180.34	410	553.5	35.89	33.35	35.54	32.58
11.75	21.00	21.00	20.50	18.00	95.04	90.72	99.36	103.68	219.54	209.56	224.06	205.23	450	607.5	36.14	34.50	36.88	33.79
12.00	28.60	25.60	24.60	21.20	95.04	95.04	99.36	108	299	267.64	268.87	251.86	560	756	39.55	35.40	35.56	33.31
12.25	30.50	28.50	27.50	22.50	95.04	95.04	99.36	108	318.86	297.95	300.56	267.3	575	776.25	41.08	38.38	38.72	34.43
12.50	31.30	30.10	28.50	25.80	99.36	99.36	103.68	108	342.10	328.98	325.04	306.50	600	810	42,23	40.61	40.13	37.84
12.75	35.00	33.00	32.00	29.80	99.36	99.36	103.68	108	382.54	360.68	364.95	354.02	610	823.5	46.45	43.80	44.32	42.99
13.00	37.60	35.40	34.40	32.60	99.36	99.36	103.68	108	410.95	386.91	392.33	387.29	625	843.75	48.71	45.86	46.50	45.90
13.25	39.50	38.00	37.50	34.50	99.36	99.36	108	108	431.72	415.32	445.5	409.86	630	850.5	50.76	48.83	52.38	48.19
13.50	39.70	38.50	37.20	36.50	103.68	99.36	108	108	452.77	420.79	441.94	433.62	640	864	52.40	48,70	51.15	50.12
13.75	39.30	36.80	36.00	34.30	103.68	103.68	108	103.68	448.21	419.70	427.68	391.18	650	877.5	51.08	47.83	48.74	44.58
14.00	39.20	36.80	35.00	33.00	99.36	103.68	108	103.68	428.44	419.70	415.8	376.36	600	810	52.89	51.81	51.33	46.46
14.25	38.50	36.00	34.00	31.50	99.36	103.68	108	103.68	420.79	410.57	403.92	359.25	560	756	55.66	54.39	53.43	47.52
14.50	37.50	35.50	31.50	29.30	99.36	103.68	108	99.36	409.86	404.87	374.22	320.24	550	742.5	55.2	54.53	50.4	43.13
14.75	36.30	34.80	30.60	28.80	95.04	103.68	108	99.36	379.49	396.89	363.53	314.77	540	729	52.06	54.44	49.87	43.18
15.00	35.00	34.50	30.00	28.00	95.04	103.68	103.68	95.04	365.90	393.47	342.14	292.72	530	715.5	51.14	54.99	47.82	40.91
15.25	33.50	32.80	29.50	27.50	90.72	103.68	99.36	95.04	334.30	374.08	322.42	287.50	515	695.25	48.08	53.80	46.38	41.35
15.50	31.90	31.40	29.60	25.60	90.72	99.36	99.36	90.72	318.34	343.19	323.52	255.47	510	688.5	46.24	49.85	46.99	37.10
15.75	30.70	27.70	27.70	25.00	90.72	95.04	99.36	90.72	306.36	289.58	302.74	249.48	505	681.75	44.94	42.48	44.41	36.59
16.00	30.20	27.00	26.50	22.80	86.4	90.72	95.04	86.4	287.02	269.44	277.04	216.69	500	675	42.52	39.92	41.04	32.10
														Average yield [%]	**45.59**	**43.21**	**42.69**	**38.83**

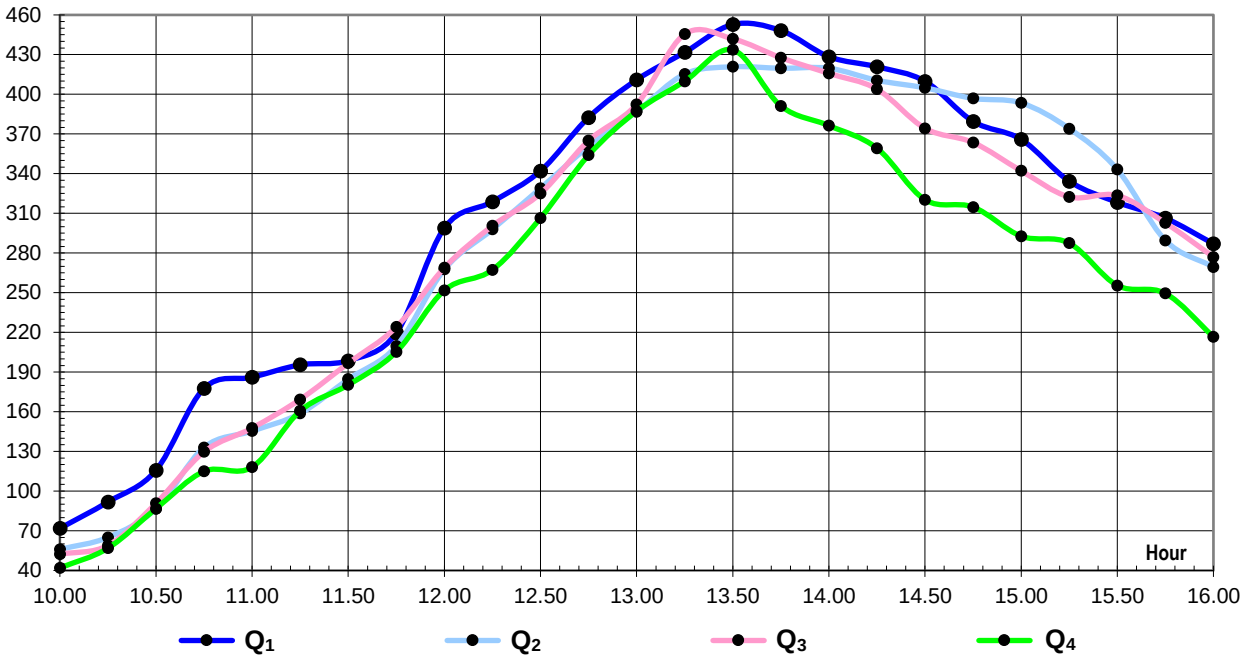

Fig. 6 - Variation of the accumulated heat on the panels for tilting in the vertical plane at 30° from the horizontal plane
Q_1 – heat accumulated on panel no. 1; Q_2 – heat accumulated on panel no. 2;
Q_3 – heat accumulated on panel no. 3; Q_4 – heat accumulated on panel no. 4

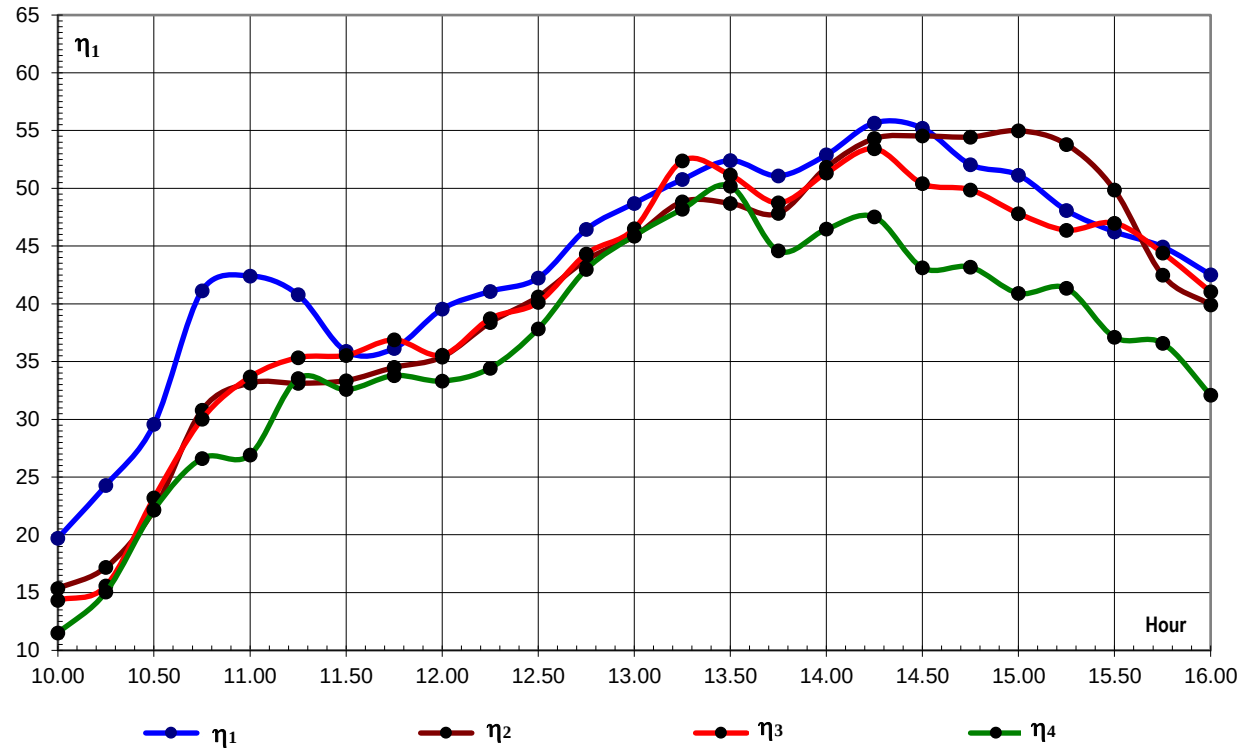

Fig. 7 - Variation of the yield at panels for tilting in the vertical plane at 30° from the horizontal plane
η_1 – yield on panel no. 1; η_2 - yield on panel no. 2; η_3 - yield on panel no. 3; η_4- yield on panel no. 4

Experiments with tilting the collectors in the vertical plane at 45°

The measurement results for the tilt position of the panels at 45° in the vertical plane and fixed orientation to the south are presented in the related diagrams. Figure 8 shows the temperature variation for each panel with measurements taken every 15 minutes between 10 a.m. and 4 p.m. The graph shows that the temperatures recorded at panel 1 (T1) are the highest. Figure 9 shows the variation of the air flows resulting from the calculation depending on the speed of the air current measured in the outlet section of the collector. Figures 10 and 11 show the variation of the heat accumulated by solar collectors during the day between 10 a.m. and 4 p.m., respectively the variation of the yields of the solar collectors resulting from the calculation.

It can be seen that the values of heat accumulated on the collectors inclined at 45° have the highest values for the collector variant "A", as well as the best efficiency.

Table 2 shows the results of the calculations performed for the temperature differences, the air flows, the accumulated heat, the total heat received from the sun and the average daily yields of the solar collectors. The values presented in the Table were processed in EXCEL with the help of relations (1-4). From the diagrams presented in Figures 10 and 11, it can also be seen that the collector variant "A" presents the highest values both for the accumulated heat and for the yield.

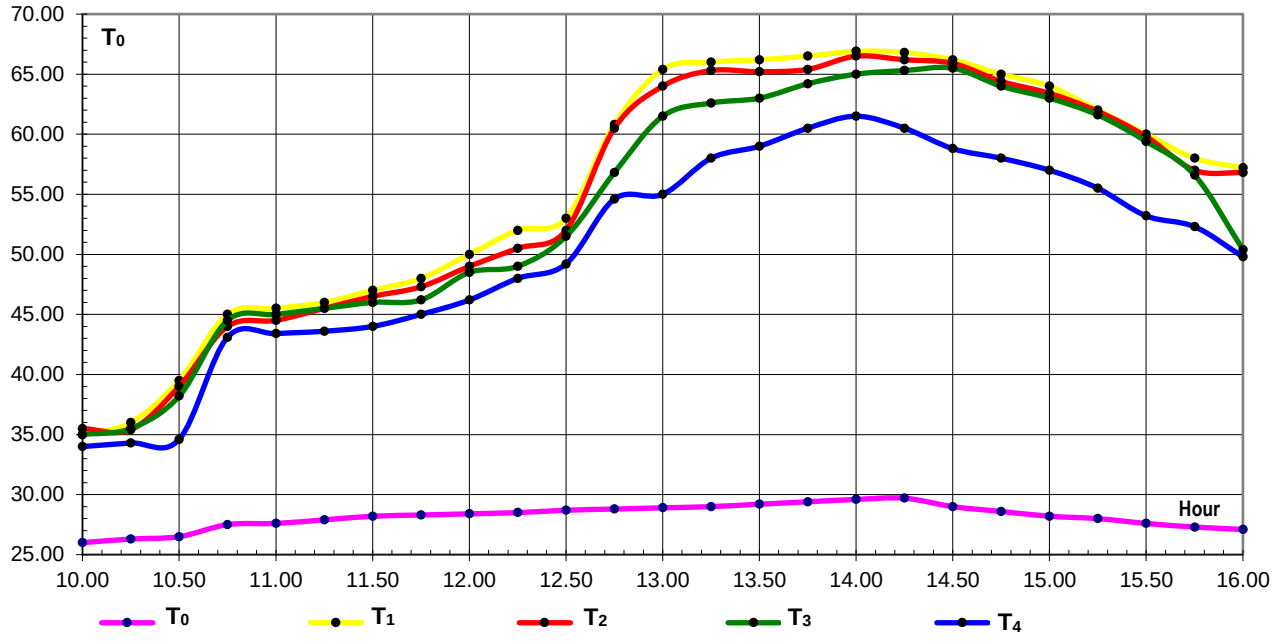

Fig. 8 - Variation of the temperature of the panels for tilting in the vertical plane at 45° from the horizontal plane T_0 – environmental temperature; T_1 - panel no. 1 temperature; T_2 - panel no. 2 temperature; T_3 - panel no. 3 temperature; T_4 - panel no. 4 temperature

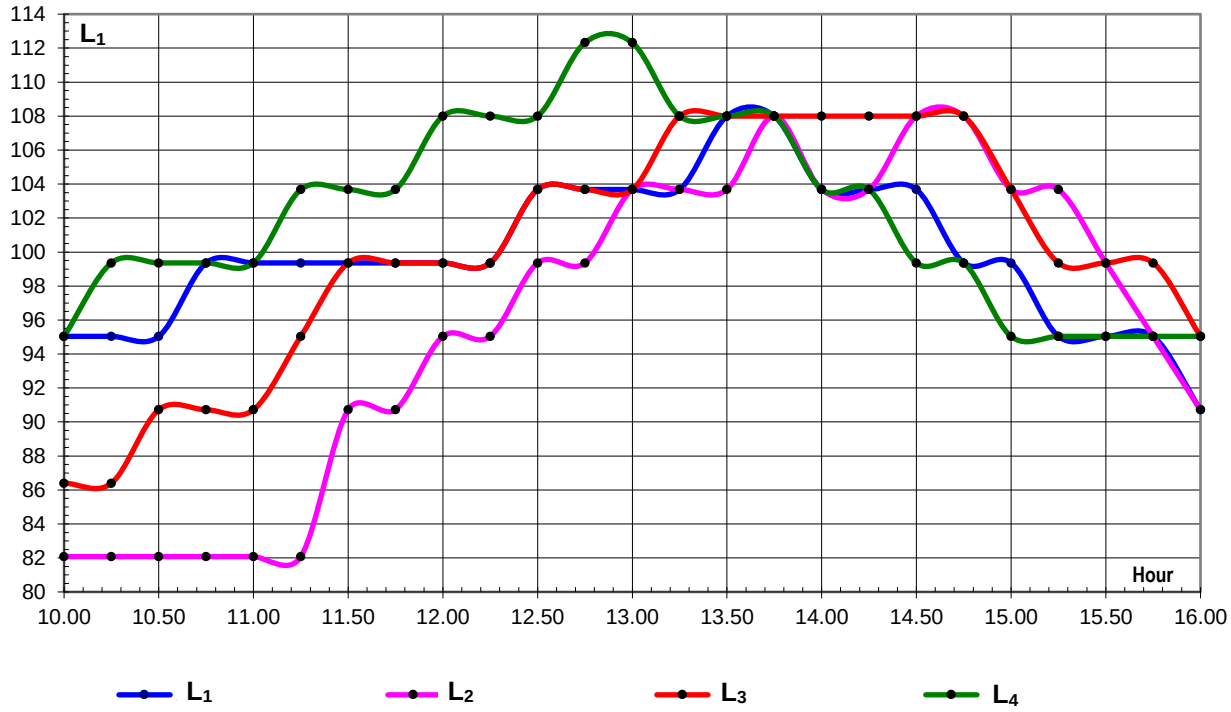

Fig. 9 - Variation of the air flows for tilting in the vertical plane at 45° from the horizontal plane L_1 – air flow to the panel no. 1; L_2 – air flow to the panel no. 2; L_3 – air flow to the panel no. 3; L_4 – air flow to the panel no. 4

Table 2

Hour	Temperature differences ($T_{panel} - T_{environment}$) [°C]				Air flows [m^3/h]				Accumulated heat [Kcal/h]				Average radiation intensity [Kcal/m^2 h]	Heat received [Kcal/h]	Yields [%]			
	Panel 1	Panel 2	Panel 3	Panel 4	Panel 1	Panel 2	Panel 3	Panel 4	Panel 1	Panel 2	Panel 3	Panel 4	-	-	Panel 1	Panel 2	Panel 3	Panel 4
10.00	9.00	9.50	9.00	8.00	95.04	82.08	86.4	95.04	94.09	85.774	85.536	83.635	270	364.5	25.81	23.53	23.47	22.95
10.25	9.70	9.10	9.20	8.00	95.04	82.08	86.4	99.36	101.41	82.162	87.437	87.437	280	378	26.83	21.74	23.13	23.13
10.50	13.00	12.50	11.70	8.10	95.04	82.08	90.72	99.36	135.91	112.86	116.76	88.53	290	391.5	34.71	28.83	29.82	22.61
10.75	17.50	16.50	17.00	15.60	99.36	82.08	90.72	99.36	191.27	148.98	169.65	170.50	300	405	47.23	36.78	41.89	42.10
11.00	17.90	16.90	17.40	15.80	99.36	82.08	90.72	99.36	195.64	152.59	173.64	172.69	325	438.75	44.59	34.78	39.58	39.36
11.25	18.10	17.60	17.60	15.70	99.36	82.08	95.04	103.68	197.83	158.91	184	179.06	355	479.25	41.28	33.16	38.39	37.36
11.50	18.80	18.30	17.80	15.80	99.36	90.72	99.36	103,68	205.48	182.62	194.55	180.20	410	553.5	37.12	32.99	35.15	32.56
11.75	19.70	19.00	17.90	16.70	99.36	90.72	99.36	103.68	215.31	189.60	195.64	190.46	540	729	29.54	26.01	26.84	26.13
12.00	21.60	20.60	20.10	17.80	99.36	95.04	99.36	108	236.08	215.36	219.68	211.46	560	756	31.23	28.49	29.06	27.97
12.25	23.50	22.00	20.50	19.50	99.36	95.04	99.36	108	256.85	230	224.06	231.66	575	776.25	33.09	29.63	28.86	29.84
12.50	24.30	23.30	22.80	20.50	103.68	99.36	103.68	108	277.14	254.66	260.03	243.54	600	810	34.21	31.44	32.10	30.07
12.75	32.00	31.70	28.00	25.80	103.68	99.36	103.68	112.32	364.95	346.46	319.33	318.76	610	823.5	44.32	42.07	38.78	38.71
13.00	36.50	35.10	32.60	26.10	103.68	103.68	103.68	112.32	416.28	400.31	371.80	322.47	625	843.75	49.34	47.44	44.06	38.22
13.25	37.00	36.30	33.60	29.00	103.68	103.68	108	108	421.98	413.99	399.17	344.52	630	850.5	49.62	48.68	46.93	40.51
13.50	37.00	36.00	33.80	29.80	108	103.68	108	108	439.56	410.57	401.54	354.02	640	864	50.88	47.52	46.48	40.98
13.75	37.10	36.00	34.80	31.10	108	108	108	108	440.75	427.68	413.42	369.47	650	877.5	50.23	48.74	47.11	42.10
14.00	37.30	36.90	35.40	31.90	103.68	103.68	108	103.68	425.40	420.84	420.55	363.81	600	810	52.52	51.96	51.92	44.92
14.25	37.10	36.50	35.60	30.80	103.68	103.68	108	103.68	423.12	416.28	422.93	351.27	560	756	55.97	55.06	55.94	46.46
14.50	37.20	36.90	36.50	29.80	103.68	108	108	99.36	424.26	438.37	433.62	325.70	520	702	60.44	62.45	61.77	46.40
14.75	36.40	35.80	35.40	29.40	99.36	108	108	99.36	397.84	425.30	420.55	321.33	500	675	58.94	63.01	62.30	47.60
15.00	35.80	35.20	34.80	28.80	99.36	103.68	103.68	95.04	391.28	401.45	396.89	301.09	475	641.25	61.02	62.60	61.89	46.95
15.25	34.00	33.90	33.60	27.50	95.04	103.68	99.36	95.04	355.45	386.62	367.23	287.50	450	607.5	58.51	63.64	60.45	47.32
15.50	32.40	32.20	31.80	25.60	95.04	99.36	99.36	95.04	338.72	351.93	347.56	267.63	440	594	57.02	59.25	58.51	45.06
15.75	30.70	29.70	29.30	25.00	95.04	95.04	99.36	95.04	320.95	310.50	320.24	261.36	435	587.25	54.65	52.87	54.53	44.51
16.00	30.10	29.70	23.30	22.70	90.72	90.72	95.04	95.04	300.37	296.38	243.59	237.31	430	580.5	51.74	51.06	41.96	40.88
Average yield [%]															**46.07**	**43.78**	**43.61**	**38.14**

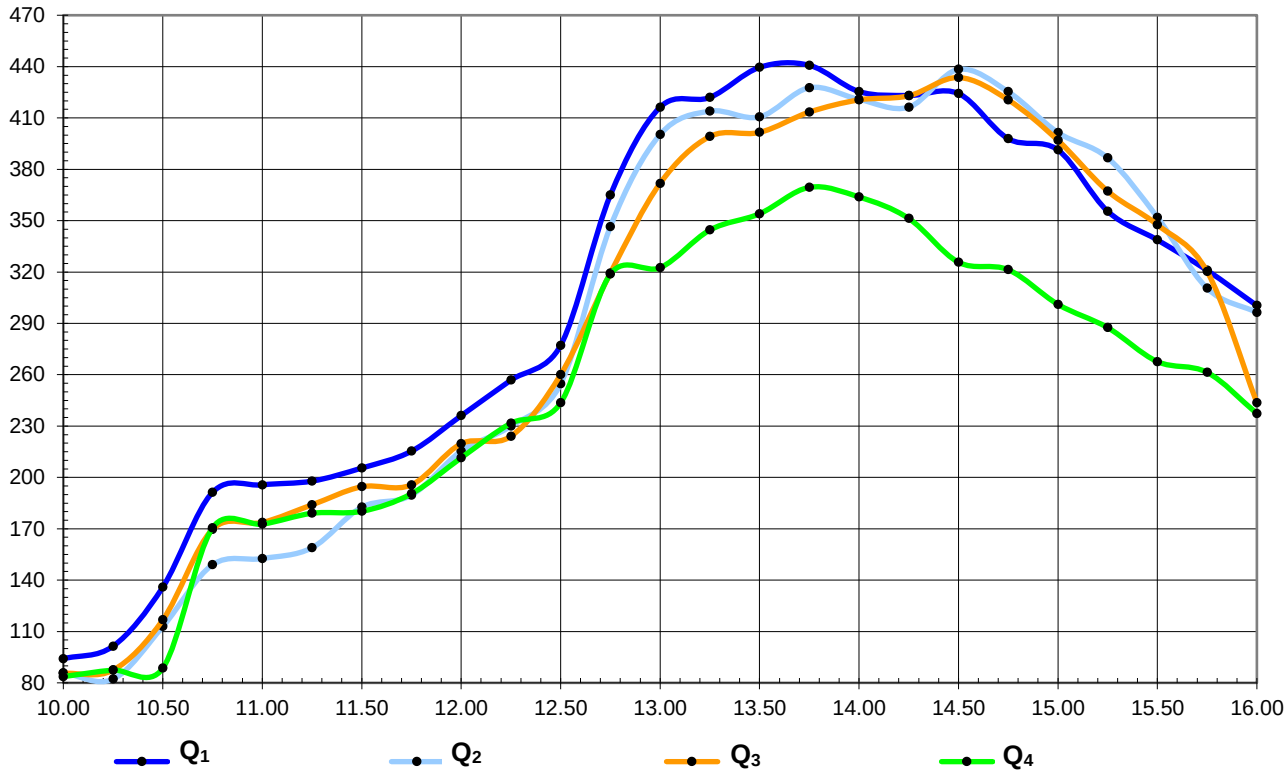

Fig. 10 - Variation of the accumulated heat for tilting in the vertical plane at 45° from the horizontal plane
Q_1 – heat accumulated on panel no. 1; Q_2 – heat accumulated on panel no. 2;
Q_3 – heat accumulated on panel no. 3; Q_4 – heat accumulated on panel no. 4

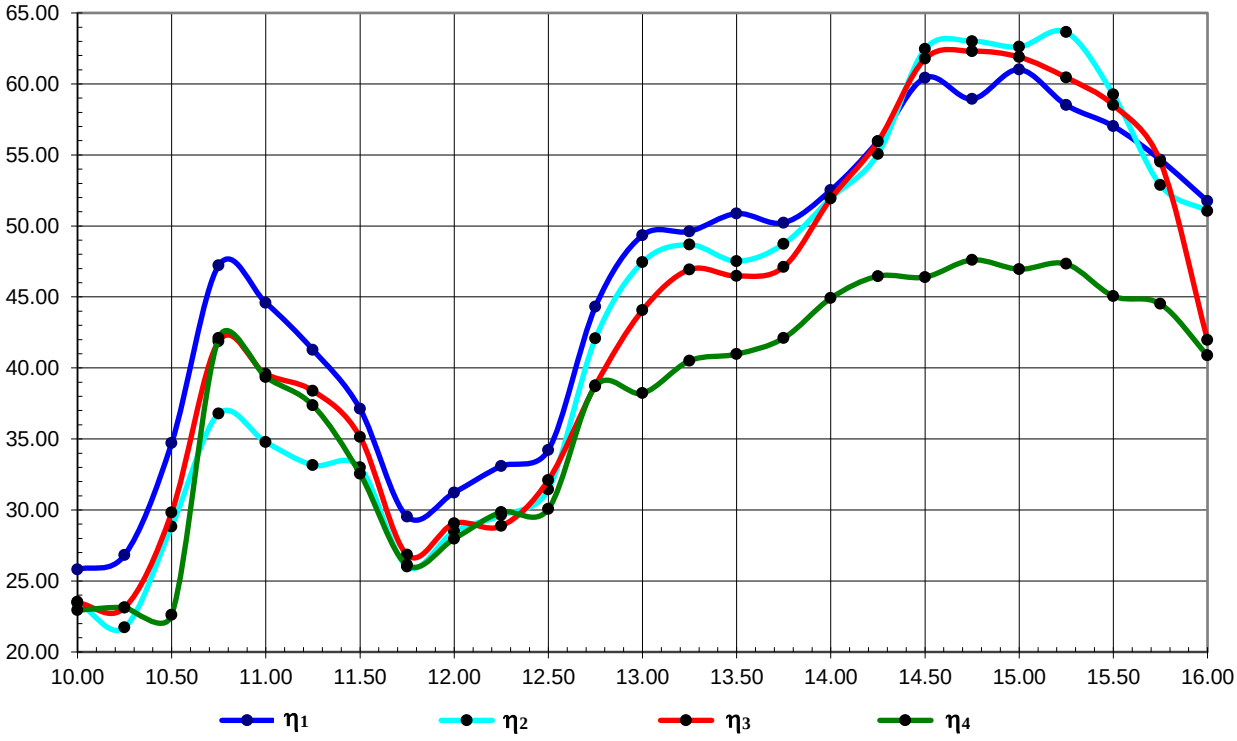

Fig. 11 - Variation of the yield at panels for tilting in the vertical plane at 45° from the horizontal plane
η_1 - yield at panel no. 1; η_2 - yield at panel no. 2;η_3 - yield at panel no. 3; η_4 - yield at panel no. 4

CONCLUSIONS

The experiments highlighted the fact that in the months of May - June in the Bucharest-Ilfov area, the angle of inclination of the solar collectors in the vertical plane is recommended to be 45°, at which the highest values for conversion yields of for solar energy into thermal energy were obtained.

As a result of the experiments carried out, it was found that of the four variants initially tested, variant A was the most efficient in terms of the heat transfer achieved, which recommends expanding the use of the installation in small and medium-sized farms for dehydrating vegetables and fruits, drying cereals and herbal medicine.

ACKNOWLEDGEMENT

This paper was supported by the Romanian Ministry of Education and Research, through the project of the Ministry of Research, Innovation and Digitalization through Program 1 - Development of the national research-development system, Subprogram 1.2 - Institutional performance - Projects for financing excellence in RDI, Contract no. 1PFE/30.12.2021.

REFERENCES

[1] Ahmed F., Sharizal Abdul Aziz M, Palaniandy P., Shaik F. (2022). A review on application of renewable energy for desalination technologies with emphasis on concentrated solar power. *Sustainable Energy Technologies and Assessments*, *53*(D), 102772. DOI: https://doi. org/10.1016/j.seta.2022.102772.

[2] Balasuadhakar A., Fisseha T., Atenafu A., Bino B. (2016). A review on passive solar dryers for agricultural products. *International Journal of Innovative Science and Research Technology, 3*, 64**–**70.

[3] Bhatia S.C., Gupta R.K. (2019). Textbook of Renewable Energy. *Woodhead Publishing India PVT. Limited*, ISBN: 938-505-995-5.

[4] Cook R.M., Torsvik H.T (2016). Climates Past and Present. Chapter 16. *Earth History and Paleogeography, Cambridge University Press*, https://www.cambridge.org/core/books/abs/earth-history-and-palaeogeography/climates-past-and-present/2FC8EE23A3F4622906BDA7DA8A7C856C

[5] Dincer I. (2000). Renewable energy and sustainable development: a crucial review. *Renewable and Sustainable Energy Reviews, 4*(2), 157–175. DOI: https://doi.org/10.1016/S1364-0321(99)00011-8.

[6] Fatai K., Oxley L., Scrimgeour F.G. (2004). Modelling the causal relationship between energy consumption and GDP in New Zealand, Australia, India, Indonesia, The Philippines and Thailand. *Mathematics and Computers in Simulation,* 64(3–4), 431–445. DOI: https://doi.org/10.1016/S0378-4754(03)00109-5.

[7] Garratt A., Petrella I., Zhang Y. (2023). Asymmetry and interdependence when evaluating US energy information administration forecasts. *Energy Economics, 121*, 106620. DOI: https://doi.org/10.1016/j.eneco.2023.106620.

[8] Găgeanu P., Vlăduţ V., Păun A., Chih I., Biriş S. (2011). Pure plant oil – source of alternative energy, Proceedings of the 39th International Symposium on Agricultural Engineering *"Actual Tasks on Agricultural Engineering",* 141**–**152, Opatija, Croatia.

[9] Hassan Q., Sameen A.Z., Salman H.M., Jaszczur M. (2023). A roadmap with strategic policy toward green hydrogen production: the case of Iraq. *Sustainability, 15*(6), 5258. DOI: https://doi.org/10.3390/su15065258.

[10] Huang W., Dai J., Xiong L. (2022). Towards a sustainable energy future: factors affecting solar-hydrogen energy production in China. *Sustainable Energy Technologies and Assessments*, *52*, 102059. DOI: https://doi.org/10.1016/j.seta.2022.102059.

[11] Hussain S.M., Jamshed W., Kumar V., Kumar V., Nisar K.S., Eid M.R., Safdar R., Abdel-Aty A.-H., Yahia I. (2021). Computational analysis of thermal energy distribution of electromagnetic Casson nanofluid across stretched sheet: shape factor effectiveness of solid-particles. *Energy Reports, 7*, 7460–7477. DOI: https://doi.org/10.1016/j.egyr.2021.10.083.

[12] Ihssen J., Braun A., Faccio G., Gajda-Schrantz K., Thony-Meyer L. (2014). Light harvesting proteins for solar fuel generation in bioengineered photoelectrochemical cells. *Current Protein & Peptide Science, 15*(4), 74–384. DOI: https://doi.org/10.2174/1389203715666140327105530.

[13] Jahid A., Monju M.K.H., Hossain M.E., Hossain M.F. (2018). Renewable energy assisted cost aware sustainable off-grid base stations with energy cooperation. *IEEE Access, 6*, 60900–60920. DOI: https://doi.org/10.1109/ ACCESS.2018.2874131.

[14] Kahraman U., Dincer I. (2022). Performance analysis of a solar based waste to energy multigeneration system. *Sustainable Energy Technology and Assessments*, *50*, 101729. DOI: https://doi.org/10.1016/j.seta.2021.101729,.
[15] Kartal M.T. (2022). The role of consumption of energy, fossil sources, nuclear energy, and renewable energy on environmental degradation in top-five carbon producing countries. *Renewable Energy, 184*, 871–880. DOI: https://doi.org/10.1016/j.renene.2021.12.022.
[16] Lindsey R. (2009). Climate and Earth's Energy Budget. *NASA - Earth Observatory*, https://earthobservatory.nasa.gov/features/EnergyBalance.
[17] Maican E., Vlăduţ V., Vilcu C., Sorică C., Dorian M., Mirea D.P., Bogăţeanu R. (2019). Hybrid renewable energy systems for isolated farms. A review. *INMATEH – Agricultural Engineering, 59*(3), 77–92. DOI: 10.35633/INMATEH-59-09.
[18] Majeed Y., Khan M.U., Waseem M., Zahid U., Mahmood F., Majeed F., Sultan M., Raza A. (2023). Renewable energy as an alternative source for energy management in agriculture. *Energy Reports, 10*, 344–359. DOI: https://doi.org/10.1016/j.egyr.2023.06.032.
[19] Marks-Bielska R., Bielski S., Pik K., Kurowska K. (2020). The importance of renewable energy sources in Poland's energy mix. *Energies, 13*(18), 4624. DOI: https://doi.org/10.3390/en13184624.
[20] Mekhilef S., Safari A., Mustaffa W.E.S., Saidur R., Omar R., Younis M.A.A. (2012). Solar energy in Malaysia: current state and prospects. *Renewable and Sustainable Energy Reviews, 16*, 386–396. DOI: https://doi.org/10.1016/j.rser.2011.08.003.
[21] Mohammed Wazed S., Hughes B.R., O'Connor D., Kaiser Calautit J. (2018). A review of sustainable solar irrigation systems for Sub-Saharan Africa. *Renewable and Sustainable Energy Reviews*, *81,* 1206–1225. DOI: https://doi.org/10.1016/j.rser.2017.08.039.
[22] Muehlbauer W. (1986). Present status of solar crop drying. *Energy in Agric*ulture, *5*, 121–138. DOI: 10.1016/0167-5826(86)90013-6.
[23] Muneer T., Maubleu S., Asif M. (2006). Prospects of solar water heating for textile industry in Pakistan. *Renewable and Sustainable Energy Reviews, 10*(1), 1**–**23. DOI: https://doi.org/10.1016/j.rser.2004.07.003.
[24] Perez M., Perez R. (2022). Update 2022 – a fundamental look at supply side energy reserves for the planet. *Solar Energy Advances*, *2*, 100014. DOI: https://doi.org/10.1016/ j.seja.2022.
[25] Saidur R., Mekhilef S. (2010). Energy use, energy savings and emission analysis in the Malaysian rubber producing industries. *Applied Energy, 87*, 2746–2758. DOI: https://doi.org/10.1016/j.apenergy.2009.12.018.
[26] Saidur R. (2010). A review on electrical motors energy use and energy savings. *Renewable and Sustainable Energy Reviews, 14*, 877–898. DOI: https://doi.org/10.1016/j. rser.2009.10.018.
[27] Salawu S., Obalalu A., Fatunmbi E., Oderinu R. (2022). Thermal Prandtl-Eyring hybridized MoS2-SiO2/C3H8O2 and SiO2-C3H8O2 nanofluids for effective solar energy absorber and entropy optimization: a solar water pump implementation. *Journal of Molecular Liquids, 361*, 119608. DOI: https://doi.org/10.1016/j.molliq.2022.119608.
[28] Tong G., Chen Q., Xu H. (2022). Passive solar energy utilization: a review of envelope material selection for Chinese solar greenhouses. *Sustainable Energy Technology and Assessments*, *50*, 101833. DOI: https://doi.org/10.1016/j.seta.2021.101833.
[29] Xiong Q., Altnji S., Tayebi T., Izadi M., Hajjar A., Sunden B., et al. (2021). A comprehensive review on the application of hybrid nanofluids in solar energy collectors. *Sustainable Energy Technology and Assessments*, *47*, 101341. DOI: https://doi.org/ 10.1016/j.seta.2021.101341.
[30] Zahraoui Y., Basir Khan M.R., Alhamrouni I., Mekhilef S., Ahmed M. (2021). Current status, scenario, and prospective of renewable energy in Algeria: a review. *Energies, 14(9),* 2354. DOI: https://doi.org/10.3390/en14092354.
[31] Zekai S. (2008). Solar Energy Fundamentals and Modeling Techniques: Atmosphere, Environment, Climate Change and Renewable Energy. *Springer,* Berlin. DOI: https://doi.org/10.1007/978-1-84800-134-3.
[32] Zhao N., Zeng X., Han S. (2013). Solar radiation estimation using sunshine hour and air pollution index in China. Energy Conversion and Management, *76*, 846–851. DOI: https://doi.org/10.1016/j.enconman.2013.08.037.

ASPECTS REGARDING THE USE OF SOLAR ENERGY IN SMALL AND MEDIUM FARMS
/
ASPECTE PRIVIND UTILIZAREA ENERGIEI SOLARE ÎN FERMELE MICI ŞI MEDII

Mario CRISTEA[1)], Nicolae-Valentin VLĂDUȚ[1*)], Georgiana MOICEANU[2*)]

[1)]INMA Bucharest / Romania; [2)]POLITEHNICA Bucharest / Romania

Corresponding authors: valentin_vladut@yahoo.com; georgiana.moiceanu@upb.ro
DOI: https://doi.org/10.35633/inmateh-72-57A

Keywords: *sun, panels, solar energy, electricity, incidence*

ABSTRACT

Considering that every day the sun generates more energy than the planet needs for daily consumption, harnessing solar energy represents one of the future solutions for clean, sustainable energy, obviously with the technological limitations related to the ability to transform this energy into electricity. The paper presents a functional model of equipment that allows the capture of solar energy using special panels, which can rotate both horizontally and vertically according to the sun, so that the incidence of rays with the radiating surface of the panels is maximum and the yields obtained at different angles of inclination in the vertical plane at 60°, respectively in the horizontal plane at 0°.

REZUMAT

Având în vedere că în fiecare zi soarele generează mai multă energeie decât planeta are nevoie pentru consumul zilnic, valorificarea energia solare reprezintă una din soluţiile de viitor pentru o energie curată, sustenabilă, evident cu limitările tehnologice legate de capacitatea de a transforma această energie în electricitate. Lucrarea prezintă un model funcţional de echipament care permite captarea energiei solare utilizând nişte panouri speciale, care se pot roti atât în plan orizontal cât şi verticla după soare, astfel încât incidenţa razelor cu suprafaţa radiantă a panourilor să fie maximă şi randamentele obţinute la diferite unghiuri de înclinaţie în plan vertical la 60°, respectiv în plan orizontal la 0°.

INTRODUCTION

Among the various possible ways, open-air sun drying is the most popular in tropical countries due to its low cost, particularly for smallholder farmers in rural areas. However, the drying process is heavily reliant on ambient circumstances and is highly susceptible to contamination from dust, rain, wind, pests, and rodents (*El Hage et al., 2018; Singh et al., 2018; Aresenoaia et al., 2019a*), resulting in low-quality goods and a reduction of farmers' income. To address these issues, numerous systems have been created, such as the greenhouse dryer (*Janjai et al., 2007; Azaizia et al., 2017; Iskandar et al., 2017; Hamdi et al., 2018*) and the hybrid solar dryer (*Amer et al., 2018; Eltawil et al., 2018*). These systems are faster, more efficient, and more sanitary, resulting in lesser crop losses compared to the traditional open-air sun drying process (*Muehlbauer, 1986; Chua and Chou, 2003; Karim and Hawlader, 2004; Tomar et al., 2017; Cârlescu et al., 2018; Arsenoaia et al., 2019b*). Moisture in raw agricultural materials is removed during solar drying using heat transfer modes such as conduction, convection, and radiation. Solar radiation travels through a transparent sheet and is kept as heat in a drying chamber or solar collector at 30-60°C.

Drying is one of the first unit activities farmers conduct in the processing chain to either increase the shelf life of their products for storage or prepare them for further processing *Ndukwu et al., 2022; Ihediwa et al., 2022a*). However, research has revealed that drying is a substantial energy consumer in many countries, accounting for 12-15% of total global agricultural energy consumption (*Samimi-Akhijahani and Arabhosseini 2018*; *Ihediwa et al., 2022b*; *Catorze et al., 2022*).

Furthermore, drying has been shown to use 6 to 30 times more energy than cooling and freezing (*Machala et al., 2022*). As a result, reliance on fossil fuels to meet heat demand during drying will emit considerable amounts of carbon into the atmosphere (*Ndukwu et al., 2023*). Thus, it is vital to switch from fossil-fueled dryers to clean energy sources (*Chowdhury et al., 2020*).

To protect the environment, most countries currently urge for a transition from fossil fuel-based dryers to renewable energy sources (*Kumar et al., 2023*). Clean technologies are being embraced in all energy sectors because they are critical to addressing and achieving the sustainable development goal, especially in rural farm areas (*Messina et al., 2022*). These goals include reducing air pollution, conserving resources, and addressing climate change. According to *Rahman et al. (2022)*, the following renewable sources are currently available: solar thermal, solar photovoltaic, wind energy, geothermal, tidal, and wave energy.

Greenhouses typically rely on carbon-based fuels, which contribute to climate change impacts, high production costs, and growing concerns about fossil fuel depletion (*Esen and Yujsel, 2013; Cabeza et al., 2014; Semple et al., 2017; Forough and Roshandel, 2018; van Beveren et al., 2019; Burg et al., 2021*). These issues require the exploitation of renewable energy resources (*Cabeza et al., 2014; Forough and Roshandel, 2018*). Solar energy is a clean, renewable, and necessary component of agriculture's sustainable energy future, including greenhouse applications *(Bakirci and Yuksel, 2011; Zhang et al., 2015; Esmaeli and Roshandel, 2020)*. However, solar energy is a recurring source of energy. Summer produces the most solar energy, whereas the biggest heating demands occur in winter (*Esen, 2000; Hesaraki et al., 2015*). Seasonal thermal energy storage is a promising approach to storing the summer heat for winter consumption (*Antoniadis and Matinopoulos, 2019; Yang et al., 2021*). Thus, heat storage devices can compensate for the mismatch between greenhouse heating demand and solar thermal energy supply (*Cabeza, 2014*).

MATERIALS AND METHODS

The solar energy capture and conversion module (figure 1) is located in an area with exposure to the sun throughout the day, at a distance that ensures minimal losses on the heat transfer network (air), from solar collectors to possible users such as a fruit drying facility. The main component sub-assemblies of the solar energy capture and conversion module are: the support frame, the solar collectors and the air tubes with a low-pressure centrifugal fan. The rotation of the solar collectors around a central pivot by 45° left-right concerning the initial south orientation position and also the orientation of the solar collectors in the vertical plane at fixed angles of 60° is done manually and checked each time with the corresponding measuring instruments. With these facilities, the variation of solar energy can be highlighted throughout the day by orienting the panels according to the position of the sun, and adjustments can be made to optimize the system's operating regime.

The solar energy capture and conversion module is composed of: a support frame; solar collectors; low-pressure centrifugal fan air ducts.

Fig. 1 – Solar energy capture and conversion module, rear view

The absorbent plate absorbs solar radiation, heats up to a temperature of 80÷120°C and radiates in the far infrared. The module has a pull-type device (figure 2) for changing the angle of inclination of the collector in the vertical plane within the limits of 30 and 60 degrees compared to the horizontal plane of the ground, for which there is an angle indicator (figure 4) with three positions of work (30, 45 and 60 degrees). The measurement of the angle of rotation in the horizontal plane is done with an indicator, with a position indexer of 15 in 15 degrees, the module being able to rotate towards sunrise or sunset depending on the position of the sun to obtain maximum efficiency of its radiation.

Fig. 2 - Angle indicator, for the vertical tilt of the pickup

The heated air ducts (figure 3) have transducers along the route to measure the temperature and air flow.

Fig. 3 – Air duct

The main characteristics of the installation are those described in part I of the article. The experiments were carried out with the installation adjusted at **an angle of 60° in the vertical plane** (maintaining at 0° in the horizontal plane), simultaneously with their rotation in the horizontal plane at 30°, 45° and 60°.

RESULTS

Experiments with tilting the collectors in the vertical plane at 60°

Figure 4 shows the results of the temperature measurement for each panel, the temperature of the environment, the calculation of the differences between the input temperature and that of the environment, as well as their average variation over a whole day (based on the measurement of the speed of the air current at the exit from the solar collectors).

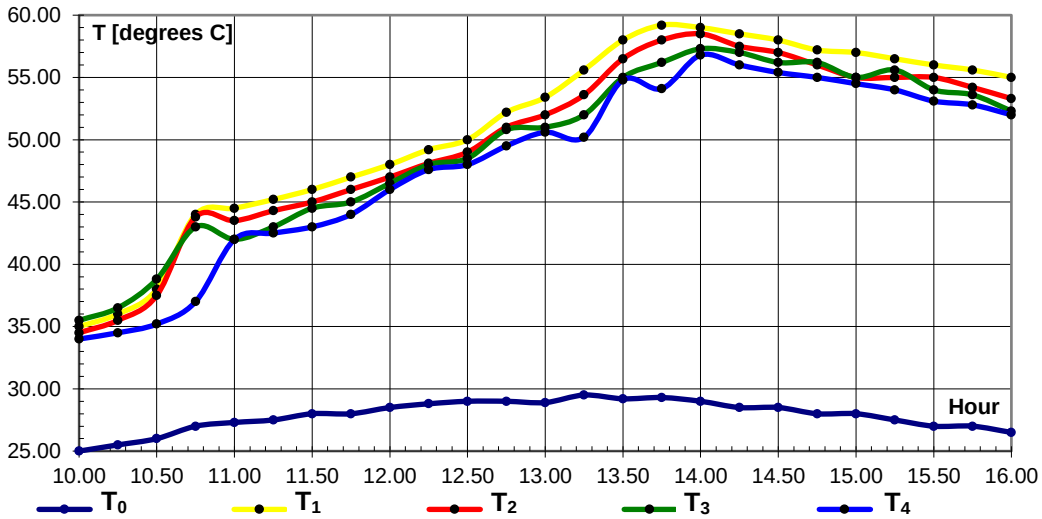

Fig. 4 - The temperature variation of the panels for tilting in the vertical plane at 60° from the horizontal
T_0 – environment temperature; T_1 - temperature panel 1; T_2 - temperature panel 2;
T_3 - temperature panel 3; T_4 - temperature panel 4

Figure 5 shows the variation of airflow rates for panels inclined in the vertical plane at 60° from the horizontal over a whole day and Figure 6 - the variation of the heat accumulated on the panels for the inclination in the vertical plane at 60° from the horizontal, at the level to each panel.

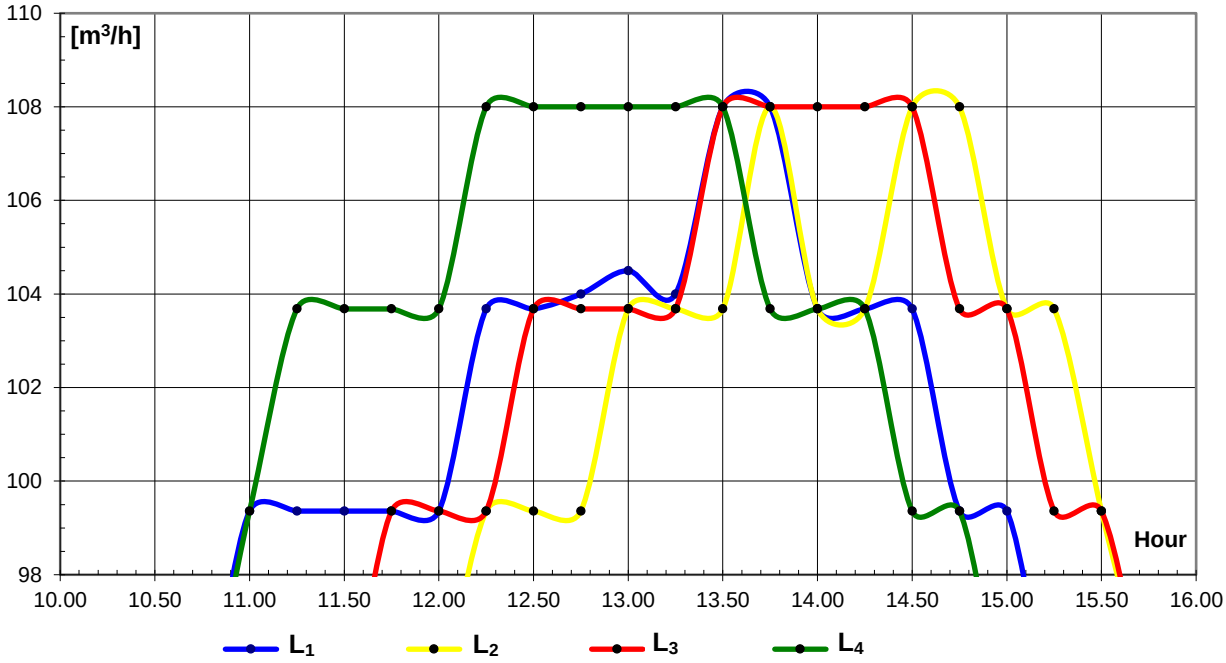

Fig. 5 - The variation of air flows at panels inclined in the vertical plane at 60° from the horizontal
L_1 – air flow to panel 1; L_2 – air flow to panel 2; L_3 – air flow to panel 3; L_4 – air flow to panel 4

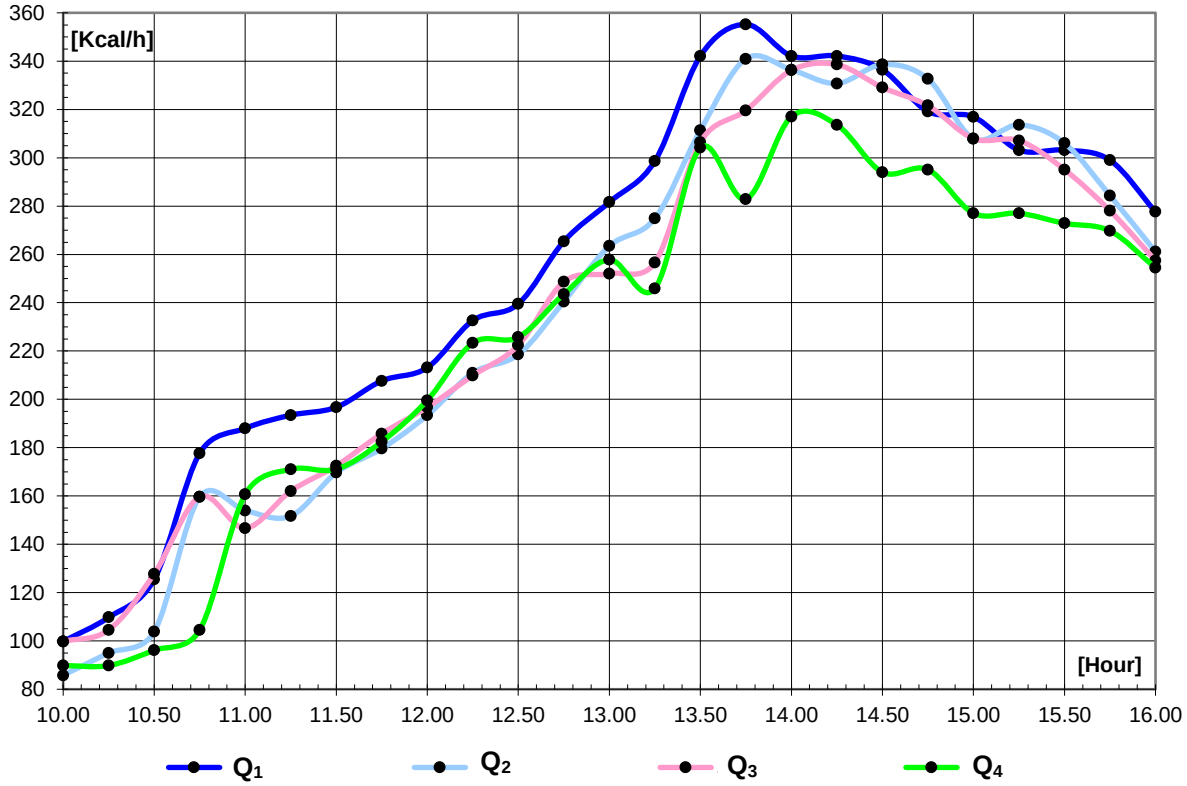

Fig. 6 - The variation of the heat accumulated on the panels for tilting in the vertical plane at 60° from the horizontal
Q_1 – heat accumulated on panel no. 1; Q_2 – heat accumulated on panel no. 2
Q_3 – heat accumulated on panel no. 3; Q_4 – heat accumulated on panel no. 4

Table 1

Hour	Temperature differences ($T_{panou} - T_{mediu}$) [°C]				Air flows [m^3/h]				Accumulated heat [Kcal/h]				Average radiation intensity [Kcal/m^2 h]	Heat received [Kcal/h]	Yields [%]			
	pan.1	pan. 2	pan.3	pan. 4	pan.1	pan. 2	pan.3	pan. 4	pan.1	pan.2	pan.3	pan.4	-	-	pan.1	pan.2	pan.3	pan.4
10.00	10.00	9.50	10.50	9.00	90.72	82.08	86.4	90.72	99.792	85.77	99.792	89.813	270	364.5	27.38	23.53	27.38	24.64
10.25	10.50	10.00	11.00	9.00	95.04	86.4	86.4	90.72	109.77	95.04	104.54	89.81	280	378	29.04	25.14	27.68	23.76
10.50	12.00	11.50	12.80	9.20	95.04	82.08	90.72	95.04	125.45	103.83	127.73	96.180	290	391.5	32.04	26.52	32.63	24.57
10.75	17.00	16.80	16.00	10.00	95.04	86.4	90.72	95.04	177.72	159.67	159.67	104.54	320	432	41.14	36.96	36.96	24.2
11.00	17.20	16.20	14.70	14.70	99.36	86.4	90.72	99.36	187.99	153.96	146.69	160.67	325	438.75	42.85	35.09	33.43	36.62
11.25	17.70	16.80	15.50	15.00	99.36	82.08	95.04	103.68	193.45	151.68	162.04	171.07	355	479.25	40.37	31.65	33.81	35.70
11.50	18.00	17.00	16.50	15.00	99.36	90.72	95.04	103.68	196.73	169.65	172.50	171.07	380	513	38.35	33.07	33.63	33.35
11.75	19.00	18.00	17.00	16.00	99.36	90.72	99.36	103.68	207.66	179.63	185.80	182.48	390	526.5	39.44	34.12	35.29	34.66
12.00	19.50	18.50	18.00	17.50	99.36	95.04	99.36	103.68	213.13	193.41	196.73	199.58	392	529.2	40.27	36.55	37.18	37.71
12.25	20.40	19.30	19.20	18.80	103.68	99.36	99.36	108	232.66	210.94	209.85	223.34	395	533.25	43.63	39.56	39.35	41.88
12.50	21.00	20.00	19.50	19.00	103.68	99.36	103.68	108	239.50	218.59	222.39	225.72	400	540	44.35	40.48	41.18	41.8
12.75	23.20	22.00	21.80	20.50	104	99.36	103.68	108	265.41	240.45	248.62	243.54	450	607.5	43.69	39.58	40.93	40.09
13.00	24.50	23.10	22.10	21.70	104.5	103.68	103.68	108	281.63	263.45	252.05	257.80	475	641.25	43.92	41.08	39.31	40.20
13.25	26.10	24.10	22.50	20.70	104	103.68	103.68	108	298.58	274.86	256.61	245.92	500	675	44.23	40.72	38.02	36.43
13.50	28.80	27.30	25.80	25,60	108	103.68	108	108	342.14	311.35	306.50	304.13	555	749.25	45.66	41.56	40.91	40.59
13.75	29.90	28.70	26.90	24.80	108	108	108	103.68	355.21	340.96	319.57	282.84	600	810	43.85	42.09	39.45	34.92
14.00	30.00	29.50	28.30	27.80	103.68	103.68	108	103.68	342.14	336.44	336.20	317.05	590	796.5	42.96	42.24	42.21	39.81
14.25	30.00	29.00	28.50	27.50	103.68	103.68	108	103.68	342.14	330.74	338.58	313.63	585	789.75	43.32	41.88	42.87	39.71
14.50	29.50	28.50	27.70	26.90	103.68	108	108	99.36	336.44	338.58	329.08	294.01	575	776.25	43.34	43.62	42.39	37.88
14.75	29.20	28.00	28.20	27.00	99.36	108	103.68	99.36	319.14	332.64	321.62	295.10	560	756	42.21	44	42.54	39.03
15.00	29.00	27.00	27.00	26.50	99.36	103.68	103.68	95.04	316.96	307.93	307.93	277.04	550	742.5	42.69	41.47	41.47	37.31
15.25	29.00	27.50	28.10	26.50	95.04	103.68	99.36	95.04	303.18	313.63	307.12	277.04	530	715.5	42.37	43.83	42.92	38.72
15.50	29.00	28.00	27.00	26.10	95.04	99.36	99.36	95.04	303.18	306.03	295.10	272.86	520	702	43.19	43.59	42.04	38.87
15.75	28.60	27.20	26.60	25.80	95.04	95.04	95.04	95.04	299.00	284.36	278.09	269.72	500	675	44.30	42.13	41.20	39.96
16.00	28.50	26.80	25.80	25.50	88.56	88.56	90.72	90.72	277.64	261.07	257.46	254.47	490	661.5	41.97	39.47	38.92	38.47
														Average yield [%]	**41.1**	**38.00**	**38.15**	**36.03**

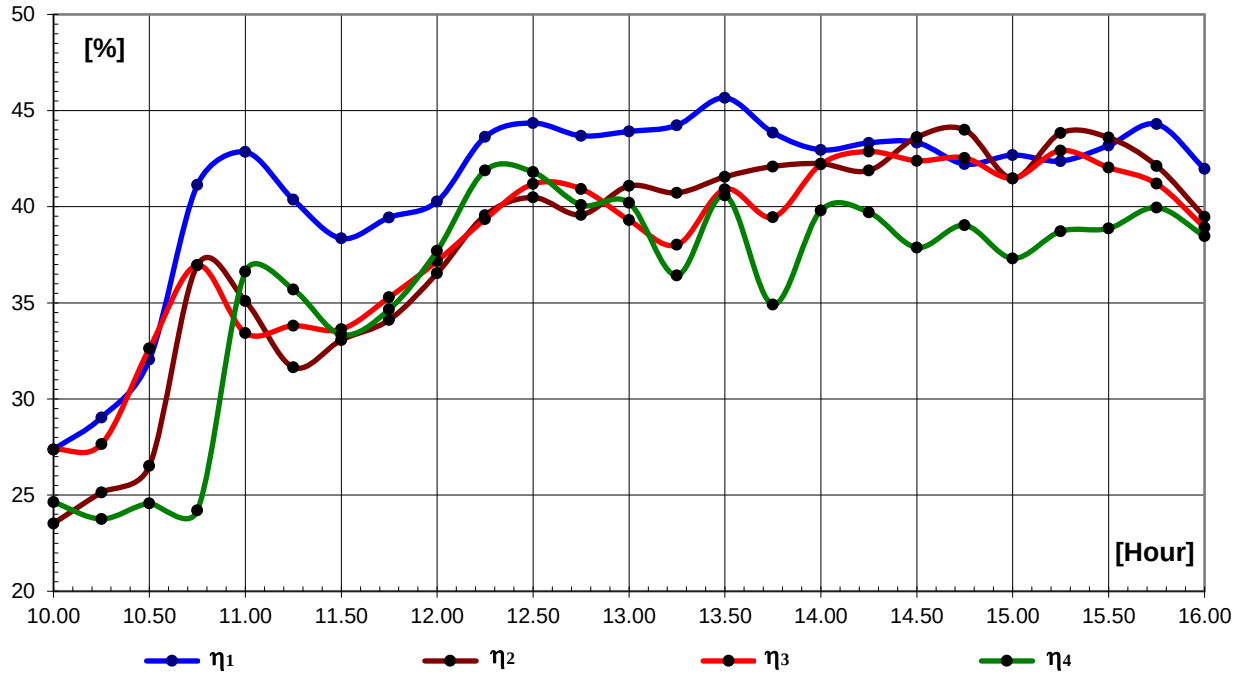

Fig. 7 - The variation of the efficiency of the panels for tilting in the vertical plane at 60° from the horizontal
η_1 - yield at panel 1; η_2 - yield at panel 2;
η_3 - yield at panel 3; η_4 - yield at panel 4

Experiments with tilting the receivers in the vertical plane at fixed angles of 30°, 45°, and 60° simultaneously with their rotation in the horizontal plane at 30°, 45° and 60°

From the integral flow of radiant energy that comes continuously from the Sun to the Earth, and which has the value of the solar constant $E_0 \pm 3\%$, (according to paper 2 E_0 =1353 W/m^2), outside the terrestrial atmosphere, a quantity reaches the earth that has a lower value (0.8-0.9 kW/m^2). This size is no longer constant but depends on the following geophysical and meteorological factors: latitude, altitude, season, day, hour, the amount of dust and water vapor in the atmosphere, as well as the angle at which the Sun's rays fall on the Earth.

At angles lower than 90° (relative to the horizontal of the place) the Sun's rays cross a larger amount of atmospheric air, so that the absorption and dispersion of radiation through the atmosphere is more pronounced than at 12 o'clock, when the thickness of the air layer is minimal.

Compared to those shown previously, the measurements presented in this chapter were made to highlight the influence of the angle of incidence of the solar rays on the surface of the collectors.

Table 2 shows the values of the angles of incidence of the solar rays with the surface of the collectors, results for fixed positions of their inclination in the vertical plane (respectively 30°, 45° and 60°), while they were rotated in the horizontal plane.

The measurements were made starting from -30° (to the East), passing through 0° (South) and continued up to +30° (to the West), from 15 degrees to 15 degrees.

It can be observed that throughout the rotation in the horizontal plane, the collector with a fixed inclination at 30° achieved angles of incidence of the sun's rays, higher than at the other inclinations. Even between 13-14 hours when the most advantageous angle is achieved, it was a maximum of 73 degrees, a fact that recommends tilting the collector at 30° as the best for the area where the experiments were carried out.

Table 3 and figure 8 show the temperature values recorded at the exit of the collectors both for fixed positions (respectively 30°, 45° and 60°) and in the case of their rotation following the position of the sun between 10-14 hours.

From the analysis of the diagram, the temperature difference recorded between the fixed collectors (T_{f1}, T_{f2}, T_{f3}, T_{f4}) and the mobile ones (T_{m1}, T_{m2}, T_{m3},T_{m4}), can be observed, highlighting also in this case the constructive variant "A", where the evolution temperature curve is the best.

Table 2

Den. no.	Hour	The angle of incidence of the sun's rays with the surface of the inclined panels in the vertical plane at:		
		30º	45º	60º
1	10	44	37	31
2	11	51	44	36
3	12	64	54	43.5
4	13	73	61	50
5	14	73	61	51

Table 3

Den. no.	Hour	Environment temperature (T_0)	Temperature at panels adjusted in vertical plane at fixed positions of:			Temperature at panels rotated in horizontal plane (from –30º to +30º) having in vertical plane fixed positions of:		
			30º (T_{f1})	45º (T_{f2})	60º (T_{f3})	30º (T_{m1})	45º (T_{m2})	60º (T_{m3})
1	10	26	40	38	44	36	46	47
2	11	27	45	42	43	54	54	48
3	12	27.5	54	50	48	62	54,5	54
4	13	28.5	60	53	55	65	55	56
5	14	27.5	66	65.4	58	67	68	60

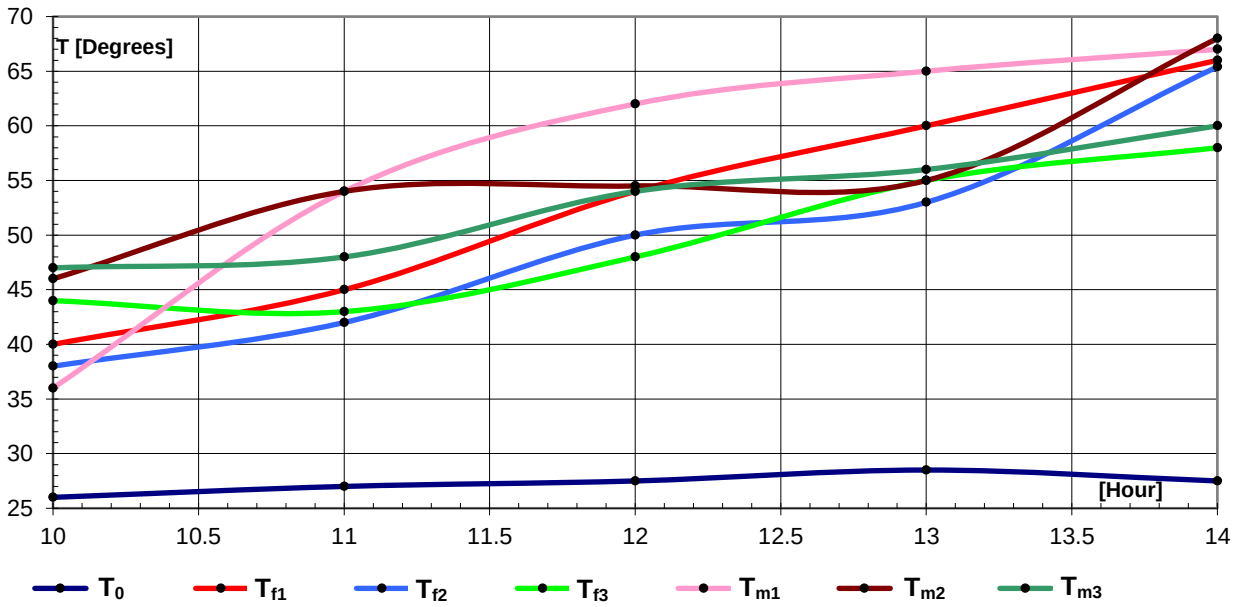

Fig. 8 - The variation of temperatures recorded at sensors with fixed positions (in the vertical plane), compared to those recorded by rotating them in the horizontal plane (respectively 30°, 45° and 60°)

CONCLUSIONS

The experiments highlighted the fact that in the months of May - June in the Bucharest-Ilfov area, at the angle of inclination of the solar collectors in the vertical plane of *60°* good yields (of converting solar energy into thermal energy) were obtained, but still lower than those obtained at the *45°* angle (presented in part I of the article).

And in this case, among the four options initially tested, option A was the most efficient in terms of heat transfer.

It is recommended that when using solar panels in the Bucharest-Ilfov area, the inclination angle of the collectors in the vertical plane should be *45°* and in the vertical plane between *30°* and 45°.

ACKNOWLEDGEMENT

This paper was supported by the Romanian Ministry of Education and Research, through the project of the Ministry of Research, Innovation and Digitalization through Program 1 - Development of the national research-development system, Subprogram 1.2 - Institutional performance - Projects for financing excellence in RDI, Contract no. 1PFE/30.12.2021.

REFERENCES

[1] Amer B.M.A., Gottschalk K., Hossain M.A. (2018). Integrated hybrid solar drying system and its drying kinetics of chamomile. *Renew. Energy* 121, 539–547.

[2] Antoniadis CN., Martinopoulos G. (2019). Optimization of a building integrated solar thermal system with seasonal storage using TRNSYS. *Renew Energy*: 56–66. https://doi.org/10.1016/j.renene.2018.03.074.

[3] Arsenoaia V., Vlăduț V., Țenu I., Voicea I., Cârlescu P. M. (2019). Mathematical modeling and numerical simulation of the drying process of seeds in a pilot plant, *INMATEH – Agricultural Engineering.* Vol.57(1), pg. 55-62.

[4] Arsenoaia V., Vlăduţ V., Ţenu I., Voicea I., Cârlescu P.M. (2019). Drying process modeling with effects of physical parameters on dehydrated seeds, *Proceedings of the 47 International Symposium on Agricultural Engineering "Actual Tasks on Agricultural Engineering",* pg. 333-342, Opatija – Croatia.

[5] Azaizia Z., Kooli S., Elkhadraoui A., Hamdi I., Guizani A. (2017). Investigation of a new solar greenhouse drying system for peppers. *Int. J. Hydrogen Energy* 42 (13), 8816–8826.

[6] Bakirci K., Yuksel B. (2011). Experimental thermal performance of a solar source heat-pump system for residential heating in cold climate region. *Appl Therm Eng*; 31: 1508–18. https://doi.org/10.1016/j.applthermaleng.2011.01.039.

[7] Burg V., Golzar F., Bowman G., Hellweg S., Roshandel R. (2021). Symbiosis opportunities between food and energy system: The potential of manure-based biogas as heating source for greenhouse production. *Journal of Industrial Ecology* 25(3): 648–62.

[8] Cabeza LF. (2014). Advances in Thermal Energy Storage Systems: Methods and Applications. *Adv Therm Energy Storage Syst Methods Appl*: 1–592, https:// doi.org/10.1016/C2013-0-16453-7.

[9] Catorze C., Tavares A.P., Cardao P., Castro A., Silva M.E., Ferreira D.W., Lopes S., Bras, I. (2022). Study of a solar energy drying system—energy savings and effect in dried food quality. *Energy Rep.* 8, 392–398. https://doi.org/10.1016/j.egyr.2022.01.070.

[10] Cârlescu P.M., Țenu I., Roșca R., Muscalu A.T, Vlăduţ N.V. (2018). CFD simulation of an innovative vertical dryer for agricultural seeds drying, *Proceedings of the 46 International Symposium on Agricultural Engineering "Actual Tasks on Agricultural Engineering",* pg. 407-418, Opatija – Croaţia.

[11] Chowdhury T., Chowdhury H., Chowdhury P., Sait M.S., Anik P., Ahamed J.U., Saidur R. (2020). A case study to application of exergy-based indicators to address the sustainability of Bangladesh residential sector. *Sustain. Energy Technol. Assessments* 37, 100615. https://doi.org/10.1016/j. seta.2019.100615.

[12] Chua K.J., Chou S.K. (2003). Low-cost drying methods for developing countries. *Trends Food Sci. Technol.* 14, 519–528.

[13] Eltawil M.A., Azam M.M., Alghannam A.O. (2018). Energy analysis of hybrid solar tunnel dryer with PV system and solar collector for drying mint (*Mentha Viridis*).

[14] El Hage H., Herez A., Ramadan M., Brazzi H., Khaled M. (2018). An investigation on solar drying: a review with economic and environmental assessment. *At. Energ*. 157, 815–829.

[15] Esen M, Yuksel T. (2013). Experimental evaluation of using various renewable energy sources for heating a greenhouse. *Energy Build*; 65:340–51. https://doi.org/ 10.1016/j.enbuild.2013.06.018.

[16] Esen M. (2000). Thermal performance of a solar-aided latent heat store used for space heating by heat pump. *Sol Energy*; 69:15–25. https://doi.org/10.1016/ S0038-092X(00)00015-3.

[17] Esmaeli H., Roshandel R. (2020). Optimal design for solar greenhouses based on climate conditions. *Renew Energy*; 145: 1255–65. https://doi.org/10.1016/j. renene.2019.06.090.

[18] Forough AB., Roshandel R. (2018). Lifetime optimization framework for a hybrid renewable energy system based on receding horizon optimization. *Energy*; 150: 617–30. https://doi.org/10.1016/j.energy.2018.02.158.

[19] Hamdi I., Kooli S., Elkhadraoui A., Azaizia Z., Abdelhamid F., Guizani A. (2018). Experimental study and numerical modeling for drying grapes under solar greenhouse. *Renew. Energy* 127, 936–946.

[20] Hesaraki A., Holmberg S., Haghighat F. (2015). Seasonal thermal energy storage with heat pumps and low temperatures in building projects - A comparative review. *Renew Sustain Energy Rev*; 43: 1199–213. https://doi.org/10.1016/j. rser.2014.12.002.

[21] Ihediwa V.E., Ndukwu M.C., Abada U.C., Ekop, I.E., Bennamoun L., Simo- Tagne M., Abam F.I. (2022). Optimization of the energy consumption, drying kinetics and evolution of thermo-physical properties of drying of forage grass for haymaking. *Heat Mass Tran*. 58 (7), 1187–1206. https://doi.org/10.1007/s00231- 021-03146-2.

[22] Ihediwa V.E., Edem Akpan G., Akuwueke L., Oriaku L., Ndubuisi C.O., Mbanasor J., Ndukwu, Macmanus C. (2022). Thermal dehydration of some forage grasses for livestock feeding: effect of different methods on moisture diffusivity and the quality of dried leaves. *Energy Nexus* 8, 100156. https://doi.org/10.1016/j.nexus.2022.100156

[23] Iskandar A.N., Ya'acob M.E., Anuar M.S. (2017). Tropical field performance of dual-pass PV tray dryer. 3rd electronic and green materials international conference. *AIP Conference Proceedings* 1885 (1), 020016.

[24] Janjai S., Khamvongsa V., Bala B.K. (2007). Development, design, and performance of a PV ventilated greenhouse dryer. *Int. Energy J.* 8, 249–258.

[25] Karim M.A., Hawlader M.N.A. (2004). Development of solar air collectors for drying applications. *Energy Convers. Manag.* 45, 329–344.

[26] Kumar M., Ravinder Kumar Sahdev S., Tawfik M.A., Noureddine E. (2023). Natural convective greenhouse vermicelli drying: thermo-environ-econo-kinetic analyses. Sustain. *Energy Technol. Assessments* 55, 103002. https://doi.org/10.1016/j.seta.2022.103002.

[27] Machala M.L., Tan F.L., Poletayev A., Khan M.I., Benson S.M. (2022). Overcoming barriers to solar dryer adoption and the promise of multi-seasonal use in India. *Energy for Sustainable Development* 68, 18–28. https://doi.org/10.1016/j.esd.2022.02.001.

[28] Ndukwu M.C., Ibeh M., Ekop I., Abada U., Etim P., Bennamoun L., Fidelis I.A., Simo-Tagne M., Gupta A. (2022). Analysis of the heat transfer coefficient, thermal effusivity and mathematical modelling of drying kinetics of a partitioned single pass low-cost solar drying of cocoyam chips with economic assessments. *Energies* 15 (12). https://doi.org/ 10.3390/en15124457.

[29] Ndukwu M.C., Bassey B.O., Fidelis I.A., Lamrani B., Bekkioui N., Wu H., Bennamoun L. et al. (2023). Energy and exergy analysis of solar dryer with triple air passage direction collector powered by a wind generator. *International Journal of Energy and Environmental Engineering* 14 (1), 63–77. https://doi.org/10.1007/s40095-022-00502-8.

[30] Rahman A., Farrok O., Haque M.M. (2022). Environmental impact of renewable energy source based electrical power plants: solar, wind, hydroelectric, biomass, geothermal, tidal, ocean, and osmotic. *Renew. Sustain. Energy Rev*. 161, 112279 https://doi.org/10.1016/j.rser.2022.112279

[31] Samimi-Akhijahani H., Arabhosseini A. (2018). Accelerating drying process of Tomato slices in a PV-assisted solar dryer using a sun tracking system. *Renew. Energy* 123, 428–438. https://doi.org/10.1016/j.renene.2018.02.056.

[32] Semple L, Carriveau R, Ting DSK. (2017). A techno-economic analysis of seasonal thermal energy storage for greenhouse applications. *Energy Build*, 154:175–87. https://doi.org/10.1016/j.enbuild.2017.08.065.

[33] Singh P., Shrivastava V., Kumar A. (2018). Recent developments in greenhouse solar drying: a review. Renew. Sustain. *Energy Rev.* 82 (3), 3250–3262.

[34] Tomar V., Tiwari G.N., Norton B. (2017). Solar dryers for tropical food preservation: thermophysics of crops, systems and components. *Sol. Energy* 154, 2–13.

[35] van Beveren PJM, Bontsema J., van Straten G., van Henten EJ. (2019). Optimal utilization of a boiler, combined heat and power installation, and heat buffers in horticultural greenhouses. *Comput Electron Agric*; 162:1035–48. https://doi.org/10.1016/ j.compag.2019.05.040.

[36] Zhang L., Xu P., Mao J., Tang X., Li Z., Shi J. (2015). A low cost seasonal solar soil heat storage system for greenhouse heating: Design and pilot study. *Appl Energy*; 156: 213–22. https://doi.org/10.1016/j.apenergy.2015.07.036.

[37] Yang T., Liu W., Kramer GJ., Sun Q. (2021). Seasonal thermal energy storage: A techno-economic literature review. *Renew Sustain Energy Rev*; 139:110732. https://doi.org/10.1016/j.rser.2021.110732.

DESIGN AND MECHANISM STUDY OF SEED FILLING ROOM WITH STAGGERED ORIENTED PLATES AND VIBRATION
/
交叉导流式振动种箱设计与机理研究

Zhiye MO[1)], Fangyuan LU*[1)], Mengqi ZHANG[1)], Chong TAO[1)], Bolong WANG[1)], Guohai ZHANG[1)], Xu MA*[2)]
[1)] School of Agricultural Engineering and Food Science, Shandong University of Technology, Zibo / China
[2)] College of Engineering, South China Agricultural University, Guangzhou / China
Tel: +8615288942032; E-mail: fangyuan-lu@foxmail.com; maxu1959@scan.edu.cn
Corresponding authors: Fangyuan Lu, Xu Ma
DOI: https://doi.org/10.35633/inmateh-72-58

Keywords: *seed filling room, staggered oriented plates, electromagnetic vibration, rice seeds*

ABSTRACT
Aiming at the existing rice mechanized seeding technology it is difficult to meet the hybrid rice low seeding volume precision seeding requirements. In this paper, based on the friction characteristics of rice seed and the theory of silo arching, the structure and parameters of seed filling room with staggered oriented plates and vibration in the quantitative seed supply device were designed. EDEM software was used to simulate the working process of the quantitative seed supply device, and it was determined that staggered oriented plates structure in the seed filling room combined with vibration could effectively prevent seed arching, thus improving the uniformity of seed supply. Finally, the results of the simulation analysis were verified by rice quantitative seed supply test. The results showed that the vibration could increase the seed supply frequency by 3.64% for large sowing weight of conventional rice and 5.52% for small sowing weight of hybrid rice. In addition, the analysis of the coefficient of variation of the seed supply frequency by quantitative seed supply devices showed that the vibration effect could increase the stability of seed supply device by 2.47 % for the conventional rice seed and 1.33 % for the hybrid rice seed, which increased the seed supply stability.

摘要
针对现有的水稻机械化播种技术难以满足杂交稻低播量精密播种要求的问题，本文基于稻种摩擦特性及料仓结拱理论，设计了定量供种装置内交叉导流式振动种箱结构参数。采用 EDEM 软件对定量供种装置的工作过程进行了离散元仿真模拟，确定了种箱内交叉导流结构结合振动作用能够有效防止种子结拱，从而提高供种均匀性。通过水稻定量供种试验，对仿真分析结果进行验证，得到振动作用可提高常规稻大播量供种频率 3.64%，提高杂交稻低播量供种频率 5.52%；通过定量供种装置供种频率变异系数分析，表明振动作用在常规稻供种时可提高供种稳定性 2.47%，杂交稻提高 1.33%，增加了供种稳定性。

INTRODUCTION
The varieties of rice grown in China are divided into conventional rice and hybrid rice, with more than 50% of the area planted in hybrid rice due to its remarkable high-yield characteristics. Among them, the planting technology of hybrid rice that obtains high yield through strong tillering ability requires less sparse planting 1-2 plants/hole (or seedling area) of seedling quantity *(Dan., 2020; Li et al., 2021; Song et al., 2023)*. To realize hybrid rice planting with fewer plants, it is necessary to improve the uniformity of sowing and adopt the precision sowing technology with low sowing rate *(Han et al., 2023; Ma et al., 2023; Song et al, .2023)*. However, it is difficult to realize precision seeding technology due to the growth characteristics of rice, that require seeding after germination, and the high water content of the seeds, which are easy to be broken by force *(Tian et al., 2022; Xia et al., 2023; Yang et al., 2023)*. The experiments showed that the quantitative seed supply performance of the two-stage and double-vibration rice seedling precision planter investigated in this paper has a significant impact on the realization of low seeding rate of hybrid rice.

Therefore, based on the theories of discrete element method, vibration mechanics and granular mechanics, this paper established a theoretical model of effective separation and uniform flow of rice seeds

Zhiye Mo, M.S. Stud. Eng; Fangyuan Lu, As. Ph.D. Eng.; Mengqi Zhang, M.S. Stud. Eng.; Chong Tao, M.S. Stud. Eng.; Bolong Wang, As. Ph.D. Eng.; Guohai Zhang, As. Ph.D. Eng., Xu MA, As. Ph.D. Eng.

under vibration, analyzed the dynamic characteristics of rice seeds under the action of seed filling room with staggered oriented plates and vibration, and studied the seed supply mechanism of the quantitative seed supply device. Through theoretical analysis combined with experimental research, the motion conditions of rice seed in seed supply device were analyzed, and the working parameters of seed supply device were optimized to improve the seed supply precision and sowing stability of hybrid rice.

MATERIAL AND METHODS

Main structure and principle

The rice seedling precision sowing quantitative seed supply device is shown in Figure.1. It is mainly composed of seed box, first seed oriented plate, electromagnetic vibration plate, second seed oriented plate, electromagnetic vibrator, adjustment door, seed cleaning brush, seed discharge wheel and other components. First seed oriented plate, vibration plate and second seed oriented plate combine to form the structure of the seed filling room with staggered oriented plates. The installation angle at which the seed oriented plates are mounted plays a crucial role in seed diversion.

The working principle of the device is that the rice seed forms a "Z-shaped" continuous seed flow in the filling area above the seed discharge wheel through the diversion effect of the three-layer staggered oriented structure, and at the same time, the funnel-shaped flow generated by the rice seeds during the seed supply process is alleviated under the action of the electromagnetic vibrator *(Lu., 2018; Yan et al., 2020; Garg et al., 2018)*. Then the seeds are filled into the groove of the seed discharge wheel in the filling area, and reach the outlet with the rotation of the seed discharge wheel. The excess rice seeds are blocked within the outlet through the flexible seed cleaning brush under the adjustment door, then the rice seeds discharge box filled in the groove of the seed discharge wheel are realized under the continuous and stable rotation of the seed discharge wheel. The structural parameters of the seed filling room with staggered oriented plates directly affect the operational performance of the seed supply mechanism.

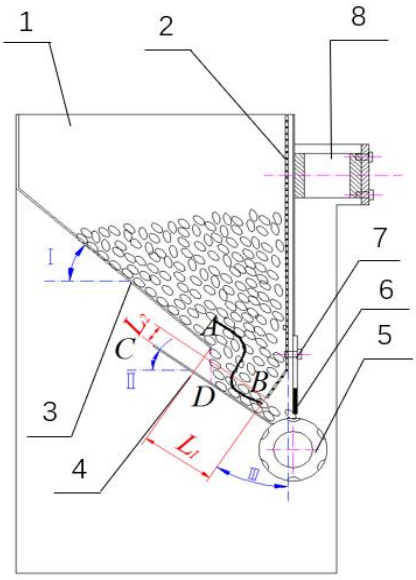

Fig. 1 - Structure diagram of quantitative seed feeding device

1 - Seed box; 2 - Electromagnetic vibration plate; 3 - First seed oriented plate; 4 - Second seed oriented plate; 5 - Seed row wheel; 6 - Cleaning brush;7 - Adjusting door; 8 - Electromagnetic vibrator

The installation angle and clearance distance of seed oriented plate play an important role in seed diversion. As shown in Figure 1, the installation angle of the first seed oriented plate is I, and the clearance distance between it and the vibration plate of the seed box is L_1; The installation angle of the second seed oriented plate is II, and the clearance distance between it and the vibration plate of the seed box is L_2. The lower inclination angle of vibration plate is III. According to the angle of repose of rice seeds and the friction coefficient *(Wang, 2010)* between seeds and the stainless steel plate (the selected material of the seed oriented plate), the inclination angle I was designed to be 45°. The inclination angle II is designed to be 37°, aiming at avoiding the excessive amount of seeds at the outlet port, and at the same time ensuring that the filling angle of the seed filling area can meet uniform and sufficient seeding of the row of seed wheels. The angle of inclination III needs to be greater than the angle of repose of the rice seeds and the static (sliding friction angle) between the seed oriented plate, so it is designed to be 45°.

Critical arching condition for rice seeds

In order to design the gap distance between the seed oriented plates, the motion characteristics of rice seeds in the seed filling room were analyzed with reference to the flow characteristics of the materials in the silo in the theory of silo unloading *(Dou, 2023)*. The flow patterns of materials in the seed filling room are mainly divided into two types: overall flow and central flow *(Sun, 2020; Ivan Kreft., 2023; Weng et al., 2023),* and central flow is the main cause of the arching phenomenon. Therefore, the structure of the seed oriented plates should be designed to avoid central flow of rice seeds in the seed box as much as possible and promote the overall flow of seeds. For this reason, taking the position between the second seed oriented plate and the vibration plate of the seed box as an example, the critical limit arching state of the seed at this position is analyzed, as shown in Figure 2.

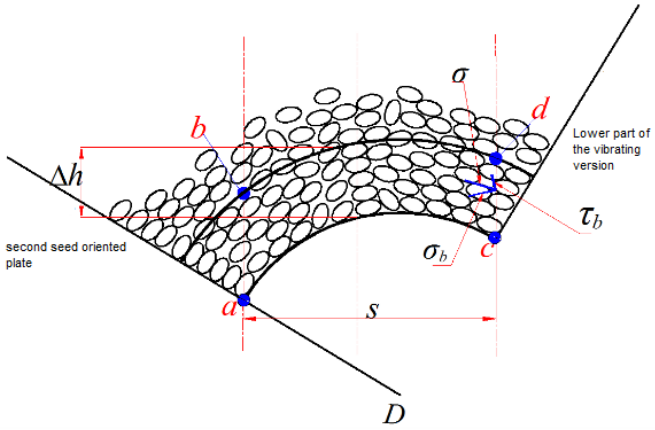

Fig. 2 - Situation of critical arch formed

Note: Create trajectory surfaces ac and bd on the knotted arch seed layer to describe the principal stresses in the knotted arch seed layer; Make vertical surfaces ab and cd upwards from points a and c perpendicular to the arched seed layer, and take the discrete unit cell abdc; Make the combined stress σ on the cd surface of the unit cell and decompose it into positive stress σ_b and tangential stress τ_b.

If A is the area of the long slit-type hole at the location of the arch between the seed oriented plates, L is the perimeter of the long slit-type hole, and the tangential stress τ_b on the cd surface is assumed to be approximately constant along the perimeter of the long slit-type hole *(Deng et al., 2013)*, then for the stabilized arching seed layer, the force balance equations are:

$$A\Delta h\rho g = L\Delta h\tau_b \quad (1)$$

where:

Δh- the height of the discrete unit abdc, [mm]; ρ- rice seed density, [kg/m^3]; g - acceleration of gravity, [m/s^2].

It is assumed that all the position points around the long slot holes are in the limit equilibrium state, and the stress Mohr's circle can be obtained:

$$\tau_b = \tau_0(1 + sin\,\phi) \quad (2)$$

where:

τ_0 - rice seed initial shear stress, [Pa]; φ- rice seed internal friction angle, [°].

For the seed box in this paper, the flow outlet section is rectangular, and the gap distance of the flow outlet is designed to be S (mm) and the length to be l (mm). According to Eq.1 and Eq.2, the gap of the flow outlet of this kind of box can be expressed as:

$$s = \frac{2\tau_0 l(1+sin\,\phi)}{l\rho g - 2\tau_0(1+sin\,\phi)} + d \quad (3)$$

where:

d - maximum size of rice seed, [mm].

Therefore, for the seed filling room with staggered oriented plates and vibration in this study, L_2 should satisfy:

$$L_2 > \frac{\tau_0(l-4-2d)(1+sin\varphi)+l\rho g(2+d)}{sin45°[2l\rho g-4\tau_0(1+sin\varphi)]} \quad (4)$$

Similarly, the above analytical method yields that L_1 should satisfy:

$$L_1 > \frac{\tau_0(l-4-2d)(1+sin\varphi)+l\rho g(2+d)}{sin53°[2log-4\tau_0(1+sin\varphi)]} \quad (5)$$

For the rice seeds, when the length of outlet hole l exceeds 600 mm, the critical arch gap S tends to be stable under the influence of outlet hole length l *(Dou, 2023).* Through the analysis of the above conditions, it is determined that L_1 is 36 mm and L_2 is 21 mm.

Discrete Element Simulation Parameter Design and Experimentations

The working process of the quantitative seed supply device was simulated and analyzed to determine if the design of seed filling room with staggered oriented plates and vibration meets the seed supply requirements of a vibratory flow type rice precision planter. The three-dimensional model of the quantitative seed supply device created by the EDEM software is shown in Figure 3, and the physical parameters and contact parameters *(Zhan et al., 2015)* of each material required for simulation are shown in Table 1. The rotation speed of the seeding wheel for hybrid rice seeds was set at 3.3 r/min, the simulation time was set at 30 s, and the movement type of the vibration plate of the seed box was sinusoidal translation with an amplitude of 0.015 mm and a frequency of 50 Hz. In order to fully study the flow state and distribution of rice seeds in different seed layer regions in the seed filling room, the rice seed particles in the seed filling room were stratified into 10 layers from the bottom to the top, as shown in Fig. 4.

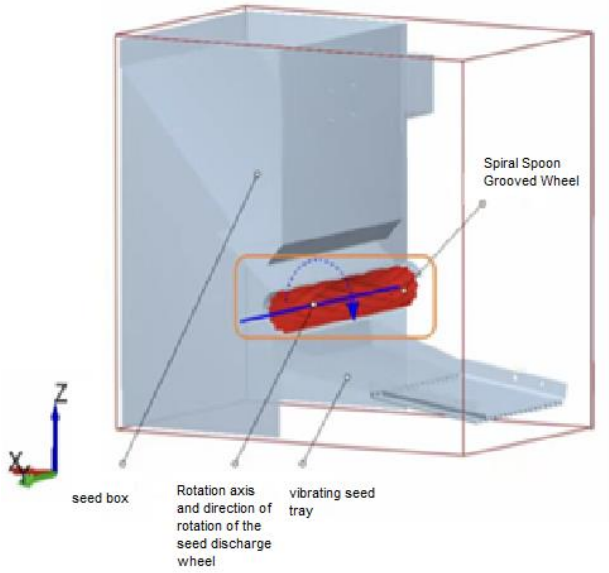

Fig. 3 - Discrete element model for quantitative seeding device

Table 1

Contact parameters between rice seeds and materials

Contact parameter	Numerical value
Rice seed and rice seed recovery coefficient	0.42
Static friction coefficient between rice seed and rice seed	0.354
Coefficient of rolling friction between rice and rice seed	0.016
Recovery coefficient of rice seed and stainless steel plate	0.52
Static friction coefficient between rice seed and stainless steel plate	0.52
Rolling friction coefficient between rice seed and stainless steel plate	0.01
Recovery coefficient of rice seed and nylon 1010 rod	0.5
Static friction coefficient between rice seed and nylon 1010 rod	0.5
Rolling friction coefficient between rice seed and nylon 1010 rod	0.02

Influence of electromagnetic vibration on the seed supply frequency

Under the same sowing condition, the vibration effect of the vibration plate was taken as the test factor, and two groups of seed supply process simulation tests were designed, one group was set with the vibration of the seed filling room, and the other group was set without the vibration.

The Settings of the remaining materials, contact parameters and motion parameters of the seeding wheel were the same, and the simulation time was 85 s (Figure 4). It can be seen from Fig. 4 that the area of the retention area generated by the vibration plate of the seed box with or without vibration is not much different, but the disconnection time of the seed layer with vibration is later than that when there is no vibration, and the vibration has a relieving effect on the "funnel flow".

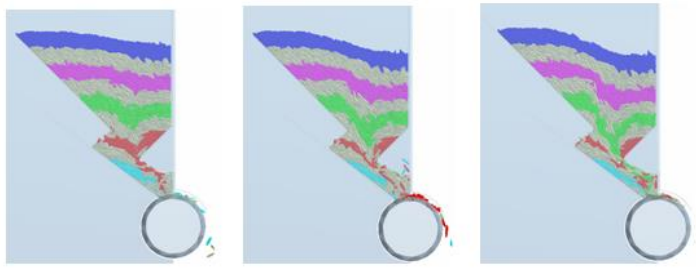

(a) vibration

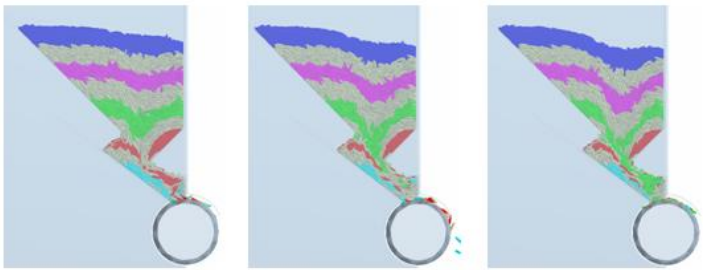

(b) vibration-free

Fig. 4 - Cross diversion seed box seeding process at small sowing quality

Note: Left, middle and right are simulation 10 s, 20 s and 30 s respectively

The variation of rice seed flow state in the seed filling room had a certain effect on the filling and discharging performance of the seed discharging wheel. As a second step, to further explore the role of the cross-conducting structure and the vibration effect on the seed flow state, the change in the number of rice seed particles in various layers was recorded according to the ten seed layers divided, and the change in the number of seeds within each seed layer over time was plotted, as shown in Fig. 5.

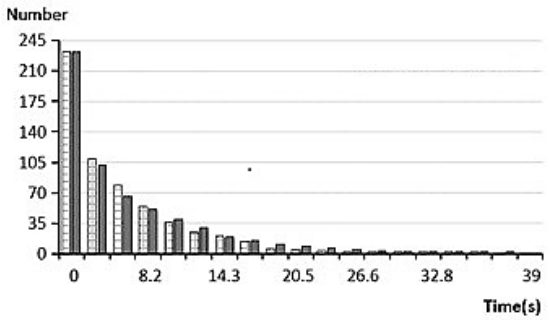

(a) Layer 1

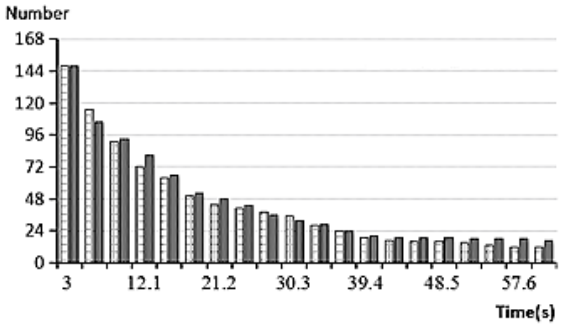

(b) Layer 2

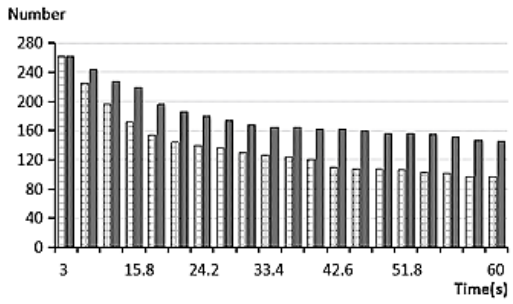

(c) Layer 3

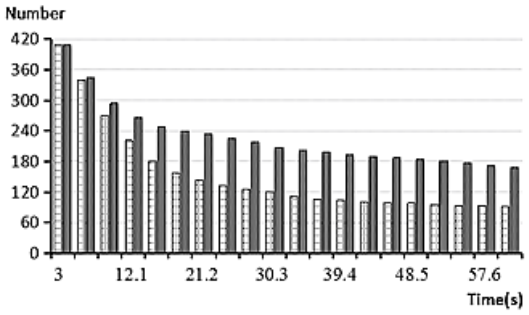

(d) Layer 4

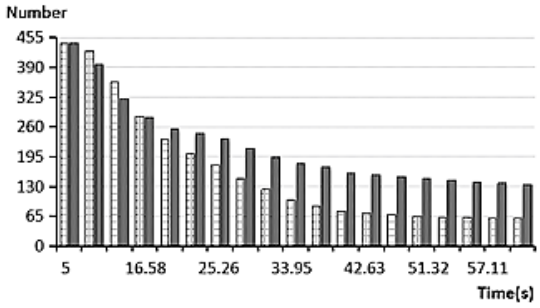

(e) Layer 5

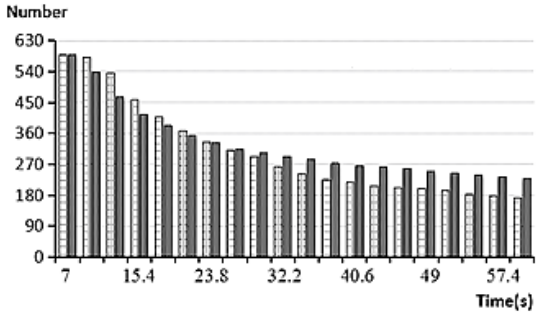

(f) Layer 6

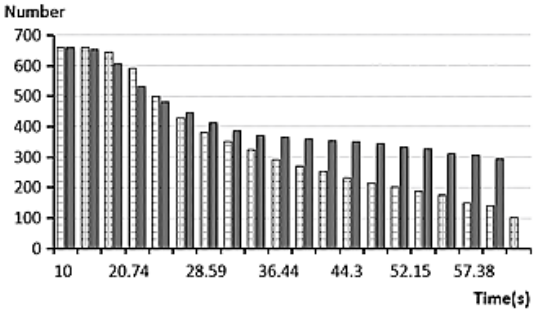

(g) Layer 7

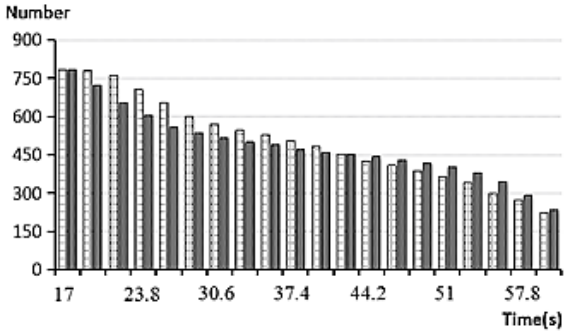

(h) Layer 8

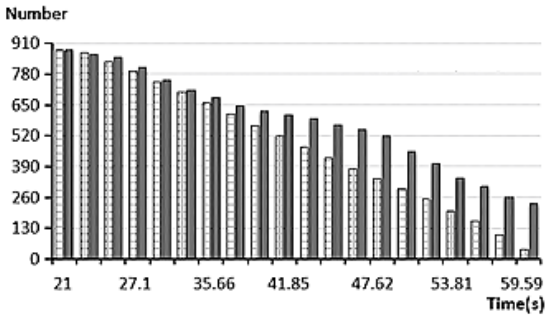

(i) Layer 9

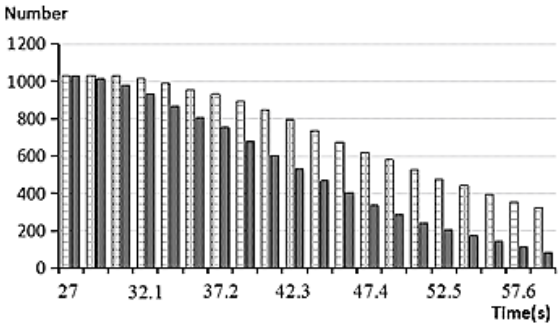

(j) Layer 10

Fig. 5 - Quantity Change chart of seeds in different seed layers varies with time

Note: :vibration :vibration-free

From Fig. 5 (a) (b) (f) (h), whether the vibration plate has vibration or not, it can be seen that the number of particles in the seed layer in the seed filling room is basically the same, indicating that the vibration does not have a significant role in influencing the time and rate of discharge of rice seeds from the 1st/2nd/6th/8th seed layer. It can be seen from Fig. 5 (c) (d) (e) (g) (i) that in the beginning, the number of rice seeds without vibration is basically the same as that with vibration, and the number of seed layers decreases faster in the subsequent vibration, indicating that the rate of rice seed discharge under vibration is higher than that without vibration.

Figure 5(j) shows the change in the number of rice seeds particles in the 10th seed layer, it can be seen the number of this layer decreases faster in the absence of vibration, which is due to the fact that with vibration this layer does not produce seed layer disconnection and the rice seeds are discharged later.

By analyzing the relationship between the number of rice seeds in various layers with time, it can be seen that the electromagnetic vibration effect increased the speed at which most of the seed layers were discharged. Further, the seed supply quality of the two sets of simulation tests was counted and the seed supply quality versus time curves were plotted for comparison in Fig. 6.

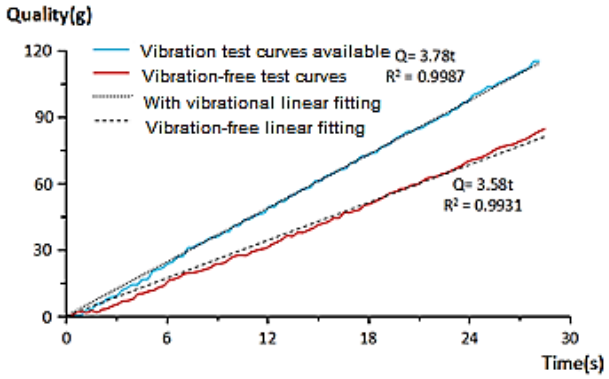

Fig. 6 - Feeding weight comparison chart of hybrid rice with or without vibration

By linear fitting of the two curves in Fig. 6, the fitted equation for the seed supply quality of the seed discharging wheel when the vibration plate of the seed filling room has vibration was obtained as:

$$Q_1 = 3.78t \quad (6)$$

where: Q_1- quality of seed supply with vibration, [g]; t- suppling time, [s].

The linear fit above is $R^2_1 = 0.9987$. Seed feeding quality of seeding discharging wheel without vibration was obtained as:

$$Q_2 = 3.58t \quad (7)$$

where: Q_2 - quality of seed supply without vibration, [g].

The linear fit above is R^2_2=0.9931. The linear fit is close to 1 for both conditions. The linear fitting degree of seed supply under vibration is higher than that without vibration which indicates that the seed supply of spiral spoon groove wheel is stable with vibration action. The feeding frequency was 3.78 g/s with vibration and 3.58 g/s without vibration, indicating that electromagnetic vibration could increase the seeding frequency of hybrid rice by about 5.59%.

The same seed efficiency analysis was carried out for conventional rice varieties according to the above method. When the vibration plate of the seed filling room in the quantitative seed supply device has vibration, the seed supply frequency of the seed discharge wheel is 10.177 g/s, and the seed supply frequency is 9.851 g/s without vibration. The results showed that the electromagnetic vibration of the quantitative seed supply device promoted the seed suppling performance of the seed discharging wheel, increased the seed feeding frequency of the device by 3.31%. According to two sets of quantitative seed supply simulation tests, the same amount of rice seed was completely discharged faster with vibration than without vibration, indicating that the seed supply efficiency of the spiral spoon type grooved wheel is higher under vibration.

RESULTS

Test materials and methods

In order to verify the accuracy of the simulation analysis, the rice quantitative seed supply test was designed. The quantitative seed supply device developed was used in the test, as shown in Figure 7.

Fig. 7 - Quantitative-seed supply device

The rice varieties used were: the hybrid rice was Peiza Taifeng, the water content of rice seed was about 27.5%, the weight of 1,000 grains was 28.20 g, and the conventional rice was Huahang 38, the water content of rice seed was about 27.38%, the weight of 1,000 grains was 27.59 g.

The vibration effect of the vibration plate of the seed box was used as the test factor. The electromagnetic vibrator was turned on and adjusted to produce an amplitude of 0.015 mm on the vibration plate there was vibration, and turned off when there was no vibration. Quantitative comparative experiments on the seed supply of conventional rice and hybrid rice by the seed supply mechanism are conducted separately.

The variation coefficient of seed frequency of seed discharge wheel was used as the evaluation index of seed suppling stability of quantitative seed supplying device, and its statistical method was as follows: after stable operation of the mechanism, seed supply tests with and without vibration were carried out under the same sowing amount (Figure 8). The mass of rice seeds discharged from the seed discharge wheel in every 5 s was respectively obtained and weighed using an electronic scale with an accuracy of 0.01 g (Figure 9). Repeated the above operation 5 times and recorded, and then the coefficient of variation of seed discharge frequency was obtained.

Fig. 8 - Seed supply trials

Fig. 9 - Weighing seeds on electronic scales

The percentage increase of seed supply frequency with vibration compared with that without vibration under the same sowing quantity was used as the index to evaluate the increase of seed supply rate by vibration effect. The statistical method was as follows: The mass of rice seeds discharged by the rotation of the seed discharge wheel for 60 s was obtained, and then the average seed supply frequency of the seed discharge wheel was calculated. The test was repeated 6 times for each group to obtain the average value, and the increase rate of the seed discharge rate with vibration was calculated compared with that without vibration, as shown in Table 2.

Test results and analysis

Table 2

Feeding frequency comparison test result of quantitative-seeds supply device

	Regular rice planting		Hybrid rice supply	
	Have vibration	Vibration-free	Have vibration	Vibration-free
Frequency of seeding rotation / (g/s)	9.96	10.01	4.73	4.46
	9.67	9.92	4.35	4.38
	10.21	9.38	4.49	4.31
	9.89	9.83	4.66	4.02
	10.13	8.96	4.71	4.59
Average feeding frequency / (g/s)	9.97	9.62	4.59	4.35
Coefficient of variation / %	2.12	4.59	3.56	4.89
Vibration feed increase rate / %	3.64		5.52	

From the results of the frequency of seed supply in Table 2, the vibration effect can increase the seed supply frequency of the quantitative seed supply device by 3.64% in the case of conventional rice and 5.52% in the case of hybrid rice. Compared with the simulation results, the relative errors of the simulation are 9.07% and 2.00% respectively, indicating that the simulation results are highly accurate. Under the condition of vibration or not, the variation coefficient of seed frequency was lower than that of seed quantity, indicating that the rice seed quantity per unit time was more stable. The stability of conventional rice and hybrid rice could be improved by 2.47% and 1.33% after the vibration effect was added to the vibration plate of seed filling room, which indicated that the electromagnetic vibration effect of vibration plate of seed filling room had more obvious effect on the stability of conventional rice.

CONCLUSIONS

(1) The quantitative seed supply device adopts the structural design of staggered oriented plates and vibration seed filling room. Through the condition analysis, the gap distance between first oriented plate and second oriented plate and the vibration plate of the seed filling room respectively was determined.

(2) The working process of the seed supply device with and without vibration was simulated, and it was obtained that the electromagnetic vibration of the vibration plate could improve the frequency and stability of seed supply. It is verified that the cross-flow structure in the seed box makes the rice seeds form a "Z-shaped" continuous seed flow, which can provide a continuous and stable seed filling volume for the seed discharge wheel.

(3) The seed supply frequency test was conducted on the quantitative seed supply mechanism to verify the conclusions of the quantitative seed supply simulation analysis. Separate quantitative seed supply tests were conducted for small sowing weight of conventional rice and larger sowing weight of hybrid rice. The results showed that the electromagnetic vibration increased the seed supply frequency of conventional rice by 3.64% and that of hybrid rice by 5.52%. Analysis of the coefficient of variation of the seed supply frequency of the seed discharge wheel indicated that the vibration improved the stability of the seed supply device by 2.47% for conventional rice and by 1.33% for low seeding rates, increasing the stability of seed supply.

REFERENCES

[1] Dou, J., (2023). Research on particle flow behavior and structural optimization in a hopper based on EDEM (基于 EDEM 的料斗内颗粒流动行为及其结构优化研究). *Wuhan University of Science and Technology,* Hubei/China.

[2] Deng, W., Li, Z., Qiu, X., Wang, W., Wu, X., Zheng, D., (2013). The Research of Rice Liquidity and Arching Based on Crossed Diversion Seed-box (基于交叉导流式种箱的稻种流动性及结拱研究). *Agricultural Mechanization Research*, Vol. 35, pp. 145-149, Heilongjiang/China.

[3] Garg, V., Mallick, S., García-Trinanes, P., (2018). An investigation into the flowability of fine powders used in pharmaceutical industries. *Powder Technology*, Vol. 336, pp. 375-382, Switzerland.

[4] Han, Q., Bing, X., Zhi, J., (2023). Study on influencing factors of hole-filling performance of rice precision direct seed-metering device with hole ejection. *Biosystems Engineering*, Vol. 233, pp. 76-92. United States.

[5] Ivan, Kreft., Aleksandra, Golob., Mateja, Germ., (2023). A Crop of High Nutritional Quality and Health Maintenance Value: The Importance of Tartary Buckwheat Breeding. *Agriculture*, Vol. 13, pp. 17-83, Switzerland.

[6] Jian, S., Yong, T., Hong, H., (2023). Molecular Breeding of Zheyou810, an Indica-Japonica Hybrid Rice Variety with Superior Quality and High Yield. *Agriculture,* Vol. 13, pp. 1807, Switzerland.

[7] Li, Z., Zou, W., Zhang, P., (2021). Effect of Seeding Density and Method on Tillering Characteristics of Mechanical Transplanting in indica Rice (播种密度和方式对机插籼稻分蘖成穗的影响). *Journal of Nuclear Agronomy*, Vol. 35, pp. 722-736, Beijing/China.

[8] Lu, F., (2018). Working mechanism analysis and experimental research on two-stage double vibration rice precision seeder (两级双振动式水稻精密播种器机理分析与试验研究). *South China Agricultural University*, Guangzhou/China.

[9] Ma, X., Chen, L., Li, Z., (2023). Furrow opener for the precision drilling nursing seedlings of hybrid rice (杂交稻精密条播育秧底土开沟装置设计与试验). *Transactions of the Chinese Society of Agricultural Engineering,* Vol. 39, pp. 1-14, Beijing/China.

[10] Sun, D., (2020). Study on Effects of Inserts in Hopper on Powder Discharge (料仓改流体对粉体下料影响的研究). *East China University of Science and Technology*, Shanghai/China.

[11] Shan, S., (2022). Physiological Mechanisms for the High Yield in Double-Season Hybrid Rice Machine-Transplanted with Less Seedlings per Hill (少本密植机插双季杂交稻高产生理机制研究). *Hunan Agricultural University*, Hunan/China.

[12] Song, W., Wan, Y., Zhou, B., (2023). Design and Experiment of combined cavity-type precision hole-drop seed-metering device for rice. *INMATEH Agricultural Engineering,* Vol. 71, pp. 25-43, Romania.

[13] Tian, L., Ding, Z., Su, Z., (2022). Design and Experiment of rotary precision hill direct seed-metering device for rice. *INMATEH Agricultural Engineering,* Vol. 66, pp. 311-320, Romania.

[14] Wen, C., Jin, H., Cai, Y.,(2023). Current Situation and Future Development Direction of Soil Covering and Compacting Technology under Precision Seeding Conditions in China. *Applied Sciences,* Vol. 13, pp. 6586, United States.

[15] Wang, C., (2010). Research of Theory and Experiment on Air Suction Cylinder Device for Tray Nursing Seedling of Super-Rice (气吸滚筒式超级稻育秧播种器的基本理论及试验研究). *Jilin University,* Jilin/China.

[16] Weng, X., Tan, D., Wang, G., (2023). CFD Simulation and Optimization of the Leaf Collecting Mechanism for the Riding-Type Tea Plucking Machine. *Agriculture*, Vol. 13, pp. 946, Switzerland

[17] Xia, Q., Zhang, W., Qi, B., (2023). Design and Experimental Study on a New Horizontal Rotary Precision Seed Metering Device for Hybrid Rice, *Agriculture*, Vol.13, pp.158, Switzerland.

[18] Yan, B., Gao, N., Meng, Z., (2020). Design and test of a gravity-assisted vacuum seed-meter for maize. *IOP Conference Series Earth and Environmental Science*, Vol. 512, pp. 012-093, Great Britain.

[19] Zhan, Z., Ya, F., Jian, J., (2015). Monitoring method of rice seeds mass in vibrating tray for vacuum-panel precision seeder. *Computers and Electronics in Agriculture*, Vol. 114, pp. 25-31, Great Britain.

TECHNICAL SOLUTIONS FOR BIOMASS ESTIMATION ACCORDING TO THE CONCEPT OF AQUACULTURE 4.0
/
SOLUȚII TEHNICE PENTRU ESTIMAREA BIOMASEI CONFORM CONCEPTULUI DE ACVACULTURĂ 4.0

Dan CUJBESCU[1)], Dragoș DUMITRU*[1)], Iulian VOICEA*[1)], Cătălin PERSU[1)], Iuliana GĂGEANU[1)], Alexandru IONESCU[1)], Ana Maria TĂBĂRAȘU[1)], Dragoș ANGHELACHE[1)]
National Institute of Research – Development for Machines and Installations Designed to Agriculture and Food Industry, Romania
Tel: 0752038668; E-mail: dumitrudragos.nicolae@gmail.com; Tel: 0752161780; E-mail: voicea_iulian@yahoo.com
DOI: https://doi.org/10.35633/inmateh-72-59

Keywords: *aquaculture; biomass estimation; aquatic environment; sensors*

ABSTRACT
Aquaculture, as a dynamic field, undergoes continuous evolution requiring continuous improvements in efficiency and new research efforts. Estimating fish biomass is an essential practice in the field of precision aquaculture, obtaining periodic information on fish biomass has been identified as an urgent need, considering the objective of optimizing daily feeding, controlling fish density and finally determining the optimal timing of harvesting. Conventional weighing methods, which often rely on manual procedures, have inherent challenges. Manual weighing processes are labor-intensive, requiring substantial time and human resources. Furthermore, manual handling of fish during weighing procedures induces considerable stress on aquatic organisms, potentially compromising their health and welfare. Consequently, there is a pressing need in the aquaculture industry to explore alternative weighing techniques that alleviate stress levels while increasing operational efficiency. In response to these challenges, contemporary research efforts have increasingly focused on the development of noninvasive and automated weighing methodologies. These innovations aim to simplify the weighing process, minimize human intervention and reduce the level of stress experienced by the fish population. However, estimating fish biomass without human intervention presents significant challenges because fish are sensitive and move freely in an environment where visibility, lighting, and stability are difficult to control. The paper analyzes technological solutions for biomass estimation according to the concept of Aquaculture 4.0.

REZUMAT
Acvacultura, ca domeniu dinamic, suferă o evoluție continuă, necesitând îmbunătățiri continue ale eficienței și eforturi noi de cercetare. Estimarea biomasei piscicole este o practică esențială în domeniul acvaculturii de precizie, obținerea de informații periodice asupra biomasei piscicole a fost identificată ca o necesitate urgentă, având în vedere obiectivul de optimizare a hrănirii zilnice, controlul densității peștilor și, în final, determinarea momentului optim de recoltare. Metodele convenționale de cântărire, care se bazează adesea pe proceduri manuale, prezintă provocări inerente. Procesele manuale de cântărire necesită multă muncă, necesită timp și resurse umane substanțiale. Mai mult, manipularea manuală a peștilor în timpul procedurilor de cântărire induce un stres considerabil asupra organismelor acvatice, putând compromite sănătatea și bunăstarea acestora. În consecință, există o nevoie presantă în industria acvaculturii de a explora tehnici alternative de cântărire care atenuează nivelurile de stres, sporind în același timp eficiența operațională. Ca răspuns la aceste provocări, eforturile de cercetare contemporane s-au concentrat din ce în ce mai mult pe dezvoltarea metodologiilor de cântărire neinvazive și automate. Aceste inovații urmăresc să simplifice procesul de cântărire, să minimizeze intervenția umană și să reducă nivelul de stres experimentat de populația de pești. Cu toate acestea, estimarea biomasei de pești fără intervenția umană prezintă provocări semnificative, deoarece peștii sunt sensibili și se mișcă liber într-un mediu în care vizibilitatea, iluminarea și stabilitatea sunt greu de controlat. Lucrarea discută soluții tehnologice pentru estimarea biomasei conform conceptului de Acvacultură 4.0.

INTRODUCTION
Aquaculture consists of a set of activities, knowledge and techniques for growing plants and some species of aquatic animals, having a particular importance in economic development and food production.

Aquaculture is experiencing rapid growth globally, driven by two significant factors: the persistent increase in demand for seafood and the depletion of fish stocks in the world's oceans. This surge in aquaculture activity underscores the urgent need for sustainable practices to avoid the pitfalls encountered in the history of European agriculture and fisheries sectors. (*FAO, 2018; Paolacci et al., 2022; Varadi et al., 2009).*

To date, traditional methodologies for estimating fish biomass have predominantly relied on manual sampling techniques. However, these approaches are frequently invasive, time-consuming, and require substantial human resources. Consequently, there exists a compelling and pressing necessity to devise noninvasive, swift, and cost-effective alternatives for this estimation process. Emerging technologies such as Machine Vision, acoustics, ambient DNA, among others, offer promising avenues for the creation of non-intrusive, expedited, and economically viable methods to estimate fish biomass in real-world scenarios (*Henriksson et al., 2021; Orduna et al., 2023; Berckmans, 2017; Yule et al., 2013; Cowley and Whitfield, 2002*).

Experimental research has underscored the pivotal role of information technologies, particularly advanced sensors and communication technologies, in expediting the evolution of new tools and methodologies aimed at enhancing the efficiency of fish biomass estimation. Nonetheless, as the demands of intensive aquaculture continue to escalate, there arises a compelling need to enhance not only the accuracy but also the intelligence level of these methodologies. In this context, fostering close collaboration between fisheries experts and engineers emerges as a fundamental approach to refining the accuracy and intelligence level of fish biomass estimation methods, as delineated by the aforementioned technologies (*Alver et al., 2005; Harvey et L., 2001; Li et al., 2019 ; Davison et al., 2015 ; Hicks et al., 2015; Marks and Klomp, 2003*).

Fish biomass, a fundamental metric in aquatic industries and fisheries management, represents the total weight of fish within a given water area. It serves as a crucial indicator for assessing the health and productivity of aquatic ecosystems, informing aquaculture practices, and guiding fisheries management decisions. The estimation of fish biomass relies on quantitative methods that integrate population counts with average weight measurements, offering valuable insights into fish populations' size, structure, and dynamics (*Johnston et al., 2023; Mihneva et al., 2023; Debroy and Seban, 2022; Cowx, 1983; Doi et al., 2015*).

Fish biomass estimation is a critical component of current aquaculture methods, covering the rigorous measurement of counting, weight, and length from the time of fry introduction until the final sale of fish. Fish biomass is a reliable metric that provides valuable information about both fish and the environment. However, calculating biomass in highly populated and protected aquatic habitats is an unavoidable and daunting challenge in modern aquaculture undertakings (*Abinaya et al., 2022; Bjerkeng et al., 1991; Proud et al., 2019; Lee et al, 2012; Shepard et al., 2015; Emmrich et al., 2012; Ríha et al., 2023; Zhang and Megrey, 2010).*

Fish biomass measurement serves as a cornerstone for evaluating recruitment rates and discerning the impacts of both fisheries management practices and environmental variables on marine systems. The dynamic nature of biomass is evident through its temporal variability, which can undergo substantial fluctuations over relatively short periods. Notably, analyses conducted by Assessment Working Groups (AWGs) under the purview of the International Council for the Exploration of the Sea (ICES) reveal significant shifts in the biomass of key species. Over the past two decades, the biomass of herring has exhibited a variation factor of 1.4, while for sprat and cod, this factor stands at 4.4, underscoring the dynamic nature of fish stocks. Nevertheless, when considering the broader context of long-term ecosystem dynamics, a mere 20-year interval appears minuscule. Climatic trends, pivotal in shaping marine environments, operate across temporal scales spanning centuries. Thus, to unravel the underlying causes of fluctuations in fish stocks, biomass estimates encompassing more extensive temporal frameworks are imperative. In this regard, extending the analysis horizon beyond short-term fluctuations becomes essential for elucidating the intricate interplay between environmental factors and the sustainability of marine ecosystems (*Thurow, 1997; Wilson et al., 2018; Chen and Andrew, 1998; Ault et al., 2018; St. John et al., 1990; Block et al., 2019; Yin et al., 2022; Lopez et al., 2016; Yulianto et al., 2015; Bianchi et al., 2021; Hossain et al., 2018; Lian et al., 2018*).

Understanding the distribution patterns of species stands as a fundamental aspect in unraveling their ecological dynamics and assessing the risks of extinction, thereby informing conservation efforts aimed at safeguarding populations. However, obtaining precise estimates of species distribution poses a significant challenge, particularly in environments characterized by intricate microhabitat topography and dense vegetation, as commonly encountered in aquatic systems. In recent years, the emergence of environmental DNA (eDNA) analysis has revolutionized the documentation of aquatic vertebrate species distributions. By detecting minute, species-specific DNA fragments suspended in the water column, eDNA offers a promising avenue to enhance the accuracy and cost-effectiveness of distribution surveys while facilitating the detection

of rare or invasive species. Noteworthy examples include the utilization of eDNA techniques to confirm the presence of bullfrog tadpoles, silver and bighead carp, as well as various frog and salamander species across diverse aquatic habitats. The application of eDNA methodologies not only broadens our understanding of species distributions but also presents a powerful tool for informing conservation strategies and ecosystem management practices in aquatic environments (*Takahara et al., 2012; Wanghe et al., 2024; Kindong et al., 2020; Murakami et al., 2020; Radinger et al, 2023; Doi et al., 2017; Kim et al., 2018*).

Fish biomass estimation without human involvement presents considerable issues since they are sensitive and move freely in an environment with challenging control over sight, lighting, and stability. The paper analyzes technological solutions for biomass estimation according to the concept of Aquaculture 4.0.

MATERIALS AND METHODS

In prevailing biomass estimation methodologies, routine sampling is conducted to determine the average weight of fish inhabiting ponds, while the quantity of extant fish is typically ascertained through a comparative analysis between the initial population count and the number of deceased fish. Hence, the estimation of fish biomass involves the multiplication of the average weight by this quantity. Nevertheless, manual sampling methodologies pose risks of physical harm or significant stress to fish, thereby impacting their well-being and developmental trajectory. Moreover, manual sampling processes typically entail substantial time investments and are associated with a labor error margin ranging between 15-25%, thereby presenting challenges in accurately gauging fish weight via noninvasive means. Additionally, while the enumeration of individuals under ordinary circumstances is feasible, quantification becomes problematic in scenarios of extensive mortality, theft, or predation incidents. The translation of recorded daily feed intake into fish biomass through the feed conversion ratio (FCR) may lack sufficient precision. Consequently, there is an imperative to adopt noninvasive, expeditious, and cost-effective approaches for fish biomass estimation to address the intensive demands prevalent in aquaculture operations (*Li et al, 2019; Mahon, 1990*).

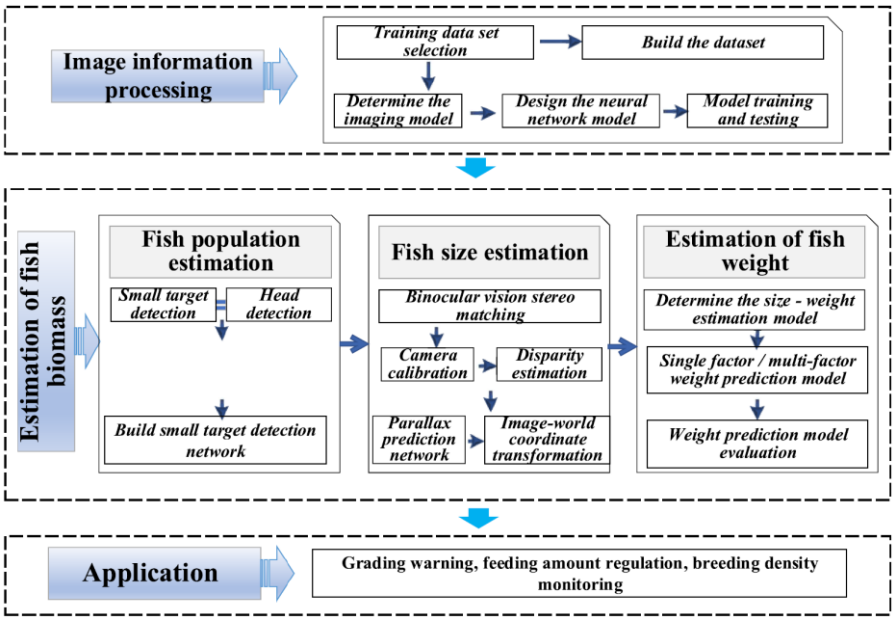

Fig. 1 - Stages of vision-based biomass estimation (*Li et al, 2019*)

Fish mass estimation holds paramount significance for farmers as it furnishes crucial fish biomass information essential for optimizing daily feeding practices, controlling stocking densities, and determining the optimal harvest time. However, the mass of fish tail fins contributes negligibly to the total body mass. Moreover, the tail fins of free-swimming fish commonly exhibit deformities or bending, thereby introducing measurement errors and consequently impairing the accuracy of mass predictions by computer vision systems. To address this challenge, a novel non-supervised method for fish tail fin removal has been proposed to enhance the development of mass prediction models based on ventral geometrical features sans the tail fin. Initially, the automated removal of fish tail fins was achieved through the utilization of the Cartesian coordinate system coupled with image processing techniques. Subsequently, distinct features were extracted from fish images both with and without the tail fin. Finally, the correlational relationship between fish mass and the extracted

features was evaluated using Partial Least Square (PLS) analysis. In this study, tail fins were systematically eliminated, and the mass estimation model based on area and area square exhibited superior performance on the test dataset, yielding a high coefficient of determination (R^2) of 0.991, a root mean square error (RMSE) of 7.10 g, a mean absolute error (MAE) of 5.36 g, and a maximum relative error (MaxRE) of 8.46% *(Hao et al., 2022*).

Length serves as a fundamental metric in the realm of aquaculture engineering, providing crucial insights into fish growth and facilitating effective monitoring protocols. In the intricate process of fish breeding, the segregation of fish based on size is imperative to optimize growth conditions and ensure favorable developmental trajectories. Furthermore, as fish reach maturity, size-based grading becomes essential to align with market demands and enhance economic value. The size of fish within breeding ponds not only serves as a barometer for growth monitoring but also aids in predicting factors such as sex and age, pivotal for management practices. Fish quality, intrinsically linked to size, underscores the significance of accurate length measurements in assessing overall product value. Traditional manual measurement techniques, however, pose inherent challenges, including the risk of fish injury or mortality and susceptibility to subjective biases. Addressing these limitations, machine vision systems emerge as a transformative solution, offering rapid, precise, non-invasive, and cost-effective approaches to fish length determination. In aquatic environments, where fish are in constant motion, acquiring accurate size measurements without physical contact presents unique challenges. Machine vision systems surmount these obstacles, providing a viable means to capture fish length data in real-time, thus revolutionizing size assessment methodologies in aquaculture settings. By harnessing advanced technology, the integration of machine vision systems heralds a new era of efficiency and accuracy in fish length measurement, facilitating informed decision-making and optimizing aquaculture practices (*Bravata et al., 2020; Dutta et al., 2016; Sture et al., 2016; Zhou et al, 2023*).

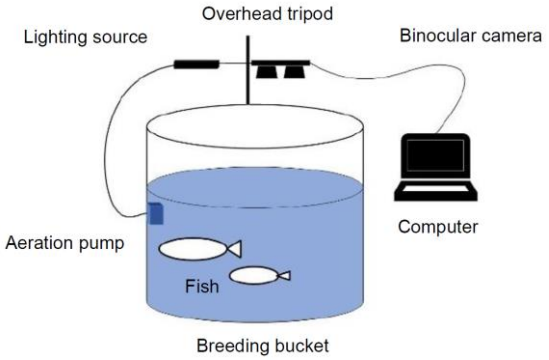

Fig. 2 - Experimental stand scheme (*Zhou et al, 2023*)

Utilizing binocular cameras equipped to capture both RGB and depth images, the acquisition of RGB-D data from fish specimens was facilitated, laying the groundwork for comprehensive analysis. Subsequently, the RGB images undergo selective segmentation employing the contrast-adaptive Grab Cut algorithm, thereby delineating distinct features and enhancing accuracy in subsequent processing stages. To discern the structural state of the fish, a skeleton extraction algorithm was deployed, designed to accommodate specimens with intricate, curved anatomies. Addressing inherent challenges associated with underwater imaging, the study meticulously analyzed and corrected errors stemming from water refraction, ensuring fidelity in measurement outcomes. Leveraging the RGB image data, optimal measurement points were identified and converted into precise 3D spatial coordinates, thereby facilitating accurate determination of fish length. The experimental results showed that the mean relative percentage error for fish length measurement was 0.9% (*Zhou et al, 2023*).

Employing advanced computer vision image processing techniques, an optimal model was developed to accurately evaluate the body weight of Asian sea bass, both with and without fins. Over the course of one month, image data of 25 randomly selected fish were systematically collected on a weekly basis. Subsequently, the collected data underwent a meticulous partitioning process, wherein a 40-60% split-test was employed. Specifically, 40% of the data, comprising 10 fish (100 images), served as training data, while the remaining 60% (15 fish; 150 images) constituted the out-samples or validation dataset. To initiate the experimental phase, a total of one hundred Asian sea bass, averaging 30 g in weight, were procured from a private fish farm and housed in two 1,000-L fiberglass tanks, accommodating 50 fish per tank. The fish were

subjected to a carefully regulated feeding regimen, receiving floating pellet feed with a minimum protein content of 35% twice daily (at 0800 h and 1700 h) until satiation. A flow-through water system was employed to maintain optimal environmental conditions within the tanks, ensuring the well-being of the fish. Each tank was equipped with three air stones to facilitate adequate oxygenation, while water quality parameters including dissolved oxygen (DO), water temperature, pH, total ammonia-nitrogen (TAN), and nitrite-nitrogen (NO_2-N) were monitored and maintained within recommended ranges. Specifically, dissolved oxygen levels, water temperature, pH, total ammonia-nitrogen, and nitrite-nitrogen were maintained above 4 mg/L, within the range of 26 - 32 degrees Celsius, within 7.5 - 8.5, less than 1 mg/L, and less than 1 mg/L, respectively. To ensure the acclimation of the fish to their new environment, feeding and monitoring protocols were rigorously implemented until the average fish weight reached the desired range of 80 to 100 g, signifying readiness for subsequent experimental procedures (*Jongjaraunsuk and Taparhudee, 2021*).

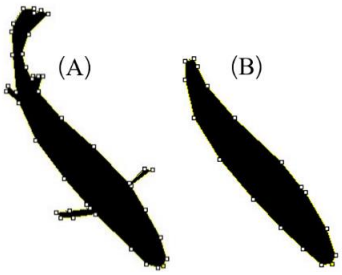

Fig. 3 - Experimental fish image (*Jongjaraunsuk and Taparhudee, 2021*)
A - with fins; B - without fins

The comparative analysis of results derived from the whole-body images and those excluding fins was conducted utilizing various statistical metrics. Specifically, the average coefficient of determination obtained from the validation dataset, comprised of 15 fish (150 images) per test ($N_{150}R^2$), and the coefficient of determination derived from the comprehensive validation dataset, consisting of 60 fish (600 images) from all tests ($N_{600}R^2$), were scrutinized using mathematical models such as RMSE (Root Mean Square Error), MAE (Mean Absolute Error), MARE (Mean Absolute Relative Error), MXAE (Maximum Absolute Error), and MXRE (Maximum Relative Error). To evaluate the significance of the mean difference between the datasets, an independent sample T-test was performed at a 95% confidence level. Statistical analysis was executed using the IBM SPSS Statistics Base 24.0 software suite for Windows, facilitating robust and comprehensive examination of the data (*Jongjaraunsuk and Taparhudee, 2021*).

Previous research has underscored the efficacy of linear mathematical models in predicting fish weight with greater accuracy and fewer errors compared to power or polynomial models. This finding has been demonstrated across various species including grey mullet (Mugill cephalus), St. Peter's fish (Sarotherodon galilaeus), common carp (Cyprinus carpio), and jade perch (Scortum barcoo). However, for large fish with an average size exceeding 1,000 g under aquaculture conditions, exploring alternative mathematical models may be warranted. For instance, in the case of sea bass ranging from 250 to 2.800 g, the utilization of a power model has been proposed in previous studies (*Konovalov et al., 2018; Viazzi et al., 2015; Zion 2012*).

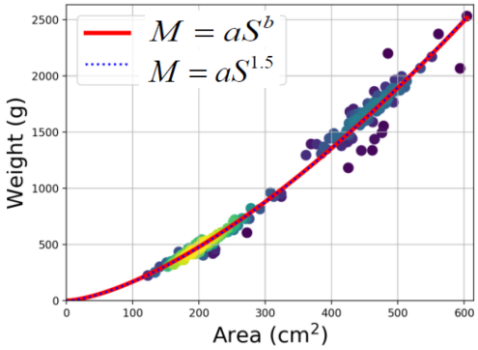

Fig. 4 - Correlation of measured fish weight (g) and manually segmented fish body image area (cm^2) (*Konovalov et al., 2018*)

Nevertheless, when comparing image formats encompassing fish with and without fins, linear modeling has been deemed sufficient in capturing the variability in fish weight accurately.

Acoustic systems, such as echo sonars or multibeam sonars, offer distinct advantages over optical methods in underwater environments. Unlike optical systems, which rely on reflected light and are subject to limitations in light level and visibility, acoustic systems produce images based on reflected sound. The emergence of high-frequency multibeam sonars, often referred to as "acoustic cameras," represents a relatively recent technological innovation initially employed for structural surveillance and inspection in marine environments. In a study conducted off the coast of French Guiana, a BlueView P900-130 acoustic camera was deployed in rocky marine habitats to assess the total abundance, size structure, and spatial distribution of a demersal fish population. The study evaluated the relevance of utilizing an acoustic camera for achieving these objectives by comparing acoustic data with those obtained from traditional fishing surveys (*Artero et al., 2021; Braga et al., 2022; Graham et al., 2004; Kim et al., 2005*).

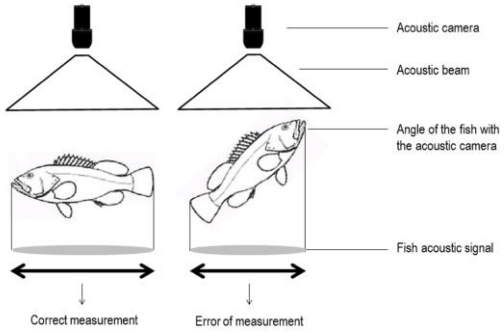

Fig. 5 - Scheme for fish measurement error using an acoustic camera (*Artero et al., 2021*)

Acoustic and computer vision techniques converge to pioneer an automated process for estimating the biomass of tuna during transfers. This innovative approach integrates a side scan sonar operating at 200 kHz and a stereo camera strategically positioned to capture the ventral perspective of the fish. These instruments serve as the primary acquisition equipment, meticulously designed to gather comprehensive data during transfer operations. A floating structure has been ingeniously devised to house the sensors between cages during transfers, effectively creating a transfer canal. This configuration facilitates seamless data acquisition as the fish migrate from the donor to the receiving cage, ensuring uninterrupted monitoring of biomass dynamics.

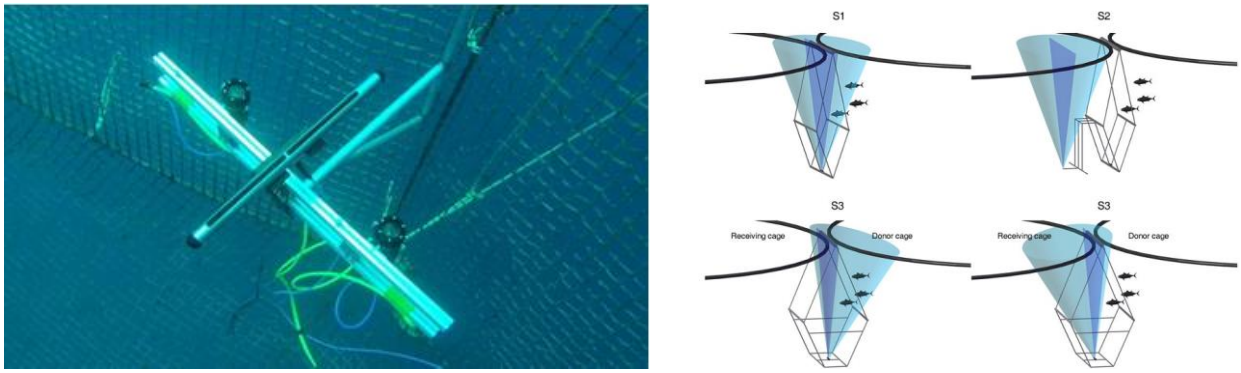

a *b*

Fig. 6 - Side scan sonar for biomass estimation of tuna during transfers, (*Puig-Pons et al., 2019*)
a – 200 kHz side scan sonar and stereo camera; b – Design of the proposed and tested floating structures.

The process of biomass assessment unfolds through a systematic methodology that involves both counting the transferred tuna and analyzing a representative sample of the stock (*Puig-Pons et al., 2019*).

In aquaculture, vision technology based on underwater robots is used for biomass estimation, solving the problem of low efficiency of traditional manual contact measurement, avoiding health issues in fish, and greatly improving work efficiency. However, the underwater environment has low visibility and many disturbances, and fish images collected based on light vision require further processing. The clarity and enhancement of underwater images based on artificial intelligence algorithms remain the focus of research. Additionally, problems such as fish body overlap, low resolution, and blurred outlines of small target fish still pose difficulties in current research.

The design and implementation of a novel Remotely Operated Vehicle (ROV) tailored for aquaculture inspection within marine environments represent a pivotal advancement aimed at furnishing essential insights into fishery nets. This ROV constitutes an integral component of the pioneering "Sea Farm" initiative. In instances where the ROV encounters operational issues, it is intended to be transported by a floating platform. Equipped with a winch, the platform facilitates the descent of the ROV into the seawater and its subsequent retrieval post-operation. The structural design incorporates three wings, each housing a dedicated thruster for propulsion. Through the coordinated efforts of these thrusters, the ROV boasts omnidirectional maneuverability, enabling efficient navigation within its marine environment (*Osen et al., 2017*).

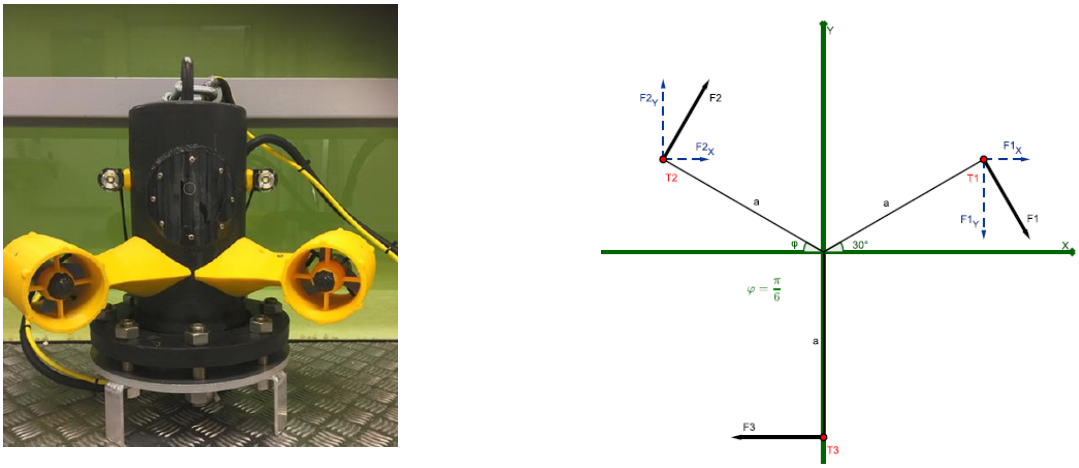

a *b*

Fig. 7 - Remotely Operated Vehicle for aquaculture, (*Osen et al., 2017*)
a – ROV prototype; b – Thruster forces.

Understanding the abundance and size distribution of fish within semi-intensive rearing systems in traditional ponds is crucial for effective sales lot planning and management. Typically, this information is acquired through sampling, which necessitates direct catch methods that are both stressful for the fish and time-consuming to manage. To achieve this objective, a portable-fixed multibeam imaging sonar employing commercial technology was employed, focused on estimating the abundance of gilthead seabream (Sparus aurata) within a fish farm's ponds through sonar image analysis (*Gutiérrez-Estrada et al., 2022*).

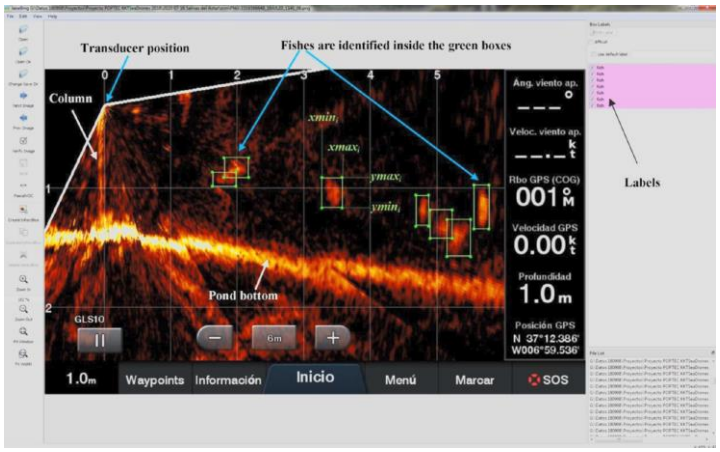

Fig. 8 - Sonar image treatment with the software LabelImg, (*Gutiérrez-Estrada et al., 2022*)

Imaging sonars (ISs) represent high-frequency acoustic devices that are experiencing growing utilization in the examination of fish populations across marine and freshwater environments. While acoustic devices offer valuable insights, they possess limitations in accurately quantifying species richness. Previous endeavors aimed at identifying fish species utilizing IS technology have predominantly concentrated on assemblages characterized by either low species richness or high morphological diversity (*Sible y et al., 2023*).

A fully automated IoT-based submersible Remotely Operated Vehicle (ROV) was designed to notify users of any detected fish diseases, enhancing overall management and health monitoring capabilities. The ROV

operation is facilitated through IoT integration and controller functionality, enabling surveillance both underwater and outside water, equipped with a plethora of features. Fish size measurement utilizing underwater cameras involves several steps. Initially, the camera captures the motion of the fish, enabling the determination of its distance from the camera. Subsequently, the system computes the "pixels per metric" ratio, which serves as a reference for size estimation:

$$Pixels\ Per\ Metric = \frac{Fish\_width}{Known\_Object\_width} \quad (1)$$

To accurately determine the size of the fish from the image, calibration is essential using a known reference object. This reference object allows for the establishment of a relationship between the number of pixels in the image and the corresponding physical distance in metric units (*Rohit et al., 2019*).

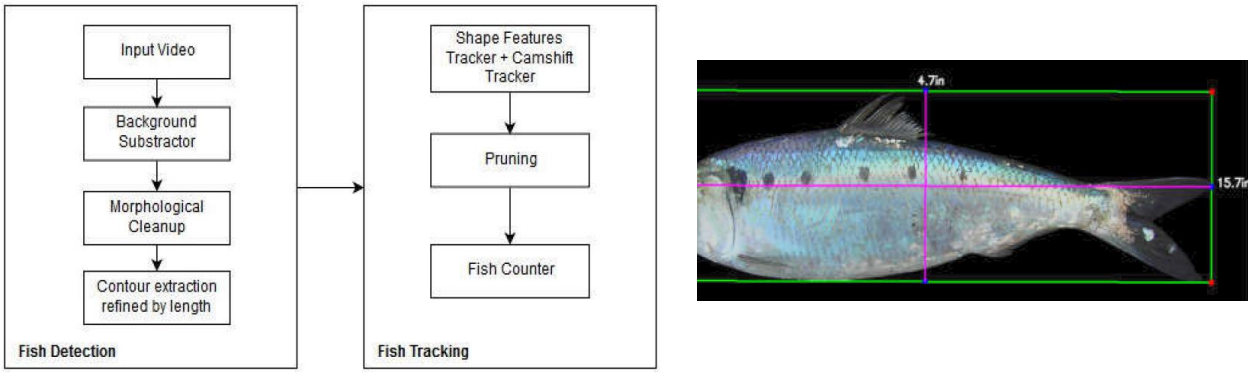

Fig. 9 - Underwater camera principle of a fully automated IoT-based ROV system, (*Rohit et al., 2019*)
a – Fish tracking and counting architecture; b – Fish Size Measurement.

Common methods of ocean remote sensing and seafloor surveying primarily involve the utilization of airborne and spaceborne hyperspectral imagers. However, the presence of the water column impedes the penetration of sunlight to deeper regions, thus constraining the range of observation. As an emerging technology, underwater hyperspectral imaging (UHI) serves as an extension of hyperspectral imaging technology adapted for air conditions, and is currently experiencing rapid advancement for applications in both shallow and deep-sea environments.

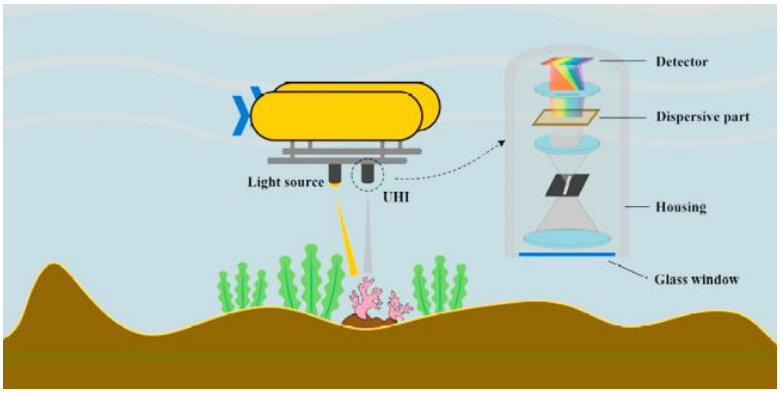

Fig. 10 - A schematic representation of underwater hyperspectral imaging (UHI) for mapping, (*Liu et al., 2020*)

UHI holds significant promise for utilization in marine fisheries and aquaculture, particularly in shallow and coastal regions. Its capabilities make it well-suited for monitoring changes in food availability, waste accumulation, and seabed composition within these environments (*Liu et al., 2020*).

RGB cameras mounted on an underwater vehicle possess the capability to capture imagery with exceptionally high spatial resolution, a fundamental requirement for ensuring precise estimation of biomass *(Overrein, 2023*).

Echo sounders enable the real-time monitoring of the complete fish population over extended periods. Nonetheless, prevailing methodologies for the automatic interpretation of echograms predominantly concentrate

on species classification, thereby inadequately encapsulating the spatiotemporal characteristics inherent in the data (*Måløy, 2020*).

Autonomous underwater vehicles (AUVs) represent unmanned submersibles programmable to navigate in three dimensions beneath the water's surface. The technological evolution necessary for their dependable deployment, mission control, performance optimization, and retrieval has undergone significant advancement over the past decade. Presently, numerous AUVs operate effectively within offshore industries and across applied and academic oceanographic disciplines. AUVs boast compact dimensions, emit minimal noise, and offer cost-effective operation, unaffected by weather conditions.

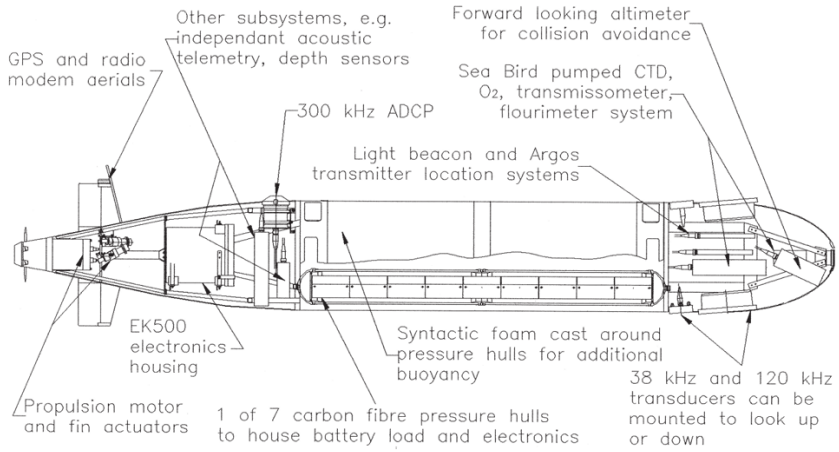

Fig. 11 - View of Autosub-2 with the payload configured for acoustic surveys of aquatic fauna - SIMRAD EK500, scientific, multi-frequency vertical echosounder (*Fernandes et al., 2003*)

Case studies demonstrate how these attributes benefit fisheries-acoustics science, drawing from past research conducted in regions like the North Sea and Southern Ocean while projecting potential future applications (*Fernandes et al., 2003*).

The SeaBED AUV is ingeniously engineered for a multifaceted exploration, encompassing photographic transects, side scan sonar, and bathymetric surveys. Its structure comprises two torpedo-like components connected by vertical struts, creating a cohesive unit for underwater operations. Despite its compact design, the AUV boasts notable dimensions: measuring 1.5 meters in length, 2.0 meters in height, and weighing approximately 250 kilograms, although the weight may fluctuate slightly depending on the payload it carries (*Tolimieri et al., 2008*).

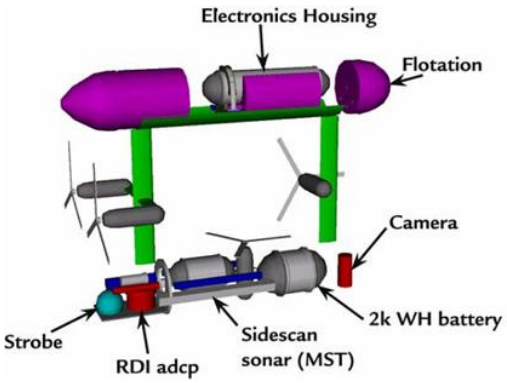

Fig. 12 - SeaBED autonomous underwater vehicle scheme, (*Tolimieri et al., 2008*)

Within the realm of marine research, the SeaBED AUV emerges as a pivotal tool, particularly in estimating the biomass of fish populations.

The aim of this paper is to provide a comprehensive overview of the evolution of various techniques utilized for mass measurement, enumeration, or direct estimation of fish biomass. This review serves as a valuable resource for researchers seeking to comprehend the current landscape of approaches to biomass estimation, providing actionable insights for enhancing the precision and efficiency of intensive fish farming practices.

RESULTS

Table 1 shows the biomass estimation technologies according to the type of underwater robots.

Table 1

The biomass estimation technologies according to the type of underwater robots

Type of Underwater Robot	Biomass Estimation Technology	Reference
ROV (Remotely Operated Vehicle)	Acoustic Imaging (sonar)	*Osen et al., 2017* *Gutiérrez-Estrada et al., 2022* *Sibley et al., 2023* *Christ and Wernli, 2014* *Rundtop and Frank, 2016* *Måløy, 2020*
	Optical Imaging (video cameras)	*Macreadie et al., 2018* *Rohit et al., 2019* *Zhang et al., 2024*
	Multispectral Imaging	*Liu et al., 2020* *Overrein, 2023*
AUV (Autonomous Underwater Vehicle)	Side scan Sonar	*Fernandes et al., 2003*
	Section Scanning Sonar	*Tolimieri et al., 2008*

Below are presented some mathematical models that contribute to the repertoire of mathematical approaches used in biomass estimation, reflecting the various methodologies used in ecological research and natural resource management.

1. *Logistic Growth Model (Verhulst, 1838):*

$$N(t) = \frac{K}{1+\frac{K-N_0}{N_0}e^{-rt}} \quad (2)$$

This model describes the growth of a population in a limited environment, where $N(t)$ represents biomass at time t, N_0 is the initial biomass, K is the carrying capacity, r is the growth rate, and e is the base of the natural logarithm.

2. *Schaefer Fish Stock Assessment Model (Schaefer, 1954):*

$$F(B) = rB(1-\frac{B}{K}) \quad (3)$$

This model uses a differential equation to estimate fish biomass (B) based on fishing rate (F), natural growth rate (r), and carrying capacity (K).

3. *Fox Model (Fox, 1970, Musick and Bonfil, 2005):*

$$B_{t+1} = B_t + rB_t\left(1-\frac{lnB_t}{lnK}\right) - C_t \quad (4)$$

The Fox surplus production model is used to estimate the surplus production of a fish stock, which represents the additional biomass that can be sustainably harvested beyond what is required to maintain the stock at its current level, where B represents biomass, K represents carrying capacity, r represents intrinsic rate of population increase and C is catch.

4. *Pella and Tomlinson Model (Pella and Tomlinson, 1969):*

$$\frac{dB}{dt} = rB(1-\frac{B}{K}) - F(B) \quad (5)$$

The Pella-Tomlinson model is based on the assumption of a logistic growth function for fish populations. The model estimates the total biomass B of the fish stock at a given time, taking into account the current biomass, the intrinsic rate of growth r, and the carrying capacity K of the environment.

$\frac{dB}{dt}$ represents the rate of change of biomass over time.

$F(B)$ represents the fishing mortality rate, which is a function of the current biomass B.

5. *Multispecies Trophic Network Model (May, 2019):*

$$\frac{dN_i}{dt} = r_i N_i (1 - \sum_{j=1}^{n} c_{ij} \frac{N_j}{K_j} \quad (6)$$

This model describes the population dynamics of species i in a trophic network, considering interactions with other species j, growth rates (r_i), carrying capacities (K_j), and consumption coefficients (c_{ij}).

6. Stochastic Differential Equations (SDE) Biomass Model (Gard, 1989):

$$dX_t = \left(\mu - \frac{\sigma^2}{2}\right) dt + \sigma dW_t \quad (7)$$

This model uses stochastic differential equations to describe biomass variations over time, where X_t represents biomass at time t, μ is the average growth rate, σ is the standard deviation of the stochastic process, and dW_t is a Brownian variation.

7. von Bertalanffy Growth Model for weight (Von Bertalanffy, 1957):

$$W(t) = W_\infty (1 - e^{-k(t-t_0)})^3 \quad (8)$$

This model describes the sigmoidal growth pattern observed in many fish species, where growth is rapid early in life, slows down as the fish approaches its maximum size, and eventually levels off, where $W(t)$ represents the weight of the fish at age t; W_∞ is the theoretical maximum asymptotic weight that the fish can reach; k is the von Bertalanffy growth coefficient, which represents the rate at which the fish approaches its maximum weight; t_0 is the theoretical age at which the weight of the fish would be zero and e is the base of the natural logarithm. The von Bertalanffy Growth Model is widely used in fisheries science and management to estimate growth parameters for fish populations, assess population dynamics, and inform fisheries management strategies.

8. Biomass Dynamic Models (Colvin et al., 2012):

Biomass Dynamic Models (BDMs) utilize a variety of equations and mathematical formulations to describe the dynamics of fish populations within ecosystems. While the specific equations used can vary depending on the model and its purpose, here are some general components and equations commonly found in Biomass Dynamic Models*:*

a. Population Growth Equation:

The population growth equation describes how the biomass of a fish population changes over time. It often includes terms for population growth, mortality, recruitment, and other factors affecting population dynamics. A basic form of the population growth equation may be represented as:

$$\frac{dN}{dt} = f(N,t) - M(N,t) \quad (9)$$

where: N represents the population biomass, t represents time, $f(N,t)$ represents the rate of population growth, $M(N,t)$ represents the rate of mortality.

b. Recruitment Equation:

The recruitment equation describes the addition of new individuals to the population. It often includes terms for spawning stock biomass, environmental conditions, and other factors influencing recruitment. A basic form of the recruitment equation may be represented as:

$$R(t) = f(S(t), E(t)) \quad (10)$$

where: $R(t)$ represents recruitment at time t, $S(t)$ represents spawning stock biomass at time t, $E(t)$ represents environmental conditions at time t.

c. Growth Equation:

The growth equation describes how individual fish grow over time. It often includes terms for growth rate, food availability, and other environmental factors. A basic form of the growth equation may be represented as:

$$\frac{dW}{dt} = G(W,t) \quad (11)$$

where: W represents individual fish weight, $G(W,t)$ represents the rate growth.

d. Fishing Mortality Equation:

The fishing mortality equation describes the impact of fishing on the fish population. It often includes terms for fishing effort, fishing mortality rates, and selectivity of fishing gear. A basic form of the fishing mortality equation may be represented as:

$$F(t) = E(t) \cdot S(t) \cdot \frac{F_{max}}{E_{max}} \quad (12)$$

where: $F(t)$ represents fishing mortality at time t, $E(t)$ represents fishing effort at time t, $S(t)$ represents selectivity of fishing gear at time t, F_{max} represents maximum fishing mortality rate, E_{max} represents maximum fishing effort.

These models represent a diverse set of mathematical approaches used for biomass estimation, incorporating advanced technologies and modern data analysis methods to provide accurate and relevant estimates in various ecological and scientific contexts.

CONCLUSIONS

By analyzing the technological solutions for biomass estimation according to the concept of Aquaculture 4.0, it can be concluded that:

- the estimation of fish biomass through the integration of optical and acoustic cameras represents a significant advancement in real-time, non-contact, non-destructive, safe, and reliable fish population assessment methodologies;
- the utilization of underwater vision for biomass estimation, coupled with the integration of data into big data platforms for decision-making processes, presents a promising avenue for enhancing the accuracy of bait casting in intelligent aquaculture practices;
- it is crucial to acknowledge the challenges posed by underwater environmental conditions, including illumination variations and multiple disturbances, which significantly increase the complexity of underwater image processing;
- future research efforts should focus on the refinement of image processing algorithms to mitigate the impact of underwater environmental disturbances on biomass estimation accuracy;
- the integration of advanced technologies, such as artificial intelligence and machine learning, holds potential for enhancing the robustness and efficiency of underwater image processing techniques;
- the integration of Machine Vision, acoustics, ambient DNA, and other innovative technologies holds immense potential for transforming the way fish biomass is estimated. By adopting non-invasive, rapid and cost-effective methodologies, timely and reliable information essential for sustainable fisheries management and conservation efforts can be obtained;
- mass prediction methods that exclude fish tail fins could more accurately estimate fish mass compared to models that incorporate tail fins. This methodology holds promise for extending mass estimation to free-swimming fish underwater in aquaculture settings.

ACKNOWLEDGEMENT

This research was supported by the Romanian Ministry of Research Innovation and Digitalization, through the project “Underwater Intelligent System (Robot) for the Protection of Life, Health and Growth Environment” – PN 23 04 01 03 – Ctr. 9N/01.01.2023 and by the Ministry of Agriculture and Rural Development – Romania - MADR through the Sectoral Project ADER 25.2.2 “Vertical Aquaponic Farm Adapted To Current Climate Changes”, Ctr. 18.07.2023.

REFERENCES

Abinaya, N. S., Susan, D., Sidharthan, R. K., (2022). Deep learning-based segmental analysis of fish for biomass estimation in an occulted environment. *Comput. Electron. Agric. 197*, 106985

Alver M. O., Alfredsen J. A., Øie G. (2005). A system for model-based biomass estimation of larvae in intensive cod larvicultures. Biomass estimation of larvae in intensive cod larvicultures. *Aquacult Int 13*, 519–541

Artero, C., Marchetti, S., Bauer, E., Viala, C., Noël, C., Koenig, C.C., Berzins, R., Lampert, L. (2021). High-Resolution Acoustic Cameras Provide Direct and Efficient Assessments of Large Demersal Fish Populations in Extremely Turbid Waters. *Appl. Sci., 11*, 1899. https://doi.org/10.3390/app11041899

Ault, J. S., Smith, S. G., Richards, B. L., Yau, A. J., Langseth, B. J., O’Malley, J. M., Boggs, C., H., Seki, M. P., DiNardo, G. T. (2018). Towards fishery-independent biomass estimation for Hawaiian Islands deepwater snappers. Fisheries research, 208, 321–328. https://doi.org/10.1016/j.fishres.2018.08.012

Berckmans, D. (2017). General introduction to precision livestock farming, *Animal Frontiers, 7*(1), 6–11. https://doi.org/10.2527/af.2017.0102

Bianchi, D., Carozza, D. A., Galbraith, E. D., Guiet, J., DeVries, T. (2021). Estimating global biomass and biogeochemical cycling of marine fish with and without fishing. Science advances, 7(41). DOI: 10.1126/sciadv.abd7554

Block, B.A., Whitlock, R., Schallert, R.J., Wilson, S., Stokesbury, M.J.W., Castleton, M., Boustany, A., (2019). Estimating natural mortality of Atlantic Bluefin tuna using acoustic telemetry. *Sci. Rep. 9* (1). https://doi.org/10.1038/s41598-019-40065-z

Braga, L. T. M. D., Giraldo, A., Godinho, A. L. (2022). Evaluation of three methods for manually counting fish in dam turbines using DIDSON. *Hydrobiologia 849*, 309–321. https://doi.org/10.1007/s10750-021-04605-x

Bravata, N., Kelly, D., Eickholt, J., Bryan, J., Miehls, S., Zielinski, D. (2020). Applications of deep convolutional neural networks to predict length, circumference, and weight from mostly dewatered images of fish. *Ecol. Evol., 10*, 9313–9325

Bjerkeng, B., Borgstrøm, R., Brabrand, Å., Faafeng, B. (1991). Fish size distribution and total fish biomass estimated by hydroacoustical methods: a statistical approach. *Fisheries Research, 11*(1), 41–73

Chen, Y., Andrew, N. (1998). Parameter estimation in modelling the dynamics of fish stock biomass: are currently used observation-error estimators reliable? *Canadian Journal of Fisheries and Aquatic Sciences, 55*(3), 749–760

Christ, R. D., Wernli, R. L. (2014). Chapter 15 - Sonar, Editor(s): Robert D. Christ, Robert L. Wernli, The ROV Manual (Second Edition), Butterworth-Heinemann, 387-424, ISBN 9780080982885. https://doi.org/10.1016/B978-0-08-098288-5.00015-4

Colvin, M. E., Pierce, C. L., & Stewart, T. W. (2012). Semidiscrete biomass dynamic modeling: an improved approach for assessing fish stock responses to pulsed harvest events. *Canadian Journal of Fisheries and Aquatic Sciences, 69*(10), 1710–1721

Cowley, P. D., Whitfield, A. K. (2002). Biomass and production estimates of a fish community in a small South African estuary. Journal of Fish Biology, 61, 74–89. https://doi.org/10.1111/j.1095-8649.2002.tb01763.x

Cowx, I. G., (1983). Review of the methods for estimating fish population size from survey removal data. Aquac. Res. 14 (2) https://doi.org/10.1111/j.1365-2109.1983. tb00057.x.

Davison, P. C., Koslow, J. A., & Kloser, R. J. (2015). Acoustic biomass estimation of mesopelagic fish: backscattering from individuals, populations, and communities. *ICES Journal of Marine Science, 72*(5), 1413-1424

Debroy, P., Seban, L. (2022). A Fish Biomass Prediction Model for Aquaponics System Using Machine Learning Algorithms. *In: Machine Learning and Autonomous Systems. Smart Innovation, Systems and Technologies, 269*. Springer, Singapore. https://doi.org/10.1007/978-981-16-7996-4_27

Doi, H., Uchii, K., Takahara, T., Matsuhashi, S., Yamanaka, H., Minamoto, T., (2015). Use of droplet digital PCR for estimation of fish abundance and biomass in environmental DNA surveys. PLoS One 10 (3). https://doi.org/10.1371/journal.pone.0122763.

Doi, H., Inui, R., Akamatsu, Y., Kanno, K., Yamanaka, H., Takahara, T., & Minamoto, T. (2017). Environmental DNA analysis for estimating the abundance and biomass of stream fish. Freshwater Biology, 62(1), 30-39. https://doi.org/10.1111/fwb.12846

Dutta, M.K., Issac, A., Minhas, N., Sarkar, B. (2016). Image processing based method to assess fish quality and freshness. *J. Food Eng.*, 177, 50–58

Emmrich, M., Winfield, I.J., Guillard, J., Rustadbakken, A., Verg` es, C., Volta, P., Jeppesen, E., Lauridsen, T.L., Brucet, S., Holmgren, K., Argillier, C., Mehner, T., (2012). Strong correspondence between gillnet catch per unit effort and hydroacoustically derived fish biomass in stratified lakes. *Freshw. Biol. 57* (12) https://doi.org/10.1111/fwb.12022

Fernandes, P.G., Stevenson, P., Brierley, A. S., Armstrong, F., Simmonds, E. J. (2003). Autonomous underwater vehicles: future platforms for fisheries acoustics, *ICES Journal of Marine Science, 60(*3), 684–691, https://doi.org/10.1016/S1054-3139(03)00038-9

Fox Jr, W. W. (1970). An exponential surplus-yield model for optimizing exploited fish populations. Transactions of the American Fisheries Society, 99(1), 80–88

Gard, T. C. (1989). Introduction to Stochastic Differential Equations. New York-Basel, Marcel Dekker Inc. 1988. XI, 234 pp., $78.-. ISBN 0–8247-7776-X (Pure and Applied Mathematics 114).

Graham, N., Jones, E. G., Reid, D. G. (2004). Review of technological advances for the study of fish behaviour in relation to demersal fishing trawls. *ICES J. Mar. Sci. J. Cons., 61*, 1036–1043

Gutiérrez-Estrada, J. C., Pulido-Calvo, I., Castro-Gutiérrez, J., Peregrín, A., López-Domínguez, S., Gómez-Bravo, F., Garrocho-Cruz, A., de la Rosa-Lucas, I. (2022). Fish abundance estimation with imaging sonar in semi-intensive aquaculture ponds, *Aquacultural* Engineering, *97*, 102235, ISSN 0144-8609. https://doi.org/10.1016/j.aquaeng.2022.102235

Hao, Y. F., Yin, H. J., Li, D. L. (2022). A novel method of fish tail fin removal for mass estimation using computer vision. *Computers and Electronics in Agriculture, 193*, 106601

Harvey E., Fletcher D., Shortis M. (2001). A comparison of the precision and accuracy of estimates of reef-fish lengths deter-mined visually by divers with estimates produced by a stereo-video system. *Fishery Bulletin-National Oceanic and Atmospheric Administration 99*(1), 63–71

Hayes, D. B., Bence, J. R., Kwak, T. J., Thompson, B. E. (2007). Abundance, biomass, and production. Analysis and interpretation of freshwater fisheries data. *American Fisheries Society, Bethesda, Maryland, 53*, 327–374

Henriksson, P. J. G., Troell, M., Banks, L. K., Belton, B., Beveridge, M. C. M., Klinger, D. H., Pelletier, N., Phillips, M. J., Tran, N. (2021). Interventions for improving the productivity and environmental performance of global aquaculture for future food security. *One Earth, 4,* 1220–1232

Hicks, B. J., Brijs, J., Daniel, A. J., Morgan, D. K., Ling, N. (2015). Biomass estimation of invasive fish. *In K. J. Collier & N. P. J. Grainger (Eds.), New Zealand Invasive Fish Management Handbook,* 116–122. Hamilton, New Zealand: Lake Ecosystem Restoration New Zealand (LERNZ) & Department of Conservation

Hossain, S. A., Hossen, M. (2018). Biomass estimation of a popular aquarium fish using an acoustic signal processing technique with three acoustic sensors. *In 2018 International Conference on Advancement in Electrical and Electronic Engineering (ICAEEE),* 1–4

Johnston, S. J., Smith, J. B., Slater, B. D., Doubek, J. P. (2023). Spatial Density, Biomass, and Composition of Crustacean Zooplankton on Lake Michigan Beaches. *Fishes, 8*, 599. https://doi.org/10.3390/fishes8120599

Jongjaraunsuk, R., Taparhudee, W. (2021). Weight Estimation of Asian Sea Bass (Lates calcarifer) Comparing Whole Body with and without Fins using Computer Vision Technique*, Walailak J Sci & Tech, 18*(10): 9495

Kindong, R., Wu, J., Gao, C., Dai, L., Tian, S., Dai, X., Chen, J., (2020). Seasonal changes in fish diversity, density, biomass, and assemblage alongside environmental variables in the Yangtze River Estuary. Environ*. Sci. Pollut. Res. 27* (20) https://doi.org/10.1007/s11356-020-08674-8.

Kim, H., Kang, D., Cho, S., Kim, M., Park, J., & Kim, K. (2018). Acoustic target strength measurements for biomass estimation of aquaculture fish, Redlip mullet (Chelon haematocheilus). *Applied Sciences, 8*(9), 1536. https://doi.org/10.3390/app8091536

Kim, K., Neretti, N., Intrator, N. (2005). Mosaicing of acoustic camera images. *IEE Proc. Radar. Sonar Navig., 152*, 263–270

Konovalov, D. A., Saleh, A., Domingos, J. A., White, R. D., Jerry, D. R. (2018). Estimating mass of harvested Asianseabass Lates calcarifer from images. *World J. Eng. Tech., 6*, 15–23.

Lee, J. B., Oh, T. Y., Yeon, I. J., Kim, B. Y., Shin, H. O., Hwang, B. K., Kyung-Hoon, L., Lee, Y. W. (2012). Estimation of demersal fish biomass using hydroacoustic and catch data in the marine ranching area (MRA) of Jeju. Journal of the Korean Society of Fisheries and Ocean Technology, 48(2), 128–136. https://doi.org/10.3796/KSFT.2012.48.2.128

Lian, Y., Huang, G., Godlewska, M., Cai, X., Li, C., Ye, S., Li, J., Li, Z. (2018). Hydroacoustic estimates of fish biomass and spatial distributions in shallow lakes. Journal of Oceanology and Limnology, 36, 587–597.

Li D., Hao Y., Duan Y. (2019). Nonintrusive methods for biomass estimation in aquaculture with emphasis on fish: a review, *Reviews in Aquaculture, 1*–2, 1-22, doi: 10.1111/raq.12388, 2019

Liu, B., Liu, Z., Men, S., Li, Y., Ding, Z., He, J., Zhao, Z. (2020). Underwater Hyperspectral Imaging Technology and Its Applications for Detecting and Mapping the Seafloor: A Review. *Sensors, 20*, 4962. https://doi.org/10.3390/s20174962

Lopez, J., Moreno, G., Boyra, G., & Dagorn, L. (2016). A model based on data from echosounder buoys to estimate biomass of fish species associated with fish aggregating devices. *Fishery Bulletin, 114*(2), 166-178. https://dx.doi.org/10.7755/fb.114.2.4

Macreadie, P. I., McLean, D. L., Thomson, P. G., Partridge, J. C., Jones, D. O. B., Gates, A. R., Benfield, M. C., Collin, S. P., Booth, D. J., Smith, L. L., Techera, E., Skropeta, D., Horton, T., Pattiaratchi, C., Bond, T., Fowler, A. M. (2018). Eyes in the sea: Unlocking the mysteries of the ocean using industrial, remotely operated vehicles (ROVs). *Science of the Total Environment, 634*, 1077–1091

May, R. M. (2019). *Stability and complexity in model ecosystems* (Vol. 1). Princeton university press

Mahon, R. (1980). Accuracy of catch-effort methods for estimating fish density and biomass in streams. *Environmental Biology of Fishes, 5*, 343–363

Marks, K. W., Klomp, K. D. (2003). Appendix Two. Fish biomass conversion equations. Atoll Research Bulletin.

Måløy, H. (2020). EchoBERT: A Transformer-Based Approach for Behavior Detection in Echograms, in *IEEE Access, 8*, 218372-218385. doi: 10.1109/ACCESS.2020.3042337

Mihneva, V., Raykov, V., Dimitrov, D. P. (2023). Summer Biomass Variability and Spatial Interactions between European Sprat (Sprattus sprattus) and Moon Jellyfish (Aurelia aurita) in the Western Part of the Black Sea. *Animals, 13*, 3691. https://doi.org/10.3390/ani13233691

Murakami, H., Yoon, S., Kasai, A., Minamoto, T., Yamamoto, S., Sakata, M.K., Horiuchi, T., Sawada, H., Kondoh, M., Yamashita, Y., Masuda, R., (2019). Dispersion and degradation of environmental DNA from caged fish in a marine environment. *Fish. Sci. 85*, 327–337. https://doi.org/10.1007/s12562-018-1282-6.

Musick, J. A., Bonfil, R. (Eds.). (2005). *Management techniques for elasmobranch fisheries* (No. 474). Food & Agriculture Org.

Orduna, C., de Meo, I., Rodríguez-Ruiz, A., Cid-Quintero, J.R., Encina, L. (2023). Seasonal Length–Weight Relationships of European Sea Bass (Dicentrarchus labrax) in Two Aquaculture Production Systems. *Fishes, 8*, 227. https://doi.org/10.3390/fishes8050227

Osen, O., Sandvik, R. I., Trygstad, J. B., Vergard, R., Houxiang, Z. (2017). A novel low cost ROV for aquaculture application, *Marine Technology Society*. http://hdl.handle.net/11250/2491512

Overrein M. M. (2023). *In situ biomass estimation of cultivated kelp using RGB imagery*. Master's thesis in Ocean Resources. NTNU Norwegian University of Science and Technology Faculty of Natural Sciences Department of Biology

Paolacci, S., Stejskal, V., Toner, D., Jansen, M. A. K. (2022). Integrated Multitrophic Aquaculture; Analysing Contributions of Different Biological Compartments to Nutrient Removal in a Duckweed-Based Water Remediation System. *Plants, 11*, 3103. https://doi.org/10.3390/plants11223103

Pella, J. J., Tomlinson, P. K. (1969). A generalized stock production model. *Inter-American tropical tuna commision, 13(3),* 421–458

Proud, R., Handegard, N. O., Kloser, R. J., Cox, M. J., & Brierley, A. S. (2019). From siphonophores to deep scattering layers: uncertainty ranges for the estimation of global mesopelagic fish biomass. *ICES Journal of Marine Science, 76*(3), 718–733

Puig-Pons, V., Muñoz-Benavent, P., Espinosa, V., Andreu-García, G., Valiente-González, J. M., Estruch, V. D., Ordóñez, P., Pérez-Arjona, I., Atienza, V., Mèlich, B., de la Gándara, F., Santaella, E. (2019). Automatic Bluefin Tuna (Thunnus thynnus) biomass estimation during transfers using acoustic and computer vision techniques, Aquacultural Engineering, 85, 22–31, ISSN 0144–8609. https://doi.org/10.1016/j.aquaeng.2019.01.005

Radinger, J., Matern, S., Klefoth, T., Wolter, C., Feldhege, F., Monk, C.T., Arlinghaus, R., (2023). Ecosystem-based management outperforms species-focused stocking for enhancing fish populations. Science 379 (6635). https://doi.org/10.1126/science.adf0895.

Říha, M., Prchalova, M., Brabec, M., Drastík, V., Muska, M., Tuser, M., Barton, D., Blabolil, P., Cech, M., Frouzova, J., Holubova, M., Jůza, T., R. Moraes, K., Rabaneda- Bueno, R., Sajdlov´ a, Z., Souza, A.T., Smejkal, M., Vasek, M., Vejrík, L., Kubecka, J., (2023). Calibration of fish biomass estimates from gillnets: step towards broader application of gillnet data. Ecol. Indic. 153, 110425 https://doi.org/10.1016/j.ecolind.2023.110425

Rohit, M. H., Barua, S., Akter, I., Karim, S. M. M., Akter, S., Lutfe Elahi, M. M. (2019). IOT Based Submersible ROV for Pisciculture, *28th IEEE International Conference on Robot and Human Interactive Communication (RO-MAN),* New Delhi, India, 1–6. doi: 10.1109/RO-MAN46459.2019.8956441

Rundtop, P., Frank, K. (2016). Experimental evaluation of hydroacoustic instruments for ROV navigation along aquaculture net pens, *Aquacultural Engineering, 74*, 143–156

Schaefer, M. B. (1954). Some aspects of the dynamics of populations important to the management of the commercial marine fisheries, *Bulletin of Inter-American Tropical Tuna Commission, 1*(2), 25–56

Shephard, S., Reid, D. G., Gerritsen, H. D., & Farnsworth, K. D. (2015). Estimating biomass, fishing mortality, and "total allowable discards" for surveyed non-target fish. *ICES journal of marine science, 72*(2), 458–466. ttps://doi.org/10.1093/icesjms/fsu146

Sibley, E. C. P., Madgett, A. S., Lawrence, J. M., Elsdon, T. S., Marnane, M. J., Fernandes, P. G. (2023). Quantifying the ability of imaging sonar to identify fish species at a subtropical artificial reef. *ICES Journal of Marine Science*, *0* , 1–13. DOI: 10.1093/icesjms/fsad156

Sture, Ø., Øye, E. R., Skavhaug, A., Mathiassen, J. R. (2016). A 3D machine vision system for quality grading of Atlantic salmon. *Comput. Electron. Agric.*, *123*, 142–148

St. John, J., Russ, G. R., & Gladstone, W. (1990). Accuracy and bias of visual estimates of numbers, size structure and biomass of a coral reef fish. *Marine Ecology Progress Series*, 253–262

Takahara, T., Minamoto, T., Yamanaka, H., Doi, H., Kawabata, Z. (2012). Estimation of Fish Biomass Using Environmental DNA. *PLoS ONE 7*(4): e35868. doi:10.1371/journal.pone.0035868

Thurow, F. (1997). Estimation of the total fish biomass in the Baltic Sea during the 20th century. *ICES Journal of Marine Science, 54*, 444–461

Tolimieri, N., Clarke, M. E., Singh, H., Goldfinger, C. (2008). *Evaluating the SeaBED AUV for Monitoring Groundfish in Untrawlable Habitat*. University of Alaska Fairbanks. 129–141. 10.4027/mhmta.2008.09.

Verhulst, P. F. (1838). Notice sur la loi que la population poursuit dans son accroissement. *Correspondance Mathématique et Physique, 10*, 113–121.

Varadi, L., Bardócz, T., Oberdieck, A. (2009). SustainAqua—Integrated Approach for a Sustainable and Healthy Freshwater Aquaculture. *SustainAqua Handbook—A Handbook for Sustainable Aquaculture. Available online: https://haki. naik. hu/sites/default/files/uploads/2018-09/sustainaqua_handbook_en. pdf (accessed on 25 April 2024).*

Viazzi, S., Hoestenberghe, S. V., Goddeeris, B., Berckmans, D. (2015). Automatic mass estimation of jadeperch Scortum barcoo by computer vision. *Aquacult. Eng., 64*, 42–8

Von Bertalanffy, L. (1957). Quantitative laws in metabolism and growth. *The quarterly review of biology, 32*(3), 217–231

Wanghe, K., Ahmad, S., Zhou, X., Tian, F., Liu, S., Zhou, B., Nabi, G., Wang, G., Li, K., Jian, S., Jiang, H., Chen, S., Niu, Y., Khan, M., I., Zhao, K. (2024). Spatially explicit estimation of freshwater fish stock biomass with limited data: A case study of an endangered endemic fish on the Tibetan Plateau, China. *Science of The Total Environment, 912*, 168717, https://doi.org/10.1016/j.scitotenv.2023.168717

Wilson, S. K., Graham, N. A. J., Holmes, T. H., MacNeil, M. A., & Ryan, N. M. (2018). Visual versus video methods for estimating reef fish biomass. *Ecological Indicators, 85*, 146–152 https://doi.org/10.1016/j.ecolind.2017.10.038

Yin, X., Yang, D., Du, R., (2022). Fishery resource evaluation in Shantou seas based on remote sensing and hydroacoustics. Fishes 7 (4). https://doi.org/10.3390/fishes7040163.

Yule, D. L., Adams, J. V., Warner, D. M., Hrabik, T. R., Kocovsky, P. M., Weidel, B. C., Rudstram, L. C., Sullivan, P. J. (2013). Evaluating analytical approaches for estimating pelagic fish biomass using simulated fish communities. *Canadian journal of fisheries and aquatic sciences, 70*(12), 1845–1857. https://doi.org/10.1139/cjfas-2013-0072

Yulianto, I., Hammer, C., Wiryawan, B., Pardede, S. T., Kartawijaya, T., Palm, H. W. (2015). Improvement of fish length estimates for underwater visual census of reef fish biomass. Journal of Applied Ichthyology, 31(2), 308-314. https://doi.org/10.1111/jai.12672

Zion, B. (2012). The use of computer vision technologies in aquaculture: A review. *Comput. Electron. Agr., 88,* 125–32

Zhang, C. I., & Megrey, B. A. (2010). A simple biomass-based length-cohort analysis for estimating biomass and fishing mortality. Transactions of the American Fisheries Society, 139(3), 911–924. https://doi.org/10.1577/T09-041.1

Zhang, T., Yang, Y., Liu, Y., Liu, C., Zhao, R., Li, D., Shi, C. (2024). Fully automatic system for fish biomass estimation based on deep neural network, *Ecological Informatics, 79,* 102399, ISSN 1574–9541. https://doi.org/10.1016/j.ecoinf.2023.102399.

Zhou, M., Shen, P., Zhu, H., Shen, Y. (2023). In-Water Fish Body-Length Measurement System Based on Stereo Vision. *Sensors, 23*, 6325. https://doi.org/10.3390/s23146325

*** FAO, (2018), *The State of World Fisheries and Aquaculture 2018 - Meeting the sustainable development goals*. Rome. Licence: CC BY-NC-SA 3.0 IGO.

STUDY ON SINGLE-BRANCH COMBING OF *Cerasus humilis*
/
钙果单枝梳脱试验研究

Shilei KANG[1,2], Junlin HE*[1,2], Tao WANG[1]
[1]College of Agricultural Engineering, Shanxi Agricultural University, Taigu 030801, China;
[2]Dryland Farm Machinery Key Technology and Equipment Key Laboratory of Shanxi Province, Taigu 030801, China
Tel: +86-0354-6288400; E-mail: hejunlin26@126.com
Corresponding author: Junlin HE
DOI: https://doi.org/10.35633/inmateh-72-60

Keywords: *Cerasus humilis*, *single-branch combing, experimental study, bench test*

ABSTRACT
In this study, a central unloading reel structure was proposed to achieve continuous harvest of Cerasus humilis, and an indoor test bench was constructed to carry out the combing test of branches. The cross-section of the comb was made of an isosceles triangle, and an orthogonal test was carried out with tooth gap, winch rotational velocity and cross-section base angle as test factors, and fruit breakage rate and leakage rate as test indicators. The results show that the tooth gap and winch rotational velocity have a significant influence on the breakage rate, and the tooth gap and section bottom angle have a significant influence on the fruit leakage rate. Considering the comprehensive loss rate, the appropriate deformation of the comb teeth and the manufacturing difficulty, the optimal values of the three test factors are 10 mm, 130 r/min, and 45°, respectively. At the same time, the maximum combing force of a single branch through the comb is 240 N through the pressure sensor of the test bench. The experimental results can be used as the basis for the structural design of continuous harvesting head.

摘要
本研究设想了一种滚筒中心卸载果实的结构以实现钙果的连续采收，制作了一个室内试验台进行整枝的梳脱试验。梳齿截面采用等腰三角形，以齿间隙、绞盘转速和截面底角为试验因素，以果实破损率和泄露率为试验指标，进行了正交试验，分析了各试验因素对各个指标的影响机制。结果表明，齿间隙和绞盘转速对破损率有着显著的影响，齿间隙和截面底角对漏果率有着显著的影响，考虑综合损失率、梳齿的适当变形和制造难度，三个试验因素的最佳值分别为：10 mm、130 r/min、45°。同时，通过试验台的压力传感器得到单个枝条通过梳齿的最大梳脱力为240 N。试验结果可以作为连续收获采摘头的结构设计依据。

INTRODUCTION
The *Cerasus humilis* tree is a tufted shrub with dense fruits at maturity, and its branches spread out and fall in all directions *(He et al., 2018)*. Its fruit is rich in calcium, which is easily absorbed by the human body, and has gradually been recognized by the market, and the planting area has expanded year by year, facing the problem of harvesting difficulties *(Chang et al., 2011)*. Vibration harvester is widely used in small fruits, such as in high-bush blueberry harvesting *(DeVetter et al., 2019; Yu et al., 2012)*. However, the research object in this paper is unable to transmit high-frequency vibration due to weak branches, and it is difficult to collect fruits. In mechanical harvesting practice, previous researchers have verified the effectiveness of combing fruit *(Du et al., 2019)*. Branches go through the comb gap, the fruit is removed, while gaining kinetic energy, and there is a tendency to splash away from the picking mechanism *(Liu et al., 2021)*. Through the analysis of the previous study, it was found that the *Cerasus humilis* could not withstand the high-speed impact, and would reach a relative static with the comb teeth in a short time after gentle combing, so the fruit could not be unloaded by backward throwing. The unloading device in this study refers to the design of a wild blueberry picking head and is arranged inside the picking head *(Farooque et al., 2014)*. In contrast, in the combing of chrysanthemums and rare Soybean pods, a higher rotation speed is required to obtain enough centrifugal force to leave the combing teeth *(Ehlert et al., 2014; Zhao et al., 2023)*, because they have different mechanical properties from *Cerasus humilis*.

[1] *Shilei KANG,As Lec.PhD. Junlin HE,Prof.Ph.D.Eng; Tao WANG,M.S. Eng.*

When the branches pass through the comb tooth gap, the comb teeth have a complex interaction relationship with the branches and fruits. During this process, the fruit may be cracked and scratched by branches *(Du et al., 2020)*. As a cantilever structure, comb teeth may be deformed and lose their working ability under the reaction of branches *(Zhao et al., 2023)*. It is of great significance to study the combing process of a single fruit-bearing branch to understand the harvest of the whole fruit tree. Therefore, a comb stripping test bench is designed to conduct physical tests on the operation effect of a single branch through comb teeth, to obtain the optimal comb structure and operating parameters, as well as the impact force of branches on comb teeth. The research results can guide the design of the structure and operation parameters of the picking head.

MATERIALS AND METHODS

Cerasus humilis combing is a group behaviour, and the time is very short, the combing process is less than 1 s, and the branches with good growth have factors that are not conducive to combing, so the stress of single fruit during combing is difficult to obtain in physical tests, and the theoretical calculation of the stress of single fruit has little significance for the group picking behaviour of *Cerasus humilis*. The performance of the population can only be known through statistics. At the same time, the impact force of the comb teeth is also an important parameter in the design of the picking device, which needs to be tested. Therefore, an indoor test bench was designed that could fully control variables. The comb teeth were still and the pruned branches were pulled through the teeth gap to observe the combing effect of the fruit, make statistics on the leakage rate and breakage rate, and study the statistical effect of fruit picking from a macro perspective. At the same time, the impact force was calculated.

Structure of the test bench

The schematic diagram of the simple comb teeth made in this study to experience the comb stripping process in the field and the envisaged continuous picking head are shown in Fig. 1. As the picking head advances with the machine, the comb teeth rotate backward around its pivot to comb the branches, and the picked fruit slides down into the device located in the centre of the reel after the comb teeth are raised higher than the pivot. The cross-section shape of comb teeth was all circular in previous studies *(Du et al., 2019; Liu et al., 2021)*, to make the simple comb easily in the Fig.1, a circular cross-section is also used. However, if from the contact point of view, under the same external force, the contact area between the fruit of the approximate sphere and the cylindrical surface is smaller than that of the triangular comb tooth, the corresponding contact stress is larger, and theoretically, greater fruit damage will be caused *(Kang et al., 2017)*. Based on the above considerations, a triangular-section comb was used in this study.

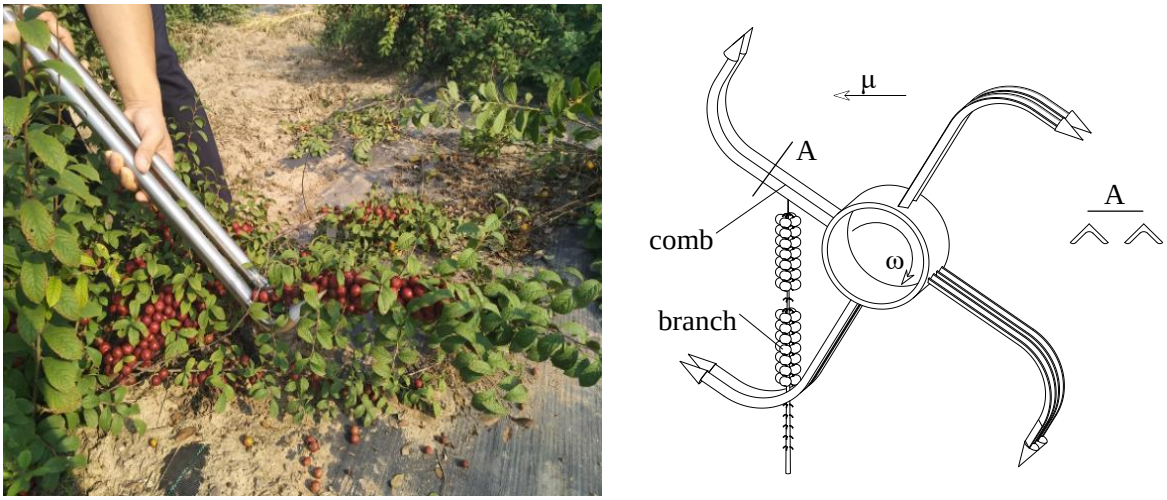

Fig. 1 - Schematic diagram of simple combing and continuous harvesting of *Cerasus humilis*

The structure of the test bench is shown in Fig 2. A winch *13* with a decelerating motor is fixed on the ground, and a speed governor *12* is provided. Two supporting platforms *1* with a height of nearly 1 m are placed, and a rectangular frame *10* is arranged between the two platforms. A pressure sensor *9* is connected to each longitudinal side of the frame. The other end of the sensor has two isosceles triangular sections of comb *8* mounted through a transverse support plate with long holes for adjusting the comb gap. The edge that forms the gap has as large a rounded corner as possible near the tooth surface to prevent scratching the fruit.

One transparent acrylic baffle 7 is placed on each side of the comb teeth to prevent the fruit from falling after the fruits are stripped, to avoid affecting fruit injury, and to facilitate subsequent statistical work. Also, some supporting sensor power supply, transmitter, and other electrical appliances are included.

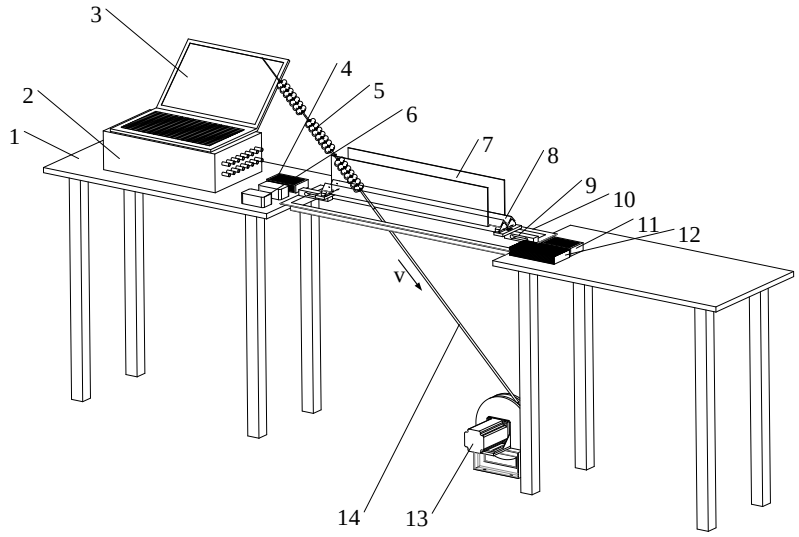

Fig. 2 - Combing test bench

1. Platform; 2. Data acquisition system; 3. Data processing software; 4. Sensor power; 5. Branch; 6. Transmitter; 7. Baffle; 8. Comb; 9. Sensor; 10. Frame; 11. Motor power; 12. Governor; 13. Gear motor and winch; 14. Rope

According to the previous combing experience of the hand-held tool, the quality of the parts above the sensor, and the peak tension of 300 N on the branch, the two pressure sensors adopted the ZEMIC L6D sensor with a measuring range of 0 ~ 200 N and a comprehensive error of ±0.02%. The transmitter is equipped with the same brand, the accuracy is 0.1%, and the output is a 0-5 V standard voltage signal. Before the test bench is installed, an electronic scale is used to test the quality of the accessories above the sensor. After the installation, the transmitter needs to be adjusted to a certain extent, so that the gravity corresponding to the mass can display the correct static voltage signal on the software. One end of the rope is connected to the root of the branch, and the other end is wound around the winch, and the tension and speed of the passing - tooth are provided by the adjustable motor to drive the winch. A nylon winch with a radius of 0.065 m is selected according to the size of the test bench.

Maximum torque required for winch

$$T_{max} = F \times r = 300 \times 0.065\ N \cdot m = 19.5\ N \cdot m \quad (1)$$

Where: F–estimated maximum tension of branch, 300 N

r–winch radius, 0.065 m

Du et al., (2019), found that the maximum speed of *Cerasus humilis* branches passing vertically through the circular-section of the comb was 0.4 m/s, which had a good effect. Through the observation of his test bench, it is found that the lack of a collecting device causes the fruit to fall after combing, so the statistical damage rate is related to the landing impact. In the continuous picking envisaged in this paper, branches and comb teeth are mostly oblique, which has better fruiting conditions. In the pre-test, it is found that the fruit spread along the comb surface and the accumulation phenomenon is not as serious as the vertical combing, so the passing-teeth speed can be faster, and good results can be obtained even when the value is lower than 1.35 m/s, which is set as the maximum linear speed at the bottom of the winch groove v.

The maximum rotational speed of the gear motor is:

$$\omega_{max} = \frac{v}{r} = \frac{1.35}{0.065} rad = 20.8\ rad/s = 198\ r/min \quad (2)$$

The maximum power of the gear motor is:

$$\mathrm{P}_{max} = \frac{T_{max} \times \omega_{max}}{9550} = \frac{19.5 \times 198}{9550} = 0.4\ kW \quad (3)$$

The motor model 6DC400-24GU is selected according to the above calculation. The maximum rotational speed is 200 r/min and the maximum torque is 19.12 N.m. Since the estimated maximum combing force is sufficient, this type of motor meets the requirements.

The gear motor spins the winch, and after the winch wraps the rope, the branch is dragged through the gap between the comb teeth.

The branch movement direction denoted by v shown in Fig.2 is pulled by the winch over the comb teeth, and the fruit is stripped by the comb teeth. The fruit has some damage phenomena, such as leakage, stuck loss, fracturing, and scratching during this process. The combing effect of the test bench is evaluated by statistics of the above loss and damage. At the same time, the comb is also affected by the impact force of the fruit, the impact force is transmitted to the two pressure sensors below. The transmitter converts the sensor signal into a standard voltage signal and then passes it into the signal collector. The signal collector and supporting software analyse the voltage signal and obtain the dynamic data of the impact force of the branch on the comb tooth.

Test materials, methods and indexes

"Nongda No. 4" *Cerasus humilis* branches were regarded as experimental materials in Juxin Modern Agriculture Demonstration Park, Taigu District, Jinzhong City, Shanxi Province, which were cut off and brought back to the laboratory on the morning of September 5, 2022. The third-year basal branches were cut from the root, the branches of this year are moderate in flexibility, dense in fruit, and many fruits seamlessly close together being the most adverse to comb and the extreme material for testing. To make the test results only affected by experimental factors, try to eliminate the difference between the test materials, the selected branches are as close as possible in terms of length, fruit number and compactness. A small number of stunted and damaged fruits were manually removed to facilitate the correct evaluation of the effect of the operation at a later stage. The fruits within 100 mm of the root were removed to facilitate the connection of the rope and eliminate the influence of the motor starting instantaneous speed instability on the test. When removing the fruit, the arrangement of the sparse fruit is not deliberate, because the sparse fruit is easy to pick, has small combing resistance, and it is not easy to leak and damage, which is not conducive to testing the effectiveness of the combing method.

Before each test, the branches were numbered, a number tag was affixed to the root, and the fruit was counted. The branch is placed on the test guide plate at the end of the comb teeth, so that it can enter the teeth smoothly when the rope pulls the root, rather than falling to the side and breaking the branch due to abnormal force. Fig. 3a and b are the images before the test. Fig. 3c and d show the distribution of fruits and branches and leaves on the surface of comb teeth after combing. It can be seen that many leaves and secondary branches with low lignification degrees were combed, and the number of leaves and secondary branches may be related to the space between comb teeth. 3e and f are the retention of leaves and secondary branches and the damage of fruits after combing.

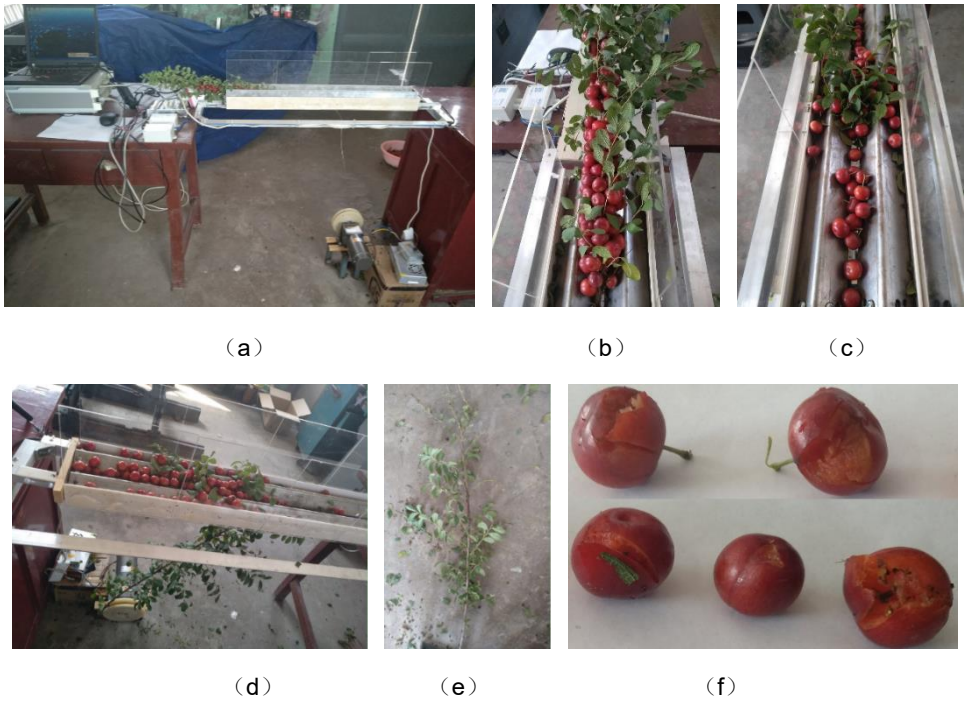

Fig. 3 - Before and after the operation of combing

Breakage rate refers to the percentage of the number of fruits with epidermal rupture in the combing process to all fruits in the whole branch, see Equation 4. Statistics were taken immediately after every test, the fallen fruits were not considered, only the damaged fruits on the tooth surface were considered, and the internal injury was not considered.

Leakage rate refers to the percentage of the fruit that is not trapped on the tooth surface as a percentage of all the fruit in the whole branch, see Equation 5. The stiffness of *Cerasus humilis* is low, a large deformation will occur when even a small force is applied, and some smaller fruits will be squeezed through the gap, more likely to occur when the gap is larger. Fruit stuck in the middle of the combs should also be regarded as lost because it is unlikely to enter the fruit-collecting device, such fruit may be crushed by subsequent branches and cause damage, and fruit that falls through the gap is lost regardless of whether it is broken or not.

$$Y_1 = \frac{N_1}{N} \times 100\% \quad (4)$$

$$Y_2 = \frac{N_2}{N} \times 100\% \quad (5)$$

Where: Y_1–breakage rate, [%];

Y_2–leakage rate, [%];

N–number of fruit before combing;

N_1–number of broken fruit;

N_2–the number of leaked fruit.

Orthogonal test

Test factor selection

It is found that the comb gap will affect the success rate of picking from the preliminary test, too big a gap will lead to more leakage, and too small a gap will cause the gap congestion and cause more serious damage to the branch. The gap of comb teeth is regarded as an important parameter of comb tooth structure, which is worth studying. According to the previous size survey of the fruit-bearing branches, the maximum diameter is about 7 mm. The secondary branches and leaves will lean on the primary branches when passing the comb gap, which increases the difficulty of passing. The comb gap is larger than the diameter of the branch, but also less than the minimum diameter of the fruit, the minimum diameter of "Nongda No. 4" *Cerasus humilis* is as low as 15 mm, 10 ~ 14 mm is considered the ideal gap range when considering a certain fruit deformation, and three levels of 10, 12, 14 mm are set.

Comb teeth with isosceles triangle section were used to replace the previous circular section in the study, and the contact between two convex curved surfaces was changed into the contact between convex and plane, and the contact area was increased theoretically *(Johnson et al., 1987)*. They are usually carried out one by one when picking large-size fruits and vegetables, a concave manipulator is used to increase the contact area *(Zhi-Guo et al., 2009)*. *Cerasus humilis* is too small to be picked one by one, and the contact area also cannot be further increased. At the same time, it also has the problem of contact angle in the triangular comb tooth, and the base angle of the isosceles triangle is specified here as the characteristic angle of the comb tooth. Different angles and different forces will cause different working effects, then the comb angle is also regarded as a factor affecting the comb effect, and 3 levels are set, respectively, 30°, 45° and 60°.

According to the author's previous research, the contact velocity of 1.18 m/s (corresponding to the drop height of 70 mm) is the critical height for yielding inside the fruit *(Kang et al., 2023)*. The contact force is complicated when the branch is combed off, it is found that the damage caused is within the acceptable range of mechanical harvest in the pre-test when the winch rotation speed does not exceed 200 r/min. At the same time, the efficiency of the operation is affected by too low speed. The speed of the branches passing through the comb was also regarded as an influencing factor, and three levels of 130, 160 and 190 r/min were set. Equation 2 was used to calculate the corresponding branch velocities, which were 0.9, 1.1 and 1.3 m/s respectively. The no-load speed was adjusted to the target value before the test.

Test method

It can be seen that the winch rotational speed, comb gap and tooth angle are the main factors affecting the operation effect from the above analysis, In order to reduce the number of test, a three-factor and three-level orthogonal test is conducted to find the optimal values of the factors, and the zero-level test is repeated five times (*Klauss et al., 2008*). The influence rule of three factors on the operation effect is studied through the analysis of variance of the test results. Data analysis software Design-Expert 12 was used to design the test, and variance analysis, model construction, and related graph drawing were performed on the test results.

RESULTS

The orthogonal test design and its physical test results data are shown in Table 1. Statistical work was carried out immediately at the end of each test, and the indicators of the last two columns were calculated.

Table 1

Test design and results

Run	Rotational speed (A) （r/min）	Comb gap (B) (mm)	Comb angle (C) (°)	Damage rate (Y_1) （%）	Leakage rate (Y_2) （%）
1	160	12	45	4.3	4.1
2	190	10	45	7.4	0
3	160	10	30	4.6	0
4	160	12	45	4.1	4.3
5	130	10	45	1.1	0
6	160	12	45	4.3	5.9
7	190	12	30	4.9	3.4
8	160	10	60	8.6	1.9
9	130	14	45	2.9	11.3
10	190	12	60	7.3	5.4
11	160	14	30	1.4	10.6
12	130	12	30	1.4	3.3
13	160	12	45	2.9	2.4
14	160	14	60	1.4	11.4
15	160	12	45	4.9	2.8
16	190	14	45	6.9	11.4
17	130	12	60	1.7	10

Linear variance analysis was performed on the damage rate, without considering the interaction between factors and the higher-order terms. The results are shown in Table 2, and the model is extremely significant (P<0.01), indicating that the influence of each test factor on the results can be analysed within the range of test values (*Zhang et al., 2018*). The change in winch rotation speed has a significant effect on the breakage rate (P<0.01), it can also be seen in Fig. 4 that the breakage rate increases from 2% to 6% as the rotation speed increases from 130 r/min to 190 r/min. The faster the relative speed, the greater the impact force must be, and the greater the possibility of breakage. So, the winch rotation speed, that is, the speed of the branches relative to the comb teeth, needs to be controlled at a low level from the point of view of the breakage rate. The change of comb gap has a significant influence on the breakage rate (P<0.01), it can also be seen in Fig. 4 that with the widening of the comb gap from 10 mm to 14 mm, the breakage rate decreases from 5% to 3%. The reason may be that the wider gap allows the branches and leaves to pass more smoothly, the crowding phenomenon is reduced, and the bearing condition of the fruit is improved. The influence of the change of comb angle on the breakage rate is not significant. As can be seen from Fig. 4, the breakage rate is slightly increased when the angle changes from 30° to 60°.

Table 2

Analysis of variance of breakage rate

Source	DF	SS	F-value	P-value	Sig
Model	3	57.22	10.97	0.0007	**
Rotational speed (A)	1	33.15	19.07	0.0008	**
Comb gap (B)	1	18.43	10.6	0.0063	**
Comb angle (C)	1	5.64	3.24	0.095	
Residual	13	20.42			
Total	16	79.82			

Notes: SS is the sum of squares, DF is degrees of freedom, Sig is significance, ** means P < 0.01, $F_{0.01}(1,13)=9.07$, $F_{0.01}(3,13)=5.74$.

The image of fruit breakage is shown in Fig. 3f. Observing the morphology of wounds, it can be found that they are not caused by tooth surface extrusion, but are scratched by lateral buds of branches. The lateral bud exerts a tangential force on the fruit when the branch passes against the fruit. The greater the pressure of the fruit, the greater the tangential force if the fruit is restricted in space at some time. The smaller the comb gap means the greater the extrusion pressure and the higher the breakage rate. When the side bud contacts the fruit at a very low speed, the fruit will be pushed away, speeding up the speed, the side bud will cut through the fruit, the faster the relative speed, the easier to cut in, and the higher the breakage rate.

The change of tooth angle can affect the compression force of fruit, but the influence of this factor on the breakage rate is not significant, which is evidence that the wound is not caused by tooth surface compression.

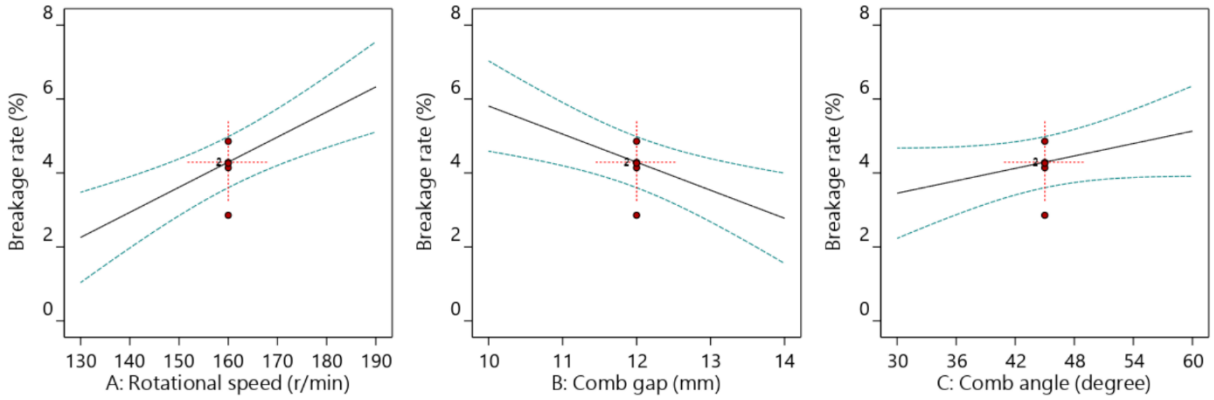

Fig. 4 - Influence of various test factors on breakage rate

Linear regression analysis was performed on the orthogonal test results of the breakage rate, and the model was obtained as shown in equation 6.

$$Y_1 = 0.068A - 0.759B + 0.056C + 0.025 \quad (6)$$

Where：A–Rotational speed of winch, [r/min];

B–Comb gap, [mm];

C–Comb angle, [°].

The coefficient of determination R^2 of the regression model is 0.77, which is not too high, probably because the consistency of agricultural materials is poor, and the number of fruits closes together on the branches and the degree of closeness are not small differences.

Linear ANOVA was performed on the leakage rate, and the results are shown in Table 3. The model was extremely significant (P<0.01). The change in winch rotational speed has no significant effect on the leakage rate. It can also be seen from Fig. 5 that the change in leakage rate is very small when the rotational speed increases from 130 r/min to 190 r/min. The change of the comb tooth gap has a significant effect on the leakage rate (P<0.01), it can also be seen in Fig. 5 that with the widening of the comb gap from 10 mm to 14 mm, the fruit leakage rate increases from 0% to 10%. The reason must be that the wider gap makes it difficult to intercept the fruit, allowing more fruit to squeeze through the gap. From the point of view of the leakage rate, the comb gap needs to be controlled at a low level. The comb angle has a significant impact on the leakage rate. It can also be seen from Fig. 5 that when the comb angle changes from 30° to 60°, the leakage rate also increases greatly. This is because the fruit wedged into the comb is also regarded as a leaked fruit, and the larger angle produces greater lateral extrusion pressure, resulting in some of the fruit getting stuck.

Table 3

Analysis of variance of leakage rate

Source	DF	SS	F-value	P-value	Sig
Model	3	248.25	32.21	<0.0001	**
Rotational speed (A)	1	2.27	0.8848	0.3640	
Comb gap (B)	1	229.59	89.39	<0.0001	**
Comb angle (C)	1	16.39	6.38	0.0253	*
Residual	13	33.4			
Total	16	281.65			

Notes: SS is the sum of squares, DF is degrees of freedom, Sig is significance, ** means P < 0.01, * means P < 0.05, $F_{0.01}(1,13)=9.07$, $F_{0.01}(3,13)=5.74$, $F_{0.05}(1,13)=4.67$, $F_{0.05}(3,13)=3.41$.

Linear regression analysis was carried out on the orthogonal test results of the leakage rate, and the model was obtained as shown in equation 7.

$$Y_2 = -0.018A + 2.679B + 0.095C - 28.406 \quad (7)$$

The coefficient of determination R^2 of the regression model is 0.85, which is slightly higher than that of the damage rate above.

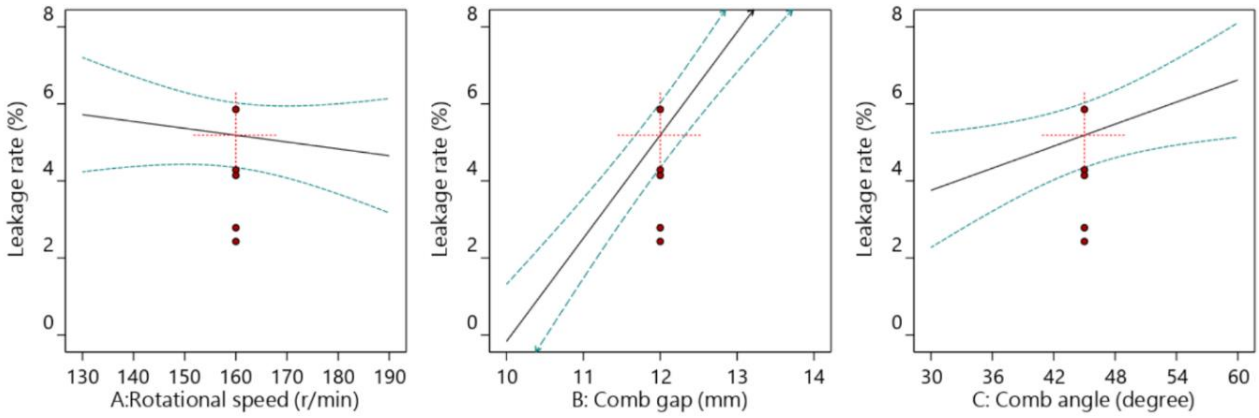

Fig. 5 Influence of each test factor on leakage rate

The reason for examining the models of breakage rate and leakage rate separately is to understand the mechanism by which each of them is affected by factors. It can be seen from the above that factors that have the greatest influence on the breakage rate are the winch rotational speed and the comb gap, while factor that has the greatest influence on the fruit leakage rate is the comb gap, and the bottom angle of the comb teeth only has a certain influence on the leakage rate. Then the combined loss rate is obtained by adding the last two columns in Table 3. The 5th test point with the smallest value is selected, with winch rotational speed of 130 r/min, comb gap of 10 mm, and bottom angle of 45°.

The selection of the results of the comb gap is in line with *Du's* mechanical theory analysis results; he believes that a smaller comb gap has smaller comb withdrawal force and fruit damage *(Du et al., 2019)*. In practice, the comb teeth should be made of materials with high stiffness, which will be subjected to horizontal and vertical impact forces when the branch is pulled off, which will widen the gap, making the actual gap greater than the ideal set value *(Arak et al., 2021)*. The base angle of 45° is selected because its fruit leakage rate is medium, and it can also be made of ready-made angle steel.

The peak value of combing force is the maximum force of branches on combing teeth during combing, which is related to the closeness of the sample fruits. This force is the key load parameter for selecting the tooth material and designing the tooth structure *(Du et al., 2021)*. Although the force–time history data corresponding to each sample is obtained in the orthogonal test, no correlation is found between several test factors, even if the correlation is not of practical significance, only the maximum value has application value. When harvesting, different measures will not be taken according to the closeness of fruits, and the closeness of fruits could not be identified, and the comb structure designed according to the maximum comb force can adapt to the different closeness of fruits. The distribution of the maximum contact force of each test is shown in Fig.6.

The average value is not used here, because the value higher than this index is ignored, and the safety and reliability of picking comb teeth designed according to this index cannot be guaranteed. The maximum comb contact force of all tests is 240 N, which has reference significance for the subsequent design.

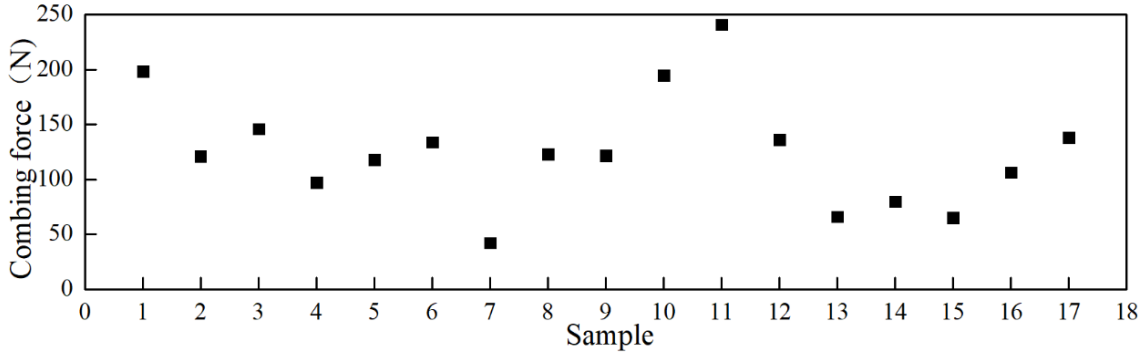

Fig. 6 - Maximum combing force of each sample

CONCLUSIONS

(1) Aiming at the assumed picking principle, a single branch combing test bench based on triangular section combs was designed. Orthogonal tests were carried out with tooth gap, tooth angle and winch speed (passing speed) as test factors, and breakage rate and leakage rate as test indexes. The influence mechanism of the test factors on each index is analysed. The factors that have a significant influence on the breakage rate are the passing speed and the gap of the comb teeth, and the gap of the comb teeth and the angle of the comb teeth have a significant influence on the leakage rate. By synthesizing the two test indexes, the optimal values of the test factors are as follows: comb gap is 10 mm; comb angle 45°; winch rotational speed 130 r/min.

(2) In the test, it was also obtained that the maximum combing force of the branches through the combing teeth was 240 N, which was much larger than the separation force of a single fruit and related to the closeness of fruits. The force is the load condition for the design of comb structure and the selection of power.

ACKNOWLEDGEMENT

This research, titled “Study on single branch combing of *Cerasus humilis*”, was funded by the project: “Shanxi Basic Research Program (Grant No. 202203021221174)”.

REFERENCES

[1] Arak, M., Liivapuu, O., Maksarov, V. V., & Olt, J. (2021). A justification of the choice of parameters for the picking reel tooth on a lowbush blueberry harvester. *Agronomy Research*, 19(3), 1329 – 1338.

[2] DeVetter, L. W., Yang, W. Q., Takeda, F., Korthuis, S., & Li, C. (2019). Modified over-the-row machine harvesters to improve northern highbush blueberry fresh fruit quality. *Agriculture*, 9(1), 13.

[3] Du, X., He, J., He, Y., & Fang, D. (2019). PARAMETER OPTIMISATION AND EXPERIMENT ON THE COMBING OF Cerasus humilis. *INMATEH-Agricultural Engineering*, 57(1).

[4] Du, X., He, J., He, Y., & Fang, D. (2020). Design and experiment of eccentric swing combing device for Cerasus humilis. *INMATEH-Agricultural Engineering*, 60(1).

[5] Du, X., Shen, T., Zhao, L., Zhang, G., Hu, A., Fang, S., ... & Yao, X. (2021). Design and experiment of the comb-brush harvesting machine with variable spacing for oil-tea camellia fruit. *International Journal of Agricultural and Biological Engineering*, 14(1), 172-177.

[6] Ehlert, D., & Beier, K. (2014). Development of picking devices for chamomile harvesters. *Journal of Applied Research on Medicinal and Aromatic Plants*, 1(3), 73-80.

[7] Farooque, A. A., Zaman, Q. U., Groulx, D., Schumann, A. W., Yarborough, D. E., & Nguyen-Quang, T. (2014). Effect of ground speed and header revolutions on the picking efficiency of a commercial wild blueberry harvester. *Applied engineering in agriculture*, 30(4), 535-546.

[8] He, Y., He, J., Du, X., & Fang, D. (2018). Design and experimental study of the finger-type lifter test bench for Cerasus humilis branches. *INMATEH-Agricultural Engineering*, 56(3).

[9] Hong Chang, Yanping Lan, Jiahua Zhou, et al., (2011), Isolation and Identification of Anthocyanins in the Fruits of Prunus humilis Bunge, *Food Science*, vol.32, issue 9, pp.59−63.

[10] Johnson, K. L., & Johnson, K. L. (1987). Contact mechanics. *Cambridge University Press*.

[11] Kang Shilei, He junlin (2017). Design and finite element analysis of harvesting device for the Cerasus humilis (钙果收获装置的设计及有限元分析). *J.Shanxiagric Univ. (Natural Science Edition)*, 36(6).

[12] Kang Shilei., Xu Yanshun., Zhou Jingpu., Tong Bing., & He Junlin. (2023). Study on the characteristics of cerasus humilis free falling impact. *INMATEH-Agricultural Engineering*, Vol.71(3), pp.725-733 https://doi.org/10.35633/inmateh-71-63

[13] Klauss, H., & Kempthorne, O. (2008). Design and Analysis of Experiments. *Introduction to Experimental Design*.

[14] Liu, S., Junlin, H. E., & Wu, N. (2021). Design and experimental study of the comb-type harvesting test bench for cerasus humilis. *INMATEH-Agricultural Engineering*, vol.63(1), pp.261-270; https://doi.org/10.35633/inmateh-63-26

[15] Yu, P., Li, C., Takeda, F., Krewer, G., Rains, G., & Hamrita, T. (2012). Quantitative evaluation of a rotary blueberry mechanical harvester using a miniature instrumented sphere. *Computers and electronics in agriculture*, 88, 25-31.

[16] Zhang, Y., Cui, Q., Li, H., Sun, D., & Hou, H. (2018). Effects of stem region, moisture content, and blade oblique angle on mechanical cutting of millet stems. *INMATEH-Agricultural Engineering*, 55(2), pp.105-112

[17] Zhao, Y., Liu, J., Yang, R., Guo, T., Zhang, J., Li, W., & Li, L. (2023). A comb-brushing-type green soybean pod harvesting equipment: *Design and experiment*. Plos one, 18(11).
[18] Zhi-Guo, L., Ji-Zhan, L., Ping-Ping, L., & Jian-Jun, Y. (2009). Study on the collision-mechanical properties of tomatoes gripped by harvesting robot fingers. *African journal of biotechnology*, 8(24).

CHERRY SEGMENTATION AND IDENTIFICATION BASED ON DeepLabV3 IN COMPLEX ORCHARD ENVIRONMENT
/
基于DeepLabV3 的复杂果园环境下樱桃分割与识别

Jinlong WU*[1,2], Ronghui MIAO[1,2]
[1] College of information science and engineering, Shanxi agricultural university, Taigu / China;
[2] College of agricultural engineering, Shanxi agricultural university, Taigu / China
Tel: +86 18503482797; E-mail: wujinlong8192@163.com
DOI: https://doi.org/10.35633/inmateh-72-61

Keywords: *DeepLabV3, cherry segmentation, complex orchard environment, residual network (ResNet), atrous convolution*

ABSTRACT
Aiming at the problems of less research on cherry segmentation and identification, with slow recognition speed and low classification accuracy in agricultural products, a method based on DeepLabV3 was proposed to realize the rapid segmentation and identification of cherry in complex orchard environment. Complex environment mainly includes front lighting, back lighting, cloudy and rainy days, single fruit, multi fruit, fruit overlap, and branch and leaf occlusion. This model proposed the Atrous Spatial Pyramid Pooling (ASPP) module to effectively extract multi-scale contextual information, and solved the problem of target segmentation at multiple scales. The obtained data was divided into training, validation and testing sets in 7:1:2 ratios, and the residual network 50 (ResNet50) was selected as backbone of the DeepLabV3. Experimental results show that the algorithm in this paper can segment cherry quickly and accurately, the mean intersection over union (MIoU) was 91.06%, the mean pixel accuracy (MPA) was 93.05%, and the kappa coefficient was 0.89, which was better than fully convolutional networks (FCN), SegNet, DeepLabV1 and DeepLabV2. It is demonstrated that this study can provide technical support for intelligent segmentation of agricultural products.

摘要
针对当前樱桃分割与识别研究较少，农产品分割与识别速度慢、分类精度低等问题，本文提出一种基于 DeepLabV3 模型的复杂果园环境下樱桃目标的快速分割与识别方法。DeepLabV3 模型提出的孔洞空间金字塔池化模块可有效地提取多尺度语境信息，解决多尺度下的目标分割难题。复杂果园环境主要包括顺光、逆光、阴雨天气、单果、多果、果实重叠和枝叶遮挡等情况。本研究选取 ResNet50 作为该模型的骨干网络，将获取的图像数据按照 7:1:2 的比例划分成训练集,验证集和测试集。实验结果表明，本文提出的方法可以对复杂果园背景下的樱桃进行快速准确分割，分割的 MIoU 值为 91.06%，MPA 值为 93.05%，kappa 系数为 0.89，均优于 FCN、SegNet、DeepLabV1 和 DeepLabV2 方法，该方法能够为农作物智能分割与识别提供技术支持。

INTRODUCTION
Cherry contains various essential amino acids for human body, it has high medicinal value and can enhance immunity. Hence, utilizing deep learning to realize the segmentation and identification for cherry is a pivotal step in the industrialization process of cherry *(Shuvo et al., 2021)*. In recent years, deep learning has been widely applied in computer vision task, focusing on solving the problems of segmentation *(Yang et al., 2019)*, detection *(Wang and He, 2021)*, recognition *(Liu et al., 2023)*, and target tracking *(Lu et al., 202*1). Among them, image segmentation is the process of understanding images at pixel levels and obtaining target category labels corresponding to each pixel, which has received widespread attention in the field of agriculture.

Recently, several researches on cherry detection and segmentation have been conducted. An image analysis algorithm for the classification of cherry in real time was developed, and histogram analysis was performed on the RGB and HSV colour spaces *(Reyes et al., 2021)*.

[1] *Jinlong Wu, Lect.; Ronghui Miao, Lect.*

[2] *Jinlong Wu, Ph.D.Stud.; Ronghui Miao, Ph.D.Stud.*

A cherry recognition method was proposed based on colour channel transform, in which the RGB colour channel was converted into the M channel in CMYK mode to realize threshold segmentation and edge detection, the experimental results showed that with high efficiency and stability, the algorithm can meet the requirements of cherry fruit recognition *(Yang et al., 2019).* An algorithm based on the improved convolutional neural network (CNN) was proposed to detect the appearance of cherry, and the results demonstrated that the accuracy was 99.4%, which was superior to other methods *(Mohammad et al., 2020).* An instance segmentation model was proposed for automated pruning decisions of sweet cherry, and the results indicated that instance segmentation was a promising approach to make automated pruning decisions in sweet cherry trees trained to the upright fruiting offshoots (UFO) architecture *(Daniel and Manoj, 2023)*. An automated method was proposed for detection of powdery mildew disease in cherry leaf images, the proposed method used an automated strategic removal of background from the image and then extracted the desired diseased portion, and a set of public arXiv e-prints data were used to test the proposed algorithm, the tested algorithm achieved accuracy of 99% *(Gupta et al., 2017)*.

The rapid and accurate segmentation of cherry in complex orchard environment are influenced by several factors: the fruits overlap with each other; the leaves would block the fruits; the lighting environment is complex; the cherry picking robot itself has limited computing resources; the low efficiency in running complex algorithms. These bring difficulties for the rapid and accurate detection of cherry. Manual picking is still the main method at present. Therefore, with scarce agricultural labour and increased picking costs, replacing manual picking with cherry picking robots has important practical significance and broad application prospects.

This paper focuses on cherry segmentation in complex orchard environment, ResNet backbone network combined with DeepLabV3 model was proposed to pre-process and segment the collected cherry images. The training and testing sets of cherry images were established to achieve segmentation and recognition, and the recognition results were analysed and evaluated.

MATERIALS AND METHODS

Data collection

The experimental cherry images were collected in Taigu orchard of Shanxi Province in May 2022. The manual data collection was carried out using an OPPO Reno5 camera model. The shooting distance between the device and the objects was 150 mm-250 mm. A total of 1251 images were collected, with an image resolution of 4032 pixels × 3024 pixels. Figure 1 shows the collected cherry images, which include complex environment such as front lighting, back lighting, cloudy and rainy days, single fruit, multi fruit, fruit overlap, and branch and leaf occlusion. The collected dataset was divided into training, validation and testing sets in 7:1:2 ratios. Seventy percent (876 images) and ten percent (125 images) were randomly selected as the training and validation sets for model training and parameter optimization. The remaining twenty percent (250 images) were used as the testing set to verify the performance of the model.

a. Back lighting+multi fruit *b. Front lighting+multi fruit* *c. Multi fruit+branch and leaf occlusion* *d. Single fruit+No occlusion* *e. Multi fruit+ rainy days*

Fig. 1 - Sample images of cherry in complex orchard environment

Dataset production

In order to ensure that the dataset can meet the PASCALVOC format, it is necessary to annotate the dataset. In this paper, the annotation tool Labelme was used to annotate the cherry images, where cherry was labelled in red, and the background was labelled in black. The annotation results were shown in figure 2.

a. Original image 1 *b. Annotation image 1* *c. Original image 2* *d. Annotation image 2* *e. Original image 3* *f. Annotation image 3*

Fig. 2 - Annotation results of partial cherry images

Cherry segmentation and identification model

This paper constructed a model for segmenting and identifying cherry based on the DeepLabV3 network. The backbone of DeepLabV3 network was ResNet. In order to reduce the parameters and accelerate the training speed of the network, the maximum pooling layer which continuously repeated in the network was removed, and the ASPP after the convolutional layer was added.

ResNet backbone

All neural networks were composed by a combination of convolutional and pooling layers before the ResNet was proposed. Generally, the more convolutional and pooling layers there are, the more comprehensive the image feature information can be obtained, and the better the learning effect of the model. However, in practical experiments, it was found that as the convolutional and pooling layers were stacked, the optimization effect actually deteriorated, and the accuracy of test and training data decreased *(Yu et al., 2022)*. This reason of the phenomenon is that the deepening of the network can lead to gradient disappearance, explosion, and degradation problems *(Zhang et al., 2022)*.

a. Gradient disappearance and explosion

Gradient disappearance: If the error gradient of each layer is less than 1, the deeper the network, the closer the gradient approaches 0 during backpropagation.

Gradient explosion: If the error gradient of each layer is greater than 1, the deeper the network, the larger the gradient value during backpropagation.

b. Degradation problem

As the number of layers increases, the prediction effect actually deteriorates. As shown in figure 3, it is evident that the training and testing performance of 56 layer network is worse than that of 20 layer network.

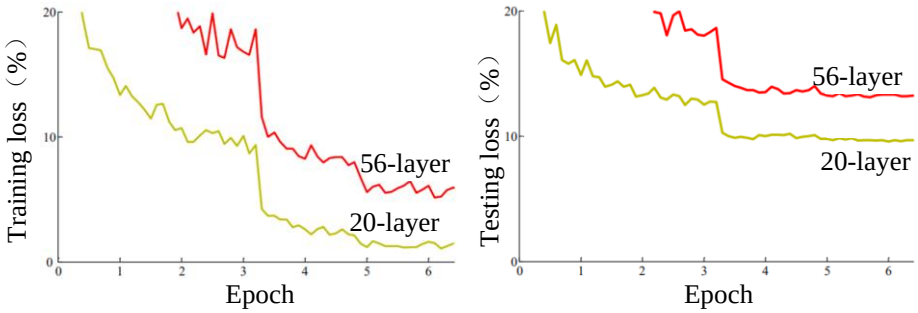

Fig. 3 - Degradation problem

There were already measures such as batch normalization (BN) to alleviate the problems of gradient explosion or disappearance. To solve the degradation problem in deep networks, certain layers of the neural network can be artificially made to skip the connections of neurons in the next layer, connect them in layers, and weaken the strong connections between each layer. In order to achieve good results and reduce degradation, *He et al. (2016)* proposed a new network structure-ResNet, this network won the first place in the classification and target detection tasks in the ImageNet contest, and the error rate was only 3.57%. Compared with the classic models such as AlexNet *(Han et al., 2017)*, VGGNet *(Noubigh et al., 2021)*, and GoogleNet, ResNet possesses prominent image classification performance, its structure can accelerate the training process of the neural networks, and improve the accuracy of the model in image classification.

ResNet is a deep learning network that implements feature extraction, which is a simplified framework for training deep learning models. ResNet has five depth structures (18, 34, 50, 101, and 152), it is composed of several small blocks, which can effectively solve the overfitting problem caused by too many layers. Each layer is composed of multiple blocks, and then form the entire network. The block contains a normal convolutional output layer, a dedicated input-output link branch. The block structure of the ResNet backbone network is shown as figure 4.

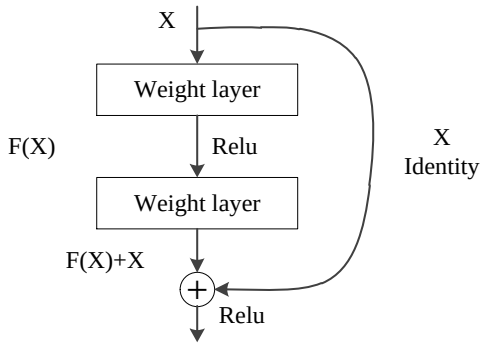

Fig. 4 – Block in ResNet

When the input is X, the learned features are denoted as $H(X)$, then the residual is $F(X)$, in which $H(X)$ is the observed value, and X is the estimated value, residual is the difference between the observed value and the estimated value. Because residual learning is easier than directly learning the original features, then the learning problem of the original features can be solved as $H(X)=F(X)+X$. When the residual is 0, the network only performs identity mapping, and the network performance will not decrease.

DeepLabV3 model

With both serial and parallel atrous convolution modules, DeepLabV3 model can achieve multi-scale object segmentation. It can extract multi-scale contextual information by the cascading and paralleling modules through various atrous rates of atrous convolution effectively *(Chen et al., 2017)*. This model proposes the ASPP module, which improves the ability of extracting global contextual information by the combination hierarchical image information. It can solve the problem of object segmentation at multiple scales, and the structure is shown in figure 5.

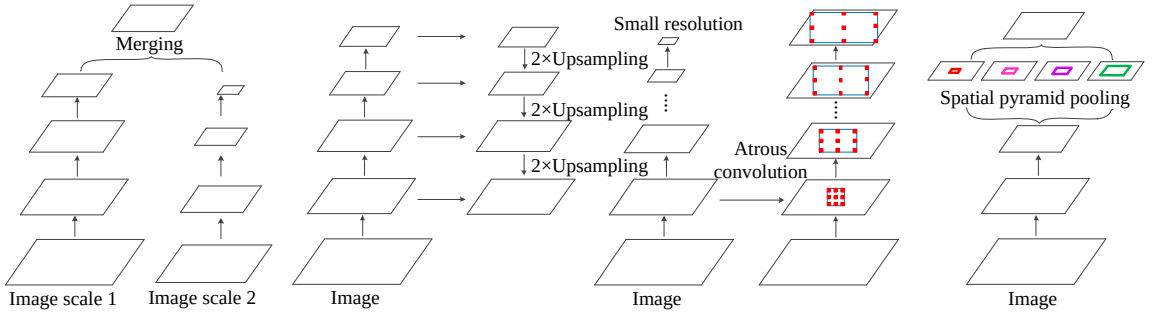

Fig. 5 – DeepLabV3 for capturing multi-scale context

Atrous convolution: In order to solve the problem of the invariance of local image spatial information transformation that hinder dense prediction tasks, atrous convolution is used for pre-training. It mainly removes the last few layers of the dense feature network by down sampling and the corresponding filter kernels for up sampling, which is equivalent to inserting holes between different filter weights to extract more compact features. And this architecture can control the resolution of deep convolutional neural networks (DCNNs) in calculating feature responses without learning new additional parameters.

Atrous space pyramid pooling *(Celik and Talu, 2022)*: This module plays a role in convolutional features to obtain corresponding contextual information through arbitrary scales.

Context module: Typically cascaded behind the model to obtain long-range contextual information, this module exists in DeepLabV1 and conditional random field recurrent neural networks (CRF-RNN).

Encoder and Decoder: Encoders are typically applied to pre trained networks for image classification. Therefore, a decoder is usually used to restore image resolution after encoder. These modules often exist in FCN, SegNet, U-Net *(Park et al., 2021)*, and RefineNet *(Viswanathan and Chu, 2005)*.

DeepLabV3 uses ResNet as the backbone network, which makes it easier to obtain global information in deeper modules. By using the last few blocks to transform them into atrous convolutions, it can maintain the computational complexity and resolution, resulting in denser feature responses and avoiding the loss of detail content in the segmentation network. Specifically, the structures of Block1 to Block4 are directly copied from the original structure of ResNet, and then Block4 is replicated three times resulting in Block 5-7. The difference between them is the use of different expansion rates, as shown in figure 6 and 7.

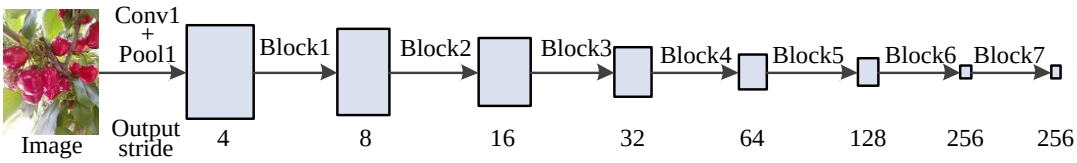

a. cascading modules with convolution while without deep layers

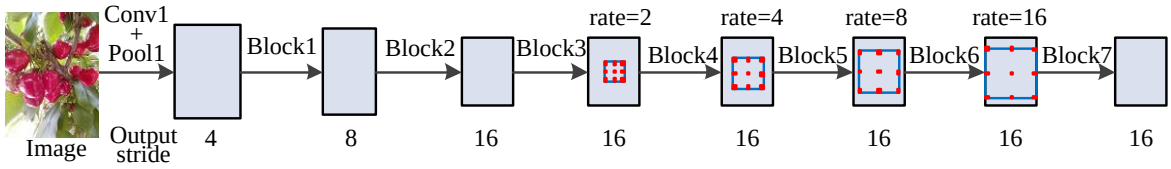

b. When output stream=16, perform atrous convolution of rate>1 after Block3

Fig. 6 – Cascading modules with inverse convolution

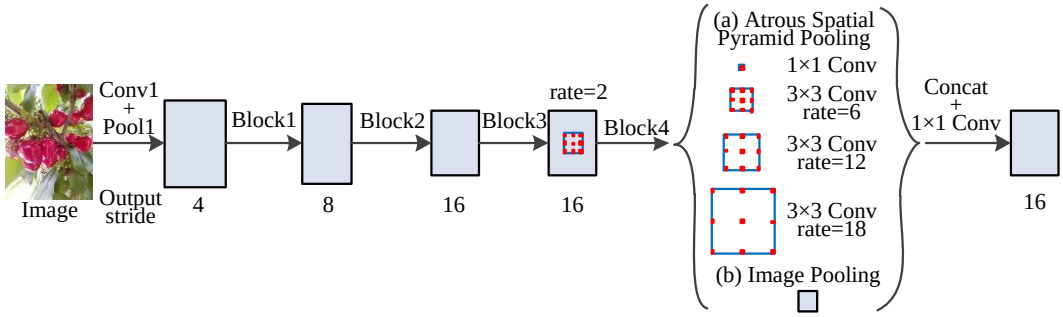

Fig. 7 – ASPP based on image level features

Model evaluation

In this paper, the confusion matrix, mean intersection over union, overall accuracy of classification, user accuracy, producer accuracy and kappa coefficient were used to evaluate the classification results. Confusion matrix is mainly used to compare the classification results with the actual measured values. Here, r is category, X_{ij} represents the percentage of category i judged as the category j by the classifier in the total number of category i; X_{ii} is the number of pixels in row i and column i in the confusion matrix (the number of correct classifications); X_{i+} and X_{+i} are the total number of pixels in row i and column i respectively; N is the total pixels.

MIoU: Inference calculation is performed separately on each category dataset. The calculated intersection of the predicted area and the actual area is divided by the union of the predicted area and the actual area, and the results obtained from all categories are averaged. The value is calculated as formulas (1) and (2).

$$IoU = \frac{TP}{TP + FP + FN} \tag{1}$$

$$MIoU = \frac{1}{k+1}\sum_{i=0}^{k}\frac{Pii}{\sum_{j=0}^{K} Pij + \sum_{j=0}^{K} Pji - Pii} \tag{2}$$

MPA: Its meaning is to calculate the proportion of correctly classified pixels for each class separately and then accumulate to calculate the average, that is, the proportion of correctly predicted pixels in the category to the total pixels (sum of diagonal element values/sum of total element values). The higher the accuracy, the better the quality of the model.

MPA first calculates the pixel accuracy (*PA*) for each class, and then averages the *PA* for all classes, as shown in formulas (3) and (4):

$$PA = \frac{\sum_{i=0}^{K} Pii}{\sum_{i=0}^{K}\sum_{j=0}^{K} Pij} \tag{3}$$

$$MPA = \frac{1}{K+1}\sum^{K}\frac{P_{ii}}{\sum^{K} P_{ij}} \tag{4}$$

Assuming there are $K+1$ classes (from class 0 to class K, which contain an empty class or background), P_{ij} represents the number of pixels that originally belongs to class i but were predicted to be class j, P_{ii} (true positives) represents the true numbers, while P_{ij} and P_{ji} are interpreted as false positives and false negatives respectively.

Overall classification accuracy (*OA*) is equal to the sum of correctly classified pixels divided by the total pixels, as shown in formula (5):

$$OA = \frac{\sum_{i=1}^{r} X_{ii}}{\sum_{i=1}^{r}\sum_{j=1}^{r} X_{ij}} \tag{5}$$

User accuracy (*UA*) indicates the probability that a certain type of sample is correctly classified, as shown in formula (6):

$$UA = \frac{X_{ii}}{X_{i+}} \tag{6}$$

Producer accuracy (*PA*) represents the probability that a certain type of sample in the classification diagram is correctly classified, as shown in formula (7):

$$PA = \frac{X_{ii}}{X_{+i}} \tag{7}$$

Kappa coefficient can make full use of the information of confusion matrix. It can be used as a comprehensive index for the evaluation of classification accuracy. The relationship between classification quality and kappa statistics are: the range of kappa coefficient is 0.0-0.2, the classification quality is “Difference”; the range of kappa coefficient is 0.2-0.4, the classification quality is “Commonly”; the range of kappa coefficient is 0.4-0.6, the classification quality is “Good”; the range of kappa coefficient is 0.6-0.8, the classification quality is “Very Good”; the range of kappa coefficient is 0.8-1.0, the classification quality is “Excellent”. The calculation formula of kappa coefficient is (8):

$$K = \frac{N\sum_{i=1}^{r} X_{ii} - \sum_{i=1}^{r}(X_{i+}X_{+i})}{N^2 - \sum_{i=1}^{r}(X_{i+}X_{+i})} \tag{8}$$

Experimental environment configuration and network parameter settings

The operating system is Windows 10, the CPU model is Intel (R) Core (TM) i7-12700F CPU@2.10GHz, the GPU model is NVIDIA GeForce RTX 3080, the running memory is 32GB, the hard drive is 1T. The programming language is Python 3.9, the deep learning framework is Python 1.13.0, and the GPU acceleration libraries are CUDA11.7 and CUDNN8.4.1.

To shorten the training time of the network, the freezing training method was adopted. When freezing the backbone network for training, the initial learning rate was 0.001, the batch processing amount was 16, and the momentum was 0.9. The network training learning rate after thawing was 0.0001, the batch size was 8, and the iteration epoch was 300.

RESULTS AND DISCUSSION

Figure 8 shows the segmentation and recognition results of cherry. In the segmentation results, 8(a) are the original images, 8(b) are the annotation images, 8(c) are the segmentation results in mask, and 8(d) are the segmentation results on the original images. In 8(b) and 8(c), red represents the cherry region, and black represents the background. The backbone network in the model is ResNet50. From figure 8(c) and 8(d), it can be seen that the DeepLabV3 model can effectively achieve segmentation of cherry in different orchard environment.

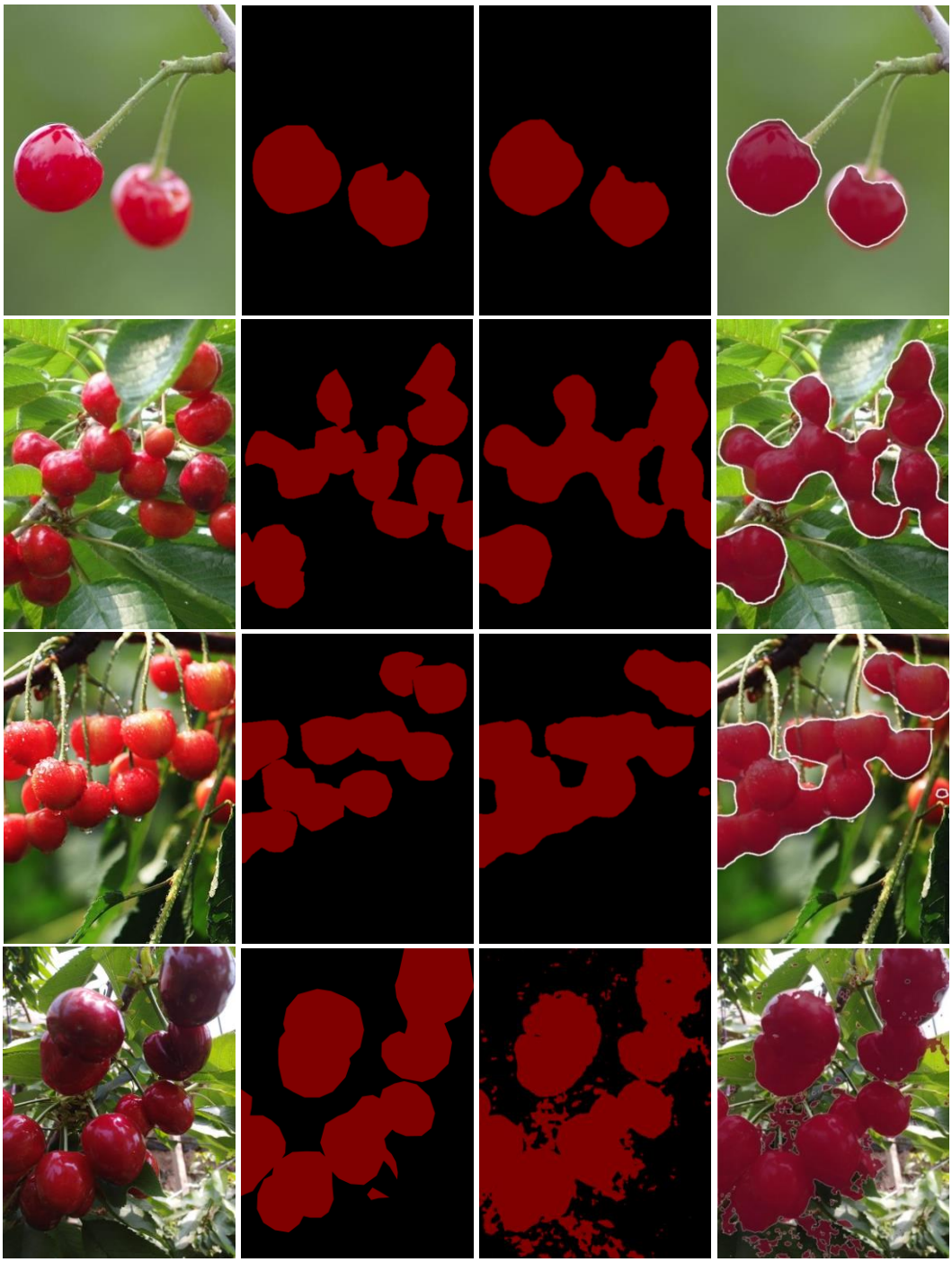

a. Original images b. Annotation images c. Segmentation results in mask d. Segmentation results on the original images

Fig. 8 – Segmentation and recognition results of cherry in DeepLabV3

Tables 1 and 2 show the confusion matrices corresponding to the classification prediction results of figure 8 (the first image), which expressed in numerical and percentage forms respectively. The former can clearly express the number of correctly and incorrectly classified pixels for different categories, while the latter can represent the accuracy of classification.

From tables 1 and 2, it can be seen that the total number of rows represents the total number of other pixels classified into that category, the total number of columns represents the true ground truth values for each category, and the diagonal elements represent the correct number of classification for each category. By calculating the sum of diagonal elements, the number of correctly classified objects can be calculated as 56397, with an overall classification accuracy of 92.53%. Table 2 shows the percentage of correct and incorrect classification for each category. It can be seen from the table that the classification accuracies of the cherry and background regions are relatively high, at 91.07% and 93.10% respectively.

Table 1

Confusion matrix of segmentation results (numerical)

Categories	Cherry	Background	Total of row
Cherry	15622	3023	18645
Background	1532	40775	42307
Total of Column	17154	43798	60952

Table 2

Confusion matrix of segmentation results (Percentage)

Categories	Cherry	Background	Total of row
Cherry	91.07	6.90	97.97
Background	8.93	93.10	102.03
Total of Column	100.00	100.00	200.00

The UA and PA of each category can also be calculated by the confusion matrix, table 3 shows the UA and PA corresponding to figure 8 (the first image). It can be seen that the UA and PA of background and cherry are both higher, which can reach over 83%.

Table 3

User accuracy and producer accuracy of classification prediction results for 9 feature vectors

Classification results	UA	UA(%)	PA	PA(%)
Cherry	15622/18645	83.79	15622/17154	91.07
Background	40775/42307	96.38	40775/43798	93.10

Identification results of different methods

Table 4 is the classification results compared with FCN, SegNet, DeepLabV1 and DeepLabV2 of the testing images. The MIoU and MPA of FCN are 78.81% and 76.54% respectively, which are the worst among all methods. Compared with traditional CNN, the input images in FCN can be of any size and the algorithm is more efficient. However, its segmentation results are not precise and not sensitive to the details of the image, at the same time, the relationship between pixels has not been fully considered, there is a lack of spatial consistency *(Wang et al., 2020)*.

The MIoU and MPA of SegNet are 89.28% and 88.45% respectively, which are better than FCN. The main reason is that SegNet utilizes the maximum pooling position index for upsampling, which not only reduces the computational complexity but also better preserves the edge information of the image *(Li et al., 2021)*.

With the upgrade of the version for DeepLab series methods, the segmentation results have also been correspondingly improved. On the basis of DeepLabV1, DeepLabV2 can achieve better performance by using multi-scale processing and ASPP. DeepLabV3 expands ASPP module to better solve segmentation problems at multiple scales *(Kwak and Sung, 2021)*. Among all the methods, the identification results of our method are the highest, the MIoU is 91.06%, the MPA is 93.05%, and kappa coefficient is 0.89, and the overall classification effect is “Good”.

Table 4

Classification results of different methods

Methods	MIoU (%)	MPA (%)	Average Kappa coefficient
FCN	78.81	76.54	0.73
SegNet	89.28	88.45	0.82
DeepLabV1	83.23	81.06	0.83
DeepLabV2	88.75	85.37	0.85
Our method	91.06	93.05	0.89

CONCLUSIONS

In this paper, DeepLabV3 was adopted to realize the rapid segmentation and identification of cherry in complex orchard environment. Compared with FCN, SegNet, DeepLabV1 and DeepLabV2, the identification results of our method are the highest, and the overall classification effect is “Good”. The algorithm in this paper can achieve cherry target segmentation in various complex backgrounds, such as front lighting, back lighting, cloudy and rainy days, single fruit, multi fruit, fruit overlap, and branch and leaf occlusion. It can provide theoretical basis for object detection, segmentation, and localization of fruits and vegetables in complex orchard environments. In image segmentation and recognition, future work can improve the network structure and introduce attention mechanisms to increase the acquisition of image feature information, thus, improving the recognition accuracy and extraction speed of the model.

The method in this paper mainly focuses on the application of intelligent cherry picking robots, and it has not been verified in embedded devices. Generally, deploying image segmentation models on embedded devices requires smaller model size and higher recognition speed. Therefore, further research is needed on the lightweight of the models while ensuring its accuracy and recognition speed, which can solve the problem of weak processing performance in embedded devices. The subsequent research on lightweight of the models will be implemented such as network pruning and efficient network structures.

ACKNOWLEDGEMENT

This research was funded by Shanxi Agricultural University Youth Science and Technology Innovation Fund, grant number 2019023; Shanxi Province Applied Basic Research Youth Project, grant number 202203021212428; Shanxi Province Applied Basic Research Youth Project, grant number 202203021212414.

REFERENCES

[1] Celik, G., & Talu, M. (2022). A new 3D MRI segmentation method based on Generative Adversarial Network and Atrous Convolution. *Biomedical Signal Processing and Control*, 71, 103155. https://doi.org/10.1016/j.bspc.2021.103155

[2] Chen, L. C., Papandreou, G., Kokkinos, I., Murphy, K., & Yuille, A. (2017). Deeplab: Semantic image segmentation with deep convolutional nets, atrous convolution, and fully connected CRFs. *IEEE transactions on pattern analysis and machine intelligence, 40*(4), 834-848. https://doi.org/10.1109/tpami.2017.2699184

[3] Daniel, B., & Manoj, K. (2023). Automated pruning decisions in dormant sweet cherry canopies using instance segmentation. *Computers and Electronics in Agriculture*, 207, 107716. https://doi.org/10.2139/ssrn.4202299

[4] Gupta, V., Sengar, N., Dutta, M., Travieso, C. & Alonso, J. (2017). Automated segmentation of powdery mildew disease from cherry leaves using image processing. *International Conference and Workshop on Bioinspired Intelligence (IWOBI), 15*(10), 27-37. https://doi.org/10.1109/iwobi.2017.8006454

[5] Han, X., Zhong, Y., Cao, L., & Zhang, L. (2017). Pre-Trained AlexNet Architecture with Pyramid Pooling and Supervision for High Spatial Resolution Remote Sensing Image Scene Classification. *Remote Sensing, 9*(8), 848. https://doi.org/10.3390/rs9080848

[6] He, K., Zhang, X., Ren, S., & Sun, J. (2016). Deep residual learning for image recognition. *In Proceedings of the IEEE conference on computer vision and pattern recognition*, 770-778. https://doi.org/10.1109/cvpr.2016.90

[7] Kwak, J., & Sung, Y. (2021). DeepLabV3-Refiner-Based Semantic Segmentation Model for Dense 3D Point Clouds. *Remote Sensing, 13*(8), 1565. https://doi.org/10.3390/rs13081565

[8] Li, Q., Wang, H., Li, B., Yanghua, T., & Li, J. (2021). IIE-SegNet: Deep semantic segmentation network with enhanced boundary based on image information entropy. *IEEE Access,* 9, 40612-40622. https://doi.org/10.1109/access.2021.3064346

[9] Liu, K., Lin, K., & Zhu, C. (2023). Research on Chinese traditional opera costume recognition based on improved YOLOv5. *Heritage Science*, *11*(1), 1727. https://doi.org/10.1186/s40494-023-00883-x

[10] Lu, P., Ding, Y., & Wang, C. (2021). Multi-small target detection and tracking based on improved YOLO and sift for drones. *International journal of innovative computing, information and control*, *17*(1), 205-224. http://www.ijicic.org/ijicic-170114.pdf

[11] Mohammad, M., Ahmad, J., Khalegh, J., & Zhang, Y. (2020). Accurate classification of cherry fruit using deep CNN based on hybrid pooling approach. Postharvest Biology and Technology, 166, 111204. https://doi.org/10.1016/j.postharvbio.2020.111204

[12] Park, J., Choi, J., Seol, S., Byun, J., & Kim, Y. (2021). A method for adequate selection of training data sets to reconstruct seismic field data using a convolutional U-Net. *Geophysics*, 1-103. https://doi.org/10.1190/geo2019-0708.1

[13] Reyes, J. F., Contreras, E., Correa, C., & Melin, P. (2021). Image analysis of real-time classification of cherry fruit from colour features. *Journal of Agricultural Engineering, 52*(4). https://doi.org/10.4081/jae.2021.1160

[14] Shuvo, M., Ahommed, R., Reza, S., & Hashem, M. (2021). CNL-UNet: A novel lightweight deep learning architecture for multimodal biomedical image segmentation with false output suppression. *Biomedical Signal Processing and Control*, 70, 102959. https://doi.org/10.1016/j.bspc.2021.102959

[15] Viswanathan, N., & Chu, C. (2005). FastPlace: efficient analytical placement using cell shifting, iterative local refinement and a hybrid net model. *IEEE Transactions on Computer-Aided Design of Integrated Circuits and Systems*, *24*(5), 722-733. https://doi.org/10.1145/981066.981072

[16] Wang, D., & He, D. (2021). Channel pruned YOLO V5s-based deep learning approach for rapid and accurate apple fruitlet detection before fruit thinning. *Biosystems Engineering*, *210*(6), 271-281. https://doi.org/10.1016/j.biosystemseng.2021.08.015

[17] Wang, Z., Xie, L., & Qi, J. (2020). Dynamic pixel-wise weighting-based fully convolutional neural networks for left ventricle segmentation in short-axis MRI. *Magnetic resonance imaging: An International journal of basic research and clinical applications, 66*(1), 131-140. https://doi.org/10.1016/j.mri.2019.08.021

[18] Yang, W., Zhang, J., Xu, Z., & Hu, K. (2019). Real-time DeepLabv3+ for pedestrian segmentation. *Journal of Optical Technology c/c of Opticheskii Zhurna*l, *86*(9), 570. https://doi.org/10.1364/jot.86.000570

[19] Yang, R., Wu, M., Bao, Z., & Zhang, P. (2019). Cherry recognition based on colour channel transform. *The 2019 International Conference on Artificial Intelligence and Computer Science*, 292-296. https://doi.org/10.1145/3349341.3349419

[20] Yu, L., Zeng, Z., Liu, A., Xie, X., Wang, H., Xu, F., & Hong, W. (2022). A Lightweight Complex-Valued DeepLabv3+ for Semantic Segmentation of PolSAR Image. *IEEE Journal of Selected Topics in Applied Earth Observations and Remote Sensing*, 15. https://doi.org/10.1109/jstars.2021.3140101

[21] Zhang, X., Bian, H., Cai, Y., Zhang, K., & Li, H. (2022). An improved tongue image segmentation algorithm based on Deeplabv3+ framework. *IET Image Processing*, 16. https://doi.org/10.1049/ipr2.12425

DESIGN AND TESTING OF A COTTON STALK CLAMP-PULLING TEST BENCH
/
棉秆对夹拉拔试验台设计与试验

Jiaxi ZHANG *[1,2], Zhenkun LI [1], Gang GUO [1], Yasenjiang BAIKELI [1], Yichao WANG [1], Jialin CAI [1], Zhenwei WANG [1,3]

[1]Xinjiang Agricultural University, School of Mechanical and Electrical Engineering, Urumqi / China;
[2]Xinjiang Key Laboratory of Intelligent Agricultural Equipment, Urumqi / China
[3] Nanjing Institute of Agricultural Mechanization, Ministry of Agriculture and Rural Affairs / China
Tel: 8613899961137; E-mail: 563810112@qq.com
Corresponding author: Zhang Jiaxi
DOI: https://doi.org/10.35633/inmateh-72-62

Keywords: *cotton stalk, displacement, pulling force, clamping force, clamping plate, friction coefficient*

ABSTRACT

In order to explore the relationship between displacement-pulling force and the change of clamping force during the clamping and pulling process of cotton stalks in the field by different types of clamps, a test bench for cotton stalks clamping and pulling was designed. Based on the combination of virtual instrument technology and external hardware, the device is programmed by Gx Works2 and LabVIEW programming software to complete the operation of the test bench clamping and pulling device and the measurement and acquisition of information. From the mapping of the collected information, the average value of the maximum uplift force on the cotton stalks was 500 N, corresponding to an upward movement of 12 mm at the root of the cotton stalks. Through the collected information the effect of two types of clamps on cotton stalks clamping and pulling was analyzed, rigid splints with the clamping force of 750 N and a linear speed of 0.18m/s having the best effect on the cotton stalks clamping and pulling. Rubber splints have the best effect on cotton stalks clamping and pulling when the clamping force is 500 N and the linear speed is 0.36 m/s. Among them, the striped rubber splint has the best effect. The collected information was subjected to analysis of variance (ANOVA), and the results showed that the coefficient of friction of the clamping plate showed a high influence on both the pull-up force and the reduction of clamping force. Based on the obtained results, it can provide a reference for the design of clamping type cotton stalk harvesting machinery.

摘要

为探讨不同类型夹板对田间棉秆夹持起拔过程中位移-起拔力之间的关系及夹持力变化情况，设计了一种棉秆对夹拉拔试验台。该装置基于虚拟仪器技术与外部硬件相结合，通过 Gx Works2 及 LabVIEW 编程软件进行编程，完成试验台夹持、起拔装置的运行及信息的测量采集。由所采集信息绘图，棉秆所受最大起拔力均值为 500N，对应棉秆根部上移 12mm。通过所采集信息分析两种夹板对棉秆夹持起拔效果，刚性夹板在夹持力 750N 线速度 0.18m/s 时对棉秆夹持起拔效果最优。橡胶夹板在夹持力 500N 线速度 0.36m/s 时对棉秆夹持起拔效果最好，其中条型纹路橡胶夹板效果最优。将所采集信息进行方差分析，结果表明，夹板摩擦系数对起拔力及夹持力减少量均呈现出高度影响。根据所得结果，可为夹持类棉秆收获机械设计提供参考。

INTRODUCTION

As one of the important cash crops in China, cotton is widely planted. In the national cotton planting area, Xinjiang is the main planting area, occupying 82.7% of the share, reaching 2.506×10^6 hm^2. Meanwhile, the cotton production in Xinjiang also occupies 89.5% of the national production, reaching 5.129×10^6 t (*Announcement of National Bureau of Statistics on cotton production in 2022, 2022*). In addition to cotton itself, cotton stalks are one of the main by-products of cotton cultivation. Cotton stalks have a wide range of applications and can be used as renewable biomass resources, poultry feed, paper making, edible mushroom culture, environmental protection materials, and other fields (*Wang Y.J. et al, 2022; Guo T.J. et al, 2018; Song X.Z. et al, 2013*). Therefore, if the recycling of cotton stalk resources can be realized, it will bring great economic benefits *(Gao R.F. et al, 2016; Fire H.X, 2021; Zhang W.Z, 2015*).

*[*1,2]Jiaxi Zhang, Prof.Ph.D.Eng.; [1]Zhenkun Li, M.S.Stud.Eng.; [1]Gang Guo, M.S.Stud.Eng.; [1]Yasenjiang Bakeli, M.S.Stud.Eng.; [1]Yichao Wang, Ph.D. Stud Eng.; [1]Jialin Cai, Ph.D. Stud Eng.; [1,3]Zhenwei Wang, Ph.D. Stud Eng.*

However, manual harvesting of cotton stalks is time-consuming and labor-intensive due to their different shapes and sizes. Therefore, the study of mechanical harvesting technology of cotton stalks has become one of the focuses of mechanization technology research in cotton production in recent years (*Xie J.H. et al, 2023*).

At present, during cotton stalk harvesting, mostly clamping type cotton stalk harvesting machinery is dominated (*Chen J.L. et al, 2018; Jian S.C. et al, 2011*). Clamping type cotton stalk harvesting machinery operation is mainly a process of clamping and pulling (*Liu X. et al, 2017; Tang Z.F. et al, 2018; Zhou S.P, 2019*). So, different types of clamping components on the cotton stalk clamping and pulling effect is different, so the clamping force, pulling force is an important theoretical basis for the design of the key components of the cotton stalk pulling. Existing cotton stalk pulling measurement devices mainly use rigid sleeves or clasps to clamp the cotton stalks, and manually or electrically drive the pulling of the cotton stalks at low speeds. The main drawbacks are that the pulling speed is too slow (*Li Y. et al, 2013*), during the pulling process, the cotton stalks are often ruptured, slipped off and so on.

Aiming at the above existing problems, this paper designs a kind of cotton straw pair clamping and pulling test bed. In the field test, different types of splints were used to clamp and pull the cotton stalks to observe the operation effect. The computer was used to collect the changes in the clamping force of the measured splints and the upward displacement of the roots of the cotton stalks corresponding to the pulling force. Through the test, the relationship between the collected information can be derived, in order to provide the basis of mechanical and structural parameters for the design of the clamping type of cotton stalk harvesting machinery.

MATERIALS AND METHODS

Overall structure

The counter clamp pulling test bench consists of a clamping device, power unit, and transmission mechanism, of which the clamping device and power unit are the main components and the structure of the whole machine is shown in Figure 1.

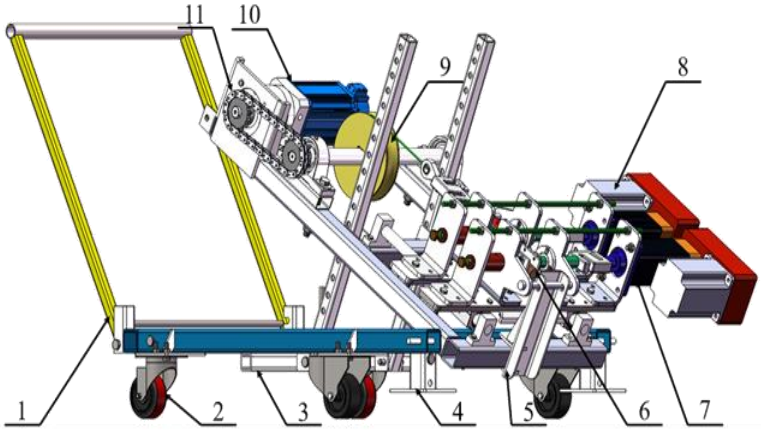

Fig. 1 - Schematic diagram of the structure of the clamping and pulling test bench

1 – Drawbar; 2 – Walking wheel; 3 – Support device; 4 – Rear support device; 5 – Fixed traction frame riser device; 6 – Cotton stalks; 7 – Clamping device Ⅰ; 8 – Clamping device Ⅱ; 9 – Pulley; 10 – Power unit; 11 – Transmission mechanism

Working principle

The working principle is to send digital signals to the programmable logic controller PLC through the computer to drive the power unit and the clamping device, to realize the clamping and pulling action on the cotton stalks. The analog signals from the pulling sensors at the clamping and pulling points are transmitted to the data acquisition card through the analog transmitter, and the data is collected by the card, and the collected data is transmitted to the LabVIEW acquisition program for data acquisition, and through analysis and calculation, the real-time data of the clamping force on the cotton stalks, the pulling force, and the upward displacement of the cotton stalks can be seen on the computer. The distance measuring sensor is directly connected to the data acquisition card for digital signal acquisition, and the edge counting acquisition module in the LabVIEW acquisition program displays and saves the acquired data in real-time. According to the measured data, the clamping force and the relationship between the pulling force and the displacement of the cotton stalks during the pulling process can be obtained. Figure 2 shows the schematic diagram of the pulling force on the cotton stalks in the field test.

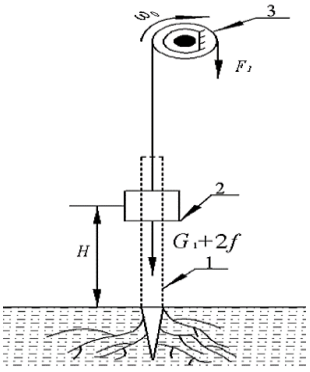

Fig. 2 - Sketch of tensile forces on cotton stalks in the field

1 – Cotton stalk main stem; 2 – Cleat; 3 – Pulley

Note: 90 degrees to pull up the cotton stalks, G_1 is the gravity of the clamping device itself, f is the force of friction, H is the clamping height, F_1 is the pulling force on the cotton stalks.

Design of key components

Design of the clamping device

The WDW-20 microcomputer-controlled electronic universal testing machine was utilized to carry out the pressure test on the measured cotton stalks. It was measured that under the same pressure, the cotton stalks did not rupture between the two materials of the clamping plate. According to the test results, it was determined that the pressure range of the cotton stalks to withstand is 0~1000 N. In view of the previous problems of the cotton stalks clamping device, the clamping device was analyzed, and the cotton stalks were prone to slip and rupture in the clamping part. In order to prevent this from happening to ensure the accuracy of the test data, a controllable electric cylinder is used as the power source of the clamping device based on the measured data when selecting the clamping device. At the same time, the head of the clamping device is installed with a tensile pressure sensor for real-time transmission of clamping force data. The schematic structure of the clamping device is shown in Figure 3.

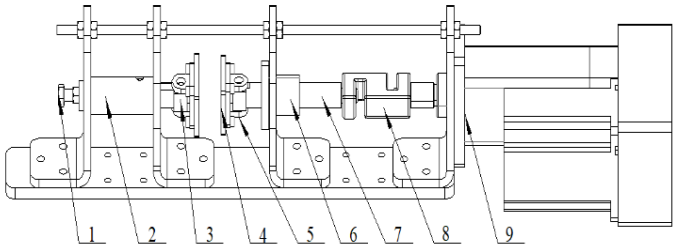

Fig. 3 - Schematic diagram of the structure of the clamping device

1 – Adjusting bolt; 2 – Adjusting sleeve; 3 – Adjustable push rod; 4 – Clamping plate; 5 – Clamping plate fixing plate; 6 – Round flange linear bearing; 7 – Pressure applying push rod; 8 – Pulling pressure sensor; 9 – Electric cylinder

Selection of electric cylinder

The working principle of the electric cylinder is: the motor drives the screw rod to rotate, realizing the axial displacement of the extended end of the electric cylinder. (*Ren M.H, 2018*). Therefore, in the process of applying pressure to the cotton stalks, the motorized cylinder is subjected to axial force-F_a, as shown in the sketch of cotton stalks subjected to clamping force in Figure 4.

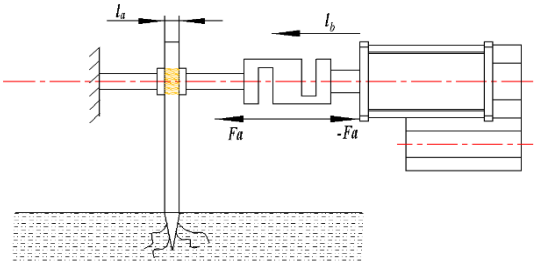

Fig. 4 - Sketch of cotton stalks subjected to clamping forces

Note: l_b is the electric cylinder stroke, l_a is the plywood spacing, F_a is the maximum clamping force

Cotton stalks are subjected to a clamping force F_a.

Therefore:

$$\left|-F_a\right| = F_a = 1000N \quad (1)$$

When selecting an electric cylinder, the most important things are load and speed. Based on the load of 1000 N and speed of 10 mm/s determined before selecting the electric cylinder, a screw with a diameter of 20 mm and a lead of 5 mm was selected. Since the average diameter of the cotton stalk is 12 mm, and the thickness of the clamp plate is 5 mm, in order to leave sufficient space between the clamp plates for clamping the cotton stalks, the clamp plate spacing (la) is designed to be 50 mm. Based on the spacing between the two clamp plates, the stroke of the electric cylinder is selected. The final choice is KDJ60 return electric cylinder with a stroke (l_b) of 50 mm. In order to select a motor that matches the electric cylinder, and the motor torque and power must meet the test requirements, the final choice is an 86-step two-phase motor with a power of 0.05kW and a reduction ratio of 1:1, providing a torque of 1.27 N·m.

Design of power unit and transmission mechanism

In order to accurately measure the pulling force on cotton stalks, and to ensure that the pulling of stalks can be rapid, the average value of the distance from the main rootstock to the ground surface of 10 sampled cotton stalks was measured. The results show that the distance from the bottom of the main rhizome to the ground surface is 180mm, therefore the velocity is set between 0.18 m/s~0.36 m/s to achieve the actual pulling speed. Therefore, the rotation speed and torque of the motor selected for the uprooting force test should meet the requirements. Furthermore, in order to avoid problems such as slipping of cotton stalks or device collision that may be caused by too high a speed, factors such as control precision, overload resistance and stable operation need to be considered in the selection of the power unit. According to the test requirements and actual operation, the final choice is a servo motor as the power source for plucking cotton stalks. In order to ensure that the pulling speed and pulling torque meet the demand or even more, a precision planetary gear reducer and servo motor with a reduction ratio of 1:10 were chosen. Regarding the transmission, the power transmission mechanism of the whole machine adopts the chain transmission and the transmission ratio of 1:1. This transmission mode helps to work in the heavy-duty low-speed and can maintain a stable average ratio. Figure 5 shows the overall schematic diagram of the power unit and transmission mechanism.

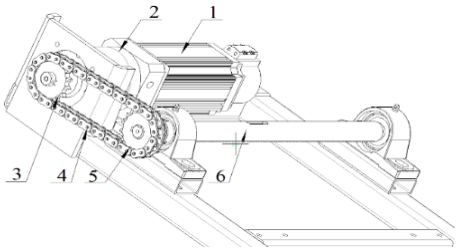

Fig. 5 - Schematic diagram of the power unit and transmission mechanism as a whole

1 – Servo motor; 2 – Precision reducer; 3 – Active sprocket; 4 – Chain; 5 – Driven sprocket; 6 – transmission output shaft

Power unit servo motor selection

Calculation of the power unit motor parameters based on the relevant parameters of the unit.

Servo motor torque calculation:

$$T_1 = F \times r \quad (2)$$

$$T_2 = \frac{T_1}{\eta \bullet \eta_1 \bullet \eta_2} \quad (3)$$

where:

r - pulley radius, 0.0145 m;

F - maximum pulling resistance F_0=2f (850 N) and clamping device's own gravity G_1 (150 N), N;

T_1 - Ideal motor torque, N;

T_2 - motor torque in actual condition, N;

η - servo motor efficiency, 0.87;

η_1 - reducer efficiency, 0.96;

η_2 - transmission efficiency between wire rope and pulley, 0.96;

Servo motor power calculation:

$$P_1 = F \times v \tag{4}$$

$$P_2 = \frac{P_1}{\eta \bullet \eta_1 \bullet \eta_2} \tag{5}$$

where:

P_1 - Ideal motor power, kW;

v - Lifting speed, m/s;

P_2 - motor power in actual condition, kW;

Calculation of servo motor speed:

$$n = \frac{v}{\pi D} \tag{6}$$

Where:

n - motor speed, r/min.

D - pulley diameter, 0.029 m;

After the above calculation, the servo motor parameters are obtained.

According to the parameters obtained, and considering the operating conditions, to prevent the motor from being damaged in the field test due to overloading and overheating, the final choice is the MIG 90ST-M02430 220 V AC servo motor, with a power of 0.75 kW, a speed of 2,500 r/min, and a torque of 2.4 N.m, which can satisfy the requirements of the test.

Design of control and measurement systems and determination of friction coefficients

Design of the control system

This control system is composed of GX Works2 programming software and a domestic Lingyi FX-32 series PLC programmable control module. Programming is done using GX Works2 programming software and communicating with the PLC module at the RS232 serial port. This PLC supports 4-channel high-speed pulse output, and the maximum pulse speed of each channel is up to 100 KHz. In this module, the Y0 and Y2 terminals output pulses, and the Y4 and Y6 terminals control the direction to realize the control of servo motors and electric cylinders. Figure 6 shows the operation control wiring diagram of the whole machine.

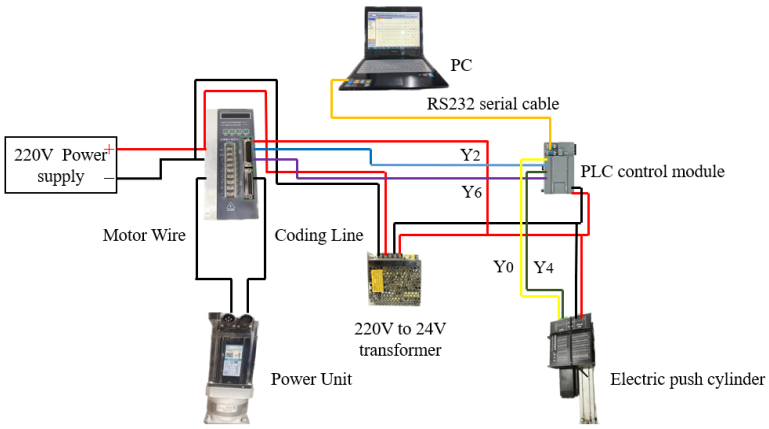

Fig. 6 - Wiring diagram of machine operation control

Design of the measurement system

This test rig requires the following measurements: the pulling force on the cotton stalks, the clamping force on the cotton stalks, and the distance traveled corresponding to the pulling force. In these three sets of measurements, the pulling force on the cotton stalks will change as the pulling distance increases. When the pulling distance reaches the pulling threshold, the cotton stalks will be subjected to the maximum pulling force.

Because this maximum pulling force exists for a very short time and is not easy to collect instantly, according to this feature, this test bench selected an Altech USB3200N type data acquisition card and LabVIEW platform measurement software combination, to collect the data of clamping force, pulling force and displacement distance. It is connected to the computer through the USB serial port and can display the collected data in real-time on the data acquisition page on the computer so that the value of each point can be recorded in time. The virtual control panel of this measurement program is divided into 5 parts: acquisition channel display area, parameter setting input area, the graphic display area of the acquired signal, numerical value display area, save path display area and the data acquisition page of the cotton stalks are shown in Figure 7.

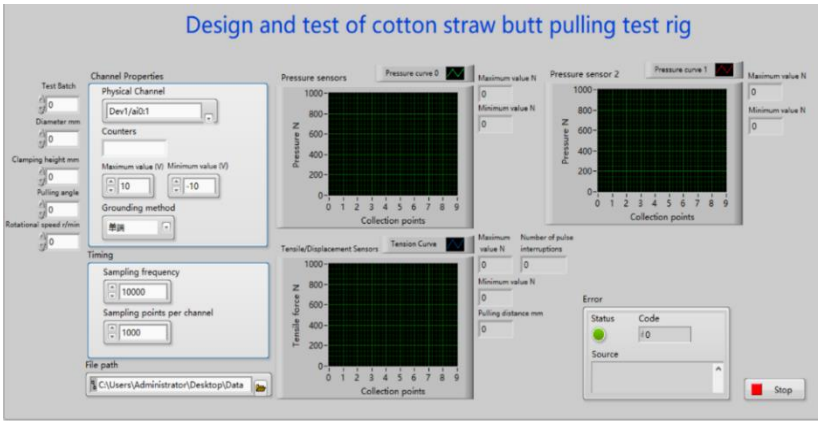

Fig. 7 - Cotton stalk data collection page

Calibration of measurement systems

Before the test, the acquisition and measurement program and the tension and pressure transducer were calibrated by running the WDW-20 microcomputer-controlled electronic universal testing machine produced by Jinan Chuanbai Instrument and Equipment Co Ltd (*Zhao B. et al, 2010*). The calibration results are shown in Table 1. The load value collected by the measurement system is compared with the load output of the universal testing machine, and the maximum relative error is only 0.2%. The calibration results show that there is a linear relationship between the load value and the output voltage signal value of the tensile transducer.

Table 1

Calibration results

Universal tester load	System measured voltage	The system measures the load	Error
[N]	[V]	[N]	[%]
100	0.361	100.13	0.13
300	1.040	300.62	0.2
600	2.019	600.37	0.061
900	3.038	900.14	0.015
1200	4.088	1200.26	0.021
1500	5.106	1498.78	-0.081
1800	6.230	1801.9	0.1
2100	7.184	2097.45	-0.12
2400	8.234	2398.64	-0.056
2800	9.598	2800.79	0.028

Determination of coefficient of friction

Measurement program

In order to determine the friction coefficient between different splints and the skin of cotton stalks, the BM-V computerized pendulum friction coefficient tester was selected to carry out the determination of the friction coefficient between different types of splints and cotton stalks, in order to obtain the accurate friction coefficients between the two, and to provide an accurate and relevant theoretical basis for the later tests.

Measurement results

The measured contact points between the cleat and the cotton stalks were measured five times (*Zhu Y.Y. et al, 2018*) and the measured pendulum values were recorded and the results are shown in Table 2.

Table 2

Measurement results

Number of tests	The determined friction coefficient value between rigid clamp and cotton stalk	The determined friction coefficient value between rubber splint and cotton stalk
1	29.9	107.2
2	30.7	107.8
3	32.1	101.7
4	28.5	106.5
5	27.3	107.5

The formula for the coefficient of friction from the pendulum tester:

$$\mu = \frac{1}{5}\sum_{i=1}^{5} X_i \frac{1}{100} \tag{7}$$

Where:

μ - measurement of coefficient of friction;

X_i - determination of pendulum value.

Substituting the five pendulum values of different types of splint tests into Equation (7), the friction coefficients between rigid splints, rubber splints, and cotton stalks were obtained as μ_1=0.297, μ_2=1.06, and for the convenience of post-test data processing, the rounded counting retention method was used so that the measured friction coefficients were retained to the second two decimal places so that μ_1=0.3, μ_2=1.06.

Experimental conditions and program design

Test condition

On March 13, 2023, tests on mechanical and displacement data collection of cotton stalks were conducted in the Polar Fly Super Cotton Field in Yuli County, Korla City, Xinjiang. The cotton field was in a post-winter irrigation condition with loose geology and a soil moisture content of 6.5%. The soil firmness was 42 kg/cm2 as measured by a soil tester, the cotton variety was Xinluzhong 46, the average plant height of the cotton stalks was 750 mm, and the spacing between the stalks was 50 mm, and the pinch point was 100 mm above the ground surface. The diameter of the cotton stalks at the clamping point was 8~12 mm. To facilitate the clamping of the cotton stalks by the fixture, the main stem and lateral branches above 300 mm from the ground surface were removed to ensure that the fixture was not affected by the influence of the lateral branches, which would lead to wide-ranging errors when clamping the cotton stalks. The test site is shown in Figure 8.

a. Test sample

b. Operational state

Fig. 8 - Field test

Test design

In order to test the clamping and pulling effect of different material pattern splints on cotton stalks, clamping force, linear velocity and friction coefficient were selected to carry out a three-factor general factorial test program, and the pull-up force and clamping force reduction were taken as the test indexes. Through the measurement data, the change curves of the pulling force and clamping force are made, and the test data are analyzed by variance. The test factors and levels are shown in Table 3. The magnitude of the clamping force was based on the data after clamping and pulling of cotton stalks in the test chamber as a reference. Under the three linear velocities measured, there was no slippage of cotton stalks at clamping forces of 500 N and above for rigid splints and 300 N and above for rubber splints. The two types of cleats did not break the cotton stalks when they were clamped at a clamping force of 1000 N or less. In order to compare the effect of both types of clamping and pulling on cotton stalks, 500 N, 750 N and 1000 N were chosen as the influencing factors.

Table 3

Test factors and levels

Levels	Clamping force A	Linear speed B	Friction coefficient C
	[N]	[m/s]	μ
-1	500	0.18	0.3
0	750	0.27	1.06
1	1000	0.36	

RESULTS AND ANALYSIS

Cotton stalk clamping force pull-up force variation curve

In the test, different materials and patterns of clamping plates were used to clamp the cotton stalks, and the perpendicular pulling angle, the same linear speed, and the equal clamping force were used as the variable control of the whole test. In this test, the clamping force and displacement-pulling force curves at a pulling speed of 0.27 m/s and a clamping force of 750 N were selected as the trends of the clamping force and pulling force in the whole test, as shown in Figure 9.

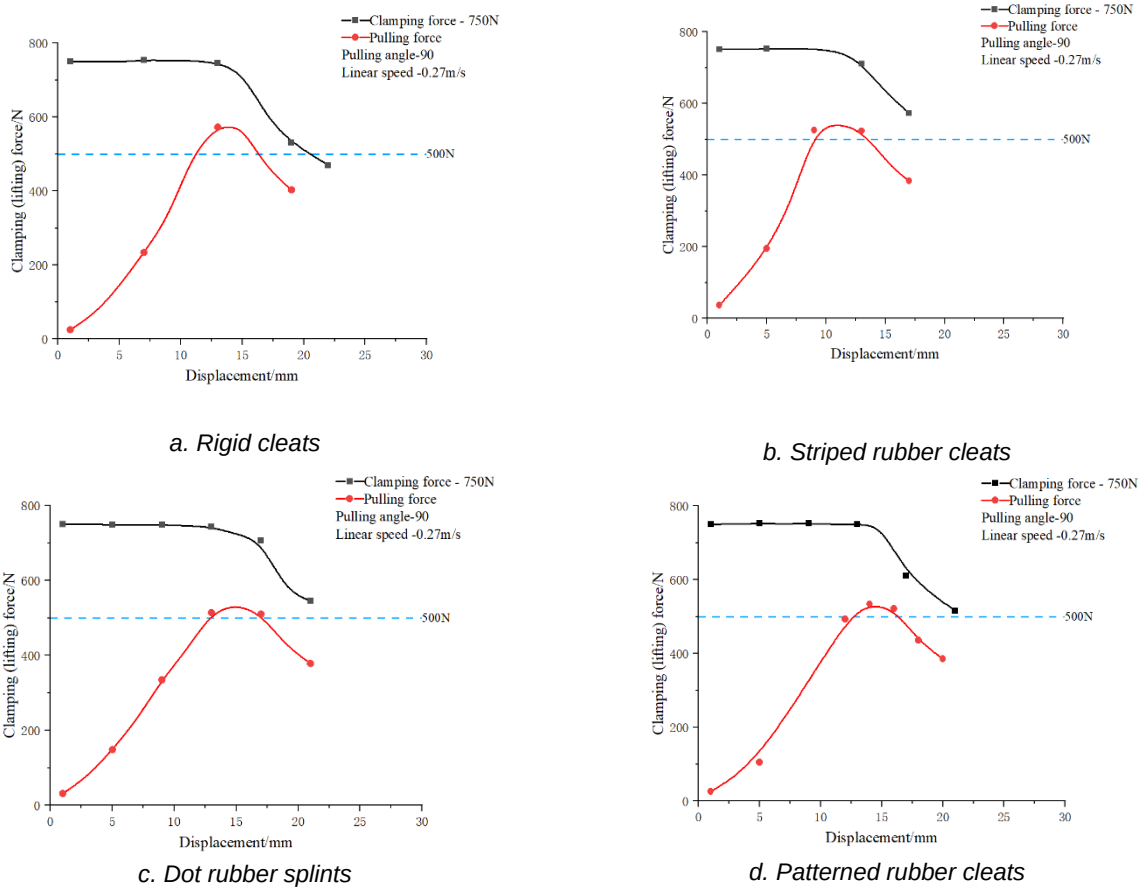

a. Rigid cleats

b. Striped rubber cleats

c. Dot rubber splints

d. Patterned rubber cleats

Fig. 9 - Clamping force, pulling force-displacement curve

The graph of clamping force, and displacement-pulling force is shown in Figure. 9, which illustrates the pulling force corresponding to the upward movement of the root of the cotton stalk by 12 mm, followed by a trend from peak to stabilization and then to zero point. At the peak of the pulling force, the clamping force tends to decrease.

Figure 9a illustrates the trends in clamping and pulling forces following the application of a rigid clamp to cotton stalks. The maximum pulling force reached approximately 500 N, at which point significant variations in the clamping force were observed, decreasing from an initial 750 N to around 400 N.

Figures 9b, 9c, and 9d depict the use of rubber clamps, differentiated by various rubber patterns as shown in Figure 10. Despite the consistent initial clamping force across these figures, variations in force are evident due to the different materials used. Specifically, Figure 9b shows the use of a striped rubber cleat; here, the trend in the graphic indicates that as the lifting force peaks, the clamping force slightly decreases from 750 N to approximately 550 N.

Figure 9c presents the polka dot rubber cleat, where the clamping force initially remains steady at 750 N. As the pulling force increases, leading to the maximum pulling force, a downward trend in clamping force is noted, correlating with the gradual uprooting of the cotton stalks, eventually stabilizing at around 510 N.

Lastly, Figure 9d utilizes a patterned rubber splint for clamping. Initially, when no pulling force is applied, the clamping force maintains a steady state of 750 N. With the progressive application of pulling force, a decrease in clamping force is observed, ultimately stabilizing at approximately 500 N as the stalks detach completely from the soil.

a. Stripes *b. Dots* *c. Pattern*

Fig. 10 - Rubber cleats

Significance analysis of test results

The results of the test were analyzed by a three-factor general factorial test using Design Expert 8.0.6 software, and the test protocol and results are shown in Table 4, and the ANOVA analysis was performed with the reduction of pull-up force and clamping force as the test indexes, and the results are shown in Table 5 and Table 6.

Table 4

Pilot program and results

NO	Clamping force A	Linear velocity B	Friction coefficient C	Pulling force	Clamping force reduction
	[N]	[m/s^{-1}]	μ	[N]	[N]
1	500	0.36	0.3	445.93	385.23
2	1000	0.27	0.3	513.43	494.67
3	1000	0.36	0.3	535.24	500.12
4	500	0.27	1.06	508.92	164.1
5	750	0.18	1.06	565.09	209.03
6	500	0.18	1.06	558.73	144.05
7	750	0.36	0.3	513.32	335.45
8	750	0.18	0.3	434.21	200.69
9	750	0.27	0.3	476.7	278.39
10	1000	0.18	1.06	563.63	263.61
11	750	0.36	1.06	535.29	282.72
12	750	0.27	1.06	491.34	238.33
13	1000	0.18	0.3	422.5	493.17
14	500	0.36	1.06	526.5	177.74
15	500	0.18	0.3	438.61	335
16	500	0.27	0.3	498.92	369.63
17	1000	0.27	1.06	494.27	302.74
18	1000	0.36	1.06	506	312.9

Table 5

Analysis of variance of pull-up force with three factors

Variance source	Sum of squares	Degree of freedom	Mean square	F value	P value
Model	29565.56	11	2687.78	4.65	0.0358
A	285.4	2	142.7	0.25	0.7886
B	695.34	2	347.67	0.6	1.06777
C	12319.79	1	12319.79	21.33	0.0036
AB	2056.68	4	514.17	0.89	1.06233
BC	14208.35	2	7104.18	12.3	0.0035
Residual	3465.2	6	577.53		
Cor Total	33030.76	17			

Table 6

Analysis of variance of clamping force reduction with three factors

Variance source	Sum of squares	Degree of freedom	Mean square	F value	P value
Model	2.22E+05	9	24626.2	26.32	< 0.0001
A	68392.2	2	34196.1	36.55	< 0.0001
B	5842.97	2	2921.48	3.12	0.0995
C	99931.32	1	99931.32	106.81	< 0.0001
AB	46944.17	2	23472.08	25.09	0.0004
BC	525.17	2	262.58	0.28	0.7624
Residual	7484.96	8	935.62		
Cor Total	2.29E+05	17			

The magnitude of the P-value in Tables 5 and 6 is the degree of influence of each parameter on the desired reflection of the test indicator, which is significant at $P < 0.05$, and on the contrary, the degree of influence is not significant. Tables 5 and 6 reflect the degree of influence of the three factors on the measured test metrics. From Table 5, it can be seen that each of the three factors has a different degree of influence on pull-up force, with the more significant effect on pull-up force being the interaction of BC. The degree of influence of the remaining factors was not significant at $P > 0.05$. Table 6 shows the ANOVA of the clamping force reduction, where $P < 0.05$ is the interaction effect of A, C, and AC, respectively, in which A and C showed a highly significant effect on the clamping force reduction. The results in Tables 5 and 6 show that in the test of whole plant uprooting of cotton stalks, A, B, and C played different degrees of influence on the reflected test indexes, with C showing a highly significant degree of influence on both test indexes.

CONCLUSIONS

(1) A cotton straw clamping and pulling test bench based on Gx Works2 and LabVIEW programming software was designed to realize the control of the power unit and pulling device of the test bench, and to collect real-time information about the force and upward displacement of the cotton straw in the process of clamping and pulling.

(2) Through the data measured after pulling the cotton stalks, it can be seen that the cotton root upward displacement of 12 mm corresponds to the maximum plucking force on cotton stalks in the average value of 500 N, and did not appear too much fluctuation. During the process of clamping and pulling the cotton stalks, the clamping force on the cotton stalks changes. Among the three linear speeds, the rigid clamp plate exhibits the optimal clamping and pulling effect on the cotton stalks at a clamping force of 750N and a linear speed of 0.18m/s, with the clamping force ultimately maintained at 500N or above. Rubber clamping had the best effect on cotton stalk clamping and pulling at a clamping force of 500 N at a linear velocity of 0.36 m/s. Under the same factors, the striped rubber clamp was superior to the remaining two patterned rubber clamps.

(3) The analysis of variance (ANOVA) of the measured test parameters showed the following conclusions at the test criterion of $P < 0.05$. In the ANOVA table of the pulling force, the significantly higher effect was the interaction of linear velocity with the coefficient of friction of the cleat with a P-value of 0.0035. In the ANOVA table of the reduction of the clamping force, it can be concluded from it that the interaction of the clamping force with the coefficient of friction at the value of $P < 0.0001$ is highly

significant. In the ANOVA table for both, it can be concluded that the coefficient of friction is the primary consideration for the clamping type of cotton stalk harvesting machinery in conducting the cotton stalk pair clamping and uprooting test for the clamping tools of the plywood type.

(4) The data were analyzed by clamping and pulling cotton stalk measurements. The maximum pulling force corresponding to the upward displacement of the cotton root was obtained. The optimal combination of different types of splints for cotton stalk clamping and pulling was obtained. By comparing the data of the same type of splint, the best pattern splint can be obtained. The measured data were analyzed by ANOVA to get the main influencing factors on the test indexes.

ACKNOWLEDGEMENT

This study was supported by the Xinjiang Uygur Autonomous Region Agricultural Science and Technology Promotion and Service Program (NTFW-2022-17), Xinjiang Uygur Autonomous Region Youth Science Foundation (2022D01B91), The National Natural Science Foundation of China (51865058).

REFERENCES

[1] Chen J.L., Cao S.L., Lu Y.T., et al., (2018), Current status and future prospects analysis of cotton stalk harvesting equipment. *Xinjiang Agricultural Mechanization*, issue 02, pp. 11-14;

[2] Fire H.X., (2021), Comprehensive Utilization of Crop Straw under the Perspective of Circular Economy. *Shanxi Agricultural Economy*, issue 14, pp. 137-138;

[3] Gao R.F., Zhang J.S., et al., (2016) Research on the development and utilization of cotton straw forage in Xinjiang. *Chinese Journal of Animal Husbandry*, vol. 52, issue 08, pp 76-80;

[4] Guo T.J., Zhang Z.J., Zhao J., et al., (2018), Analysis of the effect of steam explosion fermented cotton stalks on feeding sheep. *Transactions of the Chinese Society of Agricultural Engineering*, vol. 34, issue 07, pp. 288-293;

[5] Jian S.C., Ma J.C., Wang X.Y., et al., (2011), Research on the measurement device for cotton stalk extraction force. *Agricultural Equipment and Vehicle Engineering*, issue 06, pp. 4-6;

[6] Li Y., Zhang G.Z., Zhou Y., et al., (2013), Design and test of cotton stalk field lifting force measurement system. *Journal of Agricultural Engineering*, vol. 29, issue 18, pp. 43-50;

[7] Liu X., Sun S.L., Xiao M.T., et al., (2017), Design and experiment of a flexible clamping and pulling device for rice bowl seedlings. *Journal of Hunan Agricultural University* (Natural Science Edition), vol. 43, issue 03, pp. 324-328;

[8] Ren M.H., HOU S.X., QUAN S.P., et al., (2018), Spring fatigue testing machine loaded by servo-electric cylinder. *Engineering and Testing*, vol. 58, issue 04, pp. 87-89;

[9] Song X.S., Lei Y.F., Fu F., (2013), Preparation process and test of cotton stalk reconstituted square timber. *Journal of Agricultural Machinery*, vol. 44, issue 05, pp. 164-168;

[10] Tang Z.F., Wang H.J., Deng J.M., et al., (2018) Clamping Experiment and Simulation for High Quality String Fruit Picking. *Mechanical Design*, vol. 35, issue 11, pp. 47-52;

[11] Wang Y.J., Zhang P., Ju C.H., et al., (2022), Current situation and strategies for the recycling of cotton stalks in Xinjiang. *Cotton Science*, vol. 44, issue 06, pp. 44-49;

[12] Xie J.H., Wu S.H., Cao S.L., et al., (2023), Design and experimental study of the gripping roller-type cotton stalk pulling device. *Transactions of the Chinese Society for Agricultural Machinery*, vol. 54, issue 05, pp. 101-111;

[13] Zhang W.Z., (2015), Research on the development of China's agro-ecologization based on super-circular economy. *Hubei Social Science*, issue 11, pp. 97-101;

[14] Zhao B., Sun S.L., Wang S., et al., (2010), Research on calibration method of sensor static characteristics based on LabVIEW. *Journal of Qinghai University* (Natural Science Edition), vol. 28, issue 06, pp. 24-27;

[15] Zhou S.P, Liu Q.T, Yang D.T. et al., (2019), Design and test of vertical clamping conveyor channel leaf stripping device for sugarcane. *Journal of South China Agricultural University*, vol. 40, issue 03, pp. 117-124;

[16] Zhu Y.Y., Tang B., Chen W.H., et al., (2018) Evaluation of Uncertainty in Indication Error of Pendulum Friction Coefficient Tester. *Metrology and Testing Technology*, vol. 45, issue 06, pp. 113-114+117.

[17] ***Announcement of National Bureau of Statistics on Cotton Production in 2022, (2022). *China Information Daily.*

DESIGN AND EXPERIMENT OF MULTI-FRUIT GRIPPING AND CUTTING LINKAGE KIWIFRUIT PICKING END-EFFECTOR
/
多果夹持切割联动式猕猴桃采摘末端执行器设计与试验

Min FU*, Jianan CAI, Shike GUO, Lei CHEN, Chengmeng WANG, Gangqiang YANG, Xiaoman CUI
Northeast Forestry University, College of Mechanical and Electrical Engineering, Harbin / China;
Tel: +86 15663688203; E-mail: fumin1996@163.com
DOI: https://doi.org/10.35633/inmateh-72-63

Keywords: *kiwifruit; picking end-effector; cluster; gripping and cutting linkage*

ABSTRACT

Kiwifruit picking robots can replace manual labor for mechanized kiwifruit harvesting. However, existing picking robots encounter issues such as low separation efficiency of fruit stalks, poor stability of fruit gripping, and inaccurate identification when picking kiwifruit clusters. In response, a multi-fruit picking end-effector was designed to pick clusters of kiwifruit efficiently based on their distribution characteristics. The gripping range of the gripping device was determined based on the parameters of the spatial distribution of the fruit clusters. A multi-fruit gripping mechanics model was constructed, and the gripping force was analyzed to ensure efficient and stable fruit picking. Critical parameters of the fruit stalk separation device were determined through kinematic trajectory analysis to improve the separation efficiency of fruit stalks. Additionally, a dual-sensor fusion recognition method was proposed to identify fruit cluster locations accurately. The results of the picking experiment demonstrate that the end-effector can pick fruits in an average time of 8.28 s per cluster, with a net fruit-picking rate of 87.5% and a fruit damage rate of 7.5%. The end-effector shows a positive picking effect on kiwifruit fruits distributed in clusters. This study can serve as a reference for the development of kiwifruit-picking robots.

摘要

猕猴桃采摘机器人可替代人工劳作实现猕猴桃机械化收获。但现有采摘机器人采摘成簇分布猕猴桃时，末端执行器存在果梗分离效率低、果实夹持稳定性差、果实识别准确度低等问题。对此，本文根据猕猴桃果实的分布特征，设计了一种多果夹持切割联动式采摘末端执行器，以期实现成簇果实的快速采摘作业。根据果实簇空间分布参数确定夹持装置夹持范围，构建多果稳定夹持力学模型并对夹持力进行分析，基于运动学轨迹分析确定果梗剪切装置关键参数。在此基础上，提出了一种双传感器融合识别方法以实现果实簇位置的准确判别。采摘试验结果表明该末端执行器采摘每簇果实平均时间为 8.28s，果实净采摘率为 87.5%，果实损伤率为 7.5%，对簇生分布的猕猴桃果实有良好采摘效果。该研究可为猕猴桃采摘机器人研制提供参考。

INTRODUCTION

Kiwifruit was a highly economical fruit and was still mainly picked manually at a high cost, which was desirable for mechanical harvesting (*Fang et al., 2023*). With the rapid growth of the kiwifruit industry and its global production expected to double by 2025, manual harvesting cannot meet current market demand (*Au et al., 2022; Li et al., 2022*). The efficacy of the end-effector, as a terminal device in direct contact with the fruit, plays a crucial role in the performance of a picking robot in terms of versatility, practicality, and picking efficiency (*Bu et al., 2020*).

According to the working principle, the end-effector can be divided into three types: gripping, envelope and adsorption (*Lan et al., 2022*). Fruit stalk separation methods include pulling, cutting, and twisting. For instance, Zhi et al. designed a gripping kiwifruit-picking end-effector with bionic fingers that grip the fruits, leading to the separation of the fruit and the stalk as the end-effector rotates. Despite its simple structure, the rotating process of this end-effector can cause damage to neighboring fruits (*Zhi et al., 2023*). Similarly, Fu et al. designed a multi-fruit cutting kiwifruit picking end-effector, which allows for the aggregation of fruit clusters into the picking bin interior through an envelope and the cutting of stalks with a rotary cutter, resulting in enhanced harvesting efficiency through cluster harvesting methods. However, the rotary cutter unit of this end-effector was large and inflexible (*Fu et al., 2023*).

In another development, Wang et al., designed an apple-picking end-effector with bionic suction cups, featuring four evenly distributed suction cups on the manipulator that utilize negative vacuum pressure to produce concave deformation, enabling the cups to fit the apple's surface and adsorb it. The fruit stalk was separated through wrist rotation and dragging in a compound manner, making this picking method adaptable to different fruit shapes but suitable only for fruits with smooth surfaces (*Wang et al., 2022*). To improve the successful rate of fruit picking, Zhang et al. equipped the cherry tomato picking end-effector with Intel's RealSense D415 depth camera mounted on the side of the robotic arm base to facilitate unobstructed tomato harvesting (Zh*ang et al., 2021*). Similarly, Yu et al. utilized the DF810-HD depth camera to support the picking robot visually during tomato picking (*Yu et al., 2022*). However, it was essential to note that a single recognition sensor may need help to adapt to complex and changing harvesting environments. In addressing this challenge, Sarabu et al. devised a dual-arm picking end-effector, each arm equipped with an RGB-D depth camera, to enhance fruit recognition efficiency through cross-view recognition. Nonetheless, the high cost of the equipment poses a challenge to widespread adoption (*Sarabu et al., 2019*).

The studies outlined above have significantly informed the development of fruit-picking robots for kiwifruit and other fruits. However, the focus of previous research on end-effector has been predominantly on single-fruit picking. This limitation has led to several issues when harvesting kiwifruit distributed in clusters, such as lack of stability when gripping fruits, easy fruit detachment, and damage caused by twisting or pulling during separation from the stalks. Furthermore, using a single visual recognition sensor with low precision has also affected picking efficiency (*Jin et al., 2022*). In response to these challenges, this paper has addressed the issues above by designing a multi-fruit gripping and cutting linkage end-effector based on the characteristics of kiwifruit cluster distribution. This end-effector enables the synchronization of fruit gripping and stalk separation processes, ultimately leading to efficient harvesting of fruit clusters. Additionally, a prototype was fabricated, and a kiwifruit picking test bed was built to verify the effectiveness of this end-effector. The research results from this study can offer valuable insights for improving the efficiency of cluster fruit picking and reducing the rate of fruit damage.

MATERIALS AND METHODS

Kiwifruit distribution characteristics

Kiwifruit large-scale planting was usually carried out using a trellis planting mode, with an average row spacing of 4 m, a spacing of 2 m between trellis columns, and an average trellis height of 2 m, the fruits were distributed in a spatial range of 1.5 to 1.8 m in height from the ground, as shown in Figure 1(a). Kiwifruit hang down from the branches and were found in clusters, which come in three types: single fruit, linear cluster, and aggregation cluster, as shown in Figure 1(b). Notably, a single fruit was not surrounded by neighboring fruits, while a linear cluster typically consists of 1-2 fruits distributed on either side of the central fruit. Additionally, a maximum of two adjacent fruits can be found per fruit. The fruits within aggregation clusters display irregular distribution and usually comprise 4-6 fruits (*Ma et al., 2022*).

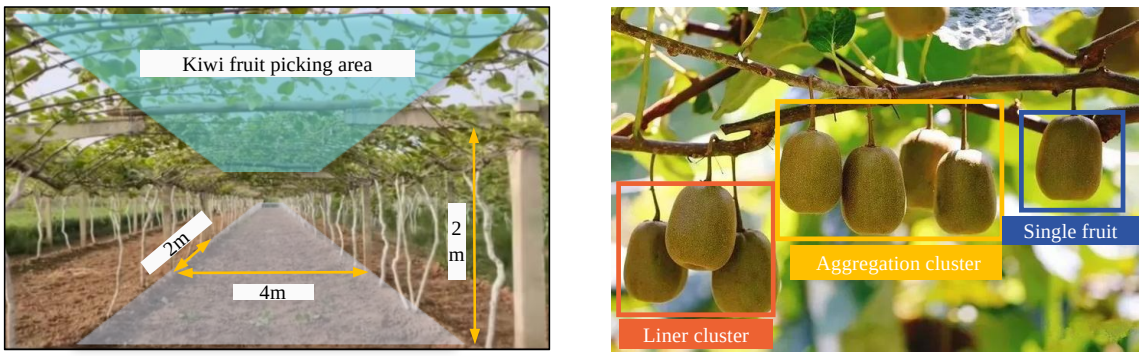

(a) Trellis planting pattern *(b) Clusters of kiwifruit*

Fig. 1 - Environment for planting kiwifruit fruits

The spatial distribution of kiwifruit fruit in the picking area affects the efficiency of the end-effector picking operation (*Li et al., 2022*). To ensure the picking success rate of the end-effector, the spatial distribution parameters of "Hongyang" kiwifruit in Nanjing Lile Agricultural Planting Base were analyzed as an example to provide a basis for the design of the end-effector for picking, as shown in Figure 2.

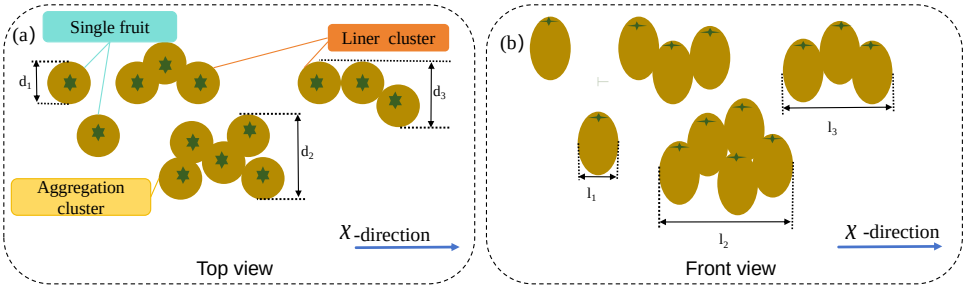

Fig. 2 - Spatial distribution of kiwifruit

Single fruit distribution length was d_1 and width was l_1; aggregation cluster distribution length d_2, distribution width l_2; linear cluster distribution length d_3, distribution width l_3. Fifteen groups were randomly selected for each growth state for the measurement of their physical parameters, the measured data can be found in Table 1.

Table 1

Spatial distribution parameters of kiwifruit

Numerical value	Single fruit length d_1[mm]	Single fruit width l_1[mm]	Aggregation cluster length d_2[mm]	Aggregation cluster width l_2 [mm]	Linear cluster length d_3[mm]	Linear cluster width l_3[mm]
maximum value	60.5	40.48	72.12	181.42	83.36	138.79
minimum value	52.3	31.26	65.23	171.23	79.21	129.41
Range	8.3	9.22	6.89	10.19	4.15	9.38
Average value	55.6	43.23	68.91	178.56	81.42	132.45

Overall structure and working principle of the end-effector

A multi-fruit gripping and cutting linkage end-effector was designed to target kiwifruit clusters' distribution characteristics, and the structure schematic was shown in Figure 3. The end-effector mainly comprises a movable gripping plate, a fixed gripping plate, a cutter, a stepper motor, a crank-rocker mechanism, and two identification sensors. A stepper motor was used as the power output. In addition, lightweight 3D printing materials were utilized in fabricating the entire machine, except the cutter and crank-rocker mechanism, ensuring the overall structure was light.

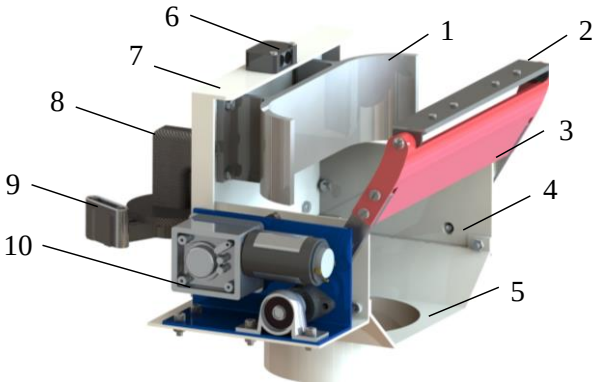

Fig. 3 - End-effector structure

1.fixed gripping plate; 2.cutter; 3 movable gripping plate; 4.sidewall plate; 5.collection cylinder; 6.color recognition sensor; 7.back plate; 8.flange holder; 9.binocular camera; 10.motor module

The working principle of the kiwifruit picking system was illustrated in Figure 4. Firstly, the end-effector was moved to the kiwifruit picking area by a robotic arm, followed by a binocular camera upward scanning the kiwifruit clusters, the target clusters were identified by clustering, and the coordinate information was acquired. Subsequently, the robotic arm elevates the end-effector to match the obtained fruit cluster coordinates for enveloping the fruit. The robotic arm stops moving when the color recognition sensor detects that all fruits have entered the fruit-gripping device. The cutter and the movable gripping plate rotate to synchronize the completion of the fruit gripping and cutting the fruit stalk action. The fruit then smoothly transitions into the fruit collection end, completing the single-picking process as it slides along the end-effector sidewall panel.

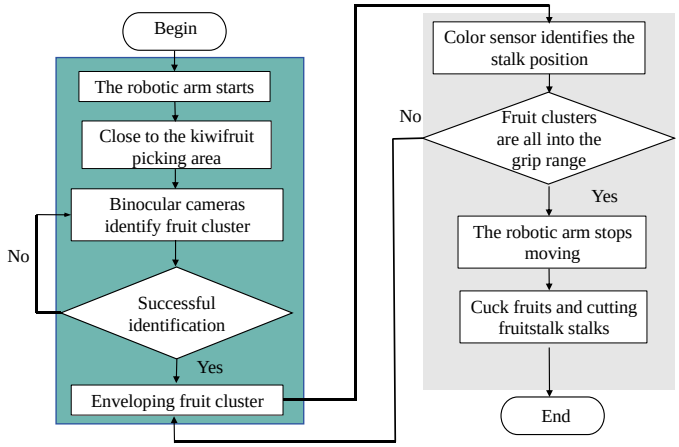

Fig. 4 - Working Principle

Parameter design of the fruit gripping device

The structure of the fruit-gripping device was illustrated in Figure 5(a). It consists of two parts: the movable and fixed gripping plates. The movable gripping plate was mounted on the crank rocker device, driven by the stepping motor, the movable gripping plate counterclockwise rotation with the fixed gripping plate to achieve a cluster of fruit stable fixture. The kiwifruit's spatial distribution parameters determined the gripping area dimensions. The design of the movable gripping plate was 160 mm in length and 45 mm in height, and the fixed gripping plate is 180 mm in length and 52 mm in height. When the gripping device comes into contact with fruit clusters, the fruits' positions may shift, resulting in a sliding zone within the 6.9-9.1 mm range from the center to the edge (*Williams et al., 2020*), as shown in Figure 5(b). This sliding zone could cause the gripping device to collide with neighboring fruits, leading to fruit drop. To mitigate this issue, the edges of both gripping plates were designed to be curved, guiding the target fruit clusters into the interior of the gripping device. This design effectively reduces the sliding zone and minimizes the risk of collision with neighboring fruits, ensuring a stable grip on the fruit cluster.

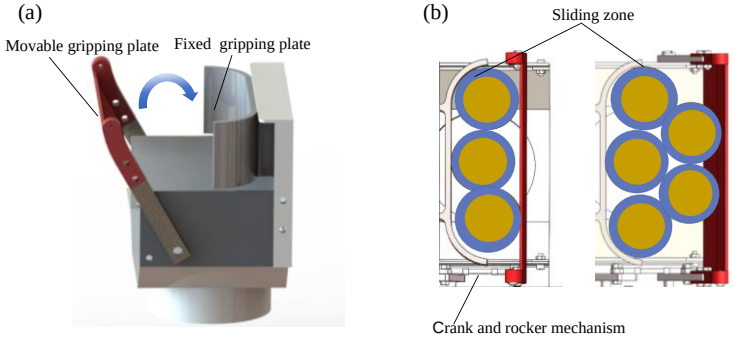

Fig. 5 - Fruit gripping device structure

To ensure the stability of the gripping device when gripping multiple fruits, it was essential to maintain an adequate gripping force. However, it was important to avoid applying excessive force that may damage the fruits during the gripping process. Therefore, it was necessary to establish a multi-fruit gripping mechanical model to determine the appropriate range of gripping force, thus ensuring both stability and the prevention of fruit damage, as shown in Figure 6.

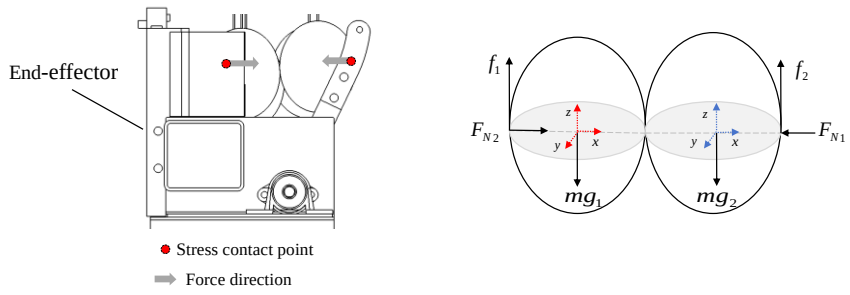

Fig. 6 - Multi-fruit gripping mechanical model

The fact that the fruit does not fall in the vertically straight direction and does not undergo relative sliding in the horizontal direction should be satisfied:

$$\begin{cases} f_1 + f_2 = mg_1 + mg_2 \\ f_1 = \mu F_{N1} \\ f_2 = \mu F_{N2} \\ F_{N1} = F_{N2} \end{cases} \quad (1)$$

where:

F_{N1} was the gripping force generated by the movable gripping plate, F_{N2} was the support force generated by the fixed gripping plate, f_1, f_2 was the maximum static friction in the perpendicular direction, mg_1, mg_2 was the gravitational force of the fruit itself, μ was the coefficient of friction.

To avoid fruit damage, the gripping force provided to the kiwifruit by the griping plate should also satisfy.

$$\frac{mg_1 + mg_2}{2\mu} \le F_{N1} \le F_b \quad (2)$$

where:

F_b was the destructive force suffered by the fruit damage, and according to the literature (*Dong et al., 2022*), the effective gripping force for the fruit not to slip is not less than 1.08 N. The kiwifruit shows significant internal damage to the pulp tissue, at which point the fruit is subjected to destructive forces in the range of 10-15 N. Considering the clamping stability and gripping damage, the preset gripping force should be between 1.08-15 N.

Design of the fruit stalk separation device

Kiwifruit stalks and fruit at the combination of the separation layer of tissue were susceptible to shear shedding (*Silwal et al., 2021*). According to the shedding characteristics of the separated layer of the fruit, a cutting fruit stalk separation device was designed as shown in Figure 7(a). The cutter was fitted on the movable gripping plate, driven by a stepping motor, to complete the operation of gripping the fruit and cutting off the stalks in turn, as shown in Figure 7(b).

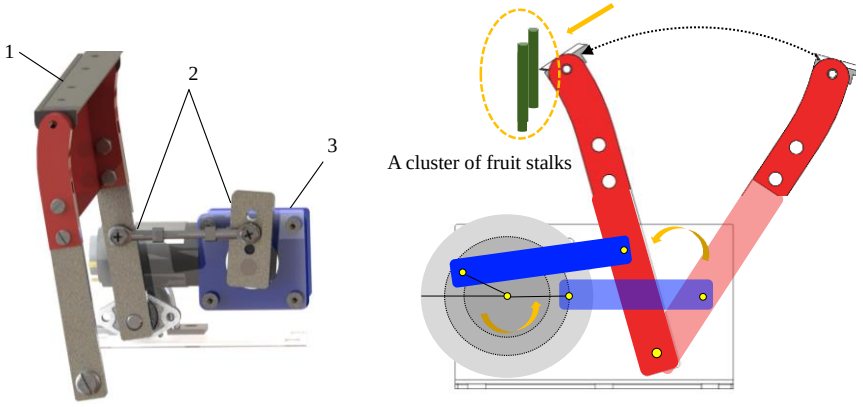

(a) Structure of fruit stalk separator *(b) Principle of operation of cutter*

Fig. 7 - Structure and working principle of the fruit stalk separator

1. Cutter; 2. Crank rocker assembly; 3. Stepper motor

When the fruit stalk separating device was in motion, it was essential to ensure a smooth fruit stalk separating process and prevent the fruit from falling off vibrations. Accordingly, a crank-rocker mechanism without sharp return characteristics was designed, and its kinematic analysis was shown in Figure 8.

The angle between the limit positions of cranks AB_1 and AB_2 was 0º, and the rocker reaches two limit positions, F_1 and F_2, during its movement. F_1 ensures that the cutter can cut the stalks sufficiently, and F_2 provides enough space between the movable and fixed gripping, the angle swept by DF_1 and DF_2 was the range of motion of the cutter.

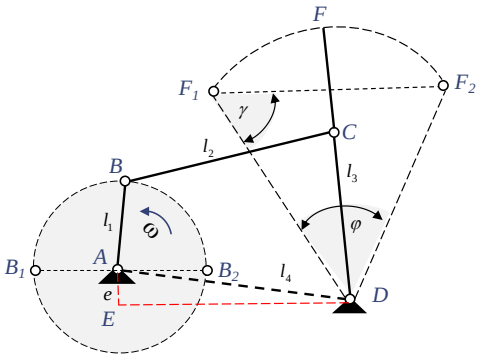

Fig. 8 - Kinematic analysis of the crank rocker mechanism

A, B, C, D indicates the crank rocker mechanism connection point; F indicates the rocker extension point; E indicates the intersection of the horizontal projection direction of the frame and the vertical projection direction; B_1, B_2 is the limit position point of the crank; C_1, C_2 is the limit position point of the rocker extension direction

According to the mechanism characteristics of the crank rocker without emergency return, it can be obtained that:

$$\begin{cases} \sin\dfrac{\varphi}{2}=\dfrac{l_1}{l_3} \\ l_1^{\,2}+l_4^{\,2}=l_2^{\,2}+l_3^{\,2} \\ e=l_3\cdot\sin\left(\dfrac{\pi}{2}-\dfrac{\varphi}{2}\right) \end{cases} \tag{3}$$

where:

l_1 indicates crank length, mm; l_2 indicates the length of connecting rod, mm; l_3 indicates the length of rocker, mm; indicates the length of frame, mm; l_4 was the horizontal projection length of frame, mm.

The crank length l_1 was calculated from Equation 3 to be 45 mm. In crank-rocker mechanism, the transmission angle γ is used to measure the force transmission performance of the mechanism. The permissible transmission angle γ is generally 40º to 50º (*El-Shakery et al., 2021*). Larger values of γ indicate better force transfer performance. In the absence of rapid return motion, the minimum transmission angle occurs γ_{min} at two positions where the crank and frame lines coincide, and the transmission angles at the two positions were equal. This can be obtained by combining with Equation 1:

$$\begin{cases} \gamma=\arccos\dfrac{l_1 l_4}{l_2 l_3} \\ l_4=\sqrt{460+l_2^{\,2}} \\ \gamma_{\min}=\arccos\dfrac{\sqrt{460+l_2^{\,2}}}{l_2^{\,2}} \end{cases} \tag{4}$$

The transmission angle γ rises sharply as l_2 increases and then tends to 60°, the longer the connecting link, the more the mass of the transmission mechanism increases. If the length is increased after 65 mm, the minimum transmission angle does not increase significantly, in order to ensure the compactness of the machine, l_2=65 mm, l_3=40 mm the minimum transmission angle at this point is 53.7°, which meets the transmission performance requirements.

Design of the fruit identification devices

The paper proposes a dual visual recognition sensor fusion method to enhance the accuracy of fruit cluster recognition during the picking phase, mainly focusing on the shape and color characteristics of kiwifruits. Initially, a binocular vision camera was mounted at the base of the end-effector to capture the spatial coordinates of kiwifruit clusters by identifying their centers at the bottom. Subsequently, the robotic arm manipulates the end-effector based on these coordinates to encase the target fruit clusters, thereby effectively averting shading between clusters and obviating interference from branches and leaves. The working principle of this process was depicted in Figure 9(a). Once all the fruit clusters were inside the gripper, the green fruit stalks were positioned above the gripping plate. A color sensor detects the green color, and the robotic arm stops moving when it detects a green signal from the fruit stalk, as illustrated in Figure 9(b). This integrated sensor fusion method ensures precise and efficient recognition of fruit clusters during the picking process.

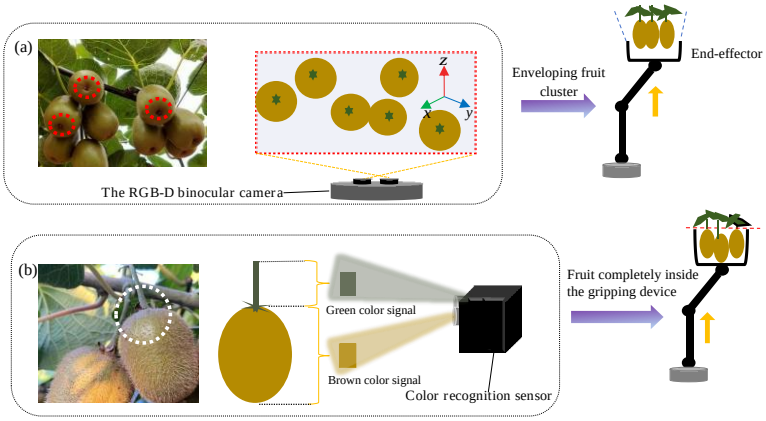

Fig. 9 - Working principle of the identification device fruit

Experimental condition

The experiment simulated a kiwifruit trellis seeding environment and was conducted in the Robotics Laboratory of the School of Mechanical and Electrical Engineering, Northeast Forestry University. The principal experimental equipment comprised a planting trellis, end-effector, AUBO-E5 robotic arm experimental bench, LegionY7000P computer, and collection device, as shown in Figure 10.

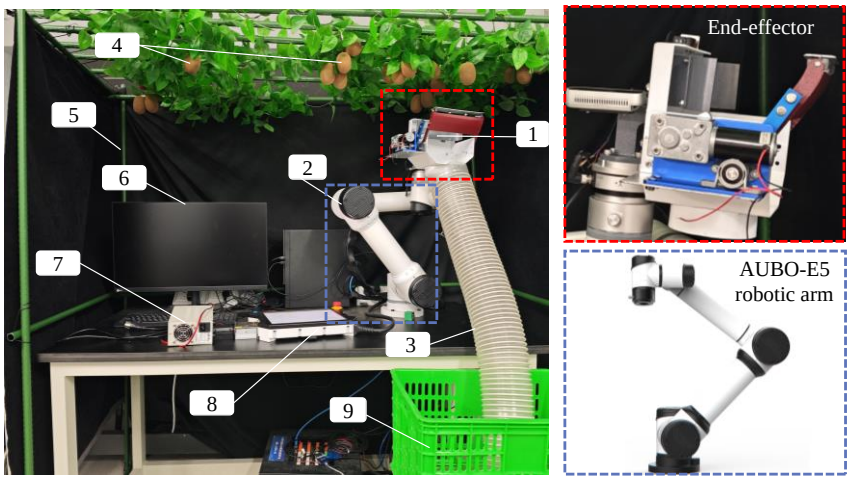

Fig. 10 - Experimental environment

1. end-effector; 2. robotic arm; 3. hose; 4. kiwifruit; 5. trellis; 6. desktop computer; 7. mobile power supply; 8. control panel; 9. collection box

Test method

The picking experiment was conducted on December 15, 2023, and the AUBO-E5 robotic arm was used to assist the end-effector in picking. 80 randomly selected kiwifruit of different shapes were used for the picking experiment to verify end-effector harvesting performance. According to the distribution characteristics of kiwifruit fruit clusters, in order to ascertain the effect of the end-effector on the picking of different types of kiwifruit fruit clusters, 80 kiwifruit were divided into 5 groups, each containing 5 clusters of the same number of fruits. Single-fruit clusters contain one fruit, linear clusters contain 2 and 3 fruits, and aggregated clusters have several 4 and 6 fruits. The average picking time per cluster, the net fruit picking rate, and the fruit damage rate are used as the evaluation indexes for fast and damage-free picking. It is defined as follows:

$$\begin{cases} P_T = t_1 - t_0/5 \\ P_C = n_1/n_2 \times 100\% \\ P_D = m_1/n_2 \times 100\% \end{cases} \quad (5)$$

where:

P_T was the average picking time per cluster, t_0 was the start time of the robotic arm driving the end-effector to reach the kiwifruit picking area. t_1 was the end time until the fruits fall into the collection device, P_C was the net fruit picking rate, n_1 was the number of harvested fruits, n_2 was the number of fruits in the picking area, and P_D was the fruit damage rate, m_1 was the number of fruits damaged by picking.

RESULTS

Picking experiments were carried out on 5 groups of 3 types of fruit clusters, and the harvesting process was shown in Figure 11. The robotic arm moves the end-effector to the fruit picking area and determines the position of the fruit by means of dual-sensor fusion recognition, after which the end-effector envelops the fruit upwards driven by the robotic arm. Subsequently, under the cooperation of the fruit gripping and fruit stalk separating device, the synchronized completion of the gripping of the fruit and cutting off the fruit stalk action, the fruit falls into the collection end. After picking, the robotic arm moved to the next picking target for picking operations.

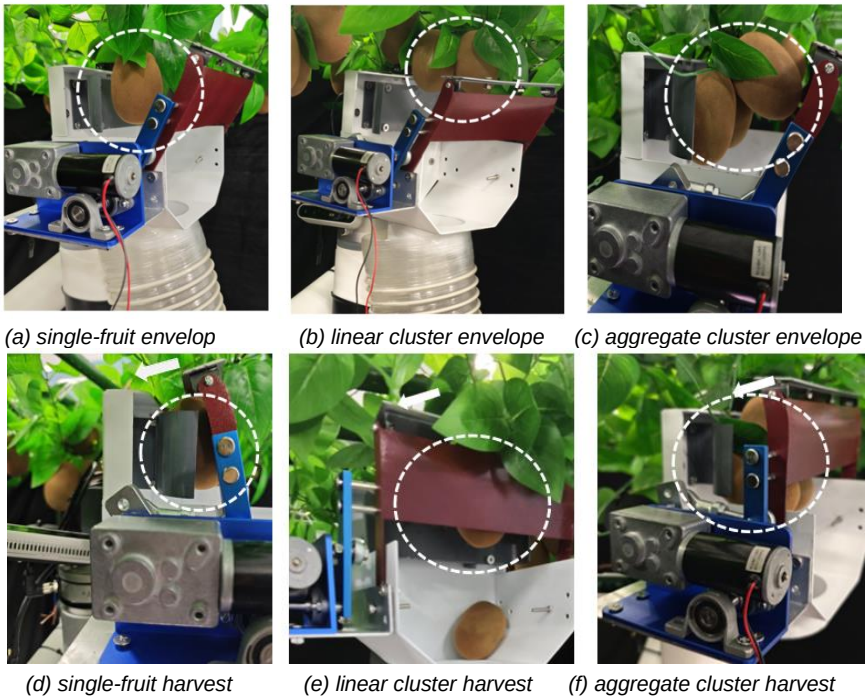

(a) single-fruit envelop *(b) linear cluster envelope* *(c) aggregate cluster envelope*

(d) single-fruit harvest *(e) linear cluster harvest* *(f) aggregate cluster harvest*

Fig. 11 - End-effector picking process

The results of the harvesting experiment were shown in Table 2.

Table 2

Results of picking experiments

Type	Number of fruits	Number of fruit clusters	Total number of fruits	Number of fruits picked	Number of failed picks	Number of fruit damage	Average picking time per cluster (s)	Net picking rate (%)	Fruit damage rate (%)
Single-fruit	1	5	5	5	0	0	6.2	100	0
Linear cluster	2	5	10	10	0	0	7.1	100	0
	3	5	15	13	1	1	7.5	86.6	6.7
Aggregate cluster	4	5	20	17	1	2	9.2	85	10
	6	5	30	25	2	3	11.4	83.3	10
Total		20	80	70	4	6	9.48	87.5	7.5

As shown in Table 3, the average picking time per cluster was 8.28 seconds, the net fruit picking rate was 87.5%, and the fruit damage rate was 7.5%. Meanwhile, the net picking rate for a single fruit was 100%, and the fruit damage rate was 0. According to the literature (*Mu et al., 2021*), the linear cluster type of fruit distribution occupies about 87% of the picking area, and the end-effector achieves an average net picking rate of 93.3% for this type of fruit cluster. The net picking rate was 100% for linear clusters with two fruits, and the fruit damage rate was 0. The net fruit picking rate for linear clusters with three fruits was 86.6%, and the fruit damage rate was 6.7%. The aggregated cluster picking operation with four and six fruits also had a net picking rate of 84.14%. Still, there was an increasing trend in the fruit destruction rate and a significant increase in the average picking time per cluster when picking aggregated cluster distribution fruit.

In summary, the designed end-effector provides excellent harvesting results for all three types of kiwifruit clusters, especially for kiwifruit distributed in single and linear clusters. Capable of meeting the current demand for kiwifruit picking in clusters. The main reason for the increase in fruit damage was that the cutter was interfered with by kiwifruit vines, which scratched the surface of the fruit. The rise in the average picking time per cluster was due to the excessive number of fruits and their disorganized distribution, which reduces the recognition efficiency of the fruit identification device.

CONCLUSIONS

(1) Aiming to address the distribution characteristics of kiwifruit fruit clusters, a multi-fruit gripping and cutting linkage picking end-effector was designed, which integrates the fruit stalk separating and fruit gripping devices, linking the gripping of fruits with the cutting of fruit stalk, simplifying the structure and improving the picking efficiency. Moreover, proposing a dual-sensor fusion recognition method enhances the accuracy of fruit cluster identification. It mitigates the impact of environmental factors on the selection of different types of kiwifruit clusters.

(2) The picking experiment showed that the end-effector picked each cluster of fruits in an average time of 8.28 s, with a net fruit picking rate of 87.5% and a fruit damage rate of 7.5%. It has a net picking rate of 93.3% for kiwifruit fruits in linear clusters with the widest distribution area, and at the same time, it has good picking effect for kiwifruit fruits distributed in single and aggregated clusters, with high picking adaptability, which can meet the current demand of mechanized picking.

ACKNOWLEDGEMENT

This paper was funded by the National Natural Science Foundation of China (Grant No.51975114).

REFERENCES

[1] Au, C. K., Redstall, M., Duke, M., Kuang, Y. C., & Lim, S. H. (2022). Obtaining the effective gripper dimensions for a kiwifruit harvesting robot using kinematic calibration procedures. *Industrial Robot: the international journal of robotics research and application*, 49(5), 865-876.

[2] Bu, L. X., Chen, C. K., Hu, G. R., Sugirbay, A., & Chen, J. (2020). Technological development of robotic apple harvesters: A review. *INMATEH-Agricultural Engineering*, 61(2), 151-164.

[3] Dong Z Y. (2022) *Research on kiwi fruit picking technology and device based on machine vision and parallel mechanical arm（基于机器视觉与并联机械臂的猕猴桃采摘技术及装置研究）*[Thesis of Master, Northwest Agriculture and Forestry University]. China Campus Repository.

[4] El-Shakery, S., Ramadan, R., & Khader, K. (2020). Analytical and Graphical Optimal Synthesis of Crank-Rocker Four Bar Mechanisms for Achieving Targeted Transmission Angle Deviations. *Jordan Journal of Mechanical & Industrial Engineering*, 14(3).

[5] Fang, W., Wu, Z., Li, W., Sun, X., Mao, W., Li, R., & Fu, L. (2023). Fruit detachment force of multiple varieties kiwifruit with different fruit-stem angles for designing universal robotic picking end-effector. *Computers and Electronics in Agriculture*, 213, 108225.

[6] Ji, W., Huang, X., Wang, S., & He, X. (2023). A Comprehensive Review of the Research of the “Eye–Brain–Hand” Harvesting System in Smart Agriculture. *Agronomy*, 13(9), 2237.

[7] Li, M., &Liu, P. (2023). A bionic adaptive end-effector with rope-driven fingers for pear fruit harvesting. *Computers and Electronics in Agriculture*, 211, 107952.

[8] Li, K., Huo, Y., Liu, Y., Shi, Y., He, Z., & Cui, Y. (2022). Design of a lightweight robotic arm for kiwifruit pollination. *Computers and Electronics in Agriculture*, 198, 107114.

[9] Lan, Y., Yan, Y., Wang, B., Song, C., & Wang, G. (2022). Current status and future development of the key technologies for intelligent pesticide spraying robots. *Trans. Chin. Soc. Agric. Eng*, 38, 30-40.

[10] Min, F. U., Shike, G. U. O., Jianan, C. A. I., Jiacheng, Z. H. O. U., & Xiaoyi, L. I. U. (2023). TRIZ-aided design and experiment of kiwifruit picking end-effector. *INMATEH-Agricultural Engineering*, 71(3).

[11] Ma, L., He, Z., Zhu, Y., Jia, L., Wang, Y., Ding, X., & Cui, Y. (2022). A Method of Grasping Detection for Kiwifruit Harvesting Robot Based on Deep Learning. *Agronomy*, 12(12), 3096.

[12] Mu, L., Cui, G., Liu, Y., Cui, Y., Fu, L., & Gejima, Y. (2020). Design and simulation of an integrated end-effector for picking kiwifruit by robot. *Information Processing in Agriculture*, 7(1), 58-71.

[13] Mu, L. (2019) *Full Field of View Information Perception and Integrated Picking Method for Kiwifruit Harvesting Robot*（*猕猴桃收获机器人的信息感知与综合采摘方法研究*）[Thesis of Master, Northwest Agriculture and Forestry University]. China Campus Repository.

[14] Sarabu, H., Ahlin, K., & Hu, A. P. (2019, July). Graph-based cooperative robot path planning in agricultural environments. In 2019 *IEEE/ASME International Conference on Advanced Intelligent Mechatronics (AIM)*. pp. 519-525. IEEE.

[15] Williams, H., Ting, C., Nejati, M., Jones, M. H., Penhall, N., Lim, J., & MacDonald, B. (2020). Improvements to and large-scale evaluation of a robotic kiwifruit harvester. *Journal of Field Robotics*, 37(2), 187-201.

[16] Wang, M., Yan, B., Zhang, S., Fan, P., Zeng, P., Shi, S., & Yang, F. (2022). Development of a Novel Biomimetic Mechanical Hand Based on Physical Characteristics of Apples. *Agriculture*, 12(11), 1871.

[17] Yu, F., Zhou, C., Yang, X., Guo, Z. H., & Chen, C. L. (2022). Design and Experiment of Tomato Picking Robot in Solar Greenhouse. *Transactions of the Chinese Society for Agricultural Machinery*, 53(1), 41-49.

[18] Zhi, H. E., Zixu, L. I., Xingting, D. I. N. G., Kai, L. I., Yinggang, S. H. I., & Yongjie, C. U. I. (2023). Design and experiment of end effect for kiwifruit harvesting based on optimal picking parameters. *INMATEH-Agricultural Engineering*, 69(1).

[19] Zhang, Q., Liu, F. P., Jiang, X. P., Xiong, Z., & Xu, C. (2021). Motion planning method and experiments of tomato bunch harvesting manipulator. *Transactions of the CSAE*, 39(7), 149-156.

RESEARCH ON THE RESPONSE MECHANISM OF CLAMPING POINT POSITION TO THE VIBRATION PROPAGATION CHARACTERISTICS OF WOODEN MATERIALS
/
夹持点位置对木质材料振动传播特性的响应机理研究

Xingdong SUN*), Yukai ZHENG, Yuhang SUI, Delin WU, Rongyan WANG, Yangyang LIU, Jianfei ZHOU
School of Engineering, Anhui Agricultural University, Hefei (230036), China
Tel: 0551-65786450; E-mail: xdsun@ahau.edu.cn
DOI: https://doi.org/10.35633/inmateh-72-64

Keywords: *clamping point, vibration frequency, geometry, vibration response, energy transfer*

ABSTRACT

Vibratory harvesting is to dislodge fruits by applying excitation force to fruit trees, so the vibration response characteristics of fruit trees are of great significance for vibratory forest and fruit harvesting machinery to realize efficient harvesting. The effects of different clamping points and vibration frequencies on vibration responsiveness and energy transfer in Broussonetia papyrifera branches are investigated in this study. The results show that the effects of different clamping point positions and vibration frequencies on the branch vibration response are mutual. The ideal distance between the clamping point position and the base of the main branch should be between 48% and 73% of the branch length, and the distance between the clamping point position and the base of the main branch increased with the increase of vibration frequency. This is because, when the clamping point is close to the base of the main branch, a higher excitation frequency increases the energy consumption at the base of the main branch, and the amount of ineffective vibration energy transferred to the base of the main branch also increases. Therefore, when the location of the clamping point is close to the base of the main branch, the suppression of high-frequency vibration at the base of the main branch is stronger than the suppression of low-frequency vibration. When the clamping point is located in the center of the branch, the overall response of the branch to vibration is better.

摘要

振动采收是通过对果树施加激振力使果实脱落，因此果树的振动响应特性对振动林果采收机械实现高效采收具有重要意义。本研究探讨了不同夹持点和振动频率对构树枝条振动响应和能量传递的影响。结果表明，不同夹持点位置和振动频率对枝条振动响应的影响是相互的。理想的夹持点位置与主枝基部之间的距离应为枝条长度的 48% 至 73%，夹持点位置与主枝基部之间的距离随着振动频率的增加而增加。这是因为，当夹持点靠近主枝基部时，较高的激振频率会增加主枝基部的能量消耗，同时传递到主枝基部的无效振动能量也会增加。因此，当夹持点位置靠近主枝基部时，对主枝基部高频振动的抑制作用强于对低频振动的抑制作用。当夹持点位于树枝中心时，树枝对振动的整体响应效果较好。

INTRODUCTION

China is the world's top producer of forest fruits (*Liu et al., 2020*). The majority of forest fruits are being harvested manually, which significantly puts more financial strain on fruit farmers. For example, 50%~70% of the entire cost is attributable to the hand harvest of apricot fruits (*Lin et al., 2016; Wang et al., 2012*). A huge labor force is needed to harvest the forest fruit once it is fully developed. Some forest fruits are not picked as a result of the decline in rural population (*Chen et al., 2019*). As a result, it is one of the best ways to increase the level of automated fruit harvesting (*Pu et al., 2023*).

The three primary categories of vibratory harvesting equipment at the moment are pneumatic, impact, and mechanical, with mechanical vibratory harvesting being the most prevalent (*Yuan et al., 2022; Liu, 2018; Xu et al., 2023*). The clamping device on vibratory harvesting equipment applies vibration to the fruit tree, which causes the fruit to vibrate until it is detached from the tree. The vibration structure, vibration amplitude, vibration frequency and other parameters of vibration harvesting machinery are studied to provide reference for the efficient operation of vibration harvesting machinery (*Fu et al., 2016; Wu et al., 2014; He et al., 2020; Pezzi et al., 2009*). The energy transmission from the clamping point to the fruit is accomplished through the fruit tree vibration, therefore, the study of fruit tree vibration response and energy transmission is crucial.

Fruit trees have a wide range of shapes in their natural growth stage, and dynamic modeling or 3D modeling combined with finite elements can be used to better understand the modal and vibrational response of fruit trees (*Sergio et al., 2020; Peng et al., 2017; Cao et al., 2023*). The research on vibration response and energy transfer under different vibration conditions can provide a better reference for the design and optimization of vibratory harvesting machinery (*Wu et al., 2022; Liu et al., 2018; Wei et al., 2017*). However, little is known about how fruit trees may efficiently use vibration energy under various vibrational conditions (*Du et al., 2012*). This research primarily examines the vibration response and energy flow transfer properties of tree branches using sinusoidal excitation force at various clamping positions and vibration frequencies. This work can serve as a theoretical guide for the later design of the clamping mechanism for vibrating harvesting equipment and the investigation of fruit trees vibration response mechanisms.

MATERIALS AND METHODS

Test materials

The test subject is 3.6 m-tall *Broussonetia papyrifera*, which is seven years old. Its trunk diameter is 39.7 mm, primary branch diameter is 25.4 mm, and secondary branch diameter is 11.7 mm. It mainly consists of two main branches and several subordinate branches (*Niu et al., 2022*). The 2D structure and the placement of the clamping point schematic diagram are shown in Fig. 1.

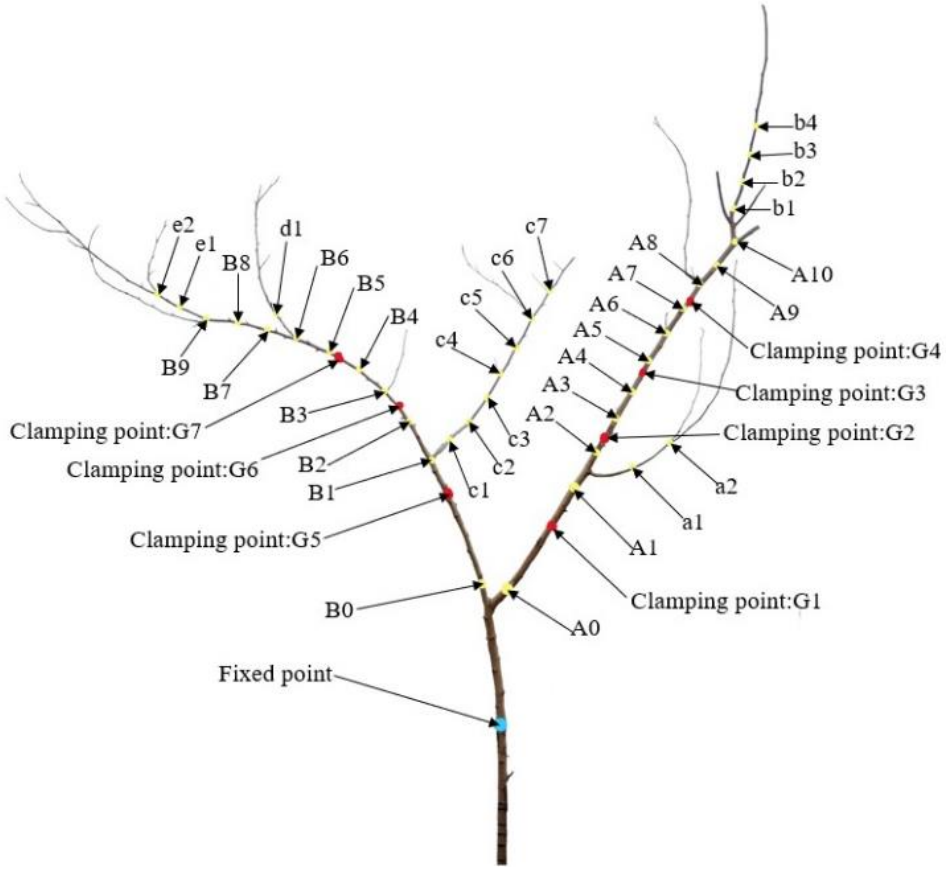

Fig. 1 - Structure of Broussonetia papyrifera

Test methods

Test equipment

Figure 2 shows the test equipment which is a homemade shaking branch type variable frequency and variable amplitude vibration harvesting device, manufactured by the Mechanical Damage and Multiscale Materials Mechanics Laboratory of Anhui Agricultural University. It comprises six-axis acceleration sensors WT61PC-485 (Range: 0~16g. Weight: 24g. Data acquisition frequency: 0~200 Hz), data acquisition system, tape measure, vernier caliper.

The rocking branch type variable frequency and vibration amplitude acquisition mechanism mainly consists of servo motor, reducer, coupling, output shaft, screw rod fixing seat, screw rod, screw rod nut, connecting rod and push rod. The overall structure of the device is a centering crank-slider mechanism. By rotating the screw, the distance between the connecting rod and the output shaft can be adjusted, thus the amplitude can be adjusted.

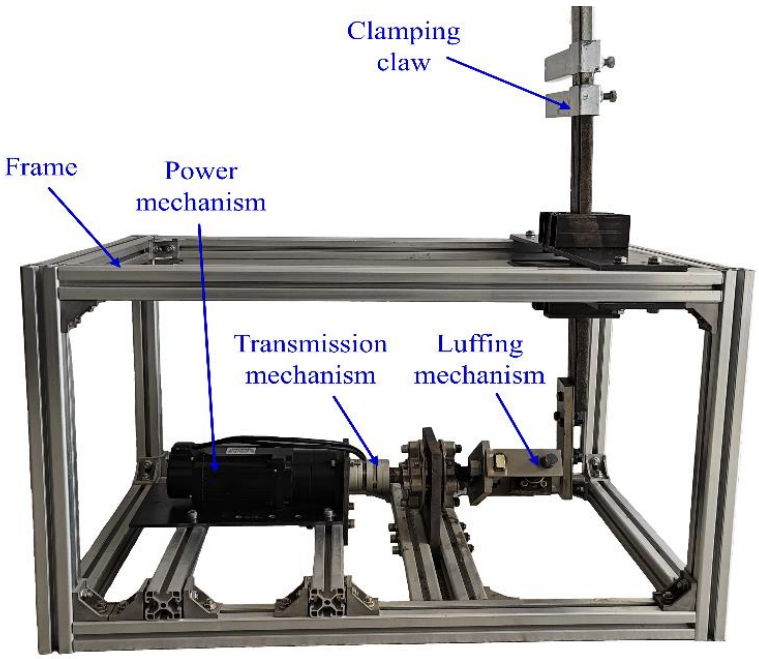

Fig. 2 - Shaking branch vibration harvesting mechanism

Testing planning

Figure 3 shows a picture of the field test of the vibration response characteristics, in which the branch clamping position was 45 cm away from the trunk, which was held in place by a tabletop clamp. Type A branches have a diameter of 21 to 34 centimeters, whereas Type B branches have a diameter of 14 to 24 centimeters. Four grasping points, G1, G2, G3, and G4, are provided on the A branch while three gripping points, G5, G6, and G7, are provided on the B branch, taking into account the manipulator's minimum gripping diameter. The distances between the different clamping points and the trunk are shown in table. 1.

Table 1

Distance between different clamping points and tree trunk

Clamping position	G1	G2	G3	G4	G5	G6	G7
Distance(cm)	45	72	99	126	45	72	99

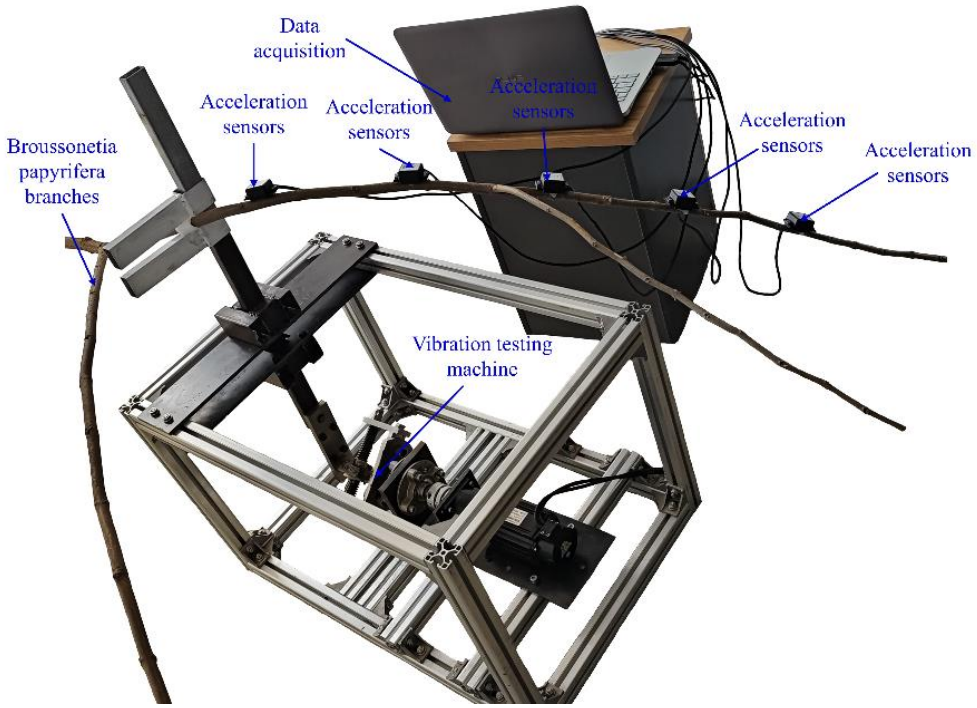

Fig. 3 - Field testing of vibration response characteristics

Monitoring sites A0 and B0 were utilized to measure the vibration response at the branch's base during vibration at a distance of 10 cm from the trunk, as illustrated in Fig. 1. It can show the intensity of the resulting vibration response at the tree trunk. This is an invalid transmission of vibration energy since the vibration of the tree trunk created in this way cannot enable the other principal branches to produce a strong enough vibration response to cause the fruit to fall off. The monitoring places A1 and B1 in Fig. 1 are used to measure the vibration response of the branches and are situated 55 cm from the trunk. In Fig. 1, the Monitoring point A2 and A1 are separated by 15 centimeters, the monitoring point B2 and B1 are separated by 15 centimeters, and the remaining sensors are separated by 10 centimeters.

These sensors are used to track the effective transfer of vibration energy as well as the response of the tree branches to vibration. Considering of the impact of branch diameter on accelerometer stability, all accelerometer attachment sites had branch sizes greater than 10 mm. The branches were clamped at various clamping points and vibrated at various vibration frequencies (2 Hz, 3 Hz, and 4 Hz), with each monitoring point measuring the acceleration of the vibration. Each series of tests was conducted three times and the average of the results was calculated, in order to confirm the accuracy of the results. The movement state of the tree branches could be used to assess the vibration response. Since the vibration was triggered by sinusoidal movement, the acceleration of different points could be integrated to obtain the maximum speed, and formula 1 could be used to calculate the maximum kinetic energy of various monitoring points on the tree branches.

$$E_i = \frac{1}{2} m_i v_i^2 = \frac{1}{2} \rho A_i (\int a_i \, dt)^2 \quad (1)$$

where:

E_i - is the kinetic energy of i monitoring point, (J);

m_i - is the mass of the i monitoring point, (m);

v_i - is the velocity of the i monitoring point, (m/s);

ρ - is the branch density, (kg/m^3);

A_i - is the branch cross sectional area, (m^2);

a_i - is the acceleration of i monitoring point, (m/s^2);

t - indicates the time, (s).

A relative kinetic energy ratio r_{ij} is established to depict kinetic energy changes at monitoring locations i and j along a transmission channel in order to more precisely illustrate the change in response at a specific location in relation to a reference point:

$$r_{ij} = \frac{E_i}{E_j} = \frac{A_i (\int a_i dt)^2}{A_j (\int a_j dt)^2} \quad (2)$$

where:

r_{ij} denotes the proportion of kinetic energy between monitoring points i and j. The cross-sectional areas of i monitoring point and j monitoring point are denoted by A_i (m^2) and A_j (m^2) respectively, whereas i monitoring point and j monitoring point acceleration are denoted by a_i (m/s^2) and a_j (m/s^2) respectively. When calculating the relative kinetic energy ratio on a branch, the value of j in formula 2 is assumed to be 1. The relative kinetic energy ratio can represent the ratio of the effective vibration energy to the ineffective vibration energy when the branch vibrates when j is monitoring point 0 and i is monitoring point at the branch's end.

RESULTS

Influence of clamping points on branch vibration

The effects of vibration on the A-branch and B-branch for various clamping points are depicted in Fig. 4 and Fig. 5 respectively. As illustrated in A2-45 in Fig. 4 (a), A3-72 in Fig. 4 (b), and A4-99 in Fig. 4 (c), with a rise in excitation frequency, the separation between the excitation point and the trunk that generates the optimal excitation response for the A branch grows. This suggests that when the excitation point is close to the base of the A branch, a lower excitation frequency generates a better vibration response. However, at high-frequencies vibration, the branches near the source of excitation generate larger damping forces, preventing effective vibration transmission. The G4 and G7 vibration clamping points have the worst overall effects on the vibration response of branches at the same vibration frequency.

This could be because the clamping point transfers the least amount of energy per unit time to the excitation points G4 and G7, which are the furthest from the branch's base and produce the least vibration in the fruiting branch.

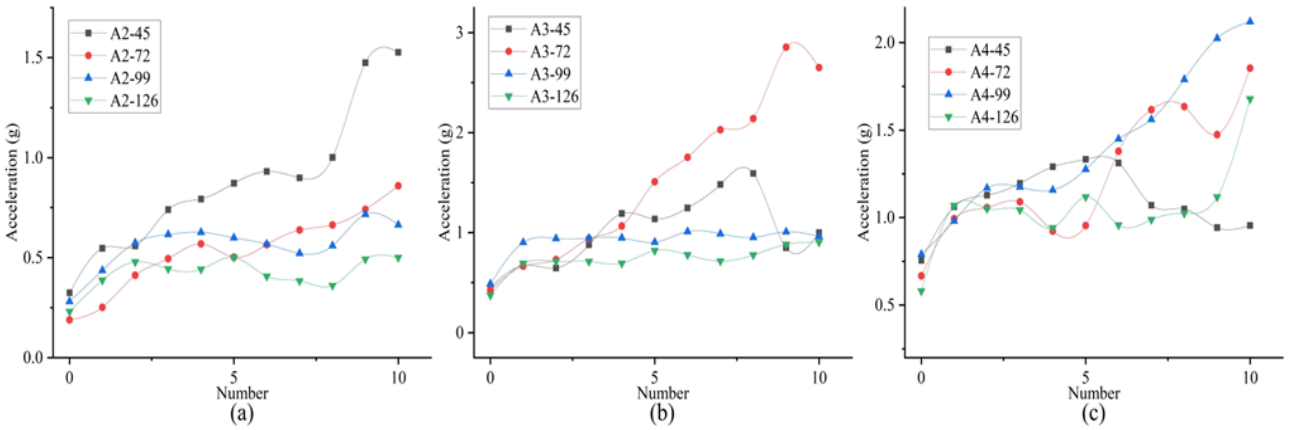

Fig. 4 - Influence of different clamping points on vibration response of A branch
(a): Vibration frequency is 2 Hz; (b): Vibration frequency is 3 Hz; (c): Vibration frequency is 4 Hz.

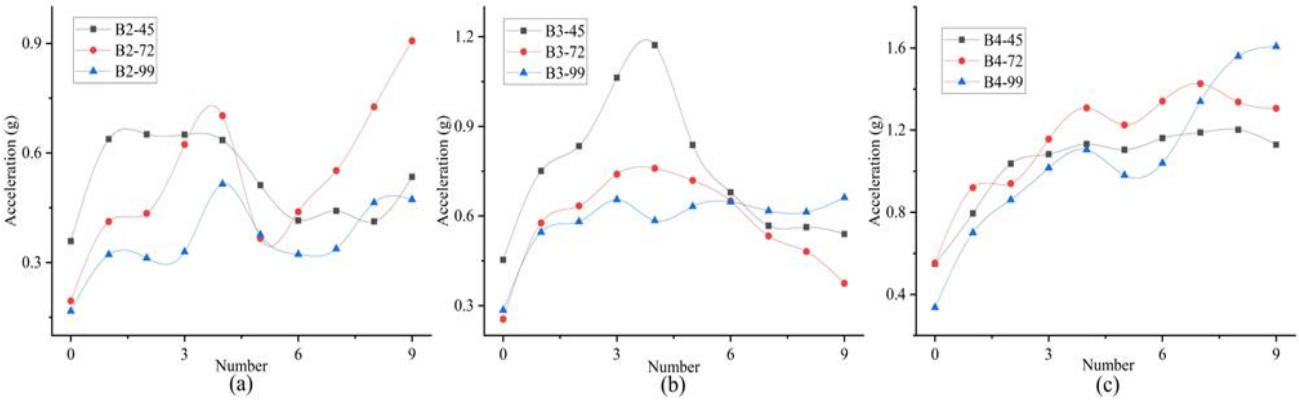

Fig. 5 - Influence of different clamping points on vibration response of B branch
(a): Vibration frequency is 2 Hz; (b): Vibration frequency is 3 Hz; (c): Vibration frequency is 4 Hz.

The relative kinetic energy ratio of each monitoring point on the A branch to the A1 monitoring point at various clamping positions is shown in Fig. 6, and the ratio of each monitoring point on the B branch to the B1 monitoring point at various clamping positions is shown in Fig. 7. The graph in Fig. 6 shows that the relative kinetic energy of A branch is significantly high near its terminal. The result in Fig. 7 shows that the relative kinetic energy of the B branch is quite high at the B4 monitoring point. This is because the branch deflection angle affects how vibrational energy is transferred. The energy transfer is typically hindered by a bigger branch deflection angle, which results in a higher relative kinetic energy ratio.

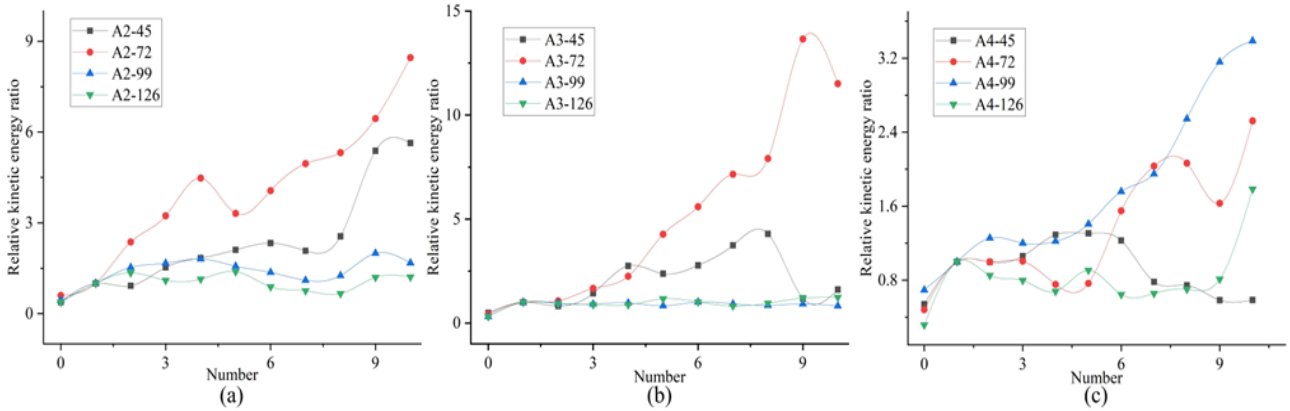

Fig. 6 - Influence of different clamping points on relative kinetic energy ratio of A branch
(a): Vibration frequency is 2 Hz; (b): Vibration frequency is 3 Hz; (c): Vibration frequency is 4 Hz.

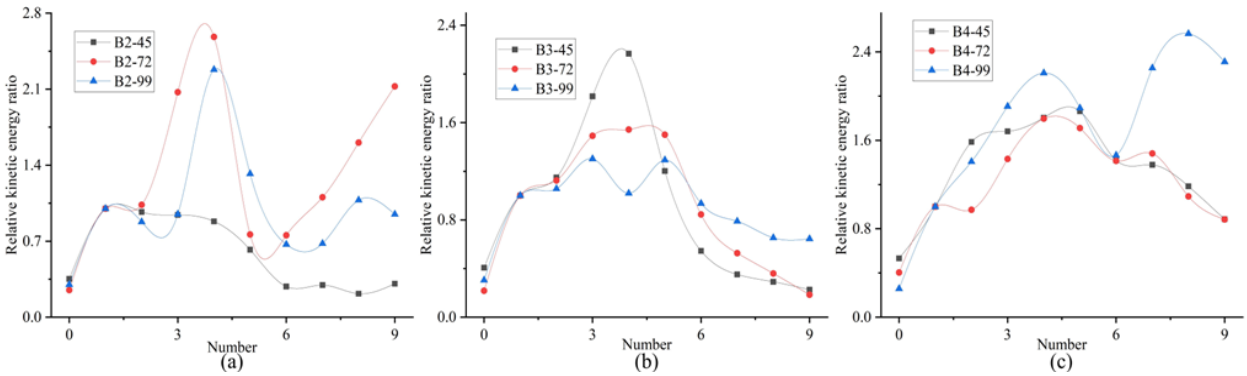

Fig. 7 - Influence of different clamping points on relative kinetic energy ratio of B branch
(a): Vibration frequency is 2 Hz; (b): Vibration frequency is 3 Hz; (c): Vibration frequency is 4 Hz.

Fig. 8 and Fig. 9 show, respectively, the vibrational effects of various vibration clamping points on the *b* branch and *c* branch. The vibration response of the secondary branch is observed to be stronger than that of the primary branch at the same vibration condition, which is favorable for the vibration shedding of fruits. It's possible that the secondary branch requires less energy to produce apparent vibration response because its diameter is substantially less than the primary branch's. Compared to the primary branch, the secondary branch's vibration response is more sensitive to changes in the clamping point's position. It demonstrates the choice of the clamping point position can significantly impact the effectiveness of fruit vibration harvesting.

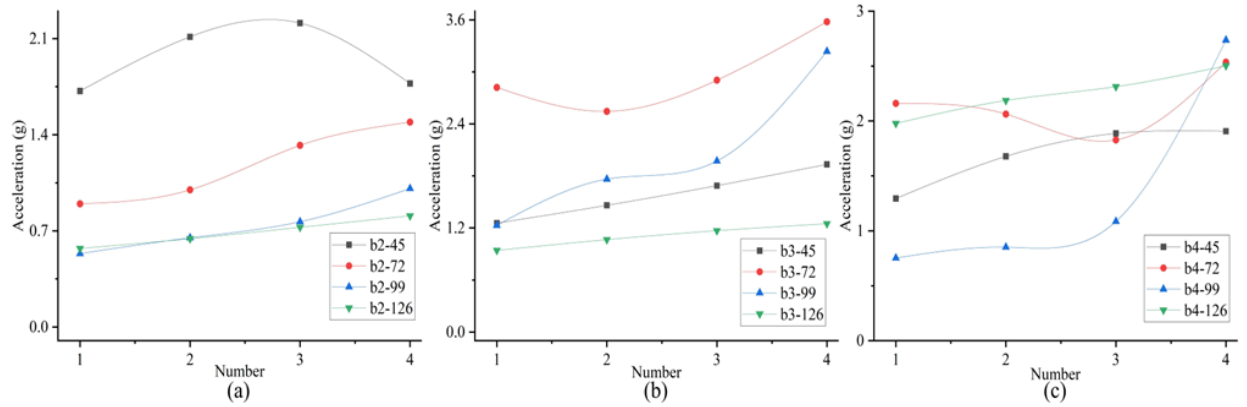

Fig. 8 - Influence of different clamping points on vibration response of b branch
(a): Vibration frequency is 2 Hz; (b): Vibration frequency is 3 Hz; (c): Vibration frequency is 4 Hz.

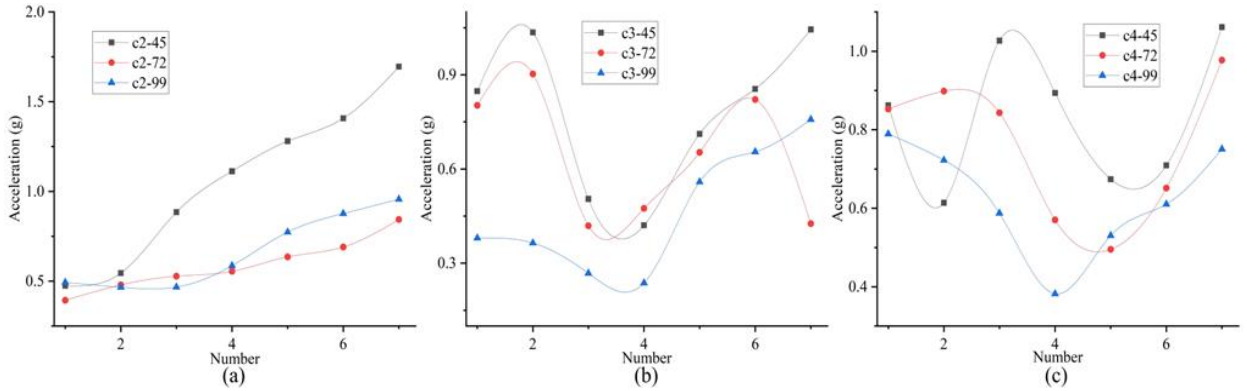

Fig. 9 - Influence of different clamping points on vibration response of c branch
(a): Vibration frequency is 2 Hz; (b): Vibration frequency is 3 Hz; (c): Vibration frequency is 4 Hz.

Influence of vibration frequency on branch vibration

Fig. 10 and Fig. 11 show, respectively the vibrational impacts of various vibration frequencies on the A branch and the B branch. It has been discovered that tree branches respond better to high frequency vibration than low frequency vibration. Under high-frequency vibration, the manipulator is able to transfer more kinetic energy to the branch clamping point with in a certain period of time, which results in higher energy density and better vibration responsiveness of the branch.

As illustrated by monitoring points 4 and 5 in Fig. 11 (a), under various vibration frequencies, the acceleration change amplitudes of the same monitoring points of branch A and branch B are different. It demonstrates how various tree branch components react differently to various vibrational frequencies. The structure of tree branches and the mechanical properties of tree materials are just two examples of the numerous elements determining how tree branches vibrate in response to various frequencies (*Liu et al., 2021*). Given that fruit trees have complicated structural and mechanical qualities as a result of their natural growing environment, it is impossible to ascertain the natural frequency of fruit trees in a timely manner. Therefore, using the resonance approach to efficiently harvest fruit is challenging.

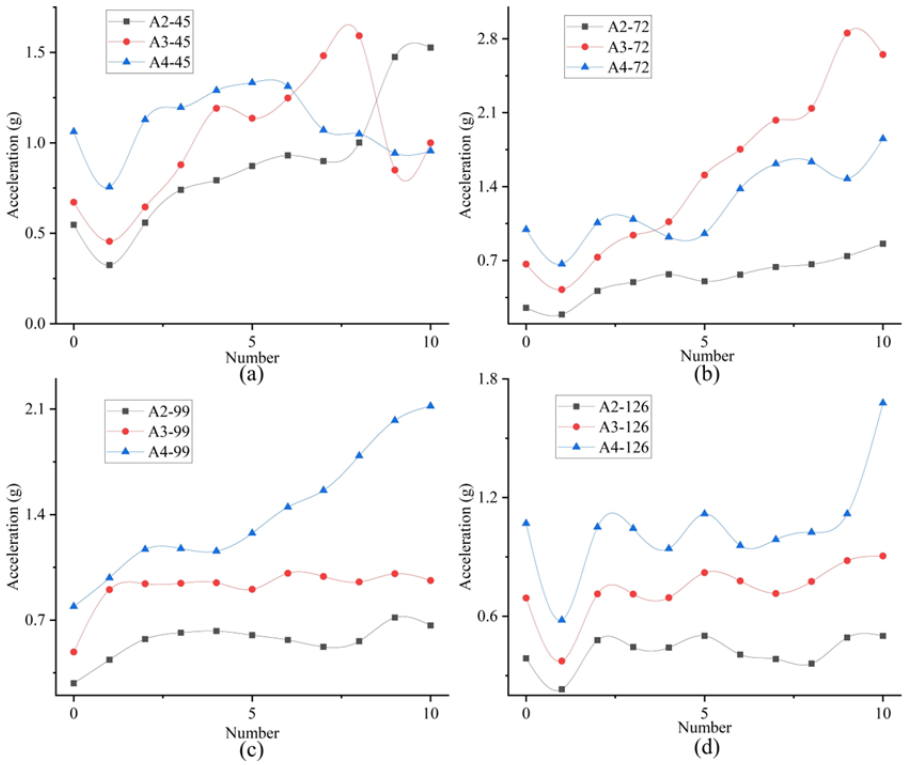

Fig. 10 - Influence of different vibration frequency on vibration response of A branch
(a): Clamping point G1; (b): Clamping point G2; (c): Clamping point G3; (d): Clamping point G4.

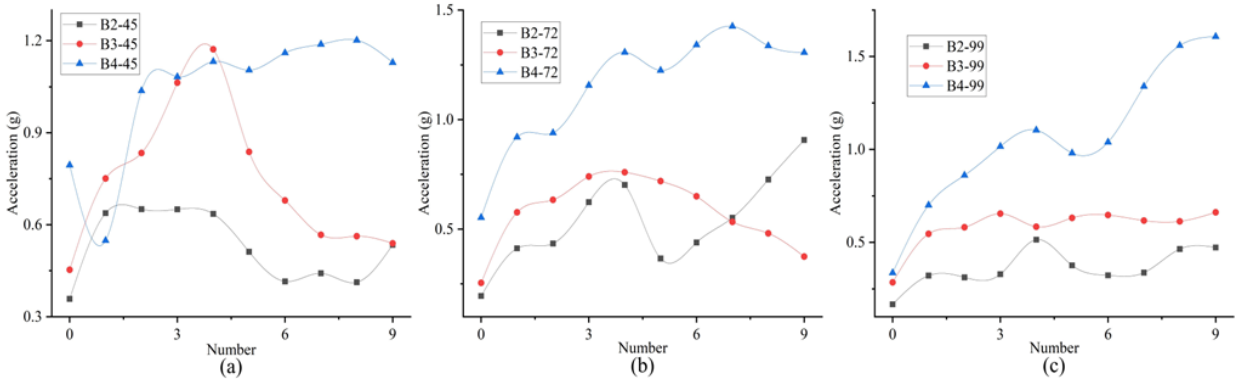

Fig. 11 - Influence of different vibration frequency on vibration response of B branch
(a): Clamping point G5, (b): Clamping point G6, (c): Clamping point G7.

Fig. 12 shows the relative kinetic energy ratio of each monitoring point of A branch to A1 monitoring point at different vibration frequency and Fig. 13 shows the relative kinetic energy ratio of each monitoring point of B branch to B1 monitoring point at different vibration frequency. High-frequency vibration can efficiently convey the vibration energy to the end of the branch when the clamping point is far from the tree trunk. When the clamping point is close to the tree trunk, high-frequency vibration makes it difficult to transfer vibration energy to the branch's end. At this time, the relative kinetic energy of monitoring point 0 is comparatively high, suggesting that more vibration energy is being transferred to the branch's base, causing in energy loss. This is because the branch's base has a considerable inhibitory impact on high-frequency vibrations, preventing the passage of high-frequency vibration energy from near the branch to the branch's end.

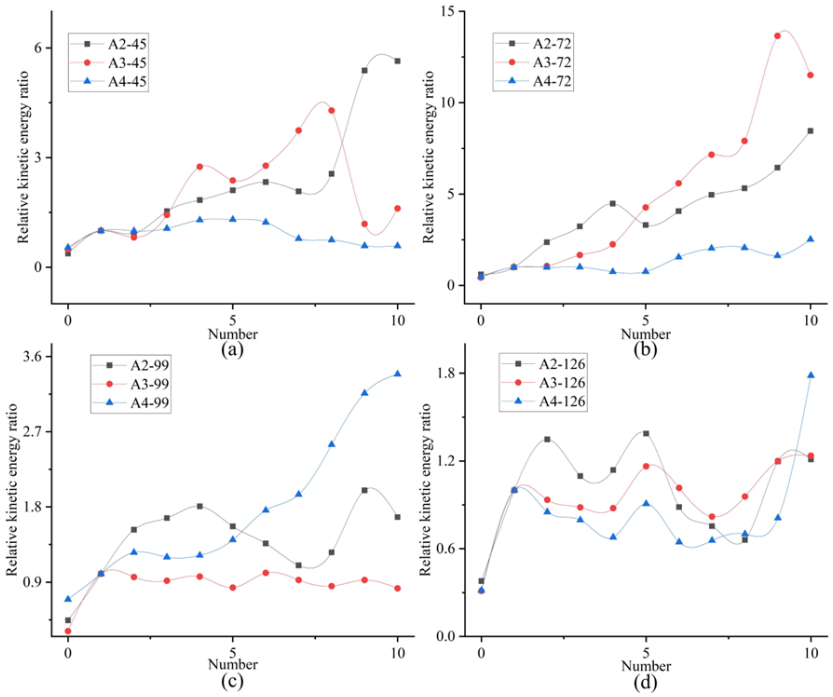

Fig. 12 - Influence of different vibration frequency on relative kinetic energy ratio of A branch (a): Clamping point G1, (b): Clamping point G2, (c): Clamping point G3, (d): Clamping point G4.

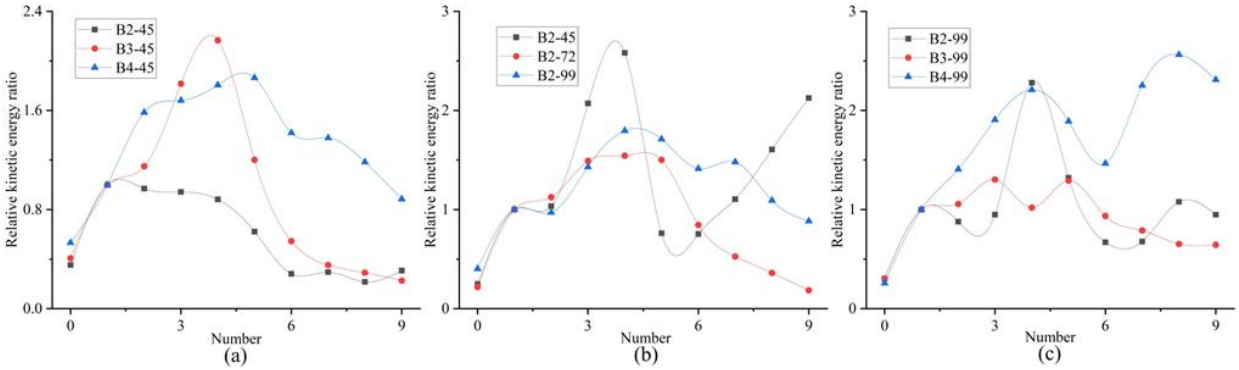

Fig. 13 - Influence of different vibration frequency on relative kinetic energy ratio of B branch (a): Clamping point G1, (b): Clamping point G2, (c): Clamping point G3.

Influence on vibration response and relative kinetic energy ratio

Fig.14 shows the vibration acceleration and relative kinetic energy ratio of A branch monitoring point 10 under various influencing variables. Fig.15 shows the vibration acceleration and relative kinetic energy ratio of B branch monitoring point 9 under various influencing variables. To better display the effective kinetic energy transferred to the branch's end and the ineffective kinetic energy transferred to the branch's bottom, the relative kinetic energy ratio in Fig.14 is the ratio of the kinetic energy of monitoring point 10 to the kinetic energy of monitoring point 0, and the relative kinetic energy ratio in Fig.15 is the ratio of the kinetic energy of monitoring point 9 to the kinetic energy of monitoring point 0. From Fig.14, it is clear that the vibration acceleration and effective kinetic energy ratio are at their best when the clamping points are 72 cm apart, with a vibration frequency of 3 Hz. From Fig.15, it is clear that the vibration acceleration and effective kinetic energy ratio are at their best when the clamping points are 99 cm apart, with a vibration frequency of 4 Hz. In order to better reflect the relations between the clamping position and the length of the branch, divide the clamping distance by the total length of the branch. It is found that when the clamping position is 48%~73% of the overall length of the branch, a better ratio of the end acceleration and relative kinetic energy of the branch can be obtained. It's that the B branch at monitoring point 3 has a wide deflection angle, resulting in ineffective vibration energy transmission to the end of the B branch when it vibrates at the clamping position of G5. When the clamping position is G7, the deflection component of the B branch efficiently prevents vibration energy from passing to the branch's base along the B branch, enhancing total energy utilization. High-frequency vibration should be applied to the clamping part away from the trunk when the secondary branches are dispersing at the ends of

the primary branches in order to maximize energy utilization and improve vibration responsiveness. When the secondary branches are evenly distributed on the primary branches, the clamping point should be in the middle of the primary branches.

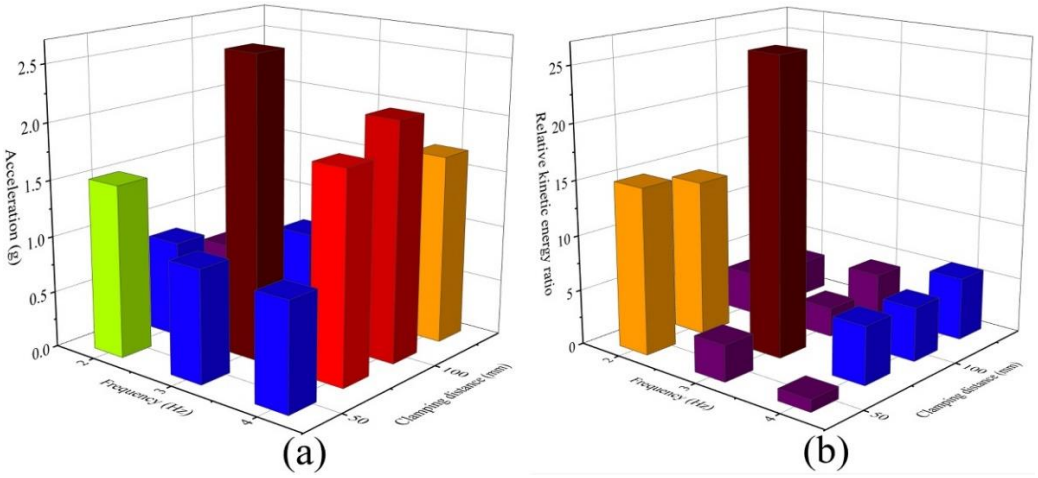

Fig. 14 - Influence of different factor on monitoring point 10 of A branch
(a): Acceleration of monitoring point 10, (b): Relative kinetic energy ratio of monitoring point 10.

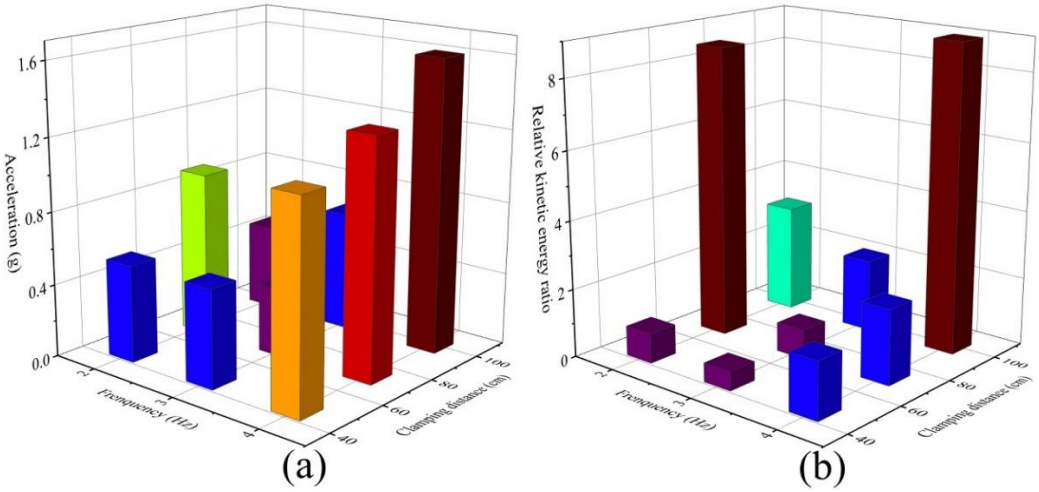

Fig. 15 - Influence of different factor on monitoring point 10 of B branch
(a): Acceleration of monitoring point 10, (b): Relative kinetic energy ratio of monitoring point 10.

CONCLUSIONS

According to the necessity and complexity of efficient vibration harvesting, this study used multiple vibration frequencies and vibration clamping positions to evaluate the vibration response and energy transfer efficiency of Broussonetia papyrifera branches. The conclusions are as follows:

(1) The vibration response of the part where the branch has a large deflection angle is greater than that of other parts of the branch, and this part can hinder the transmission of vibration energy.

(2) The ideal clamping distance should be between 48%~73% of the tree branches since it increases as the vibration frequency rises.

(3) The structural damping at the base of the branch has a more significant inhibitory effect on high-frequency vibrations than on low-frequency vibrations.

(4) When the clamping point is the middle part of the tree branch, the overall vibration response of the tree branch is better.

ACKNOWLEDGEMENT

This research was funded by the National Natural Science Foundation of China (52375228); the National Natural Science Foundation of China (52005009); the Post-Master's Enterprise Workstation in Anhui Province (2022sshqygzz012); the Key Projects of Natural Science Research Projects of Colleges and Universities in Anhui Province, China (KJ2021A0154); the Anhui Provincial Key Research and Development Program of China (202004e11020003); the Anhui Natural Science Foundation of China (2008085QE273).

REFERENCES

[1] Cao, J. L., Bai, X. P., Xu, D. C., Li, W. B., & Chen, C. C, (2023). Experiment and analysis on walnut (Juglans regia L.) shedding force based on low-frequency vibration response. *Industrial Crops and Products,* Vol. 204, pp. 117242, England.

[2] Chen, H. S., & Wang, X. P., (2019). Exploring the relationship between rural village characteristics and Chinese return migrants' participation in farming: path dependence in rural employment. *Cities,* Vol. 88, pp. 136-143, Forests, Land and Housing Division of the United Nations Economic Commission for Europe (UNECE).

[3] Du, X. Q., Chen, D., Zhang, Q., Scharf, P. A., & Whiting, M. D., (2012). Dynamic responses of sweet cherry trees under vibratory excitations. *Biosystems Engineering,* Vol. 111, pp. 305-314, England.

[4] Fu, L. S., Peng, J., Nan, Q., He, D. J., Yang, Y. G., & Cui, Y. J., (2016). Simulation of vibration harvesting mechanism for sea buckthorn. *Engineering in Agriculture, Environment and Food,* Vol. 9, pp. 101-108, Japan.

[5] He, L. Y., Liu, X. C., Du, X. Q., & Wu, C. Y., (2020). In-situ identification of shaking frequency for adaptive vibratory fruit harvesting. *Computers and Electronics in Agriculture,* Vol. 170, pp. 105245, England.

[6] Lin, H., Xu, L. Y., Xuan, Y., Zhou, W. F., & Weng, L. Y., (2016). Experimental research on the vibration mode of fruit vibration acceleration response. (林果振动加速度响应振型试验). *Journal of Forestry Engineering,* Vol. 1, pp. 100-104, Jiangsu/China.

[7] Liu, J. N., (2018). Research status and development trend of harvester based on vibration mechanism (基于振动机理的采收机研究现状及发展趋势). *Agricultural Technology & Equipment,* Vol, 3, pp. 84-85, Shanxi/China.

[8] Liu, X. W., & Guo, C. L., (2021). Study on dynamic characteristics of apple tree branches based on vibration picking (基于振动采摘的苹果树枝干动力学特性). *Journal of Forestry Engineering,* Vol. 3, pp. 120-126, Jiangsu/China.

[9] Liu, Y., Wang, H. H., Liu, Y., Yang, Y. T., & Wang, D. Z., (2020). Research progress of forest-fruit mechanized picking and sorting (林果机械采收与分选研究进展). *World Forestry Research*, Vol. 3, pp. 20-25, Beijing/China.

[10] Liu, Z. L., Wang, C. Y., Xu, Z. F., Zhang, Z., & Zhang Y. B., (2018). Study on energy of fruit trees under external excitation force (外激振力作用下果树树干能量流). *Journal of Vibration, Measurement & Diagnosis*, Vol. 1, pp. 130-135+211, Jiangsu/China.

[11] Niu, Z. j., Xu, Z., Deng, J. T., Zhang, J., Pan, S. J., & Mu, H. T. (2022). Optimal vibration parameters for olive harvesting from finite element analysis and vibration tests. *Biosystems Engineering,* Vol. 215, pp. 228-238, England.

[12] Peng, J., Xie, H. Q., Feng, Y. L., Fu, L. S., Sun, S. P., & Cui, Y. J. (2017). Simulation study of vibratory harvesting of Chinese winter jujube (Zizyphus jujuba Mill. cv. Dongzao). *Computers and Electronics in Agriculture,* Vol. 143, pp. 57-65, England.

[13] Pezzi, F., & Caprara, C. (2009). Mechanical grape harvesting: Investigation of the transmission of vibrations. *Biosystems Engineering*, Vol. 103, pp. 281-286, England.

[14] Pu, Y. J., Wang, S. M., Yang, F. Z., Ehsani, R. Z., Zhao, L. J., Li, C. S., Xie, S. Y., & Yang, M. J. (2023). Recent progress and future prospects for mechanized harvesting of fruit crops with shaking systems. *International Journal of Agricultural and Biological Engineering,* Vol. 16, pp. 1-13, Beijing/China.

[15] Sergio, C. G., Fernando, A. R., Rocío, A. C., & Jesús, A. G. R. (2020). The contribution of fruit and leaves to the dynamic response of secondary branches of orange trees. *Biosystems Engineering.* Vol. 193, pp. 149-156, England.

[16] Wang, C. Q., Xu, L. Y., Zhou, H. P., & Cui, H. (2012). Development and experiment of eccentric-type vibratory harvester for forest-fruits (偏心式林果振动采收机的研制与试验). *Transactions of the Chinese Society of Agricultural Engineering,* Vol. 16, pp. 10-16, Beijing/China.

[17] Wei, T. P., Wang, C. Y., Min, L., & Lv, M. L. (2017). Research on vibration resonance frequency of "Y-shaped" fruit trees based on Matlab (基于 MATLAB 对"Y 型"果树振动共振频率的研究). *Jiangsu Agricultural Sciences*, Vol. 3, pp. 169-172, Jiangsu/China.

[18] Wu, C. Y., He, L. Y., Du, X. Q., Chen, S. Z., & Ni, K. N. (2014). 3D reconstruction of Chinese hickory tree for dynamics analysis. *Biosystems Engineering,* Vol. 119, No. 1, pp. 69-79, England.

[19] Wu, D. L., Zhao, E. L., Jiang, S., Wang, W. W., Yuan, J. H., & Wang, k. (2022). Optimization and Experiment of canopy Parameters of Camellia oleifera Based on Energy Transfer characteristics (基于能量传递规律的油茶树冠层振动参数优化与试验). *Transactions of the Chinese Society for Agricultural Machinery*, Vol. 8, pp. 23-33, Beijing/China.

[20] Xu, X., Wang, Y. N., & Jiang, Y. M., (2023). Review of Research Advances in Fruit and Vegetable Harvesting Robots. *Journal of Electrical Engineering & Technology,* Vol. 19, pp. 773-789, South Korea.

[21] Yuan, Y. W., Bai, S. H., Niu, K., Zhou, L. M., Zhao, B., Wei, L. G., Xiong, S., & Liu, L. J. (2022). Research progress on mechanized harvesting technology and equipment for forest fruit (林果机械化采收技术与装备研究进展). *Transactions of the Chinese Society of Agricultural Engineering*, Vol. 9, pp. 53-63, Beijing/China.

DESIGN AND TESTING OF SEED PUSH WHEEL FOR HIGH-SPEED PRECISION SEED METERING DEVICE FOR CORN WITH INTERNAL SEED FILLING AND POSITIVE PRESSURE AIRFLOW

/

玉米内充气压式高速精量排种器推种轮设计与试验

Xin DU, Qianhao YU, Shufa CHEN, Qixin SUN, Han ZHANG, Changqing LIU*
School of Mechanical Engineering, Jiangsu Ocean University, Lianyungang 222005/ China
Tel: 0086-0518-85895322; E-mail: lyg_lcq@163.com
Corresponding author: Changqing Liu
DOI: https://doi.org/10.35633/inmateh-72-65

Keywords: *Precision seeding device; Seed push wheel; High-speed; Precision agriculture*

ABSTRACT

In order to improve the uniformity and stability of seed delivery and meet the requirements of precision sowing operation, a kind of seed push wheel designed to mesh with the seed discharging disk was developed. The wheel underwent theoretical analysis and experimental optimization regarding parameters such as tooth profile, tooth count, and tooth height. Using a pneumatically inflated maize precision seed-metering device as the seeding carrier, a full-factorial experiment was conducted with operational speed and tooth height as the experimental variables, and qualification rate, reseeding rate, and leakage rate as the performance indicators. A multivariate quadratic regression model was established to assess the relationships between the factors and indicators. The results indicated that optimal seed guiding performance was achieved when the seed push wheel had 9 teeth, a tooth height of 5.2–6.2 mm, and an operational speed of 9.0–12.6 km/h. This study provides a theoretical foundation and data support for the development of precision seeding technology and corresponding seed guiding devices.

摘要

为提高导种投送均匀性与稳定性，满足精量播种作业要求，设计了一种与排种盘啮合传动的推种轮，对其齿形参数、齿数、凸齿高度等因素进行了理论分析与试验优化。以气压内充式玉米精量排种器为排种载体，结合全因素试验，以作业速度和凸齿高度为试验因素，合格率、重播率和漏播率为试验指标，建立了因素与指标间的多元二次回归模型。结果表明，当推种轮齿数为 9、推种轮凸齿高度为 5.2-6.2 ㎜、作业速度为 9.0-12.6 km/h 时，导种性能最佳。本研究可为精量播种技术及配套导种装置的研制提供理论基础与数据支撑。

INTRODUCTION

Corn is an important feed, energy and industrial crop, and its cultivation area and output have ranked first in China for many years (*Yang et al., 2016*). China's per capita arable land area is less than half of the world's per capita level, in the context of sustained population growth and arable land area remains unchanged or even decreased, to ensure the efficient production of maize, that is, to improve yields is the key to solving the problem of food security (*Tang et al., 2019; Yuan et al., 2018*). Factors affecting corn yields are climate, soil conditions, seeds, planting techniques and field management techniques, among which seeding quality is one of the most important influencing factors. In order to improve the seeding quality of mechanized operations, over the years, the precision seed discharger *(Karayel et al., 2022; Kumar-Patel et al., 2021; Ospanova et al., 2024*) has been the focus of research and hot spots of single grain (precision) seeding machine, while for high-speed operations (>9 km/h) the research of smooth seeding mechanism is relatively weak, the seed guide, seeding link has become a constraint on the quality of high-speed sowing operations to further improve the "short board", there is an urgent need to develop the high-speed operation of the smooth seeding mechanism (*Liao et al., 2020*).

Xin Du, Lecturer Ph.D. Eng; Qianhao Yu, MA.Eng Stud.; Shufa Chen, Prof. Ph.D. Eng; Qixin Sun, Prof. Ph.D. Eng; Han Zhang, B.S Stud.; Changqing Liu, Lecturer Ph.D. Eng.*

Currently, improving corn seed spacing uniformity typically involves lowering the height of seed casting. However, at high speeds, the moment the seed enters the seed bed cannot fully compensate for the relative speed difference of the machine, resulting in a significant decrease in grain spacing uniformity (*Fanigliulo et al., 2022*). Additionally, the absence of synchronized contour wheels for sowing monomers with automatic depth control leads to inconsistencies in sowing depth. After the addition of synchronous contour wheels to the seeding unit, the increased seeding height necessitates the use of corrugated tubes to guide the seeds accurately into the planting furrow. However, the random movement of seeds within the tube can lead to collisions and bouncing, resulting in reduced uniformity in seed spacing (*Awad et al., 2022; Im et al., 2023*).

Liu et al. (2015) used three-dimensional reverse engineering to improve the curved seed guide tube, based on the "zero-speed seeding" method, which reduces the horizontal bouncing and slipping of the seeds. *Zhao et al. (2018)* designed a V-shaped groove paddle wheel-type seed guide component, which can actively adjust the state of seed movement after seed discharging. *Qi et al. (2015)* designed a centralized exhaust-fed corn precision seed discharger, which adopts positive pressure airflow to convey and guide seeds. *Li et al. (2020)* analysed and established the relationship and mathematical model between the length of the air-fed seed guide tube and the airflow velocity inside the tube. *Chen et al. (2012)* designed a belt-type seed guide device integrated with the transmission and seed casting mechanism, which made the seeds move to the seed casting position according to a predetermined trajectory and improved the coefficient of variation of the grain spacing. *Liu et al. (2017)* proposed a seeding technology of precise seed picking, smooth seed delivery and precise seed casting, and designed a seeding synchronous belt-type seed guide device.

The above scholars have researched various types of seed-guiding components from the aspects of component structure, parameter optimization and influencing factors, and have also made certain research progress, but they have not completely restricted the seed degrees of freedom during the seed-guiding process, and cannot avoid the collision bouncing of the seeds in the seed-guiding tubes, and the uniformity of the grain spacing during the high-speed operation is poor. In this context, in order to improve the uniformity and stability of seed guide delivery, design a kind of seed push wheel with the matching transmission of seed discharge disk, analyse the influence of each parameter on the performance of the seed guide, and validate the reasonableness of the design through the bench test, with a view to providing theoretical references and data support for the research and development of the supporting seed guide device.

MATERIALS AND METHODS

Structure and key parameters

This group designed a high-speed smooth seed delivery mechanism for corn based on full-degree-of-freedom constrained seed guiding, which is used in conjunction with the high-speed precision seed discharger for corn developed in the previous stage, the working principle and structural composition of which have been clearly described in the published literature (*Du and Liu, 2023*), and the working process can be divided into three tandem links of pushing, guiding, and casting the seed (as shown in Fig. 1).

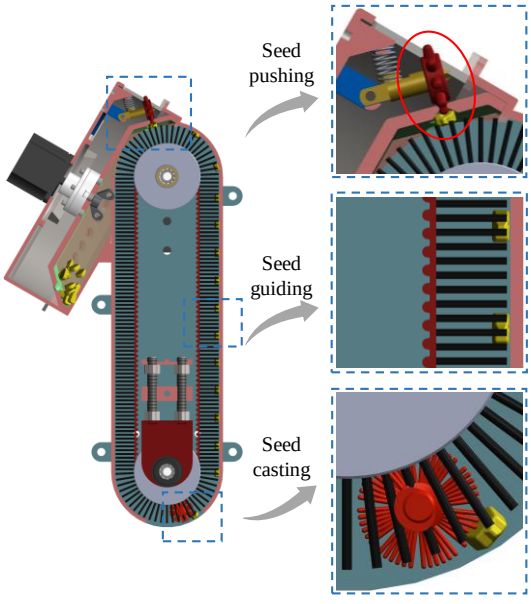

Fig. 1 – Schematic diagram of the full-degree-of-freedom constrained seed-guiding process

In order to make the seeds accurately embedded in the bristles on the brush belt, a seed push wheel setup suitable for high-speed seeding is designed by utilizing the principle of gear meshing, as shown in Fig.2. The seed push wheel consists of seed push wheel fixing device, pressure spring, seed push wheel, seed push wheel axle and bearing, etc., in which the convex teeth on the seed push wheel mesh with the type holes and concave teeth on the seed discharging disk. When working, the seed discharge disk is driven by a stepping motor to rotate, and the seed discharge disk rotates to drive the seed push wheel to follow. When the convex teeth on the seed push wheel enter the holes on the seed plate, they block airflow escape, reducing pressure on the surface of the seeds. Additionally, the increased depth of convex teeth penetration into the holes helps dislodge seeds attached to the hole surface, embedding them into the bristles of the brush.

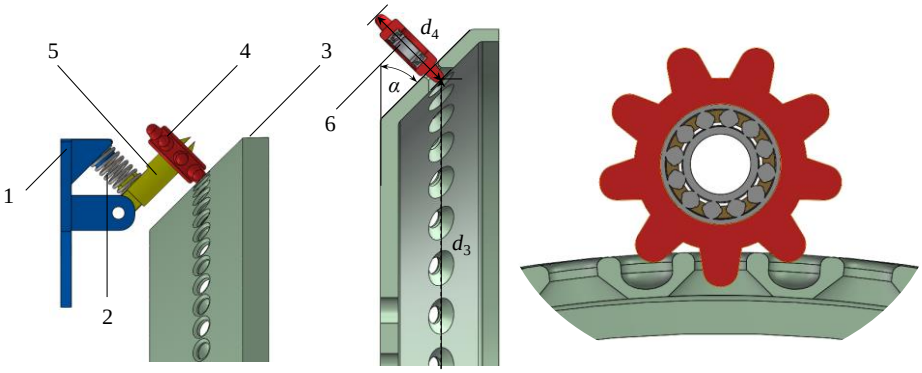

Fig. 2 – Schematic diagram of seed push wheel structure

1. seed wheel retainer 2. compression spring 3. seed discharge disk 4. seed wheel 5. seed wheel axle 6. bearing. α: cone angle; d_4: diameter of tooth apex circle; d_3: diameter of seed discharge disc at engagement

In order to make the convex teeth mesh smoothly with the concave teeth and holes, the movement between the seed pushers and seed disks should be regarded as pure rolling, and the distance between the holes on the seed disks should be equal to or a multiple of the distance between the teeth of the convex teeth of the seed pushers.

$$\frac{2\pi R}{Z} = K\frac{2\pi r}{z} \tag{1}$$

where: R is the circumferential radius of the hole in the seed discharge disk, mm; Z is the number of holes in the seed discharge disk; K is a constant, take 1 or 2; r is the radius of the base circle of the seed push wheel, mm; z is the number of teeth on the seed push wheel.

It is known that the circumferential radius R of the hole in the seed discharge disk is 99.5 mm, the number of holes Z on the seed discharge disk is 36, and the number of teeth z on the seed push wheel is 9. According to the above formula, the radius of the base circle of the seed push wheel can be obtained as 24.875 mm or 14.4375 mm, which corresponds to the K of 1 and 2, respectively. As the space available for installing the seed push device in the seed dispenser is not large, the radius of the base circle of the seed push wheel is taken to be 14.4375 mm, and at this time, K is 2, and a concave tooth is dug between every 2 holes to realize the normal meshing with the seed push wheel.

As the seed plate drives the seed push wheel's rotation, the convex teeth of the seed push wheel mesh with the concave teeth and holes on the seed plate. During this process, the engagement point on the seed plate remains constant at point B′, causing the convex teeth of the seed push wheel to slide and mesh along point B′. In order to calculate the tooth shape formula of the convex teeth, this paper adopts the "reverse method" to inverse the trajectory of B′.

As illustrated in Figure 3, assuming the seed push wheel remains stationary, the motion relationship between the seed plate and the seed push wheel remains unchanged according to the principle of relative motion. This implies that the seed plate undergoes pure rolling motion along the seed push wheel. At a certain moment, the seed plate is positioned at number 1, and the engagement point on the seed push wheel is point B, while the engagement point on the seed plate is point B′. After a period of time, when the seed plate rotates around the centre *O* of the seed push wheel by an angle *θ* and reaches position number 2, the engagement point on the seed push wheel is at point A. The trajectory of the engagement point on the seed plate, represented by B′, follows the tooth profile curve of the seed push wheel.

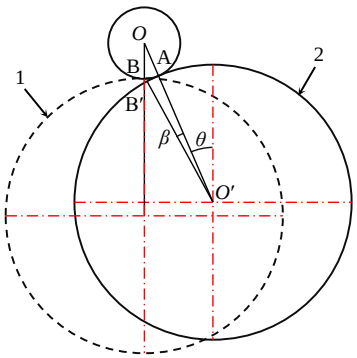

Fig. 3 – Design of convex tooth profile for seed pushers

1. initial position 2. position after relative rotation

O: seed push wheel centre; B and B′ are the initial and "post-reversal" engagement points, respectively; O′: seeding wheel centre; A: engagement point after rotation of the seed push wheel; θ: Angle of rotation of the seeding wheel around point O at the centre of the seed push wheel; β: angle of ∠AO′B′.

Establish a coordinate system with the centre *O* of the seed push wheel as the origin, so that ∠AO′B′ is *β*, then the coordinates of *O′* and *B′* are respectively:

$$O'\left[(R+r)\sin\theta,(R+r)\cos\theta\right] \tag{2}$$

$$B'\left[(R+r)\sin\theta-R\sin(\theta+\beta),(R+r)\cos\theta-R\cos(\theta+\beta)\right] \tag{3}$$

Since the form of motion between the seed discharge disk and the seed push wheel is pure rolling, according to the geometrical relationship there is:

$$\begin{cases} AB = AB' \\ \theta r = \beta R \end{cases} \tag{4}$$

i.e.

$$\beta = \frac{\theta r}{R} \tag{5}$$

From the above equation, the coordinates of B′ can be expressed as:

$$B'\left[(R+r)\sin\theta-R\sin\left(\theta\left(1+\frac{r}{R}\right)\right),(R+r)\cos\theta-R\cos\left(\theta\left(1+\frac{r}{R}\right)\right)\right] \tag{6}$$

Thus the parametric equation of the displacement curve for point B′ can be expressed as:

$$\begin{cases} x=(R+r)\sin\theta-R\sin\left(\theta\left(1+\dfrac{r}{R}\right)\right) \\ y=(R+r)\cos\theta-R\cos\left(\theta\left(1+\dfrac{r}{R}\right)\right) \end{cases} \tag{7}$$

According to the previously determined radius R of the seed discharge disk and the radius r of the base circle of the seed push wheel, the tooth shape formula of the convex teeth of the seed push wheel can be obtained as follows:

$$\begin{cases} x=113.9375\sin\theta-99.5\sin(1.1451\theta) \\ y=113.9375\cos\theta-99.5\cos(1.1451\theta) \end{cases} \tag{8}$$

Similarly, as shown in Figure 4, assuming that the push seed wheel remains stationary, assuming the seed push wheel remains stationary, the seed plate rotates counterclockwise relative to the seed push wheel.

At a certain moment, when the seed plate is positioned at number 1, the engagement point on the seed push wheel is point B, while the engagement point on the seed plate is point B′; after a period of time, when the seed discharge disc rotates around the centre of the seed push wheel *O* by an angle of *θ* and is located at the position of serial number 2, the engagement point of the seed push wheel becomes point A, and the movement trajectory of the engagement point on the seed discharge disc is B′, which is the convex tooth profile of the seed push wheel.

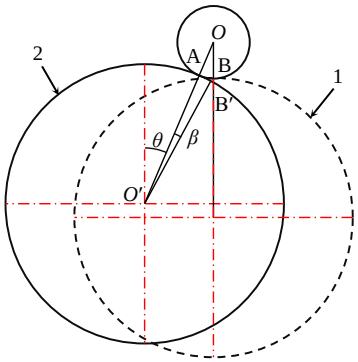

Fig. 4 – Schematic diagram of engagement and separation points

1. initial position 2. position after relative rotation

O: seed push wheel centre; B and B′ are the initial and "post-reversal" engagement points, respectively; O′: seeding wheel centre; A: engagement point after rotation of the seed push wheel; θ: Angle of rotation of the seeding wheel around point O at the centre of the seed push wheel; β: angle of ∠AO′B′.

Similar to the derivation of the tooth profile of the seeding wheel, a parametric equation for the displacement profile of the point B′ can be obtained:

$$\begin{cases} x = -(R+r)\sin\theta + R\sin\left(\theta\left(1+\dfrac{r}{R}\right)\right) \\ y = (R+r)\cos\theta - R\cos\left(\theta\left(1+\dfrac{r}{R}\right)\right) \end{cases} \tag{9}$$

Comparing Eq. (7) and Eq. (9), it can be seen that the two curves are symmetric about the y-axis.

In order to ensure that the convex teeth on the seed push wheel and the concave teeth and holes on the seed discharging disk are normally engaged, it should be ensured that when the convex teeth are disengaged from the concave teeth or holes, the next pair of teeth just start to mesh, and at this time, the convex teeth on the seed push wheel are engaged with the concave teeth and holes on the seed discharging disk at the maximum depth, as shown in Fig. 5.

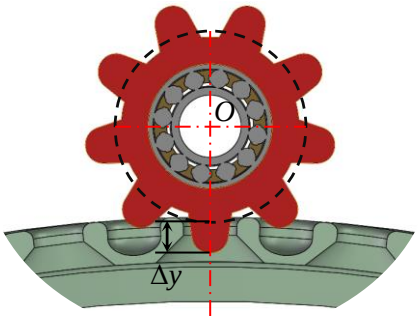

Fig. 5 – Engagement depth schematic

Δy: the maximum depth of engagement

The maximum depth of engagement Δy is the difference between the maximum value (extreme value) of the longitudinal coordinate equation of the toothing curve of the convex teeth of the seed pushers and its initial value. Since the longitudinal curve of the tooth shape of the convex teeth of the seed pushers is symmetric about the x-axis, the maximum depth of engagement Δy can be obtained by solving the parametric equation of any one of the curves, and the derivation of y.

$$y' = -113.9375\sin\theta + 99.5\times1.1415\sin(1.1451\theta) \tag{10}$$

Make $y' = 0$, then get $\theta = 0°$ or 240.4081°, will be substituted into the formula (10), the maximum value of y is 14.4375 mm or 18.64 mm, so as to get the maximum depth of engagement Δy is 0 mm or 4.2 mm. Based on the above formulas, the convex tooth profile of the seed push wheel was obtained. To prevent mechanical damage to the seeds during the pushing process and to facilitate meshing and machining, the tooth tops of the convex teeth were rounded, resulting in the convex tooth profile shown in Figure 5.

Bench testing

In order to verify the accuracy of the theoretical analysis and the hole formation performance of the internal pneumatic precision seed discharger under different working parameters, the parts were injection moulded using the Dimension Elite 3D printer (precision 0.178 mm, material ABS) produced by Stratasys Company of the United States. The seed guiding performance was tested on the JPS-12 multifunctional seed discharging test, and a layer of 1~2 mm thick grease was applied on the conveyor belt of the test stand to prevent the corn seeds from bouncing, and the test setup is shown in Figure 6. The corn variety "Zhengdan 958", which has the largest planting area in China, was utilized as the test subject.

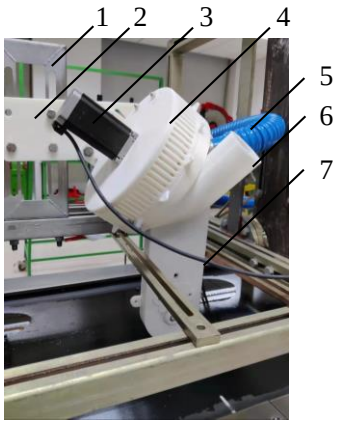

Fig. 6 – Schematic diagram of seed-guiding device bench test

1. seed dispenser fixing frame; 2. seed dispenser fixing plate; 3. seed dispenser drive motor; 4. pneumatic seed dispenser; 5. air inlet pipe; 6. seed inlet; 7. seed guide device

Test indicators

In order to evaluate the operational performance of the seed-guiding device, according to GB/T 6973-2005 Test Methods for Single Grain (Precision) Seeders, single grain rate, reseeding rate, leakage rate and grain spacing coefficient of variation are used as evaluation indexes. The formula for calculating each performance index is as follows

$$\begin{cases} Y_1 = \dfrac{n_s}{n_0} \times 100\% \\ Y_2 = \dfrac{n_d}{n_0} \times 100\% \\ Y_3 = \dfrac{n_m}{n_0} \times 100\% \end{cases} \quad (11)$$

Where: Y_1 is the qualified rate, %; Y_2 is the multiple rate, %; Y_3 is the leakage rate, %; n_s is the number of qualified seed holes, count; n_d is the number of double or more seed holes, count; n_m is the number of empty holes, count; and n_0 is the total number of holes of the test seeds, 251 holes.

Due to the length constraint of the conveyor belt, data were collected from 251 maize seed holes each time. Each treatment was repeated three times and average values were calculated. The data were organized to determine the qualified rate, multiple rate and leakage rate.

RESULTS

Number of teeth on the seed pushers

Different quantities of convex teeth on the seed push wheel result in varying linear speeds during operation. This variation alters the mechanical performance when the seed push wheel engages with the seed plate, thereby impacting the seed discharge qualification rate.

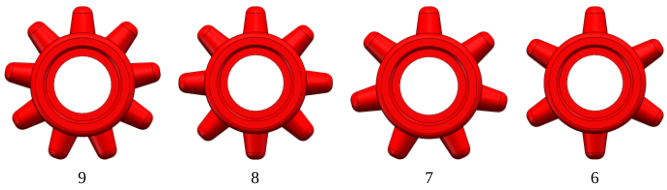

Fig. 7 – Schematic diagram of the number of teeth on the seed pushers

As shown in Fig. 7, seed pushers with different numbers of teeth were modelled in SolidWorks, and seed disks with different numbers of concave teeth were modelled considering that seed pushers were used in conjunction with seed disks. Under the conditions of operating speed of 10 km/h, air pressure of 1.6 kPa, respectively, a one-factor simulation test was carried out with the number of teeth of the seed pushers as the factor and the seed discharge pass rate as the target, and the test results were shown in Figure 8.

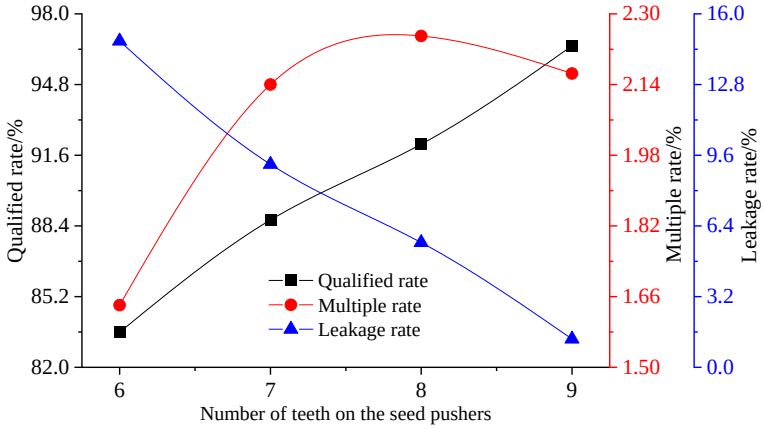

Fig. 8 – Schematic diagram of the number of teeth on the seed pushers

As shown in Figure 8, increasing the number of convex teeth on the seed push wheel leads to a linear decrease in the missing seed rate. This occurs because an increased number of convex teeth reduces the linear speed of the seed plate and ensures smoother meshing between the seed push wheel and the seed plate, minimizing vibrations in the seed plate. Consequently, the leakage rate decreases, while qualified and multiple rates improve.

Height of seed pushers' teeth

The height of the convex teeth of the seed push wheel directly affects the depth of the convex teeth into the concave teeth, which has an important impact on the timely introduction of seeds from the hole. On the premise of not affecting the normal meshing relationship between the seed push wheel and the seed discharge disk, the height of the convex teeth of the seed push wheel is set to 4.2 mm, 4.7 mm, 5.2 mm and 5.7 mm, respectively, and the height of the convex teeth of the seed push wheel is shown in Figure 9.

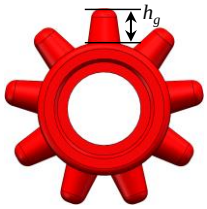

Fig. 9 – The height of the seed pushers' cams

h_g: tooth height

Under the conditions of operating speed of 10 km/h, air pressure of 1.6 kPa, the number of teeth of the seed push wheel is 9, respectively, and the height of the convex teeth of the seed push wheel is taken as the factor to carry out a one-factor simulation test with the qualified rate of seed discharging as the target, and the test results are shown in Fig. 10.

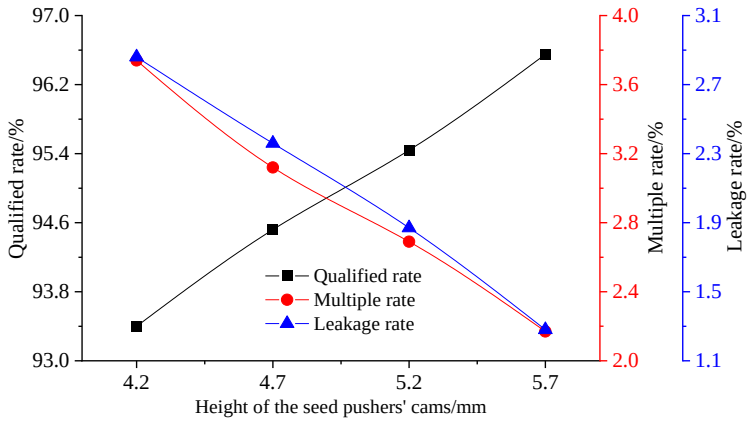

Fig. 10 – Influence of the height of the seed pushers' cams on the performance of seed discharging

As can be seen from Fig. 10, the qualified rate decreases linearly when the tooth height of the convex teeth of the seed push wheel decreases, because the seed cannot be pushed out of the surface of the moulded hole and embedded in the brush bristles in time after the tooth height decreases, resulting in an increase in the leakage rate and the re-seeding rate. Increasing the tooth height without affecting the normal engagement can push the seed away from the surface of the mould hole for a sufficiently large distance to embed the seed in the bristles.

Interactions among the factors

Based on the above analysis, the number of teeth on the seed pushers was determined to be 9. In order to study the effect of the interaction between the working speed and the height of the seed pushers' cams on the target results, a full factorial test was designed with the working speed and the height of the seed pushers' cams as the study factors, and the qualified rate, multiple rate and leakage rate were used as the study objectives.

The test scheme and test results are shown in Table 1.

Table 1

Full factorial test program and results

No.	Speed v_m (km/h)	Height h_g (mm)	Qualified y_1 (%)	Multiple y_2 (%)	Leakage y_3 (%)
1	7.2	4.7	93.17	2.38	4.45
2	7.2	5.2	94.95	2.07	2.98
3	7.2	5.7	95.66	1.69	2.65
4	7.2	6.2	95.29	1.25	3.46
5	7.2	6.7	93.85	0.73	5.42
6	9.0	4.7	93.59	2.67	3.74
7	9.0	5.2	95.40	2.36	2.25
8	9.0	5.7	96.13	1.97	1.89
9	9.0	6.2	95.80	1.52	2.69
10	9.0	6.7	94.38	1.00	4.62
11	10.8	4.7	93.68	2.76	3.56
12	10.8	5.2	95.52	2.44	2.04
13	10.8	5.7	96.29	2.05	1.66
14	10.8	6.2	95.98	1.59	2.43
15	10.8	6.7	94.59	1.06	4.35
16	12.6	4.7	93.46	2.65	3.89
17	12.6	5.2	95.33	2.32	2.35
18	12.6	5.7	96.12	1.93	1.96
19	12.6	6.2	95.84	1.46	2.70
20	12.6	6.7	94.48	0.93	4.59
21	14.4	4.7	92.91	2.34	4.75
22	14.4	5.2	94.81	2.01	3.19
23	14.4	5.7	95.63	1.61	2.77
24	14.4	6.2	95.37	1.13	3.49
25	14.4	6.7	94.05	0.59	5.36

A quadratic multiple regression was fitted to the qualified rate, multiple rate and leakage rate to obtain the regression equation

$$\begin{cases} y_1 = 20.07 + 0.8857v_m + 24.62h_g - 0.0496v_m^2 + 0.03178v_m h_g - 2.15h_g^2 \\ y_2 = -1.463 + 0.6943v_m + 0.7894h_g - 0.03086v_m^2 - 0.007v_m h_g - 0.1371h_g^2 \\ y_3 = 81.4 - 1.58v_m - 25.41h_g + 0.8047v_m^2 - 0.02478v_m h_g + 2.287h_g^2 \end{cases} \quad (12)$$

The interaction effects of the working speed and the height of the seed pushers' cams on the qualified rate, multiple rate and leakage rate are shown in Figure 11.

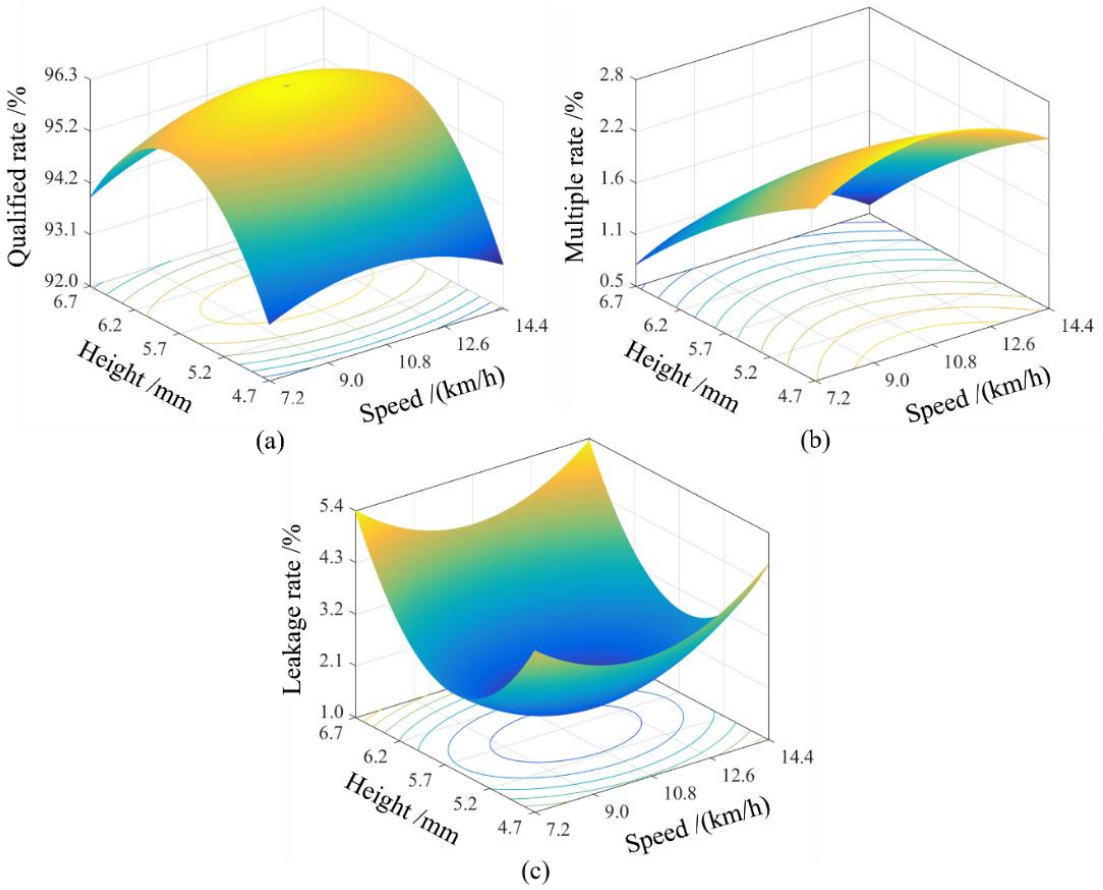

Fig. 11 – Response surface analysis of the interaction effects of factors

Fig. 11(a) shows that when the operating speed is 9.0-12.6 km/h and the height of the convex teeth of the seed pushers is 5.2-6.2 mm, the highest qualified rate is achieved. Fig. 11(b) shows that the lowest multiple rate was achieved when the operating speed was between 9.0 and 12.6 km/h and the height of the convex teeth of the seed pushers was greater than 5.7 mm. Fig. 11(c) shows that when the operating speed is 9.0-12.6 km/h and the height of the convex teeth of the seed pushers is 5.2-6.2 mm, the lowest leakage rate is achieved.

CONCLUSIONS

In this study, in order to improve the uniformity and stability of seed guide delivery, a kind of seed push wheel matched with the drive of the seed discharge tray was designed, the influence of each parameter on the performance of the seed guide was analysed, and the reasonableness of the design was verified by bench test, and it was concluded that the seed guide performance was optimal when the number of the teeth of the seed pusher wheel was 9, the height of the convex teeth of the seed pusher wheel was 5.2-6.2 mm, and the operating speed was 9.0-12.6 km/h.

ACKNOWLEDGEMENT

This work was financially supported by Natural Science Foundation of the Jiangsu Higher Education Institutions of China (23KJB210007).

REFERENCES

[1] Awad, M., Fouda, O., Abd El-reheem, S., et al. (2022). A new seed drill for planting peas on a raised-bed. *INMATEH - Agricultural Engineering, 68*(3), 681-692. http://doi.org/10.35633/inmateh-68-67.

[2] Chen X., Zhong L. (2012). Design and test on belt-type seed delivery of air-suction metering device. *Transactions of the Chinese Society of Agricultural Engineering*, *28*(22), 8-15.

[3] Du, X., Liu, C. (2023). Design and testing of the filling-plate of inner-filling positive pressure high-speed seed-metering device for maize. *Biosystems Engineering*, *228*, 1-17. http://doi.org/10.1016/j.biosystemseng.2023.02.008.

[4] Fanigiliulo, R., Grilli, R., Benigni, S., et al. (2022). Effect of sowing speed and width on spacing uniformity of precision seed drills. *INMATEH - Agricultural Engineering, 66*(1), 9-18. http://doi.org/10.35633/inmateh-66-01.

[5] Im, D., Lee, H., Kim, J., et al. (2023). Bucket size optimization for metering device in garlic planter using discrete element method. *Agriculture (Basel), 6*(13), 1199. http://doi.org/10.3390/agriculture13061199.

[6] Karayel, D., Güngör, O. & Šarauskis, E. (2022). Estimation of optimum vacuum pressure of air-suction seed-metering device of precision seeders using artificial neural network models. *Agronomy (Basel), 7*(12), 1600. http://doi.org/10.3390/agronomy12071600.

[7] Kumar-Patel, S., Bhimani, J. B., Yaduvanshi, B. K., et al. (2021). Optimization of the design and operational parameters of planter for vegetable pigeon pea (cajanus cajan l. millsp.) seed. *INMATEH - Agricultural Engineering, 63*(1), 326-334. http://doi.org/10.35633/inmateh-63-33.

[8] Li Y., Liu Y., Liu L. (2020). Distribution mechanism of airflow in seed tube of different lengths in pneumatic seeder. *Transactions of the Chinese Society for Agricultural Machinery*, *51*(06), 55-64. http://doi.org/10.6041/j.issn.1000-1298.2020.06.006.

[9] Liao Y., Li C., Liao Q., et al. (2020). Research progress of seed guiding technology and device of planter. *Transactions of the Chinese Society for Agricultural Machinery*, *51*(12), 1-14. http://doi.org/10.6041/j.issn.1000-1298.2020.12.001.

[10] Liu L., Yang H. (2015). 3D reverse engineering design on seed tube based on Geomagic Design software. *Transactions of the Chinese Society of Agricultural Engineering*, *31*(11), 40-45. http://doi.org/10.11975/j.issn.1002-6819.2015.11.006.

[11] Liu Q., He X., Yang L., et al. (2017). Effect of travel speed on seed spacing uniformity of corn seed meter. *International Journal of Agricultural and Biological Engineering*, *10*(4), 98-106. http://doi.org/10.25165/j.ijabe.20171004.2675.

[12] Ospanova, S., Aduov, M., Kapov, S., et al. (2024). The results of experimental research of a rotor seed-metering unit for sowing non-free-flowing seeds. *Journal of agricultural engineering (Pisa, Italy),* 55(1). http://doi.org/10.4081/jae.2024.1556.

[13] Qi B., Zhang D., Liu Q., et al. (2015). Design and experiment of cleaning performance in a centralized pneumatic metering device for maize. *Transactions of the Chinese Society of Agricultural Engineering*, *31*(01), 20-27. http://doi.org/10.3969/j.issn.1002-6819.2015.01.003.

[14] Tang H., Wang J., Xu C., et al. (2019). Research progress analysis on key technology of chemical fertilizer reduction and efficiency increase. *Transactions of the Chinese Society for Agricultural Machinery*, *50*(04), 1-19. http://doi.org/10.6041/j.issn.1000-1298.2019.04.001.

[15] Yang L., Yan B., Zhang D., et al. (2016). Research progress on precision planting technology of maize. *Transactions of the Chinese Society for Agricultural Machinery*, *47*(11), 38-48. http://doi.org/10.6041/j.issn.1000-1298.2016.11.006.

[16] Yuan Y., Bai H., Fang X., et al. (2018). Research progress on maize seeding and its measurement and control technology. *Transactions of the Chinese Society for Agricultural Machinery*, *49*(09), 1-18. http://doi.org/10.6041/j.issn.1000-1298.2018.09.001.

[17] Zhao S., Chen J., Wang J., et al. (2018). Design and experiment on v-groove dialing round type guiding-seed device. *Transactions of the Chinese Society for Agricultural Machinery*, *49*(6), 146-158. http://doi.org/10.6041/j.issn.1000-1298.2018.06.017.

SIMULATION ANALYSIS AND TEST OF EDEM-BASED TWIN SPIRAL PROPELLER FOR MUDFLAT AQUACULTURE
/
基于 EDEM 的滩涂养殖双螺旋推进器仿真分析与试验

Maomao ZOU[1)]; Rui ZHANG[*1)], Xiwen ZHANG[1)], Xiaoning HE[1)], Shuqi SHANG[13)], Xuegeng CHEN[12)], Zhenjia MA[1)], Moxian LI[1)], Yunkang LI[1)], Wenjie LI[1)], Haozhe WEI[1)], Yutao LI[1)]

[1)] College of Mechanical and Electrical Engineering, Qingdao Agricultural University, Qingdao 266109, China;
[2)] Shihezi University, Shihezi, 832003, China;
[3)] Key Laboratory of Intelligent Agricultural Machinery and Equipment for Saline and Alkaline Land, Ministry of Agriculture and Rural Development, 266109, China;
Tel: +86-15963011651; E-mail: 15963011651@163.com
Corresponding author: Rui ZHANG
DOI: https://doi.org/10.35633/inmateh-72-66

Keywords: *mudflat aquaculture; amphibious device; discrete element simulation; twin spiral propeller; EDEM*

ABSTRACT

Aiming at the problems of coastal ecological damage and low yield of mudflat aquaculture caused by the invasion of M. alterniflora, in order to improve the operational efficiency of mudflat wet and soft ground, and to promote the ecological balance and the development of coastal agriculture, a walking device with twin spiral propellers for muddy wet and soft ground was designed. Using EDEM simulation software to simulate and analyze, the discrete element model of muddy soil particles is established to analyze the interaction mechanism with the spiral propeller and the operation propulsion effect, and it is concluded that the spiral propeller will not produce congestion phenomenon during the operation; data are collected through several simulation tests, and the optimal parameter design of the spiral propeller structure is derived from the response surface analysis, and the spiral propeller is designed to operate at a speed of 2.416 mph in the simulation with the optimal parameter of structural design. The field test shows that the optimal height of the spiral blades is 50 mm, the total length of the drum is 2,970 mm, the helix angle of lift is 30 °, the pitch is 453 mm, and the propelling speed is 2.36 m/s. The data collected through several simulation tests are used to find the optimal parameter design of the spiral propeller structure, and the simulation speed of the spiral propeller in the optimal structural design parameter is 2.416 m/s.

摘要

针对互花米草入侵导致沿海生态破坏，滩涂养殖业低产等问题，为了提高滩涂湿软地面作业效率，促进生态平衡与沿海农业发展，设计一种泥泞湿软地面双螺旋推进器行走装置。利用 EDEM 仿真软件进行仿真分析，建立泥泞土壤颗粒的离散元模型，分析其与螺旋推进器的互作机理与作业推进效果，并探究得出螺旋推进器在作业时不会产生壅土现象；通过多次仿真试验搜集数据，经响应面分析得出螺旋推进器结构的最佳参数设计，螺旋推进器在最佳结构设计参数的仿真推进速度为 2.416m/s。田间试验验证表明，在滚筒直径为 400 mm，螺旋叶片最佳高度为 50 mm；滚筒总长为 2 970 mm，螺旋升角为 30 °，螺距为 453mm，作业推进速度为 2.36m/s。

INTRODUCTION

Mudflats are special landforms at the junction of ocean and land, which make them a unique ecosystem due to factors such as their geographic location and climatic environment. The invasion of *M. alterniflora*, which is native to the United States *(Shang et al., 2009)*, will compete for nutrients with the aquaculture products in the mudflat, leading to a substantial reduction in the production of shellfish, algae, fish and crabs, etc. In addition, *M. alterniflora* also affects the exchange capacity of seawater, which leads to a decline in water quality and induces red tides, and the large-scale flooding of *M. alterniflora* may also affect the smoothness of the waterway and impede the traffic of the harbors and terminals. As shown in Figure 1, effective management and control of the breeding and expansion of exotic species of *M. alterniflora* is urgent *(Qiao et al., 2019; Gao, 2021)*.

Maomao ZOU, Ph.D. Stud. Eng.; Rui ZHANG, Prof. Ph.D. Eng.; Xiwen ZHANG, Ph.D. Stud. Eng.; Xiaoning HE, Prof. Ph.D. Eng.; Shuqi SHANG, Prof. Ph.D. Eng.; Xuegeng CHEN, Prof. Ph.D. Eng.; Zhenjia MA, Ph.D. Stud. Eng.; Moxian LI, Ph.D. Stud. Eng.; Yunkang LI, Ph.D. Stud. Eng.; Wenjie LI, Ph.D. Stud. Eng.; Haozhe WEI, Ph.D. Stud. Eng.; Yutao LI, Ph.D. Stud. Eng.*

Fig. 1 - Coastal mudflats invaded by M. alterniflora

The current measures to control and remove *M. alterniflora (Ji et al., 2023; Zhou et al., 2023; Yin et al., 2023)* mainly include physical, chemical and biological techniques, however, the above techniques still have the problems of poor management effect, secondary pollution to the environment, and even ecological damage. Mechanical physical cleanup, as an environmentally friendly removal method, has received close attention from the industry. However, the offshore mudflat ground is always in a wet and muddy state, which makes it extremely inconvenient for the walking and transportation of conventional equipment *(Wei, 2019)*. In the face of muddy and wet mudflat ground represented by mudflats, ordinary land walking equipment often produces skidding and falling into the situation, which results in the difficulty of the operation of the conventional land walking equipment, and the development of the corresponding means of transportation due to the special geography has always been a difficult problem. In order to improve the transportation efficiency and throughput rate of such terrain, scholars at home and abroad have done a lot of research and developed many different types of walking devices, which mainly include: ordinary wheeled, tracked, multi-wheeled wide-wheeled, spiral propulsion, air cushion carrier and so on. Through checking the references, it is concluded *(Guo et al., 2014)* that among these five main types of muddy ground transportation, the air cushion transportation type has the lowest value of ground specific pressure, and the higher the value of ground specific pressure, the higher the pressure on the ground, and the easier it is to sink in the muddy ground; conversely, the less likely it is to sink in the muddy ground, and the higher the efficiency of walking. Air cushion transportation and handling is the use of gas film technology to lift and move the load, it is widely used in the field of aviation, precision or heavy instrument handling, such as airships to the launcher, transportation costs are high, not suitable for application in the field of agricultural machinery operations.

In the case of the spiral propulsion vehicle, because the ground pressure is small, the driving force is large, so the performance is strong. It is especially suitable for driving in some extreme soft and muddy terrain road surface. Spiral propulsion vehicle uses the spiral propeller as a walking mechanism; the spiral propeller is generally installed on both sides of the walking device as its main walking mechanism, through the spiral propeller and ground media (water, soil, etc.) to achieve the mutual action of the device to move forward, through the reverse rotation of the spiral propeller to achieve the device moving backward, through the two sides of the spiral propeller differential rotation to achieve the device steering walk. In the fluid, semi-fluid ground, the hollow structure of the spiral propeller can play the role of float, can effectively reduce the pressure value, so that the vehicle is not easy to fall into the ground.

The pressure value of the spiral propulsion transportation mode is second only to that of air cushion transportation, and it is a kind of idealized transportation tool suitable for traveling and operating on wet, soft and muddy ground such as river and sea shoals and marshes through the comprehensive consideration of feasibility, versatility and economy.

In order to promote the protection of offshore mudflat ecosystems and the development of coastal mudflat aquaculture and agriculture, as well as to reduce the cost and improve the efficiency of invasive species management, a shallow mudflat traveling device based on a twin-spiral propeller was designed.

MATERIALS AND METHODS

General structure and working principle

- **General structure of the traveling device**

The traveling device is mainly composed of diesel engine, twin spiral propeller, wide crawler chassis, hydraulic lifting system, reduction gearbox, class hull and other parts, as shown in Fig. 2.

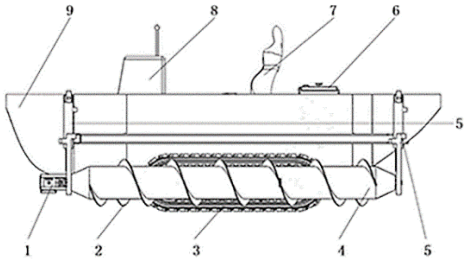

Fig. 2 - Twin spiral propeller walking device structure diagram

1. Gearbox; 2. Spiral blade; 3. Crawler walking device; 4. Spiral roller; 5. Hydraulic lifting device; 6. Diesel engine; 7. Driver's seat; 8. Operation desk; 9. Class hull

- **Working principle of twin spiral propeller walking device**

The walking device adopts diesel engine as the power source, the power of diesel engine is transmitted to the crawler gearbox through the belt to drive the crawler to walk, and then the power is transmitted to the two sides of the spiral propeller through the gear reducer box, universal drive shaft, coupling and other components to drive the spiral propeller blade to interact with the water or silt, and the reaction force is utilized to drive the walking device to realize the operation of the device.

In the offshore beach operation, this device can walk with the wide track, when encountering the phenomenon of slipping and sinking of the track on the wet and muddy ground, and the tracked walking device cannot work normally or the operation efficiency is low; it can be operated by the hydraulic lifting device through the hydraulic control handle to move down the two sides of the spiral propeller (the rotating bearing seat of the spiral propeller is connected with the hydraulic rod), so that the propeller is in contact with the ground media and the main driving wheel of the track is supported, and the propeller blades interact with the water or silt. The main driving wheel of the crawler will transfer the power to the spiral propeller through the gearbox and transmission shaft, and the rotation of the spiral propeller will realize the traveling through the mutual action with the medium.

When the tide of offshore beach operation is high, this device can float in the offshore by virtue of the hull, at this time the two sides of the spiral propeller can be used as a propeller to provide the device with power in the water, to realize the water travel.

Kinematic analysis of a twin spiral propeller

- **Preliminary design of the parameters of the twin-screw propeller**

By reviewing the relevant literature and learning to refer to other similar structure of the screw propulsion of the operating machine tools *(Sheludchenko Bogdan et al., 2022; Opeyemi Oladunjoye, 2022)*, and then after the preliminary data collection and research on the key structural parameters of the screw propeller drum diameter, helical angle of lift, helical blade height, and blade pitch parameter combination analysis *(Feng et al., 2020)*, the preliminary design of the structural parameters of the screw propeller reference range of values is shown in Table 1.

Table 1

Preliminary parameterization for screw propellers

Title	Parameters	Unit
Blade Height/d	30~70	mm
Drum diameter/D	375~425	mm
Pitch of blade/J	425~500	mm
Helix angle of lift/α	25~35	°

Discrete Element Modelling and Simulation Analysis

In order to determine the forward direction of the spiral propeller will not produce congestion phenomenon in the actual work and to determine the walking propulsion speed under different combinations of structural parameters of the spiral propeller, EDEM discrete element simulation software is used to establish a simulation model of the spiral propeller-muddy soil particles, simulate the interactions between the machine tools and the soil in the actual work, and collect multiple sets of parameters for response surface analysis to explore the optimal parameter combinations of the spiral propeller, which will provide a basis for the subsequent field experiments and optimization of the structure.

- **Discrete elemental modelling of soil particles**

Muddy soil particle model is the key factor affecting the simulation test results, according to the related research, combined with soil particle size test and related research, according to the soil characteristics of offshore beach mudland, query its soil property parameters, the soil particles were approximated to be set as a spherical model, and the radius was set to 3 mm, as shown in Fig. 3 *(Fang et al., 2016; Zeng et al., 2023)*.

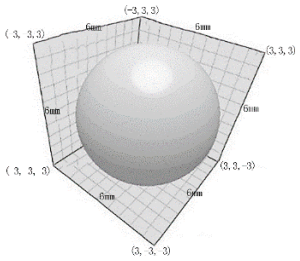

Fig. 3 - Discrete element model of soil particles

- **Modeling of soil tanks and spiral propellers**

A semi-cylindrical soil trough with a radius of 250 mm and a length of 4,510 mm was drawn using SolidWorks 3D design software and a particle factory was set up in it to generate and release soil particles, the material of the soil trough was pine wood with a density of 340 kg/m^3; the model of the spiral propeller was imported and fixed in the soil trough, the material of the spiral propeller was 316 stainless steel with a density of 8,000 kg/m^3, as shown in Figure 4. The combined 3D model of soil tank and spiral propeller was saved in STL format and imported into EDEM software.

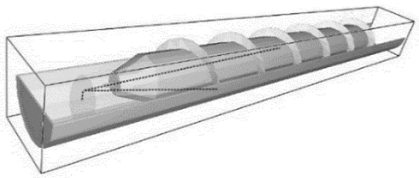

Fig. 4 - Modelling of soil flume and spiral propeller

- **Contact parameter**

The density of offshore beach soil is 1 700 kg/m^3, Poisson's ratio is 0.5, modulus of elasticity is 3.5×10^6 N/m^2, soil cohesion is 5 to 10 kPa, and the kinetic friction factor between the spiral propeller and the soil is 0.45 to 0.6, and the static friction factor is 0.76 *(Liu et al., 2015; Guo, 2016; Chen, 2023)*. The specific contact parameter ranges were determined based on relevant studies as well as the slant test method, as shown in Table 2.

Table 2

EDEM simulation contact parameter table

Title	Parameters	Unit
Soil intensity	1700	kg/m3
Poisson's ratio for soil	0.5	/
Soil cohesion	5~10	kPa
Spiral propeller – soil (kinetic friction factor)	0.45~0.6	/
Spiral propeller – soil (static friction factor)	0.76	/
Soil modulus of elasticity	3.5×106	N/m2

RESULTS

- **Simulation tests**

In order to simulate the actual working condition of the spiral propeller, a soil tank model was established with a radius of 250 mm and a length of 4,510 mm, which can make the generated soil particles completely wrap the spiral propeller, and in order to make the experiments closer to the real operating conditions, three particle factories were set up in the soil tank, which were located in front of the spiral propeller, in front of the left side, and at the back of the right side, respectively, to generate 80,000, 25,000, and 20,000 soil particles, the particle generation speed was 1.5 m/s, and the simulation was started.

Figures 5 to 8 show the simulation test of the interactions with soil particles during the operation of the spiral propeller and the velocity change of the soil particles *(Zhao et al., 2023; Song et al., 2021; Hong, 2019)*.

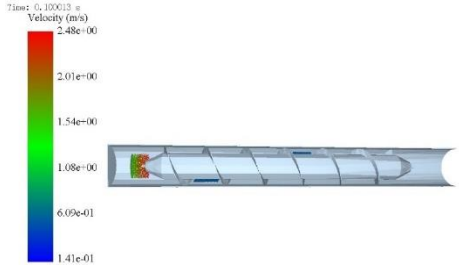

Fig.5 - 0.1s simulation test process

Fig.6 - 1s simulation test process

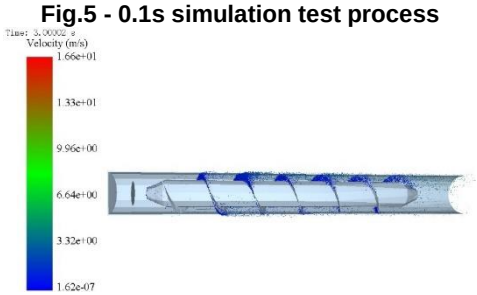

Fig. 7 - 3s simulation test process

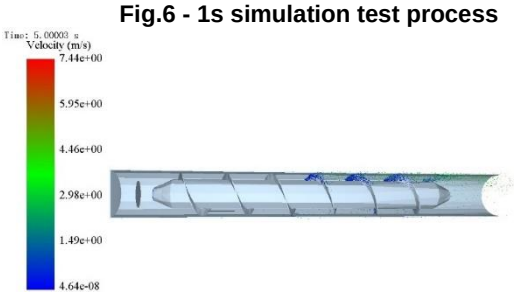

Fig. 8 - 5s simulation test process

During the experimental process, as the particle plant generates particles, the spiral propeller rotates at a speed of 4 rad/s for the soil displacement test, and the test processes of 0.1 s, 1 s, 3 s, and 5 s were recorded, respectively, and the experimental results show that the spiral propeller discharges the soil with good effect and does not generate the phenomenon of soil congestion.

In order to investigate the optimal structural parameters of the spiral propeller, several combinations of spiral propeller structural parameters (as shown in Table 3) were designed to simulate the propulsion speed and collect data.

Table 3

Experimental coding table

Level	Experimental factors			
	Drum diameter / mm	Helix angle of lift /°	Spiral blade height / mm	Pitch of blade / mm
-1	375	25	30	425
0	400	30	45	462.5
1	425	35	70	500

The propulsive velocity data of the spiral propeller under different combinations of structural parameters were obtained through multifactor and multilevel simulation tests, as shown in Table 4:

Table 4

Response surface test results

Number of tests	Experimental factors				
	Drum diameter / mm	Helix angle of lift / °	Spiral blade height / mm	Pitch of blade / mm	Speed of advancement / (m/s)
1	400	25	50	425	2.192
2	400	25	70	462.5	2.01
3	375	25	50	462.5	2.17
4	425	30	70	462.5	2.071
5	375	30	30	462.5	2.03
6	400	30	30	425	2.07
7	425	35	50	462.5	2.145
8	425	30	50	500	2.16

Number of tests	Experimental factors				
	Drum diameter / mm	Helix angle of lift / °	Spiral blade height / mm	Pitch of blade / mm	Speed of advancement / (m/s)
9	400	35	30	462.5	2.03
10	425	30	50	425	2.13
11	400	35	50	425	2.12
12	400	30	70	425	2.022
13	400	35	70	462.5	1.97
14	375	30	50	425	2.16
15	375	30	70	462.5	2.05
16	425	25	50	462.5	2.197
17	400	30	50	462.5	2.49
18	400	35	50	500	2.2
19	400	30	50	462.5	2.431
20	400	25	30	462.5	2.07
21	400	30	50	462.5	2.456
22	375	30	50	500	2.12
23	425	30	30	462.5	2.186
24	375	35	50	462.5	2.23
25	400	25	50	500	2.19
26	400	30	30	500	2.1
27	400	30	70	500	2

Table 5

Regression model ANOVA

Source of variance	Square sum	Degrees of freedom	Mean square	F-value	P-value	Significance
Model	0.4 362	14	0.0 312	17.23	<0.0 001	**Significant**
A Drum diameter	0.0 014	1	0.0 014	0.7 667	0.3 984	
B Helix angle of lift	0.0 015	1	0.0 015	0.8 273	0.3 810	
C Spiral blade height	0.0 110	1	0.0 110	6.07	0.0 298	
D Pitch of blade	0.0 005	1	0.0 005	0.2 661	0.6 153	
AB	0.0 031	1	0.0 031	1.73	0.2 125	
AC	0.0 046	1	0.0 046	2.52	0.1 385	
AD	0.0 012	1	0.0 012	0.6 773	0.4 266	
BC	0.0 000	1	0.0 000	0.0 000	1.0 000	
BD	0.0 017	1	0.0 017	0.9 294	0.3 540	
CD	0.0 007	1	0.0 007	0.3 738	0.5 524	
A2	0.0 939	1	0.0 939	51.90	<0.0 001	
B2	0.1 173	1	0.1 173	64.85	<0.0 001	
C2	0.3 680	1	0.3 680	203.45	<0.0 001	
D2	0.1 294	1	0.1 294	71.57	<0.0 001	

Source of variance	Square sum	Degrees of freedom	Mean square	F-value	P-value	Significance
Residual	0.0 217	12	0.0 018			
Lost item	0.0 199	10	0.0 020	2.27	0.3 438	**Insignificant**
Pure error	0.0 018	2	0.0 009			
Sum of all	0.4 579	26				
R^2	0.9 526					
R^2A_{dj}	0.8 973					

The quadratic polynomial regression equation obtained from the analysis of variance (ANOVA) of the results of the spiral propeller propulsive velocity sensory scoring test using the Design-Expert 13 software is:

$$\begin{aligned} Y=&2.46+0.0108A-0.0112B-0.0302C+0.0063D \\ &-0.0280AB-0.0337AC+0.0175AD+0.0000BC \\ &+0.0205BD-0.0130CD-0.1327A^2-0.1483B^2 \\ &-0.2627C^2-0.1558D^2 \end{aligned} \quad (1)$$

The regression model ANOVA results are shown in Table 5.

The interaction between AC (drum diameter and helical blade height) was the most significant (P = 0.1 385) as shown in Figure 9 by ANOVA in Table 5. The optimum combination of structural parameters is shown in Table 6.

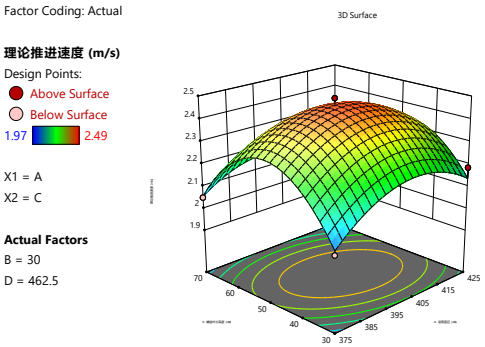

Fig. 9 - Response surface variation chart

Table 6

Optimal parameter combinations for spiral propellers

Title	Parameters	Unit
Blade Height / d	48.7 687	mm
Drum diameter / D	401.35	mm
Pitch of blade / J	463.363	mm
Helix angle of lift / α	29.7 953	°
Maximum propulsion speed / v	2.49	m/s

Test Equipment and Methods

- **Field trials**

In order to further examine the discharge propulsion capability of the designed twin spiral propeller in practical work, combined with the theoretical calculation analysis and simulation test results, a field test was conducted on April 18, 2023, in the coastal mudflat of the Blue Seed Industry Park in Wendeng District, Weihai City, Shandong Province, as shown in Figure 10.

The operating parameters of the spiral propeller selected for the test were: the diameter of the drum was 400 mm, the height of the spiral blade was 50 mm; the total length of the drum was 2,970 mm, the helical lift angle was 30°, and the pitch was 453 mm; and the traveling speed was 2.36 m/s at a diesel engine speed of 3,200 rpm.

Fig.10 - Field test of twin-spiral propeller traveling device

Relationships between slip rate, sinkage and screw propeller speed were analyzed separately in field tests. The data was also collected and plotted on a line graph using Origin software, as shown in Figures 11 and 12:

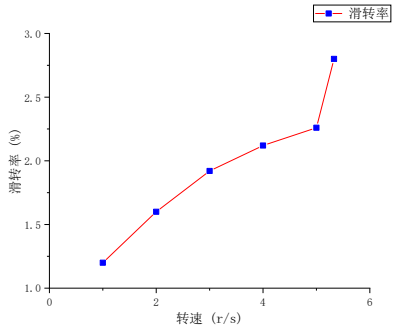

Fig. 11 - Rotation speed-slip rate relationship

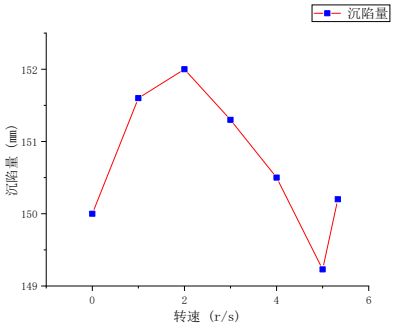

Fig. 12 - Rotation speed-sinkage relationship

CONCLUSIONS

(1) Through the study of the physical characteristics of muddy soil in coastal beaches, a spiral propeller travel device suitable for walking on muddy land was designed, and the key parameters of the spiral propeller were analyzed to obtain the optimal parameter combination of the structure.

(2) The discrete element method was used to establish a model of muddy soil particles in mud flats, and simulation analysis was carried out with the height of the spiral propeller blades and the helix angle of the blades as the test factors, and with the propelling speed of the walking device and whether congestion occurs in front of the device as the test indexes, and finally it was concluded that the designed spiral propeller does not produce congestion.

(3) The field test shows that the test results are basically consistent with the simulation results, under the design of 400 mm drum diameter, 50 mm helical blade height, 2,970 mm drum length, 30° helical angle of lift and 453 mm pitch, the propeller does not generate congestion in the forward direction, and the propulsion speed of the device reaches 2.36 m/s. The design is also consistent with the simulation results, and the design is consistent with the simulation results, and the propulsion speed of the device reaches 2.36 m/s.

ACKNOWLEDGEMENT

This research received financial support from the Key R&D Program of Shandong Province, China (No.2022CXGC010401). Thanks to the International Field Test Mechanization Association for providing us with the research foundation and platform.

REFERENCES

[1] Chen Z.X. (2023). Research on the effect of grouting lifting to reinforce soil body and preventing well wall rupture [D]（注浆抬升加固土体及防治井壁破裂效果研究）. *China University of Mining and Technology*, 001042.

[2] Fang H.M, Ji C Y. (2016). Analysis of soil motion behavior during rotary tillage based on discrete element method [J]（基于离散元法的旋耕过程土壤运动行为分析）. *Journal of Agricultural Machinery*, 47(3):22-28.

[3] Feng G., Zhou Y., Tu M. (2020). Design and test of spiral-propelled lotus root digger [J]（螺旋推进式挖

藕机的设计与试验）. *Journal of Gansu Agricultural University*, 55(04):191-199.

[4] Gao R. (2021). Impacts of mutualistic ricegrass invasion on soil physicochemical properties of coastal wetland in Huangjiatangwan [D]（互花米草入侵对黄家塘湾滨海湿地土壤理化性质的影响）. *Qufu Normal University*, 000744.

[5] Guo T.T. (2016). Experimental study on the effect of consolidation ratio on kinetic properties of pulverized clay [J]（固结比对粉质粘土动力学特性影响的试验研究）. *Advances in Geophysics*, 31(06): 2729-2734.

[6] Guo X.L, Liu J., Zhao Y. (2014). Overview of the current research status of spiral-propelled vehicles [J]（螺旋推进车研究现状概述） *Agricultural Equipment and Vehicle Engineering*, 52(04):14-17+27.

[7] Hong D.W. (2019). Research on the friction mechanical characteristics of oil pine root system and soil in the loess area of west Jin [D]（晋西黄土区油松根系与土壤的摩擦力学特性研究）. *Beijing Forestry University*, 001123.

[8] Ji Y. L., Pu S.C., Song Y. (2023). Impacts of M. alterniflora invasion on macrobenthos of salt marsh wetland in Yushan Bay [J]（互花米草入侵对乳山湾盐沼湿地大型底栖动物的影响）. *Journal of Aquatic Sciences*, 36(05):77-84.

[9] Liu Y., Chang X.Y., Li H.N. (2015). Relationships between salinity, conductivity and water content of grassy beach soils in typical coastal beaches in northern Jiangsu Province [J]（苏北典型滨海滩涂草滩土壤盐度、电导率与含水率的关系）. *Water Saving Irrigation*, (08):4-7.

[10] Opeyemi Oladunjoye, Christina Maffattone (2022). Omnidirectional All-Terrain Spiral-Driven Robot Design, *Modeling and Application in Humanitarian Demining*, 55(27):7-12.

[11] Qiao P.Y, Wang A.D., Xie B.H. (2019). Effects of herbicides on the invasive plant Miscanthus intermedius in the Yellow River Delta [J]（除草剂对黄河三角洲入侵植物互花米草的影响）. *Journal of Ecology*, 39(15):5627-5634.

[12] Qiao P.Y. (2019). Research on physical and chemical control of invasive plant Miscanthus intermedius in the Yellow River Delta [D] (黄河三角洲入侵植物互花米草物理、化学防治研究). *Inner Mongolia University*.

[13] Shang X., Guan W.B., Zhang G.S. (2009). Impacts of M. alterniflora invasion on the food web of estuarine salt marsh wetlands [J] (互花米草入侵对河口盐沼湿地食物网的影响). *Journal of Oceanography*, 31(01):132-142.

[14] Sheludchenko Bogdan, Šarauskis Egidijus, Kukharets Savelii, Zabrodskyi Andrii. (2022). Graphic analytical optimization of design and operating parameters of tires for drive wheels of agricultural machinery [J]. *Soil & Tillage Research*, 215,105227.

[15] Song S.L, Tang Z.H., Zheng X. (2021). Calibration of discrete element parameters of a post-tillage soil model for cotton fields in Xinjiang [J]（新疆棉田耕后土壤模型离散元参数标定）. *Journal of Agricultural Engineering*, 37(20):63-70.

[16] Wei X.W. (2019). Design and simulation research of automatic harvesting equipment for beach mutualistic rice grass [D]（滩涂互花米草自动收割设备设计及仿真研究）. *Dalian Ocean University*, 000134.

[17] Yin X.L, Tan C.Y., Ke Y.H. (2023). Patterns of landscape pattern evolution and driving factors of coastal salt marsh wetlands in the Yellow River Delta from 1973 to 2020 [J/OL]（1973—2020 年黄河三角洲滨海盐沼湿地景观格局演化模式和驱动因素）. *Journal of Ecology*, 2024, (01):1-14.

[18] Zeng M.J, Cong J.L., Yan Q. (2023). Design and test of chopping anti-clogging system of forage rape harvester [J/OL]（饲用油菜收获机切碎防堵系统的设计与试验）. *Journal of Shihezi University (Natural Science Edition)*, 1-9.

[19] Zhao Z., Wang D.W., He X.N., Shang S.Q., Zheng X.S., Zhu H., Xia C., Shi Y.X. (2023). Analysis and test of EDEM-based rotary tillage device for oil salsa bean [J]（基于 EDEM 的油莎豆旋耕装置分析与试验）. *Agricultural Mechanization Research*, 45(05):173-179.

Zhou Y., Jiang Z.J., Qiu G.L. (2023). Distribution of seagrass resources in China, causes of degradation and protection measures [J]（中国海草资源分布现状、退化原因与保护对策）. *Ocean and Lake*, 54(05):1248-1257.

DETERMINANTS OF AI-BASED APPLICATIONS ADOPTION IN THE AGRICULTURAL SECTOR – MULTI-GROUP ANALYSIS
/
ปัจจัยกำหนดการนำแอปพลิเคชันที่ใช้ AI มาใช้ในภาคเกษตรกรรม – การวิเคราะห์แบบหลายกลุ่ม

Vasu KEERATIVUTISEST [1)], Wornchanok CHAIYASOONTHORN[1)], Bilal KHALID[1)], Beata ŚLUSARCZYK [2,3)], Singha CHAVEESUK[*1)]

[1)] KMITL Business School, King Mongkut's Institute of Technology Ladkrabang, Thailand
[2)] North-West University, Trade and Development, Private Bag X1290, 2520 Potchefstroom, South Africa
[3)] Faculty of Management, Czestochowa University of Technology, Poland
E-mail: Singha.ch@kmitl.ac.th
DOI: https://doi.org/10.35633/inmateh-72-67

Keywords: *AI-based application, agricultural sector, artificial intelligence, organizational size, managerial support, technological competence*

ABSTRACT

This research investigated the factors determining the adoption of AI-based applications in Thailand and Poland's agricultural sectors. The study explored the sector's adoption of AI technology and its contributions to driving the market and business performance. Despite the potential of AI in the agricultural sector, its adoption rate still needs to be clarified, and its potential needs to be better understood, hence the need for the study. The research applied primary data collected from respondents working in the agricultural sector in Thailand and Poland using a structured questionnaire. A sample of 356 and 377 respondents were representative samples in Thailand and Poland, respectively. The research was driven by the hypotheses evaluated using the Structural Equation Model (SEM). The findings indicated that organizational size was the most influential determinant of AI-based applications in both countries. Another significant determinant was technological competence in both countries. Additionally, social influence was a significant determinant in Thailand, while facilitating conditions and effort expectancy were significant determinants in Poland. The multi-group analysis revealed that the two countries were not invariant; hence, the effect of independent variables on behavioral intention to adopt AI between the two countries was different. The research recommended that each country's policymakers consider its contexts differently in AI-based application adoption policies. However, improving the organizational size and technological competence would enhance the adoption of AI-based applications across the board.

INTRODUCTION

Artificial Intelligence (AI) has seen many developments recently, with the technology adopted in various industries to improve business processes and outcomes. The potential of AI in transforming businesses cannot be overstated, and its applications continue to expand, ranging from customer service to healthcare, finance, transportation, and agriculture. According to a report by *Grand View Research (2023),* in 2022, the size of the artificial intelligence market worldwide reached USD 136.55 billion and is expected to grow at an annual compound rate of 37.3% from 2023 to 2030. The report also states that the increasing adoption of AI technologies in various industries is one of the major factors driving market growth. The widespread adoption of AI is mainly due to its ability to solve complex business problems, leading to increased productivity, efficiency, and profitability (*Ayub Khan et al., 2022; Regona et al., 2022; Vinuesa et al., 2020*).

Artificial Intelligence (AI) is transforming the agricultural industry worldwide, significantly improving the efficiency and productivity of farming practices. *Van Hilten and Wolfert (2022)* inform that the AI revolution is fueled by a continual technical innovation that increases networking capability with the possibility of running tractors, spraying drones, and completely autonomous robotic farms, all probable results of AI innovation in the agricultural industry. The study by Vantage Market Research (2023) estimates that AI in the agriculture market is predicted to grow at a CAGR of 25.1% during the forecast period, reaching $4.2 billion by 2028 from $1.1 billion in 2022. The report notes that the increasing demand for food and the rising adoption of innovative farming practices are the key drivers of the growth of AI in the agriculture market. *Srivetbodee and Igel (2021)* aver that AI can help farmers optimize crop yields, reduce waste, and improve product quality while

[1] *Vasu Keerativutisest, Dr.*; *Wornchanok Chaiyasoonthorn, Assoc. Prof.*; *Bilal Khalid, Dr; Singha Chaveesuk, Assoc. Prof.*

[2,3] *Beata Ślusarczyk, Assoc. Prof.*

understanding that sustainability is vital in agriculture and continuous food availability (*Nuanphromsakul et al., 2022; Ndinojuo, 2020; Wolfert & Isakhanyan, 2022*). Srivetbodee and Igel (2021) continue that AI has been effective in helping farmers predict weather patterns, monitor soil conditions, and detect crop diseases.

In Thailand, the agricultural sector is one of the main contributors to the country's economy. According to *Statista Research Department (2022),* Thailand's agriculture, hunting, and forestry industry made a GDP contribution of around 1.38 trillion Thai baht in 2021. In Poland, the agricultural sector is also a vital part of the economy, contributing by approximately 2.22 percent to the country's GDP in 2021 (*O'Neill, 2021*). The Thailand and Poland governments support AI development in agriculture, focusing on improving the sector's efficiency and competitiveness. Both governments have been actively promoting technology in agriculture, focusing on AI, autonomous, and precision farming.

The adoption of precision farming in Thailand is still in its early stages, with only a few large-scale farms and research institutions implementing the technology. Precision farming uses data analytics, machine learning, and sensors to optimize crop yields and reduce waste (*Srivetbodee & Igel, 2021*). In Poland, precision farming is more widespread, with many farmers adopting the technology to optimize crop yields and reduce costs (*Yarashynskaya & Prus, 2022*). The adoption of autonomous farming is still in its early stages in Thailand and Poland, with only a few large-scale farms and research institutions implementing the technology (*Kernecker et al., 2020; Chaveesuk et al., 2023*). *Chaveesuk et al. (2023)* infer that autonomous farming involves using robotics and AI to automate farming processes, such as planting, harvesting, and weeding. AI is poised to affect the agricultural sector in both Thailand and Poland significantly.

While there has been significant interest in using artificial intelligence (AI) in agriculture, there needs to be more understanding of the factors that drive the adoption of AI-based applications in this sector. While AI has potential benefits in agriculture, such as improved efficiency, yield, and sustainability, there are also significant challenges related to implementing and adopting these technologies. For example, farmers may be hesitant to adopt AI-based applications due to a lack of trust in the technology or concerns about the cost or complexity of implementation. Additionally, there may be cultural and societal factors that influence the adoption of these technologies in different regions or countries. Therefore, the problem that this research aims to address is to compare the contexts of AI adoption in agriculture in Thailand and Poland. Specifically, the research will investigate the technological, economic, and sociocultural factors that influence the adoption of AI in these two countries and the strategies developed to promote their adoption and successful implementation.

By comparing the contexts of AI adoption in these two countries, the research aims to contribute to a better understanding of the factors that drive or hinder the adoption of AI-based applications in agriculture. It sheds light on the strategies that can be used to promote their adoption and success in different contexts. The novelty of this study is that it uses multi-group analysis to investigate the factors that influence the acceptance of AI-based applications in the agricultural sector, emphasizing the poor adoption of AI in agriculture as the problem. The research provided insights on enhancing AI adoption in agriculture, using statistical analysis to identify the factors influencing adoption. The findings from this research can help policymakers, farmers, and investors in the agriculture sector in Thailand, Poland, and other emerging markets by providing statistical evidence for their decisions.

MATERIALS AND METHODS

Understanding the Potential for the Application of AI in Agriculture

AI adoption in agriculture is a growing trend worldwide (*Kernecker et al., 2020; Chaveesuk et al., 2023*), including Thailand and Poland. However, the contexts of AI adoption in these two countries differ due to several factors, including technological infrastructure, economic development, and agricultural practices. Thailand who has a well-established agricultural sector is one of the world's largest rice and other crop producers. However, the country faces several challenges, such as labor shortage, climate change, and water scarcity (*Srivetbodee & Igel, 2021*), which can be addressed by adopting AI technologies in agriculture. For example, AI-based weather forecasting systems can help farmers plan their planting and harvesting schedules and optimize water usage. Moreover, AI-powered drones and robots can be used for crop monitoring, precision agriculture, and weed control, reducing labor costs and increasing productivity.

On the other hand, Poland is a relatively smaller country with a less developed agricultural sector than Thailand (*Kernecker et al., 2020*). However, the government has invested heavily in modernizing its agriculture and developing new technologies to increase productivity and efficiency (*Srivetbodee & Igel, 2021*).

AI technologies can be crucial in modernization by providing advanced data analysis tools, improving decision-making processes, and automating routine tasks. For instance, AI-based soil sensors can help farmers optimize the use of fertilizers, reduce waste, and increase yields (*Chaveesuk et al., 2023*). Although Thailand and Poland have different settings and can both benefit from the use of AI in agriculture, the precise applications of AI will rely on their unique potentials and barriers. However, AI in agriculture can aid both nations in resolving some of the most critical issues affecting their agricultural sectors and boost their competitiveness in the global market.

Technology Adoption Perspective

Embracing technological change is crucial for ensuring business success, and adopting novel technologies or new systems has been widely studied at both the individual and corporate levels. The Theory of Reasoned Action (TRA), as proposed by *Alsheibani et al. (2018)*, sheds light on how beliefs and values shape and direct people's technology adoption behaviors. On the other hand, *Ajzen (2012)* presents the Theory of Planned Behavior (TPB), which emphasizes the impact of an individual's attitude, subjective standards, and perceived behavioral control on their behavioral intentions and actions. Researchers have developed various models and frameworks to understand better what influences users' decisions about when and how to use new technologies. Davis (1986) proposed the Technology Acceptance Model (TAM), which has been validated by numerous studies and highlights the connection between behavioral intentions and actual system usage. However, TAM does not account for qualitative aspects or social forces that shape an Information System (IS) (*Lai, 2017*).

To address this limitation, Venkatesh et al. (2016) developed the Unified Theory of Acceptance and Use of Technology (UTAUT), which explains why people plan on using an IS and how they end up using it. Additionally, the Technology-Organization-Environment (TOE) paradigm, as offered by *Tornatzky et al. (1990)*, characterizes the technical and environmental factors that affect businesses' choices to accept technological innovation. Recent studies, such as those by *Cubric (2020), Mohr and Kühl (2021), Manning et al. (2022), Sood et al. (2022), Rosales et al. (2020), Na et al. (2022), and Kar et al. (2022),* have further investigated the adoption of artificial intelligence (AI) and its impact on various industries, including agriculture, food, construction, and management. These studies emphasize the importance of understanding the drivers, barriers, and social considerations for AI adoption and the critical determinants of adopting AI for sustainable development.

The Contexts of AI Adoption

Over the past few years, there has been a surge in research investigating the effects of AI in various fields. The contexts of AI adoption have been conducted by *Kelly et al. (2023), Ikumoro and Jawad (2019), Sood et al. (2022), Na et al. (2022), Sneesl et al. (2022), Mukherjee et al. (2023), and Al-Dhaen et al. (2021). Phuoc (2022)* states that while a wealth of literature explores AI's theoretical underpinnings and practical applications, there needs to be more research examining how businesses adapt to this rapidly-evolving technology. One notable example of a study that attempts to fill this gap was proposed by *Alsheibani et al. (2018)*, who put forward a framework for studying AI adoption in enterprises. However, their framework is yet to be validated through empirical testing, and little evidence supports their findings. It is challenging to build on conventional constructs and create a thorough comprehension of the factors that impact AI adoption because of the widespread nature of AI and the absence of research on its adoption at the organizational level.

To date, there has been little empirical evaluation of the social acceptability of AI, which is a critical aspect of AI adoption (*Phuoc, 2022*). Thus, further research is needed to explore the factors contributing to the acceptance of AI, including the role of organizational competence and environmental circumstances (Kelly et al., 2023). Previous research has shown that the Theory of Everything (TOE) framework helps examine the factors that facilitate or hinder AI adoption, making it a good starting point for future investigations (*Ikumoro & Jawad, 2019*). The TOE framework comprises three interconnected elements: internal technical factors, internal organizational factors, and external environmental factors (*Na et al., 2022*). To gain a better understanding of the factors that influence AI adoption in a specific industry, researchers may consider incorporating other theoretical models, such as the Technology Acceptance Model (TAM) and the Unified Theory of Acceptance and Use of Technology (UTAUT) (*Na et al., 2022; Mukherjee et al., 2023*).

Hypotheses and Research Model

According to the literature review, there is a knowledge gap on the enabling factors contributing to firms' AI adoption and how these aspects interact and impact the decision to use AI. In this study, a research approach based on the UTAUT model and Theory of Reasoned Action is proposed to understand better the success factors affecting AI adoption at the organizational level. The UTAUT model includes four fundamental

constructs: facilitating conditions, social influence, effort expectancy, and performance expectancy. The organizational context category of success variables includes technology competence, managerial support, organizational size, and AI readiness. This section presents a research model and hypothesis focusing on the Unified Theory of Acceptance and Use of Technology (UTAUT) model and organizational context as the primary determinants of AI adoption in agriculture.

UTAUT Model

The UTAUT model posits that four factors affect technology adoption: performance expectancy, effort expectancy, social influence, and facilitating conditions (*Alkhowaiter, 2022; Sood et al., 2022; Venkatesh et al., 2016*).

Facilitating Conditions

Facilitating Conditions (FC) refer to the availability of resources and support necessary for technology adoption (*Sood et al., 2022*). In AI adoption in agriculture, facilitating conditions include access to reliable internet and digital infrastructure, availability of financial resources, and technical support. The following hypothesis is formulated based on facilitating conditions:

H1: *Facilitating conditions significantly influence the adoption of AI-based applications in the agricultural sector.*

Social Influence

Social Influence (SI) refers to the influence of peers and supervisors on technology adoption (*Fulton et al., 2022; Nascimento & Meirelles, 2021*). In AI adoption in agriculture, social influence could come from peers, industry leaders, government agencies, and research institutions. Industry leaders, such as those in agriculture, can significantly drive adoption through their social influence. The following hypothesis is formulated based on social influence to investigate this influence:

H2: *Social influence significantly influences the adoption of AI-based applications in the agricultural sector.*

Effort Expectancy

Effort Expectancy (EE) refers to the ease of use of the technology (*Jain & Jain, 2022*). In the context of AI adoption in agriculture, effort expectancy could include the complexity of the technology and the ease of integration into existing farm operations. The following hypothesis is formulated based on effort expectancy to examine the claims posited by the researchers:

H3: *Effort expectancy significantly influences the adoption of AI-based applications in the agricultural sector.*

Performance Expectancy

Performance Expectancy (PE) refers to the perceived usefulness of the technology (*Kelly et al., 2023; Sneesl et al., 2022*). In the context of AI adoption in agriculture, performance expectancy could include the potential benefits of the technology, such as increased yields, reduced costs, and improved efficiency. The following hypothesis is formulated based on performance expectancy:

H4: *The adoption of AI-based applications in the agricultural sector is significantly influenced by performance expectancy in the agricultural sector.*

Organizational Context

The organizational context is another critical determinant of technology adoption. In the context of AI adoption in agriculture, the organizational context could include technology competence, managerial support, organizational size, and AI readiness.

Technology Competence

Technology Competence (TC) refers to the organization's technical expertise and experience (*Al-Sharafi et al., 2023; Zhang et al., 2022*). In AI adoption in agriculture, technology competence could include the level of expertise in using digital technologies, familiarity with AI-based applications, and the ability to integrate AI-based applications into existing farm operations. *Manning et al. (2022)* highlighted the importance of ethics in AI adoption in the food sector. The authors argued that a common language for technology adoption across the supply chain was critical for ensuring that AI-based applications were developed and deployed ethically and sustainably. *Manning and colleagues (2022)* emphasized the need for stakeholders to consider the potential ethical implications of AI adoption in the food sector and develop appropriate guidelines and frameworks for ethical technology adoption. The following hypothesis is proposed based on technology competence:

H5: *Technology competence significantly influences the adoption of AI-based applications in the agricultural sector.*

Managerial Support

Managerial Support (MS) refers to the level of support management provides for technology adoption (*Kelly et al., 2023; Sneesl et al., 2022; Balakrishnan et al., 2022*). In the context of AI adoption in agriculture, managerial support could include allocating resources, training, and support for adopting AI-based applications. AI readiness refers to the organization's preparedness for AI adoption, including its ability to handle and manage the technological, infrastructural, and human resource requirements for AI-based applications (*Cubric, 2020*). Several studies have shown that the level of AI readiness can significantly affect an organization's willingness to adopt AI-based applications in agriculture (*Mohr & Kuhl, 2021; Sood et al., 2022*). The following hypothesis is formulated based on managerial support:

H6: *Managerial support significantly influences the adoption of AI-based applications in the agricultural sector.*

Organizational Size

Organizational Size (OS) refers to the organization's size, which could affect its ability to adopt new technologies (*Alsheibani et al., 2018; Na et al., 2022*). In the context of AI adoption in agriculture, smaller organizations may need more resources and expertise to adopt AI-based applications compared to larger organizations. In a study, *Sood et al. (2022)* examined the critical determinants of AI adoption in agriculture. They found that factors such as access to funding, government support, and availability of skilled personnel were critical for enhancing AI readiness. Similarly, *Mohr and Kühl (2021)* investigated the acceptance of AI in German agriculture and identified perceived usefulness, perceived ease of use, and subjective norms as critical determinants of technology adoption. The size of a firm can influence how much it adopts new technologies. Large firms have more resources to invest in research and development (R&D) and training employees on new technologies than smaller firms. Larger firms also tend to be more stable, which means they can afford to take risks with new technologies that smaller firms cannot (*Hradecky et al., 2022*). The authors applied the Technology Acceptance Model (TAM) and the Theory of Planned Behavior (TPB) to develop a model for predicting the Intention to Adopt AI (IAA) in the agricultural sector. The following hypothesis is formulated based on organizational size:

H7: *Organizational size significantly influences the adoption of AI-based applications in the agricultural sector.*

H8: *Organizational size significantly mediates the effects of latent variables (Performance expectancy, effort expectancy, social influence, facilitating conditions, technology competence, and managerial support) on adoption of AI-based applications in the agricultural sector.*

Conceptual Framework

The conceptual framework model was developed from the advanced UTAUT model. As seen from the UTAUT model (Fig. 1), the variables used were facilitating condition, social influence, effort expectancy, and performance expectancy. From the organizational context, the variables involved were technological competence, managerial support, and organizational size. The intention to adopt was the dependent variable.

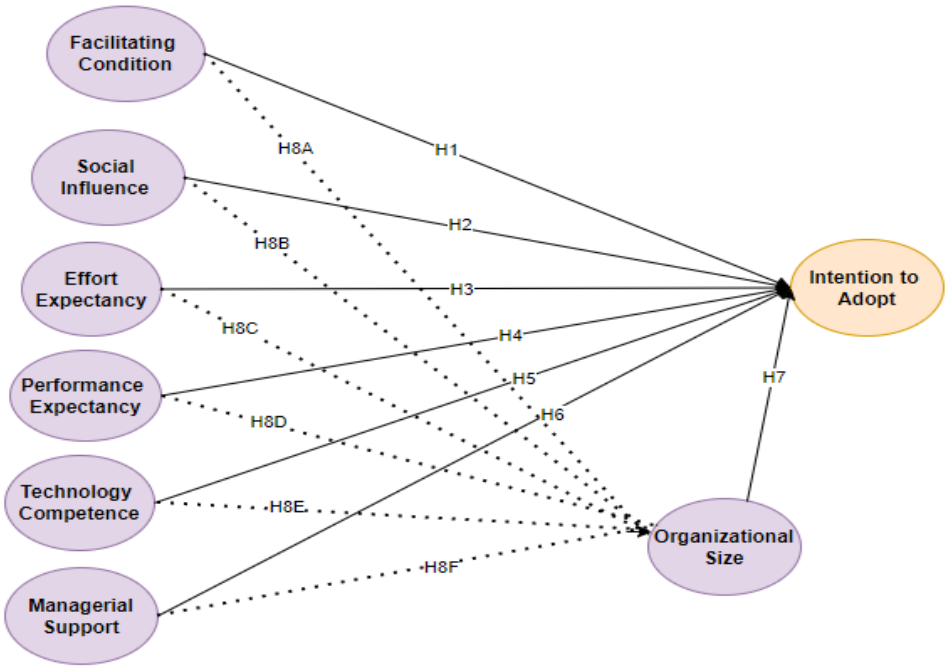

Fig. 1 - Conceptual framework of the study

Methodology

For this study, a quantitative questionnaire was adopted to collect the data. The measurement items used for various latent variables were adopted from the previous studies (Table 1). The 5-point Likert scale was adopted where (1) depicted 'strongly disagree' while (5) depicted 'strongly agree.' Four academicians were consulted to ensure the questionnaire was appropriate, and their feedback regarding the appropriateness was incorporated in redrafting the questionnaire. Since the study was conducted in Thailand and Poland, it was in English and translated into Polish and Thai.

The population of the study was the firms operating in the agricultural sector in Thailand and Poland. The focus was evaluating the factors that determine the adoption of AI-based applications in the sector by firms and other stakeholders operating in the sector. Therefore, the study subjects were individuals in managerial positions, such as human resource managers, operations managers, finance managers, and general managers. These were considered to have appropriate information regarding the adoption and use of artificial intelligence applications in their firms. The targeted sample size was 550 respondents in Thailand and 550 in Poland, totaling 1100 respondents.

A stratified random sampling technique was applied to collect primary data for the study. In both countries, the data was collected from the five central districts of Thailand and five major administrative divisions in Poland. The researchers first contacted the firms and informed on the study's intention. Then the questionnaire was sent using share email addresses to the respondents who answered and emailed back. A total of 1100 copies of the questionnaire were sent out; 550 copies of each questionnaire were sent to respondents in Poland and Thailand, respectively. Of the total sent, 362(65.82%) and 385(70.00%) were received from respondents in Thailand and Poland, respectively. After data cleaning and coding, 356(64.73%) and 377(68.55%) were deemed fit for the analysis.

Structural Equation Modeling (SEM) was applied to conduct the data analysis and to evaluate the hypothesis. However, before the actual analysis, the sample data and model fitness were evaluated for reliability and validity using the measurement model. The Confirmatory Factor Analysis (CFA), construct, convergent, and discriminant validity were analyzed. The measurement model was used to determine the relationship between the latent variables (constructs) and the observed variables (indicators). The structural model was applied to determine the causal relationship between the latent variables (*Chin et al., 2003; Muangmee et al., 2022*). The multi-group analysis evaluated the difference between Thailand and Poland regarding the determinants of AI-based applications adoption in the agricultural sector. The CFA and SEM analysis used the Analysis of Moment Structures (AMOS) software.

RESULTS

Model Evaluation

Reliability, validity, and model fitness tests assessed the measurement model's fitness. The measurement of items and constructs was used to evaluate the model. The convergent validity was estimated by evaluating the study's factor loadings for each of the observed items and the composite reliability (CR) and average variance extracted (AVE) for each construct. The factor loadings whose values were below 0.5 were below the required threshold; hence these items were removed.

Since the analysis involved a multi-group analysis, the adjustment of the CFA was made simultaneously for the two categories. For running the CFA for Thailand and Poland, the factor loadings that were below 0.5 were PE3, PE4, TC4, and TC5. These factors were removed, as they did not meet the threshold. The results after adjustment were as follows. For Thailand, the factor loadings ranged from 0.547 to 0.826, while the AVE ranged from 0.502 to 0.612. These satisfied the required threshold of 0.5 (*Chin and Gopal, 1995; Fornell and Larcker, 1981*). Additionally, the CR values ranged from 0.775 to 0.870, while the values for Cronbach's alpha ranged from 0.786 to 0.873. These values exceeded the recommended threshold of 0.7 (*Chin and Gopal, 1995; Gefen and Straub, 1997*). For the case of Poland, all the observed variable factor loadings satisfied the 0.5 threshold. The factor loadings ranged from 0.589 to 0.842. The AVE ranged from 0.547 to 0.694, which satisfied the required threshold of >5.0. The CR ranged from 0.747 to 0.896, while Cronbach's alpha ranged from 0.752 to 0.899. These values exceeded the minimum threshold of >0.70 (*Chin and Gopal, 1995; Fornell and Larcker, 1981*). As a result, the reliability and validity requirements for the study constructs were achieved.

Table 1

Model evaluation results

	Poland					Thailand				
Latent variables	**Observed Variables**	**Factor loadings**	**CR**	**AVE**	**Cronbach's alpha**	**Observed Variables**	**Factor loadings**	**CR**	**AVE**	**Cronbach's alpha**
EE	EE1	0.761	0.858	0.548	0.861	EE1	0.63	0.817	0.572	0.820
	EE2	0.697				EE2	0.657			
	EE3	0.726				EE3	0.712			
	EE4	0.724				EE4	0.724			
	EE5	0.79				EE5	0.706			
FC	FC1	0.741	0.885	0.607	0.888	FC1	0.717	0.859	0.551	0.862
	FC2	0.746				FC2	0.792			
	FC3	0.821				FC3	0.762			
	FC4	0.811				FC4	0.718			
	FC5	0.774				FC5	0.718			
IAA	IAA1	0.794	0.896	0.633	0.899	IAA1	0.786	0.870	0.573	0.873
	IAA2	0.812				IAA2	0.774			
	IAA3	0.842				IAA3	0.776			
	IAA4	0.739				IAA4	0.683			
	IAA5	0.789				IAA5	0.762			
MS	MS1	0.589	0.828	0.694	0.840	MS1	0.642	0.838	0.509	0.842
	MS2	0.711				MS2	0.733			
	MS3	0.656				MS3	0.756			
	MS4	0.751				MS4	0.734			
	MS5	0.788				MS5	0.698			
OS	OS1	0.759	0.887	0.611	0.888	OS1	0.716	0.848	0.528	0.850
	OS2	0.783				OS2	0.695			
	OS3	0.769				OS3	0.774			
	OS4	0.81				OS4	0.728			
	OS5	0.786				OS5	0.718			
PE	PE1	0.709	0.747	0.596	0.752	PE1	0.68	0.775	0.612	0.786
	PE2	0.752				PE2	0.688			
	PE5	0.649				PE5	0.547			
SI	SI1	0.812	0.867	0.567	0.871	SI1	0.703	0.834	0.502	0.835
	SI2	0.728				SI2	0.724			
	SI3	0.755				SI3	0.686			
	SI4	0.726				SI4	0.733			
	SI5	0.742				SI5	0.694			
TC	TC1	0.684	0.783	0.547	0.791	TC1	0.779	0.823	0.609	0.829
	TC2	0.796				TC2	0.826			
	TC3	0.734				TC3	0.733			

Note: FC = facilitating conditions; SI = social influence; EE = effort expectancy, PE = performance expectancy, TC = technological competence, MS = managerial support, OG = organizational size, IAA = intention to adopt AI.

In addition, the Confirmatory Factor Analysis was conducted to evaluate the measurement model fitness. Various fitness tests in Table 2 are summarized in the figure below. The fit indices are relevant in explaining how the data fit the proposed model. Scholars such as *Byrne (1994), Tucker and Lewis (1973), and Schumacker and Lomax (2010)* recommended that the required threshold for NFI, IFI, and TLI should be 0.9 and above, and GFI should be >0.80. The required threshold for the X2/df threshold is < 5.0, while the threshold for RMSEA is < 0.80 (*Kline, 2015*).

NFI (Normed Fit Index): This is a goodness-of-fit index for SEM models. It indicates how much better the model fits the data in comparison to a baseline model, usually the independence model where all variables are assumed to be uncorrelated. NFI values range between 0 and 1, where values close to 1 suggest a better

fit. IFI (Incremental Fit Index): Similar to the NFI, the IFI compares the fits of the target model to an independence model but takes into account model complexity. Like the NFI, IFI values also range from 0 to 1, with values closer to 1 indicating a better fit. TLI (Tucker-Lewis Index): This index also compares the fit of the model to that of an independence model but is adjusted for the degrees of freedom. The TLI is typically less affected by sample size than other indices. Values close to 1 indicate a good fit and values >0.95 are often considered indicative of a good fit. GFI (Goodness of Fit Index): The Goodness-of-Fit Index (GFI) is a measure of how well an estimated model fits the observed data. It varies between 0 and 1, with values closer to 1 indicating a better fit. The GFI considers the relative amount of variances and covariances that the model is able to explain. A commonly accepted threshold for a good fit in the context of GFI is 0.90 or above, although some recommend a more conservative threshold of 0.95. The Root Mean Square Error of Approximation (RMSEA) is a statistic that measures how well a model fits the population's covariance matrix, rather than the sample's covariance matrix. It is sensitive to the number of estimated parameters in the model; thus, it adjusts for model complexity. The RMSEA values range from 0 to infinity, with lower values indicating a better fit. Values of 0.05 or less are considered to indicate a close fit of the model in relation to the degrees of freedom, while values up to 0.08 represent a reasonable error of approximation. *χ2/df* (Chi-Square to Degrees of Freedom Ratio): The Chi-Square to Degrees of Freedom Ratio (*χ2/df*) is used to assess the goodness-of-fit of a model. It is calculated by dividing the model's chi-square value (*χ2*) by the degrees of freedom (*df*). A lower *χ2/df* ratio indicates a better fit. Different fields may have different thresholds for an acceptable ratio, but a common rule of thumb is that a *χ2/df* value of 2 or 3 or less signifies an acceptable fit, while some researchers might allow for higher ratios up to 5 in complex models (*Byrne, 1994; Kline, 2015; Schumacker and Lomax, 2010; Tucker and Lewis, 1973*).

For Thailand, the results were X2/df = 2.141, IFI = 0.915, CFI = 0.914, TLI = 0.903, RMSEA = 0.057. These results met the required threshold. For the case of Poland, the results were X2/df = 2.583, IFI = 0.904, CFI = 0.903, TLI = 0.890, RMSEA = 0.065. These results met the required threshold, except for TLI, which was 0.010 less, but satisfied the threshold when rounded off. For both Thailand and Poland cases, these thresholds were satisfied. This confirmed that for both Thailand and Poland, the models used for the study appropriately fit the data.

Table 2

Confirmatory factor analysis

	X2/df	IFI	CFI	TLI	RMSEA
Thailand	2.141	0.915	0.914	0.903	0.057
Poland	2.583	0.904	0.903	0.890	0.065

Empirical results

Case for Thailand

In the case of Thailand, the various factors influencing the adoption of AI in the agricultural sector were evaluated. The results indicated that the facilitating condition has an insignificant and negative influence on the intention to adopt AI (β = -0.077, p = 0.082) hence rejecting H1. Social influence significantly influenced the intention to adopt AI (β = 0.080, p = 0.049), accepting H2. Effort expectancy insignificantly influenced the intention to adopt AI (β = 0.016, p = 0.744) hence rejecting H3. Performance expectancy was found to have a negative and insignificant influence on the intention to adopt AI (β = -0.019, p = 0.684), hence rejecting H4. Technological competence significantly influenced the intention to adopt AI (β = 0.075, p = 0.003), hence accepting H5. Managerial support insignificantly influenced the intention to adopt AI (β = 0.066, p = 0.349), hence rejecting H6. The organizational size was found to significantly influence the intention to adopt AI (β = 0.931, p = 0.000), hence accepting H7. The evaluation of the mediating effect of organization size was also evaluated. The results indicated that organizational size mediated the effect of facilitating condition, effort expectancy, performance expectancy, and managerial support on intention to adopt AI. However, it did not mediate the effect of social influence and technological competence on the intention to adopt AI. The results are summarized in Table 3.

Table 3

Hypothesis results - Case for Thailand

Hypothesis	Relationship			Beta	S.E.	C.R.	P
H1	FC	→	IAA	-.077	.044	-1.741	.082
H2	SI	→	IAA	.080	.041	1.969	.049
H3	EE	→	IAA	.016	.048	.326	.744
H4	PE	→	IAA	-.019	.048	-.401	.689

Hypothesis	Relationship					Beta	S.E.	C.R.	P
H5	TC			→	IAA	.075	.026	2.944	.003
H6	MS			→	IAA	.066	.071	.937	.349
H7	OS			→	IAA	.931	.125	7.454	***
H8a	FC	→	OS	→	IAA	.228	.047	4.812	***
H8b	SI	→	OS	→	IAA	.067	.046	1.451	.147
H8c	EE	→	OS	→	IAA	.113	.056	2.037	.042
H8d	PE	→	OS	→	IAA	.206	.053	3.855	***
H8e	TC	→	OS	→	IAA	-.006	.029	-.195	.845
H8f	MS	→	OS	→	IAA	.575	.071	8.103	***

Note: *** = significant at 99% confidence level; ** = significant at 95% confidence level; FC = facilitating conditions; SI = social influence; EE = effort expectancy, PE = performance expectancy, TC = technological competence, MS = managerial support, OG = organizational size, IAA = intention to adopt AI.

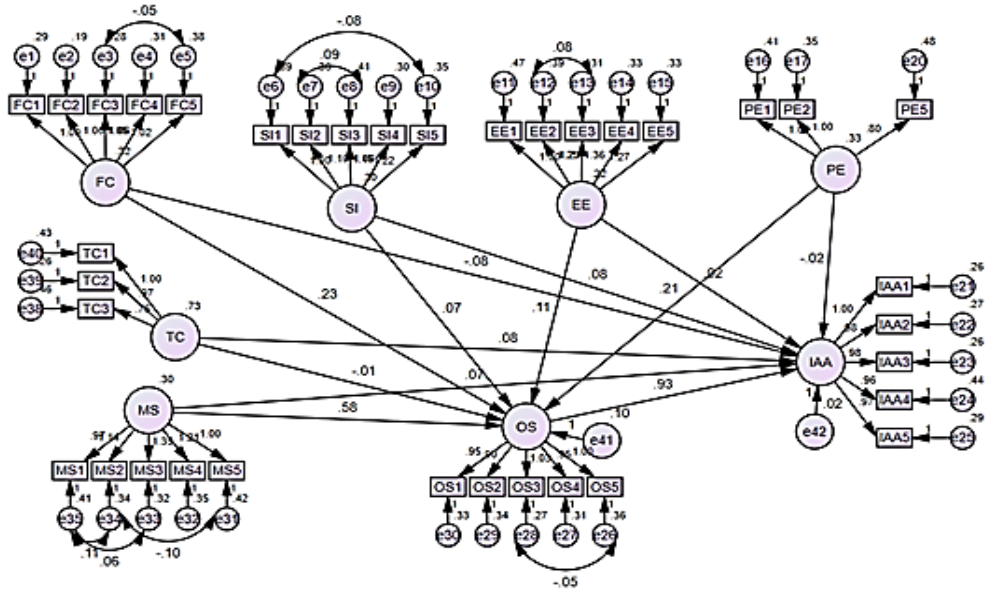

Fig. 2 - Hypothesis results - Case for Thailand

Case for Poland

In the case of Poland, the various factors influencing the adoption of AI in the agricultural sector were evaluated. The results indicated that the facilitating condition positively and significantly influences the intention to adopt AI (β = 0.088, p = 0.014) hence supporting H1. Social influence was found to have a negative and insignificant influence on the intention to adopt AI (β = -0.019, p = 0.637), hence rejecting H2. Effort expectancy was found to have a negative and significant influence on the intention to adopt AI (β = -0.125, p = 0.031) hence accepting H3. Performance expectancy was found to have an insignificant influence on the intention to adopt AI (β = 0.026, p = 0.512), hence rejecting H4. Technological competence significantly influenced the intention to adopt AI (β = 0.136, p = 0.006), hence accepting H5. Managerial support insignificantly influenced the intention to adopt AI (β = 0.080, p = 0.132), hence rejecting H6. The organizational size was found to significantly influence the intention to adopt AI (β = 0.812, p = 0.000), hence accepting H7. In addition, the mediating effect of organizational size revealed that organizational size significantly mediated the effect of all latent variables (social influence, effort expectancy, performance expectancy, technological competence, and managerial support) on the intention to adopt AI, except for facilitating conditions. The results are summarized in Table 4.

Table 4

Hypothesis results - Case for Poland

Hypothesis			Relationships	Beta	S.E.	C.R.	P
H1	FC	→	IAA	.088	.036	2.469	.014
H2	SI	→	IAA	-.019	.039	-.471	.637
H3	EE	→	IAA	-.125	.058	-2.160	.031
H4	PE	→	IAA	.026	.040	.656	.512
H5	TC	→	IAA	.136	.050	2.723	.006
H6	MS	→	IAA	.080	.053	1.507	.132
H7	OS	→	IAA	.812	.108	7.532	***

Hypothesis					Relationships	Beta	S.E.	C.R.	P
H8a	FC	→	OS	→	IAA	.031	.037	.829	.407
H8b	SI	→	OS	→	IAA	-.134	.040	-3.327	***
H8c	EE	→	OS	→	IAA	.424	.053	8.064	***
H8d	PE	→	OS	→	IAA	.152	.041	3.699	***
H8e	TC	→	OS	→	IAA	.234	.049	4.723	***
H8f	MS	→	OS	→	IAA	.409	.045	8.994	***

Note: *** = significant at 99% confidence level; ** = significant at 95% confidence level; FC = facilitating conditions; SI = social influence; EE = effort expectancy, PE = performance expectancy, TC = technological competence, MS = managerial support, OS = organizational size, IAA = intention to adopt AI.

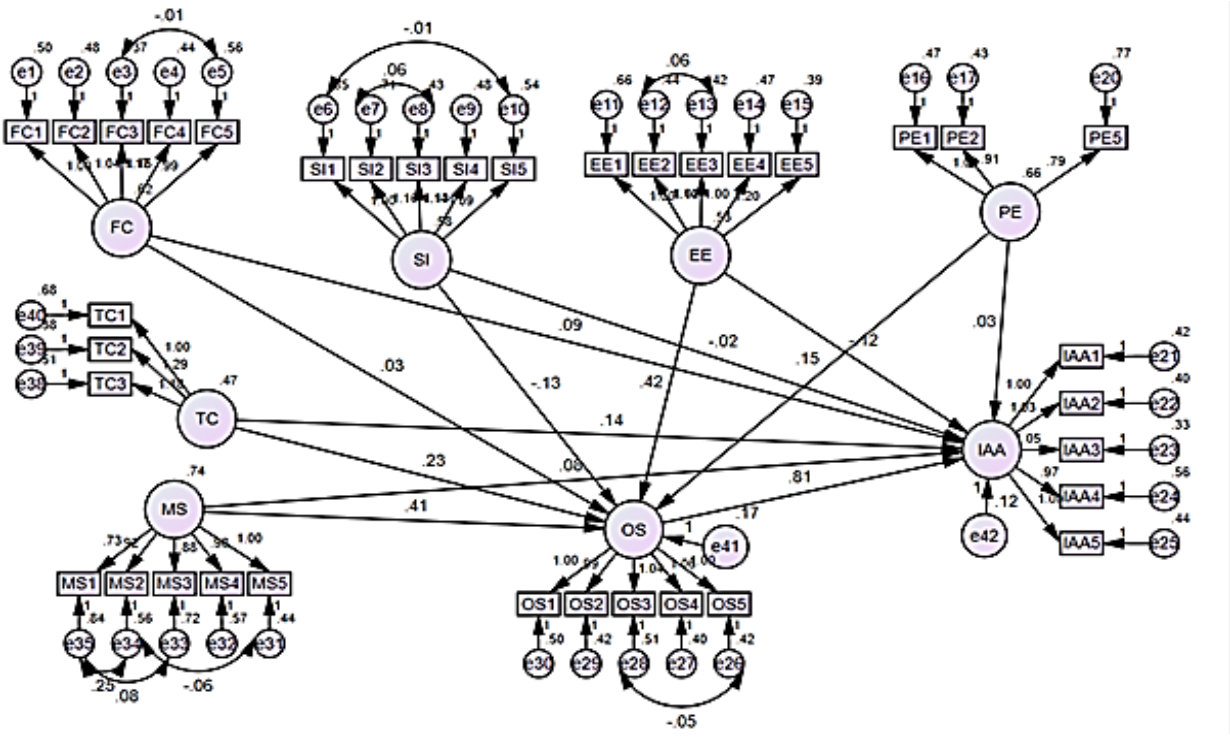

Fig. 3 - Hypothesis results - Case for Poland

Multi-group analysis

The multi-group analysis aimed to evaluate whether the two countries – Thailand and Poland – differed regarding the factors influencing behavioral intention to adopt AI in the agricultural sector. The Chi-square differences for the unconstrained and constrained models were compared. The insignificant paths for Thailand and Poland were deleted to obtain the unconstrained model. To get the constrained model, the paths were named to assume equal paths. The invariance between Thailand and Poland was evaluated by checking the difference between the chi-square and the degree of freedom. The results summarized in Table 5 below show that the Chi-square difference between the two models was 75.69 and that of degrees of freedom difference was 38. The p-value was 0.000 ($p < 0.05$). This implied that the model was not invariant (not indifferent). This meant that the two countries were different, or rather the effect of independent variables on behavioral intention to adopt AI between the two countries was different. These results show that the adoption of AI in the agricultural sector in Thailand was different.

Table 5

Multigroup analysis results

	Chi-square	df	p-val	Invariant?
Overall Model				
Unconstrained	5648.726	1152		
Fully constrained	5724.416	1190		
Number of groups		2		
Difference	75.69	38	0.000	NO

	Chi-square	df	p-val	Invariant?
Chi-square Thresholds				
90% Confidence	5651.43	1153		
Difference	2.71	1	0.100	
95% Confidence	5652.57	1153		
Difference	3.84	1	0.050	
99% Confidence	5655.36	1153		
Difference	6.63	1	0.010	

This research aimed to investigate the determinants of the adoption of AI-based applications in the agricultural sectors of Thailand and Poland, with a comparison of the two countries through a multi-group analysis. The emergence and increasing awareness of the application of artificial intelligence technology in various sectors, including the agricultural sector, drove the research. Different findings were obtained for the case of Thailand and Poland concerning the intention to adopt artificial intelligence in the agricultural sector.

In the case of Thailand, the most influential factor in the adoption of AI applications in agriculture was organizational size. According to the results, an increase of an organizational size by one unit would improve the adoption of AI by 0.931 units for the case of Thailand and 0.812 for the case of Poland. These findings are supported by *Alsheibani et al. (2018) and Kar et al. (2022)*, who indicated that organizational size is a critical aspect because it determines the ability and resources in terms of technology and human resources, which, in turn, significantly influences the ability of the firm to adopt AI technology. The organizational size was a significant mediator between other latent factors and the intention to adopt AI. This indicates that organizational size is a critical factor to consider when determining other aspects that influence the use of AI within the agricultural sector.

The second factor of significance was social influence. The results indicated that if the social influence improves by one unit, the intention to adopt AI applications in agriculture will improve by 0.080 units. Therefore, social influence is necessary to push an organization's AI technological agenda. These findings echo that of *Nascimento and Meirelles (2021),* that the influence of social settings such as peers, industry leaders, government agencies, research institutions, and supervisors of technology adoption is critical towards adopting the technology. Another factor influencing behavioral intention to adopt AI in Thailand was technological competence. These results were supported by *Zhang et al. (2022)*, who indicated that technological expertise within an organization determines how effective its adoption and use of AI technology would be. *Nascimento and Meirelles (2021)* also hold that the social influence from peers, industry leaders, government agencies, and research institutions is critical in determining the future adoption of technology.

Concerning Poland, the results indicated that the factor with the most significant influence is organizational size. The organizational size implies the number of employees, capital level, and levels of operations, among other factors critical for AI technology adoption (*Alsheibani et al., 2012*). More importantly, the organizational size significantly mediated the effect of other factors on their influence on AI adoption in Poland's agricultural sector. The second important factor was technology competence, which implies the knowledge, skills, and capability of taking advantage of the available technology, involving novation and invention. According to the results, one unit's increased technological competence would improve the behavioral intention to adopt AI applications by 0.136 units. Other factors that significantly influenced the adoption of AI in Poland's agricultural sector were facilitating conditions and effort expectancy. These results were in line with that of *Sood et al. (2022),* that the availability of resources, internet access, digital infrastructure, and financial resources are the necessary facilitating conditions that enhance technology adoption in the concerned setting or organization.

An extended analysis revealed that when comparing Thailand and Poland, the results indicated a significant variance in the determinants of adopting AI applications in the agricultural sector. For Thailand, the relevant factors include organizational size, managerial support, technological competence, effort expectancy, and social influence. For Poland, the relevant factors include organizational size, managerial support, technological competence, and facilitating conditions.

From the study, both the managerial and theoretical implications were developed. Regarding the theoretical implications, this research developed a conceptual model by borrowing from two broad perspectives – the UTAUT model and the organizational context. From the UTAUT model, the variables

used were facilitating conditions, social influence, effort expectancy, behavioral intention to adopt, and performance expectancy. From the managerial perspective, the following aspects were used - technological competence, managerial support, and organizational size. The model established the relationship between the study variables. The study added to the literature by evaluating the factors influencing the intention to adopt AI applications in the agricultural sector in Thailand and Poland by performing a multi-group analysis. From the empirical perspective, this research evaluated the factors influencing the intention to adopt AI applications in the agricultural sector. The research contributes to the literature through the findings that in Thailand, the intention to adopt AI-application in the agricultural sector is influenced by organizational size, technological competence, and social influence, while in Poland, the intention to adopt AI applications in the agricultural sector is influenced by organizational size, technological competence, effort expectancy, and facilitating conditions. Another critical implication is that regarding the adoption of AI applications in Thailand and Poland, the influencing factors are variants.

Several recommendations were developed concerning the application of AI in the agricultural sector. First, this research found that organizational size is the most influential factor in adopting AI applications in the agricultural sectors. Therefore, improving the organizational size in terms of resources, capabilities, and structures would enhance the ability to adopt AI technology. For Thailand, the other factors that should be enhanced include technological competence and social influence within an agricultural firm, which go a long way toward promoting AI adoption. For Poland, the other factors that the policymakers should improve include effort expectancy and technological competence. In addition, the facilitating condition is vital in Poland.

CONCLUSIONS

This research aimed to investigate the determinants of AI-based application adoption in the agricultural sectors in Thailand and Poland. This research was driven by the recent increased development of artificial intelligence and its application in various sectors to improve business processes and performance. AI has been considered to transform the agricultural sector through improved efficiency and productivity significantly. Two theories guided this research – the Theory for Reasoned Action (TRA), the Theory of Planned Behavior (TPB), and the Unified Theory of Acceptance and Use of Technology (UTAUT). The study used primary data collected from people working in the agricultural sectors in Thailand and Poland. From a sample target of 1100 respondents, 356 and 377 respondents in Thailand and Poland were used, respectively. The confirmatory factor analysis (CFA) was used to evaluate the model's fitness, reliability, and validity. The hypotheses were tested using Structural Equation Modeling (SEM).

The results revealed that for Thailand, the determinants for AI-based application adoption were organizational size, managerial support, technological competence, effort expectancy, and social influence. In Poland, the determinants for AI-based application adoption were organizational size, managerial support, technological competence, and facilitating conditions. The multi-group analysis revealed that the two countries were not invariant; hence the effect of independent variables on behavioral intention to adopt AI between the two countries was different. The research recommended that Thailand and Poland's agricultural sectors differ, therefore, specific factors should be considered in AI-based application adoption.

In conclusion, the adoption of AI-based applications in the agricultural sector is influenced by various determinants, including factors related to farmers' characteristics and organizational, technological, and external factors. The findings of this study highlight the importance of understanding these determinants and their respective impacts on the adoption process. By addressing the identified determinants, stakeholders in the agricultural sector can develop effective strategies to facilitate the adoption of AI-based applications and achieve their full potential in improving agricultural productivity and sustainability. However, it is important to note that adopting AI-based applications is a complex process that requires careful planning, investment, and collaboration among various stakeholders. Further research is needed to investigate the impact of these determinants in different contexts and to identify additional factors that may affect the adoption of AI-based applications in the agricultural sector.

ACKNOWLEDGEMENT

The research was carried out with financial aid and assistance from KMITL Business School, King Mongkut's Institute of Technology Ladkrabang under grant number 2565-02-12-006. The authors also acknowledge the reviewers' support, whose feedback and criticisms helped draft the published version.

REFERENCES

[1] Ajzen, I. (2012). The theory of planned behaviour. In P.A.M. Lange, A.W. Kruglanski, & E.T. Higgins (Eds.), *Handbook of Theories of Social Psychology* (pp. 438-459). Sage. https://doi.org/10.4135/9781446249215.n22

[2] Al-Dhaen, F., Hou, J., Rana, N. P., & Weerakkody, V. (2021). Advancing the understanding of the role of responsible AI in the continued use of IoMT in healthcare. *Information Systems Frontiers, 23*(6), 1-20. https://doi.org/10.1007/s10796-021-10193-x

[3] Alkhowaiter, W. A. (2022). Use and behavioural intention of m-payment in GCC countries: Extending meta-UTAUT with trust and Islamic religiosity. *Journal of Innovation & Knowledge, 7*(4), 100240. https://doi.org/10.1016/j.jik.2022.100240

[4] Al-Sharafi, M. A., Al-Emran, M., Arpaci, I., Iahad, N. A., AlQudah, A. A., Iranmanesh, M., & Al-Qaysi, N. (2023). Generation Z use of artificial intelligence products and its impact on environmental sustainability: A cross-cultural comparison. *Computers in Human Behavior, 143*, 107708. https://doi.org/10.1016/j.chb.2023.107708

[5] Alsheibani, S., Cheung, Y., & Messom, C. (2018). Artificial intelligence adoption: AI-readiness at firm-level. *PACIS*, 4, 231-245.

[6] Ayub Khan, A., Laghari, A. A., Shaikh, Z. A., Dacko-Pikiewicz, Z., & Kot, S. (2022). Internet of things (IoT) security with blockchain technology: A state-of-the-art review. *IEEE Access*, *10*, 122679-122695. https://doi.org/10.1109/ACCESS.2022.3223370

[7] Balakrishnan, J., Abed, S. S., & Jones, P. (2022). The role of meta-UTAUT factors, perceived anthropomorphism, perceived intelligence, and social self-efficacy in chatbot-based services? *Technology Forecasting and Social Change, 180*, 121692. https://doi.org/10.1016/j.techfore.2022.121692

[8] Byrne, B.M. (1994). *Structural equation modeling with EQS and EQS/Windows*. Sage Publications.

[9] Chaveesuk, S., Chaiyasoonthorn, W., Kamales, N., Dacko-Pikiewicz, Z., Liszewski, W., & Khalid, B. (2023). Evaluating the determinants of consumer adoption of autonomous vehicles in Thailand—An extended UTAUT model. *Energies, 16*(2), 855. https://doi.org/10.3390/en16020855

[10] Chin, W. W., & Gopal, A. (1995). Adoption intention in GSS: Relative importance of beliefs. ACM SIGMIS Database: *The DATABASE for Advances in Information Systems, 26*(2-3), 42-64. https://doi.org/10.1145/217278.217285

[11] Chin, W. W., Marcolin, B. L., & Newsted, P. R. (2003). A partial least squares latent variable modeling approach for measuring interaction effects: Results from a Monte Carlo simulation study and an electronic-mail emotion/adoption study. *Information Systems Research, 14*(2), 189-217. https://doi.org/10.1287/isre.14.2.189.16018

[12] Cubric, M. (2020). Drivers, barriers and social considerations for AI adoption in business and management: A tertiary study. *Technology in Society, 62*, 101257. https://doi.org/10.1016/j.techsoc.2020.101257

[13] Davis, F.D. (1986). *A technology acceptance model for empirically testing new end-user information systems: Theory and results*. [Doctoral dissertation, Sloan School of Management, MIT]. http://hdl.handle.net/1721.1/15192

[14] Fornell, C., & Larcker, D.F. (1981). Evaluating structural equation models with unobservable variables and measurement error. *Journal of Marketing Research, 18*(1), 39-50. https://doi.org/10.2307/3151312

[15] Fulton, R., Fulton, D., & Kaplan, S. (2022). Artificial intelligence: Framework of driving triggers to past, present and future applications and influencers of industry sector adoption. *arXiv*, 1-19. https://doi.org/10.48550/arXiv.2204.01518

[16] Gefen, D., & Straub, D.W. (1997). Gender differences in the perception and use of e-mail: An extension to the technology acceptance model. *MIS Quarterly, 21*(4), 389-400. https://doi.org/10.2307/249720

[17] Grand View Research. (2023). Artificial intelligence market size, share & trends analysis report by solution, by technology (deep learning, machine learning), by end-use, by region, and segment forecasts, 2023 - 2030 (Report ID: GVR-1-68038-955-5). https://www.grandviewresearch.com/industry-analysis/artificial-intelligence-ai-market

[18] Van Hilten, M., & Wolfert, S. (2022). 5G in agri-food - A review on current status, opportunities and challenges. *Computers and Electronics in Agriculture, 201*, 107291. https://doi.org/10.1016/j.compag.2022.107291

[19] Hradecky, D., Kennell, J., Cai, W., & Davidson, R. (2022). Organizational readiness to adopt artificial intelligence in the exhibition sector in Western Europe. *International Journal of Information Management, 65*, 102497.

[20] Ikumoro, A.O., & Jawad, M.S. (2019). Intention to use intelligent conversational agents in e-commerce among Malaysian SMEs: an integrated conceptual framework based on tri-theories including unified theory of acceptance, use of technology (UTAUT), and TOE. *International Journal of Academic Research in Business and Social Sciences*, *9*(11), 205-235.

[21] Jain, V., & Jain, P.P. (2022). From Industry 4.0 to Education 4.0: acceptance and use of videoconferencing applications in higher education of Oman. *Journal of Applied Research in Higher Education, 14*(3), 1079-1098. https://doi.org/10.1108/JARHE-10-2020-0378

[22] Kar, S., Kar, A. K., & Gupta, M. P. (2022). Modeling drivers and barriers of artificial intelligence adoption: Insights from a strategic management perspective. *Intelligent Systems in Accounting, Finance and Management, 28*(4), 217-238. https://doi.org/10.1002/isaf.1503

[23] Kelly, S., Kaye, S. A., & Oviedo-Trespalacios, O. (2023). What factors contribute to acceptance of artificial intelligence? A systematic review. *Telematics and Informatics, 77*, 101925. https://doi.org/10.1016/j.tele.2022.101925

[24] Kernecker, M., Knierim, A., Wurbs, A., Kraus, T., & Borges, F. (2020). Experience versus expectation: Farmers' perceptions of smart farming technologies for cropping systems across Europe. *Precision Agriculture, 21*, 34-50. https://doi.org/10.1007/s11119-019-09651-z

[25] Kline, R. B. (2015). *Principles and practice of structural equation modeling (4th ed.)*. Guilford Press.

[26] Lai, P.C. (2017). The literature review of technology adoption models and theories for the novelty technology. *Journal of Information Systems and Technology Management, 14*(1), 21-38. https://doi.org/10.4301/S1807-1775201700010000

[27] Manning, L., Brewer, S., Craigon, P. J., Frey, J., Gutierrez, A., Jacobs, N., Kanza, S., Munday, S., Sacks, J., & Pearson, S. (2022). Artificial intelligence and ethics within the food sector: Developing a common language for technology adoption across the supply chain. *Trends in Food Science & Technology, 125*, 33-42. https://doi.org/10.1016/j.tifs.2022.04.025

[28] Mohr, S., & Kühl, R. (2021). Acceptance of artificial intelligence in German agriculture: an application of the technology acceptance model and the theory of planned behavior. *Precision Agriculture, 22*(6), 1816-1844. https://doi.org/10.1007/s11119-021-09814-x

[29] Muangmee, C., Kassakorn, N., Khalid, B., Bacik, R., & Kot, S. (2022). Evaluating competitiveness in the supply chain management of small and medium scale enterprises. *Journal of Competitiveness, 14*(2), 93-112. https://doi.org/10.7441/joc.2022.03.06

[30] Mukherjee, S., Baral, M. M., Lavanya, B. L., Nagariya, R., Singh Patel, B., & Chittipaka, V. (2023). Intentions to adopt the blockchain: Investigation of the retail supply chain. *Management Decision*. Advance online publication. https://doi.org/10.1108/MD-03-2022-0369

[31] Na, S., Heo, S., Han, S., Shin, Y., Roh, Y. (2022). Acceptance model of artificial intelligence (AI)-based technologies in construction firms: Applying the Technology Acceptance Model (TAM) in combination with the Technology–Organization–Environment (TOE) framework. *Buildings, 12*(2), 90. https://doi.org/10.3390/buildings12020090

[32] Nascimento, A., & Meirelles, F. (2021). An Artificial Intelligence Adoption Model for Large and Small Businesses. *SSRN Electronic Journal*. https://dx.doi.org/10.2139/ssrn.4194043

[33] Ndinojuo, B.C. (2020). Framing biodegradable issues in selected online Nigerian newspapers: An environmental communication study. *Acta Universitatis Danubius Communicatio, 14*(1), 120-139.

[34] Nuanphromsakul, K., Szczepańska-Woszczyna, K., Kot, S., Chaveesuk, S., & Chaiyasoonthorn, W. (2022). Sustainability of rubber farmers cooperatives: Empirical evaluation of determining factors. *Agris on-Line Papers in Economics and Informatics, 14*(4), 85-96. https://doi.org/10.7160/aol.2022.140407

[35] O'Neill, A. (2023). Distribution of gross domestic product (GDP) across economic sectors Poland 2021. *Statista*. https://www.statista.com/statistics/375605/poland-gdp-distribution-across-economic-sectors/

[36] Phuoc, N.V. (2022). The critical factors impacting artificial intelligence applications adoption in Vietnam: A structural equation modeling analysis. *Economies, 10*(6), 129. https://doi.org/10.3390/economies10060129

[37] Regona, M., Yigitcanlar, T., Xia, B., & Li, R.Y.M. (2022). Opportunities and adoption challenges of AI in the construction industry: A PRISMA review. *Journal of Open Innovation: Technology, Market, and Complexity, 8*(1), 45. https://doi.org/10.3390/joitmc8010045

[38] Rosales, M.A., Jo-ann, V.M., Palconit, M.G.B., Culaba, A.B., & Dadios, E.P. (2020). Artificial intelligence: the technology adoption and impact in the Philippines. In *Proceedings of the 2020 IEEE 12th International Conference on Humanoid, Nanotechnology, Information Technology, Communication and Control, Environment, and Management (HNICEM)* (pp. 1-6). IEEE. https://doi.org/10.1109/HNICEM51257.2020.9321997

[39] Statista Research Department. (2022). GDP from agriculture, forestry, and fishing Thailand 2012 to 2021. *Statista*. https://www.statista.com/statistics/1023181/thailand-gdp-from-agriculture-forestry-and-fishing/

[40] Schumacker, R. E., & Lomax, R. G. (2010). *A beginner's guide to structural equation modeling (3rd ed.).* Lawrence Erlbaum Associates.

[41] Sneesl, R., Jusoh, Y. Y., Jabar, M. A., Abdullah, S. (2022). Revising technology adoption factors for IoT-based smart campuses: A systematic review. *Sustainability, 14*(8), 4840. https://doi.org/10.3390/su14084840

[42] Sood, A., Bhardwaj, A. K., & Sharma, R.K. (2022). Towards sustainable agriculture: key determinants of adopting artificial intelligence in agriculture. *Journal of Decision Systems, 31*(1), 1-45. https://doi.org/10.1080/12460125.2022.2154419

[43] Srivetbodee, S., & Igel, B. (2021). Digital technology adoption in agriculture: Success factors, obstacles, and impact on corporate social responsibility performance in Thailand's smart farming projects. *Thammasat Review, 24*(2), 149-170.

[44] Tornatzky, L.G., Fleischer, M., & Chakrabarti, A.K. (1990). *Processes of technological innovation*. Lexington Books.

[45] Tucker, L. R., & Lewis, C. (1973). A reliability coefficient for maximum likelihood factor analysis. *Psychometrika, 38*(1), 1-10. https://doi.org/10.1007/BF02291170

[46] Vantage Market Research. (2023). Artificial intelligence in agriculture market size worth $4.2 bn by 2028 | AI in agriculture industry expected CAGR 25.1%. https://www.globenewswire.com/news-release/2023/02/02/2600582/0/en/Artificial-Intelligence-in-Agriculture-Market-Size-Worth-4-2-Bn-by-2028-AI-in-Agriculture-Industry-Expected-CAGR-25-1-Vantage-Market-Research.html

[47] Venkatesh, V., Bala, H., & Sambamurthy, V. (2016). Implementation of an information and communication technology in a developing country: A multimethod longitudinal study in a bank in India. *Information Systems Research, 27*(3), 558-579.

[48] Vinuesa, R., Azizpour, H., Leite, I., Balaam, M., Dignum, V., Domisch, S., Felländer, A., Langhans, S.D., Tegmark, M., & Nerini, F.F. (2020). The role of artificial intelligence in achieving the Sustainable Development Goals. *Nature Communications, 11*, 233. https://doi.org/10.1038/s41467-019-14108-y

[49] Wolfert, S., & Isakhanyan, G. (2022). Sustainable agriculture by the Internet of Things – A practitioner's approach to monitor sustainability progress. *Computers and Electronics in Agriculture, 200*, 107226. https://doi.org/10.1016/j.compag.2022.107226

[50] Yarashynskaya, A., & Prus, P. (2022). Precision agriculture implementation factors and adoption potential: The case study of Polish agriculture. *Agronomy, 12*(9), 2226. https://doi.org/10.3390/agronomy12092226

[51] Zhang, B., Zhu, Y., Deng, J., Zheng, W., Liu, Y., Wang, C., & Zeng, R. (2022). I am here to assist your tourism: Predicting continuance intention to use AI-based chatbots for tourism. Does gender really matter? *International Journal of Human-Computer Interaction*. Advance online publication. https://doi.org/10.1080/10447318.2022.2124345

SATELLITE IMAGERY USAGE IN AGRICULTURE. CASE STUDY
/
UTILIZAREA IMAGINILOR SATELITARE ÎN AGRICULTURĂ. STUDIU DE CAZ

Anca Daniela MOICEANU[1)], Georgiana MOICEANU[2)], Gigel PARASCHIV*[2)], Mario CRISTEA*[3)]
[1)] Aider Association / Romania;
[2)] National University of Science and Technology "POLITEHNICA" Bucharest / Romania;
[3)] National Institute for Research-Development of Machines and Installations Designed for Agriculture and Food Industry - INMA Bucharest/ Romania;
Tel: +0745371861; E-mail: gigel.paraschiv@upb.ro and mario.cristea@yahoo.com
DOI: https://doi.org/10.35633/inmateh-72-68

Keywords: *agriculture, satellite images, NDVI index, crops.*

ABSTRACT
All sizes of farms can benefit from satellite imagery, not only big producers. When paired with artificial intelligence (AI) and deep machine learning techniques, satellite photography becomes an effective tool for monitoring agricultural conditions and anticipating issues in the field. As a result, using satellite photos to guide crop farming choices can help determine when to apply nutrients and irrigation. This paper focuses on monitoring through satellite sensors with an emphasis on the facilities offered by the European Copernicus Program through Sentinel-2 satellites the crops from a farm from Calarasi County, Borcea commune.

REZUMAT
Toate dimensiunile fermelor pot beneficia de imagini prin satelit, nu numai marii producători. Atunci când este asociată cu inteligența artificială (AI) și tehnicile profunde de învățare automată, fotografia prin satelit devine un instrument eficient pentru monitorizarea condițiilor agricole și anticiparea problemelor din domeniu. Ca rezultat, utilizarea fotografiilor din satelit pentru a ghida alegerile agricole poate ajuta la determinarea momentului în care să se aplice substanțele nutritive și irigarea. Această lucrare se concentrează pe monitorizarea prin senzori satelitari, cu accent pe facilitățile oferite de Programul european Copernicus prin sateliții Sentinel-2, a culturilor de la o fermă din județul Călărași, comuna Borcea.

INTRODUCTION

To produce more, produce better, not to pollute, not to make people sick, to remain profitable are the challenges that today's farmers must address. According to reports, agriculture is the largest consumer of water resources, accounting for 70% of the world freshwater; human consumption has tripled in the last 50 years, and resource exploitation occurs at a rate 30% higher than nature can regenerate. In this perspective, the challenges of producing more with a smaller environmental impact are evident.

Environmental conditions such as climate, topography, soil type, and latitude determine the agricultural potential of a region, but technological and social factors determine how and whether this potential is realized. Large volumes of data from multiple sources need to be transformed into information for quick and accurate decision-making, and for knowledge-based action. Remote data collection, complex analyses of historical and real-time data, and the need for accurate predictions are all essential for a sustainable future for people, farms, and the environment.

Precision agriculture, agriculture 4.0, and digital agriculture have emerged out of the necessity to bring control to a sector dependent on numerous factors. Agriculture 4.0 emerged with the technologies of the Fourth Industrial Revolution, also known as Industry 4.0, in 2011, characterized by the use of technologies such as the Internet of Things (IoT), Artificial Intelligence (AI), Big Data (BD), Cloud Computing, or other smart systems and devices for crop and farm management (*European Agricultural Machinery Association, 2016; European Agricultural Machinery, 2017; European Commission, 2017; European Parliamentary Research Service (EPRS), 2016; Zhang et al., 2020; Vladut et al., 2020*).

Agriculture 4.0, analogous to Industry 4.0, refers to integrated networks of internal and external operations. This means that digital information exists for all sectors and processes of the farm; electronic communication with external partners, suppliers, or end consumers is also established; and the transmission, processing, and analysis of data are (largely) automated (*Kovács et al., 2018; Khanal et al., 2020; Ukaegbu et. al., 2021*).

Sensors are key facilitators behind the IoT concept, thanks to technological advances that have reduced their size and made them smarter and more cost-effective. Spatial and temporal variabilities that significantly impact agricultural production can be controlled mainly through two approaches: (1) a mapping-based approach or (2) a sensor-based approach (*Araújo et al., 2021, Dainelli et al, 2023*).

In the agricultural context, Cloud Computing has gained popularity in recent years by providing (1) a cost-effective storage solution for data (text, images, video, etc.) that has significantly reduced the cost of data storage for companies; (2) intelligent computing systems to transform raw data into knowledge and further into quantitative analysis-based decisions; (3) a secure platform that allows the development of various forms of IoT. Despite numerous benefits, it comes with limitations related to data privacy and network latency (resolved through edge and fog computing) (*Sott et al., 2021*).

Big Data can play a key role in transforming data into added value for stakeholders in the agricultural chain because it can efficiently aggregate, process, and visualize large and complex datasets. Using large volumes from multiple sources, both in real-time and historical, with the ability to process, predict, and monitor, significant changes are expected in farm management and agricultural operations (*Araújo et al., 2021*).

Decision Support Systems (DSS) do not have a universally accepted definition, but according to *European Parliamentary Research Service (EPRS), (2016)*, it can be defined as a human-computer system that uses data from various sources, aiming to provide farmers with a list of advice to support their decision-making process under different circumstances. One of the most representative features of ADSS is that it does not give direct instructions or commands to farmers, as the farmer is in the position to make the final decision (*Zhai et al., 2020*).

Remote sensing, in general, is considered a technique to collect data remotely through instruments that are not in physical contact with the objects being investigated/researched/tracked/monitored. Of the entire electromagnetic spectrum, only a narrow range of wavelengths is used in remote sensing. These include energy measurements from the visible spectrum, reflected infrared, thermal infrared and microwave regions. The platforms used for these measurements are satellites, (UAVs) drones, unnamed ground vehicles (UGVs), tractors or other devices with manually operated sensors. Measurements made with sensors on tractors or handheld devices are called proximity sensors.

Satellite remote sensing today has extensive applications in various fields of activity, including agriculture. A large number of past constraints in the use of remote sensing methods for precision farming were overcome with the launch of Sentinel-2 A+B. The Sentinel-2 constellation, with an improved spatial, spectral and temporal lens, was specifically designed to address problems in the farming community, both farmers and researchers (*Segarra et al., 2020*).

The use of time series of satellite images in many applications leads to multitemporal analyses that depend on comparing the results between these images. In this respect, it is necessary to convert the digital pixel values into physical units, i.e. radiance, thus allowing an objective comparison of images and the correct determination of the nature and magnitude of changes during the analyzed period. This includes applications that rely on the use of vegetation indices. For analyses and interpretations of satellite images, as well as for establishing the degree of accuracy of the information obtained from them, additional data are needed that constitute "ground truth" (*Vorovencii, 2015*).

Among the many applications of remote sensing in agriculture, vegetation indicators (IV) are important tools to analyze the health of vegetation, because it allows to observe whether the growth is homogeneous or if the crop is subjected to some stressor. In addition, artificial intelligence models combined with remote sensing data and vegetation indices are used for harvest prediction or other applications related to crop nutrition, water stress, weed, insect or plant disease infestation, and soil properties such as organic matter content, nutrients, pH, and salinity (*Radočaj et al., 2023, Araújo et al., 2021*).

Plants interact with sunlight differently, which is called a spectral signature. Incident solar radiation can follow three paths: it can be transmitted, reflected or absorbed. The electromagnetic radiation reflected by plants contains information about their biophysical composition and physiological state, and can be measured using satellite sensors, such as those placed in ESA Sentinel-2 (*Segarra et al., 2020*).

Initially, the notion of vegetation index (VI) arose from the need to identify and delimit vegetation on multispectral images; this approach is based on the characteristics of spectral responses of vegetation in relation to other bodies on the Earth's surface (*Thieme et al., 2020*). VI are a subset of the category of spectral indices (IS) and represent one of the most widely used approaches for analyzing satellite data in the optical domain, for various applications.

VI is based solely on the interpretation of spectral responses of objects interacting with incident solar radiation. The most useful spectral ranges for vegetation surveillance by remote sensing are between 600 – 700 nm and 750 – 1350 nm. Vegetation indices are a very efficient means of monitoring and evaluating drought phenomena at image scale due to the possibilities of precise discrimination of vegetation, as well as correlations with biophysical parameters that determine the state of vegetation and turgidity such as plant height, foliar index, biomass, etc.

The Normalized Difference Vegetation Index (NDVI) is a non-linear transformation of visible (RED) and near-infrared (NIR) bands being defined as the difference between these two bands, divided by their sum (*Belgiu et al., 2018, Guzinski & Nieto, 2019, Muhammad, 2019*): NDVI = (NIR-RED)/(NIR+RED). NDVI is a "unit of measurement" of vegetation development and density and is associated with bio-physical parameters such as: biomass (tons/ha), foliar area index (LAI), very often used in crop growth models, percentage of vegetation cover of land, photosynthetic activity of vegetation. In general, NDVI values are between -1.0 and 1.0, with negative values indicating clouds or water and positive values close to 0 indicating soil not covered by vegetation, high positive NDVI values indicate sparse vegetation (0.1-0.5) to dense vegetation (>0.6).

Indirectly, NDVI is used to estimate the effects of precipitation over a certain period, to estimate the vegetation status of different crops and to estimate the quality of the environment as a habitat for different animals, pests and diseases.

Related to research done considering wheat fields it must be said that Vannoppen et al. concluded that a negative correlation was observed between high temperatures in June for spring wheat and also for winter wheat, which states as a negative impact on the yield (*Vannoppen et al, 2020*). Also, previous studies proved that using dynamic monitoring of NDVI to asses wheat trials were of help and can be further used in forecasting yields (*Duan et al, 2017; Goodwin et al, 2018)*.

Further use of NDVI as a prediction model for wheat experimental trials, is the topics studied by researchers which stated that it could help but it is more valuable if other agronomic traits are added. Thus, the results showed that the prediction accuracy was higher by 50% and lower by 10% in the root mean square error for wheat experimental trials in Spain (*Garcia-Romero et al, 2023)*.

Also, Miller et al. studied six small grain and two corn fields using NDVI, which proved that using NDVI they were able to map the soil and weather conditions in order to predict the plant's variable rate (*Miller et al, 2024*).

Considering all these factors and the continuous technological advancement, this paper utilized satellite technology on a farm in Calarasi county, Borcea commune, to determine the NDVI index, presenting the evolution of three types of crops: wheat, corn, and sunflower. The research question asked is: “What is the potential of satellite imagery in agriculture for monitoring and analyzing crop conditions, specifically focusing on the NDVI index for wheat, corn, and sunflower crops?”

MATERIALS AND METHODS

To fulfil the objective of the work, a farm from Calarasi County, Borcea commune, was chosen. Alissa Farm SA operates in the combined cultivation of oilseeds and cereals industry. Alissa Farm S.A brings together the operations of three farms: Concordia Agro, Agricom Borcea, located in Balta Ialomiţei Island (Balta Borcea), and Tudor 92, located on the terrace. The three farms were spread over a geographical area, relatively extensive, (30 km from east to west) with differences in both climate and soil properties. The most striking differences appear between terrace and island soils, therefore the technologies applied also differ with implications on economic performance. Alissa Farm manages a total area of 13,630 ha (arable, permanent, and temporary area).

The studied farm is located in an area with special importance for Romanian agriculture, being the main agricultural region in the country that includes approx. 40% of the total arable areas in Romania. Out of the total area it administers, only an area of 701.4 ha was analyzed. According to satellite measures, the selected area has an area of 690.06 ha, the analyzed plots being established with Google Earth. To accurately determine the size and to have a high degree of accuracy of satellite images, a Trimble J5 GPS was used (Figure 1). For easy highlighting of plots and easy processing and interpretation of results, a system of notations highlighted in Figure 1b has been established.

Fig. 1 - Plot determination using Google Earth, a. surface determination, b. plot monitoring

The measurements provided by the satellite were in the form of vector images with an area of 100 km^2, one for each of the 13 wavelengths, covering the light spectrum. The Sentinel products used are made available free of charge to ESA users through the Copernicus Open Access Hub environment. The platform was queried for products using the filter engines: Interrogated period 01.09.2019- 30.10.2020, Mission Sentinel – 2, the S2A* is a S2B, products S2MSISA, cloud cover [0 to 4].

The search generated 97 UTM (Universal Transverse Mercator) 35TNK products that were downloaded. Regarding the use of satellite images in the analysis, the OGOR application was used to monitor the evolution of NDVI in the analyzed area. The OGOR application works according to the following protocol:

- calculates the footprint of each product on all bands;
- generates and records FMASK rasters at UMT level from L1C products, thus classifying clouds, shadows, snow, water and pixels of clear terrain with better accuracy than that available in L2A products;
- generates and records NDVI, NDWI, and EVI rasters at UTM (Universal Transverse Mercator) level from L2A products.

Establishing in advance the coordinates of the terrain, raster images for red and green wavelength were used, by applying the formula of NDVI (B8-B4/B8+B4) and a map of vegetation was built at the date of observation. The first image downloaded was on 15.02.2020, and the following with a frequency of 5 days until dates 30.10.2020. In total, 65 images were analyzed from February to October 2020, 25 of which were removed due to cloud cover, and 40 were used for this work.

Table 1

Renaming of analyzed plots

Den. no.	Farm plot name	Rename for analysis
1	B52	A
3	B99	B
4	Bl00	C
5	B95	D
6	B96A	E
7	B96B	F
8	B102	G
9	B102A	H
10	B103A	I
1	B52	A

RESULTS

Regarding the area measured, for each plot, the deviation was calculated to ensure the accuracy of the measurements and to be able to accurately specify the results of the analysis. Thus, in the table below you can find the data on the areas of each plot of land.

Table 2

Measured surface

Plot	GPS RTK (ha)	Google Earth (ha)	Difference (GPS- GE ha)
A	83,09	81,00	+ 2,09
B	97,42	97,90	-0,48
C	96,85	97,40	-0,55
D	25,01	25,17	-0,16
E	46,27	46,89	-0,62
F	55,96	56,58	-0,62
G	122,55	123,98	-1,43
H	6,6	6,59	+0,01
I	7,8	7,78	+0,02
TOTAL	146	146,77	-0,77

Regarding the NDVI analysis on the terrain, the main results are highlighted in Figure 2.

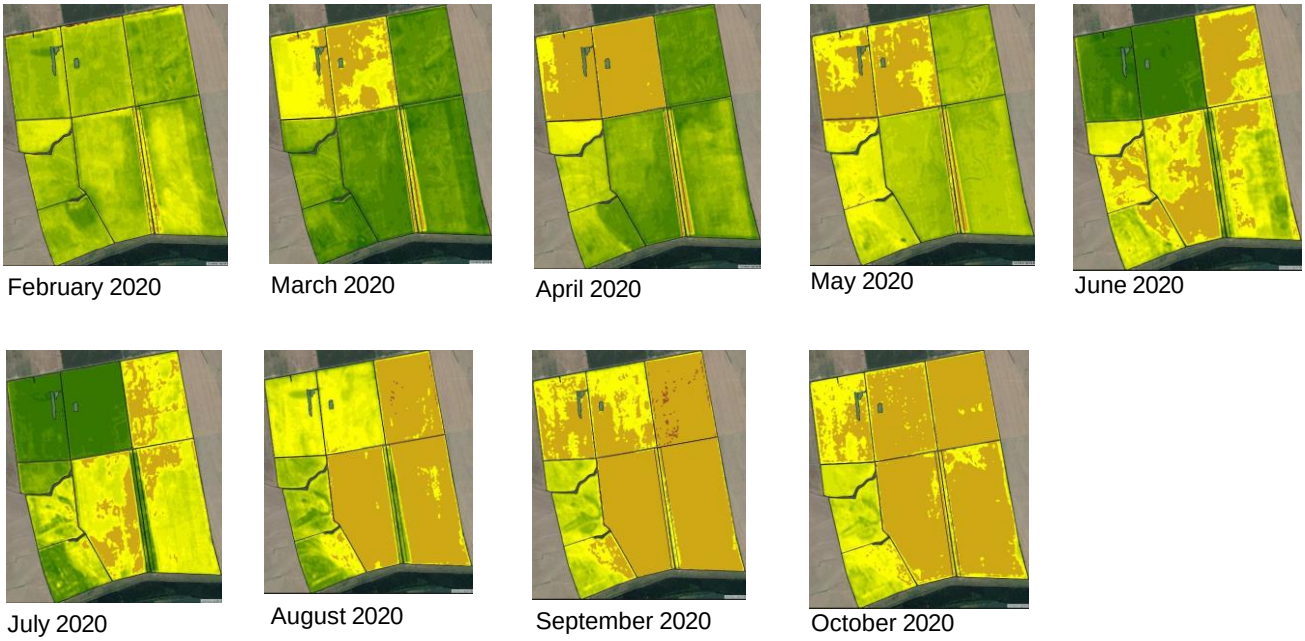

Fig. 2 - NDVI maps obtained during the analyzed period

At the same time, to compare the satellite results with those in the field, three types of crops were chosen (wheat, corn and sunflower) which were analyzed in terms of evolution using the NDVI index. The satellite images obtained in the case of wheat cultivation are shown in Figure 3.

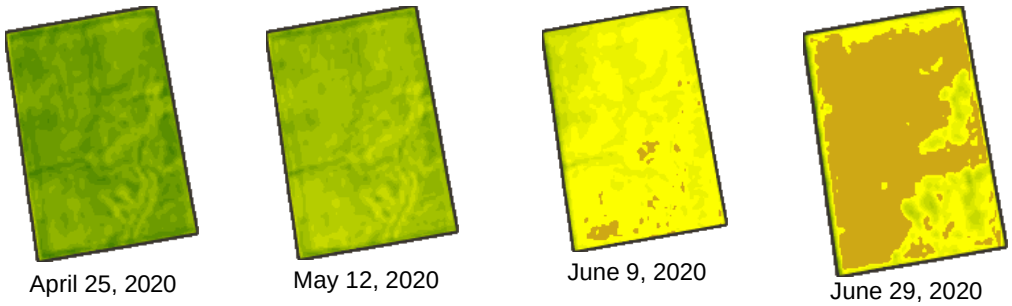

Fig. 3 - Evolution of NDVI for wheat on plot C (B100)

These images show the evolution during February and June, which, in terms of data obtained, can be seen in Figure 4 for wheat crop.

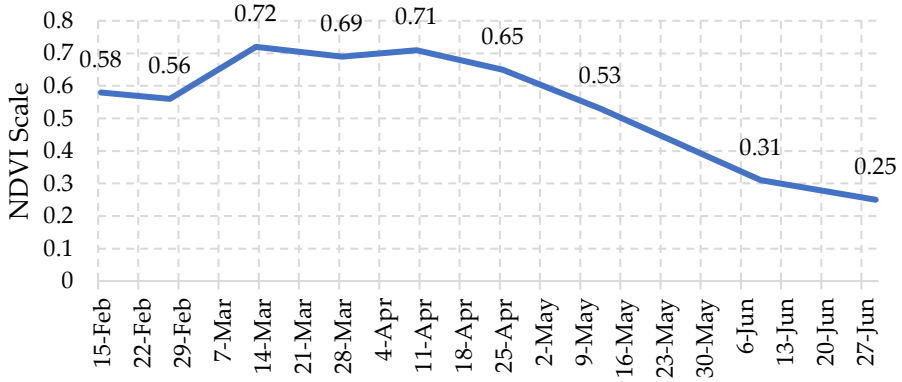

Fig.4 - Wheat crop evolution of NDVI from February to July 2020

Similarly, in Figure 5, the evolution from May to September is presented for corn crop.

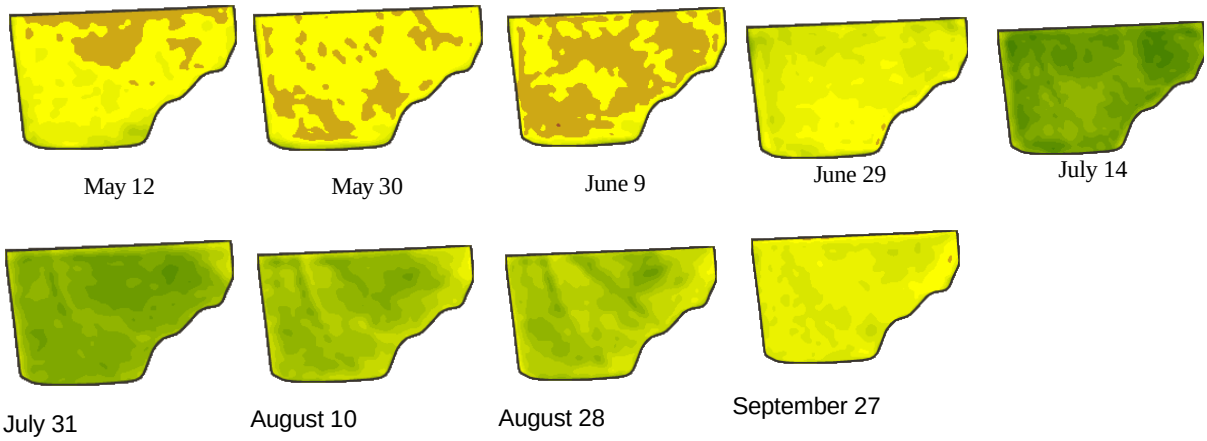

Fig. 5. NDVI evolution for corn crop. Plot D (B95).

In Figure 6, the NDVI evolution for corn crop is presented.

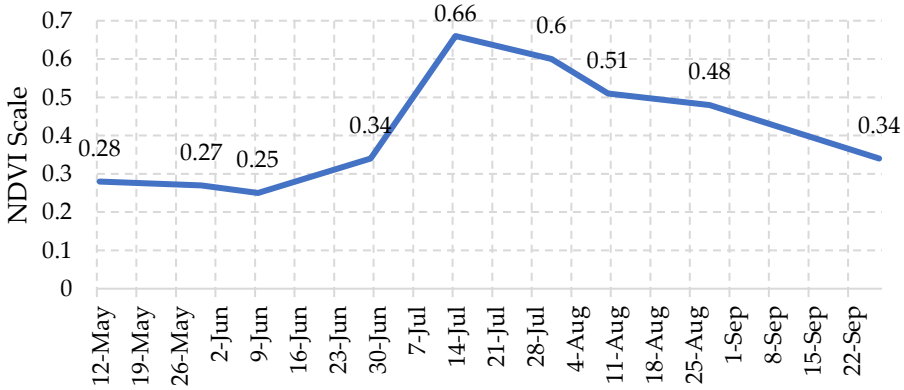

Fig. 6 - NDVI evolution of corn crop during May - September 2020

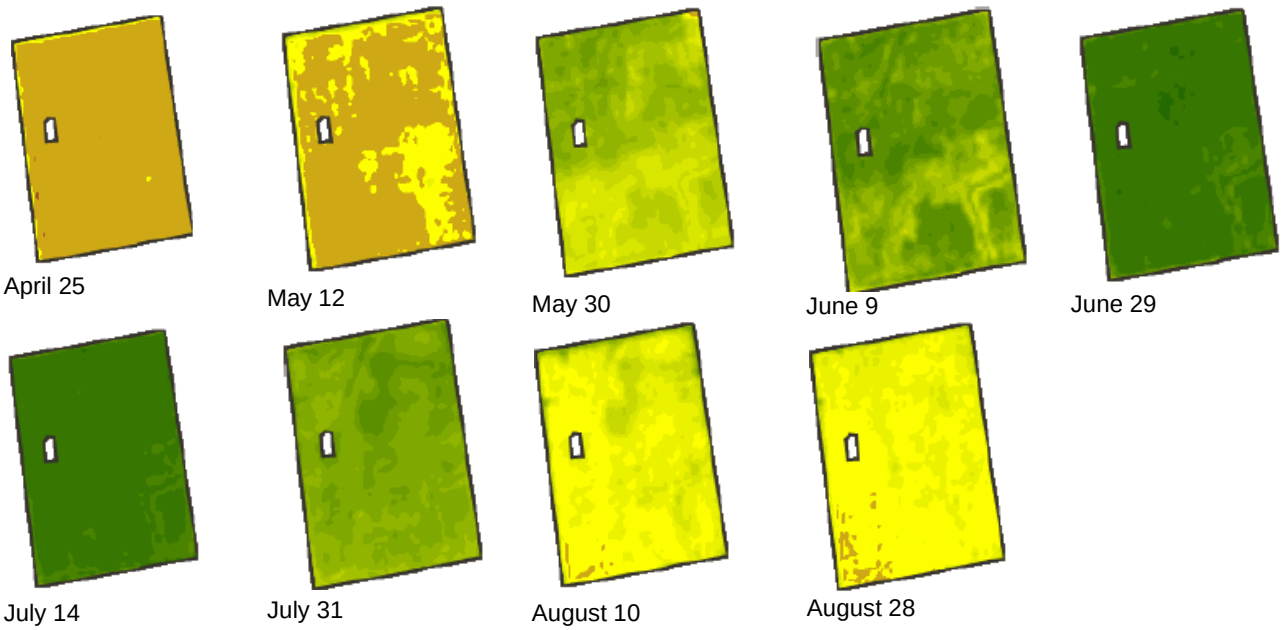

Fig. 7 - Evolution of the NDVI for sunflower cultivation on plot B (B99)

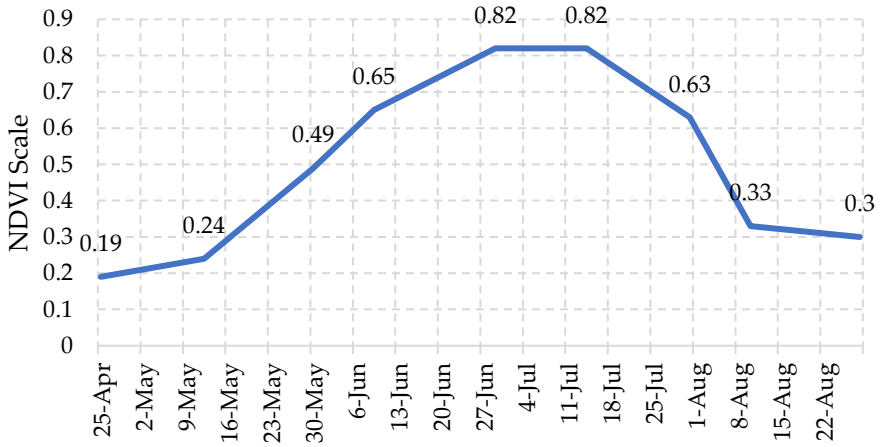

Fig. 8 - NDVI evolution for sunflower from April to August 2020

Figures 7 and 8 present the satellite images and the NDVI index for the sunflower crop.

DISCUSSION

On February 15, 2020, at the time of the first image consultation, vegetation was found on all soils selected for analysis (A – J) with an average NDVI of 0.47 on the entire analyzed area. Following the dynamics of the images over time, in March it can be observed an increase in NDVI values on plots C, G, J, and maps indicating an increase in chlorophyll content, while on the rest of the analyzed plots NDVI values were decreasing.

Going to the real land it was found that plots C, G, J were occupied by wheat crops. Thus, it was found that out of the total analyzed area, which is 690.06 ha, the area cultivated with wheat was 368.15 ha, meaning a percentage of 38.86%. The April 2020 analysis shows a decrease in NDVI values on all analyzed plots. The area under wheat (C, G, J) continued to show the highest NDVI values (mean 0.62). On the rest of the surface the indices were declining, with an average of 0.29 (A, B, H, I, D, E, F).

From the images obtained in May 2020, it can be seen that vegetation was decreasing throughout the analyzed area (A-J) with NDVI values of 0.34. In June, monitoring shows an increasing trend of NDVI on plots A, B, H, and I, reaching an average of 0.70 on June 29, 2020. On the rest of the analyzed areas, the trend is downward, more pronounced on the area occupied by wheat (C, G, J) where NDVI decreased to 0.30.

In July, the growth trend on A, B, H, I is maintained, and NDVI maps show a maximum reached on July 14, 2020 when the index values were 0.82. Going to the real land, on July 31, 2020 it was found that on plots A, B, H, I was the sunflower crop in bloom. Therefore, it follows that out of the total analyzed area (690.06 ha), 28.00% was occupied by sunflowers, meaning 193.27 ha.

Also, on the same date, it was found that wheat parcels were harvested (C, G, J), which is also visible on the NDVI map, which shows index values of 0.21. From the questions addressed to the farmer, it was found that the production on the analyzed plots was 1.5 t/ha. During the same visit, plots D, E, F were inspected and found to be cultivated with maize. The NDVI analysis shows that the maximum values for this crop were reached on July 31, 2020, with average values on plots D, E, F of 0.54. It follows that out of the total analyzed area of 690.06 ha, 18.64% was occupied by maize crops, i.e. 128.64 ha.

The analysis of August 2020 shows a decreasing trend for both sunflower (A, B, H, I) and maize (D, E, F) with average values of 0.45 for sunflower and 0.50 for corn. In September, plots A, B, H, I (sunflower) showed an average NDVI value of 0.25. From the questions addressed to the farmer, it was found out that on August 28, 2020 the sunflower was harvested, which is correctly indicated by NDVI maps. The average yield on the analyzed plots was 2.64 t/ha. NDVI indices for maize are down throughout September, averaging 0.43.

During the last field visit on October 03, 2020, it was found that corn plots (D, E, F) were not harvested, but NDVI maps showed values of 0.34. From subsequent questions addressed to the farmer, it was found out that corn was harvested on November 05, 2020 with an average yield of 2.5 t/ha.

The hardship of the year 2020 could be seen through the analysis. The 2020 production was 45% lower for corn than 2019, 41% lower for wheat production and 54% lower for sunflower. The decline was also presented in the data gathered at a national level, the drought affected the plots and could be seen throughout the maps obtained in the research.

CONCLUSIONS

Developments in precision agriculture and smart farming are meant to take farm performance to another level. One of the tools used by the new type of agriculture is remote sensing. Remote monitoring offers multiple advantages to farmers through the data it provides, replacing energy-intensive, time-consuming, and perhaps even less accurate methods of collecting field data. In this context, this paper focuses on monitoring through satellite sensors with emphasis on the facilities offered by the European Copernicus Program through Sentinel-2 satellites.

The multispectral satellite images provided by Sentinel-2 dedicated to agriculture have a spatial resolution of 10-20 m/pixel and a temporal resolution of 10 days, but the constellations (Sentinel 2A and 2B generate images every 5 days. Spectral resolution allows the determination of the physiological properties of plants, which can then be calculated and transformed into vegetation indices.

The Normalized Difference Vegetation Index (NDVI) is an index used to determine the development of vegetation in the field and is possible due to chlorophyll present in leaves that absorbs solar radiation in the red band and reflects in the NIR (near-infrared) band.

Calculating the difference between the two bands, the value of the NDVI index can be obtained, which is strongly correlated with the health of the crop.

This study demonstrated the application of satellite-derived NDVI indices to effectively monitor and analyze crop conditions over a growing season in Calarasi County, using Sentinel-2 satellite imagery.

The findings underscore the value of this approach in precision agriculture by providing timely data that can influence farming decisions.

- Wheat Harvest Timing: The NDVI analysis enabled the identification of the peak vegetative growth of wheat and the subsequent decline, indicative of the nearing harvest period. Specifically, the NDVI values for wheat plots showed a marked decrease in early July, suggesting the beginning of the harvesting activities. This temporal correlation provides a non-invasive method to monitor crop maturity and optimize harvest timings.
- Sunflower and Maize Analysis: The study also tracked the growth patterns of sunflowers and maize, with NDVI peaks reflecting key growth stages. For sunflowers, the highest NDVI readings in mid-July corresponded with full bloom, observed directly during field visits. Maize showed a gradual increase in NDVI values until late July, aligning with the critical growth phases leading up to grain filling.

- Agricultural Insights: The data revealed that the year 2020 posed significant challenges, with lower than average yields reported for maize, reflecting broader regional impacts of adverse weather conditions. This highlights the NDVI's utility in capturing the effects of environmental stressors on crop health and productivity.
- Recommendations for Future Applications: The research supports the integration of NDVI monitoring into regular agricultural practices, providing a reliable, cost-effective tool for managing crop health and optimizing resource allocation. Future studies could expand on this by incorporating additional variables such as soil moisture levels and plant phenological data to enhance the predictive accuracy of crop yield and health assessments.
- Limitations: The study's scope was initially limited due to the availability and accessibility of detailed agricultural data, such as specific hybrids used, moisture levels, and phytosanitary measures. These parameters are indeed crucial for a comprehensive agricultural assessment but often require ground-level data collection or detailed records that may not be readily accessible or available in public databases.

REFERENCES

Araújo, S. O., Peres, R. S., Barata, J., Lidon, F., & Ramalho, J. (2021) Characterizing the Agriculture 4.0 Landscape—Emerging Trends, Challenges and Opportunities. *Agronomy,* 11(4), 667. https://doi.org/10.3390/agronomy11040667

Belgiu, M., & Csillik, O. (2018) Sentinel-2 cropland mapping using pixel-based and object-based time-weighted dynamic time warping analysis. *Remote Sensing of Environment*, 204, 509–523. https://doi.org/10.1016/j.rse.2017.10.005

Dainelli, R.; Saracco, F. (2023) Bibliometric and Social Network Analysis on the Use of Satellite Imagery in Agriculture: An Entropy-Based Approach. *Agronomy*, 13, 576. https://doi.org/10.3390/agronomy13020576

Duan, T., Chapman, S. C., Guo, Y., Zheng, B. (2017). Dynamic monitoring of NDVI in wheat agronomy and breeding trials using an unmanned aerial vehicle. *F Crop Res*. 210, 71–80. doi: 10.1016/j.fcr.2017.05.025

European Agricultural Machinery Association. (2016). CEMA - European Agricultural Machinery - NEW! Drones + Smart Machines: what are the benefits in farming? https://www.cema-agri.org (accessed on 25 June 2022)

European Agricultural Machinery. (2017). Digital Farming: what does it really mean? https://www.Cema-Agri.Org/ . https://www.cema-agri.org (accessed on 15 November 2022)

European Commission. (2017). Digital Transformation Monitor Industry 4.0 in agriculture: Focus on IoT aspects. https://ati.ec.europa.eu/. (accessed on 25 August 2022)

European Parliamentary Research Service (EPRS). (2016). Precision agriculture and the future of farming in Europe. https://www.europarl.europa.eu (accessed on 13 May 2023)

Gracia-Romero A, Rufo R, Gómez-Candón D, Soriano JM, Bellvert J, Yannam VRR, Gulino D., Lopes MS (2023) Improving in-season wheat yield prediction using remote sensing and additional agronomic traits as predictors. *Front. Plant Sci.* 14:1063983. doi: 10.3389/fpls.2023.1063983

Goodwin, A. W., Lindsey, L. E., Harrison, S. K., Paul, P. A. (2018). Estimating wheat yield with normalized difference vegetation index and fractional green canopy cover. *Crop Forage Turf Man* 4 (1), 1–6. doi: 10.2134/cftm2018.04.0026

Guzinski, R., & Nieto, H. (2019). Evaluating the feasibility of using Sentinel-2 and Sentinel-3 satellites for high-resolution evapotranspiration estimations. *Remote Sensing of Environment*, 221, 157–172. https://doi.org/10.1016/j.rse.2018.11.019

Khanal, S., KC, K., Fulton, J. P., Shearer, S., & Ozkan, E. (2020), Remote Sensing in Agriculture—Accomplishments, Limitations, and Opportunities. *Remote Sensing,* 12(22), 3783. https://doi.org/10.3390/rs12223783

Kovács, I., & Husti, I. (2018), The role of digitalization in the agricultural 4.0 – how to connect the industry 4.0 to agriculture? *Hungarian Agricultural Engineering*, 33, 38–42. https://doi.org/10.17676/hae.2018.33.38

Miller O., Mondal P., Sarupria M., (2024). Sensor-based measurements of NDVI in small grain and corn fields by tractor, drone, and satellite platforms, *Crop and Environment*, 3(1), 33-42, ISSN 2773-126X,https://doi.org/10.1016/j.crope.2023.11.001

Muhammad U.H., Muhammad S. (2019), GIS & remote sensing for precision agriculture. https://Www.Technologytimes.Pk/.https://www.technologytimes.pk/2019/03/28/gis-remote-sensing-agriculture/

Radočaj, D.; Plaščak, I.; Jurišić, M. (2023), Global Navigation Satellite Systems as State-of-the-Art Solutions in Precision Agriculture: A Review of Studies Indexed in the Web of Science. *Agriculture,* 13, 1417. https://doi.org/10.3390/agriculture13071417

Segarra, J., Buchaillot, M. L., Araus, J. L., & Kefauver, S. C. (2020). Remote Sensing for Precision Agriculture: Sentinel-2 Improved Features and Applications. *Agronomy,* 10(5), 641. https://doi.org/10.3390/agronomy10050641

Sott, M. K., Nascimento, L. D. S., Foguesatto, C. R., Furstenau, L. B., Faccin, K., Zawislak, P. A., Mellado, B., Kong, J. D., Bragazzi, N. L.. (2021) Agriculture 4.0 and Smart Sensors. The Scientific Evolution of Digital Agriculture: Challenges and Opportunities. *Preprints,* Published. https://doi.org/10.20944/preprints202105.0758.v1.

Thieme, A., Yadav, S., Oddo, P. C., Fitz, J. M., McCartney, S., King, L., Keppler, J., McCarty, G. W., Hively, W. D. (2020). Using NASA Earth observations and Google Earth Engine to map winter cover crop conservation performance in the Chesapeake Bay watershed. Remote Sensing of Environment, 248, 111943. https://doi.org/10.1016/j.rse.2020.111943

Ukaegbu, U.F.; Tartibu, L.K.; Okwu, M.O.; Olayode, I.O. (2021) Development of a Light-Weight Unmanned Aerial Vehicle for Precision Agriculture. *Sensors*, 21, 4417; https://doi.org/10.3390/s21134417

Vannoppen, A.; Gobin, A.; Kotova, L.; Top, S.; De Cruz, L.; Vīksna, A.; Aniskevich, S.; Bobylev, L.; Buntemeyer, L.; Caluwaerts, S.; De Troch R., Gnatuik N., Hamdi R., Remedio R.A, Sakalli A, Van de Vyer H., Schaeybroeck B., Termonia P.,(2020) Wheat Yield Estimation from NDVI and Regional Climate Models in Latvia. *Remote Sens*., 12, 2206. https://doi.org/10.3390/rs12142206

Vladut V., Caba I.L, Constantin A-M, Voicu Gh., Maican E., Vilcu C. Lefter B. (2020), Principles of integration the agri-drones in agricultural production environments. New concepts towards Agriculture-5.0, *Annals of the University of Craiova-Agriculture, Montanology, Cadastre Series*, Vol. 51/2, DOI: 10.52846/AAMC.2021.02.70;

Vorovencii, I., (2015). Teledetecţie satelitară. Editura Matrix Rom Bucureşti. ISBN 978-606-25-0142-6. 600 pag.

Zhai, Z., Martínez, J. F., Beltran, V., Martínez, N. L. (2020). Decision support systems for agriculture 4.0: Survey and challenges. *Computers and Electronics in Agriculture,* 170, 105256. https://doi.org/10.1016/j.compag.2020.105256

Zhang, J.; Wang, C.; Yang, C.; Jiang, Z.; Zhou, G.; Wang, B.; Shi, Y.; Zhang, D.; You, L.; Xie, J. (2020). Evaluation of a UAV-Mounted Consumer Grade Camera with Different Spectral Modifications and Two Handheld Spectral Sensors for Rapeseed Growth Monitoring: Performance and Influencing Factors. *Precis. Agric.*, 21, 1092–1120; https://doi.org/10.1007/s11119-020-09710-w

DESIGN AND EXPERIMENT OF SEED-FILLING COMPONENT FOR RICE HOLE SEEDER
/
水稻穴播器取种装置设计与试验

Huyang TANG [1)], Gang WANG [1)], Bo ZHOU [1)], Yu WAN [1)], Fuming KUANG [1)], Wei XIONG [1)], Dequan ZHU [1)], Shun ZHANG *[1, 2)]

[1)] College of Engineering, Anhui Agricultural University, Hefei, Anhui, 230036, China
[2)] Engineering Laboratory of Intelligent Agricultural Machinery Equipment, Anhui, Hefei, 230036, China
Tel: +86 18856922971; E-mail addresses: shunzhang@ahau.edu.cn
DOI: https://doi.org/10.35633/inmateh-72-69

Keywords: *rice, film mulching, hole seeder, seed-filling component, DEM*

ABSTRACT
The core equipment of rice dry direct-seeding with film mulching devices shows poor adaptability to rice varieties, struggling to accommodate diverse seeding quantity for both hybrid and conventional rice varieties. A seed-filling component with unilateral and bilateral seed-filling function was designed to solve this challenge. Through theoretical analysis the key structural parameters of the seed-filling component were determined. Then Discrete Element Method (DEM) simulations were conducted to analyze the seeding performance, leading to the identification of optimal parameters for orifice width and orifice deflection angle of the seed-filling component, which are 7.7 to 8.5 mm and 1.71 to 2.41 degrees, respectively. Bench experiments using the central composite design indicates that the optimal parameters for the seed-filling component's orifice width and orifice deflection angle are 8.1 mm and 1.99 degrees, respectively. In the optimal combination of orifice parameters, for unilateral seed-filling in hybrid rice, the miss-seeding rate is 4%, the qualified rate is 84.8%, and the reseeding rate is 11.2%. For bilateral seed-filling in conventional rice, the miss-seeding rate is 4.2%, the qualified rate is 85.2%, and the reseeding rate is 10.6%. The result of field hole-seeding with film mulching is consistent with the result of indoor bench experiments, demonstrating that the seed-filling component of the hole seeder can meet the seeding requirements for rice precision direct-seeding with film mulching. This paper provides theoretical reference for the design and optimization of the seed-filling component for rice hole-seeding equipment.

摘要
针对水稻覆膜旱直播核心装备穴播器品种适应性差，难以兼用于穴播量迥异的杂交稻和常规稻覆膜播种的问题，设计了一种具有双侧充种功能的取种装置，理论分析确定了取种装置的关键结构参数，进行了排种性能的离散元EDEM仿真分析，明确了取种装置进种口宽度和型孔偏转角的取值范围，分别为7.7~8.5 mm和1.71～2.41°；中心组合试验设计方法的台架排种试验表明，最佳的取值装置进种口宽度和型孔偏转角分别为8.1 mm和1.99°，此时，单侧充种播种杂交稻，漏播率为4%、合格率为84.8%、重播率为11.2%，双侧充种播种常规稻，漏播率为4.2%、合格率为85.2%、重播率为10.6%，田间覆膜播种试验与室内台架排种试验结果一致，表明穴播器取种装置能满足水稻覆膜精量穴播的排种要求。本文为水稻穴播器取种装置的设计及优化提供理论参考依据。

INTRODUCTION
As one of the essential global cereal crops, rice holds a significant position within agricultural production. According to the statistics, in 2021, the worldwide rice cultivation area reached 160 million hectares, accounting for 10.7% of the total cultivated area for all crops, ranking only behind maize and wheat. The global rice production reached 750 million metric tons, constituting 16.8% of the total crop production (*World Food and Agriculture – Statistical Yearbook 2021*, *2021*).

Rice, known as a "water-loving crop", exhibits the highest water consumption among all crops, utilizing 25% of the global agricultural freshwater resources *(Liu et al., 2015; Tao et al., 2016*). The hole-seeding with film mulching for rice technology, achieved through surface mulching, not only reduces soil water evaporation and enhancing soil moisture retention capacity but also converts natural precipitation into effective rainfall and increases soil water storage. This approach can save 50% to 70% of irrigation water compared to conventional direct seeding methods (*Li H. et al., 2020; Sandhu et al., 2019*). In addition, traditional rice direct seeding is susceptible to the influence of weather and weed infestation (*Kakumanu et al., 2018; Singh et al., 2015*), especially during the early growth stages, which can lead to problems like poor seedling emergence or malnutrition in rice seedlings, ultimately resulting in reduced yields *(Ghosh et al., 2017*).

Film mulching not only suppresses weed growth but also raises the soil temperature on the surface, and creates a microclimate conducive to rice growth under the mulch. This microclimate ensures the necessary temperature and moisture for early seed germination, root growth, and plant development, ensuring emergence rates, survival rates and adequate nutrient supply, thereby reducing the risks associated with direct seeding of rice *(He et al., 2013; Li H. et al., 2021*). Rice seeding with film mulching can also promote soil organic carbon mineralization *(Guan et al., 2022; Yang et al., 2020*), increasing soil microbial populations, improving soil structure, enhancing enzyme activity, nutrient availability, and ultimately enhancing rice yields (*Hadden & Grelle, 2016*).

With the development of biodegradable films, the use of biodegradable properties to replace the non-degradable aspects of traditional films for rice dry direct seeding with film mulching, it's an effective means to achieve economically and environmentally friendly, which reduces costs and improves efficiency (*Yin et al., 2019*). This has become a significant driving force for the development of rice hole seeding with film mulching technology and equipment. However, suitable devices of rice mulch hole-seeding with film mulching are currently lacking. Niu Qi and others modified seed-filling component of cotton hole seeder for rice hole seeding with film mulching by using a shovel-shaped seed-filling component. But their design was relatively simple, and the seed-filling component was fixed. It required a brush to assist with the clearing of seeds. As a result, the seeding quantity couldn't be adjusted, and it couldn't accommodate the different seeding quantity requirements of various rice varieties (*Niu et al., 2016*). Hui Li used a mini shovel in combination with an independent hole seed-metering device to achieve rice hole-seeding on film. However, the structure was complex, and the seeding quantity was difficult to adjust (*Li H. et al., 2021*).

In response to the current challenge of rice mulch seeding machines that are not adaptable for seeding substantially different quantities for hybrid and conventional rice, this study aimed to design and experiment the seed-filling component. This component can be used for both unilateral and bilateral seeding, allowing for self-clearing. The goal was to achieve rice hole seeding with film mulching for various rice varieties with different seeding quantity, thus meeting the specific agronomic requirements of different rice varieties.

MATERIALS AND METHODS

Structure and working principle of hole seeder

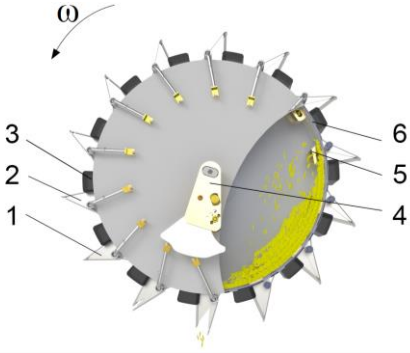

Fig. 1 - Schematic diagram of working principle of hole seeder

1. Seeding cylinder; 2. Duckbill; 3. Depth limit block; 4. Cam mechanism; 5. Seed-filling component; 6 Tile panel.

The hole seeder, is shown in Figure 1. During the seeding process, after seeds are loaded into the seed box, they descend by force of their dead weights into seeding cylinder. Positioned on bilateral of the seed-filling component secured to the tile panel are orifices. As the seeding cylinder advances through rotation, the seed-filling component undergoes synchronized rotation, causing rice seeds to be filled into it under the force of gravity lateral pressure from the surrounding rice seeds. The seed-filling component features a quantitative seed-filling space. The remaining quantitative rice seeds descend under the force of gravity, discharging the excess and re-entering the seeding cylinder. The remaining rice seeds within the seed-filling component proceed through a radial channel, entering the close state duckbill assembly as influenced by the rotational motion of the cylinder. Upon rotation of the rice-filled duckbill to its maximum soil depth, the moving duckbill, driven by the cam mechanism, opens fully and maintains this state for a specified interval. During this interval, the torsion spring accumulates energy, while the rice seeds inside the duckbill descend by gravity into the holes created by the duckbill's compression of the soil. This sequence completes the seeding process. Subsequently, as the duckbill fully disengages from the soil, the roller pendulum follower rotates to the cam's return phase. The release of energy from the torsion spring facilitates a smooth and controlled closure of the duckbill assembly.

Key parameters design of seed-filling component

The shapes and sizes of orifice inlet and outlet

As indicated in the literature (*Zhang, Li, et al., 2020*), rice seeds are filled into the orifice with their long axis aligned in the same direction as the tangential line of the seed-filling component's rotation. Based on the elliptical shape of the rice seeds, the orifice is designed to be elliptical, with its major axis aligned in the same direction as the tangential line of the rotating cylinder, as depicted in Figure 2.

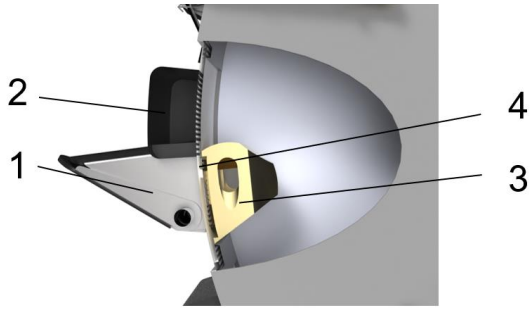

Fig. 2 - Single duckbill and seed pickup block connection diagram

1. Duckbill; 2. Depth limit block; 3. Seed-filling component; 4. Tile panel

The primary structural dimensions of the elliptical orifice are its length and width. Based on the seed-filling posture of the rice seeds, it is evident that within an equivalent range of dimensional variations, the rate per unit time seeds through the orifice is more sensitive to changes in the width dimension compared to the length dimension. Thus, the length dimension of the orifice only needs to accommodate the maximum length dimension of the rice seed, while the width dimension of the orifice must be determined experimentally based on the thickness dimension of the rice seed.

Considering the agronomic requirements of precision hole-seeding 5 to 10 seeds per hole for conventional rice, and in light of the characteristics of seed filling on bilateral of the seed-filling component, it is appropriate to fill 2 to 5 seeds on unilateral. Then the width dimension W of the orifice can be preliminarily determined within a design range using Equation (1).

$$3c_{\max} < W < 6c_{\min} \tag{1}$$

where: c is rice thickness size, mm.

To prevent rice seeds from mutually "crowding out" when entering the orifice, leading to arch, and to facilitate smooth entry of rice seeds into the radial channel of the orifice, the design of the seeds outlet is configured as a larger flow-rate square. Therefore, the orifice width and the side length of the seeds outlet should satisfy the following equation:

$$l > a_{\max} + c_{\max} \tag{2}$$

where: a is rice length size, mm; b is rice width size, mm; l is orifice width, mm.

The external dimensions of common rice seeds are summarized in Table 1 as follows:

Table 1

Rice seed outline size

Average triaxial size of rice seed (Length×Width×Thickness)	Maximum length size [mm]	Maximum width size [mm]	Maximum Thickness Size [mm]	Minimum Thickness Size [mm]
9.18×2.48×2.02	11.29	3.38	2.59	1.5

Based on Table 1 and the equations (1) and (2), the design values for the length of the orifice and side length of the seeds outlet are 14 mm. The appropriate width dimension for the orifice falls within the range of 7.7 to 8.5 mm.

Orifice deflection angle

As shown in Figure 3, by deviating the orifice at a certain angle in the opposite direction to the rotation of the seeding cylinder relative to the radial channel, the length of the orifice slope can be extended. Then the axial distance from the end face of the orifice to the vertical channel end face is reduced, contributing to the reduction of the axial dimension of the seed-filling component.

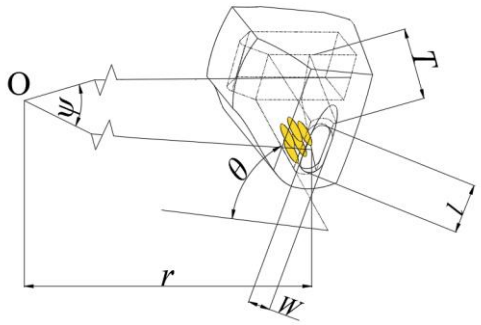

Fig. 3 - Illustration of the orifice deflection angle result

To ensure that rice seeds do not prematurely enter the radial channel during the filling and clearing phases, the value of the orifice slope angle θ needs to be determined based on the rice seed's friction angle. Theoretical analysis reveals that the orifice slope angle θ must be greater than the sliding friction angle of the rice seed. The geometric relationship between the orifice deflection angle ψ_1 and the orifice slope angle θ can be deduced from Figure 3.

$$\psi = \tan^{-1}\left(\frac{T}{\tan(0.5\pi-\theta)(r+0.5W)}\right) \tag{3}$$

where: r is distance from the geometry center of the orifice to the circle center of the seeding plate, mm; r is set to 188 mm; ψ is orifice deflection angle, (°); T is axial distance from the end face of the orifice inlet to the end face of the radial channel, mm. In this study, T is set to 9 mm.

As indicated in the literature (*Jun et al., 2021*) the coefficient of friction between rice seeds and ABS plastic is 0.5. To ensure that rice seeds does not prematurely slide into the channel during the filling phase of seed-filling component, the orifice slope angle θ should not be less than 30°. Therefore, when the orifice width is 8.1 mm, the curve of the orifice slope angle relative to the orifice deflection angle is illustrated in Figure 4:

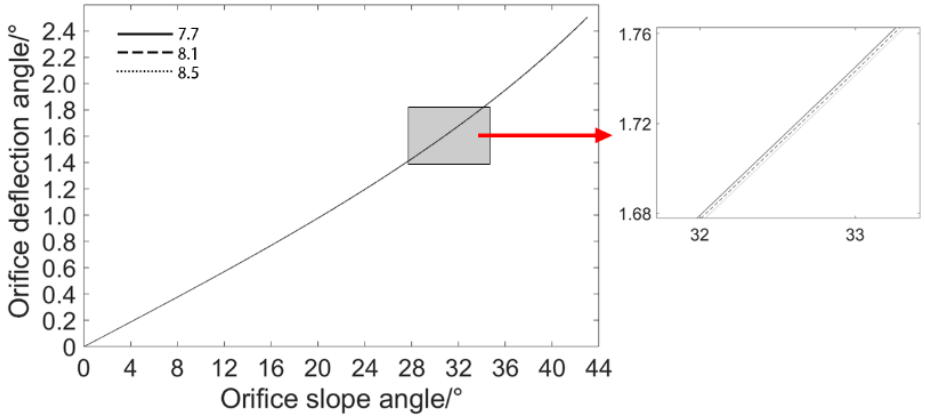

Fig. 4 - Relationship curve between orifice slope angle and orifice deflection angle

From Figure 4, it is evident that the orifice deflection angle ψ increases as the orifice slope angle θ increases. And the increase in orifice slope angle leads to a decrease in the internal seed-filling space within the orifice. Therefore, to fulfill the above requirements, the orifice deflection angle ψ should be greater than 1.60°.

Seeding performance simulation

Rice seed particle model

The experimental rice variety were selected from the conventional rice variety Huanghuazhan, which is widely grown in the lower-middle reaches of the Yangtze River in China. Based on the average triaxial dimensions of rice seeds by Huanghuazhan, and non-spherical particles modeling method based on EDEM software, multi-spherical composite approach is adopted, as illustrated in Figure 6. Since the width and thickness dimensions of rice seeds are relatively close, the width of the rice seed simulation particle is taken

as the average of the rice seed's average width and thickness dimensions, while the length of the particle is the average length dimension of the rice seed. As few filled spheres as possible were used to approximate the 3D model of the rice seed to minimize the simulation computation time.

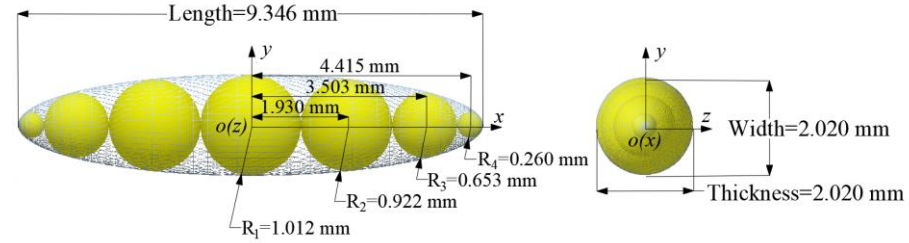

Fig. 6 - Rice seed particle model

Simulation model of hole seeding

Due to the multitude of components in the hole seeder, some of these components are not related to the seed filling process and the movement of seed particles within the seeding cylinder. To enhance simulation efficiency, the simplified hole seeder model is imported into EDEM 2022 software in STEP format. Based on the material characteristics of rice seeds and the actual materials of the hole seeder components, the material parameters for rice seed particles and each component are set, along with the contact parameters between particles and components *(Zhang, Tekeste et al., 2020)*.

The particle factory is situated within the cylinder, the particle generation method is Dynamic, the generation rate is 10000 particles/s, and the generation time is 0.2 s. Following the normal distribution characteristics of rice seed's triaxial dimensions, simulation particle sizes are set according to the standard normal distribution *(Li Y. & Xu, 2005*). As dry rice seeds have negligible adhesion forces on their surfaces, and weak electrostatic forces between the seeds are ignored, the Hertz-Mindlin no-slip contact model is selected for the simulation. The simulation model is depicted in Figure 7.

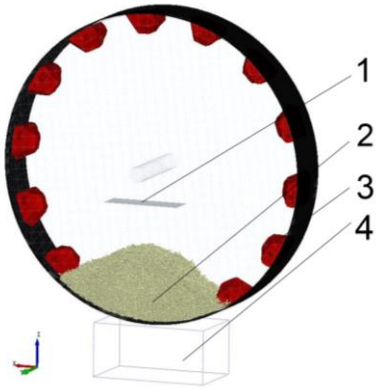

Fig. 7 - Simulation model of seeding device

1. Particle factory; 2. Rice seeds; 3. Seed-filling component; 4. Statistical unit of seed number per hole

Evaluation indicators

The experiment reference to the NY / T 987—2006 *(Standard for operating quality of hill-drop drill with film mulching*, 2006), the evaluation indicators for the hole seeder's performance are based on qualified rate, miss-seeding rate, and reseeding rate. To clarify the seed-filling pattern of seed-filling component and to avoid the influence of randomness in bilateral seed-filling on the assessment of seeding performance, considering the relatively independent unilateral seed-filling method of the seed-filling component, both simulation and bench experiment closed off unilateral orifice of the seed-filling component. This means that only the impact of unilateral seed-filling on the seed-filling component's performance is observed. Given that the recommended seeding range for conventional rice hole-seeding is 5 to 10 grains per hole, for unilateral seed filling, 2~5 seeds per hole is considered as qualified, less than 2 seeds per hole is considered as miss-seeding, and more than 5 seeds per hole is considered as reseeding. Therefore, the proportion of the total number of holes in the three results to the total number of holes in the experimental statistics is calculated, and the evaluation indexes were miss-seeding rate M (%), qualified rate Q (%), and reseeding rate R (%).

For the seeding performance simulation, a continuous count of 100 holes of rice seeds discharged by the hole seeder is taken as the experimental sample. In the bench experiment, a continuous count of 250 holes of rice seeds discharged by the hole seeder is taken as the experimental sample, and this process is repeated 2 times to account for the impact of the randomness in bench seeding on the experimental results.

Experiment design

To explore the effect of the orifice width and orifice deflection angle on the seeding performance, single factor seeding simulation tests were carried out separately. Under the condition of orifice deflection angle of 2.06°, the orifice width is set at 7.7, 7.9, 8.1, 8.3, and 8.5 mm, forming five levels.

To investigate the impact of the orifice deflection angle of the seed-filling component on the seeding performance, with an orifice of 8.1 mm, the orifice deflection angle is set at 1.60, 1.83, 2.06, 2.29, and 2.52°, forming five levels.

Bench experiment

Test materials and equipment

The experimental rice variety used was "Huanghuazhan". The experimental setup is illustrated in Figure 8. The hole seeder was driven by a direct current speed control motor (34CS85KF-490Z, Rayleigh Intelligent Technology Co., Ltd.), and a high-speed camera (i-SPEED 3 high-speed camera, Olympus Corporation, Japan) was used to count the number of seeds per hole.

Fig. 8 - Bench seeding experiment equipment

1. High-speed camera; 2. Hole seeder; 3. High-speed camera monitor; 4. Motor speed controller

Before the experiment, the high-speed camera lens was aligned with the duckbill open seeding position, and aperture and focal length were adjusted to ensure a clear view of the rice seeds being dispensed by the duckbill on the display screen. The shooting rate was set to 300 frames/s, and the resolution was set to 1280×1024. Continuous filming and recording captured the seeding situation in the seeding area when the hole seeder was stable. The recorded video was imported into the i-SPEED Suite software for frame-by-frame playback and the counting of seeding quantity per hole.

Referring to the generally operating speed of rice hole seeder with film mulching is between 0.5 to 1.2 m/s (*Jun et al., 2021*), the forward speed of cylinder is determined to be 0.8 m/s, and the rotational speed is 38 r/min.

Experimental design

In order to investigate the effects of the orifice width, orifice deflection angle, and their interaction on the seeding performance, and to determine the suitable parameter combinations, two factor central composite design was used. The levels of the factors were determined based on the single factor experiment results of seeding simulation. The experiment factors and their coded levels are presented in Table 3.

Table3

Experiment factor coding and level setting

Code	Orifice width *A*	Orifice deflection angle *B*
-1.414	7.8	1.71
-1	7.9	1.81
0	8.1	2.06
1	8.3	2.31
1.414	8.4	2.41

Field experiment

Experiment condition

To investigate field seeding performance of the hole seeder, a field experiment was conducted in June 2022 at Fenfang Village, Feixi County, Anhui Province, China. The hole seeder was assembled onto a rice hole-seeding with biodegradable film mulching machine and towed by the tractor. The experiment was carried out with reference to the *Standard for operating quality of grain film-cover hill-drop drill* NT/Y 987—2006. The forward speed of machine was set at 0.8 m/s on the field, consistent with the indoor bench experiment's operating speed of hole seeder.

After seeding, a random section of the experimental field, 20 meters in length, was selected for seed counting. Each row was continuously counted for 250 rice seeds, and this process was repeated for 8 rows. The aim was to calculate the miss-seeding rate, qualified seeding rate, and reseeding rate.

RESULTS

Analysis of seed filling process

As shown in Figure 10, this illustrates the s motion schematic of seed particles.

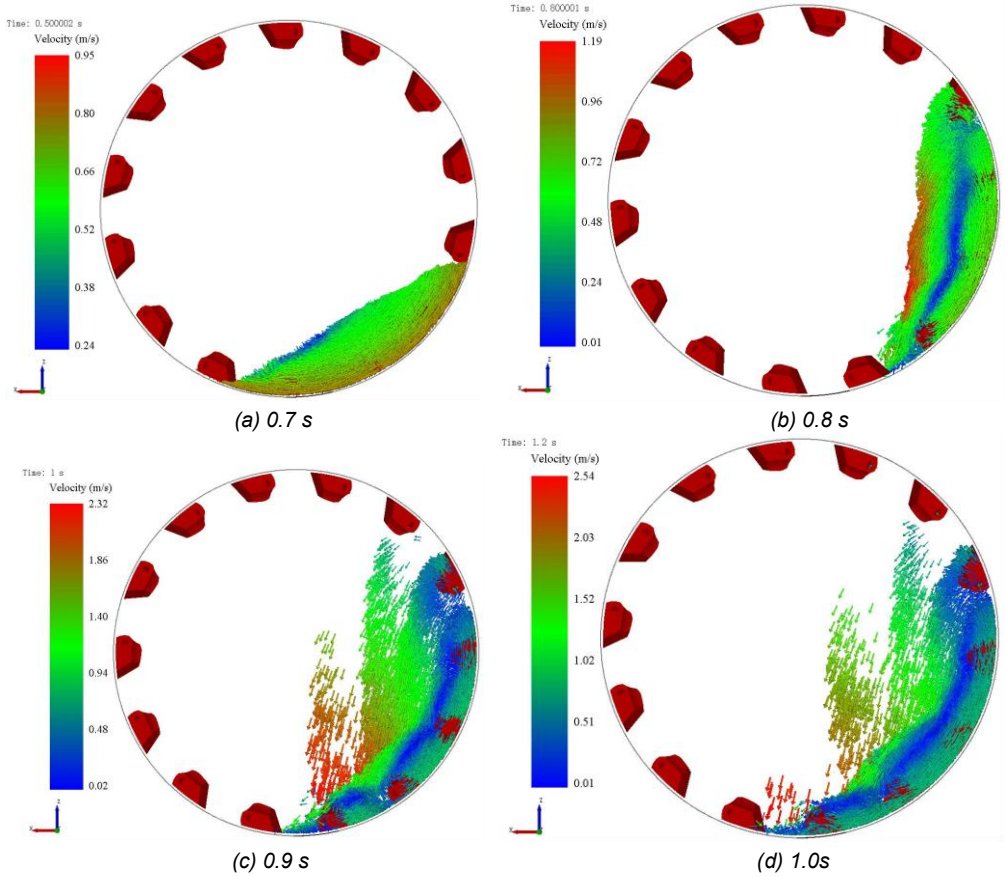

(a) 0.7 s *(b) 0.8 s*

(c) 0.9 s *(d) 1.0s*

Fig. 10 - Motion Schematic of seed particles

When seeding with the hole seeder, the particles movement process inside the seeding cylinder is shown in Figure 10, and red part represents the seed-filling component. After all the rice grain particles are generated and stabilized, the seeding cylinder begins to rotate. Driven by the seeding component and the friction of seeding cylinder's inner wall, the rice seeds move along with the cylinder, forming a semilunar shape region (Fig.10a). As the seeding cylinder continues to rotate, the semilunar seed particles are lifted to an approximate vertical state, and the surface layer of the seed particles is formed into a reflux zone under the action of gravity (Fig.10b).

As the seeding drum continues to rotate, the seeds at the top of seed-filling component slipped down followed one another, making the reflux zone increase (Fig.10c). When the hole seeder worked stably, the particles in the seeding cylinder formed three different motion regions: First, the particles close to the inner wall of the seeding cylinder rotated in synchronization with the seeding cylinder under the friction of the cylinder's inner wall and the pushing force of the seed-filling component; second, the rice seeds in the upper right area of the seed-filling component form small scattered local reflux zone; third, the reflux zone composed of the surface layer rice seeds and the refluent seeds carried away from the top of the seed-filling component (Fig.10d).

Figure 11 depicts the process of seed filling in the seed-filling component. The seed-filling component initially enters from the bottom of the seed particles (Fig.11a). As the seeding cylinder rotates, the rice seeds (in yellow) enter the seed-filling component through the orifice, approximately aligning their long axis with the tangential direction of the seed-filling component's rotation (Fig.11b). The rice seeds inside the orifice are poured onto the slope of the orifice under the influence of their self-gravity as the seed-filling component continues to rotate. Due to the limited seed-filling space of the orifice, when the slope can no longer accommodate more rice seeds pouring in, the excess rice seeds (in silver) will slide out of the orifice under the force of gravity. This achieves the self-clearing of rice seeds based on their dead weight. The quantified rice seeds poured onto the slope will continue to rotate with the seed-filling component and enter the radial channel through the seeds outlet.

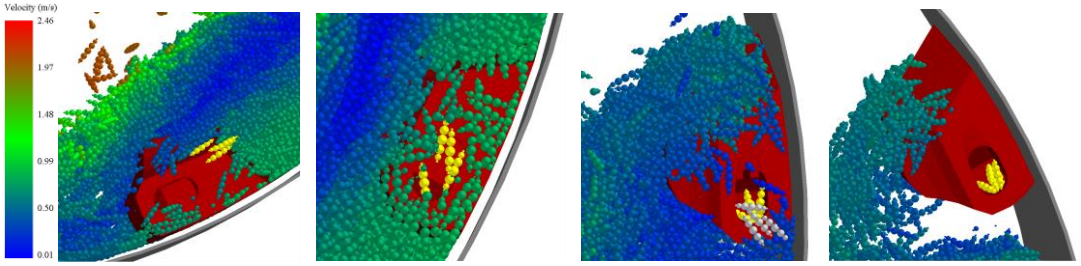

(a) (b) (c) (d)

Fig.11 - Schematic of seed filling process

Result and analysis of Central composite design

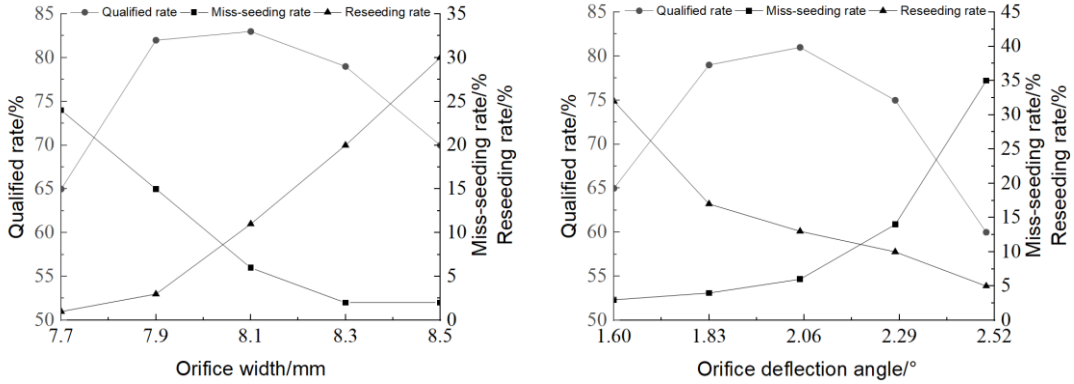

(a) (b)

Fig. 12 - Result of Central composite design

Influence of orifice width on seed filling performance are as shown in Figure 12(a), with the increase in the width of the orifice, the qualified rate of seed-filling process first increases and then decreases. The miss-seeding rate first decreases significantly and then decreases slowly, and the reseeding rate first increases slowly and then increases significantly. When the orifice width is too small, only a few rice seeds can be filled into the orifice as the seeding cylinder rotates, resulting in a high miss-seeding rate and low qualified rate and reseeding rate. As the orifice width gradually increases, multiple rice seed particles are more likely to enter the orifice, leading to a significant reduction in the miss-seeding rate and a substantial increase in the qualified rate, with a slight increase in the reseeding rate. When the orifice width becomes too large, an excessive number of rice seed particles enter the orifice, causing a further decrease in the miss-seeding rate, a significant increase in the reseeding rate, and a noticeable decrease in the qualified rate. It can be seen that the suitable orifice width should be in the range of 7.8 to 8.4 mm, at which point the qualified rate of seed-filling process is around 80%.

The experimental results of the influence of orifice width on seed filling performance, are shown in Figure 12(b). They reveal that with the increase in the orifice deflection angle, the qualified rate of seed-filling process initially increases and then decreases. The miss-seeding rate initially rises slowly and then increases rapidly, and the reseeding rate initially decreases rapidly and then decreases slowly. When the orifice deflection angle is too small, the internal seed-filling space of the orifice is relatively large, making it easier for multiple rice seed particles to lie flat on the slope inside the type hole, resulting in a low miss-seeding rate and a high reseeding rate. As the orifice deflection angle gradually increases, the internal seed-filling space of the orifice decreases, causing a slow increase in the miss-seeding rate, a substantial increase in the qualified rate, and a significant

decrease in the reseeding rate. When the orifice deflection angle becomes too large, the internal seed-filling space of the orifice is too small, and only a few rice seed particles enter the orifice, leading to a rapid increase in the miss-seeding rate, a certain decrease in the reseeding rate, and a noticeable decrease in the qualified rate. It can be seen that the suitable orifice deflection angle should be around 1.71 to 2.41 degrees, at which point the qualified rate of seed-filling process is approximately 75%.

Results and analysis of bench experiment of seeding performance

The results of the bench experiment are presented in Table 4.

Table 4

Experiment program and results of bench experiment

Experiment codes	Experiment factors		Evaluation indicators		
	X_1	X_2	M%	Q%	R%
1	7.9	1.81	4.8	78.4	16.8
2	8.3	1.81	2.2	77.6	20.2
3	7.9	2.31	6.2	81.8	12.0
4	8.3	2.31	5.2	75.6	19.2
5	7.8	2.06	6.0	83.6	10.4
6	8.4	2.06	2.4	76.4	21.2
7	8.1	1.71	1.8	78.8	19.4
8	8.1	2.41	6.2	80.2	13.6
9	8.1	2.06	4	83.4	12.6
10	8.1	2.06	4.3	84.2	11.5
11	8.1	2.06	4.4	84.0	11.6
12	8.1	2.06	4.8	85.2	10.0
13	8.1	2.06	4.2	84.6	11.2
14	8.1	2.06	4.2	84	11.8

Table 5

ANOVA table of bench test result

Source of Variance	M%				Q%				R%			
	SS	df	F	P	SS	df	F	P	SS	df	F	P
Model	24.23	5	24.83	**	137.99	5	31.09	**	203.22	5	37.35	**
X_1	9.44	1	48.37	**	36.90	1	41.57	**	83.68	1	76.89	**
X_2	14.10	1	72.26	**	1.43	1	1.61		24.51	1	22.52	**
X_1X_2	0.64	1	3.28		7.29	1	8.21		3.61	1	3.32	
X_1^2	0.03	1	0.17		44.93	1	50.62	**	42.54	1	39.08	**
X_2^2	0.00	1	0.04		54.50	1	61.40	**	55.85	1	51.31	**
Residual	1.59	8			7.10	8			8.71	8		
Lack of Fit	1.19	3	5.40	0.05	5.23	3	4.65	0.07	5.07	3	2.33	0.19
Error	0.40.	5			1.87	5			3.64	5		
Total	25.82	13			145.09	13			211.93	13		

Using Design-Expert 12 software, a regression analysis was conducted on the experimental data in Table 4 to establish quadratic regression models for the variables of miss-seeding rate, qualified rate, and reseeding rate with respect to orifice width and orifice deflection angle. The regression equations are as follows.

$$\begin{cases} M = 4.32 - 1.09A + 1.33B + 0.40AB + 0.06A^2 - 0.03B^2 \\ Q = 84.23 - 2.15A + 0.42B - 1.35AB - 2.47A^2 - 2.72B^2 \\ R = 11.45 + 3.23A - 1.75B + 0.95AB + 2.40A^2 + 2.75B^2 \end{cases} \quad (6)$$

The analysis of variance results for the experimental data in Table 4 are shown in Table 5. According to Table 5, the regression model for miss-seeding rate is significant, while the models for qualified rate and reseeding rate are highly significant. This indicates the effectiveness of the regression models for each performance evaluation indicators. The lack-of-fit terms for all regression models are not significant ($P > 0.05$), which means that there is no significant curvature lack of fit in the models. Furthermore, the determination coefficients (R^2) for each regression model are respectively 0.94, 0.95, and 0.96, which indicates that the regression model equations are highly reliable, showing a strong correlation between model predicted values and actual values. It implies that the experimental design is reasonable, and the model equations can be used for analysis and prediction of seeding performance.

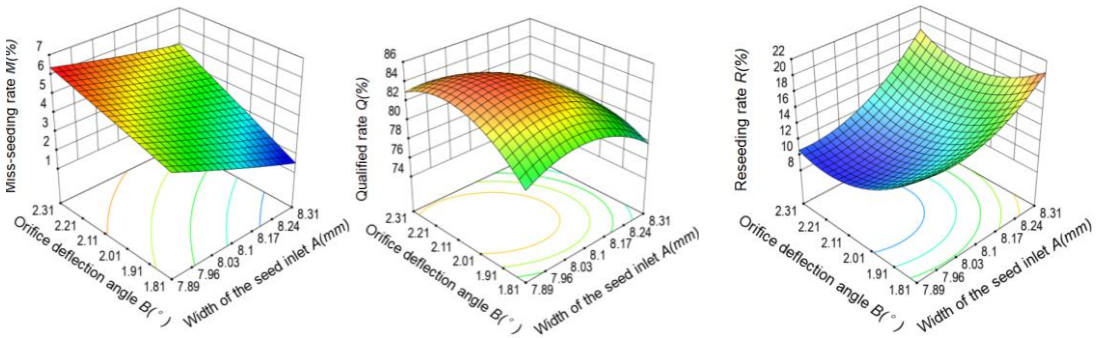

(a) Miss-seeding rate (b) Qualified rate (c) Reseeding rate

Fig. 14 - Influence of inlet width and hole deflection angle on test evaluation index

The response surface plots showing the influence of experimental factors on each evaluation indicators are presented in Figure 14. From Figure 14(a), it can be observed that when the orifice deflection angle is held constant, the miss-seeding rate decreases as the orifice width increases. Conversely, when the orifice width is held constant, the miss-seeding rate increases with the orifice deflection angle.

In Figure 14(b), it's evident that as both the orifice width and orifice deflection angle increase, the qualified rate initially rises and then declines. However, the variation in the qualified rate is more pronounced with changes in the orifice deflection angle, while changes in orifice width have a more moderate effect. This aligns with the variance analysis results, indicating that the orifice width significantly affects the qualified rate, while the influence of the orifice deflection angle is not significant. Figure 14(c) illustrates that when the orifice deflection angle is held constant, the reseeding rate first remains relatively stable and then increases rapidly as the orifice width widens. When the orifice width is constant, the reseeding rate first initially decreases and then rises with an increase in the orifice deflection angle.

Considering the changing trends of the evaluation indicators in Figure 14, it is necessary to carefully select the reasonable orifice width and orifice deflection angle to achieve a higher qualified rate and lower miss-seeding and reseeding rates.

Optimal combination of structure parameters

To obtain the optimal combination of structural parameters for the seed-filling component, achieving high qualified rate and low miss-seeding rate and reseeding rate within the range of experimental parameters, a multi-objective optimization model for the experiment structure parameters is established, as shown in Eq. (7):

$$\begin{cases} \min M(A,B) \\ \max Q(A,B) \\ \min R(A,B) \\ s.t 7.8 \le A \le 8.4 \\ 1.71 \le B \le 2.41 \end{cases} \quad (7)$$

The optimization model was solved using Design-Expert 12 software, resulting in orifice width of 8.1 mm and orifice deflection angle of 1.99°. At these optimized parameters, the seed-filling component exhibits the best seeding performance, with a miss-seeding rate of 3.95%, a qualified rate of 83.90%, and a reseeding rate of 12.15%. To verify the accuracy of the optimization results obtained, the seed-filling component with the optimized structural parameters was manufactured and subjected to bench experiments. In the unilateral seeding experiments, the results showed a miss-seeding rate of 4%, a qualified rate of 84.8%, and a reseeding rate of 11.2%. The errors in the corresponding evaluation criteria compared to the optimization results were all lower than 1%. This indicates that the validation experiment results align closely with the model predictions, further confirming the reliability of the regression model. The validation results also demonstrate that the seed-filling component with the optimized structural parameters, meets the seeding quantity requirements for hybrid rice precision direct-seeding with film mulching on unilateral seed filling process.

To meet the seeding quantity requirements for conventional rice precision direct-seeding with film mulching, the seed-filling component with the optimal structural parameters was used to conduct bilateral seeding bench experiments. The results showed a miss-seeding rate of 4.2%, a qualified rate of 85.2%, and a reseeding rate of 10.6%, which were similar to the seeding performance observed during bilateral seeding with the seed-filling component. This confirms that the designed approach of switching between bilateral and unilateral seeding to accommodate different varieties and seeding quantity is feasible.

Field experiment results

The results of field experiment are shown in Figure 15.

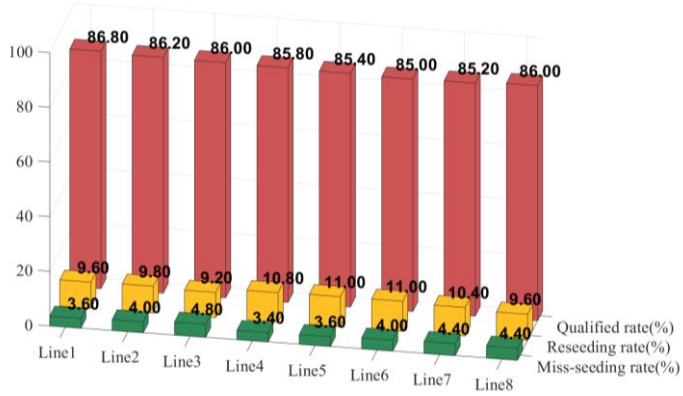

Fig. 15 - Field experiment performance test results

From Figure 15, it can be observed that the average qualified rate of each row for the field with hole seeder is 85.8%, the average miss-seeding rate is 4.03%, and the average reseeding rate is 10.17%. This indicates that the seed-filling component, which has the capability for bilateral seeding, can achieve stable seeding performance in the field and meet the seeding quantity requirements for rice precision direct-seeding with film mulching. However, in comparison to the results obtained from the beach seeding experiment, the field experiment shows a slightly lower miss-seeding rate and a slightly higher qualified rate. The reason for this difference could be attributed to the vibrations and bumps experienced by the field seeding equipment, which help seeds and the seed-filling component to exhibit relative sliding motion in the rotational direction, improving seeding performance, resulting in a reduction in miss-seeding rates, and an increase in the qualified rates. The field seeding scenario is shown in Figure 16.

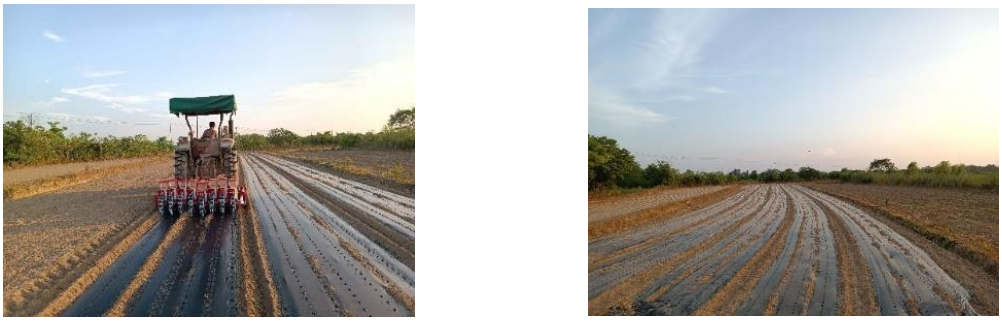

(a) Work scenario *(b) Sowing effect with biodegradable film mulching*

Fig. 16 - Field seeding experiment

CONCLUSIONS

(1) To meet the seeding quantity requirements for both hybrid rice and conventional rice, a seed-filling component with both unilateral and bilateral seeding capabilities was designed. The paper analyzed the key structural parameters of the seed-filling component based on the external characteristics of rice seeds and the quantitative seed filling method of the seed-filling component. It used DEM (Discrete Element Method) to simulate the seed-filling process of hole seeder. Single factor simulation experiment was conducted to investigate the effects of the orifice width and orifice deflection angle on the seed-filling performance. This helped determine the appropriate range of values for the key structural parameters.

(2) Central composite design between orifice width and orifice deflection angle was conducted. By using the multi-objective optimization model, the optimal structural parameter combination was determined, which consisted of an orifice width of 8.1 mm and an orifice deflection angle of 1.99°. Under this parameter combination, the unilateral seeding with the seed-filling component achieved a miss-seeding rate of 4%, a qualified rate of 84.8%, and a reseeding rate of 11.2% for hybrid rice. For conventional rice, the bilateral seeding experiments resulted in a miss-seeding rate of 4.2%, a qualified rate of 85.2%, and a reseeding rate of 10.6%, all meeting the seeding quantity requirements for rice direct-seeding with film mulching. Field seeding experiment demonstrated that the hole seeder equipped with seed-filling component had stable seeding performance.

ACKNOWLEDGEMENT

This work was supported by the National Natural Science Foundation of China, China (Grant numbers 51805005), Major Project of Natural Science Research in Universities of Anhui Province (Grant numbers KJ2021ZD0012), Key research and Development Project of Anhui Province (Grant numbers 202204c06020024) and Key programs of outstanding young talents in universities (Grant numbers gxyqZD2022016)

REFERENCES

Ghosh, D., Singh, U. P., Brahmachari, K., Singh, N. K., & Das, A. (2017). An integrated approach to weed management practices in direct-seeded rice under zero-tilled rice–wheat cropping system. *International Journal of Pest Management*, *63*(1), 37–46. https://doi.org/10.1080/09670874.2016.1213460

Guan, Z.-H., Wang, L., Turner, N. C., & Li, X. G. (2022). Plastic-film mulch affects partitioning of maize biomass and nutrients to grain. *Crop Science*, *62*(1), 315–325. https://doi.org/10.1002/csc2.20677

Hadden, D., & Grelle, A. (2016). Changing temperature response of respiration turns boreal forest from carbon sink into carbon source. *Agricultural and Forest Meteorology*, *223*, 30–38. https://doi.org/10.1016/j.agrformet.2016.03.020

He, H., Ma, F., Yang, R., Chen, L., Jia, B., Cui, J., Fan, H., Wang, X., & Li, L. (2013). Rice Performance and Water Use Efficiency under Plastic Mulching with Drip Irrigation. *PLoS ONE*, *8*(12), e83103. https://doi.org/10.1371/journal.pone.0083103

Jun, L., Dequan, Z., Qilei, T., Congyang, Y., Tingjue, W., Kang, X., Shun, Z., & Juan, L. (2021). Design and experiment of adjustable socket-wheel precision fertilizer apparatus for dry direct-seeding rice. *INMATEH-Agricultural Engineering*, *63*(1). https://doi.org/10.356.33/inmateh-63-12

Kakumanu, K. R., Kotapati, G. R., Nagothu, U. S., Kuppanan, P., & Kallam, S. R. (2018). Adaptation to climate change and variability: A case of direct seeded rice in Andhra Pradesh, India. *Journal of Water and Climate Change*, *10*(2), 419–430. https://doi.org/10.2166/wcc.2018.141

Li, H., Zeng, S., Luo, X., Fang, L., Liang, Z., & Yang, W. (2021). Design, DEM Simulation, and Field Experiments of a Novel Precision Seeder for Dry Direct-Seeded Rice with Film Mulching. *Agriculture*, *11*(5), 378. https://doi.org/10.3390/agriculture11050378

Li, H., Zeng, S., Luo, X. W., Zang, Y., Liang, Z. H., Li, X. L., Teng, S. Z., & Yang, W. W. (2020). Effects of degradable mulching film on soil temperature, seed germination and seedling growth of direct-seeded rice (ORYZA SATIVA L.). *Applied Ecology and Environmental Research*, *18*(6), 8233–8249. https://doi.org/10.15666/aeer/1806_82338249

Li Y., & Xu Y. (2005). Discrete Element Simulation on Particle Piling. *Journal of Agricultural Mechanization Research*, *2*, 57–59.

Liu, H., Hussain, S., Zheng, M., Peng, S., Huang, J., Cui, K., & Nie, L. (2015). Dry direct-seeded rice as an alternative to transplanted-flooded rice in Central China. *Agronomy for Sustainable Development*, *35*(1), 285–294. https://doi.org/10.1007/s13593-014-0239-0

Liu H., Su H., Li J., & Liu Z. (2019). Interactive Optimal Design System of Drum-type No-till Planter Mechanism. *Transactions of the Chinese Society for Agricultural Machinery*, *50*(3), 58–68.

Liu H., Wen H., Gai G., & Tang S. (2017). Design and Experiment on Passive Drum-type No-till Planter Cavitation Mechanism. *Transactions of the Chinese Society for Agricultural Machinery*, *48*(9), 53–61.

Niu Q., Wang S., & Chen X. (2016). Design of Rice Planter with Plastic Film Mulched Drip Irrigation. *Transactions of the Chinese Society for Agricultural Machinery*, *47*(S1), 90-95+102.

Sandhu, N., Subedi, S. R., Singh, V. K., Sinha, P., Kumar, S., Singh, S. P., Ghimire, S. K., Pandey, M., Yadaw, R. B., Varshney, R. K., & Kumar, A. (2019). Deciphering the genetic basis of root morphology, nutrient uptake, yield, and yield-related traits in rice under dry direct-seeded cultivation systems. *Scientific Reports*, *9*(1), Article 1. https://doi.org/10.1038/s41598-019-45770-3

Singh, M., Bhullar, M. S., & Chauhan, B. S. (2015). Influence of tillage, cover cropping, and herbicides on weeds and productivity of dry direct-seeded rice. *Soil and Tillage Research*, *147*, 39–49. https://doi.org/10.1016/j.agwat.2019.02.004

Tao, Y., Chen, Q., Peng, S., Wang, W., & Nie, L. (2016). Lower global warming potential and higher yield of wet direct-seeded rice in Central China. *Agronomy for Sustainable Development*, *36*(2), 24. https://doi.org/10.1007/s13593-016-0361-2

Yang, X., Liu, H., Mao, X., Deng, J., & Haefele, S. M. (2020). Non-flooding rice yield response to straw biochar and controlled-release fertilizer. *Agronomy Journal*, *112*(6), 4799–4809.

https://doi.org/10.1002/agj2.20430

Yin, M., Li, Y., Fang, H., & Chen, P. (2019). Biodegradable mulching film with an optimum degradation rate improves soil environment and enhances maize growth. *Agricultural Water Management*, *216*, 127–137. https://doi.org/10.1016/j.agwat.2019.02.004

Zhang S., Li Y., Wang H., Liao J., Li Z., & Zhu D. (2020). Design and Experiment of U-shaped Cavity Type Precision Hill-drop Seed-metering Device for rice. *Transactions of the Chinese Society for Agricultural Machinery*, *51*(10), 98–108.

Zhang, S., Tekeste, M. Z., Li, Y., Gaul, A., Zhu, D., & Liao, J. (2020). Scaled-up rice grain modelling for DEM calibration and the validation of hopper flow. *Biosystems Engineering*, *194*, 196–212. https://doi.org/10.1016/j.biosystemseng.2020.03.018

*** *World Food and Agriculture – Statistical Yearbook 2021.* (2021). *FAO.* https://doi.org/10.4060/cb4477en

*** *NT/Y 987—2006. (2006). Standard for operating quality of hill-drop drill with film mulching* (铺膜穴播机行业标准). National Standard of the People's Republic of China. (in Chinese)

NUMERICAL SIMULATION OF THE INFLUENCE OF SOME GEOMETRIC PARAMETERS ON THE DECONTAMINATION QUALITY OF A NON-LAMBERTIAN TYPE DETECTOR, USING A UV-C LEDs MATRIX
/
SIMULARE NUMERICĂ A INFLUENȚEI UNOR PARAMETRI GEOMETRICI ASUPRA CALITATII DECONTAMINARII UNUI RECEPTOR DE TIP NON-LAMBERTIAN, UTILIZAND O MATRICE DE LED-uri UV-C

Cristian SORICĂ[1)], Mario CRISTEA[1*)], Valentin VLĂDUȚ[1)]
[1)]INMA Bucharest, No. 6 Ion Ionescu de la Brad Blvd., Bucharest, Romania
**E-mail*: *mario.cristea@gmail.com*
DOI: https://doi.org/10.35633/inmateh-72-70

Keywords: *ultraviolet radiation UV-C, decontamination, UV-C LED, radiation intensity, UV-C dose*

ABSTRACT
The ultraviolet (UV) irradiation has been studied and used in the recent decades as a mean to inactivate various potentially harmful microorganisms, being considered an effective treatment that could limit or even avoid the use of chemical disinfectants. Within the wavelength spectrum of UV radiation, the UV-C radiation wavelength ranging between 200 and 280 nm is considered lethal to most types of microorganisms. In this paper it was studied the variation of the distribution of radiation's intensity generated by a matrix of 25 UV-C LEDs (5 x 5), (assimilated to the LED panel above a stationary conveyor), on a spherical surface (assimilated to a berry) positioned in reprezentative locations below the matrix. A fruit located under the irradiation matrix receives the strongest radiation from the LED located at the smallest distance from it, but is influenced, as a result of the superposition principle, to a lesser extent by the other LEDs within the network. It has been found that for a too small distance between the matrix of LEDs and the conveyor, the radiation dose is uneven on the surface of fruit, and by increasing this distance a radiation distribution much more uniform is obtained, but at the expense of a decrease in its intensity and an increase in the time required for irradiation, implicitly leading to an increase in operating costs. In conclusion, for the most efficient operation of the equipment, a compromise solution must be chosen.

REZUMAT
Radiatia ultravioletă (UV) a fost studiată și utilizată în ultimele decenii ca mijloc de inactivare a diferitelor microorganisme potențial dăunătoare, fiind considerată un tratament eficient care ar putea limita sau chiar evita utilizarea dezinfectanților chimici. În spectrul radiației UV, lungimea de undă a radiației UV-C cuprinsă între 200 și 280 nm este considerată letală pentru majoritatea tipurilor de microorganisme. In aceasta lucrare a fost studiata variația distribuției intensității radiației generate de o matrice de 25 LED-uri UV-C (5 x 5), (asimilate unui panou LED pozitionat deasupra unui transportor in repaos), pe o suprafață sferică (asimilată unui fruct de pădure) poziționata în locații reprezentative sub matrice. Un fruct situat sub matricea de iradiere primește cea mai puternică radiație de la LED-ul situat la cea mai mică distanță de acesta, dar este influențat, ca urmare a principiului superpozitiei, într-o măsură mai mică de celelalte LED-uri din cadrul rețelei. S-a constatat că pentru o distanță prea mică între matricea LED-urilor și transportor, doza de radiație este neuniformă pe suprafața fructelor, iar prin creșterea acestei distanțe obținem într-adevăr o distribuție a radiației mult mai uniformă, dar cu prețul scăderii intensității acesteia și creșterii timpului necesar iradierii, conducând implicit la o creștere a costurilor de exploatare. In concluzie, pentru functionarea cat mai eficienta a echipamentului trebuie aleasa o solutie de compromis.

INTRODUCTION

The ultraviolet (UV) irradiation has been studied and used in the recent decades as a mean to inactivate various potentially harmful microorganisms, being considered an effective treatment that could limit or even avoid the use of chemical disinfectants (*Romero-Martínez et al., 2022*). Within the wavelength spectrum of UV radiation, the UV-C radiation wavelength ranging between 200 and 280 nm is considered lethal to most types of microorganisms, affecting the DNA replication of these microorganisms, causing breaks of molecular chemical bonds and inducing photochemical reactions that, ultimately, lead to their inactivation.

For this reason, the non-ionizing ultraviolet radiation UV-C is used as an alternative to chemical sterilization and microbial reduction in food products and has been approved for use as a disinfectant for surface treatment of food *(US-FDA, 2002*).

UV-C is already used successfully in various fields, such as medicine, ecology, postharvest technologies etc., alone (*Rodgers et al., 2023; Calle et al., 2023; Meneses-Espinosa et al., 2023; Ruetalo et al., 2022; Yemmireddy et al., 2022; Iturralde-García et al. 2022; Cruz Mendoza et al., 2022; Berruti et al., 2021; Sorică et al., 2021*), or in combination with other methods (e.g. the use of ozone) (*Sottani et al., 2023; Dogu-Baykut et al., 2022; Martínez de Alba et al., 2021; Frigerio et al., 2021; Gutiérrez et al., 2017*).

Within the food industry, ultraviolet radiation is mainly used for disinfecting surfaces and air, complementing the cleaning measures within production facilities and storage rooms, to avoid the spread of harmful microorganisms such a wide range of viral and bacterial pathogens. As a postharvest treatment of fresh produce, UV-C irradiation has been proven beneficial to reduce respiration rates, control rot development, and delay senescence and ripening in different whole or fresh-cut fruits and vegetables, such as apples, citrus, peaches, watermelon, grape berries, tomatoes, lettuce, baby spinach and mushrooms (*de Capdeville et al., 2002; Lamikanra et al., 2005; Allende et al., 2008; Artés-Hernández et al., 2010; Escalona et al., 2010; Jiang et al., 2010; Fava et al., 2011; Manzocco et al., 2011*). Furthermore, UV-C has also been shown to elicit a range of biochemical responses in fresh produce ranging from induction of antifungal enzymes to formation of phytoalexin compounds (*Guan et al., 2012*), elements which have been positively correlated with resistance against several pathogens and reduction of physiological disorders occurring during cold storage of fruits and vegetables (*Rivera-Pastrana et al., 2007*). Another advantage of applying UV-C is the capability to improve nutraceutical properties, due to an increase of bioactive compounds with antioxidant capacity.

UV-C is almost nonexistent in nature, because it is completely absorbed in the atmosphere. Artificial sources of UV-C light are produced, mainly, by the lamps of low pressure or high / medium pressure and, more recently, light emitting diodes - LEDs. Low pressure lamps produce, essentially, monochromatic light at a wavelength of 253.7 nm, very close to the peak of germicidal efficiency, respectively 264 nm. Medium pressure lamps produce a polychromatic light on a broader spectrum. UV-C LEDs emit monochromatic light at different wavelengths between 265 nm and 285 nm. Most effective and narrow targeted on the peak of germicidal wavelength seem to be the low pressure lamps and UV-C LEDs, both emitting, almost entirely, monochromatic radiation. Although the two technologies have gained interrest for its germicidal applications, there are some differencies that bring along various advantages and disadvantages for the use of one or another. Even if the low pressure lamps have high output power for germicidal radiation, they demonstrate several disadvantages such as the necessity of warming up, low energetic efficiency and relatively short lifetime. On the other hand, UV-C LEDs show several benefits regarding the traditional UV lamps such as less electric consumption, no necessity of a warming up period, longer lifetime, greater flexibility in the wavelengths of emission and greater possibilities for configuration within the working space, yet having a low output power, emitting in very narrow wavelengths, having low energy efficiency and high directionality (*Romero-Martínez et al., 2022*).

In order to estimate the technical conditions in which an equipment can apply a certain dose of UV-C, either in a design stage or when evaluating its performance, it is necessary to know the intensity of the radiation and the time of its application in different key points, representative for the working process of the respective equipment. This already implies the knowledge of the type, technical characteristics, dimensions and layout geometry of the UV-C generators within the working space, as well as their positioning in relation to the targeted points.

There are studies that aimed to develop or numerically simulate mathematical models designed for estimating the distribution of UV-C radiation's intensity in the vicinity of a radiation source, be it a linear or point source. The most important mathematical models developed for a linear UV-C radiation source are represented by the Keitz (*Keitz, 1971*), Modest (*Modest, 1993*) or Beggs (*Beggs et al., 2000*) models, which generate quite similar results both in the immediate vicinity of the radiation source and at the distance. For a point source of radiation, the model presented by Keitz is representative, based on the inverse square law of Lambert.

In this paper it is proposed to study, through numerical simulation, the variation of the distribution of radiation's intensity generated by a matrix of UV-C LEDs (assimilated to the LED panel above a stationary conveyor), on a spherical surface (assimilated to a berry) positioned in reprezentative locations below the matrix.

MATERIALS AND METHODS

Before studying the variation of the distribution of UV-C radiation's intensity on the surface of the berries, some simplifying hypothesis were made:

- The fruits are considered to have a perfectly spherical shape;
- All fruits are the same size;
- The advance of the fruits on the conveyor is carried out without any rolling movement;
- The fruit distribution is perfectly uniform over the entire surface of the conveyor.

In the first part of the study, a comparison was made between the radiation dose received by a fruit located in the most disadvantageous position, i.e. in one of the corners (fig. 1) and in the most advantageous position from this point of view, the one located in the center (fig. 2). To simplify the calculations, it is considered that the equipment consists of a matrix of only 25 LEDs (5 x 5), located at a distance "l" between them on the two axes and at a height "h" from the conveyor.

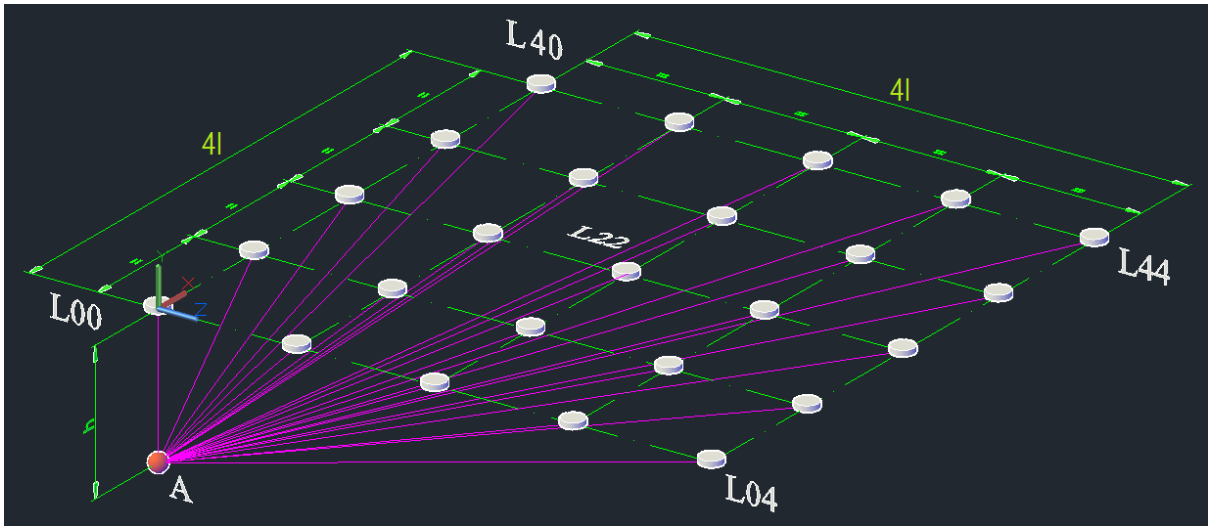

Fig. 1 - Visualization of the radiation reaching fruit "A", located below a corner of the LED array

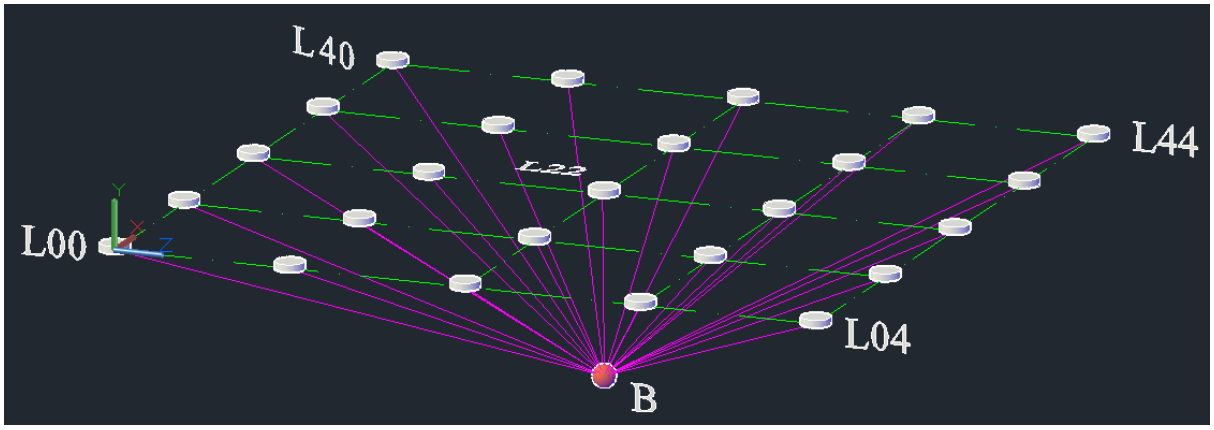

Fig. 2 - Visualization of the radiation reaching fruit "B", located below the center of the LED array

A fruit located under the irradiation matrix receives the strongest radiation from the LED located at the smallest distance from it, but is influenced, as a result of the superposition principle, to a lesser extent by the other LEDs within the network.

According to the inverse square law, the intensity of radiation "E" equals the incident luminous flux "Φ" divided by the area "S" (fig. 3) (the units of measure are adapted for the usual practice of UV-C radiation):

$$E = \frac{\emptyset}{S} = \frac{\omega \cdot I}{\omega \cdot r^2} = \frac{I}{r^2} \quad [W \cdot m^{-2}] \tag{1}$$

where: Φ is the incident luminous flux, [W];

S – the area receiving the incident luminous flux, [m^2];

ω – the solid angle [sr];

I – the luminous intensity in all directions within a solid angle, [W];

r – the radius of a sphere with L as centre, [m].

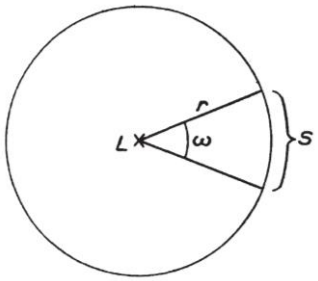

Fig. 3 - Derivation of the inverse square law (*Keitz, 1971*)

If it is imagined that the surface diminished in size to a mere point, it results that the illumination at a point in a plane perpendicular to the line joining the point and the source (the intensity of radiation "E") is equal to the luminous intensity of the source in the direction of the point, divided by the square of the distance between point and source (*Keitz, 1971*). This way the equation (1) becomes:

$$E = \frac{I}{d^2} \quad [W \cdot m^{-2}] \tag{2}$$

where: I – is the luminous intensity of the source in the direction of the point, [W];

d – is the distance between point and source, [m].

When the radiation from a source "L" falls at a point "P" on a plane "V" at an angle "α" to the normal at "P", the illumination of the plane "V" at point "P" obeys the Lambert's cosine law stating that the illumination at that point is directly proportional to the cosine of the angle "α" between the direction of incident radiation and normal to the plane in that point (fig. 4).

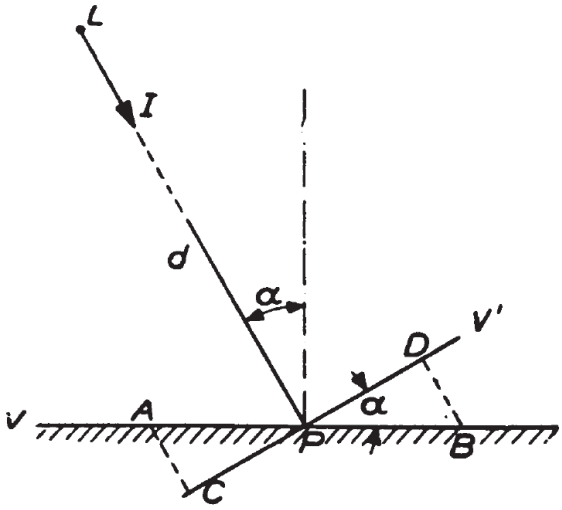

Fig. 4 - Cosine law for the illumination with oblique incidence (*Keitz, 1971*)

Using equation (2), it results:

$$E = E' \cdot \cos\alpha = \frac{I}{d^2} \cdot cos\alpha \quad [W \cdot m^{-2}] \tag{3}$$

where:

E' is the intensity of radiation at point "P" that is contained within the plane " V' " perpendicular to the line joining the point "P" and the source "L";

I and d have the significance previously described at equation (2);

α – the angle between the direction of incident radiation and normal to the plane in that point, [°].

Due to the fact that, from the initial simplifying hypothesis, the detector (the berry) is considered to has a perfectly spherical shape and not a planar surface (is a non-Lambertian detector), the cosine law does not apply to it. A fruit of radius "R" whose center is at a distance "h" from the radiation source is considered. The irradiated surface is the surface area of the spherical cap in figure 5.

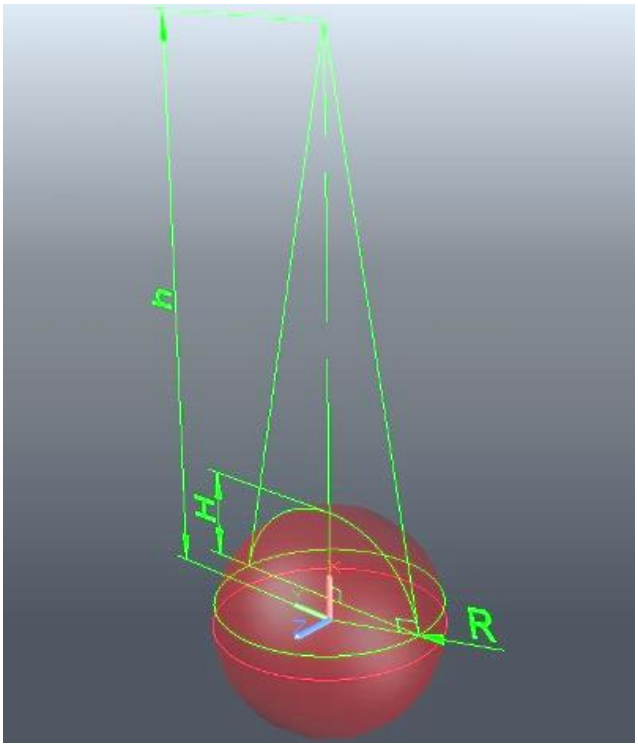

Fig. 5 - The elements that enter into the calculation of the surface area of the spherical cap

The area of the spherical cap is calculated using the relation:

$$A = 2 \cdot \pi \cdot R \cdot H \quad [m^2] \tag{4}$$

where: R is the radius of the fruit subjected to decontamination, [m];

H - the height of the spherical cap, [m].

Knowing that within the representation in figure 5, the two segments that join the radiation source and the surface of the fruit, symmetrical to the central vertical axis, are tangent to the respective surface in the two marginal points which define the chord that delimits the respective spherical cap, by expressing the half of the chord using the Pythagorean Theorem and the Theorem of the height in the right-angle triangles formed, followed by the equality of the two mathematical relations, is obtained the formula of the area depending on "h" and "R":

$$A = \frac{2 \cdot \pi \cdot R^2 (h-R)}{h} \quad [\, m^2] \tag{5}$$

Further, the dose of the absorbed radiation is defined as the intensity of radiation "E" multiplied by time "t":

$$D = E \cdot t \quad [W \cdot s \cdot m^{-2}] \tag{6}$$

where: E is the intensity of UV-C radiation within a certain point, $[W \cdot m^{-2}]$;

t – the time that this radiation intensity is applied, [s].

Knowing that the dose of the absorbed radiation is directly proportional to the intensity of radiation "E', which is inversely proportional to the square of the distance from the source, it will be determined how important the radiation received from other LEDs besides the one located exactly above the fruit is. The fruit "A", respectively fruit "B", will simultaneously accumulate several doses of irradiation starting from the strongest, due to LED "L00", respectively LED "L22", to the weakest due to LED "L44", respectively LED "L00", "L04", "L40" and "L44".

The following aspects were followed:

- The variation of the influence of each LED in the matrix on the irradiation dose to which the fruit in position "*A*", respectively "*B*", is subjected;
- The influence of the variation of the distance "h" between the matrix of LEDs and the conveyor on the distribution density of UV-C radiation;
- The variation of the irradiated surface depending on the size of the fruit and its distance from the radiation source.

RESULTS

The inverse of the square of the distances between the radiation sources and the fruit "A", respectively fruit "B" is simply calculated from the formed triangles, using the Pythagorean theorem and the data can be visualized in the following type of matrix.

$$L_A := \begin{bmatrix} \frac{1}{h^2} & \frac{1}{(1^2+h^2)} & \frac{1}{(41^2+h^2)} & \frac{1}{(91^2+h^2)} & \frac{1}{(161^2+h^2)} \\ \frac{1}{(1^2+h^2)} & \frac{1}{(21^2+h^2)} & \frac{1}{(51^2+h^2)} & \frac{1}{(101^2+h^2)} & \frac{1}{(171^2+h^2)} \\ \frac{1}{(41^2+h^2)} & \frac{1}{(51^2+h^2)} & \frac{1}{(81^2+h^2)} & \frac{1}{(131^2+h^2)} & \frac{1}{(201^2+h^2)} \\ \frac{1}{(91^2+h^2)} & \frac{1}{(101^2+h^2)} & \frac{1}{(131^2+h^2)} & \frac{1}{(181^2+h^2)} & \frac{1}{(251^2+h^2)} \\ \frac{1}{(161^2+h^2)} & \frac{1}{(171^2+h^2)} & \frac{1}{(201^2+h^2)} & \frac{1}{(251^2+h^2)} & \frac{1}{(321^2+h^2)} \end{bmatrix}$$

Fig. 6 - The matrix containing the inverse of the squares of the distances between the radiation sources and the fruit "A"

The calculation and graphics were performed using MathCAD software. The graphic based on this matrix gives us information on the influence that each LED in the network has on the irradiation dose to which the fruit is subjected (fig.7). Being a qualitative reprezentation, the calculation was simplified further by choosing conveniently the radiation intensity "I", the distance between LEDs "l", the height of LEDs matrix "h" compared to the fruits and the time "t" how long the radiation intensity is applied. All these parameters were considered equal to one unit of each.

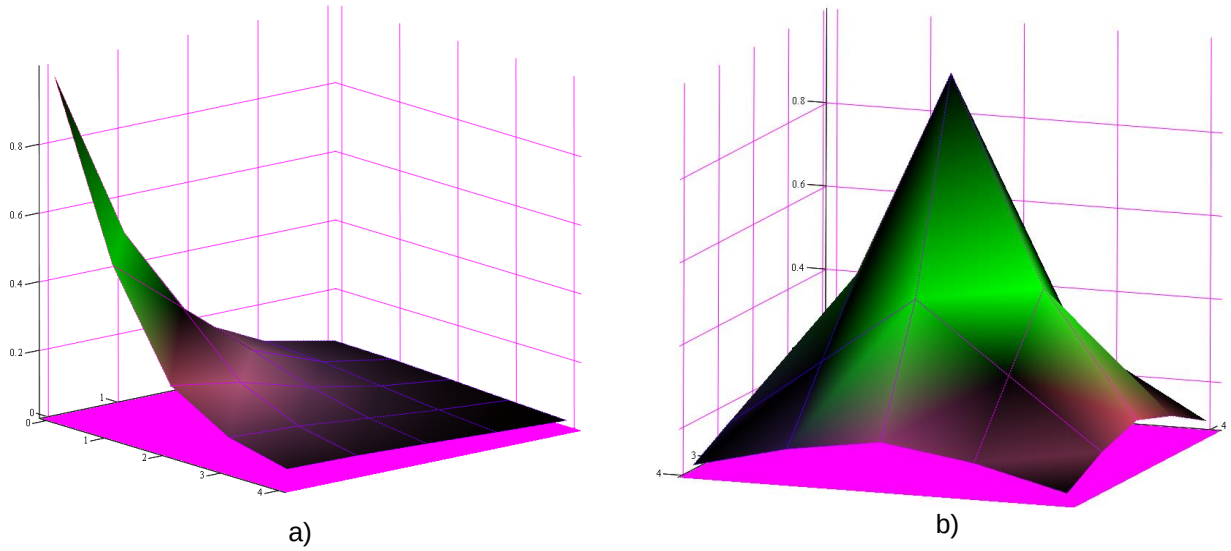

a) b)

Fig. 7 - The influence of each LED in the network on the irradiation dose to which the fruit is subjected: a) - in position "A"; b) - position "B"

From the graph (fig.7a) it can be seen that only the LEDs located in the immediate vicinity of "L00" significantly influence the level of radiation received by fruit "A", the LEDs located at a distance of "2l" have a influence of only 20% of the radiation due to "L00". From the graph in fig. 7b, it can be seen that the influence of the radiation received from the entire LED network on fruit B, located in the center, is more pronounced than in the first case. In order to study the influence of the distance "h" at which the LED matrix is located above the conveyor, on the uniformity of the radiation received by the fruits, a 2-fold reduction of the unit distance and then a 2-fold increase were taken into account. The resulting graphs are presented in fig. 8.

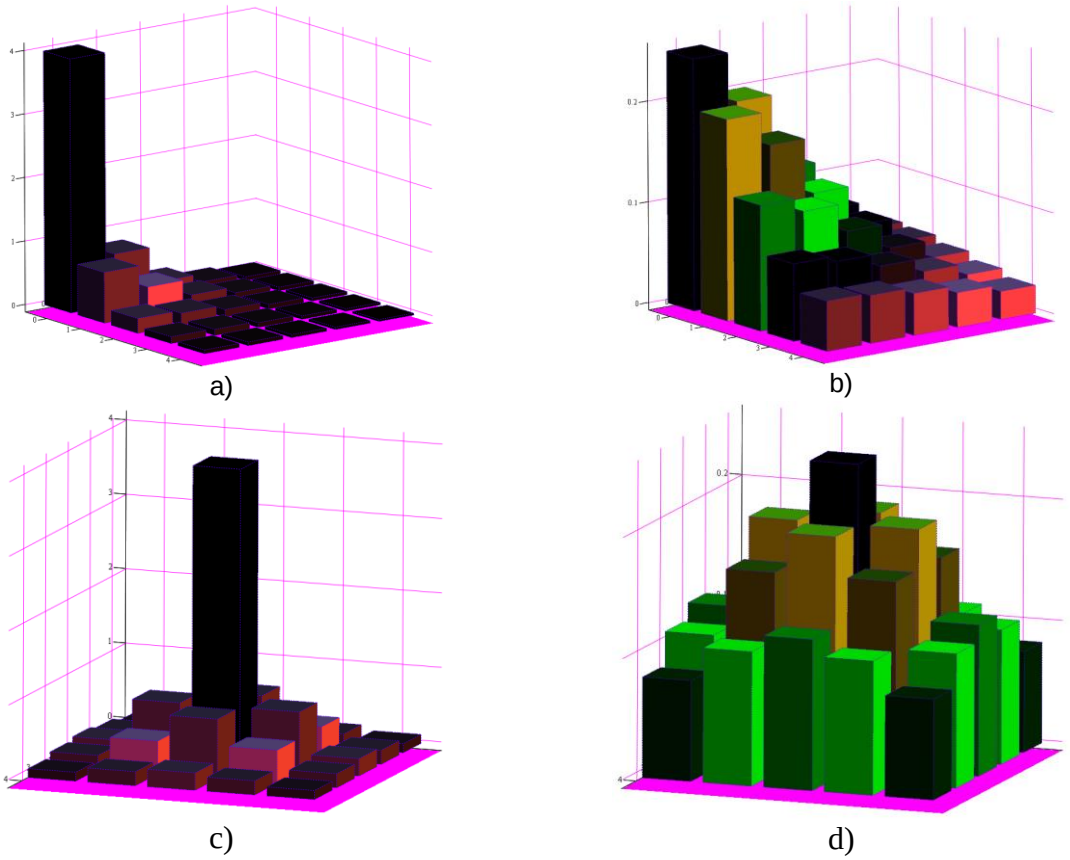

Fig. 8 - The influence of the variation of the distance "h" between the matrix of LEDs and the conveyor on the distribution density of UV-C radiation:
a) and c) – at the 2-fold reduction of the unit distance; b) and d) – at the 2-fold increase of the unit distance

From the graphs in fig. 8 it can be seen that the reduction of the distance "h" between the LED array and the conveyor leads to a reduction in the influence of the radiation coming from the adjacent LEDs, while an increase of this distance will lead to a much more uniform distribution of the radiation on the entire surface of the conveyor.

In the design stage of a fruit decontamination equipment using UV-C radiation, it must be taken into account that for a distance "h" that is too small, the radiation dose is uneven on the surface of fruit, and by increasing this distance a radiation distribution much more uniform is obtained, but at the expense of a decrease in its intensity and an increase in the time required for irradiation, implicitly leading to an increase in operating costs. In conclusion, for the most efficient operation of the equipment, a compromise solution must be chosen.

If the area A is considered a function of two variables, f(R, h), its variation can be represented graphically in a 3-dimensional space, using the MathCAD program, obtaining the graph shown in figure 9.

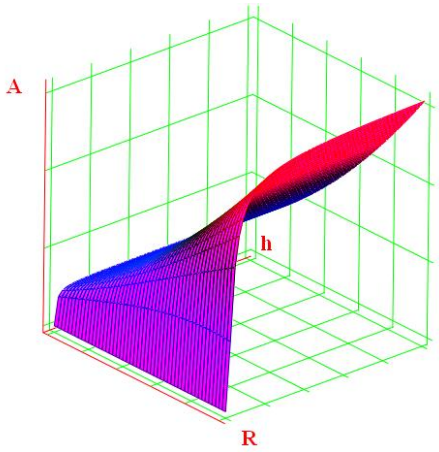

Fig. 9 - The variation of the decontaminated area of the fruit depending on its radius and the distance from UV-C source

For this study the variation of radius "R" was considered between 4 and 10 mm (blueberry) and the distance "h" was choosen between " R " and 500 mm. At the limit, the surface subjected to decontamination varied between 0 and $2\pi R^2$ (respectively half the surface of the sphere), as the distance "h" from the LEDs matrix, varies between "R" and "∞".

$$\lim_{h \to R} \frac{2 \cdot \pi \cdot R^2 \cdot (h-R)}{h} \to 0 \quad (7)$$

$$\lim_{h \to \infty} \frac{2 \cdot \pi \cdot R^2 \cdot (h-R)}{h} \to 2 \cdot \pi \cdot R^2 \quad (8)$$

A conclusion that emerges from the previously presented is that increasing the height "h" will cause an increase in the irradiated surface, but a decrease in the intensity of the incident radiation.

CONCLUSIONS

The paper has studied the variation of the distribution of radiation's intensity generated by a matrix of 25 UV-C LEDs (5 x 5), (assimilated to the LED panel above a stationary conveyor), on a spherical surface (assimilated to a berry) positioned in reprezentative locations below the matrix, respectively in the most disadvantageous positions and in the most advantageous ones.

The following conclusions were identified:

- only the LEDs located in the immediate vicinity of the corner significantly influence the level of radiation received by fruit "A". Also it can be seen that the influence of the radiation received from the entire LED network on fruit „B", located in the center, is more pronounced than in the first case.

- the reduction of the distance "h" between the LED array and the conveyor leads to a reduction in the influence of the radiation coming from the adjacent LEDs, while an increase of this distance will lead to a much more uniform distribution of the radiation on the entire surface of the conveyor.

- for a distance " h " that is too small, the radiation dose is uneven on the surface of fruit, and by increasing this distance a radiation distribution much more uniform is obtained, but at the expense of a decrease in its intensity and an increase in the time required for irradiation, implicitly leading to an increase in operating costs.

In conclusion, for the most efficient operation of the equipment, a compromise solution must be chosen.

ACKNOWLEDGEMENT

This work was supported by a grant of the Romanian Research and Innovation Ministry, through Programme 1 - Development of the national research-development system, sub-programme 1.2. Institutional performance - Projects for financing excellence in RDI, contract no. 1 PFE/2021.

REFERENCES

[1] Allende A., Selma M.V., López-Gálvez F., Villaescusa R., Gil M.I., (2008), Role of commercial sanitizers and washing systems on epiphytic microorganisms and sensory quality of fresh-cut escarole and lettuce, *Postharvest Biol. Technol*. 49, 155–163;

[2] Artés-Hernández F., Robles P., Gómez P., Tomás-Callejas A., Artés F., (2010), Low UV-C illumination for keeping overall quality of fresh-cut watermelon, *Postharvest Biol. Technol*. 55, 114–120;

[3] Beggs C. B., et al, (2000), An engineering approach to the control of Mycobacterium tuberculosis and other airborne pathogens: a UK hospital based pilot study, *Transactions of the royal society of tropical medicine and hygiene (2000),* 94,141-146.

[4] Berruti I., Nahim-Granados S., Abeledo-Lameiro M.J., Oller I., Polo-López M.I., (2021), UV-C peroxymonosulfate activation for wastewater regeneration: simultaneous inactivation of pathogens and degradation of contaminants of emerging concern, *Molecules*, 26, 4890, https://doi.org/10.3390/molecules26164890;

[5] Calle L. A., Castel J., Amaya M. E., Malo I. P., (2023), Development of an autonomous differential mobile robot for disinfection with a hybrid disinfection system, *20th International Conference on Ubiquitous Robots (UR)*, Honolulu, HI, USA, pp. 741-746, doi: 10.1109/UR57808.2023.10202383;

[6] Cruz Mendoza I., Ortiz Luna E., Dreher Pozo M., Villavicencio Vásquez M., Coello Montoya D., Chuchuca Moran G., Galarza Romero L., Yépez X., Salazar R., Romero-Peña M., Coronel León J.,

(2022), Conventional and non-conventional disinfection methods to prevent microbial contamination in minimally processed fruits and vegetables, *LWT*, Volume 165, ISSN 0023-6438, https://doi.org/10.1016/j.lwt.2022.113714;

[7] De Capdeville G., Wilson C.L., Beer S.V., Aist J.R., (2002), Alternative disease control agents induce resistance to blue mold in harvested 'red delicious' apple fruit, *Phytopathology* 92, 900–908;

[8] Dogu-Baykut Esra, Gunes Gurbuz, (2022), Effect of ultraviolet (UV-C) light and gaseous ozone on microbial and color qualities of whole black pepper seeds (Piper Nigrum L.), *Carpathian journal of food science and technology*, Volume14, Issue2, Page122-131, DOI10.34302/crpjfst/2022.14.2.10;

[9] Escalona V.H., Aguayo E., Martínez-Hernández G.B., Artés F., (2010), UV-C doses to reduce pathogen and spoilage bacterial growth in vitro and in baby spinach, *Postharvest Biol. Technol*. 56, 223–231;

[10] Fava J., Hodara K., Nieto A., Guerrero S., Alzamora S., Castro M., (2011), Structure (micro, ultra, nano), color and mechanical properties of Vitis labrusca L. (grape berry) fruits treated by hydrogen peroxide, UV-C irradiation and ultrasound, *Food Res. Int.* 44, 2938–2948;

[11] Frigerio F. et al. (2021), A safe and effective combination of UV and ozone, *2021 IEEE International Conference on Environment and Electrical Engineering and 2021 IEEE Industrial and Commercial Power Systems Europe (EEEIC / I&CPS Europe)*, Bari, Italy, pp. 1-5, doi: 10.1109/EEEIC/ICPSEurope51590.2021.9584830;

[12] Guan W., Fan X., Yan R., (2012), Effects of UV- treatment on inactivation of Escherichia coli O157:H7, microbial loads, and quality of button mushrooms, *Postharvest Biol. Technol*. 64, 119–125;

[13] Gutiérrez D.R., Chaves A.R., Rodríguez S.D.C., (2017), Use of UV-C and gaseous ozone as sanitizing agents for keeping the quality of fresh-cut rocket (Eruca sativa mill), *Journal of Food Processing and Preservation*, 41: e12968. https://doi.org/10.1111/jfpp.12968;

[14] Iturralde-García R.D., Cinco-Moroyoqui F.J., Martínez-Cruz O., Ruiz-Cruz S., Wong-Corral F.J., Borboa-Flores J., Cornejo-Ramírez Y.I., Bernal-Mercado A.T., Del-Toro-Sánchez C.L., (2022), Emerging technologies for prolonging fresh-cut fruits' quality and safety during storage, *Horticulturae 2022*, 8, 731. https://doi.org/10.3390/horticulturae8080731;

[15] Jiang T., Jahangir M., Jiang Z., Lu X., Ying T., (2010), Influence of UV-C treatment on antioxidant capacity, antioxidant enzyme activity and texture of postharvest shiitake (Lentinus edodes) mushrooms during storage, *Postharvest Biol. Technol*. 56, 209–215;

[16] Keitz H.A.E., (1971), *Light Calculations and Measurements*, Philips Technical Library, Palgrave, London, print ISBN 978-1-349-00014-2, e-ISBN 978-1-349-00012-8, https://doi.org/10.1007/978-1-349-00012-8_8;

[17] Lamikanra O., Kueneman D., Ukuku D., Bett-Garber K.L., (2005), Effect of processing under ultraviolet light on the shelf life of fresh-cut cantaloupe melon, *J. Food Sci*. 70, C534–C539;

[18] Manzocco L., Da Pieve S., Maifreni M., (2011), Impact of UV-C light on safety and quality of fresh-cut melon, *Inn. Food Sci. Emerg. Technol*. 12, 13–17;

[19] Martínez de Alba A.E., Rubio M.B., Morán-Diez M.E., Bernabéu C., Hermosa R., Monte E., (2021), Microbiological evaluation of the disinfecting potential of UV-C and UV-C plus ozone generating robots, *Microorganisms*, 9, 172. https://doi.org/10.3390/microorganisms9010172;

[20] Meneses-Espinosa E., Gálvez-López D., Rosas-Quijano R., Adriano-Anaya L., Vázquez-Ovando A., (2023), Advantages and disadvantages of using emerging technologies to increase postharvest life of fruits and vegetables, *Food Reviews International*, DOI: 10.1080/87559129.2023.2212061;

[21] Modest M. F., (1993), *Radiative Heat Transfer*, McGraw-Hill, New York;

[22] Rivera-Pastrana D.M., Bejar A.A.G., Martinez-Tellez M.A., Rivera-Dominguez M., Gonzalez-Aguilar G.A., (2007), Postharvest biochemical effects of UV-C irradiation on fruit and vegetables, *Revista Fitotecnia Mexicana*. 30, 361-372;

[23] Rodgers M., Cremers S., Bowles E., (2023), Description and results of a new method for assessing real-life performance of a UV-C disinfection robot, *Infection Prevention in Practice*, Volume 5, Issue 4, ISSN 2590-0889, https://doi.org/10.1016/j.infpip.2023.100322;

[24] Romero-Martínez L., Moreno-Andrés J., Acevedo-Merino A., Nebot E., (2022), Development of a geometrical model for the determination of the average intensity in a flow-through UV-LED reactor and validation with biodosimetry and actinometry, *Journal of Water Process Engineering*, Volume 49, 103137, ISSN 2214-7144, https://doi.org/10.1016/j.jwpe.2022.103137;

[25] Ruetalo N., Berger S., Niessner J., Schindler M., (2022), Inactivation of aerosolized SARS-CoV-2 by 254 nm UV-C irradiation, *Indoor Air. 2022*; 32:e13115. doi: 10.1111/ina.13115;

[26] Sorică C., Vlăduţ N.V., Grigore I., Cristea M., Sorică E., Pirnă I., Preda D., Duran B., (2021), Technical performances of a portable UV-C device used for the decontamination of various working spaces, *Proceedings of the 48th International Symposium on Agricultural Engineering - Actual Tasks on agricultural Engineering*, Opatija-Croatia, 2021, ISSN 1848-4425, pg. 311-320, atae.agr.hr;

[27] Sottani C., Favorido Barraza G., Frigerio F., Corica G., Robustelli della Cuna F.S., Cottica D., Grignani E., (2023), Effectiveness of a combined UV-C and ozone treatment in reducing healthcare-associated infections in hospital facilities, *Journal of Hospital Infection*, Volume 139, Pages 207-216, ISSN 0195-6701, https://doi.org/10.1016/j.jhin.2023.06.029;

[28] Yemmireddy V., Adhikari A., Moreira J., (2022), Effect of ultraviolet light treatment on microbiological safety and quality of fresh produce: An overview, *Front. Nutr.* 9:871243. doi: 10.3389/fnut.2022.871243.

[29] US-FDA, United States Food and Drug Administration, (2002), *Ultraviolet radiation for the processing and treatment of food*, Code of Federal Regulations, 21 Part 179.39.

DESIGN AND TEST OF THRESHING AND CLEANING DEVICE FOR CYPERUS ESCULENTUS L. COMBINE HARVESTER

/

油莎豆联合收获机用脱粒清选装置设计与试验

Zixuan ZHANG[1)], Honglei JIANG[1)], Xiaoning HE*[1)], Fangyan ZHANG[1)], Jiasheng WANG[1)], Dongwei WANG[1)]
[1)]College of Electromechanical Engineering, Qingdao Agricultural University, Qingdao 266109, China;
Tel: +86-19811788356; E-mail: 19811788356@163.com
DOI: https://doi.org/10.35633/inmateh-72-71

Keywords: *Cyperus esculentus L., threshing and sorting devices, field testing, design*

ABSTRACT

In response to the challenges of difficult separation and incomplete cleaning during the mechanized harvesting of Cyperus esculentus L., a combined threshing and cleaning device consisting of a fruit-picking roller, a cleaning belt, and an air-screening system was designed. The structure and working principle of this device were explained, and the main components and operating parameters were determined through theoretical analysis. Using fruit-picking roller speed, cleaning belt angle, and fan speed as evaluation indicators, a three-factor three-level field experiment was conducted based on the Box-Behnken central composite design principle. Regression models between loss rate, impurity rate, and significant factors were established, and the optimal working parameters were determined using regression equations. The results showed that when the fruit-picking roller speed was 543.7 r/min, the cleaning belt angle was 50.3°, and the fan speed was 532.4 r/min, the loss rate of sesame seed harvesting was 2.67%, and the impurity rate was 2.49%. The results of field validation experiments indicated that the average loss rate of the combined threshing and cleaning device under the optimal parameter combination was 2.88%, and the average impurity rate was 2.41%, which were consistent with the optimization results of the regression model and fully met the requirements of mechanized sesame seed harvesting production.

摘要

针对油莎豆在机械化收获过程中脱粒分离困难、清选除杂不彻底导致收获损失率、含杂率较高的难题，设计了一种摘果辊、除杂带与风筛式组合的脱粒清选装置，说明了其结构以及工作原理，通过理论分析，确定了关键零部件的主要结构以及工作参数。以摘果辊转速、除杂带倾角、风机转速为评价指标，依据 Box-Behnken 中心组合设计原理开展三水平三因素田间试验，立了损失率、含杂率与各显著因素之间的回归模型，利用回归方程解出最优工作参数，结果表明：当摘果辊转速为 543.7r/min、除杂带倾角为 50.3°、风机转速为 532.4r/min 时，油莎豆收获损失率为 2.67%，含杂率为 2.49%。田间验证试验结果表面：最优参数组合下的摘果辊与风筛式组合的脱粒清选装置平均损失率为 2.88%；平均含杂率为 2.41%，与回归模型寻优结果基本一致，完全满足油莎豆机械化收获生产需求。

INTRODUCTION

Cyperus esculentus L., also known as the tiger nut, bears fruit underground and is a metamorphic stem. (*Wang et al, 2019; Sander et al, 2023*). *Cyperus esculentus L.* has strong adaptability to drought and desertification, and its adventitious stem can produce high-quality oil, which is a new type of excellent oil crop for comprehensive desertification control and economic benefits. Currently, there is a large gap in the demand for edible vegetable oil production in China, with a high external dependence. Therefore, the development of the *Cyperus esculentus L.* industry is of great significance to improving China's self-sufficiency in edible oil and ensuring national food and oil security (*Zhao et al, 2019; Akabassi et al, 2021; Zhang et al, 2023*).

Due to the underground growth of *Cyperus esculentus L*., the small size of the beans makes it difficult to separate from soil clumps, resulting in high mechanical harvesting loss rates and low cleanliness, severely constraining the development of the *Cyperus esculentus L.* industry *(Jeroen et al, 2023)*.

Zixuan ZHANG, Ph.D. Stud. Eng; Honglei JIANG, Ph.D. Eng; Xiaoning HE, Ph.D. Stud. Eng; Fangyan ZHANG, Ph.D. Stud. Eng; Jiasheng WANG, Ph.D. Stud. Eng; Dongwei WANG, Ph.D. Stud. Eng

Currently, existing *Cyperus esculentus L.* harvesters often complete the processes of soil removal, threshing, and cleaning in a single step within the drum sieve, with only a few harvesters incorporating secondary threshing and cleaning devices. However, due to suboptimal structural or operational parameter configurations, there are issues with incomplete threshing and cleaning, leading to higher harvesting loss rates and impurity content *(Zhang et al, 2019)*.

Wei Chunnai et al. designed a threshing and cleaning device for high-input rice combine harvesters, focusing on the axial flow threshing separation device and the centrifugal fan cleaning device with dual outlets, which showed good threshing and cleaning effects *(Wei et al, 2018)*. Mao Xin et al. studied oats and threshing teeth, analyzing the effects of factors such as drum speed, feed rate, and concave screen clearance on the threshing separation performance *(Mao et al, 2022)*. Wang Dongwei et al. designed the 4HJL2 peanut combine harvester, with a cleaning device consisting of a single duct axial flow fan and a single-layer perforated flat screen, featuring simple structure and easy installation, and exhibiting good cleaning effects on peanut seedlings and straw *(Wang et al, 2013)*. Gao Lianxing et al. developed the 5XT-2Z peanut picker, with a cleaning device comprising an air suction fan and a vibrating screen; the vibrating screen removes small stones, soil clumps, and other impurities while uniformly conveying peanut pods, with the front suction port near the picking device removing small peanut leaves, stems, and other impurities, and the rear suction port removing floating peanut stems, empty pods, and other impurities *(Gao et al, 2015)*.

This study addresses the issue of existing oilseed harvester machines, which often complete the threshing and sorting process in a single step within the drum sieve during harvesting, leading to difficulties in threshing and incomplete removal of impurities. A threshing and sorting device for oilseed harvesters is proposed and the structural and operational parameters of key components are determined through theoretical analysis. Based on field experiments, the optimal operating parameter combination for the threshing and sorting device is we identified and the reliability of the results obtained from the field experiments is validated.

MATERIALS AND METHODS

Structure design

- **Complete machine structure**

The threshing and cleaning device is the main working component of mechanized harvesting for *Cyperus esculentus L*., primarily responsible for separating excavated *Cyperus esculentus L.* from large amounts of soil, clumps of grass, and other impurities *(Li et al, 2022)*. Its structural schematic is illustrated in Figure 1(a), comprising components such as the feeding conveyor belt, picking rollers, concave screens, winnowing fan, impurity removal belt, vibrating screen, and others.

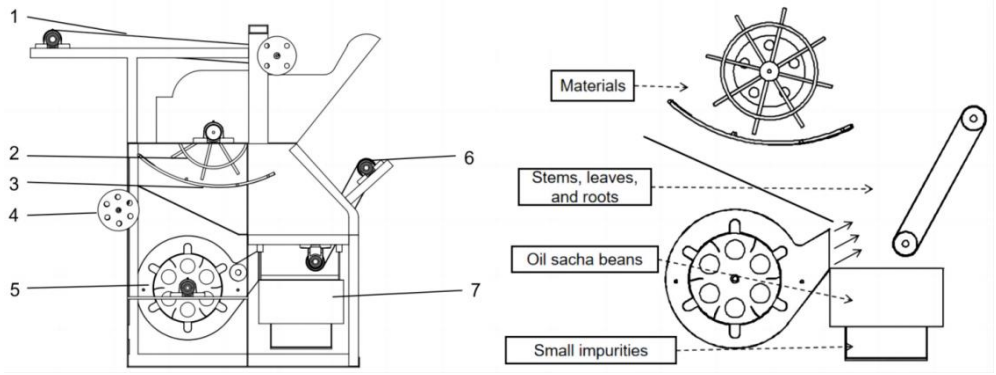

(a)overall structure *(b)working principle*

Fig. 1 - The overall structure and working principle

1. Feeding conveyor belt; 2. Picking rollers; 3. Concave screen; 4. Drive shaft; 5. Winnowing fan; 6. Impurity removal belt; 7. Vibrating screen

The working principle of the device is illustrated in Figure 1(b). Firstly, the feeding conveyor belt feeds the mixture of *Cyperus esculentus L.* plants and soil impurities, sieved preliminarily, into the threshing and cleaning device. Inside the chamber formed by the picking rollers and the concave screen, the material undergoes threshing and separation through the impact and rubbing actions of the threshing components.

After threshing, the material is separated into three parts: stems and leaves, soil, and beans. Stems and leaves fall into the vibrating screen below, where, under the action of the winnowing fan, the stems and leaves are blown onto the impurity removal belt and removed from the machine, while soil, short broken grass roots, and other fine impurities pass through the screen holes and fall onto the ground.

The design of key components

- **Design of parameters for the picking rollers**

The *Cyperus esculentus L.* plants have well-developed root systems and are prone to tillering. Several *Cyperus esculentus L.* plants often intertwine with each other, resulting in materials entering the threshing device being mostly in clumps. Therefore, it is advantageous to select threshing components with strong striking and tearing capabilities to crush clumped materials and thresh the *Cyperus esculentus L.* beans *(An et al, 2022; Fu et al, 2020)*. In this study, a nail-shaped picking element was chosen to design the picking rollers. The collision model between the nail-shaped element and *Cyperus esculentus L.* beans is shown in Figure 2. The collision area between the spherical nail-shaped element and *Cyperus esculentus L.* beans is:

$$S = \pi[R^2 - (R - h)^2] \quad (1)$$

where:

S is the collision cross-sectional area, (mm^2);

R *is* the radius of the spherical nail, (mm);

h *is the* collision compression amount, (mm).

Due to the strong striking and tearing capabilities of the nail-shaped element, considering the occurrence of damaged or rotten beans during the threshing process, the nail tip is specifically analyzed. The collision cross-sectional area of the spherical nail is significantly larger than that of a conventional nail. Under the same collision compression amount, the impact intensity on the beans is lower. To reduce damage to the beans by the nail, the tip of the nail is processed into a spherical shape, with a diameter of d = 18 mm and a length of l = 50 mm.

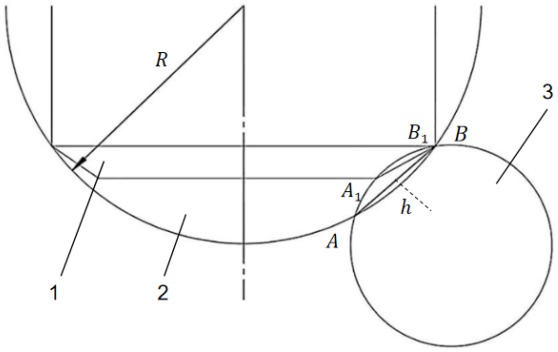

Fig. 2 - Representation of contact between nail and bean

1. Spherical nail; 2. Conventional nail; 3. Cyperus esculentus L. bean

The length of the threshing drum can be calculated using equation (2):

$$L = a(Z - 1) + 2\Delta l \quad (2)$$

where*:* a is the tooth pitch, (mm); Z is the number of threshing elements; Δl is the distance from the edge tooth to the end of the picking roller, (mm).

From equation (2), it can be calculated that the length of the picking roller is 960 mm. Currently, the commonly used diameter of picking rollers in combine harvesters is 450-650 mm *(Ge et al, 2017)*, and to avoid entanglement and blockage in the material fed into the *Cyperus esculentus L.* threshing and cleaning device, the diameter of the picking roller in this study is selected as 450 mm, as shown in Figure 3.

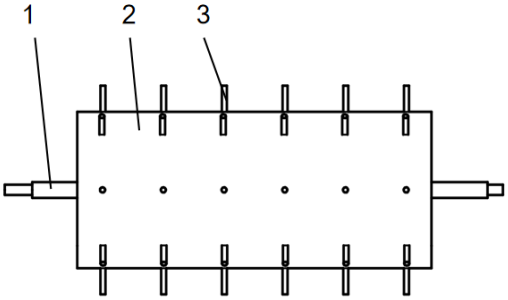

Fig. 3 - Picking roller structure

1.Picking roller drive shaft; 2. Main roller body; 3. Picking roller teeth

The threshing speed of the axial flow nail-tooth drum threshing device, which is the circumferential speed at the top of the picking roller teeth, can be initially selected as *(Ji et al, 2023)* 6-10 m/s due to the relatively hard texture of *Cyperus esculentus L.* beans. The relationship between the picking speed and the drum speed is given by the formula:

$$n = \frac{60v}{\pi D} \quad (3)$$

where*:* n is the picking roller speed, (r/min); D is the picking roller diameter, (mm).

The picking roller speed calculated from equation (3) is 347-579 r/min.

- **Design of parameters for the concave screen**

The concave screen and picking roller together form the threshing component. The concave screen mesh can comb the *Cyperus esculentus L.* beans, allowing the threshed *Cyperus esculentus L.* beans to pass through the screen under the force of gravity, while impurities such as *Cyperus esculentus L.* grass continue to move along the concave screen under the driving force of the picking roller, achieving threshing separation. Referring to existing designs and experimental results *(Dong et al, 2024)*, square aperture grid concave screens are selected, with the concave screen aperture set at 50 mm × 50 mm and the threshing gap at 20 mm.

- **Design of parameters for the winnowing fan**

The fan is installed below the picking roller, with the outlet facing the material chute. During operation, it is powered by belt drive. Due to the force of the fan, *Cyperus esculentus L.* grass, roots, soil, and other impurities are blown onto the impurity removal belt, while the threshed *Cyperus esculentus L.* beans fall into the vibrating screen *(Guo et al, 2021)*. The formula for calculating air volume is:

$$Q = \frac{q_0}{\mu\rho} \quad (4)$$

where*:* ρ is the air density, (kg/m^3); q_0 is the amount of impurities that the fan can clean in a unit of time, (3.6kg/s); μ is the mixture ratio of impurity-carrying airflow, take 0.3. Substitute 0.3 into equation (4) and solve Q = 9.28 m^3/s.

The formula for calculating blade parameters is:

$$D_2 = \frac{60\mu_2}{\pi n} \quad (5)$$

where: μ_2 is the peripheral speed of the impeller, (m/s); D_2 is the impeller outer diameter, (mm); n is the fan speed, (r/min). Based on experience, it is determined 450-550 r/min.

Obtain D_2=450 mm. Typically, the number of blades is chosen to be between 3 and 6 based on the layout and design of the whole machine. In this case, 6 blades are selected, as shown in Figure 4.

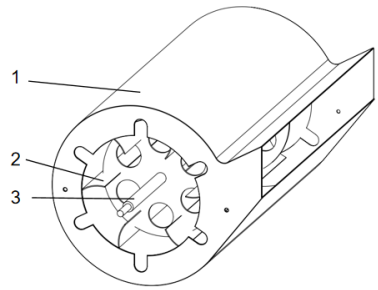

Fig. 4 - Fan impeller structure

1. Fan housing; 2. Fan blades; 3. Fan shaft

- **Design of the impurity removal belt**

The main function of the impurity removal belt is to eject a large number of clumps of grass from the machine, while the *Cyperus esculentus L.* beans carried in the clumps of grass are blocked by the impurity removal belt and fall back into the vibrating screen. To improve the efficiency of removing large impurities by the impurity removal belt and explore the main factors affecting the performance of the cleaning components, it is necessary to analyze the motion of the material on the impurity removal belt and conduct a dynamic analysis of the cleaning and impurity removal process. The force acting on the material on the impurity removal conveyor belt determines its motion stat, as shown in Figure 5.

The force acting on the material along the axial direction is:

$$\sum F_x = F_f + F_v - G\sin\alpha \tag{6}$$

where:

$$F_f = \mu G\sin\alpha, \quad F_v = \frac{\rho v^2 s}{2} \tag{7}$$

where:

α is the angle between the impurity removal conveyor belt and the horizontal plane, (°);

F_f is the friction force between the material and the impurity removal conveyor belt, (N);

F_v is the aerodynamic thrust exerted by the airflow on the material, (N);

G is the material's own gravity, (N);

S is the frontal area of the material, (mm^2);

μ is the coefficient of friction.

$$\sum F_y = N - G\cos\alpha \tag{8}$$

where:

N is the support force of the impurity removal belt on the material, (N).

From the analysis above, it is clear that the impurity removal capacity and blocking capacity of the impurity removal belt are contradictory. Referring to existing design experience *(Li et al, 2024)*, the inclination angle of the impurity removal belt is selected 50 – 60^o, and its material is chosen to be PVC grass pattern belt.

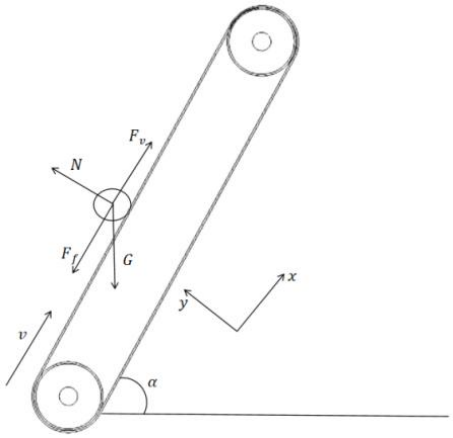

Fig. 5 - Dynamic analysis of the impurity removal process

- **Design of the vibrating screen**

The vibrating screen, together with the winnowing fan and impurity removal belt, constitutes the cleaning component. Common vibrating screens for agricultural materials include the fish scale screen, perforated screen, woven screen, and combination screen *(Han et al, 2017)*. *Cyperus esculentus L.* beans have irregular shapes and uneven surfaces, approximately spherical, and the material entering the vibrating screen contains only a small amount of soil impurities. Therefore, it is advisable to choose a screen with good screening and separating capabilities. In this study, a flat perforated screen is selected. The width of the screen surface is related to the diameter of the picking roller, while the length of the screen surface is determined by the following formula:

$$L = \frac{Q_s}{bq_s} = \frac{Q(1-\delta K)}{bq_s} \tag{9}$$

where:

Q is the feed rate of the machine per unit time, (kg/s);

Q_s is the mass of material cleaned by the vibrating screen per unit time, (kg/s);

q_s is the feed capacity that the vibrating screen can handle, (kg/m^2);

δ is the percentage of *Cyperus esculentus L.* grass and soil in the total weight of the material;

k is the performance coefficient of the threshing and cleaning unit, typically ranging from 0.6-0.9;

b is the width of the screen surface, (m).

According to Equation (9), there is L=80 cm. Considering the layout and design of the whole machine *(Yu et al, 2020; Wang et al, 2022; Hou et al, 2019)*, the length of the swinging rod is taken as 150 mm, the diameter of the eccentric wheel is 160 mm, and the eccentric radius of the eccentric wheel is 20 mm. When the crank swinging rod is in the horizontal position, the maximum amplitude of the vibrating screen is 30 mm, and the crank speed is 250 r/min. Square sieve holes are used, with a diameter of 9 mm x 9 mm.

- **Field experiments**

Prototype construction of the threshing and cleaning unit for the *Cyperus esculentus L.* bean combined harvester will be conducted. Based on the previous determinations of parameters such as the rotation speed of the picking roller, fan speed, and inclination angle of the cleaning belt, field experiments will be carried out. Through orthogonal regression analysis, the optimal combination of working parameters will be determined.

- **Experimental Materials**

The experimental prototype used in the experiment is a 4YQL-1500 trailed oil *Cyperus esculentus L.* combined harvester, whose overall structure is shown in Figure 6. The oil *Cyperus esculentus L.* combined harvester prototype consists of several key components, including the chassis, digging device, lifting and soil removal device, cylinder screen, walking device, and threshing and cleaning device. The prototype is powered by a tractor. The digging device adopts an adjustable dual oil cylinder structure, facilitating the adjustment of digging depth. The lifting and soil removal device is designed as a flat screen structure, directly connected to the digging device, capable of preliminarily removing large chunks of soil from the oil *Cyperus esculentus L.* plants and soil and conveying them into the cylinder screen. The cylinder screen is of a single-layer design, separating most of the soil through rotation, and then conveying the soil-removed oil *Cyperus esculentus L.* plants to the threshing and cleaning device via a conveyor belt.

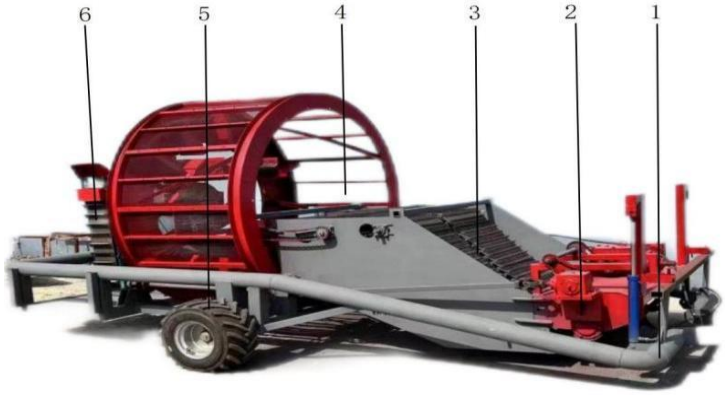

Fig. 6 - 4YQL-1500 Cyperus esculentus L. Joint Harvester

1. Chassis; 2. Digging device; 3. Lifting and soil removal device; 4. Cylinder screen; 5. Walking device; 6. Threshing and cleaning device

The experiment was conducted from October 7, 2023, to November 13, 2023, using a homemade 4YQL-1500 Cyperus esculentus L. Joint Harvester prototype at the Oil Sorghum Planting Demonstration Base in Minquan County, Henan Province. The oil sorghum used in the experiment was obtained from the Oil Sorghum Planting Demonstration Base in Minquan County, Henan Province, and the variety was "Yu Oil Sorghum No.5". Experimental instruments included the JM-B1003 electronic counting balance, TSC electronic scale, CASIO calculator, vernier caliper, protractor, etc.

- **Experimental Method**

The experiment was conducted following the methods specified in GBT 5262-2008 "General Rules for Determination Methods of Test Conditions for Agricultural Machinery", GB/T 5667 "Test Methods for Agricultural Machinery Production", and GBT25235-2010 "Combined Cleaning Sieve for Grain and Oil Machinery". Loss rate determination: Upon completion of the operation of the *Cyperus esculentus L.* harvester, impurities were collected after cleaning, and *Cyperus esculentus L.* grains were manually sorted out and weighed. Measurement of harvested *Cyperus esculentus L.* mass: After completion of the operation of the sample machine, the total weight of the Cyperus esculentus L. in the collection box was measured. Impurity content determination: After the sample machine completed harvesting, the collection box was overturned, and the *Cyperus esculentus L.* grains were poured out. Impurities were manually picked out and weighed. Loss rate and impurity content calculation are illustrated in Figures 7 and 8, respectively, and are calculated using formulas (10) and (11) as shown below.

Fig. 7 - Loss rate measurement

Fig. 8 - Impurity rate weighing

$$L_1 = \frac{Q_4}{Q_1+Q_3+Q_4} x100\% \quad (10)$$

$$L_2 = \frac{Q_1}{Q_1+Q_3} x100\% \quad (11)$$

where:

L_1 is the loss rate, (%); L_2 is the Impurity rate, (%); Q_1 is the mass of impurities carried with beans, (kg); Q_3 is the harvested bean mass, (kg); Q_4 is the impurity mass, (kg).

This experiment utilized Design-Expert 8.0.6 software for experimental design. The Box-Behnken response surface methodology with a 3-factor, 3-level design was employed. The factors chosen were the rotational speed of the fruit-picking roller (A), the inclination angle of the debris-removing belt (B), and the rotational speed of the fan (C). Loss rate (Y_1) and impurity rate (Y_2) were selected as evaluation indices.

The ranges of the selected factor levels were as follows: fruit-picking roller speed ranging from 350 to 550 rpm, debris-removing belt inclination angle ranging from 50 to 60 degrees, and fan speed ranging from 450 to 550 rpm. The factors were coded as 1, 0, and -1, respectively, and the experimental codes are detailed in Table 1.

Table 1

Factor level coding table

Levels	Factors		
	Harvester roller speed (r/min)	Angle of the debris belt (°)	Blower speed (r/min)
1	350	50	450
0	450	55	500
-1	550	60	550

Table 2

Test scheme and results

Experiment Number	Factors			Experiment Results	
	A	B	C	Y1 (%)	Y2 (%)
1	350	50	500	4.66	2.50
2	550	50	500	5.60	2.56
3	350	60	500	3.46	1.64
4	550	60	500	3.98	2.97
5	350	55	450	5.10	1.09
6	550	55	450	4.22	2.83
7	350	55	550	1.90	2.03
8	550	55	550	5.10	1.74
9	450	50	450	3.28	2.82
10	450	60	450	5.16	1.07
11	450	50	550	5.10	1.05

Table 2
(continuation)

Test scheme and results

Experiment Number	Factors			Experiment Results	
	A	B	C	Y1 (%)	Y2 (%)
12	450	60	550	1.54	2.43
13	450	55	500	2.22	2.31
14	450	55	500	2.32	1.92
15	450	55	500	3.10	1.83
16	450	55	500	2.26	1.98
17	450	55	500	2.22	2.06

- **Establishment of the regression equation and variance analysis**

For the regression model of loss rate, factors A, B, C, BC, B^2, and AC have extremely significant effects on the loss rate ($P < 0.01$), while the interaction term C^2 has a significant effect on the loss rate ($P < 0.05$). Judging by the F-values, the primary and secondary order of significance of the first-order terms on the loss rate are B, C, and A, respectively.

For the regression model of impurity rate, factors A, AB, AC, BC, and C^2 have extremely significant effects on the impurity rate ($P < 0.01$), and factor A^2 has a significant effect on the impurity rate ($P < 0.05$). Based on the F-values, the primary and secondary order of significance of the first-order terms on the impurity rate are A, B, and C, respectively.

Table 3

ANOVA for loss rate and impurity rate

Sources of Variance	Loss rate		Impurity rate	
	F	P	F	P
Model	345.43	<0. 0001	102.48	<0.0001
A	14.43	0.0067	49.32	0.0002
B	20.45	0.0027	4.11	0.0822
C	17.14	0.0043	1.92	0.2087
AB	0.36	0.5694	19.72	0.0030
AC	33.61	0.0007	50.40	0.0002
BC	59.76	<0. 0001	119.81	<0.0001
A^2	45.41	0.0003	11.74	0.0110
B^2	24.31	0.0017	5.19	0.0568
C^2	8.52	0.0224	23.29	0.0019
Lack of fit term	0.67	0. 3237	0.097	0.9577

Using Design-Expert software, multiple regression fitting analysis was conducted. After eliminating the non-significant factors, regression equations were established separately for loss rate and impurity rate with significant factors.

$$Y_1 = 2.42 + 0.47A - 0.56B - 0.52C - 0.11AB + 1.02AC - 1.36BC + 1.16A^2 + 0.85B^2 0.50C^2 \quad (12)$$

$$Y_2 = 2.02 + 0.36A - 0.10B - 0.07C + 0.32AB - 0.51AC + 0.78BC + \quad 0.24A^2 + 0.16B^2 - 0.34 \quad (13)$$

From Table 3, it can be observed that the regression models for separation rate and impurity rate are both highly significant ($P < 0.01$), while the lack of fit terms are not significant ($P > 0.05$). This indicates that the fitted regression equations are highly reliable. Therefore, optimal parameter combinations for the three factors can be determined based on the aforementioned regression models.

- **Analysis of the impact of interaction effects on experimental indicators**

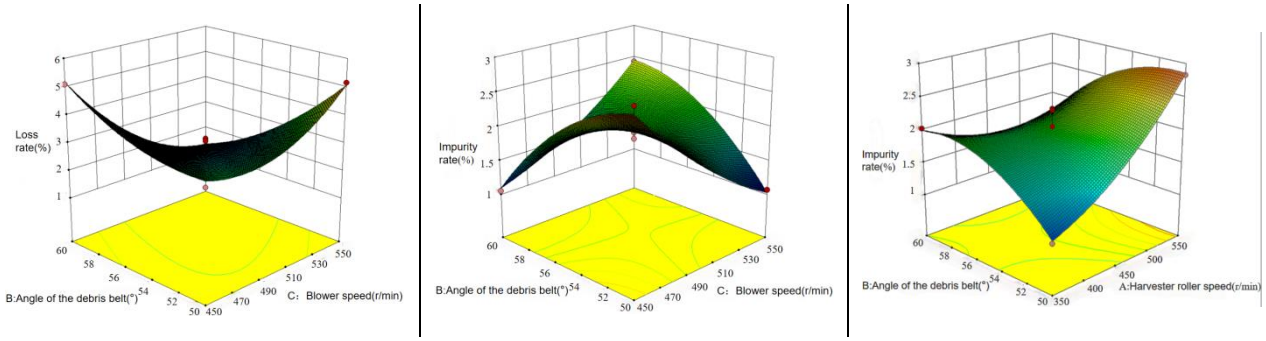

(a) **(b)** **(c)**

Fig. 9 - Response surfaces for effect of factors interaction on test indicators

The response surface of the impact of the interaction effects on the loss rate and impurity content rate was obtained through Design-Expert software, as shown in Figure 9. In Figure 10a, the contour curvature is larger compared to Figure 10b, indicating that the interaction between the inclination angle of the impurity removal belt and the fan speed has a more significant effect on the impurity content rate compared to the interaction between the inclination angle of the impurity removal belt and the roller speed. From Figure 10c, it can be observed that the loss rate is positively correlated with the fan speed and negatively correlated with the inclination angle of the impurity removal belt. The inclination angle of the impurity removal belt has a more significant impact on the response surface because as the inclination angle of the impurity removal belt increases, it can create a blocking effect on the separated *Cyperus esculentus L.* during the falling process under the action of the blowing fan airflow, leading to a rapid decrease in the loss rate.

- **Solving for the optimal combination of experimental factors**

Based on the above experimental results and regression equations, with the optimization objectives being to minimize loss rate and impurity rate, and with the optimization variables being fruit picking roller speed, inclination angle of the impurity removal belt, and fan speed, the regression model is optimized. The objective function and constraints are as follows:

$$\begin{cases} minY_1(A,B,C) \\ minY_2(A,B,C) \\ s.t. \begin{cases} 350 \le A \le 550 \\ 50 \le B \le 60 \\ 450 \le C \le 550 \end{cases} \end{cases} \quad (14)$$

The optimal operating parameters for the threshing and cleaning device are determined to be: fruit picking roller speed of 543.7 r/min, inclination angle of the impurity removal belt of 50.3°, and fan speed of 532.4 r/min. With these settings, the operational performance is optimized. Theoretical performance indicators for the optimized threshing and cleaning device are as follows: loss rate (Y_1) is 2.67%, and impurity rate (Y_2) is 2.49%.

- **Validation experiment**

Based on Table 4, the average loss rate of the traction-type oil *Cyperus esculentus L.* combined harvester's threshing and cleaning device under the optimal parameter combination obtained from the field validation experiment is 2.88%, and the average impurity rate is 2.41%, which is consistent with the results of the regression model optimization.

The machine operates smoothly during the entire operation, with outstanding threshing and cleaning effects, fully meeting the requirements for oil sunflower harvesting work. The validation experiment is depicted in Figure 10.

Table 4

Validation test results

Trial number	Loss rate	Impurity rate
1	3.03%	2.32%
2	2.57%	2.47%
3	2.65%	2.09%
4	3.28%	2.74%
Mean value	2.88%	2.41%

Fig. 10 - Verification test

CONCLUSIONS

(1) A threshing and cleaning device for a *Cyperus esculentus L.* combine harvester was designed aiming to address the challenges of completing the threshing and cleaning process within the drum sieve, leading to difficulties in threshing separation and inadequate cleaning of impurities. Through theoretical analysis, the structural and operational parameters of key components were determined.

(2) Based on the Box-Behnken experimental design principle, a field experiment with three factors and three levels was conducted using the fruit picking roller speed, the angle of the debris removal belt, and the fan speed as influencing factors, while the loss rate and impurity rate were used as evaluation indicators. The results indicate that when the fruit picking roller speed is 543.7 r/min, the angle of the debris removal belt is 50.3º, and the fan speed is 532.4 r/min, the loss rate of harvested *Cyperus esculentus L.* is 2.67%, and the impurity rate is 2.49%.

(3) Field validation experiment results show that the average loss rate of the combined fruit picking roller and wind sieve type separation and cleaning device under the optimal parameter combination is 2.88%, and the average impurity rate is 2.41%. These results are consistent with the optimization results of the regression model, fully meeting the requirements of mechanized harvesting production for *Cyperus esculentus L*.

ACKNOWLEDGEMENT

This work has been supported by Henan Provincial Major Science and Technology Project (Project No.211100110100); Youth Project of Natural Science Foundation of Shandong Province (Project No.ZR2022QE167); Shandong Province Technology Innovation Guidance Programme (Project No.YDZX2023005)

REFERENCES

[1] Akabassi G.C., Palanga K.K., Padonou E.A. (2021) A Global Systematic Review on Biology, *Production Constraints and Uses of Cyperus exculentus L. Preprints*, Vol.2, pp.42-44, United States.

[2] An S. (2022). Design and test of the separation device (油莎豆脱粒分离装置的设计与试验). *Master's degree (dissertation, Shihezi University)*. Xinjiang/China.

[3] Dong R., Xiao J., Liu W., Guo W., Wang X., Liu F. (2024). Design and test of traction oil harvester (牵引式油莎豆收获机设计与试验). *China Agricultural Machinery Chemical News*. Vol.1, pp.21-27. Jiangsu/China.

[4] Fu J., Zhang Y., Cheng C., Chen Z., Tang X., Ren L. (2020). Design and test of rigid and flexible coupling of wheat (刚柔耦合式小麦脱粒弓齿设计及试验). *Journal of Jilin University (Engineering Edition)*. Vol. 2, pp. 730-738. Jilin/China.

[5] Gao L., Li X., Guan M. (2015) Design and test of peanut fruit cleaning device with double suction outlet (双吸风口振动式花生荚果清选装置设计与试验). *Journal of Agricultural Machinery*, Vol. 46, pp. 110-117. Beijing/China.

[6] Ge Q. (2017). Design and study of key technology of longitudinal axial flow threshing drum device of combine harvester (联合收割机纵轴流脱粒滚筒装置关键技术设计与研究). *Heilongjiang Science and Technology Information*. Vol. 8, pp. 80-81. Heilongjiang/China.

[7] Guo P., Shang S., Wang D., He X., Xu N., Liu J., Dong M. (2021). Design and test of traction-type peanut picking harvester (牵引式花生捡拾收获机的设计与试验). *Agricultural mechanization research*. Vol. 12, pp. 92-97. Heilongjiang/China.

[8] Han C., Liu X., Zhang X. (2017). Design and experimental study of oil sunflower and of oil plant (油葵脱粒清选装置的设计与试验研究). *Journal of Xinjiang Agricultural University*. Vol.6 pp.454-459. Xinjiang/China.

[9] Hou J., Ren Z., Zhu H. (2022). Design and test of double-layer inclined vibration air screen castor cleaning device (双层倾斜振动风筛式蓖麻清选装置设计与试验). J*ournal of Agricultural Machinery*. Vol.S2. pp. 39-51. Beijing/China.

[10] Ji M. (2023). Design and experimental study of threshing device (横轴流油莎豆脱粒装置的设计与试验研究). *Master's degree (dissertation, Jilin Agricultural University)*. Jilin/China.

[11] Jeroen Feys, Dirk Reheul, Wolf De Smet, Shana Clercx, Sander Palmans, Gert Van de Ven & Benny De Cauwer. (2023). Effect of anaerobic soil disinfestation on tuber vitality of yellow nutsedge (*Cyperus esculentus*). *Agriculture* (8).

[12] Li J., Liu W., Zhang L. (2022). Design and testing of oil and Cyperus esculentus L. harvest equipment (油莎豆收获装备设计与试验). *Agricultural Engineering*, Vol. 4, pp. 36-39. Beijing/China.

[13] Li D., Wang D., He X., Zuo B., Zhang C., Li X. (2024). Study on the secondary clearance of peanut semi-feeding and combined harvest (花生半喂入联合收获二次清选机构研究). *China Agricultural Machinery Chemistry*. Vol. 3, pp.117-125. Jiangsu/China.

[14] Mao X., Zhao R., Yi S. (2022). Experimental study of secondary orthogonal rotation combination of naked oat threshing and separation device (裸燕麦脱粒与分离装置二次正交旋转组合试验研究). *Agricultural mechanization research*, Vol. 9, pp. 181-188. Beijing/China.

[15] Sander De Ryck, Dirk Reheul &Benny De Cauwer. (2023). Impact of regular mowing, mowing height, and grass competition on tuber number and tuber size of yellow nutsedge clonal populations (*Cyperus esculentus L.*). *Weed Research*. Vol. 6, pp. 371-381. United Kingdom.

[16] Wang R., Wang X., Xiang H. (2019). A versatile emerging oil crop (一种多用途的新兴油料作物). *Chinese fats*, Vol. 1, pp. 1-4, Shanxi/China.

[17] Wei C., Li Y., Xu L. (2018). Design and testing of feeding rice combine harvester (大喂入量水稻联合收获机脱粒清选装置的设计与试验). *Agricultural mechanization research*, Vol.8, pp.5, Heilongjiang/China.

[18] Wang D. (2013). Research on key device of peanut joint harvester (花生联合收获机关键装置的研究), *PhD (dissertation, Shenyang Agricultural University)*. PhD. Thesis. Liaoning/China.

[19] Wang L., Liu W., Li Y., Yu K. (2022). Study on shaking plate of clearing system of corn grain harvester (大喂入量玉米籽粒收获机清选系统双层筛孔抖动板研究). *Journal of Agricultural Machinery*. Vol.7 pp.92-102. Beijing/China.

[20] Yu X. (2020). Design and experimental study of small peanut fruit picker (小型花生摘果机的设计与试验研究). *Master's degree (dissertation, Xinjiang Agricultural University)*. Xinjiang/China.

[21] Zhao Y., Zou X., Zhang Y., Han Z., Zeng L., Zhang X. (2019). *Cyperus esculentus L.* High oil and high yielding variety *Cyperus esculentus L.* 1, China (油莎豆高油高产品种中油莎 1 号). *China seed industry*, Vol. 6, pp. 96-97, Beijing/China.

[22] Zhang S., Zhang R., Cao Q. (2023). Design and test of double-layer roller sieve fruit mixed separation device for oil *Cyperus esculentus L.* harvester (油莎豆收获机双层滚筒筛式果杂分离装置设计与试验). *Journal of Agricultural Machinery*, Vol. 54, pp. 148-157, Beijing/China.

[23] Zhang B., Liu J., Fan Z. (2019). Research progress on mechanized sowing and harvesting technology and equipment of saline-alkali earth oil and bean (盐碱地油莎豆机械化播种收获技术与装备研究进展). *Shandong Agricultural Science*, Vol. 51, pp. 4, Shandong/China.

DESIGN AND EXPERIMENT OF SPRAY BOOM INCLINATION CONTROL SYSTEM
/
喷杆倾角控制系统的设计与实验

Fang LI[1)], Xiaohu BAI*[2)]
[1)] School of Information and Control Engineering, Liaoning Petrochemical University, Fushun/China;
[2)] College of Engineering, Shenyang Agricultural University, Shenyang/China
E-mail: baixiaohu@syau.edu.cn
DOI: https://doi.org/10.35633/inmateh-72-72

Keywords: *CAN bus, visualization, control node, canopy mode, ground mode, dynamic monitoring*

ABSTRACT
During field operations of the spray boom sprayer, the distance between the ends of the spray boom and the height of the crop canopy affects the uniformity of spraying, requiring operators to manually adjust the spray boom to be parallel to the crop canopy, which impacts operational efficiency. This study presents the design of a boom tilt control system, consisting of a main control node, distance measurement node, vehicle tilt detection node, and spray boom tilt control node. The bus communication protocol for the spray boom tilt control system is defined according to the ISO11783 standard, and a serial communication network is designed, along with the development of a real-time dynamic monitoring interface for the spray boom. The system automatically monitors the height of the boom and the tilt of the vehicle, makes decisions based on the detection information, controls the electric actuator, and adjusts the tilt of the boom. Leveraging the advantages of fast computing speed and user-friendly human-machine interface of the PC, as well as the high cost-effectiveness and small size of the microcontroller, and the multi-master-slave structure of the CAN bus, this system can complete data acquisition, processing, and other functions required for spray boom tilt control, achieving automatic adjustment of spray boom tilt. This enhances spray uniformity and operational efficiency of the sprayer, while reducing the workload of operators.

摘要
喷杆喷雾机田间作业时，喷杆两端距离作物冠层的高度影响喷雾均匀性，需要操作人员手动将喷杆调整到与作物冠层平行，影响作业效率。本文设计了一种喷杆倾角控制系统，包括主控节点、测距节点、车体倾角检测节点和喷杆倾角控制节点。根据 ISO11783 协议定义了喷杆倾角控制系统总线通信协议，进行了串行通信网设计，开发了喷杆实时动态监控界面。本系统能自动监视喷杆高度和车体倾角，并根据检测信息做出决策，控制电动推杆，调节喷杆倾角。本系统充分发挥了 PC 机运算速度快和人机交互界面友好、单片机性价比高且体积小、CAN 总线多主从结构等优点，能够完成喷杆倾角控制所需数据的采集、处理等功能，实现喷杆倾角自动调节，从而提高喷雾均匀性和喷雾机作业效率，减轻操作人员的劳动强度。

INTRODUCTION

As of 2020, the mechanized control of various crops in China accounted for 48.5% of the total control area. The area of mechanized and intelligent plant protection operations continues to expand, with wide-width boom sprayers being widely used (*He et al., 2022*). Spray quality is one of the important factors affecting the effectiveness of pesticides, and spray uniformity is an important indicator of spray quality (*Qi et al., 1999*). The height of the nozzle relative to the target significantly affects the uniformity and drift of the spray. During field operations of boom sprayers, the harmful vertical and rolling rigid movements of the boom are the main causes of uneven spray distribution. Simulation results have shown that boom rolling can cause a spray deposition of up to 10 times the standard dose (*Roman et al., 1997*). Reducing the amplitude of vertical oscillation of the boom can reduce the coefficient of variation of the spray, thereby improving spray uniformity (*Chen et al., 2008*).

Due to the long boom of wide-width boom sprayers and the small size of the vehicle, even slight movements can cause significant displacement at the end of the boom (*Qiao et al., 2017*).

Fang Li, Lecturer, Ph.D.; Xiaohu Bai, Associate Prof., Ph.D.,Corresponding Author.

Especially when the ground excitation frequency is close to the natural frequency of the boom, the oscillation of the boom intensifies, severely affecting spray quality and even causing damage to the end of the boom touching the ground (*Cui et al., 2019*). The boom moves parallel to the ground under the influence of gravity and vertically within the plane perpendicular to the ground under the effect of ground excitation. When the sprayer is operating on sloping terrain, the height of the boom ends from the crop canopy varies, thus affecting spray uniformity. Operators need to manually adjust the boom to a parallel position with the crop canopy or the ground, which not only affects spray uniformity but also hampers operational efficiency and increases labour intensity for operators (*Li et al., 2023*).

Some research has been conducted on the control system of the spray boom. Three contact sensors are used to detect the distance between the spray boom and the ground, and a hydraulic cylinder is used to extend or retract and control the elevation or lowering of the spray boom (*Wang Songlin, 2014*). In order to keep the spray boom parallel to the crop canopy or the ground, ultrasonic sensors placed at both ends of the spray boom are used to detect the position of the spray boom. The position of the spray boom is adjusted by controlling the hydraulic cylinder using Siemens S7-200PLC and a single-chip microcomputer to achieve online adjustment of the spray boom (*Anthonis et al., 2005; Chen et al., 2013; Cui et al., 2017, 2019; Wei et al., 2015*). Multiple sensors, including laser radar, are used to measure the distance between the spray boom and the crop canopy, and a microcomputer and PLC are jointly used to control the adjustment of the spray boom height (*Wang et al., 2023*). To adjust the position of the spray boom during the operation of the sprayer, a spray boom levelling mechanism is constructed using balance cylinders, springs, and air dampers to adjust the position of the spray boom (*Wang et al., 2016*).

Therefore, this paper focuses on the design of an active suspension system for wide-width spray boom sprayers. A control system based on fieldbus technology is adopted. Ultrasonic distance sensors located at both ends of the spray boom are used to collect the height of the spray boom from the crop canopy or the ground. Tilt sensors are used to detect the attitude of the spray boom. The collected data, after removing abnormal values, is uploaded to the host computer via the fieldbus. The host computer integrates the attitude and height information of the spray boom, analyses the status of the spray boom, and controls the drive device according to the system requirements to adjust the attitude of the spray boom, thereby maintaining the height of the spray boom from the crop canopy or the ground. This improves spray uniformity, reduces the workload of operators, and enhances the efficiency of spray operations.

MATERIALS AND METHODS

THE STRUCTURE OF THE SPRAY BOOM ANGLE CONTROL SYSTEM

The overall structure of this system is shown in Figure 1. In the figure, Node 1 is responsible for measuring the vehicle body inclination angle, Node 2 and Node 3 are responsible for measuring the distance between the spray boom and the crop canopy or ground, and Node 4 is responsible for driving the electric actuator. These four nodes are installed on the spray boom and the vehicle body, so 51 series microcontrollers are used due to their high cost-effectiveness, high integration level, and strong anti-interference capabilities. The PC node is mainly responsible for analysing the data transmitted from each node and issuing commands to the control devices in each node based on the analysis results. Therefore, the entire spray boom angle control system consists of a PC, four microcontrollers, and communication lines. Due to the requirement for real-time performance in this system, a high-performance PC is selected to fully leverage the advantages of fast processor calculation speed and large storage capacity. This enables the PC to quickly perceive the various parameters in the control system and respond rapidly to on-site equipment. In addition to the PC node, the other nodes are based on the STC12C5A60S2 microcontroller, which integrates functions such as data acquisition, processing, communication, and control. These nodes are responsible for collecting the vehicle body inclination angle, measuring the height between the spray boom and the crop canopy, and controlling the angle of the spray boom.

SYSTEM HARDWARE DESIGN

Sensor selection, installation, and interface circuit design

Ultrasonic sensors have the advantages of having a constant propagation speed and direction in the same medium as the vibration direction, strong directionality, small size, fast data processing speed, high accuracy, easy installation and maintenance, and the ability to achieve non-contact measurement (*Alexandre et al., 2011*).

They are also not affected by external light, electromagnetic waves, weather, or the colour of the measured object itself, and have a certain degree of adaptability to harsh environments such as dust and smoke (*Liu, 2006*). The range of the spray boom distance from the crop canopy or ground is 10-1500 cm, and the walking speed is relatively fast, so it is required that the ranging sensor has a fast response speed and good real-time performance. In addition, the field operation environment is complex, so this paper selects the KS109 integrated ultrasonic ranging sensor produced by Guiding Technology Co., Ltd., as shown in Figure 2 (a), which has a detection range of 0.04-10 m and meets the system design requirements. The ultrasonic sensor is installed at both ends of the spray boom to measure the distance between the two ends of the spray boom and the crop canopy or ground, as shown in Figure 2 (b).

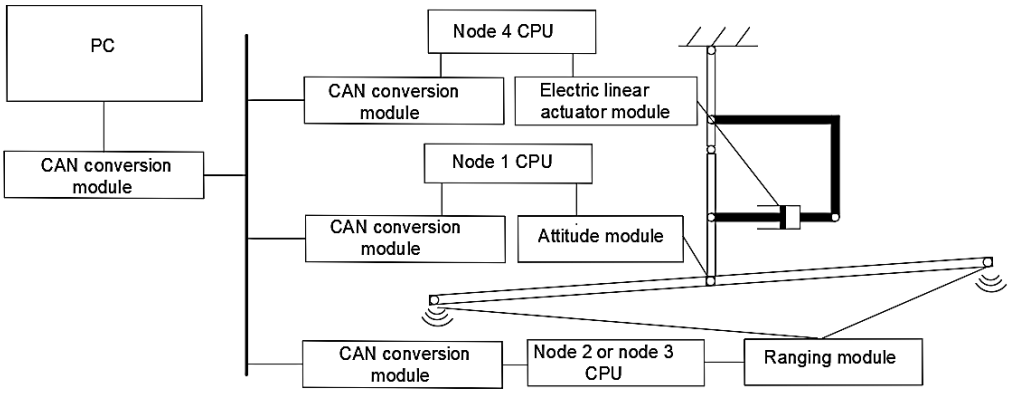

Fig. 1 - The general structure of the inclination control system of the boom

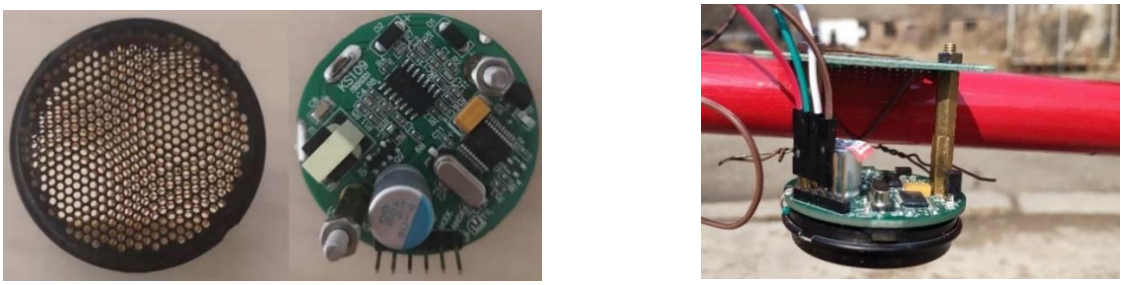

(a) Physical Picture of KS109 (b) Installation Position of KS109

Fig. 2 - KS109 ultrasonic sensor

The rotation angle of the sprayer vehicle body is an important indicator of the spray boom angle control system. This system needs to detect the swing angle of the vehicle body, and its selection also determines the performance of the spray boom angle control system. Considering the factors of speed and angular velocity sensitivity, the MPU6050 is chosen as the tilt measurement chip for this system (*Gu, 2019; He, 2020*). The WT901 uses the MPU6050 as the angle measurement chip, with a static accuracy of 0.05° and dynamic accuracy of 0.1°, which meets the system design requirements. Since the tilt sensor measures the swing angle of the vehicle body, the tilt sensor is installed on the frame as shown in Figure 3.

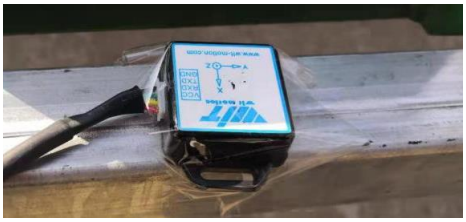

Fig. 3 - Installation position of inclination sensor

The sensor interface circuit is shown in Figure 4, which includes the interface circuits for ultrasonic ranging sensors and angle sensors. The tilt angle sensor WT901 communicates with the microcontroller through a serial port. The serial output terminal TX of WT901 is connected to the serial input terminal RXD of the microcontroller, and the serial input terminal RX of WT901 is connected to the serial output terminal TXD of the microcontroller. WT901 and the microcontroller share the same power supply. The KS109 uses an I2C interface to communicate with the microcontroller, sharing the power supply with the microcontroller.

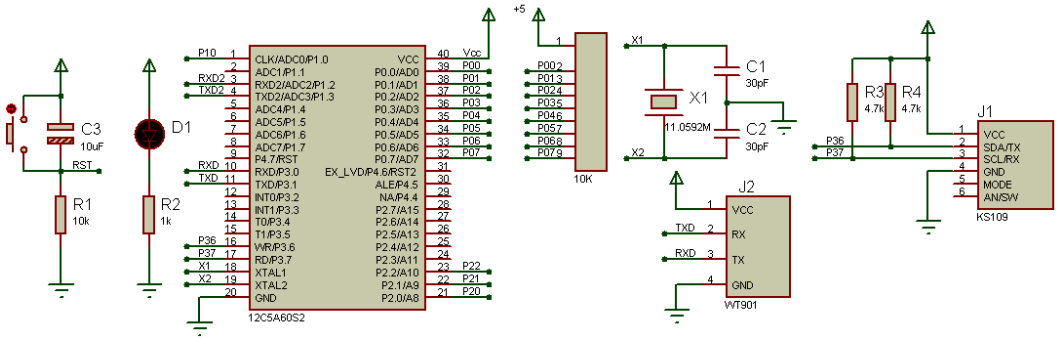

Fig. 4 - Interface circuit between the sensors and SCM

Selection and design of the drive device interface circuit

The electric actuator has advantages such as small size and high precision. It converts the rotational motion of the motor into linear motion of the actuator. It mainly consists of a motor, actuator, control device, and other mechanisms. It can be controlled by a power supply, reducing the need for pneumatic devices and reducing the overall weight of the device. Driving the electric push rod is actually driving the motor, and the I/O port of the microcontroller cannot directly drive the motor. Therefore, the AQMH3615NS driver is selected to drive the electric push rod, as shown in Figure 5(a).

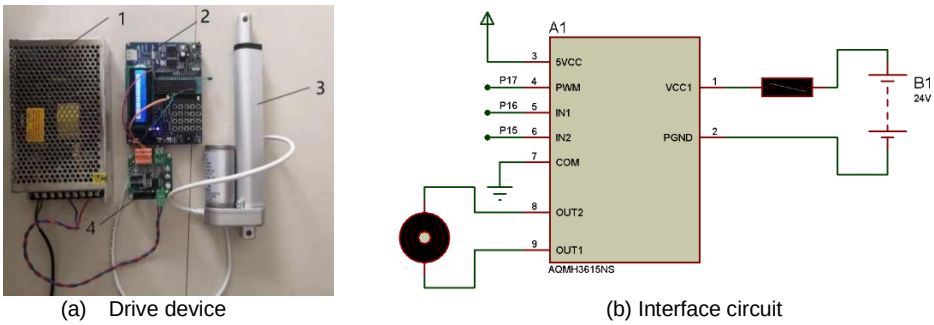

(a) Drive device (b) Interface circuit

Fig. 5 - Motor drive device and interface circuit

1. Power supply; 2. Microcontroller system board; 3. Electric actuator; 4. AQMH3615NS

The driving power supply for the electric actuator is 24 V, while the power supply for the microcontroller is 5 V. The working power supply of the motor is separated from the power supply of the microcontroller system to prevent the motor's surge current from causing the microcontroller control system to malfunction. The motor driver interface circuit is shown in Figure 5(b). The microcontroller's P1.5 and P1.6 pins are used to control the direction of the motor, and the microcontroller's P1.7 pin outputs PWM (Pulse Width Modulation) to control the DC motor's speed, thereby controlling the operating speed of the electric actuator.

Serial communication hardware circuit design

Taking into account factors such as communication transmission distance, transmission speed, bus utilization, network characteristics, transmission mode, and fault tolerance mechanisms, this system adopts a CAN bus interface. Therefore, the input and output signals of each node during communication are all CAN interface signals. The system uses CAN transceiver modules to achieve the conversion between TTL signals and CAN interface signals, as shown in Figure 6(a). To improve the reliability of the system, the bus connections between nodes are made using CAN bus connectors, as shown in Figure 6(b). Shielded cables are used for the transmission lines between nodes, with a termination resistor of 120Ω installed at the designated positions as shown in Figure 6(c).

(a)CAN conversion module (b)CAN bus connector (c)Terminal resistor

Fig. 6 - CAN bus

SOFTWARE DESIGN OF SPRAY BOOM ANGLE CONTROL SYSTEM

Distance measurement and algorithm design

Due to the influence of temperature changes on ultrasonic distance measurement, the microcontroller measures the temperature every half an hour in order to compensate for the detected values of the ultrasonic sensor. When the ultrasonic sensor detects distance, the microcontroller uses analog I2C communication to measure the distance. Since the values collected by the ultrasonic sensor are calibrated at a temperature of 25℃, and temperature has a significant impact on the speed of sound propagation, the microcontroller converts the distance detected at 25℃ to the actual distance using equation (1).

$$V = 346.675+0.607T \quad (1)$$

where:

T is the difference between the current temperature and 25°C,
V is the speed of sound propagation at the current temperature.

Since the CAN bus sends data in packets of 8 bytes, and each distance measurement takes up two bytes, the microcontroller continues to collect distance information after each measurement. After collecting distance data four times, it sends a frame of data to the CAN bus. The specific flowchart is shown in Figure 7.

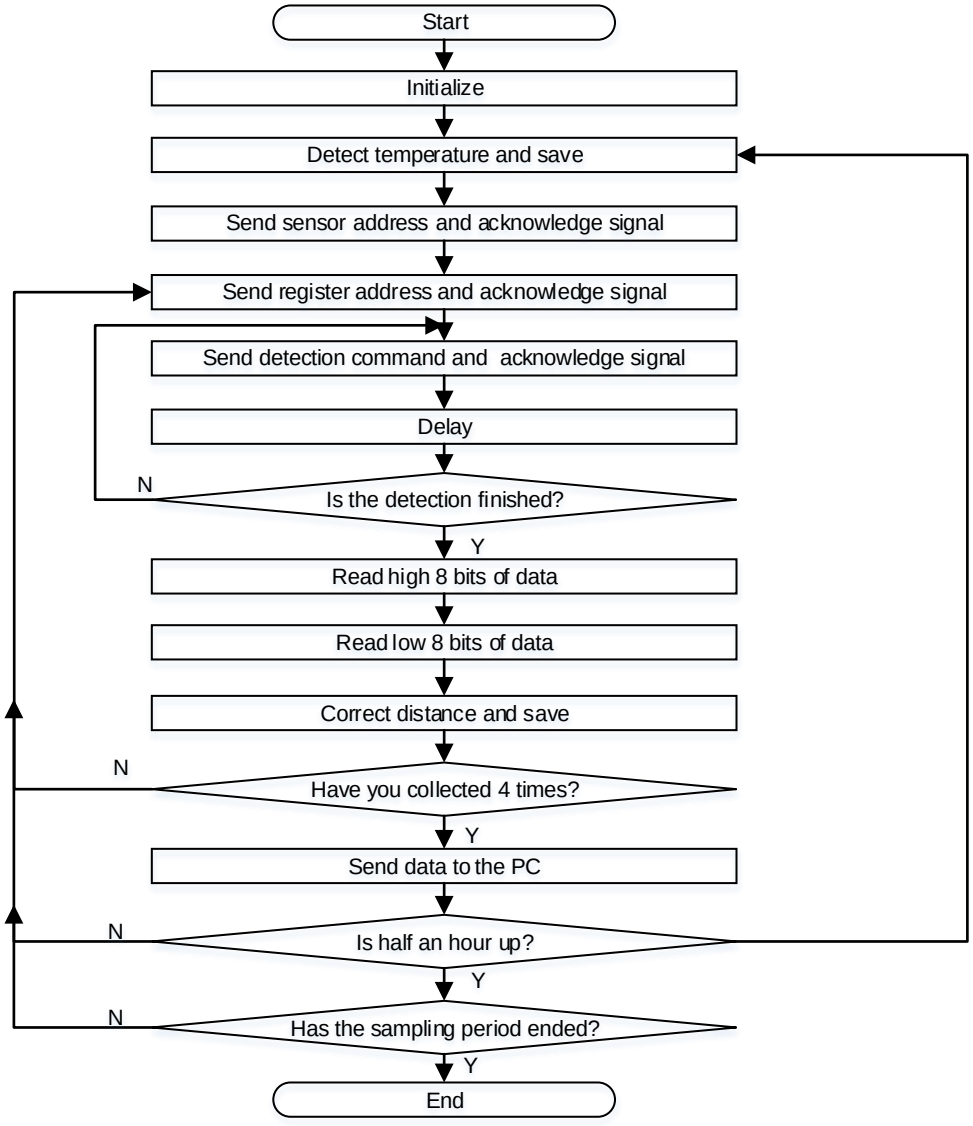

Fig. 7 - Flow diagram of distance measurement

In response to the occurrence of pests and diseases in maize crops at different growth stages, pesticide application operations are carried out. If the current monitoring is the distance between the spray rod and the crop canopy, the spray rod is adjusted to maintain the optimum distance from the crop canopy by control. As shown in Figure 9, when the spray rod passes over the crop, the distance between the spray rod and the crop canopy is maintained at the set value D_s.

In the area from point A to point B, when the set value D_s is equal to the distance value D_C measured by the ultrasonic sensor between the spray rod and the crop canopy, the spray rod remains in its current state. When the set value is greater than the measured distance value, the spray rod rotates upward; when the set value is less than the measured value, the spray rod rotates downward.

At the same time, during the 3-5 leaf stage, the ultrasonic sensor can measure the distance between it and the ground D_G. In the area without crops from point B to point C, the distance values measured by the ultrasonic waves, D_C and D_G, are basically equal. At this time, D_G is also basically equal to the measured value of the distance between the ultrasonic wave and the ground in the previous cycle. Therefore, it is considered that there are no crops under the current ultrasonic ranging sensor. Usually, the measured distance $D_C > D_S$, so the spray rod needs to be lowered according to the control requirements. If the spray rod is lowered, it is likely that the crops will collide with the agricultural machinery as the sprayer continues to move forward, damaging both the machinery and the crops. Therefore, when there is an area without crops, a virtual Dc' is fed back to the control system.

$$D_c' = D_g - \left(D_{g1} - D_{c1}\right) \quad (2)$$

where:

D_c' is the distance from the ultrasonic sensor to the crop canopy in the virtual crop-free area, m;

D_g is the distance between the ultrasonic sensor and the ground during the current sampling period, m;

D_{g1} is the distance between the ultrasonic sensor and the ground during the most recent sampling period ($Dg > Dc + hr$), m;

D_{c1} is the distance between the ultrasonic sensor and the crop canopy during the most recent sampling period ($Dg > Dc + hr$), m.

By assuming that the current crop height is the same as the crop height collected in the previous cycle, the current state of the boom is maintained. When the boom runs over the crop again, in the area between point C and D, the boom continues to maintain a parallel state with the crop canopy, as shown in Figure 8 (*Strelioff et al., 2014*).

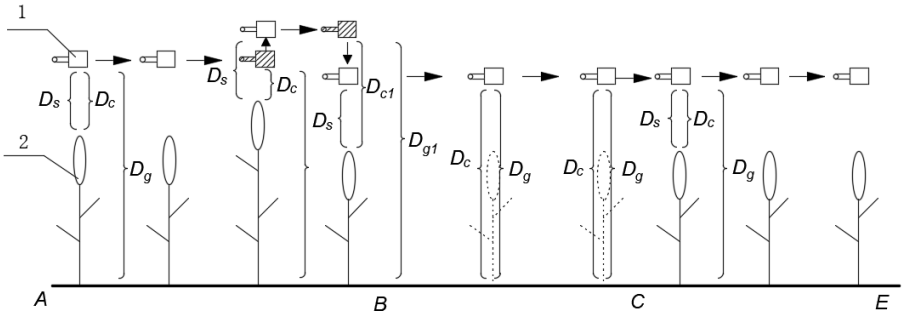

Fig. 8 - Algorithm for sparse branches and leaves

1. Ultrasonic sensor; 2. Crop

As the crop grows, after the 6-leaf stage, the corn branches and leaves become more abundant, making it difficult for ultrasonic waves to reach the ground, as shown in Figure 9. When the monitoring target remains the same, which is the distance between the boom and the crop canopy, in the area between point A and B, the system compares D_C and D_S and controls the angle of the boom. At this time, the measured D_G value is very small, and according to Equation (2), the current D_G value cannot be measured.

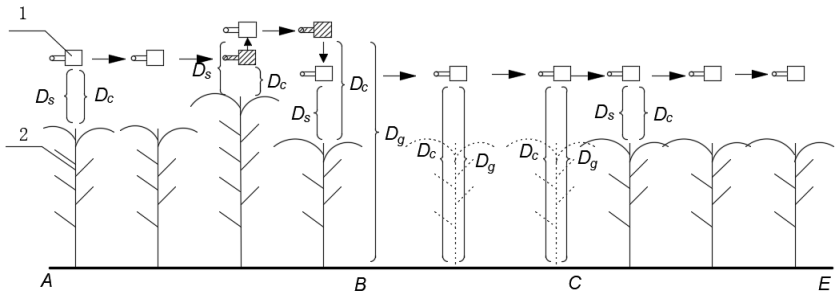

Fig. 9 - Algorithm for dense branches and leaves

1. Ultrasonic sensor; 2.Crop

When the boom enters the area BC, which is a region without crops, from the region AB where there are crops, the ultrasonic sensor near point B can collect both the distance to the crop canopy and the distance from the sensor to the ground. According to Equation (3), the distance between the ultrasonic sensor and the ground can be obtained. As the sprayer advances, when (D_G - D_C)<h_r, it can be assumed that this area is a region without crops. By using Equation (3), the distance between the ultrasonic sensor and the ground is virtually generated and then fed back to the control system.

$$D_g = \begin{cases} D_g & D_s + H_p - h_r \le D_g \le D_s + H_p + h_r \\ 0 & D_g < D_s + H_p - 25 \end{cases} \quad (3)$$

where:

D_G is the distance between the ultrasonic sensor and the ground during this sampling cycle, measured m. D_S is the distance between the sensor and the crop canopy set by the system, measured, m. H_P is the average height of the current crop, measured, m. h_r is the height of the crop ridge, m.

Vehicle body angle filtering algorithm design

When the sprayer is operating in the field, the main external excitation sources are high-frequency pulse signals and low-frequency step signals. When the wavelength is greater than 20 m and the vehicle forward speed is 2 m/s, the oscillation frequency of the vehicle is less than 0.6 rad/s. The boom should be able to fully track the ground fluctuations, and the boom can follow the vehicle's oscillation. When the oscillation frequency of the vehicle is higher than 5 rad/s, the ratio between the boom angle and the ground angle should be less than 0.2.

In order to eliminate high-frequency signal noise interference, the sampled signal is subjected to Fourier transformation to obtain the frequency of the current signal, and then signals with frequencies greater than 1 Hz are filtered out. The controller collects data N from the tilt angle sensor, applies Fourier filtering to calculate the current roll angle of the vehicle, and compares the current roll angle γi with the roll angle at the last actuation of the electro-hydraulic push rod. If equation (4) is satisfied, the roll angle of the current sampling period is sent to the PC by the controller.

$$|\gamma_i - \gamma_0| > \delta \quad (4)$$

where: γ_0 is the inclination angle of the vehicle at the last actuation of the electro-hydraulic push rod. γ_i is the inclination angle of the vehicle during the *i*-th sampling period. δ is the threshold value, and in the design, δ = 0.5.

Algorithm design for boom angle

By using the distances measured by ultrasonic sensors installed on both sides of the boom and the distance between the two sensors, the angle γ_u of the boom relative to the crop canopy or ground can be calculated. The vehicle inclination angle γ obtained from the dynamic inclination sensor data after Fourier filtering. When only the former is used as the input to the control system, vibrations caused by field ground excitation can lead to erroneous actions by the control system. When only the latter is used as the input to the control system, the system can only receive the current angle information of the boom, lacking the height of the boom relative to the crop canopy. Therefore, combining both inputs, the specific algorithm is as follows:

$$\gamma_b = \begin{cases} \gamma_{b0} & |\delta_\gamma| < \delta \\ \gamma_u & |\delta_\gamma| \ge \delta \end{cases} \quad (5)$$

where:

δ_γ represents the rate of change of the vehicle inclination angle γ; δ is the threshold value, and the optimal value is obtained through multiple experiments.γ_{b0} is the boom angle of the previous cycle.

Communication protocol and related design

In order to enable serial communication and control of agricultural machinery, the International Organization for Standardization (ISO) developed ISO 11783 based on the CAN 2.0B bus. ISO 11783 is a communication protocol that operates on top of the physical and data link layers (*Gao et al., 2019*). While the CAN 2.0B bus protocol includes both standard data frame and extended data frame formats, ISO 11783 specifically defines a complete communication standardization strategy for the extended data frame format. Therefore, this paper utilizes the extended frame format.

The extended frame format adopts the Protocol Data Unit (PDU) standard data frame format, as shown in Figure 10, which mainly includes priority (P), extended data page (EDP), data page (DP), PDU format (PF), specific PDU (PS), and source address (SA)(*Ding et al., 2019*). Referring to the ISO 11783 standard, a 29-bit identifier is defined for the spray boom control system, and the specific parameters for the 29-bit identifier are defined as shown in Table 1.

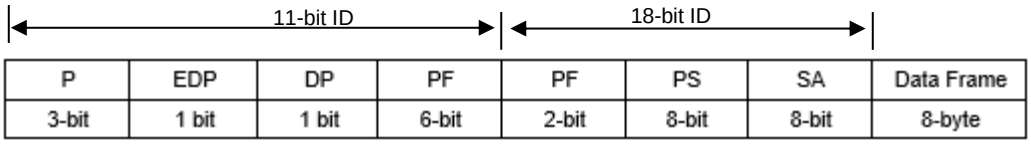

Fig. 10 - ISO 11783 PDU

In order to reduce the overhead of processing CAN signals by the processor, the following settings are made for the filter registers and mask registers, as shown in Table 2.

Table 1

Parameter definitions for 29-bit identifiers

Name	P	EDP	DP	PF	PS	SA
left	6	0	0	FE	FF	F4
right	6	0	0	FC	FF	F2
PC	3	0	0	F0	FF	00
electric actuator	6	0	0	FB	FF	F1
vehicle tilt angle	6	0	0	FA	FF	05

Table 2

Setup of CAN bus

Name	Frame format	ID	Masking filtering	Mask register	Filter register
left	Extended frame	63FEFFF4	Mask bit mode	00C00000	00F300FF
right	Extended frame	63FCFFF2	Mask bit mode	00C00000	00F300FF
PC	Extended frame	33CCFF00	Disable filtering	–	–
electric actuator	Extended frame	63EFFFF1	Mask bit mode	00C00000	00F300FF
vehicle tilt angle	Extended frame	63EEFF05	Mask bit mode	00C00000	00F300FF

In the system, the PC can not only directly read the values of each node on the CAN bus but also send commands directly to the node controlling the electric actuator. This mainly includes parameters such as the extension/retraction direction of the electric actuator and the duty cycle of the PWM waveform used to control the electric actuator.

Human-machine interface software design

To achieve real-time detection and control of the spray boom angle, this paper utilizes VC++6.0 to develop a PC program, as shown in Figure 11. The PC is responsible for receiving and sending data, analysing, processing, calculating control variables, and storing information. Each node sends the collected parameters to the PC in real-time.

The PC saves the measured distance data and vehicle tilt angle information into a database. It also uses the fuzzy ISODATA method to analyse and obtain the height of the spray boom relative to the crop canopy. The PC applies Fourier transform to filter out signals greater than 1Hz from the vehicle tilt angle. By using the distance information between the left and right spray booms and the filtered vehicle tilt angle, the current tilt angle of the spray boom is obtained. The current vehicle tilt angle serves as an input parameter. With the appropriate control algorithm, the PC determines the extension/retraction direction and the duty cycle of the input waveform for controlling the electric actuator.

The PC interface includes four sections: the main operating interface, system parameter settings, communication port settings, and data display.

The parameters that need to be set before the system runs are shown in Figure 12. First, select the operation mode. When herbicides need to be sprayed on corn during the 3-5 leaf stage, it is necessary to identify the distance between the spray boom and the ground and select 'Ground Mode'. When conducting pest and disease control, the distance between the spray boom and the canopy needs to be identified, and 'Canopy Mode' should be selected. Spray height refers to the distance between the spray boom and the canopy or ground. Due to the different targets and modes of action of pesticides, the appropriate height from the spray nozzle to the target may vary. Therefore, it is necessary to set the spray height before conducting spraying operations. The distance between the two ultrasonic sensors refers to the straight-line distance between the installation positions of the two ultrasonic ranging sensors. It is one of the parameters used to calculate the tilt angle of the spray boom.

Adjusting the threshold refers to adjusting the threshold value of the relative distance between the two ends of the spray boom and the spray target in the spray boom angle control. The system parameters that are set will be saved in the database and displayed on the main operating interface.

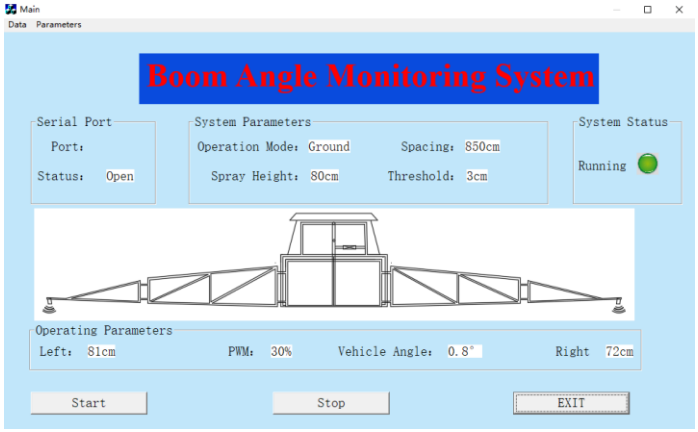

Fig. 11 - Main interface

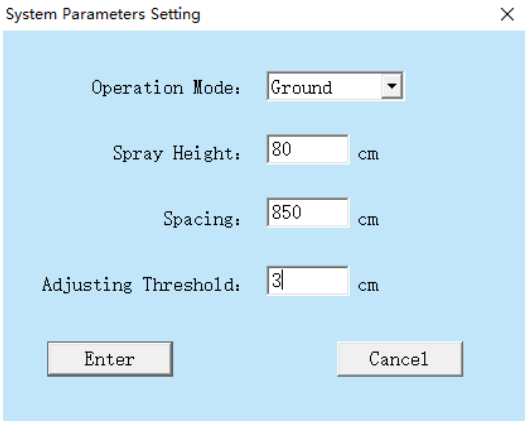

Fig. 12 - System parameters setting interface

RESULTS

In order to verify whether the design of the boom inclination control system is reasonable, the system is installed on the boom whose length is 9 m to measure the distance from the boom to the ground. After the system is running, the data shows that the menu can be used to view the collected data, the data clustered during the operation, and the control data during the system operation, as shown in Fig.13.

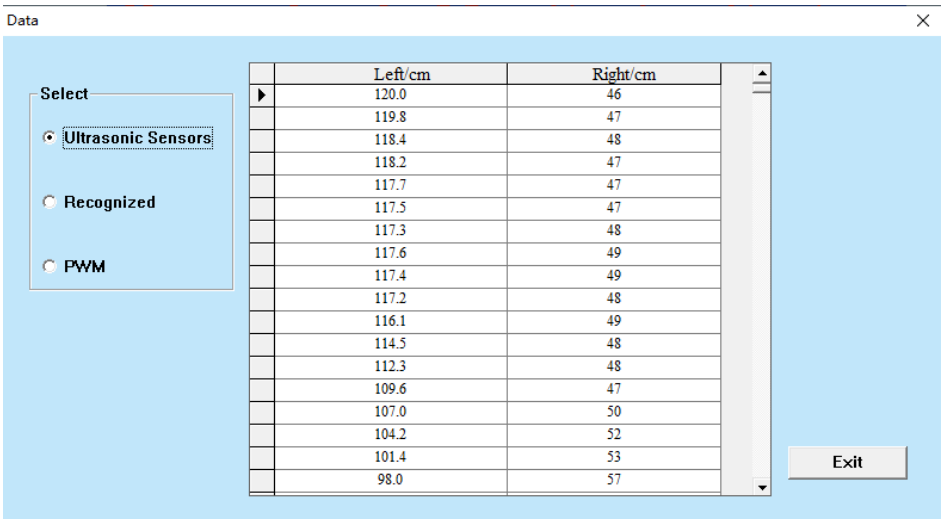

(a) Ultrasonic sensor measurement data

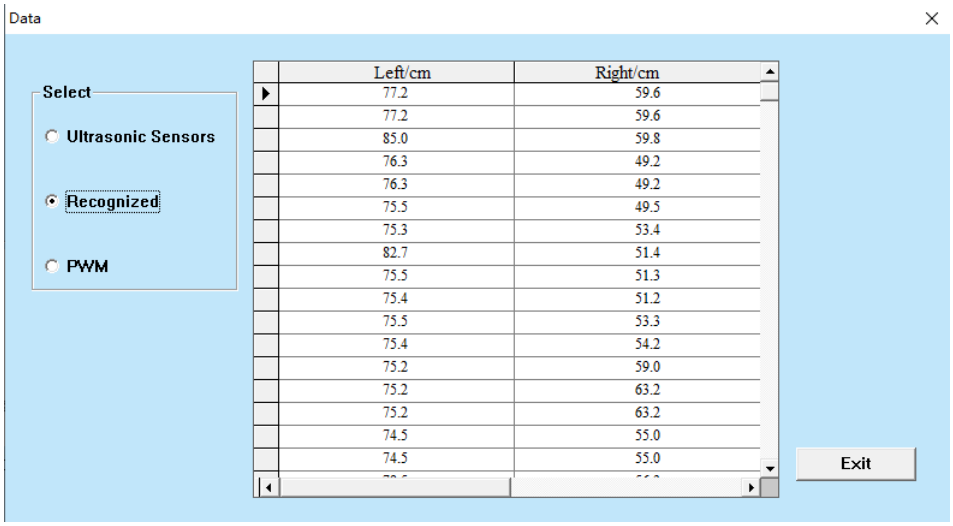

(b) Clustered data

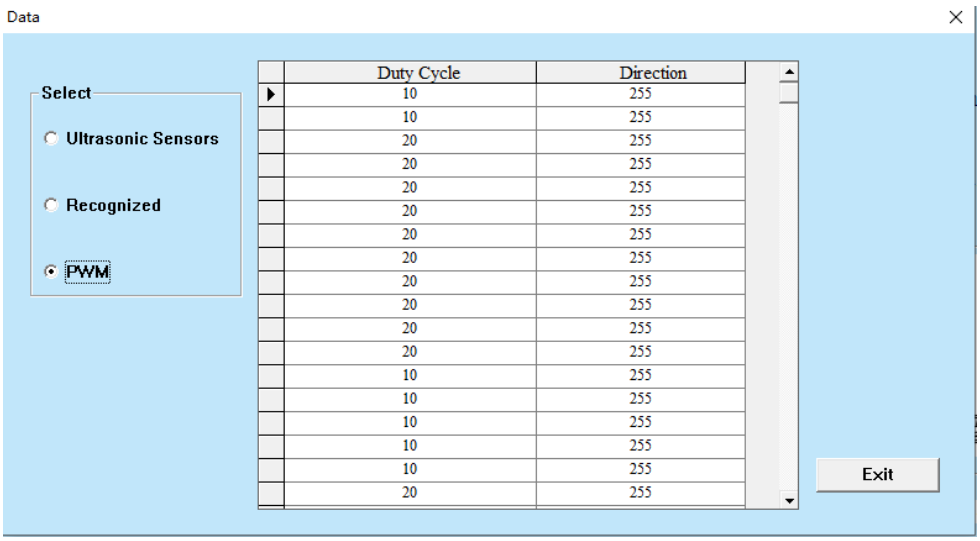

(c) Control data

Fig. 13 - Data display

CONCLUSIONS

According to the control requirements, a spray boom tilt control system based on the CAN bus was constructed, which consists of a main control node, distance measurement nodes, vehicle tilt detection nodes, and tilt control nodes. An ultrasonic sensor is used to measure the distance between the spray boom and the crop canopy or ground, a tilt sensor is used to measure the vehicle tilt angle, and an electric actuator is used to achieve real-time automatic control of the spray boom angle. The detailed design methods for the hardware and software of the real-time control system for the spray boom angle are described.

The design of a serial communication network based on the CAN bus has been completed, and the bus communication protocol for the spray boom tilt control system has been developed according to the ISO 11783 standard. This is beneficial for the standardized transmission of spray boom angle control parameters and system expansion in the future.

For the canopy mode and ground mode, a real-time dynamic monitoring system for spray boom angle was designed, which displays various parameter information in the spray boom tilt control system in real-time. The system has functions such as displaying and setting system parameters, browsing data, and automatically monitoring the tilt angle of the spray boom and making decisions based on the detection information. It drives the electric actuator to work and has a user-friendly and easy-to-operate human-machine interface.

ACKNOWLEDGEMENTS

This research was supported by talent scientific research fund of Liaoning Petrochemical University (No.2021XJJL-024).

REFERENCES

[1] He, X. (2022). Research and development of efficient plant protection equipment and precision spraying technology in China: a review (高效植保机械与精准施药技术进展). *Journal of Plant Protection*, 49(1), 389-397.

[2] Qi, L., Fu, Z. (1999). Experimental Study on Spray Deposition Uniformity (不同条件下喷雾分布试验研究). *Transactions of the Chinese Society of Agricultural Engineering*, 16 (2), 113-117.

[3] Ramon, H., Baerdemaeker, J. (1997). Spray boom motions and spray distribution: Part I-Derivation of a mathematical relation. *Journal of Agricultural Engineering Research*, 66, 23-29.

[4] Chen, Z., Wu, C., Yang, X. (2008). Spray distribution uniform of boom spraying (喷杆喷雾雾量的分布均匀性). *Journal of Jiangsu University*, (6), 465-468.

[5] Qiao, B., Ding, S., Xue, X., Cui, L., Zhuo, J., Zhang, Y. (2017). The research status and prospects on the structure of spray boom (喷雾机喷杆结构的研究现状及展望). *Journal of Agricultural Mechanization Research*, 39(11), 246-250+256.

[6] Cui, L., Xue, X. Ding, S., Le F. (2019) Development of a DSP-based electronic control system for the active spray boom suspension. *Computers and Electronics in Agriculture*, 166(2019), 105024.

[7] Li, F., Bai, X., Su, Z., Tang, S., Wang, Z., Li, F., Yu, H. (2023). Development of a control system for double-pendulum active spray boom suspension based on PSO and fuzzy PID. *Agriculture-Basel*, 13(9), 1660.

[8] Wang, S. (2014). *Design and experiments on boom height automatic adjusting system* (喷杆高度自动调节系统设计与试验研究) [Mastertal dissertation, Northwest A&F University].

[9] Anthonis, J., Audenaert, J., Ramon, H. (2005). Design optimisation for the vertical suspension of a crop sprayer boom. *Biosystems Engineering*, 90 (2), 153-160.

[10] Chen, W., Qiu, B.,Yang, N.,Yin, L. (2013). Spray boom position control system based on ultrasonic sensors (基于超声波传感器的喷杆位姿控制系统). *Journal of Agricultural Mechanization Research*, 35(3), 83-87.

[11] Cui, L., Xue, X., Ding, S., Gu, W., Chen, C, Le, F. (2017). Modeling and simulation of dynamic behavior of large spray boom with active and passive pendulum suspension (双钟摆主被动悬架式大型喷雾机喷杆动力学仿真与试验). *Transactions of the Chinese Society of Agricultural Machinery*, 48(2), 82–90.

[12] Cui, L., Xue, X., Le, F., Mao, H., Ding, S. (2019). Design and experiment of electro hydraulic active suspension for controlling the rolling motion of spray boom. *International Journal of Agricultural and Biological Engineering*, 12(4), 72–81.

[13] Wei, X., Shao, J., Miao, D., Li, L., Xie X. (2015). Online control system of spray boom height and balance (喷杆式喷雾机喷杆高度及平衡在线调控系统). *Transactions of the Chinese Society of Agricultural Machinery*, 46(8), 66–71.

[14] Wang, X., Qu, J., Xu, Y.Li, X., Xiao, Z., Wang, L. (2023). Spray Boom Height Control System of Potato Sprayer Based on Canopy Information (基于冠层信息的马铃薯喷雾机喷杆高度控制系统研究). *Transactions of the Chinese Society of Agricultural Machinery*, 54(9), 198-207.

[15] Wang, J., Yang, Z. (2016). Design and Experimental Research on Automatic Levelling Boom Sprayer (自动调平喷杆式喷药机设计与试验研究). *Journal of Agricultural Mechanization Research*. 38(7), 162-166.

[16] Alexandre, E., Santiago, P., Joan, R. (2011). Performance of an ultrasonic ranging sensor in apple tree canopies. *Sensors*, 11, 2459-2477.

[17] Liu, Y., Liu J. (2006). Application of ultrasonic range finder for mobile robotic obstacle avoidance (超声波测距仪在移动机器人避障中的应用). Chinese journal of scientific instrument, 27 (6), 1559-1560.

[18] Gu, C. (2019). Design and experimental study of a novel inclination sensor based on fiber Bragg grating (新型光纤光栅倾角传感器设计与试验研究). [Mastertal dissertation, Shenyang Jianzhu University].

[19] He, B. (2020). *Research on the algorithms of measuring force lines based on six-axis inertial sensor* (基于六轴惯性传感器的力线测定算法研究) [Mastertal dissertation, Zhe Jiang Normal University].

[20] Strelioff, W., Griffith, J., Schnaider, J., Lee, G., Hockley, D. (2014). *Height Control*. Patent. No. 8843283. USA

[21] Gao, Y., Wang, X., Yang, S., Zhai, C., Zhao, X., Zhao, C. (2019). Development of CAN-based Sowing Depth Monitoring and Evaluation System (基于 CAN 总线的播种深度监测评价系统研究). *Transactions of the Chinese Society of Agricultural Machinery*, 50(12), 23-32.

[22] Ding, Y., Liu, Y., Yang, L. (2019). Monitoring system of maize precision planter based on Android and CAN bus (基于 Android 和 CAN 总线的玉米播种机监控系统研究). *Transactions of the Chinese Society of Agricultural Machinery*, 50(12), 33-41+62.

DESIGN AND TESTING OF 4YZ-6 FRESH CORN HARVESTER GRAIN SPLITTING FRONT END COMPONENT
/
鲜食玉米联合收获机分禾前端研究与试验

Zhibo LI*), Tong YE, Meiling NIE, Haitao LAN, Xin ZHANG, Wei ZHAO
Heilongjiang Academy of Agricultural Machinery Engineering, Harbin 150000, China
Tel: +86-18745497221; E-mail: 1580322217@qq.com
DOI: https://doi.org/10.35633/inmateh-72-73

Keywords: *fresh corn, fracture, loss, components, tests*

ABSTRACT
Aiming at the problem of high cob loss in non-opposed row harvesting of 4YZ-6 fresh corn harvester, a front-end part adapted to the grain splitter of this model was designed. The structure of the front-end part was elaborated, the sliding conditions of the stalks under the action of the grain splitter were studied, the forces between the stalks and the front-end part were theoretically analyzed, and the operating effect of the front-end part was verified through field tests. The tests show that the expected operating effect is optimal when the inclination of the grain separator is 27.7°, the clamping angle of the grain splitter is 31°, the stubble height is 270 mm, and the front-end guards half width is 3.8 mm. The verification test for this parameter combination yielded a breakage rate of 8.71% and a loss rate of 9.47%, which were basically consistent with the expected values. The design of this front-end component of the grain splitter provides an effective means to reduce the loss of ears in the harvesting process of fresh corn.

摘要
针对 4YZ-6 型鲜食玉米收获机在非对行收获时果穗损失大的问题，设计了与该机型分禾器相适应的前端部件。详细阐述了前端部件的结构，研究了茎秆在分禾器作用下的滑动情况，对茎秆与前端部件之间的作用力进行了理论分析，并通过现场试验验证了前端部件的工作效果。试验表明，当谷物分离器倾角为 27.7°、谷物分割器夹角为 31°、留茬高度为 270 mm、前端护板半宽为 3.8 mm 时，预期运行效果最佳。对这一参数组合进行验证测试的结果是，破损率为8.71%，损失率为9.47%，与预期值基本一致。该分禾器前端部件的设计为减少鲜食玉米收获过程中的果穗损失提供了有效手段。

INTRODUCTION
In recent years, under the support of national policies, the fresh corn industry has been developing rapidly and its planting scale has been expanding *(Zhang et al., 2019)*. Fresh corn refers to corn harvested in the late milk ripening or early wax ripening stage and used for processing or directly consumed, including glutinous corn, sweet corn, shoot corn and colorful corn and other varieties, which are sweet, soft and nutritious, and much loved by the people *(Revilla et al., 2021).* When the harvester carries out field operations, the divider installed at the front end of the harvester takes the lead in interacting with the corn stalks, causing the stalks to move closer to the ear picking gap under the action of the divider *(Bu et al., 2016)*. With the advance of the harvester, the stem and ear enter the picking gap, so that the stem and ear are separated. Therefore, the divider needs to meet the smooth transportation of corn stalks to the picking gap, and at the same time avoid the occurrence of stalk overturning and breaking as much as possible.

Fresh corn harvest in the northeast region generally exists in August to September, when the rainy season leads to poor field conditions, in order to carry out low loss and high efficiency harvesting operation of fresh corn. some plots need to carry out non-opposite row operation. Non-opposite row operation means that the forward direction of the harvester and the forward direction of the planting machine present a certain angle, rather than parallel. In particular, fresh corn is harvested with a high-water content in the stalks, and the stalks are easy to be broken and pushed down when they touch the grain-splitting device, resulting in the loss of cobs *(Wang et al., 2021)*.

Scholars from Anhui Agricultural University used ADAMS to model and simulate the corn stalks and the grain splitter *(Guo et al., 2015)*, and through virtual orthogonal tests, it was found that the smoothness of the surface at the transition of the grain splitter can reduce the chances of the corn stalks being broken or pushed back.

Scholars from China Agricultural University pointed out that when developing a new type of corn stalk and cob combine harvesting machinery cutting table, the tip of the grain splitter is lower than 350 mm, and it is also needed to ensure that the height of the operating plane from the ground is greater than 100 mm *(Zhang et al., 2018)*. Scholars from Gansu Agricultural University conducted a study on the mechanism of vertical roller picking, pointing out that the cone angle of the grain separator and the height of the tip of the grain separator from the ground are the main factors affecting the effect of the grain separator *(Xin et al., 2020; Du et al., 2014)*. Some scholars have optimized the separating performance of the grain separator by conducting simulation experiments on the kinematic and dynamic performance of the separating device, corn plant and picking roller *(Tai et al., 2020)*. Scholars from Shandong Agricultural University evaluated the performance of the separator by analyzing the effects of the operating height of the separator and the forward speed of the harvester on the different displacements of the maize stalks in the X, Y, and Z directions at the time of harvesting *(Wang et al., 2021)*. Some scholars designed a separator suitable for the harvesting of fallen sugarcane *(Bai et al., 2021)*. Scholars from Northeast Agricultural University designed a special divider for a bionic flexible clamping spike picking cutter *(Zhu et al., 2023)*. Some scholars designed a divider for a garlic harvester to investigate the factors affecting the success rate of garlic feeding and conducted a field trial *(Zhu et al., 2023)*.

Although researchers realize that the front end of the divider has an important impact on harvesting performance, they ignore the fact that the actual operation of the harvester will result in the loss of ears due to non-opposed row operation. In the new situation of grain saving and loss reduction to ensure food security, the design of the front part of the grain splitter was carried out *(Felipe et al., 2021).* The deflection angle and force when the stalks contact with the front-end part of the grain separator are analyzed, and field tests are conducted on the key parameters of the front-end part of the grain separator, so as to verify the changes in the breakage rate of the stalks and the loss rate of the cobs, with a view to reducing the breakage rate and the loss rate of the non-opposed rows of the fresh corn harvester, and then provide theoretical support for the optimization and design of the grain separator.

MATERIALS AND METHODS

Key component design

In order to facilitate the processing and manufacturing of the harvesting device and to guarantee the structural strength of the harvesting device, the front-end components of the harvesting device are designed as shown in Fig.1. It mainly consists of a deflector plate, a front guard plate, a plug plate, a front arc plate and an intermediate arc plate. Among them, the front-end guard plate and the middle arc plate are welded with the grain separator in sequence, and the front-end components of the deflector plate, the front-end guard plate and the plug plate assembly are fastened with the grain separator through bolts. While guaranteeing that the front end of the grain separator can be replaced quickly, the amount of bending of the corn stalks by the components can be minimized.

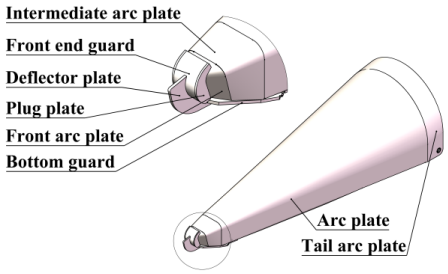

Fig. 1 - Schematic diagram of the front-end structure of the grain splitter

Stalk force analysis

When the 4YZ-6 harvester operates in non-opposed rows, the relative positions of corn stalks and the front-end parts of the divider are shown in Fig. 2, and the stalks may be distributed in the A interval, B interval, and directly on the axis of the guide plate. When the stalks are directly on the axis of the deflector plate, the corn stalks are then directed to both sides of the deflector plate by the divider, and the stalks are again in contact with the front-end guard plate, the front-tip main plate, and the intermediate arc plate.

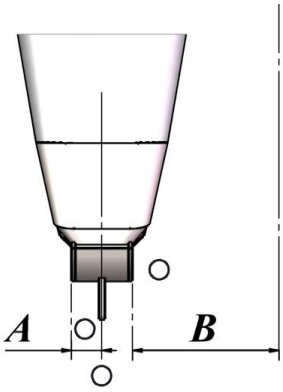

Fig. 2 - Schematic diagram of the relative positions of the stalks and the front of the grain splitter

When the stems are distributed in the interval A shown in Fig.2, between the side edge line of the deflector plate and the side edge line of the plug plate, the component that first contacts with the stems to produce the separating effect at this time is the front-end guard. As shown in Fig.3, the angle between the force F_s of the front-end component on the stalks and the forward direction of the harvester is β, then the stalks satisfy the constraint condition of not being pushed over:

$$\begin{cases} F_t = \frac{F_S}{cos\beta} \\ F_m = \lambda F_s \end{cases} \quad (1)$$

where:

λ is the coefficient of friction; F_s is the force exerted by the component on the stalk; F_m is the reaction force of the stalk on the component; F_t is a combined force in the opposite direction of forward motion; β is the angle between the combined force and the opposite direction of forward motion.

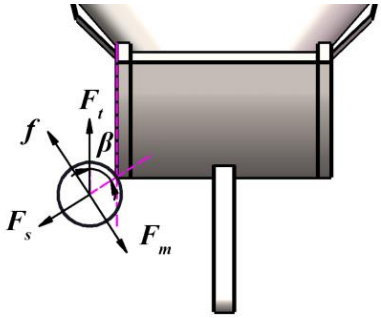

Fig. 3 - Schematic diagram of stalks touching the front-end guards

Combined with Fig.3 and Eq.1, it can be seen that when the angle of deflection of the stalk is less than the critical value of the folding angle, the constraint on whether the stalk can be pushed down at this time is that the product of the elastic force of the stalk on the front end of the divider and the half-angle cotangent value of the tip angle of the front end of the divider is greater than the friction of the front end of the divider on the stalk, i.e. Eq.2:

$$F_S cot\alpha \geq F_m \quad (2)$$

where:

α is the angle between the reaction force and the direction opposite to the forward direction.

When the stalks are distributed in the interval B shown in Fig 2, i.e., the interval from the side line of the plug plate to the side line of the middle arc plate, the edges of the components which have the effect of harvesting on the stalks at the front end of the harvesting are the plug plate, the front arc plate and the middle arc plate in order, and their force relationship is shown in Fig 4. At this time, the corn stalk is subjected to a force pointing to the center of the circle. and perpendicular to the edge of the harvesting action of F_s, the elasticity of the stem to the front end of the divider is F_t, which is opposite to the direction of the harvester. Assuming that there is no relative sliding of the stalks with the front arc plate and the middle arc plate, then there is:

$$\mathrm{F_S cot\alpha \geq F_m} \quad (3)$$

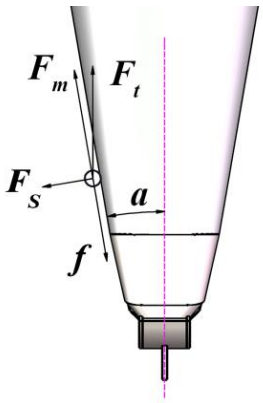

Fig. 4 - Schematic representation of the distribution of stalks in interval A

Front end guard design

From Fig.4 and Eq.3, it can be seen that the angle β between the force A and the forward direction is the key parameter to determine the breaking of the stem. When the stalks touch the front-end guard at the same time, the clamping angle of the grain splitter β takes the value close to 0. As the harvester advances, the stalk is in contact with the front end of the divider, and the force provided by the harvester points to the center of the corn stalk. At this time, as the harvester progresses, the stem is pushed down by the front guard plate. When the stalks are distributed in the interval A, and the distance between the stalks and the deflector plate is increasing, the value of the angle β is still close to 0, and the stalks are still pushed down by the front guard.

When the stalk is tangent to the side line of the blocking plate, the value of clamping angle of the grain splitter β tends to be close to 0, but when the distribution position of the stalk is close to the A interval, the clamping angle of the grain splitter β will increase, and the product of the elasticity of the stalk on the front end of the grain splitter and the cotangent value of clamping angle β is greater than the friction force of the front end of the grain splitter on the stalks, and the stalks won't be broken.

Since the value of the friction coefficient is usually between 0.2 to 0.6, combined with the change trend of the cotangent function image in the range of 0° to 90°, it can be seen that when the angle β is in the range of 59° to 78°, then the corresponding angle β takes the value of 0.6 to 0.21, and there is a possibility of the stalk being pushed over. When the value of the angle β is within the range of 78° to 90°, then the value of the angle β is less than 0.21, and the stalks will be pushed down by the front-end guard as the harvester advances. When the angle β is greater than 90°, the stalks are again tangent to the side line of the blocking plate, and the stalks enter into interval B. The stalks touch with the front guard plate axially, and the stalks move along the side of the blocking plate to the direction of the front arc plate and the middle arc plate of the divider along with the forward movement of the harvesting unit. When the divider moves to the right side of the stalks, the stalks do not touch the front end of the divider, and the stalks enter the separating gap when the harvester advances.

Through the measurement of the diameter of the stalks of Wannuo 2000 corn varieties, the average value is 25.5 mm. To sum up can be seen, when the front end guards half width is less than 7.68 mm, the stalks and the front end of the Front End Guards with the theoretical touch will not be pushed over and broken. In summary, whether the stalks are broken or not, or pushed down depends on whether the deflection angle when the stalks arrive at the tail board of the harvesting device is greater than the critical value of the deflection angle when the stalks are broken, and whether the half width of the front-end guard plate is less than 7.68 mm.

Field experiment

Inclination of the grain separator, clamping angle of the grain splitter, height of the front end of the grain splitter from the ground and front-end guards half width were selected as the evaluation indexes to explore the optimal combination of the parameters of the front end of the grain splitter for the field test.

The test period was from September 10 to September 12, 2022; the test site: 47°N planting area in the upstream township of Yian County, Qiqihar City, Heilongjiang Province; and the test equipment consisted of: a 4YX-6 fresh corn combine harvester, a Kubota GPS meter, a tape measure and a stopwatch. The 4YX-6 fresh corn harvester, shown in Fig. 5, is a 6-row fresh corn combine harvester independently developed by the Heilongjiang Provincial Research Institute of Agricultural Machinery Science and Engineering for field harvesting operations.

Fig. 5 - Field operation of 4YX-6 fresh corn combine harvester

The test variety is "Wan Nuo 2000". In accordance with the provisions of "Corn Harvesting Machinery" *(GB/T21962-2020)*, three 50 m-long horizontal non-opposed rows were randomly selected, in which the effective harvesting distance was more than 20 m, and the broken plants, diseased ears and ears with a height of 35 cm or less from the ground were removed from the test area before the test *(Lei et al., 2018)*.

Combining the above analysis with the field operation of the fresh corn harvester, the inclination of the grain separator, clamping angle of the grain separator, height of the front end of the grain separator from the ground and front end guards half width, which have a greater impact on stalk breakage and cob loss, were selected as the test factors.

In the measurement area and cleanup area, collect the missed and fallen ears (including the ear segments of more than 5 cm), weigh out the mass after stripping *(Li, 2019)*, and calculate the loss rate of ears through Eq.4.

$$S_U = \frac{M_U}{M_Z} \times 100\% \ [\%] \tag{4}$$

where:

S_U is the loss rate of ears; M_U is the lost cob mass; M_Z is the total mass harvested in the test area.

Statistics of the total number of stalks in each test area are made and the average value that is the total number of stalks in the test area is considered. After the harvester completes the harvesting operation, the number of broken stalks in the operating area are counted again and recorded. The total number of stems and the number of broken stems were calculated, and the ratio was recorded as the stem breaking rate, that is, the Eq.5:

$$Z_R = \frac{Z_U}{Z_D} \times 100\% \ [\%] \tag{5}$$

where:

Z_R is the fracture rate of stalks; Z_U is the number of broken stalks; Z_D is total number of stalks in the test area.

RESULTS

During the field test, the forward speed of the harvester was set to 6.7 km/h, and the Design-Export software was used to carry out the secondary rotary combination design test on the test data, which clarified the optimal coordination of the various parameters of the front-end device of the grain splitter *(Wang et al., 2019)*. The test factors and levels are shown in Table 1, and the selection of each level meets the requirements of field operation, and the average value of the statistical results after repeating the test three times for each test group was recorded as shown in Table 2.

Table 1

Table of factors and levels

Level	Factors			
	Inclination of the grain separator Q (°)	Clamping angle of the grain splitter J (°)	Height of divider tip from the ground H (mm)	Front end guards half width L (mm)
1	20	25	100	2.5
2	27.5	32.5	250	7.5
3	35	40	400	12.5

Table 2

Experimental program and results

Number	Factors				Indicators		Number	Factors				Indicators	
	Q	J	H	L	Z_R	S_U		Q	J	H	L	Z_R	S_U
1	20	25	100	2.5	15.79	16.78	16	35	40	400	12.5	27.82	29.26
2	35	25	100	2.5	19.74	18.14	17	20	32.5	250	7.5	12.59	14.39
3	20	40	100	2.5	13.43	15.21	18	35	32.5	250	7.5	14.85	15.47
4	35	40	100	2.5	15.14	16.42	19	27.5	25	250	7.5	19.81	20.13
5	20	25	400	2.5	19.07	20.41	20	27.5	40	250	7.5	17.77	17.59
6	35	25	400	2.5	20.28	21.38	21	27.5	32.5	100	7.5	12.41	13.92
7	20	40	400	2.5	16.79	17.77	22	27.5	32.5	400	7.5	16.32	17.55
8	35	40	400	2.5	18.22	19.24	23	27.5	32.5	250	2.5	8.26	9.27
9	20	25	100	12.5	26.47	27.13	24	27.5	32.5	250	12.5	17.91	18.84
10	35	25	100	12.5	28.59	28.07	25	27.5	32.5	250	7.5	10.6	13.65
11	20	40	100	12.5	22.9	27.18	26	27.5	32.5	250	7.5	11.64	12.84
12	35	40	100	12.5	22.51	26.58	27	27.5	32.5	250	7.5	11.72	13.16
13	20	25	400	12.5	26.75	30.00	28	27.5	32.5	250	7.5	11.59	12.95
14	35	25	400	12.5	29.58	31.53	29	27.5	32.5	250	7.5	12.08	13.30
15	20	40	400	12.5	28.31	28.61	30	27.5	32.5	250	7.5	12.19	12.92

Regression model construction and testing

Combined with the analysis of experimental data results and multiple regression fitting *(Tang et al., 2021; Liu et al., 2015)*, the analysis of variance of fracture rate of stalk Z_R is shown in Table 2. (L_1 is the level corresponding to the inclination angle of the grain sorting machine, L_2 is the level corresponding to the holding angle of the divider, L_3 is the level corresponding to the height of the divider tip from the ground, and L_4 is the level corresponding to the half width of the front guard plate). From Table 2, it can be seen that, among them, the effect of L_1, L_2, L_3, L_4, L_2L_3, L_2^2, L_3^2 on fracture rate of stalk Z_R is highly significant ($P<0.01$); the effect of L_1L_2, L_1^2 on fracture rate of stalk Z_R is more significant ($0.01<P<0.05$); the effect of L_1L_3, L_1L_4, L_2L_4, L_3L_4, L_4^2 on fracture rate of stalk Z_R was not significant ($P>0.1$). The regression sum of squares and degrees of freedom of the non-significant interaction terms were analyzed by ANOVA after incorporating them into the residual terms, which in turn led to the regression equation for the effect of each experimental factor on fracture rate of stalk Z_R as shown in Eq.6:

$$Z_R = 0.81L_1 - 1.29L_2 + 1.45L_3 + 4.67L_4 - 0.49L_1L_2 + 0.75L_2L_3 + 1.22L_1^2 + 6.29L_2^2 + 1.86L_3^2 + 12.07 \quad (6)$$

Doing a loss-of-fit test on Eq.6 yields that $P=0.1266$ is not significant ($P>0.1$), thus indicating that there are no other major factors affecting the test indicator and that there is a significant quadratic relationship between the test indicator and the test factor.

Regression model and significance test for loss rate

Combined with the analysis of the results of the experimental data and multiple regression fitting, the analysis of variance of loss rate of ears S_U is shown in Table 3. As shown in Table 3, which shows that L_1, L_2, L_3, L_4, L_1^2, L_2^2, L_3^2 have a highly significant effect on the loss rate of ears S_U ($P<0.01$); the effect of L_2L_3, L_4^2, is more significant on the loss rate of ears S_U ($0.01<P<0.05$); the effect of L_2L_4 is significant on the loss rate of ears S_U ($0.05<P<0.1$); L_1L_2, L_1L_3, L_1L_4 , L_3L_4 had a non-significant effect on loss rate of ears S_U ($P>0.1$). The regression sum of squares and degrees of freedom of the non-significant interaction terms were analyzed by ANOVA after incorporating them into the residual terms, which in turn led to the regression equation for the effect of each test factor on loss rate of ears as shown in Eq.7:

$$S_U = 0.48L_1 - 0.87L_2 + 1.46L_3 + 5.14L_4 - 0.23L_2L_3 + 0.19L_2L_4 + 1.57L_1^2 + 5.5L_2^2 + 2.37L_3^2 + 0.69L_4^2 + 13.25 \quad (7)$$

Doing a loss of fit test on Eq.7 yields $P=0.2059$ is not significant ($P>0.1$), thus indicating that there are no other major factors affecting the test indicator and that there is a significant quadratic relationship between the test indicator and the test factor.

Table 3

ANOVA of variance between stem breakage and corn ear loss rate

Indicators	Z_R					S_U				
Source	**Sum of Squares**	**df**	**Mean Square**	**F-value**	**P-value**	**Sum of Squares**	**df**	**Mean Square**	**F-value**	**P-value**
Model	1091.67	14	77.98	108.76	<0.0001***	1145.01	14	81.79	502.52	<0.0001***
L_1	11.89	1	11.89	16.58	0.001**	4.12	1	4.12	25.3	0.0001**
L_2	29.88	1	29.88	41.67	<0.0001***	13.71	1	13.71	84.25	<0.0001***
L_3	38.02	1	38.02	53.03	<0.0001***	38.49	1	38.49	236.47	<0.0001***
L_4	393.12	1	393.12	548.3	<0.0001***	476.17	1	476.17	2925.71	<0.0001***
L_1L_2	3.85	1	3.85	5.37	0.035**	0.2678	1	0.2678	1.65	0.219
L_1L_3	0.363	1	0.363	0.5063	0.4877	0.1828	1	0.1828	1.12	0.3061
L_1L_4	1.12	1	1.12	1.56	0.2308	0.3875	1	0.3875	2.38	0.1437
L_2L_3	9.11	1	9.11	12.7	0.0028**	0.8603	1	0.8603	5.29	0.0363**
L_2L_4	0.1314	1	0.1314	0.1833	0.6747	0.5513	1	0.5513	3.39	0.0856*
L_3L_4	0.1871	1	0.1871	0.2609	0.6169	0.2048	1	0.2048	1.26	0.2797
L_1^2	3.83	1	3.83	5.35	0.0354**	6.35	1	6.35	38.99	<0.0001***
L_2^2	102.39	1	102.39	142.81	<0.0001***	78.24	1	78.24	480.7	<0.0001***
L_3^2	8.98	1	8.98	12.52	0.003**	14.55	1	14.55	89.42	<0.0001***
L_4^2	0.8761	1	0.8761	1.22	0.2864	1.23	1	1.23	7.58	0.0148**
Residual	10.75	15	0.717			2.44	15	0.1628		
Lack of Fit	9.17	10	0.9168	2.89	0.1266	1.98	10	0.1981	2.15	0.2059
Pure Error	1.59	5	0.3173			0.4605	5	0.0921		
Cor Total	1102.42	29				1147.45	29			

*Note: *** means highly significant ($P < 0.01$), ** means more significant ($0.01 \leq P < 0.05$); * means significant ($0.05 \leq P < 0.1$).*

The experimental data were processed using Design-Export 13, and the response surface of the interaction of factors on fracture rate of stalk and loss rate of ears was obtained by regression equation as shown in Fig. 6.

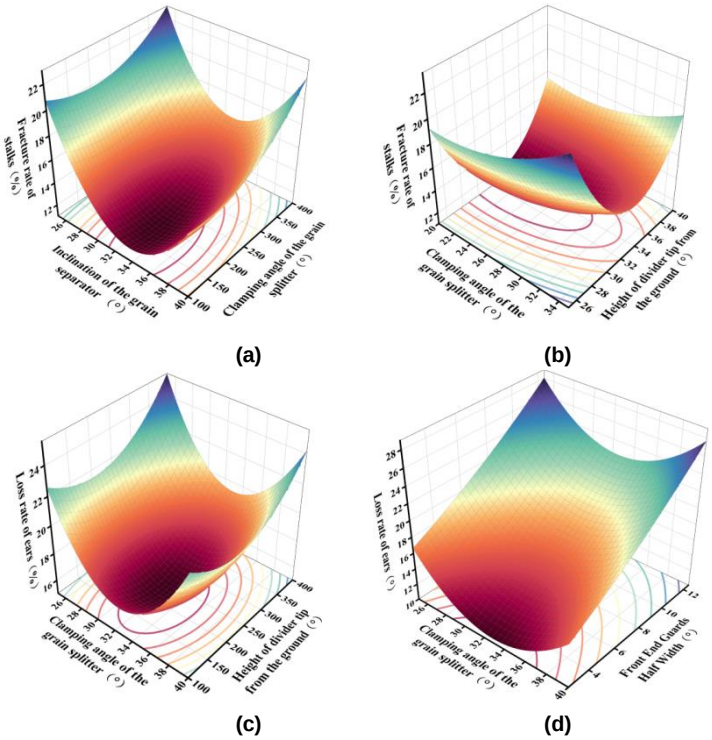

Fig. 6 - Response surface for the effect of interactions on indicators

Combined with Fig.6a, it can be seen that when the height of the front end of the grain separator is 250 mm, the half width of the front end guard plate is 7.5 m, and the inclination angle of the grain separator is kept constant, the breaking rate of the stem decreases first and then increases with the increase of the clamping angle of the grain separator. When the holding angle of the grain separator is constant, then the fracture rate of stalks with the increase of the clamping angle of the grain separator shows the trend of first decrease and then increase; when the grain separator clamping angle is constant, the fracture rate of stalks with the increase of the inclination of the grain separator is slightly showing the trend of decreasing. The reason is that the fixed width of the rear end of the grain splitter is 296 mm, with the increasing clamping angle of the grain splitter, the front edge of the grain splitter keeps approaching to the front guard plate, the short edge of the grain splitter leads to the poor effect of the grain splitter, and the deflection angle of the edge of the grain splitter and the maize stalks increases when touching, and the number of stalks pushed down and broken directly increases with the forward movement of the harvester. When the clamping angle of the grain separator is constant, the fracture rate of stalks with the increase of the inclination angle of the grain separator slightly shows a downward trend, because the inclination angle of the grain separator is constantly increasing, and the deflection angle of the corn stalks when touching them is constantly becoming smaller, the number of stems entering the snapping device increased. Therefore, in the interaction between the inclination of the grain separator and the clamping angle of the grain splitter, the clamping angle of the grain splitter is the main factor affecting the fracture rate of stalk.

In Fig. 6b it can be seen that when the clamping angle of the grain separator is 27.5° and the front end guards half width is 7.5 mm, keeping the height of the front end of the grain separator from the ground is constant, the fracture rate of stalks shows a trend of decreasing and then increasing with the increase of the clamping angle of the grain separator. The reason is that when the height of the front end of the grain separator is constant, the angle of the deflection of the stalks and the edges of the grain separator is increasing with the clamping angle of the grain separator and the amount of the fracture rate of stalks is increasing; maintaining the clamping angle of the grain separator is constant. Fracture rate of stalks showed an increasing trend with the increase of the height of the front end of the grain separator from the ground. The reason is that when the clamping angle of the grain splitter is constant, with the increasing height of the front end of the grain splitter from the ground, the stalk deflection angle increases, and the number of corn stalks broken to both sides increase. Therefore, in the interaction between the clamping angle of the grain splitter and the height of the front end of the grain splitter from the ground, the clamping angle of the grain splitter was the main factor affecting the fracture rate of stalks.

For the cob loss rate S_u, Fig.6c shows that when the clamping angle of the grain separator is 27.5° and the front end guards half width is 7.5.mm, the cob loss rate with the increase of the height of the front end of the grain separator from the ground shows a decreasing trend. The reason is that the height increase of the deflection degree of the stalks decreases, and the number of stalks smoothly entering the spike picking gap increases, the number of cobs picked increases. When the height of the front end guards half width of the grain separator from the ground is a certain height, the loss rate of ears shows a decreasing and then increasing trend. When the height of the front end of the grain splitter from the ground is constant, the loss rate of ears decreases with the increase of the clamping angle of the grain splitter. The reason is that the increase of the clamping angle of the grain splitter, the force edge of the divider increases, the number of stalks entering the spike picking gap increases, and the number of spikes lost and missed becomes less, and the loss rate of ears decreases relatively. In the interaction between the clamping angle of the grain splitter and the height of the front end of the splitter from the ground, the clamping angle of the grain splitter was the main factor affecting the loss rate of ears.

Fig.6d shows that when the inclination angle of the grain separator is 27.5°, and the height of the front end of the grain separator from the ground is 250 mm, when the clamping angle of the grain separator is maintained at a certain level, the loss rate of ears increases with the increase of the front end guards half width, because when the half width of the front end guards is increased, the wider the front end of the grain separator, the probability of the stalk touching the front end guards half width in the front section of the grain separator increases, and the stalk pushed back by the harvester increases, and the loss rate of ears increases. When the front-end guards half width is constant, the loss rate of ears increases with the increase of the clamping angle of the grain splitter, because when the clamping angle of the grain splitter increases, the force edge of the divider reduced and the fracture rate of stalks increases, resulting in an increase in the fracture rate of stalks, and the loss rate of ears increases as a result. In the interaction between clamping angle of the grain splitter and front end guards half width, the main factor affecting the loss rate of ears was the length of front end guards half width.

Combined with the fresh corn harvester field operation requirements, quadratic regression model and response surface analysis, the set constraints and mathematical models for each test factor are:

$$\begin{cases} minZ_R(L_1, L_2, L_3, L_4) \\ minS_U(L_1, L_2, L_3, L_4) \\ s.t. \begin{cases} 20° \le L_1 \le 35° \\ 25° \le L_2 \le 40° \\ 100mm \le L_3 \le 400mm \\ 2.5mm \le L_4 \le 12.5mm \end{cases} \end{cases}$$

Optimization module was applied to optimize the experimental parameters *(Zhu et al., 2023;Zhu et al., 2022)*, combined with the constraints interval to select the optimal level combination, to obtain the inclination of the grain separator of 27.7°, clamping angle of the splitter of 31°, the height of the front end of the grain separator from the ground is 270 mm and the front end guards half width of 3.8 mm, corresponding to the indicators of the stalk breakage rate of 8.63%, the loss rate of ears of 9.42%. At this time, the experimental index effect was optimal. Using the optimized front-end parameters for verification tests, the fracture rate of stalks was 8.71% and the loss rate of ears was 9.47%, which was basically the same as the optimized results, and effectively improved the fracture rate of stalks and the loss rate of ears of the fresh maize harvester in the horizontal non-opposed row operation.

CONCLUSIONS

Aiming at the problem of high stalk breakage and large cob loss in non-opposed row harvesting of fresh corn, the front part of the grain splitter was designed, and combined with the deflection angle of the stalk and the front edge of the front end of the grain splitter to the force of the contact between the corn stalk and the front end of the distributor was analyzed. and clarified the design requirement of the clamping angle of the grain splitter to be less than 59°, it provides a reference for the design of corn harvester divider.

Inclination of the grain separator, clamping angle of the grain splitter, height of the front end of the grain splitter from the ground and front end guards half width were selected as the factors, and the regression orthogonal test was conducted with the indexes of fracture rate of stalk and loss rate of ears, combined with the analysis of variance (ANOVA) and the analysis of response surface (ASRS), and it was concluded that the inclination angle of the grain splitter is 27.7°, the clamping angle of the grain splitter is 31°, the height of the front end of the grain separator from the ground is 270 mm, and the front end guards half width of 3.8 mm is the maximum of the front end guards half width. When the half-width is 3.8 mm, the expected effect is optimal, and the corresponding indexes of stalk breakage rate is 8.63% and loss rate of ears is 9.42%. The verification test on the optimized parameters yielded a stalk breakage rate of 8.71% and a cob loss rate of 9.47%, which were basically consistent with the expected results and the operation effect was ideal.

ACKNOWLEDGEMENT

This study was supported by the Heilongjiang Provincial Agricultural Science and Technology Innovation Spanning Project Agricultural Science and Technology Basic Innovation Project Excellent Youth Project (CX23YQ36), National Key Research and Development Plan (2016YFD0701900); National Corn Industry Technology System Special Project (CARS-02-28); Heilongjiang province key research and development plan project major project (2022ZX05B01) funding.

REFERENCES

[1] Bai J., Ma, S., Wang, F., Xing, H., Ma, J., & Hu, J. (2021). Field test and evaluation on crop dividers of sugarcane chopper harvester. *International Journal of Agricultural and Biological Engineering*, 14(1), 118-122.https://www.ijabe.org/index.php/ijabe/article/view/5621

[2] Becerra-Sanchez, F., & Taylor, G. (2021). Reducing post-harvest losses and improving quality in sweet corn (Zea mays L.): challenges and solutions for less food waste and improved food security. *Food and Energy Security*, 10(3), e277. https://onlinelibrary.wiley.com/doi/full/10.1002/fes3.277

[3] Bu L.X., Zhang D.L., Li T., Jia Chunyang & Cui M. (2016). Analysis and simulation of the cutting deck support device of an off-row corn harvester. *Agricultural Mechanization Research* (04), 57-60+242. DOI:10.13427/j.cnki.njyi.2016.04.012.

[4] Du, Yuefeng. (2014). *Design method and experimental research on self-propelled corn harvester in hilly and mountainous areas* (Doctoral dissertation), China Agricultural University.

[5] Guangqiang Zhu, Tianyu Li & Fujun Zhou. (2023). Design and test of a biomimetic tassel picking device for fresh corn (鲜食玉米仿生摘穗装置设计与试验). *Journal of Jilin University* (Engineering Edition) (04), 1231-1244. DOI:10.13229/j.cnki.jdxbgxb.20210767.

[6] Guangqiang Zhu, Tianyu Li & Fujun Zhou. (2022). Design and test of a flexible clamping and conveying device for bionic picking of fresh corn (鲜食玉米仿生摘穗柔性夹持输送装置设计与试验). *Journal of Jilin University* (Engineering Edition) (10), 2486-2500. DOI:10.13229/j.cnki.jdxbgxb20210308.

[7] Guo Jun Di (2017). *Performance Simulation of Corn Stalk and Harvester Cutting Table (玉米茎秆与收获机割台的性能仿真)* (Master's thesis), Anhui Agricultural University, China.

[8] Lei En, Huan Jianhua, Wang Yedong, Yang Yongbing, Liu Baohong, Lu Bingyue... & Wang, Pu. (2018). Research and Evaluation on Mechanical Harvesting Performance and Machine Harvesting Quality of Corn Yi in Yunnan. *Agricultural Mechanization Research* (04), 156-161. DOI:10.13427/j.cnki.njyi.2018.04.030.

[9] Li T.Y. (2019). *Design and test of flexible low-loss tassel picking device for fresh corn (鲜食玉米柔性低损摘穗装置设计与试验)* (Master's thesis), Northeast Agricultural University, China.

[10] Liu, Lin. (2015). *No-till planter ground wheel design and experimental research (免耕播种机地轮设计与试验研究)* (Master's Degree Thesis), Northeast Agricultural University, China.

[11] Revilla, P., Anibas, C. M., & Tracy, W. F. (2021). Sweet corn research around the world 2015–2020. *Agronomy*, 11(3), 534.https://www.mdpi.com/2073-4395/11/3/534

[12] Tai Jianjian, Li Haitao, Du Yuefeng, Guan Yunyi, Mao Enrong, Long Xinjiani (2020), Simulation analysis on the performance of splitting and picking devices of corn harvester [J]. *INMATEH Agricultural Engineering*, 62(3), pp.69-78. Romania. https://doi.org/10.35633/inmateh-62-07

[13] Wang Yikun. (2021). *Design and virtual test research on key components of corn harvester plate cutting table (玉米收获机板式割台关键部件的设计与虚拟试验研究)* [D]. Shandong Agricultural University, DOI:10.27277/d.cnki.gsdnu.2021.000584.

[14] Wang Hongxuan. (2021). *Design and experimental research on tractor-mounted multifunctional fresh corn harvester (牵引式多功能鲜食玉米收获机的设计及试验研究)* (Master's thesis, Heilongjiang Bayi Agricultural and Reclamation University). DOI:10.27122/d.cnki.ghlnu.2021.000238

[15] Wang L., Liao Y.T., Zhang Q.S., Yao L., Fu Y.K. & Liao Q.X. (2019). Research on imitation chisel-type furrow opener for oil-wheat dual-purpose precision wide no-till planter. *Journal of Agricultural Machinery* (11), 63-73.

[16] Xin Shanglong (2020). *Research on Mechanism and Key Technology of Vertical Roller Corn Harvesting (立辊式玉米摘穗机理与关键技术研究)* (PhD.Dissertation), Gansu Agricultural University. DOI: 10.27025/d.cnki.ggsnu.2020.000069

[17] Zhang Xirui, Wu Peng, Wang Keheng, Li Yue, Shang Shuqi & Zhang Xiumei. (2019). Design and test of 4YZT-2 self-propelled fresh corn pair row harvester (4YZT-2 型自走式鲜食玉米对行收获机设计与试验). *Journal of Agricultural Engineering* (13), 1-9.

[18] Zongling Zhang. (2018). *Development of new corn cob and stalk combine harvester cutting table (新型玉米穗茎联合收获机割台的研制)* (Doctoral dissertation), China Agricultural University.

[19] Zhu Guangqiang. (2023). *Research on bionic tassel picking mechanism and device for fresh corn (鲜食玉米仿生摘穗机理及装置研究)* (Ph.D. thesis), Northeast Agricultural University, China. https://link.cnki.net/doi/10.27010/d.cnki.gdbnu.2023.000012doi:10.27010/d.cnki.gdbnu.2023.000012.

[20] Zhu Z., Cheng J., Wu F., Hu Z., & Yu Z. (2023). Optimization of Operation Parameters of the Garlic Plant Divider and Lifter Mechanisms. *Agriculture*, 13(1), 189. https://www.mdpi.com/2077-0472/13/1/189

[21] Zunfeng Tang, Shuping Liu, Fujun Zhou, Tianyu Li, Jiao Li Wang & Chunyou Li. (2021). Design and test of seed production corn seed cob harvester (制种玉米种穗收获机设计与试验). *Journal of Agricultural Machinery* (07), 102-112.

EVOLUTION AND TECHNOLOGICAL DEVELOPMENT OF AUTOMATIC TRANSPLANTERS FOR VEGETABLES: A REVIEW

/

EVOLUCIÓN Y DESARROLLO TECNOLÓGICO DE LAS TRASPLANTADORAS AUTOMÁTICAS PARA HORTALIZAS: UNA REVISIÓN

Gaudencio GRANDE[1)], Martín HIDALGO-REYES[*2)], Pedro CRUZ[2)], Noe VELÁZQUEZ[3)]

[1)] Graduate Program of Agricultural Engineering and Integral Use of Water, Universidad Autonoma Chapingo / Mexico;
[*2)] Agricultural Mechanical Engineering Department, Universidad Autonoma Chapingo / Mexico;
[3)] Irrigation Department, Universidad Autonoma Chapingo / Mexico;
Tel: +525951104405; E-mail: mhidalgor@chapingo.mx
DOI: https://doi.org/10.35633/inmateh-72-74

Keywords: *automation, physical-mechanical properties, transplanting, transplant system, transplanting machine*

ABSTRACT

The main purpose of technological progress is to enhance the quality of human life. In agriculture, there has been a trend towards automating all stages of production processes. Transplanting seedlings is no exception, as it involves a repetitive and laborious process that demands significant time, depending on the extension to be transplanted. The objective of this review article was to analyze the evolution and technological development of automated transplanter prototypes by bibliometric analysis and a detailed review. Results show that the technological progress in this equipment is based on two main characteristics: (1) physical-mechanical properties of seedlings, which play a crucial role in component design, and (2) control and automation development. This means that efficiencies of over 90% and an error rate of less than 7.6% can be currently obtained for automated transplanter.

RESUMEN

El avance tecnológico ha tenido como propósito principal mejorar la calidad de vida del ser humano. En la agricultura se ha optado por automatizar todas las fases de los procesos de producción. El trasplante de plántulas no es la excepción, debido a que es un proceso repetitivo y cansado, que requiere amplios periodos de tiempo según la extensión a trasplantar. El objetivo de este artículo de revisión fue analizar la evolución y desarrollo tecnológico de los prototipos de trasplante automático de plántulas, mediante un análisis bibliométrico y una revisión detallada. Los resultados muestran que el avance tecnológico desarrollado en estos equipos se basa en dos características principales: (1) las propiedades físico-mecánicas de las plántulas, como características sobresalientes en el diseño de los componentes y, (2) el desarrollo del control y la automatización, con lo cual, actualmente se pueden obtener eficiencias superiores a 90% y una tasa de error inferior al 7.6% en el trasplante automático de plántulas.

INTRODUCTION

The evolution and technological advancement of automatic transplanters for vegetable crops mark a significant milestone in modern agriculture. These machine designs serve as transformative tools, revolutionizing traditional transplanting methods by enhancing efficiency, cutting labor costs, and refining precision in the transplanting process *(Ahmed et al., 2024)*. In recent decades, there has been remarkable progress in both the design and functionality of automatic transplanters, propelled by advancements in engineering, robotics, and precision agriculture *(Bazargani & Deemyad, 2024)*.

Vegetables comprise a group of greens and fruits such as tomatoes and are grown in open fields and greenhouses, playing a crucial role in human nutrition. They serve as antioxidants, anticancer agents, antidiabetics, and aids in reducing cardiovascular diseases *(Dias, 2019; Radovich, 2018)*. The most economically important vegetables in the world are tomatoes, bell peppers, melons and zucchinis, eggplants, cucumbers, watermelons and strawberries *(Baudoin, 2002)*.

[1] *Gaudencio GRANDE, Doctoral Stud.; Martín HIDALGO-REYES, Professor, Ph.D.; Pedro CRUZ, Professor, Ph.D.; Noe VELAZQUEZ, Professor, Ph.D.*

Transplanting is one of the tasks that requires high labor and time costs. Hence, mechanizing this task is essential for efficient operations and increased production *(Nage et al., 2023).* Currently, the most advanced transplanting machines include both semi-automated and automated models.

In contemporary agriculture, applications of robots and automated transplanters are being employed to enhance the quality and efficiency of this operation. These technologies are based on different principles, such as visual processing, aiming to reduce the damage rate to stems, leaves, and substrates *(Jin et al., 2021)*.

Automated transplanters are commonly structured with three systems: supply, manipulation, and transplant *(Jin et al., 2018)*. However, the types vary based on the working environment. Some are stationary, like the one developed by *Han et al. (2018)* for potted seedlings in a greenhouse, while others are autonomous machines designed for transplanting in elevated greenhouse cultivation *(Liu et al., 2019)*. There are also autonomous machines specifically used for transplanting in open fields *(Han et al., 2019)*.

Furthermore, various review studies have delved into the advancement and progression of automatic vegetable transplanters. *Syed et al. (2019)* primarily delved into artificial vision technology's application in automatic transplantation, aiming to enhance time efficiency, quality, and overall effectiveness. *Rasool et al. (2020)* dissected the diverse mechanisms encompassing clamps, manipulators, and end effectors of mobile, semi-automatic, and automatic transplanters, focusing specifically on onion transplantation automation. Similarly, *Habineza et al. (2023)* undertook a comparable analysis, albeit for seedlings in a broader context. *Sharma & Khar, (2022)* conducted a comprehensive examination encompassing manual, mechanical, and automatic vegetable transplanters.

Moreover, several research endeavors have explored technology and robotics' integration in transplantation methodologies, emphasizing the significance of substrates, end effectors, vision systems, and route planning *(Liu et al., 2023; Sharma et al., 2023)*.

Researchers worldwide, including those mentioned above, publish their findings in various journals, which are indexed in different databases like Scopus and Web of Science (S&WoS). Consequently, research into automated vegetable transplanters follows this trend, being no exception. The process of searching for information in these databases relies on the use of keywords. The system then displays the located documents, which are subsequently filtered by adding more specific words. In this context, bibliometric analysis serves as a tool to condense and synthesize information. It facilitates the examination of key variables, including development trends over the years, emerging areas, and collaborations among authors from different countries *(Chen et al., 2021; Donthu et al., 2021)*.

The S&WoS platforms are not designed for conducting bibliometric analyses. Therefore, extracting bibliometric information from these databases can pose a disadvantage as they may contain adverse conditions such as data duplication, and they do not analyze specific data from the study conducted in each research *(Donthu et al., 2021)*, therefore, it is necessary to complement the information with an additional review of articles obtained from other databases. In other words, a comprehensive analysis of the information is required, evaluating, discussing, and interpreting advancements and areas of opportunity related to prototypes developed for automated vegetable transplanting.

Finally, the development and evolution of automatic transplanting equipment for vegetables have proven to be highly advantageous for modern agriculture. These advancements offer a range of significant benefits, including increased efficiency and reduced labor costs, enhanced precision in seedling transplantation, minimized risk of plant damage, adaptability to diverse crops, resource optimization, and improved working conditions in the field. Clearly, these technological strides are driving a more productive, sustainable, and profitable agricultural sector, poised to revolutionize the industry and bolster global food security. However, despite the notable progress in this research domain, there remain areas necessitating further analysis. Hence, the primary objective of this study is to analyze the evolution, technological development, and engineering characteristics of prototypes for automated vegetable transplanting over the years. The analysis of this research was carried out using two tools: bibliometric analysis and a detailed review.

MATERIALS AND METHODS

Search method

The search for original documents was performed using two databases (S&WoS), in June 2023. The search was restricted to “article title, abstract, keyword” to exclude information unrelated to the topic.

For Scopus, the search equation used was TITLE-ABS-KEY (transplanting OR development AND transplanter OR design AND transplanter AND seedlings, AND automatic AND transplanter) AND (EXCLUDE(DOCTYPE , "re")) AND (EXCLUDE (DOCTYPE, "cr")) AND (EXCLUDE (DOCTYPE, "bk")),

aiming to exclude books, review articles, and conference reviews. Meanwhile, for Web of Science, the search equation used was Topic (transplanting OR development AND transplanter OR design AND transplanter AND seedlings, AND automatic AND transplanter) AND (Agricultural Engineering). Additionally, a filter was applied to exclude articles unrelated to the topic and review articles.

Bibliometric analysis

The data obtained from S&WoS was in Bibtex format with complete records and cited references. Subsequently, in the RStudio software version 2022.07.2, the two databases were merged, and information from 12 duplicate records was removed. An Excel® file was generated with a total of 243 records. Bibliometric analysis was conducted using the Biblioshiny tool in the RStudio Bibliometrix software *(Aria & Cuccurullo, 2017)*. Fig. 1 shows the flowchart for data collection, analysis, and visualization.

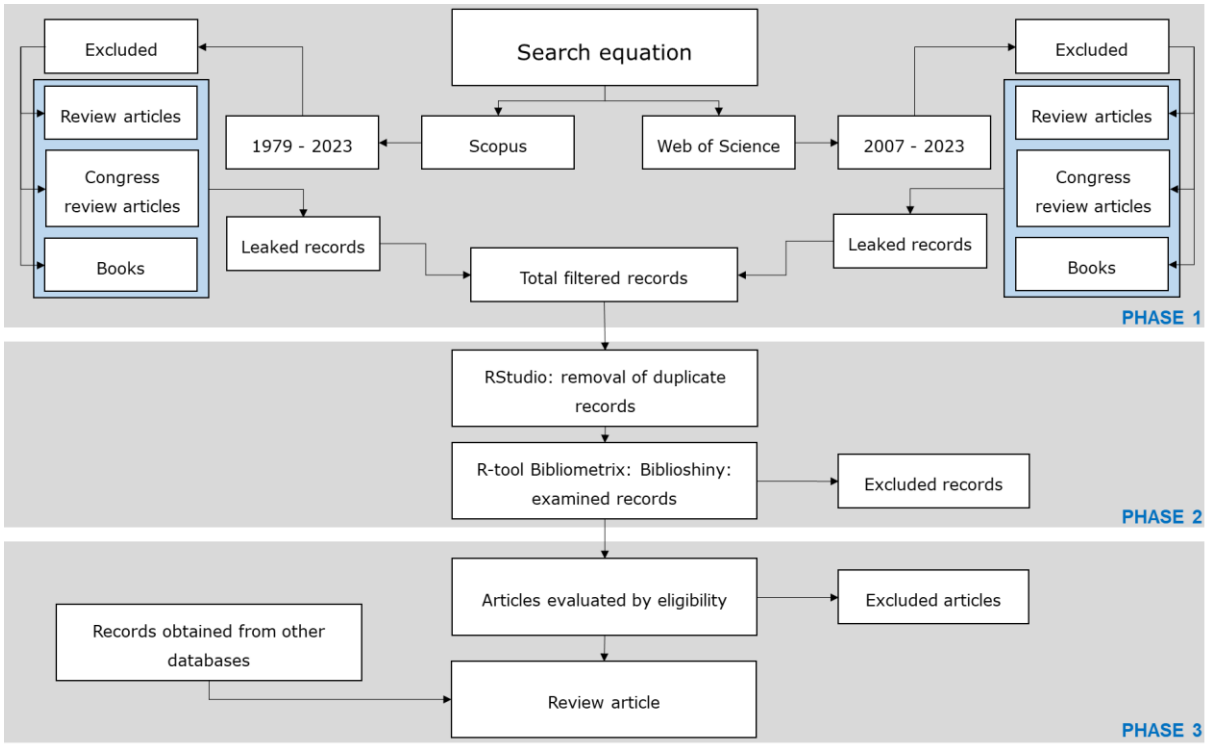

Fig. 1 – Flowchart for data search and analysis

Detailed review

In the detailed review, articles obtained from the bibliometric analysis were examined. Additionally, documents from sources beyond those used in this study were included, as they were not found in the initial S&WoS search (Fig. 1). The specific review was carried out based on the following variables in the design of equipment for automated seedling transplanting: physical and mechanical properties of seedlings, functional systems of prototypes, general characteristics, technical parameters, mechanisms and algorithms, current situation in Mexico, manufacturing costs, and areas of opportunity.

RESULTS AND DISCUSSION

The records analyzed (Table 1) were published between 1979 and 2023. A total of 243 records were analyzed, comprising 220 scientific articles and 23 conference papers.

Table 1

General information of the analyzed articles

Description	Results
Documents	243
Annual growth rate (%)	5.81
Document average age	6.63
Average citations per document	10.6
References	5128

Table 1
(continuation)

Description	Results
Documents	243
Keywords plus (ID)	1055
Author's Keywords	665
Authors	665
Authors of single-authored docs	10
Co-authors per document	4.69
International co-authorships (%)	3.292

Evolution of automated transplanting equipment

The first study related to automated transplanters was published in 1979, it refers to an automated feeder for transplanters developed by *Moden & Brewer, (1979)*. It wasn't until 1985 that the first automated transplanter for turf was recorded, achieving an efficiency of 97%. This prototype was developed by *Hauser, (1985)*.

The number of publications remained between zero and two articles per year for 28 years, totaling 13 articles. However, the boom in publications on automated transplanters began in 2008, reaching a total of five articles. This increase could be attributed to the global population growth and urbaniz ation, leading to the need to enhance food production. For instance, by 2010, more than 50% of the population already lived in cities, and it is estimated that by 2050, two-thirds of the global population will reside in urban areas due to the migration from rural to urban areas in search of better opportunities *(Van Bavel, 2013)*. One consequence of this mobility is the increased demand for food in cities, but at the same time the labor force in the countryside decreases. This situation has driven the need to automate agricultural activities to boost productivity in the fields *(FAO, 2022)*.

The evolution of transplanters aligns with the advancement of automation and data processing algorithms that require significant computational power *(Tendulkar, 2014)*. However, the rise of dual-core processors, allowing simultaneous task management, for mass consumption began in 2005 by the Intel Corporation *(Intel, 2005)*. Additionally, the implementation of Artificial Intelligence (AI) as part of automation in agriculture necessitates Graphics Processing Unit (GPU) support for the neural networks used in machine learning by researchers in the last 12 years *(Xu et al., 2021)*.

The peak in study production occurred in 2021, with a total of 35 articles. Despite the challenges the world faced due to the adversities caused by the COVID-19 pandemic, it appears that authors took advantage of the isolation period to concentrate on developing and presenting their findings on automated transplanting. The evolution of article production over the years is presented in Fig. 2.

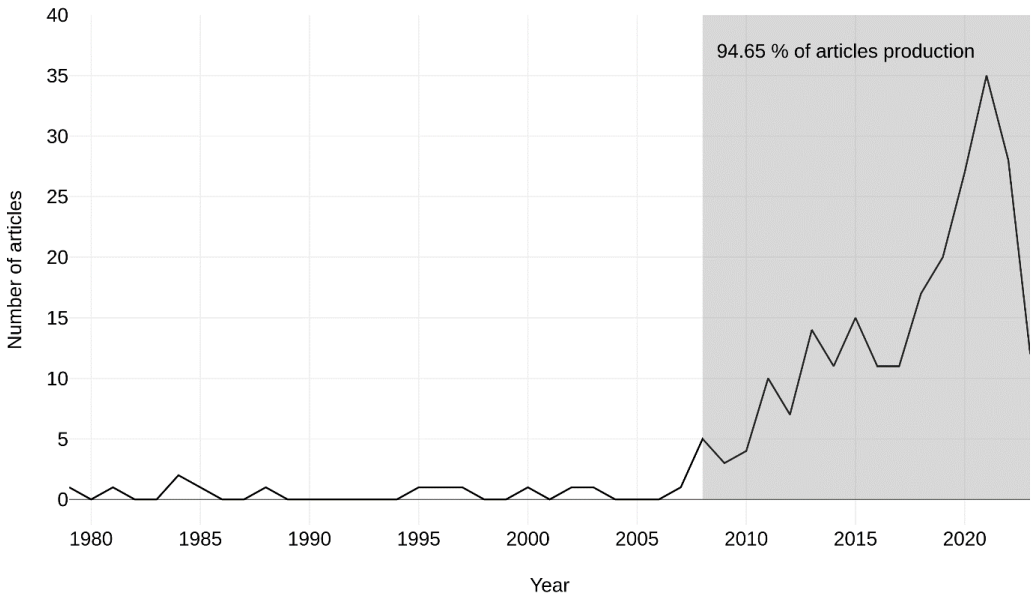

Fig. 2 – Origin and evolution of articles published between 1979 and 2023

Fig. 3 shows the 50 most frequently used keywords by the authors of the 243 analyzed documents. The term "*transplanter"* stands out as the most used, appearing in 14.4% of instances. "*Agricultural machinery"* follows with a 13.1% occurrence, and "*plug seedling"* is noted in 9% of cases. The term "*automated transplanter"* appears in only 4.1% of instances, ranking tenth in frequency. Fig. 3 shows the most used words regarding automated transplanting of vegetables.

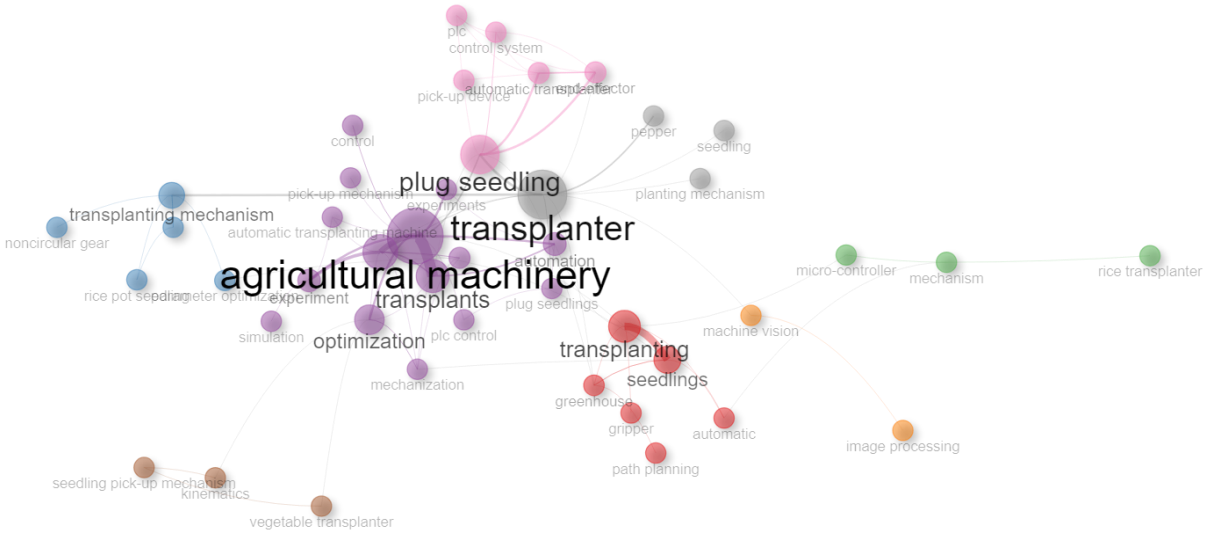

Fig. 3 – Co-occurrence network of authors' keywords

The evolution of automated transplanters is closely intertwined with technological advancements, as reflected in the keywords employed over the years. Notably, new terms such as *virtual simulation*", "*machine vision*" and "*image processing*" have emerged, signaling the influence of AI and its technological innovations in automated vegetable transplanting.

Fig. 4 shows the terms used in articles related to automated transplanters from 1979 to 2023. The parameters considered include a minimum word frequency and the number of words per year, set at five and three, respectively. The term "*transplanter*" stands out with the highest frequency, serving as the commonly used general term to describe automated transplanting in these articles.

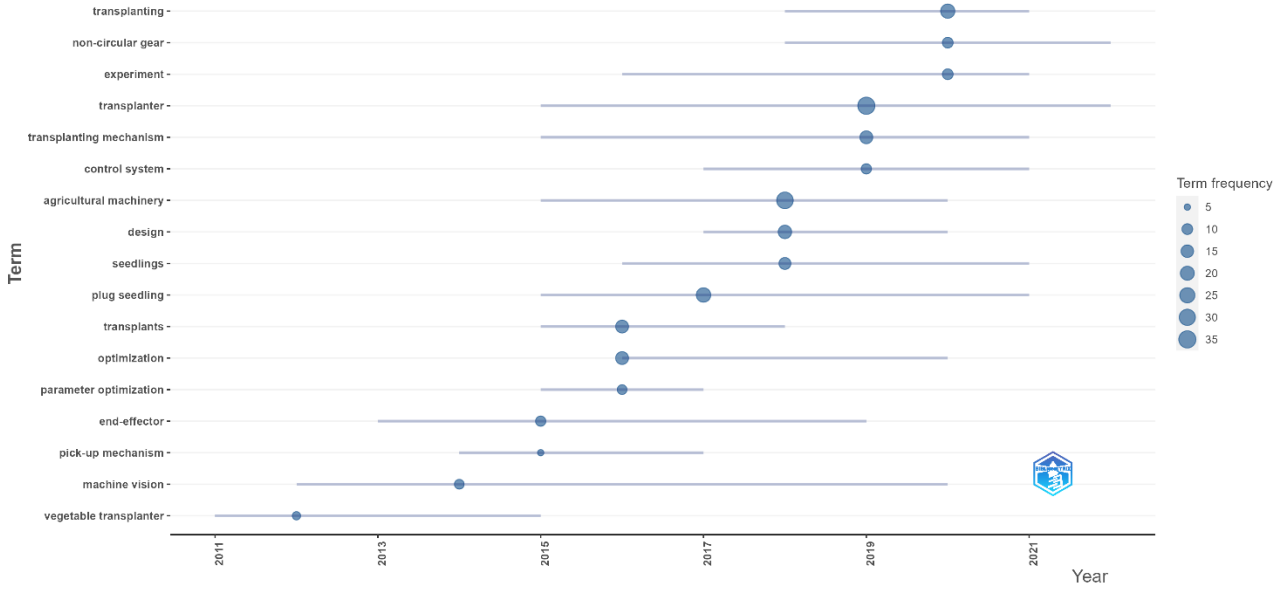

Fig. 4 – Current trends in automated transplanting-related topics

Scientific production on automated transplanters

The authors with the highest number of publications on the topic are as follows: in the first position, Hu J., Jin X., and Yu G., each with 18 published articles. The second position is held by Mao H., with a total of 17 published articles, and the third position is occupied by Han L., with 16 published articles.

The most cited authors are in the first position Kumar G. and Raheman H., each with a total of 10 citations. The second position is shared by Han L., Hu J., Kumi F., and Mao F., each with a total of seven citations, the third position is held by Ye B., with a total of five citations (Fig. 5).

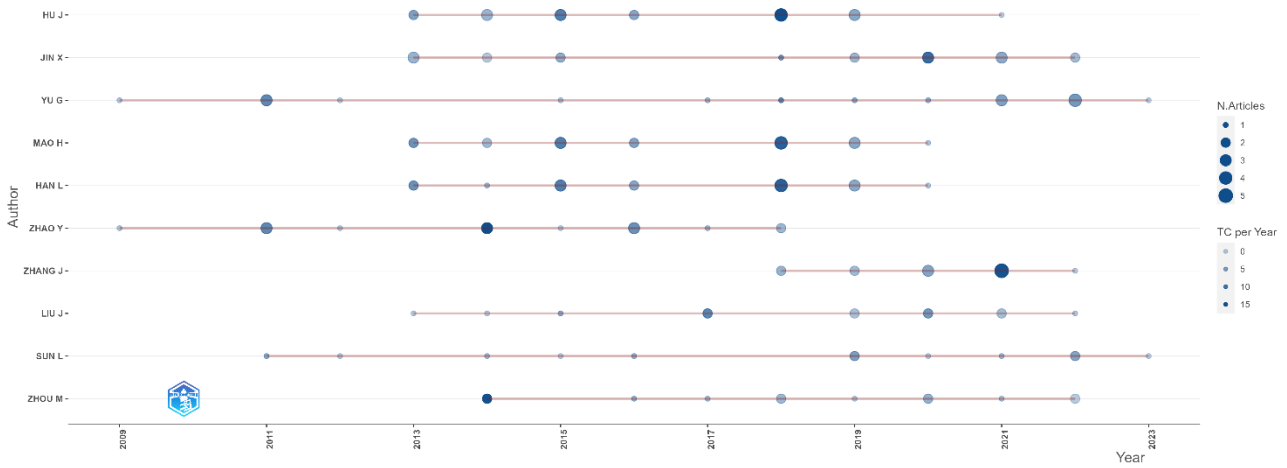

Fig. 5 – Authors' scientific production over time

The distribution of countries with the highest scientific production (Fig. 6) is indicated in blue. China, India, and the United States secure the top three positions. In the initial 28 years under analysis, the United States dominated scientific production. However, from 2007 onwards, India took the lead for six consecutive years. Yet, since 2013, China has been the leading country in scientific production on this topic. China has the highest number of citations (1645 citations), followed by India with 243 citations, and the United Kingdom in third place with 102 citations. The United States leads in collaborations, working with Spain, Bangladesh, and Korea, while China takes the second position, collaborating with Ghana and Japan. It's important to note that no information on this topic was found concerning Mexico.

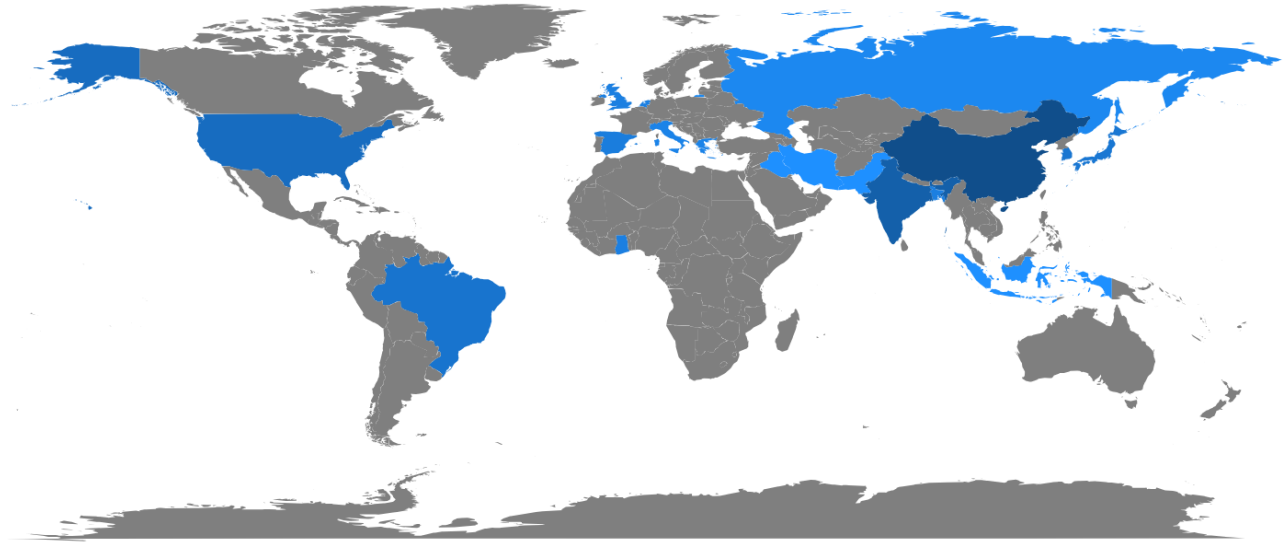

Fig. 6 – Leading countries in scientific production

Table 2 shows the most cited papers, these papers were published between 2008 and 2015, and the journals Nongye Jixie Xuebao/Transactions of the Chinese Society of Agricultural Machinery and Biosystems Engineering stand out, with the most cited articles worldwide. These documents present solutions for the process and automation of seedling transplanting.

Table 2

Most cited articles globally

Article	Authors	TC	TC/year	TC normalized
Mechanical within-row weed control for transplanted crops using computer vision	*(Tillett et al., 2008)*	102	6.38	2.90
Development of a walk-behind type hand tractor powered vegetable transplanter for paper pot seedlings	*(Kumar & Raheman, 2011)*	84	6.46	4.06
Co-robotic intra-row weed control system	*(Pérez-Ruíz et al., 2014)*	56	5.60	2.12
Design and test of automatic feed system for tray seedlings transplanter	*(Han et al., 2013)*	53	4.82	2.65
Kinematics modeling and parameters optimization of seedling pick-up mechanism of planetary gear train with eccentric gear and non-circular gear	*(Ye et al., 2011)*	51	3.92	2.46
Pincette-type end-effector using two fingers and four pins for picking up seedlings	*(Han et al., 2015)*	50	5.96	2.63
Design of automatic picking up seedling end-effector based on mechanical properties of plug seedlings	*(Han et al., 2013)*	42	3.82	2.10
Design and test of key parts on automatic transplanter for flower seedling	*(Feng et al., 2013)*	41	3.73	2.05
Development of single row automatic transplanting device for potted vegetable seedlings	*(Jin et al., 2018)*	38	6.33	2.76
Design of seedlings separation device with reciprocating movement seedling cups and its controlling system of the full-automatic plug seedling transplanter	*(Yang et al., 2018)*	37	5.14	2.22

TC– Total citations

Morphological and mechanical characteristics of seedlings

The design of any device or mechanism for an agricultural machine requires fundamental input parameters. Therefore, it is crucial to base it on the physical and mechanical characteristics of agricultural materials (*Mohsenin, 1986*). In the specific case of designing and evaluating an automated transplanter for seedlings *(Khadatkar et al., 2020)*, obtaining these parameters is essential to dimension the parts that make up the transplanting equipment. Not considering these variables would cause mechanical damage to the seedlings during transplanting and, subsequently, throughout the crop's development.

Khadatkar et al. (2021) used simulated seedlings for preliminary tests, replicating the ideal characteristics of pepper seedlings. In other words, homogeneous material was used to enhance efficiency in the prototype. Table 3 shows the physical and mechanical characteristics (seedling and root ball) used in the development and evaluation of transplanters designed by several authors.

Table 3

Characteristics of the studied seedlings and root ball

Species name	Physical and mechanical characteristics	Age (days) and #H	Substrate	Authors
Onion	-	-	-	*(Chowdhury et al., 2023)*
Chili	Height, weight, stem diameter, burst pressure, compression force and breaking force	30; 4-5	Coco peat, vermiculite and perlite (3:1:1)	*(Khadatkar et al., 2023)*
Chili	Height, canopy, moisture content and bulk density	28, 35 y 42; -	-	*(Chethan et al., 2022)*
Tomato and chili	-	30; -	-	*(Khadatkar et al., 2021)*

Species name	Physical and mechanical characteristics	Age (days) and #H	Substrate	Authors
Chili	-	-	-	*(Wen et al., 2021)*
Chili	Average stem diameter, height and weight	30; 4-5	Coco peat, vermiculite and perlite (3:1:1)	*(Khadatkar et al., 2021)*
Pepper	Height and root diameter	60; 6	-	*(Han et al., 2021)*
Cabbage	Height, failure resistance of the substrate and dimensions of the substrate	30; -	-	*(Cui et al., 2021)*
Pumpkin, pepper and tomato	Stem diameter, moisture content and pressure resistance/N	35, 30, 38; 3.5, 4.1, 5.6	-	*(Shao et al., 2021)*
Tomato	Stem height and diameter	-	-	*(Pérez-Ruiz & Slaughter, 2021)*

#H – Number of leaves

Due to the significance of the aforementioned characteristics, there are studies focused on determining specific values for these traits in a seedling based on its variety, as they are crucial for designing and evaluating automated transplanters (Table 4).

Table 4

Physical and mechanical properties studied in seedlings

Characteristics		Agricultural product (Variety)	Authors
Physical	**Mechanical**		
Age, mass, stem diameter, total height, canopy and moisture content	Impact test, stem and root ball compression test, and static friction coefficient	Chili (*Pusa Jwala*) and tomato (*Abhilash*)	*(Khadatkar et al., 2020)*
Age, height, mass, stem diameter and spreading diameter	Impact test, stem tension and compression test, and static friction angle and coefficient	Tomato (*Roma VF*)	*(Abubakar et al., 2020)*
Age, moisture content, number of leaves, height, stem diameter, mass, root ball and canopy density	Friction coefficient, stem and root ball compression test, and root ball penetration force	Tomato (*Ansal Hybrid* and *Seminis Company*), eggplant (*F1-Gaurav Hybrid* and *Pancha Ganga Seeds Company*) and cabbage (*Saint Hybrid* and *Seminis Company*)	*(Magar et al., 2023)*
Age, height of seedling and root ball, stem diameter, number of leaves, spread of leaves/millimeter and mass	Stem bending, tensile and compression test and stem clamping force until tray removal.	Bell pepper (*Xiaoxin No. 19*)	*(Shuangyan et al., 2022)*
Age, weight, bulb diameter, stem diameter, height and moisture content	Compression test and static friction coefficient	Onion (*Pusa Red*, *Set-126* and *Pusa Ridhi*)	*(Pandirwar et al., 2015)*

Obtaining the physical-mechanical parameters of each part of the seedling is crucial. Some authors focus on the stem, while others concentrate on the root ball (substrate characteristics), as demonstrated in the study conducted by *Han et al. (2013),* who conducted mechanical tests on the root balls of pumpkin seedlings. The following are the physical and mechanical characteristics to consider for the design of an automated seedling transplanter (Fig. 7). Some physical characteristics (as e, D, T) were derived from *Paneque et al., (2017),* and the remaining physical and mechanical characteristics were also used by the authors mentioned in Table 4.

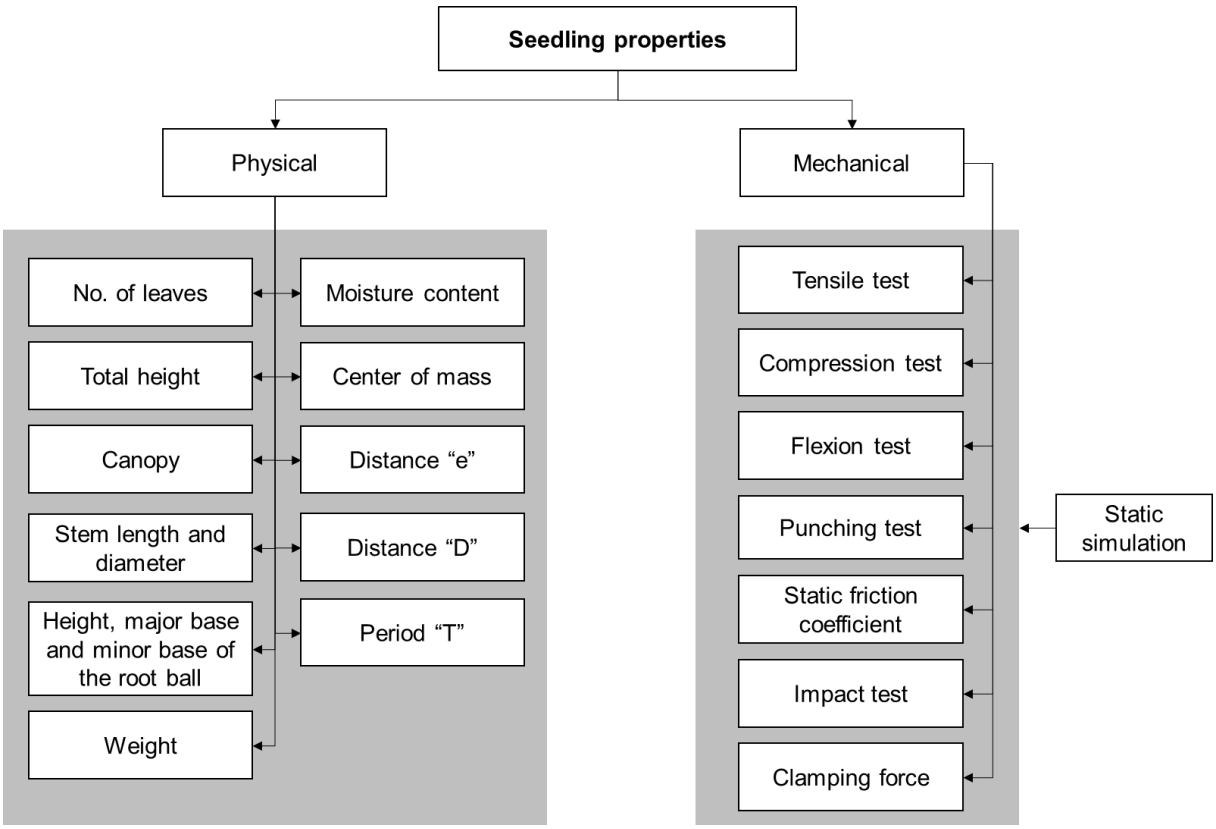

Fig. 7 – Physical and mechanical properties of seedlings included in the design and evaluation of an automated transplanter

Systems, features, and performance of transplanters

Fig. 8 shows the systems that comprise an automated transplanter. System one (Sis-1) covers the extraction of seedlings from germination trays, system two (Sis-2) handles the transportation of seedlings to the next system, and system three (Sis-3) has the function of seedling transplanting. The subfunctions of the transplanter are shown in white boxes. As with any automated machine, there are input power and input signals; on the other hand, there are output power and output signals.

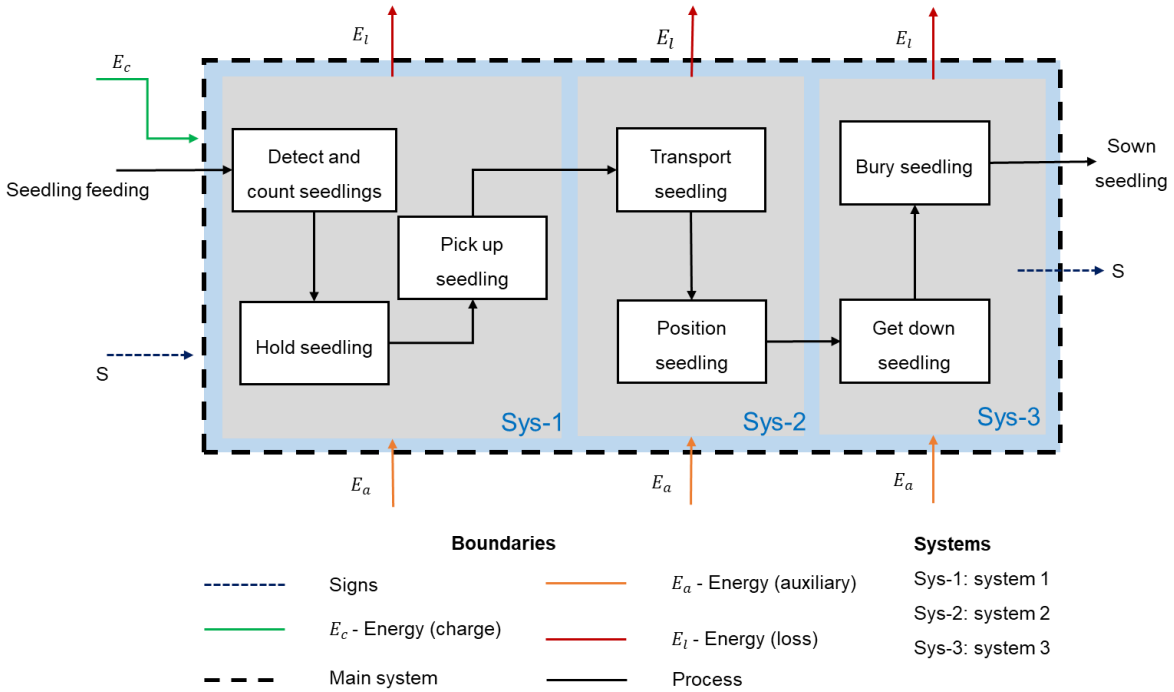

Fig. 8 – Sub-functions of a machine for automated vegetable transplanting

Table 5 shows the systems used by some authors in their research, revealing three general systems that a transplanting machine comprises. It is important to mention that all the studies shown in the table used plastic trays for germination due to their flexibility and durability, in contrast to polystyrene trays, which are more fragile and prone to break.

Table 5

Transplanter components

Seedling feeding	Extraction system (mechanism)	Transport system	Transplant system	Authors
Black plastic tray	Automatic	Automatic	Mechanic	*(Chowdhury et al., 2023)*
Black plastic tray	Manipulator with effector	Manipulator with effector	Manipulator with effector	*(Khadatkar et al., 2023)*
Black plastic tray	Manual	Gravity fall	Automatic	*(Chethan et al., 2022)*
Black plastic tray	Conveyor belt	Hopper	Automatic	*(Khadatkar et al., 2021)*
Black plastic tray	Extractor cylinder	Dosing plate automatic	Automatic	*(Wen et al., 2021)*
Black plastic tray	Spinning fingers	Metering shaft automatic	Automatic electromechanical system	*(Khadatkar et al., 2021)*
Black plastic tray	Automatic collection system		Basket type planting (Automatic)	*(Han et al., 2021)*
Black plastic tray	Conveyor belt and automatic device (mechanical arm)	Mechanical buckets	Automatic	*(Cui et al., 2021)*
Black plastic tray	Effector	Automatic chain cups	Automatic	*(Shao et al., 2021)*
Black plastic tray	Manual	Drum with 5 fingers (one seedling/finger)	Automatic	*(Pérez-Ruiz & Slaughter, 2021)*

There are several working environments in vegetable production, for example, open field with or without mulch, greenhouses with or without mulch, and greenhouses with pots. Each transplanter designed will always be focused on one or two working environments, depending on the region, production volumes and level of technology. Likewise, they have advantages and disadvantages, both in terms of production and profits. Furthermore, depending on the working environment, dimensions, weight, productivity and performance of the prototype are defined. Table 6 shows the characteristics of some transplanters developed with different working capacities.

Table 6

Properties of transplanters

Dimensions (l x w x h (mm))	Weight (kg)	NR	Work environment	Authors
875 x 1626 x 2036	690	6	Open field	*(Chowdhury et al., 2023)*
630 x 510 x 120	-	1	Open field	*(Khadatkar et al., 2023)*
940 x 680 x 890	-	1	Open field (with and without mulch)	*(Chethan et al., 2022)*
-	-	2	Open field (without mulch)	*(Khadatkar et al., 2021)*
2400 x 2200 x 1900	774	2	Open field (without mulch)	*(Wen et al., 2021)*
2030 x 1295 x 1015	210	2	Open field (laboratory experiment)	*(Khadatkar et al., 2021)*
-	-	2	Open field (without mulch)	*(Han et al., 2021)*

Dimensions (l x w x h (mm))	Weight (kg)	NR	Work environment	Authors
3100 x 3000 x 1600	-	4	Open field (without mulch)	*(Cui et al., 2021)*
-	-	-	Experimental in laboratory	*(Shao et al., 2021)*
-	-	3	Open field (without mulch)	*(Pérez-Ruiz & Slaughter, 2021)*

l- large, w- width, h- height, NR– number of rows

When testing and evaluating an automated transplanter, technical parameters such as speed and transplanting capacity are considered to determine if the prototype is efficient according to its intended working environment. These parameters, along with the number of seedlings successfully transplanted, serve as a benchmark for transplanting efficiency during a workday. Achieving a 100% success rate is challenging due to the influence of independent variables such as weight, shape, and physical dimensions of seedlings, which are inherently non-uniform. Moreover, they are susceptible to mechanical damage during extraction from germination trays, handling, and transplanting. Consequently, there is always a percentage of failure in the process. Table 7 outlines the technical parameters used in both the design and evaluation of the analyzed prototypes.

Table 7

Technical parameters of transplanters

Transplant speed (m/s)	Transplanting capacity	Successful transplant (%)	Failure (%)	Authors
0.24	-	-	-	*(Chowdhury et al., 2023)*
-	3 SG/min	90.3	7.6	*(Khadatkar et al., 2023)*
0.117-0.156	15 SG/min	-	-	*(Chethan et al., 2022)*
-	10.35 SG/min	90-92.6	4.5-5	*(Khadatkar et al., 2021)*
-	80 SG/(min*row)	92.08	3.61	*(Wen et al., 2021)*
0.556	-	90.3	2.1	*(Khadatkar et al., 2021)*
-	120 SG/min	97.5	3	*(Han et al., 2021)*
0.306	55 SG/min	93.31	3.42	*(Cui et al., 2021)*
-	6-12 SG/min	73.33-88	1-8.57	*(Shao et al., 2021)*
0.222 y 0.444	-	90	-	*(Pérez-Ruiz & Slaughter, 2021)*

SG – seedlings

There are machines designed for transplanting in greenhouses. *Hu et al., (2016)* developed and tested an automated transplanter for greenhouses, achieving a transplant success rate of 90.23%, a capacity of 120 seedlings per minute, and a planting precision within the range of 0.15-1.22 mm.

Manufacturing and operating costs

The cost of production and the selling price are features to consider in the development of automated transplanters; therefore, it is important and necessary to analyze both fixed and variable costs to justify the final cost of the prototype. It is also essential to compare the costs of manual transplanting against the costs of transplanting using an automated transplanter to determine if the prototype indeed reduces the cost of the transplanting phase.

In the analyzed works, only a few authors report the cost of their prototype. Of the total prototypes and mechanisms analyzed, 97.5% do not report the costs of the components used since they are more focused on research than on production. *Chethan et al., (2022)* mentioned that the prototype they developed does not require electricity and was constructed with locally available, inexpensive materials. They considered their prototype to be semi-automated and cost-effective.

When comparing transplanting capacities between automated and manual methods, the study found, according to *Khadatkar et al., (2021)*, that the average manual transplanting rate ranges from 2.5 to 4.5 seedlings per minute per person. Except for the prototype developed by *Khadatkar et al., (2023),* whose capacity falls within the range of manual transplanting capacity, the prototypes presented by the authors listed in Table 6 surpass traditional capacities by more than 100%. In economic terms, as reported by *Khadatkar et al., (2021)*, there was a 30.55% cost reduction in mechanically transplanting tomatoes compared to manual operations. For pepper crops, a decrease of 6.39% was observed. Therefore, it is inferred that transplanting costs will consistently be lower in a mechanical process.

Functional systems in automated transplanters

Several studies focus on one or two systems, or the development of an innovative mechanism used in transplanters. Regardless of the number of systems, their efficiency is determined by evaluating the success rate of transplanting. It is also crucial to evaluate the percentage of seedlings that remain upright, as this significantly contributes to their survival. Some of these studies include:

Hu et al., (2022) developed an integrated automated transplanting mechanism for the collection and transplantation of pepper seedlings in trays with holes. The 3D model was designed using SolidWorks, and its dynamic trajectory was modeled in Matlab. They achieved a seedling selection success rate exceeding 91.1%, a planting success rate of 78.5%, a seedling erection rate of 94.9%, and a coefficient of variation in plant spacing below 14.1%. These results demonstrated its suitability for real-field transplanting.

The pressure applied during seedling gripping poses a challenge, as it can lead to issues such as tissue damage in the stems or root ball. For this reason, various authors have developed different types of grippers. *Li et al., (2022)* designed and tested a gripper (Force Feedback) for picking up seedlings in an automated transplanter. This gripper is based on the linear Hall element. The gripping force detection system exhibited a sensitivity of 0.0693 V/N, linearity of 3.21%, a medium coefficient of determination of 0.986, and a range of 10 N. It met the requirements for gripping force during transplanting, being stable and adaptable to seedlings.

Zhou et al., (2020) developed a mechanism with a punching device for transplanting cayenne pepper seedlings into pots. The results obtained showed that the specific trajectory and transplanting mechanism met the required transplanting standards, and the success rate of seedling collection was 92.4%, confirming the correctness and feasibility of the transplanting mechanism.

On the other hand, *Chen et al., (2023)* designed a mechanism to pick up seedlings from an ejector belt, it was based on the discrete element method by using EDEM simulation software. They conducted substrate studies to determine the best variant of the proposed designs and found that when using the optimal combination of working parameters for seedling collection, they achieved a qualified seedling rate exceeding 90%, with a clod fragmentation rate of less than 20%. The seedling extraction system is effective for a transplanter in dry soil.

Modeling vegetables is a complex task that requires high computational resources. *Francis et al., (2014)* carried out a study to mathematically model the behavior of vegetables when extracting them from the root, using the Godwin and O'Dogherty equation for soil penetration tools as a foundation. They initially performed experiments with strain gauges to understand the force-time relationship of the device, indicating an initial force value of 1.1319 N. In the model under similar conditions, the force was determined to be 1.1389 N. They concluded that with this research, it is possible to optimize and design seedling collection devices for transplanting.

It is essential to consider the mechanical damage suffered by seedlings; typically, the stems and the root ball are the most affected, affecting production. *Wen et al., (2021)* reported that in the test conducted on their prototype, only 0.28% of the total used seedlings were damaged. This is considered very acceptable, as at large scales, there are minimal losses in seedlings and production costs. For instance, out of 1000 seedlings, only 3 of them are lost.

In recent years, part of the design of transplantation machines has been focused on strategies that help to optimize transplantation times. Consequently, several authors have developed algorithms to address this issue, and some of them are mentioned below. *Tong et al., (2022)* optimized the transplanting route of seedlings with multi-end effectors using an enhanced algorithm. The average calculation times they obtained for the common sequence method (CSM), greedy algorithm (GRA), greedy genetic algorithm (GGA), and improved greedy simulated annealing algorithm (IGSA) were 0.002, 0.007, 6.94, and 3.49 seconds in MATLAB

(R2019a), respectively. They commented that these algorithms can meet real-time operation requirements except for GGA. This research can be adapted to accommodate new numbers and arrangements of effectors.

He et al., (2022) designed and tested a control system for a sweet potato feeding and planting device, which consists of a pre-treatment seedling conveyor belt. According to the results obtained in the test, the average error of the seedling feeding motor speed was 4.04%, and for the planting motor speed was 3.28%. The lowest coefficient of variation (7.42%) in seedling spacing was achieved during tests at a low speed. They concluded that the system meets the control requirements for the automated seedling feeding and planting device in transplanting.

Furthermore, *Jin et al., (2021)* employed Kinect visual processing to obtain and process information about seedling height and leaf edge. They established and applied the working coordinate system of transplanting manipulator in route planning to avoid obstacles. Combining this with the inclined manipulator, they proposed the obstacle avoidance transplanting method. With this manipulator, they achieved a 4.70% leaf damage rate, a 16.67% stem bending rate, an 83.45% substrate integrity, and an 87.36% transplant quality. The transplanting time for a seedling was 8.32 seconds. The authors ensure the reduction of damage to the seedlings.

On the other hand, *Li et al., (2022)* optimized the transplant route in seedling germination trays using the improved A* algorithm for replanting. This algorithm reduced the time by 10.15 seconds compared to the Common Sequence Method (CSM) for each seedling tray. It was used to replant the cavities where the seedlings did not germinate or were defective with healthy seedlings. Additionally, it can be used for transplant route planning.

Current situation on prototype development in Mexico

In Mexico, the equipment developed for automated transplanting is scarce, with most machines being imported. However, in the course of the present research, a prototype developed in Mexico was identified. *Gutiérrez et al. (2009)* designed and built a transplanting mechanism (module) as the main component of a bare-root strawberry seedling transplanter on mulched soil. The operating principle is based on a module that remains in contact with the soil for a determined period. It features mechanisms for plastic cutting (including hiding it) and automated plant insertion into the soil. The plastic cutting had a 100% success rate; the plastic concealing activity had an efficiency of 95%; the success rate for plant placement with tweezers was 95%, and the efficiency in the verticality of the seedlings was 85%.

There is a limited amount of technology and information available on automated vegetable transplanting equipment in Mexico, although there is evidence of research work that has not been formally published. The equipment currently sold and used in the country is designed for different working conditions and focused on large growers. Therefore, there is an area of study that should be addressed, since there is a need for equipment with specifications suitable for small and medium-sized growers, who represent the majority, but have fewer possibilities of accessing automation technology because of the cost and capability.

Areas of opportunity for future research

Liu et al., (2021) conducted a design for a sweet potato transplanter based on a robotic arm. They found that the adjustment of the arm is complex as it cannot adapt to all planting terrains, negatively impacting the crop quality on ridges. Additionally, the target detection algorithm heavily relies on the quantity and quality of training images. When the transplanting environment changes, such as from a sunny day to a cloudy day, the detection results are affected. While the transplanter achieves various sweet potato transplanting methods, the single-ridge operation mode limits the efficiency of the transplanting process.

Tong et al., (2022) conducted research on optimizing the transplanting route of seedlings with multi-end effectors using the Improved Greedy Simulated Annealing (IGSA) algorithm. They proposed that, to enhance transplanting efficiency, increasing the number of end effectors would be beneficial, particularly when performing transplanting operations in dense seedling trays.

Meanwhile, *Shao et al., (2021)* developed a multi-adaptive feeding device for automated seedling plugs for a multi-seedling transplanter with six grippers. They noted that the success rate needs further improvement to meet the practical application of high-speed transplantation. They also commented that as future research, the automated feeding device could be manufactured by professionals to achieve high precision and stability.

In agriculture, the germination percentage is not 100% due to different situations such as seed quality, temperature conditions, seedbed humidity, etc. Therefore, if there were tray cavities without seedlings, the transplanting process would not be 100% complete in the furrows.

On the other hand, *Hu et al., (2022)* found issues related to the rotation speed of the mechanism they designed, as it generated vibrations that affected the transplant quality. They recommended further research into mechanisms to avoid generating vibrations when placing the plant on the ground and keeping it in a vertical position.

Paradkar et al., (2021) developed a dosing mechanism consisting of a serial robotic arm for handling seedlings in paper pots using a vegetable transplanter. They mentioned that the sources of reduced efficiencies from the ideal (100%) were due to inclinations caused by seedling transport due to friction and the operating speed of the conveyor and the damage occurred to the seedlings due to the robot arm's higher gripping force. Therefore, studying the physical-mechanical properties of seedlings is crucial for later use in the design of mechanisms used for transplanting.

Yongwei et al., (2018) recommended that, when designing the final gripper, it is crucial to consider the cultural practices specific to vegetable seedlings in the country where the mechanism will be utilized.

For the design of an automated transplanter, it's essential to define its parameters as no single machine adapts to all work scenarios. Therefore, it should be considered the cultural practices of the country, region, and the targeted type of growers, soil conditions, climate, type of germination tray, and the seedbed where the seedlings are produced. This approach aims to achieve germination rates exceeding 95% in trays, thereby optimizing the trajectories of the seedling extraction mechanism. Furthermore, the design should be accessible to small growers. Currently, most of the existing transplanters are designed for growers with large cultivation areas.

CONCLUSIONS

Automated transplanters have become very important in vegetable production because they reduce time, labor and, therefore, costs by up to 31% compared to manual transplanting; however, although this technology is expensive when developing a new prototype, it is essential not to disregard the limited availability of labor and the associated costs. Moreover, uncertainties in the quality of field operations performed by agricultural workers should be considered. Therefore, automation proves to be a favorable alternative.

The bibliometric analysis and detailed review indicate that technological progress on automated transplanters have evolved with the help of computational development. Researchers have created new prototypes for different crops, considering the conditions of their countries. However, there was limited progress in automatic transplanting (a total of 13 articles related to the topic) over 28 years, experiencing a surge in 2008 and a substantial increase in 2021 with a total of 35 published articles. Nowadays, databases of scientific articles across all fields, including automatic transplanting, are updated daily, in contrast to the previous practice of annual updates until 2007.

Several critical variables must be considered when designing an automated transplanter, such as physical and mechanical properties of seedlings. These parameters are essential for sizing and calculating the characteristics of the machine's components, ensuring they align with the intended functionality and preventing potential mechanical damage. It is also essential to test and evaluate the developed prototypes to determine the working speed, quantity of seedlings transplanted within a specified timeframe, efficiency, and percentage of failure during transplanting. Furthermore, it's important to consider the costs associated with the design, analysis, and construction time of the prototype.

Technological progress plays a pivotal role in the advancement of diverse sectors, notably in agriculture for food production and its broader economic impact. In the specific case of Mexico, it is necessary to take up the advances achieved so far in this area and develop prototypes for the automated vegetable transplanter, aligning with the unique conditions and characteristics of the country. By doing so, these transplanters can become valuable tools for small and medium-sized growers, aiding in cost reduction and integrating technology akin to that used by larger growers. This approach not only fosters competitiveness with potential producing countries and may even contribute to achieving food sovereignty.

This review article aims to show the scientific community the evolution and technological development of automatic transplanters, as well as the importance and impact of the development of technology to improve the quality, time and costs of vegetable transplanting. Limitations of this review on the development and evolution of automatic transplanters include possible study selection biases that might favor certain types of technologies or outcomes, lack of comparative studies evaluating different transplanters under various

conditions, difficulties in generalizing findings due to variability of settings and technologies, possible conflicts of interest on the part of the authors reviewed, scarcity of data on long-term performance, environmental impact, potential conflicts of interest on the part of the authors analyzed, scarcity of data on long-term performance, environmental impact, lack of long-term follow-up on durability and total cost of transplanters, as well as limitations in access to the literature that could lead to a partial view of the available evidence.

ACKNOWLEDGEMENTS

The authors of the present study thank the Consejo Nacional de Humanidades, Ciencias y Tecnologias (CONAHCyT) for the funding support. They also thank the Universidad Autonoma Chapingo and the Graduate Program in Agricultural Engineering and Integral Water Use for the funding support and facilities provided for the completion of this review article.

REFERENCES

[1] Abubakar, A. J., Iya, S. A., Aliyu, B., & Tashiwa, Y. I., (2020). Determination of physico-mechanical properties of tomato seedlings for design of a tomato transplanter. *Journal of Agricultural Engineering and Technology (JAET)*, vol. 25, no.1, pp.106–122.

[2] Ahmed, N., Zhang, B., Deng, L., Bozdar, B., Li, J., Chachar, S., Chachar, Z., Jahan, I., Talpur, A., Gishkori, M. S., Hayat, F., & Tu, P., (2024). Advancing horizons in vegetable cultivation : a journey from ageold practices to high-tech greenhouse cultivation — a review. *Frontiers in Plant Science*, vol.15, no.4, pp.1–26.

[3] Aria, M., & Cuccurullo, C., (2017). Bibliometrix: An R-tool for comprehensive science mapping analysis. *Journal of Informetrics*, vol.11, no.4, pp. 959–975.

[4] Baudoin, W. (2002). El Cultivo Protegido en Clima Mediterráneo; Estudios, FAO. In *Serie Producción y Protección Vegetales*.

[5] Bazargani, K., & Deemyad, T., (2024). Automation's Impact on Agriculture: Opportunities, Challenges, and Economic Effects. *Robotics*, vol.13, no.2, pp.33–57.

[6] Chen, J., Zhou, H., Che, H., Liu, Y., & Li, P., (2023). Optimal design of ejector belt seedling collecting mechanism based on EDEM. *INMATEH - Agricultural Engineering*, vol.69, no.1, pp.109–120.

[7] Chen, W., Ahmed, M. M., Sofiah, W. I., Isa, N. A. M., Ebrahim, N. A., & Hai, T., (2021). A Bibliometric Statistical Analysis of the Fuzzy Inference System - Based Classifiers. *IEEE Access*, vol.9, pp.77811–77829.

[8] Chethan, S., Srinivasa, K., Madivalkar, J., Mahaboob, N., & Yathisha, N., (2022). Development of Economical Plant Transplanter. *Journal of The Institution of Engineers (India): Series C*, vol.103, no.3, pp.339–345.

[9] Chowdhury, M., Reza, M. N., Ali, M., Kabir, M. S. N., Kiraga, S., Lim, S. J., Choi, I. S., & Chung, S. O., (2023). Vibration Assessment of a 12-kW Self-Propelled Riding-Type Automatic Onion Transplanter for Transplanting Performance and Operator Comfort. *Applied Sciences (Switzerland)*, vol.13, no.3, pp. 1927.

[10] Cui, Z., Guan, C., Xu, T., Fu, J., & Chen, Y., (2021). Design and Experiment of Transplanting Machine For Cabbage Substrate Block Seedlings. *INMATEH –Agricultural Engineering*, vol.64, no.2, pp.375–384.

[11] Dias, J. S., (2019). Nutritional Quality and Effect on Disease Prevention of Vegetables. *Food and Nutrition Sciences*, vol.10, no.4, 369–402.

[12] Donthu, N., Kumar, S., Mukherjee, D., Pandey, N., & Lim, W. M., (2021). How to conduct a bibliometric analysis: An overview and guidelines. *Journal of Business Research*, vol.133, no.3, pp.285–296.

[13] FAO., (2022). *The State of Food and Agriculture 2022. Leveraging Automation in Agriculture for Transforming Agrifood Systems*.

[14] Feng, Q., Wang, X., Jiang, K., Zhou, J., Zhang, R., & Ma, W., (2013). Design and test of key parts on automatic transplanter for flower seedling. *Nongye Gongcheng Xuebao/Transactions of the Chinese Society of Agricultural Engineering*, vol.29, pp.21–27.

[15] Francis, K., Mao, H., & Hu, J., (2014). Mathematical modeling of vegetable seedling root lump under pick-up force. *American Society of Agricultural and Biological Engineers Annual International Meeting 2014, ASABE 2014*, vol.5, pp.3452–3458.

[16] Gutiérrez, C., Serwatowski, R., Gracia, C., Cabrera, J. M., & Saldaña, N., (2009). Design, building and testing of a transplanting mechanism for strawberry plants of bare root on mulched soil. *Spanish Journal of Agricultural Research*, vol.7, no.4, pp.791–799.

[17] Habineza, E., Ali, M., & Chung, S., (2023). Vegetable transplanters and kinematic analysis of major mechanisms : a review. *Korean Journal of Agricultural Science*, vol.*50, no.*1, pp.113–129.

[18] Han, C., Hu, X., Zhang, J., You, J., & Li, H., (2021). Design and testing of the mechanical picking function of a high-speed seedling auto-transplanter. *Artificial Intelligence in Agriculture*, vol.5, pp.64–71.

[19] Han, C., Yang, W., Zhang, X., Guo, H., & Yin, W., (2013). Design and test of automatic feed system for tray seedlings transplanter. *Nongye Gongcheng Xuebao/Transactions of the Chinese Society of Agricultural Engineering*, vol.29, no.8, pp.51–61.

[20] Han, L. H., Mao, H. P., Hu, J. P., & Kumi, F., (2019). Development of a riding-type fully automatic transplanter for vegetable plug seedlings. *Spanish Journal of Agricultural Research*, vol.17, no.3.

[21] Han, L., Mao, H., Hu, J., Miao, X., Tian, K., & Yang, X., (2013). Experiment on mechanical property of seedling pot for automatic transplanter. *Nongye Gongcheng Xuebao/Transactions of the Chinese Society of Agricultural Engineering*, vol.29, no.2, pp.24–29.

[22] Han, L., Mao, H., Kumi, F., & Hu, J., (2018). Development of a multi-task robotic transplanting workcell for greenhouse seedlings. *Applied Engineering in Agriculture*, vol.34, no.2, pp.335–342.

[23] Han, L., Mao, H., Miao, X., Hu, J., & Yang, X., (2013). Design of automatic picking up seedling end-effector based on mechanical properties of plug seedlings. *Nongye Gongcheng Xuebao/Transactions of the Chinese Society of Agricultural Engineering*, vol.44, no.11, pp.260–265.

[24] Han, L., Mao, H., Yan, L., Hu, J., Huang, W., & Dong, L., (2015). Pincette-type End-effector Using Two Fingers and Four Pins for Picking Up Seedlings. *Nongye Jixie Xuebao/Transactions of the Chinese Society for Agricultural Machinery*, vol.46, no.7, pp.23–30.

[25] Hauser, V. L., (1985). Automatic grass transplanting machine. *Transactions of the American Society of Agricultural Engineers*, vol.28, no.6, pp.1777–1782.

[26] He, Y., Zhu, Q., Fu, W., Luo, C., Cong, Y., Qin, W., Meng, Z., Chen, L., Zhao, C., & Wu, G., (2022). Design and experiment of a control system for sweet potato seedling-feeding and planting device based on a pre-treatment seedling belt. *Journal of Agricultural Engineering*, vol.53, pp.1261.

[27] Hu, J., Zhang, C., Wang, L., & Han, L., (2016). Design and experiment on automatic greenhouse seedling transplanting machine. *Nongye Jixie Xuebao/Transactions of the Chinese Society for Agricultural Machinery*, vol.47, pp.149–154.

[28] Hu, S., Hu, M., Yan, W., & Zhang, W., (2022). Design and Experiment of an Integrated Automatic Transplanting Mechanism for Picking and Planting Pepper Hole Tray Seedlings. *Agriculture*, vol.12, pp.557.

[29] Intel. (2005). *Dual Core Era Begins, PC Makers Start Selling Intel-Based PCs*. Intel News Release. https://www.intel.com/pressroom/archive/releases/2005/20050418comp.htm

[30] Jin, X., Li, D. Y., Ma, H., Ji, J. T., Zhao, K. X., & Pang, J., (2018). Development of single row automatic transplanting device for potted vegetable seedlings. *International Journal of Agricultural and Biological Engineering*, vol.11, no.3, pp. 67–75.

[31] Jin, X., Li, R., Ji, J., Yuan, Y., & Li, M., (2021). Obstacle avoidance transplanting method on kinect visual processing. *International Journal of Agricultural and Biological Engineering*, vol.14, no.5, pp.72–78.

[32] Khadatkar, A., Gaikwad, B., & Pandirwar, A., (2020). Biometric Properties of Plug Vegetable Seedlings Relevant to the Design of Vegetable Transplanter. *Journal of Agricultural Engineering*, vol.57, no.1, pag.16–24.

[33] Khadatkar, A., Mathur, S. M., Dubey, K., & Bhusanababu, V. (2021). Development of embedded automatic transplanting system in seedling transplanters for precision agriculture. *Artificial Intelligence in Agriculture*, vol.5, pp.175–184.

[34] Khadatkar, A., Mathur, S. M., Dubey, K., & Magar, A. P., (2021). Automatic Ejection of Plug-type Seedlings using Embedded System for use in Automatic Vegetable Transplanter. *Journal of Scientific and Industrial Research*, vol.80, no.12, pp. 1042–1048.

[35] Khadatkar, A., Mathur, S. M., Rao, K. V. R., Babu, V. B., & Chaurasia, L., (2021). Comparative Performance of Automatic Transplanter with Manual Transplanting of Plug-type Vegetable Seedlings using Time-motion. *Indian Journal of Extension Education*, vol.57, no.4, pp.95–101.

[36] Khadatkar, A., Pandirwar, A. P., & Paradkar, V., (2023). Design, development and application of a compact robotic transplanter with automatic seedling picking mechanism for plug - type seedlings. *Scientific Reports*, vol.13, no.1, pp.1883–1895.

[37] Kumar, G. V. P., & Raheman, H., (2011). Development of a walk-behind type hand tractor powered vegetable transplanter for paper pot seedlings. *Biosystems Engineering*, vol.110, no.2, pp.189–197.

[38] Li, P., Yun, Z., Gao, K., Si, L., & Du, X., (2022). Design and Test of a Force Feedback Seedling Pick-Up Gripper for an Automatic Transplanter. *Agriculture*, vol.12, pp.1–17.

[39] Li, X., Wang, W., Liu, G., Li, R., & Li, F., (2022). Optimizing the Path of Plug Tray Seedling Transplanting by Using the Improved A* Algorithm. *Agriculture (Switzerland)*, vol.12, no.9, pp.1–23.

[40] Liu, J. Z., Zhao, S. Y., Li, N., Faheem, M., Zhou, T., Cai, W. J., Zhao, M. Z., Zhu, X. Y., & Li, P. P., (2019). Development and Field Test of an Autonomous Strawberry Plug Seeding Transplanter for Use in Elevated Cultivation. *American Society of Agricultural and Biological Engineers*, vol.35, no.6, pp.1067–1078.

[41] Liu, W., Tian, S., & Wang, Q., (2023). Key Technologies of Plug Tray Seedling Transplanters in Protected Agriculture : A Review. *Agriculture*, vol.*13*, pp.1488–1507.

[42] Liu, Z., Wang, X., Zheng, W., Lv, Z., & Zhang, W., (2021). Design of a Sweet Potato Transplanter Based on a Robot Arm. *Applied Sciences*, vol.11, pp.1–16.

[43] Magar, A. P., Nalawade, S. M., Walunj, A. A., Khadatkar, A., Bhangare, S. C., Bhalekar, M. N., Nimbalkar, C. A., & Gaikwad, B. B., (2023). Engineering Properties of Some Plug-type Vegetable Seedlings for Development of Automatic Vegetable Transplanter. *Journal of Agricultural Engineering (India)*, vol.60, no.1, pp.1–13.

[44] Moden, W. L., & Brewer, H. L., (1979). Automatic Bandoleer Feeder For Transplanters. *Paper - American Society of Agricultural Engineers*. https://www.scopus.com/inward/record.uri?eid=2-s2.0-85069338174&partnerID=40&md5=a76eb6762bbb3ca6b07ce327fcf7409a

[45] Mohsenin, N. N., (1986). *Physical properties of plant and animal materials* (Second Rev). Gordon and Breach Science Publishers, Inc.

[46] Nage, S. M., Mathur, S. M., & Meena, S. S., (2023). Vegetable Transplanters for India : A Review. *Agricultural Science Digest*, vol.43, no.2, pp.129–134.

[47] Pandirwar, A., Kumar, A., Mani, I., & Islam, S., (2015). Biometric properties of onion seedlings relevant to the development of onion seedling transplanter. *Journal of Applied and Natural Science*, vol.7, no.2, pp.768–773.

[48] Paneque, P. P., López, G., Mayans, P. R., Muñoz, F., & Gaytán, J. G., (2017). Fundamentos Teóricos y Análisis de Máquinas Agrícolas, vol. 1, Departamento de Publicaciones de la UACh, ISBN: 978-607-12-0532-2

[49] Paradkar, V., Raheman, H., & Rahul, K., (2021). Development of a metering mechanism with serial robotic arm for handling paper pot seedlings in a vegetable transplanter. *Artificial Intelligence in Agriculture*, vol.5, pp.52–63.

[50] Pérez-Ruiz, M., & Slaughter, D. C., (2021). Development of a precision 3-row synchronised transplanter. *Biosystems Engineering*, vol.206, pp.67–78.

[51] Pérez-Ruíz, M., Slaughter, D. C., Fathallah, F. A., Gliever, C. J., & Miller, B. J., (2014). Co-robotic intra-row weed control system. *Biosystems Engineering*, vol.126, pp.45–55.

[52] Radovich, T. J. K., (2018). Biology and Classification of Vegetables - Biology and Classification of Vegetables. In M. Siddiq & M. A. Uebersax (Eds.), *Handbook of Vegetables and Vegetable Processing,* vol. 1 (Second, Issue Jeffery 1990, pp. 1–23). John Wiley & Sons Ltd.

[53] Rasool, K., Ali, M., & Jang, B., (2020). Onion transplanting mechanisms : A review Onion transplanting mechanisms : A review. *Precision Agriculture Science and Technology*, vol.2, no.4.

[54] Shao, Y., Han, X., Xuan, G., Liu, Y., Gao, C., Wang, G., & Hu, Z., (2021). Development of a multi-adaptive feeding device for automated plug seedling transplanter. *International Journal of Agricultural and Biological Engineering*, vol.14, no.2, pp.91–96.

[55] Sharma, A., & Khar, S., (2022). Current developments in vegetable transplanters in developing countries: a comprehensive review. *International Journal of Vegetable Science*, vol.28, no.5, pp.417–440.

[56] Sharma, A., Kumawat, L., & Singh, A., (2023). Development of robotics in vegetable seedling transplantation: a future research direction. *International Journal of Vegetable Science*, vol.29, no.6, pp.577–591.

[57] Shuangyan, H., Minjuan, H., & Wenyi, Z., (2022). Experimental and simulation study on mechanical properties of stem of pepper hole seedlings. *Journal of Chinese Agricultural Mechanization*, vol.43, no.3.

[58] Syed, T. N., Lakhiar, I. A., & Chandio, F. A. (2019). Machine vision technology in agriculture : A review on the automatic seedling transplanters Machine vision technology in agriculture : A review on the automatic seedling transplanters. *International Journal of Multidisciplinary Research and Development International*, vol.6, no.12, pp.79–88.

[59] Tendulkar, P., (2014). *Mapping and Scheduling on Multi-core Processors using SMT Solvers* (Issue November) [Universite de Grenoble I - Joseph Fourier]. https://tel.archives-ouvertes.fr/tel-01087271

[60] Tillett, N. D., Hague, T., Grundy, A. C., & Dedousis, A. P., (2008). Mechanical within-row weed control for transplanted crops using computer vision. *Biosystems Engineering*, vol.99, no.2, pp.171–178.

[61] Tong, J., Qiu, Z., Zhou, H., Khawar, M., Yu, G., Wu, C., & Du, X., (2022). Optimizing the path of seedling transplanting with multi-end effectors by using an improved greedy annealing algorithm. *Computers and Electronics in Agriculture*, vol.201, no.8, pp.107276.

[62] Van Bavel, J. (2013). The world population explosion: causes, backgrounds and -projections for the future. *Facts, Views & Vision in ObGyn*, vol.5, no.4, pp.281–291.

[63] Wen, Y., Zhang, J., Tian, J., Duan, D., & Zhang, Y. (2021). Design of a traction double-row fully automatic transplanter for vegetable plug seedlings. *Computers and Electronics in Agriculture*, vol.182, no.6, pp.106017.

[64] Xu, Y., Liu, X., Cao, X., Huang, C., Liu, E., Qian, S., Liu, X., Wu, Y., Dong, F., Qiu, C. W., Qiu, J., Hua, K., Su, W., Wu, J., Xu, H., Han, Y., Fu, C., Yin, Z., Liu, M., … Zhang, J., (2021). Artificial intelligence: A powerful paradigm for scientific research. *Innovation*, vol.2, no.4.

[65] Yang, Q., Xu, L., Shi, X., Ibrar, A., Mao, H., Hu, J., & Han, L., (2018). Design of seedlings separation device with reciprocating movement seedling cups and its controlling system of the full-automatic plug seedling transplanter. *Computers and Electronics in Agriculture*, vol.147, no.8, pp.131–145.

[66] Ye, B., Yu, G., Chen, Z., & Zhao, Y., (2011). Kinematics modeling and parameters optimization of seedling pick-up mechanism of planetary gear train with eccentric gear and non-circular gear. *Nongye Gongcheng Xuebao/Transactions of the Chinese Society of Agricultural Engineering*, vol.27, no.12, pp.7–12.

[67] Yongwei, W., Zhuoliang, H., Jun, W., Chuanyu, W., Gaohong, Y., & Yanhai, T. (2018). Experiment on transplanting performance of automatic vegetable pot seedling transplanter for dry land[J]. *Transactions of the Chinese Society of Agricultural Engineering (Transactions of the CSAE)*, vol.34, no.3, pp.19–25.

[68] Zhou, M., Shan, Y., Xue, X., & Yin, D. (2020). Theoretical analysis and development of a mechanism with punching device for transplanting potted vegetable seedlings. *International Journal of Agricultural and Biological Engineering*, vol.13, no.4, pp.85–92.

TECHNOLOGIES AND CONSTRUCTIVE SOLUTIONS REGARDING THE INTER-ROW MANAGEMENT OF VINEYARD AND FRUIT TREES
/
TEHNOLOGII ȘI SOLUȚII CONSTRUCTIVE PRIVIND MANAGEMENTUL INTERVALULUI DINTRE RÂNDURILE DE VIȚĂ DE VIE ȘI POMI FRUCTIFERI

Dragoș DUMITRU[1)], Carmen BĂLȚATU[*1)], Eugen MARIN[1)], Gabriel-Valentin GHEORGHE[1)], MANEA Dragoș[1)], Marinela MATEESCU[1)], Melania-Elena CISMARU[1)]
[1)] INMA Bucharest/ Romania
E-mail: carmen.vasilachi@gmail.com
DOI: https://doi.org/10.35633/inmateh-72-75

Keywords: *vine and fruit tree management, inter-row management, sensors, intelligent system, seeder, mower.*

ABSTRACT
The management of inter-row space of vineyards and fruit trees has emerged as an essential approach in sustainable agriculture, optimizing resource use and improving ecosystem services. This paper reviews a range of innovative technologies and solutions aimed at revolutionizing line management practices. Modern sensing and monitoring systems provide real-time data on soil moisture, nutrient levels and plant health, facilitating precision row-to-row management. Furthermore, techniques for grassing the space between rows of vines and fruit trees are important for space management, ensuring good air circulation and facilitating agricultural activities such as maintenance and harvesting. In addition, the advent of inter-row seeding machines simplified the implementation of cover crops. These machines use advanced seed delivery mechanisms, precisely distributing the cover seed into the spaces between the rows. This not only encourages soil health and erosion prevention, but also mitigates weed competition, increasing the overall resilience of the agroecosystem. The purpose of this review is to discuss the combination of state-of-the-art technologies such as 3D LIDAR technology, intelligent systems used for inter-row management of vines and fruit trees, and inter-row solar panel systems, all these examples have revolutionized inter-row management in vineyards and orchards. This holistic approach optimizes resource allocation, improves soil health and encourages sustainable agricultural practices, paving the way for greener and more resilient inter-row spaces in modern agroecosystems.

REZUMAT
Managementul spațiilor între rânduri dintre viță de vie și pomi fructiferi a apărut ca o abordare esențială în agricultură durabilă, optimizarea utilizării resurselor și îmbunătățirea serviciilor eco-sistemice. Această lucrare analizează o serie de tehnologii și soluții inovatoare care vizează revoluționarea practicilor de management între rânduri. Sistemele de detectare și monitorizare moderne oferă date în timp real despre umiditatea solului, nivelurile de nutrienți și sănătatea plantelor, facilitând managementul de precizie între rânduri. Mai mult, tehnicile de înierbare a intervalului dintre rândurile de viță de vie și pomi fructiferi sunt importante pentru gestionarea spațiului, asigurarea unei bune circulații a aerului și ușurarea activităților agricole, cum ar fi lucrările de întreținere și recoltare. În plus, apariția mașinilor de semănat între rânduri a simplificat implementarea culturilor de acoperire. Aceste mașini utilizează mecanisme avansate de livrare a semințelor, distribuind cu precizie semințele de acoperire în spații între rânduri. Acest lucru nu numai că încurajează sănătatea solului și prevenirea eroziunii, dar și atenuează competiția buruienilor, sporind rezistența generală a agroecosistemului. Scopul acestei revizuiri este de a discuta despre combinarea tehnologiilor de ultimă oră, cum ar fi tehnologia 3D LIDAR, sisteme inteligente utilizate pentru managementul între rândurile de viță de vie şi pomi fructiferi şi sisteme de panouri solare amplasate între rândurile de viță de vie şi pomi fructiferi, toate aceste exemple au revoluționat managementul între rânduri în podgorii și livezi.. Această abordare holistică optimizează alocarea resurselor, îmbunătățește sănătatea solului și încurajează practicile agricole durabile, deschizând astfel calea pentru spații între rânduri mai verzi și mai rezistente în agro-ecosistemele moderne.

INTRODUCTION

Worldwide, fruit tree and vine plantations represent a very important sector in the field of agriculture, occupying large areas of land.

In the European Union, the land area dedicated to the cultivation of fruit trees and vines has a total of 11,301,345 ha, (https://www.fao.org/faostat/en/#home). The first three fruit crops that cover the largest areas of the total cultivated area are, as shown in fig.1, olive orchards, 45%, followed by vines that cover 28% of the area, and in third place are almond and other nut plantations, 11%. Other orchards covering the remaining area include: apples and pears, 5%; pome fruits (peaches, nectarines, apricots, cherries and plums) covering 4%; citrus fruits 4% and other exotic fruits (figs, avocados, kiwi, other tropical fruits and bananas) approximately 1.3%.

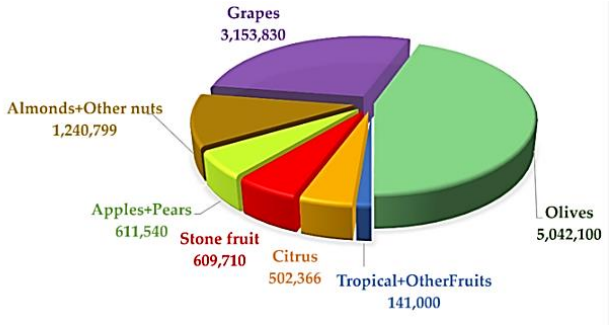

Fig. 1 - The total area at EU level of fruit tree and vine plantations
(https://www.fao.org/faostat/en/#home)

Regarding the distribution of the orchard area in the EU member countries, Spain stands out with 43% of the total area, followed by Italy with 21%, Greece with 10%, France with 8%, Portugal with 6% and Poland and Romania with 3%, as shown in fig. 2. Grapes represent an important cultural, economic and ecological feature of the Mediterranean basin, but also a cosmopolitan culture, with the largest area and the highest economic value among fruit crops globally. The EU members with the largest areas of vines are Spain, France and Italy.

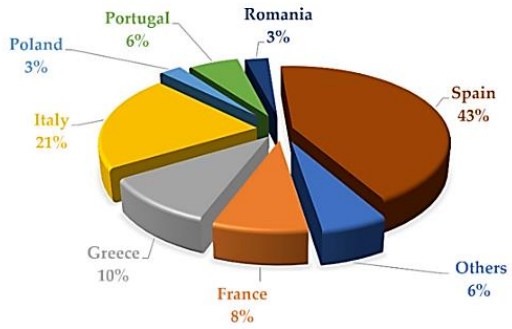

Fig. 2 - The total area at EU level of fruit tree and vine plantations
(https://www.fao.org/faostat/en/#home)

In Romania, fruit growing and viticulture play an important role in agriculture due to the favourable pedoclimatic conditions, but also due to the established fruit/vine growing areas, with tradition and high production potential.

A study carried out by the National Institute of Statistics, regarding the productive potential of fruit and viticulture plantations carried out in 2018 (National Institute of Statistics online page), shows that the total percentage of apple and pear orchards is the most considerable, respectively approx. 55050 ha of apple orchards and approx. 3231 ha of pear orchards. The apricot, peach and nectarine orchards accumulate together a total area of 4206 ha, where approximately half of this area is intended for apricot orchards, 2362 ha, followed by peach orchards 1693 ha, and the rest of 152 ha belong to the plantations of nectarine.

At the same time, vineyards represent an important area in agriculture in Romania, so that it is recognized at the EU level in 15 grape-producing countries. The official data from MADR, highlight the

evolution of the vineyard areas in recent years in which small fluctuations are observed, in 2020 approximately 173.7 thousand ha were recorded, (Ministry of Agriculture and Sustainable Development online page).

Historically, the spaces between crop rows have often been viewed as mere passages or neglected areas, left to the whims of nature. However, as concerns about soil erosion, biodiversity loss and resource scarcity have escalated, a paradigm shift has emerged. Greening the inter-row spaces has emerged as a powerful strategy to address these challenges, embracing the principles of agroecology and precision agriculture. Essentially, this practice involves planting cover crops, grasses, legumes, or even low-growing cash crops in the open spaces between primary crop rows. These secondary vegetation covers serve multiple purposes.

Erosion control techniques in agriculture, such as terracing (*Zalidis G. et. al., 2002*), or the use of cover crops (*Francis C.F. et al., 1990; Reeves D.W., et al. 1994*), break the cycle of processes that lead to soil degradation (*Lesschen J.P. et al., 2009*), however the soil remains degraded in those areas that are still rely on traditional intensive processing methods. The advantages of tillage over the use of herbicides in terms of less soil loss and runoff have been documented (*Raclot D. et. al., 2009*). In sub-humid or semi-arid environments, however, it is normal for prolonged tillage to lead to a loss of soil structure and a decrease in organic matter (OM) (*Hermle S. et al., 2008*). Erosion is responsible for OM losses of up to 21g C m^{-2} /y (*Farage P. et. al., 2009*), or up to 19% decrease in total organic carbon in treatments without organic fertilizers (Morlat, R. et.al. 2008), which means that any crop that does not include a change in OM will result in a decrease in soil carbon (*Sanchez-Maranon M. et al., 2002*).

Currently, an eco-biological method practiced in viticulture and fruit growing, which is one of the most effective soil maintenance technologies in vineyards and orchards, is the weeding of the space between the rows. The weeding of the intervals between the rows in the vineyards and fruit plantations, contributes to the conservation and enhancement of the biodiversity of the plantations and the surrounding environment, as well as to the protection and reconstruction of habitats or species, the increase of water reserves in the soil, including the maintenance and creation of landscape features or non-productive areas, in the context of climate change. A beneficial contribution of this eco-scheme also aims to ensure favourable conditions for pollinators (*AGR inteligenta, 2023*).

Viticulture, a sector with a deep history and global significance, provides an illuminating case study for the greening of inter-row spaces. Vineyards, often characterized by their orderly rows of vines, began to embrace this paradigm. For example, the distance between vine rows depends on the grape variety, soil type, and trellis system. Generally, row spacing ranges from 1.8 to 3 m, (*Grant S., 2000; Bobillet W. et. al., 2003*). Row spacing varies based on the type of fruit trees. For apple orchards, typical row spacing is around 3.6 to 5.5 m (*Gómez-del-Campo M. et al., 2020*). Planting grasses, legumes or even wildflowers between the vines not only conserves the soil, but also regulates the vigour of the vines, leading to improved grape quality. In addition, these secondary coverings act as a natural deterrent against vine diseases, alleviating the need for excessive fungicide application. While adopting row greening has numerous benefits, there are challenges. Integrating cover crops requires careful planning, taking into account factors such as water availability, climatic conditions and crop compatibility.

In this review, applications of grapevine and orchard row spacing in agriculture were discussed, with special attention to experiments and studies that have been reported in scientific papers, and analysing the advantages and constraints of using the technology in agriculture. This overview will provide guidelines for further research, the development of new ozone plant protection machines, and the expansion of its applications in agricultural production.

MATERIALS AND METHODS

Managing inter-row spaces in vineyards or orchards involves implementing various practices to optimize the space between rows of crops. This management is crucial for maintaining a healthy and productive crop, promoting soil health, controlling weeds, and facilitating efficient farm operations. Key aspects of inter-row space management are: weed control, soil fertility and nutrition, erosion control, water management, equipment and access aisles, integrated pest management, organic and sustainable practices, wildlife habitat preservation, monitoring and record keeping.

Effective inter-row space management involves a holistic approach that considers the specific needs of the crops, soil conditions, and environmental factors. Regular monitoring and adaptive management practices are essential to address changing conditions and optimize overall farm productivity.

The technologies used for row spacing management of vines and fruit trees have been used in many aspects of agriculture, such as sensors, intelligent cover system, soil vehicles, robots and seeders.

3D points, Sensors

3D LIDAR technology represents a key innovation in agriculture, with the potential to revolutionize the way vine and fruit tree crops are managed. LIDAR, which stands for "Light Detection and Ranging," uses pulses of laser light to measure distances and create detailed three-dimensional maps of the environment, as shown in fig. 3.

In the context of viticulture and fruit growing, 3D LIDAR technology can provide highly accurate and relevant information. It can measure the height and shape of trees or bushes, detecting even the smallest variations in the terrain. Thus, it helps in efficient planting planning, optimal plant spacing and uniform sunlight management. 3D LIDAR technology can also identify plant stress or disease at an early stage, enabling rapid and targeted interventions.

Benefits include increased yield, reduced wastage and more efficient use of resources such as water and pesticides. At the same time, it optimizes harvesting and maintenance methods, contributing to higher quality productions. However, for widespread and successful adoption, continued research is needed to develop LIDAR sensors that are more compact, affordable and better suited to the specific needs of viticulture and fruit growing. Ultimately, 3D LIDAR technology paves the way for more precise, sustainable and resource-efficient agriculture.

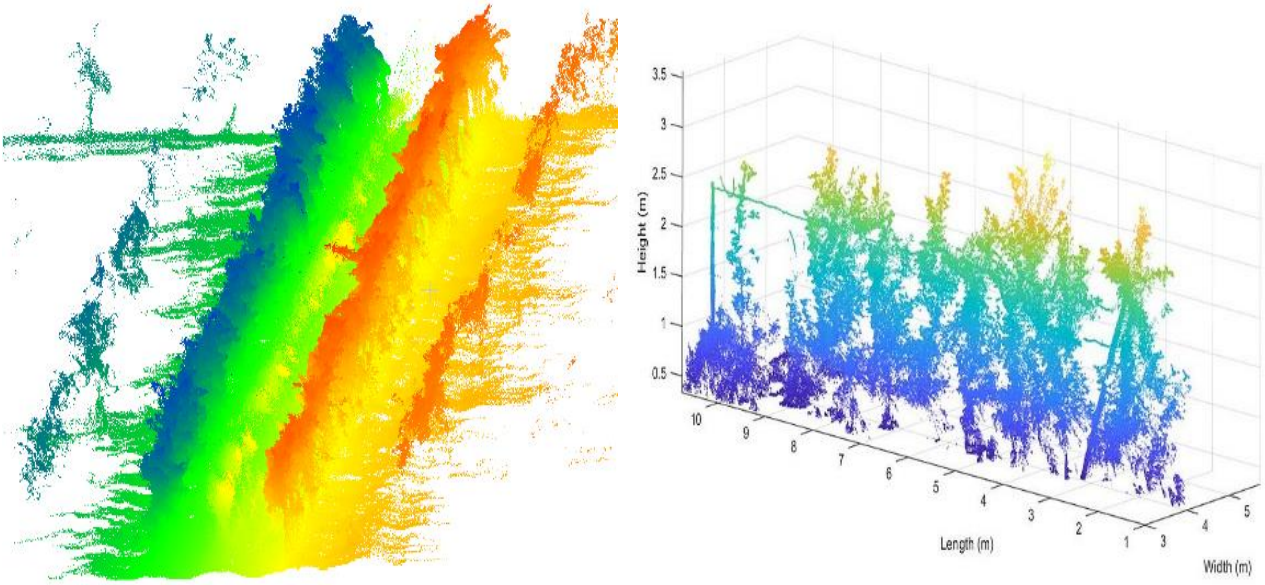

Fig. 3 - 3D LIDAR technology for vines and fruit trees
(*Biglia A. et. al, 2022, Matteo Gatti et. al, 2016*)
1 – Length; 2 – Width; 3 - Height

The article published by *Biglia A. et. al. (2022)*, proposes an innovative method for analysing 3D point clouds in vineyards, extracting information about the orientation and appearance of each row of vines. The method is based on key point detection and density-based clustering, being adaptable to different types of sensors and plant configurations. The data is obtained by multispectral cameras mounted on drones, and the algorithm is applied in three steps: detecting the centre of the vine trees, grouping these points into individual rows, and defining key points and interpolation curves for each row. The method is evaluated on various plots, achieving accurate results in row location and drone path planning. This autonomous and versatile algorithm brings significant benefits in crop monitoring and optimization of agricultural operations.

Nuno Figueiredo et. al. (2023), emphasizes the importance of automated detection of vine rows in terraced vineyards for essential agricultural objectives such as crop evaluation and yield estimation. Integrating remote sensing and artificial intelligence (AI) technologies into precision agriculture practices is essential. The text explores the use of satellite, aircraft, and drone imagery to capture vineyard data, and the application of AI algorithms, including machine learning (ML) and deep learning (DL), to analyse this imagery. Furthermore, the study investigates various ML and DL algorithms for vineyard segmentation, grape detection, and creating a 3D representation of vineyard structure. Despite the progress, the article highlights the challenges associated with row identification in terraced vineyards with curved lines due to the complexity of the land.

Gatti M. et. al. (2016), tested a new proximal sensing system called MECS-VINE® that can measure and map several parameters related to canopy development and vineyard microclimate using two array-based optical RGB image sensors and a series of microclimate sensors. The paper calibrated the canopy index (CI) derived from the MECS-VINE® system with traditional point quadrat analysis (PQA) of tree structure parameters such as number of leaf layer, fraction of tree voids and fraction of inner leaves. The work also correlated CI with other vegetative, yield and grape quality parameters such as leaf gas exchange, light interception, cutting weight, bunch weight and berry weight. They found that CI had a high correlation with PQA parameters at different tree sectors and dates, as well as with cluster weight, grain weight and light intercept. The paper also found that CI could reflect seasonal variation in tree growth and the effects of summer pruning on tree density and openness. The work suggests that the MECS-VINE® system can be a useful tool for assessing grapevine canopy structure and microclimate in a fast, accurate and non-destructive way. CI can also be used as an indicator of vine vigour, yield potential and grape quality, as well as a basis for optimizing vineyard management practices such as irrigation, fertilization, pest control and tree handling.

Hugo Moreno et. al, (2023), presents a method to obtain 3D models of vineyards using a mobile platform equipped with a LiDAR sensor and an RTK-GPS receiver. The paper aims to evaluate shoot volume and dry biomass as indicators of plant growth and health. The paper also evaluates the accuracy and performance of the LiDAR system for crop phenotyping and precision agriculture. The work demonstrates that the LiDAR system can scan large crop areas with high geometric detail and resolution, producing dense 3D point clouds that represent vine structure. The paper uses an alpha shape algorithm to generate a 3D surface that encompasses the outer points of the point cloud and calculates the volume contained by this surface as an estimate of the volume of the branches. The paper shows that there is a strong linear correlation between LiDAR-estimated branch volume and actual dry biomass measured in the field, with an R-squared value of 0.75. This suggests that the LiDAR system can reliably estimate vine cutting weight, which is an important parameter for vineyard management and yield prediction. The paper also shows that the number of LiDAR scans influences the relationship with the actual biomass measurements and has a significant effect on the different treatments. The paper finds that an R-squared value of 0.85 is obtained when comparing the average number of scans and volumes to the average dry biomass values. The paper indicates that the LiDAR system has potential applications for automated pruning, site-specific fertilization, variable rate technology and decision support systems, as it can provide fast and accurate information on crop vigour and spatial variability.

In the framework of an experimental-demonstration research project carried out by the researchers of the National Institute of Research–Development for Machines and Installations Designed for Agriculture and Food Industry-INMA Bucharest, applied research was carried out for the design, realization and testing of an equipment intended for the management of the grass cover in fruit plantations, which integrates LiDAR technology for tree trunk recognition and for the protection them while mowing the grass between the trees in a row *(https://inma.ro/wp-content/uploads/2022/12/Pagina-WEB-650-PED.pdf; Popa L. et al, 2023)*.

Fig. 4 - Intelligent Equipment for the Management of the Green Cover in Orchards in aggregate with the tractor

Intelligent systems used for inter-row management of vines and fruit trees

Intelligent soil and air systems have revolutionized agriculture through automation and efficiency. These include autonomous tractors, agricultural drones and robots used for sowing and harvesting, as shown in fig. 5.

Using technologies such as GPS, sensors and machine vision, these vehicles can precisely navigate complex agricultural terrain. They can perform various tasks such as ploughing, sowing, spraying and harvesting. Automation reduces human effort and human error, optimizing production. The vehicles can collect data on soil, plant and weather conditions, helping to make more informed crop management decisions. However, initial costs and the need for technology training remain challenges. Despite these challenges, ground vehicles continue to redefine the way modern agriculture is practiced.

Fig. 5 - Intelligent soil and air systems used for inter-row management of vines and fruit trees
(*Martina M.et al. al, 2022; Lan Y. et. al, 2021*)

Dionisio A. et. al. (2019), compare three different methods of creating 3D vineyard models based on UAV aerial imagery, ground-based LiDAR scanning, and ground-based RGB-D camera detection. The paper assesses the economic feasibility of site-specific fertilizer application based on 3D models, considering the costs and benefits of each method. The paper implies that the use of 3D models for site-specific management can reduce the environmental impact and economic cost of agrochemicals, as well as improve the quality and yield of grapevine crops.

Martina M. et al. (2022), proposes a multi-phase approach involving different unmanned aerial and ground vehicles to perform remote sensing and field operations in a vineyard. The paper describes the guidance and control strategy for the MH900 fixed-wing UAV, which is equipped with a multispectral camera, to obtain aerial images of the vineyard. The paper presents a guidance scheme that follows a snake-like path with a terrain tracking strategy and a tube-based robust model predictive control scheme that follows the reference trajectory while handling wind disturbances and constraints. The paper explains how aerial images are processed to obtain high-density 3D point clouds of vines and how these point clouds are semantically interpreted to generate low-complexity 3D meshed vine row models. The paper states that these models provide useful information for ground operations of land and rotary-wing vehicles. It discusses the design and implementation of guidance, navigation and control algorithms for the guided four-wheeled ground vehicle and the quadrotor UAV, which are used for research and spraying activities in grapevine rows. The paper shows how low-complexity 3D maps are exploited to plan the optimal path for both vehicles and how advanced control techniques are applied to ensure autonomous navigation and obstacle avoidance.

Grazia T. et al., (2019), develops and tests a system that can autonomously navigate and map a vineyard using a 2D LiDAR sensor without relying on GPS. The system aims to obtain geo-referenced images of vines for yield forecasting. The paper presents a line-based SLAM algorithm that uses vineyard rows as features to estimate the position and location of the robot. It also presents a navigation algorithm that uses the extracted lines to guide the robot along the centre of the rows and to move between them. The paper claims that these algorithms are robust and accurate in difficult and unstructured environments such as uneven terrain, overhanging branches, and long grass.

Hugo M. et al., (2020), presents a method for obtaining 3D models of vineyards using a mobile platform equipped with a LiDAR sensor and an RTK-GPS receiver. The paper aims to evaluate shoot volume and dry biomass as indicators of plant growth and health. The work demonstrates that the LiDAR system can scan large crop areas with high geometric detail and resolution, producing dense 3D point clouds that represent vine structure. The paper uses an alpha shape algorithm to generate a 3D surface that encompasses the outer points of the point cloud and calculates the volume contained by this surface as an estimate of the volume of the branches.

Biglia A. et. al., (2022), reviews how different configurations of UAV spray systems affect deposit, coverage and off-target losses in vineyards. The main argument is that the UAV flight mode is a key factor influencing the efficiency of spray application in 3D crops. The main contribution is that the paper provides empirical evidence on how the band spray mode can improve canopy deposition and reduce soil loss compared to diffuse spray modes when using UAVs for vineyard spraying. The main implication is that UAV spraying can be a viable alternative to conventional aerial spraying in vineyards if appropriate flight modes and nozzle types are selected according to crop characteristics and pest management objectives.

Samuel Marden et al., (2014), proposes a line-based algorithm for locating and navigating a robot in a difficult environment such as a vineyard. This algorithm uses plant rows as reference points to estimate the position of the robot and guide it between these rows. The authors state that this algorithm is robust and accurate in unstructured environments, such as rough terrain or tall vegetation. A prototype equipped with various sensors, such as 2D LiDAR (includes a single laser beam, for single-plane detection), IMU (inertial measurement unit), encoders, GPS and camera, is used to demonstrate the system's effectiveness. By comparing the results with high-precision data obtained from GPS and aerial LiDAR, the paper shows that the proposed algorithm has superior localization accuracy and reliability compared to traditional GPS.

A system intended for the field of robotics for the grapevine in agriculture represents a revolutionary approach in the management of wine crops. This innovative technology combines robots and automation to streamline agricultural processes related to the cultivation, maintenance and harvesting of vines. This system involves the use of specialized robots for tasks such as precise bunch cutting, plant health monitoring, proper nutrient administration and even fruit harvesting. These robots are equipped with advanced sensors to detect the needs of the plants and collect essential data about the condition of the crop. Through communication technology and real-time data analysis, robots can automatically adjust their actions to respond to changes in the environment. For example, if a bunch needs pruning to stimulate growth, robots can intervene with surgical precision. They can also detect early signs of disease or stress in plants, allowing farmers to take preventative measures. The robotics system for the vineyard in agriculture brings multiple advantages, such as increasing operational efficiency, reducing the need for human intervention and optimizing resources. Ultimately, this revolutionary technology contributes to higher yields, higher quality and increased sustainability in the wine sector.

The paper published by *Lan Y. et. al, (2021)*, proposed an orchard tree row-based navigation guidance and localization algorithm for agricultural robots. The algorithm used the trunks of the parallel planted grape trees as auxiliary information, along with the relative position provided by the IMU (inertial measurement unit), odometer and 3D LiDAR, to calculate the position and orientation of the moving robot. The paper suggests that the algorithm can be a useful tool for autonomous navigation of agricultural robots in orchards, especially in environments where GNSS (Global Navigation Satellite System) signals are weak or unavailable. The algorithm can also be applied to other crops with similar tree row structures, such as apples or citrus.

At the same time, *Lopes CM. et. al, (2016),* within a European research project called VINBOT ("Autonomous cloud-computing vineyard robot to optimize yield management and wine quality") focused on yield estimation using machine vision tools. The paper describes a real soil evaluation process carried out in an experimental vineyard with the Portuguese white grape variety Viosinho, trained on a system of vertical shoot positioning and cut spur. A sample of adjacent vines was tagged and subjected to a detailed evaluation of vegetative and reproductive data to feed a viticultural data library. The researchers report that the vines were scanned during the ripening period of the 2015 season by the VINBOT sensor head composed of a set of sensors capable of capturing vineyard images and 3D data. Real ground data was used to relate to the images taken by the sensors and to test image analysis algorithms. The paper shows that the relationships between actual and estimated yield calculated using the area occupied by the clusters in the images were high, despite a slight underestimation of the ground truth, mainly caused by cluster occlusion and factors affecting the estimation accuracy, such as tree density, position cluster, image resolution and lighting conditions.

Inter-row solar panel systems

An intelligent agricultural vine covering system is an essential technological innovation to optimize the growth and protection of wine crops, fig. 6. This advanced system combines elements of technology with the specific needs of viticulture, ensuring ideal environmental conditions for healthy plant development. By using sensors to monitor factors such as temperature, humidity, light and rain, the system can adapt coverage in real time. For example, in the event of extreme temperatures or inclement weather, the system can automatically act to close the cover, providing protection from the elements. On colder days or with less light, it can open the cover

to allow better exposure to natural light and maintain the optimal temperature. By intelligently managing the growing environment, this system contributes to maximizing crop quality and increasing yield, minimizing losses caused by external factors. In addition, automation and remote control facilitate efficient crop management, saving time and resources. The intelligent vine covering system represents a significant step forward in modern agriculture, putting technology at the service of achieving sustainable and high-quality wine production.

Fig. 6 - Inter-row solar panel systems
(*Shah et. al, 2019*)

A novel and inexpensive solution for vineyard protection that uses a covering system that can be opened and closed automatically and remotely depending on weather conditions is presented by *Karaman B. et. al, 2022*. The covering system can prevent damage to vines and grapes from natural events such as frost, hail and excessive heat or cold. The prototype consists of a DC gear motor, a control card, a solar battery, a photovoltaic panel and various sensors. The work shows that the coverage system can quickly respond to the detected data and take appropriate actions. The work uses MQTT (Lightweight Open Messaging Protocol) and a mobile application to enable remote monitoring and control of the coverage system. The work also uses the OpenWeatherMap program to obtain a three-hour weather forecast that can help anticipate and prevent potential risks. The researchers suggest that the proposed coverage system and forecasting approach may be more effective than traditional vineyard protection methods such as hail missiles, sprinklers or hail nets.

Seed sowing machines

The seed sowing machine between the rows of vines and fruit trees is an advanced and efficient technique in the field of agriculture. This specialized machine is designed to plant seeds or seedlings in the soil, in the spaces between already existing mature plants, that is, between already established rows of vines or fruit trees. By using this technology, farmers can maximize the use of available space in plantations, avoiding overcrowding and ensuring an even distribution of plants. The inter-row seeder can be programmed to plant the seeds at specific distances and appropriate depths depending on the requirements of the respective crops.

This approach not only saves time and labour, but also optimizes the plant growth process, ensuring that resources such as water, nutrients and light are efficiently distributed to each plant. In addition to increased efficiency, using the seeder between the rows reduces the risk of disease and competition between young and mature plants. However, successful implementation requires adapting the techniques to the specifics of the crops and the environment in which they grow. Thus, future research could focus on developing intelligent control systems and improving seed placement accuracy. The inter-row seeder makes a significant contribution to optimizing agricultural production through more efficient use of available resources and space.

Prakash V.B. et al., (2020), presents the design and implementation of a seed drill for intercropped fields, which can sow two types of seeds with correct spacing and depth in the agricultural field. The paper also proposes a detection algorithm based on colour features to identify the ripeness stage of each date fruit. The seed drill consists of a transport unit, a lighting and capture unit and a sorting unit. The device uses an LED light source and a Telecam camera to capture images of date fruits under a dome-shaped light box. The machine uses a paddle wheel feeder driven by stepper motors to move the Data fruits to the appropriate output ports based on their stage of ripeness. The detection algorithm uses an index based on the red, green, and blue colour components of the images to detect data fruits. The colour component coefficients are calculated by the taxonomy method. The performance of the system is evaluated by comparing it with human experts in visual sorting of date fruits. The paper suggests that the system can be improved by using other technologies that can sense the softness of the texture or by rotating the fruit in front of the camera. The paper also recommends testing the system on other date fruit varieties.

Kadu A.V. et al., (2019), presents a seed sowing machine that is made from old materials, making it cheap and available for small farms. The machine has a hopper, grooved roller, chain sprocket arrangement, soil wheel, furrow opener, seed tube and soil cover band. The machine can sow seeds of different diameters and row spacings by changing the plates on the grooved roller. The machine can also sow fertilizers along with seeds. The paper claims that the use of the proposed machine results in the uniform scattering of seeds over the field, which improves the germination rate and yield of the crop. The machine also minimizes seed and fertilizer waste by controlling seed rate and depth. The machine reduces the time and labour required for seeding, as well as the drudgery and health hazards associated with manual seeding. The paper suggests that using the BBF system with the proposed machine can improve soil fertility, moisture retention, drainage, aeration and sunlight availability for crops. The paper states that the BBF (broad bed preparation) system can save 25-30% of water and increase crop productivity by 5-10%. The paper also mentions that the BBF system allows farmers to implement various agricultural operations such as weeding, spraying, intercultural operation, irrigation.

Nemtinov V. et al., (2019), proposes the use of a self-propelled mini-pneumatic seeder with replaceable mechanical seeding devices designed and manufactured using computer technologies, advanced software and three-dimensional printing for seed selection. The paper claims that this approach can reduce the range of sowers and expand the sown seed set of different crops with a single grain feed brand. The paper tests the performance of these devices under laboratory and field conditions using different types of seeds, such as free-flowing and non-free-flowing seeds, grass seeds and bluegrass seeds. Qualitative indicators of the performance of the proposed grain-drilling fodder are determined, such as the dependence of seed supply on rotation frequency, seeding instability, uniformity of seed distribution, and energy consumption. The results obtained with the existing seeding methods and show that the proposed devices have advantages such as less labour, less time required, less seed wastage, less energy required, less pollution and more alarm and display functions.

Thenmozhi Andújar et al., (2020), aims to design and implement a radio frequency based solar controller for a seed sowing machine that can operate in three modes (slow, medium and speed) and perform seeding, spreading using an open-source software called Arduino. The paper also presents the results of testing the machine on a 45-degree inclined surface and detecting obstacles located in front and behind it. The RF Control Solar Seeder is designed to reduce skilled labour in agriculture, improve farming efficiency and save fuel cost by using electricity and solar panels. The machine can adjust the distance between the two seeds using a motor and can sow different types of seeds according to the user's choice. The machine can also spread fertilizers and plough the soil using various implements. Test results show that the machine can drive on a 45-degree inclined surface without losing balance or stability, and can detect obstacles within a 15 cm radius using ultrasonic sensors. The device can also be charged using solar panels when not in use.

Aduov M.D. etc. al, (2019), the paper aims to improve the seeding quality of non-flowing seeds, such as perennial and annual grasses, by developing and testing a new seeder design for a pneumatic seeder. The paper also presents the results of laboratory and field experiments of the proposed planter and compares them with existing planters. The new design of the seeder consists of a feed tank, a seed tube, a frame, a roller and a coulter. The seeder is capable of sowing loose, medium-flow and no-flow seeds using an auger or disc pin as a seed metering device. The constructive parameters of the seeder, such as the diameter and pitch of the screw, the diameter and number of pins on the disk, the distance between the seeds are determined by using mathematical models and formulas based on the physical and mechanical properties of the seeds and of the soil.

RESULTS

The use of technology in agriculture increases yield, reduces losses and optimizes resources. Data collection and analysis provide vital information for management decisions, such as fruit maturity status or seed distribution. These technologies have the potential to improve the productivity, quality and sustainability of wine production and more. Continuous research is needed to adapt technologies to specific agricultural requirements.

These researches aim to create an innovative technology and equipment for the sustainable development of agroecological crops, in order to use them in conditions of energy efficiency, protection of life, health and the environment.

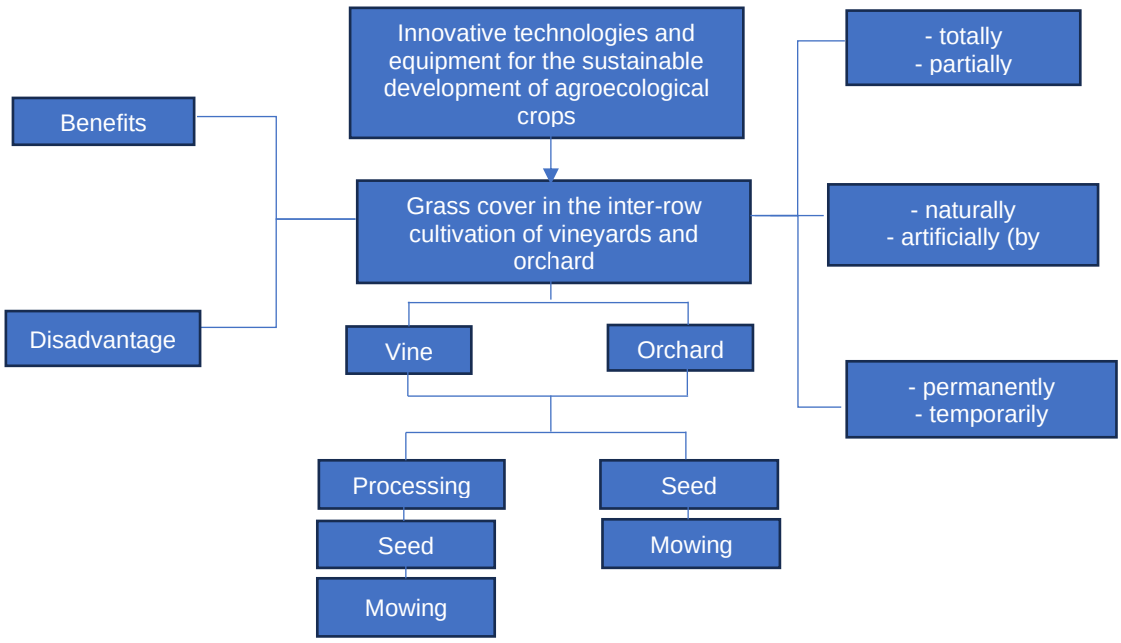

Fig. 7 - Innovative technology for greening the interval between rows of vines and fruit trees

The management of the interval between the rows of vines and fruit trees opens the opportunity to develop equipment and innovative and improved systems, which results in an increase in the quality and quantity of crops.

CONCLUSIONS

In this study, the impact and potential of using advanced technologies in the field of viticulture and fruit growing was investigated. The management of soil and light orientation, the use of 3D points and sensors, intelligent air and soil equipment, intelligent covering systems and vine robots were central to our research. The obtained results demonstrated that advanced technologies can bring significant improvements in the management of wine crops. Soil and light orientation management can optimize growing conditions by adjusting exposure angle and evenly distributing sunlight. The use of 3D points and sensors enabled detailed monitoring of land and plants, providing essential data for making accurate decisions and adapting cultivation methods. As for smart air and soil equipment, they have demonstrated increased efficiency in the precise application of nutrients and protective substances, thereby reducing waste and environmental impact. Intelligent cover systems have been able to provide crop protection against harmful weather factors, contributing to crop quality and yield. The viticulture robotics system has proven to be a promising solution for plant maintenance, monitoring and harvesting tasks. This can improve operational efficiency and free up human resources for more complex activities. Future research could explore the deeper integration of these technologies, the use of artificial intelligence for decision-making, the development of more advanced communication interfaces between agricultural devices, and the optimization of energy consumption. At the same time, more detailed assessment of the long-term costs and benefits of these technologies can contribute to their widespread adoption in the wine industry.

In conclusion, the adoption of advanced technologies in viticulture opens new perspectives for a more efficient, sustainable and quality production in the agricultural sector.

ACKNOWLEDGEMENT

The results were obtained with the support of Ministry of Research, Innovation and Digitalization through the NUCLEU Program, contract no. 9N/ 01.01.2023 project PN 23 04 02 03 “Innovative technology for covering the interval between the rows of vines and fruit trees to avoid degradation of the soil structure”, and the project “Demonstrative Model of Intelligent Equipment for the Management of the Green Cover in Orchards”, financed though The National Plan for Research, Development and Innovation 2015-2020 PN III, P2-Increasing the competitiveness of the Romanian economy through research, development and innovation, Subprogram 2.1. Competitiveness through research, development and innovation - Experimental-Demonstration Project, contract no. 960PED/30.06.2022.

REFERENCES

[1] Aduov M.D., Nukusheva S.A., Kaspakov E. Zh, Isenov K.G., Volodya K.M. and Tulegenov T.K., (2019). Substantiation of constructive parameters of the seeding machine for sowing of non-flowing grass seeds. *Mechanization in agriculture & Conserving of the resources*, *65*(2), pp.50-52. ISSN 2603-3712

[2] Andújar D., Moreno H., Bengochea-Guevara J.M., De Castro A. and Ribeiro A., (2019). Aerial imagery or on-ground detection? An economic analysis for vineyard crops. *Computers and electronics in agriculture*, *157*, pp.351-358. https://doi.org/10.1016/j.compag.2019.01.007

[3] Biglia A., Zaman S., Gay P., Ricauda A., Comba L. (2022). 3D point cloud density-based segmentation for vine rows detection and localisation, *Computers and Electronics in Agriculture, 199*, p.107166, https://doi.org/10.1016/j.compag.2022.107166

[4] Biglia A., Grella M., Bloise N., Comba L., Mozzanini E., Sopegno A., Pittarello M., Dicembrini E., Alcatrão E., Guglieri G., Balsari P., Ricauda A., Gay P. (2022). UAV-spray application in vineyards: Flight modes and spray system adjustment effects on canopy deposit, coverage, and off-target losses, *Science of the Total Environment, 845*, p.157292. https://doi.org/10.1016/j.scitotenv.2022.157292

[5] Bobillet W., Da Costa J.P., Germain C., Lavialle O., Grenier G., (2003). Row detection in high resolution remote sensing images of vine fields, *Precision agriculture Wageningen Academic* pp. 81-87 https://doi.org/10.3920/9789086865147_011

[6] Chen Y., Herrera R.A., Benitez E., Hoffmann C., Möth S., Paredes D., Plaas E., Popescu D., Rascher S., Rusch A., Sandor M., Tolle P., Willemen L., Winter S., Schwarz N. (2022). Winegrowers' decision-making: A pan-European perspective on pesticide use and inter-row management. *Journal of Rural Studies*, *94*, pp.37-53. https://doi.org/10.1016/j.jrurstud.2022.05.021

[7] Dionisio A., Moreno H., Bengochea-Guevara J., de Castro A., Ribeiro A., (2019). Aerial imagery or on-ground detection? An economic analysis for vineyard crops, *Computers and Electronics in Agriculture, Volume 157*, pp. 351-358, https://doi.org/10.1016/j.compag.2019.01.007

[8] Farage P., Ball A., McGenity T.J., Whitby C., Pretty J., (2009). Burning management and carbon sequestration of upland heather moorland in the *UK. Aust. J. Soil Res. 47* (4), 351–361. https://doi.org/10.1071/SR08095

[9] Figueiredo N., Pádua L., Cunha A., Sousa J.J, Sousa A., (2023) - Exploratory approach for automatic detection of vine rows in terrace vineyards. *Procedia Computer Science*, 219, pp.139-144. https://doi.org/10.1016/j.procs.2023.01.274

[10] Francis C.F., Thornes J.B., (1990). Runoff hydrographs from three Mediterranean vegetation cover types. In: Thornes, J. (Ed.), Vegetation and Erosion, *Processes and Environments. John Wiley & Sons, Chichester*, pp. 363–384. ISBN (Hardback): 978-0-471-92630-6

[11] Gatti M., Dosso P., Maurino M., Merli M.C., Bernizzoni F., Pirez J., Platè B., Bertuzzi G.C. and Poni S., (2016). MECS-VINE®: A new proximal sensor for segmented mapping of vigor and yield parameters on vineyard rows. *Sensors*, *16*(12), p.2009. https://doi.org/10.3390/s16122009

[12] Gomez-del-Campo M., Trentacoste E., Connor D. (2020). Long-term effects of row spacing on radiation interception, fruit characteristics and production of hedgerow olive orchard (cv. Arbequina). *Scientia Horticulturae*, *272*, p.109583. https://doi.org/10.1016/j.scienta.2020.109583Grant S., (2000). *Vine and row spacing, trellising. Practical Winery and Vineyard* ISBN: 415-479-5819

[13] Hermle S., Anken T., Leifeld J., Weisskopf P., (2008). The effect of tillage system on soil organic carbon content under moist, cold-temperate condition. *Soil Till. Res*. 98, 94–105. https://doi.org/10.1016/j.still.2007.10.010

[14] Kadu A.V., Rathod V. and Matre V., (2019). A Review on Seed Sowing Method and Alternative Method for Small Farmers. *International Journal of Research in Engineering, Science and Management*, Vol.2, Issue 7, ISSN (Online): 2581-5792

[15] Karaman B., Taskin S., Simbeye D.S., Mkiramweni M.E. and Kurtoglu A., (2023). Design and development of smart cover system for vineyards. *Smart Agricultural Technology*, *3*, p.100064. https://doi.org/10.1016/j.atech.2022.100064

[16] Lan Y., Geng L., Li W., Weixu Ran W., Yin X, Yi L. (2021). Development of a robot with 3D perception for accurate row following in vineyard, *Int J Precis Agric Aviat, 2021*; 4(2): 14–21

[17] Lan Y., Geng L., Li W., Ran W., Yin X., Yi L., (2021). Development of a robot with 3D perception for accurate row following in vineyard. *International Journal of Precision Agricultural Aviation*, *4*(2). https://ijpaa.org/index.php/ijpaa/article/view/177/156

[18] Lopes C.M., Graça J., Sastre J., Reyes M., Guzmán R., Braga R., Monteiro A., Pinto P.A., (2016). Vineyard yield estimation by VINBOT robot-preliminary results with the white variety Viosinho. In *Proceedings 11th Int. Terroir Congress. Jones, G. and Doran, N.(eds.),* pp. 458-463. Southern Oregon University, Ashland, USA. Jones, G.; Doran, N.(eds.). http://hdl.handle.net/10400.5/13128

[19] Lesschen J.P., Schoorl J.M., Cammeraat L.H., (2009), Modelling runoff and erosion for a semi-arid catchment based on hydrological connectivity to integrate plot and hillslope scale influences. *Geomorphology* 109, 174–183.

[20] Mammarella M., Comba L., Biglia A., Dabbene F., Gay P., (2022). Cooperation of unmanned systems for agricultural applications: A case study in a vineyard, Biosystems Engineering, Volume 223, Part B, pp. 81-102, https://doi.org/10.1016/j.biosystemseng.2021.12.010

[21] Marden S., Whitty W., (2014). GPS-free Localisation and Navigation of an Unmanned Ground Vehicle for Yield Forecasting in a Vineyard, Engineering, Agricultural and Food Sciences, Environmental Science, *International workshop collocated with the 13th International Conference on Intelligent Autonomous Systems* (IAS-13).

[22] Moreno H., Constantino Valero C., Bengochea-Guevara J.M., Ribeiro A., Garrido-Izard M., Andújar D., (2020). On-Ground Vineyard Reconstruction Using a LiDAR-Based Automated System, *Sensors*, 20(4), 1102; https://doi.org/10.3390/s20041102

[23] Moreno H., Andújar D., (2023), Proximal sensing for geometric characterization of vines: A review of the latest advances. *Computers and Electronics in Agriculture*, Volume 210, July 2023, 107901, https://doi.org/10.1016/j.compag.2023.107901

[24] Morlat R., Chaussod R., (2008). Long-term additions of organic amendments in a Loire valley vineyard. I. Effects on properties of a calcareous sandy soil. *Am. J. Enol. Vitic.* 59 (4), 353–363. DOI: 10.5344/ajev.2008.59.4.353

[25] Nemtinov V., Kryuchin N., Kryuchin A. and Nemtinova Y., (2019). Design and study of seeding devices for small selection seeding machines. In *E3S Web of conferences.* Vol. 126, p.00008. EDP Sciences. https://doi.org/10.1051/e3sconf/201912600008

[26] Popa L., Ciupercă R., Zaica A., Ştefan V. (2023). *Mowing equipment in orchards, with trunk detection with laser sensor*. Patent demand no. A-00764/29.11.2023. OSIM Romania

[27] Prakash V.B., Teja T.S., Krishna C., Raju N.E. and Adivi S.P., (2020). Agricultural-based seed sowing machine for intercrop fields. *https://www.researchgate.net/*

[28] Raclot D., Le Bissonnais Y., Louchart X., Andrieux P., Moussa R., Voltz M., (2009). Soil tillage and scale effects on erosion from fields to catchment in a Mediterranean vineyard area. *Agric. Ecosyst. Environ*. 134, 201–210. https://doi.org/10.1016/j.agee.2009.06.019

[29] Ramesh B., Tejaswini C. N., Ateeq S, Satyam V. (2017). Automated Agricultural System for Multipurpose Activities of Farmers. International *Journal on Recent and Innovation Trends in Computing and Communication*. Vol. 5, No. 12, https://doi.org/10.17762/ijritcc.v5i12.1351

[30] Reeves D.W., (1994) - Cover crops and erosion. In: Hatfield, J.L., Stewart B.A. (Eds.), *Crops Residue Management*. CRC Press, Boca Raton, FL, pp. 125–172

[31] Sánchez-Marañón M., Soriano M., Delgado G., Delgado R., (2002). Soil quality in Mediterranean mountain environments: effects of land use changes. *Soil Sci. Soc. Am. J.* 66, 948–958. https://doi.org/10.2136/sssaj2002.9480

[32] Shah S.F.A., Khan I. and H. A. Khan H.A., (2019). Performance Evaluation of Two Similar 100MW Solar PV Plants Located in *Environmentally Homogeneous Conditions in IEEE Access, vol. 7*, pp. 161697-161707, 2019, doi: 10.1109/ACCESS.2019.2951688

[33] Shekikhachev Y., Mishhozhev V.H., Shekikhacheva L.Z., Zhigunov R.H., Kan V., Mishhozhev K.V and (2020) - Modeling of disk sowing apparatus operation process, *IOP Conf. Ser.: Earth Environ. Sci.* 548 022004 doi: 10.1088/1755-1315/548/2/022004

[34] Tucci G., Parisi E. I., Castelli G., Errico A., Corongiu M., Sona G., Viviani E., Bresci E. and Preti F., (2019). Multi-Sensor UAV Application for Thermal Analysis on a Dry-Stone Terraced Vineyard in Rural Tuscany Landscape, *ISPRS Int. J. Geo-Inf.*, 8(2), 87; https://doi.org/10.3390/ijgi8020087

[35] Yang C., Herrera R.A., Benitez E., Hoffmann C., Möth S., Paredes D., Plaas E., Popescu D., Rascher S., Rusch A., Sandor M., Tolle P., Willemen L., Winter S., Schwarz N. (2022). Winegrowers' decision-making: A Pan-European perspective on pesticide use and inter-row management, *Journal of Rural Studies*, Vol. 94, pag. 37-53, ISSN 0743-0167, doi: 10.1016/j.jrurstud.2022.05.021.

[36] Zalidis G., Stamatiadis S., Takavakoglou V., Eskridge K., Misopolinos N., (2002). Impacts of agricultural practices on soil and water quality in the Mediterranean region and proposed assessment methodology. *Agric. Ecosyst. Environ*. 88, 137–146. https://doi.org/10.1016/S0167-8809(01)00249-3

[37] ***AGR intelligence. APIA subsidy for planting orchards and vineyards: conditions, payments per hectare. Available online: https://agrointel.ro/245940/subventie-apia-pentru-inierbarea-livezilor-si-viilor-conditii-plati-la-hectar/

[38] *** FAOSTAT. Available online: https://www.fao.org/faostat/en/#home.

[39] ***National Institute of Statistics page. Available online: https://insse.ro/cms/sites/default/files/field/publicatii/potentialul_productiv_al_/

[40] ***Ministry of Agriculture and Sustainable Development Romania. National Support Program in the wine sector 2019–2023, rev. 12. Available online: https://www.madr.ro/horticultura/viticultura-vinificatie.html

[41] ***USDA, 2000. *Interpreting Indicators of Rangeland Health*, Version 3, 2000, TR 1734- 6, BLM.

[42] *** https://inma.ro/wp-content/uploads/2022/12/Pagina-WEB-650-PED.pdf

WRITING INSTRUCTIONS

Article Types

Three types of manuscripts may be submitted:

1. **Regular articles:** These should describe new and carefully confirmed findings, and experimental procedures should be given in sufficient detail for others to verify the work. The length of a full paper should be the minimum required to describe and interpret the work clearly (max.10 pages, even number);
2. **Reviews:** Submissions of reviews and perspectives covering topics of current interest are welcome and encouraged (max.12 pages, even number).

Manuscripts should be written in English (American or British usage is accepted, but not a mixture of these) and submitted **electronically** at the following e-mail addresses: ***inmatehjournal@gmail.com***
Please be sure to include your full affiliation and e-mail address (see Sample manuscript)
The authors are responsible for the accuracy of the whole paper and references.
There are allowed 2 papers by each first author.
The text layout should be in single-column format. To avoid unnecessary errors it is strongly advised to use the "spell-check" and "grammar check" functions of your word processor.

Review Process

All manuscripts are reviewed by 2 members of the Scientifically Review Office. Decisions will be made as rapidly as possible and the journal strives to return reviewers' comments to authors in approx.3 weeks.
The editorial board will re-review manuscripts that are accepted pending revision.

NOTE:

Submission of a manuscript implies: that the work described has not been published before (excepting as an abstract or as part of a published lecture or thesis) that it is not under consideration for publication elsewhere.

1. REGULAR ARTICLES

- Manuscripts should be concise, in ***1.15 line spacing***, and should have 2 cm all over margins. The font should be ***Arial 10 pt.*** Ensure that each new paragraph is clearly indicated, using **TAB at 1 cm**.
- Title will be ***Arial 12 pt***. and explicit figures will be ***Arial 9 pt***.
- Text will be written in English.
- Chapters' titles are written by ***Arial 10 pt, Bold, Uppercase*** (e.g. **INTRODUCTION, MATERIALS AND METHODS**), between chapters is left a space for 10 pt. At the beginning of each paragraph, TAB of 1 cm.
- The paper body will be written in ***Arial 10 pt., Justify alignment***.

TITLE ***Arial 12 pt., Uppercase, Bold, Center*** *(in English language)* and ***Bold Italic*** *(in native language).*
Should be a brief phrase describing the contents of the paper. Avoid long titles; a running title of no more than 100 characters is encouraged (without spaces).

AUTHORS ***ARIAL 9, Bold, Centre alignment***
Under the paper's title, after a space (enter) 9 pt., write ***authors' names*** and ***affiliations (Arial 8 pt.-Regular)***
When the paper has more than one author, their name will be followed by a mark (Arabic numeral) as superscript if their affiliation is different. Less than 6 authors.
Corresponding author's name (next row), ***(Arial 8 pt.)***. Should be added also: phone, fax and e-mail information, for the paper corresponding author (***font: 8 pt., Italic***).

KEYWORDS ***(In English)*** about 4 to 7 words that will provide indexing references should be listed (title: ***Arial 10pt, bold italic,*** text ***Arial 10 pt., italic***).

A list of non-standard *Abbreviations* should be added. In general, non-standard abbreviations should be used only when the full term is very long and used often. Each abbreviation should be spelled out and introduced in parentheses the first time it is used in the text. Standard abbreviations (such as ATP and DNA) need not to be defined.
ABSTRACT ***(in English and Native language, Arial 10 pt.)***, the title *bold*; the text of abstract: *italic*) should be informative and completely self-explanatory, briefly present the topic, state the scope of the experiments, indicate significant data, and point out major findings and conclusions. The Abstract should be max.250 words. Complete sentences, active verbs, and the third person should be used, and the abstract should be written in the past tense. Standard nomenclature should be used and abbreviations should be avoided. No literature should be cited.
INTRODUCTION (***Arial 10 pt.)*** should provide a clear statement of the problem, the relevant literature on the subject, and the proposed approach or solution. It should be understandable to colleagues from a broad range of scientific subjects. We should refer to the current stage of researches performed in the field of the paper to be published, by quoting up-to-date specialty studies, preferably published after 2006, excepting certain referential specialty

books/studies, especially papers issued in magazines/journals/conferences/ISI quoted symposia or in other international data bases, which are well known and available.

MATERIALS AND METHODS (***Arial 10 pt.***) should be complete enough to allow experiments to be reproduced. However, only truly new procedures should be described in detail; previously published procedures should be cited, and important modifications of published procedures should be mentioned briefly. Methods in general use need not be described in detail.

RESULTS (***Arial 10 pt.***) should be clarity presented. The results should be written in the past tense when describing findings in the authors' experiments. Results should be explained, but largely, without referring to the literature. Discussion, speculation and detailed interpretation of data should not be included in the Results, but should be put into the Conclusions section.

CONCLUSIONS (***Arial 10 pt.***) The main conclusions drawn from results should be presented in a short Conclusions section. Do not include citations in this section.

Formulae, symbols and abbreviations: Formulae will be typeset in Italics (preferable with the Equation Editor of Microsoft Office 2003) and should be written or marked as such in the manuscript, unless they require a different styling. They should be referred to in the text as Equation (4) or e.g. (4). The formulae should be numbered on the right side, between brackets ***(Arial 10 pt.)***:

$$P = F \cdot v \tag{1}$$

Terms of the equation and the unit measure should be explained, e.g.

P is the power, [W];
F – force, [N];
v – speed, [m/s]

SI units must be used throughout.

Tables should be self-explanatory without reference to the text. The details of the methods used in the experiments should preferably be described in the legend instead of in the text. The same data should not be presented both in table and graph form or repeated in the text.
Table's title will be typed ***Arial 9 pt, Bold, Centered***
In the table, each row will be written Arial 9 pt, single-spaced throughout, including headings and footnotes.
The table should be numbered on the right side, ***Arial 10 pt.***

Figures ***(Arial 9 pt., Bold, Center)***should be typed in numerical order (Arabic numerals). Graphics should be high resolution (e.g.JPEG).Figure number is followed by what represent the figure or graph e.g.:

Fig.1 – Test stand

Legend: ***Arial 8 pt, Italic, Center,*** e.g.:
1 - plansifter compartments; 2- break rolls; 3 – semolina machines; 4 – reduction rolls; 5 – flour

ACKNOWLEDGMENTS (***Arial 10 pt.***) of people, grants, funds etc should be brief (*if necessarily*).

REFERENCES (***Arial 10 pt.***)
(In alphabetical order, in English and in the original publication language).
Minimum 10 references, last 10 years, minimum 3 references from the last 2 years

It can be used "*References*" tool from the *Word Editor*. **APA Style (American Psychological Association)**
https://apastyle.apa.org/style-grammar-guidelines/references/examples

All references must be provided in English
Authors are fully responsible for the accuracy of the references.

References should be **alphabetically**, with complete details, as follows:

Examples:
Books: https://apastyle.apa.org/style-grammar-guidelines/references/examples/book-references

Jackson, L. M. (2019). *The psychology of prejudice: From attitudes to social action* (2nd ed.). American Psychological Association. https://doi.org/10.1037/0000168-000
Kesharwani, P. (2020). *Nanotechnology based approaches for tuberculosis treatment*. Academic Press.
Sapolsky, R. M. (2017). *Behave: The biology of humans at our best and worst*. Penguin Books.

Torino, G. C., Rivera, D. P., Capodilupo, C. M., Nadal, K. L., & Sue, D. W. (2019). *Microaggression theory: Influence and implications*. John Wiley & Sons. https://doi.org/10.1002/9781119466642

In text:

- ***Parenthetical citations***: (Jackson, 2019; Sapolsky, 2017)
- ***Narrative citations***: Jackson (2019) and Sapolsky (2017)

Journal Article:

https://apastyle.apa.org/style-grammar-guidelines/references/examples/journal-article-references

Grady, J. S., Her, M., Moreno, G., Perez, C., & Yelinek, J. (2019). Emotions in storybooks: A comparison of storybooks that represent ethnic and racial groups in the United States. *Psychology of Popular Media Culture*, *8*(3), 207–217. https://doi.org/10.1037/ppm0000185

In text:

- ***Parenthetical citation***: (Grady et al., 2019)
- ***Narrative citation***: Grady et al. (2019)

Conference or Symposium:

https://apastyle.apa.org/style-grammar-guidelines/references/examples/conference-proceeding-references

Duckworth, A. L., Quirk, A., Gallop, R., Hoyle, R. H., Kelly, D. R., & Matthews, M. D. (2019). Cognitive and noncognitive predictors of success. *Proceedings of the National Academy of Sciences*, *USA*, *116*(47), 23499–23504. https://doi.org/10.1073/pnas.1910510116

In text:

- ***Parenthetical citation***: (Duckworth et al., 2019)
- ***Narrative citation***: Duckworth et al. (2019)

Dissertation / Thesis:

https://apastyle.apa.org/style-grammar-guidelines/references/examples/published-dissertation-references

Zambrano-Vazquez, L. (2016). *The interaction of state and trait worry on response monitoring in those with worry and obsessive-compulsive symptoms* [Doctoral dissertation, University of Arizona]. UA Campus Repository. https://repository.arizona.edu/handle/10150/620615

In text:

- ***Parenthetical citations***: (Kabir, 2016; Miranda, 2019; Zambrano-Vazquez, 2016)
- ***Narrative citations***: Kabir (2016), Miranda (2019), and Zambrano-Vazquez (2016)

https://apastyle.apa.org/style-grammar-guidelines/references/examples/unpublished-dissertation-references

Harris, L. (2014). *Instructional leadership perceptions and practices of elementary school leaders* [Unpublished doctoral dissertation]. University of Virginia.

In text:

- ***Parenthetical citation***: (Harris, 2014)
- ***Narrative citation***: Harris (2014)

Patents: Names and initials of authors, year (between brackets), patent title (Italic), patent number,country:

Grant, P. (1989). *Device for Elementary Analyses*. Patent. No.123456. USA.

Legal regulations and laws, organizations:

https://apastyle.apa.org/style-grammar-guidelines/references/examples/iso-standard-references

International Organization for Standardization. (2018). *Occupational health and safety management systems—Requirements with guidance for use* (ISO Standard No. 45001:2018). https://www.iso.org/standard/63787.html

Occupational Safety and Health Administration. (1970). *Occupational safety and health standards: Occupational health and environmental control: Occupational noise exposure* (OSHA Standard No. 1910.95). United States Department of Labor. https://www.osha.gov/laws-regs/regulations/standardnumber/1910/1910.95

In text:

- ***Parenthetical citations***: (International Organization for Standardization, 2018; Occupational Safety and Health Administration, 1970)
- ***Narrative citations***: International Organization for Standardization (2018) and Occupational Safety and Health Administration (1970)

Web references: The full URL should be given in text as a citation, if no other data are known. If the authors, year, and title of the documents are known and the reference is taken from a website, the URL address has to be mentioned after these data.

Citation in text

Please ensure that every reference cited in the text is also present in the reference list (and vice versa).

Do not cite references in the Abstract and Conclusions !.

Unpublished results, personal communications as well as URL addresses are not recommended in the references list.

Making personal quotations (one, at most) should not be allowed, unless the paper proposed to be published is a sequel of the cited paper. Articles in preparation or articles submitted for publication, unpublished, personal communications etc. should not be included in the references list.

Citations style

Text: All citations in the text may be made directly (or parenthetically) as bellow.

- ***single author:*** the author's name (without initials, unless there is ambiguity) and the year of publication:
  "as previously demonstrated *(Brown, 2010)*".
- ***two authors:*** both authors' names and the year of publication: *(Adam and Brown, 2008; Smith and Hansel, 2006; Stern and Lars, 2009)*
- ***three or more authors:*** first author's name followed by "et al." and the year of publication: "As has recently been shown *(Werner et al., 2005; Kramer et al., 2000)* have recently shown ...."

Citations of groups of references should be listed first alphabetically, then chronologically.

Units, Abbreviations, Acronyms

- Units should be metric, generally SI, and expressed in standard abbreviated form.
- Acronyms may be acceptable, but must be defined at first usage.

2. REVIEWS

Summaries, reviews and perspectives covering topics of current interest in the field, are encouraged and accepted for publication. Reviews do not have the requirements for regular articles. However, should include: (*) an introductory chapter, (**) a careful and critical presentation of the relevant aspects of the topic approached and (***) emphasis of the aspects that aren't known and require further research to progress. Reviews should be concise (max. 12 pages).

Edited by: INMA Bucharest
6, Ion Ionescu de la Brad Blvd., sect. 1, Bucharest, ROMANIA
Tel: +4021.269.32.60; Fax: +4021.269.32.73
https:// inmateh.eu
e-mail: ***inmatehjournal@gmail.com***